MAGNETOM Flash

Issue Number 100 · 5/2026
Anniversary Edition

magnetomworld.siemens-healthineers.com

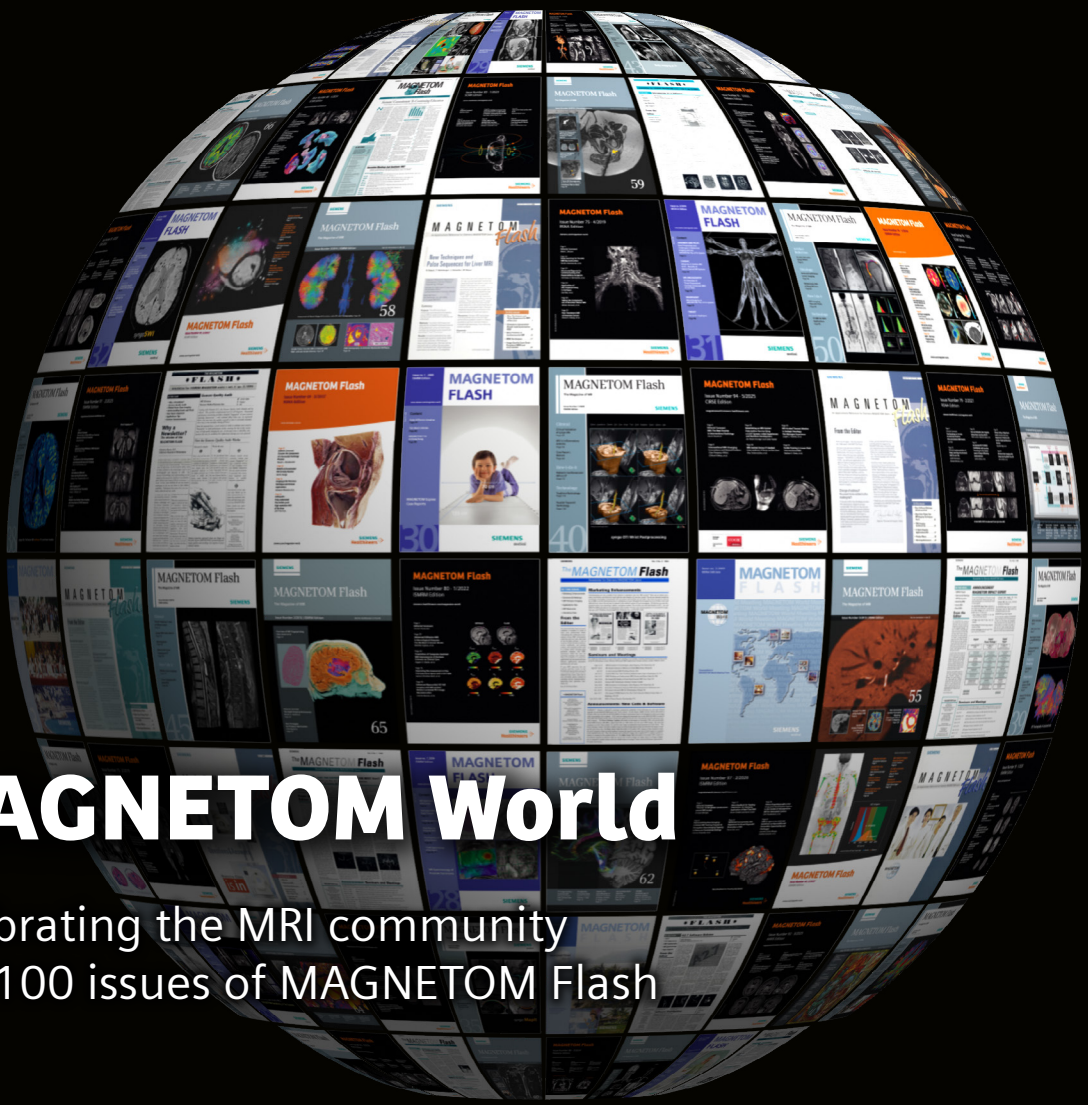

MAGNETOM World

Celebrating the MRI community
and 100 issues of MAGNETOM Flash

Not for distribution in the U.S.

SIEMENS Healthineers

A note on this special issue

Issue #100 feels like one of those rare occasions where a publication can celebrate not only its own history, but also the history of an entire professional community. Many readers will likely recognize articles they first encountered years, or even decades ago and remember where they were in their MRI journey at the time.

Since its founding in 1993, MAGNETOM Flash has served as a peer-to-peer forum for the MRI community, sharing clinical experience, practical insights, and technical innovations.

Over the years, it has become a trusted companion for generations of radiologists, radiographers, physicists, and MRI enthusiasts around the world. Many readers have known MAGNETOM Flash since their first days in MRI, as students or trainees, and have continued to follow it throughout their professional careers.

For this 100th issue, we wanted to look back. The articles collected here were selected because they reflect important milestones in MRI practice and technology, were widely read, or present enduring clinical insights from the first 99 issues. Together, they tell part of the story of MRI and of the community that has shaped its progress over the past three decades.

The articles are reprinted as they originally appeared. As a result, some affiliations, contact details, references, and web links are no longer current. We have chosen to preserve the original publications as a record of their time.

Selecting the articles for this anniversary issue was fun but no easy task, and there are many more memorable contributions that we would have loved to include. We invite readers to take a journey through the complete MAGNETOM Flash archive and rediscover past issues at
↗ **www.magnetomworld.siemens-healthineers.com/publications/magnetom-flash/archive**

Here's to the first 100 issues — and to the many conversations, collaborations, and innovations still to come.



Antje Hellwich
Editor-in-chief

Today, we are immensely proud and very grateful for what we have achieved together, thanks to the support of our incredible MAGNETOM World community.

We extend our sincere thanks to all contributors, past and present. Their willingness to share their knowledge and experience with readers from all corners of the MR world (across geographic regions and areas of expertise) is what has made MAGNETOM Flash relevant for more than three decades.

I would also like to recognize the Editors and Associate Editors who have guided MAGNETOM Flash. From its very first issue in 1993, the journal embodied its peer-to-peer philosophy under the leadership of its founding Editor-in-Chief, radiographer Christine Harris, RT(R)(MR). She was succeeded by Gary R. McNeal, MS (BME), who, together with Technical Editor Helmuth Schultze-Haakh, Ph.D., helped establish the publication in its early years. Over the following decades, Dagmar Thomsik-Schröpfer, Ph.D., Ali Nejat Bengi, M.D., Matthias Lichy, M.D., and Milind Dhamankar, M.D. each contributed their expertise and vision, ensuring that MAGNETOM Flash continued to evolve. Their dedication laid the foundation on which MAGNETOM Flash continues to build today.

THE MAGNETOM
FLASH
newsletter for SIEMENS MAGNETOM users • vol. 1 no. 1/1993

IN THIS ISSUE

- Why a Newsletter?
- Siemens Quality Audit
- Clinical Focus: Knee Imaging
- Understanding Voxels and Pixels
- New Neuro Sequences
- Applications Tips
- Seminar Announcements

Why a Newsletter?
The mission of the MAGNETOM FLASH

Christine Harris, R.T.
Children's Hospital of Philadelphia

A short while back, I attended a meeting where we discussed the lack of technologists' attendance at organized educational meetings. The lecturers were all physicians. As the lecturers spoke, most of them referred to the technologist need to be knowledgeable and educated in MRI. The amount of knowledge and understanding can be related to the success of a facility in its technologists' ability to get certain difficult techniques to work. In fact, some facilities do not use certain techniques or do not use them to their fullest capability. Techniques that some of us use routinely, others do not use at all.

It crossed my mind that there should be a communication network between the Siemens technologist and the Siemens Corporation. Siemens has always recognized the importance of educating its technologists. And continuous education is even more important now in this ever-changing world of MR. Siemens has provided technologist meetings and sponsored technologists to attend major meetings. If we, as technologists could not attend these meetings, we were out of luck until the following year. I presume that in today's cost-efficient world there are many technologists that cannot attend meetings.

What then transpired was to suggest to Siemens the idea of a Newsletter. Siemens responded with an affirmative, and the MR Newsletter was born!

This is the first issue. In order for there to be more issues, we must all work together, communicate and contribute our ideas and suggestions. This new Newsletter is for you, the Siemens user. We want it to be informative and educational. Remember, we are our own source of knowledge. Let's share the information we know.

Siemens Quality Audit

MR Division
Siemens Medical Systems, Inc.

☑ SP/SP 4000
☐ Impact
☐ P8

Starting with Numaris A2.5, the Siemens Quality Audit Module will be offered. This provides a sophisticated level of self-diagnosis. Automated performance monitoring provides a detailed "fingerprint" of your system's operating characteristic ...with minimal effort from you. As explained below, you may start the module yourself or have it activated remotely; either way, it runs overnight, during off hours.

From the measued data, a trend analysis is made to evaluate your system's "fingerprint" to track performance trends, assuring the day-to-day consistency of high-quality imaging for you. At the same time, it identifies components that may be candidates for replacement during your next planned

How the Siemens Quality Audit Works:

Your part is simple:

1

Select a day and time each week when it is convenient for you to allow the system to perform its self-checks. After the last patient has been imaged, place the appropriate phantom in the magnet and press one button to enable the Quality Audit Module. That's all you do! The rest is automatic.

We do the rest:

2

At the pre-selected time, the Audit is initiated automatically. Several key parameters of your system's performance are measured and recorded in your systems "fingerprint" for use in later analysis. If you prefer, your Siemens field service engineer will activate the Audit remotely at the specified time.

3

Siemens trained service personnel evaluate your system's "fingerprint", using a worldwide database to track emerging trends and identify components that may require attention. If warrented, they recommend equipment recalibration or possible component replacement.

4

Your Siemens service engineer then follows up on these recommendations to insure the continued reliability and high image quality of your MAGNETOM.

Please consult your user's manual for more details on this program.



Siemens proactive approach keeps our finger on the pulse of your MAGNETOM, maximizing your image quality and avoiding interruption to your clinical routine.

The MAGNETOM FLASH

Published by:
Siemens Medical Systems, Inc.
186 Wood Avenue South
Iselin, NJ 08863

Editor:
Christine Harris, R.T.
Children's Hospital of Philadelphia

Produced by:
Medical Imaging Consultants, Inc.
58 Notch Road
W. Paterson, NJ 07424

All Rights Reserved,1993
Siemens Medical Systems, Inc.

Clinical Focus: Knee Imaging

MR Imaging the Anterior Cruciate Ligament of the Knee

- SP/SP 4000
- Impact
- P8

Brian Murphy, M.D., Doctor's Hospital of Coral Gables

The anterior cruciate ligament (ACL) is a primary central stabilizing ligament in the knee. It is comprised of two bundles of fiber which attach to the anterior aspect of the tibial plateau and course posteriorly and superior into the intercondular notch to attach to the medial aspect of the lateral femoral condyl. This ligament prevents excessive anterior translation of the tibia with respect to the femur and also provides a central rotational axis for the knee.

Ideally, imaging of this small structure would be performed along its longest axis, parallel to its fibers. Traditionally, it's been stated that a 10-20 degree externally rotated knee will place the ACL in profile, so when sagittals are prescribed, there is a high probability to obtain good images of this structure. However, this still remains an "educated guess work", you may get it, you may not. Another approach is to line-up oblique slices on axial images (on medial aspect of lateral femoral condyle), again it still remains less than 100% accurate.

What has worked for us, is a method of visualizing the ACL on the coronal views and aligning oblique sagittals along its axis.

First, it is necessary to obtain "true coronals" this is, to position the knee not externally rotated, but as straight as possible - neutral. If, however, on the axial localizers the knee is rotated, we proceed to oblique the coronals along the axis of the condyles so as to obtain "true coronal views". This is a first and most important step. You will not get a good ACL if this is not followed and it will appear somewhat foreshortened if taken from a less than true coronal.

The second step is to page through the coronals and find the ACL — on the medial aspect of the lateral femoral condyle and follow it through on more than one coronal image.

Selecting a double echo sequence we are able to create different groups, the first two should be vertical, orthogonal. Each group is of seven slices with a gap of 10-20%, positioned on each meniscus (lateral and medial), then a third group of four slices with 0 gap vertical, oblique and position this group aligned with the course of the ACL on the "true coronal views".

Advantages:

a. Obtain consistently ACL views T2-weighted (more specific to determine complete vs. partial ACL tears).

b. Avoid having to run two separate sets of T2s (a separate oblique through the ACL).

c. An easy and consistent method to reproduce, helpful in centers with several MR technologists.

d. Reduces partial volume averaging which increases visualization of true signal abnormalities in the ACL.

Disadvantages:

a. If you oblique the coronals, the resulting sagittals will be double obliqued, display slice will not be supported. You may do a copy/seg store at the time of the set-up.

b. There will be some crosstalk because of the overlapping of the oblique and straight groups. You may run these interleaved and because crosstalk in T2 images with a fairly long TR is less critical than T1, this is not a significant problem.

c. The PCL and quadriceps might be missed with the oblique cuts. We obtain T1 weighted straight cuts to evaluate menisci, etc. If a PCL/quadriceps injury is suspected, we then proceed with T2-weighted sagittals acquired straight.

d. When doing left knees. The order of slices is altered. You will need to do a study/arrange by TE, then film them by selecting the study. There is no problem with right knees.

The presence of any intact taut fibers on any pulse sequence excludes a complete ligament tear. Some untorn ligaments will exhibit increased intensity in the older populations; however, some intact, taut fibers will be present. Angled ACL T2 images are usually most helpful in conjunction with the T1 coronals in differentiating partial from complete tears. Also, bone contusion sites (low intensity on T1, high on T2) in the mid to anterior lateral femoral condyle and in the posterolateral tibial plateau are frequently present with complete ACL tears and are not usually seen with tears which are only partial.

Technique:

Seq: SE_25B56_70B56 (1.0T)
Seq: SE_20B78_55B78 (1.5T)

TR=2300	Th=4mm
TE=25/70-80 (1.0T)	Gap=10-20%/0
TE=20/75-80 (1.5T)	Acq=2
Mx=192 x 256	Swap=YES
FOV=160	Filter=Fermi(weak)

SATpulse=1 TRA (th=40mm, shift=-100)

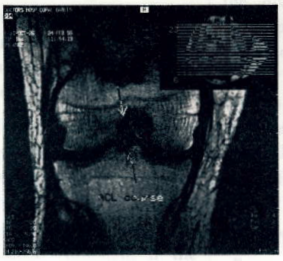

Figure 1



Figure 2

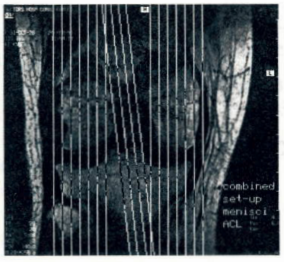

Figure 3

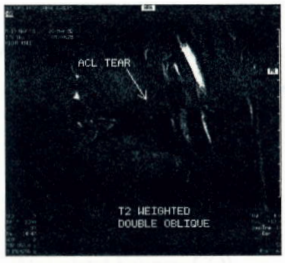

Figure 4

Figure 1 – T1-weighted coronal showing the course of the ACL. Note the set-up of the slices on an axial localizer of an externally rotated knee.

Figure 2 – T1-weighted sagittal image acquired straight.

Figure 3 – Combined set-up for menisci and ACL. This set-up requires the placement of three groups of slices.

Figure 4 – T2-weighted image acquired double oblique

Clinical Focus: Turbo Spin Echo
Principles and Clinical Applications

SP/SP4000
Impact
P8

A.J. Martinez, M.D., Dir. of MRI – North Idaho Imaging – Coeur D'Alene, ID

The two major hurdles in clinical MRI are speed and motion. Faster scanning not only improves throughput but minimizes physiologic motion. Many approaches have been utilized in the quest for more rapid methods of obtaining clinically useful images. The scan time can be calculated by the following formula:

$$\text{Scan Time} = \frac{\text{TR x \# of phase encodings x \# of acquisitions}}{\text{Echo train length}}$$

From this formula, we can surmise the following choices for decreasing scan time:

1. We can reduce TR.
2. Reduce the number of phase encodes.
3. Reduce the number of acquisitions.
4. Increase the length of the echo train and combine the data.

Turbo Spin Echo

This family of sequences was first described by Hennig as RARE (Rapid Acquisition with Relaxation Enhancement). The Siemens version of the product goes by the name of Turbo Spin Echo (TSE). The basic principle of TSE is to obtain multiple individually phase encoded echoes in a single TR. The information from these echoes is then combined to form either a single effective echo or a double effective echo (i.e. proton density and T2). The image or k-space map is thus completed in a fraction of the time that would have been required for a conventional spin echo sequence (CSE). This fraction is determined by the length of the echo train. Thus, for a given TR, if an echo train of 16 is used, imaging time would be reduced by a factor of 16 from the comparable conventional spin echo sequence.

Echo train lengths (ETL) usually vary from 3 to 16. Realistically, time savings in TSE tend to be less than 16 because adequate coverage often requires shorter ETL's. Double echo sequences also pose limitations in the ETL. Some or all of the additional time savings obtained with TSE can be traded for additional SNR by using more acquisitions. The time savings may also be traded in for the increased spatial resolution of a large matrix such as a 512 x 512 matrix.

Before prescribing a TSE sequence, several factors should be known. One should know how many slices are necessary for coverage of the anatomy under study and the acceptable TR range. This usually severely limits the ETL which can be used. The acceptable SNR, and whether a single or double echo sequence is desired, further limit the choice of sequence. Additionally, the need for GMR and its direction should be ascertained. These factors will narrow the choice of sequences significantly. At this point, the sequence which meets these criteria and offers the longest ETL will provide the maximum time savings.

The images obtained with TSE are almost exactly the same as those obtained with CSE albeit a few notable differences. Fat signal is brighter in TSE images. The brighter fat can serve to highlight bone marrow metastases on TSE T1 weighted images but significantly hinders detection of bone marrow pathology on T2 weighted images. These factors can be altered by the inter-echo spacing. This parameter has been optimized by Siemens scientists and is not offered as an operator controlled parameter. Brighter fat can be useful in assessing the neural foramina in the spine on T2 weighted images. In cases where brighter fat poses a problem, fat suppression schemes can be applied.

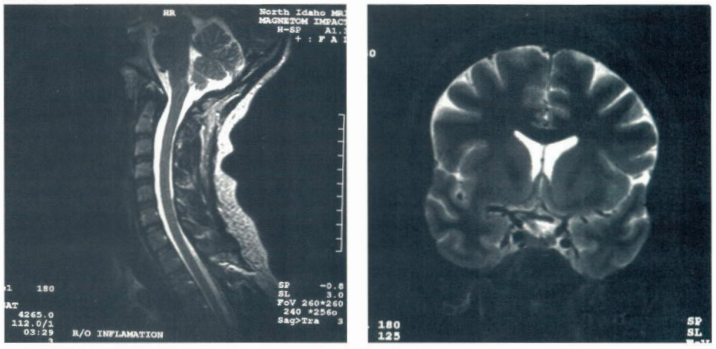

Left: TurboSE image of the sagittal cervical spine with GMR. Note the absence of flow artifact from CSF pulsation.

Right: High resolution Turbo Inversion Recovery with excellent fat suppression.

The Turbo family of data acquisition has allowed for the development of Turbo-IRABS (IRABS TurboSE) sequences. IRABS images have long been known to provide exquisite sensitivity to pathologic processes resulting in T1 and T2 prolongation. Additionally, IRABS provides homogeneous suppres- sion of fat when the appropriate TI is used. These properties have made IRABS the sequence of choice in assessing bone marrow pathology. Prior to the development of Turbo-IRABS, the IRABS sequences were hampered by low SNR, long acquisition times and motion artifacts. With the advent of Turbo-IRABS, acquisition time has been markedly shortened allowing for decreased motion artifacts. SNR can be significantly augmented by doubling or tripling the acquisitions while keeping imaging time short.

The Nuts and Bolts

In order to better understand TSE some concepts need to be defined. These include the concept of k-space, the design of the TSE sequences, the echo train length, inter-echo spacing, symmetric versus asymmetric k-space data collection schemes and shared echoes.

k-space: The information acquired through the application of an MR sequence is detected as an rf signal which has encoded contrast and spatial information. The sum of the information necessary for construction of a slice is called a k-space map. The k-space map contains this information as a complex mixture of frequencies which, when unraveled through a mathematical computation (Fourier transformation), results in the familiar image that we see and film.

An interesting feature of k-space is that the central 20% (low frequency) phase encode lines provide the vast majority of the contrast whereas the peripheral 80% (high frequency) phase-encode lines add almost nothing to contrast but provide most of the edge detail or sharpness. The contrast of the image is determined by obtaining the central phase encodings at the time TE at which the desired contrast occurs, this being the effective TE. The remainder of the edge detail information can be filled from phase encoding obtained at somewhat shorter or longer TE's.

The scheme of k-space ordering could involve either a symmetric ordering scheme or an asymmetric ordering scheme. In the case of asymmetric ordering, the phase encodings from the first echo would precede the phase encodings from the second echo and so forth. The contrast would be determined by the echo in the middle of the echo train as it would represent the central, low frequency, phase encodings. In the case of symmetric ordering, the data from each echo is split to symmetrically fill the positive and the negative phase encoding lines in a mirror image type of fashion. The last echo placed in the center of k-space to provide the desired contrast.

The inter-echo spacing (IES) is the time between echoes. This is limited by the time necessary to apply encoding gradients and GMR. In the present configuration, with the present hardware, the minimum inter-echo spacing is in the neighborhood of 12 msec. when no GMR is used and 22 msec. when GMR is applied. The IES impacts on the contrast and the quality of the image. As a general rule, most of the effects of shortening the IES are helpful. Shorter IES allows less time for dephasing effects to occur between echoes. This results in less magnetic susceptibility effects. With a shorter IES, the echoes can be clustered closer to the effective TE, thus reducing the degree of edge enhancement artifact. More slices can be obtained for a given TR. Shorter IES also reduces blurring, motion and truncation artifacts.

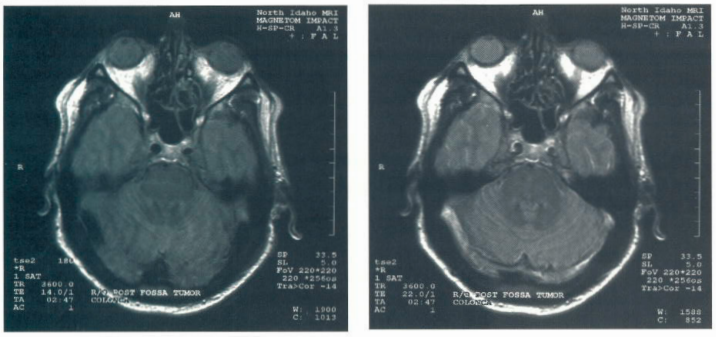

Left: TurboSE proton density weighted image of the head. No Gradient Motion Rephasing (GMR) was used. Note the presence of flow artifacts.

Right: TurboSE proton density weighted image of the head. Gradient Motion Rephasing (GMR) has been included. Note the absence of flow artifacts.

Clinical Focus: Turbo Spin Echo

The Intricacies Explained

- SP/SP4000
- Impact
- P8

Dean Kaufman, Siemens Medical Systems, Inc.

It has been said that "fast spin echo is not just *fast* spin echo" when making reference to the difference between Turbo Spin Echo (TurboSE or TSE) and just running a faster Spin Echo sequence. TurboSE is much more complex than conventional Spin Echo in many ways. In the discussion that follows, you will find a discussion of the similarities and differences between conventional Spin Echo and TurboSE and clarification of how the TurboSE parameters affect image contrast and signal-to-noise.

Both conventional Spin Echo and TurboSE refocus the echo with the use of RF pulses. This is why they are both called Spin Echo sequences. There are new parameters specific to TurboSE sequences. They are the echo train length, echo spacing and echo ordering. These parameters exist because TurboSE sequences acquire data as a train of echoes within the time allowed by the TR period, and because the raw data map of one image is actually filled with data from this series of separately acquired echoes occurring at different echo times. This differs from conventional Spin Echo imaging where the raw data from one image is filled with data acquired at only one echo time.

Because of the need to optimize these parameters within the timing of the imaging sequence, these new parameters cannot be changed by the user. This is why Siemens provides a large number of imaging sequences with various echo train lengths and effective echo times, while always attempting to minimize the interecho spacing. Selecting a sequence with a longer echo train increases the time savings, but eventually this positive effect is offset by the appearance of image artifacts.

The echo train in TurboSE also changes how the number of imaging slices are calculated. With conventional Spin Echo the maximum number of available slices is equal to TR/TE. With the TurboSE sequences the maximum number of slices is equal to the TR/the longest TE in the echo train. Therefore, as the echo train length gets longer , the number of slices per TR decreases. As with conventional Spin Echo, increasing the repetition time (TR) increases the number of potential slices one can acquire and improves the T2 contrast. TRs for TurboSE can be much longer (3000 to 5000 msec) than for conventional SE sequences to allow for good slice coverage. Echo train lengths are usually 4-15 echoes long, and provide a good compromise between scan time reduction and slice coverage for the desired range of TR values.

Parameter	Advantage	Disadvantage
Increased TR	Incr. Contrast Incr. S/N Incr. # of slices	Incr. Acq. Time Incr. Motion Artifacts
Increased TE	Incr. Contrast Decr. Edge Enhancement	Decr. S/N Incr. Mag. Suscept.
Increased Echo Train	Incr. Contrast Decr. Scan Time Incr. Range of TE's Decr. Scan Time/Slice	Decr.S/N Incr. Blurring Decr. # of slices/TR Incr. Truncation Artifact Incr. Edge Enhancement

Due to the sequence construction and spin echo reordering specific to TurboSE, there are a number of image artifacts which can manifest themselves in TurboSE. Some of these artifacts can also be seen in conventional spin echo and gradient echo images. The blurring and edge enhancement artifacts are a result of the echo reordering which must be performed with TurboSE image data. This reordering is necessary because TurboSE images are created with data from different echo times. This is the major difference between TurboSE and conventional Spin Echo. It is important to understand why these artifacts are formed in TurboSE images so they can be minimized by choosing the best possible scan parameters.

These artifacts include:

- **Blurring**
- **Truncation Artifact**
- **Motion Artifact**
- **Edge Enhancement**
- **Magnetic Susceptibility**

BLURRING

This artifact can easily be confused with motion artifact ghosts. Blurring worsens with increased echo spacing. It is caused by changes in tissue T2 during the echo train and affects tissues which have a short T2 time such as muscle, liver, and vertebral bodies. This results in the artifact getting worse when data from early echoes in the echo train are used to define the contrast.

EDGE ENHANCEMENT

This artifact is attributed to T2 decay during data collection and is manifest as increased signal at the edges of anatomic structures. This is due to data from various short echo times being used to fill the raw data which define the edges of image features.

TRUNCATION "EDGE RINGING" ARTIFACT

As in conventional Spin Echo, truncation artifact appears where there is high contrast between bright and dark anatomical structures. This artifact gets worse as the echo train length increases, and results in the acquisition of very late echoes. It is due to T2 relaxation processes occurring during the various echo acquisitions. This artifact will not be apparent with either conventional Spin Echo or TurboSE if high resolution matrices are used.

MOTION ARTIFACT

TurboSE sequences benefit from GMR (Gradient Motion Rephasing) similarly to conventional Spin Echo sequences. This is why many of the TurboSE sequences available on Siemens systems have GMR built into the sequence. It is very important to select a sequence with GMR when imaging regions which include physiological motion. When this guideline is followed, motion artifacts will not be a problem. Regions such as the spine, and body can only be successfully imaged if CSF, blood flow, and respiratory artifacts are eliminated.

MAGNETIC SUSCEPTIBILITY

This artifact is due to the dephasing of transverse magnetization. This is the very same reason magnetic susceptibility is a factor in conventional spin echo imaging. This artifact is no more of a problem with TurboSE sequences.

Above is a table summarizing the positive and negative affects of manipulating TR, TE, Echo Spacing, and Echo Train. As with most other aspects of MRI parameter optimization, there are advantages and disadvantages to manipulating each of these parameters. Gaining a thorough understanding of these tradeoffs should be a goal of anyone working with TurboSE. It is only through such an understanding that the full benefits of TurboSE can be put to use clinically.

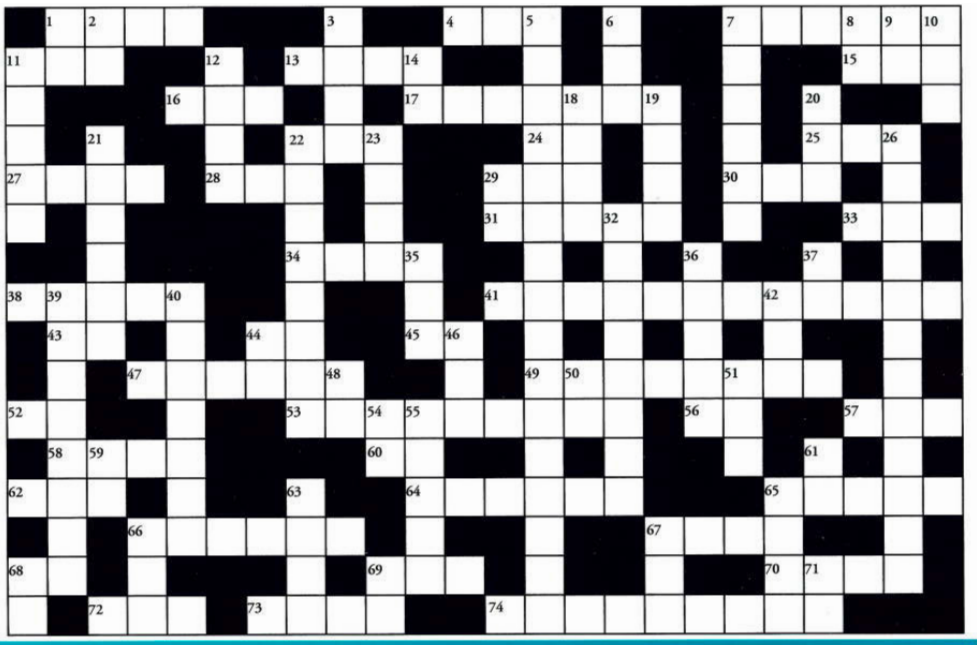

Across

1 Medical aptitude test.
4 Variable flip angle spin echo sequence.
7 Hydrocephalic babies get silastic _ _ _ _ _ _.
11 Federal agency certifies safety and efficacy.
13 Technologist registry.
15 Can generate a metal artifact.
16 Managed care genre.
17 Name of Siemens' MRI software.
22 Software that reformats additional image planes.
24 High freq. is to HF as low freq. is to _ _.
25 Biomagnetic analog of the EEG.
27 Technologist professional society.
28 MRI of the vasculature.
29 3D angiographic reconstruction software.
30 This older term was replaced by "MRI".
31 MRI can detect disease at an early _ _ _ _ _.
33 Brainstem view contains acoustic pathologies.
34 Establishes equipment manufacturers' standards.
38 Siemens' computerized service network.
41 Weakly attracted to a magnetic field.
43 Technologist degree.
44 Lateral aspect opposite left (abbrev).
45 Most sites run QA procedures in the _ _.
47 Siemens' software for non-square imaging.
49 Requires 90° and 180° RF pulses.
52 Siemens' new shielded magnet design (abbrev).
53 Alternative to time-of-flight.
56 _ _ 4000 MRI system.
57 Off-resonance MRA enhancement technique.
58 RF pulse containing a slice profile 'ramp'.
60 Physician's degree.
62 Calculation that limits RF power.
64 Siemens' 1.0T MRI system.
65 The role of applications specialists.
66 City of Siemens' USA headquarters.
67 Professional neuro society.
68 Phase encoding (abbrev).
69 Limb containing the knee.
70 MRI signal.
72 Vascular anomaly (abbrev).
73 Unspoiled gradient echo sequence.
74 Siemens USA headquarters' state.

Down

1 Physician's degree.
2 Carcinoma (abbrev).
3 _ _ _ _ around artifact.
5 Daily performance test.
6 Name of our field.
7 Pathology involving an enlarged spinal canal.
8 H _ _ (abbrev. for "slipped disk").
9 An inversion recovery sequence parameter.
10 Important image quality parameter.
11 Spoiled gradient echo sequence.
12 MRI trade show.
14 Hillary Rodham's husband's runningmate's state.
18 Main transmitter amplifier.
19 An important attribute of an MRI exam.
20 Motion rephasing technique.
21 Gad. has revitalized the imaging of this body part.
22 Siemens' MRI product name.
23 Quick magnification feature.
26 Signal refocussed without an RF pulse.
29 Pathology showing demyelination in neural tissue.
32 Linearly varying magnetic field.
35 American Hospital Association.
36 The heart TRIGGERS and the lung _ _ _ _ _.
37 It cools the magnet to supercon. temperature.
39 Best imaged with the endorectal coil.
40 First company to offer an MRA package.
42 Federal life science institute in Bethesda.
44 Type of energy specified by flip angle.
46 New functional imaging based on biomagnetism.
48 Federal hospital chain.
50 Long TR, short TE.
51 Billing codes for each examination.
54 Popular MRI contrast agent.
55 Low signal-to-noise can be due to high _ _ _ _ _.
59 Operating room.
61 Timing parameter controls amount of dephasing.
63 This puzzle's author's company (abbrev).
65 MIP allows you to view the vascular _ _ _ _.
66 Major brain vasculature.
67 Vertebral disks dehydrate with _ _ _.
68 Siemens' 0.2T MRI product.
69 Alternative to circularly polarized.
71 County (abbrev).

By: Philip A. Femano, Ph.D., President, Medical Imaging Consultants, Inc.

Find the solution on page 10

Clinical Applications of Fat Suppression Techniques

Principles and Clinical Applications

SP/SP4000
Impact
P8

Richard Patt, M.D. – Georgetown University Medical Center – Washington, D.C.

Clinical applications for fat suppression techniques remained relatively limited until two major advances in the last few years improved these techniques: improvement in RF pulses and shimming for chemically-selective FATSAT, and the increased speed and number of slices made available with Turbo Inversion Recovery (TIR) sequences. These two techniques are currently the most commonly used in routine clinical scanning and display a wide range of utility. While both FATSAT and TIR are able to provide significant suppression of signal from fat protons, these techniques are not interchangeable for all applications. In most cases, one or the other technique provides the best information; however, in some applications, using the wrong technique can lead to insufficient or incorrect diagnostic information.

If one is interested in evaluating gadolinium contrast enhancement characteristics of an area within or adjacent to fat in the body, FATSAT is the technique of choice. In general, pre- and post-contrast scans of the same area are performed using a T1-weighted FATSAT sequence. Since the high signal from fat is eliminated from the image, the image gray scale is automatically shifted and structures with a high water content become bright (bladder, blood vessels, bowel contents, etc.) The pre-gadolinium scan ensures that these normally bright structures are not confused with enhancement following gadolinium injection.

In abdominal imaging, FATSAT decreases respiratory motion artifacts by removing the bright signal from fat. This also has the effect of increasing the relative signal-to-noise ratio while providing standard spin echo imaging signal characteristics.

T2-weighted FATSAT appears to have fewer clinical uses, but has been helpful in pelvic imaging. In evaluating the periprostatic neurovascular bundle in patients with prostate cancer, TSE-T2 FATSAT has aided in the detection of tumor extension outside of the capsule of the prostate gland. It can be helpful in imaging ovarian and other adnexal masses. Imaging the orbits may also benefit from this technique.

FATSAT is not a perfect technique. It is highly dependent on magnetic field homogeneity. Individual patient shimming is becoming easier to perform with improved automation of shim programs. Performing FATSAT on regions away from isocenter such as shoulders, breasts, brachial plexus, etc. can often provide suboptimal results. It remains an operator-dependent technique, and if improperly performed can lead anywhere from uneven or no fat saturation, to partial or complete water saturation, depending on the frequency offset chosen.

Inversion recovery sequences may be used when suppression of fat signal is needed without gadolinium enhancement. These sequences provide heavily T1-weighted images. Until the ready availability of TSE IR pulse sequences, this technique was somewhat limited due to its longer imaging times and limited number of slices available, both dependent on the inversion time (TI) used. And as stated earlier, with the TI selected for fat suppression, the sensitivity for T1 changes is too low to be used with gadolinium. In fact, gadolinium administration may actually result in a "negative enhancement effect" on IRABS sequences.

There are positives and negatives to both types of fat suppression imaging,. What is most important to remember is that these are usually not interchangeable for all clinical applications. Understanding the advantages and limitations of each technique is the key to choosing which one will provide the best diagnostic images.

Neuro Imaging

T1-weighted FATSAT is useful in evaluating intraorbital lesions, especially those adjacent to the optic nerve or orbital muscles. As with other lesions adjacent to fat, enhancement following gadolinium injection can be obscured using a standard T1-weighted pulse sequence. However, by suppressing the signal intensity of fat adjacent to the pathology, enhancement is much better detected.

In the spine, T1 FATSAT following gadolinium is also useful in detecting metastasis. One must realize, though, that using the same pulse sequence without gadolinium can actually make lesions within the bone marrow less apparent. The same technique can be used in the brain to evaluate lesions involving the bones of the skull.

Body Imaging

Use of both precontrast TSE IR and postcontrast FATSAT in the neck can aid in detecting abnormal pathology such as adenopathy, primary tumors, abscess, thyroid abnormalities, and post-operative changes. In patients with suspected thyroid pathology, gadolinium-enhanced FATSAT has the advantage of not affecting possible radionuclide therapy uptake (if required) as would using iodinated contrast with a CT scan of the neck.







In the chest, FATSAT or TSE IR can be used (as it can in any part of the body) to determine whether a mass seen on standard T1-weighted imaging is composed entirely of fat; i.e. a lipoma. These are often present along the chest wall, but may be found in many parts of the body.

We have found that TSE IR sequences have occasionally been helpful in imaging the brachial plexus to better image the cords and trunks of the plexus itself by decreasing surrounding fatty signal. As this may require large fields of view over 400mm in the coronal plane to image out to both axillae, FATSAT can be less effective due to difficulties in obtaining homogeneous saturation in the lateral aspects of the magnet bore.

Breast imaging for the evaluation of cosmetic or reconstructive implants with the bilateral breast coil is a highly effective tool in diagnosing implant leak or rupture. Depending on whether single or double lumen implants are used, saline or silicone, and the mixing that can occur between silicone and saline in double lumen implants if they are ruptured, complex signal characteristics can be observed. Silicone has a T1 between fat and water. We can take advantage of this fact and, using TSE IR, select a TI that will not only null fat (TI = approx. 120-150msec) but use a TI of approximately 400msec to null the signal from silicone.

Thus, in imaging patients with breast prostheses, we perform both a "fat null" and "silicone null" sequence. The fat nulling sequence allows us to better examine the margins of the implant shell for small silicone leaks. Silicone nulling tells us whether masses along the implant are related to breast tissue or represent silicone outside a ruptured implant by behaving signal-wise the same as silicone inside the implant. Gadolinium is of no clinical benefit in the evaluation of patients with breast implants. FATSAT can be used precontrast, but due to the position of the breasts in the magnet bore, TSE IR provides more reliable suppression of fat signal from patient to patient.

Abdominal imaging has long been





plagued by the artifacts caused by motion of fat not only internally but circumferentially in the subcutaneous tissues around the body. Restraining belts, anterior saturation bands, and other means to decrease these artifacts have been used. Obviously, the ideal would be just to rid ourselves of the fat signal. IRABS imaging for liver lesion detection was used extensively with some success. Adequate resolution and slice number in a reasonable time period remained a problem until the availability of Turbo IR sequences. We tend to prefer FATSAT, however, in the upper abdomen. The signal characteristics are less complex than IR sequences, and resolution can be maintained with adequate signal to noise similar to standard SE sequences.

Precontrast FATSAT has been used to evaluate the adrenal glands, as these small structures can sometimes be all but obscured by surrounding fat on standard SE sequences. If an abnormality is found, gadolinium is administered and post-contrast FATSAT images in the same area are then obtained.

While imaging lesions within the substance of the liver does not necessarily benefit from the use of FATSAT, detecting small masses in the peripheral portion of the liver, adjacent to fat in the abdomen, is greatly improved by post-contrast FATSAT. Similarly, this same technique can be applied to masses along the peripheral margins of the kidneys.

Pre- and post-contrast T1 FATSAT is useful in imaging pancreatic masses, while TSE IR imaging may be satisfactory for imaging the spleen, when combined with standard SE sequences.

T1-weighted post-contrast FATSAT has also been used in the abdomen and pelvis to evaluate intrinsic bowel abnormalities, such as Crohn's disease and ulcerative colitis. These patients should have nothing by mouth for approximately 6 hours prior to the exam to decrease bowel motion. Post-contrast images are made immediately after a bolus of Gd-DTPA through the area of suspected bowel abnormality and show abnormal enhancement patterns in these areas.

In imaging the female pelvis, TSE IR has been used to show excellent zonal architecture within the uterus. Post-contrast FATSAT may be helpful to better distinguish tumors that spread into the adjacent pelvic fat, however. FATSAT also is helpful in minimizing the chemical shift artifact seen adjacent to solid pelvic organs when using relatively low bandwidth



sequences. In particular, this aids in better evaluating the ovaries as these small organs (much like the adrenals) are surrounded by fat and the outer margins may be obscured by chemical shift artifact on standard SE sequences.

Scanning the male pelvis for prostate carcinoma staging is usually performed without gadolinium, as the prostate is a relatively poor vascular organ and little benefit is obtained by using contrast. Accurate staging to determine appropriate therapy (surgery, radiation, or hormone therapy) is in part determined by MR's ability to evaluate the margins of the prostate gland for tumor spread into the adjacent pelvic fat. High resolution TSE IR appears very helpful in this routine evaluation, and can show impressive zonal anatomy within the gland itself.

Musculoskeletal Imaging

In adults, fat occupies the majority of the bone marrow space. While this enables us to see the dark bony cortex well, it makes the detection of lesions within the marrow often difficult. TSE IR has been used quite successfully to detect metastatic deposits in the marrow, microfractures not seen on plain film, infection (oseomyelitis), and other abnormalities. Again, the more standard signal characteristics of FATSAT make it often the better choice for detecting and evaluating lesions within the bone marrow. This must be performed with and without gadolinium, unless T2 FATSAT is employed.

Precontrast FATSAT is also used to depict the cartilage in joints, seen as a bright thin line superficial to the cortex of bone in the knee, hip, shoulder, etc. This is due to the fact that joint (articular) cartilage has a relatively high water content which stands out against the black appearance of cortical bone.

In any case of soft tissue mass that involves bone, muscle, or adjacent tissues, pre- and post-contrast FATSAT should be routinely performed. They add information about tumor extent, additional lesions in surrounding bones, invasion of surrounding tissues, etc.

Before using any of these techniques, it is important to understand their limitations and attributes. While this is not meant to represent a comprehensive use of these fat suppression techniques, it can be used as a starting point to apply these sequences in the clinical realm. New applications such as breathhold 2D FLASH with FATSAT in the abdomen and 3D gradient echo FATSAT sequences will further increase the use of these techniques.

Fat Suppression In Magnetic Resonance Imaging

SP/SP4000
Impact
P8

Helmuth Schultze-Haakh, Ph.D., Siemens Medical Systems, Inc.

When acquiring an MR image all hydrogen ions or protons whether in a water type environment or in a fatty one will be excited simultaneously. Therefore, both fat and water give relatively strong signals. This could lead to difficulties distinguishing small lesions in a fatty tissue (e.g. around the optical nerve) when using a T1-weighted contrast image, or fluid compared to other bright tissue (e.g. in the joints) in a T2-weighted contrast image. For this reason it is often important and becoming more common to suppress the fat without disturbing the other tissue signals.

There are a variety of techniques to suppress fat. Some are based on the difference in the resonance frequency of fat and water and others on the difference in the relaxation time (T1).

FATSAT

The now most common and most successful technique is FATSAT (fat-saturation). This technique is based on the fact that fat and water protons have different oscillation frequencies depending on the chemical environment of the protons.

Fat and water display two distinctive peaks. These peaks are separated by a certain frequency. To make this separation independent of the system's operating field strength a dimensionless unit is used to describe this difference; it is expressed in parts per million (ppm), and is calculated as the fat-frequency minus the water-frequency divided by the water frequency. This difference is about 3.5 ppm which translates to about 147Hz for a 1T system and 220Hz for a 1.5T system.

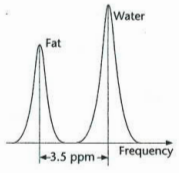

A special rf-pulse excites the protons in fat, off the water resonance and thus leaving the water protons unaffected. This acts similar to the spatial presaturation commonly used in spine imaging or MRA. Here, however, this saturation rf-pulse does not excite a spatial region, but rather a certain frequency away from water. This pulse must therefore show a very narrow range in frequencies or bandwidth in order to avoid hitting the protons in water. The SP systems actually use an off-frequency pulse which can be adjusted by the user in A2.5. A1.5 for the Impact systems includes a set of FATSAT sequences which saturate the fat by exciting both fat and water using a shallow rf-pulse, then letting the spins relax for a while which leads to a dephasing between fat and water since the spins are at different frequencies (see phase cycling below). Subsequent rf-pulses will bring the water spins into the transverse plane and the fat spins into the longitudinal plane where they will have no contribution to signal. By using a similar excitation, water can be suppressed instead of fat.

New automated shimming procedures and more reliable selection of fat saturation frequencies will make these techniques just as easy to use in the near future as the standard spin-echo sequences.

Homogeneity

As mentioned the fat and water frequencies are very close together and under normal imaging conditions the rf-pulses span a large enough range to excite both at the same time. In general, the oscillating resonance frequency of the spins is proportional to the magnetic field strength they experience. Any deviation of the field causes some spins to resonate at different frequencies than other ones in the area. This is not just due to the chemical environment of the spins but rather due to the fact that the field is not the same everywhere in the imaging area. The accuracy of the magnetic field is called its homogeneity. Slight deviations in the magnetic field causing differences in resonance frequency similar to that of the fat-water separation can be observed leading to an incomplete fat-saturation or an unwanted saturation of water in some other areas in the field when fat-saturation is used. It is therefore essential to obtain a very good magnetic field homogeneity in the area of interest by shimming the field carefully, ideally with the patient already positioned for imaging. This would make the field everywhere in the area of interest the same and hence the associated frequency of the spins residing in the same tissue. It should be clear that the success of a fat-saturation study depends largely on how well the magnetic field is shimmed. (The shimming procedure of the SP systems is described in the operator's manual.)

Phase cycling

Immediately after excitation the position of fat and water in the transverse plane is the same, they are in phase. However, since the spins experience different frequency water is "running away" from fat. The net magnetization decreases and will have a local minimum when fat and water oppose their phase orientation. After a while, however, water will "catch up" with fat again and their signal increases as they come back into the in-phase condition. This process is called phase cycling. The time period it takes for fat and water to reach the in-phase condition is the reciprocal of the separating frequency: 4.5ms at 1.5T and 6.8ms at 1T. In between fat and water are opposing.

As the echo time in a gradient echo sequence acquisition is increased some oscillation overlaying the T2* decay curve can be observed. Every time fat and water are in-phase a peak appears and whenever they are opposing a local minimum can be seen.

This fact can also be used to reduce the fat signal compared to water. If an echo time (TE) is chosen such that fat and water are opposing then fat is relatively weakened. For example, at a

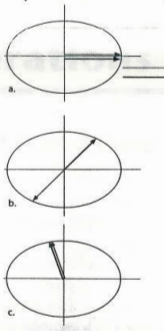

TE of 10ms fat and water are nearly in phase at 1.5T and nearly opposing at 1T. This is the reason why a TE of 10ms is used for MRA at 1T and correspondingly 7ms at 1.5T since a strong fat signal is undesirable.

Dixon Method

The "Dixon Method" also uses the fact of phase cycling. In a spin echo sequence two echoes are formed one which has fat and water in-phase (W+F) and one where they oppose (W-F). If the two images are added to each other (W+F+W-F=2W) a water image can be created and fat is suppressed. If the two images are subtracted from each other (W+F-W+F=2F) a fat image can be calculated. However, this additional post processing makes this technique somewhat tedious. It is also relatively sensitive to patient motion. Since the advent of rf selective FATSAT this technique is less popular.

IRABS

Since fat has one of the shortest longitudinal relaxation times or T1-values in the body, it relaxes relatively quickly. Starting out with a 180° rf-pulse all spins are brought into the opposite direction. As they want to be in the stable parallel direction with the external magnetic field the spins are going to relax passing the transverse plane on their way to regain signal in the longitudinal direction. If a normal spin echo excitation (90° pulse) is used to bring the spins into the transverse plane, right at the time when the fat spins are in the transverse plane, no signal is picked up by fat. Therefore, fat will remain dark. The time between the 180° inversion pulse and the 90° excitation pulse is called the inversion time (TI). Typical values for TI in a fat-suppression inversion recovery sequences are 100 to 150ms. Using longer values for TI (greater than 1500ms) one can also suppress fluid. Using a long TE and a very long TR (greater than 5000ms) this technique has been termed FLAIR (FLuid Attenuated Inversion Recovery).

There are some problems associated with IRABS:

a. To obtain a good steady state situation for all spins a relatively high TR is necessary. This might make T1-weighted contrast scans difficult and scanning times long.

b. Since the data is reconstructed using only the magnitude or amplitude of the echoe data, some signal values originally beneath the zero line are now flipped to the positive side. This leads to an ill-defined contrast behavior. This technique does not work post contrast since GdDTPA reduces T1 values. As T1 is shortened the "flipped" portion of the curve is lowered and therefore the signal reduced rather than enhanced.

On the other hand this technique has gained some wide use since it does not require the same level of homogeneity as the FATSAT techniques and can be done with standard software and hardware configurations.

Fat-suppression techniques have entered the MRI practice and are becoming more commonplace. New automated shimming procedures and more reliable selection of fat saturation frequencies will make these techniques just as easy to use in the near future as the standard spin-echo sequences. In addition, fat-saturation might even become an option for almost all sequences no matter whether they are spin-echo, gradient-echo, 2D or 3D.

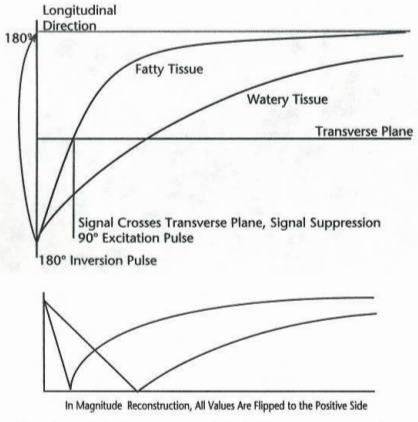

The FLASH Word Bash!

- Fill in the missing word for each statement.
- The parentheses shows the page that has a clue for that word.
- Enter each word in the corresponding entry below.
- Unscramble the eight encircled letters to find the hidden word.
- Enter the unscrambled word in the box to complete the message.
- First to fax correct answers to 201-812-9199 gets a prize.

Puzzle by:
Philip A. Femano, Ph.D., President
Medical Imaging Consultants, Inc.

1. An inversion recovery sequence which suppresses signal from fat by using a specially selected short TI is called _____. (4)

2. A technique available with A2.7 with which blood flow can be calculated by using an RF saturation pulse is called _____ tracking. (1)

3. Siemens AG has formed a research collaboration with Schering AG and eight luminary medical centers to conduct an international study on _____ diagnosis. (2)

4. New rapid 3D sequences available with the A2.7 software release which provide strong T1 weighting are called _____. (1)

5. MR Spectroscopy provides an effective method for chemical and _____ analysis. (6)

6. To facilitate the diagnosis of prostate carcinoma, Siemens has announced the availability of the _____ coil. (1)

7. In order to introduce you to the features of each new software release, Siemens plans to distribute each software version with an _____ video. (6)

8. The one-week intensive educational program offered by Siemens in New Jersey is the "MRI Essentials for _____" course. (4)

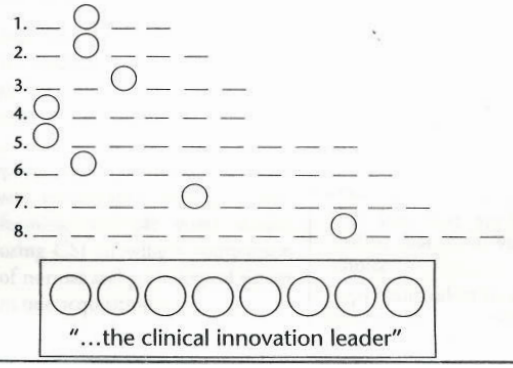

Answers to last issue's puzzle:

```
 MCAT    W   HIQ M   SHUNTS
FDA   S ARRT   U R   Y   PIN
L    HMO A NUMARIS R G   R
A B   R MPR    LF A I MEG
SMRT MRA O   MIP F NMR R
H E     G A   STAGE X   IAC
  A     NEMA   Y R G   H D
OPSIS   E   H PARAMAGNETIC
 RT I RT   AM S D T I   E
 O RECFOV   S SPINECHO N
AS   M   MAGNITUDE SP   MTS
 TONE     DO   R N   T T E
SAR N   M   IMPACT    TEACH
 T ISELIN S   N   ASNR   H
PE C    C LEG C   G   ECHO
8 AVM FISP   NEWJERSEY
```

FEATURE ARTICLE: Array Coil Design

Charles M. Anderson, M.D., Ph.D.
Ralph E. Lee, M.A., R.T.
University of California, San Francisco, CA

This article is excerpted from the Siemens MRI Coil Primer, currently under preparation by the same authors.

A new class of MR imaging coils has arrived. These so-called "array coils" have impressive sensitivity, permitting excellent images in less time. The secret to the design of these coils is that they are actually composed of many surface coils in an array, each working independently, but combining their information to yield a larger image. The array covers an extended field-of-view (FOV) as if it were one big coil, but acquires each portion of the image with the sensitivity of a surface coil. However, before describing these advanced coils, let's begin by describing the simplest coil arrangement - a single loop surface coil.

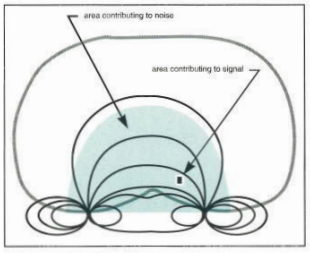

Figure 1. The effective depth of penetration of a surface coil is proportional to the diameter of the coil. The amount of MR signal contributing to each voxel of the image depends on the volume of the voxel (arrow). The amount of noise emanating from the patient's tissues and received by the coil increases with the size of the coil (shaded area). The greatest SNR, therefore, results from acquiring a coarse resolution image (large pixels) with a small coil.

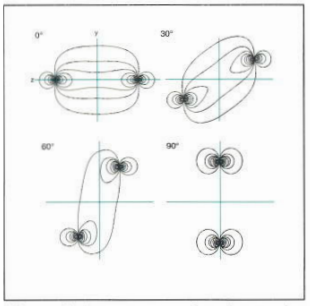

Figure 2. A sensitivity plot of a single loop surface coil as it is tilted from a coronal to a transverse plane. Note the total lack of sensitivity in the imaged volume as the coil becomes transverse.

As demonstrated in Figure 1, a plot of the sensitivity of a single loop surface coil lying under a patient's back shows that sensitivity drops rapidly with distance from the coil. The deeper one wishes to image, the greater the diameter of coil needed. However, while larger coils permit imaging of a greater FOV, they also receive more noise than do smaller coils. Therefore the extent of coverage of a coil is usually in conflict with the sensitivity of the coil.

A phenomenon which must be remembered is that sensitivity depends upon the orientation of the coil. As demonstrated in Figure 2, a sensitivity plot can be calculated for a coil which is first coronal (horizontal) and then is progressively tilted up to the transverse plane. Notice that the lines of sensitivity do not tilt with the coil but rather assume a completely new and less efficient shape. One cannot tilt a single loop surface coil towards the transverse orientation by more than about 30 degrees. This dependence on coil orientation is caused by the fact that the signal from the patient is directional; the magnetic moments of the spinning protons in the patient are precessing in the transverse plane with their axis of rotation along the axis of the bore.

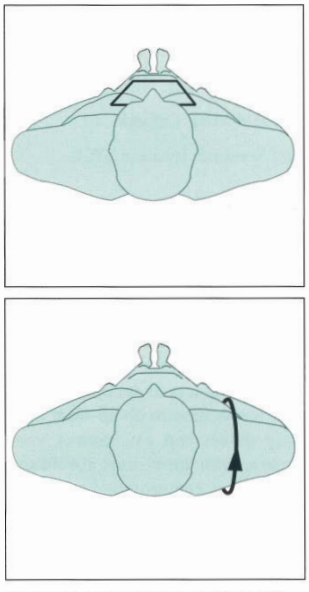

Figure 3. A single loop surface coil can be used in the coronal plane (3a), sagittal plane (3b), or anywhere in between, but not in the transverse plane.

To be most sensitive, the plane of a single loop surface coil must be parallel to the direction of the magnetic field. For super-conducting magnets (such as the MAGNETOM SP, Impact, and Vision) the magnetic field is oriented along the axis of the bore (head to foot). Single loop surface coils can be coronal or sagittal to the body, or any orientation in-between, but not transverse. Therefore, when performing an examination on any system with the magnetic field along the axis of the bore, one can orient a single loop surface coil in the coronal plane behind the spine (like the Siemens Elliptical Spine Coil in Figure 3a), or in the sagittal plane around the shoulder (like the Siemens Loop Flex Coil in Figure 3b), or in the sagittal plane worn like a bracelet around the wrist of a bent arm. One cannot, however, orient a single loop surface coil in the transverse plane with such a system.

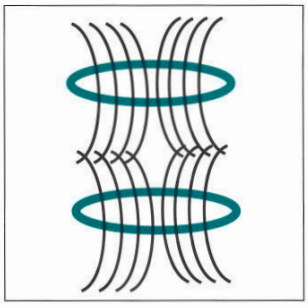

Figure 4. Helmholtz Coil: the two loops are coupled but provide good homogeneity and increase SNR in the center of the imaged volume at the expense of some loss of sensitivity immediately adjacent to each loop.

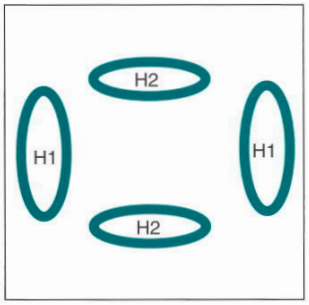

Figure 5. Circularly Polarized Coil: two mutually perpendicular Helmholtz Coils (H1 and H2) are decoupled to provide better homogeneity and better SNR than any single Helmholtz Coil.

What sort of design changes can improve the SNR beyond that achieved from a single loop surface coil? One idea to improve SNR of the coil might be to simultaneously place two independent surface coils at the same location. Unfortunately, this idea doesn't work. If two coils are parallel and lie in the same plane, the electromagnetic fields generated by the current in the first coil will be picked up by the second coil and a like current will be induced. When coils interact like this they are said to be "coupled." Coupled coils do not improve SNR since the noise detected by one coil will be received by the second coil as well.

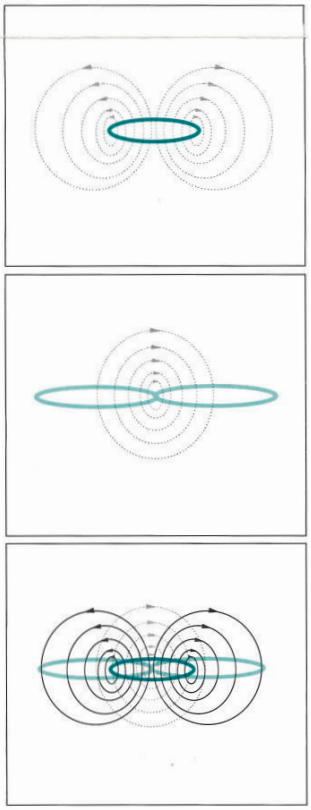

Figure 6. Uncoupled elements of a CP surface coil. (6a) Field lines of a circular surface coil. (6b) Field lines of a "figure-of-eight" coil rise up from one side of the coil and descend on the other side, since current that runs clockwise on one side is counterclockwise on the other side. (6c) When these coils are superimposed, the number of lines from the first coil which penetrate the second coil in the "up" direction are canceled by an equal number of lines in the "down" direction.

Array Coils (continued)

As shown in Figure 4, a "Helmholtz" coil is actually a pair of loop coils that are parallel to each other and separated by some distance. At normal operating distances, the two coils couple with each other and form, in effect, a new larger coil with a substantially increased area of reception. This Helmholtz arrangement improves the sensitivity in the region midway between the coils, but at the expense of sensitivity immediately adjacent to the coils. There is also an increase in noise reception resulting from increased surface area for reception. Thus, these coils provide a more uniform sensitivity throughout the entire volume between the coils as compared to a single loop surface coil. The Siemens Neck Coil and Siemens Linear Knee Coil are examples of Helmholtz designs. These are sometimes referred to as "linearly polarized" volume coils.

If two loop coils are positioned perpendicular to one another they do not couple. The electromagnetic field lines from the first coil do not pass through the second, and noise is not shared. A set of coils in this relationship is called a "circularly polarized" (CP) coil, or "quadrature" coil. This combination of coils, in effect, doubles the number of acquisitions without increasing the measurement time, since both coils are receiving from the same volume at the same time. One can arrange two Helmholtz pairs perpendicular to one another to form a "circularly polarized" volume coil, as demonstrated in Figure 5. The Siemens CP Body Coil and Siemens CP Head Coil are examples of this arrangement.

As demonstrated in Figure 6, a CP surface coil uses an ingenious arrangement of two loop coils lying in the same flat plane to construct a "circularly polarized" coil. Although the coils are physically parallel, their electromagnetic fields are "perpendicular". One coil is circular (vertical field lines) while the other coil is a figure-of-eight (horizontal field lines). With this geometry, the forward coupling caused by one half of the figure-of-eight (current in a clockwise loop) is exactly canceled by the reverse coupling generated by the other half of the figure-of-eight (a counter-clockwise loop). The Siemens CP Spine Coil and the Siemens CP Flex Coils (both the small and the large) are examples of this arrangement.

Now we are ready to discuss the "array coils" mentioned earlier. How may one acquire different locations in the body simultaneously with multiple uncoupled coils? To answer this we might look at the coupling of coils as a function of their displacement from one another. As demonstrated in figure 7, if two coils are very close together they will couple in the forward direction, but if they are very far apart they will couple in the reverse direction. If the coils are separated by a special distance (an overlap equal to about 20% of the diameter of the coil), the forward and reverse coupling will cancel. Furthermore, two CP surface coils separated by this distance will also not interact. Here at last is the secret of the array coil - it is simply a row of CP surface coils separated by the correct decoupling distance. In theory, there is no limit to the number of coils in an array. In order to be truly separate, however, the surface coils must have individual data channels. The information from each coil is reconstructed into separate images (each containing only the noise received by one small coil) and then combined to form the entire view, as demonstrated in Figure 8 for the Siemens Array Spine Coil. In that way, the total noise in the image is much less than that of a single coil covering the same area, as demonstrated in Figure 9 for the Siemens Array Body Coil.

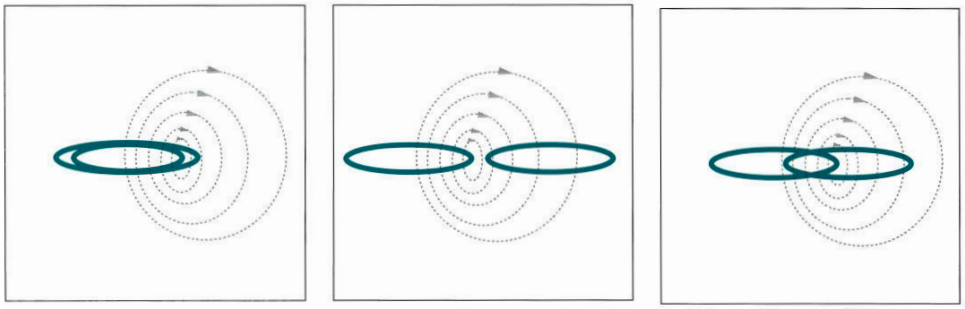

Figure 7. Two surface coils positioned at a small distance from one another will couple in the positive sense (7a). Ascending lines from the first coil enter the second coil to induce a current in the same direction. Two surface coils positioned far apart couple in the negative sense (7b). Descending lines from the first coil induce a current in the opposite direction. At an intermediate distance, the number of lines ascending in the second coil equal those descending (7c). Therefore, the forward and reverse induced currents are equal and result in a cancellation of the coupling.



Figure 8. Image from the bottom-most coil in the Spine Array Coil (8a). Images from the second (8b), third (8c), and fourth (8d) coils are acquired simultaneously through separate receiver channels and a combination of the separate images after they are acquired produces the total array coil image (8e).

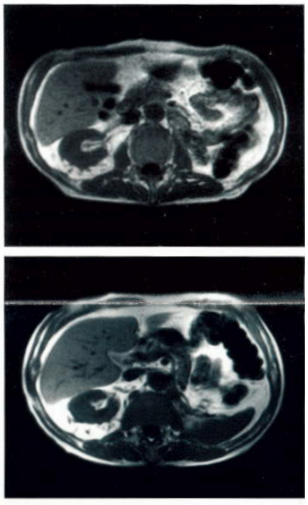

Figure 9. A breath-hold FLASH T1-weighted abdomen acquired with the standard CP Body Coil built into the scanner (9a). An identical image from the same patient with the new CP Array Body Coil (9b); note the far superior SNR.

PRODUCT ANNOUNCEMENT:

NUMARIS B21B SOFTWARE UPGRADE, MR-GUIDED PROCEDURES PACKAGE, AND KINEMATIC KNEE DEVICE FOR MAGNETOM OPEN

Anne Deery Sheehan, MS, Open Product Manager, Siemens Medical Systems, Iselin, NJ

The year 1993 started a new revolution in open MRI with the introduction of the MAGNETOM Open. Since that time, sales of open equipment have grown to more than 40% of annual MR sales. Today, Siemens announces a "new vision" for open MRI with B21B software.

NEW VISION FOR OPEN MRI

NUMARIS B21B software is the same platform that is used on the MAGNETOM Vision and Impact Expert systems. It includes many "high field" features and imaging techniques which will bring "new vision" to open MRI through expanded image contrast choices, enhanced spatial resolution and improved operator efficiency. Our "seamless" approach to R&D brings high field techniques such as TurboFLAIR, shared echo TSE, and TSE with T1 contrast to the MAGNETOM Open. This software upgrade will be installed free-of-charge for Open systems currently under Siemens service contract or warrantee. For those systems which fit neither category, the software may be purchased for $35,000.

B21B FEATURES

1. Erasable Optical disks - Simply select the optical disk drive under file/delete to erase the active side of the optical archive disk. Your drive will still recognize WORM disks, such as the Pioneer DEC 502, but now you can purchase and use the Read/Write disks, such as the Pioneer DEC 702.

2. Pixel Size Indicator - states the actual pixel size in both phase and frequency encoding directions as you change the matrix, FOV (field-of-view), and RecFOV (rectangular field-of-view).

3. Relative S/N Indicator - states the relative signal-to-noise ratio as you change the slice thickness, number of acquisitions, pixel size, and percentage of phase oversampling. The indicated S/N ratio is relative to that of the saved protocol (100% = 1.00).

phase encoding direction to adjust the FOV to the size of the imaged anatomy. This feature automatically decreases the matrix in the phase encoding direction proportional to the selected RecFOV (7/8, 6/8, 5/8, 4/8), thereby reducing the acquisition time without affecting the image resolution.

5. Phase Oversampling - for suppression of aliasing (wrap-around) in the phase encoding direction and in the partition encoding direction (for 3D scans). The amount of oversampling is freely changeable as a percentage of the selected FOV. This feature can be combined with RecFOV where desirable.

6. Measurement / History - throughout the patient exam all the measured protocols are saved in a list so they can be easily recalled, changed, or simply restarted without having to repeat the setup. This saves setup time for repeat scans or for multiple scans at the same slice locations by reusing previous slice and presat positions.

7. Measurement / Queue - setup and queue the next few protocols even during a measurement. After one protocol in the queue is completed and its images are reconstructed, the next protocol is automatically started. At any time the queue can be reviewed, paused, or modified.

8. Measurement / Position - the position platform includes a new "Image Plus" button for paging through the scout study, and also includes a new "Second Localizer" button for positioning slices on two different scout images from two perpendicular planes. This is particularly helpful when using presats and RecFOV.

9. Flexible 3D Partitions - freely selectable number of 3D partitions (in increments of 8) to allow the through-plane resolution to be easily optimized to the size and shape of the imaged anatomy.

10. Evaluate / Filter - a post-processing "adaptive filter" improves the edge enhancement to improve image quality without loss of diagnostic information. Filter parameters are freely selectable, and filtered images are stored as a new study in addition to the unfiltered images (both may be filmed if desired).

11. Integrated MAPShim - a new automated shim algorithm will replace Adjust / Gradient Offset correction to optimize the magnetic field uniformity (the old correction is still possible).

12. Integrated Fat Suppression - applied with a click of a button for some sequences. The fat signal is suppressed by use of an inversion pulse with an appropriate fixed inversion delay time (Inversion Recovery).

13. Integrated MTC - applied with a click of a button for some sequences. The bound water signal is suppressed by use of an off-resonance pulse at an appropriate frequency shift.

14. Study / Display - slices can be displayed on their localizer at the click of a button.

15. Hold / Original - toggle between magnified or scrolled images and their original display at the click of a button.

16. Evaluate / Dynamic Analysis (Optional) - user selectable combination of images with other images or with mathematical functions (add, subtract, divide, T1, T2, Z-score).

(continued on next page)

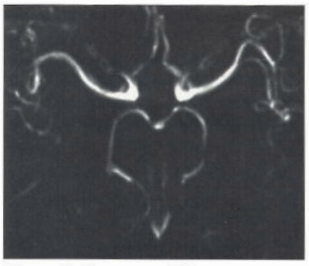

Figure 1: Transverse MIP projection of intracranial MRA acquired transversely with new multislab 3D sequence, MTS applied, 200 mm FOV.

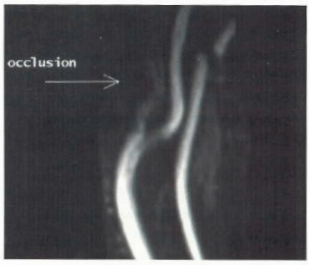

Figure 2: Sagittal MIP projection of carotid occlusion MRA acquired transversely with new sequential 2D traveling presat sequence, 200 mm FOV.

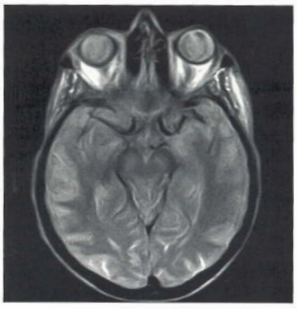



Figure 3: New dual echo TSE sequence for brains with flow compensation in both echoes, twenty 5mm slices in 6:30 min. Siemens exclusive in open MRI !

(continued from previous page)

MR-GUIDED PROCEDURES PACKAGE

The MR-Guided Procedures Package has just received FDA premarket clearance, making the MAGNETOM Open the first commercially available MRI system capable of assisting physicians during interventions. This package consists of hardware, software, and ultrafast breath-hold sequences designed to support diagnostic interventional needle biopsies and drainages. An Autodisplay feature may be used to instantly view the ultrafast breath-hold images as they are acquired on the fly, even while the measurement protocol is still running, thus providing virtually real-time tracking capabilities (fluoro-like MR acquisition).

During an interventional procedure, the interventional radiologist is guided by virtually real-time MR imaging, enabling him/her to avoid critical tissues and structures and to assure that the biopsy needle or catheter is on target when the tissue sample is taken or the drainage is started. Advantages of MR imaging for guided interventional procedures compared to other imaging modalities include radiation free imaging, excellent soft tissue contrast, the capability of arbitrary slice orientation which allows the target lesion and needle entry point to be in the same plane, and 3D volume imaging capabilities. MR-guided diagnostic procedures are well suited for anatomic areas where computed tomography or ultrasound deliver suboptimal imaging results.

The MR-Guided Procedures Package is optional. The In-Room Monitor is a separate option, but must be ordered to support the Autodisplay feature. The MR-Guided Procedures Package contains:

* Fast Imaging Sequences (up to 3 images/second, 2D, 3D, FLASH, TSE5 for T1, TSE15 for T2)
* Autodisplay of images as they are scanned
* Surgical drape for upper magnet pole
* Ergonomic chair
* Foot pedal to initiate scans
* Multipurpose 35cm diameter flexible coil
* Flexible Bore Light

KINEMATIC KNEE DEVICE

Siemens is pleased to announce commercial availability of the Kinematic Knee Device for use with the MAGNETOM Open system. This new device accessory is intended to facilitate kinematic exams through controlled positioning and movement of the knee. It can be used for examination of the left or right knee, and can be adjusted from 0 degrees to 100 degrees, in 5 degree increments. This device is not intended for dynamic examinations since this suggests an examination of the knee while forces are being applied. A new fl2d_23b24 sequence based upon the previous fl2d_25b30 sequence is especially well suited for kinematic exams.

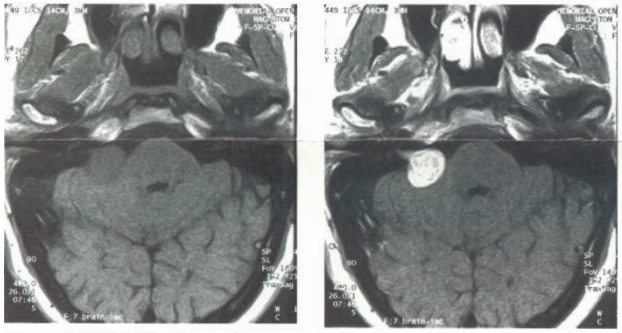

Figure 4: High field techniques benefit open MRI. RecFOV and Phase oversampling were used to obtain this aggressive 160 mm FOV, RecFOV 7/8, Phase Oversampling 25%, 3 mm slice, 7:45 min.

(a) pre-gadolinium. *(b) post-gadolinium.*

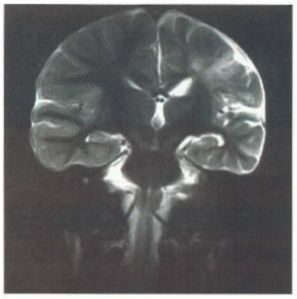

Figure 6: New Turbo IR sequence for pediatric heads with very strong white/grey matter contrast.



Figure 7: Kinematic Knee Device for static positioning of knee during kinematic exams.

MR Angiography (traveling presat band is freely selectable for head or feet)

Sequence	Description
fi3d_10rb54	Update of existing sequence, 3D partitions steps of 8
fi3d_s_10rb54	New multislab angio sequence, 3D partitions steps of 8, fixed slab overlap 0.38
fi3d_p2_10rb54	New multislab angio sequence, 3D partitions steps of 2, fixed slab overlap 0.50
fl2d_s_10rb78	Update of existing sequence
fl2d_s_14rb39	Update of existing sequence

Brain and Spine Imaging

Sequence	Description
se_25rb43_112rb17	New sequence for PD/T2 brains, flow comp in both echoes
fl2d_17b39	New sequence for Proton Density brains, faster scan and higher S/N compared to dual spin echo
tse7_117b33	New sequence for T2 brains and L-spines, faster scan and higher S/N compared to dual spin echo
tirm7_ild_93b65	New sequence for TurboFLAIR brains and spines, T2 contrast with dark fluid
tse7_114rrb65	New sequence for T2 C-spines, possible signal void with strong CSF pulsations
fl2d_46rb20	New sequence for brain hemorrhage and T2* C-spines, flow comp and variable TE
fl3d_7b98	New 3D sequence for T1 heads and spines, many slices in short scan time
fl3d_ns_8b56	Same as above, non-selective RF pulse, lower bandwidth
fi3d_7rsb195	New 3D sequence for heads and spines with very strong T2* contrast, flow comp in slice direction
ps3d_13rsb78	New 3D sequence for heads and spines with very strong T2* contrast, flow comp in slice direction
tir7_48b65	New sequence for pediatric heads with very strong white/grey matter contrast
tse240_1100b156	New sequence for myelography and cholangiography with T2 contrast so strong that only fluids are visible

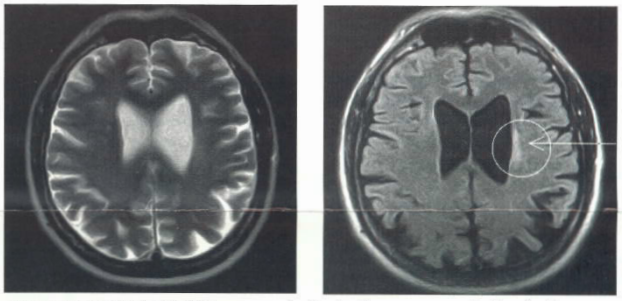

Figure 5: New Turbo FLAIR sequence for brains improves conspicuity of white matter disease. Siemens exclusive in open MRI !
(a) Turbo T2 image barely demonstrates white matter disease next to bright CSF.
(b) Turbo FLAIR image more clearly demonstrates disease next to dark CSF.

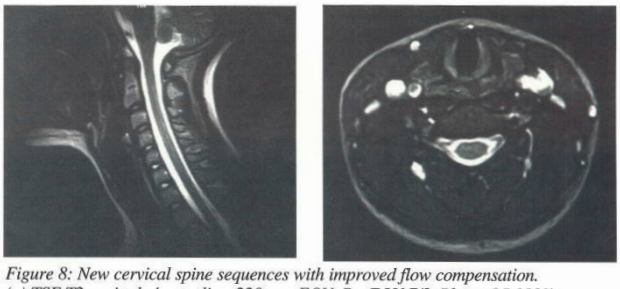

Figure 8: New cervical spine sequences with improved flow compensation.
(a) TSE T2 sagittal, 4 mm slice, 220 mm FOV, RecFOV 7/8, Phase OS 100%.
(b) Flash2D T2 transverse, 3 mm slice, 220 mm FOV.*



Figure 9: MR-Guided Procedures Package being used for interventional needle biopsy or drainage.



Figure 10: In-Room Monitor being used to operate the MR scanner and review images with Autodisplay.

CLINICAL ARTICLE:

MR IMAGING OF THE PROSTATE WITH THE CP BODY ARRAY COIL

Jeffrey C. Weinreb, MD, Director of MRI, Professor of Radiology
New York University Medical Center, New York, NY

Although most MR users believe that the endorectal coil provides a substantial improvement over the body coil for imaging the prostate, there are some practical problems with the endorectal coil that are often ignored or glossed over in the published literature. For instance, each endorectal coil costs about $100.00, and you will not get reimbursed for it. The effective depth of signal penetration is only about 4 cm. This can be a problem since the anterior aspect of the gland and bladder neck may not be well visualized with the endorectal coil alone. The images generated by an endorectal coil may also be compromised by near field high signal intensity which may obscure the posterior prostate capsule, and by ghosting artifacts from motion of the coil within the rectum during acquisition which can interfere with evaluation of the posterior prostate and the neurovascular bundles (Figure 1). Signal normalization techniques can mitigate the near field burn out but result in loss of signal in the near field, including the posterior prostate capsule. We have also found that filming the endorectal coil images can be very challenging, and to optimally evaluate the anterior and posterior fields, images may have to be viewed with two different window settings. Most users of endorectal coils will tell you that there is a pretty steep learning curve for image interpretation. If you don't do a lot of them, you may never achieve very good results.

But perhaps the biggest problem with the endorectal coil is that it is an endorectal coil. Unless you want to deal with a potential mess, the patient should have their bowel prepped prior to the exam. Furthermore, despite arguments to the contrary, placement of the endorectal coil is painful for some patients, and occasionally a patient will complain of severe pain or just not tolerate the procedure. I don't believe that glucagon really makes a substantial difference in this regard. On more than one occasion, at the completion of the exam with the endorectal coil, a patient has commented that they never want to go through that exam again. That is not terrific public relations for MRI. And don't forget the set-up time which requires that the coil be tested and tuned. We have had several occasions where the endorectal coil did not tune outside the patient, and others where it tuned outside the patient but not after it was inserted. This is reality. Sometimes the coil has to be repositioned after a scout shows that it is either too high or too low. The question we asked ourselves was "Is the endorectal coil really necessary". Can we get the same diagnostic outcome with the CP Body Array Coil?

Our experience with the CP Body Array Coil, used in conjunction with high-performance gradients and Turbo Spin Echo sequences, suggests that high quality images of the prostate may be obtained without the use of an endorectal coil. By allowing high resolution imaging of the prostate without the invasiveness and inconvenience of the endorectal coil, the CP Body Array Coil simplifies and shortens the MRI examination of the prostate, greatly increasing its acceptability to both patients and medical personnel. Some of the problems associated with endorectal coils, such as ghosting and near field high signal, are avoided (Figure 2).

Is the diagnostic accuracy with the CP Body Array Coil equivalent to that achievable with the endorectal coil? I don't know. I have not done a scientific study on the subject, and I probably never will. We did perform endorectal coil prostate MR imaging for several years before Siemens made the CP Body Array Coil available, and we subsequently performed both endorectal coil and array coil studies on a few patients. We concluded that the high resolution images we achieved using the Siemens Turbo Spin Echo sequences and CP Body Array Coil were at least as good as the endorectal coil images obtained with another manufacturer's equipment that was used in studies that reported very high quality prostate imaging. So, assuming our diagnostic skills are equal to those at other places, we should do as well. The exam is acceptable to every non-claustrophobic patient. They don't have to be prepped, there is no pain, and it goes faster. Furthermore, since there are no artifacts to contend with we no longer have to occasionally include statements in our reports like "evaluation of the neurovascular bundles and prostate capsule was limited due to ghosting artifacts". No urologist wants to receive a report like that.

Interpretation of prostate MRI is difficult under any circumstances. Gross extracapsular extension will be evaluated well with either an endorectal coil or the CP Body Array Coil. While there is no doubt that the signal-to-noise ratio at the posterior aspect of the prostate is better with the endorectal coil, there are also more artifacts. So, sometimes you will see subtle changes in the prostate contour or capsule with the endorectal coil that are not appreciated with just the CP Body Array Coil, and sometimes it is the other way around. What is the significance of these subtle changes? This is an area of controversy. Some people think that they can reliably tell which ones represent extracapsular extension and which ones represent post-biopsy or reactive changes. Personally, I think it is often a roll of the dice, and I am not certain that it matters since evidence of minimal or equivocal extracapsular extension may not preclude surgical intervention.

We use the CP Body Array Coil rather than an endorectal coil for prostate imaging, but I don't think one can be dogmatic about this subject. There are pluses and minuses of both. If you like endorectal coils, use them. If you don't, the CP Body Array Coil is a viable alternative. This approach has not won me any popularity contests with the manufacturers of endorectal coils, but you have to find these things out for yourself. Do not assume that the published results using equipment from another manufacturer necessarily apply to your equipment.

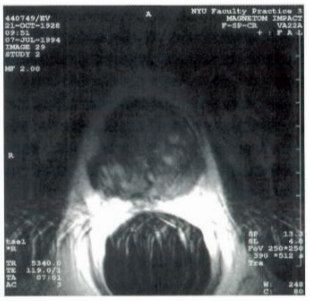

Figure 1: Endorectal coil. T2-weighted Turbo Spin Echo endorectal coil image is of no diagnostic value due to near field burn out and ghost artifacts. Most endorectal coil studies are substantially better than this, but even an occasional study like this is unacceptable.

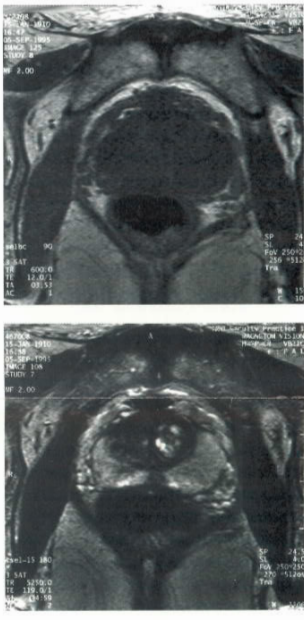

Figure 2: On a different patient, CP Body Array Coil images demonstrate no ghosting or near field high signal artifacts.
(a) T1-weighted Spin Echo.
(b) T2-weighted Turbo Spin Echo.

TECHNICAL ARTICLE:
PRINCIPLES OF LOW FIELD MR IMAGING

Helmuth Schultze-Haakh, Ph.D., MR Applications Scientist
Siemens Medical Systems, Tustin, CA

In recent years there has been an increased interest in low field MR Imaging—40 % of all MR systems sold this year were low field. There are a number of reasons for the success of such systems: lower purchasing and maintenance costs, improved magnet and gradient designs, reduced siting requirements, improved patient comfort and cooperation, as well as new and optimized applications.

ECONOMICS

In the process of evaluating the health-care situation, especially in the US, many hospital administrators are cautious in spending a lot of money for high end systems for fear that patient reimbursement might be limited and patients might not be as easily available as in the past. This might prevent the hospital from reaching the break-even point in a reasonable time. One has to look carefully into such investments and evaluate the price/performance ratio of every medical system. Advances in technology, magnet design and computer equipment have increased the value of MRI systems compared to a few years ago. Due to continual improvements in equipment performance the technical staff, radiologists, and referring physicians all have higher expectations of the technology. Also, MRI equipment has found its way into almost every radiology department, whether in-house, independent diagnostic centers or serviced by a mobile unit. The modality is widely accepted and is often the modality of choice rather than an alternative. It is for these factors that economical MR scanners are available to cover most of the daily "bread and butter" routine in radiology departments.

Specifically, the 0.2 Tesla MAGNETOM Open system is easily operated by a single technologist because all the optimized protocols and key post-processing features are fully integrated into the single console operating interface. Furthermore, the Open is more quickly and easily installed than most high field systems, and requires much lower operating costs. The break-even point is much easier to reach in a shorter time.

MAGNET DESIGN

Most low field MRI systems use either a resistive magnet or a permanent magnet. In either case, the costly cryogens used in superconductive magnets are avoided. A resistive magnet with a relatively low power consumption is used with the MAGNETOM Open system. The resistive magnet of the Open can be turned off when not needed for scanning, thus saving power and further reducing the operating costs. An added advantage in turning off the resistive magnetic is that emergency personnel and emergency equipment can safely be brought to the patient while still on the table.

There are various configurations for low field magnets—the traditional tunnel-shaped bore design, the open bore design with two opposing magnetic platforms separated by columns, or the open bore design of the MAGNETOM Open with a C-shaped magnet. Siemens has chosen the latter design for easier patient access from almost any approach to the table, making it easier for routine work as well as in emergencies. Modern magnet technology also provides much improved homogeneity as compared to a few years ago—the Open boasts only 5 ppm over a 400 mm spherical volume. With automatic shimming of the magnetic field to each patient and the virtual elimination of eddy currents, the image quality approaches that of many high field systems.

The flexible table movement of the MAGNETOM Open allows the anatomy of interest to be positioned right at the magnetic isocenter, thus reducing the need for off-center shifted imaging. The big advantage is that the magnetic field, the RF field, and the gradient fields are much more homogeneous at the isocenter, which leads to improved image quality.

SITING REQUIREMENTS

The need to build costly additions or deal with special siting restrictions is often encountered when installing high field systems. Since the fringe fields of the low field MAGNETOM Open system are significantly more confined than those of high field systems, this scanner can often be installed in the space allowed for traditional CT siting. The MAGNETOM Open system confines the 5 Gauss fringe field (pacemaker line) to within only about 2½ meters of the isocenter, the magnet is only about 1½ x 2 x 2 meters in size, and it weighs only about 12,000 kilograms. The electronics cabinet is less than 2 x 1 x 2 meters in size, and it weighs only about 1,500 kilograms.

PATIENT COMFORT AND COOPERATION

An important issue when purchasing an MRI system is the comfort, and thus the cooperation, of the patient during the scan. Pediatric patients can be more readily observed and family members can remain immediately close—even right next to the child. The spacier, brighter environment will also help reduce the occurrence of claustrophobia among patients. Due to the reduced RF heat deposition with low field systems, patient overheating is not a concern. In general, patient comfort increases cooperation, which increases image quality, which improves the diagnosis, which increases referrals, which increases revenue.

TECHNICAL CONSIDERATIONS

T1 Relaxation Times

As seen in the table below, T1 values of most tissues are about 40% lower on the 0.2 Tesla Open system (compared to 1.0 Tesla). However, fat is reduced by only 25%. Thus, fat is not quite as bright relative to other tissues on a 0.2 Tesla T1-weighted image (compared to 1.0 Tesla). The lower T1 values at lower field strengths cause an increased T1 spread at shorter repetition times (TR). Thus, for comparable T1 contrast, low field images require shorter TR's than high field images. However, when attempting to use shorter TR's, the anatomical coverage may be compromised and this may require additional scans or concatenation. Optimizing the excitation flip angle for a specific tissue and a specific TR can often improve the T1 contrast while providing sufficient coverage. Also note that, due to the lower T1 values, the inversion time (TI) for maximal fat nulling for short tau inversion recovery (STIR) sequences occurs at about 90 milliseconds on the 0.2 Tesla MAGNETOM Open system.

Sequence Bandwidth And Chemical Shift

It is well known that reducing the sequence bandwidth will also reduce the noise level of the acquisition, thus increasing the Signal-to-Noise Ratio (SNR). For example, reducing the bandwidth by one-half will increase the SNR by over 40%. But as bandwidth is reduced, the superimposed images of fat and water are slightly shifted apart by a few pixels (chemical shift artifact). The extent of this shift depends not only upon the sequence bandwidth, but also upon the slight difference in the Larmor frequencies of fat and water and upon the field strength of the MR system. Fat and water resonate at a difference of about 220 Hz at 1.5 Tesla, about 147 Hz at 1.0 Tesla, or about 29 Hz at 0.2 Tesla. The table below indicates the actual pixel shift and the relative SNR at various fields strengths and various bandwidths (Relative SNR is normalized to a value of 1.0 for a bandwidth of 78 Hz/pixel). Note that at typical bandwidths used for high field imaging (56-130 Hz/pixel), the chemical shift artifacts are easily observed (1.7-3.9 pixels). However, at typical bandwidths used for low field imaging (20-56 Hz/pixel), the chemical shift artifacts are barely observed or not at all (0.5-1.4 pixels).

Phase Cycling

The chemical shift between fat and water is 3.5 ppm, regardless of field strength. But, since different field strengths have different resonant frequencies, this translates into a chemical shift of about 220 Hz at 1.5 Tesla, about 147 Hz at 1.0 Tesla, or about 29 Hz at 0.2 Tesla. Thus, fat and water cycle in- and out-of-phase with a predictable cycle time that depends upon the field strength. The phase cycling time is the reciprocal of the chemical shift—about 4.5 milliseconds at 1.5 Tesla, about 6.8 milliseconds at 1.0 Tesla, or about 34 milliseconds at 0.2 Tesla. At 0.2 Tesla, fat and water are in-phase every 34 milliseconds (0 ms, 34 ms, 68 ms, 102 ms, ...) and out-of-phase (opposed-phase) half way between each in-phase point (17 ms, 51 ms, 85 ms, 119 ms, ...) In other words, fat and water switch from in-phase to opposed-phase every 17 ms.

The first in-phase condition always occurs at time=0, although it is

T1 Relaxation Times in Milliseconds

Tissue	1.5T	1.0T	0.2T	Rel. Difference (1.0T - 0.2T)
Fat	260	240	181	-25%
Muscle	863	730	370	-49%
Grey BM	917	809	492	-39%
White BM	783	680	388	-43%
Liver	490	430	228	-46%
Spleen	778	680	398	-41%

Bandwidth and Chemical Shift

Bandwidth (Hz/pixel)	Rel. SNR	Pixel Shift @ 1.5 Tesla	Pixel Shift @ 1.0 Tesla	Pixel Shift @ 0.2 Tesla
130	0.77	1.7	1.1	0.2
78	1.00	2.8	1.9	0.4
56	1.18	3.9	2.6	0.5
30	1.61	7.3	4.9	1.0
20	1.97	11.0	7.4	1.4
16	2.20	13.7	9.2	1.8

impossible to achieve TE=0 in an MR pulse sequence. Also, the actual field strength of many systems may be slightly different than the nominal field strength, which will slightly alter the actual cycle times.

Signal-To-Noise Ratio (SNR)

When imaging with a lower magnetic field strength, fewer protons contribute to the MR signal. This inherent limitation in signal, primarily seen on thin slices with small Fields-of-View (FOV), is often compensated by using additional signal averages (Acquisitions). This is the reason why imaging times are typically longer on low field systems as compared to high field systems. With the MAGNETOM Open, however, other factors such as sequence bandwidth and surface coil design have improved the SNR to the extent that the imaging times are not significantly longer as compared to high field systems.

ADVANCED TECHNIQUES

The MAGNETOM Open offers advanced techniques such as MR Angiography (MRA), Turbo Spin Echo (TSE), and Gradient Echo (2D and 3D). Additionally, it provides many high field applications which are not available on many other low field systems, such as FLAIR (Fluid Attenuated Inversion Recovery), DESS (Dual Echo in Steady State), MTS (Magnetization Transfer Suppression), Shared Echo TSE, RecFOV, and Phase Oversampling. Thin slices, commonly acquired on high field systems, are not only obtained with traditional 2D acquisition techniques on the Open but can also be acquired using 3D contiguous slice techniques. Traditional spin-echo sequences can be substituted with faster gradient echo sequences (FLASH) for good T1-weighting due to the inherently low susceptibility sensitivity of low field MRI systems. T2* decay much more closely resembles the true T2 decay on low field systems, making such substitutions possible.

Phase Cycling in Milliseconds

Field (T)	Freq (MHz)	Shift (Hz)	Cycle (ms)	In-Phase TE's (ms)	Opposed-Phase TE's (ms)
0.2	8.4	29	34	0, 34, 68, 102, ...	17, 51, 85, 119, ...
1.0	42	147	6.8	0, 6.8, 13.6, 20.4, ...	3.4, 10.2, 17.0, 23.8, ...
1.5	63	220	4.5	0, 4.5, 9.0, 13.5, ...	2.3, 6.8, 11.3, 15.8, ...

Clinical Principles of Diffusion Imaging

YURI WEDMID, PHD, HIGH FIELD PRODUCT MANAGER
SIEMENS MEDICAL SYSTEMS, ISELIN, NJ, USA
PHONE 908-321-3272 FAX 908-321-3287

Siemens is pleased to announce the Diffusion Imaging Package, now available with software upgrade B31B for ALL MAGNETOM VISION SYSTEMS (with/without Gradient Overdrive). This new MR OPTION is considered by many experts to be the best tool currently available for early assessment of acute stroke. Siemens is the first in the MR industry to make this important clinical application commercially available. Every competitor in the MR industry talks about Diffusion Imaging, but only Siemens "Walks The Talk". Recently, we interviewed several leading experts who have been involved with our development efforts over the past several years to determine their views on the clinical efficacy of Diffusion Imaging.

William G. Bradley, MD, PhD

PROFESSOR OF RADIOLOGY,
UNIVERSITY OF CALIFORNIA IRVINE

LONG BEACH MEMORIAL MEDICAL CENTER,
LONG BEACH, CA, USA

Siemens: What is the major message to the medical community regarding Diffusion Imaging?

Dr. Bradley: For the first time we have a way of confirming a diagnosis of stroke in time to treat it with the appropriate therapy. We should get the word out that if your patient has symptoms of stroke, get him to the hospital immediately. If your patient gets a Diffusion Imaging scan early enough, we have a better idea of what is going on. We will be able to look at the actual physiology and have a sense of whether or not the patient would benefit from a thrombolytic agent or if he might be at greater risk of hemorrhage from such an agent. With this new technology we are better able to confirm the diagnosis of early stroke within the first 24 hours, as compared to traditional MR techniques.

Siemens: What is a stroke?

Dr. Bradley: The definition of a stroke is an "acute neurologic event". There are two types of strokes: ischemic and hemorrhagic. About 85% of strokes are ischemic infarcts, which means "no blood". What usually happens is that one of the arteries supplying the brain becomes blocked by a blood clot. If the clot was formed right there, typically due to arteriosclerosis, it is called a thrombosis. Or, as more commonly happens, if the clot was formed elsewhere and becomes lodged at the stroke site, it's called an embolus. Such "embolic infarcts" have a greater chance of secondary bleeding than "thrombotic infarcts". The other type of stroke is frank hemorrhage from a ruptured aneurysm or bleeding from a vascular malformation or from a tumor. We do not know until we start imaging the patient whether he has an infarct or a bleed.

Michael Brant-Zawadski, MD

CLINICAL PROFESSOR OF RADIOLOGY,
STANFORD UNIVERSITY MEDICAL CENTER

HOAG MEMORIAL HOSPITAL,
NEWPORT BEACH, CA, USA

Siemens: What images would you use to illustrate the benefits of Diffusion Imaging in the early detection of stroke?

Dr. Brant-Zawadski: I would show the comparison between Diffusion Imaging and more conventional MR techniques, to prove the greater sensitivity of Diffusion Imaging. I would also show MR Angiography (MRA) to demonstrate the blockage of the vessels. The overall beauty of MR is that you not only see the insult in the brain tissue itself, but you also see the cause for it in the blood vessels.

Siemens: What volume of stroke patients do you see at your institution?

Dr. Brant-Zawadski: We see about 150 stroke patients per year, or about 3 per week. We have a major stroke program with advanced imaging as well as clinical research therapeutic programs for treating acute stroke, including intravenous thrombolitic therapy and neuro-protective agent therapy.

David M. Lefkowitz, MD

ASSOCIATE PROFESSOR OF RADIOLOGY
AND NEUROLOGY,
CREIGHTON UNIVERSITY

ST. JOSEPH HOSPITAL,
OMAHA, NE, USA

Siemens: How does Diffusion Imaging change the way you diagnose and treat stroke patients?

Dr. Lefkowitz: We have been using Diffusion Imaging for almost 2 years now and have scanned over 600 patients. It has really become our routine and preferred means of making the diagnosis of ischemic stroke. It has been apparent for quite some time that Diffusion Imaging is much more sensitive to stroke when it is still hyperacute, ie., within about the first 6 hours. Beyond that 6 hour window, even though you can make the diagnosis with standard MR or CT, it is generally too late to apply any of the acute stroke treatments that are becoming available commercially or on an investigational basis. Within the first 24 hours we find Diffusion Imaging to be extremely valuable simply because it more reliably separates the acute from the chronic ischemic changes. This is not an idle consideration because the pattern of acute ischemia, as has long been recognized from experience with CT and routine MRI,often reveals to us something about the mechanism of the stroke – whether it is an embolic stroke or something related to slow-flow globally, such as heart failure.

Siemens: What role does Diffusion Imaging play in diagnosing complicated clinical cases?

Dr. Lefkowitz: Elderly patients, who are at higher risk for stroke, often have fairly complicated features on their standard MR brain images. It would be impossible with any other imaging modality to pick out a very subtle lacunar infarct against a background that could be extremely complex. We have even been able to make a diagnosis of acute stroke in a person who has had prior brain surgery for a tumor followed by radiation treatment. We were still able to see the small lacunar infarct that explained an acute hemiparesis. This has not been possible without Diffusion Imaging. The more complicated the clinical background and the baseline imaging evaluation, the better Diffusion Imaging performs in comparison to other modalities. If you have a clean baseline scan, then there are certain circumstances where a CT scan or conventional MR scan might compete. But even under those circumstances, the accuracy of Diffusion Imaging within the first 24 hours far exceeds that of other imaging tools.

Steven J. Warach, MD,

ASSOCIATE PROFESSOR OF RADIOLOGY
AND NEUROLOGY,
HARVARD MEDICAL SCHOOL

BETH ISRAEL DEACONESS MEDICAL CENTER,
BOSTON, MA, USA

Siemens: What role is being played by Diffusion Imaging in discovering new therapies for stroke?

Dr. Warach: Diffusion Imaging is playing an important role. We are in the middle of a large multi-center clinical trial that is using Diffusion Imaging to determine whether a drug not only makes a patient better but actually reduces the amount of brain damage. Only with Diffusion Imaging can we detect and localize the brain damage before we give the patient the medicine. There are several other clinical trials that are being planned and will start over the next year using Diffusion Imaging. I believe that many drug companies will require that a patient receive Diffusion Imaging to be eligible for a new experimental therapy.

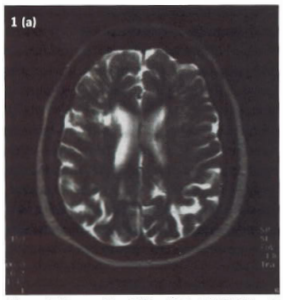

Figure 1. Conventional T2-weighted MRI (a) and CT (b) of acute stroke patient are negative.

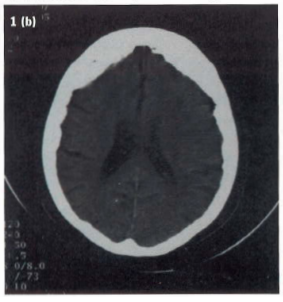

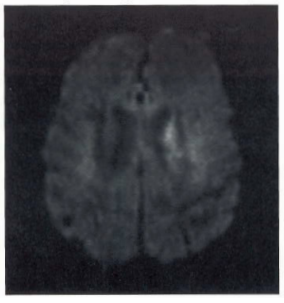

Figure 2. Diffusion Image of acute stroke patient shows the positive "light bulb" sign.

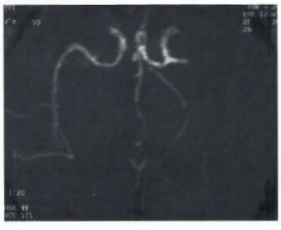

Figure 3. MR Angiogram of acute stroke patient shows the occluded vessels causing the stroke.

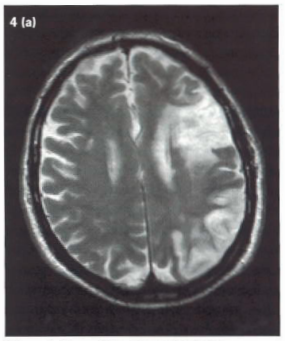

Figure 4. Comparison of a conventional T2-weighted MRI (a) with a Diffusion Image (b) demonstrates the keen ability of Diffusion Imaging to differentiate between acute stroke (bright signal) and chronic stroke (dark signal).

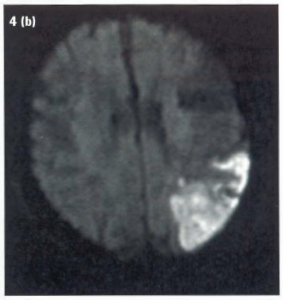

Technical Principles of Diffusion Imaging

JAMES MOORE, PHD, R&D APPLICATIONS SCIENTIST
SIEMENS MEDICAL SYSTEMS, ISELIN, NJ, USA
PHONE 908-632-2892 FAX 908-632-2813

Introduction

Diffusion-weighted MR imaging is a technique for imaging the diffusive mobility of water or other proton-containing molecules. The technique has been shown to be potentially very useful in a number of clinical applications, including acute cerebral infarction. But it has only been with the development of high performance gradient hardware and very rapid imaging techniques that diffusion-weighted imaging has become a practical tool in the clinical setting.

The diffusion of a proton spin in the presence of a magnetic field gradient has long been known to reduce the available MR signal from that spin. Figure 1 shows that as water molecules move randomly through a magnetic field gradient, the degree of phase shift will be different for each molecule. The result of the summation of the signals from molecules with different phases within an imaging voxel is a net loss in signal from that voxel. Magnetic resonance imaging pulse sequences can be designed to take advantage of this behavior. The resulting images have tissue image intensities that depend partially upon the diffusion properties of the water in the tissues

The diffusion properties of materials are usually expressed in terms of the diffusion coefficient, D. It is a measure of the distance a water molecule will move by random diffusion processes in a given amount of time. D is frequently expressed in units of mm^2/s, and the D value for free water at room temperature is approximately 2.0×10^{-3} mm^2/s. D values for brain tissues are approximately in the range 0.5 to 1.0 x 10^{-3} mm^2/s.

The degree of diffusion sensitivity of an MRI pulse sequence is usually expressed in terms of the diffusion-sensitivity b value. The MR image intensity of a substance with diffusion coefficient D, imaged using a pulse sequence with diffusion-sensitivity b, is

$$I = I_0 \exp(-b D) \exp(-TE/T2) \quad (1)$$

The image intensity therefore varies exponentially with the negative product of b and D. Tissues or materials with higher D values will have lower intensities in diffusion-weighted images. Areas of decreased diffusion coefficient (for example, as is observed in acute cerebral infarcts) appear as areas of higher image intensity. The exponential behavior depending on TE and T2 is included in equation (1) since most pulse sequences with diffusion-weighting will also have significant T2-weighting. I0 is the image intensity if there is no diffusion or T2 weighting. Clinically useful b values of 1000 s/mm^2 or more are readily attained on the MAGNETOM Vision.

Diffusion effects occur in all MRI acquisitions that use imaging gradients. The effect, however, is usually negligible compared to other sources of contrast such as T1 and T2. It is conceptually a very simple matter to modify a conventional pulse sequence so that diffusion effects will dominate the image contrast. The placement of two identical large gradient lobes on each side of the 180 degree refocusing RF pulse in a conventional spin-echo pulse sequence can add a considerable amount of diffusion-weighting to the resulting images. The diffusion sensitivity value b for this scheme can be calculated from

$$b = g^2 g_d^2 L^2 (S - L/3) \times 10^{-15} \text{ (in units s/mm2)} \quad (2)$$

where g = 268000 Radians/seconds/mT, g_d is the strength of the diffusion gradient in mT/m, L is the length of each of the two gradient pulses in milliseconds, and S is the center-to-center spacing of the two gradient pulses in milliseconds. The implementation of this scheme with conventional spin-echo pulse sequences has a serious drawback; the sequence is also very sensitive to all other sources of motion. This problem can be avoided, however, by adding diffusion-weighting to a very fast imaging technique such as Echo Planar Imaging (EPI).

Diffusion-weighted Single-shot Echo Planar Imaging

Siemens is pleased to announce the Diffusion Imaging Package, now available with software upgrade B31B for the MAGNETOM Vision system. Diffusion sensitivity is added to the basic spin-echo type EPI pulse sequence by applying a large magnetic field gradient pulse before the 180 degree refocusing RF pulse and an identical gradient pulse after the 180 degree RF pulse, as shown in Figure 2. The use of the single-shot EPI technique allows the acquisition of a single diffusion-weighted image in approximately 200 ms. This short acquisition time reduces or eliminates image artifacts due to sources such as patient motion or due to physiological processes such as CSF pulsatility. The effective echo time (TE) of the pulse sequences, which determines the degree of T2-weighting in the images, ranges between 103 and 123 ms for the various available pulse sequences.

Also included in the optional Diffusion Imaging Package are diffusion-weighted EPI pulse sequences that acquire multiple images at each slice position with the diffusion-sensitizing gradient applied in three different directions: along the slice-select, readout, and phase-encoding directions. In tissues with an inherent structure that results in different diffusion properties in different directions, the contrast in these three images will be different. For example, white matter nerve tracts will appear darker in diffusion-weighted images when the diffusion gradient is aligned with the tracts (the easiest direction for diffusion to occur) than when the diffusion gradient is applied perpendicular to the nerve tracts (Figure 3). These pulse sequences also generate an EPI image with negligible diffusion-weighting at each slice position, but that has the same T2-weighting as the diffusion-weighted images. This provides a comparison image for helping to differentiate diffusion effects from T2 effects in the diffusion-weighted images.

Artifacts in Diffusion-weighted EPI Images

The most serious drawback of the EPI-based diffusion-weighted pulse sequences is a consequence of using the EPI technique. Echo planar imaging is very sensitive to magnetic field inhomogeneities, and images are distorted wherever susceptibility effects cause field inhomogeneities. In the head, distortions are particularly noticeable at the air-tissue interfaces of the sinus cavities and at the base of the brain. In addition to distortions, magnetic susceptibility changes at boundaries can also result in hyperintense signal from those regions. These artifacts are usually recognizable, but in some situations might obscure pathology.

EPI-based diffusion-weighted imaging is also sensitive to the effects of eddy currents. The very large diffusion gradients (20 mT/m or more gradient strength for 30 milliseconds or longer) are capable of generating much larger eddy currents than are typically generated in conventional image acquisitions. EPI is also unusually sensitive to the presence of eddy currents because of the technique's inherently low bandwidth in the phase encode direction. Diffusion-weighted images can be shifted and distorted in the phase encode direction to varying degrees depending upon the direction of the diffusion gradient and the effectiveness of eddy current compensation. Another problem that the eddy currents can cause is incomplete suppression of the signal from fat. When fat is not properly suppressed in a diffusion-weighted EPI acquisition, the fat image will appear quite bright and will be displaced with respect to the water image by about one-quarter of the field of view.

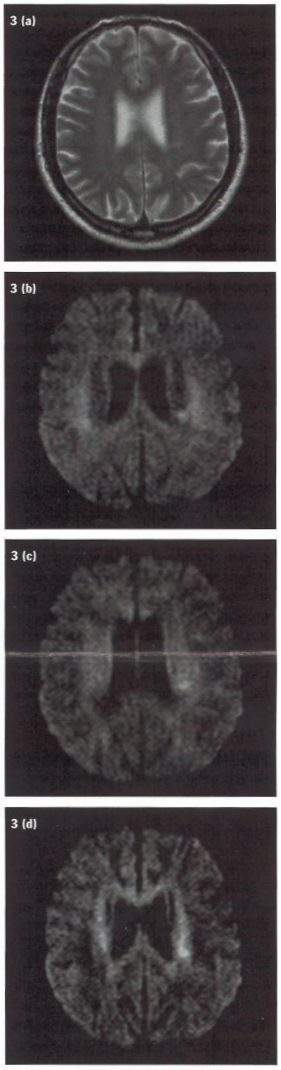

Figure 3. (a) Negative T2-weighted MRI imaged at <24 hours after onset of symptoms (exact time unknown) was also negative on CT. Positive diffusion-weighted images of same patient are encoded in three separate directions to demonstrate the importance of viewing all three images to distinguish lesions from anisotropy of brain tissues: (b) slice-select, (c) readout, (d) phase-encoding directions.

Further Reading

1. *Le Bihan D, et al. Diffusion MR Imaging: Clinical Applications. AJR 1992; 159:591-599.*
2. *Warach S, et al. Acute Human Stroke Studied by Whole Brain Echo Planar Diffusion-Weighted Magnetic Resonance Imaging. Ann. Neurol. 1995; 37:231,241.*

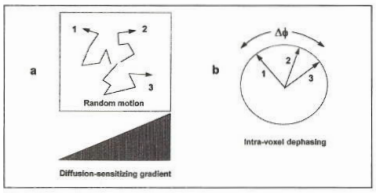

Figure 1. (a) Random motion of spins within a voxel due to diffusion. (b) The resulting intra-voxel dephasing that causes signal loss.

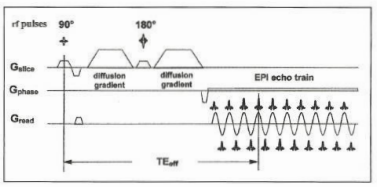

Figure 2. Diffusion-weighted single-shot EPI pulse sequence with diffusion sensitivity in the slice-select direction.

PART 1

Non-Echo-Planar Fast MR Imaging Techniques

D. Chien
Siemens AG, Medical Engineering Group, Erlangen, Germany

G. Laub
Siemens Medical Systems, MR R&D, Chicago, Mich, USA

J. Gaa
Institute for Clinical Radiology, University Hospital of Mannheim, Germany

R.R. Edelman
MRI Division, Beth Israel Deaconess, Medical Center, MRI Department, Boston, MA, USA

INTRODUCTION

Speed is of key importance in MR imaging. In the early days, MR was considered a slow imaging technique as the scan time was typically over 10-20 minutes. During the image acquisition time, any source of motion would cause image degradation. Thus, MR images were readily affected by physiologic motions and/or voluntary motions. Respiratory motions and the beating motion of the heart were particularly problematic for thoracic imaging. Abdominal imaging were often marred by respiratory motion artifacts.

In order to overcome these problems, a multitude of fast imaging techniques have been developed and tested clinically. Echo planar imaging (EPI) is currently the fastest way to generate an image. With EPI a complete image can be measured in less than 100 ms thus avoiding most of the physiologic motion artifacts. However, it requires substantial hardware modifications and is not yet in widespread use. Furthermore, it faces certain limitations, such as substantial chemical shift artifacts, limited spatial resolution, and the possibility of tissue stimulation. With this in mind, there are other fast imaging techniques that offer a broad spectrum of clinical applications. The purpose of this review is to outline the basic principles of these non-EPI fast imaging techniques. Since the field of MRI is rapidly progressing and new pulse sequences are being created all the time, we will focus on pulse sequences that are already under clinical investigations.

COVERAGE OF K-SPACE

The raw data for MR imaging is best represented by the k-space (Fig. 1). The k-space refers to the spatial frequency which is an abstract formulation of an image. k_x and k_y are given by:

$$k_x = \gamma G_x t \qquad (1)$$

$$k_y = \gamma G_y \tau \qquad (2)$$

where γ is the gyromagnetic ratio, G_x and G_y are the gradients along x and y respectively, and τ refers to the length of the phase encode gradient pulse. The units for k_x and k_y are in radians/cm. As shown in the equations, k_x and k_y are linearly proportional to the gradient strength and the time duration. The k-space domain is very helpful in interpreting MR imaging: the center points of k-space provide the overall contrast and signal of an image. The outlying k-space data points, on the other hand, contribute to the definition of edges (high spatial frequencies). A higher value for k_x and k_y denotes higher spatial frequencies and therefore higher spatial resolution, which is achieved by applying a large gradient amplitude or a longer gradient duration. The raw data in the k-space domain is transformed into the image domain by a Fourier transformation. The k-space formalism can readily be used to analyze and compare the nature of different pulse sequences with regard to image contrast and scan time.

SCAN TIME

The measurement time needed to generate a study is the time needed to collect all the necessary raw data in k-space. In conventional MR imaging, the time taken to acquire data along k_x is relatively short (in the order of msecs). Data collection along k_y is more time consuming and in conventional spin echo imaging, it takes several seconds from one k_y line to the next (for T2- weighted imaging). The scan time T_s is given by equation 3:

$$T_s = TR \bullet N_y \bullet NEX \qquad (3)$$

The scan time increases with the repetition time (TR), the number of phase encode steps (N_y), and the number of averages (NEX). As a longer TR of typically 2-3 seconds is needed for T2-weighted imaging, the scan time for a conventional spin echo T2-weighted study is in the order of 8-13 minutes for a 256 x 256 imaging matrix. With the development of new imaging techniques in combination with faster gradient systems, it is now possible to perform MR imaging substantially faster than before.

REDUCTION OF SCAN TIME

In conventional imaging strategies (both spin echo and gradient echo), each k_y line of k-space is covered in a separate TR. Therefore the scan time is given by equation (3), and faster scanning can be accomplished by reducing TR, N_y, or NEX. At the other end of the spectrum, all of k-space is covered after one single RF excitation (Fig. 2). This category of imaging techniques is referred to as single-shot imaging. A typical representative of this category is echo planar imaging (EPI). Between these two lie a range of rapid imaging techniques, in which k-space is covered in segments. Each segment contains a number of data lines (in k-space) which are acquired after each RF excitation. Consequently, the scan time is reduced, as fewer TR intervals are necessary to acquire all lines of k-space. A typical example for this category is Turbo Spin Echo, and this category is referred to as hybrid imaging, which differs itself from conventional techniques and single-shot techniques. It will be beyond the scope of this paper to include each and every one of the new techniques. Therefore, we will focus on the major ones that have demonstrated clinical applications.

The scan time can be reduced in a number of ways. These time-saving strategies can be applied to a variety of MR imaging techniques.

Reduce the number of averages (NEX).

The development of advanced RF coils (such as phased array coils) leads to major improvements in the signal-to-

noise ratio (SNR). This is particularly important in body imaging. The application of a body array coil typically improves the SNR by a factor of two. As a result, multiple averages needed in earlier days are no longer necessary. With major reduction in scan time, it is now possible to acquire abdominal images within a single breath-hold to eliminate any respiratory motion artifacts. One could even have NEX less than 1. For example, half-Fourier imaging reduces NEX to ½ and further diminishes the scan time. Half Fourier is possible due to the fact that k-space is Hermitian in nature. Based on the expected symmetry, one could generate the rest of the data acquiring only half of the data in k-space. In actual practice, slightly more than one half of the data is acquired. Consequently, the scan time is cut in half at the cost of a reduction in signal-to-noise by about SQRT(2).

Reduce the repetition time (TR).

In spin echo sequences, the TR is typically in the order of several hundred milliseconds (depending on the desired contrast). Much shorter TRs are possible with gradient echo sequences.

Currently, the minimum TR of gradient echo sequences can be as short as a few milliseconds. This is made possible by the improvement in the system hardware, in particular, the magnetic field gradient system. Due to the short TR of gradient echo sequences a variety of new clinical applications has become available, in particular 3D imaging. Note that while reducing the TR shortens the scan time (according to equation 3), it also alters the overall image contrast, as the amount of T1-weighting is changed. Special care of imaging parameters is necessary to maintain an acceptable balance between scan time and image contrast.

Acquire fewer ky lines.

In combination with a flexible rectangular field-of-view (FOV) technique fewer lines can be used to shorten the scan time. This is applicable when the region of interest is ellipsoid in the imaging slice. The image contrast and spatial resolution are maintained at the cost of a reduced signal-to-noise ratio.

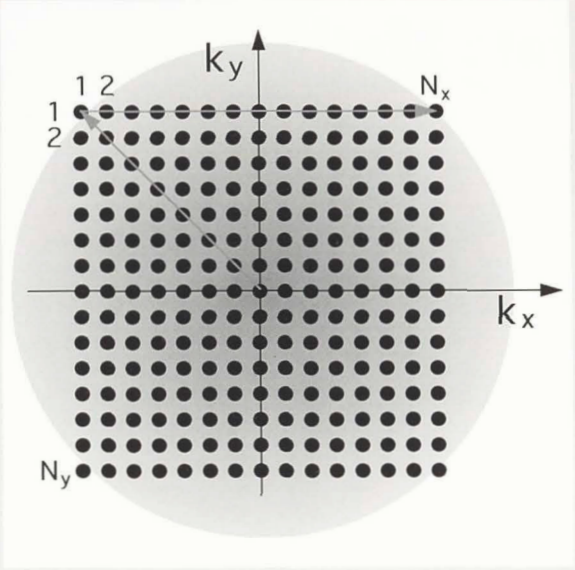

Figure 1:
k-space scanning. A set of $N_x \bullet N_y$ data points are measured to scan the raw data of the object. Points in the center of k-space define image contrast, outlying data points define the spatial resolution in the image.

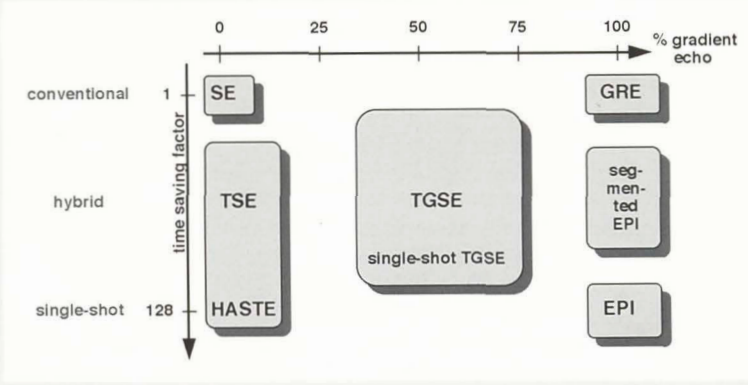

Figure 2:
k-space scanning strategies. In the conventional category one line of k-space is acquired per TR interval. Each line is acquired by sampling an echo which is created by a 180° refocussing pulse (spin echo, SE), or by gradient reversal (gradient refocused echo, GRE). Single-shot techniques scan all of k-space after one RF excitation, and provide the largest time saving factor. In between these extremes there is a variety of hybrid imaging techniques.

Part 2 to be continued in Vol.6 No.2.1999

PART 2

Non-Echo-Planar Fast MR Imaging Techniques

D. Chien
Siemens AG, Medical Engineering Group, Erlangen, Germany

G. Laub
Siemens Medical Systems, MR R&D, Chicago, IL, USA

J. Gaa
Institute for Clinical Radiology, University Hospital of Mannheim, Germany

R.R. Edelman
MRI Division, Beth Israel Deaconess, Medical Center, MRI Department, Boston, MA, USA

Continued from Part 1
MAGNETOM Flash Vol. 6 No.1

Conventional Imaging Strategies

As shown in Fig. 2a class of imaging techniques exist which are based on a more conventional way to scan k-space. Nevertheless, a variety of imaging sequences exist which are very attractive for clinical applications but still offer a significant reduction of scan time. Many of the techniques mentioned in this category are currently in clinical use.

Gradient echo imaging

As mentioned earlier, spin echo techniques usually suffer from a long scan time due to the long TR which is necessary to create the contrast. Alternatively, a different type of sequences can be applied to create the echo signal, and reduce scan time. Gradient echo imaging achieves significant reduction in scan time by eliminating the 180° pulse and shortening the TR interval from several seconds (for T2 weighted spin echo imaging) to 30 - 50 msec. Therefore, the scan time is significantly reduced from several minutes to several seconds. The introduction of gradient echo imaging enabled the acquisition of 3D data sets as 3D imaging using spin echo would be prohibitively long to acquire. Gradient echo imaging opened up a broad range of clinical applications. Among them is the imaging of flow in MR angiography.

There are different types of gradient echo sequences. The classification depends on the nature of the transverse magnetization (whether it is spoiled as in spoiled FLASH or whether it is preserved as in FISP or GRASS). Consequently, FLASH is predominantly used for T1-weighted imaging, particularly for fast breath-hold imaging in the abdomen (Fig 3), while image contrast of FISP depends on T1/T2*. Due to the steady state of the transverse magnetization in FISP, the sequence is very sensitive to motion, and even little motion, like CSF pulsation will destroy the steady state of the magnetization resulting in pulsation artifacts, or signal losses (Fig. 4).

Another variation of the gradient echo, known as PSIF (reversed FISP) or CE-FAST (contrast-enhanced FAST), generates an RF refocused echo after every other RF excitation pulse in a steady state. The effective echo time is actually larger than the TR interval, and, therefore, the image contrast of PSIF is heavily T2 weighted. Similar to FISP, however, PSIF is very vulnerable to motion, making it less useful in clinical practice. Initially, PSIF has been used for T2-weighted abdominal imaging in a breath-hold, or cholangiography, but has been found to be highly susceptible to motion or pulsations. More recently, a variant of FISP, known as TrueFISP, has become available which is less sensitive to motion effects. We will cover this in greater detail in a later section.

TurboFLASH

TurboFLASH imaging offers subsecond imaging and is useful for high speed imaging of dynamic processes such as perfusion, joint motion, and swallowing. TurboFLASH is the ultra-fast version of conventional gradient echo.

TurboFLASH imaging utilizes TR and TE at its minimum within the magnetic field gradient capabilities. TE is down to 1 to 2 ms and TR is around 5 to10 msec. Due to the short TR, TE and the small flip angle, the intrinsic contrast in TurboFLASH imaging is predominantly proton density weighted. Tissue contrast, however, is obtained by magnetization preparatory prepulses. For example, T1 contrast is generated by applying a 180° inversion prepulse prior to the echo train. Thus, TurboFLASH imaging consists of two modules: one is the magnetization preparation module to create the desired contrast and the second one is data acquisition module which consists of a train of minimum TR and TE gradient echoes (Fig. 5). Segmented TurboFLASH is a variant of TurboFLASH. It consists of acquiring segments of k-space. These segments can be triggered to specific time points in the cardiac cycle. Segmented TurboFLASH finds useful applications in cardiac imaging (breathhold CINE and MR angiography of the coronary arteries) and abdominal imaging.

A 3D version of TurboFLASH is referred to as MPRAGE (magnetization-prepared rapid gradient echo). In this case, the basic TurboFLASH period provides one plane in the three-dimensional k-space, and is repeated as many times until all of the 3D k-space data points are filled. Similar to TurboFLASH, the contrast is determined by the preceding preparing period, which in most cases is an inversion pulse followed by a wait period. MPRAGE is very useful in providing T1-weighted three-dimensional data sets of the brain in typically 3 to 5 minutes.

DESS imaging

DESS (Double Echo in Steady State) is a new technique which provides both anatomical details and pathologic information in a single 3D acquisition. It finds useful applications for orthopedic examinations. The pulse sequence diagram is as shown (Fig. 6). The DESS image is automatically generated by combining two separate images at each slice position: first, a FISP type gradient echo image which gives the anatomical details and, second, a PSIF type image which detects the presence of fluid. As stated earlier, the FISP image is T1/T2* weighted whereas the PSIF image is heavily T2 weighted and therefore has high fluid sensitivity. The 3D data set has inherently high signal-to-noise. The two steady state images are combined to form the DESS image. When used with fat suppression, only effusion or fluid stands out in the image amidst a dark tissue background. The advantage of DESS lies in its ability to depict lesion contrast in a high spatial resolution 3D

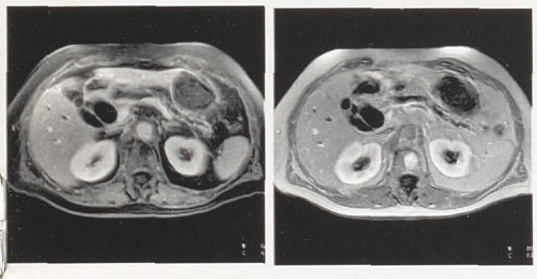

Fig. 3: FLASH imaging of the liver. Left: FLASH with fat suppression acquired in 16 s. Right: FLASH T1 imaging post contrast, 24 s acquisition time. Courtesy of Klinikum Mannheim, Germany.

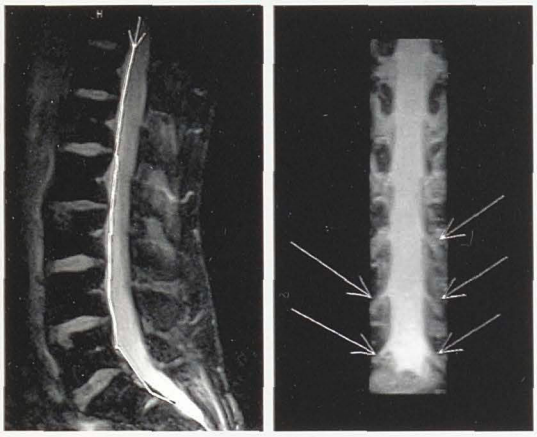

Fig. 4: FISP 3D imaging of the lumbar spine. Original data (left) with 1.6 mm slice thickness and MIP reconstruction (right).

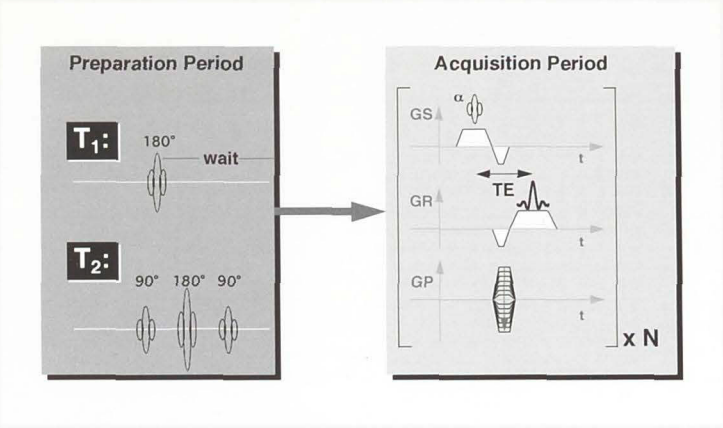

Fig. 5: TurboFLASH imaging. In the acquisition period a fast gradient echo sequence is repeated N times to fill k-space. The image contrast is created in the magnetization preparation period. For T1 contrast a 180° inversion pulse is used followed by a wait period. Alternatively, a 90° - 180° - 90° rf pulse combination can be used to create a T2 contrast.

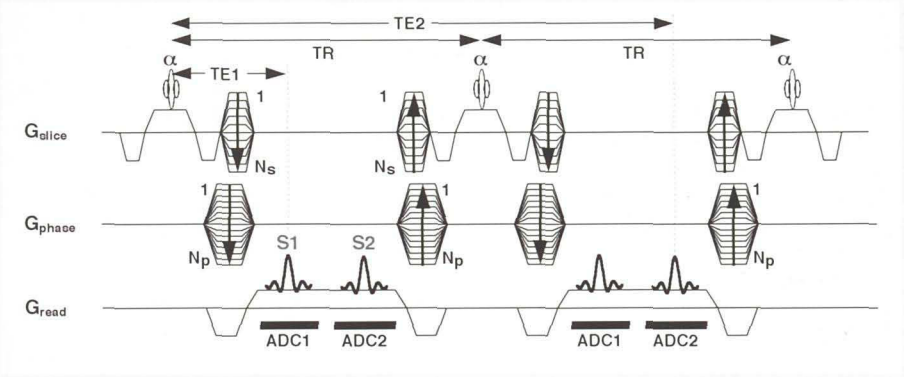

Fig. 6: The sequence combines a FISP (S1) and a PSIF (S2) signal in a single sequence. Both images are automatically superimposed to create the DESS image. The FISP signal at TE1 shows T1/T2 contrast while PSIF corresponds to the rf-rfocussed signal with a longer TE2 and is heavily T2-weighted.*

format. The data can be displayed using the 3D multiplanar reconstruction or curved reconstructions. The spatial resolution potential for DESS is 0.3 mm x 0.3 mm x 0.5 mm (Fig. 7).

TrueFISP imaging

TrueFISP is a high speed T2 imaging technique that provides very fine spatial resolution in a very short time. In the brain, it is useful for rapid imaging of trauma, stroke, and pediatric cases. A single slice can be acquired within a second, or less. A multi-slice T2-weighted acquisition is completed in about 10-15 seconds. This compares very favorably with the much longer scan times needed for conventional T2-weighted spin echo imaging. In the abdomen, it is useful for high resolution breathhold imaging (Fig. 8).



Fig. 7: DESS 3D imaging of the knee with water excitation to avoid fat signal. 1.5 mm slice thickness.

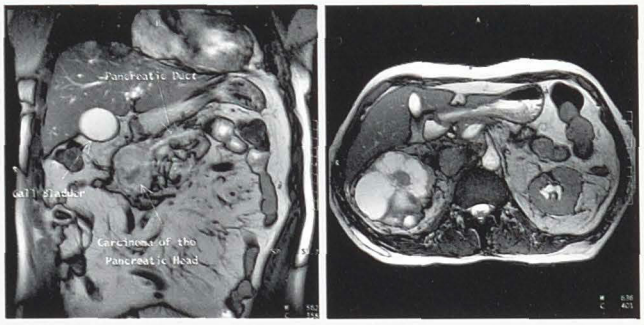

Fig. 8: TrueFISP imaging of the abdomen. Coronal study acquired in 20s (left) and axial study acquired in 13 s (right). Courtesy of Klinikum Mannheim, Germany.

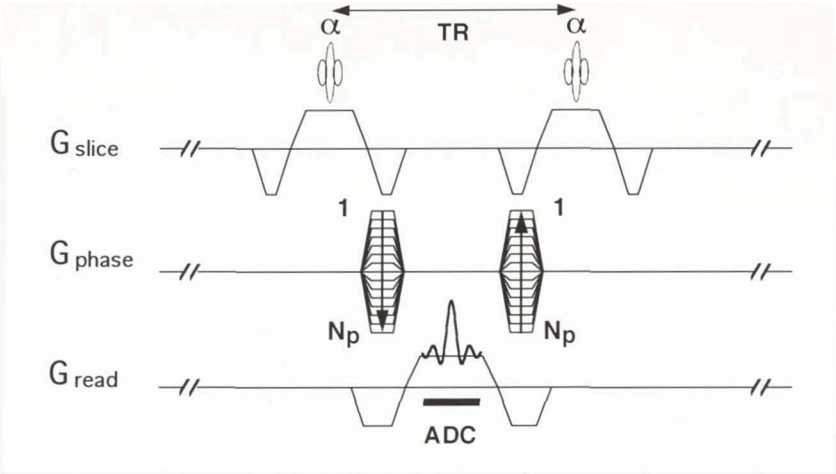

Fig. 9: TrueFISP sequence diagram. With balanceed gradients in all directions the FISP and PSIF signal will superimpose. The TR must be short to minimize dephasing errors between the gradient-refocussed echo (FISP) and the rf-refocussed echo (PSIF).

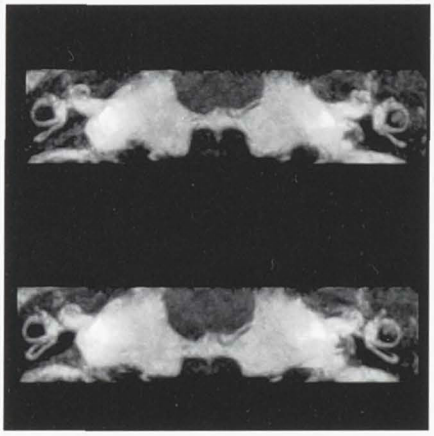

Fig. 10: CISS imaging of the inner ear, 512 matrix, 5:42 min acquisition time. Courtesy of HIA Val de Grace, Paris, France.

The pulse sequence diagram is as shown (Fig. 9). As shown in the diagram, the gradient pulses are completely balanced in all 3 directions for TrueFISP imaging. As a result, TrueFISP is inherently flow compensated and useful for imaging moving structures such as CSF. The image contrast is primarily T2-weighted. T1 weighting is small due to the fact that T1 relaxation time is typically 10 times longer than that of T2.

There are severe system requirements for TrueFISP. Strong gradients and fast pulses are needed to make the FISP and PSIF echoes coincide in time. The TR is made as short as possible (around 5 msec). In addition, high field homogeneity is needed to ensure that the FISP and PSIF echoes occur at the same time. Good magnet design and high quality shimming enables the acquisition of TrueFISP. For high speed T2 imaging using TrueFISP, a magnetization preparation scheme is used to minimize the time for the magnetization to reach steady state.

CISS imaging

A new high speed imaging technique is CISS (constructive interference in the steady state) which offers rapid, high resolution T2 weighted imaging. The signal is based on TrueFISP. Each image is generated by the combination of two separately acquired TrueFISP images. The two source images are created with two CISS sequences which differ only in its RF pulse scheme. The 3D implementation of CISS imaging provides sub-millimeter resolution T2-weighted imaging of the inner ear and cranial nerve (Fig. 10).

Hybrid Imaging Techniques

In the conventional imaging techniques, one phase encode line is acquired per TR. In high speed imaging, new techniques utilize a mixture of the above strategies to complete an image in a shorter time. We will start with the turbo spin echo and discuss the principles of these different imaging techniques.

Turbo Spin Echo

In conventional spin echo imaging, each phase encode line is covered in a TR period. Turbo spin echo, or TSE (also known as fast spin echo) speeds up the imaging process by acquiring several phase encode lines per TR. To do this, multiple 180° pulses are applied after the initial 90° pulse (Fig. 11). Each resulting spin echo is individually phase encoded.

The overall contrast is determined by the echoes at the central portion of the k-space domain. The effective echo time (TE_{eff}) is therefore the echo time of the zero phase encode step. Contrast can be modified by reordering of k-space. A long effective TE is used to generate T2 weighted images. Typically, TR is in the order of 3-4 seconds to acquire slices covering the whole brain.

In spin echo imaging, the echo amplitude is constant from one phase encode step to the next. The signal is acquired in the presence of steady state magnetization. Turbo spin echo, on the other hand, acquires the signal in the presence of changing signal intensity (Fig. 11). As shown in the diagram, the amplitude of each of the successive spin echoes is not constant. Rather, it decreases according to T2 decay. This could lead to blurring in the image if the amount of signal variation is substantial (for example, over a long echo train). The modification in the point spread function leads to a reduction in the edge sharpness. The edge sharpness is only affected along the phase encode direction and it is less noticeable in long T2 components. Questions have been raised regarding the potential loss of small object definition in turbo spin echo images. The amount of blurring, however, can largely be avoided by appropriate choice of data acquisition schemes. The use of short echo spacing reduces the amount of signal variation. This does require high performance gradients that allow the echo spacing to be as short as possible.

There are some differences between conventional spin echo and turbo spin echo images. One of the differences is the signal intensity of fat. Fat can appear bright in T2-weighted turbo spin echo images (Fig. 12). This has been attributed to lengthening of the T2 due to j-coupling. Another key difference between turbo spin echo images and spin echo images is reduced flow artifacts in turbo spin echo images. This is due to the application of multiple 180° pulses in TSE sequences.

Scan time for turbo spin echo imaging is substantial shorter than that needed for spin echo imaging. The scan time is shortened by a factor of N where N is the number of 180° pulses. Depending on the gradient strength and its performance, N can be larger than 30. As a result, the scan time may be reduced by over 30 times. The practical limitation on N is the gradient performance (and the echo spacing).

Due to substantial savings in scan time, turbo spin echo imaging has largely replaced conventional spin echo imaging for head and spine imaging on systems that have the gradient performance to provide the short echo spacing. Optimized TSE sequences offer high resolution and good contrast behavior in a much shorter time compared to conventional spin echo imaging.

Turbo gradient spin echo imaging

Turbo gradient spin echo, or TGSE (also known as GRASE) offers spin echo contrast with high spatial resolution and speed. It is even faster than turbo spin echo. The increased efficiency in data acquisition can be utilized to shorten the scan time or to achieve higher spatial resolution.

In its basic implementation, each spin echo is accompanied by two gradient echoes (Fig. 13). The scan time is reduced by an additional factor M, where M is the number of echoes per 180° pulse. For example, when there are two gradient echoes generated per spin echo (one gradient echo on each side of the spin echo), then M = 3. This results in quite substantial savings in time. This reduction in scan time can be used to benefit high resolution imaging. For example, for 512 matrix and a TR of 2 sec, the following shows the calculation of the scan time:

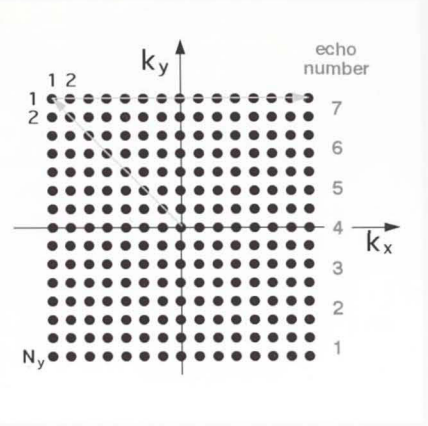

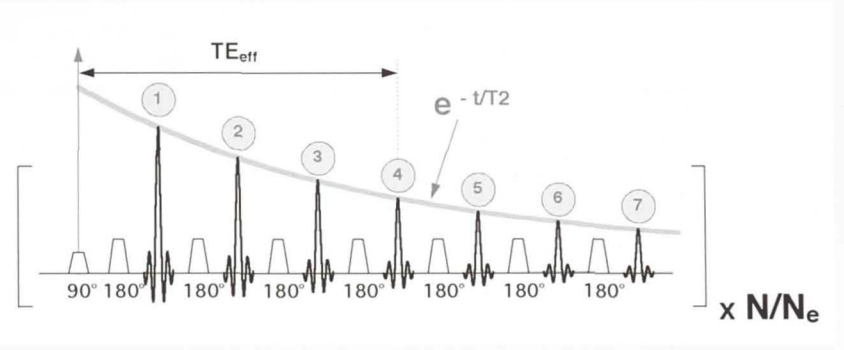

Fig. 11: Turbo Spin Echo sequence. A series of 180° refocusing pulses produces multiple spin echoes. Each echo is phase encoded (phase encode gradients are omitted for simplicity) to fill one line of k-space as shown in the diagram below. The echo number in the center of k-space defines the contrast of the TSE sequence. The sequence is repeated N/Ne times until k-space is completely filled.



Fig. 12: Turbo Spin Echo imaging of the head, 5 mm slice thickness, 512 matrix, 3:56 min acquisition time. Courtesy of Klinikum Mannheim, Germany.

Scan time (SE) = (2 x 512) sec = 17 min

Scan time (TSE) = (2 x 512)/6 sec = 2.8 min for N = 6

Scan time (TGSE) = (2 x 512)/(6 x 3) sec = 56 sec for N = 6, M = 3

When acquiring data in TGSE, the k-space is completed in 3 major segments, as shown in Fig. 13. The spin echoes are used to fill the center of k-space while the gradient echoes are used to fill the outer parts of k space. As a result, the tissue contrast in the images is similar to spin echo imaging (Fig. 14). Compared with turbo spin echo, more signals are sampled per 180° pulse. To minimize the time between the successive 180° pulses, strong and fast gradients are needed.

Single-Shot Imaging Techniques

In contrast to the imaging strategies from before all of k-space is acquired after one RF excitation in single-shot imaging. A well-known example for this category is echo-planar imaging, EPI. While this technique has been published very early in MR imaging it took a long time to implement EPI on commercially available imaging systems. Due to the single-shot nature of EPI all of k-space must be acquired within the lifetime of the magnetization depending on the T2* relaxation times. Consequently, data acquisition must be finished in typically 100 msec, or shorter. As such, EPI demands for very fast gradient switching capabilities. Even with the fastest gradients available EPI is still vulnerable to local susceptibility effects resulting in local image distortions, or signal losses. Other techniques, based on multiple spin echoes do not suffer from T2* effects, and, therefore, are more robust in clinical practice.

RARE

RARE (**R**apid **A**cquisition with **R**elaxation **E**nhancement) applies a 90° excitation pulse followed by a long train of 180° refocusing pulses. A series of spin echoes are generated by the refocusing pulses and each echo is individually phase encoded. The contrast depends on the position of the central phase encode step. With linear phase encoding the effective echo time is relatively long. Assuming an echo spacing of 10 msec, and 200 lines, the effective echo time is 200/2 x 10 msec = 1000 msec, and, therefore, only species with a long T2 relaxation time will appear bright in the image. Consequently, RARE imaging is useful for MR cholangiography, myelography, and urography.

HASTE

HASTE (Half-Fourier single shot turbo spin echo) offers subsecond T2-weighted imaging. The technique utilizes a 90° excitation followed by a train of RF refocused echoes, similar to RARE. In contrast to RARE the effective echo time of HASTE is much shorter as it starts filling k-space in the center of k-space with the first echoes of the echo train as demonstrated in Fig. 15. Additionally, due to the half-Fourier technique which is incorporated into HASTE, the scan time is further cut in two. With NEX = 1/2, 128 echoes are acquired to give a 256 x 256 matrix image. A single slice can be acquired within a fraction of a second. Contrast is similar to turbo spin echo (true T2 weighting and low susceptibility weighting). The technique allows management of uncooperative patients because of its speed and sequential slice capability. Furthermore, HASTE is particularly useful for imaging patients who are unable to breath-hold for T2-weighted abdominal studies and for MR cholangiography (Fig. 16). An additional inversion pulse preceeding the 90° excitation pulse is incorporated into the sequence to create T1 sensitivity.

Summary

Conventional spin echo pulse sequences have formed the basis for clinical MR imaging since the modality was introduced. A variety of novel techniques have been proposed which dramatically speed up the image acquisition time and make possible applications which are otherwise not feasible. In addition, images with much improved spatial resolution can now be obtained. The introduction of new techniques continue to expand the clinical applications of MR imaging. A number of these techniques have overcome the intrinsic problems facing EPI. These techniques have come into the main stream of clinical imaging and will continue to contribute to improved diagnostic capability.

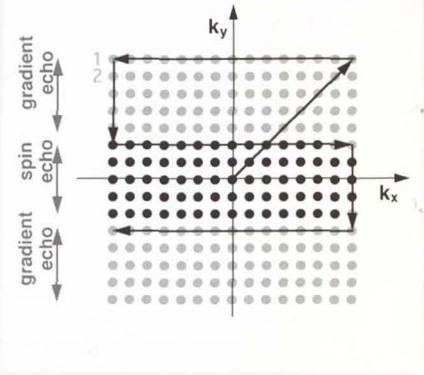



Fig. 14: Turbo Gradient Spin Echo imaging with 1024 matrix, 3 mm slice thickness, 4:04 min acquisition time. Courtesy of Lund university Hospital, Sweden.

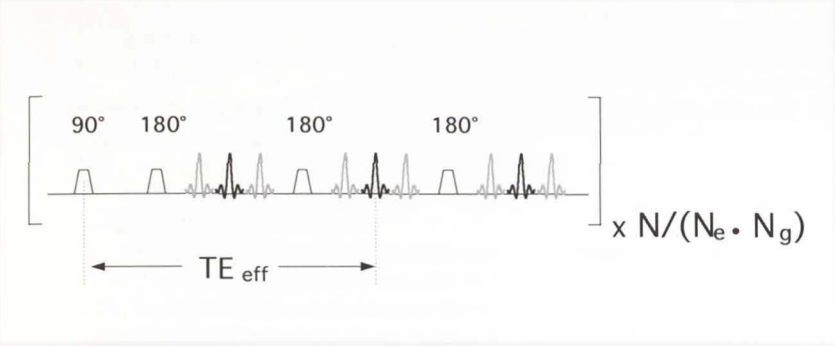

Fig. 13: Turbo Gradient Spin Echo sequence diagram. In contrast to TSE additional gradient echoes are generated on both sides of the spin echo by gradient reversal. The spin echoes are positioned in the center of k-space, and gradient echoes are used to fill the outer lines of k-space.



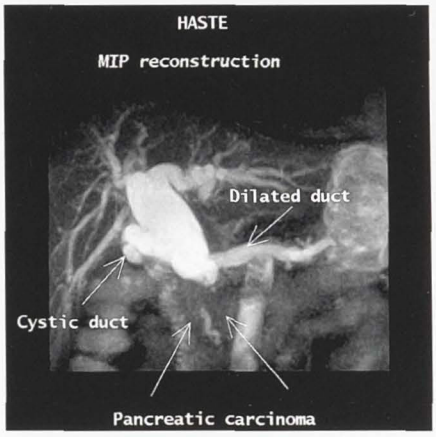

Fig. 16: HASTE imaging of the abdomen acquired in 12s (left). MR Cholangiography of the same patient acquired with HASTE and reconstructed using MIP; acquisition time 16s.
Courtesy of Klinikum Mannheim, Germany.

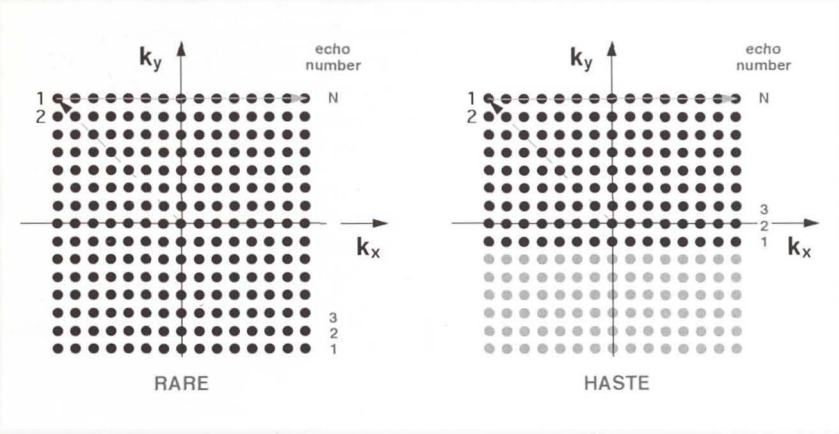

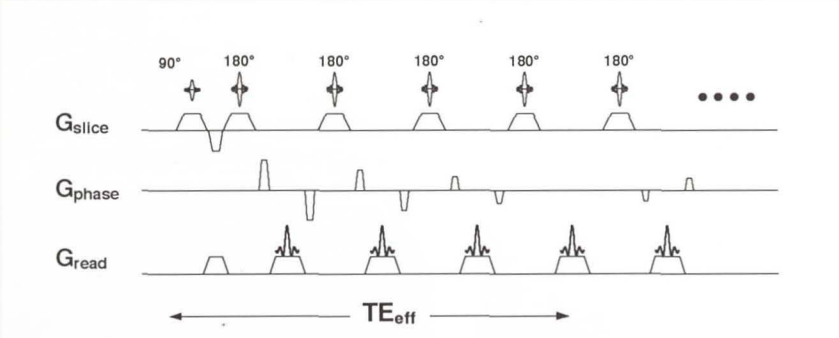

Fig. 15: k-space scanning with RARE and HASTE. A series of 180° rf refocusing pulses generates an echo train. Each echo is individually phase encoded similar to TurboSE. With RARE, k-space is filled in a linear fashion starting from top to bottom. With HASTE, k-space filling is started in the center towards the top of k-space. The other half of k-space is extrapolated with a Half-Fourier technique.

MAGNETOM Flash Archive

Explore the complete MAGNETOM Flash archive, from the first issue published in 1993 to the latest editions.

For more than 30 years, MAGNETOM Flash has provided clinically relevant, peer-to-peer information on MRI — sharing practical experience, technical insights, protocols, and clinical applications from the MR community.
Browse the archive and discover how MRI has evolved over the decades, as documented by the people who use it every day.

Go to
magnetomword.siemens-healthineers.com/publications/magnetom-flash/archive

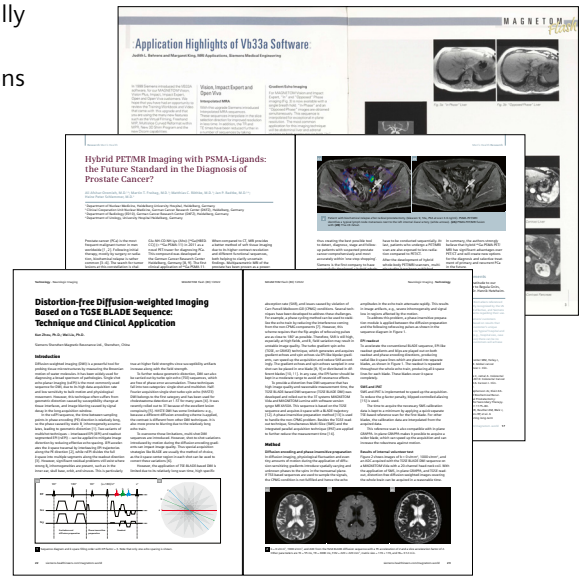



SIEMENS

Vol. 8 · No.1 · 2001

MAGNETOM Flash

An Applications Reference for Siemens MAGNETOM Users

:MRI in Pediatric Radiology – Possibilities and Limitations of Low Field Magnetic Resonance Imaging:

M. Wagner, P. Kreissler[1], R. Kuth[1], T. Rupprecht

Department of Pediatric Radiology
Hospital and Outpatient Clinic for Children and Adolescents
(Professor Dr. W. Rascher, Director)
Friedrich-Alexander University, Erlangen-Nuremberg

[1] Siemens Medical Engineering, MR Research and Development, Erlangen, Germany

Technical Characteristics – Monitoring and Sedation of Patients – Possible Interventions – Disadvantages in Comparison to High-Field Magnetic Resonance Systems – Fields of Application – Typical Diagnoses – Prospects and Perspectives

Abstract:

MRI has been used in pediatric imaging for several years. It provides excellent anatomic detail and tissue characterization combined with the advantage that it is not associated with the application of ionizing radiation to the radiation sensitive infant organism. Low field MRI provides some additional advantages like a lower rate of sedations, easier monitoring of sedated patients and the option of interventional examination and therapy. The disadvantages, however, are the slightly prolonged examination times and the lower signal-to-noise ratio compared to high-field MR scanners. In the future, new techniques using modern gradient echo sequences will provide fast imaging methods with a very high signal-to-noise ratio which

continuation next page

** Prior to 3 weeks out of the body, infant imaging is not determined to be safe.*

:In this issue:

- ***Low-Field MRI in Pediatric Radiology – Possibilities and Limitations of the Method 1***
- ***Diffusion and Perfusion Weighted MRI in Acute Neurological Studies 12***
- ***Advancements in MRI Scanner technology lead to improved functional imaging 18***
- ***Application News – Software Release B33F for MAGNETOM Open / Open viva 22***
- ***Product News – CP Body Array Flex Coil and CP Body Extender ... 28***

continuation from title

could partially replace conventional x-ray imaging. In the presented article we report our experiences in low-field MR imaging of pediatric patients. The possibilities as well as the limitations of this imaging modality are pointed out.

Keywords: MRI, low-field MRI, children, sedation and monitoring.

Introduction

Magnetic resonance imaging is an imaging modality free of ionizing radiation. For this reason, especially in pediatric patients*, it is frequently applied. The development of low-field magnetic resonance imaging systems in recent years has opened up new avenues for the use of diagnostic MR imaging in pediatric radiology. On the one hand, magnetic resonance imaging using field strengths of around 0.2 Tesla (T) is subject to physical limitations compared to traditional high-field magnetic resonance technology; on the other hand, though, the different construction of these systems (open design) results in improved opportunities for patient monitoring and new possibilities for interventional procedures.

From the Editor

Change of address? Would you like to be added to our mailing list?

In the US, please contact the Applications Helpline (phone 1-800-888-SIEM (7436) in the US) and give us your name and business address (no home addresses, please). MAGNETOM Flash is distributed outside the US by local Siemens offices. Please contact me and I will make sure that you are included on your local support office's distribution list.

We hope you will find the information in this issue of MAGNETOM Flash helpful.

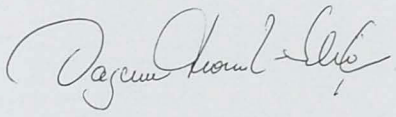

Dagmar Thomsik-Schroepfer, Editor

For the last two-and-a-half years, an open low-field magnetic resonance system from Siemens (MAGNETOM Open) has been installed in the Hospital and Outpatient Clinic for Children and Adolescents at Erlangen-Nuremberg University. This paper is a presentation of our experiences using this method as well as a collection of interesting patients.

Opportunities and Limitations of Open Magnetic Resonance in the "Routine" Examinations

We have examined approximately 1500 children in the last two and a half years using magnetic resonance imaging (MRI). Approximately 80 % of these examinations involved indications in the central nervous system (CNS); 15% involved thoracic diseases, diseases of the abdomen, and diseases of the musculo-skeletal system; finally, 5 % of these examinations involved congenital heart defects.

In the following, we present a selection of typical diagnoses for each individual group of examination indications, and discuss the opportunities and limitations of the method.

Examinations of CNS

Magnetic resonance imaging is a standard diagnostic technique for the CNS (1,2). In pediatric medicine, it is used in the case of congenital diseases (deformities in the brain or spinal cord [figs. 1-3], metabolic defects [4]); for tumor location; for follow-up of tumors [5], hydrocephalus, and chronic inflammatory diseases [6]; as an imaging technique in cases of convulsions [7] or equivocal neurological symptoms; and in the diagnosis of infarctions or hemorrhage [8]. Figures 1-9 present a range of typical diagnostic situations.

All customary examination procedures for the CNS area are also available in low-field magnetic resonance tomography. In some cases, the inferior signal-to-noise ratio due to physical constraints results in a slight increase in examination time over that required for a high-field examination. As figs. 1, 4 and 9 demonstrate, inversion recovery (IR) sequences are outstandingly well suited to improve and clear imaging of gyration. At the present time, image quality in angiography sequences [figs. 1, 8, 9] is still inferior to that obtainable in a high-field system. In case of doubt, the MR tomography results should be verified using color Doppler sonography and quantified by pulsed Doppler sonography [figure 1].

Currently, the principal technical limitation on low-field MRI in the CNS area is in imaging very thin slices. Slice thicknesses of 1-2 mm, which we and many other institutions use for planning surgical interventions for epilepsy, can be successfully achieved using 3D sequences. Images can be reconstructed with a slice thickness of 2 mm when a Fast Low-Angle Shot (FLASH) 3D examination is conducted. The datasets are obtained in a way suitable for image fusion using single-photon emission computed tomography (SPECT) and magnetic encephalography (MEG) examinations [figure 10].

As a result of the inferior signal-to-noise ratio, currently neither functional MR sequences nor spectroscopy can be realized on low-field magnetic resonance systems. At the moment, this is the only real limitation on this examination method in the field of pediatric CNS diagnosis.

Cardiac and Thoracic Examinations

MRI has been a standard technique for some years now in the diagnostic imaging of the thorax and anomalies of the great vessels (3-5). But it is also possible using this technology to produce good quality images of congenital cardiac defects and anomalies in the thoracic venous course, as well as anomalies in the area of the trachea (6-9).

Finally, there are textural anomalies of the myocardium (arrhythmogenic right ventricle) that can be diagnosed almost exclusively with MRI (10). Here, T1-weighted spin echo sequences in all 3 orientations (axial, coronal, sagittal) are chiefly used. In addition, double oblique sequences are used for imaging of the course of the aorta.

In recent years, we have examined 5 children whose severe ventricular arrhythmias led clinically and electrocardiographically to the suspicion of an arrhythmogenic right ventricle. This suspicion was confirmed in three of the children by means of a cardiac low-field magnetic resonance examination.



Fig. 1a

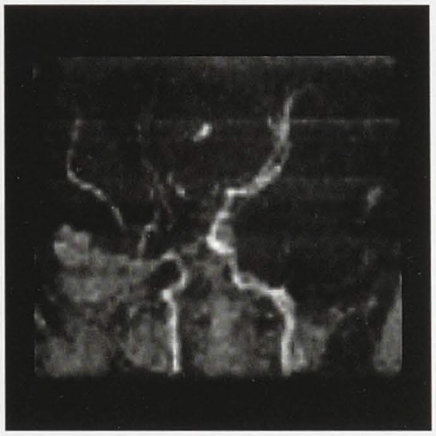

Fig. 1b

Figure 1a: Two-month-old boy with congenital malformation of the right cerebral hemisphere which is lisencephalic and smaller than the left hemisphere which appears normal.

Figure 1b: MR angiography of the same patient revealed a missing lenticulostriate artery which was confirmed by Doppler sonography. Additionally, the right anterior cerebral artery was missing in this patient. If the malformation was the result of an early intrauterine infarction or caused by a primary malformation of the arteries is not known. The quality of MR angiography is poorer compared to high-field imaging and is even more difficult to interpret in this patient, due to small size of the anatomic structures.



Fig. 2a

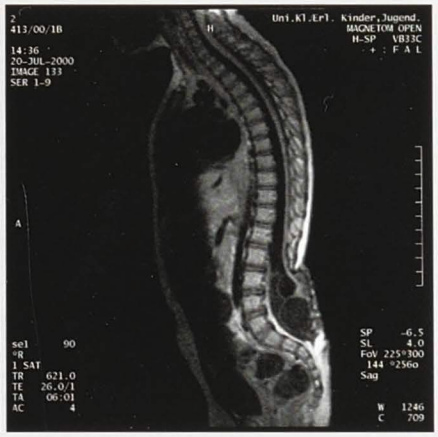

Fig. 2b

Figure 2a: T1-weighted image of a two-year-old girl with postoperative spina bifida and Chiari II malformation. The typical features of the malformation are seen in the medial sagittal plane. Low posterior fossa contents with herniated tonsils and elongated fourth ventricle, partial agenesis of the corpus callosum as well as polymicrogyria, a large massa intermedia and the beaking of the tectum are characteristics of this malformation.

Figure 2b: Midsagittal T1-weighted spin echo of the spine in the same patient. The large lumbar defect is easily depicted. The spinal cord is fixed to the operation site indicating a tethered cord which in this patient had become symptomatic in terms of a decrease of the motor function of the left leg. Additionally, two arachnoid cysts are noted at the lower end of the spinal cord.

Figure 3a: Eleven-month-old patient with frontal encephalocele. The T1-weighted coronal spin echo revealed a small cele within the nasal cavity. The intracranial connection is clearly depicted. Note the wide arachnoid space which is considered normal in the young child.

Figure 3b: Sagittal T1-weighted spin echo sequence of the same patient. The encephalocele is seen very softly within the nasopharynx, occluding most of the right upper airway.

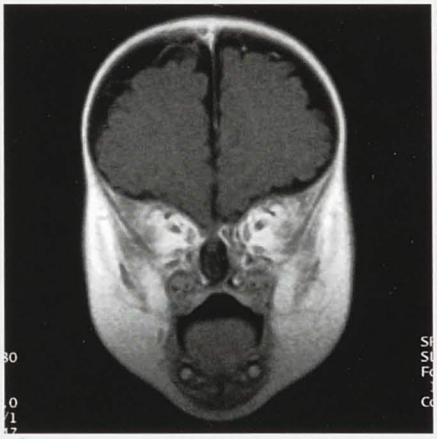

Fig. 3a

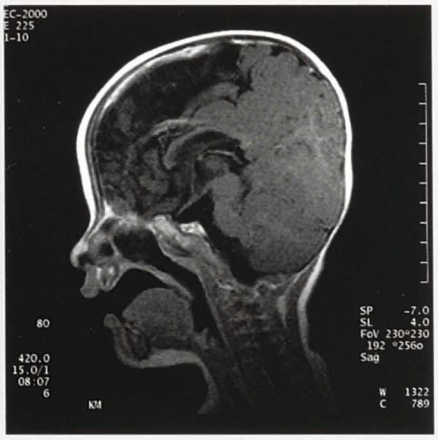

Fig. 3b



Fig. 4a



Fig. 4b

Figure 4a: 14 year-old girl with mucopolysaccharidosis III (Sanfilippo) and severe physical and mental retardation. Axial T2-weighted spin echo shows dilated ventricles and severe atrophy of the brain.

Figure 4b: Sagittal IR sequence of the same patient. The atrophy is easily depicted. Most of the white matter is destroyed in this patient secondary to the underlying disease. However, exact differentiation of the white and gray matter is no longer possible in this patient.



Fig. 5a



Fig. 5b

Figure 5a: Sagittal T1-weighted spin echo of a seven year-old patient presenting with upper extremity paresis. The image shows an intraspinal tumor over 3 cervical segments. Partial destruction of the seventh cervical vertebra is present.

Figure 5b: Postoperative T1 weighted spin echo of the same patient. No residual tumor is seen within the spinal canal. A fine syrinx is observed as well as a persistent spinal edema causing a mild thickening of the spinal cord. Note the scarring and the partial resection of the spinous processes at the operation site.
Definite histology is pending.

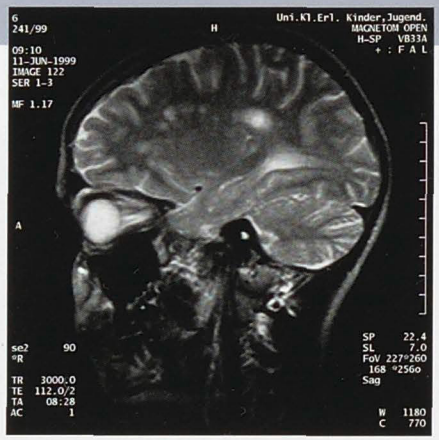

Fig. 6

Figure 6: Sagittal T2-weighted image of a 14 year-old girl suffering from cerebral involvement of systemic lupus erythematodus. The areas of cerebral vasculitis are easily depicted as regions of high signal intensity.



Fig. 7a

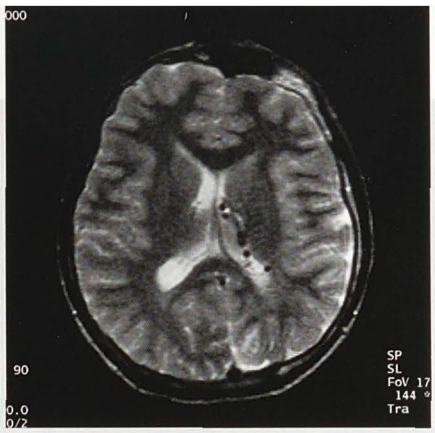

Fig. 7b

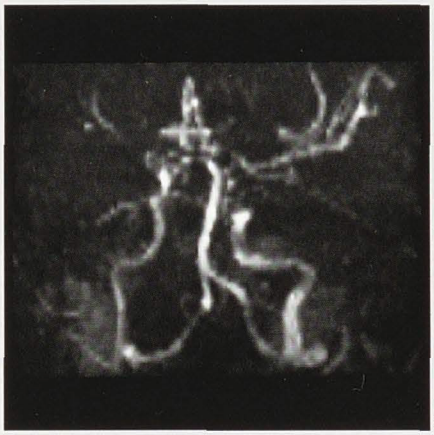

Fig. 8a

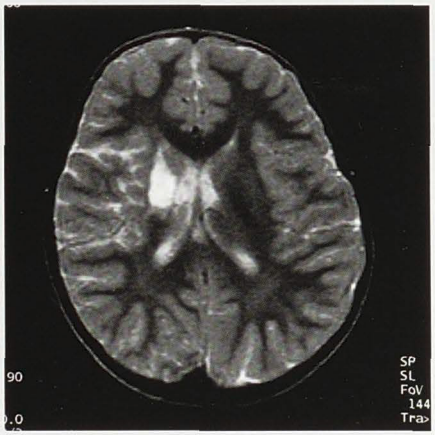

Fig. 8b

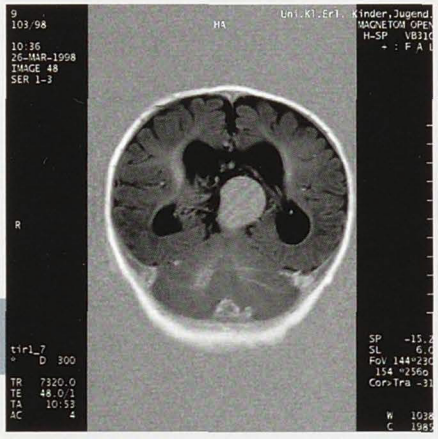

Fig. 9a

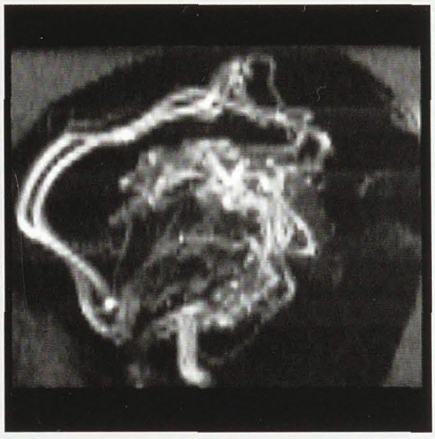

Fig. 9b

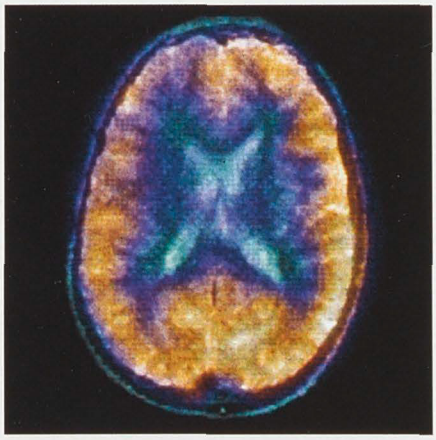

Fig. 10

Figure 10: Image fusion from a FLASH 3D examination using interictual single-photon emission computed tomography (SPECT) of a 6-year-old patient with therapy-resistant cerebral convulsive disorder associated with Rasmussen's encephalitis. The image shows a frontally reduced perfusion, with basal accentuation. The image was reconstructed in a slice thickness of 2 mm. The datasets were obtained in a way suitable for image fusion using single-photon emission computed tomography (SPECT) and magnetic encephalography (MEG) examination. (Image fusion: Dr. Platsch, Nuclear Medicine Clinic, University of Erlangen/Nuremberg).

Figure 7a: 16 year-old boy with Sturge-Weber disease. Coronal T1-weighted image after contrast enhancement. Left cerebral hemiatrophy with and associated expansion of the subdural space. Cortical and meningeal contrast enhancement due to multiple vascular malformations is observed within the left hemisphere.

Figure 7b: Same patient, axial T2-weighted image. The hemiatrophy and expansion of the arachnoid space is observed in this plane as well. Note the expansion of the left frontal sinus consistent with the cerebral hemiatrophy. In addition to that, multiple enlarged vessels are seen within the left choroid plexus which were identified as veins in an additionally performed venous MR-angiography.

Figure 8a: Cerebral MR-angiography. Occlusion of the right middle cerebral artery (MCA) in a four-year-old girl with an infarction of the right MCA.

Figure 8b: T2-weighted spin echo sequence of the same patient. The large periventricular defect is readily apparent as well as the concomitant atrophy of the surrounding gyri.

Figure 9a: Four month-old girl with large vein of Galen aneurysm following interventional angiography with coil and fibrin glue embolization of the aneurysm (Professor W. Huk, Neuroradiology, University Clinic Erlangen/Nuremberg). Coronal IR sequence. The aneurysm is easily depicted.

Figure 9b: MR-angiography, sagittal view of the same patient. The supplying vessels are clearly imaged while the aneurysm itself showed a minimal flow, indicating residual perfusion after the embolization. A complete thrombosis of the aneurysm ensued.

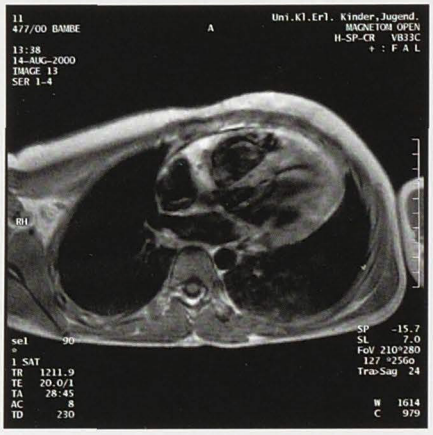

Fig. 11



Fig. 13a

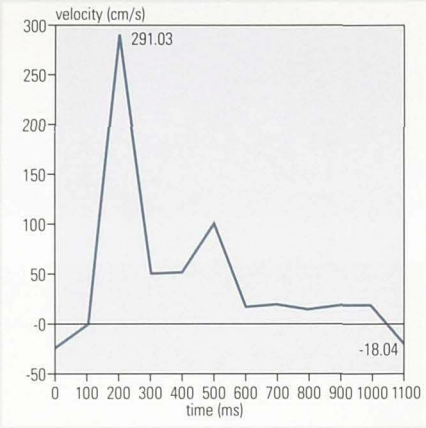

Fig. 13b

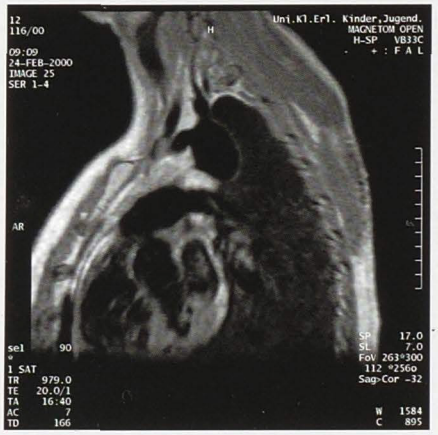

Fig. 12

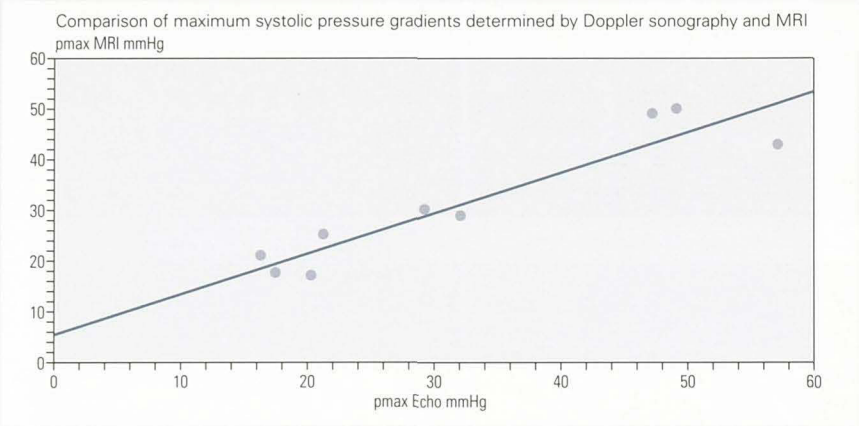

Fig. 14

Figure 11: Cardiac MR images (modified longitudinal axis with cardiac triggering) of a 12 year-old boy suffering ventricular tachycardia. The pronounced thinning of the right ventricular wall and the increased signal intensity within the right ventricular myocardium are typical evidence for fatty degeneration consistent with an arrhythmogenic right ventricle.

Figure 12: 16 year-old boy with coarctation of the aorta status post repair in his infancy. Routine follow-up MRI. Modified long axis T1-weighted spin echo with cardiac triggering. A large aneurysm of the aorta at the former operation site was diagnosed. In addition, an aneurysm of the left carotid artery was clearly depicted on the images. The patient underwent surgical repair of the aneurysms.

Figure 13a: Cardiac MRI of a 14 year-old patient status post repair of a coarctation of the aorta. The MRI revealed a hypoplastic aortic arch with prestenotic enlargement of the ascending aorta.

Figure 13b: Flow curve for the same patient. The result in the post-stenotic segment is a maximum systolic flow velocity of 291 cm/sec., which (in accordance with the modified Bernoulli equation) corresponds to a calculated pressure gradient of 34 mm Hg. A slight diastolic gradient is suggested.

Figure 14: Comparison of maximum systolic pressure gradients (pmax) for 9 patients determined by Doppler sonography and by magnetic resonance tomography. The difference between the two methods appears to be acceptable at high pressure gradients ($r = 0.93$, $p < 0.001$). The pressure gradient was calculated from the maximum flow velocities using the modified Bernoulli equation ($\Delta pmax = 4v2$).

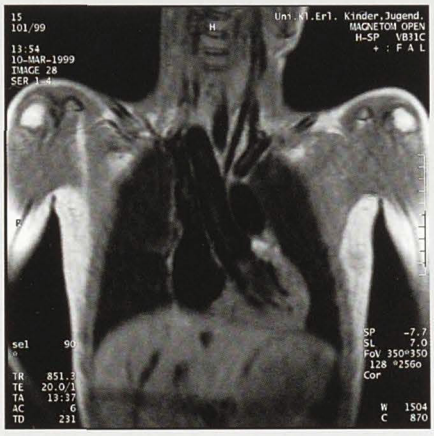

Fig. 15a

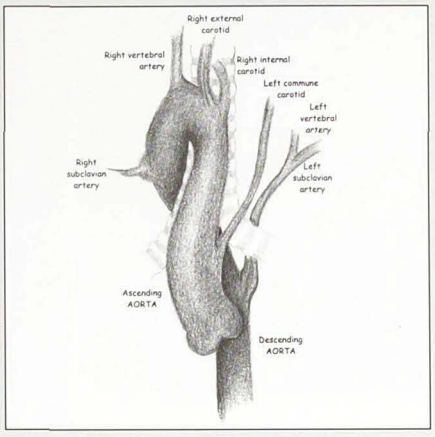

Fig. 15b

Figure 15a: Cardiac MRI in a 13 year-old girl with right cervical aortic arch. The ascending aorta is elongated and orientated to the right. The left carotid artery is easily depicted in this slice.

Figure 15b: Anatomical sketch of the right cervical aortic arch. The aortic arch is drawn up and deflected to the right. The right external and internal carotid arteries arise as independent vessels from the aortic arch; the right subclavian artery arises from an aortic diverticulum. The descending aorta intersects the central line and runs along the left side in the thoracic region. The left subclavian artery arises aberrantly from a diverticulum. (Modified from Finch MA, in: Amplatz, Moller, Radiology of Congenital Heart Disease; 1992, p. 1031).

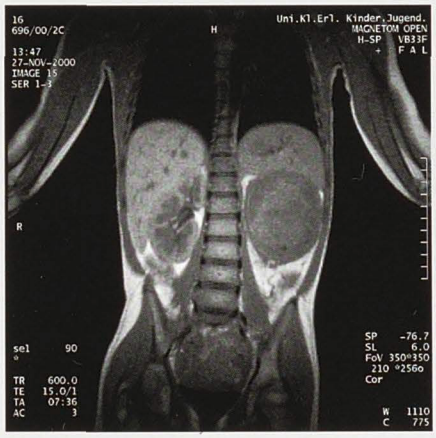

Fig. 16a

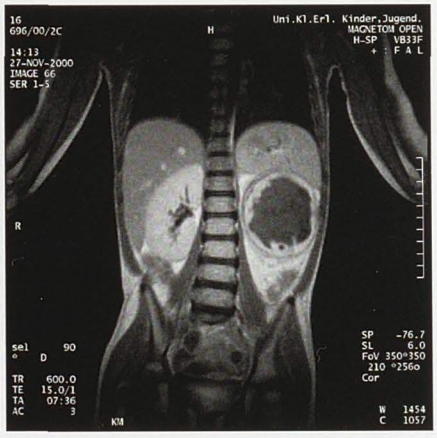

Fig. 16b

Figure 16a: 4 ½ year-old girl presenting with a large abdominal tumor. Coronal T1-weighted image without contrast enhancement. A large left-sided abdominal mass with heterogeneous medium-signal-intensity is seen, while the left kidney could not be located.

Figure 16b: Same slice after contrast medium injection. A heterogeneous contrast enhancement was seen while the right kidney showed no pathological contrast enhancement. Histology confirmed a unilateral Wilms' tumor.

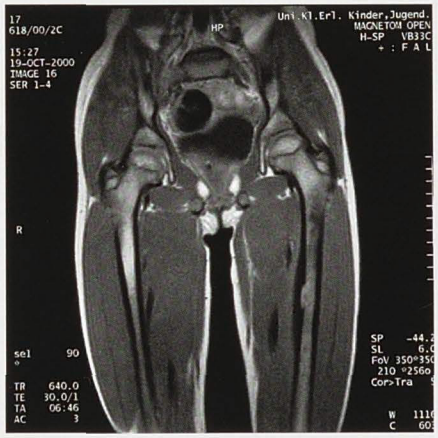

Fig. 17a

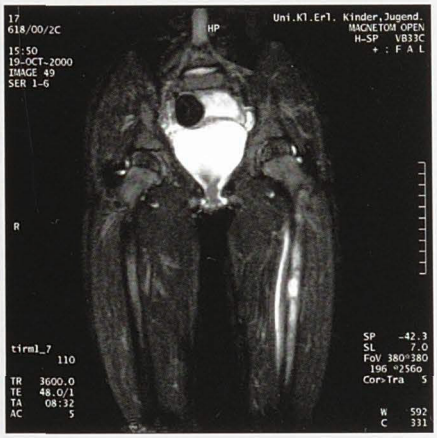

Fig. 17b

Figure 17a: 7 year-old girl presenting with swelling and pain of the left thigh. X-ray revealed a cystic process with periostal reaction. Coronal T1-weighted image without contrast enhancement. The isointense process is clearly seen within the proximal femur. Cortical thickening and periostal reaction are observed as well as an involvement of the surrounding soft tissues.

Figure 17b: Coronal fat suppressed sequence of the same patient. An increased signal intensity is noted at the site of the process as well as a bone edema involving most of the femur diaphysis and the surrounding soft tissue. Histology of the process revealed chronic osteomyelitis. Malignancy was the most important differential diagnosis and has to be excluded by histology in such cases.

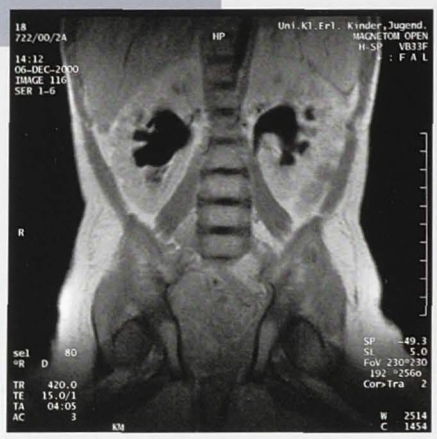

Fig. 18a



Fig. 18b



Fig. 18c

Figure 18a: Coronal T1-weighted spin echo after Gadolinium administration in an 11 month-old boy with a presacral mass of unknown origin. The mass is seen at the lower boarder of the image. Additionally, marked dilatation of both renal pelvices is noted.

Figure 18b: More anterior slice of the same patient. The bladder is dilated and shifted to the right. The bladder neck is clearly seen. The tumor compresses the urethra leading to massive urine retention in this patient. As no contrast medium is collected in the bladder during the investigation an inhibited urinary excretion may be assumed secondary to the morphological findings.

Figure 18c: Sagittal T1-weighted image after contrast enhancement of the same patient. The presacral mass is clearly seen. After contrast enhancement it showed a heterogeneous signal intensity. In the sagittal plane the intraspinal spread of the tumor is easily depicted. Histology is pending. Note the only mild motion artifacts (respiration, bowel movement) which are notably less pronounced than they would be in high-field MR imaging.



Figure 19: Typical examination of a conscious little girl. There is direct visual and physical contact with the child during the examination, which has a positive effect on the cooperation of the young patient.



Fig. 20a

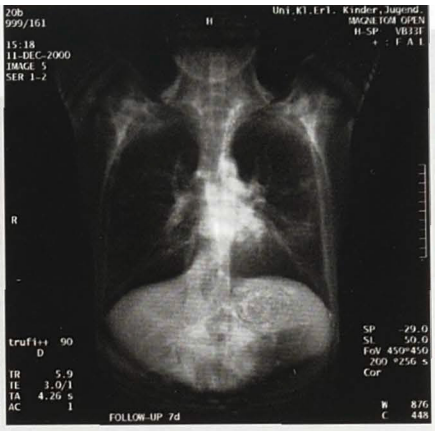

Fig. 20b



Fig. 21

Figure 20a: Fast thick-slice MRI of the lung in a 16 year-old boy with cystic fibrosis. Multiple patchy areas of increased signal are noted consistent with diffuse pneumonia. Interstitial disease is seen in its typical streaky appearance. Additionally, hilar attenuation is noted. Acquisition time for 3 slices (slice thickness 50 mm each) covering the whole thorax 3.6 sec!

Figure 20b: Follow-up of the same patient after 1 week of treatment. The pneumonic infiltrates have markedly resolved indicating the usefulness of thick-slice MRI to diagnose and later follow up acute changes in patients with chronic lung disease.

Figure 21: Fast thick-slice true FISP imaging of the paranasal sinuses in an eight year old girl presenting with fever. The left maxillary sinus is completely mucous-filled. The ethmoidal cells were involved while the sphenoid sinus was found to be free of infection. Despite antibiotic therapy the girl developed an orbital phlegmon which resolved within three days of IV antibiotic treatment. Acquisition time per slice 1.7 sec!

Fig. 11 shows as an example the cardiac low-field MR results for a twelve-year-old boy (modified longitudinal axis). In addition to electro-physiological criteria, the cardiac low-field MR diagnosis is a mainstay in diagnosing this clinical picture.

Coarctation of the aorta is the most easily imaged congenital cardiac anomaly. In our clinic, patients are regularly subjected to a follow-up MR examination after surgical repair of a coarctation in order to detect as early as possible the development of any restenosis or an aortic aneurysm. The method also enables good pre-operative aortic imaging of the morphological isthmus. In addition to the morphological image, it is also possible using MRI with the newly developed phase-sensitive flow measurement sequences to evaluate the hemodynamic relevance of the stenosis.

Figure 12 presents an aneurysm formation of the aortic arch following surgical repair of a coarctation of the aorta in a 16 year-old boy; figures 13a-b show the morphological image of a hypoplasic aortic arch and the flow curve. Figure 14 is a comparison of the pressure gradients of 9 children determined by Doppler sonography and by MRI, respectively.

As a result of the good quality image of both the vascular system and the trachea provided by MRI, anomalies of the great vessels can often be better evaluated by that technology than by angiography or bronchography.

Figure 15a shows the results for a patient whose right cervical aortic arch was diagnosed using sonography. Low-field MRI here enables easy imaging of the relationship between the bronchial and vascular structures.

Figure 15b visualizes the findings in an anatomical diagram.

Low-field MRI is also a valuable method in the field of thoracic and cardiac diagnosis; here, though, its usefulness is restricted by its somewhat inferior signal-to-noise ratio with very thin slices. Here at the Hospital and Outpatient Clinic for Children and Adolescents at the University of Erlangen, we have succeeded for the first time in establishing functional low-field MR sequences that also enable quantitative flow measurement in the region of the great vessels.

In the future, it will also be necessary to realize additional functional sequences (ejection fraction, cardiac output) for low-field diagnostics. This seems feasible in terms of the physics involved, although here too one must expect that examination times will be lengthier than they are for comparable high-field examinations.

Abdominal Examinations

The most salient feature of abdominal diagnosis in pediatric imaging is the limited degree of patient cooperation compared to adults. MRI that are customary in use with adult patients (breath-hold examinations) are of only limited practical value in pediatrics (11). This difficulty must be overcome by an optimized examination process that includes the patient's regular and even breathing (breath triggering, special sequences that perform an averaging of individual lines rather than of the entire image), and, if necessary, pharmaceutical sedation.

Figure 16 shows the examination of an infant with a central Wilms' tumor of the left kidney; figures 18a-c depict the MR results for an 11 month-old boy with a low abdominal tumor. Special line-averaged sequences for better suppression of motion artifacts due to breathing were not applied in this patient because of the even breathing during sedation.

Overall, MR diagnosis is a valuable component of pediatric abdominal imaging. Here, and especially in the case of diagnosis of intra-abdominal tumors, examination should be conducted following the administration of contrast medium. MRI is often superior to CT examination here, especially in connection with the extent of paravertebral tumors in the vertebral canal, as shown in the examples in figures 5 and 18 of tumors with intraspinal dissemination or origin in the vertebral canal.

For examinations in the abdomen, the use of special sequences for artifact suppression and an examination technique that accommodates the special needs of pediatric patients are recommended.

Musculoskeletal Examinations

MR imaging of the musculoskeletal system is less frequently performed in pediatric patients. X-ray is still the imaging method of choice for bone evaluation. Indications for MRI are better differentiation of bone defects diagnosed on radiographs (tumors, infections, benign cysts), secondary imaging when clinical findings cannot be explained by the radiographic finding, especially when the condition is caused by a soft tissue process, rheumatic disease and follow-up of musculoskeletal tumors. One of the important indications is the diagnosis and follow-up of osteomyelitis in pediatric patients as radiographs are often negative while MRI might reveal a skeletal edema consistent with the disease before any other imaging method becomes positive. In addition to the routine sequences with and without contrast enhancement, special fat suppressed sequences should therefore always be performed when evaluating the pediatric musculoskeletal system [figure 17].

Design-dependent Features Affecting Patient Monitoring and Sedation

The open design of the MAGNETOM Open system provides good visual and physical contact during the entire examination and thus facilitates patient monitoring; this is particularly advantageous when pharmaceutical sedatives are used. In our experience, the presence of the mother during the examination and the possibility of direct physical contact with her have a very positive effect on the cooperation of non-sedated children. Fig. 19 shows the process of a typical examination.

Special Technical Monitoring Features

We use a monitoring system from Bruker (Maglife) for technical monitoring of patients in our department; this system enables continuous measurement of transcutaneous pCO_2 and pO_2, capillary oxygen saturation, and terminal expiratory CO_2, as well as oscillatory and invasive arterial blood pressure measurement. The routine monitoring of sedated patients chiefly involves the measurement of capillary oxygen saturation and of the oscillatory blood pressure.

In our experience, the use of this monitoring system in its standard commercially available form results in considerable RF interference, with a significant deleterious effect on the quality of MR tomography images. This is the result of the increased sensitivity of open MRI systems to RF interference, which can reach the receiving coil more easily than it is the case for closed tubes with better shielding.

We have solved this problem by developing additional RF shielding for the monitoring system. This shielding is already available from the companies involved.

Overall, the ease of patient monitoring is significantly increased by the open system design: direct access to the patient is always available, and even malfunctions occurring during the examination process (for example, sensor dislocations) can easily be corrected without delay or interruption of the investigation.

Sedation of Uncooperative Children

In a retrospective and prospective study conducted in 1997-1998, we compared a cohort of children requiring sedation during use of our current system with data for 111 patients examined by us using a closed high-field MR system. Strikingly, we found that the sedation and anesthesia rate for our patients had decreased significantly, from 47 % to 27 % ($p < 0.001$), following introduction of the open magnetic resonance tomograph. This is principally the result of a considerably lower sedation rate for the age group up to 10 years (12).

Table 1 presents an overview of the sedation rate in a closed magnetic resonance system versus the sedation rate in an open system, broken down into 2 age groups. In the age group over 10 years, the decision for pharmaceutical sedation is determined by the patient's physical condition (for example, intensive care patients) or mental situation (statomotoric and mental retardation) rather than the design of the system and the examination process (13,14).

Examinations in high-field systems at our clinic were conducted exclusively using general anesthesia. In our experience, this can almost always be avoided in an open MRI, where sedation combining 0.2 mg/kg KG etomidate and 0.2 mg/kg body weight midazolam is sufficient for nearly all patients to ensure an uninterrupted examination. Although there have been no incidents during sedation in the last two and a half years, the presence of an investigator with experience in pediatric intensive medicine is necessary.

	Open Low-Field System *(Sedation)*	***Closed High-Field System*** *(General Anesthesia)*	***Significance Level***
Age ≤ 120 Months *examined/sedated*	*232/68 (29%)*	*84/51 (61%)*	*$p < 0.0001$*
Age > 120 Months *examined/sedated*	*42/6 (14%)*	*25/1 (4%)*	*n.s.*
Total *examined/sedated*	*274/74 (27%)*	*111/51 (47%)*	*$p < 0.001$*

Table 1:
Overview of sedation rates in a closed magnetic resonance system in comparison to an open magnetic resonance system, broken down into 2 age groups.

Interventions

Not only does the open system design allow for better contact with the patient in respect to monitoring, but it also enables intervention for diagnostic and therapeutic purposes. The open system design makes it easier to reach the target regions. Fast sequences can be used to track the needle in real time during a biopsy. These interventions can be performed with short-term pharmaceutical sedation.

In our center, for example, we performed a biopsie in a 7-year-old boy with status post treated oncological disease and current suspicion of a metastasis in a vertebral body. The conventional MRI of the spine had shown a destroyed thoracic vertebra. As an increased sensitivity to ionizing radiation was included in the differential diagnosis of this patient the puncture had to be undertaken under radiation free conditions. The biopsy was performed in a dorso-lateral position using MR monitoring. Necrotic tissue was confirmed histologically. The necrosis of the vertebral body was assumed to be a radiation side-effect resulting from the patient's increased sensitivity to radiation as further proven in the fibroblast cultures. Another patient who underwent an interventional biopsy presented with a cystic intra-abdominal lymphangioma. During the procedure a sclerosing agent (OK 432) was injected into the lymphangioma.

Overall, our experience shows that interventional procedures are easily performed in the open MR system. Methodological difficulties do arise, however, in the positioning of MR slice orientation for interventions; the use of markings on the body surface or needle probings at likely points of access can make this complicated. Further development of biopsy holders for automatic needle positioning would significantly increase the importance of MR-supported interventions by simplifying the necessary methods.

Prospects and Perspectives

While low-field MRI provides obvious advantages in the areas of sedation and patient access, this method's principal limitation lies in its inferior signal-to-noise ratio in comparison with high-field systems. If modern gradient echo sequences, for example, are used with considerably increased slice thicknesses to counteract this, the method will allow for MR images that are – in theoretical physical terms – qualitatively better than those obtained with high-field systems: some of the artifacts that occur with MRI increase with increasing field strength. With the use of very thick slices in the area of body diameter, projection volume images can be obtained that can be interpreted similar to conventional X-ray images in the area of the lung or the paranasal sinuses.

As an example, figure 20a shows the volume projection examination using thick slices in the area of the lung of a patient with cystic fibrosis. The follow up image [figure 20b] shows that acute changes are clearly noted and radiation free follow-up is possible. At a very short examination time (1.2-3.6 seconds), this examination method might be used in the future as an alternative to conventional X-ray examination of the thorax in pediatrics. This is currently being investigated in a prospective study conducted at our clinic (15). Due to the extremely fast imaging real-time MRI during respiration can also be performed easily. Another possible perspective is the fast imaging of the paranasal sinuses as presented in figure 21.

Conclusion

MRI is an important element in pediatric diagnostic imaging. Without using ionizing radiation, it provides outstanding imaging of anatomical relationships and tissue limits. In the low-field range, the open system design provides significant advantages such as a decrease in sedation rates, easier monitoring of sedated patients, and interventional diagnostics and therapy. At the same time, examination times are slightly lengthened and the signal-to-noise ratio is slightly inferior to those for high-field MR systems.

The future prospects for low-field MRI are new methods relying on modern gradient echo systems, which will enable fast imaging with a high signal-to-noise ratio. In some areas, these methods could come to supplant conventional X-ray exposures.

Literature

1. Fagan SJ, Byrd SE, Chuang HS, et al: Head and Spine Imaging; in Cohen MD and Edwards MK. (eds): Magnetic Resonance Imaging of Children. Philadelphia, BC Decker, Inc. 1990, pp 85-540.

2. Kangarloo H, Bach AM, Hilfer CL, et al. Chest MRI in children. Radiol Clin North Am 1998;8:1040-1046.

3. Klein MV, Hesselink JR: Brain: Indications, Techniques, and Atlas; in Edelmann RR, Hesselink JR and Zlatkin MB. (eds): Clinical Magnetic Resonance Imaging. Philadelphia, WB Saunders Company, 1996, pp 457-981.

4. Kuharik MA: Sedation, Anesthesia, and Patient Monitoring; in Cohen MD and Edwards MK. (eds): Magnetic Resonance Imaging of Children. Philadelphia, BC Decker, Inc, 1990, pp 75-84.

5. Link KM, Lesko NM: Congenital Heart Disease; in Edelmann RR, Hesselink JR and Zlatkin MB. (eds): Clinical Magnetic Resonance Imaging. Philadelphia, WB Saunders Company, 1996, pp 1683-1710.

6. Malmgren N, Hochbergs P, Holmqvist C, Sandström S, Laurin S, Björkhem G. Complex congenital heart malformation evaluated with MR imaging at 0.3 T. Pediatr Radiol 1996;26:470-477.

7. Mc Kenna W et al. Diagnosis of arrhythmogenic right ventricular dysplasia/ cardiomyopathia. British Heart Journal 1994;71:215-218.

8. Rupprecht T, König M, Nitz WR, Hofbeck M, Singer H, Böwing B. Möglichkeiten der Niederfeld NMR-Diagnostik bei kardiopulmonalen Erkrankungen im Kindesalter. Monatsschr Kinderheilkd 1997;145 (S1): S 155 (Abstract)

9. Rupprecht T, Böwing B, Rascher W, Kuth R, Deimling M. Steady State Free Precession Projektions NMR - Eine Alternative zu konventionellen Röntgenthorax Untersuchungen? Ergebnisse einer pädiatrischen Pilotstudie. Radiologe 1999;8:732-733. (Abstract)

10. Siegel MJ. Chest applications of magnetic resonance imaging in children. Top Magn Reson Imaging 1990;3:1-23.

11. Sieverding L, Jung W I, Fleiter T H, et al. Progress of MRI and variation of the diagnostic procedure in congenital and acquired heart disease. Klin Pädiatr 1992;204:340-347.

12. Rupprecht T, Kuth R, Böwing B, Gerling S, Wagner M, Rascher W. Sedation and Monitoring of Pediatric Patients undergoing Open Low Field MRI. Acta Paediatr 2000;89:1077-1081.

13. Carr JJ, Hatabu H, Gefter WB: Thorax; in Edelmann RR, Hesselink JR and Zlatkin MB. (eds): Clinical Magnetic Resonance Imaging. Philadelphia, WB Sunders Company, 1996, pp 1615-1682.

14. Cohen MD: Gastrointestinal System; in Cohen MD and Edwards MK. (eds): Magnetic Resonance Imaging of Children. Philadelphia, BC Decker, Inc. 1990, pp 611-678.

15. Volle E, Park W, Kaufmann HJ. MRI examination and monitoring of pediatric patients under sedation. Pediatr Radiol 1996;26:280-281.

T. Rupprecht, MD
University Pediatric Hospital
Loschgestrasse 15
D-91054 Erlangen
Germany

Advancements in MRI Scanner Technology Lead to Improved Functional Imaging

A. G. Sorensen
MGH-NMR Center, Massachusetts General Hospital, Charlestown, USA

Introduction

MRI has generally excelled at depicting anatomic changes in the brain. Over the past decade, however, MRI has increasingly been used to image physiologic changes in the brain, including changes associated with brain function and dysfunction. Responding to the demand for physiologic imaging, equipment capabilities are beginning to be expanded; this in turn is allowing improvements in physiologic brain imaging to begin to reach clinical practice. This article will review a few of the basic technical advances that suggest near term and long term clinical applications. Clinical image examples shown in this article have been acquired on a Siemens 1.5T MAGNETOM Sonata and a 3T MAGNETOM Allegra system.

The Need for More SNR

Perhaps as much or more than any other MRI technique, physiologic imaging is limited by the signal to noise ratio (SNR). Broadly defined, physiologic imaging, also termed functional imaging includes diffusion-weighted imaging (DWI); perfusion-weighted imaging (PWI), including techniques with and without exogenous contrast agents; brain activation imaging using blood oxygen level-dependent (BOLD) and blood flow techniques; and various other experimental techniques. Physiological imaging also includes spectroscopic imaging; although issues surrounding spectroscopic techniques warrant a separate discussion than will be undertaken here, to first approximation many of the same technical requirements imposed by the already mentioned advanced techniques are also needed by spectroscopic imaging. Conversely, spectroscopic imaging stands to benefit from the hardware and software advances that have been recently made just as other types of physiological imaging do.

MR Signal Increases with Field Strength

Investigators have used numerous approaches to try to overcome these SNR limitations. Many of these techniques such as acquiring multiple signal averages, use of surface coils, and sequence optimization often still leave physiologic imaging limited by SNR. As a result, additional approaches are being utilized. One approach is to move to higher field strengths. Work at a number of institutions has confirmed that higher field strength does indeed provide improvements in SNR and thereby in imaging performance for physiological imaging. Fig. 1 shows an example of this for BOLD imaging in a cognitive paradigm. Because BOLD imaging detects only a small change in signal compared to background fluctuations, the improvement in SNR translates effectively into a reduction in background fluctuations and therefore improved statistical confidence regarding what changes represent signal and what changes represent noise. This improvement in raw SNR by moving to higher field will benefit most if not all forms of functional imaging. Many investigators believe that such improved SNR will be essential if functional imaging is to meet its full clinical potential.

Overcoming High Field Artifacts

Some investigators have felt that moving to higher field strength such as 3T might come at too great a cost. In particular, since the susceptibility sensitivity also increases roughly linearly with field strength, there has been some concern that in areas near the base of the skull or in the posterior fossa there would be artifacts that would preclude gaining useful information from the brain in these areas. However, this does not appear to be necessarily the case. We have found that by moving to thinner slices (something that one wishes to do typically with increased SNR anyway), the intravoxel dephasing and incoherence is decreased (as a result of the smaller voxel size) and in fact susceptibility effects can decrease. An example of this is shown in fig. 2, where single shot echo-planar imaging is obtained throughout the brain including the cerebellum and brain stem and down in to the superior cervical spine without image degradation.

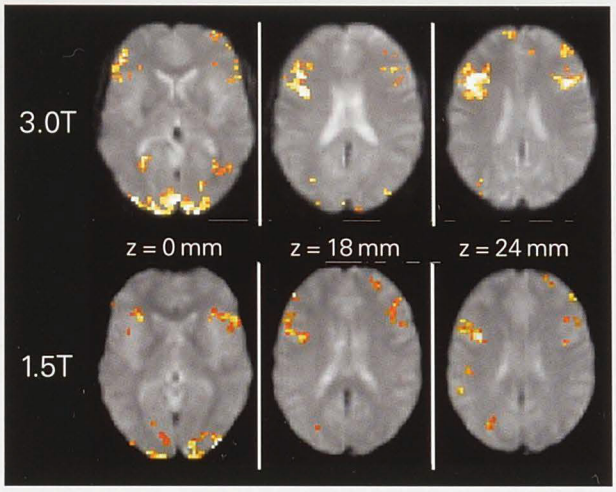

Figure 1
3T versus 1.5T activation. Comparison of activation in a group of subjects performing a word-generation task to visual stimuli at 3.0T (top row) and at 1.5T (bottom row).

Note the more extensive and stronger (as evidenced by the higher intensity color) activation in all regions. Note that additional noise is not produced, but rather additional signal consonant with the type of paradigm used.

Courtesy of Russell Poldrack, PhD.

Figure 2
Coverage at 3.0T of brain, cerebellum/ brainstem, and superior cervical spine.

Note the lack of warping, signal dropout, or other overt signs of susceptibility effects.

Technical parameters:
Gradient Echo EPI, 3.0T, TR 3000 ms, TE 50 ms, 3 mm slice thickness, no gap, single shot interleaved acquisition, 48 slices.

Courtesy of Larry Wald, PhD.

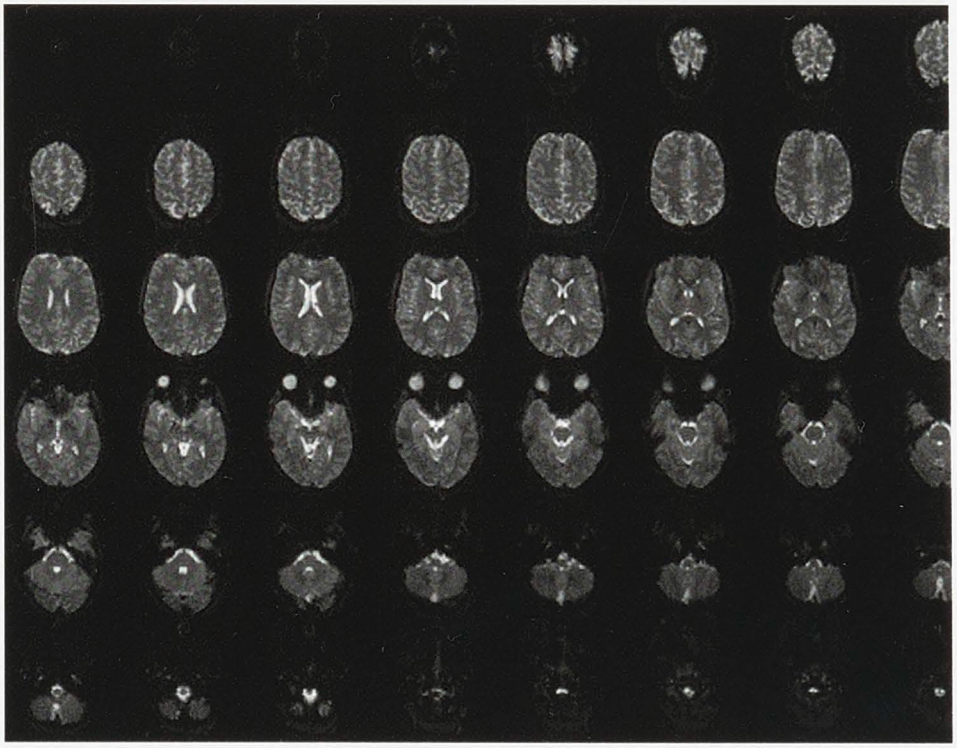

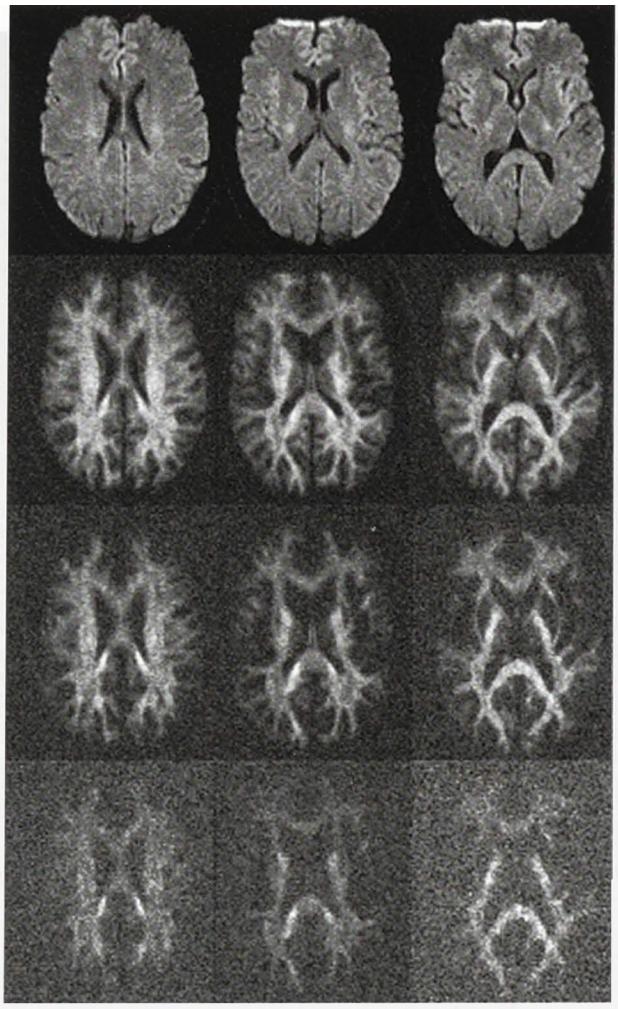

Figure 3
Very high b value diffusion weighted imaging. All images are trace-weighted from full tensor acquisitions at 1.5T with a 40 mT/m system. Images through the brain in this normal volunteer demonstrate routine appearance at b = 1,000 s/mm² (top row, 3 signal averages).

Note that at b = 5,000 s/mm², there is now marked gray-white contrast present whereas at 1,000 s/mm² there is little contrast (and what contrast is present at b = 1,000 is based mainly on T_2 differences). However, at b = 5,000 s/mm² (second row, 12 signal averages) there are clearly new phenomena occurring including apparently different rates of water diffusion in gray versus white matter, as well as a drop in signal to noise ratio due to the very high b value used.

This trend continues at b = 10,000 s/mm² (third row, 20 signal averages), where there are still increased gray-white differences compared to b = 1,000 s/mm², until at b = 20,000 s/mm² the gray matter is essentially invisible. This is probably due to non-monoexponential decay in the brain, but this is a matter of ongoing research.

Note that even for b = 20,000 s/mm² on a 40 mT/m system with all three axes able to operate simultaneously the TE is 136 ms (as compared to 67 ms for b = 1,000 s/mm²). This makes the visualization of white matter possible at b = 20,000 s/mm2 with 20 signal averages; if less SNR were available (if, for example, the TE was substantially longer), many more signal averages would be needed since SNR goes as the square root of the number of signal averages.

Note that the system is capable of 40 mT/m in all three gradient directions simultaneously, for a net performance of (square root of 3 times 40 mT/m) approximately 69 mT/m.

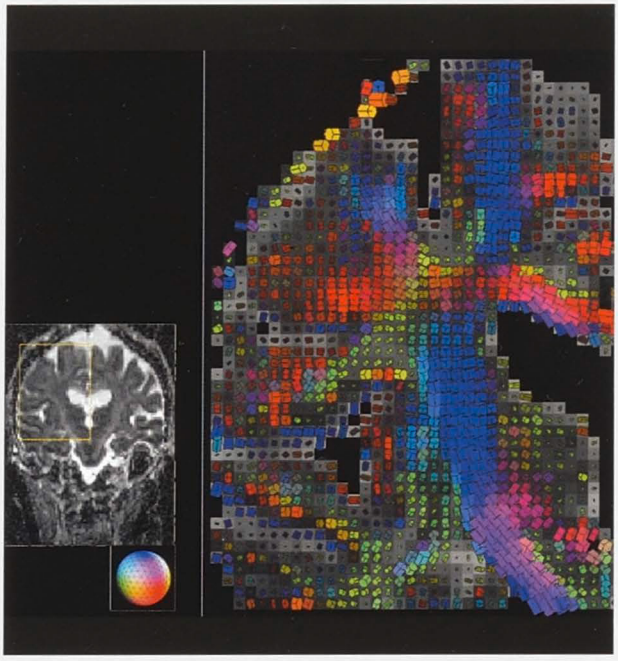

Figure 4
Diffusion tensor tractography of the in vivo human brain.*

This tractography study is from a 68 year old female with motor weakness but no evidence on any imaging study (including this tractography study) of any physical defect.

The multicolor area is an enlarge-ment of a coronal section through the brain.

The eigenvalues and eigenvectors were then computed, weighted by the fractional anisotropy in the image, and overlaid on to an anatomic scan.

Note the clear directionality of the fiber bundles including the corpus callosum, cortico-spinal tracts, and subcortical U fibers.

Data were obtained on a 1.5 T system with 40 mT/m gradients and 18 signal averages of a single tensor acquisition sequence.

Courtesy of Mette Wiegell, David Tuch, and Van Wedeen MD.

Balanced System Architecture

Other approaches to improving SNR can be as important and as helpful as the increase in field strength. Indeed, the entire MRI system must be engineered to optimize SNR at each step: the magnetic field, the gradient subsystem, the RF chain, and the computer systems to handle both control of the system and the acquisition and processing of the data that are obtained. For example, it is well known that surface coils can improve SNR in a local area just underneath or near the surface coil. Numerous groups have demonstrated that one approach to improving SNR over a larger area than just a surface coil is to create arrays of surface coils. However, for functional imaging, an array-aware system is not enough. The RF receivers and digitizing hardware must be able to handle the high throughput of data on each of the multiple channels, rather than just on a single channel if phased array functional imaging is to actually be usable. This means four, eight, or more fast receivers, something that needs to be deliberately engineered in to the MR system. Similar issues arise with the computational chain: there is no point in having fast RF and gradient hardware to sample the magnetization rapidly if the computing subsystem cannot store or process the incoming data.

Gradient System Performance

A key subsystem that has been a focus of improvement recently is the gradient subsystem. While slew rates on the order of 100 T/m/s were once considered to be high, such systems are now underpowered for the rapid read-out pulse sequences in use today. Similarly, while peak gradient strength of 20 mT/m was only recently considered high performance, many users find their needs for peak gradient strength to keep increasing well beyond the 40 mT/m routinely offered today. This need for high peak gradient performance is particularly true in diffusion-weighted MR imaging. Fig. 3 demonstrates images from a normal volunteer taken at multiple high b values, including up to b = 20,000 s/mm^2. (Normal DWI is obtained at b = 1,000 s/mm^2). Such very high b value images are highly dependent on adequate SNR, since the large diffusion gradients cause extensive signal loss. By increasing peak gradient strength, one can shorten the duration of the gradient pulses and markedly reduce the overall echo time of a given pulse sequence. Because diffusion-weighted images typically have long TE values (due to the long diffusion gradient pulse length), decreasing the TE from 100 ms (typical with gradient capabilities of approximately 20 mT/m) to TE of 65 ms (typical with gradient capabilities of 40 mT/m) one can expect a doubling of SNR. Particularly because very high b values are highly dependent on peak gradient strength and amplifier duty cycle, engineering the system from the ground up to handle such advanced performance requirements is essential.

Towards New Frontiers in Neuroscience

Once these systems are in place, however, the type and quality of functional imaging that can be done is dramatically increased. To close with just a single example, Fig. 4 demonstrates diffusion tensor tractography* performed using 40 mT/m gradients at 1.5 T in the brain. The type of tractography and the resolution available are highly dependent on the shortened TE, the faster gradient and RF performance, the amplifier capabilites, and the computer control and data processing subsystems. With the advent of this type of functional imaging, diagnoses of more subtle abnormalities and insight into more complex disease processes will be available in ways that were heretofore unavailable.

** This information about diffusion tensor tractography is preliminary. The product is under development and not commercially available in the U.S., and its future availability cannot be ensured.*

Author's address

A. Gregory Sorensen, MD
MGH-NMR Center
Massachusetts General Hospital
Building 149, 13th Street
Charlestown, MA 02129
USA

MAGNETOM Harmony, Symphony, Sonata Maestro Class – A New Degree of Perfection

Dagmar Thomsik-Schröpfer, PhD, Siemens Medical Solution, Market Segment Manager High Field



At the RSNA 2001 Siemens Medical Solutions introduced the next step in development for their main product line MAGNETOM Harmony, Symphony and Sonata: the Maestro Class. New systems are delivered with Maestro Class already. And it is available for the already existing systems as an upgrade. The obvious change are new covers.

Within the soul of Maestro Class you find intelligence, speed and innovative applications.

Maestro Class is in telligence – to make MR easier!

We use technology in an intelligent way to make MR even easier to use. Many routine processes are automated, making them faster and simpler.

Inline Technology – Processing instead of Post-processing

The complete exam is finished as soon as image acquisition is finished. Inline technology uses an intelligent on-the-fly feedback loop to control scanning, reconstruction and processing. Thus motion is detected and corrected on the acquired image and unwanted information is no longer filling up your harddisk.

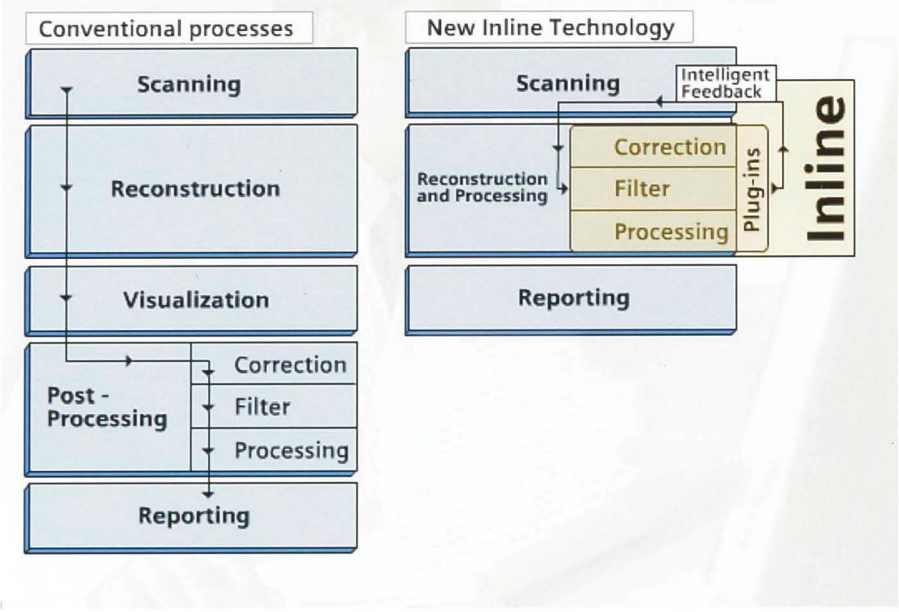

PACE Prospective Acquisition and CorrEction – Motion under control!

1D PACE allows exams with free breathing and is the perfect alternative to breath hold scanning. The user defines the expiration phase in which data are accepted. The Inline display shows the diaphragm position. Thus respiratory motion is detected. For imaging only the selected phases are taken resulting in high image quality in free breathing.

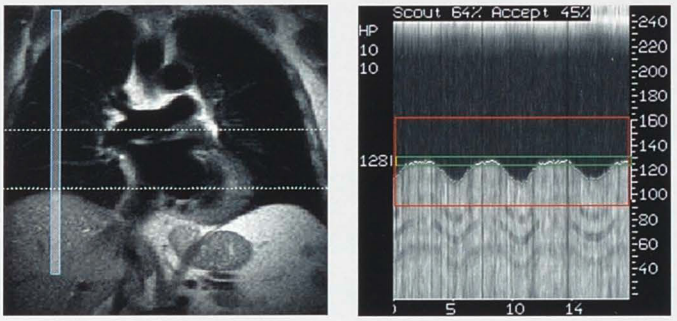

Inline display of diaphragm positon

Define expiration phase to accept data

2D PACE improves selectivity and precision in abdominal MRI. It is a robust technique that automatically aligns each multi breath hold.
2D PACE compensates unwanted patient movement.

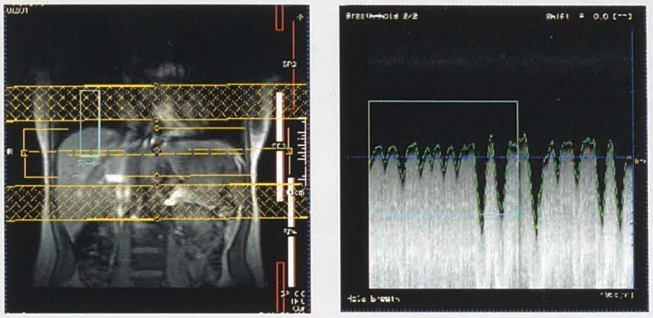

Multi breath holding with 2D PACE control

3D PACE* virtually freezes patient motion. It improves selectivity and increases selectivity. This is beneficial e.g. in functional MRI for precise neurosurgical planning.

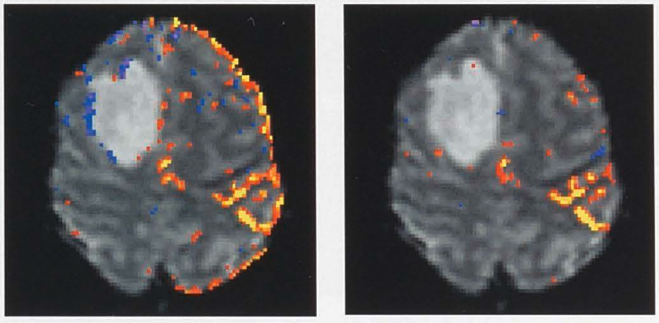

None *3D PACE*

Processing Plug-ins – provide unmatched flexibility

Simplify routine procedures by selecting various checkboxes on the according *syngo* task cards (e.g. Subtraction, MIP, SuperMIP, t-test) or by creating own macros.

Maestro UI – Your cockpit for dynamic MRI

This ergonomic and easy-to-use interface supports the clinical workflow. A quick overview is provided by Image Stamps.

The Phoenix* feature is a drag and drop function. An existing image is selected via the Browser and simply placed into the measurement queue. All image parameters.are extracted and placed into the exam task card.

syngo scan assistant

Changing one MR parameter inevitably means adjusting other parameters. The *syngo* Scan Assistant makes the effect visible and suggests further parameters in case of conflict.

Inline Movie for cine studies

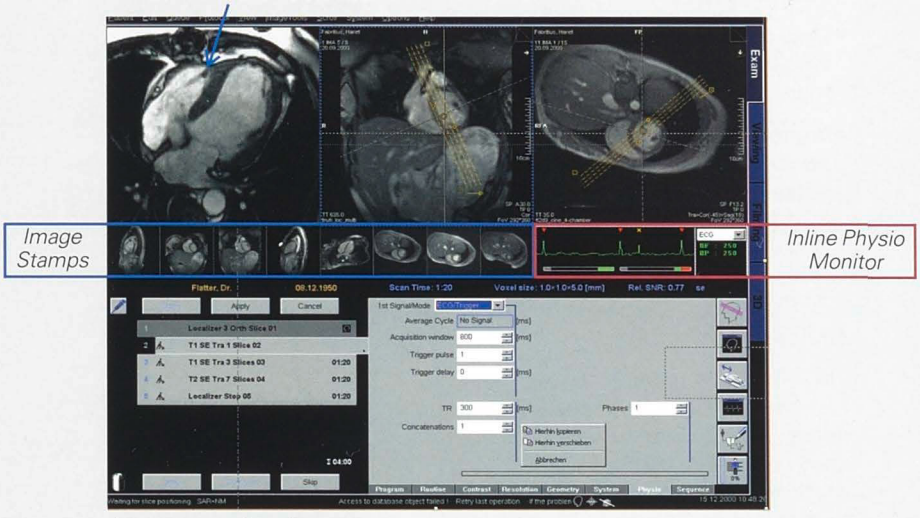

Maestro user Interface

Maestro Class

is in creased speed to make MR faster!

The Solution to speed up acquisition times is iPAT – Integrated Parallel Acquisition Techniques.

- Integrated feature
- Integrated into the MAGNETOM IPA coil concept, use up to 8 independent channels
- Integrated Auto-calibration
- Combines the convenience of IPA and iPAT for many applications

PAT factor 2 is Standard!

Maestro Class for MAGNETOM Harmony, Symphony and Sonata *features iPAT with a speed factor of 2* as standard and is IPA compatible. The benefits are:

- Higher patient comfort – Shorter breath holds in abdominal imaging increase patient comfort; due to the short acquisition times
- Higher temporal resolution – in abdominal and cardiac MRI, e.g. dynamic 3D VIBE liver imaging, cine cardiac imaging
- Less blurring artifacts through the whole body due to shorter measurement times
- Improved diagnostic confidence in stroke imaging - shorter measurement times possible, higher resolution, FEWER *distortion artifacts in single-shot EPI*

PAT Plus – iPAT factor 4*

iPAT-Plus with speed factor 4 combines high speed imaging with the 8 channel neuro array coil and the 6 channel body array coil to push demanding *applications, e.g. stroke imaging, even* further.

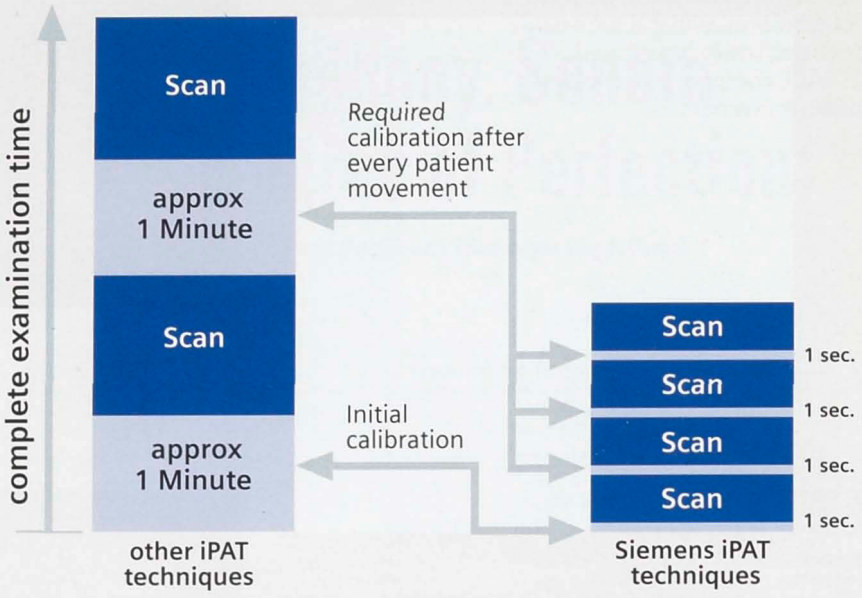



without *iPAT*, TA 1:24 min.



PAT factor 4, 24 s.



without *iPAT*, 20 s.

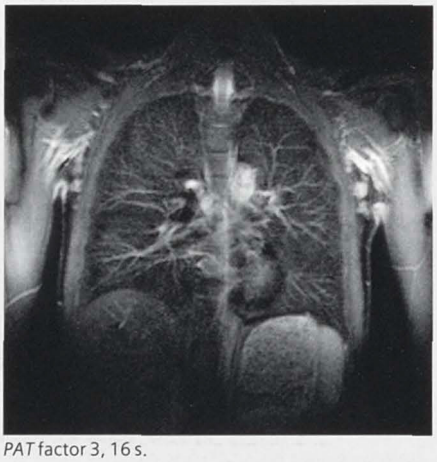

PAT factor 3, 16 s.

Maestro Class

is in novative applications

Expand MR and open new application areas

Neuro MRI – One-stop stroke examination in less than 5 minutes

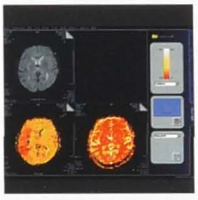

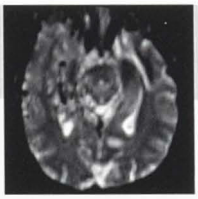

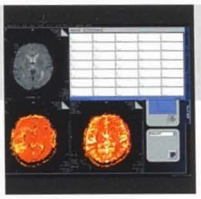

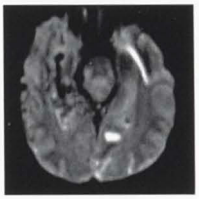

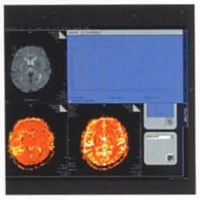

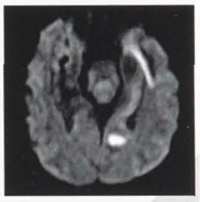

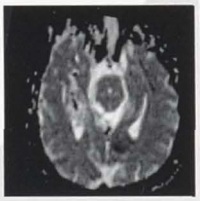

Parameter map calculations*, such as time to peak as well as relative MTT*, relative CBF*, relative CBV* are done automatically using Inline Technology.

Diffusion-weighted MRI (DWI) in combination with Perfusion-weighted MRI is highly sensitive to early cerebral ischemia (within the first 30 minutes to 6 hours). It may predict the severity of the stroke and the outcome of the recovery.

The **ADC** (Apparent Diffusion Coefficient) map helps to estimate the age of stroke lesions. Calculate ADC maps automatically with Inline Technology at the end of the scan.

Trace-weighted images help to differentiate infarcted regions compared to normal tissue. They can be acquired directly in a single-shot exam or by combining individual diffusion-weighted images.

High resolution imaging with various contrast provides: perfect anatomical images, visualiz ation of pathological tissue.



MR Angiography is an easy add-on to show details in vessels according to tissue/ pathology

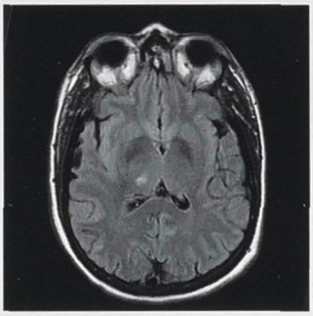

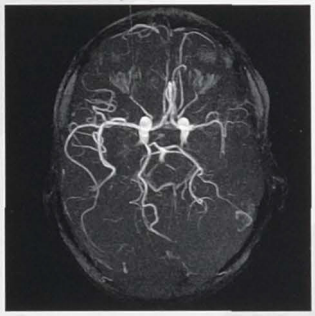

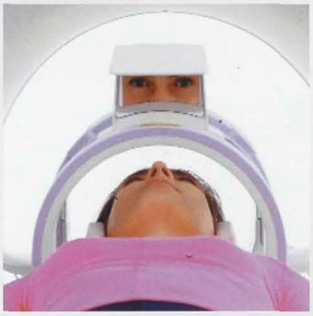

Easy patient set-up with high comfort for the patient

MR Spectroscopy is getting easier keeping the high flexibility for research

- **Easy and efficient** "single-button" Spectroscopy, with spectra annotation and quantification at a mouse-click.
- **Free slice positioning** – tailor slice position and orientation to your patient!
- **High research flexibility** – allows to interact with the whole procedure for the research approach
- 3D CSI for complete anatomical coverage. For faster 3D CSI weighted encoding can be chosen
- Fully automated post-processing of data with instant display, e.g.
  - Spectral maps displaying spectra in the selected voxels
  - Metabolite images* are showing the voxel dependent peak intensities or peak ratios as grayscale or color overlay onto a reference image
  - Table of metabolites for simple reporting
- 31P and multi nuclear* spectroscopy do benefit from the post processing functionality in the same extent



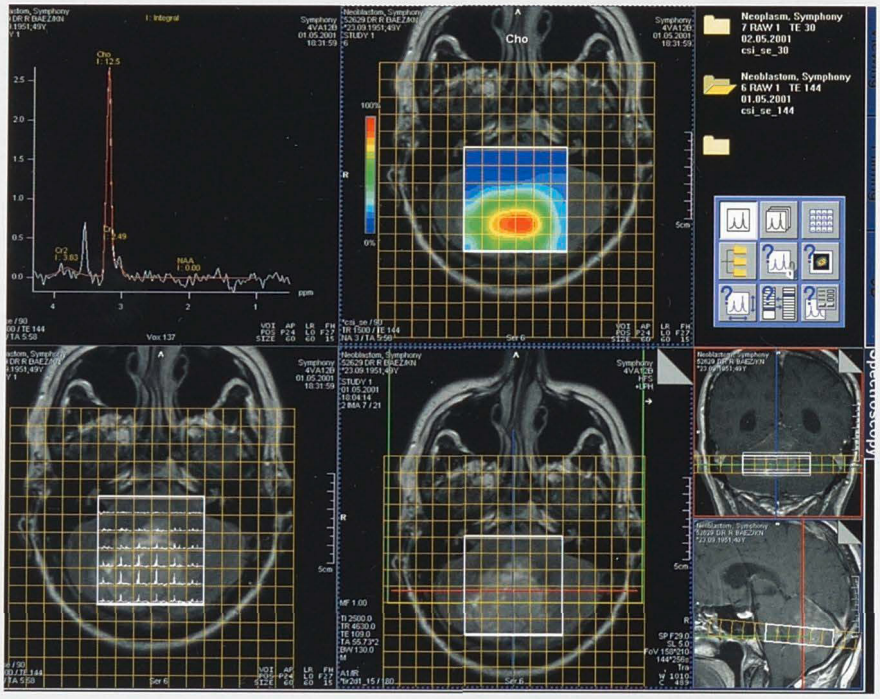

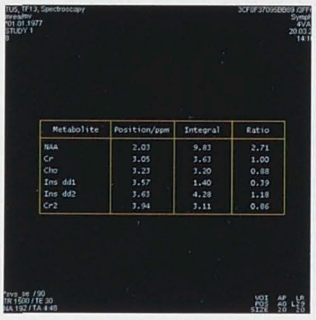

MR Angiography – Easy and completely automated – High resolution peripheral MRA from diaphragmatic level to distal vessels

Use Body and CP Head Array Coil or a set up of multiple CP array coils with automated table movement using Integrated Panoramic Array (IPA) and Integrated Panoramic Positioning (IPP).

Optimized workflow is only a mouse click away!

Combination of Body Coil and CP Head Array Coil allows to get a vessel overview and can be used for post operative exams



or



Get a **maximum coverage of 1.5 m** (5 feet) in 4 steps by combining our Peripheral CP Angio Array Coil, the CP Body Array Flex Coil and the Large Field of View Adapter. Used e.g. for pre-operative planning

The scan program for the whole examination is already programmed using the **Maestro User Interface** with its multi level scouts, automatic table travel and pre and post contrast scanning. Each mearsurement (no. of slices, matrix) can be individually adjusted to the patient anatomy

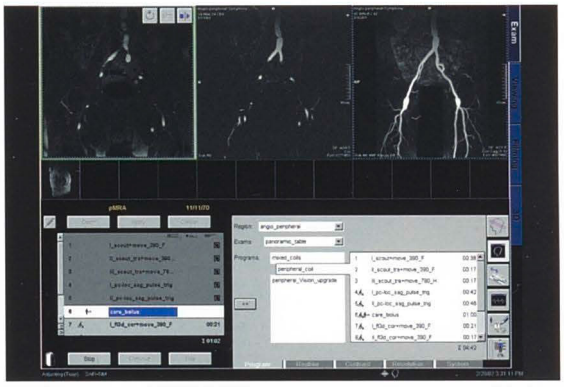

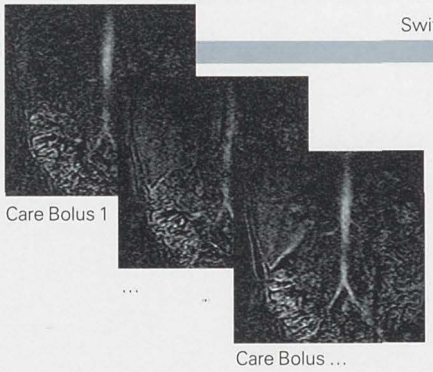

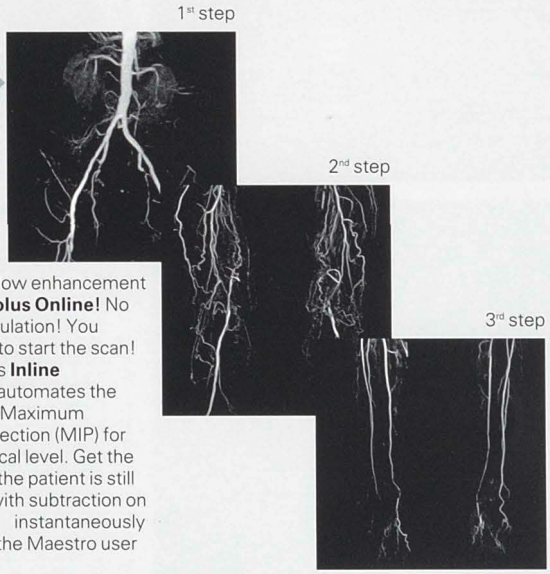

Watch the inflow enhancement using **Care Bolus Online!** No guess,no calculation! You decide when to start the scan! Maestro Class **Inline Technology** automates the calculation of Maximum Intensity Projection (MIP) for each anatomical level. Get the results while the patient is still on the table with subtraction on the fly. MIP is instantaneously displayed on the Maestro user interface.

Body MRI – VIBE and iPAT – Expand your diagnosis

Combine VIBE and iPAT to speed up your body exams by a factor of 2 standard. This ultra fast imaging technique allows to visualize even earlier arterial phase in liver imaging which may open the way to new diagnoses.



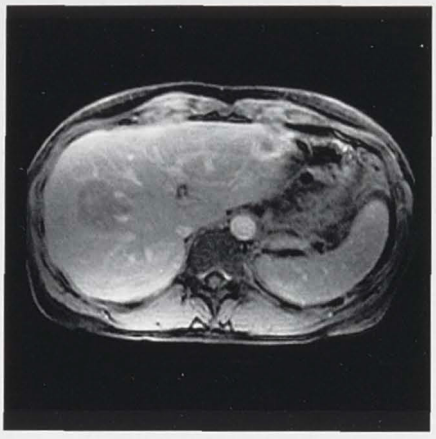

Hepato cellular carcinoma
Courtesy of University Erlangen

Cardiac MRI – One-stop shop cardiac examination in just 16 Minutes





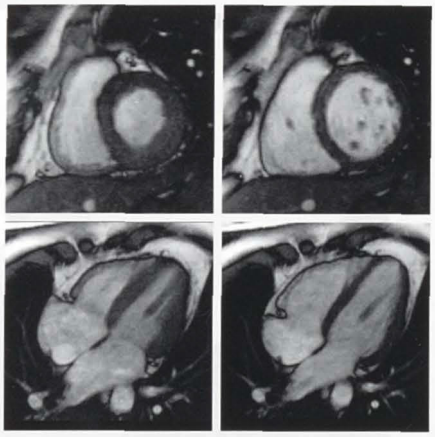

Morphology

- Display your results automatically with the Auto Movie function
- Image stamps can be loaded into the movie function, the post processing card or into the measurement queue

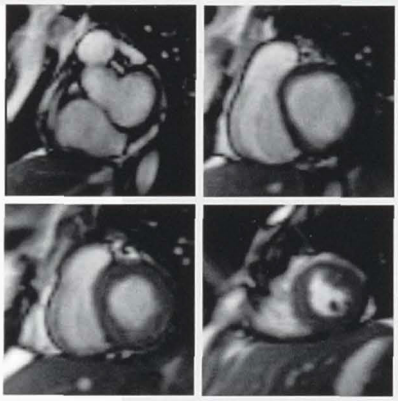

Function

Real time TrueFISP allows rapid assessment of ventricular function

** Information about features with syngo MR 2002B is being provided for planning purposes. The product requires 510(k) review and is not commercially available in the U.S.*



Siemens Ultra High-Field Program

www.SiemensMedical.com

A91100-M-Z730-1-7600

The Siemens commitment to 3 Tesla can easily be seen in our leading product line in the Ultra High-Field segment. MAGNETOM® Allegra – See the Mind. Dedicated to brain imaging, this most compact 3T scanner is equipped with the strongest gradients in the market. MAGNETOM Trio – See the Body. The Trio is your system for whole body applications in the 3T Ultra High-Field sector. It offers a full 40 cm Field of View and is the shortest 3T scanner allowing clinical whole-body imaging at 3 Tesla.

Siemens **Medical Solutions** that help

SIEMENS
medical

SENSE and SMASH
Physical Principle, Advantages

Matthias Blasche, Siemens AG, Medical Solutions, MR Marketing, Erlangen

Introduction

The need for shorter measurement times in magnetic resonance imaging is as old as the procedure itself. Shorter overall examination times increase productivity and patient comfort. Breath-hold times can be reduced. Dynamic processes, such as the beating heart, can be scanned with higher temporal resolution.

In traditional imaging, spatial resolution is attained by switching the gradient fields. Each echo is individually encoded. Thus, the speed of a measurement is the result of how quickly the spatial encoding of an individual echo can be performed sequentially.

One possibility of reducing measurement time without compromising resolution is to reduce the number of echoes measured. This results in a rectangular field of view (RecFOV). If, however, the field of view is selected to be smaller than the size of the object, so-called aliasing is the result. Thus, with traditional techniques, the possibility of reducing measurement times with a rectangular field of view is limited by the patient's anatomy.

Shared Characteristics of SENSE and SMASH

In contrast to traditional sequential measurement techniques, SENSE and SMASH are parallel imaging techniques. The spatial resolution of the image is no longer determined solely by the acquired, gradient-encoded echoes. With SENSE and SMASH, additional spatial information is obtained from the spatial variation in the coil intensity profiles during measurement with array coils. Thus, fewer echoes are measured with SENSE and SMASH than would be needed to obtain the desired resolution with a traditional technique.

In simple terms, this is nothing more than a measurement with a rectangular field of view (RecFOV). The only "trick" with SENSE and SMASH is the elimination of the aliasing that occurs with traditional techniques. This is the result of the additional information that one can gain from the intensity profiles of the individual coils during measurement with array coils. SENSE and SMASH use different methods to obtain this information.

The Physical Principle of SENSE

During a measurement with a single coil, the signal intensity of a pixel located at (x,y) is given as:

$$P(x,y) = S(x,y) \cdot C(x,y) +$$
$$S(x+FoV_{Phase},y) \cdot C(x+FoV_{Phase},y)$$

S(x,y) is the (coil-independent) signal intensity, indicated by the tissue and sequence parameters, of the measurement object at location (x,y). C(x,y) describes the coil sensitivity (=coil profile) at location (x,y).

The second addend describes the aliasing. The aliasing appears in the image if the anatomical structure extends to the location $(x+FoV_{Phase},y)$ and at the same time the coil demonstrates a significant sensitivity at this location, that is to say, if both $S(x+FoV_{Phase},y)$ and $C(x+FoV_{Phase},y)$ are greater than zero. (For purposes of clarity, the formula above considers only aliasing of the first magnitude.)

The actual signal intensity and the undesired aliasing cannot be distinguished when measuring with only one coil. It is different, however, when measurement is performed with array coils. Additional information can be obtained as a result of the different coil profiles of the individual coil elements.

The principle of the SENSE technique is explained in the following simple example with 2 coil elements (Fig. 1):

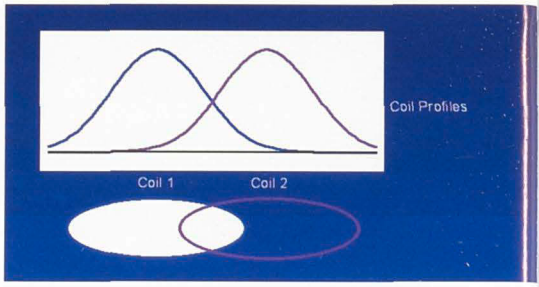

Figure 1:
Coil profiles of individual coils in a simple 2-coil array

In the case of a measurement with a 2-coil array, the signal intensity of a pixel at the location is the result of both portions measured with the single elements:

$$P1(x,y) = S(x,y) \,.\, C1(x,y) +$$
$$S(x+FoV_{Phase},y) \,.\, C1(x+FoV_{Phase},y)$$

$$P2(x,y) = S(x,y) \,.\, C2(x,y) +$$
$$S(x+FoV_{Phase},y) \,.\, C2(x+FoV_{Phase},y)$$

If the coil profiles C1 and C2 are known at all locations (e.g., as the result of a suitable reference measurement), the actual signal intensities can be separated from the undesirable aliasing using this system of equations.

Thus, if the coil profiles are known, the correct image can be calculated using the individual images measured by the array-coil elements. The SENSE technique is a modified image reconstruction in the image space. The maximum reduction in measurement time is determined by the number of coil elements.

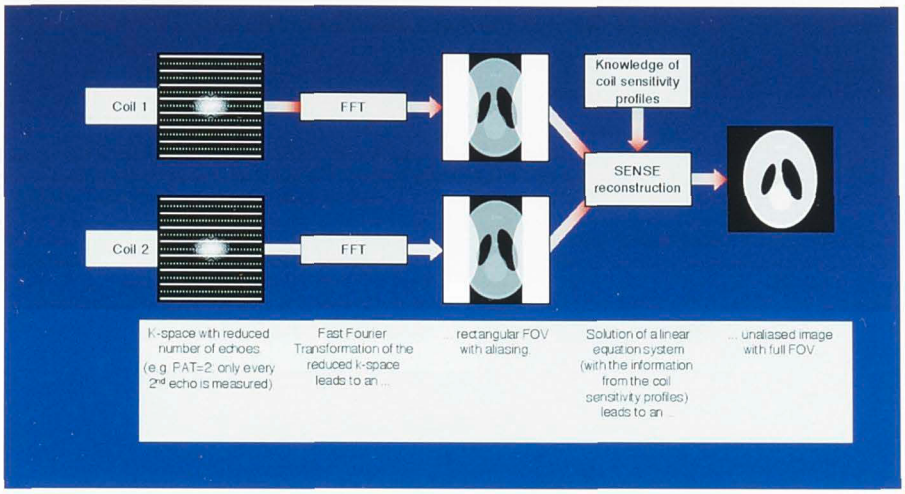

Figure 2:
How does SENSE work?

These superpositions of the coil profiles are quite similar to traditional gradient encodings. Thus, these superpositions can be used to increase the number of (gradient-encoded) echoes measured. To a certain extent, the "gaps" in the raw data matrix that occur during measurement with a reduced number of measured echoes (RecFOV) can be closed. The raw data matrix is completed in this way, and no more aliasing occurs . As with SENSE, the maximum reduction in measurement time is equal to the number of coil elements.

The Physical Principle of SMASH

Unlike SENSE, SMASH is based on a modified image reconstruction in the k-space. Compared to traditional techniques, measured (gradient-encoded) echoes are replaced by "artificial" echoes. Spatial information is imprinted onto these artificial echoes by an encoding using the coil sensitivities.

First, linear superpositions are formed for the signals of the individual coils. Fig. 3 illustrates this with the simple example of a 2-coil array.

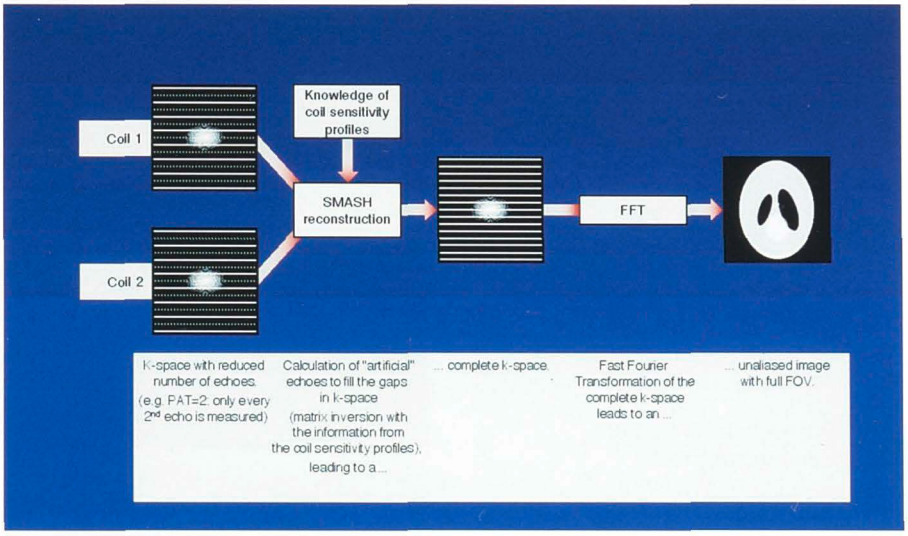

Fig. 4:
How does SMASH work ?

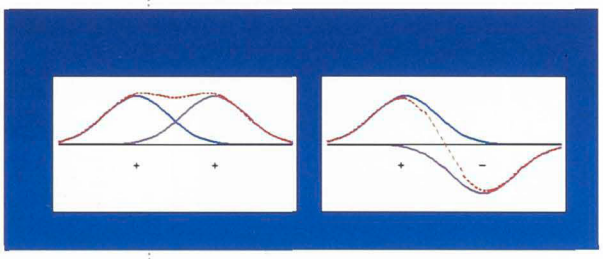

Figure 3:
Linear superposition (dotted line) of the individual coil sensitivity profiles

Advantages of SENSE and SMASH
Case study

The patient was a 68 year old male with numbness of his fingers and impaired balance. An MR study was conducted to evaluate for cervical spondylotic myelopathy. The patient was unable to hold still in the scanner because of severe pain. Scanning at conventional speed (and even at an PAT factor of 2) yielded images with excessive motion artifacts. By using an PAT factor of 4, scan time was shortened sufficiently to acquire artifact-free images, allowing accurate diagnosis (Fig. 5).

1. Reduced acquisition times

With SENSE and SMASH, images can be produced in a shorter time (though with a lower signal to noise ratio). The maximum reduction in acquisition time is determined by the number of array coil elements.

Moving organs (for example, the heart) can be more clearly imaged, and dynamic processes (for example, transit of contrast agent) can be measured with higher temporal resolution.

Shorter scan times (and shorter breath-hold times) lead to improved patient compliance, with implications for image quality (e.g. less patient movement in the scanner, hence fewer motion artifacts). Patient comfort is also enhanced. (Figure 5)

2. Shorter echo trains for single-shot methods

A second advantage is that echo trains can be shortened for single-shot methods (single-shot EPI, single-shot TSE, HASTE) while maintaining the same resolution.

Shorter echo trains for single-shot procedures result in lower "T2 filtering" (or "T2* filtering") of the raw data. As a result, the images are more sharply focused, with fewer susceptibility artifacts and distortions.

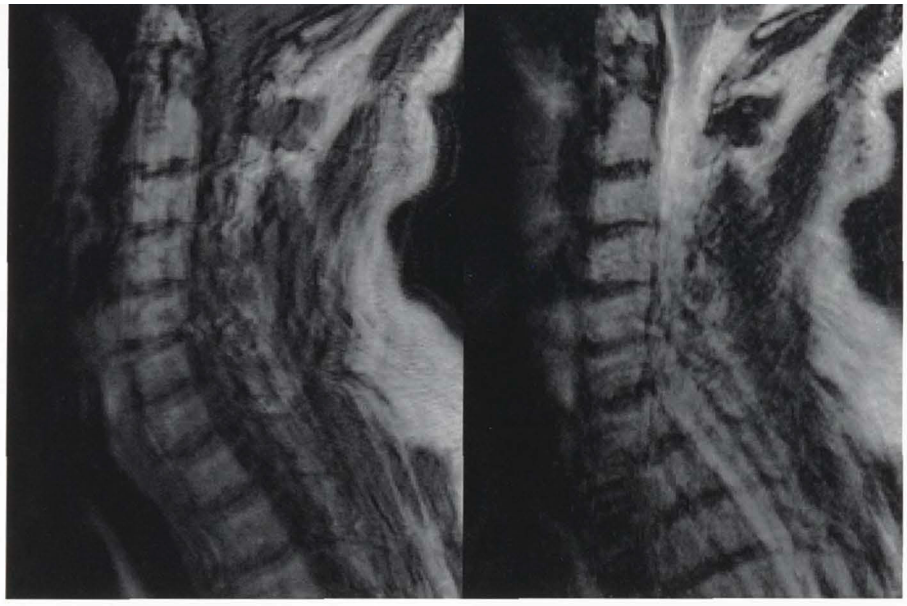

T1, conventional speed.
Acquisition time: 3:06 min

T2, conventional speed.
Acquisition time: 3:48 min



T1, iPAT 4x
Acquisition time: 37 sec

T2, iPAT 4x
Acquisition time: 41 sec

Figure 5:
Time-Critical MR Imaging of the Cervical Spine (Clinical case and images, courtesy of Edmond, A. Knopp, M.D., New York University School of Medicine)

Literature:

1. Weiger M, Pruessmann KP, Boesiger P. Cardiac Real-Time Imaging Using SENSE.
Magnetic Resonance in Medicine 43, 177-184 (2000)

2. Sodickson DK, Griswold MA, Jakob PM. SMASH Imaging.
MRI Clinics of North America, Vol. 7, No. 2, 237-254 (May 1999)

3. Internet page of Beth Israel Deaconess Medical Center, Boston:
http://www.bidmc.harvard.edu/cmr/smash.html

What happens when you have an MRI scan?

Help your little patients lose their fear – with Lottie

Lottie is an adventurous little lamb that loves to skateboard. But poor Lottie had an accident and may have broken her ankle. Now instead of leaping, she can only limp. Lottie is off to the hospital for an MRI scan. This engaging story by Professor Rolf Vosshenrich and Sylvia Graupner explains to children what it's like to have an MRI scan in a way they can understand.

We offer Lotti's story as a children's book in 23 languages (PDF) and as video in 6 languages. You can also order hard copies of the book in German, English, and Spanish.

The material is available at
www.siemens-healthineers.com/magnetom-world

Go to **> Publications > MR Basics**





20 Years of Development and a Constantly Improving Performance = MAGNETOM

Peter Kreisler, Ph.D.
Collaborations and Applications ,
Erlangen, Germany

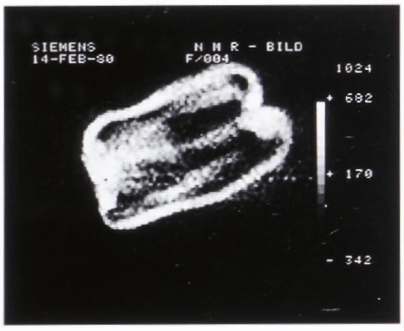

Figure 1 *The first MR image from Siemens: Red pepper*

Working in the field of MR for almost 20 years, it has been really impressive to see the developmental steps that have taken place over this time. Siemens' involvement with MR development began in the late seventies, but it was the first images of a red pepper in1980 which were to some extent the "starting signal" to set Siemens off to a flying start in the field of MAGNETOM product development (Fig. 1).

An 0.2T prototype system was the first Siemens MR to be installed in a clinical environment. The system – based on a resistive 0.2T magnet – was installed at the Medizinische Hochschule of Hanover (MHH), Germany. In 1983, the first MAGNETOM with a super-conducting 0.35T magnet was delivered to the Mallinckrodt Institute in St. Louis/ USA. This system was the first member of a product family that has increased in size and in technical and clinical performance.

Let's look at some of the components and subsystems.

Magnets

The early super-conducting magnets were relatively large (2.55 m long) and heavy (~8 tons for 1.5T), they had a large fringe field since they were not shielded at all, and they required very frequent liquid gas refills (nitrogen every two weeks and helium every 6 weeks). Over the years passive iron shielding was introduced – with weights of 21 t and 31 t (Fig. 2); active shielding was created; the magnets became smaller and lighter; additional nitrogen was no longer needed and the refill intervals for helium were extended to more than a year. One interesting developmental step was the introduction of a magnet system with an integrated helium liquefier: the Helicon. However, because of new magnet designs and helium saving developments, the direct integration of a liquefier turned out to be no longer economically beneficial and the development was discontinued. Today's magnet trends are towards increased openness, lower helium consumption and lower total costs.

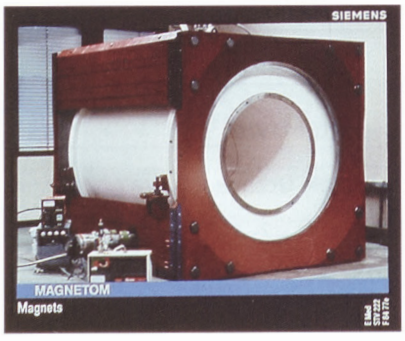

Figure 2 *Magnets with passive shielding. 21 t or 31 t of iron was needed to reduce the magnetic fringe field.*

Space requirements

The magnet's fringe field is one of the parameters that define the space requirement of an MR system. Another parameter is the amount of hardware needed. The first systems in the 1980s comprised a total of 12 cabinets fully packed with electronics. As we all know from the revolutionary changes in computer technology, electronics became integrated to a very high degree. The entire system electronics and supplies can be put into two cabinets today, with a much higher performance than in the past.

Gradients

The gradients used for spatial encoding – as for several contrast mechanisms – are one of the essential components for MR imaging. Tremendous improvements have been developed and implemented over the last two decades.
The following table summarizes the main steps.

2003

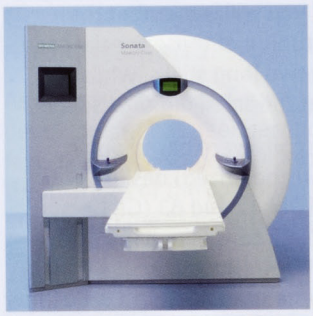





MAGNETOM Trio

MAGNETOM Maestro Class

MAGNETOM Rhapsody

MAGNETOM Harmony, Symphony, Sonata (*syngo* based), Concerto

MAGNETOM Allegra

MAGNETOM Harmony, Symphony, Sonata

MAGNETOM Vision Plus, Open Viva

MAGNETOM Impact Expert

MAGNETOM Vision, Open

MAGNETOM Impact, P8

MAGNETOM SP and SP 4000

MAGNETOM 42/63 (GBS 2)

MAGNETOM M/H (GBS 1)

1983

0.2T Prototype



1983		
MAGNETOM M	3 mT/m	1.5 ms
1986		
MAGNETOM SP	10 mT/m	1 ms
1991		
MAGNETOM Vision	25 mT/m	0.6 ms
1999		
MAGNETOM Sonata	40 mT/m	0.2 ms
1999		
MAGNETOM Allegra	40 mT/m	0.1 ms

And the development continues. In 2002, the prototype of a gradient insert coil, especially for head and small animal studies, has been created with a gradient strength of 80 mT/m and a rise-time as short as 0.1 ms (800 T/m/s).

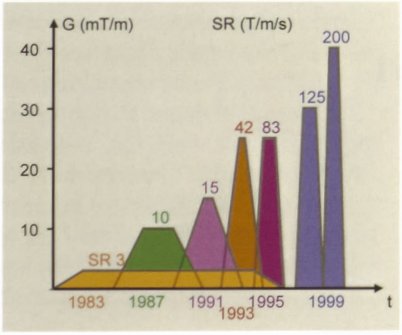

Even more important than these horse power numbers are the improved and advanced applications that became available based on this powerful hardware. Think about the fast imaging techniques in ce-MRA and abdominal imaging, think about EPI in diffusion weighted scans, or look at all the "bread and butter scans" – like the fast T2-weighted sequences routinely used today.

RF System

The first units were delivered with an integrated body coil and a head coil – nothing more. Knowing that a higher signal-to-noise ratio was essential for the future success of MR, our physicists and engineers started the development of dedicated surface coils and smaller volume coils: they created the 10 cm eye/ear coil (Fig. 3), a breast coil and an extremity coil, and a spine coil would follow. also soon be available.



Figure 3

Some of you will remember the manual tuning of these special coils with the two long sticks, whilst staring at the small digital display.

All these coils were based on an LP (linearly polarized) design. With MAGNETOM 42 and 63 (GBS2 systems), CP coils (circularly polarized) were introduced, with a gain in signal-to-noise of 40%. In 1991, the first prototypes of array coils were delivered, a development which resulted in the Integrated Panoramic Array (IPA) concept, introduced with MAGNETOM Harmony and Symphony (Fig.4). And today, the IPA coils form the basis for the parallel imaging techniques like mSENSE and Grappa which are now integrated into the MAGNETOM Maestro Class product line.

All these developments have helped to broaden the range of applications by increasing the signal-to-noise and/or by increasing the speed of the examinations.

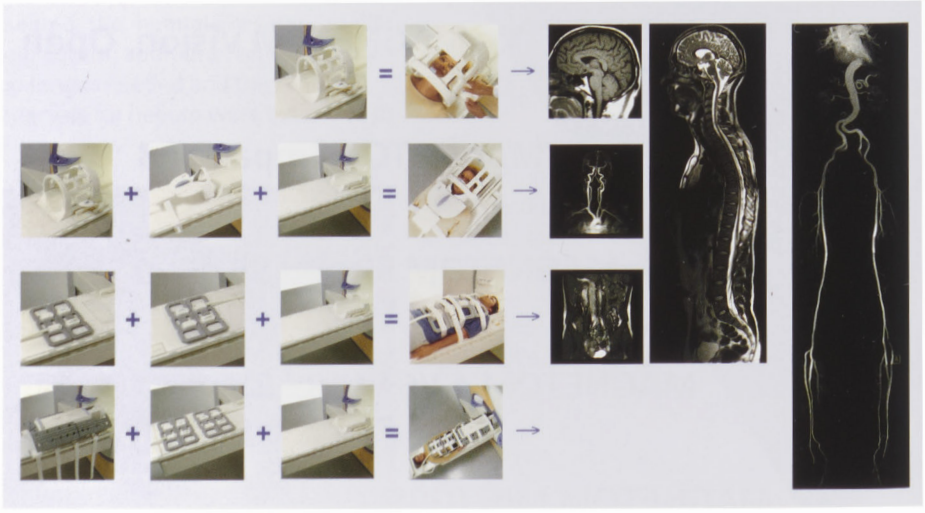

Figure 4 *IPA Coil Combinations, iPAT compatible!*

Computer configuration and data handling

As already mentioned, computer development has been terrifically fast. This has also been reflected in the changes of the computer configuration in the MAGNETOM systems:

VAX11/730 and VAX 11/750 together with a BSP11 image processor in the GBS1 systems, MicroVax2 and later Microvax 4000 in the MAGNETOM SP systems, then replaced by Sparc2 and turboSparc in combination with the SMI 5 for fast image reconstruction and today the combination of high performance PC systems with GHz processors.

Just remember the increase in speed for the image reconstruction by using the 2D Fourier transformation. 1984: 6.8 seconds per image in full 256^2 matrix, and today less than 6 ms.

Or consider the amount of data generated. In 1983, typically much less than 100 images per patient were measured. The images were filmed with analog monitor based cameras like the MULTISPOT M. Some of the "most interesting" images were stored digitally on a floppy disc (three images per side). Today hundreds to thousands of images are the result of a complete patient examination with new challenges for processing, networking and archiving.

Sequences

The NUMARIS software for the first MAGNETOM system enabled the user to perform Spin-Echo measurements – T1 and T2 weighted – and T1 weighted Inversion-Recovery scans.

Virtually from the start, quantitative T1 and T2 calculations could be performed, hoping that by knowing T1 and T2, all tissue types were characterized. But there is a larger variability between the human tissues, and additional contrasts and parameters are used for diagnosis.

Scan times were rather long in the early 80's. A T2 weighted scan using a spin-echo sequence took easily a quarter of an hour. All developers sought faster sequences. Let's look at some steps:

1983:
Spin Echo

1985:
Half Fourier

1987:
Gradient Echoes FLASH and FISP

1989:
Turbo-FLASH

1990:
Turbo Spin Echo

followed by hybrid-techniques like Turbo Gradient-Spin-Echo, and the single shot techniques , tse240, HASTE, segmented gradient-echo sequences, and finally EPI.

In the meantime, EPI has become an indispensable tool in brain-imaging and brain-research. The single shot scan times can be cut down to less than 50ms for a single image.

Or remember the steps in MR-Angiography, starting in 1985/86 with FLASH2D for sequential slice-by-slice measurement in a time-of-flight manner. The technique became extended to 3D, to automized 3D multi-slab and to the faster Turbo-MRA. No contrast agent is required. Nevertheless, the MR-angio scan of the carotids typically took more than 10 minutes. And now? More and more MRA scans are performed with fast 3D-gradient-echo sequences, using Gadolinium-based contrast-agents and CARE-Bolus techniques. A 3D scan of the carotid arteries takes only a few seconds. Dynamic angio scans can be performed with good temporal resolution. Today, MR-Angio is applied from head to toe.

Over the years, therefore, Siemens has been the first to develop unique sequences and imaging techniques that increased speed and resolution, or offered new contrasts or new applications, such as MP-RAGE, CISS, DESS, HASTE and TrueFISP.

And finally, let's not forget spectroscopy, the oldest MR technique. Spectroscopy has been a tool for chemical research since the 1940's. And the MAGNETOM systems offered spectroscopy capabilities almost from the start. In 1984, 1.5T MAGNETOM systems allowed phosphorus spectroscopy, in 1985 a sodium head coil was available as a product together with sequences for imaging, and shortly after fluorine spectroscopy was put into the product. Today, clinical spectroscopy is mainly done with hydrogen protons, but there is still a lot of interest in the use of other nuclei. To bring spectroscopy to clinical routine, its use – scanning and post-processing – must be easy. With the *syngo* based software, a lot of effort has been put into a stream-lined workflow for spectroscopic examinations.

Overall, we can look back over twenty years of exciting and fascinating developments. And we are looking forward to further developments that will make the future even more exciting.

1983



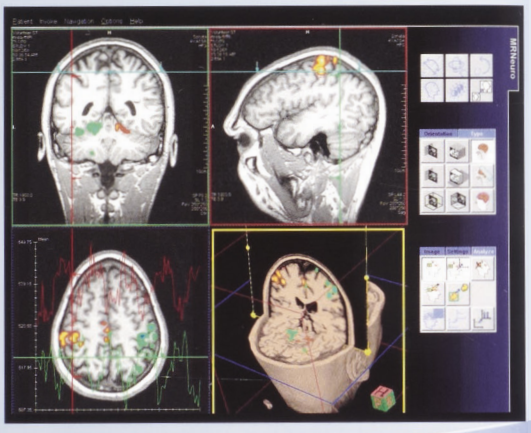

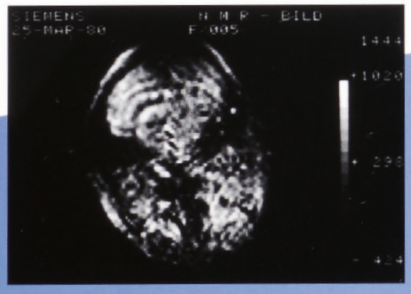
SIEMENS
N M R - BILD
F/005

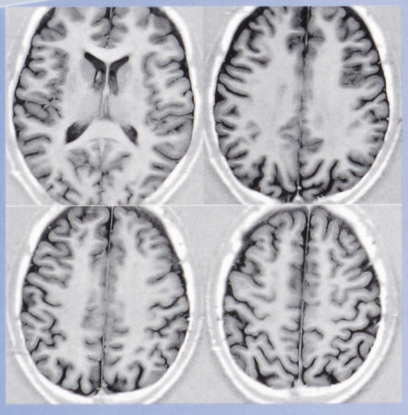

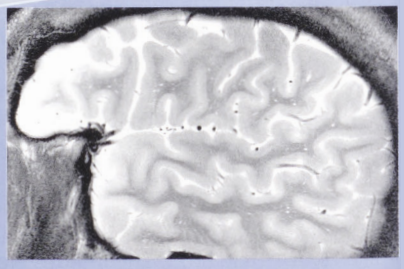

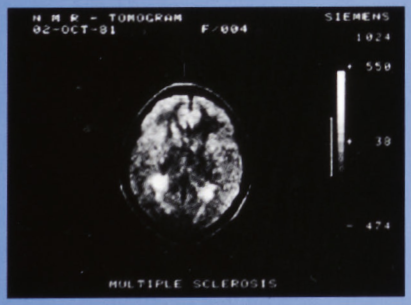
N M R - TOMOGRAM
02-OCT-91
F/004
SIEMENS
MULTIPLE SCLEROSIS


N M R - TOMOGRAM
01-OCT-91
F/002
SIEMENS
SPONGIOBLASTOMA

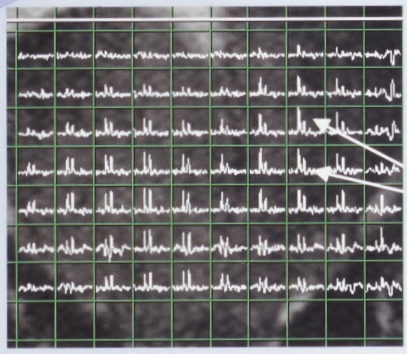

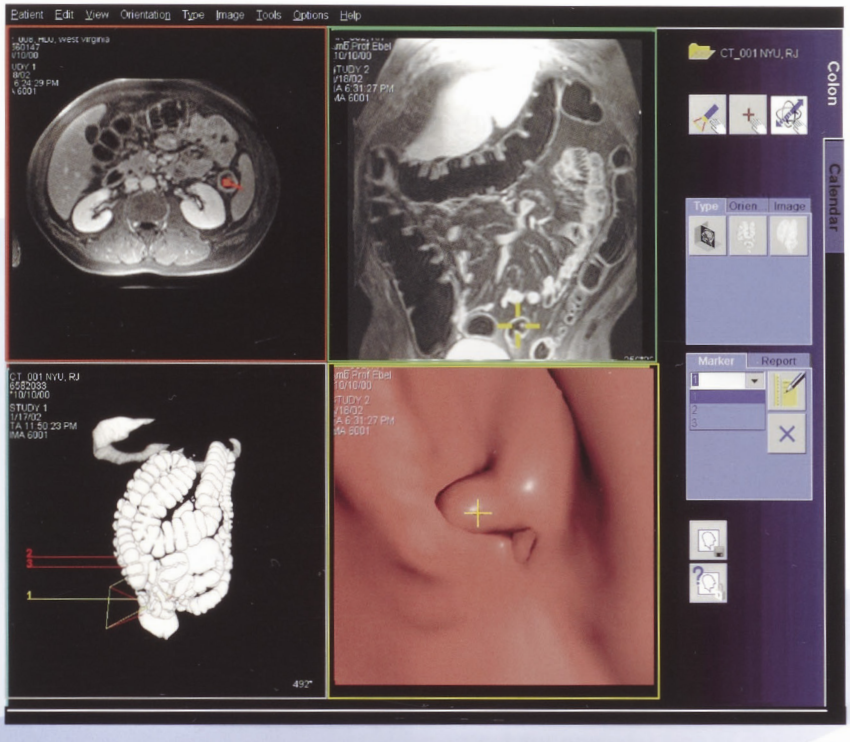
Patient Edit View Orientation Type Image Tools Options Help
CT_001 NYU, RJ
Colon
Calendar
Type
Orien
Image
Marker
Report

2003

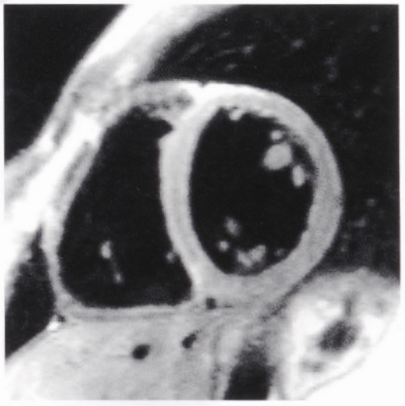

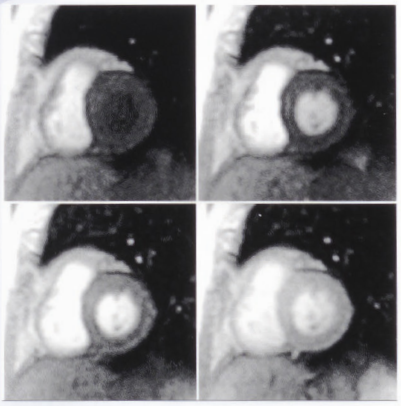

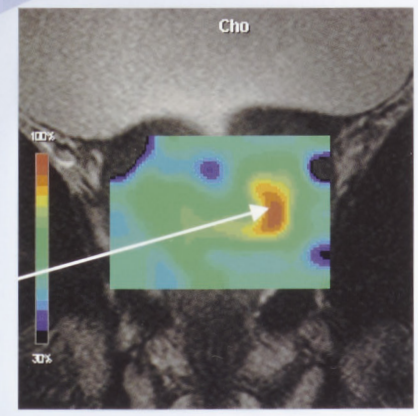
Cho
100%
30%

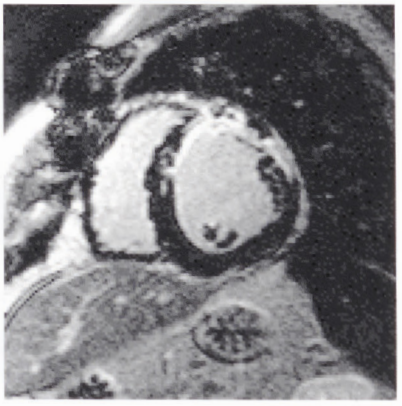

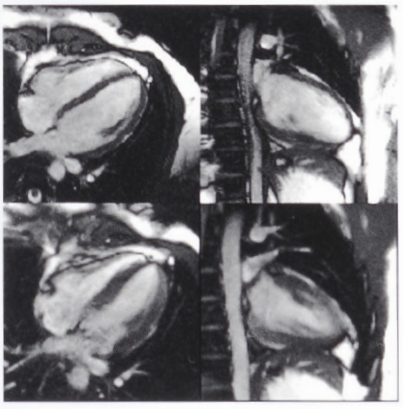

iPAT Applications in Clinical Routine and Beyond: Imaging from Head to Toe

Olaf Dietrich, Ph.D.
Stefan O. Schoenberg, M.D.

Department of Clinical Radiology – Großhadern
(Chairman: Maximilian F. Reiser, M.D.), Ludwig-Maximilians-University of Munich, Germany

Correspondence:
Dr. Olaf Dietrich
Ludwig-Maximilians-University of Munich
Department of Clinical Radiology – Großhadern
Marchioninistraße 15
D-81377 Munich
Germany

Introduction

With the release of *syngo* MR 2002B, an important new feature has become available for routine examination: integrated Parallel Acquisition Techniques (iPAT). The general idea behind iPAT is to acquire image data simultaneously by two or more receiver coils with different spatial sensitivities. Initially, this technique was motivated by the wish to accelerate image acquisition without reducing the spatial resolution of the image. However, it turned out that iPAT provides several other advantages in various MR applications.

Technical background

Acquisition of MR images works by subsequently acquiring phase-encoded lines in k-space. These lines of data are finally transformed into the image slice (or slab, in the case of 3D acquisitions) by a mathematical process called Fourrier transformation. An important property of data in k-space is that the density or "distance" of the lines in k-space corresponds inversely to the field of view (FOV) of the final image, whereas the data range in k-space corresponds to the spatial resolution of the image. Therefore, reducing the line sampling density by a factor of 2 (by not acquiring every other line) leads to an image with half the FOV in phase-encoding direction in comparison with the original image. In this case, the acquisition time is also reduced by a factor of 2 as is well known from using rectangular FOVs. iPAT methods use exactly this effect to accelerate image acquisition, but without decreasing the FOV due to a special iPAT image reconstruction. Using the complementary data from the different receiver coils, the "missing" lines in k-space can be calculated during image reconstruction.

There are two groups of iPAT algorithms: algorithms that explicitly calculate missing k-space lines before Fourier transforming the data, and algorithms that first reconstruct images with reduced FOV for all receiver coil elements and then merge these different images into one with full FOV. *syngo* MR 2002B provides both types of algorithms. GeneRalized Auto-calibrating Partially Parallel Acquisition (GRAPPA) is an algorithm of the first type [1] and is based on another well-known algorithm of the same class called SiMultaneous Acquisition of Spatial Harmonics (SMASH) [2]. The best-known algorithm of the second type has been called SENSitivity-Encoded (SENSE) MRI [3] and a modified SENSE algorithm called mSENSE is available under *syngo* MR 2002B. It depends on the specific application, such as the anatomical region and pulse sequence, as to which of these two iPAT algorithms will yield better image quality.

Both GRAPPA and mSENSE algorithms require some additional information about the spatial coil sensitivities, i.e. which part of the FOV is covered by each coil element. This information can be acquired as a separate extra scan with low resolution or, typical for the GRAPPA and mSENSE algorithm, by additionally acquiring some of the missing data lines in the center of k-space (so-called reference lines) integrated into the acquisition.

Generally, the signal-to-noise ratio (SNR) in iPAT images is decreased compared to acquisitions with the full k-space data. This is the same effect as in conventional imaging with rectangular FOV: acquiring fewer lines in k-space decreases the SNR of the image. Additionally, iPAT images suffer an SNR loss due to the special reconstruction scheme: this effect depends on the efficacy of the

geometry of coil distribution and is described by the so-called "geometry factor" *g* [3].

Advantages and disadvantages of iPAT

The obvious advantage of iPAT is the acceleration of imaging due to the reduced number of phase-encoding lines to be acquired. With an acceleration factor (or PAT factor) of 2, i.e. acquisition of only every second line in k-space, the imaging time is reduced by close to 50 % depending on the number of reference lines. This can be used to decrease the overall examination time and thus improve the patient throughput and examination efficacy. Alternatively, the spatial image resolution can be improved in an iPAT scan compared to a conventional scan of the same duration. Both shorter scan times and higher resolution are especially important in breath-hold imaging: either breath-hold times can be shortened or the spatial resolution can be improved without prolonging the breath-hold time.

Another important iPAT application is dynamic imaging, such as measurements of perfusion or cardiac function, because image acceleration allows for a higher temporal resolution. However, as mentioned above, the resulting SNR will be decreased compared to non-iPAT acquisitions, so iPAT is especially useful for high-SNR applications like contrast-enhanced angiography.

Using iPAT to acquire more averages in the same total scan time can improve image quality, particularly in anatomical areas that are prone to motion artifacts. iPAT imaging is less sensitive to motion, because every single acquisition is shorter than in a conventional sequence. By averaging image data, the iPAT-related SNR loss is almost compensated and remaining motion artifacts are further reduced.

Single-shot pulse sequences, like echo-planar imaging (EPI) or half-Fourier acquired single-shot turbo spin echo (HASTE), often suffer from image artifacts due to their long echo trains. EPI is especially sensitive to susceptibility artifacts, whereas HASTE images often appear blurred due to the T2-related signal decay during the readout of the echo train. Both problems can be reduced by applying iPAT to shorten the length of the echo train without loss of spatial resolution. In contrast to other pulse sequences, single-shot methods can even gain SNR due to iPAT because late echoes with relatively low signal intensity that are acquired in conventional sequences are not contained in the shortened iPAT echo train.

In conclusion, iPAT can be advantageous in very different applications with very different ways of using iPAT. This is demonstrated in the following sections with examples ranging from clinical routine imaging to advanced study protocols. Imaging in all presented applications is performed on a 1.5 T MAGNETOM Sonata Maestro Class system. Standard sequences are used in most cases; however, some applications require sequences from special "work in progress" (WIP) packages by Siemens Medical Solutions*.

Diffusion tensor imaging

Diffusion tensor imaging (DTI) is an advanced MR imaging technique for measuring the strength, anisotropy, and direction of water diffusion in tissue. The term "water diffusion" refers to the property of all water molecules to move stochastically due to their thermal energy (Brownian motion). The extent of this motion is restricted by tissue properties, particularly by the cellular microstructure and the spatial orientation of cells. Especially in fiber structures like muscle tissue or the cerebral white matter, molecular motion is restricted by cell membranes or myelin sheaths, and molecules move preferably parallel to the fiber direction whereas diffusion orthogonal to the fiber direction is decreased. Thus, the resulting water diffusion is anisotropic. Information about the diffusion strength (apparent diffusion coefficient, ADC), diffusion anisotropy, and diffusion direction are contained in the so-called diffusion tensor, a mathematical object (symmetric 3x3 matrix) consisting of 6 independent numbers.

The most common pulse sequences to measure the diffusion tensor are diffusion-weighted EPI sequences with diffusion gradients applied in at least six different directions [4, 5]. Single-shot EPI sequences have the advantage that imaging is fast (about 100 ms/image) and thus very insensitive to motion. However, EPI sequences are very prone to susceptibility artifacts manifesting as distortions in the frontal brain and the cranial base. This disadvantage can be overcome by using iPAT sequences to shorten the length of the EPI gradient echo train. Hence, we use a spin echo EPI diffusion sequence with GRAPPA reconstruction, an acceleration factor of 2, and 24 reference lines for DTI examinations. A dedicated iPAT head coil consisting of 8 surface coil elements (Fig. 1) provides the required number of receiver channels.

Acquisition with the 8-channel head coil results in images with an improved SNR compared to the standard quadrature head coil (Fig. 2).

** The information about this product is preliminary. The product is under development and is not commercially available in the U.S., and its future availability cannot be ensured.*

This can be explained by the smaller diameter of the 8-channel head coil (24 cm vs. 26 cm) and the reduced coil size in cranio-caudal direction. Images were acquired with a 128x128 matrix in 36 slices, 230x230 mm² FOV, phase-encoding in anterior-posterior direction, a slice thickness of 3.6 mm, 10 averages, and an iPAT factor of 2 (24 reference lines); the echo time was 71 ms and the repeat time 6000 ms. DTI with iPAT displays less distortion artifacts than DTI with conventional EPI sequences (Fig. 3). Evaluating the diffusion-weighted images, parameter maps with the mean ADC, the diffusion anisotropy, and the main direction of diffusion can be calculated (Fig. 4). Although an N/2 artifact in phase-encoding direction (anterior-posterior) is visible in some of the original EPI images, this artifact seems not to influence the calculated parameter maps. An additional advantage of iPAT imaging is the reduced duration of the readout that allows for the acquisition of an increased number of slices within the given repetition time (TR) compared to conventional sequences, e.g., 38 slices without iPAT vs. 50 slices with iPAT given a TR of 6000 ms.



Figure 1 *8-channel phased-array head coil for acquisition of iPAT data. 8 surface coil elements are located cylindrically around the AP axis; the inner diameter of the coil is 24 cm.*

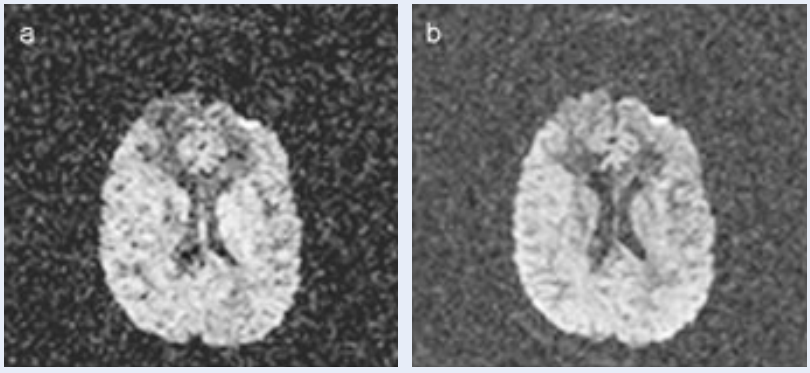

Figure 2 *Comparison of SNR with standard head coil (a) and 8-channel head coil (b). Both images are acquired with identical sequence parameters (diffusion-weighted EPI sequence, b = 1000 s/mm², no averaging) and without iPAT.*

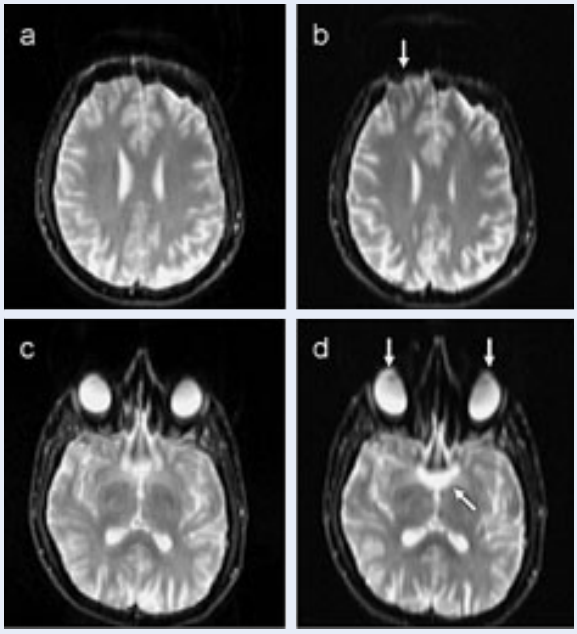

Figure 3 *Comparison of spin echo EPI images in two slices with (a, c) and without (b, d) iPAT (GRAPPA algorithm). Some obvious susceptibility artifacts are marked with arrows in (b) and (d).*

Larynx imaging

Magnetic resonance imaging of the larynx is difficult due to tissue motion caused by swallowing and respiration [6]. Generally, MR pulse sequences with long acquisition times are more sensitive to motion than fast imaging sequences or even single-shot sequences. Therefore, MRI of the larynx at conventional speed often leads to images with excessive motion artifacts.

Since moving organs like the larynx can be more clearly visualized by reducing the image acquisition time,

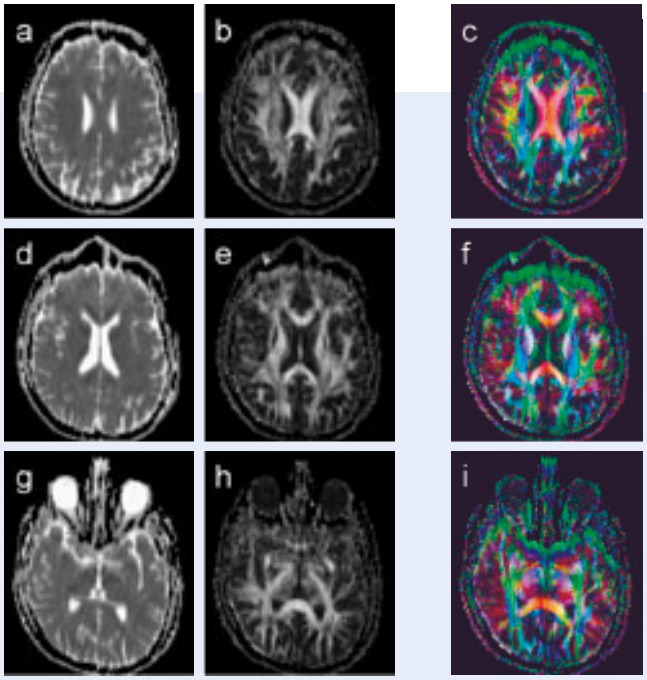

Figure 4 *Examples of DTI evaluation from diffusion-weighted iPAT images: ADC map (a, d, g) with diffusion coefficients from 0 (black) to 2.5x10 $^{-3}$ mm^2/s (white); fractional anisotropy (b, e, h) from 0 (black) to 1 (white); color-coded main diffusion direction (c, f, i), left-right: red, anterior-posterior: green, cranio-caudal: blue. Note especially the high anisotropy and left-right diffusion direction in the corpus callosum.*

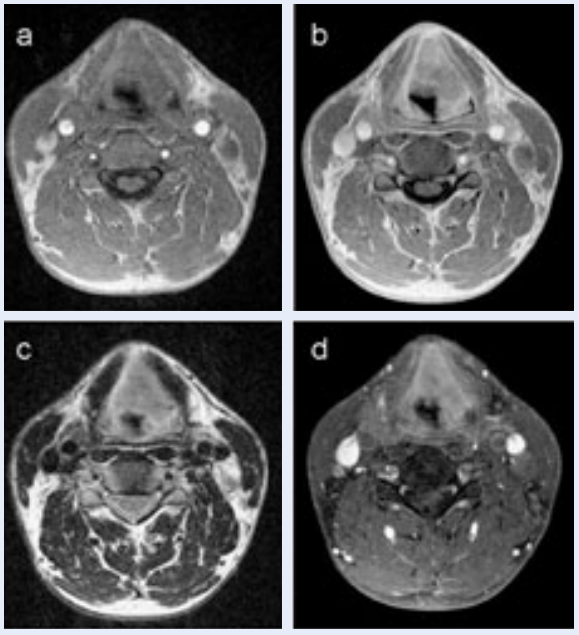

Figure 5 *Axial MRI scan through the supraglottic larynx, all images show the same scan position. The images demonstrate a large supraglottic tumor infiltrating the preepiglottic space, the left paraglottic space and the left aryepiglottic fold.*
(a) T1-weighted image showing muscle-isointense tumor.
(b) T1-weighted image demonstrating contrast-enhancement of the tumor.
(c) T2-weighted axial image showing slightly hyperintense tumor tissue.
(d) T1-weighted fatsat image demonstrating contrast enhancement of the tumor. Spinocellular carcinoma was found at surgery.

iPAT sequences can reduce the sensitivity to motion artifacts by accelerating image acquisition while maintaining the same image resolution. Thus, we use T1-weighted and T2-weighted iPAT sequences for routine larynx imaging, e.g. in patients suffering from suspected laryngeal carcinoma. A pair of dedicated iPAT surface coil systems with 2x6 coil elements is arranged around the lower part of the head and neck of the patient. To compensate for the iPAT intrinsic SNR loss, we increase the number of acquisitions to 5 (T1-weighted gradient echo sequence with TR/TE = 176 ms/4.8 ms, 24* iPAT reference lines) and 3 (T2-weighted TSE sequence with TR/TE = 3970 ms/89 ms, echo train length 15, 45* iPAT reference lines). Both sequences have a 512x384 matrix, a FOV of 300x281.3 mm^2 and a slice thickness of 3.5 mm. The GRAPPA algorithm is used for iPAT reconstruction.

The acquired images show a better delineation of tumor extent and less motion artifacts than MRI using non-iPAT techniques, thus allowing accurate diagnosis of laryngeal carcinoma (Fig. 5). In our experience, MRI with iPAT using a flexible 12-element phased-array coil is suitable for reliable diagnosis when laryngeal carcinoma is suspected. Generally, in imaging moving tissue it appears preferable to acquire more averages with reduced imaging time using iPAT and thus gain images with identical resolution and comparable SNR but less motion artifacts than in conventional non-iPAT imaging.

** In each case the actual number of lines measured is half the number of reference lines mentioned in the text. This is due to the fact that every other line is already part of the iPAT scan.*

Lung imaging

MR screening of infiltrates

Radiological lung screening is typically performed either by conventional x-ray (CXR) examination or by high-resolution computed tomography (HR-CT) of the thorax and therefore exposes patients to a considerable amount of radiation, particularly after repeated examinations. This radiation dose could be reduced by using MRI as screening modality instead of x-ray based methods. Unfortunately, MRI of the lung is still a technical challenge because of the very low proton density of the lung tissue and the strong variation of susceptibility leading to very short T2* relaxation times. Both factors together are the reason for very low MR signal intensities from lung parenchyma and hence for a low SNR. A further difficulty in lung MRI is tissue motion because of respiration and cardiac motion.

The introduction of iPAT opened new possibilities to lung imaging with T2-weighted HASTE sequences. The main disadvantage of conventional HASTE sequences is the blurring of images caused by the long echo train and the T2-related signal decay during its readout; this effect severely limited the actual maximum image resolution [7]. By using iPAT, the echo train can be reduced to half of its original length and thus blurring artifacts are reduced. Since late echoes with low signal intensity are not acquired, SNR can even improve compared to non-iPAT sequences. Additionally, the image acquisition is accelerated such that more slices can be acquired during one breath-hold period.

To evaluate the use of iPAT HASTE sequences for lung screening, we compared HR-CT and MR images in immunosuppressed patients with symptoms of pneumonia but normal

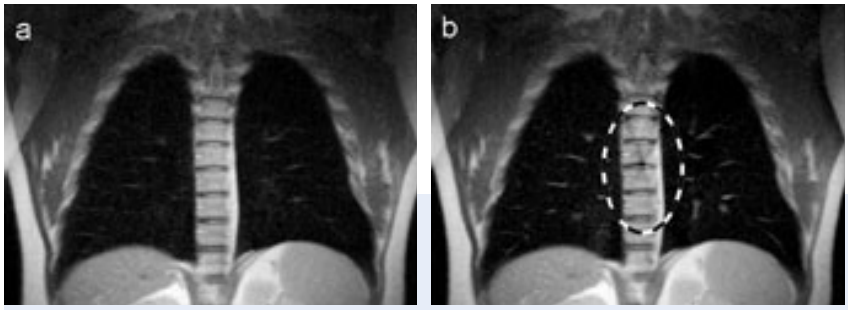

Figure 6 *iPAT HASTE images of a healthy volunteer reconstructed with GRAPPA (a) and mSENSE (b) algorithm. Note the reconstruction artifacts superimposing the spine in (b).*

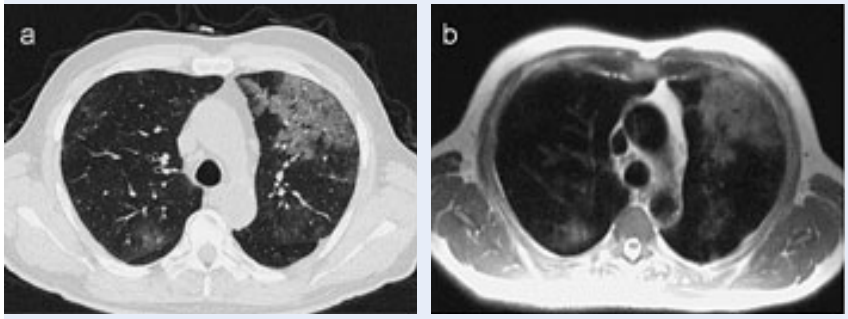

Figure 7 *Ground glass infiltrate in immunosuppressed patient. Multi-detector HR-CT (a) and iPAT HASTE MRI (b).*

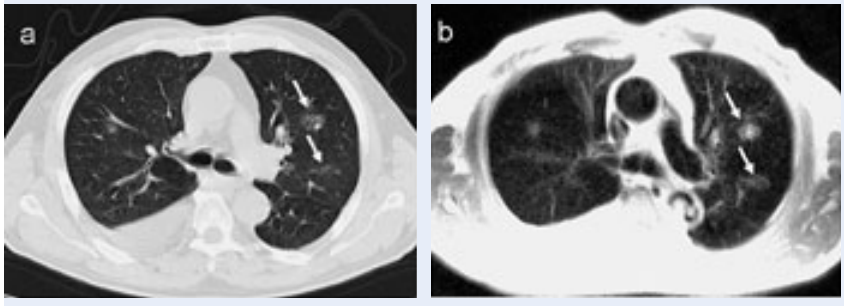

Figure 8 *Small irregular infiltrates in immunosuppressed patient. Multi-detector HR-CT (a) and iPAT HASTE MRI (b).*

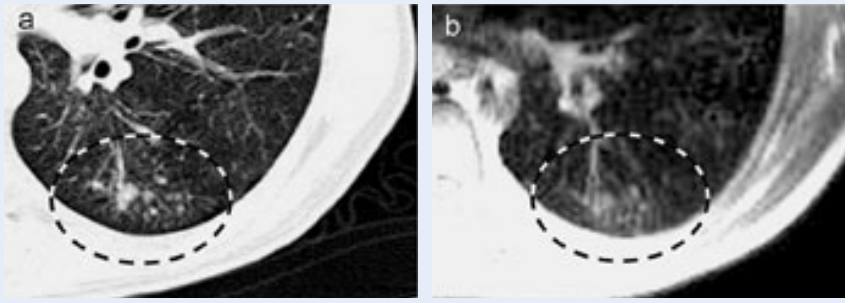

Figure 9 *Discrete atypical infiltrates in immunosuppressed patient. Multi-detector HR-CT (a) and iPAT HASTE MRI (b).*

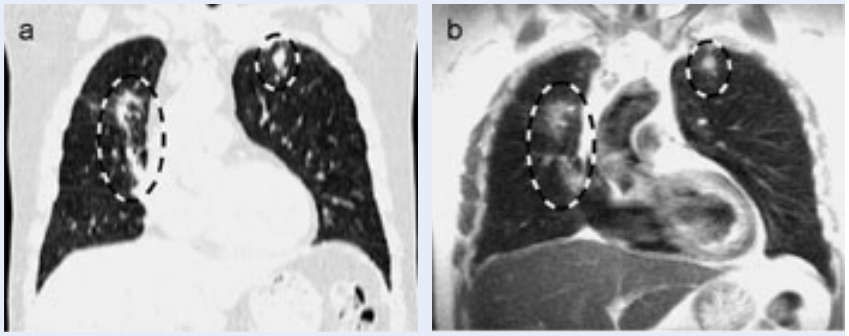

Figure 10 *Discrete atypical infiltrates in immunosuppressed patient. Multi-detector HR-CT (a) and iPAT HASTE MRI (b).*

or unspecific CXR. After comparing iPAT images reconstructed with the GRAPPA and mSENSE algorithm (Fig. 6), we decided to use the GRAPPA algorithm because of the occurrence of reconstruction artifacts in the image center of the mSENSE images. Coronal slices of the lung are acquired with a FOV of 400x400 mm^2 and a resolution of 320x320 pixels; axial slices with a FOV of 400x320 mm^2 and a 320x256 matrix. The slice thickness is 8 mm and the TE is 27 ms in both sequences. To reduce the echo train length as far as possible, a Siemens WIP* sequence was used. Examples of the findings are shown in Figs. 7-10.

We found that lung MRI with iPAT HASTE sequences is nearly as good as HR-CT for the detection of pulmonary infiltrates with only few false-negative and false-positive cases such that MRI can be recommended especially as a follow-up tool after initial HR-CT diagnosis.

MR angiography and perfusion imaging

Contrast-enhanced vascular lung MRI requires a good spatial resolution and – especially in the case of perfusion imaging – also a good temporal resolution. Both are limited by the breath-hold duration for the patient rather than by SNR considerations due to the high-contrast situation in contrast-enhanced MRI. Experiences on MR perfusion imaging of the lung are still limited and various approaches like conventional FLASH and HASTE sequences or flow-sensitive inversion recovery techniques are used [8-10]. However, using iPAT techniques, both temporal and spatial resolution can be significantly

** The information about this product is preliminary. The product is under development and is not commercially available in the U.S., and its future availability cannot be ensured.*

increased compared with conventional imaging.

We therefore added iPAT FLASH sequences to our protocol for 3D contrast-enhanced MR angiography (MRA) and MR perfusion imaging of patients with primary and secondary pulmonary arterial hypertension. Using GRAPPA with the optimized 12-element iPAT coil, a temporal resolution of 1.2 seconds per phase is possible for dynamic perfusion imaging, acquiring 25 dynamic phases in 30 seconds; the image resolution is 1.5x3.0x4.0 mm^3 acquired with a 256x128 matrix in 24 slices. High resolution angiograms can be acquired with a 512 matrix (0.8x1.0x1.6 mm^3 voxel size) in 20 seconds breath-hold time. For both dynamic perfusion and high-resolution angiography, an iPAT acceleration factor of 2 is used with 24 reference lines*.

Image examples of these sequences are shown in Figs. 11 and 12. Using the parallel acquisition technique, excellent visualization of subsegmental vessels is possible in the angiographic images. Time-resolved perfusion imaging allows a reliable detection of small segmental and subsegmental perfusion defects. Using non-iPAT methods, visualization of perfusion defects and intravascular thrombi is generally possible as well, although with lower temporal and spatial resolution than using iPAT methods. In conclusion, we could substantially improve the temporal resolution as well as the spatial resolution by using iPAT.

Functional cardiac imaging

Global and regional cardiac function

Cardiac magnetic resonance imaging has been extensively used in the assessment of global and regional myocardial function. There is no doubt that MRI represents the current standard of reference. Although dataset acquisition can be performed in virtually any plane, the calculation of functional parameters is most commonly based on a stack of slices in double oblique short-axis orientation. To allow for high spatial as well as high temporal resolution, the current sequence techniques acquire a single-slice cine data set each breath-hold. Although innovations of recent years allowed for a speed up of techniques, a completion of a standardized functional study still takes about 10-15 minutes including patient recovery periods. Real-time imaging techniques using steady-state free precession (SSFP) sequences such as TrueFISP, allow for a major speed up in data acquisition due to the completion of a short-axis dataset within a single breath-hold [11, 12]. However, this comes along with a restriction in spatial and temporal resolution. And in terms of volumetric accuracy, temporal resolution is far more crucial than spatial resolution as recently shown by Miller and co-workers [13]. The current recommendation for functional cardiac imaging requests a temporal resolution of 50 ms or even better.

iPAT allows this criterion to be met when implemented in conjunction with real-time TrueFISP. Compared to previous studies performed by Barkhausen and Lee [11, 12], the temporal resolution that can be achieved is in the order of 45-50 ms. And as most recently shown, this improvement in temporal resolution now leads to an accuracy of results comparable to that of segmented TrueFISP [14] (Figs. 13-16); the iPAT images are acquired with an acceleration factor of 2 and 12 reference lines. Accordingly, iPAT not only allows for dramatic time savings in cardiac function analysis without

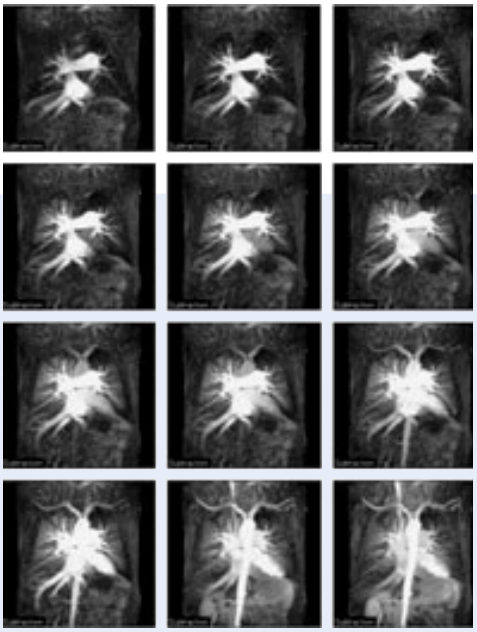

Figure 11 *Dynamic pulmonary perfusion imaging using iPAT to acquire a slab of 24 images each 1.2 seconds. Perfusion defects are shown in the left upper lobe and right lower lobe.*



Figure 12 *Example of an iPAT high-resolution pulmonary MR angiography of the same patient as in Fig. 11. A significant reduction of arterial enhancement can be demonstrated in the left upper lobe and right lower lobe due to central thromboembolic occlusions.*

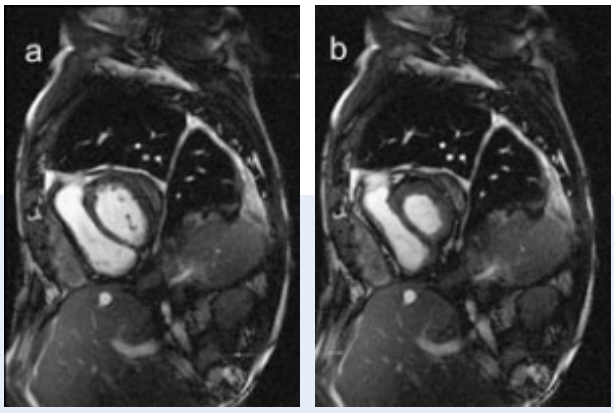

Figure 13 *Short axis view of a male patient with impaired right ventricular function due to pericardial disease. Images acquired with a segmented TrueFISP technique showing diastole (a) and systole (b).*

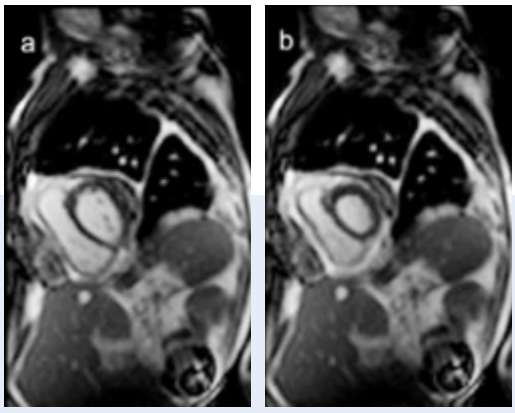

Figure 14 *A single slice of the multi-slice iPAT real-time cine data set at exactly the same slice position as in Fig. 13. Comparable time points in (a) diastole and (b) systole.*

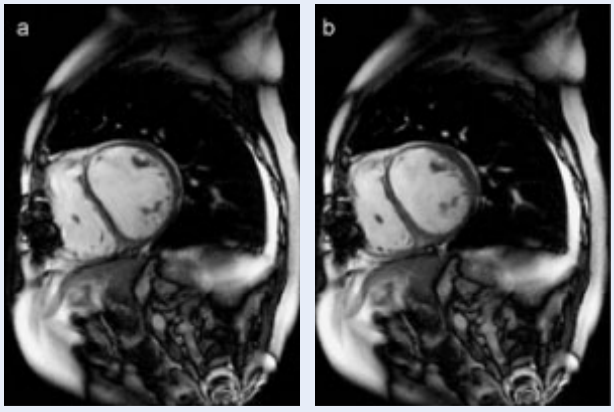

Figure 15 *Patient after myocardial infarction with ischemic dilatating cardiomyopathy. Diastolic (a) and systolic (b) images acquired with segmented TrueFISP show almost no change in ventricular shape (ejection fraction < 25 %).*

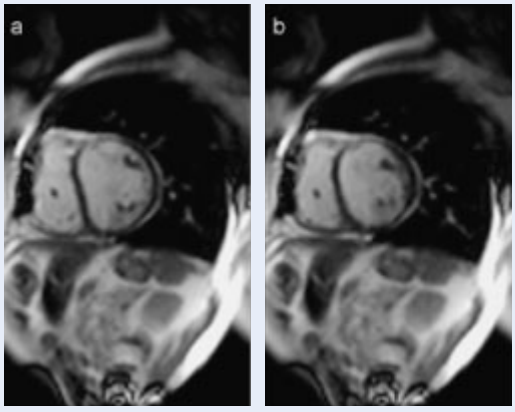

Figure 16 *Comparison with Fig. 15 at identical slice position. iPAT real-time TrueFISP shows the same marked thinning of the anterior wall without change within diastole (a) and systole (b).*

** In each case the actual number of lines measured is half the number of reference lines mentioned in the text. This is due to the fact that every other line is already part of the iPAT scan.*

losing accuracy of volumetric results, but even allows for a multiplanar data acquisition within a single breath-hold.

Based on experiences and comparisons, the GRAPPA reconstruction shows a more robust image quality in cardiac MRI than mSENSE [1]. Due to the higher sensitivity of SENSE-related methods to folding artifacts, these techniques seem to be less useful in cardiac imaging because of the necessary larger FOV that leads either to an additional loss of spatial resolution or to loss of acquisition time when more phase-encoding lines are acquired. Apart from the use of iPAT with real-time techniques, it also allows for a further improvement of spatial or temporal resolution in segmented single-slice acquisitions compared to standard techniques (Fig. 17). In general, when using cine TrueFISP techniques, the loss in SNR due to iPAT is almost negligible.

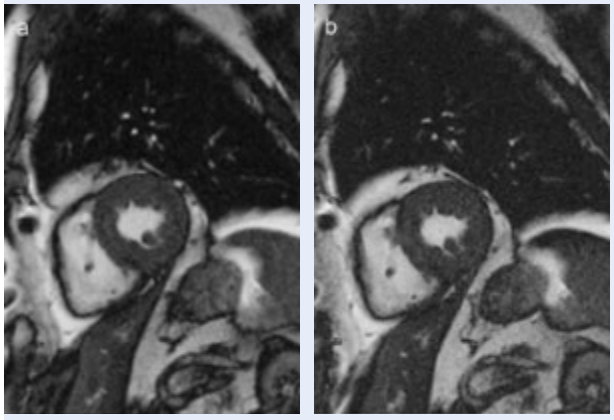

Figure 17 *Combination of segmented cine TrueFISP with iPAT. In comparison to standard techniques (a; pixel size 1.5x1.5 mm²), the use of iPAT allows for a marked increase of spatial resolution (b; pixel size 1x1 mm²).*

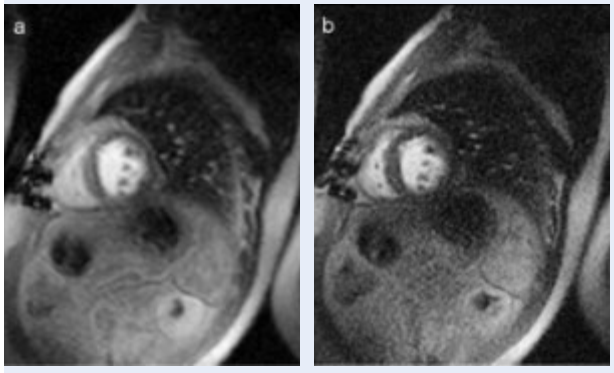

Figure 18 *Images of MR perfusion data sets using a saturation recovery TurboFLASH technique. Comparison of a non-iPAT TurboFLASH technique (a) with an iPAT (GRAPPA) TurboFLASH technique (b). There is considerable more noise within the iPAT image which hampers depiction of perfusion abnormalities based on the low SNR.*

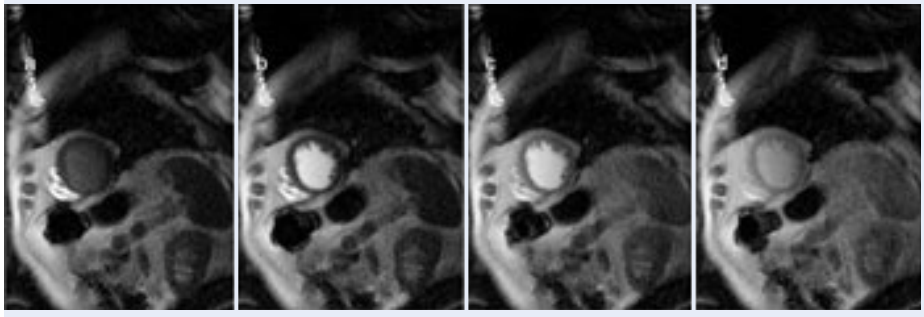

Figure 19 *Saturation recovery TrueFISP perfusion images combined with iPAT (GRAPPA) and a high in-plane resolution of 2.1x2.1 mm². In contrast to saturation recovery TurboFLASH, the spatial resolution is still high enough to follow signal dynamics.*

Myocardial perfusion imaging*

Myocardial perfusion imaging is a promising and rapidly increasing field in cardiac MRI. The rapid development of scanner hardware allows also for an improvement in sequence technologies which has been of a major benefit in techniques that require an ultra-fast data acquisition such as myocardial perfusion imaging. MR perfusion imaging has intrinsic benefits compared to routinely used techniques of nuclear medicine such as single photon emission computed tomography (SPECT) imaging or even positron emission tomography (PET) which represents the current gold standard in clinical perfusion imaging. Apart from the higher spatial resolution and lack of radiation exposure, myocardial MR perfusion imaging has no attenuation problem related to anatomical limitations.

** The information about this product is preliminary. The product is under development and is not commercially available in the U.S., and its future availability cannot be ensured.*

With the use of magnetization-prepared TurboFLASH techniques, however, such as saturation recovery TurboFLASH, the SNR has reached a limit (Fig. 18). Therefore a combination with iPAT techniques seems to be of less benefit, as a further loss in SNR is produced. Newly developed techniques for myocardial perfusion imaging based on SSFP techniques are currently under investigation [15]. In comparison with TurboFLASH techniques, these sequences (available as Siemens WIP package) show a considerable higher intrinsic SNR, therefore allowing for a minimal to moderate loss of SNR when combined with iPAT (Fig. 19).

Liver imaging

MR liver imaging is most severely restricted by respiratory movement. Therefore, image quality was considerably improved with the introduction of T2-weighted turbo spin echo (TSE) and single-shot sequences. With these techniques, breath-hold examinations of the liver became possible, which most authors consider superior to conventional spin echo sequences [16-18]. Generally, a maximum breath-hold time of about 20 seconds, tolerable even for patients in bad health condition, is a limiting parameter for all sequences used for liver imaging.

Respiratory-triggered T2-weighted sequences have been studied as an alternative to the breath-hold strategy with contradictory results [16, 19, 20]. An advantage of respiratory-triggered sequences is the ability to perform high-resolution examinations with 5 mm slice thickness which has not been possible with breath-hold sequences due to the limited breath-hold time. An attempt to overcome this limitation of breath-hold imaging by examinations with multiple breath-holds such that the liver is examined in several stacks of slices, may result in parts of the liver being missed if the patient does not meet the same position of the diaphragm in all stacks [19].

The development of iPAT allows for a substantial reduction of acquisition time, and thus breath-hold sequences with improved spatial resolution can be used. 2D navigator-based techniques, as the Prospective Acquisition Correction (PACE) technique, known from cardiac imaging, can adapt the stacks of slices according to the respiratory position by registering the diaphragm position, so that the whole liver can be covered even if the patient does not hold his breath at the same position [21].

We compared four high-resolution T2-weighted sequences with 5 mm slice thickness and a 320x240-256 matrix for routine liver imaging: a breath-hold TSE sequence with and without iPAT and PACE (echo train length: 27, TR = 2120 ms, TE = 87 ms, 4 breath-hold cycles, iPAT factor 2, 24 reference lines*), and a respiratory-triggered TSE sequence with and without iPAT (echo train length: 25, min. TR = 2680 ms, TE = 117 ms, iPAT factor 2, 24 reference lines). All images were acquired with a 12-element surface coil system optimized for iPAT applications. A respiration belt was used for triggering. The aim was to demonstrate the feasibility of iPAT and PACE for T2-weighted liver imaging and to evaluate image quality of the different sequences.

Image examples of all sequences are shown in Figs. 20 and 21. In general, imaging with iPAT reduced the acquisition time by almost 50% without visible SNR loss. Comparing breath-hold and respiratory-triggered techniques, the latter turned out to be more robust in patients whereas no difference in image quality was observed in volunteers. An explanation for this result is that patients have more difficulty with the breath-hold period of up to 20 seconds. In conclusion, iPAT liver examinations with respiratory triggering appear to be the most robust approach for clinical routine examinations.

** In each case the actual number of lines measured is half the number of reference lines mentioned in the text. This is due to the fact that every other line is already part of the iPAT scan.*

High-resolution renal MR angiography

Three dimensional gadolinium-enhanced magnetic resonance angiography (3D-Gd-MRA) has gained high popularity as a non-invasive imaging alternative for grading of renal artery stenosis [22]. High accuracies of over 90 % have been reported by numerous researchers in the past five years [23]. Nevertheless, the technique is still notoriously known for over-grading high-grade renal artery stenoses and missing low-grade lesions, thereby limiting its overall clinical acceptance [24]. A recent Dutch multi-center trial presented less encouraging results with overall accuracies of only 85 % compared to DSA. In addition, no reliable data on grading of stenoses of the more distal main renal artery or segmental arteries exists yet [25].

One major limiting factor is spatial resolution. For standard breath-hold acquisitions with bolus administration of extracellular, non-intravascular gadolinium chelates, the maximum achievable spatial resolution represents a compromise between scan time, anatomic coverage and SNR. Current imaging protocols usually obtain images with a maximum of 1.5 mm^3 isotropic resolution which still represents 5 to 7 fold less than that of digital subtraction angiography

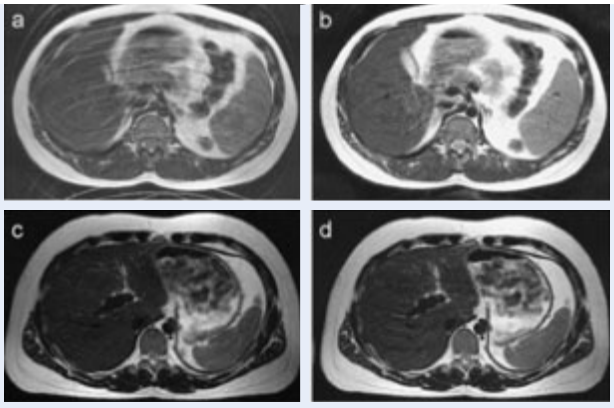

Figure 20 *Examples of T2-weighted liver images: Breath-hold sequence without iPAT (a) and with iPAT (b), respiratory triggering without iPAT (c) and with iPAT (d). Note the markedly reduced artifacts in the breath-hold sequence with iPAT (b) of this subject, who had problems holding his breath. Respiratory triggering as well compensated this problem.*

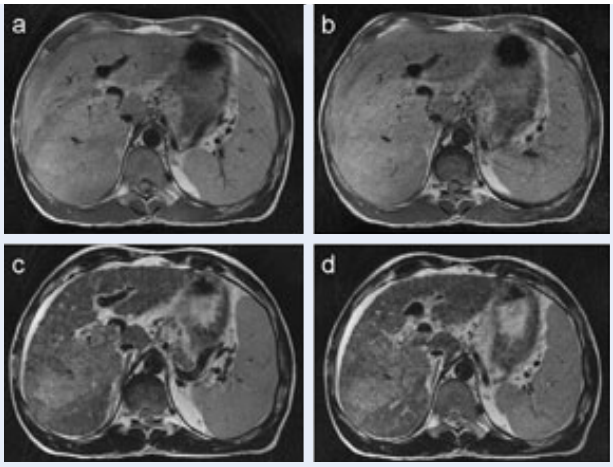

Figure 21 *Examples of T2-weighted liver images: Breath-hold sequence without iPAT (a) and with iPAT (b), respiratory triggering without iPAT (c) and with iPAT (d). Respiratory triggering shows less motion artifacts and better delineation of the diffuse HCC due to better T2 contrast.*

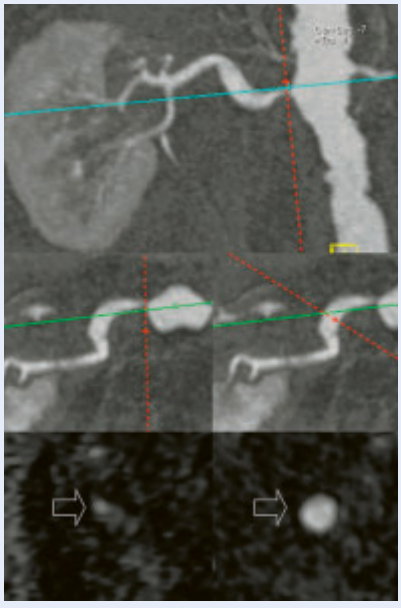

Figure 22 *Multiplanar reformats of a high-resolution 3D-Gd-MRA. In the cross-sectional reformats of the vessel (lower image series) even the area of the stenotic lumen can be clearly demonstrated due to the isotropic spatial resolution.*

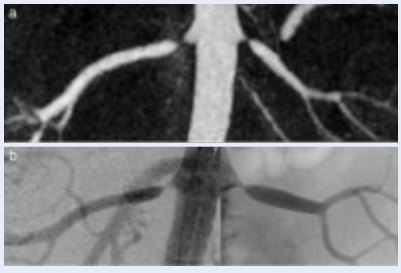

Figure 23 *Coronal MIP image of high-resolution MRA with iPAT (a) reveals excellent agreement to DSA (b). Both high-grade renal artery stenoses are seen including the residual vessel lumen. Note the absence of any major aliasing artifacts in the center of the image.*

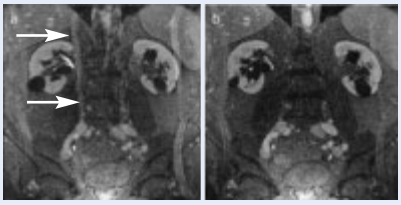

Figure 24 *Comparison of propagated aliasing artifacts in the same patient using the mSENSE (a) and GRAPPA (b) algorithm. The field of view was on purpose set to only 32 cm to enforce aliasing of the arms. In the mSENSE images severe artifacts occur in the center of the image (arrows) while these artifacts are virtually absent on the GRAPPA images.*

(DSA). In a renal artery with a diameter of 7-8 mm, an isotropic voxel size of at least 1 mm^3 is required for accurate depiction of a 90 % reduction in lumen diameter.

Parallel acquisition techniques allow for improvement of spatial resolution without prolonging data acquisition and are well suited for images with a high SNR such as 3D-Gd-MRA. Based on previous calculations, it is expected that voxel sizes of less than 1 mm^3 are substantially limited by SNR constraints [26]. Therefore, it was our aim to increase spatial resolution to maximum values within this range. The iPAT strategy was applied on an 8-channel MAGNETOM Sonata Maestro Class System in combination with a fast 3D FLASH sequence (TR = 3.79, TE = 1.3, Bandwidth = 350 Hz/pixel, flip angle = 25°). Nearly isotropic data sets with a spatial resolution of 0.8x0.8x1 mm^3 could be acquired within 23 seconds [27]. For signal reception the 12-element array coil system was used. An acceleration factor of 2 was used with 24 reference lines for auto-calibration of the coils. For data acquisition and reconstruction, the GRAPPA and mSENSE algorithms were compared in terms of artifacts. To improve the contrast-to-noise ratio, the one molar contrast agent gadobutrol (Gadovist®, Schering AG, Germany) was administered at a dose of 1.25 mmol/kg body weight with an injection rate of 2 ml/s.

In the iPAT images, SNR decreased by a factor of about 1.5 compared to the data without iPAT. This decrease in SNR could be visually noticed in the source images, however the intravascular signal was still acceptable. In the MIP images, the overall decrease in SNR was hardly detected.

The high-resolution renal 3D-Gd-MRA data sets were compared to selective x-ray angiography in more than 20 patients with renal artery stenosis ranging from 20 % luminal narrowing to occlusion. Image analysis of the isotropic data sets consisted of multiplanar reformats along the vessel axis to assess the degree of diameter reduction. In addition, reformats perpendicular to the vessel axis were performed to assess the degree of reduction of vessel area. Using multiplanar reformats the degree of stenosis was correctly assessed in 18 of 20 patients. In 2 cases, the degree of stenosis was overestimated. However, when reformats were performed in the isotropic data sets perpendicular to the vessel axis, all stenoses could be correctly identified compared to x-ray angiography (Figs. 22 and 23).

One limitation is the propagation of aliasing artifacts into the center of the image. These artifacts could be theoretically avoided by extending the FOV in the left-right direction so that no aliasing occurs at all. In clinical practice, however, this would mean a substantial increase in scan time, in particular in large patients. In addition, not all patients are able to put their arms over their heads. Therefore some degree of aliasing into the margins of the FOV has to be accepted. Using the GRAPPA algorithm, artifacts propagating from tissue outside the FOV into the center of the image were kept at a minimum. Only slight ring-like artifacts occurred, which did not affect the image interpretation. However, when the mSENSE technique was alternatively used, these artifacts were more severe (Fig. 24).

In conclusion, high-resolution renal 3D-Gd-MRA using iPAT allows for substantial improvement of spatial resolution, thereby increasing diagnostic accuracy compared to digital subtraction angiography. Using the GRAPPA based algorithm, artifacts propagating into the center of the FOV can be kept at a minimum.

Whole-body imaging

Because of the recent improvements in hardware and software and the lack of ionizing radiation, magnetic resonance imaging has become a candidate for screening imaging [28]. We have developed an MR examination which combines well established components including functional cardiac imaging together with myocardial perfusion* imaging, imaging of the lung, brain, an overall view of liver, kidneys, spleen, and pancreas, as well as the arterial system.

The whole-body examination is performed in two parts. In the first part, the patient is in a head first position; the spine array, two body arrays, and a head array are used as receiver coils. In the second part, the patient is in a feet first position; the spine array, the large FOV adapter, one or two body arrays (depending on the height of the patient), and the peripheral angio array are used as receiver coils. iPAT with an acceleration factor of two is applied for most scans of the examination including real-time TrueFISP imaging of the heart (Fig. 25), high-resolution imaging of the lung (Fig. 26) as well as dynamic cardiac perfusion* MRI with TrueFISP. In addition, iPAT of 3D-Gd-MRA in combination with the large FOV adapter is performed for all studies allowing a total scan time of only 62 seconds to cover the area from the thoracic aorta down to the toes at a spatial resolution of less than 1.4x1.0x1.5 mm^3 (Fig. 27).

By applying the GRAPPA algorithm with its integrated auto-calibration scan, it is possible to use flexible combinations of receiver coils with a flexible choice of iPAT directions and

** The information about this product is preliminary. The product is under development and is not commercially available in the U.S., and its future availability cannot be ensured.*

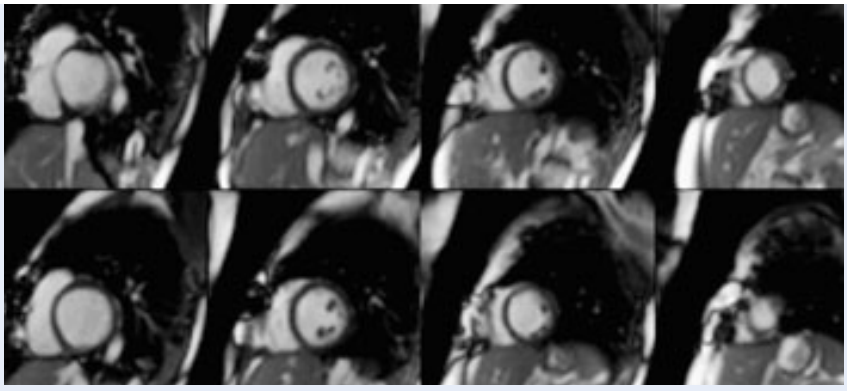

Figure 25 *Single breath-hold evaluation of global cardiac function with real-time iPAT TrueFISP.*

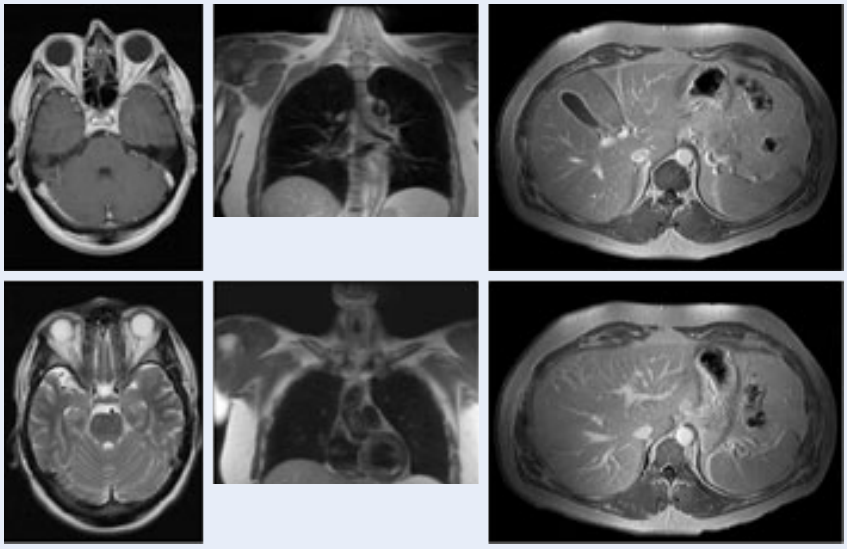

Figure 26 *Imaging of the brain, lungs, and abdomen as part of the whole-body screening examination.*



Figure 27 *Example of gadolinium-enhanced MR angiography as part of the whole-body screening examination. Note the excellent visualization of vessel segments down to the pedal arch. No stenoses are present.*

to move the patient table for different iPAT acquisitions. The advantage of iPAT in this kind of exam is the coverage of a large anatomic region and gain of time.

In the last two months twenty individuals, referred by their physician while participating in a manager healthcare program, underwent the whole-body scan in our department. All twenty individuals tolerated the MR examination well. Compared to the conventional examination techniques like ultrasound and ECG, we have established a more comprehensive exam within reasonable scan time. First results of pathologic findings (scar in lung, aortic stenosis, renal artery stenosis) show good correlation with the gold standard examinations.

Conclusion

This overview on applications and ongoing studies in different areas of the body supports the current trend to use parallel imaging in the majority of clinical scan protocols. The general advantages of parallel imaging are now well established. This includes the possibility for higher spatial resolution for 3D-Gd-MRA with shorter breath-holds, thereby potentially improving the accuracy of this technique for grading of renal artery stenosis. The combination of time-resolved and high-resolution 3D-Gd-MRA improves the detection and differentiation of pulmonary hypertension. The use of shorter echo trains for single shot HASTE or echo planar imaging results in less image distortion and less signal decay. Initial results show benefits for EPI diffusion tensor imaging in the brain as well as detection of early infiltrates in the lung with HASTE imaging. Imaging with multiple averages in shorter acquisition times improves visualization of tumors in areas with increased motion such as the larynx. Higher temporal resolution improves the accuracy of cardiac real-time techniques using SSFP sequences to measure global cardiac function within a single breath-hold.

In addition to the general benefits of parallel imaging, the iPAT methods GRAPPA and mSENSE feature some unique advantages. Artifacts in the center of coronal images resulting from aliasing of tissue outside the FOV are substantially suppressed using the GRAPPA algorithm. The iPAT algorithms with auto-calibration integrated into the individual scan are less sensitive to patient motion than other parallel imaging techniques with a single measurement of the coil sensitivity profiles at the start of the examination. In addition, the IPA™ (Integrated Panoramic Array) allows a flexible combination of multiple receiver coil systems. Therefore, large anatomic coverage with various receiver coils and a flexible choice of the iPAT directions is possible. This is particularly helpful for whole-body imaging where multiple receiver coil systems are combined to scan the entire body with parallel imaging techniques. Scan time for a complete cardiovascular exam is substantially reduced while spatial and temporal resolution of the individual scans are preserved.

In conclusion, iPAT can be used to improve most clinical protocols for comprehensive morphologic and functional imaging. Depending on the specific application its main advantages are a decrease in imaging artifacts or an increase in speed, spatial, or temporal resolution.



Co-workers on parallel imaging

Roger Eibel (pulmonary imaging)
Wilhelm Flatz (imaging of the larynx)
Peter Herzog (pulmonary imaging)
Armin Huber (cardiac imaging)
Wolfgang Klinger (MR technician)
Harald Kramer (whole-body imaging and screening)
Konstantin Nikolaou (cardiac imaging and pulmonary imaging)
Carola Schmid (MR technician)
Frank Stadie (MR technician)
Robert Stahl (diffusion tensor imaging)
Anja Struwe (MR technician)
Bernd J. Wintersperger (cardiac imaging)
Christoph Zech (abdominal imaging)

Acknowledgements

We would like to thank the Magnetic Resonance Development Department of Siemens Medical Systems and especially Mathias Nittka, Berthold Kiefer, and Rolf Sauter for their technical support.

References:

[1] *Griswold MA, Jakob PM, Heidemann RM, Nittka M, Jellus V, Wang J, Kiefer B, Haase A. Generalized autocalibrating partially parallel acquisitions (GRAPPA). Magn Reson Med 2002; 47: 1202–1210*

[2] *Sodickson DK, Manning WJ. Simultaneous acquisition of spatial harmonics (SMASH): fast imaging with radiofrequency coil arrays. Magn Reson Med 1997; 38: 591–603*

[3] *Pruessmann KP, Weiger M, Scheidegger MB, Boesiger P. SENSE: sensitivity encoding for fast MRI. Magn Reson Med 1999; 42: 952–962*

[4] *Basser PJ, Pierpaoli C. A simplified method to measure the diffusion tensor from seven MR images. Magn Reson Med 1998; 39: 928–934*

[5] *Le Bihan D, Mangin JF, Poupon C, Clark CA, Pappata S, Molko N, Chabriat H. Diffusion tensor imaging: concepts and applications. J Magn Reson Imaging 2001; 13: 534–546*

[6] *Keberl M, Kenn W, Hahn D. Current concepts in imaging of laryngeal and hypopharyngeal cancer. Eur Radiol 2002; 12: 1672–1683*

[7] *Biederer J, Busse I, Grimm J, Reuter M, Muhle C, Freitag S, Heller M. Sensitivity of MRI in detecting alveolar Infiltrates: Experimental studies. Rofo Fortschr Geb Rontgenstr Neuen Bildgeb Verfahr 2002; 174: 1033–1039*

[8] *Amundsen T, Torheim G, Kvistad KA, Waage A, Bjermer L, Nordlid KK, Johnsen H, Asberg A, Haraldseth O. Perfusion abnormalities in pulmonary embolism studied with perfusion MRI and ventilation-perfusion scintigraphy: an intra-modality and inter-modality agreement study. J Magn Reson Imaging 2002; 15: 386–394*

[9] *Hatabu H, Tadamura E, Prasad PV, Chen Q, Buxton R, Edelman RR. Noninvasive pulmonary perfusion imaging by STAR-HASTE sequence. Magn Reson Med 2000; 44: 808–812*

[10] *Mai VM, Hagspiel KD, Christopher JM, Do HM, Altes T, Knight-Scott J, Stith AL, Maier T, Berr SS. Perfusion imaging of the human lung using flow-sensitive alternating inversion recovery with an extra radiofrequency pulse (FAIRER). Magn Reson Imaging 1999; 17: 355–361*

[11] *Barkhausen J, Goyen M, Ruhm SG, Eggebrecht H, Debatin JF, Ladd ME. Assessment of ventricular function with single breath-hold real-time steady-state free precession cine MR imaging. Am J Roentgenol 2002; 178: 731–735*

[12] *Lee VS, Resnick D, Bundy JM, Simonetti OP, Lee P, Weinreb JC. Cardiac function: MR evaluation in one breath hold with real-time true fast imaging with steady-state precession. Radiology 2002; 222: 835–842*

[13] *Miller S, Simonetti OP, Carr J, Kramer U, Finn JP. MR imaging of the heart with cine true fast imaging with steady-state precession: influence of spatial and temporal resolutions on left ventricular functional parameters. Radiology 2002; 223: 263–269*

[14] *Wintersperger BJ, Nikolaou K, Dietrich O, Rieber, J, Nittka M, Reiser MF, Schoenberg SO. Single breath-hold real-time cine MR imaging: Improved temporal resolution using generalized autocalibrating partially parallel acquisition (GRAPPA) algorithm. Eur Radiol 2003; 13: 1931–1936*

[15] *Schreiber WG, Schmitt M, Kalden P, Mohrs OK, Kreitner KF, Thelen M. Dynamic contrast-enhanced myocardial perfusion imaging using saturation-prepared TrueFISP. J Magn Reson Imaging 2002; 16: 641–652*

[16] *Katayama M, Masui T, Kobayashi S, Ito T, Takahashi M, Sakahara H, Nozaki A, Kabasawa H. Fat-suppressed T2-weighted MRI of the liver: comparison of respiratory-triggered fast spin-echo, breath-hold single-shot fast spin-echo, and breath-hold fast-recovery fast spin-echo sequences. J Magn Reson Imaging 2001; 14: 439–449*

[17] *Gaa J, Hatabu H, Jenkins RL, Finn JP, Edelman RR. Liver masses: replacement of conventional T2-weighted spin-echo MR imaging with breath-hold MR imaging. Radiology 1996; 200: 459–464*

[18] *Hori M, Murakami T, Kim T, Kanematsu M, Tsuda K, Takahashi S, Takamura M, Hoshi H, Nakamura H. Single breath-hold T2-weighted MR imaging of the liver: value of single-shot fast spin-echo and multishot spin-echo echoplanar imaging. AJR Am J Roentgenol 2000; 174: 1423–1431*

[19] *Augui J, Vignaux O, Argaud C, Coste J, Gouya H, Legmann P. Liver: T2-weighted MR imaging with breath-hold fast-recovery optimized fast spin-echo compared with breath-hold half-Fourier and non-breath-hold respiratory-triggered fast spin-echo pulse sequences. Radiology 2002; 223: 853–859*

[20] *Tang Y, Yamashita Y, Namimoto T, Abe Y, Takahashi M. Liver T2-weighted MR imaging: comparison of fast and conventional half-Fourier single-shot turbo spin-echo, breath-hold turbo spin-echo, and respiratory-triggered turbo spin-echo sequences. Radiology 1997; 203: 766–772*

[21] *Liu YL, Riederer SJ, Rossman PJ, Grimm RC, Debbins JP, Ehman RL. A monitoring, feed-back, and triggering system for reproducible breath-hold MR imaging. Magn Reson Med 1993; 30: 507–511*

[22] *Prince MR, Narasimham DL, Stanley JC, Chenevert TL, Williams DM, Marx MV, Cho KJ. Breath-hold gadolinium-enhanced MR angiography of the abdominal aorta and its major branches. Radiology 1995; 197: 785–792*

[23] *Dong Q, Schoenberg SO, Carlos RC, Neimatallah M, Cho KJ, Williams DM, Kazanjian SN, Prince MR. Diagnosis of renal vascular disease. Radiographics 1999; 19: 1535–1554*

[24] *Schoenberg SO, Bock M, Knopp MV, Essig M, Laub G, Hawighorst H, Zuna I, Kallinowski F, van Kaick G. Renal arteries: Optimization of 3D Gadolinium MR Angiography with bolus-timing independent fast multiphase acquisition in a single breath-hold. Radiology 1999; 201: 667–676*

[25] *Schoenberg SO, Knopp MV, Londy F, Krishnan S, Zuna I, Lang N, Essig M, Hawighorst H, Maki JH, Stafford-Johnson D, Kallinowski F, Chenevert TL, Prince MR. Morphologic and functional magnetic resonance imaging of renal artery stenosis: a multireader tricenter study. J Am Soc Nephrology 2002; 13: 158–169.*

[26] *Heid O. The outer limits of contrast enhanced MR angio (gradient performance, resolution, speed, etc). In: Proceedings of the tenth international workshop on magnetic resonance angiography, Park City, Utah. The International MR Angio Club 1998: 75*

[27] *Schoenberg SO, Rieger J, Johannson LO, Dietrich O, Bock M, Prince MR, Reiser MF. Diagnosis of renal artery stenosis with magnetic resonance angiography – update 2003. Nephrol Dial Transplant 2003, 18: 1252–1256*

[28] *Goyen M, Herborn CU, Kroger K, Lauenstein TC, Debatin JF, Ruehm SG. Detection of atherosclerosis: systemic imaging for systemic disease with whole-body three-dimensional MR angiography/initial experience. Radiology 2003; 227: 277–282*



Tim will change MR forever.

It's a whole new way to think about MR. Going beyond incremental enhancements in magnet technology and gradient power to something radically different. A transforming technology that shifts the spotlight onto a new and tremendously innovative RF system and matrix coil design. Tim technology is a unique combination of features that will launch the next era in powerful MR advances. From revolutionary acquisition quality to breakthrough applications and remarkable profitability. It's opening up new worlds of possibility.

- Tim is a revolutionary. **Select exams, not coils.** [76 x 32] Up to 76 seamlessly integrated matrix coil elements and up to 32 RF channels combined to create one Total imaging matrix.

- Tim sees all. **Local becomes total.** True 205 cm (6′ 9″) seamless, whole-body anatomical coverage with no coil reconfiguration or patient repositioning.

- Tim knows no boundaries. **Parallel in all directions.** Head to toe, front to back, and side to side for unlimited Parallel Imaging.

A Quantum Leap in MR Tomography: Tim [76x32]

MRI is about to become radically faster and more flexible, enabling entirely new applications thanks to a powerful new partner: Tim – Total imaging matrix.

By Carol Milano,
Dr. Christoph Zindel, M.D.

This fall, Siemens will be introducing Tim, a revolutionary new addition to the traditional MRI process. Tim, the unique Total imaging matrix technology, brings MR tomography greater performance than it has ever had before.

In the past, MR technology was limited to array coils offering a maximum of only eight receiving channels. Until Siemens introduced the unique IPA (Integrated Panoramic Array) concept in 1997, the possibility of varying the combination of coils for scanning larger areas of the body has been very limited or even nonexistent. Now, for the first time in the history of MR, the user can individually select the specific exams for the desired anatomy – and no longer has to deal with patient repositioning or coil reconfigurations. Tim features as many as 76 (!) seamlessly integrated coil elements, along with exactly 32 independent receiver channels. These can be used flexibly in any combination to create a whole-body imaging matrix, supporting a total field of view of 205 cm (6' 9"). Conventional metastases evaluation of the whole body, however, requires changing coils and repositioning the patient for each anatomical area of interest, e.g. head, thoracic, abdominal, pelvis, etc... With the introduction of Tim, workflow and patient comfort level are vastly improved by simplifying the MR process and shortening examination times. Both the matrix coils and the patient need only be positioned once for all desired exams, as multiple channels allow a unique and almost unlimited scanning flexibility.

Scan times cut in half

Usually, even with the existing coil concept, only about a 150-cm field of view could be scanned with surface coils and a sufficient signal-to-noise ratio (SNR). For whole-body coverage, the patient needs to be repositioned, i.e. the coil setup has to be reconfigured. The only alternative, up to now, has been to perform whole-body MR imaging without surface coils, i.e. just with the integrated body coil, which, however, significantly reduces image quality. Thus, MRI technicians have always had to choose in the past between total body coverage and adequate image quality. Tim erases that difficult decision by allowing up to 100 percent more SNR. The result: up to 205 cm (6' 9") can now be scanned at maximum SNR – requiring only 12 minutes. That's a phenomenal time reduction of more than 50 percent!

Tim can help making accurate diagnoses, even for extremely complex imaging needs. Tim's flexibility means that if something unexpected is spotted, the region of interest can be expanded instantly, without any repositioning of the patient or any coil reconfigurations.

Unlimited parallel imaging

Tim's reach is virtually boundless. Today, so-called Parallel Imaging (Parallel Acquisition Technique, PAT) already allows faster acquisition with high image quality. This is a distinct advantage, for instance, in MRIs of moving organs, because motion artefacts are significantly reduced or even eliminated. Unfortunately, the disadvantages of PAT include limited fields of view, usually based on the specific PAT coils required, and a finite number of receiver channels. Here, Tim shows its real added value. It removes all those negatives by allowing Parallel Imaging along the patient's entire body in a total field of view of 205 cm. The very highest PAT factors are now available in all three dimensions: from head to feet, anterior to posterior, and left to right. That means that the highest acquisition speeds and image resolutions can be achieved without the need for any specific PAT coils.

Intelligent assistance

Tim goes even further to intelligently assist with MRIs: For the first time, it makes Parallel Imaging easy by recommending the maximum PAT factors for whichever application is selected. And the Tim Assistant helps finding the selected coil elements, correct patient position, and appropriate MR protocol, assuring the integrated Parallel Acquisition Technique (iPAT) configuration for each particular need. Siemens continues to uncompromisingly pursue its goal of truly optimizing workflow: With Tim's new Intelligent Coil Control, technicians can control all coils, both fixed and flexible, and their corresponding elements. This is all aimed at making Parallel Imaging easy and more efficient, as well as integrating it into the clinical routine.

In addition, with iPAT, Siemens offers two forms of PAT: GRAPPA (Generalized Autocalibrating Partial Parallel Acquisition) and mSENSE (modified Sensitivity Encoding), thus increasing flexibility for the different requirements of MR applications. Thanks to Tim and its broad iPAT capabilities, outstanding image quality is achieved along with high-speed acquisition performance and improved SNR.



The first MRI system equipped with Tim Technology.

Tim redefines the term "freedom in MRI" by taking a quantum leap beyond the boundaries of array coils to a breakthrough matrix coil concept.

Whole-body functionality with [76 x 32]

Tim features three performance levels: the top-of-the-line Tim [76x32] (i.e. 76 seamlessly integrated coil elements and 32 receiver channels), which not only accommodates clinical routine and demanding research, but is also open for all future applications, such as interventional procedures. Tim [76x18], with 18 anatomically optimized independent receiver channels, provides Parallel Imaging in the full 50-cm field of view, and Tim [32x8] for high-end clinical routine. There is a level for every need.

World premiere

When and where can you meet Tim? Tim will make its debut at the 89th Scientific Assembly and Annual Meeting of the Radiology Society of North America, beginning in Chicago on November 30. Also in November, the first Tim systems will be installed at key facilities in New York and Tübingen, Germany. As part of a special publication on science and health innovations, Siemens recently used Tim technology to perform a whole-body scan on Hannah Stockbauer, one of the most successful female swimmers in German history. Hannah, 21, who won three gold medals this summer at the 10th FINA World Swimming Championships in Barcelona, is currently doing an internship at Siemens.



German Swim world champion 2003, Hannah Stockbauer, in a whole-body MRI scan.

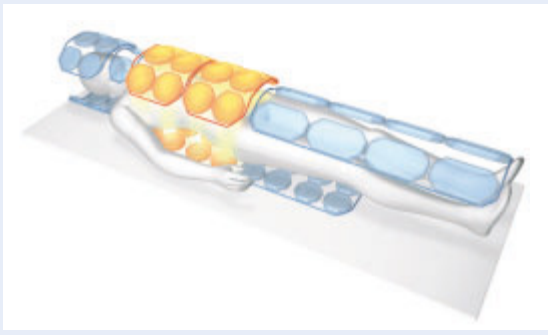

Up to 76 seamlessly integrated coil elements and up to 32 RF channels combined to create one Total imaging matrix.

Tim enables MR users to freely and flexibly combine up to 76 seamlessly integrated coil elements and up to 32 RF channels to one Total imaging matrix. No manual coil reconfiguration during the exam. No patient repositioning either. Giving them total, multi-channel whole-body imaging, seamlessly. If during the course of an exam unexpected findings appear, the anatomical region of interest can be expanded immediately. Tim enables streamlined true whole-body imaging with a total field of view (FoV) of up 205 cm (6' 9") – in surface coil quality and with up to 100 percent increase in signal-to-noise ratio (SNR). Tim opens up a whole new world of clinical applications, from whole-body to local MRI. New approaches for cancer staging, visualization of systemic diseases like rheumatic or vessel diseases, or MR angiography. Radiologists will see more than ever before: detailed morphology, leading to an unparalleled level of confidence in all physician's diagnoses while at the same time shortening exam times and streamlining workflow.

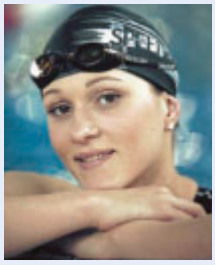

Hannah Stockbauer

High-speed PAT Factors in all 3 dimensions

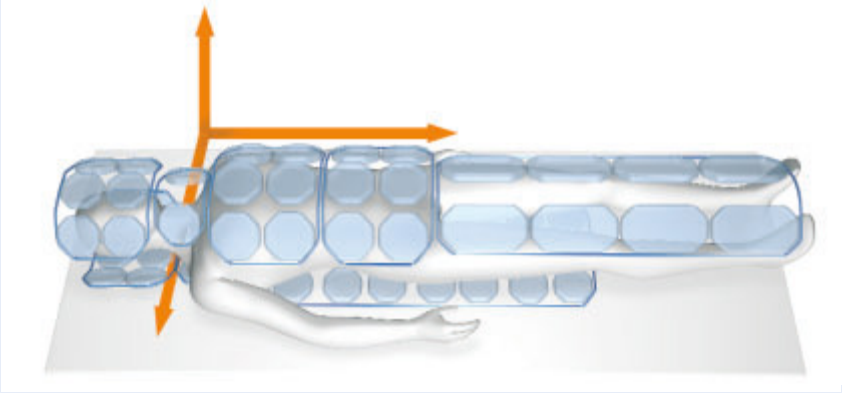

Redefined and optimized Parallel Imaging thanks to the new Total imaging matrix technology. With Tim, high-speed PAT factors (Parallel Acquisition Techniques) can be applied in all three dimensions. Supporting the highest acquisition speeds and image resolutions. Tim allows full iPAT functionality including iPAT² with PAT factors up to 12. Highest image quality is provided by up to 100 % more SNR for the most clinically exceptional and relevant images. And: no specific PAT coils are required. The Tim Assistant intelligently helps to make Parallel Imaging easy by recommending the appropriate PAT factors for the selected application.



Redefining the concept of time: With Tim, matrix coils only need to be positioned once. This dramatically reduces patient set-up.



Easier for everyone: With Tim nearly all MR procedures can be performed as feet-first exams.

The benefits of Tim and MAGNETOM Avanto at a glance

Clinical benefits:

- Outstanding image quality with up to 100 percent more SNR, for whole-body and local MR imaging
- A total FoV of 205 cm can be scanned without any coil reconfigurations or patient repositioning
- Excellent temporal resolution with the strongest gradients currently available in the industry
- Unlimited Parallel Imaging seamlessly throughout the whole-body, and in all directions. No specific PAT coils required
- True whole-body MR enables first-ever optimized visualization and staging of systemic diseases

Business benefits:

- More patients per day due to the highest workflow efficiency
- More referrals due to greatly expanded MR services and applications
- Attracting more technicians due to most advanced MR system
- Less siting costs due to AudioComfort and less noise damping
- Always state-of-the-art technology with the MAGNETOM Evolve program
- More revenue with less operating costs, powerful return on investment

Patient benefits:

- Stress-free MRI with reduced exam time (patients need to be positioned only once, and a high-quality whole-body MRI can take as little as 12 minutes)
- Virtually all applications can be performed feet first, thus reducing patient anxiety
- Breath holding reduced by up to 50 percent
- 97 percent less acoustic noise with AudioComfort
- Less burden due to ultralight-weighted coils

Introducing MAGNETOM Avanto: The Revolution Begins Now

Carol Milano,
Dr. Christoph Zindel, M.D.

True whole-body functionality is now available, thanks to Siemens' new high-end 1.5T MRI system, MAGNETOM Avanto – the very first Tim system. Harnessing the power of Tim technology, MAGNETOM Avanto is able to deliver faster and more precise results than ever before for systemic diseases. This holistic approach provides benefits for many other examinations, such as clarifications of vessel and rheumatic diseases as well as preventional exams. Tim makes MAGNETOM Avanto not only more versatile, but also more efficient. As a result, MRI facilities can broaden their offerings and expand into other, totally new application areas. The state-of-the-art MAGNETOM Avanto offers performance without compromises: Having to choose between high performance and high acoustic noise levels or low performance and quietness – this decision is no longer necessary. With MAGNETOM Avanto's AudioComfort, the strongest and fastest gradient systems with field strength of up to 45 mT/m and a slew rate of 200 T/m/s are combined, with a reduction of acoustic noise of up to 30 dB(A), equal to 97 percent.

Workflow automation

MAGNETOM Avanto is surprisingly easy to use. By intelligently automating the workflow path, it makes both the work environment and the staff more comfortable. The entire system, including hardware and software, together with the matrix coils and the 10 (!) table-integrated plugs, are consistent with Siemens' commitment to ergonomic design. This design virtually eliminates many time-consuming manual steps, including coil reconfigurations and patient repositioning, while significantly reducing table operation. The telescopic matrix patient table is perfectly suited for whole-body workflow and helps to increase the available workspace in the MR room. Tim helps MAGNETOM Avanto to accelerate patient setup, scan times and exams. Inline technology, enabling processing instead of post-processing provides immediate clinical results – in realtime – for procedures such as prospective motion correction (PACE), diffusion,



Head-neck ce-MRA with excellent separation of the arteries from the veins.

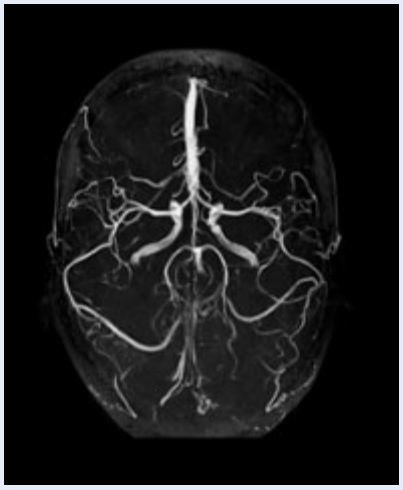

High-resolution 3D Time of Flight (ToF) MR Angio with excellent visualization of peripheral vasculature.

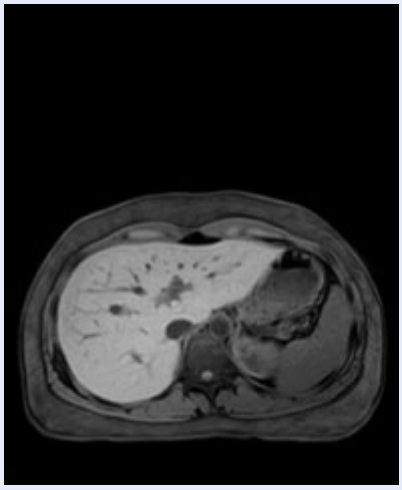

T1-weighted FLASH 2D fat suppressed transverse image.



perfusion, MR angiograms, and fMRI (BOLD), supporting also fast, precise visualization of systemic diseases. Another Siemens innovation, Phoenix, makes it possible to save, extract, and set up MR protocols in less than 30 seconds. With Phoenix, what you see is what you get: Just drag and drop a DICOM image and use the MR protocol to reproduce it. With the new AutoAlign, using a standard adult three-dimensional brain, automatic slice positioning in the brain is possible for the first time ever. AutoAlign helps to make MR brain exams more reproducible which is especially important for follow-up exams. In combination with Phoenix, it can be also used to distribute predefined MR protocols from one scanner to another within the same institution.

From a business perspective, MAGNETOM Avanto allows MR labs to do more with less: more patients per day, more referrals due to new applications, and higher diagnostic confidence as a result of the impressive image quality – all coupled with lower operating and siting costs. Another plus for the business side: Because Siemens has attained zero helium boil-off, there is far less

MAGNETOM Avanto is the first system with Total imaging matrix technology. It features exceptional image quality by utilizing the highest signal-to-noise ratio possible. MAGNETOM Avanto has the most comprehensive and innovative application range available today. Tim has met his match.

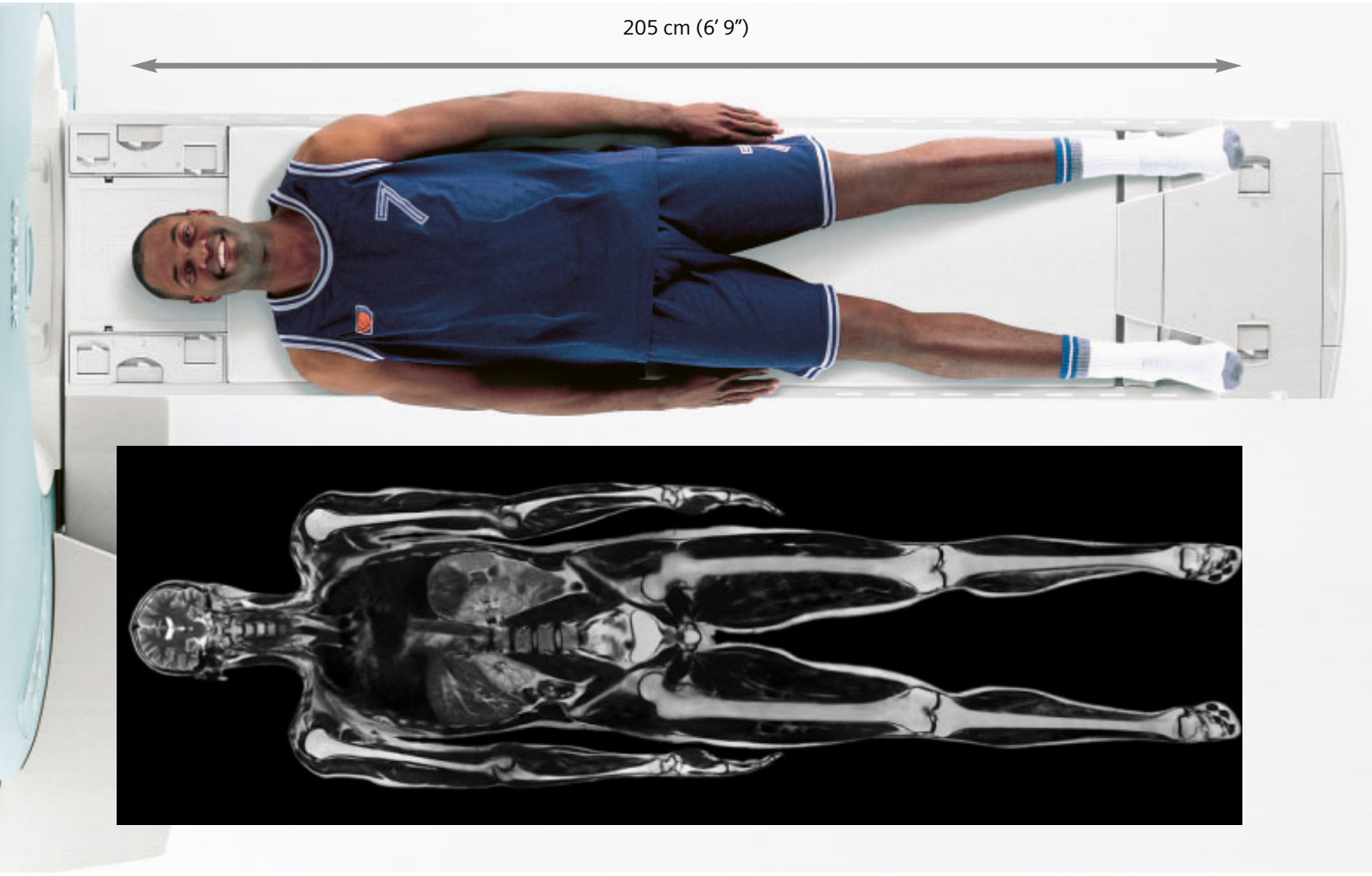

MAGNETOM Avanto, the first Tim-operated system, enables whole-body imaging of up to 205 cm (6′ 9″) – in as little as 12 minutes.

downtime for refilling the magnet, and more uptime for the system.

Higher patient satisfaction

Often, patients become anxious because of the acoustic noise during an MRI procedure. They will be very grateful for MAGNETOM Avanto's AudioComfort concept, featuring multiple and integrated measures to significantly reduce noise levels. For example, special casting for gradient coils and magnet encapsulation help to achieve reductions of up to 97 percent without sacrificing the high-performance gradients needed for demanding applications. Therefore, ear protection or headphones are no longer mandatory. Patient comfort is also enhanced due to ultra-light-weight Body Matrix coils. Weighing only 950 grams, they are far more comfortable and will make a major difference to very ill cardiac or cancer patients suffering from pain. For claustrophobic patients, the fact that virtually all MR exams can now be carried out in the feet-first position is a critical factor. Most scans can easily be performed with the head outside the bore.

With MAGNETOM Avanto, exam times are shortened and acquisition speed is peerless – welcome improvements for both medical staff and patients. Frail patients will also be very relieved that breath-holding time is reduced by up to 50 percent.

MAGNETOM Avanto's examination table can be lowered down to just 47 cm (18.5 inches), making it accessible to virtually any patient, even children and the elderly.



Flexible combination of seamlessly integrated coil elements for coverage of large anatomical areas. This entire CNS was imaged without patient repositioning or coil reconfiguration.

Without any movement restrictions, the table also supports obese patients weighing up to 200 kilograms (400 lbs).

The exciting future of MR

With MAGNETOM Evolve, the easy upgrade program from Siemens, MRI facilities will be able to keep up with any future changes in MR. And Siemens' integrated customer care program Life will be available to meet each customer's evolving needs. Evolution – and revolution – are what Tim is all about. The powerful, cutting-edge abilities of Tim and MAGNETOM Avanto are vanguards of change, integrating state-of-the-art medical technology, information technology, and clinical services to increase efficiency, satisfy patients, ease pressures on staff, and strengthen any facility's position in the medical sector. Tim has launched a new era, pushing MR to new limits while opening the door to an exciting world of possibilities beyond.

Author: *New York-based medical writer Carol Milano has contributed to the New York Daily News, Los Angeles Times, Science and Health, and Woman's Day, as well as numerous trade publications and online magazines for the medical profession. She is also a longtime adjunct professor at New York University and the author of two business books.*

Author: *Dr. Christoph Zindel, M.D., is Director of Segment Management at Siemens Medical Solutions' MR division.*

Perfusion MRI and MRS for Brain Tumors

Meng Law[1], M.D.; N. Salibi[2], Ph.D.; E.A. Knopp[1], M.D.

[1] New York University school of Medicine, New York, NY, USA

[2] Siemens Medical Solutions USA, Inc, Malvern, PA, USA

Introduction

Advanced MRI techniques, such as MR spectroscopy, diffusion and perfusion MR imaging can give important *in vivo* physiological and metabolic information, complementing morphologic findings from conventional MRI in the clinical setting. Combining perfusion MRI and MR spectroscopy will help in solving difficult cases and increase confidence in making a diagnosis.

Techniques

Brain tumor MR Imaging protocol: typical parameters for brain tumor imaging at 1.5 Tesla are shown in Table 1. Perfusion MRI exams are performed with TR/TE = 1,000 ms/ 54 ms; field of view 210 mm x 210 mm; section thickness 3-8 mm (typically 5 mm); matrix 128 x 128; in-plane voxel size 1.8 x 1.8 mm; intersection gap 0%-30%; flip angle 30°; signal bandwidth 1,470 Hz/pixel. Ten slices are usually obtained to cover the entire lesion volume as identified on T2-weighted images. A series of 60 multi-slice acquisitions are acquired at 1-second intervals. The combination of a 1,000-msec repetition time and a 30° flip angle ensures that T1 effects are minimized. The first 10 acquisitions are performed prior to the contrast agent injection to establish a pre-contrast baseline. At the 10th acquisition, gadopentetate dimeglumine (0.1 mmol/kg) is injected with a power injector at a flow rate of 3-5 ml/sec through the intravenous catheter (18-22 gauge), the contrast agent injection is immediately followed by a bolus injection of saline (total of 20 ml at the same rate).

Proton MRSI protocol

The volume of interest is confirmed with scout HASTE (Half-Fourier Acquisition Single-Shot Turbo-Spin-Echo) images (TR/TE/excitations = 15 ms/6 ms/1; inversion time of 500 ms). Ten 5 mm sections are obtained with a 1 minute 15 seconds scan in the axial, coronal, and sagittal planes. Depending on lesion size, a volume selective 2D or 3D CSI sequence with TR/TE = 1,500 ms/ 144 ms (or 1500ms /30ms) is used for MRSI. A measurement at TE = 288 ms was initially included in the protocol and dropped later. As demonstrated in the examples below, this measurement provided no additional clinical information, although it contributed to a better understanding of the behavior of metabolite signals at various TEs. The hybrid multivoxel CSI technique uses a PRESS double spin echo scheme for pre-selection of a volume of interest (VOI) that is usually defined to include the abnormality as well as normal-appearing brain tissue when possible. To prevent strong contribution to the spectra from subcutaneous fat signals, the VOI is completely enclosed within the brain and positioned at the center of the phase-encoded field of view (FOV), which is large enough to prevent wraparound artifact. For lesions that are cortically based or near the skull base, the VOI can be rotated, and up to 8 outer volume saturation (OVS) slabs can be placed over the skull (Fig. 1). A typical VOI consists of an 80 mm x 80 mm region placed within a 160 mm x 160 mm FOV on a 10 mm to 20 mm slice. A 16 x 16 phase-encoding matrix gives an 8 x 8 array of spectra in the VOI with an in plane resolution of 10 mm x 10 mm. Although the acquired 2D or 3D CSI data set can be measured with a higher spatial resolution, to save time interpolation is sometimes used to reduce the effective voxel size. Spatial resolution is set by adjusting the FOV and matrix size while keeping the measurement time at 8 minutes or less. A second 3D (or 2D) CSI sequence is also obtained (time permitting) with TR/TE = 1500 ms/30 ms (Table 1).

Clinical Applications of Perfusion MR and MR Spectroscopy in Brain Tumors

Assessment of Glioma Grade
Combined Perfusion MRI and MR Spectroscopy in the clinical setting provide complementary information that can be used for prospective grading of gliomas. This has important clinical utility to the neurosurgeon and neuro-oncologist (Figs. 2-5). For example, high-grade gliomas generally have higher relative cerebral blood volume rCBV* measurements and Cho levels than low grade gliomas [1].

Gliomatosis Cerebri
Gliomatosis cerebri is characterized by involvement of at least two lobes of the brain by a glial cell tumor of neuroepithelial origin with relative preservation of neuronal architecture [2]. Gliomatosis cerebri, which refers to the contiguous involvement of different regions of the brain, must be differentiated from multi-centric glioma, which is defined as multiple foci of tumor in different sites. Histopathologically, there is a lack of vascular hyperplasia in gliomatosis cerebri; this accounts for the relatively low rCBV* measurements, mean

Table 1 *Brain tumor imaging protocol.*

Sequence	TR (ms)	TE (ms)	Flip Angle /TI	Acq/NEX	Thickness (mm)	No. Slices	Matrix	FOV (mm)	Acq. time (min.sec)
Scout/Localizer	15	6	NA	1	8	3	256	280	0.19
Axial T1	600	14	90	2	5	20	256	210	3.36
Axial FLAIR	9000	110	180/2500	1	5	20	256	210	3.56
Axial T2	3400	119	180	1	5	20	256	210	1.36
1. Dual Echo/PD	3400	16	180	1	5	26	256	256	7.59#
Diffusion/ADC	3400	95	NA	3	5	20	128	210	1.15
2. DTI*	4000	95	NA	4	5	20	128	210	1.56
PERFUSION MRI	**1000**	**54**	**30 degrees**	**60 (1/s)**	**3 to 8**	**10**	**128**	**210**	**1**
Post Gd T1	600	14	90	1	5	20	256	210	3.36
MRSI	**1500** **1500**	**144** **30**	**90 2D CSI** **90 3D CSI**	**3** **1**	**10** **10**	**1** **8**	**16 x 16** **12 x 12**	**160** **160**	**6.05** **7.53**
3. MP Rage	1100	4.38	15	1	0.9	192	256	230	3.33

Note: Total imaging time is approximately 30 mins. The optional sequences are:

1. *Dual echo T2 – Proton density for patients in a stereotactic headframe, acquired instead of the FLAIR. Larger field of view (FOV) and square FOV (256x256) are used to match the software in the operating room for stereotactic biopsy or resection. No angulation.*
2. *Diffusion Tensor Imaging (DTI in 12 directions).*
3. *MPRage – reconstructed in the axial, coronal and sagittal planes. TI denotes Inversion Time.*

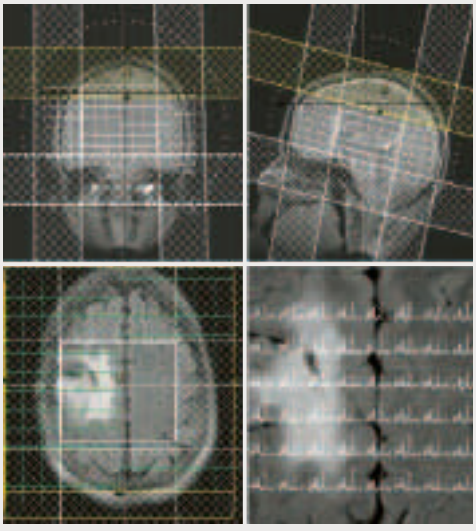

Figure 1

**WIP: The information about this product is preliminary. The product is under development and is not commercially available in the US and its future availability cannot be ensured.*

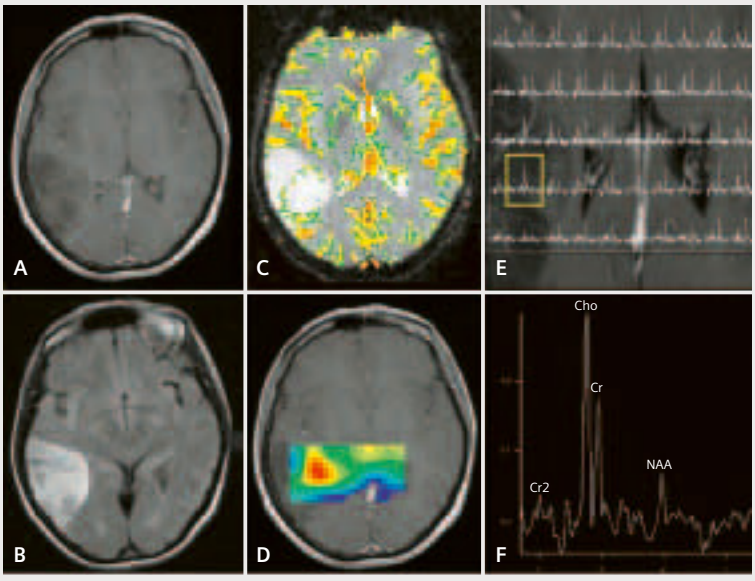

Figure 2 *A 52-year-old woman with a histologically confirmed grade II/IV glioma. A: Axial T1-weighted image post-gadolinium shows a lesion in the right temporo-parietal region with low signal and minimal enhancement. B: Axial FLAIR image shows increase in T2 signal within the lesion with minimal edema. C: Gradient-echo axial perfusion MRI with rCBV* color overlay map, shows a low rCBV* of 1.70 in keeping with a low-grade glioma. There is a thin rim of slightly increased perfusion at the margin of the lesion. D: Cho color overlay metabolite map showing the region of increased Cho, which sometimes does not correspond to the region of highest rCBV* seen on the perfusion MRI study in C. This may be due to the fact that MRSI and perfusion MRI are measuring different parameters of tumoral activity. E: Spectral map shows regions of Cho elevation only within the region of abnormal signal indicating a lack of tumor infiltration in the peritumoral region in this grade II lesion. F: Spectrum (TE 144 ms) showing Cho elevation with respect to Cr and NAA within the tumor. Data were acquired on a 1.5T MAGNETOM Symphony.*

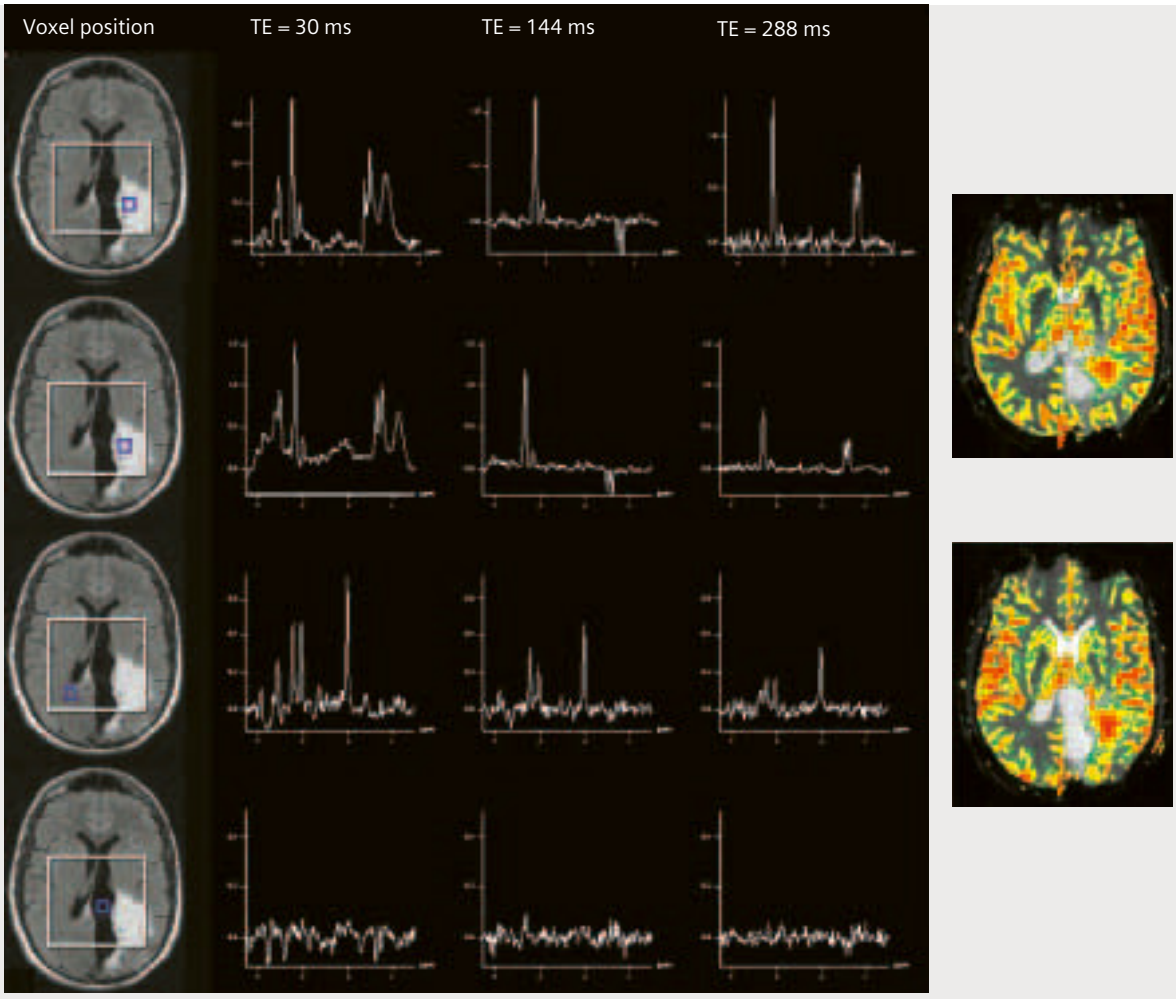

Figure 3 *MRSI and perfusion MRI images from a patient demonstrating recurrent high-grade glioma within the left parietal region. Images illustrate typical features of spectra at different echo times (TE). A: The first column of images shows axial FLAIR images with the voxel position corresponding to the spectra in the same row. Short TE (30 ms), intermediate TE (144 ms), and long TE (288 ms) spectra are displayed in the second, third, and fourth column respectively. In the fifth column corresponding rCBV* color overlay maps, (B), and (C), of the recurrent glioma demonstrate evidence of increased rCBV* in regions of significant Cho elevation. The 1st and 2nd rows of (A) represent spectra from a voxel within the recurrent tumor demonstrating marked elevation in Cho relative to Cr and NAA. There is also a lactate peak that is inverted at the intermediate TE of 144 ms and upright at TEs of 30 and 288 ms. Note that myo-inositol, Glx (Glutamine/Glutamate) and lipid peaks are more readily appreciated at the short TE (2nd row, 30 ms). There is an elevated Glx complex of peaks (2.05-2.5 ppm). (In addition to the Glx, there may be a very small NAA peak that disappears at long TE because of T2 decay). The 3rd row displays spectra from a voxel within normal appearing contralateral brain. Note the decrease in signal (from metabolites) relative to baseline noise at longer echo time (288 ms) due to the T2 decay of signal from metabolites at longer echo time. The 4th row displays a voxel in the ventricles, where the lack of metabolites within CSF results in a noisy spectrum, seen at all echo times (30, 144 and 288 ms). Data were acquired on a 1.5T MAGNETOM Symphony.*

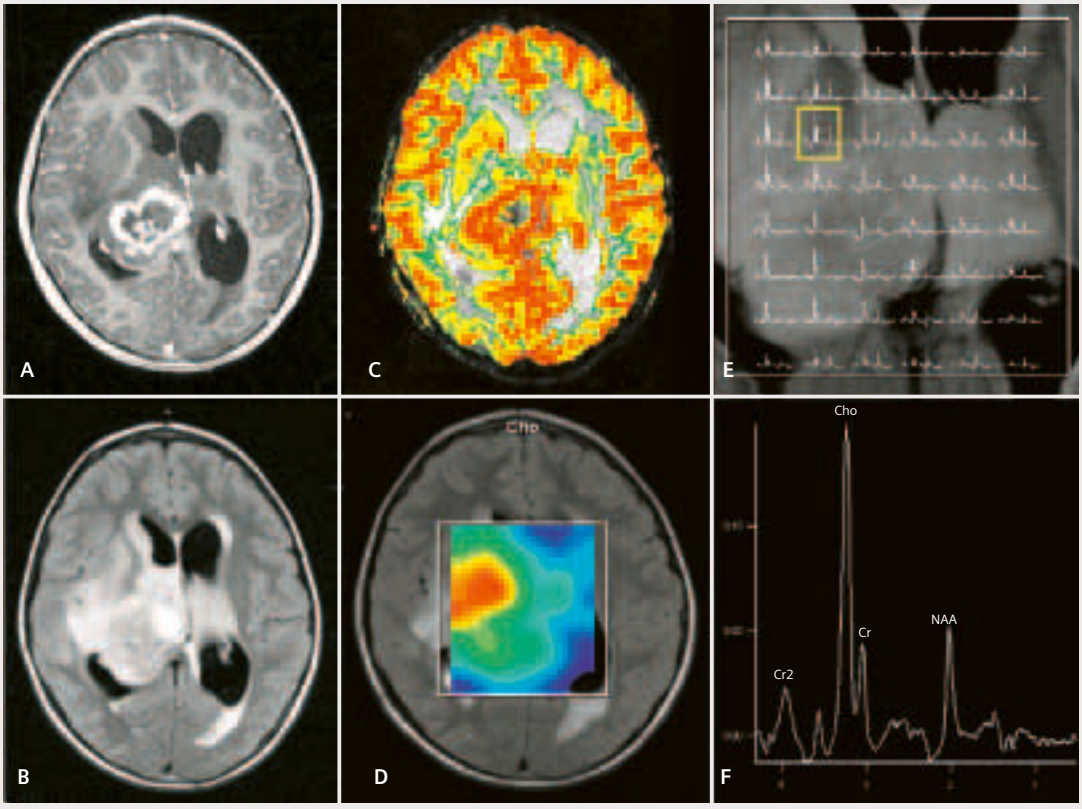

Figure 4 *A 70-year-old woman with a histologically confirmed grade III/IV glioma. A: Post-gadolinium Axial T1-weighted image shows a lesion in the right thalamic region with heterogeneous peripheral contrast enhancement and a central cystic/necrotic region. B: Axial FLAIR image shows increase in T2 signal within the lesion with moderate surrounding edema. The patient also has hydrocephalus and trans-ependymal edema around the ventricles. C: Gradient-echo axial perfusion MRI with rCBV* color overlay map, shows a high rCBV* of 3.70 in keeping with a high-grade glioma. There is a thick rind of marked increased perfusion. D: Cho color overlay metabolite map showing the region of increased Cho, which again does not correspond exactly to the region of highest rCBV* seen on the perfusion MRI study in C. E: Spectral map shows regions of Cho elevation within the region of abnormal signal as well as tumor infiltration beyond the region of enhancement, anteriorly and potentially across the midline into the left thalamus. The central areas do not demonstrate substantial amount of lipids/lactate as compared to a grade IV lesion. F: Spectrum (TE 144 ms) from the peritumoral region showing marked Cho elevation with respect to Cr and NAA indicating tumor infiltration. Data were acquired on a 1.5T MAGNETOM Symphony.*

**WIP: The information about this product is preliminary. The product is under development and is not commercially available in the US and its future availability cannot be ensured.*

1.02±0.42 [3], in (Fig. 6). Normal Cho, elevated myo-Inositol, and decreased NAA have been demonstrated with MRS in gliomatosis cerebri [4] (Fig. 6). The combination of these spectroscopy findings and reduced perfusion suggest that gliomatosis cerebri can be differentiated from high-grade multicentric glioma.

Metastatic Neoplasms

A solitary brain metastases may be indistinguishable from a primary glioma by conventional MRI imaging. The pathophysiology of the peri-tumoral region of gliomas and metastases is well known by neurosurgeons and neuro-pathologists. High-grade gliomas are known to be infiltrating tumors, with tumoral tissue infiltrating along vascular channels, whereas in metastases, the peri-tumoral region contains no infiltrating tumor cells or vascular endothelial proliferation and is almost purely vasogenic edema [5-7]. In the differentiation of glioma from metastases, finding high Cho and high rCBV* in the peri-tumoral region of a lesion (Figs. 7-8) is more likely to represent glioma rather than metastases [7].

Non-Neoplastic Mimics – Cerebrovascular Injury

The clinical differentiation between a cerebral infarct and glioma is usually straightforward, with acute cerebrovascular events presenting with notable neurologic symptoms and signs. Diffusion-weighted imaging is also extremely sensitive and time efficient in demonstrating ischemia and infarction. However, in some clinical instances where the clinical history and diffusion-weighted imaging is somewhat confusing (Fig. 9), MRSI and perfusion MRI can be used to differentiate a surgical lesion (tumor) from a non-surgical lesion

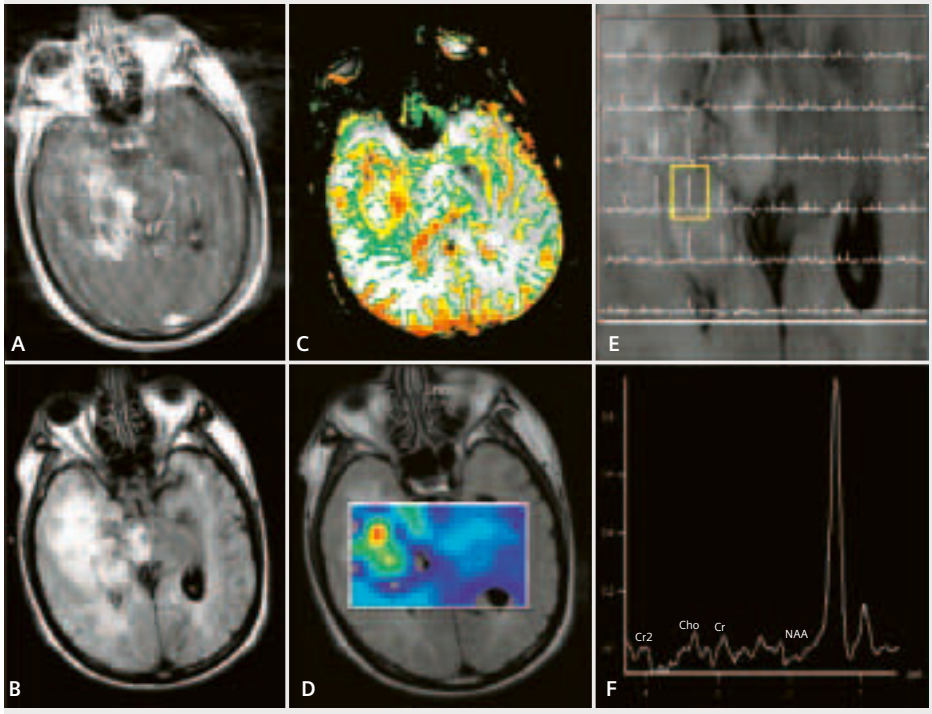

Figure 5 *A 60-year-old man with a histologically confirmed grade IV/IV glioma. A: Post-gadolinium axial T1-weighted image (motion degraded) shows a lesion in the right temporal region with heterogeneous peripheral contrast enhancement and central necrosis. B: Axial FLAIR image shows increase in T2 signal within the lesion with marked surrounding edema/tumor infiltration. There is also infiltration into the right occipital region and right midbrain. C: Gradient-echo axial perfusion MRI with rCBV* color overlay map, shows a high rCBV* of 8.90 in keeping with a grade IV glioma. There is increased perfusion around the periphery of the lesion with decreased perfusion within the necrotic center. D: Cho color overlay metabolite map showing the region of increased Cho which corresponds to the regions of high rCBV* seen on the perfusion MRI study in C. E: Spectral map shows regions of lipid within the region of abnormal signal indicating necrosis in a glioblastoma multiforme. F: Spectrum (TE 30 ms) showing marked lipids elevation (primarily aliphatic methylene groups [-CH2-] of fatty acids at 1.2-1.4 ppm). Data were acquired on a 1.5T MAGNETOM Symphony.*

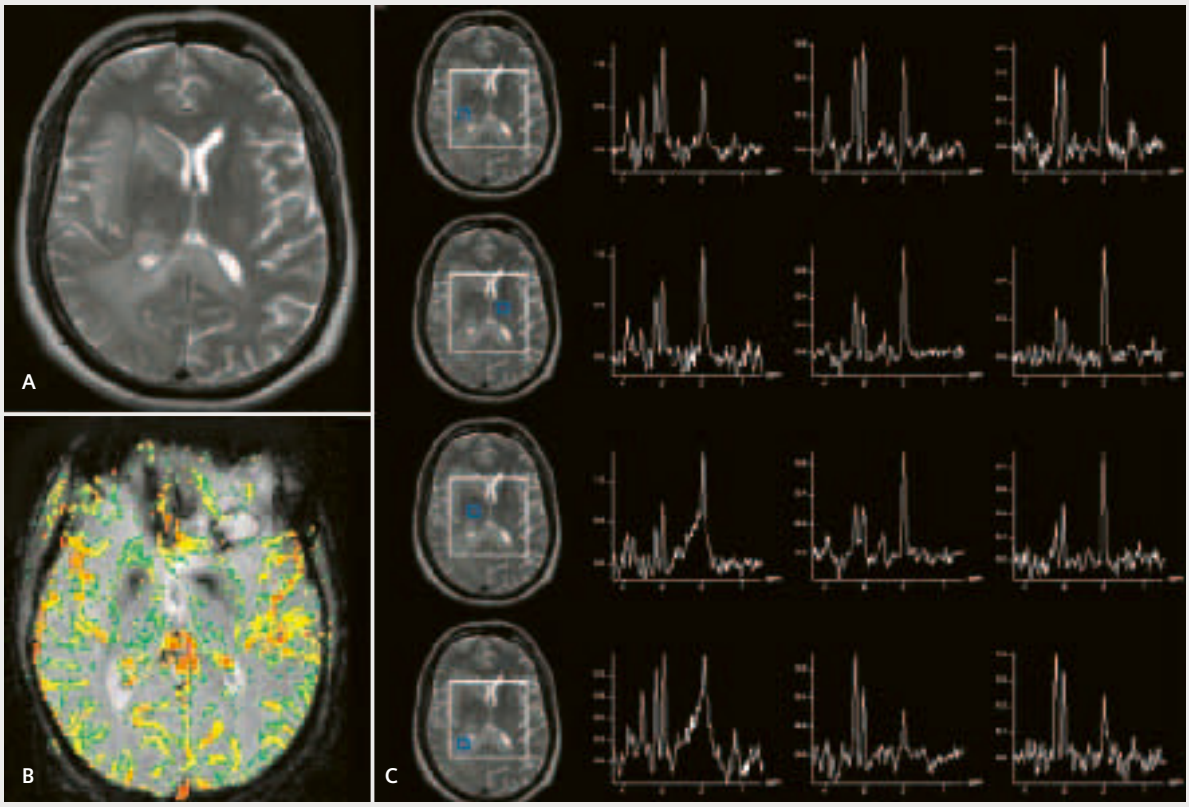

Figure 6 *A: Axial T2-weighted image shows extensive hyperintensity involving the right hemispheric white matter. Contiguous involvement of at least two lobes of the brain is characteristic of gliomatosis cerebri. B: Gradient echo perfusion MRI with rCBV* color overlay demonstrating reduced perfusion. Mean rCBV* was 1.02. C: Multi-TE MRSI of gliomatosis cerebri. The first column shows axial T2-weighted images with the voxel position corresponding to the spectra in the same row. Short TE (30 ms), intermediate TE (144 ms), and long TE (288 ms) spectra are displayed in the second, third, and fourth columns respectively. The 1st row demonstrates spectra from within the tumor, at short TE, there is elevation in myo-inositol and decrease in NAA without appreciable increase in Cho seen at all echo times (30, 144 and 288 ms). The 2nd and 3rd row demonstrate normal spectra from within the normal appearing contralateral brain and the relatively unaffected right thalamus respectively. The 4th row demonstrates elevation in myo-inositol at short TE (30 ms) and some elevation in Cho within the tumor. Myo-inositol elevation in the setting of normal Cho has been described in gliomatosis cerebri (4). Increased Cho/Cr and Cho/NAA have also been described with longer TE's (3). Data were acquired on a 1.5T MAGNETOM Symphony.*

**WIP: The information about this product is preliminary. The product is under development and is not commercially available in the US and its future availability cannot be ensured.*

(stroke). Strokes generally demonstrate increased mean transit time (MTT), and decreased CBF [8-13]. Strokes may demonstrate elevated or decreased rCBV*. In contrast, tumors generally demonstrate increased rCBV* and CBF*. Review of the MTT, CBF* and rCBV* measurements and color overlay maps will not only demonstrate substantial reduction in perfusion in a stroke compared with a tumor but it will conform to a vascular territory (Fig. 9).

An initial inspection of spectroscopy data obtained in a stroke will demonstrate Cho/Cr elevation due to cell membrane destruction and demyelination, as well as decrease in NAA from neuronal and axonal damage. Lactate is also demonstrated for up to 6 weeks and sometimes beyond, initially from anaerobic glycolysis, then later from macrophage activity and persistent ischemia [14]. However, the major difference between a stroke and tumor can best be appreciated by comparing a spectrum from within the stroke to a spectrum from contralateral healthy tissue, which can be done with a multi-voxel MRSI acquisition. The primary difference is a reduction in all metabolites in stroke compared with the contralateral normal brain. Cr, as an energy marker, is particularly reduced in stroke. Even though there may be Cho/Cr elevation and NAA/Cr decrease, when comparing the Cho to normal contralateral Cho(n), there will be a reduction in the Cho/Cho(n) ratio. This demonstrates the value of directly comparing abnormal with normal metabolite levels and measuring Cho/Cho(n) Cho/Cr(n) and NAA/NAA(n) ratios which may increase the specificity somewhat in characterizing mass lesions in the clinical setting when absolute quantification, relative to an external standard cannot be made.

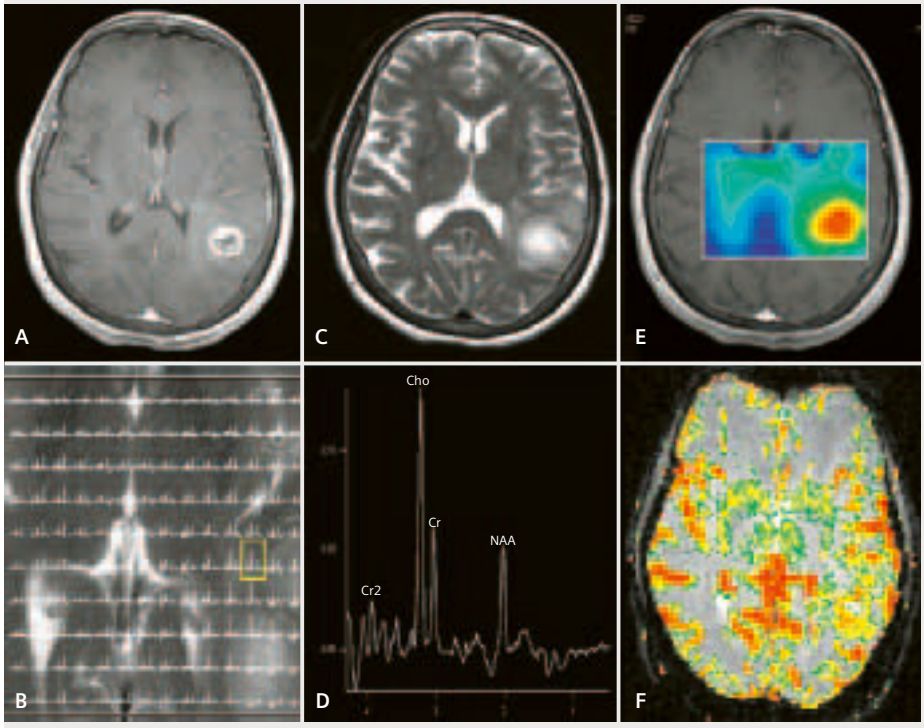

Figure 7 *A glioblastoma multiforme. A: Axial T1-weighted image post-gadolinium shows a peripherally enhancing mass with heterogeneous signal intensity and central necrosis in the left parietal region. B: Axial T2-weighted image demonstrates moderate surrounding T2 signal abnormality, which is likely to represent infiltrating tumor and edema. C: Cho metabolite color overlay demonstrates elevation in Cho in and around the region of enhancement and T2 signal abnormality. D: MRSI (TE 144 ms) spectral map confirms the increase in Cho within the lesion as well as within the abnormal T2 signal anteriorly. E: Spectrum (TE 144 ms) from within the anterior peri-tumoral region demonstrating increase in Cho/Cr and in Cho/NAA from tumoral infiltration of adjacent peri-tumoral tissues. F: Gradient-echo axial perfusion MRI with rCBV* color overlay show increase in vascularity within the enhancing tumor as well as in the peritumoral region anteriorly. These MRSI and perfusion MRI findings in the peritumoral region help to differentiate an infiltrating primary high-grade glioma from a metastasis. Data were acquired on a 3T MAGNETOM Allegra.*

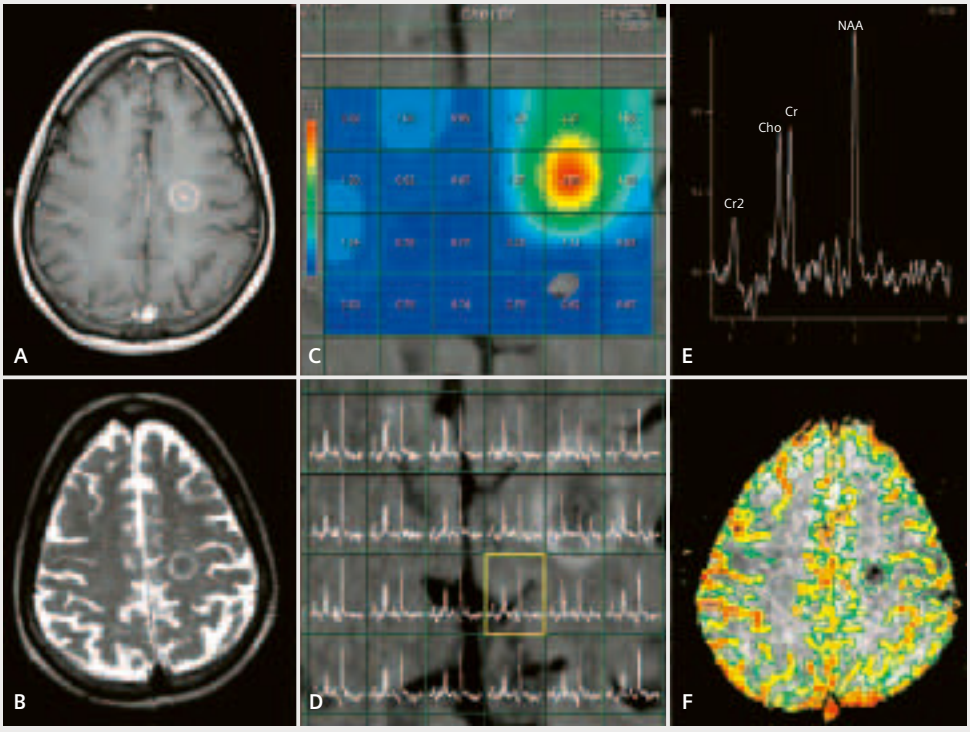

Figure 8 *60 year-old-woman with a metastasis from breast carcinoma. A: Axial T1-weighted image post-gadolinium shows a well defined mass in the left frontal region. B: Axial T2-weighted image demonstrates negligible edema surrounding this lesion. C: Cho metabolite color overlay demonstrates Cho/Cr elevation within the tumor and in voxels where there is partial volume averaging with the tumor. D: MRSI (TE 144 ms) spectral map demonstrates no elevation in Cho within voxels in the peri-tumoral region of the lesion, indicating a non-infiltrating lesion like a metastasis. E: Spectrum (TE 144 ms) from a voxel in the peri-tumoral region with normal metabolite peaks. F: Gradient-echo axial perfusion MRI with rCBV* color overlay may demonstrate increase in tumor vascularity confined to the enhancing tumor but not within the peri-tumoral region. Data were acquired on a 1.5T MAGNETOM Symphony.*

**WIP: The information about this product is preliminary. The product is under development and is not commercially available in the US and its future availability cannot be ensured.*

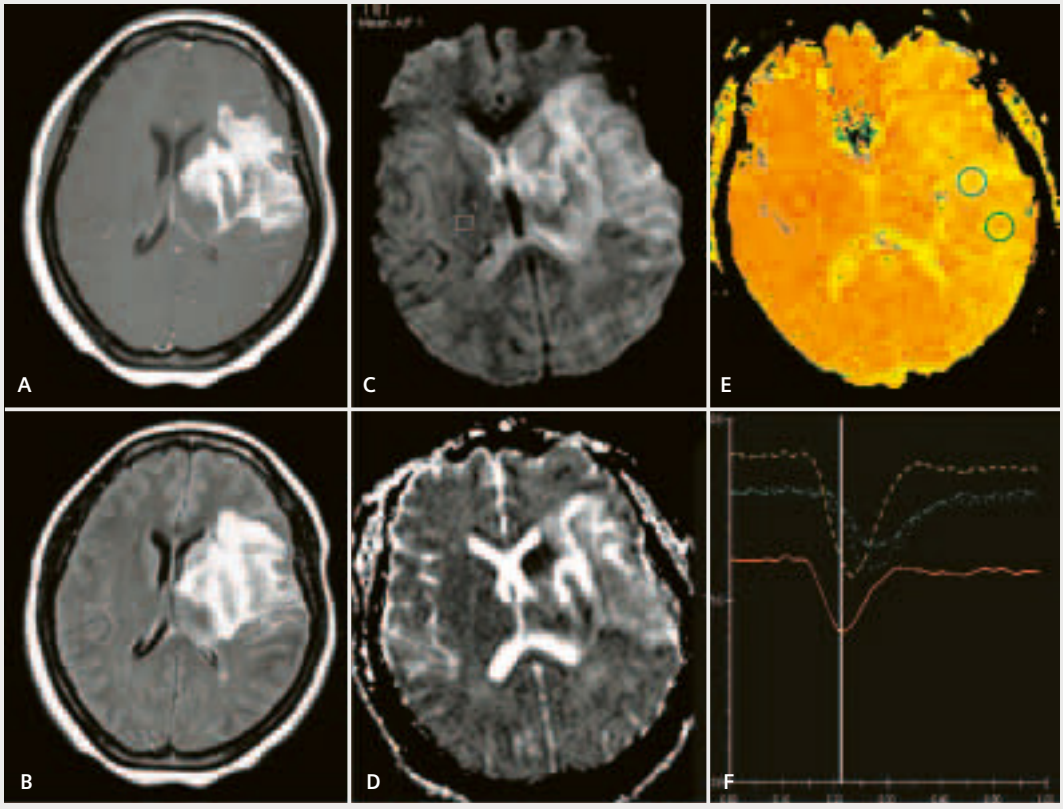

Figure 9 *45-year-old-woman presenting with a 10-day history of right arm and leg weakness: The clinical and final diagnosis was a left middle cerebral artery territory stroke, however conventional MRI, including diffusion weighted imaging was inconclusive. A: Axial T1-weighted image post-gadolinium demonstrates abnormal enhancement in the left hemisphere involving gray and white matter. B: Axial FLAIR image demonstrates abnormal T2 signal as well as some mass effect. There is a small amount of edema. C: Diffusion-weighted image (B = 1000) demonstrating some increase in signal. D: The ADC map also shows areas of increased signal, which may represent "T2-shine-through effect" as well as some areas of decrease signal, which may represent true diffusion restriction. These findings on diffusion are sometimes also seen in very heterogeneous high-grade gliomas. E: Gradient-echo axial perfusion MRI with mean transit time (MTT) color overlay demonstrating prolongation in the MTT throughout the entire middle cerebral artery (MCA) territory in keeping with left MCA ischemia. F: Signal intensity versus time curves color coded to the 4 ROIs placed on the MTT maps, demonstrating prolongation in MTT in the green, blue and to a lesser extent the yellow ROIs. The red ROI indicates normal MTT in the contralateral hemisphere. The delay in MTT and reduced CBF* in the MCA distribution is in keeping with a stroke. Data were acquired on a 1.5T MAGNETOM Symphony.*

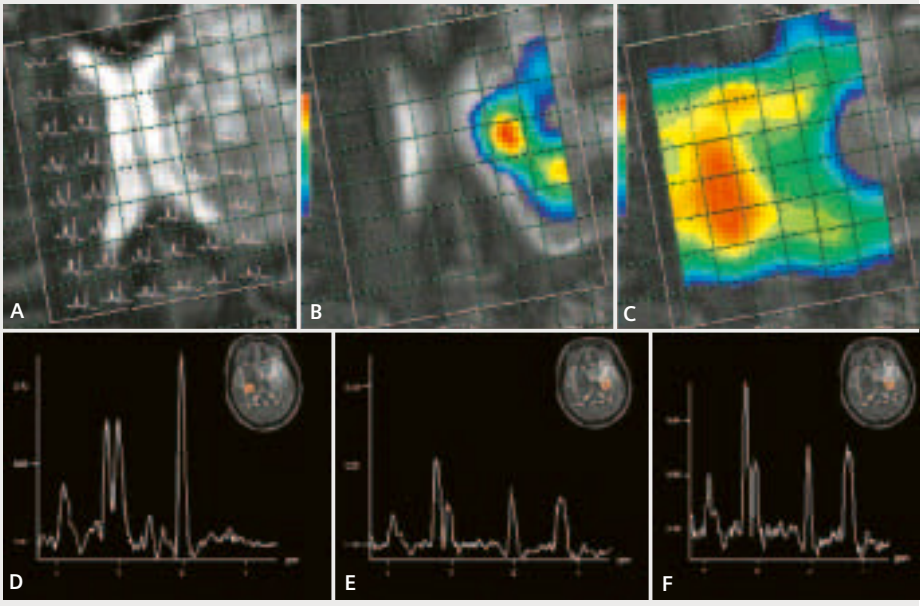

Figure 10 *45-year-old-woman with a left MCA stroke. A: MRSI (TE 144 ms) spectral map demonstrating an increase in Cho/Cr within the abnormal voxels in the left hemisphere, however, there is an overall decrease in metabolites when compared with the right hemisphere. B: The Cho/Cr metabolite ratio color overlay map shows increase in Cho/Cr, which can be misinterpreted for a neoplastic process. C: The Cho metabolite color overlay demonstrates a decrease in Cho (but NOT Cho/Cr) when compared with the right hemisphere. D: MRSI (TE 144 ms) showing a spectrum from the normal right hemisphere. Note is made of the vertical scale and the normal Cho level [Cho (n)], which is used as a control for comparing the abnormal side. E: A spectrum from the abnormal left side displayed on the same scale as the spectrum in D. It shows a decrease in all metabolites including choline, which indicates an ischemic rather than neoplastic process. F: The same spectrum from E scaled to the highest peak in the spectrum i.e choline may be misinterpreted as a neoplastic process. This display illustrates the pitfall of reading a spectrum without a contralateral control. Finding substantial reduction in Cr, Cho and NAA by comparing a spectrum with the normal contralateral control can increase the specificity and exclude a neoplastic process in favor of infarct in this case. Data were acquired on a 1.5T MAGNETOM Symphony.*

**WIP: The information about this product is preliminary. The product is under development and is not commercially available in the US and its future availability cannot be ensured.*

References

[1] *Law M, Yang S, Wang H, et al. Glioma Grading: Sensitivity, Specificity and Predictive Value of Perfusion MRI and Proton Spectroscopic Imaging compared with Conventional MR Imaging. AJNR 2003 24: 1989-1998.*

[2] *Kleihues P, Cavanee P. WHO Classification of Tumors: Pathology and Genetic of Tumours of the Nervous System. Lyon: IARC Press, 2000.*

[3] *Yang S, Wetzel S, Law M, et al. Dynamic contrast-enhanced T2*-weighted MR imaging of gliomatosis cerebri. AJNR Am J Neuroradiol 2002; 23:350-355.*

[4] *Saraf-Lavi E, Bowen BC, Pattany PM, et al. Proton MR Spectroscopy of Gliomatosis Cerebri: Case Report of Elevated Myoinositol with Normal Choline Levels. AJNR 2003; 24:946-951.*

[5] *Burger PC. Classification, grading, and patterns of spread of malignant gliomas. Neurosurgical topics: malignant cerebral glioma. America Association of Neurological Surgeons. Park Ridge, Ill, 1990; 3-17.*

[6] *Burger PC, Vogel FS, Green SB, et al. Glioblastoma multiforme and anaplastic astrocytoma: Pathologic criteria and prognostic implications. Cancer 1985; 56:1106-1111.*

[7] *Law M, Cha S, Knopp EA, et al. High-Grade Gliomas and Solitary Metastases: Differentiation by Using Perfusion and Proton Spectroscopic MR Imaging. Radiology 2002; 222:715-721.*

[8] *Karonen J, Liu Y, Vanninen R, et al. Combined Perfusion- and Diffusion-weighted MR Imaging in Acute Ischemic Stroke during the 1st Week: A Longitudinal Study. Radiology 2000; 217:886-894.*

[9] *Sorensen AG, Copen WA, Ostergaard L, et al. Hyperacute stroke: simultaneous measurement of relative cerebral blood volume, relative cerebral blood flow, and mean transit time. Radiology 1999; 210:519-527*

[10] *Sorensen AG, Buonanno FS, Gonzalez RG, et al. Hyperacute stroke: evaluation with combined multisection diffusion-weighted and hemodynamically weighted echo-planar MR imaging. Radiology 1996; 199:391-401.*

[11] *Hatazawa J, Shimosegawa E, Toyoshima H, et al. Cerebral blood volume in acute brain infarction: A combined study with dynamic susceptibility contrast MRI and 99 mTc-HMPAO-SPECT. Stroke 1999; 30:800-806.*

[12] *Crosby D, Simonson T, Fisher D, et al. Echo-planar MR Imaging: correlation of intracranial perfusion-sensitive imaging with cerebral angiography. Society of Magnetic Resonance 1994; 277.*

[13] *Saunders DE. MR spectroscopy in stroke. Br Med Bull 2000; 56:334-345.*

MAGNETOM C! ...
...is Changing the Face of Mid-Field MRI

Stefan Domalski

Siemens AG
Medical Solutions,
Magnetic Resonance Division,
Market Segment Manager Open Systems, Erlangen, Germany

MAGNETOM World Events around the globe

On July 19, 2004 a new member of the MAGNETOM family achieved US market clearance – MAGNETOM C! – the first open MAGNETOM operating at 0.35T. It is also a member of the MAGNETOM Open family together with the 0.2T MAGNETOM Concerto and the 1.5T MAGNETOM Espree.



The first MAGNETOM C! installed in Europe being delivered to the Eduardus Hospital in Cologne, Germany.

The MAGNETOM C! is an open MRI system based on over 25 years of Siemens MR experience, following the tradition of spearheading the innovations in open MRI. A high-field gradient system with 24 mT/m and a true multi-channel RF system with up to four channels and coils able to cover up to 100 cm (25") field of view are built into the most compact magnet in mid-field, reducing claustrophobia to the minimum. The system is equipped with iPAT parallel acquisition techniques and multi-directional motion correction 2D PACE for fast and robust examinations.

The MAGNETOM C! was introduced to the MR community during a global series of MAGNETOM World events that began in July at the Caravelle Hotel in Ho-Chi-Minh City, Vietnam, where 86 MR experts from all over Asia were the first to see the new system and its potential.

The first MAGNETOM C! in Asia was installed at the Airforce General Hospital in Beijing, China in June 2004. Following the first clinical studies, 150 guests were invited to its official inauguration at the Shangri-La hotel in Beijing, at which Prof. Zhang Wanshi shared his initial experiences of working with the new system. MR users from all over the world have taken the opportunity to check out the MAGNETOM C! in Beijing in the first couple of months after installation and appreciated the exceptional image quality and easy handling of the system.
The HOSPEQ exhibition at the Beijing exhibition center was the first trade show world-wide featuring the MAGNETOM C!

In Europe, the first MAGNETOM C! was installed on September 4 at the Eduardus Hospital in Cologne, Germany, while the first US system went to the Physicians Imaging Center in Dallas, Texas.

This before meeting the public at the "Open MRI in Clinical Practice" meeting in Las Vegas, Nevada, side by side with the MAGNETOM Espree.

The MAGNETOM C! has been developed and is manufactured at the new Siemens MR facility in Shenzhen, China – evidence of the Siemens philosophy of being close to customers anywhere in the world. In addition to research, development and manufacturing, a Headquarter Support Center (HSC) for MR will be set up in Shenzhen, complementing the two existing centers in Erlangen, Germany and Cary, North Carolina, USA with a center in the Asian time zone. The center in Shenzhen has started operations and supports not only the MAGNETOM C! but also all other MAGNETOM systems.



The MAGNETOM C! was introduced to the customers in USA with a presentation at the Open MRI in Clinical Practice Meeting and a reception at the Hard Rock Hotel.



MAGNETOM C! appearing from a cloud of mist and lights at the inauguration event at the Shangri-La Hotel, Beijing, China on Aug 7, 2004.



Delegates at the MAGNETOM C! inauguration meeting on June 12, 2004 at the Caravelle Hotel in Ho-Chi-Minh City, Vietnam.



Prof. Zhang Wanshi from Airforce General Hospital in Beijing, China in front of his new MAGNETOM C!, the first system in the world was installed in June 2004.



T2 TSE Restore, 3 steps, 512 matrix, 345 mm FoV, SL 4.0 mm.



T2 TSE Restore, 512 matrix, 280 mm FoV, SL 3.0 mm.

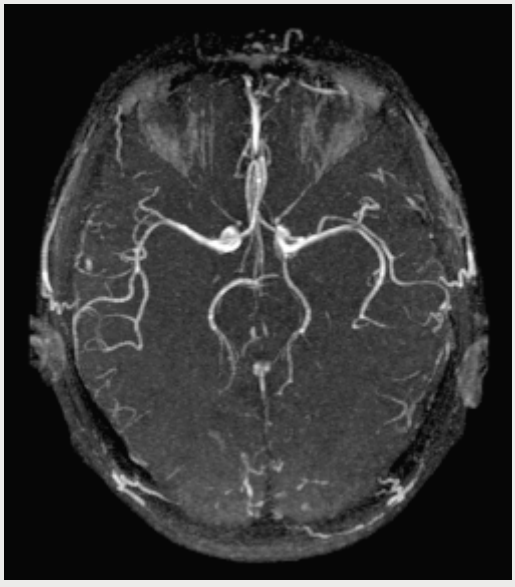

3D MIP, FLASH 2D, 512 matrix, 221 mm FoV, SL 78 mm.

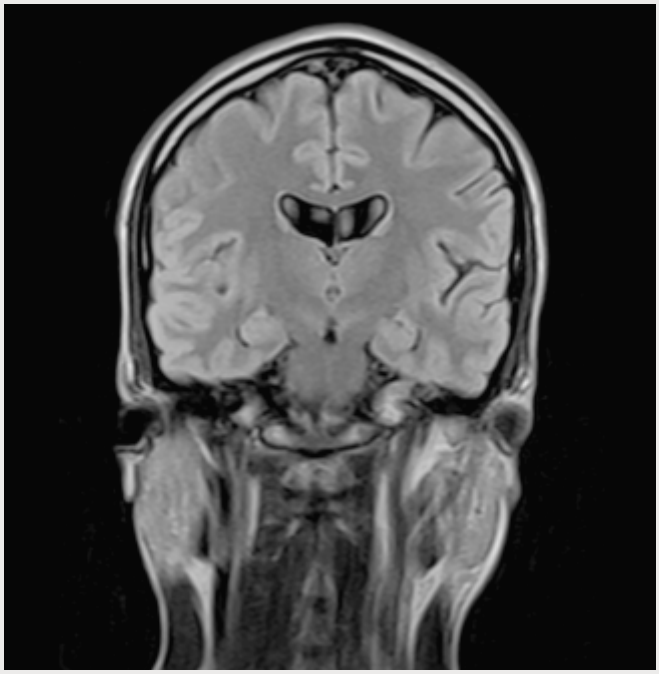

TIRM Dark Fluid, 512 matrix, 239 mm FoV, SL 5.0 mm.

MAGNETOM C!

Image Gallery

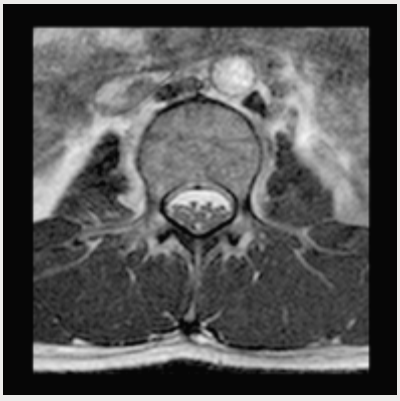

3D CISS, 512 matrix, 216 mm FoV, SL 3.0 mm.

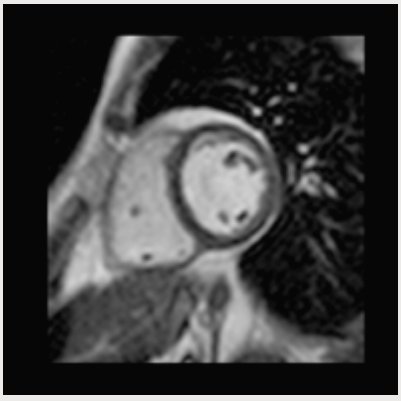

TrueFISP 2D, 256 matrix, 263 mm FoV, SL 8.0 mm.

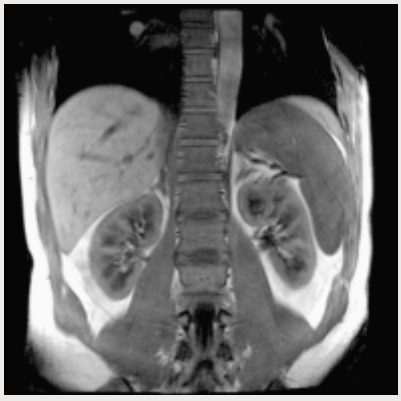

FLASH 2D, 512 matrix, 363 mm FoV, SL 6.0 mm.

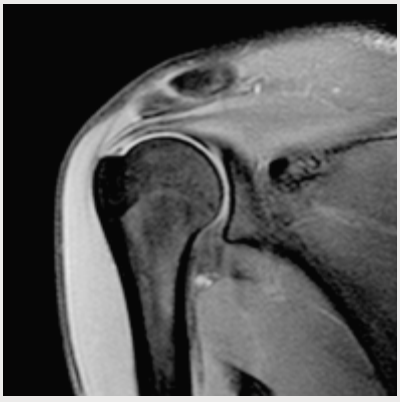

FLASH 3D we, 384 matrix, 146 mm FoV, SL 3.5 mm.



TSE Restore, 640 matrix, 250 mm FoV, SL 4.0 mm.

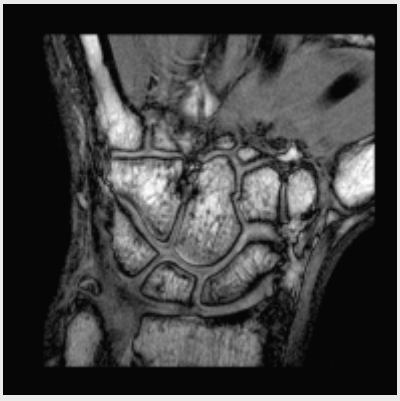

3D DESS, 512 matrix, 115 mm FoV, SL 2.0 mm.



TSE Restore, PAT x 2, 512 matrix, 180 mm FoV, SL 4.0 mm.



FLASH 2D we, 256 matrix, 160 mm FoV, Courtesy of Eduardus Hospital, Cologne, Germany.



TSE Restore, 512 matrix, 300 mm FoV, SL 4.0 mm, Courtesy of Prof. Zhang Wanshi, Airforce General Hospital, Beijing, P.R. China.



FLASH 2D we, 256 matrix, 160 mm FoV, SL 4.0 mm, Courtesy of Eduardus Hospital, Cologne, Germany.



3D MRCP with 2D PACE multi directional motion correction algorithm, Courtesy of Hai Nan Nong Ken Sanya Hospital, P.R. China.



Cine FLASH 2D with tagging, Courtesy of Prof. Zhang Wanshi, Airforce General Hospital, Beijing, P.R. China.

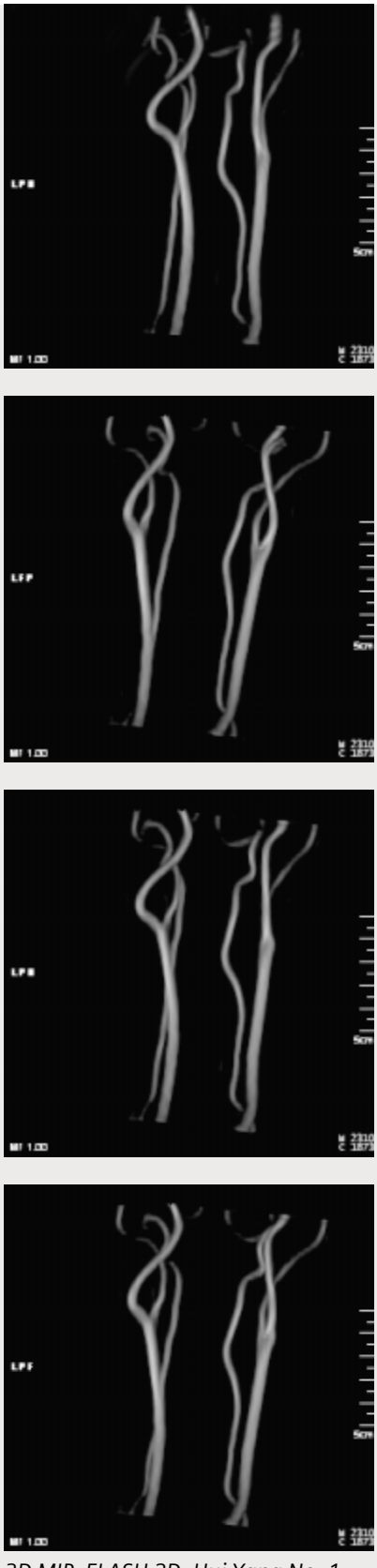

3D MIP, FLASH 2D, Hui Yang No. 1 People's Hospital, Hui Yang, P.R. China.

MAGNETOM C!

Image Gallery



FLASH 2D, 512 matrix, 350 mm FoV, SL 8.0 mm, Courtesy of Hui Yang No. 1 People's Hospital, Hui Yang, P.R. China.

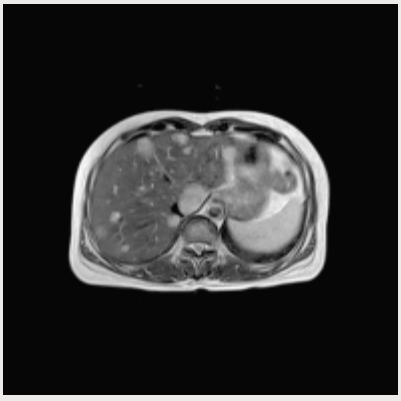

Triple contrast TSE, 512 matrix, 350 mm FoV, SL 10.0 mm, Courtesy of Hui Yang No. 1 People's Hospital, Hui Yang, P.R. China.



3D HASTE, 192 matrix, 250 mm FoV, SL 8.0 mm, Courtesy of Hui Yang No. 1 People's Hospital, Hui Yang, P.R. China.



TSE Restore with PAT x 2, 256 matrix, 260 mm FoV, SL 4.0 mm in 2:11 min.

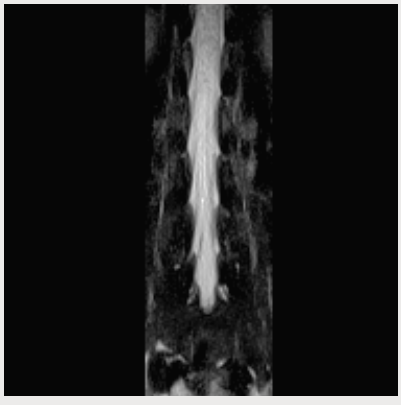

3D MIP of 3D HASTE, 192 matrix, 250 mm FoV, SL 45 mm.

All You Want to Know about FatSat

David Purdy, Ph.D.

MR R&D
Research & Collaborations,
USA

Quick FatSat

What is Quick FatSat and why do we need it ?
Fat and water saturation pulses take so much time compared to the rest of a gradient echo sequence that acquisition times become nearly as long as the corresponding spin echo sequence. In standard saturation mode, saturation pulses are applied before every phase-encoding step of every slice. The quick saturation mode provides a significant reduction in imaging time by using fewer saturation pulses while maintaining a reasonable level of fat or water suppression. This technique is only available for the gradient echo sequence.

How is Quick FatSat used with *syngo*?
Choose two or more slices to ensure that the Saturation mode selection is active in the Saturation subcard of the Geometry card. Select Saturation mode = Quick. Then select Q-fat sat or Q-water sat.

Quality versus imaging time
In quick saturation mode, gradient echo slices are acquired with varying degrees of saturation. The "strong" option gives more slices with good fat saturation in a relatively short imaging time. Even shorter acquisition times are available with the "weak" option, which also gives some slices with good fat saturation, but permits more of the slices to have poorer saturation. This allows the user to adjust the trade-off between imaging time and fat saturation quality when speed is essential, often for breath-hold imaging.

Quick FatSat with 2D Multislice
Since the effect of a saturation pulse does not disappear immediately, and since the GRE sequence acquires data rapidly, one Fourier line from several slices can be acquired after a single saturation pulse. Naturally, the first slice acquired following the saturation pulse will show better saturation than the last, so the user is allowed some control over how many slices are acquired before the next saturation.

For strong Quick fat sat mode, the system acquires as many different slices as possible between FatSat pulses, provided that the time between saturation pulses does not exceed about 50 ms. This amounts to roughly four slices between saturation pulses, greatly increasing the time efficiency of the sequence. For the "weak" fat sat mode, the time between saturation pulses does not exceed about 75 ms, further increasing time efficiency at the cost of poorer fat suppression for a few of the slices.

You can obtain the maximum number of slices per FatSat pulse if you increase the number of slices to the final value, rather than decreasing the number.

If only two slices are acquired, there are only two slices between saturation pulses, and there is no difference between "strong" and "weak" quick saturation modes. The same will usually be true for three and four slice protocols. The gradient echo sequence does not change the FatSat flip angle to create brighter or darker fat.

If only one slice is acquired, the saturation pulse must be applied for each phase encoding, so there is no difference between quick saturation mode and standard mode.

Quick FatSat with 2D Sequential Slice
The saturation pulse must be applied for each phase encoding, so there is no difference between quick saturation mode and standard mode.

Quick FatSat with the 3D GRE Sequence
For a single slab (or multiple, sequential slabs), the quick and standard saturation modes are identical. For multiple interleaved slabs, the quick mode works as described above for interleaved slices. For 3D, users should select the "weak" Q-fat sat mode to avoid a system problem with the "strong" mode. For a faster acquisition with good fat suppression, a water excitation pulse should be considered.

Quick FatSat: Some Examples

A concrete example is helpful for explaining how Quick FatSat works. Here is my test case :

I used the gradient echo sequence on a MAGNETOM Symphony Quantum, regular gradient mode, regular RF mode, 260 Hz/pixel bandwidth, one segment, minimum TE, and minimum TR. For acquisition time measurements, I used a 256 x 256 matrix.

To describe what is happening, I need to define a couple of words. I will call that part of the sequence that excites the slice, phase-encodes it, and reads out the data the "imaging module." The duration of the imaging module is the same as the minimum TR of the sequence (without saturation pulses) when one slice is imaged. This is a few milliseconds longer than TE. For my test case, TE is 3.76 ms and the imaging module takes 7.7 ms.

I will call the FatSat RF pulse and the following spoiler gradient the "FatSat module." For the GRE sequence, the FatSat or Water sat module takes about 20 milliseconds.

The operation of the quick saturation mode is governed by several concepts or rules.

Rules:

1. The effectiveness of the FatSat pulse decays over time: 30 ms after the pulse, the fat suppression is only "fair"; 55 ms after the pulse, the suppression is just adequate. For the standard FatSat technique, only one imaging module is placed after each FatSat module, so that the strongest saturation is obtained. However, additional imaging modules (e.g., slices) may be placed after the first. This reduces imaging time. Images reconstructed from these later imaging modules will have poorer fat saturation.
2. The time between the imaging modules for a particular slice is TR. To avoid serious artifacts, the TR for all 256 Fourier lines must be the same.
3. To maintain the same clinical contrast for every slice, the TR of each slice should be the same.
4. To avoid artifacts, the time between the FatSat module and the imaging module for a particular slice should be the same for all 256 Fourier lines.
5. It is not necessary for the time between FatSat pulses to be constant.

These considerations lead naturally to the Quick saturation method: more than one imaging module may be placed after a FatSat module. This technique was originated by Dr. Paul Finn (U.S. patent 5.633.586). The sequence diagrams are rather different for one slice, a few slices, and many slices, and I will treat these separately.

Quick Sat – Small number of slices

The advantage of Quick saturation is most easily diagrammed for two slices.

Figure 1 shows a two-slice interleaved multislice sequence with standard FatSat:

Each imaging module acquires one Fourier line, and each is directly preceded by a FatSat module. Each Fourier line has good fat suppression, and the two images do also. TR is the sum of the durations of two FatSat and two imaging modules (20 + 20 + 7.7 + 7.7 = 55.4 ms). The time between the centers of the FatSat modules is (20 + 7.7 = 27.7 ms). The desirable short acquisition time of the GRE sequence is lost when FatSat is added in this manner – the FatSat module takes up 20/27.7 = 72% of the overall imaging time.

The Quick saturation mode saves time by inserting the imaging modules for slice 2 immediately after the modules for slice 1 (Figure 2). This eliminates half (256) of the FatSat modules from the acquisition. The fat suppression for slice 2 is not as good as that for slice 1, but it is acceptable as long as not too much time has elapsed between the FatSat pulse and the second slice module. The *syngo* Quick sat mode guarantees this.

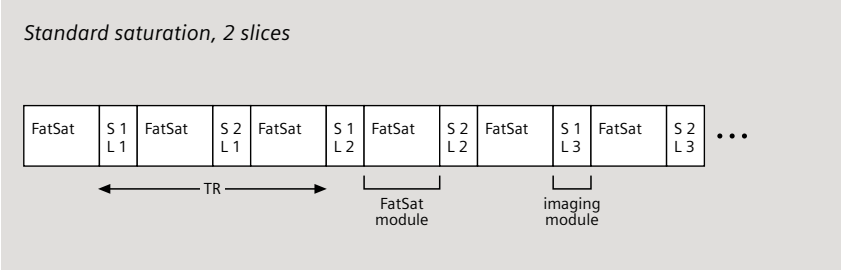

Figure 1 *Each imaging module is labeled with the spatial slice position (S) and the Fourier line number (L). The horizontal axis is time. The 2 slice, 256 line acquisition has 512 FatSat modules.*

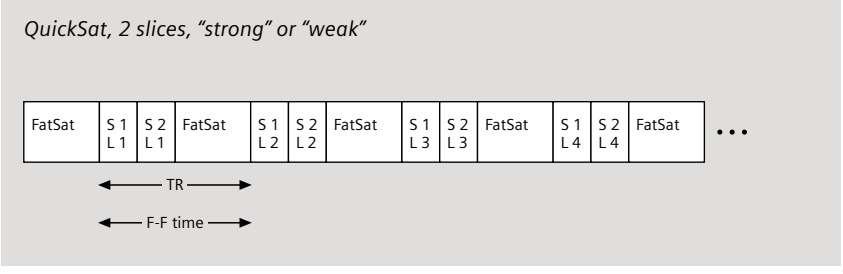

Figure 2 *Compared to the standard saturation mode in Figure 1, the FatSat module now only takes up 56% of the total imaging time. The time between FatSat modules (center-to-center or end-to-end) is labeled "F-F time."*

TR has been reduced to one FatSat module and two imaging modules (20 + 7.7 + 7.7 = 35.4 ms), and the total imaging time (256 x TR) has been reduced from 14.2 seconds in standard mode to 9.1 seconds in Quick sat mode, a time saving of 36%.

The fat saturation of the second slice in Figure 2 is still fairly good, so more imaging modules (slices) may be added between the FatSat pulses. Since each additional slice has poorer saturation, we cannot insert too many slices between FatSat modules. The user is given some control over the tradeoff between speed and FatSat quality. In "strong" mode, the FatSat-to-FatSat time (measured from the pulse centers) will not exceed about 50 milliseconds (four slices for our test case). In "weak" mode, the time limit is about 75 ms (seven slices for our test case). One measure of the efficiency of these modes is how much time is wasted on the long FatSat pulses. When we acquire 4 slices per FatSat, only 39% of the acquisition time is spent on the FatSat module, for 7 slices per FatSat, only 27%.

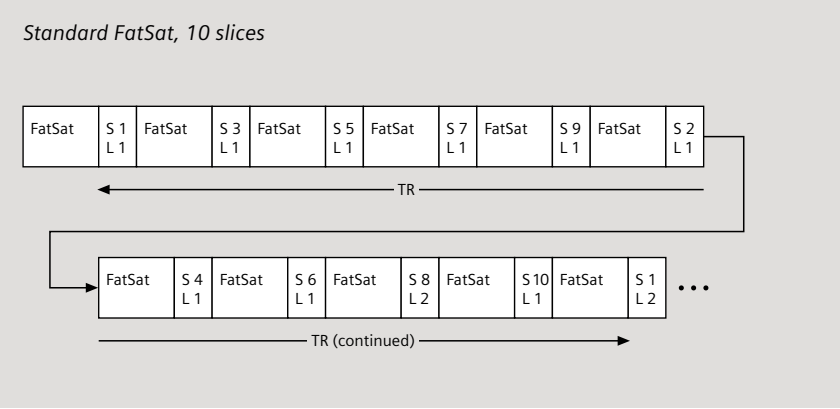

Figure 3 *TR is the duration of ten FatSat pulses and ten imaging modules. As in Figure 1, the FatSat module takes up 72% of the overall imaging time.*

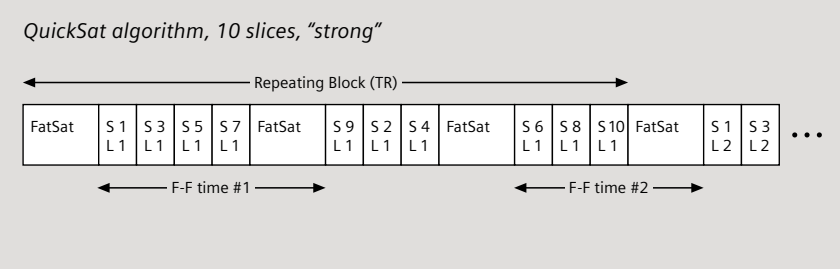

Figure 4 *TR is the duration of three FatSat pulses and ten imaging modules. The FatSat module takes up 44% of the overall imaging time.*

Quick Sat – Large number of slices

The pattern of FatSat and imaging modules changes when we request more slices. Figure 3 shows 10 interleaved slices acquired in standard FatSat mode. The slice numbers represent physical positions, and the interleaving is assumed to be odd slices before even (Fig. 3).

Figure 4 shows 10 interleaved slices in "strong" Quick sat mode. For this example, only 4 slices are permitted after each FatSat pulse (Fig. 4).

The maximum time between FatSat pulses is 50.8 ms, just at the limit for the "strong" algorithm. The TR for any one slice is constant (Rule #2), because the slice only appears once in the repeating block. The TR for all of the slices is the same (Rule #3), because the 10-slice block repeats. The time between a FatSat pulse and a particular slice is constant (Rule #4) for the same reason. The time between the first and the second FatSat pulses is longer than between the other FatSat pulses – this does not cause significant artifacts (Rule #5). It is important to note that slices 1, 9, and 6 are acquired directly following a FatSat pulse, and will show maximal fat suppression. Slices 3, 2, and 8 will show somewhat less suppression, and slices 5, 4, and 10 less still.

Figure 4 should make it clear that the sequence in this example is most efficient when the number of requested slices is a multiple of four, but it is not possible to make the 10-slice sequence more efficient by having four imaging modules between every pair of FatSat modules. Figure 5 shows that the pattern does not repeat after 10 slices.

The first TR for slice 1 is the duration of 10 imaging modules and 2 FatSat modules, but the next TR for this slice is 10 imaging modules and 3 FatSat modules. This violates Rule #2, and would lead to unacceptable artifacts. Rule #4 is also violated.

For quick saturation, "weak" mode gains time efficiency at the cost of a few slices with diminished fat suppression. For the example case, seven imaging modules can be

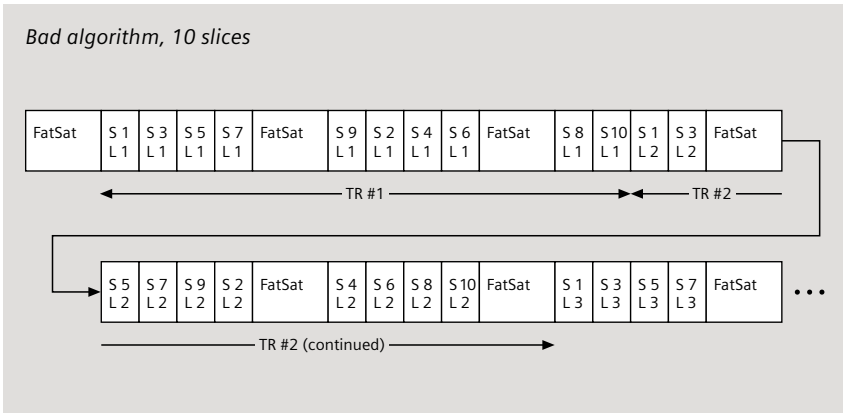

Figure 5 *Four imaging modules are placed between each pair of FatSat pulses. TR #2 continues from the first line to the second.*

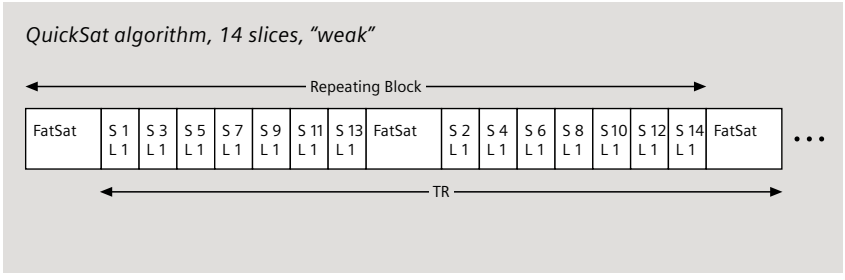

Figure 6 *TR is the duration of two FatSat modules and fourteen imaging modules. Only 27% of the acquisition time is spent for FatSat.*

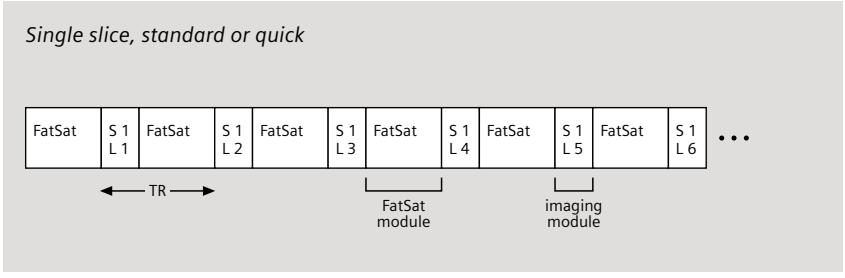

Figure 7 *The only imaging module that could be inserted after slice 1, line 1 would be slice 1, line 2, and this would create Fourier lines with very different TRs (Rule #2), leading to artifacts.*

inserted between the FatSat pulses without exceeding the 75 ms FatSat-to-FatSat limit. Figure 6 shows a 14-slice example.

Note that slices 1 and 2 in the "weak" example of Figure 7 have the same strong fat suppression as slices 1, 9, and 8 in the "strong" example of Figure 4. The only slices in Figure 6 that have weaker saturation than the slices of Figure 4 are slices 9, 11, 13, 10, 12, and 14.

Quick Sat – No "weak" and "strong" for small numbers of slices

The weak and strong modes for quick saturation are only relevant when the number of requested slices is larger than the number that are allowed between FatSat pulses for "strong" mode. For our example, "strong" mode allows as many as four slices between FatSat modules; there is no difference between "weak" and "strong" protocols for 2-, 3-, or 4-slice protocols.

No Quick Sat for single slice

Although permitted by the user interface, there is no Quick sat mode for single-slice protocols. Standard saturation, Quick weak saturation, and Quick strong saturation all follow the pattern of Figure 7.

No Quick Sat for sequential slices

Since sequential slice mode acquires one slice at a time, each slice follows the pattern of Figure 7. Quick saturation is permitted by the user interface (no harm is done), but standard saturation is performed.

Improving slice efficiency for breath-holds

There is a trick that you can use to shorten certain scans by 2-4 seconds.

Quick fat saturation is very useful for time-critical imaging tasks such as breath-hold imaging. To acquire as many slices as possible during the breath-hold, we want to get as many slices between the FatSat pulses as possible. This means using a high receiver bandwidth, the shortest possible TR, and "weak" mode. For example, using weak mode and a bandwidth of 490 Hz/pixel, it is possible to obtain one Fourier line from 12 slices between the FatSat pulses. With this bandwidth and 114 lines, each additional slice adds 0.5 s to the imaging time, and each FatSat pulse adds 2.16 s. The sequence acquires 12 slices in (12 x 0.5 + 2.16) = 8.16 s, or 1.47 slices per second. The efficiency drops when one more slice (13 total) is requested, because an additional FatSat pulse must be added, and the imaging time is (13 x 0.5 + 2 x 2.16) = 10.82 s, or 1.20 slices per second.

Unfortunately, the maximum number of slices acquired between FatSat pulses varies, depending on how the user types in the number of slices. To obtain the maximum number of slices in the minimum acquisition time for breath-hold applications, use the arrow to increase the number of slices one by one, allowing the system to compute the new TR and acquisition time for each step. You will notice a larger jump in TR and acquisition time when the next FatSat pulse is added. For certain numbers of slices, fewer slices per FatSat will be available when you decrease the number of slices one by one. If you need to decrease the number of slices, reduce the number by at least six slices, reset TR to its minimum value, and begin to increase the number again.

Here are the results for the example above. TR increases by about 4 ms as each slice is added. TR jumps an additional 19 ms as each FatSat pulse is added. The acquisition time is TR times the number of lines. We expect to get 12 slices per FatSat, and we do indeed get 36 slices with three FatSat pulses. However, if we decrease the number of slices to the final value, we can get as few as 9 slices for one FatSat pulse.

Quick Sat for 3D MRA Sequences

A different kind of quick saturation is used for some of the 3D angiography sequences in single-slab or sequential slab modes. This allows the acquisition of data for many phase-encoding steps after each FatSat pulse. Because there are fewer 3D (slice) encodings than in-plane (line) encodings, these sequences acquire all of the 3D phase encodings after each FatSat. For a reasonable number of 3D partitions, say 32 or more, it is not possible to maintain good saturation for all of the encodings, so the important central encodings are

Slices	Minimum TR as you increase the no. of slices	Minimum TR as you decrease the no. of slices
1	24	(same) (24)
2	28	(same)
(. . .)		
9	59	(same)
10	63 ----------	82
11	68 ----------	87
12	91	(same)
(. . .)		
20	126	(same)
21	131	(same)
22	135 ----------	154
23	140 ----------	159
24	163	(same)
(. . .)		
33	203	(same)
34	207	(same)
35	211 ----------	230
36	216 ----------	235
37	239	(same)

acquired first (“centric reordering”). This ensures that large regions of fat are uniformly saturated in all of the reconstructed slices. This is the standard mode of fat saturation for these sequences; the user does not need to select any special “quick” mode.

Quick Sat – Summary

Quick saturation mode is very suitable for breath-hold abdominal examinations, where acquisition speed is much more important than slice-to-slice uniformity of fat suppression.

Conventional FatSat – Strong and weak modes

What are these modes?
For conventional (not Quick) FatSat, “strong” mode gives darker fat than “weak” mode.

Why do we use weak mode ?
Weak FatSat mode prevents the bone marrow from becoming completely black, enabling visualization of marrow lesions. It also keeps the signal from ligaments hypointense. Each slice has essentially the same degree of fat saturation.

With which sequences can we use weak and strong modes ?
“Weak” and “strong” modes are available for RF refocused sequences (SE, TSE, TGSE, and HASTE). Only standard saturation mode is permitted for these sequences; there is no “quick” option. In “strong” mode, an optimized FatSat flip angle is used to ensure the smallest signal from fat. This angle varies with TR and the number of slices. In “weak” mode, a fixed flip angle of 90° is used. Imaging time is the same for both modes.

Standard saturation mode is available for the gradient echo sequences, but only with a fixed FatSat flip angle – there is no “strong” or “weak” option.

Spin Echo “weak” and “strong” versus Gradient Echo “weak” and “strong”

For RF-refocused (SE, TSE, TGSE, HASTE) sequences, "weak” and "strong” adjust the fat brightness of all of the slices together by changing the FatSat pulse tip angle. The strong mode optimizes the tip angle for the number of slices and TR. The weak mode uses a fixed tip angle – the low end of the range of strong values. Except for shim problems, all of the slices for one measurement should have the same fat brightness. Some physicians want very dark bone marrow, and use “strong” mode. Others feel that marrow lesions are more easily seen if the marrow is gray, and use the “weak” mode.

The words “weak” and “strong” have a completely different meaning for the Quick sat mode of the GRE sequence. When many slices are acquired, one group of slices will have good saturation, another group will show less saturation, the next group even less saturation, and so on. In “strong” mode, the slice group showing the least fat suppression will still have relatively good suppression. “Weak” mode allows faster acquisitions, but the slice group showing the least fat suppression will have only adequate suppression. These modes allow the user some choice over this tradeoff. Both “weak” and "strong” modes will give some slices with good saturation, but we cannot use Quick fat sat for consistent control of bone marrow brightness.

Diffusion-Weighted MR Imaging for Diagnosis of Liver Metastases

Bachir Taouli, M.D.

**Department of Radiology,
NYU Medical Center,
New York, USA**

Liver metastases are the most frequently encountered malignant lesions, most frequently related to colorectal, lung and breast carcinomas. Diagnosis of liver metastases can be obtained with ultrasound (which suffers from limited sensitivity), CT and MR imaging before and after intravenous contrast injection. In some instances, metastases can be difficult to differentiate from benign lesions such as hemangiomas or focal nodular hyperplasias (FNH), and therefore an accurate method of characterization is necessary to avoid unnecessary treatments and anxiety for patients. In addition, in patients with known liver metastases undergoing surgical resection, an accurate detection of metastases is necessary for the surgical planning.

Diffusion is the thermally induced motion of water molecules in biological tissues, called Brownian motion. With the addition of motion probing gradient (MPG) pulses, magnetic resonance imaging (MRI) – by means of the apparent diffusion coefficient (ADC) measurement – is currently the best imaging technique for in vivo quantification of the combined effects of capillary perfusion and diffusion.

Diffusion-weighted imaging (DWI) is possible by using diffusion gradients on each side of the 180° pulse when using single-shot Spin Echo echoplanar imaging (EPI) sequences, using various b-values. The b-value represents the diffusion factor (measured in s/mm^2) and represents the strength of the diffusion gradients. The ideal b-value for lesion characterization is a trade-off between signal attenuation and perfusion contamination, this is generally possible using b-values between 300-1000 s/mm^2 for liver imaging. Pure diffusion images are obtained when using b-values > 1000 s/mm^2, however images will be limited by signal loss.

The ADC (measured in mm^2/s) represents the slope of the curve of signal intensity vs. b-value, and is calculated using the following formula: ADC = (-1/b) Log S1/S0; where b = diffusion factor, S_0 = signal intensity (SI) for b= 0 (before application of diffusion gradient), S_1 = SI after application of diffusion gradient.

The primary application of diffusion-weighted imaging has been in brain imaging. With the advent of EPI technique, DWI of the abdomen has become possible with fast imaging times minimizing the effect of gross physiologic motion from respiration and cardiac movement. DWI can be used to detect and characterize liver lesions (including malignant lesions), and also for treatment follow-up.

Protocol used in our institution

At NYU medical center, for DWI of the liver, we use breath-hold single shot EPI sequences on 1.5T (MAGNETOM Sonata and MAGNETOM Avanto), using CP array surface coils, a pulse trigger to minimize artifacts from heart beating [1]. We use a short TR (1300 ms) to decrease the acquisition time, and the shortest possible TE (approximately 50-70 ms. depending on the b-value) close to the T2 of the liver (which is approximately 50 ms at 1.5T). We use parallel imaging (GRAPPA 2) in order to decrease distortion artifacts, acquisition time as well as to get the shortest possible TE [2]. The matrix size is 128 x 128, with a large FoV in order to decrease ghosting artifacts, and a slice thickness of 7-8 mm. We use typically b-values of 0-50-500-1000 s/mm^2.

Role of DWI for detection of liver lesions

There is limited data on the use of DWI for lesion detection. For example, a recent study from the Netherlands [3] showed that DWI with small b-values < 50 s/mm^2 giving black-blood images can potentially replace the routine Turbo Spin Echo T2 for lesion detection. Fig. 1 shows images in a normal volunteer using small diffusion gradients.

DWI for characterization of liver lesions and diagnosis of liver metastases

DWI represents a potential new tool for the characterization of liver metastases, and differentiation of benign from malignant liver lesions. DWI is non invasive, requires no contrast injection, and can be performed within a breath-hold.

Most of previous studies have used DWI to characterize liver lesions, and have shown that benign lesions – such as liver cysts and hemangiomas – show higher ADCs than malignant lesions – such as hepatocellular carcinomas and metastases [4-8]. This is likely related to free water motion in benign lesions, and restricted water motion in the presence of tumor. However, ADC values are often variable from a study to another, partially related to different equipment and different b-values. ADCs tend to be larger when using small b-values, because the signal attenuation due to diffusion plays only a minor role in that case, and ADC values are contaminated by microperfusion. When higher b-values

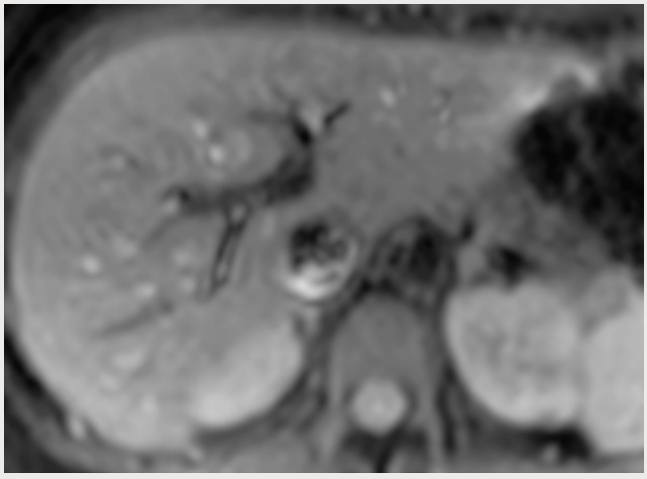

Figure 1a

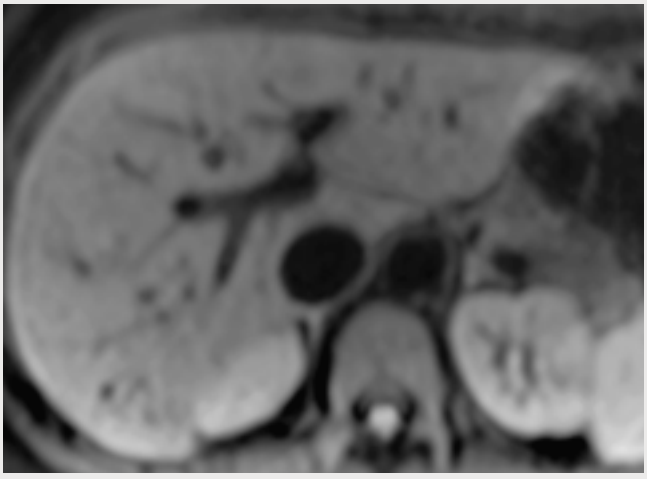

Figure 1b

Figure 1 (a, b) *Diffusion-weighted images in a 31-year-old normal volunteer. Single-shot EPI images without application of a diffusion gradient (b = 0 s/mm²) and after application of a small diffusion gradient of b = 50 s/mm² (b, black-blood image). Note complete vessel darkening on b. This allows easier detection of liver lesions which will not attenuate at this small b-value.*

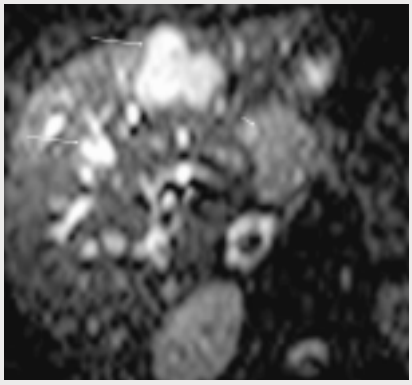

Figure 2a

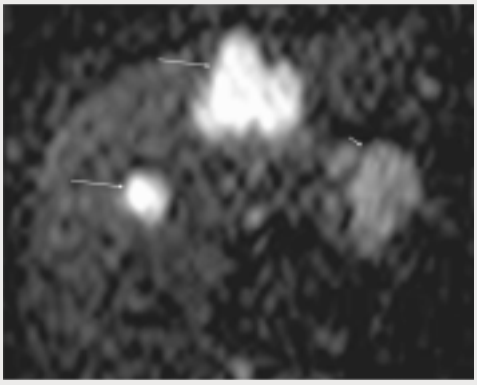

Figure 2b

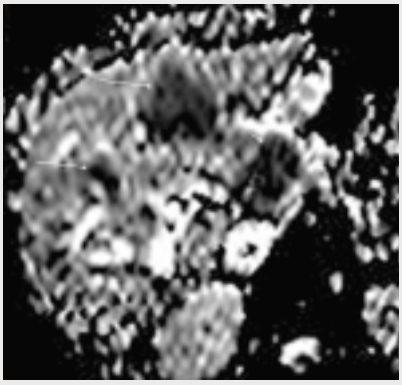

Figure 2c

Figure 2 (a-c) *33-year-old man with liver metastases from pancreatic islet cell tumor. Diffusion-weighted images obtained using single-shot EPI for b = 0 s/mm² (a) and b = 500 s/mm² (b), without parallel imaging, show metastases of the right and the left liver lobes (long arrows) in high signal, with no attenuation at b = 500 s/mm². The primary tumor is located in the pancreatic head (short arrow). These lesions can be easily confused for hemangiomas. ADC measured on the mapping image (c) was very low (0.5 x 10⁻³ mm²/s).*

are used, ADCs tend to decrease, in relation with less perfusion contamination. We showed in a previous study [8] a significant difference between ADCs of benign and malignant lesions ($2.45 \pm 0.96 \times 10^{-3}$ and $1.08 \pm 0.50 \times 10^{-3}$ mm²/s for b = 0 and 500 s/mm²; respectively, $p < 0.001$). The mean ± SD ADCs ($\times 10^{-3}$ mm²/s) of the different groups of lesions were: metastases 0.94 ± 0.60, hepatocellular carcinomas 1.33 ± 0.13, FNH / adenomas 1.75 ± 0.46, hemangiomas 2.95 ± 0.67 and cysts 3.63 ± 0.56 [8]. Using a threshold ADC value of 1.5×10^{-3} mm²/s, we were able to differentiate benign from malignant lesions with 84% sensitivity and 89% specificity. Potential limitations will include necrotic and cystic metastases, where ADC might be elevated, and the diagnosis will then rely on post-contrast images. Fig. 2 and 3 show examples of patients with liver metastases.

DWI for follow-up of treated liver metastases

DWI can potentially be used to follow treated metastases, whether using systemic or local chemotherapy (transarterial catheter chemoembolization), or local treatment (such as radiofrequency or cryoablation). A recent study has shown the usefulness of DWI over routine contrast-enhanced MRI for prediction of hepatocellular carcinoma necrosis in cirrhotic patients [9]. An animal study has also shown a good correlation between response to therapy and ADC changes [10, 11].

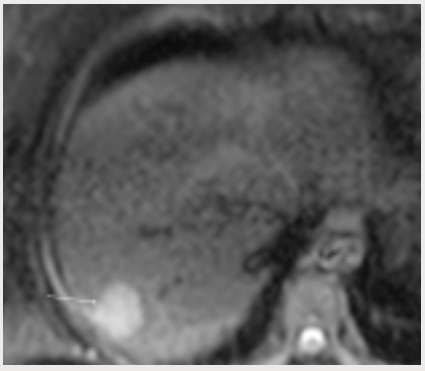

Figure 3a

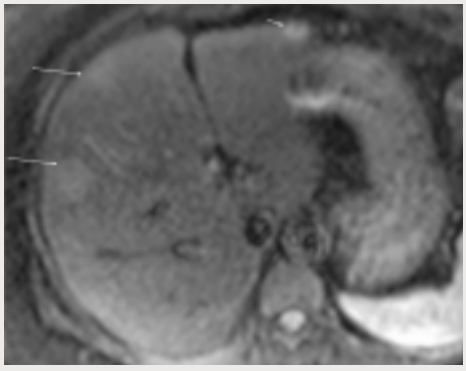

Figure 3b

Figure 3(a-e) *34-year-old patient with liver metastases from colon cancer. Diffusion-weighted images obtained with single-shot EPI and parallel imaging, b-values of 0 (a, b) and b = 500 s/mm² (c, d) show multiple hyperintense liver lesions, with no attenuation on diffusion-weighted images. In particular, there is a sub-centimeter lesion in the lateral left lobe (short arrow) not seen on the routine axial TSE T2 (e) images.*

Future improvements in image quality

3T technology will be potentially able to provide better image quality in relation with improved signal. However, susceptibility and distortion artifacts with EPI sequences may also be increased [12].

Conclusion

DWI allows functional imaging of liver lesions and liver disease. The acceptance of DWI into routine practice will be parallel to the new developments in sequences and also to the improved experience of the radiologists in this area.

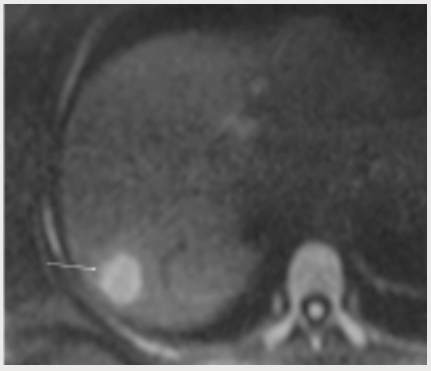

Figure 3c

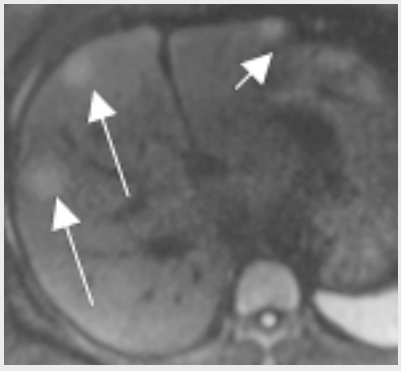

Figure 3d

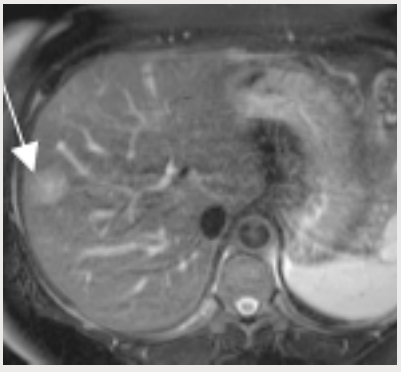

Figure 3e

References

[1] *Murtz P, Flacke S, Traber F, van den Brink JS, Gieseke J, Schild HH. Abdomen: diffusion-weighted MR imaging with pulse-triggered single-shot sequences. Radiology 2002; 224:258-264.*

[2] *Taouli B, Martin AJ, Qayyum A, et al. Parallel imaging and diffusion tensor imaging for diffusion-weighted MRI of the liver: preliminary experience in healthy volunteers. AJR Am J Roentgenol 2004; 183:677-680.*

[3] *Hussain SM, De Becker J, Hop WC, Dwarkasing S, Wielopolski PA. Can a single-shot black-blood T2-weighted spin-echo echo-planar imaging sequence with sensitivity encoding replace the respiratory-triggered turbo spin-echo sequence for the liver? An optimization and feasibility study. J Magn Reson Imaging 2005; 21:219-229.*

[4] *Muller MF, Prasad P, Siewert B, Nissenbaum MA, Raptopoulos V, Edelman RR. Abdominal diffusion mapping with use of a whole-body echo-planar system. Radiology 1994; 190:475-478.*

[5] *Namimoto T, Yamashita Y, Sumi S, Tang Y, Takahashi M. Focal liver masses: characterization with diffusion-weighted echo-planar MR imaging. Radiology 1997; 204:739-744.*

[6] *Kim T, Murakami T, Takahashi S, Hori M, Tsuda K, Nakamura H. Diffusion-weighted single-shot echoplanar MR imaging for liver disease. AJR Am J Roentgenol 1999; 173:393-398.*

[7] *Ichikawa T, Haradome H, Hachiya J, Nitatori T, Araki T. Diffusion-weighted MR imaging with single-shot echo-planar imaging in the upper abdomen: preliminary clinical experience in 61 patients. Abdom Imaging 1999; 24:456-461.*

[8] *Taouli B, Vilgrain V, Dumont E, Daire JL, Fan B, Menu Y. Evaluation of liver diffusion isotropy and characterization of focal hepatic lesions with two single-shot echo-planar MR imaging sequences: prospective study in 66 patients. Radiology 2003; 226:71-78.*

[9] *Kamel IR, Bluemke DA, Ramsey D, et al. Role of diffusion-weighted imaging in estimating tumor necrosis after chemoembolization of hepatocellular carcinoma. AJR Am J Roentgenol 2003; 181:708-710.*

[10] *Roth Y, Tichler T, Kostenich G, et al. High-b-value diffusion-weighted MR imaging for pretreatment prediction and early monitoring of tumor response to therapy in mice. Radiology 2004; 232:685-692.*

[11] *Herneth AM, Guccione S, Bednarski M. Apparent diffusion coefficient: a quantitative parameter for in vivo tumor characterization. Eur J Radiol 2003; 45:208-213.*

[12] *Kuhl CK, Textor J, Gieseke J, et al. Acute and subacute ischemic stroke at high-field-strength (3.0-T) diffusion-weighted MR imaging: intraindividual comparative study. Radiology 2005; 234:509-516.*

T2-Weighted 3D MR Imaging of the Torso – First Clinical Experiences with SPACE

M. P. Lichy, M.D.[1]
W. Horger[2]
J. P. Mugler, Ph.D.[3]
Marion I. Menzel, Ph.D.[2]
Berthold Kiefer, Ph.D.[2]
H.-P. Schlemmer, M.D.[1]

[1] Department for Radiological Diagnostics, University Tübingen, Germany
[2] Siemens AG Medical Solutions, MR Division, Erlangen, Germany
[3] University of Virginia, Radiology and Biomedical Engineering, USA

Introduction:

MRT provides the best soft tissue contrast of all imaging methodologies. Based on the technological advances (e.g. coil technology, parallel imaging), magnetic resonance is also able to image large body areals during an examination. The acquisition of larger anatomical regions is frequently the basis for an improved understanding of the pathologies involved. Oncology proves this point better than most. In addition to accurate diagnoses of local tumor expansion, both rather demanding with respect to resolution and contrast, large anatomical regions are required to fully acquire the actual tumor expansion.

This is the only way to provide for an exact as well as clinically useful planning of individual treatment strategies.

Until now, high-speed acquisition of large volumes with high resolution was the domain of multi-slice computed tomography (MS CT). The newest generation of Spiral MS CTs allows for a quick realization of 3D data records in the submillimeter range. But it is the possibility of retrospective reconstruction of random image planes that provides for an additional decisive advantage when dealing with complex relationships between anatomical structures and pathological changes. Based on the poor soft tissue contrasting when compared to MRT, MS CT as such rarely suffices for an exact evaluation of the pathology involved.

Using the newest generation of Spiral MS CTs, isotropic 3D data records in the submillimeter range can be realized within a short period of time. However, there is also the possibility of retrospectively reconstructing random image planes that represents a decisive advantage for complex relationships between anatomical structures and pathological changes.

Based on the poor soft tissue contrast obtained as compared to MRT, MS CT is frequently not capable on its own to provide satisfactory statements in regard to exact evaluations of the pathology involved. As a result, the necessity of combining different examination modalities – unfortunately this also leads to a delay in therapeutic treatments – increases overall treatment costs in the final analysis.

Therefore the demand for real three-dimensional imaging (that is, with the isotropy of the voxels) has been present in MRT for some time now. It was successfully resolved by using gradient-echo based (GRE) MR sequences for T1-weighted (w) imaging. For this reason, these techniques used in modern MRT are a permanent feature of examination protocols and an important part in the evaluation of pathologies. Even though T2-similar contrasts are possible with the help of GRE MR sequences (examples in this case are the MEDIC or DESS sequences), for optimal image contrast with T2-weighting, a Spin Echo or Turbo Spin Echo (TSE) is required. The introduction of SPACE sequence technology (Sampling Perfection with Application optimized Contrasts using different flip angle Evolutions; SPACE) is an important prerequisites for using T2-weighted 3D imaging:

1. T2-weighted image contrast (SPACE is a variant of TSE),
2. true isotropic 3D data records with high resolution (voxel size ≤ 1 mm^3)
3. use of a large Field of View (FoV) and finally,
4. clinically acceptable measurement times [1, 2, 3].

Meeting these requirements is all the more important, because more questions will find their way into the clinical MR tomographic routine since the introduction of the Tim (Total imaging matrix) technology. These, based on the necessary acquiring of large FoVs, were previously the sole domain of MS CT. [4].

Application methods and their first clinical results

When using SPACE* for image generation in the torso, a number of factors have to be observed. Pulsations of large vessels and respiratory motion cannot limit image quality as compared to conventional MRT. In addition, the previously available patient preparation techniques have to be maintained. Since October 2004, SPACE is used within the framework of clinical routine for patients requiring high resolution T2-weighted 3D imaging as compared to conventional 2D MRT. Key emphasis are pathologies of the pelvis and the spine. Whenever necessary, (for example, for staging rectal carcinoma) an additional retrograde filling of the rectum with ultrasound gel is performed.To keep intestinal motion quiet as a function of the body weight, up to 1 or 2 vials of buscopan (n-butyle scopolamine) will be administered intravenously. The following were used as default values for previous routine applications of

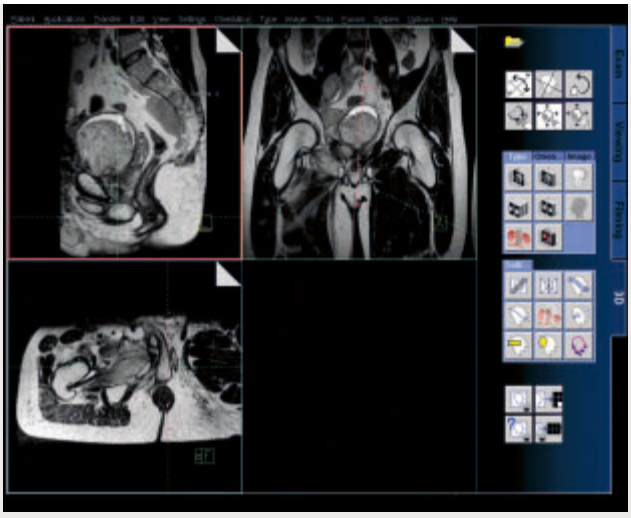

Figure 1 *T2 SPACE with PAT 3 of the pelvis.*
35-year-old patient with extended rhabdomyosarcoma invading into the bladder.
3D imaging with 1 mm³ isotropic spatial resolution allows retrospective slice prescription in any orientation needed.

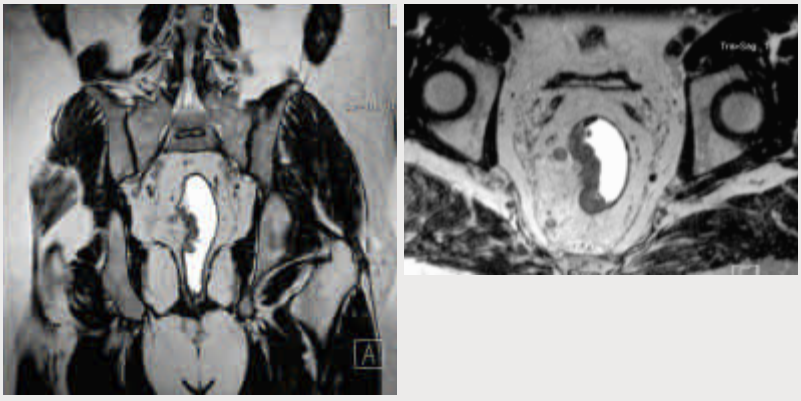

Figure 2 *T2 SPACE with PAT 3 of the pelvis 1 mm³ isotropic spatial resolution.*

43-year-old patient with rectum carcinoma with transgression of lamina propria /T3).
The 3D dataset was acquired in coronal orientation (left) and reconstructed in axial direction (right).



Figure 3 *T2 SPACE with PAT 3 of the spine. 1 mm³ isotropic spatial resolution.*

Female 13-year-old patient with
- *Arnold Chiari III*
- *Scoliosis*
- *Multiple segmentation disorders of the spine*

The isotropic 3D dataset acquired in coronal orientation (left) and a curved-cut reconstruction along the spine (right).

** The information about this application is preliminary. The application is under development and is not commercially available in the U.S., and its future availability cannot be ensured.*

SPACE: TR/TE = 1500/124 ms, 2 averages, Field of View (FoV) = 380 mm, 144 slices per slab, base matrix = 384, iPAT Factor = 3 (GRAPPA, 24 reference lines, triple matrix mode), Turbo Factor = 71, resulting isotropic voxel size $(1.0\ mm)^3$ (no interpolation), resulting measurement time 10 min, 32 seconds. It should be noted as well that the repetition time (TR) is shorter by using a restore pulse. All measurements are performed at a MAGNETOM Avanto system. Depending on the region to be examined, a variable combination of body and spine Matrix coils were implemented (when displaying the cervical spine/neck, an additional neck, head coil combination was used).

During the first 50 patients (21 females, 29 males, medium age 49 years, minimum 2 and maximum 79 years), the following regions were examined with SPACE: pelvis n = 30, lower spinal column n = 12, upper spinal column n = 6, extremities n = 4. Of 10 patients, the entire cohort was transferred for staging of a rectal carcinoma and a rectal filling with ultrasound gel was performed. In 2 cases, the entire spine was imaged using an automatic table feed followed by combining the images with a composing function of the scanner. Although it was possible to observe changes in the contrast characteristics of individual tissues to one another by using a restore pulse and variable flip angles (that theoretically led to a slight T1-dependency), the diagnostic quality obtained was not limited. Also, every case showed that the signal-to-noise ratio (SNR) was equivalent to conventional 2D T2-weighted imaging.

The same applies to the contrast-to-noise impression (CNR) of the SPACE sequence with respect to the diagnostic quality. Again, it can be considered equal to conventional T2-weighted imaging. We did not observe an increase in artifacts caused by e.g. metallic clips or implantations [5].

Conclusion and future considerations

What is decisive in using SPACE combined with Tim in the torso is the fact that the display of complex anatomical and pathological interactions and changes is possible in routine applications by means of MRT. It allows for the visualization of systemic disease aspects (for example, complete display of scoliosis) and enables at the same time a detailed view of the local situation (for example, proof of a small syrinx). In addition, this technology combines the advantages of T2-weighted MRT with high resolution and true 3D imaging.

Another critical point that deserves mentioning in our initial clinical experience is the fact that the diagnostic advantages are fully applied only in the presence of a widely available reconstruction software. This is especially important within the framework of interdisciplinary discussions. Our institute uses the SPACE sequence exclusively as required by the speciality – especially for planning large operative spinal column or pelvic interventions. Multiplanar reconstructions are dialog-driven via the radiologist or operator. Additional research is required to determine whether SPACE is suitable for replacing the previous 2D T2-weighted sequences used with previous examination protocols.

Bibliography

[1] *Mugler III JP, Kiefer B, Brookeman JR. Three-dimensional T2-weighted imaging of the brain using very long Spin Echo trains. Proceedings of the International Society for Magnetic Resonance in Medicine 687; 2000. Eighth Meeting, Denver.*

[2] *Mugler III JP, Wald LL, Brookeman JR. T2-weighted 3D Spin Echo train imaging of the brain at 3 Tesla: Reduced power deposition using low flip-angle refocusing RF pulses. Proceedings of the International Society for Magnetic Resonance in Medicine 438; 2001. Ninth Meeting, Glasgow.*

[3] *Mugler JP III, Meyer H, Kiefer B. Practical implementation of optimized tissue-specific prescribed signal evolutions for improved turbo-Spin Echo imaging. Proceedings of the International Society for Magnetic Resonance in Medicine 203; 2003. Eleventh Meeting, Toronto.*

[4] *Schlemmer HP, Schafer J, Pfannenberg C, Radny P, Korchidi S, Muller-Horvat C, Nagele T, Tomaschko K, Fenchel M, Claussen CD. Fast whole-body assessment of metastatic disease using a novel magnetic resonance imaging system: initial experiences. Invest Radiol. 2005 Feb;40(2):64-71.*

[5] *Lichy M, Wietek B, Mugler JP III, Horger W, Menzel M, Müller-Horvat C, Siegmann K, Martirosian P, Claussen C, Schick F, Schlemmer HP. WHole-body applications of isotropic high resolution T2-weighted MRI with a single slabe 3D-TSE based sequence optimized for high sampling efficiencies, called SPACE – initial clinical experiences. International Society for Magnetic Resonance in Medicine 2005. Thirtheenth Meeting, Miami.*

The information about this application is preliminary. The application is under development and is not commercially available in the U.S., and its future availability cannot be ensured.

Advances in Cardiac MRI at 3T – Benefits of Multi-Channel MR Systems

Bernd J. Wintersperger, M.D.; Stefan O. Schoenberg, M.D.; Olaf Dietrich, Ph.D; Maximilian F. Reiser, M.D.

Department of Clinical Radiology, University Hospitals-Grosshadern, Ludwig-Maximilians-University, Munich, Germany

Introduction

The challenges for cardiac MR imaging are three-fold: spatial and temporal resolution, signal-to-noise ratio and the limitations induced by the need for breath-hold imaging (Figure 1). With the advance of multi-channel whole-body MRI systems at 3T, all these limitations can now be effectively overcome. Parallel acquisition techniques (PAT) allow increasing temporal or spatial resolution at virtually no costs in acquisition time. The higher field strength at 3T makes up for the loss of signal-to-noise ratio (SNR) induced by fast scanning with PAT. With the combination of PAT and 3T, real-time acquisitions have now become feasible without obviating the need for breath-hold cardiac MRI (Figure 1).

Different Aspects of MR imaging

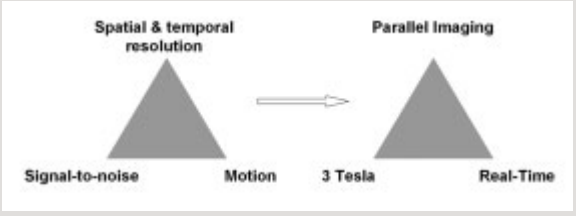

[Figure 1] *Relationship of different aspects of MR imaging specially in respect to resolution, SNR and motion (left); possible solutions to the problems as offered by 3T multi-channel MRI.*

Basic Concepts of Parallel Imaging at 3T

The concept of parallel imaging is the under-sampling of k-space by sampling only every n^{th} line in k-space compared to a full k-space acquisition. This reduces the acquisition time to 1/n of the non-accelerated acquisition and is typically referred to as imaging with an acceleration or reduction factor R. However, parallel imaging requires multi-element coils for spatially resolved signal detection. The so-called coil sensitivity profiles are then used to reconstruct an image equivalent to a full k-space acquisition without increase in acquisition time and without aliasing artifacts caused by under-sampling. Parallel imaging and 3T have a unique synergistic effect. One limitation of 3T MRI is the higher specific absorption rate (SAR) induced by the higher Larmor frequency of the RF pulses, which is effectively compensated by parallel imaging where fewer RF pulses are required to sample an equivalent data set. Nevertheless, the lower SNR induced by the use of PAT which decreases the SNR by at least a factor of one over the square root of the acceleration factor ($1/\sqrt{R}$) is nicely compensated by the higher SNR at 3T. Looking at the performance of PAT at 3T compared to 1.5T, it is easy to see that the loss of SNR introduced by an acceleration factor of R=4 with parallel imaging is approximately compensated by the SNR increase of a factor of 2 from 1.5 to 3.0T. Therefore a four-fold gain in acquisition speed is feasible at 3 Tesla with virtually no penalty in SNR compared to 1.5T.

These methodological advantages result in a number of shifts of paradigms in cardiac MRI at 3T:

- Multi-breath-hold imaging becomes single breath-hold imaging.
- 128 matrix becomes 256 matrix.
- Gated breath-hold CINE MRI becomes free breathing real-time CINE MRI.
- 2D CINE cardiac MRI becomes 3D CINE cardiac MRI.

Cardiac CINE MRI @ MAGNETOM Trio with Tim

It has already effectively been shown that single breath-hold multi-slice cardiac MRI is feasible already at 1.5T. In a study by Wintersperger et al., 11 short axis slices using TrueFISP cardiac functional analysis have been feasible within a single breath-hold of ~20 heart beats (1). As other studies have shown that temporal resolution is more critical for the accuracy of cardiac function analysis than spatial resolution (2), a temporal resolution of <50ms could have been maintained in this study with an acquisition matrix of 128 (1). For those

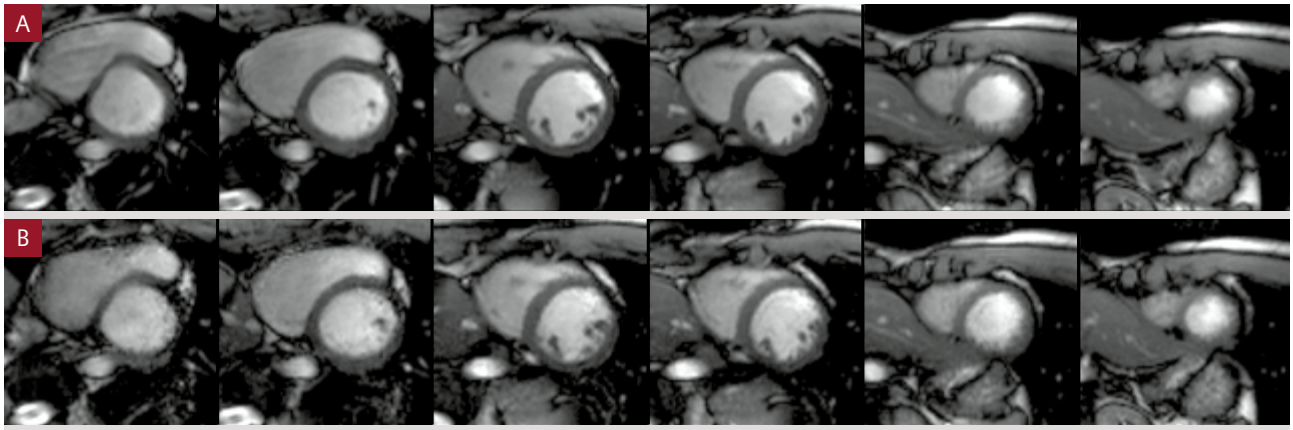

[Figure 2] *Comparison of (a) segmented CINE TrueFSIP acquiring a single slice per breath-hold and (b) fourfold (R=4) TSENSE accelerated CINE TrueFISP with whole short axis data acquired in just 2 breath-holds on a MAGNETOM Trio, A Tim System. Note that the slightly increased noise does not interfere with depictability of subtle details.*

studies typically an acceleration factor of R=2 was used with a GRAPPA (generalized auto-calibrating partially parallel acquisition) reconstruction algorithm. A limitation of the integrated auto-calibration in the GRAPPA algorithm in CINE imaging is caused by the fact that within each image frame additional central lines in k-space (reference lines) have to be acquired for auto-calibration of the coil sensitivity profiles. This results in a net loss of the effective acceleration factor R which is typically reduced by approximately 20–40%, depending on the number of reference lines. More recent reconstruction algorithms such as TSENSE or TGRAPPA effectively overcome this limitation by eliminating the need for additional reference line or ACS (auto-calibration signal) measurements by exploiting the data of an interleaved k-space line sampling covering the full k-space in subsequent dynamic CINE frames (3, 4). These techniques allow for a marked acceleration of CINE TrueFISP imaging as already shown at 1.5T by Reeder et al. with no significant loss in image quality and accuracy for cardiac functional analysis at R=3 (5). The combination of the TSENSE algorithm with higher field strengths and multi-channel MRI at 3T exceeds this performance by far.

On a MAGNETOM Trio, A Tim System, four-fold faster cardiac acquisitions at full 256 matrix size with no loss in diagnostic accuracy compared to the unaccelerated images have been successfully demonstrated in clinical applications. In a study of 10 patients with myocardial infarction, an excellent visualization of regional wall motion abnormalities and evaluation of global ventricular function was possible due to the high spatial and temporal resolution of a full 256 matrix and 50 ms temporal resolution in a multi-slice approach (Figure 2). This is a clear gain in diagnostic accuracy for single breath-hold cardiac MRI compared to 1.5T, since it has been shown earlier that with real-time CINE regional function analysis is not reliably feasible at 1.5T due to the limits in spatial resolution. Another advantage of the combination of parallel imaging with a multi-channel MAGNETOM Trio, A Tim System compared to conventional 3T MRI scanner is that the under-sampling of k-space with parallel acquisition techniques results in the possible use of higher flip angles for TrueFISP imaging. Due to the square relationship between the excitation angle and the specific absorption rate (SAR), cardiac MRI at 3T was traditionally limited to lower flip angles within the range of ~40° to 50°. Using TSENSE in combination with a MAGNETOM Trio, A Tim System, flip angles of 60° or even higher could be realized resulting in a better blood-to-myocardium contrast. The contrast of multi-slice acquisitions at 3T accelerated by T-SENSE is therefore comparable to unaccelerated images at 1.5T.

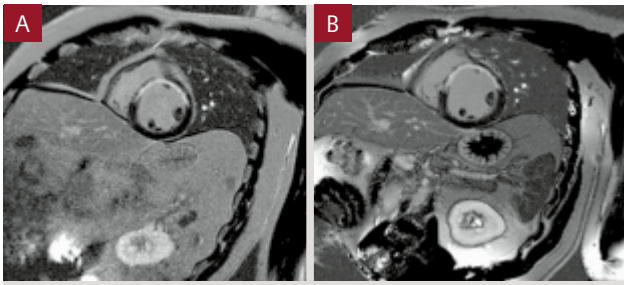

[Figure 3] *PSIR single-shot TrueFISP in a patient with extensive LAD infarction; while this technique at 1.5T (a) comes along with a considerable level of noise, at 3T (b) image quality improves also based on the substantial lower noise level.*

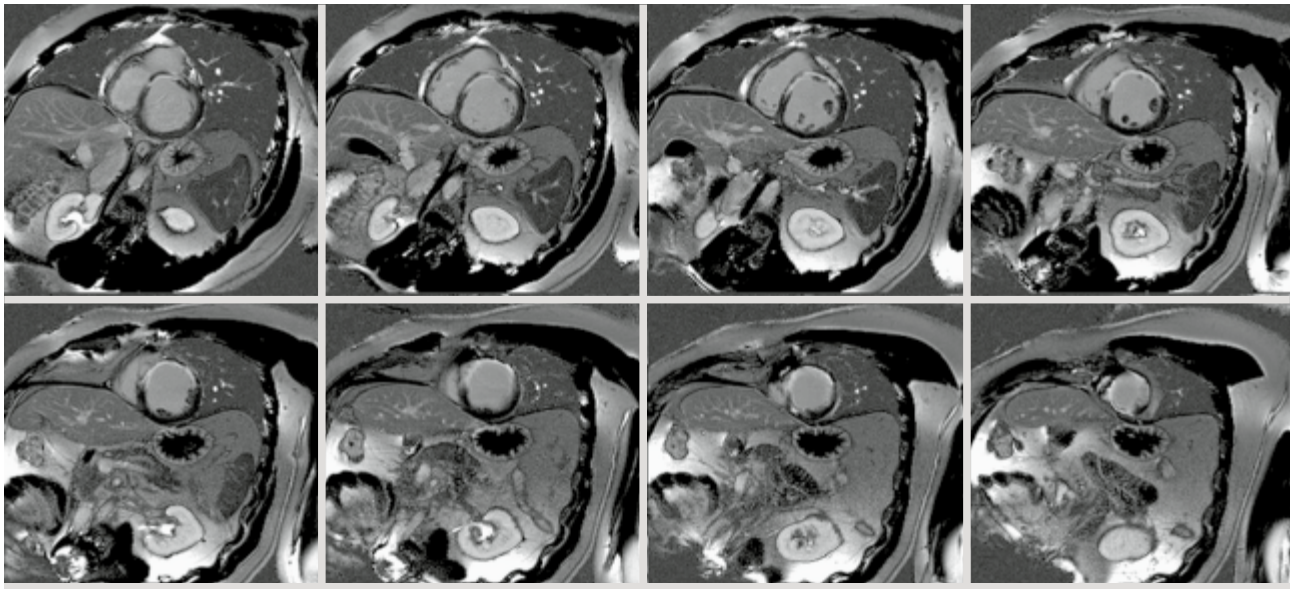

[Figure 4] *MAGNETOM Trio, A Tim System short axis data set acquired in multiple breath-holds using a segmented PSIR TrueFISP technique showing the whole extent of the LAD infarction in the same patient as shown in figure 3.*

Delayed Enhancement* @ MAGNETOM Trio, A Tim System

Additionally, for use in delayed enhancement (DE) imaging assessing myocardial infarction and viability, multi-channel 3T MRI allow for new possibilities and options. Despite all the effectiveness and value of DE imaging for assessment of myocardial infarction, this technique remains quite time-intensive in clinical routine due to the need for inversion time adjustments to allow optimized contrast between the infarcted and normal myocardium. Already at 1.5T it had been shown that a new technique termed phase sensitive IR (PSIR) reconstruction obviates the need for exact optimization of the inversion time (6).

Huber et al. demonstrated that PSIR allows an accurate assessment of the area of infarcted myocardium at virtually any arbitrary chosen inversion time (7). The combination with TrueFISP based acquisition speeds up data sampling allowing single breath-hold multi-slice coverage of the entire left ventricle for the exact assessment of the extent of myocardial infarction (8). However at 1.5T these images are somewhat noisy and sometimes influenced by artifacts due to the ambiguousness of the phase information at low signal-to-noise ratios (Figure 3). At 3T the higher SNR allows for excellent multi-slice single breath-holds TrueFISP PSIR imaging of the entire left ventricle with high image quality (Figure 4). The combination with PAT techniques like GRAPPA again allows preventing possible SAR limitations using TrueFISP at 3T.

If TSENSE TrueFISP acquisitions of cardiac function and PSIR TrueFISP acquisition of delayed contrast enhancements are combined at multi-channel 3T MRI, a complete assessment of function and viability with high temporal and spatial resolution is feasible with only a few breath-holds.

At 3T the contrast-to-noise ratio of the TrueFISP based PSIR technique even exceeds the SNR of the best technique at hand used 1.5T, e.g. segmented TurboFLASH magnitude reconstruction. Comparing the accuracy of single breath-hold multi-slice acquisitions to time intensive multi-breath-hold single slice acquisitions, it has been shown that the limits of agreement between both are smaller at 3T compared to 1.5T.

Myocardial Perfusion* @ MAGNETOM Trio with Tim

While CINE MRI and viability imaging have already been daily clinical routine techniques on 1.5T with sufficient high SNR levels, myocardial perfusion imaging has been a promising tool for the evaluation of coronary artery disease for years but never really took off for widespread use. This has been mainly based on limited SNR performance, artifacts and variable coexisting sequence techniques. At 3T one can envision that due the higher SNR the quality of TurboFLASH techniques, the best evaluated standard in myocardial perfusion imaging, will dramatically improve therefore enabling a reliable time-signal analysis and accurate assessment of myocardial perfusion (Figure 5). The gain in SNR could par-

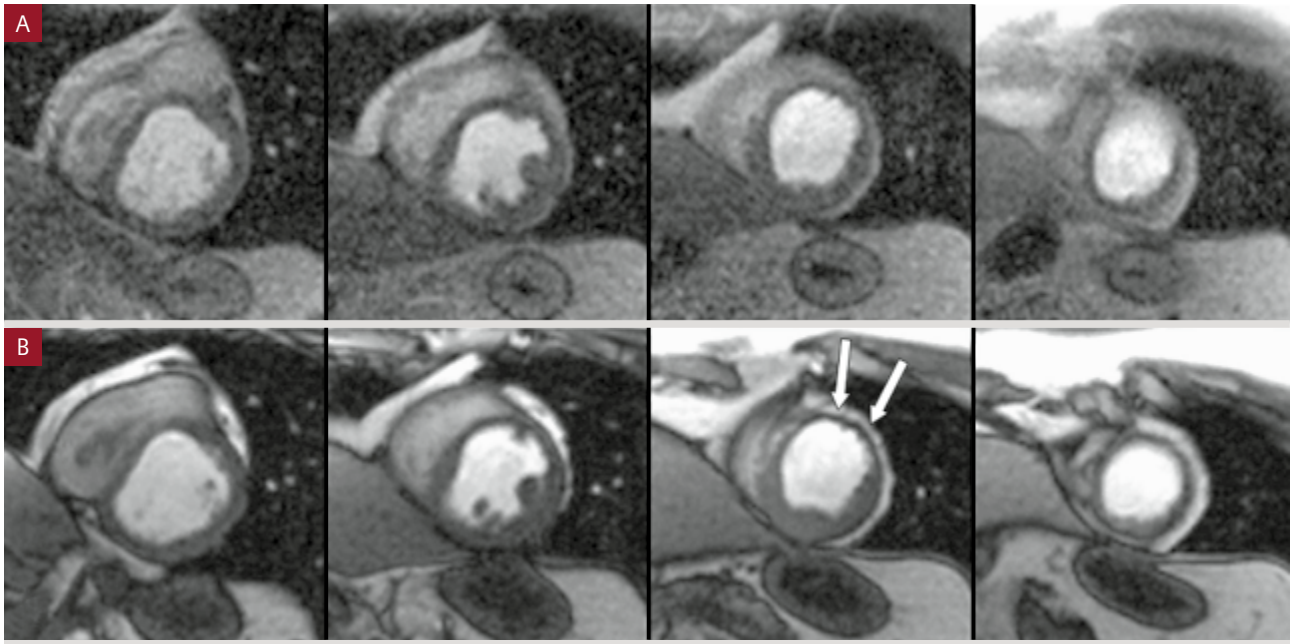

[Figure 5] *IR TurboFLASH myocardial perfusion imaging: (a) four slice data set acquired at 1.5T shows a considerable high noise level possibly interfering with quantitative analysis. (b) Data set of same patient acquired with MAGNETOM Trio, A Tim System using the same technique shows markedly reduced noise and allows better delineation of the hypoperfusion in the infarcted anterior wall (arrows).*

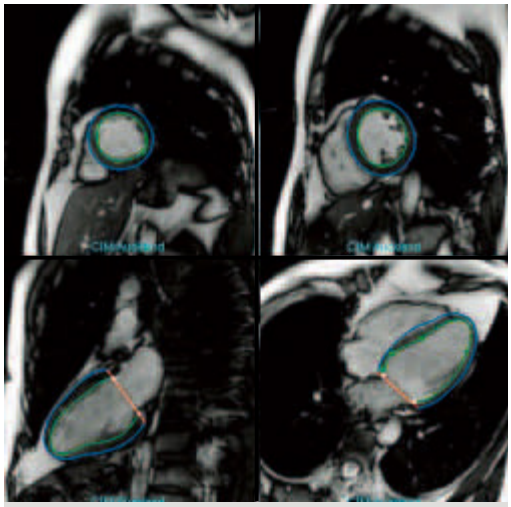

[Figure 6] *T-SENSE CINE data set showing the automated contouring of the endo- and epicardial border in multiple planes. This technique allows for better detection of valve planes and therefore increased accuracy. Functional Information of the circumferential contraction though is maintained by incorporated short axis images.*

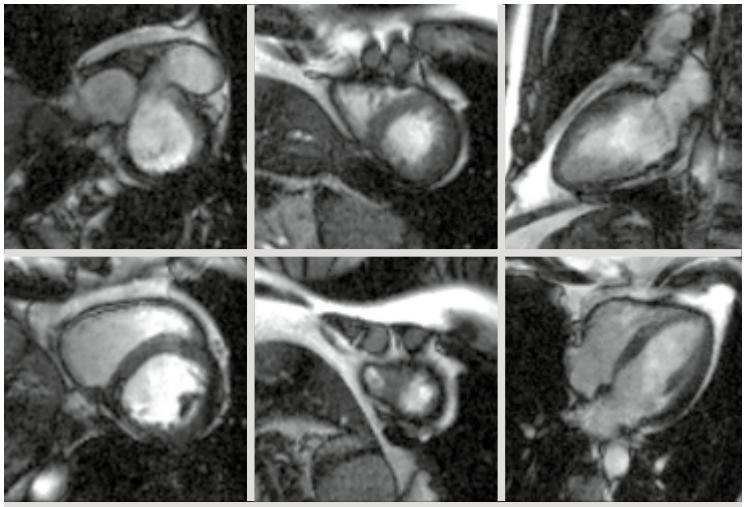

[Figure 7] *The data sampling acceleration in CINE imaging of the heart by PAT (T-SENSE) allows not only for fast acquisition of short axis data but also multiplanar data sets without the need of data registration to avoid mismatch of the data.*

*The information about this product is preliminary. The product is under developement and is not commercially available in the US. and its future availability cannot be assured.

tially be invested in even higher spatial/temporal resolution using higher acceleration factors with PAT (e.g. TENSE) or enabling coverage of the entire short axis during first pass perfusion.

Future Developments

The introduction of 4D function analysis tools allows changing the approach for cardiac functional assessment (9). Although the use of the Simpsons' rule with a contiguous coverage along the entire short axis from the apex to the AV-valve plane has major benefits in terms of accuracy based on its 3D modeling, the valve plane itself could much better be identified in 2- and 4-chamber views. The 4D analysis software allows combining the information of long and short axis cardiac MRI including a computerized LV model thereby reducing the number of required short axis views (Figure 6). This ideally combines with single breath-hold cardiac MRI at 3T accelerated with T-SENSE, since one breath-hold is sufficient to require 5–6 slices with sufficiently high temporal and spatial resolution for this analysis (Figure 7). Therefore one can envision a single breath-hold, highly accurate assessment of the LV function by the combination of MAGNETOM Trio, A Tim System and 4D Argus Software.

With the advent of multi-channel scanner systems, new dedicated coil arrays might be developed that meet the high number of the receiver channels of the MAGNETOM Trio, A Tim System ("32 elements meet 32 channels"). In a preliminary research study in collaboration with RAPID Biomedical, a dedicated flexible cardiac coil was used in close cooperation with the team of Dr. Mark Griswold. Results exceeded those already obtained at 1.5T with a previous prototype of the coil (5). Acceleration factors of 6 for TSENSE cine TrueFISP cardiac function analysis were feasible at virtually no loss in diagnostic image quality. In combination with real-time acquisitions instead of segmented CINE techniques, this would allow new three-dimensional insights in the true physiologic cardiac function without hemodynamic changes based on breath-hold induced intrathoracic pressure variations. As already shown in preliminary studies, this has promising clinical applications for the assessment of diseases such as constrictive pericarditis and the differentiation from restrictive cardiomyopathy (10).

Summary

Cardiac MRI was initially not considered the primary application for 3T due to problems with the high SAR and a number of artifacts particularly for the use of steady-state free precession techniques (TrueFISP). The advent of multi-channel cardiac MRI systems in combination with new acquisition strategies such as TSENSE and TGRAPPA now has vastly overcome these limitations and even shown new possibilities for improved diagnosis of cardiac diseases at higher field strengths.

Acknowledgement

The authors also acknowledge the work of the entire cardiac team of the Department of Clinical Radiology: Kerstin Bauner, M.D., Denise Friedrich RT, Armin Huber, M.D., Michele Picciolo, RT, Frank Stadie, RT, and of Siemens Medical Solutions: Andreas Greiser Ph.D., Edgar Müller, Ph.D., Michaela Schmidt, RT, Katrin Sprung, RT.

This work was in part supported by the "Verein zur Förderung der Forschung und Entwicklung der Magnetresonanztomographie e.V."

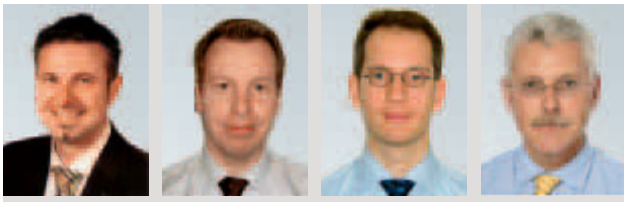

Authors (left to right): Bernd J. Wintersperger, M.D.; Stefan O. Schoenberg, M.D.; Olaf Dietrich, Ph.D; Maximilian F. Reiser, M.D.

References

[1] Wintersperger BJ, Nikolaou K, Dietrich O, et al. Single breath-hold real-time cine MR imaging: improved temporal resolution using generalized auto-calibrating partially parallel acquisition (GRAPPA) algorithm. Eur Radiol 2003; 13:1931–1936.

[2] Miller S, Simonetti OP, Carr J, Kramer U, Finn JP. MR Imaging of the heart with cine true fast imaging with steady-state precession: influence of spatial and temporal resolutions on left ventricular functional parameters. Radiology 2002; 223:263–269.

[3] Kellman P, Epstein FH, McVeigh ER. Adaptive sensitivity encoding incorporating temporal filtering (TSENSE). Magn Reson Med 2001; 45:846-852.

[4] Breuer FA, Kellman P, Griswold MA, Jakob PM. Dynamic auto-calibrated parallel imaging using temporal GRAPPA (TGRAPPA). Magn Reson Med 2005; 53:981–985.

[5] Reeder SB, Wintersperger BJ, Dietrich O, et al. Cardiac CINE SSFP imaging with parallel acquisition techniques and a 32-channel cardiac coil: evaluation of SNR performance. Mag Reson Med 2005; in press.

[6] Kellman P, Arai AE, McVeigh ER, Aletras AH. Phase-sensitive inversion recovery for detecting myocardial infarction using gadolinium-delayed hyperenhancement. Magn Reson Med 2002; 47:372–383.

[7] Huber AM, Schoenberg SO, Hayes C, et al. Value of phase-sensitive Inversion Recovery (PSIR) for Detection of Myocardial Infarction. Radiology 2005; in press.

[8] Huber AM, Schoenberg SO, Spannagl B, et al. Single shot inversion recovery TrueFISP for assessment of myocardial infarction. Am J Roentgenol 2005; accepted.

[9] Young AA, Cowan BR, Thrupp SF, Hedley WJ, Dell'Italia LJ. Left ventricular mass and volume: fast calculation with guide-point modeling on MR images. Radiology 2000; 216:597–602.

[10] Francone M, Dymarkowski S, Kalantzi M, Bogaert J. Real-time cine MRI of ventricular septal motion: a novel approach to assess ventricular coupling. J Magn Reson Imaging 2005; 21:305–309.

Software Compensation for Patient Position Enabling Reproducible Slice Positioning – AutoAlign

Katherine T. Scott, Ph.D.

Siemens Medical Solutions, Inc., Malvern, PA, USA

Whether repeat-scanning the same patient for follow-up in a clinical environment or performing comparison studies on different subjects, AutoAlign enables reproducible prescription of slice positions and orientations in neuroimaging studies, without technologist intervention and, in routine use, without retrieval of previously archived datasets.

MRI examinations generally begin with the acquisition of a rapid localizer scan, from which slices for subsequent scans are manually prescribed. If a follow-up examination is performed on the same subject some time later, exactly duplicating the previous slice positions and orientations requires identification of the same anatomical landmarks in the new images. Since the subject is never identically positioned in the scanner and RF coil from one scan session to the next, these may be difficult to locate, especially if changing pathology is present. High precision is required to track small changes in serial studies of e.g. lesion load. However since in-plane resolution is typically higher than through-plane resolution, minor errors in slice positioning can greatly affect resulting measurements. Several studies have shown that less variability is introduced by multiple observers reading the data than by errors due to repositioning in serial scanning multiple sclerosis, brain atrophy, tumors, stroke etc. [1, 2]. For group comparison studies, natural anatomical variability precludes acquisition of identical datasets, but consistent slice prescription techniques are required to enable acquisition of images that can confidently be compared side-by-side i.e. observed differences should reflect true anatomical variation and not be due to variations in slice prescription.

At the heart of the technique is the AutoAlign Atlas, which was created from segmented and co-registered MRI images

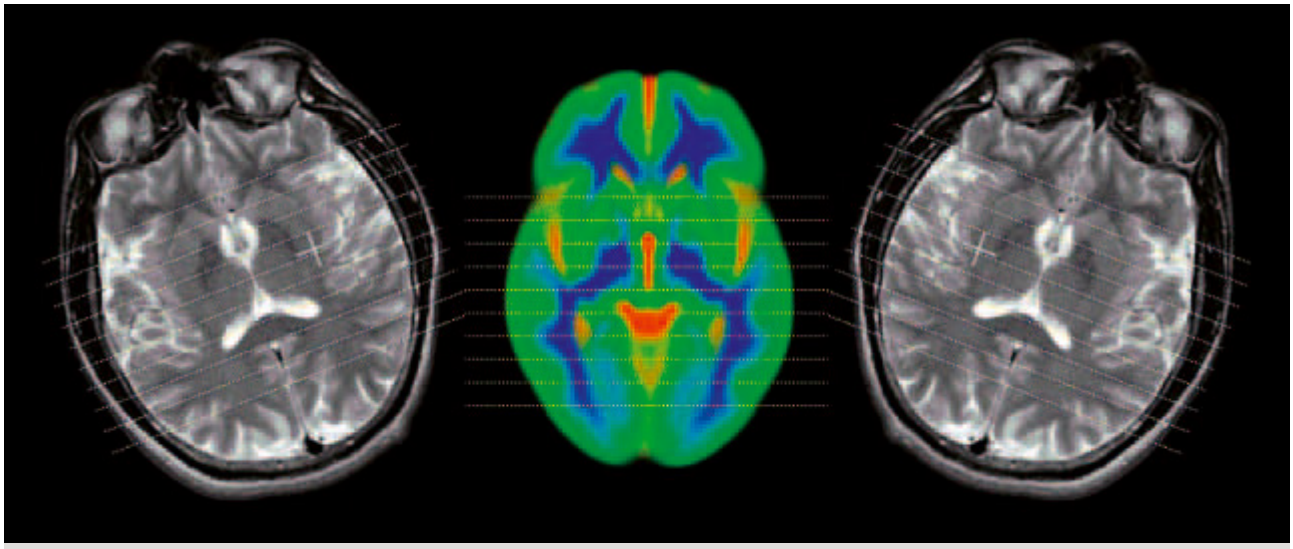

[Figure 1] *AutoAlign registers localizer images to the Atlas, enabling slice parameters saved in protocols or previously run on an individual subject, to be correctly positioned and oriented, irrespective of the position of the head. No additional manual adjustment by the technologist is required – alignment is automatic and reproducible.*

[3, 4] of the brains of a group of 400 adult subjects, both normal and abnormal. This composite dataset, contains two types of probabilistic information: the likelihood that a particular type of tissue (white matter, gray matter, CSF, etc.) will occur at any given location; and the intensities to be expected from the different tissue types in MRI images acquired with selected parameters specified at particular field strengths. The probabilistic information relating to the pathology and location are also inherent in the atlas, increasing the robustness of the method in the presence of disease. Each examination begins with the AutoAlign localizer, a 40 s scan during which both proton density and T1-weighted volumes of the brain are acquired and registered to the Atlas. Registration is done using a rigid body alignment process which incorporates the contrast and tissue classification information. The series of rotations and translations required to optimally align the images with the atlas is saved as a matrix, which is applied to define slice positions and orientations in subsequent scans. In-plane rotation of the imaging slab is a feature that increases the accuracy of positioning as compared to manual slice prescription, since this is often not routinely used in a clinical environment. No anatomical landmarks are used in the process i.e. the whole brain is aligned with the atlas, enabling rapid computation with accurate results as demonstrated in both intra and inter subject studies [2, 5].

AutoAlign in different cases

Once the AutoAlign localizer has been run, protocols are run without operator intervention i.e. no "tweaking" of the slice positions or orientations is necessary – see Figures 1 and 3. Using this method, the same subject can be scanned repeatedly on the same system, on different systems at different field strengths and at different sites. In all cases, the same slices will be prescribed without reference to any prior imaging study. In the case of comparative studies of different subjects, matching slice positions will automatically be selected. AutoAlign is equally applicable in a number of different cases – exactly how it would be used depends on the desired application:

1. **Existing protocols –** The simplest and most universally applicable method is to scan the subject(s) using existing protocols as they have been saved on the scanner. In this case, the protocols have been set up with predefined slice orientations relative to the Atlas and registration of the brain to the Atlas ensures that the slice orientations are always correct, irrespective of the orientation of the head and without retrieval of archived images. Subjects could be scanned on different systems or at other sites without

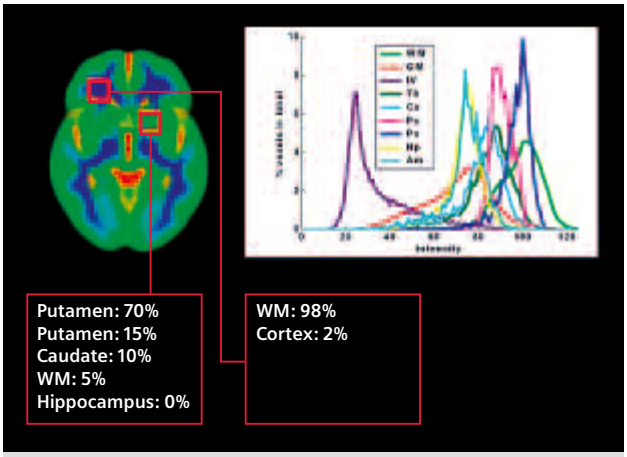

[Figure 2] *The AutoAlign Atlas (left) contains probabilistic information on the likelihood of certain tissues appearing at a particular location in the brain, as well as the signal intensities expected from different tissue types. Intensity histograms from T1-weighted images are shown for a variety of neuroanatomical structures (right) – white matter (WM), cortical gray matter (GM), lateral ventrical (LV), Thalamus (Th), Caudate (Ca), Putamen (Pu), Pallidum (Pa), Hippocampus (Hp) and Amygdala (Am). Incorporation of spatial information and the dual contrast provided by the AutoAlign localizer enables separation of the distributions that would not be possible using intensities alone. Figure reproduced with permission from Reference 3.*

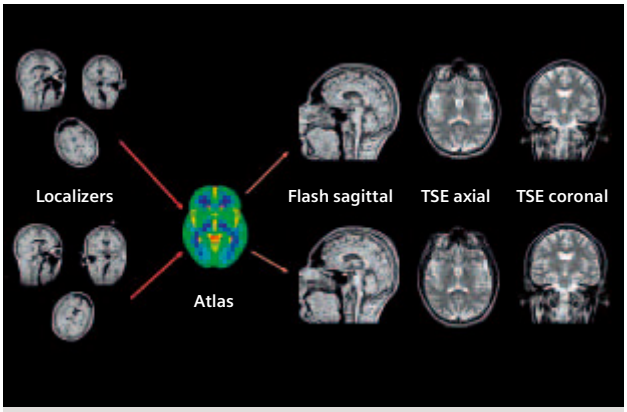

[Figure 3] *Repeat scanning of the same subject. On the left hand side are the 3-plane localizers showing the position of the head for the two scan sessions. AutoAlign registration of the images to the Atlas enables the slices on the right hand side to be acquired without altering the scan prescription. Sagittal, axial and coronal slices are shown for the two studies – each has the same slice number as the corresponding slice in the previous study.*

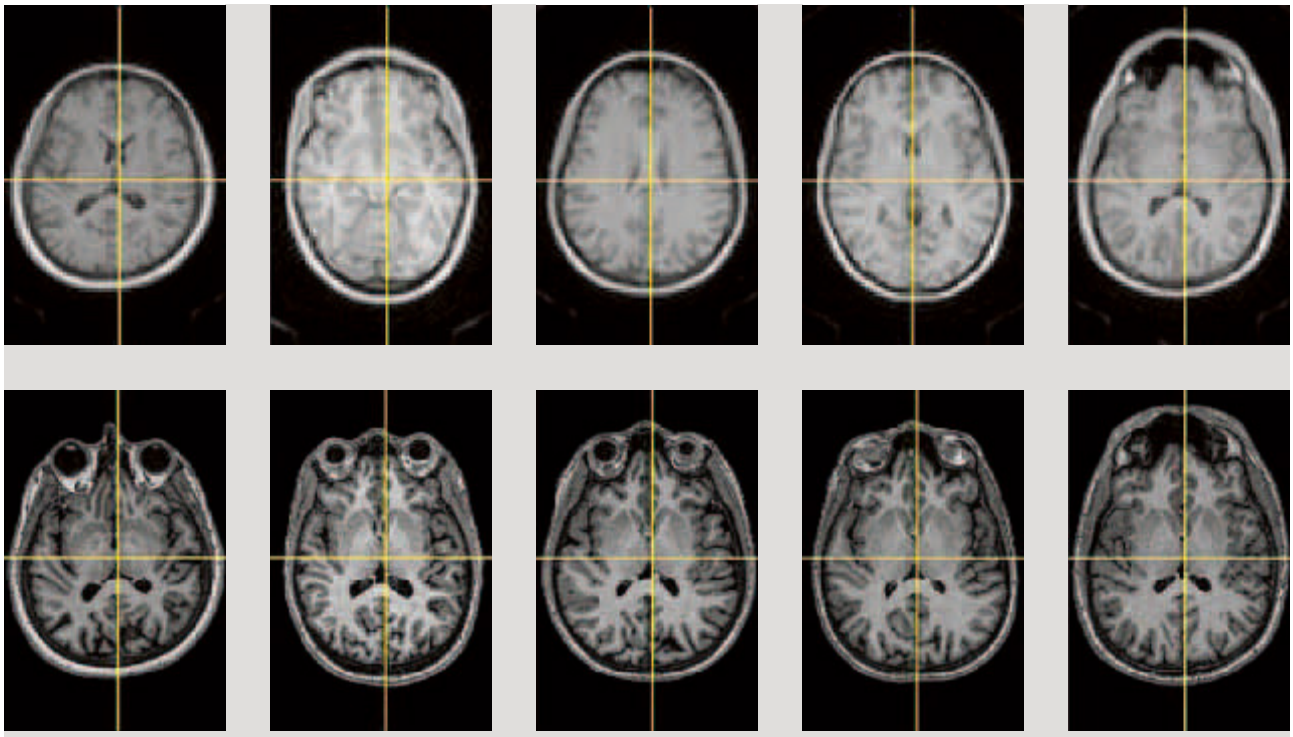

[Figure 4] *Five different subjects scanned with the same protocol. Localizer images before automatic alignment are shown at the top; MPRAGE (Magnetization Prepared RApid Gradient Echo) images incorporating AutoAlign in the row beneath. Good midline alignment and left-right symmetry are observed in the aligned images as well as close slice selection across subjects. Reproduced with permission from Reference 5.*



[Figure 5] *Planning on the Atlas. Using the AutoAlign patient enables protocols to be planned directly on the Atlas. Note that this is a probabilistic composite of 400 brains, hence the "blurred" appearance. Since anatomic landmarks are not used in the whole brain alignment, their absence in these views is not relevant in planning site specific protocols. For individualized protocols, planning on the actual patient images at the first visit and saving the protocols, will enable reproducible slice scanning (using anatomical landmarks if required) on that subject at a future visit.*



[Figure 6] *Same subject scanned in three different scanners and at two different field strengths - images from 1.5T MAGNETOM Sonata (left), 1.5T MAGNETOM Symphony with Quantum gradient system (centre), 3T MAGNETOM Trio (right). Note the consistent alignment of the brain, while the non-rigid anatomy, such as the spinal cord, varies across the images.*

further protocol management.

2. **Site specific protocols –** It is recognized that different radiologists at different sites will have their own preferred protocols that may differ from those delivered as standard with the system. In this case, technologists can create protocols with the preferred parameters that will be standard for the site and save them. When the AutoAlign localizer is run at a subsequent session (or on a different patient), the slice positions and orientations will automatically be correctly applied to the subject without operator intervention or reference to archived images. If protocol uniformity across scanners (or at other sites) is desired, it is necessary to recreate the slice prescription on each scanner. This can be carried out manually, by importing an electronic protocol exported from a scanner with the desired slice positions and orientations, or by using the Phoenix functionality (i.e. image-based automatic protocol parameter retrieval) and saving the protocols – see later.
3. **Individual (patient specific) protocols –** Finally, in some cases it may be desirable to create a protocol for a specific patient, rather than using a standard imaging protocol. Cases where this might be applicable include adapting the imaging volume to conform with patient pathology, performing additional examinations not usually incorporated in the standard protocol, or for an imaging study where a particular feature or orientation is desired e.g. AC-PC line exactly in the axial plane. This protocol could be saved and used in the same manner as described previously, but this would be one situation where retrieval of archived images may be the preferred option. In this case, using AutoAlign and Phoenix together, enables repetition of the study in the same manner as previously performed on an individual patient. Phoenix recreates the previous protocol and AutoAlign ensures that slices are again correctly positioned and oriented, irrespective of the position of the head.

Site specific or patient specific protocols that use AutoAlign may be created in a number of different ways.

A: Planning directly on the Atlas (AutoAlign patient). This is the most generic form and is useful for setting up routine clinical protocols i.e. site specific protocols.

B: Planning on the current subject. Useful for a time series on the same patient (patient specific protocols) or as an alternative to planning site specific protocols directly on the Atlas, if the subject is representative of the subsequent subjects.

C: Manually entering the offset, tilt and rotation parameters. Most useful for the specification of study protocols e.g. for clinical trials involving multi-center studies, to ensure uniformity across sites.

D: Importing electronic protocols from another scanner where protocols contain the correct offsets and orientations. Helpful in transferring sets of protocols between scanners at one site or for studies at multiple centers.

E: Phoenix in images from another scanner or site, acquired using protocols with the desired slice parameters. Of use in keeping individual scanner protocols consistent across systems and/or in multi center trials.

In each case, at the end of each step in the protocol creation process, the protocol must be saved to the exam database.

All of the Siemens head sequences support AutoAlign and may be saved with the desired slice orientations and positions during planning. Slice positions may be graphically displayed on a 3-plane localizer to monitor during the course of the examination and it is always possible for the technologist

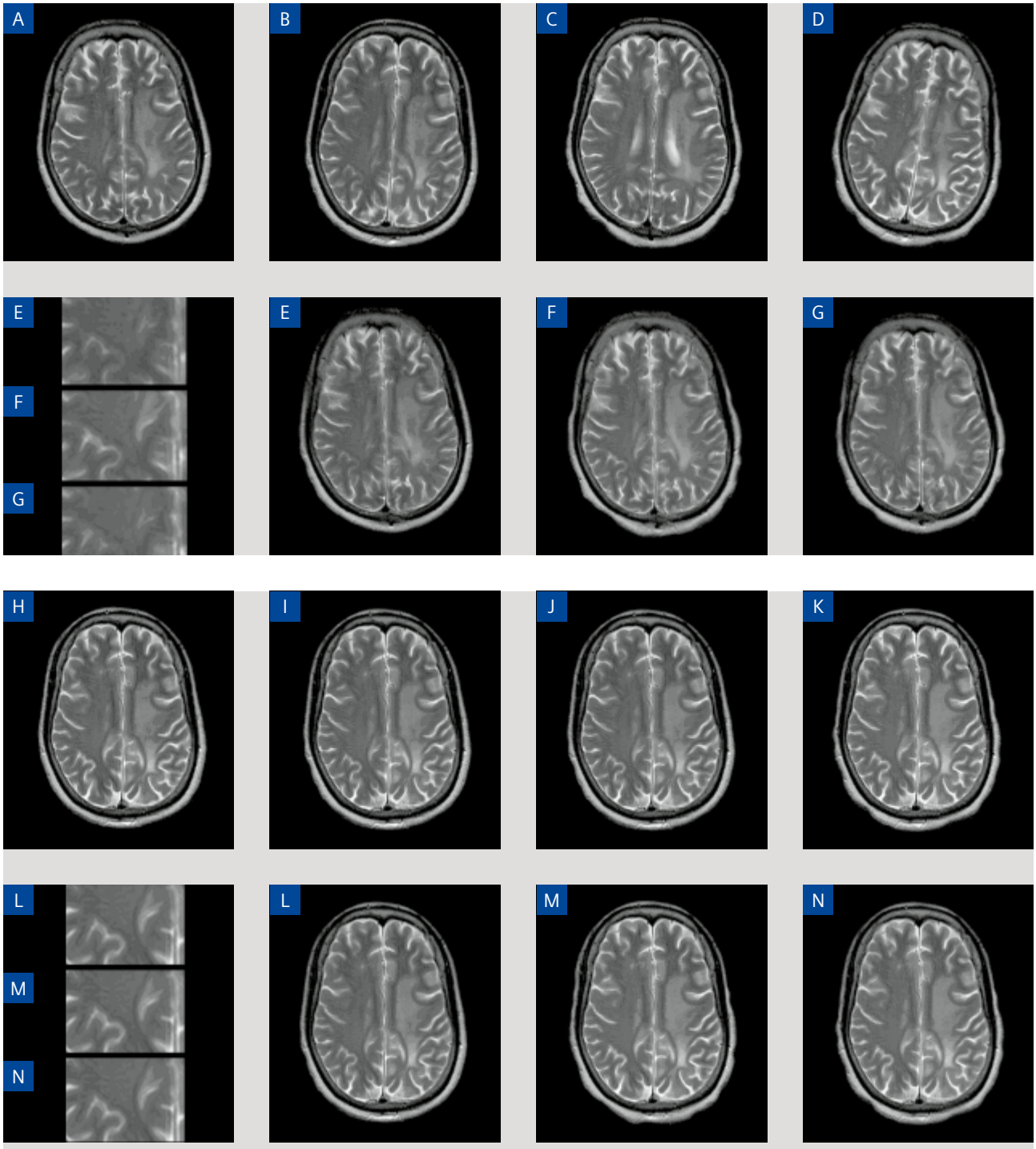

[Figure 7] *Scan – rescan of the same patient with manual slice prescription (upper panel) and using AutoAlign (lower panel) a total of four times with each method. Manually aligned TSE (Turbo Spin Echo) images (A–D) and AutoAligned images (H–K) are shown in the top half of each panel. Images after co-registration of the follow-up series (E, F, G and L, M, N) to the initial series (A and H) are shown in the bottom half of each panel. Finally, a zoomed section of the co-registered images is displayed in the lower left pane of each panel. Note the higher variation in the manually aligned slices (A-D) versus the automatically aligned slices (L–N), as well as the slight blurring caused by the co-registration procedure. Figure courtesy of Dr. Thomas Benner.*

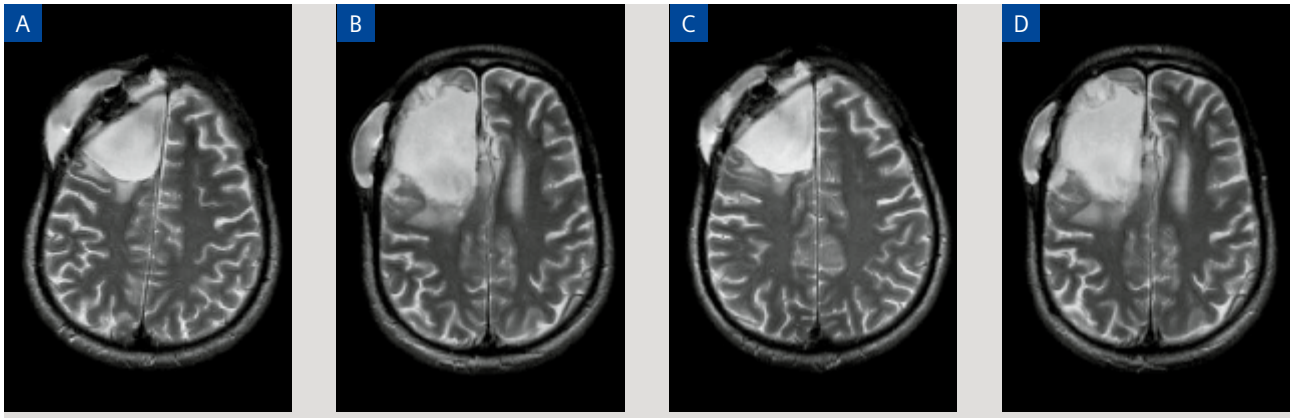

[Figure 8] *Comparison of manual alignment by the technologist (A, C) and AutoAlign (B, D) in TSE images for initial and follow up visit of tumor patient. Midline rotation errors reflected in the images on the left were caused by failure to adjust rotation in the acquisition plane (axial), whereas this was automatically corrected by AutoAlign. On systems where in-plane rotation is not possible, this can only be achieved by repositioning the patient.*

to over-ride the prescribed slices if desired, but naturally this overrides the benefits of the AutoAlign feature and should only be carried out if absolutely necessary e.g. if major surgery or large pathological changes cause the AutoAlign procedure to fail. Manually aligning the slices will disable AutoAlign for that scan only – subsequent ones will continue to use the feature unless it is actively turned off or the patient is closed, a new patient is registered, the patient table is moved or the scanner is rebooted.

The atlas is – as of today – not designed for pediatric patients or those with large areas of resected anatomy (however, it is possible to include your own Atlas). Gross changes in patient position during the scan session will also cause errors in subsequent scan positioning and the AutoAlign localizer can be rerun at any time during the study to correct for this, but should not usually be required. Since no landmarks are used in the alignment process of the slices to the Atlas, prescribing slices relative to specific anatomical landmarks in a single subject will result in excellent alignment upon rescanning of the same subject, but will not be consistent from this subject to another. The latter is an example of where patient specific protocols should be used.

Conclusion

AutoAlign enables rapid patient throughput with increased reproducibility and reduced dependence on operator expertise. Both serial scanning of the same patient and comparative studies of different subjects at different field strengths and/or at different sites are possible, without fiducial markers or reference to previously archived images. Brain imaging protocols benefit from the increased positioning reliability enabled by AutoAlign and only in the case of patient specific protocols is it necessary to retrieve archived images. In this case the use of AutoAlign and Phoenix together enable the correct imaging slices and protocols to be quickly defined and rescanned.

References

[1] Benner, T., Wisco, J.J., van der Kouwe, A., Fischl, B., Sorensen, A.G., 2004. Accuracy and repeatability of automatic slice positioning compared with manual slice positioning. 12th Meeting of the ISMRM, Kyoto, Japan.

[2] Benner, T. et al. Comparison of Manual and Automatic Slice Positioning of Brain MR Images. Radiology – in press.

[3] Fischl, B., Salat, D.H., Busa, E., Albert, M., Dietrich, M., Haselgrove, C., van der Kouwe, A., Killiany, R., Kennedy, D., Klaveness, S., Montillo, A., Makris, N., Rosen, B., Dale, A.M., 2002. Whole brain segmentation: automated labeling of neuroanatomical structures in the human brain. Neuron 33, 341–355.

[4] Fischl, B., Salat, D.H., van der Kouwe, A.J., Makris, N., Segonne, F., Quinn, B.T., Dale, A.M., 2004. Sequence-independent segmentation of magnetic resonance images. NeuroImage 23 (Suppl. 1), S69–S84.

[5] van der Kouwe, A.J., Benner, T., Fischl, B., Schmitt, F., Salat, D., Harder, M., Sorensen, A.G., Dale, A.M.2005. On-line automatic slice positioning for brain MR imaging. Neuroimage 27, 222–230.

Acknowledgements

I am deeply indebted to Drs. Thomas Benner and Andre van der Kouwe from the Martinos Center for Biomedical Imaging at Massachusetts General Hospital for extensive discussions on the subject matter, for allowing me the use of their images as examples, and for their thoughtful comments and suggestions.

A Practical Approach to Lung MRI at 1.5T

Jürgen Biederer, M.D.[1,2]; Michael Puderbach, M.D.[2]; Christian Hintze, M.D.[2]

[1]University Hospital Schleswig-Holstein Campus Kiel (UKSH), Department of Diagnostic Radiology, Kiel, Germany
[2]German Cancer Research Center (DKFZ), Department of Radiology, Heidelberg, Germany

Introduction

The value of MRI in imaging cardiac and large vessel disease is widely accepted, but the largest organ of the thorax, the lung, is usually investigated with X-ray and CT. MRI suffers from well-known limitations such as constant artifacts from heart pulsation or respiration and the low signal intensity of the aerated lung. This results from low overall proton density in combination with high susceptibility artifacts at air-tissue interfaces. The broadly accepted routine indications for MRI of the chest are instead focused on soft tissue processes such as chest wall masses or tumors of the mediastinum. The excellent contrast and the capacity of MR to produce cross sectional images or three-dimensional data sets in any orientation designate it as the ideal tool for this purpose. However, X-ray and CT are constantly criticized for the associated radiation exposure, in particular where applied for frequent follow-up examinations of children, or during pregnancy. A non-invasive method for follow-up of lung diseases during clinical trials or for physiologic research is therefore highly desirable. Since the recent technical developments in the field have contributed to overcome the well-known limitations of lung MRI, we can now recommend a comprehensive routine imaging protocol for the whole chest including lung parenchyma diseases.

Clinical method description

To match the criteria of a comprehensive imaging protocol for clinical routine, the recommended protocol needs to keep within a reasonable time frame of 15 to 30 minutes. It uses fast sequences for single- or multiple breathhold imaging and does not require cardiac or respiratory triggering. This facilitates patient positioning and shortens the room time. Limited information on cardiac pathology is provided with the single shot T2-HASTE and the free-breathing True-FISP. If further cardiac imaging is planned, ECG-triggering would be needed. The key to high image quality without respiratory motion artifacts is appropriate instruction of the patient. Nevertheless, the T2-HASTE as well as the free breathing TrueFISP are robust against breathing motion and can therefore be applied even with completely uncooperative patients. The vessel imaging capacity of the TrueFISP will even allow detection of large central pulmonary emboli in dyspneic patients. Only one sequence – the optional high-resolution – T2-TSE uses a navigator.

We present below a basic protocol for non contrast-enhanced MRI of the lung, followed by recommendations for additional contrast-enhanced and functional imaging (table 1). This would be applicable to children from 8–10 years and adults. For younger children, spatial resolution and Field of View

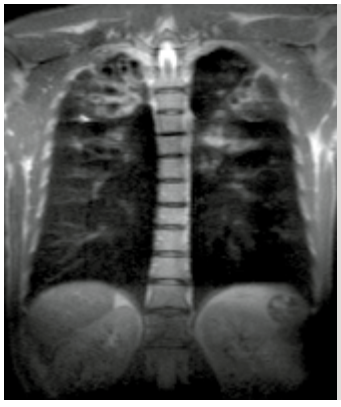

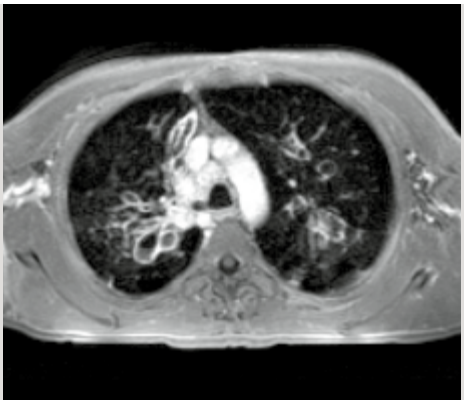

[Figure 1] *45-year-old male with cystic fibrosis of the lung. Bronchiectases in both upper lung lobes with mucous plugging being represented by bright signal on the T2-weighted HASTE (left image) and intermediate signal of the mucus within the bright signal of the contrast-enhanced bronchus walls in the transverse 3D-GRE (VIBE) sequence. For recommended sequence parameters see table 1.*

(FoV) would need to be adjusted. All components are based on common MR sequence components of current standard installations. In detail, they refer to 1.5T MAGNETOM Avanto protocols and a Body Matrix coil for thoracic imaging, but they would also be applicable to MAGNETOM Sonata and MAGNETOM Symphony installations with minimal adjustments. Where parallel acquisition techniques are not available, multi-breathhold acquisitions can be used instead. If a navigator is not available, a respiration belt could be used instead. For all coronal sequences (except for perfusion and angiography to save reconstruction time), distortion correction ("large FoV") is activated and excitation order is interleaved, where appropriate.

Basic protocol for non-contrast enhanced MRI of the lung

The imaging protocol starts with a gradient echo localizer in inspiration. The first sequences are acquired in breathhold, usually starting with the coronal T2-HASTE followed by the transverse T1-weighted 3D-GRE (VIBE). After this the first set of coronal SS-GRE sequences is acquired in free breathing, giving the patient some time to recover from the breathhold maneuvers. This is followed by the T2-TIRM image series, which is acquired with multiple breathholds. Anatomic coverage should include the upper abdomen with liver and adrenal glands. This basic protocol may be completed with the single slice dynamic SS-GRE series for diaphragmatic function. For this series, the patient is instructed to breathe deeply. Total room time up to here will be approximately 15 minutes.

This basic protocol covers a range of routine indications, e.g. follow-up examinations in children with cystic fibrosis (Fig. 1) [1]. The sensitivity for lung nodules larger than 4 mm ranges

Indications for the basic protocol

- pneumonia (T2-HASTE, TrueFISP)
- atelectasis (all sequences)
- cystic fibrosis (T2-HASTE, VIBE)
- tuberculosis (T2-HASTE, TrueFISP)
- nodule detection (TIRM, T2-HASTE, VIBE)
- mediastinal masses (VIBE, T2-TIRM) (lymphoma, goiter, cyst (Fig. 4), thymoma)
- interstitial lung disease (plus HR T2-TSE)
- diaphragmatic paralysis (TrueFISP)
- acute pulmonary embolism (TrueFISP)

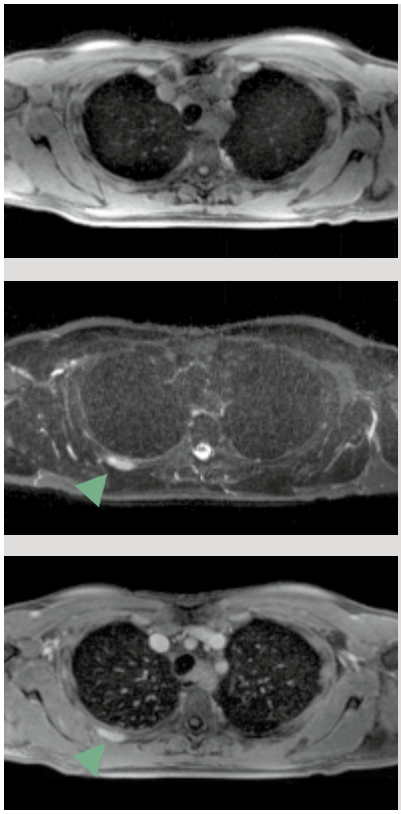

[Figure 2] *62-year-old male with suspected bronchial carcinoma. Bone metastasis of the third right rib hardly detectable on the non-contrast enhanced VIBE, but with high signal on T2-TIRM and intensive enhancement after i.v. administration of contrast material.*



[Figure 3] *46-year-old female with suspected bronchial carcinoma after incidental detection of a hilar mass on chest x-ray. The single image of the coronal TrueFISP series (upper image) and the high resolution navigated T2-TSE image (lower image), both acquired during free breathing, show a well defined cystic formation in the lower part of the right hilus with water-equivalent signal of the content. Histology after surgical resection confirmed a bronchogenic cyst. For recommended sequence parameters see table 1.*

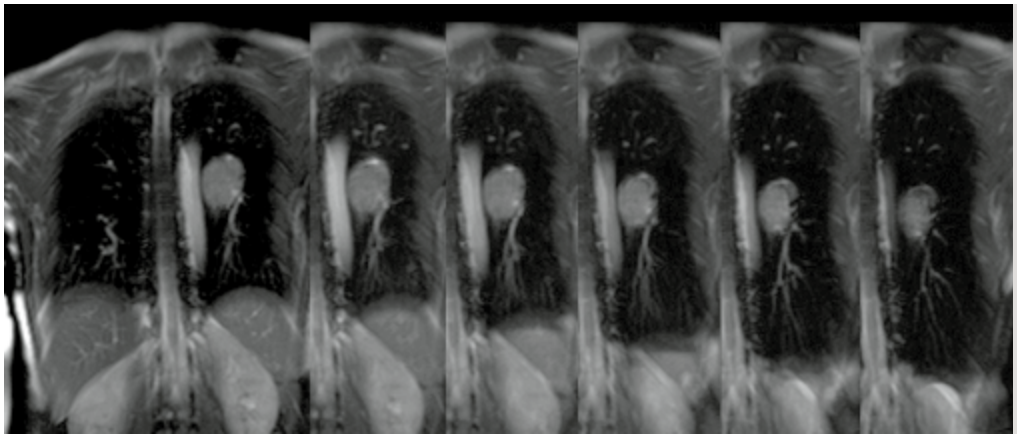

[Figure 4] *48-year-old female with suspected lung cancer. The dynamic TrueFISP series in coronal position demonstrates tumor and diaphragm motion during a deep inspiration maneuver. (left to right). For recommended sequence parameters see table 1.*

between 80 and 90% and reaches 100% for nodules larger than 8 mm [2, 3]. Depending on the water content, nodules can be detected either on the VIBE or on the HASTE and T2-TIRM images. Atelectasis and tumor can be well distinguished on T2-weighted sequences, especially if the high resolution T2-TSE is added. If MRI is applied for staging of lung malignancies with non-contrast enhanced images, T2-TIRM is an obligatory protocol component for the detection of bone metastases [4] (Fig. 2). The dynamic coronal TrueFISP acquisitions allow estimating diaphragmatic function and the mobility of intrathoracic masses (Fig. 3). This particular part provides additional functional information to the morphologic images and is one of the essential differences between lung MRI and any other common imaging modalities [5].

Basic protocol including contrast enhanced MRI of the lung

For routine purposes it might appear sufficient to conclude the study, if the non-enhanced scans show completely normal findings. Nevertheless, application of i.v. contrast material markedly improves the diagnostic yield of 3D-GRE imaging of the lung by the clearer depiction of vessels, hilar structures and pleural enhancement. Parenchymal disease and solid pathologies are also enhanced. Thus, a study to exclude pulmonary malignancies e.g. for staging purposes should usually comprise a contrast enhanced series, preferably with a fat-saturated 3D-GRE sequence. Contrast enhancement is also necessary for pleural processes (empyema, abscess, metastatic spread of carcinoma, mesothelioma) or for the further evaluation of solid masses, as well as for functional imaging or angiography. If it is intended to include a contrast-enhanced series, the 3D-GRE (VIBE) sequence in the pre-contrast series should be applied with fat-saturation to allow for a direct comparison of contrast uptake. Contrast material: 0.2 mmol/kg i.v. per hand or power injector. The contrast enhanced VIBE extends the range of indications for the protocol towards lung cancer and malignant and infectious pleural processes [6]. It is important to know that calcified nodules or masses may be invisible either on the non-contrast enhanced as well as on the contrast enhanced images. In most cases, this reflects benign findings but might be crucial e.g. for the staging of osteosarcoma.

Indications for additional CE-VIBE

- lung cancer
- pleural spread of carcinoma
- pleural effusion of unknown origin
- mesothelioma
- neurogenic tumours of the mediastinum
- mediastinitis
- vasculitis (e.g. Wegener's disease)

Lung perfusion imaging

The basic principle of contrast-enhanced perfusion MRI is a dynamic MR image acquisition following an intravenous bolus injection of a paramagnetic contrast agent. Perfusion MRI of the lung requires a high temporal resolution in order to visualize the peak enhancement of the lung parenchyma. The recommended fast acquisition technique is based on iPAT (integrated Parallel Acquisition Techniques) and data sharing. It allows for a 3D data acquisition with a temporal resolution of 1.5 seconds per image [7]. The resulting 4D-data set can be displayed with the "Mean Curve" application, which allows one to scroll through the series in a single image position or to scroll through the images of a 3D data set obtained at a single time point. A quick, semi-quantita-

Indications for perfusion MRI

- emphysema (indirectly)
- pulmonary hypertension
- acute and chronic pulmonary embolism

tive analysis of contrast-enhanced perfusion MRI data consists of the calculation of signal time curves, SNR and contrast-to-noise ratios (CNR) using region-of-interest (ROI) analysis of the signal of the lung tissue. For documentation, contrast-enhanced 3D perfusion MRI is usually processed by subtraction of mask image data acquired before contrast bolus arrival (Fig. 5). Since the acquisition time and diagnostic yield are at least the same as for a test bolus, the dynamic perfusion series may be used to prepare the angiogram. A disadvantage compared to the test bolus method is the additional time needed for image post-processing and the slightly higher amount of contrast medium (0.07 mmol/kg patient weight). To allow for an exact calculation of the time points for the angiograms, injection speed and the volume of the bolus plus sodium chloride chaser should be the same as for the following angiogram.

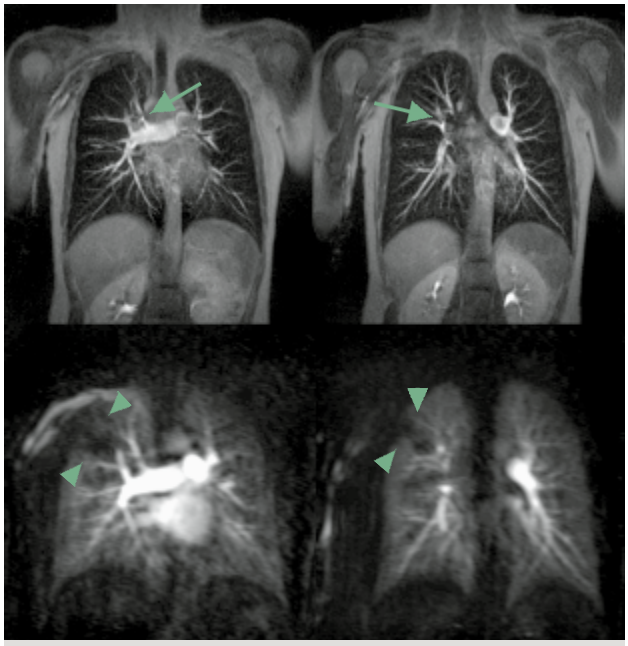

[Figure 5] *39-year-old female with suspected pulmonary artery hypertension. 10 mm MIP reconstruction of the coronal CE-MRA (3D-FLASH; upper pair of images) demonstrating small emboli in the right upper lobe artery as incidental finding (arrows). 20 mm MIP of the subtracted perfusion sequences (TREAT Perfusion, lower pair of images) show corresponding hypoperfusion in dependent parts of the right upper lung lobe (arrowheads). For recommended sequence parameters see table 1.*

Pulmonary angiography

Contrast-enhanced MRA uses a T1-weighted 3D-FLASH acquisition after intravenous injection of a paramagnetic MR contrast agent. A short TR allows for breathhold acquisitions and a short TE minimizes background signal and susceptibility artifacts. The flip angle of 25 degree produces a high contrast between lung tissue and the vessels. Adequate breathhold and exact timing of the contrast agent (0.1 mmol/kg at 5 ml/s followed by a 20 ml sodium chloride chaser, time to center 8.7 s) with an automatic power injector are essential prerequisites. Three acquisitions (non-contrast enhanced, centered on the peak signal of the pulmonary artery and centered on the peak signal of the aorta) are appreciated. For comprehensive viewing, we recommend use of the 3D-tool for multi planar reformation (MPR) or maximum intensity projections (MIP). The combination of 4D MRA perfusion and CE-MR angiography provides a useful alternative to perfusion scintigraphy and CT angiography, thus extending the range of indications for lung MRI by a considerable number of clinical conditions, e.g. suspected pulmonary embolism in pregnancy [8]:

Indications covered by lung CE-MRA

- pulmonary hypertension
- acute and chronic pulmonary embolism
- AV-malformation (e.g. M. Osler)
- pulmonary sequestration
- Swyer-James-Syndrom
- pulmonary artery aneurysms
- pulmonay vein anomalies
- masses of the hila
- tumour invasion a. pulmonalis / aorta

Respiration-triggered high resolution T2-TSE

Further options to extend the standard protocol are T1- and T2-weighted Spin Echo (SE) or Turbo Spin Echo (TSE) sequences with respiratory triggering (or gating). T1-weighted images are usually recommended for the detection of lymph nodes and tumor infiltration into the chest wall, but only the T2-weighted sequences contribute to the evaluation of lung

Indications to add HR-TSE

- interstitial lung disease
- lymphangitic spread of carcinoma
- differentiation of tumour/atelectasis
- masses with chest wall infiltration
- collateral findings (liver, adrenals)

parenchyma pathology and provide equal information about the chest wall and mediastinum. Since these triggered sequences are time-consuming, we recommend the inclusion of only one additional T2-TSE series into the protocol, since all aspects are covered by the previous sequences.

Conclusion

The proposed imaging protocol covers a wide range of clinical indications for lung imaging and may be used for routine purposes whenever it is mandatory to avoid radiation exposure as far as possible (e.g. in childhood and pregnancy). Moreover, its potential capacity to add functional information such as analysis of diaphragm motion and lung perfusion studies make it more that just a surrogate for chest x-ray and CT. The suggested sequences for lung MRI can be easily set up on state-of-the-art MR scanners by using the Phoenix sample files from www.siemens.com/MAGNETOM-World.

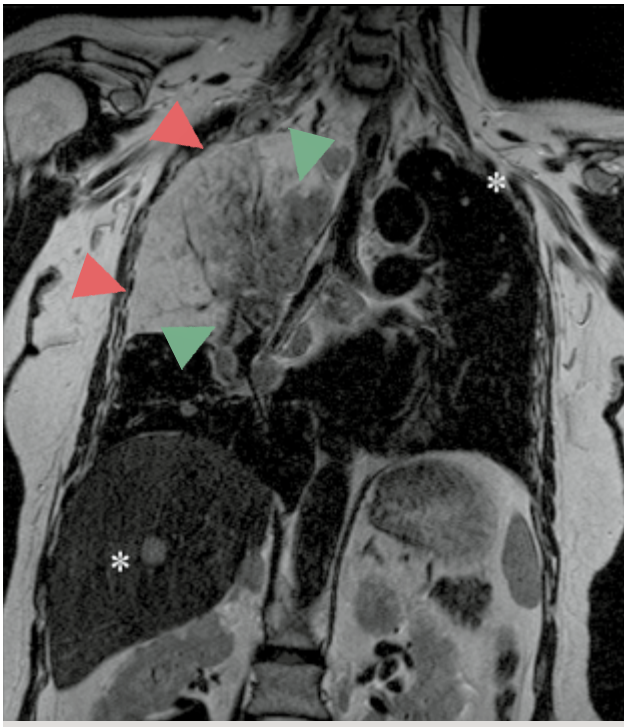

[Figure 6] *50-year-old female with large metastases from breast cancer. The T2-weighted respiration triggered TSE images show a clear difference of tumor (intermediate signal intensity on T2-weighted image green arrowheads) and atelectatic lung (high signal on T2-weighted image red arrowheads). Further pulmonary and hepatic metastases are indicated by stars. For recommended sequence parameters see table 1.*

Abbreviations

CE	Contrast enhanced
GRE	Gradient echo
HASTE	A Turbo Spin Echo technique
HR	High resolution
MRA	MR Angiography
SS GRE	Single shot gradient echo
TIRM	Turbo Inversion Recovery Magnitude
TrueFISP	a gradient echo sequence that provides the highest signal of all steady state sequences. FISP: Fast Imaging with Steady Precession
TSE	Turbo spin echo
TWIST	Time resolved 3D MR angiography
VIBE	Volume Interpolated Breathhold Examination

Further Reading

[1] Eichinger M, Puderbach M, Fink C, Gahr J, Ley S, Plathow C, Tuengerthal S, Zuna I, Muller FM, Kauczor HU. Contrast-enhanced 3D MRI of lung perfusion in children with cystic fibrosis-initial results. Eur Radiol. 2006 May 4; [Epub ahead of print].

[2] Biederer J, Schoene A, Freitag S, Heller M. Simulated pulmonary nodules implanted in a dedicated porcine chest phantom: Sensitivity of MR imaging for detection. Radiology 2003; 227: 475–483.

[3] Biederer J, Both M, Graessner J, Liess C, Jakob P, Reuter M, Heller M. Lung morphology: Fast MR imaging assessment with a volumetric interpolated breath-hold technique: Initial experience with Patients. Radiology 2003; 226: 242–249.

[4] C. Hintze, J. Biederer, H. W. Wenz, R. Eberhardt, H. U. Kauczor. MRI in staging of lung cancer. Radiologe. 2006; 46: 251–259.

[5] Plathow C, Klopp M, Fink C, Sandner A, Hof H, Puderbach M, Herth F, Schmahl A, Kauczor HU. Quantitative analysis of lung and tumour mobility: comparison of two time-resolved MRI sequences. Br J Radiol. 2005; 78: 836–840.

[6] Both M, Schultze J, Reuter M, Bewig B, Hubner R, Bobis I, Noth R, Heller M, Biederer J. Fast T1- and T2-weighted pulmonary MR-imaging in patients with bronchial carcinoma. Eur J Radiol. 2005; 53: 478–488.

[7] Fink C, Puderbach M, Bock M, Lodemann K, Zuna I, Schmaehl A, Delorme S, Kauczor H.-U. Regional Lung Perfusion: Assessment with Partially Parallel Three-dimensional MR Imaging. Radiology 2004; 231: 175–184.

[8] Scarsbrook AF, Evans AL, Owen AR, Gleeson FV. Diagnosis of suspected venous thromboembolic disease in pregnancy. Clin Radiol. 2006 Jan; 61(1): 1–12.

Sequence parameters for MRI of the lung

	Non-CE lung MRI						Perf.	MRA	CE	T2-HR
Basic protocol 15'	x	x	x	x	x	x				(x)
Basic/CE 20'	x	x	x	x	x	x			x	(x)
Functional 30'	x	x	x	x	x	x	x	x	x	(x)
Siemens name	gre	haste	Fl3d _vibe	tfiseg	tse	tfiseg	Fl3d	Fl3d_ce _ce_ff	Fl3d _vibe	tse
Sequence	2D-Flash localizer	T2-HASTE	VIBE	True FISP	T2-TIRM	True FISP	4D MRA Perf.	3D-Flash Angio	VIBE	T2-TSE at
Respiratory phase	insp./bh.	insp./bh.	insp./bh	tidal	insp./bh	in./exp.	insp.	insp.	insp./bh	free
Slice orientation	c/t/s	cor	tra	cor	tra	cor	cor	cor	tra	cor
TA (min:s)	0:10	0:18	0:20	0:56	1:28	0:19	0:29	0:21	0:20	5:05+
Slices per acquisition	7	30	72	≤128	32x4	1	32x20	120	72	45
Preparation	A>P/R>L	R>L	A>P	R>L	A>P	R>L	R>L	R>L	A>P	R>L
FoV (mm) [FoV phase %]	500 [100]	450 [100]	400 [87.5]	450 [100]	400 [75]	400 [100]	500 [100]	500 [83.3]	400 [87.5]	500 [79.7]
Base resolution	256	256	256	256	320	256	256	384	256	512
Phase resolution (%)	75	100	100	100	75	66	54	90	100	75
Slice thickness (mm)	10	8	4	4	6	10	5	1.6	4	4
Phase partial Fourier	6/8	4/8	off	off	off	off	6/8	6/8	off	5/8
Pixel size (mm)	2.6x2.0	1.8x1.8	1.6x1.6	1.8x1.8	1.7x1.3	2.4x1.6	3.6x2.0	1.2x1.0	1.6x1.6	1.3x1.0
Distance factor	50%	0%	20%	-50/0%	10%	n.a.	20%	20%	20%	10%
TR (ms)	8.9	600	3.15	437.2	3500	317.1	1.64	2.75	3.15	1700
TE (ms)	4.38	31	1.38	1.16	106	1.14	0.64	1.12	1.38	100
Flip-angle (degr.)	30°	180°	8°	80	150	67	40	25	8°	150
Band width (Hz/pixel)	180	610	500	1030	252	980	1220	384	500	195
iPAT [no. of ref. lines]	0	2 [14]	2 [35]	2 [25]	2 [66]	2 [24]	2 [24]	2 [24]	2 [35]	2 [46]
Large FoV (dist. corr.)	off	on	off	on	off	off	off	off	off	on
Comments	cor/sag A>P/tra. R>L	2 concatenations ("interleaved")	FatSat, if CE VIBE is planned	Distance factor -50% WIP-Package	TI 150 ms, 5 concatenations	60 measurements at 3/second	20 measurements 1.5 s each. Reduce FA, if SAR limit exceeded	To be run pre-contrast and pul./aortic phase (8.7 s time to center)	With FatSat activated Identical with 3	Navigator needed 5 concatenations

syngo TimCT – Continuous Table Move, Powered by Tim

Mathias Blasche

Siemens Medical Solutions, Erlangen, Germany

Scanning with Continuous Table Move (CTM) is a very new and exciting technology for all applications that require large anatomical coverage, beyond the scanners intrinsic field-of-view (FoV). As publications show [1–30], CTM has so far been possible only on prototype scanners, with significant modifications to the MR system.

Siemens is proud to introduce *syngo* TimCT – Continuous Table move, powered by Tim (Total imaging matrix) for the new T-class generation of Tim systems. The following chapters will discuss the physical principles of Continuous Table Move, the benefits, the scanner requirements and the Siemens implementation of Continuous Table Move: *syngo* TimCT.

TimCT – Physical Principles

There are many possible methods for Continuous Table Move, the main differentiators being the readout direction (parallel or orthogonal to the direction of table movement) and the imaging method (2D or 3D). In the literature, we find examples of a large variety of methods, e.g.

1. 2D transversal sequential scans [19, 22, 26]
2. 2D transversal multi-slice scans [13, 15, 20, 21]
3. 3D transversal scans [16, 18, 23, 24, 27]
4. 2D and 3D radial transversal scans [3, 28]
5. 3D coronal scans [1, 2, 4–6, 8–12, 14, 17, 25, 29, 30]

In the following, we will concentrate on the methods 1 and 5 of this list since these are the first implementations of the new Siemens product, *syngo* TimCT.

Transversal 2D Sequential

The transversal orientation is useful when one is interested in the whole extension of anatomy in both the left-right direction (x) and the anterior-posterior direction (y). The sequential mode makes sense with fast sequences (e.g., TurboFLASH, HASTE, single shot EPI) where the complete phase-encoding of the single slice can be applied without pauses.

With "Transversal 2D Sequential", each slice, in axial orientation, is measured completely before proceeding to the next slice. The sequential method is different from conventional multi-slice scans (e.g., with Spin Echo) where a stack of slices is excited in an interleaved fashion.

In conventional imaging, one would plan a stack of slices at isocenter, scan all these slices sequentially, move the table by a distance equaling the thickness of the slice stack, and repeat this process until the entire scan range is covered (Fig. 1A).

This approach has some disadvantages:

a) The "outer" slices of the stack (indicated in Fig. 1 by the darker and brighter shades) are out of isocenter in a region of lower magnet homogeneity and lower gradient linearity, possibly degrading image quality.
b) Scan efficiency is compromised since it is interrupted by table moves without scanning.
c) Planning of the slice stacks is more cumbersome and time-consuming since each slice stack has to be planned exactly adjacent to its neighbors.

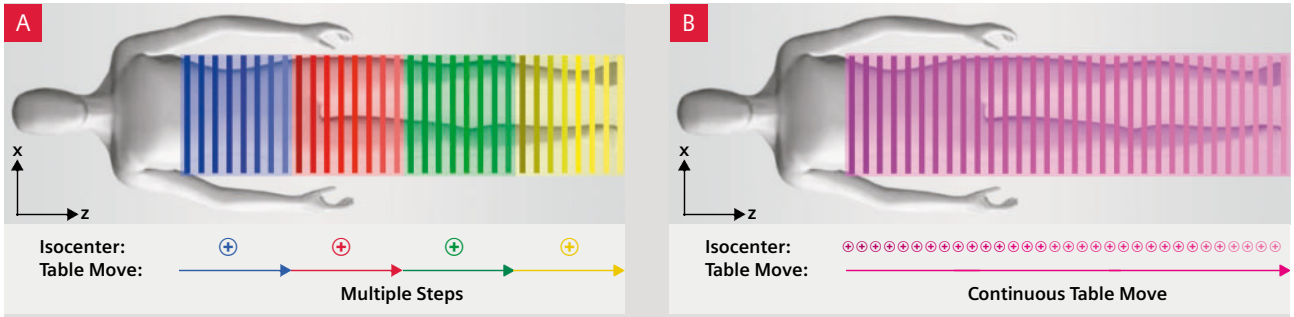

[Figure 1] *Transversal 2D sequential scanning with (A) conventional multi-step approach and with (B) Continuous Table Move. Each colored line represents a transversal image.*

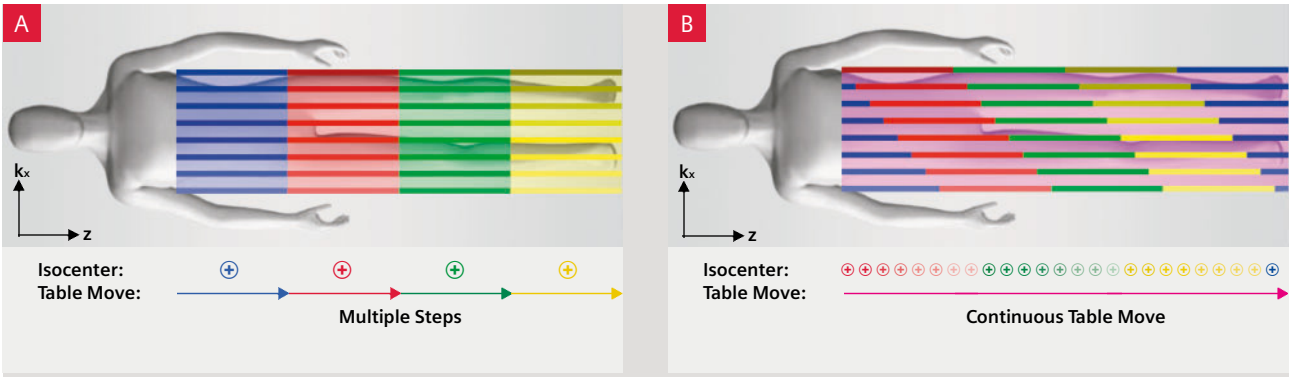

[Figure 2] *Coronal 3D acquisition with (A) conventional multi-step approach and with (B) Continuous Table Move in hybrid k-space (z-k_x). k_x is the in-plane phase-encoding direction (left-right), while k_y (anterior-posterior, not shown) is the through-plane partition-encoding direction. Each colored line represents one partition-encoding loop, Fourier-transformed in the readout direction, z. Each color represents a complete in-plane plus through-plane encoding-cycle of one slab (in case of CTM, "virtual slab").*

"Transversal 2D Sequential" is the most intuitive method when thinking about Continuous Table Move. Each slice is exactly scanned at isocenter (indicated by identical shades of purple of lines and isocenter symbols in Fig. 1B), while the table is constantly moving.

The table velocity for "Transversal 2D Sequential" with gapless axial slices is the slice thickness divided by the scan time per slice:

$$V_{Table} = \frac{Thk_{Slice}}{N_{Phase} \cdot TR} = \frac{Thk_{Slice}}{TA}$$

Continuous Table Move with the "Transversal 2D Sequential" approach is advantageous in the following aspects:

a) Each slice is scanned at isocenter, in a region of optimal magnet homogeneity and gradient linearity, optimizing image quality.
b) Since no time is required for table movements while scanning is suspended, Continuous Table Move offers higher scan time efficiency.
c) Workflow is also facilitated by the fact that the whole slice stack can be planned in one seamless block.

The method "Transversal 2D Sequential" is implemented in TimCT FastView, used for easy extended-FoV localizer imaging. It is based on a fast TurboFLASH sequence (refer to chapter "TimCT Product Implementation" for more details).

Coronal 3D

The coronal orientation is beneficial if the region of interest has a large extension in the cranio-caudal direction (z) and the left-right direction (x), but when it is not necessary to cover the whole anatomy in the anterior-posterior direction (y). These conditions are exactly met by peripheral angiography, explaining the fact that most CTM publications about the "Coronal 3D" method cover this application.

The conventional approach to cover the entire peripheral vasculature is to acquire multiple coronal 3D slabs with overlapping regions (overlaps omitted in Fig. 2 for simplicity).

Although this multi-step approach is well-established and yields very good results in clinical routine, there are a couple of intrinsic disadvantages:

a) Scan efficiency is compromised since it is interrupted by table movements without scanning.
b) Planning of the coronal slabs is more cumbersome and time-consuming since typically all slabs are aligned individually in order to seamlessly cover the whole peripheral vasculature with defined overlaps.
c) The individual slabs have to be composed to get the complete vasculature in one resulting image (although this can be done automatically with the Inline Composer).
d) The resulting composed image may suffer from "boundary artifacts", i.e. shading or signal differences at the edges of the (previously) independent 3D slabs.

As with multi-step conventional imaging, there are also "subsets" of the total scan range with Continuous Table Move. Each subset represents one complete cycle of in-plane and through-plane phase-encoding, N_x x N_y. We will call the extension of each subset in z-direction the "intrinsic FoV", or FoV_z. FoV_z is analogous to the FoV in the multi-step approach. Due to the continuous table movement, these subsets are "sheared" in hybrid k-space (z-k_x), see Fig. 2B. The echoes in z-direction are Fourier-transformed and combined. Fourier

transformations in the two remaining directions, x and y, will result in one single large FoV of the total scan range. This method, with the echo readout in z-direction, was first proposed by Kruger et al. in a publication from 2002 [1].
The maximum table velocity can be calculated by setting into relation (a) the time it takes to perform a complete encoding cycle N_x x N_y x TR to (b) the time it takes to move the table by one FoV_z. This yields:

$$V_{Table} = \frac{FoV_z}{N_x \cdot N_y \cdot TR}$$

A table velocity smaller than this maximum value is analogous to an overlap of slabs in the conventional multi-step approach. It becomes clear from this formula that the intrinsic FoV in z-direction has an effect on the achievable table velocity V_{Table} and/or spatial resolution N_x x N_y.
"Coronal 3D" with Continuous Table Move offers some significant advantages compared to the multi-step approach:

a) There are no scanning pauses for table moves, scan time efficiency is maximized.
b) Planning is straight-forward, no more difficult than planning of a single stationary FoV: The total scan range can be flexibly increased or decreased in a continuous manner, not only in multiples of the intrinsic z-FoV.
c) The total scan range is one single entity – it is "intrinsically composed".
d) The smooth scanning process will result in less boundary artifacts.

The method "Coronal 3D" is implemented in TimCT Angiography, based on a fast 3D FLASH sequence (refer to chapter "TimCT Product Implementation" for more details).

Benefits of *syngo* TimCT

When scanning a large scan range, Continuous Table Move (CTM) has many advantages compared to multi-step approaches:

Workflow

Fast workflow is probably the biggest advantage of CTM:
Easier and faster examination prescription: The setup of the examination is extremely easy. With an integrated implementation like TimCT, it is no more complicated than, for example, a conventional stationary head scan.
Reduced post-processing: Multi-step approaches can require extensive post-processing [30]. With CTM, the anatomy of the whole scan range – or any part of it in detail – can be viewed directly, without the need of any composing processing.
TimCT also supports Inline multiplanar reconstruction (MPR), Inline Subtraction and Inline maximum intensity projection (MIP): Processing is done automatically at the end of the scan, without any user interaction.

Speed

CTM has higher scan time efficiency than multi-step approaches because there are no scanning pauses during table motion. [1, 2, 17] The higher scan time efficiency is especially beneficial for contrast-enhanced MR angiography where short scan times are dictated by physiology, i.e. blood velocity.
Certain sequence techniques require dummy RF pulses in the beginning to achieve a steady state. With multi-step approaches, these need to be repeated at every level [1, 2] – which is not necessary with CTM.

Image Quality

With CTM, scans are always done exactly at isocenter, i.e. in the region of maximum homogeneity. This directly translates into improved image quality.
Especially ultrashort magnets with lower homogeneity can benefit from CTM. Continuous Table Move can significantly facilitate large-coverage scans with ultrashort magnets. [21, 22, 27]
Being intrinsically continuous, CTM provides seamless images, without the boundary artifacts that are sometimes visible in composed multi-step images. [1, 2]

Patient Comfort

A CTM scan is a smooth process without repeated scan-move-stop procedures. The less frequent "table jerking" increases patient comfort. [9]

Be Ready for the Future

syngo TimCT – Continuous Table move, powered by Tim – offers CT-like scanning with MR. And like Spiral CT, TimCT offers a huge potential. Tremendous improvements for many applications are already visible on the horizon, e.g. interactive or even automatic adaptation of table velocity, controlled by bolus speed [8, 29]; simultaneous acquisition of multiple contrasts in one table stroke [15]; combination of Continuous Table Move with dynamic imaging [4, 5, 7]; tumor staging [19] – to name just a few.

MR – CT Analogies

Although magnetic resonance imaging (MRI) and computed tomography (CT) are fundamentally different in the way the images are generated, there are some striking analogies in the historical development of both modalities.



MR in the 80s – The Decade of Magnets

One could call the 80s the "decade of magnets". The main topic at that time was the question for the optimal field strength – 0.5T, 1T or 1.5T. MR systems at that time had only one RF channel and slow gradients.

The CT analogy at that time was the question for the best detector material, gas or solid state. CT scanners in the 80s had slow rotation times and only one detector ring.

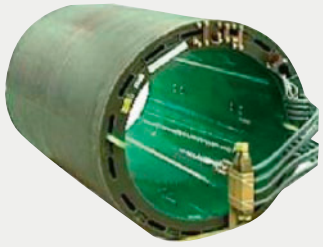

MR in the 90s – The Decade of Gradients

Gradient performance was the most critical question in the 90s. Both gradient amplitude and slew rate were increased by orders of magnitude, up to the limit where gradient performance is no longer limited by technology, but by the patient's peripheral nerve stimulation limit.

At the same time, CT saw an increase in rotation speed, up to more than 3 rotations per second.

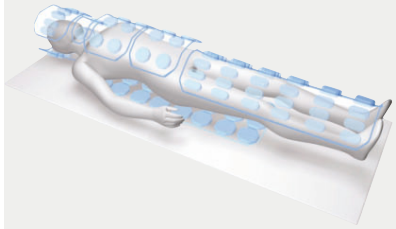

MR in the 2000s – The Decade of RF

RF technology and Parallel Imaging have been the primary focus in this decade, with an increase of the number of RF channels and the development of "high-density" coils. Siemens introduced Integrated Panoramic Array (IPA) as early as 1997, and Tim (Total imaging matrix) technology in 2003, with up to 102 seamlessly integrated coil elements and up to 32 truly independent RF channels. There is even a prototype with 128 RF channels. Tim offers high flexibility, accuracy and speed, with high PAT factors in all body regions and all directions.

The CT analogy to RF technology is multi-detector technology, also offering larger coverage in less time, with higher image quality and spatial resolution.

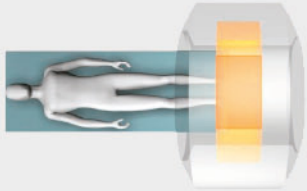



MR in 2006 – TimCT

Now, in 2006, Siemens pioneers TimCT – Continuous Table move, powered by Tim. Peripheral run-off studies can be done faster, and TimCT tremendously facilitates the workflow. The potential of TimCT for peripheral angiography and for other applications is huge.

MR's TimCT is very similar to CT's spiral technology. Both technologies enable seamless scanning – with high speed and ease of use.

Actually, spiral CT scanners have been available for more than 15 years. One might take this as a proof point that it was about time that MR caught up with CT in this technological perspective. Actually we expect that MR systems without TimCT capabilities will be similarly shunned in a few years as CT scanners without spiral capabilities would be today.

Requirements for *syngo* TimCT

Scanning with Continuous Table Move (in analogy to Spiral CT) and not wasting time for multiple Scan–Stop–Adjust procedures sounds straight-forward and easy. However, it is not trivial. The MR system has to meet numerous requirements to make TimCT possible. Here is a list of all the technical requirements and how these are met by *syngo* TimCT.

Table Requirements	
■ **Shielded table drive** The electronics of the patient table need to be shielded. An unshielded table would result in electronic interferences and consequently image artifacts.	***syngo* TimCT ✓** Actually, the patient tables of all Tim systems are shielded. Siemens had the vision of TimCT years ago and prepared the scanners accordingly – which made it much easier to implement TimCT and makes it easier to upgrade to TimCT, too.
■ **Software-enabled table motion** For routine clinical use, manual table motion is of course no alternative. It is imperative that the table can be moved from the console, easily and flexibly. The remote table move capabilities need to cover the whole scanning distance.	***syngo* TimCT ✓** Software-enabled table motion is standard with all Tim systems. One major aspect here is that the cables of the Tim coils are very short and – unique to Siemens – plug into the table, thus reducing the risk that the cables get jammed during the table move.
■ **Control of table speed with high accuracy** For sub-millimeter image resolution, the accuracy of the patient table has to be accordingly high. Furthermore, software-controlled sub-pixel correction has to be implemented. [1]	***syngo* TimCT ✓** All Tim systems feature an accurate control of table speed and position. In addition, a sub-pixel software correction is implemented with TimCT.
Software Requirements	
■ **Sequences** Imaging sequences supporting Continuous Table Move are required.	***syngo* TimCT ✓** TimCT FastView and TimCT Angiography are available with the new T-class generation of scanners (software *syngo* MR B15). The flexible architecture of IDEA, our sequence programming tool, facilitates the development of TimCT sequences.
■ **Image processing** The measured raw data need to be corrected, processed and displayed automatically in order to guarantee a smooth workflow.	***syngo* TimCT ✓** With TimCT, image processing is fully integrated, including corrections (see below), fully automated image reconstruction of the full FoV, Inline MPR, and Inline Subtraction & Inline MIP for angiography.
■ **Graphical slice positioning** Beyond the "standard" capabilities, graphical slice positioning needs to offer specific features, e.g. independent control of intrinsic FoV and total scan range, control of active coil elements etc.	***syngo* TimCT ✓** With the Tim Planning Suite, we were already prepared for most aspects of TimCT graphical slice positioning. With T-class, an intuitive (color-based) control of intrinsic FoV and total scan range has been added.

Software Requirements	
■ **Adjustments** Frequency, transmitter and receiver adjustments must be available over the whole scan range.	*syngo* TimCT ✓ Frequency and transmitter adjustments are performed in a short TimCT Adjustment scan, also during table motion. A time-consuming receiver adjustment is in general not required with all Tim systems, due to the large dynamic range of the receiver.
Image Quality Requirements	
■ **High SNR and high spatial resolution** The requirements for optimal diagnostic quality can only be met with surface coils. In comparison to an integrated body coil, surface coils offer 2-4 times more signal-to-noise ratio (SNR). The benefit of surface coils has often been mentioned in the literature [5, 8, 16, 17, 29].	*syngo* TimCT ✓ With his readily available Matrix coils, Tim is the ideal basis for TimCT. The "high-density" Matrix coils offer highest SNR in all body regions which can easily be translated into high spatial resolution and short scan times.
■ **Gradient non-linearity correction** It is known from the literature that gradient non-linearity correction is basically a must for Continuous Table Move scanning. Without this correction, the lateral anatomy would become blurry – the farther outside of isocenter, the worse [6, 25].	*syngo* TimCT ✓ Inline gradient non-linearity correction is fully integrated into TimCT and automatically performed.
■ **Phase correction** A phase correction in the readout direction is required for coronal scans, in order to avoid a shading pattern in the reconstructed images [11].	*syngo* TimCT ✓ Phase correction is fully implemented with TimCT Angiography.
Speed Requirements	
■ **Parallel Imaging** Parallel Acquisition Techniques (PAT) have become accepted for the majority of applications. PAT is an *essential* tool for higher speed. Especially for peripheral angiography, short scan times (to follow the contrast bolus) combined with high spatial resolution (to be able to diagnose also small vessels and pathologies) are critical [30].	*syngo* TimCT ✓ Again it comes back to Tim, with "high-density" coils in all body regions, enabling Parallel Acquisition Techniques (PAT) in all directions. TimCT is compatible with iPAT using Tim's unique Matrix coil design. Note that Parallel Imaging can *only* be performed with surface coils, not with an integrated body coil. See section "Coil Technology Requirements" below.
■ **Calibration for Parallel Imaging** Coil calibration for Parallel Imaging needs to be possible with a continuously moving table. Many implementations today rely on separate calibration scans that are not integrated into the scan. A large number of these calibration scans would be necessary to cover the whole scan range which would result in very long examination times and low productivity.	*syngo* TimCT ✓ The Auto-Calibration algorithm, standard with Siemens iPAT (integrated Parallel Acquisition Techniques), is the ideal solution for Parallel Imaging with Continuous Table Move. The benefits of Auto-Calibration are covered in [30].

Coil Technology Requirements	
■ **Connection of multiple coils** Given the fact that good diagnostic image quality can only be achieved with surface coils, it needs to be possible to connect all surface coils simultaneously for full anatomical coverage.	*syngo* TimCT ✓ Beside having a "high density" of coil elements for optimal image quality, one of the major benefits of Tim is the possibility to simultaneously connect up to 10 coils, with up to 102/76 (3T/1.5T) seamlessly integrated coil elements.
■ **Flexible coil combinations** For flexible coverage of arbitrary regions-of-interest, coil combinations are required.	*syngo* TimCT ✓ With Tim all Matrix coils can be combined for seamless anatomical coverage. Elements from different coils can be used simultaneously.
■ **Surface coils plug into patient table** With multiple coils being connected for large anatomical coverage, coil cables need to be short and integrated into the table. Long coil cables (e.g. attached to the magnet front) create safety issues during table movement.	*syngo* TimCT ✓ All Matrix coils have very short coil cables that directly plug into the patient table.
■ **Automatic coil detection** With a large scan range being covered by multiple coils, it would be extremely cumbersome and time-consuming if the user had to "teach" the system the exact location of each coil element. Therefore, the exact position of each coil has to be detected automatically.	*syngo* TimCT ✓ All Tim systems feature AutoCoilDetect. All coil elements are automatically detected in the localizer scan and depicted in the graphical slice positioning.
■ **Dynamic coil switching** Beyond the detection of the coils, it is also necessary to automatically activate and de-activate the coil elements during Continuous Table Move. It would be next to impossible to manually pre-select the coil switching for a continuous scan during table motion. For a discussion of the benefits of dynamic coil switching see [30].	*syngo* TimCT ✓ With AutoCoilDetect (see above), the Tim systems were already prepared for the next step, AutoCoilSelect. Now, the user does not need to take care of coil selections at all, boosting workflow and robustness – and being one of the major revolutionary features that make TimCT possible.
Patient Safety Requirements	
■ **SAR monitor** SAR values need to be known for all body locations.	*syngo* TimCT ✓ SAR is checked for the whole scan range in a short TimCT Adjustment scan.

In summary

As the literature about Continuous Table Move (CTM) shows, only a few sites worldwide have been working on CTM. The reason for this is the long list of very challenging technical requirements for Continuous Table Move.

All CTM sites so far have been pure prototype installations that have to cope with limitations including a) external control for table motion, b) external image processing, c) scans with the body coil only, no surface coils, and d) no Parallel Acquisition Techniques.

With Tim, Siemens has the ideal platform for the implementation of TimCT. This is expressed with "*syngo* TimCT – powered by Tim".

syngo TimCT Product Implementation

syngo TimCT FastView

TimCT FastView is an extremely fast localizer sequence. It is based on a sequential TurboFLASH sequence, i.e. all slices are acquired in a sequential mode. Each slice is scanned at isocenter while the table is moving. The slice orientation is axial.

The rather coarse spatial resolution allows very fast scanning, with a table velocity as high as 5 cm/sec – e.g., 150 cm can be covered in just 30 seconds.

Benefits of TimCT FastView:

- Inline Technology is implemented: With Inline MPR, sagittal and coronal reformats are automatically generated on the fly.
- TimCT FastView can be immediately performed without any adjustments. SAR (specific absorption rate) is extremely low since only small flip angles are used. TimCT FastView is done with the integrated body coil and can be done independently of any coil used for the specific examination.
- TimCT FastView can even be initiated without laser light positioning, using a preset (user-definable) scan range that e.g. covers the whole spine. This has the potential to increase productivity due to shorter patient setup times.

TimCT FastView is standard with all T-class systems.

syngo TimCT Angiography

TimCT Angiography is optimized for contrast-enhanced peripheral run-off studies in coronal (or sagittal) orientation. It is a high-resolution 3D sequence. TimCT Angiography has the full flexibility of all parameters, as in a "conventional" scan. Additionally, the total scan range can be flexibly increased beyond the intrinsic FoV of the scanner.

Benefits of TimCT Angiography:

- Workflow is facilitated since the whole process is completely automated. The setup of the scan is easier than a conventional multi-step approach, planning steps are reduced by up to 50%. Inline Subtraction and Inline MIP, all automatically processed with Inline Technology, further increase the examination speed.
- TimCT Angiography offers maximum scan time efficiency – no scan interrupts during table move phases as in conventional multi-step approaches. Consequently, the contrast bolus can be tracked faster and/or with higher spatial resolution.
- Tim technology, AutoCoilDetect and AutoCoilSelect, all exclusive to Siemens, make it possible to perform TimCT Angiography with optimal image quality, i.e. with a signal-to-noise ratio that can only be achieved with surface coils.

TimCT Angiography is an option for all T-class systems.

syngo TimCT Adjustments

The TimCT Adjustments cover all adjustments that are required to run a TimCT scan with optimal image quality, fast workflow and full patient safety.

The TimCT Adjustments include Frequency Adjustment, Transmitter Adjustments, SAR Monitoring, AutoCoilDetect and AutoCoilSelect for all locations of the whole scan range. The adjusted values are then dynamically applied to the TimCT measurement on the fly. All connected coils are automically detected during the TimCT Adjustments and then automatically selected during the TimCT measurement.

TimCT FastView does not require adjustments (see above).

The TimCT Adjustments can be run in combination with TimCT FastView (prior to TimCT Angiography), or they will be automatically performed with TimCT Angiography if they have not been done before.

The TimCT Adjustments are very fast and are performed with a table velocity of 5 cm/sec.

Prerequisites

T-class and *syngo* TimCT are available for

- MAGNETOM Trio, A Tim system
- MAGNETOM Avanto
- MAGNETOM Espree
- MAGNETOM Symphony, A Tim system

syngo TimCT is exclusive to the new generation T-class systems, introduced at the RSNA 2006. All Tim systems are upgradable to T-class.

syngo TimCT is compatible with 18 and 32 RF channels, i.e. Tim [76x18] and Tim [76x32] for 1.5T systems, and Tim [102x18] and Tim [102x32] for 3T.

The maximum scan range of all Tim systems is sufficient for a complete peripheral run-off study, i.e. from the renal arteries to the feet. Whole-body coverage is possible with the Telescopic Table which is part of the Tim Whole-Body Suite (optional).

Literature
[1] Kruger DJ, Riederer SJ, Grimm RC, Rossman PJ. Continuously moving table data acquisition method for long FoV contrast-enhanced MRA and whole-body MRI. Magn Reson Med 2002; 47: 224–231.
[2] Zhu Y, Dumoulin CL. Extended Field-of-View Imaging With Table Translation and Frequency Sweeping. Magn Reson Med 2003; 49: 1106–1112.
[3] Shankaranarayanan a, Herfkens R, Hargreaves BM, Polzin JA, Santos JM, Brittain JH. Helical MR: Continuously moving table axial imaging with radial acquisitions. Magn Reson Med 2003; 50: 1053–1060.
[4] Madhuranthakam AJ, Kruger DG, Riederer SJ, Glockner JF, Hu HH. Time-resolved contrast enhanced MRA for extended FoV moving table imaging. In: Proceedings of the 11th Annual Meeting of ISMRM 2003. p 256.
[5] Madhuranthakam AJ, Kruger DG, Riederer SJ, Glockner JF, Hu HH. Time-resolved 3D contrast-enhanced MRA of an extended FoV using continuous table motion. Magn Reson Med 2004; 51: 568–576.
[6] Polzin JA, Kruger DG, Gurr DH, Brittain JH, Riederer SJ. Correction for gradient nonlinearities in continuously moving table MR imaging. Magn Reson Med 2004; 52: 181–187.
[7] Fain SB, Browning FJ, Polzin JA, Du J, Zhou Y, Block WF, Grist TM, Mistretta CA. Floating Table Isotropic Projection (FLIPR) Acquisition: A time-resolved 3D method for extended field-of-view MRI during continuous table motion. Magn Reson Med 2005; 52: 1093–1102.
[8] Kruger DG, Riederer SJ, Polzin JA, Madhuranthakam AJ, Hu HH, Glockner JF. Dual-velocity continuously moving table acquisition for contrast-enhanced peripheral Magnetic Resonance angiography. Magn Reson Med 2005; 53: 110–117.
[9] Keupp J, Aldefeld B, Börnert P. Continuously moving table SENSE imaging. Magn Reson Med 2005; 53: 217–220.
[10] Hu HH, Madhuranthakam AJ, Kruger DG, Glockner JF, Riederer SJ. Variable field of view for spatial resolution improvement in continuously moving table magnetic resonance imaging. Magn Reson Med 2005; 54: 146–151.
[11] Kruger DG, Riederer SJ, Rossman PJ, Mostardi PM, Madhuranthakam AJ, Hu HH. Recovery of phase inconsistencies in continuously moving table extended field of view Magnetic Resonance Imaging acquisitions. Magn Reson Med 2005; 54: 712–717.
[12] Hu HH, Madhuranthakam AJ, Kruger DG, Glockner JF, Riederer SJ. Continuously moving table MRI with SENSE: Application in peripheral contrast enhanced MR angiography. Magn Reson Med 2005; 54: 1025–1031.
[13] Fautz HP, Kannengiesser SAR. Sliding Multi-Slice (SMS): A New Technique for Minimum FoV Usage in Axial Continuously Moving-Table Acquisitions. Magn Reson Med 2006; 55: 363–370.
[14] Madhuranthakam AJ, Hu HH, Kruger DG, Riederer SJ. Numerical equilibration of signal intensity and spatial resolution in time-resolved continuously moving-table imaging. Magn Reson Med 2005; 55: 694–699.
[15] Sommer G, Fautz HP, Ludwig U, Hennig J. Multicontrast sequences with continuous table motion: A novel acquisition technique for extended field of view imaging. Magn Reson Med 2006; 55: 918–922.
[16] Aldefeld B, Börnert P, Keupp J. Continuously moving table 3D MRI with lateral frequency-encoding direction. Magn Reson Med 2006; 55: 1210–1216.
[17] Madhuranthakam AJ, Hu HH, Kruger DG, Glockner JF, Riederer SJ. Contrast-enhanced MR angiography of the peripheral vasculature with a continuously moving table and modified elliptical centric acquisition. Radiology 2006; 240: 222–229.
[18] Aldefeld B, Börnert P, Keupp J, Nehrke K. Respiratory-Gated Continuously Moving Table 3D MRI. In: Proceedings of the 14th Annual Meeting of ISMRM 2006. p 212.
[19] Brauck K, Zenge M, Stock F, Mark L, Vogt F, Barkhausen J. Multi-contrast whole-body 2D axial MR imaging during continuous table movement for tumor staging. In: Proceedings of the 14th Annual Meeting of ISMRM 2006. p 1793.
[20] Sommer G, Ludwig UA, Fautz HP, Schäfer O. Abdominal imaging with extended field of view in rectal cancer using a continuously moving table: A feasability study. In: Proceedings of the 14th Annual Meeting of ISMRM 2006. p 1801.
[21] Sommer G, Ludwig UA, Schäfer O, Fautz HP. One-breath-hold acquisition of the whole abdomen in one minute using continuously moving table. In: Proceedings of the 14th Annual Meeting of ISMRM 2006. p 2269.
[22] Zielonka A, Kinner S, Zenge MO, Ladd ME, Ladd SC. Do we need suspended breathing with real-time axial continuously moving table MR imaging? In: Proceedings of the 14th Annual Meeting of ISMRM 2006. p 2270.
[23] Börnert P, Aldefeld B, Keupp J, Eggers H. Two approaches to water/fat selective whole-body continuously moving table 3D imaging. In: Proceedings of the 14th Annual Meeting of ISMRM 2006. p 2271.
[24] Börnert P, Aldefeld B, Eggers H, Keupp J. Fast whole-body 3D water/fat scoring. In: Proceedings of the 14th Annual Meeting of ISMRM 2006. p 2305.
[25] Grimm RC, Kruger DG, Polzin JA, Riederer SJ. Sub-second 3D image reconstruction with gradwarp correction in moving table MRI. In: Proceedings of the 14th Annual Meeting of ISMRM 2006. p 2367.
[26] Kinner S, Zielonka A, Zenge MO, Ladd SC, Ladd ME. Whole-body MR imaging with continuously moving table and multiplanar reformations: toward parameter optimization for SSFP imaging in patient examinations. In: Proceedings of the 14th Annual Meeting of ISMRM 2006. p 2421.
[27] Zenge MO, Ladd ME, Quick HH. A novel reconstruction method for axial 3D data acquisition during continuous table movement. In: Proceedings of the 14th Annual Meeting of ISMRM 2006. p 2944.
[28] Börnert P, Aldefeld B, Keupp J. Whole-Body 3D Continuously Moving Table Imaging using Radial and Spiral Sampling. In: Proceedings of the 14th Annual Meeting of ISMRM 2006. p 3018.
[29] Sabati M, Lauzon ML, Mahallati H, Frayne R. Interactive continuously moving table (iCMT) large field-of-view real-time MRI. Magn Reson Med 2006; 55: 1202–1209.
[30] Zenge MO, Vogt FM, Brauck K, Jökel M, Barkhausen J, Kannengiesser S, Ladd ME, Quick HH. High-resolution continuously acquired peripheral MR angiography featuring partial parallel imaging GRAPPA. Magn Reson Med 2006; 56: 859–865.

syngo TimCT – a Novel Concept for Whole-Body MRI

O. Schaefer[1], T. Baumann[1], G. Pache[1], D. Paul[2], M. Langer[1]

[1] *Department of Radiology, University Hospital Freiburg, Germany*
[2] *Department of Radiology, Medical Physics, University Hospital Freiburg, Germany*

Introduction

The application of whole-body MRI for staging of malignant diseases is increasingly accepted by clinicians. Results underlining the diagnostic significance of the procedure are encouraging [1, 2]. Parallel imaging (iPAT), multiple Matrix coils and receiver channels (Total imaging matrix, Tim) opened the door for high-resolution whole-body MRI. The work of Fautz and Kannengiesser [3] formed the basis of the current clinical applications of the novel technique termed TimCT, which utilizes continuously moving table acquisition to generate images of excellent diagnostic quality. Thus, an extended volume coverage is now possible within one examination in order to gain information from organ systems distant from the primary region of interest to complete one-step staging or to significantly reduce examination time. Currently, we routinely perform TimCT for rectal cancer staging and follow-up of patients with Crohn's disease.

Technique

The purpose of Continuous Table Move MRI is to extend the field-of-view (FoV) in axial direction beyond the scanner's available scan region with a temporally and spatially seamless acquisition. The sliding multislice technique (SMS) was introduced in 2006 by Fautz et al. to minimize the required axial FoV without compromising image quality. The SMS uses a segmented multi-slice acquisition pattern, which samples the same phase-encoding step of any anatomical slice at the same spatial position in the scanner's axial FoV. The implementation of this special pattern avoids discontinuities between the images along the slice axis, for example, gradient non-linearity, because all z-dependent scan properties are encoded identically for all slices. The full k-space data of any slice is collected while the slice moves through the scanner from one scan position to the next (Continuous Table Move, CTM). The simultaneous acquisition of multiple slices is possible by just shifting the acquisition trajectories of different slices in time.

SMS implemented in the TimCT product can be applied to single-shot sequences (like FLASH) as well as to multi-shot sequences (like TSE). We now routinely perform a T1-weighted contrast-enhanced FLASH sequence with an initial breath-hold phase of 20 s to ensure artifact-free imaging of the liver and a free-breathing TIRM sequence. For both sequences the table speed is set to 1 cm per second. The sequence parameters are summarized in Table 1.

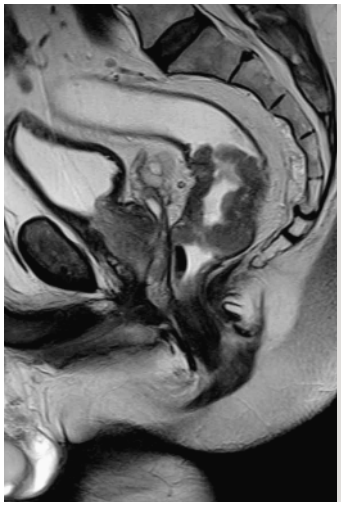

[Figure 1] *Example of T3 rectal cancer depicted on a sagittal T2-weighted TSE from our high-resolution pelvic MRI protocol.*

Clinical applications

High-resolution pelvic MRI represents the current gold standard of local staging of rectal cancer [4]. No other state-of-the-art imaging modality has the ability to directly visualize the relationship between tumor and resection margin. To overcome step-by-step staging of rectal cancer patients using different imaging modalities, we integrated TimCT into a high-resolution imaging protocol for initial work-up and surveillance. With TimCT we perform both, an axial breath-hold contrast-enhanced T1-weighted FLASH sequence in a portal dominant phase to detect liver metastases and retroperitoneal lymph nodes, and an axial free-breathing TIRM sequence to cover the lungs, whole abdomen and pelvis to depict lung

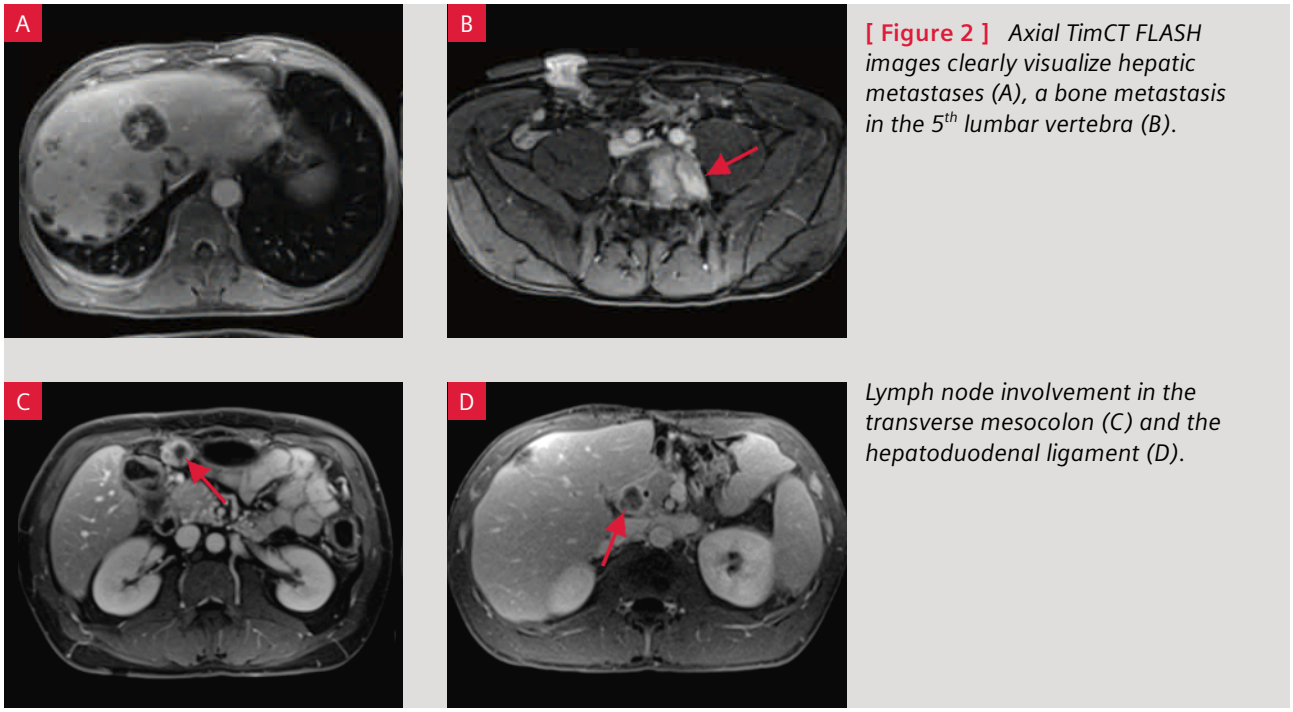

[Figure 2] *Axial TimCT FLASH images clearly visualize hepatic metastases (A), a bone metastasis in the 5th lumbar vertebra (B). Lymph node involvement in the transverse mesocolon (C) and the hepatoduodenal ligament (D).*

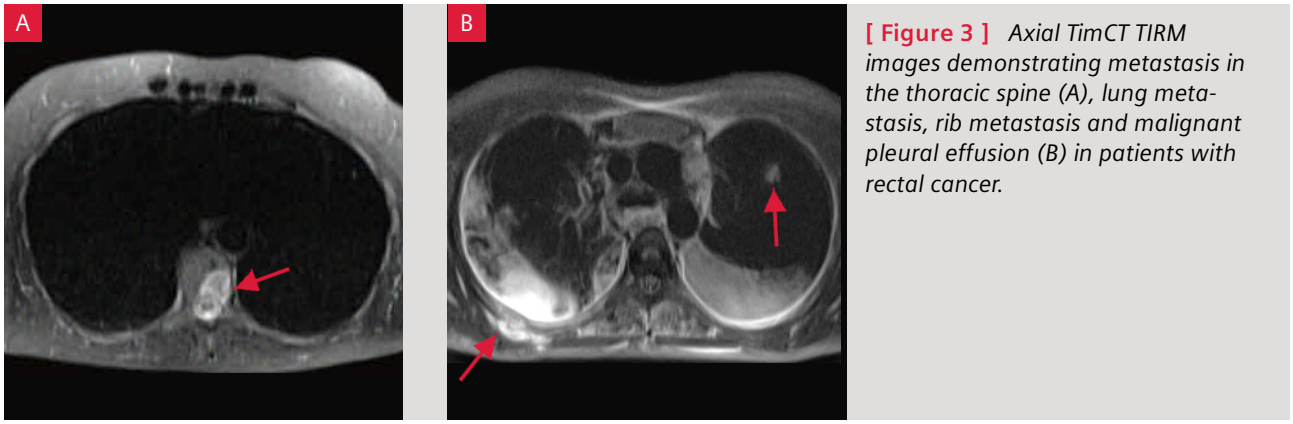

[Figure 3] *Axial TimCT TIRM images demonstrating metastasis in the thoracic spine (A), lung metastasis, rib metastasis and malignant pleural effusion (B) in patients with rectal cancer.*

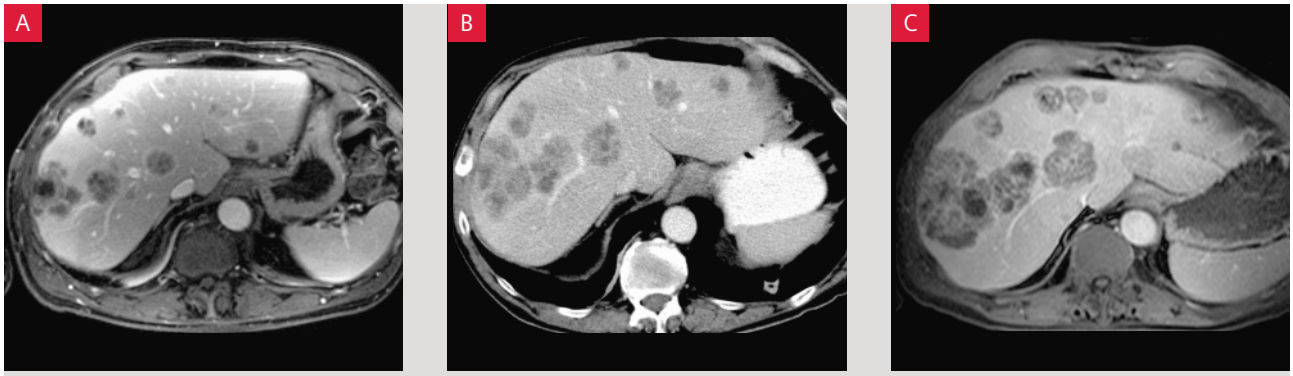

[Figure 4] *The comparison between (A) TimCT FLASH, (B) multi-slice CT and (C) conventional FLASH show the excellent lesion detection in this patient with recurrent rectal cancer and multiple metastases.*

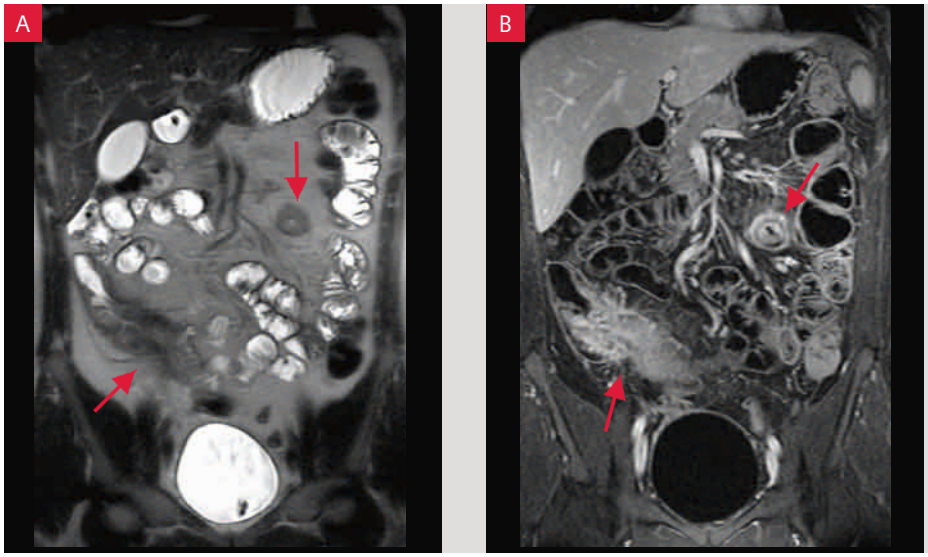

[Figure 5] *Coronal HASTE (A) and contrast-enhanced VIBE (B) images derived from our Hydro-MRI protocol show manifestations of Crohn's disease with an inflammatory conglomerate and a skip lesion at the level of the proximal jejunum.*

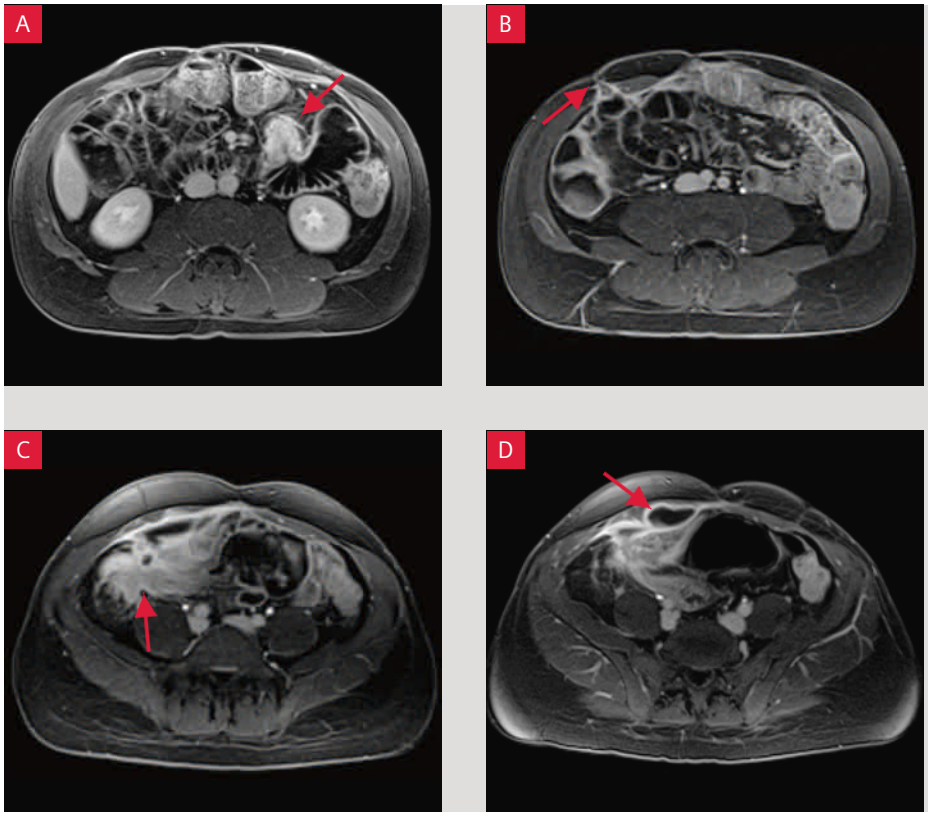

[Figure 6] *Axial TimCT FLASH images of the same patient clearly demonstrate the skip lesion (A), an enterocutaneous fistula (B). The inflammatory conglomerate (C) and an abscess in the rectus abdominis muscle (D).*

lesions, lymph nodes and bone marrow infiltration. Our experiences with TimCT for staging of rectal cancer patients are promising. The image quality has turned out to be comparable to that of a stationary upper abdomen protocol. Moreover, no differences in lesion detectability were found between TimCT and multi-slice CT (MSCT) regarding liver metastases and malignant lymph nodes.

MR-Enteroclysis is an established imaging technique for the evaluation of Crohn's disease since the degree of disease activity, presence of bowel wall pathology and extraintestinal manifestations of the disease (e.g. abscesses, fistulas) are accurately assessed [5]. For patient follow-up, Hydro-MRI is recommended by several working groups. Simplification and acceleration of the imaging protocol is of special interest, as

Crohn patients require repeated MRI during the course of the disease. However, the integration of Continuous Table Move MRI into a Hydro-MRI protocol for the evaluation of Crohn's disease has so far not been described. Our experiences with TimCT for the evaluation of patients with Crohn's disease are encouraging. The diagnostic sensitivity was found to be excellent compared to conventional axial multi-stage breath-hold sequences. Additionally, a marked reduction in total examination time can be achieved if TimCT is used.

Conclusion

syngo TimCT seems to be a promising adjunct to both rectal cancer staging and Hydro-MRI for follow-up of patients with known Crohn's disease. Scan efficiency and image quality are attributes of this upcoming technique. Furthermore, this new imaging modality is applicable to short-bore scanners like MAGNETOM Espree. In our opinion TimCT represents the next milestone in the evolution of whole-body MRI.



Prof. M. Langer, M.D. (left), O. Schaefer, M.D. (right)

Table 1: Sequence parameters for *syngo* TimCT

	TimCT-FLASH	TimCT-TIRM
TR	102 ms	3568 ms
TE	2.03 ms	101.22 ms
Slice thickness	5.0 mm	6.0 mm
Matrix	320 x 224	320 x 200
FoV	350 x 263 mm	400 x 250 mm
Pixel bandwidth	300 Hz/pixel	445 Hz/pixel
Flip angle	70°	60°
Slices/package	17	8
No. of packages	5	16
Pixel size	1.4 x 1.1 x 5.0 mm	1.6 x 1.1 x 6.0 mm
Parallel imaging	GRAPPA, factor 2	
Acquisition time	1 min.	4 min.

References
[1] Schaefer JF, Schlemmer HP. Total-body MR-imaging in oncology. Eur Radiol. 2006; 16: 2000–15.
[2] Schmidt GP, Baur-Melnyk A, Herzog P, et al. High-resolution whole-body magnetic resonance image tumor staging with the use of parallel imaging versus dual-modality positron emission tomography-computed tomography: experience on a 32-channel system. Invest Radiol. 2005; 40: 743–53.
[3] Fautz HP, Kannengiesser SA. Sliding multislice (SMS): a new technique for minimum FoV usage in axial continuously moving-table acquisitions. Magn Reson Med. 2006; 55: 363–70.
[4] Klessen C, Rogalla P, Taupitz M. Local staging of rectal cancer: the current role of MRI. Eur Radiol. 2006 Sep 29 [Epub ahead of print].
[5] Mackalski BA, Bernstein CN. New diagnostic imaging tools for inflammatory bowel disease. Gut. 2006; 55: 733–41.

Small Animal Imaging on 1.5T MR Systems

J. Schulz[1, 2], M. Korn[1], M. Requardt[2], M. Bock[1]

[1]DKFZ, Dept. of Medical Physics in Radiology, Heidelberg, Germany
[2]Siemens Medical Solutions, Erlangen, Germany

Introduction

In recent years an increasing number of small animal studies have been performed since MR Imaging (MRI) offers an excellent soft tissue contrast, enables imaging in arbitrary slice orientations and does not use ionizing radiation. MRI is especially suited for longitudinal studies where, for example, the influence of a drug treatment is studied in the same animal over several weeks. Small animal MRI is usually performed using dedicated MRI systems with high field strengths ($B_0 > 4$ Tesla) and bore sizes that are chosen depending on the size of animals. Since small animal imaging facilities are not necessarily available in clinical research institutions, in these environments the existing clinical whole-body MR imaging systems have been utilized for small animal MRI [1].
Besides their availability, clinical MR imaging systems offer further advantages. Firstly, small animal studies at clinical field strengths ($B_0 = 1.5-3$ Tesla) yield image contrasts that are comparable to image contrasts in clinical studies since relaxation times are field-strength dependent. Secondly, susceptibility and chemical shift artifacts are smaller at lower field strength so that the delineation of tissue interfaces is facilitated. Finally, a clinical MR system with optimized user interface is easier to use, the same operating personnel can perform both animal and human studies and a large variety of imaging and post-processing protocols and applications exists.
Clinical whole-body MRI systems offer a cost-effective imaging alternative to dedicated small animal MR systems if only a limited number of small animal studies is performed and a sufficient amount of imaging time is available (e.g. during night times). Though feasible, small animal MRI at clinical systems is challenging due to the lower signal-to-noise ratio (SNR), the limited spatial resolution and the shortage of appropriate animal handling and supervision hardware (e.g. ECG monitoring). In this article we describe several hardware and software modifications to enable small animal studies at 1.5T and 3T MRI systems. For a comparison of dedicated small animal MRI systems and clinical MRI units, refer to Box 1.
For those researchers looking for a dedicated small animal MRI system with clinical user interface, the ClinScan 7T MR system has been developed (ClinScan, Bruker BioSpin, Ettlingen, Germany). ClinScan combines high-performance small animal gradient systems and radio-frequency hardware with the clinically known *syngo* control software and applications.

Small Animal RF Coils

A 4,000 times weaker MR signal is measured in a mouse (weight: 25 g) than in a 100 kg man if the same imaging RF coil is used, because the spatial resolution needs to be scaled relative to the anatomy so that a typical clinical voxel size of 10 mm³ scales down to 0.0025 mm³ in a mouse [2]. To overcome this SNR limitation the field strength can be increased, although the SNR gain is approximately proportional to the ratio of the field strengths only. A much higher gain in SNR is achieved if smaller rf coils are used [3], [4]. As in human studies, the size of the coil is governed by the imaging application and different coils will be required for whole-body mouse MRI or mouse head imaging.
Initial animal experiments can be performed on clinical systems using existing loop coils. Loop coils are available in various diameters (4, 7, 11 cm) and for all clinical field strengths (1.5 and 3T), and allow imaging without modification to the MR system.
To further optimize mouse imaging at 1.5T we constructed a dedicated receive-only coil prototype which is connected to the existing flex interface of the MR system. The solenoid receive coil has a 36 mm diameter and is 90 mm long to conveniently accommodate a medium-



1 The photograph shows three different RF coils in an MR system: the receive-only coil prototype (left), a head coil (center) and a flex loop coil (right). In addition, a new series of loop coils are available with 3, 7 and 11 cm diameter to be used with a new 4-channel preamplifier module. These coils are available for 1.5 and 3T, whereas the shown coil is only available for 1 and 1.5T systems.

size mouse of 30 g body weight (Fig. 1). For comparison, gradient and spin echo images of an ex-vivo mouse were acquired with the mouse coil, a small loop coil and the head coil (Fig. 2). The head coil is much larger than the mouse and thus provides a good homogeneity over the whole sample. Unfortunately, due to the low filling factor, the SNR is compromised. The small loop coil offers the highest SNR at the center; however, SNR rapidly decreases with distance from the coil center. The dedicated mouse coil provides a slightly lower SNR, but is homogeneous over the whole sample so that whole-body mouse imaging becomes possible.
Quantitative SNR comparisons were measured in a phantom setup (cylindrical phantom, 35 ml physiologic saline solution, 0.5% Gd-DTPA) (Fig. 3). The results in Tab. 1 show that the mouse coil has the highest SNR when averaged over the dimensions of the mouse. A homogeneous and high SNR is important, for example, in tumor studies where the location of metastases is not known a priori [5] or in phenotyping experiments that aim to detect small morphologic changes [2].
A further advantage of clinical MR systems is the possibility of imaging several animals simultaneously [6]. Several small animal coils can be mounted side by side in the large bore of the clinical MR magnet [7]. In principle, the dedicated mouse coils described above can be utilized for simultaneous imaging, however, special care must be taken to avoid coupling between the coils.

	Clinical MR systems at reasonable resolutions	Dedicated small animal MR systems
Field strength B_0	*1.5 – 3.0 Tesla*	*7 – 11 Tesla*
Gradient strength G	*30 – 45 mT/m*	*50 – 1000 mT/m*
Slew rate	*100 – 200 T/m/s*	*400 – 1200 T/m/s*
Coil diameter	*4 – 15 cm*	*1 – 6 cm*
TR / TE *(for a gradient echo sequence)*	*10 – 25 ms / 5 – 12 ms*	*3 ms / 1.5 ms*
T1 contrast	*Excellent, moderate T_1-relaxation, short repetitions*	*Longer TR required (T_1 increases with B_0)*
T2 contrast	*Acceptable. Suffers from low SNR.*	*Good*
Single Shot EPI	*Not applicable due to insufficient gradient strength / EPI only with high number of segments.*	*Possible*
Consequences	*Morphologic imaging is possible with competitive quality but with long measurement times.*	*Full range of applications possible. SN is **not** 1000 times better.*

Box 1: Comparison of a clinical MR system and dedicated small animal MR units.

Coil	Diameter [mm]	Length [mm]	SNR_{max}	SNR_{ave}
Head coil	*~290*	*~320*	*6*	*6*
Flex loop small	*~30*	*20 (casing)*	*144*	*70*
Mouse coil	*36*	*90*	*89*	*78*

Tab. 1: SNR comparison for three different coils.

Anaesthesia and Life Support

Small animals need to be anesthetized during MR imaging. The anaesthetic of choice is currently isofluorane, a gaseous anaesthetic which is applied through an MR-compatible ventilator. Though simple to use, isoflurane is known to affect physiological parameters – myocardial blood flow, for example, is highly sensitive to isoflurane concentration [8].
A cost-effective, although more complicated, alternative to gaseous anaesthesia is the injection of Xylazine/Ketamine. For this procedure it is important to supervise the depth of anaesthesia by monitoring, for example, breathing frequency. ECG and respiratory triggering are challenging as the typical respiratory rate of mice is about 150 per minute and the heart rate is around 600 beats per minute, i.e. about 10 times faster than in humans. Nevertheless, breathing monitoring can be achieved by connecting a paediatric breathing sensor (VitalAire, Altmannstein, Germany) to the animal (Figs. 4/5). Triggered measurements are not possible since the respiratory triggering algorithm of the patient monitoring unit (PMU) detects only respiratory cycles greater than 1 s.
To circumvent problems with ECG and respiratory triggering, self-gating methods can also be used to directly measure the heart beat-correlated and breathing-correlated variations of the MR signal. This elegant concept requires modifications to the pulse sequence [9].
Under anaesthesia, animals frequently lower their body temperature, and the additional cooling by the anaesthetic gas flow can lead to potentially lethal hypothermia. To maintain their body temperature, mice require warming, whereas with rats it may be sufficient to thermally isolate the animal. A cost-effective solution for warming is to blow warm air over the animal, which can be achieved with, for example, an external hairdryer connected to a coil housing by a long flexible tube. Another solution is a radiative heating system with halogen light bulbs that are placed at a sufficiently large distance from the coil to prevent artifacts (Fig. 6).

Pulse Sequence Optimization

Small animal imaging with clinical MRI systems is already feasible without major system modifications (refer to Box 2 for

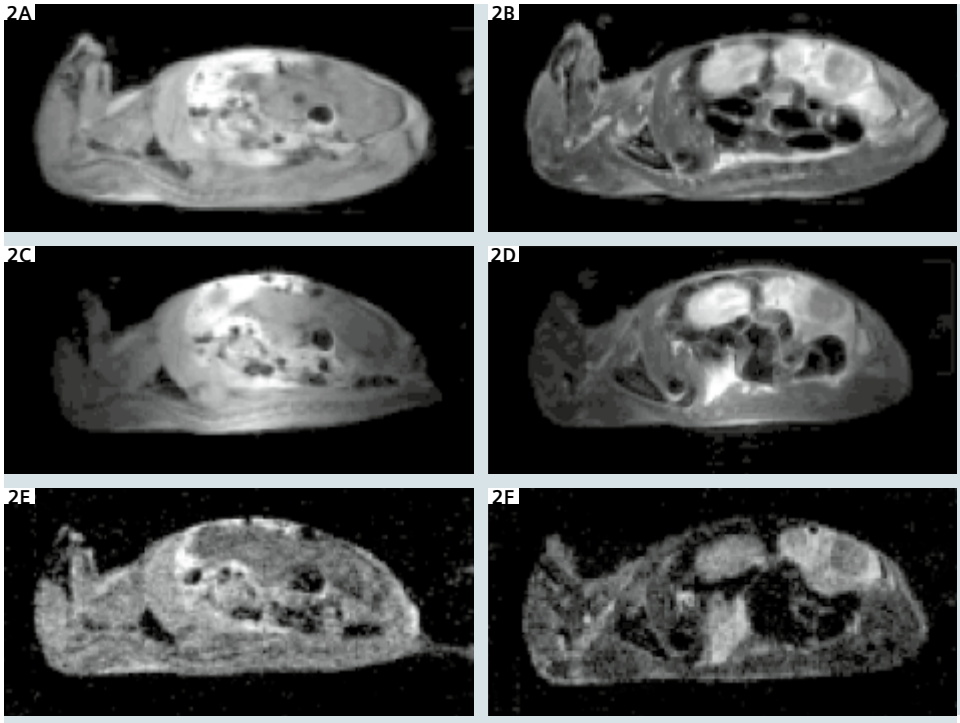

2 Visual signal-to-noise (SNR) comparison for three different imaging coils.

A, B: dedicated mouse coil

C, D: flex loop small

E, F: head coil

In the 3D gradient echo images (left) as well as in the 2D T2-weighted TSE images (right) the whole mouse is optimally visualized in the mouse coil, whereas a slightly higher SNR is seen in the shorter loop coil, although only a limited portion of the mouse is illuminated.

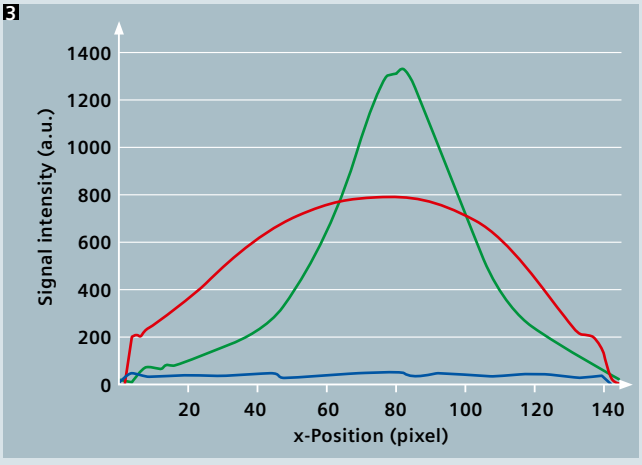

3 MR-signal intensities along a homogeneous 10 cm long phantom, acquired in the head-coil (blue), flex-loop-small (green) and the dedicated mouse coil (red).

possible pitfalls). To further improve image quality, pulse sequences can be adapted to the small field of view.
For mouse imaging, an approximately 10-fold greater absolute spatial resolution (0.1 mm) is required as for humans (1 mm). The spatial resolution Δx in an MR system is given by (see e.g. [10])

$$\Delta x = \frac{1}{G_x \gamma} \cdot BW \qquad (1)$$

where G_x is the gradient strength in read-out direction, BW the receiver bandwidth per pixel and γ denotes the gyromagnetic ratio (42.577 MHz/T for ^1H). At constant BW the spatial resolution can be increased by increasing the readout gradient strength, although gradient amplitudes are limited to typical values between 30 and 40 mT/m. Therefore, at maximum gradient strength the only possibility of achieving smaller pixel sizes is to lower the receiver bandwidth. But smaller bandwidths result in stronger chemical

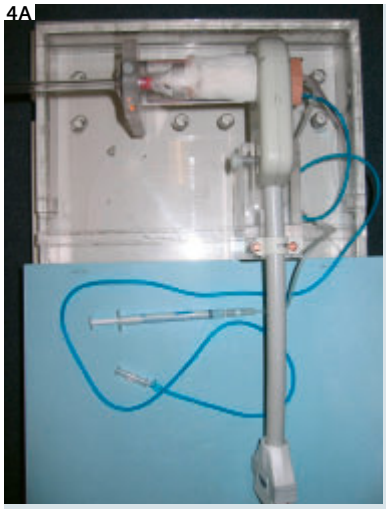

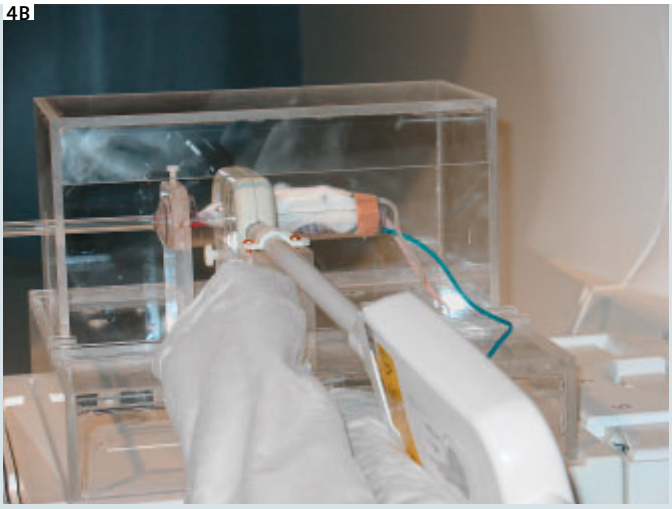

4 A, B: Acrylic glass box and a syringe filled with narcotic agents and connected to a butterfly located in the abdomen. The blue tube belongs to the paediatric respiratory sensor and can be connected with an adapter to the standard ECG/Respiratory-module.

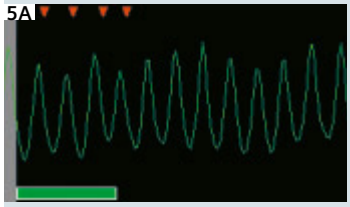

Deep anaesthesia 4 cycles/s
Green bar = 1s

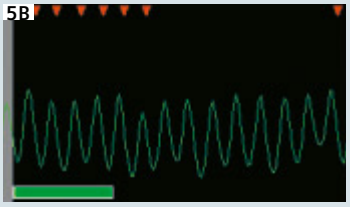

Anaesthesia becomes weak,
6 respiratory cycles/s,
a new injection is needed.

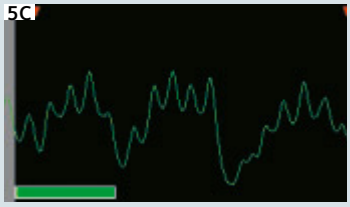

Mouse is awakening
Hurry up!

5 A–C: The respiratory sensor counts the number of breaths per second thus monitoring the physiological status of the animal.

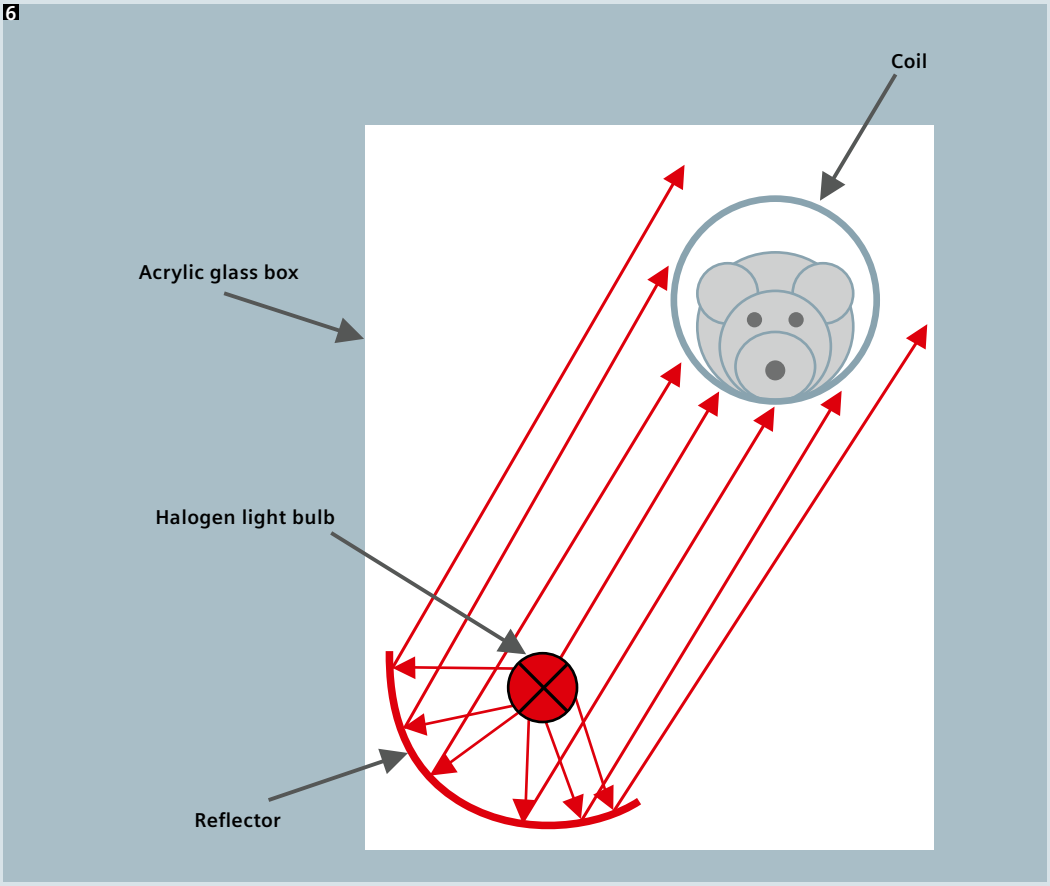

6 Schematic of a radiative heating system with a halogen light bulb in the coil setup.

Possible Pitfalls of Small Animal Imaging at Clinical MR Systems

- Compared to human applications, the trade-off between temporal and spatial resolution is even more pronounced since, for example, the heart rate is significantly higher. In particular, first pass contrast agent studies are thus difficult to perform.
- Chemical shift: In very small structures a shift between the fat and the water signal of a few pixels aggravates interpretation of images. The chemical shift artifacts increase at low bandwidths.
- Fat saturation: Higher order shimming is not possible due to the shim coil design – effectively, only linear shims can be adjusted since they are realized by gradients.
- Steady state free precession (TrueFISP) sequences: Longer TRs create significant banding artifacts. Unfortunately, shorter TRs are only possible with stronger gradients (gradient inserts).
- ECG-Triggering: Sampling rates and filters for ECG systems are currently optimized for human applications. At high heart rates, blood signal suppression cannot be achieved with inversion recovery preparation (black blood). Other options (dephasing, saturation) are still possible.

Box 2: Possible pitfalls

shift artifacts (i.e. position shifts of fat vs. water), which can only be reduced by increasing the bandwidth.
Gradient amplitudes of clinical MR scanners are often confined to about 70% of the maximum gradient strength to allow angulating the image slices at all times [11], [12]. When a slice is angulated against the physical axes x, y and z, slice selection, phase encoding and readout gradients are realized as a combination of the x-, y- and z-gradients. If, for example, the maximum gradient strength is applied in phase encoding direction, a higher gradient amplitude than physically achievable might be necessary. Limiting the gradient amplitudes avoids this gradient overflow condition and pulse sequences can always be realized. In small animal imaging slice angulation is often of minor importance. To fully exploit the available gradient strength for small animal imaging we have designed pulse sequences where the possibility to angulate slices is switched off. In Fig. 7 these sequences are compared with conventional pulse sequences with restricted gradient amplitudes. At constant BW the optimized sequences can achieve approximately a 40% higher spatial resolution, or, if chemical shift artifacts are a limiting factor, the increased gradient amplitudes can be used to increase the readout bandwidth. Equation 1 is also valid for the slice selection direction: here, the slice thickness depends on the slice selection gradient and on the bandwidth of the rf pulse. Thus, in addition to increasing the slice selection gradient, dedicated rf pulses with low bandwidth were implemented to achieve sub-millimeter slice thicknesses. In general, these rf pulses are longer than their conventional counterparts which results in prolonged minimal echo times. The optimizations for high resolution imaging are shown in the example of a Turbo Spin Echo (TSE) pulse sequence. At a 1.5T system (MAGNETOM Symphony) with G_{max} = 30 mT/m the minimal slice thickness could be reduced to 0.24 mm compared to the conventional TSE pulse sequence with 0.7 mm. In Fig. 8 image examples of a new-born mouse are shown which were obtained with the optimized TSE sequence (T2-weighted: TR 3000 ms / TE 98 ms / FoV 40×28 mm^2/ matrix 136×192 / 15 slices / slice thickness 0.24 mm / number of averages 350 / echo train length: 7; T1-weighted: TR 756 ms / TE 27 ms / FoV 40×27 mm^2 / matrix 128×192 / 15 slices / slice thickness 0.24 mm / number of averages 200). Another possibility of increasing the resolution in slice selection direction is the use of 3D imaging techniques. Here, slice resolution is defined by a second phase encoding which can achieve a similar resolution as the in-plane phase encoding. However, 3D techniques are difficult to combine with spin echo acquisitions because the long TRs necessary to establish the SE contrast lead to excessive imaging times. Gradient echo techniques such as FLASH, however, naturally lend themselves to 3D encoding, and spatial resolutions of 100 µm can be achieved in reasonable imaging times of about 1 hour (Fig. 9). The imaging parameters were: TR 20.3 ms / TE 7.2 ms / FoV 100×50 mm^2/ matrix 1024×512×218/ partition thickness 100 µm.

Gradient Inserts

Higher spatial resolution can be achieved with shorter TEs and TRs if the gradient amplitude is increased. For small animal

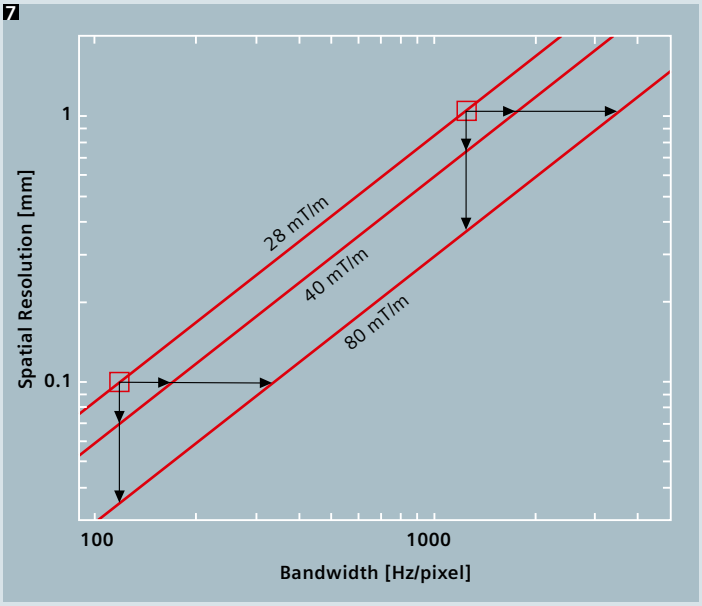

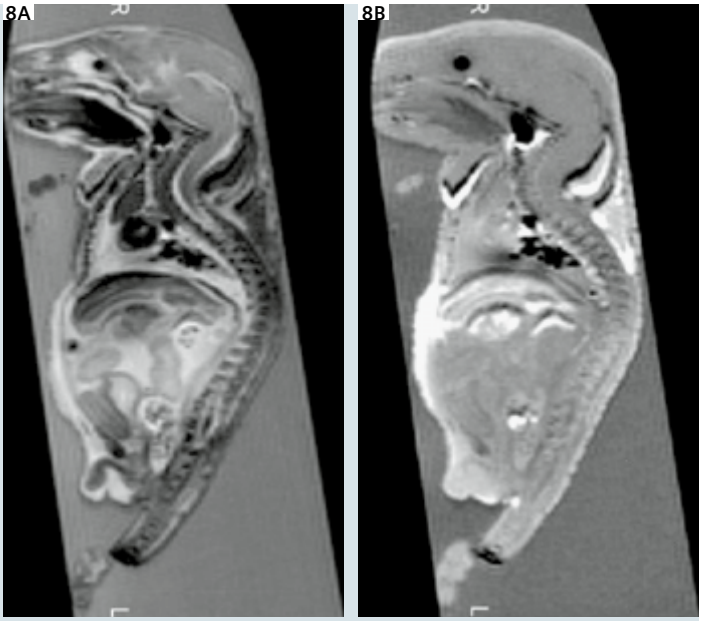

7 Plot of the minimum spatial resolution as a function of readout bandwidth. The absolute gradient amplitude of the clinical MR system (40 mT/m, in this example) is significantly higher than the maximum gradient strength for tilted slices (here: 28 mT/m). If slice angulation is switched off, the higher gradient amplitude can be used which allows either reducing the pixel size or increasing the readout bandwidth. Alternatively, a gradient insert can deliver a gradient amplitude of 80 mT/m or even more.

8 A T2-weighted (A) and a T1-weighted (B) TSE *ex vivo* image of a new-born mouse. A spatial resolution of 240 × 210 × 210 µm³ was achieved and a signal-to-noise ratio of about 50 was observed in the animal's brain.

MRI at clinical systems this may be realized by so-called gradient inserts, i.e. small additional gradient coils, which provide gradient amplitudes of 80 mT/m and more over a limited FoV. This requires additional gradient hardware which is a cost-factor, and the set-up of the small animal imaging system will become more time-consuming.

Parametric Imaging

In addition to the morphologic information, MRI offers several functional imaging techniques such as diffusion imaging, flow measurements, temperature mapping, and relaxometry. The latter is of special importance in small animal studies where often magnetically labelled substances are investigated. To assess the concentration of these substances after administration, preferably the local change of the relaxation times T1, T2 and T2* is measured. The concentration information is then used, for example, to quantify organ perfusion, an important parameter in tissue viability studies. In addition, relaxation studies can be used to measure local vessel sizes (vessel size imaging [13]) which might help to differentiate normal from tumour tissue. Finally, relaxation time measurements can be used to optimize the image contrast: Thus the T1 information can be utilised to suppress signals from tissue using an inversion recovery preparation with an appropriately selected TI [14].

The very fast contrast agent transit in the animals' vascular system makes relaxometry studies difficult to perform during first pass. Additionally, echo planar imaging (EPI) cannot be used for data acquisition, since the low acquisition bandwidths associated with the limited gradient amplitudes lead to very long EPI echo trains. Despite these restrictions, conventional relaxometry pulse sequences for the measurement of T1, T2, and T2* and existing post-processing tools can be applied.

A standard method to determine the longitudinal relaxation time T1 is the saturation recovery (SR) or inversion recovery (IR) technique, where the longitudinal magnetisation is prepared with a 90° (SR) or a 180° (IR) pulse. After a recovery delay TI an image is acquired with a single-shot acquisition module (e.g. HASTE). This procedure is repeated for different TIs, and T1 is calculated from the signal recovery on a pixel-by-pixel basis. In particular, the combination of SR signal preparation with a turboFLASH readout module is advantageous, and the established T1 contrast is maximised when data are acquired with centric k-space reordering [15]. For small animal applications we have additionally implemented a segmented SR turboFLASH acquisition technique, which further reduces image blurring due to variable T1 contrast during data acquisition (Fig. 10).

To measure T1 in larger volumes (e.g. in a solid tumour and the surrounding tissue), variable flip-angle methods can also be applied. Here, a series of 3D FLASH data sets is acquired and T1 is calculated using the known signal equation. This

9

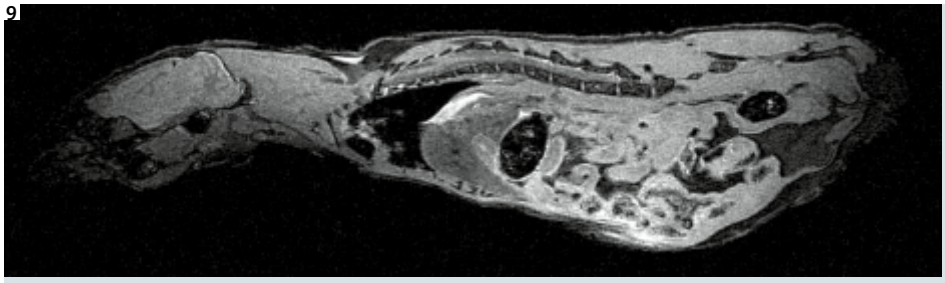

9 A 3D FLASH *ex vivo* image of a mouse with an isotropic resolution of 100 µm. The mouse was prepared by MR staining [2] using Gd-DTPA. Thus, a good T1-contrast could be achieved with a short-TR FLASH sequence resulting in a measurement time of only 48 min.

10A

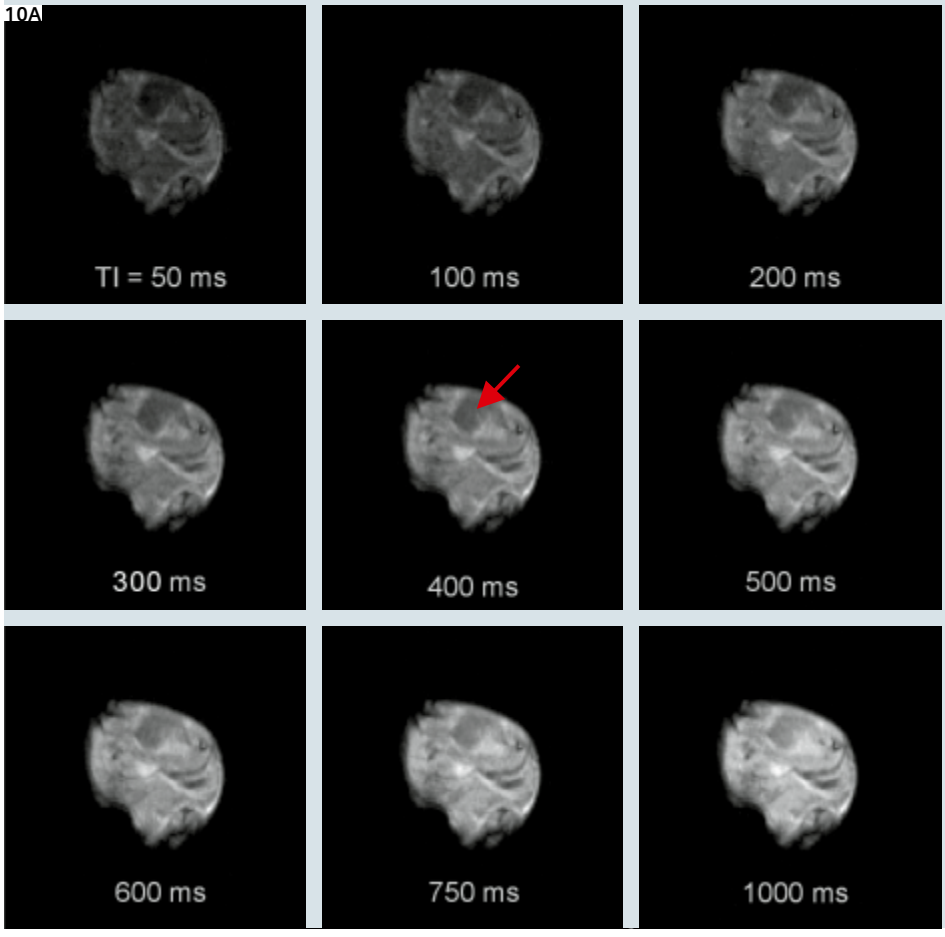

10 A: Transverse saturation recovery TurboFLASH images of a mouse tumor model (arrow). The saturation recovery delay time TI between preparation and data read-out varied between 50 ms and 1000 ms.

B: The signal intensity in a region of interest in the mouse tumor against the saturation recovery delay time TI. The exponential fit gives a spin-lattice relaxation time T1 = 1089 ms.

10B

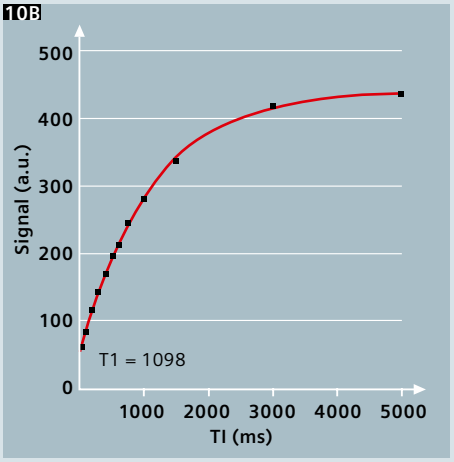

technique has the additional advantage that the computation of the relaxation times can be simplified using a linearised form of the FLASH equation [16].
The quantification of the transverse relaxation times T2 and T2* is performed with multi-echo pulse sequences, where signal is multiply refocused using either spin echoes (T2) or gradient echoes (T2*). A multi spin echo pulse sequence with up to 32 echoes is implemented for T2 measurements, and T2 post-processing (i.e. the calculation of T2 maps) is available within the standard *syngo* environment. Multi-echo T2* measurement sequences are currently developed, and due to the similarity in the signal equation, the same post-processing tools can be utilised. In the application of either technique care must be taken that noise does not adversely affect the T2/T2* mapping results. Image noise at long echo times can lead to an overestimation of T2/T2* - in the post-processing software this is considered by a manually selectable amplitude threshold, which should be set to about 3–5 times the mean of the noise amplitude.

Conclusion

Small animal MRI with clinical 1.5T MRI systems gives sufficient image quality. Existing RF coils and standard pulse sequences can be utilized although, for some applications, even better results can be achieved with optimized rf coils and dedicated pulse sequences.

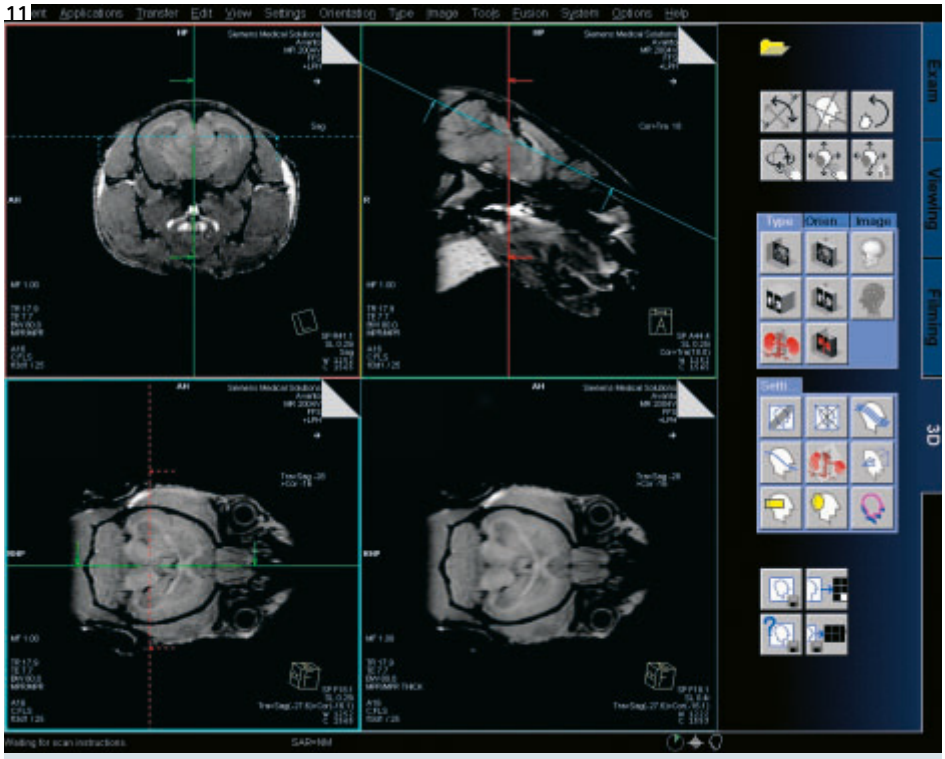

11 High resolution T1-weighted images showing the fine sub-structures of the cerebellum were acquired with a standard VIBE sequence (45 minutes *in vivo* scan, resolution 125 x 125 x 250 µm³). To achieve a high SNR, a 3D-measurement with large volume coverage, a high number of partitions, and a moderate number of averages was performed. For contrast effects, the SNR can be increased by reconstructing thicker slices (see lower right quadrant). Each necessary orientation can be calculated via 3D-MPR (3D multi-planar reformatting), i.e. only one data set has to be acquired and all orientations can be derived from these data.





12 A, B: T2-weighted standard TSE images are shown (6 slabs, 8 partitions/slab, 2 concatenations, compensation of T2-decay). The left measurement took 35 minutes for a 180 x 180 x 500 µm³ resolution. The image on the right shows 125 x 125 x 400 µm³ resolution. The measurement time was 2 h.

References

1 Wolf RF, Lam KH, Mooyaart EL, Bleichrodt RP, Nieuwenhuis P, Schakenraad JM. Magnetic resonance imaging using a clinical whole body system: an introduction to a useful technique in small animal experiments. Lab Anim. 26(3): 222–7 (1992).
2 Johnson GA, Cofer GP, Fubara B, Gewalt SL, Hedlund LW, Maronpot RR. Magnetic resonance histology for morphologic phenotyping. J Magn Reson Imaging. 16: 423–9 (2002).
3 Hoult DI, Richards RE. The Signal-to-Noise Ratio of the Nuclear Magnetic Resonance Experiment. J Magn Reson 24: 71–85 (1976).
4 Darrasse L, Ginefri JC. Perspectives with cryogenic RF probes in biomedical MRI. Biochimie 85: 915–937 (2003).
5 Lewis JS, Achilef S, Garbow JR, Laforest R, Welch MJ. Small animal imaging: current technology and perspectives for oncological imaging. Eur J Cancer 38(16):2173–2188 (2002).
6 Bock NA, Konyer NB, Henkelman RM. Multiple-mouse MRI. Magn Reson Med. 49(1): 158–67(2003).
7 Umathum R, Mangalathu Arumana J, Semmler W, Bock M. A Solenoid Receive Array for Multi-Mouse Imaging at 1.5T. Proc. Intl. Soc. Mag. Reson. Med. 13 (2005).
8 Kober F, Iltis I, Cozzone PJ, Bernard M. Myocardial blood flow mapping in mice using high-resolution spin labeling magnetic resonance imaging: Influence of ketamine/xylazine and isoflurane anesthesia. MRM 53(3): 601–606 (2005).
9 Larson AC, White RD, Laub G, McVeigh ER, Li D. Simonetti OP. Self-Gated Cardiac Cine MRI. Magn Reson Med 51: 93–102 (2004).
10 Bernstein MA, King KF, Zhou XJ. Handbook of MRI Pulse Sequences. Elsevier Science & Technology (2004).
11 Bernstein MA, Licato PE. Angle-dependent utilization of gradient hardware for oblique MR imaging. J Magn Reson Imaging 4: 105–108 (1994)
12 Atalar E, McVeigh ER. Minimization of dead-periods in MRI pulse sequences for imaging oblique planes. Magn Reson Med 32: 773–777 (1994).
13 Kiselev VG, Strecker R, Ziyeh S, Speck O, Hennig J. Vessel size imaging in humans. Magn Reson Med. 2005 Mar; 53(3): 553–63.
14 Essig M, Bock M. Contrast optimization of fluid-attenuated inversion-recovery (FLAIR) MR imaging in patients with high CSF blood or protein content. Magn Reson Med. 2000 May; 43(5): 764–7.
15 Bluml S, Schad LR, Stepanow B, Lorenz WJ. Spin-lattice relaxation time measurement by means of a TurboFLASH technique. Magn Reson Med. 1993 Sep; 30(3): 289–95.
16 Cheng HL, Wright GA. Rapid high-resolution T(1) mapping by variable flip angles: accurate and precise measurements in the presence of radiofrequency field inhomogeneity. Magn Reson Med. 2006 Mar;55(3): 566–74.

High-Resolution Small Animal Imaging on 3T Clinical MR Scanners

Robin M. Heidemann[1], Deepu R. Pillai[2], Felix Schlachetzki[2], Thomas Steinberger[3], Titus Lanz[3], Ulrich Bogdahn[2]

[1]*Siemens Medical Solutions, Erlangen, Germany*
[2]*Dept. of Neurology, University Hospital of Regensburg, Regensburg, Germany*
[3]*RAPID Biomedical, Rimpar, Germany*

Introduction

Whenever the subject of small animal imaging comes up, people imply the use of dedicated small animal high field MR scanners with field strengths in the range of 7T to 17.6T. Currently, only few research facilities rely on conventional clinical MR scanners with field strengths of 1.5T to 3.0T for small animal studies. It is quite interesting to note that these "low field" systems also offer some advantages for small animal studies and a closer look at the options available can be of some importance.
In comparison to clinical MR scanners, dedicated small animal systems offer higher field strengths as well as stronger and faster gradients. This available high field strength directly translates into a higher signal-to-noise ratio (SNR) even though it comes at a price. There are four primary field-strength related effects which can diminish image quality.
Susceptibility effects: Living organisms are made up of various soft tissue types, air cavities and bones, all with different magnetic susceptibility values. Large susceptibility jumps, resulting from sudden transitions between tissues with significant susceptibility differences, can cause local field inhomogeneities in conjunction with the high main field in MRI. These inhomogeneities, which scale with the magnetic field strength, act as additional local gradients and are responsible for local deformations of the object geometry in the resulting MRI image.
T2* relaxation: The MR signal in general decays with a time constant T2*, which is otherwise known as the apparent T2. In addition to the tissue-dependent transversal- or T2 relaxation of the underlying tissue, other effects are also included in this phenomenon. For instance, unavoidable inhomogeneities of the main magnetic field, the afore mentioned susceptibility jumps and effects such as flow and diffusion lead to a shortening in the relaxation time constant T2*. Whenever the readout train of an imaging sequence is not small compared to T2*, the T2* relaxation will affect the MR signal. Ultrafast imaging techniques like Echo Planar Imaging (EPI), Turbo Spin Echo (TSE) or HASTE are particularly plagued by a

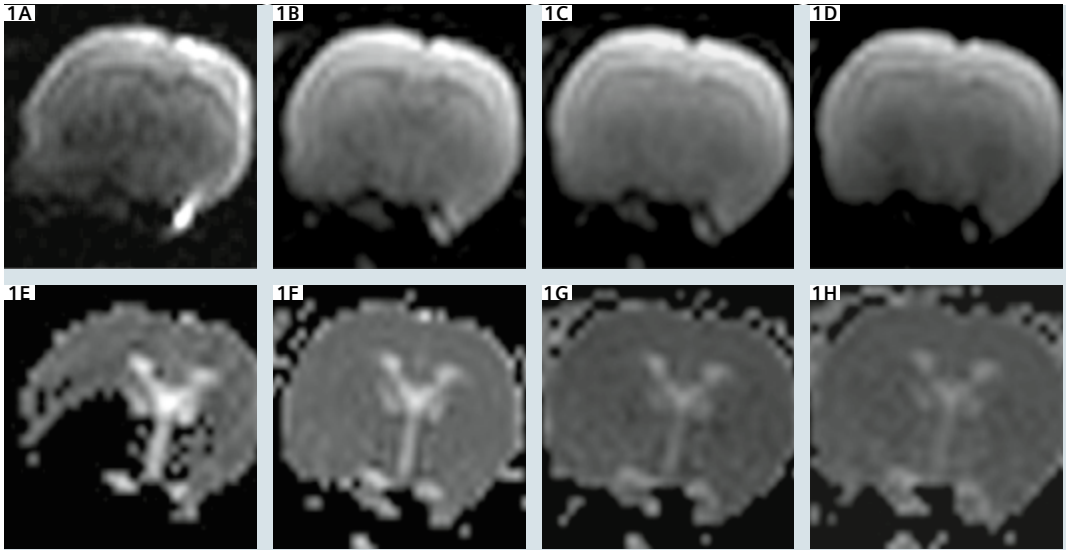

1 Single-shot diffusion-weighted (DW) EPI of the rat brain on a clinical MR scanner (MAGNETOM Allegra) at 3T using a 4-channel phased array head coil for the rat.

A–D: DW EPI with b = 1000 s/mm² using iPAT (*syngo* GRAPPA) with PAT factors of 1, 2, 3 and 4 (from A to D).

E–H: Corresponding ADC maps.

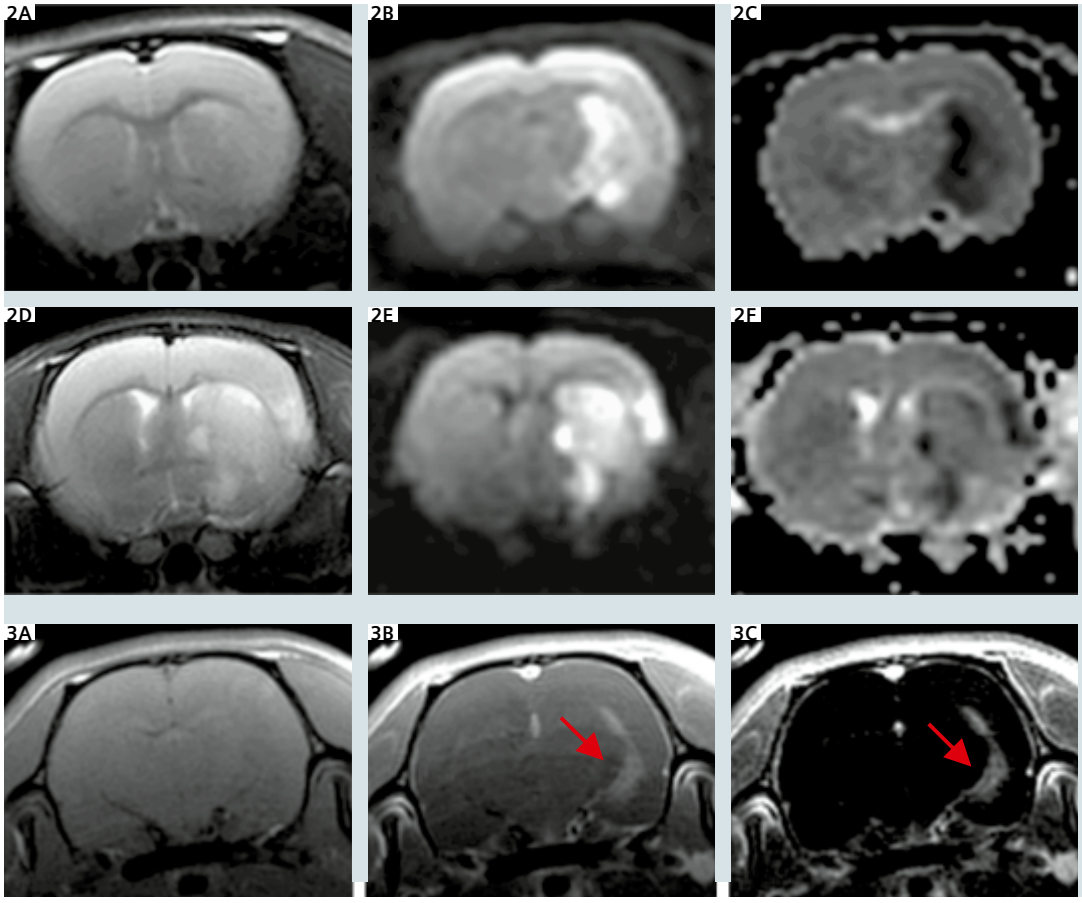

2 Small animal stroke imaging on a clinical MR scanner (MANGETOM Allegra) at 3T using a 4-channel phased array head coil for the rat.

A–C: Rat A, 6 h after occlusion.

D–F: Rat B, 36 h after occlusion. (A and D) *T2*-weighted TSE, (B and E) DW EPI with PAT factor 3, (C and F) corresponding ADC maps.

3 Small animal post-contrast study on a clinical MR scanner (MAGNETOM Allegra) at 3T using a 4-channel phased array head coil for the rat: Rat A, 8 h after occlusion. The arrow indicates MR contrast agent leakage.
A: Pre-contrast acquisition
B: Post-contrast acquisition 30 min after injection of the contrast agent.
C: Subtraction image demonstrates the region of the blood-brain-barrier (BBB) damage.

strong signal loss due to T2* relaxation. This signal attenuation is responsible for significant image blurring and produces a loss of small object contrast. The signal decay in high-field systems occurs much faster than at lower field strengths, as the T2* values at these higher fields are significantly shorter.

T1 relaxation: The magnetic field strength also affects the longitudinal or T1 relaxation. In general, there is no rule which describes the effect of the magnetic field on the T1 times of different tissues. These irregular and often unpredictable changes in T1 values lead to a different contrast behavior of MRI sequences at high field strength as compared to low field strength, which can be partially compensated by the use of a longer repetition time (TR), but this also implies a prolonged total acquisition time.

Specific absorption rate: Another high-field specific problem is the specific absorption rate (SAR), or the amount of energy (Watt x time) from high-frequency pulses absorbed by the body per unit time and weight. As an example, the transition from 1.5T to 3.0T generally increases the SAR value by a factor of four. In general, imaging protocols which run at low field strength have to be adapted for higher field strength to stay below the SAR limit, e.g. by the use of a longer TR, which also prolongs the total acquisition time.

It is clear that clinical low field systems cannot compete in terms of SNR with dedicated small animal high field systems, but the field strength related problems described above are smaller at lower field strengths. This is of major importance for examinations based on fast imaging techniques, such as EPI or HASTE. Further, the use of parallel imaging (integrated Parallel Acquisition Technique, iPAT), which is routinely available on clinical MR scanners, improves the image quality of such studies. The animal handling for the experimental set up is easier, because clinical scanners offer more space than dedicated small animal systems.

In this study, we demonstrate that high image quality small animal imaging on clinical MR scanners can be obtained in acquisition times comparable to those used for human examinations. This enables a direct transfer of findings and protocols from the small animal model onto human studies, performed on the same MR system. Short acquisition times directly translate into a higher throughput, which is of major importance for large small animal studies. Additionally, a shorter scan time means less stress for the animal itself, which will reduce the mortality rate. The properties of small animal imaging on clinical MR systems described above can finally be used to reduce the total costs of large small animal studies.

Methods

Animal care and all experimental procedures were conducted in accordance with German laws governing animal care and with the European Communities Council

Protocol	Standard human	Animal model
T2-weighted TSE	*0.6 x 0.4 x 5.0 mm* *1 min 20 s*	*0.2 x 0.2 x 1.5 mm* *2 min 18 s*
T1-weighted SE	*1.0 x 1.0 x 3.0 mm* *5 min 19 s*	*0.2 x 0.2 x 1.0 mm* *8 min 4 s*
DW EPI	*1.8 x 1.8 x 5.0 mm* *1 min 14 s*	*0.5 x 0.5 x 1.6 mm* *2 min 20 s*

Tab 1: Comparison between the standard MR protocols used for clinical human examinations and adapted small imaging protocols. The resolution and the total acquisition time are listed for the three protocols used for stroke examination.

Directive (86/609/EEC). Protocols were approved by the Ethics Committee for animal research of the local authorities.
All experiments were performed on 3T clinical MR scanners; either on a MAGNETOM Allegra (Siemens Medical Solutions, Erlangen, Germany) or on a MAGNETOM Trio, A Tim System (Siemens Medical Solutions, Erlangen, Germany). The Allegra was equipped with a 4-channel phased array head coil and a 4-channel phased array spine coil for the rat (RAPID Biomedical, Rimpar, Germany), while the Tim Trio was equipped with an 8-channel phased array whole body coil for the mouse (RAPID Biomedical, Rimpar, Germany).

Results

A conventional diffusion-weighted (DW) EPI examination of a healthy rat brain is shown in Fig. 1A. In comparison, Figs. 1B–1D show a series of DW EPI acquisitions with PAT factors from 2 to 4 using *syngo* GRAPPA [1]. The in-plane resolution being 500 µm and the slice thickness is 1.6 mm. Corresponding ADC maps can be found in the bottom row of Fig. 1.
Images obtained from a rat model of cerebral ischemia (Rat A, 6 h after Middle Cerebral Artery Occlusion (MCAO)) are shown in Figs. 2A–2C. While the images in Figs. 2D–2F are from a different rat (Rat B) acquired 36 hrs after occlusion. T2-weighted TSE images are shown in Fig. 2A and Fig. 2D. The in-plane resolution is 200 µm with a 1.5 mm slice thickness. The total acquisition time of the TSE study was 2 min 18 s, with 11 slices. The corresponding DW EPI (b = 1000 s/mm^2) images with a PAT factor of 3 are shown in Figs. 2B and 2E. The in-plane resolution is 500 µm and the slice thickness is 1.6 mm. The total acquisition time of the DW EPI study with three directions and four b values was 2 min 20 s. Calculated ADC maps are shown in Figs. 2C and 2F.
Results from a post contrast T1-weighted study to detect the blood-brain-barrier (BBB) permeability can be seen in Fig. 3. The acquisition time of each examination was 8 min 4 s, with the same in plane resolution as for the TSE study. Table 1 shows a direct comparison between the standard and the adapted small animal protocol parameters, in terms of resolution and total acquisition time.
Images obtained from a small animal model of hemorrhagic stroke acquired 2 hrs after blood injection are shown in Fig. 4. A single slice from a T2-weighted TSE acquisition is shown in Fig. 4A. The in plane resolution is 200 µm with a 1.0 mm slice thickness. The total acquisition time of the TSE study with 11 slices using 3 averages was 2 min 18 s. The corresponding susceptibility-weighted image is shown in Fig. 4B. Here, the in plane resolution is 400 µm with 1.6 mm slice thickness. The total acquisition time of the T2*-weighted gradient echo (GRE) sequence with 11 slices, using 2 averages was 1 min 76 s.
Single sagittal sections from two animals of a spinal contusion injury are shown in Fig. 5. The T2-weighted TSE acquisitions have an in-plane resolution of 200 µm with a slice thickness of 400 µm. The total acquisition time of the TSE study using 3 averages and 11 slices in 2 concatenations was 5 min 35 s. These images were acquired without respiratory or cardiac gating, which would improve the overall image quality. A series of whole mouse images with PAT factors from 1 to 4 is shown in Fig. 6. Those images were obtained on a MAGNETOM Trio, A Tim System using an 8-channel phased array whole-body coil for the mouse. With the same set up, a contrast enhanced 3D FLASH acquisition was performed on a mouse with congested kidneys (Fig. 7). This study was obtained with a PAT factor of 2. The acquisition of this dataset with an isotropic resolution of 300 µm took about 4 min.

Discussion

In EPI the use of iPAT reduces blurring due to T2* relaxation and distortions due to off-resonance effects significantly [2]. It has been shown that this effect is especially important for stroke detection using DW EPI [3]. Further, the use of iPAT allows one to shorten the echo time (TE), in the example shown in Fig. 1, from 174 ms down to 77 ms. The reduction of TE increases the signal-to-noise ratio (SNR), which can balance out the inherent loss in SNR due to the use of iPAT in a certain range. The use of iPAT for DW EPI of small animals on a 3T clinical MR scanner is essential to obtain high image quality. In terms of off-resonance distortion reduction and achievable SNR, iPAT with an acceleration factor of 3 is found to perform best for this specific set up.
The feasibility of small animal imaging after experimental transient ischemia on a 3T clinical MR scanner is demonstrated in Figs. 2 and 3. High resolution, high quality images were obtained using standard Siemens product sequences with some protocol adaptations for the small

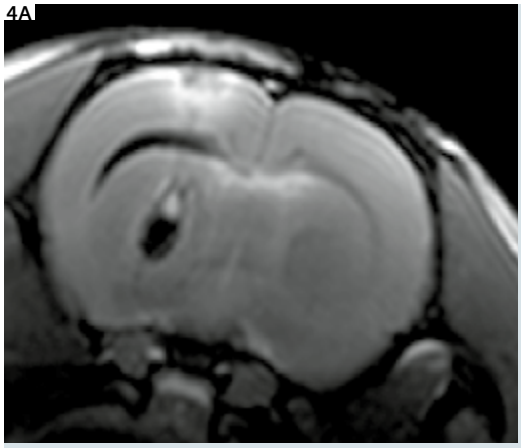

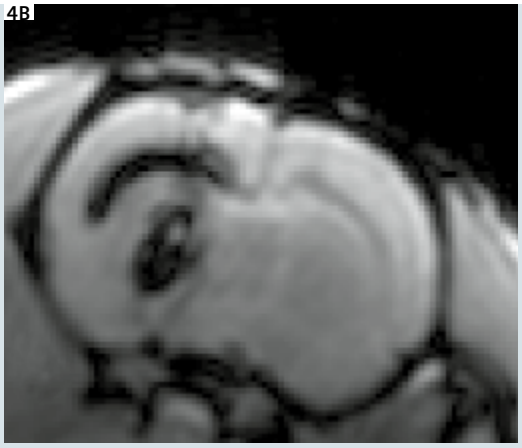

4 Small animal hemorrhagic stroke imaging on a clinical MR scanner (MAGNETOM Allegra) at 3T using a 4-channel phased array head coil for the rat:

A: T2-weighted TSE acquisition.

B: T2*-weighted GRE acquisition.

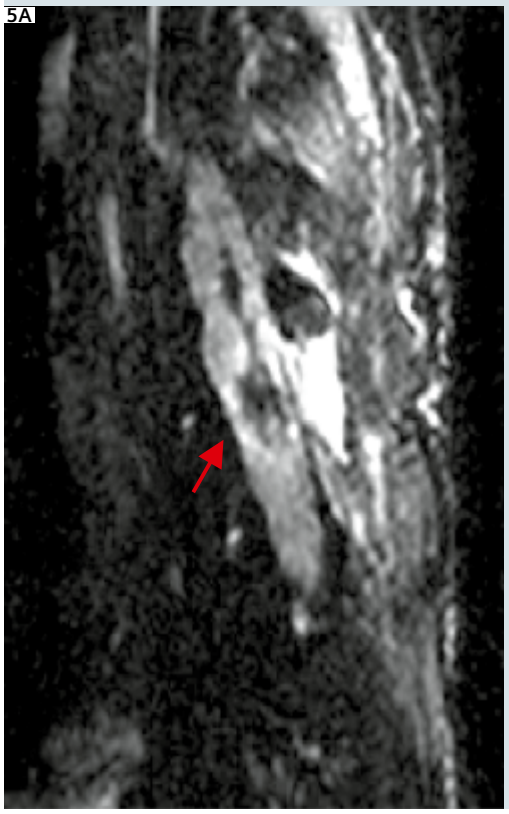

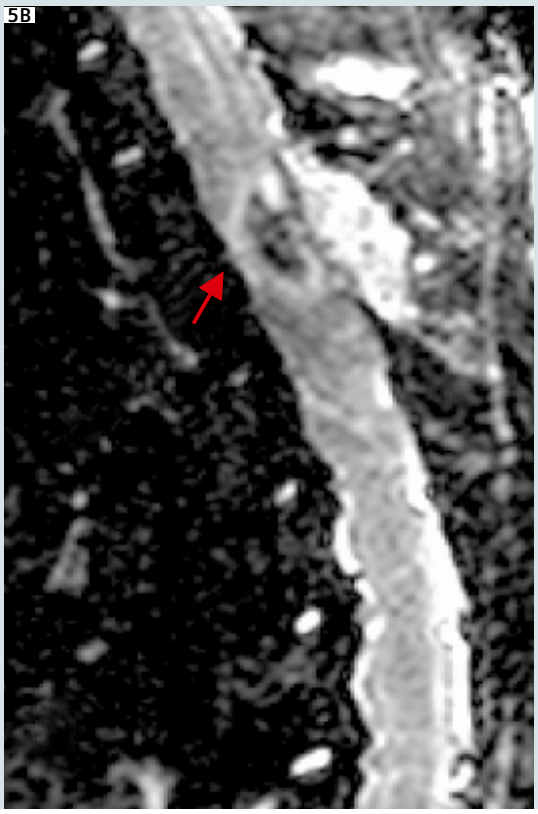

5 Imaging of spinal cord injury in rats on a clinical MR scanner (MAGNETOM Allegra) at 3T using a 4-channel phased array spine coil for the rat: T2-weighted TSE sequence with 200 µm in plane resolution and 400 µm slice thickness.

field of view and the high resolution. As shown in Table 1, the total acquisition time is comparable to standard imaging protocols used for human examinations. Besides a 4-channel phased array head coil for the rat and the animal handling system, no specific hardware had to be used. To achieve sufficient SNR in the high resolution small animal experiments, it was necessary to use more averages or to turn off the partial Fourier option, which explains the longer acquisition times compared to the standard human protocols. As can be seen in Fig. 6, the use of iPAT in combination with the HASTE sequence [4] helps to increase the resolution of those acquisitions.

Conclusion

High resolution small animal imaging on 3T clinical MR scanners can be realized in scan times comparable to those used for human examinations. Since all imaging protocol parameters fall in a tolerable range for human applications, a direct transfer of the knowledge gained with those small animal models to human studies is possible.
The short acquisition times can be used to increase the animal throughput of the system and can reduce the mortality rate due to examination stress. Finally, this approach can reduce the overall cost of studies with a large number of small animals being examined.

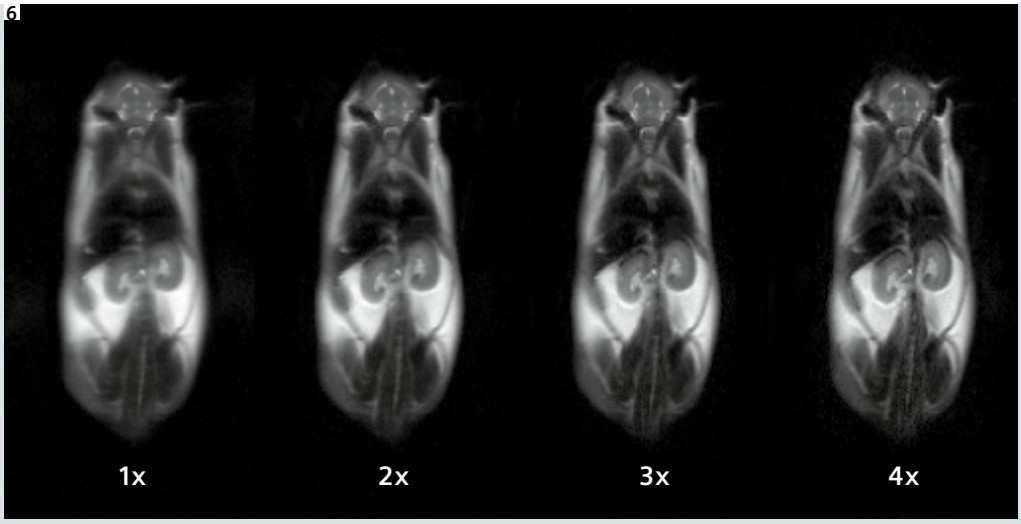

6 Imaging of a whole mouse on a clinical MR scanner (MAGNETOM Trio, A Tim System) at 3T using an 8-channel phased array Body Matrix coil for the mouse: T2-weighted HASTE sequence with PAT acceleration factors from 1 to 4.

Images courtesy of Herbert Reinl, Grosshadern, Munic, Germany.

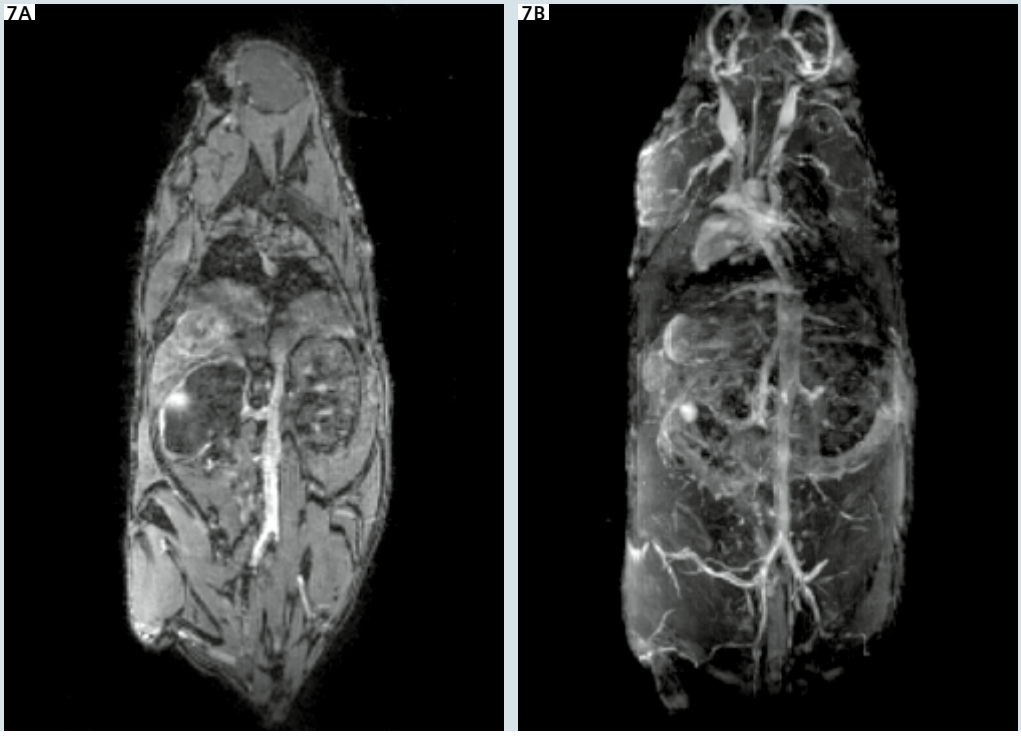

7 Imaging of a whole mouse with congested kidneys on a clinical MR scanner (MAGNETOM Trio, A Tim System) at 3T using an 8-channel phased array whole-body coil for the mouse: 3D FLASH with PAT factor 2.

Images courtesy of Herbert Reinl, Grosshadern, Munic, Germany.

Acknowledgement

This work was supported by Siemens Medical Solutions and the Bavarian Research Foundation (Grant 570/3).

References

1 Griswold MA, Jakob PM, Heidemann RM, Nittka M, Jellus V, Wang J, Kiefer B, Haase A. Generalized autocalibrating partially parallel acquisitions (GRAPPA). Magn Reson Med 2002; 47: 1202–1210.

2 Griswold MA, Jakob PM, Chen Q, Goldfarb J, Manning WJ, Edelman RR, Sodickson DK. Resolution enhancement in single-shot imaging using simultaneous acquisition of spatial harmonics (SMASH). Magn Reson Med 1999; 41: 1236–1245.

3 Bammer R, Keeling SL, Augustin M, Pruessmann KP, Wolf R, Stollberger R, Hartung HP, Fazekas F. Improved diffusion-weighted single-shot echo-planar imaging (EPI) in stroke using sensitivity encoding (SENSE). Magn Reson Med 2001; 46: 548–554.

4 Heidemann RM, Griswold MA, Kiefer B, Nittka M, Wang J, Jellus V, Jakob PM. Resolution enhancement in lung ^{1}H imaging using parallel imaging methods. Magn Reson Med 2003; 49: 391–394.

Pushing the Boundaries of MR with Siemens MAGNETOM 7T

John Grinstead, Ph.D.; Siemens Medical Solutions USA, Inc.

Introduction

There has been a continual push towards higher and higher magnetic field strengths in MR, motivated primarily by the approximately linear increase in signal-to-noise ratio (SNR) with magnetic field strength. In the 1990s, 3 Tesla research systems were pushing the boundaries of the time. The engineering challenges at 3 Tesla led to technical improvements in areas such as RF technology. After considerable engineering efforts, 3 Tesla scanners made the transition to true clinical systems. Today, the technology is pushing forward again, this time to 7 Tesla. More challenges exist at 7 Tesla. These challenges are also opportunities to push innovation in MR technology even further, which will benefit all field strengths.

The MAGNETOM 7T System

7 Tesla MR systems are investigational devices and are not available for clinical use or diagnosis, but only for clinical research purposes.
Siemens is taking its expertise in RF technology and high-quality gradients and applying it to 7T. The MAGNETOM 7T offers 32 independent RF channels, and uses the proven fast and reliable whole-body MAGNETOM Avanto gradients. In addition, all Siemens 7T systems use the same advanced applications software platform as on our clinical systems.
The MAGNETOM 7T comes with a Siemens-approved CP transmit-receive head coil. The improvement in image quality due to a higher signal-to-noise ratio at 7T compared to a comparable transmit-receive coil on the 3T MAGNETOM Trio, A Tim System, is shown in Fig. 1. Of course, the Tim Trio is capable of much better SNR by using, for example, the 12-element receive-only Head Matrix coil, which is standard on the Trio, A Tim System. Multi-channel RF coils with higher SNR are also available at 7T. We used the CP coils because it allows a fair direct comparison, as for both field strengths the coil geometry is similar.
Whole-body 7T magnets are large unshielded magnets with a 2.4 meter outer diameter and 3.4 meter length, compared to standard 1.5T systems that have a 2 meter outer diameter and a 1.2 meter length. Because the magnets are unshielded, unlike modern clinical magnets, passive iron shielding is needed in the scanner room walls to minimize the floor

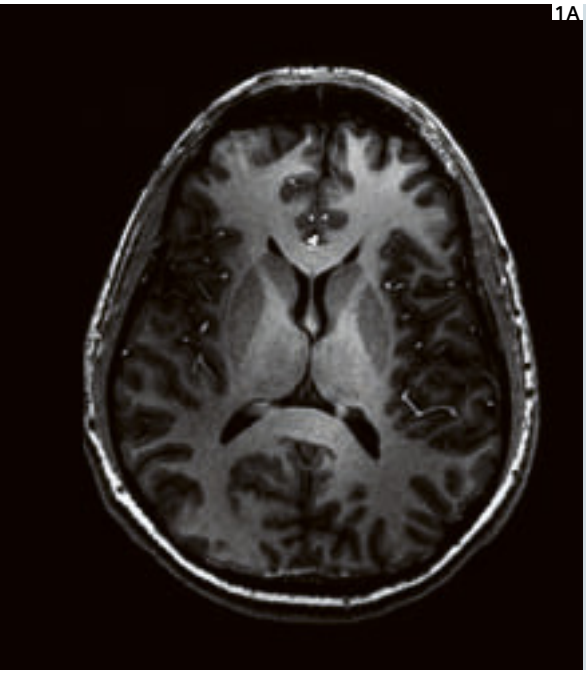

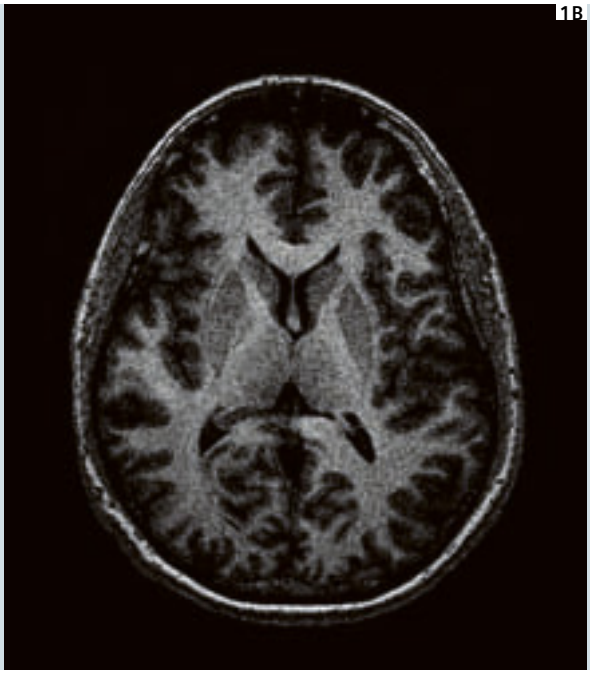

1 Comparison using transmit-receive volume coils at 7T (A) and 3T (B) for a T1-weighted MPRAGE sequence at 1 x 1 x 2 mm resolution.

Courtesy of W. Rooney and C. Springer, Oregon Health and Science University, Portland, OR, USA.

space footprint by restricting the 5 gauss line which is considered the safe boundary for the general public, such as those with cardiac pacemakers. This can require between 200 and 400 metric tons of iron, and the associated construction costs are significant.
Partly because of this, and also because the majority of 7T studies to date involve neuro applications, a head-only 7T system is also available. The first such 7T system has already been installed at the Center for Imaging in Biomedicine in Lausanne, Switzerland. This is an actively shielded head-only magnet that does not require iron shielding. It also has head-only gradients that are approximately twice as powerful and fast as whole-body gradients (80 mT/m, 400 T/m/s), which is possible because of the reduced size of the gradients for head-only applications.

7 Tesla RF Coil Technology

Siemens is a proven leader in RF technology with its Total imaging matrix (Tim) technology, currently offering 32 independent RF channels with a scalable Open Architecture. This expertise, combined with strong collaborations with leading research institutions across the world, is an essential element for success to get the most out of the greater MR signal at 7T. Coil design is more challenging at ultra high field due to dielectric effects. Multiple coil designs are being explored at several institutions. A few examples of multi-channel RF coils built by industrial and academic partners are shown in Fig. 2.

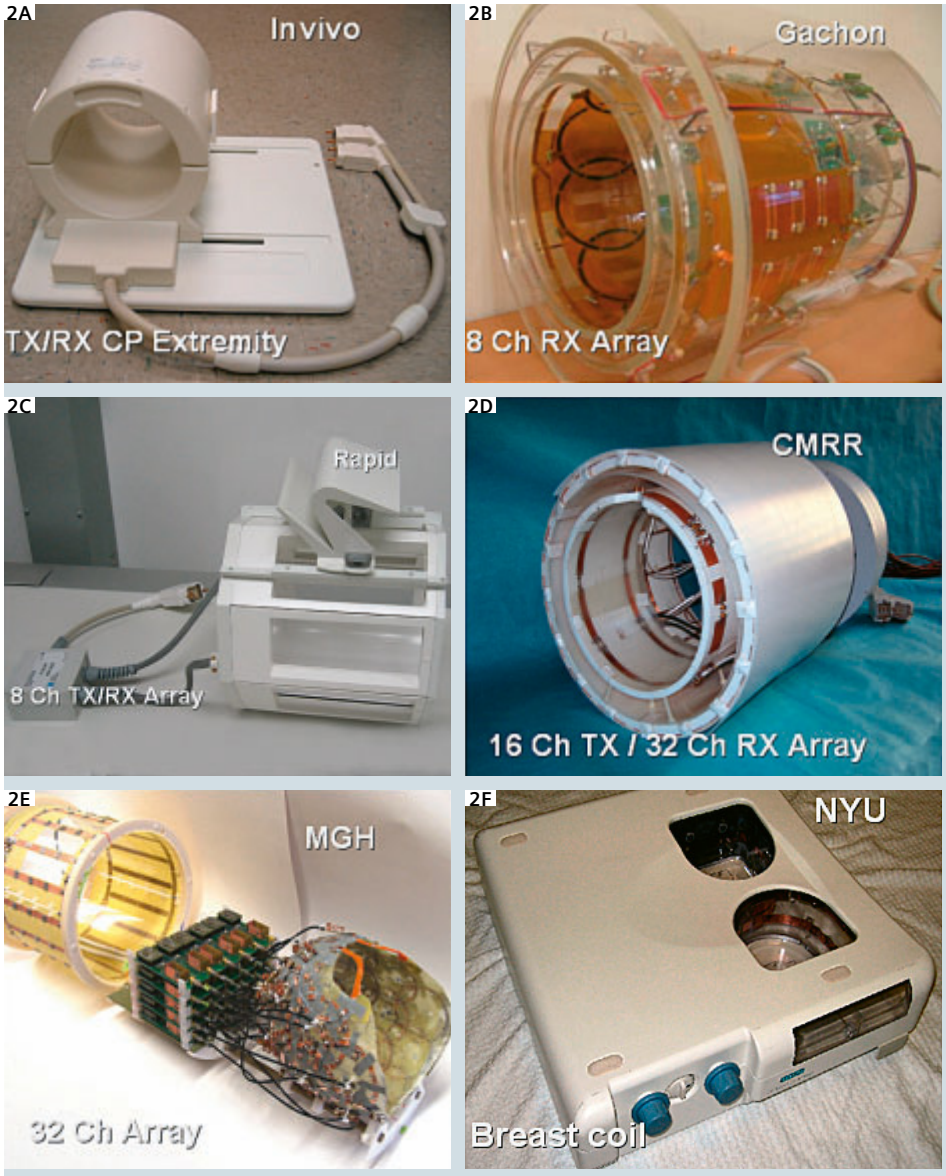

2 A few examples of RF coils built by industrial and academic partners:
A: CP Transmit/receive (TX/RX) extremity coil, Invivo
B: 8-channel RX array, Gachon Medical School, Seoul, Korea
C: 8-channel TX/RX array, Rapid Medical
D: 16-channel TX / 32 RX array, Center for MR Research, Minneapolis, MN, USA
E: 32-channel RX array, MGH Martinos Center, Boston, MA, USA
F: Breast coil, New York University, New York City, NY, USA

Signal and Contrast Improvements at 7 Tesla

As already mentioned, the primary reason to go up to 7 Tesla is to get more MR signal. The extra signal can be traded for a reduced imaging time by either reduced averaging or the use of integrated Parallel Imaging (iPAT) with high PAT factors. The extra signal can also be used to acquire exceptionally high resolution images in a scan time not possible at lower field strengths. Fig. 3 shows extremely high resolution ex vivo imaging of the temporal lobe (100 µm isotropic voxels), visualizing the entorhinal cortex islands related to the development of Alzheimer's disease. Fig. 4 is an in vivo coronal T1-weighted MPRAGE acquisition with 0.45 x 0.45 x 1 mm resolution, acquired with a 32-channel phased array coil, showing fine anatomical detail. Orthopedic imaging can also benefit from increased resolution and is being actively developed at 7T. Fig. 5 shows an image of the knee acquired with 0.35 x 0.35 x 4 mm voxels. The basis of the functional MRI (fMRI) signal is blood-oxygenation level dependent (BOLD) contrast, which generally increases quadratically with the magnetic field. This

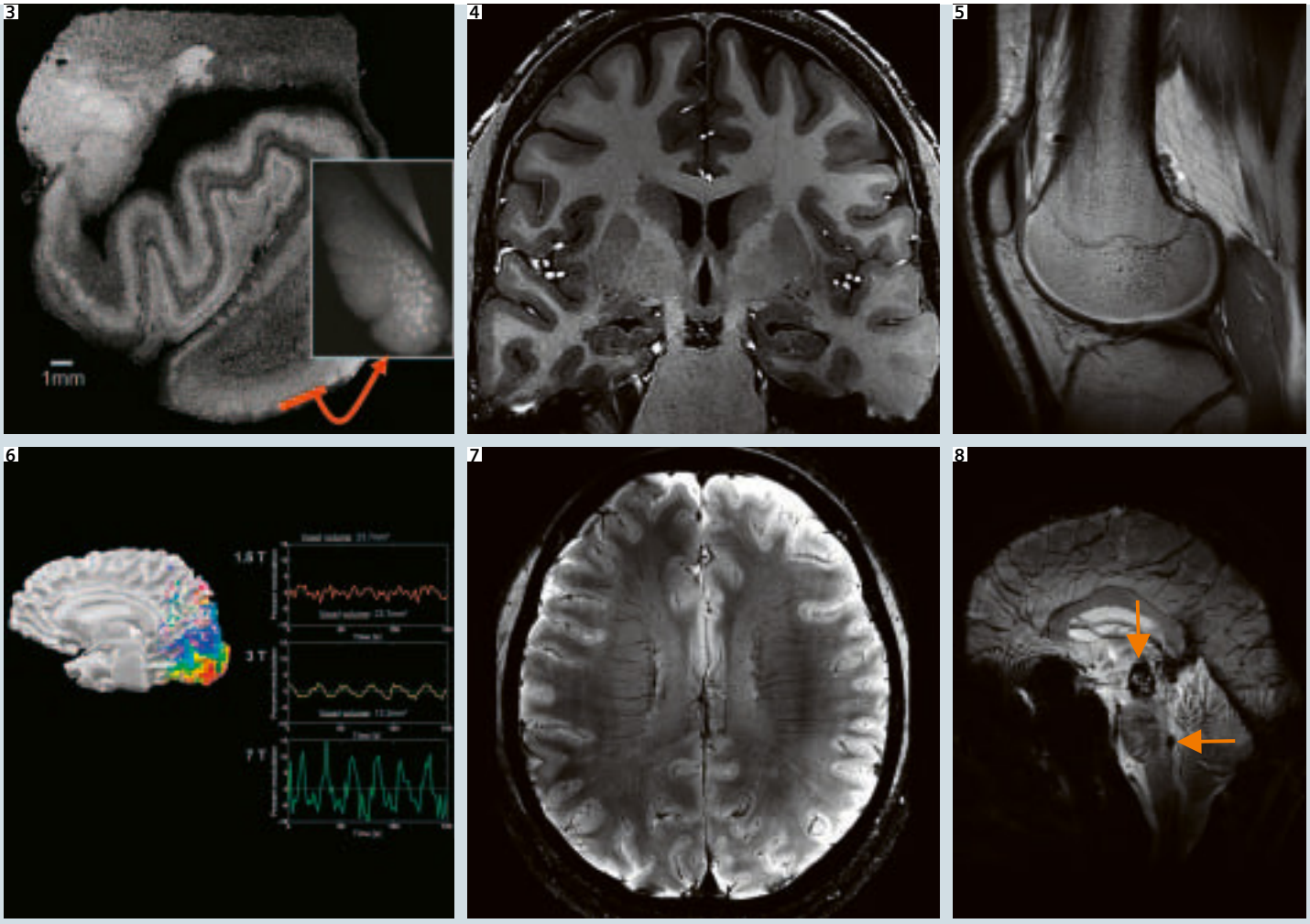

3 **Ex vivo images of the temporal lobe with 100 µm isotropic resolution, visualizing the entorhinal cortex islands related to the development of Alzheimer's disease.**

Courtesy of B. Fischl, L. Wald et al., MGH Martinos Center, Boston, MA, USA.

4 **A coronal T1-weighted MPRAGE image with 0.45 x 0.45 x 1 mm resolution, acquired with a 32-channel phased array coil.**

Courtesy of G. Wiggins, C. Wiggins, L. Wald et al., MGH Martinos Center, Boston, MA, USA.

5 **Knee image acquired at 0.35 x 0.35 x 4 mm resolution.**

Courtesy of M. Ladd, Erwin-Hahn-Institute for Magnetic Resonance, Essen, Germany.

6 **The plots show the increased BOLD (Blood Oxygen Level Dependent) signal change with field strength in a region of the occipital cortex throughout a series of fMRI measurements.**

Courtesy of H. Scheich, A. Brechmann, J. Stadler, Institute for Neuro-Biology, Magdeburg, Germany.

means the BOLD related signal change at 7T can be more than 5 times as much as 3T. Fig. 6 compares BOLD signal plots for a region of interest in the occipital cortex for optimized protocols at 1.5, 3, and 7 Tesla, showing a strong increase in the BOLD response with field strength. The higher magnetic susceptibility differences between venous blood and tissue can also be used for venous anatomical imaging. Fig. 7 depicts small veins in the corpus callosum and white matter; Fig. 8 shows a lower venous anomaly and cavernoma. Figure 9 is an extremely high resolution T2*-weighted gradient echo image with 0.22 x 0.22 x 1 mm voxels at two different zoom levels, showing a very high level of detail and many tiny blood vessels penetrating the cortex. This amount of resolution and venous sensitivity makes it possible to use gradient echo imaging to see microvascular changes in the initial stage of Multiple Sclerosis lesion development in vivo, which has not been seen at lower field strengths (Fig. 10). One can now see the small veins around which these lesions develop.

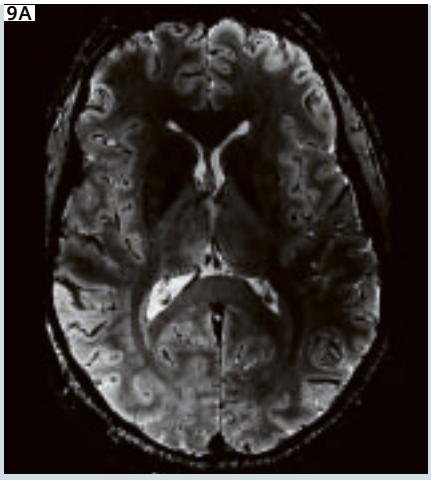

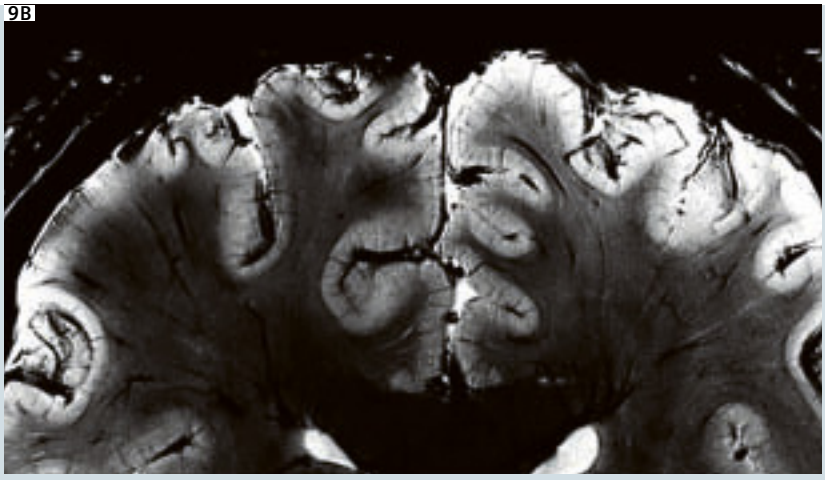

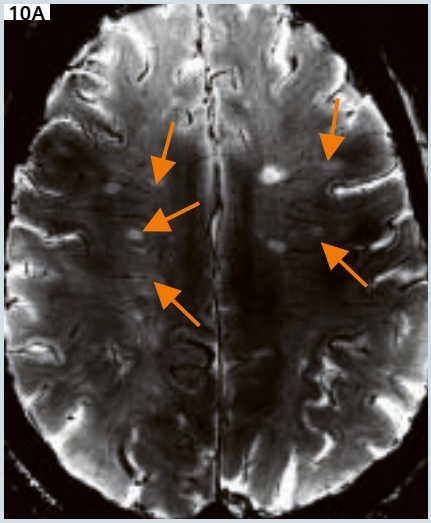

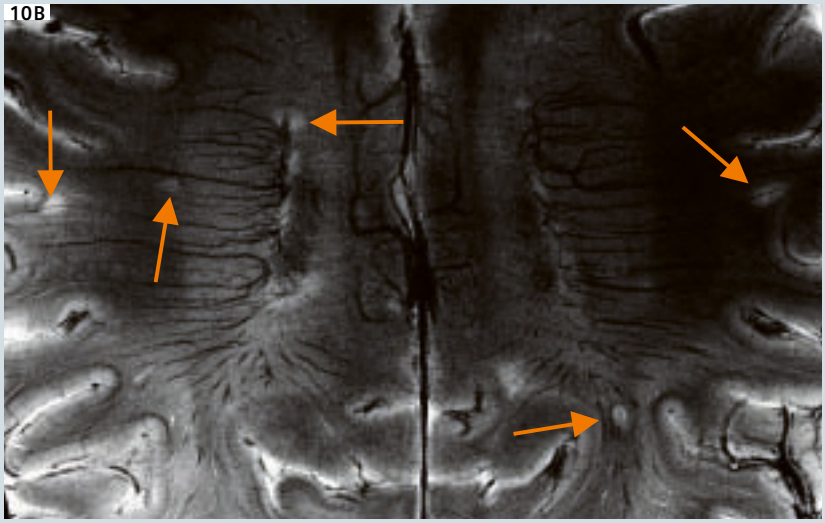

7 **Depiction of the veins in the corpus callosum and white matter.**

Courtesy of Z. Cho, Gachon Medical School, Seoul, Korea.

8 **Lower venous anomaly and cavernoma.**

Courtesy of M. Ladd, R. Forsting, Erwin-Hahn-Institute for Magnetic Resonance, Essen, Germany.

9 **High-resolution T2*-weighted gradient echo image with 0.22 x 0.22 x 1 mm voxels at two different zoom levels, showing many tiny blood vessels penetrating the cortex.**

Courtesy of G. Wiggins, C. Wiggins, L. Wald et al., MGH Martinos Center, Boston, MA, USA.

10 **(A) Microvascular changes in the initial stage of Multiple Sclerosis lesion development. (B) The small veins around which the lesions develop are visible.**

Courtesy of Y. Ge, R. Grossman, New York University, School of Medicine, New York City, USA.

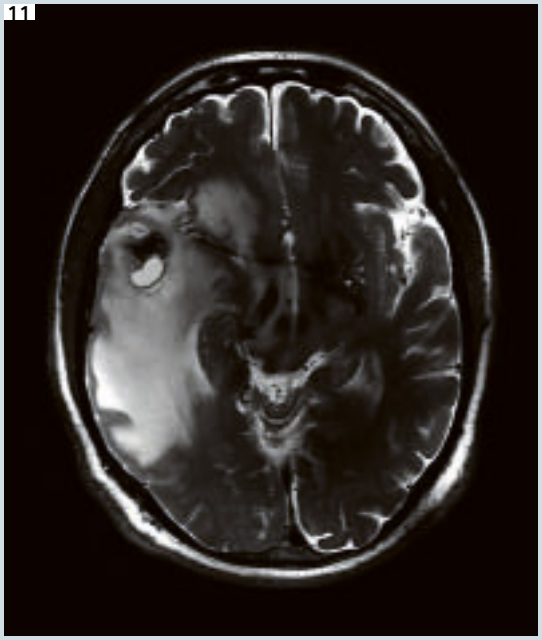

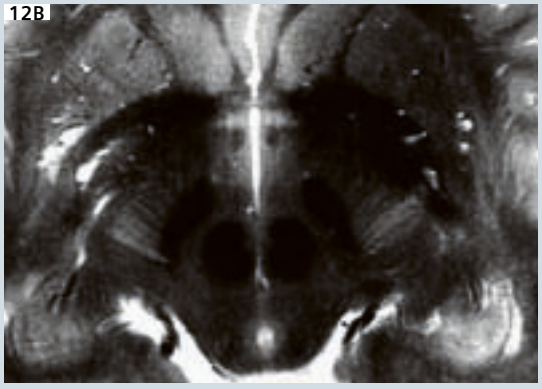

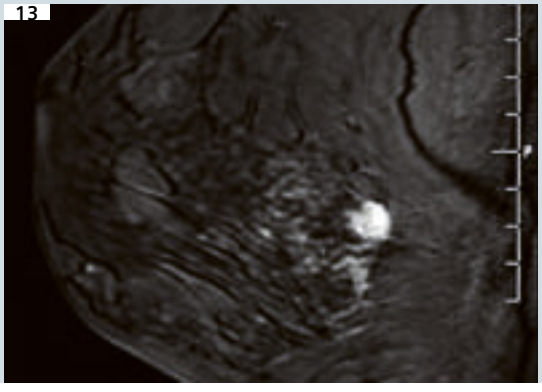

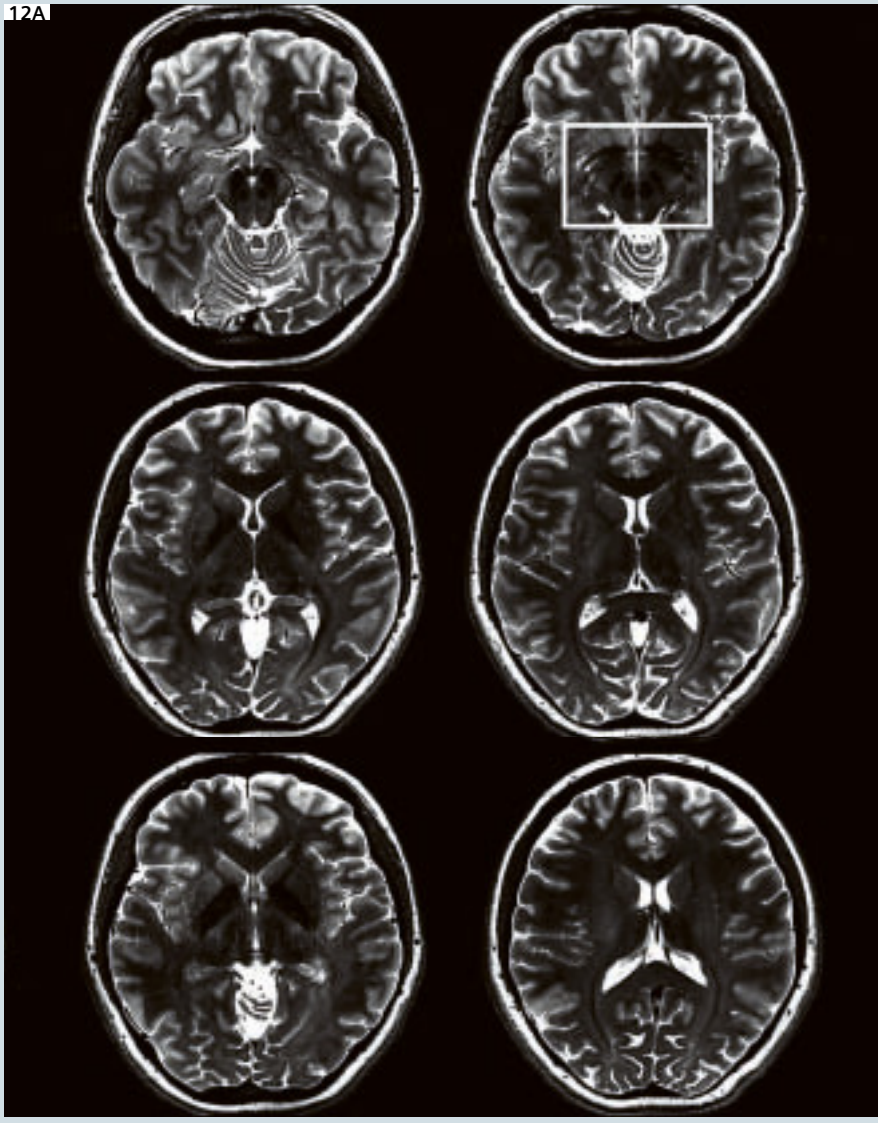

11 **T2-weighted image of glioblastoma using an 8-channel coil.**

Courtesy of M. Ladd, Erwin-Hahn-Institute for Magnetic Resonance, Essen, Germany.

12 **(A) Several slices from a T2-weighted turbo spin echo sequence. The zoomed section (B) shows high contrast between deep brain structures that have high iron content.**

Courtesy of E. Auerbach, C. Snyder, Gözübüyük, G. Adriany, T. Vaughan, K. Ugurbil, Center for MR Research, Minneapolis, MN, USA.

13 **Breast lesion post-contrast.**

Courtesy of R. Lee, L. Moy, New York University, School of Medicine, New York City, USA.

Fig. 11 is a T2-weighted image using an 8-channel coil demonstrating excellent contrast and resolution in examining glioblastoma. Fig. 12 contains several slices from a high resolution T2-weighted turbo spin echo using a 32-channel head coil with PAT factor of 2, 1024 x 1024 matrix, and 0.18 x 0.18 x 2 mm voxels. The zoomed section shows the high contrast of deep brain structures having relatively high iron content caused by the increased iron susceptibility effects at 7T.

Contrast agents have stronger effects at higher field due to both increased magnetic susceptibility and increased T1. This allows the use of smaller contrast doses or potentially can increase the lesion conspicuity post-injection. Fig. 13 shows initial results in the breast with good tumor contrast in the glandular tissues.

Conclusion

Development on 7 Tesla systems is progressing rapidly, and the user base is constantly growing with more than 10 MAGNETOM 7T systems already in operation. Although the siting, magnet size, engineering challenges, and associated costs are significant, the benefits of higher MR signal and contrast are allowing us to begin to see things not seen before. Technical advances at 7 Tesla should also benefit lower field strengths, and keep them at the forefront of MR research, making it worth the investment in applications and hardware development.

Parallel Transmission (pTX) Technology*

MR Imaging with an 8-Channel RF Transmit Array

Franz X. Hebrank[1], Lawrence L. Wald[2], Vijayanand Alagappan[2], Elfar Adalsteinsson[3], Kawin Setsompop[3], Adam Zelinski[3], Ulrich Fontius[4], Juergen Nistler[4], Franz Schmitt[4]

[1]*Siemens Medical Solutions, Charlestown, MA, USA*
[2]*Massachusetts General Hospital (MGH) Martinos Center, Charlestown, MA, USA*
[3]*Massachusetts Institute of Technology (MIT), Cambridge, MA, USA*
[4]*Siemens Medical Solutions, Erlangen, Germany*

Introduction

In recent years there has been a trend towards higher field strength in MR imaging. Nowadays 3 Tesla is already routinely used for clinical imaging, and there is a tendency to move towards even higher field strengths for human imaging, like 7T. But besides the many potential advantages of ultra-high field MRI, there are also some methodological challenges like the destructive interference of transmit RF fields within a typical volume coil [1, 2]. These effects arise when the RF wavelength reaches the dimension of the human head or body and can lead to center brightening in the head at 7T (Fig.1) and shading in abdominal imaging at 3T. The spatial variations of the B_1 field lead to reduced tissue contrast and inhomogeneous image intensity. Several methods have been explored to compensate for these spatial variations of the transmit field. These methods include the application of shaped 2D and 3D RF pulses [3] or "RF shimming", where the channels of the transmitting coil are driven with tunable global RF-phase and amplitude in order to optimize the homogeneity of the resulting B_1 field [4, 5, 6].
So far 2D and 3D RF pulses were not practical in clinical MR imaging, since the duration of the pulses is too long for normal sequences. Parallel transmission (pTX) techniques have demonstrated the feasibility of accelerating time consuming 2D and 3D excitation pulses, to accommodate clinical sequences [3, 4, 7]. Another challenge linked to the design of tailored 2D and 3D RF pulses and RF shimming is the need for a transmit coil with preferably highly decoupled elements. On current coil designs this requirement is often reduced to a high degree of decoupling between next neighboring elements.
This article describes the design and setup of a parallel Transmission (pTX) prototype Siemens MAGNETOM Trio, A Tim System equipped with an 8-channel transmit array. This prototype MR system was used in combination with two different TX coils to acquire phantom and in vivo images with 1 to 8 fold accelerated 2D and 3D RF pulses.

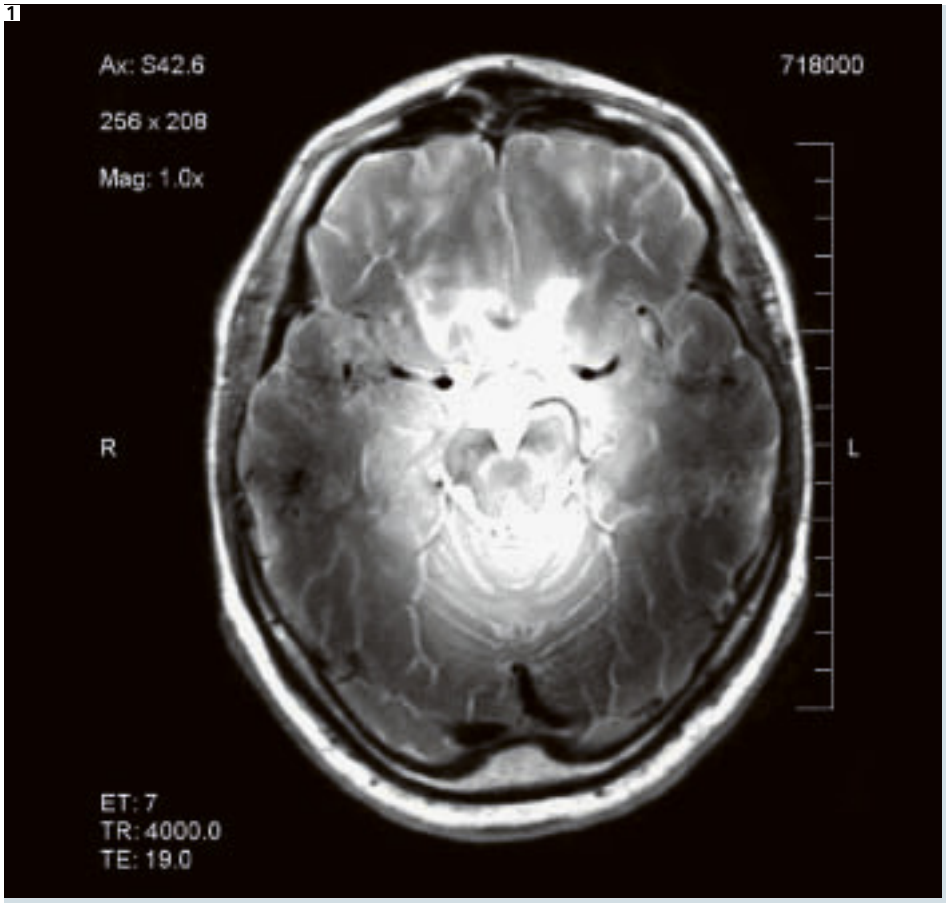

1 Center brightening in the head at 7T.

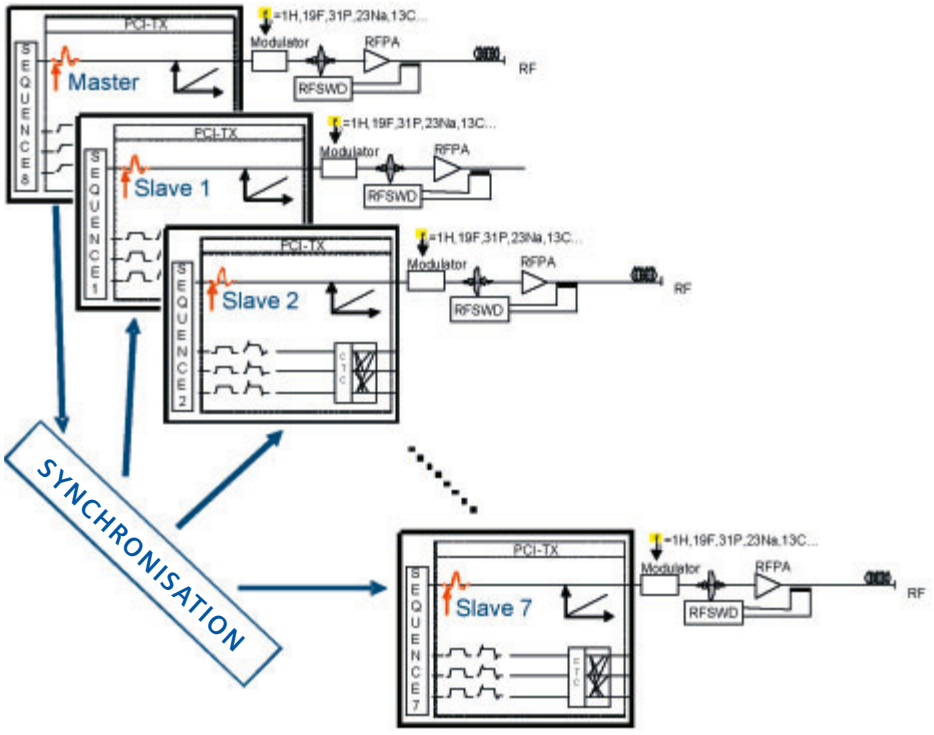

2 Block diagram of the Transmit Array system.

3 SAR simulations in the head.

4 Transmit only 8-channel. head coil.

Experimental Setup

System setup

A prototype 8-channel transmit array in a master-slave configuration was used, with one measurement control unit acting as the "master" controlling the other 7 "slaves" [8]. The transmit array was attached to a 3T MAGNETOM Trio, A Tim System, hence the primary console of the scanner was determined as the master (Fig. 2). Cloning the standard Siemens measurement control unit (MPCU) for all 7 slaves enables to run 8 independent sequences with individual RF shapes and characteristics, individual B_0 eddy current compensation and 3 additional gradient channels per unit, which can be used for gradient array [9] or dynamic shimming applications. Each of the 8 independent RF pulses is amplified by a separate 8 kW Dressler RF amplifier. For safety reasons, each channel includes its own independent RF power monitor (SAR supervision) which will switch off the RF in each channel if the SAR limit in any of the channels is exceeded. Moreover, the SAR settings can be configured for each channel individually limiting the peak power and the average power within the 6 minutes and 10 seconds time interval according to the IEC 60601-2-33 standard.

SAR calculation and safety concept

To ensure the safe operation and fulfillment of the IEC limits for SAR of the system in human imaging, the power limits were calculated before starting with the in vivo experiments. For this purpose a commercial program was used, which applies the Finite Integration Technique (FIT). The simulations were performed for the 8-channel head coil and the 8-channel body coil. The worst case SAR was calculated by summation of the E-field magnitude of all coil elements for all voxels in the human model. These worst case E-fields and the knowledge of the tissue properties were used to calculate the 10 g averaged local SAR and the whole-body SAR (Fig. 3). The calculated whole-body SAR was scaled down until the local SAR limits were fulfilled. These new whole-body SAR limits were divided by the number of transmit channels and were applied to the SAR supervision of each channel. With this concept the RF safety concerning whole-body and local SAR limits is guaranteed, even if one or more of the amplifiers will fail.

Transmit coils

Two different 8-channel coils were used for parallel transmission:
The first coil is a pTX only head coil (Fig. 4), which was used for the RF excitation in combination with the body coil receiving the RF signals [10]. This TX only coil was designed as a degenerated birdcage coil (DBC) [11], which basically can be used in two mode configurations, using either the eight "loop mode" basis set or the orthogonal birdcage modes as driven by an 8 x 8 Butler matrix [12]. The Butler matrix has 8 coaxial inputs and 8 coaxial outputs, which can therefore produce

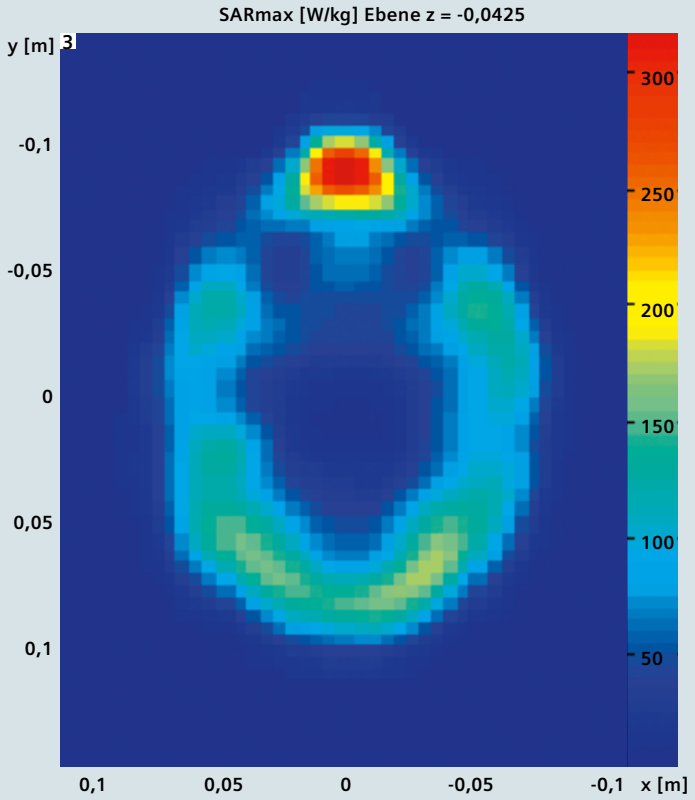

3

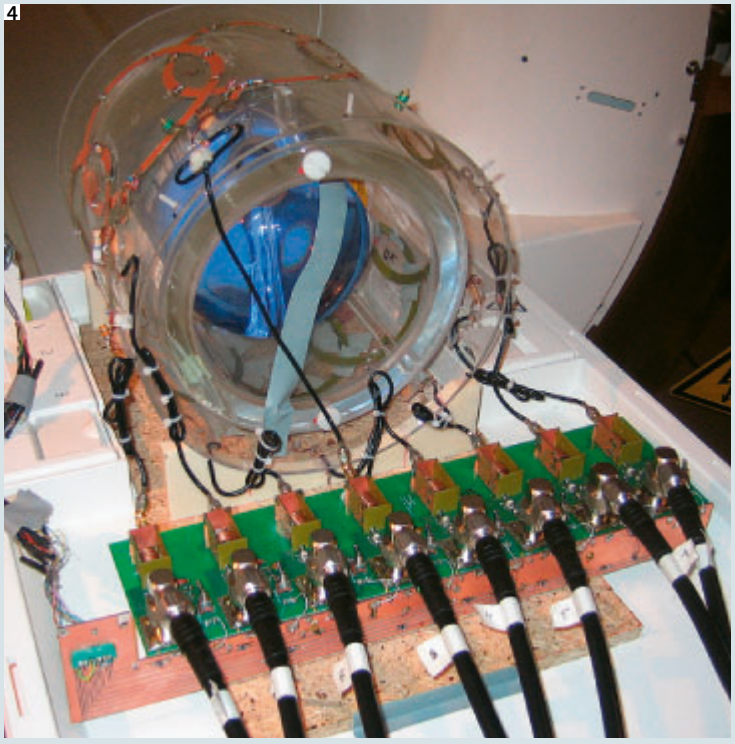
4

8 independent modes. The big advantage of using the modes of a birdcage coil excited by a Butler matrix is that they form naturally decoupled orthogonal modes which do not require additional decoupling strategies. This decoupling is essential for a parallel transmission methodology, since – similar to a parallel receive array – the capability of a transmit array to accelerate the spatially tailored excitation pulses depends on the spatially differing B_1 profiles of the individual array elements.

The second coil used for the experiments is an 8-channel TX/RX body coil, which also allowed the insertion of a Butler matrix into the TX and the RX path to generate orthogonal modes [13].

With both coils in a first step the magnitude and phase profiles of the transmitted B_1 field have been measured. To avoid an interference with the receive coil profile this measurement was performed for both 8-channel coils using the uniform standard CP mode of the scanner body coil for RF reception. The amplitude and phase of these B_1 fields were then used for the calculation of the RF pulse shapes as described in the next section.

RF pulse design

Different RF waveforms in the low flip angle domain were calculated based on the formalism used by Grissom et al. [14]. For excitation we used two types of gradient trajectories [3]:

The first trajectory consisted of a 2D excitation with a spiral trajectory in (k_x, k_y) and no encoding in z-direction. This 2D trajectory can be used to excite a high resolution target profile in the 2D plane. With this pulse design accelerations of integer factors of 2 through 8 can be utilized by successively increasing separation between the turns in the k-space trajectory. At a gradient amplitude of 35 mT/m and a slew rate of 150 T/m/s the duration of these 2D pulses could be reduced from 9.47 ms in the unaccelerated case (R =1) to 2.42 ms for R = 4, 1.64 ms for R = 6 and only 1.26 ms for R = 8 respectively. Therefore the R = 8 accelerated pulse was 7.5 times shorter than the unaccelerated pulse, which will make their application in clinical pulse sequences possible.

The second trajectory consisted of a 3D k-space excitation using a set of line segments or "spokes" in the k_z direction placed at regular intervals in the (k_x, k_y) plane [3, 15, 16, 17]. Using a sinc-like RF waveform during the transversal of each spoke achieves a sharp slice selection in z but with low resolution control of the in-plane magnetization profile. Two versions of these trajectories were designed and tested: one with 4 spokes with a pulse length of 3.42 ms and one with 1 spoke with a pulse length of 1.2 ms. With such a trajectory it is possible to achieve a uniform excitation across the phantom despite the nonuniform nature of the 8 individual excitation profiles.

Image examples

Phantom measurements

The 2D trajectory in combination with the 8-channel pTX head coil was used to excite a high-resolution spatial pattern of letters in the (x, y) plane. The resolution for this experiment was set to 5 mm with a FoV of 180 mm. Fig. 5 shows the image using an acceleration factor of R = 4. The high resolution "Tim TX" logo (Fig. 6) was also acquired using the 2D trajectory with an acceleration of R = 4. For this image parallel transmit and parallel receive have been used simultaneously by employing the 8-channel TX/RX body coil for excitation and the standard Siemens 12-channel Head Matrix coil for reception of the data. Fig. 7 shows as an example the image of a phantom using the 3D homogenous excitation with 4 spokes and an acceleration factor of R = 4. For this measurement the RF pulse duration was 3.42 ms.



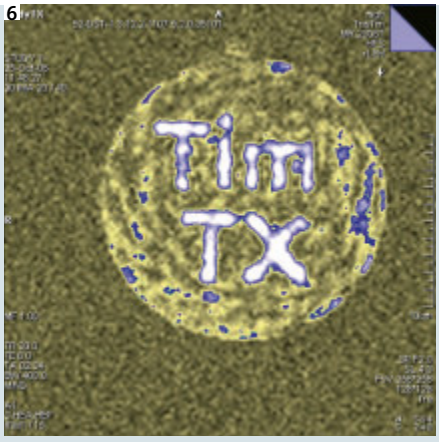

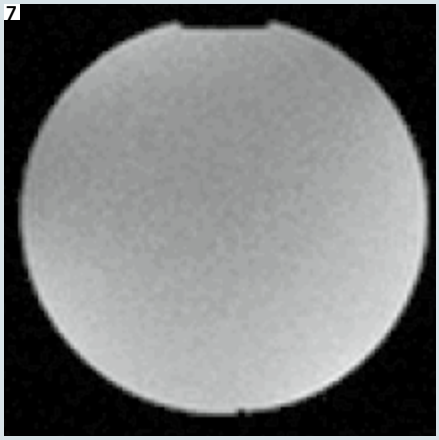

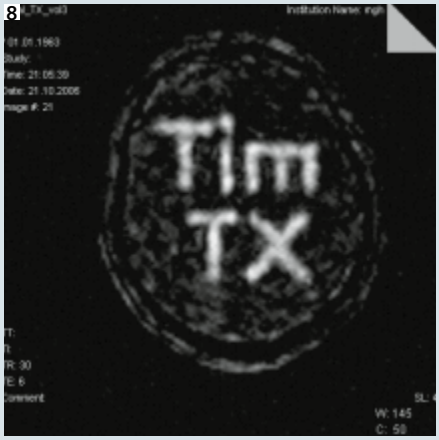

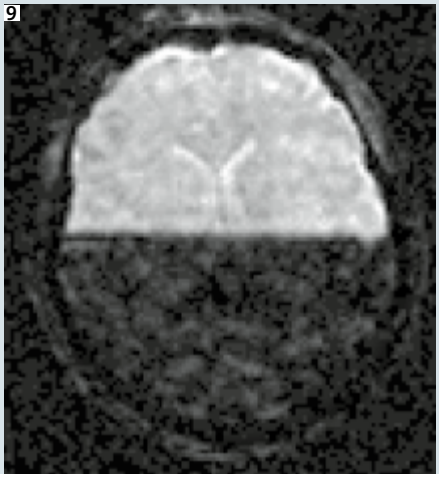



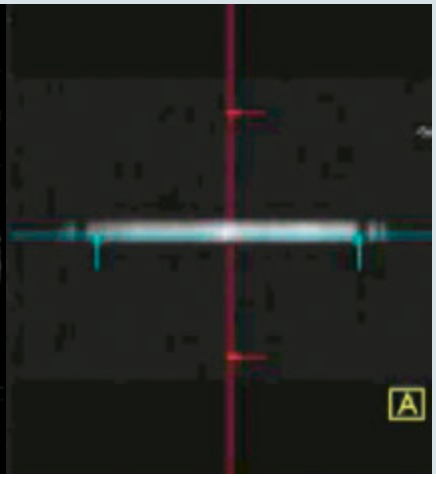

5 MIT logo excitation using a 2D trajectory and the TX head coil, R = 4.

6 "Tim TX logo", 2D excitation with body coil, acquisition with 12-channel Head Matrix coil, R = 4.

7 3D homogenous excitation using the 4 spokes trajectory.

8 "Tim TX" logo in the human head acquired with the TX head coil using an acceleration of 4.

9 "Half brain" excitation with the TX head coil, R = 4.

10 3D excitation of a homogenous slice in the brain using the TX/RX body coil for excitation.

11 3D excitation of a homogeneous slice in the human torso using the TX/RX body coil for excitation.

In vivo measurements

Using the TX only head coil for excitation and the 2D trajectory with an acceleration factor R = 4 the "Tim TX" logo could also be excited in the human brain (Fig. 8). Moreover with this coil/pulse configuration we were also able to excite only one half of the subject's brain (Fig. 9) using an acceleration factor of R = 4. Excitation of homogeneous brightness profiles in the head (Fig. 10) and the torso (Fig. 11) were obtained with the TX 8-channel body coil using the 3D pulses with a 4 spokes design as described above.

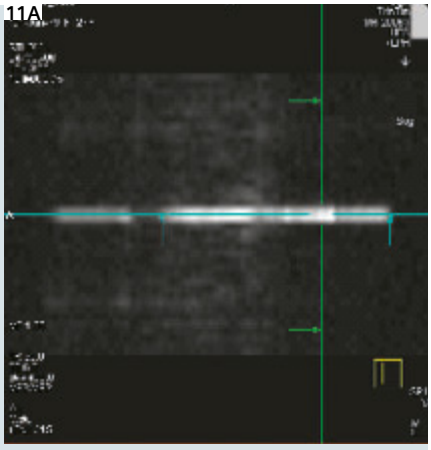

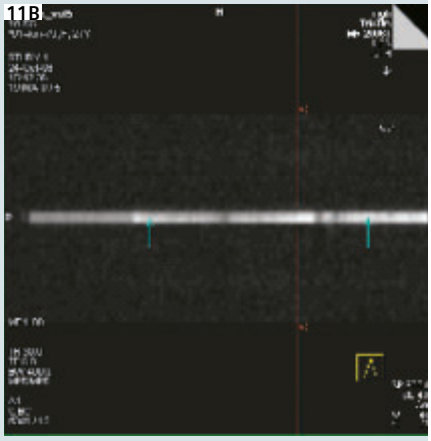

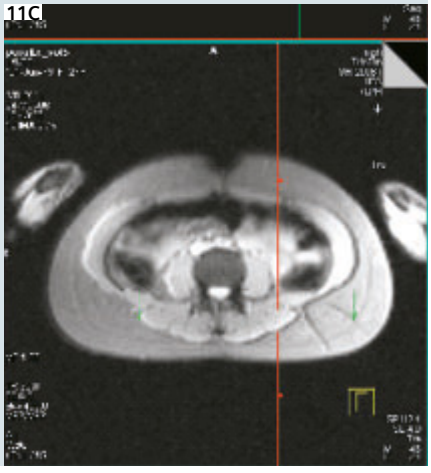

Conclusion

We have developed a new setup of a parallel Transmission (pTX) prototype Siemens MAGNETOM Trio, A Tim System equipped with an 8-channel transmit array. This new scanner was successfully tested in combination with two different 8-channel coils and two different RF pulse designs. With this combination of modified software and hardware we were able to acquire phantom and in vivo images with homogeneous signal distribution and high resolution spatial patterns. First results with the pTX array are very promising and raise the possibility of performing highly homogeneous head and whole-body imaging not only at 3T but furthermore at ultra high field strength like 7T, where destructive interference of transmit RF fields can lead to clinically compromised image quality. Moreover the design of 2D trajectories in combination with acceleration factors of up to 8 also raise the possibility to use these 2D pulses in clinical sequences, where the duration of the RF pulse is crucial.

* WIP – Works in Progress. The information is preliminary. The sequence is under development and not commercially available in the U.S., and its future availability cannot be ensured.

References

1 Hoult DI, Phil D. Sensitivity and power deposition in a high-field imaging experiment. J Magn Reson Imaging 2000; 12(1): 46–67.
2 Collins CM, Liu W, Schreiber W, Yang QX, Smith MB. Central brightening due to constructive interference with, without, and despite dielectric resonance. J Magn Reson Imaging 2005; 21(2): 192–196.
3 Setsompop K, Wald LL, Alagappan V, Gagoski B, Hebrank F, Fontius F, Schmitt F, Adalsteinsson E. Parallel RF Transmission with Eight Channels at 3 Tesla. Magn Reson Med 2006; 56(5): 1163–1171.
4 Katscher U, Bornert P, Leussler C, van den Brink JS. Transmit SENSE. Magn Reson Med 2003; 49(1): 144–150.
5 Vaughan, J.T., DelaBarre, L., Snyder, C., Adriany, G., Collins, C., Van de Moortele, P-F., Moeller, S., Ritter J., Strupp, J., Andersen, P., Tian, J., Smith, M., Ugurbil, K., RF Image Optimization at 7T & 9.4T, 2005, ISMRM. Miami Beach, Florida, USA. p. 953.
6 Adriany, G., Van de Moortele, P-F., Wiesinger, F., Moeller, S., Strupp, J., Andersen, P., Snyder, C., Zhang, X., Chen, W., Pruessmann, K.P., Boesiger, P., Vaughan, J.T., Ugurbil, K., Transmit and receive transmission line arrays for 7 Tesla parallel imaging. Magn Reson Med, 2005. 53(2): p. 434–445
7 Zhu Y. Parallel excitation with an array of transmit coils. Magn Reson Med 2004; 51(4): 775–784.
8 Fontius U., et al., A Flexible 8-Channel RF Transmit Array System for Parallel Excitation, 2006, ISMRM, Seattle, Washington, USA, p. 127
9 Parker DL, Hadley JR. Multiple-Region Gradient Arrays for Extended Field of View, Increased Performance, and Reduced Nerve Stimulation in Magnetic Resonance Imaging, Magn Reson Med, 2006; 56 (6): 1251–1260.
10 Alagappan V, Nistler J, Adalsteinsson E, Setsompop K, Fontius U, Vester M, Wiggins GC, Hebrank F, Renz W, Schmitt F, Wald LL. A degenerate Mode Band-Pass Birdcage for Accelerated Parallel excitation. Submitted for Magn Reson Med.
11 Lin FH, Kwong KK, Huang IJ, Belliveau JW, Wald LL. Degenerate mode birdcage volume coil for sensitivity-encoded imaging. Magn Reson Med 2003; 50(5): 1107–1111.
12 Moody HJ. The systematic design of the Butler matrix. IEEE Transaction on Antenna and Propagation 1964: 786–788.
13 Nistler J. et al, Using a mode concept to reduce hardware efforts for multi channel transmit array, 2006, ISMRM, Seattle, Washington, USA, p. 2024
14 Grissom W, Yip C-Y, Noll DC. A new method for the design of RF pulses in Transmit SENSE, Proceedings of the 2nd International Workshop on Parallel Imaging, Zurich, Switzerland 2004. p. 95.
15 Saekho S, Boada FE, Noll DC, Stenger VA. Small tip angle three-dimensional tailored radiofrequency slab-select pulse for reduced B1 inhomogeneity at 3 T. Magn Reson Med 2005; 53(2): 479–484.
16 Ulloa J, P. I, Hajnal JV. Exploring 3D RF shimming for slice selective imaging. 2005; ISMRM. Miami Beach, Florida, USA. p 21.
17 Saekho S, Yip C-Y, Noll DC, Boada FE, Stenger VA. A Fast-kz 3D Tailored RF Pulse for Reduced B1 Inhomogeneity. 2005; ISMRM. Miami Beach, Florida, USA. p 22.

Acknowledgments

We would like to thank Melanie Schmitt for her valuable assistance in the preparation of this article.

Diffusion-Weighted Imaging in Breast MRI* – An Easy Way to Improve Specificity

Dr. Evelyn Wenkel, M.D.[1]; Dr. Christian Geppert, Ph.D.[2]; Prof. Dr. Michael Uder, M.D.[1]; Dr. Berthold Kiefer, Ph.D.[2]; Prof. Dr. Werner Bautz, M.D.[1]; Dr. Rolf Janka, M.D.[1]

[1] *University Hospital Erlangen, Radiology, Erlangen, Germany*
[2] *Siemens Medical Solutions, Erlangen, Germany*

Introduction

Classic breast magnetic resonance imaging (MRI) is based on the enhancement pattern of lesions in dynamic breast MRI, and morphologic changes [1–3]. With these two criteria breast MRI has a sensitivity of about 85–99% in detecting malignant breast lesions [1–10]. However, there is an overlap of these criteria with benign lesions which leads to a reported specificity of about 40 to 80% [1, 10, 11]. There is an increasing number of congress abstracts and published studies that the specificity of breast MRI could be increased using diffusion-weighted (DW) sequences [12–16]. DW MRI is based on the principle that random motion of molecules during the interval of excitation and signal measurement reduces the amplitude of the resulting signal. The application of appropriate pulse sequences (using, for example, bipolar gradient pulses in one or several directions) allows the measurement of the signal cancellation due to diffusion in the given direction. While normal tissue exhibits gross signal loss, areas with restricted motion of molecules like densely packed tumor cells show less signal loss and become bright in diffusion-weighted images. The value of the diffusion of water in tissue is called the apparent diffusion coefficient (ADC). Based on the diffusion-weighted images an ADC map can be calculated which shows the ADC value of each voxel in every slice. Restricted water movement in tumors with high cellularity leads to smaller ADC values [13]. In some organs, especially the brain, the direction of the diffusion contains important information which can be used, for example, for tracking of fibers by diffusion tensor imaging in many directions. However, in tumor clusters the diffusion is vastly restricted in every direction and therefore it is sufficient to measure DWI of the breast in just one orientation. In most applications the diffusion gradients are integrated in echo planar imaging (EPI) sequences which exhibit high signal intensity in areas with restricted diffusion as well as in fatty tissue. Furthermore, the fat signal is displaced in the direction of the chemical shift as compared to the water signal. This makes fat saturation techniques necessary to identify

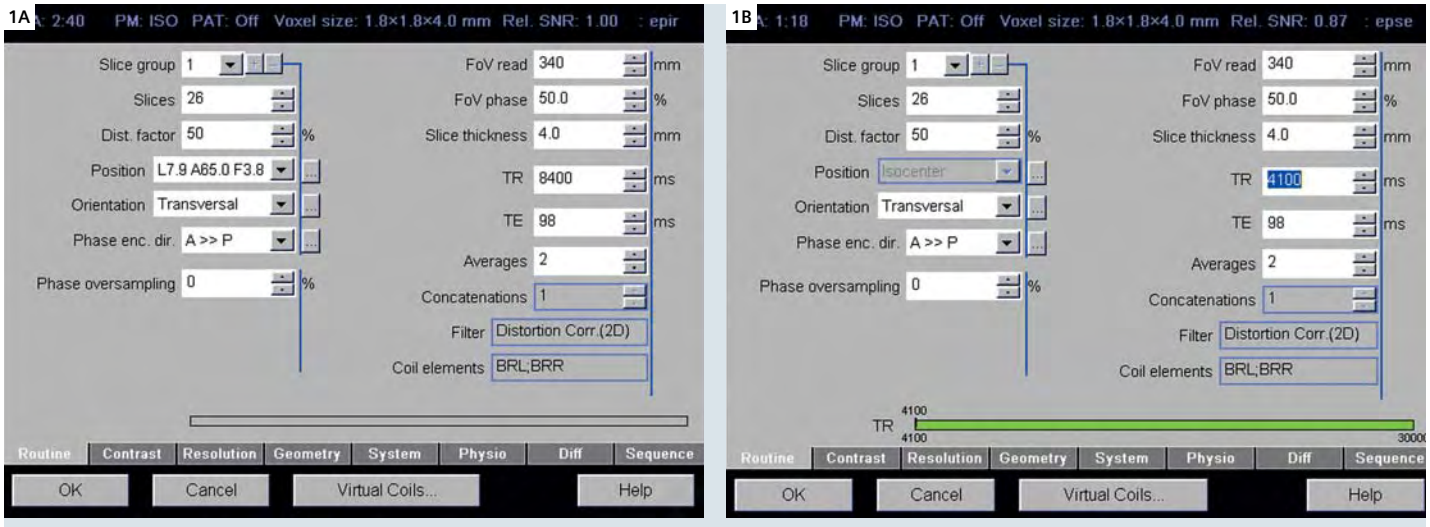

1 Sequence card of the diffusion-weighted EPI STIR **(A)** and the diffusionweighted EPI fs sequence **(B)**.

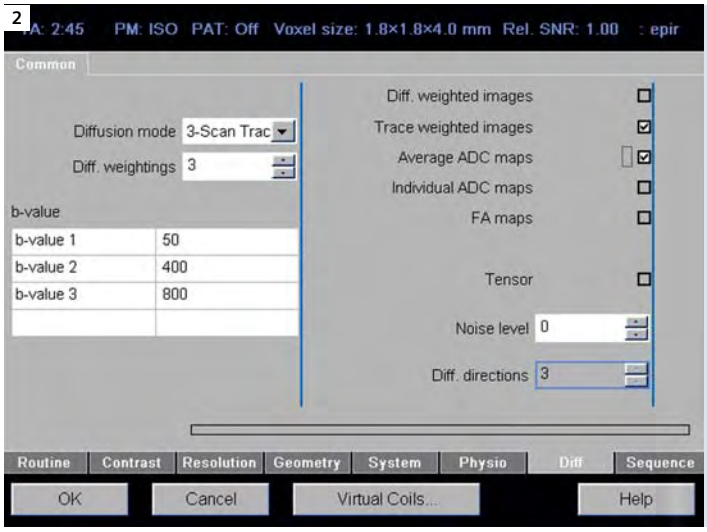

2 Parameters in the diffusion card.

the lesions in the diffusion-weighted images. There are two main possibilities for fat saturation: spectral fat saturation (fs) and a 180° pre-pulse with a short inversion time (STIR or TIRM).
In *syngo* MR B13 both methods can be applied. In our setup we acquire the DW images in axial slice orientation using echo planar imaging pulse sequences incorporating diffusion gradients. TR/TE/TI for the inversion recovery diffusion-weighted EPI (DW EPI STIR) are 8400/98/180 ms (Fig. 1A). The fat saturated diffusion weighted EPI (DW EPI fs) pulse sequence is scanned with a TR = 4100 ms and a TE = 98 msec (Fig.1B). Both sequences are acquired with a FoV of 340 x 170 mm, matrix: 192 x 96 and a slice thickness of 4 mm. We apply the DW sequences prior to the dynamic scan as the T1 relaxation due to the contrast agent will cause changes to the inversion of the tissue and thus can have a strong impact. All DW measurements were acquired with two averages of 26 slices and b-values of 50, 400 and 800 using 3-scan trace calculation, i.e. the sum of the diagonal elements D_{xx}, D_{yy} and D_{zz} of the diffusion tensor is calculated for each slice position and b-value (Fig. 2). With the MAGNETOM Avanto scanner the DW EPI STIR takes 2:40 minutes while DW EPI fs is performed in 1:18 minute. ADC maps are calculated automatically on the basis of the b50, b400 and b800 images using the scanner software. As mentioned above we suppose that a diffusion gradient in just one direction would also lead to sufficient results.

Image interpretation

Image interpretation starts like conventional breast MRI. If a lesion is visualized in the dynamic scan (Fig. 3) it has to be identified in the corresponding slice of the diffusion weighted images. As a second step, a region-of-interest (ROI) is drawn in the centre of the lesion on the b-800 DWI and copied to the ADC map (Fig. 4). The scanner software provides the mean value within the ROI which equals the ADC value (multiplied by 10^{-3} mm²/s). If the lesion is not visible in the b-800 images, the location of the lesion can be identified in the b-400 or b-50 image. Where the lesion is not visible in the b-50, b-400 or the b-800 image the ADC value cannot be evaluated. Lesions smaller than 5 mm and lesions with central necrosis and an enhancing rim smaller than 5 mm are often hard to delineate in the DWI or lead to wrong ADC values. So we do not recommend evaluating such lesions with DWI.

Results of DWI of the breast

In a pilot study with 56 patients and 69 histologically proven lesions > 5 mm only 5/69 lesions could not be evaluated with DW-MRI [17]. Three of these five lesions were not visible in the DWI sequences and therefore could not be matched with the ADC map. Histology of these lesions were one septated invasive lobular carcinoma with two tumor portions of 9 and 6 mm, one recurrent invasive ductal carcinoma with a maximum diameter of 10 mm in the MRI and one tubulolobular invasive carcinoma with 7 mm. In two patients the DWI images were not evaluable due to patient movement. ADC values were finally measured in 51 women (age 50

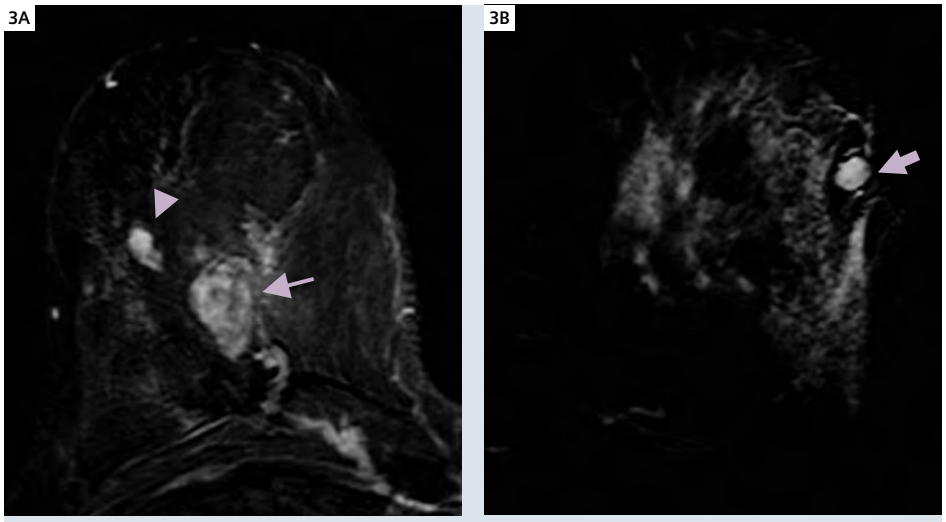

3 Your diagnosis? Subtraced image of the dynamic contrast enhanced sequence: **(A)** 45- year-old woman with a palpable mass and two suspicious lesions with blurred borders. The bigger one with inhomogeneous contrast enhancement (small arrow) and a smaller non-palpable lesion with nearly homogenous enhancement. **(B)** 41-year-old woman with a suspicious lesion in mammography and a sharp lined lesion in the outer-upper quadrant (big arrow).

Table 1: Histology of 69 lesions with DW sequences

Histology, N = 69	IDC	ILC	DCIS	Rare	FA	FD	BP	total
Evaluated	39	6	1	3	8	6	1	64
Not evaluated	2	2	0	1	0	0	0	5

IDC: invasive ductal carcinoma, ILC: invasive lobular carcinoma, DCIS: ductal carcinoma in situ, Rare: rare malignant tumors (medullary, tubular carcinoma, carcinosarcoma, angiosarcoma), FA: fibroadenoma, FD: fibrocystic disease, BP: benign phylloides tumor.

Table 2: Apparent diffusion coefficient (ADC) values (10^{-3} mm²/s) of all evaluated lesions (b = benign, m = malignant) in both MR diffusion weighted sequences

			ADC values (10^{-3} mm²/s)							
	n		Mean ± SD		Maximum		Minimum		95% CI	
	b	m	b	m	b	m	b	m	b	m
DW EPI STIR	15	45	1.92 ± 0.53	0.91 ± 0.24	3.20	1.43	1.10	0.35	1.62-2.22	0.83-0.98
DW EPI fs	15	49	1.76 ± 0.42	0.90 ± 0.18	2.58	1.19	1.21	0.34	1.53-2.00	0.85-0.96

SD: Standard deviation, EPI STIR: echo planar imaging with short time inversion recovery, EPI fs: echo planar imaging with spectral fat saturation.

years ± 15 years) with 64 focal mass lesions (15 benign, 49 malignant).
The mean longest diameter of the evaluated lesions was 17 ± 10 mm (benign 17 ± 10 mm, malignant lesions 17 ± 10 mm). The size of the ROI for the ADC value calculation was 24 ± 11 mm² (benign 27 ± 13 mm², malignant lesions 23 ± 10 mm²). There was no statistical difference of the size of the lesions or the ROI between benign or malignant masses. In the DW EPI STIR sequence the ADC values of 4 lesions could not be evaluated correctly due to patient movement between the b-50 and the b-800 sequence. So the ADC values of 60 lesions in the DW EPI STIR sequence and 64 lesions in the DW EPI fs sequence were evaluated (table 2). Lesion delineation was significantly better in the EPI fs sequence than in the EPI STIR sequence.
The mean ADC values were 1.92 ± 0.53 and 1.76 ± 0.42 x 10^{-3} mm²/s in benign lesions (DW EPI STIR and, DW EPI fs), and 0.91 ± 0.24 and 0.90 ± 0.18 x 10^{-3} mm²/s in malignant lesions, respectively. There was a highly significant difference in ADC values between benign and malignant lesions in both DW sequences. In the DW EPI STIR sequence the range of the ADC values of benign lesions was 1.10 – 3.20 x 10^{-3} mm²/s (95% CI: 1.62 – 2.22 x 10^{-3} mm²/s) and in malignant lesions 0.35 – 1.43 x 10^{-3} mm²/s (95% CI: 0.83 – 0.98 x 10^{-3} mm²/s, table 2). Assuming a threshold of 1.26 x 10-3 mm²/s for the DW EPI STIR sequence, 1/15 benign lesion and 1/45 malignant lesion would be misdiagnosed. In the DW EPI fs sequence the range of ADC values of benign lesions was 1.21 – 2.58 x 10^{-3} mm²/s (95% CI: 1.53 – 2.00 x 10^{-3} mm²/s) and of malignant lesions 0.34 –1.19 x 10^{-3} mm²/s (95% CI: 0.85 – 0.96 x 10^{-3} mm²/s) . There was no overlap in the ADC values of benign and malignant lesions in the DW EPI fs sequence.

Discussion

Detection of breast lesions has become more sensitive in mammography, ultrasound and MRI due to technical developments in the last years. Digital mammography seems to be more sensitive for breast lesion detection in dense breasts [18]. Higher spatial resolution leads to higher detection rates in ultrasound [19] and MRI.
However, the characterization of the detected lesions can be difficult. Up to now breast MRI is analyzed according to morphologic criteria, the enhancement kinetics and the T2 characteristic of breast lesions. However, all these criteria show an overlap between benign and malignant lesions [2, 4, 20-22]. In this situation an additional feature to characterize suspicious lesions would be helpful in order to decrease the number of invasive breast procedures. Prior studies with breast MRI and DWI have already addressed this question and show promising results [13-15]. In our study we compared two different DW sequences, an EPI STIR sequence and an EPI sequence with spectral fat saturation. Both DW sequences revealed a significant difference between ADC values of malignant and benign breast lesions. Comparing both sequences there was no overlap between the ADC values of benign and malignant breast lesions in the DW

sequence with spectral fat saturation. Assuming a threshold of 1.26 x 10^{-3} mm²/s, 2/60 lesions (1 benign and 1 malignant) would have been misclassified in the DW EPI STIR sequence.

In our opinion placement of the ROI is the crucial point in analyzing DWI. In most prior studies the ROI was placed with direct reference to the subtracted images of the dynamic contrast enhanced sequence. However, the spatial localization of a lesion in the dynamic contrast enhanced sequence is not necessarily the same as in the DW images due to distortion of echo planar images or patient movement between the DW sequence and the dynamic contrast enhanced sequence. Especially in small lesions this may lead to inadequate placement of the ROI. To overcome this problem the easiest and possibly more exact method to evaluate the ADC value is to localize the lesion in the contrast enhanced sequence, match it with the corresponding lesion in the DWI, select a ROI in the DWI and copy this ROI to the ADC map (Fig. 4). Using this method, lesion delineation in the DW sequence plays an important role for ADC measurement. In terms of lesion delineation the EPI fs sequence was significantly better than the EPI STIR sequence. This can be explained with the reduced signal-to-noise ratio (SNR) with inversion recovery as opposed to fat saturation.

Lesion delineation may also have an impact on the ADC map. Calculating the ADC map is a voxel per voxel analysis in the b-50, b-400 and b-800 DWI. A good delineation of the lesion in all three DW measurements should result in a sharp edged and homogenous ADC map of this lesion and vice versa. In our study the better lesion delineation in the DW EPI fs sequence corresponded with a significant lower standard deviation within the ROI in the ADC measurements.

There are some limitations of DW MRI of the breast. Patient movement between the acquisitions of the three DW sequences leads to wrong ADC values. In our study four lesions scanned with the EPI STIR

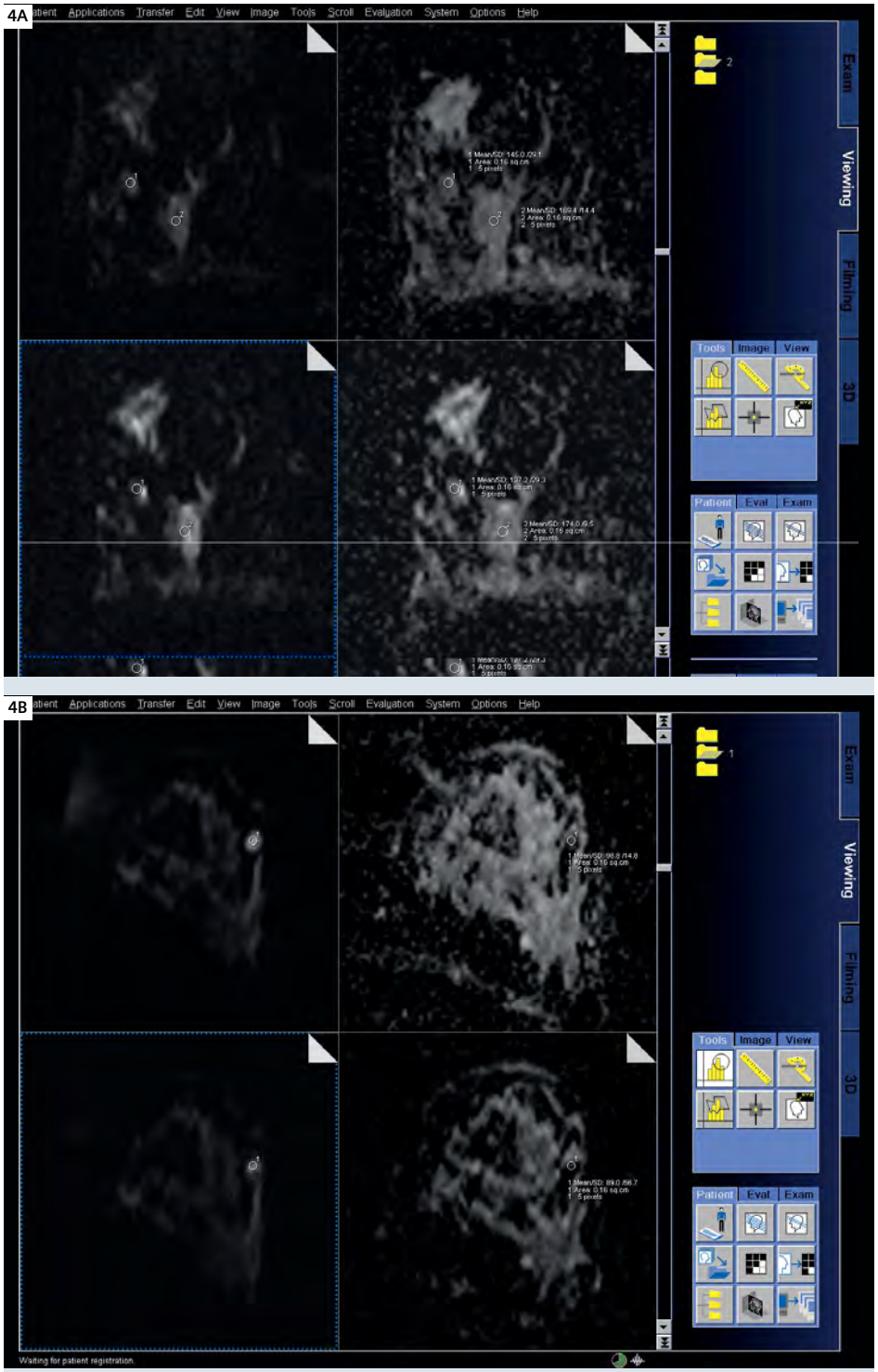

4 DWI (b=800, left side) of the corresponding lesions in figure 3 and the calculated ADC-maps (right side). Upper row: DW EPI fs, lower row DW EPI STIR. A region of interest was drawn in the centre of the lesions and copied in the ADC-map. **(A)** The ADC value of the bigger lesion reveals 1,7 x 10^{-3} mm²/s and the EPI fs and EPI STIR sequence. The ADC value of the smaller lesion is 1.5 x 10^{-3} mm²/s (EPI fs) and 1.4 x 10^{-3} mm²/s (EPI STIR). Histology of both lesions was a fibroadenoma. **(B)** The ADC value of the solitary lesion is 1.0 and 0.9 x 10^{-3} mm²/s (DW EPI fs and DW EPI STIR) Histology of the lesion was an invasive ductal carcinoma.

sequence were excluded from the evaluation due to patient movement. The reason for this may be the longer acquisition time of the EPI STIR sequence compared to the EPI fs sequence (2 min 40 s vs. 1 min 18 s) which makes patient movement more likely. But even under optimal circumstances DWI can fail to categorize breast lesions. Some lesions cannot be visualized in the DWI and therefore the exact localization of the ROI in the ADC map cannot be determined. In our study 3/69 lesions were not visualized in DWI and could not be evaluated. This ratio would be higher if lesions smaller than 5 mm had been analyzed. However, according to Liberman et al. there is a low likelihood of cancer in lesions smaller than 5 mm [23]. Malignant lesions with central necrosis often show high ADC values in the area of necrosis [24, 25] and the rim of the lesion may be too thin for correct ROI placement. Non focal mass lesions as often seen in DCIS may not be categorized correctly with DWI even with a small ROI due to diffuse tumor spread and partial volume effects [15]. Carcinoma with very high signal intensities in T2-weighted images – like mucinous tumors – could result in misleading ADC values due to different tumor cell packing compared to classic intraductal breast cancer [26]. Despite these limitations DWI of the breast provides additional information to characterize focal breast lesions in a fast and easy way and will hopefully help to reduce invasive procedures.

*Some of the concepts and information presented in this paper are based on research and are not commercially available in the U.S.

Conclusion

DW MRI of the breast with EPI fs and EPI STIR sequences has a high potential to differentiate between benign and malignant breast lesions. Due to significantly better lesion delineation, better selectivity and shorter acquisition time the DW EPI fs sequence is superior.



The authors: Dr. Evelyn Wenkel M.D. (left) and Dr. Rolf Janka, M.D. (right) from the University Hospital Erlangen, Radiology, Erlangen, Germany.

References

1 Macura KJ, Ouwerkerk R, Jacobs MA, et al. Patterns of enhancement on breast MR images: interpretation and imaging pitfalls. Radiographics 2006; 26:1719-1734; quiz 1719.
2 Schnall MD, Blume J, Bluemke DA, et al. Diagnostic architectural and dynamic features at breast MR imaging: multicenter study. Radiology 2006; 238:42-53.
3 Szabo BK, Aspelin P, Wiberg MK, et al. Dynamic MR imaging of the breast. Analysis of kinetic and morphologic diagnostic criteria. Acta Radiol 2003; 44:379-386.
4 Bluemke DA, Gatsonis CA, Chen MH, et al. Magnetic resonance imaging of the breast prior to biopsy. Jama 2004; 292:2735-2742.
5 Wiener JI, Schilling KJ, Adami C, et al. Assessment of suspected breast cancer by MRI: a prospective clinical trial using a combined kinetic and morphologic analysis. AJR Am J Roentgenol 2005; 184:878-886.
6 Bedrosian I, Mick R, Orel SG, et al. Changes in the surgical management of patients with breast carcinoma based on preoperative magnetic resonance imaging. Cancer 2003; 98:468-473.
7 Heywang-Kobrunner SH, Bick U, Bradley WG, Jr., et al. International investigation of breast MRI: results of a multicentre study (11 sites) concerning diagnostic parameters for contrast-enhanced MRI based on 519 histopathologically correlated lesions. Eur Radiol 2001; 11:531-546.
8 Kaiser WA. [Magnetic resonance tomography of the breast. The results of 253 examinations]. Dtsch Med Wochenschr 1989; 114:1351-1357.
9 Kinkel K, Helbich TH, Esserman LJ, et al. Dynamic high-spatial-resolution MR imaging of suspicious breast lesions: diagnostic criteria and interobserver variability. AJR Am J Roentgenol 2000; 175:35-43.
10 Kuhl CK, Mielcareck P, Klaschik S, et al. Dynamic breast MR imaging: are signal intensity time course data useful for differential diagnosis of enhancing lesions? Radiology 1999; 211:101-110.
11 Fischer U, Kopka L and Grabbe E. Breast carcinoma: effect of preoperative contrast-enhanced MR imaging on the therapeutic approach. Radiology 1999; 213:881-888.
12. Sinha S, Lucas-Quesada FA, Sinha U, et al. In vivo diffusion-weighted MRI of the breast: potential for lesion characterization. J Magn Reson Imaging 2002; 15:693-704.
13 Guo Y, Cai YQ, Cai ZL, et al. Differentiation of clinically benign and malignant breast lesions using diffusion-weighted imaging. J Magn Reson Imaging 2002; 16:172-178.
14 Rubesova E, Grell AS, De Maertelaer V, et al. Quantitative diffusion imaging in breast cancer: a clinical prospective study. J Magn Reson Imaging 2006; 24:319-324.
15 Woodhams R, Matsunaga K, Iwabuchi K, et al. Diffusion-weighted imaging of malignant breast tumors: the usefulness of apparent diffusion coefficient (ADC) value and ADC map for the detection of malignant breast tumors and evaluation of cancer extension. J Comput Assist Tomogr 2005; 29:644-649.
16 Kuroki Y, Nasu K, Kuroki S, et al. Diffusion-weighted imaging of breast cancer with the sensitivity encoding technique: analysis of the apparent diffusion coefficient value. Magn Reson Med Sci 2004; 3:79-85.
17 Wenkel E, Geppert C, Schulz-Wendtland R, et al. Diffusion weighted imaging in breast MRI comparison of two different pulse sequences. Acad Radiol 2007; 14:1077-1083.
18 Pisano ED, Gatsonis C, Hendrick E, et al. Diagnostic performance of digital versus film mammography for breast-cancer screening. N Engl J Med 2005; 353:1773-1783.
19 Schulz-Wendtland R, Bock K, Aichinger U, et al. [Ultrasound examination of the breast with 7.5 MHz and 13 MHz-transducers: scope for improving diagnostic accuracy in complementary breast diagnostics?]. Ultraschall Med 2005; 26:209-215.
20 Bartella L, Liberman L, Morris EA, et al. Nonpalpable mammographically occult invasive breast cancers detected by MRI. AJR Am J Roentgenol 2006; 186:865-870.
21 Kuhl CK, Klaschik S, Mielcarek P, et al. Do T2 weighted pulse sequences help with the differential diagnosis of enhancing lesions in dynamic breast MRI? J Magn Reson Imaging 1999; 9:187-196.
22 Nunes LW, Schnall MD and Orel SG. Update of breast MR imaging architectural interpretation model. Radiology 2001; 219:484-494.
23 Liberman L, Mason G, Morris EA, et al. Does size matter? Positive predictive value of MRI-detected breast lesions as a function of lesion size. AJR Am J Roentgenol 2006; 186:426-430.
24 Chang SC, Lai PH, Chen WL, et al. Diffusion-weighted MRI features of brain abscess and cystic or necrotic brain tumors: comparison with conventional MRI. Clin Imaging 2002; 26:227-236.
25 Dorenbeck U, Butz B, Schlaier J, et al. Diffusion-weighted echo-planar MRI of the brain with calculated ADCs: a useful tool in the differential diagnosis of tumor necrosis from abscess? J Neuroimaging 2003; 13:330-338.
26 Kawashima M, Tamaki Y, Nonaka T, et al. MR imaging of mucinous carcinoma of the breast. AJR Am J Roentgenol 2002; 179:179-183.

Potential Role of Multi b Factor Diffusion-Weighted Imaging of the Breast*

Mitsuhiro Tozaki, M.D.[1], Katsuya Maruyama[2]

[1]*Breast Center, Kameda Medical Center, Chiba, Japan*
[2]*Siemens-Asahi Medical Technologies LTD., Tokyo, Japan*

Introduction

Diffusion-weighted imaging (DWI) is characterized by extremely high contrast resolution, and it has been applied to diagnose early-stage cerebral infarction. When used to image the body, however, strong artifacts are created by the non-uniformity of the magnetic field. Recent development of MR technology has nearly overcome this obstacle and enabled the clinical application of diffusion-weighted imaging. DWI has shown great promise in the detection of any tumor type throughout the entire body.

Regarding breast DWI, the potential role of apparent diffusion coefficient (ADC) value in characterizing breast lesions has been reported. In the preliminary results, the ADC value may be an effective parameter in distinguishing between benign and malignant breast lesions because tumor cellularity has a significant influence on the ADC values. On the other hand, the VIBE (volumetric interpolated breathhold examination) sequence with iPAT (integrated parallel acquisition techniques), which allows high-spatial-resolution images with isotropic voxels to be obtained, improves the quality of breast MR examinations dramatically (Table and Figs. 1–3). Following this development, it is debatable whether DWI of the breast is useful or not in routine clinical MR examinations.

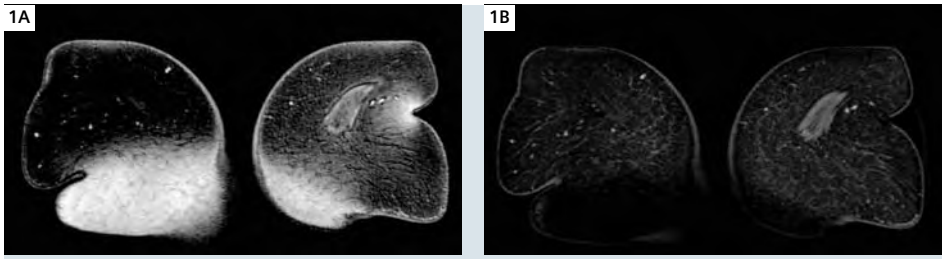

1 Breast measurements with the VIBE sequence and Fat Sat using CHESS **(A)** and SPAIR **(B)**. SPAIR utilizes adiabatic fat suppression pulses which have also been optimized with respect to their frequency selective profile. Thus the sensitivity to B1-inhomogeneities is reduced.

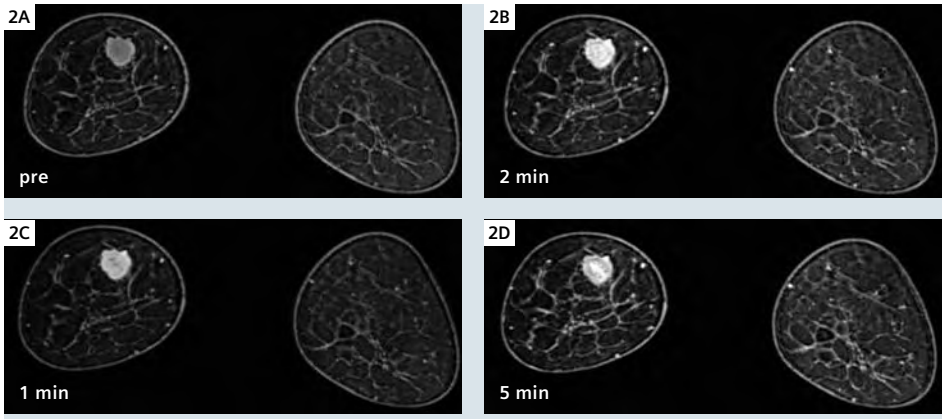

2 Dynamic protocol using VIBE with iPAT: High resolution 3D dynamic acquisitions with fat saturation (SPAIR) using a PAT factor of 2. Both breasts were examined in the coronal plane on the first, second, and fifth-phase dynamic images.

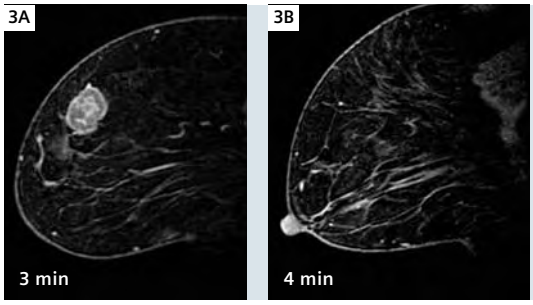

3 High resolution imaging using VIBE without iPAT in the same patient as Fig. 2: Bilateral breasts were sagittally examined on images obtained in the third **(A)** and fourth phases **(B)**. **(A)** Right breast. **(B)** Left breast.

The impact of DWI

Tumor detection

Unfortunately, there was no evidence that sensitivity and accuracy of breast cancer detection by DWI are higher than

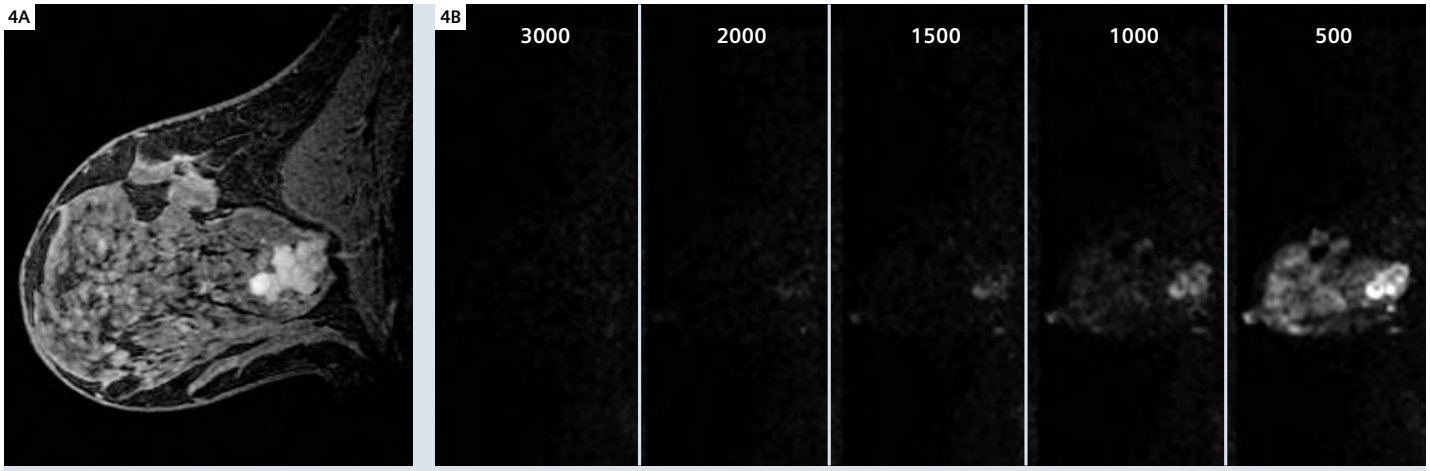

4 Sagittal MPR images of diffusion-weighted imaging, showing a fibroadenoma. This benign tumor appears hyperintense on b 500–1500 images.

that by standard contrast-enhanced MRI. In fact, it is insufficient to detect small breast cancer or ductal carcinoma in situ (DCIS). Tumor angiogenesis and increasing cellularity are developed simultaneously in breast cancer. However, the detection of the presence of angiogenesis by perfusion MR imaging using Gd-DTPA contrast agent is more sensitive than that of the degree of increasing cellularity by DWI. In these circumstances, screening MRI without the use of contrast agent has come up for discussion in Japan. Breast cancer is the leading cause of cancer deaths among Japanese women, and among this group it tends to occur in the late forties. Because the limitations of X-ray mammography are well known in dense breast tissue, screening for breast cancer with ultrasound has just started in Japan. One of the current problems of screening ultrasound is that too many benign hypoechoic nodules are depicted. In our hospital, the clinical usefulness of non-contrast MRI that combines DWI and T1-, T2-weighted imaging has been investigated prospectively for the patients with equivocal or suspicious findings on screening ultrasound.

Differential analysis: multi b factor DWI
Regarding the differentiation between benign and malignant lesions, the ADC value may be an effective parameter. Up to the present, only the diagnostic cut-off value of ADC has been evaluated and discussed. However, there is the overlap in ADC values. We try to make categorization using multi b factor DWI. In the differen-

Table 1: Protocols

	sequence	orientation	voxel size	TA	TE	TR
localizer	gre	3 orientation	2.1x1.6x6mm	0:35	4,22	9,2
t1_fl3d_cor_in-phase_FS(-)	fl3d_vibe	coronal	1x1x3mm	0:52	4,76	8
t2_tse_sag_R_fs_SPAIR	tse_rst_ire	sag (right)	0.6x0.6x3mm	1:18	97	4780
t2_tse_sag_L_fs_SPAIR	tse_rst_ire	sag (left)	0.6x0.6x3mm	1:18	97	4780
DWI_ep2d_cor_fs_SPAIR	ep2d_diff_pace	coronal	3x3x3mm	2:24	96	8000
Dyn_t1_fl3d_vibe_cor_fs_SPAIR	fl3d_vibe	coronal	1x0.7x0.9mm	1:00 x 3	2,29	5,23
t1_fl3d_vibe_sag_R_fs_SPAIR	fl3d_vibe	sag (right)	0.6x0.6x1.2mm	1:00	2,22	4:04
t1_fl3d_vibe_sag_L_fs_SPAIR	fl3d_vibe	sag (left)	0.6x0.6x1.2mm	1:00	2,22	4:04
Delay_t1_fl3d_vibe_cor_SPAIR	fl3d_vibe	coronal	1x0.7x0.9mm	1:00	2,29	5,23
svs_se_ub2_270_breast	svs_se_ub2	transversal	15x15x15mm	7:01	270	1620

tial diagnosis of breast lesions, categorization of the lesions, such as ACR-BI-RADS and scoring system (Göttingen score, Jena score, and MARIBS (Magnetic Resonance Imaging in Breast Screening)), is essential. In our hospital we perform categorization visually based on multi-b-factor DWI, always applying the same window level and width (Figs. 4, 5).

Monitoring the therapeutic response

After one or two cycles of chemotherapy there are substantial changes in the contrast enhancement pattern, which are observed even before measurable changes of the tumor size occur. However, contrast enhancement patterns may lead to misleading findings and false-negative results due to the effects of chemotherapeutic agents. In contrast, DWI and ^{1}H MR spectroscopy show great promise in the observation of the direct effects of chemotherapeutic agents. ^{1}H MR spectroscopy is a promising molecular-based method, although the chemotherapeutic changes can be observed within a limited region (single voxel) that, in advanced cases, may be smaller than the breast cancer itself. We believed that DWI has additional information in monitoring the therapeutic response of locally advanced breast can-

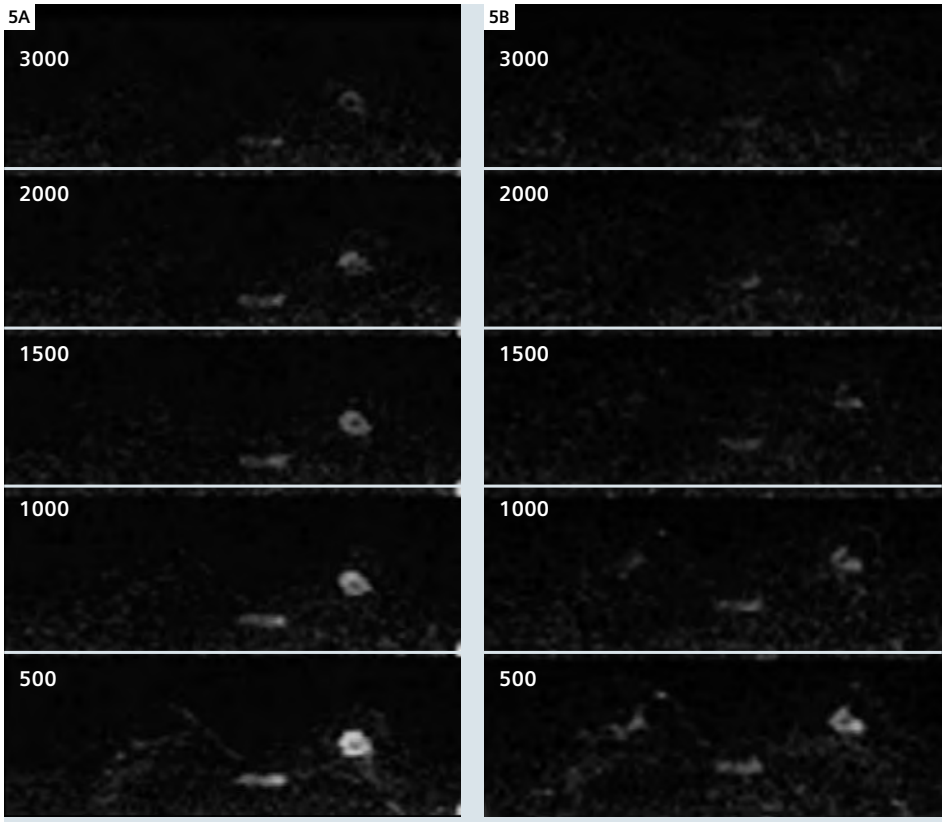

5 Transeverse MPR images of diffusion-weighted imaging, showing a breast cancer in the left breast. DWI before **(A)** and after **(B)** chemotherapy. Signal intensity and size of the tumor are reduced after chemotherapy.

FA	FoV read	FoV phase	slice thickness (mm)	matrix (base resolution)	matrix (phase resolution)	iPAT (Acce)	Fat Sat	band width
20	400	100	6	256	75%	off	off	230
25	330	100	3	320	100%	GRAPPA (2)	off	320
150(refo)	160	100	3	256	100%	off	SPAIR	300
150(refo)	160	100	3	256	100%	off	SPAIR	300
3scan-trace	330	100	3	110	100%	GRAPPA (2)	SPAIR	1684*
12	330	100	0,9	448	71%	GRAPPA (2)	SPAIR	430**
15	160	100	1,2	256	100%	off	SPAIR	390
15	160	100	1,2	256	100%	off	SPAIR	390
12	330	100	0,9	448	71%	GRAPPA (2)	SPAIR	430
90							spectral suppresion	1000

*b1=500,b2=1000,b3=1500,b4=2000,b5=3000; **pre+ 2 measurements

cer patients (Fig. 5). In addition, diffusion-weighted images are thought to be a useful guide for placing a volume of interest (VOI) within a breast tumor in order to measure the 1H MR spectrum.
There is, however, a pitfall in the use of ADC values. Figure 6 shows a patient with breast cancer before and after neoadjuvant chemotherapy. Before chemotherapy, cancer was visible on b 3000 images and had a low ADC value (0.69 x 10^{-3} mm^2/s). After chemotherapy, the cancer decreased in size as observed on both contrast-enhanced MRI and DWI. The lesion was visible on b 2000 images and had an ADC value (0.64 x 10^{-3} mm^2/s) similar to the pre-therapy value. Despite the decrease in tumor size due to the chemotherapeutic effect, cellularity changes within the lesion were of variable degree (Fig. 6). In short, decreasing cellularity of breast cancer has occurred inhomogeneously within the tumor and may be independent useful information, compared with morphology and vascular permeability.

Conclusion

It is debatable whether DWI of the breast is useful or not in the clinical MR examinations. However, DWI is the only sequence able to visualize breast cancers with a high rate on non- or pre-contrast enhanced MRI. We should continuously evaluate the potential role and limitations of this Cellularity-weighted Imaging. Further investigation and prospective study incorporating the visual assessment of multi b factor DWI is necessary.

*Some of the concepts and information presented in this paper are based on research and are not commercially available in the U.S.

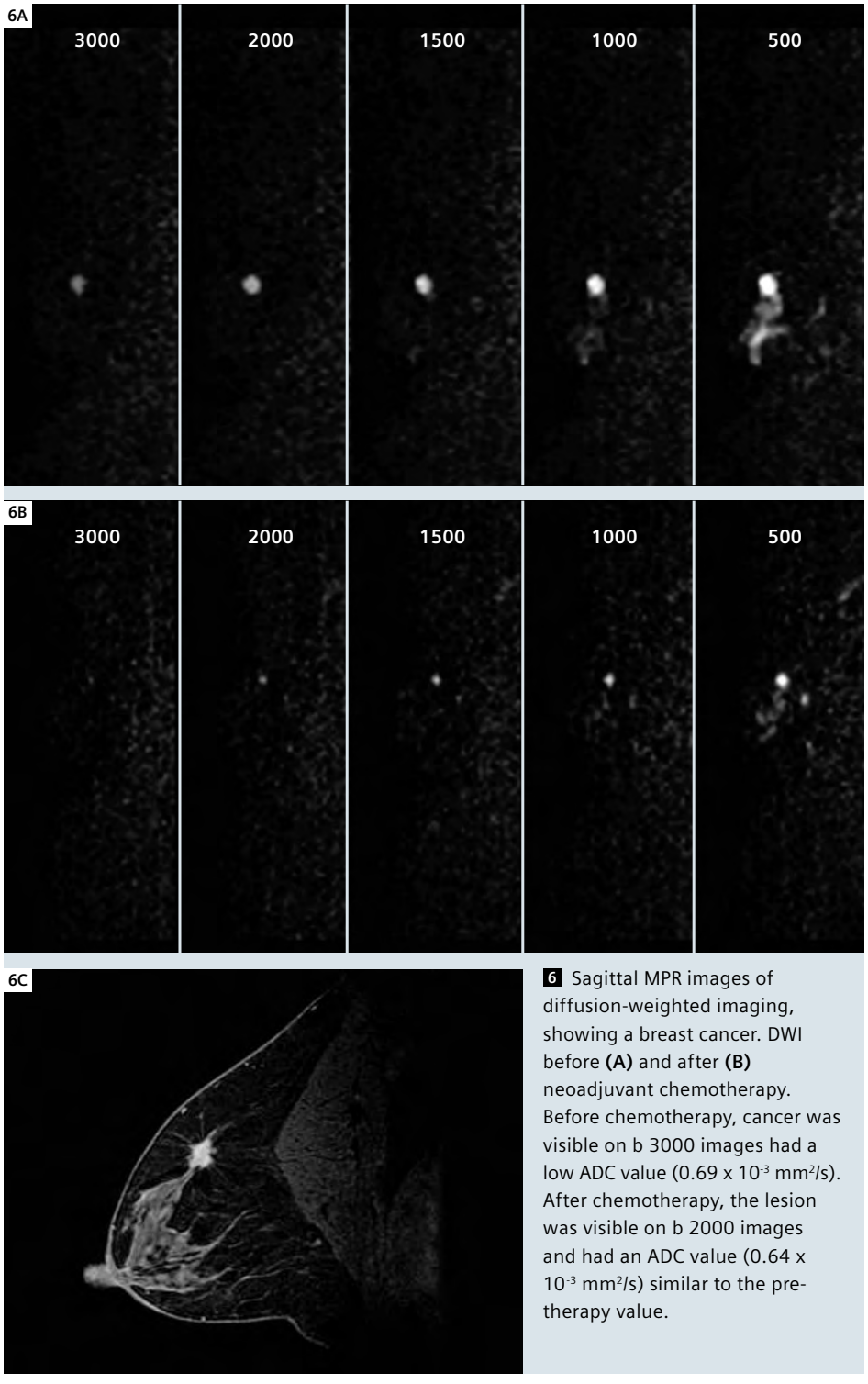

6 Sagittal MPR images of diffusion-weighted imaging, showing a breast cancer. DWI before **(A)** and after **(B)** neoadjuvant chemotherapy. Before chemotherapy, cancer was visible on b 3000 images had a low ADC value (0.69 x 10^{-3} mm^2/s). After chemotherapy, the lesion was visible on b 2000 images and had an ADC value (0.64 x 10^{-3} mm^2/s) similar to the pre-therapy value.

Arterial Spin Labeled Perfusion MRI

John A. Detre, M.D.

Center for Functional Neuroimaging, Department of Neurology and Radiology, University of Pennsylvania, Philadelphia, PA, USA

Perfusion refers to the delivery of oxygen and nutrients to tissues by means of blood flow and is one of the most fundamental physiological parameters. Disorders of perfusion also account for most of the leading causes of medical disability and mortality. While measurements of perfusion are of direct diagnostic value in vascular disorders, perfusion measurements also serve as biomarkers for a broader range of physiological and pathophysiological functions. A close coupling between cerebral blood flow and metabolism allows regional brain function to be assessed through measurements of cerebral perfusion and increased vascularity of neoplasms allows tumor perfusion to be used as a measure of tumor grade and to monitor the response to tumor therapy.

Classical tissue perfusion is measured using a diffusible tracer that can exchange between the vascular compartment and tissue. This yields a perfusion measurement in units of milliliters of blood flow per gram of tissue per unit time (ml/g/min). However, owing to the relative ease of inferring hemodynamic function from the passage of an intravascular tracer, the term "perfusion imaging" has also been applied to measurements of perfusion-related parameters such as mean transit time and blood volume that can be related to perfusion through the Central Volume Principle. In the field of MRI, most people associate the concept of perfusion imaging with dynamic susceptibility contrast imaging using a relaxation contrast agent. However, there are also several methods for the measurement of classical tissue perfusion using MRI. Diffusible tracers that can be monitored with MRI include fluorinated halocarbons [1], deuterated water ($^{2}H2O$) [2, 3], ^{17}O-water [4], and potentially ^{13}C labeled hydrocarbons.

Magnetically labeled endogenous blood water can also be used as a tracer for perfusion MRI. To accomplish this, the longitudinal magnetization of arterial blood water must be manipulated so that it differs from the tissue magnetization. It is quite analogous to the use of 15O-water for PET perfusion imaging except that the magnetic tracer decays with T1 instead of a radioactive decay and the ASL

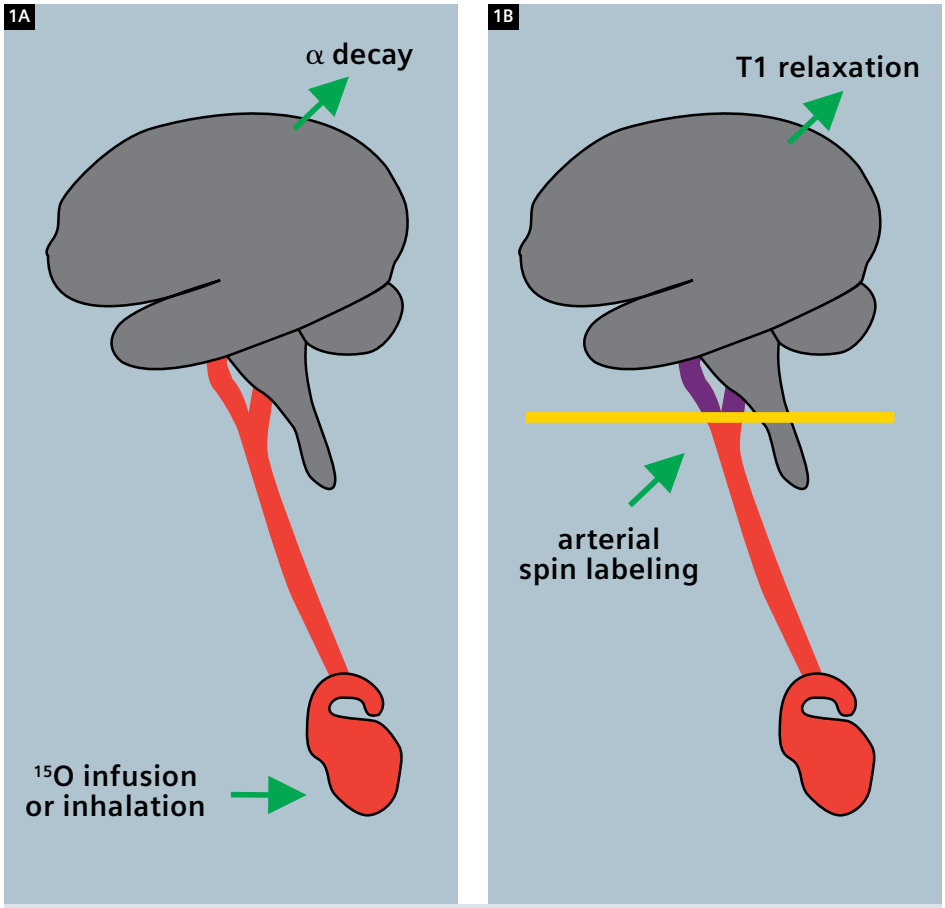

1 Concept of Arterial Spin Labeling (ASL), comparing 15O-PET (Fig. 1A)) and ASL (Fig. 1B) approaches. In ASL, endogenous arterial blood water is magnetically labeled instead of exogenously administered tracer, and the magnetic label decays with T1 instead of radioactive decay (α).

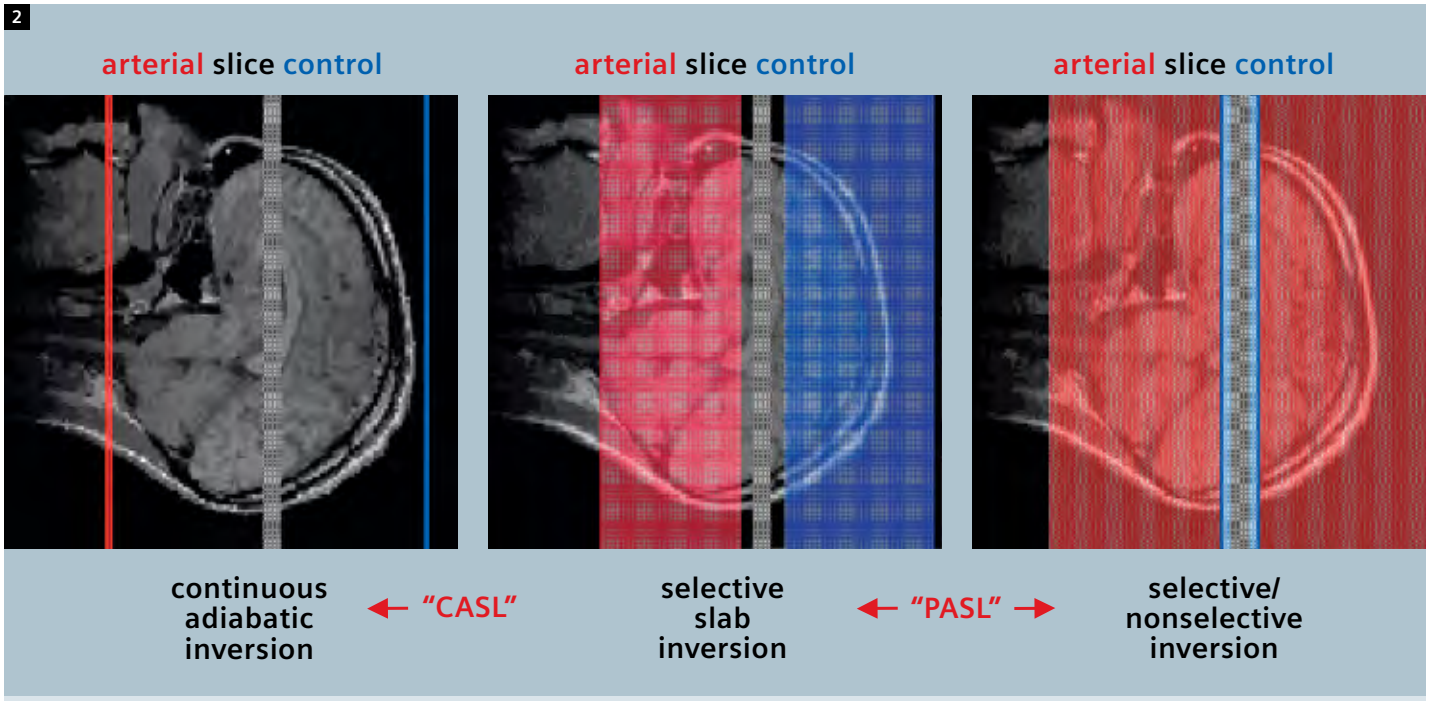

2 Schematic diagram illustrating arterial spin labeling strategies. Continuous ASL (CASL, left) labels arterial spins as they flow through a labeling plane. Pulsed ASL (PASL, middle and right) labels arterial spins using a spatially selective labeling pulse. Applications to single-slice imaging are illustrated for simplicity. Somewhat more complex schemes are used for multislice imaging.

approach is completely noninvasive. Because T1 relaxation is approximately 100 times faster than the radioactive decay rate of 15O, only a small amount of labeled water accumulates, though the temporal resolution is also correspondingly higher. The subtle difference between images acquired with and without arterial spin labeling (ASL) can be modeled to derive a calculated blood flow image showing perfusion in ml/g/min at each voxel. Key parameters required for ASL quantification include knowledge or assumptions about the T1 values in blood and tissue, the labeling efficiency, and the arterial transit time [5, 6]. ASL can be combined with any imaging sequence and theoretically provides a flow image that is completely independent of scanning parameters; As such, it represents one of the few MRI contrast mechanisms for which the physiological basis is really well understood. In practice, most ASL measurements are made with some compromises trading off sensitivity and convenience for a less pure measurement of tissue blood flow.

Arterial spin labeling can be accomplished using a variety of approaches and in nearly any organ. Most ASL has been carried out in the brain because the arterial supply is extremely well defined and perfusion to brain tissue is high. However, ASL studies have also successfully been carried out in kidney, lung, retina, heart, and skeletal muscle. The most common ASL approaches use either pulsed labeling (PASL) with an instantaneous spatially selective saturation or inversion pulse [7], or continuous labeling (CASL), most typically by flow driven adiabatic fast passage [8]. In some PASL methods, a spatially selective inversion pulse is administered to the tissue rather than to arterial blood [9]. More recently there have also been efforts label based on velocity rather than spatial selectivity for tissue arterial supply [10]. The first publication on ASL perfusion MRI actually used pseudocontinuous saturation to dephase arterial blood water in the neck of a rat [11]. Prior to that time, the idea of labeling arterial blood water had been considered primarily as a means for visualizing intraluminal flow in arteries and veins [12, 13]. Continuous labeling schemes allow brain magnetization to reach a steady-state that maximizes the signal difference between labeled and unlabeled conditions [14], though this occurs at the expense of both increased SAR deposition and magnetization transfer effects that complicate both the accurate measurement of the control (unlabeled) condition, and the extension to multislice imaging. Some groups have addressed this using a separate labeling coil [15], while others have pursued single coil approaches [16]. The myriad technical details of ASL implementation are beyond the scope of this article, but key advances have focused on improved labeling, improved measurements of the subtle effects of ASL on tissue signal, and improved modeling of measured signal changes in terms of tissue blood flow. For CBF, current tech-

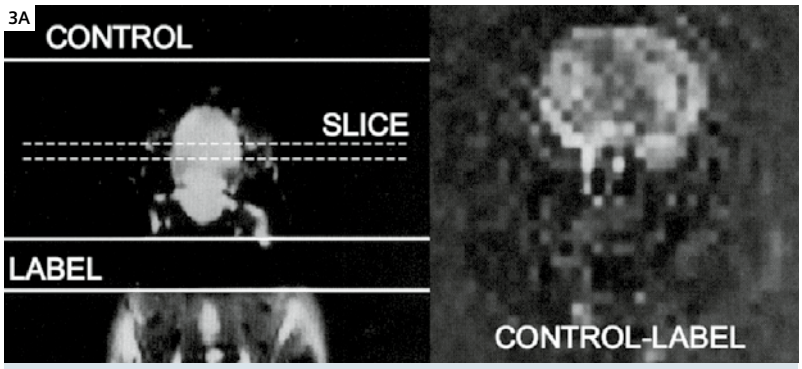

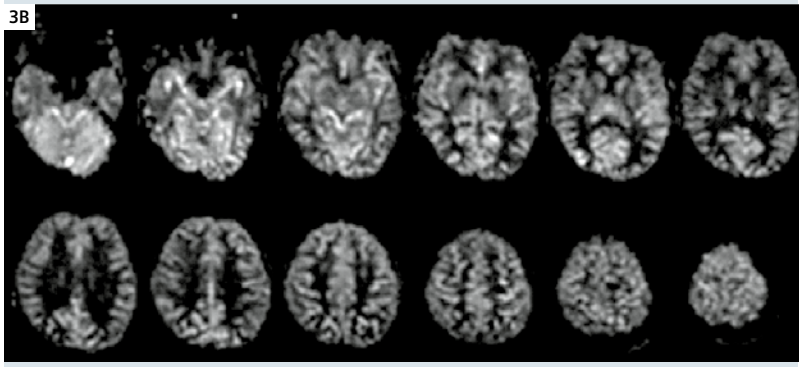

3 The original demonstration of ASL using pseudocontinuous ASL in the rat brain [11]. **(Fig. 3A)**
Multislice PASL of human brain acquired from a normal volunteer at 3T [18]. **(Fig. 3B)**

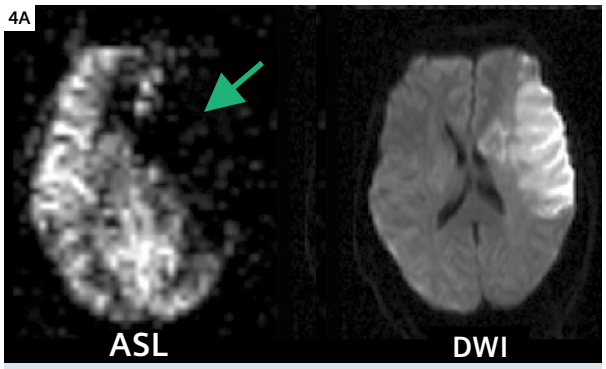

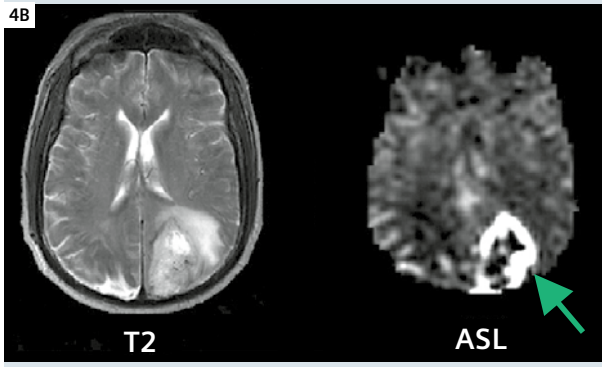

4 Representative clinical applications of ASL showing hypoperfusion in an acute stroke **(Fig. 4A)** and hyperperfusion in a glioblastoma **(Fig. 4B)**. For more details on clinical applications of ASL see [31].

nology provides a reasonably good whole-brain image in just a few minutes of scanning. ASL methods particularly benefit from high magnetic field trengths because not only is the sensitivity higher, but T1 also lengthens, allowing more label to accumulate [17, 18]. ASL methods also benefit from the increased sensitivity provided by multicoil receivers and are minimally degraded by parallel imaging [19]. The use of a body transmitter benefits PASL by allowing a larger region for arterial inversion but necessitates a more elaborate approach for CASL, termed pseudo-continuous labeling [20].

In clinical neuroscience, while the application of ASL perfusion MRI to the diagnosis and management of acute stroke is both obvious and feasible, the clinical utility of ASL is likely much broader since only a minority of acute stroke patients undergo MRI. ASL perfusion MRI could greatly enhance the evaluation of both TIA (Transient Ischemic Attack) and chronic cerebrovascular disease by quantifying regional CBF in specific vascular territories where interventions may be planned, or by allowing the effects of pharmacological therapies on CBF to be evaluated. Several approaches now also exist for selective arterial labeling, allowing the perfusion distribution of specific arteries to be assessed independently [21, 22]. A challenge in the application of ASL to cerebrovascular disorders is that sensitivity decreases in regions with very low CBF and the presence of prolonged arterial transit times that can create regions of apparent hyperperfusion when labeled spins remain in large vessels due to prolonged arterial transit times. This artifact is usually easy to recognize and can be verified by the addition of spoiler gradients that dephase coherently flowing spins. Arterial transit times can even be quantified by comparing ASL images with and without spoiler gradients [23], providing access to a novel physiological parameter that likely reflects the recruitment collateral flow sources. Another significant application of ASL is in degenerative diseases, where specific patterns of hypoperfusion may be used to aid in differential diagnosis of disorders such as Alzheimer's disease [24] and frontotemporal dementia [25]. Finally, as noted above, perfusion of brain tumors typically correlates with their grade and potentially their response to therapies [26]. Undoubtedly, the clinical availability of noninvasive and quantitative CBF imaging will lead to numerous additional applications as further experience with this modality develops.

In basic neuroscience, ASL perfusion MRI can be used to localize task activation in a manner similar to BOLD fMRI (Blood Oxygen Level Dependent functional MR Imaging). Indeed, ASL based contrast derived from inversion recovery imaging of task activation was included in one of the earliest reports of fMRI in human brain [28]. Although relative CBF can be inferred from ASL images acquired without control labeling, acquisition of both labeled and control pairs are required for quantification of CBF. While this reduces the temporal resolution of ASL perfusion fMRI as compared to BOLD fMRI, it also

dramatically changes the noise properties of the data, providing sensitivity over much longer timescales [29]. ASL perfusion fMRI can also be used as a measure of brain function at rest, independent of any sensorimotor or cognitive task, and reveals regional changes in brain function associated with development [30], behavioral states [31], or genetic traits [32]. Because ASL measures a purely biological parameter, it should also be particularly valuable for multisite studies examining brain function on a variety of scanner platforms or longitudinally.

A limitation in the widespread use and dissemination of ASL perfusion MRI has been the absence of product sequences provided by vendors. The recent development of an ASL product by Siemens should help alleviate this limitation, at least for Siemens users. Other vendors will hopefully follow suit. The Siemens ASL product provides a robust PASL sequence with echoplanar readout and online calculation of CBF maps from the acquired data. Many of us involved in the early development and validation of ASL perfusion MRI are eager to see it translated to routine clinical use.

Dr. Detre is an inventor of ASL technology and has received royalties from the University of Pennsylvania for its licensure.

References

1 Eleff, S.M., M.D. Schnall, L. Ligetti, M. Osbakken, V.H. Subramanian, B. Chance and J.S.J. Leigh, Concurrent measurement of cerebral blood flow, sodium, lactate, and high-energy phosphate metabolism using 19F, 23Na, 1H, and 31P nuclear magnetic resonance spectroscopy. Magn. Reson. Med., 1988. 7: p. 412-24.
2 Ackerman, J.J., C.S. Ewy, N.N. Becker and R.A. Shalwitz, Deuterium nuclear magnetic resonance measurements of blood flow and tissue perfusion employing 2H2O as a freely diffusible tracer. Proc Natl Acad Sci U S A, 1987. 84(12): p. 4099-102.
3 Detre, J.A., V.H. Subramanian, M.D. Mitchell, D.S. Smith, A. Kobayashi, A. Zaman and J.S. Leigh, Measurement of regional cerebral blood flow in cat brain using intracarotid 2H2O and 2H NMR imaging. Magn. Reson. Med., 1990. 14: p. 389-395.
4 Pekar, J., L. Ligeti, Z. Ruttner, R.C. Lyon, T.M. Sinnwell, P. van Gelderen, D. Fiat, C.T. Moonen and A.C. McLaughlin, In vivo measurement of cerebral oxygen consumption and blood flow using 17O magnetic resonance imaging. Magn Reson Med, 1991. 21(2): p. 313-9.
5 Alsop, D.C. and J.A. Detre, Reduced transit-time sensitivity in noninvasive magnetic resonance imaging of human cerebral blood flow. J. Cereb. Blood Flow Metab., 1996. 16: p. 1236-1249.
6 Buxton, R.B., L.R. Frank, E.C. Wong, B. Siewert, S. Warach and R.R. Edelman, A general kinetic model for quantitative perfusion imaging with arterial spin labeling. Magn Reson Med, 1998. 40(3): p. 383-96.
7 Wong, E.C., R.B. Buxton and L.R. Frank, Implementation of quantitative perfusion imaging techniques for functional brain mapping using pulsed arterial spin labeling. NMR Biomed, 1997. 10(4-5): p. 237-49.
8 Williams, D.S., J.A. Detre, J.S. Leigh and A.P. Koretsky, Magnetic resonance imaging of perfusion using spin inversion of arterial water. Proc. Natl. Acad. Sci. USA, 1992. 89: p. 212-216.
9 Kim, S.G., Quantification of relative cerebral blood flow change by flow-sensitive alternating inversion recovery (FAIR) technique: application to functional mapping. Magn. Reson. Med., 1995. 34: p. 293-301.
10 Wong, E.C., M. Cronin, W.C. Wu, B. Inglis, L.R. Frank and T.T. Liu, Velocity-selective arterial spin labeling. Magn Reson Med, 2006. 55(6): p. 1334-41.
11 Detre, J.A., J.S. Leigh, D.S. Williams and A.P. Koretsky, Perfusion imaging. Magn. Reson. Med., 1992. 23: p. 37-45.
12 Sardashti, M., D.G. Schwartzberg, G.P. Stomp and W.T. Dixon, Spin labeling angiography of the carotids by presaturation and simplified adiabatic inversion. Magn. Reson. Med., 1990. 15: p. 192-200.
13 Singer, J.R. and L.E. Crooks, Nuclear magnetic resonance blood flow measurements in the human brain. Science, 1983. 221(4611): p. 654-6.
14 Wong, E.C., R.B. Buxton and L.R. Frank, A theoretical and experimental comparison of continuous and pulsed arterial spin labeling techniques for quantitative perfusion imaging. Magn Reson Med, 1998. 40(3): p. 348-55.
15 Zaharchuk, G., P.J. Ledden, K.K. Kwong, T.G. Reese, B.R. Rosen and L.L. Wald, Multislice perfusion and perfusion territory imaging in humans with separate label and image coils. Magn. Reson. Med., 1999. 41: p. 1093-8.
16 Alsop, D.C. and J.A. Detre, Multisection cerebral blood flow MR imaging with continuous arterial spin labeling. Radiology, 1998. 208: p. 410-16.
17 Wang, J., D.C. Alsop, L. Li, J. Listerud, J.B. Gonzalez-At, M.D. Schnall and J.A. Detre, Comparison of quantitative perfusion imaging using arterial spin labeling at 1.5 and 4.0 Tesla. Magn Reson Med, 2002. 48(2): p. 242-54.
18 Wang, J., Y. Zhang, R.L. Wolf, A.C. Roc, D.C. Alsop and J.A. Detre, Amplitude-modulated Continuous Arterial Spin-labeling 3.0-T Perfusion MR Imaging with a Single Coil: Feasibility Study. Radiology, 2005. 235: p. 218-28.
19 Wang, Z., J. Wang, T.J. Connick, G.S. Wetmore and J.A. Detre, Continuous ASL perfusion MRI with an array coil and parallel imaging at 3T. Magn Reson Med, 2005. 54(3): p. 732-7.
20 Garcia, D.M., C. de Bazelaire and D. Alsop, Pseudo-continuous Flow Driven Adiabatic Inversion for Arterial Spin Labeling. ISMRM 13th Scientific Meeting Proceedings, 2005: p. 37.
21 Hendrikse, J., J. van der Grond, H. Lu, P.C. van Zijl and X. Golay, Flow territory mapping of the cerebral arteries with regional perfusion MRI. Stroke, 2004. 35(4): p. 882-7.
22 Werner, R., K. Alfke, T. Schaeffter, A. Nabavi, H.M. Mehdorn and O. Jansen, Brain perfusion territory imaging applying oblique-plane arterial spin labeling with a standard send/receive head coil. Magn Reson Med, 2004. 52(6): p. 1443-7.
23 Wang, J., D.C. Alsop, H.K. Song, J.A. Maldjian, K. Tang, A.E. Salvucci and J.A. Detre, Arterial transit time imaging with flow encoding arterial spin tagging (FEAST). Magn Reson Med, 2003. 50(3): p. 599-607.
24 Alsop, D.C., J.A. Detre and M. Grossman, Assessment of cerebral blood flow in Alzheimer's disease by spin-labeled magnetic resonance imaging. Ann Neurol, 2000. 47(1): p. 93-100.
25 Du, A.T., G.H. Jahng, S. Hayasaka, J.H. Kramer, H.J. Rosen, M.L. Gorno-Tempini, K.P. Rankin, B.L. Miller, M.W. Weiner and N. Schuff, Hypoperfusion in frontotemporal dementia and Alzheimer disease by arterial spin labeling MRI. Neurology, 2006. 67(7): p. 1215-20.
26 Wolf, R.L., J. Wang, S. Wang, E.R. Melhem, M. O'Rourke D, K.D. Judy and J.A. Detre, Grading of CNS neoplasms using continuous arterial spin labeled perfusion MR imaging at 3 Tesla. J Magn Reson Imaging, 2005. 22(4): p. 475-482.
27 Wolf, R.L. and J.A. Detre, Clinical neuroimaging using arterial spin-labeled perfusion magnetic resonance imaging. Neurotherapeutics, 2007. 4(3): p. 346-59.
28 Kwong, K.K., J.W. Belliveau, D.A. Chesler, I.E. Goldberg, R.M. Weisskoff, B.P. Poncelet, D.N. Kennedy, B.E. Hoppel, M.S. Cohen and R. Turner, Dynamic magnetic resonance imaging of human brain activity during primary sensory stimulation. Proc. Natl. Acad. Sci. USA, 1992. 89: p. 5675-5679.
29 Aguirre, G.K., J.A. Detre and D.C. Alsop, Experimental design and the relative sensitivity of BOLD and perfusion fMRI. Neuroimage, 2002. 15: p. 488-500.
30 Wang, Z., M. Fernandez-Seara, D.C. Alsop, W.C. Liu, J.F. Flax, A.A. Benasich and J.A. Detre, Assessment of functional development in normal infant brain using arterial spin labeled perfusion MRI. Neuroimage, 2008. 39(3): p. 973-8.
31 Wang, J., H. Rao, G.S. Wetmore, P.M. Furlan, M. Korczykowski, D.F. Dinges and J.A. Detre, Perfusion functional MRI reveals cerebral blood flow pattern under psychological stress. Proc Natl Acad Sci U S A, 2005. 102(49): p. 17804-9.
32 Rao, H., S.J. Gillihan, J. Wang, M. Korczykowski, G.M. Sankoorikal, K.A. Kaercher, E.S. Brodkin, J.A. Detre and M.J. Farah, Genetic variation in serotonin transporter alters resting brain function in healthy individuals. Biol Psychiatry, 2007. 62(6): p. 600-6.

Highly Parallel Detection for MRI

Lawrence L. Wald[1, 2]; Graham Wiggins[1]

[1]Athinoula A. Martinos Center for Biomedical Imaging, Department of Radiology, Massachusetts General Hospital and Harvard Medical School, Boston, MA, USA
[2]Harvard-MIT Division of Health Sciences and Technology, Cambridge, MA, USA

Introduction

Over the past two decades, phased array detection of the MR signal has benefited from a focused and sustained engineering effort. From the introduction of the first local coils on the MAGENTOM platform in 1983, the advantages of surface coil detection could be seen. The inception of array technology in the early 1990's, where a few coils were used to extend surface coil coverage and sensitivity, clearly demonstrated the power of extending the surface coil concept with arrays. The important clinical benefit of being able to match the reception strategy to individual clinical targets was not achieved until the introduction of the Integrated Panoramic Array (IPA) on the MAGNETOM Symphony in 1997. Here, the user controls the selection of the array elements from a larger array placed on the patient. While a seemingly simple and obvious extension in flexibility, the engineering challenge of seamlessly integrating the IPA methodology is belied by its continued lack of repetition within the industry.

The final step in extending array technology came from the recognition that optimal linear combinations of the coil elements could preserve much of the sensitivity and iPAT (integrated Parallel Acquisition Technique) capability of a larger array and provide a tradeoff between signal homogeneity, sensitivity and iPAT performance. Thus, while preserving the flexibility of the IPA concept, Tim (Total imaging matrix) significantly extended performance, leading to today's state-of-the-art in array technology where the practitioner has the ability to place over a hundred receive elements on the patient and combine them into up to 32 independent receive channels with a sophisticated mode-mixing matrix designed to optimize coverage, sensitivity and iPAT acceleration.

So, what is left to improve upon? Past success drives future development, and Tim technology has done much to fuel speculation about what the ultimate limits of array detection technology are for sensitivity and iPAT capability. In this article we examine theoretical limitations in parallel imaging technology: the so-called "ultimate SNR (signal-to-noise ratio)" and "ultimate g-factor (geometry-factor)", a measure for coil efficiency regarding its iPAT performance. Finally, we try to identify future directions for parallel RF hardware based on the conclusion that there are still significant gains possible. In particular, we wish to explore how parallel imaging technology might benefit if the coil designer was unconstrained by the number of RF channels available on the instrument. Toward this goal, the introduction of a prototype MAGNETOM Trio, A Tim System with 128 independent receive channels has given us the opportunity to move beyond theory and try to realize the potential benefits of highly parallel array detection.

> "While preserving the flexibility of the IPA concept, Tim significantly extended performance."

In these "highly parallel detectors", the role of the image encoding is no less important than the role of signal detection. While we continue to think of the gradient coil as the principal "encoder" of the MR image, this view is becoming outdated. With iPAT squared (iPAT^2) methodology – iPAT in 2 dimensions, acceleration rates above 10-fold can be achieved with Tim technology. Thus, the gradients account for as little as 10% of the encoding; the rest of the burden being placed on the receive array. In this scenario, the role of the MR detector array begins to more resemble the electroencephalography (EEG) or magnetoencephalography (MEG) detector. In these devices all of the spatial information is derived from the detector geometry. Although there appears to be limits on the ability of the array to encode spatial information distant from the coils, the MEG/EEG case can serve to educate us on the extraction of useful spatial information when faced with an ill-conditioned inverse problem. We are only beginning to explore the potential of these methods much less the hardware needs of this unusual regime.

Basic signal and noise considerations

A principal design goal is to inductively tightly-couple the receive coil to the pre-

cessing nuclear magnetization. Because the spins in the body lie in an ionic bath (salt water), the coil is also tightly coupled to randomly fluctuating fields produced by ionic currents. The currents that happen to have frequencies within the bandwidth of the RF receiver appear as spatially uniform Gaussian distributed noise in the complex image. An equivalent picture is produced by a reciprocity argument. Here, the effectiveness of the receive coil is proportional to its efficiency as a transmit coil. The receive noise power is proportional to the power dissipated in the conductive tissue through eddy current damping (driving the ions with the electric field associated with the changing transmit field.) In either picture, the same basic rules of thumb arise. The more effective the receive coil is at detecting the spins, the more effective it will be at receiving the noise. Thus, once "body noise dominance" has been achieved, gains in SNR can only be achieved by limiting the volume of tissue contributing the noise. For example, the coil should only interact with tissue that is of interest; tissue outside of the imaging field of view (FoV) but within the region of coil sensitivity produces only unwanted noise. Arrays take advantage of this principle by their "divide and conquer" method, where each individual array element sees only a limited "noise" region.

Three related sensitivity figures of merit for the array coil are of interest:

a) the SNR as a function of position for un-accelerated scans,

b) a similar SNR map for accelerated scans and

c) the maximum acceleration achievable with an acceptable g-factor penalty. The g-factor penalty is the ratio of the unaccelerated to accelerated SNR corrected for the reduced scan time (which contributes a factor of the square root of the acceleration rate). General simulations of array coils are challenging since there are a near infinite number of design choices. Nevertheless, analyzing arrays of identical coil elements arranged to cover simple sample geometries (such as spherical or planar regions) can provide insight into more complicated variations. One particularly illuminating approach for understanding the future benefits of larger array configurations is to analyze how the SNR is affected by a larger and larger number of array elements covering the same area [1, 2]. Studies of this kind have analyzed planar [1] and spherical arrays [2].

"The quest for higher sensitivity and improved encoding acceleration both drive exploration of the logical expansion of the array approach: increasing the number of elements and reducing the size of the receive coils."

In the planar case [1], a square region was tiled with N = 1, 4, 16 and 64 square array elements in a 1x1, 2x2, 4x4 and 8x8 configuration. The coils were overlapped by the width of the conductor and were modeled as being 1 cm above an infinite half-space of lossy salt water (σ = 0.72 S/m). The coils were assumed to have no inductive coupling (e.g. from perfect preamplifier decoupling or decoupling networks) but the noise correlation from their shared view of the sample noise was calculated using a full-wave analysis. The SNR was then calculated as a function of depth from the center of the array. The SNR near the array was found to scale approximately with the number of array elements per side (i.e. with $\sqrt{}$ where N is the total element count). Thus, a 4-fold potential sensitivity gain can be expected for tissue near the array by moving from a modest number of array elements (N = 4) to a "large-N" array (N = 64). This gain is, however, lost for deeper tissue (depths approximately equal to the lateral size of the overall array). On the other hand, there is no depth at which an array of fewer elements outperforms the arrays with more elements. Thus large gains near the surface are potentially achievable at the cost of an added number of receive channels and a less homogeneous sensitivity profile. The reception inhomogeniety has become increasingly less problematic with the arrival of robust normalization algorithms, such as the Normalize and Prescan Normalize features on *syngo*.

In a separate modeling study, circular coils were uniformly distributed in both a gapped and overlapped configuration around a 22 cm diameter sphere of conductive dielectric material modeling biological tissue [2]. N = 8, 12, 16, 20, 26, 32 and 64 circular coils were tiled on the sphere. In addition to the noise from body loading, the coils were assigned a non-body noise level determined from typical copper and preamplifier noise contributions. In addition to modeling SNR for un-accelerated scans, this work modeled the additional g-factor penalty incurred in accelerated imaging and examined the SNR as a function of B_0 and compared the model results to that expected from the so-called "ultimate" SNR; the highest achievable SNR obtainable with an arbitrarily large array whose individual sensitivity basis set satisfying Maxwell's equations [3–5].

In the spherical case, the results were qualitatively similar to the planar case. The largest gains achieved by increasing the number of array elements (N) occurred near the coil elements. At a radius of

*Works in progress (WIP). The information about this product is preliminary. The product is under development and not commercially available in the U.S., and its future availability cannot be ensured.

9 cm in the 22 cm diameter sphere, the SNR of the unaccelerated image at 1.5T increased 3.5-fold when the number of loops was increased from 8 to 32. In this case, the dependence on N was observed to be closer to linear with N compared with the $\sqrt{}$ seen near the planar array. Like the planar case, however, the benefits were considerably smaller more distant from the array elements. At the center of the sphere the unaccelerated 1.5T SNR increased only ~5% with the 4-fold increase in N. At higher field strength, there was more room for improvement at the center of the object. At 7.5T for example, only a very small region in the center of the phantom was within 10% of the ultimate SNR levels for a 64-channel array [6].

Accelerated imaging showed even larger gains as coil elements were added, especially for high acceleration rates. For example at Rate = 3, the g-factor penalty was 1.4-fold larger for the 8-channel array compared to the 32-channel. At Rate = 4, this widened to a factor of 2. The final accelerated image benefits from both the intrinsic sensitivity improvements as well as the g-factor gains. An additional finding of this study was an improved SNR for the overlapping array configuration compared to the gapped configuration for the largest N coils for both unaccelerated and accelerated scans. For the smaller array, the gapped array was beneficial for accelerated scans; a result seen by other studies [7, 8].

"Ultimate" SNR of arrays

Several studies have examined the upper bound on sensitivity and spatial encoding capabilities of coil arrays. The concept of the "ultimate" SNR achievable by an RF coil was introduced by Ocali and Atalar [5]. An arbitrary coil sensitivity profile outside a sample was generated from a complete set of basis functions satisfying Maxwell's equations (either plane waves or spherical harmonics) and a linear combination was found that maximized the SNR at a given location in the sample. This work was expanded to include the SNR of accelerated imaging [3, 4]. The ultimate SNR for accelerated imaging is found by analyzing the performance of the complete basis set.

The first interesting conclusion of this analysis is that the sensitivity of MR detection is intrinsically limited. The significance of this for future array designs, of course, hinges on how close current array designs are to this theoretical ceiling. Comparing actual designs (such has the arrays of circular coils tiling a spherical phantom reviewed above), suggest that a 32-channel array is close to the theoretical limit at the center of the phantom [2]. Happily for the employment prospects of array designers, there is substantial room for improvement towards the periphery. At a radial location equal to 80% of the coil radius, there is still a factor of 7 to go before the theoretical limit is achieved [2].

The ultimate limitation of the ability of the array for spatial encoding (iPAT) is likely imposed by a fundamental smoothness to the coil sensitivity patterns in regions free of current sources. This fact of nature derives from Maxwell's equations. Both studies examining the ultimate acceleration limits point out a steep drop in the SNR for accelerations above about R = 4 or 5 [3, 4]. For example, after this rate, the g-factor penalty was seen to rise exponentially with acceleration rate for locations near the center of the spherical sample [3]. Both studies found that moving to higher B_0 field strength postponed the rapid deterioration of SNR for rates above 4x. As with the unaccelerated SNR, the situation improves as you move closer to the array elements. Here the proximity to the wires provides more rapidly varying spatial profiles. This proximity effect allowed the 64-element array of McDougall and Wright [9] to achieve credible images with an acceleration rates of 64-fold; considerably higher than the 4 to 5-fold limit suggested by the ultimate sensitivity analysis which focused on regions far from the array.

Highly parallel arrays in practice

Historical experience with array coils quickly showed that signal detection efficiency improved with even a modest number of surface coils and that the reception uniformity and reconstruction burden could be handled with simple post-processing algorithms such as the Normalize and Prescan Normalize feature. The use of surface coils was thus able to expand into the traditional role of volume coil structures. The quest for higher sensitivity and improved encoding acceleration both drive exploration of the logical expansion of the array approach: increasing the number of elements and reducing the size of the receive coils (to cover a fixed anatomical territory). With other manufacturer's likely to follow the Tim system's technology, at least in channel count, 32 receive channels is becoming the new standard, and multiple groups are developing torso / cardiac [10, 11], and brain [12] [13, 14] arrays for these instruments.

Although exploring arrays of N > 32 channels clearly risks hitting the limits identified by the studies of the ultimate sensitivity for MR, the theory suggests there is room for improvement and such important limitations must be extensively explored experimentally. We have therefore gone on to build such arrays explicitly to determine the potential capabilities and practical limitations of even larger-N arrays (96 and 128 channels). The overall picture of these two efforts has been to support the case that parallel imaging strategies can receive expanding benefits from these "large-N" arrays.

Close fitting brain arrays with 32 and 90 and 96 channels

Preliminary experience in highly parallel acquisition strategies using helmet shaped geometries of circular receive coils has concentrated on building and testing brain array prototypes for 1.5T, 3T, and 7T. Tests so far include 23 and 90-channel arrays for 1.5T [15] and 32 and 96-channel

arrays for 3T [12] and 32-channel arrays for 7T. All of the arrays were built onto a helmet shaped former that conforms closely to the head. The tiling strategy for the individual circular surface coils was based on the combination of hexagonal and pentagonal symmetry of the soccer ball or the Buckminister-Fullerene molecule. Coil elements are circular, receive-only loop coils.

Figure 2 shows sensitivity maps from the 32 and 96-channel brain arrays and compares them to the standard 12-channel coil. While the 32 and 96-channel arrays are matched in size, the 12-channel coil employs a larger shell, likely exchanging the ability to accommodate a wider variety of patients with sensitivity. The larger arrays show considerable gains in the cortex with much smaller gains in the center of the head. Nonetheless, the gains in the cortex are substantial, with nearly 10-fold increases in peripheral regions allowing the images of Figs. 3 and 4 which show brain MR images acquired with voxel volumes about 5-fold smaller than conventional acquisitions.

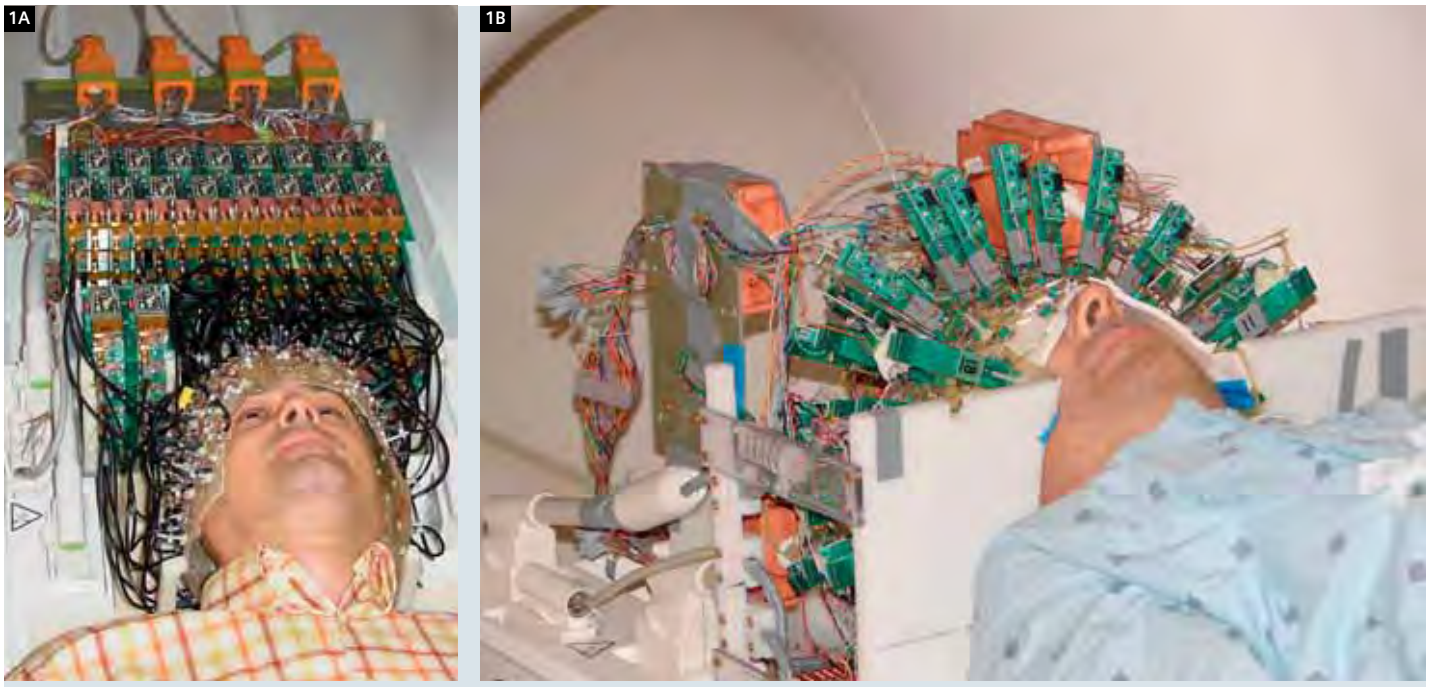

1 Graham Wiggins, one of the authors, tests the 90-channel 1.5T brain array prototype (left) and the 96-channel 3T array prototype (right). The system is a prototype 128-channel MAGNETOM Trio, A Tim System.

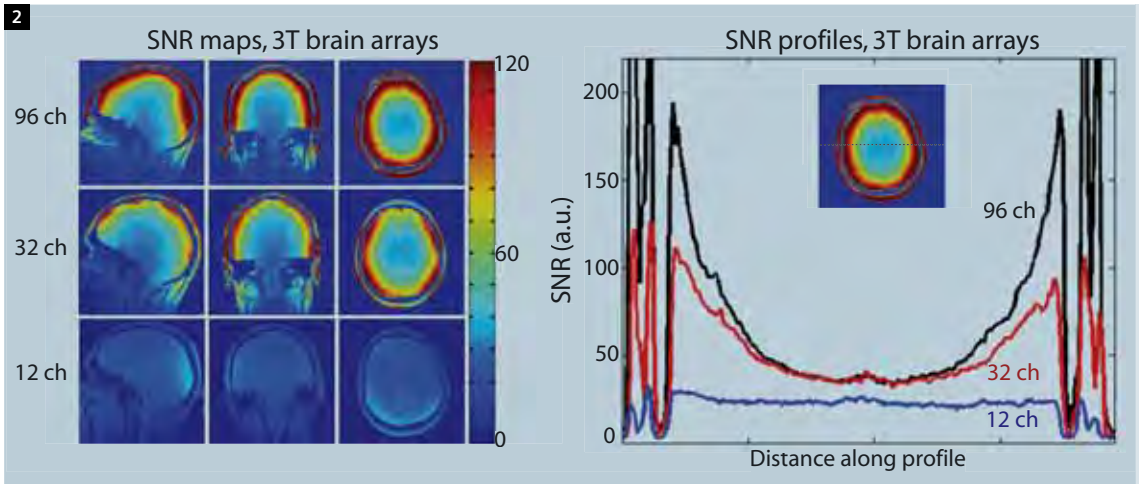

2 Sensitivity comparison of 12, 32 and 96-channel brain arrays at 3T. In the distal cortex, substantial sensitivity improvements are seen as the number of channels is increased.

*Works in progress (WIP). The information about this product is preliminary. The product is under development and not commercially available in the U.S., and its future availability cannot be ensured.

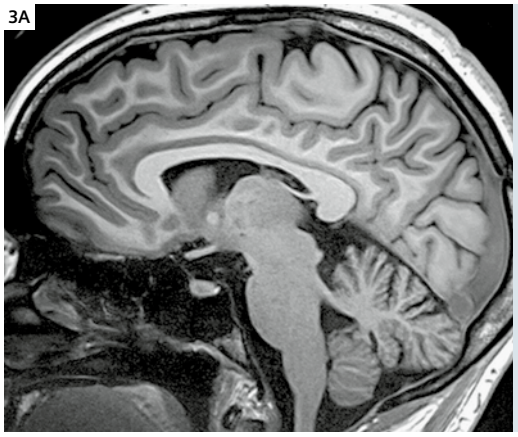

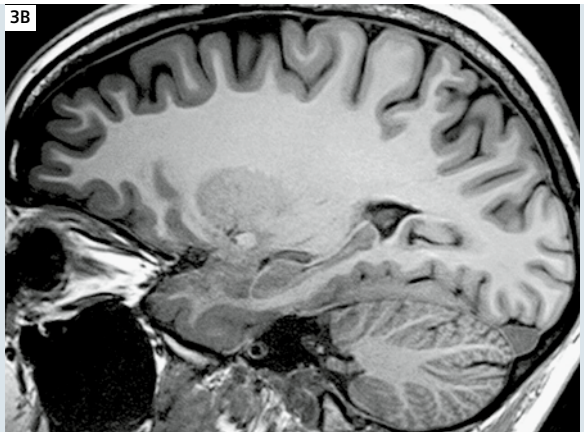

3 3 Tesla MPRAGE with a 32-channel coil (left). 500 µm in-plane resolution with a 1 mm partition thickness.
8 minutes acquisition time.

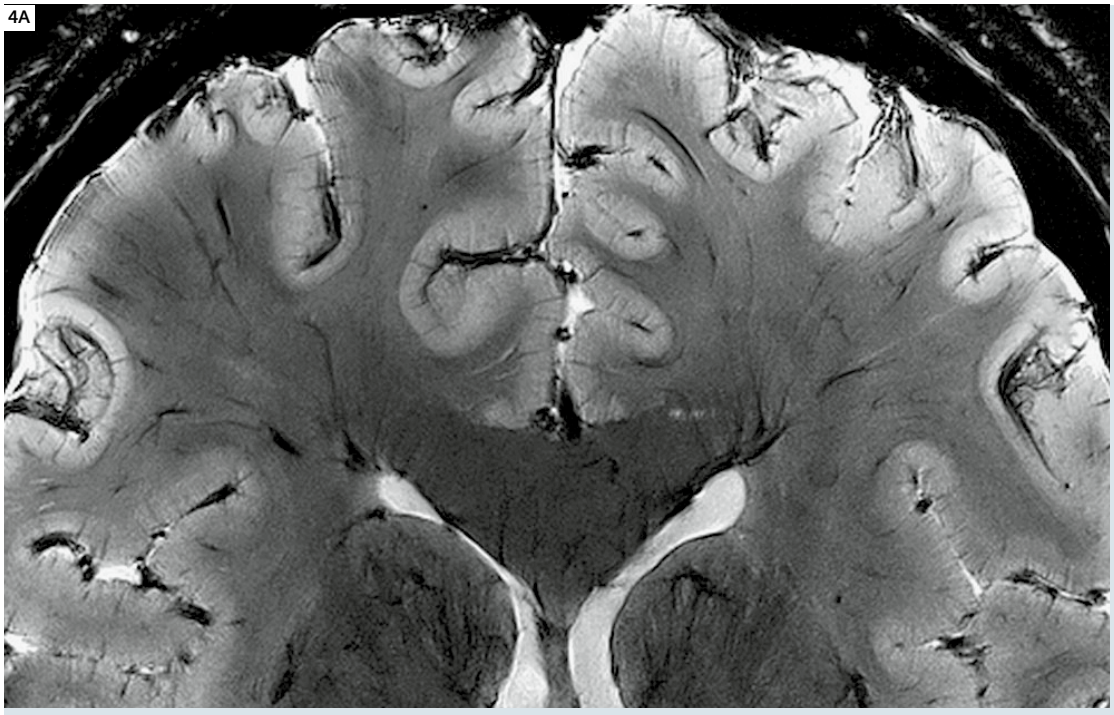

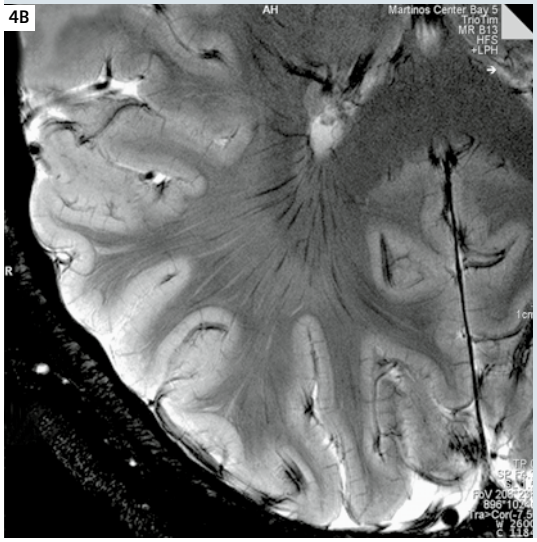

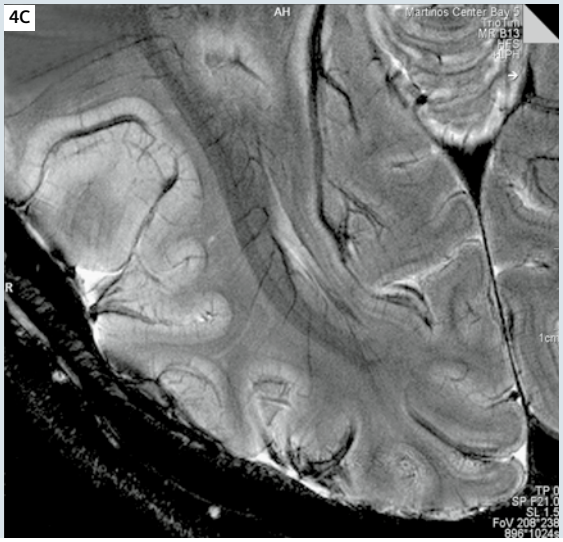

4 7 Tesla T2*-weighted imaging with a 32-channel coil. 220 µm in-plane resolution (1024 matrix) with a 1 mm slice thickness, TR/TE = 500 ms / 25 ms.
8 minutes acquisition time.

g-factor noise penalties for a given acceleration are obtained by measuring the noise correlation matrix (using a noise image acquired with no RF excitation) and coil sensitivity maps in a head shaped phantom [16]. Figure 5 shows the improved ability of the arrays for accelerated imaging. Shown is the percentage of the maximum achievable SNR, a measure related to the g-factor penalty (% SNR = 1/g) for 2 through 6-fold acceleration (conventional iPAT) as well as PAT² (acceleration in two phase encode directions) with accelerations up to 20-fold. For the higher acceleration factors, sensitivity gains up to 3-fold are seen (e.g. the R = 5 with 96 channels compared to 12 channels.) For 2-fold accelerations, extremely high accelerations (e.g. R = 4x4) are possible with the 96-channel coil. While the 32-channel coil performs significantly better with acceleration than the 12-channel coils, it still does not appear to truly push the 6x intrinsic limit identified in the ultimate g-factor calculations [3, 4]. The 96-channel array, however, appears to be close to achieving this limit.

5

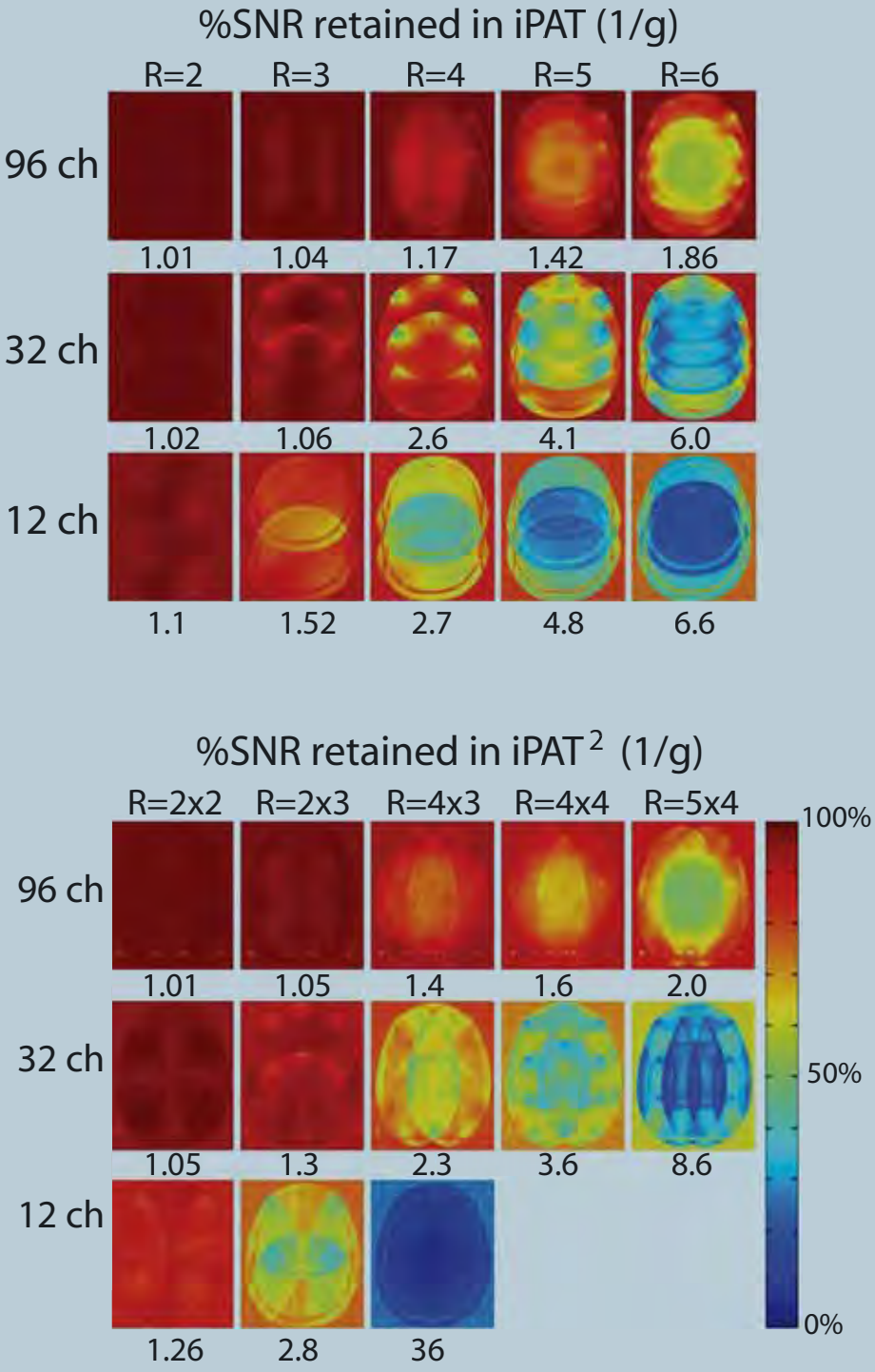

5 g-factor results for 2 thru 6x acceleration for iPAT imaging and R = 2 x 2 thru R = 5 x 4 acceleration for PAT². Maps are displayed as 1/g to allow visualization on the same scale. The maximum g-factor in the slice is given below each map. Each increase in the number of elements suggests the potential for an additional step in iPAT acceleration.

* Works in progress (WIP). The information about this product is preliminary. The product is under development and not commercially available in the U.S., and its future availability cannot be ensured.

Figure 6 shows a section of a high resolution 3D FLASH image accelerated 12-fold (3x in one direction and 4x in the other) with the 32-channel 3T coil. The 1 mm spatial resolution volume acquisition was acquired in 1:20 min. Figure 7 shows spin echo EPI (echo planar imaging) acquired at millimeter resolution with single shot encoding to freeze motion. The high acceleration rates which shorten the duration of the EPI readout train help prevent geometric distortion from the susceptibility effects in the frontal lobes as well as preventing significant T2* filtering of the image during the readout.

128-channel array for cardiac MRI

Perhaps no other application has more intrinsic need for improved accelerated imaging than 3D breathhold coronary angiograms. This motivated the extension of the "large N" array concept from brain arrays to cardiac imaging. Our prototype coil (Fig. 8) is closely contoured to the body with a "clam-shell" geometry with 68 posterior and 60 anterior elements of 75 mm diameter and arranged in a continuous overlapped array of hexagonal symmetry to minimize nearest neighbor coupling. The array was designed around accelerated imaging. For example, retaining only a subset of the elements near the heart would have likely produced similar sensitivity for non-accelerated imaging since coil elements distant from the heart contribute little to the SNR. But the accelerated image requires localized coil elements in these areas to assist with unaliasing the accelerated image.

6

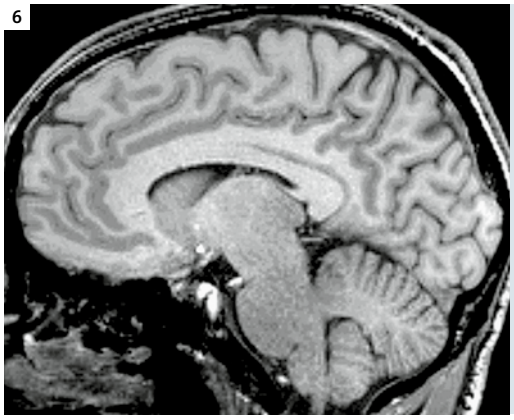

6 A highly accelerated 3D FLASH scan acquired with the 32-channel 3T helmet array. Image was accelerated 12-fold, 4-fold in the in-plane phase encode direction and 3-fold in the thru plane phase encode direction. Image time 1:20 min, image resolution 1 mm isotropic.

7

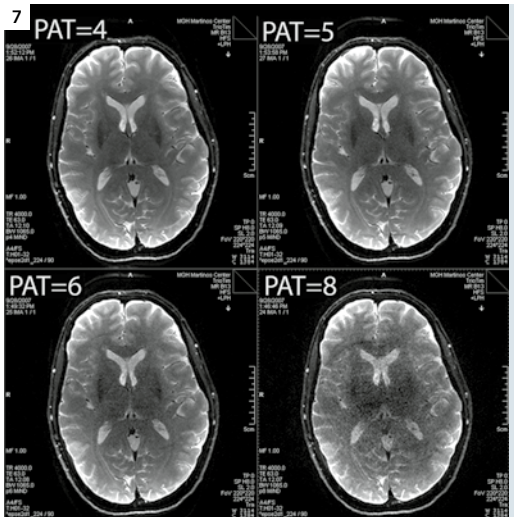

7 Highly accelerated, high resolution single shot spin echo EPI acquired with the 96-channel 3T array. Tolerable artifact and noise amplification for PAT factor up to 6x. SE-EPI, 224 x 224 matrix, 220 mm, 2 mm slice thickness, TR/TE = 4 s/63 ms. Single shot encoding, with but 4 averages.

8

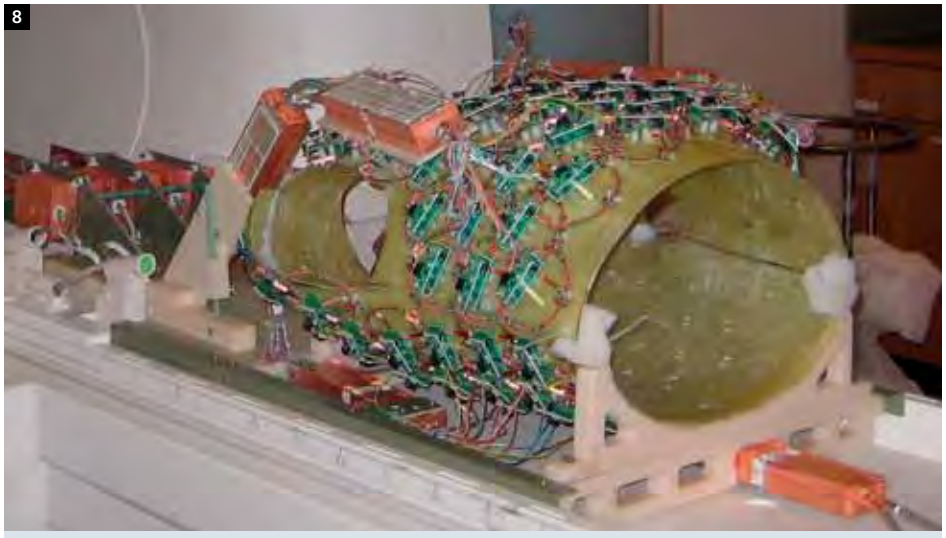

8 Prototype of a 128-channel cardiac coil. Coil is built on a fiberglass former molded to the chest shape of a 180 lbs male. The coil opens "clam-shell" style for patient access. PAT factor up to 6x. SE-EPI, 224 x 224 matrix, 220 mm, 2 mm slice thickness, TR/TE = 4 s/63 ms. Single shot encoding, with but 4 averages.

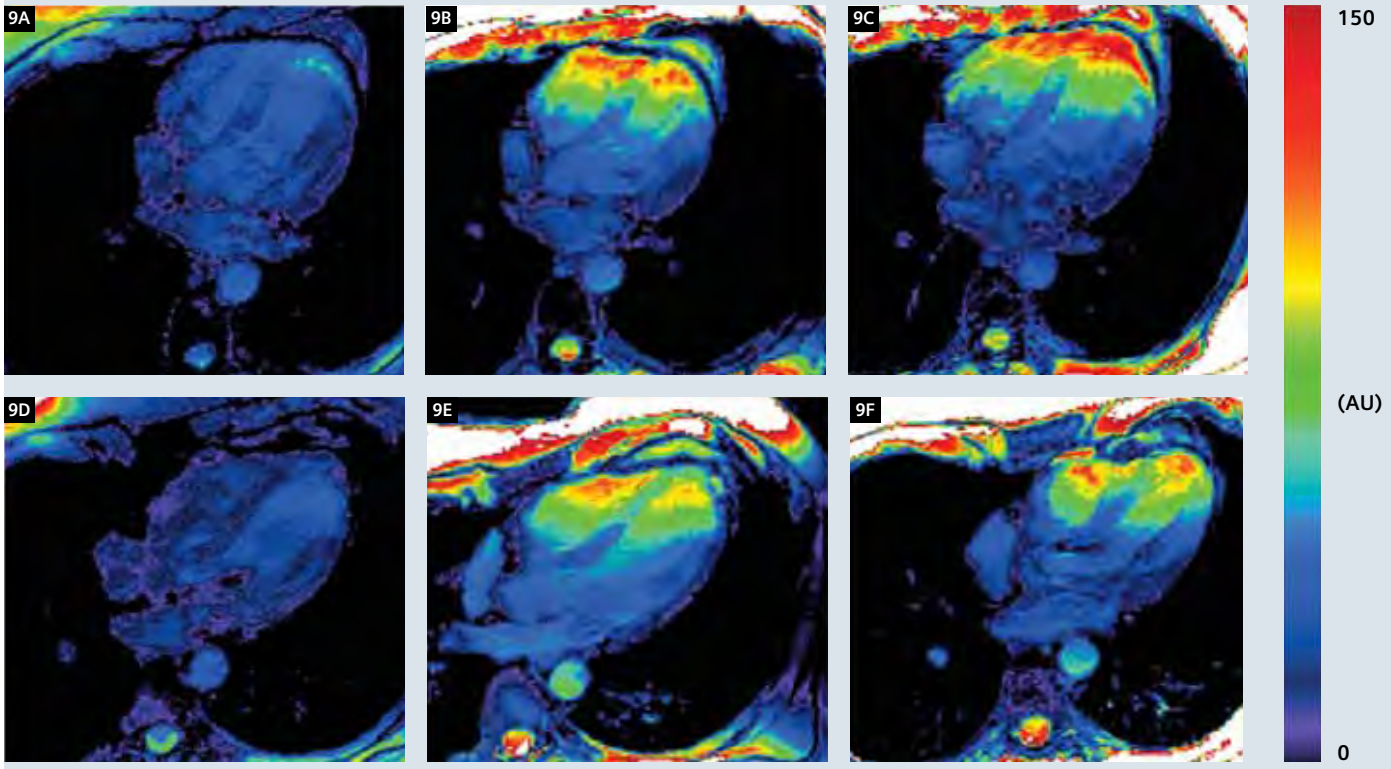

9 SNR in the heart for 24, 32 and 128-channel arrays. The 24 and 128-channel arrays have similar spatial coverage, and the 32 and 128-channel arrays have similar element sizes (and thus similar sensitivity for unaccelerated imaging).

Figure 9 shows SNR maps in the heart with this coil as well as two commercial arrays. Only modest sensitivity improvements are seen relative to the 32-channel coil, which uses similar sized elements (but only covers areas near the heart.) The 128-channel coil distinguishes itself for highly accelerated imaging with maximum g-factor values at higher acceleration factors improved by a factor of 2 or more over that of the 32-channel coil. For example, at rate 5 acceleration in the head-foot direction, the maximum g-factor of the 128-channel coil reached only 1.2, and was 2.5 for the 32-channel coil. Rate 7 acceleration in the left-right direction produced a maximum g-factor value of 1.7 (128-channel array) compared to 3.4 (32-channel array).

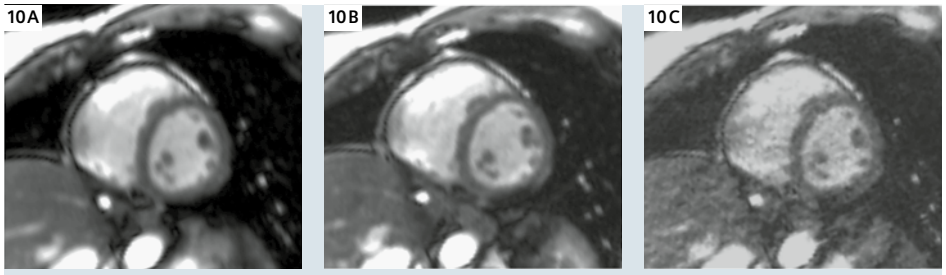

10 High-resolution, highly accelerated 2D cine imaging performed in a female volunteer with the 128-channel cardiac coil. The SSFP cine images shown were acquired with a slice thickness of 6 mm and an in-plane resolution of 1.9 x 2.9 mm. The following acceleration factors were used: **(A)** rate 1, **(B)** rate 4, **(C)** rate 7. The rate 1 and rate 4 images remain almost identical **(A, B)**, and the rate 7 images remain fully diagnostic with well-preserved blood tissue contrast and well-defined fine anatomical features.

* Works in progress (WIP). The information about this product is preliminary. The product is under development and not commercially available in the U.S., and its future availability cannot be ensured.

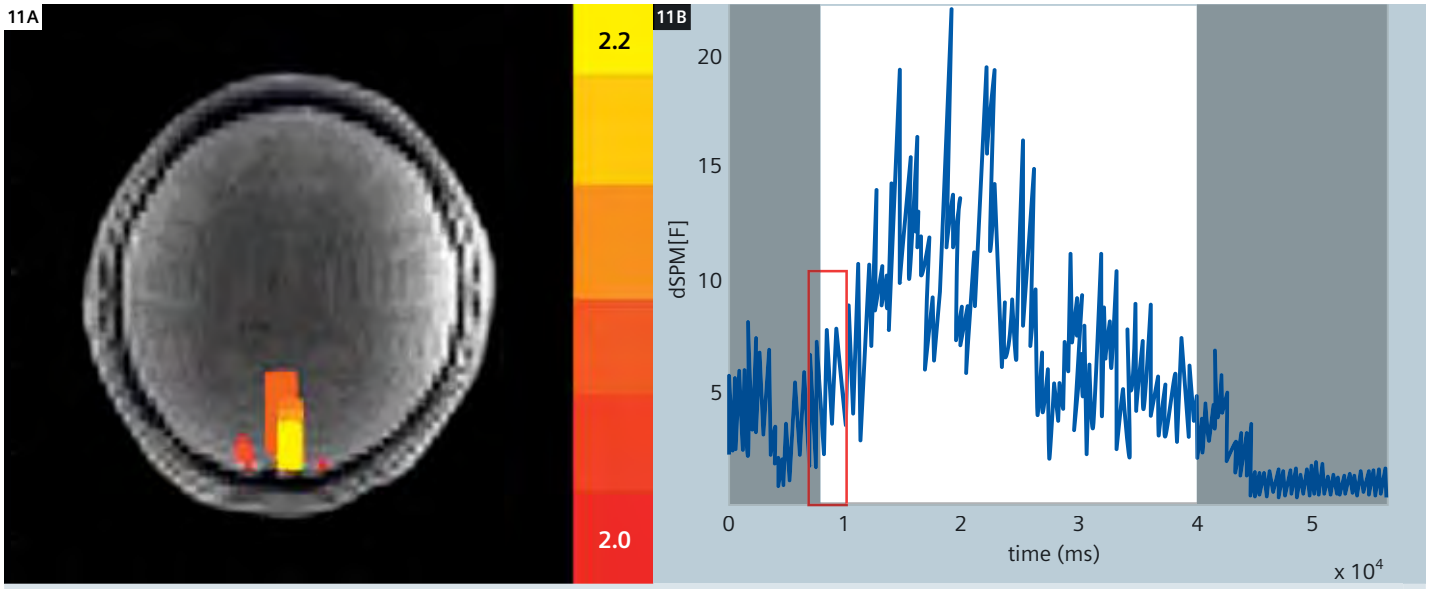

11 InI (MR Inverse Imaging) reconstructed statistical estimates of BOLD visual activation acquired with the 90-channel brain array. Spatial maps (left) and time series of one epoch. Temporal resolution of 20 ms was achieved with a PRESTO sequence and no phase encoding. Modulation at frequencies corresponding to the respiratory and cardiac rates are clearly visible in the time-course.

Result courtesy of FaHsuan Lin, MGH, Boston, USA.

Extreme encoding with large arrays

With current clinical systems (e.g. 32-channel), the reduction of a 10 minute volume scan to less than 1 minute with 12-fold acceleration is possible with modest increase in noise beyond the standard tradeoff between SNR and acquisition time. With even more channels (64 and 96), credible imaging can take place with truly minimal use of the gradients (for example a single readout to form an image). McDougall and Wright constructed a specialized 64-element planar array to demonstrate the potential for very high frame rate imaging acquired with no phase encode steps (e.g. all the information in this direction provided by array localization). Since the imaging is performed in a single readout, they refer to the resulting highly accelerated image as a Single Echo Acquisition (SEA) [9, 17]. Because the readout can be performed in a few milliseconds, frame rates of up to 200 fps were achievable, providing the ability to stop-motion in a paddle wheel phantom rotating at 60 rpm. In addition to illustrating the excellent image quality (considering the 64-fold acceleration and total acquisition time of 8 ms!), their images show the potential for extreme robustness to motion.

MR Inverse Imaging (MR InI)

Using a completely different reconstruction strategy, SEA imaging was acquired in the brain using the 32 and 90-channel brain array described above. The goal was not to detect images per se, but localize the source regions of dynamic change within the brain during functional activation. In this case the goal of the MR image reconstruction resembles MEG/EEG source localization. Here, we seek statistical best estimates of the source locations and associated time courses given the spatial and temporal information available by applying the inverse solution methods used in MEG/EEG source localization. In the example shown in Fig. 8, the temporal information comes from a 50 fps PRESTO sequence acquired with no phase encoding. PRESTO was used at achieve the long TE needed for BOLD fMRI (blood oxygen level dependent functional MR imaging). The spatial information was provided by the readout gradient (L-R direction) and the 90-channel array (A-P direction). Because of the similarity of the reconstruction to the MEG/EEG inverse problem, this approach was called MR Inverse Imaging (MR InI) [18].

Unlike conventional parallel imaging where lack of sufficient spatial information from the array manifests itself as noise amplification (g-factor), the same problem in InI produces reduced ability to spatially localize the changes; namely, a greatly reduced spatial resolution. Here, "sources" refers to the areas of the brain with dynamically altered signal with respect to user defined baseline condition. Since spatial localization is provided in one direction by the array and in the other by conventional frequency encoding, the InI method as implemented is a 1D method with slice select and standard frequency encoding providing the other spatial dimensions. It could potentially be expanded to 2D or even 3D. The 2D case is thus a Single Echo Acquisition, and the 3D case is potentially a single sample of the signal with no use of gradients. For the 90-channel array, the spatial resolution of

the activation localization in the 2D case was 3 mm in the readout direction and estimated to vary from just over 1 cm near the array to about 3 cm deep within the head.

Thus, in the MEG-like inverse problem, the reduced ability of the array to provide spatial information in the center of the head (where the coil profiles are too smooth to provide high spatial resolution information) translates to a deteriorated spatial resolution in these regions. Since the SNR of MR imaging scales as the cube of the voxel dimensions, a small increase in voxel dimensions may make up for reduced spatial encoding accuracy since statistical estimates will be more robust due to the higher signal levels in the larger voxels. Thus the InI method can be viewed as coping with the encoding limitations in the center of the head by adjusting the spatial resolution accordingly. Figure 11 shows the InI reconstructed statistical estimates of the stimulus correlated changes associated with a block design visual stimulus. Also shown is the reconstructed time-course for the activated area. A temporal resolution of 50 frames per second was achieved. At this temporal resolution, many physiological modulations such as the cardiac and respiratory modulations are not temporally aliased (as they normally are) and thus potentially easily removable from the data. Figure 12 shows the extension of the InI method to 3D imaging, here the InI reconstruction is done in the right-left direction and the other spatial directions are encoded with conventional 2D EPI. Thus, in the time it takes to acquire a conventional EPI slice (about 80 ms), the 3D InI method can do whole-head fMRI, improving temporal resolutions as much as 30-fold.

Figure 12 shows visual fMRI acquired at a whole-brain temporal resolution of 10 frames per second. The ability to significantly improve the temporal resolution of fMRI using these extreme parallel acceleration methods offers several exciting possibilities. Firstly, this will be a necessary technology for future attempts to image direct neuronal manifestations of neuronal activation (as opposed to relatively slow and more indirect hemodynamic

12

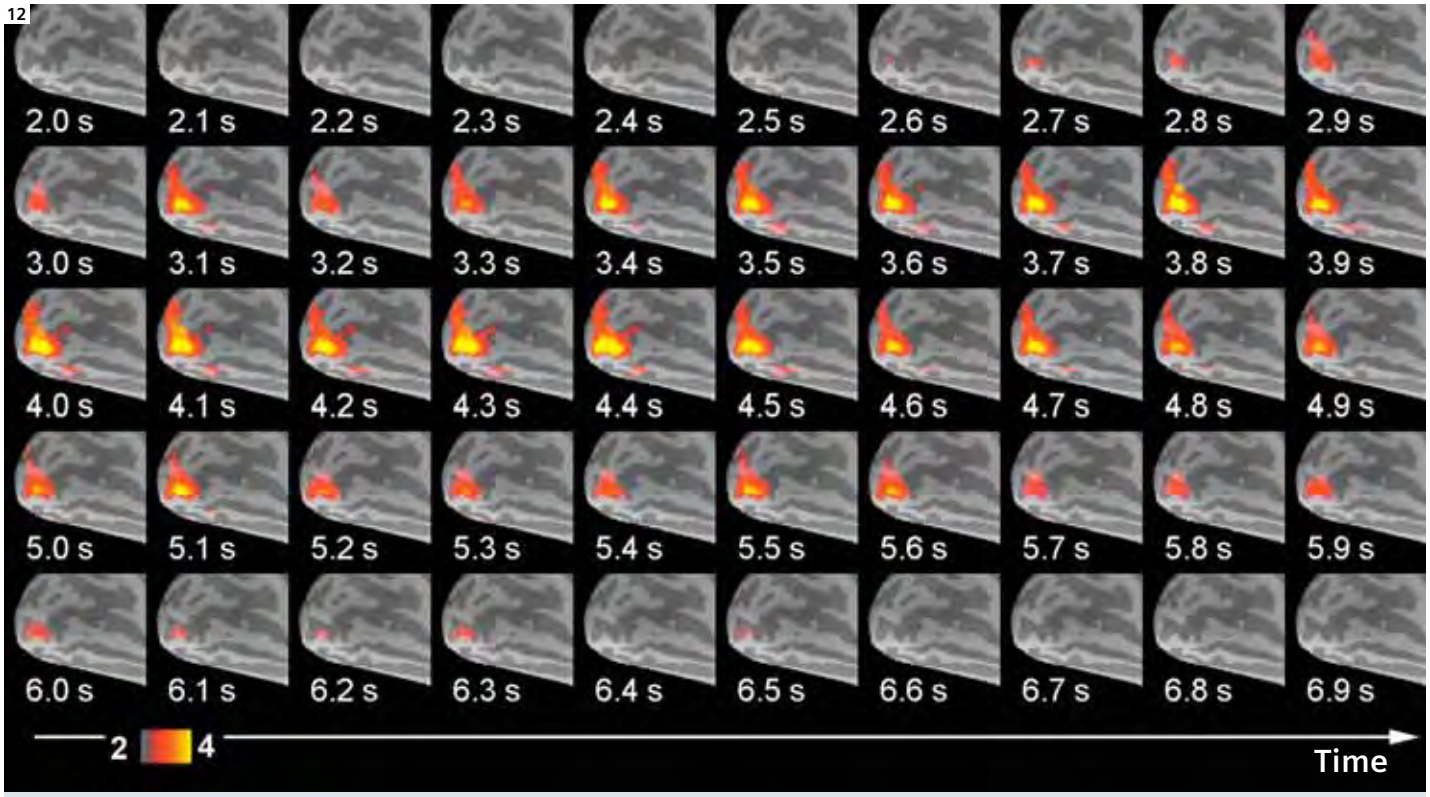

12 3D InI reconstructed statistical estimates of BOLD visual activation across the whole brain at 10 fps. Activation averaged across 5 subjects is shown on a representation of the inflated occipital pole.

Result courtesy of FaHsuan Lin, MGH, Boston, USA.

* Works in progress (WIP). The information about this product is preliminary. The product is under development and not commercially available in the U.S., and its future availability cannot be ensured.

effects.) MEG and EEG show these evoked responses are typically bipolar and of a duration of 30 ms or less. Thus, imaging strategies with order of magnitude improvements in the temporal resolution are needed to unambiguously resolve these events. The ability to temporally resolve significant sources of physiological modulation in the data, such as respiratory and cardiac cycle effects will also improve statistical inference in BOLD fMRI. Finally, with 3D InI there is the potential for truly silent fMRI studies of the auditory system since all gradient waveforms can be eliminated.

Conclusion

While the technical issues of building arrays with large numbers of receive elements are challenging, both the theoretical simulations and the experimental prototypes suggest the potential for substantial benefits, especially for accelerated image encoding. The synergy between large receive arrays, higher field strength systems, and the Tim methodology also suggest that these methods will continue to evolve together in a productive way. This is seen on the theoretical side where the sensitivity gains for accelerated imaging as a function of the number of array elements were seen to improve at higher field and also on the practical side where constructing a small receive coil which is body noise dominated is easier at higher field strength.

Perhaps even more intriguing than being able to substantially improve conventional imaging, is the ability to perform new types of imaging. Realization of this potential is in its infancy but will likely have its first and largest implications for encoding-limited imaging such as high resolution 3D imaging, spectroscopic imaging, and dynamic imaging such as functional imaging.

Acknowledgements

We would like to thank Andreas Potthast, Franz Hebrank and Franz Schmitt of Siemens Medical Systems for their contribution to the large-N brain array and receiver configurations, Melanie Schmitt of MGH who developed the cardiac array, Chris Wiggins of MGH (Currently of NeuroSpin, CEA Saclay France) for his contribution to high resolution 7T studies, and FaHsuan Lin of MGH for results from the inverse imaging reconstruction method. We would like to acknowledge support from the NCRR of the NIH, grant 5P41RR014075-05, the NIH grants 1RO1EB000790 and 1R01EB006847 and the MIND Institute for Mental Illness and Neuroscience Discovery.

References

1 Wright, S.M. and L.L. Wald, Theory and application of array coils in MR spectroscopy. NMR Biomed, 1997. 10(8): p. 394-410.
2 Wiesinger, F., N. DeZanche, and K.P. Pruessmann. Approaching Ultimate SNR with Finite Coil Arrays. in Proceedings of the ISMRM. 2005. Miami FL.
3 Wiesinger, F., P. Boesiger, and K.P. Pruessmann, Electrodynamics and ultimate SNR in parallel MR imaging. Magn Reson Med, 2004. 52(2): p. 376-90.
4 Ohliger, M.A., A.K. Grant, and D.K. Sodickson, Ultimate intrinsic signal-to-noise ratio for parallel MRI: electromagnetic field considerations. Magn Reson Med, 2003. 50(5): p. 1018-30.
5 Ocali, O. and E. Atalar, Ultimate intrinsic signal-to-noise ratio in MRI. Magn Reson Med, 1998. 39(3): p. 462-73.
6 Wiesinger, F., N. DeZanche, and K.P. Pruessmann, Approaching Ultimate SNR with Finite Coil Arrays, in ISMRM 13th Annual Scientific Meeting, presentation 672. 2005: Miami FL.
7 Weiger, M., et al., Specific coil design for SENSE: a six-element cardiac array. Magn Reson Med, 2001. 45(3): p. 495-504.
8 de Zwart, J.A., et al., Design of a SENSE-optimized high-sensitivity MRI receive coil for brain imaging. Magn Reson Med, 2002. 47(6): p. 1218-27.
9 McDougall, M.P. and S.M. Wright, 64-channel array coil for single echo acquisition magnetic resonance imaging. Magn Reson Med, 2005. 54(2): p. 386-92.
10 Zhu, Y., et al., Highly parallel volumetric imaging with a 32-element RF coil array. Magn Reson Med, 2004. 52(4): p. 869-77.
11 Sodickson, D.K., et al., Rapid volumetric MRI using parallel imaging with order-of-magnitude accelerations and a 32-element RF coil array: feasibility and implications. Acad Radiol, 2005. 12(5): p. 626-35.
12 Wiggins, G., et al. A 32 Channel Receive-only Phased Array Head Coil for 3T with Novel Geodesic Tiling Geometry. in Proceed. International Soc. of Magnetic Resonance in Medicine. 2005. Miami FL.
13 Moeller, S., et al. Parallel Imaging Performance for Densely Spaced Coils in Phase Arrays at Ultra High Field Strength in Proceed of the 12th Annual ISMRM meeting. 2004. Kyoto Japan.
14 Cline, H., et al. 32 channel head array for highly accelerated parallel imaging. in Proceedings of the 12th annual meeting of ISMRM. 2004. Kyoto Japan.
15 Wiggins, G., et al. A 96-channel MRI System with 23- and 90-channel Phase Array Head Coils at 1.5 Tesla. in Proceed. International Soc. of Magnetic Resonance in Medicine. 2005. Miami FL.
16 Pruessmann, K.P., et al., SENSE: sensitivity encoding for fast MRI. Magn Reson Med, 1999. 42(5): p. 952-62.
17 McDougall, M.P. and S.M. Wright, Phase compensation in single echo acquisition imaging. Phase effects of voxel-sized coils in planar and cylindrical arrays. IEEE Eng Med Biol Mag, 2005. 24(6): p. 17-22.
18 Lin, F.H., et al., Dynamic magnetic resonance inverse imaging of human brain function. Magn Reson Med, 2006. submitted.

Detection and Characterization of Focal Liver Lesions using Respiratory-Triggered Diffusion-Weighted MR Imaging (DWI)

Konstantin Holzapfel; Melanie Bruegel; Matthias Eiber; Ernst J. Rummeny; Jochen Gaa

Department of Radiology, Technical University Munich, Germany

Diffusion-weighted MR imaging (DWI), theoretically described as far back as the 1950s and 1960s by Carr/Purcell and Stejskal/Tanner [1, 2], has become an established method in neuroradiology since the introduction of the intravoxel incoherent motion technique by Le Bihan and coworkers in 1988 [3]. Due to a number of technical challenges, the use of DWI was initially confined to the brain with its low incidence of movement artifacts and the high homogeneity and signal-to-noise ratio (SNR) of brain tissue. Physiological motion artifacts (e.g. motility of the bowel, cardiac pulsation, respiratory motions) and the heterogeneous composition of many extracranial organs had precluded the application of DWI in body imaging until a series of technologic advances such as the development of echo-planar imaging (EPI), high-gradient amplitudes, multichannel coils and parallel imaging techniques enabled the acquisition of high quality diffusion-weighted images of the body. Over the last few years, DWI has become increasingly used in extracranial organs to detect and characterize tumors for the functional evaluation of different organs and for response evaluation in oncology (for review see [4, 5]).

The term 'diffusion' defines the random thermally induced motion of water molecules in biologic tissues ('Brownian motion'). The addition of motion probing gradient (MPG) pulses to MR sequences allows quantifying the combined effects of capillary perfusion ('pseudodiffusion') and diffusion in vivo by means of the apparent diffusion coefficient (ADC). For DWI, diffusion gradients are applied before and after the 180°-pulse of a single-shot spin-echo echoplanar imaging (SSEPI) sequence, for example. The b-value represents the diffusion factor [s/mm^2] and represents amplitude and duration of the diffusion gradients. The ADC [mm^2/s] describes the slope of the curve of signal intensity vs. b-value, and is calculated using the following formula: $ADC = (\ln SI_1/SI_2)/(b_2-b_1)$ where b_1 and b_2 are motion-probing gradient factors (diffusion factors) of sequences S_1 and S_2, and SI_1 and SI_2 are signal intensities in these sequences.

Liver DWI protocol used in our institution [6]

At the Department of Radiology of the Technical University of Munich we use a SSEPI sequence at a 1.5T scanner (MAGNETOM Avanto) for DWI. MR imaging is performed with two six-channel body phased array coils anterior and two spine clusters (three channels each) posterior. As image quality of respiratory-triggered sequences has been shown to be superior to breath-hold sequences, we obtain diffusion-weighted images applying respiratory-triggering using prospective acquisition correction (PACE). A single-shot EPI readout is preceded by a diffusion-sensitizing block consisting of two 180° radiofrequency pulses and four motion probing gradient (MPG) pulses in order to reduce the influence of eddy currents compared to the conventional Stejskal-Tanner preparation. The technical parameters are as follows: echo time: 69 ms; echo train length: 58; echo spacing: 0.69; receiver bandwidth: 1,736 Hz/pixel; spectral fat saturation; field of view: 263 × 350 mm; matrix: 144 × 192; number of signal averages: 3; section thickness: 5 mm; intersection gap: 0.5 mm; 30–45 transverse sections acquired; ≈ 4–6 min acquisition time, b-values of 50, 300 and 600 s/mm^2. Integrated parallel imaging techniques (iPAT) by means of generalized autocalibrating partially parallel acquisitions (GRAPPA) with a twofold acceleration factor is used to shorten the echo train length.

Detection of focal liver lesions using DWI

Over the last few years several studies have investigated the use of DWI in the detection of focal liver lesions (FLL). DWI was superior to T2-weighted sequences [7–10] and to superparamagnetic iron oxide (SPIO)-enhanced MR imaging in the detection of focal liver lesions [11]. The detection of small FLLs in particular seems to be significantly improved by DWI [7, 9, 10] (Fig. 1). High SNRs and high lesion-to-liver signal intensity ratios are seen especially at low b values alleviating the depiction of focal liver lesions. In addition, the 'black blood effect' of diffusion-weighted images makes it easier to distinguish small FLLs from hepatic vessels. Furthermore, DWI seems to improve the perceptibility of FLLs, especially of hepatocellular car-

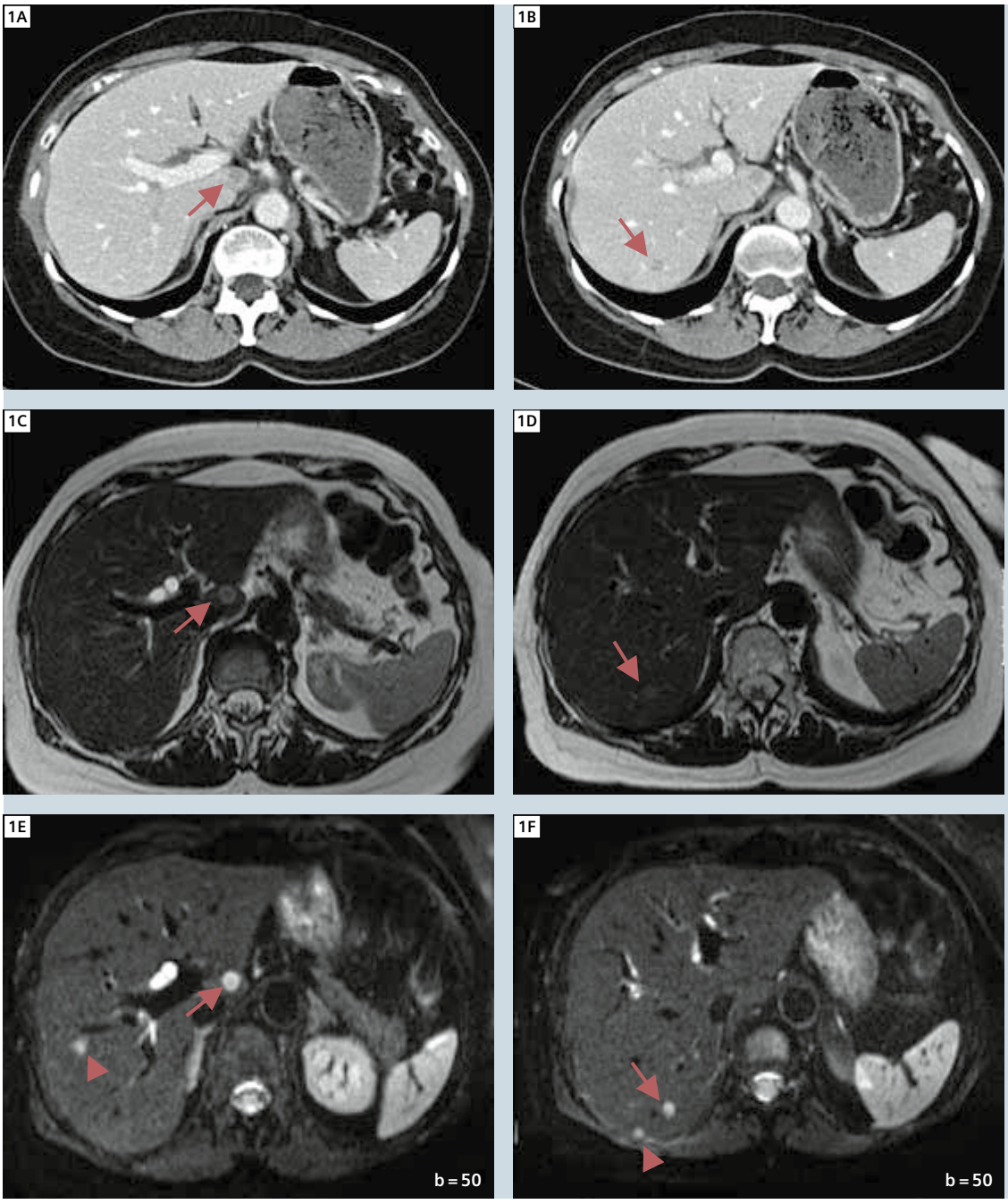

1 Detection of focal liver lesions using DWI. Multi-slice CT (MSCT, A, B), T2-weighted TSE (C, D) and diffusion-weighted SSEPI MR images (E, F) of a patient with breast cancer. On MSCT and T2-weighted MR images one liver metastasis can be seen on each image (arrows). However, on diffusion-weighted images on each slice an additional metastasis can be identified that cannot be seen on MSCT and T2-weighted MR images (arrowheads).

cinomas (HCCs) in patients with liver cirrhosis as that the heterogeneity and increased signal intensity of the cirrhotic liver parenchyma as a result of nodular regeneration, fibrosis, and scarring appears to be less pronounced on DWI compared to T2-weighted images [7]. However, in one study DWI was inferior to Manganese dipyridoxyl-diphosphate (MnDPDP)-enhanced MRI in the detection of FLLs [12] and the potential benefit of DWI in association or compared with conventional gadolinium-enhanced liver MR imaging remains to be investigated [7].

Characterization of focal liver lesions using DWI

Differences in cellularity between benign and malignant liver lesions resulting in different diffusion properties of water protons within these lesions are reflected by different ADC values measured by DWI. Typically, benign liver lesions like cysts or hemangiomas that are hypocellular compared to liver parenchyma allow relatively unhindered diffusion of water protons resulting in high ADC values (e.g. ~ 2 × 10–3 mm^2/s in hemangiomas, ~ 3 × 10–3 mm^2/s in cysts) compared to low ADC values in commonly hypercellular malignant liver lesions such as metastases or HCCs (e.g. 1.1 – 1.3 × 10–3 mm^2/s in HCCs and 1.1 – 1.4 × 10–3 mm^2/s in metastases) where diffusion of water protons is

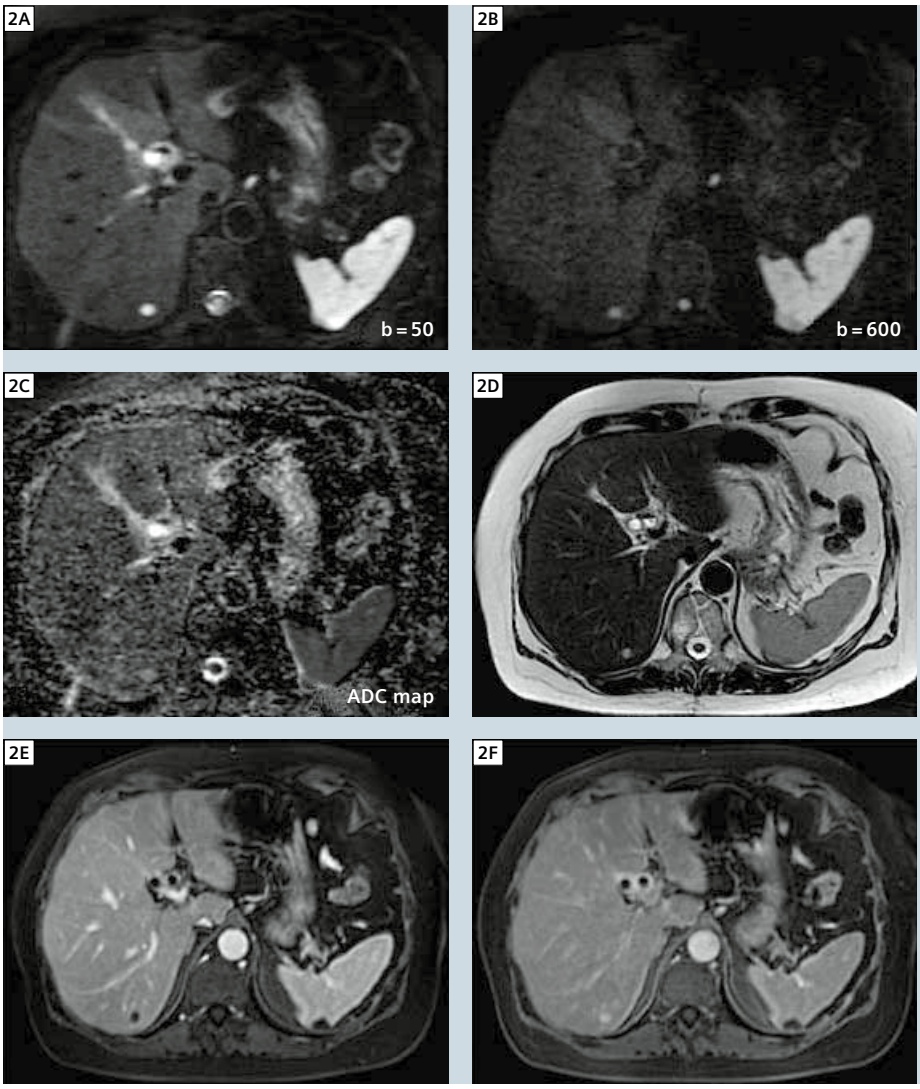

2 Characterization of focal liver lesions by DWI. Diffusion-weighted SSEPI (A–C), T2-weighted TSE (D) and Gd-enhanced T1-weighted MR images (3D Volume Interpolated Breathhold Examination [VIBE] with fat saturation, E, F) in a patient with pancreatic cancer. A small focal liver lesion in segment 7 is hyperintense on the b-50 image (A), shows signal loss at a high b-value (B) and thus, a moderately high ADC value (1.96 × 10–3 mm^2/s, c) typically seen in hemangiomas. The lesion is hyperintense on the T2-weighted image (D) and shows centripetal enhancement on dynamic post-contrast images (E, F), features typical for hemangiomas.

more restricted [6] (Figs. 2, 3). Thus, several studies have identified significantly lower ADC values in malignant compared to benign FLLs [6, 7, 13]. A feasible threshold ADC for differentiating benign from malignant FLLs would be 1.5 – 1.7 × 10–3 mm^2/s [6]. As in the brain, secondary to highly viscous pus containing proteinaceous fluid and necrotic cells, hepatic abscesses show extremely low ADC values in most cases and therefore are an exception to this rule [14, 15]. However, the differentiation between benign solid FLLs like focal nodular hyperplasia (FNHs) and adenomas from malignant lesions often is impossible by DWI as there is considerable overlap of ADC values between both groups. Furthermore, although mean ADC values of hemangiomas and metastases are significantly different, characterizing a single liver lesion by means of the ADC value prospectively can be difficult. Thus, in our opinion, DWI should be used as a complementary method in the characterization of FLLs.

DWI for response evaluation of treated liver tumors

The value of DWI in the detection and prediction of tumor response to chemotherapy, radiation therapy, or other modalities is increasingly studied. Effective anticancer treatment results in lysis of tumor cells, loss of cell membrane integrity, increased extracellular space, and, consequently, an increase in water diffusion reflected by a rising ADC value [5]. Promising animal studies report a significant rise in ADC values in patients with HCC who respond to transcatheter arterial chemoembolization [16]. In addition, amongst patients with colorectal hepatic metastases, an increase in ADC was observed in those with at least a partial response to treatment, while no ADC increase was observed in non-responders [17]. Furthermore, in the same study, metastases with low baseline ADC values have been shown to respond better to chemotherapy than tumors that exhibit high pre-treatment ADC values [17]. One possible explanation is that tumors with high pre-treatment ADC values are likely to be more necrotic than those with low values. Necrotic tumors frequently are hypoxic, acidotic, and poorly perfused, leading to diminished sensitivity to chemotherapy and to radiation therapy [5].

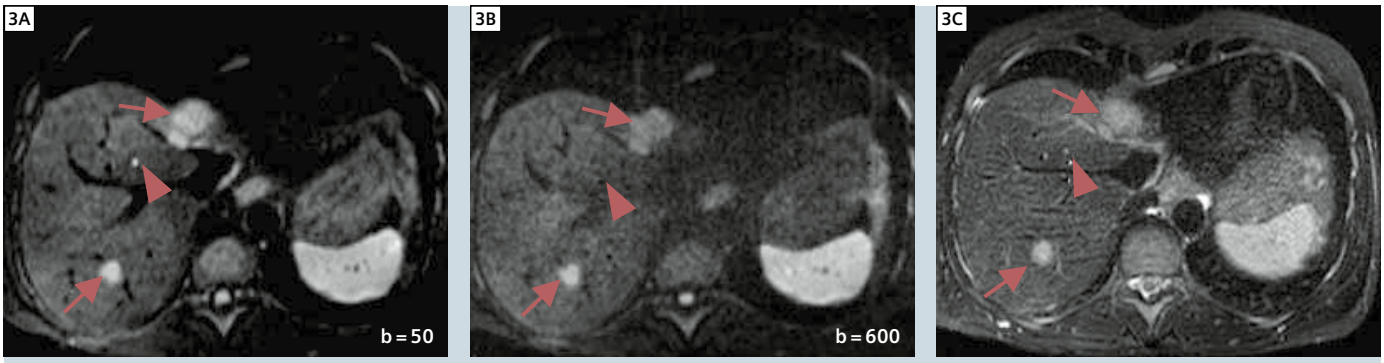

3 Characterization of focal liver lesions by DWI. Diffusion-weighted SSEPI (A, B) and fat-saturated T2-weighted TSE MR images (C) in a patient with rectal cancer. Two metastases (arrows) are hyperintense both on the b-50 (A) and b-600 image (B) resulting in low ADC values (1.18 and 1.27 × 10–3 mm²/s, respectively) typically seen in malignant liver lesions. A small cyst (arrowhead) is hyperintense on the b-50 image (A) but shows considerable signal loss on the b-600 image (B) resulting in a high ADC value (2.79 × 10–3 mm²/s). Note that on the T2-weighted image the small cyst can hardly be differentiated from a small metastasis (C).

Conclusion

In summary, DWI is a valuable tool in the detection of FLLs, especially with regard to small lesions. In the characterization of FLLs, DWI is of use as an additional, complementary method being interpreted in conjunction with other MR sequences. Finally, DWI seems to have great potential in the response evaluation of treated liver tumors: This has to be investigated in further studies.

Contact
Konstantin Holzapfel, M.D.
Technical University Munich
Dept. of Radiology
holzapfel@roe.med.tum.de

References

1 Carr HY, Purcell EM (1954) Effects of diffusion on free precession in nuclear magnetic resonance experiments. Phys Rev 94:630–638.
2 Stejskal EO, Tanner JE (1965) Spin diffusion measurements: spin echoes in the presence of a time-dependent field gradient. J Chem Phys 42:288–292.
3 Le Bihan D, Breton E, Lallemand D, Aubin ML, Vignaud J, Laval-Jeantet M (1988) Separation of diffusion and perfusion in intravoxel incoherent motion MR imaging. Radiology 168:497–505.
4 Thoeny HC, De Keyzer F (2007) Extracranial applications of diffusion-weighted magnetic resonance imaging. Eur Radiol 17:1385–1393.
5 Koh DM, Collins DJ (2007) Diffusion-weighted MRI in the body: applications and challenges in oncology. AJR Am J Roentgenol 188:1622–1635.
6 Bruegel M, Holzapfel K, Gaa J, Woertler K, Waldt S, Kiefer B, Stemmer A, Ganter C, Rummeny EJ (2008) Characterization of focal liver lesions by ADC measurements using a respiratory triggered diffusion-weighted single-shot echo-planar MR imaging technique. Eur Radiol 18:477–485.
7 Parikh T, Drew SJ, Lee VS, Wong S, Hecht EM, Babb JS, Taouli B (2008) Focal liver lesion detection and characterization with diffusion-weighted MR imaging: comparison with standard breath-hold T2-weighted imaging. Radiology 246:812–822.
8 Zech CJ, Herrmann KA, Dietrich O, Horger W, Reiser MF, Schoenberg SO (2008) Black-blood diffusion-weighted EPI acquisition of the liver with parallel imaging: comparison with a standard T2-weighted sequence for detection of focal liver lesions.Invest Radiol 43:261–266.
9 Coenegrachts K, Delanote J, Ter Beek L, Haspeslagh M, Bipat S, Stoker J, Van Kerkhove F, Steyaert L, Rigauts H, Casselman JW (2007) Improved focal liver lesion detection: comparison of single-shot diffusion-weighted echoplanar and single-shot T2 weighted turbo spin echo techniques. Br J Radiol 80:524–531.
10 Bruegel M, Gaa J, Waldt S, Woertler K, Holzapfel K, Kiefer B, Rummeny EJ (2008) Diagnosis of hepatic metastases: comparison of respiration-triggered diffusion-weighted echo-planar MRI and five T2-weighted turbo spin-echo sequences. AJR Am J Roentgenol (in press).
11 Nasu K, Kuroki Y, Nawano S, Kuroki S, Tsukamoto T, Yamamoto S, Motoori K, Ueda T (2006) Hepatic metastases: diffusion-weighted sensitivity-encoding versus SPIO-enhanced MR imaging. Radiology 239:122–130.
12 Koh DM, Brown G, Riddell AM, Scurr E, Collins DJ, Allen SD, Chau I, Cunningham D, deSouza NM, Leach MO, Husband JE (2008) Detection of colorectal hepatic metastases using MnDPDP MR imaging and diffusion-weighted imaging (DWI) alone and in combination. Eur Radiol 18:903–910.
13 Taouli B, Vilgrain V, Dumont E, Daire JL, Fan B, Menu Y (2003) Evaluation of liver diffusion isotropy and characterization of focal hepatic lesions with two single-shot echo-planar MR imaging sequences: prospective study in 66 patients. Radiology 226:71–78.
14 Chan JH, Tsui EY, Luk SH, Fung AS, Yuen MK, Szeto ML, Cheung YK, Wong KP (2001) Diffusion-weighted MR imaging of the liver: distinguishing hepatic abscess from cystic or necrotic tumor. Abdom Imaging 26:161–165.
15 Holzapfel K, Rummeny E, Gaa J (2007) Diffusion-weighted MR imaging of hepatic abscesses: possibility of different apparent diffusion coefficient (ADC)-values in early and mature abscess formation. Abdom Imaging 32:538–539.
16 Chen CY, Li CW, Kuo YT, Jaw TS, Wu DK, Jao JC, Hsu JS, Liu GC (2006) Early response of hepatocellular carcinoma to transcatheter arterial chemoembolization: choline levels and MR diffusion constants--initial experience. Radiology 239:448–456.
17 Koh DM, Scurr E, Collins D, Kanber B, Norman A, Leach MO, Husband JE (2007) Predicting response of colorectal hepatic metastasis: value of pretreatment apparent diffusion coefficients. AJR Am J Roentgenol 188:1001–1008.









What if one size fits them all?



MAGNETOM Espree – the first open bore MRI for any patient.

With the shortest 1.5T magnet in the industry and its 70 cm inner diameter, MAGNETOM® Espree provides 1.5T high-field power with the highest level of patient comfort. Powered by Tim® (Total imaging matrix) technology, MAGNETOM Espree provides a new level of flexibility, accuracy, and speed. The combination of ultimate patient comfort and superb image quality will attract new referrals and will maximize your patient throughput.
www.siemens.com/healthcare +49 69 797 6420

Answers for life.

SIEMENS

MR-Z1098-1-7600

Questions & Answers on Hardware Topics

Jörg Stapf; Rolf Heinrichs; Matthias Nittka, Ph.D.

Siemens Healthcare, Erlangen, Germany

Q: What is the principle of "Zero-Helium Boil Off"?

A: Super-conducting magnets require built-in overdimensional thermos flasks for maintaining super-conductivity in cryostats (Fig. 1).
To ensure that the liquid helium used as coolant does not boil off too quickly, the helium dewar has to be very well insulated to reduce, for example, heat conduction and radiation. For this purpose, the helium vessel is suspended by materials that are poor heat conductors, such as GFK or reinforced carbon fiber materials. Furthermore, heat bridges are reduced as much as possible. The housing is evacuated to prevent convection currents. Irradiation on the helium vessel is reduced by Kelvin shields and super-insulating foils.
If the helium boiling off re-condenses via a 4K cold head, at least statically the magnet no longer boils off or consumes helium. The second stage extends into a volume connected to the helium vessel where it cools and re-liquifies the gas. Since it is not easy to regulate the performance of the cold head, the excess refrigeration capacity is compensated for by a heater so that the working pressure in the helium vessel remains constant.
Eddy currents caused by gradient activity lead to additional heat transfer into the helium vessel.
If the sum of heat transferred is less than that of the refrigeration capacity of the cold head, a "zero boil off" system is obtained.
To maintain this state, the cold head has to be in continuous operation, and the line voltage as well as the chilled water supply should not fail, at all, or at worst, only briefly.
Normally, liquid helium is lost only within the framework of service activities, such as ramping or replacing cold heads. Unfortunately, liquid helium will also boil off when both the line voltage and chilled water supply fail for more than 3 hours.

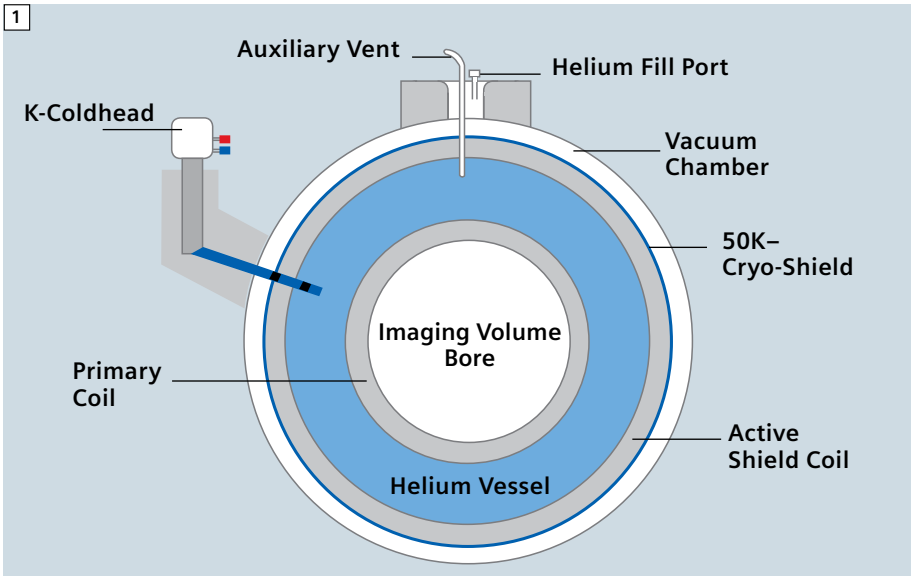

1 MR system.

Q: What is the difference between the different RF pulse types?

A: The RF pulse types are pure sequence parameters. This means they are not allocated to a hardware feature. By comparison, the Matrix Mode, for example, actually affects the surface coils (modes: CP, Dual, Triple depending on the coil).
The RF pulse types allow flexible control of the RF pulses (radio frequency pulses) of the sequences, for exciting or refocusing the MR signals and for various other applications:

- The "Normal" mode is optimized to cover a broad sequence application range providing for a well-defined slice profile.
- The "Fast" mode is implemented for time-critical protocols when rather short echo times are required. For this reason, it uses very short RF pulses.

A disadvantage of the "Fast" mode is that shorter RF pulses are normally accompanied by increased RF exposure for the patient (increase in the specific absorption rate).

- The "Low SAR" mode addresses high-performance protocols that may exceed the allowed SAR threshold. Usually, longer RF pulses are used, i.e., the RF-power output decreases.

One of the resulting disadvantages is that longer RF pulses increase the minimal timing of fast sequences. However, this is not required for all applications. It is important that every sequence defines the actual pulses that stand behind the RF pulse types and is able to change them at any time depending on other parameters.

Intravoxel Incoherent Motion (IVIM)* *f*-maps of Pancreatic Lesions

Re, Thomas Joseph, M.D., MSEE[1]; Klauss, Miriam, M.D.[2]; Lemke, Andreas, MSc[3,4]; Laun, Frederik, Ph.D.[4]; Simon, Dirk, MSc[1]; Delorme, Stefan, M.D.[1]; Stieltjes, Bram, M.D.[1]

[1]German Cancer Research Center (DKFZ), Department of Radiology – E 010, Heidelberg, Germany
[2]Department of Diagnostic Radiology, University of Heidelberg, Heidelberg, Germany
[3]Department of Computer Assisted Clinical Medicine, University of Heidelberg, Mannheim, Faculty of Medicine, Mannheim, Germany
[4]German Cancer Research Center (DKFZ), Department of Physics in Radiology – E 020, Heidelberg, Germany

Abstract

Purpose: To illustrate our experience using diffusion-weighted (DW) derived IVIM perfusion fraction *f* images (*f*-maps) for the delineation of solid pancreatic lesions. Particular attention is given to the comparison of this experimental technique with the clinically established technique of ADC-mapping.

Methods: Seven representative cases (1 healthy volunteer, 4 pancreatic adenocarcinoma cases, and 2 pancreatitis cases) are presented. Each were examined with contrast-enhanced T1 and T2-weighted magnetic resonance (MR) and with echo-planar MR diffusion-weighted imaging (DWI) using eleven different b-values ranging from 0–800 s/mm². The DWI data was fitted to both the "Incoherent Intra-Voxel Motion" (IVIM) model and a linear apparent diffusion constant (ADC) equation, and the perfusion fraction *f* and ADC-maps were calculated. As a novel approach, ADC and *f*-map data was combined to identify vascular (high perfusion but low ADC) or bile duct (low perfusion but high ADC) voxels which were then color tagged on the *f*-map images.

Results / Conclusion: When compared to ADC-maps, *f*-maps improved the distinction between lesion and vessels, while ADC-maps more accurately identified adjacent pancreatic ducts. Images which integrate f and ADC data provided better lesion delineation than could be achieved with either technique alone. Since *f*-maps do not require ionizing radiation nor contrast agent, they could be considered an alternative to CT and contrast-enhanced MRI techniques in patients with specific contraindications as well as in screening and follow-up imaging programs.

Introduction

Contrast-enhanced magnetic resonance (MR) and computed tomography (CT) imaging are currently the standard imaging modalities for pancreatic lesions [1–3]. Their high diagnostic value unconsidered, they require intravenous contrast agent and, in the case of CT, ionizing radiation. Diffusion-weighted imaging (DWI) could prove a non-invasive alternative, since recent advances in scanner technologies, fast pulse sequences and parallel imaging have permitted its use in the abdomen where organ motion and tissue inhomogeneity have long prevented robust diffusion measurements [4–6]. Reports have shown that the DWI-derived apparent diffusion constant (ADC) can be used to monitor the pancreatic exocrine function in chronic pancreatitis [7, 8], for characterizing cystic lesions of the pancreas [9], and for detecting pancreatic cancer, which has a significantly lower ADC value than normal pancreas tissue [10–12].
Recently there has been growing interest in extracting perfusion information from diffusion-weighted data based on the intravoxel incoherent motion (IVIM) model [13–15] first presented by LeBihan in 1986 [16, 17]. In this model, the diffusion-weighted signal is considered to be effected by two distinct types of molecular motion: *diffusion*, due to thermal Brownian motion, and *perfusion*, due to the microcirculation in capillaries. The IVIM model is represented mathematically by the equation:

$$\frac{S}{S_0} = (1-f)\, e^{-bD} + f e^{-b(D+D^*)}$$

where S/S_0 is the signal decay measured in each individual voxel in the diffusion-weighted image, the b-value represents the strength of the diffusion weighting, D is the diffusion constant, D* is the pseudo diffusion coefficient, and *f* is the perfusion fraction. This equation is a biexponential with the first term representing the pure diffusion influence on the diffusion-weighted signal, while the second term represents the pure perfusion influence on the diffusion-weighted signal. The perfusion fraction (*f*) indicates the relative influence of the second perfusion term and thus is correlated to the perfusion or microcirculation in the capillaries of the tissue under study. In a recent work, *f* was shown to be significantly lower within pancreatic tumors than in healthy pancreatic tissue [18]. Another study showed similar results for chronic pancreatitis mass formations [19]. Furthermore, *f* was shown to be

quantitatively superior to both ADC and D for characterizing pancreatic lesions [18]. Images created by mapping the f parameter as a gray scale (f-maps), hold important clinical information for both diagnosing and differentiating pancreatic lesions, but so far the reading of f-maps is unfamiliar to general radiologists. Thus, this pictorial essay aims to familiarize the clinician with this emerging imaging method. This work was generated within a cooperative project of Siemens Healthcare and the German national cancer center, diagnostic imaging for radio-oncology.

Materials and methods

Study population

This work was generated within a cooperative project of Siemens Healthcare and the German national cancer center, diagnostic imaging for radio-oncology. The study protocol was approved by the Institutional Review Board. Informed consent was obtained from all subjects prior to the examination. In 2008 (June-December), 3 healthy volunteers, 14 patients with histopathologically proven pancreatic carcinoma (11 men and 3 women, age range 43–82, mean age 62.6) and 8 histopathologically verified pancreatitis patients (7 men and 1 woman, age range 40–74, mean age 55.5) were included consecutively during this period.

MR examination

MR imaging was performed using a 1.5T scanner (MAGNETOM Avanto, Siemens Healthcare, Erlangen, Germany) with a maximum gradient strength of 45 mT/m using a six-element body-phased array coil and a 24-channel spine array coil. The routine pancreatic MR imaging protocol for the patient group consisted of TrueFISP imaging sequences (sagital, axial and coronal) (TR/TE = 437.2/1.16 ms), breathhold (in expiration) dual gradient echo (2D) T1-weighted (T1w) imaging in transversal orientation (TR/TE = 110/4.82 ms), breathhold (expiration) single-shot turbo spin-echo T2-weighted (T2w) imaging in transversal and coronal orientation (TR/TE = 250/20 ms) and MR cholangiopancreatography in breathhold (expiration) single-shot turbo spin-echo (TR/TE = 4500/789 ms).

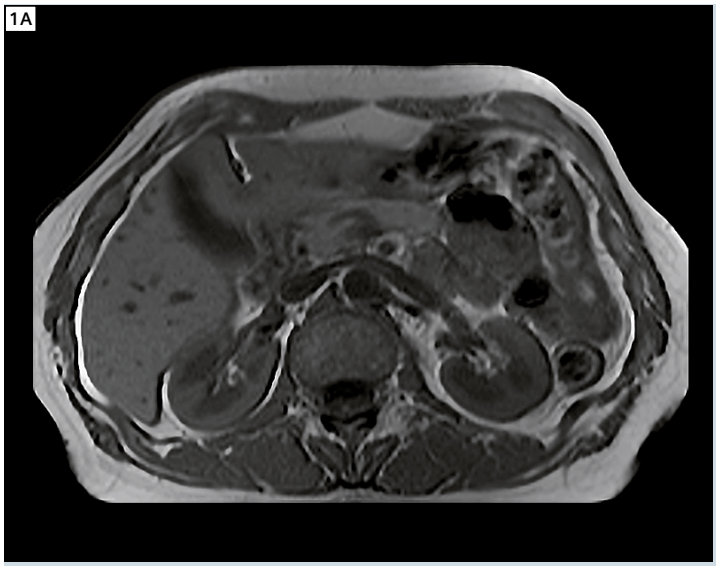

1 Axial T1-weighted image of a healthy volunteer.

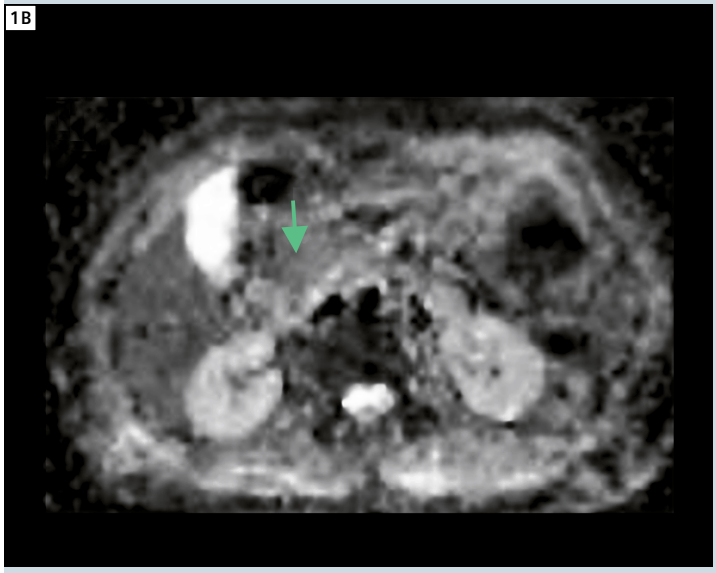

1 In the ADC-map it can be seen that the pancreas (green arrow) appears isointense to the liver.

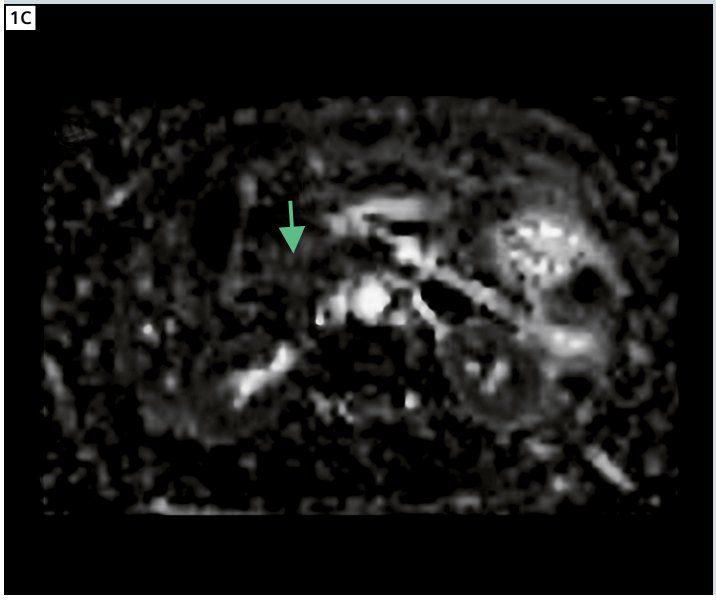

1 In the f-map, the pancreas (green arrow) shows a mixed hypo- and hyperintense signal.



2 Axial contrast-enhanced CT **(A)**, contrast-enhanced T1w image **(B)** and T2w image **(C)** for a patient with chronic pancreatitis with calcifications (red arrows) within the pancreatic head (see CT on the left) as well as pancreatic cancer (green arrowhead). The dilated pancreatic duct can also be appreciated (yellow arrows). (T = tumor; DP = ductus pancreaticus).

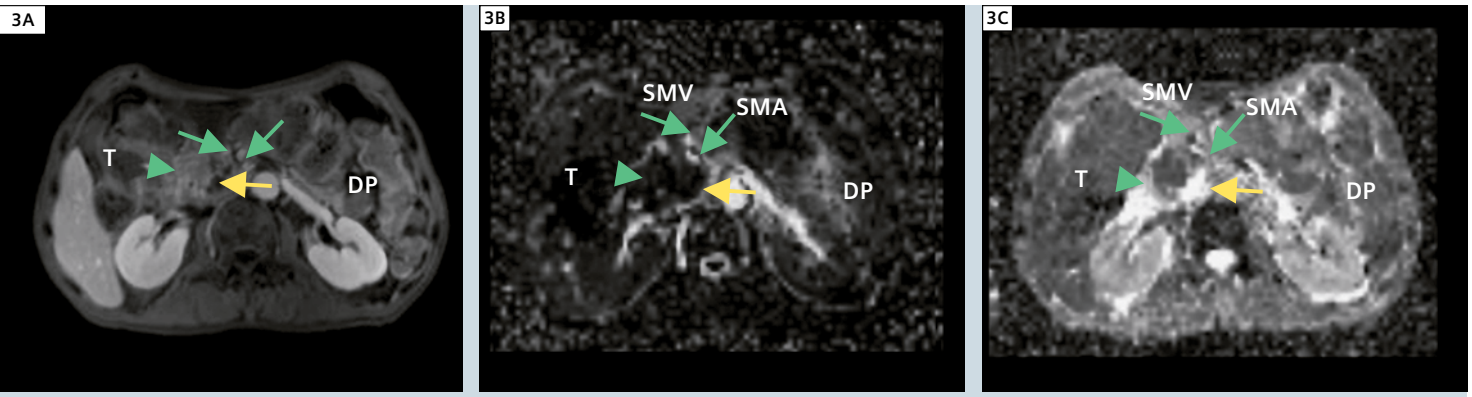

3 Axial T1w image **(A)**, f-map **(B)** and ADC map **(C)** in the same patient with pancreatic cancer as shown in figure 2. The carcinoma can be seen as a hypointense area in both the f and the ADC-map (green arrowhead). Note that the hypointense area in the f-map is larger than that in the ADC-map because in the f-map the dilated pancreatic duct (long arrows) adjacent to the tumor is as hypointense as the tumor itself. Also appreciated in these images are the superior mesenteric artery (SMA) and superior mesenteric vein (SMV) (green arrows), which both appear bright in the f-map and in the T1w image. In the ADC-map, the SMV is visible but the SMA is not. The tumor is more easily evidenced in the f-map than in the conventional imaging. (T = tumor; DP = ductus pancreaticus (yellow arrow); SMA = superior mesenteric artery; SMV = superior mesenteric vein).

DWI was performed in addition to the routine MR imaging protocol. Diffusion-weighted images were acquired using a single-shot echo-planar imaging (SE-EPI) pulse sequence in end expiration breath-hold with the following imaging parameters: TR = 1300 ms, TE = 60 ms, FOV = 350 × 273 mm², matrix size = 100 × 78, 14 slices, slice thickness/gap = 5/0.25 mm, 4 averages, bandwidth = 3000 Hz/Px, k-space based parallel imaging technique (*syngo* GRAPPA; Siemens Healthcare) used with an acceleration factor of two, b-values = 0, 25, 50, 75, 100, 150, 200, 300, 400, 600 and 800 s/mm² and a total measurement time of twelve minutes. The diffusion weighting was accomplished with a twice-refocused spin echo (TRSE) diffusion preparation and three orthogonal gradient directions (1,1,-1/2), (1,-1/2,1) and (-1/2,1,1) to obtain trace-weighted images. The acquisition was separated into blocks (b0, b25), (b0, b50)...(b0, b800) and each block was acquired in a single breathhold (TA = 26 s) to avoid motion artifacts.

CT examination

Computed tomography (CT) scans of the patients were obtained from referring institutions.

Post processing and data analysis

DW-images were post-processed using software developed in-house based on the open source imaging software ImageJ (http://rsb.info.nih.gov/ij) applying two approaches:

- biexponential Levenberg-Marquardt based fitting to the IVIM-model equation (1) (see above) separating the contribution of microperfusion and real diffusion in a DWI measurement. In this fit, the perfusion fraction f and the diffusion coefficient D were taken as free parameters, whereas the pseudo Diffusion Coefficient D* was fixed at 20 µm²/ms.
- monoexponential linear least squares fitting to equation (2):

$$\ln \frac{S}{S_0} = -b(ADC)$$

using the total set of b-values yielding the Apparent Diffusion Coefficient ADC. The f parameter obtained through the first approach and the ADC parameter obtained through the second approach were mapped as a gray scale to create multi-slice f-map and ADC-maps.
For two specific cases, the f and ADC data were combined to identify vascular

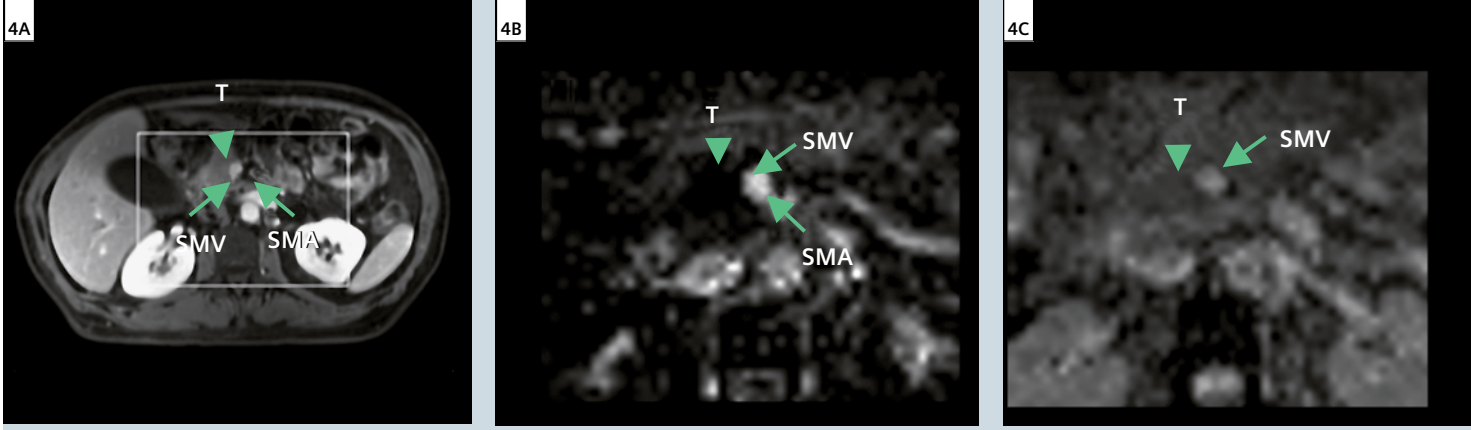

4 Patient with pancreatic cancer tumor in the head of the pancreas (green arrowhead). The tumor is better delineated in the f-map **(B)** than in the ADC-map **(C)**. Contact with the adjacent superior mesenteric vein (SMV) can be seen in all three images. Note that the superior mesenteric artery (SMA) is visible in the f-map but not in the ADC-map. T1w image **(A)** also provided for comparison. (white rectangle in T1w image = region displayed in other images; T = tumor; SMA = superior mesenteric artery; SMV = superior mesenteric vein).

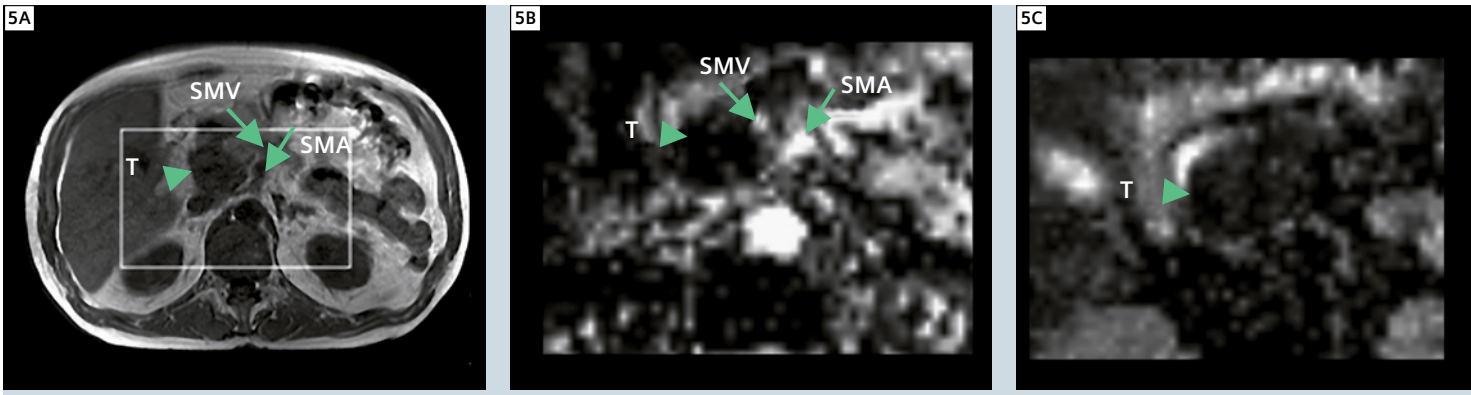

5 Axial T1w image **(A)**, f-map **(B)** and ADC-map **(C)** in a patient with pancreatic cancer in the head of the pancreas (green arrowhead). The tumor margins are better seen in the f-map than in the ADC-map. Furthermore, the superior mesenteric artery (SMA) and vein (SMV) can be seen in the f-map (green arrows) but not in the ADC-map. (White rectangle in T1w image = region displayed in other images; T = tumor; SMA = superior mesenteric artery; SMV = superior mesenteric vein).

and bile duct voxels. Voxels with high perfusion ($f > 0.35$) but low ADC (ADC between 0.81 and 2.1 μm^2/ms) were classified as vascular while those with low perfusion ($f < 0.15$) but high ADC (ADC between 1.5 and 2.5 µm2/ms) were classified as ductal. A color overlay was then used to depict vascular (red) and bile duct (blue) voxels on the f-maps. Images and parameter maps were read by two experienced radiologists in consensus. Pancreatic lesions were first identified in the routine CT and MR images. The lesions were then visually identified in the corresponding ADC and f-maps.

Results

Healthy volunteer

An example of normal ADC and f-map findings, taken from one of the healthy volunteers is provided in figure 1. It can be seen that the pancreas (arrow) appears isointense to the liver in the ADC-map. In the f-map, the pancreas shows a mixed hypo- and hyperintense signal.

Pancreatic adenocarcinoma

Four cases of histopathologically confirmed adenocarcinoma are shown in figures 2 through 6.

Figure 2 shows a venous phase contrast CT, venous phase contrast T1w and T2w MRI for the first carcinoma case in which a lesion in the head of the pancreas is hypodense in CT and hypointense in both T1w and T2w MRI. Also note the dilated pancreatic duct (DP). The ADC, and f-map for this case, presented in figure 3, clearly show the lesion as an area of low apparent diffusion on the ADC and hypo-perfusion (hypointense) on the f-map. Compared to the healthy volunteer, note the extensive area of hypointensity in both the f-map and the ADC in the tumor region. Also note that the tumor stands out most prominently on the f-map. Furthermore, vessels are best delineated and hyperintense on the f-map. However, there is no clear demarcation between the tumor and the dilated duct on the f-map. This is better seen on the ADC map where the duct is relatively hyperintense when compared to the tumor.

Figure 4 shows a venous phase T1w, ADC and f-map for the second carcinoma patient. The lesion again appears as hypointense in T1w, as well as on both the ADC and f-map. Again, note the superior depiction of the tumor in the f-map where once more the vessels in the vicinity of the tumor are delineated

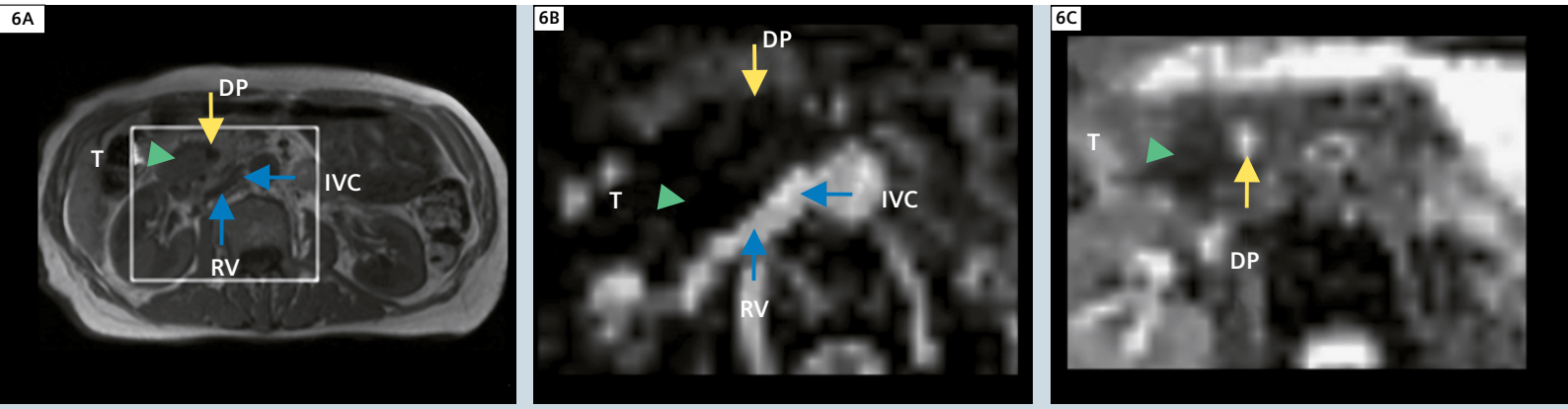

6 Patient with a pancreatic cancer in the head of the pancreas. Like in the case presented in figure 3, in the *f*-map **(B)** the lesion can not be separately distinguished from the adjacent dilated pancreatic duct (DP), whereas the structures can be readily told apart in the ADC-map **(C)**. However, the *f*-map provides much better visualization of the vasculature than the ADC-map, i.e., one can identify the inferior vena cava (IVC), renal vein (RV) and aorta **(A)**. T1w image (A) also provided for comparison. (White rectangle in T1w image = region displayed in other images; T = tumor; IVC = inf. vena cava, RV = renal vein, A = aorta).

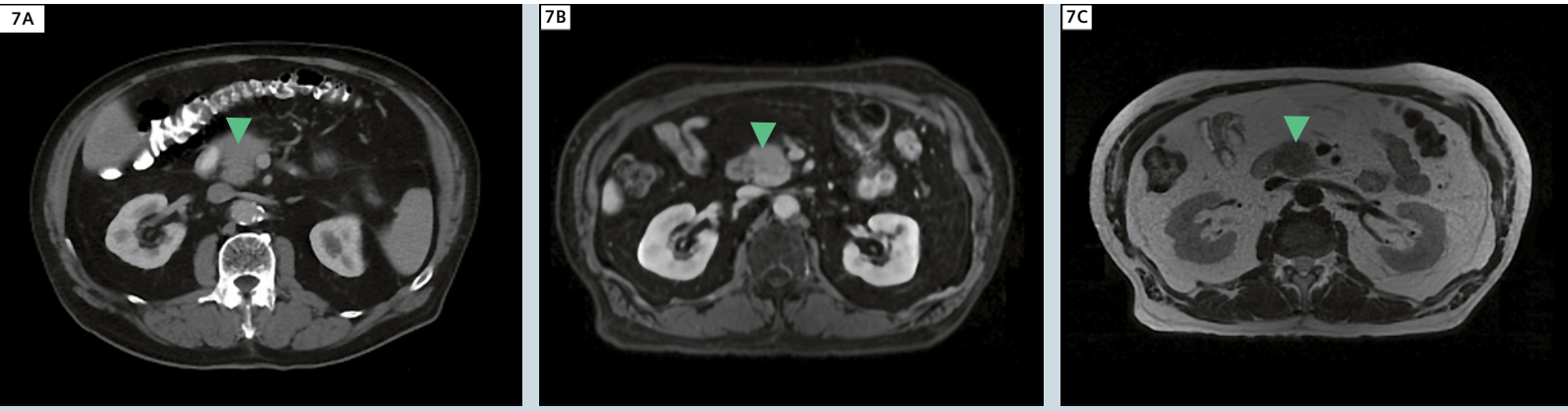

7 Axial venous phase contrast-enhanced CT **(A)**, portal phase contrast-enhanced T1w **(B)** and T2w **(C)** images of patient with histopathologically proven chronic pancreatitis in the head of the pancreas (green arrowhead). Note the mass-forming aspect of the lesion, and absence of calcifications in the CT.

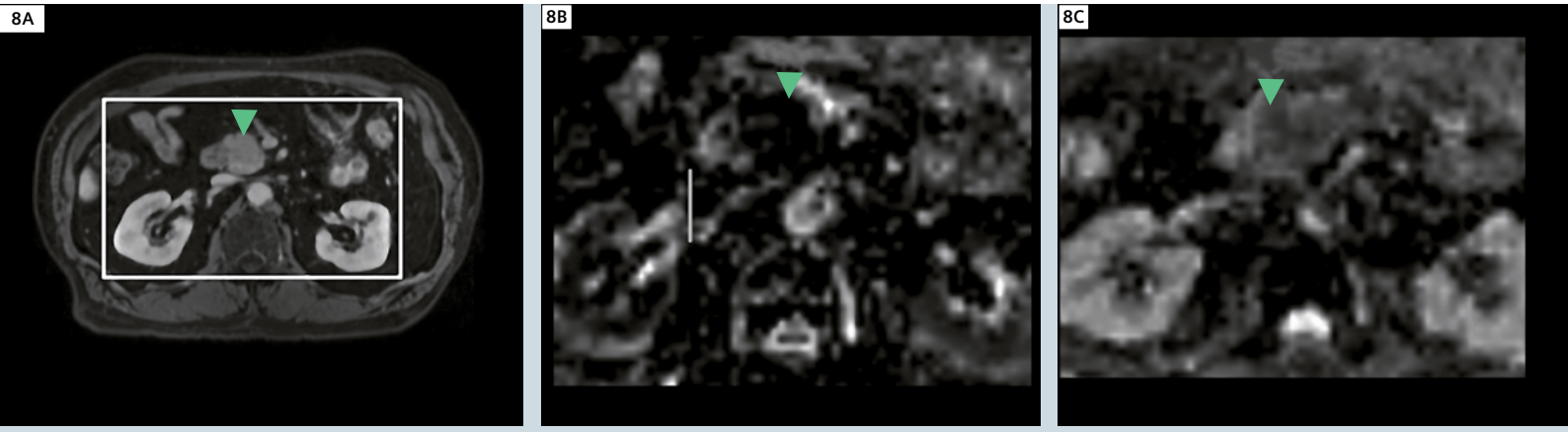

8 Axial portal phase contrast-enhanced T1w **(A)**, *f*-map **(B)** and ADC-map **(C)** of the pancreatitis patient from figure 6. In the contrast-enhanced MRI a slightly hypointense lesion can be seen in the head of the pancreas (large white arrow). It appears markedly hypointense in the *f*-map and only slightly hypointense on the ADC-map (white rectangle in T1w image = region displayed in other images).

clearly and appear hyperintense. Since no pancreatic duct is present in this slice, the tumor size is depicted accurately in the *f*-map.
In the third carcinoma patient (Fig. 5), once more the tumor appears hypointense on the *f*-map. Again, tumor contrast on the *f*-map (5B) is higher than in the ADC-map (5C). In this case, the tumor appears larger than it is on the ADC-map because it is hardly discriminated from the neighboring vessel, whereas the *f*-map, where the vessels are clearly seen as hyperintense, shows the tumor's correct size.
Contrary the previous case, the carcinoma in the fourth cancer patient (Fig. 6) is overestimated in the *f*-map when compared to the ADC-map because it lies close to the dilated duct, and both are hypointense. In the ADC-map, the duct appears hyperintense and is thus more readily distinguishable from the lesion as previously seen in patient two (Fig. 4).

Chronic pancreatitis

Two cases of histopathologically confirmed pancreatitis mass lesions are shown in figures 7 through 9.
Figure 7 shows the venous phase contrast-enhanced CT, portal phase contrast-enhanced T1w, and T2w for the first pancreatitis patient. Note the mass-forming aspect of the lesion. On the ADC and *f*-maps for the same case (Fig. 8), the pancreatitis lesion can be outlined as clearly hypointense in the *f*-map. In the ADC-map, the lesion is partly hypo- and partly isointense compared to the surrounding tissue, and therefore hard to delineate. Note again that the poor lesion/vessel contrast might cause an overestimation of the total lesion size in the ADC-map (e.g. figure 5).
Figure 9 shows similar venous phase T1w, ADC, and *f*-maps where the mass-forming pancreatitis is hypodense in the CT and hypointense in T1w/T2w images. Compared to the previous case, note that the lesion is hard to detect on both the conventional MRI and the ADC-map, but that it stands out in stark contrast against both the non-affected pancreatic parenchyma and the surrounding vessels in the *f*-map.

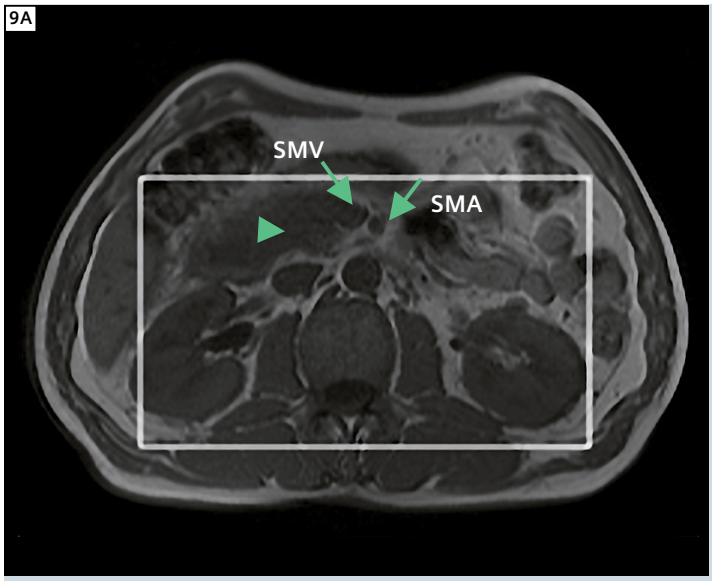

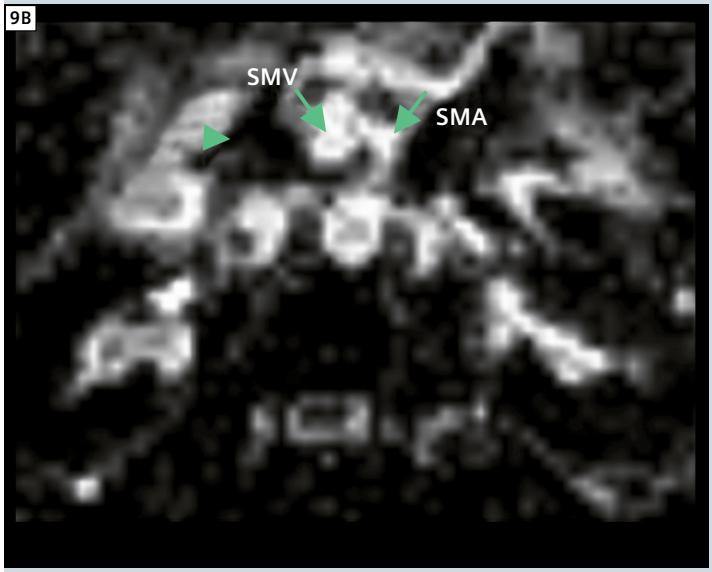

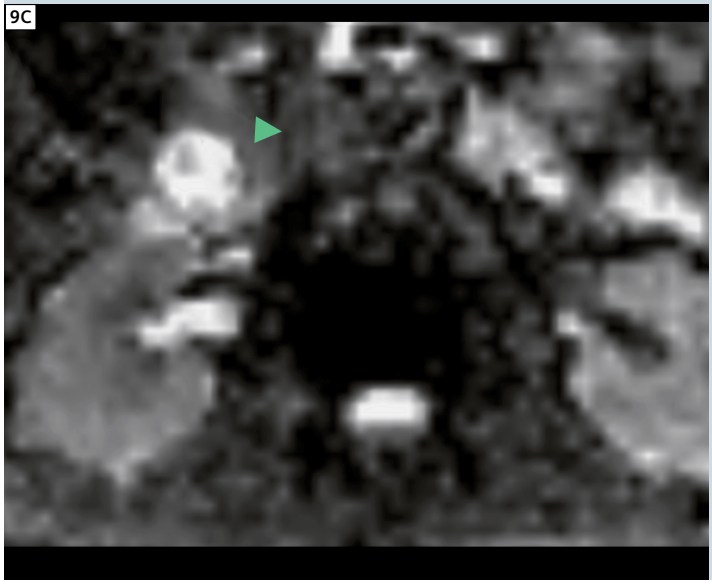

9 Axial T1w **(A)**, *f*-map **(B)** and ADC-map **(C)** for a second patient with histopathologically proven chronic pancreatitis with mass-formation in the head of the pancreas (green arrowhead). The lesion is seen as a well-delineated, hypointense area in the *f*-map, while it is less clearly delineated in the ADC-map. Also well-delineated in the *f*-map as in the T1w image, are the superior mesenteric vein (SMV) and superior mesenteric artery (SMA) (green arrows). (SMA = superior mesenteric artery; SMV = superior mesenteric vein).

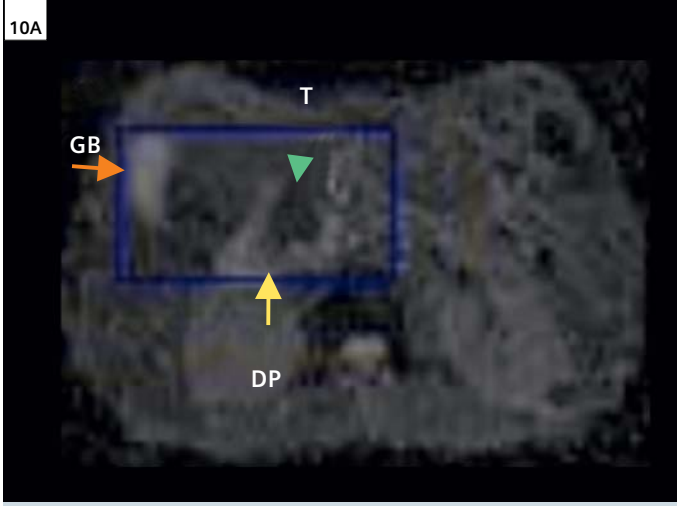

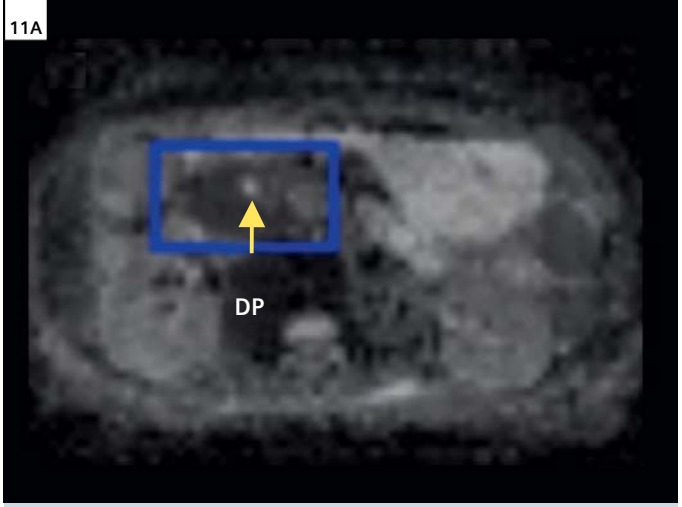

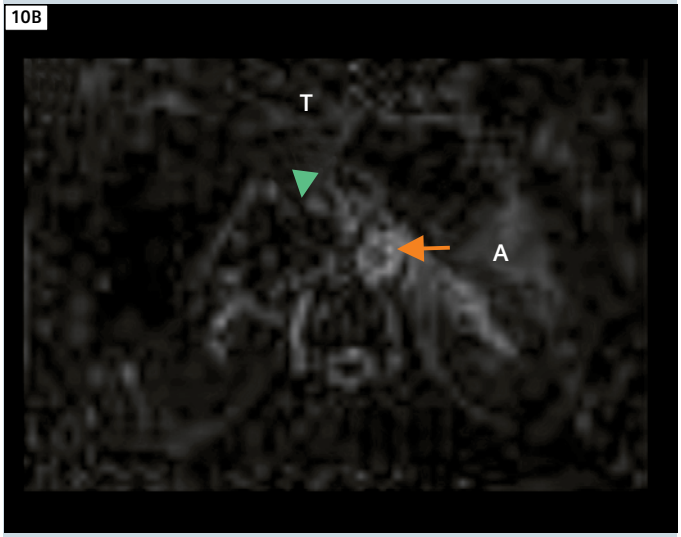

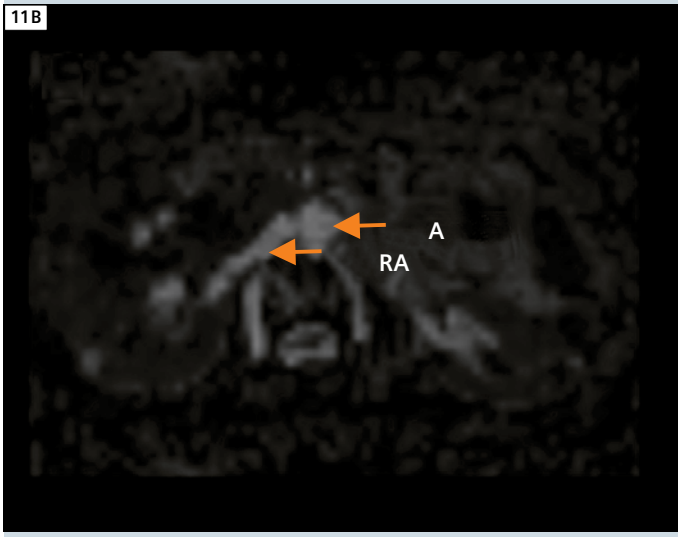

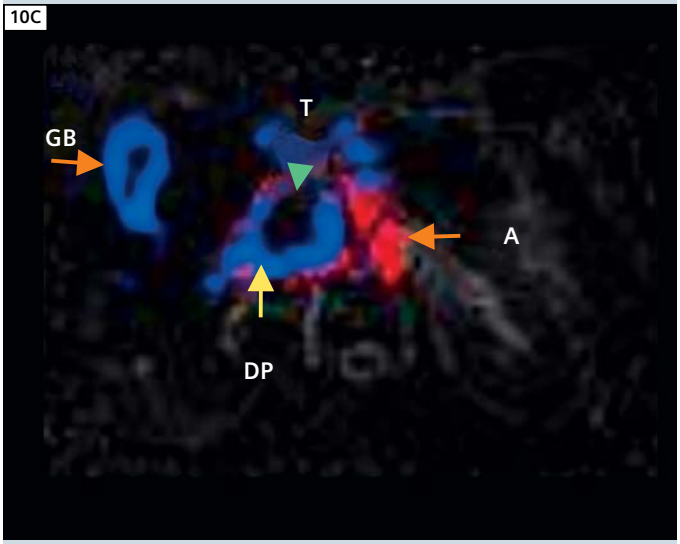

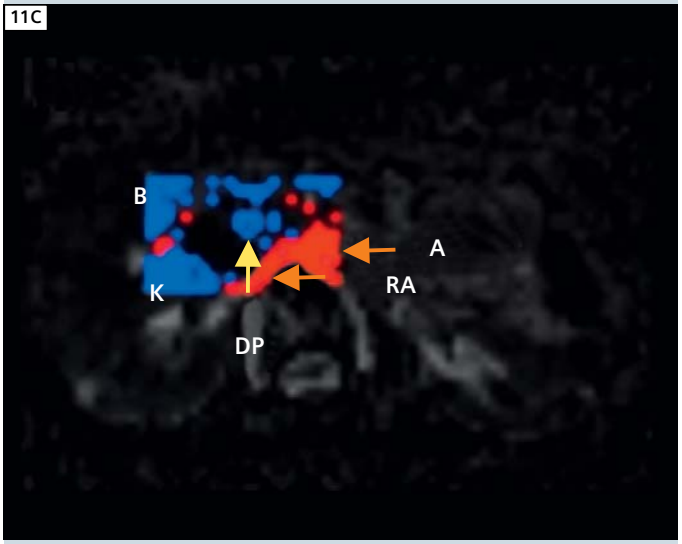

10 Axial ADC-map **(A)** and f-map **(B)** of the pancreatic carcinoma case previously presented in figures 2 and 3 along with an image which integrates both ADC- and f-map data **(C)**. In the integrated image **(C)**, a color mask is used to segment vascular (red) and ductal (blue) voxels according to f and ADC ranges described in the text. Note that the tumor is best delineated in the f-map if the pancreatic duct, which due to its curved path almost completely surrounds the tumor, is color-tagged according to the integrated data. (Dark blue rectangle in ADC-map = region of interest for calculating the color overlay; T = tumor; GB = gall bladder; DP = ductus pancreaticus; A = aorta).

11 Patient previously presented in figure 6 with the ADC **(A)** and f-map **(B)**. Image **(C)** shows the f-map with a vascular (red) and ductal (blue) segmentation overlay calculated by integrating the ADC and f data. Note that the pancreatic duct inside the tumor region can be readily identified on the f-map only with the help of the overlay. (Dark blue rectangle in ADC-map = region of interest for calculating color overlay; T = tumor; GB = gall bladder; DP = ductus pancreaticus; A = aorta; K = kidney; B = bowel).

f-maps with an ADC overlay

As seen in the previous cases, the f-map is superior to the ADC-map considering tumor detection in general. Also, the f-maps show an increased tumor/vessel contrast when compared to the ADC-maps, but have the disadvantage that adjacent ductal structures may coalesce with the tumor. To circumvent this, we developed a method to integrate both f and ADC in single parameter images where based on their unique combination of ranges of f and ADC values, voxels were tagged as belonging to either vessels, ducts, or solid tissue.

In figure 10, the f and ADC-maps of the patient previously presented in figures 1 and 2 are presented once more (10A, B). Figure 10C shows a color overlay on the f-map where the pancreatic duct, the gall bladder and the bile ducts are marked blue and the vessels are marked red, defined by the previously described f and ADC ranges. Note that the tumor size can now be estimated correctly. Figure 11 shows the patient previously presented in figure 6 with the ADC and f-map (11A, B). Note that the duct inside the tumor region can be readily identified on the f-map when the color tags are used. Other areas also marked blue include the kidney and the bowel.

Conclusion

in the cases presented, IVIM-based f-maps calculated from multiple b-value-weighted magnetic resonance data enabled the delineation of pancreatic lesions and demonstrated advantages over ADC imaging in their ability to distinguish vessels from low-perfused lesions, a crucial element of pancreatic cancer staging. However, which is less apt for distinguishing between lesion and pancreatic or bile ducts as were the ADC-maps. By considering both ADC and f-maps in combination, better lesion delineation can be achieved than by considering either parameter separately. Concerning lesion pathology differentiation: based on the current experience, it does not seem possible to differentiate between pancreatic carcinoma and pancreatitis using only the imaging aspects of the lesion in the f-map. Further research should elucidate the potential of quantitative approaches as means to address this issue. An advantage of ADC and f-maps when compared to the current imaging standards of concentional CT and ceMRI, is that neither technique uses ionizing radiation nor contrast agent. Since the acquisition takes only approximately 10 minutes, they may be not only safer but also more cost-effective than CT or conventional MRI. Combined ADC/f-maps may be particularly well suited for the assessment of lesions in patients who can not tolerate contrast agents. In these cases, appropriately combined non-contrast agent T1w/T2w MRI, ADC and f-maps would be recommended. This combination of non-invasive, non-contrast agent techniques, also shows promise as a screening method for post-treatment follow-up.

*WIP - Work in progress. This information about this product is preliminary. The product is under development and not commercially available in the U.S., and its future availability cannot be ensured.

References

1 Gemmel C, Eickhoff A, Helmstadter L, et al. Pancreatic cancer screening: state of the art. Expert Rev Gastroenterol Hepatol 2009;3:89–96.
2 Tamm EP, Silverman PM, Charnsangavej C, et al. Diagnosis, staging, and surveillance of pancreatic cancer. AJR Am J Roentgenol 2003;180:1311–1323.
3 Tamm EP, Bhosale PR, Lee JH. Pancreatic Ductal Adenocarcinoma: Ultrasound, Computed Tomography, and Magnetic Resonance Imaging Features. Semin Ultrasound CT MRI 2007;28:330–338.
4 Colagrande S, Carbone SF, Carusi LM, Cova M, Villari N. Magnetic resonance diffusion-weighted imaging: extraneurological applications. Radiol med (2006) 111:392–419.
5 Koh DM, Collins DJ Diffusion-weighted MRI in the body: applications and challenges in oncology. AJR Am J Roentgenol 2007;188:1622–1635.
6 Yoshikawa T, Kawamitsu H, Mitchell D, Ohno Y, Ku Y, Seo Y, Fujii M, Sugimura K. ADC Measurement of Abdominal Organs and Lesions Using Parallel Imaging Technique, AJR 2006;187:1521–1530.
7 Czako L. Diagnosis of early-stage chronic pancreatitis by secretin-enhanced magnetic resonance cholangiopancreatography. J Gastroenterol 2007; 42[Suppl XVII]:113–117.
8 Balci NC, Momtahen AJ, Akduman EI, Alkaade S, Bilgin M, Burton FR. Diffusion-weighted MRI of the pancreas: correlation with secretin endoscopic pancreatic function test (ePFT). Acad Radiol. 2008 Oct;15(10):1264–8.
9 Inan N, Arslan A, Akansel G, Anik Y, Demirci A. Diffusion-weighted imaging in the differential diagnosis of cystic lesions of the pancreas. AJR Am J Roentgenol. 2008 Oct;191(4):1115–21.
10 Fattahi R, Balci NC, Perman WH, Hsueh EC, Alkaade S, Havlioglu N, Burton FR. Pancreatic diffusion-weighted imaging (DWI): comparison between mass-forming focal pancreatitis (FP), pancreatic cancer (PC), and normal pancreas. J Magn Reson Imaging. 2009 Feb;29(2):350–6.
11 Matsuki M, Inada Y, Nakai G, et al. Diffusion-weighed MR imaging of pancreatic carcinoma. Abdom Imaging 2007;32:481-483.
12 Muraoka N, Uematsu H, Kimura H, et al. Apparent diffusion coefficient in pancreatic cancer: characterization and histopathological correlations. J Magn Reson Imaging 2008;27:1302–1308.
13 Le Bihan D. Intravoxel incoherent motion perfusion MR imaging: a wake-up call. Radiology. 2008 Dec; 249(3): 748–52.
14 Lee SS, Byun JH, Park BJ, Park SH, Kim N, Park B, Kim JK, Lee MG. Quantitative analysis of diffusion-weighted magnetic resonance imaging of the pancreas: usefulness in characterizing solid pancreatic masses. J Magn Reson Imaging 2008;28:928–936.
15 Luciani A, Vignaud A, Cavet M, Nhieu JT, Mallat A, Ruel L, Laurent A, Deux JF, Brugieres P, Rahmouni A. Liver cirrhosis: intravoxel incoherent motion MR imaging-pilot study. Radiology. 2008 Dec;249(3):748–52.
16 Le Bihan D MR imaging of incoherent motions: application to diffusion and perfusion in neurologic disorders. Radiology 1986;161:401–407.
17 Le Bihan D Seperation of Diffusion and Perfusion in Intra Voxel Incoherent Motion MR Imaging Radiology 1988;168:497–505.
18 Lemke A, Schad LR, Laun F, Stieltjes B. Differentiation of pancreas carcinoma from healthy pancreatic tissue using a wide range of b-values: Comparison of ADC and IVIM parameters. Proc. Intl. Soc. Mag. Reson. Med. 17 (2009):666.
19 M. Klauss, A. Lemke, K. Grünberg, M. N. Wente, H-U. Kauczor, S. Delorme, L. Grenacher, and B. Stieltjes. Evaluation of low and high b-values for the differentiation between pancreatic carcinoma and chronic pancreatitis using Diffusion-Weighted Imaging. Proc. Intl. Soc. Mag. Reson. Med. 17 (2009): 4031.

Contact
Bram Stieltjes, M.D.
German Cancer Research Center (DKFZ)
Department of Radiology - E 010
Im Neuenheimer Feld 280
69120 Heidelberg
Germany
Tel.: +49(0)6221 42-2492
b.stieltjes@dkfz.de

32-Channel Head Coil Imaging at 3T

Thomas Benner

Athinoula A. Martinos Center for Biomedical Imaging, Department of Radiology, Massachusetts General Hospital and Harvard Medical School, Boston, MA, USA

The new 32-channel head coil for 3T provides considerable benefits over the standard Head Matrix coil. The coil sensitivity and therefore signal-to-noise ratio (SNR) is increased over the whole head [1]. Parallel imaging performance (better g-factor) is increased in any direction, including 2D acceleration for 3D imaging [2]. In practice, these advantages translate into image data with better quality where higher SNR, less distortion in EPI scans, higher resolution or shorter scan times can be traded off. All data in this report were acquired on a 3T MAGNETOM Trio, A Tim System scanner (software version *syngo* MR B15A, SP2). Two scan sessions were performed on a healthy appearing volunteer. In one session the standard 12-channel Head Matrix coil was used. In another session the 32-channel head coil was used.

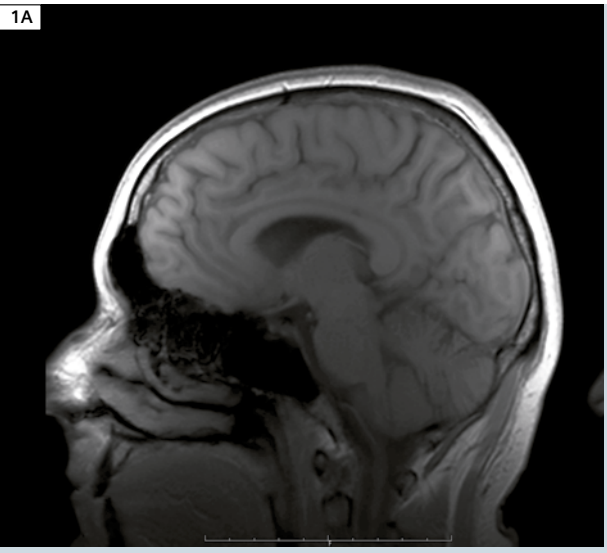

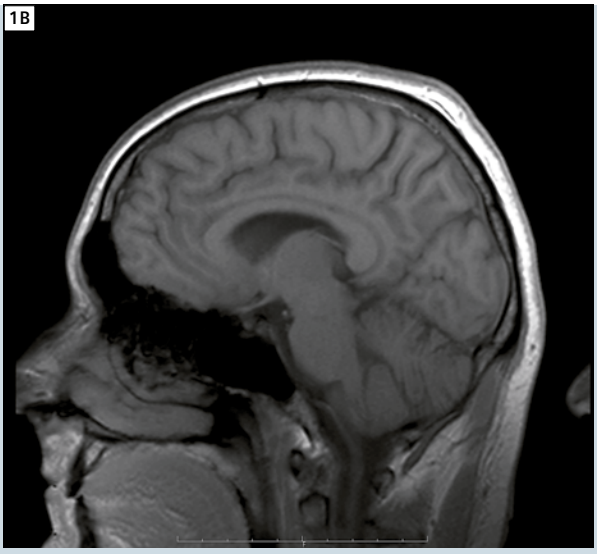

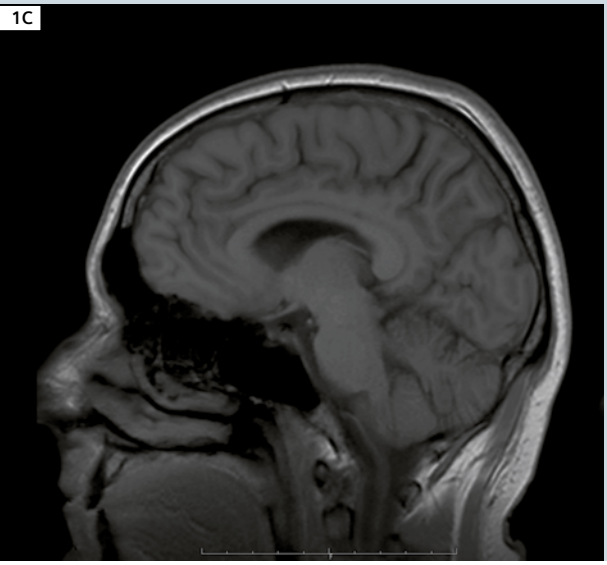

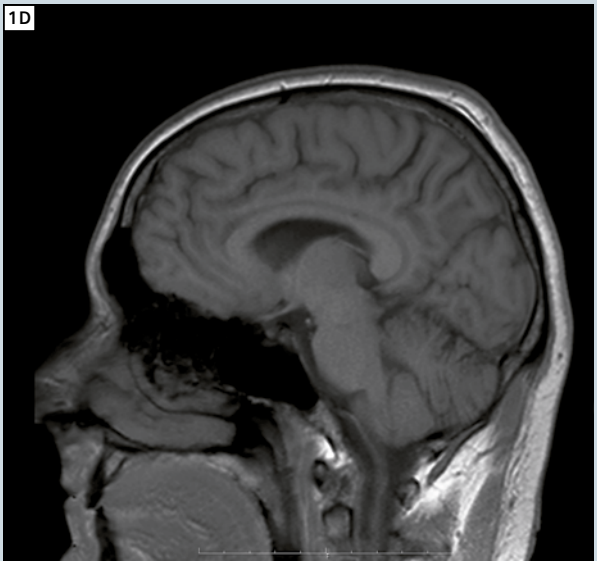

1 T1w 2D FLASH (sagittal orientation, PAT factor 2): top row: unfiltered images; bottom row: pre-scan normalized images; left column: 32-channel head coil; right column: Head Matrix coil. **32, Matrix:** T1w 2D FLASH (sagittal orientation, PAT factor 2), TR 280 ms, TE 2.57 ms, FOV 230 × 230 mm², matrix 256 × 256, 25 slices, slice thickness 5 mm, distance factor 20%, bandwidth 270 Hz/pixel, flip angle 70°, 1 acquisition, PAT mode GRAPPA, acceleration factor PE 2, reference lines PE 24, matrix coil mode auto (triple), reference scan mode integrated, coil combine mode adaptive combine, TA 0:39 min.

To ensure matching slice prescription, AutoAlign was run at the beginning of the session as well as in the middle of the session to adjust for potential subject motion during the study [3–5]. The following examples compare the 32-channel head coil to the Head Matrix coil in terms of image homogeneity, SNR, and parallel imaging performance.

Image homogeneity

The strong gradient of the coil sensitivities of the 32-channel head coil leads to a larger gradient of signal intensities from areas close to the coil elements to areas more distant from the coil elements as compared to the Matrix coil. Therefore, application of the pre-scan normalize filter is essential for homogeneous signal intensities over the whole scan volume. As can be seen from

2

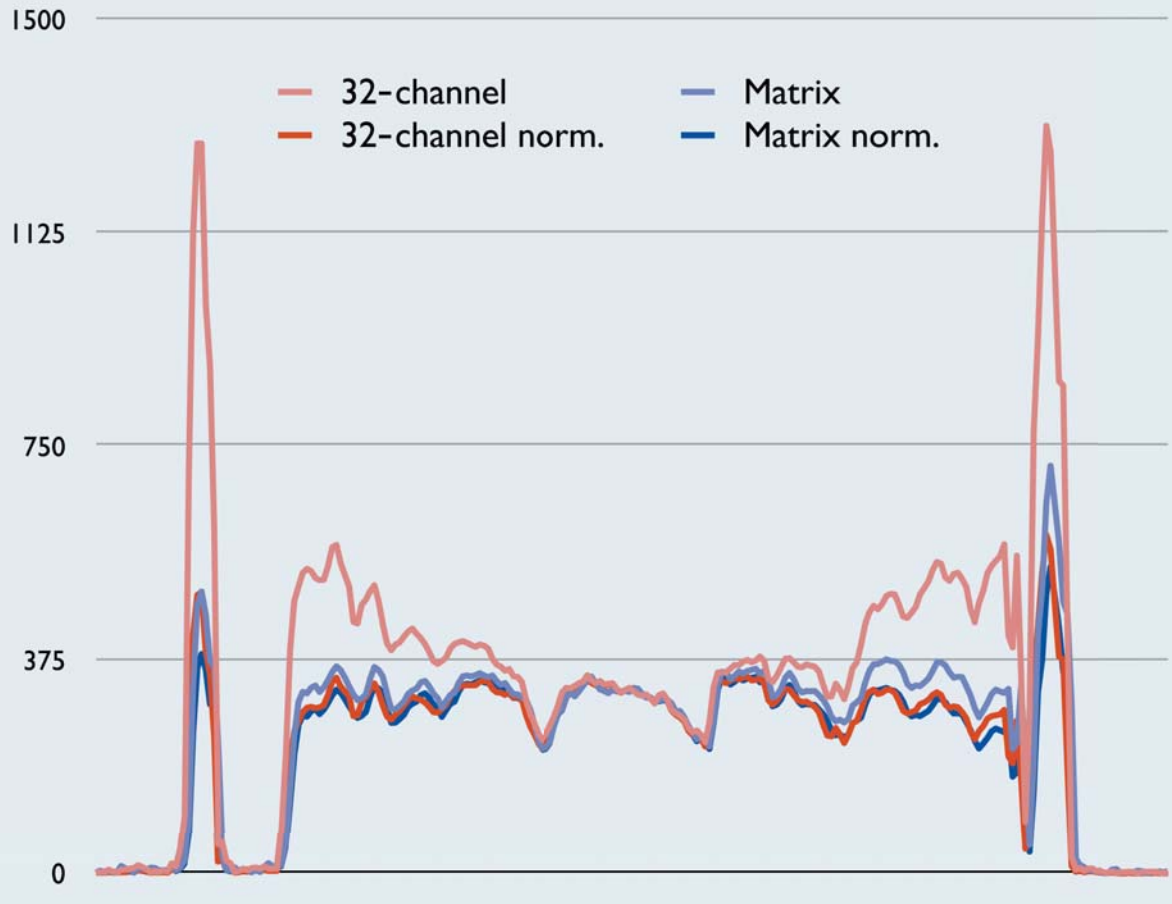

2 T1w 2D FLASH (sagittal orientation, PAT factor 2); horizontal signal intensity profiles for the center row of the images shown in Fig. 1, normalized to the mean signal intensity of the middle 16 pixels. Note the close match of the signal intensity profiles between 32-channel head coil and Head Matrix coil, demonstrating how well pre-scan normalize works. It also shows the very good performance of AutoAlign to align the slice prescription from one session to the other.

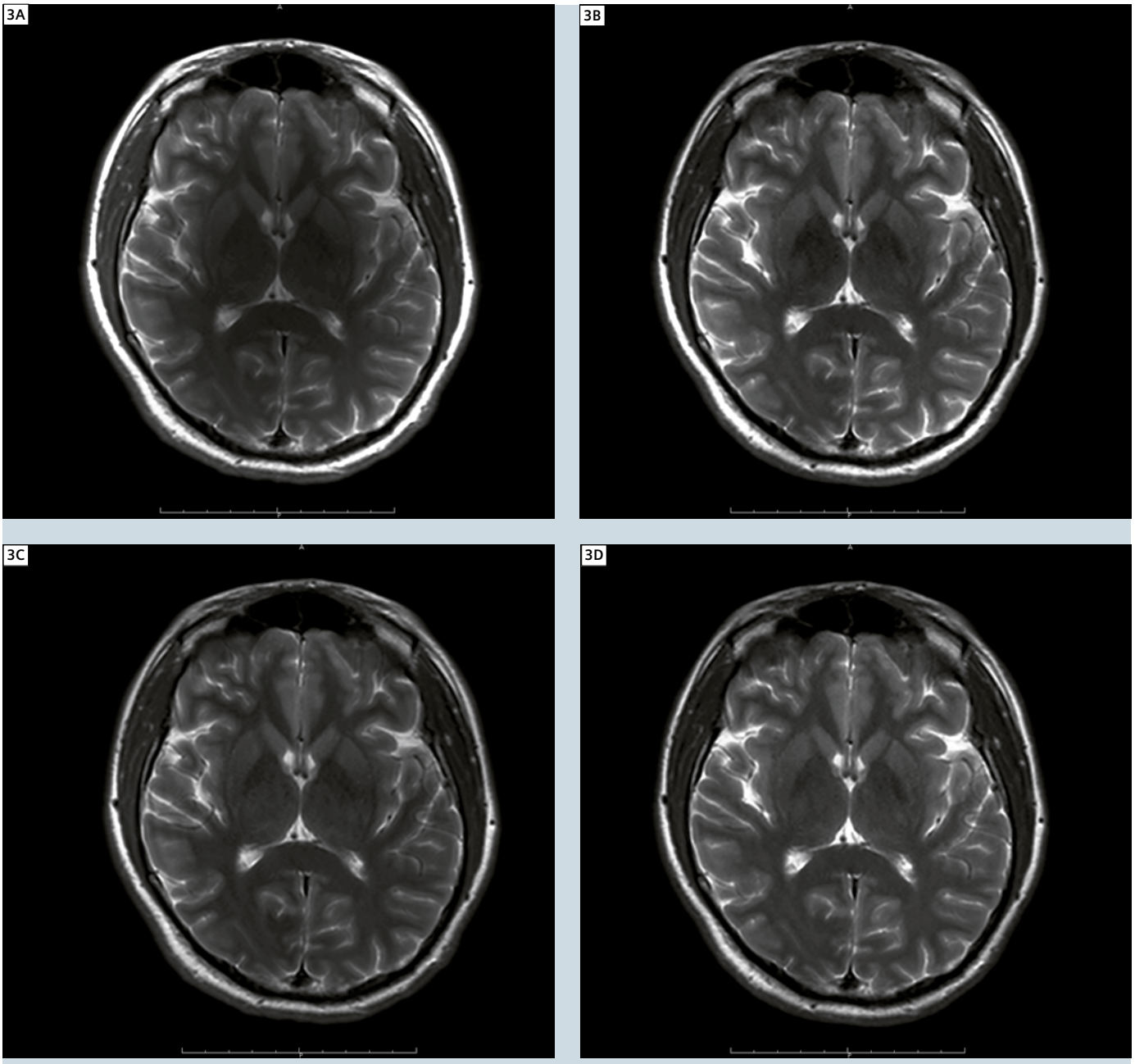

3 T2w TSE (transversal orientation, PAT factor 2); top row: unfiltered images; bottom row: pre-scan normalized images; left column: 32-channel head coil; right column: Head Matrix coil. **32, Matrix:** T2w TSE (transversal orientation, PAT factor 2, TR 6210 ms, TE 84 ms, FOV 220 × 192.5 mm², matrix 256 × 224, 25 slices, slice thickness 5 mm, distance factor 20%, bandwidth 260 Hz/pixel, flip angle 120°, turbo factor 26, 1 acquisition, PAT mode GRAPPA, acceleration factor PE 2, reference lines PE 35, matrix coil mode auto (triple), reference scan mode integrated, coil combine mode adaptive combine, TA 0:39 min.

4

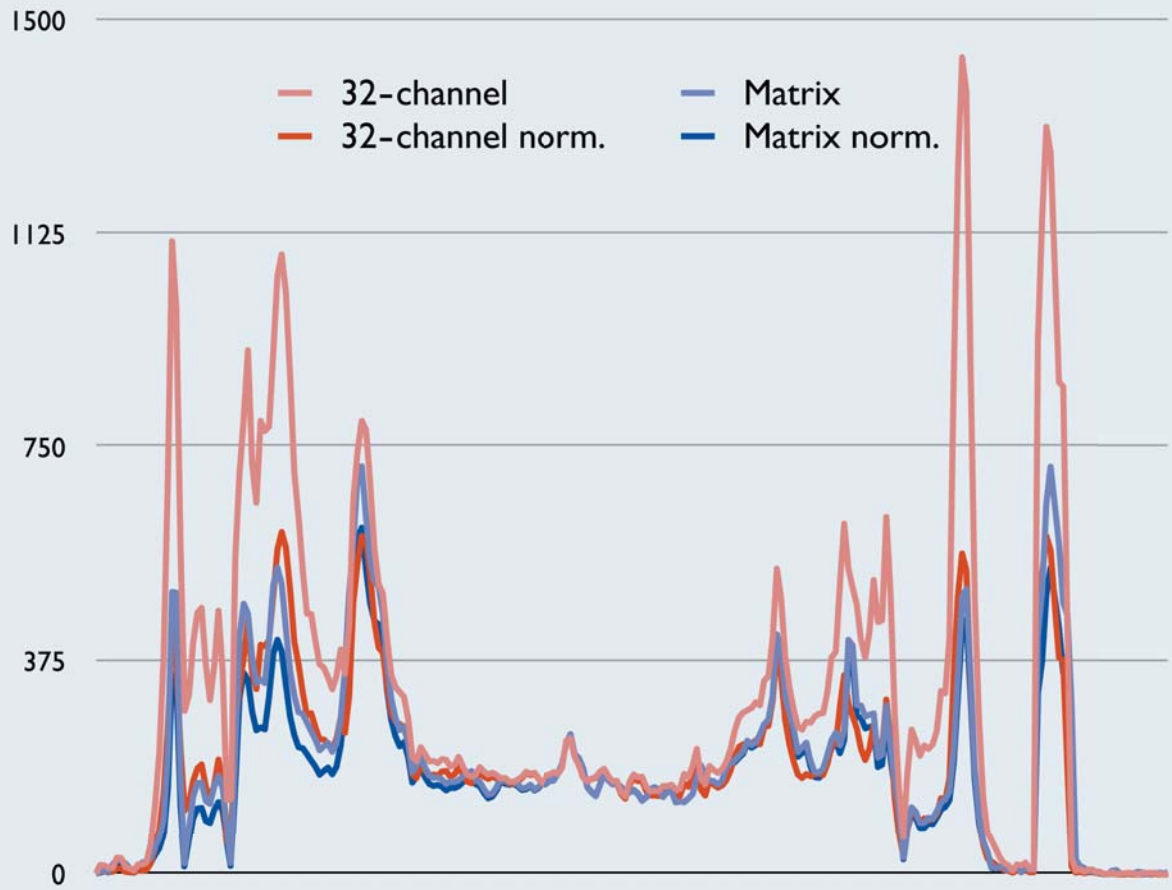

4 T2w TSE (transversal orientation, PAT factor 2; horizontal signal intensity profiles for the center row of the images shown in Fig. 3, normalized to the mean signal intensity of the middle 16 pixels. Note the close match of the signal intensity profiles between 32-channel head coil and Head Matrix coil, demonstrating how well pre-scan normalize works. It also shows the very good performance of auto-align to align the slice prescription from one session to the other.

Figures 1–4, the pre-scan normalize filter works well for both head coils. In case of the 32-channel head coil where the signal intensities become very high towards the periphery of the brain, application of the pre-scan normalize filter results in a flattened signal intensity profile very similar to that of the Head Matrix coil after application of the pre-scan normalize filter. Note, though, that the SNR gain of the 32-channel coil is retained. In comparison, the pre-scan normalize filter has little effect on the images from the Matrix coil.

SNR

Compared to the Head Matrix coil the SNR of the 32-channel head coil is ~20% better at the center of the brain and at least 100% better at the periphery of the brain [1]. The improved SNR can be easily appreciated in Fig. 5. A gradient of SNR from the periphery to the center of the brain can be seen for both coils. Increasing the PAT factor from 2 to 3 causes a drop in SNR that is more noticeable when using the Matrix coil, especially in the center of the brain, demonstrating the better g-factor of the 32-channel head coil.

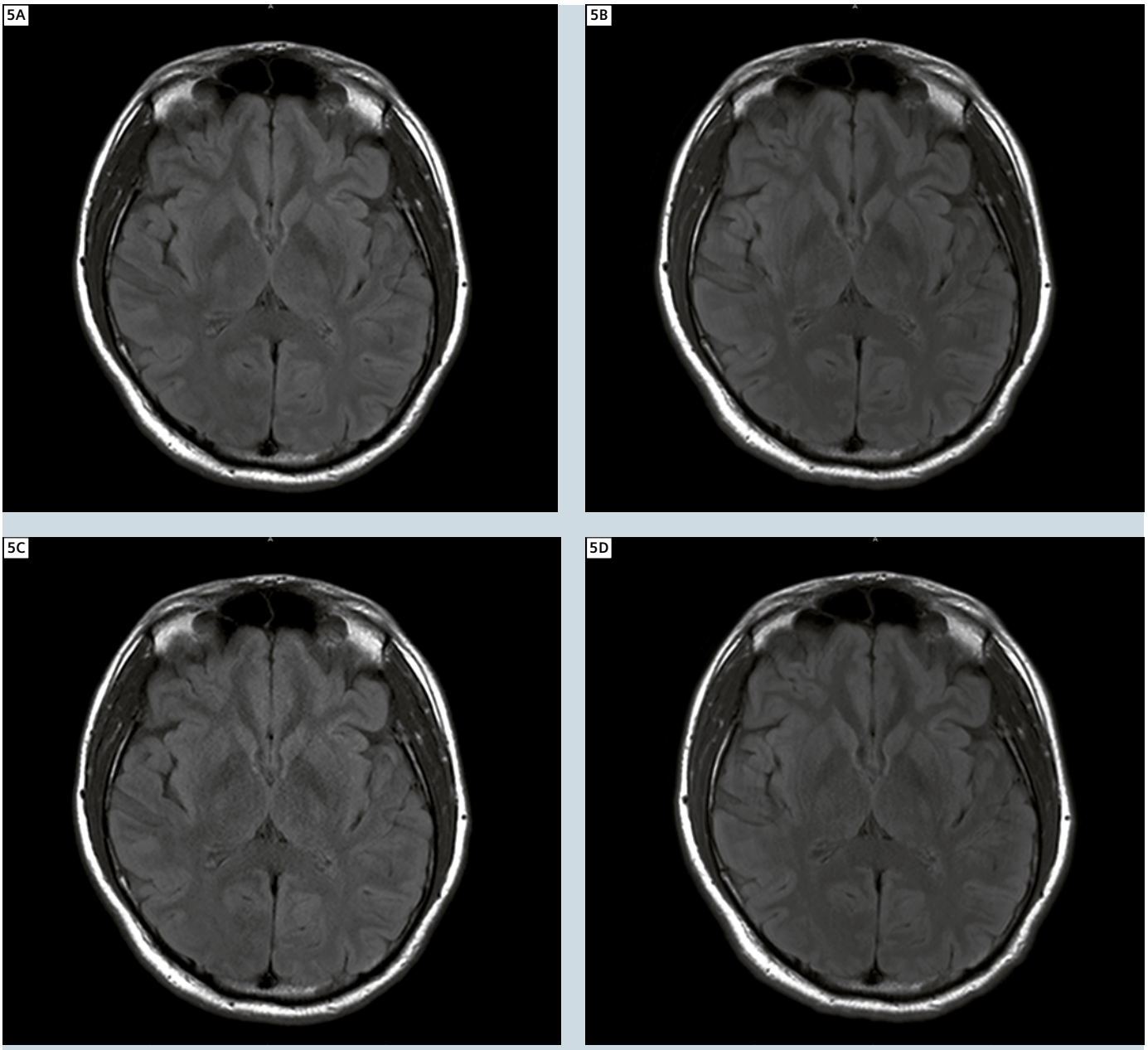

5 T2w TIRM (DarkFluid, transversal orientation, PAT factor 2 / 3); top row: PAT 2; bottom row: PAT 3; left column: 32-channel head coil; right column: Head Matrix coil. **32, Matrix:** T2w TIRM (DarkFluid, transversal orientation, PAT factor 2), TR 7000 ms, TE 81 ms, TI 2500 ms, FOV 220 × 192.5 mm², matrix 256 × 224, 25 slices, slice thickness 5 mm, distance factor 20%, bandwidth 271 Hz/pixel, flip angle 120°, turbo factor 16, 1 acquisition, 2 concatenations, PAT mode GRAPPA, acceleration factor PE 2, reference lines PE 31, matrix coil mode auto (triple), reference scan mode integrated, coil combine mode adaptive combine, pre-scan normalize filter, TA 2:08 min; **32, Matrix:** T2w TIRM (DarkFluid, transversal orientation, PAT factor 3), same as above but for: acceleration factor PE 3, reference lines PE 32, TA 1:40 min.

While image quality (SNR) is better when using the 32-channel head coil compared to Head Matrix coil at an PAT factor of 2, the difference becomes much more obvious when using an PAT factor of 2×2 (Fig. 6). Image quality of the PAT 2×2 scan with the 32-channel head coil (scan time 2:42 min) is comparable to the image quality of the PAT 2 scan with the Head Matrix coil (scan time 4:43 min) i.e. a 43% reduction of scan time can be achieved without image quality loss.

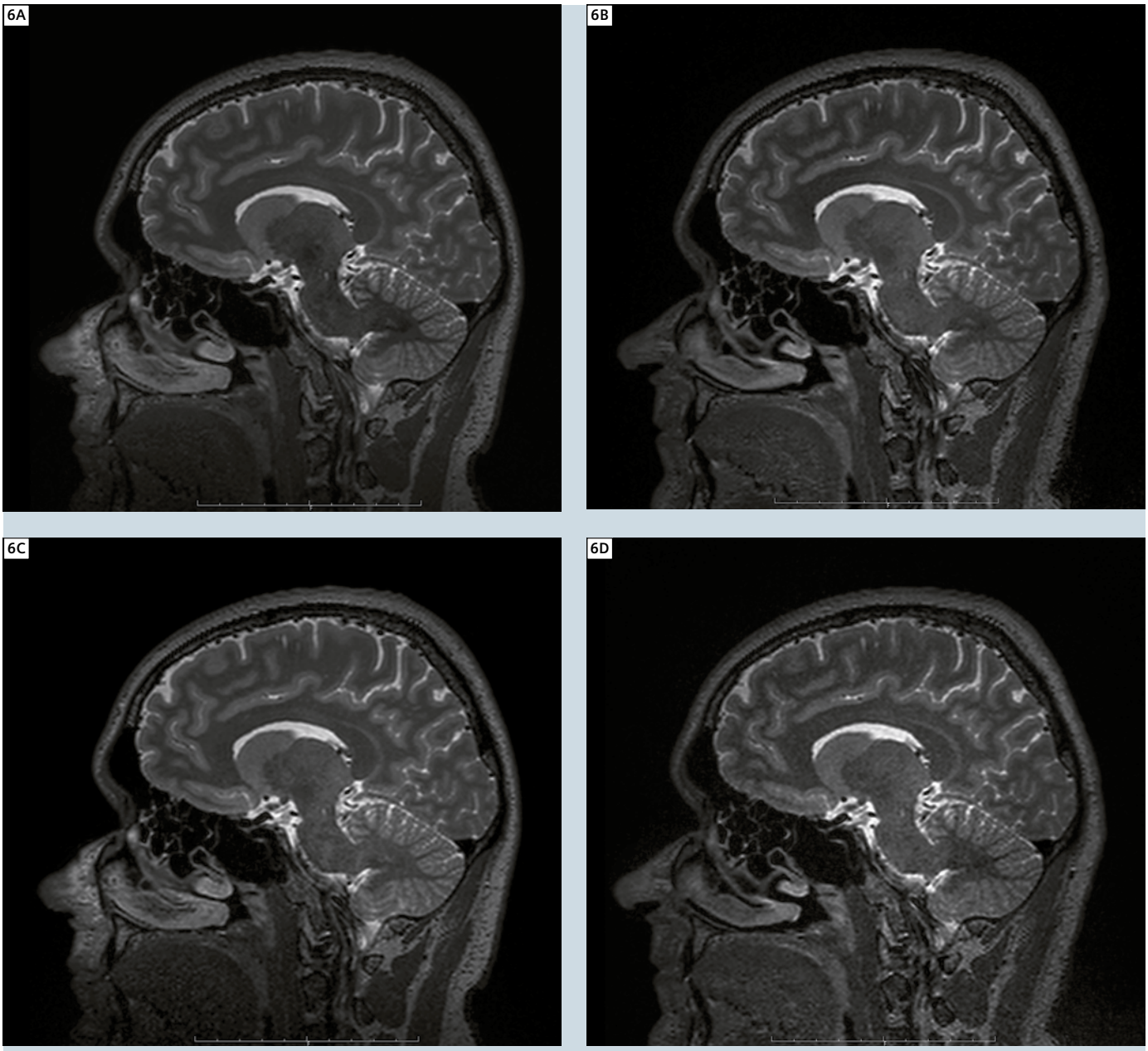

6 Isotropic T2w 3D SPACE (sagittal orientation, PAT factor 2 / 2x2); top row: PAT 2; bottom row: PAT 2×2; left column: 32-channel head coil; right column: Head Matrix coil. **32, Matrix:** Isotropic T2w 3D SPACE (sagittal orientation, PAT factor of 2), TR 3200 ms, TE 403 ms, FOV 250 × 250 mm², matrix 256 × 256, 176 slices per slab, slice thickness 1 mm, bandwidth 751 Hz/pixel, turbo factor 141, 1 acquisition, PAT mode GRAPPA, acceleration factor PE 2, reference lines PE 24, acceleration factor 3D 1, matrix coil mode auto (triple), reference scan mode integrated, coil combine mode adaptive combine, pre-scan normalize filter, TA 4:43 min; **32, Matrix:** Isotropic T2w 3D SPACE (sagittal orientation, PAT factor 2x2), same as above but for: acceleration factor 3D 2, reference lines 3D 24, TA 2:42 min.

Parallel imaging

Figures 7 and 8 demonstrate parallel imaging performance of the two head coils with increasing PAT factor for DTI (Diffusion Tensor Imaging) scans. At a PAT factor of 4 the image data becomes unusable for the Matrix coil while the 32-channel coil still provides reasonable image quality. Image quality of the 32-channel head coil data with PAT factors 3 and 4 compares well with image quality of the Matrix coil at PAT factors 2 and 3, respectively. The figures also

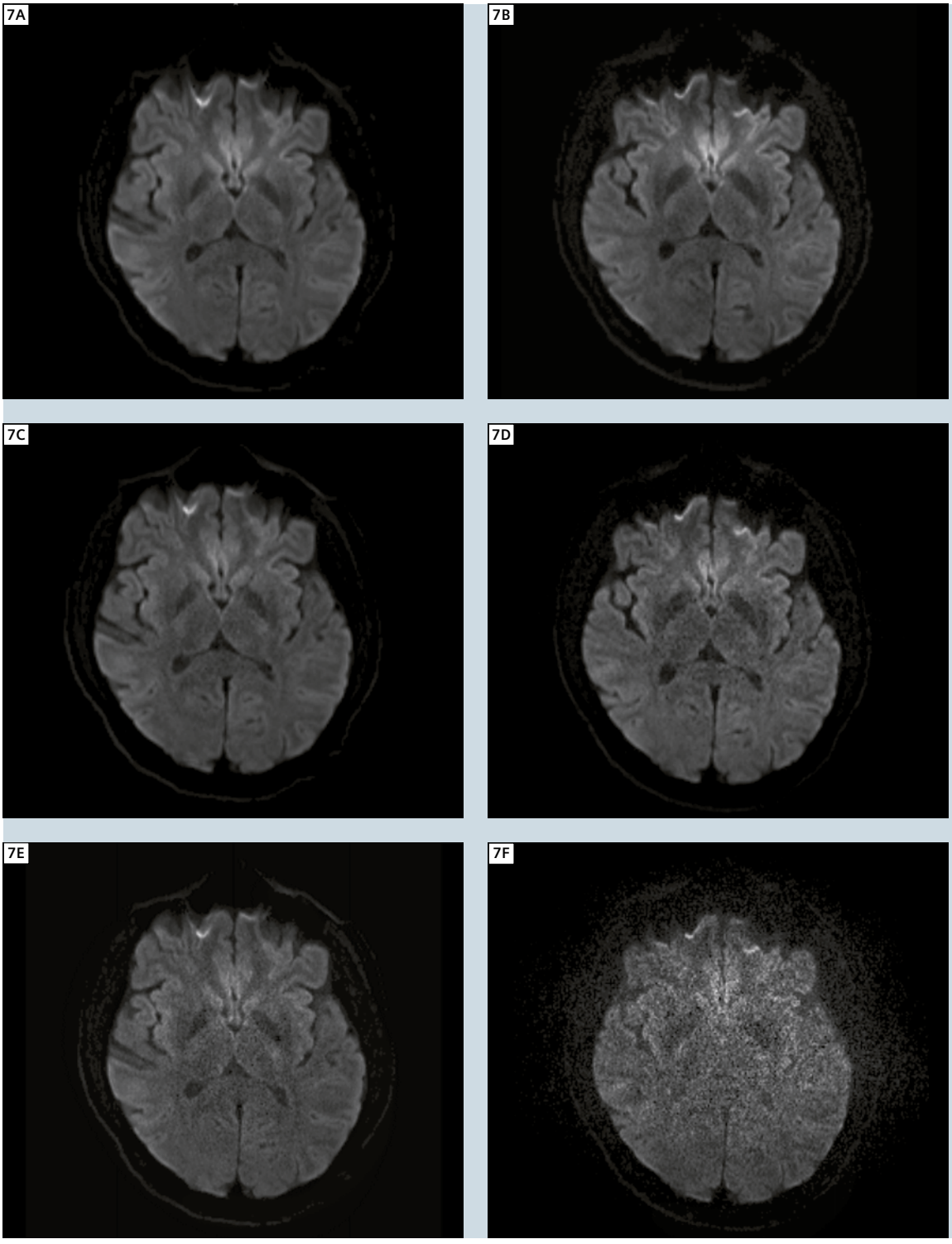

7 Diffusion-weighted imaging (DWI) 2D EPI (transversal orientation, 6 diffusion directions (MDDW), PAT factor 2 / 3 / 4); top row: PAT 2; middle row: PAT 3; bottom row: PAT 4; left column: 32-channel head coil; right column: Head Matrix coil. **32, Matrix:** DWI 2D EPI (transversal orientation, 6 diffusion directions (MDDW), PAT factor 2), TR 3900 ms, TE 94 ms, FOV 220 × 220 mm², matrix 192 × 192, phase partial Fourier 6/8, 25 slices, slice thickness 5 mm, distance factor 20%, bandwidth 1184 Hz/pixel, 1 acquisition, 2 diffusion weightings, b1 0 s/mm², b_2 1000 s/mm², 6 diffusion directions, PAT mode GRAPPA, acceleration factor PE 2, reference lines PE 40, matrix coil mode auto (triple), reference scan mode separate, coil combine mode adaptive combine, pre-scan normalize filter, TA 0:41 min; **32, Matrix:** DWI 2D EPI (transversal orientation, 6 diffusion directions (MDDW), PAT factor 3), same as above but for: acceleration factor PE 3, reference lines PE 48, TA 0:41 min; **32, Matrix:** DWI 2D EPI (transversal orientation, 6 diffusion directions (MDDW), PAT factor 4), same as above but for: acceleration factor PE 4, reference lines PE 128, TA 0:49 min.

show a decrease in distortions with increasing PAT factor because of the shorter EPI readout. Scan times are 0:41 min, 0:41 min and 0:49 min for PAT factors of 2, 3 and 4, respectively. In the case of EPI, scan times are not reduced with increasing PAT factor as is typically the case for non EPI scans. This is due to the increased number of PAT reference scans that are required with higher PAT factors.

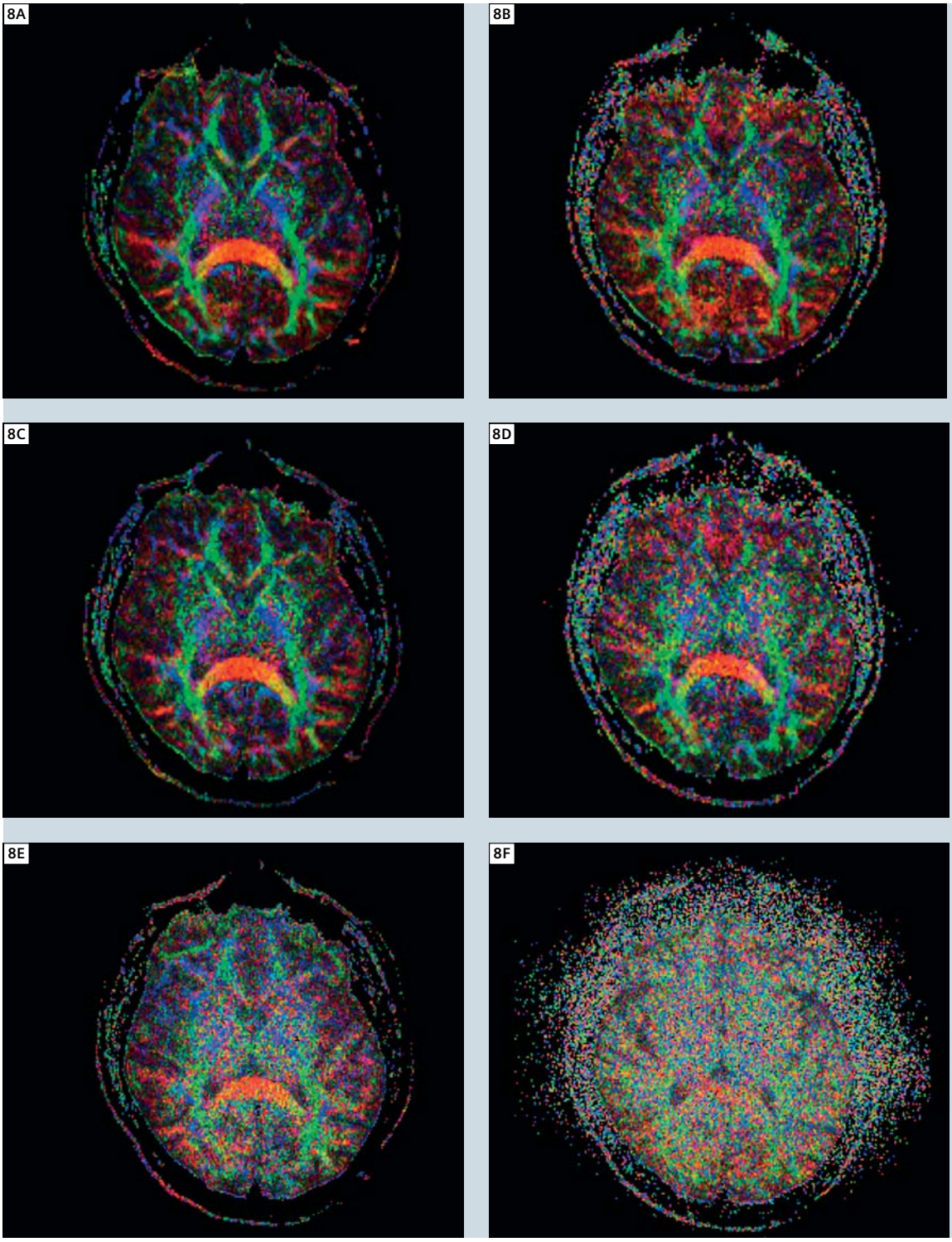

8 Diffusion-weighted imaging (DWI) 2D EPI (transversal orientation, 6 diffusion directions (MDDW), PAT factor 2 / 3 / 4); top row: PAT 2; middle row: PAT 3; bottom row: PAT 4; left column: 32-channel head coil; right column: Head Matrix coil. **32, Matrix:** DWI 2D EPI (transversal orientation, 6 diffusion directions (MDDW), PAT factor 2), TR 3900 ms, TE 94 ms, FOV 220 × 220 mm², matrix 192 × 192, phase partial Fourier 6/8, 25 slices, slice thickness 5 mm, distance factor 20%, bandwidth 1184 Hz/pixel, 1 acquisition, 2 diffusion weightings, b1 0 s/mm², b_2 1000 s/mm², 6 diffusion directions, PAT mode GRAPPA, acceleration factor PE 2, reference lines PE 40, matrix coil mode auto (triple), reference scan mode separate, coil combine mode adaptive combine, pre-scan normalize filter, TA 0:41 min; **32, Matrix:** DWI 2D EPI (transversal orientation, 6 diffusion directions (MDDW), PAT factor 3), same as above but for: acceleration factor PE 3, reference lines PE 48, TA 0:41 min; **32, Matrix:** DWI 2D EPI (transversal orientation, 6 diffusion directions (MDDW), PAT factor 4), same as above but for: acceleration factor PE 4, reference lines PE 128, TA 0:49 min.

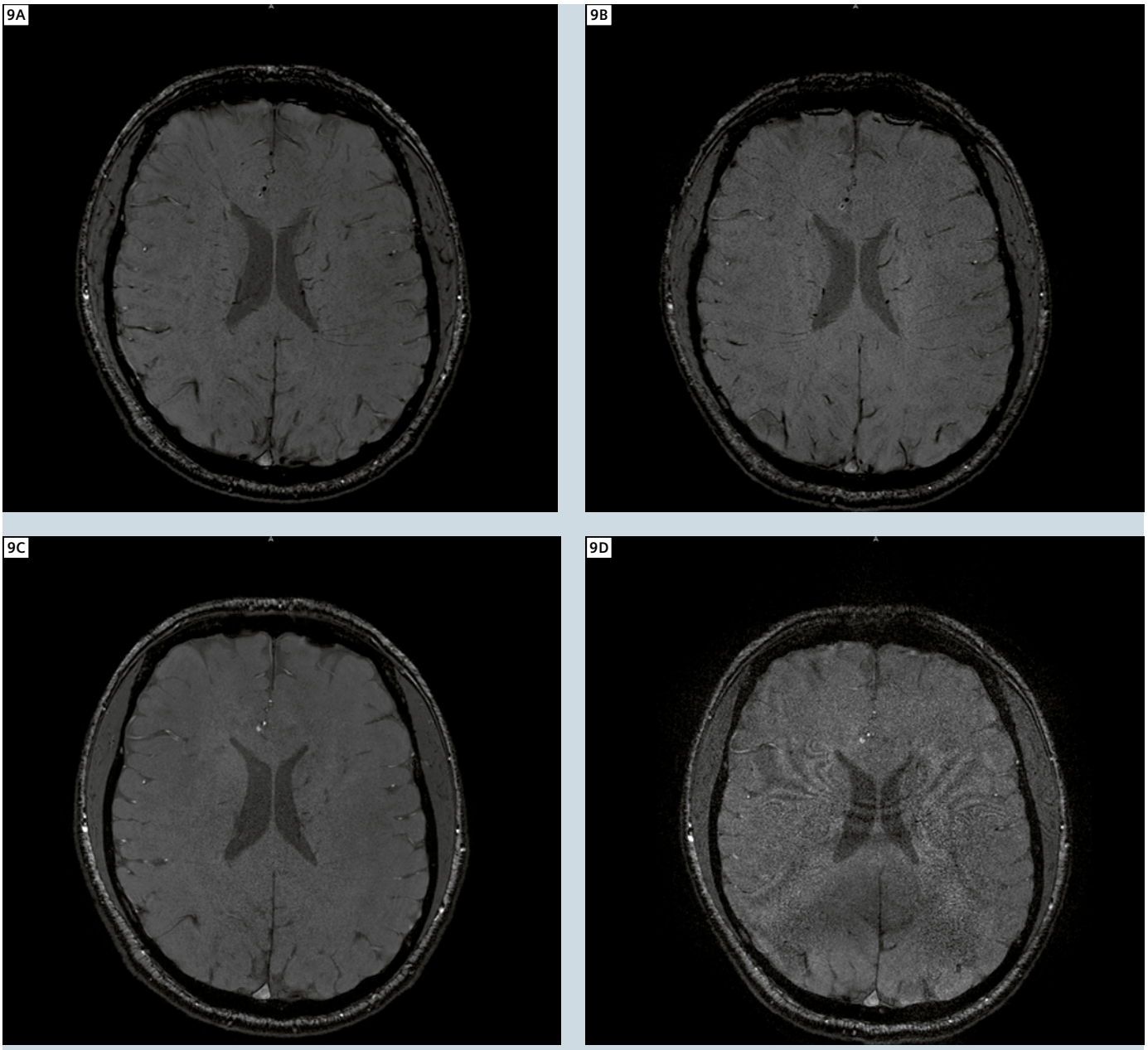

9 Susceptibility-weighted imaging (SWI) 3D FLASH (transversal orientation, PAT factor 2): PAT 2; bottom row: PAT 2x2; left column: 32-channel head coil; right column: Head Matrix coil. **32, Matrix:** SWI 3D FLASH (transversal orientation, PAT factor 2), TR 28 ms, TE 20 ms, FOV 230 × 179.6 mm², matrix 448 × 297, 72 slices per slab, slice thickness 1.2 mm, slice oversampling 22.2%, bandwidth 120 Hz/pixel, flip angle 15°, 1 acquisition, PAT mode GRAPPA, acceleration factor PE 2, reference lines PE 24, acceleration factor 3D 1, matrix coil mode auto (triple), reference scan mode integrated, coil combine mode adaptive combine, pre-scan normalize filter, TA 6:38 min; **32, Matrix:** SWI 3D FLASH (transversal orientation, PAT factor 2x2), same as above but for: acceleration factor 3D 2, reference lines 3D 24, TA 3:17 min.



32-channel head coil.

Figure 9 again demonstrates the better g-factor of the 32-channel head coil compared to the Head Matrix coil. While image quality is acceptable when using the Matrix coil at PAT 2, it becomes unacceptable when using an acceleration factor of 2×2. At this setting, the 32-channel head coil still performs well. At similar image quality, a 50% reduction of scan time from 6:38 min to 3:17 min is achievable with the 32-channel head coil.

Conclusions

The 32-channel head coil provides better performance compared to the Head Matrix coil in terms of SNR and parallel imaging capabilities. The SNR is improved over the whole head with the periphery of the brain benefitting the most. Because of the almost 3x number of coil elements, parallel imaging performance is improved i.e. the acceleration factor can be increased without imaging artifacts and with an SNR that is comparable to that of the Matrix coil at a lower PAT factor. It should also be noted that acceleration is possible in any direction with the 32-channel head coil since the coil elements are distributed on a helmet shaped geometry, thereby allowing arbitrary slice prescriptions without having to consider the direction of the acceleration.

Because of the helmet shaped form that conforms closely to the head, the 32-channel head coil has the disadvantage that some subjects with large head circumference will not be able to fit into the coil and will have to be scanned using the Matrix coil instead. Image reconstruction times can be slightly increased as well when using the 32-channel head coil since about 3 times the data volume has to be processed. However, this is not a problem in routine imaging when using the high-end image reconstruction computer.

References

1 Stapf J. 32-Channel Phased-Array Head Coil for 1.5T and 3T. MAGNETOM Flash 1/2008, 45.
2 Wald LL; Wiggins G. Highly Parallel Detection for MRI. MAGNETOM Flash 1/2008, 34–44.
3 van der Kouwe AJ, Benner T, Fischl B, Schmitt F, Salat DH, Harder M, Sorensen AG, Dale AM. On-line automatic slice positioning for brain MR imaging. Neuroimage. 2005 Aug 1;27(1):222–230.
4 Benner T, Wisco JJ, van der Kouwe AJ, Fischl B, Vangel MG, Hochberg FH, Sorensen AG. Comparison of manual and automatic section positioning of brain MR images. Radiology. 2006 Apr;239(1):246–254.
5 Scott KT. Software Compensation for Patient Position Enabling Reproducible Slice Positioning – AutoAlign. MAGNETOM Flash 1/2006, 98–103.

Contact
Thomas Benner
Athinoula A. Martinos Center
for Biomedical Imaging
Dept. of Radiology
Massachusetts General Hospital
and Harvard Medical School
Boston, MA
USA
benner@nmr.mgh.harvard.edu

First Clinical Experiences with a Prototype* of a Novel Cardiac Workflow Engine

Russell Bull, MRCP, FRCR.; Matthew Benbow

Royal Bournemouth Hospital, Bournemouth, UK

Introduction

In November 2007 a novel cardiac work in progress (WIP) software package was introduced on our 1.5T Siemens MAGNETOM Avanto MRI system (high-order shim, 32-channels, SQ gradients). This WIP system automates or augments most user interactions during cardiac scanning. For localization of standard cardiac planes users select anatomical reference points on the heart, supported by guidance images and text (Fig. 1). The software then calculates all cardiac planes automatically and applies them to all subsequent measurements. Sequences are automatically adapted to the patients heart rate and breath-hold capability according to the exam settings entered by the user (Fig. 2). The field-of-view is automatically adjusted for each combination of planes to fit the individual patient. Reliable, robust protocols can be constructed ensuring a comprehensive cardiac exam but still allowing enough flexibility to add additional sequences such as flow, tagged grid, constriction tests, etc.

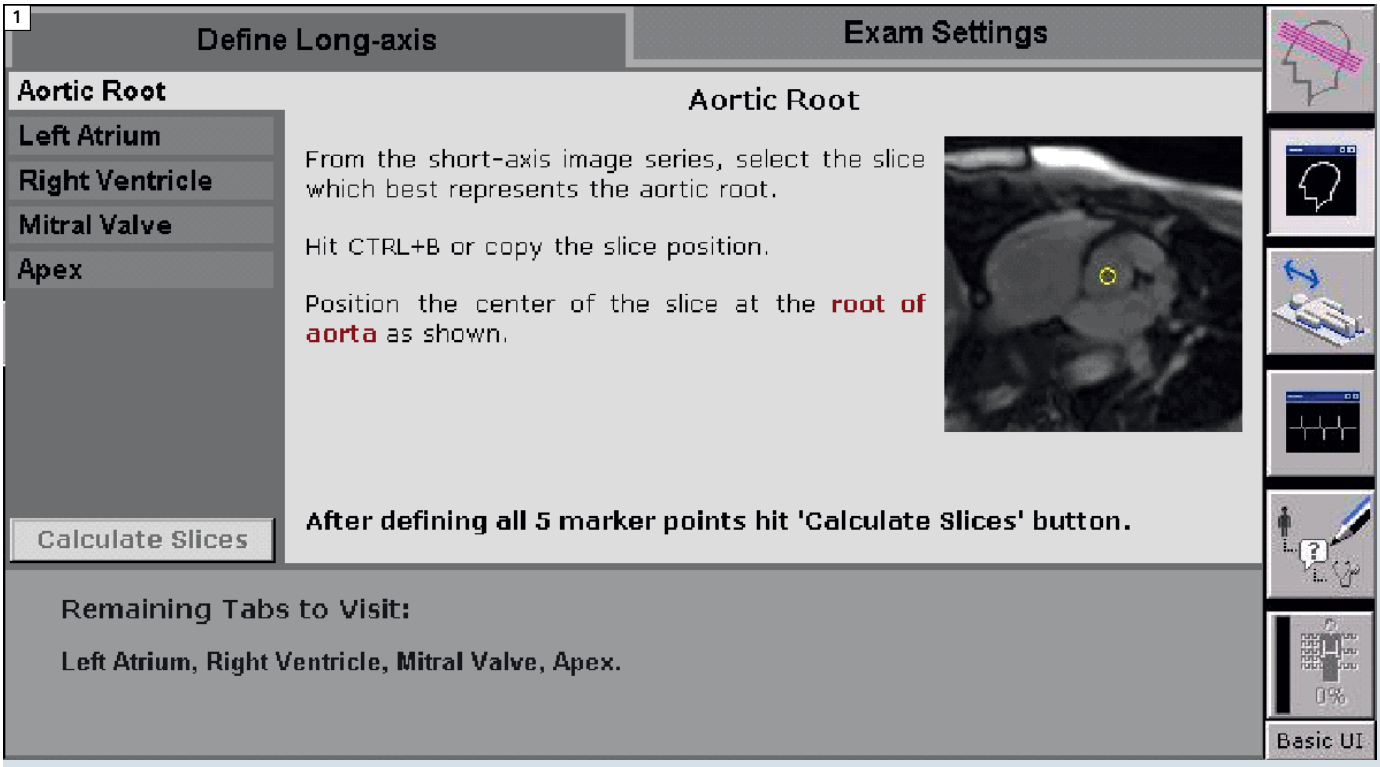

1 Novel way of localization of the heart: The user marks five anatomical landmarks. To find the landmarks, guiding text and example images are displayed. These landmarks are consecutively used to calculate all cardiac planes.

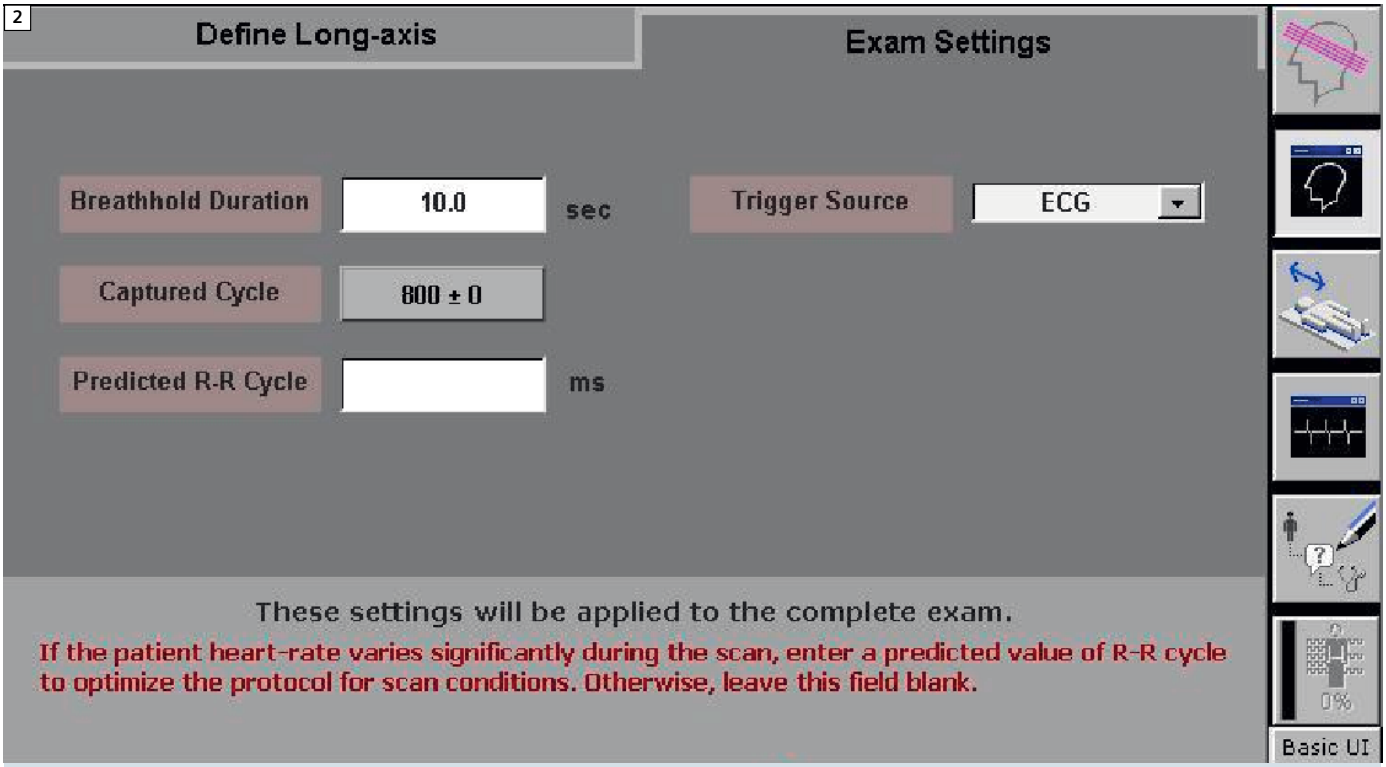

2 Exam Settings – Patient-centric parameters which globally influence the whole exam and are used to initialize the scan protocols.

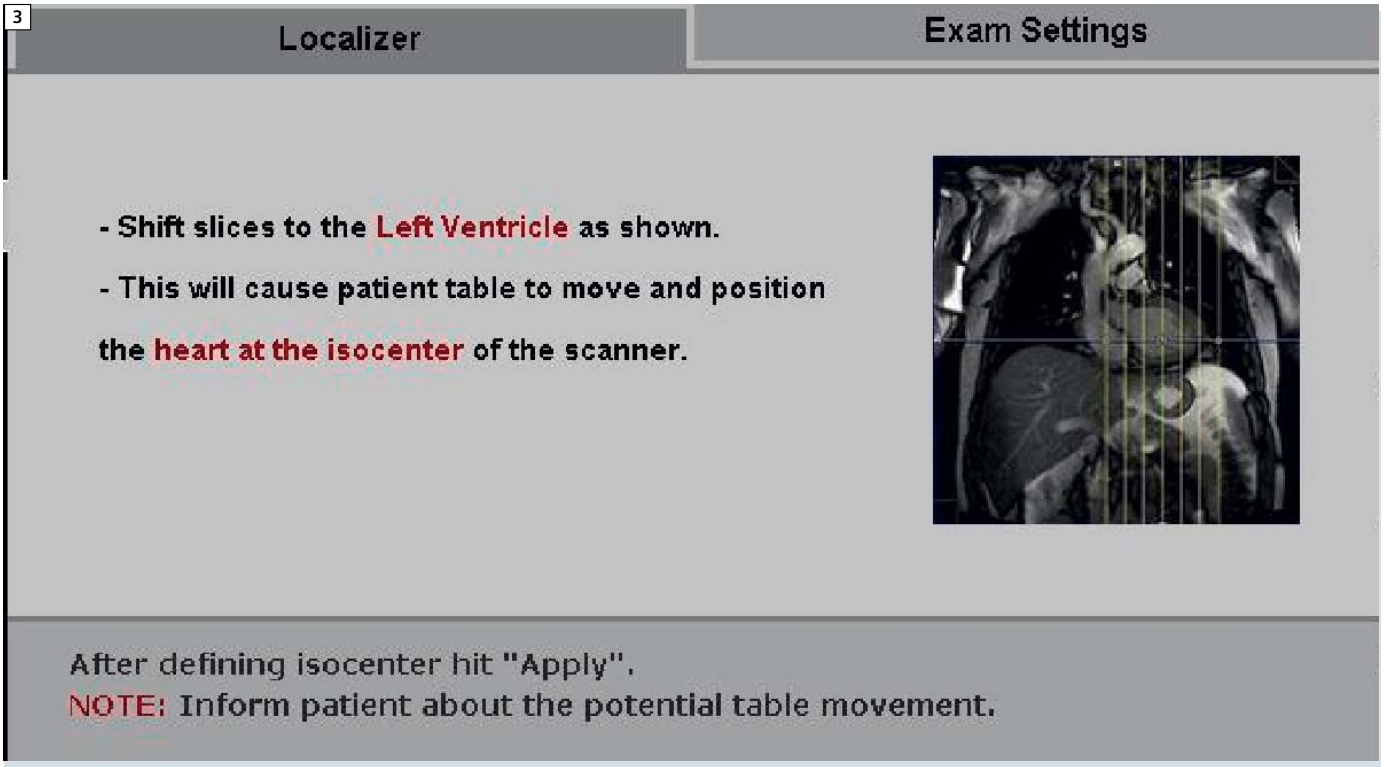

3 Iso-center scanning. Support by guidance images and text the user can move the left ventricle to the iso-center to ensure high scan quality

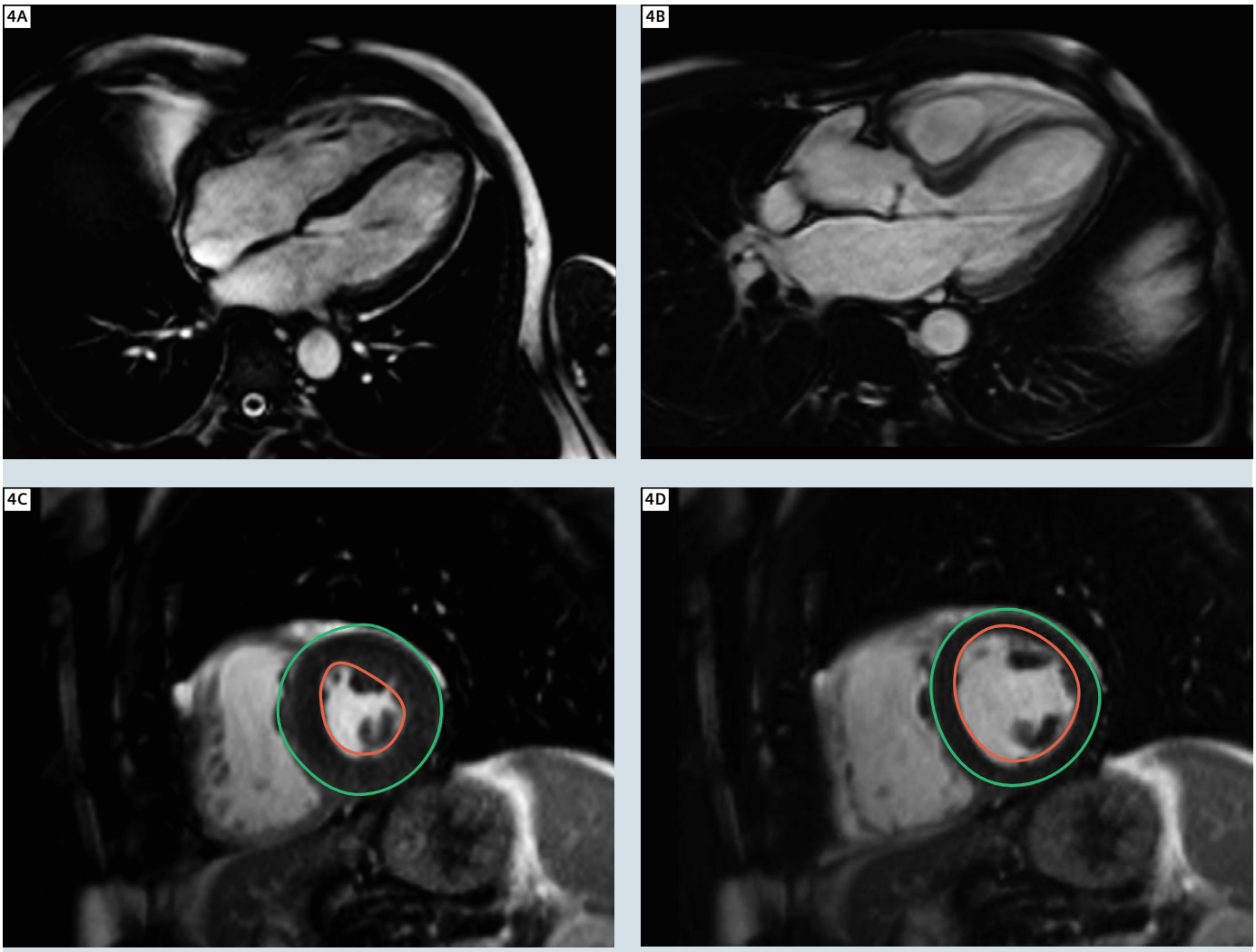

4 Examplatory cine-images from a typical CMR exam, performed after the introduction of the WIP software package, scanned by a less experienced technologist. A standard 4-chamber view is shown in **4A**. No manual adjustments were required, not even for dedicated planes like the LVOT (left ventricular outflow tract). Segmentation of the left ventricular wall on the short axis **(4C, D)** was calculated by the integrated Inline segmentation tool and required no interaction neither by the technologist nor the radiologist.

Clinical setting

The Royal Bournemouth is an acute-care general hospital (900 beds) with a large regional cardiac unit performing over 2500 procedures per year. The cardiac MRI (CMR) service started in 2004, initially providing basic structural information only. CMR stress exams started in 2007. Our patient population is almost exclusively adult. CMR is used to provide structural and functional information and is used particularly for planning revascularisation strategies in patients with known coronary artery disease.

Extensive process-mapping was undertaken in order to identify areas in which the scanning process could be accelerated. Even with these changes, stress heart exams required a time-slot of 1 hour using conventional software. There were also major issues regarding

5A

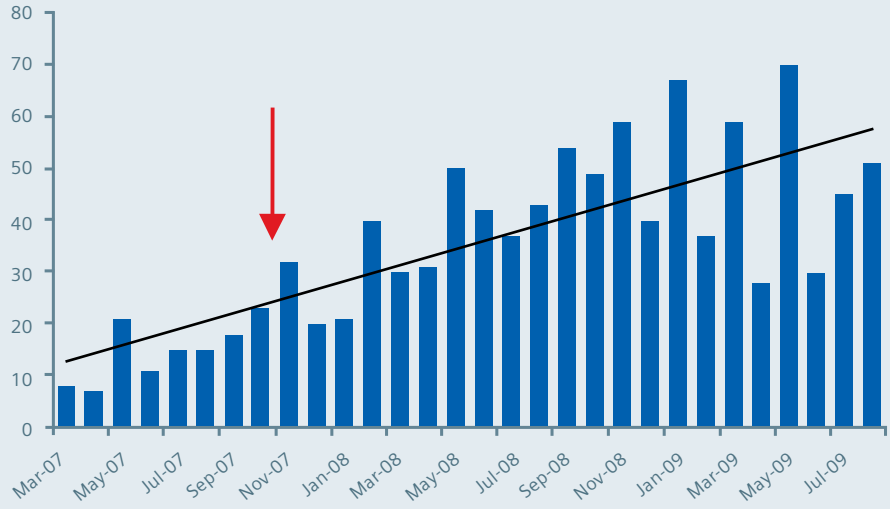

5A Development of the number of stress CMR studies per month performed at our institution (red arrow: cardiac prototype installed). Note that at our institution during this timeframe all cardiac MR exams were reported by only two cardiac radiologists; variations in patient throughput from month to month have now been addressed by appointment of a cardiac radiology fellow.

5B

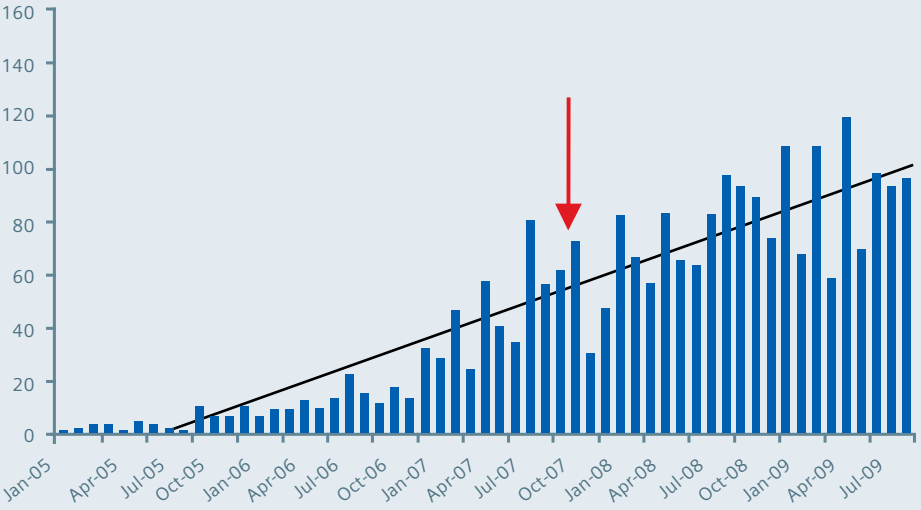

5B Total number of all CMR studies per month (red arrow – cardiac prototype installed).

staff training due to the complexity of the procedures and the lack of familiarity with cardiac anatomy and cardiac planes.

Clinical experiences

The cardiac WIP software has transformed the scanning process for cardiac MRI patients. The most difficult MR examination has become much more straightforward and now, even relatively inexperienced staff members are able to scan cardiac patients quickly and efficiently. The increased scanning speed has raised throughput by 50%**, now allowing 6 patients to be scanned in a 4 hour session rather than only 4 before. This software enables us to scan over 1000 cardiac patients per year in a general department, scanning up to 120 cases per month using only 10% of total scanning capacity. The prototype

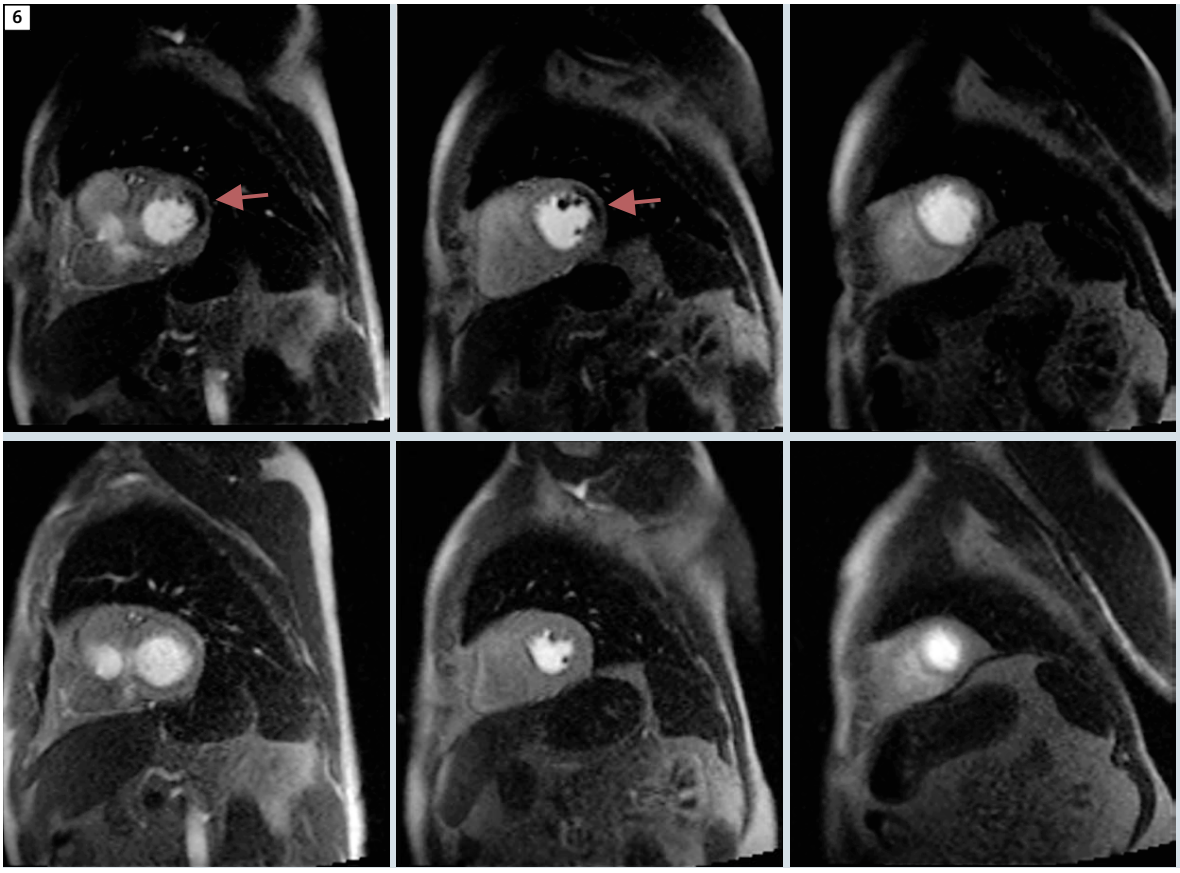

6 Short axis stress CMR images using cardiac prototype showing lateral wall subendocardial defect (arrow) secondary to circumflex lesion (upper row). This resolved following successful stenting (lower row).

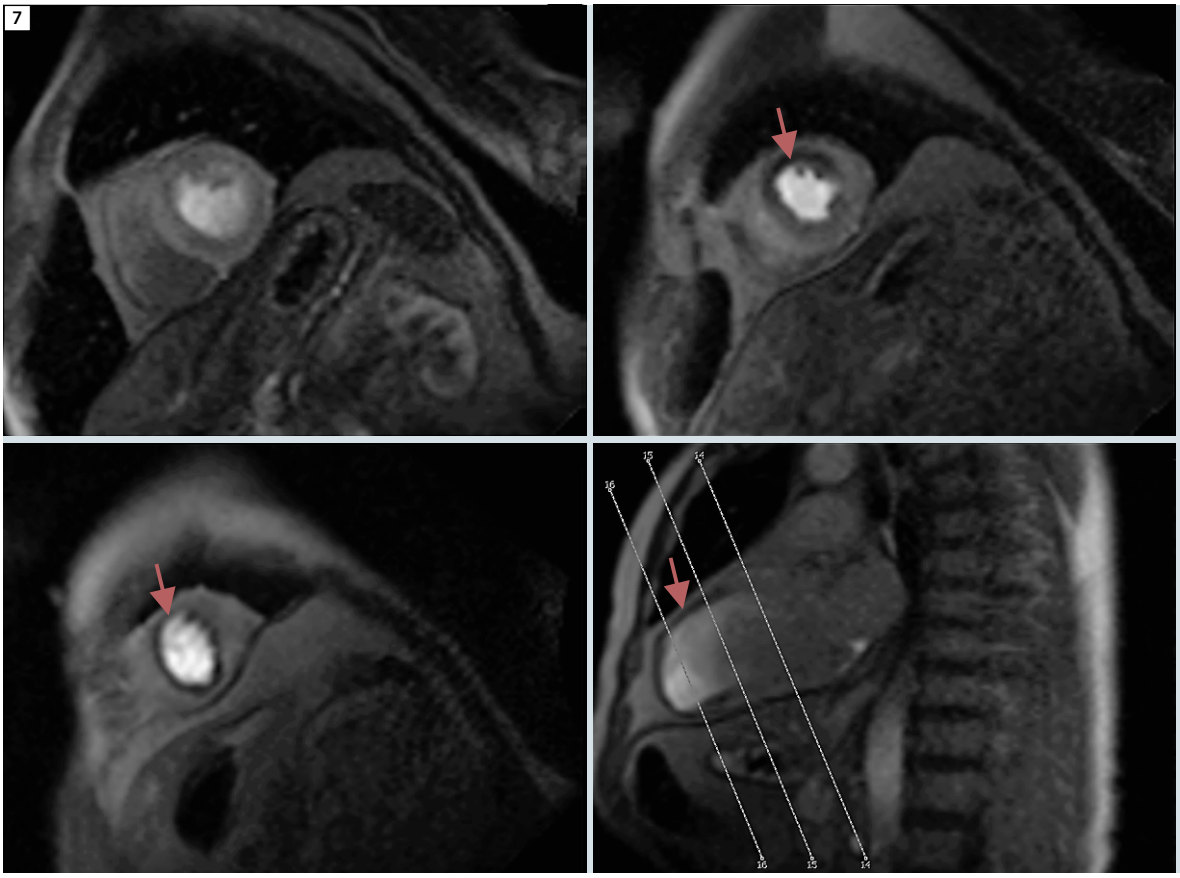

7 Stress CMR using cardiac prototype showing anterior wall/apical subendocardial defect (arrow) secondary to critical mid-LAD lesion. The prototype always acquires 3 short axis stress images and adaptively includes additional selected views if R-R interval allows (additional 2-chamber view shown in Fig. 8).

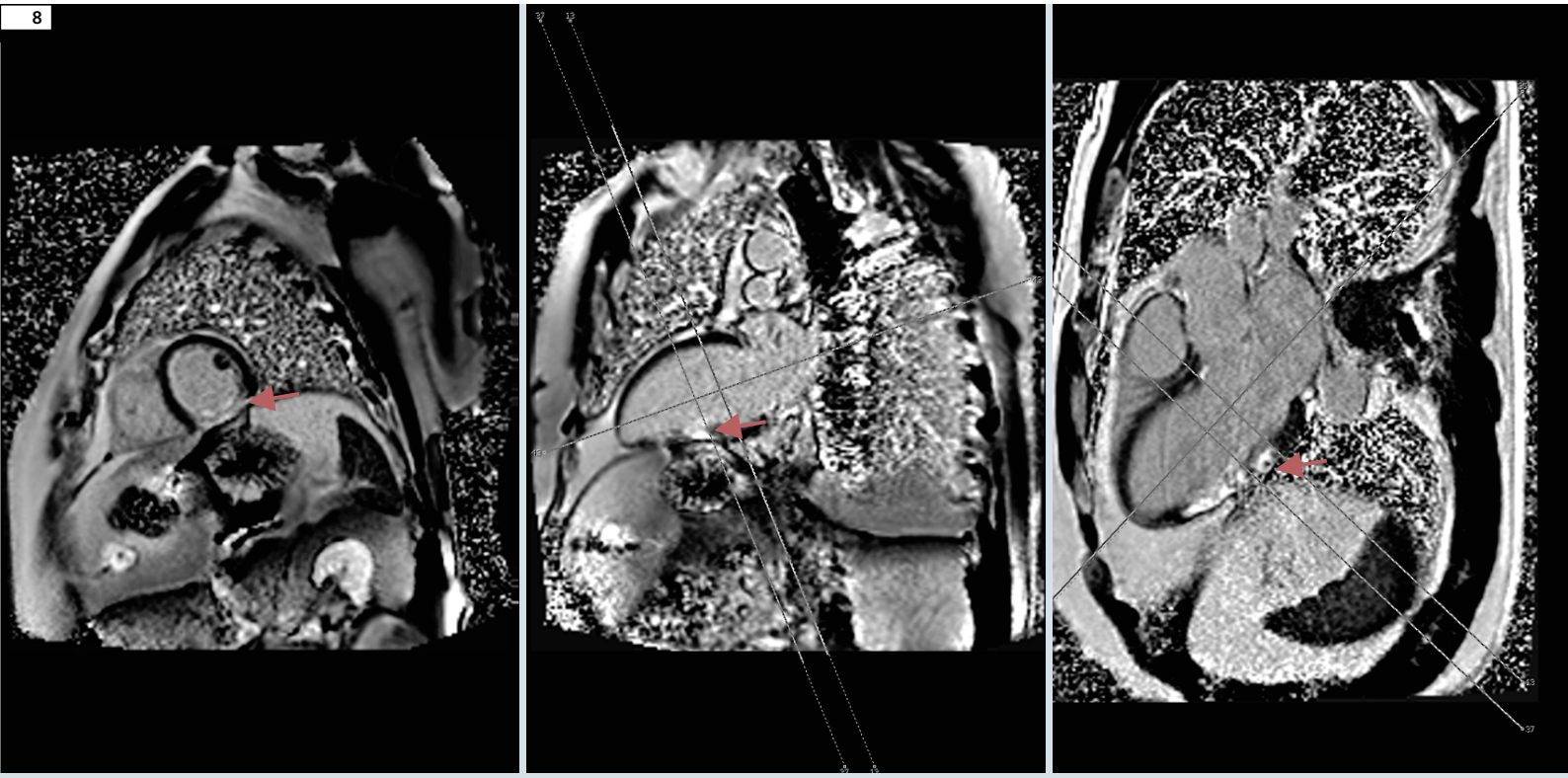

8 Short axis, 2-chamber and LVOT PSIR images showing old inferior infarct (arrow).



Dr. Russel Bull and Matthew Benbow (left).

has made training easier and scanning much simpler and faster thus enabling incorporation of cardiac examinations into the workload of a busy general hospital. All 16 scanning staff now perform cardiac examinations compared with just 3 before. The imaging results are now much more robust and quality is consistently high due to standardization. The increased speed has also made the scanning process more pleasant for patients, particularly for those suffering from claustrophobia.

*WIP – Work in progress. The information about this product is preliminary. The product is under development and not commercially available in the U.S., and its future availability cannot be ensured.
**Results may vary. Data on file.

Contact
Dr. Russell Bull , MRCP, FRCR
Consultant Radiologist
Royal Bournemouth Hospital
Castle Lane East
Bournemouth
UK
Russell.Bull@rbch.nhs.uk

IMRIS*neuro* 70 cm Bore 3T in Intra-Operative Neurosurgery

Jeanne Elliott

IMRIS, Winnipeg, Manitoba, Canada

1



1 IMRIS*neuro* 3T system. *(Image courtesy of: the Seaman Family MR Research Centre, Foothills Medical Centre, Calgary, Alberta, Canada.)*

The first IMRIS*neuro* system using a MAGNETOM Verio 3T magnet was installed at the Foothills Medical Centre in Calgary, Canada in early 2009.

Physicians appreciate High Field MR

The Seaman Family MR Research Centre at Foothills Medical Centre, under the leadership of Dr. Garnette Sutherland recently upgraded their 10-year old prototype 1.5T magnet to the latest IMRIS*neuro* with 3T MAGNETOM Verio technology. After successfully treating more than 1,000 neurosurgical patients using the 1.5T technology, the centre was ready to upgrade its capabilities. It became clear that the 3T Verio system including Diffusion Tensor Imaging (*syngo* DTI) and functional MRI would add significant value to surgical planning and intra-operative imaging.

The benefits of applying MR imaging during surgery has been recognized for many years. However, more recently the field has seen major growth in awareness and usage of MR guided imaging for neurosurgery. Many peer reviewed articles report the benefits of MR imaging including one, which concluded that in 41% of cases, the use of intra-operative MRI resulted in extended tumor resection. A different study concluded that in 27.5% of cases the original surgical plan was altered based on the intra-operative MR findings.

Many of the original observations were often based on past generation high field intra-operative MR technologies. They provided good image quality, but lacked the ability to deliver efficient workflow as the patient had to be moved to the MRI. Seeking the best in intra-operative MR technology, leading institutes like Barnes-Jewish Hospital (St. Louis, MO, USA), Johns Hopkins Hospital (Baltimore, ML, USA), Mayo Clinic (Jacksonville, FL, USA), Cleveland Clinic (Cleveland, OH, USA), Seaman Family MR Research Centre (Calgary, Canada), and PLA 301 Army Hospital (Beijing, China) have selected IMRIS*neuro*. These systems include the 1.5T MAGNETOM Espree or the 3T MAGNETOM Verio magnets and provide superior imaging capabilities with a technology workflow that brings MR to the patient. When the MR scanner is not in the operating room, the surgical team has full 360-degree access to the patient, and relocation of the magnetic field enhances operating room safety.

IMRIS*neuro* with the Siemens Verio or Espree magnets provide industry-leading capability and may also be used for diag-

2

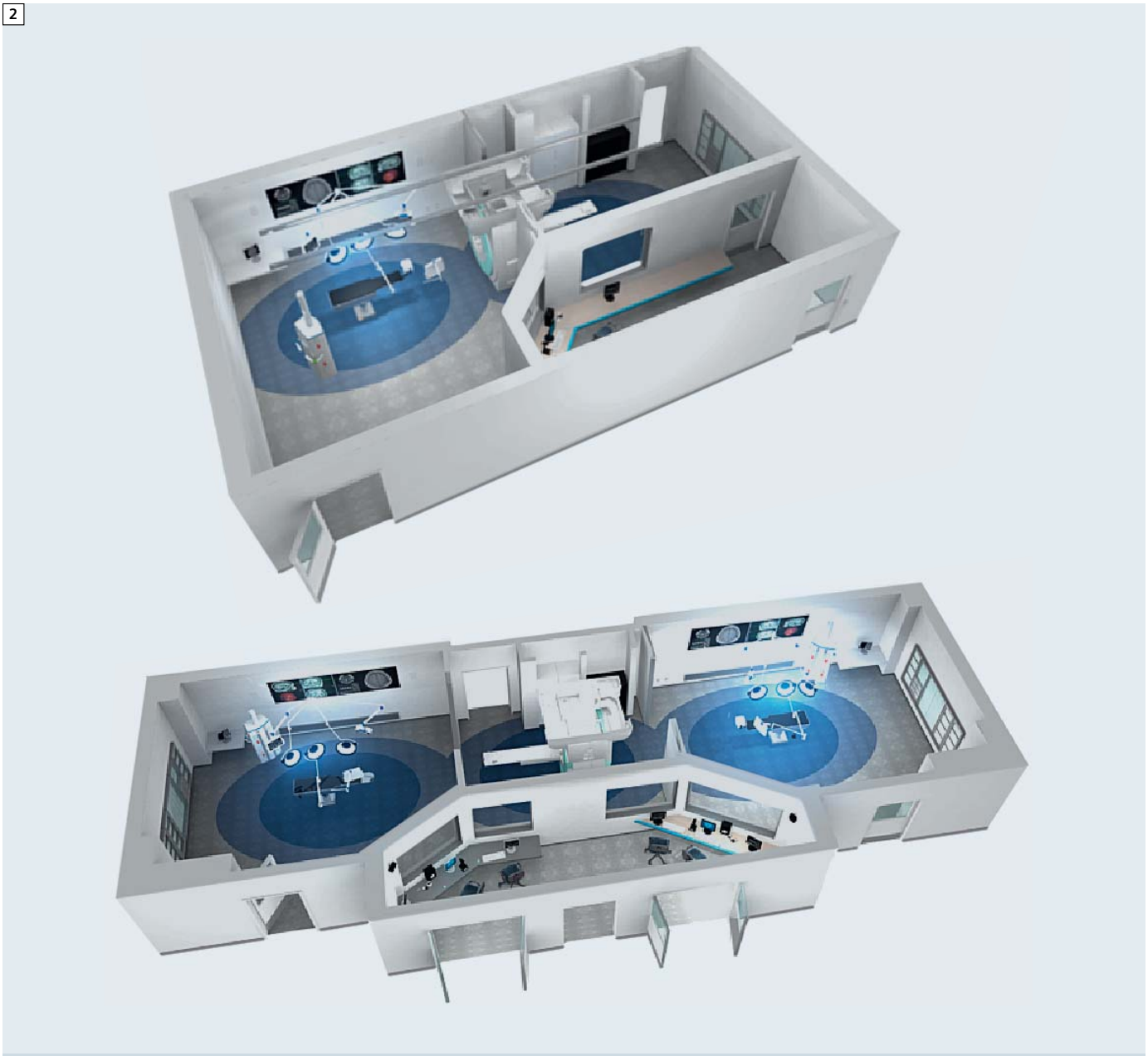

2 IMRIS*neuro* 2-room and 3-room configurations.

nostic examination of non-surgical patients who require the service of anesthesia or critical support. The IMRIS*neuro* solution is available in five configurations that allow the use of the 3T or 1.5T magnets for routine diagnostic imaging procedures while the system is not in use intra-operatively. For centers with significant surgical volumes, the magnet can move between two separate operating rooms further enhancing efficiency and the ability to offer better patient care.

Clinical cases with IMRIS*neuro* 3T MAGNETOM Verio

The moving magnet concept began with Dr. Garnette Sutherland's desire to bring the imaging benefits of an MRI to the neurosurgical operating room environment. His motivation was to preserve the current surgical workflow and to avoid moving the positioned surgical patient. IMRIS translated Dr. Sutherland's concept to pioneer the original 1.5T moving magnet design. More than 10-years later, Dr. Sutherland is also the first in the world to use the advanced IMRIS*neuro* with 3T MAGNETOM Verio: "The images obtained using the upgraded 3T intra-operative MRI system are of remarkable quality. The new system has been used for over 75 surgeries, in surgical planning, assessment during surgical dissection and for quality assurance. We have taken advantage of complex imaging techniques including fibre tracking, MR angiography and the rapid image pro-

cessing software. I am pleased that this innovation has turned into a commercial product that has gone on to benefit close to 3000 patients throughout the world."
It is well understood in normal MR diagnostic scans that 3T image quality offers superior resolution and definition of soft tissue structures in the brain versus 1.5T. Initial intra-operative experience with the 3T MAGNETOM Verio shows the same advantages existing in image quality before, during and after surgery. The state-of-the-art imaging techniques and rapid processing times characteristic of the 1.5T are enhanced through the inherent higher signal-to-noise ratio (SNR) of the 3T. Surgical planning intra-operative MR images were obtained from a 61-year-old woman with a left subtentorial meningioma. Diffusion tensor imaging (*syngo* DTI) sequences show well the relationship of fibers to the tumor. Interdissection images (not shown) demonstrated deformation for the fiber tracks as a result of tumor removal. Knowledge of these relationships increased the safety of tumor resection.

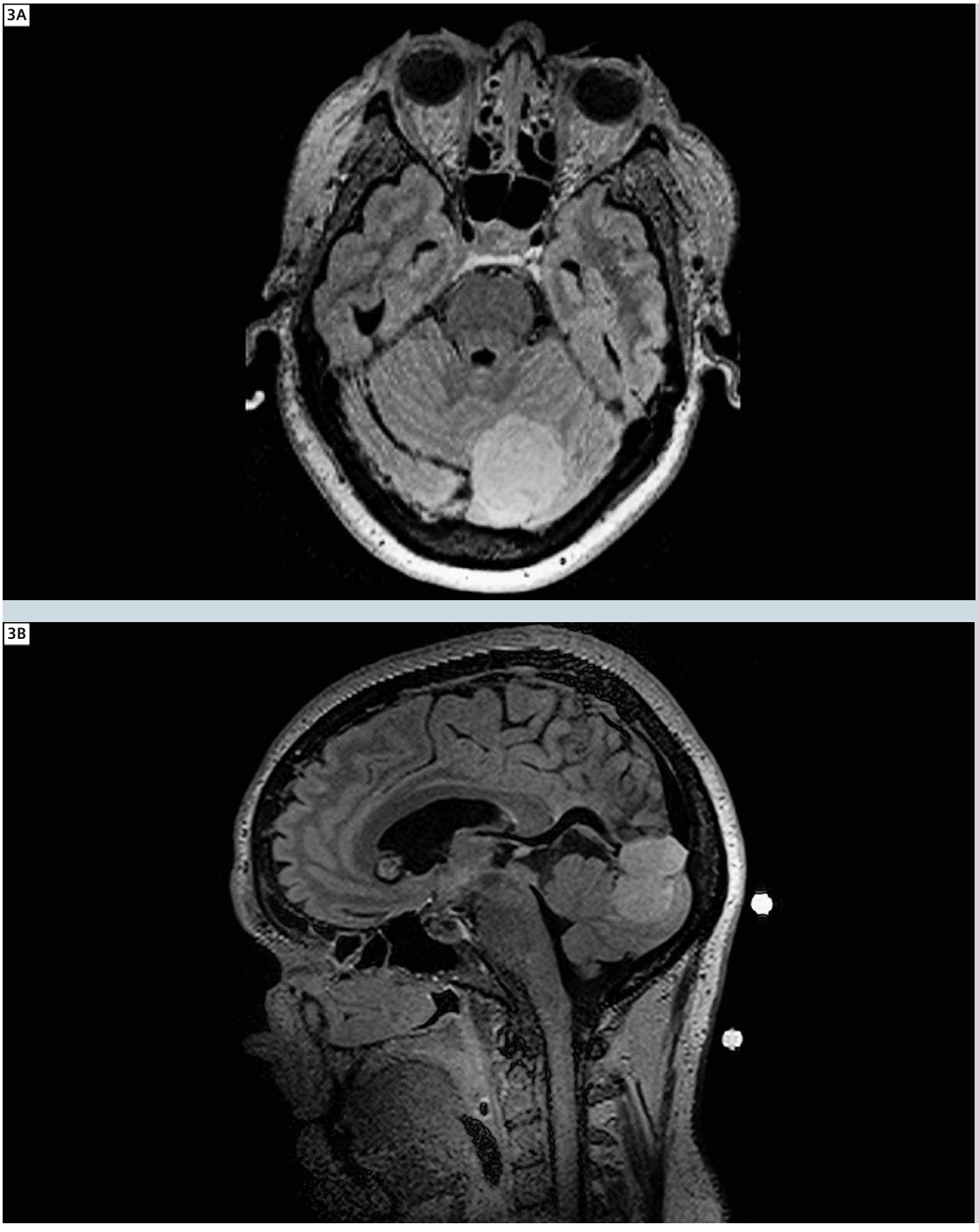

3 3T intra-operative. (*Images courtesy of the Seaman Family MR Research Centre, Foothills Medical Centre, Calgary, Alberta Canada 2009).*

New and additional clinical applications

The unique wide bore 70 cm 3T MAGNETOM Verio system is extremely valuable for intra-operative and interventional procedures. More often than not, interventional procedures require specialized patient positioning that can only be fully achieved with the 70 cm bore MAGNETOM Verio and Espree magnets. Positioning patients in lateral or prone positions is easily achievable with the use of wide bore, moving MR technology from IMRIS.

Excellent patient positioning and imaging capability is further supported by the enhancements made to the IMRIS*neuro* surgical bed. This newly developed surgical table is MR-compatible and X-Ray translucent for spine imaging and applications. The bed allows use of a single plane X-ray system in combination with MR imaging in the operating room (OR).

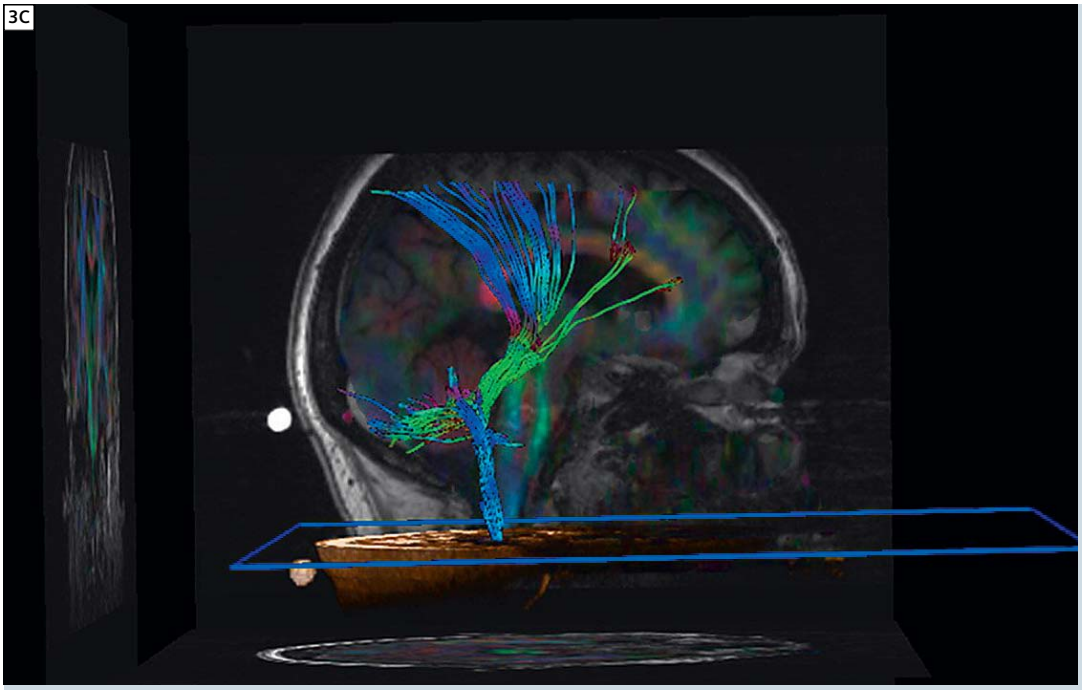

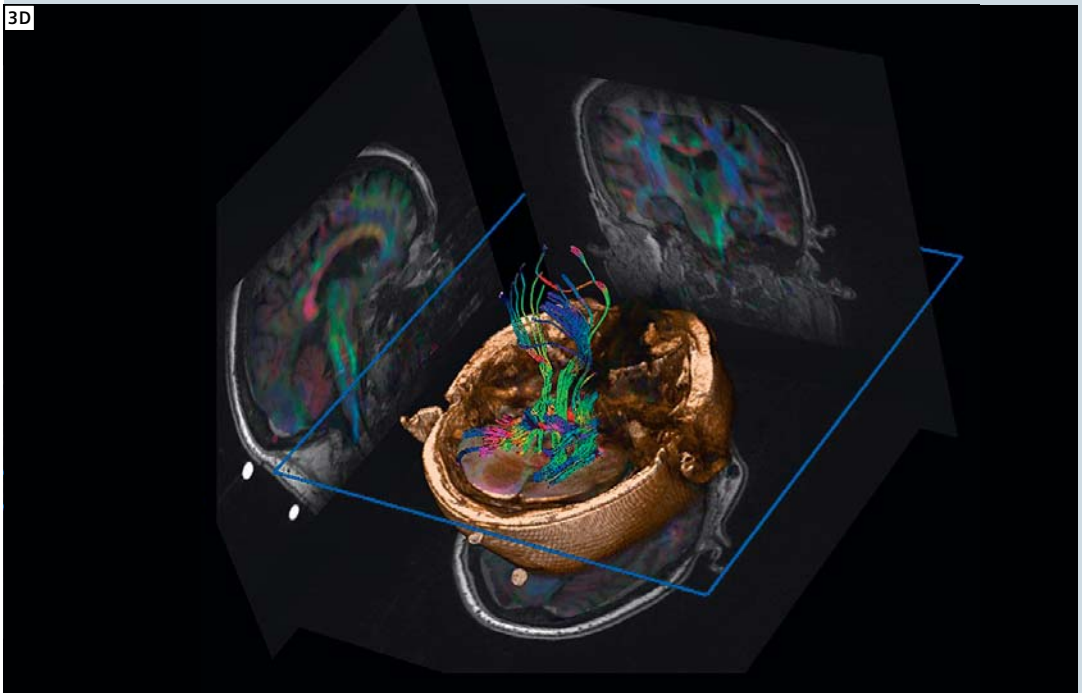

3 3T intra-operative. (*Images courtesy of the Seaman Family MR Research Centre, Foothills Medical Centre, Calgary, Alberta Canada 2009).*

4 IMRIS*neuro* surgical bed and collage images of prone/lateral/supine positioning. *(Images courtesy of IMRIS, Inc., Canada, 2009.)*







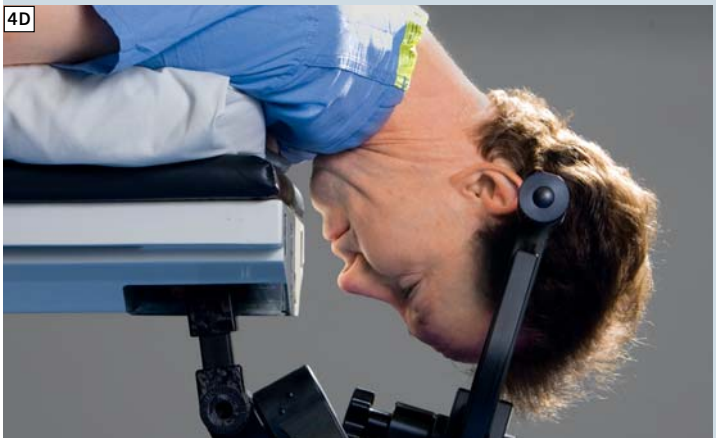

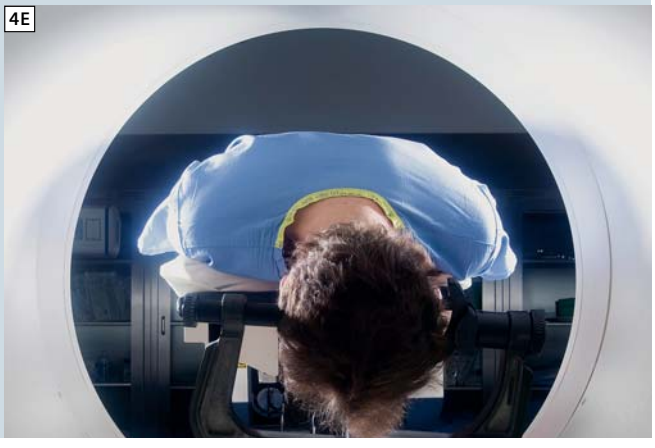



5 IMRIS$_{NV}$ and IMRIS$_{cardio}$

Future applications and technologies

IMRIS is widening the use of its image guided therapy solutions by expanding into new applications, combining 3T or 1.5T MR with single and bi-plane X-ray systems. IMRIS$_{NV}$ and IMRIS$_{cardio}$ are unique and advanced interventional suites providing an imaging environment that physicians may apply in providing stroke management and neurovascular care and in performing structural cardiac and minimally invasive procedures.

References

1 Intraoperative Visualization for Resection of Gliomas Nimsky C, Ganslandt O, Buchfelder M, Fahlbusch R. "Intraoperative visualization for resection of gliomas: the role of functional neuronavigation and intraoperative 1.5T MRI". Neurological Research 28(5): 482–7, July 2006.

2 Intraoperative High-Field-Strength MR Imaging: Implementation and Experience in 200 Patients. Nimsky C, Ganslandt O, von Keller B, Romstöck J, Fahlbusch R. 'Intraoperative High-Field Strength MR Imaging: Implementation and Experience in 200 Patients." Radiology 2004; 233:67–78.

Contact
Jeanne Elliott
IMRIS
100 – 1370 Sony Place
Winnipeg, Manitoba
Canada, R3T 1N5
jelliott@imris.com

Diagnostic Relevant Reduction of Motion Artifacts in the Posterior Fossa by *syngo* BLADE Imaging

T. von Kalle[1]; B. Blank[2]; C. Fabig-Moritz[1]; P. Müller-Abt[1]; M. Zieger[1]; K. Wohlfarth[3]; P. Winkler[1]

[1]*Department of Pediatric Radiology, Olgahospital Klinikum Stuttgart, Germany*
[2]*Department of Pediatric Oncology, Hematology and Immunology, Olgahospital Klinikum Stuttgart, Germany*
[3]*Siemens Healthcare, Erlangen, Germany*

1

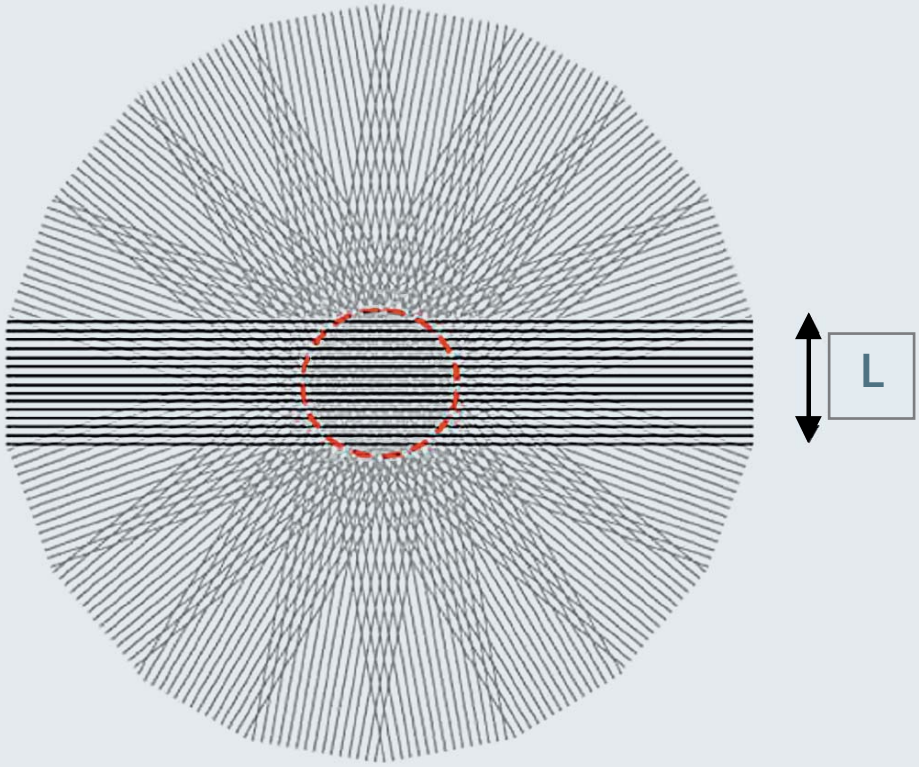

1 k-space trajectory in BLADE imaging. The k-space is covered by a series of blades each of which consists of the lowest phase encoding lines. The centre of the k-space (red circle) with diameter L is resampled for every blade. Data are then combined to a high resolution image.

Although movement and pulsation artifacts are a frequent problem in daily routine [1–4] especially in the diagnostics of pediatric patients, only few articles on this topic can be found in the literature. According to our experience mainly MR images of the posterior fossa, the cerebellum and the brain stem, may be significantly impaired by artifacts from pulsatile flow of blood or cerebrospinal fluid even without patient head movement [5, 6]. Sedation or general anesthesia rarely influence these pulsation or flow artifacts. However, accurate assessment of small brain lesions is essential in many pediatric patients, especially in those with malignant brain tumors. MR imaging with "rotating blade-like k-space covering" (BLADE) and "Periodically Rotated Overlapping Parallel Lines with Enhanced Reconstruction" (PROPELLER) have been shown to effectively reduce artifacts in healthy volunteers and adult patients [7, 8, 9], as well as in pediatric patients [4, 10] and therefore have the potential to reduce the frequency of anesthesia in children. As these MR techniques reduce motion artifacts by fast segmental image acquisition combined with mathematical algorithms, we assumed that it might at

the same time reduce the visibility of small brain lesions. We therefore compared the image quality of two T2-weighted fluid attenuated inversion recovery (T2w FLAIR) sequences with different k-space trajectories (conventional Cartesian and BLADE) with respect to artifacts and depiction of small hyperintense brain lesions [5].

Imaging techniques

We used a 1.5T scanner (MAGNETOM Avanto, Siemens Healthcare, Erlangen, Germany) and the Siemens 12-channel head matrix coil.
For each patient we compared two sequences with transverse 4 mm sections (gap 10%) that were applied in identical slice positions:
1. The T2w FLAIR standard sequence, a spin-echo sequence with conventional rectilinear Cartesian k-space trajectories (image parameters: TI 2500 ms, TR 9000 ms, TE 100 ms, BW 150 Hz/pixel, turbo factor 19, TA160 s, FOV 230 x 230 mm, matrix 256 x 256).
2. The BLADE FLAIR sequence with rotating blade-like k-space trajectories (image parameters: TI 2500 ms, TR 9000 ms, TE 107 ms, BW 250 Hz/pixel, turbo factor 29, TA 260 s, BLADE-Coverage 130 %, FOV 230 x 230 mm, matrix 256 x 256).
During the acquisition of both sequences children were encouraged not to move their head. They were offered video films or audio programs during the examination.

BLADE technique

syngo BLADE is the product name of the motion insensitive Siemens turbo-spin-echo sequence which utilizes the PROPELLER k-space trajectory [11].
The technique is approved for diagnostic MR examinations of patients. It consists of blade-like rotating k-space coverage. During each echo train of a BLADE sequence the lowest phase encoding lines of a conventional rectilinear k-space are acquired. The number of lines, which depends on the length of the echo train, determines the resolution of the image. During the acquisition process the direction of this "blade" is rotated around the k-space centre such that the complete series covers the whole k-space (Fig. 1). Images can be displayed with or without an additional motion correction algorithm.

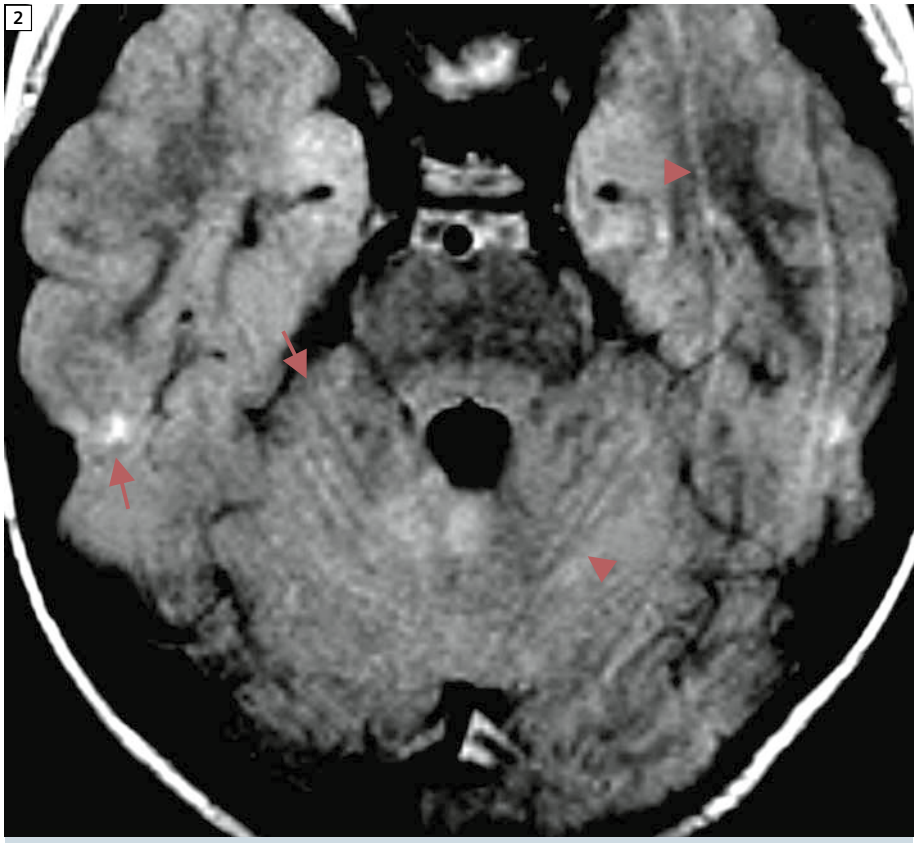

2 Movement artifacts caused by head movements (arrowheads) and pulsation artifacts caused by pulsatile flow (arrows). T2w FLAIR sequence with conventional rectilinear k-space trajectories.

Patients

The typical hyperintense white matter abnormalities in the cerebellum of patients with neurofibromatosis type 1 (NF 1) [12] served the purpose of our study to assess and compare the visibility of small and low contrast lesions.
We re-evaluated images of children with NF 1, who had been routinely scanned for optic pathway gliomas and who had been examined with T2w FLAIR sequences of both techniques. 26 patients, 10 girls and 16 boys from 2 years 7 months to 17 years (median age 8 years 5 months) were included in the study.

Image evaluation

Four experienced pediatric radiologists independently assessed unlabeled images of both FLAIR sequences of each patient. Structures of the posterior fossa, cerebellum and brain stem, were evaluated according to the presence of movement artifacts (caused by head movements) or pulsation artifacts (caused by pulsatile flow of blood and/or cerebrospinal fluid) (Fig. 2), their differentiation from lesions, and their delineation from the surrounding tissue by contrast (difference in signal intensities) and edge definition (clearly or poorly defined margins) as has been described elsewhere

Table 1: Scores for movement and pulsation artifacts, and the differentiation of artifacts and lesions in the posterior fossa.

	Conventional		*syngo* BLADE	
	yes	no	yes	no
Movement	29	75	4	100
Pulsation	99	5	25	79
Differentiation lesion/artefacts	53	30	81	2

Yes = artifacts present, lesions and artifacts distinguishable. No = artifacts not present, lesions and artifact not distinguishable. Maximum score for each sequence = 104. Last line. Patients with neither artifacts nor lesions were excluded. Results of statistical tests cf Table 2.

[5] The transverse diameters of the largest and smallest lesions were measured in both sequences of each patient. Signal intensities of a representative lesion and the adjacent normal brain tissue were measured. [5]

Discussion

Techniques with rotating blade-like k-space covering (BLADE) [9], with periodically rotated overlapping parallel lines with enhanced reconstruction (PROPELLER) [8,10], and with k-space alignment similar to a trellis [13] have been shown to effectively reduce artifacts in T1- and T2-weighted images. Studies on pediatric [4] and adult patients [7] found a comparable detectability of lesions in contrast-enhanced T1-weighted images of FLAIR BLADE sequences and conventional spin-echo sequences. However, image quality and delineation of small or poorly delineated lesions in MR images in T2-weighted FLAIR acquired with these techniques have not been systematically studied.

In our study, all observers found more pulsation artifacts than movement artifacts in images of both the conventional and the *syngo* BLADE sequence (Table 1). Artifacts were reported significantly less often in images acquired with BLADE technique than in images with rectilinear k-space trajectory (Table 1 and 2). These results confirm that artifacts caused by pulsation, flow and motion are significantly reduced by the BLADE technique in comparison to the standard sequence with conventional

Table 2: Posterior fossa. Comparison of conventional vs. BLADE images. McNemar's test. p-values for each observer. Cohen's kappa for interobserver agreement.

	Presence of movement artifacts	Presence of pulsation artifacts	Differentiation of lesions and artifacts	Delineation of lesions	
				Edge definition	Contrast
Observer 1	0.03	0.02	0.04	> 0.05	> 0.05
Observer 2	0.02	0.00002	0.002	0.0027	0.0009
Observer 3	0.041	0.000007	0.001	> 0.05	> 0.05
Observer 4	0.013	0.00002	0.013	> 0.05	> 0.05
Cohen's kappa	0.34	0.37	0.72	0.11	0.01

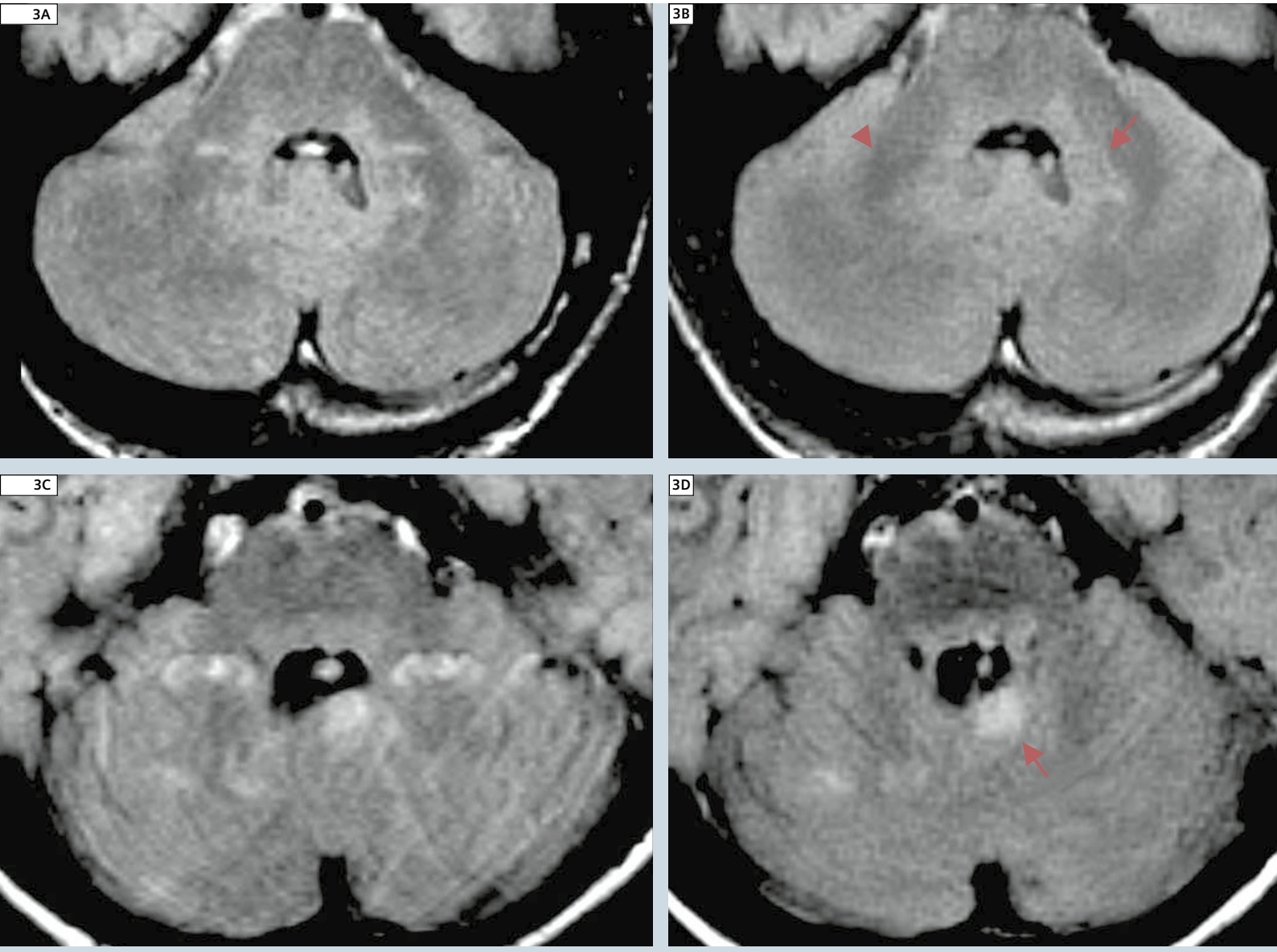

3 T2w FLAIR images of the posterior fossa of two different patients. Rectilinear k-space coverage (left), BLADE (right). Lesions typical of neurofibromatosis type 1: low contrast confluent (arrowhead), high contrast round (arrow). Artifacts and lesions not reliably distinguishable in conventional images (left).

rectilinear k-space covering. As the children were encouraged not to move during the examination, there were only moderate to minor movement artifacts even in conventional T2w FLAIR images. Pulsation artifacts were more frequent and more severe in conventional images and sometimes also present in BLADE images. Ratings of subtle movement artifacts in conventional images and subtle pulsation artifacts in BLADE images led to an only fair interobserver agreement (Cohen's kappa < 0.4, Table 2). These artifacts did not disturb the depiction of lesions.

There was good observer agreement (Cohen's kappa 0.74, Table 2) that artifacts compromised the assessment of lesions more often and more severely in conventional T2w FLAIR images than in BLADE images. In 6 of all 26 patients (23%) observers agreed that in conventional T2w FLAIR images they could not differentiate lesions from artifacts in the posterior fossa, rendering nearly a fourth of the examinations with conventional k-space trajectory inadequate for a reliable diagnosis. In none of the BLADE sequences more than one observer considered artifacts and lesions to be indistinguishable (Fig. 3).

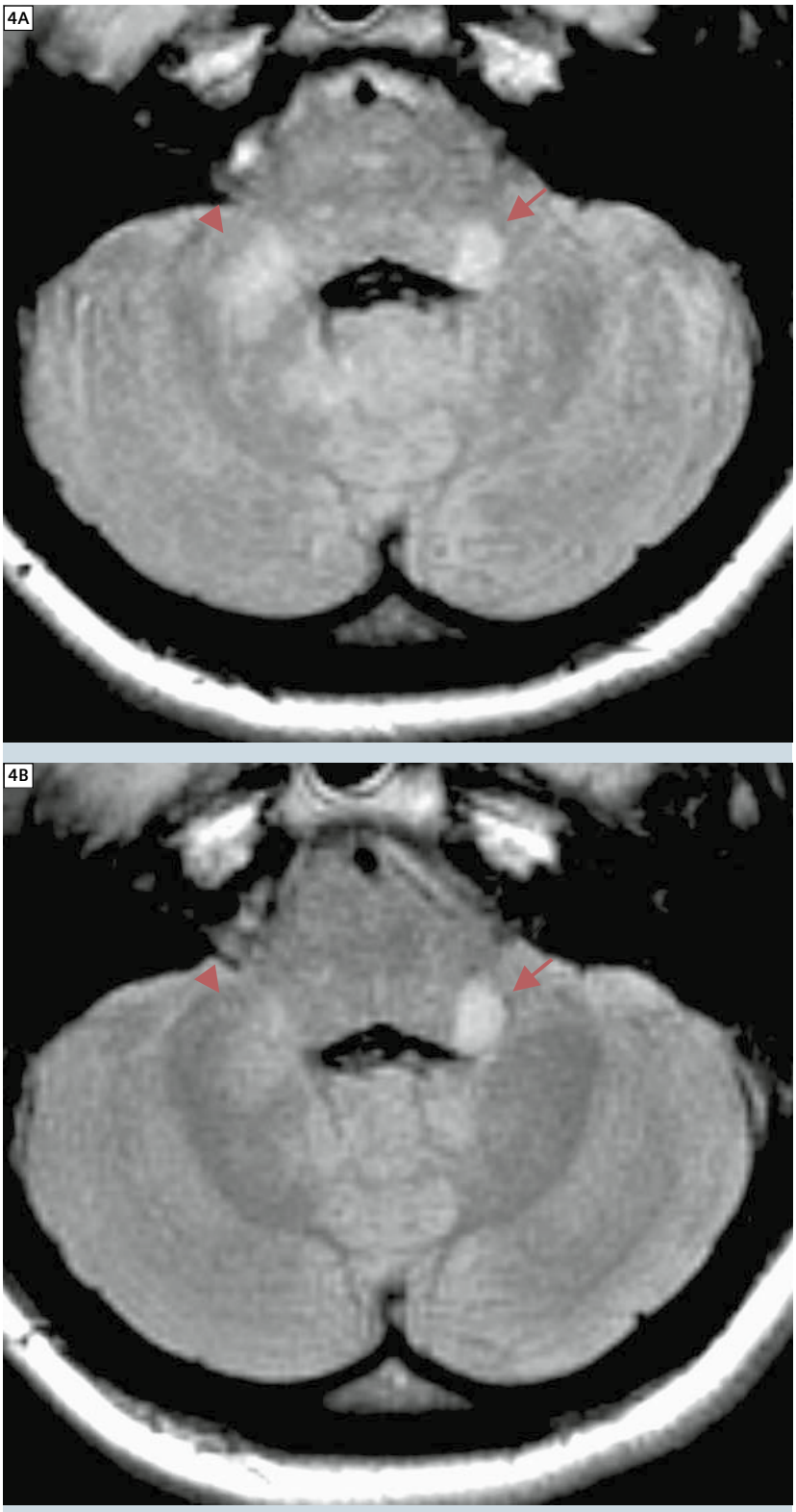

4 Absence of major artifacts and comparable visibility of lesions in images of both techniques (T2w FLAIR: rectilinear k-space top, BLADE bottom), low contrast confluent (arrowhead), high contrast round (arrow).

As Gill et al. reported for their sample [12], most hyperintense lesions in the thalami, brain stem and cerebellum were confluent or diffuse with poorly defined edges. A smaller number of lesions were well circumscribed with edges that were distinct from the adjacent normal tissue. Mean ratios of signal intensities were only slightly lower in the posterior fossa than in cerebrum and midbrain.

If lesions were not obscured by artifacts, visibility of lesions with both clearly and poorly defined edges appeared to be comparable in images of both techniques (Fig. 4). Observers' comparisons of both imaging techniques according to contrast and edge definition did not reveal consistently significant differences for lesions of the posterior fossa (Table 2). There only was a tendency to better edge definition in BLADE images. Visibility of lesions also was independent of size. Even the smallest lesions of our sample (2–3 mm) were equally depicted by both techniques.

BLADE technique is based on standard image acquisition techniques and therefore has the advantage of providing image characteristics equal to standard sequences. As an alternative to *syngo* BLADE imaging, pulsation artifacts may be identified by a second data acquisition after changing the phase encoding direction [1] or the slice orientation, with the disadvantage of a longer examination time and the higher risk of movement artifacts. Reduction of motion artifacts in non-sedated children can also be achieved by rapid sequences (e.g. single shot techniques) which, in neuroimaging, have the disadvantages of a poorer differentiation of gray and white matter [3, 10,14] and a lower spatial resolution [15].

Observers of our study had the subjective impression that the appearance of FLAIR BLADE images differed slightly from that of conventional images which did not impair image quality and lesion detectability (Figs. 3 and 4). These subtle differences have already been reported for PROPELLER technique [2]. BLADE images might therefore be identified by experienced radiologists despite "blinding". We have, however, not identified bias due to this fact in our study.
In our study, data acquisition time and image reconstruction time together were approximately 2–3 minutes longer for *syngo* BLADE sequences than for conventional FLAIR sequences. The advantage of artifact reduction by the BLADE technique clearly outweighed the prolonged duration.
There are limitations of our retrospective study: We were not able to measure the degree of patients' movements. Therefore, like other investigators [2, 4, 9], we can only assume that these parameters were similar in statistical mean throughout the examination. As both sequences were performed successively, pulsation and flow artifacts were also assumed as unchanged for both acquisitions. For our retrospective analysis we had to accept that in addition to the k-space trajectory some of the parameters of both sequences were not identical. As the BLADE technique benefits from long echo trains, a turbo factor had been chosen that was larger than that of our routine T2w FLAIR sequence. However, a change of these parameters would have had only minor influence on motion artefacts, and presumably would not have changed the quality of results. Prospective studies of a larger patient group could avoid these shortcomings.

Conclusion

BLADE technique reduces movement and pulsation artifacts in T2w FLAIR images without relevant loss of image quality. It therefore markedly improves depiction of small and low contrast brain lesions in children in the posterior fossa of pediatric patients. This can be crucial especially in patients after surgery of malignant brain tumors. In the absence of major artifacts lesions of all sizes were depicted in comparable quality by both techniques.

References

1 Böck JC, Neumann K, Sander B, Schmidt D, Schörner W (1991) Prepontine artifacts due to pulsation of cerebrospinal fluid in T_2-weighted coronal MRI. Clinical relevance, incidence and a technique for efficient artefact suppression. RoeFo 154: 202-205.
2 Forbes KP, Pipe JG, Bird CR, Heiserman JE (2001) PROPELLER MRI: Clinical testing of a novel technique for quantification and compensation of head motion. J Magn Reson Imaging 14: 215-222.
3 Penzkofer AK, Pfluger T, Pochmann Y, Meissner O, Leisinger G (2002) MR imaging of the brain in pediatric patients: Diagnostic value of HASTE sequences. AJR 179: 509-514.
4 Alibek S, Adamietz B, Cavallaro A, Stemmer A, Anders K, Kramer M, Bautz W, Staatz G (2008) Contrast-enhanced T1-weighted fluid-attenuated inversion-recovery BLADE Magnetic Resonance Imaging of the brain: An alternative to spin-echo technique for detection of brain lesions in the unsedated pediatric patient? Acad Radiol 15: 986-995.
5 Von Kalle T, Blank B, Fabig-Moritz C, Müller-Abt P, Zieger M, Wohlfarth K, Winkler P (2009) reduced artefacts and improved assessment of hyperintense brain lesions with BLADE MR imaging in patients with neurofibromatosis type 1. Pediatr Radiol 39: 1216-1222.
Kallmes DF, Hui FK, Mugler JP III (2001) Suppression of cerebrospinal fluid and blood flow artifacts in FLAIR MR imaging with a single-slab three-dimensional pulse sequence: Initial experience. Radiographics 221: 251-255.
6 Naganawa S, Satake H, Iwano S, Kawai H, Kubota S, Komada T, Kawamura M, Sakurai Y, Fukatsu H (2008) Contrast-enhanced MR imaging of the brain using T1-weighted FLAIR with BLADE compared with a conventional spin-echo sequence. Eur Radiol 18: 337-342.
7 Forbes KP, Pipe JG, Karis JP, Heiserman JE (2002) Improved image quality and detection of acute cerebral infarction with PROPELLER diffusion-weighted MR imaging. Radiology 225:551-555.
8 Wintersperger BJ, Runge VM, Biswas J, Nelson CB, Stemmer A, Simonetta AB, Reiser MF, Naul LG, Schoenberg SO (2006) Brain magnetic resonance imaging at 3 Tesla using BLADE compared with standard rectilinear data sampling. Invest Radio 41: 586-592.
9 Forbes KP, Pipe JG, Karis JP, Farthing V, Heiserman JE (2003) Brain imaging in the unsedated pediatric patient: Comparison of periodically rotated overlapping parallel lines with enhanced reconstruction and single-shot fast spin-echo sequences. AJNR 24: 794-798.
10 Pipe JG (1999) Motion correction with PROPELLER MRI: Application to head motion and free-breathing cardiac imaging. Magn Reson Med 42: 963-969.
11 Gill DS, Hyman SL, Steinberg A, North KN (2006): Age-related findings on MRI in neurofibromatosis type 1. Pediatr Radiol 36: 1048-1056.
12 Maclaren JR, Bones PJ, Millane RP, Watts R (2008) MRI with TRELLIS: a novel approach to motion correction. Magn Res Imaging 26: 474-483.
13 Iskandar BJ, Sansone JM, Medow J, Rowley HA (2004) The use of quick-brain magnetic resonance imaging in the evaluation of shunt-treated hydrocephalus. J Neurosurg (Pediatrics 2) 101: 147-151.
14 Ba-Ssalamah A, Schick S, Heimberger K, Linnau KF, Schibany N, Prokesch R, Trattnig S (2000) Ultrafast magnetic resonance imaging of the brain. Magn Reson Imaging 18: 237-43.

Contact
Thekla v. Kalle, M.D.
Department of Pediatric Radiology
Olgahospital Klinikum Stuttgart
Bismarckstr. 8
70176 Stuttgart
Germany
Phone: +49 (0) 711/ 278-04
t.vonkalle@klinikum-stuttgart.de
www.klinikum-stuttgart.de

4D Flow MR Imaging

Alex Barker; Jelena Bock; Ramona Lorenz; Michael Markl

Department of Radiology, Medical Physics, University Hospital Freiburg, Germany

Introduction

Magnetic Resonance Imaging (MRI) techniques provide non-invasive, highly accurate anatomic depictions of the heart and vessels. The intrinsic motion sensitivity of MRI can be used to image vessels with phase contrast (PC) MR-angiography, or to quantify blood flow [1–3].

Traditionally, MR imaging of flow is accomplished using methods that resolve two spatial dimensions (2D) in individual slices [4]. Alternatively, 3D spatial encoding offers the possibility of isotropic high spatial resolution and thus the ability to measure and visualize the temporal evolution of complex flow patterns in a 3D-volume. In this context, ECG synchronized flow-sensitive 3D MRI using 3-directional velocity encoding (also termed 'flow-sensitive 4D MRI', '4D Flow MRI', 'time-resolved 3D velocity mapping' or '4D PC-MRI') can be employed to detect and visualize global and local blood flow characteristics in targeted vascular regions (aorta, cranial arteries, carotid arteries, etc.) [5, 6]. The nature of such datasets (3 spatial dimensions, 3 blood flow velocity directions, and time) points towards the potential of flow-sensitive 4D MRI to provide detailed quantitative flow and vessel wall parameters with complete vascular coverage. A number of recent studies have indicated the potential of flow-sensitive 4D-MRI for the detailed visualization of complex flow patterns associated with healthy and pathologic hemodynamics [7–12].

Over the past few years, flow-sensitive 4D MR imaging has systematically improved to the point that it is possible to reliably acquire comprehensive flow information within reasonable scan times on routine clinical MR systems. However, the subsequent analysis and visualization of complex, three-directional blood flow within a 3D volume is still time consuming, and advanced data processing and 3D visualization tools are necessary.

In this article we report the first experiences with a new software prototype* for analysis of 4D Flow data, developed by Siemens Healthcare in cooperation with the Medical Physics group at the University Hospital Freiburg, Germany. After a brief overview of MR imaging and data analysis methods, we present their application for the evaluation of flow-sensitive 4D MRI in different vascular territories in the human body.

4D Flow MR Imaging

Modern phase contrast MR imaging allows for the simultaneous acquisition of 3D morphology and time-resolved blood flow velocities in 3 directions. Due to the large amount of data collected, the acquisition timing relies on an efficient synchronization with cardiac and respiratory motion. Image acquisition is therefore based on an ECG-synchronized fast gradient echo sequence with short echo and repetition times in the order of TE = 2–4 ms and TR = 5–7 ms. For thoracic and abdominal applications, additional respiration control using navigator gating is necessary to avoid breathing artifacts. A number of recent methodological improvements (parallel imaging, adaptive respiration control with increased efficiency, etc.) allow for the acquisition of flow-sensitive 4D MRI data with reasonable scan times in the order of 10–20 minutes. Ultimately, the total scan time will depend on the heart rate and efficiency of respiration control in the individual patient. Typical imaging parameters providing full spatial and temporal coverage of different cardiovascular regions of interest are summarized in table 1.

*Works in Progress. The product is under development and is not commercially available in the U.S. and its future availability cannot be ensured.

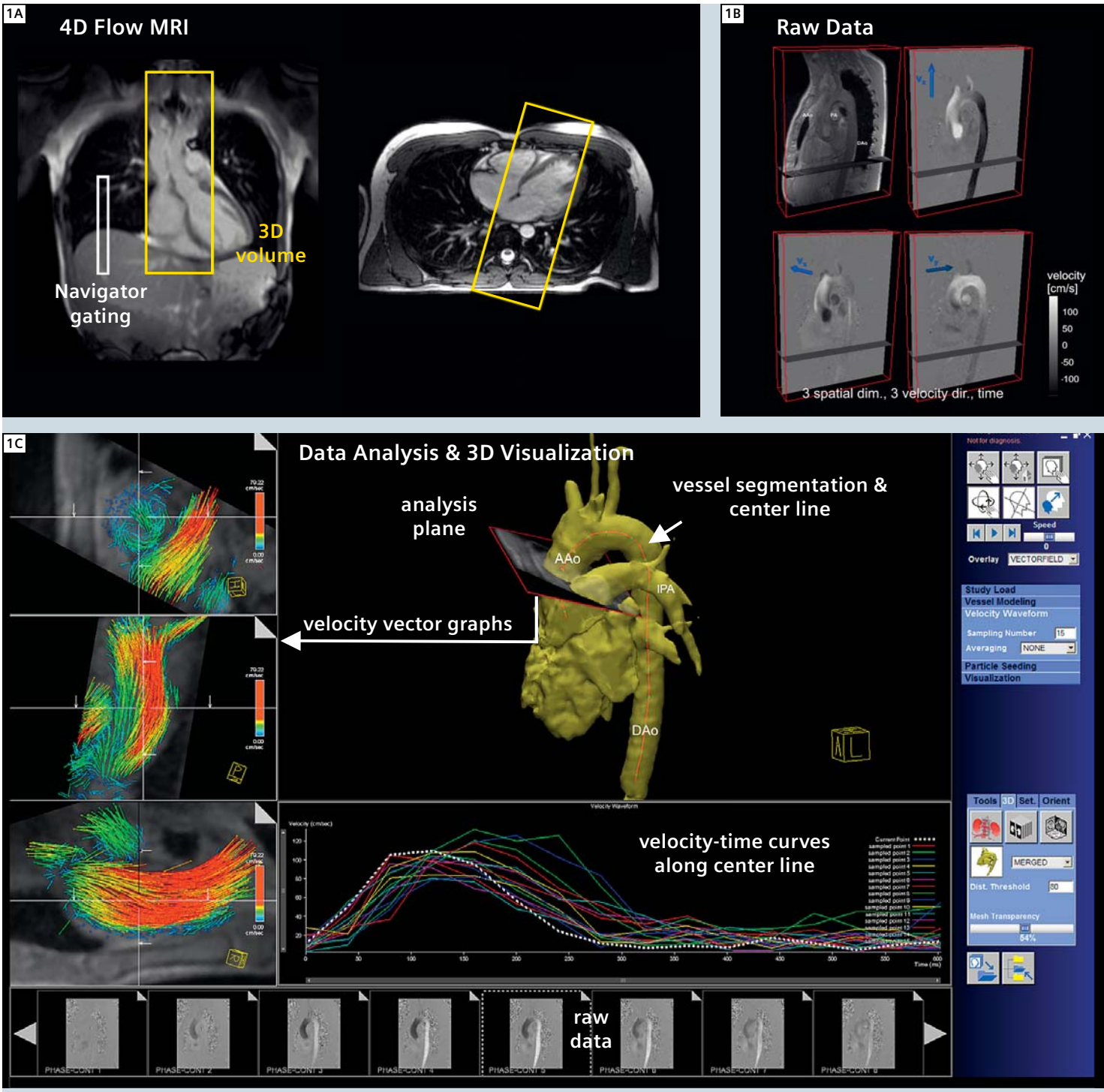

1 Schematic summary of the data acquisition and analysis strategy for flow-sensitive 4D MRI in the thoracic aorta. **A:** For 4D Flow imaging, a sagittal oblique volume covering the entire thoracic aorta is used. Data acquisition is synchronized with the cardiac cycle (ECG gating) and performed during free breathing using adaptive respiration control based on navigator gating of the lung-liver interface. **B:** The 4D Flow raw data, directly after reconstruction consist of the magnitude (top left) and the three sets of velocity encoded phase difference images (v_x, v_y and v_z). These images depict a single sagittal oblique slice at one systolic time point within the acquired 3D volume. Each velocity image represents quantitative velocity components along one encoding direction in which the gray-scale values correspond to the velocity magnitude and direction. **C:** 4D Flow data analysis prototype. 3D flow visualization in the same thoracic aorta is shown in figure 2. AAo: ascending aorta, DAo: descending aorta, IPA: left pulmonary artery.

Table 1: Typical scan parameters for flow-sensitive 4D MRI in different vascular territories. Velocity sensitivity refers to the maximum blood flow velocity that can be measured without fold-over artifacts (velocity aliasing).

application	spatial resolution	temporal resolution	navigator gating	velocity sensitivity
aorta & pulmonary artery	2.2 mm^3	40 ms	lung-liver interface	100 –150 cm/s
carotid arteries	1.2 mm^3	45 – 50 ms	–	100 cm/s
intracranial arteries	1 mm^3	45 – 50 ms	–	80 cm/s
portal venous system	2.1 mm^3	45 ms	spleen-liver interface	50 cm/s
iliac & femoral arteries	2 mm^3	40 ms	–	80 –100 cm/s

4D Flow analysis and 3D visualization

Flow-sensitive 4D MRI obtains, for each voxel within a 3D-volume and at each measured time point of the cardiac cycle, anatomical and three-directional velocity information. The 4D nature of the data frees the operator from choosing predefined examination planes within the vascular system of interest and offers the opportunity to quantify blood flow at any desired location within the data volume.

The new 4D Flow analysis software was developed to allow for a straightforward and time-efficient analysis of flow characteristics directly following data acquisition. Post-scan, the 4D Flow data can be directly loaded into the software prototype, providing a basic toolbox necessary to produce 3D anatomic and flow visualization. This includes 3D vessel geometry rendering by a combination of thresholding and segmentation, options to semi-automatically or interactively define 2D analysis planes, and automated calculation of vessel center lines. Analysis planes can be manually sized, angulated and used to display regional blood flow velocities as vector fields or to show velocity-time curves along the center line.

Currently implemented features for data analysis and 3D visualization include:

- Direct loading and database storage of 4D Flow raw data.
- Combined vessel lumen thresholding and segmentation to depict 3D vascular geometry/anatomy.
- Interactive 3D data manipulation and 4D (3D + time) viewing.
- Interactive 'point and click' definition of analysis planes and vessel center line calculation.
- Calculation of mean velocity-time curves in analysis planes longitudinally along vessel center line.
- Flow visualization based on time-resolved 3D pathlines originating from multiple and freely selectable emitter planes and locations (including the option to color code according to local absolute blood flow velocity or by vascular origin).
- Planar flow visualization as vector graphs or color coded overlay.

A summary of representative 4D Flow data acquisition and analysis in the thoracic aorta is illustrated in figure 1. The 4D Flow prototype and its different features to display and evaluate raw data, vessel geometry, vessel center line, interactively positioned analysis planes, and velocity-time curves are shown in figure 1C. The 3D flow visualization results, using time-resolved 3D pathlines are depicted in figure 2.

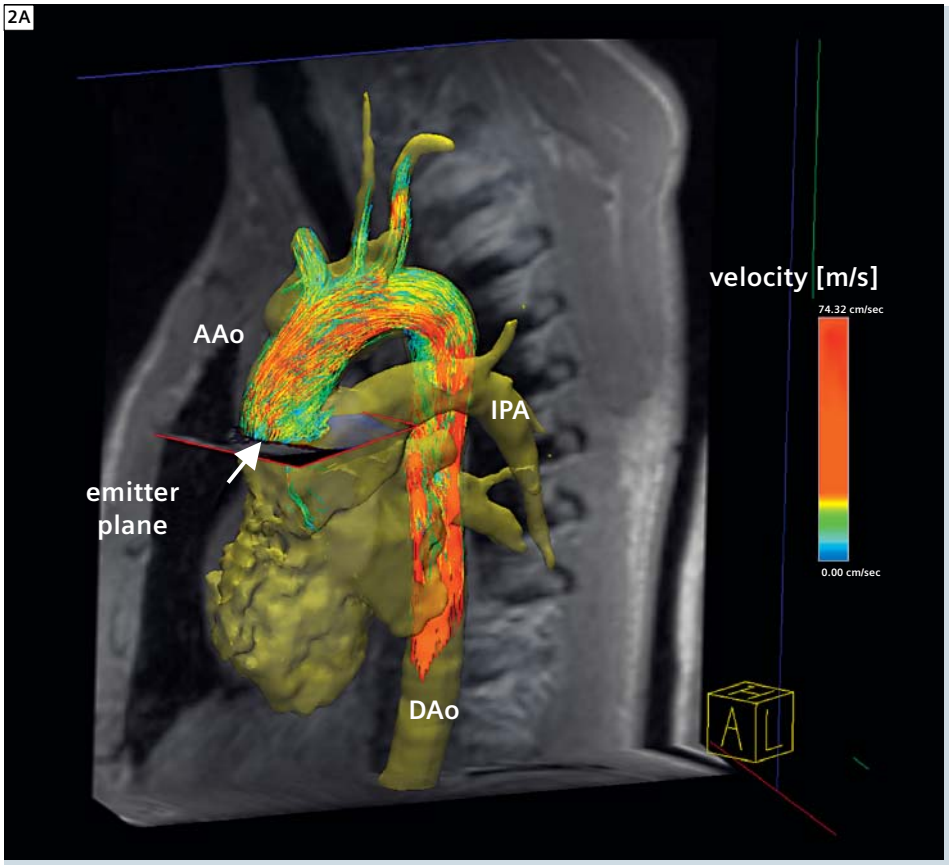

2A Time-resolved 3D pathlines in a normal thoracic aorta during peak systole. **A:** All traces originate from two emitter planes in the ascending aorta and proximal descending aorta (not shown). Color coding reflects the local absolute blood flow velocity.

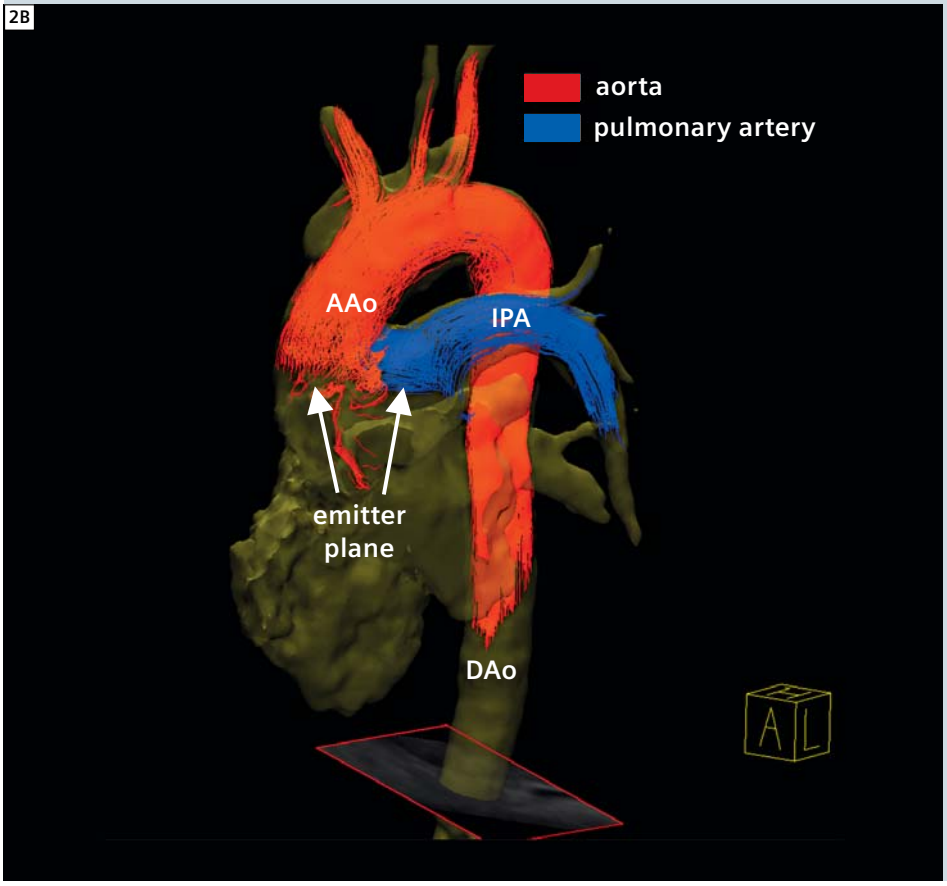

2B **B:** Flow visualization by 3D pathlines in the aorta and pulmonary system. Color coding according to the origin of the traces (red = aorta, blue = pulmonary artery) allows for a clear separation of aortic and pulmonary flow channels which can help understanding complex flow patterns or mixing of flows of different origin. AAo: ascending aorta, DAo: descending aorta, IPA: left pulmonary artery.

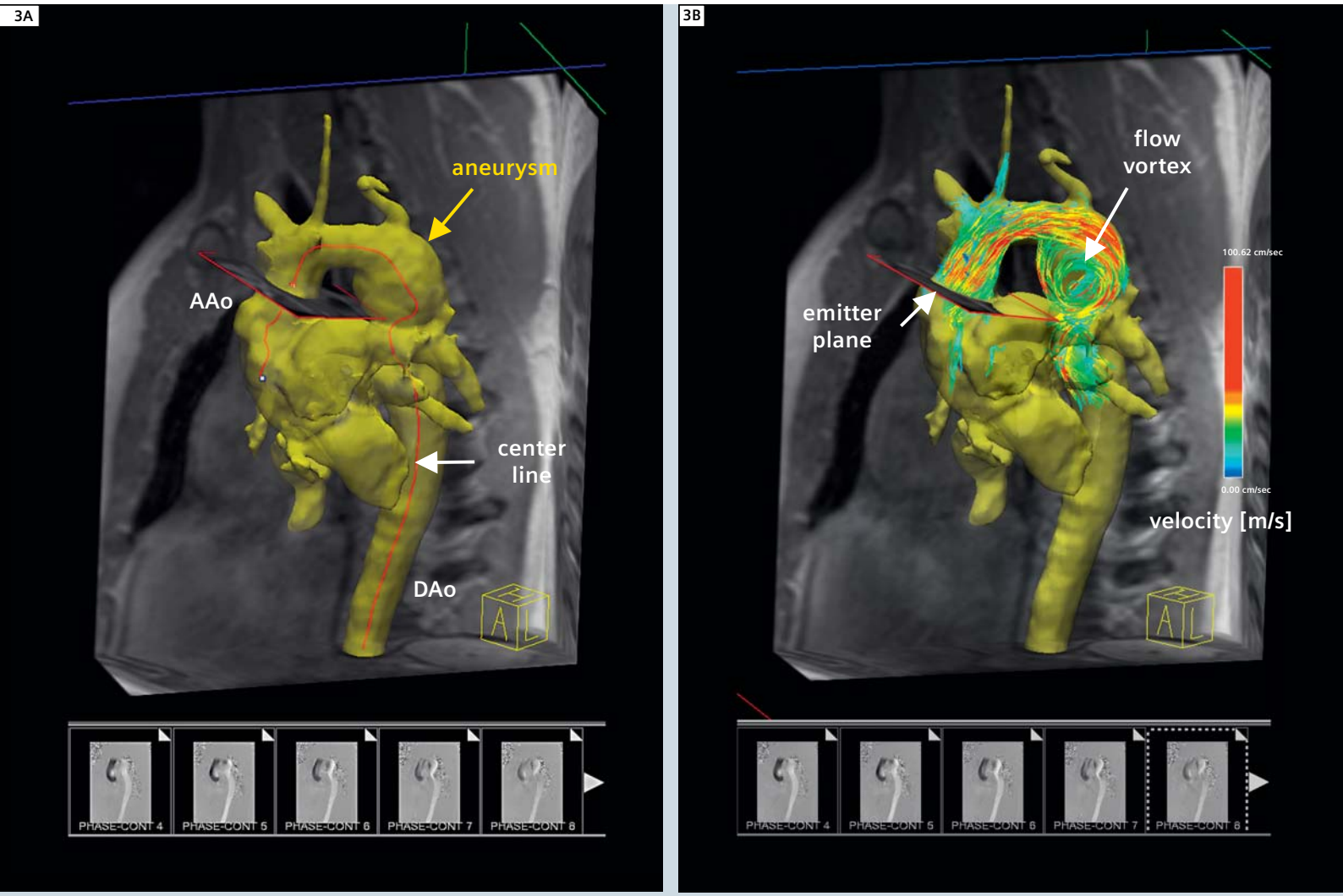

3 3D flow pattern development in the thoracic aorta in a patient with tubular hypoplasia of the aortic arch and an aneurysm of the proximal descending aorta (yellow arrow, diameter = 4.2 cm). 3D pathlines within the segmented aortic lumen clearly illustrate increased flow along the outer aneurysm wall and formation of a pronounced flow vortex within the aneurysm. The possibility to detect flow patterns such as vortex flow or identify regions with increased velocities may help to identify regions with abnormal flow and altered shear forces acting on the vessel wall. It is known from the literature that unfavorable shear forces at the vessel wall can change endothelial function and create areas at risk for vascular remodeling. The identification of such flow patterns may thus help to identify previously not assessable markers for the progression of disease or development of secondary pathologies such as aneurysms or dissections. AAo: ascending aorta, DAo: descending aorta.

Applications

In the following examples, a number of different vascular territories are presented to illustrate the utility of the new 4D flow analysis software prototype for the comprehensive evaluation of vascular hemodynamics. Figure 3 shows results from the combined visualization of vessel geometry and 3D flow patterns clearly illustrating altered flow patterns and marked vortex flow in a thoracic aortic aneurysm. The dynamics of normal portal venous flow supplying the liver are depicted in figure 4 demonstrating the subsequent filling of the portal vein and its main branches. Figure 5 shows the hemodynamic environment in a carotid bifurcation belonging to a patient with a moderate stenosis of the internal carotid artery. Note that for all patients, the flow sensitive 4D MRI data reflects the true underlying time-resolved blood flow velocity vector field and it is therefore possible to quantify blood flow velocities as shown by the velocity-time curves along the vessel center lines in figures 1 and 5. More details for each case are provided in the legends of figures 3–5.

The current 4D Flow prototype offers a new and time efficient tool to evaluate

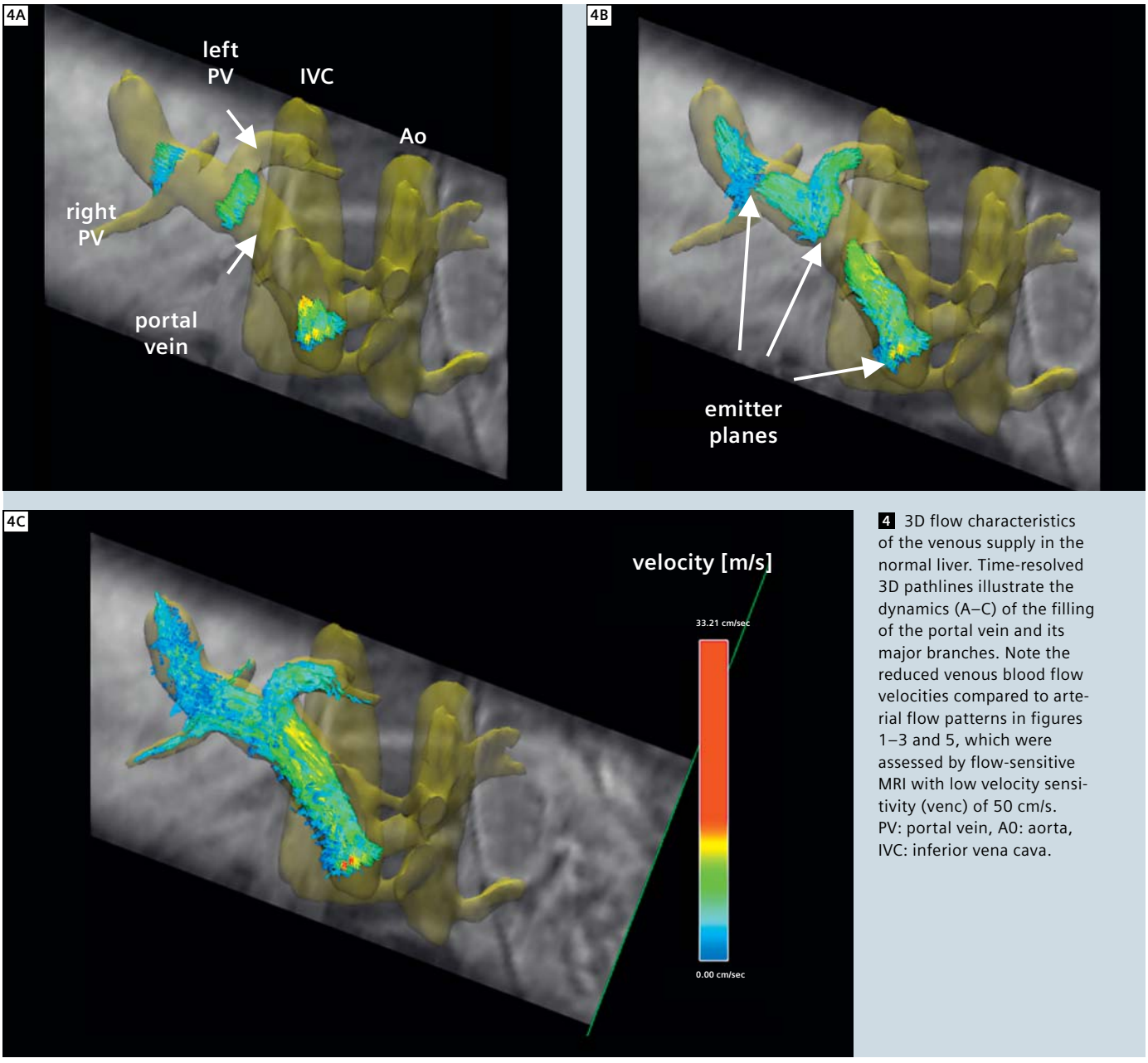

4 3D flow characteristics of the venous supply in the normal liver. Time-resolved 3D pathlines illustrate the dynamics (A–C) of the filling of the portal vein and its major branches. Note the reduced venous blood flow velocities compared to arterial flow patterns in figures 1–3 and 5, which were assessed by flow-sensitive MRI with low velocity sensitivity (venc) of 50 cm/s. PV: portal vein, A0: aorta, IVC: inferior vena cava.

4D flow data and has demonstrated its potential for analysis of arterial and venous hemodynamics in different vascular territories. Further improvements of this first software prototype include the implementation of correction algorithms for eddy currents and velocity aliasing as well as improved reporting and presentation functionality. In addition, supplementary refinements regarding flexible quantification of flow parameters (e.g. peak systolic velocities, regurgitant fraction) and derived parameters (e.g. wall shear stress, pressure differences) will enable a comprehensive evaluation of the structural and functional information embedded in 4D flow data.

In summary, the new 4D Flow analysis prototype provides an important first step for the efficient evaluation of vascular hemodynamics – providing a foundation for the adaptation of this technique in the clinical workflow. Further software additions and testing at multiple centers will also provide the opportunity to improve clinical acceptance of flow-sensitive 4D MRI, including the identification of important clinical applications and to streamline future developments.

5

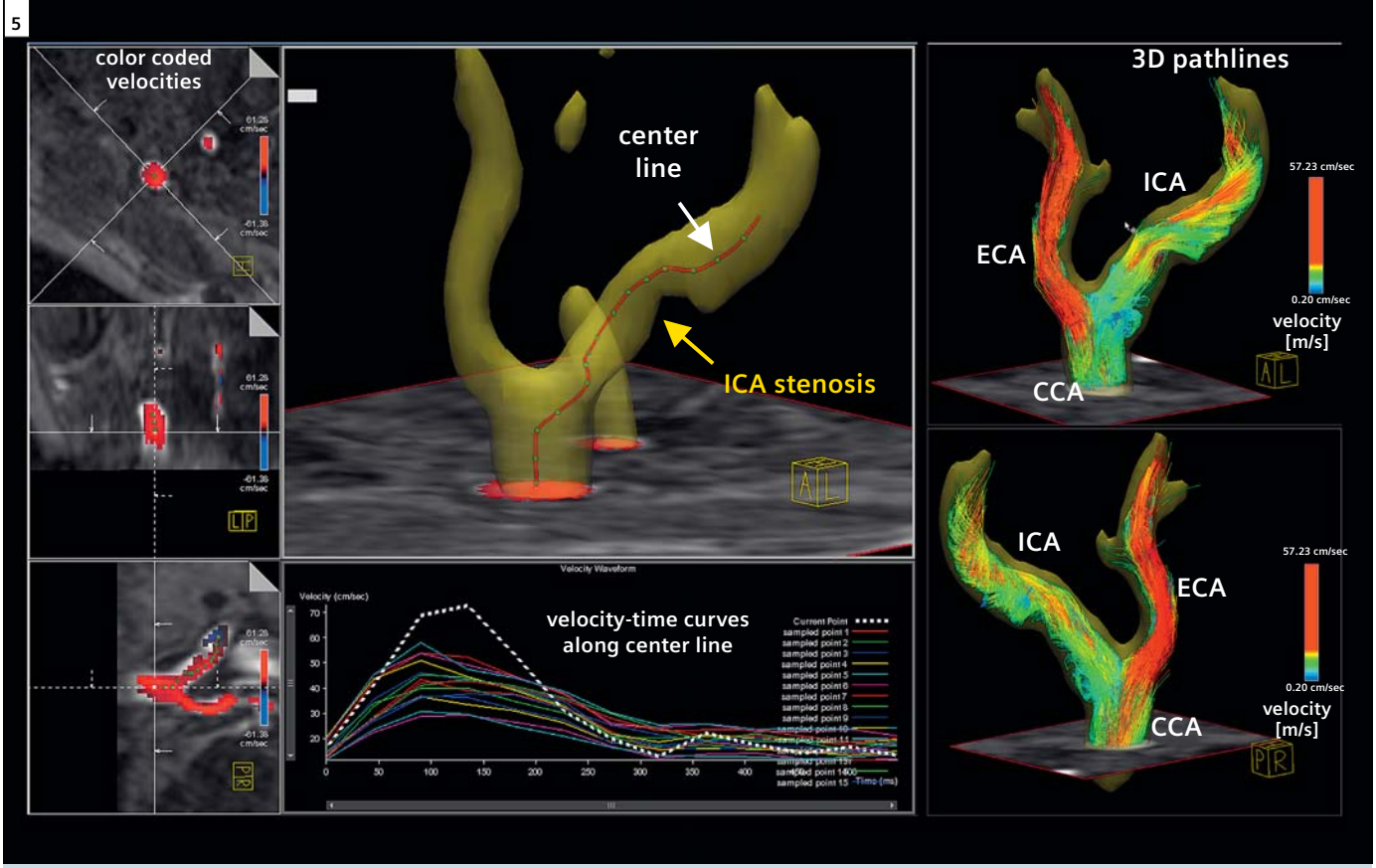

5 Visualization of 3D blood flow characteristics in the carotid bifurcation in a patient with moderate (40%) stenosis of the internal carotid artery (ICA). Thresholding using 3D PC-MR angiography derived form the 4D Flow data and subsequent vessel segmentation allowed for the depiction of the geometry of the carotid bifurcation. The definition of a vessel centerline from the common (CCA) into the internal carotid artery was used to calculate blood flow velocity – time curves in analysis planes along the center line. 3D flow visualization using time-resolved pathlines revealed straight flow through the stenosis and considerably enhanced helix flow within the post-stenotic dilatation. ECA = external carotid artery.



Left to right: Ramona Lorenz, Jelena Bock, Michael Markl, Alex Barker

Contact
PD. Dr. Michael Markl
Department of Radiology, Medical Physics
University Hospital Freiburg, Germany
Phone: +49 761 270 3832
Fax: +49 761 270 3831
michael.markl@uniklinik-freiburg.de

References

1 Firmin DN, Nayler GL, Kilner PJ, Longmore DB. The application of phase shifts in NMR for flow measurement. Magn Reson Med 1990; 14(2):230-241.
2 Dumoulin CL. Phase contrast MR angiography techniques. Magn Reson Imaging Clin N Am 1995;3(3):399-411.
3 Bock J, Frydrychowicz A, Stalder AF, Bley TA, Burkhardt H, Hennig J, Markl M. 4D phase contrast MRI at 3 T: effect of standard and blood-pool contrast agents on SNR, PC-MRA, and blood flow visualization. Magn Reson Med 2010;63(2):330-338.
4 Pelc NJ, Herfkens RJ, Shimakawa A, Enzmann DR. Phase contrast cine magnetic resonance imaging. Magn Reson Q 1991;7(4):229-254.
5 Wigstrom L, Sjoqvist L, Wranne B. Temporally resolved 3D phase-contrast imaging. Magn Reson Med 1996;36(5):800-803.
6 Markl M, Harloff A, Bley TA, Zaitsev M, Jung B, Weigang E, Langer M, Hennig J, Frydrychowicz A. Time-resolved 3D MR velocity mapping at 3T: improved navigator-gated assessment of vascular anatomy and blood flow. J Magn Reson Imaging 2007;25(4):824-831.
7 Frydrychowicz A, Winterer JT, Zaitsev M, Jung B, Hennig J, Langer M, Markl M. Visualization of iliac and proximal femoral artery hemodynamics using time-resolved 3D phase contrast MRI at 3T. J Magn Reson Imaging 2007;25(5):1085-1092.
8 Wetzel S, Meckel S, Frydrychowicz A, Bonati L, Radue EW, Scheffler K, Hennig J, Markl M. In vivo assessment and visualization of intracranial arterial hemodynamics with flow-sensitized 4D MR imaging at 3T. AJNR Am J Neuroradiol 2007;28(3):433-438.
9 Harloff A, Albrecht F, Spreer J, Stalder AF, Bock J, Frydrychowicz A, Schollhorn J, Hetzel A, Schumacher M, Hennig J, Markl M. 3D blood flow characteristics in the carotid artery bifurcation assessed by flow-sensitive 4D MRI at 3T. Magn Reson Med 2009;61(1):65-74.
10 Uribe S, Beerbaum P, Sorensen TS, Rasmusson A, Razavi R, Schaeffter T. Four-dimensional (4D) flow of the whole heart and great vessels using real-time respiratory self-gating. Magn Reson Med 2009;62(4):984-992.
11 Hope MD, Hope TA, Meadows AK, Ordovas KG, Urbania TH, Alley MT, Higgins CB. Bicuspid aortic valve: four-dimensional MR evaluation of ascending aortic systolic flow patterns. Radiology 2010;255(1):53-61.
12 Stankovic Z, Frydrychowicz A, Csatari Z, Panther E, Deibert P, Euringer W, Kreisel W, Russe M, Bauer S, Langer M, Markl M. MR-based visualization and quantification of three-dimensional flow characteristics in the portal venous system. J Magn Reson Imaging 2010;32(2):466-475.

3T MR Imaging of Peripheral Nerves Using 3D Diffusion-Weighted PSIF Technique

Avneesh Chhabra[1], M.D.; Theodore Soldatos[1], M.D.; Aaron Flammang[1]; Wesley Gilson[1]; Abraham Padua[2]; John A Carrino[1], M.D., M.P.H.

[1]Johns Hopkins University, Baltimore, MD, USA
[2]Siemens Healthcare, MR RD Management, Malvern, PA, USA

High-resolution magnetic resonance (MR) Neurography is a novel imaging technique, which enables multiplanar imaging of peripheral nerves, as well as diagnosis and localization of entrapment and non-entrapment peripheral neuropathies related to etiologies, such as inflammation, tumor and trauma. Typically, MR Neurography techniques utilize a combination of fat-saturated T2-weighted, short inversion time recovery (STIR), or T2 spectral adiabatic inversion recovery turbo spin echo (T2 SPAIR TSE) images for the detection of the nerve signal, contour and size changes, as well as T1-weighted spin echo or fluid attenuated long inversion recovery (FLAIR) images for the anatomic assessment of the involved areas, based on the abundant intra- and perineural fat. However, the diagnostic ability of conventional MR Neurography is limited in the evaluation of smaller peripheral nerves of the axial and appendicular skeleton, where the similar caliber and T2 signal intensity of peripheral nerves and adjacent vessels render discrimination of the above structures difficult, if not impossible. Since nerve injuries and entrapments commonly lead to effacement of perineural fat in the area of involvement, T1-weighted images are often not helpful. In addition, an attempt to sup-

Table 1: Acquisition parameters for 3D-PSIF at 3T

The typical acquisition parameters employed for the 3D-PSIF sequence in a Siemens 3T MAGNETOM Verio scanner. The spatial resolution of this technique yields 0.9 x 0.9 x 0.9 mm voxel sizes and, whenever possible, this dimension is preserved. When examining areas requiring larger or smaller coverage, the scan matrix and the FOV are adjusted accordingly. This and number of slices are all that is changed. Scan time is typically kept below 6 minutes 30 seconds through the use of parallel acquisition. High quality thin MIP projections are rendered for display purposes.

Acquisition parameter	Value
Slabs	1
FOV	172 mm
Slice thickness	0.9 mm
TR	12 ms
TE	4.1 ms
Averages	1
Coil	8-channel knee coil
PAT	GRAPPA 2
Flip angle	30
Fat suppression	Water Excitation Normal
Diffusion mode	Phase
Diffusion moment mT/m*ms	85
Diffusion directions	1
Dimension	3D
Elliptical scanning	On
Asymmetric echo	Off
Receiver bandwidth	230 Hz/Px
Acquisition time	4 min 37 sec

press vascular signal with saturation bands often fails in distal locations of the body, as the peripheral nerves frequently course through various obliquities.
Due to recent advances in 3T MR imaging with incorporation of optimized extremity coils and new pulse sequences, 3-dimensional high-resolution and high-contrast demonstration of the peripheral nerves is possible.
The 3-dimensional diffusion-weighted sequence based on reversed fast imaging with steady-state precession (3D-PSIF) has been recently implemented in high-resolution MR Neurography imaging protocols and has a potential to overcome most of the above mentioned challenges in small peripheral nerve imaging. The 3D-PSIF is a balanced gradient echo steady-state free precession (SSFP or PSIF) sequence with inherent features of a spin-echo sequence, as compared with other unbalanced spoiled or refocused gradient-echo techniques, such as fast low-angle shot (FLASH), fast field-echo, and gradient recall acquisition using steady-states (GRASS or FISP). Therefore, the 3D-PSIF sequence demonstrates less influence of local magnetic field inhomogeneities on the spin relaxation. The water-excitation technique enables uniform fat suppression and is unaffected by the chemical shift effect. Although 3D-PSIF may also be performed without fat saturation, fat-suppressed images usually provide better nerve-to-background contrast ratio. In addition, the application of diffusion moment provides suppression of water signal. In most cases, a diffusion moment value of 80–90 mT/m*ms provides an acceptable compromise in peripheral nerve-to-background contrast and image signal-to-noise ratios (SNR). Since the signal depends strongly on the steady-state condition, all moving structures, such as flowing blood, demonstrate a loss of signal intensity. As a result, the high T2 signal intensity of peripheral nerves is effectively differentiated from the nulled signal of adjacent vessels (Figs. 1, 2). Although 3D-PSIF images provide predominantly T2 contrast, there is a potential to perform post-contrast imag-



1 Sagittal 3D-PSIF image of the forearm and wrist demonstrates the median nerve (arrow) along its entire course.



2 Coronal 3D-PSIF image of the lumbosacral plexus demonstrates excellent discrimination of the nerve roots from adjacent soft-tissue structures.

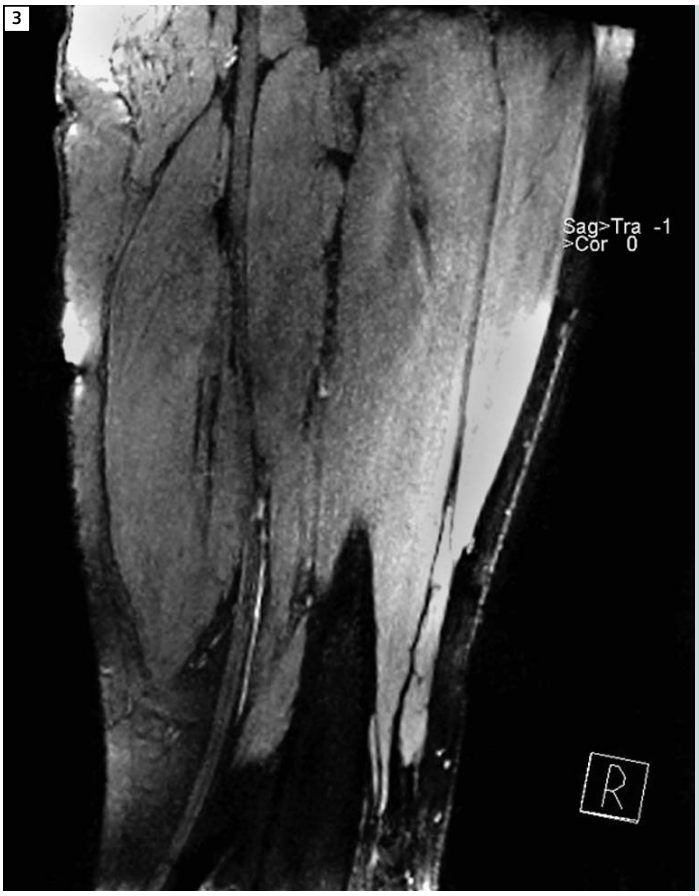

3 Coronal 3D-PSIF maximum intensity projection (MIP) of the thigh demonstrates the course of the sciatic nerve.

ing following administration of intravenous gadolinium. In 3D-PSIF imaging, the acquisition of isotropic voxels enables the data set to be reformatted into any imaging plane without significant loss of resolution. The latter feature may provide confirmation of anatomic continuity, as well as identification of branching, focal enlargement, course deviation and/or displacement of peripheral nerves. In addition, maximum intensity projections (MIPs) can be employed to further enhance the conspicuity of the nerves and provide images, which can be distributed to referring physicians for better depiction and understanding of nerve anatomy and pathology (Fig. 3). Table 1 displays the typical acquisition parameters employed for the 3D-PSIF sequence in a Siemens 3T MAGNETOM Verio scanner. In clinical practice, 3D-PSIF has proven more efficient than the conventional STIR and T2 SPAIR TSE sequences in differentiating small peripheral nerves from adjacent vessels. In the extremities, and particularly distal to the knee and elbow joints, the commonly encountered T2 hyperintense subcutaneous and/or fascial edema restricts the identification of small peripheral nerves on conventional T2-weighted sequences. In contrast, the inherent diffusion sensitive gradients of 3D-PSIF enable selective suppression of the water signal of the stationary subcutaneous and fascial edema, thus improving the conspicuity of small peripheral nerves in the above areas. On the other hand, the inherent high TE values of 3D-PSIF images result in lower SNR as compared to conventional fat-saturated T2-weighted images, which remain superior in delineating the fascicular structure of the nerves. In post-contrast imaging, as compared to the three-dimensional volumetric interpolated breathhold examination (3D VIBE) sequence, the 3D-PSIF technique provides better visualization of the nerve fascicles, as well as more adequate assessment of the anatomic relationship between fascicles and enhancing intraneural and/or extraneural tumors.
In summary, the 3D-PSIF sequence with high spatial resolution and high contrast provides reliable and objective identification of peripheral nerve anatomy and may be incorporated as part of the high-resolution MR study of peripheral nerves, whenever accurate nerve localization and/or pre-surgical evaluation are required.



→ Don't miss the talks on peripheral nerve imaging on www.siemens.com/magnetom-world

- Imaging of peripheral nerves – status quo by Mirko Pham University of Heidelberg, Germany
- Peripheral nerve imaging from head to toe by Meng Quan-Fei. The First Affiliated Hospital of Sun Yat-sen University, Guangzhou, China

Contact
John A. Carrino, M.D., M.P.H.
Associate Professor of Radiology and Orthopedic Surgery
Section Chief, Musculoskeletal Radiology
The Russel H. Morgan Department of Radiology and Radiological Science
601 North Caroline St. /JHOC 5165
Baltimore, MD 21287-0856
USA
carrino@jhmi.edu

Advantages of MSK Imaging at 3 Tesla with special focus on Spine and Tumor Imaging

Marc-André Weber, M.D., M.Sc.

Diagnostic and Interventional Radiology, University Hospital Heidelberg, Germany

Background

In 2009, our institution, the Department of Diagnostic and Interventional Radiology, had to decide for a replacement of an existing 1.0 Tesla MR system with conventional coil technology and a bore-size of 60 cm at the Department of Orthopedics with the main departments Orthopedics and Traumatology as well as Paraplegiology and Rehabilitation Medicine. While the clinicians were satisfied with the robustness of imaging in case of metal implants with the old scanner, compromises in image resolution and relatively long examination times as well as the missing capabilities of the old system for scanning multiple regions of interest within one examination without the need for patient repositioning did limit the usage of MRI. In addition, due to the limited signal-to-noise ratio (SNR) as a result of the low field strength and old coil technology implemented in this system, the increasing clinical demand for widening the application of MRI to include, for example, molecular assessment of cartilage repair or multi-region tumor staging in children and adults could not be fulfilled sufficiently in a clinical environment.
The advantages of 3 Tesla especially for orthopedic imaging are well known: increase in SNR (proportional increase of the SNR with the increase of the field strength) and less prominent effect of B1 inhomogeneity on image quality for most areas of interest in musculoskeletal (MSK) imaging (knee, shoulder, ankle, wrist etc.) results in clearly improved image quality (resolution wise) and / or faster scan times. However, for advanced spine imaging as well as tumor staging, the "dielectric shading" effects would again have limited the usability of the MRI scanner. But with the development of anatomy optimized amplitude and phase transmission settings for homogenous B1 radio-frequency (RF) transmission and in combination with further optimizations of the magnet and gradient design (TrueForm technology), local signal drop out at 3T can be reduced significantly if not even eliminated practically. Another limitation of higher field strength is the higher energy deposit within tissue, resulting in higher specific absorption rate (SAR). And finally, metallic implants will result also in increased signal drop due to pronounced susceptibility artifacts [Fries 2008, Baudendistel 2004]. But these effects with negative impact on the image quality and examination time can again significantly be reduced if not compensated by new MR technology (e.g. adopting sequence techniques and application of parallel imaging techniques). Finally, we were convinced that the advantages of the 3T technology available with the new scanner generation do outweigh the disadvantages significantly. In spring 2009 we therefore decided for replacement of our old 1T scanner by a 3T MAGNETOM Verio.
We would like to present below some interesting cases out of our daily clinical routine which demonstrate the advantages of MSK imaging at 3T with special focus on spine and tumor imaging.

Case 1

As a center dealing with a high number of patients with hemi-/ paraplegia, cerebral palsy as well as scoliosis, the 70 cm open-bore system has the advantage of a very flexible patient positioning. As demonstrated in figure 1B, especially severe contractions of the extremities often seen in these patients do require sufficient space in the anterior-posterior direction. In figure 1A our MR-compatible wheelchair is shown, which enables an easy and relative fast patient transport into the scanner.

1A



1B



1 Patient with contractions of the lower extremities. MR-compatible wheelchair for easy patient transport.

Flexible patient positioning in the 70 cm open-bore system.

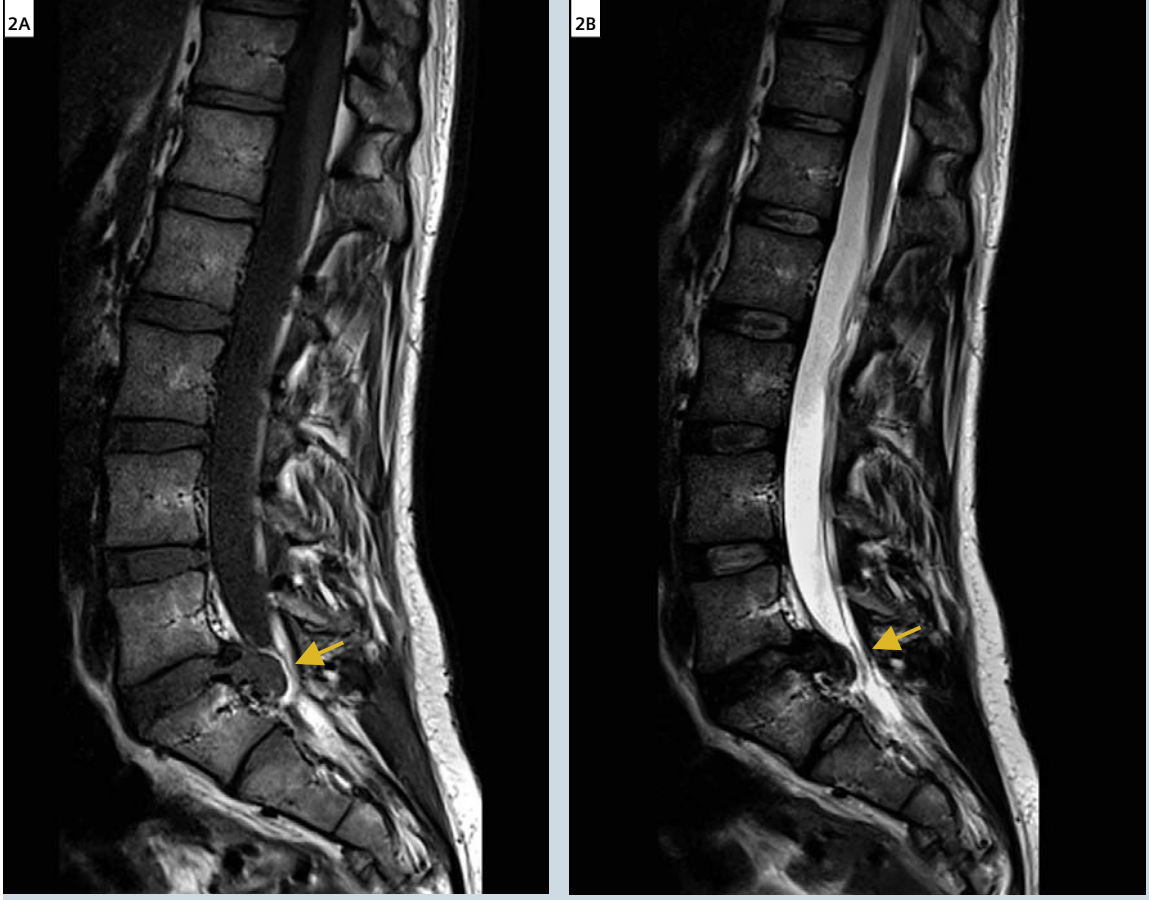

2 **A)** T1w TSE sagittal
B) T2w TSE sagittal

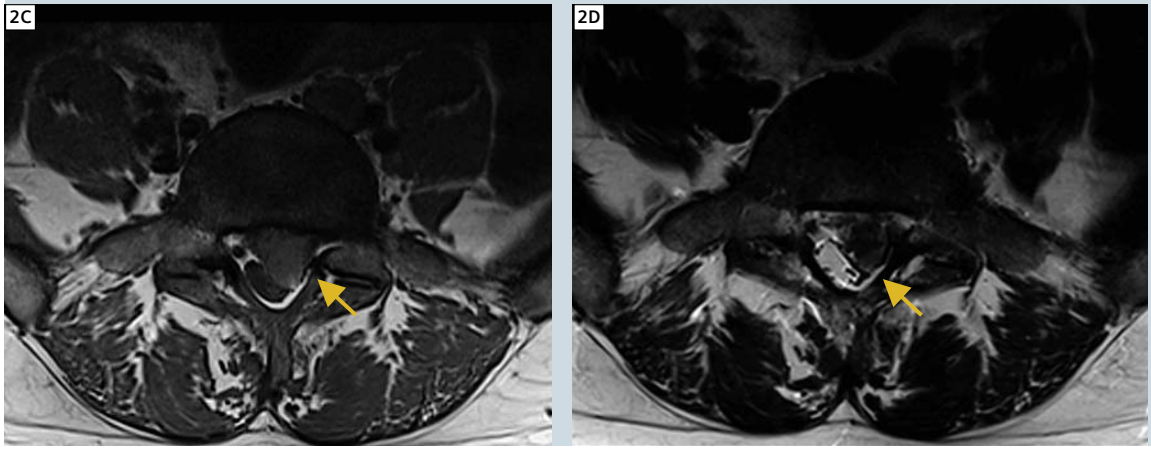

C) T1w TSE axial (oblique)
D) T2w TSE axial (oblique)

Case 2

This case demonstrates our standard imaging strategy in case of lower back pain. We apply mainly turbo spin-echo (TSE) sequences for this purpose. Sequence parameters for the shown images are:
T1w TSE sagittal: resolution (0.7 x 0.7 x 3.0) mm^3, TR 684 ms, TE 12 ms, TA 2:48 min (fig. 2A).
T2w TSE sagittal: resolution (0.7 x 0.7 x 3.0) mm^3, TR 3650 ms, TE 113 ms, TA 3:00 min (fig. 2B).
T1w TSE axial (oblique): resolution (0.7 x 0.7 x 3.0) mm^3, TR 969 ms, TE 12 ms, TA 3:09 min (fig. 2C).
T2w TSE axial (oblique): resolution (0.7 x 0.7 x 4.0) mm^3, TR 5060, TE 115 ms, TA 2:59 min (fig. 2D).
With a total scan time of less than 15 minutes, this protocol focuses on a fast assessment of the lumbar spine. However, because of the higher signal-to-noise contribution of the 3 Tesla system in combination with the integrated multi-channel spine coil, also a relatively high sub-millimeter in-plane resolution at slice thicknesses of 3 mm for sagittal and transversal planes is achieved.
In this particular case, a medio-lateral large hernia of the intervertebral disc of L5/S1 with compression of the left nerve root is seen (arrows).

Case 3

In case of malignancies or inflammation, however, we have to expand our clinical routine protocol. This case shows selected images of a 63-year-old male patient with known spinal astrocytoma WHO grade III. This patient underwent chemo- and radiotherapy and presented at our institution with clinically stable paraplegia at the level of Th5. A swollen myelon can be seen in this follow-up exam at the height of the irradiated tumor at the height of thoracic vertebra 6–8. On post-contrast T1w MRI, an inhomogeneous medullar enhancement can be seen (arrow). Note that the patient also underwent laminectomy and that a residual seroma can be detected. Enhancement within the vertebra was stable over a long period of time and based also on CT imaging, this finding has to be classified as a hemangioma of the 9th thoracic vertebra.



3 **A)** T1w TSE sagittal
B) T2w TSE sagittal
C) ce T1w sagittal with fat-saturation
D) ce T1w axial (oblique)

Case 4

43-year-old male patient, who underwent a dorsal stabilization after traumatic fracture of vertebra Th10 and had complete paraplegia below this segment. On conventional x-ray, the spine fusion from Th9 to Th11 is shown (fig. 4A). Figure 4B shows an MRI which was performed at our institution with our old 1 Tesla scanner. While artifacts caused by metallic implants on the 1T exam with the chosen sequences are less prominent compared to imaging at 3T (compare Fig. 4C), SNR and therefore in-plane resolution was low in the 1T exam and a further evaluation of the tethering of the myelon was not possible. The high SNR of the 3T scan allowed for a high in-plane resolution (Fig. 4C, D) and also for T2w 3D imaging (*syngo* SPACE, Fig. 4E).The capability of evaluating the whole area of interest with the SPACE sequence at highest resolution and contrast in any orientation allowed further evaluation of the reason for the dorsal dislocation of the myelon starting at the height of Th6.

Based on this MRI exam, the suspicion of an arachnoidal cyst was supported leading to a dorsal dislocation and compression of the myelon. Even the slight arachnoidal web could be detected on the SPACE sequence (red arrow in Fig. 4D).
Slice thickness for sagittal T2w images were 3 mm for both examinations at 1 and 3 Tesla, respectively. Resolution of the *syngo* SPACE exam was (0.7 x 0.7 x 0.7) mm^3.

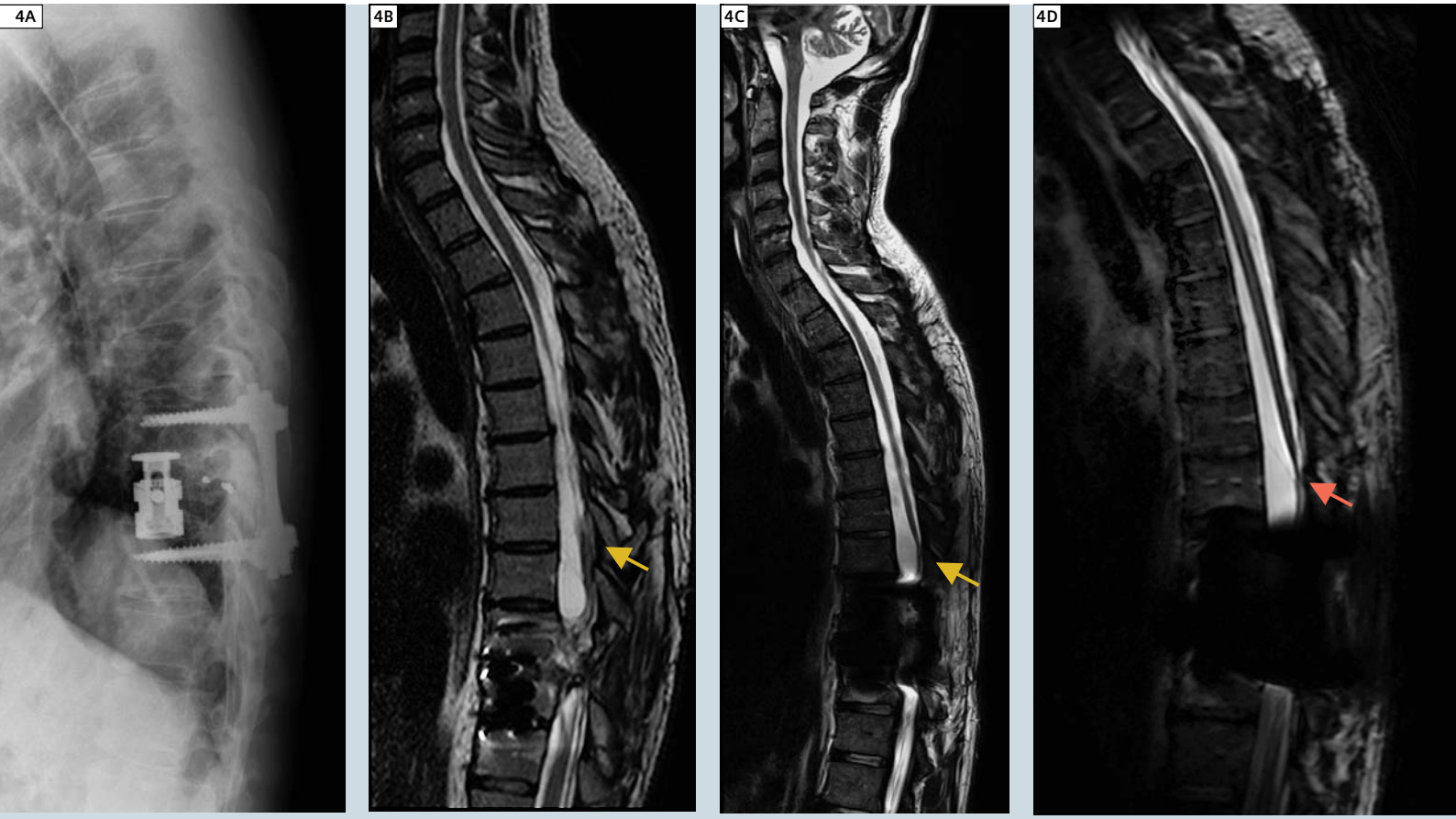

4 **A)** Conventional x-ray **B)** T2w sagittal at 1T **C)** T2w sagittal at 3T **D)** T2w *syngo* SPACE at 3T

Case 5

66-year-old female patient with molecular pathology confirmed Ewing sarcoma of the right humerus. After initial tumor excision in 2009 and osteosynthesis, the patient presented with an extensive recurrence of the tumor within four months. Figure 5A demonstrates the large tumor with infiltration also of the bone marrow. In addition, diffuse oedema is shown (arrowhead in 5A). Figure 5B also shows a large lymph node metastasis (arrow). Therefore, before again operating on the humerus, the orthopaedic tumor surgeon wants to know whether more lesions are present. Thus, a whole-body scan was added (Fig. 5C), demonstrating also multiple osseous filiae (arrows in 5C) of the pelvis and spine. No evidence of high risk or presence of a pathologic fracture was found.

By selecting appropriate imaging techniques, imaging at 3T even with metal implants present and off-center positioning can result in excellent image quality. The achievable superior resolution clearly increases confidence about extension of a tumor and impairment of anatomical structures. In addition, the capability of scanning large areas of interest up to whole-body without compromise in image quality and within a clinical acceptable setting (time and patient-comfort wise) is a prerequisite for any sufficient oncologic decision making and is highly esteemed by our tumor surgeons, especially to detect skip lesions that would distinctly influence the therapeutic concept. The superior capability of evaluating changes within the bone marrow including diffuse tumor infiltration is a particularly big advantage in our patient cohort.



5 A) Coronal ce T1w with fat saturation.

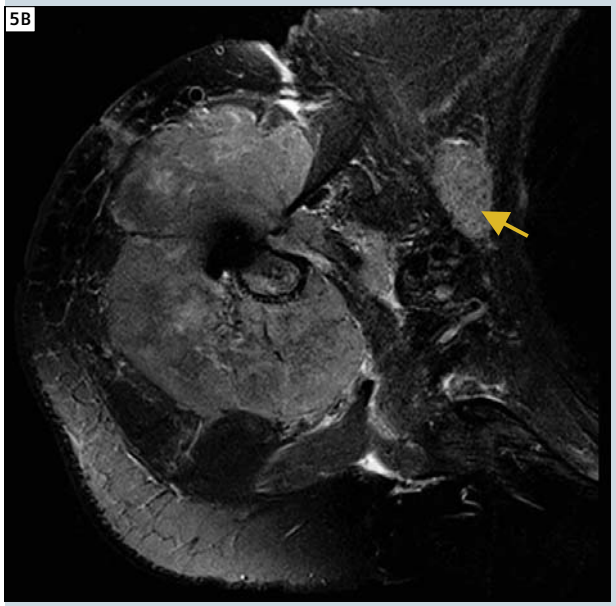

B) Axial ce T1w with fat saturation.

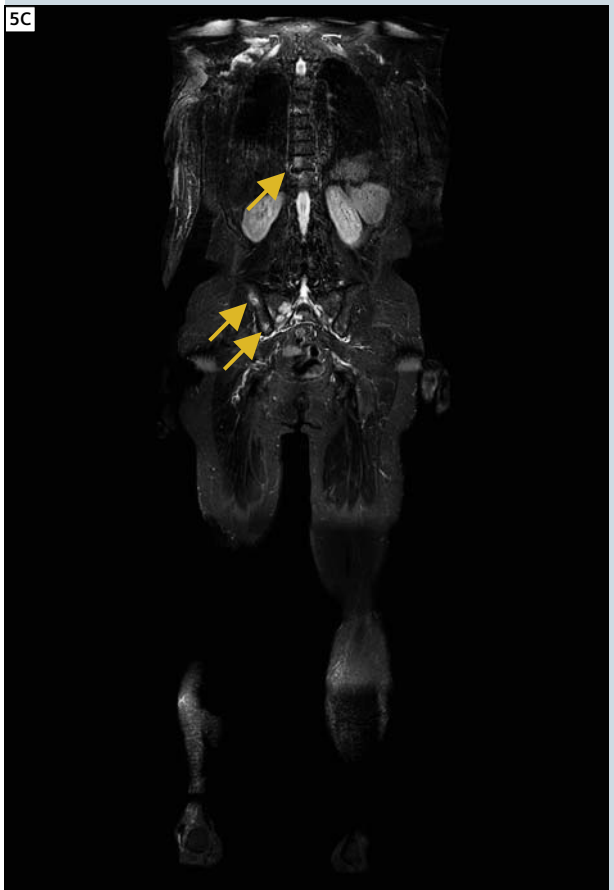

C) Coronal T2w whole-body with fat saturation.

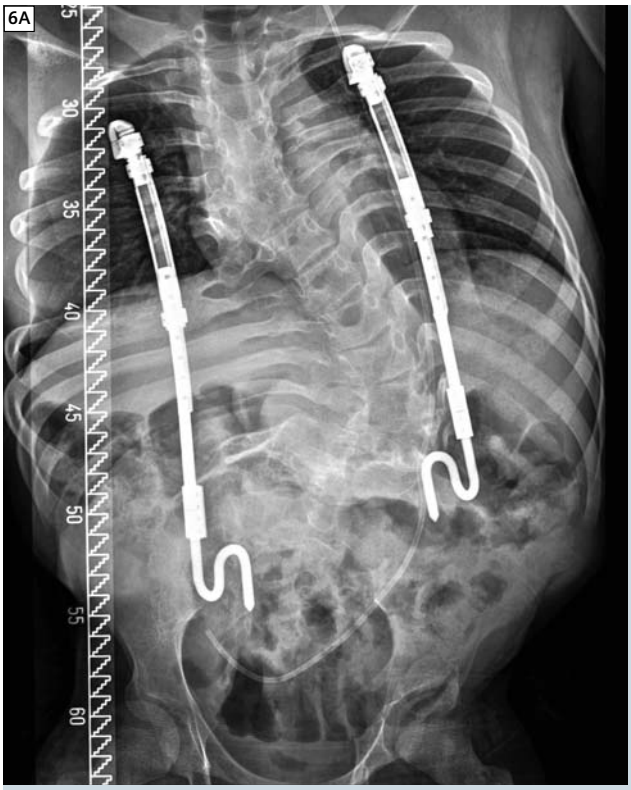



6 **A)** Conventional x-ray **B)** T2w sagittal at 1T

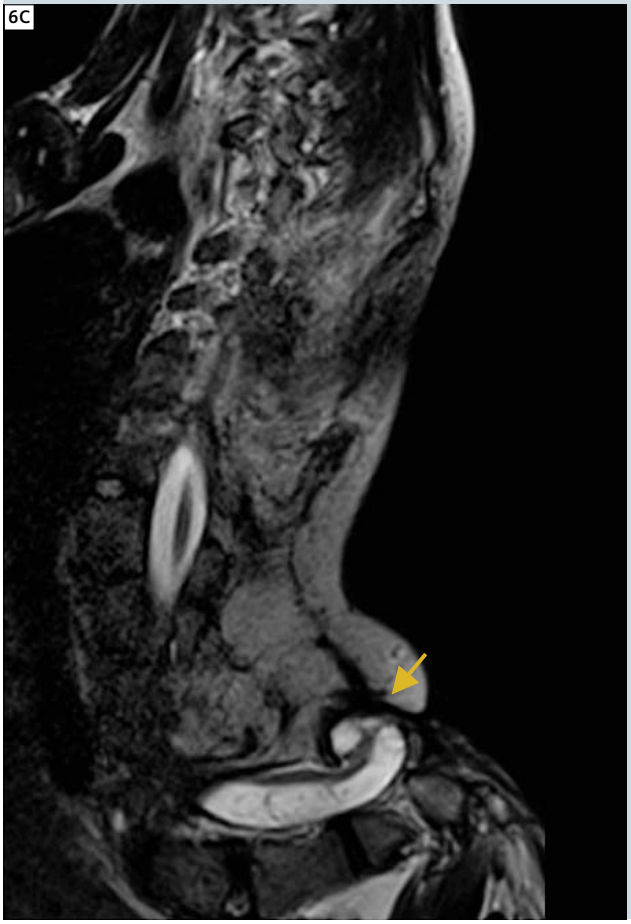

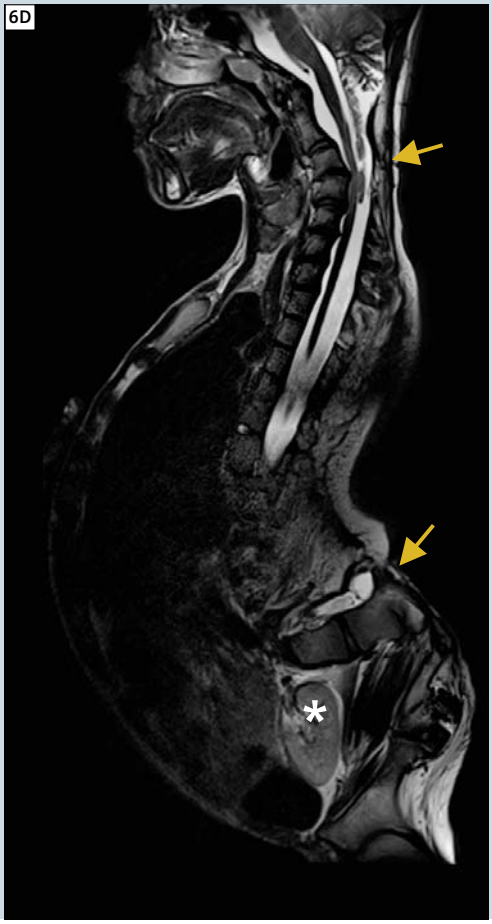

C) T2w sagittal at 3T **D)** T2w *syngo* SPACE at 3T

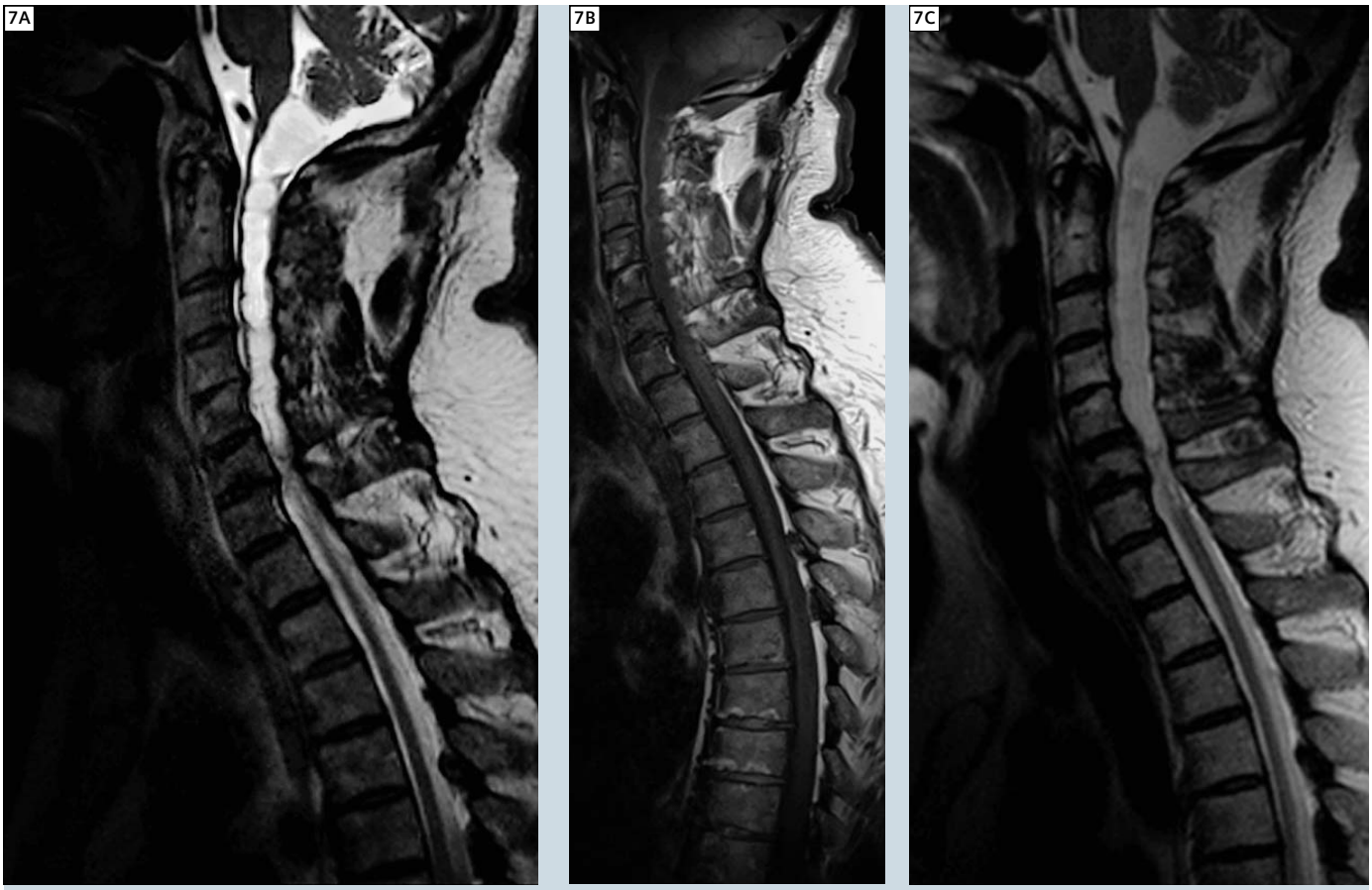

7 **A)** T2w sagittal at 3T **B)** T1w sagittal at 3T **C)** T2w sagittal at 1T

Case 6

Complex congenital malformation of the central nervous system, as well as the spine, requires also evaluation of the whole systemic aspect of disease. In this case, we show images from a 15-year-old boy with Arnold Chiari II malformation and lumbal meningomyelocele (closed by surgery after birth). Because of severe and progedient complex scoliosis, this patient also underwent a dorsal spine fusion of Th9 downwards to the pelvis with VEPTR instruments and underwent multiple extensions (conventional x-ray Fig. 6A).
Figures 6B and C do show the image quality difference between 1 and 3T exam (both 3 mm slice thickness). Again, the superior SNR and in-plane resolution allows for a more detailed assessment of the meningomyelocele (arrows). Especially T2w 3D imaging allows for a detailed assessment of all aspects of the impairment of the central nervous system including the myelon and nerve roots. Figure 6D shows the results of a *syngo* SPACE exam of the whole spine. The meningomyelocele is resolved in detail (arrow) as well as the displacement of the cerebellum as part of the Arnold Chiari malformation. Also tethering of the myelon, which is important for the orthopaedic surgeons to know about because it must be resolved before any operation to the spine, is well depicted. Note also the displacement of inner organs in this case (asterisk marks one of the kidneys).

Case 7

Exam of a 59-year-old male patient with complete tetraplagia at the level of C5 and secondary syringobulbia starting at the vermis down to the 6th thoracic vertebra as a consequence of a bathing accident in 1968. The patient received arachnolysis and dural plastic as specific therapy, as well as a wound examination because of a liquor pad. The *syngo* SPACE exam (Fig. 7A) shows multiple horizontal septae, which divide the syrinx and might hinder CSF exchange and thus might cause extension of the syrinx. The 3 Tesla T2-weighted image (Fig. 7A) better delineates the septae than the 1 Tesla T2-weighted image (Fig. 7C). In this case, a complete suppression of the liquor was seen on FLAIR images (not shown), suggesting communication of the multiple cystic lesions and the subarachnoid space.







8 **A)** Coronal and **B, C)** sagittal reconstructions based on 3D T2w imaging.

Case 8

Intramedullar formation of cavities can often be found as a consequence of widening of the central canal (hydro myelia) or outside the central canal (syringomyelia) as result of traumatic events or space occupying lesions / tumors or as a malformation. T2w images of a 7-year-old boy are shown, showing a syringomyelia affecting the whole myelon (holocord syrinx).

Case 9

10-year-old girl with meningomyelocele, paraparesis, spina bifida and rotation skoliosis is shown. In addition, partial fusion of the first and second lumbar vertebra is present as well as dysplasia of the 12th thoracic vertebra. Imaging was conducted for planning of specific therapy including instrumented dorsal spine fusion and decompression of the spinal canal. For optimal outcome and for best risk stratification of such a therapy, detailed information not only about the complexity of the disorders of the spine but also of the myelon and nerve roots is essential. CT (volume rendering shown in Fig. 9A) as well as 3T MRI demonstrated in detail the known left convex rotation scoliosis of the thoraco-lumbal spine. Syrinx from level Th3 down to the conus is visualized by MRI (arrows in Figs. 9B–D). In addition, starting at the height of Th6, a T2w hypointense, T1w isointense to the myelon, linear and parallel to the myelon running structure can be delineated that might resemble a scarred cord. Most probably this structure represents split cord malformation e.g. diastematomyelia.

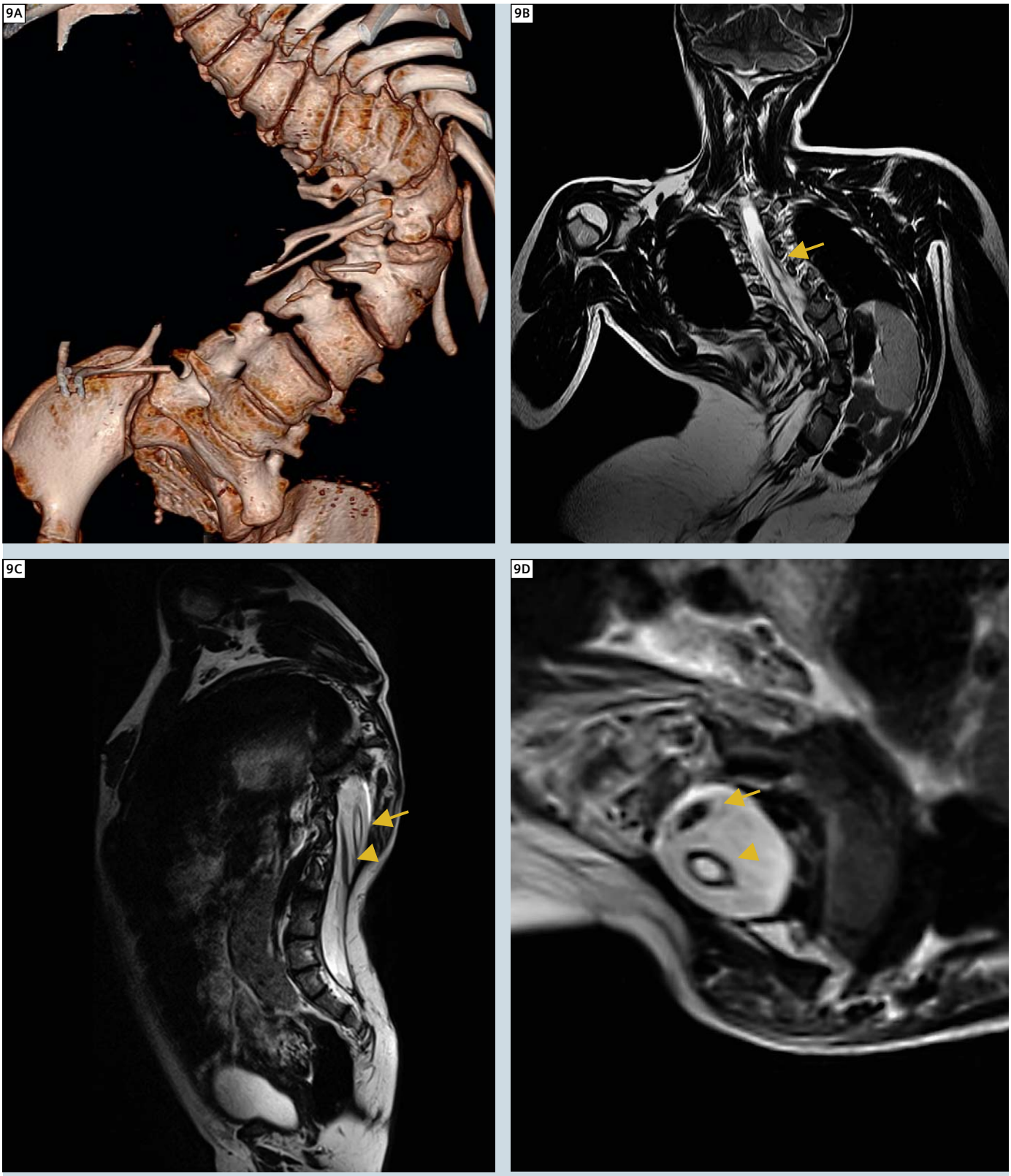

8 **A)** Volume Rendering Technique (VRT) of a CT scan. **B)** Coronal, **C)** sagittal and **D)** oblique reconstructions based on 3D T2w imaging.

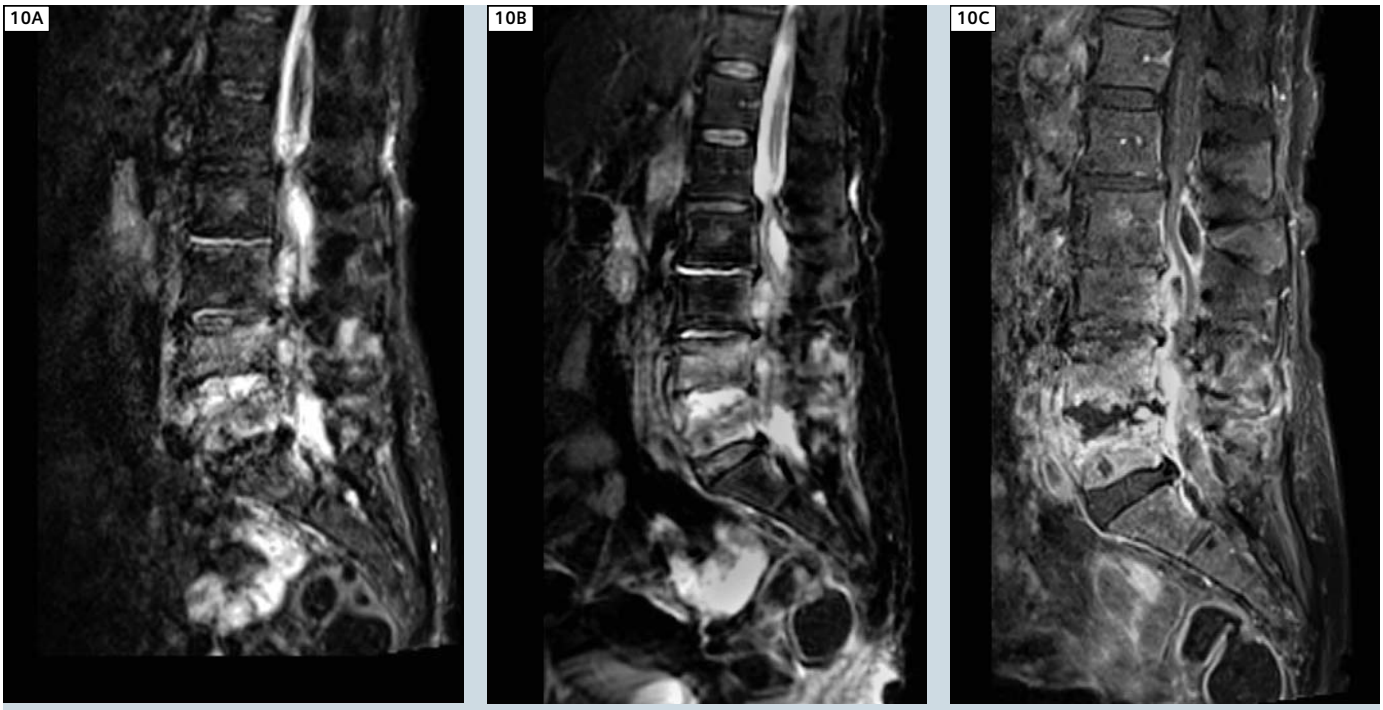

10 **A)** T2w sagittal with severe motion artifacts. **B)** T2w sagittal with *syngo* BLADE technique. **C)** ce T1w sagittal with fat saturation.

Case 10

Results of an MRI scan of an 87-year-old female patient with dementia and severe back pain are shown. Severe motion artifacts were present (Fig. 10A) but could be compensated by applying motion-insensitive (*syngo* BLADE; Fig. 10B) MR sequences and fast sequences with parallel imaging (post-contrast T1w image; Fig. 10C). Spondylodiscitis and complete destruction of the intervertebral space of L5/4 is seen. In addition, multiple epidural abscesses can be seen. The patient underwent surgery with dorsal and ventral spine fusion, open discectomy and laminectomy as well as drainage.

Conclusion

Although the adoption to the higher field strength of 3T, new coil technology and multi-region exams were challenges to radiologists, technologist and referring clinicians and do require a (short) transition phase, the clinical advantages are significant, as shown with this case series. After approximately one year of operation, the installation of the 3T open bore system with TrueForm technology has clearly improved our diagnostic potential as well as widened the indications for MRI and has lead to improved patient care. The system is therefore well received among our clinical colleagues, resulting also in a significant increase of referrals during the last year. In addition, the patient comfort of the open bore system has resulted in a higher acceptance of MRI by patients.

Acknowledgements

The excellent cooperation regarding brain and spine imaging with Prof. Dr. Stefan Hähnel and Dr. Leonie Jestaedt from the Department of Neuroradiology at the University Hospital Heidelberg (Head: Prof. Dr. Martin Bendszus) is gratefully acknowledged.

References

1 Fries P, Runge VM, Kirchin MA, Watkins DM, Buecker A, Schneider G. Magnetic resonance imaging of the spine at 3 Tesla. Semin Musculoskelet Radiol. 2008 Sep;12(3):238-52.
2 Baudendistel KT, Heverhagen JT, Knopp MV. Clinical MR at 3 Tesla: current status. Radiologe 2004;44(1):11-8.

Contact
Marc-André Weber, M.D., M.Sc.
Professor of Radiology
Head of Musculoskeletal Radiology
Department of Diagnostic and Interventional Radiology
University Hospital Heidelberg
Im Neuenheimer Feld 110
69120 Heidelberg
Germany
Phone: +49 6221-966601
Fax: +49 6221-966640
MarcAndre.Weber@med.uni-heidelberg.de

Fat Suppression Techniques – a Short Overview

Wilhelm Horger; Berthold Kiefer

Siemens Healthcare, Erlangen, Germany

Introduction and background

Fat-suppression is an integral part of nearly any routine MR application. Insufficient elimination of the fat signal or even saturation of tissue of interest in an MR image can have severe consequences and therefore the knowledge about available fat-suppression techniques and their individual advantages and disadvantages are required. The purpose of this article is to provide a short technical overview of the main fat-suppression techniques available for clinical routine.

All techniques for fat suppression are based on the fact that – due to the different chemical environment – hydrogen nuclei in water and in fat-tissue have different values for some MRI-relevant parameters, mainly the relaxation time and the resonance frequency

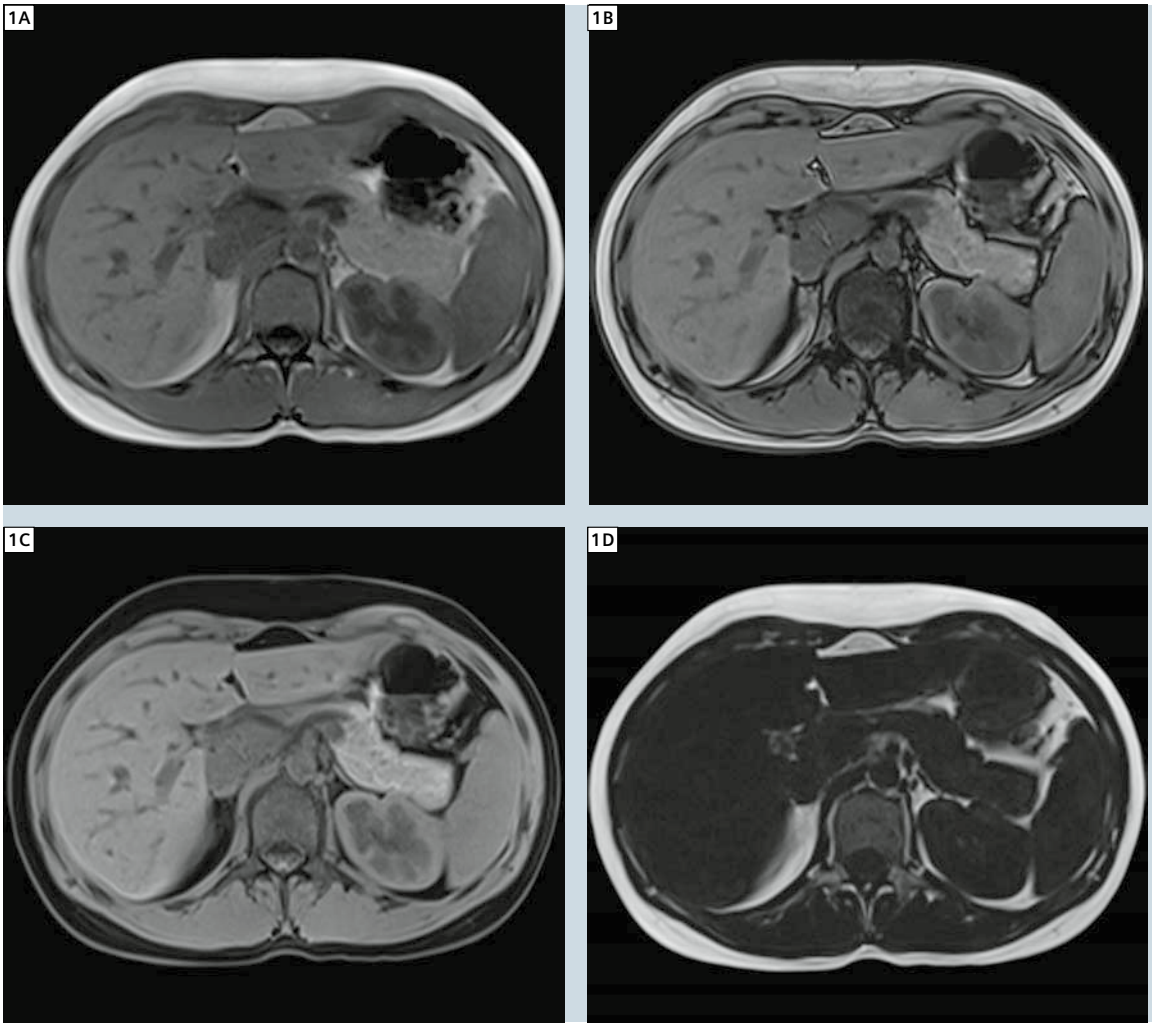

1 Dixon technique (VIBE). Four contrasts generated in one breathhold:
1A: in-phase
1B: opposed-phase
1C: water image
1D: fat image

2

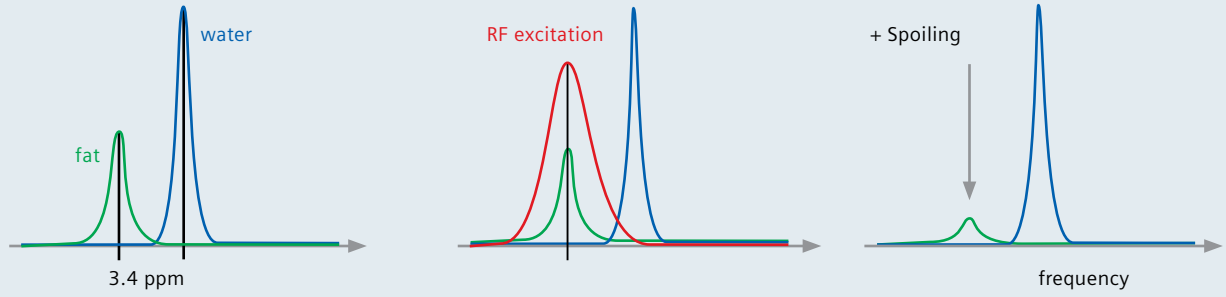

2 Spectral fat saturation.

(chemical shift). These differences can be used to selectively suppress or reduce the signal of fat bound protons. Thus one can differentiate between two types of fat-suppression techniques:

a) Relaxation-dependant (e.g. STIR)

b) Chemical shift-dependant methods (e.g. Dixon technique (available for VIBE and TSE sequence techniques), spectral fat saturation, water excitation and SPAIR).

Dixon technique

The Dixon technique is based on the chemical shift i.e. the difference in resonance frequencies between fat and water-bound protons. With this technique two images are acquired. In the first image the signal from fat-protons and from water-protons are 'in phase'; in the second they are 'opposed phase'. A separate fat and water-image can then be calculated. The Dixon method is integrated into the VIBE sequence and TSE sequence (compare Fig. 1).

Dixon delivers up to 4 contrasts in one measurement: in-phase, opposed-phase, water and fat images.

Advantages of the Dixon technique:

- Insensitive to B_0 and B_1 inhomogeneities.
- 4 contrasts delivered in one measurement.

Disadvantage of the Dixon technique:

- Increases minimal TR because in- and opposed phase data must be acquired. This can be compensated by using integrated Parallel Acquisition Techniques (iPAT).

Spectral fat saturation

This technique is based on the chemical shift (3.4 ppm) i.e. the difference in resonance frequencies between fat- and water-bound protons. The application of a narrow band frequency selective radio-frequency (RF) pulse excites mainly fat-bound protons. This transversal magnetization is destroyed afterwards by spoiler gradients, thus no fat magnetization is left for imaging (compare figure 2).

For spectral fat saturation, a 'Quick-Fat-Sat' setting is available. If this feature is selected, not every slice excitation is preceded by a preparation pulse. This means:

- Shorter possible TR;
- Shorter breath-hold examinations (e.g. VIBE, recommended 40 lines/shot).

Two FatSat modes (strong/weak) are also available. Basically, the user can select how much of the fat signal is contributing to the MR image. In the 'strong' mode a nearly full suppression is achieved, whereas in the 'weak' modus, anatomical information of fatty tissue is partially preserved.

3

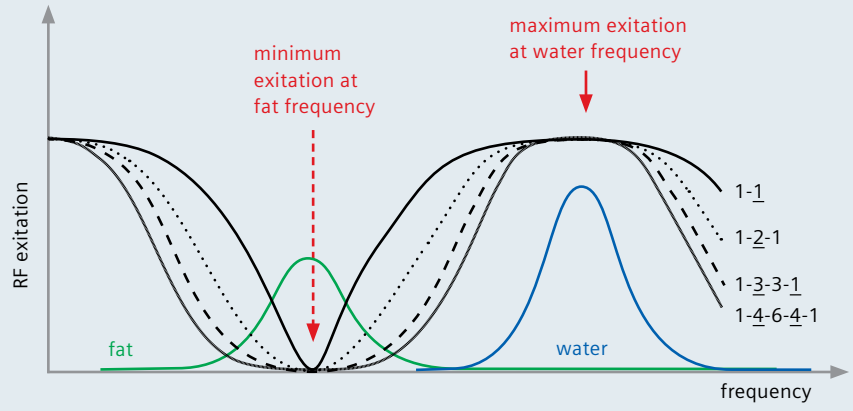

3 Water Excitation.

Advantages of spectral fat saturation:

- Tissue contrast is not affected;
- Quick-FatSat can be applied for increased performance.

Disadvantages of spectral fat saturation:

- Sensitive to B_0 and B_1 inhomogeneities;
- Additional preparation pulse increases minimal TR and total measurement time or reduces maximum number of slices (partially compensated by Quick-Fat Sat).

Water excitation

This technique is based on the chemical shift i.e. the difference in resonance frequencies between fat and water-bound protons. No additional preparation pulse is necessary. Instead, a special excitation pulse (binomial pulse) is used with the spectral excitation profile (minimum excitation of fat bound protons, maximum excitation of water-bound protons) (compare Fig. 3).

Advantages of water excitation:

- Reduced sensitivity to B_1 inhomogeneities.

Disadvantages of water excitation:

- Increased min TE, TR and total measurement time or reduced maximum number of slices.

Fat suppression with Inversion Recovery

In clinical routine, two types of inversion recovery techniques are applied: SPAIR (Spectrally Adiabatic Inversion Recovery) method, and Short TI Inversion Recovery (STIR; in principal identical to TIRM (Turbo Inversion Recovery Magnetization) technique).

4

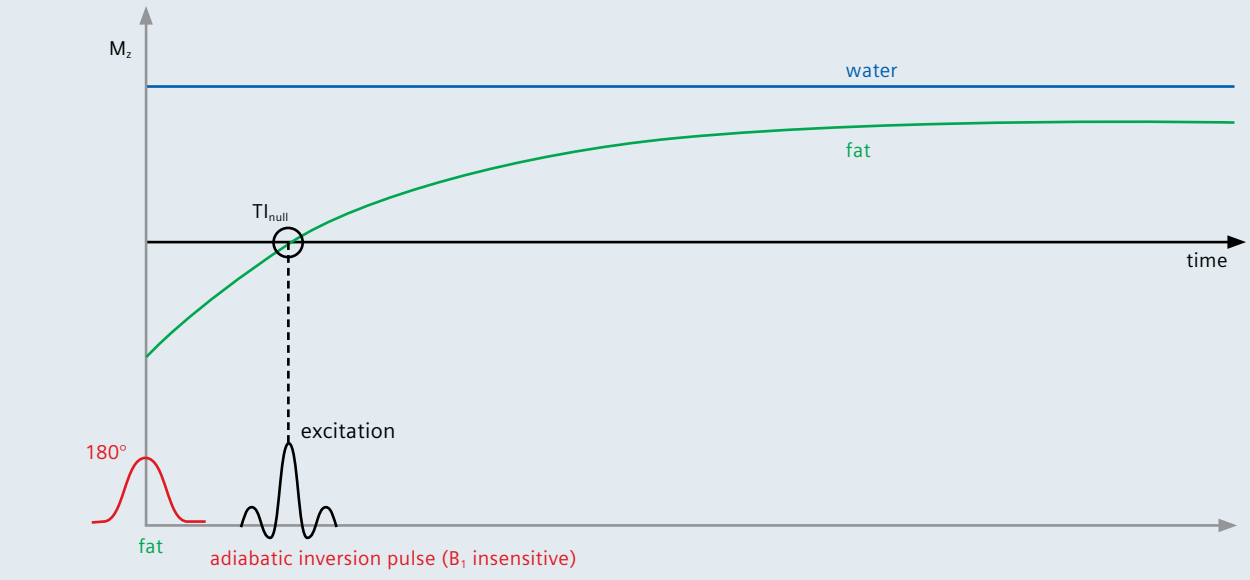

4 SPAIR technique.

5

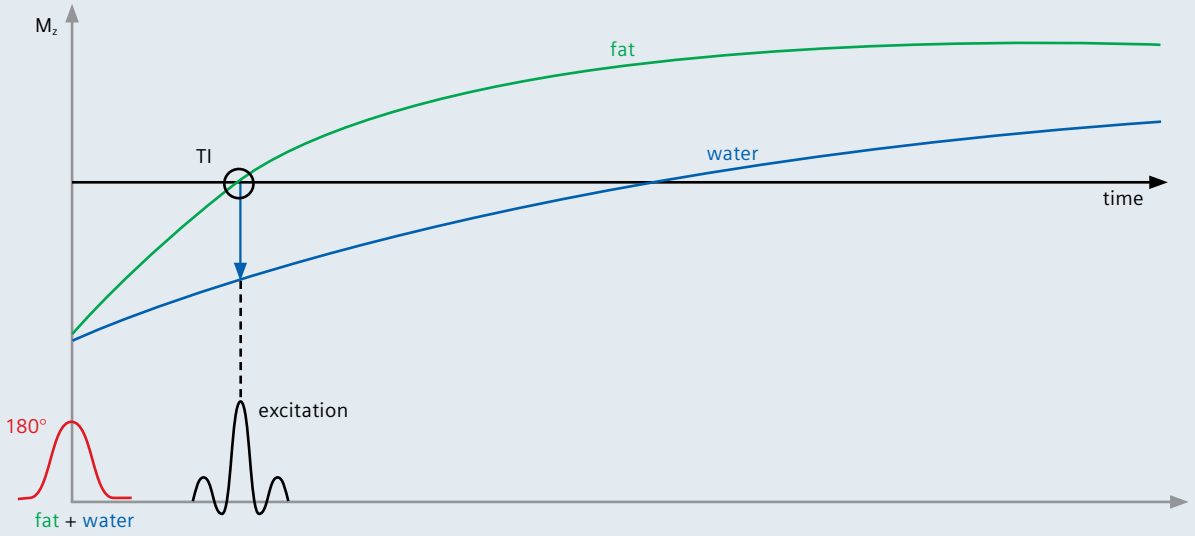

5 STIR technique.

SPAIR technique (Spectrally Adiabatic Inversion Recovery)

SPAIR is an alternative to the conventional spectral fat saturation. A spectrally selective adiabatic inversion pulse excites only fat spins, thus no STIR like contrast is created. With gradient spoiling the transverse magnetization is destroyed. The inversion time TI is such that the longitudinal magnetization of fat at the time when the excitation pulse is applied is zero, so fat spins will not contribute to the MR signal (compare Fig. 4).

Advantages of SPAIR:

- Insensitive to B_1 inhomogeneity;
- Tissue contrast is not affected.

Disadvantages of SPAIR:

- Increased minimal TR or reduced maximal number of slices due to more complex preparation pulse (partially compensated by Quick-Fat Sat).

STIR (Short TI Inversion Recovery)

This relaxation-dependant technique is based on the different relaxation behavior of water and fat tissue. Fat has a much shorter T1 relaxation time than other tissues. Prior to the excitation pulse of the sequence an inversion pulse (= 180°) is applied which inverts the spins of all tissue and fat protons. This is followed by T1 relaxation. When choosing TI such that the longitudinal magnetization of fat at the time when the excitation pulse is applied is zero, the fat spins will not contribute to the MR signal. STIR images have an inverted T1 contrast: Tissue with long T1 appears brighter than tissue with short T1 (compare Fig. 5).

Advantages of STIR:

- Insensitive to B_0 inhomogeneities.

Disadvantages of STIR:

- Additional inversion pulse increases minimal TR and total measurement time or reduces maximum number of slices;
- Tissue contrast is affected, SNR is reduced.

Contact
Wilhelm Horger
Siemens AG
H IM MR PLM-AW ONCO
Allee am Roethelheimpark 2
D-91052 Erlangen
Germany
wilhelm.horger@siemens.com

→ In this article, the Siemens nomenclature is used. A list of MRI acronyms for a variety of MR techniques and different vendors as well as a booklet with detailed description of MR terms can be found at our MAGNETOM World Internet site. Follow the QR code or visit us at **www.siemens.com/magnetom-world** and go to **MR Basics** under **Publications**.

Frequently Asked Questions: Diffusion-Weighted Imaging (DWI)

Joachim Graessner, Dipl. Ing.

Siemens Healthcare, Hamburg, Germany

Background

MR diffusion-weighted imaging (DWI) has ceased to be used only in brain applications for several years. The utilization of whole body DWI is becoming a standard application in routine imaging. Whole body DWI has become as valuable as T2 contrast in tumor imaging and it allows to characterize tissue properties. Due to the more frequent use of DWI, questions are often asked with regard to the background, application, and interpretation of whole body DWI and its calculated Apparent Diffusion Coefficient (ADC) images.
The following will answer some of these questions.

What is diffusion?

Molecular diffusion is the random movement of molecules – in our case water (H_2O) – within tissues propelled by thermal energy. The contribution of intra- and extra-cellular (interstitial) movement to the total diffusion is still under investigation.

How is MR sensitizing the tissue for diffusion effects?

Within the spin echo preparation period of an EPI sequence, two strong gradient pulses are played out around the 180° pulse. The first pulse dephases the magnetization of moving and static spins and the second pulse rephases only static spins 100% while moving i.e. diffusing spins acquire non-zero phase dispersion, resulting in a stronger signal dampening of tissues with fast diffusion compared to tissues with slow diffusion. Free water experiences the strongest signal attenuation at higher b-values.

What does the b-value mean?

The b-value identifies the measurement's sensitivity to diffusion and determines the strength and duration of the diffusion gradients. It combines the following physical factors into one b-value and is measured in s/mm² [1].

$$b = \gamma^2 G^2 \delta^2 (\Delta - \delta/3)$$

The signal ratio diffusion-weighted to non diffusion-weighted signal is:

$$\frac{S}{S_0} = e^{-\gamma^2 G^2 \delta^2 (\Delta - \delta/3) D} = e^{-bD}$$

- S_0 – signal intensity without the diffusion weighting
- S – diffusion-weighted signal
- γ – gyromagnetic ratio
- G – amplitude of the two diffusion gradient pulses
- δ – duration of the pulses
- Δ – time between the two pulses
- D – diffusion coefficient is a measure of the strength (velocity) of diffusion in tissue. The stronger the diffusion, the greater the diffusion coefficient, i.e. the ADC in our in vivo case.

If you choose the b-value the reciprocal magnitude of the expected ADC (D) in the focus tissue you make the exponent of the exponential function being '-1'. This means your signal **S** is reduced to about 37% of its initial value $\mathbf{S_0}$.

What is the optimum b-value?

A b-value of zero delivers a T2-weighted EPI image for anatomical reference. The b-values should attenuate the healthy background tissue more than the lesion at a level so that the intensity differences are about a factor of two at a comfortable signal-to-noise ratio (SNR) level i.e. there is signal left in the highest b-value image.
In the range of clinically-relevant b-values (up to approximately 1,000), then the greater the b-value, the stronger the diffusion weighting and the higher

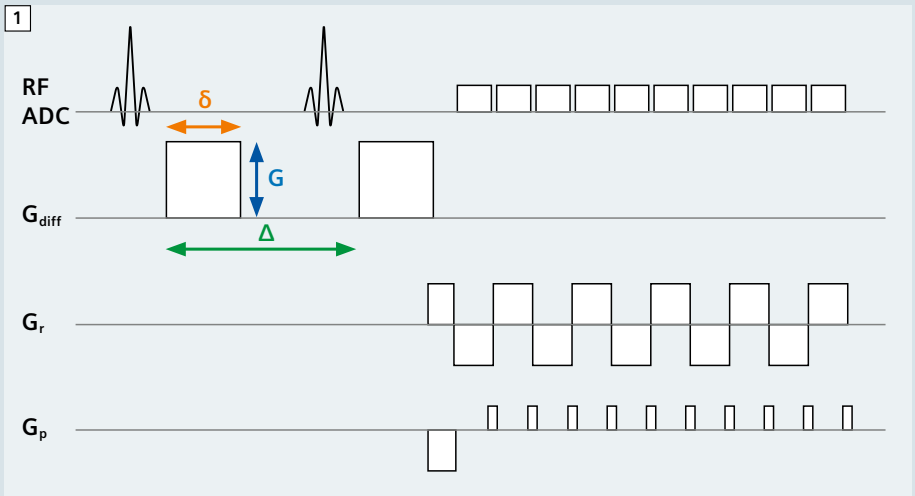

1 Sequence diagram of an EPI diffusion-weighted sequence illustrating the physical quantities of the b-value.



2A b = 0. No diffusion weighting, low-resolution T2 image.



2B b = 500. Intermediately diffusion-weighted image.

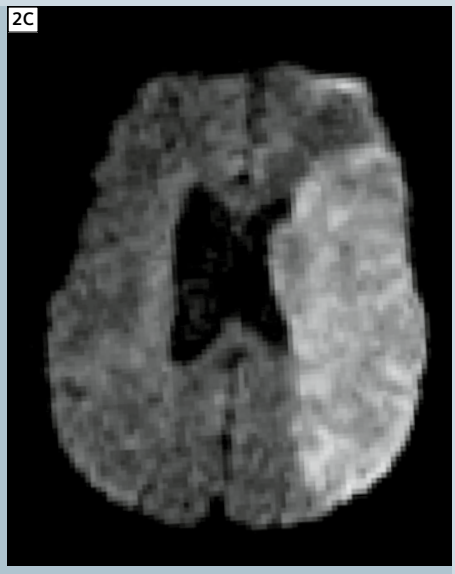

2C b = 1000. Strongly diffusion-weighted image.

the contrast in pathogenic regions. Shown below are examples of three b-values: b 0, b 500, and b 1000 s/mm^2. The proper b-value has approximately 80% of the reciprocal ADC value of normal background tissue. Keep in mind that higher b-values may pronounce lesions even more at the price of poor SNR due to longer TEs and increased susceptibility. This can be compensated by increasing averages, which result in longer scan times. Changing the b-value immediately influences other parameters like minimal TE, slice thickness and FOV as well as maximum matrix at a given optimal bandwidth. Furthermore anisotropy of tissues, like white matter, also influences the choice [2].

Why are a minimum of three directions measured for each high b-value?
Diffusion may be different in all three dimensions, like in white matter. Fibers exhibit longer free path in the longitudinal direction than perpendicular to it. The ADC images are therefore different depending on the sensitizing direction. This information is collected by applying diffusion gradients in all three dimensions. For example, in the case of commissures, diffusion is severely limited perpendicular to the fibers due to the surrounding myelin layer. In contrast, there are few or no limitations along the fibers. Anisotropy may have a strong effect on measurement results. To measure the diffusion strength independent of anisotropy, diffusion images of different orientation are measured and averaged.

Why should I measure three b-values for a DWI protocol when two would be enough for calculating ADC?
While two b-values are sufficient for creating an ADC image, the selection of three b-values (b 0, b 500, b 1000) delivers a more accurate calculation of the ADC values. The lower SNR of the b 1000 images introduces a higher standard deviation of the ADC which is partially compensated by the median value of b500.
Here is an example of two ADC images, the first acquired with three b-values and the second with two b-values.

What is a trace image?
The 'trace image' displays the geometric averaging of all three directional measurements, resulting in trace-weighted images. It suppresses to some extent anisotropy information and focuses on differences in signal attenuation. Like the ADC map, the trace-weighted map shows the strength of the diffusion and not its orientation.

Why do we need ADC images, and what does the 'A' in ADC stand for?
In addition to diffusion contrast, diffu-

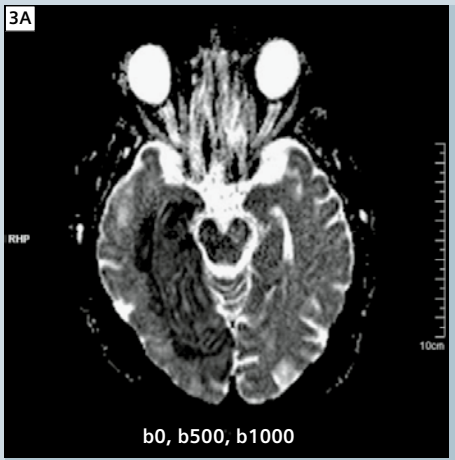

3A ADC calculated from 3 b-values (0, 500, 1000).

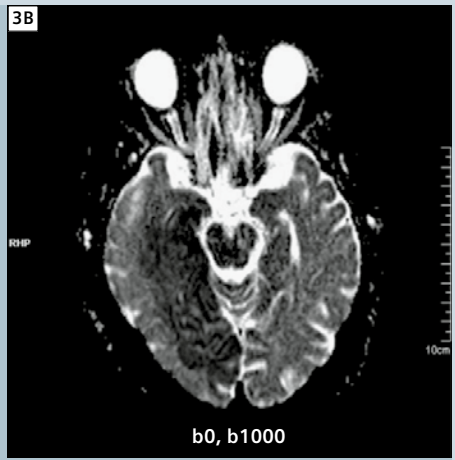

3B ADC calculated from 2 b-values (0, 1000).

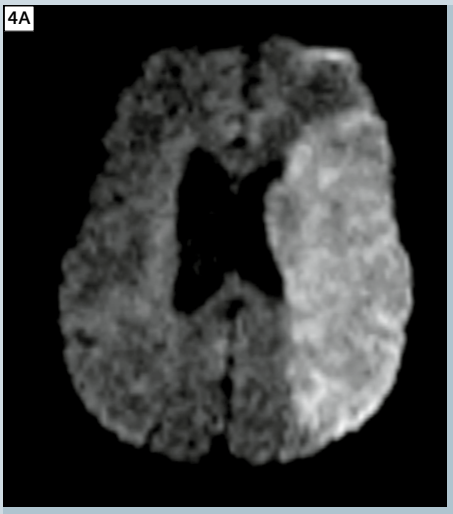

4A b1000 image; infarct is brighter than normal tissue.



4B ADC Image; infarct appears darker than normal tissue.

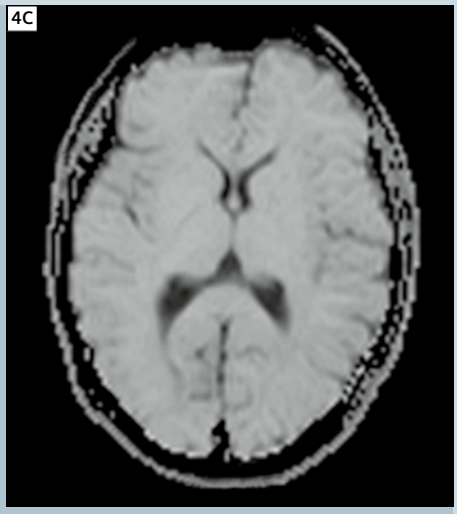

4C Exponential-Map

sion images also have an overlaying T2 contrast. In regions with long T2, this can simulate reduced diffusion ('T2 Shine-Through'). These portions of the signal can be eliminated by calculating a pure diffusion coefficient.
The 'A' stands for apparent because we do not measure the pure diffusion coefficient (D or DC). In living tissue the diffusion process is superimposed by capillary pseudo diffusion and gross motion to which the MR measurement is also very sensitive.

How is the ADC calculated?
Having measured a set of at least 2 different b-value images (e.g., b 0 and b 1000 s/mm²) the system calculates pixel by pixel the ADC by linear regression. The ADC pixel values together form the ADC map. On a half logarithmic scale, the signal decay delivers a straight tilted line whose slope provides the ADC. The faster the signal decay the steeper the slope and the higher the ADC.
The Diffusion image (b 1000) below displays reduced diffusion as hyperintense (brighter pixels); in contrast the ADC map displays it as hypointense (darker pixels).

Why are some lesions typically brighter than the background brain tissue on the higher b-value image and darker on the ADC map?
Due to the nature of certain lesions and their missing perfusion, the cells swell and hinder a normal diffusion; i.e., the mean free path is shorter. Water molecules cannot move as far in the damaged tissue as in normal tissue. As a result, the ADC is lower and appears darker than the surrounding normal tissue.

Which benefit does the calculation of an exponential map deliver?
The exponential map or image is calculated by dividing the maximal b-value diffusion-weighted image by the b_0 image. Mathematically the exponential map displays the negative exponential of the ADC; it is a synthetic diffusion-weighted image without T2 'shine-through' effect.
The contrast behaviour is similar to the high b-value image [3].

How do I get the ADC value out of my ADC image and what is the right unit?
Place a region of interest (ROI) on the ADC map and record the mean value in that ROI. A value of 850 intensity points is to be interpreted as 0.85 10^{-3} mm²/s. This is valid for software versions since *syngo* MR B13. Systems with A-level software (e.g., *syngo* MR A30) and *syngo* MR B11, a mean value of 85 delivers the result above.

There are many publications on DWI and ADC. But why are there so many different unit and digits used for ADCs?
Currently, there is no consensus about applied units in DWI. You will find all of the following units which are equal (*syngo* MR B13).

A mean intensity of 1000 is equal to:
1.0*µm²/ms or intensity times 10^{-3}
1.0*10^{-3} mm²/s or intensity times 10^{-6}
1.0*10^{-5} cm²/s or intensity times 10^{-8}
1.0*10^{-9} m²/s or intensity times 10^{-12}
Also found:
1000*10^{-6} mm²/s
1000*µm²/s

Why does the ADC have a unit of an area/time although diffusion occurs in all three dimensions?
By definition, the diffusion coefficient is defined as the product of 1/3 times medial velocity times mean free path:

$$D = 1/3 * v' * l$$

The unit is an area per time.

Why is there a lack of standardization for the choice of b-values in whole body DWI?
As a relatively new application body DWI is on its way to become a technique with recommended b-values and measurement conditions. See cited reference [4] for further information.

Why do most body and liver DWI protocols start with b-value 50 s/mm²?
The selection of a low b-value larger than zero provides suppression of large vessels which makes lesions more con-

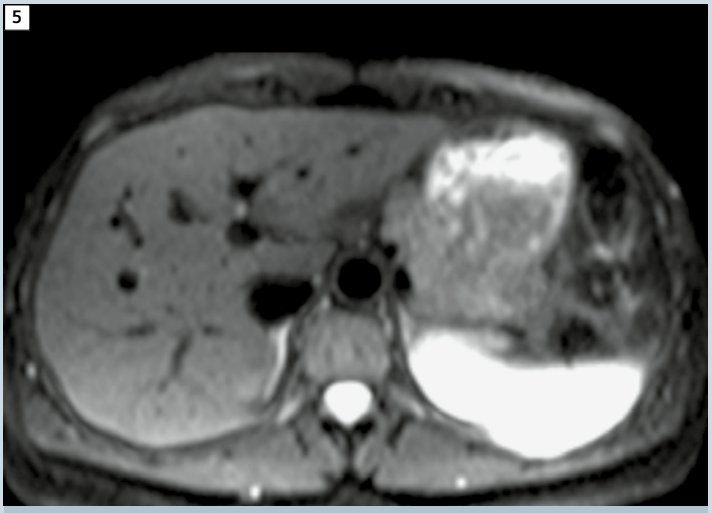

5 b50 image of normal liver at 3T.

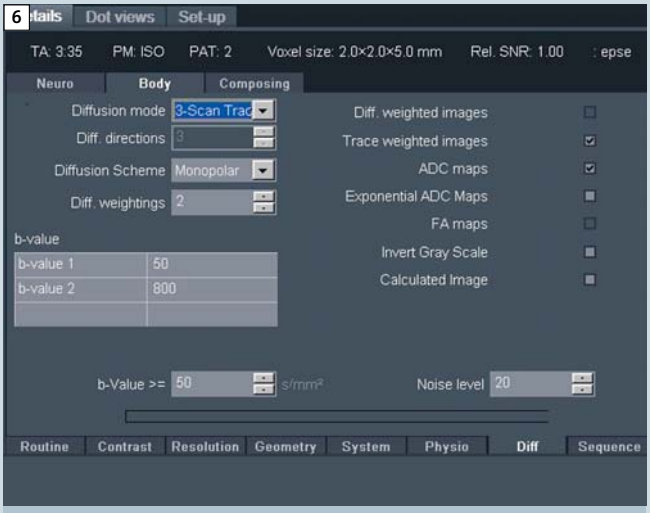

6 *syngo* body-diffusion card in software version *syngo* MR D11A.

spicuous. The calculation of the tissue ADC can be more accurate when starting with even higher b-values like 100 or 200 to omit the contribution of flow and micro vascular effects. Low b-values more often serve as anatomical reference. In software level *syngo* MR D11A and above you can delimit the b-values for ADC calculation on the body diffusion application card of the protocol.

Why do liver diffusion-weighted images look darker on 3T than 1.5T?

The T2 and T2* relaxations times for liver tissue, and other tissues as well, are considerably shorter as the field strength increases The overall signal is therefore diminished at 3T, even at lower b-values, due to the relatively long echo times (TE) used in DWI [5].

Which new DWI features are introduced with software version *syngo* MR D11A for MAGNETOM Aera and Skyra?

There is a new 'body diffusion' application card with many new applications:

- diffusion scheme monopolar/bipolar
- start ADC calculation for b > = ...
- exponential ADC; no T2 shine-through
- invert gray scale ("PET-like" image)
- calculated image of artificial b-values plus
- choice of dynamic field correction
- improved fat saturation schemes

What should I know when scanning liquids in phantoms with DWI sequences?

Firstly, the liquids should not move in the phantom bottle. Flowing liquid in the phantom would cause artificially strong diffusion and results in low intensity DWI images with inaccurately long ADC values.

Secondly, the diffusion coefficient is also strongly temperature dependent. Pure water has a diffusion coefficient of about 3 *10^{-3} mm²/s (exactly: 2.96) at body temperature of 37 °C (98.6 °F). Water of 0 °C (32 °F) has a diffusion coefficient of 1.12 * 10^{-3} mm²/s. This could serve as a standard for different machines.

Additional reading

In addition to the comprehensive Siemens applications guide, "Diffusion/Perfusion Imaging", there is literature [6] available which covers neuro and body diffusion. (Listed according to year of publication):

Derek K. Jones: Diffusion MRI: Theory, Methods, and Applications; Oxford University Press

Bachir Taouli: Extra-Cranial Applications of Diffusion-Weighted MRI; Cambridge University Press

Dow-Mu Koh: Diffusion-Weighted MR Imaging: Applications in the Body; Springer

Heidi Johansen-Berg: Diffusion MRI: From Quantitative Measurement to In-Vivo Neuroanatomy; Academic Press

References

1 Le Bihan D, Breton E, Lallemand D, Grenier P, Cabanis E, Laval-Jeantet M (1986). MR imaging of intravoxel incoherent motions; application to diffusion and Perfusion in neurologic disorders. Radiology. 161: 401-407.

2 Kingsley PB, Monahan WG (2004) Selection of the Optimum b Factor for Diffusion-Weighted Magnetic Resonance Imaging Assessment of Ischemic Stroke. MRM 51: 996-1001.

3 Provenzale JM, Engelter ST, Petrella JR, Smith JS, MacFall JA (1998). Use of MR Exponential Diffusion-Weighted Images to eradicate T2 "Shine-Through" Effect. AJR. 172:537-539.

4 Padhani AR, Liu G, Mu-Koh D, Chenevert TL, Thoeny HC, Takahara T, Dzik-Jurasz A, Ross BD, Van Cauteren M, Collins D, Hammoud DA, Rustin GJS, Taouli B, Choyke PL (2009). Diffusion-Weighted Magnetic Resonance Imaging as a Cancer Biomarker: Consensus and Recommendations. NEOPLASIA.11 (2): 102-125.

5 de Bazelaire CMJ, Duhamel GD, Rofsky NM, Alsop DC (2004).MR Imaging Relaxation Times of Abdominal and Pelvic Tissues in Vivo at 3.0 T. Radiology 230: 652-659.

6 Hagmann P, Jonasson L, Maeder P, Thiran JP, Van Wedeen J, Meuli R (2006). Understanding Diffusion MR Imaging Techniques: From Scalar Diffusion-weighted Imaging to Diffusion Tensor Imaging and Beyond. Radiographics 26: 205-223.

Contact
Joachim Graessner, Dipl. Ing.
Siemens Healthcare
GER H IM BM MR
Lindenplatz 2
20099 Hamburg
Germany
joachim.graessner@siemens.com

Whole-Body MR/PET Hybrid Imaging: Technical Considerations, Clinical Workflow, and Initial Results

Harald H. Quick, PhD[1]; Ralf Ladebeck, PhD[2]; Jens-Christoph Georgi, PhD[2]

[1]*Institute of Medical Physics (IMP), Friedrich-Alexander University Erlangen-Nürnberg, Erlangen, Germany*
[2]*Siemens AG Healthcare Sector, Erlangen, Germany*

MR/PET – Advent of a new hybrid imaging modality

These days we are eyewitnesses to an exciting new hybrid imaging modality to enter the clinical arena, namely simultaneous whole-body MR/PET imaging. Envisioning the combination of the excellent soft tissue contrast, high spatial and temporal resolution, and functional tissue parameters that MR provides with the high sensitivity of PET, different technical approaches have been pursued by researchers and by the industry to work on the integration of two formerly 'non-integrable' imaging modalities. With the recent introduction of the Biograph mMR, Siemens has launched a 3.0 Tesla whole-body MR hybrid system that hosts in its isocenter a fully integrated PET detector and that with its 60 cm patient bore enables whole-body simultaneous MR/PET imaging.

Researchers, radiologists, and nuclear medicine physicians have been waiting and actively been working on the advent of this hybrid imaging modality for a long time [1–3]. A detailed overview about the pre-clinical developments, the rationale to combine MR and PET as well as the steps which were necessary for integrating these imaging modalities to allow simultaneous scanning can be found in the article by Beyer et al. 'MR/PET – Hybrid Imaging for the Next Decade', published in the supplement of issue 3/2010, RSNA edition of MAGNETOM Flash. Now that whole-body MR/PET has entered clinical practice, we have a starting point to evaluate the full clinical potential of the modality, to research for and to validate new imaging applications, and to ultimately establish this imaging modality in early diagnosis of oncologic, neurologic, cardiologic, and many more diseases.

As more and more research and clinical sites come on board during the months and years ahead, let's take a first look into the technology and explore what specifics such an integrated MR/PET hybrid system brings with it. We will then also explore the workflow of a MR/PET whole-body hybrid exam and present first image examples from clinical findings.

Technical integration of MR and PET

The Biograph mMR hybrid imaging system fully integrates the MR and the PET imaging modality into one imaging system. In order to ensure such a high level of integration, we have to overcome numerous physical and technical preconditions and challenges. The potential physical interactions of both modalities in both directions – PET on MRI and MRI on PET – are manifold. Full integration of a PET system into an MRI environment requires technical solutions for three groups of potential electromagnetic interaction:

1) the strong static magnetic B_0-field for spin alignment,
2) the electromagnetic changing fields of the gradient system (G_{xyz}) for spatial signal encoding, and
3) the radiofrequency (RF) B_1-field for MR signal excitation and MR signal readout.

→ The QR code is your direct link to Thomas Beyer's article on the history of combining PET with MRI, the rationale to do so and challenges which had to be overcome. You will also find the article at **www.siemens.com/magnetom-world**

1

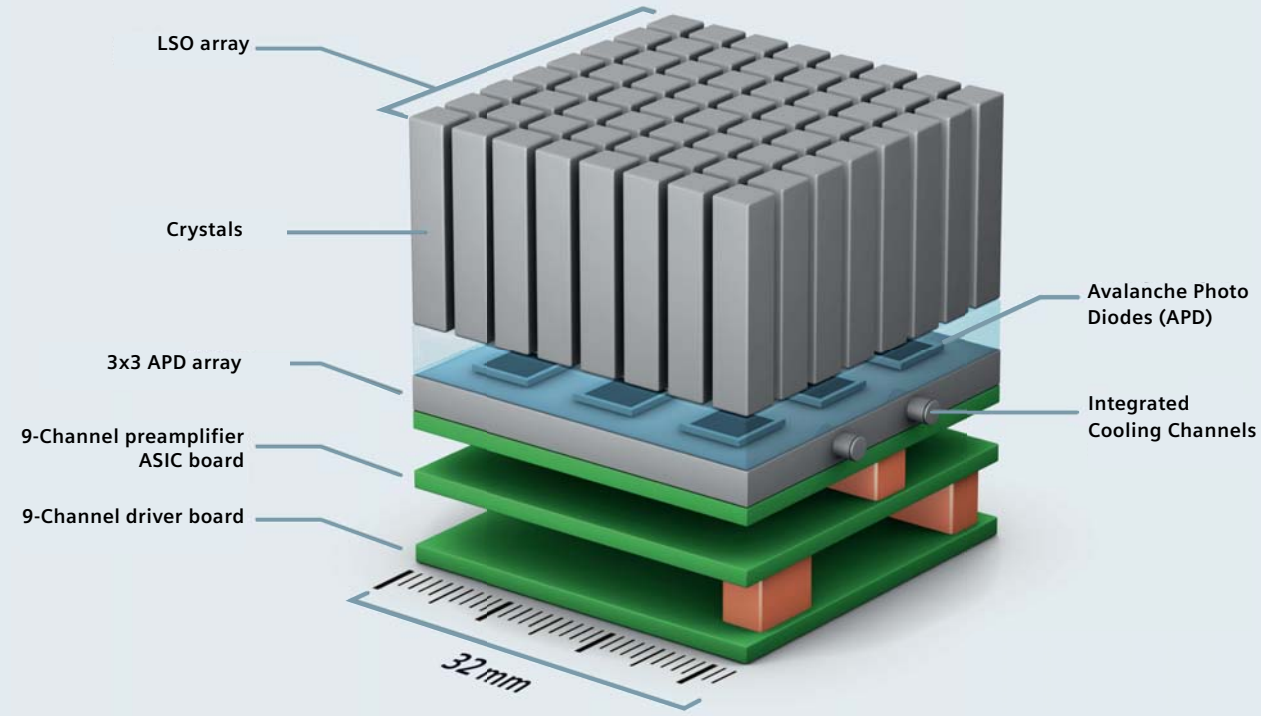

1 Pet detector assembly for mMR. 64 Lutetium Oxyorthosilicate (LSO) crystals form one block that transforms 511 keV gamma quanta into light flashes. Light events in the LSO crystals are detected by a 3x3 array of avalanche photo diodes (ADP). 9-channel preamplifiers and driver boards as well as integrated water cooling completes each detector block. This detector assembly is characterized by its small size, can be designed free of magnetic components, and performs in strong magnetic fields. 56 such blocks form one detector ring, 8 rings form the PET detector assembly in the Biograph mMR that spans a longitudinal field-of-view (FOV) of 25.8 cm.

PET hardware and PET signals must not be disturbed by any of these fields. Equally, for full and unlimited MRI system performance, PET must not disturb any of these electromagnetic MR fields and signals.

Numerous technical solutions were thus required for PET integration into an MRI system. The most important key technology enabler was the development of detectors and photo diodes that are able to detect the 511 keV PET gamma quanta following an annihilation event inside of a strong magnetic field. What worked well in established PET and in hybrid PET/CT systems in the form of scintillation crystal blocks read out by photomultiplier tubes (PMT), had to be replaced for the MR/PET integration since the PMTs are very susceptible to magnetic fields. The current detector solution for simultaneous MR/PET is a combination of Lutetium Oxyorthosilicate (LSO) crystals and Avalanche Photo Diodes (APD) able to detect gamma quanta even inside strong magnetic fields and convert the detected events from scintillation light to electrical signals (Fig. 1A) [4]. Another advantage of the combination LSO crystal and APD diodes compared to PMT is that they do not require as much space and thus can be integrated inside of an MRI bore. Siemens' 70 cm magnet bore technology is clearly another precondition to integrate the PET detectors inside the limited space of an MRI system and at the same time to leave enough space to eventually end up with an inner whole-body bore diameter of 60 cm – as has been clinical standard for MRI magnet bore diameter in the past. In the Biograph mMR hybrid system, 56 LSO-APD detector blocks, each with a block area of 32 x 32 mm^2, are aligned circumferentially to form one PET detector ring. 8 rings form the full PET detector unit, spanning a length of 25.8 cm in z-direction (for comparison: conventional/standard PET-CT systems have an axial field-of-view (FOV) of less than 20 cm and high-end PET-CT systems nowadays have a FOV of approximately 22 cm). Each LSO crystal, which are put together to form than the LSO-APD block, has a size of 4 x 4 x 20 mm^3 which is the finest crystal dimension in the market for clinical PET systems; the crystal size has a direct impact on the achievable PET resolution.

2

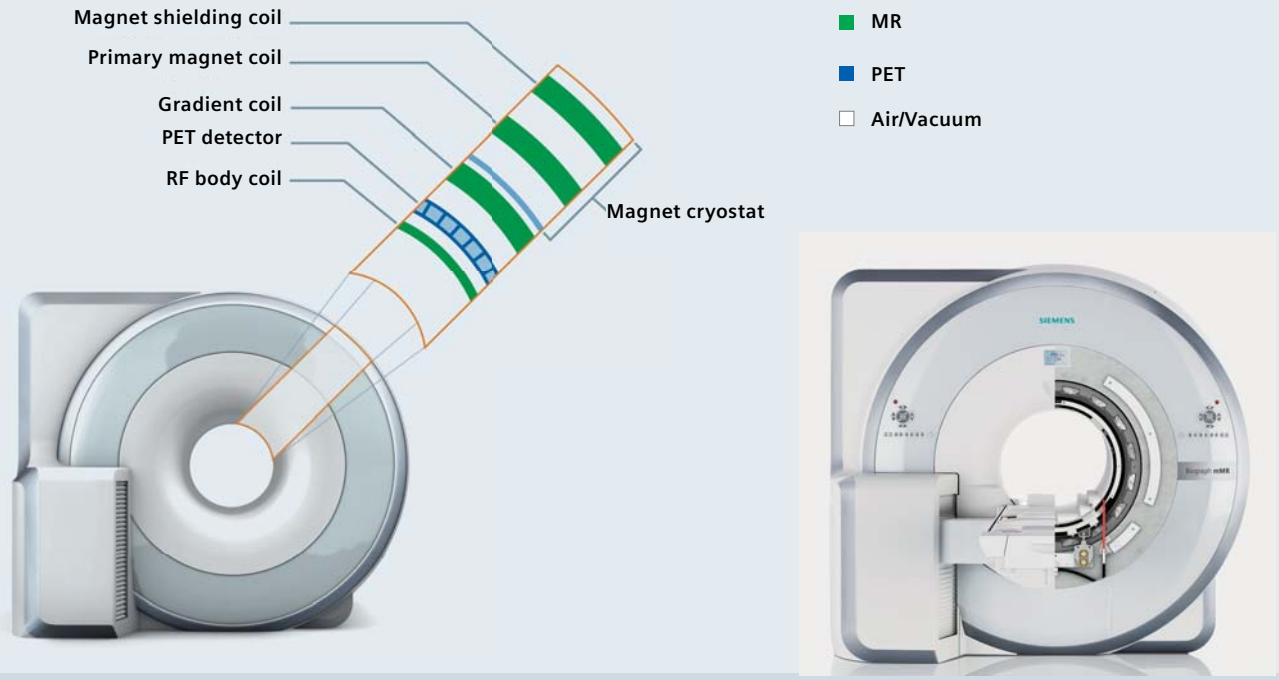

2 Schematic drawing and photograph showing the integration of the PET detectors in the MR hardware structure of the Biograph mMR. From the inside to the outside: RF body coil, PET detector, gradient coil assembly, primary magnet coil, and magnet shielding coil. The latter two magnet coil assemblies are contained in the helium filled magnet cryostat. The MR/PET integration as shown requires that the PET detector works within strong static and dynamic magnetic fields, and does not disturb any of the associated electromagnetic MR fields. The PET detector must not disturb the static B_0-field, the gradient fields nor the RF transmission and reception. Additionally, in this configuration the RF body coil needs to be designed 'PET transparent' with little attenuation of gamma quanta.

How has the integration of the PET detector unit into the MR environment been performed technically? Seen from the perspective of the signals emitting patient, the hardware layer structure of the hybrid system is as follows: The innermost layer in the magnet bore is formed by the signal transmitting and receiving RF body coil with its RF shield, shielding the RF coil towards the other structures in the bore. The PET detector rings are located behind the RF coil and its RF shield. The layer behind the PET detector unit is formed by the gradient coil assembly encompassing gradient coils for spatial MR signal encoding in all three dimensions of the scanner coordinate system. The outer layer structure is formed by the magnet cryostat containing the liquid helium for magnet cooling as well as the superconducting magnet winding producing the 3.0 Tesla static magnetic B_0-field (Fig. 2). The individual hardware components as well as the whole hardware assembly are optimized towards MR and PET signal detection with no signal disturbances in either direction. A technical precondition to fulfill these requirements is that the RF body coil should be 'PET transparent' such that gamma quanta emitted by the patient are not attenuated by the RF body hardware. An additional consequence is that the PET detectors need to be non-magnetic and 'gradient transparent' in order to not distort the linearity of the fast switching gradient fields. The PET detectors require stable temperatures over time of around 20°C temperature, which has been achieved by implementing water cooling into the APDs (Fig. 1). Analog electrical signals and water cooling are conducted from the PET detector in the isocenter of the magnet bore to the back end of the MR/PET system. All PET detector electronics are hermetically shielded by copper elements in order not to emit RF signals that potentially could disturb the weak MR RF signals or contribute to increased overall RF noise, leading to decreased signal-to-noise-ratio (SNR) in MRI measurements. With regard to potential interaction with the three groups of electromagnetic fields in an MRI surrounding, all components of the PET detector and electronics must be absolutely non-magnetic, must be absolutely RF shielded and must be optimized to eliminate susceptibility to eddy currents. Eddy currents potentially interact with the strong and fast switching magnetic gradient fields for spatial MR signal encoding. When switching gradient fields, according to Lorentz' induction law, eddy currents are induced into neighboring electrically conducting structures. Unwanted eddy currents thus counteract the effect of fast switching linear gradient fields, potentially leading to reduced rise times, reduced amplitudes, and reduced gradient linearities, resulting in an overall reduced gradient performance and non-linear geometrical distortions in MR imaging.

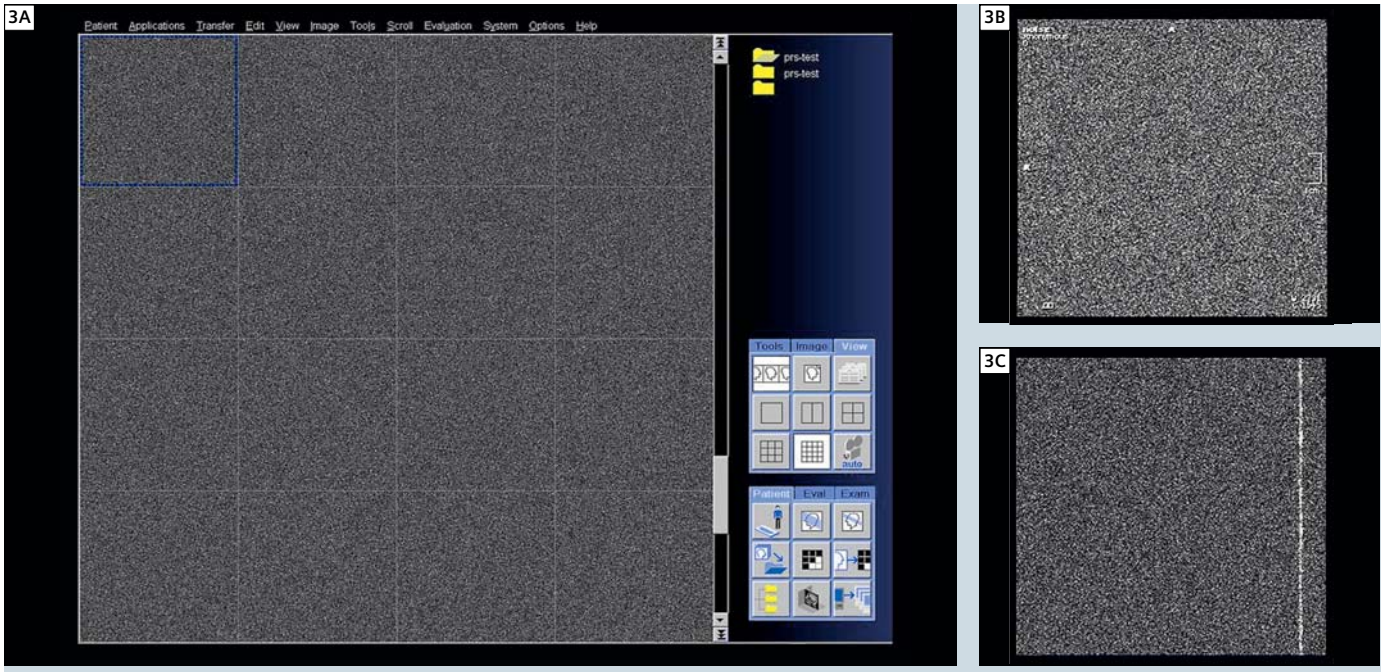

3 System integration testing: RF noise check. Images in **(A)** show results of an RF noise detection routine in MR imaging that was acquired while the PET detector unit was simultaneously activated. In this noise check, the RF receivers of the MR system are stepped through a frequency range of ±250 kHz around the Larmor center frequency in intervals of 10 kHz. The panel in **(A)** shows a selection of 4x4 images, each representing a frequency range of 10 kHz. The individual noise images here show neither increased noise nor any other discrete enhancement. Zoom-in **(B)**. This result of the RF noise check indicates uncompromised shielding of the electronic PET components over the whole receiver bandwidths of the MR system. Just to demonstrate the effect of disturbing RF noise, image **(C)** shows a single measurement disturbed by a discrete RF signal (vertical stripe on the right side of the image) that has been provoked by opening the two doors of the RF cabin during measurement.

System integration testing

Early system integration testing of the Biograph mMR hybrid MR/PET system has been performed at the Institute of Medical Physics (IMP), University of Erlangen, Germany, in close collaboration with Siemens Healthcare, Erlangen, Germany. Successful system integration needs to be explored and verified in numerous systematic technical and phantom testing experiments. This requires testing in both directions to answer the following questions: Is PET performance influenced by the MR? Is MR performance influenced by the PET? MR testing encompasses testing for potential interactions with RF, B_0, and G_{xyz}, and related artifacts. PET testing encompasses testing for count rates, detector performance, signal homogeneity, and artifacts [5].

Figure 3 shows RF noise testing – a routine system performance test in MRI. In this test, the RF receiver chain is set to a high receiver gain and then stepped in steps of 10 kHz through a varying bandwidth ranging from -250 kHz to +250 kHz around the Larmor center frequency of the 3.0 Tesla MR system. This is performed twice: Once with PET switched off, and again with the PET hardware switched on. Thus subtle differences in the overall noise level or discrete RF noise frequencies with/without PET can be detected.

Static magnetic B_0-field homogeneity testing encompasses measurements of the static magnetic field homogeneity with/without PET detectors inside of the system. The difference between both measurements can be visualized and evaluated in B_0 difference field maps in three spatial dimensions. Thus subtle differences in the B_0 static magnetic field homogeneity can be detected and displayed within ppm accuracy. In the Biograph mMR system the magnetic field homogeneity is specified with ≤6 ppm standard deviation V_{rms} (volume root-mean square) over an elliptical volume of 50 cm diameter in the x-y-plane and 45 cm in z-direction. In system integration testing the measurements with/without PET detector installed did not reveal any influence of the PET detector on the B_0-field homogeneity of the MR system.

Also the gradient system performance with its parameters amplitude (mT/m), slew rate (T/m/s) and overall linearity has to be evaluated twice with/without PET detectors to determine possible variations from the gradient systems specifications. Measurements have confirmed that the gradient systems performance in the Biograph mMR system is in the specifications – 45 mT/m maximum amplitude for all three gradient axes, 200 T/m/s maximum slew rate, and thus compares well to a system without PET integrated in the magnet bore. This is a major precondition to take full advantage of numerous whole-body imaging

4



4 The Biograph mMR system installation at the Institute of Medical Physics, University of Erlangen. Both imaging modalities – MR and PET – are fully integrated into one MR/PET hybrid system.

5

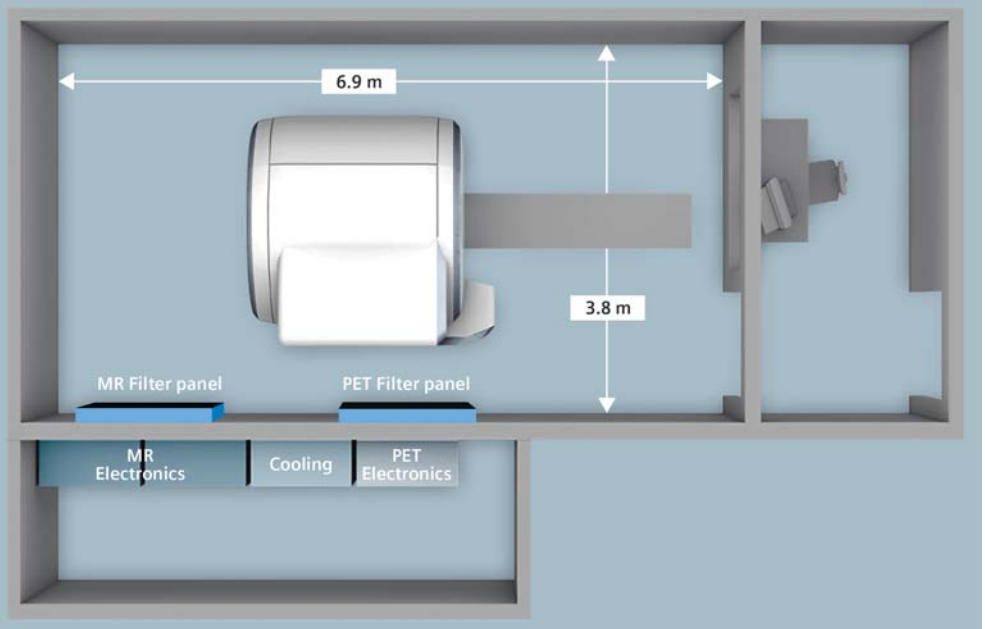

5 Schematic showing the compact siting of the Biograph mMR system and its hardware components. In comparison to an MR-only installation, the MR/PET installation adds only another filter panel and one extra cabinet for the PET electronics to the installation site.

sequences providing anatomical and functional tissue information simultaneously with a combined data acquisition with PET: Diffusion-weighted imaging (DWI), diffusion tensor imaging (DTI), arterial spin labeling (ASL), functional MRI (fMRI), MR spectroscopy, time-of-flight angiography (TOF-MRA), dynamic cardiac acquisitions, etc., to name only a few. Finally the PET systems performance has also to be tested for the potential influences of the strong magnetic field by gradient fields, or by RF interactions. Such testing performed according to NEMA standards [5] twice outside and inside of the MRI system and during system integration testing did not reveal any deviations from the PET performance without MRI surrounding.

Siting specifics

With this new hybrid imaging systems generation, combining the non-radiating imaging modality MRI with the nuclear medicine imaging modality PET, a couple of technical and logistical particularities have to be considered when it comes to siting of such a hybrid system. The high degree of system integration in case of the Biograph mMR helps to reduce the space that is required for system installation. This holds true for the scanner room as well as for the technical equipment room. The installation only requires a minimum of 33 m^2 of installation space for the scanner, electronics and console room. Figure 4 shows the Biograph mMR installation at the Institute of Medical Physics (IMP), University of Erlangen, Germany. When compared to the installation of a conventional standalone MR system, the MR/PET hybrid system does not require additional space in the scanner room and only requires one additional cabinet in the technical equipment room (Fig. 5). Water cooling infrastructure is shared for both the gradient system and for the PET detectors. The additional cabinet in the technical equipment room contains the PET electronics and computers for signal processing and image reconstruction, respectively. Another requirement for the MR/PET hybrid system installation is a second filter panel in the RF cabin to

feed the PET signals and associated cables through the wall between the system room and the technical equipment room. During the MR/PET systems installation at the Institute of Medical Physics, University of Erlangen, a second RF shielded door was installed in the RF cabin. Although not a necessity, this installation at the IMP enables a patient to be brought directly from the 'active waiting' controlled area into the scanner room which then becomes a temporal control area and thus not affecting the operator room with radiation at any time. Thus personnel, researchers and potential visitors can stay in the operator room while switching patients in the scanner room.

RF coils and associated attenuation correction

Like its MR-only siblings, the Biograph mMR MR/PET hybrid system is equipped with a full set of RF coils and associated RF architecture – the well established Tim technology (Tim, Total imaging matrix, Siemens Healthcare). The Tim RF system provides seamless coverage of the patient's body with integrated surface coils from head to toe (Fig. 6). The coils are each equipped with multiple RF coil channels providing a high coil element density for high SNR gain as well as parallel imaging capabilities with high acceleration factors in three spatial dimensions. While this integrated RF surface coil concept today is well established in MRI, its use in a combined MR/PET hybrid imaging system is a novelty and prerequisite for seamless whole-body MR/PET acquisitions. The RF surface coils that cover the patient's body for optimal MR signal performance are at the same time in the FOV of the PET detectors. Thus all RF surface coils now have to be also optimized towards PET-transparency, i.e. such coils should attenuate gamma quanta to only a minor extent, for optimized PET performance. This also holds true for all other hardware equipment – MR or PET related – that potentially accompanies the patient's body when traveling through the PET-FOV, e.g. RF surface coils, the patient table, cables, connectors, patient monitoring equipment, etc. [6]. Here one can differentiate between 'rigid and stationary' equipment such as the patient table, the RF spine array coil as well as the RF head coil, and between 'flexible and non-stationary' equipment such as the flexible RF Body Matrix array coils. 'Rigid' here means stable in its form and geometry. 'Stationary' in this context means non-moving relative to the patient table whose position is known to the imaging coordinate system at any point in time when moving in the scanner bore.

The PET signal attenuation and scatter of rigid and stationary equipment can be compensated for by straightforward attenuation correction (AC) methods. For example, the RF head coil (Fig. 7A) is scanned in a CT (computed tomography)

6

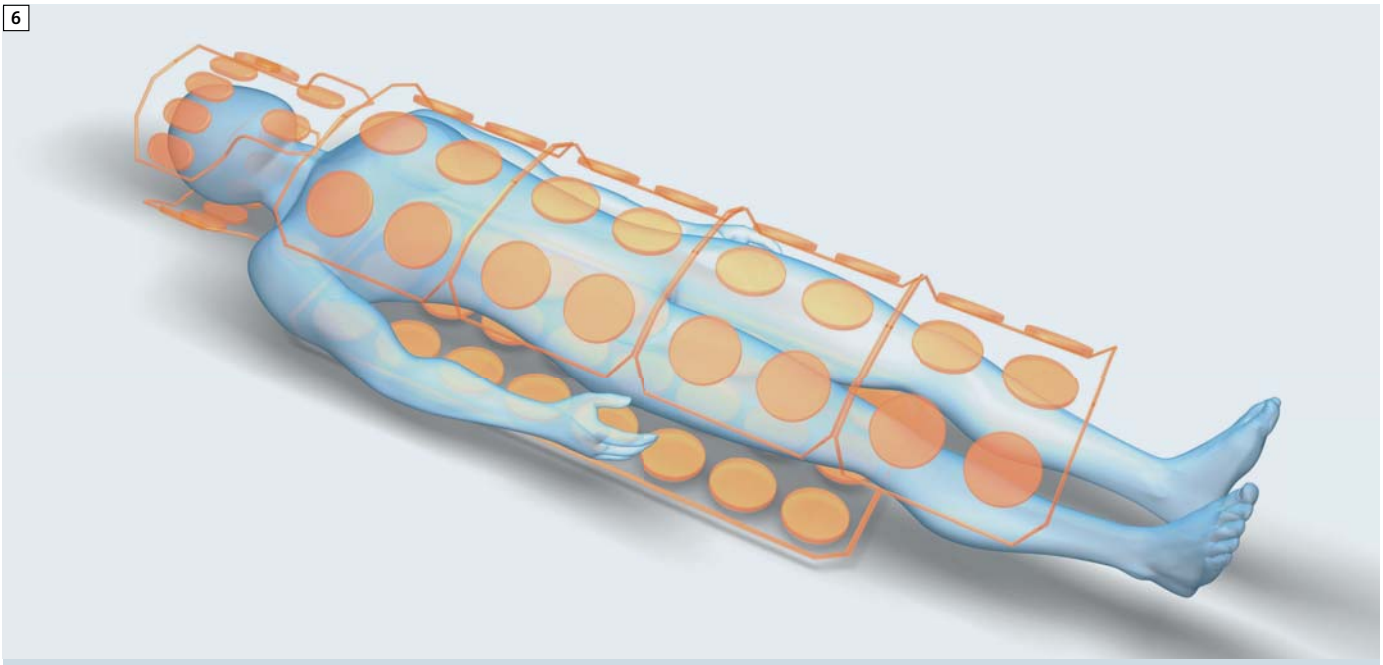

6 The Biograph mMR is equipped with the Tim (Total imaging matrix) RF coil technology consisting of multiple integrated surface coils that cover the patient's body from head to toe with up to 102 RF coil elements connected to 32 RF receivers. This multi-channel phased array RF coil configuration enables parallel imaging and whole-body MR data acquisition with optimized signal-to-noise (SNR) performance. In simultaneous MR/PET hybrid imaging, the surface RF coils are located between the radioactivity emitting patient and the PET detectors. As a consequence, the RF coils should be designed to be as PET-transparent as possible.



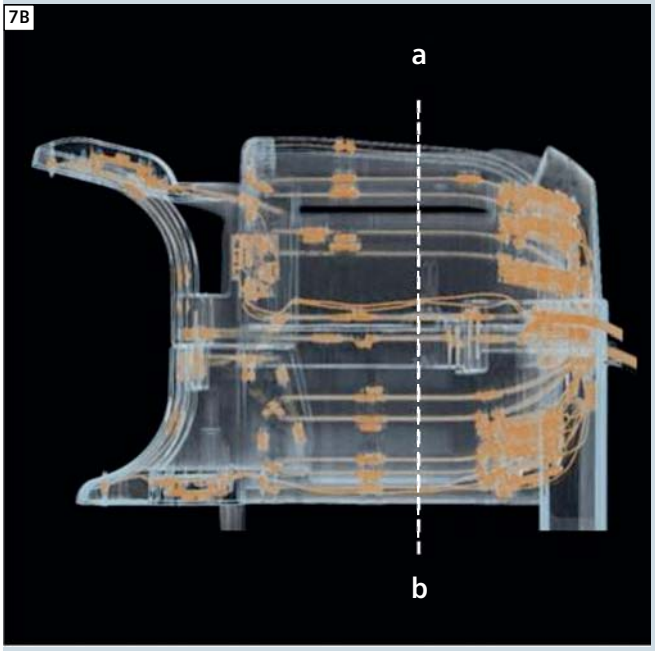

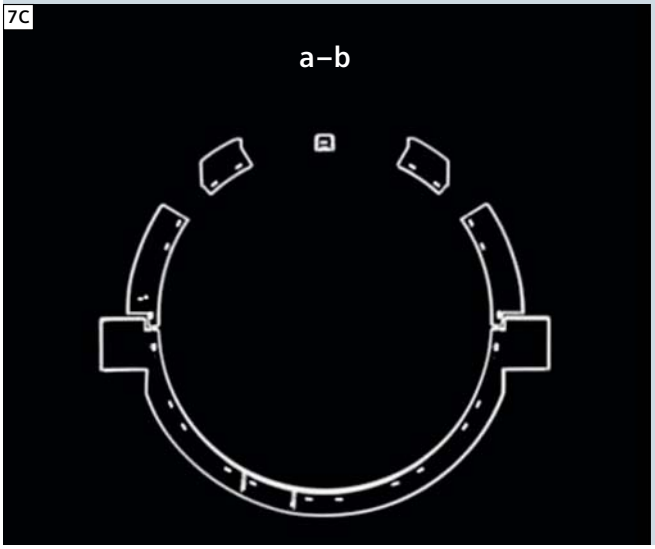

7A **(A)** A head/neck RF coil that was designed and optimized towards PET-transparency for use in simultaneous MR/PET hybrid imaging. This RF coil serves as an example of a rigid hardware component that is stationary at its known position with regard to the patient table. **(B)** 3D CT-scan of this rigid RF coil. Such a CT-scan provides hardware attenuation values that can be transformed from the CT's 100 keV energy level to the 511 keV energy level of PET in order to derive a PET-equivalent attenuation map (μ-map), shown in image **(C)**. The μ -map in **(C)** has been acquired at level a–b as shown in image **(B)**.

system once and a 3-dimensional map of attenuation values is thus generated (Fig. 7B). X-ray based CT attenuation values in general are in the energy range of about 70–120 keV and thus have to be converted to the 511 keV energy level of the gamma quanta emitted in PET. A 3D graphical representation of the obtained attenuation values 'μ-map' with 511 keV attenuation values is then generated (Fig. 7C). This CT-based registration of 3D attenuation values has to be performed once for each rigid hardware component and then the according μ-map becomes part of the PET image reconstruction process. By linking the RF spine – or RF head coils – position relative to the patient's table position, the relevant AC μ-map for each table position is automatically selected by the system for PET image reconstruction. The flexible and non-stationary Body Matrix RF array coils covering the patient's body cannot be attenuation-corrected in the same manner. Here the geometry and position of the coils attenuating structures depend on the patient's individual anatomy and on the individual situation of the patient exam and thus cannot be easily predicted by MR imaging. Here the emphasis lies on designing flexible and moving RF coils as PET-transparent as possible. For the Biograph mMR system, the associated RF coils have been further optimized in this regard. Potential design parameters for RF coil optimization are the choice of materials, the geometry, and the overall assembly. The ultimate goal of such an RF coil design optimization process is to maximize SNR and signal performance for MR while not disturbing PET-imaging.

Attenuation correction for tissue

A necessity in PET-based imaging is the correction for attenuation and scatter resulting not just from the hardware in the PET FOV (e.g. patient table, and RF coils as described above) but also from the patient's body, i.e. the anatomic distribution of soft tissues, air, and bones in the individual patient. Such tissue AC in PET-only systems traditionally has been performed by rotation of radioac-

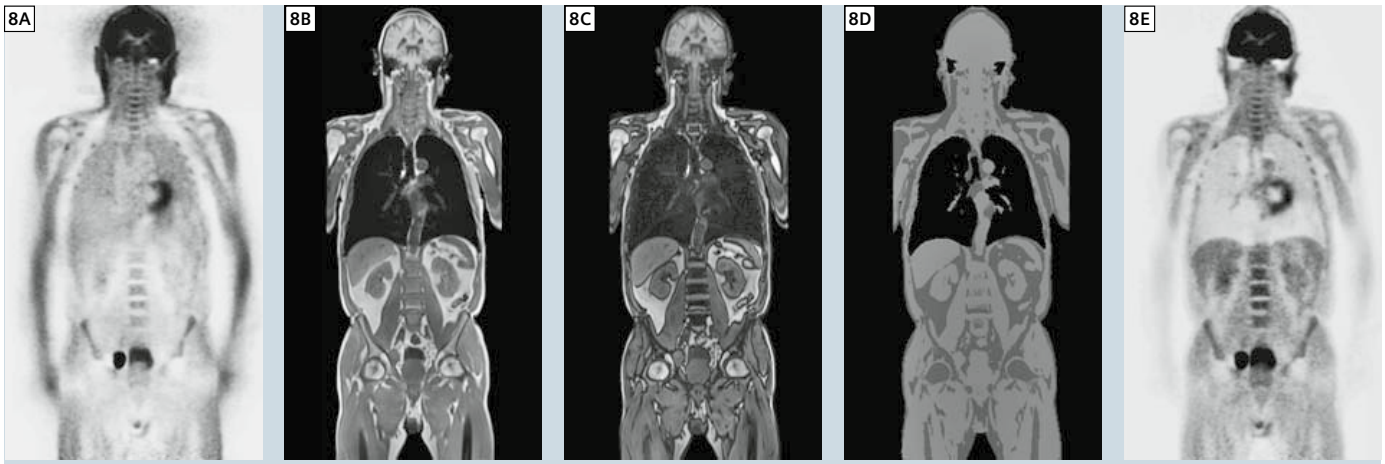

8 Soft-tissue attenuation correction (AC) based on MR imaging. **(A)** Uncorrected whole-body PET scan showing relative activity enhancement in the lungs and on the outer contours of the patient. **(B and C)** Dixon MR sequence providing separate water/fat 'in-phase' and 'opposed phase' images that serve as basis for soft-tissue segmentation. **(D)** Segmented tissue groups (air, fat, muscle, lungs) that can be assigned to 511 keV attenuation maps. **(E)** Resulting attenuation corrected whole-body PET scan of the initial data set **(A)**.

tive ^{68}Ge 511 keV sources around the patient and detection of the attenuated transmission signals 'behind' the patient. From a number of projections, a topography of attenuation values (μ-map) could be reconstructed. This was a relatively time-consuming process, since the ^{68}Ge-source needed to be rotated at a relatively slow speed in order to achieve a significant count rate for each projection angle.

In modern PET/CT hybrid systems, the hardware (e.g. patient table) and the patient tissue μ-map are generated straightforwardly from a fast (potentially low-dose) 3D CT scan provided by the build-in CT scanner. Attenuation values are converted from the 70–120 keV energy level to 511 keV and thus a fast individual and reliably AC μ-map of the patient and any hardware accessories in the PET FOV is obtained.

In a combined MR/PET hybrid system tissue attenuation has to be obtained in a completely different way. Since no CT-like attenuation information is available in such a hybrid system, tissue AC necessary for PET image reconstruction needs to be based on MR images. The problem is the non-irradiative nature of MR imaging, based on proton densities and T1 and T2 relaxation parameters, rather than on the attenuation of radiation in tissue. MR-based AC of tissues also leads to the problem that air and bone are depicted in black the vast majority of MR imaging sequences turning air and bone hardly distinguishable, in CT and PET imaging on the other hand air and bone show minimal and maximal attenuation values, respectively. Different methods have been described in the recent literature, that deal with MR-based AC for tissue [7–9]. Those methods can be separated in atlas-based or atlas-supported methods and in image segmentation based efforts. In the latter, the gray values provided by selected sequences are registered to different tissue classes resulting in tissue segmentation. Depending on the sequence type used, air, lung, fat, muscle, and bones might be segmented and provided with according PET correction values. In the current implementation of the Biograph mMR system, tissue attenuation and scatter correction is performed twice. The head/neck region is attenuation-corrected with the help of a UTE (ultrashort echo time) sequence [10, 11] providing segmentation also of the bone which in this region takes a large percentage of the imaged volume. All other body parts are attenuation-corrected by a Dixon technique providing two images where water and fat are 'in phase' and in 'opposed phase'. This allows for reconstruction of fat-only, water-only and of fat-water images and results in tissue segmentation of air, fat, muscle, and lungs (Fig. 8) [8]. Bone is not accounted for in this approach. Initial results in patient imaging have shown that this approach works reliably and provides results that are comparable to corrected images form PET/CT in the same individual. The ultimate impact of this and other MR-based AC methods on PET-quantification and determination of standard uptake values (SUV) has not yet been determined and is subject to current investigations and further research efforts.

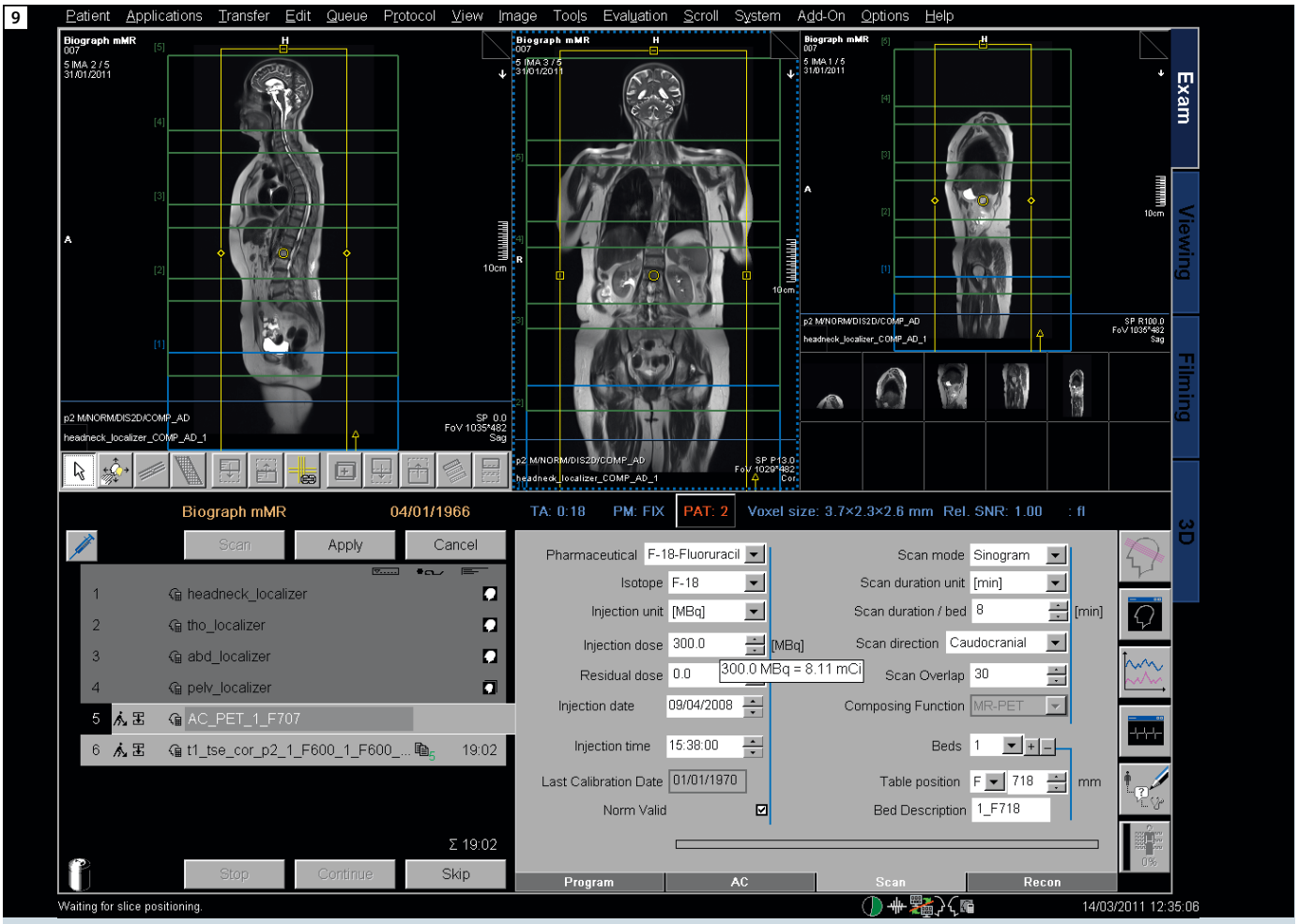

9 Screenshot of the *syngo* user interface during planning of a MR/PET examination. The image panel shows multi-station MR localizers in sagittal (left and right) and coronal (middle) orientation. Displayed with a yellow frame is the FOV of the AC MR sequence for tissue attenuation correction. Green and blue frames show graphical planning of the individual bed positions of the MR and PET data acquisition. In the lower half the planning of the MR/PET acquisition is currently ongoing.

Imaging workflow

From a procedural point-of-view the imaging workflow of a whole-body MR/PET examination on the Biograph mMR is very similar to a whole-body MRI examination. First the patient is prepared on the patient table. For that purpose the earlier described dedicated mMR Tim RF coils (head and neck coil, spine coil, and up to four body matrix coils) are positioned underneath, on and around the patient's body, respectively. In this context the Tim RF coil technology is a prerequisite for seamless whole-body imaging without RF coil replacement and patient repositioning.
Following patient preparation a localizer MR scan is performed covering the region to be examined. Making use of the *syngo* software functionality the localizer scan, as well as any further MR scan can be loaded per drag and drop from a predefined list of protocols and can also be adjusted according the user's specific needs and saved afterwards as individualized protocols, similar to customization of MR protocols. Based on the localizer scan the combined MR/PET scan then is planned.
Figure 9 shows the user interface for examination planning. The yellow boxes in the graphical slice positioning section indicate the acquisition volume for the MR sequences used in the attenuation and scatter correction. The green and blue boxes indicate the acquisition volume of the respective PET bed positions. The overlap between the bed positions is variable. When the planning for the AC sequence is finished and the scan is started, automatically the simultaneous acquisition of the PET starts as well and – bed position per bed position – the simultaneous acquisition of PET, MR AC scan, and any further MR scan for anatomy and function is performed (Fig. 10). Additional MR sequences (beyond the AC scans) for assessment of anatomy and function can be chosen individually for each bed position. For a typical MR/PET scan using ^{18}F-FDG for tumor staging, the overall scan time is defined not necessarily only by the PET acquisition time per bed and number of required

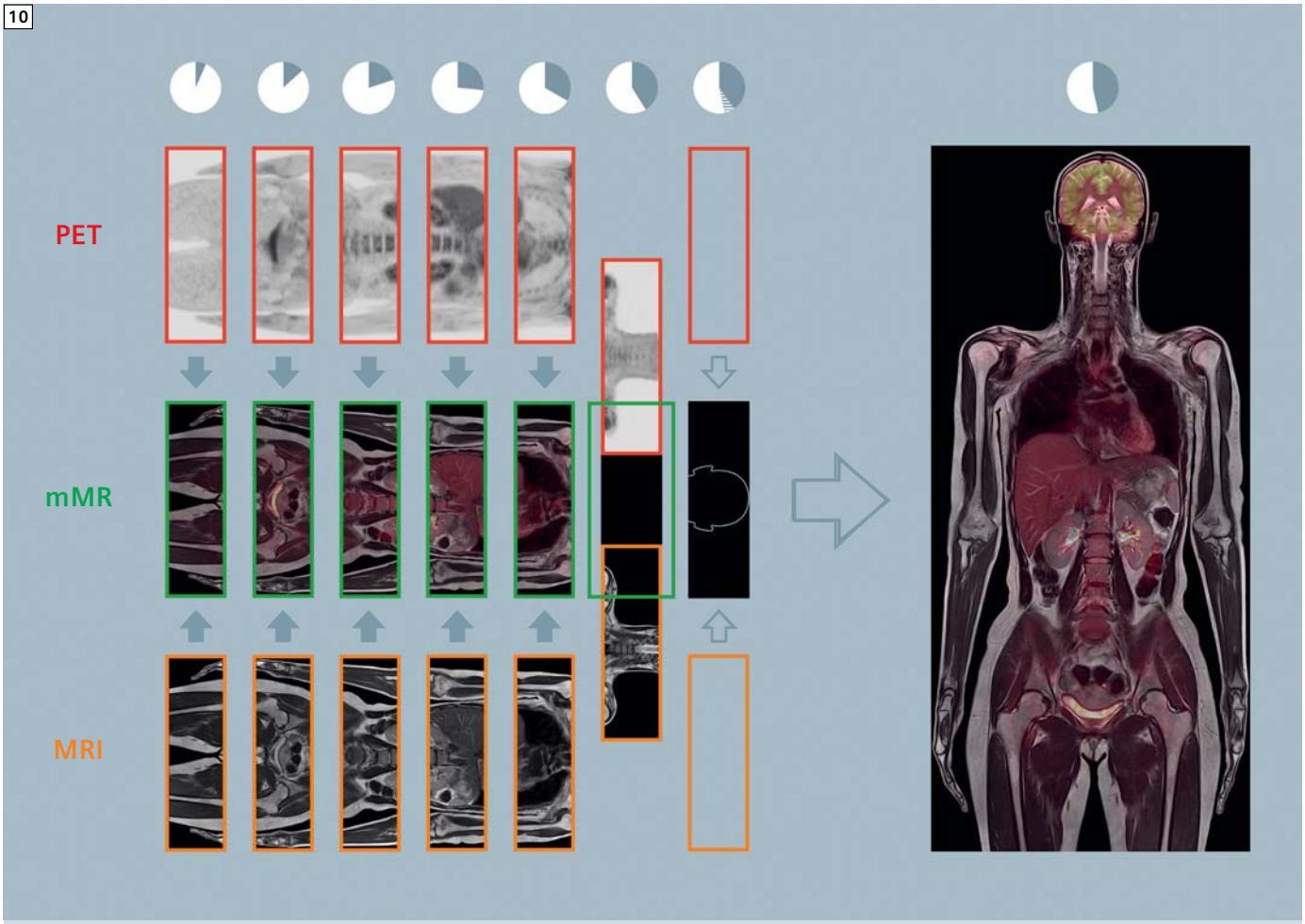

10 MR/PET simultaneous imaging workflow. MR and PET data acquisition is performed simultaneously during a multi-step examination with 6–7 bed positions for whole-body coverage. Depending on the selection of MR imaging sequences, such a whole-body MR/PET hybrid imaging study is regularly completed in about 20–30 minutes.

bed postitions to cover the region-of-interest; in contrast to PET/CT, the acquisition time necessary for MR imaging can be the limiting factor with respect to the total scan time of a mMR exam. However, the additional MR scan time is not lost: Further MR sequences may add to the acquisition time of a specific bed position. This additional time can then directly be used for longer PET data acquisition, translating not only into improved PET image quality but allowing the collection of dynamic PET data (this includes also gating / triggering of PET data). The acquisition of single bed positions for simultaneous MRI and PET, e.g. for dynamic MR/PET studies of the brain, is clinically possible and it should be emphasized that this possibility is also a direct consequence of the large z-axis coverage by the PET detectors, allowing to scan the whole brain or the liver without the need of repositioning over a longer time-period.

Combining PET data and multiple MR sequences will increase the amount of images and complexity of reading, not only for whole-body applications. Therefore an intuitive and powerful tool for evaluating mMR examinations was developed in parallel to the scanner hardware. After the acquisition of the MR/PET data the dedicated mMR Reader based on *syngo*.via and delivered with the Biograph mMR system can be used for image reading and diagnosis. It has been developed for efficient and seamless integration of the new modality into clinical workflow; this includes automatically loading and displaying images for the whole body and specific anatomical regions in MR only, PET only and MR/PET fusion. The client-server-based software supports reading and diagnosing by an MRI and a PET expert (also on different days and in different rooms) in several regards including advanced findings navigation and also by automatically merging these individual findings into one joint report.





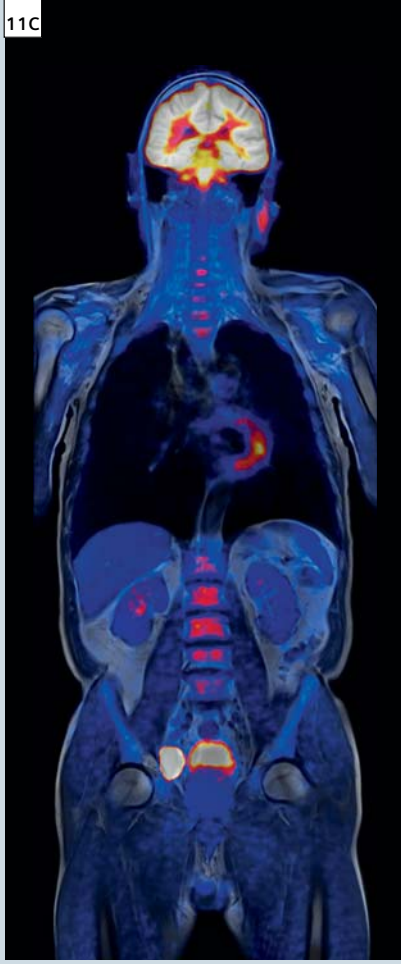

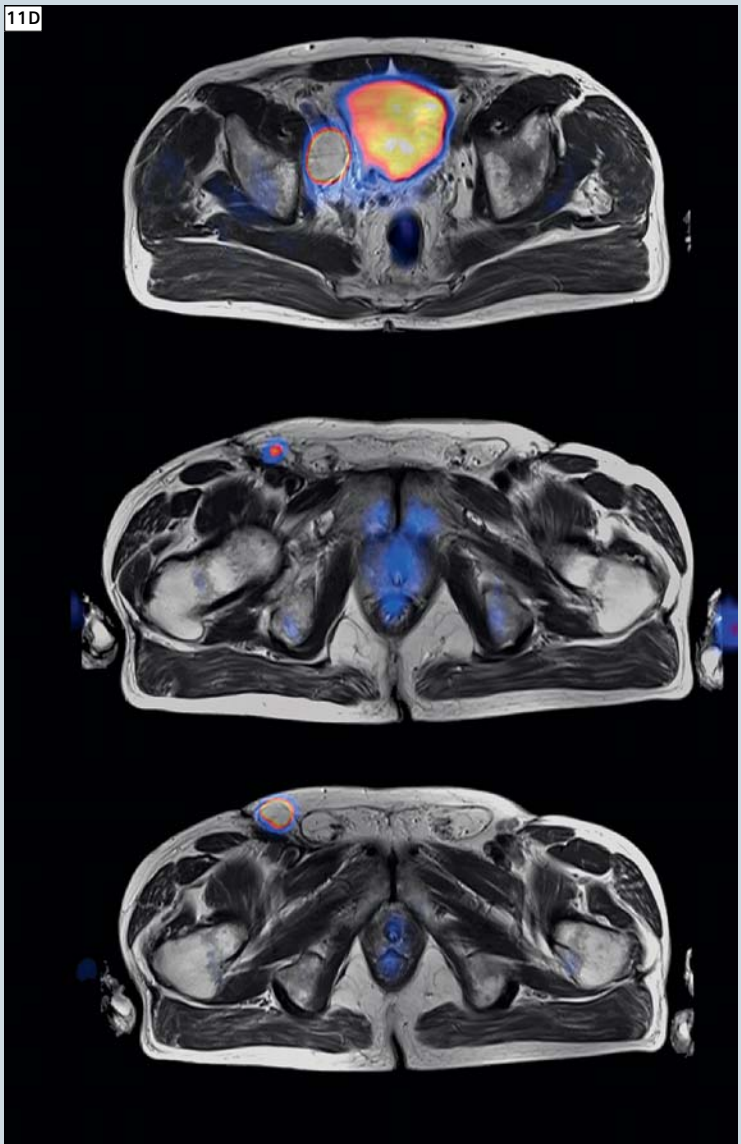

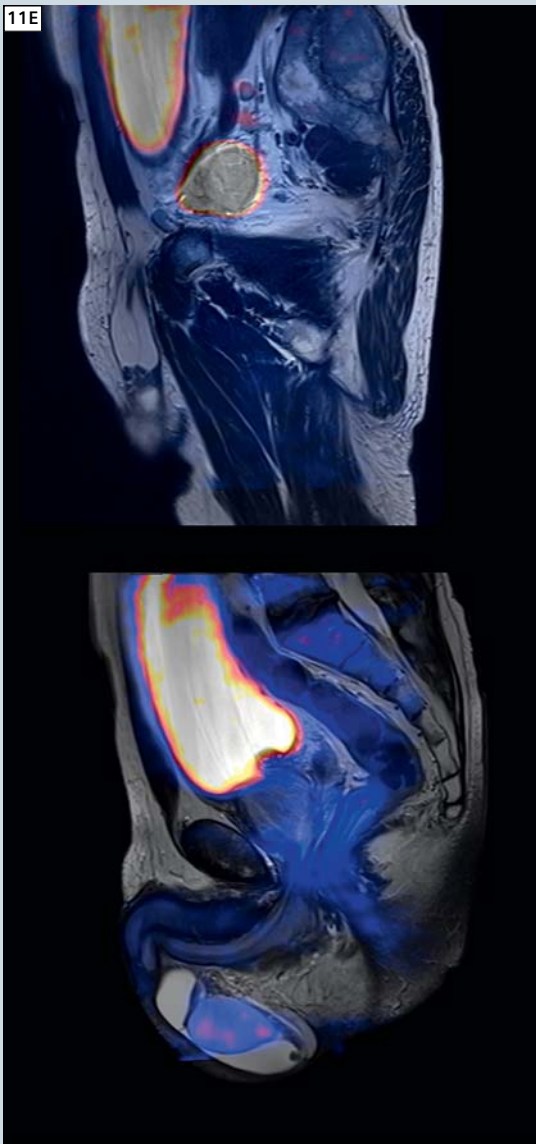

11 Patient with lymph node filiae following a history of a penis carcinoma. Images **(A–C)** show whole-body T1-weighted MR image **(A),** attenuation corrected PET **(B)**, and MR/PET hybrid images **(C)** in a coronal orientation, that were all simultaneously acquired in a multi-station/multi-bed acquisition mode. MRI in this whole-body study **(A)** displays anatomical structures with exquisite detail and excellent soft-tissue contrast. PET **(B)** and the combined MR/PET hybrid image **(C)** in this coronal overview show enhanced tracer activity in one lymph node on the right side of the patient. The axial and sagittal reformates of the MR/PET hybrid data **(D, wE)** reveal two additional lymph nodes with focal tracer activity on the right side.

First clinical examples

An early study was initiated in 2010 at the Institute of Medical Physics (IMP), University of Erlangen, in cooperation with Siemens AG Healthcare Sector, Erlangen. This study aimed at system integration testing and at showing system performance and full operationality by scanning first patients. For acquiring these images, the study was setup as follows: Patients referred to PET/CT scanning were recruited from the Nuclear Medicine Department of the nearby University Hospital Erlangen. Patients had been injected the radioactive tracer ^{18}F-Fluordesoxyglucose (FDG) and had already undergone their PET/CT examination immediately before participating in the MR/PET hybrid imaging examination. This study design thus also had the benefit that the preceding PET/CT examination could serve as a 'gold standard' comparison for subsequent MR/PET imaging. No additional FDG injection or increased radiation dose was necessary. Due to the scanning PET/CT first, however, patients involved in this study had their MR/PET examination on average about 120 min after the injection of FDG. This is about 60 min later than the PET scan would usually have been performed after ^{18}F-FDG-injection. With the given half life time of 108 min for ^{18}F-FDG, this has the effect that activity and thus count rate have already decreased since the PET/CT examination and additionally, FDG has been metabolized during a longer time window than usual. In our study, the effect of decreased activity has been compensated for by longer PET measurement times per bed position (i.e. 6 minutes instead of 2–3 minutes per bed position).

Figure 11 shows a whole-body MR/PET study of a patient with a history of a penis carcinoma with R0 resection of the tumor and now suspicion of tumor recurrence (lymph node metastases). The MR/PET study in this case revealed multiple lymph node filiae inguinal and iliacal, which can be displayed in fine detail in PET and in MRI. These findings correlate well with the findings of the preceding PET/CT examination (not shown).
Figure 12 shows a brain MR/PET study of a lung cancer patient for therapy effectivness control with a history of 2 resected brain metastases. No increased activity or any other signs of recurrence or malignancy could be observed – neither in the PET nor in the MR images. This also correlates with the findings of the associated PET/CT examination (not shown).

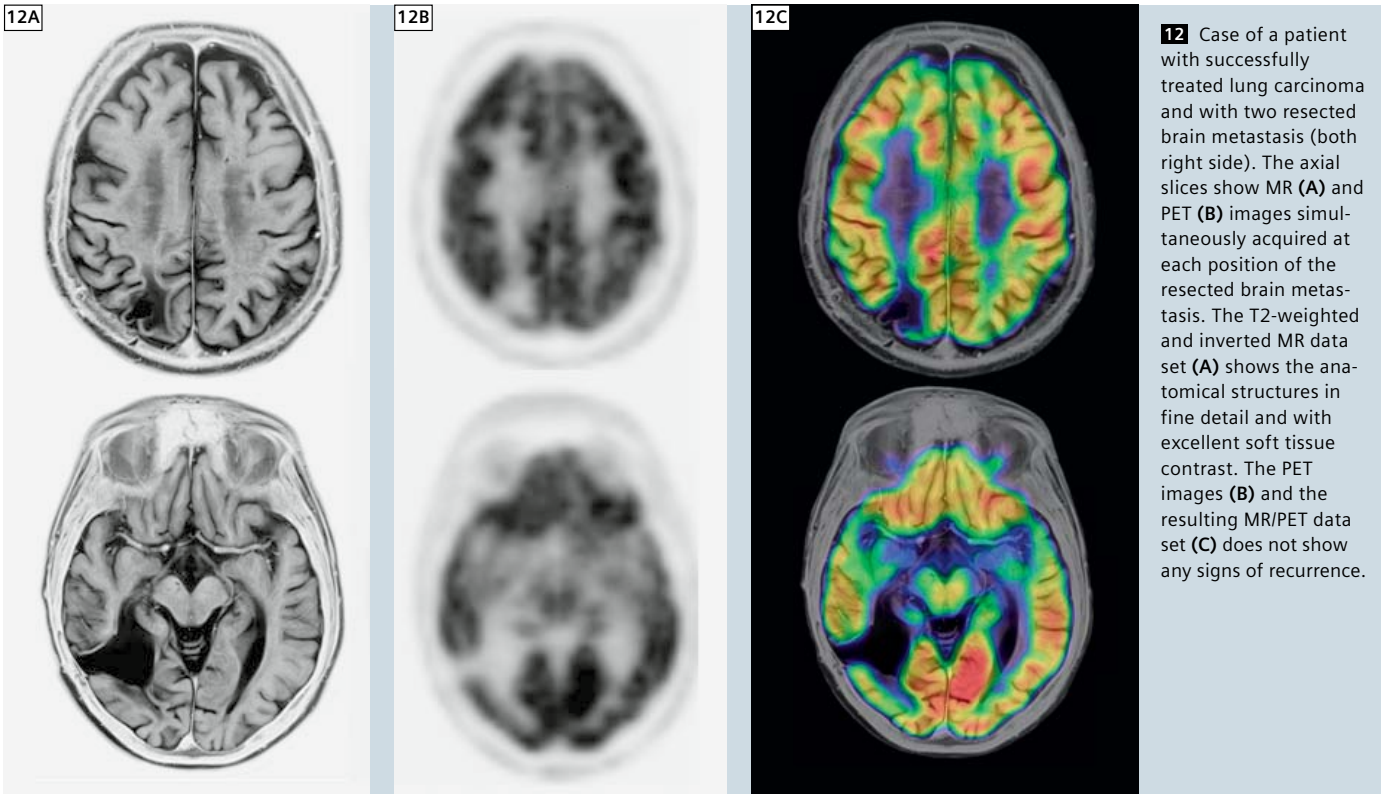

12 Case of a patient with successfully treated lung carcinoma and with two resected brain metastasis (both right side). The axial slices show MR **(A)** and PET **(B)** images simultaneously acquired at each position of the resected brain metastasis. The T2-weighted and inverted MR data set **(A)** shows the anatomical structures in fine detail and with excellent soft tissue contrast. The PET images **(B)** and the resulting MR/PET data set **(C)** does not show any signs of recurrence.

Status and outlook

The long-awaited hybrid imaging modality enabling simultaneous whole-body MR/PET imaging has entered the clinical arena. On the physics and hardware level, this opens up completely new options for clinical imaging research. MR-based hardware and tissue attenuation correction (AC) and MR-based motion correction (MC) for PET imaging are only two examples of current active fields of research. The development of RF coils intended not only for their intended diagnostic application and MR imaging performance but also for their PET-transparency is another research field. On the clinical imaging level, this new hybrid imaging modality demands clinical evaluation especially given the wealth of new diagnostic information generated by the integration of both imaging modalities. Here a special area of interest will focus on the streamlining and optimization of the imaging workflow of simultaneous MR and PET imaging. The ultimate goal is the maximization of multi-modal diagnostic information within a minimum of acquisition time.

Acknowledgements

The authors would like to thank Dr. Matthias Lichy, Dr. Jürgen Kampmeier, and Heike Weh, all Siemens Healthcare Sector, Erlangen, Germany, for in depth discussions and for their support in preparing figures for this article. The authors are also grateful to Prof. Dr. Torsten Kuwert, Prof. Dr. Michael Uder, Dr. Michael Lell, all University Hospital Erlangen, Germany, and to Dr. Alexander Cavalaro, ISI Erlangen, for their help in patient recruitment and personal support.

References

1. Pichler BJ, Judenhofer MS, Wehrl HF. PET/MRI hybrid imaging: devices and initial results. Eur Radiol. 2008; 18:1077-86. Review.
2. Antoch G, Bockisch A. Combined PET/MRI: a new dimension in whole-body oncology imaging? Eur J Nucl Med Mol Imaging. 2009; 36 Suppl 1:S113-20. Review.
3. Wehrl HF, Sauter AW, Judenhofer MS, Pichler BJ. Combined PET/MR imaging--technology and applications. Technol Cancer Res Treat. 2010; 9:5-20.
4. Pichler BJ, Wehrl HF, Kolb A, Judenhofer MS. Positron emission tomography/magnetic resonance imaging: the next generation of multimodality imaging? Semin Nucl Med. 2008; 38:199-208. Review.
5. Delso G, Martinez MJ, Torres I, Ladebeck R, Michel C, Nekolla S, Ziegler SI. Monte Carlo simulations of the count rate performance of a clinical whole-body MR/PET scanner. Med Phys. 2009; 36:4126-35.
6. Delso G, Martinez-Möller A, Bundschuh RA, Ladebeck R, Candidus Y, Faul D, Ziegler SI. Evaluation of the attenuation properties of MR equipment for its use in a whole-body PET/MR scanner. Phys Med Biol. 2010; 55:4361-74.
7. Beyer T, Weigert M, Quick HH, Pietrzyk U, Vogt F, Palm C, Antoch G, Müller SP, Bockisch A. MR-based attenuation correction for torso-PET/MR imaging: pitfalls in mapping MR to CT data. Eur J Nucl Med Mol Imaging. 2008; 35:1142-6.
8. Martinez-Möller A, Souvatzoglou M, Delso G, Bundschuh RA, Chefd'hotel C, Ziegler SI, Navab N, Schwaiger M, Nekolla SG. Tissue classification as a potential approach for attenuation correction in whole-body PET/MRI: evaluation with PET/CT data. J Nucl Med. 2009; 50:520-6.
9. Schulz V, Torres-Espallardo I, Renisch S, Hu Z, Ojha N, Börnert P, Perkuhn M, Niendorf T, Schäfer WM. Automatic, three-segment, MR-based attenuation correction for whole-body PET/MR data. Brockmann H, Krohn T, Buhl A, Günther RW, Mottaghy FM, Krombach GA. Eur J Nucl Med Mol Imaging. 2011; 38:138-52.
10. Waldman A, Rees JH, Brock CS, Robson MD, Gatehouse PD, Bydder GM. MRI of the brain with ultra-short echo-time pulse sequences. Neuroradiology. 2003; 45:887-92.
11. Robson MD, Bydder GM. Clinical ultrashort echo time imaging of bone and other connective tissues. NMR Biomed. 2006; 19:765-80. Review.

Contact
Prof. Dr. Harald H. Quick, PhD
Director of MR-Imaging
Institute of Medical Physics (IMP)
Friedrich-Alexander-University (FAU)
Erlangen-Nürnberg
Henkestr. 91
91052 Erlangen
Germany
Phone: +49 9131 85 25900
Harald.Quick@imp.uni-erlangen.de

Dr. Jens-Christoph Georgi, PhD
Global Product Manager Biograph mMR
Siemens AG Healthcare Sector
MR MK O
Karl-Schall-Str. 6
91052 Erlangen
Germany
Phone: +49 9131 84 4701
Jens-Christoph.Georgi@siemens.com

Integrated Whole Body MR/PET Imaging. First Examples of Clinical Application

A. Drzezga; A.J. Beer; S. Fürst; S. Ziegler; S.G. Nekolla; M. Schwaiger

Technische Universität München, Klinik und Poliklinik für Nuklearmedizin, Klinikum rechts der Isar, Munich, Germany

Introduction

Over the last decade, development of hybrid-imaging instrumentation has been among the innovations with the strongest impact on diagnostic imaging in clinical everyday routine. The driving force behind these developments is the considerable extent to which several different imaging modalities show complementary rather than redundant features. Consequently, it is logical to bundle the particular strengths of different modalities, and to compensate particular deficits of one modality with capabilities of another by combination of the different modalities into one hybrid instrument. Hybrid PET/CT entered the market in around 2000 and became a major success, thereby quickly obviating the demand for PET-only scanners. This success has been strongly driven by oncological applications, combining the high sensitivity of PET with the anatomical precision of CT. The coupling of ^{18}F-FDG, a tracer for metabolic activity with CT, has especially proved highly valuable: FDG-PET allows the sensitive detection of tumor cells and the estimation of their viability (e.g. for therapy control); CT complements the exact anatomic localization of suspect lesions and has a very high sensitivity for small lesions which are missed by PET due to limited resolution or movement artifacts (e.g. in the lung).

However, CT has some specific limitations, the most apparent being the relatively low soft-tissue contrast. This represents a disadvantage particularly for diagnostic questions directed to body regions which are defined by a complex regional arrangement of different adjacent soft tissue structures, e.g. the brain, the head-and-neck region or the pelvis. In contrast to CT, MR-imaging is distinguished by the ability to provide excellent soft-tissue contrast. This is the main reason why corresponding diagnostic problems are typically directed to MRI as the first-line imaging procedure of choice rather than to CT. This includes questions concerning e.g. neurological disorders, brain tumors, conditions in the head and neck region, abdominal/hepatic and pelvic masses and musculoskeletal problems.

For many of these diagnostic questions, PET has demonstrated a high added value as a complementary test in itself, whilst frequently being performed in addition to mandatory MRI-tests (see A. Padhani 'Multiparametric imaging of tumors – an emerging paradime', MAGNETOM Flash #45 3/2010, Research Supplement). Thus, the value of a combination of PET with MRI seems obvious. However, the development of such hybrid MR/PET instrumentation has been hampered for a long time primarily by technical obstacles which have been harder to overcome compared to the combination of PET and CT. Whereas the latter both represent modalities working with radiation (although in different wavelengths) and can thus be combined more easily, PET and MRI are based on entirely different image acquisition principles. The strong magnetic field required for MR-image acquisition is severely affecting the acquisition of the PET-signal. In particular, the conventional photomultiplier technique commonly used for obtaining the PET signal does not work properly in a magnetic field. To circumvent this limitation, platforms have been developed in which spatially separate MR- and PET-scanners are connected by means of a moving table. The patient is positioned on this table and undergoes first PET and then MR imaging, without having to get up from the table between the scans. However, these solutions do not allow simultaneous image acquisition and they are of course associated with lengthy examination protocols and with the risk of patient movement.

With the introduction of the so-called APDs (Avalanche Photodiodes) into PET-

instrumentation this problem has been solved more elegantly. APDs function in strong magnetic fields and can be used to substitute conventional photomultipliers to acquire information in the MR-scanner. The advent of this technology has allowed the industry to produce a first generation of hybrid MR-scanners in which a true integration of both modalities in a single machine has been realized (see H. Quick 'Whole-body MR/PET hybrid imaging' page 88 in this issue of MAGNETOM Flash). This principle was first successfully demonstrated by means of small head-only PET-scanners (PET-insert) which have been installed in conventional MR-scanners (see T. Beyer et al. 'MR/PET-hybrid imaging for the next decade', MAGNETOM Flash #45 3/2010 Research Supplement). Several studies have been performed in this prototype system since and proved the practicability of the concept [1–4].

On the basis of this prototype, a dedicated whole-body MR/PET system has now been developed. In November 2010, the world's first integrated clinical whole-body MR/PET scanner (Siemens Biograph mMR) was installed in the Department of Nuclear Medicine at the Technische Universität München (TUM), in Munich, Germany. The scanner is now operated by a consortium between the directors of Nuclear Medicine (Prof. Dr. Markus Schwaiger) and Radiology (Prof. Dr. Ernst Rummeny) from TUM and the directors of Nuclear Medicine (Prof. Peter Bartenstein) and Radiology (Prof. Dr. Maximilan Reiser) from the Ludwig-Maximilians-Universität, München. The setup of the first scanner of this type in Germany (and of three identical scanners which will be established in 2011 in Essen, Leipzig and Tübingen) has been made possible by funding of the German Research Foundation (DFG, Deutsche Forschungsgemeinschaft).

The Biograph mMR MR/PET-scanner is constituted by a high end 3T MR-scanner which harbours a fully functional state-of-the-art PET system within the gantry. The PET-system covers a field of view (25.8 cm) which is larger than in any other existing PET-camera. This allows to obtain multimodal (MR&PET) image information simultaneously in an extended region and to cover the entire body with a limited number of bed positions in short time. For further technical details on the system see page 88 in this issue of MAGNETOM Flash.

Opportunities of the MR/PET-system

From a clinical point of view, this system offers a number of obvious advantages:

1. Reduction in examination time

In comparison to clinical CT-examinations, MR-scans can often be relatively time-consuming. The recently introduced whole-body MR/PET scanner now allows the acquisition of MR and PET information in a truly simultaneous approach, i.e. in regional alignment at exactly the same time, thereby reducing not only the number of examination appointments (i.e. the visits patients have to make to the imaging department) but also cutting the required examination time approximately in half (as compared to two separate examinations). This option of 'one-stop shop' examinations represents a major gain in patient comfort for patients requiring both MR and PET examinations and also reduces the required time of the medical personnel to acquire the requested imaging information.

2. Regional coregistration

The acquisition of PET and MR-information in exactly overlapping anatomical positions also offers clear advantages: Precise coregistration of the PET-signal with the underlying anatomical information is assured as the risk of patient movement or changes in organ position (e.g. in bowel positions, different bladder filling status) between the acquisition of the two modalities is reduced, and thus potential misalignment is minimized. Due to the lack of radiation exposure by the MR-image acquisition, anatomical scans can be added/repeated to achieve optimal anatomical information.

3. Simultaneity of acquisition

The newly introduced integrated MR/PET scanners for the first time allow truly simultaneous acquisition of imaging information from two different modalities of the same region at the same time. This opens a completely new dimension in hybrid imaging. Even established PET/CT technology only allows the acquisition of CT and PET in the same system but not at exactly the same time and region, as the two modalities/acquisition procedures are cascaded one after the other. The simultaneous acquisition of MR and PET information opens the opportunity to address many new scientific questions, which may be translated into clinical application, e.g. to cross-evaluate the value of different imaging tests under identical examination conditions or to improve understanding of disease pathophysiology by shedding light on the interrelation between different pathological processes. Simultaneous acquisition may also allow the following of organ and/or patient movement over time allowing for motion correction [2] and also the combination of information on motility with other functional information provided by PET (e.g. information on viability/perfusion derived from PET-imaging with information on wall movement in cardiac examinations).

4. Exposure to ionizing radiation

Radiation exposure based on clinical imaging tests is currently a much-discussed topic. Compared to PET/CT, hybrid MR/PET offers the chance to reduce ionizing radiation exposure without loss of diagnostic information. MRI will probably allow anatomical allocation of the PET-signal with comparable precision as known from CT. In some cases the combination of PET-imaging with appropriate diagnostic MR-imaging procedures may be of superior diagnostic value with considerably lower radiation exposure as compared to the combination of PET and diagnostic CT.

5. Complementary/superior diagnostic value of MR/PET compared to PET/CT
It is well known that MRI has complementary features to CT. The most obvious being the higher soft-tissue contrast. As mentioned above, combined MR/PET may be of obviously higher diagnostic value compared to PET/CT for indications and in body regions which would usually be approached using MRI rather than CT (see clinical examples below). In this regard MR/PET may represent a complementary imaging technique to PET/CT in the future just as MR itself represents a complementary imaging technique to CT nowadays.

6. Opportunities for scientific applications
The MR/PET-system opens a large number of potential scientific applications. Among these is the unique option to establish previously unknown interrelations between different measures of pathology and physiology in the human body such as structure and function, perfusion and metabolism, tissue diffusivity and cell proliferation etc. This may allow to improve the understanding of healthy organ function and to detect causal relationships in disease pathogenesis potentially leading to new therapeutic approaches.
For clinical diagnosis, combined MR/PET may allow the development of integrated multiparametric markers for more sensitive and more specific diagnosis, therapy planning and evaluation [5]. Several previous studies using separate modalities point to a potentially high scientific and clinical benefit from multimodal imaging approaches using MR/PET [e.g. 5–7].

Challenges of the MR/PET system

Like every new system, combined MR/PET still has a number of apparent challenges:

1. Attenuation correction
In PET/CT systems, low-dose CT scans are used to estimate the expected attenuation of the radiation emitted from a specific body region. In contrast to CT, MR imaging does not provide information on tissue specific photon absorption, but rather on tissue type/class. However, it has been demonstrated that by means of a set of specific MR-sequences (Dixon imaging or chemical shift imaging) suitable attenuation maps can be calculated, which allow an approximation of 511 keV photon attenuation correction with sufficient reliability [8]. The dual point VIBE T1-weighted Dixon sequence used for attenuation correction in the Biograph mMR can be acquired quickly for each bed position (e.g. in the thorax during one breathhold), practically not increasing the examination time. However, the current approach of tissue classification with the Dixon sequence is not yet fully satisfying, it is prone to metal artifacts, attenuation by bones is not considered and truncation artifacts may occur due to the limited transaxial field-of-view of the MR/PET scanner (particularly of the upper limbs). The compensation for these artifacts is currently a matter of ongoing research. Moreover, it can be anticipated that different sequences for attenuation correction will be used in specific areas of the body. For the head e.g., bone probably cannot be neglected completely for truly accurate AC, especially for the skull base. Therefore in this region, the application of ultrashort TE (UTE) sequences might be favourable, which allows for delineation of the bone, thus leading to more exact attenuation maps (μ-maps) as compared to the Dixon imaging approach.

2. Anatomical allocation of PET-findings
The low dose CT scan of the whole body as acquired in conventional PET/CT provides limited diagnostic information but it allows a rough anatomical allocation of suspect PET-findings with sufficient reliability in many cases. For precise attribution diagnostic contrast-enhanced CT scans can be acquired in very short time and provide excellent anatomical information. By contrast, MR-sequences can be comparably slow and it may not be feasible to always acquire whole-body MR-information with high resolution in due time. However, it seems likely that the Dixon-sequences used for attenuation correction of the PET-data also can be used for anatomical allocation of PET-findings with very satisfying results. These whole-body images can then be complemented by added high-resolution MR-sequences in particular regions of interest.

3. MR-specific diagnostic limitations
It is expected that MR/PET will be inferior to PET/CT for indications which are commonly addressed with better diagnostic value by CT, e.g. small pulmonary lesions. It remains to be evaluated for which indications MR/PET is superior or equal to PET/CT and for which indications PET/CT will remain the method of choice.

4. Workflow
The high costs for this type of imaging instrumentation will require elaborate logistics regarding patient flow, occupancy of the scanner, selection of examination procedures etc., to assure efficient utilization of the scanner. The combined acquisition of MR and PET information defines the need for specially educated medical personnel experienced with both modalities.

5. Design of suitable imaging protocols
The large number of available MR-sequences and of different PET-tracers exponentiates the number of potential combinations of imaging tests. This will define the need to develop optimized imaging algorithms for specific diagnostic questions, which ensure the selection of the most beneficial combinations.

Examples for clinical applications

1. Oncology

Case 1 Patient with a cervical Non-Hodgkin lymphoma.

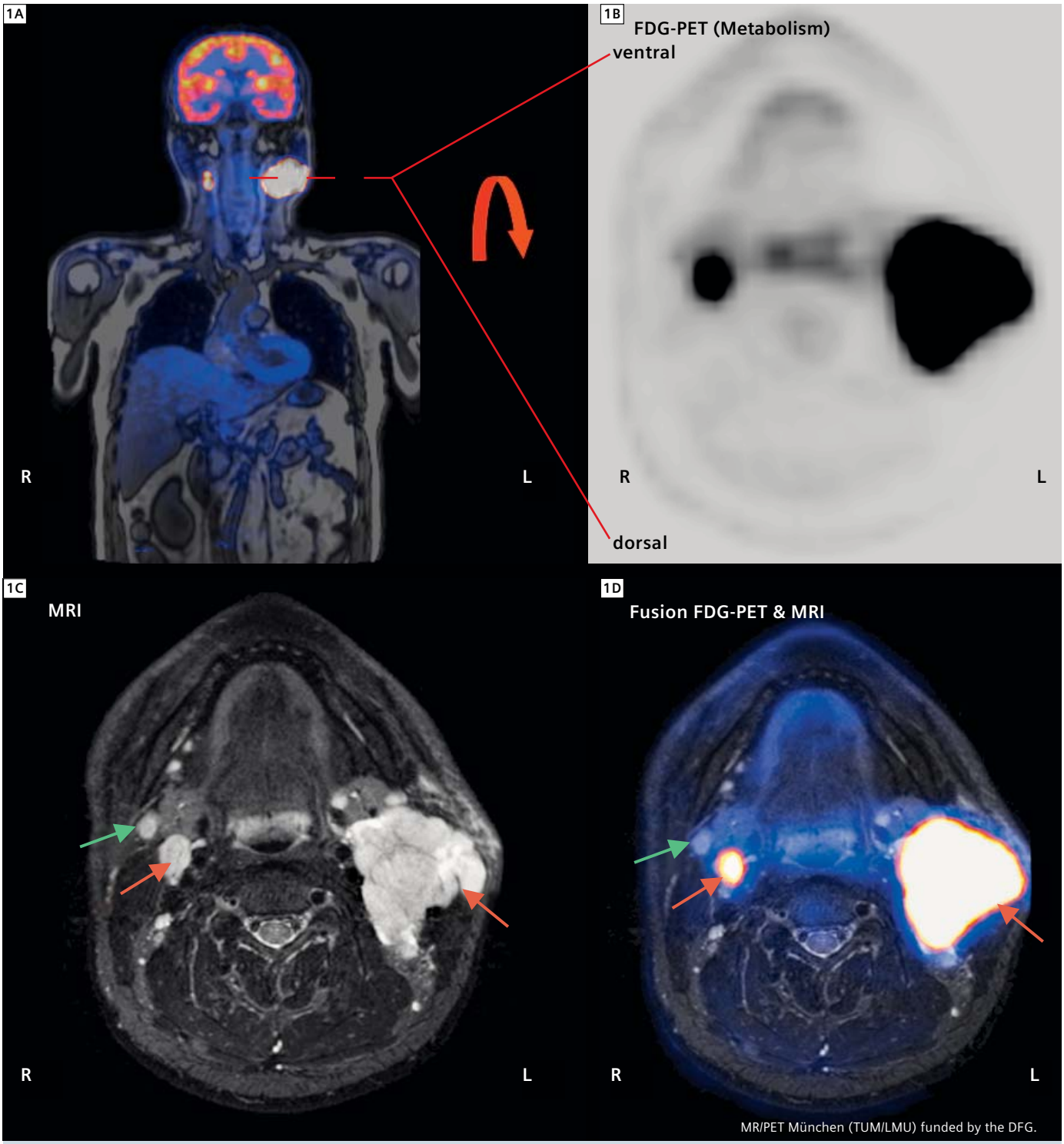

1 **A:** Overview using the opposed phase of the MR AC Dixon sequence. **B:** Axial slice of the ^{18}F-FDG-PET image, demonstrating tumor-suspect increased metabolism in two lesions (left and the right lateral). **C:** Axial MRI (STIR sequence) demonstrating the high tissue contrast. Several cervical lymph nodes are apparent, some enlarged. **D:** Overlay of PET and MRI, easily tumor-typical (red arrows) and non tumor-typical findings (green arrow) can be identified and allocated anatomically.

Case 2 Patient with a Neuroendocrine tumor.

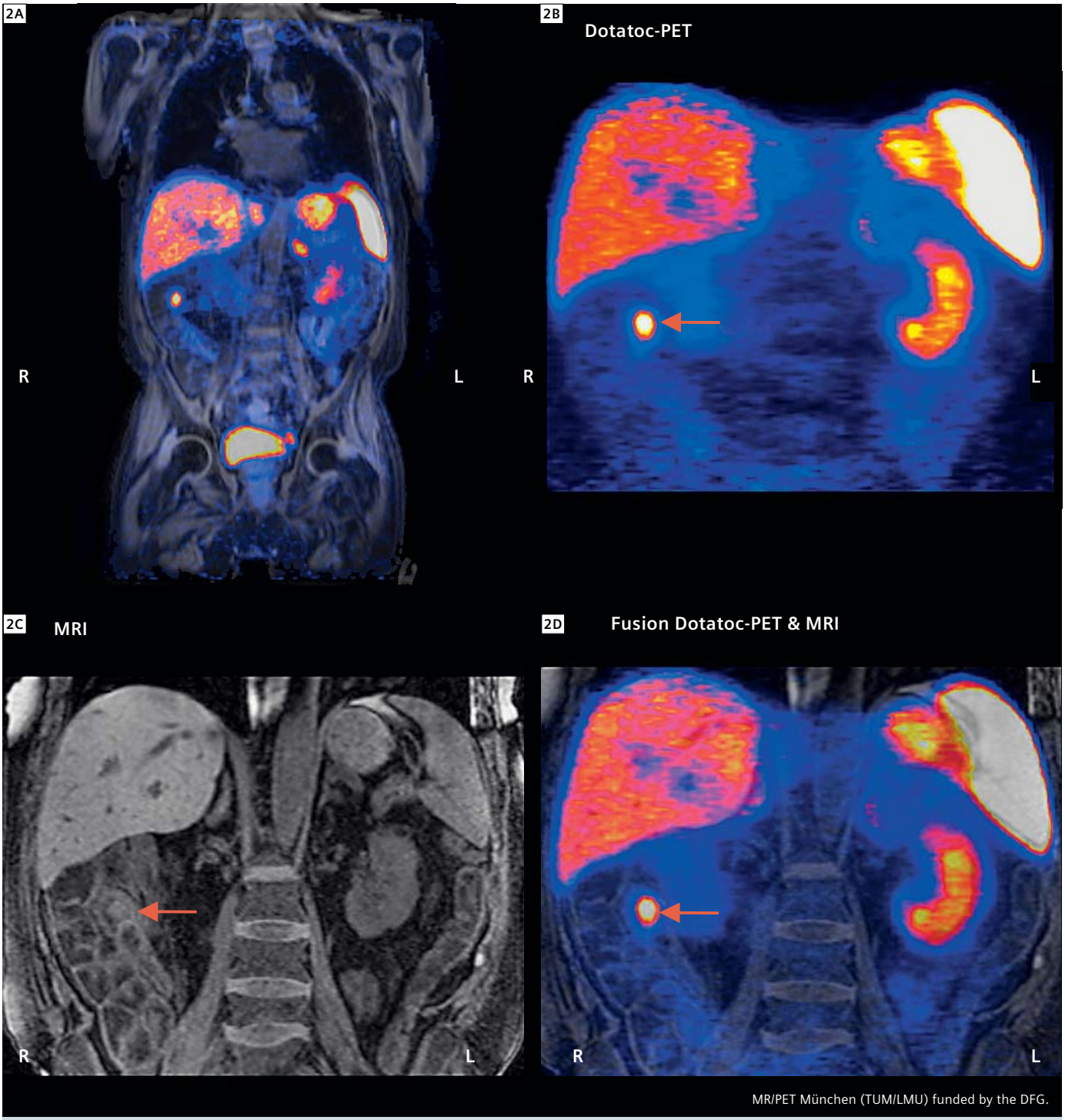

2 **A:** Overview using the water image of the MR AC Dixon sequence. Note the area of intense focal tracer uptake in the right upper quadrant of the abdomen, projecting on the region of the terminal ilium. There is a small bladder diverticulum of the left lateral bladder wall with tracer retention as accidental finding. **B:** PET-findings with ^{68}Ga-DOTATOC, a tracer binding to somatostatine-receptors which are expressed frequently on neuroendocrine tumors. An intense focal tracer-uptake can be found in the abdomen. **C:** MR-image, fat-suppressed coronal T1w breathold VIBE sequence. **D:** Fusion of PET and MR-findings. An excellent identification and anatomical allocation of the tumor is possible by combination of PET and MRI findings. No additional suspect lesions are apparent.

Case 3 Patient with bone metastases of a prostate cancer.

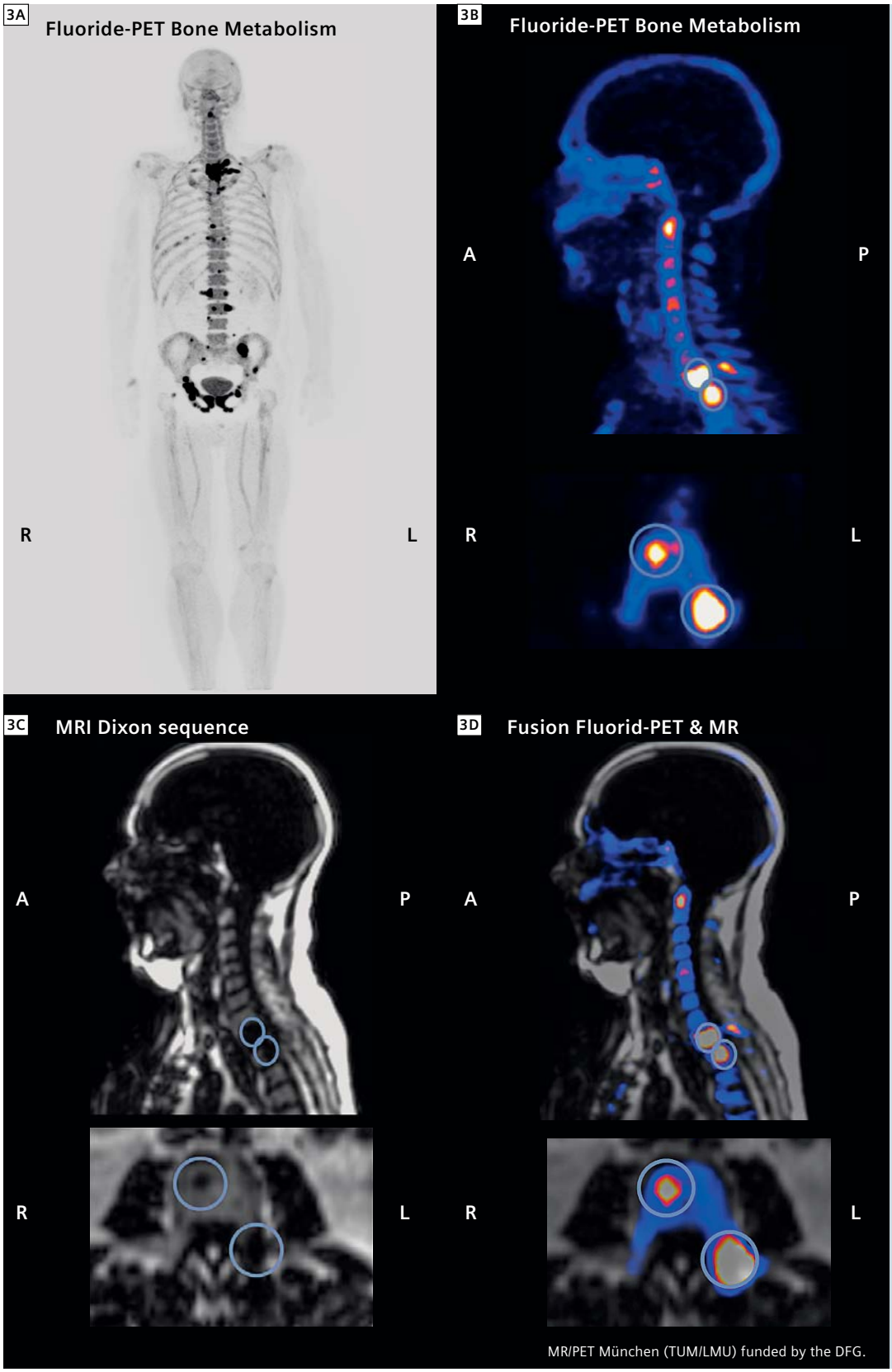

3 **A:** Overview of the ^{18}F-Fluoride PET scan. **B:** PET-findings. **C:** MR-image, sagittal fat-weighted MR AC Dixon sequence. **D:** Fusion of PET and MR-findings. Upper row: sagittal slices, Lower row: axial slices. The Fluoride-PET scan shows a number of suspect lesions in the skeleton, likely corresponding to bone metastases of the prostate-cancer. On the MR- and the fusion-images it is apparent that in the region of the increased PET-tracer uptake, displacement of the bone marrow has occurred, underlining the suspicion of bone metastases.

MR/PET München (TUM/LMU) funded by the DFG.

2. Neurology

Case 4 Patient with a glioblastoma multiforme.

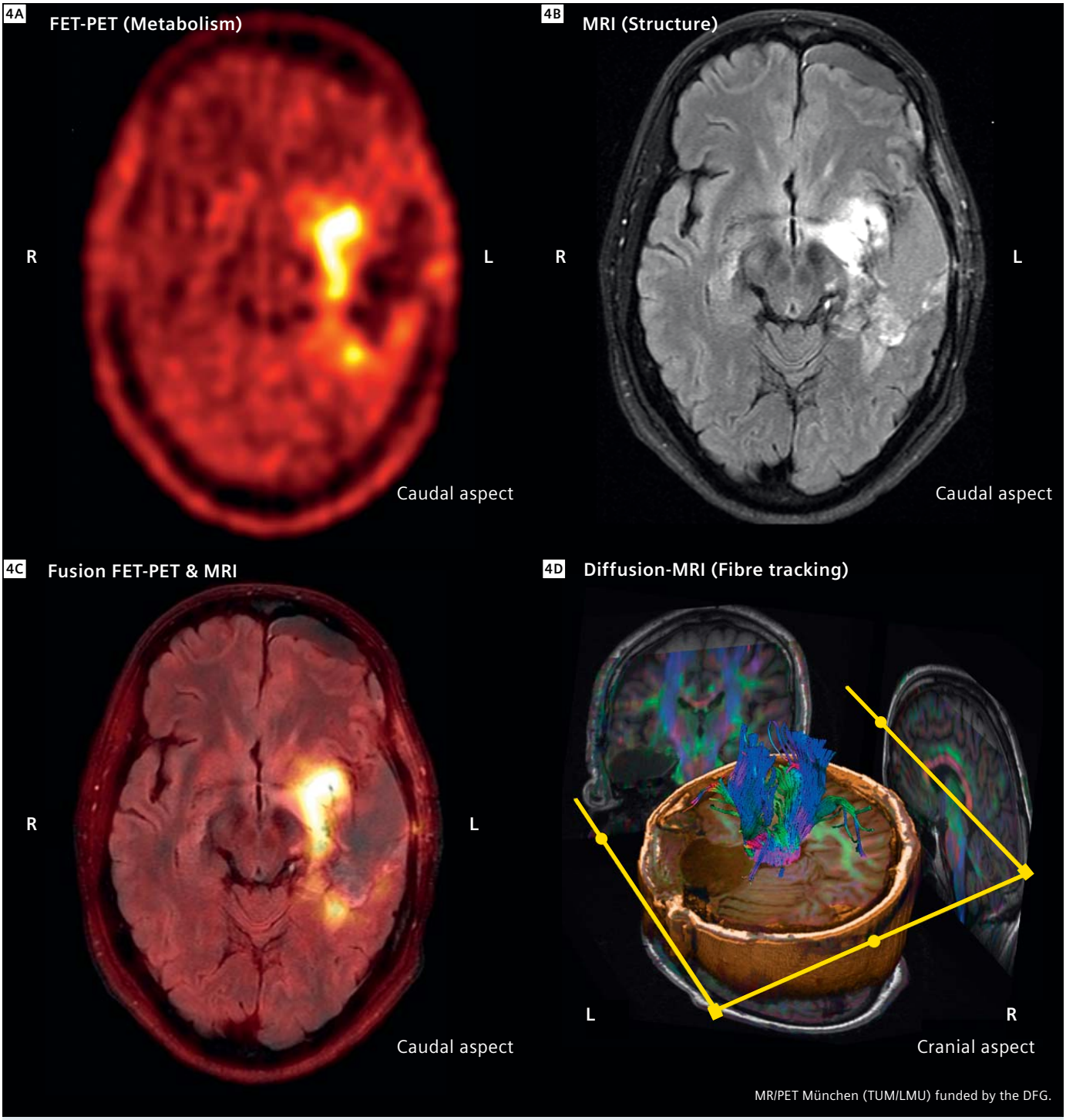

4 **A:** ^{18}F-FET PET scan. The tracer FET represents a measure of the amino acid metabolism and allows the sensitive identification of brain tumor tissue which is characterized by high amino acid turnover, in contrast to healthy brain tissue. A strong tracer uptake is visible around a previous resection area, suspect for remaining/recurrent brain tumor tissue. **B:** MR-image, axial FLAIR-sequence, demonstrating a region of hyper intensity around the area of resection, potentially representing edema and/or gliosis, but also vital tumor tissue cannot be excluded. Moreover, a left frontopolar hygroma is seen. **C:** Fusion of PET and MR-findings, allowing excellent anatomical allocation of the vital tumor tissue in reference to anatomical structures and abnormalities in the MR-image. **D:** Fibre-tracking based on a diffusion-tensor MR dataset, demonstrating the course of neuronal axons alongside the resection area.

Case 5 Patient with Alzheimer's disease.

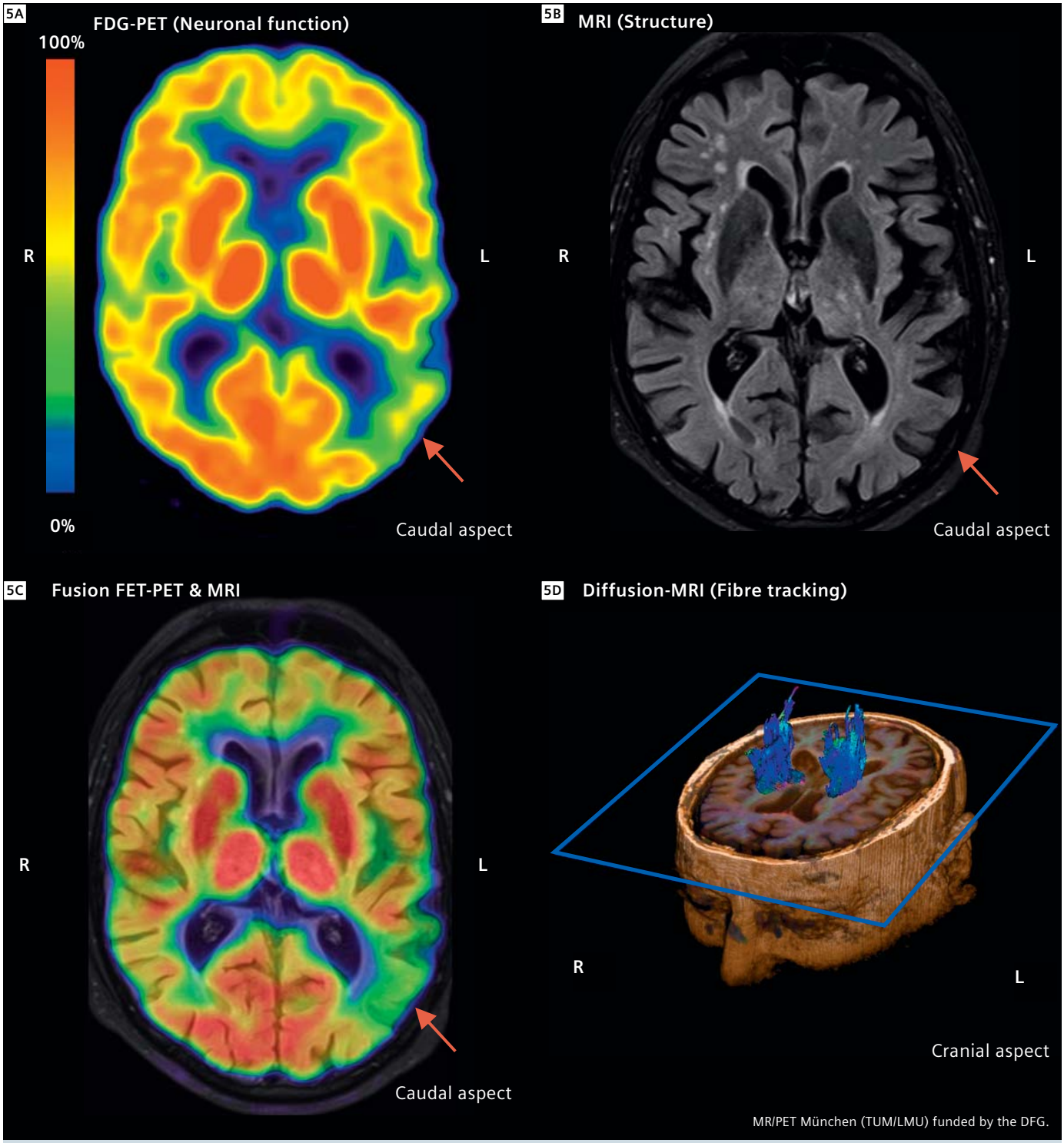

5 **A:** ^{18}F-FDG-PET of the brain, which represents a measure of neuronal function. Areas with reduced neuronal function in consequence of ongoing neurodegenerative processes are displayed in green-yellow (left temporoparietal cortex, see red arrow), healthy brain regions in orange-red. **B:** MR-image, axial FLAIR-sequence. Brain anatomy can be displayed in high resolution, cerebral atrophy is apparent in widespread regions, predominantly on the left side. **C:** In the MR/PET fusion regional allocation of hypometabolism and brain substance loss is possible. **D:** Fibre-tracking based on a diffusion-tensor MR dataset, demonstrating the course of neuronal axons in the brain of the patient.

3. Cardiology

Case 6 MR/PET of the heart.

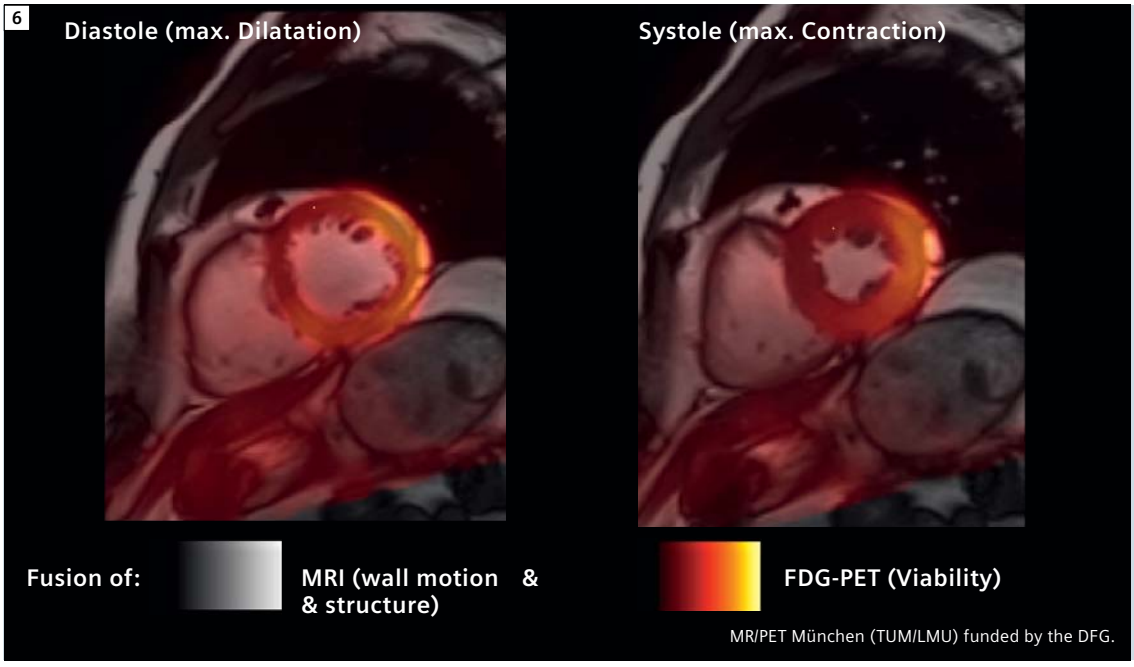

6 Assessment of the metabolism of cardiac tissue with the tracer ^{18}F-FDG allows the identification of viable myocardium. Simultaneous acquisition of wall motion and myocardial anatomy can be performed using MRI. The combination allows the exact attribution of functional aspects to underlying regional metabolic conditions/viability.

Conclusions

- First clinical imaging studies demonstrate successful clinical applicability of integrated whole body MR/PET.
- Attenuation correction of the PET signal using appropriate MR-derived attenuation maps appears to be feasible with sufficient reliability for most cases. Some problems (lack of accurate bone-detection, truncation artifacts) are a matter of ongoing research.
- From a diagnostic perspective, superiority of MR/PET compared to PET/CT can be foreseen for indications/body regions, which would preferably be approached by MRI rather than by CT, due to the superior soft tissue contrast of MRI. Examples are:
  Oncology: Head and neck tumors, masses in the pelvis/abdomen (e.g. prostate cancer), carcinoma of unknown primary, whole-body imaging
  Neurology: Brain tumors, epilepsy, dementia, stroke
  Cardiology: Regional function (wall motion) and scar detection (late enhancement) versus myocardial perfusion and tissue viability
- It remains to be evaluated for which indications MR/PET is superior or equal to PET/CT and for which indications PET/CT will remain the method of choice. MR/PET will probably be inferior to PET/CT for indications which are commonly addressed with better diagnostic value by CT, e.g. pulmonary lesions.
- The expected high costs for this type of imaging procedure will require elaborate logistics regarding patient flow, examination procedures, occupancy of the scanner etc., to ensure efficient utilization.
- The large number of available MR-sequences and of different PET-tracers exponentiates the number of potential combinations of imaging tests. This will define the need to develop optimized imaging algorithms for specific diagnostic questions.

References
1 Catana, C., et al., MRI-assisted PET motion correction for neurologic studies in an integrated MR-PET scanner. J Nucl Med. 52(1): p. 154-61.
2 Catana, C., et al., Toward implementing an MRI-based PET attenuation-correction method for neurologic studies on the MR-PET brain prototype. J Nucl Med. 51(9): p. 1431-8.
3 Herzog, H., et al., High resolution BrainPET combined with simultaneous MRI. Nuklearmedizin. 50(2).
4 Schlemmer, H.P., et al., Simultaneous MR/PET imaging of the human brain: feasibility study. Radiology, 2008. 248(3): p. 1028-35.
5 Beer, A.J., et al., Radionuclide and hybrid imaging of recurrent prostate cancer. Lancet Oncol. 12(2): p. 181-91.
6 Metz S, Ganter C, Lorenzen S, van Marwick S, Herrmann K, Lordick F, Nekolla SG, Rummeny EJ, Wester HJ, Brix G, Schwaiger M, Beer AJ. Phenotyping of tumor biology in patients by multimodality multiparametric imaging: relationship of microcirculation, alphavbeta3 expression, and glucose metabolism. J Nucl Med. 2010 Nov; 51(11):1691-8. Epub 2010 Oct 18.
7 Drzezga A, Becker AJ, Van Dijk K, Sreenivasan A, Talukdar T, Sullivan C, Schultz AP, Sepulcre J, Putcha D, Greve D, Johnson KA, Sperling RA. Neuronal dysfunction and disconnection of cortical hubs in non-demented subjects with elevated amyloid-burden. Brain. 2011, in press.
8 Martinez-Moller, A., et al., Tissue classification as a potential approach for attenuation correction in whole-body PET/MRI: evaluation with PET/CT data. J Nucl Med, 2009. 50(4): p. 520-6.

Contact
Alexander Drzezga, MD
Technische Universität München
Klinik und Poliklinik für Nuklearmedizin
Klinikum rechts der Isar
Ismaninger Str. 22
D-81675 Munich
Germany
phone: +49 89 4140 7722
a.drzezga@lrz.tum.de

TOGETHER WE MOVE FORWARD IN THE FIGHT AGAINST CANCER

When two leading companies join forces in the fight against cancer, it broadens the realm of what's possible. That's why Varian and Siemens have partnered. Siemens' advanced diagnostic imaging capabilities coupled with Varian's powerful delivery systems and treatment planning tools give even more of an edge in the pursuit of our common goal: to **EnVision better cancer care**. Together we offer more personalized treatment and expanded care options that aid you in making the best possible decisions for your patients—with confidence. By gathering our strengths, we have the energy and vision to better help healthcare professionals detect, diagnose and treat cancer while paving the way for the future of cancer care.

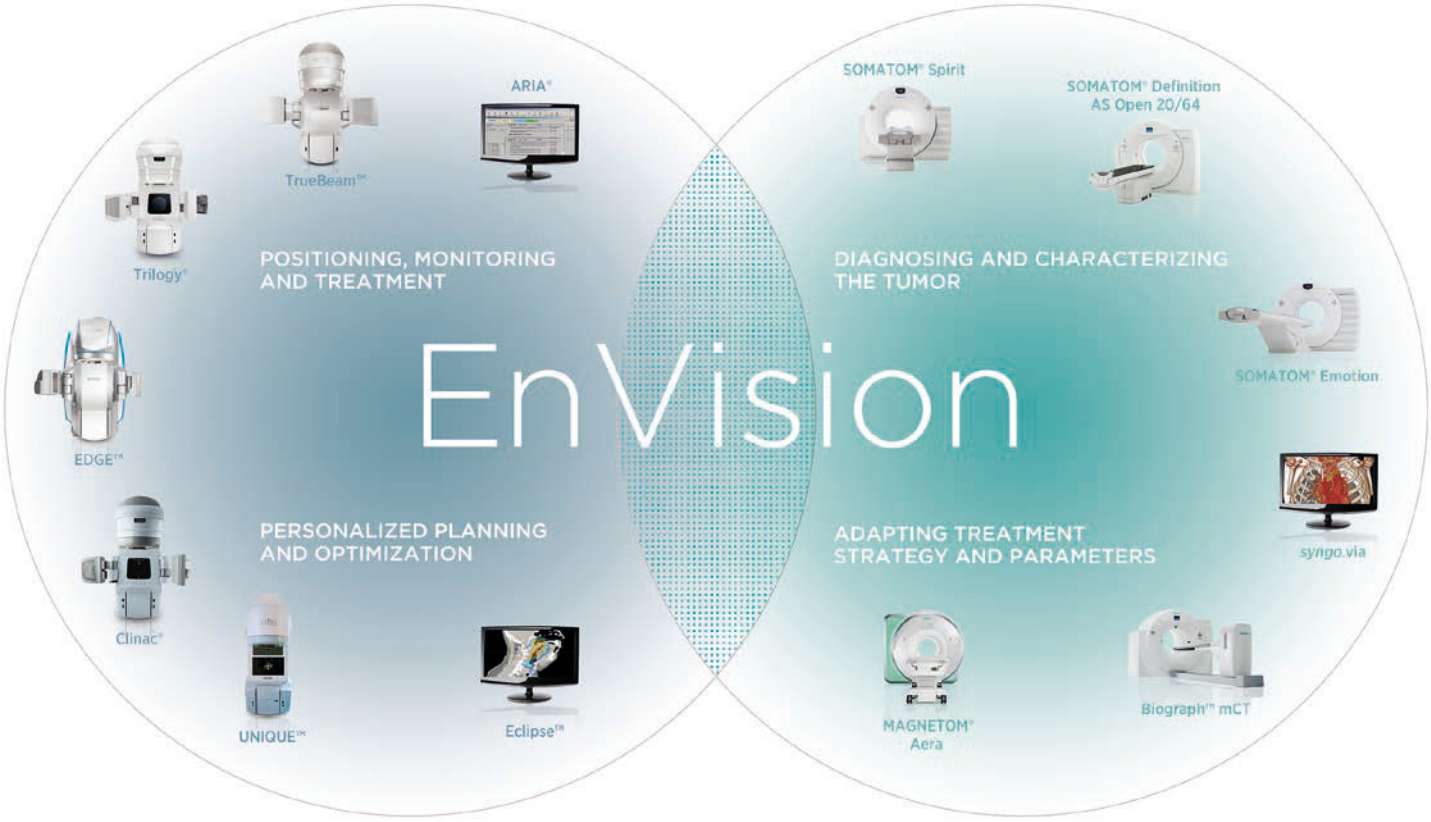

VARIAN medical systems

SIEMENS
Strategic Partner of Varian for Radiation Therapy

© 2013 Varian, Varian Medical Systems, Trilogy, and ARIA are registered trademarks, and TrueBeam, Edge Radiosurgery and Eclipse are trademarks of Varian Medical Systems, Inc. All other trademarks are property of Siemens AG.

Varian Medical Systems
International AG
Zug, Switzerland
Tel: +41 - 41 749 88 44
Fax: +41 - 41 740 33 40
varian.com
info.europe@varian.com

Global Siemens Healthcare Headquarters
Siemens AG
Healthcare Sector
Henkestrasse 127
91052 Erlangen, Germany
Tel: +49 9131 84-0
siemens.com/healthcare

Find out more at **varian.com/envision**

Neuroimaging as a Clinical Tool in Surgical Planning and Guidance for Pediatric Epilepsy

Binjian Sun, Ph.D.; Robert Flamini, M.D.; Susan Palasis, M.D.; Richard A. Jones, Ph.D.

Children's Healthcare of Atlanta, Department of Radiology, Atlanta, GA, USA

Epilepsy is the fourth most common neurological disorder in all ages. According to the Epilepsy Foundation, 1% of the population is expected to develop epilepsy before 20 years of age. Extra-temporal cortical resection is the most common curative epilepsy surgery in infants* and children, whereas temporal lobectomy is the most common in adults. Children with intractable epilepsy may benefit from early surgical intervention to avoid the potential negative effects of continued seizures and prolonged use of anti-epilepsy drugs on cognitive and psychosocial development and to increase the chances of post-operative neurological reorganization due to the inherent functional plasticity of the pediatric brain. Tellez-Zenteno et al. surveyed 3557 (697 non-lesional, 2860 lesional) temporal and extra-temporal epilepsy data from children for whom structural MRI was used to define the patient as being lesional or non-lesional and who then underwent surgery [1]. The meta-analysis revealed the seizure free post-surgery rate was 45% for non-lesional patients and 81% for lesional patients. This highlights the importance of successfully locating, and characterizing, the epileptogenic zone (EZ), which is defined as the volume of brain tissue responsible for the generation of seizures and whose removal consequently leads to freedom from seizures. It is important to characterize the structural lesion because the spatial relationship of the lesion to the EZ varies between different types of lesions. For most brain

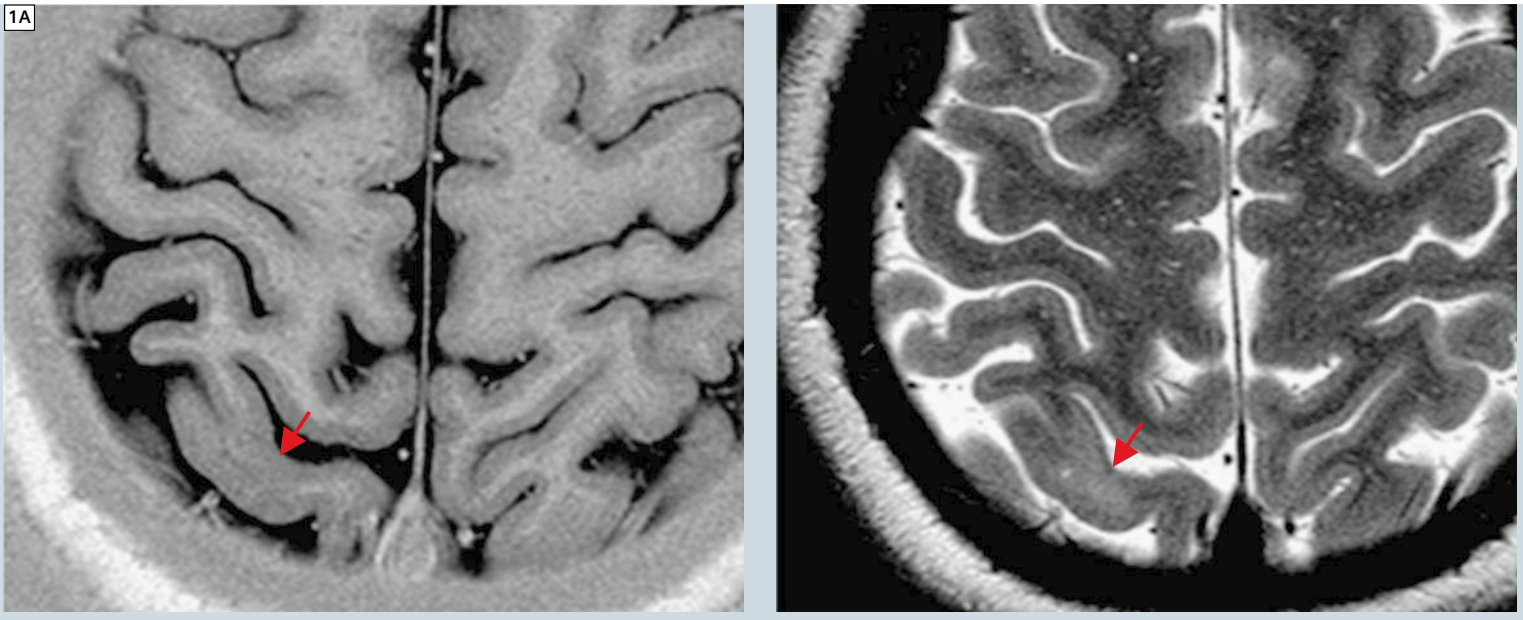

1A Inversion recovery and T2-weighted images acquired with high spatial resolution on a 3T MAGNETOM Trio scanner. A subtle lesion (red arrows) can be seen that is hypo- and hyper-intense on the IR and T2-weighted images respectively.

tumors, removal of the lesion, including the immediate margins of tissue around the lesion, will lead to freedom from seizures in a high percentage of patients. However, in the case of focal cortical dysplasia, removal of the lesion and its margins frequently does not lead to freedom from seizures, implying that the EZ extends beyond the visible lesion in this case. As with any surgery there are potential risks as well as benefits, in particular that the epileptogenic focus may share, or be in close proximity, to eloquent cortex. Thus it is not uncommon for patients to suffer from varying degrees of neurocognitive decline post-surgery. For patients with temporal lobe epilepsy (TLE) the decline is predominately manifested as verbal or visual memory impairment [2–5]. For example, one study showed that TLE patients suffered an average of 11% verbal memory decline following TL resection [4]. Another, more recent, study revealed that although group level comparison shows no significant verbal intellectual loss, roughly 10% of TLE children experienced a significant decline in verbal functioning following TL resection [5]. Hence thorough and meticulous pre-surgical assessments are necessary to address both aspects of the surgical outcome, i.e., post-surgical seizure activity and neurological functioning. Neuroimaging is now routinely prescribed for TLE patients who are potential candidates for temporal lobectomy. The neuroimaging assessment includes video EEG monitoring, structural neuroimaging (MRI), functional cerebral imaging such as fMRI, Single Photon Emission Computed Tomography (SPECT) and Positron Emission Tomography (PET). The results of these evaluations can be used individually, or collectively, to:

1) Localize and characterize the epileptogenic focus and thus help the physician to determine if surgical resection of the extratemporal cortex is appropriate.

2) Identify both the laterality of functions such as language and the location of patient-specific, functionally important, cortical regions and white matter tracts that should, if possible, be spared by surgery.

Localization of epileptogenic focus

The brain lesions associated with pharmacoresistant epilepsy are often subtle and require special expertise for their detection and characterization. In addition, the use of a dedicated epilepsy protocol, rather than a standard brain protocol, has been shown to offer improved lesion detection [6]. Dedicated TL epilepsy protocols include high spatial resolution thin slice, T1 and T2-weighted coronal and axial imaging with the coronal images being acquired in an oblique plane perpendicular to the long axis of the hippocampus when evaluating TLE. It has also been shown that the use of a 3T magnet and phased array coils further improves the sensitivity of lesion detection, when compared to 1.5T results [7]. Figure 1 illustrates two cases where epileptogenic foci were identified on high resolution anatomical MR images. To date, most studies have shown that interictal diffusion imaging is not helpful for lesion localization [8]. Changes in the diffusion tensor have been detected

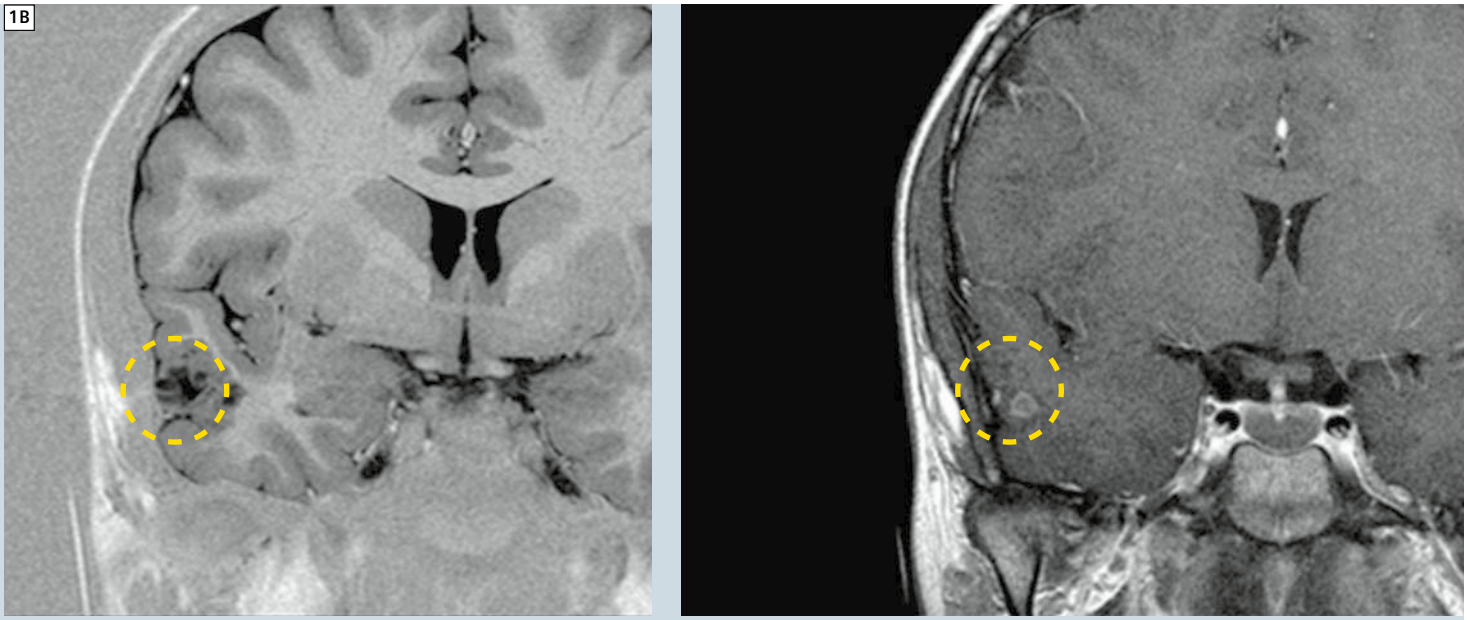

1B Inversion recovery and post-gadolinium T1 images identifying a small cystic lesion (yellow circles) in temporal lobe.

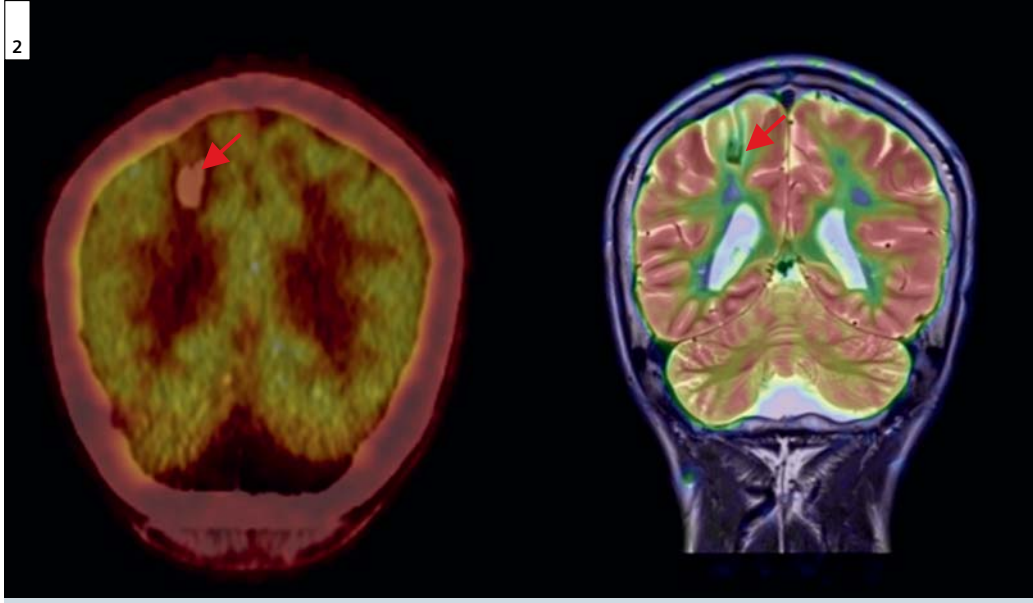

2 Fused PET-CT (left) and PET-MR images of a patient with tuberous sclerosis. The PET images detected regions of hypometabolism in three of the multiple sub-cortical tubers (only one is shown (red arrows)) allowing these to be identified as the possible seizure foci.

but in general do not reach statistical significance even at the group level [9]. This may be, in part, due to partial volume effects from the poor spatial resolution typically used for diffusion studies. The development of higher resolution techniques for diffusion imaging may change this in the future.
In a small portion of our epilepsy surgery population, PET is used to assist the localization of epileptogenic focus. Due to the poor resolution of PET images, CT and/or MRI are also performed on this group of patients. The PET images are then coregistered with CT and MR results in order to allow the anatomical location of areas of poor perfusion to be more accurately identified. Figure 2 shows a case where an epileptogenic lesion was identified on the fused PET-CT and PET-MR images.
Another technique that is used more frequently at our institution for the localization of the EZ is SISCOM (Subtraction Ictal SPECT Co-registered to MRI). This technique combines SPECT studies of a tracer that reflects cerebral perfusion, with the studies being acquired both ictally (during a seizure) and an interictally (between seizures) [10, 11]. Conventionally, side-by-side visual analysis of ictal and interictal SPECT images can be used for lesion identification. However, the interpretation of the images can be quite difficult due to differences in the injected dose, tracer uptake and decay, patient head position, and slice positioning. To address these problems, the SISCOM technique registers the two SPECT scans using a mutual information based registration algorithm (we do an initial crude manual registration in order to avoid problems with local maxima of the registration algorithm) and then normalizes the two SPECT scans prior to computing a difference image that represents a semi-quantitative map of the cerebral blood flow changes occurring during the seizure [10]. Unfortunately, the poor spatial resolution and contrast of the SPECT images complicate the determination of the exact anatomical location of any seizure focus detected on the differential image. For this reason, the differential image is subsequently coregistered to and then represented as a color overlay on a T1-weighted volumetric MR image in order to better localize the lesion. One study showed that the localization of epileptic foci is 88.2% for SISCOM but only 39.2% for side-by-side inspection of SPECT images [11]. Figure 3 shows the SPECT data, the processed difference image and the fused SISCOM images for a patient with TLE.
Using the information from SISCOM and/or video-EEG to further refine the epilepsy protocol can allow an experienced radiologist to detect focal cortical dysplasia in patients who were considered non-lesional on the standard epilepsy protocol [12]. While SISCOM can be a very useful technique, it is rather time and labor intensive as the injection must be performed promptly after the seizure for the technique to work properly. The seizure must also be of sufficient duration and of the type that typically occurs in that patient (video EEG is required to verify this).
For patients scheduled for TL resection, intracranial EEG recordings are performed in some cases in order to provide additional information of the location of the epileptogenic focus, or to better define functional cortex that needs to be spared. If lesions have been identified by structural MRI or an area of abnormal perfusion has been identified on the SISCOM study, the results of these studies are used to guide the grid placement. In our hospital, we used the Stealth station navigation system by Medtronic to guide the electrode grid placement. For the structural images, the procedure is straightforward. For the SISCOM images, the procedure is a little more involved and requires the following steps:

1) Register the differential SPECT image to the anatomical MRI.
2) Color code the differential image.
3) Fuse the color coded SISCOM to the MR image on the navigation system.

After grid placement, the patients are observed using continuous EEG video monitoring in order to detect seizures. Once a seizure is identified, the electrodes showing the strongest activity at the time of the seizure can be localized. In order to identify the spatial location of these electrodes a CT scan of the electrode grid is obtained, preferably performed immediately post-surgery in order to minimize the swelling caused by post-surgical edema. Co-registering of the CT scan to a structural MRI volume is performed using the fusion tool on the MultiModality Workplace (Leonardo). The neurologists and radiologists can then determine the spatial location of the electrodes closest to the source of the seizure activity. Figure 4 illustrates a case of CT grid and MRI co-registration.

Identification of laterality and functional cortex

Traditionally, a neuropsychological evaluation called the Wada test is performed to determine which side of the brain is responsible for certain vital cognitive functions, specifically language and memory. The Wada test consists of a standard neuropsychological assessment performed in conjunction with intracarotid injections of sodium amytal. The drug is injected into one hemisphere at a time inactivating language and/or memory function in that hemisphere in order to evaluate the contralateral hemisphere. The patient is engaged in a series of language and memory related tests during and after the Amytal effect. The results of the test are then used to estimate the potential functional effects of the surgery in language and memory, and help in planning the surgical approach. When localization of function to a particular area of the brain is required electro-cortical stimulation (ECS) was traditionally used. This test requires that electrodes are placed on the surface of the brain and direct stimulation of the electrodes on the exposed brain is then performed to map regionally specific function. As the patient has to interact with the surgeon for this test the actual mapping has to be performed under local, rather than general, anaesthetic.

Recently, fMRI has emerged as a non-invasive alternative method for lateralizing the language and motor networks, and to a lesser degree – memory, in cooperative children with epilepsy [13–15]. Brain mapping with fMRI has also revolutionized the evaluation of patients undergoing epilepsy surgery by providing a non-invasive method for identifying critical brain areas to spare during resection and offering a powerful tool for studying neural plasticity. There are numerous advantages of fMRI over other conventional modes in terms of language mapping: fMRI is non-invasive, does not carry the risk of either the WADA test or ECS, and different paradigms can be utilized to map different cognitive functions. Unlike the WADA test and ECS, fMRI can be readily repeated to confirm findings, and can both lateralize and localize different aspects of language functions. Correlation of fMRI results with those obtained using ECS show good, but not perfect, agreement. For language paradigms, when allowing for up to 10 mm between the activated areas using the two techniques, the sensitivity of fMRI to detect the language areas was between 67 and 100% depending on the paradigm [16]. It should be noted that the intrinsic resolution of fMRI studies is typically in excess of 3 mm and the smoothing used in the post-processing increases this to 5 mm or more.

For the pediatric population, impaired language is the most common adverse consequence of TL surgery. At our institution, language mapping is performed using one or more of three novel fMRI paradigms. The language paradigms were developed in conjunction with the Children's National Medical Center and are designed to target both expressive and receptive language processing. They were specifically developed for the assessment of the BOLD response in the language cortex of children and young adults under clinical conditions. Specifically, the following three tasks are employed, each using a block design:

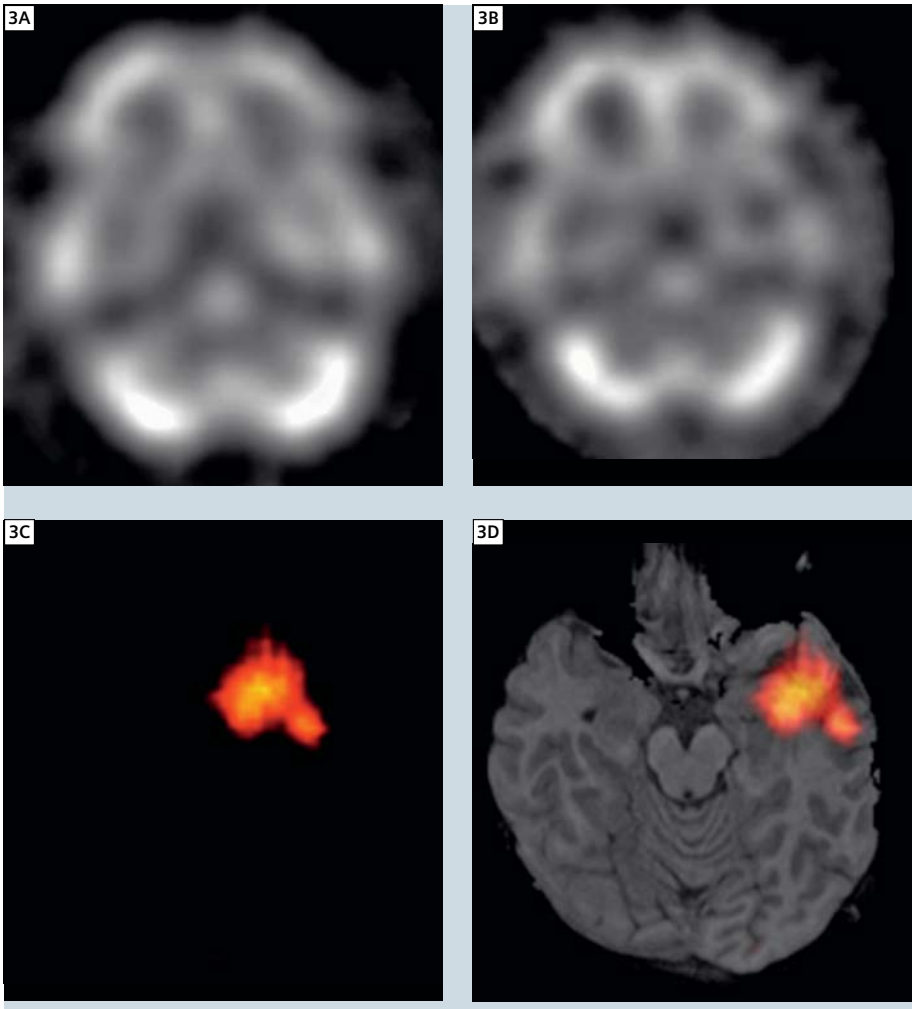

3 SISCOM result for a pediatric patient with TLE (**3A**). Ictal SPECT (**3B**). Interictal SPECT (**3C**). Differential SPECT and (**3D**) SISCOM result.

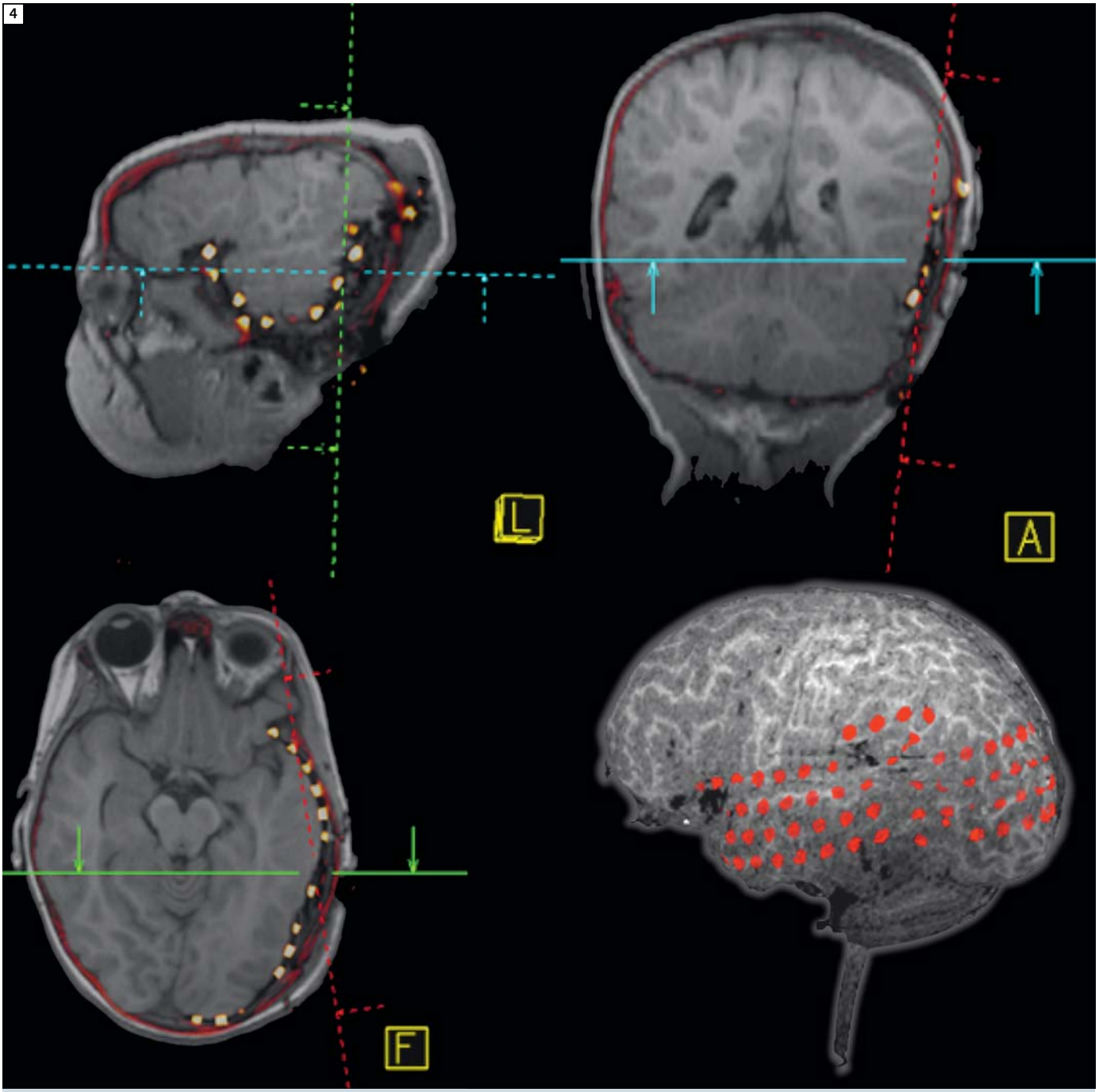

4 This case illustrates CT grid and MRI co-registration. Registration and initial visualization were achieved with 3D task card on a Siemens MultiModality Workplace (Leonardo). The electrodes can be seen as yellow/white area on the fused image due to their high intensity (i.e. high attenuation) on the CT images, areas of bone can be seen in red due to the relatively high attenuation of bone. The 3D representation was generated using in-house software which segments the CT scan to remove the bone and brain tissue and then provides an overview of the position of the grids on the surface of the brain.

5

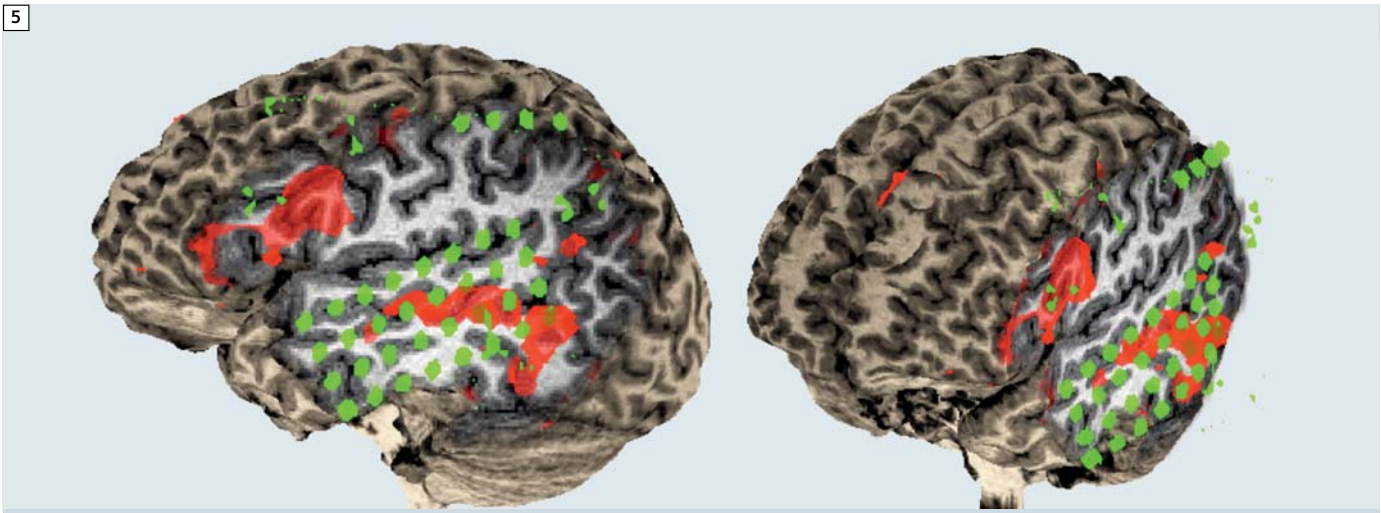

5 A case illustrating CT grid, fMRI (ADDT) activation and MRI co-registration. The CT electrodes are highlighted in green and the fMRI activations are rendered in red.

a) Auditory category decision task (AU CAT): A category is presented followed by a series of words. Participants are instructed to press a button if a word belongs to the specified category;
b) Auditory description decision task (ADDT): A description of an object is presented to the participants. The participants are required to press a button when the description is consistent with the matched object;
c) Listening to stories (Listening): Stories based on Gray Oral Reading Test are presented with pseudorandom inserted beeping sounds. Participants are instructed to press a button when a beep is heard while listening to the story. The participants are told that they will be questioned on the story after the scan in order to try and ensure that the participant pays attention to the story.
The rest condition for all three paradigms consists of reverse speech of the experimental condition with intermittent beeps as cues for button presses. All paradigms comprise five 30 second task blocks and five 30 second control (rest) blocks, resulting in a total duration of five minutes. Participants are instructed to press a single button for correct answers or upon hearing a beep (70% true and 30% false for task condition, matching number of button pushes for the corresponding control condition) during the course of the experiment. The responses are collected and inspected for the purposes of task monitoring and evaluation of response accuracy. The paradigms are also graded for skill and the appropriate version is selected for each participant based on his/her neuropsychological test score. All MRI scans are conducted on a Siemens 3T MAGNETOM Trio scanner equipped with 8-channel receive only head coil. A gradient echo EPI with TR = 3 sec and TE = 36 milliseconds and a nominal spatial resolution of 3.0 mm^3 is used for the fMRI studies. Oblique axial slicing is chosen for the fMRI acquisitions in order to increase coverage and reduce susceptibility effects. Inline fMRI analysis is done within the BOLD task card. Pediatric neuroradiologists and neuropsychologists use these results to determine the laterality of language and to locate the cortical regions implicated in language. The results are communicated to the neurosurgeons so that an optimized surgery plan can be developed. In some cases, the fMRI results along with CT grid and/or SISCOM results are all uploaded to the navigation system and used for realtime surgery guidance. For such purposes, the fMRI data is processed with FSL (www.fmrib.ox.ac.uk/fsl) and the statistical parametric maps are exported in DICOM format, which is required by our navigation system. Briefly, the fMRI data is pre-processed using the standard options and then analyzed using a general linear model, the resulting spatial statistical maps are then projected back to the corresponding anatomical MRIs and fed to the navigation software. Figure 5 shows a case where we simultaneously overlaid a CT grid scan (segmented to exclude brain tissue and bones) and the ADDT fMRI result on the anatomical MRI image. Diffusion tensor imaging (DTI) can also be used to map the major white matter pathways which project into the temporal lobe and this information can be used by the surgeons to try and spare these regions and hence preserve the communication with other regions of the brain. To achieve this goal,

white matter tracts connecting vital cortical regions (as identified by fMRI) are traced on DTI images, and those tracts are then uploaded onto the navigation system for surgical guidance. The DTI data is acquired axially using a 30 directions EPI sequence (b = 1000 sec/mm^2), 5 b = 0 scans, TR/TE = 8900/96 ms, a parallel imaging factor of 2 and a nominal spatial resolution of 2 mm^3. Our radiologists first review the DTI results produced by Neuro3D on the Siemens console and determine if DTI guidance is appropriate. If so whole brain tractography using the FACT algorithm is performed. The relevant fiber tracts are generated using the fMRI results as seed/target points. Binary masks are then created from the fiber tracts (voxels in the path of the tracts are assigned value 1 while others are assigned value 0). The resulting binary images are exported as DICOM images and sent to the navigation system (in a similar manner to the SISCOM and fMRI results) where they can be used to highlight the fiber tracts to be avoided during surgery.

These imaging techniques are now a routine part of the clinical workup for all of the epilepsy patients at our institution. They have greatly improved our ability to detect focal lesions, to minimize the detrimental effects of epilepsy surgery and to provide improved guidance to the neurosurgeon.

References

1 Tellez-Zenteno, J.F., et al., Surgical outcomes in lesional and non-lesional epilepsy: a systematic review and meta-analysis. Epilepsy Res, 2010. 89(2–3): p. 310-8.
2 Binder, J.R., et al., A comparison of two fMRI methods for predicting verbal memory decline after left temporal lobectomy: language lateralization versus hippocampal activation asymmetry. Epilepsia, 2010. 51(4): p. 618-26.
3 Helmstaedter, C. and C.E. Elger, Cognitive consequences of two-thirds anterior temporal lobectomy on verbal memory in 144 patients: a three-month follow-up study. Epilepsia, 1996. 37(2): p. 171-80.
4 Ojemann, G.A. and C.B. Dodrill, Verbal memory deficits after left temporal lobectomy for epilepsy. Mechanism and intraoperative prediction. J. Neurosurg, 1985. 62(1): p. 101-7.
5 Westerveld, M., et al., Temporal lobectomy in children: cognitive outcome. J Neurosurg, 2000. 92(1): p. 24-30.
6 Von Oertzen, J., et al., Standard magnetic resonance imaging is inadequate for patients with refractory focal epilepsy. J Neurol Neurosurg Psychiatry, 2002. 73(6): p. 643-7.
7 Knake, S., et al., 3T phased array MRI improves the presurgical evaluation in focal epilepsies: a prospective study. Neurology, 2005. 65(7): p. 1026-31.
8 Wehner, T., et al., The value of interictal diffusion-weighted imaging in lateralizing temporal lobe epilepsy. Neurology, 2007. 68(2): p. 122-7.
9 Widjaja, E., et al., Subcortical alterations in tissue microstructure adjacent to focal cortical dysplasia: detection at diffusion-tensor MR imaging by using magnetoencephalographic dipole cluster localization. Radiology, 2009. 251(1): p. 206-15.
10 Nehlig, A., et al., Ictal and interictal perfusion variations measured by SISCOM analysis in typical childhood absence seizures. Epileptic Disord, 2004. 6(4): p. 247-53.
11 O'Brien, T.J., et al., Subtraction ictal SPECT co-registered to MRI improves clinical usefulness of SPECT in localizing the surgical seizure focus. Neurology, 1998. 50(2): p. 445-54.
12 Ruggieri, P.M., et al., Neuroimaging of the cortical dysplasias. Neurology, 2004. 62(6 Suppl 3): p. S27-9.
13 Binder, J.R., et al., Determination of language dominance using functional MRI: a comparison with the Wada test. Neurology, 1996. 46(4): p. 978-84.
14 Gaillard, W.D., C.B. Grandin, and B. Xu, Developmental aspects of pediatric fMRI: considerations for image acquisition, analysis, and interpretation. Neuroimage, 2001. 13(2): p. 239-49.
15 Saykin, A.J., et al., Language before and after temporal lobectomy: specificity of acute changes and relation to early risk factors. Epilepsia, 1995. 36(11): p. 1071-7.
16 FitzGerald, D.B., et al., Location of language in the cortex: a comparison between functional MR imaging and electrocortical stimulation. AJNR Am J Neuroradiol, 1997. 18(8): p. 1529-39.

Contact
Richard A. Jones
Department of Radiology
Children's Healthcare of Atlanta
1001 Johnson Ferry Road
Atlanta, GA 30342
USA
Richard.Jones@choa.org

*MR scanning has not been established as safe for imaging fetuses and infants under two years of age. The responsible physician must evaluate the benefit of the MRI examination in comparison to other imaging procedures.

3T MR Imaging of Cartilage using 3D Dual Echo Steady State (DESS)

Rashmi S. Thakkar, M.D.[1]; Aaron J Flammang, MBA-BSRT (R) (MR)[2]; Avneesh Chhabra, M.D.[1]; Abraham Padua, RT (R)[3]; John A. Carrino, M.D., M.P.H.[1]

[1]Johns Hopkins University School of Medicine, Russell H. Morgan Department of Radiology and Radiological Science, Baltimore, MD, USA
[2]Siemens Corporate Research (CAMI), Baltimore, MD, USA
[3]Siemens Healthcare, Malvern, PA, USA

Introduction

Magnetic resonance imaging (MRI), with its excellent soft tissue contrast is currently the best imaging technique available for the assessment of articular cartilage [1]. In the detection of cartilage defects, three-dimensional (3D) MRI is particularly useful because cartilage is a thin sheet wrapped around complex anatomical structure. Isotropic, high resolution voxels enable reformatting of images into more convenient planes for viewing.

An MRI technique specifically for imaging cartilage should be able to accurately assess cartilage thickness and volume, depict morphological changes and show subtleties within the cartilage while minimizing artifactual signal alterations. In addition, it is necessary to evaluate subchondral bone for abnormalities. 3T MR scanners with multichannel dedicated coils allow to obtain image data with high resolution as well as sufficient signal-to-noise ratio (SNR) and contrast-to-noise ratio (CNR) [2]. Conventional spin echo and turbo spin echo sequences (T1, T2, and PD with or without fat suppression) as well as gradient echo techniques (incoherent GRE sequence, such as FLASH and coherent or steady state sequence, such as DESS) have been used for many years in cartilage imaging. Spin echo based approaches have clearly dominated due mostly to efficiency with respect to scan time.

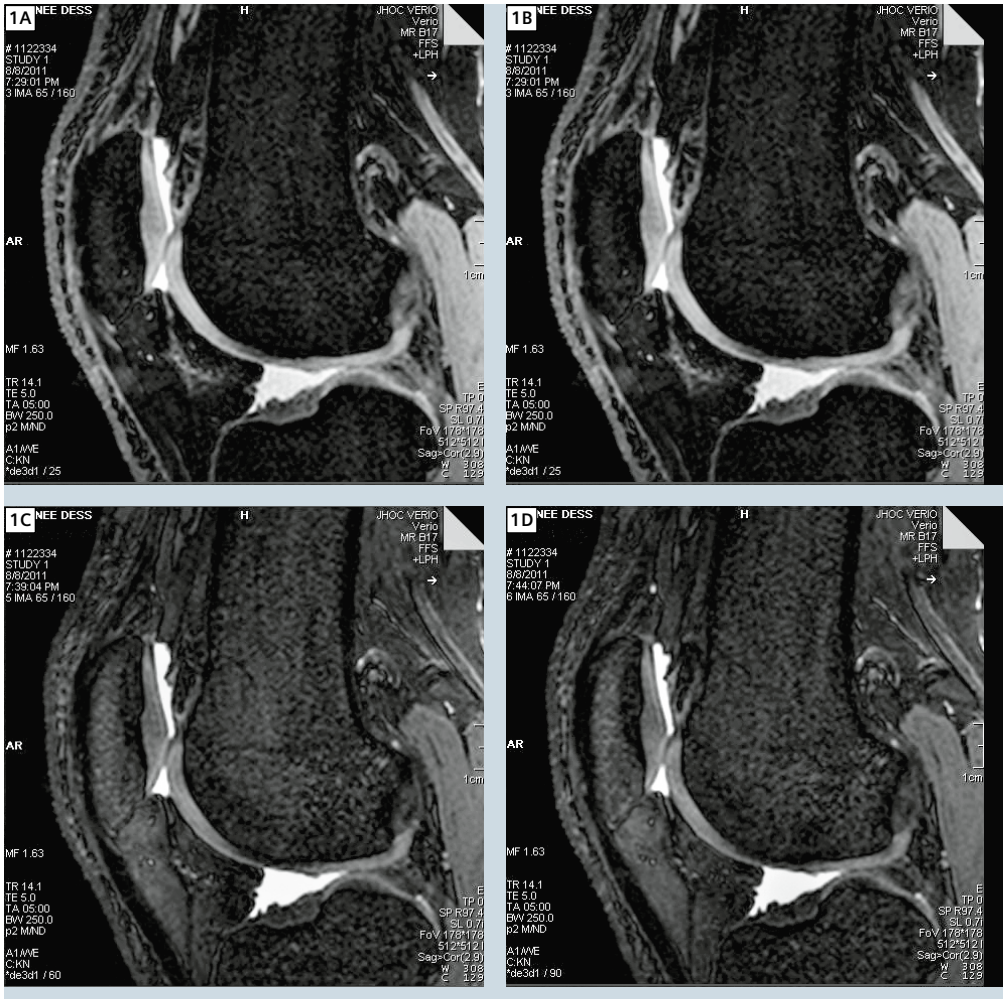

1 Sagittal water selective 3D DESS imaging of the knee (TR/TE 14.1/5 ms) at various flip angles (1A = 25°, 1B = 45°, 1C = 60°, 1D = 90°). With the flip angle of 60° there is highest signal intensity of synovial fluid with highest contrast-to-noise ratio of the cartilage.

In this article, we would like to describe the use of Dual Echo Steady State (DESS) in imaging of the articular cartilage on the Siemens MAGNETOM Verio.

DESS

Dual Echo Steady State (DESS) is a 3D coherent (steady state) GRE sequence. Steady state sequences (FISP, TrueFISP, DESS, PSIF, CISS) have two major characteristics. First, TR is too short for transverse magnetization to decay before the next RF pulse is applied. Second, slice selective (or slab selective) RF pulses are evenly spaced. When phase-coherent RF pulses of the same flip angle are applied with a constant TR that is shorter than the T2 of the tissue, a dynamic equilibrium is achieved between transverse magnetization (TM) and longitudinal magnetization (LM) [3]. Once this equilibrium is reached, two types of signals are produced. The first type is post excitation signal (S+) that consists of free induction decay (FID) arising from the most recent RF pulse. The second signal is an echo reformation that occurs prior to excitation (S–) and results when residual echo is refocused at the time of the subsequent RF pulse [4].
Based on the theory of Bruder et al. [5], the simultaneous acquisition of two separate, steady state, free precession (SSFP) echoes allows the formation of two MR images with clearly different contrasts: S+ = FISP (fast imaging steady precession); and S– = PSIF (reversed FISP). DESS combines these signals into one by applying a sum of squares calculation to both echoes. The PSIF part of the sequence leads to a high T2 contrast, whereas the FISP part provides representative morphological images with a contrast dominated by the T1/T2 ratio. In principle, the different T2 weightings of both echoes (and images), allows the calculation of quantitative T2 maps with a certain functional dependence on T1 based on the chosen flip angle. Hence, the DESS sequence has the potential advantage to combine morphological and functional analysis from the same data set with high

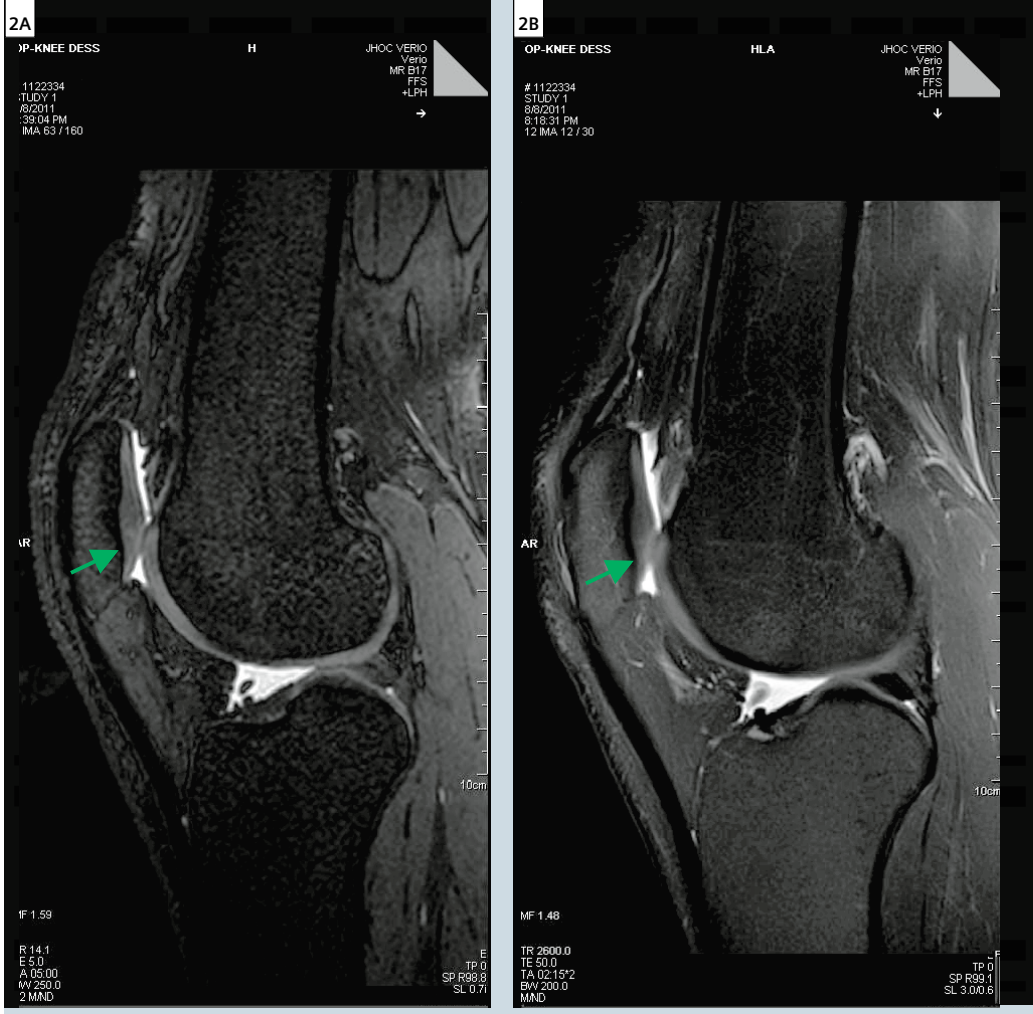

2 Sagittal MRI image of the knee. **(2A)** 3D DESS (TR/TE 14.1/5 ms) at flip angle 60°. **(2B)** 2D proton density with fat saturation (TR/TE 2600/50 ms). PD fat sat **(2B)** shows partial volume averaging of the cartilage of patella and femur, not seen in the 3D DESS sequence **(2A)** due to isotropic imaging. Also note better evaluation of menisci and ligamentum mucosum on the FSPD sequence.

DESS sequence		SNR	CNR (synovial fluid SNR – cartilage SNR)
FA 25°	Cartilage Synovial fluid	30.8 62.9	32.1
FA 45°	Cartilage Synovial fluid	24.38 86.22	61.84
FA 60°	Cartilage Synovial fluid	42.64 198.88	156.24
FA 90°	Cartilage Synovial fluid	25.7 121.22	95.5

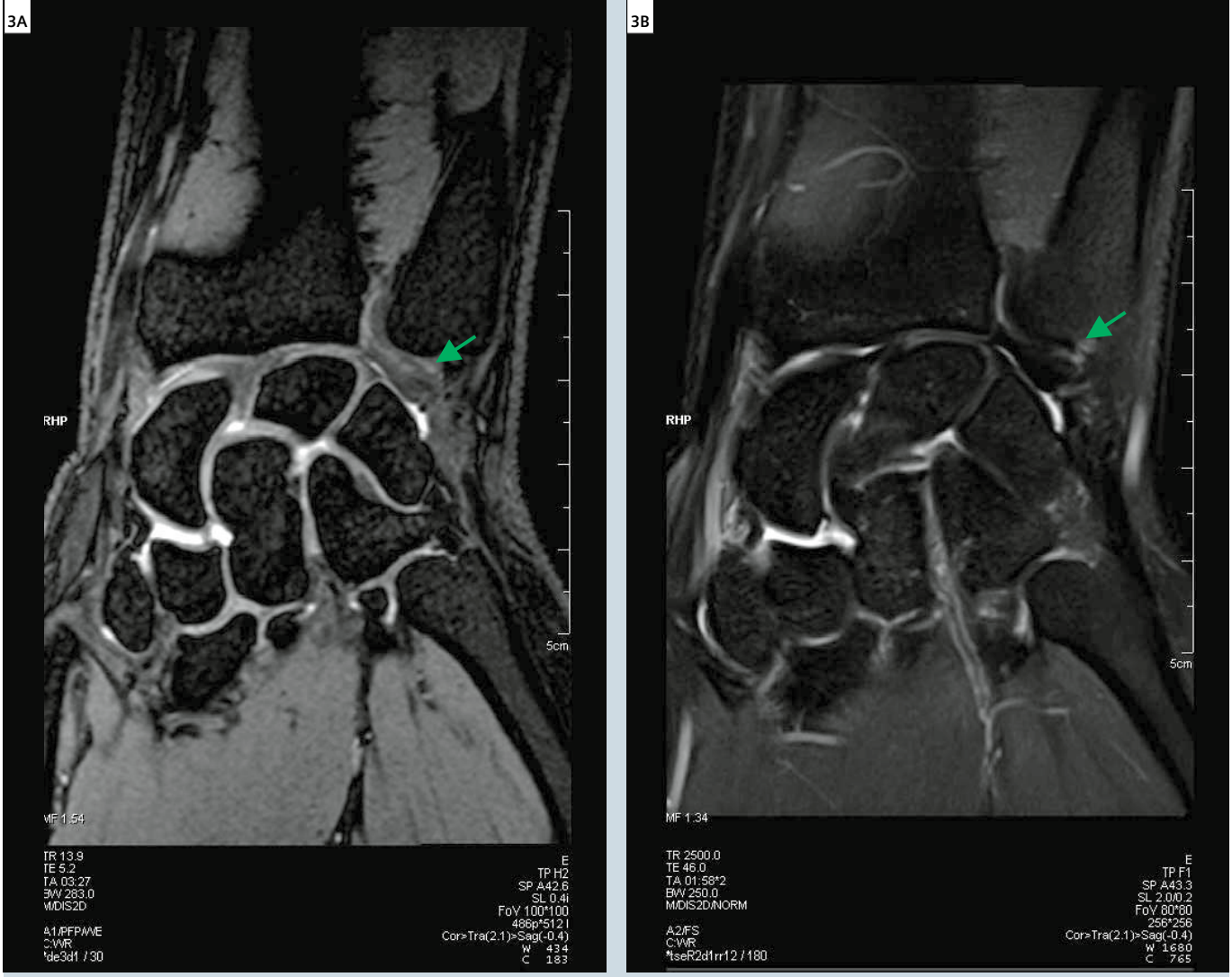

3 Coronal MRI image of the wrist joint. **(3A)** 3D DESS (TR/TE 13.9/5.2 ms) FA 30° and **(3B)** 2D proton density with fat saturation (TR/TE 2500/46 ms). The arrow marks the triangular fibro-cartilage complex of the wrist joint.

resolution in a relatively short imaging time [6]. In DESS, two or more gradient echoes are acquired. Each of these group of echoes are separated by a refocusing pulse and the combined data results in higher T2* weighting, creating high signal in cartilage and synovial fluid [7].

The most important parameter which needs to be kept in mind while acquiring a DESS is the flip angle (FA). According to Hardy et al. [8], the appropriate flip angle for the 3D DESS sequence is 60 degrees. At this point, SNR and cartilage-synovial fluid CNR is highest. In figure 1, we show the knee joint at flip angles of 25, 45, 60 and 90 degrees with the table showing SNR and CNR at various angles. At FA >60°, cartilage-synovial fluid contrast decreased along a curve obtained by the theoretical formula irrespective of TR [9].

Cartilage-synovial fluid contrast is comparable between water excited 3D DESS with a 60° FA and fat suppressed turbo spin echo proton density, which is commonly used for depicting cartilage. With both techniques, signal intensity of cartilage is intermediate and that of synovial fluid is high. Compared to 2D fat suppressed turbo spin echo proton density, slice thickness is typically thinner, suggesting the possibility that 3D DESS is capable of detecting smaller cartilage defects than the 2D technique. Lee et al. [10] have shown that fat suppressed 3D gradient echo sequences are better than 2D fat suppressed proton density sequences for differentiating grade 3 and grade 4 articular cartilage defects.

Water excited or fat suppressed 3D gradient echo imaging is recommended for measuring the exact cartilage thickness without partial volume artifacts, even though the CNR ratio between cartilage and bone marrow is relatively poor [11]. Chemical shift artifact can affect the cartilage-bone interface and fat suppression helps to reduce this. The disadvantages of 3D gradient echo imaging techniques are relatively long scan time, suboptimal contrast of other intra-articular and periarticular structures and metallic susceptibility artifacts. Fat suppressed turbo spin echo proton density is superior for other intra-articular and periarticular structures and is obtained in short imaging time, but it has the previously mentioned disadvantage of partial volume effects (Fig. 2).

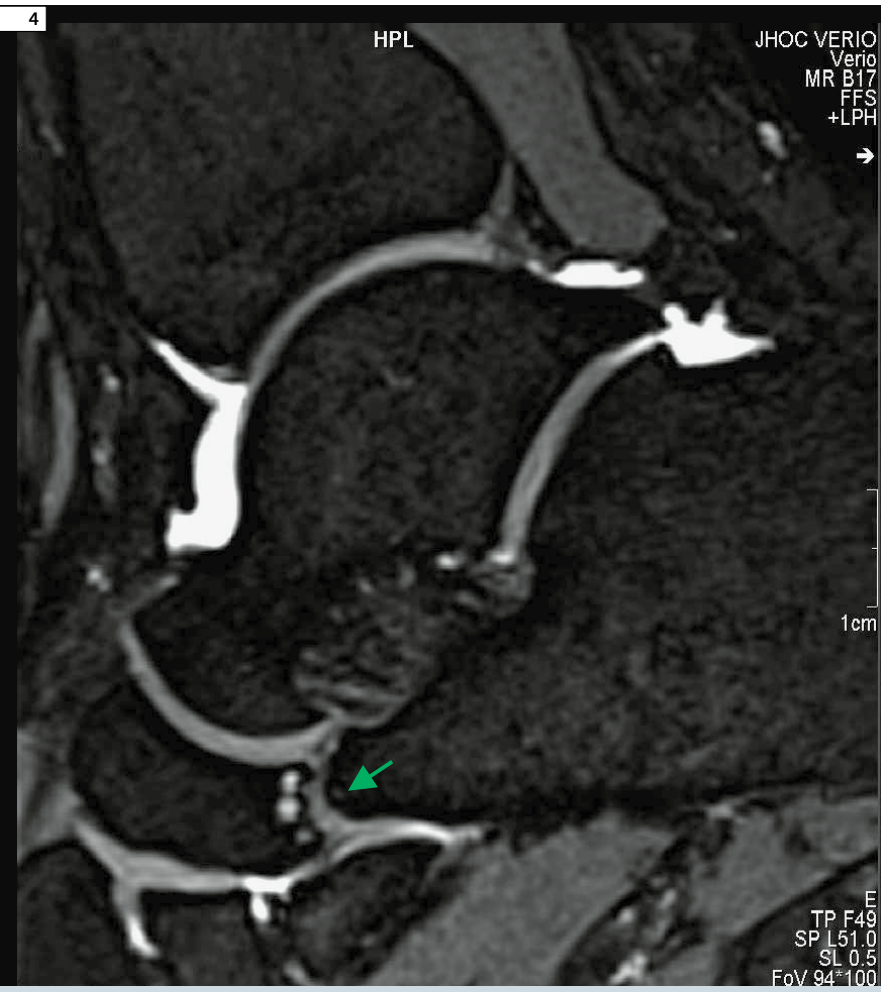

4 Sagittal 3D DESS image of the ankle joint showing the normal articular cartilage. Also note the fibrous calcaneonavicular coalition (arrow).

Clinical implications

3D DESS allows quantitative assessment of cartilage thickness and volume with good accuracy and precision [12]. In comparison with other 3D GRE techniques tested in longitudinal knee osteoarthritis trial, DESS imaging exhibited similar sensitivity to changes in knee cartilage thickness over time [13]. It can be used in other joints such as ankle and wrist; however, there has been no comparative study between DESS and other 3D sequences in imaging of small joints (Figs. 3, 4).

Summary

Cartilage imaging using the 3D DESS technique has many advantages including higher SNR, increased cartilage to fluid contrast and isotropic resolution, which helps to reduce partial volume effects.

Contact
John A. Carrino, M.D., M.P.H.
Associate Professor of Radiology and Orthopaedic Surgery
The Russel H. Morgan Department of Radiology and Radiological Science
Johns Hopkins University School of Medicine
601 North Caroline St. / JHOC 5165
Baltimore, MD
USA
carrino@jhmi.edu

References

1 Gold GE, Chen CA, Koo S, Hargreaves BA, Bangerter NK. Recent advances in MRI of articular cartilage. AJR Am J Roentgenol 2009 Sep;193(3):628-638.
2 Kornaat PR, Reeder SB, Koo S, Brittain JH, Yu H, Andriacchi TP, et al. MR imaging of articular cartilage at 1.5T and 3.0T: comparison of SPGR and SSFP sequences. Osteoarthritis Cartilage 2005 Apr;13(4):338-344.
3 Chavhan GB, Babyn PS, Jankharia BG, Cheng HM, Shroff MM. Steady-State MR Imaging Sequences: Physics, Classification, and Clinical Applications1. Radiographics July-August 2008 July-August 2008;28(4):1147-1160.
4 Gyngell ML. The application of steady-state free precession in rapid 2DFT NMR imaging: FAST and CE-FAST sequences. Magn Reson Imaging 1988 Jul-Aug;6(4):415-419.
5 Bruder H, Fischer H, Graumann R, Deimling M. A new steady-state imaging sequence for simultaneous acquisition of two MR images with clearly different contrasts. Magn Reson Med 1988 May;7(1):35-42.
6 Welsch GH, Scheffler K, Mamisch TC, Hughes T, Millington S, Deimling M, et al. Rapid estimation of cartilage T2 based on double echo at steady state (DESS) with 3 Tesla. Magn Reson Med 2009 Aug;62(2):544-549.
7 Crema MD, Roemer FW, Marra MD, Burstein D, Gold GE, Eckstein F, et al. Articular Cartilage in the Knee: Current MR Imaging Techniques and Applications in Clinical Practice and Research. Radiographics January-February 2011 January-February 2011;31(1):37-61.
8 Hardy PA, Recht MP, Piraino D, Thomasson D. Optimization of a dual echo in the steady state (DESS) free-precession sequence for imaging cartilage. J Magn Reson Imaging 1996 Mar-Apr;6(2):329-335.
9 Moriya S, Miki Y, Yokobayashi T, Ishikawa M. Three-dimensional double-echo steady-state (3D-DESS) magnetic resonance imaging of the knee: contrast optimization by adjusting flip angle. Acta Radiol 2009 Jun;50(5):507-511.
10 Lee SY, Jee WH, Kim SK, Koh IJ, Kim JM. Differentiation between grade 3 and grade 4 articular cartilage defects of the knee: fat-suppressed proton density-weighted versus fat-suppressed three-dimensional gradient-echo MRI. Acta Radiol 2010 May;51(4):455-461.
11 Gold GE, McCauley TR, Gray ML, Disler DG. Special Focus Session. Radiographics 2003 September 01;23(5):1227-1242.
12 Eckstein F, Hudelmaier M, Wirth W, Kiefer B, Jackson R, Yu J, et al. Double echo steady state magnetic resonance imaging of knee articular cartilage at 3 Tesla: a pilot study for the Osteoarthritis Initiative. Ann Rheum Dis 2006 Apr;65(4):433-441.
13 Wirth W, Nevitt M, Hellio Le Graverand MP, Benichou O, Dreher D, Davies RY, et al. Sensitivity to change of cartilage morphometry using coronal FLASH, sagittal DESS, and coronal MPR DESS protocols--comparative data from the Osteoarthritis Initiative (OAI). Osteoarthritis Cartilage 2010 Apr;18(4): 547-554.

Magnetic Resonance Elastography: Proven Indications, Challenges and Future Considerations

Sudharshan Parthasarathy, MS[1]; Bradley D. Bolster, Jr, Ph.D.[2]; Frank H. Miller, M.D.[3]

[1]Chicago Medical School, Rosalind Franklin University of Medicine, North Chicago, IL, USA
[2]Siemens Healthcare, Rochester, MN, USA
[3]Northwestern Memorial Hospital, Northwestern University Feinberg School of Medicine, Department of Radiology, Chicago, IL, USA

Introduction

Magnetic Resonance Elastography (MRE)* is a rapidly developing, non-invasive, accurate and reproducible imaging technique to assess the mechanical properties of tissue, which are dramatically affected by pathological disease processes such as inflammation, cancer and fibrosis. Physicians have long relied on the 'palpation' of tissue as a qualitative diagnostic tool in the detection of these pathologies, but this technique is limited to only superficial organs and pathologies and lacks objectivity [1]. Developed by Dr. Richard Ehman and colleagues at Mayo Clinic, MRE serves as a technique to quantitatively evaluate the propagation of mechanical shear waves through tissue. Using a modified phase-contrast magnetic resonance imaging (MRI) technique that generates spatial maps and measurements of shear wave displacement patterns called elastograms, MRE can be implemented onto a conventional MRI system with a few hardware and software modifications [2]. While the technique has been reported in a variety of organs including brain [3–7], breast [8–12], blood vessels, heart [13–15], lung [16–20], pancreas and kidneys [21, 22], MRE is developing as a safe, reliable and non-invasive alternative to liver biopsy in the detection and staging of chronic liver fibrosis [2, 23–26]. To date, MRE has also been compared to other non-invasive imaging techniques including ultrasound-based transient elastography (TE) [27], diffusion-weighed imaging (DWI) [24] and conventional MR imaging markers [28]. It may be used to monitor treatment response or disease progression. Moreover, MRE has also been investigated in helping to identify individuals with steatohepatitis in patients with non-alcoholic fatty liver [29], characterize hepatic tumors [30], assess fibrosis in pediatric populations [31] and liver transplant patients with recurrent

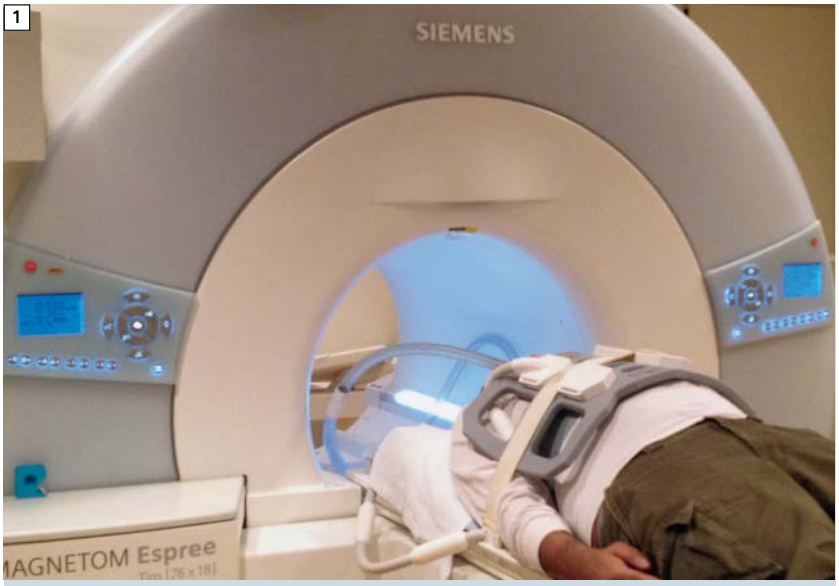

1 Photograph of an acoustical active and passive driver system for MRE with connecting tubing. The active driver is shielded from the imaging magnet and delivers vibrational energy to the passive driver at 60 Hz through the connecting tube. The passive driver is placed across the right anterior chest wall to deliver vibrations transcostally into the liver.

hepatitis C [32] and serve as a guide for MR-guided biopsies [33]. The following provides a summary of some of the proven indications, challenges and future considerations for MRE as an evolving imaging technique.

MRE protocol in our institution

MRE is well tolerated by patients, it is non-invasive and does not require contrast material. To perform hepatic MRE, mechanical waves are generated in the liver with a special MRI-compatible driver system (Resoundant Inc, Rochester, MN, USA). The system consists of an active driver, located outside the magnet room, which generates continuous low frequency vibrations. These vibrations are transmitted via a flexible tube to a drum-like passive driver (19 cm diameter, 1.5 cm thick flat and disc shaped), which is placed directly against the anterior right chest wall over the liver and held in place by an abdominal binder (Fig. 1). The propagating shear waves are imaged with a modified phase difference gradient-echo sequence which incorporates first moment nulled cyclic motion encoding gradients sensitive to through-plane motion. The Resoundant system is synchronized to these gradients via a trigger provided by the imager. The trigger time is stepped to provide a sample of the propagating wave field at four different phase offsets. The parameters of the MRE sequence are as follows: repetition time (TR) / echo time (TE), 50/22.9 msec; flip angle 25°; bandwidth 260 Hz/pixel; acquisition matrix 256 x 64; section thickness 5 mm; field-of-view (FOV) 390 x 390 mm^2. The scanning time of each trans-axial slice is 21 seconds with breath-hold. Four trans-axial slices at different anatomic levels are acquired. The resulting phase images depicting the waves in the liver for each slice are automatically processed using an inversion algorithm to generate quantitative images depicting the stiffness of the liver (elastograms) [23, 34–36].

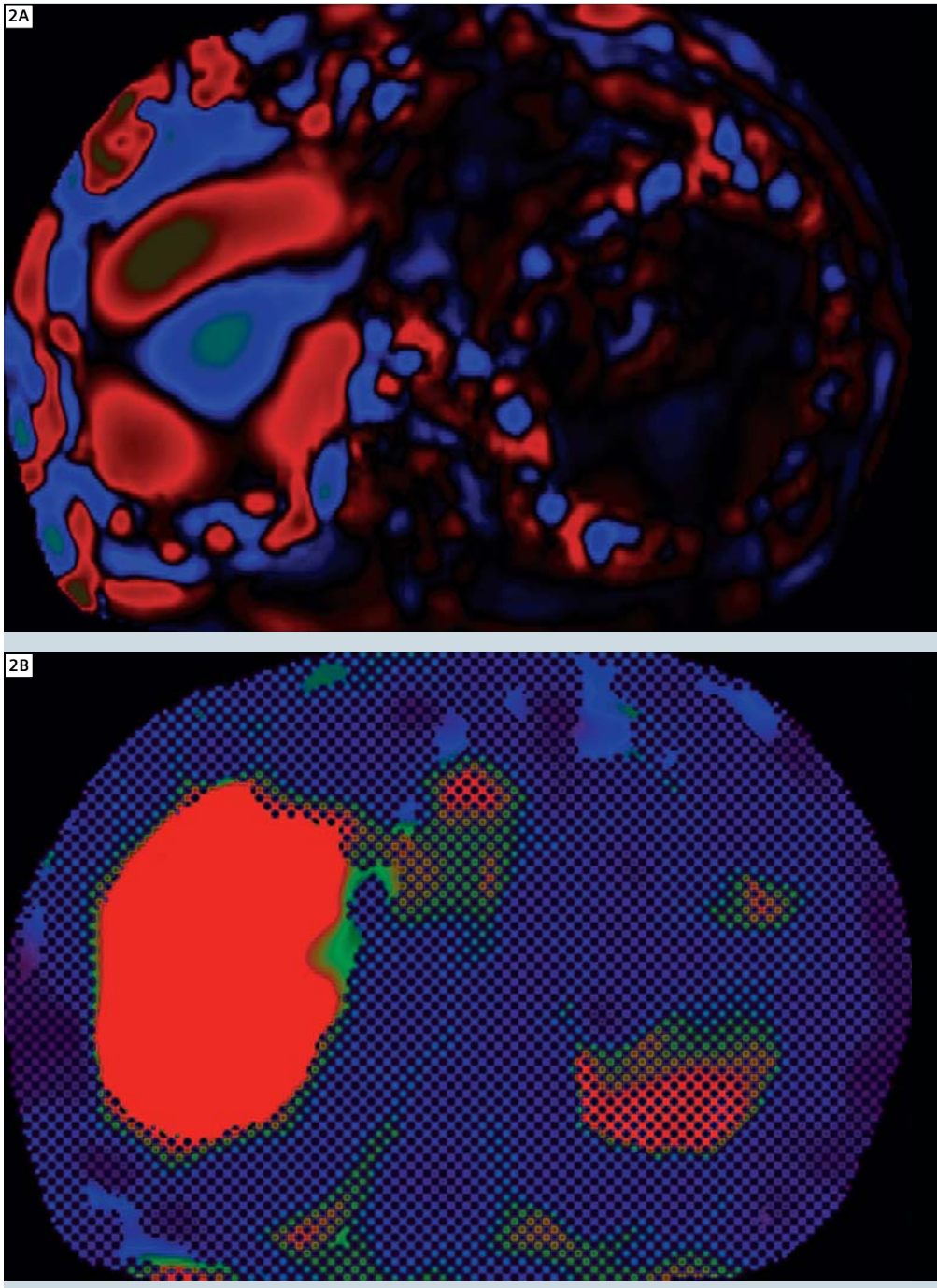

2 **(2A)** Wave image shows the propagation of the shear waves through the hepatic parenchyma. **(2B)** Color-coded elastogram shows markedly elevated stiffness values with a mean 15 kPa consistent from severe fibrosis.

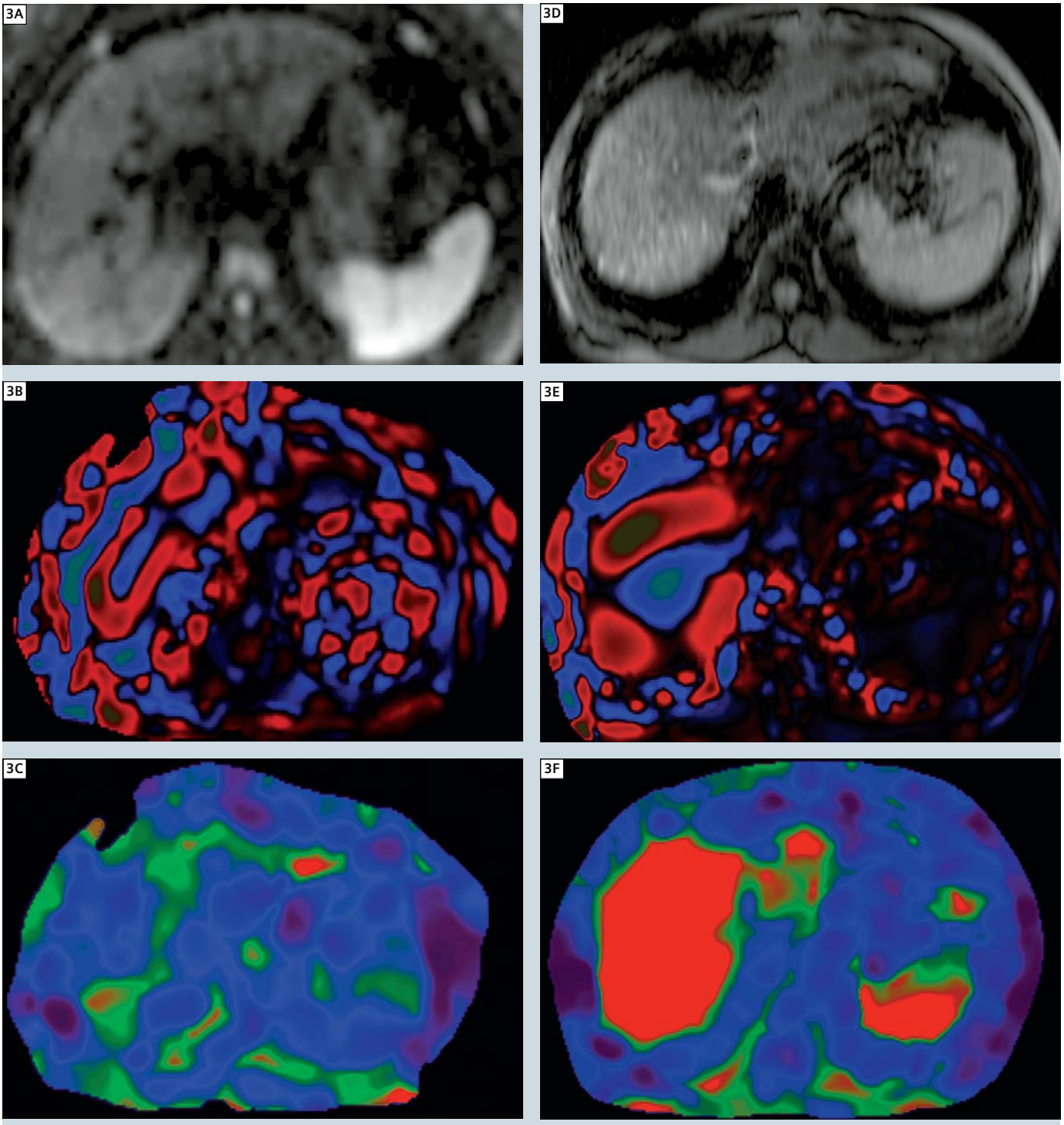

3 Example anatomic images, wave images and shear stiffness maps (elastograms) in a normal patient with elevated liver enzymes **(3A–C)** and biopsy-proven stage 4 fibrosis (F4) **(3D–F)**. Shear stiffness was measured to be 2.1 kPa in the normal patient and 14 kPa in the patient with F4 fibrosis.

MR Elastography analysis

To analyze the MRE results, regions of interest (ROI) are placed on the MR elastograms. When placing an ROI, care is taken to avoid bile ducts and large vessels within the liver, motion artifacts, the region immediately below the driver, and the left lobe of liver (which is prone to artifacts due to transmitted cardiac motion). For the measurement of shear stiffness using MRE, the ROIs are first visually transposed onto the wave images to ensure that they were placed in regions with adequate wave quality. A region is determined to have adequate wave quality if the propagating waves had both good amplitude and the presence of a clear dominant propagation direction. Subsequently, the ROI locations are visually transposed onto the quantitative elastogram image and mean stiffness values (in kilopascals, kPa) are calculated (Figs. 2A, B).

MRE in the detection and staging of liver fibrosis

Liver biopsy is currently the gold standard for detecting fibrosis and cirrhosis. As an invasive procedure, it has an increased risk for potential complications such as procedural pain, bleeding, pneumothorax, biliary tree puncture and death (approximately 1 in 10,000–12,000) [37]. From a clinical perspective, one of the greatest limitations with biopsy is a significant sampling error of up to 14.5% and 25% when determining presence or absence of cirrhosis [38]. Based on recent studies, MRE is receiving attention as a non-invasive alternative. Thus far, MRE has shown that it can be an accurate method for both the detection (Figs. 3A–F) and staging (Figs. 4A–D) of hepatic fibrosis [2, 23–26]. Receiver operating characteristic (ROC) analysis by Yin et al. comparing 50 patients with biopsy-proven liver disease and 35 healthy controls showed 98% sensitivity and 99% specificity for the detection of liver fibrosis with a shear stiffness cutoff value of 2.93 kPa [26]. ROC analysis also showed that MRE was able to discriminate between patients that had moderate to severe fibrosis (F2-F4) and those that had mild fibrosis based on the METAVIR histopathological staging system (F0-F1) [26]. The ability to distinguish moderate to severe fibrosis from mild fibrosis is clinically significant, as treatment is advised for a score of F2 of greater by the American Association for the study of liver diseases [39]. More recent studies by Wang et al. [24], Rustogi et al. [28], Kim et al. [40] and Huwart et al. [25] have demonstrated comparable sensitivity and specificity ranges (Table 1).

MRE versus other non-invasive assessments of liver fibrosis

Studies have also begun to compare MRE to other non-invasive techniques in the detection and staging of liver fibrosis. One study of 141 patients with chronic liver disease comparing MRE and ultrasound transient elastography (TE) showed that MRE had a higher technical success rate (94%) than TE (84%) [25]. In addition, areas under the curve (AUC) in ROC analysis for MRE were significantly larger than those of TE, aspartate aminotransferase to platelets ratio index (APRI), and the combination of TE and APRI [25]. Significantly, MRE measurements did not seem to be influenced by the presence of obesity or ascites, which cause TE to fail, or steatohepatitis [41]. Furthermore, MRE evaluates a global view of the liver, whereas TE looks at only a 1 cm x 4 cm area over the right liver edge. While TE has also demonstrated excellent sensitivity and specificity for the detection of fibrosis compared to biopsy, it has reduced values of 70% and 80% , respectively, compared to MRE (86% and 85% respectively) [26] in the detection of intermediate stages of fibrosis (F2-F4) [42].

More recently, the diagnostic performance of MRE was compared to diffusion-weighted imaging (DWI). ROC analysis showed that MRE had greater accuracy in assessing the severity of fibrosis compared with DWI using histopathology as a reference standard. In a group of 76 patients [32], MRE had greater predictive ability in distinguishing the stages of liver fibrosis than DWI [24]. Specifically, MRE showed greater capability than DWI in discriminating stages F2 or greater, F3 or greater and F4 as shown as significant differences in AUC analysis. While stiffness values on MRE increased in relation to increasing severity of fibrosis, no consistent relationship between apparent diffusion coefficient (ADC) values and stage of fibrosis was shown.

Another recent study has compared the diagnostic accuracy of MRE and conventional anatomic MR imaging features in the diagnosis of severe hepatic fibrosis and cirrhosis [28]. Three readers independently assessed 72 patients with liver biopsy for conventional imaging features such as caudate to right lobe ratios and expanded gallbladder fossa sign compared with shear stiffness values from MR elastograms. Sensitivity, specificity and diagnostic accuracy was calculated and intra-class correlation coefficient was used to assess inter-reader reproducibility. MRE proved to be a more accurate and reproducible technique compared to conventional imaging features with a higher intra-class correlation coefficient and better diagnostic accuracy.

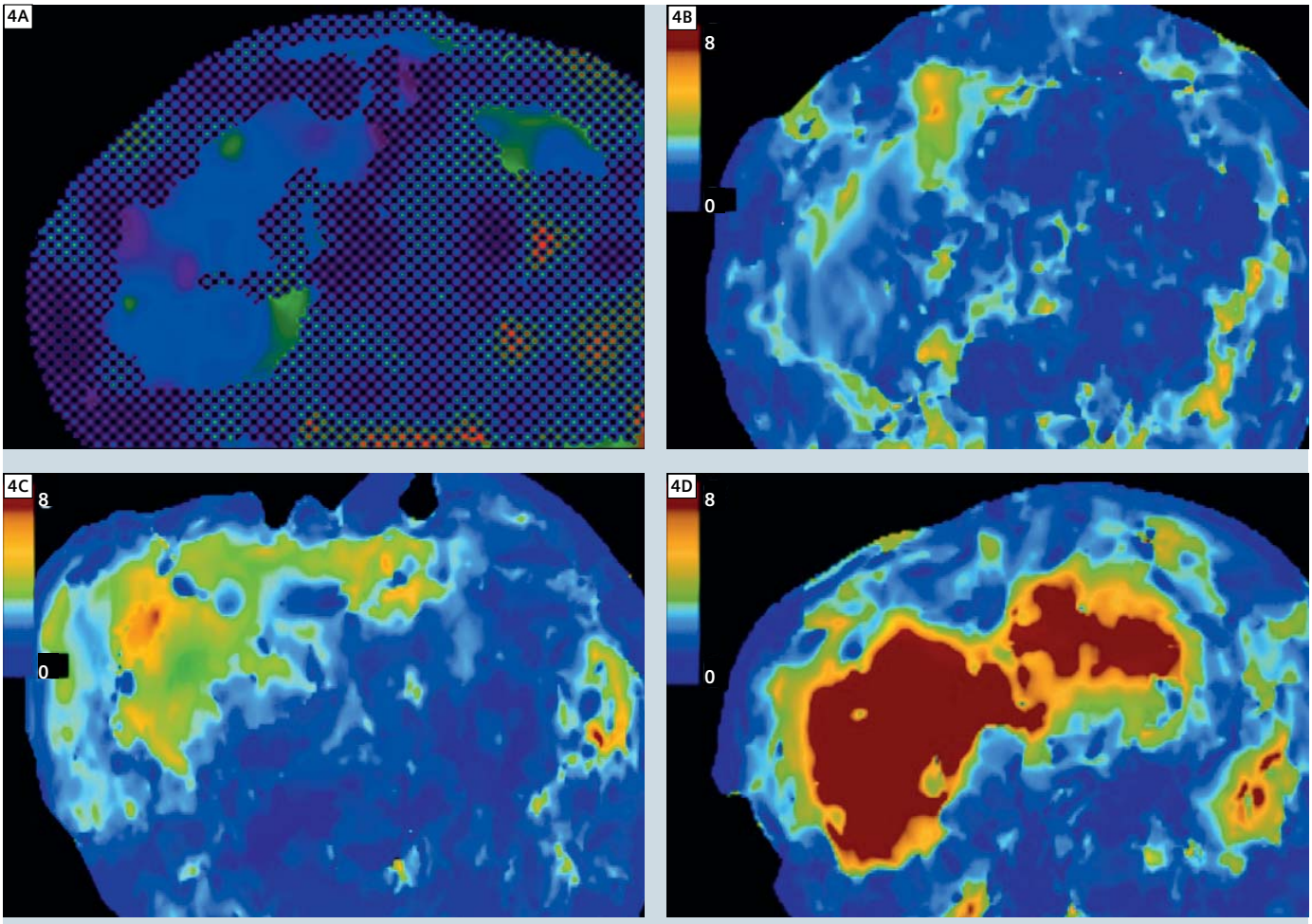

4 Liver stiffness values (kPa) represented through elastograms increased in parallel with the degree of fibrosis (stages F0-F4). **(4A)** Shear stiffness was measured to be 2.1 kPa in normal liver tissue, **(4B)** 2.9 kPa in fibrosis stage F1, **(4C)** 4.1 kPa in fibrosis stage F2, and **(4D)** 10.5 kPa in fibrosis stage F4.

MRE for the early detection of non-alcoholic steatohepatitis (NASH)

Associated with obesity and type 2 diabetes mellitus, non-alcoholic fatty liver disease (NAFLD) is a clinical condition now estimated to affect 1 in 3 adults in the US [43]. Up to 25% of NAFLD patients develop non-alcoholic steatohepatitis (NASH), which can progress to cirrhosis in susceptible individuals [44]. Since a diagnosis of NASH currently requires an invasive liver biopsy to help detect and stage liver cell injury, MRE has been investigated as an alternative technique that could help in early detection. Using a rat model of fatty liver disease, Salameh et al. showed that MRE could help to discriminate the presence of steatohepatitis from simple steotosis before the onset of fibrosis [45]. This led to a retrospective study of 58 NAFLD patients to investigate the variation of liver stiffness in patients ranging from simple steatosis to NASH. MRE was able to show that NAFLD patients with NASH but no fibrosis had higher hepatic stiffness measurements than patients with simple steatosis [29] (Fig. 4).

MRE in the characterization of liver tumors

While it is well known that cirrhosis is the strongest predisposing factor for the development of hepatocellular carcinoma (HCC), the detection of small tumors presents the greatest challenge to imaging in HCC [46]. The application of MRE to HCC may be a promising tool in the characterization of hepatic tumors. A preliminary investigation has shown that malignant liver tumors have a significantly greater mean shear stiffness than benign liver tumors as well as normal liver tissue parenchyma by estab-

Table 1: Selected diagnostic ranges of MRE-assessed hepatic fibrosis in patients with chronic liver disease from various studies.

Reference	N	Cutoff	Sensitivity	Specificity	Liver Stiffness, kPa
Yin et al.	85	F0-1:F2-4	86	85	4.9
		F0-2:F3-4	78	96	6.7
Huwart et al.	88	F0-1:F2-4	98	100	2.5
		F0-2:F3-4	95	100	3.1
Huwart et al.	133	F0-1:F2-4	100	91	2.5
		F0-2:F3-4	91	97	3.1
Kim et al.	55	F0-1:F2-4	89	87	3.1
Wang et al.	76	F0-1:F:2-4	91	97	5.4
		F0-2:F3-F4	92	95	5.9

lishing a cutoff value of 5 kPa [30]. Since the technique can be readily combined as a complement to conventional MRI of the abdomen, it shows potential in further characterization and early detection of liver tumors [47]. A potential limitation may be in the cirrhotic liver where the background liver may be as stiff as the HCC but further investigation will be required.

MRE in the assessment of fibrosis in liver transplant recipients

MRE has also been compared to various biomarkers to assess efficacy in the staging of fibrosis in liver transplant recipients with recurrent hepatitis C (HCV) with HCC [32]. While limited by graft complications, MRE and serum panels like FIBROSpectII have high sensitivity in detecting fibrosis from recurrent HCV, but are limited by poor specificity and positive predictive value (PPV). MRE could avert the need for liver biopsy, as values below the MRE and FIBROSpectII cutoffs strongly suggested the absence of fibrosis in transplant recipients with recurrent HCV.

Challenges / difficulties with MRE

Future challenges and difficulties with MRE lie mainly in further technical development. The widespread use of MRE relies on the same technology and infrastructure as conventional MR imaging, and so claustrophobic or very obese patients and those with contraindications to MRI will be excluded from investigation due to an inability to enter the scanner. Other challenges include technical failure in patients with hemochromatosis and iron overload conditions because of signal-to-noise limitations [25]. Falsely elevated shear stiffness values have been reported in regions just below the passive driver used to generate shear waves. Liver stiffness can be increased without the presence of fibrosis in pathological processes such as inflammation, hepatic congestion, and vascular abnormalities [24, 28]. Since MRE is a relatively new technique, improved driver technologies [48] and refined imaging sequences [49] are currently under development to produce more accurate shear stiffness values and improve signal-to-noise ratios. Moreover, in its bid to replace liver biopsy as a non-invasive technique in the staging of detection of liver fibrosis, MRE must be evaluated for cost-effectiveness versus other non-invasive techniques. While researchers have proposed diagnostic algorithms to help define how to stage fibrosis incorporating these techniques, these algorithms are yet to be externally validated in independent populations.

Conclusions and future outlook

MRE has received considerable interest as a quantitative technique to assess the same information evaluated pathology by the more qualitative clinical tool of palpation. As a non-invasive, accurate and reproducible technique, it is receiving consideration as a viable alternative to liver biopsy for the diagnosis and staging of hepatic fibrosis. Since many applications of MRE are currently under investigation in the liver, heart, brain and kidney, it is likely that MRE will continue to elucidate invaluable information about tissue structure and function. As the field continues to evolve rapidly, this information should help to guide clinicians and researchers improve clinical outcomes and management.

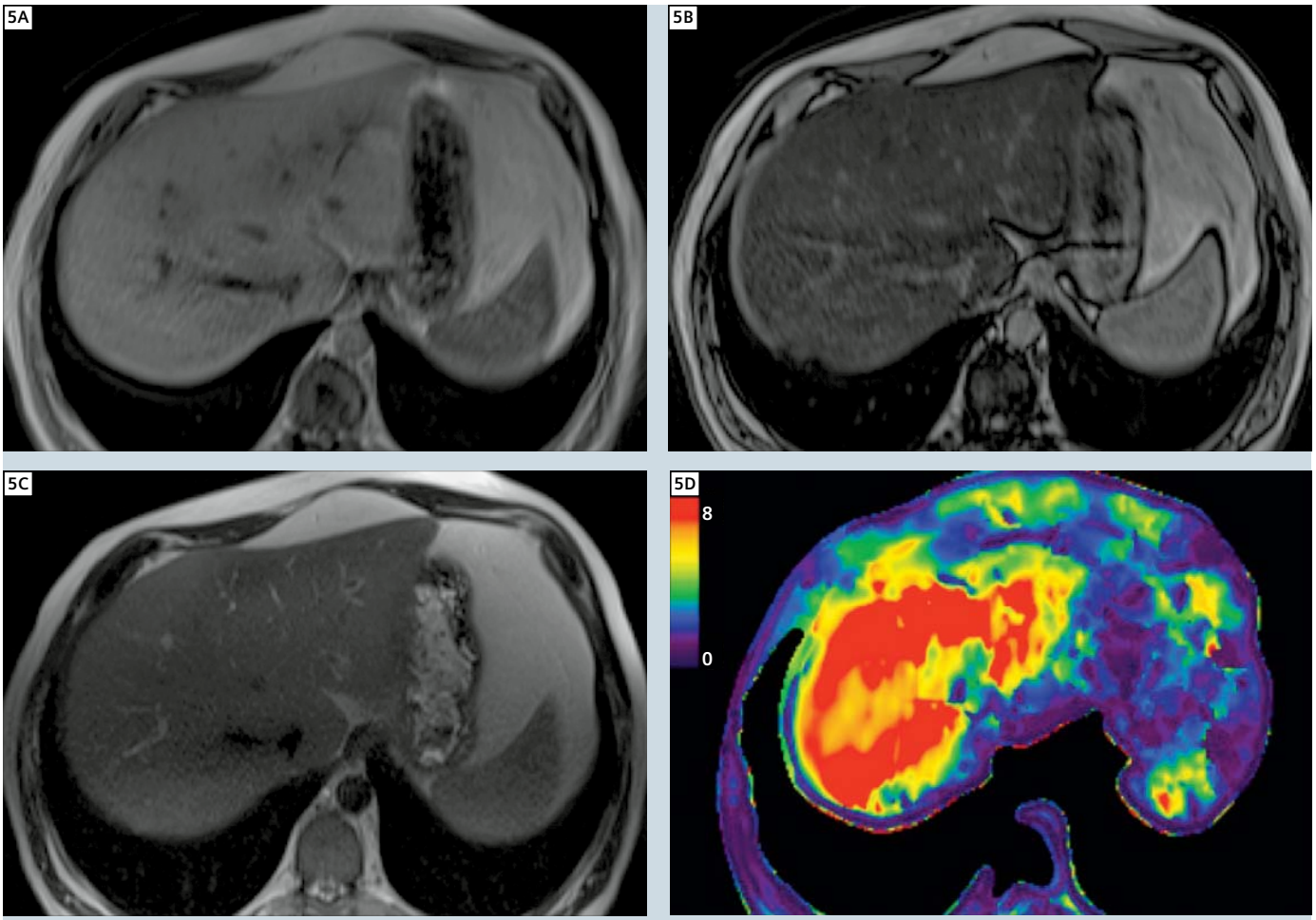

5 **(5A)** In-phase (top left) and **(5B)** out-phase (top right) images show significant SI decrease, suggesting a diagnosis of non-alcoholic steatohepatitis (NASH). **(5C)** Liver cirrhosis cannot be identified based on routine T2-weighted image (bottom left). **(5D)** MRE elastogram (bottom right) shows shear stiffness of 7.51 kPa, suggesting fibrosis stage F4.

Acknowledgement

The authors thank Bradley Bolster, Saurabh Shah, and Sven Zuehlsdorff of Siemens Healthcare and Dr. Richard Ehman of Mayo Clinic for their development of the MR technology used in this study and for the support of our program and reviewing this article. We would also like to acknowledge the hard work of Charles Fasanati RT and Judy Wood RT for the program's success.

References

1 Mariappan YK, Glaser KJ, Ehman RL. Magnetic resonance elastography: a review. Clin Anat. 2010;23(5):497-511.
2 Yin M, Chen J, Glaser KJ, Talwalkar JA, Ehman RL. Abdominal magnetic resonance elastography. Topics in magnetic resonance imaging : TMRI. 2009;20(2):79-87.
3 Kruse SA, Rose GH, Glaser KJ, et al. Magnetic resonance elastography of the brain. NeuroImage. 2008;39(1):231-7.
4 Green MA, Bilston LE, Sinkus R. In vivo brain viscoelastic properties measured by magnetic resonance elastography. NMR in biomedicine. 2008;21(7):755-64.
5 Sack I, Beierbach B, Hamhaber U, Klatt D, Braun J. Non-invasive measurement of brain viscoelasticity using magnetic resonance elastography. NMR in biomedicine. 2008;21(3):265-71.
6 Streitberger KJ, Wiener E, Hoffmann J, et al. In vivo viscoelastic properties of the brain in normal pressure hydrocephalus. NMR in biomedicine. 2010.
7 Streitberger KJ, Sack I, Krefting D, et al. Brain viscoelasticity alteration in chronic-progressive multiple sclerosis. PloS one. 2012;7(1):e29888.
8 McKnight AL, Kugel JL, Rossman PJ, Manduca A, Hartmann LC, Ehman RL. MR elastography of breast cancer: preliminary results. AJR American journal of roentgenology. 2002;178(6):1411-7.
9 Van Houten EE, Doyley MM, Kennedy FE, Weaver JB, Paulsen KD. Initial in vivo experience with steady-state subzone-based MR elastography of the human breast. JMRI. 2003;17(1):72-85.
10 Sinkus R, Siegmann K, Xydeas T, Tanter M, Claussen C, Fink M. MR elastography of breast lesions: understanding the solid/liquid duality

can improve the specificity of contrast-enhanced MR mammography. Magnetic resonance in medicine. 2007;58(6):1135-44.
11 Doyley MM, Perreard I, Patterson AJ, Weaver JB, Paulsen KM. The performance of steady-state harmonic magnetic resonance elastography when applied to viscoelastic materials. Medical physics. 2010;37(8):3970-9.
12 Plewes DB, Bishop J, Samani A, Sciarretta J. Visualization and quantification of breast cancer biomechanical properties with magnetic resonance elastography. Physics in medicine and biology. 2000;45(6):1591-610.
13 Kolipaka A, McGee KP, Manduca A, Anavekar N, Ehman RL, Araoz PA. In vivo assessment of MR elastography-derived effective end-diastolic myocardial stiffness under different loading conditions. JMRI. 2011;33(5):1224-8.
14 Elgeti T, Laule M, Kaufels N, et al. Cardiac MR elastography: comparison with left ventricular pressure measurement. Journal of cardiovascular magnetic resonance : official journal of the Society for Cardiovascular Magnetic Resonance. 2009;11:44.
15 Sack I, Rump J, Elgeti T, Samani A, Braun J. MR elastography of the human heart: noninvasive assessment of myocardial elasticity changes by shear wave amplitude variations. Magnetic resonance in medicine. 2009;61(3):668-77.
16 Mariappan YK, Kolipaka A, Manduca A, et al. Magnetic resonance elastography of the lung parenchyma in an in situ porcine model with a noninvasive mechanical driver: correlation of shear stiffness with trans-respiratory system pressures. Magnetic resonance in medicine. 2012;67(1):210-7.
17 Mariappan YK, Glaser KJ, Hubmayr RD, Manduca A, Ehman RL, McGee KP. MR elastography of human lung parenchyma: technical development, theoretical modeling and in vivo validation. JMRI. 2011;33(6):1351-61.
18 McGee KP, Hubmayr RD, Levin D, Ehman RL. Feasibility of quantifying the mechanical properties of lung parenchyma in a small-animal model using (1)H magnetic resonance elastography (MRE). JMRI. 2009;29(4):838-45.
19 McGee KP, Hubmayr RD, Ehman RL. MR elastography of the lung with hyperpolarized 3He. Magnetic resonance in medicine. 2008;59(1):14-8.
20 Goss BC, McGee KP, Ehman EC, Manduca A, Ehman RL. Magnetic resonance elastography of the lung: technical feasibility. Magnetic resonance in medicine. 2006;56(5):1060-6.
21 Warner L, Yin M, Glaser KJ, et al. Noninvasive In vivo assessment of renal tissue elasticity during graded renal ischemia using MR elastography. Investigative radiology. 2011;46(8):509-14.
22 Shah NS, Kruse SA, Lager DJ, et al. Evaluation of renal parenchymal disease in a rat model with magnetic resonance elastography. Magnetic resonance in medicine. 2004;52(1):56-64.
23 Rouviere O, Yin M, Dresner MA, et al. MR elastography of the liver: preliminary results. Radiology. 2006;240(2):440-8.
24 Wang Y, Ganger DR, Levitsky J, et al. Assessment of chronic hepatitis and fibrosis: comparison of MR elastography and diffusion-weighted imaging. AJR American journal of roentgenology. 2011;196(3):553-61.
25 Huwart L, Sempoux C, Vicaut E, et al. Magnetic resonance elastography for the noninvasive staging of liver fibrosis. Gastroenterology. 2008;135(1):32-40.
26 Yin M, Talwalkar JA, Glaser KJ, et al. Assessment of hepatic fibrosis with magnetic resonance elastography. Clinical gastroenterology and hepatology : the official clinical practice journal of the American Gastroenterological Association. 2007;5(10):1207-13 e2.
27 Huwart L, van Beers BE. MR elastography. Gastroenterologie clinique et biologique. 2008;32(6 Suppl 1):68-72.
28 Rustogi R, Horowitz J, Harmath C, et al. Accuracy of MR elastography and anatomic MR imaging features in the diagnosis of severe hepatic fibrosis and cirrhosis. JMRI. 2012.
29 Chen J, Talwalkar JA, Yin M, Glaser KJ, Sanderson SO, Ehman RL. Early detection of nonalcoholic steatohepatitis in patients with nonalcoholic fatty liver disease by using MR elastography. Radiology. 2011;259(3):749-56.
30 Venkatesh SK, Yin M, Glockner JF, et al. MR elastography of liver tumors: preliminary results. AJR American journal of roentgenology. 2008;190(6):1534-40.
31 Binkovitz LA, El-Youssef M, Glaser KJ, Yin M, Binkovitz AK, Ehman RL. Pediatric MR elastography of hepatic fibrosis: principles, technique and early clinical experience. Pediatric radiology. 2011.
32 Lee VS, Miller FH, Omary RA, et al. Magnetic resonance elastography and biomarkers to assess fibrosis from recurrent hepatitis C in liver transplant recipients. Transplantation. 2011;92(5):581-6.
33 Perumpail R, Jin N, Wang Y, et al. Real-time MR-guided Biopsies to Target Focal Hepatic Fibrosis Detected with Magnetic Resonance Elastography. International Society for Magnetic Resonance in Medicine; 2010.
34 Manduca A, Oliphant TE, Dresner MA, et al. Magnetic resonance elastography: non-invasive mapping of tissue elasticity. Medical image analysis. 2001;5(4):237-54.
35 Muthupillai R, Lomas DJ, Rossman PJ, Greenleaf JF, Manduca A, Ehman RL. Magnetic resonance elastography by direct visualization of propagating acoustic strain waves. Science. 1995;269(5232):1854-7.
36 Taouli B, Ehman RL, Reeder SB. Advanced MRI methods for assessment of chronic liver disease. AJR American journal of roentgenology. 2009;193(1):14-27.
37 Carey E, Carey WD. Noninvasive tests for liver disease, fibrosis, and cirrhosis: Is liver biopsy obsolete? Cleveland Clinic journal of medicine. 2010;77(8):519-27.
38 Regev A, Berho M, Jeffers LJ, et al. Sampling error and intraobserver variation in liver biopsy in patients with chronic HCV infection. The American journal of gastroenterology. 2002;97(10):2614-8.
39 Strader DB, Wright T, Thomas DL, Seeff LB. Diagnosis, management, and treatment of hepatitis C. Hepatology. 2004;39(4):1147-71.
40 Kim BH, Lee JM, Lee YJ, et al. MR elastography for noninvasive assessment of hepatic fibrosis: experience from a tertiary center in Asia. JMRI. 2011;34(5):1110-6.
41 Talwalkar JA. Elastography for detecting hepatic fibrosis: options and considerations. Gastroenterology. 2008;135(1):299-302.
42 Talwalkar JA, Kurtz DM, Schoenleber SJ, West CP, Montori VM. Ultrasound-based transient elastography for the detection of hepatic fibrosis: systematic review and meta-analysis. Clinical gastroenterology and hepatology. 2007;5(10):1214-20.
43 Browning JD, Szczepaniak LS, Dobbins R, et al. Prevalence of hepatic steatosis in an urban population in the United States: impact of ethnicity. Hepatology. 2004;40(6):1387-95.
44 Fassio E, Alvarez E, Dominguez N, Landeira G, Longo C. Natural history of nonalcoholic steatohepatitis: a longitudinal study of repeat liver biopsies. Hepatology. 2004;40(4):820-6.
45 Salameh N, Larrat B, Abarca-Quinones J, et al. Early detection of steatohepatitis in fatty rat liver by using MR elastography. Radiology. 2009;253(1):90-7.
46 Willatt JM, Hussain HK, Adusumilli S, Marrero JA. MR Imaging of hepatocellular carcinoma in the cirrhotic liver: challenges and controversies. Radiology. 2008;247(2):311-30.
47 Lee JM, Choi BI. Hepatocellular nodules in liver cirrhosis: MR evaluation. Abdominal imaging. 2011;36(3):282-9.
48 Mariappan YK, Rossman PJ, Glaser KJ, Manduca A, Ehman RL. Magnetic resonance elastography with a phased-array acoustic driver system. Magnetic resonance in medicine. 2009;61(3):678-85.
49 Faria SC, Ganesan K, Mwangi I, et al. MR imaging of liver fibrosis: current state of the art. Radiographics. 2009;29(6):1615-35.

Contact
Frank H. Miller, M.D.
Professor of Radiology
Chief, Body Imaging Section
Medical Director MR Imaging
Department of Radiology
Northwestern University
Feinberg School of Medicine
676 N. St. Clair, Suite 800
Chicago, Illinois 60611
USA
Phone: +001 312-695-3775
Fax: +001 312-695-5645
fmiller@northwestern.edu

Controlled Aliasing in Parallel Imaging Results in Higher Acceleration (CAIPIRINHA)

Felix Breuer[1]; Martin Blaimer[1]; Mark Griswold[2]; Peter Jakob[1,3]

[1]Research Center, Magnetic Resonance Bavaria e.V (MRB), Würzburg, Germany
[2]Case Center for Imaging Research, Case Western Reserve University and University Hospitals, Cleveland, OH, USA
[3]Dept. of Experimental Physics 5, University of Würzburg, Würzburg, Germany

1

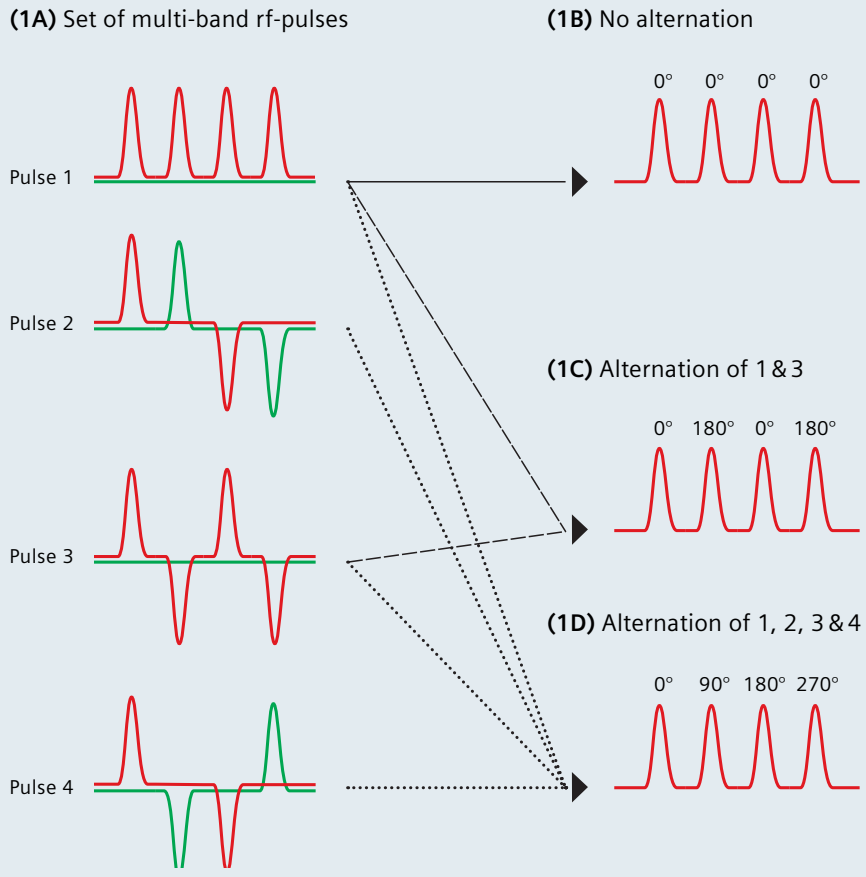

1 Multi-slice excitation with alternating rf-pulses taken from **(1A)** a set of 4 rf-pulses with different phase modulations (pulse 1 to 4) allows one to provide the individual slices with well defined phase-cycles along the phase encoding direction. The real part (red) and imaginary part (green) of the pulses are plotted. **(1B)** Using only one pulse (e.g. pulse 1) no phase-cycle is provided (0°, 0°, 0°, 0°). **(1C)** Alternation between pulses 1 and 3 yield no phase-cycle for slice 1 and 3 and an 180° phase cycle for slices 2 and 4 (0, 180°, 0, 180°). **(1D)** Alternation of all 4 pulses allows one to provide all the individual slices with an individual phase-cycle (0, 90°, 180°, 270°).

Introduction

Image acquisition time is one of the most important considerations for clinical magnetic resonance imaging (MRI). The development of multi-coil receiver hardware as well as dedicated parallel MRI (pMRI) reconstruction methods such as SENSE [1] and GRAPPA [2] allowed for significant decrease of acquisition times in almost all clinical applications. Thus, today, pMRI plays a substantial role in everyday clinical routine.

pMRI operates by reducing the amount of data necessary to form an image. In the Cartesian case, this is usually accomplished by uniformly undersampling the k-space (e.g. skipping every other phase-encoding line) resulting in so-called 'aliasing artifacts' in the image domain. pMRI reconstruction methods seek to compensate the lack of spatial encoding by taking into account the spatial sensitivity information, provided by a multi-coil receiver array. Unfortunately, the pMRI concept is intrinsically associated with a signal-to-noise (SNR) loss compared to a fully encoded image. The SNR is

a) reduced by the square root of the acceleration factor, simply due to the fact that less data is acquired, and

b) by the so-called g-factor, depending strongly on the encoding capabilities of the underlying receiver array.

Thus, pMRI is often limited to applications with sufficiently high base SNR, such as volumetric imaging methods. With the newest generation of MR scanners

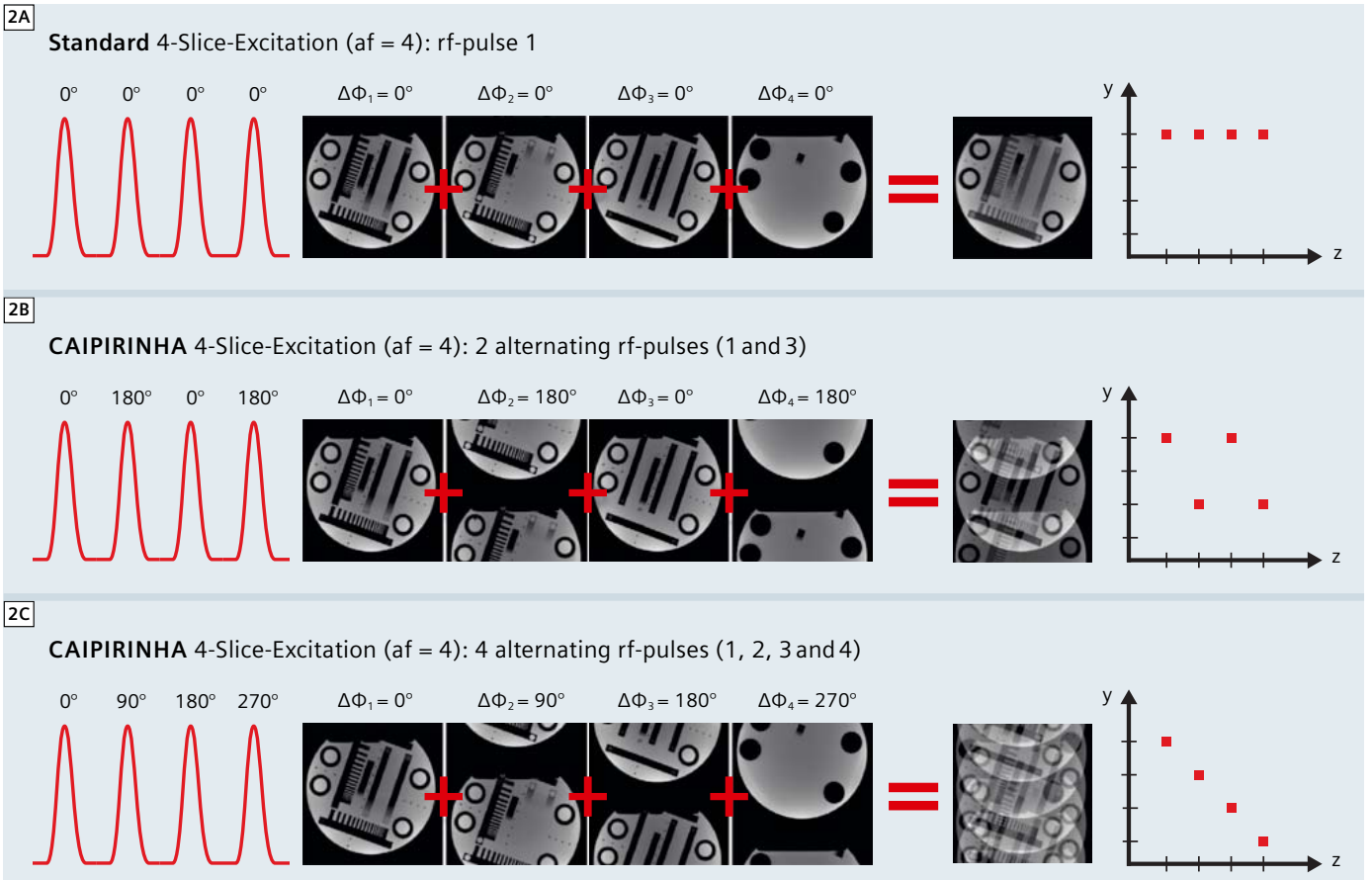

2 **(2A)** Standard 4 times accelerated simultaneous 4-slice-experiment. The same pulse is applied for subsequent excitations (phase encoding lines), resulting in all 4 slices projected onto each other. **(2B)** CAIPIRINHA 4-times accelerated simultaneous 4-slice-experiment alternating between e.g. pulses 1 and 3 for subsequent excitations, thereby providing slice 2 and slice 4 with a 180° phase cycle. According to the Fourier Shift Theorem, slices 2 and 4 appear shifted by half of the FOV with respect to slices 1 and 3 in the resulting folded image. **(2C)** CAIPIRINHA 4-times accelerated simultaneous 4-slice-experiment alternating between pulse 1, 2, 3 and 4 for subsequent excitations, thereby providing each slice with a different phase-cycle (0°, 90°,180°, 270°). Each slice appears shifted by FOV/4 with respect to their adjacent slice in the folded image.

providing up to 128 independent receiver channels, further scan time reductions are potentially achievable. However, in conventional 2D clinical imaging, parallel imaging today is still restricted to relatively moderate scan time reductions (acceleration factors of 2 to 3) due to intrinsic limitations in the coil sensitivity variations along one phase encoding direction (1D parallel imaging). In 3D and simultaneous multi-slice imaging, parallel encoding can be carried out in two encoding directions (2D parallel imaging), thereby employing the sensitivity variations in both directions, as has been demonstrated in, for example, 2D SENSE [3] and MS SENSE [4]. This concept has been shown to significantly improve the reconstruction conditions, allowing for higher accelerations of the acquisition (>3). However, both techniques require sufficient sensitivity variations in two encoding directions for successful image reconstruction and therefore strongly depend on the underlying coil geometry. As mentioned above, spatial encoding with a receiver array is associated with a certain noise amplification known as 'g-factor noise'. Quantitative g-factor estimation methods have been derived for SENSE [1] and GRAPPA reconstructions [5] and serve as a quality metric for pMRI reconstructions. One important approach to reduce this g-factor noise for a given application is the optimization of the receiver array geometry (e.g. number of coils, coil arrangement) towards the application at hand. However, hardware limitations, the diversity of patient weight and size, the need for flexibility regarding a wider range of applications, as well as sequence or protocol specific considerations, hamper the viability.

The **CAIPRINHA** concept (**C**ontrolled **A**liasing **I**n **P**arallel **I**maging **R**esults **IN** **H**igher **A**cceleration) allows one to partially overcome these requirements and limitations by modifying the aliasing conditions in a well defined manner. This is done already during the data acquisition by modifying the rf-excitation or gradient encoding scheme in

3

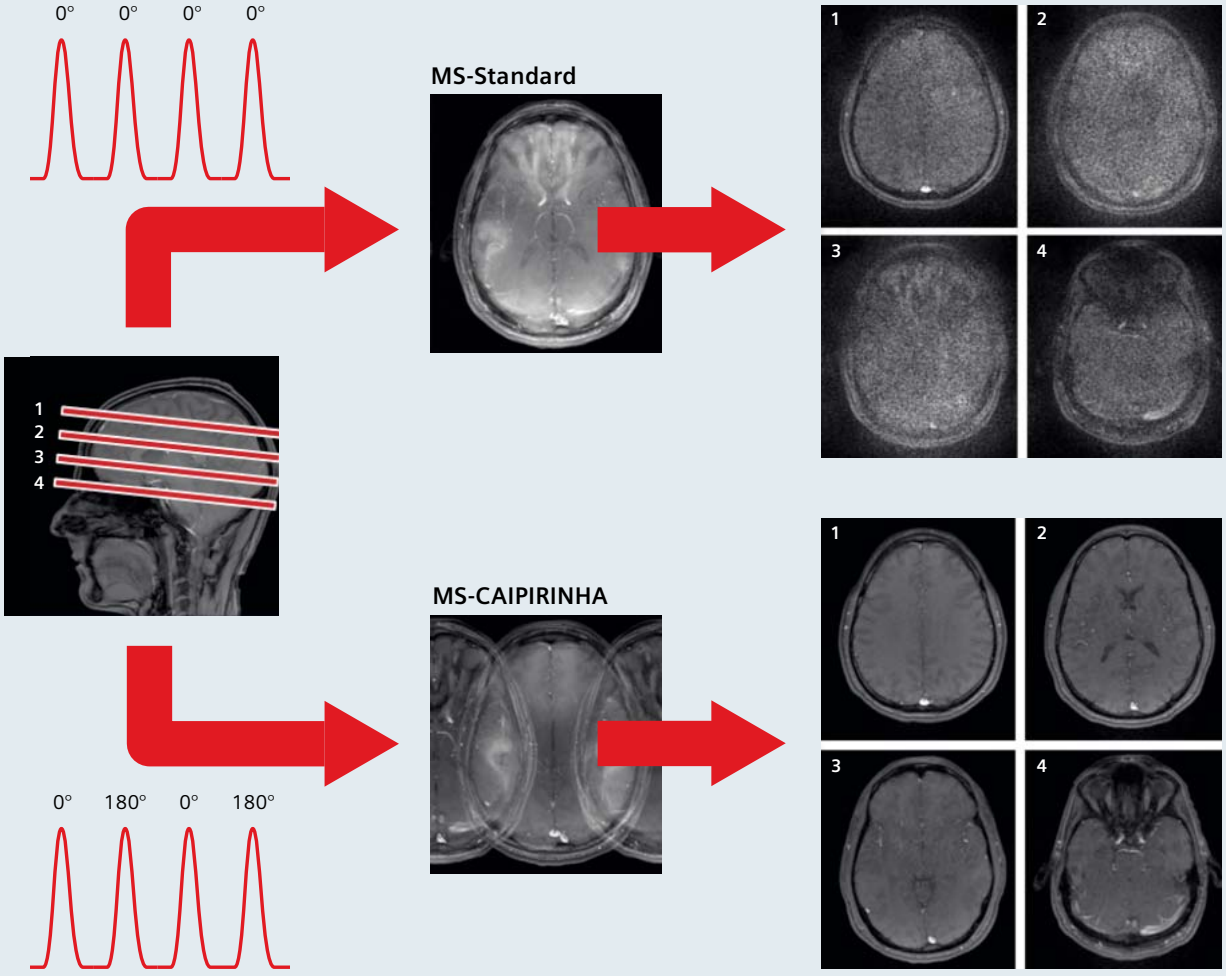

3 In vivo brain example: 4 x accelerated simultaneous 4-slice experiment using no phase cycling (MS-Standard) results in superimposition of all the slices directly on top of each other. Due to the lack of sufficient sensitivity variations along the slice direction strong noise amplifications can be observed after GRAPPA reconstruction. Using MS-CAIPIRINHA, employing 2 alternating multi-band rf-pulses, slices 2 and 4 appear shifted with respect to slices 1 and 3 in the folded image. In this way sensitivity variations in the phase encoding direction (LR) can be used in addition to the sensitivity variations available in the slice direction. The concept results in significantly improved image quality after GRAPPA reconstruction. Imaging parameters: 3T MAGNETOM Skyra, TE 3.4 ms, TR 100 ms, FA 50°, FOV 178 x 220 mm², matrix 208 x 320, slice thickness 4 mm, distance factor 300 %.

order to use the coil encoding power of the underlying receiver array to full capacity. The concept has been successfully applied so far to simultaneous multi-slice imaging (MS-CAIPIRINHA) [6] and 3D imaging where data reduction can be carried out in two phase-encoding directions (2D-CAIPIRINHA) [7]. In addition, both strategies can be extended to the third remaining direction, namely the read-out direction, by utilizing e.g. zig-zag shaped read-out trajectories [8]. The following provides a brief overview of MS-CAIPIRINHA and 2D-CAIPIRINHA.

Improving parallel imaging performance with CAIPIRINHA

MS-CAIPIRINHA

Simultaneous multi-slice imaging offers an SNR benefit over standard single-slice imaging and comprises rf-excitations with specialized multi-band pulses as displayed in Figure 1. After multi-band excitation the received signals will accrue from all the slices (bands) and thus are subject to the subsequent gradient encoding sequence. Simply replacing the standard single-slice excitation pulse with a multi-slice pulse in an MR imaging sequence will therefore result in an image with all the simultaneously excited slices projected onto each other (Fig. 2A). As mentioned above, the parallel imaging concept provides an elegant way to separate multiple image signals which are aliased into one image pixel. Thus, sufficient sensitivity variations of the underlying receiver array

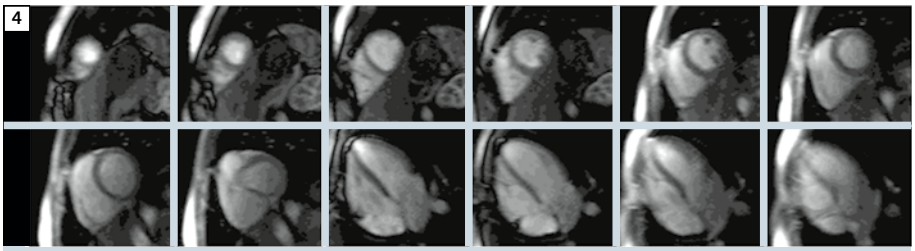

4 In vivo cardiac example: The MS-CAIPIRINHA approach enables the acquisition of up to 6 slices per cardiac cycle. Here, 12 slices are acquired within 2 cardiac cycles (8 slices in short axis view and 4 in the long axis). Imaging parameters: 1.5T MAGNETOM Avanto, 32-channel cardiac array (Rapid Biomedical, Würzburg, Germany); Sequence: SR-TrueFISP, CAIPIRINHA phase cycle +90°/-90°; FOV 320 x 260 mm², matrix 128 x 77, resolution 2.5 x 3.4 mm², slice thickness 10 mm, distance factor (two-slice pulse) of short/long axis: 200%/100%; partial Fourier 6/8, measurements: 20, TR 2.8 ms, TI 120 ms, TE 1.4 ms, FA 50°, reconstruction algorithm GRAPPA (R=3). *Images courtesy of Daniel Stäb.*

along the slice direction will then allow for separation of the slices using adapted standard pMRI reconstruction algorithms [4, 9]. However, in cases where the sensitivity variations along the slice direction are not sufficient e.g. as a result of small slice distances or suboptimal coil geometry, the pMRI reconstruction will fail and result in large noise amplification. Sensitivity variations, potentially available along the other spatial directions, here the phase-encoding direction, are not employed.

It has been demonstrated that increasing the field-of-view (FOV) by the number of simultaneously excited slices allows the individual slices to be shifted with respect to each other in an extended FOV (along the phase-encoding) [10, 11] such that the slices show no superposition. A similar concept is Hadamard aided rf-encoding [12]. The required shifts mentioned above can be accomplished by employing dedicated alternating multi-band rf-pulses providing the individual bands with well-defined phase-cycles along the phase-encoding direction (e.g using the set of rf-pulses displayed in Fig. 1). Due to the volumetric excitation this approach offers a benefit in SNR efficiency of square root of the number of simultaneously excited slices compared to single slice acquisitions, however at the cost of increased pulse energy deposition.

Using this concept in combination with image acceleration (fewer phase-encoding steps) superimposed slices with individual shifts along the phase-encoding direction can be realized by employing alternation of rf-pulses taken e.g. from the set of pulses given in Fig. 1. A four-slice excitation at an acceleration of af = 4 using only rf-pulse 1 yields a superimposition of 4 image pixels originating from all the 4 slices at the same location in the phase-encoding direction (Fig. 2A). Employing an alternation of rf-pulses (e.g. pulse 1 and pulse 3, or pulses 1, 2, 3 and 4) the individual slices can be shifted with respect to each other in the FOV (Figs. 2B, C). In this way, as demonstrated in the corresponding z_y-plots, aliased pixels may now originate from both different slices and different locations in the phase-encoding direction in a well defined manner (MS-CAIPIRINHA), thereby allowing the pMRI reconstruction to take advantage of sensitivity variations in the slice and the phase encoding direction.

The benefit of MS-CAIPIRINHA is demonstrated in vivo employing a 4 times accelerated simultaneous 4-slice experiment: Figure 3 shows 4 slices in a volunteer's brain (slice positions are indicated in the sagittal brain image), which are excited simultaneously using specialized multi-band rf-pulses taken from the set of pulses given in Figure 1A. In the case of non-alternating rf-pulses [4] (MS-Standard), each slice is subject to the same phase cycle along the phase-encoding direction (LR). The slices appear projected directly on top of each other, thereby allowing the pMRI reconstruction (here GRAPPA-SENSE hybrid [9]) only to use sensitivity variations available in the slice direction. Due to the relatively small slice distances, the relatively high acceleration factor (af = 4) and the limited sensitivity variations provided by the coil array in the slice-direction, the reconstruction results in large noise amplifications and thus unacceptable image quality. However, using a MS-CAIPIRINHA acquisition in combination with an adapted GRAPPA reconstruction, the folded image pixels can now be separated almost without any noise amplification. In this example, an MS-CAIPIRINHA scheme as depicted in Figure 2B has been employed. Alternation of pulses 1 and 3 provides slices 2 and 4 with a 180° phase-cycle along the phase encoding direction causing these slices to appear shifted by FOV/2 with respect to the slices 1 and 3 which had no phase modulation. Thus, in this case, MS-CAIPIRINHA allowed the acquisition of 4 slices in the same time normally required or a single slice without losing SNR.

In addition, the applicability of MS-CAIPIRINHA to cardiac perfusion imaging is demonstrated in Figure 4. A two-slice CAIPIRINHA saturation recovery TrueFSIP sequence has been employed using a total acceleration of af = 3. This allows for the acquisition of 12 slices (8 slices in the short axis view and 4 in the long axis) in only two cardiac cycles. A repetition of the sequence during contrast agent uptake has the potential for cardiac perfusion imaging with significantly increased spatial coverage in high temporal resolution [13].

2D-CAIPIRINHA

In contrast to conventional 2D imaging where only one phase-encoding direction is available for scan-time reduction (1D pMRI), 3D volumetric imaging with a second phase encoding direction offers the potential to choose the direction in which undersampling is performed, or even to split the acceleration between the two phase-encoding directions (2D pMRI). Given a receiver array geometry providing sensitivity variations in both phase encoding directions, this

5

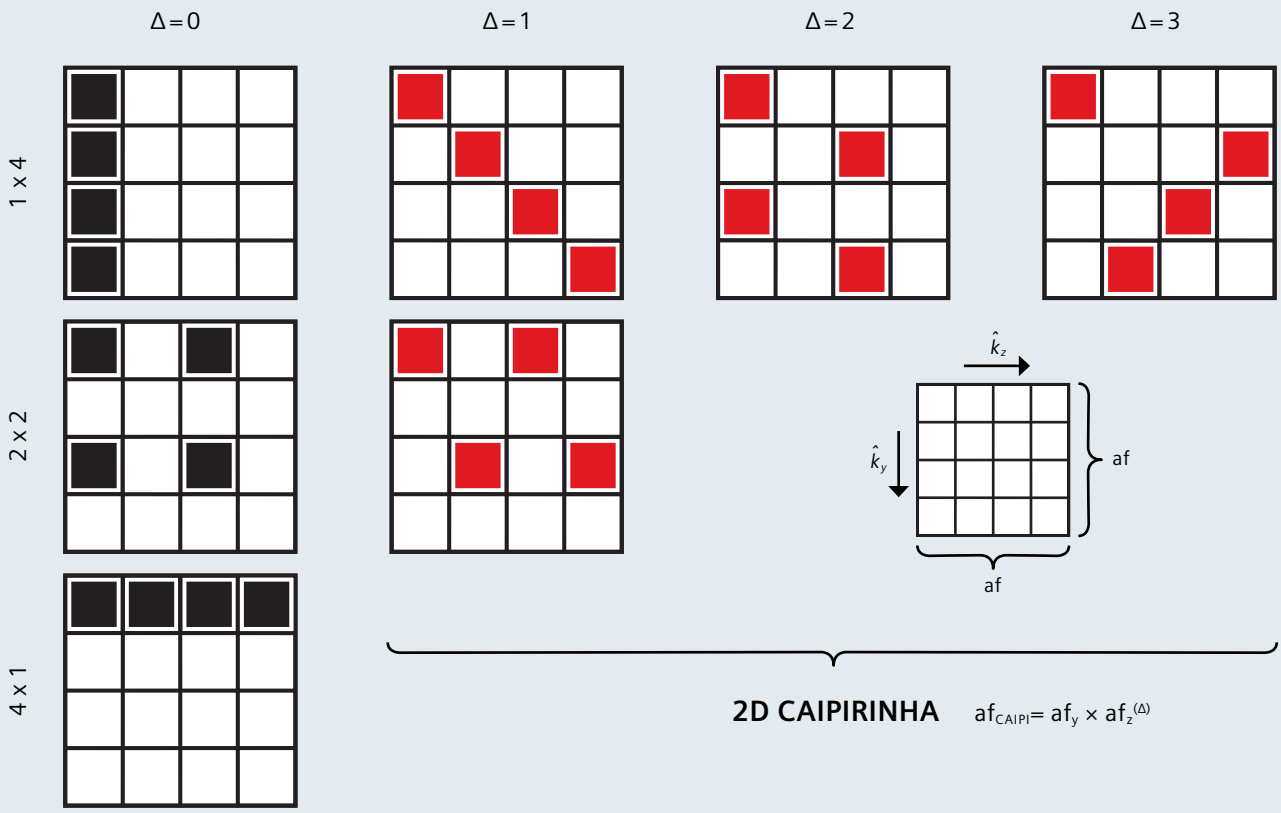

5 Procedure of generating 2D-CAIPIRINHA sampling patterns for a given total acceleration factor, here af = 4. All possible sampling schemes can be represented by an af x af elementary cell with af sampling positions to fill. For each undersampling rate in the k_y direction (af_y) multiple patterns can be created by shifting sampling positions at row k_y in the k_z direction by a different amount Δ, whereas Δ runs from 0 to af_z-1, and $af_z = af/af_y$. Sampling patterns without shift (Δ = 0) are 2D standard acquisitions, while all the other patterns are represented by 2D-CAIPIRINHA-type acquisitions ($af = af_y \times af_z^{(\Delta)}$) indicated by the red sampling positions.

strategy has shown the potential to allow for higher total image accelerations compared to undersampling schemes restricted to only one direction [4, 5]. However, since the sensitivity variations available for the pMRI reconstruction depend not only on the coil geometry but also on the image position and orientation, the choice of the FOVs and encoding directions as well as the object position, size and shape, the right choice of the undersampling rate for the individual phase-encoding directions is not easily predictable and remains a challenging task. Thus, in many applications the reconstructed images suffer from severe residual artifacts or strong noise amplifications, depending on the choices made by the operator.

Again, the CAIPIRINHA concept has shown to partially overcome these limitations. It has been realized that, besides the standard rectangular sampling patterns with undersampling using simple integer reductions, many other patterns are conceivable where the sampling positions are shifted from their original positions in the 2D phase encoding scheme. Here we restrict ourselves to sampling positions on so-called 'sheared grids' which form periodic lattices [14] resulting in exactly af superimposed image pixels at an acceleration factor of af as it is the case in all standard rectangular patterns. The procedure of generating the available 2D-CAIPIRINHA patterns is schematically displayed in Figure 5 for a total image acceleration of af = 4. The sampling schemes can be represented by an af x af elementary cell with af sampling positions to fill. For each undersampling rate in the k_y direction (af_y) multiple patterns can be created by shifting sampling positions at row k_y in the k_z direction by a different amount d, whereas d runs from 0 to af_z-1, and $af_z = af/af_y$. Sampling patterns without shift (d = 0) are 2D standard acquisitions, while all the other patterns are represented by 2D-CAIPIRINHA-type acquisitions. This concept can also be used for prime number accelerations (af = 2, 3, 5 ...) where standard accelerations only allow undersampling in one of the phase encoding directions. The required shifts in k-space can simply be realized by applying additional gradient offsets to the phase encoding gradient tables. These 2D-CAIPIRINHA sampling patterns, analogous to the phase-cycles in simultaneous

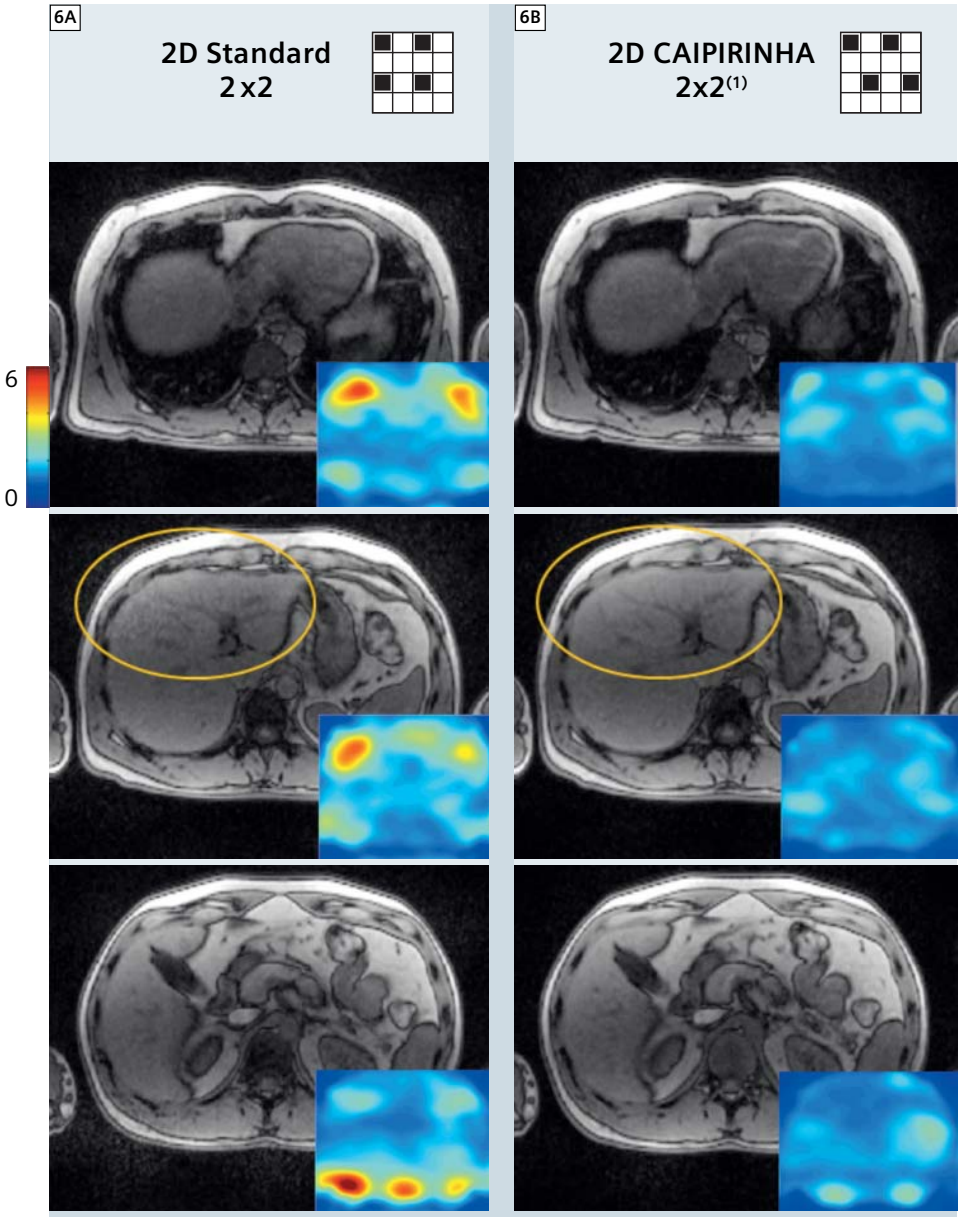

6 In vivo liver example; volunteer: Compared are GRAPPA reconstructions (3 example slices) derived from two different reduction schemes **(6A)** Standard 2x2 and **(6B)** 2D-CAIPIRINHA 2x2(1). In addition, the corresponding GRAPPA g-factor maps are displayed. In the indicated region the SNR benefit of 2D-CAIPIRINHA can be appreciated.
Imaging details: 1.5T MAGNETOM Avanto, 6-channel body matrix coil and 6-channel spine matrix coil; VIBE af = 4, extra reference scan matrix 32 x 24 x 24. FOV 400 x 312.5 mm², matrix 320 x 170 x 50 GRAPPA, total acquisition time 9 s breath-hold.

multi-slice imaging, modify the appearance of aliasing in 2D parallel imaging compared to conventional rectangular reduction schemes and have the potential to relax the requirements of integer reductions to great extent. This is demonstrated in more detail in the original publication [7]. By shifting the sampling positions in a well-directed manner, aliasing can be shifted in such a way that sensitivity variations provided by the underlying receiver array are employed more efficiently. In some cases the amount of aliasing can even be reduced. These modified aliasing conditions may then result in a further improvement in parallel imaging reconstruction conditions and therefore in better image quality. Recently, this concept has also been extended to more generalized sampling schemes which are not restricted to sheared grids [15].
In order to demonstrate the benefit of 2D-CAIPIRINHA in vivo, two subsequent accelerated (af = 4) abdominal 9 s breath-hold VIBE experiments have been carried out on a volunteer. In Figure 6 GRAPPA reconstructions from three out of 50 slices from
a) a standard 2x2 and
b) a 2D-CAIPIRINHA 2x2(1)
acquisition are displayed. In addition, the corresponding g-factor maps of the GRAPPA reconstructions are displayed as a quantitative measure of image quality. As indicated by the lower g-factor values in the 2D-CAIPIRINHA reconstructions the improved image quality can clearly be observed, even on a visual scale (see region indicated by the orange circle).
Furthermore, the improvements in image quality associated with 2D-CAIPIRINHA are demonstrated taking four different T1-weighted 3D FLASH experiments of a volunteer's brain with different acceleration factors and acquisition schemes (Fig. 7). The acquisitions compared are
a) standard 2x2,
b) 2D-CAIPIRINHA 2x2(1),
c) 2D-CAIPIRINHA 1x5(2) and
d) standard 5x1 scheme.
Displayed are the central sections of the reconstructed 3D image data in the sagittal, coronal and axial view in addition to the corresponding quantitative g-factor maps. Comparing reconstruction results from af = 4 (7A) and (7B) the improvement of 2D-CAIPIRINHA can clearly be appreciated. Comparing results from af = 5 (7C) and (7D) the gain in SNR is even more obvious. In this case the parallel imaging performance of 2D-CAIPIRINHA 1x5(2) (7C) compares pretty well with the standard af = 4 (2x2) acquisition employed in (7A). While the 2D-CAIPIRINHA patterns in general appear to be more tolerant against user influence and suboptimal patient positioning, the automatic

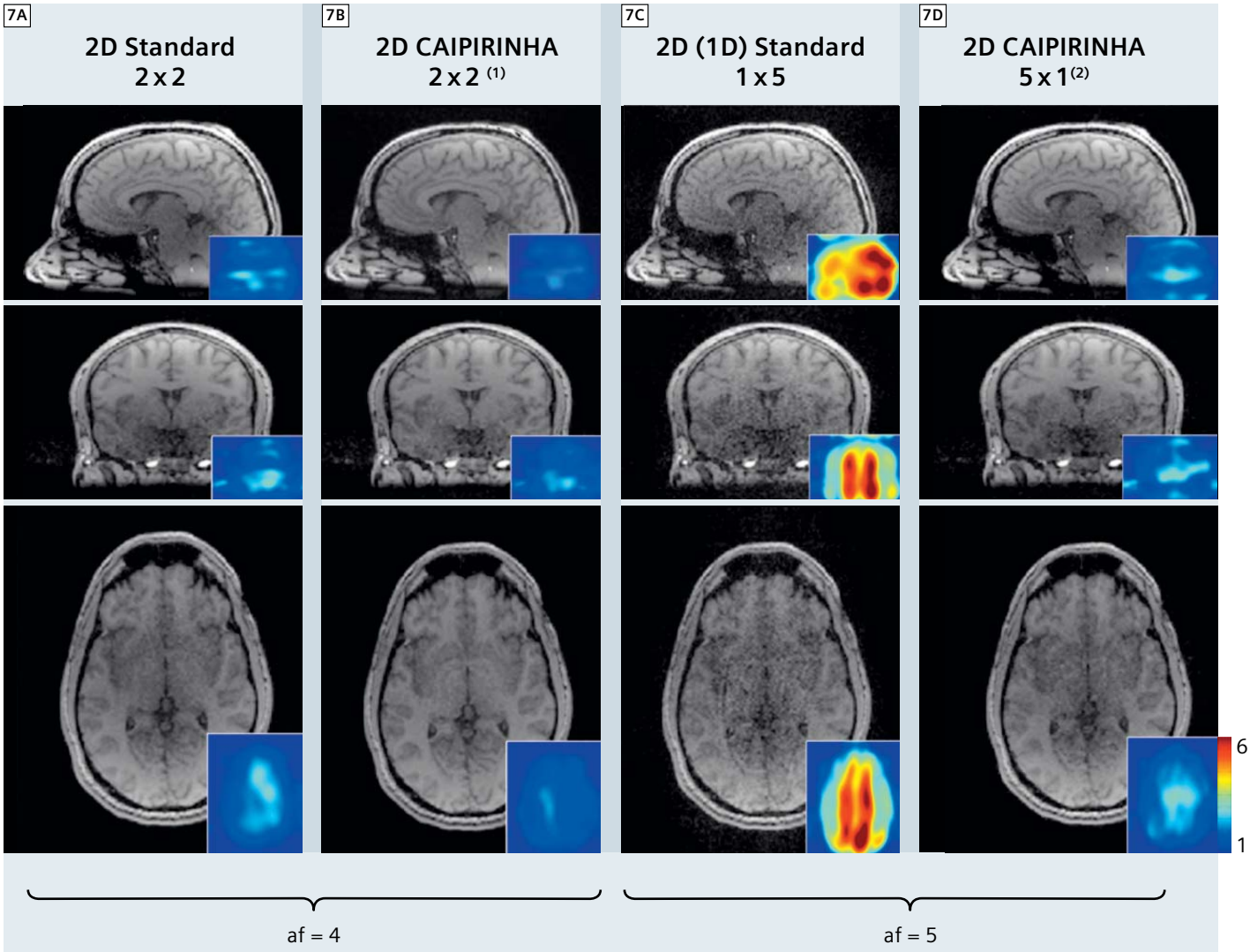

7 In vivo 3D FLASH brain imaging using different acceleration schemes: **(7A)** Standard 2x2 **(7B)** 2D-CAIPIRINHA 2x2[1] **(7C)** Standard 5x1 **(7D)** 2D-CAIPIRINHA 1x5[2]. Displayed are central slices in the sagittal, coronal and axial view. In addition the corresponding GRAPPA g-factor maps are shown.
Imaging details: 3T MAGNETOM Skyra, 20-channel head neck matrix coil, 3D FLASH, GRAPPA with extra reference scan, matrix 32 x 32 x 32, TE / TR 4.3 ms / 16 ms, FA 35°, FOV 256 x 208 x 204 mm³, matrix 256 x 168 x 144; partial Fourier factor 7/8, total scan time 1 min 40 s (af = 4) and 1 min 16 s (af = 5).

extraction of the optimal pattern for the given imaging setup remains a challenging task and has not been sufficiently answered.

Conclusion

In all current parallel imaging techniques, aliasing artifacts resulting from an undersampled acquisition are removed by a specialized pMRI image reconstruction algorithm. The CAIPIRINHA concept aims at modifying the appearance of the aliasing artifacts already during the acquisition to improve the following parallel image reconstruction procedure. Specifically, this concept has been successfully applied to simultaneous multi-slice imaging (MS-CAIPIRINHA) and 3D imaging (2D-CAIPIRINHA).

MS-CAIPIRINHA

Aliasing in simultaneous multi-slice acquisitions can be modified already during the acquisition by employing alternating rf-pulses for subsequent phase encoding lines, thereby allowing the imprint of the individual slices with individual phase-cycles causing the slices to appear shifted with respect to each other thereby improving the reconstruction process minimizing g-factor related noise enhancements. Thus, a CAIPIRINHA-type 4 slice excitation with low g-factor values (close to 1) allows the acquisition of 4 slices in the same time usually required for 1 slice without

loss of SNR. Recently, the MS-CAIPIRINHA concept has been also successfully applied to more advanced acquisition schemes such as SSFP [13] EPI [16] and radial [17] simultaneous multi-slice imaging.

However, it is important to note that multi-slice excitations are associated with significantly increased energy deposition, currently limiting the method to a moderate number of simultaneously excited slices, and/or to low flip angles. However, recently, a promising concept for reducing the rf power of multi-band pulses has been introduced [18]. Thus, MS-CAIPIRINHA is expected to become a powerful strategy in the near future allowing to significantly accelerate many clinical protocols in almost preserved image quality.

2D-CAIPIRINHA

In conventional pMRI accelerated 3D imaging, data reduction is performed in two spatial dimensions simultaneously by integer-valued undersampling in each phase encoding direction. Though sensitivity variations can be exploited in two spatial dimensions, this sampling strategy provides suboptimal encoding performance. The 2D-CAIPIRINHA strategy similar to MS-CAIPIRINHA modifies aliasing in a controlled manner already during the data acquisition. This is accomplished by shifting sampling positions in the two dimensional phase encoding scheme with respect to each other. In this way, at certain image acceleration values, an optimal sampling pattern can be found which minimizes signal overlap and at the same time allows one to efficiently take advantage of all the sensitivity variations provided by the coil array in the 2D phase encoding plane. Thus, 2D-CAIPIRINHA provides optimal reconstruction performance given a certain coil configuration and object shape, and therefore results in optimal image reconstruction quality.

Acknowledgments

The authors thank Daniel Neumann from the Research Center Magnetic Resonance Bavaria (MRB), Würzburg, Germany and Daniel Stäb from the Institute for Diagnostic Radiology, University Hospital Würzburg, Germany for providing material.

In addition, the authors are extremely grateful for receiving continuing support from the colleagues from Siemens Healthcare, especially Stephan Kannengiesser, Dominik Nickel, Berthold Kiefer, Mathias Nittka, Vladimir Jellus and Randall Kroeker.

References

1 Pruessmann KP, Weiger M, Scheidegger B, Boesiger P. SENSE: sensitivity encoding for fast MRI. Magn Reson Med 1999; 42:952-962.
2 Griswold MA, Jakob PM, Heidemann RM, Nittka M, Jellus V, Wang J, Kiefer B, Haase A. GeneRalized Autocalibrating Partially Parallel Acquisitions (GRAPPA). Magn Reson Med 2002; 47:1202-1210.
3 Weiger M, Pruessmann KP, Boesiger P. 2D SENSE for faster 3D MRI. MAGMA. 2002 Mar; 14(1):10-9.
4 Larkman DJ, Hajnal JV, Herlihy AH, Coutts GA, Young IR, Ehnholm G. Use of multicoil arrays for separation of signal from multiple slices simultaneously excited. J Magn Reson Imaging. 2001 Feb; 13(2):313-7.
5 Breuer FA, Kannengiesser SA, Blaimer M, Seiberlich N, Jakob PM, Griswold MA. General formulation for quantitative G-factor calculation in GRAPPA reconstructions. Magn Reson Med. 2009 Sep;62(3):739-46.
6 Breuer FA, Blaimer M, Heidemann RM, Mueller MF, Griswold MA, Jakob PM. Controlled Aliasing in Parallel Imaging Results in Higher Acceleration (CAIPIRINHA) for Multislice Imaging. Magn Reson Med 2005; 53:684-691.
7 Breuer FA, Blaimer M, Mueller MF, Seiberlich N, Heidemann RM, Griswold MA, Jakob PM. Controlled aliasing in volumetric parallel imaging (2D CAIPIRINHA). Magn Reson Med. 2006 Mar;55(3):549-56.
8 Breuer FA, Moriguchi H, Seiberlich N, Blaimer M, Jakob PM, Duerk JL, Griswold MA. Zigzag sampling for improved parallel imaging. Magn Reson Med. 2008 Aug;60(2):474-8.
9 Blaimer M, Breuer FA, Seiberlich N, Mueller MF, Heidemann RM, Jellus V, Wiggins G, Wald LL, Griswold MA, Jakob PM. Accelerated volumetric MRI with a SENSE/GRAPPA combination. J Magn Reson Imaging. 2006 Aug;24(2):444-50.
10 Muller S. Simultaneous multislice imaging (SIMUSIM) for improved cardiac imaging. Magn Reson Med. 1989 Apr;10(1):145-55.
11 Glover GH. Phase-offset multiplanar (POMP) volume imaging: a new technique. J Magn Reson Imaging. 1991 Jul-Aug; 1(4):457-61.
12 Souza SP, Szumowski J, Dumoulin CL, Plewes DP, Glover G. SIMA: simultaneous multislice acquisition of MR images by Hadamard-encoded excitation. J Comput Assist Tomogr. 1988 Nov-Dec;12(6):1026-30.
13 Stäb D, Ritter CO, Breuer FA, Weng AM, Hahn D, Köstler H. CAIPIRINHA accelerated SSFP imaging. Magn Reson Med. 2011 Jan;65(1):157-64
14 Willis NP and Bresler Y. Optimal scan design for time varying tomographic imaging {II}: Efficient design and experimental validation. IEEE Trans. Image Processing, 1995 May; 4: 654-666.
15 Wu B, Millane RP, Watts R, Bones PJ. Improved matrix inversion in image plane parallel MRI. Magn Reson Imaging. 2009 Sep;27(7):942-53.
16 Setsompop K, Gagoski BA, Polimeni JR, Witzel T, Wedeen VJ, Wald LL. Blipped-controlled aliasing in parallel imaging for simultaneous multislice Echo Planar Imaging with reduced g-factor penalty. Magn Reson Med. 2011 Aug 19.
17 Yutzy SR, Seiberlich N, Duerk JL, Griswold MA. Improvements in multislice parallel imaging using radial CAIPIRINHA. Magn Reson Med. 2011 Jun;65(6):1630-7.
18 Norris DG, Koopmans PJ, Boyacioğlu R, Barth M. Power independent of number of slices radiofrequency pulses for low-power simultaneous multislice excitation. Magn Reson Med. 2011 Nov;66(5):1234-40.

Contact
Dr. Felix Breuer
Research Center
Magnetic Resonance Bavaria e.V (MRB)
Am Hubland
97074 Würzburg
Germany
Phone: +49 (0) 931 318 3060
Fax: +49 (0) 931 318 4680
breuer@mr-bavaria.de

The Signal-to-Noise Indicator or How to Navigate the 'Bermuda Triangle'

Joachim Graessner, Dipl. Ing.

Siemens Healthcare, Hamburg, Germany

1

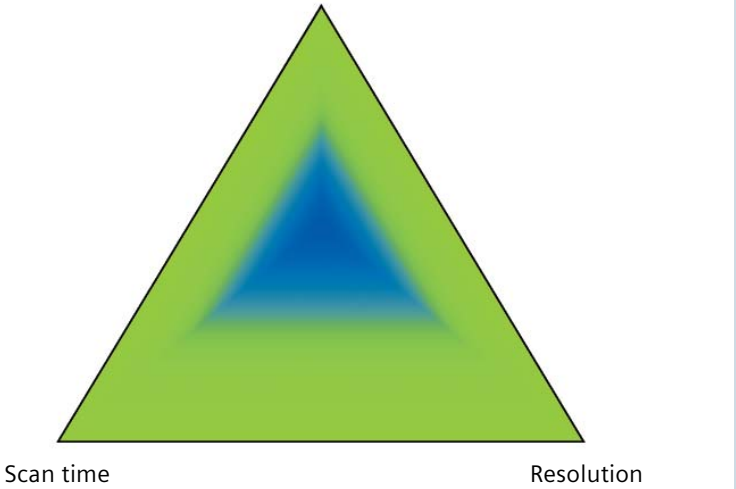

1 'Bermuda Triangle' of dependant MR quantities.

We observe quite often that people feel uneasy with the interpretation of the numbers the signal-to-noise (S/N) indicator shows on the *syngo* program-card. "May I change the protocol although the SNR indicator shows a value of 0.3?" "Why does oversampling improve S/N? The larger FOV only covers more air." Such questions and many more will be answered in this article. We will take away the mystery of parameter changes and explain their mutual dependencies (Fig. 1).

What is signal-to-noise?

The total MR-signal is a mixture of the signal from the pure MR experiment plus thermal noise and other sources of noise. A measure of quality for a medical image is the ratio of the signal-intensity in the object divided by the signal-intensity of the noise (SNR) typically measured in the air outside the body.

Why is the SNR relative?

The SNR indicator of a saved protocol always shows the value 1.00 or 100%. Changing certain MR parameters changes this indicator value but only relative to the initially stored version of this protocol. After saving the performed parameter changes the SNR indicator switches back to the value of 1.00. Do not use this value for comparisons between different protocols!

Which parameters influence the SNR indicator?

There are several parameters which alter the signal S. Or, looking at the equation, the signal S is proportional to certain parameters.

$S_{2D} \sim 1/\text{sqrt}(BW) * \Delta x * \Delta y * \Delta z * \text{sqrt}(AC * N_{pe})$

$S_{3D} \sim 1/\text{sqrt}(BW) * \Delta x * \Delta y * \Delta z * \text{sqrt}(AC * N_{pe} * N_{3D})$

- BW – bandwidth in Hz/pixel
- Δx – inplane resolution in x-direction: FOV_x / N_{re}
- Δy – inplane resolution in y-direction: FOV_y / N_{pe}
- Δz – Slice thickness or partition thickness in 3D case: slab-thickness/ N_{3D}
- AC – Averages: number of excitations per same encoding step
- N_{re} – Base matrix size in read direction
- N_{pe} – Number of phase encoding steps
- N_{3D} – Number of phase encoding steps in 3D direction or Z-direction

For our problem we are only looking for dependencies with respect to resolution, i.e. voxel size, total number of acquired echoes (number of phase encoding steps), number of averages (number of excitations) and readout-properties such as bandwidth per pixel. Parameters determining contrast like TE, TR, TI and flip angle as well as the sequence type, field strength and coil type do not play any role for the SNR indicator (Fig. 2).

2



2 Headline of the parameter card in the *syngo* MR B/C/D-software versions.

What does the resolution indicator show?

In *syngo* MR A/B/C software versions you get with mouse-over on the resolution field a display of values down to an accuracy of 1/100 mm. In the *syngo* MR D-version you additionally get a display of the measured and the calculated resolution (Fig. 3).
Example:
1.00 x 1.00 x 1.00 mm = Δx * Δy * Δz

What does the scan time indicator show?

The measurement time (TA) depends on the product of TR time, number of averages AC, number of phase encodings, and number of 3D encodings and may be divided by the Turbo factor TF, EPI factor and time saving factors from sampling strategies like iPAT and Halffourier.
$TA_{2D} = [(TR * AC * N_{pe}) / (TF * PAT_{2D})] +$ Prep + Intro
$TA_{3D} = [(TR * AC * N_{pe} * N_{3D}) /$ $(TF \times PAT_{2D} * PAT_{3D})] +$ Prep + Intro

- Prep – preparation pulses at the beginning of a sequence to bring the magnetization into steady state. This takes a few seconds.
- Intro – 3 gradient knockings at the beginning of a protocol to warn the patient; can be switched off for breath-hold series on the sequence card.

What do these values tell me?

Fortunately the MR software does all these calculations for you. When changing parameters of a given protocol which already delivered decent image quality you get an idea of how the scan time, the resolution and the relative SNR change compared to the initial protocol setup. A protocol with a lot of reserve in SNR can still deliver good image quality, even with an SNR indicator on 0.1. But

3

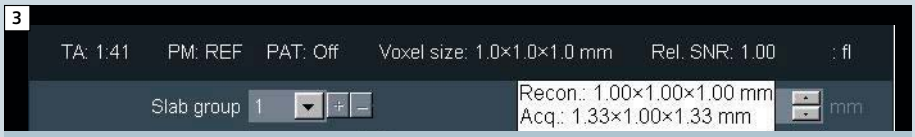

3 Mouse-over on voxel size in the *syngo* MR D-software version.

Table 1: Changing the number of phase encoding steps and averages affects scan time TA, pixel size and relative SNR.

FOV (mm)	Matrix N_{pe} x N_{re}	AC	TA a.u.	Pixel size (mm^2)	Rel. SNR a.u.	Explanation
512	256 x 256	2	1	2 x 2	**4.00**	4 times the pixel size
256	128 x 128	2	0.5	2 x 2	**2.83** = (4 / √2) = 2 * √2	4 times the pixel size and 2 times less N_{pe}
256	128 x 256	2	0.5	2 x 1	**1.41** = (2 / √2) = √2	twice the pixel size, but 2 times less N_{pe}
256	256 x 256	4	2	1 x 1	**1.41** = √2	twice the number of ACs
256	**256 x 256**	**2**	**1**	**1 x 1**	**1.00**	**start protocol (reference)**
256	256 x 256	1	0.5	1 x 1	**0.71** = (1 / √2)	half the number of ACs
256	256 x 512	2	1	1 x 0.5	**0.5**	half the pixel size
256	512 x 512	2	2	0.5 x 0.5	**0.35** = (0.25 * √2)	quarter pixel size, but 2 times more N_{pe}
128	256 x 256	2	1	0.5 x 0.5	**0.25**	quarter pixel size

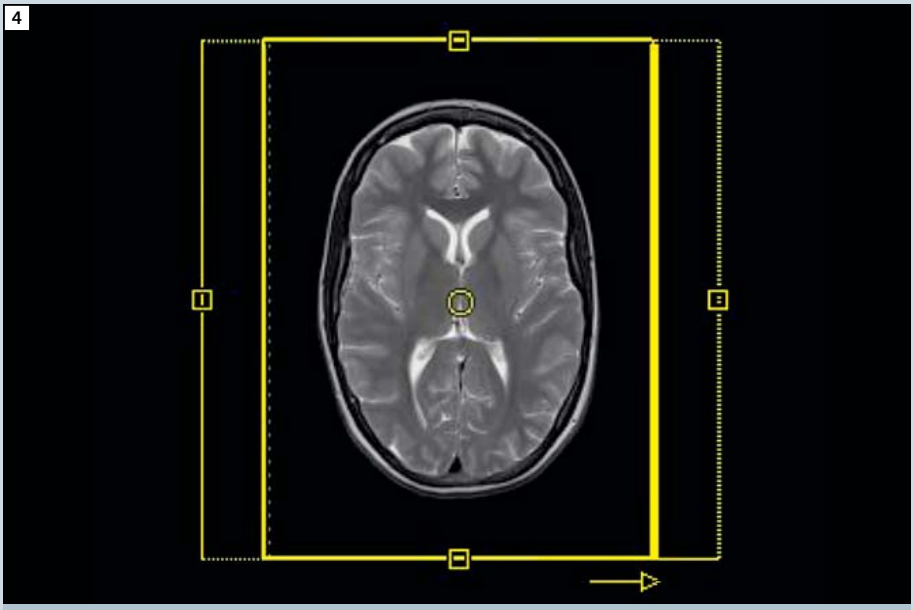

4 33% phase oversampling applied on a 75% phase FOV.

when you already pushed resolution and scan time to a level where the images start to get noisy, a further change with a resulting SNR of 0.9 could result in an unacceptable quality. As said, the SNR indicator shows a relative quantity. It depends on the starting conditions.
You will always have to sacrifice one or two items when optimizing the third one.
Better resolution in less scan time with higher SNR is impossible unless you change the measurement conditions like field strength or type of RF coil.

Table 1 gives an example:
- Bandwidth and slice thickness are assumed constant
- No iPAT and quadratic FOV
- Pixel size x slice thickness = Voxel size

Obviously the factor square root of two ($\sqrt{2}$) plays an important role when diminishing or enlarging certain MR parameters by a factor of two. Only alterations of the slice thickness change the SNR indicator linearly. All other parameters go with the square root of the change factor up or down.

Table 2: How MR parameters affect TA, resolution and SNR.

Parameter	Measurement time TA	Resolution	SNR
Matrix ↑	↑	↑	↓
Fields-of-view (FOV) ↑	–	↓	↑
Slice thickness ↑	–	↓	↑
Bandwidth per pixel ↑	(↓)*	–	↓
Averages AC ↑	↑	–	↑
Phase oversampling ↑	↑	–	↑
Rectangular FOV ↓	↓	–	↓
iPAT factor ↑	↓	–	↓
Partial Fourier factor ↑	↓	–	↓

* only if TR can be shortened

Why does phase oversampling improve the S/N?

Oversampling in phase direction acquires more encoding steps and thus increases SNR. Each independently-sampled phase encoding step adds a portion to the total SNR. Each echo contains information about the whole image; there are no echoes which collect data in the air.
Figure 4 shows a special case with 75% phase FOV combined with 33% phase oversampling (PhOS). Compared to 100% phase FOV with no PhOS you have the same SNR, scan time and resolution. The same is true for a setup with 100% PhOS and half the number of ACs or instead iPAT = 2.

Why does the SNR not increase with more reference lines in GRAPPA mode?

Because the number of reference lines are not included in the formula. The

Table 3: Parameters for SNR discovery protocols.

	SE 2D	TSE 2D	GRE 3D	GRE 2D
Sequence name	tse	tse	gre	gre
Dimension	2D	2D	3D	2D
FOV read	256	256	256	256
FOV phase	100%	100%	100%	100%
Base resolution	256	256	256	256
Phase resolution	100%	100%	100%	100%
Slice thickness	5 mm	5 mm	1 mm	5 mm
TR	467 ms	3050 ms	5.5 ms	235 ms
TE	12 ms	107 ms	2.35 ms	5 ms
AC	2	2	2	2
iPAT	none	none	none	none
Bandwidth	130	130	390	260
Slice/Slices per slab	5	10	64	5
Flipangle	90	180	25	70
Turbo factor	1	9	n.a.	n.a.
Introduction	deselect	deselect	deselect	deselect
Coil	8/12/16-	channel	head	coil
TA	4:00 min	3:00 min	3:00 min	2:00 min
Resolution	1.0 x 1.0 x 5.0	1.0 x 1.0 x 5.0	1.0 x 1.0 x 1.0	1.0 x 1.0 x 5.0
Rel. SNR	1.00	1.00	1.00	1.00

same is true for interpolation. But the SNR actually benefits in most sequences from the additionally sampled number of reference lines using the 'integrated' mode.

Why does allowed partial Fourier not change scan time in a TSE sequence?

Partial Fourier in a TSE sequence only shortens the echo train length. This gives you the opportunity to shorten TR and gain some scan time if appropriate for the contrast.

Is there a rule of thumb for changes in the SNR indicator?

A red arrow in Table 2 indicates for both directions a drawback compared to our positive expectations of shorter scan times, better resolution and SNR. There is always at least one red arrow accompanying a black arrow.

How can I get a feeling for the amount of change in the SNR indicator?

Generate a protocol with the parameters shown in Table 3, save it and than play around with the MR parameters and discover their influence on SNR, TA and resolution. The TRs were chosen that way to get round scan times, which will have slight deviations when changing the number of averages AC. These few seconds are due to the preparation phase at

Table 4: Influence of the voxel size on total volume and SNR.

SVS voxel size (mm^3)	approx. UI values (mm^3)	Volume (cm^3)	Rel. SNR a.u.
20 x 20 x 20	20 x 20 x 20	8	1.00
18.1 x 18.1 x 18.1	18 x 18 x 18	6	0.75
15.9 x 15.9 x 15.9	16 x 16 x 16	4	0.5
12.6 x 12.6 x 12.6	13 x 13 x 13	2	0.25
10 x 10 x 10	10 x 10 x 10	1	0.125
7.9 x 7.9 x 7.9	8 x 8 x 8	0.5	0.063
6.3 x 6.3 x 6.3	6 x 6 x 6	0.25	0.031
5 x 5 x 5	5 x 5 x 5	0.125	0.016

the very beginning of a protocol which is played out only once.

Is there anything different with spectroscopy protocols?

In single voxel spectroscopy (SVS) you have to be aware of the fact that a slight decrease in the side length of a single voxel will result in a large change to the measured volume, i.e. dramatic decrease in SNR, which can rarely be compensated by an increase of averages (Table 4). CSI protocols can deliver much smaller voxels than SVS due to higher number of encoding steps in two or three dimensions. But this has to be paid for by longer scan times and a more global shim situation.

→ Visit www.siemens.com/magnetom-world to download training files in .edx format. Training files are available for software versions *syngo* MR D11D, *syngo* MR B15 and *syngo* MR B17.



References

Recommended literature for the curious reader in the order of increasing physical depth:

1 "Magnets, Spins and Resonances"; Siemens 2003.
2 "Magnets, Flow and Artifacts"; Siemens 2004.
3 "The Physics of Clinical MR Taught Through Images": Runge, Nitz, Schmeets; Thieme 2008.
4 "Questions & Answers in MRI": Elster, Burdette; Mosby 2001.
5 "MRI the Basics": Hashemi, Bradley, Lisanti; LWW 2010.
6 "MRI from Picture to Proton": McRobbie, Moore, Graves, Prince; Cambridge 2007.

Especially recommended for the German speaking community:

7 „Praxiskurs MRT": Nitz, Runge; Thieme 2011.
8 „MRT-Guide für MTRA/RT": Nitz; Thieme 2012.

Contact
Joachim Graessner, Dipl.Ing.
Siemens AG Healthcare
GER H IM BM MR
Lindenplatz 2
20099 Hamburg
Germany
joachim.graessner@siemens.com

syngo WARP – Metal Artifact Reduction Techniques in Magnetic Resonance Imaging

Theresa Bachschmidt; Ferdinand Lipps, Ph.D.; Mathias Nittka, Ph.D.

Siemens Healthcare, Erlangen, Germany

The term WARP summarizes methods to minimize the impact of metal implants on image quality.

Challenges

Metals have highly different susceptibility constants compared to tissue. When metallic implants are present in the MRI examination, the static magnetic field in their vicinity is manipulated by strong local off-resonances induced by the implants. The degree of field distortions depends on the shape, the location and the material properties of the metal implant.

Distortions of the static magnetic field result in:

- Intra-voxel dephasing: Signal voids are visible as black areas in the image.
- Changes in tissue contrast: Failure of fat suppression and saturation bands.
- In-plane distortion: The local field offset leads to a shift of image pixels in the readout encoding (i.e. frequency encoding) direction.
- Through-plane distortion: The local field offset leads to curved and frayed slices instead of the expected flat image plane (Fig. 1).

Since both in-plane and through-plane distortions shift image pixels away from their real positions, image geometry appears to be distorted. In both cases, regions with severe field changes will lead to signal voids visible as black spots and signal pileups visible as bright spots. However, it makes sense to distinguish between in- and through-plane artifacts, since different techniques are needed to reduce these types of artifacts.

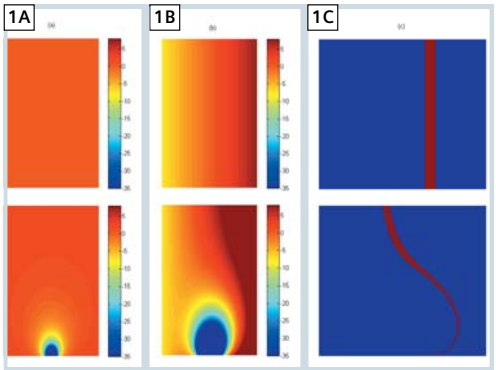

1 The upper row visualizes the ideal case of slice selection, while the lower row displays the effects on the slice selection by a distorted background field: **(1A)** B_0 field map in slice select direction, **(1B)** B_0 field map in direction of slice encoding with superimposed magnetic gradient field for excitation, and **(1C)** position of the excited slice.

Approaches to avoid metal artifacts

Imaging in the presence of metal implants is mostly based on (turbo) spin echo sequences due to its high immunity with regard to signal dephasing induced by local off-resonances.
In the following, three approaches to reduce metal artifacts are presented, that have shown promising results in clinical settings. Figure 2 depicts their effects *in-vivo* compared to imaging with standard protocols. Although other techniques exist, they are often constrained by excessive scan times or special hardware requirements.

High bandwidth sequence parameters

Basic acquisition parameters are adjusted to what is called high bandwidth (BW) parameters to make the MR sequence less sensitive to field distortions.
What is done:
The bandwidth of both the excitation pulse and the signal readout is increased.
What it effects:
A high bandwidth sequences reduces the through-plane distortion of the slice profile. This implies less severe variations of the apparent slice thickness, i.e. the amount of signal voids and pileups is reduced compared to standard protocols with a low bandwidth.
A high signal readout bandwidth

Implant imaging at 3T:
There is a significant difference between MR imaging at 3T and 1.5T. In contrast to common clinical imaging, higher field strength does not necessarily imply better image quality for patients with metal implants. Apart from increased safety concerns, the level of image distortions scales with the strength of the static field, i.e. the level of artifacts is higher at 3T than at 1.5T. Additionally, the efficiency of artifact reduction techniques is reduced by the increased SAR constrains at 3T.

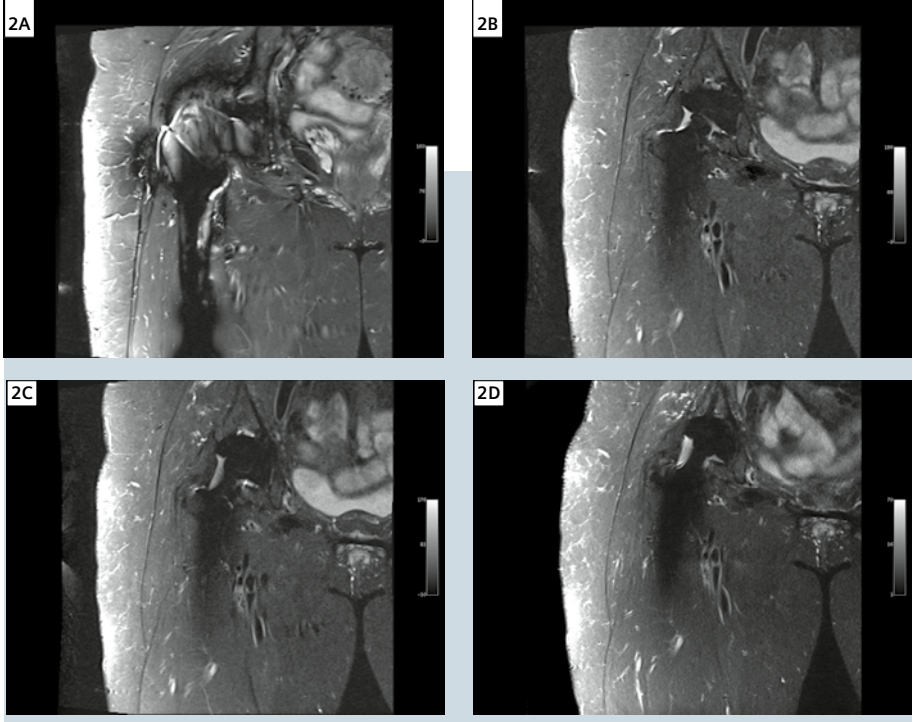

2 Image comparison: **(2A)** standard protocol, **(2B)** high BW, **(2C)** VAT* and **(2D)** SEMAC**.

addresses in-plane distortions: Intravoxel signal dephasing and geometrical shift in the readout encoding direction are reduced. Consequently, the image has less signal voids and less pileup artifacts related to in-plane distortions.
The main drawback of high bandwidth protocols is reduced signal-to-noise ratio (SNR) and increased specific absorption rate (SAR). High bandwidth sequences are very demanding in terms of scanner hardware, mainly gradient and RF power performance. Ultimately, the RF power applied by high bandwidth RF pulses is limited by the patient (SAR). Hence, the RF pulse bandwidth is more affected by these restrictions and in-plane artifact reduction is more efficient.

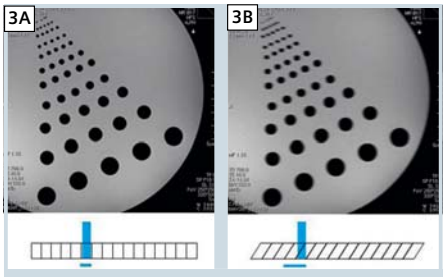

3 VAT* blurring caused by the shearing of the slice: **(3A)** Image without VAT: the signal of a vertical structure (vertical blue line) is well localized in a pixel (horizontal blue line); **(3B)** blurred image with VAT: The vertical structure appears smeared over multiple pixels.

VAT* (View Angle Tilting)

VAT is a modified sequence acquisition scheme that is able to compensate for in-plane distortions. It can be easily implemented into a turbo spin echo (TSE) sequence.
What is done:
Simultaneously with the conventional readout gradient, an additional readout gradient is applied along the slice selective direction. Its amplitude equals the one applied during the excitation RF pulse.
What it means:
The additional gradient causes shearing of the imaged pixels, as if the slice were viewed at an angle. From a different point-of-view, the VAT gradient brings back all excited spins within the RF bandwidth and local off-resonances are cancelled exactly. Hence, the pixel shift in readout direction is fully compensated.
What it effects:
In-plane distortions, more precisely those along the readout direction, are corrected. However, VAT may cause blurring of the image caused by two separate effects. One cause is the geometric slice shear, causing edges to be smeared out along the shearing direction (Fig. 3). This effect can be reduced by using thin slices and a high resolution. The second source of blurring is a low-pass filter superimposed on the signal readout by the additional VAT gradient. This can be reduced by a short readout duration.

SEMAC** (Slice Encoding for Metal Artifact Correction)

SEMAC is based on a 2D TSE sequence. An additional encoding dimension is introduced to enable the correction of through-plane distortions.
What is done:
Each slice is additionally phase-encoded in the third dimension, very similar to a 3D scan. This provides information on how the slice profile is distorted, such that signal shifted perpendicular to the image plane can be corrected by post-processing during image reconstruction.
What it effects:
Gross through-plane artifacts, which usually cannot be handled efficiently by high bandwidth parameters, can be corrected. In particular, imaging of large metal structures like full knee or hip replacements is being studied. This method is very time-consuming. Despite the use of advanced undersampling techniques, such as partial Fourier and parallel imaging, it is challenging to achieve scan times acceptable for routine examinations.

**510(k) pending. Not for sale in the U.S. and in other countries.*

***WIP: Work in progress. SEMAC is currently under development; is not for sale in the U.S. Its future availability cannot be guaranteed.*

Disclaimer:
MR imaging of patients with metallic implants brings specific risks. However, certain implants are approved by the governing regulatory bodies to be MR conditionally safe. For such implants, the previously mentioned warning may not be applicable. Please contact the implant manufacturer for the specific conditional information. The conditions for MR safety are the responsibility of the implant manufacturer, not of Siemens.

Contact
Mathias Nittka, Ph.D.
Siemens Healthcare
MR PI ORTH
Postbox 32 60
91050 Erlangen
Germany
Phone: +49 (9131) 84-4460
mathias.nittka@siemens.com

Whole-Body Diffusion-Weighted MRI of the Bone Marrow in Health and Disease

Anwar R. Padhani[1]; Hassan Douis[2]; Peter Gall[3]

[1]Paul Strickland Scanner Centre, Mount Vernon Cancer Centre, Northwood, Middlesex, UK
[2]Department of Radiology, Royal Orthopaedic Hospital, Birmingham, UK
[3]Siemens Healthcare, Erlangen, Germany

Background

A comprehensive imaging assessment of the skeletal bone marrow requires a multimodal approach because no one technique is able to evaluate all aspects of bone health. Thus, ^{99m}Tc-MDP skeletal scintigraphy and ^{18}F-Na PET evaluate osteoblastic function, ultrashort TE and CT scans evaluate the structural properties of bone and the osteolytic activity of osteoclasts. Non-specific PET tracers can evaluate bone marrow/tumor membrane transporters and metabolism. Relevant tracers include ^{18}F-flurodeoxyglucose (FDG) for glucose metabolism, ^{11}C/^{18}F-thymidine (FLT) for DNA synthesis, ^{11}C/^{18}F-acetate for fatty acid synthesis, ^{11}C-methionine for protein synthesis and ^{11}C/^{18}F-choline for cell membrane synthesis and degradation [1]. Tumor specific tracers include ^{18}F-FES (fluoroestradiol for breast cancer), ^{18}F-FDHT (fluorodihydrotestosterone for prostate cancer) and engineered antibody fragments that target tumor cell-surface targets such as HER-2/neu (for breast cancer) and prostate specific membrane antigen (PSMA) [2]. Dynamic contrast-enhanced MRI (DCE-MRI) can evaluate the vascularisation of bone marrow and its cellular content can be assessed using Dixon and diffusion MRI techniques. These techniques have variable clinical availability and whole-body imaging capability.

In recent years, whole-body MRI has emerged as an excellent imaging modality for the evaluation of normal bone, of bone marrow infiltration and the detec-

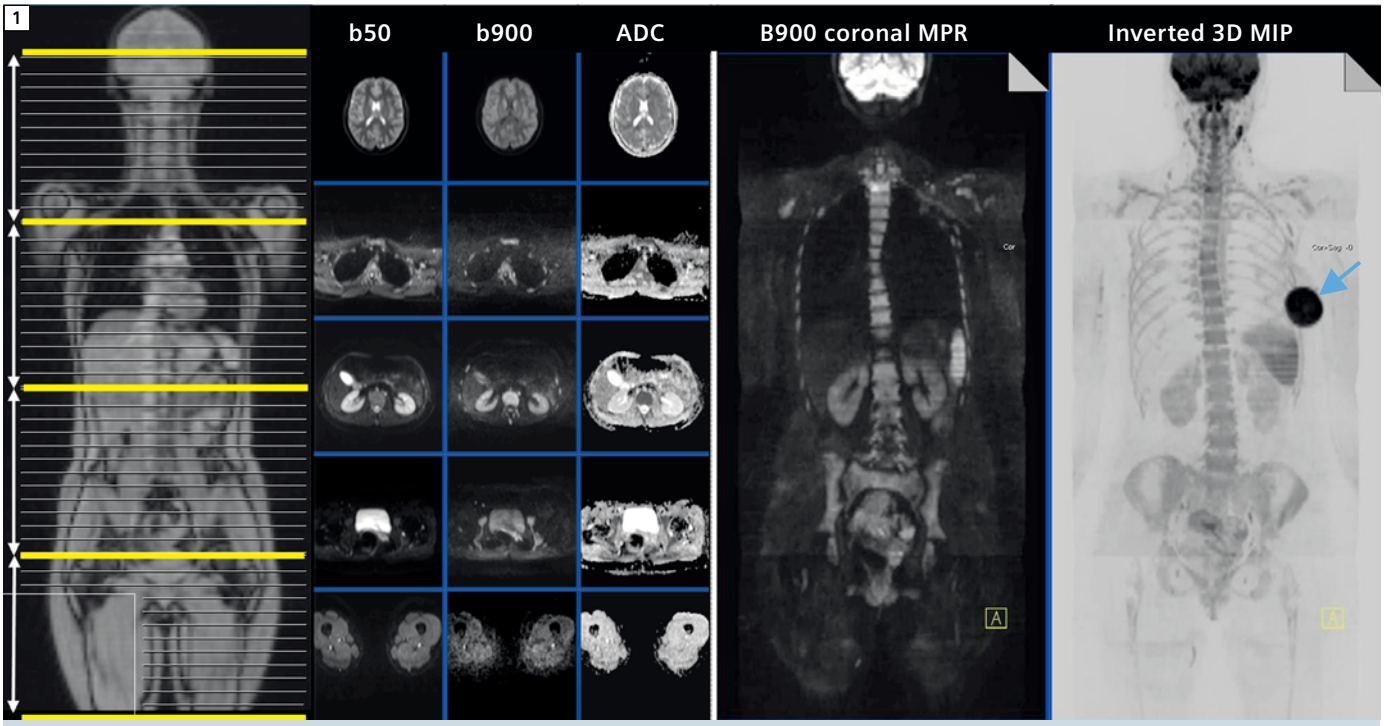

1 WB-DWI workflow. 27-year-old-woman with sarcomatoid left breast cancer (arrow). The bone marrow pattern is normal for this age. Axial DWI from the skull base to the mid-thigh is performed using 2 b-values (50 and 900 s/mm²) with a slice thickness of 5 mm in 4 stations. The b900 images are reconstructed into the coronal plane (5 mm) and displayed as thick 3D MIPs (inverted grey scale). ADC images are computed inline with mono-exponential fitting of b50 and b900 signal intensities.

tion of skeletal metastases due to its exquisite soft tissue contrast, high spatial resolution and lack of ionizing radiation [3]. Whole-body MRI is particularly attractive for children* and young adults because it lacks ionizing radiation. Despite its high sensitivity and high specificity for the detection of skeletal metastases, whole-body MRI has not been widely adopted into daily clinical practice. This is predominantly due to the fact, that whole-body MRI performed with conventional sequences has to be tailored for each tumor type, has long examination times, often requires the administration of intravenous contrast and importantly, it is time consuming to analyse and report [4]. However, there is a strong clinical need for whole-body tumor assessments particularly for cancer patients.

Whole-body diffusion-weighted MRI (WB-DWI) is a new powerful adjunct to anatomical whole-body MRI because it provides a functional assessment of disease burden, can quantify disease extent, does not require the administration of exogenous contrast medium and can be performed in reasonably short examination times. Furthermore, WB-DWI can improve the reading and test performance of anatomical whole-body MR examinations because areas of increased cellularity are depicted as regions of high signal-intensity, therefore allowing an 'at-a-glance' assessment of disease burden and distribution [5]. Whole-body DWI is emerging as a particularly promising imaging technique in the detection, assessment of extent and therapy monitoring of skeletal metastases [6] because it is sensitive to bone marrow cellular density, the relative proportion of fat and marrow cells, water content and bone marrow perfusion.

Technique of whole-body DWI

Most modern high-field MRI systems possess echo-planar and parallel imaging capabilities and allow the use of high-performance gradients which together with phased-array multichannel surface coils, make it feasible for WB-DWI to be implemented into clinical practice. Currently we find that WB-DWI

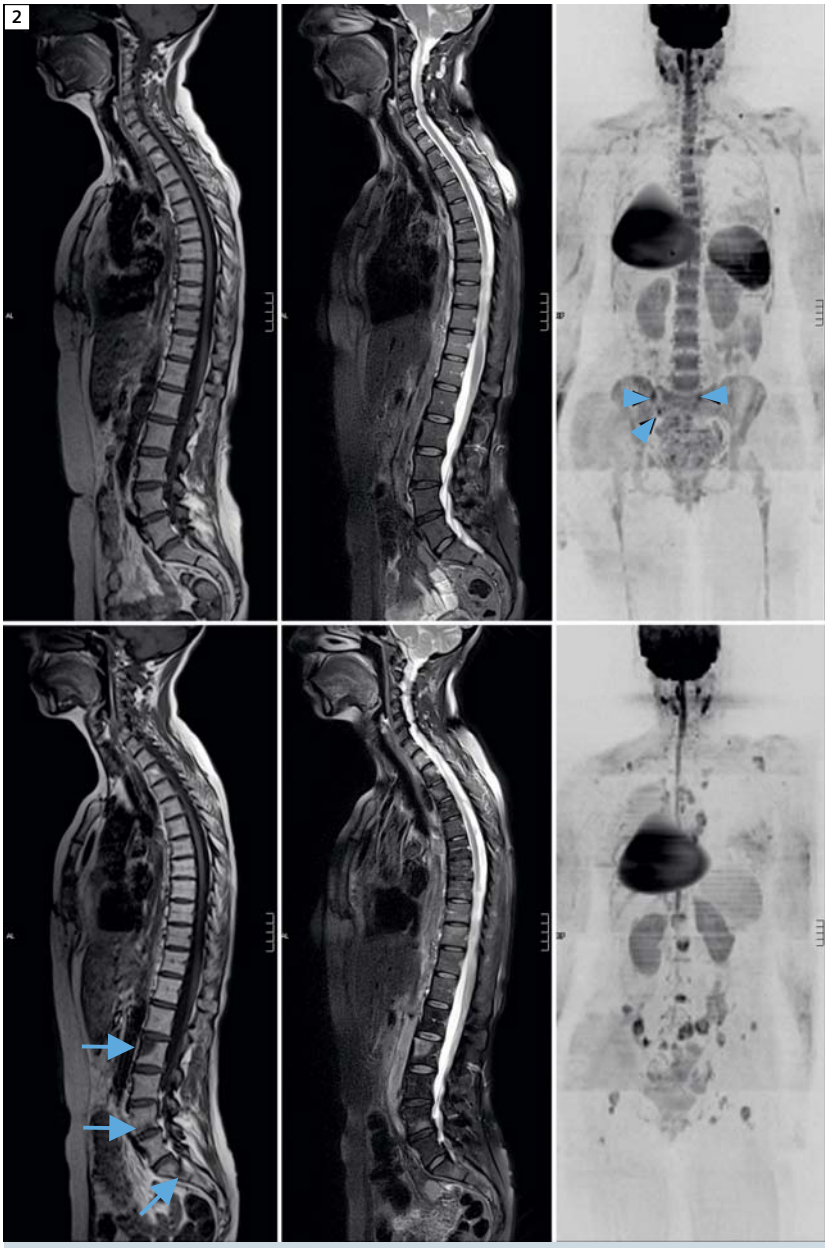

2 Bone marrow hypoplasia due to chemotherapy with disease progression. 49-year-old-woman with metastatic breast cancer before and after 3 cycles of carboplatin chemotherapy. Both rows left-to-right: spine T1-weighted spin-echo, spine T2-weighted spin-echo with spectral fat saturation and b900 3D MIP (inverted scale) images. Top row before chemotherapy shows normal background bone marrow pattern with superimposed small volume bone metastases (arrow heads). Bottom row after chemotherapy shows marked disease progression with enlarging and new bony metastases (arrows). Note that bone marrow hypoplasia has developed in the ribs, spine and pelvis. Note reductions of signal intensity of the spleen secondary to iron deposition due to blood transfusions. There is a right sided silicone containing breast enhancement bra pad in place on both examinations.

*MR scanning has not been established as safe for imaging fetuses and infants under two years of age. The responsible physician must evaluate the benefit of the MRI examination in comparison to other imaging procedures.



3 Bone marrow hypoplasia due to aromatase inhibitor therapy. 56-year-old post-menopausal woman with estrogen receptor positive breast cancer on long term anastrozole therapy. Long term therapy of aromatase inhibitors such as anastrozole put women at greater risk for of osteoporosis which in turn leads to increased bone marrow fat. Left-to-right: spinal T1-weighted GRE sequence (from the scout views), T1-weighted spin-echo, T2-weighted spin-echo with spectral fat saturation and b900 3D MIP (inverted scale) images. There is some loss of vertebral height of the D9 vertebral body. Note the visibility of the entire length of the spinal cord on the 3D inverted MIP images and ready visibility of the dorsal nerve root ganglia of the brachial and lumbar plexuses. Focal high-signal lesions over the left chest are due to an acneiform rash on the skin.

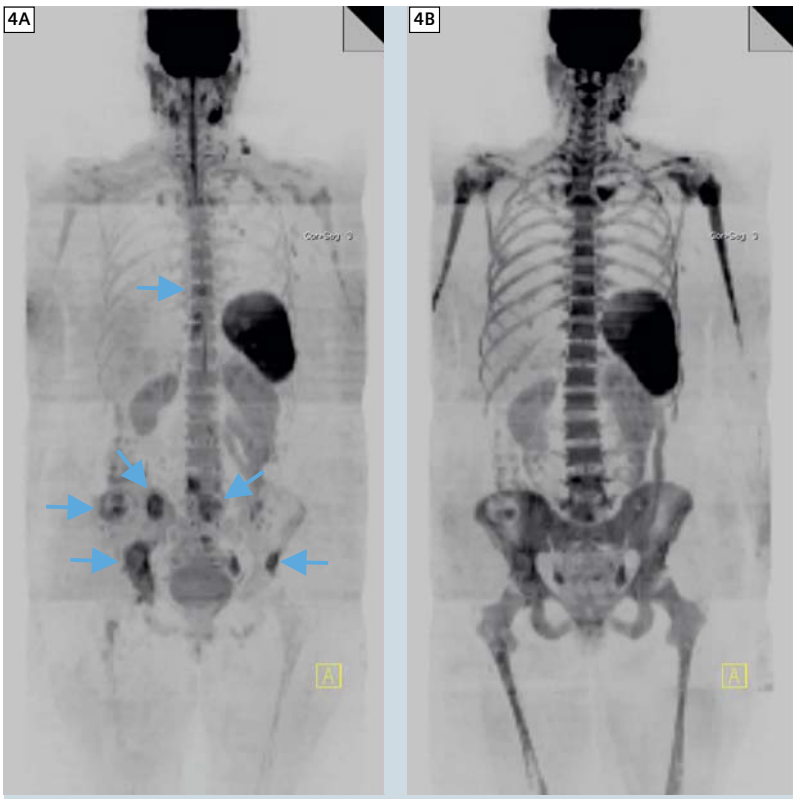

4 Bone marrow hyperplasia induced by chemotherapy with G-CSF therapy. 50-year-old woman with metastatic breast cancer before and after 3 cycles of erubulin chemotherapy with growth-colony stimulating factor (G-CSF) given to prevent neutropenia. b900 3D MIP (inverted scale) images. Left image show multiple bone metastases (arrows). Right image after 3 cycles of chemotherapy shows increases in signal intensity of the bone marrow leading to the decreased visibility of the bone metastases. The splenic size has also increased. The increased signal intensity of the background bone marrow should not be misinterpreted as malignant progression.

is best performed at 1.5T using multiple surface coils for signal reception which allows uniform fat-suppression over large fields-of-view. Although imaging at 3T increases the signal-to-noise ratio, WB-DWI remains challenging because of increased susceptibility artifacts and poorer fat suppression.

A multiple-averaged, free-breathing technique is most commonly used for data acquisition. In general, the use of two diffusion sensitizing gradients is sufficient to enable good quality, clinically useable images to be acquired. Low b-value black-blood (50 s/mm^2) combined with high b-value (800–1000 s/mm^2) images are used in combination for anatomic depiction, disease detection and for the calculation of apparent diffusion coefficient (ADC) values [5, 7]. Our preferred method for fat suppression uses inversion recovery because it allows uniform fat suppression over large fields-of-view [8].

Our institutional protocol combines whole-body MRI and whole-body DWI done on a 1.5T MAGNETOM Avanto scanner (Siemens Healthcare, Erlangen, Germany) equipped with a continuous moving table option and total imaging matrix (Tim) body surface coils. First, conventional sagittal T1-weighted and T2-weighted fat-suppressed images of the spine are obtained. Subsequently, axial T1-weighted and STIR images from the skull vault to the mid-thigh are acquired using continuous table movement employing multiple breath-holds for image acquisitions of the chest, abdomen, pelvis and upper thighs. Axial DWI from the skull vault to the mid-thigh is then performed using b-values of 50 s/mm^2 and a b-value of 900 s/mm^2 with a slice thickness of 5 mm. The axial DWI acquisition is usually achieved in 4 contiguous stations using a free-breathing technique, with each station taking approximately 6 minutes to acquire. The high b-value images are then reconstructed in orthogonal planes as thin multiplanar reconstructions (5 mm) and as thick 3D maximum intensity projections (MIPs) which are usually displayed using an inverted grey scale. ADC maps are computed inline with system soft-

ware using mono-exponential fitting in which each voxel reflects the tissue diffusivity (units: $\mu m^2/s$) (Fig. 1).

Bone marrow imaging on WB-DWI

In order to be able to utilize WB-DWI in the detection, characterization and treatment assessment of skeletal metastases, it is vital to be familiar with the signal distribution of normal bone marrow on high b-value images. Normal adult bone marrow distribution becomes established by the age of 25 years with mixed red bone marrow found in the axial skeleton, the humeral and femoral proximal metaphyses whilst yellow marrow is found in the appendicular skeleton. Thereafter, conversion of red marrow regions to yellow marrow occurs at a slow rate, the speed of conversion being dependent on patient gender and underlying medical conditions [9]. It is thought that the reduced water content [9], the larger-sized fat cells, the hydrophobic nature of fat and poorer perfusion all contribute to lower signal intensities and ADC values of the yellow bone marrow. On the other hand, with increasing cellularity and water content and greater perfusion, mixed yellow-red bone marrow returns higher signal intensities and paradoxically higher ADC values [5, 10–12]. The changing distribution of the normal marrow is exquisitely demonstrated on WB-DWI (Fig. 1). Similarly, both bone marrow hypo- and hypercellularity are also well depicted on WB-DWI. Common causes for bone marrow hypocellularity include chemotherapy (Fig. 2), radiotherapy, myeloproliferative disorders (e.g. myelofibrosis, myelodysplasia), non-malignant marrow disorders (e.g. aplastic anemia), old age and osteoporosis (including drug induced), chronic disease (e.g. renal failure, chronic liver disease, rheumatoid arthritis) and prolonged immobility. In contrast, relative bone marrow hypercellularity is observed in children and adolescents, chronic anaemia, in smokers, chronic cardiac failure, in pregnancy and in patients treated with hematopoietic growth factors such as granulocyte-colony stimulating factors (G-CSF). On WB-DWI, bone marrow hypocellularity demonstrates decreased signal intensity on high b-value images with the increased visibility of the spinal cord (Fig. 3). Marrow hypercellularity presents as diffuse increases in signal intensity on high b-values [5, 6]. Changes in background bone marrow cellularity can affect the visibility of bone marrow metastases. Bony metastases can become less conspicuous against increasing background signal intensities when growth colony stimulating factor (G-CSF) is used to prevent chemotherapy induced neutropenia (Fig. 4). On the other hand, the detection of bone metastases is improved in bone marrow that is relatively hypocellular, for example in the older patient or after chemotherapy (Fig. 2).



5 Poor visibility of treated metastases and osteoblastic metastases. 69-year-old man with metastatic prostate cancer on long term, third line hormonal therapy with abiraterone being evaluated for rising serum prostate specific antigen (PSA) levels. He has had an excellent response to 2 years of treatment with residual abnormalities in his bone marrow visible on T1-weighted **(5A)** and T2-weighted **(5B** with fat suppression**)** spinal images. No hyperintensity is seen on the b900 3D MIP (inverted scale) image **(5C)** indicating the absence of osteolytic disease. Bone scan **(5D)** shows a focal area of osteoblastic uptake in the intertrochanteric region of the left femur (arrow) which is not visible as a discrete region on the b900 3D inverted MIP image.

Skeletal metastases detection

On WB-DWI, skeletal metastases appear as focal or diffuse areas of high signal intensity on high b-values (Figs. 2, 4, 5). It is, however, important to emphasize that WB-DWI should not be performed nor interpreted in isolation but rather has to be considered as a valued adjunct to anatomical whole-body MRI and therefore needs to be interpreted in conjunction with conventional WB-MRI studies [13]. This assertion has been highlighted in a recent meta-analysis which demonstrated that the high sensitivity of WB-DWI to detect metastases was at the expense of specificity [3]. Causes for false-positive findings are bone marrow edema caused by fractures, osteoarthritis, infection, bone infarcts, vertebral hemangiomas, isolated bone marrow islands and bone marrow hyperplasia due to G-CSF (Fig. 4). However, many of these false-positive findings can be overcome by correlating high b-value DW images with ADC maps and anatomical sequences [5].

In contrast, causes for false-negative findings are low levels of bone marrow infiltration such as in smoldering multiple myeloma or when background bone marrow hyperplasia obscures the pres-

ence of metastases. Similarly, the detection of skeletal metastases on WB-DWI may be impaired in areas of macroscopic movement such as the anterior ribs and sternum. Visibility of skull vault infiltrations can be impaired because of the adjacent high signal of the brain. The visibility of skull base disease is impaired because of susceptibility effects. Another important cause for false-negative findings is successfully treated malignant disease and sclerotic metastases (Fig. 5). In general, lytic lesions are better detected than sclerotic or treated lesions on WB-DWI. This is due to the lower water and cellular content of sclerotic and treated metastases [10, 14]. Diffusion-weighted MRI is better at detecting skeletal lesions from smaller cancer cell size infiltrations such as those due to breast cancer, myeloma, lymphoma and small cell tumors such as neuroendocrine tumors compared to bony metastases from clear cell cancers of the kidneys.

Therapy assessment of skeletal metastases on WB-DWI

Successful treatment of skeletal metastases is characterized by tumor cell death which results in increased water diffusivity. On WB-DWI, this leads to marked increases of ADC values. The extent of ADC increases after successful therapy is thought to be related to mechanism of tumor cell death. It has been proposed that therapies which result in necrotic cell death may result in higher ADC values than treatment regimes which result in non-necrotic tumor cell death. This is thought to be due to the fact that necrotic cell death is associated with an inflammatory response which results in increased tissue water. Signal intensity changes on high b-values images after successful therapy are more

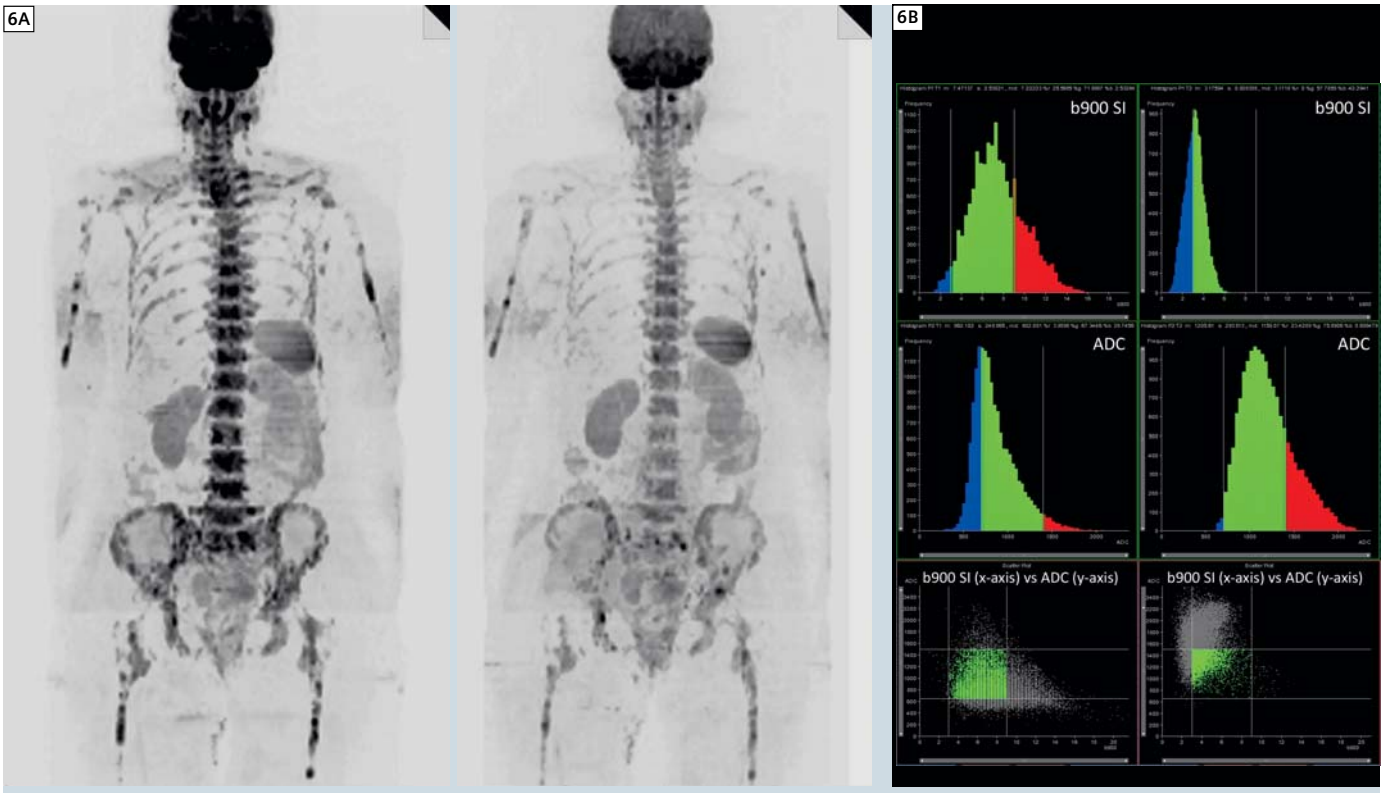

6 Therapy response in metastatic breast cancer. Serial changes in a 64-year-old woman with metastatic breast cancer responding to treatment with FEC (Fluorouracil (5FU), epirubicin and cyclophosphamide) chemotherapy with bisphosphonates. **(6A)** b900 3D MIP (inverted scale) images before (left column) and after 3 cycles of treatment (right column). A diffuse pattern of metastatic bone disease is seen pre-treatment that decreases in extent and signal intensity indicating disease response. There are a few focal areas of persistent signal hyperintensity post-therapy indicating likely active disease. **(6B)** Histogram analysis of a pelvic volume of interest defined on b900 images of the pre-treatment examination and applied to the second examination after robust image registration. Threshold histograms of muscle normalized b900 signal intensity (top row) and ADC values (middle row), and pixel scatter plots (bottom row) of normalized b900 signal intensity (x-axis) and ADC values (y-axis). The control lines on the histograms and scatter plots are placed on 3 and 9 for normalized b900 signal intensity and 650 and 1500 $\mu m^2/s$ for ADC values. The histograms show reductions in signal intensity (more blue pixels and less overall spread) on top row accompanied by increases in ADC values (more green and red pixels). Note how the pixel scatter plot moves to the top left. Analyses were done using OncoTreat* software (Works-in-progress, Siemens Healthcare, Erlangen, Germany).

*This information about this product is preliminary. The product is under development and not commercially available in the U.S., and its future availability cannot be ensured.

varied, but in most cases decreases in signal intensity are seen (Fig. 6). Occasionally, successful treatment response may demonstrate persistent high signal intensity on high b-value images but with an associated increase in ADC-values. This appearance is termed 'T2 shine-through' and is due to tumor necrosis. It is thus prudent to always correlate high b-value images with ADC values when interpreting WB-DWI in order to avoid misinterpreting persistent high signal intensity on high b-value images as non-responding disease. Another pattern is a decrease in signal intensity on high b-values associated with unchanged ADC values or slight decreases in ADC values. Our experience from comparison with CT examinations, Dixon images and anatomical MRI studies suggests that this pattern may be due to sclerosis or fibrosis. We have classified this pattern as indeterminate and therefore take into account other radiological and clinical findings for response assessment.
By contrast, patients who fail to respond to therapy usually demonstrate persistent or increasing bone marrow hyperintensity on high b-value images. In the context of disease progression, a decrease or no change in ADC values can be observed because of increasing in tumor cell density within the confines of a fixed bone marrow space. Small increases in ADC values can also be observed in progressive disease (but of a much smaller magnitude compared to responding lesions). For this reason we use an upper ADC cut-off value derived from untreated patients in order to differentiate responders from non-responders. This cut-off value is likely to be dependent on the choice of b-values utilized and the tumor type [5, 6].

Clinical indications

At our institution, we have performed more than 1,200 WB-MRI examinations incorporating diffusion MRI in the last four years using it for bone marrow metastasis detection and therapy monitoring for a variety of cancer types – principally in breast and prostate cancer and multiple myeloma. It is increasingly being used for the evaluation of patients with melanoma, lymphoma and renal cancer. We have also found it valuable for the examination of children* and young adults, pregnant* women with cancer and in patients with impaired renal function or allergies when there is a contraindication to the intravenous injection of contrast medium.

Conclusions

WB-DWI has emerged as a powerful imaging tool in the detection, characterization and for monitoring of treatment response of tumors. It particularly excels in the detection and disease extent assessment of bone marrow lesions as well as in the evaluation of therapy response of skeletal lesions. It is however important to emphasize the fact that WB-DWI has to be interpreted in conjunction with conventional whole-body MRI sequences in order to avoid pitfalls in diagnoses. There is an urgent need to better understand the biologic basis of treatment-related changes. Furthermore response criteria need to be established and tested in prospective clinical studies. Nevertheless, WB-DWI demonstrates great potential in the evaluation of bone marrow lesions because it is quick to perform, can be incorporated into standard clinical protocols and can potentially answer clinical questions regarding tumor response more reliably than conventional imaging modalities.

*MR scanning has not been established as safe for imaging fetuses and infants under two years of age. The responsible physician must evaluate the benefit of the MRI examination in comparison to other imaging procedures.

Contact
Prof. Anwar R. Padhani, MBBS FRCP FRCR
Paul Strickland Scanner Centre
Mount Vernon Cancer Centre
Rickmansworth Road
Northwood
Middlesex HA6 2RN
United Kingdom
Phone: +44-(0) 1923-844751
Fax: +44-(0) 1923-844600
anwar.padhani@stricklandscanner.org.uk

References

1. Jadvar H. Prostate cancer: PET with 18F-FDG, 18F- or 11C-acetate, and 18F- or 11C-choline. J Nucl Med 2011;52:81-89.
2. Mankoff DA, Link JM, Linden HM, Sundararajan L, Krohn KA. Tumor receptor imaging. J Nucl Med 2008;49 Suppl 2:149S-163S.
3. Wu LM, Gu HY, Zheng J, et al. Diagnostic value of whole-body magnetic resonance imaging for bone metastases: a systematic review and meta-analysis. J Magn Reson Imaging 2011;34:128-135.
4. Schmidt GP, Reiser MF, Baur-Melnyk A. Whole-body MRI for the staging and follow-up of patients with metastasis. Eur J Radiol 2009;70:393-400.
5. Padhani AR, Koh DM, Collins DJ. Whole-body diffusion-weighted MR imaging in cancer: current status and research directions. Radiology 2011;261:700-718.
6. Padhani AR, Gogbashian A. Bony metastases: assessing response to therapy with whole-body diffusion MRI. Cancer Imaging 2011;11 Spec No A:S129-145.
7. Padhani AR. Diffusion magnetic resonance imaging in cancer patient management. Semin Radiat Oncol 2011;21:119-140.
8. Koh DM, Blackledge M, Padhani AR, et al. Whole-Body Diffusion-Weighted MRI: Tips, Tricks, and Pitfalls. AJR Am J Roentgenol 2012;199:252-262.
9. Hwang S, Panicek DM. Magnetic resonance imaging of bone marrow in oncology, Part 1. Skeletal Radiol 2007;36:913-920.
10. Messiou C, Collins DJ, Morgan VA, Desouza NM. Optimising diffusion weighted MRI for imaging metastatic and myeloma bone disease and assessing reproducibility. Eur Radiol 2011;21:1713-1718.
11. Hillengass J, Bauerle T, Bartl R, et al. Diffusion-weighted imaging for non-invasive and quantitative monitoring of bone marrow infiltration in patients with monoclonal plasma cell disease: a comparative study with histology. Br J Haematol 2011;153:721-728.
12. Nonomura Y, Yasumoto M, Yoshimura R, et al. Relationship between bone marrow cellularity and apparent diffusion coefficient. J Magn Reson Imaging 2001;13:757-760.
13. Lecouvet FE, El Mouedden J, Collette L, et al. Can whole-body magnetic resonance imaging with diffusion-weighted imaging replace Tc 99m bone scanning and computed tomography for single-step detection of metastases in patients with high-risk prostate cancer? Eur Urol 2012;62:68-75.
14. Eiber M, Holzapfel K, Ganter C, et al. Whole-body MRI including diffusion-weighted imaging (DWI) for patients with recurring prostate cancer: Technical feasibility and assessment of lesion conspicuity in DWI. J Magn Reson Imaging 2011;33:1160-1170.

Biochemical MRI in Musculoskeletal Applications

Siegfried Trattnig; Štefan Zbýň; Vladimir Juras; Pavol Szomolanyi; Stephan Domayer; Iris-Melanie Noebauer-Huhmann; Goetz Welsch; Benjamin Schmitt

MR Centre – High field MR, Department of Radiology, Medical University of Vienna/Vienna General Hospital, Vienna, Austria

1. Biochemical MRI assessment of cartilage and cartilage repair

To visualize the constitution of articular cartilage and cartilage repair tissue, a variety of different MRI methods are available. Considering the composition of healthy hyaline articular cartilage, these methods can depict relatively specifically either one component of cartilage or a combination of different components. Although some more recent techniques, in particular CEST, have not yet been validated sufficiently, studies have shown promising initial results. Articular cartilage is complex, dense, connective tissue that relies on the diffusion of solutes for nutrition [1]. Responsible for the biomechanical properties of articular cartilage is the extracellular matrix, mainly composed of water (~75%), collagen (~20%), and proteoglycan aggregates (~5%) [1, 2]. Water either freely moves throughout the matrix or is bound to macromolecules. Collagen in hyaline cartilage is largely type II, which creates a stable network throughout the cartilage. The negatively-charged proteoglycans are composed of a central core protein to which glycosaminoglycans (GAG) are bound.

1.1) Proteoglycan-sensitive MRI techniques

Although no MRI sequence is really 100% specific for only proteoglycans or collagens, there are MRI methods that reportedly focus mainly on one component of articular cartilage. The negatively-charged proteoglycan, composed of a central core protein to which GAG are bound, can be visualized by delayed gadolinium-enhanced MRI of cartilage (dGEMRIC*) [3], sodium MR imaging [4, 5], and, very recently, chemical exchange-dependent saturation transfer (CEST) [6]. Of these techniques, only dGEMRIC has so far become clinically useful in cartilage repair imaging.

a) Delayed gadolinium-enhanced MRI of cartilage (dGEMRIC)*

GAG are important to the cartilage tissue's biochemical and biomechanical function. GAG are the main source of fixed charge density (FCD) in cartilage, and are often decreased in the early stages of cartilage degeneration [7], or in repar-

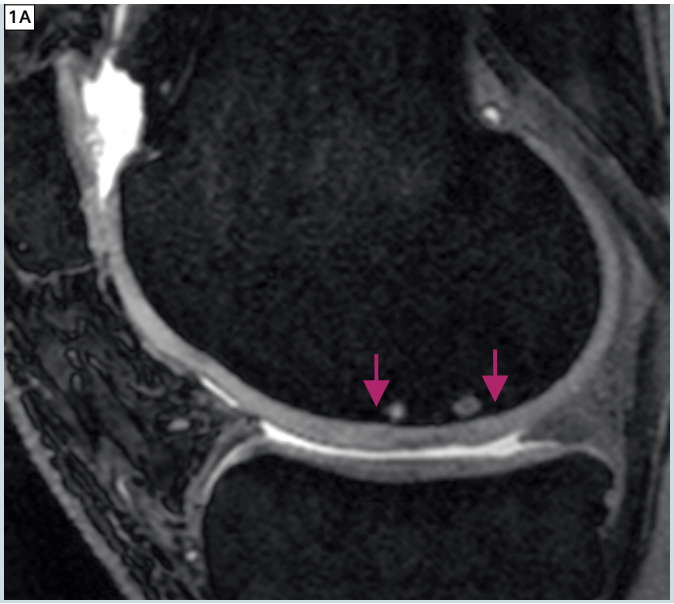

1 **(1A)** Shows a sagittal 3D GRE image in a patient after microfracturing at 3T. In the area of microfracture only slight thinning of the cartilage layer can be seen. **(1B)** Precontrast* T1-map shows no difference in T1 relaxation times in the repair tissue; however, in the postcontrast* image **(1C)** a significant drop in T1 values in the repair tissue can be seen, which corresponds to a low glycosaminoglycan content.

ative cartilage after cartilage repair [8]. Intravenously administered gadolinium diethylenetriamine pentaacetate anion, ($Gd\text{-}DTPA^{2-}$) penetrates the cartilage through both the articular surface and the subchondral bone. The contrast equilibrates in inverse relation to the FCD, which is, in turn, directly related to the GAG concentration. Therefore, T1, which is determined by the Gd-DTPA2- concentration, becomes a specific measure of tissue GAG concentration, suggesting that $Gd\text{-}DTPA^{2-}$ enhanced MRI has the potential to monitor the GAG content of cartilage in vivo [9]. Thus, T1-mapping, enhanced by delayed administration of $Gd\text{-}DTPA^{2-}$ (T1 dGEMRIC*), can be considered the most widely used methodology for detecting proteoglycan depletion in articular cartilage (Fig. 1), and has shown promising results [10, 11].
As differences in pre-contrast values between cartilage repair tissue and normal hyaline cartilage are larger compared to early cartilage degeneration, in cartilage repair tissue, the pre-contrast T1 values must also be calculated [8]. The concentration of GAG is represented by delta ΔR1, i.e., the difference in relaxation rate (R1=1/T1) between $T1_{precontrast}$ and $T1_{postcontrast}$. Thus, the sequence must be performed twice, for pre-contrast and delayed post-contrast T1-mapping. This increases the total scan time, and requires a break in between the two MRI scans, where the contrast agent must be administered and a delay of at least 90 minutes after injection is needed for penetration of the contrast agent into the cartilage. Scan time reduction, compared to the standard inversion recovery (IR) evaluation, has been achieved with a new approach using fast T1-mapping based on GRE-technique [12]. Although the 90-minute delay is still required, this might increase the clinical applicability of the dGEMRIC* technique. Other drawbacks of dGEMRIC* are the use of i. v. contrast agent administration, the necessity of a double dose of contrast agent, and the fact that uptake and distribution of contrast agent is not only dominated by GAG.
Since GAG content is responsible for cartilage function, particularly its tensile strength, the monitoring of the development of GAG content in cartilage repair tissues may provide information about the quality of the repair tissue. A study by our group showed that dGEMRIC* was able to differentiate between different cartilage repair tissues with higher delta ΔR1 values, and thus, lower GAG content, in cartilage repair tissue after MFX, compared to MACT [13]. The applicability of this technique has also been shown in regions other than the knee joint [14–16].

b) 23Na (Sodium) imaging of cartilage

The major advantage of sodium MRI in musculoskeletal applications is that it is highly specific for glycosaminoglycan content, and, since the sodium from surrounding structures in the joint is low (< 50 mM), cartilage can be visualized with very high contrast without the requirement for any exogenous contrast agent, such as with dGEMRIC*.
The recent proliferation of 7T[1] whole-body MRI scanners in clinical research centers has had a significant impact on sodium MRI and its potential for clinical use. Since signal-to-noise (SNR) scales linearly with increasing field strength, and because of the lack of B_1 penetration and B_0 susceptibility that pose problems with proton imaging, sodium MRI can be particularly advantageous at higher fields. The low gyromagnetic ratio of sodium also means significantly lower power deposition compared with proton imaging, which thus reduces SAR problems at 7T[1]. It is, therefore, very likely that the improved SNR sodium MRI at 7T[1] can provide a robust tool for quantitative imaging of MSK structures in particular cartilage. Although sodium MRI has high specificity and does not require any exogenous contrast agent, it does require special hardware capabilities (multinuclear) and specialized RF coils [5].

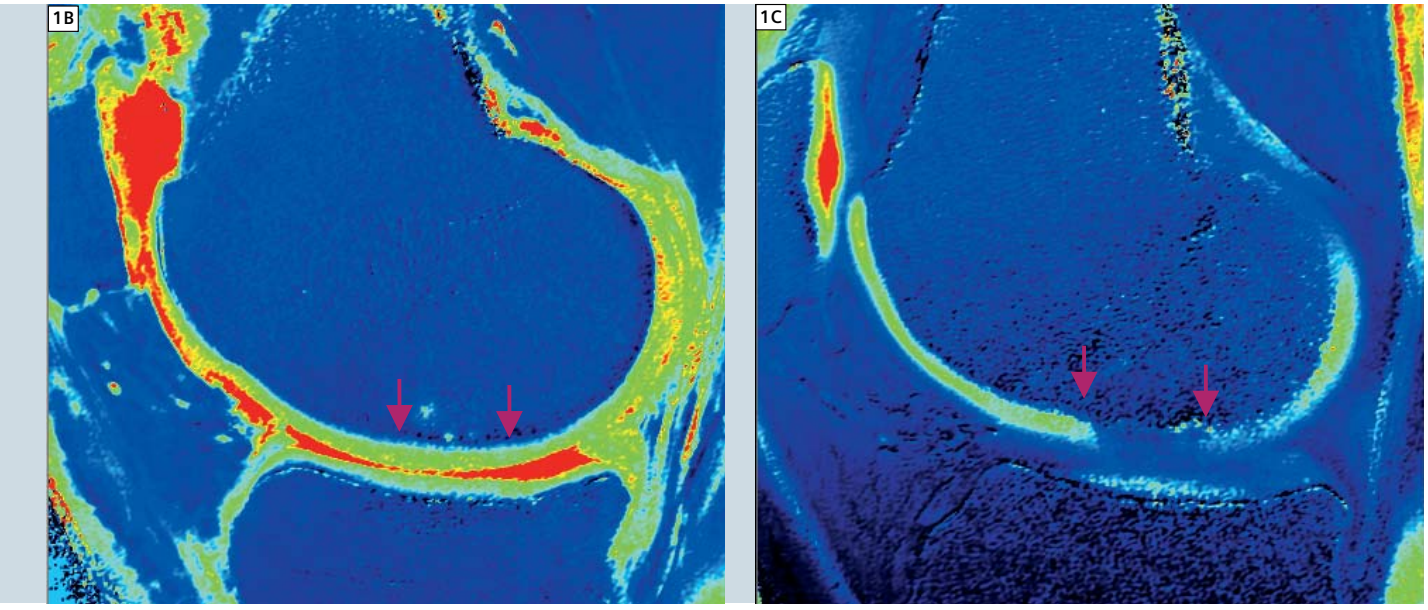



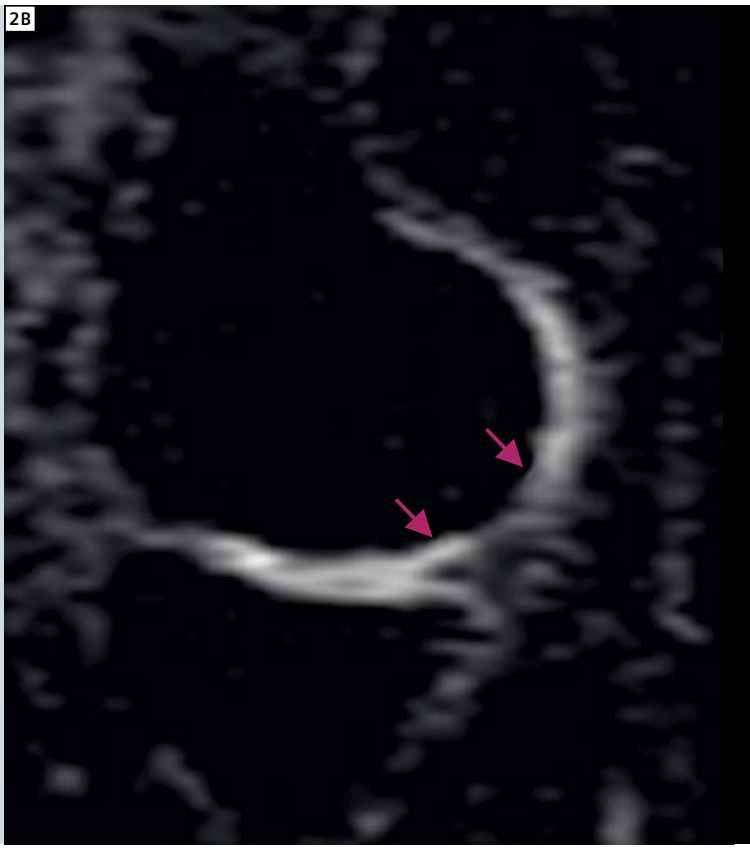

With the application of a 7T whole-body system and a modified 3D GRE optimized for sodium imaging and dedicated multi-element sodium coils, we performed a series of clinical studies.
In a small group of 12 patients after matrix-associated autologous chondrocyte transplantation (MACT), sodium imaging enabled the differentiation between sodium content, and thus GAG in the transplants, compared to native, healthy cartilage. In all patients, the sodium SNR was lower in the repair tissue compared to healthy cartilage.
A good correlation between sodium imaging and dGEMRIC* in the quantification of GAG content was found in patients after MACT [17].
In another study, 18 patients who had different cartilage repair surgeries (nine bone marrow stimulation (BMS) and nine MACT patients), age-matched, with similar postoperative intervals and defect locations, were examined with sodium imaging. Sodium SNR was significantly lower in BMS ($p < .001$) and MACT ($p = .002$) repair tissue, compared to reference cartilage. These differences were influenced by surgery type, but not by age and follow-up interval. Although sodium SNR was not different between the reference cartilage in the MACT and BMS patients ($p = .528$), it was significantly higher in MACT than in BMS repair tissue ($p = .002$). There was no difference between the magnetic resonance observation of cartilage repair tissue (MOCART) scores for MACT and BMS patients ($p = .889$). No correlation was observed between the MOCART score and repair tissue SNR with sodium imaging ($R = .111$). Our results suggest that MACT provides higher GAG content and, therefore, higher-quality repair tissue compared to the BMS techniques. Sodium MR imaging at 7T[1] (Fig. 2) might be beneficial in the non-invasive evaluation of cartilage repair procedure efficacy in the knee [18].
Similar studies in patients after long-term autologous osteochondral transplantation (AOT) in which hyaline cartilage is transplanted, and in patients after patella dislocation, have demonstrated the potential of sodium imaging in the detection of early stages of cartilage degeneration [19].

c) Chemical Exchange Saturation Transfer (CEST)

Chemical exchange between bulk water protons and protons bound to solutes can be visualized with MR imaging [20] by using the saturation transfer (ST) technique, a common approach in nuclear magnetic resonance (NMR) [21]. Consequently, the corresponding MR imaging scheme is referred to as CEST MRI [22, 23]. In principle, CEST MRI relies on a reduction of bulk water MR signal as a consequence of selective saturation of off-resonant (solute) spins and subsequent chemical transfer of the saturation to spins of bulk water [24].
A prerequisite for observation of CEST phenomena within a chemical environment is the abundance of sufficiently labile solute protons that are in contact

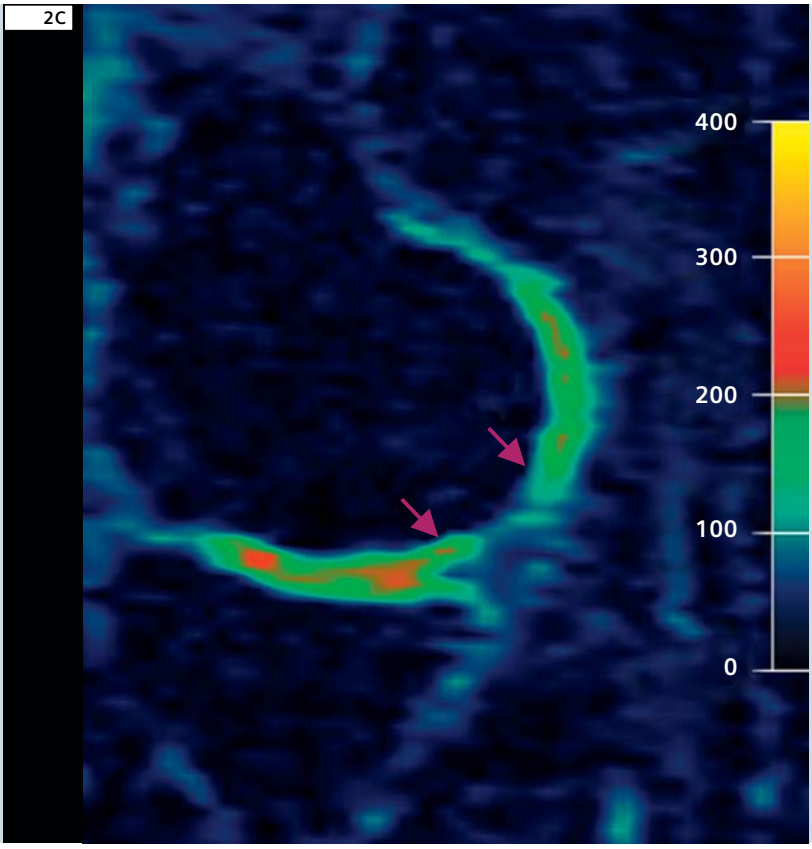

2 Sagittal images of the knee of a 43-year-old woman obtained 42 months after MFX cartilage repair procedure. The proton-density-weighted 2D-TSE image with fat suppression **(2A)**, sodium 3D-GRE image **(2B)**, and color-coded sodium 3D-GRE image **(2C)**. The cartilage repair tissue is situated between the two arrows. Color scale represents the sodium signal intensity values.

with bulk water. The offset of the resonance frequency of the labile protons (Δω) in Hz must be greater than the exchange rate *(k)* to provide CEST effects that can be distinguished from direct water saturation. For example, hydroxyl and amide protons of GAG were shown to be suited for CEST experiments (gagCEST) due to their chemical exchange properties [25]: GAG –OH protons resonate at frequency offsets of 1 and 1.5–2 ppm downfield from bulk water, and *k* can be on the order of up to 1000 s^{-1} [26]. This means that magnetic field strengths greater than 3 Tesla are beneficial for gagCEST experiments, as the condition $\Delta\omega > k$ will be increasingly fulfilled. At higher fields, i.e., with increasing frequency differences, the confounding direct water saturation (RF spillover) decreases. In combination with longer T1 relaxation times, this factor makes ultra high field strengths, such as 7T[1], potentially favorable for CEST experiments. Consequently, gagCEST imaging was first demonstrated to be a sensitive biomarker for cartilage GAG content in *in vitro* studies of bovine cartilage at 11.7T[1] [25].

Since the introduction of the gagCEST imaging, more studies have been performed on animal and human subjects to assess the feasibility of gagCEST imaging *in vivo* [27–29], and a large palette of imaging sequences for fast and reliable detection of CEST effects have been proposed [27, 30–32]. The vast majority of techniques is based on repetitive image acquisition with pre-saturation at different offset frequencies (Δω), which allows plotting of the remaining bulk water signal (M_{Sat}), normalized to a reference (M_{Ref}), against the RF pre-saturation offset (z-spectrum). In the z-spectrum, CEST effects appear asymmetric with respect to the water resonance and, thus, calculation of the asymmetry of the magnetization transfer ratio, (Eq. 1) ($MTR_{asym}(\Delta\omega) = (M_{Sat}(-\Delta\omega) - M_{Sat}(+\Delta\omega))/M_{Ref}$), provides a positive measure of CEST effects. In first order, the magnitude of MTR_{asym} values in cartilage scales linearly with the ratio of GAG protons to bulk water protons.

gagCEST imaging (Fig. 3) was shown to be a valuable tool for the non-invasive assessment of GAG content *in vivo*. For example, we could demonstrate that gagCEST can be used to reliably detect GAG in the knee cartilage of patients after cartilage repair surgery [33]. In this study, which was performed at 7T[1], a 3D GRE-based gagCEST measurement technique was used, and results from ^{23}Na MRI served as a reference for GAG measurements. Moreover, the potential of gagCEST for GAG evaluation in intervertebral discs (IVD) at 3T has been demonstrated in healthy volunteers [34, 35] and in patients with lower back pain [36]. Given the results from the latter studies on IVDs from our group, it is reasonable to assume that gagCEST can also be used to assess cartilage GAG content at 3T. Thus, the indicated potential of gagCEST for the clinical routine is tremendous because it also offers advantages compared to other GAG-sen-



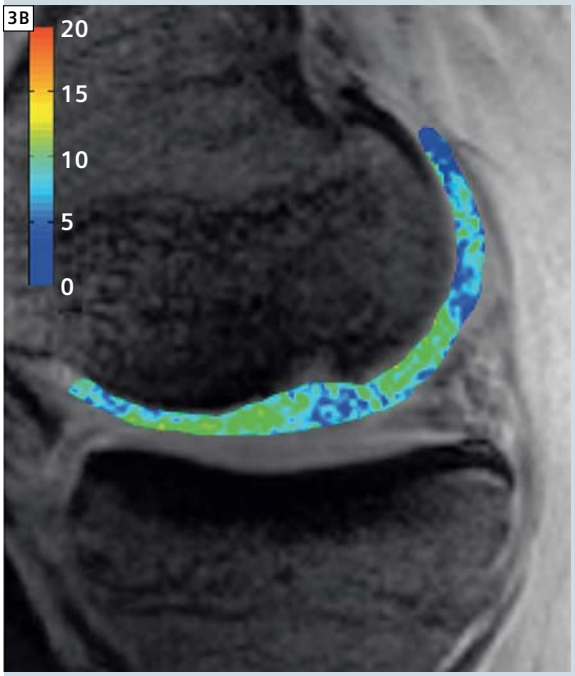

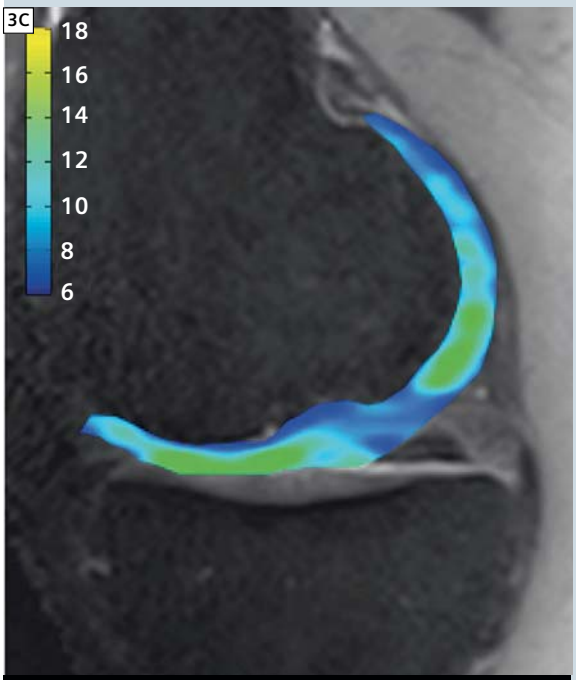

3 High-spatial-resolution **(3A)** morphologic, **(3B)** gagCEST, and **(3C)** 23 Na MR images of the knee joint cartilage of a patient after MFX in the medial femoral condyle. Color bars on (3B) and (3C) represent MTR asym values summed over offsets from 0 to 1.3 ppm (gagCEST) and sodium SNRs, respectively. Both techniques show decreased signals in repair tissue compared to surrounding native tissue.

sitive imaging techniques, such as dGEMRIC* and sodium imaging. These advantages include the relatively short acquisition time, which covers the entire volume of a knee joint in ~10 minutes [33], no administration of contrast agent, and simple implementation into a standard imaging protocol.

1.2) Collagen and water-sensitive MRI techniques

Although the differentiation of particular components of articular cartilage that are visualized by a specific sequence is not entirely possible, the classic biochemical MR methodology that focuses on the collagen content of articular cartilage is T2-mapping [37]. In addition to the transverse relaxation time (T2) of articular cartilage, recently, T2* relaxation is being discussed for the depiction of the collagen matrix [38]. Magnetization transfer contrast (MTC) might also play a more important role in future approaches [39].

T2 relaxation time mapping

The transverse relaxation time (T2) of cartilage is a sensitive parameter for the evaluation of changes in water and collagen content and tissue anisotropy [37]. Cartilage T2 reflects the interaction of water and the extracellular matrix on a molecular level. The collagen fiber orientation defines the layers of articular cartilage. Thus, the three-dimensional organization and curvature of the collagen network, influenced by water mobility, the proteoglycan orientation, and the resulting magic angle at 55° (with respect to the main magnetic field B_0) influence the appearance of T2 [40, 41]. In healthy articular cartilage, an increase in T2 values from deep to superficial cartilage layers can be observed, based on the anisotropy of collagen fibers running perpendicular to cortical bone in the deep layer of cartilage [42]. Histologically validated animal studies have shown this zonal increase in T2 values as a marker of hyaline or hyaline-like cartilage structure after cartilage repair procedures in the knee [43, 44]. To visualize this zonal variation *in vivo*, high spatial resolution

is essential, which can already be achieved with high-field MR, together with dedicated multi-channel coils in clinical approaches (Fig. 4). In cartilage repair tissue, global (bulk) T2 values, as well as line profiles, have shown an increase in the early post-operative follow-up period, which might enable visualization of cartilage repair maturation [45]. Another study by our group further showed the ability of zonal T2 evaluation to differentiate cartilage repair tissue after microfracture (MFX) and MACT [46]. Whereas cartilage repair tissue after MFX – histologically seen as fibrocartilage – shows no zonal increase from deep to superficial cartilage aspects, repair tissue after MACT – histologically reported as hyaline-like – shows a significant stratification.

The current evidence shows that the quality of the repair tissue is the key to success in the long term. Patients with repair tissue similar to the native articular cartilage are more likely to have good mid-term results, and in the knee, cell-based techniques result more often in hyaline-like repair tissue than does microfracturing.

In addition to the knee joint, studies have been performed to analyze different repair surgery techniques in the ankle joint. The initial results at 3T were highly surprising; the average T2 value of the repair tissue after microfracture did not differ significantly from the repair tissue after matrix associated autologous chondrocyte transplantation (MACT). These results were very different from the analyses in the knee, but did, however, agree with the clinical evidence in the literature.

A major drawback of T2-mapping in the ankle was that the SNR even at 3T was not sufficient to perform a zonal analysis of the very thin cartilage layer of the talus. Based on the results in the knee, this might be crucial for characterizing the quality of cartilage repair tissue, as the zonal T2 variation correlates with the degree of organization of the collagen network, and therefore, with the general quality of the repair tissue.

The optimization of the multi-echo spin echo T2-mapping algorithm for 7T yielded a high SNR, better resolution within a clinically feasible scan time, and enabled us to perform an initial comparison of 20 cases after microfracture and MACT of the ankle joint cartilage. The analysis confirmed that there was no significant difference between the average T2 values of the repair tissue after either technique. The major advance was, however, the possibility of a zonal analysis of the healthy cartilage in asymptomatic volunteers, and in patients after cartilage repair [47].

The values of the superficial layer of the repair tissue were comparable to those of articular cartilage; however, there was a substantial difference in the deep layer. A significantly higher T2 was demonstrated for the repair tissue when compared to the healthy reference. Again, there was no difference between the cartilage repair techniques. T2-mapping yielded repair tissue with comparable properties in the MR analysis, which further substantiates the notion that cartilage repair of the ankle cannot be compared to the knee. Bone marrow stimulation techniques are less invasive and less costly than MACT, and might yield a comparable or even better outcome for this joint. It should be noted that the evidence does not allow for

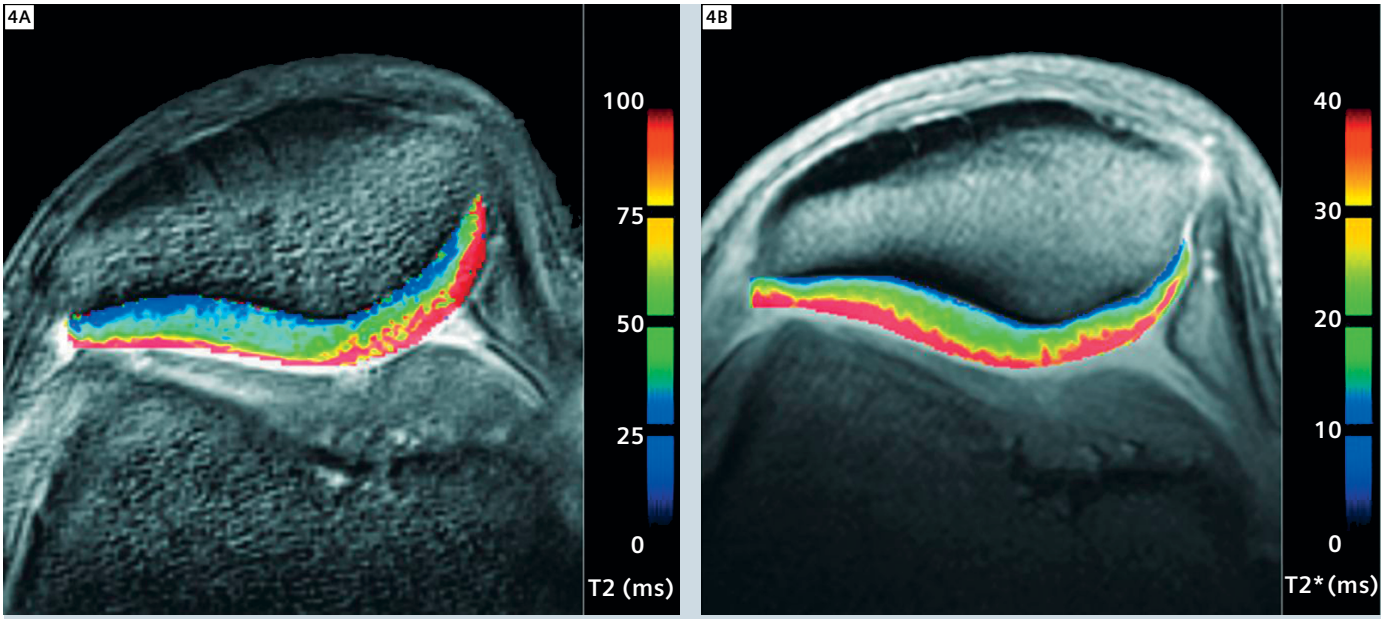

4 Axial T2-maps **(4A)** and T2*-map **(4B)** of the cartilage layer of the patella at 7 Tesla[1] nicely demonstrate the zonal variation in the collagen fiber network in cartilage in this volunteer.

a conclusion at this time; however, biochemical MRI can be of substantial help in determining future treatment algorithms in this field.
In osteoarthritis, however, T2-mapping has shown varying results [48–50] and the role of T2 as an absolute quantification parameter must be further analyzed. Thus, it is not yet totally clear whether a slight increase or decrease in T2 relaxation times can be correlated to morphological changes. Nevertheless, T2-mapping seems to offer potential in this area as well. Conclusions would be more easily derived, however, from a longitudinal evaluation of the same subject, with MRI performed at the same time of day.

2. Biochemical MRI assessment of the intervertebral disc

For biochemical MR imaging of the intervertebral disc (IVD), the following MR methods and techniques were optimized by our group: T2-mapping; T2*-mapping; diffusion-weighted imaging at 3 Tesla; and recently, sodium imaging at 7 Tesla; and Chemical Exchange Saturation Transfer (CEST) at 3 Tesla (Fig. 5).
In an initial trial on 34 patients with lower back pain but without radicular symptoms we compared standard morphological MRI at 3T with T2-mapping [51, 52]. For T2-mapping, all discs of the lumbar spine were analyzed by classification into five equally-sized regions-of-interest (ROI) (20% each) in the sagittal plane, where the anterior and posterior 20% were defined anatomically as the annulus fibrosus (AF) and the 60% area in between the anterior and posterior represented the nucleus pulposus (NP) of the IVD. We found a good correlation between the morphological Pfirrmann classification and T2 relaxation time values. To further increase the sensitivity of the analysis, the posterior annulus fibrosus was further subdivided into two 10% ROIs to consider the axial load on the posterior column of the spine. This analysis provided a possible marker for the early stage of disc degeneration [51].
Furthermore, a comparison of quantitative T2 values of the IVD with conventional MRI findings of the spine at 3T was performed [53]. In a total of 265 discs, there were 39 focal herniations, 10 annular tears, 123 disc bulgings, and 103 normal discs. We found a statistically significant difference between the nucleus pulposus T2 values in discs with annular tears and all other groups with the discs with annular tears, showing significantly lower T2 values compared to discs without annular tears. The difference in NP T2 values between discs with focal herniations and normal discs was also significant. However, no significant difference was found between NP T2 values between disc bulging and disc herniation. Thus, for the first time, quantitative T2-mapping of the NP at 3 Tesla demonstrated significant differences in T2 values between different dislocations of the discs of the lumbar spine.
In addition, methodologically, T2-mapping of the IVD was compared to T2*-mapping at 3 Tesla in 30 patients with lower back pain [54]. The highest variation with an increase of T2 and T2* values from the AF to NP was found in Pfirrmann grade I and decreased with higher Pfirrmann grades II-IV. In addition to T2-mapping, T2*-mapping revealed further changes in the posterior annulus fibrosus. The correlation between T2 and T2*-mapping showed a moderate correlation of 0.21 to 0.356. The clear differentiation between different stages

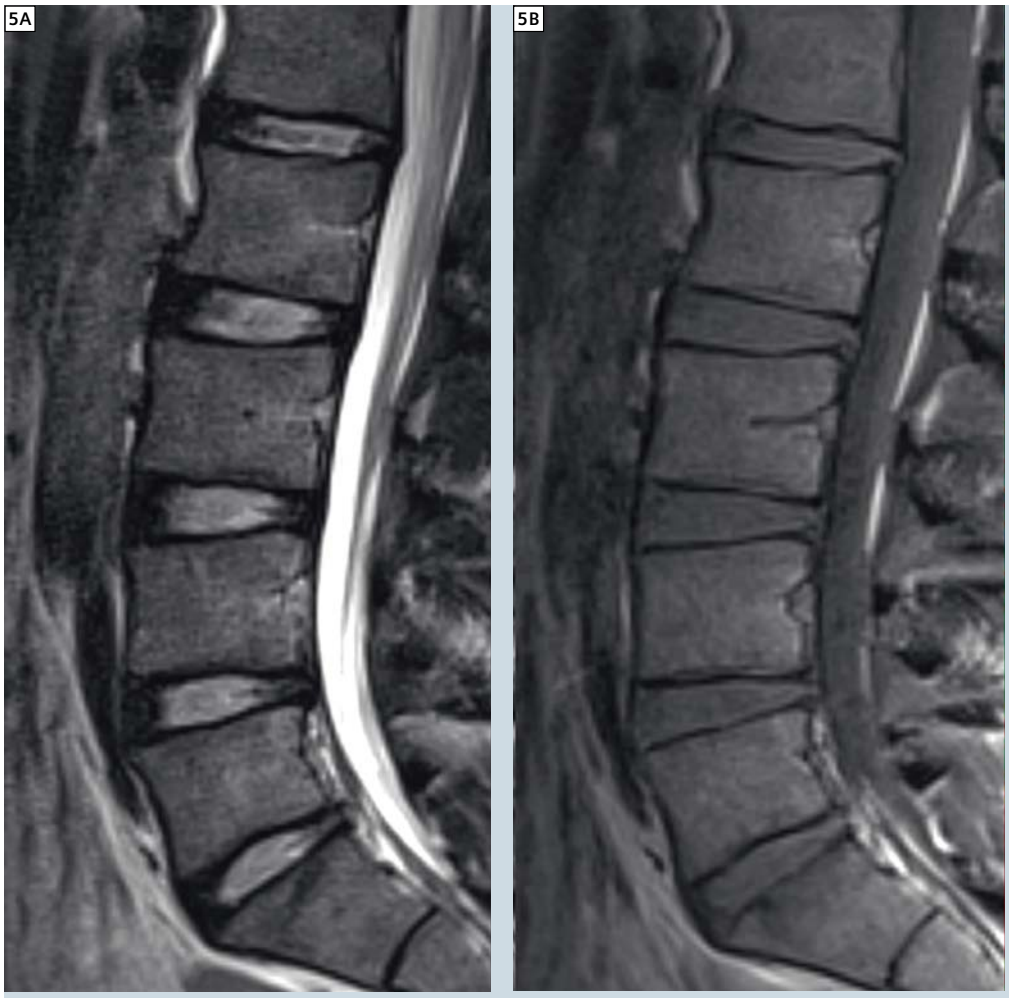

5 Comparison of morphological and biochemical imaging of the intervertebral discs of the lumbar spine in a healthy volunteer using T2 FSE **(5A)**, T1 FSE **(5B)**, T2-map **(5C)**, and T2*-map **(5D)**.

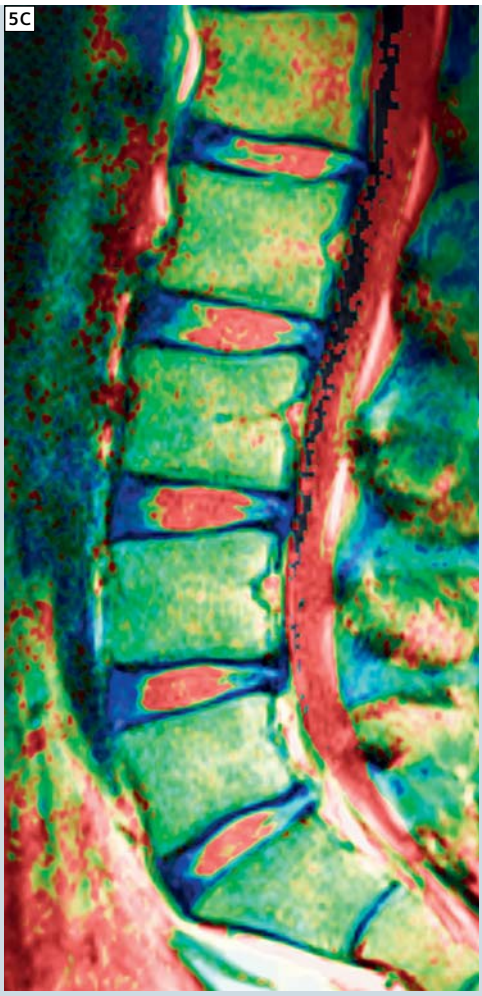
5C

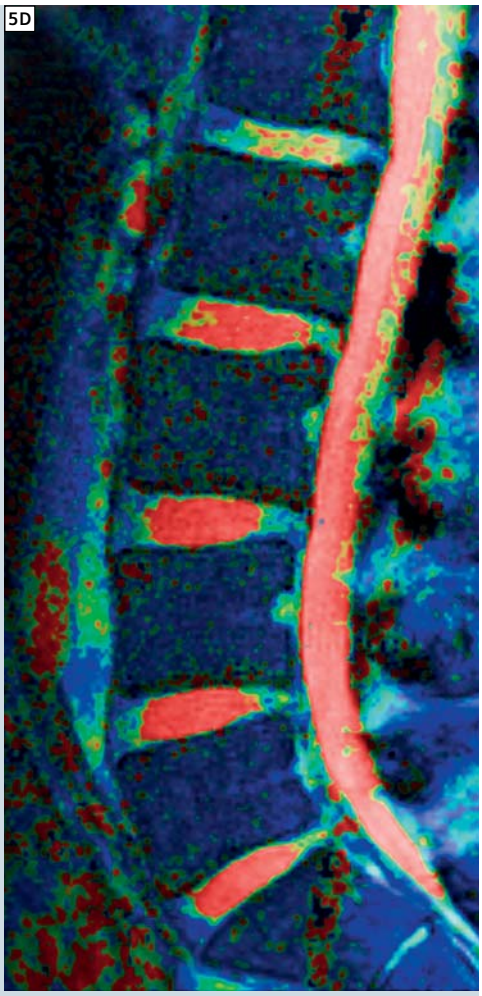
5D

of disc degeneration and the possibility of quantification by T2 and T2*-mapping may provide a new tool for a more sensitive monitoring of different therapies in patients with lower back pain. In a preliminary study, sodium imaging of the IVD of the lumbar spine at 7 Tesla was compared with T2-mapping and morphological grading by the Pfirrmann classification. No correlation was found between sodium imaging and T2-mapping, confirming that both methods detect different components of the IVD [55].

3. Biochemical MRI assessment of tendons

3.1) Sodium imaging of tendons

Tendons, which are dense, fibrous connective tissues, are often affected by tendinopathy. This clinical condition is defined as a syndrome of tendon pain, tenderness, and swelling that affects tendon function. Morphologically, degeneration of the Achilles tendon, for example, leads to thickening of the tendon [56]. Tendinopathy is accompanied by a disaggregation of the microfibrillar bundles due to the greater quantities of water and proteoglycan macromolecules. In chronic Achilles tendinopathy, biochemical alterations presage macroscopic changes [57]. Glycosaminoglycan (GAG) content was observed to be doubled in pathologic tendons in biochemical studies [58]. In a study our group, the feasibility of sodium magnetic resonance imaging at 7T[1] for the diagnosis of Achilles tendinopathy was investigated [59]. The cohort comprised twenty healthy volunteers with no history of pain in the Achilles tendon and eight patients with clinical findings of chronic Achilles tendinopathy. We used a three-dimensional gradient-echo sequence optimized for sodium imaging. The parameters were as follows: TR 17 msec, TE 8.34 msec, FOV 199 x 199 mm, section thickness 3 mm, flip angle 50°; 12 signals acquired, acquisition matrix 224 x 224 pixels. The total measurement time for sodium imaging, including flip angle calibration and localizers, was about 32 minutes. Moreover, five fresh human cadaver lower legs from four different subjects (mean age of 48 ± 8 years) were used as a reference for sodium signal and GAG content relation. These samples were analyzed biochemically to obtain GAG and water content. The study found that the mean bulk sodium SNR was 4.9 ± 2.1 in healthy control subjects and 9.3 ± 2.3 in patients with Achilles tendinopathy, and that the difference between the means was statistically significant. The correlation between sodium SNR values acquired from three regions of five cadaver Achilles tendons and GAG content was found to be high, with a Pearson coefficient of 0.71.

This study showed a statistically significant increase in sodium SNR in patients with Achilles tendinopathy, compared with healthy tendons (Fig. 6C). Moreover, the study also revealed abnormal sodium signal values in the whole tendon, although morphologically focal abnormalities with focal thickening were seen. This suggests that the Achilles tendon is affected diffusely in tendinopathy rather than focally. Sodium signal values mostly correspond to GAG content in the Achilles tendon, which, as shown in *in vitro* studies, is increased with tendinopathy [59]. It has been shown that, despite the relatively challenging techni-

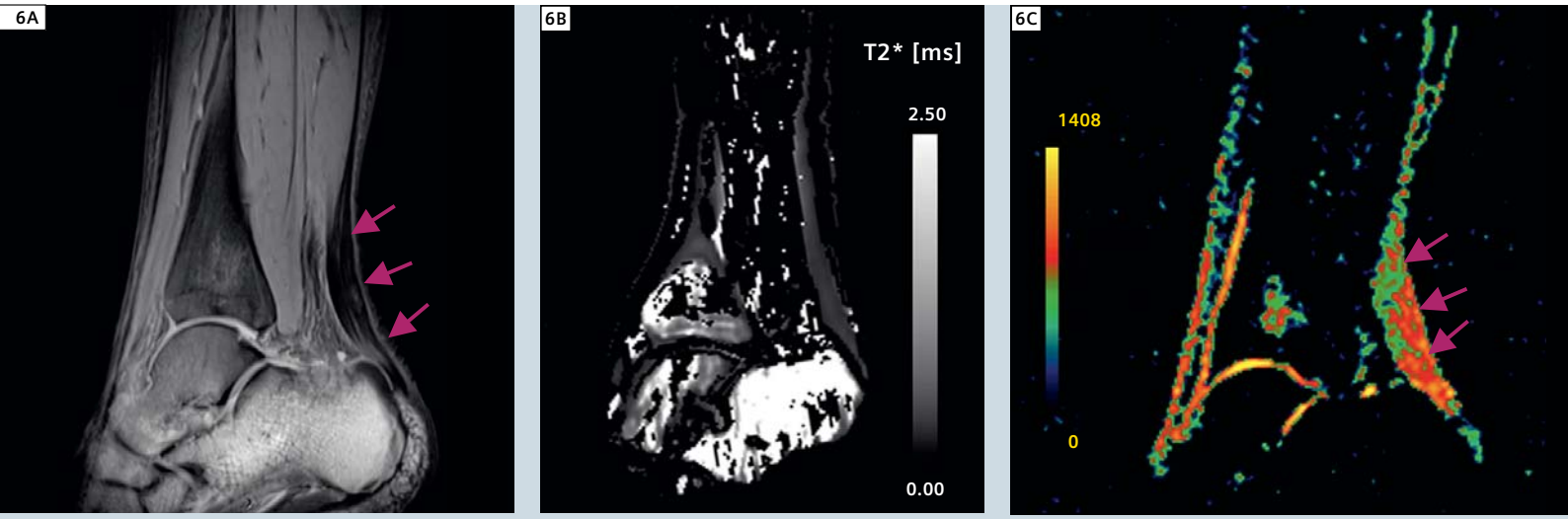

6 Morphological image **(6A)**, T2*-map measured by 3D-UTE multi-echo sequence **(6B)** acquired at different echo times (minimal TE 0.07 ms, maximal TE 9.0 ms), sodium image **(6C)** of a patient with chronic Achilotendinitis. Sodium image shows increased sodium SNR and thus higher GAG content.

cal requirements of sodium MRI, it is possible to clinically use sodium MRI for diagnostic purposes in the Achilles tendon *in vivo*.

3.2) Quantitative analysis of T2* in the Achilles tendon at 7 Tesla[1]

With the recent hardware and software developments, MRI is still more often used clinically for the evaluation of the Achilles tendon. Modern MRI methods provide direct access to signal from fast-relaxing tissues, such as tendons. Since the relaxation times in the AT are on the order of 1 ms, a very short echo time (TE) must be used to acquire signal from the tendon. These methods were successfully used to detect partial or total tendon rupture or even the degenerative processes in the tendon tissue [56]. Pathological and consecutive repair processes may lead to collagen fiber alterations, and thus, relaxation properties may be changed [60]. This results in signal alterations and changes in relaxation properties of the bound and free water molecules. Quantitative analysis of the relaxation and/or diffusion constants of the AT, such as T1, T2*, T1ρ, or ADC, may provide additional information about the tendon condition. On conventional high-field MR systems, several parameters have been investigated in the past as prospective markers for Achilles tendon degeneration, such as T2, T2*, T1ρ, ADC, and magnetization transfer [61–65]. It was shown spectroscopically that T2* decay in the Achilles tendon demonstrates a multi-component nature [66]. The MR signals from the second, third, and fourth components are difficult to acquire on conventional clinical MR systems, since these have a relatively small component ratio compared to the first component. The first component has the highest ratio, but it is in the submillisecond range and can therefore hardly be acquired with conventional echo times (~5 ms). Recent sequence development allows the acquisition of a signal from these tissues. The most important sequences used in MR imaging of highly organized tissues are two- and three-dimensional ultra-short echo time sequences (2D- and 3D-UTE), variable echo time sequences (VTE), and an acquisition-weighted stack of spirals (AWSOS) sequence. Du and colleagues observed a T2* of 0.78 ± 0.07 ms at 3T, using a 2D-UTE sequence [67]. Regional dependencies of T2* within the Achilles tendon were described by Robson et al. [61]. Ultra high field MRI provides a substantial increase in the SNR ratio of fast-relaxing tissue types [68]. In a recent study, we used a 3D-UTE sequence at 7T[1] to estimate T2* in tendons in order to investigate the potential feasibility of using this parameter as a marker for Achilles tendinopathy [69]. An SNR increase between 3 and 7T[1] was observed in this study as well. T2* was acquired by fitting bi-component exponential functions, and both short (T2*s) and long (T2*l) components were evaluated. With regard to the comparison of patients and volunteers at 7T[1], the bulk T2*s was significantly higher in patients, although the bulk T2*l difference was not statistically significant. This study suggests that ultra-short bi-component T2* measurements in the human Achilles tendon *in vivo* are feasible using a 3D-UTE sequence, with high accuracy at 7T[1] (Fig. 6B). Although it is difficult to separate the water and collagen fibers in the Achilles tendon; T2* reflects the overall condition of AT as an interplay between the amount of water and the organization of collagen macromolecules. The observed differences between T2*s in healthy and pathological tendons suggest that advanced quantitative imaging of the human Achilles tendon may provide additional information to standard clinical imaging in reasonably short MR data acquisition times. Quantitative analysis of T2* may be a promising marker for the diagnosis of early tendinopathy in the Achilles tendon [69].

In conclusion, ultra high field MRI at 7T[1] offers the advantage of higher resolution imaging for morphological information, and improves spatial resolution in T2-mapping, which enables an evaluation of the zonal variation of even thin cartilage layers and significantly improves sensitivity for other nuclei, such as 23Na. This plays an important role in MSK imaging, since sodium correlates directly with GAG content. In addition, the GAG-specific CEST technique also benefits from the ultra high field. This will provide new insights into the normal and abnormal physiology of musculoskeletal tissues, and will, therefore, provide new in vivo clinical applications.

Acknowledgment

The authors would like to thank the Editorial office of **European Radiology, Osteoarthritis and Cartilage and Radiology** for permissions to use figures from previously published articles.

* A licensed physician may choose to use FDA-approved contrast agents in conjunction with an MRI exam, based on his/her medical opinion and discretion and in accordance with the instructions for use and indications for use supplied by the pharmaceutical manufacturer for the contrast agents.

[1] Works in Progress in the USA. The information about this product is preliminary. The product is under development and is not commercially available in the U.S. and its future availability cannot be ensured. The 7T system is an investigational device. Limited by U.S. federal law to investigational use. This research system is not cleared, approved or licensed in any jurisdiction for patient examinations. This research system is not labelled according to applicable medical device law and therefore may only be used for volunteer or patient examinations in the context of clinical studies according to applicable law.

References

1 Buckwalter JA, Mankin HJ (1998) *Articular cartilage: Degeneration and osteoarthritis, repair, regeneration, and transplantation*. Instructional Course Lectures, Vol 47 – 1998 **47**, 487-504.

2 Poole AR, Kojima T, Yasuda T, et al (2001) *Composition and structure of articular cartilage – A template for tissue repair.* Clinical Orthopaedics and Related Research, S26-S33.

3 Burstein D, Velyvis J, Scott KT, et al (2001) *Protocol issues for delayed Gd(DTPA)(2-)-enhanced MRI: (dGEMRIC) for clinical evaluation of articular cartilage*. Magnetic Resonance in Medicine **45**, 36-41.

4 Bashir A, Gray ML, Burstein D (1996) *Gd-DTPA(2-) as a measure of cartilage degradation*. Magnetic Resonance in Med. **36**, 665-673.

5 Borthakur A, Shapiro EM, Beers J, et al (2000) *Sensitivity of MRI to proteoglycan depletion in cartilage: comparison of sodium and proton MRI.* Osteoarthritis and Cartilage **8**, 288-293.

6 Ling W, Regatte RR, Navon G, et al (2008b) *Assessment of glycosaminoglycan concentration in vivo by chemical exchange-dependent saturation transfer (gagCEST).* Proceedings of the National Academy of Sciences of the United States of America **105**, 2266-2270.

7 Burstein D, Bashir A, Gray ML (2000) *MRI techniques in early stages of cartilage disease.* Investigative Radiology **35**, 622-638.

8 Watanabe A, Wada Y, Obata T, et al (2006) *Delayed gadolinium-enhanced MR to determine glycosaminoglycan concentration in reparative cartilage after autologous chondrocyte implantation: Preliminary results.* Radiology **239**, 201-208.

9 Bashir A, Gray ML, Boutin RD, et al (1997) *Glycosaminoglycan in articular cartilage: In vivo assessment with delayed Gd(DTPA)(2-)-enhanced MR imaging.* Radiology **205**, 551-558.

10 Tiderius CJ, Olsson LE, Leander P, et al (2003) *Delayed gadolinium-enhanced MRI of cartilage (dGEMRIC) in early knee osteoarthritis.* Magnetic Resonance in Medicine **49**, 488-492.

11 Williams A, Gillis A, McKenzie C, et al (2004) *Glycosaminoglycan distribution in cartilage as determined by delayed gadolinium-enhanced MRI of cartilage (dGEMRIC): Potential clinical applications.* American Journal of Roentgenology **182**, 167-172.

12 Trattnig S, Marlovits S, Gebetsroither S, et al (2007) *Three-dimensional delayed gadolinium-enhanced MRI of cartilage (dGEMRIC) for in vivo evaluation of reparative cartilage after matrix-associated autologous chondrocyte transplantation at 3.0T: Preliminary results.* Journal of Magnetic Resonance Imaging **26**, 974-982.

13 Trattnig S, Mamisch TC, Pinker K, et al (2008) *Differentiating normal hyaline cartilage from post-surgical repair tissue using fast gradient echo imaging in delayed gadolinium-enhanced MRI (dGEMRIC) at 3 Tesla.* European Radiology **18,** 1251-1259.

14 Kim YJ, Jaramillo D, Millis MB, et al (2003) *Assessment of early osteoarthritis in hip dysplasia with delayed gadolinium-enhanced magnetic resonance imaging of cartilage.* Journal of Bone and Joint Surgery-American Volume **85A**, 1987-1992.

15 Vaga S, Raimondi MT, Caiani EG, et al (2008) *Quantitative assessment of intervertebral disc glycosaminoglycan distribution by gadolinium-enhanced MRI in orthopedic patients.* Magnetic Resonance in Medicine **59**, 85-95.

16 Williams A, Shetty SK, Burstein D, et al (2008) *Delayed gadolinium enhanced MRI of cartilage (dGEMRIC) of the first carpometacarpal (1CMC) joint: a feasibility study.* Osteoarthritis and Cartilage **16**, 530-532.

17 Trattnig S, Welsch GH, Juras V, et al (2010) (23) *Na MR Imaging at 7 T after Knee Matrix-associated Autologous Chondrocyte Transplantation: Preliminary Results.* Radiology **257**, 175-184.

18 Zbyn S, Stelzeneder D, Welsch GH, et al *Evaluation of native hyaline cartilage and repair tissue after two cartilage repair surgery techniques with (23)Na MR imaging at 7 T: initial experience.* Osteoarthritis Cartilage **20**, 837-45.

19 Krusche-Mandl I, Schmitt B, Zak L, et al *Long-term results 8 years after autologous osteo-chondral transplantation: 7 T gagCEST and sodium magnetic resonance imaging with morphological and clinical correlation.* Osteoarthritis Cartilage **20**, 357-63.

20 Guivel-Scharen V, Sinnwell T, Wolff SD, et al (1998) *Detection of proton chemical exchange between metabolites and water in biological tissues.* Journal of Magnetic Resonance **133**, 36-45 DOI: S1090-7807(98)91440-9 [pii] 10.1006/jmre.1998.1440.

21 Forsen S, Hoffman RA (1963) *Study of Moderately Rapid Chemical Exchange Reactions by Means of Nuclear Magnetic Double Resonance.* Journal of Chemical Physics **39**, 2892.

22 Ward KM, Aletras AH, Balaban RS (2000) *A new class of contrast agents for MRI based on proton chemical exchange dependent saturation transfer (CEST).* Journal of Magnetic Resonance **143**, 79-87 DOI: 10.1006/jmre.1999.1956 S1090-7807(99)91956-0 [pii].

23 Ward KM, Balaban RS (2000) *Determination of pH using water protons and chemical exchange dependent saturation transfer (CEST).* Magnetic Resonance in Medicine **44**, 799-802 DOI: 10.1002/1522-2594(200011)44:5<799::AID-MRM18>3.0.CO;2-S [pii].

24 Zhou JY, van Zijl PCM (2006) *Chemical exchange saturation transfer imaging and spectroscopy.* Progress in Nuclear Magnetic Resonance Spectroscopy **48,** 109-136 DOI: DOI 10.1016/j.pnmrs.2006.01.001.

25 Ling W, Regatte RR, Schweitzer ME, et al (2008) *Characterization of bovine patellar cartilage by NMR.* Nmr in Biomedicine **21**, 289-295 DOI: Doi 10.1002/Nbm.1193.

26 Ling W, Regatte RR, Navon G, et al (2008) *Assessment of glycosaminoglycan concentration in vivo by chemical exchange-dependent saturation transfer (gagCEST).* Proc Natl Acad Sci U S A **105**, 2266-70 DOI: 0707666105 [pii] 10.1073/pnas.0707666105.

27 Schmitt B, Bock M, Stieltjes B, et al. *A new, 3D GRE based CEST imaging method for clinical application and verification with gagCEST in articular cartilage.* in *Proceedings 18th Scientific Meeting, International Society for Magnetic Resonance in Medicine.* 2010. Stockholm.

28 Vinogradov E, Ivanishev A, Grant AK, et al. *CEST and Sodium Imaging of Glycosaminoglycans in-vivo in the 3T: Preliminary Results.* in *Proceedings 18th Scientific Meeting, International Society for Magnetic Resonance in Medicine.* 2010. Stockholm.

29 Fenty M, Kassey V, Kogan F, et al. *Feasibility of CEST imaging on the guinea pig stifle at 9.4 T.* in *Proceedings 19th Scientific Meeting, International Society for Magnetic Resonance in Medicine.* 2011. Montreal.

30 Vinogradov E, Lenkinski RE. *Detection of Glycosaminoglycans using Positive CEST approach.* in *Proceedings 18th Scientific Meeting, International Society for Magnetic Resonance in Medicine.* 2010. Stockholm.
31 Varma G, Alsop DC, Lenkinski RE, et al. *Optimization of pulsed-gagCEST at 3.0T.* in *Proceedings 19th Scientific Meeting, International Society for Magnetic Resonance in Medicine*. 2011. Montreal.
32 Varma G, Lenkinski RE, Vinogradov E. *Keyhole Chemical Exchange Saturation Transfer.* in *Proceedings 19th Scientific Meeting, International Society for Magnetic Resonance in Medicine.* 2011. Montreal.
33 Schmitt B, Zbyn S, Stelzeneder D, et al (2011) *Cartilage quality assessment by using glycosaminoglycan chemical exchange saturation transfer and (23)Na MR imaging at 7 T.* Radiology **260,** 257-64 DOI: 10.1148/radiol.11101841.˙
34 Ling W, Saar G, Regatte R, et al. *Assessing the Inververtebral Disc via gagCEST.* in *Proceedings 17th Scientific Meeting, International Society for Magnetic Resonance in Medicine.* 2009. Honolulu.
35 Kim M, Chan Q, Anthony MP, et al (2011) *Assessment of glycosaminoglycan distribution in human lumbar intervertebral discs using chemical exchange saturation transfer at 3 T: feasibility and initial experience.* NMR in Biomedicine **24,** 1137-44 DOI: 10.1002/nbm.1671.˙
36 Haneder S, Apprich S, Schmitt B, et al (2012) *Glycosaminoglycan content in intervertebral discs using chemical exchange saturation transfer at 3T MRI: preliminary results in patients with low back pain.* European Radiology **Accepted for Publication.**
37 Mosher TJ, Dardzinski BJ (2004) *Cartilage MRI T2 relaxation time mapping: Overview and applications.* Seminars in Musculoskeletal Radiology **8**, 355-368.
38 Welsch GH, Mamisch TC, Hughes T, et al (2008) *In vivo biochemical 7.0 Tesla magnetic resonance - Preliminary results of dGEMRIC, zonal T2, and T2* mapping of articular cartilage.* Investigative Radiology **43**, 619-626.
39 Welsch GH, Trattnig S, Scheffler K, et al (2008) *Magnetization transfer contrast and T2 mapping in the evaluation of cartilage repair tissue with 3T MRI.* Journal of Magnetic Resonance Imaging **28**, 979-986.
40 Goodwin DW, Zhu HQ, Dunn JF (2000) *In vitro MR imaging of hyaline cartilage: Correlation with scanning electron microscopy.* American Journal of Roentgenology **174**, 405-409.
41 Goodwin DW, Wadghiri YZ, Dunn JF (1998) *Micro-imaging of articular cartilage: T2, proton density, and the magic angle effect.* Academic Radiology **5**, 790-798.
42 Smith HE, Mosher TJ, Dardzinski BJ, et al (2001) *Spatial variation in cartilage T2 of the knee.* Journal of Magnetic Resonance Imaging **14**, 50-55.
43 Watrin-Pinzano A, Ruaud JP, Cheli Y, et al (2004) *Evaluation of cartilage repair tissue after biomaterial implantation in rat patella by using T2 mapping.* Magnetic Resonance Materials in Physics Biology and Medicine **17**, 219-228.
44 White LM, Sussman MS, Hurtig M, et al (2006) *Cartilage T2 assessment: Differentiation of normal hyaline cartilage and reparative tissue after arthroscopic cartilage repair in equine subjects.* Radiology **241**, 407-414.
45 Trattnig S, Mamisch TC, Welsch GH, et al (2007) *Quantitative T-2 mapping of matrix-associated autologous chondrocyte transplantcation at 3 Tesla – An in vivo cross-sectional study.* Investigative Radiology **42**, 442-448.
46 Welsch GH, Mamisch TC, Domayer SE, et al (2008) *Cartilage T2 assessment at 3-T MR imaging: In vivo differentiation of normal hyaline cartilage from reparative tissue after two cartilage repair procedures – Initial experience.* Radiology **247**, 154-161.
47 Domayer SE, Apprich S, Stelzeneder D, et al *Cartilage repair of the ankle: first results of T2 mapping at 7.0 T after microfracture and matrix associated autologous cartilage transplantation.* Osteoarthritis Cartilage **20**, 829-36.
48 David-Vaudey E, Ghosh S, Ries M, et al (2004) *T-2 relaxation time measurements in osteoarthritis.* Magnetic Resonance Imaging **22**, 673-682.
49 Dunn TC, Lu Y, Jin H, et al (2004) *T2 relaxation time of cartilage at MR imaging: Comparison with severity of knee osteoarthritis.* Radiology **232**, 592-598.
50 Burstein D, Gray ML (2006) *Is MRI fulfilling its promise for molecular imaging of cartilage in arthritis?* Osteoarthritis and Cartilage **14**, 1087-1090.
51 Stelzeneder D, Welsch GH, Kovacs BK, et al *Quantitative T2 evaluation at 3.0T compared to morphological grading of the lumbar intervertebral disc: a standardized evaluation approach in patients with low back pain.* Eur J Radiol **81**, 324-30.
52 Stelzeneder D, Messner A, Vlychou M, et al *Quantitative in vivo MRI evaluation of lumbar facet joints and intervertebral discs using axial T2 mapping.* Eur Radiol **21,** 2388-95.
53 Trattnig S, Stelzeneder D, Goed S, et al *Lumbar intervertebral disc abnormalities: comparison of quantitative T2 mapping with conventional MR at 3.0 T.* Eur Radiol **20**, 2715-22.
54 Welsch GH, Trattnig S, Paternostro-Sluga T, et al *Parametric T2 and T2* mapping techniques to visualize intervertebral disc degeneration in patients with low back pain: initial results on the clinical use of 3.0 Tesla MRI.* Skeletal Radiol **40**, 543-51.
55 Noebauer-Huhmann IM, Juras V, Pfirrmann C, et al (in press) *Sodium Imaging of the Lumbar Intervertebral Disc at 7T: Correlation with T2 Mapping and Modified Pfirrmann Score at 3T. Preliminary results.* Radiology.
56 Schweitzer ME, Karasick D (2000) *MR imaging of disorders of the Achilles tendon.* AJR Am J Roentgenol **175**, 613-25.
57 Samiric T, Parkinson J, Ilic MZ, et al (2009) *Changes in the composition of the extracellular matrix in patellar tendinopathy.* Matrix Biol **28**, 230-6.
58 Fu SC, Chan KM, Rolf CG (2007) *Increased deposition of sulfated glycosaminoglycans in human patellar tendinopathy.* Clin J Sport Med **17**, 129-34.
59 Juras V, Zbyn S, Pressl C, et al (2012) *Sodium MR Imaging of Achilles Tendinopathy at 7 T: Preliminary Results.* Radiology **262**, 199-205.
60 Gelberman RH, Manske PR, Vande Berg JS, et al (1984) *Flexor tendon repair in vitro: a comparative histologic study of the rabbit, chicken, dog, and monkey.* J Orthop Res **2**, 39-48.
61 Robson MD, Benjamin M, Gishen P, et al (2004) *Magnetic resonance imaging of the Achilles tendon using ultrashort TE (UTE) pulse sequences.* Clin Radiol **59**, 727-35.
62 Hodgson RJ, Evans R, Wright P, et al (2011) *Quantitative magnetization transfer ultrashort echo time imaging of the Achilles tendon.* Magn Reson Med **65**, 1372-6.
63 Du J, Carl M, Diaz E, et al (2010) *Ultrashort TE T1rho (UTE T1rho) imaging of the Achilles tendon and meniscus.* Magn Reson Med **64**, 834-42.
64 Fechete R, Demco DE, Eliav U, et al (2005) *Self-diffusion anisotropy of water in sheep Achilles tendon.* NMR Biomed **18**, 577-86.
65 Henkelman RM, Stanisz GJ, Kim JK, et al (1994) *Anisotropy of NMR properties of tissues.* Magn Reson Med **32**, 592-601.
66 Peto S, Gillis P (1990) *Fiber-to-field angle dependence of proton nuclear magnetic relaxation in collagen.* Magn Reson Imaging **8**, 705-12.
67 Du J, Chiang AJT, Chung CB, et al (2010) *Orientational analysis of the Achilles tendon and enthesis using an ultrashort echo time spectroscopic imaging sequence.* Magnetic Resonance Imaging **28**, 178-184.
68 Regatte RR, Schweitzer ME (2007) *Ultra-high-field MRI of the musculoskeletal system at 7.0T.* J Magn Reson Imaging **25**, 262-9.
69 Juras V, Zbyn S, Pressl C, et al (2012) *Regional Variations of T2* in Healthy and Pathologic Achilles Tendon In Vivo at 7 Tesla: Preliminary Results.* Magnetic resonance in Medicine **In Press.**

Contact
Prof.Siegfried Trattnig, M.D.
MR Center – High field MR
Department of Radiology
Medical University of Vienna/Vienna
General Hospital
Lazarettgasse 14
A-1090 Vienna
Austria
Phone: +43 1 40 400 6460
Fax.: +43 1 40 400 6475
siegfried.trattnig@meduniwien.ac.at

The magazine of MR

MAGNETOM Flash

turns 50...

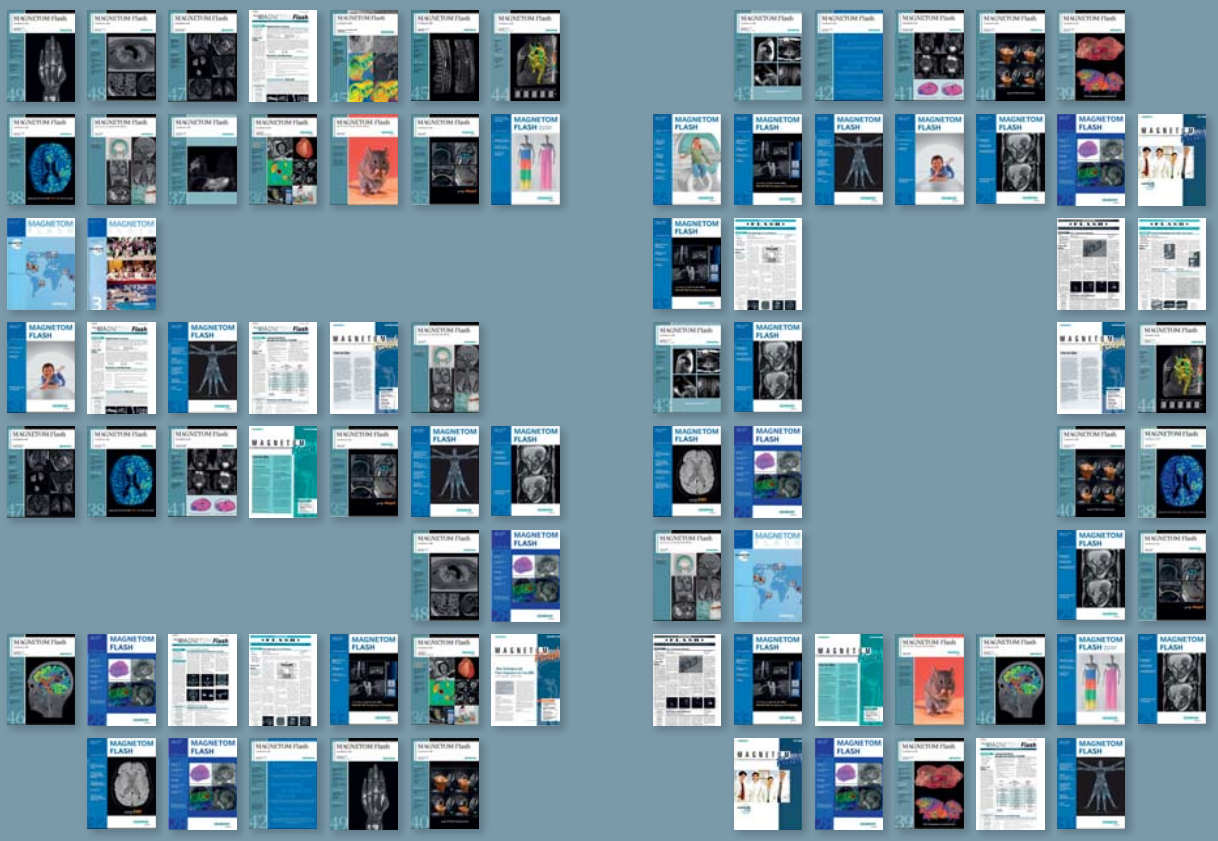

...and says thank you to all authors and readers.

With the first issue published in 1993 we are not celebrating our 50th birthday, but issue no. 50.
From the very beginning, MAGNETOM Flash was a cooperation between Siemens Healthcare and MAGNETOM users.
The first editor of the newspaper sized publication was Christine Harris, R.T. at Children's Hospital of Philadelphia, USA and the focus of the 'newsletter' was a communication network between Technologists and the Siemens Corporation. As the newsletter developed into a magazine the target group grew to include radiologists, physicists, cardiologists and researchers.
What did not change is the involvement of you - our readers. Being part of the MAGNETOM World, the community for all Siemens MR users worldwide, the magazine is affording you a platform to contribute and expand your knowledge.
We welcome your feedback, questions and comments – please contact us at **magnetomworld.med@siemens.com**.

www.siemens.com/magnetom-world – communications keeping you up-to-date.

Magnetic Resonance Neurography – Techniques and Interpretation

Avneesh Chhabra, M.D.[1]; Abraham Padua Jr., Ph.D.[2]; Aaron Flammang, MBA[2]; Wesley Gilson, Ph.D.[2]; John A. Carrino, M.D., M.P.H.[1]

[1]*Department of Radiology & Radiological Science, Johns Hopkins University, Baltimore, MD, USA*
[2]*Siemens Healthcare, Malvern, PA, USA and Erlangen, Germany*

Introduction

Magnetic resonance neurography (MRN), akin to angiography, is an ever-advancing technology for multiplanar depiction of normal and abnormal peripheral nerves. This article will highlight various 2D and 3D pulse sequences available for non-selective and selective nerve visualization as well as their functional evaluation. Related interpretation pearls and pitfalls are discussed.

Techniques

MRN is best performed on 3 Tesla (T) scanners with dedicated extremity or wrap around flex coils as they can provide higher signal-to-noise ratio (SNR), which is essential to enhance the smallest structure in the neurovascular bundle, namely the peripheral nerves [1].

On current 1.5T scanners (MAGNETOM Aera, MAGNETOM Avanto), 2D (dimensional) imaging can be performed with near-similar resolution as on 3T scanners, however 3D imaging is often limited, especially if smaller voxels are used or fat suppression is applied. On the other hand, if there is metal in the field-of-view, in order to mitigate susceptibility artifacts and for superior nerve visualization, 1.5T imaging is often favored.
2D pulse sequences include high resolution (base resolution 256 or higher, in plane resolution 0.3–0.4 mm) T1-weighted and fat suppressed T2w images. Uniform fat suppression is essential to avoid artifactual increase in nerve signal intensity. Options include frequency selective fat suppression (fsT2w), short tau inversion recovery (STIR), and spectral adiabatic inversion recovery (SPAIR), or 2-point or 3-point Dixon techniques. fsT2w is often limited due to loss of fat saturation along the curvatures of extremities, especially in large subjects. STIR works well for 3D imaging with excellent fat suppression, however for 2D imaging it is often marred by poor SNR, excessive SAR (specific absorption rate) deposition and pulsation artifacts. SPAIR works well as it provides better fat suppression than fsT2w and higher SNR than STIR. It has virtually no pulsation artifacts and is also relatively SAR favorable (Fig. 1). It comes in weak and strong contrast versions. The authors prefer the strong version as it provides isointense signal in normal nerves [2].

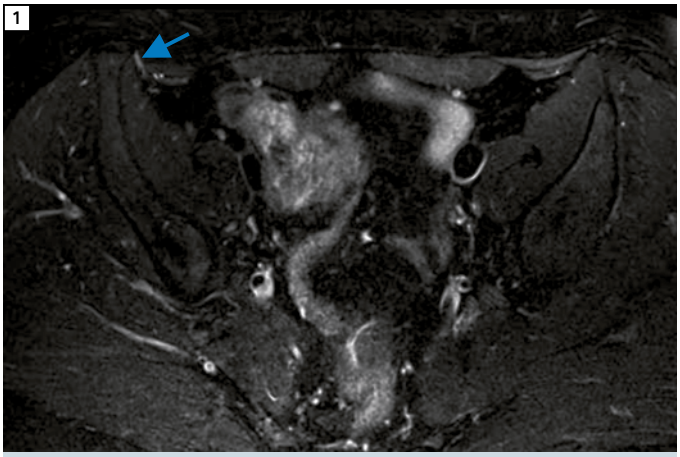

1 Meralgia Paresthetica. Young woman with right anterolateral thigh pain and suspected lateral femoral cutaneous (LFCN) nerve abnormality. Axial T2 SPAIR image shows uniform fat suppression and abnormally hyperintense right LFCN (arrow) in keeping with clinical diagnosis of meralgia paresthetica.

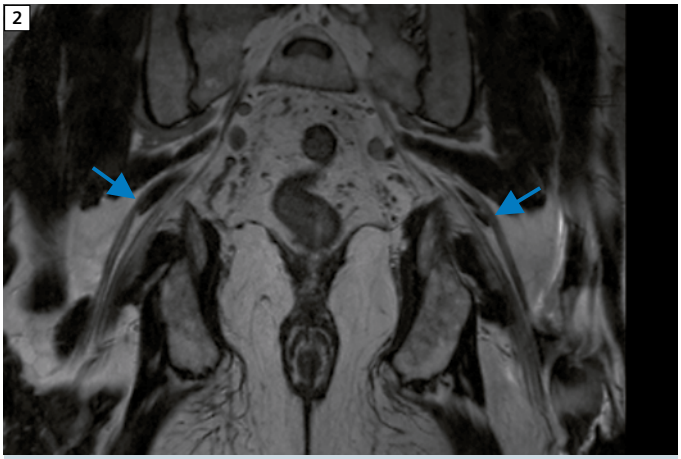

2 T2 SPACE. Coronal non-fat suppressed T2 SPACE image through the pelvis shows bilaterally split sciatic nerves (arrows) in this patient with no symptoms of sciatica.

Dixon technique applied with T2w imaging gives separate water and fat images and also provides excellent fat suppression with higher SNR and contrast-to-noise ratio than STIR or SPAIR.

3D pulse sequences can be divided into anatomic and functional techniques. Anatomic techniques are further divided into nerve non-selective and nerve selective sequences. Nerve non-selective techniques include T1w imaging, namely VIBE (volume interpolated breathhold examination, T1 3DGRE) or MPRAGE (3D GRE); and T2w multislab acquisition, namely SPACE (sampling perfection with application optimized contrasts using varying flip angle evolutions) [3]. SPACE is heavily used in MRN examinations as isotropic spine echo type imaging can obtained using SPACE in a variety of contrasts (T1, PD, T2, STIR, and SPAIR) with constant or variable echo times (Fig. 2). The authors use VIBE for pre- and post-contrast imaging, and otherwise mostly use 3D imaging with fluid sensitive contrast. 3D STIR SPACE provides best fat suppression for the brachial and LS plexus while 3D SPAIR SPACE provides higher SNR along with good fat suppression for extremity imaging (Figs. 3, 4). Dixon T2w imaging also provides excellent images of the brachial plexus, however currently can be acquired in 2D mode only (Fig. 5). Others such as 3D PD SPACE with variable echo time can produce similar image quality and allows multiplanar reconstruction (Fig. 6). Currently, 3D STIR SPACE and SPAIR SPACE sequences are most widely used and are time tested. Maximum intensity projections (MIP) of acquired images or their curved planar reformats produce excellent quality nerve images along their long axis. It remains to be seen if other techniques, such as Dixon with SPACE, can be obtained within acceptable time periods and provide the necessary isotropic spatial and good contrast resolution.

3D nerve selective imaging includes diffusion-weighting (DW) with a small b-value (80–200 s/mm^2) to suppress flowing blood. It is a fine balance as one adds diffusion gradient to the 3D imaging, as it reduces SNR and can degrade image quality while providing the benefit of vascular flow signal suppression for selec-

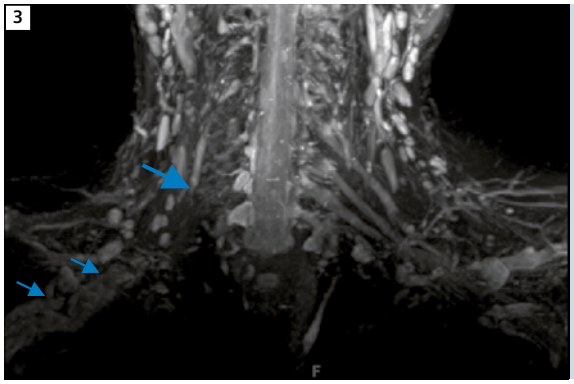

3 3D STIR SPACE. 24-year-old man with recent motor vehicle accident and flail right arm. MIP image from coronal 3D STIR SPACE sequence shows transected right L5 nerve (large arrow). Notice torn, retracted and bunched up remaining right brachial plexus (small arrows).

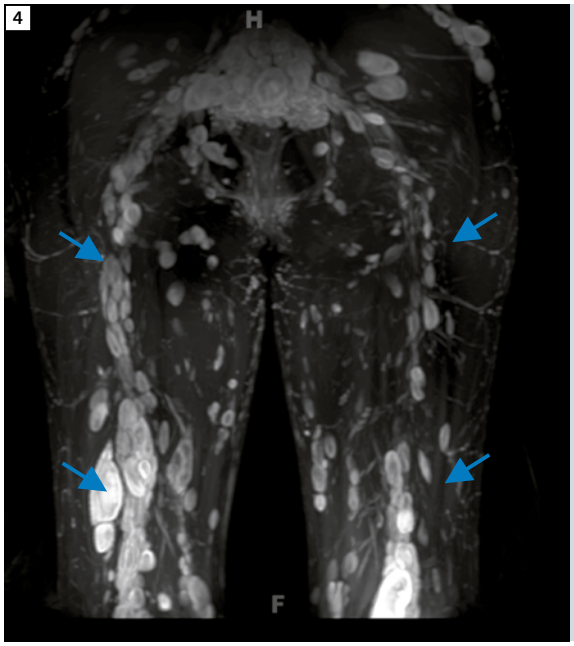

4 SPAIR SPACE. MIP image from coronal 3D SPAIR SPACE sequence shows multifocal nodular enlargement of bilateral sciatic nerves, infiltrated by numerous neurofibromas (arrows) in this known case of NF type I.

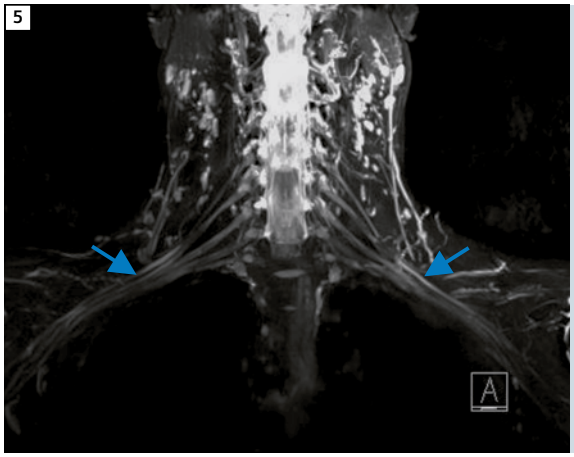

5 T2 Dixon. MIP image from coronal 2D T2 Dixon sequence shows excellent depiction of normal bilateral brachial plexuses (arrows) in a healthy volunteer.

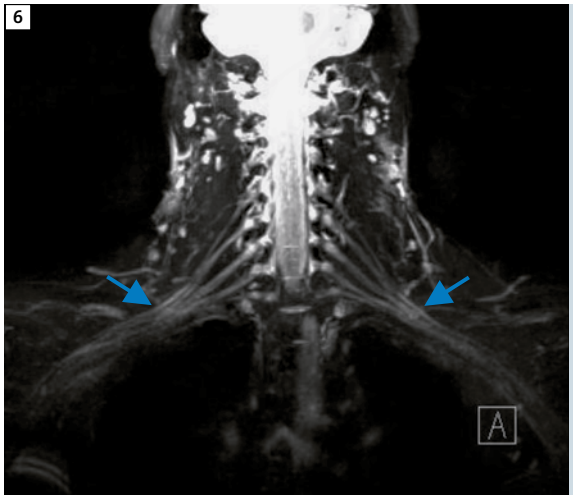

6 PD variable 3D SPACE. MIP image from coronal PD variable 3D SPACE sequence shows excellent depiction of normal bilateral brachial plexuses (arrows) in a healthy volunteer.

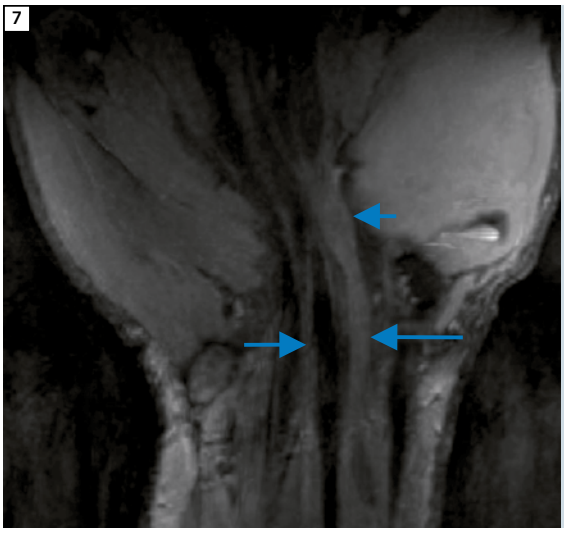

7 3D DW PSIF. Young woman with persistent carpal tunnel symptoms following a prior transverse carpal ligament release. Notice normal median (large arrow) and ulnar nerves (medium arrow) proximal to the carpal tunnel. A neuroma in continuity is seen along the distal aspect of the carpal tunnel (smallest arrow). Notice selective nerve depiction with excellent vascular signal suppression

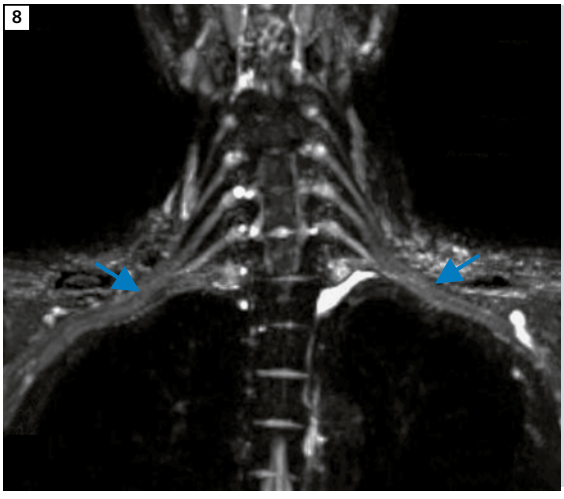

8 3D DW SPACE. MIP image from coronal DW 3D STIR SPACE sequence shows selective depiction of normal bilateral brachial plexuses (arrows) in a healthy volunteer. However note decreased SNR due to added diffusion component.

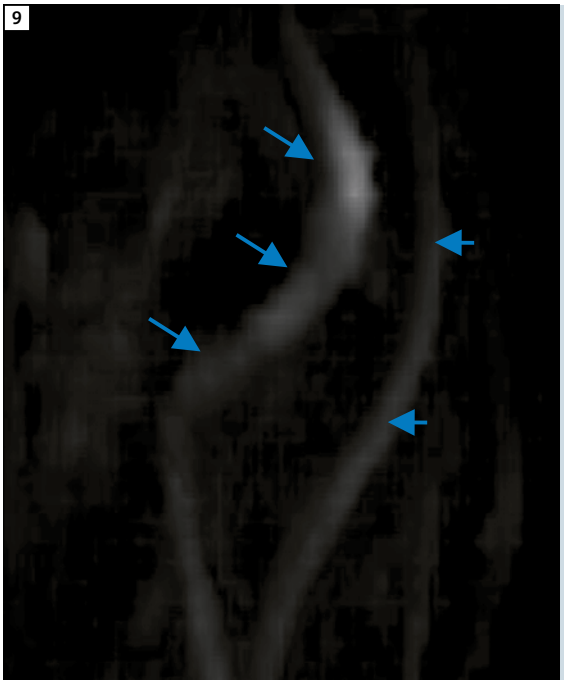

9 DTI. MIP coronal tensor image with inverted grey scale from axial DTI sequence shows enlarged ulnar nerve with abnormally low FA and high ADC values in this case of re-entrapped ulnar nerve at the site of prior anterior transposition (large arrows). Notice normal median nerve (small arrows).

tive nerve imaging. The sequences include 3D DW PSIF (reversed steady state free precession) and DW STIR SPACE. 3D DW PSIF is very susceptible to local inhomogeneity, motion artifacts, breathing artifacts, and poor fat suppression. Water selective fat suppression currently works well with PSIF [4, 5]. With appropriate technique, it provides excellent nerve selective images (Fig. 7). MIP images from DW PSIF and DW SPACE provide good nerve selective depiction (Fig. 8). With further pulse sequence development, one can look at adding Dixon to DW PSIF or try to improve DW SPACE sequence that can be obtained in acceptable time periods while keep the advantages of nerve selectivity. A typical lumbosacral plexus protocol has been highlighted in Table 1. Normal nerves do not enhance as they are outside the blood-nerve barrier. Contrast imaging (gadolinium based agent) does not add much in trauma or entrapment neuropathy cases as these are mostly subacute cases. In these cases, only denervated muscles enhance, the demonstration of which is already visible on T1w and fat suppressed fluid sensitive images. Contrast administration is, however, recommended in other cases, such as suspected neural and perineural mass lesions, polyneuropathy conditions including lymphoma, amyloidosis, demyelinating neuropathies, hereditary neuropathies, etc.

Functional imaging of the peripheral nerves primarily includes diffusion tensor imaging (DTI). It has been exploited in various extremity and plexus peripheral nerves in the last few years and continuous refinements are being made. Single shot echo planar imaging (EPI) is the technique used in most centers and multiple diffusion moments (b-values) are applied to obtain functional parameter of apparent diffusion coefficient (ADC) [6]. At least 6 directions of interrogation are needed for DTI, although most authors have used 12–20 directions to obtain reproducible data. The authors use 3 diffusion moments (0, 800, 1000 s/mm^2) and 12 directions of interrogation. Tight echo spacing, frequency selective fat suppression, auto-shimming before image acquisition and no motion degradation

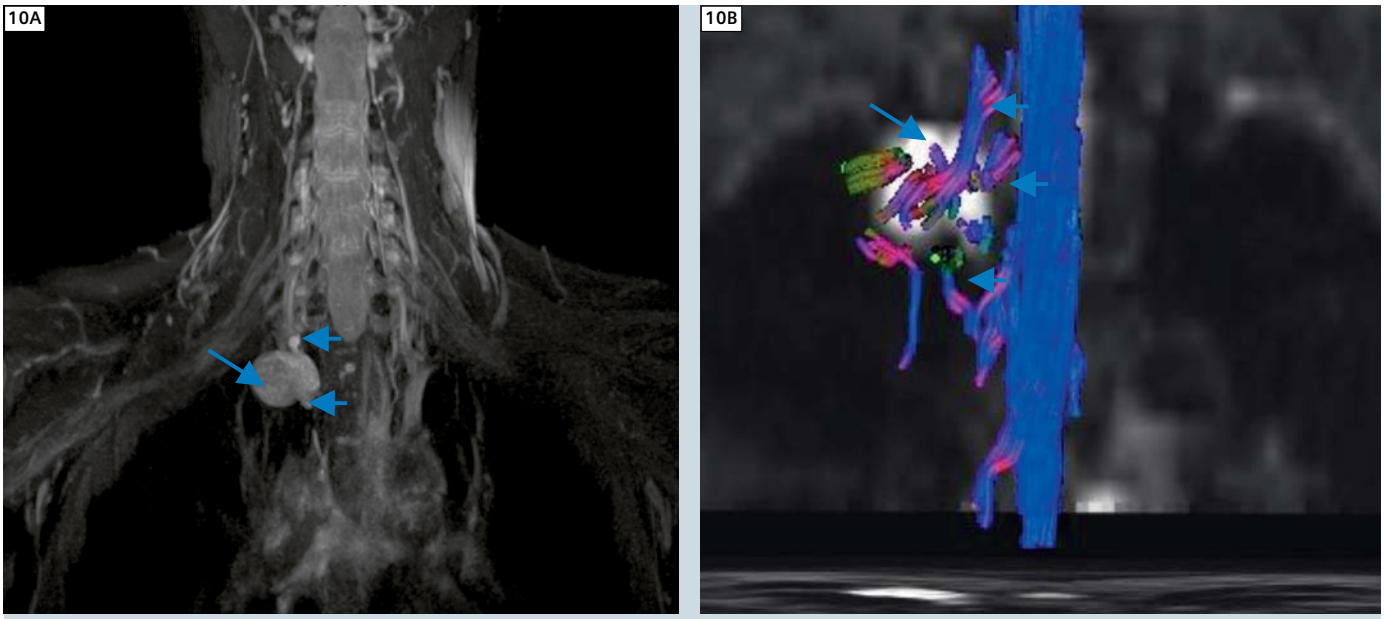

10 3D STIR SPACE and DTI. MIP image from coronal 3D STIR SPACE sequence **(10A)** shows normal depiction of normal bilateral brachial plexuses in a 39-year-old woman with incidentally detected lesion on chest CT (not shown). A peripheral nerve sheath tumor (large arrow) is nicely depicted in close relation to paraspinal T1 and T2 ganglia (small arrows). The lesion showed high ADC values in keeping with a benign lesion. Tractography image from DTI **(10B)** shows the nerve roots (small arrows) draped over the lesion (large arrow) without involvement.

Table 1: The imaging protocol employed in the magnetic resonance neurography examination for the LS plexus.

MR sequence	Slice thickness (mm)	TR / TE (ms)	TF	Base resolution (pixels)
Axial T1	4	800/12	6	832
Coronal T1	4	960/12	5	384
Axial T2 SPAIR	4	4890/80	22	256
Sagittal T2 3D SPACE	1	1000/97	81	256
Sagittal STIR	4	3700/18	22	256
Coronal STIR 3D SPACE	1.5	1500/91	41	256

are essential to obtain good and reproducible DTI data. Axial images obtained with 4–5 mm slice thickness with 0 gap can be reconstructed in multiple planes without artifacts (Fig. 9). These images then allow accurate tensor calculation, fractional anisotropy (FA) measurements and tractography. DTI has proven useful in non-invasive pre- and post-operative evaluation of carpal tunnel syndrome patients and peripheral nerve sheath tumors (PNST) as the involved nerves show reduced FA values that improve over time with treatment [7]. The benign PNSTs show higher ADC values than their malignant counterparts and tractography differences exist among different tumor types depending upon internal fascicular involvement or mere displacement [8] (Fig. 10). Further investigations are underway to evaluate the role of DTI in other types of neuropathies.

Interpretation pearls and pitfalls

While image generation is getting easier with high field MR techniques, the radiologists should learn to correctly interpret these high quality examinations. There is a steep learning curve for those who spend time with attention to detail, since nerve architecture is easily visible to the fascicular and perineurium level. One should learn normal nerve anatomy, variations, diagnostic pearls and pitfalls while obtaining all the information possible from clinical findings and available electrodiagnostic test results. Electrodiagnostic tests are also limited by false negative or indeterminate results, especially in deeply located nerves. So, while these results are helpful, one

should not get biased by negative results. The reader should follow a stepwise approach to imaging diagnosis:

1. Image quality – is it adequate and is fat suppression uniform? Are the nerves visible adequately and can the nerves be separately evaluated from adjacent vessels or compared side to side if the contralateral portion of body is available, such as in pelvic imaging. Recognize normal nerves and their variations (bifid nerve, split nerve with muscle belly intervening, intramuscular course of the nerve, etc.)
2. Look for orthopedic internal derangements which can mimic similar neuropathic symptoms or are potential cause of traction neuropathy, such as spondylosis, plantar fasciitis, tibialis posterior dysfunction, etc.
3. Look for clues of disseminated or systemic causes of neuropathy: one nerve abnormal over long distance away from entrapment sites or multiple regional nerves abnormal. This may happen in diabetic neuropathy, demyelinating neuropathies, hereditary neuropathy, vasculitis or toxic metabolic conditions. Usually hereditary neuropathy results in symmetric disease as compared to acquired conditions. Clinical findings should be correlated for insights into above diagnoses.
4. Look for focal area of nerve abnormality, abnormal T2 hyperintensity (approaching adjacent venous signal intensity) and / or fascicular abnormality (enlargement / effacement from edema / discontinuity) indicating entrapment or injury in the correct clinical scenario. If the nerve is really abnormal, the signal intensity will persist over few to many sections along its length versus signal change from a magic angle artifact. The nerve further enlarges with worsening neuropathy forming a pseudoneuroma in entrapment and neuroma in injury (lost partial or complete fascicular continuity with heterogeneous appearance) [9]. The nerve abnormality is generally worst at the site of insult and it fades gradually proximally and distally. Abrupt change in nerve intensity from bright-black-bright signal (Triple B sign) usually means severe focal neuropathy and a potential surgical case. Painful neuroma in continuity and nerve discontinuity in functionally important nerves also require surgical repair/reconstruction. Long standing neuropathy, such as in diabetes, can lead to atrophic appearance of the nerve with fascicular atrophy and intra-epineurial fatty proliferation / replacement.
5. Evaluate regional muscles. As a rule, the muscle denervation changes are distal to the site of insult. If muscle changes are patchy or widespread in different nerve territories or associated with fascial edema, the diagnosis could be myopathy / myositis rather than denervation change. The diagnosis can be made with confidence if regional nerves are normal.
6. In case of a mass lesion, further characterize the lesion into neural or perineural masses. Age, clinical findings and anatomic MRN plus DTI are useful in the imaging evaluation of neural masses. Perineural lesions are further evaluated based on anatomic imaging and contrast evaluation into lipoma, ganglion cyst, hematoma, and abscess etc.
7. Finally, look for prior local surgical changes or nerve repair/reconstruction changes. The signal alteration may persist but in successful cases, the signal decreases within the nerves and denervation changes in the muscle resolve. In worsening nerve degeneration cases, the nerve signal approaches fluid signal and persists till the nerve atrophy starts, while the regional muscles undergo continued fatty replacement and atrophy [10]. Correlation with prior imaging studies is essential in these cases.

To conclude, magnetic resonance neurography is an exciting imaging technique that affords multiplanar anatomic and functional depiction of peripheral nerves and their related lesions. Appropriate imaging and accurate interpretation are essential components of successful performance of this ever advancing technique.

References
1 Chhabra A, Lee PP, Bizzell C, Soldatos T. 3 Tesla MR neurography-technique, interpretation, and pitfalls. Skeletal Radiol 2011; 40:1249-1260.
2 Chhabra A, Andreisek G, Soldatos T, et al. MR neurography: past, present, and future. AJR Am J Roentgenol 2011; 197:583-591.
3 Vargas MI, Viallon M, Nguyen D, Beaulieu JY, Delavelle J, Becker M. New approaches in imaging of the brachial plexus. Eur J Radiol. 2010 May;74(2):403-10.
4 Zhang Z, Song L, Meng Q, et al. Morphological analysis in patients with sciatica: a magnetic resonance imaging study using three-dimensional high-resolution diffusion-weighted magnetic resonance neurography techniques. Spine (Phila Pa 1976) 2009; 34:E245-250.
5 Chhabra A, Soldatos T, Subhawong TK, Machado AJ, Thawait SK, Wang KC, Padua A Jr, Flammang AJ, Williams EH, Carrino JA. The application of three-dimensional diffusion-weighted PSIF technique in peripheral nerve imaging of the distal extremities. J Magn Reson Imaging. 2011 Oct;34(4):962-7.
6 Viallon M, Vargas MI, Jlassi H, Lovblad KO, Delavelle J. High-resolution and functional magnetic resonance imaging of the brachial plexus using an isotropic 3D T2 STIR (Short Term Inversion Recovery) SPACE sequence and diffusion tensor imaging. Eur Radiol 2008; 18:1018-1023.
7 Guggenberger R, Eppenberger P, Markovic D, Nanz D, Chhabra A, Pruessmann KP, Andreisek G. MR neurography of the median nerve at 3.0T: Optimization of diffusion tensor imaging and fiber tractography. Eur J Radiol. 2012 Apr 19. [Epub ahead of print]
8 Chhabra A, Thakkar RS, Gustav A et al. Anatomic MR imaging and functional diffusion tensor imaging of peripheral nerve tumor and tumor like conditions. AJNR 2012 (in press).
9 Chhabra A, Williams EH, Wang KC, Dellon AL, Carrino JA. MR neurography of neuromas related to nerve injury and entrapment with surgical correlation. AJNR Am J Neuroradiol; 31:1363-1368.
10 Chhabra A, Subhawong TK, Williams EH, Wang KC, Hashemi S, Thawait SK, Carrino JA. High-resolution MR neurography: evaluation before repeat tarsal tunnel surgery. AJR Am J Roentgenol. 2011 Jul;197(1):175-83.

Contact
Avneesh Chhabra, M.D.
Assistant Professor Radiology &
Orthopedic Surgery
Russell H Morgan Department
of Radiology & Radiological Science
Johns Hopkins University, Baltimore, MD
USA
achhabr6@jhmi.edu

High-Resolution DWI in Brain and Spinal Cord with *syngo* RESOLVE[1]

Julien Cohen-Adad

Department of Electrical Engineering, Ecole Polytechnique de Montreal, QC, Canada
A. A. Martinos Center for Biomedical Imaging, Massachusetts General Hospital, Harvard Medical School, Charlestown, MA, USA

Abstract

In this paper we present some applications of the *syngo* RESOLVE[1] sequence that enable high-resolution diffusion-weighted imaging. The sequence is based on a readout-segmented EPI strategy, allowing susceptibility distortions and T2* blurring to be minimized. The RESOLVE[1] sequence can be combined with other acquisition strategies such as reduced field-of-view (FOV) and parallel imaging, to provide state-of-the-art tractography of the full brain and cervical spinal cord. The RESOLVE[1] sequence could be of particular interest for ultra high field systems where artifacts due to susceptibility and reduced T2 values are more severe. At all field strengths, the sequence promises to be useful in a number of clinical applications to characterize the diffusion properties of pathology with high resolution and a low level of image artifact.

1. Introduction

1.1. Diffusion-weighted imaging

Diffusion-weighted MRI makes it possible to map white matter architecture in the central nervous system based on the measurement of water diffusion [11]. The technique works by using MRI sequences that are sensitized to the microscopic motion of water molecules, which are in constant motion in biological tissues (Brownian motion). Using the well-known pulse sequence introduced by Stejskal and Tanner in 1965 [29], it is possible to quantify the extent of water displacement in a given direction. This sequence consists of magnetic field gradient pulses (diffusion-encoding gradients) that are applied before and after a 180° radiofrequency (RF) refocusing pulse. The first gradient pulse dephases the precessing nuclear spins that generate the signal in MRI. In the theoretical case of static molecules, the second gradient pulse completely rephases the spins and there is no attenuation due to the application of the gradients. However, if water molecules move during the application of this pair of gradients, spins are dephased and signal decreases as a function of the magnitude of the displacement, leading to a so-called diffusion-weighted signal. The magnitude by which the signal is weighted by diffusion is dictated by the so-called *b-value*, which depends on the length and amplitude of the applied diffusion-encoding gradients, as well as the duration between the first and the second gradient pulse (also called diffusion time). By applying diffusion gradients in various directions (e.g., 20 directions equally sampled on a sphere), it is possible to estimate the rate and direction of water diffusion. For example in pure water, molecules diffuse equally in all directions, hence the diffusion is described as *isotropic*. Conversely, in mesenchymal structures such as the white matter or muscles, water diffuses preferentially along the direction of the fiber. In such a case, the diffusion is *anisotropic* [3].

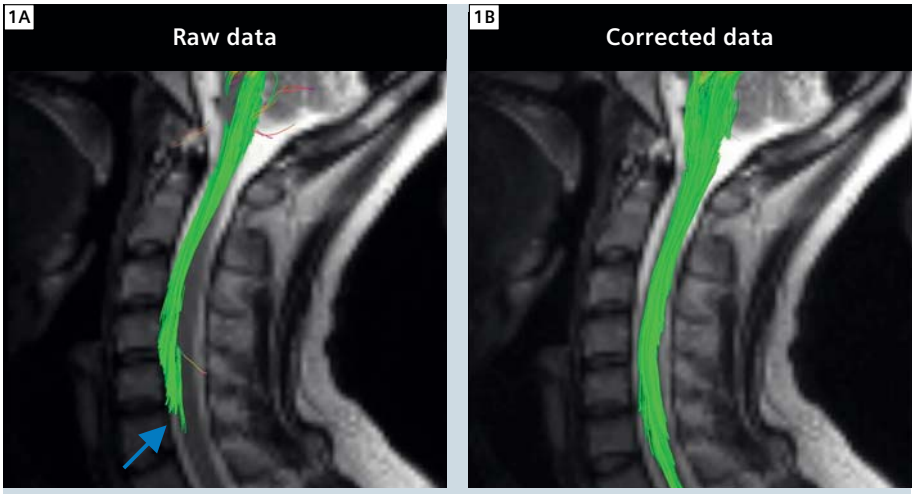

1 Tractography in a healthy subject, overlaid on a distortion-free anatomical image (fast spin echo). **(1A)** shows tractography performed on the raw data (i.e., without correction). **(1B)** shows tractography performed on the same dataset, after distortion correction using the reversed-gradient technique [13]. A false apparent interruption of the tracts is observed on the data hampered by susceptibility distortions. Acquisition was performed using the standard EPI sequence with the following parameters: sagittal orientation, TR/TE = 4000/86 ms, 1.8 mm isotropic, R = 2 acceleration. Tractography was seeded from a slice located at C1 vertebral level.

[1]The software is pending 510(k) clearance, and is not yet commercially available in the United States and in other countries.

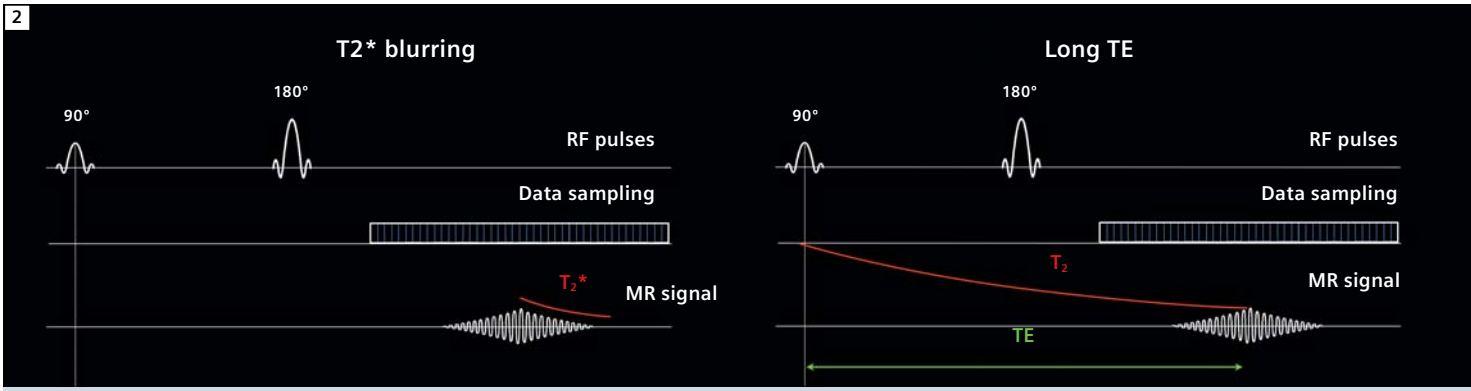

2 The left panel illustrates the origin of the T2* blurring effect, which is caused by T2* dephasing during *k*-space (raw data) sampling. The right panel illustrates the consequence of a long TE due to the combination of the diffusion-encoding gradients and the extended data sampling interval, resulting in low SNR data.

1.2. DTI and tractography

After acquiring a set of diffusion-weighted data, it is possible to compute a parametric model representing the main diffusion direction at each voxel [2]. This type of model is described by a tensor and is usually represented graphically as a 3D ellipsoid. This technique is known as Diffusion Tensor Imaging (DTI) and makes it possible to derive metrics such as fractional anisotropy (FA), mean diffusivity and axial and radial diffusivities. These metrics are relevant as they have been shown to correlate with demyelination and axonal degeneration [28] and can therefore be used to obtain markers of demyelination in multiple sclerosis [26], spinal cord injury [7] or amyotrophic lateral sclerosis [8].

Having modeled the diffusion tensor, it is possible to reconstruct global axonal pathways by linking every voxel with a similar eigenvector (principal axis of the diffusion tensor) to its neighbors. This procedure is called fiber tracking or tractography [18]. It should be mentioned however that the reconstructed fiber bundles do not represent *real* axonal tracts but rather represent the path where water diffuses preferentially. It is therefore an indirect measure of axon orientation. Hence, tractography results should be handled with care since they may not represent the real pathway of axons [14]. For instance, false negatives could be induced by the presence of crossing fibers, which would artificially decrease the FA and stop the tracking procedure. Inversely, false positives could be induced by fibrous structures such as scar tissue, in which water diffusion also has anisotropic properties [27]. In such cases, fiber tracking can become fiber *tricking*.

To illustrate the need for caution, Figure 1 shows an example of tractography performed in a healthy subject, before and after correction for susceptibility artifacts, which can induce strong image distortions in the phase-encoding direction (antero-posterior in this example). On the 'raw data' (1A), a false apparent interruption of the tracts is clearly observed, and can be misinterpreted as an interruption of the white matter tracts. However, this apparent interruption is simply due to susceptibility distortions, as can be seen on the 'corrected data' (1B). This result suggests two things: *(I)* a careful assessment of the image data is essential before further processing is applied and *(II)* susceptibility-induced distortions should be minimized by an appropriate choice of data acquisition technique. This might ultimately reduce the need for quality assessment, which is not often possible in clinical routine. This brings us to the next section on how to reduce susceptibility artifact during the acquisition.

1.3. Artifacts in diffusion-weighted imaging

In this section we will mostly focus on susceptibility artifacts and T2* blurring. Other artifacts exist in diffusion-weighted imaging [15], but are not in the scope of the presence article.

Single-shot echo planar imaging (ss-EPI) is an ultra-fast imaging sequence that makes it possible to acquire a full slice within a single repetition time (TR) [16]. To achieve this, spatial encoding gradients are played out rapidly along two gradient axes (e.g. X and Y) in order to sample all raw data (or *k*-space) points in a 'single shot' after an RF excitation pulse. By applying the EPI readout directly after the excitation pulse, a gradient echo image can be generated. Alternatively, an RF refocusing pulse can be inserted between the excitation and EPI readout to produce a spin echo image, which has reduced susceptibility-induced signal loss, but has the same sensitivity to susceptibility-based distortions. An oscillating readout gradient is applied along one axis (e.g. X), consisting of a series of gradient pulses with alternating polarity and each of these readout gradient pulses is used to sample a single line of *k*-space. A short phase-encoding gradient or 'blip' is applied along an orthogonal gradient axis (e.g. Y), so that each readout gradient corresponds to a different line of *k*-space in the Y direction. While acquisition of a full line a *k*-space in the read-

out direction is obtained rapidly (in about 1 ms), the acquisition of *k*-space data along the phase-encoding direction takes much more time. For example, for a 128×128 matrix, acquisition of the full *k*-space can take more than 100 ms. During that time, spins experience dephasing due to local B_0-inhomogeneities. These undesirable inhomogeneities are typically induced at interfaces between structures with different susceptibility properties, such as air/tissue or bone/muscle. As a result, phase errors accumulate in the phase-encoding direction, causing geometric distortions in the reconstructed image in that direction. EPI sequences are fast and particularly appropriate for diffusion-weighted experiments [31] where multiple datasets need to be acquired in a clinically acceptable time with low sensitivity to motion-induced phase error [17]. However single-shot EPI also has the disadvantage that it is particularly sensitive to susceptibility-related geometric distortions. Reduction of susceptibility artifacts can be achieved by sampling the *k*-space faster, which decreases the accumulation of the phase errors. Faster acquisition can be achieved by reducing the echo spacing, which is defined as the total time between the application of two phase-encode blips. Echo spacing can be reduced by *(I)* increasing the readout bandwidth, *(II)* reducing the number of phase lines by reducing the FOV (because the sampling density in *k*-space defines the FOV in the image domain) and *(III)* combining several subsampled *k*-space acquisitions (multi-shot). In addition to susceptibility artifacts, T2* blurring can be induced due to the relatively long sampling of *k*-space, during which T2* relaxation occur (Figure 2, left). This effect is more pronounced in regions with large B_0 inhomogeneities. Another undesirable effect of the long sampling is that it will impose a relatively long echo time (TE) (Figure 2, right). As a result, the recorded signal amplitude will be small due to the relatively short transverse relaxation (T2) in white matter (about 70 ms at 3T). This effect is critical since SNR is proportional to exp(-TE/T2), therefore even a small increase of TE (several ms) can substantially reduce the signal-to-noise ratio (SNR).

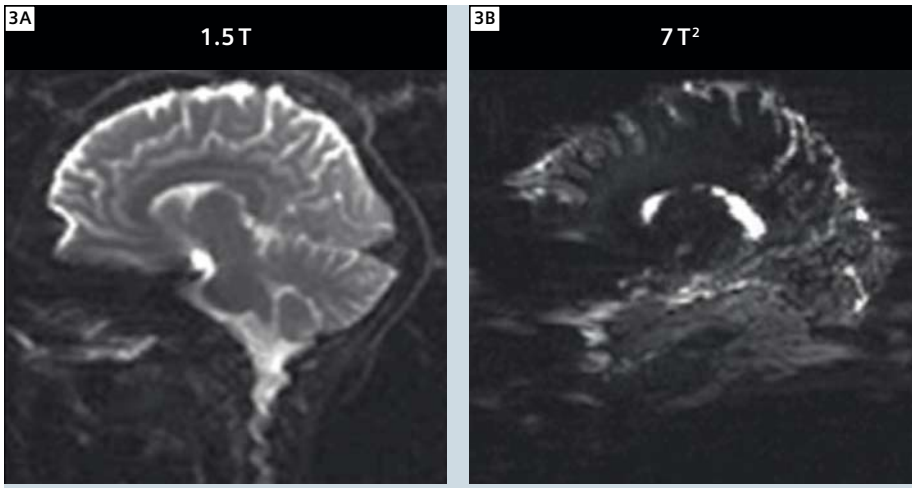

3 Comparison of single-shot EPI at 1.5T **(3A)** and 7T[2] **(3B)**.



4 Benefits of faster sampling for: *(I)* reducing susceptibility distortions (less accumulation of phase errors), *(II)* reducing T2* blurring (faster sampling) and *(III)* enabling shorter TE (due to the faster sampling of *k*-space, which in turn brings the center of the readout window closer to the 180° pulse).

All these limitations become even more problematic at higher field, where T2 is reduced (about 50 ms at 7T) and B_0 homogeneity is more difficult to achieve, resulting in a greater level of susceptibility artifact. Figure 3 shows an example of the high-field degradation in image quality when using the standard single-shot EPI technique at 1.5T and 7T[2].

To summarize, the main issues encountered with diffusion-weighting EPI are:

- **Susceptibility artifacts**, which are caused by an accumulation of phase error during the readout, leading to image distortions.
- **T2* blurring**, which is caused by the long data sampling interval during the readout, leading to a broadening of the point spread function and a blurring of the reconstructed image.
- **Long TE**, which is imposed by a combination of the diffusion-encoding gradients and the long data sampling interval and results in low SNR.

These three arguments provide motivation for a reduction in the sampling time, which will address all these issues, as illustrated in Figure 4.

[2]The 7T system is a research system only. It cannot be used outside of a research study.

2. Multi-shot techniques and *syngo* RESOLVE[1]

As described in the previous section, susceptibility artifacts and T2* blurring can be reduced by decreasing the sampling time (or the effective echo spacing). In EPI, this can be done by skipping lines of *k*-space in the phase-encoding direction (also called interleaved EPI). Multi-shot techniques consist of acquiring several sub-sampled images and combining them to reconstruct a full *k*-space data set. An example of a 2-shot interleaved EPI acquisition is illustrated in Figure 5. In this approach, the first image is acquired by only filling even lines of *k*-space, while the second image is acquired by filling the odd lines. Then, both data sets are combined in order to obtain the full *k*-space data that is required for image reconstruction. The key aspect is that each of the sub-sampled data sets is acquired twice as fast as in the single-shot case, which reduces the effective echo spacing by a factor two, and hence also reduces the distortions by a factor of 2. However, one disadvantage of the interleaved EPI approach is that the overall acquisition time is longer than single-shot techniques (because multiple TR intervals are required acquire all data required to form an image). Another disadvantage is that phase errors due to motion (from subject or physiology) can occur between the acquisition of different interleaves, which can lead to severe ghosting artifacts [6].

To overcome the mismatch between different data interleaves, one can acquire navigator echoes that monitor phase errors and correct them before image reconstruction. At their introduction, navigator echoes consisted in single line of *k*-space acquired at the center, which was used to apply a linear phase correction in the readout direction [1, 20]. Later, 2D navigator echoes enabled linear phase correction both in the readout- and in the phase-encoding directions [4]. More recently, non-linear approaches have been introduced [17], which is particularly important for diffusion-weighted imaging of the brain, where cerebrospinal fluid pulsation leads to non-rigid-body brain motion that results in non-linear phase errors if the motion occurs during the application of the diffusion-encoding gradients. 2D non-linear phase correction is most easily applied when each shot in the multi-shot data acquisition samples a contiguous set of data points from a sub-region of *k*-space. In this case, the Nyquist sampling condition is fulfilled and the phase correction can be applied as a complex multiplication in image space. The interleaved EPI sampling scheme does not fulfill this local Nyquist sampling condition and results in aliased signal contributions that complicate the phase correction procedure.

2.1. Readout-segmented EPI

An alternative to the interleaved approach is to perform readout-segmented EPI [25]. In readout-segmented EPI, *k*-space is filled with a series of concatenated segments in the readout direction (Figure 6), corresponding to shorter readout gradient pulses and an overall reduction in the length of the EPI readout As with interleaved EPI, the shorter readout time results in a reduction in the level of susceptibility-based distortion.

2.2. Diffusion-weighted readout-segmented EPI

One advantage of readout-segmented EPI compared to phase-segmented (or interleaved) EPI is that each segment consists of a Nyquist-sampled region of *k*-space that is well suited to the application of 2D non-linear phase correction, as described above. This property of the readout-segmented EPI sampling scheme was first exploited by Porter et al. [24] who proposed the sequence shown in figure 7 for application to diffusion-

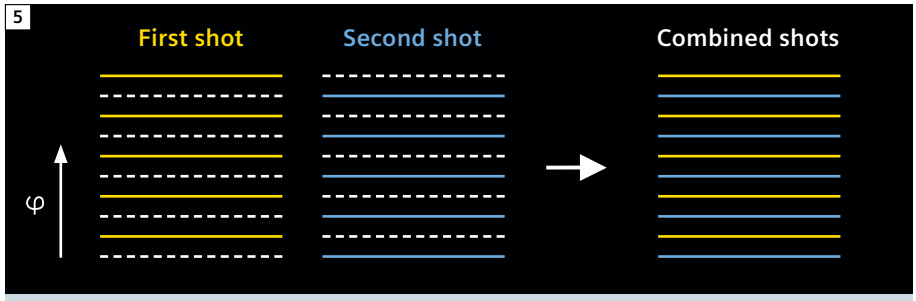

5 Segmented EPI along the phase-encode direction (interleaved EPI). *(I)* Acquire several shots of sub-sampled *k*-space, *(II)* concatenate all shots and *(III)* reconstruct image. Each shot is sub-sampled, resulting in a shorter data sampling interval and reduced distortion.

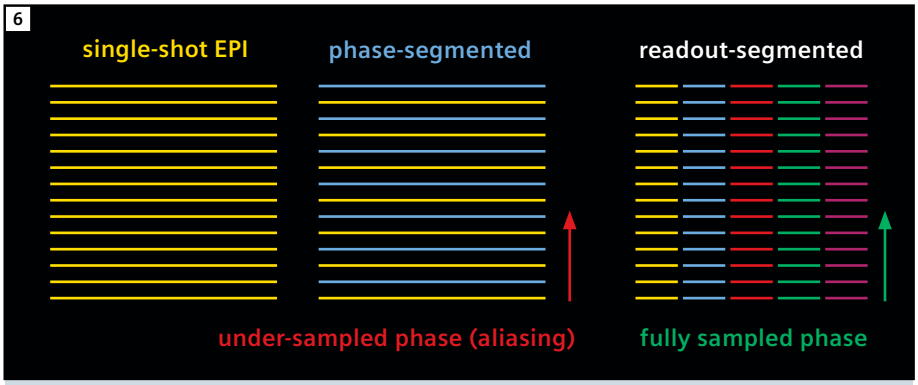

6 Schematic of *k*-space acquired using a conventional single-shot EPI (left), phase-segmented or interleaved EPI (middle) and readout-segmented EPI (right). In the phase-segmented EPI, the data for each shot is sub-sampled in the phase-encoding direction, which induces aliasing and therefore difficulties in correcting for phase-to-phase errors using advanced 2D non-linear techniques. However in readout-segmented EPI, all phase-encode lines are acquired in each shot, therefore there is no aliasing.

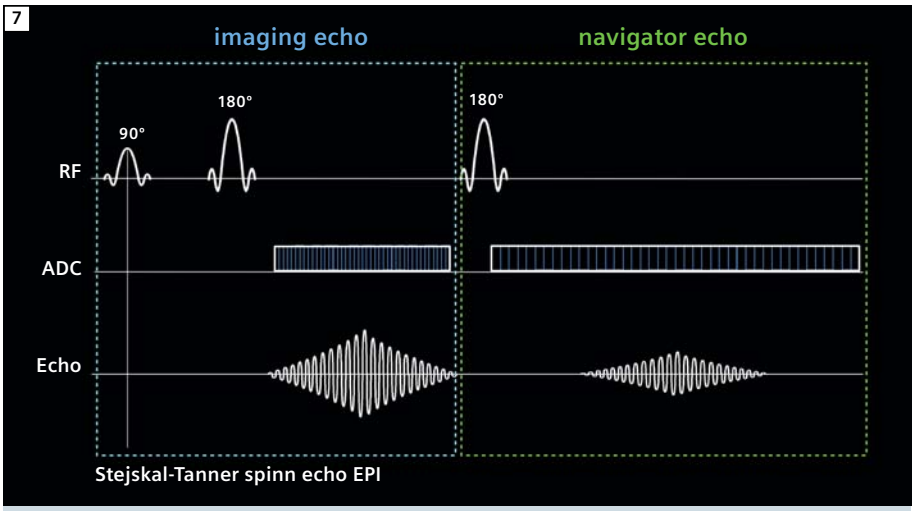

7 Simplified pulse diagram of the RESOLVE sequence (gradients are not represented).

weighted imaging. The sequence consists of an imaging echo, which is used to sample the standard readout-segmented EPI data, and a 2D navigator echo, in which a low resolution EPI readout is used to sample the center of *k*-space at each shot. The sequence was subsequently modified to support parallel imaging [22] using GRAPPA [10]. This made it possible to further shorten the readout time with a corresponding additional reduction in the level of susceptibility artifact. The resulting sequence has been given the acronym RESOLVE[1] (Readout Segmentation Of Long Variable Echo-trains).

2.3. Reacquisition technique

In some cases, the level of motion-induced phase error can be too severe for a reliable phase correction due to signal voids in the navigator images. Although physiological gating strategies can be employed to mitigate these effects, they do not address all sources of motion and can significantly increase acquisition time. To avoid the residual artifacts associated with these occasional extreme phase errors, the RESOLVE[1] sequence uses a reacquisition strategy to identify and re-measure corrupt readout segments that cannot be reliably phase corrected. This method is based on an original concept that was proposed for interleaved EPI and 1D navigator echoes [19], but uses an adapted real-time algorithm, which has been optimized for the combination of 2D navigator data and the readout-segmented EPI sampling scheme [21]. For a comprehensive description of the RESOLVE[1] sequence, including the adaptions for parallel imaging and data reacquisition, the reader is referred to [23].

3. Application of the RESOLVE[1] sequence

To illustrate the benefits of the RESOLVE[1] sequence, Figure 8 shows a comparison between the conventional single-shot EPI (8A) and RESOLVE[1] (8B). Acquisition parameters were:

RESOLVE: Axial slices, TR 3800 ms, TE 80 ms, 4 nex, 12-4 mm thick slices with 0.4 mm gap, 320 × 256 matrix, b=700 s/mm^2 only in slice direction (S-I), GRAPPA x 2, segment 21, FOV 163 mm, acquisition time 6–7 min (depending on reacquisition).

Single-shot EPI: Axial slices, TR 3800 ms, TE 102 ms, 32 nex, 12–4 mm thick slices with 0.4 mm gap, 192 × 192 matrix, b=700 s/mm^2 only in slice direction (S-I), GRAPPA x 2, FOV 220 mm, acquisition time 2 min 15 sec.

All scans were performed at 3T using a 32-channel array head coil.

Images represent an axial mean diffusion-weighted image located in the lower brain region, which is well-known for its susceptibility artifacts due to the sinuses and temporal poles. In the ss-EPI image, strong susceptibility artifacts can be observed as image and signal distortions. For example, the temporal region not only shows image distortion along the phase-encoding direction (antero-posterior), but also shows increase of signal intensity caused by the overlap of distorted voxels (arrow). This spurious signal increase could be falsely interpreted as pathological. Conversely in the RESOLVE[1] image, the same region shows a substantial reduction in this susceptibility artifact. In addition, an overall blurring can be observed on the ss-EPI image, which is caused by the relatively long *k*-space sampling relative to the T2* decay. Reducing the sampling time also reduces this T2* blurring, as can be seen on the RESOLVE[1] image, where the image appears sharper, making it possible to delineated white and gray matter with greater precision.

3.1. 1×1×1 mm^3 resolution full brain at 7T

With the RESOLVE[1] sequence it is possible to acquire high-resolution images without the large increase in susceptibility and T2* artifacts that would affect an ss-EPI acquisition. In one study at 7T, the sequence was used to perform full brain diffusion-weighted imaging at 1×1×1 mm^3 resolution [12]. The study was performed on a whole-body scanner (MAGNETOM 7T[2], Siemens Healthcare, Erlangen, Germany) with a 24-channel RF receive coil (Nova Medical, Wilmington, MA, USA). Acquisition parameters were: 104 axial slices, matrix 220×220, FOV 220 mm, slice thickness 1 mm (no gap), TR 7500 ms, TE 76 ms, 7 readout segments, 30 diffusion-weighting directions at a b-value of 1000 s/mm^2, acquisition time was 78 min. The diffusion-weighted images were filtered with a two-stage hybrid image restoration procedure, corrected for subject motion and registered to a T1-weighted anatomical image (1 mm resolution) of the same participant. For each voxel, multiple fiber orientations were modeled by constrained spherical deconvolution [30] followed by whole-brain fiber-tracking using

MRtrix (http://www.brain.org.au/software)[3].
Figure 9 shows results of the fiber orientation distribution function (ODF) and tractography centered over the pre-motor cortex. The spatial consistency of the fiber ODF demonstrates the high SNR of the data (Figure 9B). Tractography successfully demonstrated intersection of the corpus callosum (CC, pink), the corona radiata (CR, blue) and the superior longitudinal fasciculus (SLF, green, tracks not shown).
The same data were processed using track-density imaging [5], which makes it possible to reconstruct fiber bundles at 200 µm resolution. Figure 10 shows the results at the three orientations in order to appreciate the 1 mm isotropic resolution. The views are centered over the thalamus. The ultra-high resolution in combination with high SNR and low susceptibility artifacts provide an unprecedented level of detail about the anatomical organization of the thalamus. The ability of the sequence to provide full brain coverage at an isotropic resolution of 1 mm made it possible to reconstruct track density images of the whole brain with no orientation bias.

3.2. Spinal cord DTI at 3T

Another powerful application of the RESOLVE sequence is the spinal cord. Indeed, spinal cord DTI is particularly challenging due to *(I)* the small cross-sectional size of the spinal cord, which requires high spatial resolution, resulting in low SNR at standard imaging times; *(II)* susceptibility artifacts, which are caused by inhomogeneous magnetic field in the spinal region due to the close proximity of tissue with very different magnetic susceptibility (tissue, bone, air, cartilage) and *(III)* physiological-related motion due to respiration, heart beat, cerebrospinal fluid pulsation. The first two arguments (small size and susceptibility artifacts) are particularly well suited for the RESOLVE[1] sequence, as this

[3]MRtrix is not a Siemens Healthcare product. Siemens bears no responsibility for this product including, but not limited to, its regulatory status. Further information about the software can be found at the website listed.

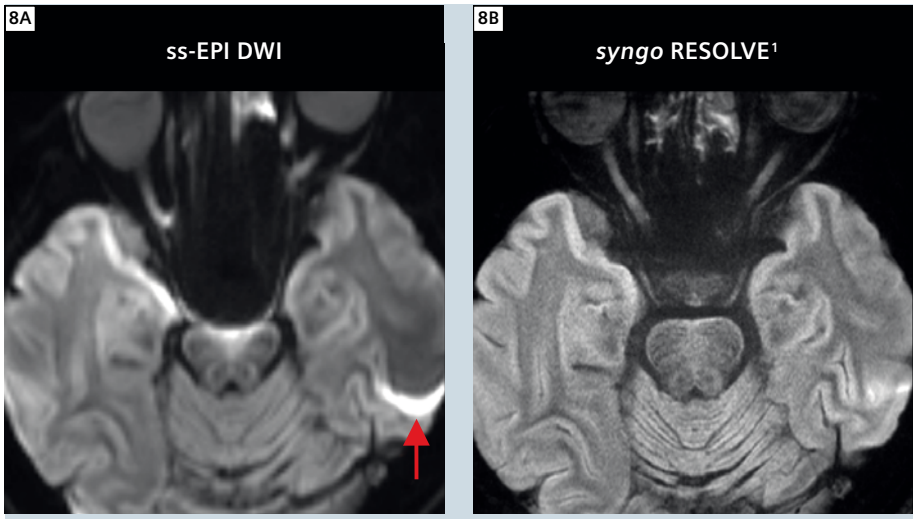

8 Comparison of standard single-shot EPI sequence **(8A)** and *syngo* RESOLVE[1] **(8B)**. Susceptibility distortions are substantially reduced on the RESOLVE[1] image. For example, the temporal region of the ss-EPI image not only shows image distortion along the phase-encoding direction (antero-posterior), but also shows an increase in signal intensity caused by the overlap of distorted voxels (arrow). Sharper image with RESOLVE[1] also comes from faster sampling, via reduction of T2* blurring. *Images courtesy of Professor Naganawa, Nagoya University School of Medicine, Japan.*

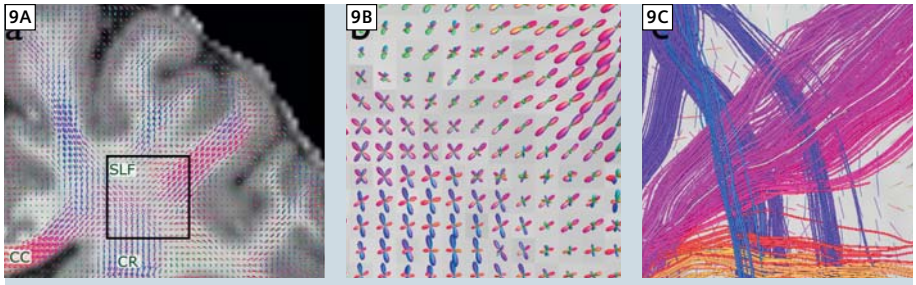

9 High angular resolution diffusion imaging results from 1 mm isotropic resolution. **(9A)** Coronal view centered in the pre-motor region at the intersection between corpus callosum (CC), superior longitudinal fasciculus (SLF) and corona radiate (CR). **(9B)** Orientation distribution functions (ODF) showing crossing of the major pathways. **(9C)** Tractography results showing intersection of the CC (pink) and CR (blue). *Images courtesy of Drs. Robin Heidemann and Alfred Anwander, MPI Leipzig, Germany.*

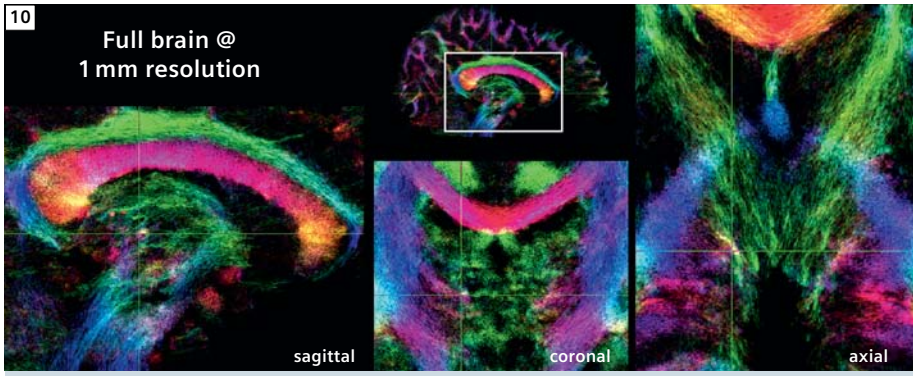

10 Track density image with 200 µm resolution. Fine details of the structure of the thalamus are visible. *Image courtesy of Drs. Robin Heidemann and Alfred Anwander, MPI Leipzig, Germany.*

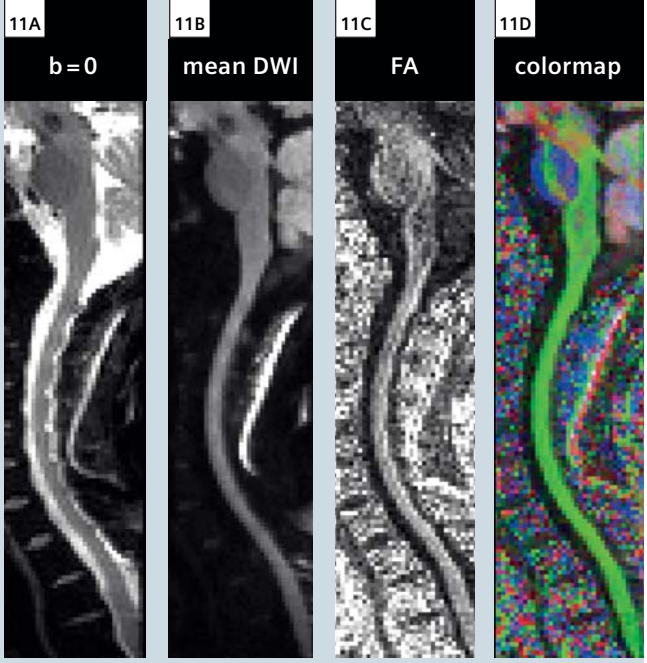

11 Human cervical spinal cord. 1.7 mm isotropic, 3 shots, R = 3, TE 74 ms, Cardiac gating, b 800 s/mm², 30 directions in 8 min.

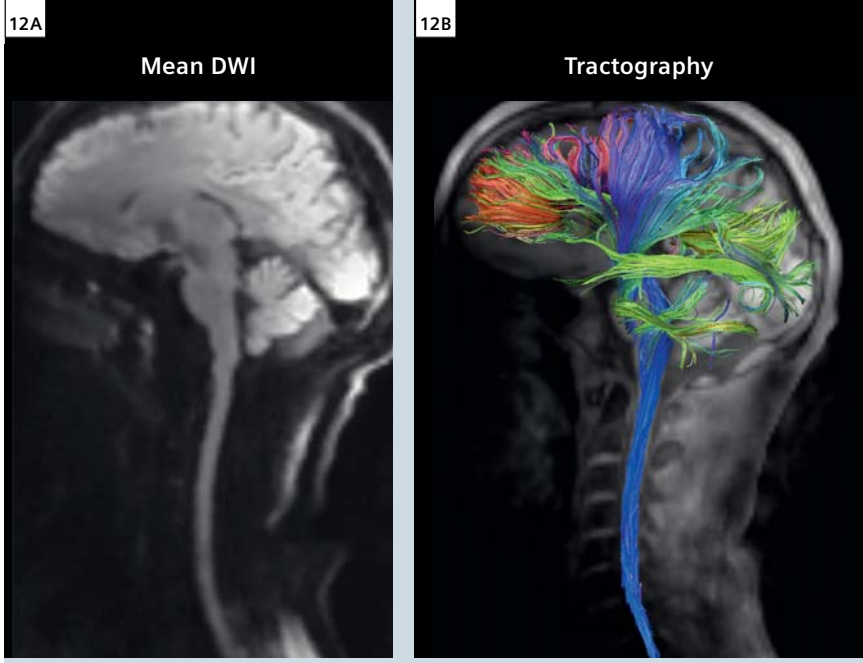

12 Sagittal view of the mean diffusion-weighted images **(12A)** and fiber tractography overlaid on the anatomical image **(12B)**. Almost no distortions are observed, which makes it possible to explore white matter connections from cortical areas down to the spinal cord without spurious interruptions.

sequence provides high SNR and enables reduction of susceptibility distortions. The last challenge (physiological motion) is a typical cause of failure for segmented approaches, however the non-linear 2D phase correction combined with the reacquisition scheme enabled in the RESOLVE[1] sequence ensures low sensitivity to physiological motion.

An example of the RESOLVE[1] in the spinal cord is shown in Figure 11. To further improve image quality, the RESOLVE[1] sequence was used with parallel imaging using the GRAPPA algorithm [10] to further reduce susceptibility artifacts and shorten the TE. To maximize the capabilities of parallel imaging, a dedicated 32-channel head/spine coil was used, which enables up to 4× acceleration [9]. Acquisition parameters were: 1.7 mm isotropic, 3 shots, R = 3 acceleration (iPAT3), TE 74 ms, Cardiac gating, b 800 s/mm², 30 directions, acquisition time 8 min. The sequence only used 3 shots (i.e., 3 segments per *k*-space), therefore the acquisition was relatively short. Although minor distortions are still visible on the b = 0 image at the level of each intervertebral disk, the spinal cord itself is not affected by these intervertebral distortions as assessed by the mean diffusion-weighted image, the fractional anisotropy (FA) map and the FA color map. Note the particularly high spatial resolution (1.7 mm isotropic, 4.9 mm³ voxel volume), which is rarely achieved in spinal cord imaging.

One particularly difficult acquisition is when one wants to image the full brain and spinal cord. The challenge of B_0-inhomogeneity can be partially overcome when only the spinal cord is imaged by adjusting the shim volume within an elongated box that nicely encompasses the spinal cord. However, when the FOV includes both the brain and spinal cord, it is a difficult for the shimming algorithm to find appropriate fitting coefficients for ensuring B_0-homogeneity both in the brain and spinal cord, due to the complex geometry and the presence of several susceptibility interfaces (sinuses, temporal poles, brainstem, intervertebral disks and lungs). This type of acquisition is therefore particularly well-suited to the RESOLVE[1] sequence.

Images were acquired with the following parameters: 2.2 mm isotropic resolution, matrix 138 × 104, TR ~ 15000 ms (cardiac gating), TE 66 ms, 3 shots, R = 3 acceleration, b 800 s/mm², 30 diffusion-weighting directions, acquisition time 10:45 min. Images were further corrected for residual susceptibility-distortions in the thoracic region (due to the close proximity with the lungs), using the reversed gradient technique [13]. Tractography was performed using the Diffusion Toolkit[3] (deterministic FACT algorithm) and displayed with TrackVis[3] (http://www.trackvis.org/). Diffusion-weighted images were then registered to the 1 mm isotropic anatomical image (MPRAGE). Results are shown in Figure 12 and demonstrate reduction of susceptibility artifacts, enabling to explore connections within and between the brain, brainstem and cervical spinal cord.

4. Conclusion

syngo RESOLVE[1] is a useful sequence for acquiring high-quality diffusion-weighted images thanks to the reduction of susceptibility distortion, reduction of T2* blurring, shorter TE (and hence high SNR) and robust correction for motion-induced artifacts. The RESOLVE sequence has shown promising tractography results in the brain and spinal cord, the latter being known for suffering from severe susceptibility artifacts using standard sequences. The RESOLVE sequence can be combined with other acquisition strategies such as reduced field-of-view and parallel imaging. Potential applica-

[3]Diffusion Toolkit and TrackVis are not Siemens Healthcare products. Siemens bears no responsibility for these products including, but not limited to, their regulatory status. Further information about the software can be found at the website listed.

tions in research include the study of white matter architecture in the brain, brainstem and spinal cord, and also the possibility to study fine structure such as the thalamus and the gray nuclei. In clinical application, the reduced level of susceptibility artifact with the RESOLVE[1] sequence can provide better interpretation of abnormalities in white matter pathology. Although acceptable image quality can already be obtained using the conventional single-shot EPI sequence providing shimming is successful, this procedure is strongly user-dependent, subject-dependent and structure-dependent. Because this variability is not acceptable in clinical routine, the RESOLVE[1] sequence has the potential to ensure robust image quality. Moreover, the RESOLVE[1] sequence may be particularly useful in cases where patients have metallic implants, notably in spinal cord injury, where assessing the integrity of spinal pathway would be of tremendous help for patient prognosis.

5. Acknowledgements

The author wishes to thank Drs. Lawrence Wald, Thomas Witzel, Kawin Setsompop and Boris Keil at the *A. A. Martinos Center for Biomedical Imaging*, Alfred Anwander at the *Max Planck Institut* and Drs. David Porter, Keith Heberlein, Himanshu Bhat, Robin Heidemann and Ignacio Vallines at *Siemens Healthcare*. This study was supported by NIH-P41RR14075 and National Multiple Sclerosis Society (FG 1892A1/1).

[1]The software is pending 510(k) clearance, and is not yet commercially available in the United States and in other countries.
[2]The 7T system is a research system only. It cannot be used outside of a research study.

References

1 Anderson, A.W., Gore, J.C., 1994. Analysis and correction of motion artifacts in diffusion weighted imaging. Magn Reson Med 32, 379-387.
2 Basser, P.J., Mattiello, J., LeBihan, D., 1994. Estimation of the effective self-diffusion tensor from the NMR spin echo. J Magn Reson 103, 247-254.
3 Beaulieu, C., 2002. The basis of anisotropic water diffusion in the nervous system – a technical review. NMR Biomed 15, 435-455.
4 Butts, K., Pauly, J., de Crespigny, A., Moseley, M., 1997. Isotropic diffusion-weighted and spiral-navigated interleaved EPI for routine imaging of acute stroke. Magn Reson Med 38, 741-749.
5 Calamante, F., Tournier, J.-D., Jackson, G.D., Connelly, A., 2010. Track-density imaging (TDI): super-resolution white matter imaging using whole-brain track-density mapping. NeuroImage 53, 1233-1243.
6 Clark, C.A., Barker, G.J., Tofts, P.S., 2000. Improved reduction of motion artifacts in diffusion imaging using navigator echoes and velocity compensation. J Magn Reson 142, 358-363.
7 Cohen-Adad, J., El Mendili, M.-M., Lehéricy, S., Pradat, P.-F., Blancho, S., Rossignol, S., Benali, H., 2011a. Demyelination and degeneration in the injured human spinal cord detected with diffusion and magnetization transfer MRI. NeuroImage 55, 1024-1033.
8 Cohen-Adad, J., El Mendili, M.M., Morizot-Koutlidis, R., Lehericy, S., Meininger, V., Blancho, S., Rossignol, S., Benali, H., Pradat, P.-F., 2012. Involvement of spinal sensory pathway in ALS and specificity of cord atrophy to lower motor neuron degeneration. Amyotroph Lateral Scler doi:10.3109/17482968.2012.701308.
9 Cohen-Adad, J., Mareyam, A., Keil, B., Polimeni, J.R., Wald, L.L., 2011b. 32-channel RF coil optimized for brain and cervical spinal cord at 3 T. Magn Reson Med 66, 1198-1208.
10 Griswold, M.A., Jakob, P.M., Heidemann, R.M., Nittka, M., Jellus, V., Wang, J., Kiefer, B., Haase, A., 2002. Generalized autocalibrating partially parallel acquisitions (GRAPPA). Magn Reson Med 47, 1202-1210.
11 Hagmann, P., Jonasson, L., Maeder, P., Thiran, J.P., Wedeen, V.J., Meuli, R., 2006. Understanding diffusion MR imaging techniques: from scalar diffusion-weighted imaging to diffusion tensor imaging and beyond. Radiographics 26 Suppl 1, S205-223.
12 Heidemann, R.M., Porter, D.A., Anwander, A., Feiweier, T., Calamante, F., Tournier, J.-D., Lohmann, G., Meyer, H., Knoesche, T.R., Turner, R., 2011. Whole-Brain, Multi-Shot, Diffusion-Weighted Imaging in Humans at 7T with 1 mm Isotropic Resolution. Proceedings of the 19th Annual Meeting of ISMRM, Montreal, Canada 541.
13 Holland, D., Kuperman, J.M., Dale, A.M., 2010. Efficient correction of inhomogeneous static magnetic field-induced distortion in Echo Planar Imaging. NeuroImage 50, 175-183.
14 Johansen-Berg, H., Behrens, T.E., 2006. Just pretty pictures? What diffusion tractography can add in clinical neuroscience. Curr Opin Neurol 19, 379-385.
15 Le Bihan, D., Mangin, J.F., Poupon, C., Clark, C.A., Pappata, S., Molko, N., Chabriat, H., 2001. Diffusion tensor imaging: concepts and applications. J Magn Reson Imaging 13, 534-546.
16 Mansfield, P., 1977. Multi-planar image formation using NMR spin echoes. J. Phys. C: Solid State Phys. 10, L55-58.
17 Miller, K.L., Pauly, J.M., 2003. Nonlinear phase correction for navigated diffusion imaging. Magn Reson Med 50, 343-353.
18 Mori, S., Zhang, J., 2006. Principles of diffusion tensor imaging and its applications to basic neuroscience research. Neuron 51, 527-539.
19 Nguyen, Q., Clemence, M., Thornton, J., Ordidge, R., 1999. Isotropic diffusion-weighted multishot imaging using automatic reacquisition. Proceedings of the 7th Annual Meeting of ISMRM, Philadelphia, USA, 559.
20 Ordidge, R.J., Helpern, J.A., Qing, Z.X., Knight, R.A., Nagesh, V., 1994. Correction of motional artifacts in diffusion-weighted MR images using navigator echoes. Magn Reson Imaging 12, 455-460.
21 Porter, D.A., 2006. 2D-navigator-based re-acquisition for motion artefact suppression in multi-Shot, diffusion-weighted Imaging. Proceedings of the 14th Annual Meeting of ISMRM, Seattle, USA, 1047.
22 Porter, D.A., Heidemann, R., 2006. Multi-Shot, Diffusion-Weighted Imaging at 3T using readout-segmented EPI and GRAPPA. Proceedings of the 14th Annual Meeting of ISMRM, Seattle, USA, 1046.
23 Porter, D.A., Heidemann, R.M., 2009. High resolution diffusion-weighted imaging using readout-segmented echo-planar imaging, parallel imaging and a two-dimensional navigator-based reacquisition. Magn Reson Med 62, 468-475.
24 Porter, D.A., Mueller, E., 2004. Multi-shot diffusion-weighted EPI with readout mosaic segmentation and 2D navigator correction. Proceedings of the 12th Annual Meeting of ISMRM, Kyoto, Japan, 442.
25 Robson, M.D., Anderson, A.W., Gore, J.C., 1997. Diffusion-weighted multiple shot echo planar imaging of humans without navigation. Magn Reson Med 38, 82-88.
26 Schmierer, K., Wheeler-Kingshott, C.A.M., Boulby, P.A., Scaravilli, F., Altmann, D.R., Barker, G.J., Tofts, P.S., Miller, D.H., 2007. Diffusion tensor imaging of post mortem multiple sclerosis brain. NeuroImage 35, 467-477.
27 Schwartz, E.D., Duda, J., Shumsky, J.S., Cooper, E.T., Gee, J., 2005. Spinal cord diffusion tensor imaging and fiber tracking can identify white matter tract disruption and glial scar orientation following lateral funiculotomy. J Neurotrauma 22, 1388-1398.
28 Song, S.K., Sun, S.W., Ju, W.K., Lin, S.J., Cross, A.H., Neufeld, A.H., 2003. Diffusion tensor imaging detects and differentiates axon and myelin degeneration in mouse optic nerve after retinal ischemia. NeuroImage 20, 1714-1722.
29 Stejskal, E.O., Tanner, J.E., 1965. Spin Diffusion Measurements: Spin Echoes in the Presence of a Time-Dependent Field Gradient. J Chem Phys 42, 288-292.
30 Tournier, J.D., Calamante, F., Connelly, A., 2007. Robust determination of the fibre orientation distribution in diffusion MRI: non-negativity constrained super-resolved spherical deconvolution. NeuroImage 35, 1459-1472.
31 Turner, R., Le Bihan, D., 1990. Single-shot diffusion imaging at 2.0 Tesla. J Magn Reson 86, 445-452.

Contact
Julien Cohen-Adad, Ph.D.
Department of Electrical Engineering
Ecole Polytechnique de Montreal
2900 Edouard-Montpetit Bld.
Montreal, QC, H3T 1J4
Canada
Phone: +1 514-340-4711
Fax: +1 514-340-4611
jcohen@polymtl.ca

Get your free copy of the PI-RADS Scoring Image Atlas

Visit us at
www.siemens.com/magnetom-world
Go to > Publications > Subscriptions > MRI Poster



Read the comprehensive article

"PI-RADS Classification: Structured Reporting for MRI of the Prostate"

by Matthias Röthke et al.
in MAGNETOM Flash 4/2013
page 30-38.

Available for download at
www.siemens.com/magnetom-world

SIEMENS

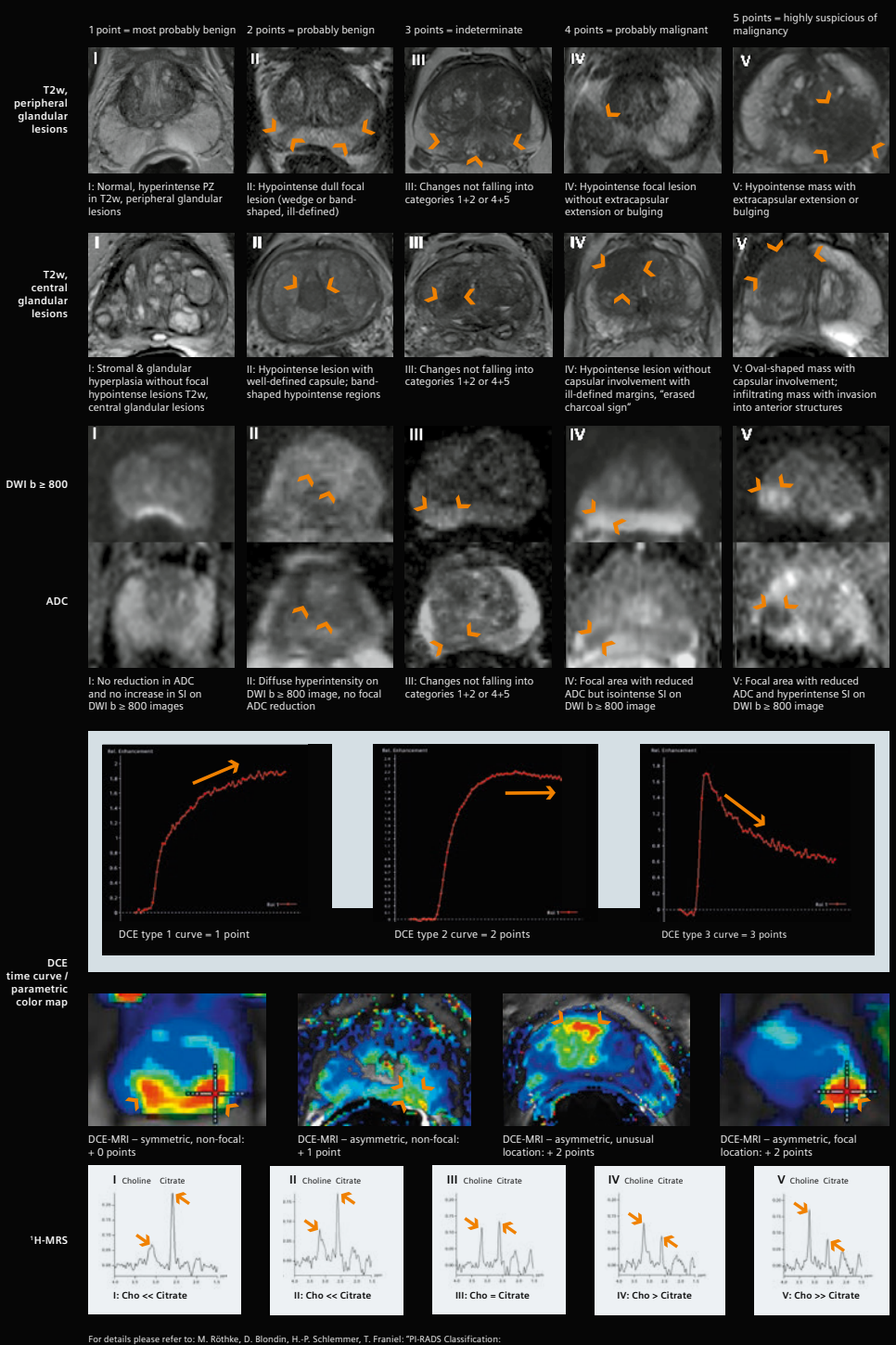

For details please refer to: M. Röthke, D. Blondin, H.-P. Schlemmer, T. Franiel: "PI-RADS Classification: Structured Reporting for MRI of the Prostate", MAGNETOM Flash issue 4/2013, ASTRO edition, page 30-38.

www.siemens.com/magnetom-world

PI-RADS SCORING Image Atlas

Prostate MRI

Answers for life.

Myocardial First-Pass Perfusion Imaging with High Resolution and Extended Coverage Using Multi-Slice CAIPIRINHA

Daniel Stäb, Dipl. Phys.[1,2]; Felix A. Breuer, Ph.D.[3]; Christian O. Ritter, M.D.[1]; Andreas Greiser, Ph.D.[4]; Dietbert Hahn, M.D.[1]; Herbert Köstler, Ph.D.[1,2]

[1]Institute of Radiology, University of Würzburg, Würzburg, Germany
[2]Comprehensive Heart Failure Center (CHFC), Würzburg, Germany
[3]Research Center Magnetic Resonance Bavaria (MRB), Würzburg, Germany
[4]Siemens Healthcare, Erlangen, Germany

Background

Contrast-enhanced myocardial first-pass perfusion MR imaging (MRI) is a powerful clinical tool for the detection of coronary artery disease [1–4]. Fast gradient echo sequences are employed to visualize the contrast uptake in the myocardium with a series of saturation prepared images. However, the technique is strictly limited by physiological constraints. Within every RR-interval, only a few slices can be acquired with low spatial resolution, while both high resolution and high coverage are required for distinguishing subendocardial and transmural infarcted areas [5] and facilitating their localization, respectively.
Acceleration techniques like parallel imaging (pMRI) have recently shown their suitability for improving the spatial resolution in myocardial first-pass perfusion MRI [5–7]. Within clinical settings, 3 to 4 slices can be acquired every heartbeat with a spatial resolution of about $2.0 \times 2.0\,mm^2$ in plane [6]. However, for increasing anatomic coverage [8], standard parallel imaging is rather ineffective, as it entails significant reductions of the signal-to-noise ratio (SNR):

a) In order to sample more slices every RR-interval, each single-slice measurement has to be shortened by a certain acceleration factor R, which

1A **Conventional MS-CAIPIRINHA** for coverage extension
Multi-slice excitation and rf phase cycling

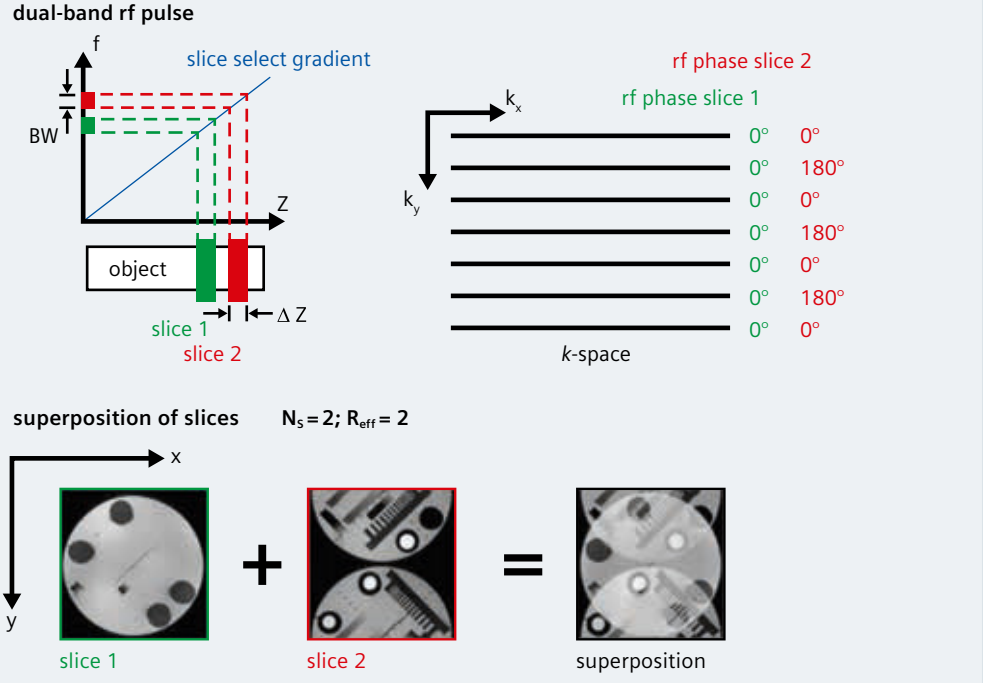

1A MS-CAIPIRINHA with two slices simultaneously excited ($N_S = 2$). A dual-band rf pulse is utilized to excite two slices at the same time (BW = excitation bandwidth). During data acquisition, each slice is provided with an individual rf phase cycle. A slice specific constant rf phase increment is employed (0° in slice 1, 180° in slice 2) between succeeding excitations. Consequently, the two slices appear shifted by ½ FOV with respect to each other. In this way, the overlapping pixels originate not only from different slices, but also from different locations along the phase encoding direction (y), facilitating a robust slice separation using pMRI reconstruction techniques. Using the two-slice excitation, effectively a two-fold acceleration is achieved ($R_{eff} = 2$).

inevitably comes along with an √R-fold SNR reduction.

b) During image reconstruction, the SNR is further reduced by the so-called geometry (g)-factor [9], an inhomogeneous noise-amplification depending on the encoding capabilities of the receiver array.

In addition, unless segmented acquisition techniques are utilized [10], the saturation recovery (SR) magnetization preparation has to be taken into account:

c) The preparation cannot be accelerated itself. Hence, the acceleration factor R has to be higher than the factor by which the coverage is extended. This leads to an increase of the SNR-reduction discussed in (a).

d) Subsequent to the preparation, the signal increases almost linearly with time. Thus, shortening the acquisition by a factor of R is linked to an additional R-fold SNR-loss.

As demonstrated recently [11], most of these limitations can be overcome by employing the **MS-CAIPIRINHA** (**M**ulti-**S**lice **C**ontrolled **A**liasing **I**n **P**arallel **I**maging **R**esults **IN** **H**igher **A**cceleration) concept [12, 13] for simultaneous 2D multi-slice imaging. By simultaneously scanning multiple slices in the time conventionally required for the acquisition of one single slice, this technique enables a significant increase in anatomic coverage. Since image acquisition time is preserved with respect to the single-slice measurement, the technique does not experience any SNR reductions despite the g-factor noise amplification of the required pMRI reconstruction [11, 12]. The MS-CAIPIRINHA concept can also be employed with acceleration factors that are higher than the number of slices excited at the same time. By utilizing this acceleration for increasing spatial resolution, the technique facilitates myocardial first-pass perfusion examinations with extended anatomic coverage and high spatial resolution.

A short overview of the concept is set out below, followed by a presentation of *in-vivo* studies that demonstrate the capabilities of MS-CAIPIRINHA in contrast-enhanced myocardial first-pass perfusion MRI.

1B **MS-CAIPIRINHA with $R_{eff} > N_s$** for improving coverage and resolution
Multi-slice excitation, *k*-space undersampling and rf phase cycling

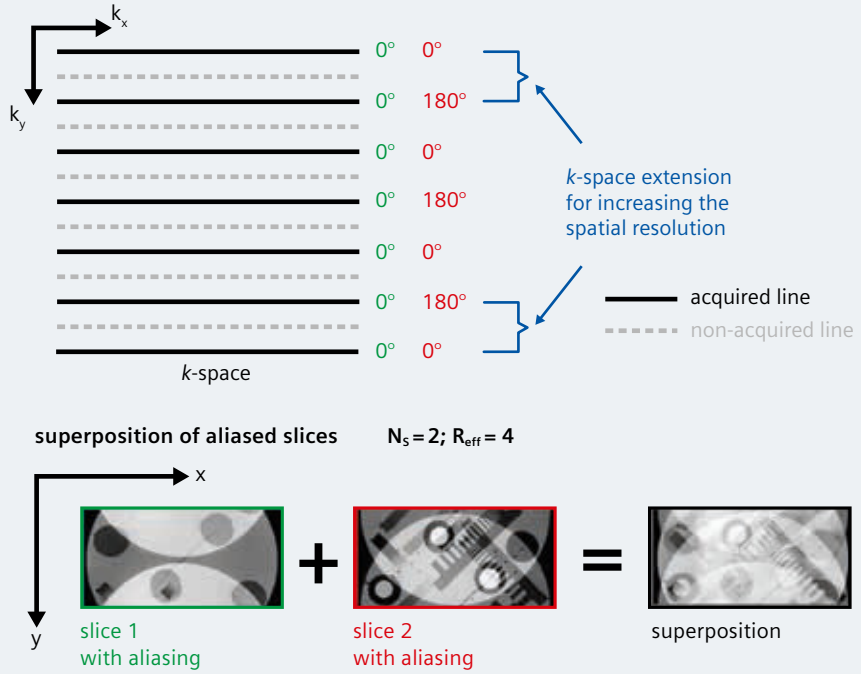

1B MS-CAIPIRINHA with an effective acceleration factor higher than the number of slices excited simultaneously. Again, two slices are excited at the same time employing the same rf phase cycles as in (1A), but *k*-space is undersampled by a factor of two. The slices and their undersampling-induced aliasing artifacts appear shifted with respect to each other by ½ FOV and can be separated using pMRI reconstruction techniques. Effectively, a four-fold acceleration is achieved (R_{eff} = 4). The additional acceleration can be employed to extend *k*-space and to improve the spatial resolution.

Improving anatomic coverage and spatial resolution with MS-CAIPIRINHA

MS-CAIPIRINHA

The MS-CAIPIRINHA concept [12, 13] is based on a coinstantaneous excitation of multiple slices, which is accomplished by means of multi-band radiofrequency (rf) pulses (Fig. 1A). Being subject to the identical gradient encoding procedure, the simultaneously excited slices appear superimposed on each other, unless the individual slices are provided with different rf phase cycles. In MS-CAIPIRINHA, the latter is done in a well-defined manner in order to control the aliasing of the simultaneously excited slices. Making use of the Fourier shift theorem, dedicated slice specific rf phase cycles are employed to shift the slices with respect to each other in the field-of-view (FOV) (Fig. 1A). The slice separation is performed using pMRI reconstruction techniques. However, the shift of the slices causes superimposed pixels to originate from not only different slices, but also different locations along the phase encoding direction. Thus, the MS-CAIPIRINHA concept allows the pMRI reconstruction to take advantage of coil sensitivity variations along two dimensions and to perform the slice separation with low g-factor noise amplification [12].

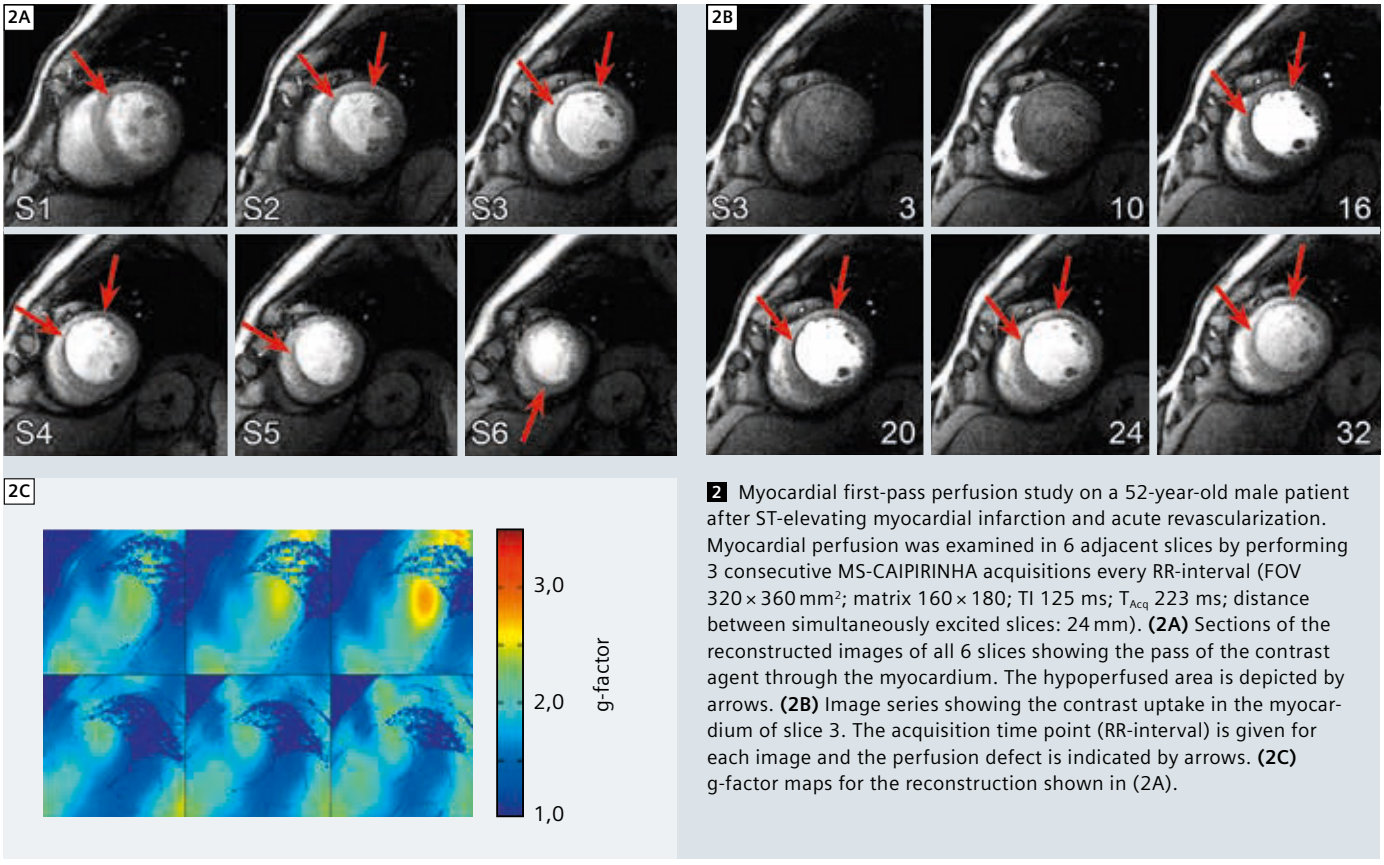

2 Myocardial first-pass perfusion study on a 52-year-old male patient after ST-elevating myocardial infarction and acute revascularization. Myocardial perfusion was examined in 6 adjacent slices by performing 3 consecutive MS-CAIPIRINHA acquisitions every RR-interval (FOV 320 × 360 mm²; matrix 160 × 180; TI 125 ms; T_{Acq} 223 ms; distance between simultaneously excited slices: 24 mm). **(2A)** Sections of the reconstructed images of all 6 slices showing the pass of the contrast agent through the myocardium. The hypoperfused area is depicted by arrows. **(2B)** Image series showing the contrast uptake in the myocardium of slice 3. The acquisition time point (RR-interval) is given for each image and the perfusion defect is indicated by arrows. **(2C)** g-factor maps for the reconstruction shown in (2A).

By conserving image acquisition time with respect to an equivalent single-slice measurement, the technique is not subject to any further SNR penalties. MS-CAIPIRINHA hence allows extending the coverage in 2D multi-slice imaging in a very efficient manner. Applied to myocardial first-pass perfusion imaging, the concept facilitates the acquisition of 6 slices every heartbeat with an image quality that is comparable to that of conventional 3-slice examinations [11].

Additional acceleration

While extending the coverage can be accomplished by simultaneous multi-slice excitation, improving the spatial resolution requires additional *k*-space data to be sampled during image acquisition. Of course, as the FOV and the image acquisition time are to be conserved, this can only be achieved by means of additional acceleration. However, the effective acceleration factor of MS-CAIPIRINHA is not restricted to the number of slices excited simultaneously. By applying simultaneous multi-slice excitation to an imaging protocol with reduced phase FOV, i.e. equidistant *k*-space undersampling, supplementary in-plane acceleration can be incorporated (Fig. 1B). The rf phase modulation forces the two simultaneously excited slices and their in-plane aliasing artifacts to be shifted with respect to each other in the FOV. As before, image reconstruction and slice separation is performed utilizing pMRI methods. Employed like this, the MS-CAIPIRINHA concept facilitates an increase of both, anatomic coverage and spatial resolution with high SNR efficiency. Since image acquisition time does not have to be shortened, SNR is only affected by the voxel size and the noise amplification of the pMRI reconstruction.

Imaging

Perfusion datasets were obtained from several volunteers and patients. The study was approved by the local Ethics Committee and written informed consent was obtained from all subjects. All examinations were performed on a clinical 3T MAGNETOM Trio, a Tim system (Siemens AG, Healthcare Sector, Erlangen, Germany), using a dedicated 32-channel cardiac array coil (Siemens AG, Healthcare Sector, Erlangen, Germany) for signal reception. Myocardial perfusion was assessed using a SR FLASH sequence (FOV 320 × 300-360 mm²; matrix 160 × 150-180; TI 110-125 ms; TR 2.8 ms; TE 1.44 ms; T_{Acq} 191-223 ms; slice thickness 8 mm; flip angle 12°). Two slices were excited at the same time (distance between simultaneously excited slices: 24-32 mm) and shifted by ½ FOV with respect to each other by respectively providing the first and second slice with a 0° and 180° rf phase cycle. In order to realize a spatial resolution of 2.0 × 2.0 mm² within the imaging plane, *k*-space was undersampled by a factor of 2.5, resulting in an overall effective acceleration factor of 5.

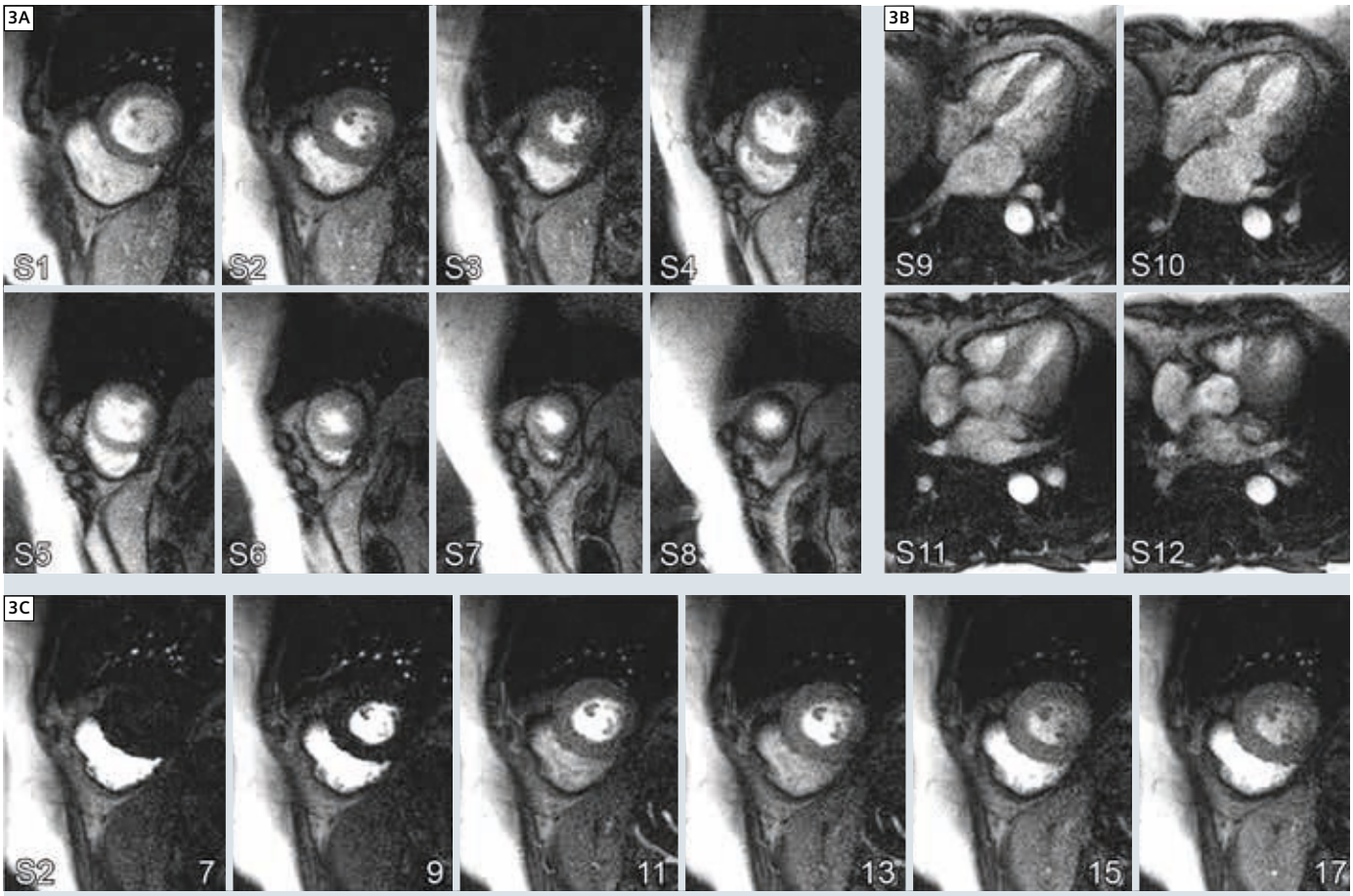

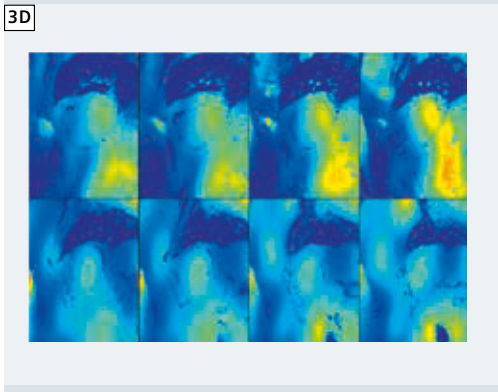

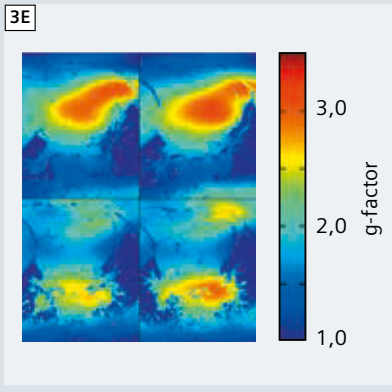

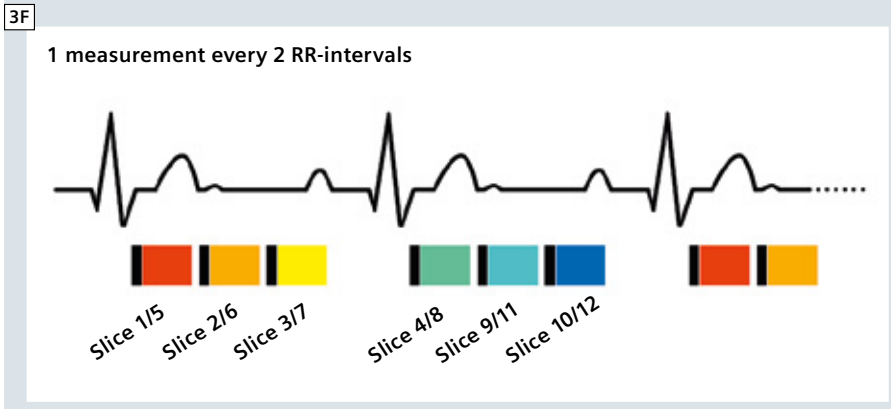

3 Myocardial first-pass perfusion study on a 51-year-old female volunteer with whole heart coverage. 6 consecutive MS-CAIPIRINHA acquisitions were performed every two RR-intervals (FOV 320 × 300 mm²; matrix 160 x 150; TI 110 ms; T_{Acq} 191 ms; distance between simultaneously excited short/long axis slices: 32/16 mm). **(3A)** Sections of the reconstructed short axis images. **(3B)** Sections of the reconstructed long axis images. **(3C)** Series of image sections showing the contrast uptake in the myocardium of slice 2. The acquisition time point (RR-interval) is given for each image. **(3D)** g-factor maps for the reconstructions shown in (3A). **(3E)** g-factor maps for the reconstructions shown in (3B). **(3F)** Measurement scheme. The acquisition was performed with a temporal resolution of 1 measurement every 2 RR-intervals.

All first-pass perfusion measurements were conducted in rest over a total of 40 heartbeats. All subjects were asked to hold their breaths during the acquisition as long as possible. Every RR-interval, 3 to 4 consecutive MS-CAIPIRINHA acquisitions were performed in order to sample the contrast uptake of the myocardium. For contrast enhancement, a contrast agent bolus (4 ml, Gadobutrol, Bayer HealthCare, Berlin, Germany) followed by a 20 ml saline flush was administered at the beginning of each perfusion scan. Image reconstruction was performed using an offline GRAPPA [14] reconstruction. The according weights were determined from a separate full FOV calibration scan. To evaluate the GRAPPA reconstruction, an additional noise scan was obtained and the g-factor noise enhancement was quantified [15]. All calculations were performed on a standalone PC using Matlab (The MathWorks, Natick, MA, USA).

Results

Figure 2 shows the results of a myocardial first-pass perfusion examination with 6-slices on a 52-year-old male patient (91 kg, 185 cm) on the fourth day after STEMI (ST-elevating myocardial infarction) and acute revascularization. Sections of the reconstructed images of all examined slices are depicted, showing the first pass of contrast agent through the myocardium (Fig. 2A). Also displayed is a series of image sections demonstrating contrast uptake in slice 3 (Fig. 2B). The GRAPPA reconstruction separated the simultaneously excited slices without visible artifacts. The g-factor maps (Fig. 2C) indicate generally low noise amplification. Thus, in comparison to the high effective acceleration factor of 5, the images provide excellent image quality. Both contrast and SNR allow for a clear delineation of the subendocardial hypoperfused area within the anterior and septal wall of the myocardium (arrows).
The results of a first-pass perfusion study with whole heart coverage are displayed in Fig. 3. In a 51-year-old female volunteer, first pass perfusion was examined in eight short (Fig. 3A) and four long axis slices (Fig. 3B). In order to accomplish the 12-slice examination and to achieve whole heart coverage, temporal resolution was reduced by a factor of two with respect to the examination displayed in Fig. 2. The contrast uptake of the myocardium was sampled with 1 measurement every two RR-intervals by performing 3 out of 6 consecutive double-slice MS-CAIPIRINHA acquisitions every heartbeat (Fig. 3F). Image reconstruction could be performed without visible artifacts and generally low noise amplification (Figs. 3D and E). Only in a few regions, the g-factor maps show moderate noise enhancement. In the images, the myocardium is homogeneously contrasted and the contrast agent uptake is clearly visible (Fig. 3C).
The findings of a first-pass perfusion study in a 48-year-old male patient (80 kg, 183 cm) on the eighth day after STEMI and acute revascularization are presented in Fig. 4. An overall of 8 slices were acquired with a temporal resolution of 1 measurement every RR-interval by performing 4 consecutive MS-CAIPIRINHA acquisitions after each ECG trigger pulse. Sections of the reconstructed images, showing the first pass of contrast agent through the myocardium in all 8 slices (Fig. 4A) are depicted together with sections demonstrating the process of contrast uptake in slice 5 (Fig. 4B). Despite the breathing motion (Fig. 4D), the GRAPPA reconstruction performed robustly and separated the slices without significant artifacts. The g-factor noise amplification is generally low and moderate within a few areas (Fig. 4C). In the images, the hypoperfused subendocardial region in the anterior wall can be clearly identified (arrows). As can be seen from the enlarged section of slice 5 (Fig. 4F), the technique provides sufficient spatial resolution to distinguish between subendocardial and transmural perfusion defects. These findings correspond well to the results of a subsequently performed Late Enhancement study (Fig. 4E) delineating a transmural infarction zone of the anterior wall (midventricular to apical).

Discussion

Contrast-enhanced myocardial first-pass perfusion MRI with significantly extended anatomic coverage and high spatial resolution can be successfully performed by employing the MS-CAIPIRINHA concept for simultaneous multi-slice imaging. Basically, two different acceleration approaches are combined: the simultaneous excitation of two slices on the one hand and *k*-space undersampling on the other. While the first directly doubles the number of slices acquired, the second provides sufficient acceleration for improving the spatial resolution. The proposed imaging protocols provide an effective acceleration factor of 5, which is sufficient for the acquisition of 6 to 8 slices every RR-interval with a high spatial resolution of $2.0 \times 2.0 \times 8\,mm^3$. Correspondingly, whole heart coverage can be achieved by sampling 12 slices with a temporal resolution of 1 measurement every 2 RR-intervals. Since the slices can be planned with individual thickness and pairwise specific orientation, the concept thereby provides high flexibility. With image acquisition times of 191 ms, it also supports stress examinations in 6 slices up to a peak heart rate of 104 bpm.
Employing a dedicated 32-channel cardiac array coil, the image reconstructions could be performed without significant reconstruction artifacts and only low to moderate g-factor noise amplification. Also in presence of breathing motion, the GRAPPA reconstruction performed robustly. The images provided sufficient SNR and contrast between blood, myocardium and lung tissue to delineate small perfusion defects and to differentiate between subendocardial and transmural hypoperfused areas.
Compared to conventional parallel MRI, the MS-CAIPIRINHA concept benefits from the high SNR efficiency discussed earlier. Simultaneous multi-slice excitation allows increasing the coverage without supplementary *k*-space under-

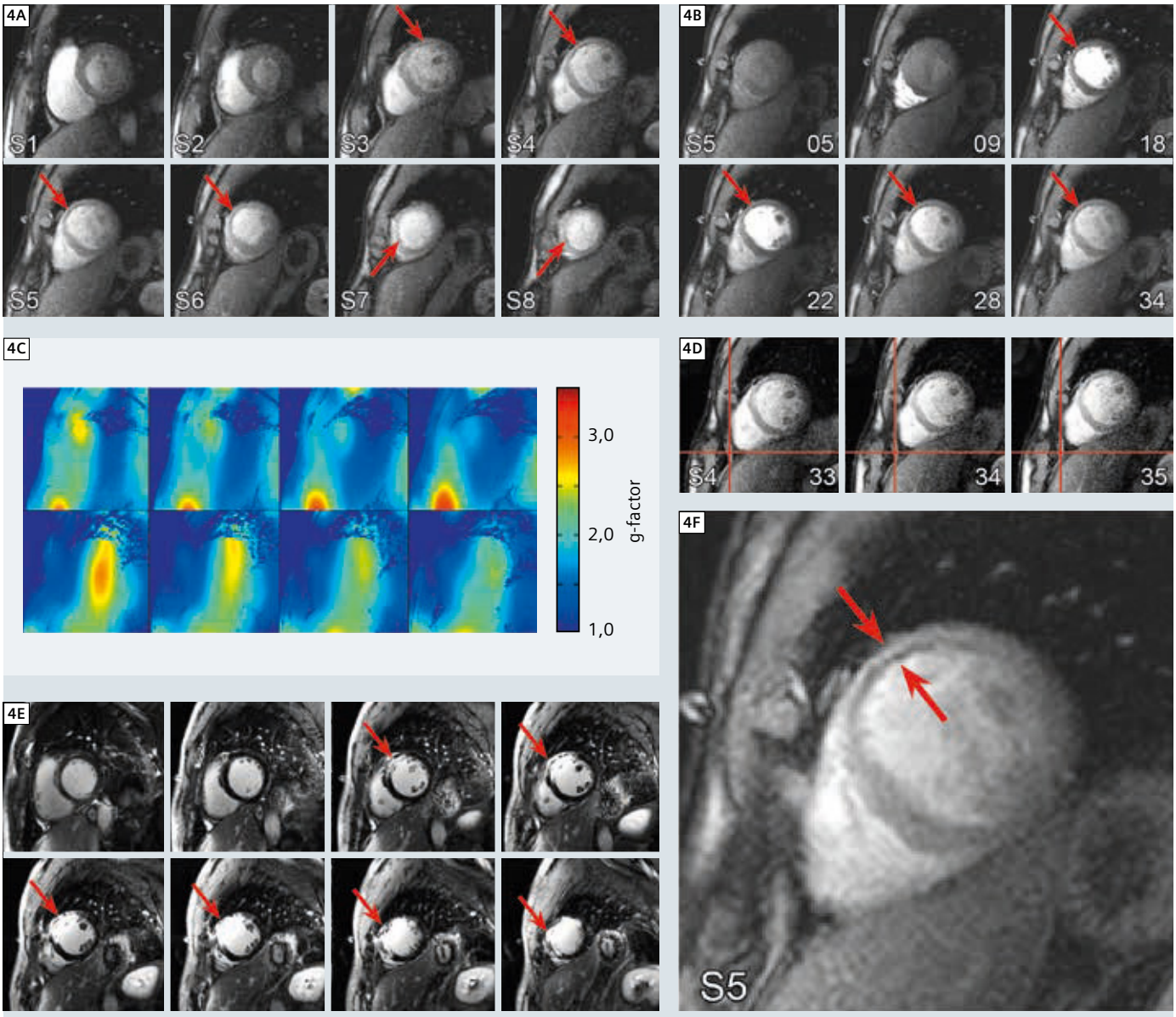

4 Myocardial first-pass perfusion study on a 48-year-old male patient after ST-elevating myocardial infarction and acute revascularization. 8 slices were acquired every RR-interval by performing 4 consecutive MS-CAIPIRINHA acquisitions (FOV 320 × 300 mm²; matrix 160 × 150; TI 110 ms; T_{Acq} 191 ms; flip angle 10°; distance between simultaneously excited slices: 32 mm). **(4A)** Sections of the reconstructed images of all 8 slices showing the first pass of the contrast agent through the myocardium. The hypoperfused area is depicted by arrows. **(4B)** Image series showing the contrast uptake in the myocardium of slice 5. The acquisition time point (RR-interval) is given for each image and the perfusion defect is indicated by arrows. **(4C)** g-factor maps for the reconstruction shown in (4A). **(4D)** Displacement of the heart due to breathing motion, example for slice 4. **(4E)** Late gadolinium enhancement. **(4F)** Enlarged section of slice 5. The technique allows distinguishing between subendocardial and transmural perfusion defects.

sampling. At the same time the g-factor noise amplification is minimized by exploiting coil sensitivity variations in both, slice and phase encoding direction. Thus, despite the doubled anatomic coverage, the image quality obtained is comparable to that of an accelerated measurement with standard coverage and high spatial resolution [5]. An important feature of the MS-CAIPIRINHA concept in myocardial first-pass perfusion MRI is the frame-by-frame reconstruction, which prevents the reconstructed images to be affected by temporal blurring. Moreover, arrhythmia and breathing motion only impact the underlying time frame and not the whole image series, as it is likely for reconstruction techniques incorporating the temporal domain [16–19].

Simultaneous multi-slice excitation is, of course, linked to an increase in the amount of energy that is deployed to the subject under investigation. Thus, limitations have to be expected at higher field strengths or when using sequences with larger flip angles, such as TrueFISP. At 1.5 Tesla, the application of the MS-CAIPIRINHA concept to TrueFISP has been successfully demonstrated utilizing advanced rf phase cycling [11].
In all *in-vivo* examinations, the distance between the two slices excited simultaneously was maximized in order to make use of the highest possible coil sensitivity variations in slice direction and to minimize the g-factor penalty. Thus, the spatial distance between consecutively acquired cardiac phases is large which might be a possible drawback for correlating hypoperfused regions of the myocardium. While the latter was feasible for all *in-vivo* studies, slice distance naturally can be reduced at the expense of slightly more noise enhancement.

Conclusion

Utilizing the MS-CAIPIRINHA concept for simultaneous multi-slice imaging, contrast-enhanced myocardial first-pass perfusion MRI can be performed with an anatomic coverage of 6 to 8 slices every heart beat and a high spatial resolution of $2.0 \times 2.0 \times 8\,mm^3$. Based on the simultaneous excitation of multiple slices, the concept provides significantly higher SNR than conventional in-plane acceleration techniques with identical acceleration factor and facilitates an accurate image reconstruction with only low to moderate g-factor noise amplification. Taking into account the high flexibility, simple applicability and short reconstruction times in addition to the high robustness in presence of breathing motion or arrhythmia, the concept can be considered a promising candidate for clinical perfusion studies.

Acknowledgements

The authors would like to thank the Deutsche Forschungsgemeinschaft (DFG) *and* the Federal Ministry of Education and Research (BMBF), Germany *for grant support.*

Contact
Daniel Stäb
Institute of Radiology
University of Würzburg
Oberdürrbacher Str. 6
97080 Würzburg
Germany
staeb@roentgen.uni-wuerzburg.de

References

1 Atkinson DJ, Burnstein D, Edelman RR. First-pass cardiac perfusion: evaluation with ultrafast MR imaging. Radiology 1990; 174:757–762.
2 Wilke N, Jerosch-Herold M, Wang Y, Yimei H, Christensen BV, Stillman E, Ugurbil K, McDonald K, Wilson RF. Myocardial Perfusion Reserve: Assessment with Multisection, Quantitative, First-Pass MR Imaging. Radiology 1997; 204:373–384.
3 Rieber J, Huber A, Erhard I, Mueller S, Schweyer M, Koenig A, Schiele TM, Theisen K, Siebert U, Schoenberg SO, Reiser M, Klauss V. Cardiac magnetic resonance perfusion imaging for the functional assessment of coronary artery disease: a comparison with coronary angiography and fractional flow reserve. Eur Heart J 2006; 27:1465–1471.
4 Schwitter J, Nanz D, Kneifel S, Bertschinger K, Büchi M, Knüsel PR, Marincek B, Lüscher TF, Schulthess GK. Assessment of Myocardial Perfusion in Coronary Artery Disease by Magnetic Resonance. Circulation 2001; 103:2230–2235.
5 Ritter CO, del Savio K, Brackertz A, Beer M, Hahn D, Köstler H. High-resolution MRI for the quantitative evaluation of subendocardial and subepicardial perfusion under pharmacological stress and at rest. RoFo 2007; 179:945–952.
6 Strach K, Meyer C, Thomas D, Naehle CP, Schmitz C, Litt H, Bernstein A, Cheng B, Schild H, Sommer T. High-resolution myocardial perfusion imaging at 3 T: comparison to 1.5 T in healthy volunteers. Eur Radiol 2007; 17:1829–1835.
7 Jung B, Honal M, Hennig J, Markl M. k-t-Space accelerated myocardial perfusion. J Magn Reson Imag 2008; 28:1080–1085.
8 Köstler H, Sandstede JJW, Lipke C, Landschütz W, Beer M, Hahn D. Auto-SENSE perfusion imaging of the whole human heart. J Magn Reson Imag 2003; 18:702–708.
9 Pruessmann KP, Weiger M, Scheidegger MB, Boesiger P. SENSE: sensitivity encoding for fast MRI. Magn Reson Med 1999; 42:952–962.
10 Kellman P, Derbyshire JA, Agyeman KO, McVeigh ER, Arai AE. Extended coverage first-pass perfusion imaging using slice-interleaved TSENSE. Magn Reson Med 2004; 51:200–204.
11 Stäb D, Ritter CO, Breuer FA, Weng AM, Hahn D, Köstler H. CAIPIRINHA accelerated SSFP imaging. Magn Reson Med 2011; 65:157–164.
12 Breuer FA, Blaimer M, Heidemann RM, Mueller MF, Griswold MA, Jakob PM. Controlled aliasing in parallel imaging results in higher acceleration (CAIPIRINHA) for multi-slice imaging. Magn Reson Med 2005; 53:684–691.
13 Breuer F, Blaimer M, Griswold M, Jakob P. Controlled Aliasing in Parallel Imaging Results in Higher Acceleration (CAIPIRINHA). Magnetom Flash 2012; 49:135–142.
14 Griswold MA, Jakob PM, Heidemann RM, Nittka M, Jellus V, Wang J, Kiefer B, Haase A. Generalized autocalibrating partially parallel acquisitions (GRAPPA). Magn Reson Med 2002; 47:1202–1210.
15 Breuer FA, Kannengiesser SAR, Blaimer M, Seiberlich N, Jakob PM, Griswold MA. General formulation for quantitative G-factor calculation in GRAPPA reconstructions. Magn Reson Med 2009; 62:739–746.
16 Adluru G, Awate SP, Tasdizen T, Whitaker RT, Dibella EVR. Temporally constrained reconstruction of dynamic cardiac perfusion MRI. Magn Reson Med 2007; 57: 1027–1036.
17 Otazo R, Kim D, Axel L, Sodickson DK. Combination of compressed sensing and parallel imaging for highly accelerated first-pass cardiac perfusion MRI. Magn Reson Med 2010; 64:767–776.
18 Ge L, Kino A, Griswold M, Mistretta C, Carr JC, Li D. Myocardial perfusion MRI with sliding-window conjugate-gradient HYPR. Magn Reson Med 2009; 62:835–839.
19 Plein S, Kozerke S, Suerder D, Luescher TF, Greenwood JP, Boesiger P, Schwitter J. High spatial resolution myocardial perfusion cardiac magnetic resonance for the detection of coronary artery disease. Eur Heart J 2008; 29:2148–2155.

Introduction to Advanced Techniques in MR Neuroimaging

Bernhard Schuknecht, M.D.; Krisztina Baràth, M.D.

Diagnostic, Vascular and Interventional Neuroradiology, Medizinisch Radiologisches Institut MRI Zürich, Bethanien Hospital, Zürich, Switzerland

Functional MRI (fMRI)

Functional magnetic resonance imaging (fMRI) is based on the blood oxygenation level dependent (BOLD) effect. BOLD contrast rises with neural activation and depends on the variables blood flow and oxygenation. Augmentation of regional cerebral blood flow (CBF) is accompanied by a local increase in oxygen extraction due to a rise in the cerebral metabolic rate of oxygen consumption. The ferrous iron in deoxyhemoglobin adopts paramagnetic properties contrary to the

fMRI and DTI of a brain tumor: function and structure

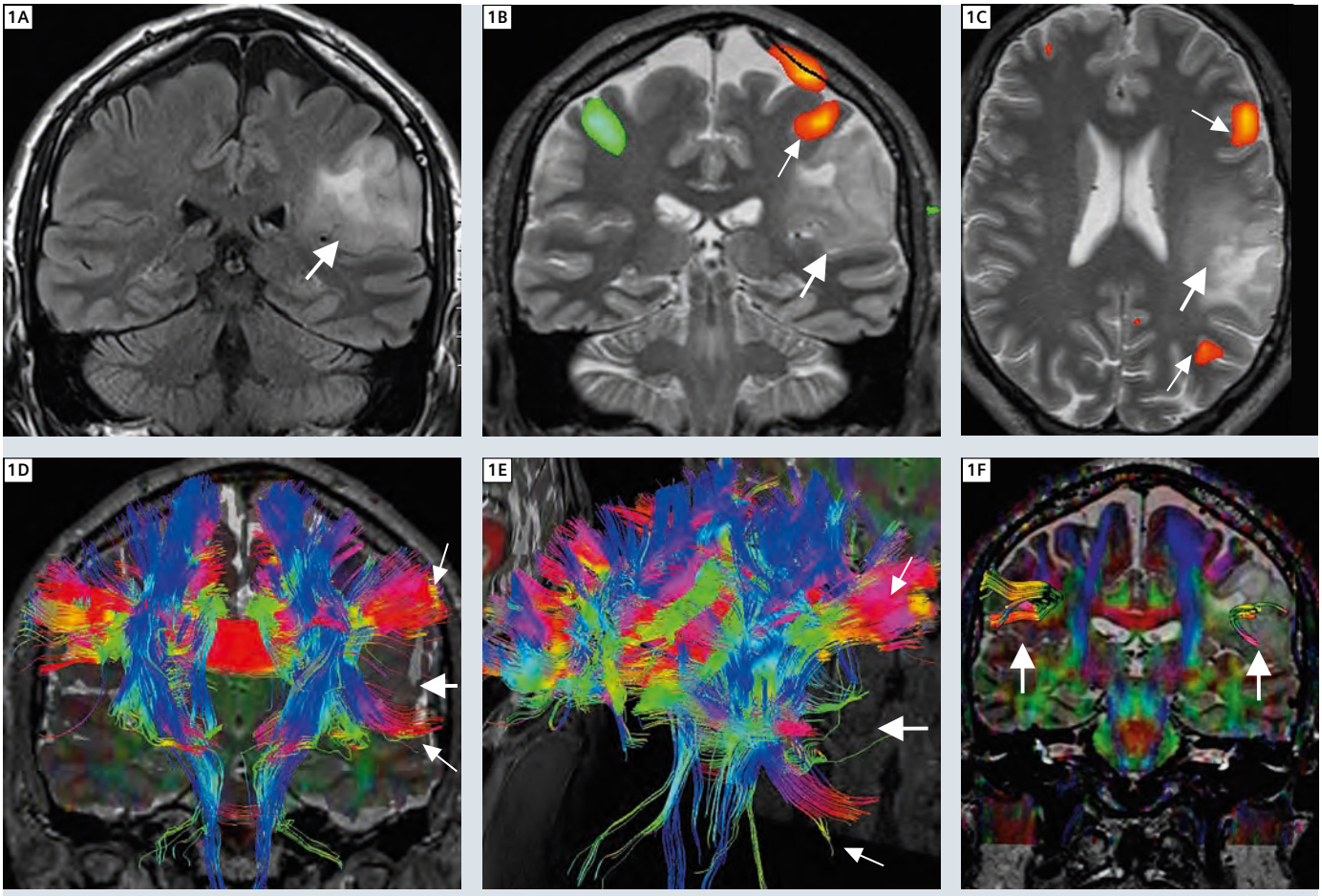

1 **(1A)** Brain tumor (oligodendroglioma) (arrow) in the subcentral gyrus/inferior parietal lobule on the left shown on a FLAIR sequence. **(1B)** Activation of the primary motor cortex (thin arrow) close to the tumor (arrow) during finger tapping. Red = movement on the right, Green = movement on the left. **(1C)** Activation of the motor speech area and the sensory speech area (thin arrows) far away from the tumor (arrow). The DTI sequence **(1D–E)** shows the deviated U-fibers (thin arrow) due to the tumor (arrow).
The Broca- and Wernicke areas are connected through the arcuate fibers, which makes a combination of fMRI and DTI for the preoperative planning necessary. **(1F)** The thinning of the left arcuate fibers indicates an infiltration of the speech-network.

diamagnetic effect in oxyhemoglobin. This results in a susceptibility induced field shift and leads to an increase in T2* value and a signal increase in T2* gradient echo or echo planar imaging (EPI) studies. The high sensitivity of EPI sequences enables real time visualization of activation of different parts of the brain in comparison to a resting state. In a functional MR paradigm the patient is asked to alternatively perform tasks or is stimulated to trigger several processes or emotions. Threshold functional MRI activation maps are spatially addressed (Fig. 1A) and therefore typically overlaid in colour on a high resolution anatomical T1 MPRAGE or SPACE FLAIR MR image (Figs. 1B, C).

fMRI was first employed for mapping of neuronal activation during visual perception tasks and motor activation in the early nineties. Since then fMRI has evolved into an invaluable research tool, e.g. in cognitive neuroscience or neuropharmacology as well as a routinely applied clinical MR technique.

Clinical applications comprise mainly neurosurgical planning in order to determine resection margins in relation to functional 'eloquent' areas. With fMRI brain functional plasticity may also be visualized in recovery after stroke or surgery. Furthermore fMRI can be used to evaluate specific brain functions in a range of neuro-degenerative diseases. Despite existing limitations of fMRI, a significant increase in spatial and temporal resolution has been achieved in order to improve localization of specific brain function and individualize treatment.

Diffusion Tensor Tractography (Diffusion Tensor Imaging, DTI)

DTI is a non-invasive MR technique to study brain tissue composition and architecture *in vivo*. DTI is based on the concept that water diffusion is anisotropic in organized tissues. Cerebral white matter is composed of axons, myelin sheaths and neuroglia which are aligned to form fiber tracts. DTI provides information on water diffusion properties regarding the extent of diffusion anisotropy and its orientation. A pair of magnetic dephasing and rephasing field gradients is successively applied in distinct directions in 3D space. The resulting images exhibit signal attenuation in the direction of the applied gradient which is proportional to water diffusivity. The largest principal axis of the diffusion tensor aligns with the predominant fiber orientation in an MRI voxel. A diffusion tensor or the mean diffusivity may be estimated from as few as 6 diffusion-weighted images acquired along non-collinear directions and 1 minimally = T2-weighted (b_0) image. From the diffusion tensor, the DTI indices derived include the mean diffusion coefficient (ADC), calculated eigenvalues and eigenvectors and an index of diffusion anisotropy, e.g. fractional anisotropy (FA). To achieve a high signal-to-noise ratio DTI employs more than the minimum of 6 diffusion-weighting angulations and/or acquires repeated measurements of diffusion directions. Despite substantial improvement in technique, spatial resolution of DTI in the order of 1–4 mm per dimension, reflects limitations imposed by using a macroscopic technique to visualize microscopic restrictions.

DTI is performed in combination with fMRI for preoperative localization of fiber tracts in proximity to a lesion (Figs. 1D–F), and for preoperative differentiation of white matter tract infiltration from displacement in patients with low grade glioma in particular.

Following hemorrhagic or ischemic stroke and trauma DTI has become an important tool to assess white matter tract involvement beyond findings by morphologic imaging. This holds also true for white matter alterations in patients suffering from neurodegenerative and movement disorders, and to visualize secondary neurodegeneration in inflammatory conditions such as multiple sclerosis.

Diffusion-Weighted Imaging (DWI)

Diffusion-weighted MR imaging renders microscopic molecular motion of water visible within tissues. The anisotropic nature of diffusion in the brain can be visualized by comparing images obtained with DWI gradients applied in three orthogonal directions. DWI consists of an echo planar spin-echo T2w pulse sequence. Alternative DWI sequences are based on a single-shot gradient or single-shot fast spin-echo technique, 'line-scan' and spiral DWI technique. The signal intensity obtained by DWI corresponds to the signal on T2w images decreased by a signal amount that is related to the rate of diffusion in the direction of the applied gradients. Pathology therefore is reflected by high signal on diffusion-weighted images and by decreased signal on apparent diffusion coefficient (ADC) maps.

While DWI is highly sensitive in reflecting the physical properties of diffusion, the observation of restricted water diffusion is relatively non-specific for pathology. Restricted diffusion is the earliest detectable MR sign of ischemia. However diffusion changes are also seen with infection, inflammation and neoplasms. In an abscess restricted diffusion and low ADC values are attributed to increased fluid viscosity and higher cellularity present in pus. Metastases and tumors may have a similar appearance to an abscess on morphologic images but present with normal diffusion and high ADC values in areas of necrosis.

DWI is gaining increasing importance in oncology both for the initial diagnosis and as a sensitive tool to assess tumor response to treatment. Low ADC values in a lesion are an indicator for a malignant compression fracture in the spine as well as for malignant lymphadenopathy in the neck. In cerebral gliomas ADC values inversely correlate with the grading of gliomas, and low values indicate the higher grade component in a 'mixed' glioma. Lower ADC values in the edema of gliomas compared to metastases are an early sign of brain infiltration beyond macroscopic visible margins. Restricted diffusion in the early postoperative phase is more likely to correspond to ischemia and reparative changes, while after 6–8 weeks may indicate true progression or pseudoprogression. Increasing ADC values in a solid lesion like a glioma, lymphoma or metastasis are a more sensitive

parameter to chemo-radiotherapy treatment response than the contrast enhanced T1 images.
Metastases and glial tumors can be differentiated by low ADC due to their high grade cellularity (metastases) and by areas of high ADC due to necrosis (glial tumors) (Figs. 2A–D).

Perfusion-MRI (PWI = Perfusion-weighted imaging)

Perfusion MRI relies on two different techniques: dynamic contrast enhanced (DCE) perfusion MRI consists of a T1w 3D FLASH sequence which is used to depict cerebral microcirculation and is a direct measure of vascular permeability. On the other hand dynamic susceptibility contrast (DSC) MR perfusion is based on a gradient-echo echo planar sequence. DSC provides a measure of vascularity, mircovascular density or relative cerebral blood volume (rCBV) and therefore is complementary to DCE perfusion. Both sequences require a bolus of contrast media injected into a peripheral vein.

Diffusion in glioma and metastasis: cellularity and tissue ultrastructure

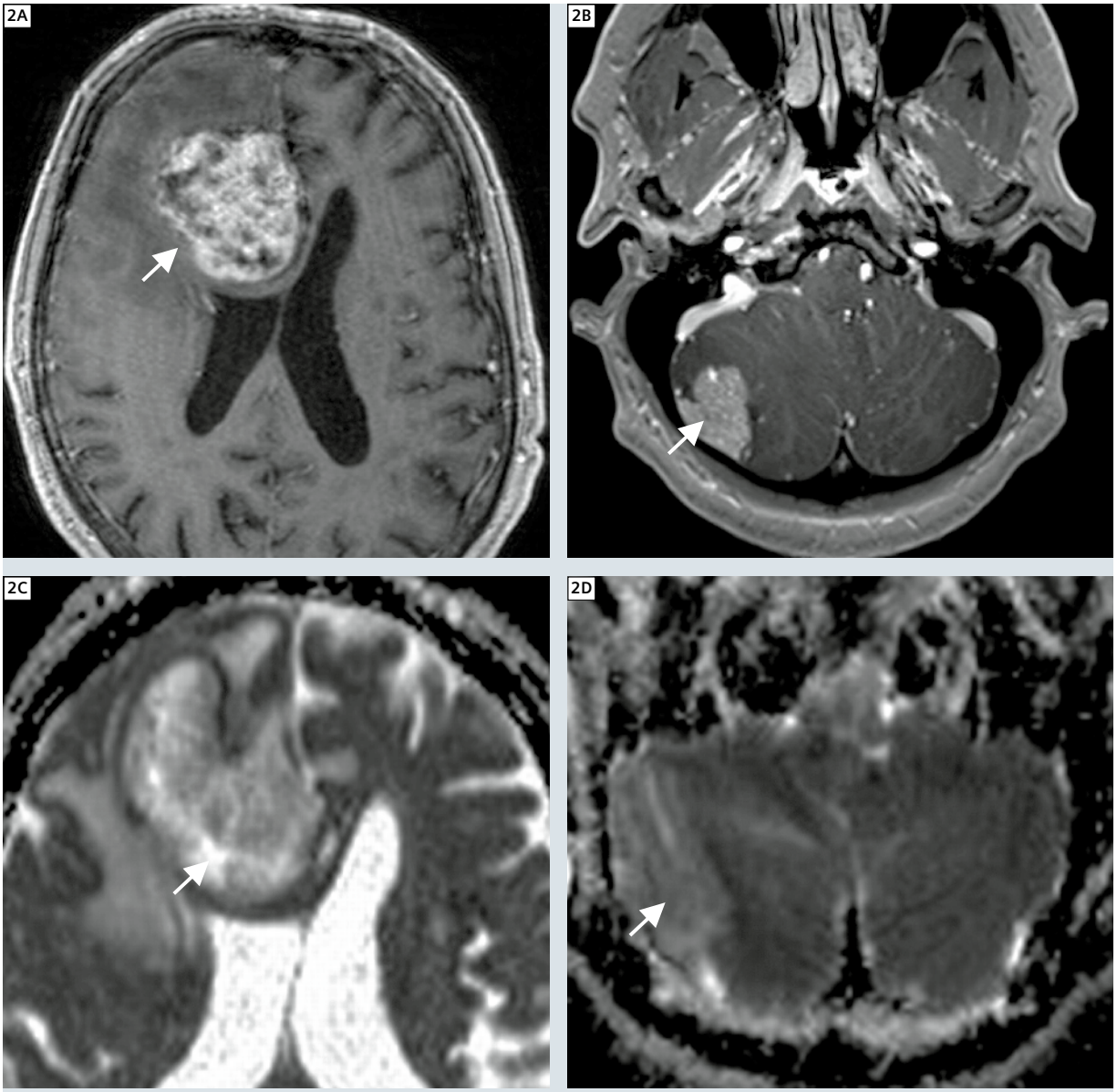

2 Contrast enhanced MRI does not reliably distinguish a glioblastoma multiforme **(2A)** from a metastasis **(2B)**. Focal high ADC values (bright) indicate necrotic components in a glioma (arrow **2C**). Low ADC values represent a solid metastasis **(2B)** as in this case or a lymphoma with dense cellularity **(2D)**. ADC values are lower within the edema of a glioma due to microscopic infiltration which is usually not present within the edema of a metastasis.

Perfusion MR in combination with diffusion-weighted imaging has been routinely applied in the setting of acute stroke. The initial perfusion – diffusion mismatch correlates with the ischemic penumbra, the tissue at risk and the extent of the definite infarct size.
In brain neoplasms vascular proliferation and neoangiogenesis are hallmarks of differentiation to higher grades of malignancy. rCBV values as obtained by DSC show a significant correlation with tumor grade (Figs. 3 A–C), microvascular density and in case of increase predict malignant transformation. Frequently, changes of these parameters during cytostatic, anti-angiogenic and radiation therapy (Figs. 4A–C) precede tumor volume reduction. DCE is applied to assess the degree of tumor angiogenesis and vessel permeability. Dynamic contrast enhanced perfusion (DCE) in combination with dynamic susceptibility contrast (DSC) perfusion (Fig. 5B) and MR spectroscopy (Fig. 6C) is applied to distinguish treatment related effects (pseudoprogression or pseudoresponse) from true progression and true response respectively.

Perfusion and diffusion in brain tumor imaging: vascularisation, neo-angiogenesis, capillary permeability – cellularity vs. extracellular space

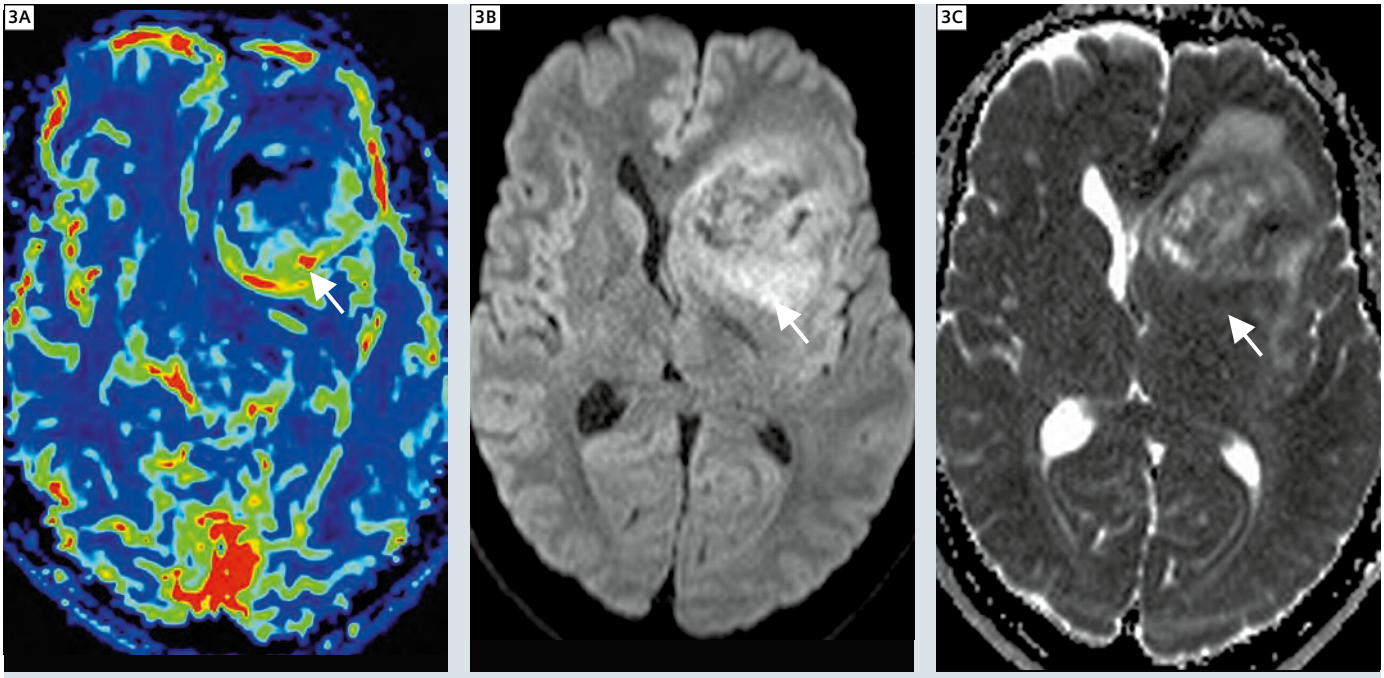

3 Perfusion MRI of a anaplastic glioma with high rCBV within the component of higher maligancy in the posterior part (arrow **3A**) with restricted diffusion **(3B)** and low ADC values **(3C)** as additional signs of a highly cellular anaplastic component.

Treatment monitoring: decreased vascularity

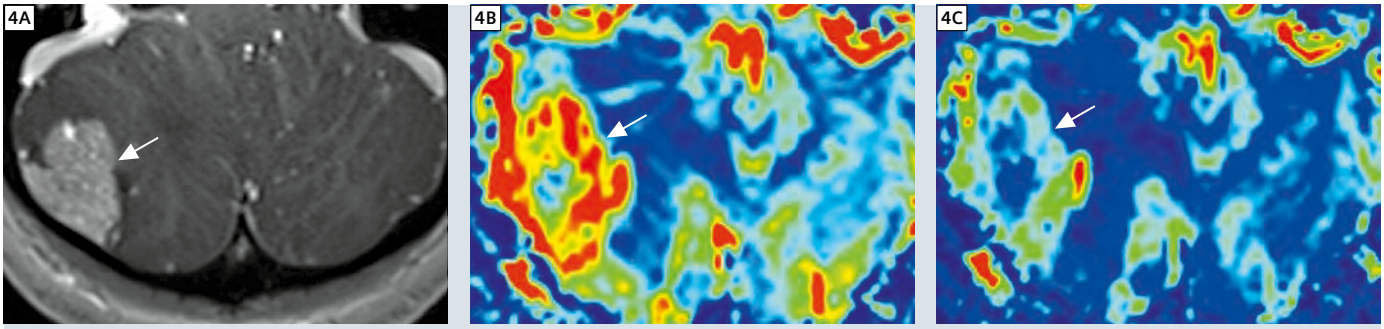

4 **(4A)** Cerebellar metastasis of renal cell carcinoma with subtle peripheral vessels indicated on the contrast enhanced T1w image. DSC perfusion MRI depicts markedly increased vascularity within the entire metastasis with high rCBV values before **(4B)** and with decreased rCBV values under radiotherapy **(4C)**.

Treatment related effects: low perfusion – low cellularity

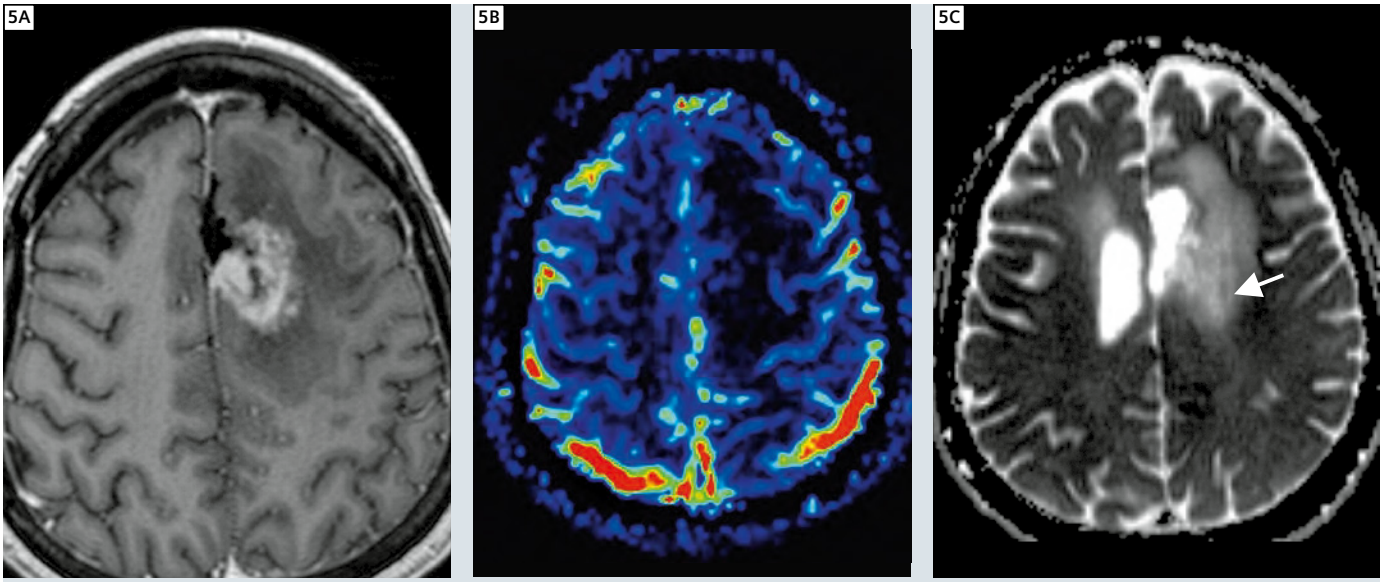

5 T1w contrast enhanced image one year following resection and chemo-radiotherapy of a glioblastoma. Recurrence and treatment related necrosis cannot be reliably differentiated based on morphology **(5A)**. Perfusion MRI depicts low rCBV values **(5B)** contrary to high rCBV values indicating recurrence in a high grade glioma (compare to Fig. 3A). High ADC values **(5C)** denote low cellularity indicative of a necrosis confirmed by subsequent histology.

ASL Arterial Spin labelling

MR imaging with ASL is an alternative method to measure perfusion. Contrary to dynamic contrast enhanced (DCE) and dynamic susceptibility contrast (DSC) perfusion MRI, ASL uses electromagnetically labelled arterial blood water as a freely diffusible intrinsic tracer. In clinical applications, the ASL technique proved reproducible and reliable to assess cerebral blood flow (CBF) despite a relatively low signal intensity-to-noise ratio. ASL has been evaluated in various pathological states including cerebrovascular and neurodegenerative disease and for the assessment of glioma grading and tumor angiogenesis. Quantitative assessment of blood flow in gliomas by ASL yielded results and reproducibility comparable to DSC perfusion MR imaging.

MR Spectroscopy (MRS)

MR spectroscopy provides a measure of brain metabolic composition or chemistry. Each metabolite appears at a specific ppm (Fig. 6 A–C), and each one reflects specific cellular and biochemical processes. N-Acetyl-Aspartat (NAA) is a neuronal marker and decreases with any disease that adversely affects neuronal integrity. Creatine provides a measure of energy stores. Choline is a measure of increased cellular turnover and is elevated in tumors and inflammatory processes. Lactate is a marker of oxygen deficiency, lipids of tissue necrosis and myoinositol of granulation tissue (gliosis).

Indication of MRS:

- differential diagnosis of low-grade and high-grade tumors
- monitoring under radio-chemotherapy
- differentiation of recurrent tumor from secondary necrosis due to therapy

Susceptibility-Weighted Imaging (SWI)

SWI is a modified 3D gradient-echo technique which exploits the susceptibility differences between tissues and uses the phase image to detect these differences. The magnitude and phase data are combined to produce an enhanced contrast magnitude image which is exquisitely sensitive to products of blood-deterioration (DeoxyHB, MetHB and Hämosiderin) (Fig. 7 A–D).
Iron depositions can be the result of an untreated high blood pressure and accompanied by a gliosis could be a sign of a brain damage. Residual blood after a stroke, amyloid angiopathy or brain injury can be easily detected with gradient-echo sequences, such as SWI or T2*.

Indications of SWI:

- micro-bleedings in hypertension and vascular dementia
- superficial bleedings in amyloid angiopathy
- hemorrhagic contusion and diffuse axonal injury after brain trauma
- iron deposition in neurodegenerativ diseases

MR Spectroscopy: tumor progression vs. pseudoprogression

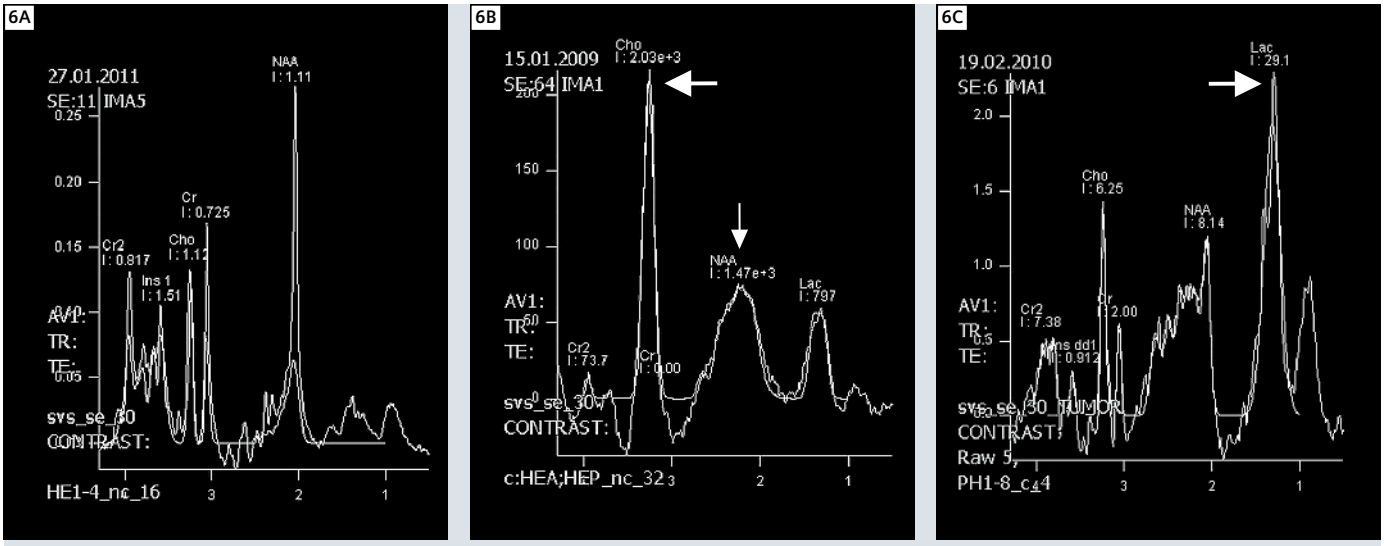

6 **(6A)** Normal spectrum. **(6B)** Spectrum of an Oligodendroglioma with high Cholin as a marker of a high proliferation-rate (thick arrow) and with low NAA as a marker of lost neuronal integrity (thin arrow). **(6C)** Spectrum of a therapy-induced necrosis with low Cholin and NAA and with high Lactate as a sign of oxygen deficiency (thick arrow).

Iron deposition after trauma, in hypertension and in amyloid angiopathy

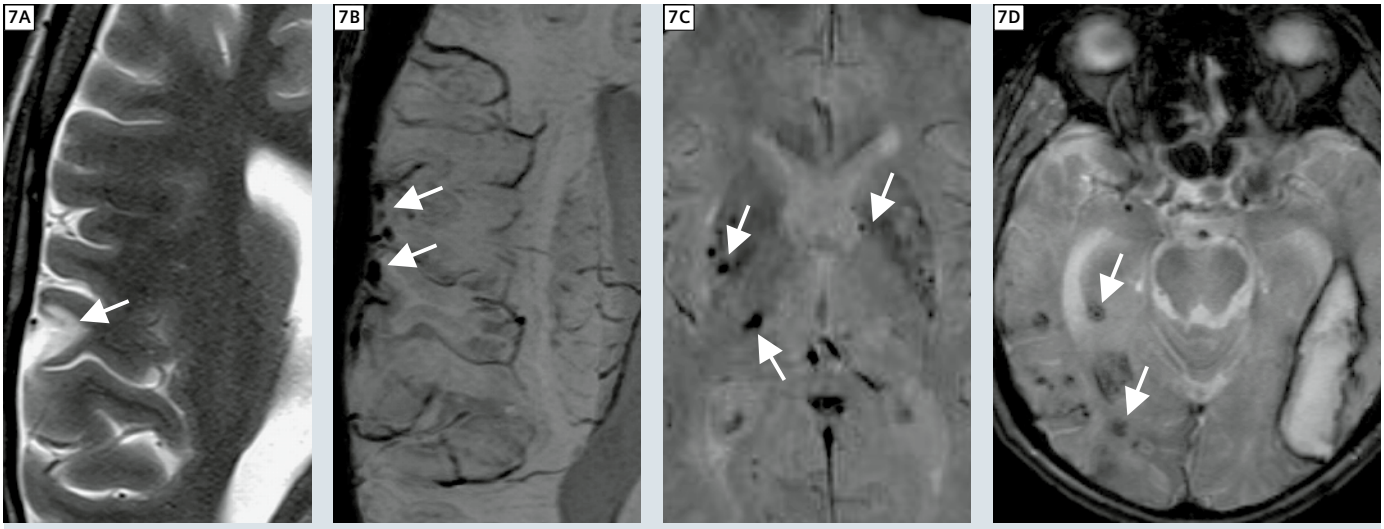

7 **(7A)** Circumscribed cortical gliosis (arrow) after brain injury without visible micro-bleeding on the T2-weighted image. **(7B)** Same patient with the same localization with well visible micro-bleedings (arrows) on SWI. **(7C)** Hypertensive small micro-bleedings in the basal ganglia and in the thalamus. **(7D)** Amyloid angiopathy with a large intraparenchymal bleeding on the left and with multiple superficial micro-bleedings on the right (arrows).

Advanced imaging in cerebrovascular diseases and vascular lesions

Contrast enhanced MR Angiography (MRA) is a well established complementary examination to Doppler sonography and in most cases replacement for digital subtraction angiography by producing high-quality static images.

Time resolved MR Angiography

The latest MRA technique is time resolved or 4D MRA with a time resolution of <0.7 s. This method is capable of capturing the dynamic filling of vessels, thus demonstrating the arterial, capillary and the venous phase of the cerebral circulation, similar to digital subtraction angiography (DSA). Hemodynamic changes caused by arterial stenoses and occlusions can be well

detected and dural arteriovenous fistulas (Figs. 8A, B) or arteriovenous malformations can be easily diagnosed. 4D MRA can contribute to the preoperative evaluation and characterization of a tumor by its degree of vascularization (Figs. 9A–F).

Indication of 4D MR Angiography

- hemodynamic changes due to an arterial stenosis or occlusion
- dural arteriovenous fistulas
- vascular malformations of the brain, face or neck

Advanced MR imaging of inflammatory demyelinating diseases of the central nervous system

Advanced MR techniques have revolutionized the recognition and characterization of white matter disease. MR imaging is required to depict the presence and location of inflammatory lesions within the optic nerve, the brain and spinal cord. The morphology and distribution of lesions along the ventricular lining and perimedullary veins, in juxtacortical and infratentorial location may permit a tentative diagnosis. The acuity of lesions is assessed based on the presence of contrast enhancement or by alterations in the composition of neurometabolites in MR spectroscopy when large and unusual lesions or diffuse white matter changes are present. Follow-up examinations by high resolution MR sequences are of major importance to depict 'dissemination in time'.

3D Fluid-Attenuated Inversion Recovery Sequence (FLAIR SPACE)

provides a higher spatial resolution with 0.8 to 1 mm isotropic slices and inherent contrast resolution in comparison to T2-weighted (Fig. 10A) and proton den-

4D MRA of a dural arteriovenous fistula – high temporal resolution

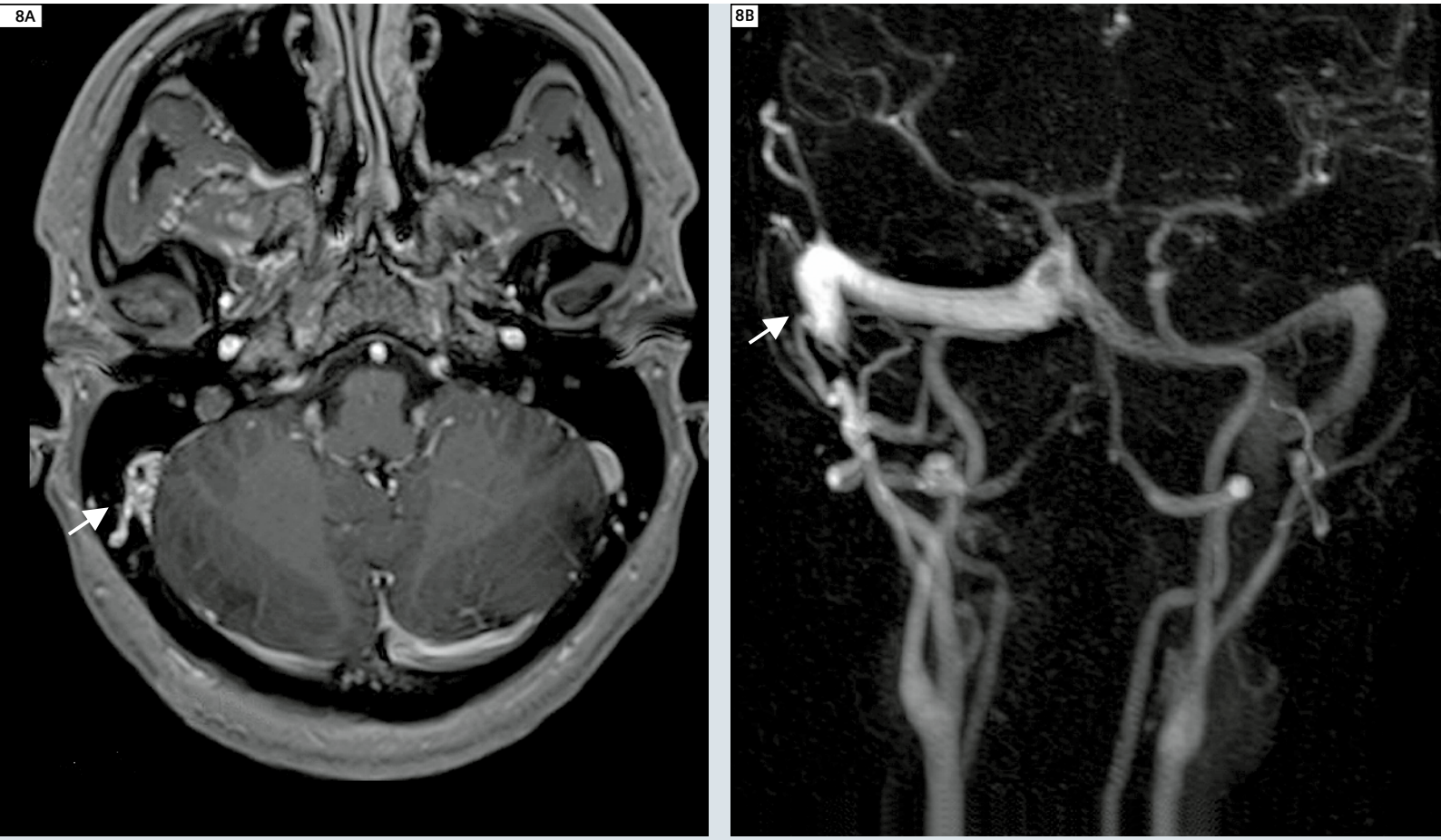

8 **(8A)** Contrast enhanced MRI shows a filling defect of the right sigmoid sinus (arrow). **(8B)** The 4D MRA depicts the arterial filling of the sinus as sign of a dural arteriovenous fistula (arrow) with origin from the branches of the external carotid artery.

sity-weighted images (Fig. 10B) and 2D standard FLAIR sequences. Higher resolution is beneficial due to better recognition of small demyelinating lesions on the initial examination: This holds particularly true in locations such as the brainstem, at the temporal horns, corpus callosum and in juxta- and cortical location. On follow-up examinations, isotropic 3D multiplanar reconstructions facilitate comparison and increase sensitivity to recognize new lesions. High inherent contrast allows to better differentiate cortical and juxtacortical lesions (Fig. 10C) similar to the 3D DIR sequence. Furthermore 3D FLAIR permits to differentiate acute and old lesions and to distinguish demyelination from perilesional edema and concomitant neurodegenration of white matter tracts.

3D T1 MPRAGE sequence

provides isotropic resolution (0.8 to 1 mm) and thus sensitivity in recognition of small contrast enhancing lesions. High accuracy in detecting focal axonal destruction requires reassessment of the current concept of the frequency and distribution of 'dark holes' which are a common finding with this new sequence.

3D Double Inversion-Recovery (DIR) sequence

is characterized by a high sensitivity to depict cortical (Fig. 10D) and deep grey matter involvement due to high signal of the lesions relative to the low white and grey matter signal intensity. 3D SPACE DIR sequence is equivalent to 3D FLAIR SPACE to depict white matter infra- and supratentorial lesions. The sequence appears sligthly superior to recognize focal and generalized cortical grey matter volume loss in the vicinity of subcortical lesions and as a sign of neurodegeneration respectively.

4D MRA for demonstrating tumor perfusion: diagnostic and preoperative information

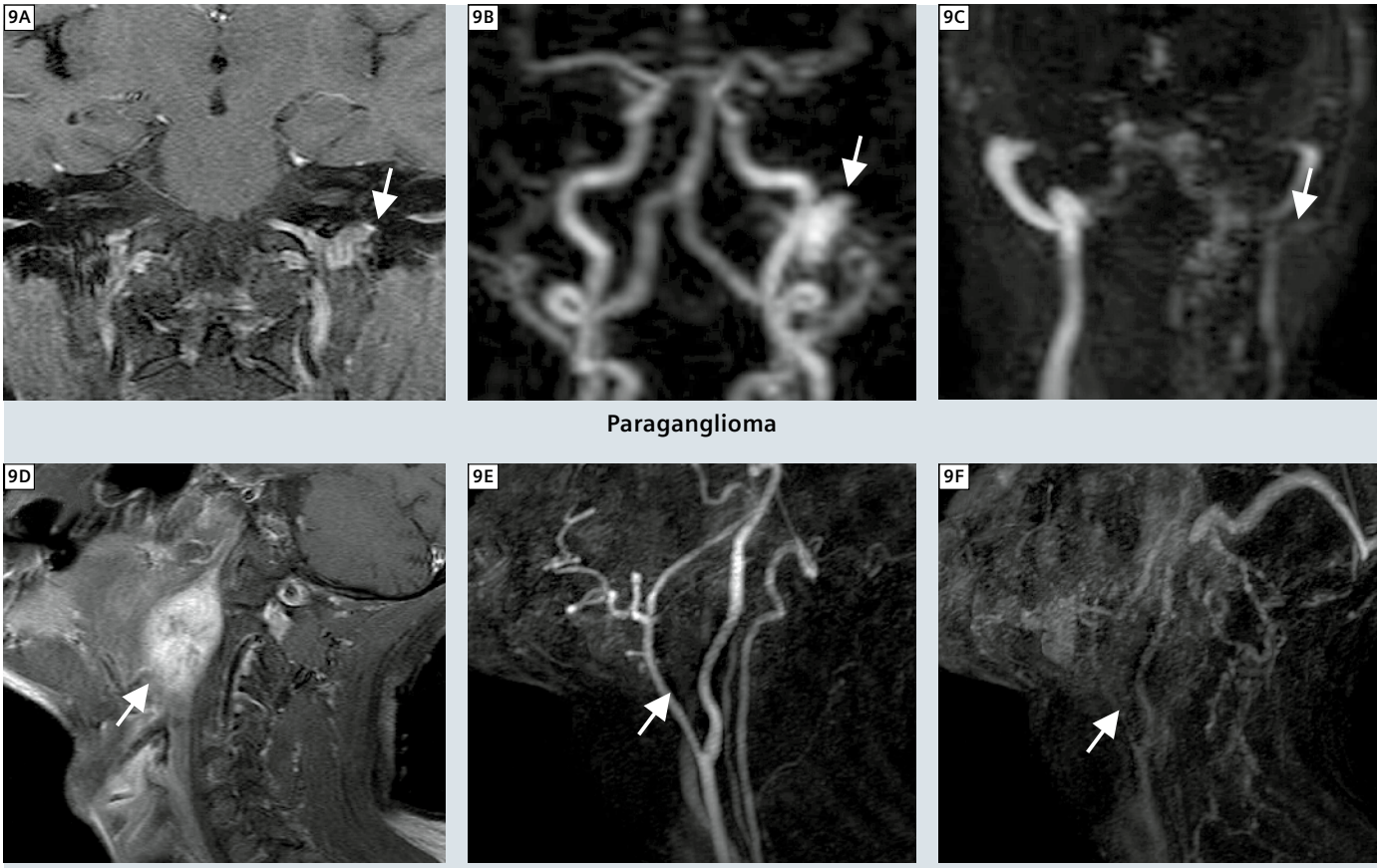

9 The similar location, morphology and signal intensity of a paraganglioma (glomus tumor) and neurinoma (arrows: **9A, C**) makes the differentiation sometimes challenging. The 4D MRA however, demonstrates the difference clearly: a paraganglioma shows an early and strong tumor filling **(9B)**, and early washout in the venous phase **(9C)** whereas a vagal neurinoma **(9D)** exhibits no macrsocopic vascularization in the arterial **(9E)** and venous **(9F)** phase.

New sequences: increased sensitivity to gray and white matter involvement by demyelination

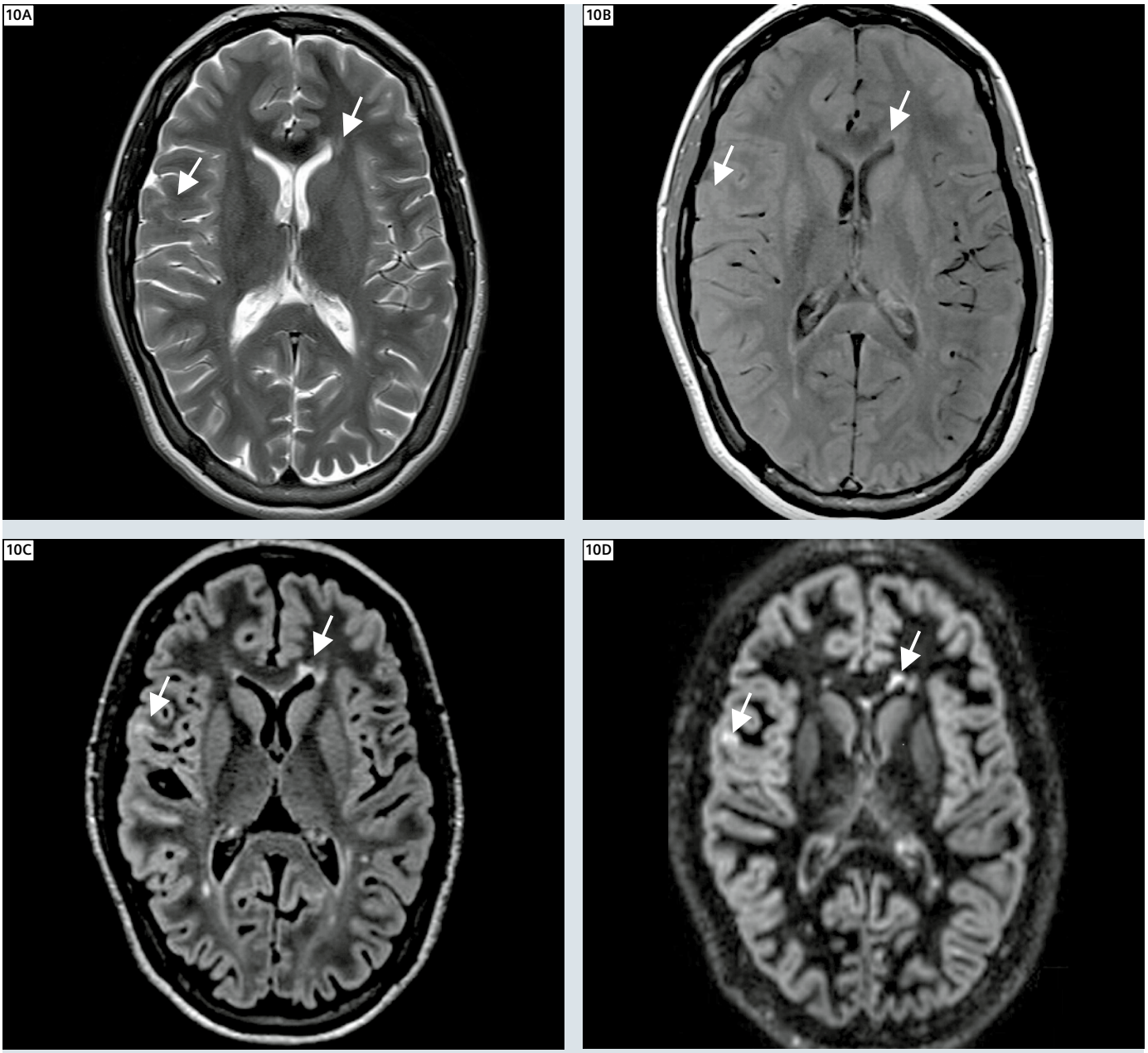

10 Axial T2w **(10A)** and PD images **(10B)** hardly allow recognition of demyelinating lesions indicated by arrows within the forceps minor of the corpus callosum and in intracortical location within the subcentral gyrus. Images are acquired with 3.5 mm contiguous slices. Improved delineation of the corresponding lesions and significant more demyelinating plaques in the 3D FLAIR **(10C)** und 3D SPACE DIR sequence **(10D)** acquired at 1.0 and 1 mm slice thickness respectively.

Inflammatory demyelinating disease: new 3D sequences yield higher diagnostic accuracy, improved clinical and imaging correlation, and more precise follow-up assessment.

Contact
Prof. Bernhard Schuknecht, M.D.
Diagnostic, Vascular and
Interventional Neuroradiology
Medizinisch Radiologisches Institut MRI Zürich
Bahnhofplatz 3
8001 Zürich
Switzerland
image-solution@ggaweb.ch

MAGNETOM Aera – Combining Throughput and Highest Quality MRI in an Optimized Clinical Workflow

Johan Dehem, M.D.

VZW Jan Yperman, Ieper, Belgium

We have been using the 1.5T MAGNETOM Aera for a year now and it is perhaps time to reflect on how the system is performing in a busy environment. My experiences with the MAGNETOM Aera are summarized in this article.
Compared to our earlier 1.5T MAGNETOM Symphony a Tim system, MAGNETOM Aera's new RF system – Tim 4G – introduces signal increase that is used to scan at higher resolution than before whilst keeping the same acquisition time or can be combined with parallel imaging for higher speed.

Section 1: fast brain imaging with Tim 4G and Dot

In our center we use eight sequences for brain evaluation in a 20-minute time slot that includes getting the patient in and out of the MRI suite. Figure 1 shows the details of the brain protocol we follow.
The Brain Dot Engine helps us to acquire all brain examinations with consistent accurate coverage from the foramen magnum up to the vertex and from left to right or anteroposterior without fault, which is possible irrespective of the experience level of the operators. Moreover, Brain Dot Engine starts with an AutoAlign 3D localizer which is mapped to the Tailarach space, and as a result sequence planning is automated according to the reference space independent of patient positioning / habitus.
This is especially convenient in follow-up examinations, such as in this case of demyelinating disease or tumor, resulting in a more reliable and comfortable comparison of the examinations at different time points (Fig. 2).

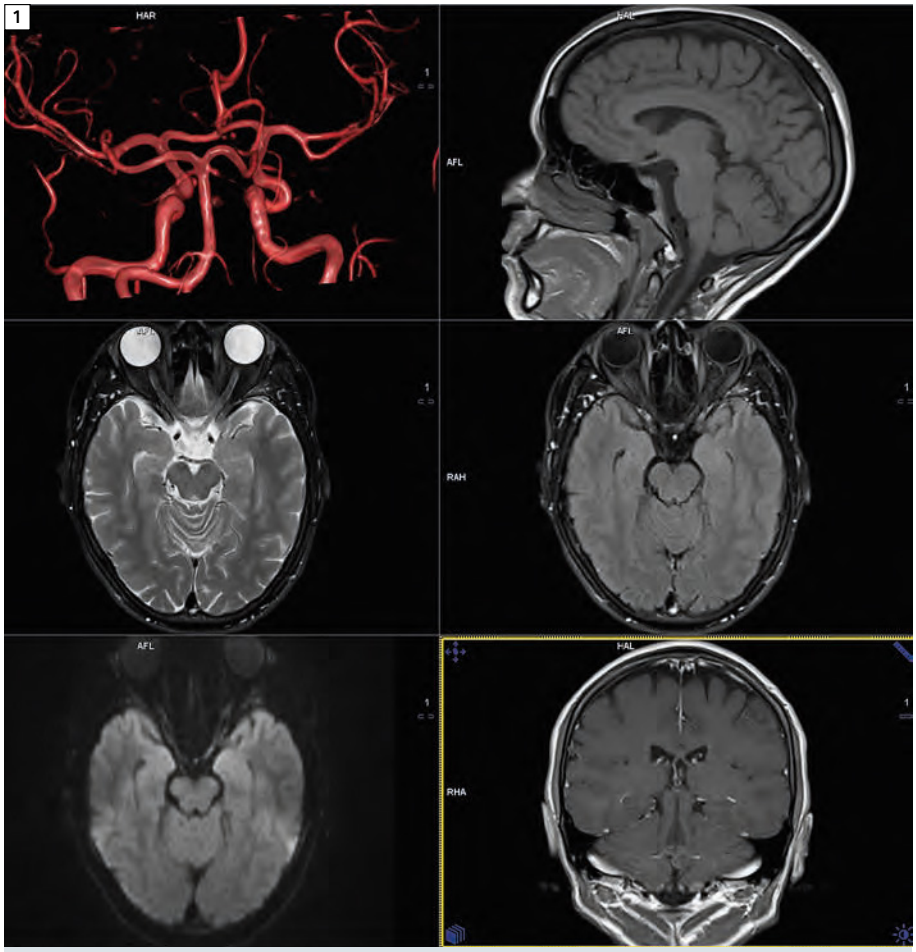

1 Sequence details of our 20-minute brain evaluation:
1. T2*w EPI, 23 slices, 5 mm in 9.7 sec, 0.9 x 0.9 x 5 (FOV 185 x 220, matrix 216 x 256) res
2. T1w sag SE, 4 mm slices in 2:09 min, 0.7 x 0.7 x 4 (FOV 290 x 223, matrix 246 x 320) res
3. T2w ax TSE, 25 slices, 4 mm in 01:34 min, 0.5 x 0.5 x 4 (FOV 171 x 221, matrix 256 x 384)
4. T2w FLAIR, 23 slices, 5 mm in 32 sec x 2 0.8 x 0.8 x 5 (FOV 211 x 211, matrix 205 x 256)
5. DWI EPI *b*50, *b*500, *b*1000, 69 slices in 1:30 min (1.2 x 1.2 x 5, FOV 216 x 231, matrix 174 x 188)
6. 3D TOF 3 slabs, 116 slices in 2:44 min, 0.4 x 0.4 x 0.5 mm isotropic (FOV 141 x 181, matrix 376 x 512)
7. T1w cor TSE, 22 4 mm slices in 1:34 min, 0.8 x 0.8 x 4 (FOV 174 x 200, matrix 213 x 256)
8. T1w ax SE 22 4 mm slices in 2:34 min, 0.9 x 0.9 x 5 (FOV 174 x 200, matrix 213 x 256)

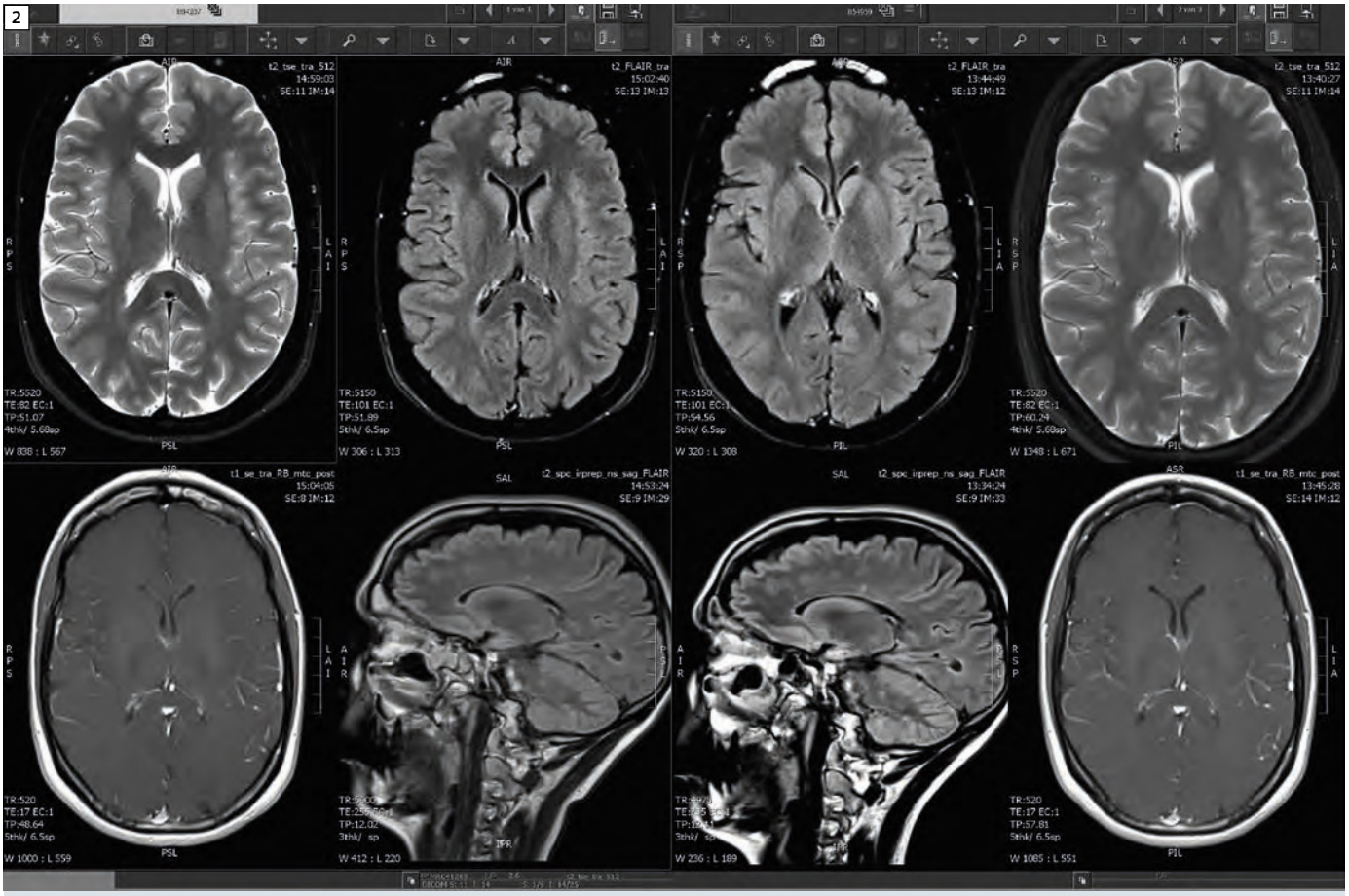

2 Follow-up examination at different time-points in demyelinating disease. Even the small lesions are comparable since anatomy is depicted consistently, independent of operator and patient positions even on a different PACS system and on the viewing system of the referring physician.

Section 2: 16-channel MSK coils

The new RF system enables the use of 16-channel MSK coils like the Shoulder, Foot/Ankle and Hand/Wrist coils.
The new wrist coil gives abundant signal and superb detail. The wrist coil has grown, in fact, to a 16-channel hand-wrist coil (Fig. 3), which is quite convenient for both the patient and the operators and helps faster setup times. Many patients have combined hand/wrist pathology and symptoms, and extended coverage is a huge benefit. Since it is easy to position the hand in the Hand/Wrist coil, examining the fingers has become very straightforward. Figure 4 shows a young butcher who suffered from a deep wound in the index finger. You still can notice the susceptibility artifacts on the coronal STIR and GRE (Figs. 4D, E). One week later the young man can no longer flex the distal interphalangeal joint (DIP) of the index finger. MRI nicely depicts the torn deep flexor retracted to the proximal phalanx in the tendon sheet (Figs. 4H, I). All these images have an in-plane resolution of 0.5 mm, a slice thickness of 2.3 mm or less and scanning times of 1.30 min or less thanks to the higher signal from the high-channel coil.
Since this coil is so successful for fingers, it could also be used for toes. This is the flexibility with Tim.
Figure 5 shows images of a middle-aged man, who suffers from a "tingling pain sensation" in the forefoot intermetatarsal space III-IV and numb feeling in digit IV. A T2 hyperintense, T1 hypointense dumbbell shaped lesion bulging between the metatarsal heads III-IV is clearly demonstrated (Figs. 5A, B, C) confirming the clinical suspicion of Morton neuroma.



3 16-channel Hand/Wrist coil.

Section 3: reduction of susceptibility artifacts caused by metal

MRI is challenging in the presence of metal. MAGNETOM Aera came equipped with *syngo* WARP with high bandwidth TSE and TSE STIR protocols and an

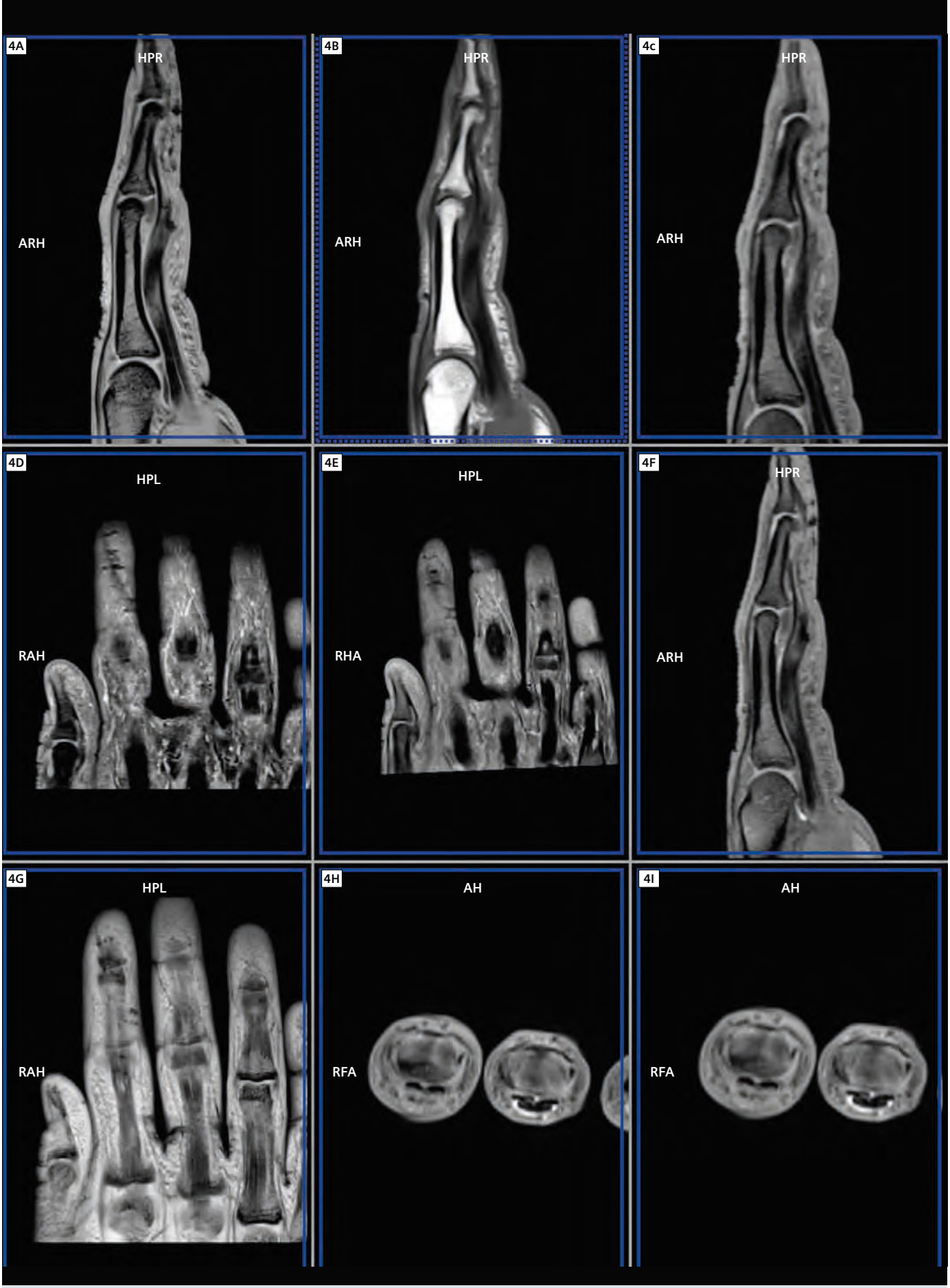

4 Superb details in a case of trauma to index finger in 1:30 min per sequence.

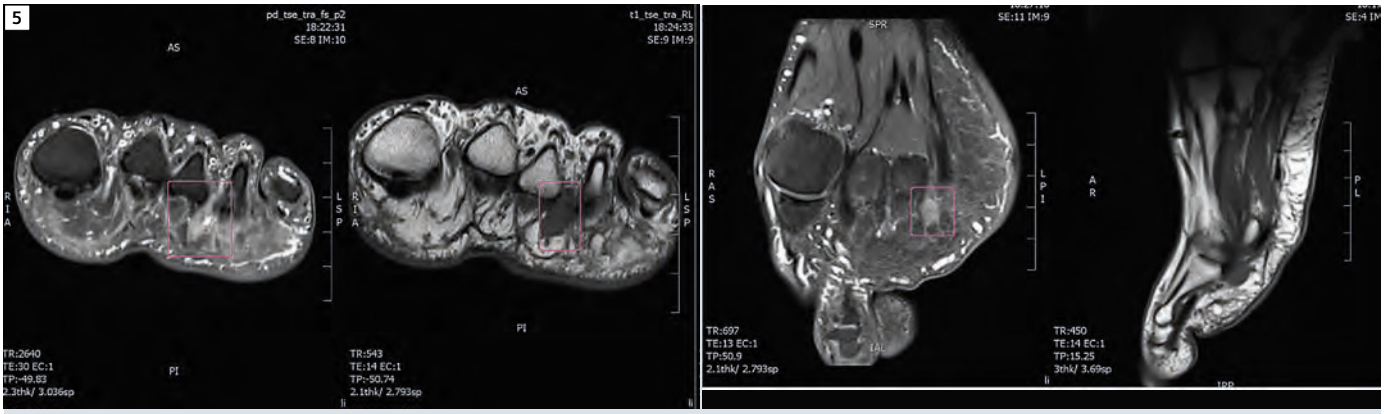

5 Toe imaging using the 16-channel Hand/Wrist coil. Excellent image quality showing Morton neuroma between the metatarsal heads III and IV.

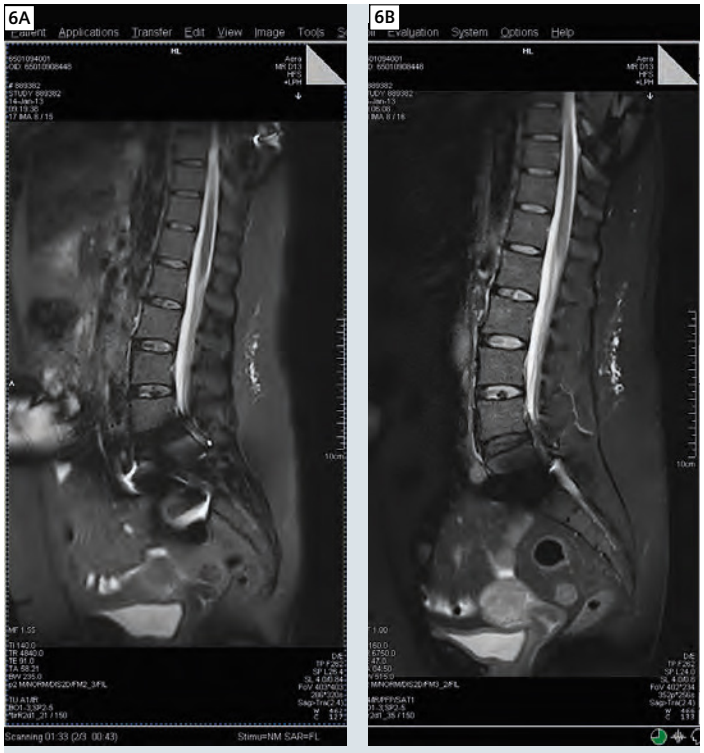

6 T2w TIR versus T2w TIR WARP demonstrates dramatic improvement in image quality with the disc L5-S1 showing up on the WARP images only **(Fig. 6B)**.

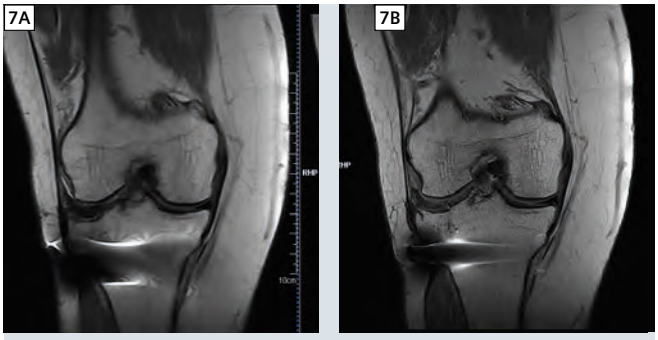

7 T1-weighted coronal imaging degraded by artifacts **(7A)**. T1 VAT WARP does the job **(7B)**.

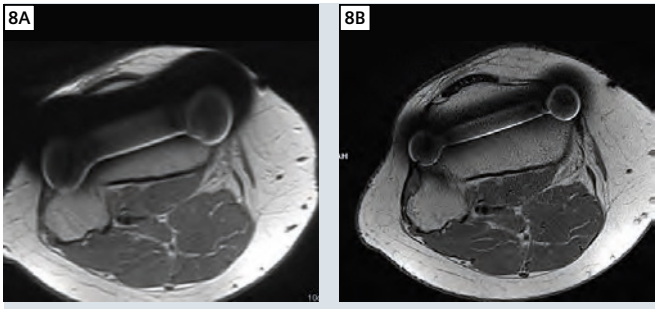

8 Proton density-weighted axial image largely degraded **(8A)**. PD VAT WARP nicely demonstrates the material and recovers the distortion **(8B)**.

optional VAT (View Angle Tilting) technique. In Figures 6–8 I share some examples of real day-to-day cases.
Figures 7 and 8 show images of a female patient who has had osteosynthesis for tibial plateau fracture following a skiing accident 20 years ago. She had an MRI of the knee, after another skiing accident. WARP helped reduce susceptibility artifacts for better image quality and confidence in diagnosis.

Section 4: faster imaging with CAIPIRINHA

CAIPIRINHA (Controlled Aliasing in Parallel Imaging Results in Higher Acceleration) is a new parallel imaging technique from Siemens.
The new RF system and high channel coils (Body 18) provide the signal that is needed, whilst the parallel imaging with fourfold acceleration with CAIPIRINHIA offers the speed required to maintain short breath-holds even at large coverage in the z-direction and thin slices. The short breath-holds are a real game changer especially in the case of elderly patients, but even young and fit patients benefit.
No trade-off between thick slice / large coverage or thin slice / partial coverage is necessary: we always scan full coverage with thin slices. Examination of the abdo-

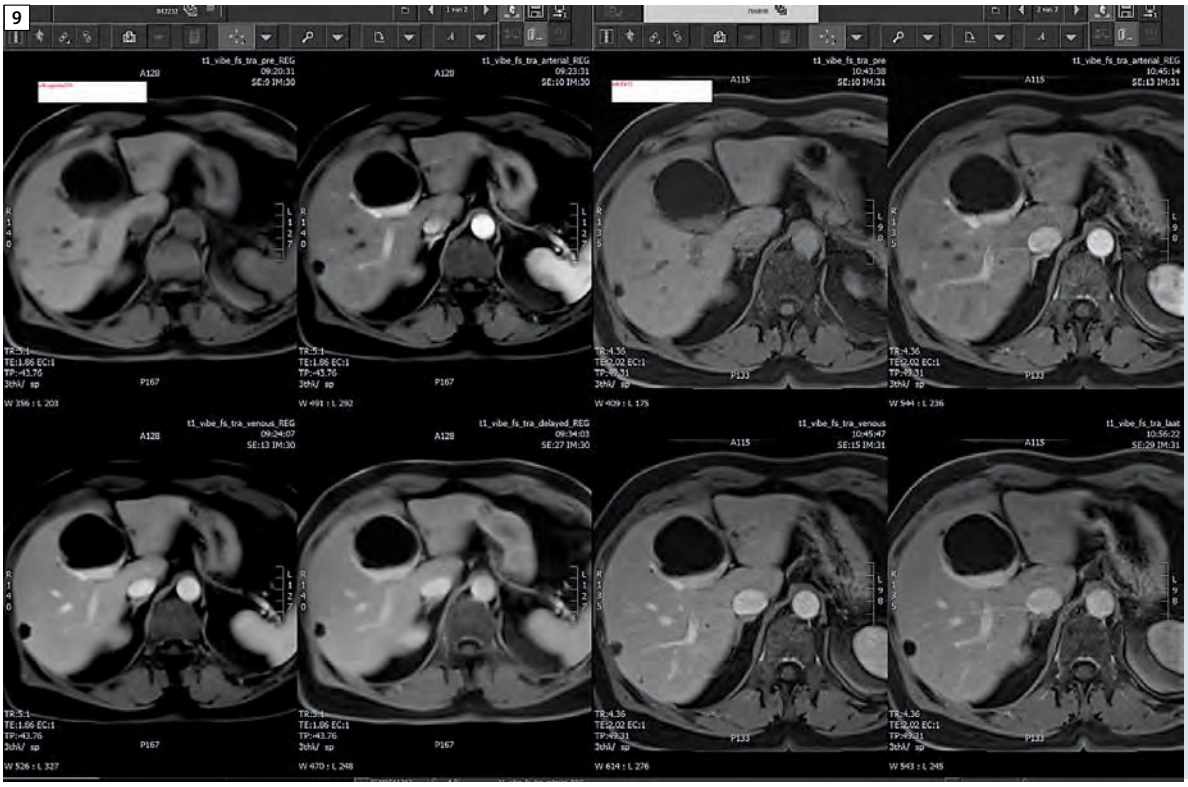

9 CAIPIRINHA PAT4 in 10 sec compared to PAT2 in 21 sec with same slice thickness and in-plane resolution.

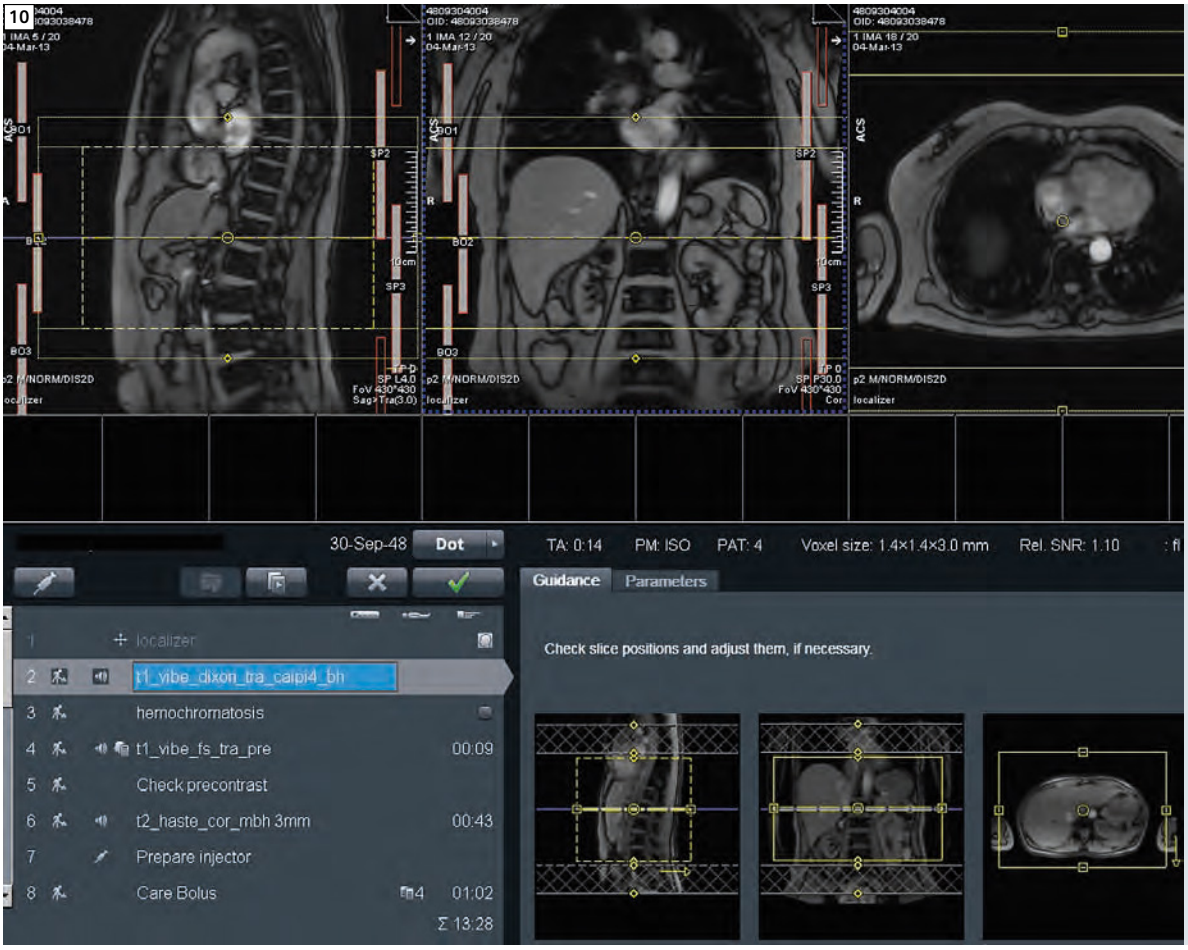

10 With CAIPIRINHA no trade-off between thick slice / large coverage or thin slice / partial coverage is necessary: we always scan full coverage with thin slices. The coverage is well seen in this screenshot (yellow dotted box top left, or yellow bold box top middle).

men and thorax benefits greatly from the Aera system. It all fits perfectly together. Here are some examples.
More signal in less scanning time! Figure 9 demonstrates how, in a liver examination in the same patient examined with CAIPI4, the images with a breath-hold of 10 sec have more signal than the same images (same slice thickness and in-plane resolution) with iPAT2 and 21 sec breath-hold.
MRI examination of the thorax – although more rare – follows the same rules as the abdomen: sequences should be fast enough for the patient to cooperate. Figure 11 gives an example of a metastatic lung carcinoma where PET-CT was not able to exclude or confirm chest wall invasion. MRI was ordered and it turned out to be quite an easy job on MRI, having the short breath-hold CAIPIRINHA PAT 4 VIBE sequences. Even this patient, who clearly is in a bad condition,

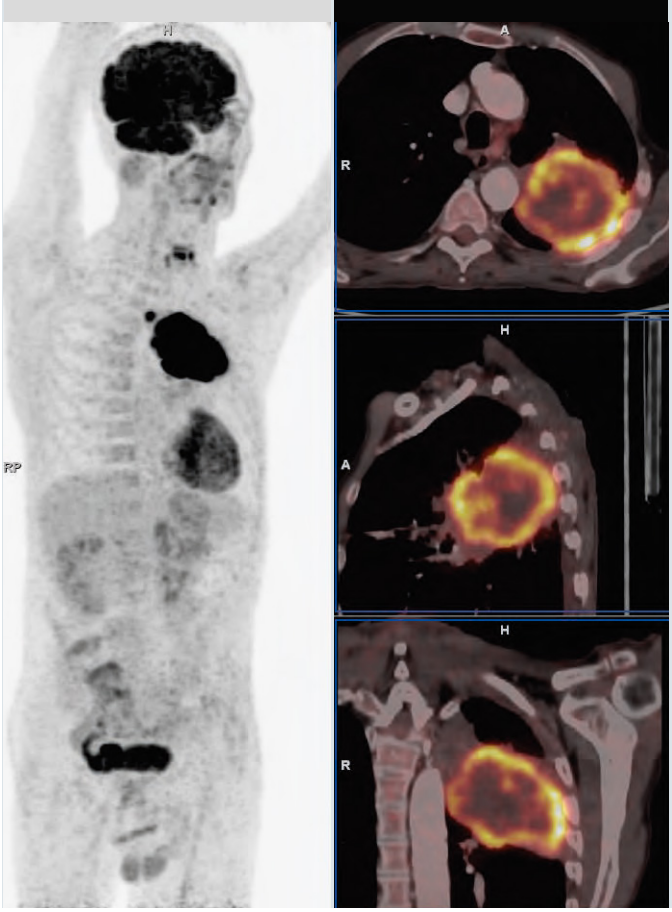

11 A case of a metastatic lung carcinoma where PET-CT was not able to exclude or confirm chest wall invasion.

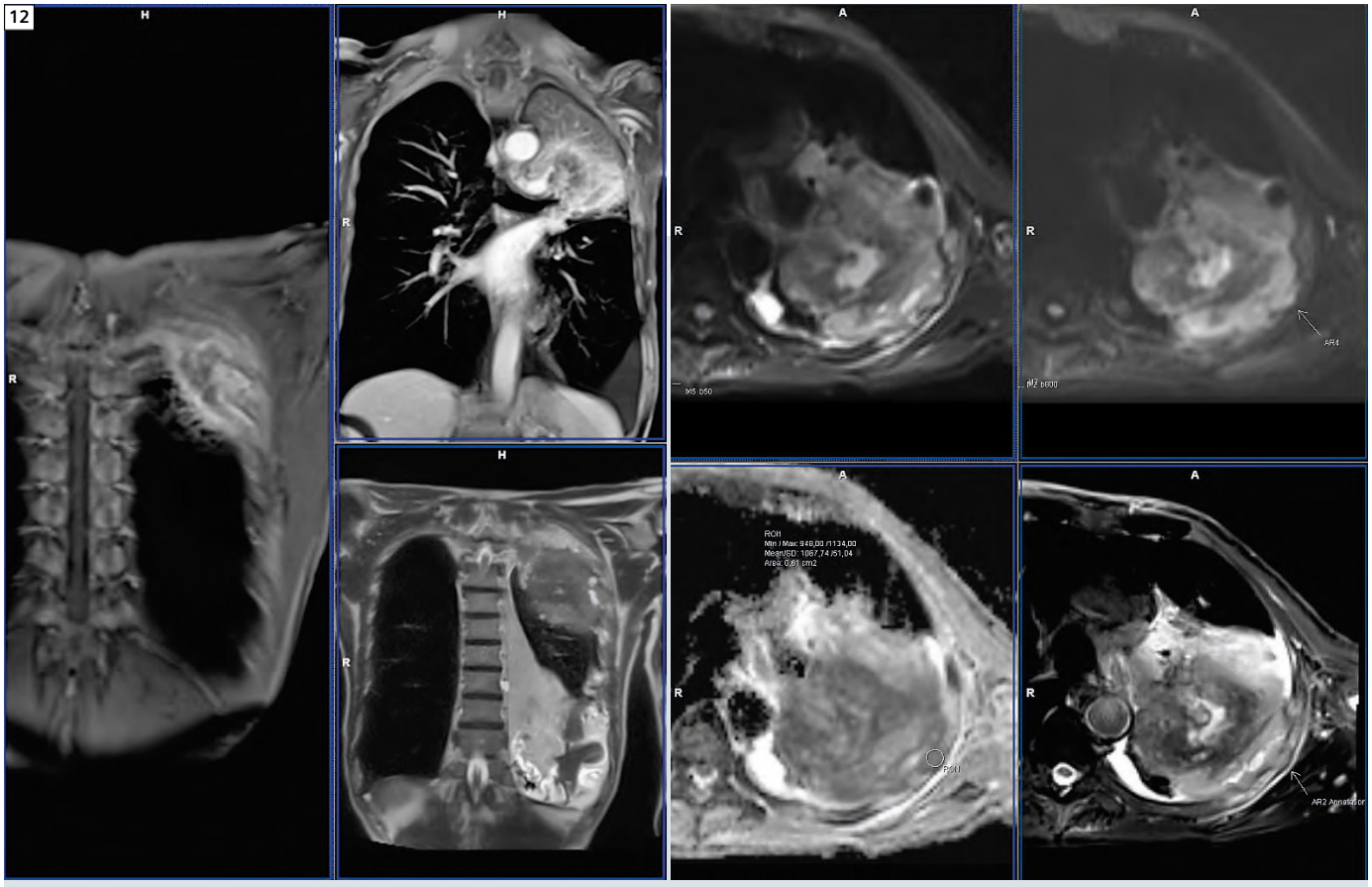

12 CAIPIRINHA PAT4 VIBE post-contrast coronal showing the tumor (arrow) and lateral and dorsal chest wall invasion (small arrows). Axial T2w BLADE and free breathing DWI show the chest wall invasion with actual rib invasion.

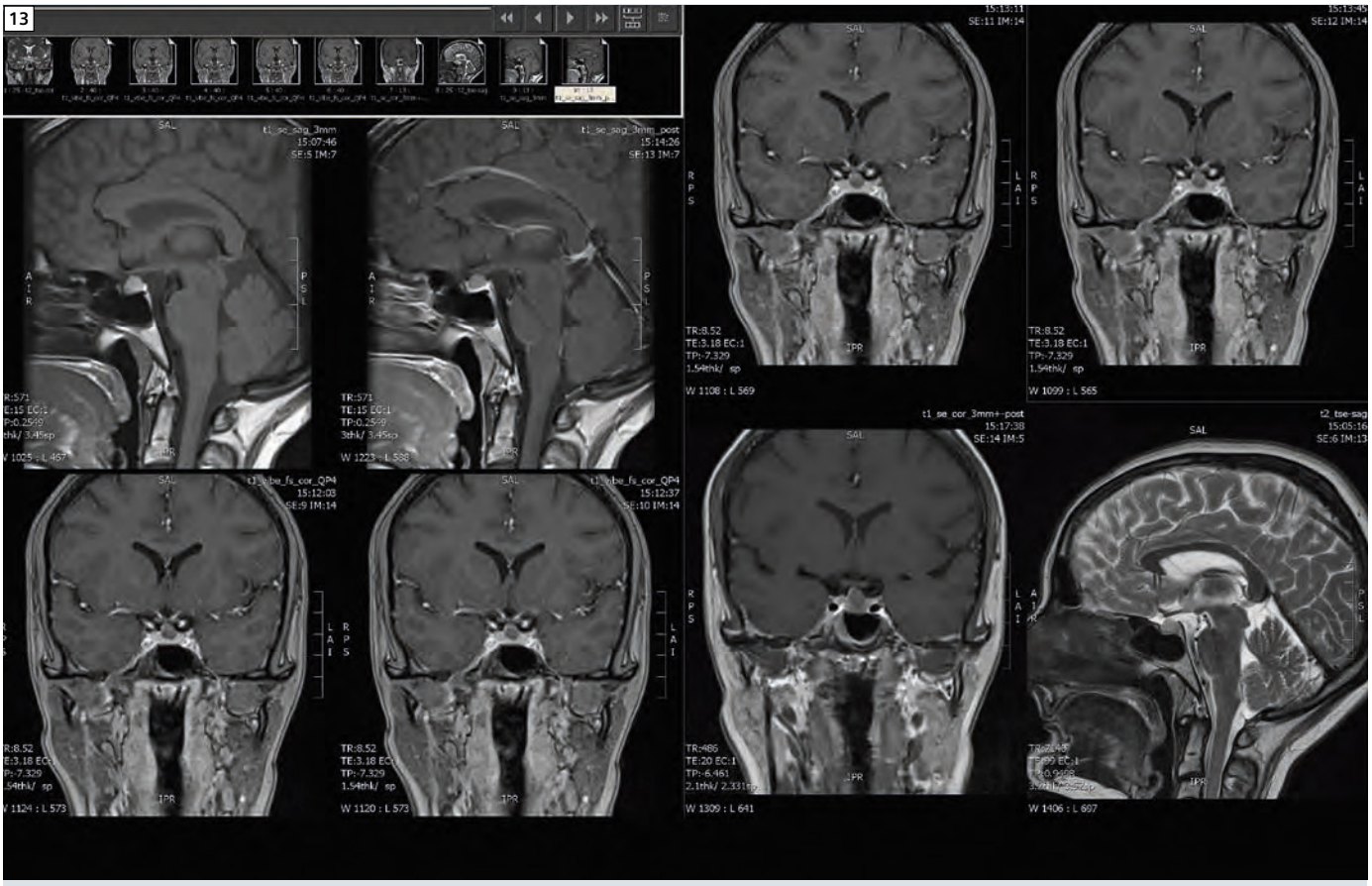

13 Coronal dynamic sella imaging with CAIPI PAT4 VIBE in 34 seconds.

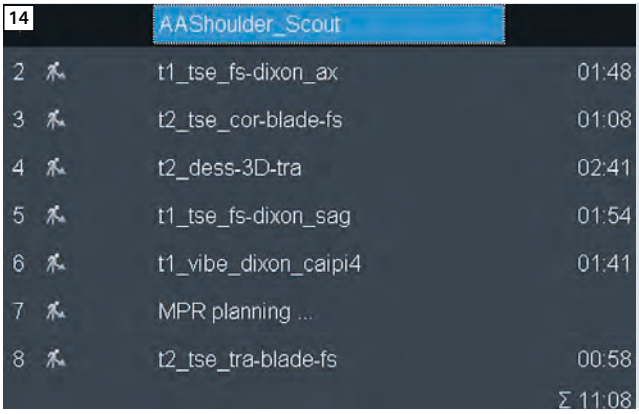

14 Screenshot showing 1.41 min CAIPI VIBE Dixon for 3D shoulder imaging. High SNR due to the 16-channel MSK coils allows us to use these fast sequences.

cooperated and tolerated the exam well. Invasion in the lateral and dorsal chest wall is readily depicted in both axial and coronal enhanced images. Axial T2w BLADE and free breathing diffusion-weighted imaging (DWI) confirm the chest wall invasion with actual rib invasion and the malignant nature is clearly translated in low ADC values of the lesion (Fig. 12). Maybe we don't have the fancy colors, like PET does, but we do have the diagnosis!

CAIPIRINHA can be used in other regions, too. Figure 13 shows images of a female patient who underwent a brain scan in search of a (post-traumatic?) cause of the headaches. A small mass in the sella was incidentally found. Coronal dynamic VIBE imaging provides a means to assess the perfusion of the sella and pick up smaller lesions e.g. adenomas as demonstrated in this examination. The VIBE sequence is pimped using CAIPIRINHA with 4-fold acceleration, providing 40 high res 1.5 mm slice thickness images every 34 seconds, and dramatically improving detection rate. The acquisition speed makes it possible to complete this examination within the same 20-minute time slot.

At our center, shoulder examination is mostly done after arthrogram. This can cause some discomfort and the fast scanning of patients is the best option to avoid movement artifacts. *syngo* BLADE helps reduce motion artifacts. However CAIPIRINHA is a huge benefit here. We acquire a 3D VIBE Dixon fatsat with CAIPI PAT4 in 1:41 min. The screenshot in Figure 14 shows the details of our shoulder protocol.

Section 5: the Large Joint Dot Engine for shoulder imaging

The AutoAlign tool in the Dot Engine helps technologists to plan more quickly and accurately, with reduced operator-depen

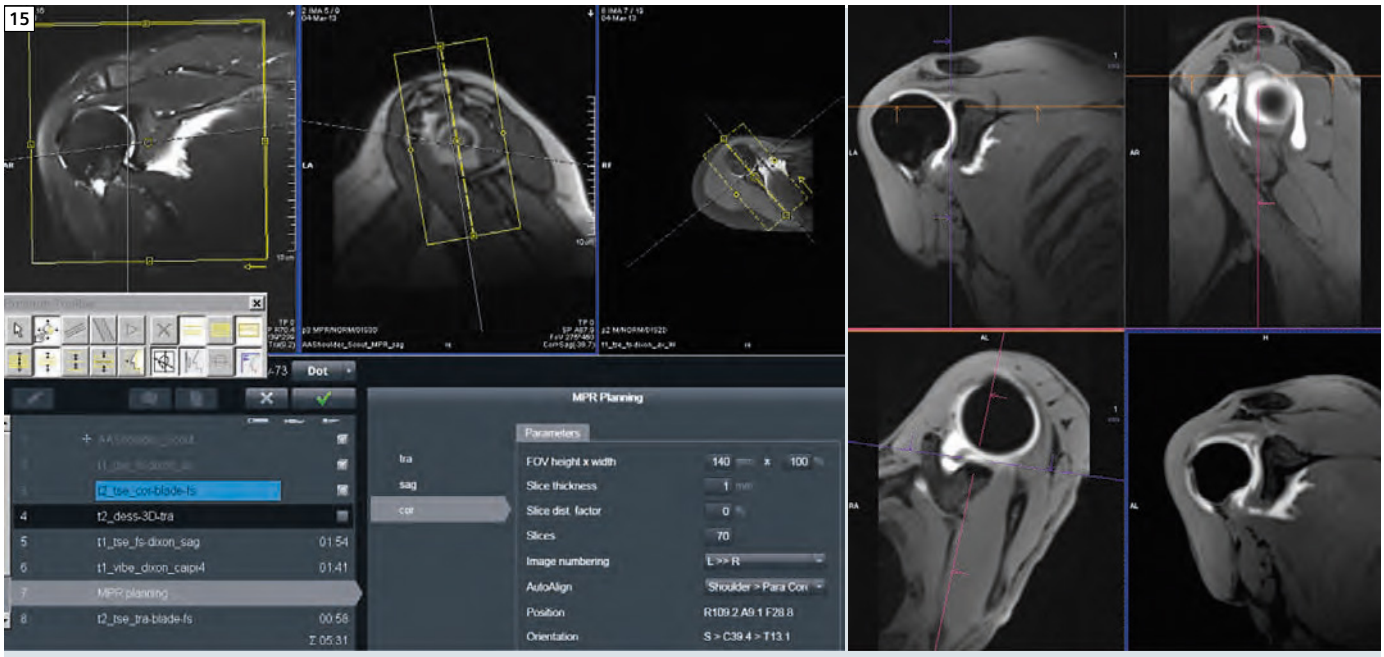

15 Shoulder Dot screenshot showing Inline MPR planning and VIBE CIAPI reformats.

dent variation. Figure 15 shows the sequences used and a total exam time of 11:08 minutes.

Two 3D blocks are scanned: 3D VIBE Dixon fatsat with CAIPI PAT4 (1:41 min) and 3D DESS fatsat (2:41 min) are acquired. These are reconstructed in axial, paracoronal and parasagittal planes inline, rather than in post-processing, thanks to the Inline MPR function of Dot. While still planning the sequences, the technologist already plans the multi-planar reconstruction so that the MPRs are available for reporting without delay as depicted. This produces an incremental benefit in workflow.

Section 6: liver imaging with Abdomen Dot Engine

Dot has many smart tools that help improve efficiency, consistency, reproducibility and throughput. AutoAlign is one tool I mentioned above in Brain Dot. The Abdomen Dot Engine actually provides several operator-independent tools: with AutoAlign for liver, and AutoCoverage, you always have the complete anatomy covered, ensuring good quality images with fewer incidences requiring repeat scans. This is a significant benefit of Dot and it holds true when we image obese patients, too.

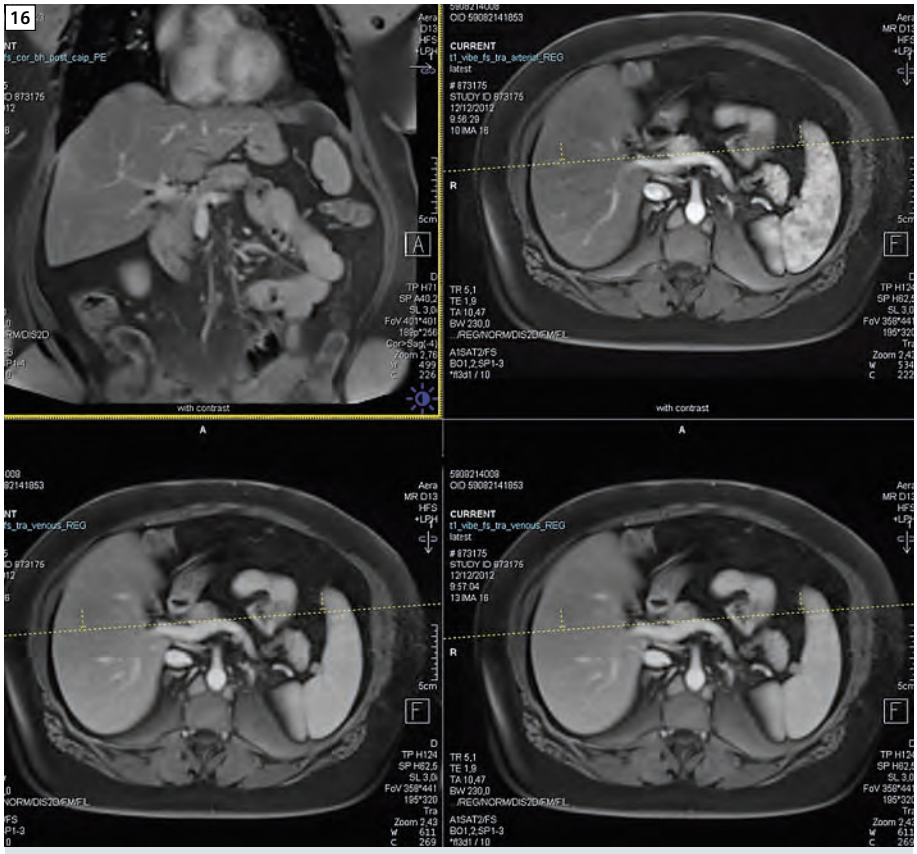

16 Excellent image quality, fat suppression and coverage in an obese patient in 10.7 sec (breath-hold).

MAGNETOM Aera's 70 cm open bore enables some larger patients to fit for the first time in their lives inside an MRI machine. But even if we did manage to fit such a patient inside the previous MRI scanner, we still ran into the problems of too much noise and of breath-holds that were too long to cover all the phase encoding steps needed in an obese patient. The increased signal available on the Aera tackles the noise problem and the CAIPIRINHA technique gives you a fourfold parallel imaging factor (without additional noise) resulting in acceptable breath-hold times (10.7 sec) even in large patients. Again, it all fits perfectly together!

Abdomen Dot enables easier, faster and more consequent – less operator-dependent – sequence planning and execution with AutoCommand tools where breath-hold commands are given by the system in a language the patient understands. The Abdomen Dot features ABLE (add-in for Automatic Breath-hold Liver Exams) where the system actually triggers on bolus arrival to ensure a pure arterial phase even in cirrhotic liver patients where timing of the bolus could be a challenge for less experienced technologists (Fig. 17).

Non-rigid liver registration of dynamic VIBE series is an automatic step done within the ABLE function to save all phases registered in the database, which enables faster and more accurate reading and reporting.

Different contrasts scans (*b*50 – *b*800 DWI and ADC map & T2w BLADE) can be in similar anatomical positions as close as possible to the multi-phase dynamic scans due to smart AutoCoverage functionality in Abdomen Dot. The example of a cirrhotic liver in Figure 18 will clearly illustrate the efficiency in reading.

This holds true within the scope of a single examination but becomes even more important when comparing examinations at different time points (Fig. 19). Having imaged and sent the images to the PACS in registered series turns out to be of great benefit for reading and reporting in follow-up examinations. This registration process allows for synchronized scrolling up and down simultaneously in the registered series even in a bare bone viewing system used by, for example, the referring physician. Figure 19 shows how convenient it was to reevaluate the liver on MRI in a case of invasive adenocarcinoma of the sigmoid colon. Comparing exams from 2011 and 2013 even on a bare bone viewing system: the Dot registration provides all the synchronization that is needed.

Section 7: excellent images in the head/neck region

Whereas in the old days fatsat could be problematic in the cervicothoracic region, TSE Dixon really assists with impeccable fatsat images and having the T2w or T1w TSE images for free.

Figure 20 gives a nice example of metastatic melanoma after gadolinium enhancement: no artifacts in the base of the neck! DWI has also improved due to the gradient power enabling short TE thus minimizing artifacts.

The next two examples of DWI in the neck highlight the importance of ADC maps. High signal on the high *b*-value DWI and low ADC value confirm the malignant nature of the metastatic melanoma.

DWI can help in determining the nature of lesions, such as in the small benign mixed tumor (BMT) of the right parotid gland with high ADC value depicted in Figure 22.

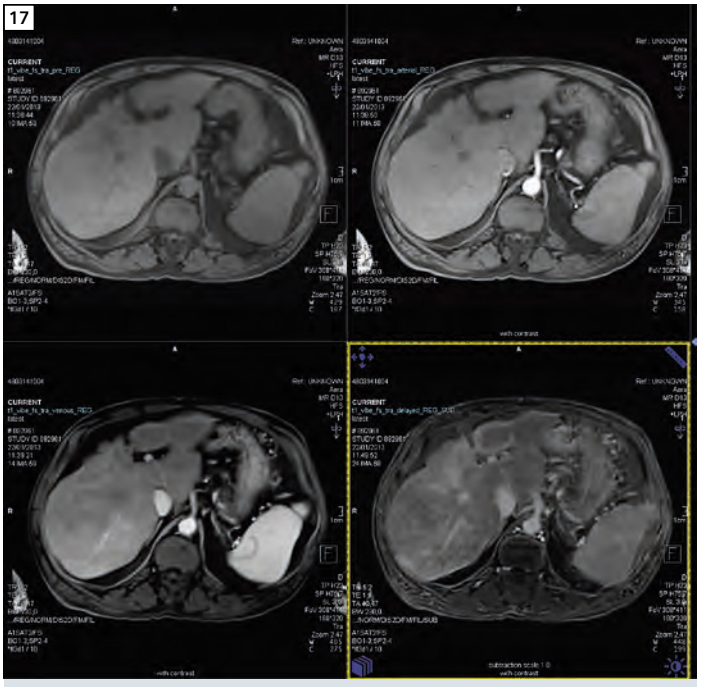

17 Abdomen Dot ABLE technique helps ensure accurate dynamic liver phases even in cirrhotic livers.

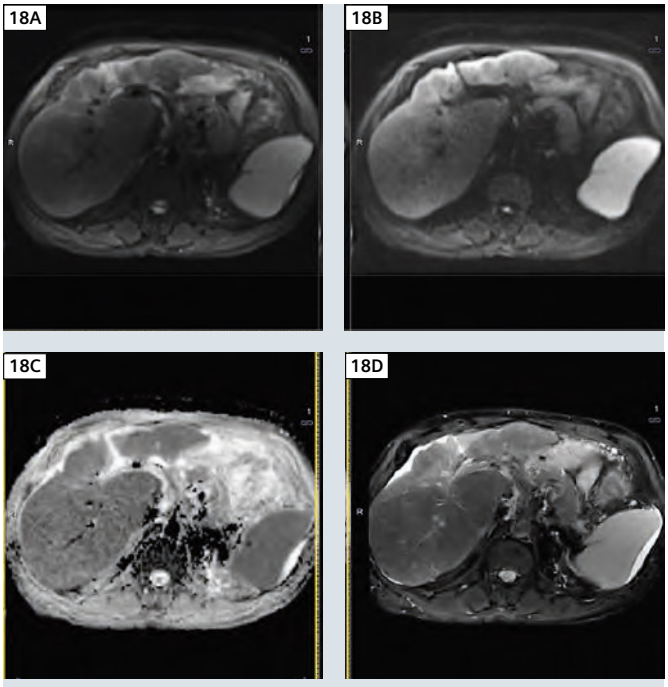

18 **(18A)** VIBE, **(18B)** DWI, **(18C)** ADC map and **(18D)** T2w BLADE all at almost similar slice positions. This helps in faster and more accurate reading and reporting.

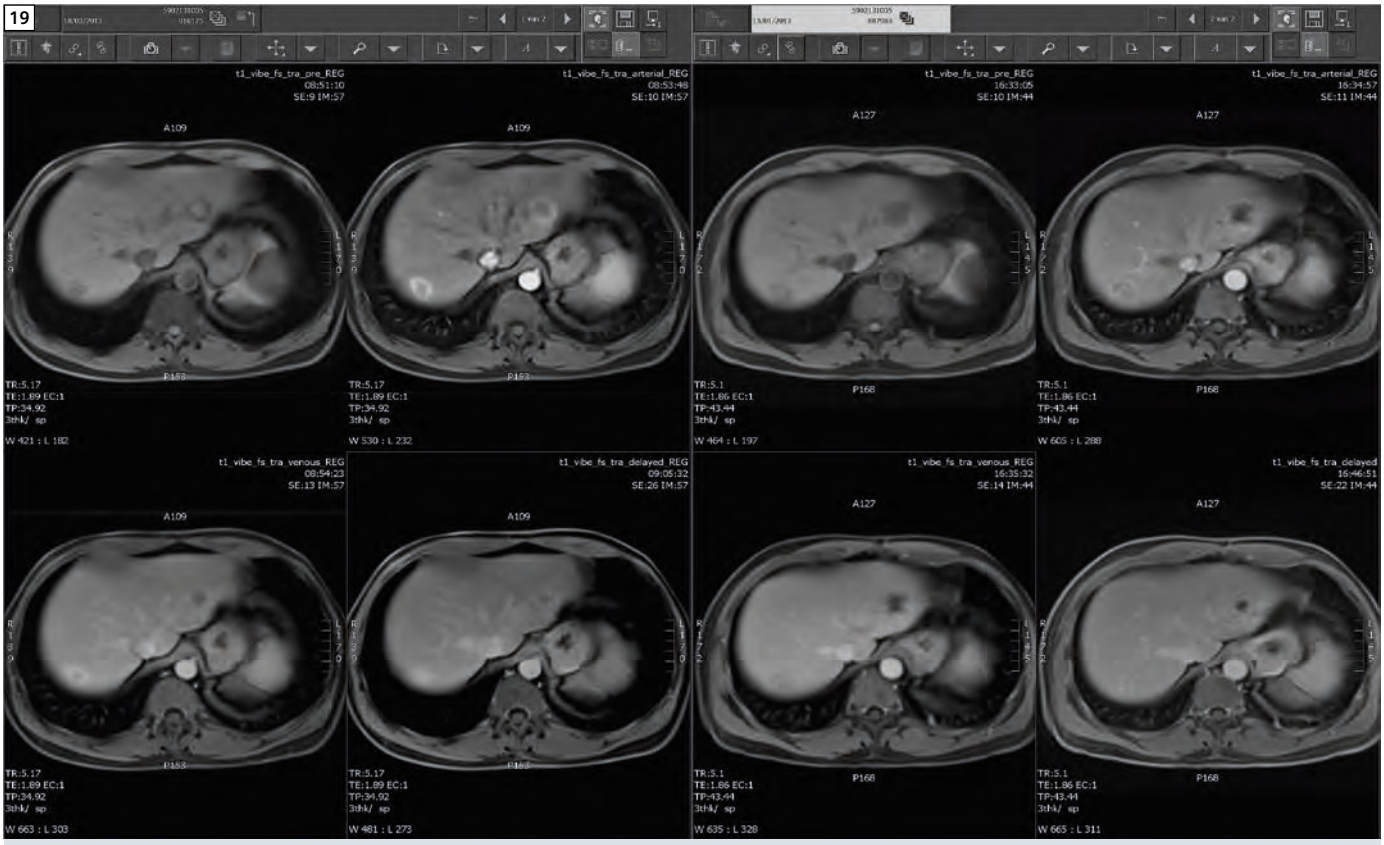

19 Shows the relevance of liver registration and synchronized viewing for efficiency.

Section 8: leveraging *syngo*.via

Presenting the roadmap to vascular surgeons has been made easier and better with *syngo*.via. The MIP and composing functionality helps us to integrate three 4D datasets for angiography of the aorta and lower limbs into one dataset and to present the roadmap to the vascular surgeons – something that we do in every case. Cardiac evaluation is done on *syngo*.via and, again, instead of having to leave my reporting system to go to the workstation, I simply push the *syngo*.via button and do my evaluations. Another area where I use *syngo*.via is for volume calculations. Volume calculating helps me out with every acoustic neuroma and for prostate (benign prostate hypertrophy). The inline registration in the Dot engines really helps with the multi timepoint follow up of 90% of cases: it gives me the series synchronized and sends them in that registered way to my non-intelligent, bare bone viewing station (the reporting

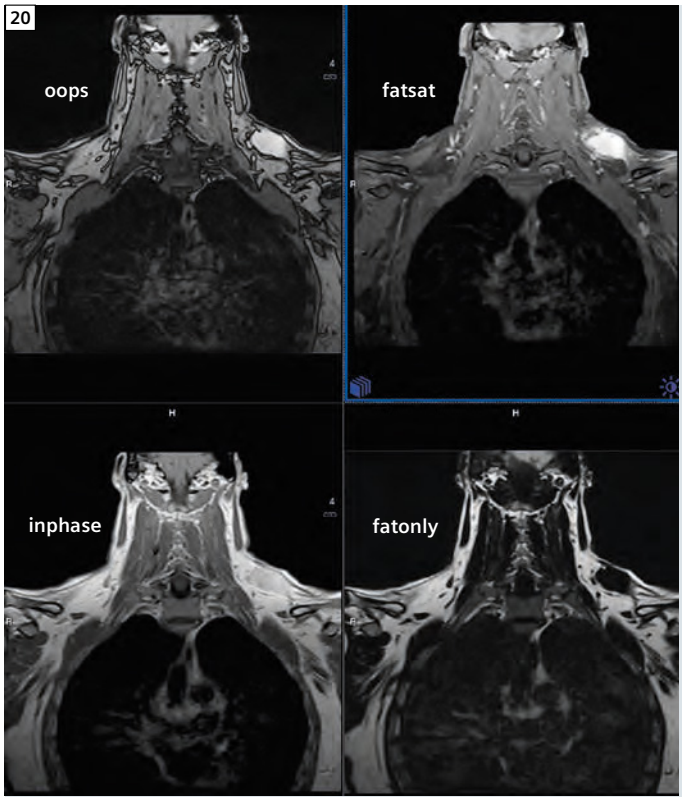

20 TSE Dixon showing In-phase, Out-of-phase, fat and water coronal in a case of metastatic melanoma post-contrast.)

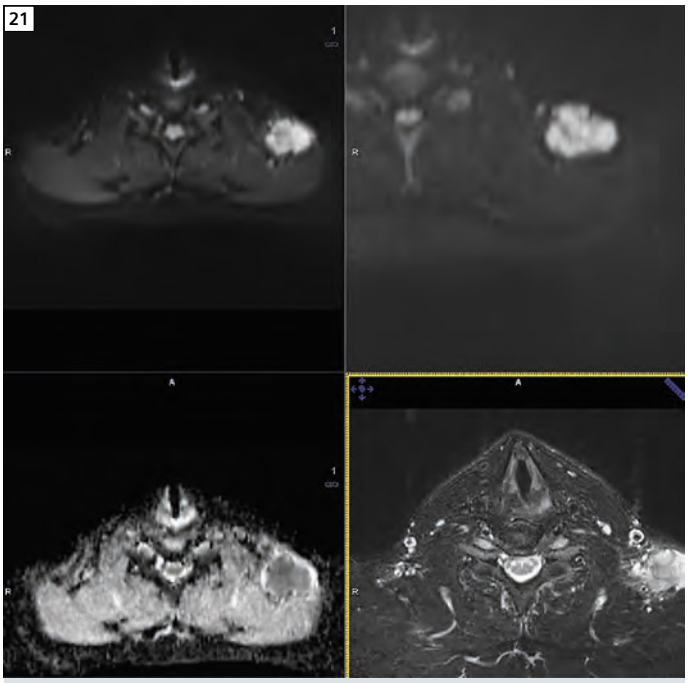

21 CAIPIRINHA, axial, DWI, ADC map and Fatsat T2w axial?? Showing low ADC (arrow) metastatic melonoma.

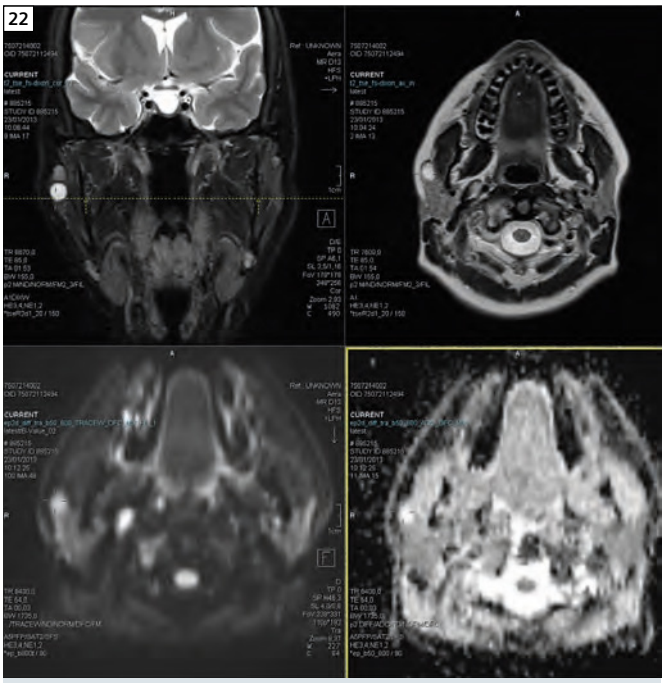

22 Coronal T2w TSE, T2w axial showing hyperintense lesion. DWI and ADC map with high ADC (arrow) help confirm benign mixed tumor diagnosis.

system). This synchronization-registration assists in most of the brain and abdomen cases. *syngo*.via helps in reading difficult cases, where I like to compare, for example, not only the registered axial slices but also coronal slices, the free breathing DWI and other contrasts. When this is required, I simply push the *syngo*.via button on my viewing station and get my patient opened up in *syngo*.via. It makes reading and reporting not only faster but also more accurate.

Conclusion

The new RF, high-channel coils, gain in SNR, faster techniques like CAIPIRINHA, new metal implant imaging possibilities, Dot features and *syngo*.via all are a perfect fit and the MAGNETOM Aera truly combines throughput and highest quality MR imaging in an optimized clinical workflow.

Contact
Johan Dehem, M.D
VZW Jan Yperman
Ieper
Belgium
johan.dehem@gmail.com

Further information

Visit us at
www.siemens.com/magnetom-world
to listen to Dr. Dehem's talk on **Highest Quality Imaging in an Optimized Clinical Workflow** given during the lunch symposium at the 15th International MRI Symposium MR 2013 in Garmisch-Partenkirchen, Germany.

Go to
www.siemens.com/magnetom-world > Clinical Corner > Clinical Talks





Johan Dehem, M.D.
VZW Jan Yperman
(Ieper, Belgium)

Parallel Transmission and its Clinical Implementation: Enabling new Clinical Imaging Paradigms

Fernando Boada[1]; Tim Shepherd[1]; Andrew Rosenkrantz[1]; Eric E. Sigmund[1]; Jurgen Fütterer[2]; Hersh Chandarana[1]; Mari Hagiwara[1]; Henry Rusinek[1]; Artem Mikheev[1]; Mary Bruno[1]; Christian Geppert[3]; Christopher Glielmi[3]; Josef Pfeuffer[3]

[1]*Department of Radiology NYU Langone Medical Center, New York, NY, USA*
[2]*Department of Radiology, Radboud University Nijmegen Medical Centre, Nijmegen, The Netherlands*
[3]*Siemens Healthcare*

Introduction

The use of multiple and independent receive channels to accelerate MR data acquisition has enabled numerous clinical applications that are now part of the standard clinical workflow at state-of-the-art imaging centers. Parallel transmission (pTX) was, likewise, introduced as a means to enable and improve the use of extended RF excitations schemes such as multidimensional spatially-selective excitation, which, although conceptually powerful, were previously rendered impractical due to their long RF pulse durations.

The 3T MAGNETOM Skyra is the first clinical system to feature a parallel transmission architecture capable of enabling applications beyond B_1 shimming. This revolutionary capability allows enhancing the performance and reliability of several imaging sequences that are essential for advanced clinical applications. These enhancements are particularly significant at 3T, where B_1 field inhomogeneity can be problematic over large fields-of-view (FOV). We present several examples where the role of this technology demonstrates clinical benefits by enabling previously impractical imaging paradigms and/or improving the performance of existing ones.

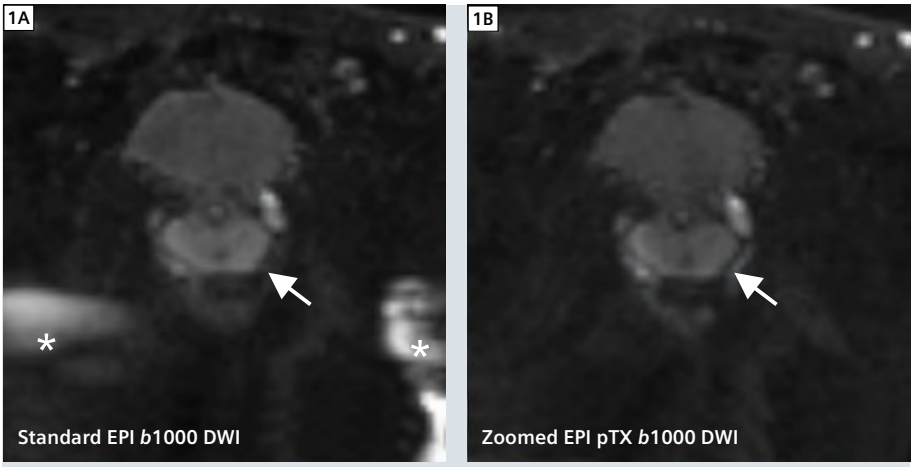

1 Standard *b*1000 image **(1A)** shows wrap artifact (*) not present on zoomed EPI image **(1B)**. There is greater clarity of prostate capsule on zoomed EPI (arrow, 1A and 1B).

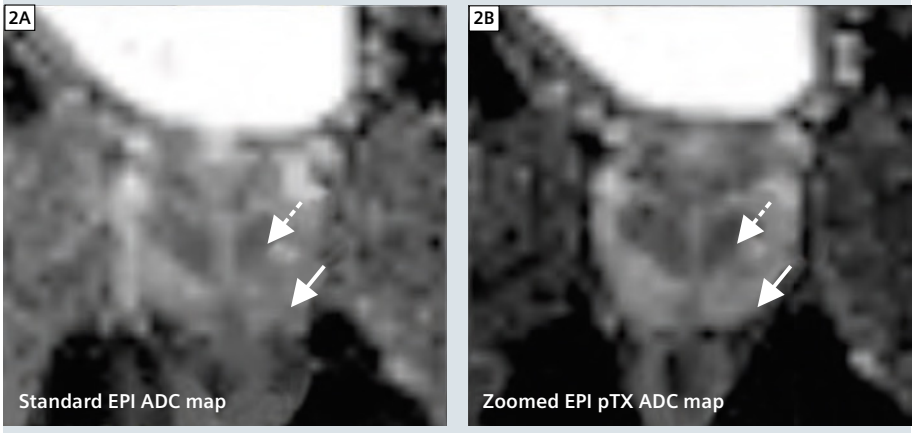

2 There is greater clarity of prostate capsule (solid arrow) and of transition zone boundary (dotted arrow) on zoomed EPI image **(2B)** than on standard EPI **(2A)**.

Table 1: Comparison of standard and zoomed DWI.

Feature	Standard EPI	Zoomed EPI
b1000 s/mm² images		
Absence of ghosting artifact	3.8 ± 0.4	4.3 ± 0.5
Absence of wrap artifact	3.7 ± 0.8	4.7 ± 0.5
Clarity of prostate capsule	4.0 ± 0.0	4.8 ± 0.4
Clarity of peri-urethral region	3.5 ± 0.5	4.2 ± 1.0
Overall image quality	3.7 ± 0.5	4.0 ± 0.6
ADC maps		
Reduced distortion of prostate	3.5 ± 0.5	3.8 ± 0.4
Clarity of transition zone boundary	3.2 ± 0.8	3.5 ± 0.4
Clarity of prostate capsule	3.2 ± 9.4	3.8 ± 0.4
Overall image quality	3.2 ± 0.4	3.7 ± 0.5
ADC (x 10^{-3} mm^2/s)	1.34 ± 0.3	1.41 ± 0.8

Skyra pTX architecture

The Skyra pTX system builds upon the existing clinical MAGNETOM Skyra platform, namely, a 3T magnet with a 70 cm patient bore diameter and parallel RF excitation via two fully independent, phase-coherent RF channels (TimTX TrueShape). The two pTX RF channels allow extended dynamic RF excitation schemes using a two-channel RF body coil. State-of-the-art imaging gradients (45 mT/m peak amplitude, 200 mT/m/s slew rate) and a full complement of Tim 4G multi-channel receive coils round out the hardware configuration of the system. The scanner operates under software version *syngo* MR D13C providing full access to further new technologies such as Dot, *syngo* REVEAL etc. While there are pTX features that can be applied during the adjustments (patient-specific B_1-shimming, volume-selective B_1-shimming), we have focused on the improved sequences and applications which provide new features with pTX. This includes 2D-selective RF pulses with an echo-planar TX trajectory that excite a selective volume (so-called 'inner-volume') and allows to reduce the FOV in the phase direction [1, 2] for zoomed echo planar imaging (EPI) (*syngo* ZOOMit).

[§] Firevoxel and Igor Pro are not Siemens Healthcare products. Siemens bears no responsibility for these products including, but not limited to, their regulatory status.

Prostate imaging

Diffusion-weighted imaging (DWI) is a critical sequence for prostate cancer detection and localization, but often suffers from spatial-distortion EPI artifacts related to the field inhomogeneity induced by the neighboring air spaces; these challenges can be more problematic at 3T. In this challenging imaging scenario, 2D-selective zoomed EPI in conjunction with a more homogeneous localized (B_1-shimmed) RF excitation can be particularly helpful. The impact of zoomed EPI on image quality of prostate DWI at 3T was assessed in six volunteers who underwent prostate MRI using an 18-channel body matrix receive coil. Scans included a single-shot EPI DWI sequence (*b*-values 50, 500, and 1000 s/mm²) performed with a regular sinc pulse ('Standard') and with the advanced 2D spatially selective RF pulse ('ZOOMit') combined with a reduced FOV approach (zoomed EPI). The *b*1000 images and ADC maps were assessed for various image quality measures on a scale from 1 to 5 (5 = highest image quality). Also, peripheral zone (PZ) ADC and estimated signal-to-noise (eSNR: determined as mean/SD of PZ) on *b*1000 images were measured. These measures were compared between standard and zoomed EPI.

Compared with standard EPI, zoomed EPI *b*1000 images showed improvements in ghosting, wraparound artifacts, clarity of prostate capsule, and clarity of peri-urethral region (Fig. 1, Table 1). By contrast, zoomed EPI ADC maps showed improvements in clarity of prostate capsule and overall image quality (Fig. 2). eSNR was nearly identical between standard and zoomed EPI *b*1000 images. The prostate showed a small increase in mean ADC on zoomed EPI images (mean increase 0.07 x 10^{-3} mm^2/s). However, ADC reproducibility between standard and zoomed EPI DWI remained high (mean coefficient of variability of ADC (4.4 ± 4.0)%, range 0.3 to 11.0%).

This preliminary assessment showed improvements in numerous measures relating to artifacts and anatomic clarity

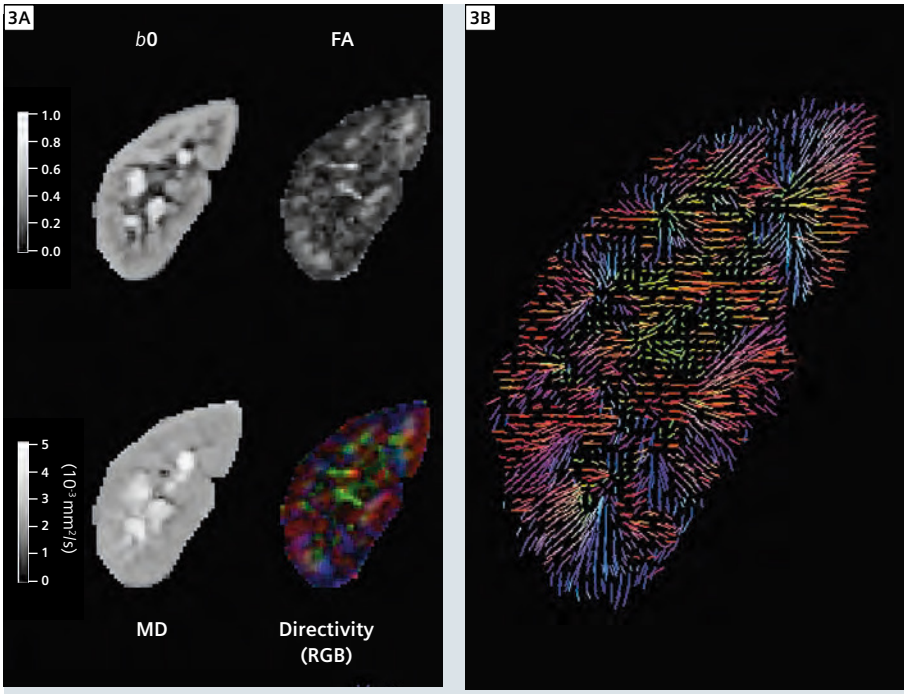

3 Kidney Zoomed-EPI DTI images.
(3A) Images obtained with *b*0 sec/mm², fractional anisotropy (FA) map, mean diffusivity (MD) map, and direction-encoded color map. Medullary anisotropy is evident in the FA map.
(3B) Color-coded primary diffusion eigenvectors display radial pattern of medullary tubules.

when applying 2D-selective zoomed EPI with for prostate DWI at 3T. While the FOV was held fixed to ensure comparability between the sequences, the use of a smaller FOV is easily achieved with zoomed EPI and currently under investigation. Nonetheless, even without this adjustment, zoomed DW-EPI using 2-channel pTX has potential to improve image quality for DWI of the prostate at 3T.

Renal imaging

Diffusion-tensor imaging (DTI) uses multiple diffusion sensitizing directions to evaluate anisotropic microstructure and is a promising imaging technique for the functional assessment of kidneys. Microstructure is a key factor in renal physiology, where cortex contains randomly oriented structures, while medulla holds more aligned vessel and tubular networks. Kidney DTI has shown that renal medulla has inherently higher fractional anisotropy (FA) in comparison with the isotropic cortex [2-4]. However, kidney DTI using single-shot spin-echo EPI typically suffers from imaging artifacts such as field-inhomogeneity-related distortions, and low spatial resolution due to the matrix size and long echo trains required for abdominal imaging. In this context, shortening the echo train length could reduce the aforementioned distortions. To achieve the same level of spatial resolution, while keeping a shorter echo train length, the imaging FOV must be reduced along the phase direction by the same factor used to shorten the echo train length. Zoomed EPI achieves such a goal through the use of 2D-selective RF excitation.
Four consecutive healthy volunteers without any history of renal disease (three males, one female; mean age 28 (24-30 years); non-fasting conditions) were imaged on the Skyra pTX system. Free-breathing single-shot 2D-selective zoomed EPI DW images were acquired with reduced FOV in the left-right direction with the following parameters: 10-14 coronal slices, slice thickness 4 mm, no gap; FOV of 83 x 400 mm; 64 x 308 acquisition matrix, 1.3 mm resolution, TR 4000 ms; TE 65 ms; six diffusion directions; monopolar diffusion gradients; two *b*-values (*b*0 and *b*500 s/mm²); parallel imaging (GRAPPA) factor of two and scan time 5:28 min. An additional saturation band was applied to suppress signal from the left side of the body extending slightly beyond the stop-band. Right kidney images were co-registered by using a two-dimensional rigid body transform algorithm, and MR images at the same *b*-value and direction were then averaged by using locally developed software (Firevoxel[§]). DT processing was performed with custom software written in Igor Pro[§] (Wavemetrics, Portland, OR, USA). Parametric maps were generated of DTI eigenvalues λ_i and eigenvectors, mean diffusivity (MD) and fractional anisotropy (FA). The ZOOMit DTI technique allowed for high quality diffusion images of the kidney with reduced blurring and distortion (Fig. 3) compared to full FOV EPI DTI. Medullary anisotropy and radial orientation pattern was evident in all volunteers (e.g. Fig. 3). The medullary / cortical MD and FA values were 2.04 ± 0.14 / 2.21 ± 0.12 μm²/ms, and 0.34 ± 0.08 / 0.13 ± 0.04, respectively, consistent with literature [3-5]. MD showed significantly higher, and FA significantly lower, cortical than medullary values. ZOOMit DTI may be valuable for clinical assessment of kidney pathology, particularly for applications closely scrutinizing corticomedullary differentiation.

Breast imaging

Diffusion-weighted imaging (DWI) of the breast is increasingly used for the differential diagnosis and treatment response monitoring of breast cancer. Conventional EPI techniques are prone to characteristic artifacts, such as susceptibility artifacts, image blurring and spatial distortion resulting from gradient nonlinearity and eddy currents. Thus, there can be a significant mismatch in lesion appearance and position between morphologic sequences and EPI which can potentially affect the diagnostic accuracy. In addition, the strong demand

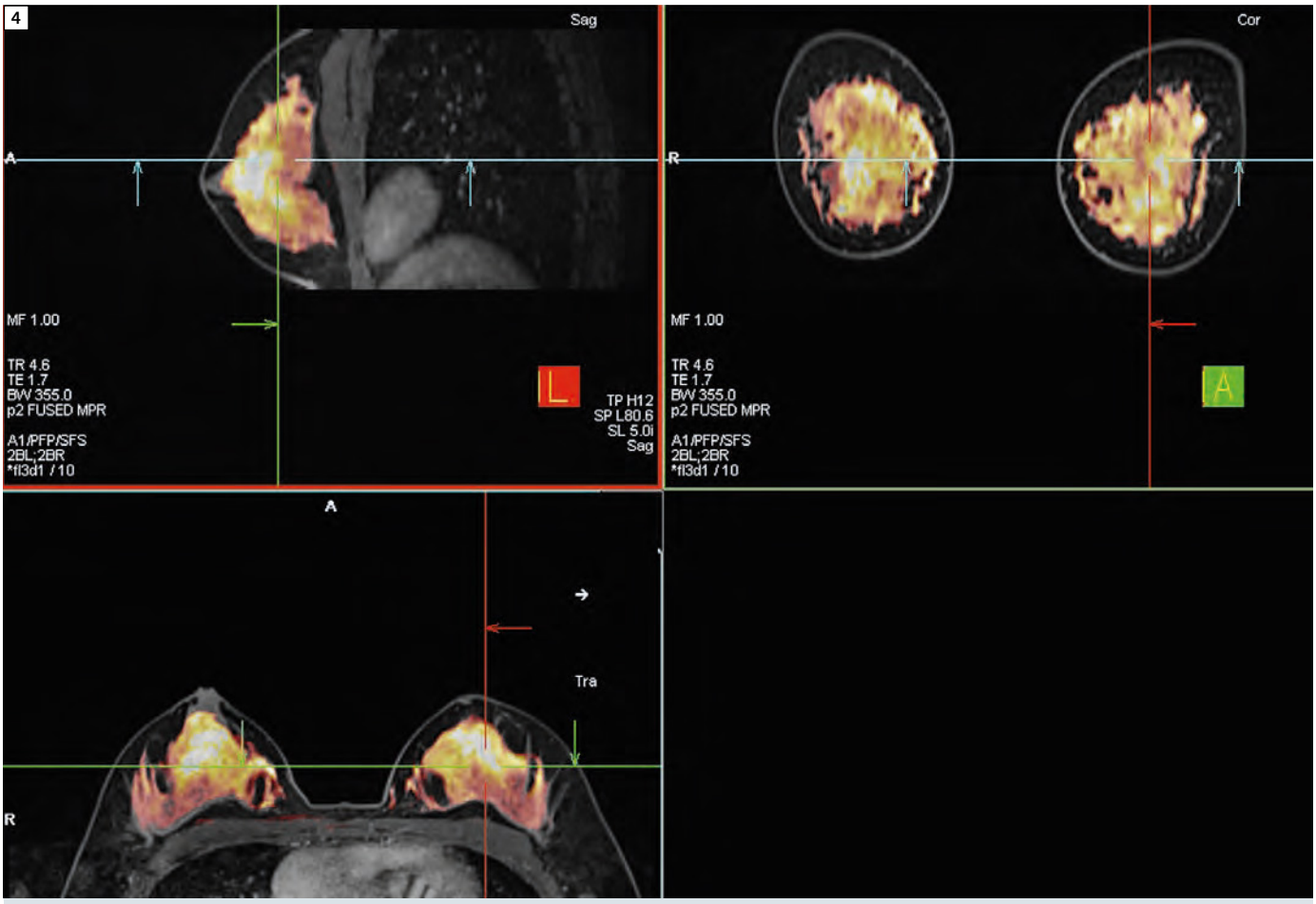

4 T1-weighted VIBE fused with a diffusion-weighted (*b*400) dataset.

on the gradient system limits the spatial resolution to only moderate in-plane resolution around 1.8 x 1.8 mm² or even coarser. Thus spatially-selective excitation with EPI ZOOMit was applied to a) mitigate the spatial distortion by shortening the phase encode burden and the echo train length and b) to allow the user to restrict the acquisition volume to the breast alone resulting in a higher spatial resolution.

3 healthy subjects were scanned using a 4-channel combined (biopsy and diagnostic) breast coil. For comparison, in both protocols 24 axial slices were acquired with three b-values in 3-scan trace mode with GRAPPA factor of 2. The nominal in-plane resolution was 1.8 x 1.8 mm² vs 1.3 x 1.3 mm² for zoomed EPI where the FOV could be reduced from 332 to 260 mm as well as the

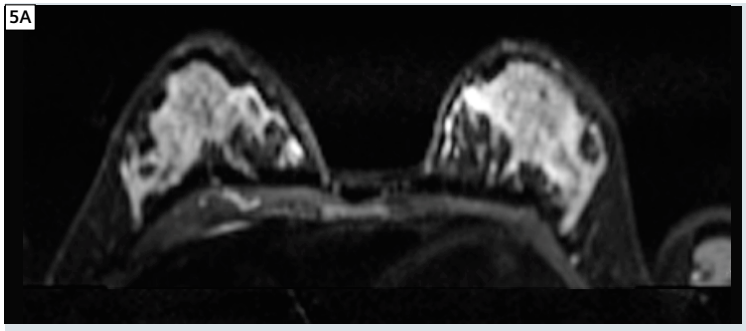

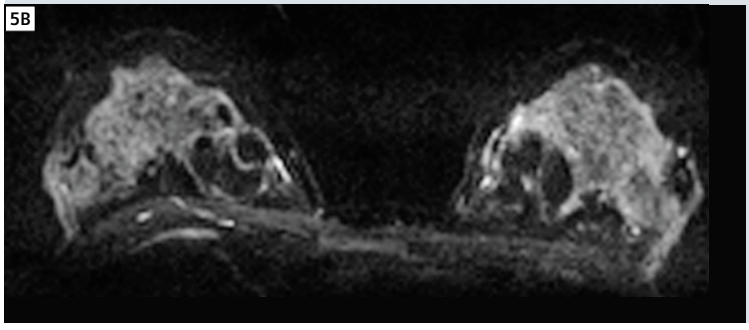

5 Standard DW-EPI **(5A)** and zoomed EPI **(5B)**.

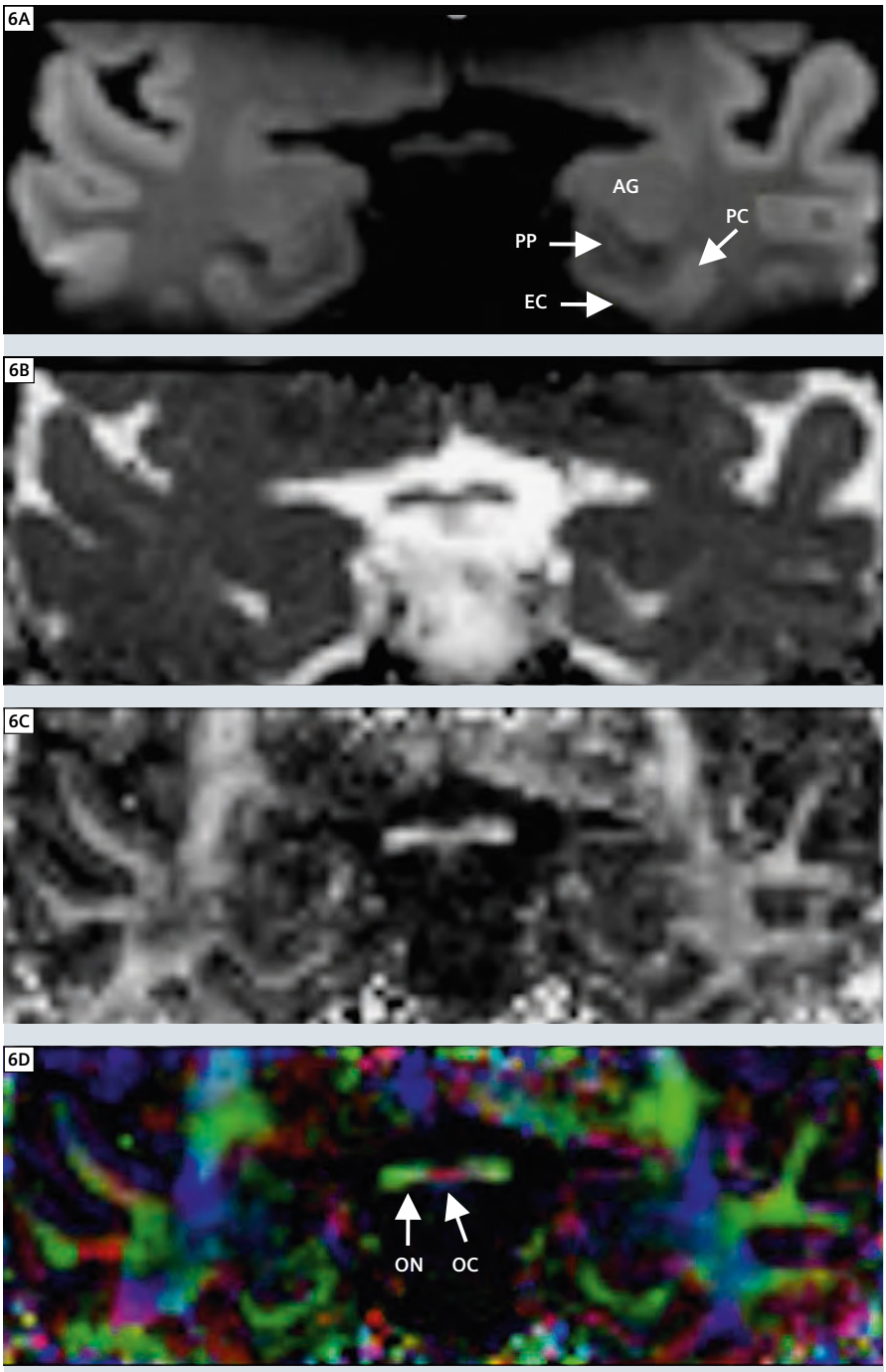

6 1.2 mm in-plane resolution reduced FOV diffusion tensor images of the medial temporal lobes using the *syngo* ZOOMit application with single-shot EPI (top to bottom: diffusion trace, ADC, FA and color orientation map). This particular coronal slice at the level of the uncus and amygdala (AG) demonstrates distortion-free quantitative diffusion in several regions affected by early Alzheimer's disease including the perirhinal cortex (PC), entorhinal cortex (EC) and perforate pathway (PP) in the subjacent white matter. Without the reduced number of phase encoding steps enabled by ZOOMit, these structures are often severely distorted by susceptibility generated from air spaces in the subjacent temporal bone.

matrix slightly increased (192 x 78 to 200 x 78). Both protocols were set up for comparable acquisition times, 3:53 min ('standard') and 3:39 min (ZOOMit). Figure 4 shows an overlay of a T1-weighted VIBE with a diffusion-weighted (*b*400) dataset in multi-planar reconstruction to illustrate the excellent co-registration and resolution. In Figure 5 the comparison between standard DW-EPI (top) with the described ZOOMit DWI protocol (bottom) is shown. There is a clear improvement regarding resolution and distortion, in this example the reduced SNR however is obvious as well. This is due to two reasons, first due to increased echo time with a longer RF pulse; but secondly also a *higher resolution* protocol was acquired. In signal-starved situations, such as fatty breasts higher averaging might still be advised. Clinically, the higher spatial resolution allows the more accurate DWI evaluation of enhancing foci and small non-mass enhancement on MRI. ZOOMit DWI shows potential to mitigate spatial distortions commonly observed in standard EPI. Further developments and investigations are anticipated to balance SNR and spatial resolution, as well as a quantitative comparison including measured ADC and reduction of artifacts. The preliminary data suggest that using ZOOMit DWI can enable higher spatial resolution in breast applications at reduced distortions when supported by sufficient SNR.

Medial Temporal lobe imaging

The hippocampus and entorhinal cortex form a critical neuronal circuit for declarative memory formation that is often altered by different pathologies, including Alzheimer's disease. Unfortunately, standard single-shot EPI DTI fails to properly characterize the medial temporal lobe structures and their functional connectivity due to geometric distortions from subjacent temporal bone airspaces. In this setting, the 2D-selective RF excitation approach using a Skyra pTX system can be used to overcome these distortions at 3T and, therefore, quantify

diffusion tensor properties for specific medial temporal lobe structures.
To evaluate the role of ZOOMit EPI in this setting, five healthy human volunteers were imaged using the 20-channel head/neck receive coil. Single-shot EPI diffusion-weighted images with fat saturation were obtained (TR 2200 ms, TE 83 ms, NEX 15, acquisition time 8 min, 10 gradient directions, *b*800 s/mm^2) using ZOOMit EPI. The protocol used a 13.3 x 4.4 cm FOV (read x-phase axes) with 1.5 mm in-plane resolution (90 x 30 image matrix). 18 contiguous 3 mm thick oblique coronal slices were obtained orthogonal to the long axis of the temporal lobe with the most posterior slice prescribed tangential to the vertical portion of the hippocampal tail. ZOOMit DW images had acceptable signal-to-noise (6.6 ± 1.1 @ *b*800 s/mm^2) and significantly reduced geometric distortions from subjacent temporal bone airspaces compared to full FOV acquisitions. Diffusion-weighted images resolved specific components of the medial temporal lobes such as the entorhinal cortex (EC), perforant pathway white matter (PP), hippocampal head, subiculum, dentate gyrus (DG), molecular and neuronal layers of the hippocampus (CA1). Quantitative data (Table 2) was consistent with prior DTI parameter values from human hippocampus autopsy samples [5]. Color fiber orientation maps demonstrated coherence from CA1 neuron apical dendrites as previously shown [5] and data may allow tractography of the perforant pathway between the entorhinal cortex and hippocampus. The central portion of the color fiber orientation map (Fig. 6) also demonstrates the midline optic chiasm (OC, red) and paired, anterior coursing optic nerves (ON, green, 4.5 mm diameter). This is a nice illustration of the capability for ZOOMit diffusion to also achieve sufficient resolution to accurately measure diffusion parameters in cranial nerves. Similar results have been observed for the trigeminal nerves and may provide improved diagnosis/monitoring for trigeminal neuralgia.

Table 2: Quantitative diffusion values using zoomed diffusion.

Region	Mean diffusivity (x 10-3 mm^2/s)	Fractional Anisotropy
CA1	0.82 ± 0.04	0.25 ± 0.06
DG	0.86 ± 0.06	0.27 ± 0.06
ERC	0.77 ± 0.08	0.32 ± 0.07
PP	0.81 ± 0.07	0.40 ± 0.08

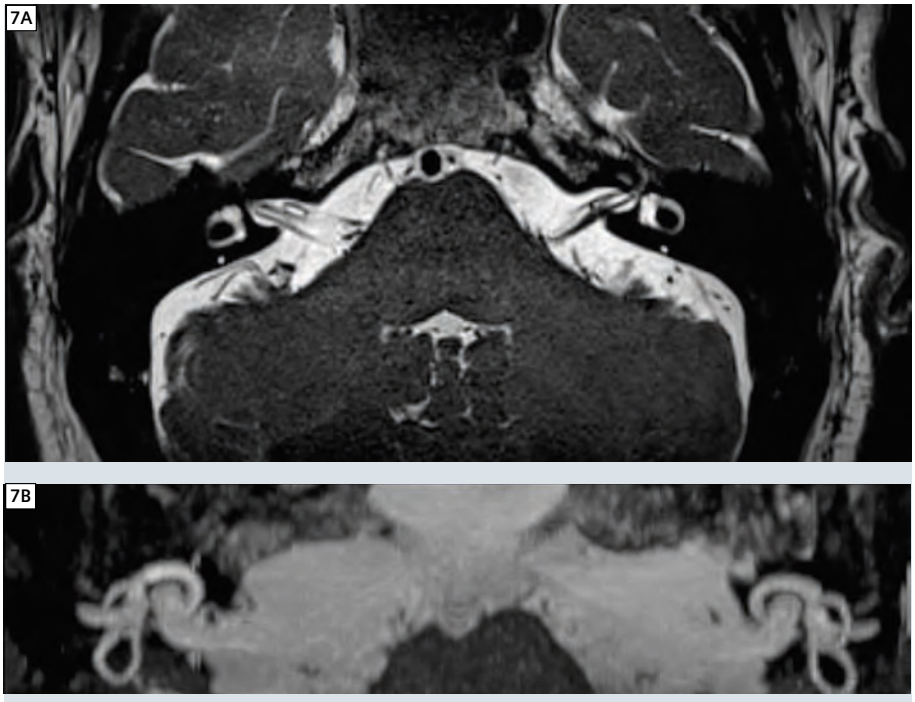

7 Zoomed T2-weighted SPACE of the IAC **(7A)** and thin maximum intensity projection **(7B)**.

ZOOMit SPACE

Similarly to ZOOMit EPI, SPACE with reduced FOV using ZOOMit can increase acquisition efficiency enabling improved spatial resolution or T2-weighting for a given scan duration. For example, ZOOMit SPACE was acquired using the 20-channel head/neck receive coil to visualize the internal auditory canal (IAC) in a patient with Meniere's disease (axial orientation, TR 1000 ms, TE 125 ms, 2 averages, echo train length of 54, 160 x 80mm FOV, 2 x 2 x 0.5 mm resolution, flip angle 100 degrees, BW: 255 Hz/Px, acquisition time 2:31 min). The acquisition time in this case was approx. 50% shorter then with the non-zoomed reference protocol. As shown in Figure 7, this case shows clear anatomical features including cochlear and vestibular nerves, as well as posterior and lateral semi-circu-

lar canals in an axial slice (top) and thin maximum intensity projection (bottom). Another application is depicted in Figure 8 using ZOOMit SPACE in the prostate. This example was acquired using a combination of the body-18 and spine coil elements. TR 2000 ms, TE 99 ms, echo train length of 57 and 600 Hz/pixel at 320 x 160 matrix and 72 slices; using a 230 x 115 FOV this resulted in a voxel size of 0.7 x 0.8 x 1 mm at a total acquisition time of 7:15 min providing the capabilities of reformatting the data in any orientation.

Conclusions

The results shown clearly demonstrate that 2D-selective RF excitation on a 2-channel pTX system enables zoomed EPI acquisitions on 3T scanners that can significantly reduce the limitations imposed by spatial distortions due to field inhomogeneity. Together with the inherent ability to simultaneously improve excitation inhomogeneity while providing effective reduced FOV implementations, the TimTX TrueShape clinical platform is ideally suited to fully capitalize on a wide range of improved imaging approaches that require a practical and fully integrated multi-channel transmission platform. These approaches have been previously demonstrated to be of significant value in similarly challenging imaging settings, albeit at the expense of requiring a complex hardware set up due to the lack of commercially available, fully-integrated, multi-channel transmission platforms. The introduction of the clinical Skyra TimTX TrueShape platform is poised to have a significant impact on the clinical implementation of such powerful imaging tools.

For further scientific details of the above shown studies, please refer to Proc ISMRM 2013 abstract numbers (#): #3390 (prostate), #1554 (kidney), #1739 (breast), #3021 (neuro).

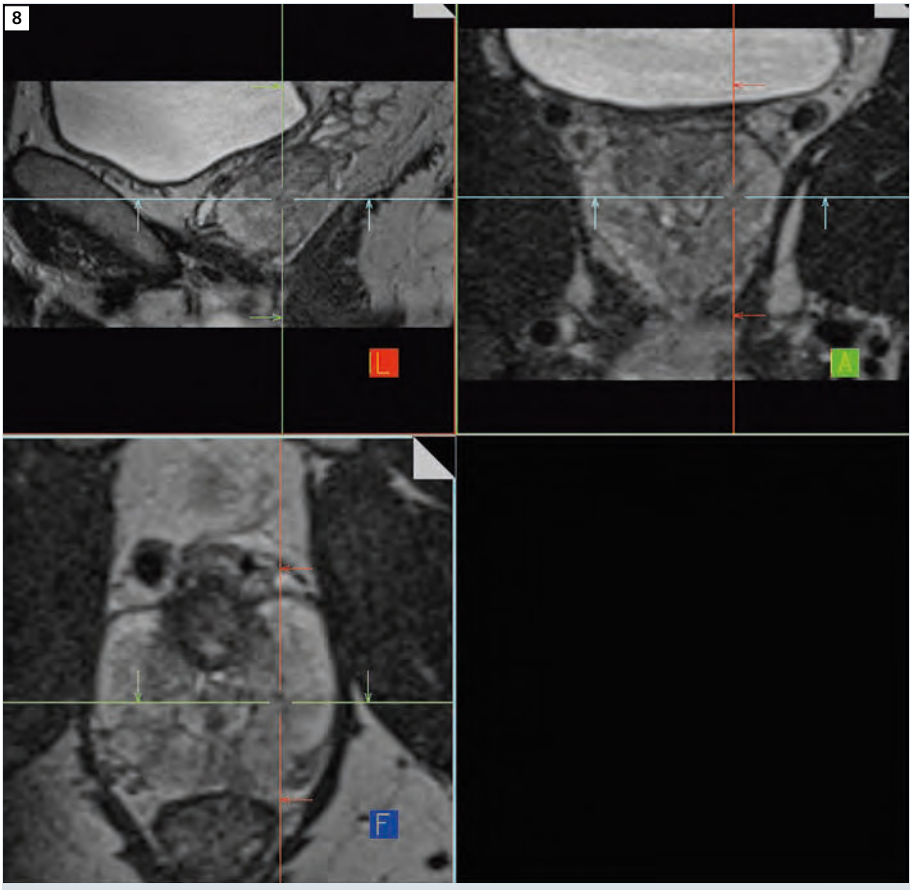

8 Zoomed T2-weighted SPACE of the prostate (MPR).

References

1 Rieseberg S, Frahm J, Finsterbusch J. Two-dimensional spatially-selective RF excitation pulses in echo-planar imaging. Magn Reson Med. 2002 Jun;47(6):1186-93.
2 Schneider R et al. Evaluation of 2D RF echo planar pulse designs for parallel transmission. Proc ISMRM 2012 #3459.
3 Ries M, et al. Diffusion tensor MRI of the human kidney. JMRI 2001;14(1):42-49.
4 Notohamiprodjo M et al. Diffusion tensor imaging of the kidney with parallel imaging: Initial clinical experience. Invest Radiol 2008;43(10):677-685.
5 Sigmund EE et al. Intravoxel incoherent motion and diffusion-tensor imaging in renal tissue under hydration and furosemide flow challenges. Radiology 2012;263(3):758-769.
6 Shepherd TM et al. diffusion tensor microscopy indicates the cytoarchitectural basis for diffusion Anisotropy in the human hippocampus. AJNR 2007;28:958-964.

Contact
Fernando Boada
Department of Radiology
NYU Langone Medical Center
660 1st Avenue
New York, NY 10016
USA
fernando.boada@nyumc.org

Bandwidth in MRI?

Joachim Graessner, Dipl.-Ing.

Siemens Healthcare, Hamburg, Germany

Questions about the term 'bandwidth' are most frequently asked during MR trainings and discussions regarding MR parameters and image quality.
This article is intended to clarify the meaning of bandwidth in MRI, to show dependencies with other MR parameters, and to give hints for daily routine work and protocol optimization.
The bandwidth occurs twice in the course of an MR sequence (Fig.1): during transmission describing properties of the radiofrequency (RF) pulses and during reception of the MR signal.

Transmission phase

During transmission you have to apply RF pulses which contain a certain range of frequencies, i.e., bandwidth, to excite a discrete slice thickness or volume while a local gradient is on as well. The bandwidth typically lies in the range of a

1

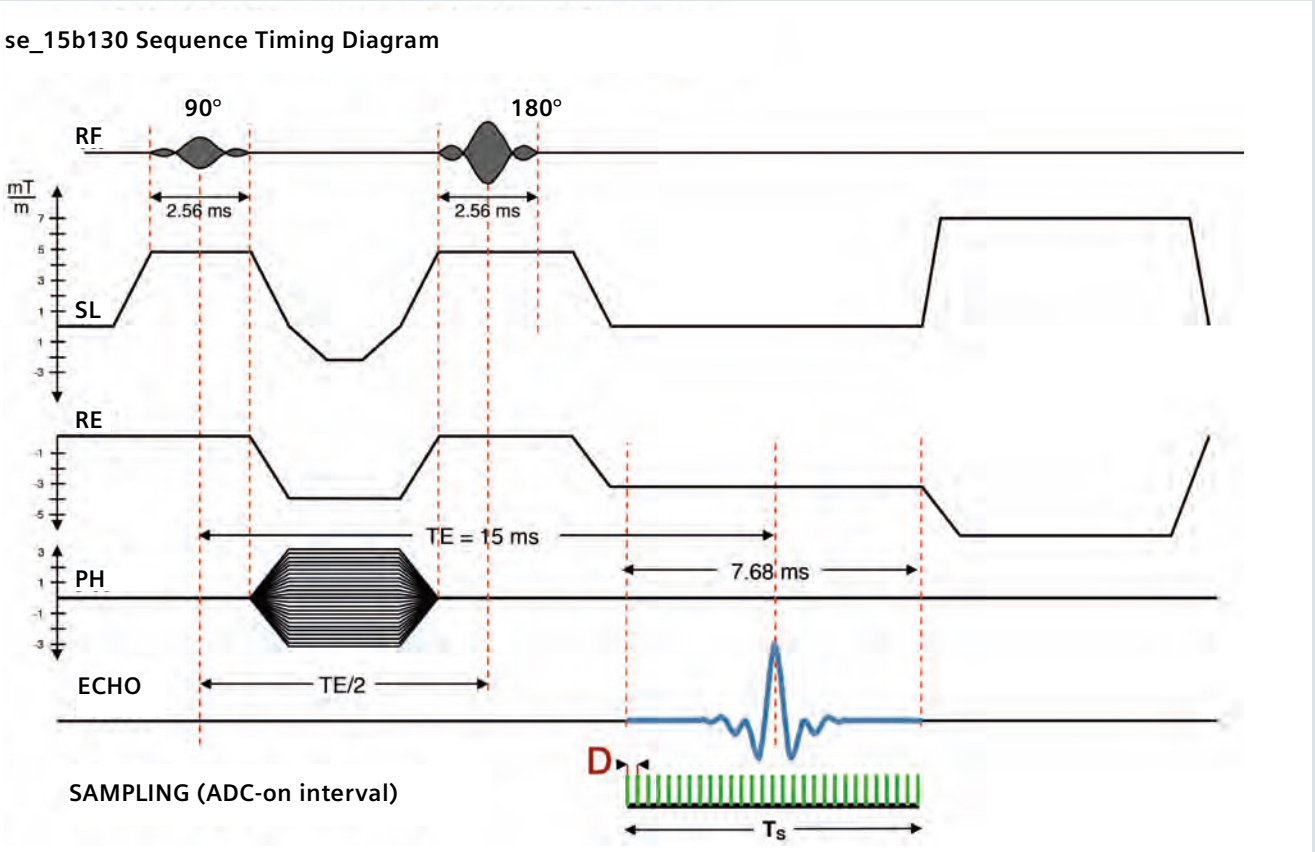

1 Sequence timing for se15_b130.

few kilohertz (kHz). The *syngo* user interface offers three types of pulses for most sequences in the Sequence parameter card, part 2: Low SAR, Normal, and Fast (Fig.2).
Pros and Cons for RF pulse types with timing examples:

Low SAR (3.84 ms)
- Longer RF pulse with good slice profile
- Reduced SAR values (lower amplitude)
- Less crosstalk between slice; narrower gaps tolerated
- Longer minimum TEs and TRs

Normal (2.56 ms)
- Normal RF pulse with good slice profile
- Optimized SAR behavior

Fast (1.28 ms)
- Shorter RF pulse, with a compromised slice profile
- Higher SAR compared to the other modes (higher amplitude)
- Shorter echo spacing (ES)
- Opportunity for shorter TEs and TRs
- Fewer susceptibility artifacts

The 'Fast' mode is mainly applied in sequences where measurement speed and short echo spacing (ES) – the time from one echo to the next echo – is essential for good image quality: HASTE, EPI, TrueFISP, and TurboFlash. These modes can be combined with up to three gradient modes: Whisper, Normal and Fast. The gradient modes influence the slew rate of the gradient pulses, or the steepness of the ramps from zero to full gradient strength and back. The trade-off for faster sequence timing with shorter TEs and TRs usually results in more noise and a higher potential for peripheral stimulation.

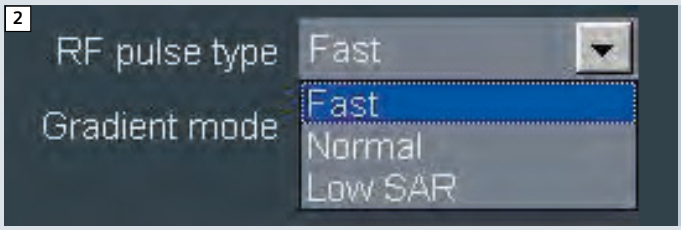

2 RF pulse types.

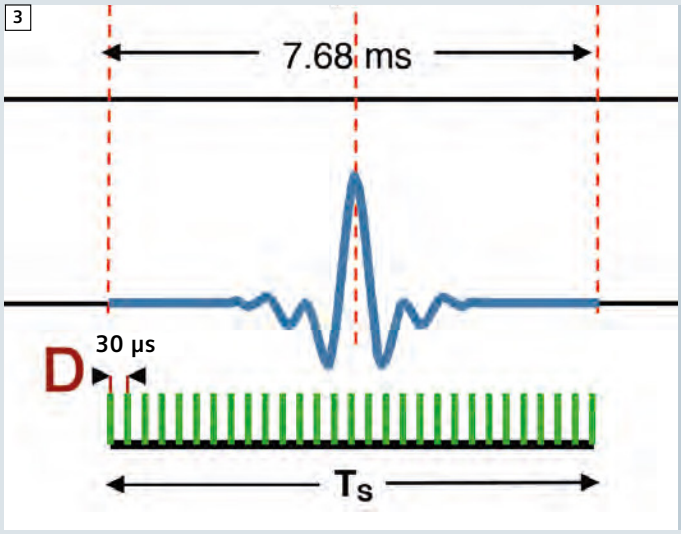

3 Sampling time T_s and dwell time D.



4 Bandwidth in the *syngo* user interface.

Reception phase

When the echo signal appears, a read-out gradient is switched on and the analog-digital-converter (ADC) samples this signal. The gradient encodes different rows of frequencies into signal; the time-amplitude integral defines the measured field-of-view (FOV). The ADC is virtually asking the echo-signal (e.g., every 30 microsecond (µs)) how high its amplitude is and writes these values in a digital fashion into the memory of the image computer. This time is called the dwell time D. For a 256 base matrix this process has to be repeated 256 times. The whole sample period T_s will be in this example (Fig. 3):
T_s = 256 x 30 µs = 7.680 ms

T_s = N x D with N = matrix in read

The frequency content of this sampled signal is the reciprocal of the dwell time:

f = 1/D.

In the above example it is roughly 33 kHz.
The magic term bandwidth (BW) is the reciprocal of the total sampling time T_s and has the unit of Hz/pixel:

Bandwidth: BW = 1/ T_s [Hz/pixel]

The parameter 'Bandwidth' is found on the Sequence parameter card, part 1 (Fig. 4).
The bandwidth describes in a simplified manner which frequency range from our analyzed echo signal is transferred into one pixel:
1. lower left pixel: 0-130 Hz
2. lower left pixel 130-260 Hz
and so forth. If you continue this fill-up task to the last pixel of a 256 matrix you end up with 33 kHz in the lower right pixel.

5

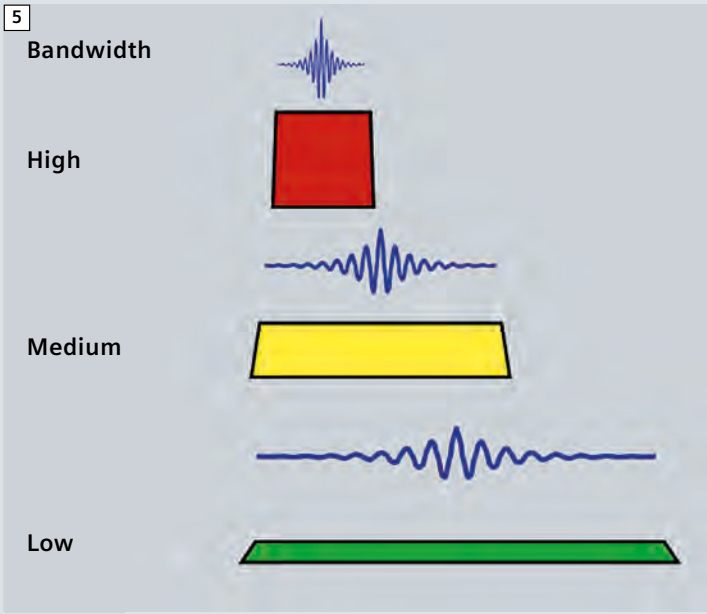

5 Influence of receive bandwidth on readout time and gradient amplitude.

6

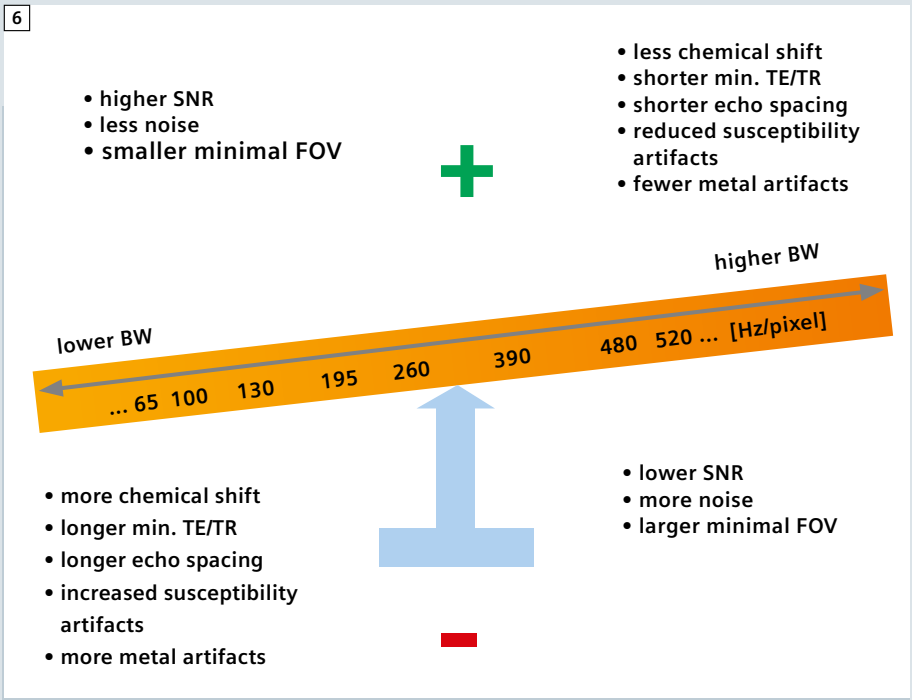

6 Influence of bandwidth on other parameters.

Increasing the bandwidth reduces the sampling time T_s and shortens the sequence timing, allowing shorter TE and TR values and vice versa (Fig. 5). The disadvantage of a higher bandwidth is the larger amount of noise which is sampled due to larger frequency range. This translates into a lower signal-to-noise-ratio (SNR). A slightly bumpy analogy is a motorway, where you have a speed limit and the number of cars per hour is limited. If you increase the speed limit, more cars will pass per hour and the noise for the neighbors rises as well.

On the positive side we have the shorter echo spacing (ES) which delivers less blurring in the images. The lipid signal in turbo spin echo protocols is also influenced by the echo spacing and the turbo factor (TF) [1]; the shorter the ES and the higher the TF, the brighter the fat in TSE protocols. The larger readout (RE) gradient amplitude needed for a high BW protocol increases the minimally adjustable FOV (Fig. 6). Furthermore, high bandwidth protocols play an important role in metal artifact reduced scanning. Shorter optimized excitation pulses combined with short readout intervals and short ES enables fewer distortions due to conditional implants. This feature is enhanced with optimized protocols which use WARP and VAT (view angle tilting) [2–4].

Last but not least, the chemical shift between water and fat gets smaller with high BW and larger with lower BW. This feature is of less importance for fatsat protocols. Fat resonates at an approximately 3.3 ppm lower frequency than water. Although commonly excited in the first part of a sequence, fat and water from the same physical place answer with different frequencies. In the above mentioned sorting process of frequency ranges into pixels we have to face a missorting. Fat will always appear shifted to lower frequencies by a certain amount of pixel in the readout direction. The only exception is the EPI sequence where we have a very strong chemical shift artifact in the phase encoding direction (PH) due to the long sampling period producing echoes. This very long sampling period in the order of >40 ms or more translates into a quite low bandwidth (<25 Hz/pixel). Fatsat is therefore mandatory for EPI measurements.

The chemical shift in readout direction is indicated as a mouse-over tooltip on the bandwidth field in the Sequence parameter card, part 1 (Fig. 7).

As one can see, chemical shift is not a big issue at low field strengths (Table 1). It is getting important at 1.5T and above for the range of practical bandwidth of a few hundreds Hz/pixel. But with the rise of the magnetic field the resolution typically goes up as well, keeping the abso-

lute chemical shift in millimeters reasonably low. A protocol at 3T with a bandwidth of 195 Hz/pixel and an inplane resolution of 0.3 mm creates an absolute chemical shift of less than 0.7 mm. Figure 8 demonstrates in an exaggerated way the artificial movement of the intervertebral discs (orange) towards the upper vertebrae or the spinal cord depending on the chosen readout direction and bandwidth option. The low bandwidth examples should be avoided in daily routine, although one may gain SNR and shorter scan time with lower bandwidth protocols.

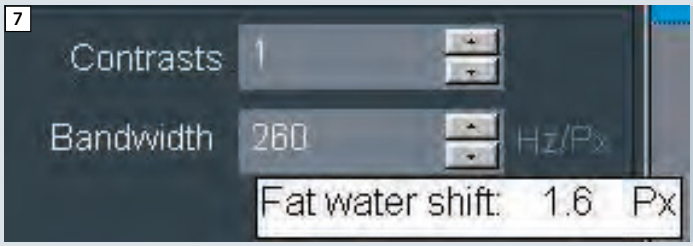

7 Tooltip shows absolute chemical shift in number of pixels (Px) at 3T.

Table 2 shows the effects of optimizing a TSE protocol with respect to change of bandwidth and resolution for a 1.5T scanner. Identical SNR is the border condition for these four examples. TE was kept in the mid thirty ms range. The penalty for better resolution is usually longer measurement time. Personal taste and application dictates the parameters chosen.

Starting with protocol B, one can speed up the scan by halving the bandwidth to

Table 1: Absolute pixel shift for different field strengths.

Bandwidth*	Readout time	Chemical Shift* 0.35T	Chemical Shift* 1T	Chemical Shift* 1.5T	Chemical Shift* 3T	Chemical Shift* 7T	Relative SNR change*
[Hz/pixel]	[ms]	[pixel]	[pixel]	[pixel]	[pixel]	[pixel]	[%]
3000	0.330	0.017	0.05	0.075	0.15	0.3	-79
2000	0.500	0.025	0. 07	0.1	0.2	0.5	-74
1000	1.000	0.05	0.1	0.2	0.4	1.0	-64
520	1.920	0.09	0.3	0.4	0.8	1.9	-50
480	2.080	0.1	0.3	0.4	0.9	2.1	-48
390	2.560	0.13	0.35	0.5	1.1	2.5	-42
260	3.840	0.2	0.5	0.8	1.6	3.8	-29
195	5.120	0.25	0.7	1.1	2.2	5.1	-18
130	**7.680**	**0.4**	**1.1**	**1.6**	**3.2**	**7.6**	**0**
100	1.000	0.5	1.4	2.1	4.2	9.9	14
78	12.280	0.6	1.8	2.7	5.4	12.7	29
65	15.380	0.8	2.1	3.2	6.4	15.2	41
50	20.000	1.0	2.8	4.2	8.4	19.8	61

*Rounded values for convenience.

8

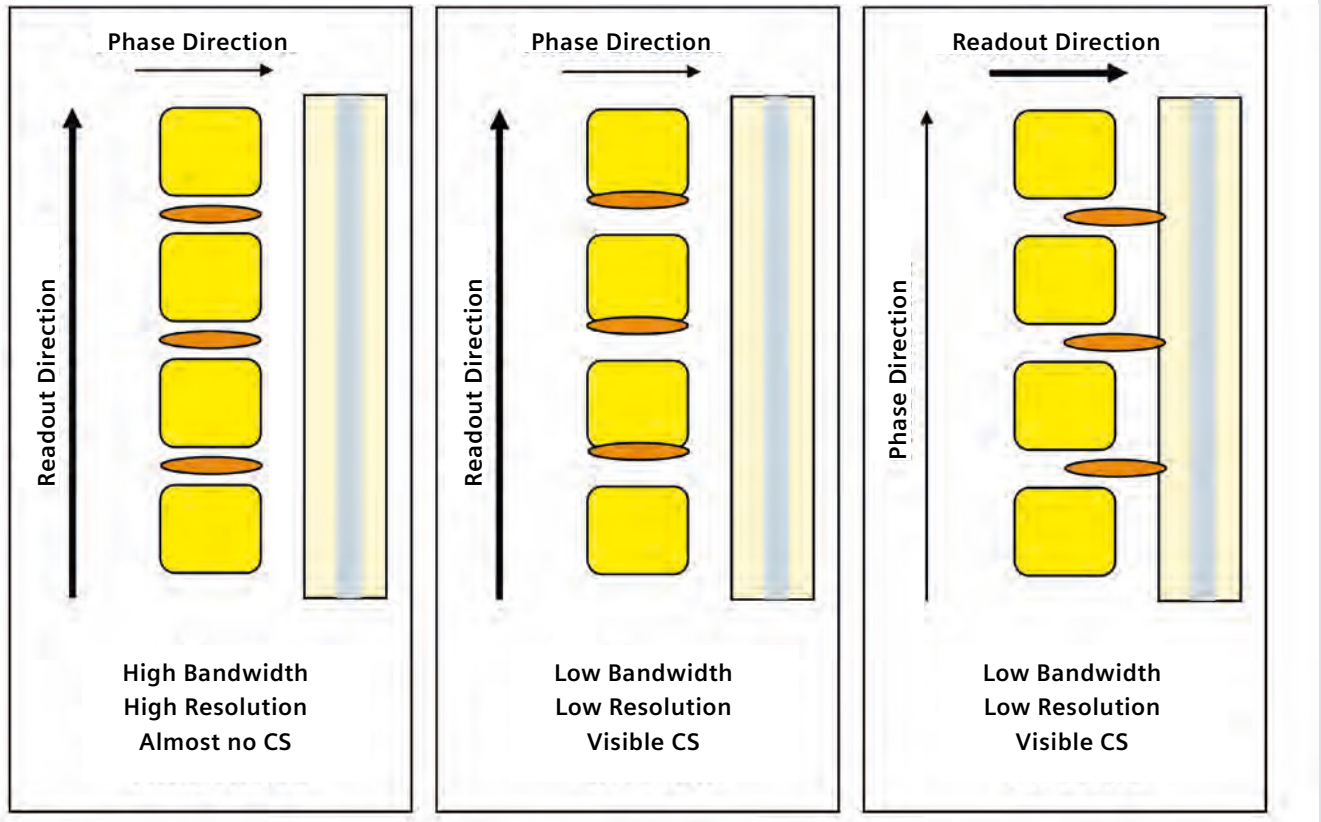

8 Chemical shift (CS) on an example sagittal spine.

compensate for the SNR loss coming from the reduction of acquisitions. An increase of the inplane resolution in protocol C and D results in an obvious prolongation of the scan time which could be kept tolerable when reducing the bandwidth. In example D partial Fourier, i.e., reducing the measured turbofactor, allows a TR minimization for an acceptable scan time. One could save further time in this example by a decrease of phase oversampling, which was chosen 100% for a phase encoding in head-feet direction to minimize flow artifacts from the arteries; a slight increase of the FOV, e.g., to 200 mm, could compensate for this SNR reducing step though sacrificing some hundreds of a mm inplane resolution.

On a 3T system one should at least increase the bandwidth by 50% and save time by adjusting the other parameters. The higher signal of 3T supports this measure.

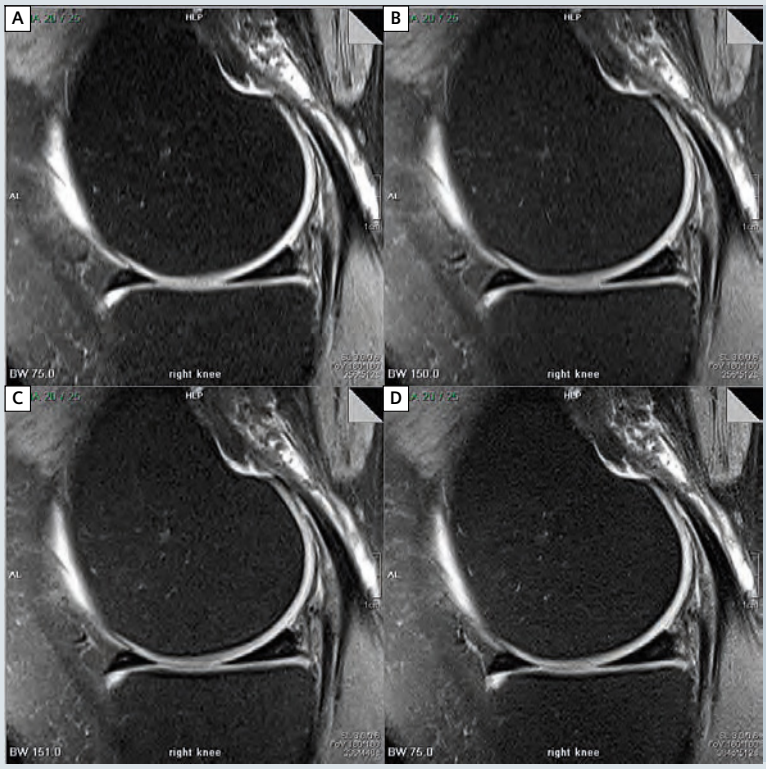

9 Image examples for table 2.

Table 2: Protocol optimization.

Knee sagittal, 25 slices, FOV 180 mm, 3 mm, matrix 512 x 256, TF 7, weak Fatsat, 100% Phase OS, iPAT 2, 15-channel coil, identical SNR.

#	Parameter	Bandwidth	Matrix	Resolution	Scantime	TR	TE	Echo-spacing	Ava-rages	partial Fourier	rel. SNR
	Unit	[Hz/pixel]	-	mm²	min:s	ms	ms	ms	-	-	-
A	low BW normal Resolu-tion*	75	256 x 512	0.7 x 0.35 = **0.245**	2:46	4020	36	17.8	1	off	1
B	high BW normal Resolu-tion*	150	256 x 512	0.7 x 0.35 = **0.245**	3:32	2770	34	11.2	2	off	1
C	high BW higher Resolution	150	336 x 448	0.54 x 0.4 = **0.216**	**4:43**	2870	34	11.7	2	off	1
D	low BW higher Resolu-tion*	75	384 x 512	0.47 x 0.35 = **0.165**	**6:04**	3240	37	18.7	2	on	1

* In Accordance to the German MR Guidelines (BÄ)

Further reading

1. Magnets, Spins and Resonances; Siemens 2003.
2. Magnets, Flow and Artifacts; Siemens 2004.
3. The Physics of Clinical MR Taught Through Images: Runge, Nitz, Schmeets; Thieme 2008.
4. MRI the Basics: Hashemi, Bradley, Lisanti; LWW 2010.
5. Handbook of MRI Sequences: Bernstein, King, Zhou; Elsevier 2004.
6. MRI from Picture to Proton: McRobbie, Moore, Graves, Prince; Cambridge 2007.

Especially recommended for the German speaking community:

7. Praxiskurs MRT: Nitz, Runge; Thieme 2011.
8. MRT-Guide für MTRA/RT: Nitz; Thieme 2012.

Helpful links

The Impact of Bandwidth on MR Image Quality: Chen Lin, 2012.
http://www.indiana.edu/~mri/seminars/slides/The%20Imapct%20of%20Bandwidth%20on%20MRI%20Image%20Quality%20CL20120324.pdf

Metal Artifact Reduction in MRI – High Bandwidth Techniques, SEMAC, and VAT: Val Runge, 2013.
http://www.clinicalmri.com/pdf/Garmisch/2_Garmisch_2013_Metal_artifact_reduction.pdf

References

1 Piraino D, Hardy PA, Schils JP, Richmond BJ, Tkach JA, Belhobek GH. (1993). Fast Spin-Echo Imaging of the Knee: Factors Influencing Contrast. JMRI 3:835-842.
2 Ulbrich EJ, Sutter R, Ranieri FA, Nittka M, Pfirrmann CW (2012). STIR Sequence With Increased Receiver Bandwidth of the Inversion Pulse for Reduction of Metallic Artifacts. AJR 199: 735-742.
3 Sutter R, Ulbrich EJ, Jellus V, Nittka M, Pfirrmann CWA (2012). Reduction of Metal Artifacts in Patients with Total Hip Arthroplasty with Slice-encoding Metal Artifact Correction and View-Angle Tilting MR Imaging. Radiology 265: 204-214.
4 Koch KM, Hargreaves BA, Butts Pauly K, Chen W, Gold GE, King KF (2010). Magnetic Resonance Imaging Near Metal Implants. JMRI 32: 773-787.

Contact
Joachim Graessner, Dipl.Ing.
Siemens AG Healthcare
GER H IM BM MR
Lindenplatz 2
20099 Hamburg
Germany
joachim.graessner@siemens.com

The New, High-Performance MR Gradient System XR 80/200. Design, Benefits and Safe Operation

Daniel Fischer; Eva Eberlein

Siemens Healthcare, Erlangen, Germany

Introduction

At the RSNA 2012, Siemens introduced MAGNETOM Prisma*, a new 3 Tesla MR imaging (MRI) scanner. This system is designed to fit the needs of those involved primarily in research activities. The foundation of the system is a new 3T magnet, based on the proven MAGNETOM Trio. It provides the same robust base as Trio did – with high homogeneity, only now with zero helium boil-off. MAGNETOM Prisma combines Siemens' latest technological advancements in MR signal transmit and receive technologies – TimTX TrueShape and Tim 4G technology, with the latter forming the backbone of other Siemens MR scanners 1.5T MAGNETOM Aera and 3T MAGNETOM Skyra. Both technologies have shown an increase in image quality and imaging speed, proving their value in a number of clinical MRI applications [1]. On top of these components, MAGNETOM Prisma includes XR 80/200, a new, high-end gradient system that delivers high gradient amplitudes and fast switching capabilities in a combination that is currently unmatched in the market.

This article is to provide insight into the evolution of the new gradient engine: a brief history of gradients in MR, the technical aspects surrounding the XR gradient engine, safety mechanisms, as well as the benefits that MR applications stand to gain from the outstanding performance.

*The product is still under development and not commercially available yet. Its future availability cannot be ensured.

1

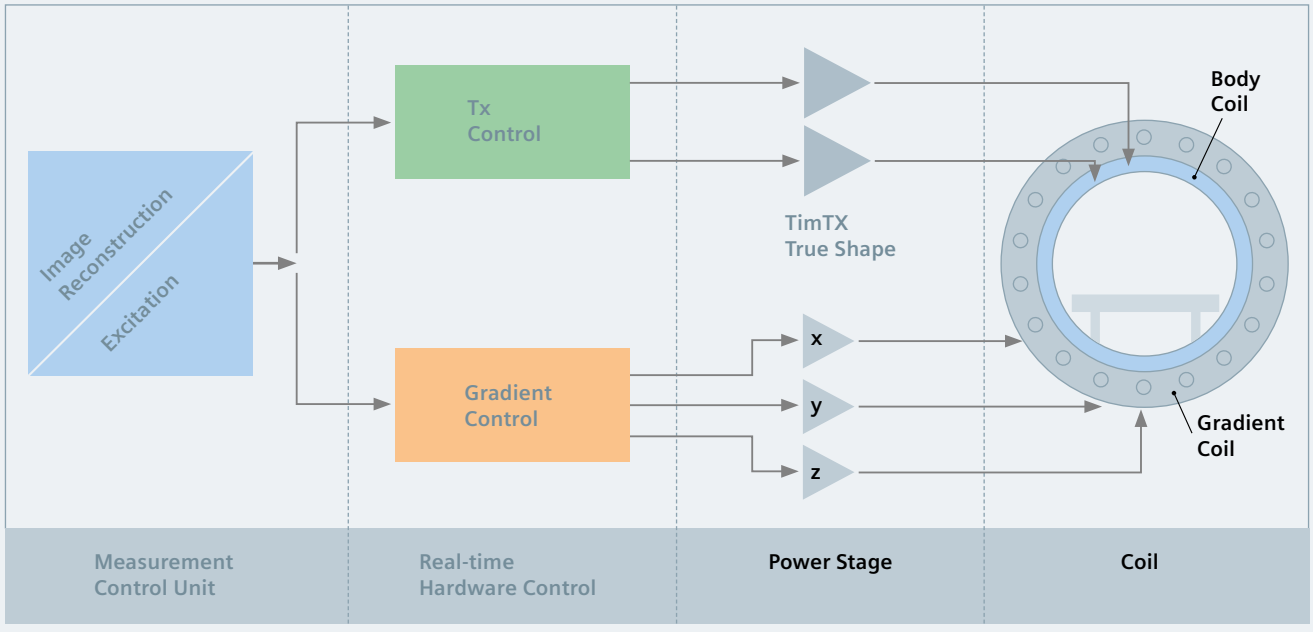

1 Excitation chain of an MR scanner.

A few words on gradients

The gradient system is one of the major sub-systems of any MR scanner. It plays a key role in the creation of the MR image by providing a means to:
1) spatially select a region that should be imaged and
2) encode the contents of this region.
Both selection and encoding are done by applying electric current to the gradient coil, thus creating a field slope on any one of the physical axes x, y, or z. Through precise timing of these additional fields, or gradients, a specific section of an object can be selected and then encoded. By altering the physical characteristics of the selected image region, it can be seen that the gradients have a tremendous influence on the overall quality of the acquired image.
In order to create a gradient pulse in the context of an MR measurement, a lot has to happen, and it all has to happen very fast. The gradient sub-system can be generalized as a chain of several individual units that receive data from their previous neighbor on the chain, process it, and then pass it down the chain to their next neighbor. First in this chain is the measurement control unit, which controls the entire MR pulse sequence and image reconstruction task. This unit has the task of 'ordering' not only gradient pulses, but also the necessary RF pulses and performing the reconstruction algorithms on the received MR data.
The 'ordered' gradient pulse information is passed onto the next unit, the gradient control module, which works digitally and in sub-millisecond intervals, executing the desired gradient pulse forms in real-time and performing algorithms on these wave forms in order to compensate for effects such as eddy currents, delays, and other gradient-field-induced abnormalities. Next, the small-signal unit processes the digital signal further and converts it into an analog signal, to be fed into the power stage. Here, the signal is amplified and finally fed to the last member of the chain, the gradient coil, in which the rapidly flowing current creates a gradient field in the region of interest.
The two main performance characteristics of any gradient sub-system are the maximum attainable amplitude (Gmax), which is measured in millitesla per meter (mT/m), and the slew rate (SR), which describes how fast a gradient can attain a desired amplitude and is measured in Tesla per meter per second (T/m/s). Ideally, the gradient sub-system is designed in a way to allow the highest amount of performance (Gmax and SR) without having to compromise one measure for the other. It is not uncommon to find clinical scanners with a Gmax anywhere from 33 mT/m to 45 mT/m, while slew rates can vary from 100 T/m/s to 200 T/m/s.
To get an idea as to how gradient performance has evolved over the past 30 years: In 1983 the first super-conducting 0.35T clinical Siemens MAGNETOM system, was commissioned in St. Louis, USA and could deliver a maximum gradient amplitude of 3 mT/m and a slew rate of 3 T/m/s. Ten years later in 1993, the MAGNETOM Vision was introduced and set a new standard in gradient performance for clinical systems with a maximum amplitude of 25 mT/m and a slew rate of 42 T/m/s. Shifting to the new century, MAGNETOM Avanto, the first Tim system, was introduced in 2003 and boasted gradients with a 45 mT/m maximum amplitude and a 200 slew rate. MAGNETOM Prisma raises the gradient performance bar again, delivering maximum gradient amplitude of 80 mT/m and a slew rate of 200. In very few industries has there been such a dramatic enhancement in performance in such a short period of time.
So what are the benefits of maximum amplitude and slew rate? The gradient sub-system has a direct influence on the spatial resolution and acquisition time of the MR image [4]. By increasing the performance of the gradient sub-system, you can increase the spatial resolution and decrease the acquisition time. In terms of MR images, increased gradient performance translates into more signal-to-noise (SNR), fewer distortions, higher in-plane resolution and thinner slices. In short, better image quality. Fast imaging techniques such as echo planar imaging (EPI) and turbo spin echo (TSE) have evolved and thrived in part because of the higher performance that gradient sub-systems have been able to offer. Diffusion-weighted imaging (DWI) benefits greatly as well because there is a direct relation of the measured ADC data to the square of the diffusion gradient amplitudes. By utilizing higher gradient amplitudes, higher levels of SNR can be achieved, improving DWI and making it even more relevant in the clinical and research environments.
The technical challenge in designing a gradient system is two-fold. On one hand, the desire exists to deliver outstanding performance, which allows the user to realize the previously mentioned imaging benefits. On the other hand, guaranteeing safe operation is paramount. Striking the right balance of performance and safety is the key guiding principle in this process. The characteristics of high gradient performance and safety are largely dependent on the design of the analog components in the gradient sub-system, namely the power amplifier and gradient coil, and play a major role in achieving the desired image quality results. However, the surrounding digital infrastructure also contributes significantly. The following sections give an overview of the XR gradient system in the MAGNETOM Prisma.

The XR gradient system

The XR gradient is a key component of the technological foundation upon which the MAGNETOM Prisma is built. This gradient is capable of driving maximum amplitudes of up to 80 mT/m with a slew rate of 200 T/m/s, on each axis, simultaneously. Let's take a deeper look at these aspects as they relate to designing the XR gradient system.
The gradient coil can truly be considered a masterpiece of engineering as it brings a number of separate topics together: physics, electro-magnetics, thermodynamics, mechanics, and manufacturing. As the gradient coil is responsible for precisely encoding the physical characteristics within the measurement volume, it is imperative that particular attention be paid to its design. The XR gradient coil itself is constructed of numerous

2

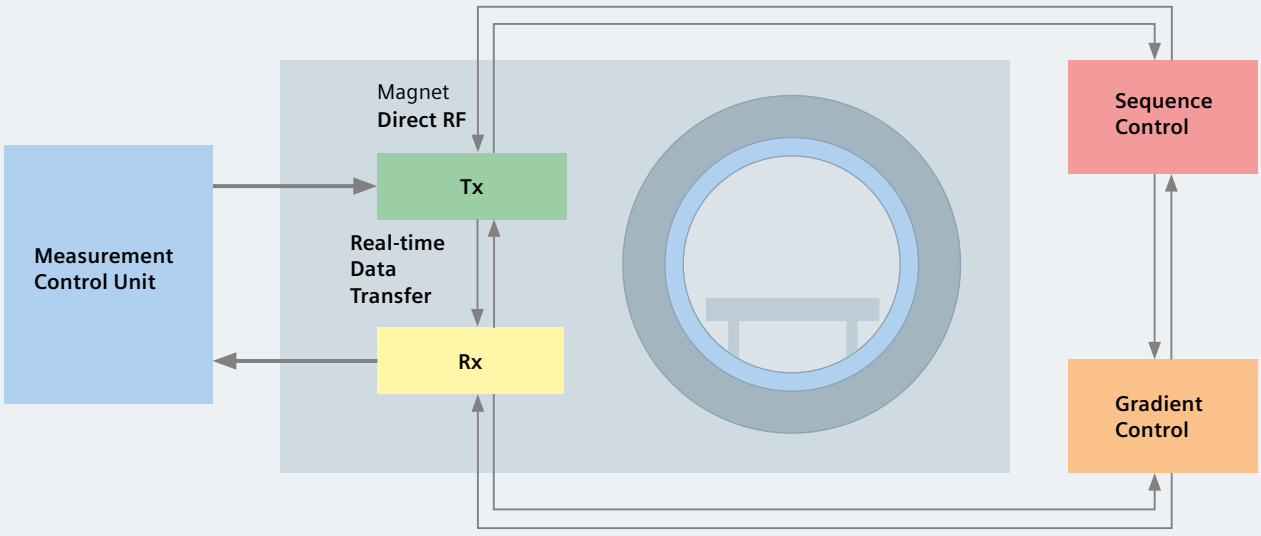

2 Tim 4G control architecture.

individual layers of different materials, making the coil substantially thicker and, as a result, much heavier than conventional gradient coils. These layers all have a specific function – whether the conductors to create and adjust the gradient fields, the isolation layers to aid in protection from RF disturbances as well as those potentially induced by the coil itself, or the fill layers to ensure a stable and rigid coil. Additionally, a number of these layers are dedicated water-cooling. High gradient performance delivers a strong, stable and linear gradient field. A byproduct of all of this current is induced mechanical vibration [3] and thermal noise as well as heat as a result of simple electrical resistance. Through an efficient force compensation design on all axes, these vibrations can be reduced to a minimum. The sheer size of the gradient coil plays to its advantage, whilst the mass of the coil helps reduce vibrations, acoustic noise, and eddy currents further. Heat must still be dealt with as efficiently as possible. Failure to do so can result in a decrease in contrast and an increase in susceptibility artifacts due to a thermally induced drift of the B_0 frequency, a common effect with fast imaging techniques such as EPI. With this in mind, the designers of the XR gradient coil utilized a special conductive material that allows thermal energy to be transferred easily to the coolant flowing through these layers in the coil. Each cooling layer is then placed next to a coil conductor, effectively giving each axis its own individual cooling source. In total, the MAGNETOM Prisma has the ability to cool up to 60 kW, thus ensuring that any thermal energy created by the system is also removed from the system, guaranteeing stability and performance at the same time.

Driving the gradient coil is a power amplifier system designed specifically to handle the needs of such a high-performance gradient system. Modular in design and small in footprint, the solid-state amplifier provides 2250 V at maximum voltage for fast switching gradients and up to 900A of peak current for high-amplitude pulses, which this amplifier can achieve simultaneously. It has the total specified power available to it at all times – there is no need to switch to a special hardware mode which would create some compromise with respect to maximum amplitude or slew rate. It is these specific capabilities that made this amplifier so attractive for the renowned high-performance gradient system supplied by Siemens for the Human Connectome Project (HCP). For this project, two unique MR systems were built, using this amplifier specifically for neurological research. One such system is able to deliver up to 300 mT/m of peak gradient amplitude with a slew rate of 200 T/m/s!

While power is important to drive performance, it is just as important to have the ability to accurately reproduce the pulses from scan to scan. Unless the unit controlling the amplifier and thus the gradient coil is deterministic and precise in its functionality, then stable performance of the entire system cannot be guaranteed. The gradient control unit of the XR gradient system consists of a real-time digital signal-processing unit working in sub-millisecond intervals to control the entire operation of the gradient system as requested by the MR sequence. Like many other control units critical to the MR system functionality, the gradient control unit contains a vast amount of intelligence. It has the ability to influence the state of the entire MR

system through an intelligent real-time data transfer, realized via a fiber-optic communication network. Through this real-time data transfer, which is common on all Tim 4G MR scanners and made possible by DirectRF, all components that rely on data produced by the gradient system – be it for fine-tuning of the RF transmit/receive systems, patient safety data collection, or supplying algorithms with data, can receive it in real-time and integrate it into their data processing chain. The gradient control unit is part of an intelligent network and plays an integral part not only in the operation of the XR gradients, but also the entire MAGNETOM Prisma.

Safe operation

Unfortunately we cannot continuously increase the amplitudes and slew rates of our gradient pulses and reap their benefits. A rapidly changing magnetic field, which is essentially what MR gradients are meant to produce, have been shown to produce physiological effects such as peripheral nerve stimulation (PNS) in humans [2]. These effects can be uncomfortable. All MR systems with agradient system that has the potential to stimulate must provide measures in order to ensure that this does not occur. How is it possible to maximize performance of the gradient system while maintaining safe operation under these conditions?

The XR gradient system, like all other Tim 4G scanners, employs several safety measures (or layers) in order to allow the user to not only maximize the performance of the gradient system, but also to ensure that the patient is in no way harmed and safe at all times. Feeding off the vast knowledge that has been accumulated through projects such as the Human Connectome Project, the MAGNETOM Prisma employs three main layers of safety.

First – the prediction. A so-called 'look-ahead', or prediction monitor examines the critical pulses in a measurement protocol and determines whether or not it will be possible to run the protocol without exceeding the stimulation limit. If it is deemed that the protocol will exceed stimulation limits, then the user is presented with a set of possibilities as to how to adjust the protocol, allowing it to run. If the MR protocol checks out OK, then it is allowed to run. Prior to the actual execution of the sequence, the look-ahead monitor sends measurement parameters to the second safety layer – the online monitor.

The online monitor has the task of calculating the current stimulation level and checking this against that calculated by the prediction model. Each calculation occurs at regular sub-millisecond intervals during a running sequence. Should at any time during a running sequence the measured levels exceed the predicted levels, the measurement is stopped. Upon completion of a measurement, the prediction model obtains the final stimulation results from the online monitor and does a comparison: does the calculated prediction model stimulation correlate with the actual measured stimulation? By checking the prediction model with the online calculation, there is the added security that the hardware is performing as intended and the user is receiving the maximum performance available. If there were a discrepancy, the user would be notified of this.

The third and final safety layer involves Tim 4G technology. We are not referring to the high-density coils that Tim 4G is known for, but rather the infrastructure that makes it possible to integrate them flawlessly into a complex system.

Through the intense use of fiber optics that enable the DirectRF real-time data transfer, the scanner can digitally transmit large amounts of raw data over dedicated channels from the receivers located directly at the magnet, to the measurement control unit located in the equipment room in a fast and efficient manner. At the same time, other MR components, such as the transmitter or gradient controller, utilize the same fiber optic technology to communicate with each other, at all times, and in real-time. By doing so, the free exchange of information between MR-critical components is possible. Information such as measurement results, calibration data, status updates, and safety information is broadcast over this 'network' at all times to all components. Should one component in this network exhibit abnormal behavior, this is registered and the scanner is immediately brought into a safe state. Fiber optics is just part of the digital backbone that makes Tim 4G possible – not just for excellent image quality, but also for robust communication and safe operation of all components at the scanner.

Outlook

The XR 80/200 gradient system of the MAGNETOM Prisma sets a new standard in gradient performance. The design of a unique gradient coil that is easily able to handle the stresses demanded by MR researchers, coupled with a powerful amplifier and an intelligent control system make this the gradient system the perfect centerpiece for a 3T MR research platform. Ensuring safe operation is of the utmost importance, and multiple, redundant layers of safety make this possible. Many MR applications will surely benefit from the gradient power that the XR 80/200 gradient system provides. Adding the technologies TimTX TrueShape, Tim 4G, and a solid 3T magnet to the XR gradients and you get MAGNETOM Prisma – a powerful and flexible tool that will offer MR researchers innumerable possibilities.

References

1 Boada, Shepherd, Rosenkrantz, Sigmund, Fütterer, Chandarana, Hagiwara, Rusinek, Mikheev, Bruno, Geppert, Glielmi, Pfeuffer, Parallel Transmission and its Clinical Implementation: Enabling new Clinical Imaging Paradigms, MAGNETOM Flash 2/2013, Vol. 52, pp 104ff.

2 Reily, J.P., Medical and Biological Engineering and Computing March 1989, Volume 27, Issue 2, pp 101-110.

3 Mansfield, Haywood, Coxon – Active Acoustic Control in Gradient Coils for MRI Magnetic Resonance in Medicine 46:807–818 (2001).

4 Cohen, Echo Planer Imaginer and functional MRI. Appeared in Bandetti and Moonen: Functional MRI 2000, 137-149.

Contact
Daniel Fischer
Siemens Healthcare
IM MR PI PPM
daniel.df.fischer@siemens.com

Optimizing MRI for Radiation Oncology: Initial Investigations

James Balter[1]; Yue Cao[1]; Hesheng Wang[1]; Ke Huang[1]; Shu-Hui Hsu[1]; Martin Requardt[2]; Steven M. Shea[3]

[1] Department of Radiation Oncology, University of Michigan, Ann Arbor, MI, USA
[2] Siemens Healthcare, Erlangen, Germany
[3] Siemens Corporation, Corporate Technology, Baltimore, USA

Introduction

The superior soft tissue contrast, as well as potential for probing molecular composition and physiological behavior of tumors and normal tissues and their changes in response to therapy, makes MRI a tempting alternative to CT as a primary means of supporting the various processes involved in radiation therapy treatment planning and delivery. Obvious examples of the benefit of MRI over CT include target delineation of intracranial lesions, nasopharyngeal lesions, normal critical organs such as the spinal cord, tumors in the liver, and the boundaries of the prostate gland and likely cancerous regions within the prostate gland. For brachytherapy planning for cervical cancer, a recent GEC-ESTRO report directly recommends a change from traditional point-based prescriptions based primarily on applicator geometry, to volumetric treatment plans and prescriptions aided by soft tissue visualization, specifically improved by the use of MRI. MRI-based maps of diffusion and perfusion have demonstrated potential for predicting therapeutic outcome for tumors as well as normal tissues, and current clinical trials seek to validate their roles and performance as a means to individualize therapy to improve outcomes (minimize toxicity and improve local tumor control). In addition to these advantages, MRI has been initially investigated as a means to better map the movement and deformation of organs over time and due to physiological processes such as breathing.

The historically accepted challenges in using MRI for primary patient modeling in radiation oncology have included distortion, lack of electron density information, and lack of integrated optimized systems to scan patients immobilized in treatment configuration.

MRI 'simulator' system

Over the past several years, we have investigated the feasibility of MRI systems to function in the same roles that CT scanners have for the past 10–15 years, that is as primary tools for patient modeling for radiation therapy. These efforts have accelerated in the past years with the installation of a dedicated MRI 'simulator' at the University of Michigan, based on a 3T wide-bore scanner (MAGNETOM Skyra, Siemens Healthcare, Erlangen, Germany), outfitted with a laser marking system (LAP, Lueneburg, Germany) and separate detachable couch tops supporting brachytherapy and external beam radiation therapy applications.



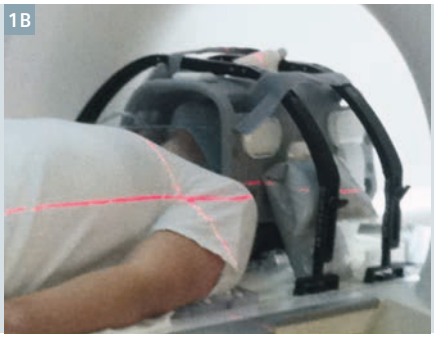

1

MRI simulation system shows a volunteer in position for initial setup wearing a customized face mask **(1A)**. Close-up view of anterior coil setup and crosshairs from laser marking system **(1B)**.

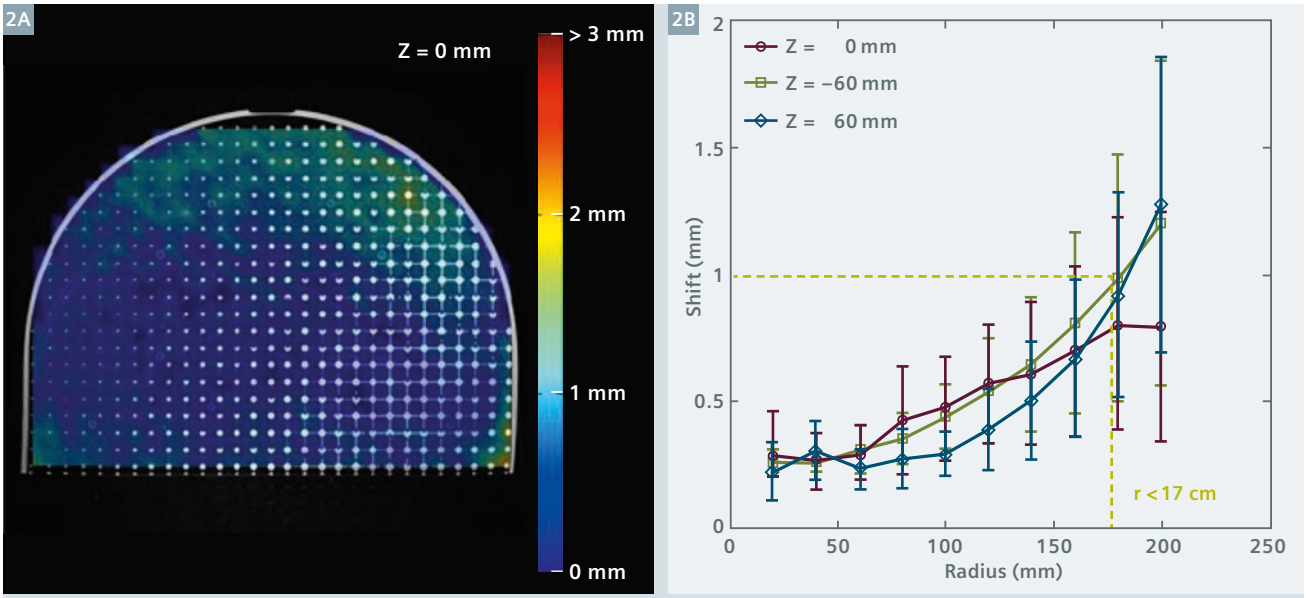

2 Colorwash of measured distortion through an axial plane of the distortion phantom **(2A)**. Magnitude of distortion-induced shifts in circles of increasing radius from the bore center in axial planes at the center and +/– 6 cm along the bore **(2B)**.

The process of integrating MRI into the standard workflow of radiation oncology requires attention be paid to a number of specific areas of system design and performance. In our instance, we chose a system that could potentially support both external beam therapy as well as brachytherapy. The brachytherapy requirement played a specific role in some of our design choices. As the high-dose-rate (HDR) brachytherapy system was housed in a room across the hall from the MRI suite, a room design was created that permitted the direct transfer of patients from MRI scanning to treatment. Typically brachytherapy treatment has involved transferring patients to and from imaging systems, a process that could potentially influence the treatment geometry and changes the dose delivered away from that planned. Treating a patient directly without moving them has significant advantages for geometric integrity as well as patient comfort. To facilitate such treatments, a detachable couch was chosen as part of the magnet specifications, and two such couches were specifically purchased to support simultaneous treatment of patients on the couch used for MRI scanning and scanning of other patients for subsequent external beam treatments.

To support external beam radiotherapy, patients need to be scanned in positions and configurations that can be reproduced at treatment. In addition to necessitating a wide bore MRI scanner, an indexed flat table top insert was purchased from a company that specializes in radiation therapy immobilization systems (Civco, Kalona, IA, USA). A number of immobilization accessories were customized for use in the MRI environment, most notably a head and neck mask attachment system. To support high quality scanning of patients in treatment position without interfering with their configuration for treatment, a series of attachments to hold surface coils (primarily 18-channel body coils) relatively close to the patient without touching are used.

Initial commissioning and tests

To commission the system, a number of tests were performed in addition to the standard processes for MRI acceptance and quality assurance. The laser system was calibrated to the scanner coordinates through imaging of a phantom with externally visible laser alignment markings and internal MRI-identifiable coordinates indicating the nominal laser intersection, and end-to-end tests were performed on phantoms and volunteers to establish the accuracy of isocenter marking using MRI scans as a source of input.

To characterize system-level distortion, a custom phantom was developed to fill the bore of the magnet (with perimeter space reserved for testing the 18-channel body coil if desired). The resulting phantom was a roughly cylindrical section with a sampling volume measuring 46.5 cm at the base, with a height of 35 cm, and a thickness of 16.8 cm. This sampling volume was embedded with a three-dimensional array of interconnected spheres, separated by 7 mm center-to-center distances. The resulting system provided a uniform grid of 4689 points to sample the local distortion. The phantom was initially scanned using a 3D, T1-weighted, spoiled gradient echo imaging sequence (VIBE, TR 4.39 ms and TE 2.03 ms, bandwidth 445 Hz/pixel) to acquire a volume with field-of-view of 500 × 500 × 170 mm with a spatial resolution of 0.98 × 0.98 × 1 mm. Standard 3D shimming was used for scanning, and 3D distortion correction was applied to the images prior

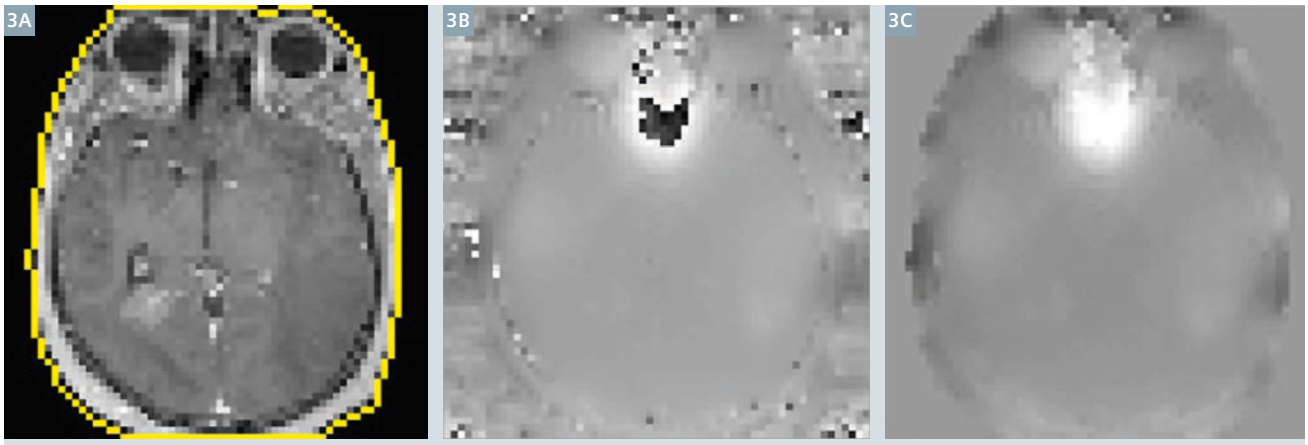

3 T1-weighted image with external contour delineated as a mask **(3A)**. The B_0 inhomogeneity map acquired from this subject **(3B)** was unwrapped within the boundaries of the mask, yielding the resulting distortion map **(3C)**.
Reprinted with permission from Wang H, Balter J, Cao Y. Patient-induced susceptibility effect on geometric distortion of clinical brain MRI for radiation treatment planning on a 3T scanner. Phys Med Biol 58(3):465-77, 2013.

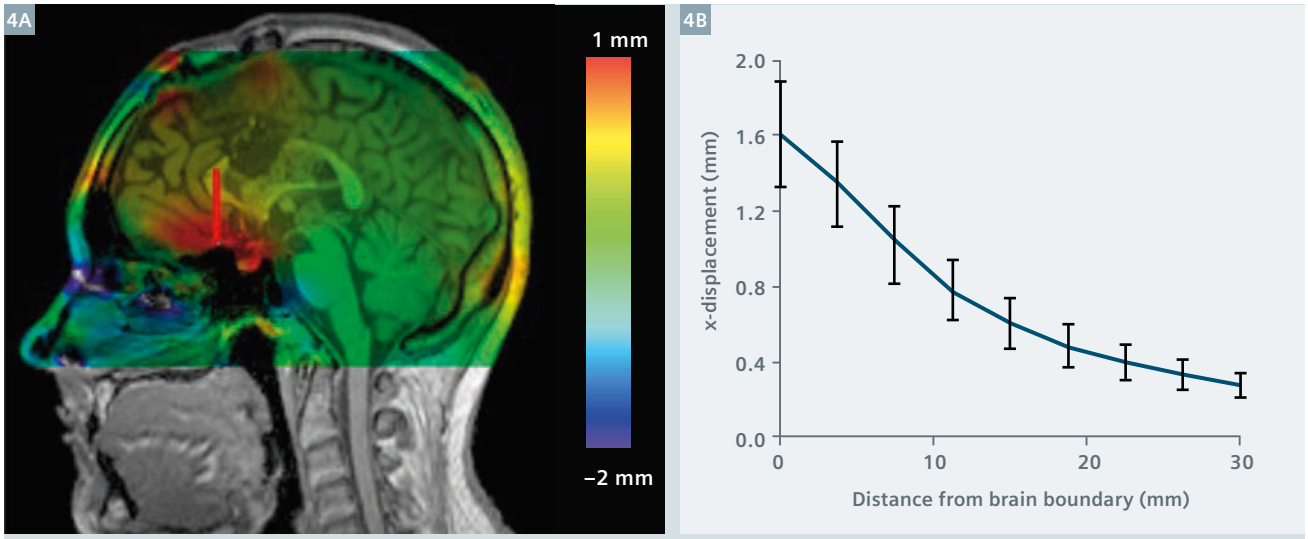

4 Colorwash of distortion-induced displacements through a sagittal plane of a subject **(4A)**. Analysis of displacements along a line moving away from the sinus (red line in fig. 4A) shows the falloff of distortion due to susceptibility differences as a function of distance from the interface **(4B)**.
Reprinted with permission from Wang H, Balter J, Cao Y. Patient-induced susceptibility effect on geometric distortion of clinical brain MRI for radiation treatment planning on a 3T scanner. Phys Med Biol 58(3):465-77, 2013.

to analysis. For this initial test, the body coil integrated into the magnet was used. Automated analysis of the images localized the sphere centers, yielding a deformation vector field that described the influence of system-level distortion on the measured sphere locations. This initial test demonstrated the accuracy of coordinate mapping via this scanning protocol, with average 3D distortions of less than 1 mm at radii of up to 17 cm in planes through the bore center as well as +/– 6 cm along the bore length. Of note, scanning was performed using the *syngo* MR D11 software version. Future tests will be performed on the *syngo* MR D13 release.

To begin to assess the impact of subject-induced susceptibility on distortions, B_0 inhomogeneity maps were acquired during routine patient scanning and analyzed (for 19 patients) under an IRB-approved protocol. These maps were acquired using a 2D, double-echo, spoiled gradient echo sequence (GRE field mapping TE_1 4.92 ms, TE_2 7.38 ms, TR 400 ms, flip angle 60 degrees, voxel size 3.5 × 3.5 × 3.75 mm), masked by the boundaries of the head acquired from T1-weighted images, and unwrapped using an algorithm from the Oxford Center for Functional Magnetic Resonance Imaging of the Brain [1]. The resulting maps showed homogeneity

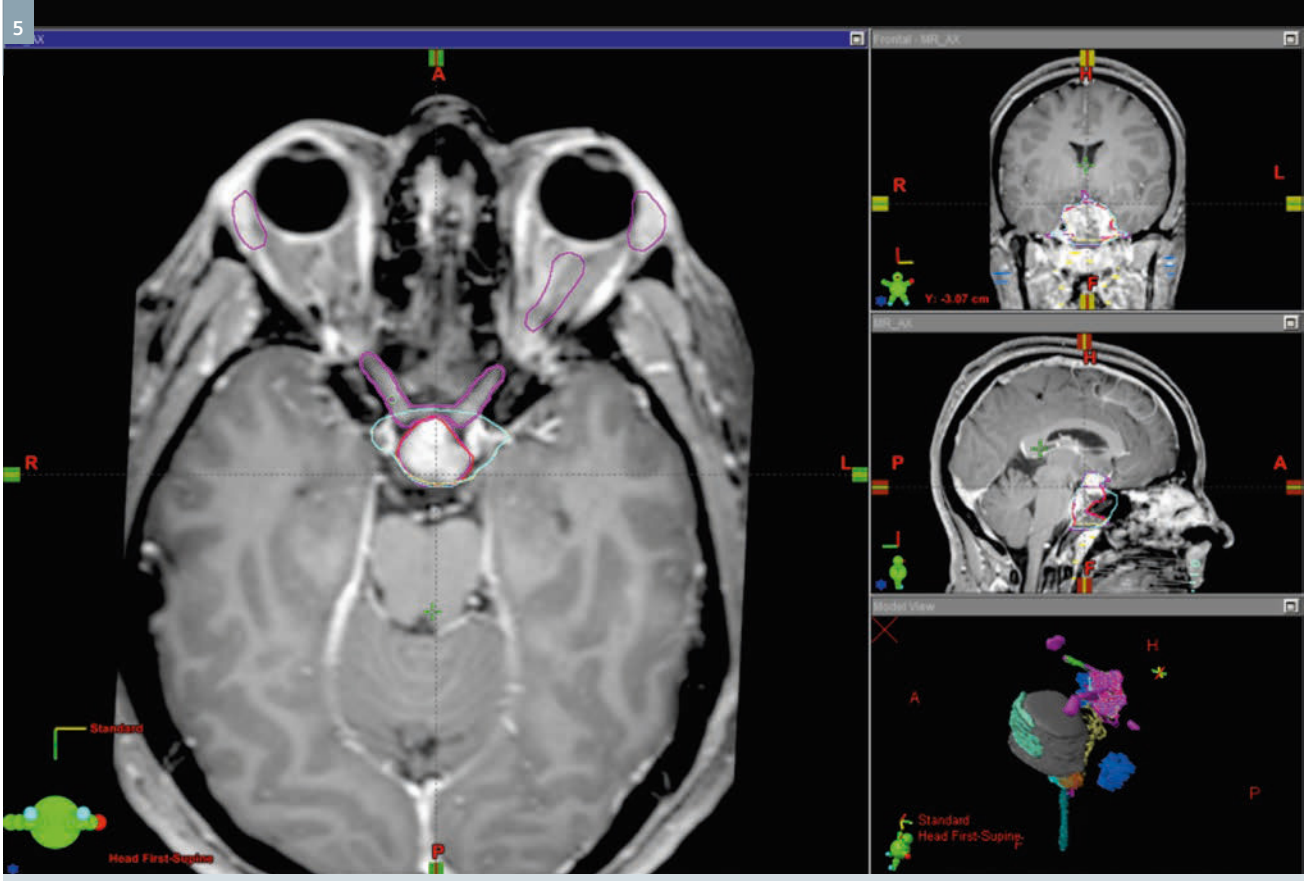

5 Post-contrast T1-weighted images of a patient scanned in an immobilization mask using an anterior 18-channel body surface coil and a posterior 4-channel small soft coil and displayed in a radiation therapy treatment planning system (Eclipse, Varian, Palo Alto, CA, USA). Various delineated structures shown are used to guide optimization of intensity-modulated radiation therapy.

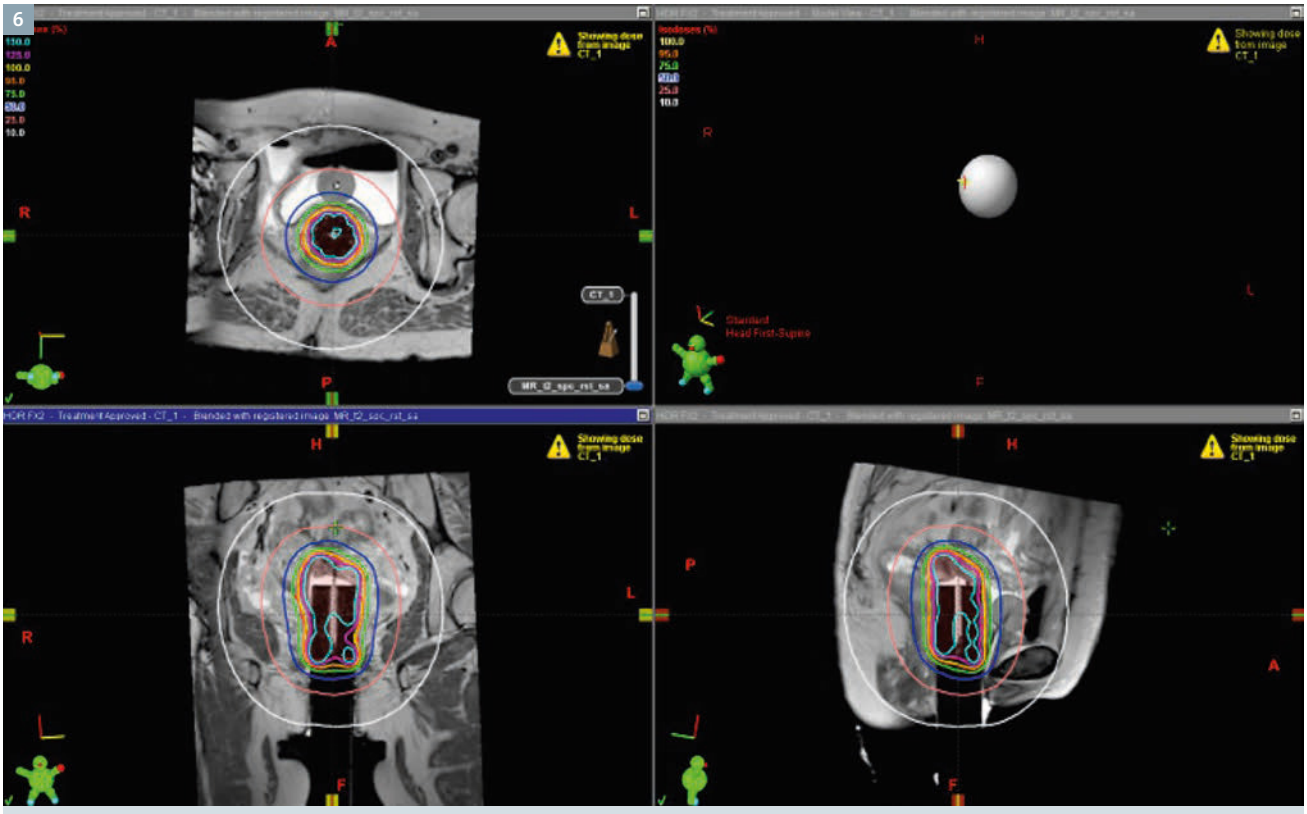

6 Display from a brachytherapy treatment planning system (Brachyvision, Varian, Palo Also, CA, USA) showing orthogonal planes through cylindrical applicator implanted in a patient. Source locations (red dashes through the center of the applicator) are shown, as well as radiation isodose lines.

of 0.035 ppm or less over 88.5% of a 22 cm diameter sphere, and 0.1 ppm or less for 100% of this volume.

These inhomogeneity maps were applied to calculate distortions from a typical clinical brain imaging sequence (3D T1-weighted MPRAGE sequence with TE 2.5 ms, Siemens TR 1900 ms, TI 900 ms, flip angle 9 degrees, voxel size 1.35 × 1.35 × 0.9 mm, frequency-encoding sampling rate of 180 Hz/pixel). On these images, 86.9% of the volume of the head was displaced less than 0.5 mm, 97.4% was displaced less than 1 mm, and 99.9% of voxels exhibited less than 2 mm displacement. The largest distortions occurred at interfaces with significant susceptibility differences, most notably those between the brain and either metal implants or (more significantly) adjacent air cavities. In the location with the largest displacement (interface with the sinus), the average displacement of 1.6 mm at the interface falls to below 1 mm approximately 7 mm away.

Examples of clinical use

We have implemented a number of scanning protocols in our first year of operation. Routine scans are performed for patients with intracranial lesions of all forms, as well as for those with nasopharyngeal tumors, hepatocellular carcinoma, and certain spinal and pelvic lesions. Routine use of the system for MRI-based brachytherapy of patients with cervical cancer using a ring and tandem system is currently pending modification of part of the applicator for safety and image quality reasons, although patients undergoing other implants (e.g. cylinders) have had MRI scans to support treatment planning.

Summary

We have implemented the initial phase of MRI-based radiation oncology simulation in our department, and have scanned over 300 patients since operations began just over one year ago. The system demonstrates sufficient geometric accuracy for supporting radiation oncology decisions for external beam radiation therapy, as well as brachytherapy. Work is ongoing in optimizing MRI scanning techniques for radiation oncology in various parts of the body and for various diseases. In addition to current and future work in optimizing MRI for use in routine radiation therapy, a variety of research protocols are underway using this system. A major current focus is on using MRI without CT for external beam radiation therapy. Results of these efforts will be presented in future articles.

References
1 Jenkinson M. Fast, automated, N-dimensional phase-unwrapping algorithm. Magn Reson Med. 2003 Jan;49(1):193-7.
2 Dimopoulos JC, Petrow P, Tanderup K, Petric P, Berger D, Kirisits C, Pedersen EM, van Limbergen E, Haie-Meder C, Pötter R. Recommendations from Gynaecological (GYN) GEC-ESTRO Working Group (IV): Basic principles and parameters for MR imaging within the frame of image based adaptive cervix cancer brachytherapy. Radiother Oncol 103(1):113-22, 2012.
3 Wang H, Balter J, Cao Y. Patient-induced susceptibility effect on geometric distortion of clinical brain MRI for radiation treatment planning on a 3T scanner. Phys Med Biol 58(3):465-77, 2013.



Contact

James M. Balter, Ph.D., FAAPM
Professor and co-director,
Physics division
Department of Radiation Oncology
University of Michigan
Ann Arbor, MI
USA
Phone: +1(734)936-9486
jbalter@umich.edu

Improving the Robustness of Clinical T1-Weighted MRI Using Radial VIBE

Kai Tobias Block[1]; Hersh Chandarana[1]; Girish Fatterpekar[1]; Mari Hagiwara[1]; Sarah Milla[1]; Thomas Mulholland[1]; Mary Bruno[1]; Christian Geppert[2]; Daniel K. Sodickson[1]

[1] Department of Radiology, NYU Langone Medical Center, New York, NY, USA
[2] Siemens Medical Solutions, New York, NY, USA

Introduction

Despite the tremendous developments that MR imaging has made over the last decades, one of the major limitations of conventional MRI is its pronounced sensitivity to motion, which requires strict immobility of the patient during the data acquisition. In clinical practice, however, suppression of motion is often not possible. As a consequence, MR images frequently show motion artifacts that appear as shifted object copies, which are well-known as 'ghosting' artifacts and which, depending on the artifact strength, can potentially obscure important diagnostic information. Ghosting artifacts pose a particular problem for abdominopelvic exams that need to be performed during suspended respiration. Because many patients struggle to adequately hold breath during the scan, the number of exams with suboptimal image quality is relatively high. This has impaired the acceptance of MRI as an imaging modality of choice in many abdominopelvic indications. Other widely utilized MRI applications such as head and neck imaging are also often affected by motion-induced ghosting artifacts, e.g., if patients are anxious, or if wthey cannot suppress swallowing or coughing during the exam.

Radial *k*-space acquisition scheme

The high sensitivity to motion results from the data-sampling strategy used in conventional MR imaging to spatially resolve the object. Conventional sequences acquire the data space (*k*-space) using a sampling scheme along parallel lines (Fig. 1A), which is usually referred to as 'Cartesian' sampling. The acquired parallel lines differ by a fixed difference in the signal phase, which is why the scheme is also called 'phase encoding' principle. However, if the object moves during the exam, phase offsets are created that disturb the phase-encoding scheme. In a simplified view, it can be thought of as jittering of the sampled lines, which causes gaps in the *k*-space coverage and results in aliasing artifacts along the phase-encoding direction from improper data sampling. Hence, the Cartesian geometry is inherently prone to motion-induced phase distortions. Even if navigation or triggering techniques are used to minimize phase inconsistencies within the acquired data, a certain amount of residual ghosting artifacts is almost always present.

The situation can be improved when changing the *k*-space acquisition to a different sampling geometry. One promising alternative is the 'radial' sampling scheme, which acquires the data along rotated spokes (Fig. 1B). Due to the overlap of the spokes in the center, gaps in the *k*-space coverage cannot occur if individual spokes are 'jittered' and, therefore, appearance of ghosting artifacts is not possible with this scheme. Furthermore, the overlap has a motion-averaging effect. Data inconsistencies can instead lead to 'streak' artifacts. However, in most cases the streaks have only a mild effect on the image quality, and they can easily be identified as artifacts due to their characteristic visual appearance (e.g., Fig. 3B). Because the artifacts appear mainly as 'texture' added to the underlying object, the likelihood that lesions get obscured is significantly lower than for the more dominant Cartesian ghosting artifacts.

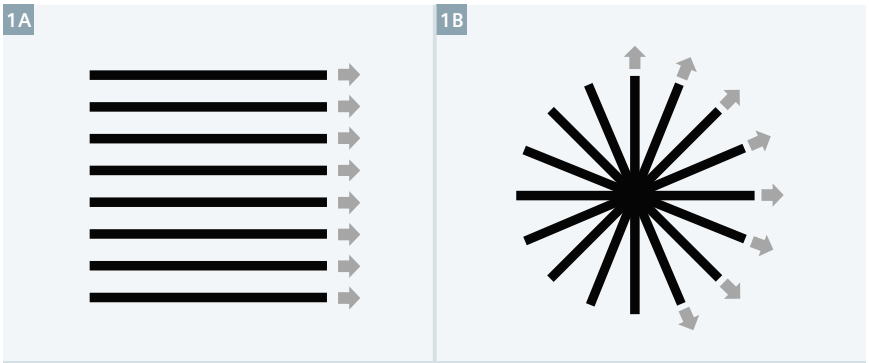

1 **(1A)** Conventional 'Cartesian' MRI sampling scheme along parallel lines, and **(1B)** radial sampling scheme along rotated spokes that overlap in the center of *k*-space.

Interestingly, although the advantages for clinical applications seem clear and although the idea of radial sampling has been known since the early days of MRI, the technique has not been widely employed in clinical practice so far. Radial sampling was first described by Lauterbur in his seminal MRI paper from 1973 [1]. However, because practical implementation required coping with a number of technical complexities, it was soon replaced by the Cartesian acquisition scheme which could be more easily and more robustly implemented on early MRI systems. These technical complexities include a more sophisticated image reconstruction, higher required homogeneity of the magnetic field, and the need for much more accurate and precise generation of time-varying gradient fields. Consequently, radial sampling has only been used sporadically in research projects while clinically established techniques are currently almost exclusively based on the Cartesian scheme.

Over the last several years, however, it has become possible to resolve the majority of issues that prevented a practical application of radial sampling, in part through improvements of the MR hardware designs and in part through new algorithmic developments. Therefore, it is now for the first time feasible to utilize radial acquisitions routinely on unmodified clinical MRI systems, with sufficient reliability and robustness for clinical applications and with image quality comparable to that of the conventional Cartesian scans.

Radial VIBE sequence

The Radial VIBE sequence* is the first available works-in-progress sequence for Siemens MR systems that integrates these developments for volumetric acquisitions and provides radial *k*-space sampling in a fully seamless way, aiming at achieving higher robustness to motion and flow effects in daily practice. It is based on the conventional product VIBE sequence, which is an optimized T1-weighted 3D gradient echo sequence (3D FLASH) with various fat-saturation options. Radial sampling has been implemented using a 3D 'stack-of-stars' approach, which acquires the k_x-k_y plane along radial spokes and the k_z dimension with conventional sampling, resulting in cylindrical *k*-space coverage (see Fig. 2). This trajectory design enables use of time-efficient fat-saturation methods, such as Quick FatSat or SPAIR, with minimal artifact strength, which is important as radial scans should be performed with fat suppression for most applications. Although Cartesian acquisition steps are employed along the k_z dimension, a high degree of motion robustness is achieved due to the use of an incoherent temporal acquisition order. The Radial VIBE sequence can be used on the full range of Siemens MR systems, including systems from the B-line generation (e.g., MAGNETOM Avanto, Trio, Verio) and D-line generation (e.g., MAGNETOM Skyra, Aera), and it can also be used on the Biograph mMR MR-PET system as well as Siemens' 7T** systems. Because the sequence does not require any modification of the MR hardware or reconstruction system, it can be deployed to installed systems and used clinically for fat-saturated T1-weighted exams as a motion-robust alternative to 3D GRE, VIBE, MPRAGE, or 2D TSE sequences.

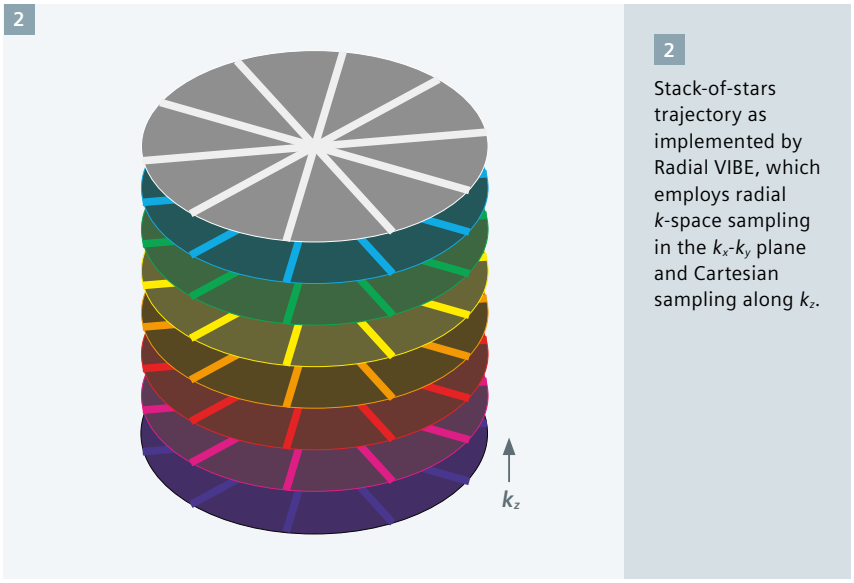

2 Stack-of-stars trajectory as implemented by Radial VIBE, which employs radial *k*-space sampling in the k_x-k_y plane and Cartesian sampling along k_z.

* Radial VIBE is a prototype for StarVIBE. StarVIBE is now 510k released and is available for 1.5T MAGNETOM Aera and 3T MAGNETOM Skyra. Radial VIBE is work in progress.

** The product is under development and not commercially available yet. Its future availability cannot be ensured. This research system is not cleared, approved or licensed in any jurisdiction for patient examinations. This research system is not labelled according to applicable medical device law and therefore may only be used for volunteer or patient examinations in the context of clinical studies according to applicable law.

Clinical applications and results

Over the last two years, the sequence has been tested extensively at NYU Langone Medical Center to evaluate the achievable image quality across various MR systems in daily routine applications. Radial VIBE scans were added to clinical protocols under IRB approval in more than 5000 patient exams and compared to established reference protocols. Several clinical studies have been performed or are ongoing that investigate the improvement in diagnostic accuracy resulting from the absence of ghosting artifacts.

Free-breathing abdominal imaging

A key application of the Radial VIBE sequence is imaging of the abdomen and/or pelvis before and after injection of a contrast medium, which is conventionally performed during suspended respiration. With Radial VIBE, it is possible to acquire the data during continued shallow breathing, which therefore can be the preferred exam strategy for patients who are unable to sustain the normally

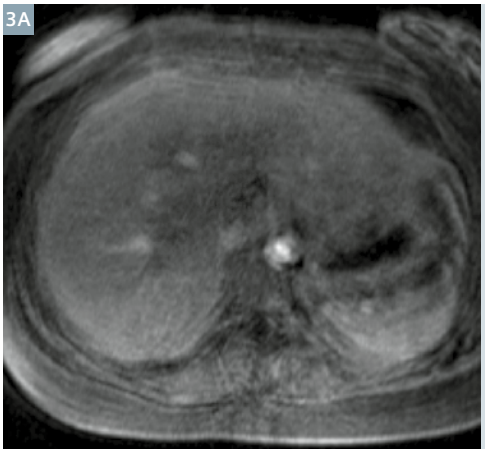

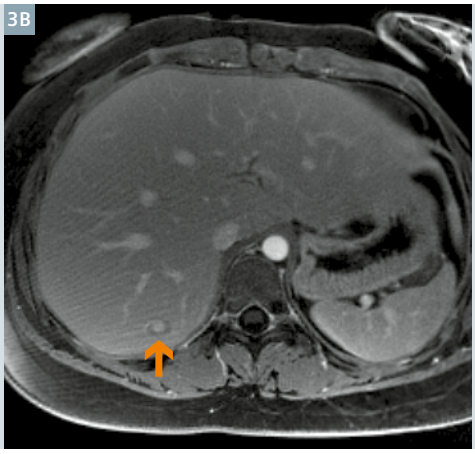

3

(3A) Conventional VIBE exam of a patient failing to hold breath during the acquisition and **(3B)** Radial VIBE acquisition during free breathing. Radial VIBE provides significantly higher image quality and reveals a lesion in the liver (arrow) not seen on the conventional scan

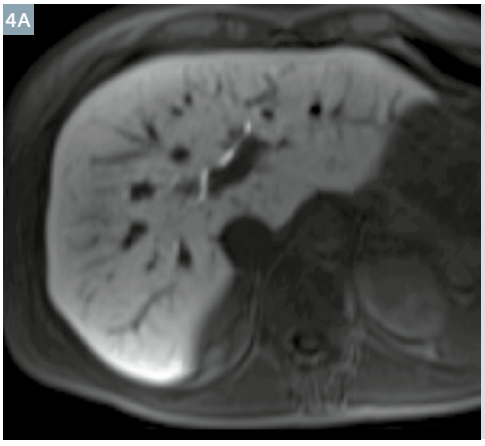



4

(4A) Conventional breath-hold VIBE exam of a patient 20 min after injection of Gadoxetate Disodium. **(4B)** Because Radial VIBE exams can be performed during continued respiration, data can be acquired over longer time, resulting in clearly improved resolution (here 1.0 mm isotropic).

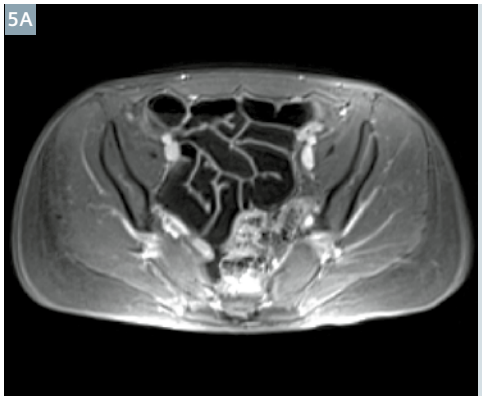

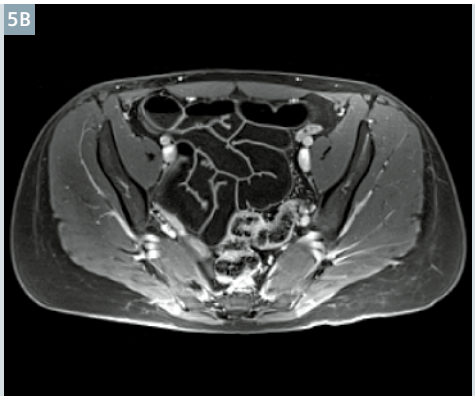

5

MR enterography using **(5A)** conventional VIBE and **(5B)** Radial VIBE acquisition. The higher motion robustness achieved with Radial VIBE leads to sharper images and improved resolution.

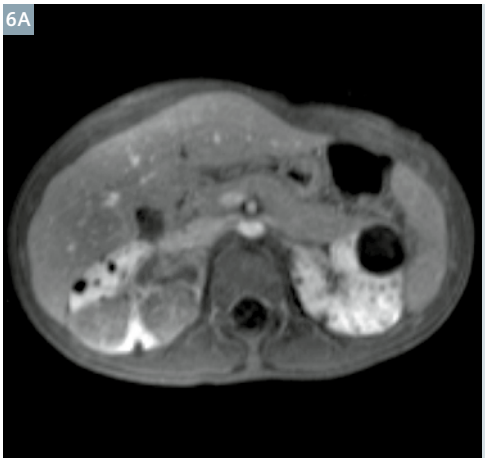

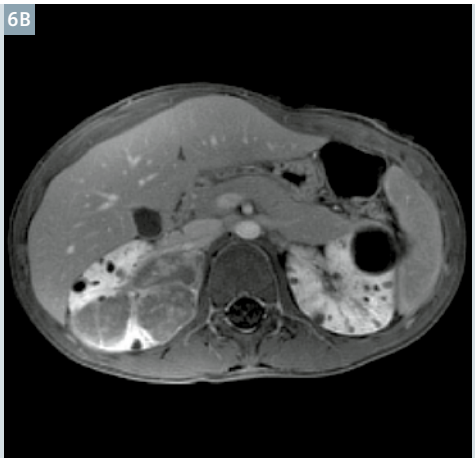

6

Abdominopelvic exam of a sedated pediatric patient with Tuberous Sclerosis. **(6A)** Because suspending respiration is not possible under deep sedation, conventional exams are affected by respiration artifacts. **(6B)** Radial VIBE provides significantly sharper images with improved spatial resolution, as visible from the small cysts in the kidneys.

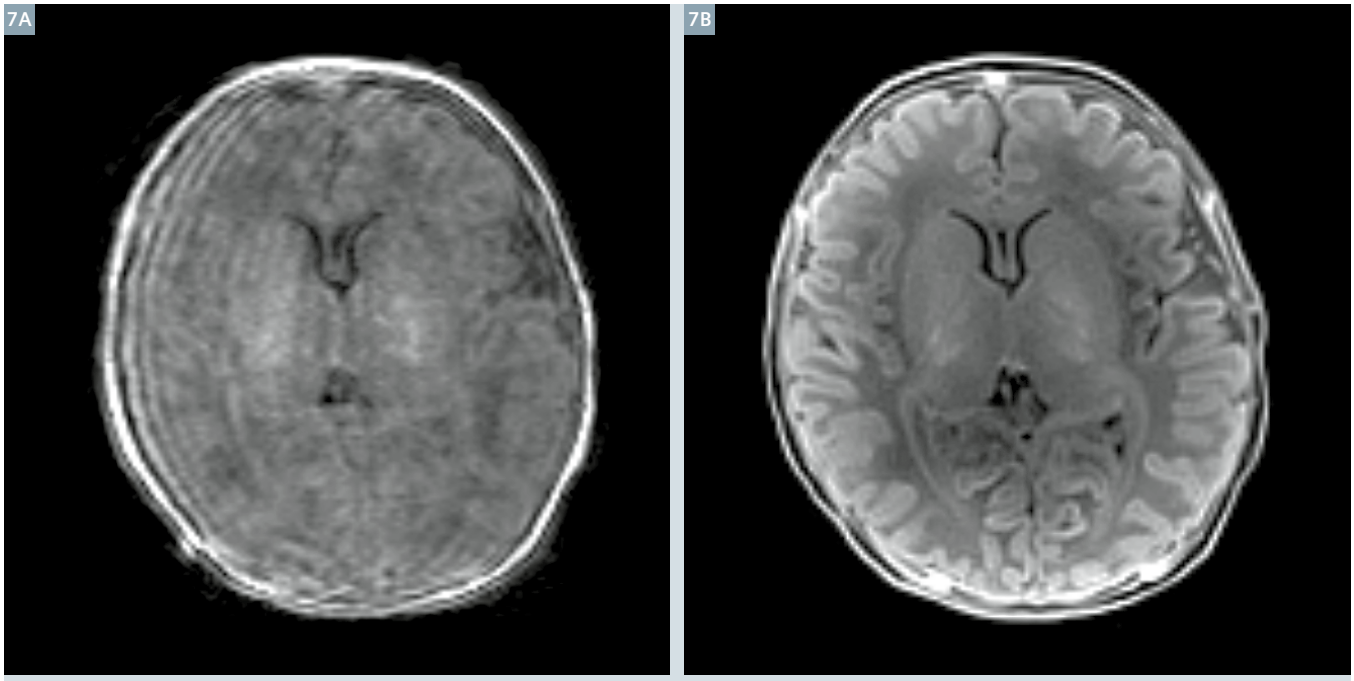

7 Brain exam of a 4-day-old* patient using **(7A)** conventional MPRAGE and **(7B)** Radial VIBE sequence. Due to vigorous patient activity, the MPRAGE scan is affected by strong ghosting artifacts, while Radial VIBE provides diagnostic image quality.

*MR scanning has not been established as safe for imaging fetuses and infants less than two years of age. The responsible physician must evaluate the benefits of the MR examination compared to those of other imaging procedures.

required breath-hold time, such as elderly or severely sick patients. A blinded-reader study by Chandarana et al. demonstrated that the average image quality obtained with free-breathing radial acquisition is comparable to conventional breath-hold exams and significantly better than free-breathing exams with Cartesian acquisition [2]. As an example, figure 3 compares a free-breathing Radial VIBE exam to a conventional Cartesian exam of a patient with insufficient breath-hold capability. The Radial VIBE image is affected by a certain amount of streak artifacts but clearly depicts a lesion in the right lobe of the liver, which is fully obscured in the Cartesian scan.

High-resolution abdominopelvic imaging

The ability to acquire data during continued respiration also has advantages for the examination of patients with proper breath-hold capacity. With conventional Cartesian sequences, the achievable spatial resolution in abdominopelvic exams is limited by the amount of *k*-space data obtainable within typical breath-hold durations of less than 20 sec. Because Radial VIBE eliminates the need for breath holding, it is possible to sample data over several minutes and, thus, to increase the spatial resolution by a significant factor. Figure 4 demonstrates this possibility for an isotropic 1 mm high-resolution scan of the liver 20 min after injection of Gadoxetate Disodium, which provides clearly sharper visualization of the biliary duct compared to the corresponding Cartesian protocol. In figure 5, the achievable resolution improvement is shown for the case of MR enterography, which is another good candidate for Radial VIBE due to the higher overall robustness to the bowel motion.

Pediatric imaging

During the clinical evaluation phase, Radial VIBE demonstrated particular value for the application in pediatric* patients. Pediatric exams are often conducted under general anesthesia or deep sedation, which makes active breath holding impossible. Therefore, conventional abdominopelvic scans are in most cases affected by respiration artifacts that impair the achievable effective resolution and diagnostic accuracy. Due to the inherent motion robustness, much sharper and crisper images are obtained with Radial VIBE, as evident from the depiction of small cysts in the kidneys of a patient with Tuberous Sclerosis shown in figure 6. A retrospective blinded-reader study of our case collection revealed that 8% of all lesions were only identified with Radial VIBE but missed in the corresponding Cartesian reference exams [3].

In young neonatal patients, sedation is usually avoided due to the higher risk of potential adverse effects. Imaging these patients is challenging because they often move spontaneously in the scanner. Also in this patient cohort Radial VIBE provides improved image quality and reliability, which is demonstrated in figure 7 for a brain exam of a 4-day-old patient, in this case compared to a Cartesian MPRAGE protocol.

*MR scanning has not been established as safe for imaging fetuses and infants less than two years of age. The responsible physician must evaluate the benefits of the MR examination compared to those of other imaging procedures.

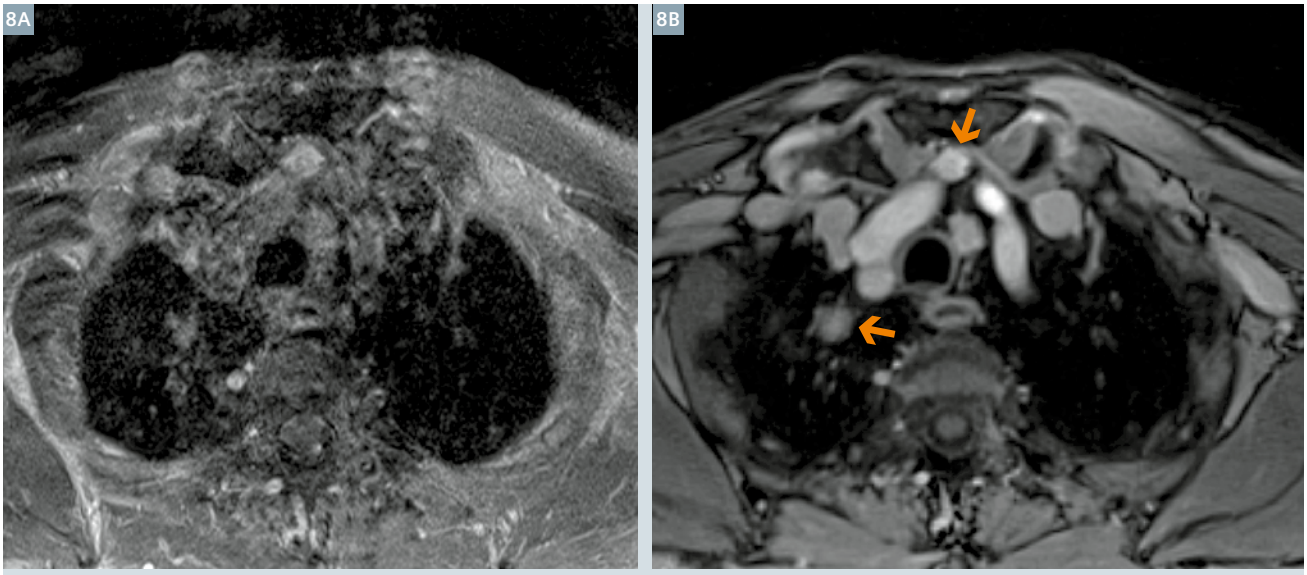

8 Examination of the neck and upper chest using **(8A)** a conventional 2D TSE sequence and **(8B)** Radial VIBE. Because of the respiration and strong blood flow, the TSE scan shows drastic artifacts. Two suspicious lesions are more clearly visible on the Radial VIBE exam (arrows).

Imaging of the neck and upper chest

Although imaging of the head and neck region appears less critical at first glance, severe motion-related artifacts occur quite often in routine exams. Conventional neck protocols usually include slice-selective T1-weighted TSE sequences, which are especially sensitive to motion and flow. If patients are unable to suppress swallowing or coughing during the acquisition, images are rendered non-diagnostic. Furthermore, adequate examination of the upper chest region is often not possible because of drastic artifacts from respiration and strong blood flow in the proximity of the heart. Radial VIBE exams are a promising alternative for this application and are largely unaffected by swallowing, minor head movements, or flow, which is illustrated in figure 8. The sequence also maintains a convincing sensitivity to chest lesions in the presence of respiratory motion [4]. Because Radial VIBE scans are immune to ghosting artifacts, exams can be performed with high isotropic spatial resolution, which allows for retrospective reconstruction in multiple planes (MPRs). In this way, it is possible to substitute multiple conventional slice-selective protocols in varying orientation with a single Radial VIBE high-resolution scan. A representative example is shown in figure 9.

Imaging of the orbits, inner auditory canal, and full brain

Finally, the sequence also offers improved sharpness and clarity for the examination of the orbits. When patients move the eyes or change the position of the eyelids during the exam, conventional protocols show a band of strong ghosting artifacts along the phase-encoding direction, which can make identifying pathologies a difficult task. Radial VIBE provides cleaner depiction of the optic nerves and improved suppression of intra- and extraconal fat [5]. Flow effects from surrounding larger blood vessels can lead to mild streak patterns but are less prominent than for most Cartesian protocols and can be additionally attenuated with the use of parallel saturation bands. The possibility to create high-resolution MPRs is another advantage of using Radial VIBE for this application, which is demonstrated in figure 10 for a patient with optic nerve sheath meningioma. In a similar way, the sequence can be applied for examinations of the inner auditory canal (IAC) or the full brain, in which a particularly high sharpness of vessel structures is achieved.

Conclusion

The large number of successful patient exams of various body parts conducted with Radial VIBE over the last two years demonstrates that radial sampling is now robust and reliable for routine use on standard clinical MR systems. Due to the higher resistance to patient motion and the absence of ghosting artifacts, improved image quality can be obtained in applications where motion-induced image artifacts are a common problem. In particular, the Radial VIBE sequence enables exams of the abdomen and upper chest during continued shallow respiration, which can be a significant advantage for patients that struggle to adequately hold breath. Furthermore, the sequence enables reconfiguring exam protocols towards higher spatial resolution and allows consolidating redundant acquisitions into MPR-capable isotropic scans. Because the sequence works robustly on existing MRI hardware, Radial VIBE has the potential to find broad application as motion-robust T1-weighted sequence alternative and will complement the spectrum of clinically established imaging protocols.



9 Neck exam using transversal Radial VIBE acquisition with 1 mm isotropic resolution. Due to the robustness to swallowing and minor head motion, high quality 3D scans are possible that can be reconstructed in multiple planes (MPR). This enables consolidating redundant 2D protocols with varying scan orientation.

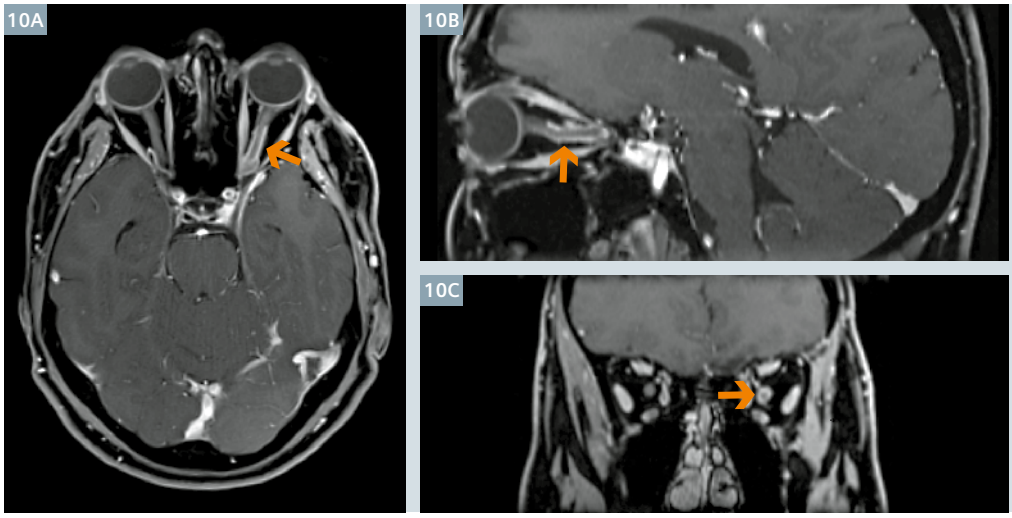

10 Multiplanar reconstructions of a transversal Radial VIBE exam with 0.8 mm resolution. The sequence achieves good fat suppression and provides sharp depiction of the optic nerves without artifacts from eye motion. An abnormal contrast enhancement of the left optic nerve is clearly visible (arrows), which is indicative of an optic nerve sheath meningioma.

References

1 Lauterbur PD. *Image formation by induced local interactions: Examples employing nuclear magnetic resonance.* Nature 242:190–191, 1973.

2 Chandarana H, Block KT, Rosenkrantz AB, Lim RP, Kim D, Mossa DJ, Babb JS, Kiefer B, Lee VS. *Free-breathing radial 3D fat-suppressed T1-weighted gradient echo sequence: a viable alternative for contrast-enhanced liver imaging in patients unable to suspend respiration.* Invest Radiology 46(10):648-53, 2011.

3 Chandarana H, Block KT, Winfeld JM, Lala SV, Mazori D, Giuffrida E, Babb JS, Milla S. *Free-breathing contrast-enhanced T1-weighted gradient-echo imaging with radial k-space sampling for paediatric abdominopelvic MRI.* European Radiology, September 2013.

4 Chandarana H, Heacock L, Rakheja R, Demello LR, Bonavita J, Block KT, Geppert C, Babb JS, Friedman KP. *Pulmonary Nodules in Patients with Primary Malignancy: Comparison of Hybrid PET/MR and PET/CT Imaging.* Radiology 268(3):874-81, 2013.

5 Bangiyev L, Raz E, Block KT, Hagiwara M, Yu E, Fatterpekar GM. *Contrast-enhanced radial 3D fat-suppressed T1-weighted gradient echo (Radial-VIBE) sequence: A viable and potentially superior alternative to conventional T1-MPRAGE with water excitation and fat-suppressed contrast-enhanced T1W sequence for evaluation of the orbit.* ASNR Annual Meeting 2013: O-413.



Contact

Tobias Block, Ph.D.
Assistant Professor of Radiology
New York University
School of Medicine
Center for Biomedical Imaging
New York, NY 10016
USA
tobias.block@nyumc.org

Making MRI Scanning Quieter: Optimized TSE Sequences with Parallel Imaging

Eric Y. Pierre[1]; David Grodzki[2]; Bjoern Heismann[2]; Gunhild Aandal[3, 5]; Vikas Gulani[1, 3]; Jeffrey Sunshine[3]; Mark Schluchter[4]; Kecheng Liu[6]; Mark A. Griswold[1, 3]

[1]Biomedical Engineering, Case Western Reserve University, Cleveland, Ohio, USA
[2]Siemens Healthcare, Erlangen, Germany
[3]Radiology, Case Western Reserve University, Cleveland, Ohio, USA
[4]Division of Biostatistics, Case Western Reserve Univeristy, Cleveland, Ohio, USA
[5]Haraldsplass Deaconess Hospital, Bergen, Norway
[6]Siemens Medical Solutions, USA Inc., Malvern, Pennsylvania, USA

Introduction

Turbo Spin-Echo sequences at 1.5T can generate noise at over 100dB$_A$ inside the bore [1–3]. This noise is equivalent to standing 5 meters away from a jackhammer [3], and would be even louder on higher field systems. Despite the use of ear-protective equipment, reducing the Sound Pressure Level (SPL) generated by these standard clinical sequences could noticeably improve patient comfort [4]. MRI pulse sequences mostly generate acoustic noise because of rapidly varying gradient waveforms: The resulting Lorentz forces applied on the gradient coils make the entire scanner structure vibrate [5]. To circumvent this issue, several hardware solutions have been proposed. For example, the whole gradient coil can be enclosed in a vacuum chamber [6–8], or gradient field rotation can be performed mechanically [9]. While these solutions achieve significant noise reduction for all types of sequences, they can noticeably increase manufacturing cost, and can even decrease gradient efficiency. Mechanical and acoustic balanced designs of gradient coil systems including windings performing active acoustic control have also been considered and investigated [10, 11].

Modifying and/or optimizing pulse sequences can also reduce acoustic noise effectively. One such solution is to time the ramping up and ramping down of the gradient waveforms so that the induced scanner vibrations cancel each other out [12]. Another approach is to use lower gradient amplitude and slew rates of the gradient waveforms [13]. By low-pass filtering the gradient, vibration frequencies for which the acoustic response of the gradient coil is high can be avoided.

Elaborate redesigns of gradient waveforms coupled with parallel imaging have demonstrated further reduction

1

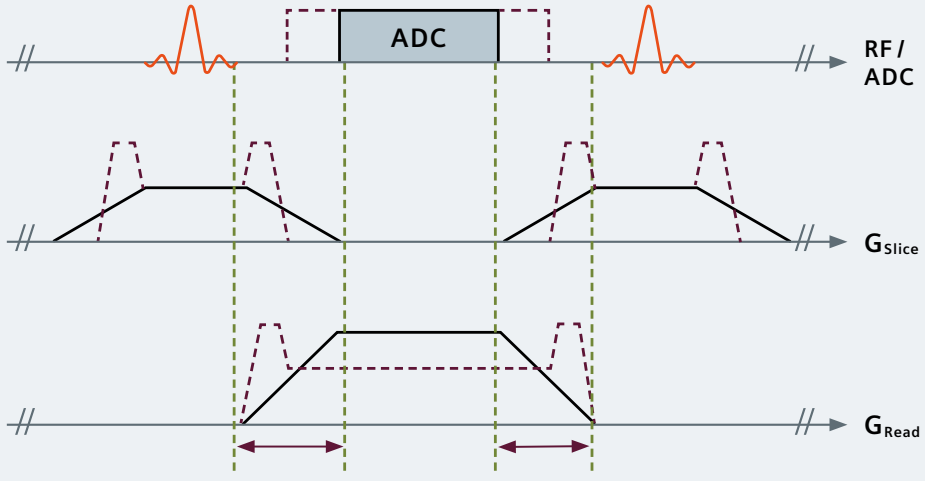

1 Comparison of conventional sequence (dashed lines) with quiet sequence (solid lines). The reduction of ADC represents a BW increase.

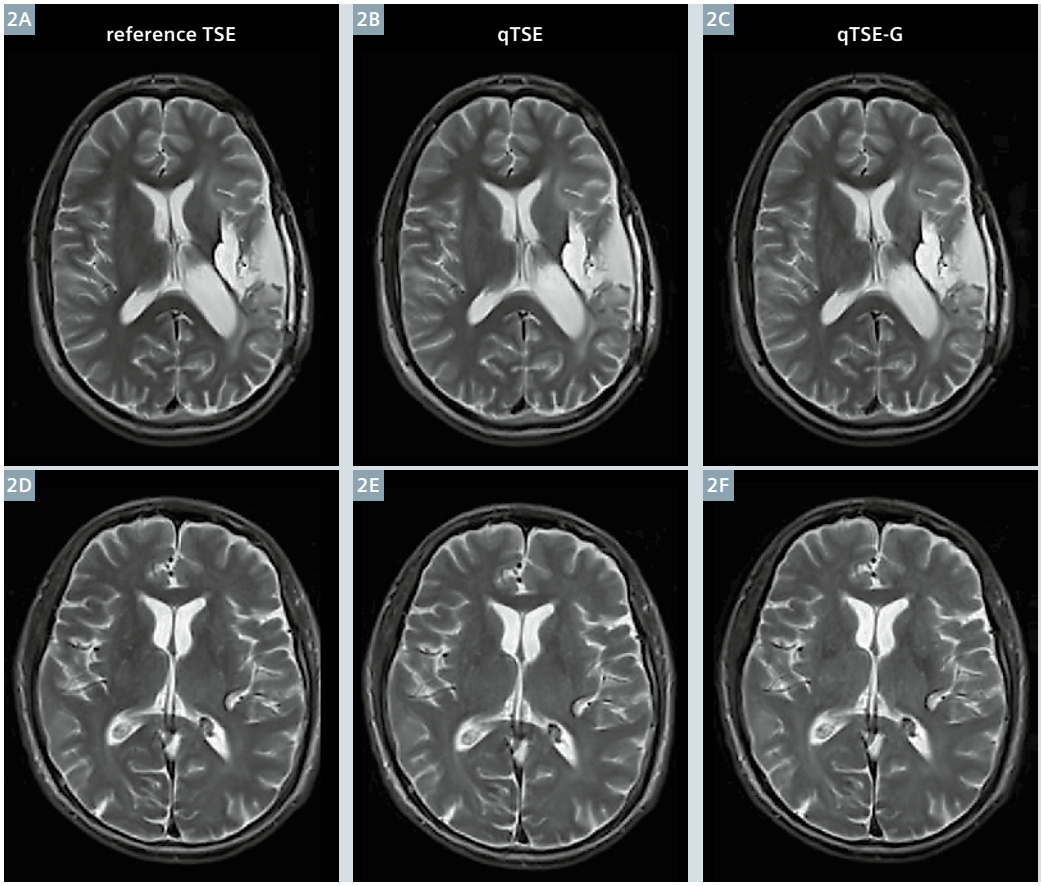

2

Representative slices from 2 patients acquired with the reference TSE sequence (left column), the qTSE sequence (center column) and the qTSE-G sequence (right column).

of acoustic noise in Echo Planar Imaging (EPI) [14, 15]. The reduction was achieved by counterbalancing lengthened gradient waveforms with increased acquisition speed, thereby reducing acoustic noise without increasing acquisition time while maintaining inter-echo spacing, only at cost of signal-to-noise ratio (SNR). By extending such principles to other generally-used standard clinical MR sequences, this article demonstrates that with minor SNR reductions (≤ 10%), effective reduction in acoustic noise can be further achieved without noticeable degrade of diagnostic information or imaging time, as well as without sacrificing gradient efficiency.

Two types of modifications in a T2-weighted Turbo Spin-Echo (TSE) sequence were investigated for acoustic noise reduction: First by solely modifying the gradient waveforms and second by additionally using GRAPPA at a reduction factor of two (R=2)*. Comparative SPL measurements at the bore were performed between standard TSE, quiet TSE (qTSE)* and quiet TSE with GRAPPA (qTSE-G)*. A statistical analysis of comparative scores from a reader's study was conducted.

Methods

The gradient waveforms of the TSE sequence were optimized with an automatic gradient optimization algorithm that extends any slope duration to its maximum and reduces the number of slopes to their minimum. For instance, with minor changes in protocols, spoiling and crusher gradient lobes are replaced by long rising or descending slopes, while maintaining the crusher moment unchanged. To keep the same total acquisition time, the reduction of the gradient slew rate is constrained by the fixed inter-echo spacing. The decreased slew rate of readout gradient will slightly reduce readout sampling time (Fig. 1). In consequence, the readout bandwidth (BW) increases slightly, with a tradeoff between reduction of SPL and SNR loss.

* WIP, the product is currently under development and is not for sale in the US and other countries. Its future availability cannot be ensured.

In addition, parallel acquisition could be further employed to reduce the echo-train length, i.e. number of echoes per train, by a factor of R. Keeping the acquisition time constant, the inter-echo spacing can be extended by R, allowing further stretching of the gradient moments. This effectively represents a benefit of parallel imaging acceleration in acoustic noise reduction rather than imaging time reduction.

The acquisition protocols changes are as follows: The readout BW was increased by about 10%, from 107 Hz/pixel in the standard protocol to 125 Hz/pixel. The effective TR/TE were increased from 5000/93 ms to 5180/85 ms, which resulted in only a 3 second increase in acquisition time, from 1:37 min to 1:40 min. The qTSE-G parameters were identical to the qTSE protocol, but with use of GRAPPA with R=2. For both qTSE and qTSE-G protocols, and the gradient slopes were maximally stretched as illustrated in figure 1.

Table 1: Comparison of dB_A values

Sequence type	Standard TSE	qTSE	qTSE-G	Background
LAEQ (30 sec average)	92.5	81.3	72.7	53.0
Max Peak	102.8	95.8	92.0	77.7

Comparison of dB_A values for standard TSE, qTSE, qTSE-G sequences, and measured background noise. Measurements were performed inside the bore at patient head position using a 2238 Mediator sound level meter (Brueel & Kjaer GmbH, Bremen, Germany).

Table 2: Ratings by readers

Sequence type	All techniques compared to themselves	qTSE : TSE	qTSE-G : TSE
Reader #1	0.35 ± 0.40 (0.06, 0.64) p = 0.02	-0.20 ± 0.26 (-0.38, -0.02) p = 0.04	0.20 ± 0.59 (-0.22, 0.62) p = 0.31
Reader #2	-0.03 ± 0.11 (-0.11, 0.04) p = 0.34	1.30 ± 1.96 (-0.10, 2.70) p = 0.07	3.95 ± 0.86 (3.33, 4.57) p < 0.0001
Reader #3	0 ± 0 –	0.73 ± 1.59 (-0.41, 1.86) p = 0.18	3.08 ± 1.25 (2.18, 3.97) p < 0.0001
Average	0.11 ± 0.14 (0.01, 0.21) p = 0.04	0.61 ± 1.17 (-0.23, 1.45) p = 0.13	2.41 ± 0.80 (1.83, 2.98) p < 0.0001

Mean and standard deviation, 95% confidence interval, and p-value of the scores given by each radiologist to the different types of image volume pairs after self-bias correction. Positive score show preference of the right volume over the left volume, on a -10 to +10 scale.

In-vivo studies were performed on a 3T MAGNETOM Verio MRI scanner (Siemens Healthcare, Erlangen, Germany) with a 12-channel head coil with patients admitted for head examination. Informed consent was obtained from the volunteer before the start of the study in accordance with IRB protocol. A total of 10 different patient scannings were performed, each comparing standard TSE images with qTSE and qTSE-G images. The image resolution (192 × 256 matrix), number of slices (26), slice thickness (5 mm) and slice orientation were kept identical throughout the 3 different acquisitions.

To measure acoustic noise level LAEQ (Equivalent Continuous Sound Level in A-weighting) with 30 seconds average and peak values, a professional device, 2238 Mediator sound level meter (Brueel & Kjaer GmbH, Bremen, Germany), was used, which was placed inside the bore at patient head position. The background noise is mainly generated by the cold-head pump and the ventilation among other sources.

To evaluate the image quality, a total of 7 image-volume-pairs were assembled from each of the 10 patient datasets. The first 2 pairs compared qTSE with TSE volumes, alternatively with qTSE on the left and TSE on the right. Similarly, another 2 pairs compared qTSE-G with TSE volumes in both left-right orders randomly. Finally, 3 pairs were assembled with the same volume on the left and right, which consist of TSE vs. TSE, qTSE vs. TSE, and qTSE-G vs. qTSE-G volumes, respectively.

All 70 volume pairs were presented in the same random order to 3 trained radiologists blinded to the acquisition technique, who were asked the following question: "On a scale from -10 to +10, how much better is the image quality of the volume on the right compared to the volume on the left, with a positive score indicating superiority of the right volume, and 0 representing no difference in quality between left and right?". The graphical user interface used for the reading allowed user-navigation through the paired-volume slices, and simultaneous image windowing of the 2 displayed images.

To avoid possible left-right bias, the average of the qTSE vs. TSE score and the TSE vs. qTSE score multiplied by -1 was then calculated for each reader's reading on each patient. The average of the corrected scores across readers was then computed for each patient. Corrected scores were calculated in the same way for the qTSE-G vs. TSE comparison. One-sample t-tests were used to test whether the mean average reader scores differed from zero, and 95% confidence intervals (CI) for the mean scores were also calculated. One-sample t-tests and CI were also carried out using each reader's scores

3

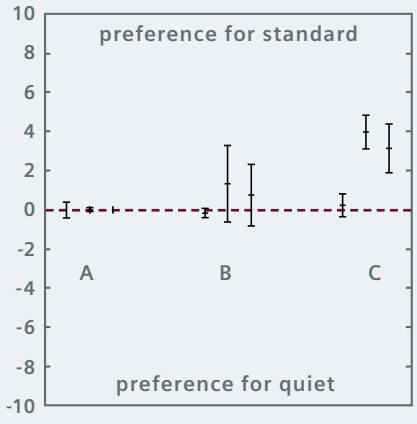

A. self image comparison (all methods)
($p < 0.05$)

B. qTSE vs. standard TSE
Non significant difference for all 3 readers
($p = 0.20$, $p = 0.06$, $p = 0.18$)

C. qTSE+GRAPPA vs. standard TSE
($p < 0.0001$)

3
(A) 95% confidence intervals for averages scores by readers for volumes compared to themselves; (B) qTSE vs. standard TSE; and (C) qTSE-G vs. standard TSE. Positive scores show preference for standard TSE in the last two cases.

separately. A reader's average rating of these three self-comparisons using images from each patient were averaged, and then the three reader averages were averaged for each patient. A t-test was used to test whether the average of the reader ratings across patients differed from zero. One-sample t-tests and CI were also carried out for each reader separately.

Results

The respective average and peak SPL in [dB_A] measurements for standard TSE, qTSE and qTSE-G protocols are listed in table 1. The achieved reduction of average SPL for qTSE and qTSE-G were 10 dB_A and near 20 dB_A (30 seconds average), respectively.

Discussion

Optimizing the gradient waveforms alone with a 10% increase in bandwidth achieves an 11 dB_A SPL reduction (Table 1), with little cost to image quality (Fig. 3). These results are in accordance with [16] though here the measurements were made directly at the bore. This cost might be more noticeable with lower SNR systems, however in this configuration, no statistically significant difference in image quality was observed (Table 2), making gradient redesign a viable solution to make TSE sequences quieter.

With additional use of Parallel Imaging, the modified quiet TSE sequence allows on average a 20 dB_A reduction in SPL (Table 1). The modified sequence had an effect on in image quality (Fig. 3): The average preference score across readers for standard TSE images over qTSE-G images was +2.41 ($p<0.0001$, Table 2), and the 95% confidence interval places its true value between +1.8 and +3. However it should be noted that this change in image quality is to be expected as Parallel Imaging was used. In compensation, the reduction of acoustic noise was highly effective: the SPL at the bore of the standard TSE sequence was 39.5 dB_A higher than the background noise, compared to 19.7 dB_A for the modified sequence.

Conclusion

In comparison with standard MR sequences, gradient wave modifications in TSE sequence coupled with Parallel Imaging can achieve over a factor 10 of acoustic noise reduction, yielding an improved patient comfort with nearly identical diagnostic information and imaging time. Without any hardware modifications or upgrade, both proposals described in this article, qTSE and qTSE-G, can be easily implemented on a conventional MRI system for routine clinical applications. In addition, scanning on a high field system with multiple channel coils, such as the 32-channel head coil, provides more flexibility to make MRI scanning quieter.

* Work in progress: The product is still under development and not commercially available yet. Its future availability cannot be ensured.

References

1 Shellock FG, Morisoli SM, Ziarati M. Measurement of acoustic noise during MR imaging: evaluation of six "worst-case" pulse sequences. Radiology 1994;191:91–93.
2 McJury M, Blug A, Joerger C, Condon B, Wyper D. Acoustic noise levels during magnetic resonance imaging scanning at 1.5 T. Br J Radiol 1994;67:413–415.
3 McJury M. Acoustic noise levels generated during high field MR imaging. Clin Radiol 1995;50:331–334.
4 Quirk ME, Letendre AJ, Ciottone RA, Lingley JF. Anxiety in patients undergoing MR imaging. Radiology 1989;170:463–466.
5 Hedeen R, Edelstein W. Characterization and prediction of gradient acoustic noise in MR imagers. Magn Reson Med 2005;37:7–10.
6 Katsunuma A, Takamori H, Sakakura Y, Hamamura Y, Ogo Y, Katayama R. Quiet MRI with novel acoustic noise reduction. MAGMA 2002;13:139–44.
7 Edelstein WA, Hedeen RA, Mallozzi RP, El-Hamamsy SA, Ackermann RA, Havens TJ. Making MRI quieter. Magn Reson Imaging 2002;20:155–63.
8 Edelstein WA, Kidane TK, Taracila V, Baig TN, Eagan TP, Cheng Y-CN, Brown RW, Mallick J a. Active-passive gradient shielding for MRI acoustic noise reduction. Magn Reson Med 2005;53:1013–7.
9 Cho ZH, Chung ST, Chung JY, Park SH, Kim JS, Moon CH, Hong IK. A new silent magnetic resonance imaging using a rotating DC gradient. Magn Reson Med 1998;39:317–21.
10 Mansfield P, Haywood B. Principles of active acoustic control in gradient coil design. MAGMA 2000;10:147–51.
11 Haywood B, Chapman B, Mansfield P. Model gradient coil employing active acoustic control for MRI. MAGMA 2007;20:223–31.

12 Shou X, Chen X, Derakhshan J, Eagan T, Baig T, Shvartsman S, Duerk J, Brown R. The suppression of selected acoustic frequencies in MRI. Appl Acoust 2010;71:191–200.
13 Hennel F, Girard F, Loenneker T. "Silent" MRI with soft gradient pulses. Magn Reson Med 1999;42:6–10.
14 De Zwart J, Vangelderen P, Kellman P, Duyn J. Reduction of Gradient Acoustic Noise in MRI Using SENSE-EPI. Neuroimage 2002;16:1151–1155.
15 Witzel T, Wald LL. Methods for Functional Brain Imaging. Massachusetts Institute of Technology; 2011.
16 Pierre EY, Grodzki D, Heismann B, Liu K, Griswold MA. Reduction of Acoustic Noise to Improve Patient Comfort Through Optimized Sequence Design. In: Proceedings of the 21st Annual Meeting of ISRMRM. Vol. 42. Salt Lake City, USA; 2013. p. 256.

Contact

Eric Y. Pierre, Ph.D.
Department of Biomedical Engineering
Case Western Reserve University
319 Wickenden Building
10900 Euclid Avenue
Cleveland, OH 44106-7207
USA
Phone: +1 (216)-368-4063
pierre@case.edu


Eric Pierre


Gunhild Aandal


Vikas Gulani


Jeffrey Sunshine


Mark Schluchter


Kecheng Liu


Mark Griswold



RESOLVE: A Powerful Tool for Imaging the Pediatric Spine

Laura L. Hayes[1]; David A. Porter[2]; Richard A. Jones[1, 3]; Susan Palasis[1]; J. Damien Grattan-Smith[1]

[1]Department of Radiology, Children's Healthcare of Atlanta at Scottish Rite, Atlanta, GA, USA
[2]Siemens AG, Healthcare Sector, Erlangen, Germany
[3]Department of Radiology, Emory University, Atlanta, GA, USA

Introduction

Diffusion-weighted imaging (DWI) is one of the most powerful imaging tools available to radiologists today. DWI of the brain revolutionized neuroimaging when it was introduced in the mid-1990s. Until recently, clinically useful DWI of the spine has not been possible using standard single shot EPI techniques due to susceptibility artifacts and the need for higher spatial resolution. The novel 2D-navigator-corrected readout-segmented EPI sequence known as RESOLVE (REadout Segmentation Of Long Variable Echo trains) can obtain images with higher spatial resolution and reduced distortion of the spine related to susceptibility, pulsations, respiration, and motion [1]. This is especially helpful when imaging children where the small size of their spine/cord, prominent CSF and arterial pulsations, and higher pulse and respiratory rates compared to adults can pose significant limitations on the quality of the images obtained. Motion artifacts that notoriously plague every facet of pediatric imaging are also reduced with RESOLVE. RESOLVE is proving to be a valuable sequence for the evaluation of numerous pathological states of the pediatric spine.

Sequence description

RESOLVE [1, 2] is a multi-shot, diffusion-weighted sequence, which is based on the readout-segmented echo-planar imaging (rs-EPI) sampling scheme [3]. The sequence incorporates a 2D non-linear correction for motion-induced phase errors [4] and supports iPAT using GRAPPA [5]. The rs-EPI method only samples a subset of raw data points in the readout direction, making it possible to use a very short EPI echo spacing with a typical value of 360 µs. This is significantly shorter than the echo spacing used for single-shot EPI (ss-EPI), which reduces the level of susceptibility and blurring

1

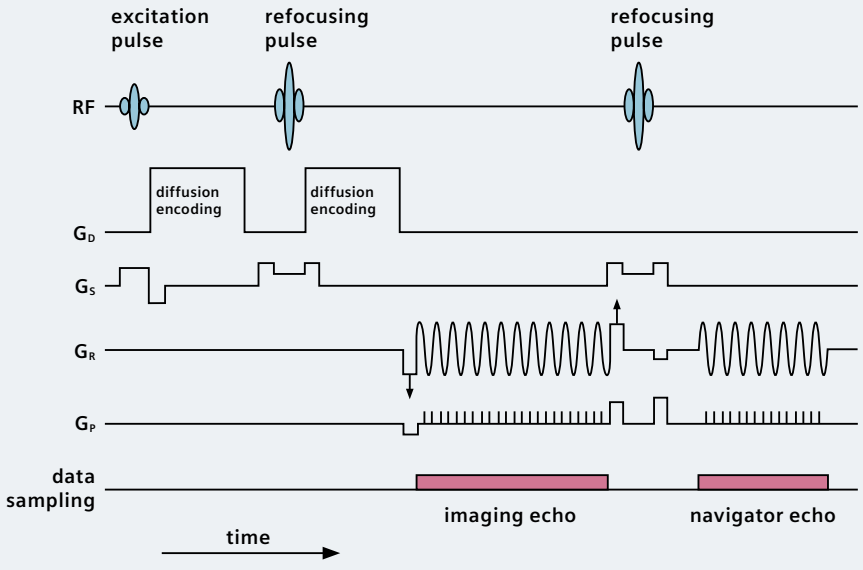

1 Pulse diagram for the RESOLVE sequence. The figure shows radiofrequency (RF) pulses and magnetic field gradient pulses for diffusion-encoding (G_D) and for spatial encoding along slice (G_S), readout (G_R) and phase-encoding (G_P) directions. The gradients with the ↟ symbol have an amplitude that is varied at each spin excitation to control an offset in the k_x direction, so that a different readout segment is sampled by the imaging echo at each shot. In contrast, the navigator echo always samples a fixed 2D region at the centre of *k*-space.

artifacts and makes it possible to acquire images with a higher spatial resolution.

In general, multi-shot, diffusion-weighted sequences are susceptible to image artifacts that arise from motion during the diffusion preparation, resulting in shot-to-shot phase errors. Navigator phase correction [6, 7] can address this problem by sampling data from the center of *k*-space at each shot; these data are then used to monitor and correct the phase variation between shots. CSF pulsation around the brain and spinal cord causes non-rigid-body motion, resulting in a 2D non-linear phase variation in image space, which requires 2D navigator data to perform a correction [4]. The rs-EPI sampling scheme is particularly well-suited to this type of correction because, unlike the more commonly used interleaved EPI sequence, the Nyquist sampling condition is fulfilled at each shot and there are no aliased signal contributions in the image domain to interfere with the phase correction procedure.

As shown in figure 1, following a spin excitation and diffusion preparation, the RESOLVE sequence uses two EPI readouts to acquire data from two spin echoes respectively at each shot. The first spin echo is used to sample a region of *k*-space, known as a readout segment, in which contiguous data samples are collected for all phase-encoding (k_y) points and for a subset of readout (k_x) points. A variable pre-phase gradient is applied along the readout (*x*) axis before the EPI readout to control an offset along k_x, so that a different readout segment is sampled at each shot. As shown in the *k*-space trajectory in figure 2, data from multiple readout segments are combined to provide full *k*-space coverage; typical protocols require 5, 7 or 9 shots to acquire the full data set, depending on the spatial resolution. The second spin echo shown in figure 1 is used to sample the central readout segment at each shot, thereby providing data for the 2D non-linear navigator correction. This is performed as a complex multiplication in the image domain before the data from the individual segments are combined to form the final image.

2

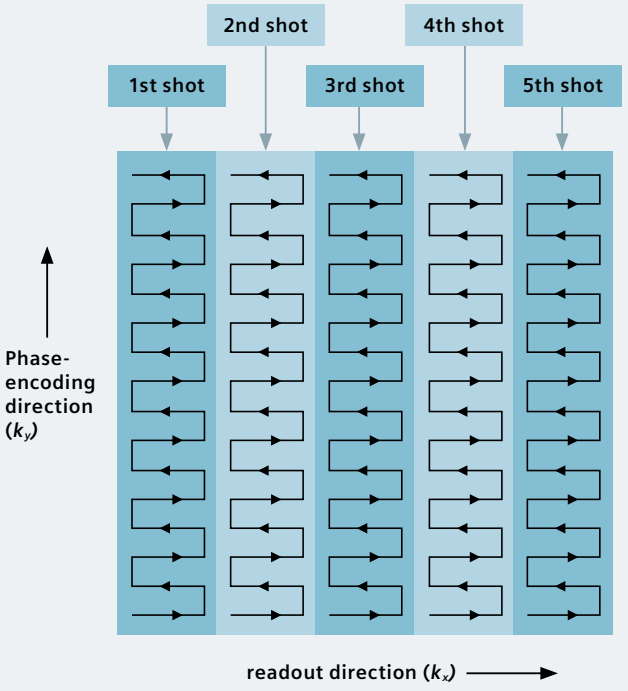

2 Diagram showing the *k*-space sampling scheme used for the imaging echo in the RESOLVE sequence. In this example, a five shot acquisition is used which divides *k*-space into five segments along the readout direction. Within each shot, an EPI readout is used to sample all phase-encoding (k_y) points and a subset of readout (k_x) points. The second (navigator) echo is always used to sample the central readout segment, providing 2D reference data from the center of *k*-space, which are used to perform a non-linear phase correction.

To further reduce the effect of motion-induced phase errors, the RESOLVE sequence uses a reacquisition scheme [8], which has been adapted to the case of a 2D navigator [9]. This ensures that readout segments with severe phase errors, which cannot be removed by the 2D navigator correction, are discarded and replaced by reacquired data.

Currently useful applications:
1. Tumor
a. Intradural
i. Drop metastases

DWI of the brain has revolutionized the sensitivity of MR in diagnosis, staging, and follow-up of children with central nervous system (CNS) tumors [10]. Likewise DWI of the spine is demonstrating the ability to reveal spinal disease that may not be visible on conventional MR sequences in children with primary brain tumors [11] (Figs. 3–5). Many of the primary CNS tumors that metastasize to the spine have a hypercellular tumor matrix. Primitive neuro-ectodermal tumors (PNETs) consist of small, round cells with scanty cytoplasm and have an extremely high cellular density with a high nuclear-to-cytoplasmic index. The total water content of these tumors is low, and their densely packed cellular nature results in restricted diffusion. The physical characteristics of these tumors render them sensitive to detection by DWI. Due to their high grade and often high degree of necrosis, they may not exhibit enhancement on conventional imaging sequences that currently are the standard imaging method for detection of drop metastasis. Medulloblastoma, a PNET, is the second most common neoplasm of the CNS in children and has pathologic features that make it optimal for

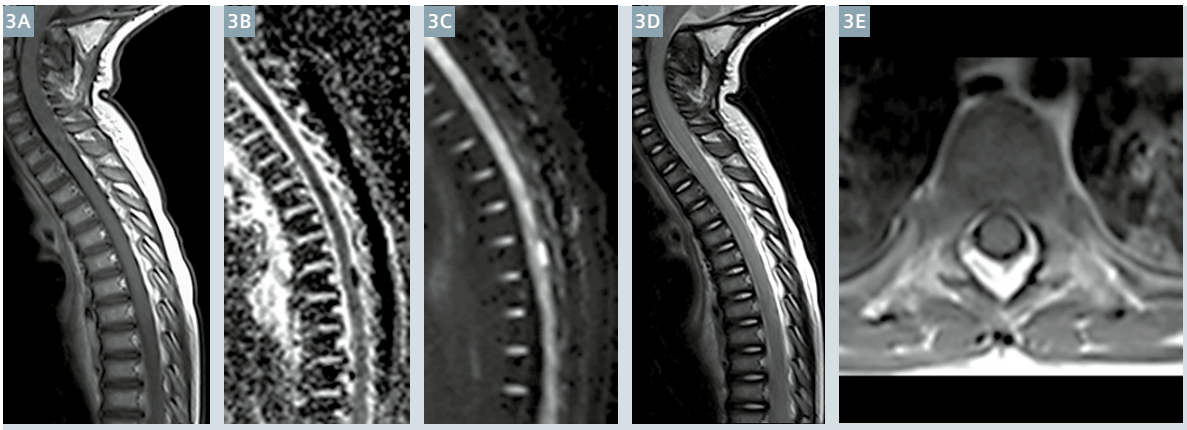

3 2-year-old girl* with ataxia and vomiting found to have a large posterior fossa tumor that restricted diffusion and demonstrated minimal enhancement, consistent with an atypical rhabdoid teratoid tumor (ATRT). Initial MRI scan of the spine: Sagittal T1 post-contrast **(3A)**, ADC map **(3B)**, isotropic DWI **(3C)**, sagital T2 **(3D)**, and axial T1 post-contrast image at the level of interest **(3E)** demonstrate the lack of any abnormal signal or enhancement **(3A, D, E)** at the location of the nodular diffusion abnormality at the dorsal aspect of the thoracic cord **(3B, C)**.

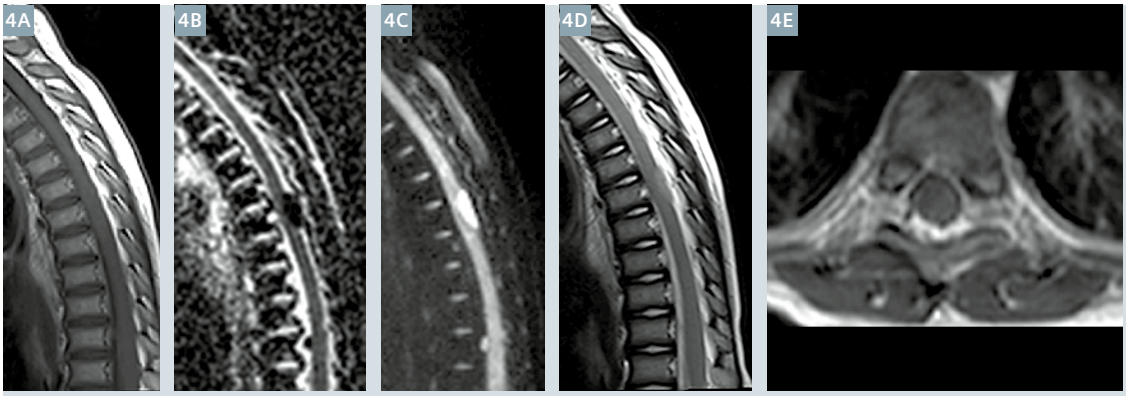

4 Follow up scan two months later. Sagittal T1 post-contrast **(4A)**, ADC map **(4B)**, isotropic DWI **(4C)**, sagittal T2 **(4D)**, and axial T1 post-contrast image at the level of interest **(4E)** demonstrate interval increase in the size of the previously visualized nodular diffusion abnormality, now also seen on the T2 image as well. Another nodular diffusion abnormality along the ventral aspect of the lower thoracic cord is now clearly visible. Note the continued lack of conspicuity on the T1 post-contrast images **(4A, E)**.

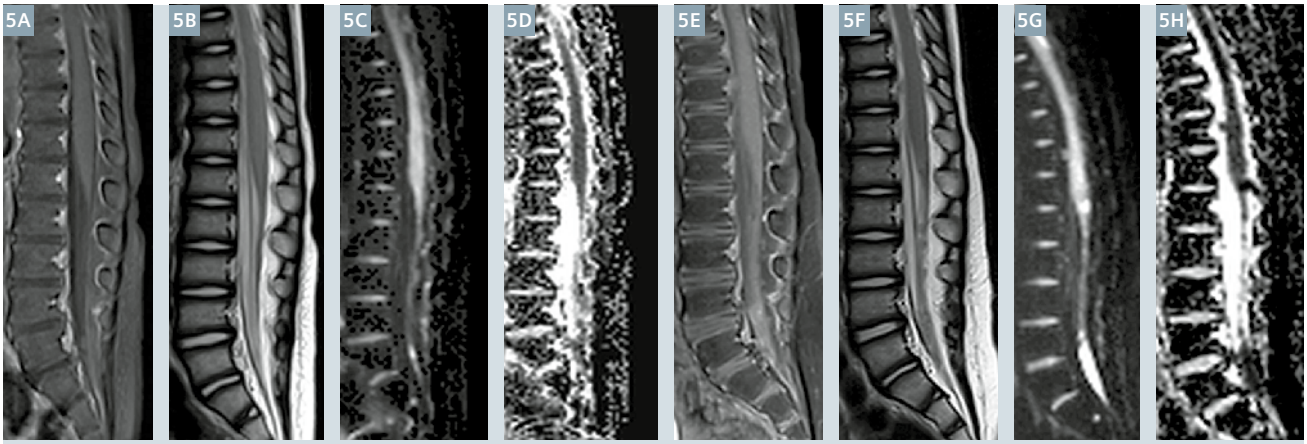

5 Images of the thoracolumbar spine from initial scan **(5A–D)** and follow-up scan two months later **(5E–H)**. Initially negative T1 post-contrast **(5A)** and T2 image **(5B)** with possible tiny, nodular diffusion abnormality along the distal cauda equina on isotropic DWI **(5C)** and ADC map **(5D)**. Follow-up T1 post-contrast image demonstrates enhancement within the distal thecal sac **(5E)**; T2 image demonstrates nodularity along the cauda equina and within the distal thecal sac **(5F)**; isotropic DWI **(5G)** and ADC map **(5H)** demonstrate nodular and clumpy areas of restricted diffusion consistent with drop metastases.

evaluation with DWI. Other CNS tumors that can restrict diffusion and spread to the spine include other PNETs such as atypical teratoid rhabdoid tumor (ATRT), as well as ependymoma, glioblastoma multiforme, germinoma, and choroid plexus carcinoma.

ii. Primary cord tumor

Just as in the brain, DWI is helpful in narrowing the differential diagnosis of primary spinal tumors (Fig. 6). Diffusion tensor imaging (DTI) can be used to visualize ordered white matter tracts of the spinal cord in an effort to further characterize a mass. It is helpful to determine whether the lesion displaces the tracts or infiltrates between them. Identification of white matter tracts can ultimately assist in surgical planning as well [12].

iii. Epidermoid

Restricted diffusion within a solitary intradural cyst is essentially pathognomonic for an epidermoid cyst (Fig. 7). The restricted diffusion within these cysts is related to their squamous epithelial contents. Epidermoids are often congenital and can be related to tethered cords, a common indication for spine MRI in children. Arachnoid cysts and epidermoid cysts can be easily differentiated with DWI [13].

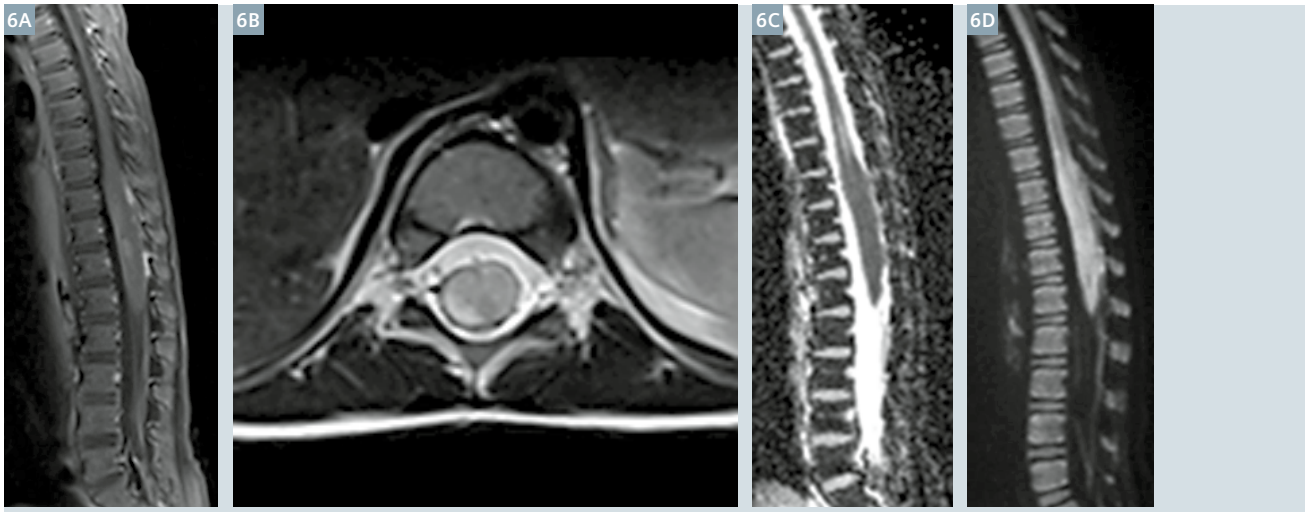

6 2-year-old boy* with limping and back pain. Sagittal T1 post-contrast **(6A)** and axial T2 images **(6B)** demonstrate an intramedullary mass involving the conus medullaris. There is mild enhancement of the lesion, and the mass is iso- to hyperintense on T2. ADC map **(6C)** reveals isointensity of the mass with the normal cord, corresponding to an iso- to hyperintense appearance on the isotropic DWI image **(6D)**. This excludes a densely cellular lesion such as PNET, and is consistent with a lower grade lesion such as a diffuse leptomeningeal neuroepithelial tumor (DLNT) as in this case.

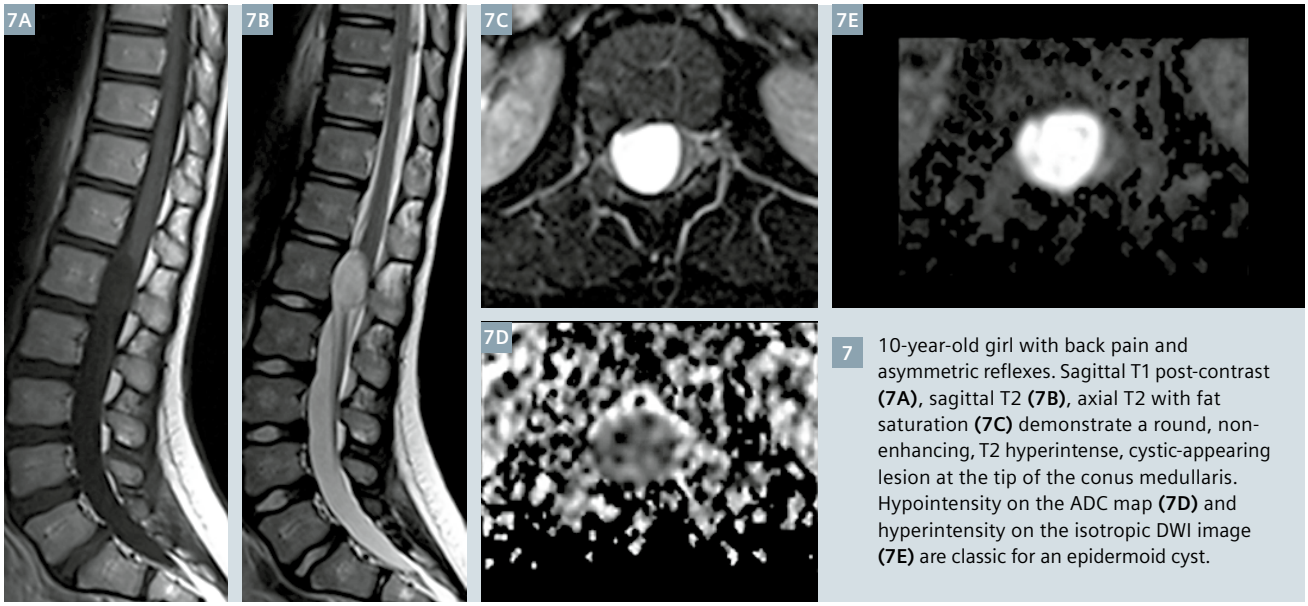

7 10-year-old girl with back pain and asymmetric reflexes. Sagittal T1 post-contrast **(7A)**, sagittal T2 **(7B)**, axial T2 with fat saturation **(7C)** demonstrate a round, non-enhancing, T2 hyperintense, cystic-appearing lesion at the tip of the conus medullaris. Hypointensity on the ADC map **(7D)** and hyperintensity on the isotropic DWI image **(7E)** are classic for an epidermoid cyst.

b. Extradural

i. Vertebral/paravertebral/ metastatic tumors

As previously discussed, spine DWI is particularly well-suited to pediatric oncologic imaging due to the high frequency of densely cellular tumors that occur in children. These tumors can be found both intra- and extradurally within the spine. Pediatric extradural tumors that lend themselves to DWI detection include neuroblastoma, leukemia, lymphoma, rhabdomyosarcoma, and Ewing sarcoma (Fig. 8). The unifying pathologic feature of these tumors is that they are comprised of small, round, blue cells. In the case of primary vertebral Ewing sarcoma, DWI not only assists with tumor detection but also in differentiation from other vertebral lesions that can have a similar appearance on conventional imaging sequences such as eosinophilic granuloma and chordoma (Fig. 9).

Diffusion-weighted imaging can also be a useful tool for distinguishing acute benign osteoporotic from malignant vertebral compression fractures. Increased water motion is typically present in post-traumatic benign compression fractures resulting in low or iso-intense signal on DWI and high ADC values on ADC maps [14]. In contrast, pathologic compression fractures related to densely cellular tumors such as lymphoma have restricted diffusion with hyperintensity on DWI and hypointensity on ADC maps [15] (Fig. 10).

2. Infarction

DWI is a powerful tool in the identification of spinal cord infarction, sometimes revealing restricted diffusion in the cord even before changes on the T1 or T2-weighted images develop [16]. Spinal cord infarctions in children are rare, but can occur in such settings as spinal arteriovenous malformations (AVMs) and fibrocartilaginous emboli. The latter are caused by retrograde migration of nucleus pulposis from the intervertebral disk into the spinal microcirculation [17]. This is usually caused by a minor physical trauma or a physical effort in conjunction with Valsalva [16]. Acute spinal cord infarcts present with severe pain followed by a rapidly progressive paraplegia/tetraplegia and loss of reflexes. MR images reveal cord swelling, increased T2 signal, and

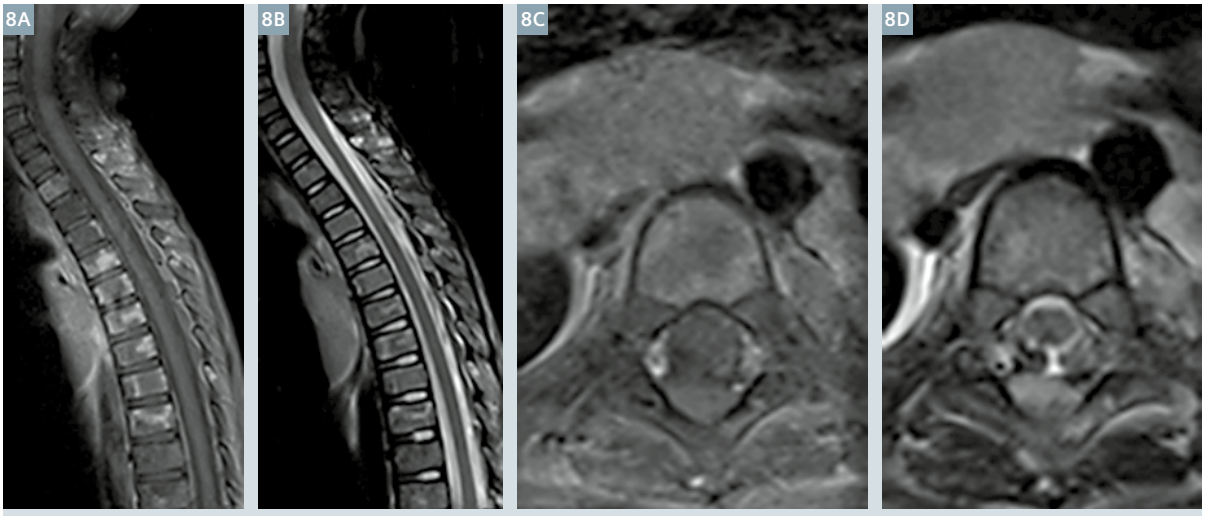

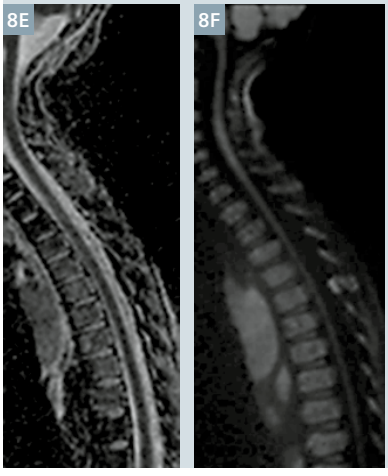

8 6-year-old boy with intermittent fevers, bilateral leg pain, and abdominal mass. Sagittal T1 post-contrast with fat saturation **(8A)**, sagittal T2 **(8B)**, axial T1 post-contrast with fat-saturation **(8C)**, axial T2 with fat-saturation **(8D)**, sagittal ADC map **(8E)** and isotropic DWI **(8F)** images demonstrate a large paraspinal mass invading the central spinal canal. Restricted diffusion within the mass is consistent with neuroblastoma. Note the epidural involvement at the dorsal aspect of T5, well delineated on the isotropic DWI sequence. Extensive metastatic disease involving the vertebral bodies is also apparent.

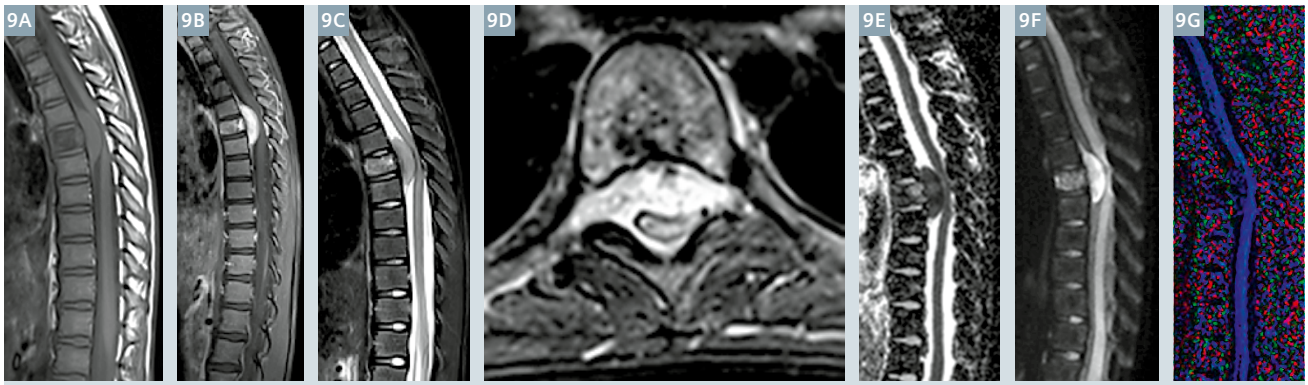

9 8-year-old boy with ataxia. Sagittal pre-contrast T1 **(9A)** and post-contrast T1 with fat saturation **(9B)**, sagittal and axial T2 with fat saturation **(9C, D)**, sagittal ADC **(9E)**, isotropic DWI **(9F)**, and color FA (fractional anisotropy) map **(9G)** reveal a large, enhancing epidural mass involving the T6 vertebral body producing cord compression. Restricted diffusion in the mass **(9E, F)** is typical for Ewing sarcoma.

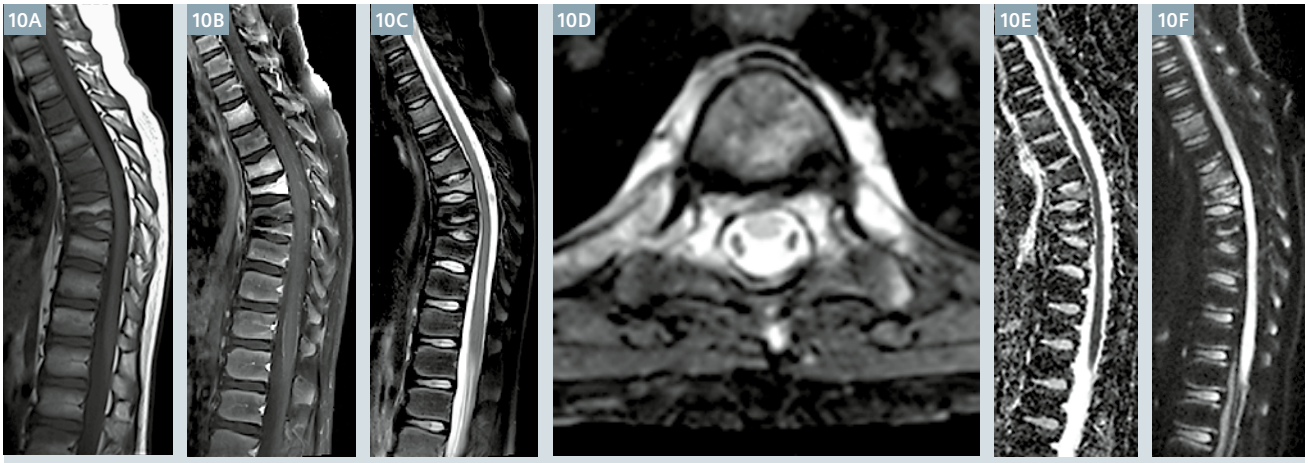

10 10-year-old boy with back pain. Sagittal pre-contrast T1 **(10A)**, post-contrast T1 with fat saturation **(10B)**, sagittal and axial T2 with fat saturation **(10C, D)**, ADC map **(10E)** and isotropic DWI **(10F)** images demonstrate multilevel compression fractures with enhancement of the involved vertebral bodies, low signal on ADC maps, and marked hyperintensity on DWI. Findings are consistent with leukemia/lymphoma. Chronic relapsing multifocal osteomyelitis is one differential consideration.

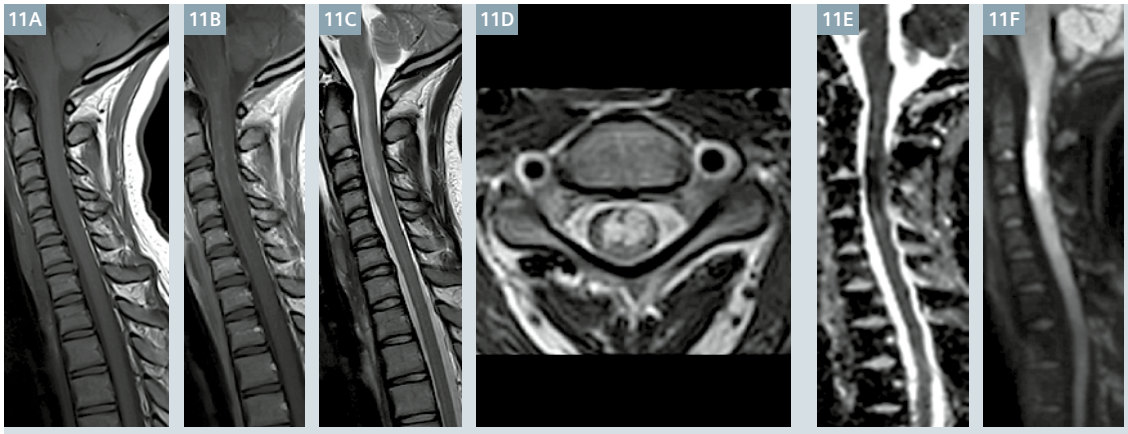

11 17-year-old girl with acute onset of neck pain followed by flaccid tetraparesis. Sagittal pre- and post-contrast T1 **(11A, B)** and sagittal and axial T2 **(11C, D)** images demonstrate intrinsic T2 hyperintensity within the cord from the level of the cervicomedullary junction to the level of C4. There is corresponding hypointensity with minimal enhancement on T1. Sagittal ADC map **(11E)** demonstrates marked hypointensity within the cord at these levels, and isotropic DWI image **(11F)** demonstrates hyperintensity consistent with acute cord infarction.

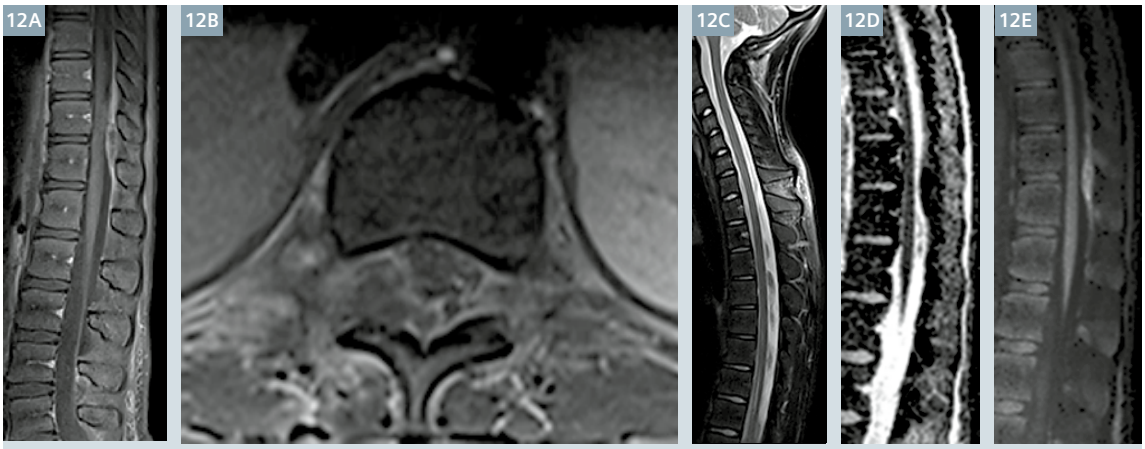

12 12-year-old girl with back pain, fever, and CSF pleocytosis. Sagittal and axial T1 post-contrast with fat saturation **(12A, B)**, sagittal T2 with fat saturation **(12C)**, sagittal ADC map **(12D)**, and isotropic DWI **(12E)** images reveal an epidural collection with irregular enhancement with associated paraspinal soft tissue edema. There is corresponding hypointensity on the ADC map with well-defined hyperintensity on isotropic DWI in keeping with restricted diffusion in an abscess.

markedly restricted diffusion [18] (Fig. 11). Spinal cord infarcts secondary to fibrocartilaginous emboli can demonstrate loss of expected T2-hyperintensity in the disk and loss of disk height.

DWI can aid in the differentiation of acute infarction from inflammatory conditions such as transverse myelitis, a condition not uncommon in children. While restricted diffusion can be seen with transverse myelitis once vasogenic edema becomes cytotoxic, the ADC values are typically not as low as those seen with acute infarction. Further studies are needed to evaluate these differences.

3. Infection

Infection involving the spine is frequently encountered in children. Osteomyelitis, diskitis, and epidural abscesses are common ailments, caused by hematological seeding of bacteria and often manifested with fever, pain, and/or limp. Abscesses can be surgical emergencies due to their potential for cord compression that requires emergent surgical intervention before permanent cord damage ensues. Prompt and accurate imaging detection is critical, and can be assisted by the use of spine DWI. Both osseous and epidural/intradural abscesses restrict diffusion, appearing markedly hyperintense on isotropic trace images and dark on ADC maps [19]. Polymorphonuclear leukocytes and necrotic debris in abscesses restricts water motion, a characteristic that can help differentiate abscesses from simple or mildly proteinaceous fluid collections. Abscess formation is often more conspicuous on DWI than on conventional images. DWI can also identify the extent of the abscess and assist in identifying multifocal disease that may not otherwise be apparent (Fig. 12).

Future directions

DWI shows promise in the evaluation of numerous pathological states of the pediatric spine. More research is needed in regards to demyelinating disease such as multiple sclerosis and spinal cord trauma such as SCIWORA (Spinal Cord Injury Without Radiographic Abnormality) in an effort to improve lesion detection and contribute to a prompt and accurate prognosis.

Several technical developments could further improve the quality of spine DWI images, specifically the use of coils with larger numbers of elements (which has improved diffusion imaging of the brain in recent years) and the use of multi-band to improve the efficiency of the image acquisition [20, 21]. Work also needs to be done to determine the optimum b-values for spine imaging as a range of values has been used in the literature.

As RESOLVE becomes more readily available in the community, it should serve to revolutionize spine imaging just as DWI did when it was introduced into routine MR imaging of the brain. DWI of the brain is currently standard-of-care in MR imaging, and we expect that DWI of the spine will become part of the standard of care for spine imaging in the near future.

Conclusions

RESOLVE DWI is a powerful imaging tool for evaluation of spinal pathology. Images presented in this article demonstrate that this technique is exquisitely helpful in the work-up of numerous pathological conditions of the spine affecting children, including tumor, infarction, and infection.

*Siemens Disclaimer: MR scanning has not been established as safe for imaging fetuses and infants less than two years of age. The responsible physician must evaluate the benefits of the MR examination compared to those of other imaging procedures.

References

1 Porter DA, Heidemann RM. High resolution diffusion weighted imaging using readout segmented echo planar imaging, parallel imaging and a two dimensional navigator based reacquisition. Magn Reson Med 2009;62:468-475.
2 Porter DA, Mueller E. Multi-shot diffusion-weighted EPI with readout mosaic segmentation and 2D navigator correction. In: Proceedings of the 12th Annual Meeting of ISMRM, Kyoto, Japan, 2004. p442.
3 Robson MD, Anderson AW, Gore JC. Diffusion-weighted multiple-shot echo planar imaging of humans without navigation. Magn Reson Med 1997; 38:82-88.
4 Miller KL, Pauly JP. Nonlinear phase correction for navigated diffusion imaging. Magn Reson Med 2003;50:343–353.
5 Griswold MA, Jakob PM, Heidemann RM, Nittka M, Jellus V, Wang J, Kiefer B, Haase A. GeneRalized Autocalibrating Partially Parallel Acquisitions (GRAPPA). Magn Reson Med 2002;47:1202-1210.
6 Ordidge RJ, Helpern JA, Qing ZX, Knight RA, Nagesh V. Correction of motional artefacts in diffusion-weighted MR images using navigator echoes. Magn Reson Imag 1994; 12:455-460.
7 Anderson AW, Gore JC. Analysis and correction of motion artifacts in diffusion weighted imaging. Magn Reson Med 1994;32:379-387.
8 Nguyen Q, Clemence M, Thornton J, Ordidge RJ, Isotropic diffusion-weighted multishot imaging using automatic reacquisition. In: Proceedings of the 7th Annual Meeting of ISMRM, Philadelphia, USA, 1999. p 559.
9 Porter DA. 2D-navigator-based re-acquisition for motion artefact suppression in multi-Shot, diffusion-weighted Imaging. In: Proceedings of the 14th Annual Meeting of ISMRM, Seattle, USA, 2006. p1047.
10 Moffat BA, Chenevert TL, Lawrence TS et al. Functional diffusion map: a noninvasive MRI biomarker for early stratification of clinical brain tumor response. PNAS 2005; 102(15): 5524-5529.
11 Hayes LL, Jones RA, Palasis S, Aguilera D, Porter DA. Drop metastases to the pediatric spine revealed with diffusion-weighted MR imaging. Pediatr Radiol 2012;42(8): 1009-13.
12 Tanenbaum LN. Clinical applications of diffusion imaging in the spine. Magn Reson Imaging Clin N Am 2013;21(2): 229-320.
13 Kukreja K, Manzano G, Ragheb J, Medina LS. Differentiation between pediatric spinal arachnoid cyst and epidermoid-dermoid cysts: is diffusion-weighted MRI useful? Pediatr Radiol 2007;37(6):556-60
14 Rumpel H, Chong Y, Porter DA, Chan LL. Benign versus metastatic vertebral compression fractures: combined diffusion-weighted MRI and MR spectroscopy aids differentiation. Eur Radiol 2013;23(2):541-50.
15 Baur A, Stäbler A, Brüning R, Bartl R, Krödel A, Reiser M, Deimling M. Diffusion-weighted MR imaging of bone marrow: differentiation of benign versus pathologic compression fractures. Radiology 1998;207(2):349-56.
16 Manara R, Calderone M, Severino MS, Citton V, Toldo I, Laverda AM, Sartori S. Spinal cord infarction due to fibrocartilaginous embolism: the role of diffusion weighted imaging and short-tau inversion recovery sequences. J Child Neurol 2010;25(8):1024-8.
17. Reisner A, Gary MF, Chern JJ, Grattan-Smith JD. Spinal cord infarction following minor trauma in children: fibrocartilaginous embolism as a putative cause. J Neurosurg Pediatr 2013;11(4):445-50.
18 Tsang BK, Foster E, Kam A, Storey E. Diffusion weighted imaging with trace diffusion weighted imaging, the apparent diffusion coefficient and exponential images in the diagnosis of spinal cord infarction. J Clin Neurosci 2013;20(11): 1630-2.
19 Eastwood JD, Vollmer RT, Provenzale JM. Diffusion-weighted imaging in a patient with vertebral and epidural abscesses. AJNR 2002;(23): 496-498.
20 Setsompop K, Gagoski BA, Polimeni JR, Witzel T, Wedeen VJ, Wald LL. Blipped-controlled aliasing in parallel imaging for simultaneous multislice echo planar imaging with reduced g-factor penalty. Magn Reson Med 2012;67:1210–1224.
21 Frost R, Porter DA, Douaud G, Jezzard P, Miller KL. Reduction of diffusion-weighted readout-segmented EPI scan time using a blipped-CAIPI modification. In: Proceedings of the 20th Annual Meeting of ISMRM, 2012 (abstract 116).



Contact

Laura L. Hayes, M.D.
Children's Healthcare of Atlanta at Scottish Rite
1001 Johnson Ferry Road NE
Atlanta, GA 30342
USA
laura.hayes@choa.org

Amide Proton Transfer MRI in Patients with High-Grade and Low-Grade Gliomas

Yan Bai[1]; Panli Zuo[2]; Benjamin Schmitt[3]; Dapeng Shi[1]; Jinyuan Zhou[4]; Meiyun Wang[1]

[1]Department of Radiology, Henan Provincial People's Hospital, Zhengzhou, Henan, China
[2]Siemens Healthcare, MR Collaborations NE Asia
[3]Siemens Healthcare, Erlangen, Germany
[4]Department of Radiology, Johns Hopkins University, Baltimore, MD, USA

Introduction

The grading of gliomas has clinical significance in determining a treatment strategy and evaluating prognosis. Despite the accumulated knowledge in clinical practice, differentiating high-grade and low-grade gliomas has persistently posed a dilemma for radiologists in many cases, because of the overlapping imaging findings on conventional MR imaging. One of the differences between solid tumors and normal tissue is the acidic micro-environment around the tumor caused by hydrolysis of Amide Proton Transfer (APT) and an upregulated anaerobic metabolism. As a consequence of the increased intracellular generation of acidic values, the transport of acidic compounds to the extracellular space is upregulated correspondingly to prevent the cellular metabolism from breaking down, which, in turn, can result in slightly increased intracellular pH values [1]. APT is a new MRI technique which detects endogenous mobile proteins and peptides in biotissues, such as tumors [2]. Previous studies have showed that APT MRI is sensitive to changes in cellular pH and protein concentration [3]. Here we used APT MRI, which does not require exogenous contrast agents, as a tool to distinguish high-grade and low-grade gliomas.

Theory

Chemical exchange-dependent saturation transfer (CEST) imaging, which was introduced by Balaban in the early 1990s, is a type of magnetization transfer (MT) imaging to measure exchangeable protons in proteins. As shown in figure 1, the low-concentration proteins are labeled by saturating their exchangeable protons (e.g., hydroxyl, amine, and amide) via selective radio-frequency (RF) irradiation at their specific resonance frequency, and then the labeled protons are transferred to the bulk water via chemical exchange at an exchange rate. The

1

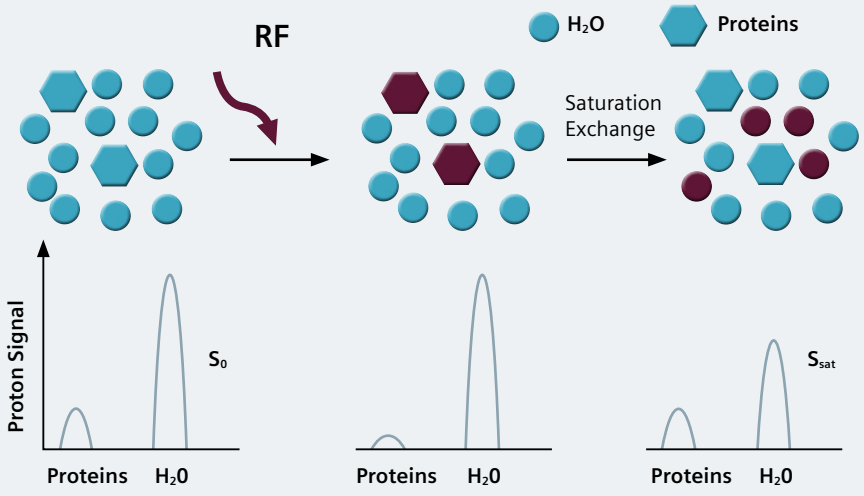

1 A schematic of chemical exchange saturation transfer (CEST). Water and proteins are two pools of protons and have distinct chemical shifts. Protons of proteins are saturated at their specific resonance frequency via RF irradiation. This saturation is transferred to water and decreases the water signal.

solute protons are always at a very low concentration and hard to detect directly using standard MR protocols. However, after a certain time of continuous transfer, this effect decreases the MRI signal and the protons are detected indirectly through the attenuation of the water signal. This effect is measured by using the ratio of water signals with (S_{sat}) and without saturation (S_0).

For the CEST analysis, the most common metric used is the magnetization transfer asymmetry (MTR_{asym}) analysis by subtracting the right and left MT ratio ($MTR=1-S_{sat}/S_0$) to reduce the interference of the coexisting conventional MR and direct saturation effects:

$$MTR_{asym} = S_{sat}(-\Delta\omega)/S_0 - S_{sat}(+\Delta\omega)/S_0 \quad (1)$$

in which $\Delta\omega$ is the frequency difference with water. Plotting MTR with the saturation frequency gives a Z-spectrum (also called CEST spectrum). The amide protons resonate at 8.3 ppm of the proton MR spectrum (3.5 ppm to water signal) and are used for amide proton transfer (APT) imaging.

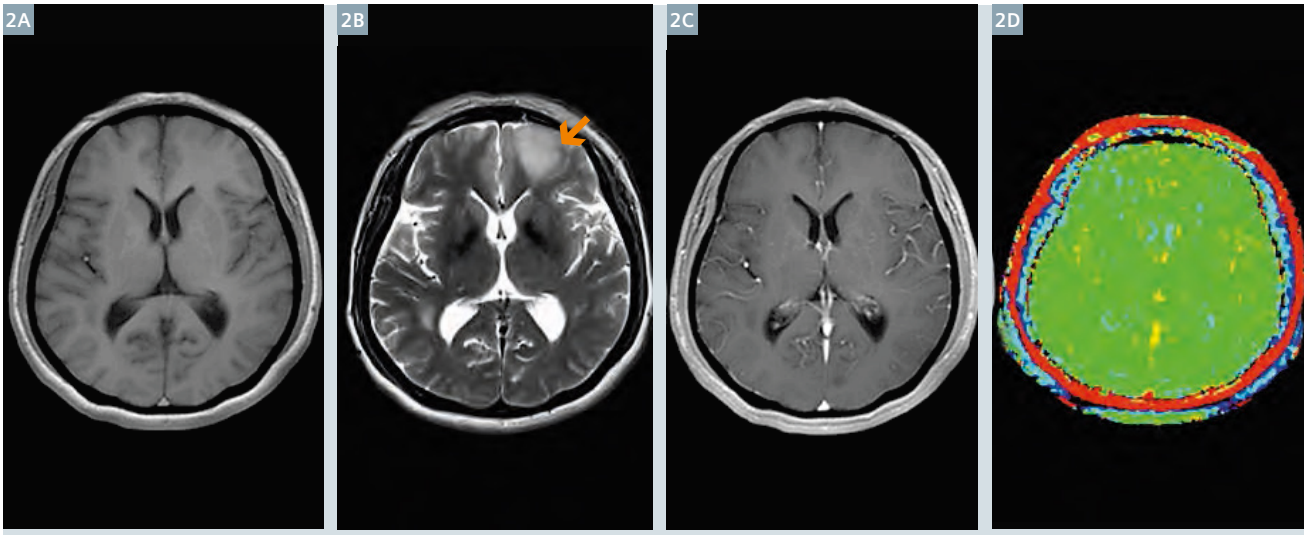

2 51-year-old female patient with astrocytomas (WHO grade II) in the left frontal lobe. **(2A)** T1-weighted image; **(2B)** T2-weighted image; **(2C)** Post-gadolinium T1-weighted image; **(2D)** APT map.

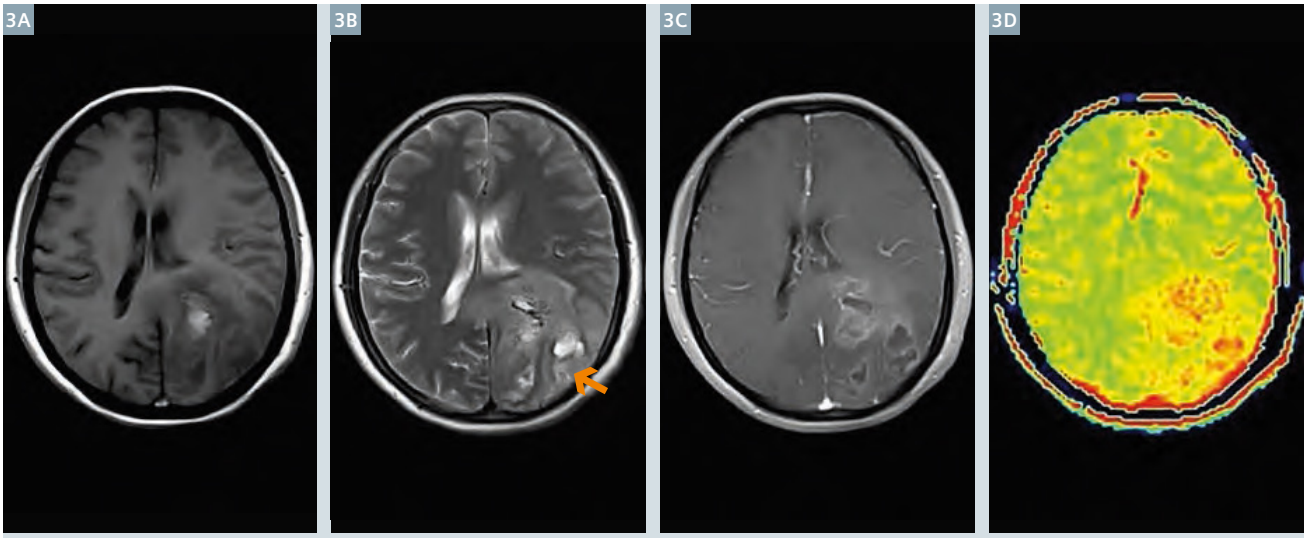

3 47-year-old male patient with glioblastoma (WHO grade IV) in the left occipital lobe. **(3A)** T1-weighted image; **(3B)** T2-weighted image; **(3C)** Post-gadolinium T1-weighted image; **(3D)** APT map.

Patient history

Case 1 is a 51-year-old female patient with astrocytomas (WHO grade II) in the left frontal lobe (Fig. 2). She had neurologic complaints including dizziness, nausea and vomiting for 5 hours before the MRI examination.

Case 2 is a 47-year-old male patient with glioblastoma (WHO grade IV) in the left occipital lobe (Fig. 3). He had a two months history of insomnia and a five hours history of complaints including dizziness, nausea and vomiting before the MRI examination.

Sequence details

The patients were examined at a 3T MR system (MAGNETOM Trio a Tim System, Siemens AG, Erlangen, Germany). The APT images were acquired using a GRE-based CEST* WIP sequence with the following parameters: TR 3200 ms, TE 2.87 ms, FA 10 degrees, slice thickness 5 mm. The saturation module was applied before the imaging readout. Four RF pulses were repeated for 21 different offset frequencies from +5 to -5 ppm (interval is 0.5 ppm) with respect to the water frequency. MTR asymmetry analysis at the offset around 3.5 ppm is calculated to obtain APT images.

*WIP, the product is currently under development and is not for sale in the US and other countries. Its future availability cannot be ensured.

Imaging findings

In Case 1, the low-grade glioma in the left frontal lobe is not very apparent on the T1-weighted image (Fig. 2A), but shows hyperintensity on the T2-weighted image (Fig. 2B). No enhancement is revealed on the contrast-enhanced T1-weighted image (Fig. 2C). The APT map demonstrates the tumor's isointensity (Fig. 2D).

In Case 2 the solid part of the high grade glioma shows hypointensity on the T1-weighted image (Fig. 3A) and heterogeneous hyperintensity on the T2-weighted image (Fig. 3B). The hemorrhage area in the tumor shows isointensity to hyperintensity on the T1-weighted image (Fig. 3A) and hyperintensity on the T2-weighted image (Fig. 3B). Irregular enhancement is revealed on contrast-enhanced T1-weighted image (Fig. 3C). The APT map demonstrates that the tumor, including the solid and hemorrhage components, is hyperintense (Fig. 3D).

Conclusion

Our preliminary results demonstrate that this GRE-based CEST sequence can provide APT images with good quality. It has been shown that intracellular pH is almost the same in tumor and in normal tissue. High APT signal in high-grade cerebral gliomas is usually due to high protein concentration [2, 3]. The non-invasive technique of APT may be a useful tool to detect the mobile cellular proteins and an upward pH shift *in vivo*. It has the potential to be an alternative imaging modality to improve the diagnostic accuracy in grading gliomas.

References
1 Zhou J, Lal B, Wilson DA, et al. Amide Proton Transfer (APT) Contrast for Imaging of Brain Tumors. Magn Reson Med. 2003;50:1120-1126.
2 Zhou J, Blakeley JO, Hua J, et al. Practical data acquisition method for human brain tumor amide proton transfer (APT) imaging. Magn Reson Med. 2008;60(4):842-849.
3 Zhou J, Tryggestad E, Wen Z , et al. Differentiation between glioma and radiation necrosis using molecular magnetic resonance imaging of endogenous proteins and peptides. Nat Med. 2011;17(1):130-134.



Contact

Meiyun Wang, M.D., Ph.D.
Associate Director
Department of Radiology
Henan Provincial People's Hospital
Zhengzhou, Henan 450003
China
Phone: +86-371-6558-0267(0)
marian9999@163.com

Case Series: Minimally Invasive 3 Tesla Interventional MRI

Kemal Tuncali, M.D.

Brigham and Women's Hospital, Dept. of Radiology, Boston, MA, USA

Case 1

76-year-old man with cirrhosis was discovered to have a 2.5 cm lesion in segment 4/8 of the liver suspicious for a hepatocellular carcinoma (HCC). This was visualized on a 1.5 Tesla MRI study only with the use of i.v. contrast. It was not seen by ultrasound or CT scan. Hence, MRI-guided biopsy was performed in 3 Tesla MRI (MAGNETOM Verio, Siemens Healthcare, Erlangen, Germany).

Using spine coil elements and body matrix coil, the lesion is seen as a T1 hyperintense mass (Fig. 1). This was used to guide 22 gauge MRI-compatible needles into the mass and Fine-needle aspiration (FNA) biopsy was performed under local anesthesia and i.v. procedural sedation. The patient tolerated the procedure well without complications and the pathology proved the lesion to be an HCC.



1 MRI guided liver biopsy. Intraprocedural axial T1-weighted SPGR (VIBE) shows liver lesion and biopsy needle*.

Case 2

65-year-old woman with history of breast cancer and a newly discovered 1.3 cm left kidney upper pole lesion suspicious for tumor. To differentiate between metastasis versus a renal origin tumor, percutaneous biopsy was indicated. However, this small renal mass was embedded in the renal parenchyma and very difficult to see with other imaging modalities except for MRI where it was well visualized even without the use of i.v. contrast material. 3T MRI (MAGNETOM Verio, Siemens Healthcare, Erlangen, Germany) with spine coil elements and body matrix coil was used for imaging.

Axial T2w TSE respiratory triggered sequence (BLADE) provided excellent visualization of the small lesion and needle location (18 gauge MRI-compatible) with minimal artifact (Fig. 2). The procedure was performed under local anesthesia and i.v. procedural sedation. The patient tolerated the procedure well without complications. Pathology showed mucinous tubular and spindle cell carcinoma, a low grade primary cancer of the kidney.

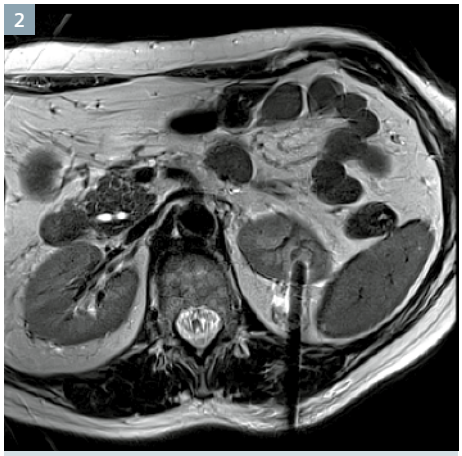

2 MRI guided kidney biopsy. Intraprocedural axial T2w respiratory triggered TSE (BLADE) shows the 18 gauge biopsy needle in the small renal mass.

*Metal: The MRI restrictions (if any) of the metal implant must be considered prior to patient undergoing MRI exam. MR imaging of patients with metallic implants brings specific risks. However, certain implants are approved by the governing regulatory bodies to be MR conditionally safe. For such implants, the previously considered prior to patient undergoing MRI exam. MR imaging of patients with metallic implants brings specific risks. However, certain implants are approved by the governing regulatory bodies to be MR conditionally safe. For such implants, the previously mentioned warning may not be applicable. Please contact the implant manufacturer for the specific conditional information. The conditions for MR safety are the responsibility of the implant manufacturer, not of Siemens.

Case 3

57-year-old woman with a 2 cm left kidney upper pole biopsy proven renal cell carcinoma. Its small size and intraparenchymal location in the upper pole renders it challenging for partial nephrectomy. Since it is well seen on MRI, cryoablation using MRI guidance was preferred as a minimally-invasive nephron-sparing treatment option. 3T MRI (MAGNETOM Verio, Siemens Healthcare, Erlangen, Germany) with spine coil elements and an 11 cm loop coil was used for imaging.

Axial and sagittal HASTE sequence was used to place three 17 gauge MRI-compatible cryoablation probes (Galil Medical, Plymouth, PA USA) and to monitor the ablation (Fig. 3). This helped cover the tumor completely while preventing injury to adjacent pancreas and adrenal gland. The procedure was performed in the prone position under general anesthesia without complications.

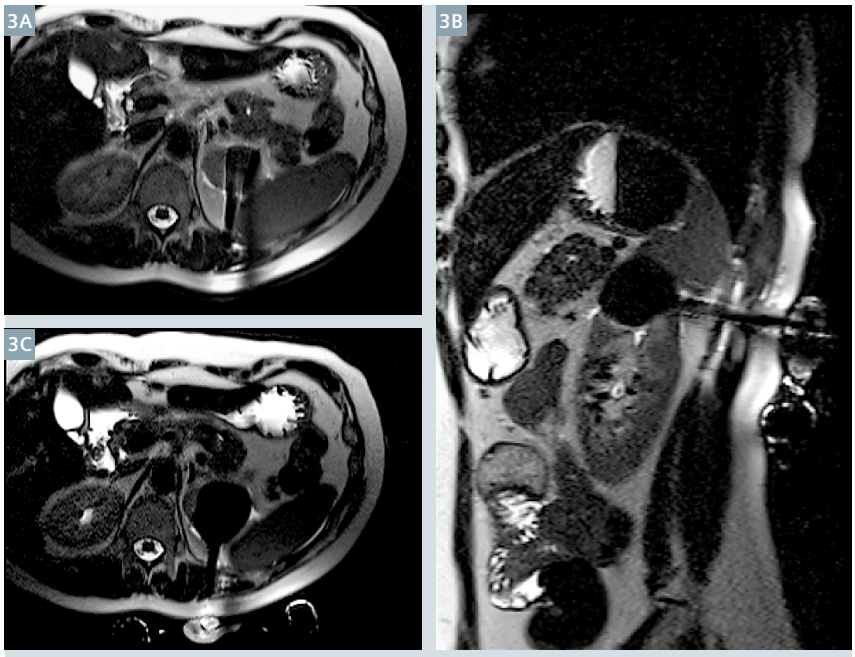

3 **Cryoablation of native renal mass.**
(3A) Intraprocedural axial T2w HASTE shows two of the probes in the renal tumor. **(3B)** Sagittal T2w HASTE obtained 10 min into the 2nd freezing cycle shows the iceball close to adjacent pancreas but without overlap.
(3C) Axial T2w HASTE obtained at the end of the 2nd 15 min freezing cycle shows that the iceball has eclipsed the tumor and is close to the adjacent adrenal gland but without overlap.

Case 4

68-year-old man with a 2.9 cm left lower pole biopsy proven renal cell carcinoma, discovered during hematuria workup. Due to comorbid coronary artery disease, patient was referred for minimally invasive, nephron sparing image-guided cryoablation. MRI guidance was preferred due to tumor proximity to ureter to minimize risk of injury. 3T MRI (MAGNETOM Verio, Siemens Healthcare, Erlangen, Germany) with spine coil elements and body matrix coil was used for imaging. Axial T2W HASTE sequence was used to place three 17 gauge MRI-compatible cryoablation probes (Galil Medical, Plymouth, PA USA) and to monitor the ablation (Fig. 4). This ensured covering the tumor completely while preventing injury to adjacent ureter. The procedure was performed in the prone position under local anesthesia and i.v. procedural sedation. The patient tolerated the procedure well without complications.

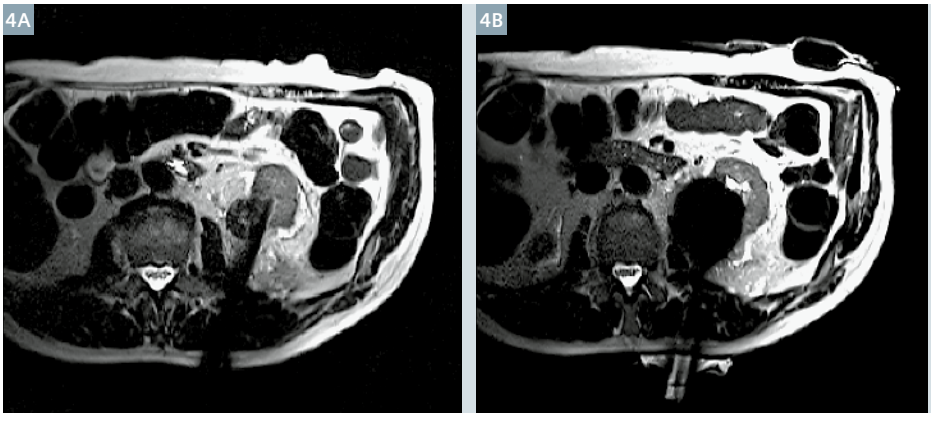

4 **Cryoablation of native renal mass.**
(4A) Intraprocedural axial T2w HASTE shows first of the three probes being placed in the renal tumor.
(4B) Intraprocedural axial T2w HASTE obtained at the end of the 2nd 15 min freezing cycle shows that the iceball has eclipsed the tumor without overlapping adjacent proximal ureter.

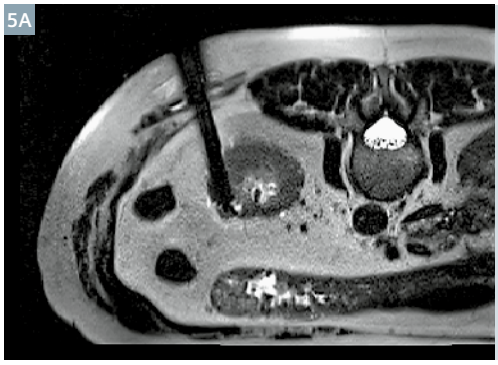

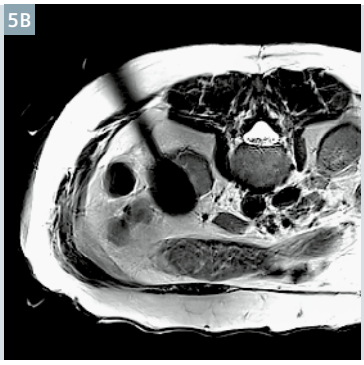

5

Cryoablation of native renal mass.
(5A) Intraprocedural axial T2w HASTE shows first of the three probes being placed in the renal tumor.
(5B) Intraprocedural axial T2w respiratory triggered TSE (BLADE) obtained at the end of the 2nd 15 min freezing cycle shows that the iceball has eclipsed the tumor without overlaping adjacent colonic wall.

Case 5

68-year-old man with 2.4 cm left lower pole renal cell carcinoma. Due to history of lung cancer, cutaneous T-cell lymphoma and chronic lymphocytic leukemia, he was referred for percutaneous cryoablation as a minimally invasive, nephron sparing treatment option.

3T MRI (MAGNETOM Verio, Siemens Healthcare, Erlangen, Germany) with spine coil elements and body matrix coil was used for imaging. Axial T2w HASTE sequence was used to place three 17 gauge MRI-compatible cryoablation probes (Galil Medical, Plymouth, PA USA) (Fig. 5A). Then, for more detailed monitoring of the ablation, we utilized an axial T2w respiratory triggered TSE (BLADE) sequence (Fig. 5B). This ensured covering the tumor completely while preventing injury to adjacent colon. The procedure was performed in the prone position under local anesthesia and i.v. procedural sedation. The patient tolerated the procedure well without complications.

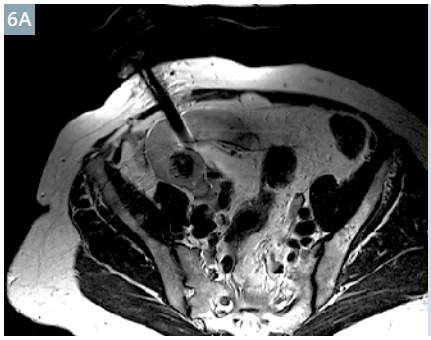

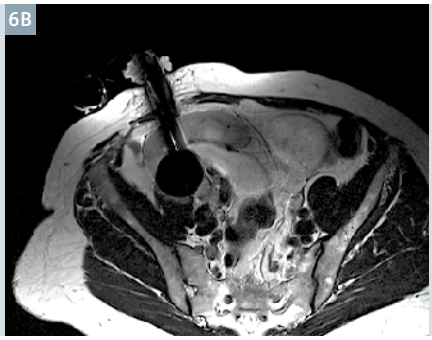

6

Cryoablation of renal transplant mass.
(6A) Intraprocedural axial T2w TSE shows first of the three probes being placed in the renal tumor.
(6B) Intraprocedural axial T2w TSE obtained at the end of the 2nd 15 min freezing cycle shows that the iceball has eclipsed the tumor without overlaping adjacent renal pelvis.

Case 6

66-year-old woman with a 2.1 cm biopsy proven renal cell carcinoma inside of a renal transplant located in her right lower abdomen. She was referred for percutaneous cryoablation as a minimally-invasive nephron-sparing treatment option. The tumor margins were not well seen on ultrasound or CT scan due to its small size and intraparenchymal location.

However, MRI showed the tumor very well. 3T MRI (MAGNETOM Verio, Siemens Healthcare, Erlangen, Germany) with spine coil elements and an 11 cm loop coil was used for imaging.

Axial T2w TSE sequence was used to place three 17 gauge MRI-compatible cryoablation probes (Galil Medical, Plymouth, PA USA) and to monitor the ablation (Fig. 6). This ensured covering the tumor completely while preventing injury to adjacent renal pelvis and ureter. The procedure was performed in the supine position under local anesthesia and i.v. procedural sedation. The patient tolerated the procedure well without complications.



Contact

Kemal Tuncali, M.D.
Brigham and Women's Hospital
Department of Radiology
75 Francis St
Boston, MA 02115, USA
ktuncali@partners.org

GRASP: Tackling the Challenges of Abdominopelvic DCE-MRI

Kai Tobias Block[1]; Li Feng[1]; Robert Grimm[2]; Hersh Chandarana[1]; Ricardo Otazo[1]; Christian Geppert[2]; Daniel K. Sodickson[1]

[1] Department of Radiology, NYU Langone Medical Center, New York, NY, USA
[2] Siemens Healthcare, Erlangen, Germany

Introduction

Dynamic contrast-enhanced (DCE) T1-weighted acquisition after injection of a gadolinium-based contrast agent is an integral part of most diagnostic abdominopelvic MRI examinations and essential for identifying and properly characterizing lesions and tumors, such as the hepatocellular carcinoma (HCC) or renal cancer [1]. Because tumors show a specific temporal contrast-enhancement pattern, it is necessary to obtain images of the whole region-of-interest at multiple short time points following the injection. While technically infeasible years ago, parallel-imaging acceleration techniques such as GRAPPA [2] have made it possible to achieve the required acquisition speed using standard clinical MRI systems, so that these scans can nowadays be performed at almost all imaging centers.

However, in routine practice abdominopelvic DCE-MRI exams remain challenging and the failure rates are undesirably high.

One main challenge is that the data has to be collected precisely at defined time points relative to the arrival time of the contrast agent in the aorta (see Fig. 1). To this end, usually a small test bolus is injected prior to the actual diagnostic scan and monitored using a bolus-tracking sequence to determine the patient-specific circulation delay [3]. Once estimated, the delay is then incorporated into the timing calculation of the dynamic scans, which are scheduled relative to the injection time of the contrast dose. This procedure is, of course, prone to inaccuracies and mistakes – with the potential risk of missing the important arterial phase (AP) of contrast enhancement. As additional complication, the dynamic acquisitions have to be performed during a strict breath hold of the patient and, thus, need to be properly synchronized with breath-hold commands. While the latter can be automated using computer-controlled voice instructions [3], it cannot be guaranteed that the patient is actually following these breath-hold instructions. Continued respiration occurs due to various reasons, including inability to hold breath for the scan duration (usually ~15 sec per acquisition), hearing or language problems, and uncertainty when exactly to stop breathing after hearing the command. Especially elderly or severely sick patients often struggle to properly suspend respiration, resulting in compromised or even fully non-diagnostic image quality. A particular problem here is that once the injection has been done, the acquisitions cannot be repeated before the contrast agent has been extracted from the body, which takes several hours and requires

1

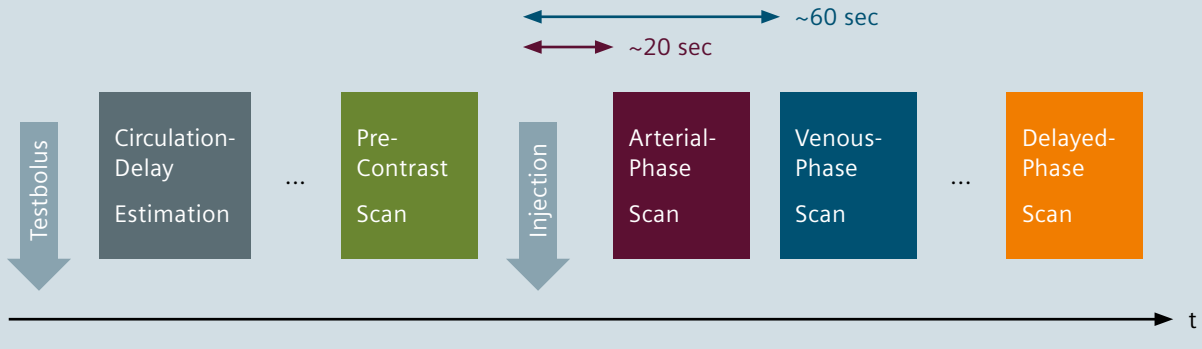

1 Conventional scheme for abdominopelvic DCE-MRI exams, starting with the injection of a test bolus to determine the circulation delay. Afterwards, a pre-contrast image is acquired as well as images in arterial, venous, and delayed phases of contrast enhancement. The acquisitions must be properly timed relative to the injection and accounting for the circulation delay, which makes the procedure prone to timing errors. Furthermore, the scans need to be performed during breath holding.

rescheduling of the examination on a different day. Strongly compromised image quality is also obtained when examining sedated or anesthetized patients, where suspending the respiration is not possible at all.

DCE-MRI with continuous radial acquisition

The requirement to perform abdominal scans during breath-holding results from the high motion sensitivity of conventional MRI techniques, as motion translates into appearance of numerous overlapping object copies known as ghosting artifacts. This problem can be ameliorated by using non-Cartesian acquisition techniques such as radial *k*-space sampling, which inherently prevent the appearance of motion-induced ghosting artifacts. Radial scanning techniques, such as the Radial VIBE or StarVIBE sequence [4], have recently become available for routine imaging, and it has been demonstrated that these sequences can be used to image the abdomen during free breathing [5]. However, the higher motion robustness of radial *k*-space trajectories comes at the price of lower scan efficiency. With typical scan durations of around 60 sec per image volume, sequences such as Radial VIBE are by itself too slow for dynamic abdominopelvic imaging as it would be impossible to separate the arterial and venous phases of enhancement.

To overcome this problem, our group has recently developed a technique called GRASP* that enables using the Radial VIBE sequence for DCE-MRI applications and that resolves many of the aforementioned challenges [6]. The key idea of GRASP is that, instead of performing several individual acquisitions for the required time points, data is acquired continuously throughout the whole exam while the contrast agent is injected (see Fig. 2). Image sets for the needed time points are then calculated from the continuously acquired data using an iterative reconstruction procedure (as described in the next section).

*WIP, the product is currently under development and is not for sale in the US and in other countries. Its future availability cannot be ensured.

This concept leads to a significant simplification of the overall clinical workflow. Because data is acquired all the time during the examination, it is not necessary anymore to determine the circulation delay using a test bolus. Also, the possibility of missing one of the important enhancement phases as a result of a timing or synchronization error is eliminated. Furthermore, because based on radial *k*-space acquisition, GRASP examinations can be performed during continued breathing [7], which removes the need for breath-hold commands, improves patient comfort, and makes the technique well-suited for patients where holding breath is impossible, such as pediatric** patients. Hence, with GRASP, the formerly complex and stressful abdominopelvic DCE-MRI exams now become a simple one-click procedure.

** MR scanning has not been established as safe for imaging fetuses and infants under two years of age. The responsible physician must evaluate the benefit of the MRI examination in comparison to other imaging procedures.

2

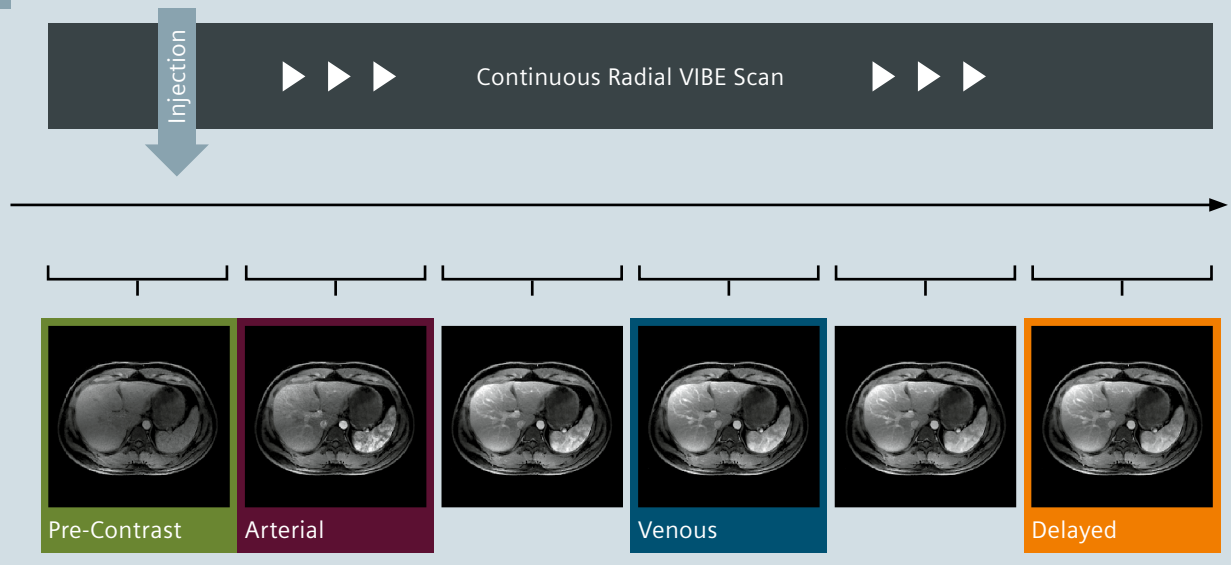

2 GRASP scheme for DCE-MRI, which uses a single continuous acquisition while the contrast agent is injected. Because radial sampling of k-space is used, the data can be acquired during free breathing. Images are calculated from the continuous data using an iterative reconstruction that allows selecting the desired time points and temporal resolution retrospectively. This eliminates the possibility of timing errors and leads to significant simplification of the workflow.

Technical background

On a technical level, GRASP combines several concepts for MRI scan acceleration that have been described previously as individual techniques. The data acquisition is based on the radial golden-angle ordering scheme, which was originally proposed by Winkelmann et al. [8]. When acquiring radial data with constant angular increment of 111.25 degrees (referred to as 'golden angle' because it corresponds to 180 degrees multiplied by the golden ratio), successively sampled radial spokes always add complementary *k*-space information to the previously acquired data, and any number of grouped spokes cover *k*-space approximately uniformly. This means that if data is acquired continuously over some time, any number of successively acquired spokes can be combined into an individual image (e.g., 144 spokes for low temporal resolution, or 21 spokes for high temporal resolution). Furthermore, the reconstruction window can be placed at any time point of the scan. In other words, it is possible to retrospectively decide which temporal resolution and which time points should be reconstructed.

When grouping only few spokes into each image to achieve high temporal resolution, as needed in DCE-MRI for separating the phases of enhancement, the data available for each time point is highly incomplete or, according to MR terminology, undersampled. For radial sequences, this means that the images are affected by severe 'streak' artifacts, which render the images diagnostically unusable. However, GRASP applies two known tricks to suppress this effect and to recover artifact-free images from the undersampled data: Compressed sensing [9] and parallel imaging [10]. The use of compressed sensing is motivated from the fact that the streak artifacts lead to strongly flickering patterns if viewed along time, whereas the true contrast enhancement occurs in a 'smooth' non-flickering fashion. In other words, flickering pixel intensities can be considered as artificial effects. Therefore, artifact-free images can be obtained by employing an iterative reconstruction procedure that, during each calculation step, matches the solution with the available undersampled data and, in addition, suppresses flickering pixels. Mathematically, this is achieved by calculating the total variation (TV) of each pixel along time and using this value as penalty measure during the iterations (because the true solution should have low total variation). By running the iterative procedure for a certain number of iterations, the streak artifacts disappear and the underlying true solution is recovered – even for severely undersampled data. As second mechanism, parallel imaging is integrated into the iterative scheme by using a CG-SENSE-type formalism [11], which contributes to the suppression of streaking artifacts by exploiting local coil sensitivities. Due to the synergistic combination of these two MR acceleration techniques, GRASP is able to compensate for the lower scan efficiency of radial sampling and achieves even higher temporal resolution than possible with most conventional DCE-MRI techniques. The key advantage, however, consists in the aforementioned workflow simplification.

Clinical integration and evaluation

The downside of using such an iterative reconstruction approach is that the image calculation involves a very computationally demanding numerical process (because the solution has to be mapped between image space and radial *k*-space over and over again). This property is not specific to GRASP and applies to other compressed-sensing techniques likewise. However, a difference is that the amount of data acquired during continuous GRASP acquisitions is enormous (up to 10 GB per scan). Processing such a vast amount of data with the described algorithm is not feasible using the computer components of current clinical MRI scanners, as the MRI systems would be blocked from clinical scanning for an unacceptable long time. Hence, for validating the feasibility of the GRASP technique in actual clinical practice, it was necessary for us to derive a workflow-friendly solution that completely circumvents the normal reconstruction pipeline. Therefore, we developed an offline-processing framework [12] that automatically transfers the acquired GRASP data from our various clinical MRI scanners to a central reconstruction server. Incoming reconstruction tasks are queued according to urgency (clinical vs. research scan) and processed with a parallelized and performance-optimized C++ implementation of the GRASP algorithm. Upon completion, the reconstructed images are sent into the clinical PACS without any user interaction. Our radiologists can then read the GRASP exams side-by-side with other scans that were reconstructed directly on the MRI scanner. Using our current reconstruction server with 64 CPU cores, GRASP images are available in the PACS within 5 to 45 minutes after the exam (depending on the exact scan/reconstruction protocol). With this seamless integration of the GRASP prototype into our routine clinical workflow, a stable solution is now in place to evaluate the technique in a large number of patients and across our different MRI systems. Over the last two years, already several thousand GRASP reconstructions have been performed at our institution, and the setup has recently also been disseminated to multiple collaboration sites for an independent evaluation.

Initial applications

As the development of GRASP was aimed at improving abdominal DCE-MRI, liver and kidney scans are logically among the main applications. Figure 3 shows exemplary images from a free-breathing GRASP liver exam of an adult patient, which are free from the typical MRI ghosting artifacts for continued respiration. In this reconstruction, 55 spokes were combined into each image, which yields a temporal resolution of 8.8 sec per image volume and fulfills the timing requirements for diagnostic abdominal DCE-MRI. However, a very powerful feature of GRASP is that the same dataset can be reconstructed with different temporal resolution as well.

When grouping only 13 spokes into each image, the resulting temporal resolution is 2.1 sec and, thus, fast enough for quantitative tissue-perfusion analysis. Researchers in our group are currently exploring this possibility for assessment of the liver function via dual-input dual-compartment modeling [13] and for assessment of the kidney function via estimation of the glomerular filtration rate (GFR). The key advantage here is that the perfusion information is obtained simultaneously without need for additional contrast injection or scan time. Thus, in the future, the GRASP concept might not only help to make abdominal examinations more robust but also provide new diagnostic measures.

Due to the high scan efficiency and simple workflow, GRASP is also very interesting for dynamic imaging of the prostate [14], which has become the GRASP application with the largest clinical scan volume at our institution. In prostate DCE-MRI, which is also with conventional techniques acquired during free breathing due to the required long readout (to properly capture the contrast washout), the main benefit of using GRASP consists in the higher achievable resolution (both spatially and temporally), which translates into an improved detectability and characterization of small tumors. Figure 4 shows images from our current GRASP protocol with 1.1 x 1.1 x 3.0 mm spatial and 2.2 sec temporal resolution, which represents a significant improvement in comparison to our former protocol and allows more precise assessment of the uptake/washout characteristics of suspicious lesions. In this application, data is acquired over a total duration of 5:38 min while the contrast agent is injected 20 sec after the start of the scan to ensure that sufficient pre-contrast data is available. In addition to the higher resolution, also the motion robustness of GRASP contributes to the achieved improvement in image clarity, as conventional prostate scans are often affected by ghosting artifacts caused by motion of the rectum or adjacent bowel loops.

Because GRASP handles such motion effects in a relatively benign manner, our clinical researchers have started

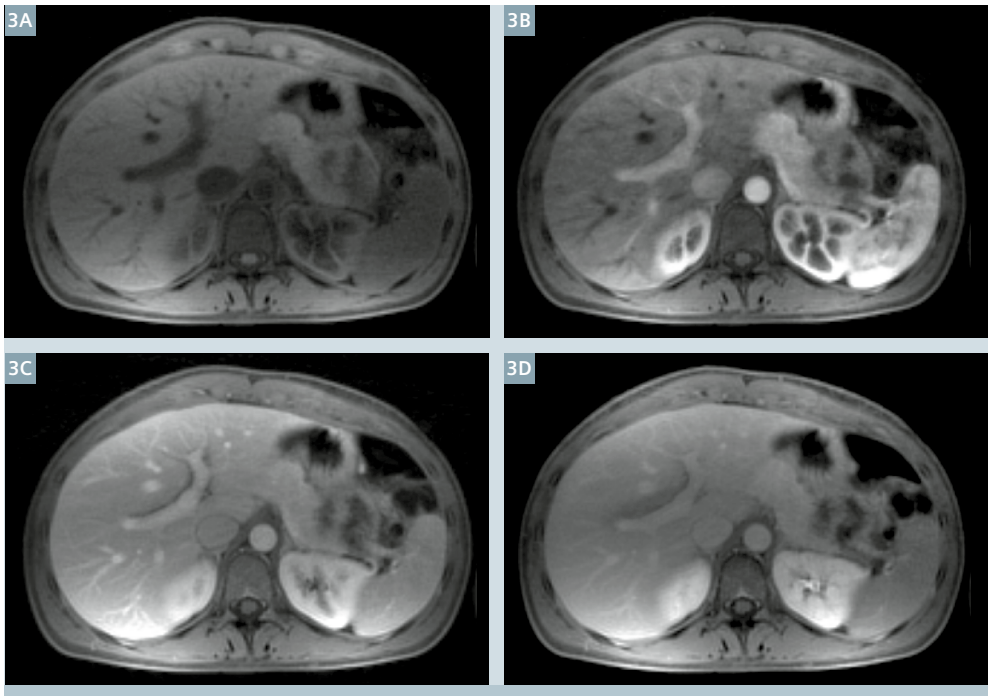

3 Free-breathing dynamic liver GRASP exam in an adult patient. Shown are images of the **(3A)** pre-contrast, **(3B)** arterial, **(3C)** venous, and **(3D)** delayed phase of enhancement. The reconstruction used 55 spokes per frame, corresponding to 8.8 sec per image (spatial resolution 1.5 x 1.5 x 3.0 mm, acquired at 1.5 Tesla).

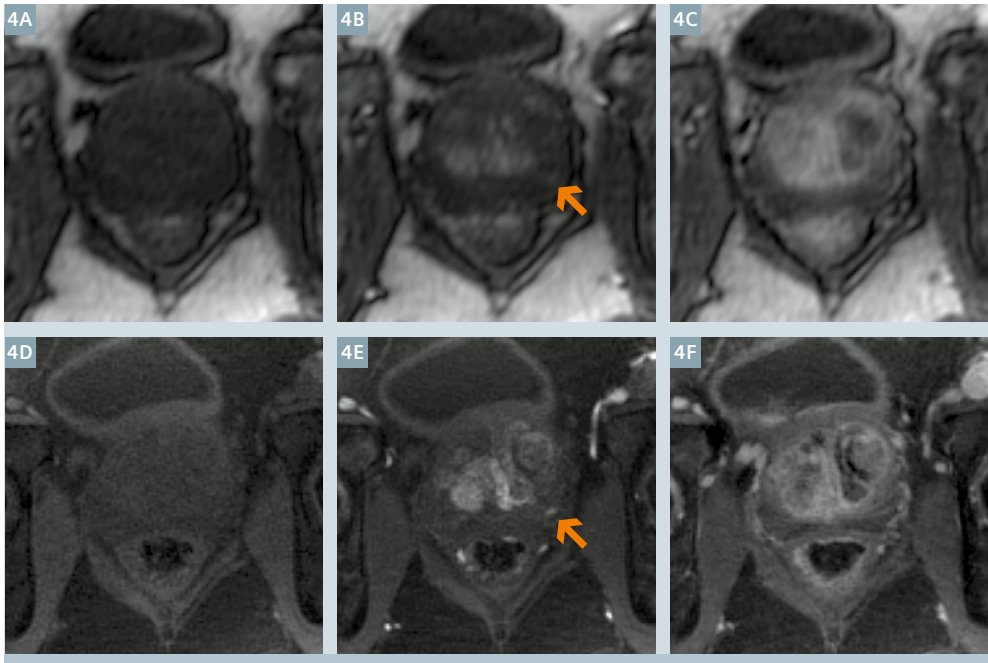

4 Dynamic prostate exam in a patient on active surveillance using **(4A, B, C)** conventional 3D FLASH with 5.5 sec temporal resolution and **(4D, E, F)** GRASP with 2.2 sec temporal resolution (both acquired at 3 Tesla). Images are shown from **(4A, D)** before the injection, **(4B, E)** the time of contrast arrival, and **(4C, F)** a late phase. Due to the higher spatial resolution (1.1 mm vs. 1.9 mm), a suspicious lesion in the peripheral zone with early enhancement and rapid washout (arrow) is more clearly visible on the GRASP scan. Note that the GRASP acquisition used fat suppression due to the off-resonance behavior of radial k-space sampling [4].

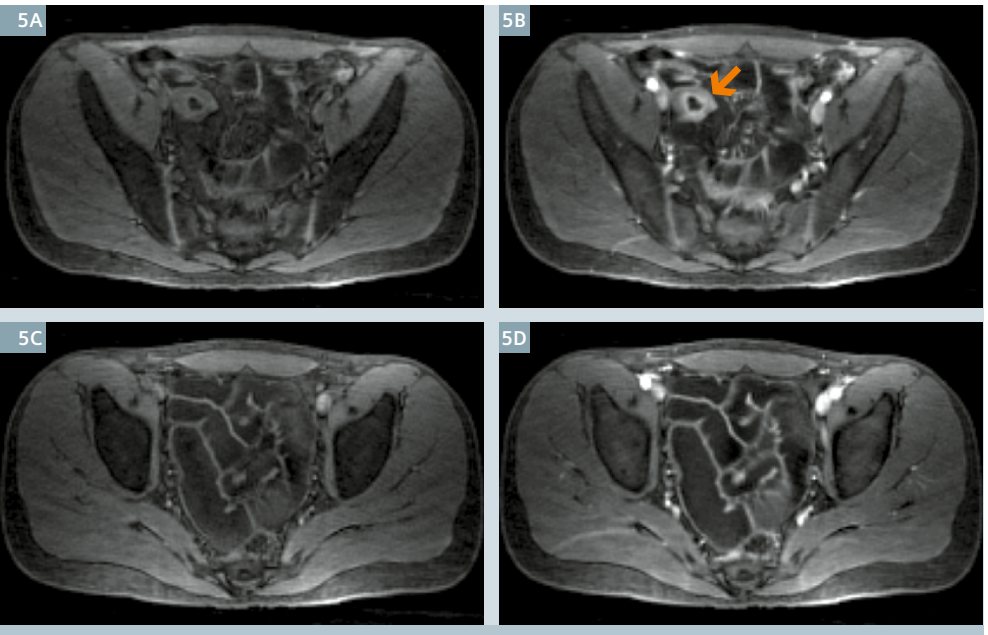

5 Bowel imaging using GRASP in a patient with Crohn's disease (acquired at 1.5 Tesla). Shown are time points **(5A, C)** before and **(5B, D)** shortly after the contrast injection. In the upper images **(5A, B)**, a bowel section with increased wall thickness and mucosal hyperenhancement can be seen (arrow), which indicates active inflammation. For comparison, the lower row **(5C, D)** shows a different slice with normal-appearing bowel sections.

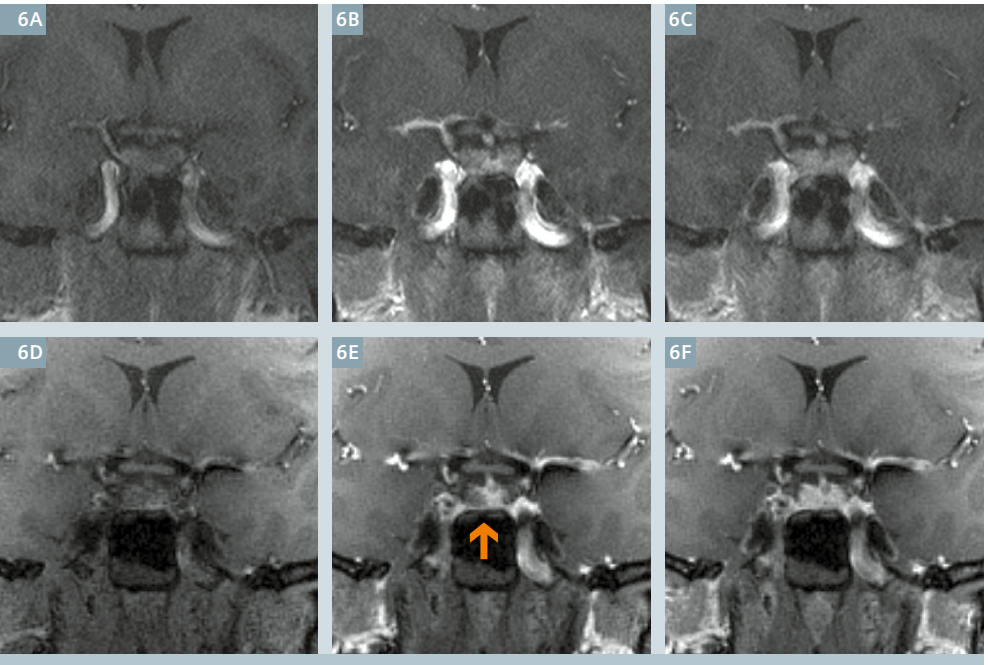

6 Dynamic imaging of the pituitary gland using **(6A, B, C)** a conventional 2D GRE sequence and **(6D, E, F)** GRASP (both acquired at 3 Tesla). Shown are images **(6A, D)** before the injection, **(6B, E)** shortly after contrast arrival, and **(6C, F)** at a later phase. A small area with delayed contrast uptake is visible in the inferior right gland (arrow), which likely reflects a microadenoma. Because of much thinner slices (1 mm vs. 3 mm) and higher overall image quality, such findings are easier to identify with GRASP.

using GRASP also for bowel imaging to investigate inflammatory bowel diseases such as Crohn's disease [15]. Inflamed bowel sections are characterized by increased wall thickness and reduced motility, as well as increased vascularity. Therefore, these bowel sections can be easily identified on GRASP scans, as shown in Figure 5. In addition, signal-enhancement curves can be generated from region-of-interests of the dynamic GRASP images and used to calculate quantitative perfusion measures that have been found to correlate with inflammation [15]. These parameters can potentially be used to non-invasively predict disease progression as well as response to treatments. Again, an advantage is that the perfusion images are obtained together with morphologic information from the same dataset through GRASP reconstruction with variable temporal resolution.

Finally, applications of GRASP are of course not confined to abdominopelvic imaging. GRASP can be used as robust imaging technique for any other dynamic T1-weighted examination as well, and a large portion of our recent GRASP scans are actually done in the head and neck region, including dynamic imaging of the orbits, the neck, and the pituitary gland. In the latter application, it is again the improvement in spatial resolution that makes GRASP attractive. When compared to our previously employed 2D GRE protocol (see Fig. 6), GRASP provides much higher spatial resolution along the slice direction and, thus, makes it easier to accurately localize tiny lesions such as microadenomas or small cysts. The possibility to incorporate also perfusion information into the diagnosis adds to its value [16].

Additional motion compensation

So, is GRASP now the ultimate solution for abdominopelvic DCE-MRI? Unfortunately, not quite yet. Our clinical evaluation showed that free-breathing abdominal GRASP exams work well in many patients with convincing results, but in a certain percentage of patients the image quality is still suboptimal. The problem here is that some patients perform deep respiration in

the moment when the contrast agent is injected, most likely because they are surprised by the sudden onset of the injection and the resulting sensation. Some patients even start to cough, so that the liver and adjacent organs rapidly move up and down by up to 10 cm during the initial circulations of the contrast agent. While GRASP handles moderate motion relatively well, compromised image quality is obtained if the data for each time point is affected by strong inconsistencies due to varying motion states. For example, if during 50% of the spokes the liver was in an end-expiratory position and during the other 50% of the data in an end-inspiratory position, GRASP will not be able to find one reconstruction that is consistent with both of these motion states. As a result, the images show motion blurring and streak artifacts.

However, since GRASP is based on radial sampling, it is possible to apply additional tricks to resolve this situation. Because all of the spokes pass through the center of *k*-space, it is possible to extract a respiration curve from the *k*-space center that indicates how the patient was breathing during the examination [17]. This is possible because the percentage of (dark) lung tissue in the field-of-view changes during respiration, which leads to a modulation of the total signal power. The latter is reflected by the signal intensity at the *k*-space center, which therefore can be used to generate the respiration curve. Once it is known from the curve what the respiratory state for each acquired spoke was, the data can be sorted according to the respiratory state and the GRASP reconstruction can be extended to treat the respiratory state as an extra dimension, which allows freezing the respiration in the reconstructed images [18]. This extended approach, which we call XD-GRASP*, is still under active development and accompanied by a further increase of the computational complexity. However, as shown in Figure 7, initial results look promising and we are convinced that the motion-compensated XD-GRASP approach is a leap towards the future of abdominopelvic DCE-MRI, soon delivering 100% reliability in every patient and at every imaging center, regardless of the patient's cooperation and regardless of the operator's training level.

Conclusion

GRASP is a new concept to simplify DCE-MRI exams by acquiring all information using a single continuous scan instead of several individual scans, which eliminates the possibility of timing or synchronization mistakes. Because GRASP is based on radial sampling, acquisitions can be performed during free breathing, thus making abdominal DCE-MRI accessible for patients unable hold breath. Sufficiently high acquisition speed is achieved by synergistically combining the compressed-sensing and parallel-imaging principles. Due to use of the golden-angle scheme, the temporal resolution and desired image time points can selected retrospectively, which enables reconstructing both morphologic and perfusion information from the same exam. GRASP has already been tested in thousands of patient exams in our routine practice, making it one of the first compressed-sensing techniques that have been evaluated on a large scale for clinical feasibility. While results are convincing for patients with regular breathing activity, limitations still exist for those patients performing deep respiration/coughing during the injection. This remaining issue is now being addressed by integrating active motion compensation based on the radial self-navigation principle.

References

1 Elsayes KM, Narra VR, Yin Y, Mukundan G, Lammle M, Brown JJ. Focal hepatic lesions: diagnostic value of enhancement pattern approach with contrast-enhanced 3D gradient-echo MR imaging. Radiographics. 2005 Sep-Oct;25(5):1299-1320.

2 Griswold MA, Jakob PM, Heidemann RM, Nittka M, Jellus V, Wang J, Kiefer B, Haase A. Generalized autocalibrating partially parallel acquisitions (GRAPPA). Magn Reson Med. 2002 Jun;47(6):1202-1210.

3 Martin DR, Sharma P, Kitajima H. Challenges and Clinical Value of Automated and Patient-Specific Dynamically Timed Contrast-Enhanced Liver MRI Examination. Siemens MAGNETOM Flash 3/2009:40-45.

4 Block KT, Chandarana H, Milla S, Bruno M, Mulholland T, Fatterpekar G, Hagiwara M, Grimm R, Geppert C, Kiefer B, Sodickson DK. Towards Routine Clinical Use of Radial Stack-of-Stars 3D Gradient-Echo Sequences for Reducing Motion Sensitivity. J Korean Soc Magn Reson Med. 2014 Jun;18(2):87-106.

5 Chandarana H, Block TK, Rosenkrantz AB, Lim RP, Kim D, Mossa DJ, Babb JS, Kiefer B, Lee VS. Free-breathing radial 3D fat-suppressed T1-weighted gradient echo sequence: a viable alternative for contrast-enhanced liver imaging in patients unable to suspend respiration. Invest Radiol. 2011 Oct;46(10):648-53.

6 Feng L, Grimm R, Block KT, Chandarana H, Kim S, Xu J, Axel L, Sodickson DK, Otazo R. Golden-angle radial sparse parallel MRI: Combination of compressed

*WIP, the product is currently under development and is not for sale in the US and other countries. Its future availability cannot be ensured.

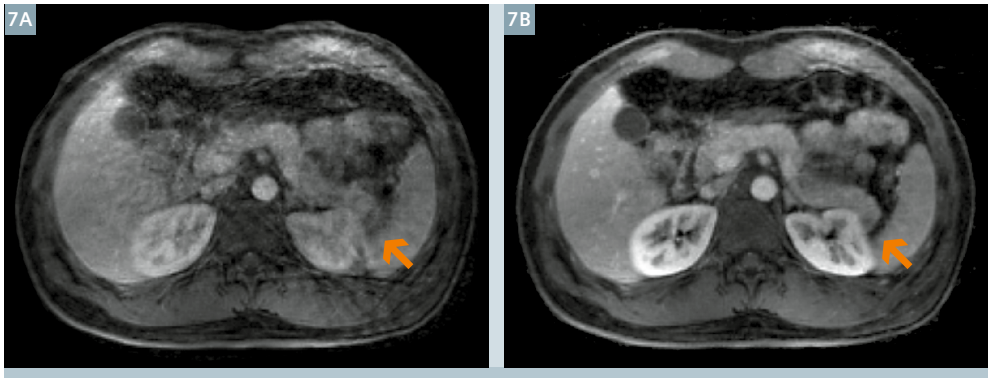

7 GRASP liver exam of a patient breathing deeply after the injection. Due to the inconsistent motion state of the acquired data, the normal GRASP reconstruction **(7A)** is affected by streak artifacts and motion blurring (arrow). These artifacts are clearly reduced when employing XD-GRASP with additional motion compensation **(7B)**.

sensing, parallel imaging, and golden-angle radial sampling for fast and flexible dynamic volumetric MRI. Magn Reson Med. 2014 Sep;72(3):707-717.
7 Chandarana H, Feng L, Block TK, Rosenkrantz AB, Lim RP, Babb JS, Sodickson DK, Otazo R. Free-breathing contrast-enhanced multiphase MRI of the liver using a combination of compressed sensing, parallel imaging, and golden-angle radial sampling. Invest Radiol. 2013 Jan;48(1):10-16.
8 Winkelmann S, Schaeffter T, Koehler T, Eggers H, Doessel O. An optimal radial profile order based on the Golden Ratio for time-resolved MRI. IEEE Trans Med Imaging. 2007 Jan;26(1):68-76.
9 Lustig M, Donoho D, Pauly JM. Sparse MRI: The application of compressed sensing for rapid MR imaging. Magn Reson Med. 2007 Dec;58(6):1182-1195.
10 Pruessmann KP, Weiger M, Börnert P, Boesiger P. Advances in sensitivity encoding with arbitrary *k*-space trajectories. Magn Reson Med. 2001 Oct;46(4):638-651.
11 Block KT, Uecker M, Frahm J. Undersampled radial MRI with multiple coils. Iterative image reconstruction using a total variation constraint. Magn Reson Med. 2007 Jun;57(6):1086-1098.
12 Information and free download available at http://ktblock.de/yarra
13 Chandarana H, Block TK, Ream J, Mikheev A, Sigal SH, Otazo R, Rusinek H. Estimating Liver Perfusion From Free-breathing Continuously Acquired Dynamic Gd-EOB-DTPA Enhanced Acquisition With Compressed Sensing Reconstruction. Invest Radiol. In press.
14 Rosenkrantz AB, Geppert C, Grimm R, Block TK, Glielmi C, Feng L, Otazo R, Ream JM, Romolo MM, Taneja SS, Sodickson DK, Chandarana H. Dynamic contrast-enhanced MRI of the prostate with high spatiotemporal resolution using compressed sensing,parallel imaging, and continuous golden-angle radial sampling: Preliminary experience. J Magn Reson Imaging. 2014 May 16. Epub ahead of print.
15 Ream JM, Doshi AM, Block KT, Kim S, Otazo R, Feng L, Chandarana H. High Spatiotemporal Dynamic Contrast-Enhanced MRI of the Small Bowel in Active Crohn's Terminal Ileitis using Compressed Sensing, Parallel Imaging, and Golden-Angle Radial Sampling. In Proc. Intl. Soc. Mag. Reson. Med. 22 (2014): 4292.
16 Espagnet CR, Bangiyev L, Block KT, Grimm R, Feng L, Ruggiero V, Babb J, Davis A, Sodickson DK, Fatterpekar G. High resolution DCE MRI of the Pituitary gland using Radial K space Aquisition with Compressed Sensing Reconstruction. In Proc. Intl. Soc. Mag. Reson. Med. 22 (2014): 4669.
17 Grimm R, Bauer S, Kiefer B, Hornegger J, Block KT. Optimal Channel Selection for Respiratory Self-Gating Signals. In Proc. Intl. Soc. Mag. Reson. Med. 21 (2013): 3749.
18 Feng L, Liu J, Block KT, Xu J, Axel L, Sodickson DK, Otazo R. Compressed Sensing Reconstruction with an Additional Respiratory-Phase Dimension for Free-Breathing Imaging. In Proc. Intl. Soc. Mag. Reson. Med. 21 (2013): 606.



Contact

Dr. Kai Tobias Block
Center for Biomedical Imaging
NYU Langone Medical Center
660 First Avenue
New York, NY 10016
USA
tobias.block@nyumc.org

Growth with Body MRI.



Are you facing challenges in Body MRI? With us you will be able to solve them!

Find out how we do that and see what other MAGNETOM users say:

www.siemens.com/body-mri

Slice Order (Slice Timing) for fMRI Evaluation

Joachim Graessner, Dipl. Ing.

Siemens Healthcare, Hamburg, Germany

This article focuses on the temporal order of slices in EPI-BOLD experiments such as slice timing, which is essential at least for event-related paradigms.

The first thing to keep in mind is the difference between the "Multi-slice mode" and "Series" parameters (Fig. 1). The latter requires our attention for our topic slice order.

The **Multi-slice mode** describes the way slices are excited within one TR interval:

- Interleaved measurement means line-by-line data acquisition of all slices in the repetition time TR starting with the first and ending with the last phase encoding step for normal sequences, such as spin echo or gradient echo.
- For an EPI sequence the Multi-slice mode = Interleaved is is actually a Single-Shot mode.

The **Series** parameter influences the excitation order of a stack of slices. You can select Ascending, Descending or Interleaved (Fig. 2).

The interleaved mode is usually chosen to minimize crosstalk between the slices.

In ascending and interleaved mode, the direction of transverse slice excitation is always from foot to head. In descending mode the direction changes to head to foot for axial slices. (Fig. 3)

All examples are valid for transverse slices only, meaning the orientation parameter with a leading "TRA > .... ".

In interleaved mode the number of slices determines which slice is excited first when image numbering feet to head is used:

- Even number of slices: slice number 2 first
- Odd number of slices: slice number 1 first

Example: Image numbering F>>H

- 36 slices: even number of slices (Fig. 4)
  – Order: **2**,4,6,8,10,...., 34,36,**1**,3,5,7,10,....,33,35
- 35 slices: odd number of slices (Fig. 5)
  – Order: **1**,3,5,7,10,...., 33,35,**2**,4,6,8,10,....,32,34



1 GEOMETRY/COMMON card; "Multi-slice mode" and "Series" parameters.

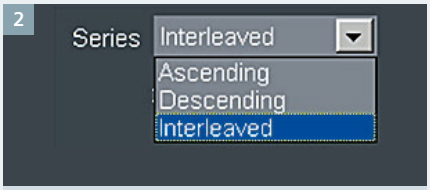

2 Choices for parameter "Series".

3

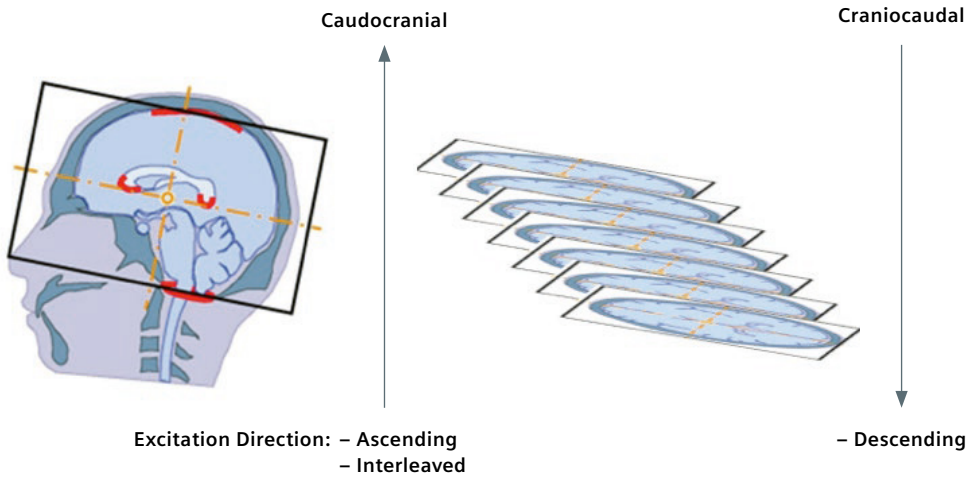

3 Slice excitation direction depending on "Series Mode" = Ascending; Descending; Interleaved.

4

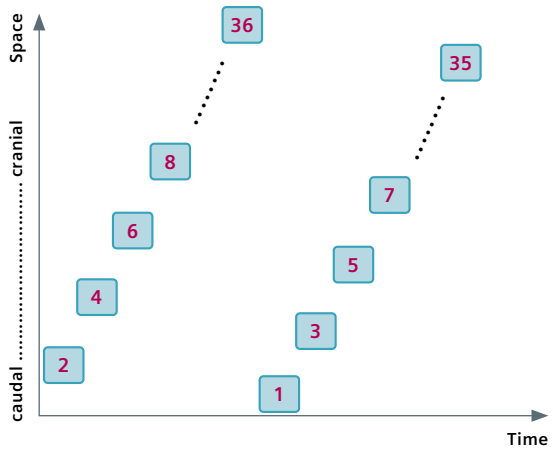

4 Even number of slices; Series = Interleaved; Image Numbering F>>H.

5

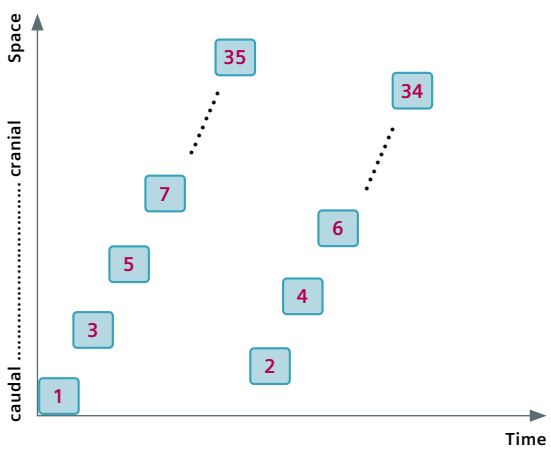

5 Odd number of slices; Series = Interleaved; Image Numbering F>>H.

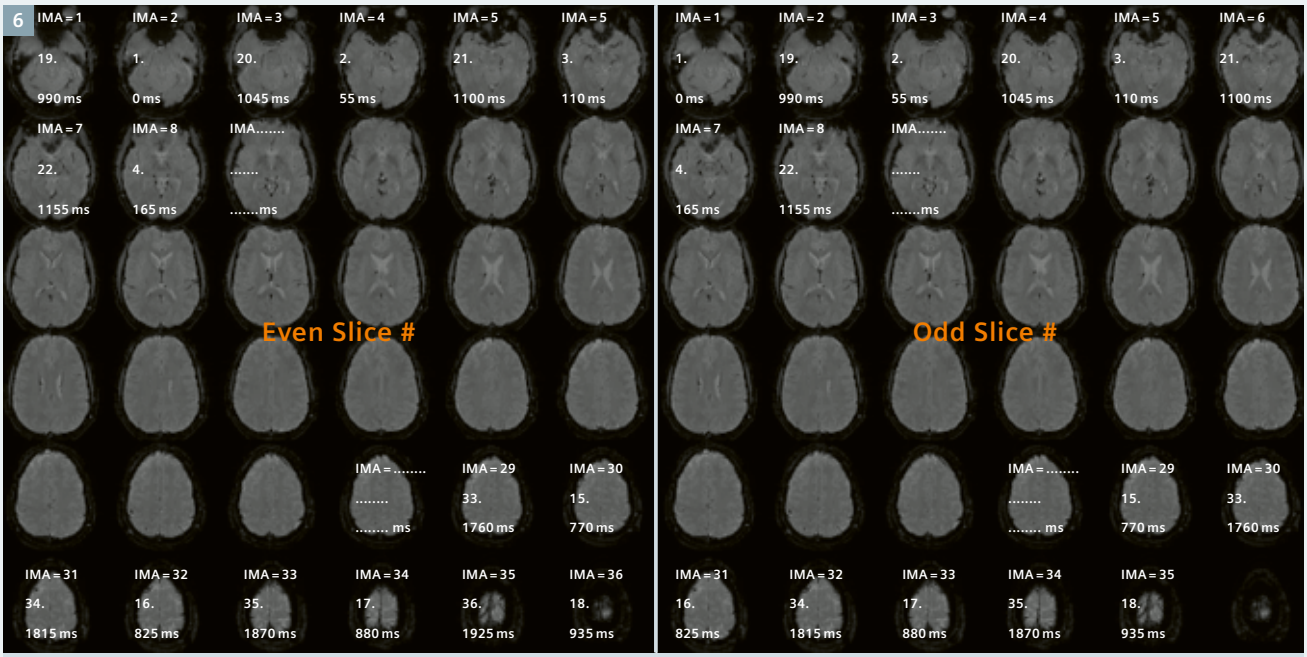

6 Mosaic images with even/odd number of slices; Series = Interleaved; Image Numbering F>>H.

The EPI mosaic in figure 6 shows a series containing 36/35 interleaved measured slices with text overlays for image numbers, excitation order number and relative offset time. The latter value can be extracted from the DICOM header in tag (0019,1029) „MosaicRefAcqTimes" together with tag (0008,0032) „Acquisition time" to calculate the absolute time of an image.

The displayed slice numbers in this example are identical to the image numbers of the series as long as the default setting for image numbering is used: Transversal F>>H on parameter card System/Miscellaneous (Fig. 7)

Do not use the mode H>>F because this complicates the numbering and you will have to sort images manually in most fMRI post-processing tools. The excitation of the slices in this case also starts caudally with the highest image numbers counting backwards! The rule with even or odd image numbers is not applicable. Furthermore, the images are displayed in a reverse order on the mosaic images. When used accidentally, the excitation order is shown below.

Example: Image numbering H>>F

- 36 slices: Even number
  – Order: **35**,33,31,29,....,
    3,1,**36**,34,32,30,...4,2
- 35 slices: Odd number
  – Order: **35**,33,31,29,....,
    3,1,**34**,32,30,28,...4,2

Please make sure that your evaluation software takes care of the slice order specified above.

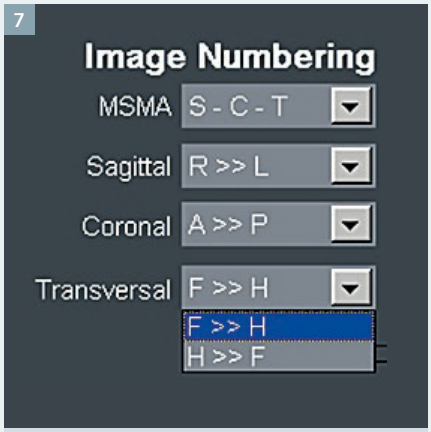

7 Parameter card SYSTEM/MISCELLANEOUS; Image Numbering Transversal F>>H.



Contact

Joachim Graessner, Dipl. Ing.
Siemens AG Healthcare
RC-DE COC NB CM
Lindenplatz 2
20099 Hamburg
Germany
joachim.graessner@siemens.com

Cardiac Dot Engine: Significant Time Reduction at Cardiac Magnetic Resonance Imaging

Jesús Ciro Pueyo, M.D., Ph.D.[1]; Paula García-Barquín, M.D.[1]; Laura Romina Zalazar, M.D.[1]; José Miguel Madrid, M.D.[1]; Jon Etxano, M.D.[1]; Efrén Ojeda, M.Sc.[2]; Óscar Fernández[3]

[1] Department of Radiology, Clínica Universidad de Navarra, Pamplona, Spain
[2] Siemens Healthcare, Erlangen, Germany
[3] Siemens Healthcare Getafe (Madrid), Spain

Introduction

Cardiac Magnetic Resonance (CMR) has rapidly developed and is now the technique of choice in the study of multiple heart diseases and an important tool for planning revascularization strategies in patients with coronary artery disease [1]. It allows the assessment of cardiac morphology and function. Therefore, it provides important information about tissue characterization by detecting the first steps of the ischemic cascade through perfusion sequences. An appropriate assessment of myocardial viability can be performed with delayed enhancement sequences [2].

However, CMR is not without certain limitations. Firstly, it requires skilled personnel with a good knowledge of cardiac anatomy and cardiac planes. Secondly, the scan times for CMR studies are substantially longer than for other types of study (with up to more than an hour on stress heart exams) and remain a limiting factor in the recruitment of patients suffering from claustrophobia.

In order to reduce CMR scan times, the Cardiac Dot Engine has been developed. It is a new software technology from Siemens Healthcare, which offers a review of CMR fully guided and suited to the needs of the patient.

The system guides you through a series of graphical illustrations selecting some anatomical reference points on the heart. The software then performs an automatic planning of the different cardiac planes without the need for user intervention. It also allows you to obtain superimposable slices in all sequences of the study, increasing confidence in our diagnoses [3].

Clinical experience

Our experience with the Dot software began in June 2013. To date, we have performed in our center over 272 CMR studies of which 60% are stress studies after administration of adenosine. All

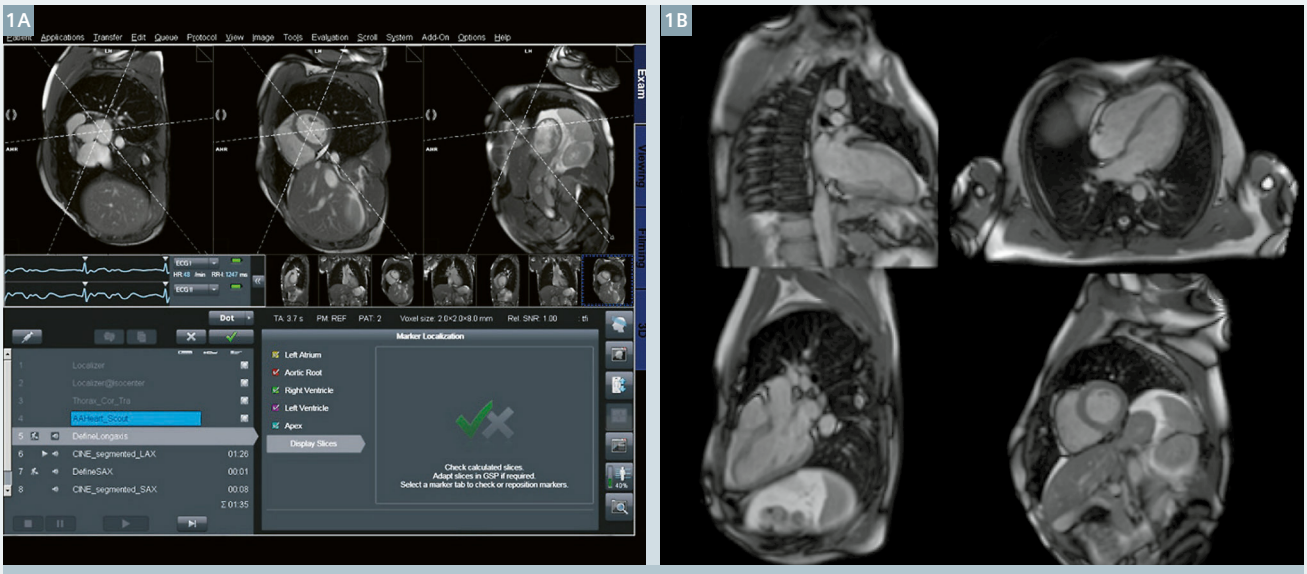

1 Automatic planning of the different cardiac axis with Cardiac Dot Engine.

studies have been performed under medical supervision and have been reproducible and high-quality diagnostic scans. During this time, we have observed a significant reduction of the average scan time.

We therefore proposed the following study to assess the time saved by using the Cardiac Dot Engine in both conventional and stress studies, compared to standard cardiac scans.

Materials and methods

Study design and patients
We have retrospectively reviewed a total of 194 patients consecutively between October 2012 and March 2014 with CMR studies performed at our Siemens 1.5T system (MAGNETOM Aera XQ) with an 18-channel body matrix coil.

For the correct categorization of the study we took into account some variables:

- First, the type of study of stress or conventional CMR. The technical specifications of both protocol studies are summarized in Table 1.
- Second, the use of Short Tau Inversion Recovery (STIR) sequences. We usually use this sequence for patients with suspected acute disease or suspicion of infiltrative heart disease.
- Third, the use of the Cardiac Dot Engine or conventional software.

Depending on the different variables, we obtained eight groups comparing the average scan time with the Cardiac Dot Engine and without it (conventional software).

The total examination time comprises the time from the beginning until the end of each scan.

The image quality of the studies has been assessed by a radiologist with over 20 years of experience on a 10-point scale (1 = poor to 10 = excellent).

The statistical analysis has been performed using a Student's T-test for independent samples to compare means. SPSS Statistics software 20.0 (IBM corporation, Armonk, NY, USA) has been used.

Table 1

Conventional CMR	Stress CMR
Localizer	Localizer
HASTE	HASTE
AAHeart-Scout	AAHeart-Scout
Function 4-chamber	Function 4-chamber
Dynamic rest (Gadovist® 0.1 mmol/kg, 4 ml/s)	Dynamic stress adenosine (Gadovist® 0.1 mmol/kg, 4 ml/s)
Function 2 + 3-chamber	Function 2 + 3-chamber
Function short-axis	Function short-axis
Delayed enhancement	Delayed enhancement
	Dynamic rest (Gadovist® 0.1 mmol/kg, 4 ml/s)

Specifications of both study protocols (stress and conventional CMR) performed at our Siemens 1.5T MAGNETOM Aera XQ.

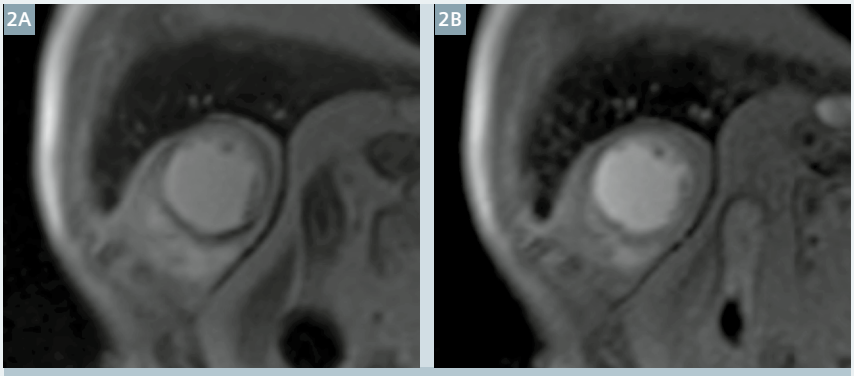

2 MR images show positive findings on stress study in a 53-year-old man with chest pain. The inferolateral wall stress-induced perfusion shows a defect **(2A)** that corresponds with a stenosis involving the left circumflex artery (LCX), disappearing in the dynamic perfusion study **(2B)**.These findings were confirmed on subsequent invasive angiography with successful coronary stenting of the stenosis.

Results

The image quality of all studies obtained a result between 9 and 10.

For conventional CMR studies with STIR sequences (58 patients) statistically significant differences in the average examination time using the Cardiac Dot Engine (t = 39.1 min +/- 12.1) have been observed, reducing the average examination time by 26.5 minutes compared to examination times using conventional software (t = 65.6 min +/- 14.1) (P = .003).

For stress CMR studies with STIR sequences (27 patients) a statistically significant decrease of the examination time has been observed with a reduction of 19.7 minutes (t = 45.11 min +/- 14.7) using the Cardiac Dot Engine compared to (t = 64.9 min +/- 7.8) examination times using conventional software (P = .001).

Furthermore, for CMR studies without STIR sequences (31 patients) a significant mean reduction of the examination time of 15.5 minutes has been found, which has been also statistically significant (t = 57.7 min +/- 14.7) compared to (t = 42.2 min +/- 16.1) (P= .001).

Stress CMR studies without STIR sequences (78 patients) have also shown mean examination times of (t = 44.6 min +/- 16.8) using the Cardiac Dot Engine compared to (t = 65.1 min +/- 22.3) using the conventional software, which means a time reduction of 20.4 min (P = .002) (Table 2).

Discussion and limitations

Our study is not without limitations.

First of all, it is a retrospective study, which has inherent disadvantages.

There are also independent variables that may alter the average examination time. For example, at the time of infusion of adenosine, as a rule, there is a cardiologist present. The mean arrival time of the cardiologist is (t = 4.8 min +/- 7.1), which introduces a considerable delay.

There may also be glitches that force the study to be repeated, although this is very rare. This process, however, rarely extends beyond 5 minutes.

Another factor that may have extended the examination times at the beginning of this study is the universal training of all MRI personnel. It has been observed that during the initial learning phase, after the introduction of the Cardiac Dot Engine, the average examination times have been longer than afterwards. However, once the basic handling of the Dot Engine has been learned, the Cardiac Dot Engine has a fast learning curve without requirement of highly specialized technologists.

Conclusion

The Cardiac Dot Engine introduces patient benefit by providing systematically reproducible and efficient studies that consistently reduce examination time, resulting in increased efficiency, reduced costs and improved patient satisfaction without ever sacrificing high-quality diagnostic images.

Table 2

Time reduction in cardiac magnetic resonance

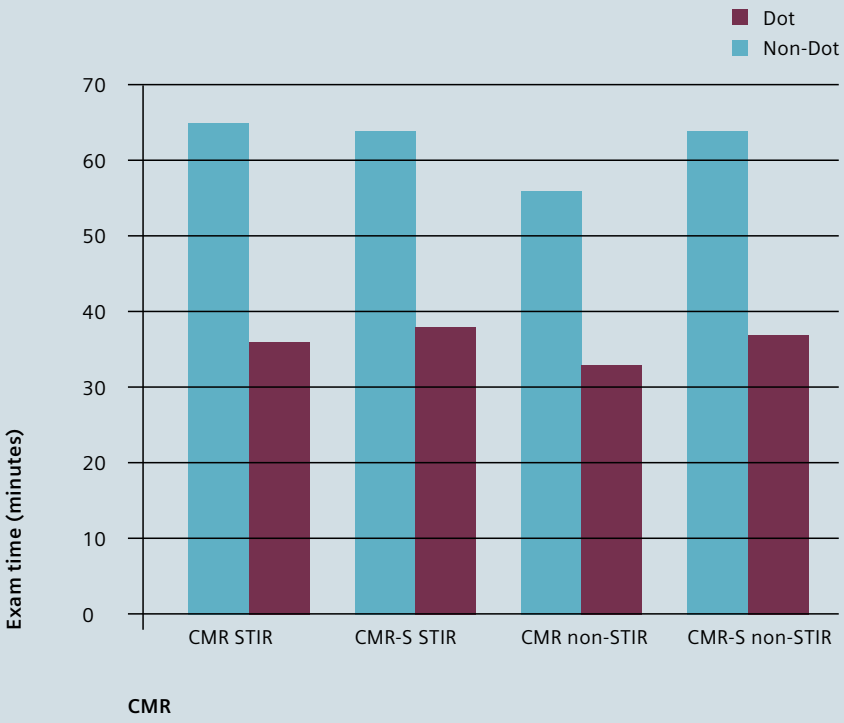

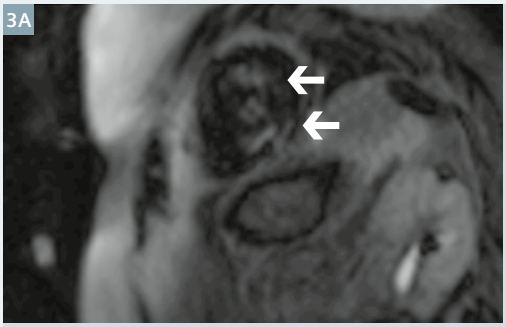

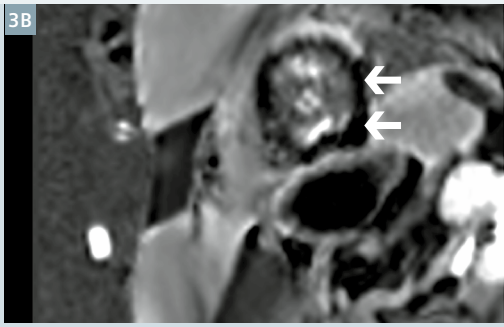

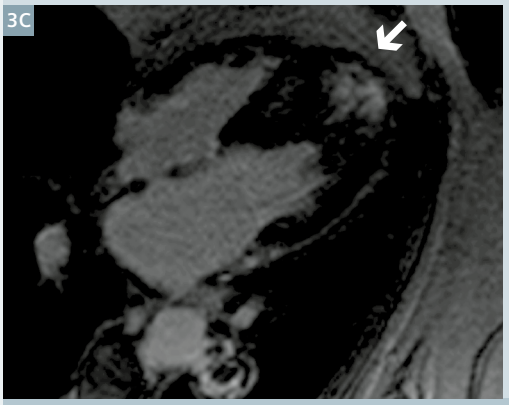



3 Short axis **(3A, B)** and four-chamber-view **(3C, D)** demonstrates hypertrophic changes as well as delayed contrast enhancement in the apex in a 43-year-old man with hypertrophic cardiomyopathy.

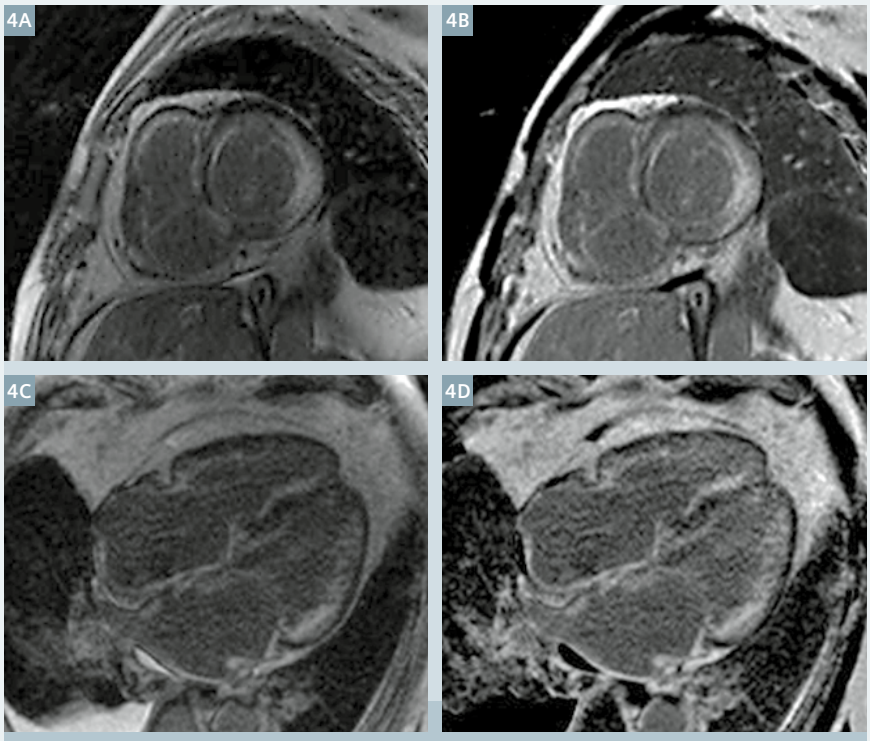

4 Delayed enhancement in the short axis **(4A, B)** and four-chamber-view **(4C, D)** reveals the presence of a diffuse patchy enhancement pattern, very suggestive of cardiac amyloidosis in a patient with congestive heart failure. A cardiac biopsy confirmed the diagnosis.

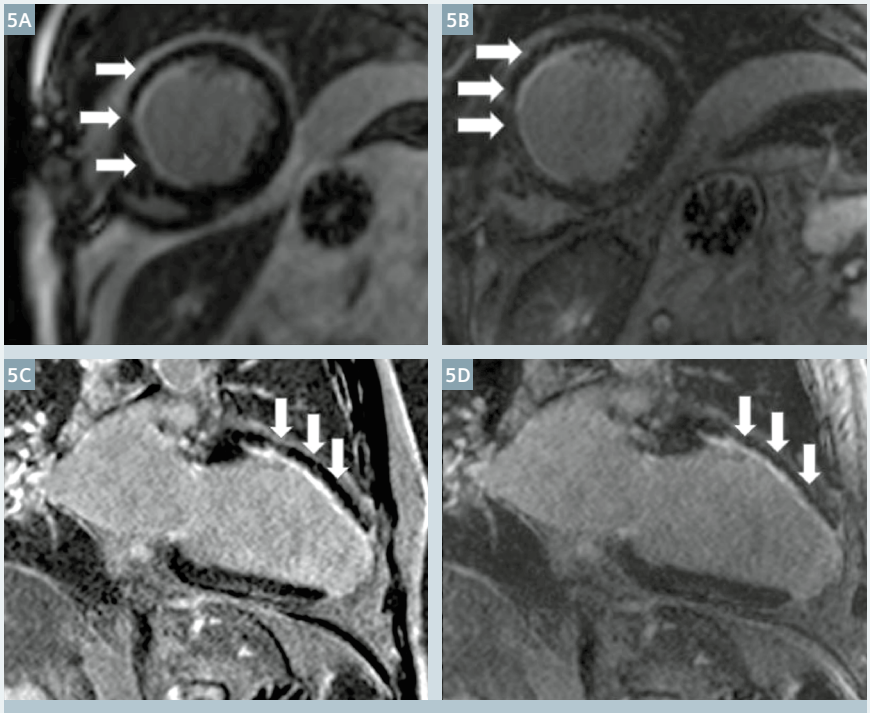

5 **(5A, B)** Short axis and **(5C, D)** two-chamber-view of delayed enhancement sequences. Arrows point to the septal wall of this patient, showing a severe subendocardial hyperenhancement that represents the region of myocardial infarction in the territory of left anterior descending (LAD) and the left circumflex artery (LCX).

Acknowledgements

The authors would like to thank all the members of the Cardiac MRI team from the Clínica Universidad de Navarra (CUN) and the MRI nurses for their valuable participation, helpfulness and support during the study, and also a very important acknowledgment to our colleagues from Siemens Healthcare, especially Efrén Ojeda, for his continuous support and contribution.

References

1 McMurray JJ, Adamopoulos S, Anker SD, Auricchio A, Böhm M, Dickstein K et al. ESC guidelines for the diagnosis and treatment of acute and chronic heart failure 2012. Eur J Heart Fail. 2012 Aug;14(8):803-69.

2 Montalescot G, Sechtem U, Achenbach S, Andreotti F, Arden C, Budaj A et al. 2013 ESC guidelines on the management of stable coronary artery disease: the Task Force on the management of stable coronary artery disease of the European Society of Cardiology. Eur Heart J. 2013 Oct;34(38):2949-3003.

3 Moenninghoff C, Umutlu L, Kloeters C, Ringelstein A, Ladd ME, Sombetzki A et al. Workflow efficiency of two 1.5 T MR scanners with and without an automated user interface for head examinations. Acad Radiol. 2013 Jun;20(6):721-30.



Contact

Jesús Ciro Pueyo, M.D., Ph.D.
Department of Radiology
Clínica Universidad de Navarra
Av. Pio XII, 36
31008 Pamplona
Spain
Phone: +34 948255400
Fax: +34 948296500
jpueyo@unav.es

"The best way to predict the future is to invent it."

Theodore Edward Hook, 1825

Magnetic Resonance Imaging at Siemens: A success story

Ingo Zenger; Antje Hellwich

Siemens Healthcare, Erlangen, Germany

In 1983 the first Siemens MRI system bearing the MAGNETOM name was installed at Mallinckrodt Institute of Radiology, in St. Louis, Missouri, USA. That was thirty years ago.

Today MAGNETOM systems feature our integrated Tim coil technology; our unique Dot scanning software; our applications, which continue to set trends in imaging; and naturally also the design of our MRI systems, which makes scans increasingly efficient for MAGNETOM users and increasingly patient-friendly. Let's take a look back and see how we got there.



1 The very first MAGNETOM system in 1983.

Making the invisible visible

On November 8, 1895, Wilhelm Conrad Röntgen revolutionized the field of medical diagnostics when he discovered X-rays. Over time, researchers developed other imaging methods to help doctors diagnose disease: Computed tomography, ultrasound, and nuclear medicine all use different techniques, each one supplying especially good images for specific scans. In the second half of the 20th century, scientists also began researching the fundamentals of a technology that turned out to be outstanding for medical imaging purposes: Magnetic resonance imaging (MRI).

In 1946, two physicists independently discovered the principle of magnetic resonance: Felix Bloch and Edward Mills Purcell showed that atomic nuclei in a magnetic field tilt when they are excited by a high-frequency electromagnetic field. If this high-frequency field is switched off, the atoms release the energy they have absorbed and return to their original state. By making this discovery, Block and Purcell laid the technical foundations for magnetic resonance imaging. It was an accomplishment for which they shared the Nobel Prize in Physics in 1952.

In 1950, Erwin Hahn proved that atomic nuclei generate an echo – a 'spin echo' – when they are influenced with two high-frequency pulses. But magnetic resonance remained a slow and imprecise method until 1968, when a group of researchers from Zurich made groundbreaking

Innovation track

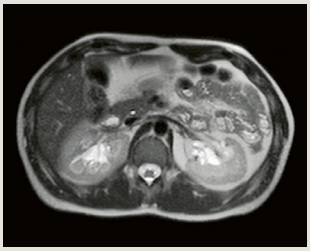

First passive direct magnetic shielding

1984

progress in enhancing its sensitivity. Richard Ernst, Weston Anderson, and Kurt Wüthrich improved the pulse excitation and used a new method to analyze the resonance signal. This made magnetic resonance technology about a thousand times faster and significantly more sensitive. Ernst went on to receive the Nobel Prize in Chemistry in 1991 for this achievement.

In the years that followed, magnetic resonance imaging became an important analytical method suitable for solids, liquids, and gases – until, in 1971, Raymond Damadian showed that it could also be used to distinguish between tumors and healthy tissue. Modern MRI technology is considered to have been born in 1973, when chemist Paul C. Lauterbur and physicist Sir Peter Mansfield were the first to make it possible to visualize a fluid-filled object. The two men together received the Nobel Prize in Medicine in 2003 for their groundbreaking work in developing MRI technology.

Early history at Siemens

Siemens recognized the new method's potential and displayed great interest in research and development involving this technology. Engineers at the Siemens research lab used magnetic resonance to study the qualities of plastics back in 1959. In 1965, the company hired a man who would play a significant role in shaping the development of MRI in the years to come: The physicist Alexander Ganssen (Fig. 2). Ganssen became intrigued by magnetic nuclear resonance while still a student, and remained true to this passion for the rest of his life. At Siemens, his research focused on MR techniques for medical diagnostics. He developed a system that was built in 1966 and patented a year later: The world's first unit that used magnetic resonance to measure a patient's blood flow at the carotid artery or arm.

On February 1, 1978 Siemens began to develop an MRI system.

Alexander Ganssen engaged physicist Arnulf Oppelt to manage the project and the team built the first MRI prototype: A 0.1-tesla system with a magnet already able to fit a person's whole body. This magnet was ordered from Oxford Instruments Ltd. – later to become Siemens Magnet Technologies. This experimental system (Fig. 3A) was completed in a wooden shed built specifically for the purpose (Fig. 4). To avoid disrupting the magnetic field, the building was constructed without any magnetic parts – not even a single steel nail. Even so, the researchers still struggled with issues: The power supply to the magnet fluctuated, and since the frequency of the nuclear resonance was in the same range as that of radio waves, the physicists received shortwave broadcasts instead of MRI signals in the evening. To solve this problem, they built a Faraday cage around the magnet to shield it (Fig. 3B).



2 Alexander Ganssen, around 1954.

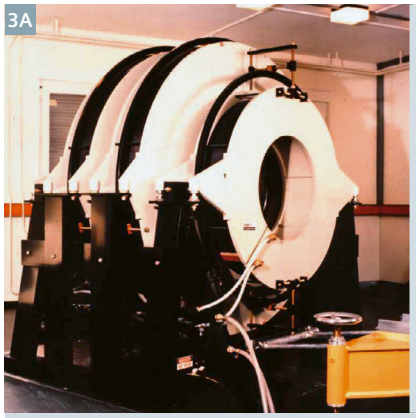



3 **(3A)** Air-cooled 0.1 Tesla magnet, 1978. **(3B)** 0.1T magnet with Faraday cage, 1979.

1989



First actively shielded 1T system

1993

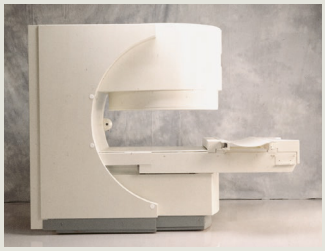

First open MR 0.2T system

In 1979, Oppelt's team looked around for a suitable test object, ultimately deciding on a green bell pepper (Fig. 5), since "It would definitely hold still, it was big enough to stand in for a human organ, and you could also cut it open to ascertain the similarity between the potential image and its anatomy." The team's research soon brought further successes. The first image of a human skull followed just a few months later, in March 1980 (Fig. 6). Ganssen himself volunteered for the scan, which took only eight minutes – already significantly shorter than the amount of time needed to scan the bell pepper just a few months before.

In September 1980 the first few patients were scanned using an MRI system (Fig. 8). The early scanning process was not very comfortable for the test subjects, who had to crawl into the magnet – which was a very tight fit – on a wooden board.

Over the course of the year in 1981, the engineers significantly enhanced the MRI system's image quality. A second pilot unit was built, this time with a field strength of 0.2T. Ernst Zeitler, a radiologist in Nuremberg, Germany, used the new system to scan his patients. By then, the images were so good that tumors in the head or abdomen and changes in the brains of patients with multiple sclerosis could be localized. "The potential that MRI technology had for diagnostic purposes was clear in 1981, when we saw the first tumor in a head scan," Oppelt says.

It wasn't long before the superconducting magnets made it possible to achieve higher field strengths, and the third pilot system reached 0.5T. Soon after Siemens began developing 1.5T magnets.

In early 1983, the time had come: At Hannover Medical School, Germany, Siemens installed the first MRI system to be tested in a clinical setting to ensure that it was suitable for day-to-day clinical use. The system's centerpiece was an oil-cooled, normally conductive 0.2T magnet. The testing went so well that Siemens ramped up product development efforts, establishing the new Magnetic Resonance Business Unit within the Medical Technology Division. Not long after that Siemens installed the first 0.35T MAGNETOM system at the Mallinckrodt Institute of Radiology, in St. Louis, MO, USA (Fig. 9). This made Siemens one of the first providers worldwide to offer magnetic resonance imaging for clinical applications.

The first MAGNETOM systems were available in different field strengths (0.35, 0.5 and 1.5 tesla). Once the system had been set up in the shielded MRI room, the magnet was cooled to minus 269 degrees Celsius using liquid nitrogen and liquid helium and then charged with electricity. After that, no further electrical power to the magnet was needed, and the power supply was permanently cut off. The helium and nitrogen, however, slowly evaporated, so regular replenishments were necessary – the first MAGNETOM systems used about two liters of nitrogen and half a liter of helium per hour (Fig. 10). Today's advanced MAGNETOM systems rely on 'zero helium boil-off' technology, which allows MRI systems to keep running in normal operation without using up any helium.

In December 1983, Klinikum Charlottenburg, a hospital operated by Freie



4 The wooden building used as the first MRI research lab, Erlangen, 1979.



5 MR image of a green bell pepper, November 1979.



6 Alexander Ganssen's head, 1980. 128 matrix, 8 minutes.

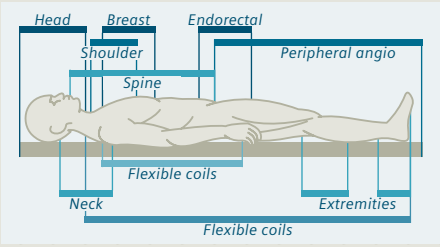

1997 — *First integrated Panoramic Array Coil concept for whole body imaging*



2001 — *MAGNETOM World*

The MRI community consisting of internet platform, MAGNETOM Flash magazine and MAGNETOM World Summits

Universität Berlin, became the first university medical center in Germany to receive an MRI system with superconducting magnets from Siemens (Fig. 11). From then until June 1984, Siemens shipped 14 MAGNETOM systems to destinations all over the world. That same month, the U.S. Food and Drug Administration granted the MAGNETOM its final approval for the U.S. market. In 1986, Siemens became the first manufacturer of MRI systems to win approval for 1.5-tesla systems in Japan.

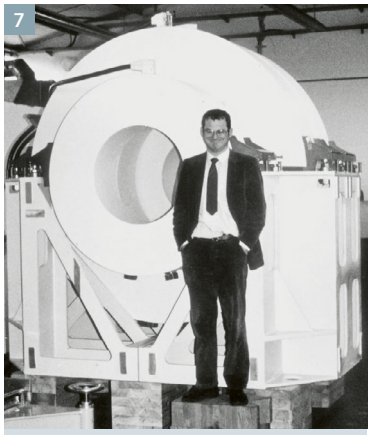

7 Arnulf Oppelt with the 0.1T MRI prototype, 1981.

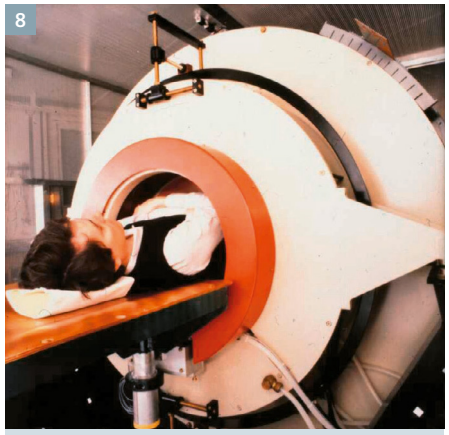

8 A whole-body scan using the pilot system, 1980.



9 The first MAGNETOM, St. Louis, 1983.

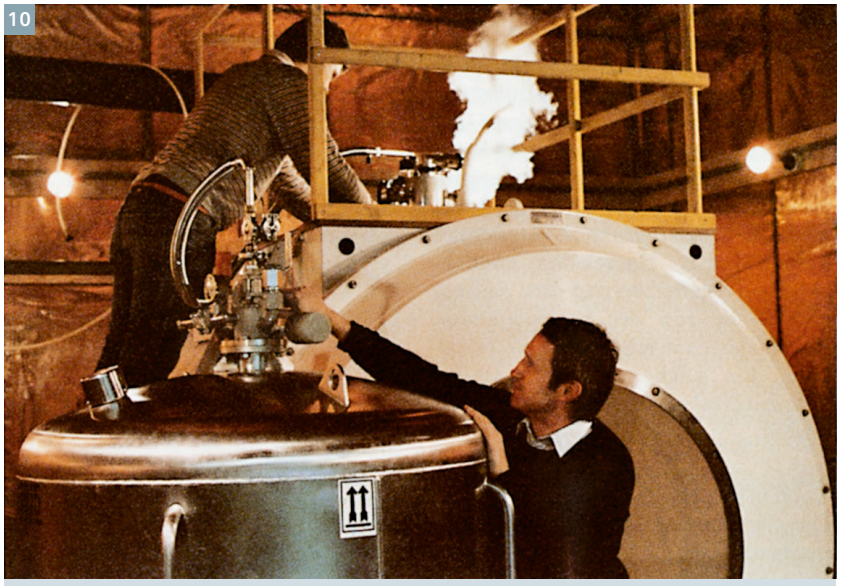

10 Replenishing helium in the early 80s.

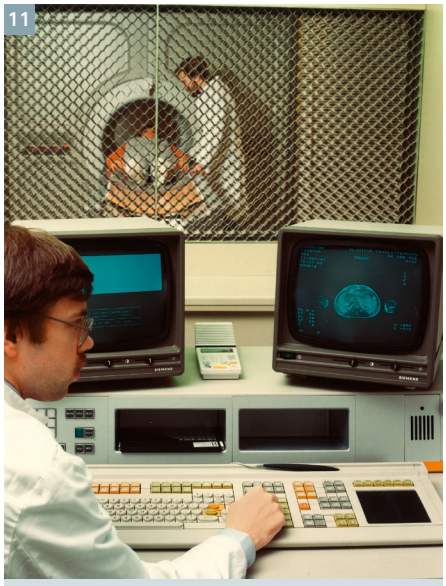

11 Klinikum Charlottenburg, operated by Freie Universität Berlin, 1983.

2003

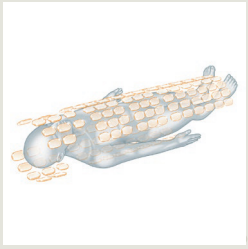

New Technology Tim RF and coil technology

2004



First Open Bore (70 cm) system

12

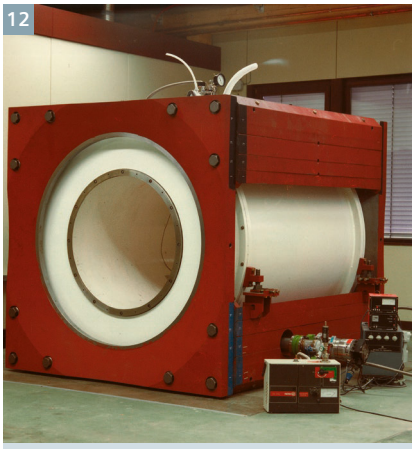

12 Magnet shielding, 1984.

13

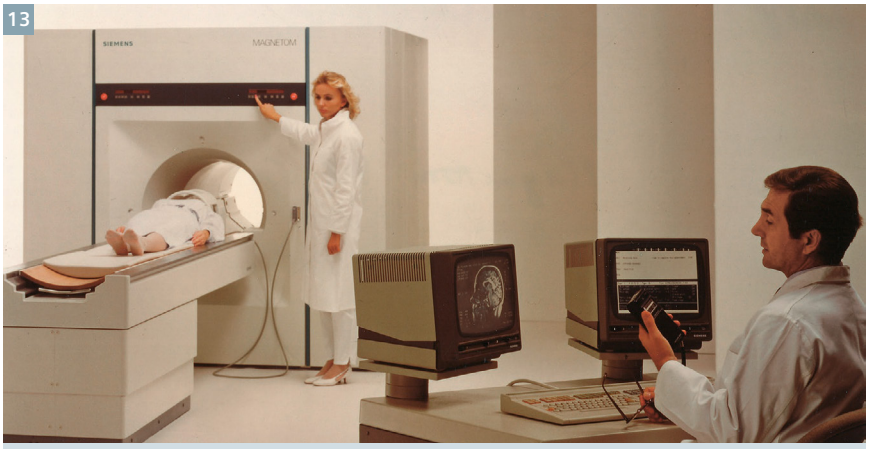

13 Actively shielded 1T MAGNETOM 42 SPE.

The magnets used in the first MRI systems lacked any shielding for the magnetic field and therefore could only be installed in rooms measuring at least 40 m². So Siemens developed a superconducting magnet with a stray field about five times smaller. This design, found nowhere else in the world, shielded the magnetic field through 'self shielding', where a cage-shaped shield conducted the stray field back to the magnet. These magnets required only a quarter of the space. Many of the changes that rooms had previously needed in order to accommodate an MRI system were no longer necessary, cutting installation costs (Fig. 12).

In 1989, Siemens launched a 1.0-tesla system with an actively shielded magnet, the MAGNETOM 42 SPE (Fig. 13). Active shielding means that in addition to the coils that generate the magnetic field, there are also coils installed on the magnet itself, which weaken the magnetic field toward the outside – where no magnetic field is needed for imaging purposes. It was followed in 1991 by an MRI system with an actively shielded 1.0-tesla whole-body magnet operated via an intuitive user interface similar to that of a PC: The MAGNETOM Impact (Fig. 14).

Even as these performance gains were being made, Siemens was also introducing a number of technological innovations that unlocked new diagnostic possibilities, shortened scan times, and reduced power consumption. As early as 1985, the company was able to cut scanning time nearly in half by using a 'half-Fourier imaging'. In this measurement technique, only about half the data was determined through direct measurements, while the other half was reconstructed mathematically.

14



14 MAGNETOM Impact, 1991.

Open and standardized

By the early 1990s, MRI had become an integral part of everyday clinical practice. In 1992, the standard was 20 patients in eight hours. However, some patients felt uncomfortable



New Technology
Dot workflow engines and Tim 4G

2009



15 Using the MAGNETOM Open to monitor an operation at Cleveland University in 1994.

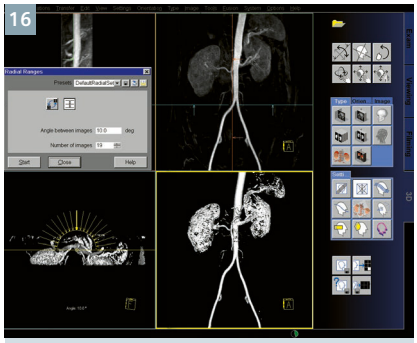

16 Angiography with *syngo*, 2001.

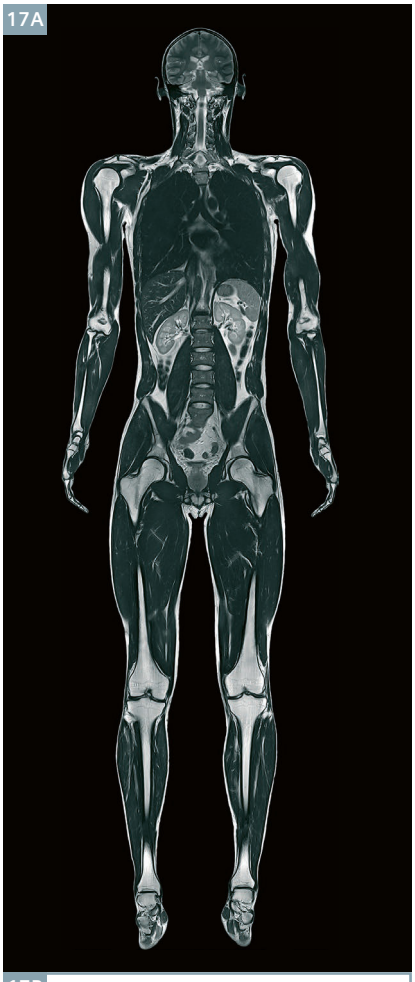

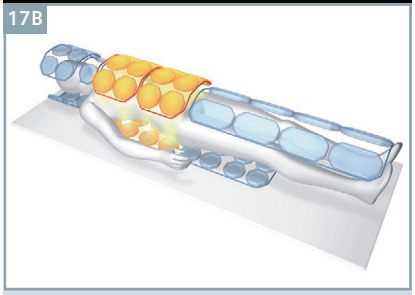

17 **A, B:** Whole-body imaging with Tim (Total imaging matrix).

when they were moved into the MRI system's narrow bore. In 1993, Siemens succeeded in making MRI accessible to everyone by introducing the first truly open MRI system, the MAGNETOM Open.

The 0.2T MAGNETOM Open even made it possible to monitor patients during surgery (Fig. 15).

The software used for the Siemens MRI systems in the 1990s was structured similarly to PC software, so it was already much more intuitive to use than the software for the first MRI systems. However, MRI and CT or other imaging systems from the same manufacturer had always used different software interfaces – which operators had to learn individually. Around the turn of the 21st century, Siemens became the first medical technology manufacturer to craft a standardized user interface for all of its systems: *syngo* software (Fig. 16). When a hospital or medical practice purchases a new system from Siemens, the learning curve for staff is much shorter.

From then on, all imaging systems from Siemens featured standardized operation.

In late 2003, Tim – the Total imaging matrix – revolutionized MRI (Fig. 17). The centerpiece of Tim technology is the completely innovative HF coils that collect data based on a matrix concept.

Whole-body scans without changing coils and without repositioning the patient finally came true. Tim makes it possible to produce images of the entire body from head to toe in a single pass, since the matrix coils cover all areas of the body at the same high level of detail. Scanning the entire body is possible in about twelve minutes for patients as much as 2.05 meters tall.

Tim represents tremendous technological progress in image quality, significantly lower patient preparation time, and shorter scanning times, but it also has additional advantages for operators and patients. Patient comfort is also

2010

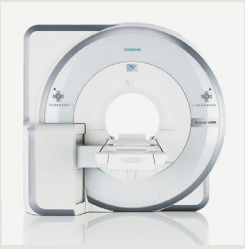

First MR-PET Biograph mMR

2011



First parallel transmit application: Tim TX TrueShape



18 MAGNETOM Espree, the world's first 1.5-tesla system with a 70-centimeter open bore.

enhanced by light-weight coils: At just 950 grams, the body matrix coil is lighter than some winter bed comforters. Tim technology allows patients to be positioned feet first for almost all scans – a big relief for many patients, since it means the head can stay outside the tube. Siemens combined all of these features in the MAGNETOM Avanto, which was commissioned for clinical operation at University Hospital Tübingen, Germany on November 25, 2003.

A few months later, Tim technology, working in tandem with optimization of components such as the magnet, gradient system, and receiver electronics, enabled another milestone in magnetic resonance imaging: The MAGNETOM Espree was the world's first 1.5-tesla system with a 70-centimeter opening (Fig. 18). This allowed invasive procedures and gave obese patients unrestricted access to high-field MRI for the first time.

*QISS is pending 510(k) clearance and is not commercially available in the US.

Biograph mMR	first simultaneous acquired MR-PET images across all body regions
FLASH	fast imaging
PACE	inline motion correction for fMRI
ASL	non-contrast MRI perfusion
AutoAlign	standardized, reproducible patient scan positioning
SWI	new insights with susceptibility-weighted imaging
DTI task card	easy visualization of fiber tracks
SPACE	high-speed TSE imaging in 3D
TrueFISP cine	excellent blood-tissue contrast and cardiac function
Inline Dynamic Signal	fully automated myocardial perfusion analysis incl. motion correction and quantification of myocardial first pass perfusion with Cardiac Dot Engine
Delayed Enhancement	visualization of myocardial scar and fibrosis
Inline VF	inline analysis of ventricular function
TWIST	low-dose time resolved MR Angiography with high resolution in space and time
QISS*	non-CE MR Angiography technology
Cardiac Dot Engine	standardizes Cardiovascular MR examinations with workflow guidance and automation
Tissue4D	pharmakokinetic modeling of dynamic studies
TimCT	moving table whole-body MR imaging
TWIST-VIBE	always the right contrast in dynamic liver MRI
StarVIBE	free-breathing contrast-enhanced body imaging
GRAPPA	small FOVs with parallel imaging in *k*-space
WARP	minimizing artifacts from metal implants
MapIt	quantitative cartilage characterization
Phoenix	drag and drop protocol sharing
Inline	motion correction and analysis such as MIPs and ADC maps on the fly
Dot Engines	automated and personalized scanning for each body region

19 Leading applications developed together with our international collaboration partners.



FREEZEit
body imaging

Innovation drives our success

2014

Siemens engineers have since worked on technologies and software that further improve and support Tim technology. The *syngo* software has received numerous new MRI applications that further enhance comfort and convenience, expand the range of scanning options (Fig. 19).

Healthcare providers face mounting pressure to work on a cost-optimized basis while also offering the very best in diagnosis and treatment. Technological innovations and enhanced productivity play a large role in achieving this balance. In 2009, Siemens launched the fourth generation of Tim technology (Tim 4G) as well as Dot – Day optimizing throughput – technology (Fig. 20). Dot simplifies workflows, thereby boosting productivity by as much as 30 percent. It uses images and text to guide operators step by step through the scanning process, even during complex scans.

Another technological breakthrough from Siemens has unlocked completely new views of the inside of the human body in 2010: The Biograph mMR system combines MRI and PET (Fig. 21). These two methods have different strengths, and they supply complementary information on diseases.

On the journey from fundamental research in the wooden shed to world market leadership in MRI technology, Siemens has grown around the globe. With production sites in Erlangen (Germany), Oxford (UK), Shenzhen (China) and Joinville (Brazil) Siemens has all the technology and capabilities needed to build state-of-the-art MRI systems entirely from a single source. The sites work seamlessly together on research and development. Ongoing investments give rise to numerous innovations that add to the product family and are adjusted to meet the needs of the various markets Siemens serves. At all of the locations, the superior standard of quality that applies to development and production activities is supplemented by consulting and other services for customers from all over the world.

This retrospective shows the impressive development of this technology from the early days to the first commercial steps and right through to today's technology and market leadership.

Many innovations from Siemens have changed the world. With MRI, we have been unlocking new possibilities for 30 years now – what we once dreamed about is now reality. And today's dreams will become tomorrow's reality.

Further reading

If you are interested in the whole story of MRI development at Siemens, please visit

www.siemens.com/magnetom-world > Publications > MR Basics

where you will find a 43-page booklet with many more images and all the details on 30 years of innovation at Siemens.

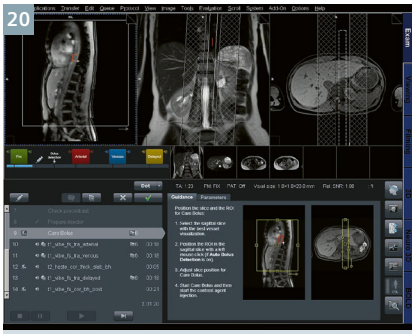

20 Screenshot of a Dot Engine.

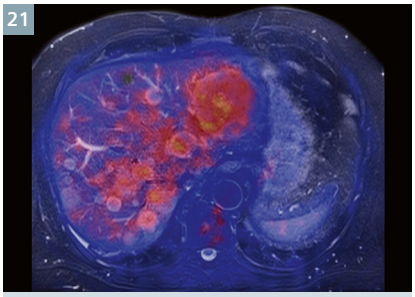

21 Molecular MR image generated with Biograph mMR at TU Munich, Germany in 2011.



22 Since 2001 the MAGNETOM World offers a platform to meet, discuss and exchange valuable information with your peers.

Myocardial T1 Mapping – Comparison of Techniques

Kelvin Chow, Ph.D.; Richard Thompson, Ph.D.

Department of Biomedical Engineering, University of Alberta, Edmonton, Canada

Introduction

Diffuse myocardial fibrosis and other remodeling of the myocardial extracellular space are common pathological features of many cardiac diseases [1]. These changes can be measured non-invasively using magnetic resonance imaging (MRI) through changes in native (non-contrast) myocardial T1 relaxation times, post-contrast T1 times, and derived estimates of extracellular volume (ECV) using both native and post-contrast T1 values. Numerous clinical studies have found correlations between both myocardial T1 and ECV measurements and various metrics of disease severity in patient populations including heart failure [2], dilated cardiomyopathy [3], and amyloidosis [4]. These findings have also been further validated by histological correlations to MRI fibrosis measurements in human studies of aortic stenosis and hypertrophic cardiomyopathy, as well as infiltrative diseases such as amyloidosis [5-8]. A large single-centre study of myocardial ECV in consecutive patients showed increased ECV to be an independent predictor of short-term mortality [9], demonstrating its prognostic importance.

The ability to quickly and reliably assess diffuse myocardial fibrosis using MRI makes T1 and ECV promising surrogate biomarkers with the potential for widespread clinical utility [10-12]. This optimism has led to the development of a multitude of techniques for their measurement, each with unique properties, advantages, and disadvantages. Three major classes of T1 measurement techniques are reviewed here in order to provide insight into differences in reported T1 and ECV values and determine the most appropriate technique for potential new studies.

T1 mapping techniques

Continuous Look-Locker techniques

The classic Look-Locker experiment consists of a series of measurements using a train of radiofrequency (RF) pulses with a short repetition time (TR) to more efficiently sample the T1 recovery curve [13]. This is commonly implemented using an inversion pulse followed by a continuous spoiled gradient recalled echo (GRE) readout [14] (Fig. 1A). Magnetization perturbation caused by the repeated RF excitations causes a shortening of the apparent relaxation time (T1*) and a reduction in the equilibrium magnetization. However, assuming that the TR << T1 and a flip angle <10° is used, the true T1 value can be calculated when using a standard 3-parameter exponential recovery model by applying the commonly termed "Look-Locker correction factor" [15] (Fig. 2A):

$$\text{Signal} = A - B*\exp(-TI/T1^*) \quad \text{[Eq. 1]}$$

$$T1 = (B/A - 1)T1^* \quad \text{[Eq. 2]}$$

Cardiac Look-Locker implementations typically use gated-segmented imaging readouts, with between 15-30 images acquired at different effective inversion recovery (TI) times and cardiac phases in a single breath-hold (Table 1). This *k*-space segmentation results in images with less temporal blurring compared to single-shot images, but with increased sensitivity to artifacts from poor breath-holding.

Table 1

	Continuous Look-Locker [3, 50]	MOLLI (Intermittent Look-Locker) [6, 18, 23, 29, 30, 49]	SASHA (Independently magnetization-preparation) [37, 44, 45]
Readout	GRE	bSSFP	bSSFP
k-space acquisition	segmented	single-shot	single-shot
Preparation pulse	inversion	inversion	saturation
Number of images	15-30	7-11	11 (variable)
Duration	1 breath-hold	9-18 heartbeats	11 heartbeats typical (variable)
Base matrix size	176-192	192-256	192-256
Flip angle	10-12°	35°	70°
Myocardial T1 (1.5T)	Not reported	939-1011 ms	1174 ms
Normal ECV (1.5T)	25%	25-27%	18-22%

Comparison of typical pulse sequence parameters between three major classes of myocardial T1 mapping sequences.

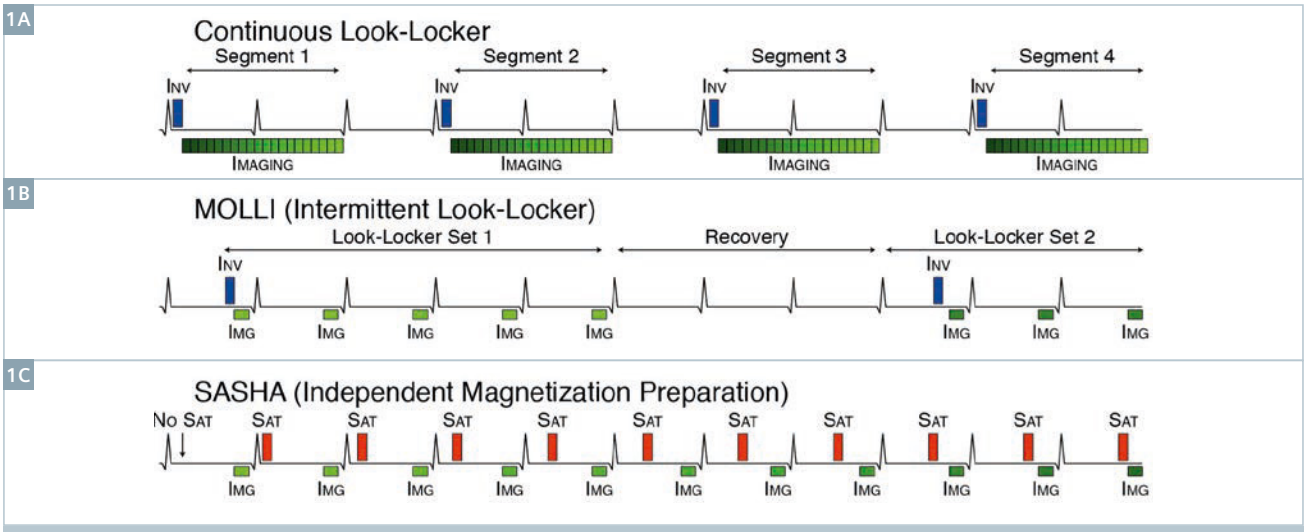

1 Pulse sequence diagram of three major classes of myocardial T1 mapping sequences. **(1A)** A continuous Look-Locker sequence acquires many segmented images following an inversion pulse. **(1B)** The MOLLI sequence consists of Look-Locker sets, each containing multiple single shot images following a single inversion, with recovery periods between sets. **(1C)** The SASHA sequence is composed of a non-saturated single-shot image followed by a series of images at variable saturation recovery times, with only a single image following each saturation pulse.

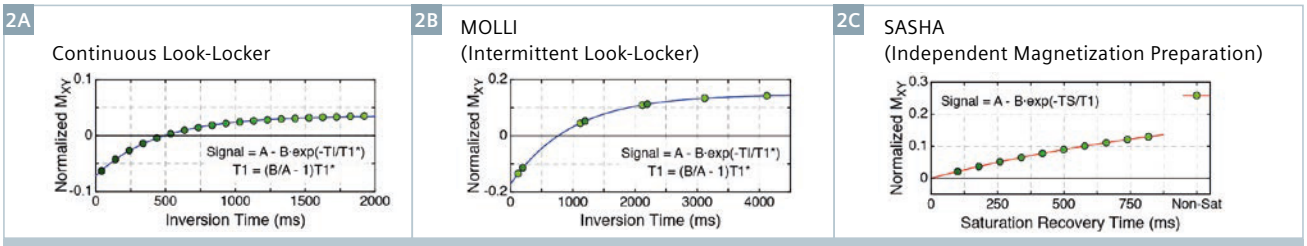

2 Sampling of the T1 recovery curve for three major classes of myocardial T1 mapping sequences. **(2A)** Continuous Look-Locker sequences have many data points along the recovery curve, but have lower SNR due to the low flip angle GRE readout. **(2B)** Samples of the recovery curve in MOLLI are clustered, with the spacing between clusters approximately equal to the R-R interval. The spacing within the clusters is determined by the "TI increment" between Look-Locker sets. Data is shown for a 5(3)3 scheme with an 80 ms TI increment. Both continuous and intermittent Look-Locker techniques generally use the "Look-Locker correction factor" to estimate true T1 values. **(2C)** The SASHA sequence samples a saturation recovery curve instead of an inversion recovery curve, with many data points at comparatively short TS times. A non-saturated image is assigned an infinitely long TS time and acts as an anchor point.

Look-Locker sequences with a continuous balanced steady-state free precession (bSSFP[1]) imaging readout such as the Small Animal Look-Locker Inversion recovery (SALLI) [16] and Multi-Contrast Late Enhancement (MCLE[1]) sequences [17] have been used to improve blood-tissue contrast and overall signal yield compared to GRE. These sequences also utilize the cardiac phase information to generate a cine-like time series for analysis of cardiac function.

Continuous Look-Locker sequences provide excellent sampling of the inversion recovery curve, but the cardiac motion between images that is intrinsic to the sequence design can be problematic for T1 quantification. Continuous through-plane cardiac motion in a typical short-axis slice results in signal enhancement as unexcited spins move into the imaging plane, modulating the shape of the recovery curve and potentially confounding calculated T1 values. Additionally, data analysis is time consuming because the myocardium must be manually contoured for each image separately and parametric T1 pixel maps cannot be readily generated.

Intermittent Look-Locker techniques

The MOdified Look-Locker Inversion recovery (MOLLI[1]) technique overcomes many of the challenges associated with cardiac and respiratory motion by using 'intermittent' cardiac-gated single-shot readouts instead of continuous readouts [18]. The sequence consists of multiple 'Look-Locker sets', each of which contains an inversion pulse followed by gated single-shot images at a consistent cardiac phase in several sequential heartbeats (Fig. 1B). As sampling of the recovery curve in each set is limited and also determined by the heart rate, Look-Locker sets are repeated with slightly incremented TI values and separated by several heartbeats to allow magnetization recovery. MOLLI images also generally use bSSFP readouts to improve blood-tissue contrast as well

as overall signal yield, although a GRE variant has been used at 7T[2] [19].

Implementations vary in the number of Look-Locker sets and the number of images in each set, which are commonly indicated with a series of numbers such as 3(3)3(3)5. In this naming convention [20], the parentheses indicate the number of recovery heartbeats between sets and all other numbers indicate the number of images in each set. In this example, 3(3)3(3)5 describes the original MOLLI implementation with three Look-Locker sets containing 3, 3, and 5 images and each set separated by 3 heartbeats for recovery. The choice of sampling pattern affects not only the total breath-hold duration, but also the variability of calculated T1 values and potential heart rate dependent T1 errors.

With good breath-holding, the consistent cardiac phase between MOLLI images simplifies data analysis by allowing regions of interest (ROIs) to be drawn for all images simultaneously. Consistent spatial positions between images allows parametric T1 maps to be generated, which provide an invaluable visual tool for identifying spatial patterns of T1 abnormalities. While myocardial T1 mapping was feasible with other techniques prior to MOLLI, the simplicity of a single breath-hold acquisition and straightforward analysis contributed to its success and helped to spur the growth of the T1 mapping field as a whole.

Similar to the continuous Look-Locker techniques, the measured apparent T1 time, termed T1*, from MOLLI data is generally shorter than the true T1 time due to magnetization perturbation by the image readouts. Conventional MOLLI analysis uses the standard Look-Locker correction factor (Eq. 2) to estimate the true T1 value. However, MOLLI's intermittent bSSFP readouts result in notable differences in the magnetization time-course compared to the continuous GRE readouts for which the correction factor was derived. This difference in magnetization progression gives rise to errors in MOLLI T1 values that are systematically dependent on multiple factors and well characterized [20]. Briefly, MOLLI T1 values are generally systematically underestimated with reduced T2 values [21, 22], increased T1 values [18, 23, 24], high heart rates [18, 23], increased off-resonance [25], poor inversion efficiency [26, 27], and magnetization transfer (MT) effects [28]. The magnitude of T1 errors from these factors is dependent on various aspects on the sequence implementation, resulting in a wide range of calculated MOLLI T1 values. For example, various studies of healthy subjects using 3(3)3(3)5 MOLLI at 1.5T have reported average myocardial T1 values of 939±24 ms (n=20) [29], 1011±41 ms (n=10) [30], and 950±21 ms (n=102) [31]. Despite moderate differences in mean T1 values between studies, the coefficient of variation within a given study is 2.2-4.0%, suggesting that healthy myocardial MOLLI T1 values are stable and consistent within a specific sequence implementation.

While a number of MOLLI's systematic dependencies are deeply rooted in the use of the Look-Locker correction factor for an intermittent bSSFP Look-Locker readout, other dependencies have been mitigated through a combination of sequence modifications and alternative image reconstruction algorithms. For example, heart rate dependence in certain MOLLI implementations is largely due to incomplete magnetization recovery between Look-Locker sets. By ordering the Look-Locker sets from longest to shortest, such as the 5(3)3, 4(1)3(1)2, and 5(1)1(1)1 patterns, and defining the recovery durations in seconds instead of heartbeats [32], heart rate dependence is significantly reduced. A conditional fitting algorithm used in the shortened MOLLI (ShMOLLI[1]) sequence, where images from later Look-Locker sets are discarded when fitting long T1 values or if the residual fit error is too great, further improves heart rate insensitivity [23]. An optimized adiabatic inversion pulse was also found to increase the accuracy of the MOLLI sequence [27], and more complex MOLLI T1 calculation techniques utilizing Bloch equation simulations [33] have also been developed to account for other dependencies. However, as these improvements bring MOLLI T1 values closer to the true T1 value, it is important to be mindful that newer implementations are no longer directly comparable to reported literature values from previous, less accurate implementations.

Although systematic errors in MOLLI T1 values are conceptually undesirable when trying to accurately quantify true T1 values, the primary goal of most T1 mapping is to reliably quantify myocardial fibrosis. This more pragmatic view asserts that well characterized systematic errors are tolerable, provided that MOLLI T1 values are a reproducible biomarker that is sensitive to fibrosis. This perspective is supported by extensive published literature using the MOLLI techniques in a wide variety of cardiomyopathies. Furthermore, the influence of T2 values and MT on native MOLLI T1 values may actually increase its sensitivity to overall cardiac disease, as common pathologic changes in T2 and MT also increase native MOLLI T1 values. However, variability in factors such as flip angle and off-resonance is dependent on MRI system design and shimming, but still cause artifactual changes in MOLLI T1 values. Thus MOLLI's systematic dependencies are simultaneously an advantage and a disadvantage. While they may increase sensitivity of MOLLI T1 values as a biomarker for overall cardiac disease, there is the potential for misinterpretation because it may be difficult to rule out non-pathological confounders as the underlying cause of MOLLI T1 derived ECV abnormalities.

Intermittent Look-Locker can also be performed using a saturation recovery preparation, such as in the MLLSR sequence [34]. As an ideal saturation pulse nullifies longitudinal magnetization regardless of the magnetization before it, recovery periods between Look-Locker sets are no longer required and thus more images can be acquired in the same total duration. However, as MLLSR still fundamentally uses an intermittent Look-Locker acquisition, it has similar characteristics to the MOLLI sequences, with underestimated

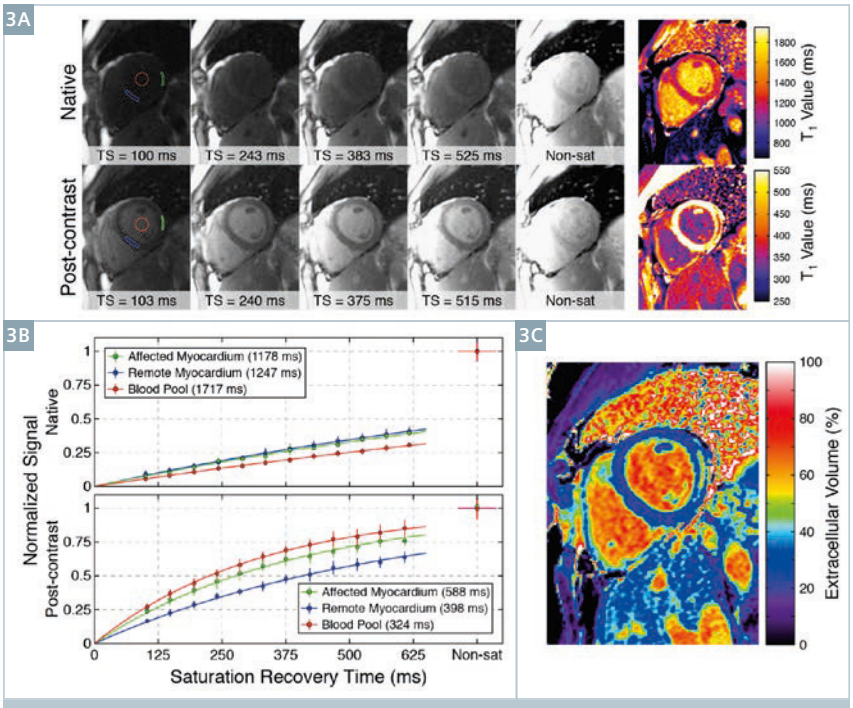

3 T1 and ECV mapping in a subject with myocarditis. **(3A)** Sample raw images from native (top) and post-contrast (bottom) SASHA-VFA T1 mapping and resulting T1 maps (right). Non-saturated images are window-leveled independently to allow better visualization. Images were motion corrected using Siemens HeartFreeze and T1 maps were generated on the scanner. ROIs drawn in the affected myocardium (green), remote myocardium (blue) and blood pool (red) are shown in the shortest TS image only. **(3B)** Signal intensities and 2-parameter best-fit curves are shown for each ROI in native (top) and post-contrast (bottom) data. **(3C)** ECV map was calculated by co-registering native and post-contrast T1 maps. *Data courtesy Drs. Peter Kellman and Andrew Arai at the National Institutes of Health.*

apparent T1* values that cannot be accurately corrected with direct application of the Look-Locker correction factor in Eq. 2.

Independently magnetization-preparation techniques

Both continuous and intermittent Look-Locker sequences acquire multiple images after a single magnetization preparation (inversion or saturation) pulse as a means of reducing the total scan time and providing a wide range of sampled recovery times. In comparison, the SR-TFL [35], SAP-T1 [36], and SAturation-recovery single-SHot Acquisition (SASHA[1]) sequences [37] acquire only a single image after each saturation pulse. As ideal saturation pulses reset the longitudinal magnetization regardless of the initial state, each image is independently magnetization prepared, and thus the magnetization time-course in each image readout is independent of other image readouts. The SASHA sequence consists of a non-prepared 'anchor' image, followed by a series of saturation recovery images in sequential heartbeats (Fig. 1C). Images are gated single-shot bSSFP readouts, similar to the MOLLI sequence (Table 1), but have significantly poorer blood-tissue contrast. SASHA images and analysis from a subject with myocarditis are shown in Fig. 3.

T1 values calculated from SASHA data using a 3-parameter model (Eq. 1) have been shown to be highly accurate and robust over a wide range of T1, T2, flip angles, heart rates, off-resonance values, and magnetization transfer effects [20, 28, 37]. However, the dynamic range of signal intensities in SASHA is nearly half that of MOLLI due to its saturation recovery preparation, resulting in significantly higher SASHA T1 variability [20]. SASHA data acquired using a variable flip angle (VFA) readout and using a 2-parameter model for T1 calculation has been recently shown to have coefficients of variation similar to MOLLI measurements while maintaining SASHA's accuracy [38]. VFA images were also shown to consistently reduce image artifacts associated with off-resonance effects. However, VFA readouts further reduce blood tissue-contrast in the anchor image, potentially reducing the effectiveness of motion correction algorithms and impairing visual identification of the myocardial boundaries when contouring on raw images.

The number of acquired SASHA images is flexible and can be reduced in subjects with diminished breath-hold capabilities at the expense of increased variability. The original SASHA sequence used saturation recovery times (TS) linearly spanning the range of values possible while keeping the saturation and imaging in the same heartbeat to maximize the number of acquired images in a fixed duration. Longer TS times may better sample the recovery curve for long T1 values and can be achieved by imaging in a separate heartbeat from the saturation pulse, such as in the SR-TFL sequence [35] and the recent SMART$_1$Map sequence [39]. Recent work numerically optimizing saturation recovery times for 3-parameter [40] and 2-parameter [41] models found clustered sampling patterns with repeated TS times result in moderate reductions in T1 variability.

The robustness of the SASHA sequence to systematic confounders makes it an attractive candidate for T1 mapping in new study protocols. While SASHA is a relatively new sequence with less clinical and histological validation compared to more established techniques, studies with SASHA in patients with heart failure [37], anthracycline cardiotoxicity remodelling [42], and Fabry disease [43] have findings consistent with established literature. Nevertheless, the lack of established values and difficulty comparing values between techniques make SASHA a difficult choice for sites where data has already been acquired with another technique.

Discussion

Absolute native myocardial T1 values vary significantly between imaging sequences, with 15-20% lower values with MOLLI compared to SASHA [44, 45] due to MOLLI's systematic underestimation [20]. ECV values are derived using both native and post-contrast T1 measurements in the blood and myocardium and thus systematic T1 errors, which may be different between each of these measurements, result in even larger differences between sequences (Table 1). Therefore, caution must be exercised when comparing literature values, and a recent consensus statement on T1 mapping recommends that site-specific normative values be established for any given T1 mapping sequence implementation [46].

In clinical practice, breath-hold motion commonly causes errors in T1 maps as signal intensity changes between images are caused by spatial misalignment instead of magnetization recovery. Although manually adjusting ROIs between images can overcome some motion effects, this process increases analysis time and effort. A robust non-rigid image registration algorithm designed for the large changes in image contrast in MOLLI data was found to significantly reduce apparent motion between images and improve T1 map quality [47]. In the Siemens implementation found in the MyoMaps package, T1 maps are generated from motion corrected images on the scanner console directly. This immediate feedback allows the operator to easily detect poor quality data sets and repeat the acquisition and enables focused investigations within the same study, as T1 abnormalities can be detected in real-time.

By extending the image registration algorithm to co-register native (non-contrast) and post-contrast T1 maps and using hematocrit values with automated blood pool segmentation, parametric ECV maps can also be generated [48, 49]. ECV image maps are more easily interpretable than T1 maps because they represent a physiologically relevant parameter and the ability to generate these in a semi-automated manner greatly improves analysis workflow. The uncertainty in T1 values from fitting measured data to the exponential recovery model can be quantified by converting fit residuals into a standard deviation with the same units as T1 values [32]. This approach can be further extended to calculating uncertainties in derived ECV values. These uncertainty maps provide valuable context in interpreting the likelihood of whether T1 and ECV abnormalities are simply due to measurement noise.

Conclusions

Myocardial T1 mapping is an active and exciting field of research, driven by a strong clinical motivation to detect diffuse myocardial fibrosis that is so ubiquitous in cardiac disease. A number of techniques are commonly used for T1 mapping, each with unique advantages and disadvantages. While direct comparison of values between these techniques is complicated by different systematic dependencies between sequences, the ability of each technique described here to detect fibrosis is supported by clinical evidence and literature. The most appropriate technique for any given study depends on considerations such as the image quality of single-shot images in subjects with smaller or thinner hearts and fast heart rates, the likelihood of variations in known confounders, and the need to compare values to existing literature. Commercial availability of a T1 mapping sequence in MyoMaps provides broad clinical access to this technology, and is a significant step towards the adoption of T1 mapping as a clinical standard for quantifying myocardial fibrosis.

References

1 Mewton N, Liu CY, Croisille P, Bluemke DA, Lima JAC. Assessment of myocardial fibrosis with cardiovascular magnetic resonance. J Am Coll Cardiol 2011;57:891–903. doi: 10.1016/j.jacc.2010.11.013.
2 Iles L, Pfluger H, Phrommintikul A, Cherayath J, Aksit P, Gupta SN, Kaye DM, Taylor AJ. Evaluation of diffuse myocardial fibrosis in heart failure with cardiac magnetic resonance contrast-enhanced T1 mapping. J Am Coll Cardiol 2008;52:1574–1580. doi: 10.1016/j.jacc.2008.06.049.
3 Jerosch-Herold M, Sheridan DC, Kushner JD, Nauman D, Burgess D, Dutton D, Alharethi R, Li D, Hershberger RE. Cardiac magnetic resonance imaging of myocardial contrast uptake and blood flow in patients affected with idiopathic or familial dilated cardiomyopathy. Am J Physiol Heart Circ Physiol 2008;295:H1234–H1242. doi: 10.1152/ajpheart.00429.2008.
4 Karamitsos TD, Piechnik SK, Banypersad SM, et al. Noncontrast T1 mapping for the diagnosis of cardiac amyloidosis. JACC Cardiovasc Imaging 2013;6:488–497. doi: 10.1016/j.jcmg.2012.11.013.
5 Flett AS, Hayward MP, Ashworth MT, Hansen MS, Taylor AM, Elliott PM, McGregor C, Moon JC. Equilibrium contrast cardiovascular magnetic resonance for the measurement of diffuse myocardial fibrosis: preliminary validation in humans. Circulation 2010;122:138–144. doi: 10.1161/CIRCULATIONAHA.109.930636.
6 Fontana M, White SK, Banypersad SM, Sado DM, Maestrini V, Flett AS, Piechnik SK, Neubauer S, Roberts N, Moon JC. Comparison of T1 mapping techniques for ECV quantification. Histological validation and reproducibility of ShMOLLI versus multibreath-hold T1 quantification equilibrium contrast CMR. J Cardiovasc Magn Reson 2012;14:88. doi: 10.1186/1532-429X-14-88.
7 Bull S, White SK, Piechnik SK, et al. Human non-contrast T1 values and correlation with histology in diffuse fibrosis. Heart 2013;99:932–937. doi: 10.1136/heartjnl-2012-303052.
8 White SK, Sado DM, Fontana M, et al. T1 Mapping for Myocardial Extracellular Volume Measurement by CMR: Bolus Only Versus Primed Infusion Technique. JACC Cardiovasc Imaging 2013;6:955–962. doi: doi: 10.1016/j.jcmg.2013.01.011.
9 Wong TC, Piehler K, Meier CG, et al. Association between extracellular matrix expansion quantified by cardiovascular magnetic resonance and short-term mortality. Circulation 2012;126:1206–1216. doi: 10.1161/CIRCULATIONAHA.111.089409.
10 Ferrari VA, Witschey WRT, Zhou R. Cardiac magnetic resonance assessment of myocardial fibrosis: honing new clinical tools. Circ Cardiovasc Imaging 2011;4:604–606. doi: 10.1161/CIRCIMAGING.111.969204.
11 Lima JAC. The promise of myocardial fibrosis assessment by T1 mapping. JACC Cardiovasc Imaging 2013;6:485–487. doi: 10.1016/j.jcmg.2012.11.014.
12 Moon JC, Treibel TA, Schelbert EB. T1 Mapping for Diffuse Myocardial Fibrosis. J Am Coll Cardiol 2013;62:1288–1289. doi: 10.1016/j.jacc.2013.05.077.

13 Look D, Locker D. Time Saving in Measurement of NMR and EPR Relaxation Times. Review of Scientific Instruments 1970;41:250–251. doi: 10.1063/1.1684482.
14 Haase A, Matthaei D, Bartkowski R, Dühmke E, Leibfritz D. Inversion recovery snapshot FLASH MR imaging. J Comput Assist Tomogr 1989;13:1036–1040.
15 Deichmann R, Haase A. Quantification of T1 values by SNAPSHOT-FLASH NMR imaging. J Magn Reson 1992;96:608–612. doi: doi: DOI: 10.1016/0022-2364(92)90347-A.
16 Messroghli DR, Nordmeyer S, Buehrer M, et al. Small Animal Look-Locker Inversion Recovery (SALLI) for Simultaneous Generation of Cardiac T1 Maps and Cine and Inversion Recovery–prepared Images at High Heart Rates: Initial Experience. Radiology 2011;261:258–265. doi: 10.1148/radiol.11101943.
17 Connelly KA, Detsky JS, Graham JJ, Paul G, Vijayaragavan R, Dick AJ, Wright GA. Multicontrast late gadolinium enhancement imaging enables viability and wall motion assessment in a single acquisition with reduced scan times. J Magn Reson Imaging 2009;30:771–777. doi: 10.1002/jmri.21907.
18 Messroghli DR, Radjenovic A, Kozerke S, Higgins DM, Sivananthan MU, Ridgway JP. Modified Look-Locker inversion recovery (MOLLI) for high-resolution T1 mapping of the heart. Magn Reson Med 2004;52:141–146. doi: 10.1002/mrm.20110.
19 Rodgers CT, Piechnik SK, DelaBarre LJ, Van de Moortele P-F, Snyder CJ, Neubauer S, Robson MD, Vaughan JT. Inversion recovery at 7 T in the human myocardium: Measurement of T1, inversion efficiency and B1 (+). Magn Reson Med 2013;70:1038–1046. doi: 10.1002/mrm.24548.
20 Kellman P, Hansen MS. T1-mapping in the heart: accuracy and precision. J Cardiovasc Magn Reson 2014;16:2. doi: 10.1186/1532-429X-16-2.
21 Chow K, Flewitt JA, Pagano JJ, Green JD, Friedrich MG, Thompson RB. T2-dependent errors in MOLLI T1 values: simulations, phantoms, and in-vivo studies. J Cardiovasc Magn Reson 2012;14:P281.
22 Gai ND, Stehning C, Nacif M, Bluemke DA. Modified Look-Locker T1 evaluation using Bloch simulations: human and phantom validation. Magn Reson Med 2013;69:329–336. doi: 10.1002/mrm.24251.
23 Piechnik SK, Ferreira VM, Dall'Armellina E, Cochlin LE, Greiser A, Neubauer S, Robson MD. Shortened Modified Look-Locker Inversion recovery (ShMOLLI) for clinical myocardial T1-mapping at 1.5 and 3 T within a 9 heartbeat breathhold. J Cardiovasc Magn Reson 2010;12:69. doi: 10.1186/1532-429X-12-69.
24 Lee JJ, Liu S, Nacif MS, Ugander M, Han J, Kawel N, Sibley CT, Kellman P, Arai AE, Bluemke DA. Myocardial T1 and extracellular volume fraction mapping at 3 tesla. J Cardiovasc Magn Reson 2011;13:75. doi: 10.1186/1532-429X-13-75.
25 Kellman P, Herzka DA, Arai AE, Hansen MS. Influence of Off-resonance in myocardial T1-mapping using SSFP based MOLLI method. J Cardiovasc Magn Reson 2013;15:63. doi: 10.1186/1532-429X-15-63.
26 Chow K, Flewitt JA, Pagano JJ, Green JD, Friedrich MG, Thompson RB. MOLLI T1 Values Have Systematic T2 and Inversion Efficiency Dependent Errors. Proc Intl Soc Magn Reson Med 2012. p. 395.
27 Kellman P, Herzka DA, Hansen MS. Adiabatic inversion pulses for myocardial T1 mapping. Magn Reson Med 2014;71:1428–1434. doi: 10.1002/mrm.24793.
28 Robson MD, Piechnik SK, Tunnicliffe EM, Neubauer S. T1 measurements in the human myocardium: The effects of magnetization transfer on the SASHA and MOLLI sequences. Magn Reson Med 2013. doi: 10.1002/mrm.24867.
29 Messroghli DR, Greiser A, Fröhlich M, Dietz R, Schulz-Menger J. Optimization and validation of a fully-integrated pulse sequence for modified look-locker inversion-recovery (MOLLI) T1 mapping of the heart. J Magn Reson Imaging 2007;26:1081–1086. doi: 10.1002/jmri.21119.
30 Kawel N, Nacif M, Santini F, Liu S, Bremerich J, Arai AE, Bluemke DA. Partition coefficients for gadolinium chelates in the normal myocardium: Comparison of gadopentetate dimeglumine and gadobenate dimeglumine. J Magn Reson Imaging 2012;36:733–737. doi: 10.1002/jmri.23651.
31 Dabir D, Child N, Kalra A, et al. Reference values for healthy human myocardium using a T1 mapping methodology: results from the International T1 Multicenter cardiovascular magnetic resonance study. J Cardiovasc Magn Reson 2014;16:69. doi: 10.1186/s12968-014-0069-x.
32 Kellman P, Arai AE, Xue H. T1 and extracellular volume mapping in the heart: estimation of error maps and the influence of noise on precision. J Cardiovasc Magn Reson 2013;15:56. doi: 10.1186/1532-429X-15-56.
33 Shao J, Nguyen K-L, Natsuaki Y, Spottiswoode B, Hu P. Instantaneous signal loss simulation (InSiL): An improved algorithm for myocardial T1 mapping using the MOLLI sequence. J Magn Reson Imaging 2014. doi: 10.1002/jmri.24599.
34 Song T, Stainsby JA, Ho VB, Hood MN, Slavin GS. Flexible cardiac T(1) mapping using a modified look-locker acquisition with saturation recovery. Magn Reson Med 2012;67:622–627. doi: 10.1002/mrm.24137.
35 Wacker CM, Bock M, Hartlep AW, Beck G, van Kaick G, Ertl G, Bauer WR, Schad LR. Changes in myocardial oxygenation and perfusion under pharmacological stress with dipyridamole: assessment using T*2 and T1 measurements. Magn Reson Med 1999;41:686–695.
36 Higgins DM, Ridgway JP, Radjenovic A, Sivananthan UM, Smith MA. T1 measurement using a short acquisition period for quantitative cardiac applications. Med Phys 2005;32:1738–1746.
37 Chow K, Flewitt JA, Green JD, Pagano JJ, Friedrich MG, Thompson RB. Saturation recovery single-shot acquisition (SASHA) for myocardial T1 mapping. Magn Reson Med 2014;71:2082–2095. doi: 10.1002/mrm.24878.
38 Chow K, Spottiswoode B, Pagano JJ, Thompson R. Improved precision in SASHA T1 mapping with a variable flip angle readout. J Cardiovasc Magn Reson 2014;16:M9.
39 Slavin GS, Hood MN, Ho VB, Stainsby JA. Breath-Held Myocardial T1 Mapping Using Multiple Single-Point Saturation Recovery. Proc Intl Soc Magn Reson Med, Vol. 20. 2012. p. 1244.
40 Akçakaya M, Weingärtner S, Roujol S, Nezafat R. On the selection of sampling points for myocardial T1 mapping. Magn Reson Med 2014. doi: 10.1002/mrm.25285.
41 Kellman P, Xue H, Chow K, Spottiswoode BS, Arai AE, Thompson RB. Optimized saturation recovery protocols for T1-mapping in the heart: influence of sampling strategies on precision. J Cardiovasc Magn Reson 2014;16:55. doi: 10.1186/s12968-014-0055-3.
42 Tham E, Chow K, Spavor M, Pagano JJ, Haykowsky MJ, Thompson RB. Degree of diffuse fibrosis measured by MRI correlates with LV remodelling in childhood cancer survivors after anthracycline chemotherapy. J Cardiovasc Magn Reson 2011;13:P276.
43 Thompson RB, Chow K, Khan A, Chan A, Shanks M, Paterson I, Oudit GY. T_1 mapping with cardiovascular MRI is highly sensitive for Fabry disease independent of hypertrophy and sex. Circ Cardiovasc Imaging 2013;6:637–645. doi: 10.1161/CIRCIMAGING.113.000482.
44 Flewitt JA, Chow K, Pagano JJ, Green JD, Friedrich MG, Thompson RB. Effect of Systematic T1 Errors on Lambda Calculations: Comparison of Different T1 Mapping Techniques. Proc Intl Soc Magn Reson Med, Vol. 20. 2012. p. 3370.
45 Roujol S, Weingärtner S, Foppa M, Chow K, Kawaji K, Ngo LH, Kellman P, Manning WJ, Thompson RB, Nezafat R. Accuracy, Precision, and Reproducibility of Four T1 Mapping Sequences: A Head-to-Head Comparison of MOLLI, ShMOLLI, SASHA, and SAPPHIRE. Radiology 2014;272:683–689. doi: 10.1148/radiol.14140296.
46 Moon JC, Messroghli DR, Kellman P, et al. Myocardial T1 mapping and extracellular volume quantification: a Society for Cardiovascular Magnetic Resonance (SCMR) and CMR

Working Group of the European Society of Cardiology consensus statement. J Cardiovasc Magn Reson 2013;15:92. doi: 10.1186/1532-429X-15-92.

47 Xue H, Shah S, Greiser A, Guetter C, Littmann A, Jolly M-P, Arai AE, Zuehlsdorff S, Guehring J, Kellman P. Motion correction for myocardial T1 mapping using image registration with synthetic image estimation. Magn Reson Med 2012;67:1644–1655. doi: 10.1002/mrm.23153.

48 Kellman P, Wilson JR, Xue H, Ugander M, Arai AE. Extracellular volume fraction mapping in the myocardium, part 1: evaluation of an automated method. J Cardiovasc Magn Reson 2012;14:63. doi: 10.1186/1532-429X-14-63.

49 Kellman P, Wilson JR, Xue H, Bandettini WP, Shanbhag SM, Druey KM, Ugander M, Arai AE. Extracellular volume fraction mapping in the myocardium, part 2: initial clinical experience. J Cardiovasc Magn Reson 2012;14:64. doi: 10.1186/1532-429X-14-64.

50 Neilan TG, Coelho-Filho OR, Shah RV, et al. Myocardial extracellular volume fraction from T1 measurements in healthy volunteers and mice: relationship to aging and cardiac dimensions. JACC Cardiovasc Imaging 2013;6:672–683. doi: 10.1016/j.jcmg.2012.09.020.



Contact

Kelvin Chow, Ph.D.
1098 Research Transition Facility
Department of Biomedical Engineering
University of Alberta
Edmonton AB T6G 2V2
Canada
kelvin.chow@ualberta.ca



Contact

Dr. Richard Thompson, Associate Professor
1098 Research Transition Facility
Department of Biomedical Engineering
University of Alberta
Edmonton AB T6G 2V2
Canada
Phone: +1 (780) 492-8665
richard.thompson@ualberta.ca

[1] The product is still under development and not commercially available yet. Its future availability cannot be ensured.

[2] MAGNETOM 7T is ongoing research. All data shown are acquired using a non-commercial system under institutional review board permission. MAGNETOM 7T is still under development and not commercially available yet. Its future availability cannot be ensured.

Practical Considerations for the Evaluation of the Neuroforamina in Routine Spine Imaging at 3T. A Case Series

Thuy D. Do; Marc-André Weber

Clinic of Diagnostic and Interventional Radiology, University Hospital Heidelberg, Germany

Introduction

Pathologies of the neuroforamina are one of the most frequent indications for spine surgery. When imaging the neuroforamina usually sagittal and axial planes are acquired to delineate these pathologies. However, in a relatively small, but clinically not negligible, 29% of cases where root impingement was surgically confirmed, lateral root compression was underestimated in standard MRI with standard MR planes (axial/sagittal). Moreover, Bartynski et al. estimated the rate of successful prediction of a root impingement with such a standard MRI at only 72% [1]. Consequently there is a need to optimize the procedure for spine MRI to reliably evaluate nerve root impingement in a potential preoperative setting. By obtaining parasagittal sequences and by performing oblique image reconstructions, one can generate images that are strictly axial cuts through the neuroforamina. This allows for a better evaluation of the nerve enlargement, the disappearance of the nerve surrounding fat, and the provision of T2-neuropathy signals. The application of multiplanar reconstructions, e.g. for sacral nerves, has already been postulated and practiced on CT scans in clinical routine [2]. However, in clinical reality, MRI protocols often still use strictly axial and sagittal 2D planes, resulting in the above-mentioned challenges. In the following cases we present some practical aspects on the imaging protocols used to improve visualization of neuroforaminal pathologies.

Imaging of neuroforaminal pathologies at 3T

At our institute we mainly apply 3T MRI for evaluation of neurforaminal pathologies. The main advantage of imaging at 3T is the proportional increase of signal-to-noise ratio (SNR), enabling a clear reduction in slice thickness. Even in clinical realistic routine exams, the slice thickness can be reduced to even less than 3 mm for 2D T2-weighted MRI sequences. High SNR also provides better in-plane resolution as well as spatial resolution of the anatomical structures to be evaluated [5]. Although the disadvantages of MR imaging at 3T, such as dielectric shading effects, have to be taken into consideration, many of these limitations have been overcome, or are at least less pronounced, compared to the first clinical generation of 3T MR systems. Nevertheless, it should be emphasized that these dielectric shading effects do play a role in the application of 3T for spine imaging and must be addressed alongside other issues such as increased specific absorption rates. Most of the practical considerations in this case series, however, also apply for spine imaging at 1.5T.

All examinations presented in this article were performed on a 3T MRI scanner (MAGNETOM Verio, Siemens Healthcare, Erlangen, Germany) using the integrated multi-channel spine coil and – for imaging of the cervical spine – the head/neck coil.

Conclusion

Questions concerning pathologies of the neuroforamina, multiplanar reconstructions and/or additional angulated imaging sequences (at a 45° oblique view towards the standard sagittal plane) of the spine should particularly be included in routine examinations for improved delineation and depiction of neuroforaminal pathologies, especially if there is a need to evaluate surgical therapy. Whenever possible, a 3D sequence is preferred and thus post-imaging reconstructions can be compiled that not merely reduce examination time but also offers advantages for multiple planar reconstructions as well as simplifying the MR exam. In other cases, e.g. when dealing with metal instrumentation or motion artifacts due to pain, faster additional T2w sequences can be applied. Kinematic MRI might be beneficial for revealing disc bulges, which are not shown by traditional neutral views and should be considered also in a routine clinical setting for evaluation of the cervical spine.

Acknowledgment

The excellent technical assistance from Mrs. Sandra Kauczor and Joanna Weihrauch-Mohr is gratefully acknowledged.

Case 1: Parasagittal oriented T2-weighted sequences

An MRI exam of a 51-year-old male patient suffering pain within the cervical spine predominantly on the left side for the last four years. No focal neurologic symptoms were present. This case shows the value of parasagittal-oriented 2D MR sequences for improved confidence in diagnoses. In the parasagittal sequences, a focal mediolateral protrusion of the disc C3/C4-vertebra with compression of the left C3 spinal nerve can be easily delineated.

The disc herniation is less obvious due to partial volume effects and could have been missed on the standard sagittal planes, whereas the oblique parasagittal sequence nicely depicts the left sided protrusion (arrows). The parasagittal planes were planned as a 45° oblique angulated plane to the median and perpendicular to the neuroforamina. This case illustrates that by relying only on standard sagittal and axial 2D MRI for depicting the cervical spine and relatively thick slices (>3 mm), the diagnostic information may be limited for a proper evaluation of the nerve roots. In addition to the said protrusion, an old fracture of the spinous process C7 and Th1 was diagnosed.

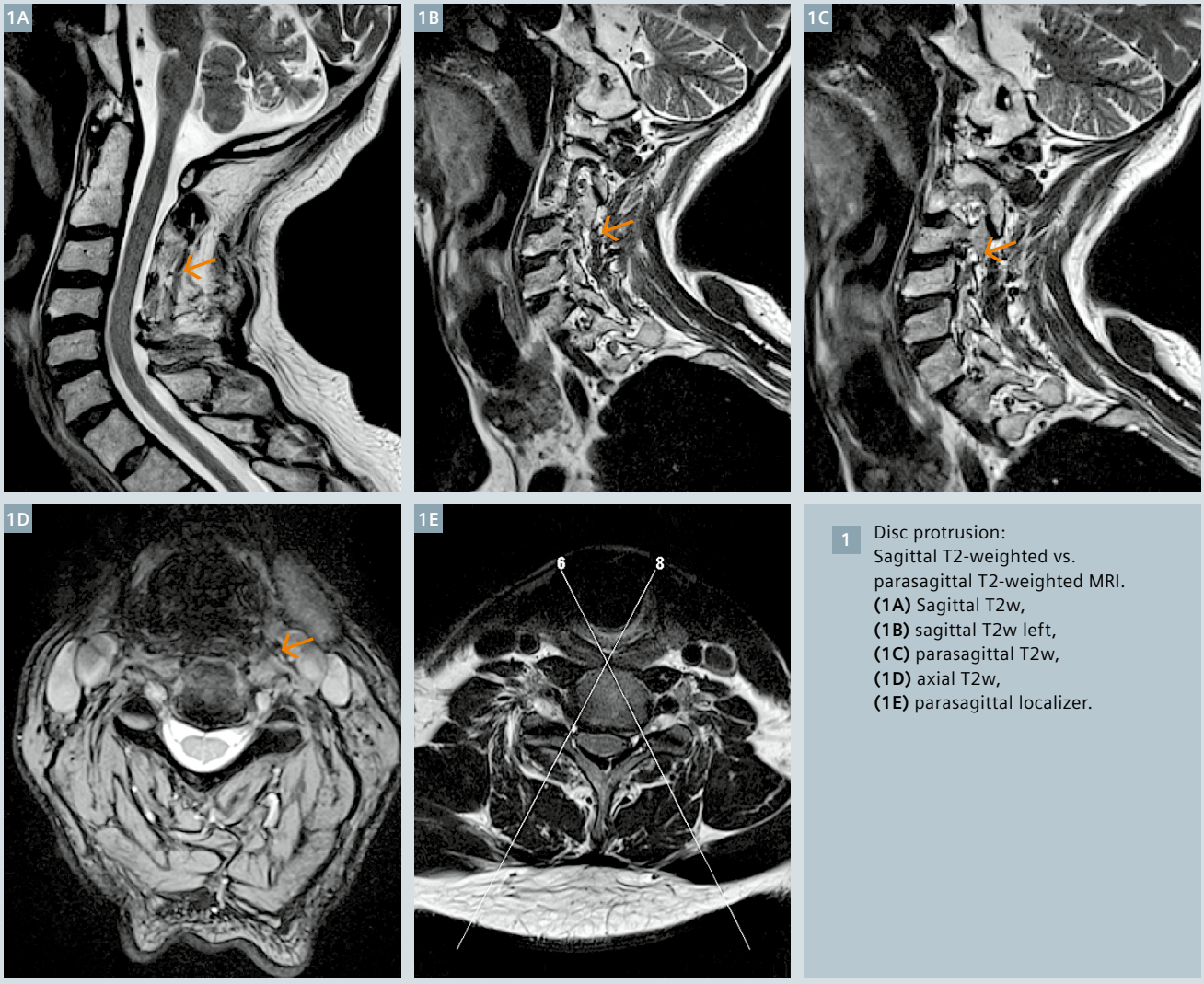

1 Disc protrusion:
Sagittal T2-weighted vs. parasagittal T2-weighted MRI.
(1A) Sagittal T2w,
(1B) sagittal T2w left,
(1C) parasagittal T2w,
(1D) axial T2w,
(1E) parasagittal localizer.

		TA [min]	Matrix	FOV [mm]	Slices	ST	TR [ms]	TE [ms]
Cervical spine	Parasagittal T2w TSE	2:13	384	260	11	2	2690	110

Table 1: Parasagittal T2-weighted TSE sequence used in this case for improved visualization of the neuroforamina.

Case 2: 3D T2-weighted sequences and parasagittal image plane reconstructions

In contrast to oblique-oriented 2D MR sequences, 3D MR sequences allow in retrospect any necessary reformation and are less dependent on accurate planning of the exam. Furthermore, there are obvious time benefits where multiple planes are needed. However, the differences in contrast and image impression (high resolution in-plane versus isotropic voxels resulting in thin slices with reduced in-plane resolution) compared with conventional 2D MRI sequences should be mentioned, even though they are not covered in this article.

In this case, MR images were made of a 52-year-old male who presented with pain in the lower back, radiating in the legs. Standard 2D MRI based on axial and (para-) sagittal planes showed disc protrusion of the L4-S1 vertebra with the maximum of the herniation at the L4/L5 segment. There was a narrowing more of the right neuroforamen than of the left neuroforamen at the L4/L5 segment due to the disc protrusion as well as spondylarthritis.

In addition to the standard MRI protocol, we used a balanced steady-state free precession sequence (TrueFISP), which provides a high signal intensity of the cerebrospinal fluid. As shown in figure 2B, the oblique reconstruction improves the confidence of the finding. With its short acquisition time, this TrueFISP sequence is also less sensitive to motion artifacts. To achieve a similar contrast of the cerebrospinal fluid other sequences can also be used, e.g. 3D CISS sequences. However, it should be pointed out that at 3T we must also keep the flip angles under observation because of their effect on the specific absorption rate (SAR) [3].

One drawback of the TrueFISP sequence is the so-called dark banding artifact which can be met by acquiring images at different phase offset angles. Another alternative would be the application of the SPACE sequence for T2w 3D imaging at 3T.

By allowing multiplanar oblique reconstructions, the additional 3D sequence reduces the risk of missing neuroforamen encroachment, without the need for further sequences and without increasing the complexity of the procedure for the MR scan. Although the lumbar neuroforamina have a nearly sagittal orientation to the lumbar spine and are in most cases well depicted with traditional location of planes, these additional images provided by the TrueFISP that depict the neuroforamina en face facilitate the detection of even minor encroachments. In addition, the higher spatial resolution can improve the diagnostic confidence for the conventional planes e.g. as shown in this case, for a strictly axial orientation (Fig. 2C).

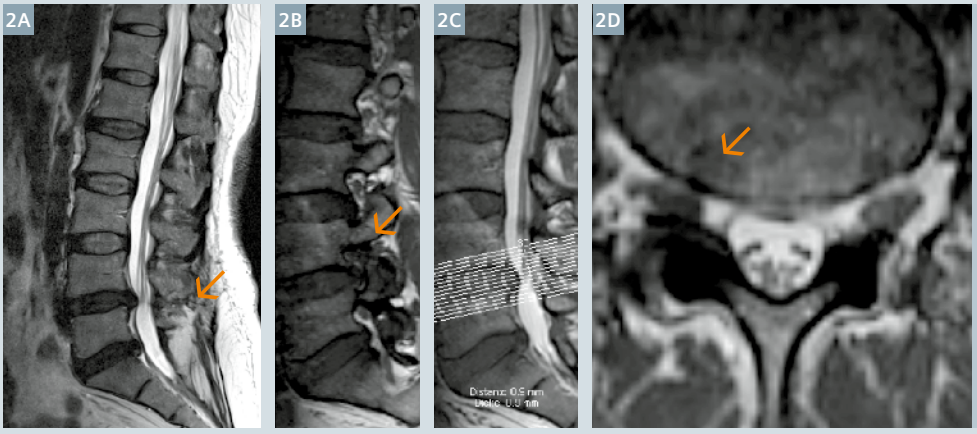

2 Disc protrusion: Sagittal T2-weighted sequence vs. parasagittal TrueFISP reconstructions and strictly axial reconstructions along the disc. **(2A)** Sagittal T2w, **(2B)** parasagittal reconstruction, **(2C)** localizer, **(2D)** axial reconstruction.

		TA [min]	Matrix	FOV [mm]	Slices	ST	TR [ms]	TE [ms]
Sequence	Cor TrueFISP 3D	4:26	256	220	80	0.9	4.86	2.43
Lumbar spine reconstructions	Axial		256		Variable	1	4.86	2.43
	Parasagittal reconstruction angulated towards the neuroforamina		256		Variable 30	1	4.86	2.43

Table 2: TrueFISP sequence and parasagittal reconstructions.

Case 3: Parasagittal and oblique oriented MR sequences in case of indwelling metal

In this case MRI images were made of a 76-year-old female who presented with a one-year history of back pain spreading more in her right than her left leg. Two years ago a spacer between the spinous processes L4/L5 had been implanted at another hospital.

In this case, a conventional parasagittal plane represents a good option for postoperative imaging, since metal susceptibility artifacts are avoided. But depending on the implant used and its configuration, the usage of double oblique planes offers the opportunity that the artifact generated by the osteosynthesis instrumentation moves out of the field-of-view. We prefer conventional T2-weighted TSE sequences in patients with surgical hardware and in combination with different angulations: Often good, robust imaging is feasible even with the pronounced sensitivity of 3T towards artifacts introduced by these implants. Since 3D gradient echo sequences, like the MEDIC, are more prone to susceptibility artifacts, they do not represent the backbone of our protocol. However, for instance 3D SPACE sequences have the advantage of post-imaging reconstructions which may be required especially in very complex cases and instrumentation e.g. severe scoliosis and rotation of the spine. As demonstrated in figure 4, the instrumentation does not affect the diagnostic quality of the MR scan and the neuroforamina can be assessed adequately.

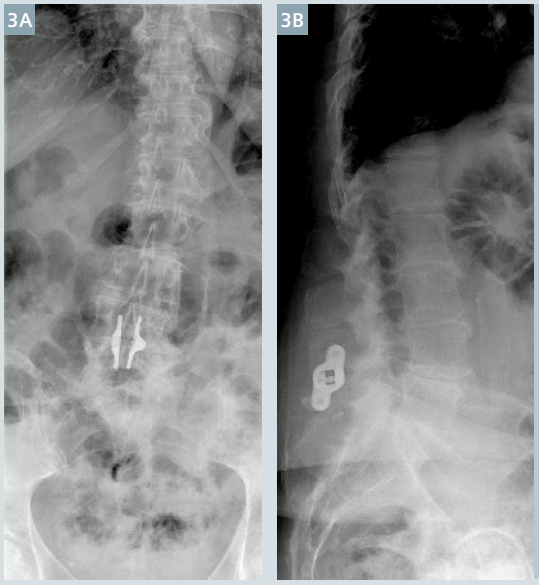

3 X-rays of lumbar spine with osteosynthesis material between the spinous process L4/L5.

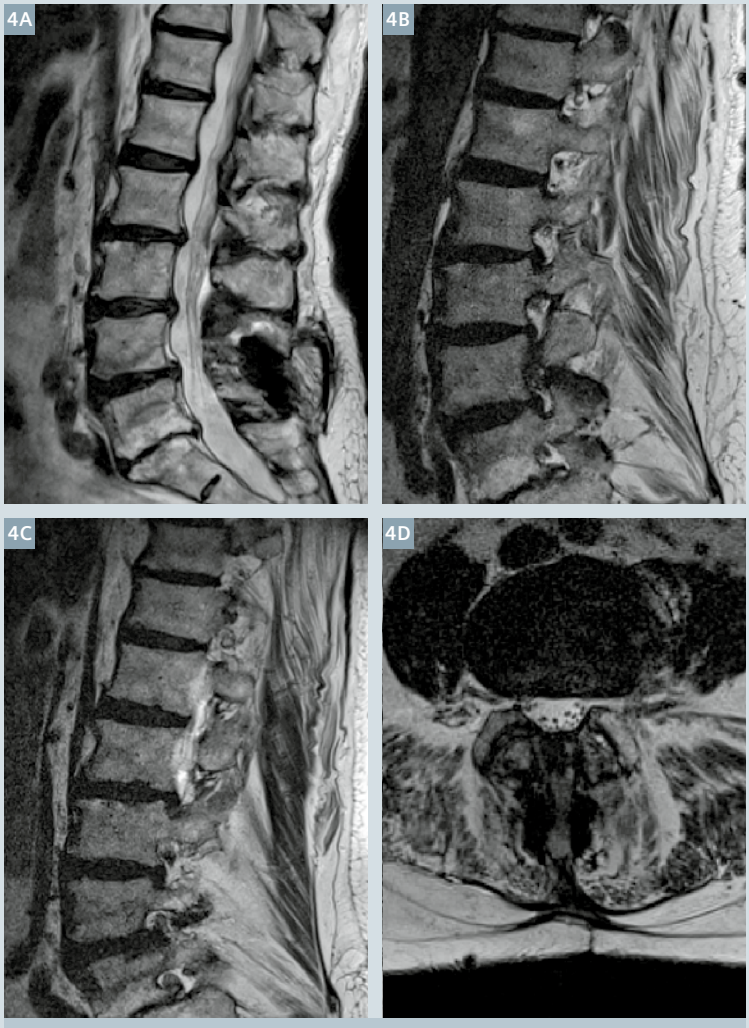

4 Sagittal vs. parasagittal oriented T2-weighted TSE sequences. **(4A)** Sagittal T2w, **(4B)** parasagittal T2w left, **(4C)** parasagittal T2w right, **(4D)** axial T2w.

Case 4: Additional value of dynamic MRI sequences

For the evaluation of pathologies of the cervical spine in particular, dynamic MRI sequences can add important clinical information, obtained within a routine clinical setting. In this case, a 42-year-old man with persisting pain in the cervical spine presented for MR reevaluation after a car accident two years ago. He has no focal paresis, only paresthesia in his left thumb. The kinematic MRI comprised of ultrafast sequences (e.g. T2-weighted HASTE) at 30° inclination and reclination. At the neutral position a disc bulge and myelopathy signal are denoted at the C6/C7 level indicating the cause of the symptoms. The disc bulge was significantly increased in extension (reclination) position (Fig. 5C). This case illustrates well the valuable information obtained by adding a 30-second sequence to the standard MRI protocol. Sometimes abnormalities can only be depicted – or are better depicted – by flexion or extension of the spine so that the symptoms are at their maximum. This method may be restricted, apart from contraindications, if there is severe pain that renders the patient unable to bear this position. Nevertheless, the application of a HASTE sequence represents a good approach that allows in most cases such a dynamic scan. Other sequences, like conventional 2D TSE, or even 3D sequences like SPACE or TrueFISP do, of course, offer all the advantages discussed above, but they are coupled with longer examination times and sequence-dependant challenges such as sensitivity to metal artifacts [4].

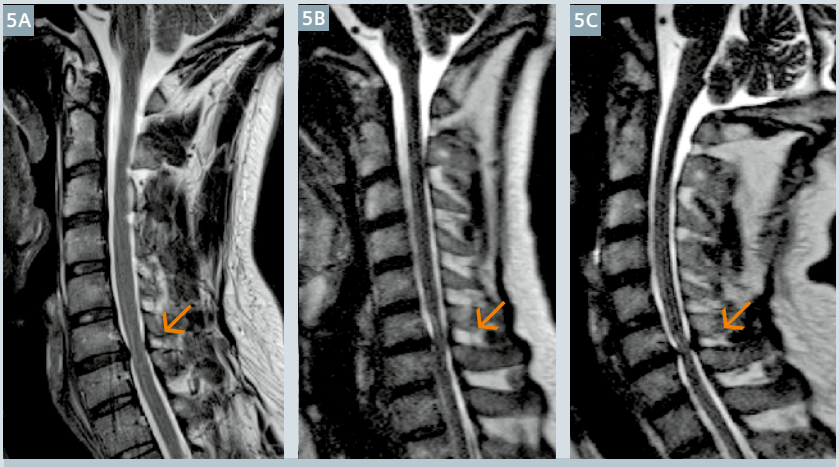

5 Conventional sagittal T2w vs. dynamic T2w MRI.
(5A) Sagittal T2w, **(5B)** T2w HASTE inclination, **(5C)** T2w HASTE reclination.

		TA [min]	Matrix	FOV [mm]	Slices	ST	TR [ms]	TE [ms]
Cervical spine inclination	T2w HASTE sag	0:30	320	250	15	3	1000	249
reclination	T2w HASTE sag	0:30	320	250	15	3	1000	249

Table 3: Dynamic sequences.

References

1 Bartynski, W.S. and L. Lin, Lumbar root compression in the lateral recess: MR imaging, conventional myelography, and CT myelography comparison with surgical confirmation. AJNR Am J Neuroradiol, 2003. 24(3): p. 348-60.

2 Yang, J., et al., Application of MPR in sacral nerve injury during sacral fracture. J Trauma, 2011. 70(6): p. 1489-94.

3 Baskaran, V., et al., Myelographic MR imaging of the cervical spine with a 3D true fast imaging with steady-state precession technique: initial experience. Radiology, 2003. 227(2): p. 585-92.

4 Gerigk, L., et al., Dynamic magnetic resonance imaging of the cervical spine with high-resolution 3-dimensional T2-imaging. Clin Neuroradiol, 2012. 22(1): p. 93-9.

5 Shapiro, M., Imaging of the spine at 3 tesla. Neuroimaging Clin N Am, 2012. 22(2): p. 315-41, xi-xii.

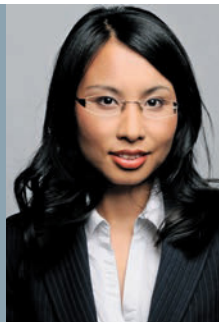

Thuy D. Do

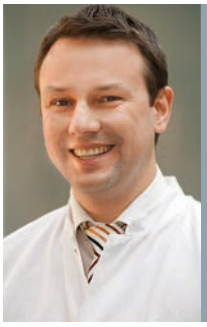

Marc-André Weber

Contact

Marc-André Weber, M.D., M.Sc.
Professor of Radiology
Heidelberg University Hospital
Diagnostic and Interventional Radiology
Im Neuenheimer Feld 110
69120 Heidelberg, Germany
MarcAndre.Weber@med.uni-heidelberg.de

MR-Guided Biopsies of the Prostate in Supine Patient Position

Florian Schneider, M.D.[1]; Martin Requardt, Ph.D.[2]; Gregor Thörmer, Ph.D.[2]; Karl Engelhard, M.D.

[1] Diagnostic Radiology, Martha-Maria Hospital Nürnberg, Germany
[2] Siemens Healthcare, Magnetic Resonance, Erlangen, Germany

Introduction

Prompted by elevated PSA levels, more than a million men in the United States alone have to undergo transrectal ultrasound (TRUS)-guided prostate biopsy to clarify suspicion for prostate cancer per year [1]. Unlike pathways for other malignancies, biopsy of the prostate is performed by standardized, systematic but essentially random sampling [2]. The major limitation of this approach is that clinically *in*significant cancers are often identified by chance while, even more important, clinically *significant* cancers may remain undetected [3, 4]. As a result of this uncertainty, more than one-third of men whose first biopsy was negative are rebiopsied within 5 years [1].

Over recent years, multiparametric magnetic resonance imaging (mpMRI), combining the morphological assessment of T2-weighted (T2w) imaging with different functional imaging techniques such as diffusion-weighted imaging (DWI) and dynamic contrast enhanced imaging (DCE) has become a mature tool for localizing and visualizing suspicious foci in the prostate.

Consequently, advances are being made in the way that biopsies are performed, with the aim to integrate the additional information into the biopsy workflow: Cognitive registration, in-bore MR guided biopsy and MR/US fusion biopsies are the most commonly used techniques to improve prostate cancer detection with targeted biopsy.

While both cognitive integration and MR/US fusion biopsies have been shown to improve the cancer detection rate [5], prostate biopsies performed under direct MR guidance are indicated in patients where MR imaging identified lesions that are either very small or located in areas difficult to reach with standard TRUS-guided biopsy. Another indication might be in patients showing a clear discrepancy between the histopathological findings of TRUS-biopsy and imaging results.

In the following, we report on our clinical experience with a customized approach and a simplified biopsy workflow for MR-guided prostate biopsies where the patient lies in supine position.

Case 1

Due to a contraindication for digital rectal examination and transrectal ultrasound because of rectal stenosis, a 72-year-old, biopsy-naive patient with continuously rising PSA levels (last: 12 ng/ml) was referred to our institution for diagnostic prostate MRI. Scans were performed with high-channel surface coils only using a MAGNETOM Skyra 3T system.

The protocol consisted of axial, coronal and sagittal T2-weighed TSE scans (TR 8300 ms, TE 107 ms, slice thickness 3.0 mm, FOV 160 mm, matrix 320, TA 3:11 min); axial diffusion-weighted imaging with RESOLVE (TR 4190 ms, TE 69 ms, slice thickness 3.0 mm, FOV 160 mm, matrix 114, TA 4:42 min) and axial DCE scans (TR 5.08 ms, TE 1.77 ms, slice thickness 3.5 mm, FOV 260 mm, matrix 192, TA 8:1 s, 35 repetitions).

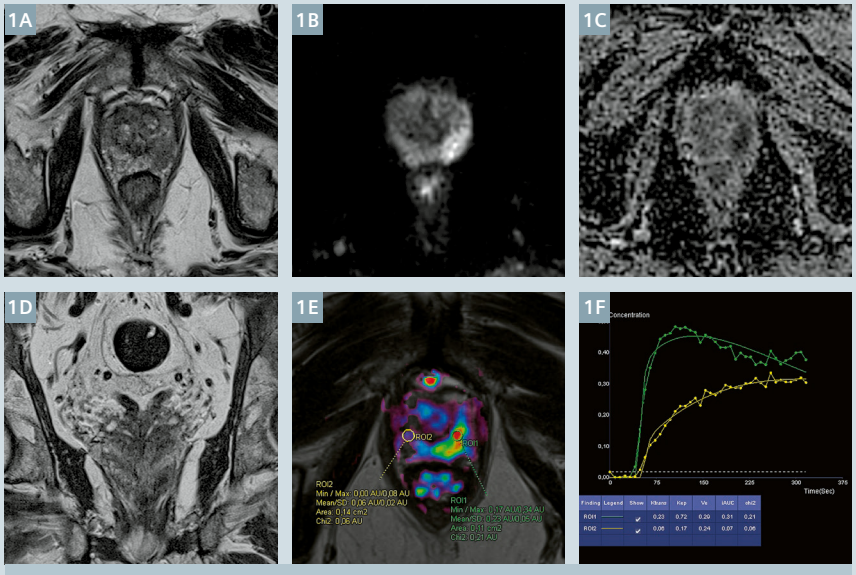

1 Transversal T2w TSE images **(1A)** demonstrating a suspicious lesion within the left peripheral zone with correspondingly increased signal in the b = 800 s/mm² image **(1B)**, diffusion restriction in the ADC map **(1C)**. The lesion can be confirmed in the coronal T2w images **(1D)**. The parametric map **(1E, K^{trans})** shows a clear focal lesion with a highly suspicious curve **(1F)**.

Dynamic contrast-enhanced images were post-processed using *syngo*.via Tissue 4D.

As illustrated in Figure 1, a lesion in the apical third of the prostate was visible in T2-weighted images as a hypointense, lenticular shaped structure extending more than 1.5 cm with corresponding diffusion-restriction and suspect, focal contrast uptake as well as wash-out in the DCE series. Consequently, the patient was referred to MRI-guided prostate biopsy of the highly suspicious areal in the gland.

Biopsy was performed in a wide-bore MAGNETOM Aera 1.5T system with the patient in supine lithotomy position using a tailored positioning device (Fig. 2, Invivo Germany, Schwerin, Germany). Intra-procedural imaging was undertaken using a combination of a flexible 4-channel coil underneath the patients back and a standard 18-channel body coil positioned on the pelvis of the patient. First, a small, contrast-filled tube was inserted to the patient's rectum and fixated with a highly flexible MR-compatible arm. To define the target for biopsy, fast T2-weighted scans (TR 5000 ms, TE 100 ms, slice thickness 3.5 mm, FOV 200 mm, matrix 256, TA 1:45 min) were performed, while the position and orientation of the contrast-filled needle guide was imaged using a 3D fat suppressed TrueFISP sequence and visualized with a 3D maximum intensity projection (MIP) technique. By simply positioning the center mark of a slice block (Fig. 3, yellow circle) in the center of the lesion, the orientation of the needle guide with respect to the target was checked and the trajectory of the needle guide was iteratively corrected to point to the target. In the given case, only one iteration (repositioning of the needle guide, control scan) was necessary. After contentedly positioning the needle guide, the actual fully-automated biopsy device was inserted and two samples from slightly different positions were taken (Fig. 4). Histopathology revealed a 3 + 3 = 6 acinar adenocarcinoma.



2 Setup with the customized biopsy device. Patient will be positioned in supine position. A flexible arm (arrow) holds the contrast filled needle guide which is used to define the trajectory to the target and to insert the actual biopsy needle.

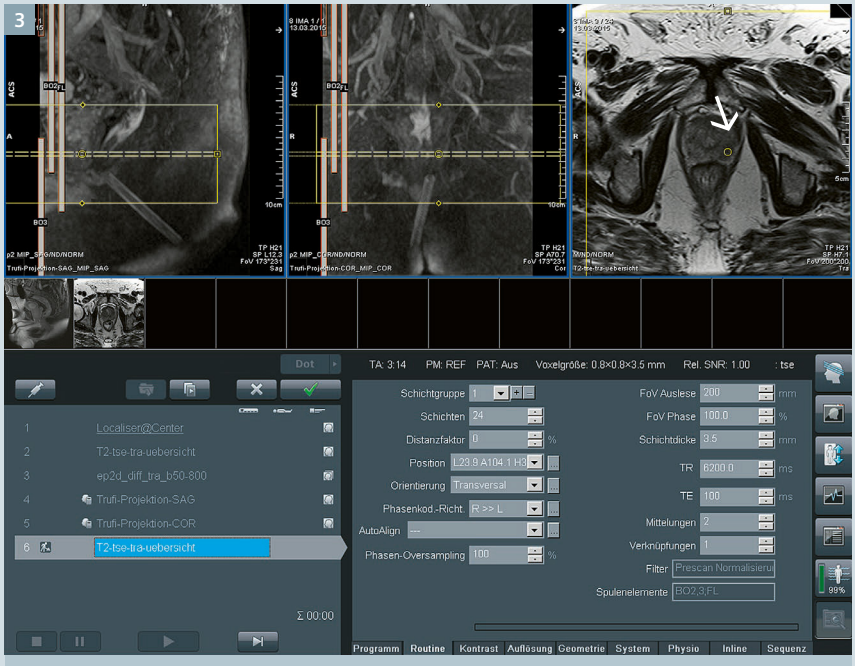

3 Control images to confirm the correct positioning of the needle guide. The center mark (yellow circle, right image) was positioned on the lesion to be biopsied. The left and middle images confirm that the contrast filled needle guide (visible as two bright lines) directly points to the target (yellow circle, arrow).

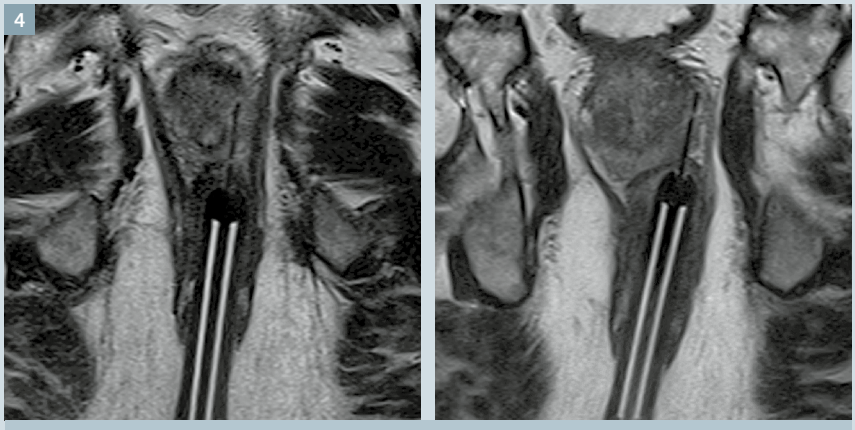

4 Fast, double-oblique T2w TSE control images confirming the right position of the needle in the lesion before tissue sampling.

Case 2

Patient presented at our department with constantly high PSA values (03/2015: 10.8 ng/ml; 04/2015: 13.0 ng/ml) with a referral for prostate MRI. Diagnostic multiparametric prostate MRI was performed on our 1.5T MAGNETOM Aera and revealed two relatively small lesions in the right and left peripheral zone (Fig. 5). The lesion in the right peripheral zone was selected for MR target biopsy due to better accessibility. During the MR-guided biopsy session, two samples were taken from different positions (Fig. 6). The one taken from the periphery revealed an acinar adenocarcinoma with a Gleason Score of 6 (3 + 3) while the other sample even showed a more aggressive pattern (Gleason Score 3 + 4 = 7).

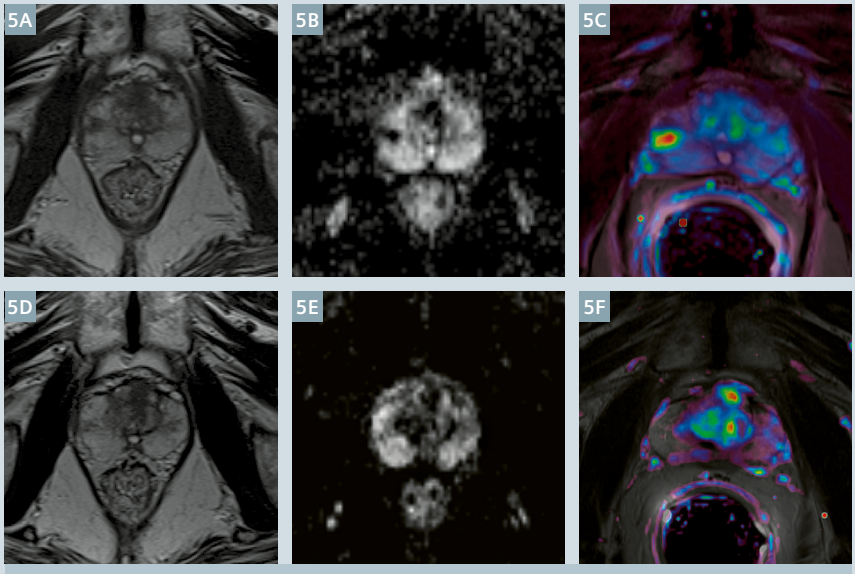

5 Axial T2w TSE **(5A, D)**, ADC map **(5B, E)**, and K^{trans} maps **(5C, F)**.

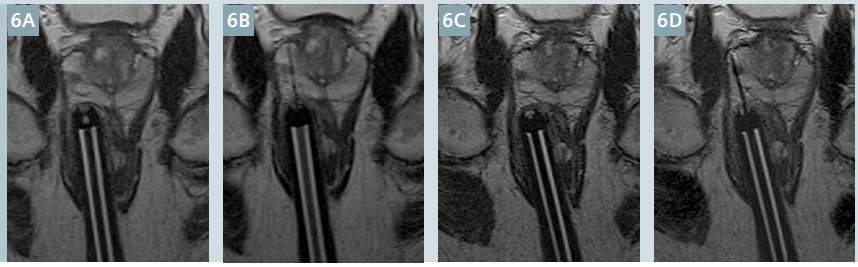

6 After planning the biopsy trajectory **(6A)** the needle was inserted and an oblique control scan was performed. The control scan **(6B)** clearly shows that only the periphery of the lesion is targeted. After minimal repositioning of the needle guide **(6C)** the needle was reinserted and control scan shows optimal positioning of the needle in the lesion.

Summary

Targeted biopsies of the prostate under direct MRI-guidance are a reasonable complement to ultrasound biopsy techniques. As shown in the second case presented here, exact targeting of the most suspicious portion of a tumor is crucial for correct classification and consequently best therapy decisions. Especially in case of relatively small lesions, direct MR-guidance has clear advantages over fusion techniques which are always susceptible to intrinsic sources of registration errors.

The targeting procedure presented here, does not require any additional software equipment or extra planning PCs, since it is solely based on standard sequences and planning tools provided with the scanner. Biopsies in a supine position, as performed in Nuremberg, may further improve the acceptance and applicability of MR guided biopsies of the prostate especially in obese, dyspnoeic or elderly individuals.

References

1 Welch HG, Fisher ES, Gottlieb DJ, Barry MJ. Detection of prostate cancer via biopsy in the Medicare-SEER population during the PSA era. J Natl Cancer Inst 2007;99:1395–1400.
2 Churukanti G1, Siddiqui MM1. Prostate cancer: MRI-TRUS fusion biopsy versus 12-core systematic biopsy. Nat Rev Urol. 2015;12:369-71.
3 Sinnott M, Falzarano SM, Hernandez AV et al. Discrepancy in prostate cancer localization between biopsy and prostatectomy specimens in patients with unilateral positive biopsy: implications for focal therapy.Prostate 2012; 72: 1179–86.
4 Epstein JI, Feng Z, Trock BJ, Pierorazio PM. Upgrading and downgrading of prostate cancer from biopsy to radical prostatectomy: incidence and predictive factors using the modified Gleason grading system and factoring in tertiary grades. Eur Urol 2012; 61: 1019–24.
5 Sonn GA, et al. Targeted biopsy in the detection of prostate cancer using an office based magnetic resonance ultrasound fusion device. J Urol. 2013;189: 86-91.



Contact

Florian Schneider, M.D.
Martha-Maria Hospital
Radiology Department
Stadenstr. 58
90491 Nürnberg
Germany
Phone: +49 (0) 911 959-1151
Florian.M.Schneider@web.de

Self-Navigated Free-Breathing High-Resolution 3D Cardiac Imaging: A New Sequence for Assessing Cardiovascular Congenital Malformations

Pierre Monney, M.D.[1]; Davide Piccini[2]; Grégoire Berchier[1]; Tobias Rutz, M.D.[1]; Gabriella Vincenti[1]; Milan Prša, M.D.[3]; Nicole Sekarski, M.D.[3]; Matthias Stuber, Ph.D.[4]; Juerg Schwitter, M.D.[1]

[1] Division of Cardiology and Cardiac MR Center, University Hospital of Lausanne (CHUV), Lausanne, Switzerland
[2] Advanced Clinical Imaging Technology, Siemens Healthcare IM BM PI, Lausanne, Switzerland
[3] Unit of Pediatric Cardiology, Department of Pediatrics, University Hospital Lausanne (CHUV), Lausanne, Switzerland
[4] Department of Radiology, University Hospital (CHUV) and University of Lausanne (UNIL) / Center for Biomedical Imaging, (CIBM), Lausanne, Switzerland

Introduction

Congenital cardiac malformations occur in 9.1 per 1,000 live births [1] and range from simple defects including bicuspid aortic valve or isolated restrictive ventricular septal defect, to complex malformations requiring surgical correction or palliation early in life. While the neonatal mortality with such complex malformations remained stable, an important increase in life expectancy has been achieved with the advances in surgical treatment and the majority of the patients can nowadays reach adulthood [2].

As a consequence of this increase in life expectancy, the population of adult patients with congenital heart disease is growing [3]. Despite an optimal surgical correction or palliation, a regular follow-up of these patients is mandatory as they remain at higher risk for long-term cardiac complications including arrhythmia and heart failure [4, 5]. Cardiac imaging plays an important role in the follow-up of these patients to assess the morphology and function of the cardiac chambers and the valves, and to assess the integrity of any surgically implanted material. While echocardiography is used as the first-line imaging modality for initial diagnosis and follow-up assessments, cardiac magnetic resonance (CMR) is the

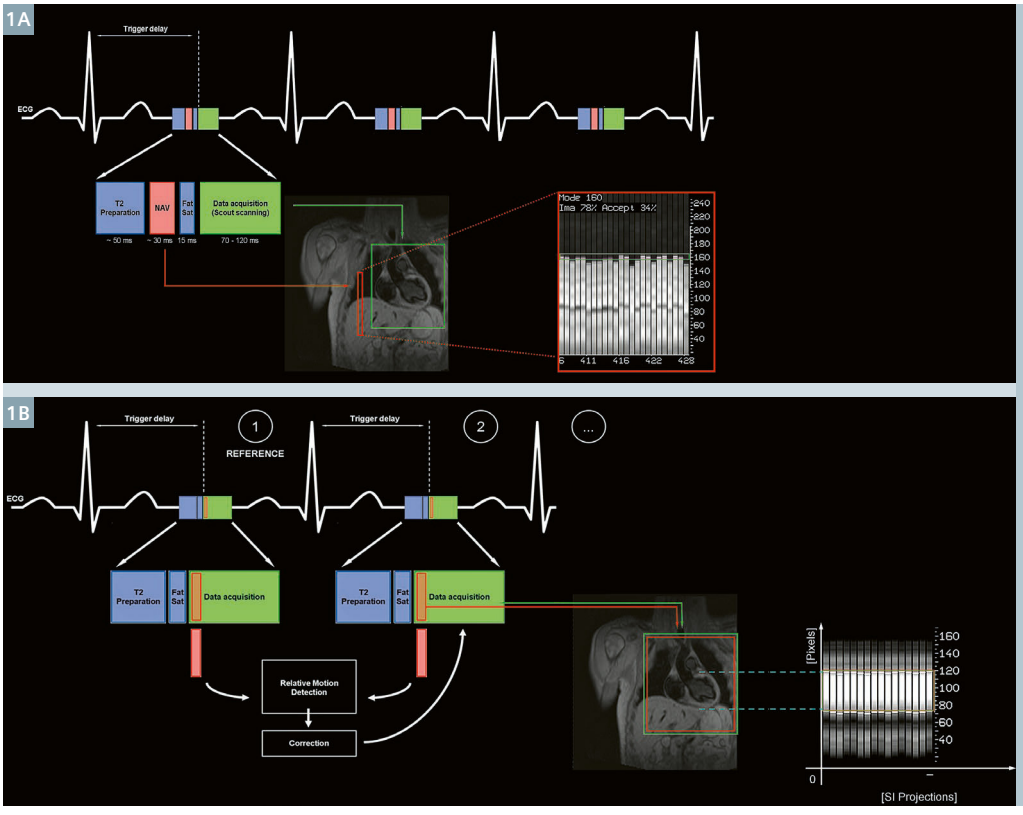

1 (**1A**) To consistently acquire data at the same respiratory position, a narrow acceptance window is defined, corresponding to the end-expiration, and only data acquired within this window are utilized in the final image reconstruction, while all other data segments are rejected and reacquired later during the scan. (**1B**) The position of the heart at the beginning of each data segment is compared with a reference position, i.e. the position of the ventricular blood-pool at the very first data segment, and automatically corrected for respiratory motion before the data are sent to the reconstruction pipeline.

modality of choice for the assessment of the right ventricle, the pulmonary arteries and veins, and for imaging extracardiac shunts or conduits [5].

Several consensus papers from scientific societies provide recommendations for standard CMR protocols adapted to the different cardiac malformations [6-9]. Three-dimensional whole-heart acquisitions are now routinely performed, especially for more complex malformations, as they allow the acquisition of a full volume of data during one single imaging sequence, including the heart and the intrathoracic vessels. This volume of data can be explored freely and specific 2D images can be extracted in any plane orientation during post-processing.

As CMR acquisitions are relatively slow and a high spatial resolution is required, the acquisition has to be segmented over several heartbeats. Additionally, the amount of data is so large that it cannot be acquired during one single breath-hold and respiratory motion compensation is needed for an adequate data acquisition during free-breathing.

Self-navigation: a new concept for respiratory motion compensation

Initially developed for coronary artery visualization, three-dimensional whole-heart navigator-based acquisitions have been used for over a decade to also assess the complex anatomy of congenital cardiac malformations [10]. These sequences rely on diaphragmatic respiratory navigation, where a pencil-beam navigator, usually placed on the dome of the right hemi-diaphragm, detects the respiratory position of the liver-lung interface along the superior-inferior direction for every heartbeat [11]. To consistently acquire data at the same respiratory position, a narrow acceptance window is defined, corresponding to the end-expiration, and only data acquired within this window are utilized in the final image reconstruction, while all other data segments are rejected and reacquired later during the scan (Fig. 1A). However, respiratory motion of the right hemidiaphragm and the heart are not tightly coupled, in particular during irregular breathing, when this correlation changes. As a result, data quality, especially during longer scans, can be inadequate if patients start to breath irregularly. In addition, with the navigator approach, acquisition duration is unpredictable and scan efficiency is typically in the order of 40% [12].

In order to address these limitations, respiratory self-navigation has been developed for coronary artery imaging [13-15]. With this strategy, the position of the heart itself is monitored over time and this approach should therefore also be robust in cases of irregular breathing. In addition, the respiratory motion information is extracted directly from the ventricular blood-pool signal throughout the respiratory cycle, so that navigator placement is not needed [13]. The prototype imaging sequence consists of a segmented 3D radial acquisition, intrinsically robust against motion, undersampling and foldover artifacts, with T2 and fat-saturation pre-pulses, and a balanced Steady-State Free Precessing (bSSFP) readout. The arrangement of the radial lines in *k*-space follows a spiral phyllotaxis pattern [16], with the first radial line of each acquired data segment (at each heartbeat) being consistently oriented in the superior-inferior direction, allowing for a 1D-detection of the cardiac displacement during the respiratory cycle. The position of the heart at the beginning of each data segment is thus compared with a reference position, i.e. the position of the ventricular blood-pool at the very first data segment, and automatically corrected for respiratory motion before the data are sent to the reconstruction pipeline (Fig. 1B). With this acquisition scheme, the respiratory motion correction reliably tracks the heart position and scan efficiency is typically 100%.

Characteristics of the sequence and planning strategy

With the current version of this prototype sequence[1], a cubic field-of-view of 180-240 mm^3 is acquired with a 3D isotropic spatial resolution of 0.9-1.15 mm^3. Other important imaging parameters are TR 3.1 ms, TE 1.65 ms, matrix size (192)^3, receiver bandwidth 898 Hz/pixel, and RF excitation angle of 90°-115°. The trigger delay is selected to match one of the quiescent periods of the cardiac cycle – either mid-diastole or end-systole – previously identified on a standard four-chamber cine acquisition of the heart. The temporal resolution is adapted to the duration of the quiescent cardiac period, and may range from 18 to over 100 ms. A higher temporal resolution (= a lower number of lines per segment) has to be compensated by a higher number of heartbeats (= a higher number of shots) to ensure an adequate filling of the *k*-space. As a rule of thumb, we made sure that a minimum of 20% of the Nyquist sampling of *k*-space lines (= number of shots x number of lines per segment) were acquired, corresponding to a 6 to 12-minute scan duration, depending on the heart rate of the patient. The Nyquist undersampling ratio can be easily assessed by a tooltip that pops up when hovering the mouse pointer over the 'Radial Views' parameter in the Resolution tab.

The self-navigated 3D whole-heart acquisition is easy to use, as it avoids the placement of a pencil-beam navigator on the right hemi-diaphragm. The planning of the sequence is performed in two steps: 1) the *coil-localizer sequence* (allowing an automated selection of the receiver coils that will best detect the blood-pool signal for respiratory navigation) [17], and 2) the *data acquisition sequence*. The coil-localizer sequence is first selected, and the planning is simply using the axial, sagittal and coronal localizers. On each of these orthogonal planes, the cubic volume of acquisition is displayed as a square field-of-view, which has to be cen-

[1] The product is still under development and not commercially available yet. Its future availability cannot be ensured.

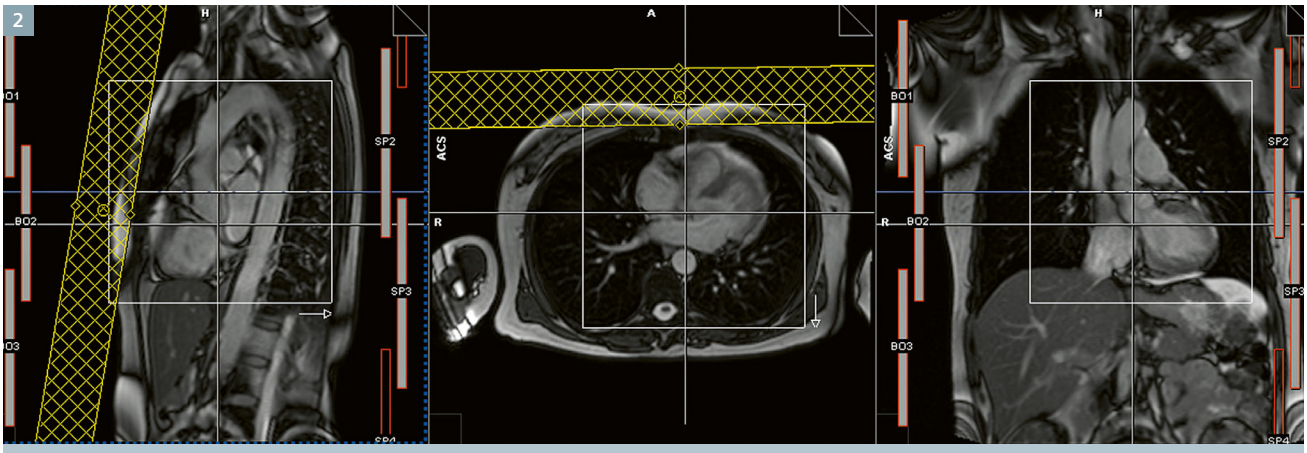

2 The cubic field-of-view is simply placed on the heart, while keeping the left ventricular blood-pool roughly in the center. A saturation band is placed on the anterior thoracic fat to reduce striking artifacts.

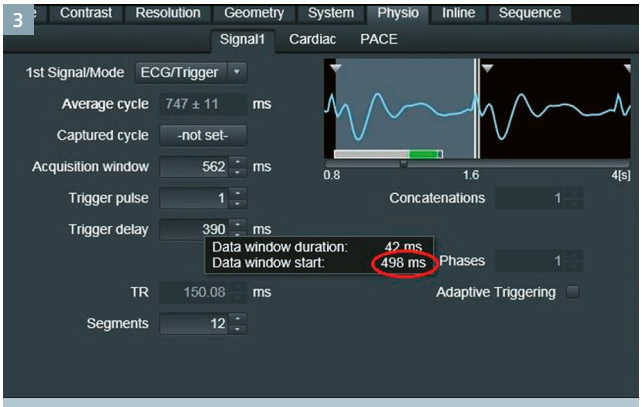

3 The trigger delay is selected, such that the data window start matches the onset of the quiescent period previously identified.

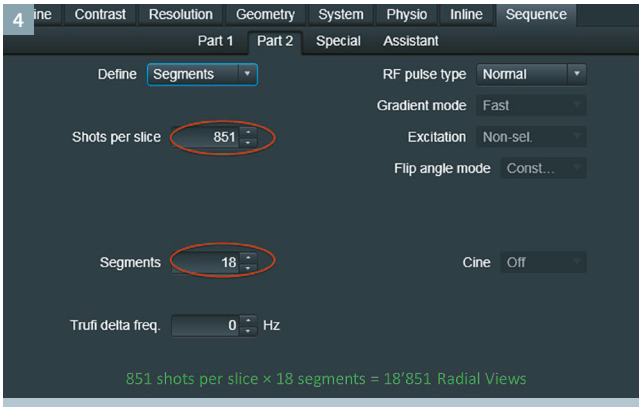

4 Depending on the duration of the quiescent period, the duration of the acquisition window can be modified, together with the number of heartbeats of acquisition (shots per slice), in order to keep the number of acquired *k*-space profiles over the above mentioned 20% of the Nyquist limit.

tered on the left ventricular blood-pool. A saturation band is placed on the anterior thoracic fat to reduce striking artifacts (Fig. 2). The coil-localizer sequence is started without a breath-hold, typically lasting a total of about 10 sec. The data acquisition sequence is then opened, and the positions of the acquisition volume and of the saturation band are simply copied from the coil-localizer sequence. The trigger delay is selected, such that the data window start matches the onset of the quiescent period previously identified (Fig. 3). Depending on the duration of the quiescent period, the duration of the acquisition window can be modified, together with the number of heartbeats of acquisition (shots per slice), in order to keep the number of acquired *k*-space profiles over the above mentioned 20% of the Nyquist limit (Fig. 4). The sequence is then started during free-breathing, and the quality of respiratory tracking can be checked in real time throughout the data acquisition, using the inline monitor (Fig. 5).

Experience in patients with congenital heart disease

Early experience with 3D self-navigated cardiac imaging was gained from small series of volunteers aiming at the visualization of the coronary arteries [13-15]. These early

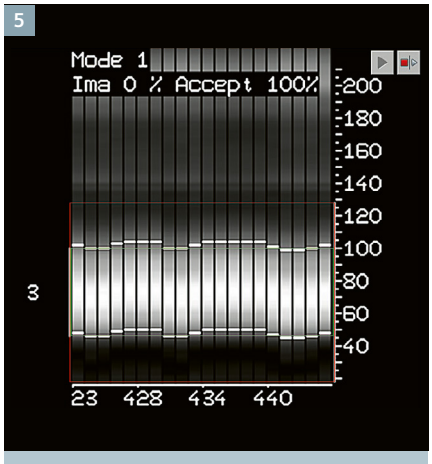

5 The quality of respiratory tracking can be checked in real time throughout the data acquisition, using the inline monitor.

studies reported a good performance of the sequence with an image quality that was equal or better than that obtained with conventional diaphragm navigation [13]. The first single-center experience on patients was also reported for coronary artery assessment [14]. 78 patients were included, and the self-navigated 3D sequence was used with a spatial resolution of 1.15 x 1.15 x 1.15 mm^3. The proximal segments of the coronary arteries were visualized in 92% of cases and the distal segments in 56%. When compared to invasive coronary angiography (available for comparison in 31 patients), the sensitivity and specificity for the detection of a significant coronary artery stenosis were 65% and 85%, respectively.

The first experience using the sequence for the characterization of congenital heart malformations was recently reported in a single-center series of 105 patients [18]. All examinations were performed on a 1.5T MAGNETOM Aera (Siemens Healthcare, Erlangen, Germany). The cohort included patients with ages ranging from 2 to 56 years (55% were males), and 44% had a complex cardiac malformation. The majority of the datasets (87%) were acquired after intravenous contrast injection (Gadovist, Bayer Schering Pharma, Zurich, Switzerland). While no direct head-to-head comparison with the conventional 3D whole-heart imaging sequence using diaphragm navigation was performed, this study aimed to assess the diagnostic performance and the image quality obtained with the new self-navigated sequence.

Using the 3D whole-heart self-navigated sequence alone, the systematic segmental anatomy of the heart and great vessels was correctly described in 93% to 96% of cases (by two different readers) and 93% to 95% of the residual uncorrected defects were correctly identified. Images were of diagnostic quality in 90% of cases and 70% were of good to excellent quality. Injection of intravenous contrast before image acquisition was associated with an improvement in image quality, resulting in a diagnostic image quality in 94% and a good to excellent image quality in 77% of the contrast-enhanced datasets.
The origin and proximal course of the coronary arteries were visualized in 93%, 87% and 98% of the cases for the left anterior descending, left circumflex and right coronary artery, respectively, and all four patients of the cohort with an abnormal course of the coronary arteries were correctly identified. Finally, the measurement of the great arteries' diameters were very robust with a high intra-observer (coefficient of variation 3.5%) and inter-observer (coefficient of variation 5.0%) agreement.

27% of the patients were of pediatric[2] age (age <16) and the performance of the self-navigated 3D sequence also showed good results in this population. Despite the fact that fewer datasets were of good to excellent quality in children, a diagnostic image quality was obtained as frequently as in adult patients. This slight reduction in image quality might be attributed to a shorter quiescent period of the cardiac cycle with higher heart rates, or to the fact that dephasing artifacts, which may occur with high-velocity flows, more severely obscured the small vascular structures of pediatric patients.

Figure 6 shows 2D images reconstructed from a 3D whole-heart dataset acquired with self-navigation in a 47-year-old man with unoperated pulmonary atresia with a ventricular septal defect (VSD). 6A shows a large anterior mal-alignment VSD (*) with an overriding aorta. The branch pulmonary arteries are hypoplastic (6B) and there is fibrous atresia of the main pulmonary artery, located immediately behind the left atrial appendage (arrow on 6C).

[2] MR scanning has not been established as safe for imaging fetuses and infants under two years of age. The responsible physician must evaluate the benefit of the MRI examination in comparison to other imaging procedures.

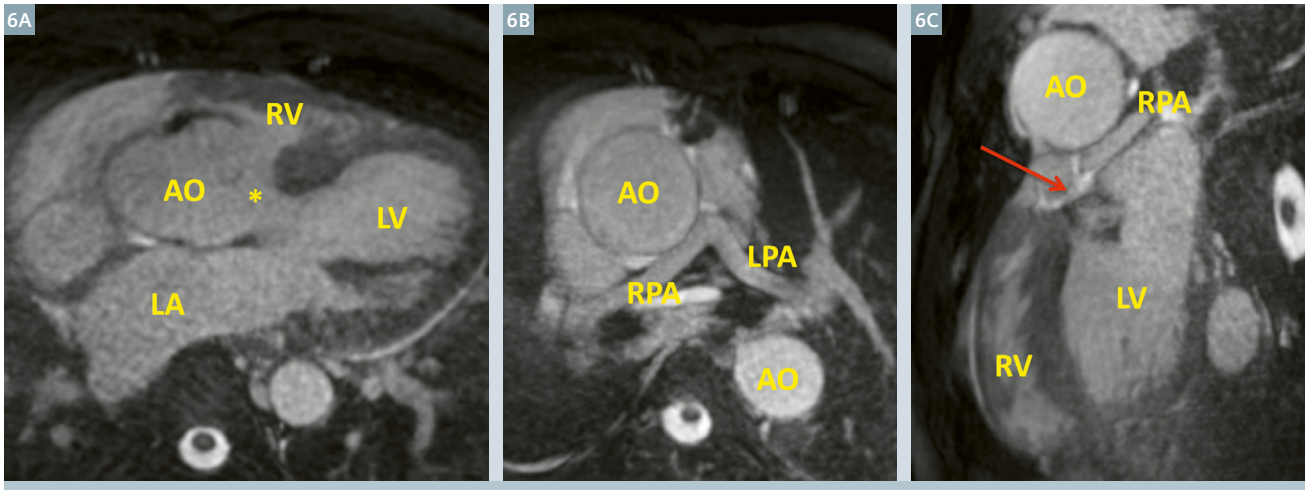

6 2D images reconstructed from a 3D whole-heart dataset acquired with self-navigation in a 47-year-old man with unoperated pulmonary atresia with a ventricular septal defect (VSD). **6A** shows a large anterior mal-alignment VSD (*) with an overriding aorta. The branch pulmonary arteries are hypoplastic (**6B**) and there is fibrous atresia of the main pulmonary artery, located immediately behind the left atrial appendage (arrow on **6C**).

Another example of complex cardiac anatomy is presented in Figure 7. This 27-year-old patient was born with right atrial isomerism, complete atrio-ventricular septal defect, total anomalous pulmonary venous return (TAPVR) and a single ventricle of right ventricular morphology. He underwent surgical correction of the TAPVR, followed by a bilateral Glenn operation and an extracardiac Fontan operation. 7A shows a large central liver and no spleen. The inferior vena cava (IVC) is located anterior to the descending aorta (AO). 7B shows the single ventricle with the typical characteristics of a right ventricle, connected to the ascending aorta. The systemic venous return is presented on 7C: both the right-sided superior vena cava (SVC) and the persistent left SVC are connected to the pulmonary arteries (bilateral Glenn), whereas the IVC is connected to the left pulmonary artery through an extracardiac conduit. 7D shows the normal-sized branch pulmonary arteries.

Good performance of the 3D self-navigated cardiac sequence is also demonstrated in children [18], as shown in the example presented in Figure 8. This 6-year-old patient, born with d-transposition of the great arteries, underwent an arterial switch operation. To connect the aorta to the left ventricle and the

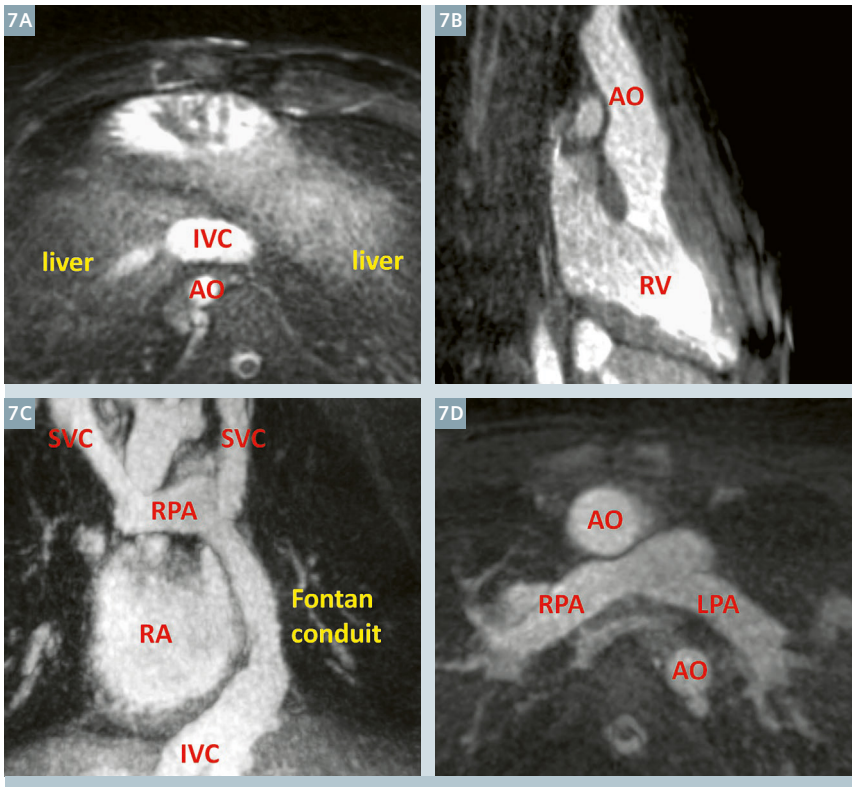

7 This 27-year-old patient was born with right atrial isomerism, complete atrio-ventricular septal defect, total anomalous pulmonary venous return (TAPVR) and a single ventricle of right ventricular morphology. He underwent surgical correction of the TAPVR, followed by a bilateral Glenn operation and an extracardiac Fontan operation. **7A** shows a large central liver and no spleen. The inferior vena cava (IVC) is located anterior to the descending aorta (AO). **7B** shows the single ventricle with the typical characteristics of a right ventricle, connected to the ascending aorta. The systemic venous return is presented on **7C**: both the right-sided superior vena cava (SVC) and the persistent left SVC are connected to the pulmonary arteries (bilateral Glenn), whereas the IVC is connected to the left pulmonary artery through an extracardiac conduit. **7D** shows the normal-sized branch pulmonary arteries.

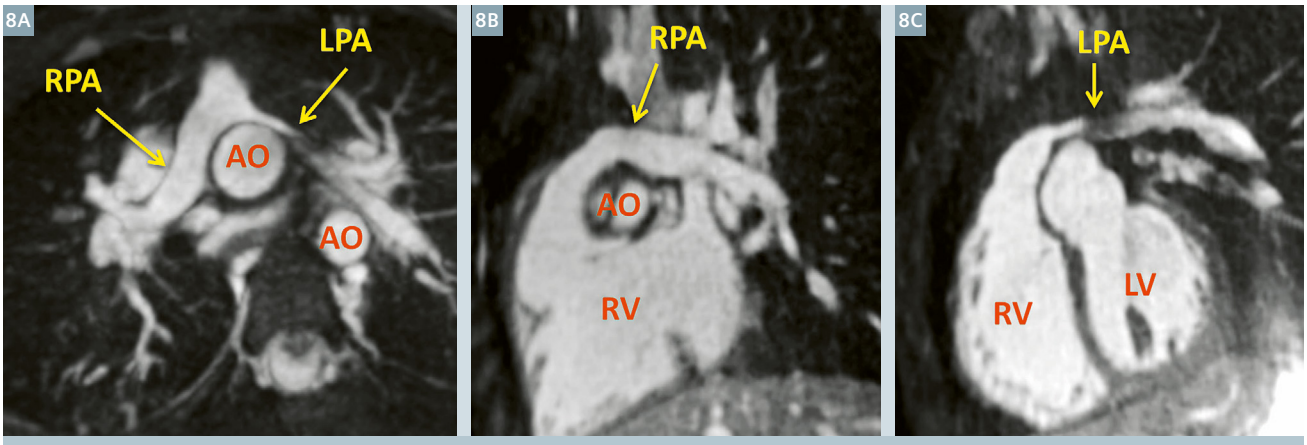

8 This 6-year-old patient, born with d-transposition of the great arteries, underwent an arterial switch operation. To connect the aorta to the left ventricle and the pulmonary artery to the right ventricle, the main pulmonary artery has to be displaced anteriorly to the ascending aorta by the surgeon. **8A** shows the typical anterior position of the main pulmonary artery with the branch pulmonary arteries running on either side of the aorta. In this patient, the right pulmonary artery is of normal size (**8B**) while the left pulmonary artery appears compressed by the ascending aorta. Flow acceleration in the LPA induces dephasing of the spins and appears as a low-signal artifact in the vessel (**8C**).

pulmonary artery to the right ventricle, the main pulmonary artery has to be displaced anteriorly to the ascending aorta by the surgeon. 8A shows the typical anterior position of the main pulmonary artery with the branch pulmonary arteries running on either side of the aorta. In this patient, the right pulmonary artery is of normal size (8B) while the left pulmonary artery appears compressed by the ascending aorta. Flow acceleration in the LPA induces dephasing of the spins and appears as a low-signal artifact in the vessel (8C).

Abnormal origin or course of the coronary arteries can be successfully detected with this sequence, as shown in Figure 9. This 4-year-old patient is known for a surgically corrected tetralogy of Fallot, associated with a coronary abnormality. As shown on 9A, all 3 coronary arteries originate from a single main stem connected to the right coronary sinus of the aortic root. On 9B, the course of the left anterior descending artery (LAD) is anterior to the main pulmonary artery. The left circumflex artery (LCx) has a proximal course between the aorta and the atria (9C), while the right coronary artery (RCA) has a normal course around the tricuspid annulus (9D). Such morphology – especially the presence of a LAD running anterior to the main pulmonary artery, is associated with a risk of coronary artery damage during the surgical correction of the right ventricular outflow tract obstruction. A precise identification of the coronary anatomy in these patients is therefore essential.

Discussion and conclusion

The self-navigated 3D cardiac imaging sequence is characterized by a great ease of use and a low operator interaction. The radial acquisition scheme renders the sequence immune to foldover artifacts and a high isotropic resolution is obtained over a relatively large field-of-view. The temporal resolution can be individually adapted to the heart rate, i.e. the duration of the quiescent period of the cardiac cycle, resulting in a 6 to 12 min acquisition duration, which can be known *a priori*.

With these characteristics, the sequence can be easily added to the standard imaging protocol of patients with congenital cardiac malformations. The performance of the sequence was considered very good in this population with a diagnostic image quality obtained in 94% of contrast-enhanced datasets and 93 to 96% of residual defects correctly detected. Despite the fact that very young children <2 years old were not included in the reported study, the performance of this sequence was good in the pediatric population[2] as well [18].

Further improvements are likely to be implemented to this sequence in the future, including the development of 3D rather than 1D respiratory motion compensation algorithms [19, 20], or strategies to selectively remove *k*-space lines associated with extreme respiratory positions [21], which were shown to further improve image quality.

In conclusion, the 3D self-navigated cardiac imaging sequence is characterized by its high robustness while providing high temporal and high isotropic spatial resolution. It may serve as an attractive tool for the three-dimensional assessment of congenital heart malformations in adults and children.

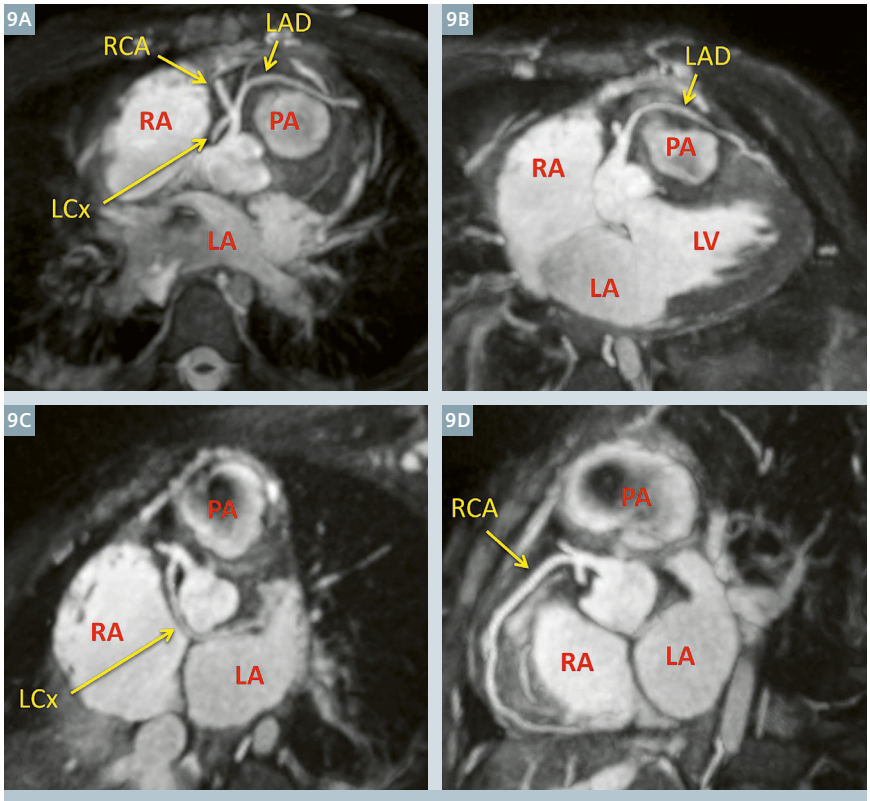

9 This 4-year-old patient has surgically corrected tetralogy of Fallot, associated with a coronary abnormality. As shown on **9A**, all 3 coronary arteries originate from a single main stem connected to the right coronary sinus of the aortic root. On **9B**, the course of the left anterior descending artery (LAD) is anterior to the main pulmonary artery. The left circumflex artery (LCx) has a proximal course between the aorta and the atria (**9C**), while the right coronary artery (RCA) has a normal course around the tricuspid annulus (**9D**).

Acknowledgement

The authors would like to thank all the members of the Center for Cardiac Magnetic Resonance of the

[2] MR scanning has not been established as safe for imaging fetuses and infants under two years of age. The responsible physician must evaluate the benefit of the MRI examination in comparison to other imaging procedures.

CHUV (CRMC, Prof Juerg Schwitter MD) and of the Center for Cardiovascular MR Research (CVMR, Prof Matthias Stuber PhD), as well as the MR technologists team at the CHUV for their active and excellent collaboration during this study. An important acknowledgement also goes to our colleagues from the pediatric cardiology unit and from the adult congenital heart disease clinic at the CHUV, Lausanne. Finally, we want to thank the Siemens Healthcare MR cardio team of Edgar Müller in Erlangen.

References

1 van der Linde D, Konings EE, Slager MA, et al. Birth prevalence of congenital heart disease worldwide: a systematic review and meta-analysis. Journal of the American College of Cardiology 2011;58:2241-7.

2 Wren C, O'Sullivan JJ. Survival with congenital heart disease and need for follow up in adult life. Heart 2001;85:438-43.

3 Marelli AJ, Mackie AS, Ionescu-Ittu R, Rahme E, Pilote L. Congenital heart disease in the general population: changing prevalence and age distribution. Circulation 2007;115:163-72.

4 Bouchardy J, Therrien J, Pilote L, et al. Atrial arrhythmias in adults with congenital heart disease. Circulation 2009;120:1679-86.

5 Baumgartner H, Bonhoeffer P, De Groot NM, et al. ESC Guidelines for the management of grown-up congenital heart disease (new version 2010). European heart journal 2010;31:2915-57.

6 Kilner PJ, Geva T, Kaemmerer H, Trindade PT, Schwitter J, Webb GD. Recommendations for cardiovascular magnetic resonance in adults with congenital heart disease from the respective working groups of the European Society of Cardiology. European heart journal 2010;31:794-805.

7 Kilner P, Valsangiacomo Buechel E, Schwitter J. Congenital Heart Diseases in Adults. In: Schwitter J, ed. CMR Update. 2. Edition ed. Lausanne, Switzerland: Schwitter, J. www.herz-mri.ch; 2012:136-55.

8 Fratz S, Chung T, Greil GF, et al. Guidelines and protocols for cardiovascular magnetic resonance in children and adults with congenital heart disease: SCMR expert consensus group on congenital heart disease. Journal of cardiovascular magnetic resonance : official journal of the Society for Cardiovascular Magnetic Resonance 2013;15:51.

9 Valsangiacomo Buechel ER, Grosse-Wortmann L, Fratz S, et al. Indications for cardiovascular magnetic resonance in children with congenital and acquired heart disease: an expert consensus paper of the Imaging Working Group of the AEPC and the Cardiovascular Magnetic Resonance Section of the EACVI. European heart journal cardiovascular Imaging 2015;16:281-97.

10 Sorensen TS, Korperich H, Greil GF, et al. Operator-independent isotropic three-dimensional magnetic resonance imaging for morphology in congenital heart disease: a validation study. Circulation 2004;110:163-9.

11 Wang Y, Rossman PJ, Grimm RC, Riederer SJ, Ehman RL. Navigator-echo-based real-time respiratory gating and triggering for reduction of respiration effects in three-dimensional coronary MR angiography. Radiology 1996;198:55-60.

12 Kato S, Kitagawa K, Ishida N, et al. Assessment of coronary artery disease using magnetic resonance coronary angiography: a national multicenter trial. J Am Coll Cardiol 2010;56:983-91.

13 Piccini D, Littmann A, Nielles-Vallespin S, Zenge MO. Respiratory self-navigation for whole-heart bright-blood coronary MRI: methods for robust isolation and automatic segmentation of the blood pool. Magnetic resonance in medicine 2012;68:571-9.

14 Piccini D, Monney P, Sierro C, et al. Respiratory self-navigated postcontrast whole-heart coronary MR angiography: initial experience in patients. Radiology 2014;270:378-86.

15 Stehning C, Bornert P, Nehrke K, Eggers H, Stuber M. Free-breathing whole-heart coronary MRA with 3D radial SSFP and self-navigated image reconstruction. Magnetic resonance in medicine 2005;54:476-80.

16 Piccini D, Littmann A, Nielles-Vallespin S, Zenge MO. Spiral phyllotaxis: the natural way to construct a 3D radial trajectory in MRI. Magnetic resonance in medicine 2011;66:1049-56.

17 Piccini D, Marechal B, Coppo S, et al. Automated and Subject-Specific Coil Selection for Respiratory Self-Navigation in Coronary MRA. Proc Intl Soc Mag Reson Med. Milan2014:2503.

18 Monney P, Piccini D, Rutz T, et al. Single centre experience of the application of self navigated 3D whole heart cardiovascular magnetic resonance for the assessment of cardiac anatomy in congenital heart disease. Journal of cardiovascular magnetic resonance : official journal of the Society for Cardiovascular Magnetic Resonance 2015;17:55.

19 Henningsson M, Prieto C, Chiribiri A, Vaillant G, Razavi R, Botnar RM. Whole-heart coronary MRA with 3D affine motion correction using 3D image-based navigation. Magnetic resonance in medicine 2014;71:173-81.

20 Pang J, Sharif B, Arsanjani R, et al. Accelerated whole-heart coronary MRA using motion-corrected sensitivity encoding with three-dimensional projection reconstruction. Magnetic resonance in medicine 2014.

21 Chaptinel J, Piccini D, Coppo S, Bonanno G, Schwitter J, Stuber M. Optimized Data Selection for 3D Radial Self-Navigated Whole-Heart Coronary MRA. MRA Club; 2013; New York City, New York, USA.

Further reading

For more images and quantitative analyses on this study, please refer to the newly published paper in Reference 18.

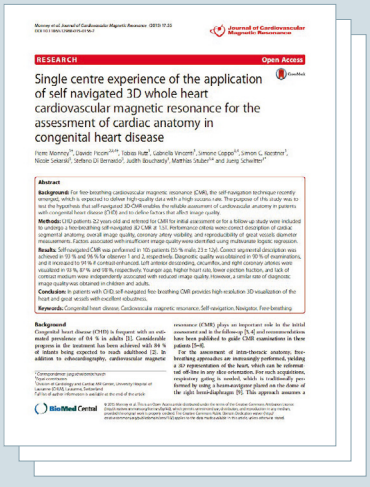



Pierre Monney



Juerg Schwitter

Contact

Professor Juerg Schwitter
Médecin Chef Cardiologie
Directeur du Centre de la RM Cardiaque du CHUV
Centre Hospitalier Universitaire Vaudois – CHUV
Rue du Bugnon 46, 1011 Lausanne, Switzerland
Phone: +41 21 314 0012
jurg.schwitter@chuv.ch
www.cardiologie.chuv.ch

CAIPIRINHA – Revisited

Felix Breuer[1], Martin Blaimer[1], Mark Griswold[2], Peter Jakob[3]

[1] Research Center, Magnetic Resonance Bavaria e.V. (MRB), Würzburg, Germany
[2] Case Center for Imaging Research, Case Western Reserve University, Cleveland, OH, USA
[3] Würzburg University, Department of Experimental Physics 5 and Research Center, Magnetic Resonance Bavaria e.V. (MRB), Würzburg, Germany

Introduction

Image acquisition time is one of the most important considerations for clinical magnetic resonance imaging (MRI). The development of multi-coil receiver hardware as well as dedicated parallel acquisition techniques (PAT) and respective reconstruction methods allowed for significant decrease of acquisition times in almost all clinical applications. This, for example, enables much shorter breath-holds in abdominal MRI and improves the temporal resolution of dynamic scans but can also be applied to improve image quality while keeping the acquisition time constant. Thus, today, parallel imaging techniques play a substantial role in everyday clinical routine.

Every parallel imaging technique combines (1) a specific acquisition scheme of *k*-space data with a (2) respective reconstruction method.

(1) **Parallel acquisition** operates by reducing the amount of data necessary to form an image. In the Cartesian case, this is usually accomplished by uniformly undersampling the *k*-space (e.g. skipping every other phase-encoding line) resulting in so-called 'aliasing artifacts' in the image domain.

(2) **Parallel reconstruction** methods seek to compensate the lack of spatial encoding by taking into account the spatial sensitivity information, provided by a multi-coil receiver array and can be divided into 2 main groups (Fig. 1): algorithms that combine undersampled images from the individual coil elements in the image domain to a global image, e.g. SENSE [1]. And algorithms that combine the frequency information of each coil

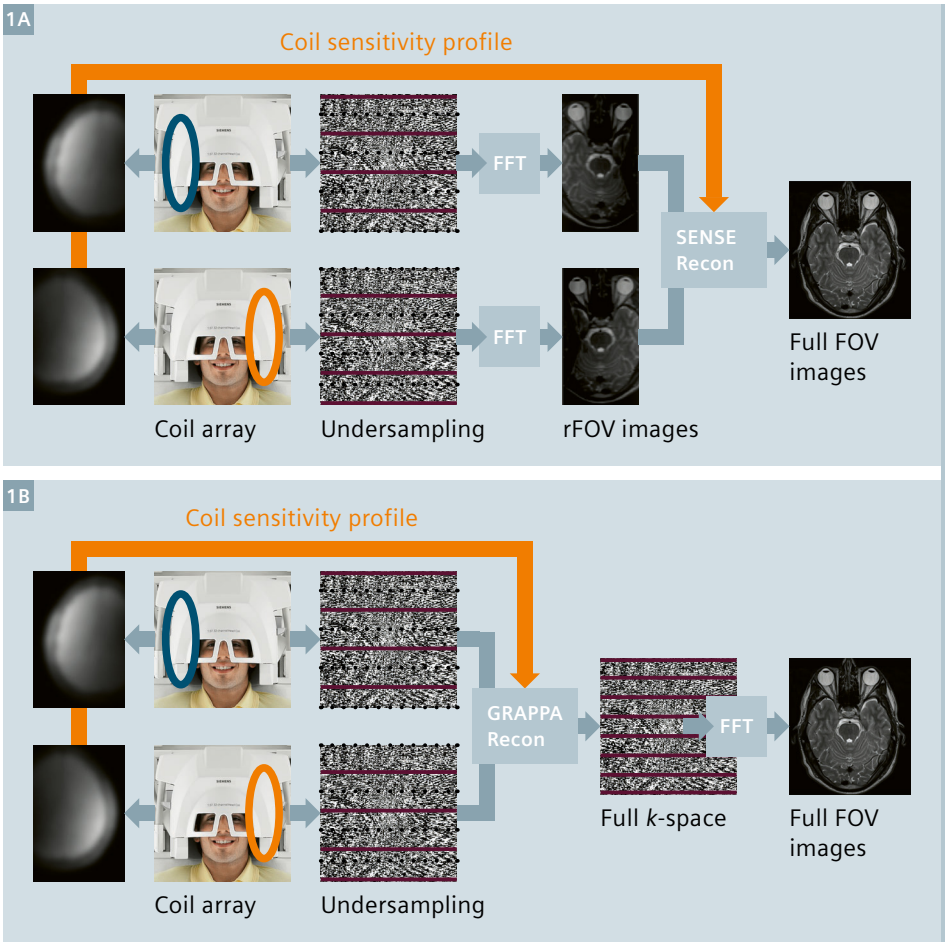

1 Procedure of reconstructing the image information from undersampled datasets with SENSE (**1A**, image based) and GRAPPA (**1B**, *k*-space based). Coil sensitivity profiles and frequency information is received with individual coil elements. With SENSE, reduced FOV images are reconstructed first and unaliased afterwards using the sensitivity information. With GRAPPA the sensitivity information from each coil element is used right at the beginning to calculate missing echos followed by Fourier transformation.

element in the *k*-space domain before Fourier transformation, e.g. GRAPPA [2].

Unfortunately, the PAT concept is intrinsically associated with a signal-to-noise (SNR) loss compared to a fully encoded image. The SNR is reduced

a) by the square root of the acceleration factor, simply due to the fact that less data is acquired, and

b) by the so-called *g*-factor, depending strongly on the encoding capabilities of the underlying receiver array.

Thus, PAT is often limited to applications with sufficiently high base SNR, such as volumetric imaging methods. With the newest generation of MR systems providing up to 128 independent receiver channels, further scan time reductions are potentially achievable. However, in conventional 2D clinical imaging, parallel imaging today is still restricted to relatively moderate scan time reductions (PAT factors of 2-3) due to intrinsic limitations in the coil sensitivity variations along one phase-encoding direction (1D parallel imaging). In 3D and simultaneous multi-slice imaging, parallel encoding can be carried out in two encoding directions (PAT^2 or 2D parallel imaging), thereby employing the sensitivity variations in both phase-encoding directions, as has been demonstrated in, for example, 2D SENSE [3] and MS SENSE [4]. This concept has been shown to significantly improve the reconstruction conditions, allowing for higher accelerations of the acquisition (>3). However, both techniques require sufficient sensitivity variations in two encoding directions for successful image reconstruction and therefore strongly depend on the underlying coil geometry, which is described by the *g*-factor. As mentioned above, spatial encoding with a receiver array is associated with a certain noise amplification known as '*g*-factor noise'. Quantitative *g*-factor estimation methods have been derived for SENSE [1] and GRAPPA reconstructions [5] and serve as a quality metric for PAT reconstructions. One important approach to reduce this *g*-factor noise for a given application is the optimization of the receiver array geometry (e.g. number of coils, coil arrangement) towards the application at hand. However, hardware limitations, the diversity of patient weight and size, the need for flexibility regarding a wider range of applications, as well as sequence or protocol specific considerations, hamper the viability.

The CAIPIRINHA concept (Controlled Aliasing In Parallel Imaging Results IN Higher Acceleration) is a specific data acquisition technique that allows to partially overcome these requirements and limitations by modifying the aliasing conditions in a well defined manner. This leads to an improved *g*-factor when compared to standard acquisition with the same acceleration factor. CAIPIRINHA takes effect already during the data acquisition by modifying the RF excitation or gradient encoding scheme in order to use the coil encoding power of the underlying receiver array to full capacity. The concept has been successfully applied so far to 3D imaging where data reduction can be carried out in two phase-encoding directions (2D-CAIPIRINHA) [7] and simultaneous multi-slice imaging (MS-CAIPIRINHA) [6]. In addition, both strategies can be extended to the third remaining direction, namely the read-out direction, by utilizing e.g. zig-zag-shaped read-out trajectories [8] or wave-CAIPI [9, 10]. The following provides a brief overview of 2D-CAIPIRINHA and S-CAIPIRINHA.

Improving parallel imaging performance with CAIPIRINHA

2D-CAIPIRINHA

In contrast to conventional 2D imaging where only one phase-encoding direction is available for scan-time reduction (1D PAT), 3D volumetric imaging with a second phase-encoding direction offers the potential to choose the direction in which undersampling is performed, or even to accelerate in both phase-encoding directions at the same time (2D PAT / PAT^2), where the total PAT factor is the product of the acceleration factors in the individual phase-encoding directions, e.g. 2 x 3 = 6. Given a receiver array geometry providing sensitivity variations in

2

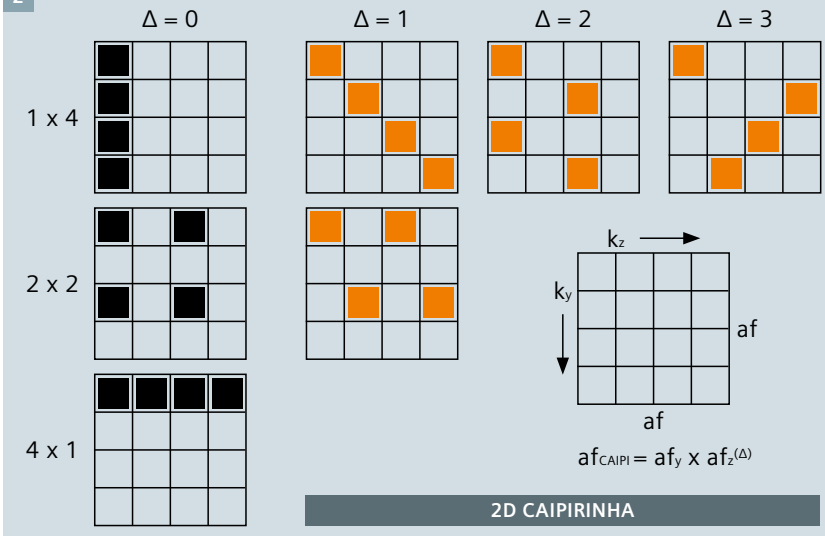

2 Procedure of generating 2D-CAIPIRINHA sampling patterns for a given total acceleration factor, here PAT = 4. All possible sampling schemes can be represented by a PAT x PAT elementary cell with PAT sampling positions to fill. For each undersampling rate in the k_y direction (PAT_y), multiple patterns can be created by shifting sampling positions at row k_y in the k_z direction by a different amount Δ, whereas Δ runs from 0 to PAT_{z-1}, and PAT_z = PAT/PAT_y. Sampling patterns without shift (Δ = 0) are 2D PAT standard acquisitions, while all the other patterns are represented by 2D-CAIPIRINHA-type acquisitions (PAT = PAT_y x PAT_z (Δ)) indicated by the red sampling positions.

both phase-encoding directions, this strategy has shown the potential to allow for higher total image accelerations compared to undersampling schemes restricted to only one direction [4, 5]. However, since the sensitivity variations available for the PAT reconstruction depend not only on the coil geometry but also on the image position and orientation, the FOVs and encoding directions as well as the object position, size and shape, the right choice of the undersampling rate for the individual phase-encoding directions is not easily predictable and remains a challenging task. Thus, in many applications the reconstructed images suffer from severe residual artifacts or strong noise amplifications, depending on the choices made by the operator.

Again, the CAIPIRINHA concept has shown to partially overcome these limitations. It has been realized that, besides the standard rectangular sampling patterns with undersampling using simple integer reductions, many other patterns are conceivable where the sampling positions are shifted from their original positions in the 2D phase-encoding scheme. Here, we restrict ourselves to sampling positions on so-called 'sheared grids' which form periodic lattices [16] resulting in exactly PAT superimposed image pixels at an acceleration factor of PAT as it is the case in all standard rectangular patterns. The procedure of generating the available **2D-CAIPIRINHA** patterns is schematically displayed in Figure 2 for a total image acceleration of PAT = 4. The sampling schemes can be represented by a PAT x PAT elementary cell with PAT sampling positions to fill. For each undersampling rate in the ky direction (PAT_y), multiple patterns can be created by shifting sampling positions at row ky in the kz direction by a different amount d, whereas d runs from 0 to PAT_{z-1}, and PAT_z = PAT /PAT_y. Sampling patterns without shift (d = 0) are 2D standard acquisitions, while all the other patterns are represented by 2D-CAIPIRINHA-type acquisitions. This concept can also be used for prime number accelerations (PAT = 2, 3, 5 ...) where standard accelerations only allow undersampling in one of the phase-encoding directions. The required shifts in *k*-space can simply be realized by applying additional gradient offsets to the phase-encoding gradient tables. These 2D-CAIPIRINHA sampling patterns, analogous to the phase-cycles in simultaneous multi-slice imaging, modify the appearance of aliasing in 2D parallel imaging compared to conventional rectangular reduction schemes and have the potential to relax the requirements of integer reductions to great extent. This is demonstrated in more detail in the original publication [7]. By shifting the sampling positions in a well-directed manner, aliasing can be shifted in such a way that sensitivity variations provided by the underlying receiver array are employed more efficiently. In some cases, the amount

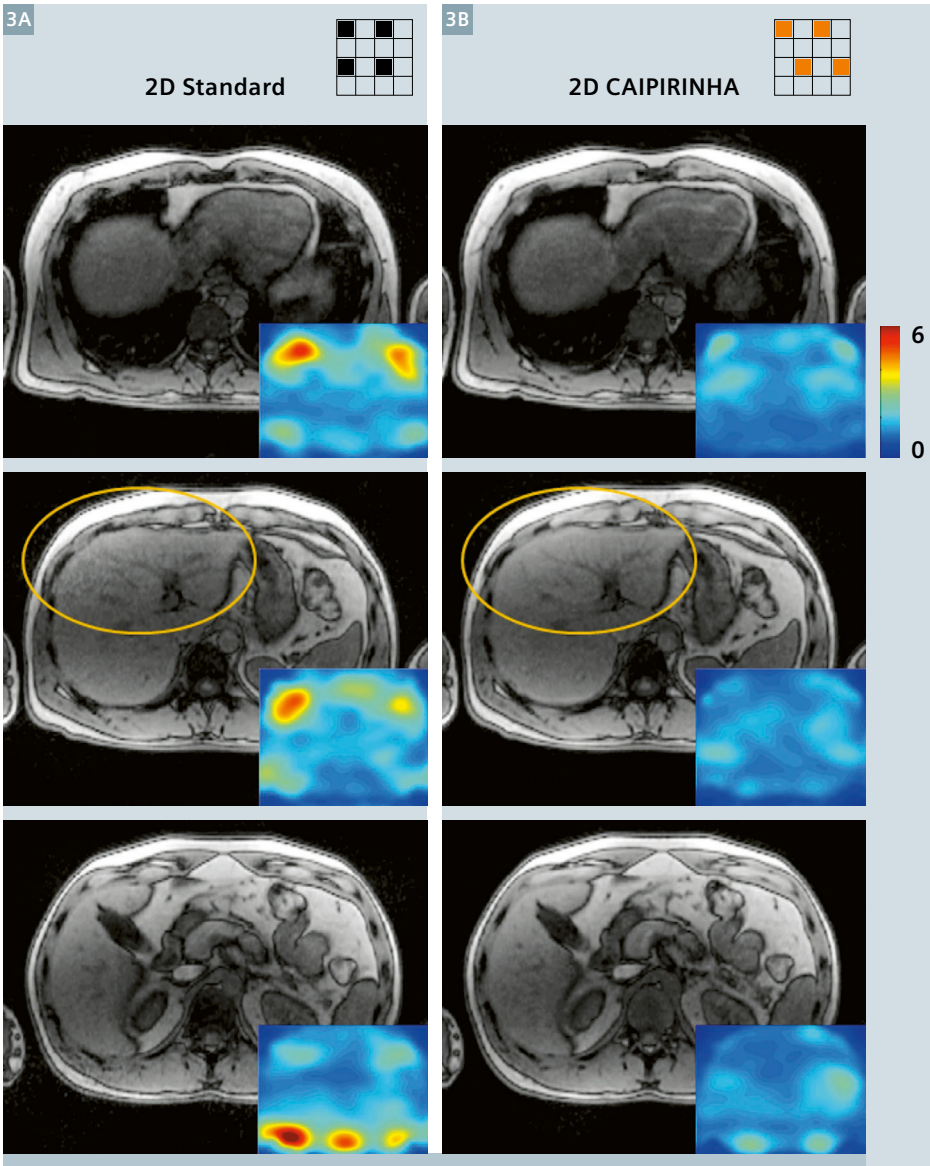

3 *In vivo* liver example; volunteer: Compared are GRAPPA reconstructions (3 example slices) derived from two different reduction schemes **(3A)** Standard 2 x 2 and **(3B)** 2D-CAIPIRINHA 2 x $2^{(1)}$. In addition, the corresponding GRAPPA *g*-factor maps are displayed. In the indicated region the SNR benefit of 2D-CAIPIRINHA can be appreciated.

Imaging details: 1.5T MAGNETOM Avanto, 6-channel body matrix coil combined with 6 channels from the spine matrix coil; VIBE PAT = 4, extra reference scan matrix 32 x 24 x 24. FOV 400 x 312.5 mm^2, matrix 320 x 170 x 50, total acquisition time 9 s breath-hold.

of aliasing can even be reduced. These modified aliasing conditions may then result in a further improvement in parallel imaging reconstruction conditions and therefore in better image quality. Recently, this concept has also been extended to more generalized sampling schemes which are not restricted to sheared grids [17].

In order to demonstrate the benefit of 2D-CAIPIRINHA in vivo, two subsequent accelerated (PAT = 4) abdominal 9 s breath-hold VIBE experiments were carried out on a volunteer. In Figure 3, GRAPPA reconstructions from three out of 50 slices from

a) a standard 2D-PAT 2 x 2 and

b) a 2D-CAIPIRINHA 2 x 2[1]

acquisitions are displayed. In addition, the corresponding *g*-factor maps of the GRAPPA reconstructions are displayed as a quantitative measure of image quality. As indicated by the lower *g*-factor values in the 2D-CAIPIRINHA reconstructions, the improvement of image quality can clearly be observed, even on a visual scale (see region indicated by the orange circle).

Furthermore, the improvements in image quality associated with 2D-CAIPIRINHA are demonstrated taking four different T1-weighted 3D FLASH experiments of a volunteer's brain with different acceleration factors and acquisition schemes (Fig. 4). The acquisitions compared are

a) a standard 2D-PAT 2 x 2,

b) a 2D-CAIPIRINHA 2 x 2[1],

c) a 2D-CAIPIRINHA 1 x 5[2] and

d) a standard 1D-PAT 5 x 1 scheme.

Displayed are the central sections of the reconstructed 3D image data in the sagittal, coronal and axial view in addition to the corresponding quantitative *g*-factor maps. Comparing reconstruction results from PAT = 4 (a) and (b), the improvement of 2D-CAIPIRINHA can clearly be appreciated. Comparing results from PAT = 5 (c) and (d), the gain in SNR is even more obvious. In this case, the parallel imaging performance of 2D-CAIPIRINHA 1 x 5[2] (c) compares pretty well with the standard PAT = 4 (2 x 2) acquisition employed in (a).

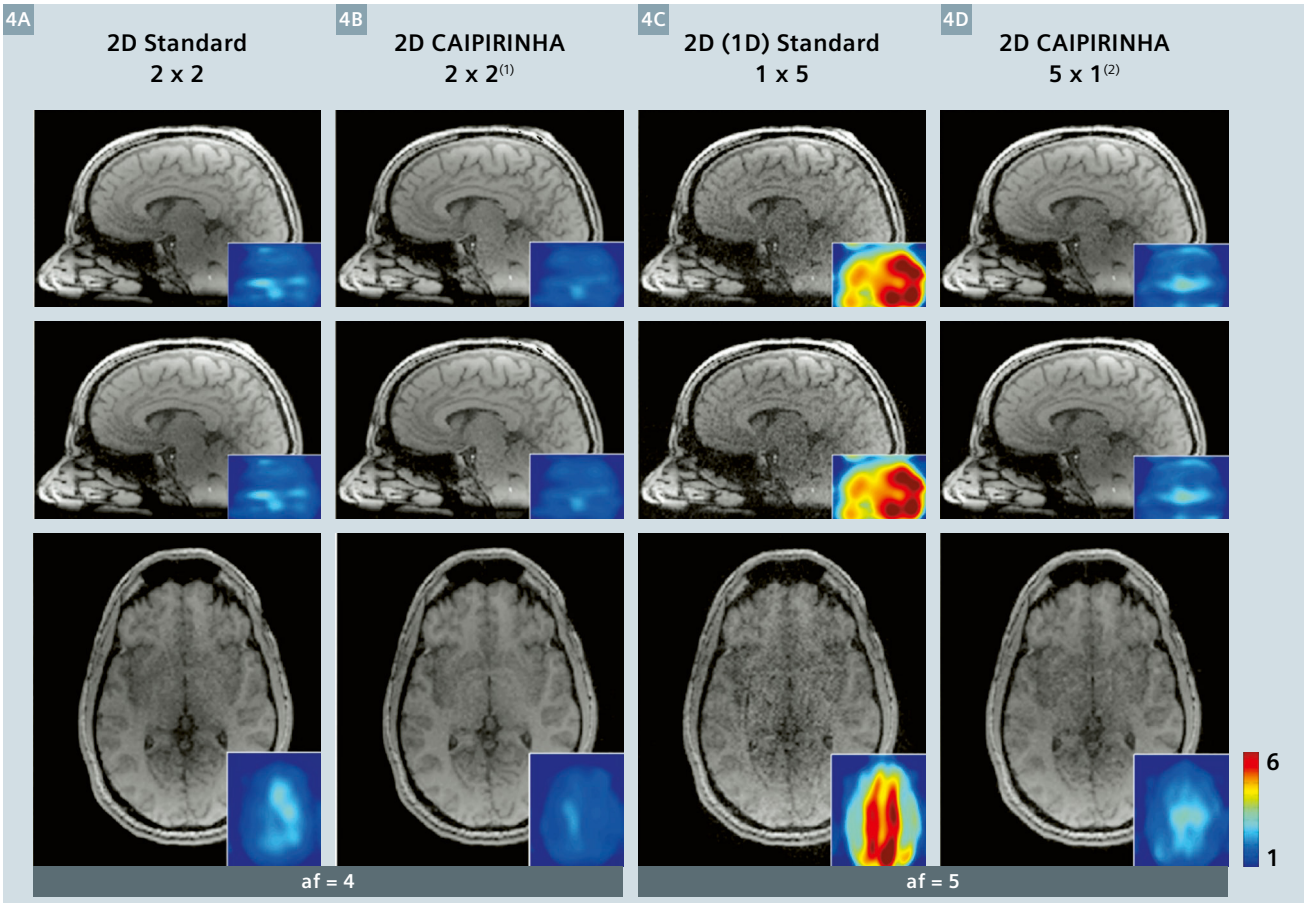

3 *In vivo* 3D FLASH brain imaging using different acceleration schemes: **(4A)** Standard 2D-PAT 2 x 2 **(4B)** 2D-CAIPIRINHA 2 x 2[1] **(4C)** Standard 1D-PAT 5 x 1 **(4D)** 2D-CAIPIRINHA 1 x 5[2]. Displayed are central slices in the sagittal, coronal and axial views. In addition, the corresponding GRAPPA *g*-factor maps are shown.

Imaging details: 3T MAGNETOM Skyra, 20-channel head-neck matrix coil, 3D FLASH, GRAPPA with extra reference scan, matrix 32 x 32 x 32, TE / TR 4.3 ms / 16 ms, FA 35°, FOV 256 x 208 x 204 mm³, matrix 256 x 168 x 144; partial Fourier factor 7/8, total scan time 1 min 40 s (PAT = 4) and 1 min 16 s (PAT = 5).

5A

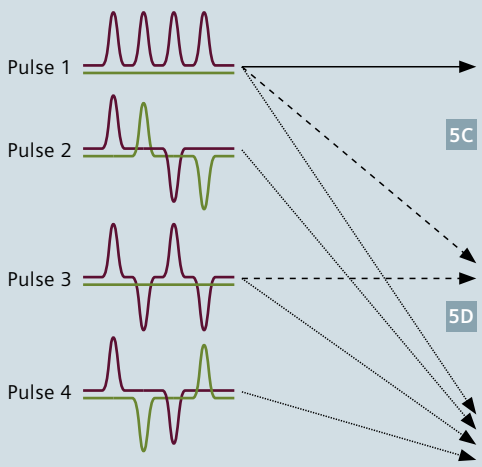

5B

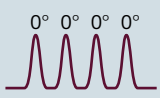

5C

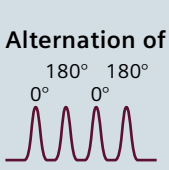

5D

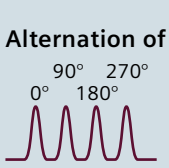

5 Multi-slice excitation with alternating RF pulses taken from **(5A)** a set of 4 RF pulses with different phase modulations (pulse 1 to 4) allows one to provide the individual slices with well defined phase-cycles along the phase-encoding direction. The real part (red) and imaginary part (green) of the pulses are plotted. **(5B)** Using only one pulse (e.g. pulse 1), no phase-cycle is provided (0°, 0°, 0°, 0°). **(5C)** Alternation between pulses 1 and 3 yield no phase-cycle for slice 1 and 3 and an 180° phase cycle for slices 2 and 4 (0, 180°, 0, 180°). **(5D)** Alternation of all 4 pulses allows one to provide all the individual slices with an individual phase-cycle (0, 90°, 180°, 270°).

6A

Standard 4-slice-excitation (SMS = 4): RF pulse 1

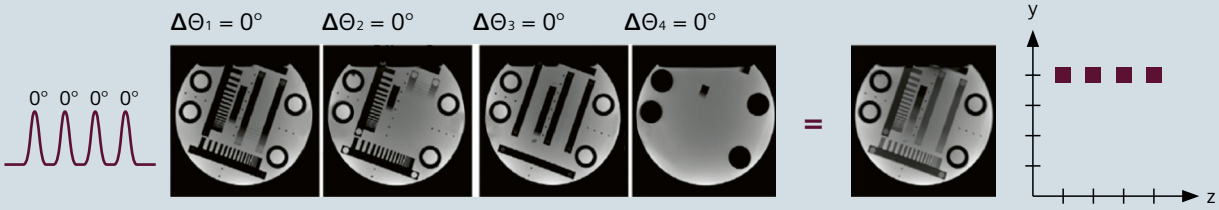

6B

CAIPIRINHA 4-slice-excitation (SMS = 4): 2 alternating RF pulses (1 & 3)

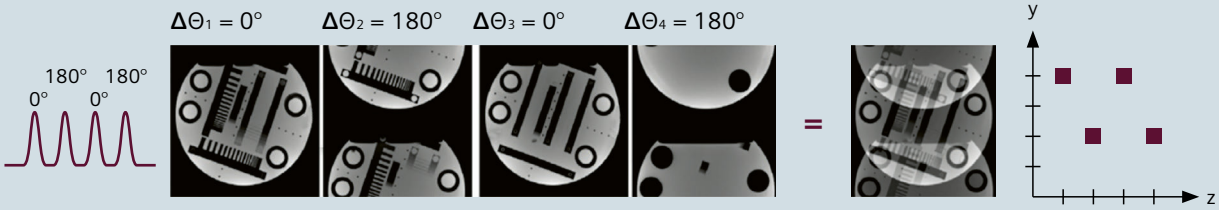

6C

CAIPIRINHA 4-slice-excitation (SMS = 4): 4 alternating RF pulses (1, 2, 3 & 4)

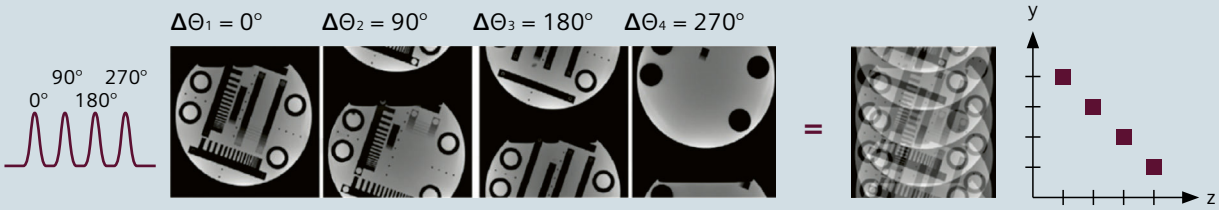

6 **(6A)** Standard 4-times-accelerated simultaneous 4-slice experiment. The same pulse is applied for subsequent excitations (phase-encoding lines), resulting in all 4 slices projected onto each other. **(6B)** CAIPIRINHA 4-times accelerated simultaneous 4-slice-experiment alternating between e.g. pulses 1 and 3 for subsequent excitations, thereby providing slice 2 and slice 4 with a 180° phase cycle. According to the Fourier Shift Theorem, slices 2 and 4 appear shifted by half of the FOV with respect to slices 1 and 3 in the resulting folded image. **(6C)** CAIPIRINHA 4-times-accelerated simultaneous 4-slice experiment alternating between pulse 1, 2, 3 and 4 for subsequent excitations, thereby providing each slice with a different phase-cycle (0°, 90°,180°, 270°). Each slice appears shifted by FOV/4 with respect to their adjacent slice in the folded image.

While the 2D-CAIPIRINHA patterns in general appear to be more tolerant against user influence and suboptimal patient positioning, the automated extraction of the optimal pattern for the given imaging setup remains a challenging task and has not been sufficiently answered.

MS-CAIPIRINHA

Simultaneous multi-slice (SMS) imaging offers an SNR benefit over standard single-slice imaging which may be either translated into shorter acquisition times or higher spatial resolution. SMS comprises RF excitations with specialized multi-band pulses as displayed in Figure 5. After multi-band excitation, the received signals will accrue from all the slices (bands) and thus are subject to the subsequent gradient-encoding sequence. Simply replacing the standard single-slice excitation pulse with a multi-slice pulse in an MR imaging sequence will therefore result in an image with all the simultaneously excited slices projected onto each other (Figure 6A). As mentioned above, the parallel imaging concept provides an elegant way to separate multiple image signals which are aliased into one image pixel. Thus, sufficient sensitivity variations of the underlying receiver array along the slice direction will then allow for separation of the slices using adapted standard PAT reconstruction algorithms [4, 11]. However, in cases where the sensitivity variations along the slice direction are not sufficient, e.g. as a result of small slice distances or suboptimal coil geometry, the PAT reconstruction will fail and result in large noise amplification. Sensitivity variations, potentially available along the other spatial directions, here the phase-encoding direction, are not employed.

It has been demonstrated that increasing the field-of-view (FOV) by the number of simultaneously excited slices allows the individual slices to be shifted with respect to each other in an extended FOV (along the phase-encoding) [12, 13] such that the slices show no superposition. A similar concept is Hadamard-aided RF encoding [14]. The required shifts mentioned above can be accomplished by employing dedicated alternating multi-band RF pulses providing the individual bands with well-defined phase-cycles along the phase-encoding direction (e.g using the set of RF pulses displayed in Figure 5). Due to the volumetric excitation, this approach offers a benefit in SNR efficiency of square root of the number of simultaneously excited slices compared to single-slice acquisitions, however at the cost of increased pulse energy deposition.

Using this concept in combination with image acceleration (fewer phase-encoding steps), superimposed slices with individual shifts along the phase-encoding direction can be realized by employing alternation of RF pulses taken, e.g. from the set of pulses given in Figure 5. A four-slice excitation at an acceleration of PAT = 4 using only RF pulse 1 yields a superimposition of 4 image pixels originating from all the 4 slices at the same location in the phase-encoding direction (Fig. 6A). Employing an alternation of RF pulses (e.g. pulse 1 and pulse 3, or pulses 1, 2, 3 and 4), the individual slices can be shifted with respect to each other in the FOV (Figs. 6B, C). In this way, as demonstrated in the corresponding *zy*-plots, aliased pixels may now originate from both different slices and different locations in the phase-encoding direction in a well defined manner (MS-CAIPIRINHA), thereby allowing the PAT reconstruction to take advantage of sensitivity variations in the slice and the phase-encoding direction, resulting in lower *g*-factors and consequently a higher SNR.

The benefit of MS-CAIPIRINHA is demonstrated *in vivo* employing a 4-times-accelerated simultaneous 4-slice experiment: Figure 7 shows 4 slices in a volunteer's brain (slice positions are indicated in the sagittal brain image), which are excited simultaneously using specialized multi-band RF pulses taken from the set of pulses given in Figure 5A. In the case of non-alternating RF pulses [4] (MS-Standard), each slice is subject to the same phase cycle along the phase-encoding direction (LR). The slices appear projected directly on top of each other, thereby allowing the PAT reconstruction (here GRAPPA-SENSE hybrid [11]) only to use sensitivity variations available in the slice direction. Due to the relatively small slice distances, the relatively high acceleration factor (PAT = 4) and the limited sensitivity variations provided by the coil array in the slice direction, the reconstruction results in large noise amplifications and thus unacceptable image quality. However, using a MS-CAIPIRINHA acquisition in combination with an adapted GRAPPA reconstruction, the folded image pixels can now be separated almost without any noise amplification.
In this example, an MS-CAIPIRINHA scheme as depicted in Figure 6B has been employed. Alternation of pulses 1 and 3 provides slices 2 and 4 with a 180° phase-cycle along the phase-encoding direction, causing these slices to appear shifted by FOV/2 with respect to the slices 1 and 3 which had no phase modulation. Thus, in this case, MS-CAIPIRINHA allowed the acquisition of 4 slices in the same time normally required for a single slice without losing SNR.

In addition, the applicability of MS-CAIPIRINHA to cardiac perfusion imaging is demonstrated in Figure 8. A two-slice CAIPIRINHA saturation recovery TrueFISP sequence has been employed using a total acceleration of PAT = 3. This allows for the acquisition of 12 slices (8 slices in the short-axis view and 4 in the long axis) in only two cardiac cycles. A repetition of the sequence during contrast agent uptake has the potential for cardiac perfusion imaging with significantly increased spatial coverage in high temporal resolution [15].

Conclusion

In all current parallel acquisition techniques, aliasing artifacts resulting from an undersampled acquisition are removed by a specialized PAT image reconstruction algorithm. The CAIPIRINHA concept aims on modifying the appearance of the aliasing artifacts already during the acquisition to improve the following parallel image reconstruction procedure. Specifically, this concept has been successfully applied to 3D imag-

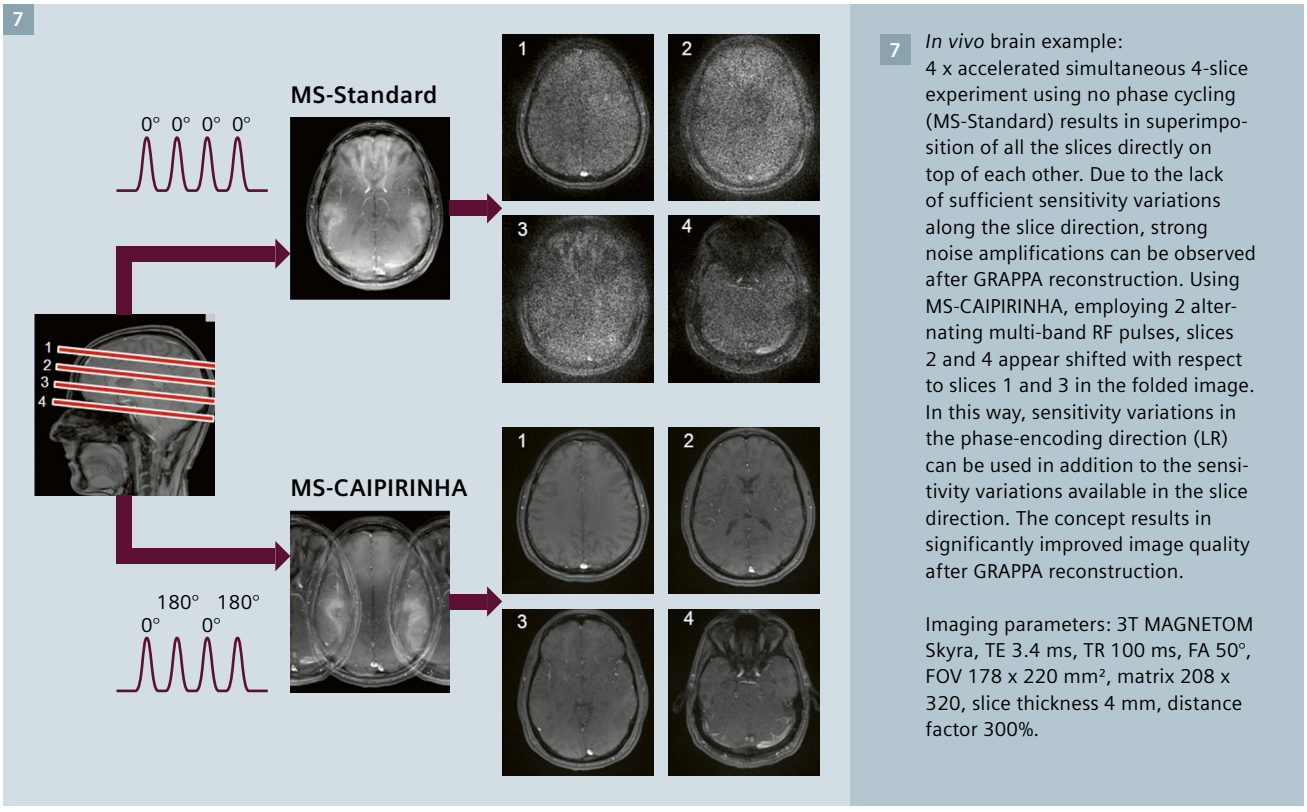

7 *In vivo* brain example: 4 x accelerated simultaneous 4-slice experiment using no phase cycling (MS-Standard) results in superimposition of all the slices directly on top of each other. Due to the lack of sufficient sensitivity variations along the slice direction, strong noise amplifications can be observed after GRAPPA reconstruction. Using MS-CAIPIRINHA, employing 2 alternating multi-band RF pulses, slices 2 and 4 appear shifted with respect to slices 1 and 3 in the folded image. In this way, sensitivity variations in the phase-encoding direction (LR) can be used in addition to the sensitivity variations available in the slice direction. The concept results in significantly improved image quality after GRAPPA reconstruction.

Imaging parameters: 3T MAGNETOM Skyra, TE 3.4 ms, TR 100 ms, FA 50°, FOV 178 x 220 mm², matrix 208 x 320, slice thickness 4 mm, distance factor 300%.

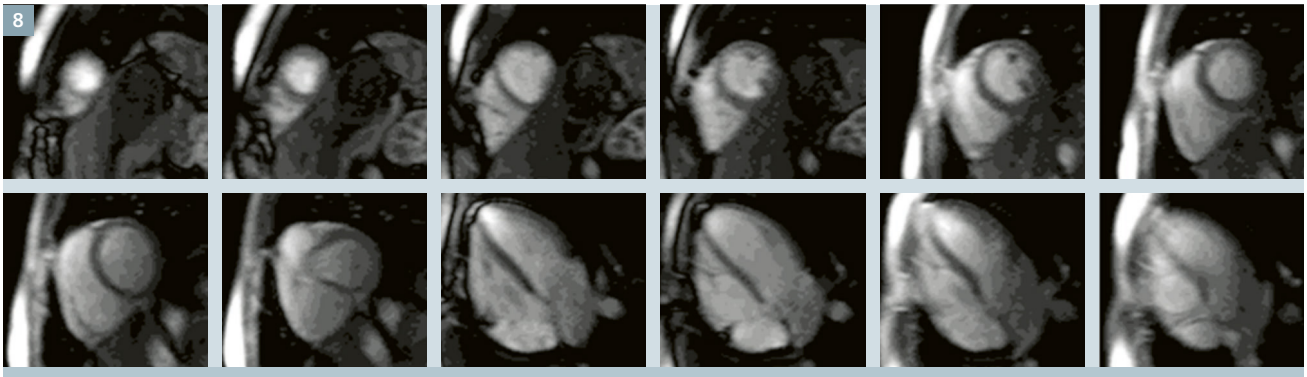

8 *In vivo* cardiac example: The MS-CAIPIRINHA approach enables the acquisition of up to 6 slices per cardiac cycle. Here, 12 slices are acquired within 2 cardiac cycles (8 slices in short-axis view and 4 in the long axis).

Imaging parameters: 1.5 T MAGNETOM Avanto, 32-channel cardiac array (Rapid Biomedical, Würzburg, Germany); Sequence: SR-TrueFISP, CAIPIRINHA phase cycle +90°/-90°; FOV 320 x 260 mm², matrix: 128 x 77, resolution 2.5 x 3.4 mm², slice thickness 10 mm, distance factor (two-slice pulse) of short/long axis: 200%/100%; partial Fourier 6/8, measurements: 20, TR 2.8 ms, TI 120 ms, TE 1.4 ms, FA 50°, reconstruction algorithm GRAPPA (R=3). *Images courtesy of Daniel Stäb.*

ing (2D-CAIPIRINHA) and clinically even to the often more routinely used 2D sequences (TSE; ss-EPI) with simultaneous multi-slice imaging (MS-CAIPIRINHA).

2D-CAIPIRINHA

In conventional PAT-accelerated 3D imaging, data reduction is performed in two spatial dimensions simultaneously by integer-valued undersampling in each phase-encoding direction. Though sensitivity variations can be exploited in two spatial dimensions, this sampling strategy provides suboptimal encoding performance. The 2D-CAIPIRINHA strategy modifies aliasing in a controlled manner already during the data acquisition. This is accomplished by shifting sampling positions in the two-dimensional phase-encoding scheme with respect to each other. In this way, at certain image acceleration values, an optimal sampling pattern can be found which minimizes signal overlap and at the same time allows one to efficiently take advantage of all the sensitivity variations provided by the coil array in the 2D phase-encoding plane. Thus, 2D-CAIPIRINHA provides optimal reconstruction performance given a certain coil configuration and object shape, and therefore results in optimal image reconstruction quality.

MS-CAIPIRINHA

Similar to 2D-CAIPIRINHA, aliasing in simultaneous multi-slice acquisitions can be modified already during the acquisition by employing alternating RF pulses for subsequent phase-encoding lines, thereby allowing the imprint of the individual slices with individual phase-cycles causing the slices to appear shifted with respect to each other thereby improving the reconstruction process minimizing *g*-factor-related noise enhancements. Thus, a CAIPIRINHA-type 4-slice excitation with low *g*-factor values (close to 1) allows the acquisition of 4 slices in the same time usually required for 1 slice without loss of SNR. The initial approach of alternating RF pulses introduced here, however, is not applicable for single-shot sequences such as EPI where only a single RF pulse is used to acquire all lines of *k*-space. Innovative concepts like blipped-CAIPINHA (see also the Article by Kawin Setsompop) where additional gradient magnetic fields are used during the readout to generate the required phase modulations allow to apply SMS to more advanced acquisition schemes such as SSFP [15] EPI [18] and radial [19] simultaneous multi-slice imaging.

However, it is important to note that multi-slice excitations are associated with significantly increased energy deposition, currently limiting the method to a moderate number of simultaneously excited slices, and/or to low flip angles. However, recently, a promising concept for reducing the RF power of multi-band pulses has been introduced [20]. Thus, MS-CAIPIRINHA is expected to become a powerful strategy in the near future allowing for significantly acceleration of many clinical protocols while almost preserving image quality.

Acknowledgments

The authors would like to thank Daniel Neumann from the *Research Center Magnetic Resonance Bavaria (MRB), Würzburg, Germany* and Daniel Stäb from the *Institute for Diagnostic Radiology, University Hospital Würzburg, Germany* for providing material.

In addition, the authors are extremely grateful for receiving continuing support from the colleagues from *Siemens Healthcare*, especially Stephan Kannengiesser, Dominik Nickel, Berthold Kiefer, Mathias Nittka, Vladimir Jellus and Randall Kroeker.

References

1 Pruessmann KP, Weiger M, Scheidegger B, Boesiger P. SENSE: sensitivity encoding for fast MRI. Magn Reson Med 1999; 42:952-962.
2 Griswold MA, Jakob PM, Heidemann RM, Nittka M, Jellus V, Wang J, Kiefer B, Haase A. GeneRalized Autocalibrating Partially Parallel Acqusitions (GRAPPA). Magn Reson Med 2002; 47:1202-1210.
3 Weiger M, Pruessmann KP, Boesiger P. 2D SENSE for faster 3D MRI. MAGMA. 2002 Mar; 14(1):10-9.
4 Larkman DJ, Hajnal JV, Herlihy AH, Coutts GA, Young IR, Ehnholm G. Use of multicoil arrays for separation of signal from multiple slices simultaneously excited. J Magn Reson Imaging. 2001 Feb; 13(2):313-7.
5 Breuer FA, Kannengiesser SA, Blaimer M, Seiberlich N, Jakob PM, Griswold MA. General formulation for quantitative G-factor calculation in GRAPPA reconstructions. Magn Reson Med. 2009 Sep;62(3):739-46.
6 Breuer FA, Blaimer M, Heidemann RM, Mueller MF, Griswold MA, Jakob PM. Controlled Aliasing in Parallel Imaging Results in Higher Acceleration (CAIPIRINHA) for Multislice Imaging. Magn Reson Med 2005; 53:684-691.
7 Breuer FA, Blaimer M, Mueller MF, Seiberlich N, Heidemann RM, Griswold MA, Jakob PM. Controlled aliasing in volumetric parallel imaging (2D CAIPIRINHA). Magn Reson Med. 2006 Mar;55(3):549-56.
8 Breuer FA, Moriguchi H, Seiberlich N, Blaimer M, Jakob PM, Duerk JL, Griswold MA. Zigzag sampling for improved parallel imaging. Magn Reson Med. 2008 Aug;60(2):474-8.
9 Bilgic B, Gagoski BA, Cauley SF, Fan AP, Polimeni JR, Grant PE, Wald LL, Setsompop K. Wave-CAIPI for highly accelerated 3D imaging. Magn Reson Med. 2015 Jun;73(6):2152-62.
10 Gagoski BA, Bilgic B, Eichner C, Bhat H, Grant PE, Wald LL, Setsompop K. RARE/turbo spin echo imaging with Simultaneous Multislice Wave-CAIPI. Magn Reson Med. 2015 Mar;73(3):929-38.
11 Blaimer M, Breuer FA, Seiberlich N, Mueller MF, Heidemann RM, Jellus V, Wiggins G, Wald LL, Griswold MA, Jakob PM. Accelerated volumetric MRI with a SENSE/GRAPPA combination. J Magn Reson Imaging. 2006 Aug;24(2):444-50.
12 Muller S. Simultaneous multislice imaging (SIMUSIM) for improved cardiac imaging. Magn Reson Med. 1989 Apr;10(1):145-55.
13 Glover GH. Phase-offset multiplanar (POMP) volume imaging: a new technique. J Magn Reson Imaging. 1991 Jul-Aug; 1(4):457-61.
14 Souza SP, Szumowski J, Dumoulin CL, Plewes DP, Glover G. SIMA: simultaneous multislice acquisition of MR images by Hadamard-encoded excitation. J Comput Assist Tomogr. 1988 Nov-Dec;12(6):1026-30.
15 Stäb D, Ritter CO, Breuer FA, Weng AM, Hahn D, Köstler H. CAIPIRINHA accelerated SSFP imaging. Magn Reson Med. 2011 Jan;65(1):157-64
16 Willis NP and Bresler Y. Optimal scan design for time varying tomographic imaging {II}: Efficient design and experimental validation. IEEE Trans. Image Processing, 1995 May; 4: 654-666.
17 Wu B, Millane RP, Watts R, Bones PJ. Improved matrix inversion in image plane parallel MRI. Magn Reson Imaging. 2009 Sep;27(7):942-53.
18 Setsompop K, Gagoski BA, Polimeni JR, Witzel T, Wedeen VJ, Wald LL. Blipped-controlled aliasing in parallel imaging for simultaneous multislice Echo Planar Imaging with reduced g-factor penalty. Magn Reson Med. 2011 Aug 19.
19 Yutzy SR, Seiberlich N, Duerk JL, Griswold MA. Improvements in multislice parallel imaging using radial CAIPIRINHA. Magn Reson Med. 2011 Jun;65(6):1630-7.
20 Norris DG, Koopmans PJ, Boyacioğlu R, Barth M. Power independent of number of slices radiofrequency pulses for low-power simultaneous multislice excitation. Magn Reson Med. 2011 Nov;66(5):1234-40.

Contact

Dr. Felix Breuer
Research Center
Magnetic Resonance Bavaria e.V. (MRB)
Am Hubland
97074 Würzburg, Germany
Phone: +49 (0) 931 318 3060
Fax: +49 (0) 931 318 4680
breuer@mr-bavaria.de



Advancing Diffusion MRI Using Simultaneous Multi-Slice Echo Planar Imaging

Kawin Setsompop[1, 2]; Stephen F. Cauley[1, 2]; Lawrence L. Wald[1, 2]

[1] Martinos Center for Biomedical Imaging, Department of Radiology, Massachusetts General Hospital, Charlestown, MA, USA
[2] Department of Radiology, Harvard Medical School, Boston, MA, USA

Introduction

There has been a recent significant interest in the use of parallel imaging based Simultaneous Multi-Slice (SMS) acquisition [1] to increase the temporal efficiency of many imaging sequences in MRI. In particular, the use of SMS for diffusion MRI (dMRI) and functional MRI (fMRI) has fundamentally changed the scope of studies that clinicians and researchers are able to perform with these imaging sequences. For dMRI, SMS has opened up the possibility of obtaining information from many more diffusion encoding directions in a limited timeframe, to enable more complex/advanced diffusion acquisitions to be performed in clinical and neuroscientific settings.

Due to the use of diffusion encoding gradients in dMRI, large temporally and spatially varying phase contamination exists, which hampers the utility of multi-shot acquisitions. As such, dMRI acquisitions are often based on rapid single-shot 2D spin-echo EPI sequence. This sequence provides high quality imaging but at a cost of being highly inefficient. Figure 1 shows the sequence diagram for such acquisition, where a single 2D imaging slice is excited, after which diffusion encoding is performed and the data for that particular slice is then readout/received using EPI encoding. This process is repeated multiple times, once for each imaging slice, until whole-brain coverage is achieved. As depicted, the diffusion encoding period can represent a significant portion of the acquisition time. This diffusion encoding is performed using magnetic field gradient pulses which provide encoding to the whole imaging volume. However, for each acquisition period, only a single slice is excited and acquired, and the lengthy diffusion encoding has to be repeated for all imaging slices, leading to large inefficiency.

1

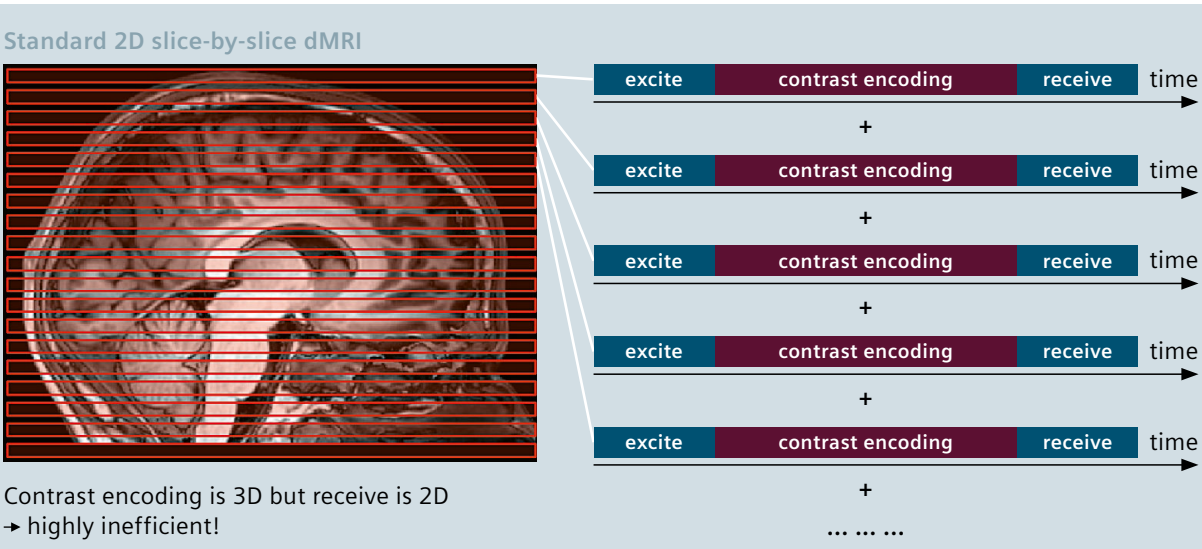

1 The inefficiency of standard 2D DWI techniques is illustrated. Although the lengthy diffusion contrast-encoding encompasses the entire volume, only a single slice is acquired. Simultaneous multi-slice enables the concurrent acquisition of several imaging slices during a single diffusion encoding. Unlike typical in-plane acceleration techniques, which only shorten the receive portion of the acquisition, SMS allows for proportional reductions in total scan time as the multiband factor is increased.

The use of conventional 2D parallel imaging acceleration [2-4] in dMRI can reduce the number of phase encoding steps of EPI which reduces image distortion and blurring artifacts. However, such technique does not provide significant acceleration to dMRI, since they only shorten the EPI encoding period and not the other components of the data acquisition, in particular the lengthy diffusion encoding. The use of simultaneous multi-slice (SMS) acceleration [1], on the other hand, allows for the concurrent acquisition of several imaging slices (the slices will appear collapsed before reconstruction) during each acquisition period, thereby reducing the number of acquisition periods needed to perform volumetric acquisition. Thus, SMS is much more effective at providing scan time reduction in dMRI, where the total scan time is now reduced by a factor equal to the number of simultaneously excited slices (multiband (MB) factor). Additionally, unlike conventional parallel imaging, SMS does not shorten the EPI encoding period and is not affected by the undesirable $\sqrt{R}$ SNR penalty of conventional parallel imaging.

Several SMS methods have been applied to single shot SMS-EPI, including Wideband imaging [5, 6], Simultaneous Image Refocusing (SIR) [7, 8] and parallel image reconstruction based multi-slice imaging [9, 10]. However, the presence of significant artifact and/or signal-to-noise (SNR) loss from these methods have prevented their wide scale adoption in dMRI. In particular, parallel imaging based multi-slice imaging suffers from high *g*-factor noise amplification in brain MRI. This is due to the fact that the imaging field-of-view (FOV) along the slice direction is typically small for brain acquisitions, causing the aliased voxels of the simultaneously acquired slices to be spatially close which makes it hard to tease them apart. An improved parallel imaging strategy termed CAIPIRINHA [11], which creates an inter-slice image shift between simultaneously acquired slices to increase the distance between the aliased voxels has been proposed as a way to reduce the *g*-factor penalty associated with SMS. The CAIPIRINHA method creates an inter-slice shift by utilizing a different RF pulse for the data acquisition of each *k*-space line, where each RF pulse is designed to induce a different phase modulation to each of the slices that are being acquired simultaneously. This is feasible for multi-shot acquisitions but not for single-shot EPI where only a single RF pulse is used to acquire all lines of *k*-space. An initial attempt to adopt CAIPIRINHA for single-shot EPI acquisitions was performed by Nunes *et al*. [9]. Here, a Wideband-like approach was used in the phase encoding and readout directions to increase the distance between aliased voxels. However, this resulted in voxel tilting (blurring) artifacts and heavily restricted the distance that could be imposed between aliased voxels. In this article, we describe the blipped-CAIPIRINHA method [12] which is a modification of Nunes' approach, to generate the desired voxel shifts in the phase encoding direction without tilting artifacts. This approach has provided us with the ability to perform high quality parallel imaging based SMS-EPI acquisition that can be used to significantly shorten dMRI acquisition time.

Blipped-CAIPIRINHA

The blipped-CAIPIRINHA method utilizes additional G_z magnetic field gradient blips during the EPI readout. Figure 2 shows the standard G_x and G_y gradients of the EPI encoding, along with these additional G_z gradient blips. These G_z blips are applied concurrently with the G_y phase encoding blips to create a different phase modulation between the simultaneously excited slices for the data acquisition of each *k*-space line. For this example, the G_z blips are being applied to create a FOV/2 shift along the phase encoding (PE) direction between two simultaneously acquired slices (collapsed image shown in top-right of Figure 2). In order to create the desired inter-slice shift, an appropriate gradient blip area must be used for these G_z blips. Specifically, in the example in

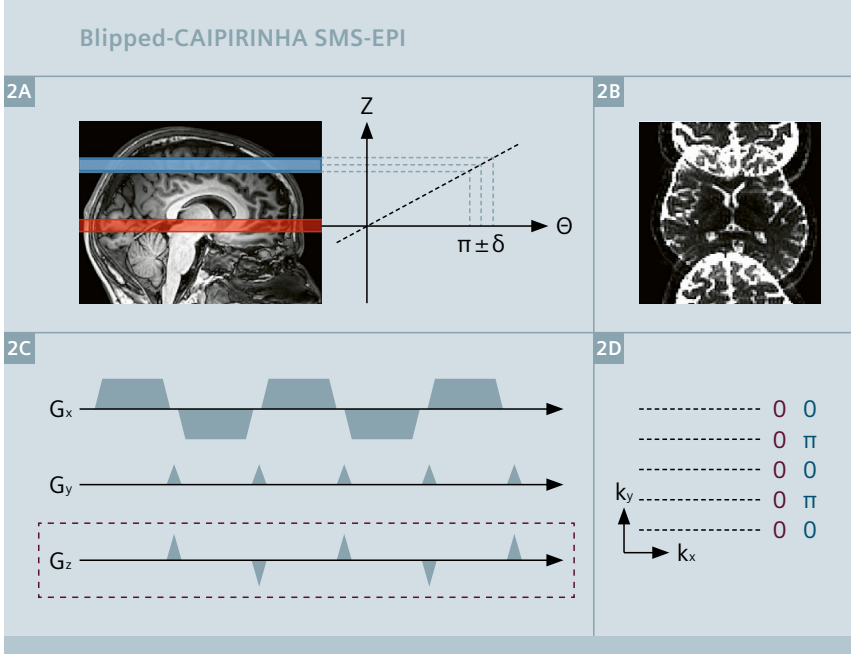

2 A blipped-CAIPIRINHA SMS-EPI gradient scheme applied across the X, Y and Z (Readout, Phase-Encode, and Slice) axes is illustrated. The G_z gradient blips required to create a FOV/2 shift between two simultaneously acquired slices are shown (collapsed image in **2B**). The blipped-CAIPIRINHA method varies the sign of the G_z gradient blips in order to avoid accumulation of through-slice phase variation, which would result in voxel titling artifacts. The accumulated phase applied to each of the k_y lines are shown for the two slices **(2D).**

Figure 2, each G_z blip will have to create a π phase increment to the spins located at the upper slice (blue) and no increment to the lower slice (red). The phase modulations along k_y caused by the G_z blip train are shown on the lower-right of Figure 2, for the upper (blue) and lower (red) imaging slices. With no phase modulation to the lower slice, this slice remains unaffected. On the other hand, the linear phase moduation along k_y at π phase increment for the top slice causes this slice to shift by FOV/2 along the PE direction. As such, a desired FOV/2 inter-slice shift is achieved.

It is important to note that each G_z blip will also introduce a small phase variation 2δ across the finitely thick slices being acquired as shown in Figure 2. This through-slice phase variation created by each blip will result in a very minor signal attenuation (typically less than 1%).
The important concept in blipped-CAIPIRINHA is the utilization of alternating positive and negative gradient blips to limit ability of the gradient moment and this through-slice phase variation to accumulate during the EPI encode and cause significant signal attenuation. This solves the issue of the Wideband approach where only positive G_z blips are employed which results in accumulation of through-slice dephasing and voxel tilting artifacts. Thus, the blipped-CAIPIRINHA method facilitates efficient CAIPIRINHA controlled aliasing schemes for simultaneously acquired slices in EPI. This can be seen clearly when examining the 3× slice-accelerated (SMS 3) example acquired using a 32-channel head coil at 3T shown in Figure 3. Here, the *g*-factor associated with FOV/2 shift and no-shift parallel imaging reconstructions are compared (both with slice-GRAPPA reconstruction). When no-shift was applied between the simultaneously acquired slices, the average retained SNR (1 / *g*-factor) dropped significantly to 68%. The blipped-CAIPIRINHA method with FOV/2 shift retained over 99% of the SNR, while removing the 3.5 voxel tilt that would have been present with the standard wideband approach. Thereby, blipped-CAIPIRINHA enables three times faster acquisitions in dMRI without incurring significant SNR penalty. (Note that in some regions the retained SNR is slightly greater than unity indicating some noise cancellation in the reconstruction process as previously demonstrated in low acceleration in-plane GRAPPA acquisitions [13]).

3 SMS-3 Blipped-CAIPIRINHA with 32-channel head coil

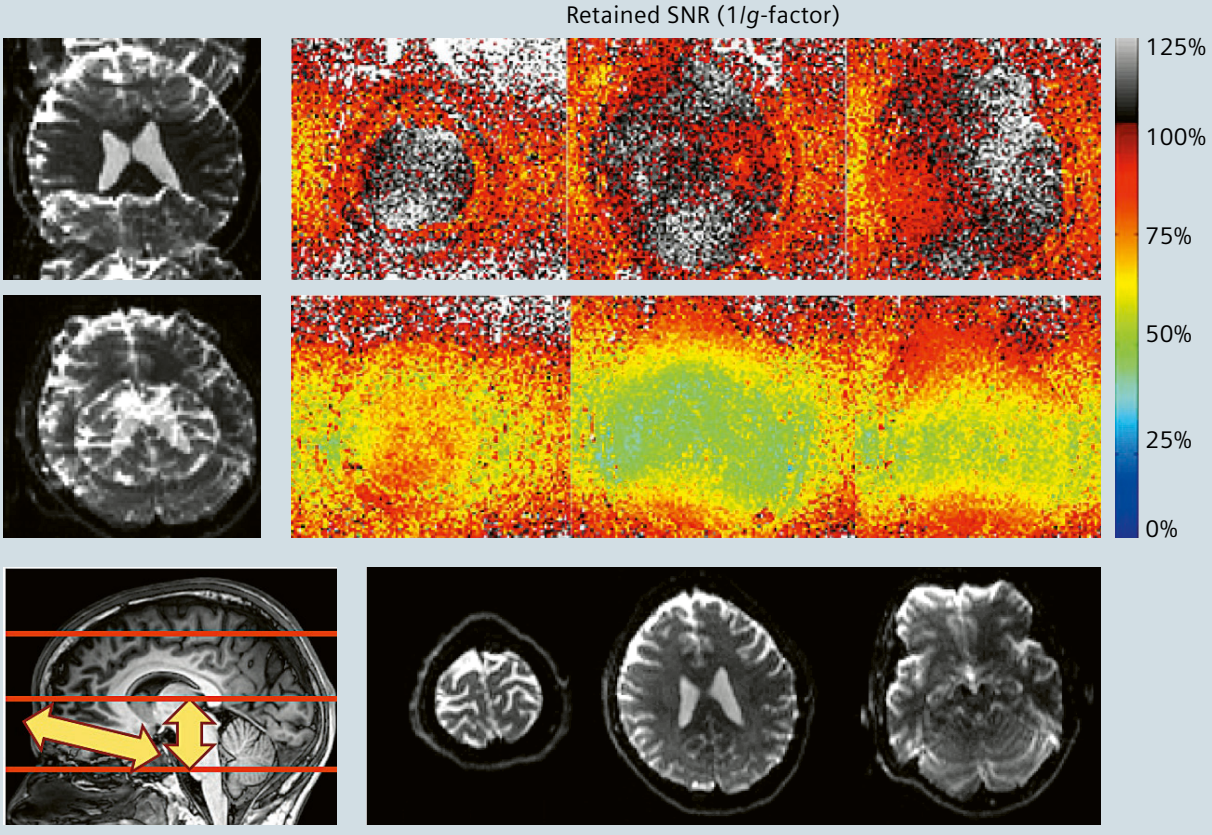

3 SMS-EPI at SMS-3 acceleration acquired at 3T using Siemens' 32-channel coil. The *g*-factor associated with FOV/2 shift and no-shift parallel imaging reconstructions are compared. The retained SNR (1 / *g*-factor), when no-shift was applied dropped significantly to 68%. The blipped-CAIPIRINHA method with FOV/2 shift retained over 99% of the SNR, while avoiding the 3.5 voxel tilt associated with standard wideband approaches.

RF pulse design and image reconstruction

When considering the use of blipped-CAIPIRINHA for high slice acceleration factors, there are several sequence design and image reconstruction aspects that need to be carefully developed. Of particular importance to diffusion-weighted imaging (DWI) is the design of the multiband RF pulse that allows for multiple slices to be simultaneously excited in SMS acquisitions. Multiband RF pulses cause an increase in SAR, which is especially problematic for DWI since it relies on high SAR spin-echo 90-180 pulses. At SMS-3 acceleration, the use of the VERSE algorithm [14] has been shown to provide adequate SAR reduction for *in vivo* DWI at 3T [15]. However, the benefit of SAR reduction from VERSE comes at a cost of slice profile distortion at off-resonance frequencies. This can be mitigated by the use of the SLR algorithm for RF pulse design along with a high time-bandwidth product that improves the slice-profile quality prior to the application of VERSE. Figure 4 (A, B) shows multiband 90-180 pulses with slice acceleration factor 3 designed using both the SLR and VERSE algorithms. Figure 4A shows the VERSE 90 and 180 RF pulses along with corresponding gradient pulses. Figure 4B shows the comparison of slice-profiles obtained from a standard single-slice 90-180 RF pulse pair and those obtained from the slice acceleration factor 3 RF pulse pair. Here, the high-quality slice profiles are achieved at both on resonance and 50 Hz off-resonance.

In addition to the combined design of VERSE and SLR, a number of other approaches have been developed to reduce both SAR and peak-power of MB pulses. These techniques are particularly beneficial at higher slice accelerations and/or for ultra-high field imaging. In order to reduce peak-power, a phase optimization scheme [16], a pulse time-shift method [17] and a combined approach [18, 19] of phase optimization with the use of 90° and 180° pulses with spatially-varying phases that combine to provide a flat spin-echo excitation phase have been

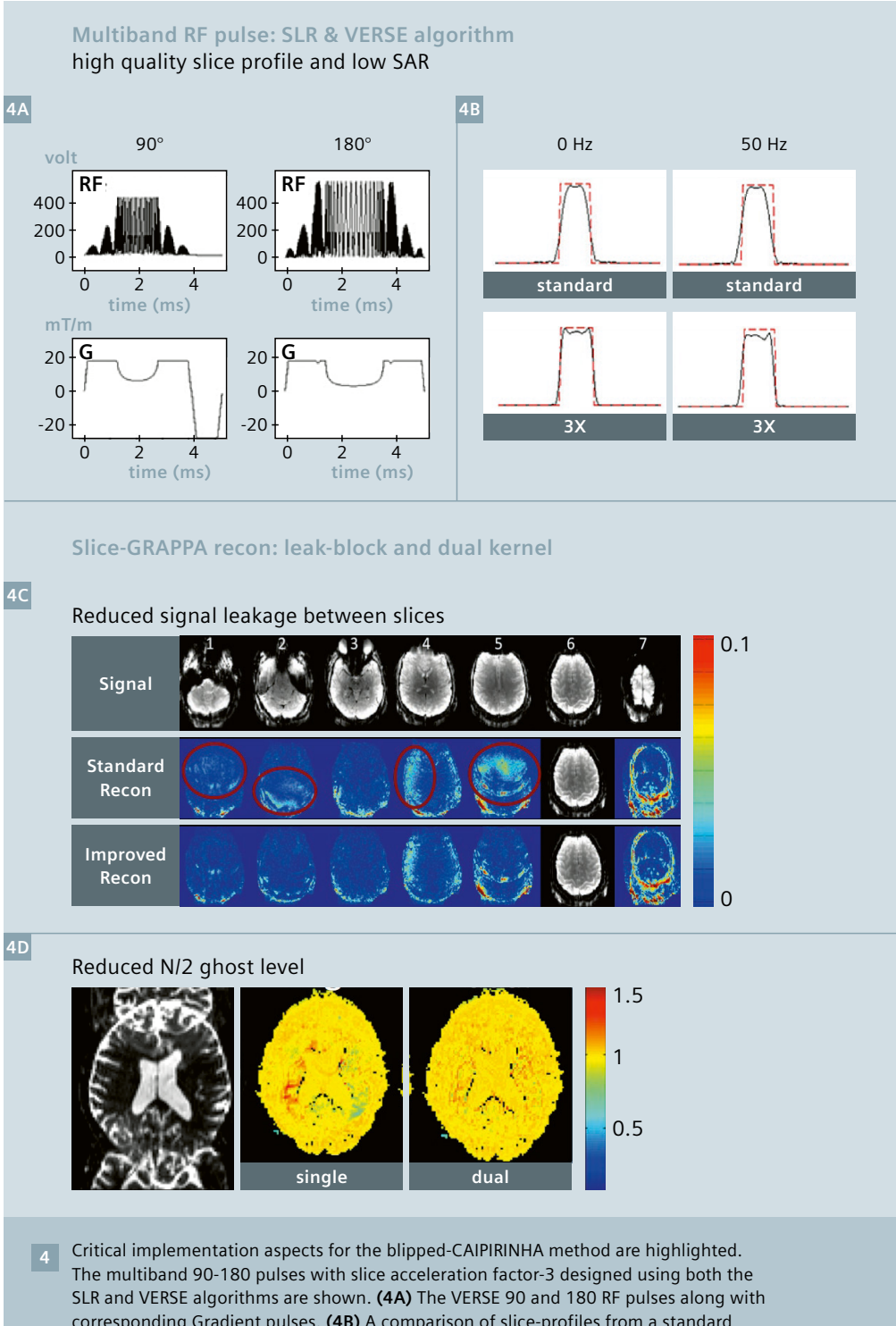

4 Critical implementation aspects for the blipped-CAIPIRINHA method are highlighted. The multiband 90-180 pulses with slice acceleration factor-3 designed using both the SLR and VERSE algorithms are shown. **(4A)** The VERSE 90 and 180 RF pulses along with corresponding Gradient pulses. **(4B)** A comparison of slice-profiles from a standard single-slice 90-180 RF pulse pair and those obtained from the slice acceleration factor 3 RF pulse pair. These pulses are necessary to ensure image quality while limiting peak-power and SAR. The benefits of the 'LeakBlock' Slice-GRAPPA reconstruction technique in reducing leakage signal contamination between simultaneously acquired slices is shown **(4C)**.The individual leakage signal contaminations onto the 6th imaging slice (for a SMS 7 acquisition) are greatly reduced when compared with standard slice-GRAPPA reconstruction. The use of 'dual kernel' slice-GRAPPA to separate SMS 3 blipped-CAIPIRINHA EPI with FOV/2 shift data is shown **(4D)**. The dual kernels operate specifically to the even and the odd lines of the slice-collapsed *k*-space data, and enable clean separation of both of the slice data and associated ghost (prior to the application of typical ghost correction).

proposed. In addition, the Power Independent of Number of Slices (PINS) [20] and MultiPINS [21] RF pulse designs have been proposed as a strategy to excite/refocus a large number of imaging slices simultaneously without increasing peak power or SAR.

A number of techniques have been developed in order to improve the quality of SMS-EPI image reconstruction. The original SENSE/GRAPPA approach for SMS reconstruction [22] has been modified to facilitate CAIPIRINHA acquisitions with inter-slice FOV shifts [23-25]. Slice-GRAPPA [12], which has been widely-used for blipped-CAIPIRINHA SMS-EPI reconstruction, has been redesigned to provide robust reconstruction through a 'LeakBlock' technique [26]. This technique reduces the leakage signal contamination between simultaneously acquired slices and has been shown to improve temporal stability at high accelerations. Figure 4C shows a comparison of signal leakage contamination in the standard and the improved LeakBlock slice-GRAPPA reconstructions for blipped-CAIPIRINHA acquisition at SMS-7 using a 32-channel head coil. It can be clearly seen that the individual leakage signal contaminations onto the 6th imaging slice are greatly reduced using the LeakBlock reconstruction.

Another important consideration for SMS-EPI reconstruction is in the minimization of N/2 image ghosting artifacts. For SMS-EPI, this is a particular concern since a different slice-specific ghost correction could be required for each of the simultaneously acquired imaging slices (due to differences in phase error of the N/2 ghost for different slice locations). Thus, the N/2 ghost cannot be cleanly removed from the slice-collapsed dataset prior to the parallel imaging (slice-unaliasing) reconstruction. The use of a 'dual kernel' slice-GRAPPA, where separate GRAPPA kernels are applied to the even and the odd lines of the slice-collapsed *k*-space data has been shown to overcome this issue [15]. This method enables a clean separation of both of the slice data and associated ghost, prior to the application of typical ghost correction.

Figure 4D shows a comparison of the N/2 ghost artifact level for an SMS-3 blipped-CAIPIRINHA SMS-EPI with FOV/2 shift reconstructed using i) single kernel slice-GRAPPA and ii) dual kernel slice-GRAPPA approaches. Note that the ghost artifact of the top imaging slice in the SMS acquisition lands directly in the center of the imaging FOV of the middle imaging slice (due to the FOV/2 inter-slice shift). This prevents the single kernel slice-GRAPPA approach from accurately unaliasing the ghosting artifact. Figure 4 shows the corresponding large reconstruction artifact in the center of the middle imaging slice. With the use of dual kernel slice-GRAPPA, this artifact has been mitigated. The dual kernel approach has been successfully applied to SENSE/GRAPPA reconstruction [27] and an extension of the method has been used to overcome artifacts associated with phase-encode line bunching [28]. Finally, for SENSE based reconstruction of SMS data, a slice-specific phase error of the ghost artifact has been successfully incorporated into the parallel imaging reconstruction [29].

Diffusion-weighted imaging applications

With the careful design of RF pulses and the image reconstruction framework, blipped-CAIPIRINHA allows for the efficient acquisition of high quality SMS-EPI data for DWI. In clinical settings, where time is limited, DWI is often restricted to only a small number of diffusion encoding directions. This constrains studies to only examine the most basic diffusion information, such as the apparent diffusion coefficient (ADC). With the use of blipped-CAIPIRINHA SMS-EPI, diffusion-weighted acquisitions can be accelerated robustly by 3-fold to provide high quality data with negligible SNR loss and artifact levels. This has allowed for more diffusion directions to be obtained in a clinically relevant time-frame, enabling more complex diffusion models/metrics (e.g. Fractional Anisotropy (FA), Diffusion Kurtosis, and fiber tracking) to be considered. Figure 5 demonstrates the use of blipped-CAIPIRINHA to achieve 3-fold acceleration for typical neuroimaging acquisitions based upon Diffusion Tensor Imaging (DTI), Q-ball, and Diffusion Spectrum Imaging (DSI). Here, the color FA, Orientation Distribution Function (ODF), and the fiber tracking results from these diffusion models are compared using standard SMS-1 and blipped-CAIPIRINHA SMS-3 acquisitions. In all cases, the high quality of the results is maintained at a 3-fold speed up with the blipped-CAIPIRINHA technique.

There is a growing interest in the application of DWI to areas outside the brain, where it has also proven to be highly sensitive to tissue abnormalities. Similar to the neuroimaging applications described above, blipped-CAIPIRINHA SMS-EPI can play a role in speeding up acquisitions in the body. Here, a large in-plane FOV has to be encoded and in-plane acceleration (typically a factor of 2) is used to reduce image distortion. While accelerations in the slice and in-plane directions are compatible, the use of both can lead to a high total acceleration factor (the product of the two acceleration factors) and result in higher *g*-factor noise amplifications. For the DWI applications where SNR is inherently low, it is desirable to keep the noise penalty to a minimum. Thus, a combined SMS-2 and in-plane-2 acceleration strategy is typically employed for blipped-CAIPIRINHA SMS-EPI in the body.

Figure 6 shows DWI results for liver, whole-body, and breast imaging from a standard in-plane-2 acceleration with and without the inclusion of blipped-CAIPIRINHA SMS factor 2. The imaging results are near identical, with the blipped-CAIPIRINHA acquisition providing a 2-fold speed up in imaging time. This is particularly useful for whole-body DWI, where a large number of imaging slices are acquired. Reducing these lengthy scans (often ~20 minutes is required for standard diffusion scans focusing on the basic ADC metric) will have a significant impact on the wide-spread adoption of whole-body DWI in clinical settings.

5

3x Faster brain dMRI

Q-ball: 12 min → 4 min

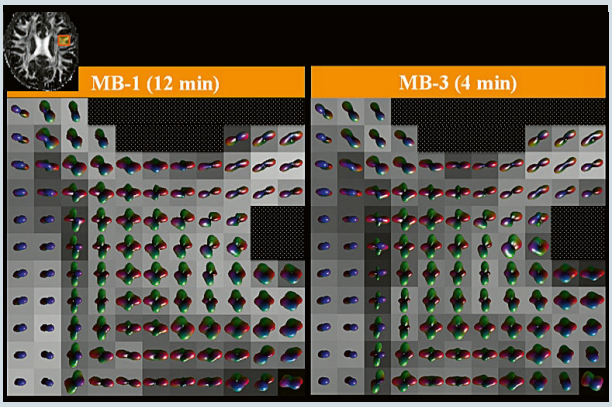

DTI: 10 min → 3 min

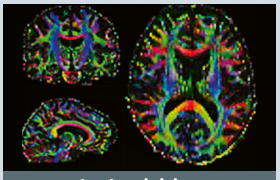

1x Aquisition

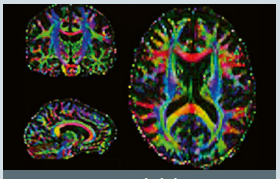

3x Aquisition

DSI: 45 min → 15 min

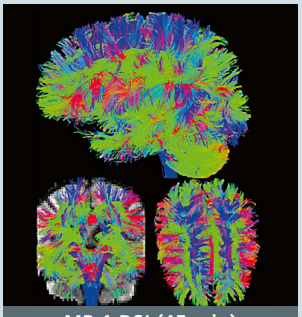

MB-1 DSI (45 min)

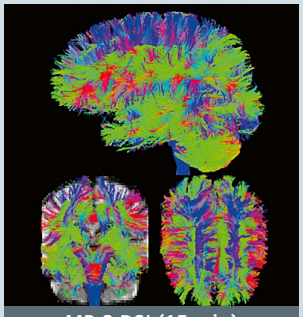

MB-3 DSI (15 min)

5 Diffusion Tensor Imaging, Q-ball, and Diffusion Spectrum Imaging are compared using standard SMS 1 and blipped-CAIPIRINHA SMS 3 acquisitions at 3T using Siemens' 32-channel head coil. The high level of similarities in color FA, Orientation Distribution Function, and the fiber tracking results can be clearly seen.

6

Applications outside of the brain

Liver diffusion

b = 50



SMS-1

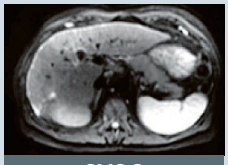

SMS-2

b = 400



SMS-1



SMS-2

b = 800



SMS-1



SMS-2

ADC

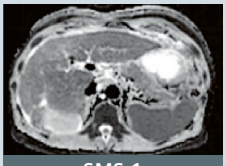

SMS-1



SMS-2

Whole-body diffusion

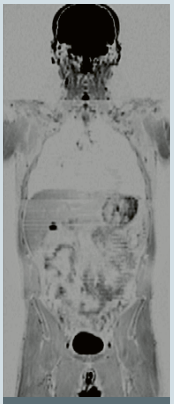

SMS-1

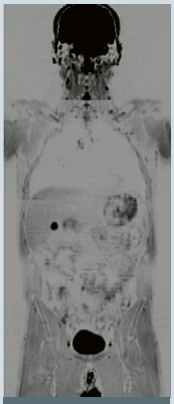

SMS-2

Breast diffusion

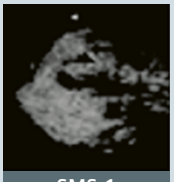

SMS-1

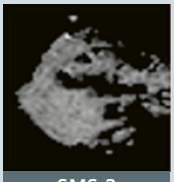

SMS-2

6 Emerging applications of DWI in the body are demonstrated. Blipped-CAIPIRINHA with SMS 2 and in-plane GRAPPA 2 was used in large FOV body diffusion. Relative to conventional DWI with in-plane GRAPPA 2, similar image quality can be seen. Blipped-CAIPIRINHA SMS enables effective combination of in-plane GRAPPA acceleration which is critical for the reduction of distortions especially in large FOV DWI of the body. With blipped-CAIPIRINHA SMS-EPI, scan time reductions to a factor of 2 with similar image quality can be obtained for the liver, breast, and whole-body DWI.

References

1 Larkman DJ, Hajnal J V, Herlihy AH, Coutts GA, Young IR, Ehnholm G. Use of multicoil arrays for separation of signal from multiple slices simultaneously excited. J Magn Reson imaging. 2001;13:313–7.
2 Pruessmann KP, Weiger M, Scheidegger MB, Boesiger P. SENSE: sensitivity encoding for fast MRI. Magn Reson Med [Internet]. 1999 Nov;42(5):952–62. Available from: 10.1002/(SICI)1522-2594(199911)42:5<952::AID-MRM16>3.0.CO;2-S.
3 Griswold MA, Jakob PM, Heidemann RM, Nittka M, Jellus V, Wang J, et al. Generalized autocalibrating partially parallel acquisitions (GRAPPA). Magn Reson Med [Internet]. 2002 Jun [cited 2014 Jan 21];47(6):1202–10. Available from: http://www.ncbi.nlm.nih.gov/pubmed/12111967.
4 Sodickson DK, Manning WJ. Simultaneous acquisition of spatial harmonics (SMASH): fast imaging with radiofrequency coil arrays. Magn Reson Med [Internet]. 1997 Oct;38(4):591–603. Available from: http://www.ncbi.nlm.nih.gov/pubmed/9324327.
5 Paley MNJ, Lee KJ, Wild JM, Griffiths PD, Whitby EH. Simultaneous parallel inclined readout image technique. Magn Reson Imaging [Internet]. 2006 Jun [cited 2014 Sep 9];24(5):557–62. Available from: http://www.ncbi.nlm.nih.gov/pubmed/16735176.
6 Weaver JB. Simultaneous Multislice Acquisition of MR Images. 1988;284:275–84.
7 Feinberg D a., Reese TG, Wedeen VJ. Simultaneous echo refocusing in EPI. Magn Reson Med. 2002;48(1):1–5.
8 Reese TG, Benner T, Wang R, Feinberg D a., Van Wedeen J. Halving imaging time of whole brain diffusion spectrum imaging and diffusion tractography using simultaneous image refocusing in EPI. J Magn Reson Imaging. 2009;29(3):517–22.
9 Nunes RG, Hajnal J V, Golay X, Larkman DJ. Simultaneous slice excitation and reconstruction for single shot EPI . Proc Intl Soc Mag Reson Med. 2006. p. 293.
10 Moeller S, Yacoub E, Olman C a, Auerbach EJ, Strupp J, Harel N, et al. Multiband multislice GE-EPI at 7 tesla, with 16-fold acceleration using partial parallel imaging with application to high spatial and temporal whole-brain fMRI. Magn Reson Med [Internet]. 2010 May [cited 2014 Jan 21];63(5):1144–53. Available from: http://www.pubmedcentral.nih.gov/articlerender.fcgi?artid=2906244&tool=pmcentrez&rendertype=abstract.
11 Breuer FA, Blaimer M, Heidemann RM, Mueller MF, Griswold MA, Jakob PM. Controlled aliasing in parallel imaging results in higher acceleration (CAIPIRINHA) for multi-slice imaging. Magn Reson Med. 2005;53:684–91.
12 Setsompop K, Gagoski BA, Polimeni JR, Witzel T, Wedeen VJ, Wald LL. Blipped-controlled aliasing in parallel imaging for simultaneous multislice echo planar imaging with reduced g-factor penalty. Magn Reson Med [Internet]. 2012 May [cited 2014 Jan 21];67(5):1210–24. Available from: http://www.pubmedcentral.nih.gov/articlerender.fcgi?artid=3323676&tool=pmcentrez&rendertype=abstract.
13 Polimeni JR, Wiggins GC, Wald LL. Characterization of artifacts and noise enhancement introduced by GRAPPA reconstructions. Proc Intl Soc Mag Reson Med. 2008. p. 1286.
14 Conolly SM, Nishimura DG, Macovski A, Glover GH. Variable-rate selective excitation. J Magn Reson [Internet]. 1988 Jul [cited 2012 Jul 4];78(3):440–58. Available from: http://linkinghub.elsevier.com/retrieve/pii/002223648890131X.
15 Setsompop K, Cohen-Adad J, Gagoski BA, Raij T, Yendiki A, Keil B, et al. Improving diffusion MRI using simultaneous multi-slice echo planar imaging. Neuroimage [Internet]. Elsevier Inc.; 2012 Oct 15 [cited 2014 Jan 30];63(1):569–80. Available from: http://www.pubmedcentral.nih.gov/articlerender.fcgi?artid=3429710&tool=pmcentrez&rendertype=abstract.
16 Wong E. Optimized phase schedules for minimizing peak RF power in simultaneous multi-slice RF excitation pulses. Proc Intl Soc Mag Reson Med [Internet]. 2012 [cited 2014 Jan 21]. p. 2209. Available from: http://scholar.google.com/scholar?hl=en&btnG=Search&q=intitle:Optimized+phase+schedules+for+minimizing+peak+RF+power+in+simultaneous+multi-slice+RF+excitation+pulses#0.
17 Auerbach EJ, Xu J, Yacoub E, Moeller S, Uğurbil K. Multiband accelerated spin-echo echo planar imaging with reduced peak RF power using time-shifted RF pulses. Magn Reson Med. 2013 May;69(5):1261–7.
18 Zhu K, Kerr AB, Pauly JM. Nonlinear-Phase Multiband 90°-180° RF Pair With Reduced Peak Power. Proc Intl Soc Mag Reson Med. 2014. p. 1440.
19 Sharma A, Bammer R, Stenger VA, Grissom W a. Low peak power multiband spokes pulses for B 1 + inhomogeneity-compensated simultaneous multislice excitation in high field MRI. Magn Reson Med [Internet]. 2015;doi: 10.1002/mrm.25455. Available from: http://doi.wiley.com/10.1002/mrm.25455.
20 Norris DG, Koopmans PJ, Boyacioğlu R, Barth M. Power Independent of Number of Slices (PINS) radiofrequency pulses for low-power simultaneous multislice excitation. Magn Reson Med [Internet]. 2011 Nov [cited 2014 Jan 10];66(5):1234–40. Available from: http://www.ncbi.nlm.nih.gov/pubmed/22009706.
21 Eichner C, Wald LL, Setsompop K. A low power radiofrequency pulse for simultaneous multislice excitation and refocusing. Magn Reson Med [Internet]. 2014 Oct [cited 2014 Sep 25];72:949–58. Available from: http://www.ncbi.nlm.nih.gov/pubmed/25103999.
22 Blaimer M, Breuer F a, Seiberlich N, Mueller MF, Heidemann RM, Jellus V, et al. Accelerated volumetric MRI with a SENSE/GRAPPA combination. J Magn Reson imaging [Internet]. 2006 Aug [cited 2014 Oct 13];24(2):444–50. Available from: http://www.ncbi.nlm.nih.gov/pubmed/16786571.
23 Stäb D, Ritter CO, Breuer F a, Weng AM, Hahn D, Köstler H. CAIPIRINHA accelerated SSFP imaging. Magn Reson Med. 2011;65:157–64.
24 Blaimer M, Choli M, Jakob PM, Griswold M a, Breuer F a. Multiband phase-constrained parallel MRI. Magn Reson Med [Internet]. 2013 Apr [cited 2014 Jul 21];69(4):974–80. Available from: http://www.pubmedcentral.nih.gov/articlerender.fcgi?artid=3606646&tool=pmcentrez&rendertype=abstract.
25 Moeller S, Vu AT, Auerbach E, Ugurbil K, Yacoub E. RO extended FOV SENSE/GRAPPA for multiband imaging with FOV shift. Proc Intl Soc Mag Reson Med. 2014. p. 4396.
26 Cauley SF, Polimeni JR, Bhat H, Wald LL, Setsompop K. Interslice leakage artifact reduction technique for simultaneous multislice acquisitions. Magn Reson Med [Internet]. 2014 [cited 2014 Jan 28];72:93–102. Available from: http://www.ncbi.nlm.nih.gov/pubmed/23963964.
27 Koopmans PJ, Poser BA, Breuer FA. 2D-SENSE-GRAPPA For Fast, Ghosting-Robust Reconstruction of In-Plane and Slice Accelerated Blipped-CAIPI-EPI. Proc Intl Soc Mag Reson Med. 2015. p. 2410.
28 Moeller S, Auerbach EJ, Vu AT, Lenglet C, Sotiropoulos SN, Ugurbil K, et al. EPI 2D ghost correction and integration with multiband : application to diffusion imaging at 7T. Proc Intl Soc Mag Reson Med. 2015. p. 248.
29 Zhu K, Dougherty RF, Takahashi A, Pauly J, Kerr AB. Nyquist Ghosting Correction For Simultaneous Multislice Echo Planar Imaging. 2014. p. 647.



Contact

Kawin Setsompop
Massachusetts General Hospital
Martinos Center for Biomedical Imaging
Building 75, Room 2.102, 13th Street
Charlestown, MA, 02129, USA
Phone: +1 617-669-6640
kawin@nmr.mgh.harvard.edu

High-Resolution Diffusion-Weighted Neuroimaging at 3T and 7T with Simultaneous Multi-Slice RESOLVE

Robert Frost[1]; Peter J. Koopmans[1]; George W. Harston[2]; James Kennedy[2]; Peter Jezzard[1]; Karla L. Miller[1]; David A. Porter[3]

[1] FMRIB Centre, Nuffield Department of Clinical Neurosciences, University of Oxford, Oxford, UK
[2] Radcliffe Department of Medicine, University of Oxford, Oxford, UK
[3] Fraunhofer Institute for Medical Image Computing MEVIS, Bremen, Germany

Introduction

Single-shot echo-planar imaging

Diffusion-weighted imaging is an important tool in both clinical imaging and neuroscience research. Its widespread use is due to the advent of the single-shot echo-planar imaging (ss-EPI) sequence [1], which is relatively immune to motion-related diffusion-encoding artifacts because all the required data for each image are acquired in a single 'shot' after the diffusion encoding. This insensitivity to motion, particularly cardiac-related brain pulsation, and the ability to rapidly acquire a multi-slice volume are the reasons why, 25 years after it was first introduced [2], spin echo ss-EPI remains the most commonly-used diffusion imaging sequence for the assessment of acute stroke [3] and white matter anisotropy [4]. However, ss-EPI suffers from the well-known geometric distortion artifact as well as the more subtle blurring due to T2* decay of the signal. These issues limit the achievable spatial resolution, particlularly at high field strengths where increased artifact levels directly undermine the goal of improved spatial resolution.

RESOLVE

One approach to overcoming these limitations is to use diffusion-weighted, readout-segmented EPI (RESOLVE) [5] which is becoming established as an alternative to ss-EPI that provides improved image quality in a wide range of clinical applications throughout the body [6-14].

RESOLVE belongs to a family of sequences that have addressed the ghosting and blurring artifacts that arise in multi-shot diffusion imaging due to phase inconsistencies between the shots. RESOLVE measures the motion-related phase caused by the diffusion encoding in a so-called 'navigator' echo acquired at the centre of *k*-space (see Fig. 1A). The navigator phase information is acquired after every shot of the multi-shot image and is used to correct motion-induced phase errors to generate an artifact-free image [15, 16].

A particular advantage of the readout-segmented approach to multi-shot image acquisition [17] (shown in Fig. 1B) is that an efficient 2D non-linear navigator phase correction [18]

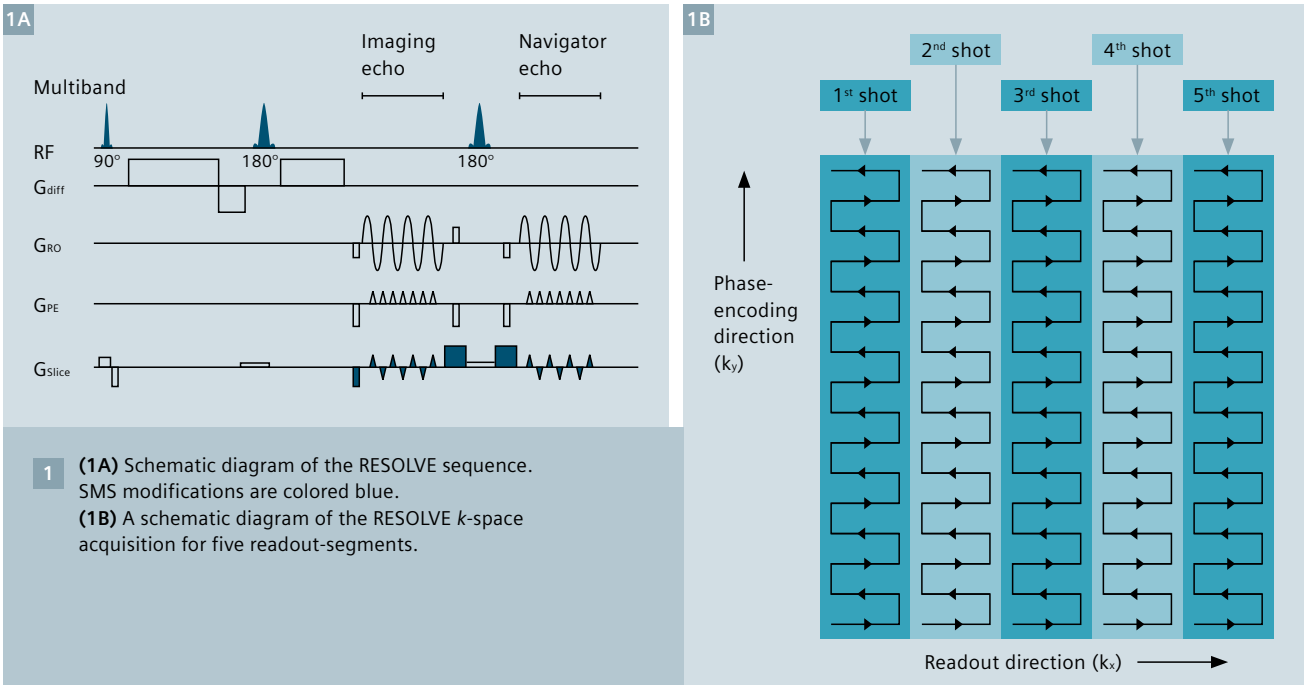

1 **(1A)** Schematic diagram of the RESOLVE sequence. SMS modifications are colored blue. **(1B)** A schematic diagram of the RESOLVE *k*-space acquisition for five readout-segments.

can be used because the *k*-space data sampling fulfils the Nyquist condition, which avoids the confounding effects of aliased signal contributions. A related feature of RESOLVE that is necessary for robust diffusion imaging, is a navigator-based selective reacquisition that identifies shots with particularly severe motion-induced phase corruption and reacquires them [19, 20].

The possibility of multi-shot acquisition with RESOLVE reduces sensitivity to distortion and T2* blurring artifacts in comparison to ss-EPI. Images are less distorted because the phase evolution time between adjacent *k*-space lines (echo-spacing) is shorter and T2* blurring is reduced because the total duration of each shot is shorter. Both features are consequences of acquiring sub-sets of *k*-space in multiple shots or repetition times (TRs) rather than encoding the whole of *k*-space in a single shot. This makes it possible to acquire high-spatial-resolution diffusion-weighted images because the sequence avoids the severe limitations seen with ss-EPI, where there is a trade-off between resolution and the level of geometric distortion and blurring.

RESOLVE can also be combined with GRAPPA [21] to further reduce the effective echo-spacing and readout duration [22]. The reduced duration of the EPI readout with RESOLVE compared to ss-EPI also results in a shorter echo time (TE), which reduces signal loss due to T2 decay; this is particularly significant at ultra-high field strengths, such as 7T, due to the shorter T2 decay times.

Simultaneous multi-slice RESOLVE

Acquiring multiple shots to form each image increases the RESOLVE scan time compared to ss-EPI. Techniques to accelerate the sequence are therefore important for routine clinical use and to increase the number of diffusion-weighted directions for diffusion tensor imaging (DTI) or tractography. Two advances that reduce RESOLVE scan times have recently been demonstrated: 1) readout partial Fourier (PF) acquisition [23] and 2) simultaneous multi-slice (SMS) acceleration [24, 25]. These two techniques are compatible and can, in combination, deliver substantial reductions in the RESOLVE scan time, thereby making whole-brain studies with multiple diffusion directions feasible.

At 7T, radiofrequency (RF) heating constraints often lead to extended scan times and this is exacerbated when acquiring multiple slices simultaneously with SMS acceleration, which, in itself, increases the specific absorption rate (SAR). These effects can be mitigated by using low-SAR 'Power Independent of Number of Slices' (PINS) RF pulses [26], which make SMS acceleration possible at 7T. The PINS technique has therefore been combined with SMS RESOLVE to enable 1 mm isotropic DTI at ultra-high field [27].

The recent work described in this article demonstrates how time-efficient, high-resolution SMS RESOLVE[1] images have important advantages over ss-EPI for clinical stroke imaging and for DTI. In addition, the article shows how the combination of PINS and SMS RESOLVE makes it possible to acquire high-resolution, whole-brain DTI at ultra-high field.

SMS RESOLVE

SMS acquires data from multiple slices together and extracts the slice-specific information using a parallel imaging reconstruction [28]. As fewer slice excitations are required to cover the volume, the TR can be reduced, thereby accelerating the scan and increasing the SNR efficiency. A crucial feature of EPI-based SMS is the blipped-CAIPIRINHA modification that improves SNR by reducing the *g*-factor [29] of the reconstruction, which is achieved by imparting differential in-plane shifts of adjacent slices using slice gradients during the EPI readout [30-33].

The SMS modifications to RESOLVE [24, 25] are shown in Figure 1A (colored blue). Data were acquired on a MAGNETOM Verio 3T and an actively-shielded MAGNETOM 7T[2]. Figure 2 shows examples of SMS RESOLVE images with 26 slices acquired at 3T in 2:14 min with a nominal pixel size of 1 × 1 × 5 mm, an SMS acceleration factor (R_{slice}) of 2 and an in-plane GRAPPA acceleration factor (R_{PE}) of 2; single-shot EPI images acquired in 55 s are provided for comparison.

[1] The product is still under development and not commercially available yet. Its future availability cannot be ensured.
[2] MAGNETOM 7T is ongoing research. All data shown are acquired using a non-commercial system under institutional review board permission. MAGNETOM 7T is still under development and not commercially available yet. Its future availability cannot be ensured.

2

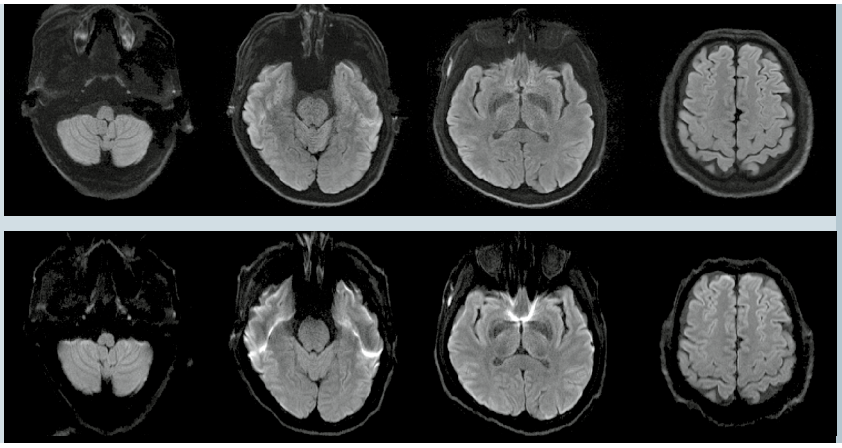

2 Comparison of nominal 1 × 1 × 5 mm resolution trace-weighted images between SMS RESOLVE (top row) and ss-EPI (bottom row) acquired at 3T with 26 slices.

The SMS RESOLVE images show a significant reduction in distortions and T2* blurring compared to the ss-EPI images.

The single-shot EPI images acquired in this study used a routine clinical protocol with a partial Fourier (PF) factor of 6/8 in the phase-encode direction to reduce the echo time (TE) and thereby boost SNR. The images were reconstructed in the standard way using zero-filling (ZF) which creates additional blurring in the phase-encode direction. Despite this blurring, it is standard practice to use ZF with diffusion-weighted ss-EPI because it is more robust than other PF reconstruction algorithms in the presence of motion-induced phase imparted during the diffusion preparation [34].

Comparisons with standard ss-EPI in this study did not use SMS to accelerate the ss-EPI scans. SMS would reduce the scan times and increase the SNR efficiency of the ss-EPI acquisitions, but the image quality, which is the focus of the comparisons, would not be affected.

Clinical stroke imaging with SMS RESOLVE

SMS RESOLVE scans can be a viable clinical alternative to standard ss-EPI DWI for stroke diagnosis, which is typically acquired using an isotropic resolution of around 2 mm. SMS RESOLVE with $R_{slice} = 2$ and $R_{PE} = 2$ can reliably acquire high-quality data at higher resolution with reduced distortion and blurring artifacts. Figure 3 demonstrates the improved image quality provided by SMS RESOLVE with a 1.5 mm isotropic resolution (78 slices) compared to typically-acquired lower-resolution ss-EPI images with $R_{PE} = 2$ and a nominal pixel size of 1.8 × 1.8 × 2 mm with 0.6 mm slice gap (50 slices). The following comparisons (Figs. 4-6) show matched 3:20 min scan times and 1.5 mm isotropic resolution (78 slices) for SMS RESOLVE versus ss-EPI (3 averages) and indicate further potential advantages of using SMS RESOLVE.

3

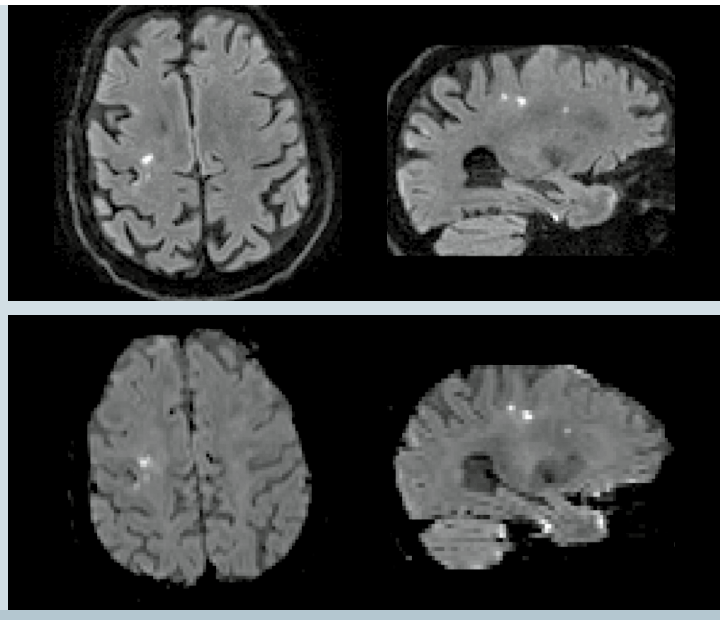

3 Comparison of 1.5 mm isotropic SMS RESOLVE (top row) and 1.8 × 1.8 × 2 mm with 0.6 mm slice gap ss-EPI images (bottom row) acquired at 3T. The images show a right subcortical infarct. The SMS RESOLVE and ss-EPI scans acquired 78 and 50 slices, respectively.

Reduced distortion artifact confounds

SMS RESOLVE has fewer confounding 'signal pile-up' artifacts caused by distortion, in the posterior fossa, brainstem and in proximity to the sinuses, especially the frontal sinus. The improvements are especially apparent in Figures 4 and 5, which show the similarity in appearance of infarcts and signal pile-up artifact in the ss-EPI images. Suppressing these artifacts in the SMS RESOLVE images improves the recognition of regions of true restricted diffusion.

Improved quantification of infarct volume

Previous clinical imaging studies in stroke [10] and of pelvic tumors in radiotherapy planning applications [12] have confirmed that RESOLVE provides an improved geometric distortion performance when compared to ss-EPI; similar benefits are to be expected when SMS RESOLVE images are used to estimate infarct volume in acute stroke. The importance of accurately tracking infarct volume in acute stroke imaging has recently been identified in the Acute Stroke Imaging Research Roadmap II [35]. However, the accuracy of quantifying infarct volume from standard ss-EPI images is limited by the substantial distortion and blurring artifacts. In particular, subtle injuries depicted in Figure 6 are better defined in the SMS RESOLVE images.

7T DTI with PINS SMS RESOLVE

RESOLVE DWI becomes more advantageous at higher resolution because the corresponding ss-EPI acquisitions require an increase in both the echo-spacing and the number of echoes to increase resolution along the readout and phase-encoding axes respectively; this results in a substantial increase in the level of distortion and T2* blurring. These effects become particularly significant at 7T due to amplification of susceptibility and reduced relaxation times. In the case of RESOLVE, the higher resolution in the readout direction is achieved by increasing the number of readout segments, or shots, without a change in echo spacing and only the number of echoes is increased; in this case, there is no increase in distortion at higher resolution and T2* blurring is substantially less than in the ss-EPI case.

However, the technical capability to perform DWI with small voxel sizes and

4A

SMS RESOLVE

ss-EPI

4B

SMS RESOLVE

ss-EPI

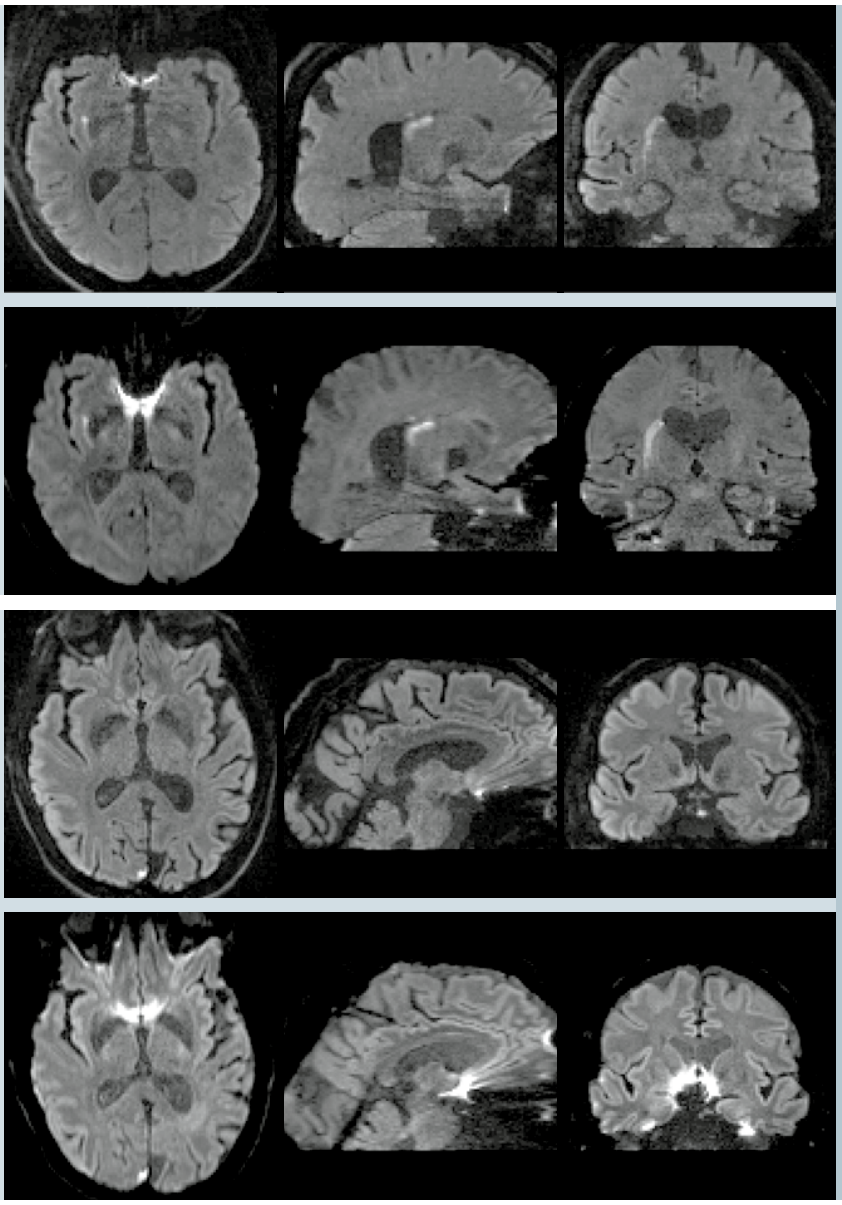

4 Comparison of 1.5 mm isotropic SMS RESOLVE (top row) and ss-EPI images (bottom row) acquired at 3T highlighting the reduction of signal pile up artifact caused by geometric distortions. Panel **(4A)** shows a right lenticulostriate artery infarct and panel **(4B)** shows a right occipital infarct. 78 slices were acquired in both scans.

5

SMS RESOLVE

ss-EPI

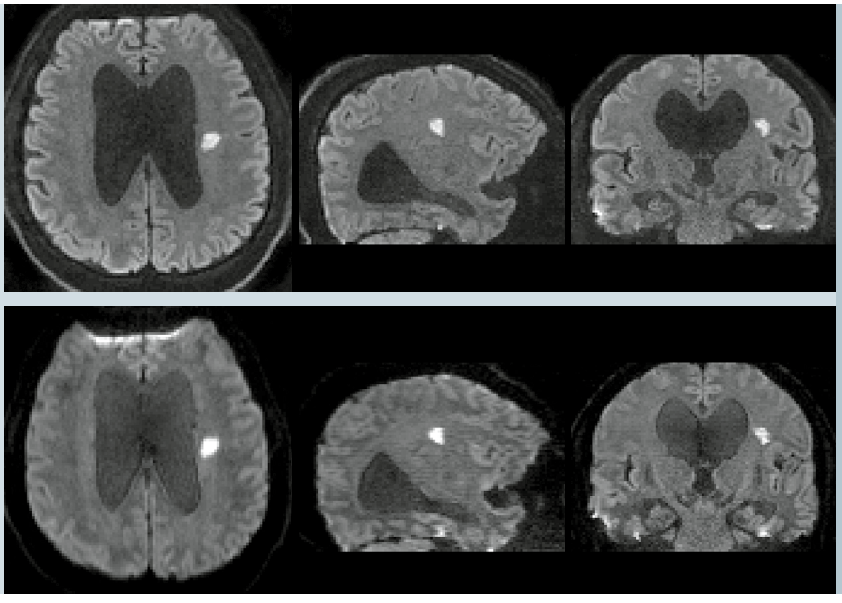

5 Comparison of 1.5 mm isotropic SMS RESOLVE (top row) and ss-EPI images (bottom row) acquired at 3T highlighting the reduction of geometric distortion in proximity to the frontal sinuses. The images show a left lacunar infarct. 78 slices were acquired in both scans.

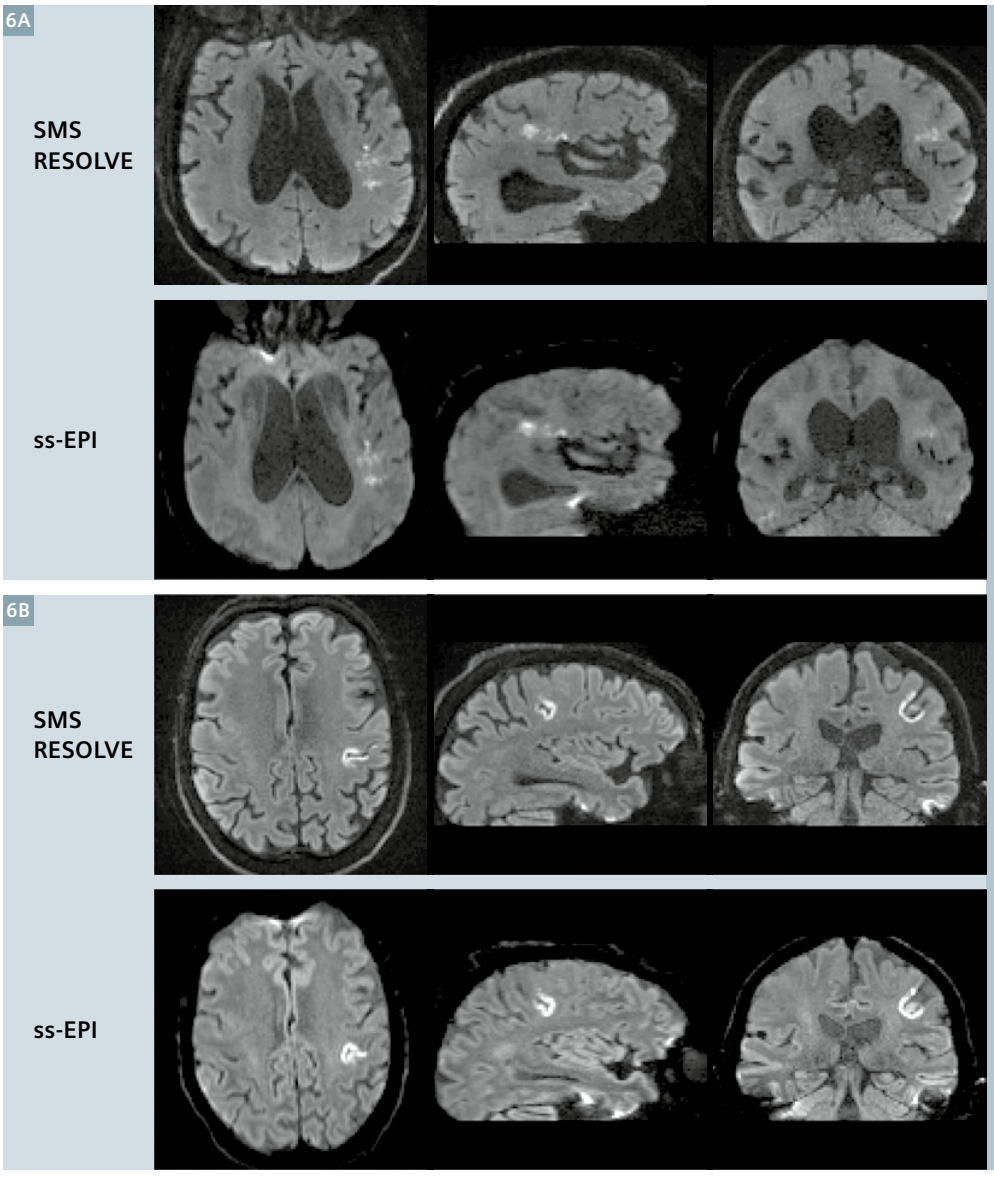

6 Comparison of 1.5 mm isotropic SMS RESOLVE (top row) and ss-EPI images (bottom row) acquired at 3T highlighting the improved depiction of subtle injuries with SMS RESOLVE. Confounding signal pile-up artifacts in the ss-EPI images are also reduced with SMS RESOLVE. Panel **(6A)** shows a left middle cerebral artery territory subcortical infarct and panel **(6B)** shows left middle cerebral artery territory cortical infarcts. 78 slices were acquired in both scans.

a low level of T2* blurring is compromised by the corresponding reduction in SNR, which is already inherently low in DWI due to signal attenuation at high b-value. For isotropic resolution with a small slice thickness, SNR efficiency is further reduced by the requirement to use long TR times to accommodate the increased number of slices. Strategies for increasing SNR and maximising acceleration therefore have an important role to play when using RESOLVE to perform high-resolution DTI.

One way to meet these goals is to perform imaging studies at higher B_0 field strength, where there is increased SNR and improved performance of parallel imaging because the coil sensitivities are more distinct [36]. There are however a number of additional challenges at 7T, including B_0 and RF inhomogeneity, SAR constraints and shorter T2 values than at lower field strengths. The combination of PINS and SMS RESOLVE has the potential to meet these challenges and provide a technique that can exploit the potential benefits of diffusion-weighted imaging at 7T. In particular, the shortened readout time reduces distortion, T2* blurring and the effects of signal loss due to T2 decay, and the low-SAR PINS RF pulses allow high slice-acceleration factors to be used with low TR, resulting in high SNR efficiency.

SMS RESOLVE at 7T

As shown previously in studies without SMS, the RESOLVE acquisition scheme is inherently less sensitive to the very high level of B_0 distortion and T2* blurring that affects ss-EPI at 7T [37]. Figure 7 demonstrates how these benefits can also be seen when the technique is combined with slice acceleration to reduce scan time; the figure compares 1.2 mm isotropic SMS RESOLVE images using $R_{slice} = 3$ and $R_{PE} = 2$ with standard ss-EPI images (also with $R_{PE} = 2$). The SMS RESOLVE scan with 99 slices was acquired with 6 segments (6/7 readout PF), 0.32 ms echo-spacing, 32 b = 1000 s/mm² diffusion directions, and with 4 interspersed low-b-value images in 35 min. A consequence of the

7

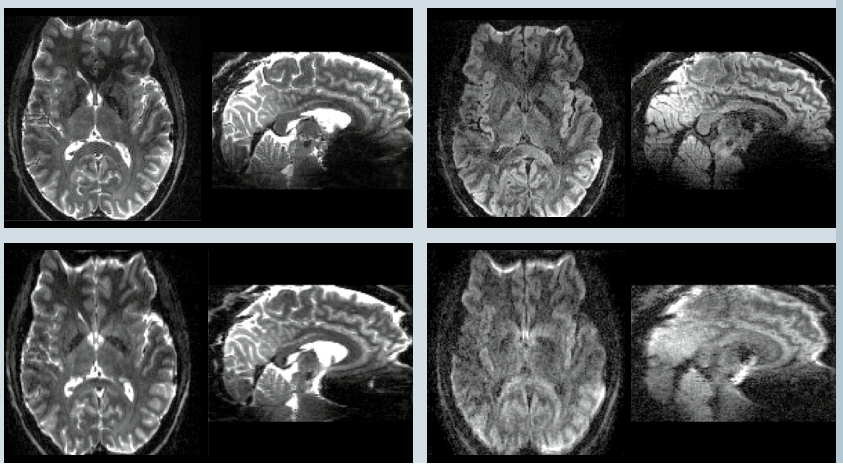

7 Comparison of 1.2 mm isotropic SMS RESOLVE (top row) and ss-EPI images (bottom row) acquired at 7T (99 slices) highlighting the reduction of geometric distortion and blurring with SMS RESOLVE.

8

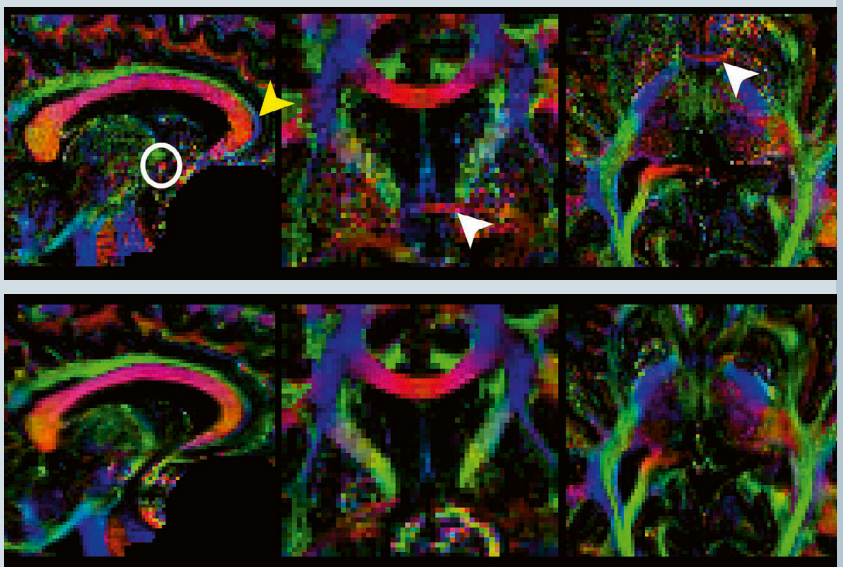

8 7T DTI results comparing blurring and distortion in 1.2 mm isotropic SMS RESOLVE and ss-EPI acquisitions with 99 slices. Color-coded maps of the principal diffusion direction weighted by the fractional anisotropy are shown. The SMS RESOLVE data show the anterior commissure (white circle and arrows), which is not present in the ss-EPI data. SMS RESOLVE also exhibits reduced blurring and distortion in the cingulum (yellow arrow). Color code: green, anterior–posterior; blue, superior–inferior; red, left–right.

artifact reduction is highlighted in the color-coded principal diffusion direction (PDD) maps weighted by the fractional anisotropy (FA) of Figure 8. The thin anterior commissure tract is missing in the ss-EPI data (in both the matched slice and the surrounding slices) because it is in a region of high distortion but it is clearly visualised in the SMS RESOLVE images. However, in this first proof of principle, the SMS RESOLVE data utilized standard (non-PINS) RF pulses, which resulted in SAR limitations that necessitated an increased TR, and, as such, the ideal 3-fold scan time reduction could not be achieved.

PINS SMS RESOLVE at 7T

PINS RF pulses directly address the SAR restriction that otherwise limits the SMS

9

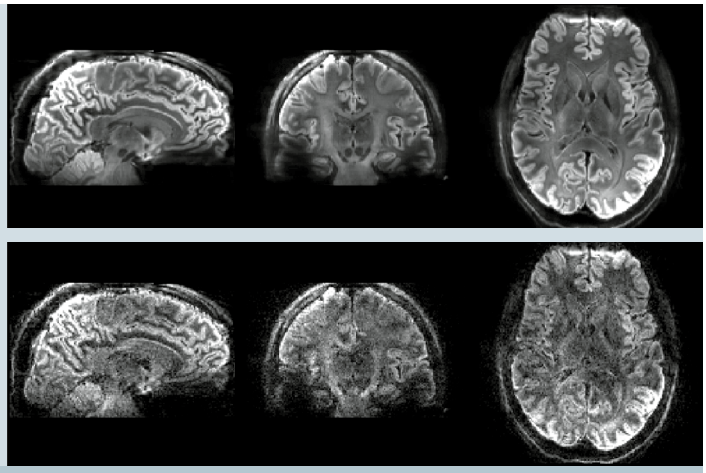

9 1.2 mm isotropic PINS SMS RESOLVE images (99 slices) acquired at 7T with b = 800 s/mm². The mean of 80 diffusion directions (top row) and a single diffusion direction are shown (bottom row).

scan-time reduction that can be realized at 7T. Figure 9 shows 1.2 mm isotropic images with 99 slices acquired using PINS SMS RESOLVE [27] with 80 diffusion-gradient directions and 12 averages with low b-value in a scan time of 38 minutes; the data were acquired without readout partial Fourier using $R_{slice} = 3$, $R_{PE} = 2$, five readout segments, an echo-spacing of 0.38 ms and b = 800 s/mm^2; the figure shows the mean of all the diffusion-weighted images and data from a single diffusion direction. The color-coded PDD FA map in Figure 10 highlights the fine tract resolution and good contrast of these data.

Figure 11 shows data from a PINS SMS RESOLVE scan with 1 mm isotro-

10

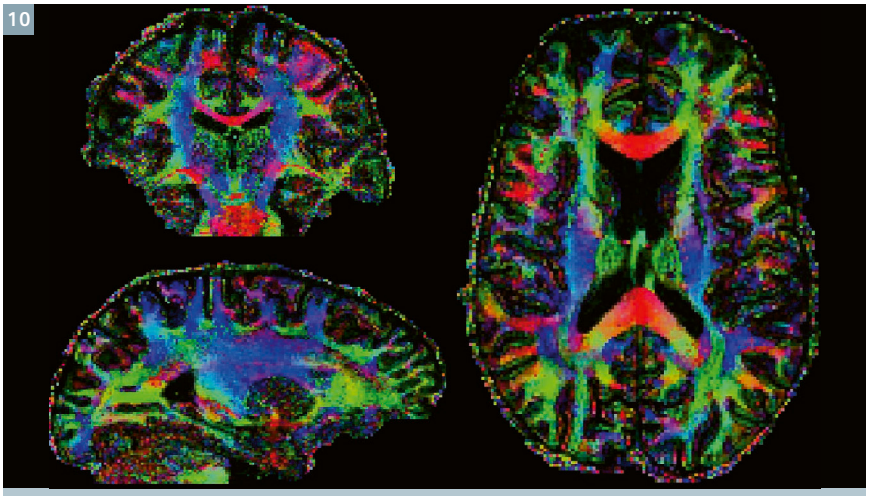

10 7T DTI results of a 1.2 mm isotropic PINS SMS RESOLVE acquisition (99 slices) demonstrating fine resolution and good contrast of the anisotropy. Color-coded maps of the principal diffusion direction weighted by the fractional anisotropy are shown. Color code: green, anterior–posterior; blue, superior–inferior; red, left–right.

11

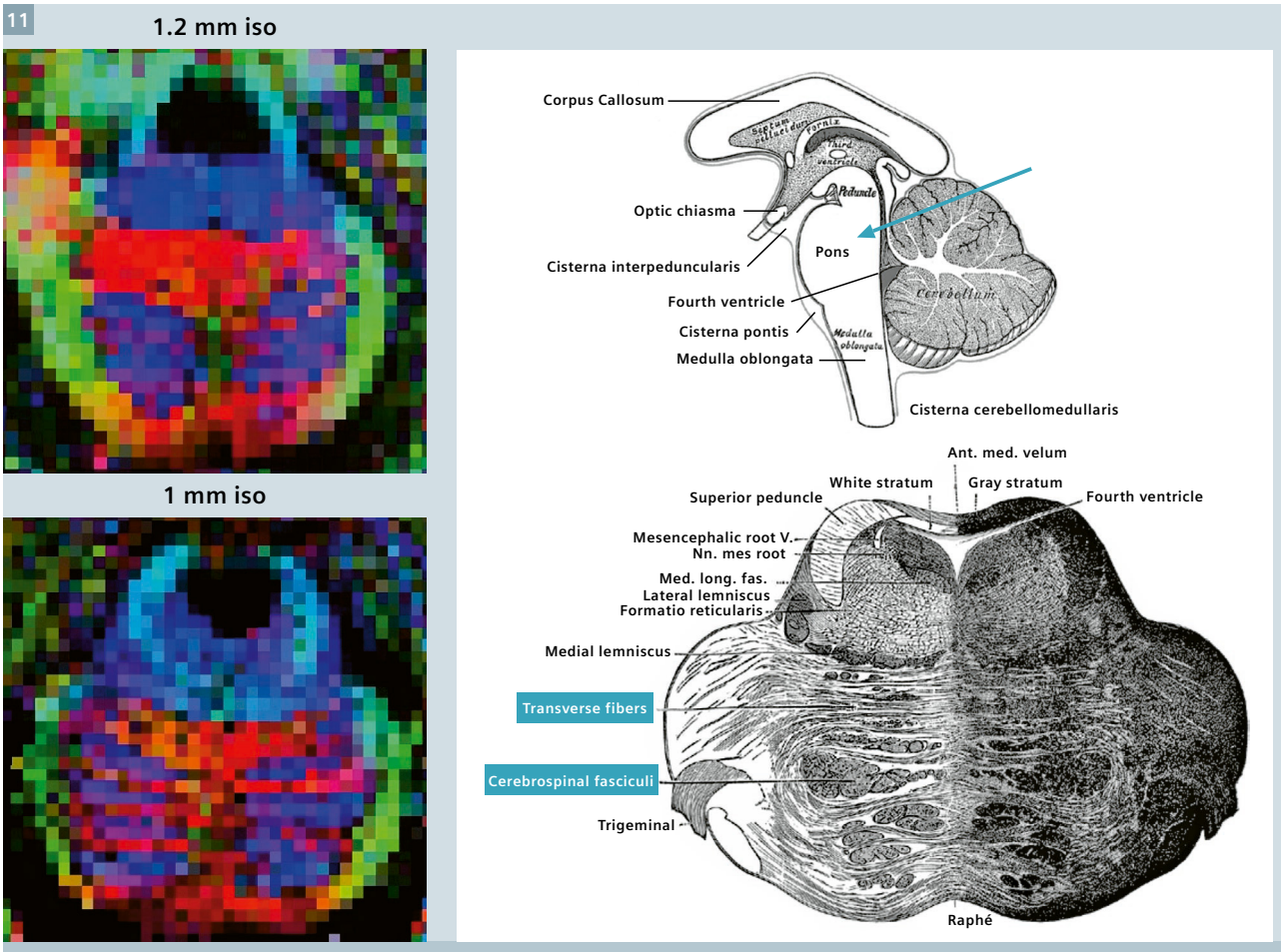

11 7T DTI results comparing 1.2 mm and 1 mm isotropic PINS SMS RESOLVE acquisitions. The thin transverse pontocerebellar fibers are more clearly resolved in the 1 mm isotropic images (in a different healthy volunteer). The transverse pontocerebellar fibers (running right-left, colored red) interdigitate with the cerebrospinal fasciculi (running superior-inferior, colored blue). The 1.2 mm and 1 mm acquisitions acquired 99 and 117 slices, respectively. Color-coded maps of the principal diffusion direction weighted by the fractional anisotropy are shown. Color code: green, anterior–posterior; blue, superior–inferior; red, left–right. *The anatomical drawings are adaped from Gray's Anatomy (1918).*

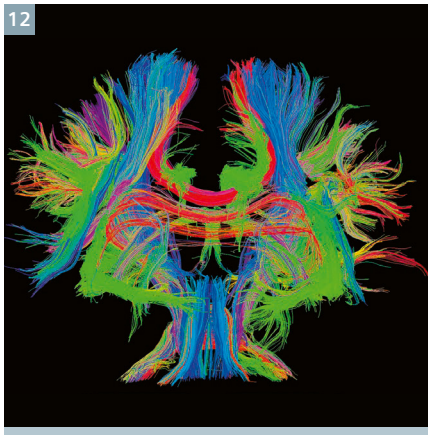

12 7T tractography generated from 1 mm isotropic PINS SMS RESOLVE data with 117 slices. Color code: green, anterior–posterior; blue, superior–inferior; red, left–right.

pic resolution and 117 slices in a scan time of 45 minutes; the images were acquired with $R_{slice} = 3$, $R_{PE} = 2$ using 3 readout segments (3/5 readout PF), an echo spacing of 0.40 ms, 60 scans at b = 580 s/mm², 60 scans at b = 1160 s/mm² and 13 scans with low b-value. This, in comparison with the 1.2 mm isotropic data suggests potential advantages of high-resolution DTI by showing improved depiction (in a different subject) of the transverse pontocerebellar fibers (running right-left) that interdigitate with the cerebrospinal fasciculi (running superior-inferior). An example of whole-brain tractography with the 1 mm isotropic data is shown in Figure 12. This image was generated using the Diffusion Toolkit and TrackVis [38].

In summary, PINS RF pulses make it possible to acquire high-resolution RESOLVE at 7T with a slice-acceleration factor of three; this enables acquisition protocols with a large number of diffusion directions and multiple b-value shells with acquisition times that are acceptable for neuroscientific applications. Data sets of this type provide valuable input for advanced tractography analyses that probe secondary fiber populations. The preliminary results acquired with the technique suggest that the SMS RESOLVE sequence could become a powerful tool for *in vivo* tractography of fine structure.

Other applications of SMS RESOLVE

In addition to the brain imaging applications reported in this paper, preliminary work reported elsewhere has shown that SMS RESOLVE can provide data for combined tractography studies of the brain and cervical spine [39]. Studies of this type are not possible with ss-EPI due to the high level of susceptibility-based distortion around the spinal cord. The SMS RESOLVE technique has also been applied to diffusion-weighted breast imaging of healthy volunteers, demonstrating acquisitions with reduced acquisition times with potential application in clinical studies of breast tumors [40], where the standard RESOLVE technique has been shown to provide a clinical benefit [8].

As an alternative to the SMS RESOLVE technique described in this paper, a simultaneous, multi-slab acquisition method has also been proposed, in which a 3D-encoded version of the RESOLVE sequence [41] is used to simultaneously encode data in multiple slabs [42].

Conclusion

The results shown in this paper demonstrate that SMS RESOLVE makes it possible to perform diffusion-weighted imaging of the whole brain with isotropic resolution and shortened scan times that are suitable for clinical stroke protocols. The improved image quality compared to ss-EPI provides a clearer depiction of infarcts with fewer confounding susceptibility artifacts and the reduction in geometrical distortion is expected to provide a more accurate quantification of lesion volume.

This paper has also shown how the SMS RESOLVE technique can be combined with PINS RF pulses to exploit slice-acceleration at 7T without the constraints of high SAR, making it possible to acquire high-quality data sets for advanced tractography studies which require a large number of diffusion-gradient directions. The technique also promises to enhance clinical diffusion-weighted imaging at 7T, for which preliminary studies with the standard RESOLVE technique are producing promising results [43].

SMS RESOLVE is an appealing alternative to standard ss-EPI DWI with potential benefits for clinical and scientific applications in the brain and other organs. The clinical benefit of the standard RESOLVE technique has been established in a large number of studies, but there is typically an acquisition-time penalty relative to lower-quality image acquisitions with ss-EPI. This limitation is much less prohibitive when RESOLVE is combined with SMS and readout PF to accelerate the scans and this combination increases the potential of the technique to substantially improve the quality of diffusion-weighted imaging in a wide variety of applications.

Acknowledgements

We thank the NIHR Oxford Biomedical Research Centre and the Medical Research Council for funding. PK acknowledges funding by the Wellcome Trust [WT100092MA]. We are also grateful for funding to the NIHR Clinical Research Network, the Dunhill Medical Trust [grant number: OSRP1/1006] and the Centre of Excellence for Personalized Healthcare funded by the Wellcome Trust and Engineering and Physical Sciences Research Council [grant number: WT088877/Z/09/Z]. We thank Thorsten Feiweier of Siemens Healthcare for the diffusion preparation module used in this work. We also thank Juliet Semple and Peter Manley for assistance with data acquisition and are grateful for the facilities provided by the Oxford Acute Vascular Imaging Centre (AVIC).

References

1 Mansfield P, Pykett IL. Biological and medical imaging by NMR Journal of Magnetic Resonance (1969) 1978;29:355–373.
2 Turner R, Le Bihan D, Maier J, Vavrek R, Hedges LK, Pekar J. Echo-planar imaging of intravoxel incoherent motion. Radiology 1990;177:407–414.
3 Warach S, Gaa J, Siewert B, Wielopolski P, Edelman RR. Acute human stroke studied by whole brain echo planar diffusion-weighted magnetic resonance imaging. Ann Neurol 1995;37:231–241.
4 Basser PJ, Mattiello J, LeBihan D.

Estimation of the effective self-diffusion tensor from the NMR spin echo. J Magn Reson B 1994;103:247–254.
5 Porter DA, Heidemann RM. High resolution diffusion-weighted imaging using readout-segmented echo-planar imaging, parallel imaging and a two-dimensional navigator-based reacquisition. Magn Reson Med 2009;62:468–475.
6 Hayes LL, Jones RA, Palasis S, Aguilera D, Porter DA. Drop metastases to the pediatric spine revealed with diffusion-weighted MR imaging. Pediatr Radiol 2012;42:1009–1013.
7 Rumpel H, Chong Y, Porter DA, Chan LL. Benign versus metastatic vertebral compression fractures: combined diffusion-weighted MRI and MR spectroscopy aids differentiation. Eur Radiol 2013;23:541–550.
8 Bogner W, Pinker-Domenig K, Bickel H, Chmelik M, Weber M, Helbich TH, Trattnig S, Gruber S. Readout-segmented Echo-planar Imaging Improves the Diagnostic Performance of Diffusion-weighted MR Breast Examinations at 3.0 T Radiology 2012;263:64–76.
9 Wisner DJ, Rogers N, Deshpande VS, Newitt DN, Laub GA, Porter DA, Kornak J, Joe BN, Hylton NM. High-resolution diffusion-weighted imaging for the separation of benign from malignant BI-RADS 4/5 lesions found on breast MRI at 3T Journal of Magnetic Resonance Imaging 2014;40:674–681.
10 Morelli J, Porter D, Ai F, Gerdes C, Saettele M, Feiweier T, Padua A, Dix J, Marra M, Rangaswamy R, Runge V. Clinical evaluation of single-shot and readout-segmented diffusion-weighted imaging in stroke patients at 3 T. Acta Radiol 2013;54:299–306.
11 Thian YL, Xie W, Porter DA, Weileng Ang B. Readout-segmented echo-planar imaging for diffusion-weighted imaging in the pelvis at 3T-A feasibility study. Acad Radiol 2014;21:531–537.
12 Foltz WD, Porter DA, Simeonov A, Aleong A, Jaffray D, Chung P, Han K, Ménard C. Readout-segmented echo-planar diffusion-weighted imaging improves geometric performance for image-guided radiation therapy of pelvic tumors Radiotherapy and Oncology.
13 Tokoro H, Fujinaga Y, Ohya A, Ueda K, Shiobara A, Kitou Y, Ueda H, Kadoya M. Usefulness of free-breathing readout-segmented echo-planar imaging (RESOLVE) for detection of malignant liver tumors: comparison with single-shot echo-planar imaging (SS-EPI). Eur J Radiol 2014;83:1728–1733.
14 Friedli I, Crowe LA, Viallon M, Porter DA, Martin P, de Seigneux S, Vallee J. Improvement of renal diffusion-weighted magnetic resonance imaging with readout-segmented echo-planar imaging at 3T. Magn Reson Imaging 2015;33:701–708.
15 Ordidge RJ, Helpern JA, Qing ZX, Knight RA, Nagesh V. Correction of motional artifacts in diffusion-weighted MR images using navigator echoes. Magn Reson Imaging 1994;12:455–460.
16 Anderson AW, Gore JC. Analysis and correction of motion artifacts in diffusion weighted imaging. Magn Reson Med 1994;32:379–387.
17 Robson MD, Anderson AW, Gore JC. Diffusion-weighted multiple shot echo planar imaging of humans without navigation. Magn Reson Med 1997;38:82–88.
18 Miller KL, Pauly JM. Nonlinear phase correction for navigated diffusion imaging. Magn Reson Med 2003;50:343–353.
19 Nguyen Q, Clemence M, Ordidge RJ. The use of intelligent re-acquisition to reduce scan time in MRI degraded by motion. In: Proceedings of the 6th Annual Meeting of ISMRM, 1998 (abstract 134).
20 Porter DA. 2D-navigator-based re-acquisition for motion artefact suppression in multi-shot, diffusion-weighted imaging. In: Proceedings of the 14th Annual Meeting of ISMRM, 2006 (abstract 1047).
21 Griswold MA, Jakob PM, Heidemann RM, Nittka M, Jellus V, Wang J, Kiefer B, Haase A. Generalized autocalibrating partially parallel acquisitions (GRAPPA). Magn Reson Med 2002;47:1202–1210.
22 Porter DA, Heidemann RM. Multi-shot, diffusion-weighted imaging at 3T using readout-segmented EPI and GRAPPA In: Proceedings of the 14th Annual Meeting of ISMRM, Seattle, Washington, USA, 2006 (abstract 1046).
23 Frost R, Porter DA, Miller KL, Jezzard P. Implementation and assessment of diffusion-weighted partial Fourier readout-segmented echo-planar imaging. Magn Reson Med 2012;68:441–451.
24 Frost R, Porter DA, Douaud G, Jezzard P, Miller KL. Reduction of diffusion-weighted readout-segmented EPI scan time using a blipped-CAIPI modification. In: Proceedings of the 20th Annual Meeting of ISMRM, 2012 (abstract 116).
25 Frost R, Jezzard P, Douaud G, Clare S, Porter DA, Miller KL. Scan time reduction for readout-segmented EPI using simultaneous multislice acceleration: Diffusion-weighted imaging at 3 and 7 tesla. Magn Reson Med 2015;74:136–149.
26 Norris DG, Koopmans PJ, Boyacioglu R, Barth M. Power Independent of Number of Slices (PINS) radiofrequency pulses for low-power simultaneous multislice excitation. Magn Reson Med 2011;66:1234–1240.
27 Koopmans PJ, Frost R, Porter DA, Wu W, Jezzard P, Miller KL, Barth M. Diffusion-weighted readout-segmented EPI using PINS simultaneous multislice imaging. In: Proceedings of the 23rd Annual Meeting of ISMRM, 2015 (abstract 959).
28 Larkman DJ, Hajnal JV, Herlihy AH, Coutts GA, Young IR, Ehnholm G. Use of multicoil arrays for separation of signal from multiple slices simultaneously excited. J Magn Reson Imaging 2001;13:313–317.
29 Pruessmann KP, Weiger M, Scheidegger MB, Boesiger P. SENSE: sensitivity encoding for fast MRI. Magn Reson Med 1999;42:952–962.
30 Breuer FA, Blaimer M, Heidemann RM, Mueller MF, Griswold MA, Jakob PM. Controlled aliasing in parallel imaging results in higher acceleration (CAIPIRINHA) for multi-slice imaging. Magn Reson Med 2005;53:684–691.
31 Nunes RG, Hajnal JV, Golay X, Larkman DJ. Simultaneous slice excitation and reconstruction for single shot EPI. In: Proceedings of the 14th Annual Meeting of ISMRM, 2006 (abstract 293).
32 Setsompop K, Cohen-Adad JA, McNab JA, Gagoski B, Wedeen VJ, Wald LL. Improving SNR per unit time in diffusion Imaging using a blipped-CAIPIRINHA simultaneous multi-slice EPI acquisition. In: Proceedings of the 18th Annual Meeting of ISMRM, 2010 (abstract 187).
33 Setsompop K, Gagoski BA, Polimeni JR, Witzel T, Wedeen VJ, Wald LL. Blipped-controlled aliasing in parallel imaging for simultaneous multislice echo planar imaging with reduced g-factor penalty. Magn Reson Med 2012;67:1210–1224.
34 Robson MD, Porter DA. Reconstruction as a source of artifact in non-gated single-shot diffusion-weighted EPI. Magn Reson Imaging 2005;23:899–905.
35 Wintermark M, Albers GW, Broderick JP, Demchuk AM, Fiebach JB, Fiehler J, Grotta JC, Houser G, Jovin TG, Lees KR, Lev MH, Liebeskind DS, Luby M, Muir KW, Parsons MW, von Kummer R, Wardlaw JM, Wu O, Yoo AJ, Alexandrov AV, Alger JR, Aviv RI, Bammer R, Baron J, Calamante F, Campbell BCV, Carpenter TC, Christensen S, Copen WA, Derdeyn CP, Haley ECJ, Khatri P, Kudo K, Lansberg MG, Latour LL, Lee T, Leigh R, Lin W, Lyden P, Mair G, Menon BK, Michel P, Mikulik R, Nogueira RG, Ostergaard L, Pedraza S, Riedel CH, Rowley HA, Sanelli PC, Sasaki M, Saver JL, Schaefer PW, Schellinger PD, Tsivgoulis G, Wechsler LR, White PM, Zaharchuk G, Zaidat OO, Davis SM, Donnan GA, Furlan AJ, Hacke W, Kang D, Kidwell C, Thijs VN, Thomalla G, Warach SJ. Acute Stroke Imaging Research Roadmap II. Stroke 2013;44:2628–2639.
36 Wiesinger F, Van de Moortele P, Adriany G, De Zanche N, Ugurbil K, Pruessmann KP. Potential and feasibility of parallel MRI at high field NMR in Biomedicine 2006;19:368–378.
37 Heidemann RM, Porter DA, Anwander A, Feiweier T, Heberlein K, Knosche TR, Turner R. Diffusion imaging in humans at 7T using readout-segmented EPI and

GRAPPA. Magn Reson Med 2010;64:9–14.
38 Wang R, Benner T, Sorensen AG, Wedeen VJ. Diffusion Toolkit: a software package for diffusion imaging data processing and tractography. In: Proceedings of the 15th Annual Meeting of ISMRM, 2007 (abstract 3720).
39 Liu W, Bhat H, Cohen-Adad J, Setsompop K, Wang D, Beck T, Cauley SF, Zhou K, Porter DA. Large-FOV tractography of the brain and spinal cord with reduced scan time: a study using diffusion-weighted readout-segmented EPI and simultaneous multi-slice acceleration In: Proceedings of the 23rd Annual Meeting of ISMRM, 2015 (abstract 4434).
40 Liu W, Bhat H, Weiland E, Wang D, Beck T, Cauley SF, Porter DA. Readout-segmented EPI with simultaneous, multi-slice acceleration for the rapid acquisition of high-resolution, diffusion-weighted images of the breast In: Proceedings of the 23rd Annual Meeting of ISMRM, 2015 (abstract 1605).
41 Frost R, Miller KL, Tijssen RHN, Porter DA, Jezzard P. 3D Multi-slab diffusion-weighted readout-segmented EPI with real-time cardiac-reordered k-space acquisition. Magn Reson Med 2014;72:1565–1579.
42 Frost R, Jezzard P, Porter DA, Tijssen RHN, Miller KL. Simultaneous multi-slab acquisition in 3D multi-slab diffusion-weighted readout-segmented echo-planar imaging. In: Proceedings of the 21st Annual Meeting of ISMRM, 2013 (abstract 3176).
43 Bogner W, Pinker K, Zaric O, Baltzer P, Minarikova L, Porter D, Bago-Horvath Z, Dubsky P, Helbich TH, Trattnig S, Gruber S. Bilateral diffusion-weighted MR imaging of breast tumors with submillimeter resolution using readout-segmented echo-planar imaging at 7 T. Radiology 2015;274:74–84.

Contact

Dr. Robert Frost
FMRIB Centre
John Radcliffe Hospital
Oxford OX3 9DU
UK
robert.frost@ndcn.ox.ac.uk

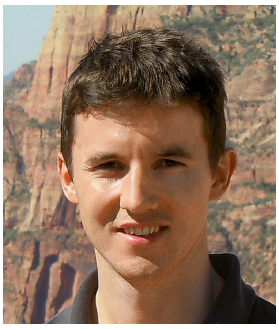

Learn more!

Don’t miss the talks of experienced and renowned experts on all aspects of MR imaging at:

www.siemens.com/magnetom-world



Multislice accelerated RESOLVE for time-efficient, high-resolution diffusion imging

Robert Frost, PhD
FMRIB Centre, University of Oxford

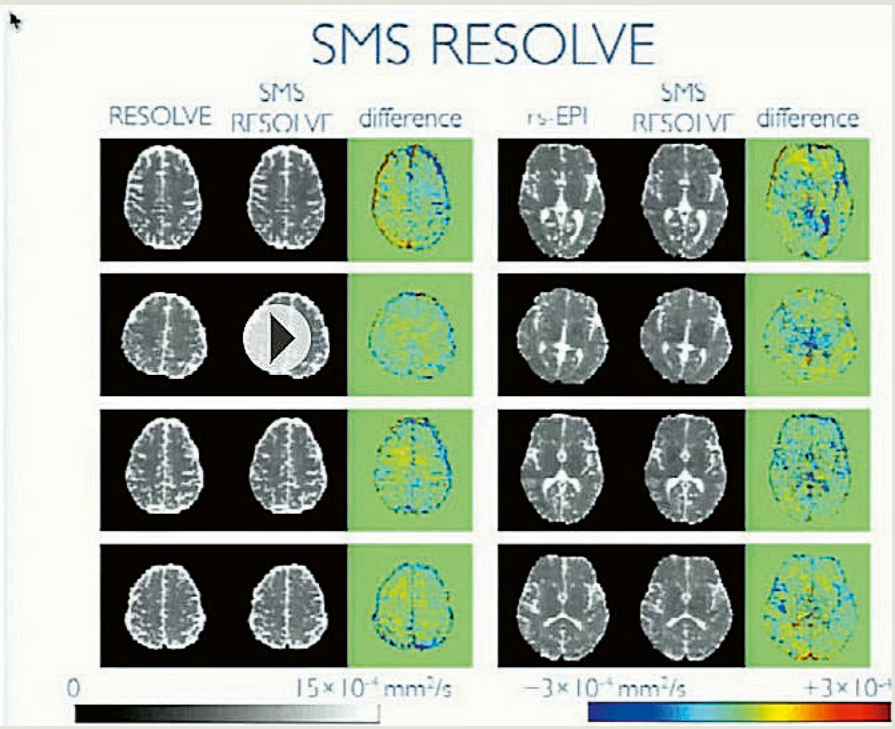

Epilepsy Imaging with Simultaneous Multi-Slice Turbo Spin Echo

Michael Kean, FSMRT[1,2]; Dr Lee Coleman, BSc MB ChB FRANZCR[1,2]; Sonal Josan, Ph.D.[3]; Benjamin Schmitt, Ph.D.[3]

[1] Royal Children's Hospital, Melbourne, Australia
[2] Murdoch Children's Research Institute Parkville, Melbourne, Australia
[3] Siemens Healthcare, Melbourne, Australia

Background

In today's modern pediatric epilepsy protocols, high-resolution, T2-weighted (T2w) imaging plays a very important role in evaluating patients who present with epilepsy. At our institution, the use of 3T combined with high-density receive arrays has improved our diagnostic sensitivity and specificity for the detection of small cortically-based lesions.

Historically, 3D T1-weighted volume acquisitions such as MPRAGE have been integral in identifying small areas of cortical dysplasia. In previous iterations of epilepsy protocols, the T2-weighted imaging has been the Achilles heel of the examination due to inefficient use of the available TR and long scan times but with the increased signal-to-noise (SNR) ratios attributed to modern scanners, T2-weighted acquisitions are improving the diagnostic accuracy of scans.

The ability to reduce the sequence acquisition time has been the ultimate goal for pulse sequence developers since Hennig et al. [1] published their work on RARE imaging. As with most advances in pulse sequence development, clinicians are usually quite reserved in transitioning the current gold standard protocols due to the potential differences in signal intensity and tissue contrasts demonstrated by these acquisitions [2, 3].

The next advancement to significantly reduce T2w acquisition times were techniques proposed by Pruessmann [4, 5] and Griswold [6] using reconstruction algorithms that used the unique properties coil array geometry to undersample data resulting in reduced scan times at the cost of a reduction in SNR.

Several authors have proposed modifications to these techniques to reduce the amount of noise encoded into the images and further reduce scan times, one of the most significant was Breuer [7] with the development of phase and slice-based acceleration – CAIPIRINHA.

Recently several authors [9-12] have proposed the implementation of

Case 1

Figure 1 demonstrates a coronal T2w slice orientated perpendicular to the hippocampus. This slice was chosen to demonstrate the capabilities of the sequence because of the complex anatomy and potential for artifacts originating from physiological sources. It demonstrates the image quality achievable using SMS TSE with a significant reduction in scan time. Importantly, when the images were de-identified, the only reliable factor used by the radiologist in identifying the gold standard TSE was the higher signal intensity of CSF. The reduction of CSF signal was attributed to saturation effects associated with the application of the SMS RF pulse. The overall impression was that the accelerated acquisition appeared slightly sharper and this was probably due to slightly altered noise level associated with parallel imaging reconstruction.



TSE, 4:05 min



TSE_Accel 2, 2:30 min

CAIPIRINHA based reconstruction methods into conventional turbo spin echo to accelerate T2w acquisitions without the SNR penalties associated with data undersampling reconstruction methods. The implementation of simultaneous multi-slice (SMS) sequences into routine imaging will enable a more efficient TR-to-slice ratio, the potential to use higher echo train lengths while staying within current SAR restrictions, and reduced scan times. More importantly, these techniques can help overcome some of the limitations of conventional parallel imaging techniques such as *g*-factor penalties and SNR loss with undersampling.

The cases presented here are our initial experience with SMS TSE[1] in clinical epilepsy cases. All acquisitions were anatomically matched to an equivalent standard T2w TSE acquired on a MAGNETOM Trio or MAGNETOM Verio 3T (with software verison *syngo* MR B17) using the product 32-channel head coil. A whole-brain high-resolution T2 coronal with non-interpolated resolution of 0.5 x 0.6 x 2.5 mm^3 was achieved in all acquisitions. All images were evaluated for signal-to-noise, contrast-to-noise, image sharpness, artifacts, reconstruction faults, diagnostic confidence and lesion detectability.

Conclusion

Our initial experience with SMS TSE with a slice acceleration factor of 2 in conjunction with in-plane parallel imaging acceleration factor of 2 is very encouraging, producing scans of a similarly high diagnostic quality when compared to our gold standard TSE (with in-plane parallel imaging acceleration factor of 2) in much shorter scan times. Modifications to the protocol have enabled our team to incorporate slice accelerated TSE into protocols developed for our pediatric[2] epilepsy program.

As with many variations to pulse sequences, our team had concerns

[1] The product is still under development and not commercially available yet. Its future availability cannot be ensured.

Case 2

10-year-old patient presented with seizures. Preliminary imaging demonstrated a dysembryoplastic neuroepithelial tumour (DNET) in the right anterior temporal lobe.

The images demonstrate a complex lesion involving the anterior component of the right temporal lobe.

Both sequences equally demonstrate the complex nature of the lesion including small cysts, calcification including blurring and loss of grey and white matter.

There is slight anatomical disparity with the comparative images as there was patient movement between the acquisitions.

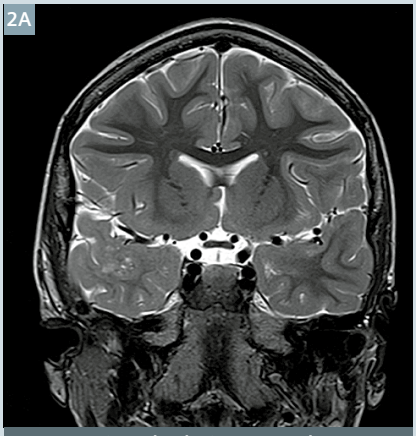

Standard T2w coronal

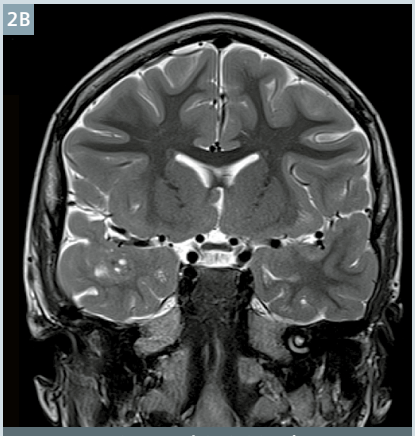

TSE Accel 2, 2:39 min

Case 3

5-year-old patient presented to our Epilepsy unit with aphasia and seizures originating from left anterior temporal lobe. A comprehensive epilepsy protocol was undertaken including comparative TSE and SMS TSE high-resolution T2-weighted coronal images aligned perpendicular to the hippocampus.

The images demonstrate a complex lesion adjacent to the left MCA involving the left anterior temporal lobe and amygdala. Based on the imaging characteristics, the lesion probably represents a dysembryoblastic neuroepithelial tumor (DNET).

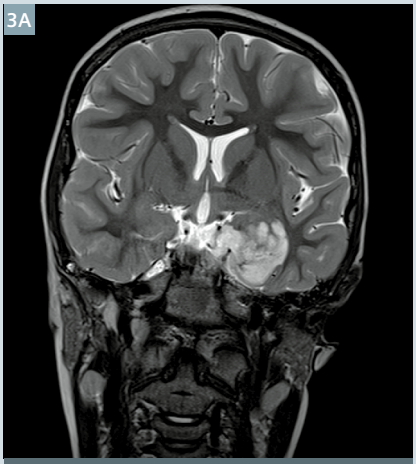

Standard T2w coronal

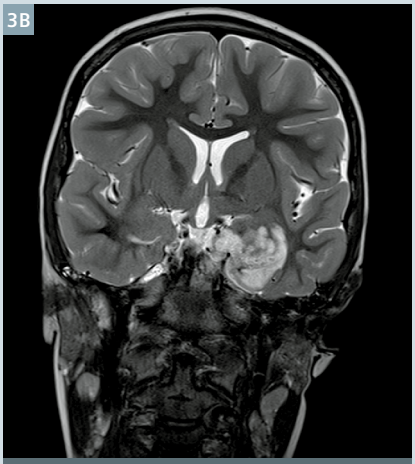

TSE Accel 2, 2:39 min

Case 4

11-year-old with periventricular nodular heterotopia (PVNH) for further evaluation of the PVNH and to demonstrate any right occipital focal cortical dysplasia.

The images demonstrate a complex malformation of cortical development with clear delineation of multiple areas of PVNH and occipital polymicrogyria.

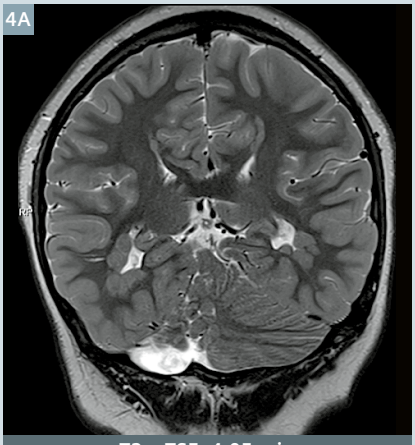

T2w TSE, 4:05 min

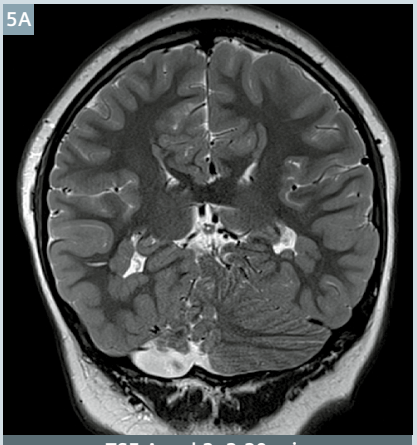

TSE Accel 2, 2:20 min

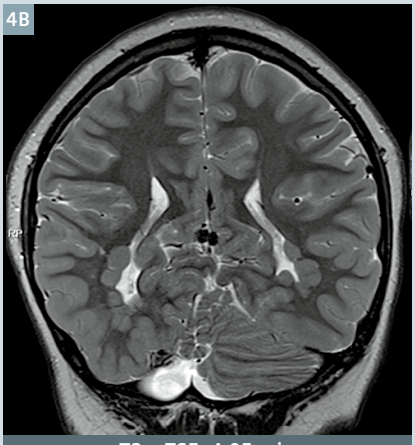

T2w TSE, 4:05 min

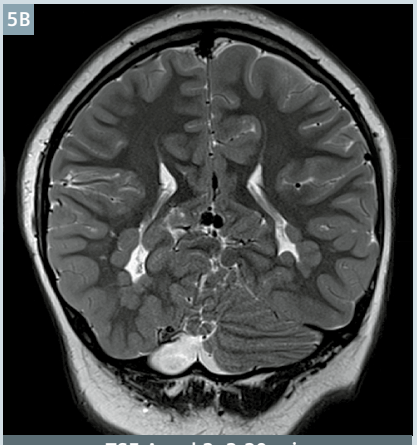

TSE Accel 2, 2:20 min

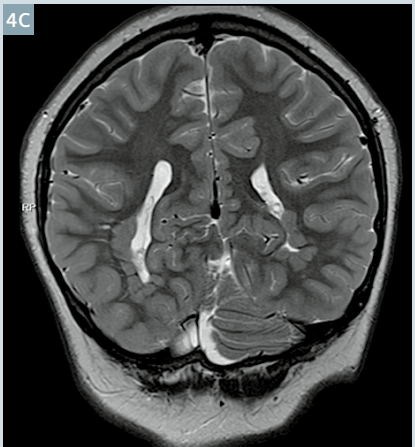

T2w TSE, 4:05 min

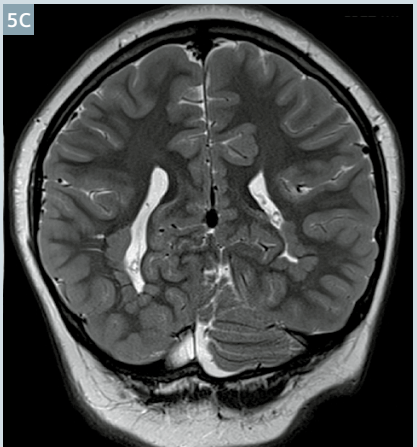

TSE Accel 2, 2:20 min

over a number of factors that would potentially impact on the diagnostic quality of the scans:

1. Sequence RF pulse techniques to reduce the SAR of the acquisition would influence image sharpness. The concern related to the implementation of low SAR VERSE pulses would increase echo-spacing has been unfounded and the general impression is that the accelerated T2 acquisitions appear sharper.
2. The reduction of CSF signal, potential loss of grey matter / white matter ratio and general SNR were highlighted as potential areas that would limit clinical integration. A number of scans on complex cerebral infections were undertaken to evaluate the diagnostic accuracy of the sequence and this comparison demonstrated equal diagnostic quality between the two sequences, with no significant difference in contrast to noise ratios in grey matter and white matter or CSF pulsation artifacts. The initial comments were that these concerns were similar to the transition from spin echo to TSE and then TSE with hyper-echo.
3. The acquisition and reconstruction strategy could invoke inter-slice leakage that could influence image quality. This has not been demonstrated to affect image quality as we expect a maximum leakage factor of less than 5%.
4. SMS TSE would have limited clinical utility due to SAR limitations. As with all MR sequences, there are numerous options to facilitate SAR management and we have obtained scans using low-SAR and normal RF pulses. The goal is to operate the system in normal operating mode and as such we tend to use low SAR RF pulses in the majority of cases.

[2] MR scanning has not been established as safe for imaging fetuses and infants under two years of age. The responsible physician must evaluate the benefit of the MRI examination in comparison to other imaging procedures.

The team has also started using the sequence in brain tumor imaging with very encouraging results. We have developed acquisition strategies to obtain high-resolution thin slice whole-brain coverage using acceleration factors of 3 in under 24 seconds for a limited clinical indication.

Acknowledgements

The authors wish to acknowledge the expertise of the Children's MRI Centre Staff, the assistance of Dr Simone Mandelstam for reviewing images, Dr Dingxin Wang and Siemens Healthcare for access to VB17_sliceaccel_WIP1003.

References

1 Hennig, J., Nauerth, A. & Friedburg, H., 1986. RARE imaging: a fast imaging method for clinical MR. Magnetic Resonance in Medicine : 3(6), pp.823–833.
2 Prenger, E.C. et al., 1994. Comparison of T2 weighted spin echo and fast spin echo techniques in the evaluation of myelination. : JMRI, 4(2), pp.179–184.
3 Patola, W.B. et al., 2001. A comparison of conventional spin-echo and fast spin-echo in the detection of multiple sclerosis.: JMRI, 13(5), pp.657–667.
4 Pruessmann, K.P. et al., 1999. SENSE: sensitivity encoding for fast MRI. Magnetic Resonance in Medicine : 42(5), pp.952–962.
5 Pruessmann, K.P. et al., 2001. Advances in sensitivity encoding with arbitrary k-space trajectories. Magn Reson in Med : 46(4), pp.638–651.
6 Griswold MA, Jakob PM, Heidemann RM, et al. Generalized autocali-brating partially parallel acquisitions (GRAPPA). Magn Reson Med. 2002;47:1202–1210
7 Breuer, F.A. et al., 2005. Controlled aliasing in parallel imaging results in higher acceleration (CAIPIRINHA) for multi-slice imaging. Magnetic Resonance in Medicine : 53(3), pp.684–691.
8 Eichner, C. et al., 2013. Slice accelerated gradient-echo spin-echo dynamic susceptibility contrast imaging with blipped CAIPI for increased slice coverage. Magnetic Resonance in Medicine 72(3), pp.770–778.
10 Gagoski, B.A. et al., 2015. RARE/turbo spin echo imaging with simultaneous multislice Wave-CAIPI. Magnetic resonance in medicine : 73(3), pp.929–938.
11 Bilgic, B. et al., 2014. Wave-CAIPI for highly accelerated 3D imaging. Magnetic Resonance in Medicine : 73(6), pp.2152–2162.
12 Wang, D 2014 Multiband Slice Accelerated TSE: Application in Brain Imaging. Proc Int Soc Mag Reson Med 22 , 4317

Contact

Michael Kean, FSMRT
Chief MRI Technologist
The Royal Children's Hospital
Flemington Road
Parkville Victoria 3052
Australia
michael.kean@rch.org.au



Learn more!

Don't miss the talks of experienced and renowned experts on all aspects of pediatric MR imaging at:

www.siemens.com/magnetom-world



Body MRI and Whole-Body Staging in Pediatric Patients

Günther Schneider

Saarland University Hospital
(Homburg, Germany)



Urogenitary Malformations and Their Imaging Features

J. Damian Grattan-Smith

Children's Healthcare of Atlanta
(Atlanta, GA, USA)



Running Pediatric MRI as an Effective Clinical and Cost Centre

Thomas Vogl

Frankfurt University Hospital
(Frankfurt/Main, Germany)

Cardiac Diffusion Tensor MRI Using Simultaneous Multi-Slice Acquisition with a Blipped-CAIPIRINHA Readout

Choukri Mekkaoui[1]; Timothy G. Reese[1]; Marcel P. Jackowski[2]; Himanshu Bhat[3]; David E. Sosnovik[1,4]

[1] Athinoula A. Martinos Center for Biomedical Imaging, Department of Radiology, Massachusetts General Hospital, Harvard Medical School, Boston, MA, USA
[2] Department of Computer Science, Institute of Mathematics and Statistics, University of São Paulo, São Paulo, Brazil
[3] Siemens Healthcare, Charlestown, MA, USA
[4] Cardiovascular Research Center, Cardiology Division, Massachusetts General Hospital, Harvard Medical School, Boston, MA, USA

Background

Heart muscle is highly anisotropic with an intricate microstructure, well suited to characterization with diffusion tensor imaging (DTI) [1]. The most widely used measure of fiber organization in the myocardium is the helix angle (HA), simply defined as the inclination of the myofiber out of the local short-axis plane. Myofibers in the subendocardium have a positive HA, while those in the subepicardium have a negative HA [1, 2]. These myofibers are further arranged into laminar sheets, which slide against each other allowing the myocardium to thicken during systole [3, 4]. Alterations of this microstructure due to heart disease affect its mechanical efficiency and also could contribute to arrhythmias [5, 6]. These microstructural changes can precede symptoms and thus a non-invasive evaluation could be of significant clinical value.

The motion of the heart is five orders of magnitude greater than the self-diffusion of water. Therefore, approaches that are sensitive to the microscopic diffusion of water, but not to cardiac motion and strain, are needed for successful *in vivo* imaging [7-9]. One approach to enable *in vivo* DTI uses a diffusion-encoded stimulated echo (STE) sequence (Fig. 1), which can be implemented on most clinical scanners [10, 11]. The diffusion-encoded STE sequence is played out over two successive heartbeats. The first and second 90° excitation pulses are applied in the first heartbeat, and the third excitation pulse in the second heartbeat. The diffusion-encoding gradients are monopolar and placed immediately after the first and third excitation pulses. The main appeal of the STE approach is its conceptual immunity to cardiac motion. Ideally, each monopolar diffusion gradient occurs at exactly the same time in two sequential R-R intervals. Hence, not only is the phase due to the diffusion-encoding gradient unwound, but the influence of cardiac motion on the phase of the magnetization also is unwound.

The use of a STE sequence, however, introduces a high degree of inefficiency into the acquisition due to the dual-gated acquisition. Additionally, the STE is half the amplitude of a spin-echo. Consequently most investigators have used ~8 averages per slice in order to achieve sufficient signal-to-noise (SNR) during diffusion-encoded STE acquisitions, taking 5-7 minutes per slice [12]. The inefficiency of the STE approach frequently requires the anatomical coverage of the acquisition to be compromised. For instance, only 3 short-axis slices can be imaged in ~15 minutes, which covers only 25% of the myocardium [12]. New approaches to improve anatomical coverage and reduce scan time are thus sorely needed. The development of simultaneous multi-slice (SMS) acquisition using a blipped Controlled Aliasing in Parallel Imaging (blipped-CAIPIRINHA) readout holds great promise [13, 14], and could play a key role in facilitating the more widespread use of cardiac DTI.

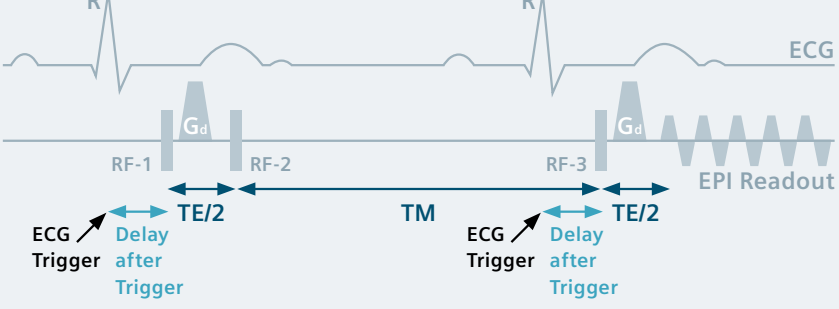

1 Dual gated stimulated echo (STE) sequence. Three 90° excitation pulses (RF) are applied over two successive heartbeats. The excitation (RF-1), refocusing (RF-3), and diffusion dephase and rephrase occur at the same time in the R-R intervals, thereby exploiting periodicity of heart motion to rewind motion related dephasing. Additionally, the long diffusion time (including TM), allows a sufficient b-value to be produced on clinical scanners without the need for an excessively long TE.

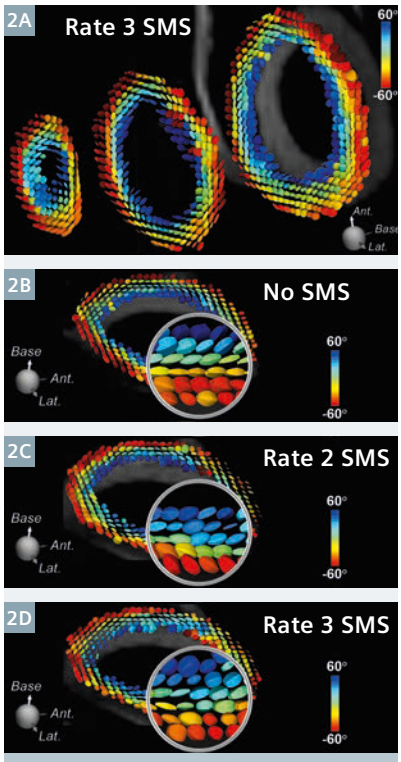

2 **(2A)** Simultaneous acquisition of 3 slices with rate 3 SMS. The gap between the slices is 500% of slice thickness. The tensor field is represented by supertoroids color-coded by HA. Supertoroid fields resulting from no SMS **(2B)**, rate 2 **(2C)**, and rate 3 **(2D)** SMS acquisitions of the same mid-ventricular slice are consistent with the transmural change in HA from positive in the subendocardium to negative in the subepicardium.

Implementation

The technical details of SMS excitation using blipped-CAIPIRINHA are described in detail in the SMS Supplement of MAGNETOM Flash (63) 3/2015. The technique has been used extensively in the brain [13, 14], and preliminary experience with it in the heart appears promising [15]. In the current article, we describe our experience with this technique for cardiac DTI in healthy volunteers.

Breath-hold DTI was performed on a clinical 3T scanner (MAGNETOM Skyra, Siemens Healthcare, Erlangen, Germany) with a 34-element receive coil[1] (18 anterior and 16 posterior elements). Images were acquired with a diffusion-encoded STE sequence, which was volume-selected in the phase-encode axis using a slab selective radiofrequency (RF) pulse. Acquisition parameters included: FOV 360 x 180 mm, resolution 2.5 x 2.5 x 8 mm^3, in-plane GRAPPA rate 2, TE 34 ms, b-value 500 s/mm^2, 10 diffusion-encoding directions, and 8 averages. Twelve short-axis slices were acquired in the systolic sweet spot of the cardiac cycle to mitigate strain effects [11, 16]. Imaging was performed with no SMS, and rates 2 and 3 SMS. HA was derived from the diffusion tensor, which was estimated from the diffusion-weighted images. Fiber tracts were constructed by integrating the primary eigenvector field into streamlines using an adaptive 5th order Runge-Kutta approach [5].

Results and impact

With no SMS, 96 breath-holds were required to cover the entire LV. Using rate 2 SMS, this was reduced to 48 breath-holds, and with rate 3 SMS to 32. With rate 3 SMS, the acquisition time was approximately 20 minutes for whole-heart coverage. Image quality was well preserved using both rates 2 and 3 SMS. This is demonstrated in Figure 2, where the diffusion tensor in each voxel is represented by the supertoroidal model [17]. The glyphs are parameterized by the magnitude and orientation derived from the diffusion tensor and color-coded by HA. The transmural evolution in HA from positive in the subendocardium to negative in the subepicardium is well resolved in all 3 slices with rate 3 SMS. Glyph fields using rates 2 and 3 SMS of a mid-ventricular slice compare favorably with those acquired with no SMS, and are consistent with expected transmural evolution in HA.

Tractography of the heart has previously been performed over a small anatomical range (3-5 slices) or with

[1] The product is still under development and not commercially available yet. Its future availability cannot be ensured.

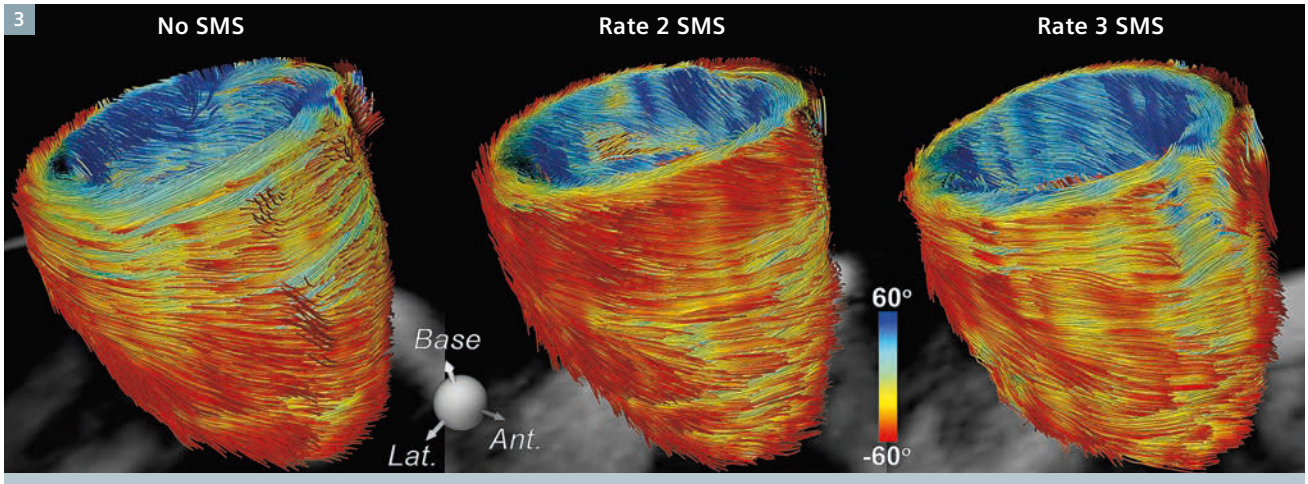

3 Tractography of the entire LV, color-coded by HA, of the same subject imaged with no SMS, and rates 2 and 3 SMS. Tracts obtained using rates 2 and 3 SMS compare favorably and are in agreement with those obtained with no SMS.

very large slice gaps. Meaningful tractography requires the entire heart to be imaged without any slice gaps. With no SMS, this takes over 60 minutes to acquire. However, as shown in Figure 3, fiber tracts of the entire LV were successfully obtained with rates 2 and 3 SMS, and are qualitatively comparable with those obtained with no SMS.

Discussion

DTI of the heart has the potential to improve the understanding, diagnosis and management of a range of cardiovascular diseases. However, the main limitation is long scan times. With current techniques, the acquisition of 3 short-axis slices takes ~20 minutes. We demonstrated that using SMS, scan time was reduced by 3-fold. The simultaneous acquisition of 3 slices (basal, medial, and apical), as shown in Figure 2, takes ~5 minutes. While imaging only 3 slices yields limited coverage of the LV, the utility of this approach has been demonstrated in first-pass perfusion studies of the heart [18]. The additional acquisition of DTI images in the same 3 short-axis slices would add little time to a clinical study and could be of substantial value.

DTI of the entire heart, while more demanding, could provide a unique way to evaluate myocardial microstructure. SMS combined with further technical advances may facilitate the clinical translation of whole-heart DTI, enabling the reliable characterization of myocardial structure in a wide range of patients with cardiac diseases.

References

1 Streeter DD, Jr., Spotnitz HM, Patel DP, Ross J, Jr., Sonnenblick EH. Fiber orientation in the canine left ventricle during diastole and systole. Circ Res. 1969;24(3):339-47.

2 Scollan DF, Holmes A, Winslow R, Forder J. Histological validation of myocardial microstructure obtained from diffusion tensor magnetic resonance imaging. Am J Physiol. 1998;275(6 Pt 2):H2308-18.

3 LeGrice IJ, Smaill BH, Chai LZ, Edgar SG, Gavin JB, Hunter PJ. Laminar structure of the heart: ventricular myocyte arrangement and connective tissue architecture in the dog. Am J Physiol. 1995;269(2 Pt 2):H571-82.

4 Dou J, Tseng WY, Reese TG, Wedeen VJ. Combined diffusion and strain MRI reveals structure and function of human myocardial laminar sheets in vivo. Magn Reson Med. 2003;50(1):107-13.

5 Mekkaoui C, Huang S, Chen HH, Dai G, Reese TG, Kostis WJ et al. Fiber architecture in remodeled myocardium revealed with a quantitative diffusion CMR tractography framework and histological validation. J Cardiovasc Magn Reson. 2012;14:70.

6 Trayanova NA. Whole-heart modeling: applications to cardiac electrophysiology and electromechanics. Circ Res. 2011;108(1):113-28.

7 Sosnovik DE, Wang R, Dai G, Reese TG, Wedeen VJ. Diffusion MR tractography of the heart. J Cardiovasc Magn Reson. 2009;11:47.

8 Nguyen C, Fan Z, Sharif B, He Y, Dharmakumar R, Berman DS et al. In vivo three-dimensional high resolution cardiac diffusion-weighted MRI: a motion compensated diffusion-prepared balanced steady-state free precession approach. Magn Reson Med. 2014;72(5):1257-67. doi:10.1002/mrm.25038.

9 Gamper U, Boesiger P, Kozerke S. Diffusion imaging of the in vivo heart using spin echoes--considerations on bulk motion sensitivity. Magn Reson Med. 2007;57(2):331-7. doi:10.1002/mrm.21127.

10 Reese TG, Weisskoff RM, Smith RN, Rosen BR, Dinsmore RE, Wedeen VJ. Imaging myocardial fiber architecture in vivo with magnetic resonance. Magn Reson Med. 1995;34(6):786-91.

11 Tseng WY, Reese TG, Weisskoff RM, Wedeen VJ. Cardiac diffusion tensor MRI in vivo without strain correction. Magn Reson Med. 1999;42(2):393-403.

12 Nielles-Vallespin S, Mekkaoui C, Gatehouse P, Reese TG, Keegan J, Ferreira PF et al. In vivo diffusion tensor MRI of the human heart: reproducibility of breath-hold and navigator-based approaches. Magn Reson Med. 2013;70(2):454-65.

13 Setsompop K, Cohen-Adad J, Gagoski BA, Raij T, Yendiki A, Keil B et al. Improving diffusion MRI using simultaneous multi-slice echo planar imaging. NeuroImage. 2012;63(1):569-80. doi:10.1016/j.neuroimage.2012.06.033.

14 Setsompop K, Gagoski BA, Polimeni JR, Witzel T, Wedeen VJ, Wald LL. Blipped-controlled aliasing in parallel imaging for simultaneous multislice echo planar imaging with reduced g-factor penalty. Magn Reson Med. 2012;67(5):1210-24. doi:10.1002/mrm.23097.

15 Lau AZ, Tunnicliffe EM, Frost R, Koopmans PJ, Tyler DJ, Robson MD. Accelerated human cardiac diffusion tensor imaging using simultaneous multislice imaging. Magn Reson Med. 2015;73(3):995-1004. doi:10.1002/mrm.25200.

16 Stoeck CT, Kalinowska A, von Deuster C, Harmer J, Chan RW, Niemann M et al. Dual-phase cardiac diffusion tensor imaging with strain correction. PLoS One. 2014;9(9):e107159. doi:10.1371/journal.pone.0107159.

17 Mekkaoui C, Chen IY, Chen HH, Kostis WJ, Pereira F, Jackowski MP et al. Differential response of the left and right ventricles to pressure overload revealed with diffusion tensor MRI tractography of the heart in vivo. Journal of Cardiovascular Magnetic Resonance. 2015;17(Suppl 1):O3-O. doi:10.1186/1532-429X-17-S1-O3.

18 Stab D, Wech T, Breuer FA, Weng AM, Ritter CO, Hahn D et al. High resolution myocardial first-pass perfusion imaging with extended anatomic coverage. J Magn Reson Imaging. 2014;39(6):1575-87. doi:10.1002/jmri.24303.



Timothy G. Reese



Choukri Mekkaoui

Contact

Choukri Mekkaoui
Athinoula A. Martinos Center for Biomedical Imaging
149 13th Street
Charlestown, MA 02129, USA
Phone: +1 617 724-3407
Fax: 617 726-7422
mekkaoui@nmr.mgh.harvard.edu

Overview of Magnetic Resonance Fingerprinting

Simone Coppo[1]; Bhairav B. Mehta[1]; Debra McGivney[1]; Dan Ma[1]; Yong Chen[1]; Yun Jiang[2]; Jesse Hamilton[2]; Shivani Pahwa[1]; Chaitra Badve[1]; Nicole Seiberlich[1]; Mark Griswold[1,2]; Vikas Gulani[1]

Departments of Radiology (1) and Biomedical Engineering (2), Case Western Reserve University, University Hospitals Case Medical Center, Cleveland, OH, USA

Introduction

Magnetic Resonance Imaging (MRI) is a powerful diagnostic, prognostic and therapy assessment tool due to its versatile nature as compared to other imaging modalities, as MRI allows the user to probe and measure various kinds of information (T1, T2, B_0, diffusion, perfusion, etc.). However, MRI has the drawback of being slow compared to other diagnostic tools, and is generally qualitative, where the contrast between tissues, rather than absolute measurements from single tissues, is the primary means of information that is used to characterize an underlying pathology. While this information has proven extremely valuable for diagnosis, prognosis, and therapeutic assessment, the lack of quantification limits objective evaluation, leads to a variability in interpretation, and potentially limits the utility of the technology in some clinical scenarios.

To overcome this limitation, significant effort has been put into developing quantitative approaches that can measure tissue proprieties such as T1 and T2 relaxation times. Quantifying tissue proprieties allows physicians to better distinguish between healthy and pathological tissue [1] in an absolute sense, makes it easier to objectively compare different exams in follow-up studies [2], and could be more representative of the underlying changes at the cellular level [3, 4] than standard weighted imaging. Quantitative imaging is crucial in the assessment of disease settings presenting subtle features such as cardiac diffuse fibrosis [5], iron [6] or fat deposition in the liver [7]. Additionally, there are various clinical settings in which multiple features such as T1, T2, diffusion, etc. add up synergistically to drastically improve the information for diagnosis, prognosis and/or therapeutic assessment.

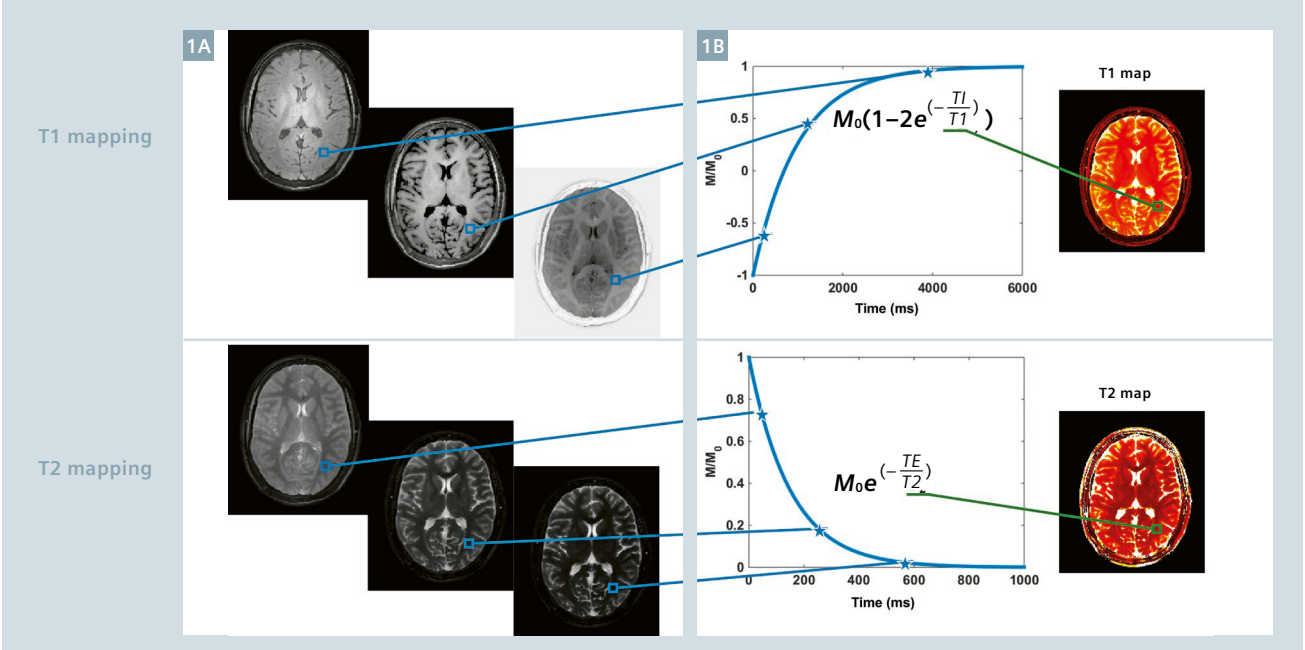

1 Conventional parametric mapping approaches. Example of conventional T1 (above) and T2 (below) mapping techniques. **(1A)** Several fully sampled images are acquired one after the other with different inversion time (for T1) or echo time (for T2). **(1B)** An exponential fitting is performed using the multiple values of each voxel and the relaxation or decay time is the one that provides the best fit.

While quantitative imaging has been a long-standing goal of the MR community, a drawback encountered in early conventional quantitative imaging was the reduced time efficiency compared to qualitative imaging. Early conventional approaches for T1 and T2 mapping involved measuring one parameter at a time. These techniques relied on the acquisitions of several images, each with one specific acquisition parameter that varies for each image while the others were kept constant (Fig. 1A). The obtained images were subsequently fitted with a mathematical model to estimate the one parameter of interest, for example the relaxation time (T1) [8] or the time of signal decay (T2) [9] (Fig. 1B). This process had to be repeated for each parameter of interest. The need for keeping all except one sequence parameter and signal state constant and the limitation of assessing one parameter at a time made these approaches extremely time-inefficient because of the prolonged scan time and thus not suitable for a clinical environment where interscan motion can render such approaches infeasible. In recent times, several approaches have been proposed to shorten the acquisition time [10–13] or to provide combined T1 and T2 measurements [14–18] within a single acquisition. However, major barriers remain to clinical adoption, most notably a simultaneous need for rapid and accurate quantification.

To overcome the common drawbacks of quantitative imaging, Magnetic Resonance Fingerprinting (MRF)[1] [19–21] has been recently developed. This technique aims at providing simultaneous measurements of multiple parameters such as T1, T2, relative spin density, B_0 inhomogeneity (off-resonance frequency), etc., using a single, time-efficient acquisition. MRF completely changes the way quantitative MRI is performed with an entirely different approach from that of conventional techniques. Instead of performing an acquisition with all but one sequence parameter constant, MRF relies on deliberately varying acquisition parameters in a pseudorandom fashion such that each tissue generates a unique signal evolution. It is possible to simulate signal evolutions from first principles using different physical models for a wide variety of tissue parameter combinations, which are collected together in a database called dictionary. After the acquisition, a pattern recognition algorithm is used to find the dictionary entry that best represents the acquired signal evolution of each voxel. The parameters that were used to simulate the resulting best match are then assigned to the voxel. This process is analogous to the fingerprinting identification process used by forensic experts to identify persons of interest. The acquired signal evolution is unique for each tissue and can be seen as the collected fingerprint that has to be identified. The dictionary is equivalent to the database where all the known fingerprints are stored, together with all the information relative to each person. In the forensic case, each fingerprint points to the feature identification of the associated person such as name, height, weight, eye color, date of birth, etc. Similarly, in the case of MRF, each fingerprint in the dictionary points to the MR related identification features of the associated tissue such as T1, T2, relative spin density, B_0, diffusion, etc. After the acquisition, the fingerprint contained in a voxel is compared with all the entries in the dictionary. The dictionary entry that best matches the acquired fingerprint is considered a positive match, meaning that the tissue represented in the voxel has been identified. All the known parameters relative to that fingerprint can then be retrieved from the dictionary and assigned to the voxel. The uniqueness of the different signal components and the accuracy with which the dictionary is simulated are two crucial components for the correct estimation of the tissue parameters.

This paper attempts to describe the basic concepts of MRF and illustrate some clinical applications.

Acquisition sequence

Standard quantitative MR imaging approaches require several acquisitions, each one of which constantly repeats the same acquisition pattern, such as radiofrequency excitation angle (flip angle, FA), repetition time (TR) and gradient patterns, until all required data in the Fourier domain (also called *k*-space) are obtained. Each image is then reconstructed using the Fourier transform and a nonlinear fitting process is applied to each voxel. With MRF, instead, the flip angle, the TR and the trajectory (Fig. 2A, B) vary in a pseudorandom fashion throughout the acquisition; when implemented properly, this generates uncorrelated signals for each tissue, providing the unique fingerprints that are used to recognize the tissue. The initial implementation of MRF [19] was based on a balanced steady-state free-precession (bSSFP or TrueFISP) sequence because of its sensitivity to T1, T2 and off-resonance frequency, and because the steady-state signal generated by this sequence has been thoroughly studied [22]. The FA (Fig. 2A) varies in a sinusoidal fashion to smoothly vary the transient state of the magnetization, ranging from 0° to 60° and from 0° to 30° alternatively, with a period of 250 time points, or images. On top of this signal, a random variation is added to induce differences in the time evolutions from tissues with similar parameters. After each half period (250 images), 50 flip angles are set to 0° to allow for signal recovery. The TR variations, instead, are based on Perlin noise [23] which ranges from 9.34 ms to 12 ms. These are only examples of how the parameters can be randomly varied. Other random patterns have been tested [19, 24] showing that MRF is not limited to one specified set of parameters.

An inversion recovery pulse is played out at the beginning of the acquisition sequence to enhance T1 differences between tissues (Fig. 2B). For each TR, a heavily undersampled

[1] The product is still under development and not commercially available yet. Its future availability cannot be ensured. As this is a research topic in predevelopment, all results shown are preliminary in nature and do not allow for generalizations or conclusions to be drawn. Product realization and features therein cannot be assured as the product may undergo futher design iterations.

image is reconstructed (Fig. 2C). It can be noticed how the base image series are not useful by themselves, but each voxel contains a signature fingerprint that will be used later on for the matching (identification). The total number of images acquired (also referred to as 'time points') can vary from acquisition to acquisition, ranging from 1000 [19] to 2500 [21] as function of the image resolution, the undersampling ratio, the matching approach used, etc. In most cases, we have used a variable-density spiral trajectory [25] designed to have a minimum time gradient and zero moment compensation for the acquisition. For example, we have successfully used a trajectory for a 128 x 128 matrix size that requires one interleaf to fully sample the center of *k*-space and 48 interleaves to fully sample the outer region of *k*-space. In the case of a 256 x 256 matrix, a trajectory requiring 24 interleaves to fully sample the inner region and 48 interleaves to fully sample the outer region can be used instead. Within each TR, one interleaf is acquired and used to reconstruct an image (or time point). The interleaf in the following TR is then rotated by 7.5° (≈ 2π/48) compared to the previous one.

The MRF framework is not only limited to a TrueFISP-based acquisition, but can be virtually applied to any kind of sequence. As an example, the MRF framework has been applied to a steady-state precession sequence (FISP) [20] to avoid the banding artifacts that can appear in wide field-of-view scans or in a high-field-strength scanner. The FISP sequence is still sensitive to T1 and T2 components but is less sensitive to off-resonance frequency. This is caused by the unbalanced gradient within every TR which results in the signal to be the sum of the spins within a voxel, making the sequence immune to banding artifacts. The unbalanced gradient, though, leads the FISP sequence to have a shorter transient state com-

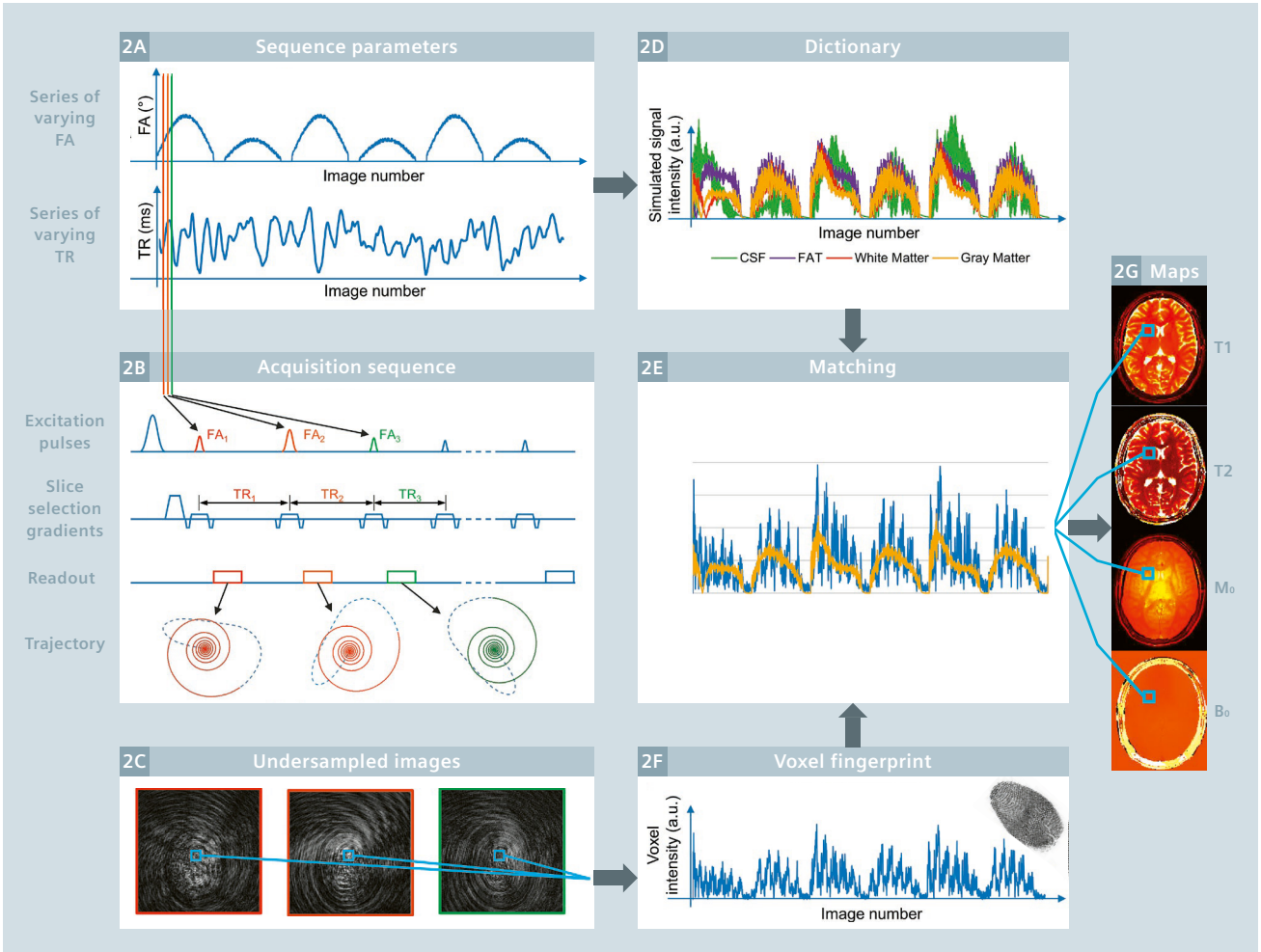

2 Flow chart of the MRF framework. **(2A)** Example of variable FA and TR used for a TrueFISP acquisition. **(2B)** Sequence diagram showing the excitation pulses, slice selection gradients, readout and *k*-space trajectory for each TR; **(2C)** Example of three undersampled images acquired in three different TR. **(2D)** Examples of four dictionary entries representing four main tissues: cerebrospinal fluid (CSF) (T1 = 5000 ms, T2 = 500 ms), fat (T1 = 400 ms, T2 = 53 ms), white matter (T1 = 850 ms, T2 = 50 ms), gray matter (T1 = 1300 ms, T2 = 85 ms); **(2E)** Matching of a voxel fingerprint with the closest entry in the dictionary, which allows to retrieve the tissue features represented by that voxel; **(2F)** intensity variation of a voxel across the undersampled images (fingerprint); **(2G)** parameter maps obtained repeating the matching process for each voxel.

pared to the TrueFISP. For this reason, the pseudorandom FA variation needs to be generated slightly differently than in the case of the TrueFISP sequence, in order to keep incoherence between the signal and undersampling artifacts and to be able to identify the underlying fingerprint. The FA variation is thus generated based on sinusoidal variation in which the maximum reached FA for each half period randomly changes, ranging from 5° to 90°. The TR variation is always based on a Perlin noise pattern which ranges from 11.5 ms to 14 ms.

	TrueFISP			FISP		
Parameter	**Min value**	**Max value**	**Step size**	**Min value**	**Max value**	**Step size**
T1 (ms)	100	2000	20	20	3000	10
	2000	5000	300	3000	5000	200
T2 (ms)	20	100	5	10	300	5
	100	200	10	300	500	50
	200	1900	200	500	900	200
Off-resonance (Hz)	-250	-190	20			
	-50	50	1			
	190	250	20			

Table 1: Ranges and step sizes used for the dictionary creation in case of a TrueFISP sequence (left) or FISP sequence (right).

Dictionary generation

The dictionary can be seen as the heart of the MRF framework; it is the database that contains all physiologically possible signal evolutions that may be observed from the acquisition and that makes it possible to recognize the tissue within each voxel. MRF, like the forensic fingerprinting identification process, is effective only when a database large enough to contain all the potential candidates is available. In MRF, the dictionary is generated on a computer using algorithms that simulate the spin behavior during the acquisition and thus predict the realistic signal evolution. In case of a TrueFISP-based acquisition, the Bloch equations [26] are used to simulate the various effects of the acquisition sequence on the spins, given a set of tissue parameters of interest (Fig. 2D). The information that can be retrieved with MRF is thus related to how and what physical effects are simulated. In the initial stages of development, MRF includes the simulation of T1, T2 and off-resonance, but more tissue features can be simulated and extracted, such as partial volume [19], diffusion [27] and perfusion [28].

A critical aspect of the dictionary is its size: to ensure the identification of any possible tissue parameter present in the acquisition, a wide combination of T1, T2 and off-resonance frequency need to be simulated. A standard TrueFISP dictionary with the parameter ranges as shown in Table 1 leads to a total of 363,624 possible combinations and includes the parameter values that are commonly found in the human body. The computation of such a dictionary for 1000 time points takes about 2.5 minutes on a standard desktop computer using a C++ based script and reaches 2.5 GB of memory size. A further increase in the dictionary size and/or resolution would increase the accuracy of the obtained maps at the expenses of an increase in the reconstruction time and memory requirements [19].

The simulation of a FISP acquisition is computed differently compared to the one described above. Since the FISP acquisition requires the simulation of multiple isochromats at different frequencies, which are then combined together, the simulation process through Bloch equations can be time consuming. An alternative time-efficient simulation is the extended phase graph (EPG) formalism [29], where a spin system affected by the sequence can be represented as discrete set of phase states, ideal to simulate the signal evolution of spins strongly dephased by unbalanced gradients. The FISP sequence is less sensitive to off-resonance effects compared to the TrueFISP acquisition, so the corresponding dictionary includes only the T1 and T2 relaxation times (Table 1) as the parameters of interest. This leads to 18,838 dictionary entries that can be computed in about 8 minutes on a standard desktop computer, and that generates a dictionary of about 1.2 GB.

Regardless of which sequence is used, the dictionary needs to be computed only once beforehand. It can then be used on the scanner, where it is used to reconstruct each MRF acquisition acquired with the sequence parameters that were simulated.

Matching

After the data acquisition, the fingerprint of each voxel (Fig. 2F) is normalized to unit norm and compared with all the normalized dictionary entries to identify the tissue in a given voxel (Fig. 2E). The simplest version of the matching is performed by taking the inner product between the voxel signal and each simulated fingerprint signal; the entry that returns the highest value is considered to be the one that best represents the tissue properties, and the respective T1, T2 and off-resonance values are assigned to the voxel (Fig. 2G). The relative spin density (M_0) map, instead, is computed as the scaling factor between the acquired and the simulated fingerprints. The inner product has been demonstrated to be a robust operation and is able to correctly classify the tissues even in case of low SNR due to undersampling or even in the presence of a limited amount of motion artifacts [19].

This approach has also the potential of distinguishing different tissue components present within a single voxel (partial volume effect) thanks

to the incoherence between different signal evolutions. The fingerprint (S) of a voxel containing different tissue can be seen as the weighted sum (w) of the different components (D): S = Dw. It has been shown [19] that, if the different components are known a priori, the appropriate inverse solution of the previous equation – $(D)^{-1}S = w$, where $(D)^{-1}$ represents the pseudoinverse of D – will provide the weight of each different tissue for each voxel [19,31].

The pattern recognition algorithm is performed on the scanner for every acquisition, so it is crucial for the clinical usefulness of the MR framework that this operation is performed in a reasonable time. While the direct matching using the inner product is accurate, it can take up to about 160 seconds to match a 2D slice of 128 x 128 base resolution, 1000 time points with a dictionary counting 363 624 entries. Similarly it takes about 30 seconds to match a 2D image with 256 x 256 voxels, 1000 time points and 18,838 dictionary entries for a FISP reconstruction.

The matching can be potentially accelerated by compressing the dictionary either in the time dimension or in the parameter combinations dimension, thus reducing the total number of comparisons that need to be performed. It has been shown [31] that the singular value decomposition (SVD) can be applied to compress the dictionary in the time dimension and reduce the matching time by a factor of 3.4 times for a TrueFISP dictionary and up to a factor of 4.8 times for a FISP dictionary. The SVD-based dictionary compression has less than 2% of reduction in the accuracy of the estimated parameters. In this approach, the dictionary is projected into a subspace of lower dimension spanned by the first 25-200 singular vectors obtained from the SVD. The acquired fingerprint is projected onto the same subspace, and the matching is performed using the projected signal and the compressed dictionary. This framework reduces the number of calculations, thus reducing the final computation time despite the added operation of data projection on the subspace.

An alternative approach for reducing computational time for matching is by reducing the parameter combination dimension. A fast group matching algorithm [32] has been developed, where dictionary entries that have strong correlations are grouped together and a new signal that best represents the group is generated. The matching is thus subdivided in two steps; at first the acquired fingerprint is matched with the representing signal of each group, and only groups that return the highest correlation are kept in consideration. Then matching is used to find the best fit between the fingerprint and the remaining dictionary entries for the assignment of the parameters. This algorithm reduces the matching computation speed of one order of magnitude compared to the SVD compression and two orders of magnitude compared to the direct matching with no significant loss in the quality of the match. Techniques such as this make it feasible to implement MRF in a clinical manner.

Undersampling and motion

In MRF, the obtained parameter maps are the result of a pattern recognition algorithm as opposed to conventional reconstruction techniques, which allows MRF to be more robust to various image artifacts. This effect is strengthened by the random variation of FA, TR and trajectory which not only aim at differentiating the fingerprints from different tissues, but also aim at increasing the incoherence between the fingerprints. The matching can recognize the underlying signal evolutions even in low signal-to-noise or accelerated conditions as long as the noise or undersampling artifacts are incoherent with the signal. Additionally, just like in forensic fingerprinting, a correct identification is possible even with the use of blurry or partial fingerprints, the MR counterpart is also capable of providing parametric maps without any residual motion artifacts in case of a fingerprint partially corrupted by motion [19].

Volunteer acquisitions

MRF acquisitions have been tested in volunteers in 2D brain, abdominal, and cardiac scans. All *in vivo* experiments were performed under the Institutional Review Board guidelines and each subject signed informed consent prior to the data acquisition. The scans were performed on a 3T MAGNETOM Skyra system with a 20-channel head coil or a phased array 18-channel body coil plus spine coil. For the brain scans, the variable acquisition parameters (FA and TR) were set as described above and 3000 time points were acquired; the FOV was 300 x 300 mm, the slice thickness was 5 mm and the matrix size was 256 x 256. The acquisition time was 38 s for a 2D TrueFISP slice and 41 s for the FISP acquisition. The cardiac MRF scans were acquired using a modified pulse sequence with ECG triggering to restrict data collection to mid-diastole [35]. A total of 768 time points were acquired over a 16-heartbeats breathhold using a scan window of 250 ms with FOV 300 x 300 mm, slice thickness 8 mm, and matrix size 192 x 192 [35]. For the abdominal and cardiac imaging, the trajectory and acquisition protocols were adapted as described in references [21, 35] respectively. The dictionaries were computed as described above and SVD based matching was used for parameter estimation.

Figure 3 shows the maps obtained from volunteer scans in the brain (Fig. 3A), abdomen (Fig. 3B), and heart (Fig. 3C). Both FISP and TrueFISP MRF provide comparable high resolution multiparametric tissue maps. The FISP acquisition has the drawback of not providing the off-resonance information, but it has the advantage of being insensitive to banding artifacts. Therefore, FISP MRF is advantageous for body imaging, where the sharp susceptibility transitions and the need for a large field-of-view would lead to banding artifacts with a balanced SSFP acquisition.

The values obtained with MRF maps are generally in good agreement with the standard mapping techniques [20] and with the literature value of tissue parameters [19, 24], as shown in table 2. It can be noticed, though,

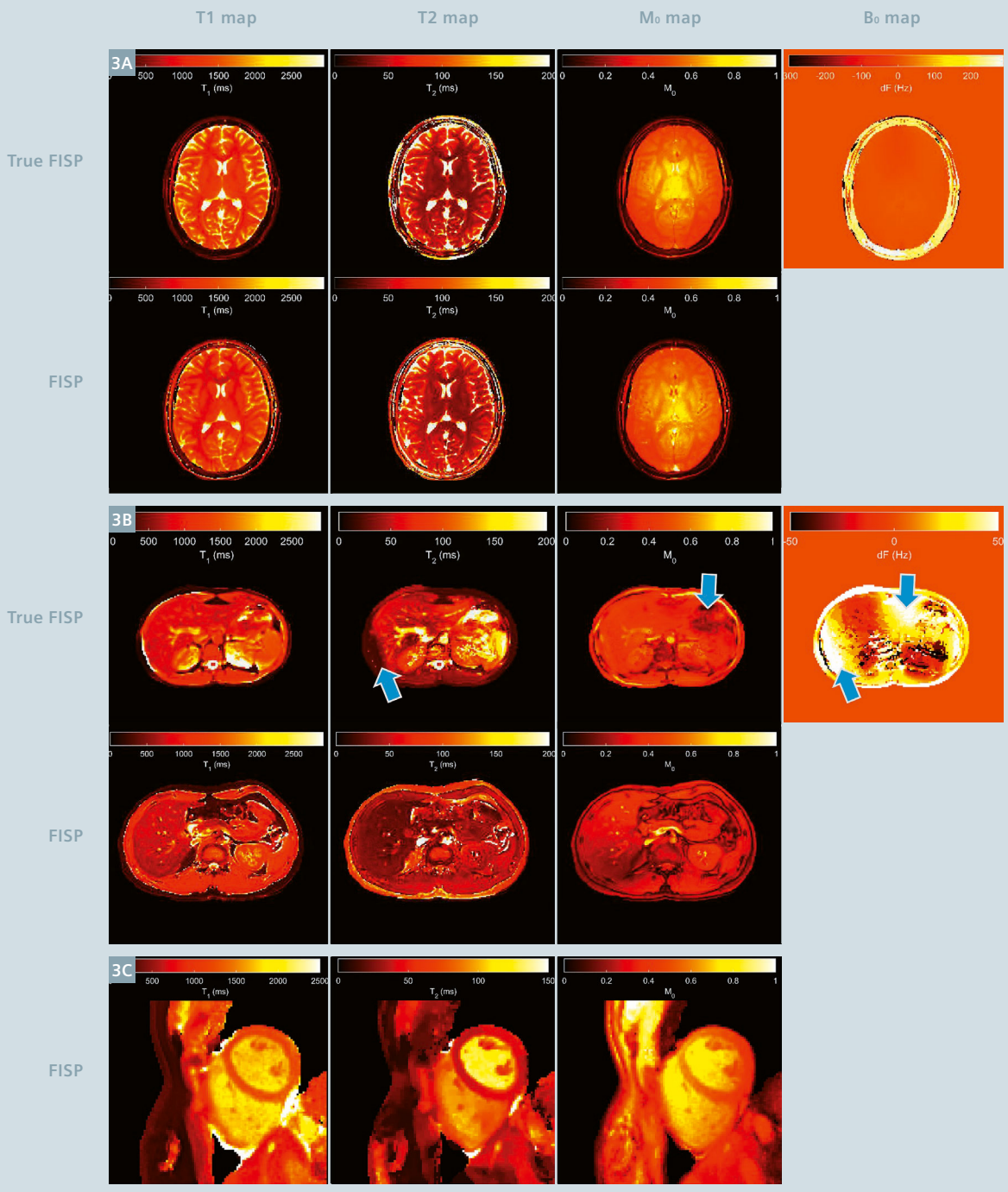

3 Examples of T1, T2, relative spin density (M_0) and off-resonance (B_0) maps acquired in two volunteers with a TrueFISP and a FISP acquisition. **(3A)** Single 2D slice of a head scan. **(3B)** Single 2D slice of an abdominal scan. **(3C)** Single 2D slice of diastolic cardiac scan in short axis view. In the T2 and B_0 map obtained from the TrueFISP acquisition, banding artifacts due to field inhomogeneity are visible (blue arrows).

	T1 (ms)		T2 (ms)	
Tissue	**MRF**	**Literature**	**MRF**	**Literature**
White matter	685 ± 33 [19]	608–756 [34, 40–42]	65 ± 4 [19]	54–81 [34, 40–42]
	781 ± 61 [20]	788–898 [43]	65 ± 6 [20]	78–80 [43]
Gray matter	1180 ± 104 [19]	998–1304 [34, 40–42]	97 ± 5.9 [19]	78–98 [34, 40–42]
	1193 ± 65 [20]	1286–1393 [43]	109 ± 11 [20]	99–117 [43]
Cerebrospinal fluid	4880 ± 379 [19]	4103–5400 [34, 40–42]	550 ± 251 [19]	1800–2460 [34, 40–42]
Liver	745 ± 65 [21]	809 ± 71 [44]	31 ± 6 [21]	34 ± 4 [44]
Kidney medulla	1702 ± 205 [21]	1545 ± 142 [44]	60 ± 21 [21]	81 ± 8 [44]
Kidney cortex	1314 ± 77 [21]	1142 ± 154 [44]	47 ± 10 [21]	76 ± 7 [44]
Skeletal muscle	1100 ± 59 [21]	1017 ± 78 [45]	44 ± 9 [21]	50 ± 4 [46]
Fat	253 ± 42 [21]	343 ± 37 [45]	77 ± 16 [21]	68 ± 4 [44]

Table 2: List of T1 and T2 relaxation times measured with MRF for different tissues and comparison with the value available in literature.

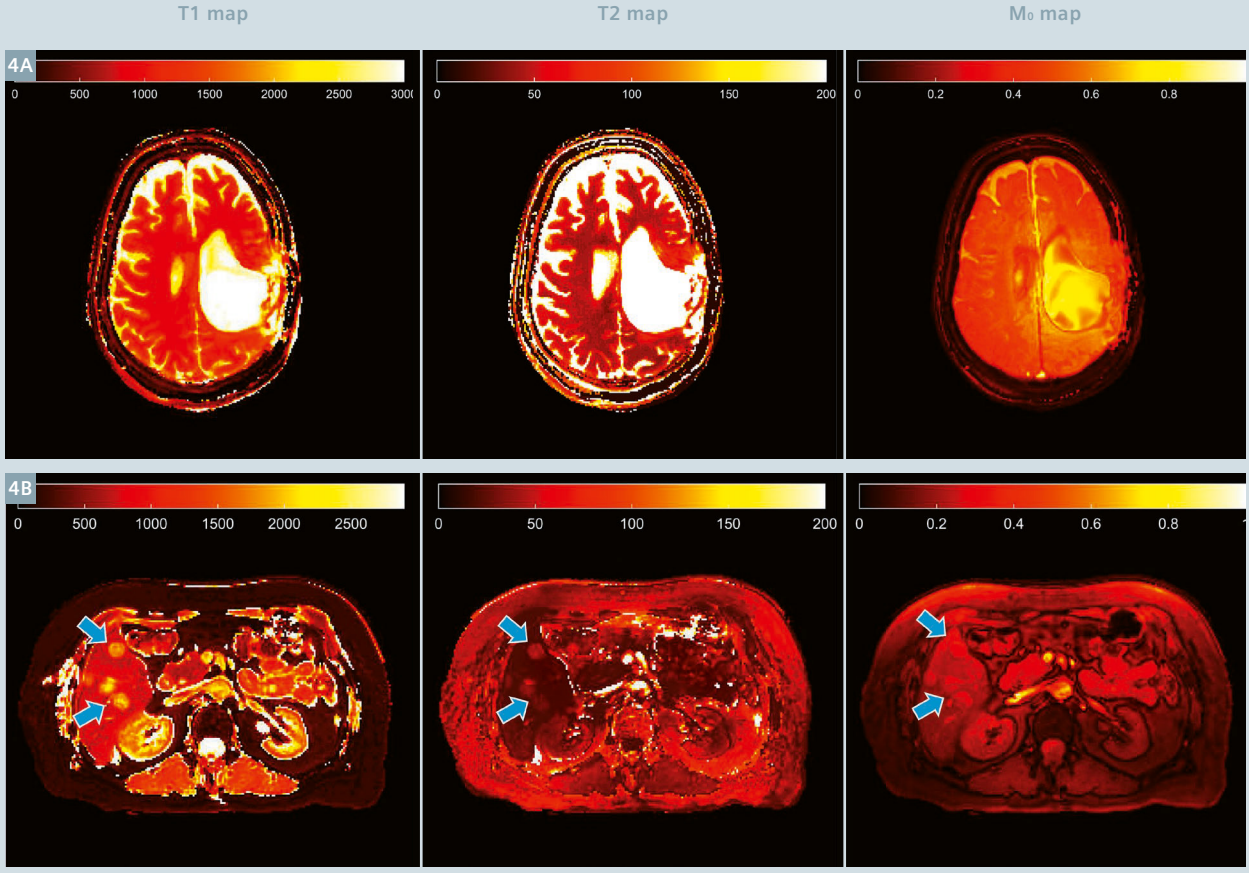

4 Example of patient results. Quantitative T1, T2 and relative spin density (M_0) maps obtained using the FISP protocol for brain [16] and abdomen acquisitions [20]. **(4A)** Maps of a patient with a brain tumor; **(4B)** 69-year-old patient with metastatic breast cancer. The metastasis (blue arrows) presents an increase in all tissue parameters, compared to the surrounding tissues.

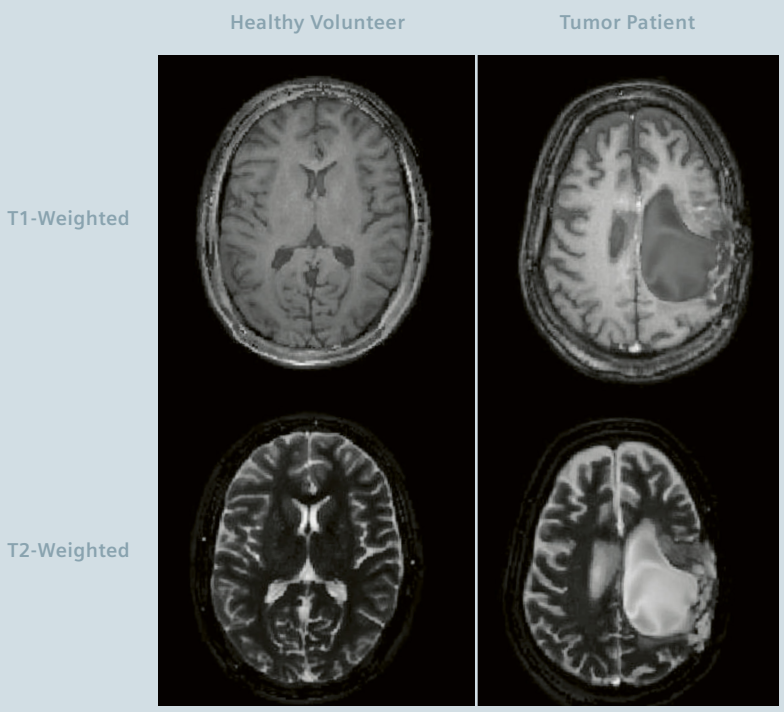

5 Synthetic generation of conventional images. Example of T1-weighted and T2-weighed images from a healthy volunteer and a patient with brain tumor, reconstructed starting from the T1, T2 and M_0 maps obtained from the FISP MRF maps of Figure 3 and 4.

that there is a mismatch in the values of CSF and fat. The CSF T2 discrepancy between MRF and literature value can be explained by through-plane motion of the fluid that was not taken into account in the dictionary simulation [19]. The fat T1 discrepancy, instead, is mainly due to the intentionally low T1 dictionary resolution (100 ms) for the range 100–600 ms used for that study [21].

The MRF efficiency is extremely high compared to traditional mapping approaches [19–21] as well as rapid combined T1 and T2 mapping methods like DESPOT [19, 36]. The high efficiency and accuracy of the MRF framework enable parametric mapping to be performed in a clinically relevant acquisition time without loss of information. In this way, multiparametric mapping can be translated to the clinical environment.

Patient acquisitions

The MRF framework has also been successfully tested on patients. Figure 4 shows the feasibility of brain and abdominal MRF in a clinical environment. Data were acquired with the previously described FISP acquisitions on patients with a brain tumor and breast cancer metastatic to the liver (Fig. 4). Longer T1 relaxation time can be observed in the metastatic lesions compared to the surrounding tissues. It has been shown in six patients with metastatic adenocarcinoma that the mean T1 and T2 values in the metastatic adenocarcinoma were on the order of 1673 ± 331 ms and 43 ± 13 ms, respectively. Those values are significantly higher than the ones of the surrounding tissues (840 ± 113 ms and 28 ± 3 ms, respectively) [21]. Recent studies investigate the possibility of predicting response of tumor to treatment using tissue relaxation times; e.g. the T1 relaxation time can potentially be an indicator of chemotherapy response [35, 36]. Fast multiparametric mapping can thus open the path to the creation of a multiproperty space that might allow a deeper characterization and understanding of the conditions and evolutions of determined pathologies.

Synthetic weighted images

It is also possible to retrospectively calculate and estimate 'standard' weighted images from the multiple parameter maps obtained from an MRF scan. Figure 5 shows an example of T1-weighted and T2-weighted acquisition calculated from the FISP T1 and T2 maps of the volunteer and patient head scan shown above.

Conclusions

Magnetic resonance fingerprinting is a novel framework for MRI, where the pulse sequence design is not aimed at acquiring images, but at directly measuring tissue properties. In MRF, the sequence generates unique signal evolutions, or fingerprints, for each different tissue and matches it with a set of theoretical signal evolutions to measure several tissue properties within a single acquisition. Once the tissue features are measured, it is possible to directly know several tissue-specific properties that can synergistically provide all the information to improve diagnosis, prognosis and/or therapeutic assessment. In this work, only two MRF implementations have been shown, but the MRF framework has the potential to allow more freedom in the sequence design compared to standard MRI sequences, since the parameters can be randomly varied. Thanks to this freedom, a whole new world of possibilities of acquisition and reconstruction strategies that can probe and measure new features have been opened up for our community to explore.

This paper focused on T1, T2, M_0 and B_0 characterization, but the MRF is not limited to that. Several work are being performed to exploit the potential of MRF including: diffusion

[27], arterial spin labeling [28, 42, 43] and chemical exchange [44].

The pattern recognition nature of MRF makes the acquisition robust to artifacts like undersampling and motion, yielding high efficiency, accuracy and robustness that are critical for the successful integration of a multiparametric mapping technique into the clinical environment. Moreover, the increased efficiency and robustness to artifacts compared to standard MR imaging approaches could potentially reduce the time and thus the costs of MRI exams, making it more affordable and more competitive in comparison to other imaging modalities.

References

1 Larsson H, Frederiksen J. Assessment of demyelination, edema, and gliosis by in vivo determination of T1 and T2 in the brain of patients with acute attack of multiple sclerosis. Magn Reson Med [Internet]. 1989;348:337–48. Available from: http://onlinelibrary.wiley.com/doi/10.1002/mrm.1910110308/abstract
2 Usman AA, Taimen K, Wasielewski M, et al. Cardiac magnetic resonance T2 mapping in the monitoring and follow-up of acute cardiac transplant rejection: a pilot study. Circ Cardiovasc Imaging [Internet]. 2012;5(6):782–90. Available from: http://www.ncbi.nlm.nih.gov/pubmed/23071145
3 Payne AR, Berry C, Kellman P, et al. Bright-blood T 2-weighted MRI has high diagnostic accuracy for myocardial hemorrhage in myocardial infarction a preclinical validation study in swine. Circ Cardiovasc Imaging. 2011;4(6):738–45.
4 Van Heeswijk RB, Feliciano H, Bongard C, et al. Free-breathing 3 T magnetic resonance T2-mapping of the heart. JACC Cardiovasc Imaging [Internet]. 2012 Dec;5(12):1231–9. Available from: http://www.ncbi.nlm.nih.gov/pubmed/23236973
5 Iles L, Pfluger H, Phrommintikul A, et al. Evaluation of Diffuse Myocardial Fibrosis in Heart Failure With Cardiac Magnetic Resonance Contrast-Enhanced T1 Mapping. J Am Coll Cardiol. 2008;52(19):1574–80.
6 Hernando D, Levin YS, Sirlin CB, Reeder SB. Quantification of liver iron with MRI: state of the art and remaining challenges. J Magn Reson Imaging [Internet]. 2014 Nov;40(5):1003–21. Available from: http://www.pubmedcentral.nih.gov/articlerender.fcgi?artid=4308740&tool=pmcentrez&rendertype=abstract
7 Reeder SB, Cruite I, Hamilton G, Sirlin CB. Quantitative assessment of liver fat with magnetic resonance imaging and spectroscopy. J Magn Reson Imaging [Internet]. 2011 Oct;34(4):729–49. Available from: http://www.ncbi.nlm.nih.gov/pubmed/21928307
8 Look DC, Locker DR. Time saving in measurement of NMR and EPR relaxation times. Rev Sci Instrum. 1970;41(2):250–1.
9 Huang TY, Liu YJ, Stemmer A, Poncelet BP. T2 measurement of the human myocardium using a T 2-prepared transient-state trueFISP sequence. Magn Reson Med. 2007;57:960–6.
10 Mehta BB, Chen X, Bilchick KC, Salerno M, Epstein FH. Accelerated and navigator-gated look-locker imaging for cardiac T1 estimation (ANGIE): Development and application to T1 mapping of the right ventricle. Magn Reson Med. 2015;73(1):150–60.
11 Zhu DC, Penn RD. Full-brain T1 mapping through inversion recovery fast spin echo imaging with time-efficient slice ordering. Magn Reson Med. 2005;54(3):725–31.
12 Cheng H-LM, Wright GA. Rapid High-Resolution T1 Mapping by Variable Flip Angles: Accurate and Precise Measurements in the Presence of Radiofrequency Field Inhomogeneity. Magn Reson Med. 2006;55:566–76.
13 Doneva M, Börnert P, Eggers H, Stehning C, Sénégas J, Mertins A. Compressed sensing reconstruction for magnetic resonance parameter mapping. Magn Reson Med. 2010;64(4):1114–20.
14 Deoni SCL, Rutt BK, Peters TM. Rapid combined T1 and T2 mapping using gradient recalled acquisition in the steady state. Magn Reson Med. 2003;49(3):515–26.
15 Blume U, Lockie T, Stehning C, et al. Interleaved T1 and T2 relaxation time mapping for cardiac applications. J Magn Reson Imaging. 2009;29:480–7.
16 Warntjes JBM, Dahlqvist O, Lundberg P. Novel method for rapid, simultaneous T1, T2*, and proton density quantification. Magn Reson Med. 2007;57(3):528–37.
17 Schmitt P, Griswold MA, Jakob PM, et al. Inversion recovery TrueFISP: quantification of T(1), T(2), and spin density. Magn Reson Med. 2004;51(4):661–7.
18 Ehses P, Seiberlich N, Ma D, et al. IR TrueFISP with a golden-ratio-based radial readout: Fast quantification of T1, T2, and proton density. Magn Reson Med. 2013;69(1):71–81.
19 Ma D, Gulani V, Liu K, et al. Magnetic resonance fingerprinting. Nature [Internet]. 2013;495(7440):187–92.
20 Jiang Y, Ma D, Seiberlich N, Gulani V, Griswold M a. MR fingerprinting using fast imaging with steady state precession (FISP) with spiral readout. Magn Reson Med [Internet]. 2014;. Available from: http://www.ncbi.nlm.nih.gov/pubmed/25491018
21 Chen Y, Jiang Y, Pahva Shivani, et al. MR Fingerprinting for Rapid Quantitative Abdominal Imaging. Radiology. 2016;000(0):1–9.
22 Schmitt P, Griswold MA, Gulani V, Haase A, Flentje M, Jakob PM. A simple geometrical description of the TrueFISP ideal transient and steady-state signal. Magn Reson Med. 2006;55(1):177–86.
23 Perlin K. An image synthesizer. ACM SIGGRAPH Comput Graph. 1985;19(3):287–96.
24 Ma D, Pierre EY, Jiang Y, et al. Music-based magnetic resonance fingerprinting to improve patient comfort during MRI examinations. Magn Reson Med [Internet]. 2015; Available from: http://doi.wiley.com/10.1002/mrm.25818
25 Lee JH, Hargreaves B a., Hu BS, Nishimura DG. Fast 3D Imaging Using Variable-Density Spiral Trajectories with Applications to Limb Perfusion. Magn Reson Med. 2003;50(6):1276–85.
26 Bloch F. Nuclear induction. Phys Rev. 1946;70:460–85.
27 Jiang Y, Wright KL, Seiberlich N, Gulani V, Griswold MA. Simultaneous T1, T2, diffusion and proton density quantification with MR fingerprinting. In: In proceedings of the 22nd annual meeting of ISMRM meeting & exhibition in Milan, Italy. 2014. p. 28.
28 Wright KL, Ma D, Jiang Y, Gulani V, Griswold MA, Luis H-G. Theoretical framework for MR fingerprinting with ASL: simultaneous quantification of CBF, transit time, and T1. In: In proceedings of the 22nd annual meeting of ISMRM meeting & exhibition in Milan, Italy. 2014. p. 417.
29 Weigel M, Schwenk S, Kiselev VG, Scheffler K, Hennig J. Extended phase graphs with anisotropic diffusion. J Magn Reson. 2010;205(2):276–85.
30 Deshmane AV, Ma D, Jiang Y, et al. Validation of Tissue Characterization in Mixed Voxels Using MR Fingerprinting. In: In proceedings of the 22nd annual meeting of ISMRM meeting & exhibition in Milan, Italy. 2014. p. 0094.
31 McGivney D, Pierre E, Ma D, et al. SVD Compression for Magnetic Resonance Fingerprinting in the Time Domain. IEEE Trans Med Imaging. 2014;0062(12):1–13.
32 Cauley SF, Setsompop K, Ma D, et al. Fast group matching for MR fingerprinting reconstruction. Magn Reson Med [Internet]. 2014;00. Available from: http://dx.doi.org/10.1002/mrm.25439
33 Hamilton JI, Jiang Y, Chen Y, et al. MRF for Rapid Quantification of Myocardial T1, T2, and Proton Spin Density. Magn Reson Med. 2016;In press.

34 Deoni SCL, Peters TM, Rutt BK. High-resolution T1 and T2 mapping of the brain in a clinically acceptable time with DESPOT1 and DESPOT2. Magn Reson Med. 2005;53(1):237–41.

35 Jamin Y, Tucker ER, Poon ES, et al. Evaluation of Clinically Translatable MR Imaging Biomarkers of Therapeutic Response in the TH- MYCN Transgenic Mouse Model of Neuroblastoma. Radiology. 2012.

36 Weidensteiner C, Allegrini PR, Sticker-Jantscheff M, Romanet V, Ferretti S, McSheehy PM. Tumour T1 changes in vivo are highly predictive of response to chemotherapy and reflect the number of viable tumour cells - a preclinical MR study in mice. BMC Cancer. 2014;14(1):88.

37 Christen T, Pannetier NA, Ni WW, et al. MR vascular fingerprinting: A new approach to compute cerebral blood volume, mean vessel radius, and oxygenation maps in the human brain. Neuroimage [Internet]. 2014 Apr 1 [cited 2015 Nov 19];89:262–70. Available from: http://www.pubmedcentral.nih.gov/articlerender.fcgi?artid=3940168&tool=pmcentrez&rendertype=abstract

38 Pan S, Mao D, Peiying L, Yang L, Babu W, Hanzhang L. Arterial Spin Labeling without control/label pairing and post-labeling delay: an MR fingerprinting implementation. In: In proceedings of the 23rd annual meeting of ISMRM meeting & exhibition in Toronto, Canada. 2015. p. 0276.

39 Hamilton JI, Deshmane AV, Stephanie H, Griswold MA, Seiberlich N. Magnetic Resonance Fingerprinting with Chemical Exchange (MRF-X) for Quantification of Subvoxel T1, T2, Volume Fraction, and Exchange Rate. In: In proceedings of the 23rd annual meeting of ISMRM meeting & exhibition in Toronto, Canada. 2015. p. 0329.

40 Vymazal J, Righini A, Brooks RA, et al. T1 and T2 in the Brain of Healthy Subjects, Patients with Parkinson Disease, and Patients with Multiple System Atrophy: Relation to Iron Content. Radiology. 1999;211(2):489–95.

41 Whittall KP, MacKay AL, Graeb DA, Nugent RA, Li DK, Paty DW. In vivo measurement of T2 distributions and water contents in normal human brain. Magn Reson Med. 1997;37(1):34–43.

42 Poon CS, Henkelman RM. Practical T2 quantitation for clinical applications. J Magn Reson Imaging. 1992;2(5):541–53.

43 Wansapura JP, Holland SK, Dunn RS, Ball WS. NMR relaxation times in the human brain at 3.0 tesla. J Magn Reson Imaging. 1999;9(4):531–8.

44 de Bazelaire CM, Duhamel GD, Rofsky NM, Alsop DC. MR imaging relaxation times of abdominal and pelvic tissues measured in vivo at 3.0 T: preliminary results. Radiology. 2004;230(3):652–9.

45 Chen Y, Lee GR, Aandal G, et al. Rapid volumetric t1 mapping of the abdomen using three-dimensional through-time spiral GRAPPA. Magnetic Resonance in Medicine. 2016 Apr;75(4):1457-65.

46 Stanisz GJ, Odrobina EE, Pun J, et al. T1, T2 relaxation and magnetization transfer in tissue at 3T. Magn Reson Med [Internet]. 2005/08/09 ed. 2005;54(3):507–12. Available from: http://www.ncbi.nlm.nih.gov/pubmed/16086319.

Contact

Vikas Gulani, M.D.
Department of Radiology
Case Western Reserve University
University Hospitals Case Medical Center
11100 Euclid Ave
Bolwell Building, Room B120
Cleveland, OH 44106
USA
vxg46@case.edu



Permeability Imaging of Parotid Tumors with Golden-Angle Radial Sparse Parallel MR Imaging (GRASP)

Sohil H. Patel, M.D.[1]; Hersh Chandarana, M.D.[1]; Kai Tobias Block, Ph.D.[1]; Robert Grimm, Ph.D.[2]; Girish Fatterpekar, M.D.[1]

[1] Department of Radiology, NYU Langone Medical Center, New York, NY, USA
[2] Siemens Healthcare, Erlangen, Germany

Introduction

A range of pathologic processes may affect the parotid gland. These vary from benign processes such as reactive lymph nodes, pleomorphic adenoma, and Warthin's tumor, to malignancies such as adenocarcinoma, adenoid cystic carcinoma, and mucoepidermoid carcinoma. Neoplasms of the parotid gland can pose a diagnostic challenge because conventional imaging features cannot differentiate benign from malignant lesions with complete certainty [1]. In conventional MRI examinations, most neoplasms of the parotid gland enhance with intravenous contrast. Therefore, the presence of enhancement, while essential to the identification and mapping of parotid neoplasms, does not differentiate between different tumor subtypes. To further obfuscate clinical management, the most common benign tumor of the parotid gland (pleomorphic adenoma) can occasionally dedifferentiate into a malignant tumor [2]. Moreover, the accuracy of fine needle biopsy of parotid neoplasms can occasionally be limited due to sampling errors [3].

GRASP

Golden-Angle Radial Sparse Parallel MR Imaging (GRASP[1]) is a novel imaging technique that combines golden-angle radial stack-of-stars sampling with a compressed sensing reconstruction [4], enabling motion-robust imaging at high spatial and temporal resolution. GRASP allows a characterization of the dynamic contrast curve of parotid tumors. Numerous features of the contrast curve can be easily assessed, such as the wash-in and wash-out contrast slopes, the time-to-maximum-enhancement, area under the curve, and peak enhancement. Each of these features may differ amongst various parotid neoplasms, and provide an additional non-invasive method of interrogating parotid neoplasms. In addition, GRASP produces high-resolution, fat-suppressed images with excellent motion robustness allowing for precise localization and mapping of parotid neoplasms.

[1] The product is still under development and not commercially available yet. Its future availability cannot be ensured.

Clinical cases

Two cases are included for illustration. Figure 1 shows GRASP imaging data of a parotid mass in a 67-year-old male.

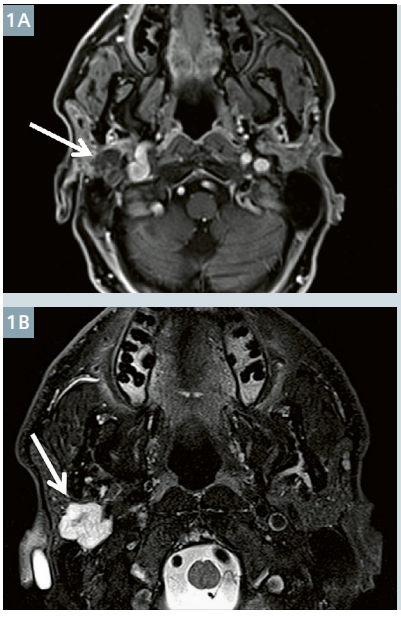

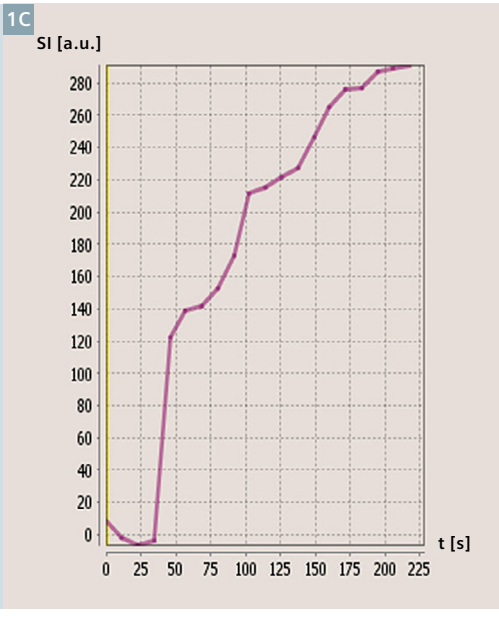

1 67-year-old male patient with a right parotid pleomorphic adenoma. **(1A)** Composite GRASP image shows a lobulated mass in the right parotid gland demonstrating mild enhancement (arrow). **(1B)** T2-weighted imaging demonstrates hyperintense signal in the lesion (arrow). **(1C)** Dynamic contrast curve shows continuous gradual wash-in of contrast material during the image acquisition.

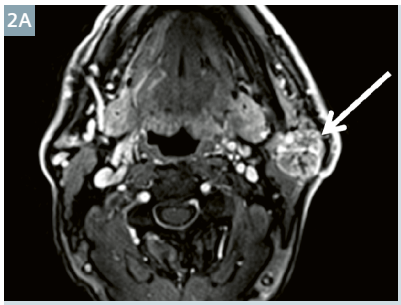

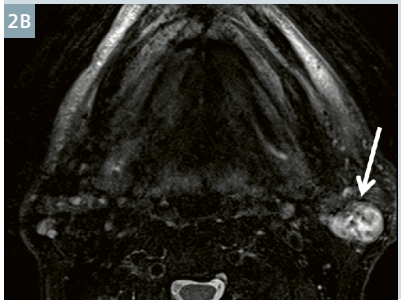

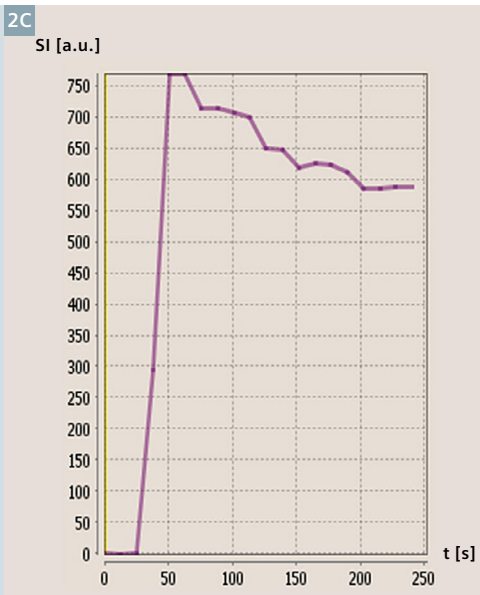

2 68-year-old male patient with a left parotid Warthin's tumor. **(2A)** Composite GRASP image shows a lobulated mass in the left parotid gland demonstrating moderate enhancement (arrow). **(2B)** T2-weighted imaging demonstrates predominantly hyperintense signal in the lesion (arrow). **(2C)** Dynamic contrast curve shows steep wash-in slope, sharp early peak of contrast enhancement, and more gradual wash-out of contrast material.

Figure 1A is a high-resolution post-contrast image demonstrating that the mass has mild heterogeneous enhancement, and contains lobulated margins. Figure 1B shows that the lesion is hyperintense on T2-weighted imaging. Figure 1C demonstrates the dynamic contrast curve after processing of the GRASP data. The contrast curve demonstrates a gradual and continuously rising wash-in of contrast material. The imaging appearance and contrast curve characteristics were consistent with a pleomorphic adenoma [5], and this proved to be the case on pathologic analysis.

Figure 2 shows GRASP imaging data of a left parotid mass in a 68-year-old male. Figure 2A shows that the mass demonstrates moderately avid heterogeneous enhancement, and contains lobulated margins. Figure 2B shows that the lesion is predominantly hyperintense on T2-weighted imaging. Figure 2C demonstrates the dynamic contrast curve, which is strikingly different than the case shown in Figure 1. In this case, the contrast curve shows a sharp wash-in, an early peak, and relatively early wash-out of contrast material. Though the conventional imaging characteristics in this case were non-specific, the contrast curve was characteristic of a Warthin's tumor [5], which proved to be the case upon pathologic analysis.

Conclusion

Improving the diagnostic specificity in assessing parotid neoplasms is only one among many potential applications for GRASP in the head and neck. Examples include assessment of lymph node status in cancer patients, differentiation of tumor recurrence from inflammation in treated patients, or differentiation of tumor types in other organs of the head and neck. At our institution, GRASP is performed in all of our clinical head and neck MRI scans, and it routinely impacts on our diagnostic performance.

References

1 Christe A, Waldherr C, Hallett R, Zbaeren P, Thoeny H. MR imaging of parotid tumors: typical lesion characteristics in MR imaging improve discrimination between benign and malignant disease. AJNR American journal of neuroradiology. 2011;32(7):1202-7. doi:10.3174/ajnr.A2520.

2 Antony J, Gopalan V, Smith RA, Lam AK. Carcinoma ex pleomorphic adenoma: a comprehensive review of clinical, pathological and molecular data. Head and neck pathology. 2012;6(1):1-9. doi:10.1007/s12105-011-0281-z.

3 Daneshbod Y, Daneshbod K, Khademi B. Diagnostic difficulties in the interpretation of fine needle aspirate samples in salivary lesions: diagnostic pitfalls revisited. Acta cytologica. 2009;53(1):53-70.

4 Feng L, Grimm R, Block KT, Chandarana H, Kim S, Xu J, Axel L, Sodickson DK, Otazo R. Golden-angle radial sparse parallel MRI: combination of compressed sensing, parallel imaging, and golden-angle radial sampling for fast and flexible dynamic volumetric MRI. Magn Reson Med. 2014.

5 Dong Y, Lei GW, Wang SW, Zheng SW, Ge Y, Wei FC. Diagnostic value of CT perfusion imaging for parotid neoplasms. Dento maxillo facial radiology.

6 Chandarana H, Feng L, Block TK, Rosenkrantz AB, Lim RP, Babb JS, Sodickson DK, Otazo R. Free-breathing contrast-enhanced multiphase MRI of the liver using a combination of compressed sensing, parallel imaging, and golden-angle radial sampling.Invest Radiol 2013 Jan;48(1):10-6.

7 Chandarana H, Block TK, Ream J, Mikheev A, Sigal SH, Otazo R, Rusinek H. Estimating liver perfusion from free-breathing continuously acquired dynamic gadolinium-ethoxybenzyl-diethylenetriamine pentaacetic acid-enhanced acquisition with compressed sensing reconstruction. Invest Radiol. 2015 Feb;50(2):88-94. 2014;43(1):20130237. doi:10.1259/dmfr.20130237.

Contact

Sohil H. Patel, M.D.
Department of Radiology
New York University
Langone Medical Center
660 1st Ave
New York , NY 10016
USA
sohil.patel@nyumc.org

Diffusion-Weighted MR Mammography (DWI-MRM) – Potential in the Clarification of Suspicious Lesions Detected by X-Ray Mammography

Sebastian Bickelhaupt[1]; Frederik Laun[2]; Wolfgang Lederer[3]; Heidi Daniel[4]; Anne Stieber[5]; Stefan Delorme[1]; Heinz-Peter Schlemmer[1]

[1] German Cancer Research Center (DKFZ), Radiology Department, Heidelberg, Germany
[2] German Cancer Research Center (DKFZ), Medical Physics in Radiology Department, Heidelberg, Germany
[3] Radiology Group Practice at the ATOS Clinic, Heidelberg, Germany
[4] Mannheim Radiology Center (RZM), Mannheim, Germany
[5] Department of Diagnostic and Interventional Radiology at the Heidelberg University Hospital, Heidelberg, Germany

Abstract

Diffusion-weighted MR mammography (DWI-MRM) maps the diffusion of water molecules in body tissue and could also contribute to a further increase in the diagnostic certainty of breast diagnostics. The advantages offered by DWI-MRM include short examination and evaluation times and the omission of administering contrast media containing gadolinium. In addition to its integration as a component of conventional MR mammography protocols, a shortened and contrast medium free DWI-MRM protocol (DWI, T2 TSE, T2 SPAIR/STIR) might be of independent diagnostic value for specific indications, e.g. the noninvasive clarification of suspicious lesions in X-ray mammography. The establishment of a quality assurance concept and device-specific optimization for breast diagnostics has proved especially valuable in ensuring the data quality of such a shortened DWI-MRM protocol. The initially published data from a bicentric study indicate that a high level of sensitivity and specificity can be achieved for the clarification of suspicious lesions in X-ray mammography with this concept.

Introduction

False-positive findings in X-ray mammography may lead to further clarification examinations up to and including invasive measures such as tissue biopsies performed on healthy women [1, 2]. For the widely established breast cancer screening programs, this was described by the work group "International Agency for Research on Cancer (IARC)" in their Statement 2015 as a significant risk posed by breast cancer screening programs [3]. For women participating in breast cancer screening programs, the risk of obtaining a false-positive result in X-ray mammography is estimated to be 20% for those who undergo 10 screening examinations (in Germany, at two-year intervals and between the ages of 50 and 69 years) [1]. Based on the statistically processed biopsy results of the German breast cancer screening program, over 50% of the biopsies indicated in the context of the current clarification strategies result in benign histopathological findings [4]. It should be noted here that, especially in a screening program, continual balancing takes place between sufficient sensitivity and an optimally high specificity; moreover, the effects of a possible shift in this balance (belated detection vs. higher rate of false-positive findings) therefore have to be

1

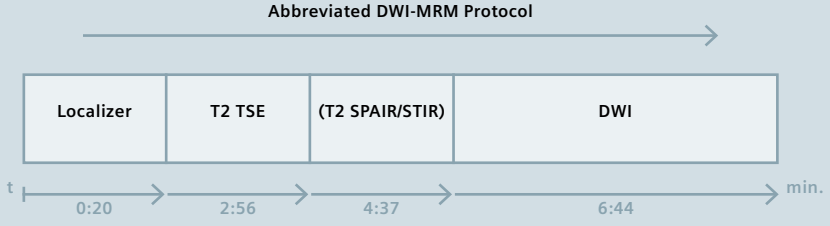

1 Sequence of the shortened, scientific DWI-MRM protocol in the study setting.

thouroughly discussed. The (further) development of imaging techniques in order to lower the rate of false-positive findings leading to the performance of invasive measures on the women concerned, and concurrently, in order to obtain a high sensitivity for the detection of malignant tumors, is therefore an essential task of radiological research. Further technical developments of existing techniques, e.g. modern ultrasound procedures by means of elastography, could further increase the diagnostic certainty in breast imaging under certain conditions [5]. Newer complementary techniques not previously considered in the breast cancer screening program on a regular basis, e.g. magnetic resonance imaging (MRI), also could lead to an improvement of diagnostic certainty if optimally adapted for screening purposes. The auspicious use of shortened contrast agent enhanced sequences in a screening collective has recently been demonstrated [6]. However, in addition to conventional sequences (T1, T2 TSE, T2 SPAIR/STIR, contrast agent enhanced), the contrast medium free, diffusion-weighted (DWI) sequence might also contribute to the further improvement of breast cancer screening [7, 8].

Diffusion-weighted MR mammography

Diffusion-weighted magnetic resonance imaging (DWI-MRI) enables the visual display and quantification of the Brownian motion of water molecules in body tissue [9]. Since the diffusion of water molecules in body tissue enables us to draw conclusions regarding tissue characteristics beyond the limits of pure image morphology, this technology is increasingly gaining interest, especially for the characterization of tissue in the field of oncological imaging [10]. In this way, DWI has established itself as an integral component of many oncological MRI protocols and has been integrated in the PI-RADS classification. It is used e.g. in the diagnostics of prostate carcinomas as the leading sequence for the detection of carcinomas of the peripheral zone [11].

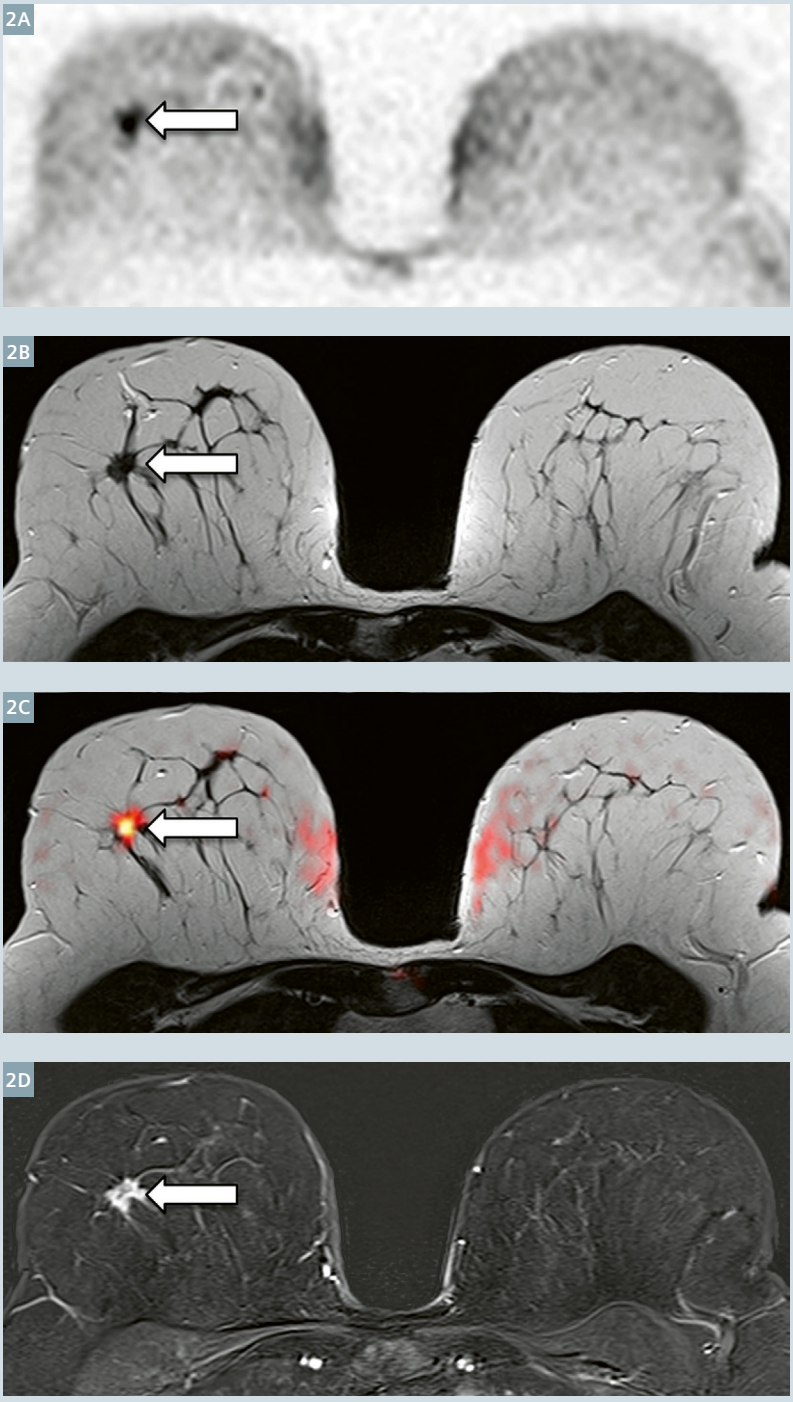

2 Example of a lesion radiologically detected as BIRADS 5 in a mammography screening. **(2A)** RESOLVE DWI with b-value of 1500 s/mm² and clear demarcation of a diffusion-restricted focal lesion. **(2B)** T2-TSE sequence with suspiciously configured, spiculated lesion. **(2C)** Fusion imaging from T2-TSE and DWI (PET-CLUT) with congruent focus. **(2D)** DCE-MRI with likewise clear, contrast-enhanced lesion. Histopathology: Invasive ductal mammary carcinoma.

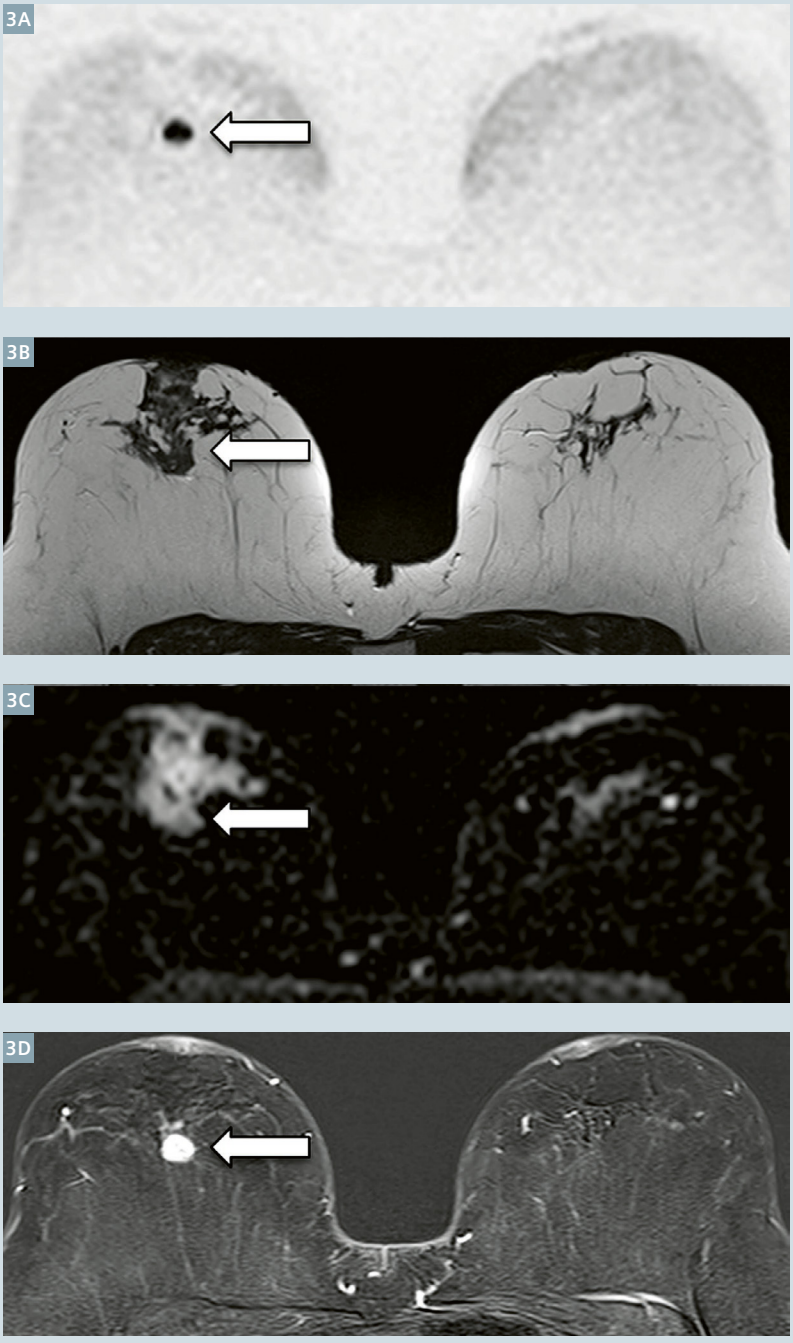

3 Participant in the mammography screening program with conspicuous lesion in the right breast. **(3A)** RESOLVE DWI with b-value of 1500 s/mm² and distinct, diffusion-restricted focal lesion. **(3B)** T2-TSE sequence with corresponding lesion, somewhat difficult to delimit in the gland tissue. **(3C)** Apparent diffusion coefficient (ADC) map. **(3D)** DCE-MRI with contrast-enhanced lesion. Histopathology: Invasive ductal mammary carcinoma.

The DWI-MRI technique allows for insights into various different biophysiological compartments: The determination of intravoxel incoherent motion (IVIM) enables conclusions concerning the perfusion behavior of the tissue under examination and uses low b-values [12]. The diffusion in the tissue can be quantified with the apparent diffusion coefficient (ADC) [13]. With high b-values, the free perfusion of the water begins to play a less predominant role and, based on the signal intensity curves, conclusions can be made regarding the spatial restriction of motion (kurtosis) [14].

The evaluation of diffusion-weighted sequences (DWI) as an integral module or as an additive component in breast diagnostics was the objective of several studies in recent years, which were partially summarized in a review by Thomassin-Naggara et al. in 2013 [13]. As an additive technique, DWI is chiefly researched as a means of increasing the specificity of conventional contrast agent enhanced (dynamic contrast enhanced) DCE-MRM protocols [13]. Recently published studies have shown that, in terms of a contrast medium free, shortened MRM using only DWI and morphological (T2-weighted-TSE, T2-weighted-SPAIR) sequences, DWI-MRM could exhibit its own diagnostic value under certain conditions [7, 8, 15]. The advantages offered by DWI-MRM include short examination times and dispensing with the administering of contrast media containing gadolinium. The latter benefit is especially important in light of the ongoing discussion concerning the accumulation of contrast media containing gadolinium in the brain after repeated application [16-18]. Scientific studies have provided morphological image-based and histopathological evidence of deposits of gadolinium in the brains of patients following repeated intravenous application in which preparation-dependent differences between linear and macrocyclic contrast media appeared [19]. The clinical relevance of these findings is currently still the controversial

subject of multiple studies. However, in the case of screening programs involving recurring examinations of participants primarily regarded as healthy, a technique which is as gentle as possible and at the same time of high diagnostic quality is very important for the guidance and acceptance of the measure.

In an initial study concerning the use of a contrast medium free DWI-MRM protocol (DWI, STIR, T2-TSE) as a diagnostic technique in breast cancer diagnostics, the work of Telegrafo et al. showed a sensitivity of 94% and a specificity of 79% [8]. DWI-MRM might prove especially valuable in the clarification of lesions previously detected and classified as suspicious by means of other diagnostic techniques. The possibilities offered by DWI-MRM for quantification with independent multiparametric aspects (IVIM, kurtosis, ADC) could play a role here. In a multicenter study concerning the application of DWI-MRM as an additional measure for clarifying conspicuous findings in the mammography screening program, a study project involving the German Cancer Research Center (DKFZ) and regional screening units was implemented to evaluate the diagnostic significance of a contrast medium free, shortened DWI-MRM performed prior to biopsies. A multilevel study concept enabled the translational establishment of a quality-assured DWI-MRM with subsequent implementation of the actual study project here.

Challenges and establishment of the quality-assured DWI-MRM

In addition to the advantages of DWI-MRM, methodic and technical challenges and limitations must be observed. Despite the use of DWI sequences in breast diagnostics in the scientific and clinical setting, no national or international standardization has occurred yet regarding the decisive sequence parameters. The b-values and slice thicknesses/resolutions selected in routine clinical protocols thus vary greatly and the values are not infrequently selected too low. However, the selection of the b-values is very significant, especially for achieving a sufficient suppression of normal tissue and the T2 shine-through effect. Since the spatial resolution also is much lower than for DCE-MRM, e.g. partial volume effects must be considered in the optimization and standardization. Device-specific optimization of DWI-MRM is therefore an essential prerequisite for its effective and diagnostically significant application in breast diagnostics. If suboptimal parameters without a dedicated device-specific optimization are selected, this can influence the diagnostic significance substantially. Thus, for example, with b-values that are selected inadequately low, due to the missing suppression of the breast parenchyma and any possible benign compactions, false-positive lesions which complicate diagnostic assessment often can be found. For this reason, numerous b-values covering a broad spectrum should be acquired in order to have reliable data points for the calculation of the ADC. Moreover, a very high b-value in the range of 1000-1500 mm/s² should also be included in the protocol [20]. Therefore, device-optimized standardization of the MRI systems was performed in the study centers participating in the study project as part of a multilevel standardization process. Furthermore, a dedicated DWI-MRI phantom was developed by the Medical Physics Department and then established in all study centers with a quality assurance program. The phantom comprises a hollow cylindrical body containing several inserted tubes of varying diameter. A solution with high and low ADC values is placed in these tubes, thus simulating benign and malignant lesions of varying size. Device-optimized, comparable DWI-MRM findings as well as consistent quality could be ensured throughout the course of the study via regular check measurements.

Perspectives of DWI-MRM

The initial data of our multicenter study project indicated the possibility that a significant percentage of the false-positive findings from the breast cancer screening program can be detected as such only by using DWI-MRM as an additional clarification modality [7]. The number of unnecessary invasive biopsies could possibly be reduced considerably hereby. Although this method exhibited a high sensitivity in the first study evaluation, it still was apparent that lesions (e.g. DCIS lesions) also could be missed. The published early results here refer to a collective of 50 women with BI-RADS 4/5 lesions and a biopsy indication which subsequently resulted from the screening clarification. A sensitivity of 92% and a negative predictive value of 92% resulted for DWI-MRM [7]. DWI-MRM did not appear to be less advantageous compared to contrast agent enhanced DCE-MRM for this indication. Just as single-image MIPs (maximum intensity projections) can be evaluated for DCE-MRM, we tested the MIP display technique in the early data evaluation. This showed that high b-values (b = 1500 mm/s²) resulted in a sufficient suppression of the regular mammary gland tissue and fatty tissue, thus enabling a MIP projection. Regarding the reading function, the MIP technique shows the benefit a shorter evaluation time offers to the radiologist in contrast to the use of single slices. These were used for further morphological assessment in conjunction with the T2-weighted sequences only in cases involving anomalies.

No statement could be made to date or can possibly be made in the future within the scope of our study project as to what extent DWI-MRM could represent a possible alternative screening modality. Likewise, the objective of the study is not to evaluate the universal comparability of DWI-MRM and DCE-MRM, but rather, to investigate a dedicated indication, the clarification of suspicious findings

by means of noninvasive imaging where other diagnostic techniques have been exhausted. The initial results encourage us to perform further studies in order to evaluate use of the DWI-MRM technique as a procedure in breast cancer diagnostics.

Summary

Apart from the use of DWI as an additional component of conventional contrast agent enhanced MRM a shortened and contrast medium free DWI-MRM protocol (DWI, T2 TSE, T2 SPAIR/STIR) might be singularly significant in breast cancer diagnostics for specific indications. This concerns e.g. the noninvasive clarification of suspicious lesions from (screening) X-ray mammography before diagnosing an indication for biopsy. The advantages offered by DWI-MRM here include short examination and interpretation times, as well as the omission of any intravenous administering of contrast media containing gadolinium. In particular, the establishment of the quality assurance concept escribed above has proved valuable as a means of ensuring data quality. A device-specific optimization of imaging quality has proven indispensable in the preliminary stages of multicenter study projects. The initially published results from our first bicentric study project indicate that a high level of sensitivity and specificity can be achieved for the further clarification of suspicious lesions in X-ray mammograms with this concept.

The implementation of further studies dealing with DWI-MRM in breast cancer diagnostics is therefore ppropriate.

References

1 Hofvind S, Ponti A, Patnick J, et al. False-positive results in mammographic screening for breast cancer in Europe: a literature review and survey of service screening programmes. Journal of Medical Screening 2012;19:57-66.
2 Payne JI, Martin T, Caines JS, Duggan R. The Burden of False-Positive Results in Analog and Digital Screening Mammography: Experience of the Nova Scotia Breast Screening Program. Canadian Association of Radiologists Journal 2014;65:315-20.
3 Lauby-Secretan B, Scoccianti C, Loomis D, et al. Breast-Cancer Screening — Viewpoint of the IARC Working Group. New England Journal of Medicine 2015;372:2353-8.
4 Berlin CMgKM. Evaluation-Report 2010. Results of the Mammography-Screening-Program in Germany. 2014.
5 Golatta M, Schweitzer-Martin M. Evaluation of virtual touch tissue imaging quantification, a new shear wave velocity imaging method, for breast lesion assessment by ultrasound. 2014;2014:960262.
6 Kuhl CK, Schrading S, Strobel K, Schild HH, Hilgers R-D, Bieling HB. Abbreviated Breast Magnetic Resonance Imaging (MRI): First Postcontrast Subtracted Images and Maximum-Intensity Projection—A Novel Approach to Breast Cancer Screening With MRI. Journal of Clinical Oncology 2014;32:2304-10.
7 Bickelhaupt S, Laun FB, Tesdorff J, et al. Fast and Noninvasive Characterization of Suspicious Lesions Detected at Breast Cancer X-Ray Screening: Capability of Diffusion-weighted MR Imaging with MIPs. Radiology 2015:150425.
8 Telegrafo M, Rella L, Stabile Ianora AA, Angelelli G, Moschetta M. Unenhanced breast MRI (STIR, T2-weighted TSE, DWIBS): An accurate and alternative strategy for detecting and differentiating breast lesions. Magn Reson Imaging 2015;33:951-5.
9 Le Bihan D, Breton E. Imagerie de diffusion in-vivo par résonance. C R Acad Sci (Paris) 1985; 301 (15):1109–12.
10 Freitag MT, Bickelhaupt S, Ziener C, et al. [Selected clinically established and scientific techniques of diffusion-weighted MRI: In the context of imaging in oncology]. Der Radiologe 2016;56:137-47.
11 Weinreb JC BJ, Choyke PL, Cornud F, Haider MA, Macura KJ, Margolis D, Schnall MD, Shtern F, Tempany CM, Thoeny HC, Verma S. Weinreb JC. PI-RADS Prostate Imaging-Reporting and Data System:2015,Version 2. Eur Urol 2016;69(1):16-40
12 Panek R, Borri M, Orton M, et al. Evaluation of diffusion models in breast cancer. Medical physics 2015;42:4833-9.
13 Thomassin-Naggara I, De Bazelaire C, Chopier J, Bazot M, Marsault C, Trop I. Diffusion-weighted MR imaging of the breast: Advantages and pitfalls. European Journal of Radiology 2013;82:435-43.
14 Jensen JH, Helpern JA, Ramani A, Lu H, Kaczynski K. Diffusional kurtosis imaging: the quantification of non-gaussian water diffusion by means of magnetic resonance imaging. Magnetic resonance in medicine 2005;53:1432-40.
15 Kul S, Oguz S, Eyuboglu I, Komurcuoglu O. Can unenhanced breast MRI be used to decrease negative biopsy rates? Diagnostic and interventional radiology (Ankara, Turkey) 2015;21:287-92.
16 Errante Y, Cirimele V, Mallio CA, Di Lazzaro V, Zobel BB, Quattrocchi CC. Progressive increase of T1 signal intensity of the dentate nucleus on unenhanced magnetic resonance images is associated with cumulative doses of intravenously administered gadodiamide in patients with normal renal function, suggesting dechelation. Invest Radiol 2014;49:685-90.
17 Kanda T, Ishii K, Kawaguchi H, Kitajima K, Takenaka D. High signal intensity in the dentate nucleus and globus pallidus on unenhanced T1-weighted MR images: relationship with increasing cumulative dose of a gadolinium-based contrast material. Radiology 2014;270:834-41.
18 McDonald RJ, McDonald JS, Kallmes DF, et al. Intracranial Gadolinium Deposition after Contrast-enhanced MR Imaging. Radiology 2015;275:772-82.
19 Radbruch A, Weberling LD, Kieslich PJ, et al. Gadolinium retention in the dentate nucleus and globus pallidus is dependent on the class of contrast agent. Radiology 2015;275:783-91.
20 Tamura T, Murakami S, Naito K, Yamada T, Fujimoto T, Kikkawa T. Investigation of the optimal b-value to detect breast tumors with diffusion weighted imaging by 1.5-T MRI. Cancer imaging : the official publication of the International Cancer Imaging Society 2014;14:11.



Contact

Sebastian Bickelhaupt, M.D.
German Cancer Research Center (DKFZ)
Im Neuenheimer Feld 280
69126 Heidelberg
Germany
Phone: +49 6221 422603
Fax: +49 6221 422615
S.Bickelhaupt@dkfz.de

Long-term Experience with MR Upgrades

Christos Loupatatzis, M.D; Christoforos Stoupis, M.D.

MRI AG Spital Maennedorf, Switzerland

In this article we share some of our experiences over the last few years with MR upgrades.

The MRI AG Spital Maennedorf is located beside Lake Zurich in Switzerland and is one of the leading MR-centers in the region. With its close relationship to the academic hospital Maennedorf and to specialized practitioners with a variety of subspecialties including Orthopedics, Trauma-/General-/Hand- and Neuro-Surgery, Neurology, Psychiatry, Gastroenterology, Urology, Gynecology and Angiology we receive requests for MR examinations all over the body ("from head to toe"). We therefore need an MRI scanner able to perform all kinds of examinations at a very high level. Our referring physicians recognize the high quality of our work and our participation in radiology boards and meetings (e.g. European School of Radiology). Without the proper technical equipment it would not be possible to sustain this high level.

In 2007 the decision was made to acquire a MAGNETOM Avanto 1.5T MRI system (Siemens Healthcare, Erlangen, Germany). This scanner worked consistently over the years to provide very good image quality. Nevertheless, always aiming to optimize our image quality and performance, in 2013 we became one of the first MRI centers in Switzerland to perform a fit upgrade, accompanied by a Dot upgrade. Notwithstanding the acquisition of additional diagnostic tools during the first years (such as spectroscopy,

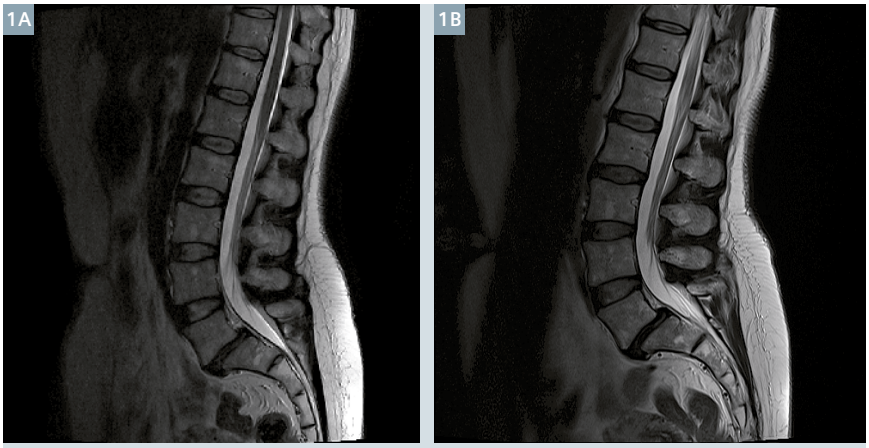

TR 4000 ms, TE 122 ms, TA 3 min, 12 slices, FOV 317 x 320, matrix 754 x 896, SL 4.0 mm

TR 3250 ms, TE 91 ms, TA 3:31 min, 15 slices, FOV 300 x 300, matrix 307 x 512, SL 4.0 mm

1 46-year-old female patient. T2w sagittal images of the lumbar spine, before **(1A)** and after **(1B)** MAGNETOM Avanto^{fit} upgrade. Note the improved image quality in 1B (i.e. better delineation of the nerve roots).

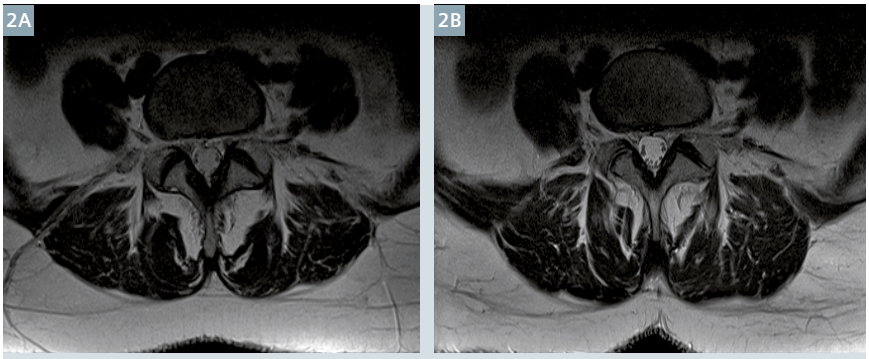

TR 3100 ms, TE 108 ms, TA 3:03 min, 15 slices, FOV 248 x 250, matrix 311 x 448, SL 4.0 mm

TR 3800 ms, TE 108 ms, TA 2:58 min, 16 slices, FOV 200 x 200, matrix 269 x 448, SL 4.0 mm

2 Same patient as in Figure 1. T2w axial images of the lumbar spine, before **(2A)** and after **(2B)** MAGNETOM Avanto^{fit} upgrade. In 2B note the possibility to reduce the FOV and therefore improved image resolution, in shorter acquisition time (i.e. the nerve roots).

perfusion imaging and susceptibility-weighted imaging), this fit upgrade was our first major MR upgrade.
A second major step has been our update to software version *syngo* MR E11C. A milestone in this context was our participation as a CPF ("Customer Preference Feedback") reference center for the *syngo* MR E11C software version in 2015/2016.

Avanto^{fit} and first Dot engine experiences

Despite the high image quality of the MAGNETOM Avanto system, we needed firstly to respond to our referring physicians' demands for the best image quality, and secondly to stay competitive as a leading MRI center amongst the increasing number of 3T systems available in the Zurich area. We decided on the Avanto^{fit} upgrade instead of buying a new scanner, a solution we thought would be more cost efficient and less time consuming. Since we have only one MRI scanner, we could not afford the time required for the de-installation and a new installation, whereas an upgrade would reduce the downtime of the system to a couple of days.

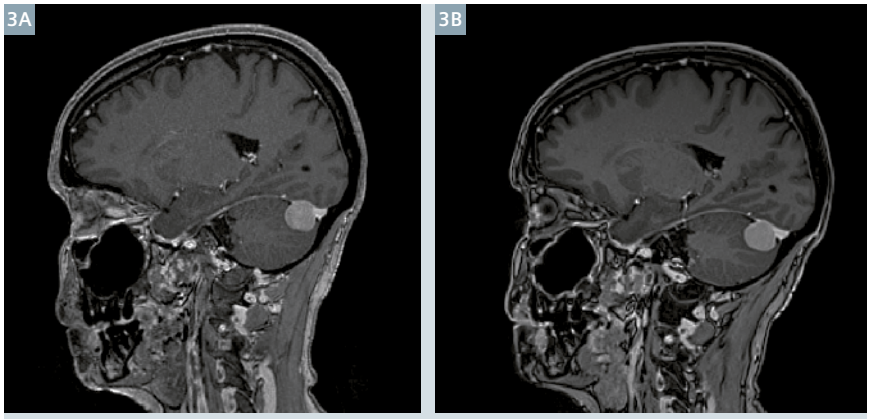

TR 2060 ms, TE 3.4 ms, TI 1100 ms, TA 5:11 min, 208 slices, FOV 250 x 250, matrix 320 x 320, SL 0.9 mm

TR 2000 ms, TE 2.5 ms, TI 900 ms, TA 5:01 min, 208 slices, FOV 250 x 250, matrix 288 x 288, SL 0.9 mm

3 54-year-old female patient. 3D-MPRAGE-sequence of the brain after contrast administration before **(3A)** and after **(3B)** MAGNETOM Avanto^{fit} upgrade showing a meningeoma of the cerebellar tentorium. Note the much better image quality in less acquisition time in 3B (i.e. the delineation of the cortical matter).

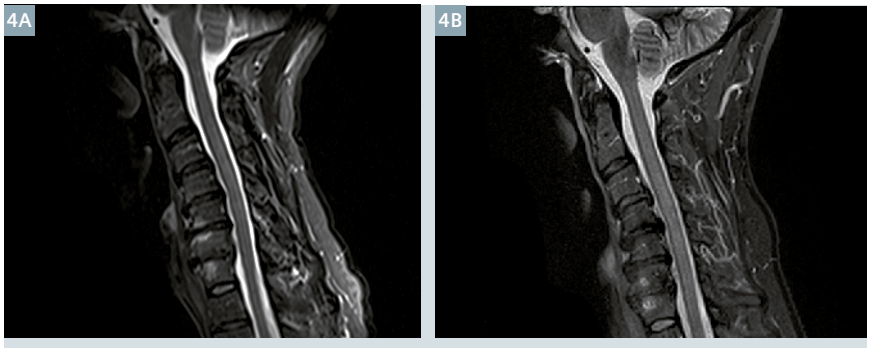

TR 3500 ms, TE 91 ms, TA 3:27 min, 12 slices, FOV 280 x 280, matrix 384 x 512, SL 3.5 mm

TR 3500 ms, TE 29 ms, TA 3:47 min, 12 slices, FOV 220 x 220, matrix 515 x 512, SL 3.0 mm

4 45-year-old male patient. STIR sagittal images of the cervical spine, before **(4A)** and after **(4B)** MAGNETOM Avanto^{fit} upgrade. Note the possibility to reduce both the FOV and the slice-thickness with minimal increase in acquisition time, and with a superior image quality in 4B (i.e. the subtle signal intensity changes of the spinal cord).

We decided to carry out this fit upgrade during the summer holiday season, when most of our referring physicians were on holiday. Following the fit upgrade installation we received one week's intensive support from our Siemens MR Application Specialist, since obviously an adjustment of all our sequence protocols was necessary. This intensive and time-consuming period after installation was followed by a two-month period of further protocol optimization, with the help of the application specialist, adapting the initial protocols after gaining some experience with the new system. In retrospect, all of our efforts were worthwhile.

The improvement of the image quality was obvious in all examinations over the whole body. External neurologists and orthopedic surgeons mentioned that our image quality was so good that they thought we bought a 3T-system (Figs. 1, 2).
This fit upgrade had two benefits of a 1.5T over a 3T system: Less susceptibility artifacts, specifically in abdominal imaging, as well as patient security and fewer limitations in case of intracorporeal medical devices such as prosthetic cardiac valves etc. This was definitively the right choice for our institution.

In brain-imaging specifically the 3D-MPRAGE-sequence became much crispier and clearer (Fig. 3) and the RESOLVE-diffusion showed significantly less artifacts in comparison to the standard EPI diffusion.
In spine-imaging we were able to reduce the field-of-view (FOV) and therefore increase the resolution with even higher signal-to-noise ratio (SNR) (Fig. 4). In shoulder-imaging, the new Shoulder 16-channel coil not only gave better image quality, but also increased patient comfort when positioned. In knee-imaging, the new 15-channel Tx/Rx Knee coil produced images of a quality superior to the previous system (Fig. 5). The only disadvantage is that obese patients and patients after trauma unable to stretch-out their knee do not fit into this coil: For those cases we still use the previous Extremity coil with an additional adapter in order to enable

the link with the new system. Special mention should go to the Hand/Wrist 16 coil and Foot/Ankle 16 coil for their convenience for the patient and for enabling the scan of very small structures (such as a finger joint) or the whole hand, and the foot without moving the target area within the coil (for example imaging a distal joint or a proximal joint; Fig. 6).

Feedback from our technologists tells us that one of the advantages of the fit upgrade is the much easier handling of the coils with the new innovative SlideConnect system and the new in-room display at the scanner, which enables the technologist to get information about the coils before leaving the scanner room. Additionally the display provides patient-data-information, ECG-waves, etc.

Definitely one of the biggest steps of evolution and advantage of the new system is the standardization of the exam protocols using the Dot engines in routine examinations. The first Dot engines we used were the Brain and the Spine Dot Engines. The Brain Dot Engine, with AutoAlign, its automatic anatomic orientation, not only helps less experienced technologists to reliably find the anatomic landmarks for an optimal examination, but also guides the radiologist in the comparison of the image-planes in follow-up brain studies such as in multiple sclerosis patients, because of the identical slice orientation and slice-positioning.

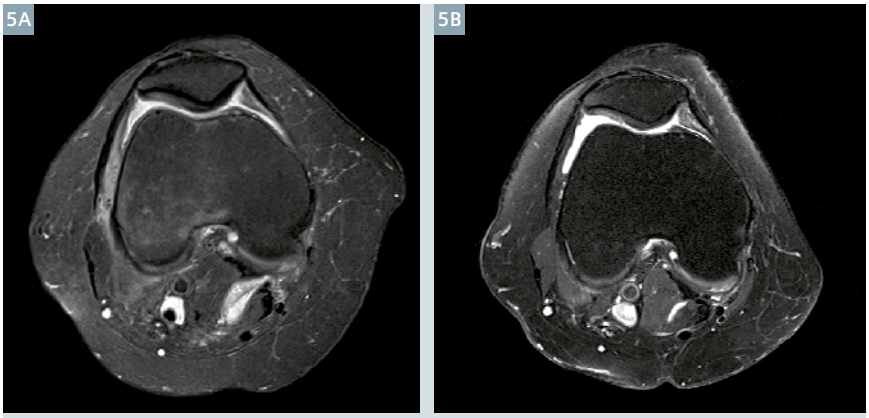

TR 2120 ms, TE 41 ms, TA 2:14:2 min, 32 slices, FOV 160 x 160, matrix 240 x 320, SL 3 mm

TR 3600, TE 45 ms, TA 3:10 min, 30 slices, FOV 160 x 160, matrix 269 x 448, SL 3 mm

5 75-year-old female patient. Proton Density-weighted fat sat (PDfs) axial images of the knee before **(5A)** and after **(5B)** MAGNETOM Avanto^{fit} upgrade, using the new 15 channel knee coil. Note the much better image quality in 5B (i.e. in the retropatellar cartilage).



TR 3010 ms, TE 26 ms, TA 2:09 min, 20 slices, FOV 186 x 220, matrix 345 x 512, SL 2 mm

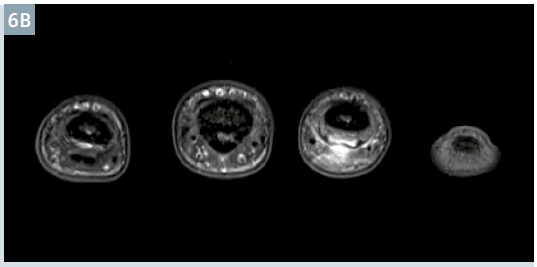

TR 4200 ms, TE 28 ms, TA 3:31 min, 25 slices, FOV 96 x 110, matrix 353 x 448, SL 3 mm

6 15-year-old male patient with rupture of the flexor digitorum profundus tendon (4th finger). Note the high quality images: **(6A)** Coronal PDfs image showing the rectracted tendon and **(6B)** axial PDfs image showing the empty space, where the tendon should be.

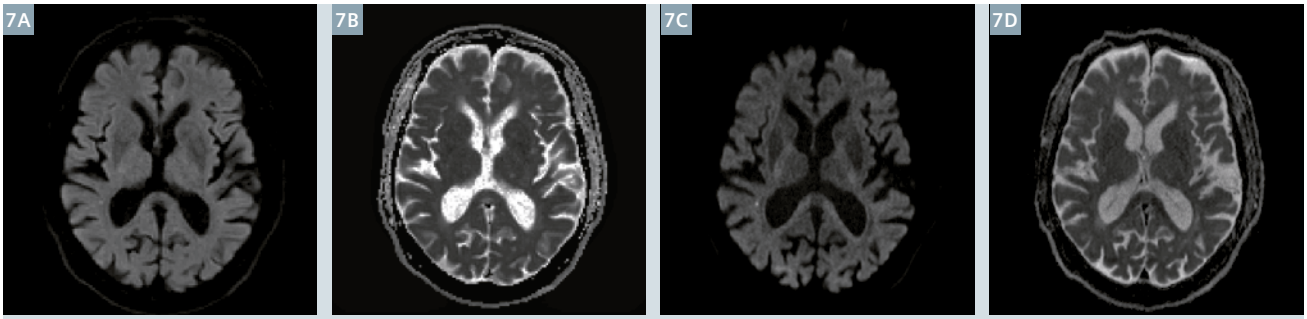

TR 4000 ms, TE 64 ms, SL 5 mm, TA 1:34 ms, 25 slices, b-value 1000

TR 3000 ms, TE 83 ms, SL 2.5 mm, TA 2:40 ms, 40 slices, b-value 2000

7 71-year-old male patient with focal acute embolic ischemia within the Meyer's loop on the right hemisphere (standard RESOLVE Diffusion **(7A)** b1000 image, **(7B)** ADC map). Note the much better visibility of the pathology using thinner slices and higher b-value (modified SMS-Diffusion **(7C)** b2000 image, **(7D)** ADC map). Because of the Simultaneous Multi-Slice acquisition, the image quality is very good **(7C, D)**, even with a b-value of 2000. (Also see Table 1.)

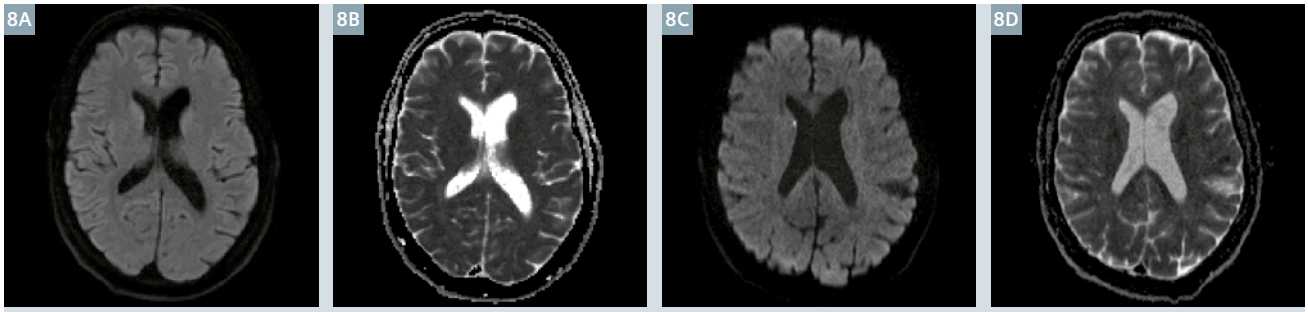

TR 4000 ms, TE 64 ms, SL 5 mm, TA 1:34 ms, 25 slices, b-value 1000

TR 3200 ms, TE 83 ms, SL 2.5 mm, TA 2:51 ms, 40 slices, b-value 2000

8 56-year-old male patient with focal acute lacunar infarct in the head of the right caudate nucleus, only visible in the modified SMS-Diffusion sequence **(8C, D)**. No visibility of the pathology at all in the standard 5 mm RESOLVE diffusion **(8A, B)**. Standard RESOLVE Diffusion **(8A)** b1000 image, **(8B)** ADC map; modified SMS-Diffusion **(8C)** b2000 image, **(8D)** ADC map. (Also see Table 1.)

The Spine Dot Engine was very useful in ensuring a complete coverage of the spine, even for patients with scoliosis. The automatic labelling of the axial slices is very much appreciated by our referring spine-surgeons, helping them to look quickly through the images even as hard-copy films, which many of them still share and discuss with their patients, rather than the primary images taken from CD.

Update to *syngo* MR E11C

The update to the new software version *syngo* MR E11C has had profound benefits for our team. Whilst we faced major software layout changes, we also benefited from new possibilities and opportunities by using the new workflow and a number of new Dot engines.

Perhaps the most important improvement in image quality due to *syngo* MR E11C is simultaneous multi-slice (SMS) diffusion-imaging. Realizing the possibilities of high SNR and time-efficiency of this sequence, one of our first modifications for brain imaging was to create a 2.5 mm thin sliced sequence with a b-value of 2000 s/mm². This modification was initially scrutinized by the Siemens-developers, who were quickly convinced of the advantages of this modification. With such a high b-value the conspicuity of acute ischemic lesions increased dramatically. Using the very robust RESOLVE diffusion (b-value 1000 s/mm², 5 mm slice thickness) as a standard sequence, we sometimes doubted the interpretation of our findings as to whether or not there was an ischemic lesion. However, using the modified SMS-diffusion, we were able to eliminate these doubts in all cases. Therefore this sequence found its way into our standard stroke protocol (Figs. 7, 8, Tab. 1).

	Original parameters	Parameters for SMS Diffusion in stroke protocol
Voxel size (mm)	0.6 x 0.6 x 4.0	0.6 x 0.6 x 2.5
PAT	4	4
Accelerator factor slice	2	2
Slices	28	40
Position	Isocenter	L2.8 A26.4 H21.7 mm
Orientation	Transversal	T > C-4.1 > S-2.1
FOV (mm)	220	230
Slices (mm)	4	2.5
TR (ms)	4000	3200
TE (ms)	97	83
Coil elements	HE 1-4	HE 1-4; NE1,2
AutoAlign	–	Head > Brain
Initial position (L x P x H) (mm)	Isocenter	0 x 17 x 2.8
System adjustments		
B1 Shim mode	TrueForm	None
Diffusion mode	4-scan trace	4-scan trace
Diffusion scheme	bipolar	monopolar
Diffusion-weightings		
b-value 1	0 s/mm²	0 s/mm²
b-value 2	1000 s/mm²	2000 s/mm²
Sequence part 1		
Echo spacing (ms)	1.04	0.91
Bandwidth (Hz/Px)	1042	1240
TA (min)	1:17	2:51

Table 1: Modified parameters of Simultaneous Multi-Slice (SMS) Diffusion for standard stroke protocol.

A substantial improvement of the new *syngo* MR E11 software has been the new ability with the Dot Cockpit to create and combine Dot protocols in a definitively easier way than in prior software versions. With a basic instruction we were able to create our own new Dot-protocols, according to our local needs, without reliance on an application specialist.

Initially, the acceptance of the Abdomen Dot Engine was suboptimal: being used to manually adapting the positioning of various parameters (e.g. slice, slab, FOV etc.) to the patients' anatomy and cooperation, we had to learn a more passive role during the acquisition of the examination. Nevertheless, the vast advantages of a guided workflow and automatic adaption of field-of-view and number of slices to the individual anatomy with AutoCoverage soon convinced us – especially for the liver. Less experienced technologists in particular appreciated the automatism for the more challenging abdominal studies. The automatic breathing commands in the Dot Engine allowed us to standardize the timing of our arterial phase in liver imaging by using the bolus-tracking technique with automatic bolus detection, thereby enabling us to acquire a consistent arterial phase, independent of patients' cardiac output. This contrast phase stability has been particularly useful in the follow-up of patients with liver cirrhosis and screening for hepatocellular carcinoma. As to time-efficiency, the new fast BLADE technique allowed a much quicker T2 acquisition of the liver, especially when using a gated technique (Fig. 9), and the coronal T1 3D acquisition became much faster by using FREEZEit and the StarVIBE (T1 VIBE CAIPIRINHA) technique. The DynaVIBE offers the possibility of multi-arterial phase acquisition, although some institutions prefer only one well-timed arterial phase with bolus-tracking. The StarVIBE technique minimizes breathing artefacts, and is especially useful with patients who are not able to hold their breath, or deaf patients. This was also one of the sequences we modified with the assistance of Siemens creating a test-version[1] of a dynamic StarVIBE sequence, which enabled dynamic liver imaging with decent image quality even with totally uncooperative patients (Fig. 10, Tab. 2). Liver-evaluation techniques with quantification of fat and iron-deposition within the liver are completing an advanced evaluation of liver pathologies.

A new innovative technique with the potential to revolutionize MR-Angiography is the Quiescent-Interval Single-Shot (QISS) sequence. This is the first reasonable alternative to contrast-enhanced angiography, in particular peripheral angiography

[1] WIP, the product is currently under development and is not for sale in the US and in other countries. Its future availability cannot be ensured.

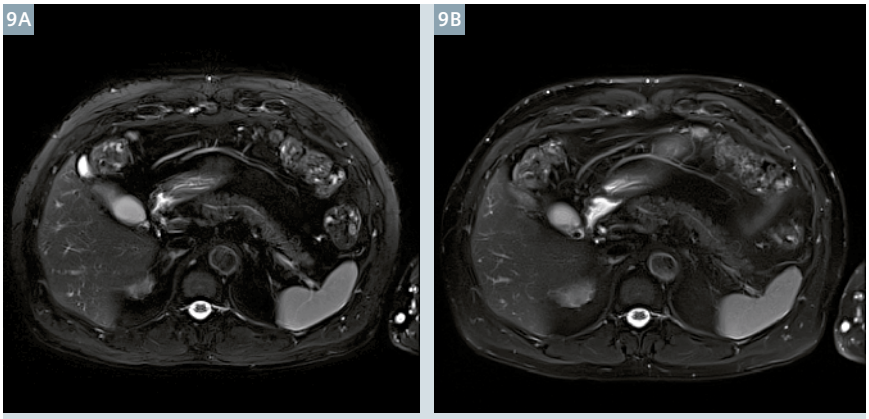

TR 5325.3 ms, TE 96 ms, TA 46.06 x 5, FOV 380 x 380, matrix 320 x 320, SL 6 mm

TR 5274.1, TE 83 ms, TA 22.77 x 5, FOV 380 x 380, matrix 320 x 320, SL 6 mm

9 Abdominal imaging of a 64-year-old male patient. Comparison between T2w fs-acquisition of the liver with gated T2 BLADE **(9A)** and T2w fast BLADE technique **(9B)**. Note the sharper image contrast and better visibility of the gallbladder stone in less than half of the time in T2w fast BLADE in **9B**.

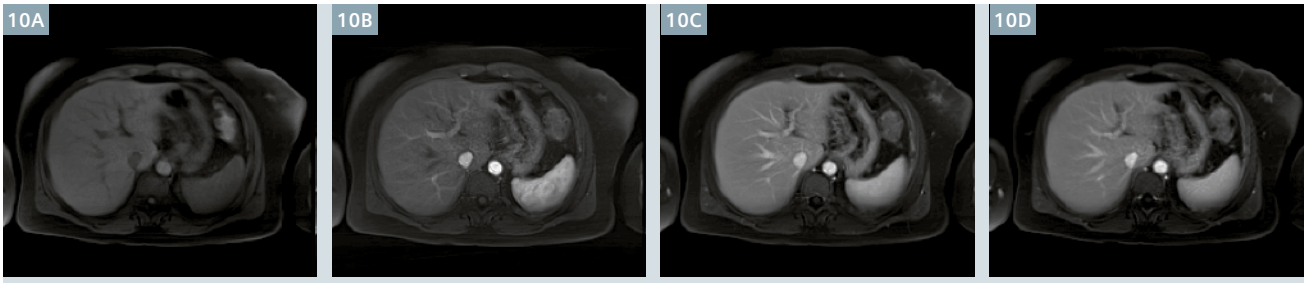

TR 3.3 ms, TE 1.4 ms, TA 21.35 sec, SL 4 mm, FOV 380 x 380

10 46-year-old female patient, immigrant, unable to understand the language in which the breathing commands were spoken. Modified StarVIBE sequence was used to acquire dynamic imaging before and after contrast-enhancement: **(10A)** without contrast medium, **(10B)** late arterial phase, **(10C)** first hepatovenous phase, **(10D)** second hepatovenous phase. Note the sharp organ contours and the well delineated anatomic structures without breath-hold imaging in different phases (each phase less than 22 seconds). (Also see table 2)

	Original parameters	Parameters for T1 StarVIBE dynamic liver imaging
Voxel size (mm)	1.2 x 1.2 x 3.0	1.7 x 1.7 x 4.0
Slab group		
Position	Isocenter	Isocenter
Orientation	Transversal	Transversal
Rotation	0.00 deg	90 deg
Phase directions	A - P	R - L
Slice oversampling	44.5%	0.0%
Slices per slab	72	52
FOV (mm)	380	380
Slice thickness (mm)	3	4
TR (ms)	2.83	3.26
TE (ms)	1.48	1.44
Flip angle	9 deg	10 deg
Lines per shot	56	18
Coil elements	BO1-3;SP2,3	BO1-3;SP2-4
Contrast – Dynamic		
Multiple series	Each measurement	Off
Resolution		
Base resolution	320	224
Radial views	680	220
System adjustments		
B1 Shim mode	TrueForm	Off
Sequence part 1		
Bandwidth (Hz/Px)	820	600
Sequence Assistant		
Allowed delay	60 s	–
TA (min)	2:53	0:21

Table 2: Modified parameters for dynamic liver imaging for totally uncooperative patients.

of lower extremity arteries (Fig. 11). Furthermore the QISS sequence can visualize arterial vessels in the lower leg each time without any overlay of venous vessels, which may happen in contrast-enhanced angiography. Knowing the adverse effects of contrast-media discussed in recent years, such as nephrogenic systemic fibrosis (NSF) and gadolinium accumulation in the brain, and having recently had the personal experience of a very rare life-threatening anaphylactic shock due to gadolinium administration, we do appreciate any development in this direction.

Summary

Our long-term experience with MR upgrades is a real success story. Technical innovations lead to better image quality and faster examination protocols, help improve the comfort and safety of the patients through the MR-examination, and especially help increase the radiologists' confidence in the final diagnosis. Therefore, an increased image quality that convinces the referring physician is an improvement in the quality of our product that we hope will lead to a better patient outcome.

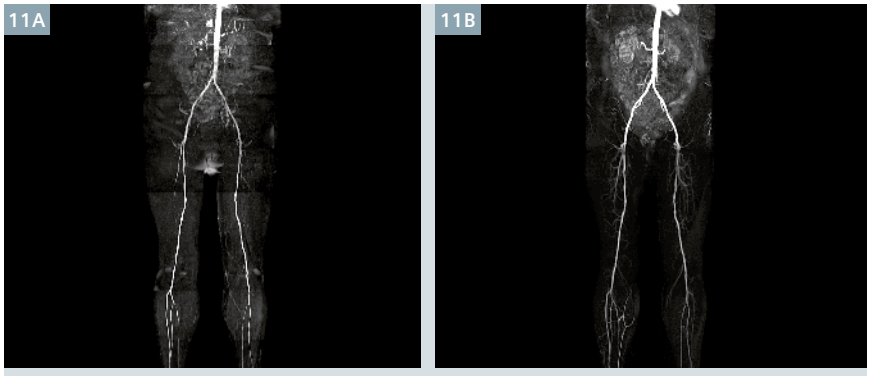

TR 544.4, TE 1.7, TT 475.0, TI 345.0 — TR 3.0, TE 1.0

11 71-year-old female patient. Comparison between MR Angiography (MRA) with QISS technique without intravenous contrast administration **(11A)** and MRA with intravenous contrast administration (gadobenate dimeglumine) **(11B)**. Note the comparable image quality in **(11A)** without intravenous contrast. One of the additional benefits of the QISS technique is the lack of overlapping venous artifacts as seen sometimes in contrast-enhanced MRA.



Contact

Christos Loupatatzis, M.D.
Spital Maennedorf
Department of Radiology
Asylstrasse 10
8708 Maennedorf
Switzerland
Phone: +44 922 20 10
c.loupatatzis@spitalmaennedorf.ch

Iron Quantification with LiverLab

Stephan Kannengiesser, Ph.D.

Siemens Healthineers, MR Oncology Applications, Erlangen, Germany

Multi-echo Dixon VIBE contained in LiverLab provides liver fat fraction values which are corrected for the effects of transversal relaxation. By doing this, it also provides a simultaneous estimation of that transversal relaxation time T2*, which is corrected for fat signal effects, herefafter called $T2_c$*. The reciprocal value of this estimate, fat-corrected $R2_c$* = 1/ $T2_c$*, can be used, within limits, to assess liver iron concentration (LIC). This note provides some guidelines for doing that.

MR liver iron quantification

Liver iron content is an important clinical biomarker. It can be assessed by various methods, including biopsy, which is still considered to be the gold standard but potentially harmful for the patient and suffering from a large sampling variability. It is also possible to use biomagnetic susceptibility measured with SQUID devices, but these are few and far between.

Alternatively, the effect of iron on the MR signal can be exploited. One such technique uses the transverse relaxation rate R2 = 1/T2 from spin-echo images, calibrated against biopsy [1], and this has been cast into a commercial product with regulatory approval: FerriScan (Resonance Health, Claremont, WA, Australia). Another, larger group of published techniques uses the transverse relaxation rate R2* = 1/T2* from 2D gradient-echo images, also calibrated against biopsy [2-5]. Unfortunately, these calibrations vary, if not by very much. Potential reasons for these variations are differences in the reference histology procedure [6], but also in data acquisition, and probably most importantly, in the R2* evaluation procedures, and there mainly in how they deal with noise. Some techniques use a constant noise offset as model parameter, others subtract a measured noise level, or truncate the number of echoes used. Fortunately, it seems that different techniques, despite different calibrations, lead to comparable LIC values [7]. However, the previously published methods do not take fat signal effects into account.

In order for the $R2_c$* to be truly quantitative, the data fitting procedure needs to correct for confounding effects, in particular image noise and signal modulations from fat [8]. A disadvantage of taking the fat signal into account is that any erroneous swaps of fat and water not only lead to errors in the estimation of the fat fraction (in that case, it is *not* equal to one minus the water fraction), but also to a confounded estimation of $R2_c$*. An important additional effect to consider is that liver R2* scales almost linearly with field strength [9, 10].

R2* from multi-echo Dixon VIBE

The multi-step adaptive fitting approach in [11] was originally designed for fat quantification, and its signal model contains terms for water and fat, as well as R2*; the inner fitting step uses magnitude data; appropriate protocols have to be used so that the later echo images still have sufficient signal-to-noise ratio (SNR).

Protocol design

In general, measurement protocols for R2* estimation need echo times which are as short as possible to capture rapid signal decay [5]. On the other hand, the initial water/fat separation step in multi-echo Dixon VIBE works best when the first two echo times are at or near opposed- and in-phase. At 3T, these two requirements are not in conflict (the first opposed-phase echo time is 1.23 ms), but at 1.5T, echo times near opposed- and in-phase are preferred. To reduce noise bias, the SNR of the acquisition should be as high as possible, so smaller image matrices and moderate parallel imaging (iPAT) acceleration factors are helpful. Asymmetric data acquisition should be avoided [12]. Finally, since the later echoes will always be dominated by noise if R2* is very high, it may be advantageous to use only 4 instead of the standard number of 6 echoes. Recommended protocols are listed in Table 1.

	1.5T	3T
TE [ms]	1.1, 2.2, 3.3, 4.4 (5.5, 9.5)[1]	min, typ. 1.1, 2.2, 3.3, ...
Matrix	160	
Bandwidth [Hz/pixel]	typ. 1100 for minimum first TE	
Flip angle [°]	6[2]	5[2]
TR [ms]	min, typ. 11	
Asymmetric echo	off	
Partial Fourier	off	
Parallel imaging	CAIPIRINHA x3 (abdomen preset: PE x1, 3D x3, reordering shift 2)	

Table 1: Recommended protocol values for iron estimation with multi-echo Dixon VIBE.

[1] At very high R2*, leaving out the later echoes will help to avoid noise bias.
[2] Depending on TR. Higher flip angles will improve SNR, but introduce a T1 bias in the fat fraction values.

Data interpretation

A mean $R2_c^*$ can be measured from the corresponding parameter maps via a region-of-interest (ROI) using any viewing software. In multi-echo Dixon VIBE, one grey scale unit corresponds to 1 s^{-1}, as it is also noted in the DICOM image comment. This value can then be multiplied with the iron calibration conversion factor of choice (see below). Several ROIs in different slices can be used to assess spatial heterogeneity of liver iron overload, or to average results. As long as the inline liver segmentation contained in LiverLab was successful, the average R2* across the entire liver can also be used, but it has to be noted that structures inside the liver which are not liver parenchyma, e.g. large vessels, are not automatically excluded.

Iron calibration

So far, no direct iron calibration for fat-corrected $R2_c^*$ against biopsy has been published. However, initial comparisons between $R2_c^*$ and LIC from FerriScan come to similar conclusions [13, 14]. Figure 1 lists a number of iron calibration curves.

Noise bias on magnitude images will in general lead to under-estimation of R2*, and requires an increased calibration factor. Depending on the noise level, this effect sets in when T2* approaches twice the first TE, which is typically ~1 ms. Consequently, R2* values above 500 s^{-1} should always be assumed to be under-estimated; this means that currently severe iron overload cannot be reliably detected at 3T using LiverLab. It can, however, be assumed that R2* estimates are reproducible up to ~1000 s^{-1} as long as the protocol is held constant, the setup of patient and receive coils is comparable, and that there are no fat/water swaps, which would make follow-up examinations possible.

Trying to summarize the current state of knowledge, and taking into account the tendencies of the individual original techniques to under- or over-estimate R2*, a tentative working value for converting $R2_c^*$ from multi-echo Dixon VIBE in units of s^{-1} into LIC in units of mg/g dry weight (dw) at 1.5T seems to be approximately 0.032 mg/g Fe_{dw}/s^{-1}, e.g.

Examplary calculation for 1.5T

$R2_c^* = 200\ s^{-1}$

$\rightarrow LIC = 0.032 \cdot 200\ mg/g\ Fe_{dw}$
$= 6.4\ mg/g\ Fe_{dw}$

Most iron calibrations contain, beside the proportionality factor, an offset in mg/g Fe_{dw}, which is positive for some calibrations, and negative for others. In the absence of further evidence, we suggest to assume this offset to be zero, which seems to be supported by simulations [15]. Using the field-strength dependence as reported in [9], and typical Larmor frequency values of Siemens MR scanners, this translates into a conversion factor at 3T of approximately 0.017 mg/g Fe_{dw}/s^{-1}. Table 2 summarizes values which take into account an assumed under-estimation towards high R2* values.

However, for now, the LIC values calculated using LiverLab always have to be interpreted with care by an experienced user.

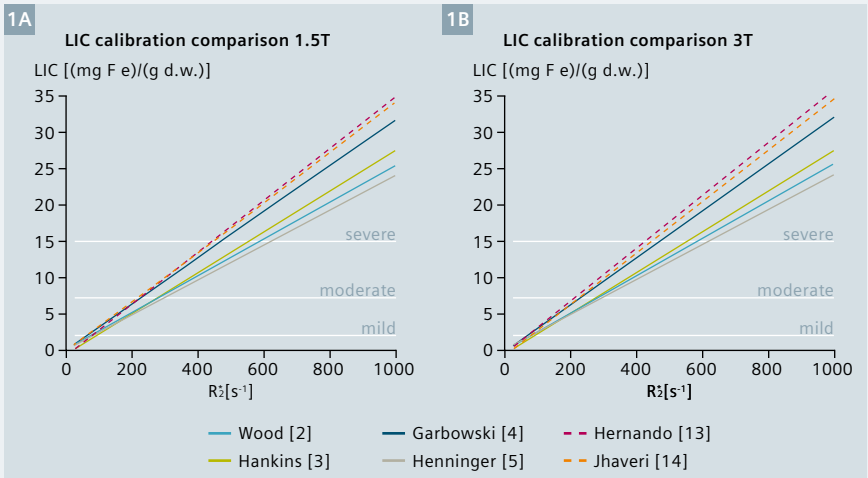

1 Existing iron calibrations. **(1A)** 1.5T; solid lines are calibrated against biopsy results, dashed lines are calibrated against FerriScan. **(1B)** 3T; there are no biopsy-based calibrations; results projected from 1.5T using [9], except Hernando [8].

	1.5T	3T[3]
mild (LIC ≥ 2 mg/g Fe_{dw})	65 s^{-1}	115 s^{-1}
moderate (LIC ≥ 7 mg/g Fe_{dw})	215 s^{-1}	400 s^{-1}
severe (LIC ≥ 15 mg/g Fe_{dw})	440 s^{-1}	n/a

Values in this table are a tentative and preliminary projection from existing studies, taking into account some expected under-estimation of R2* given the current limits of implementation in LiverLab.

Results will vary depending on protocol settings and image SNR, as well as on future changes in the algorithm.

Data interpretation and diagnostic conclusions are solely in the responsibility of the user.

Table 2: Tentative cut-off values of $R2_c^*$ from multi-echo Dixon VIBE for different grades of liver iron overload.

[3] 3T values are projected from 1.5T values using [9].

Offline processing of individual echoes

Multi-echo Dixon VIBE allows exporting the individual echoes in addition to the parameter maps. In challenging cases, or when an external cross-calibration is desired, these can be processed manually with custom software, see for example [16].

Likewise, the data acquisition protocols of existing iron calibrations, e.g. [3], or the signal-intensity ratio method described in [17], can easily be reproduced using the product 2D GRE sequence, and the results compared to those of LiverLab as long as the appropriate post-processing is used.

Conclusion and outlook

Although multi-echo Dixon VIBE from LiverLab was originally designed for liver fat evaluation, the $R2_c$* values, used with care, allow estimating liver iron concentration within limits.

There are predevelopment activities and ongoing studies to extend multi-echo Dixon VIBE to properly calibrated iron quantification in a future software version. We encourage all users of LiverLab to share their experience using the current product version.

Contact

Stephan Kannengiesser
Siemens Healthcare GmbH
MR PI TIO ONCO
Postbox 32 60
91050 Erlangen
Germany
Phone: +49 (1525) 4689516
stephan.kannengiesser@siemens.com



References

1 St Pierre TG, Clark PR, Chua-anusorn W, et al. Noninvasive measurement and imaging of liver iron concentrations using proton magnetic resonance. Blood 2005;105:855-861.
2 Wood JC, Enriquez C, Ghugre N, et al. MRI R2 and R2* mapping accurately estimates hepatic iron concentration in transfusion-dependent thalassemia and sickle cell disease patients. Blood 2005;106:1460-1465.
3 Hankins JS, McCarville MB, Loeffler RB, et al. R2* magnetic resonance imaging of the liver in patients with iron overload. Blood 2009;113:4853-4855.
4 Garbowski MW, Carpenter JP, Smith G, et al. Biopsy-based calibration of T2* magnetic resonance for estimation of liver iron concentration and comparison with R2 Ferriscan. J Cardiovasc Magn Reson 2014;16:40-50.
5 Henninger B, Zoller H, Rauch s, et al. R2* relaxometry for the quantification of hepatic iron overload: Biopsy-based calibration and comparison with the literature. RöFo 2015;187:472-479.
6 Butensky E, Fischer R, Hudes M, et al. Variability in hepatic iron concentration in percutaneous needle biopsy specimens from patients with transfusional hemosiderosis. Am J Clin Pathol 2005;123:146-152.
7 Meloni A, Rienhoff HY, Jones A, et al. The use of appropriate calibration curves corrects for systematic differences in liver R2* values measured using different software packages. Br J Haematol 2013.
8 Hernando D, Levin YS, Sirlin CB, et al. Quantification of liver iron with MRI: state of the art and remaining challenges. J Magn Reson Imaging 2014;40:1003-1021.
9 Storey P, Thompson AA, Carqueville CL, et al. R2* imaging of transfusional iron burden at 3T and comparison with 1.5T. J Magn Reson Imaging 2007;25:540-547.
10 Meloni A, Positano V, Keilberg P, et al. Feasibility, reproducibility, and reliability for the T2* iron evaluation at 3T in comparison with 1.5T. Magn Reson Med 2012;68:543-551.
11 Zhong X, Nickel MD, Kannengiesser S, et al. Liver fat quantification using a multi-step adaptive fitting approach with multi-echo GRE imaging. Magn Reson Med 2014;72:1353-1365.
12 Storey P, Liu YW, and Novikov DS. Artifact-free T2* mapping without post hoc corrections. Proc ISMRM 2015;23:442.
13 Hernando D, Quazi N, and Reeder SB. Calibration of confounder-corrected R2* for liver iron quantification at 1.5T and 3T: preliminary results. Proc ISMRM 2013;21:4194.
14 Jhaveri K, Kannengiesser S, Sadougi N, et al. A prospective study comparing R2* derived liver iron concentration (LIC) with noise-corrected post processing of data against FerriScan reported LIC in patients with liver iron overload. Proc ISMRM 2016;24:3854.
15 Ghugre NR, Doyle EK, Storey P, et al. Relaxivity-iron calibration in hepatic iron overload: Predictions of a Monte Carlo model. Magn Reson Med 2015;74:879-883.
16 Fernandes JL, and Kalaf JM. Increasing productivity in myocardial and liver T2* acquisition and analysis. MAGNETOM Flash 2015;1:28-32 (www.ironcalculator.com).
17 Gandon Y, Olivié D, Guyader D, et al. Non-invasive assessment of hepatic iron stores by MRI. Lancet 2004; 363:357-362 (www.ironbymr.fr).

Further Reading

An Efficient Workflow for Quantifying Hepatic Lipid and Iron Deposition using LiverLab

Puneet Sharma, Diego Martin (University of Arizona, Tucson, AZ, USA), MAGNETOM Flash #58 (3/2014)

Case Study LiverLab

Stephan Kannengiesser et al. (Siemens Healthcare, Erlangen, Germany), MAGNETOM Flash #58 (3/2014)

The articles are online at

www.siemens.com/magnetom-world

Free-breathing Late Enhancement Imaging: Phase Sensitive Inversion Recovery (PSIR) with Respiratory Motion Corrected (MOCO) Averaging

Peter Kellman; Hui Xue; Michael S. Hansen

National Heart, Lung, and Blood Institute, National Institutes of Health, DHHS, Bethesda, MD, USA

Introduction

Late gadolinium enhancement (LGE) has become a gold standard in myocardial viability assessment [1, 2] providing excellent depiction of myocardial infarction (MI) and macroscopic scarring. The use of late enhancement in the diagnosis of ischemic heart disease and in guiding revascularization therapy has gained wide acceptance. More recently, late enhancement has been playing a broader role in characterizing fibrosis in non-ischemic cardiomyopathies [3,4], and in measurement of scar resulting from treatment of cardiac arrhythmias using radiofrequency ablation [5]. As the use of late enhancement imaging has matured and as the span of applications has widened, clinicians are examining late enhancement images for more subtle indication of fibrosis and the demands on image quality have grown [6].

Breath-held (BH), segmented FLASH has been the gold standard for LGE for many years [7] and is widely used with great success when patients are cooperative and can hold their breath. In instances where poor breath-holding results in ghost artifacts, single shot SSFP imaging has been used as an alternative. However, while single shot imaging mitigates ghosting artifacts, it generally has compromised spatial resolution and image quality compared to BH FLASH. Therefore, the single shot approaches are less sensitive to detection of subtle LGE and to detection of small lesions [8]. The development of PSIR LGE with respiratory motion corrected (MOCO) averaging[1] [6, 9, 10] has led to a free-breathing (FB) approach which achieves the robustness of single shot approaches and the resolution and image quality of BH segmented FLASH. In addition to elimination of ghosting artifacts due to poor breath-holds (Fig. 1), the PSIR MOCO LGE is inherently less sensitive to arrhythmias.

In addition to being easier on the patients, free-breathing PSIR MOCO LGE eliminates pauses between BH slices and is therefore faster to acquire than a BH stack. Free-breathing, MOCO LGE greatly simplifies the clinical workflow, particularly since LGE is typically at the end of the study where patient compliance is frequently a problem. PSIR MOCO LGE has been demonstrated to improve the image quality in both pediatric[2] [11] and adult populations [12]. It has been shown to make a significant improvement in the most vulnerable population of sick patients [12].

[1] The product is still under development and not commercially available yet. Its future availability cannot be ensured.

[2] MR scanning has not been established as safe for imaging fetuses and infants less than two years of age. The responsible physician must evaluate the benefits of the MR examination compared to those of other imaging procedures.

1

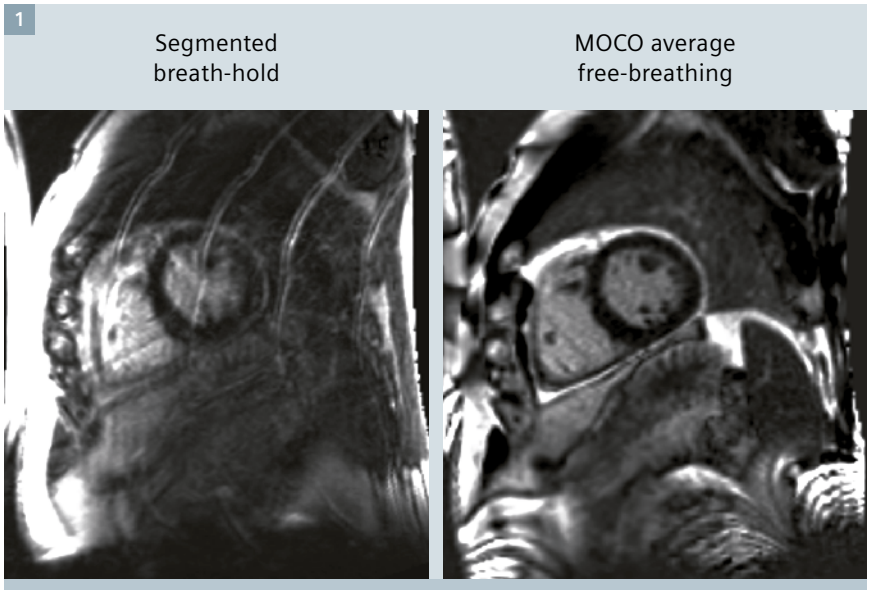

1 Free-breathing, MOCO PSIR LGE images eliminate ghosting artifacts and achieve high SNR by means of respiratory motion corrected averaging [6].

In a study of 390 consecutive patients [12], it was concluded that: "Myocardial infarction detection and quantification are similar between MOCO-LGE and BH-LGE when BH-LGE can be acquired well, but BH-LGE quality deteriorates with patient vulnerability. Acquisition time, image quality, diagnostic confidence, and the number of successfully scanned patients are superior with MOCO-LGE, which extends LGE-based risk stratification to include patients with vulnerability confirmed by outcomes." A number of sites have adopted PSIR MOCO LGE as their sole means of LGE imaging and combined they have been performing over 10,000 studies annually for the past several years.

Respiratory MOCO averaging can offer SNR improvements well beyond what is possible using BH FLASH by further increasing the number of averages. Therefore, with PSIR MOCO LGE, higher spatial resolution or thinner slices are achievable in clinical practice. Furthermore, PSIR MOCO LGE has been integrated with dark blood PSIR to provide improved contrast of subendocardial MI with the adjacent bright blood pool.

Key points/implications:

- Free-breathing imaging is easier for the patient
- Improves clinical workflow
- Free-breathing imaging reduces artifacts
- Improves diagnostic quality
- Is highly effective for the most vulnerable population

Free-breathing approach

Motion correction may be used to correct respiratory motion [9, 10] in the case of free-breathing acquisition, or diaphragmatic drift in the case of breath-holding. The SNR for individual single shot PSIR-SSFP images is slightly worse than segmented PSIR-FLASH due to the increase in bandwidth, despite the increase in flip angle. However, the SNR of single shot PSIR-SSFP may be significantly improved by averaging multiple repeated measurements (Fig. 2). Typically, using 8 PSIR images acquired in 16 heartbeats provides an SNR comparable or better than the FLASH protocol for approximately the same duration and may be extended to a larger number of averages since the acquisition is not breath-held. Parallel imaging at higher acceleration factors may be used to reduce the imaging duration in diastole to achieve higher spatial resolution or reduce motion blur at higher heart rates. Use of non-rigid motion correction provides correction over the full FOV in a fully automated fashion. Selective averaging may be used to discard images that do not meet similarity criteria due to through plane motion [10]. This retrospective image based navigator strategy is robust and simple to use, thereby eliminating the complexity and unreliability of prospective navigators.

2

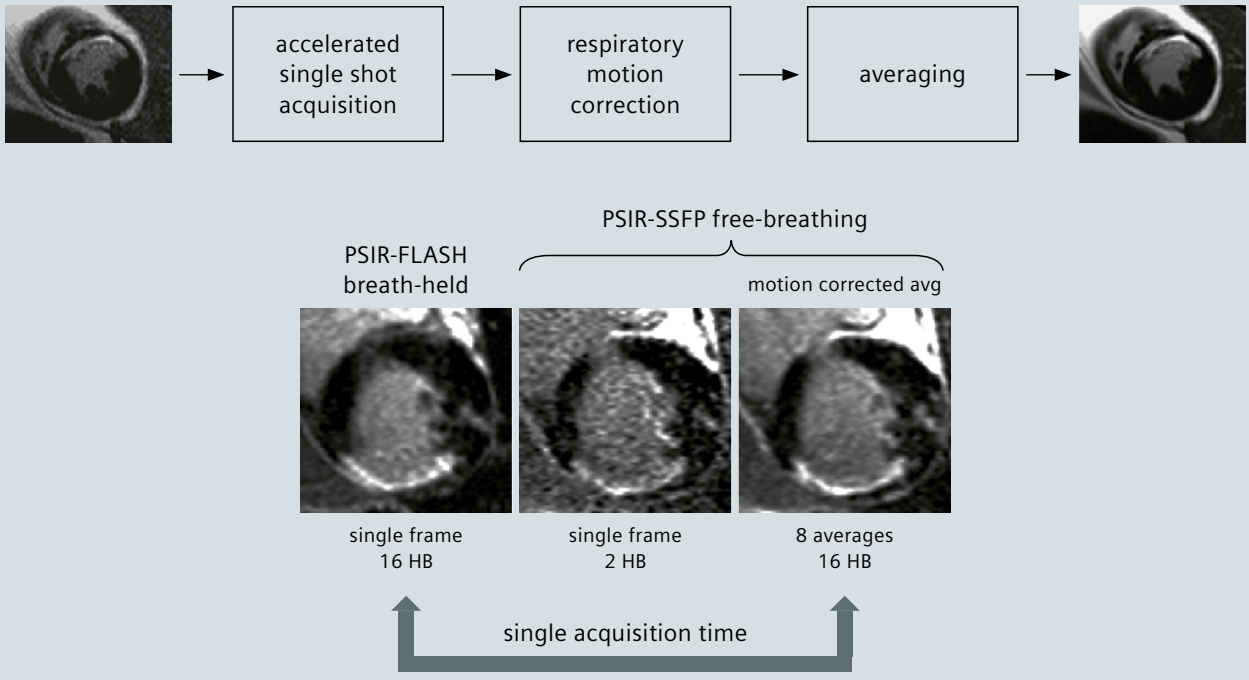

2 Respiratory motion corrected averaging strategy using accelerated single shot imaging to mitigate artifacts and motion corrected averaging to increase SNR [6].

Imaging protocols

PSIR MOCO LGE has been integrated with a number of imaging protocols to include SSFP, FLASH, and multi-echo GRE for water fat separated LGE, and dark blood (DB) PSIR LGE (Fig. 3). Typical parameters for these protocols are listed in Table 1. Additionally, early gadolinium enhancement (EGE) protocols use reduced averaging for more rapid multi-slice coverage, and higher spatial resolution protocols (e.g. 256 x 224 or 320 x 244) use higher parallel imaging acceleration (PAT) factors and increased averaging.

3



3 Simplified diagram of sequence for PSIR LGE with interleaved acquisition of IR and PD images on alternate heartbeats (top) and dark blood (DB) PSIR LGE using IR-T2 RF preparation. Readout may be single-shot SSFP, FLASH, or multi-echo GRE for water fat separated PSIR LGE imaging.

	Bright Blood (BB)		Dark Blood (DB)	Fat Water (FW)
Preparation	Inversion Preparation		Inversion Preparation & T2 preparation	Inversion Preparation
Readout (single shot)	SSFP FA_{IR} = 50° FA_{PD} = 8°	FLASH FA_{IR} = 10° FA_{PD} = 5°	SSFP FA_{IR} = 50° FA_{PD} = 8°	3-echo GRE (FA_{IR} = 25°, FA_{PD} = 5°) monopolar readout
Typical FOV / resolution	360 x 270 mm² 1.4 x 1.9 x 8 mm³			360 x 270 mm² 1.4 x 2.2 x 8 mm³
Matrix size	256 x 144 (parallel imaging factor 2)			256 x 123 (parallel imaging factor 3)
Number of acquired measurements	8		16	9
T2 prep TE	n/a		10 - 40 ms	n/a
TE / TR	1.2/2.8 ms	1.25/3.1 ms	1.2/2.8 ms	(1.5,3.8, 6.1)/7.2 ms
ECG triggering	Inversions every 2 RR (HR < 90 bpm) Inversions every 3 RR (HR > 90 bpm)			

Table 1: Typical imaging parameters for various PSIR LGE MOCO protocols.

PSIR motion corrected averaging

Non-rigid image registration is used to correct respiratory motion between repeated measurements acquired during normal free-breathing PSIR LGE imaging [6, 9, 10]. The motion correction (MOCO) is done independently for the IR and proton density (PD) images and the MOCO averaged complex images are co-registered prior to the PSIR demodulation step (Fig. 4, current implementation). The non-rigid image registration corrects in-plane motion and through-plane motion is dealt with by discarding 50% of the acquired measurements which are most dissimilar. The selection of the reference frame used for image registration as well as which frames to be discarded is based on the similarity of frames as estimated from a global mean square difference metric [10]. In this way, the retrospective image-based strategy averages the most frequent respiratory phase which is typically at end-expiration. The co-registered MOCO PD image is used for both PSIR demodulation, which preserves the sign of the IR signal by removing the background phase, as well as for correcting the surface coil intensity roll-off (Fig. 5). To improve the reliability of IR/PD co-registration which is critical for both PSIR demodulation and surface coil intensity correction, a volume preserving non-rigid co-registration is used to deal with the challenge of different contrasts between IR and PD images.

In dark blood imaging protocols SNR is typically lower due to T2 weighting and more averages are needed compared to the bright blood PSIR MOCO protocol. Likewise, for higher spatial resolution with higher PAT factors and smaller voxels, the loss in SNR in raw images may be compensated for by increased averaging.

Implementation

The PSIR MOCO implementation has evolved over the last several years and has achieved high quality and reliability used at a large number of sites in their clinical workflow. Initial off-line implementations [9, 10] were quickly

4

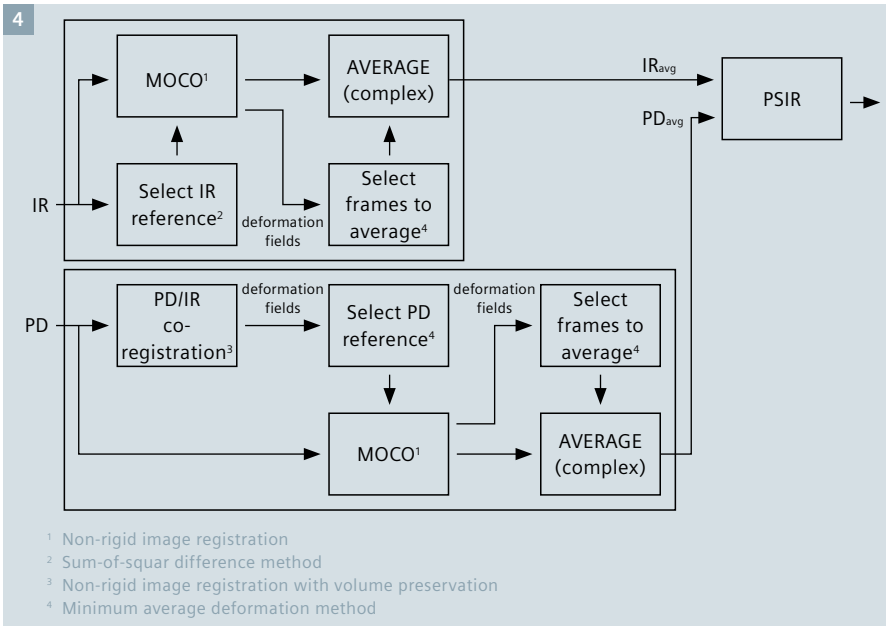

[1] Non-rigid image registration
[2] Sum-of-squar difference method
[3] Non-rigid image registration with volume preservation
[4] Minimum average deformation method

4 Current strategy for free-breathing, respiratory motion corrected averaging and PSIR demodulation.

5

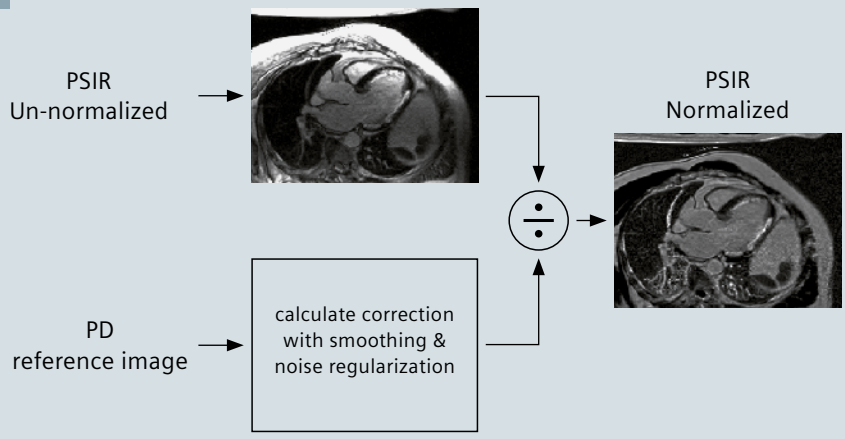

5 Correction of surface coil intensity roll-off used the proton density (PD) magnitude image after MOCO averaging.

moved to the scanner as works-in-progress (WIP) packages as part of co-development between NIH and Siemens under a cooperative research and development agreement (CRADA). Initial WIPs began in 2007 with WIP 373 (*syngo* MR B13A) for MAGNETOM Avanto and Espree, and were re-released with various improvements over the ensuing years.

Initial implementations applied respiratory MOCO and averaging directly to the individual single shot SSFP images, and significant through plane motion was dealt with by discarding frames as described above. Subsequent development applied MOCO averaging independently to the IR and PD, and performed the PSIR between IR and PD after motion corrected averaging. This mitigated artifacts arising due to respiratory motion between IR and PD. Early versions would output a number of intermediate series to include the raw images, MOCO images, as well the averages. As the development matured, the final versions output only the MOCO average.

A recent development has been the implementation of the PSIR MOCO reconstruction using the Gadgetron image reconstruction framework [13]. The Gadgetron framework provides increased speed and 'on-the-fly' reconstruction for multi-slice acquisitions. On-the-fly reconstruction immediately starts the computation when the image acquisition of the first slice is completed. For a scan covering multiple slices, this scheme allows image display during the acquisition of a stack of slices. Gadgetron software may be installed on the *syngo* MR E11 platforms (1.5T MAGNETOM Aera, 3T MAGNETOM Skyra and Prisma) to run on the scanner's image reconstruction computer (MARS) or may be run on an external computer connected over the network (currently a C2P with NIH research collaboration partners). Using on-the-fly reconstruction, the time to complete the full stack of slices (9 slices/8 measurements) is approximately 6 or 8 seconds after completion of the acquisition, when performed on a 24 core external Linux PC or 16 core MARS, respectively. For on-the-fly reconstruction, all measurements for a given slice are acquired consecutively (inner loop).

PSIR MOCO LGE

Free-breathing PSIR MOCO LGE protocols are now widely used at a number of clinical research sites. At many of these sites, the free-breathing protocol is used exclusively since it saves time and provides excellent quality. Examples of late enhancement for a wide range of patterns (Fig. 6) in both ischemic and non-ischemic heart disease illustrate that PSIR MOCO provides excellent image quality and high spatial resolution to detect small focal enhancement as well as more subtle enhancement.

The typical acquisition of a SAX stack of 9-slices (Fig. 7) is acquired in 9 slices × 8 measurements × 2 RR = 144 heart beats = 2:24 min at 60 bpm. The reconstruction is performed 'on-the-fly' and is completed within 10 seconds of the end of scan. Long axis views may be prescribed individually or as multi-slice. When prescribing long axis views off of free-breathing SAX images, the long axis may be at a different respiratory position and possibly not optimal. Some sites find it simpler to prescribe a parallel stack of 3 long axis slices for each view (Fig. 8) to ensure acquisition of the best position.

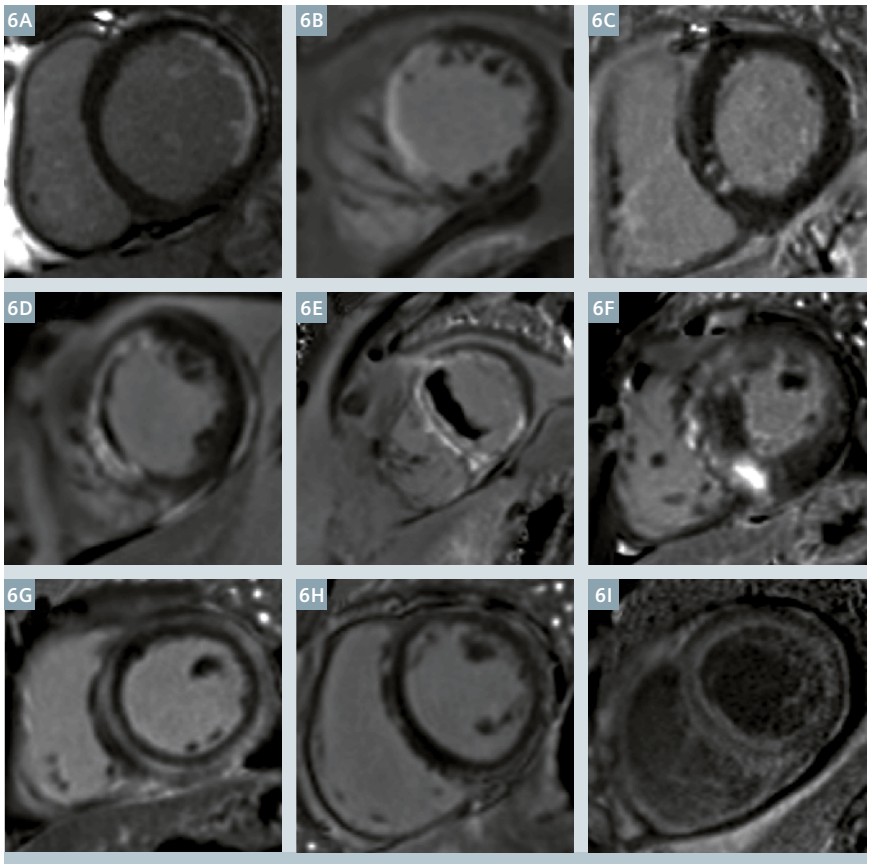

6 Examples of free-breathing PSIR MOCO LGE images illustrating the a variety of late enhancement patterns: (**6A**) sub-endocardial chronic MI, (**6B**) transmural chronic MI, (**6C**) small focal scar, (**6D**) acute MI with dark core due to microvascular obstruction (MVO), (**6E**) MI with thrombus, (**6F**) heterogeneous focal enhancement in a patient with HCM, (**6G**) mid-wall enhancement in patient with myocarditis, (**6H**) sub-epicardial enhancement in patient with myocarditis, and (**6I**) subendocardial fibrosis in patient with amyloidosis.

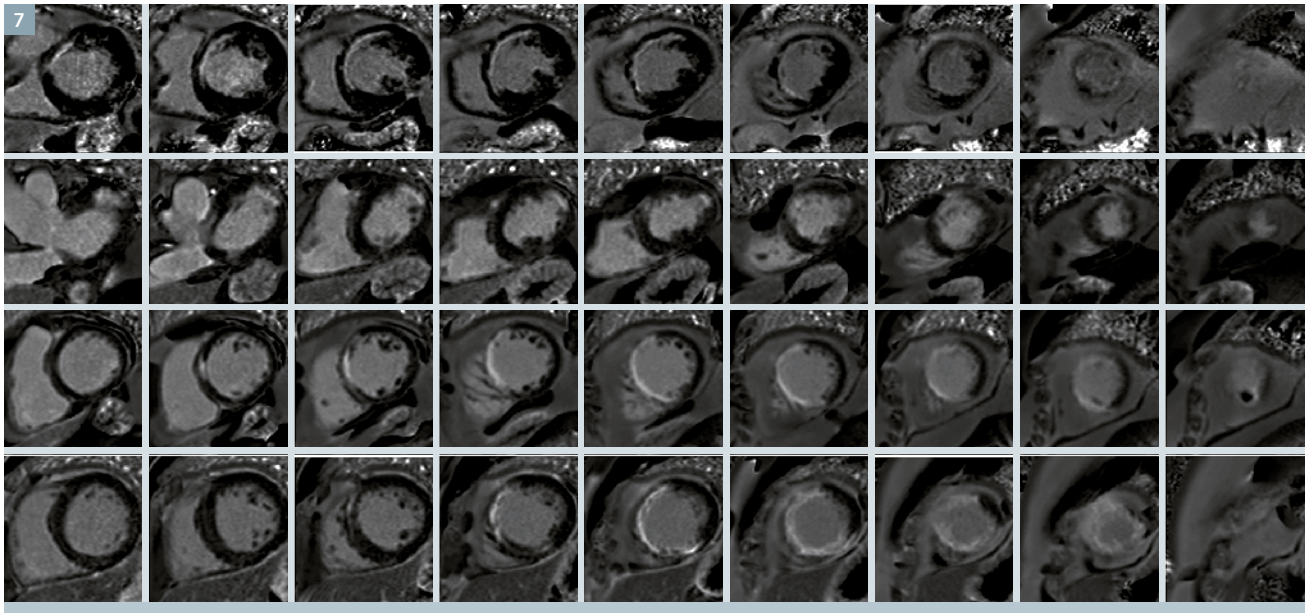

7 Examples of free-breathing acquisition of stacks of 9 short axis slices using PSIR MOCO LGE acquired and reconstructed on-the-fly in approximately 2.5 min, depending on heart rate.

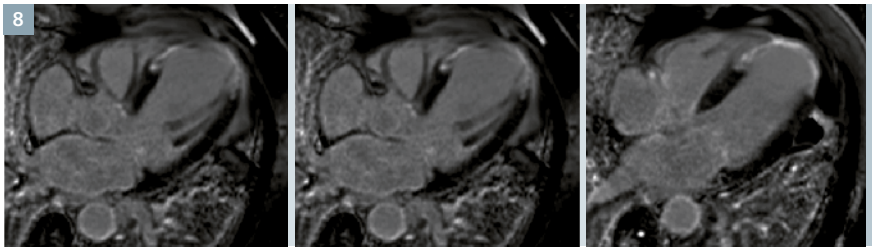

8 Example of free-breathing acquisition of a stack of 3 parallel long axis slices to ensure that the 4-chamber view is correctly obtained when prescribed off images that are potentially at a different respiratory position.

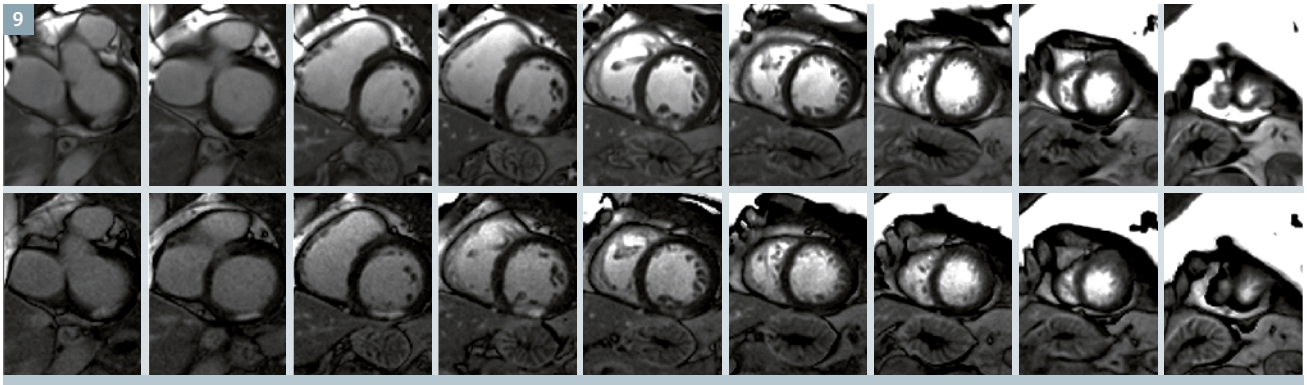

9 Comparison of 9 slice short axis stack acquired at 3T using the free-breathing PSIR MOCO LGE with SSFP (top) and FLASH (bottom) readouts, respectively.

The PSIR MOCO protocol most frequently used is the SSFP based protocol. A FLASH based protocol has also been tested, and is beneficial in situations with large off-resonance variations that are difficult to shim. There is a reduction in SNR that may be compensated by increased averaging. A comparison of SSFP and FLASH protocols at 3T is shown in Fig. 9 using the same averaging (protocols in Table 1).

Early enhancement imaging

Early gadolinium enhancement (EGE) during the phase between 1-5 minutes following gadolinium administration is often more sensitive to detection of edema, thrombus, or microvascular obstruction (MVO). MVO may be less apparent for LGE when the gadolinium may reach the MI core. Furthermore, in the case of acute MI, the early enhancement may show the area at risk since the edematous tissue will experience a more rapid early enhancement than the central core. Similarly the edematous region in acute myocarditis is more conspicuous in early phase.

The free-breathing PSIR MOCO LGE protocol may be used for EGE without tiring the patient. The EGE may use the same LGE protocol, or may use a reduced number of averages, e.g. 4, in order that a full SAX stack can be acquired in just over minute, in cases where better time resolution is desired.

Dark Blood PSIR LGE

Late-enhancement imaging typically achieves excellent contrast between infarcted and normal myocardium. However, the contrast between the MI and the blood pool is frequently suboptimal. A large fraction of infarctions caused by coronary artery disease are sub-endocardial and thus adjacent to the blood pool. The contrast between the blood and MI in the inversion recovery (IR) image depends on variables such as contrast agent dosage, time from gadolinium administration, clearance rate, and imaging parameters. Blood velocity may also have a role in the contrast, even though non-slice-selective IR is used. Therefore, as a result of mechanisms that are not fully characterized or controlled, it is not infrequent that sub-endocardial MIs are difficult to detect or clearly delineate.

A dark blood (DB) LGE may be achieved by combining a T2 preparation [14–16] with IR. In these schemes, the myocardial signal is reduced relative to the blood signal thereby reducing the inversion times to null the myocardium. In this way, it is possible to null both the myocardium and the blood at the same time. The order of the T2 and IR preparations may be applied as T2-IR [16] or IR-T2 [14]. Both of these previously reported schemes used a FLASH readout. We combined an IR-T2 with a single shot SSFP readout and respiratory motion corrected averaging to achieve the acceptable SNR while maintaining the desired spatial and temporal resolution. In this manner, imaging is conducted free-breathing which has benefits for image quality, patient comfort, and clinical workflow. Furthermore, by using a PSIR reconstruction [17] the blood signal may be made darker than the myocardium (i.e. negative signal values) thereby providing contrast between the blood and both the MI and remote myocardium [15].

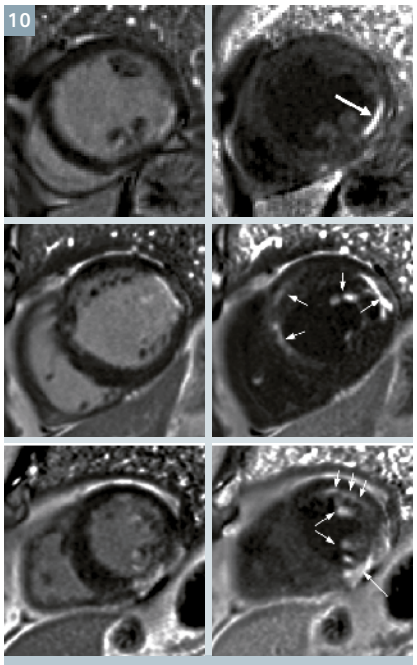

10 Examples of bright blood (left) and dark blood (DB) (right) PSIR MOCO LGE illustrating improved contrast between subendocardial MI and blood pool. The areas of scar indicated by LGE are more conspicuous on the DB PSIR images (see arrows) and in some cases might have been missed entirely in the bright blood PSIR images.

Dark blood LGE schemes provide contrast between the MI and the blood pool at the expense of SNR. However, the SNR cost of the proposed DB may be recovered by increased averaging. The DB PSIR MOCO LGE protocol in Table 1 achieves comparable contrast-to-noise ratio (CNR) between the MI and myocardium as the conventional bright blood protocol.

Free-breathing, dark blood PSIR LGE imaging has been demonstrated to improve the visualization of subendocardial MI and fibrosis in cases with low contrast with adjacent blood pool (Fig. 10). The proposed method also improves visualization of thin walled fibrous structures such as atrial walls and valves, as well as papillary muscles.

Fat water separated late enhancement

Lipomatous metaplasia is prevalent in chronic myocardial infarction (MI) [18] and other nonischemic cardiomyopathies. Using conventional late enhancement imaging, it is difficult to discriminate between fibrosis and intramyocardial fat since both have low T1 and appear bright. Furthermore, the presence of fat may create image artifacts due to the chemical shift of fat or the bright epicardial fat signal may obscure the subepicardium. Using fat-water separated late-enhancement imaging it is possible to distinguish the fibrosis from fat with improved sensitivity and to avoid erroneous tissue classification [19]. Detecting the presence of fibrofatty

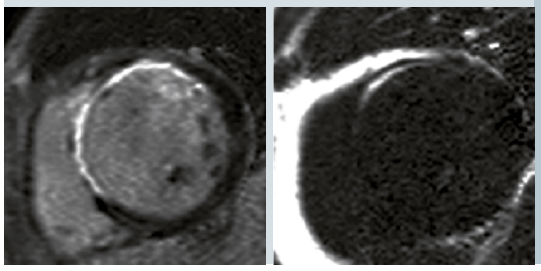

11 Patient with chronic MI in anteroseptal region with lipomatous metaplasia seen in fat-water separated PSIR MOCO LGE [19].



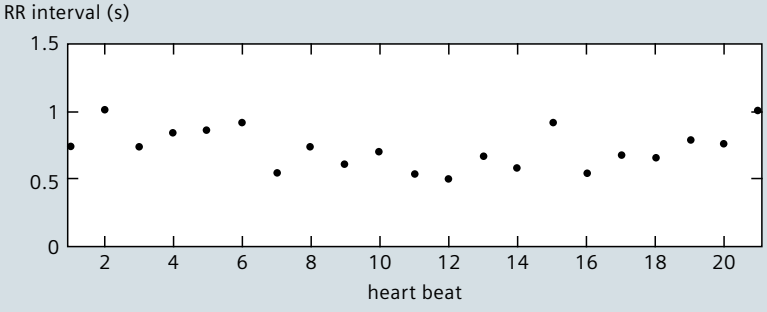

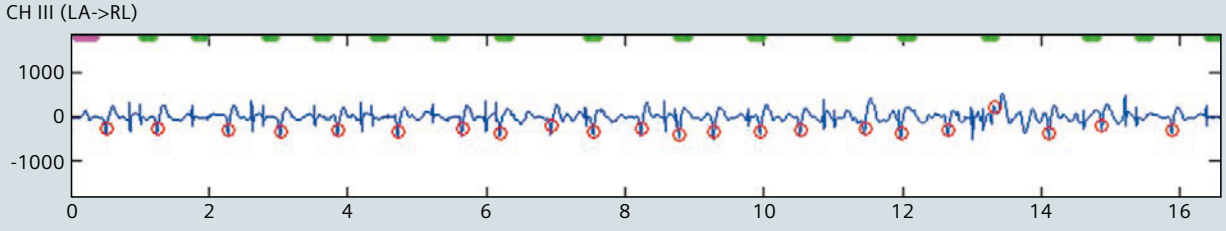

12 Free-breathing, PSIR MOCO LGE in patient with chronic MI in atrial fibrillation (shown at SCMR 2014 Annual Scientific Meeting, Real-time imaging: in case of atrial fibrillation, Kellman P).

infiltration or other intramyocardial fat may have diagnostic value. The presence of intramyocardial fat may form a substrate for arrhythmias due to the lower electrical conductivity of fat. It has been shown that fibrofatty infiltration of the myocardium is associated with sudden death, and therefore noninvasive detection could have prognostic value. Fat water separated imaging may be performed free-breathing [20] with multi-echo PSIR MOCO LGE (Table 1). An example of lipomatous metaplasia in chronic MI is shown in Fig. 11. It is also used to improve visualization of pericardial disease and in general mass characterization.

Insensitive to arrhythmias

The free-breathing PSIR MOCO LGE imaging based on single shot imaging is inherently insensitive to arrhythmias since it is free from ghosting artifacts experienced with breath-held segmented acquisitions. In patients with arrhythmias during scanning, there may be some variation in the cardiac phase of repeated measurements depending on the precise nature of the variation. It is possible to retrospectively discard heart beats outside of specified criteria, however in practice the MOCO average has been found to be relatively insensitive to a large variation in RR intervals and is even robust in subjects with atrial fibrillation (Fig. 12). Furthermore, some patients experience arrhythmias that are brought on or worsened by breath-holding, and are in sinus rhythm during normal free-breathing.

Discussion

The free-breathing approach to LGE using PSIR MOCO performs reliably with excellent image quality. The image is often better than breath-held LGE in the most vulnerable population that cannot breath-hold [12] and for pediatric subjects[3] [11]. The paradigm shift to free-breathing CMR has benefits to the clinical workflow in terms of speed, ease of use, and patient comfort. A number of other free-breathing protocols that incorporate retrospective MOCO have been recently developed and allow for a complete free-breathing CMR study to include real-time cine function [21, 22], T2-SSFP [23], T2* mapping [24], and myocardial perfusion mapping [25]. These afford a significant reduction in overall exam time when combined. The PSIR MOCO LGE has been adopted at a number of sites as the new standard and is widely used.

[3] MR scanning has not been established as safe for imaging fetuses and infants less than two years of age. The responsible physician must evaluate the benefits of the MR examination compared to those of other imaging procedures.

Acknowledgements

We would like to acknowledge our colleagues at Siemens, in particular Xiaoming Bi and Randall Kroeker, for their role in development of the PSIR MOCO LGE WIP, and to our numerous clinical collaborators for their insights and clinical examples: Andrew E. Arai, W. Patricia Bandettini, Erik B. Schelbert, James C. Moon, Marianna Fontana, Martin Ugander, Patricia Feuchter, Cavan McGurk, Sofie Olsson, Jenny Rasck, Sarah Anderson, and Christine Mancini.

Supported by the National Heart, Lung and Blood Institute, National Institutes of Health by the Division of Intramural Research.

References

1 Fieno DS, Kim RJ, Chen E, Lomasney JW, Klocke FJ, Judd RM. Contrast-Enhanced Magnetic Resonance Imaging of Myocardium at Risk Distinction Between Reversible and. 2000;36:1985–91.
2 Kim RJ, Fieno DS, Parrish TB, Harris K, Chen E-L, Simonetti O, et al. Relationship of MRI Delayed Contrast Enhancement to Irreversible Injury, Infarct Age, and Contractile Function. Circulation. 1999;100:1992–2002.
3 Bohl S, Wassmuth R, Abdel-Aty H, Rudolph A, Messroghli D, Dietz R, et al. Delayed enhancement cardiac magnetic resonance imaging reveals typical patterns of myocardial injury in patients with various forms of non-ischemic heart disease. Int. J. Cardiovasc. Imaging. 2008;24:597–607.
4 Hunold P, Schlosser T, Vogt FM, Eggebrecht H, Schmermund A, Bruder O, et al. Myocardial Late Enhancement in Contrast-Enhanced Cardiac MRI: Distinction Between Infarction and Non-Infarction-Related Disease. AJR. Am. J. Roentgenol. 2005;184:1420–6.
5 Vergara GR, Marrouche NF. Tailored management of atrial fibrillation using a LGE-MRI based model: from the clinic to the electrophysiology laboratory. J. Cardiovasc. Electrophysiol. 2011;22:481–7.
6 Kellman P, Arai AE. Cardiac imaging techniques for physicians: Late enhancement. J. Magn. Reson. Imaging. 2012;36:529–42.
7 Kim RJ, Shah DJ, Judd RM. How We Perform Delayed Enhancement Imaging. J. Cardiovasc. Magn. Reson. 2003;5:505–14.
8 Lee D, Wu E, Chung Y, Simonetti O, Elliot M, Holly T, et al. Comparison Between Single Shot TrueFISP and Segmented TurboFLASH for the Detection of Myocardial Infarction. J. Cardiovasc. Magn. Reson. 2003;5:79–80.
9 Kellman P, Larson AC, Hsu L-Y, Chung Y-C, Simonetti OP, McVeigh ER, et al. Motion-corrected free-breathing delayed enhancement imaging of myocardial infarction. Magn. Reson. Med. 2005;53:194–200.
10 Ledesma-Carbayo MJ, Kellman P, Hsu L-Y, Arai AE, McVeigh ER. Motion corrected free-breathing delayed-enhancement imaging of myocardial infarction using nonrigid registration. J. Magn. Reson. Imaging. 2007;26:184–90.
11 Olivieri L, Cross R, O'Brien KJ, Xue H, Kellman P, Hansen MS. Free-breathing motion-corrected late-gadolinium-enhancement imaging improves image quality in children. Pediatr. Radiol. Pediatric Radiology; 2016;46:983–90.
12 Piehler KM, Wong TC, Puntil KS, Zareba KM, Lin K, Harris DM, et al. Free-Breathing, Motion-Corrected Late Gadolinium Enhancement Is Robust and Extends Risk Stratification to Vulnerable Patients. Circ. Cardiovasc. Imaging. 2013;6:423–32.
13 Hansen MS, Sørensen TS. Gadgetron: an open source framework for medical image reconstruction. Magn. Reson. Med. 2013;69:1768–76.
14 Basha T, Roujol S, Kissinger K V, Goddu B, Manning WJ, Nezafat R. Black blood late gadolinium enhancement using combined T2 magnetization preparation and inversion recovery. J. Cardiovasc. Magn. Reson. BioMed Central Ltd; 2015;17:O14.
15 Kellman P, Xue H, Olivieri LJ, Cross RR, Grant EK, Fontana M, Ugander M, Moon JC, Hansen MS. Dark blood Late Enhancement Imaging. J. Cardiovasc. Magn. Reson. 2016; In press.
16 Liu C-Y, Wieben O, Brittain JH, Reeder SB. Improved delayed enhanced myocardial imaging with T2-Prep inversion recovery magnetization preparation. J. Magn. Reson. Imaging. 2008;28:1280–6.
17 Kellman P, Arai AE, Mcveigh ER, Aletras AH. Phase-Sensitive Inversion Recovery for Detecting Myocardial Infarction Using Gadolinium-Delayed Hyperenhancement. Magn. Reson. Med. 2002;383:372–83.

18 Mordi I, Radjenovic A, Stanton T, Gardner RS, McPhaden A, Carrick D, et al. Prevalence and Prognostic Significance of Lipomatous Metaplasia in Patients With Prior Myocardial Infarction. JACC. Cardiovasc. Imaging. American College of Cardiology Foundation; 2014;1–2.
19 Kellman P, Hernando D, Arai AE. Myocardial Fat Imaging. Curr. Cardiovasc. Imaging Rep. 2010;3:83–91.
20 Kellman P, Hernando D, Shah S, Chefdhotel C, Liang Z-P, Arai A. Free-breathing, single shot fat-water separated cardiac imaging with motion corrected averaging. ISMRM 2010 Sci. Meet. 2010;18:3662.
21 Kellman P, Chefd'hotel C, Lorenz CH, Mancini C, Arai AE, McVeigh ER. Fully automatic, retrospective enhancement of real-time acquired cardiac cine MR images using image-based navigators and respiratory motion-corrected averaging. Magn. Reson. Med. 2008;59:771–8.
22 Xue H, Kellman P, LaRocca G, Arai AE, Hansen MS. High spatial and temporal resolution retrospective cine cardiovascular magnetic resonance from shortened free breathing real-time acquisitions. J. Cardiovasc. Magn. Reson. 2013;15:102.
23 Kellman P, Aletras AH, Mancini C, McVeigh ER, Arai AE. T2-prepared SSFP improves diagnostic confidence in edema imaging in acute myocardial infarction compared to turbo spin echo. Magn. Reson. Med. 2007;57:891–7.
24 Kellman P, Xue H, Spottiswoode BS, Sandino CM, Hansen MS, Abdel-Gadir A, et al. Free-breathing T2* mapping using respiratory motion corrected averaging. J. Cardiovasc. Magn. Reson. 2015;17:3.
25 Xue H, Hansen MS, Nielles-vallespin S, Arai AE, Kellman P. Inline quantitative myocardial perfusion flow mapping. JCMR/ISMRM Workshop. 2016;18:4–6.

Contact

Peter Kellman
National Heart, Lung, and Blood Institute
National Institutes of Health, DHHS
10 Center Drive MSC-1061
Bethesda, MD 20892
USA
kellman@nih.gov



Siemens' global MRI community offers peer-to-peer support and information. Radiologists, physicists, cardiologists, and technologists, have all contributed with publications, presentations, training documents, case studies, and more – all freely available to you via this unique network.

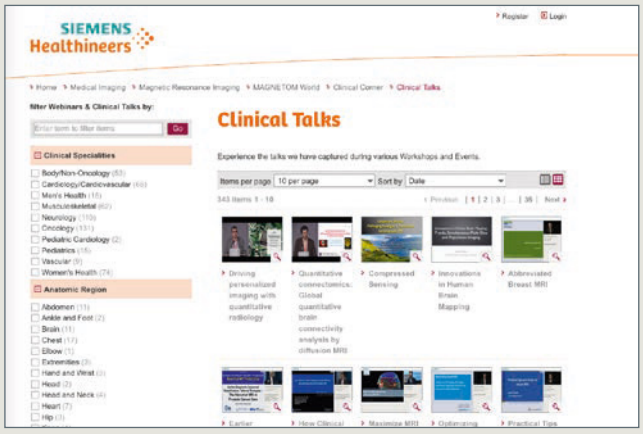

Don't miss the >300 lectures and presentations by international and renowned experts in the field on all aspects of MR imaging that will allow you to be exposed to new ideas and alternative approaches.

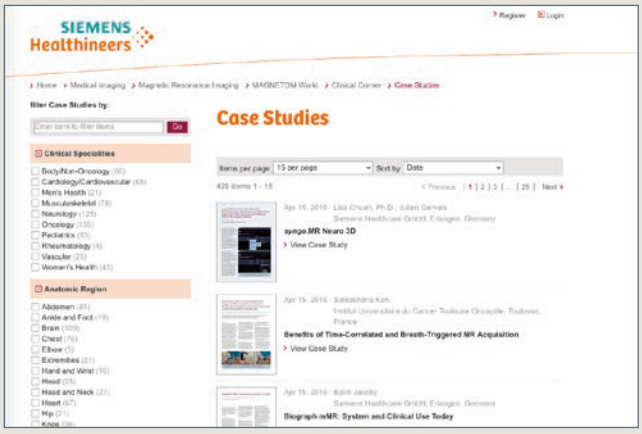

The centerpiece of the MAGNETOM World Internet platform consists of MAGNETOM users' results. Here you will find case reports, articles and application tips allowing you to optimize your daily work.

Put the advantages of the MAGNETOM World to work for you!

www.siemens.com/magnetom-world

Clinical Neuroimaging at 7T Compared to Lower Field: a Photo Essay

Stephen E. Jones, Ph.D., M.D.[1]; Emmanuel Obusez, M.D.[1]; Sehong Oh, Ph.D.[1]; Irene Wang, Ph.D.[2]; Mark Lowe, Ph.D.[1]

Imaging Institute (1), Epilepsy Center (2), Cleveland Clinic, Cleveland, OH, USA

Introduction

The recent introduction of a clinical 7T human MRI scanner continues the progress of increasing field strength, ever since the invention of MRI. While research is understandably emphasized as the initial application when a new higher field MRI system is commercially introduced, inevitably clinical applications become the majority appliation. Similarly, such 7T scanners as are currently available are used mainly for research. However, with anticipated FDA approval in the next few years, 7T MRI will become clinically available. While the research utility of 7T is already clear, especially in functional brain imaging using BOLD fMRI [1-4], the clinical utility is uncertain at this time.

The main advantage of using higher magentic field is an increased signal from precessing magnetic moments, which scales as the field strength increases [5]. The increased signal improves images in several ways: Images with the same voxel size but higher signal-to-noise ratio (SNR), images with smaller voxels but the same SNR, or images with the same SNR but scanned faster (for example less averaging would be needed). It is likely that the second advantage yielding higher spatial resolution will be the principle clinical advantage of 7T.

The goal of this paper is to illustrate the potential advantages of 7T in clinical neuroimaging, by imaging a variety of neurological diseases at 7T and directly comparing them to lower field imaging (typically 3T) in the same patient.

Amytrophic lateral sclerosis	14
Dementia	1
Epilepsy	66
Multiple Sclerosis	18
Parkinsons disease	2
Traumatic brain injury	22
Tumors (brain)	6
Tumors (eye)	3
Vasculitis	2
Total	134

Sequences	$TR/TE_1/TE_2$ (ms)	FOV (mm^2)	Matrix	Slice thickness (mm)
Coronal FLAIR	8360/111	170	320 x 320	4
Axial FLAIR	8360/117	201	224 x 192	4
Axial 3D GRE	9.8/4.76	256	256 x 256	1
Coronal 3D GRE	11/4.92	230	224 x 256	1.25
Axial MPRAGE	1800/3.12	256	256 x 256	1
SWI	49/40	220	224 x 204	3

Table 1: 1.5T sequence parameters

Sequences	$TR/TE_1/TE_2$ (ms)	FOV (mm^2)	Matrix	Slice thickness (mm)
Coronal FLAIR	8100/115	180	240 x 192	3
Axial FLAIR	8640/128	180	256 x 204	3
Axial 3D GRE	4000/112	180	320 x 320	3
Coronal 3D GRE	10/4.6	256	256 x 256	1
Axial MPRAGE	1900/2.54	256	256 x 256	1
SWI	27/20	210	256 x 256	2.5

Table 2: 3T sequence parameters.

MRI technique

Currently the 7T system[1] is not FDA approved, and this study was approved by our institutional IRB for the strict purpose of comparing imaging features of neuropathology at 7T to imaging features obtained previously at lower field on an FDA approved clinical scanner. Exclusion criteria included implants not validated as safe at 7T, body weight less than 30 kg, inability to lay motionless while in MRI, claustrophobia, and a normal MRI at lower field.

The 7 tesla whole-body MRI system used at Cleveland Clinic is a Siemens MAGNETOM with an Agilent 830AS magnet. For all the studies presented here, a head-only CP transmit/32-channel phased-array receive coil (Nova Medical, Wilmington, MA, USA) was used. Sequences used in the following figures were: FLAIR, MP2RAGE, SWI, and GRE, as well as TSE T2 in the lower field scans. In order to focus on the qualitative features of the differences in imaging results, we list the complete scan protocols here and in individual figures highlight spatial resolution differences between the different field strength images. Although slight variations in clinical scan prescriptions exist across the scanner installations at Cleveland Clinic, the basic scan protocol for each at 1.5T and 3T are shown in Tables 1 and 2, respectively.

For 7T the scan protocols are:

Coronal and transverse 2D FLAIR TSE sequence
- TR/TE = 9000/124 ms
- FOV = 192 x 192 mm²
- slice number = 45
- slice thickness = 2 mm
- In-plane resolution = 0.75 x 0.75 mm²
- TI = 2600 ms
- matrix = 256 x 256
- GRAPPA 3
- bandwidth 244 Hz/pixel
- scan time = 3:02 min

Axial and/or sagittal T1-weighted MP2RAGE
- TR/TE = 6000/2.99 ms
- FOV = 240 x 240 mm²
- slice number = 192
- resolution = 0.75 mm³ isotropic voxel
- flip angle = 4° and 5°
- TI1/TI2 = 700/2600 ms
- Matrix = 320 x 320 6/8 partial Fourier in k_y and k_z
- GRAPPA 3
- bandwidth 240 Hz/pixel
- scan time = 9:48 min

T2*-weighted GRE
- TR/TE = 2290/17.8 ms
- FOV = 192 x 192 mm²
- slice number = 60
- slice thickness = 1.5 mm
- In-plane resolution = 0.38 x 0.38 mm²
- flip angle = 250
- matrix = 512 x 512
- GRAPPA 2
- bandwidth 40 Hz/pixel
- scan time =10:08 min

Transverse 3D SWI sequence
- TR/TE = 23/15 ms
- FOV = 220 x 220 mm²
- slice number = 144
- resolution = 0.49 x 0.49 x 0.8 mm³
- flip angle =20°

[1] MAGNETOM 7T is ongoing research. All data shown are acquired using a non-commercial system under institutional review board permission. MAGNETOM 7T is still under development and not commercially available yet. Its future availability cannot be ensured.

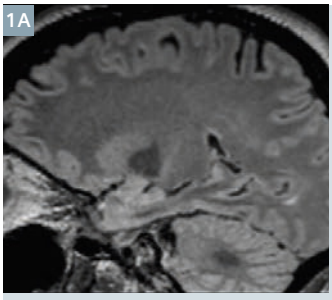

3T 5000/393/1800 [TR/TE/TI]

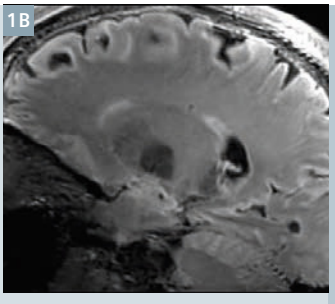

7T 7000/380/2100

1 Example of increased SNR in a FLAIR sequence from a 7T image **(1B)** compared to a 3T image **(1A)** in different patients. For comparison purposes, similar sequences were used that had the same voxel size (1 x 1 x 1 mm). In the flat region of anterior white matter, the SNR was 32.3 for 7T and 16.0 for 3T. While the increased SNR at 7T is apparent as a 'flatter' appearance of the white matter, this may not yield additional clinical benefit for most neurological disease, which would benefit more from using the increased SNR to enable smaller voxels and higher spatial resolution with the same SNR [5, 6].

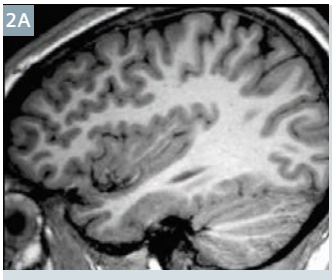

3T 1 x 1 x 1.2 mm
2300/2.98/900

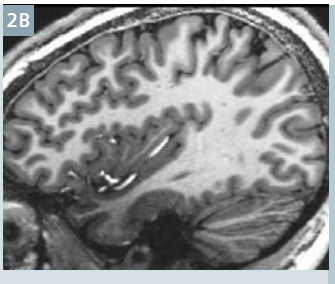

7T 0.75 x 0.75 x 0.75 mm
6000/2.99

2 Example of increased contrast-to-noise ratio (CNR) in a T1-weighted sequence, with 7T MP2RAGE **(2B)** and a 3T MPRAGE **(2A)**. The CNR of signal in white matter to gray matter is 18.3 (7T) and 9.9 (3T). This increased distinction between the gray-white interface is very important in the evaluation of a class of lesions causing epilepsy. In addition, any lesion embedded within white matter that follows gray matter signal characteristics will have increased conspicuity [7, 8].





3 Example of increased in-plane resolution, with 7T MP2RAGE **(3B)** and 3T MPRAGE **(3A)**. The in-plane voxel size is 0.75 x 0.75 mm (7T) and 1.0 x 1.0 mm (3T). Although the decrease in linear size is only 25%, this small change can noticeably improve image quality, as seen in the improved detail of the cerebellar folia. Also contributing to visual improvement at 7T is a thinner slice, being 0.75 mm compared with 1.2 mm for 3T, which provides less volume averaging and thereby sharper images [7-9].

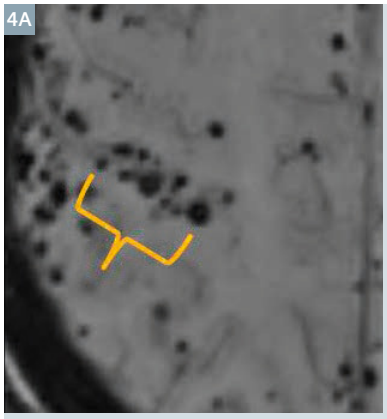

3T SWI 0.82 x 0.82 x 2.5 mm

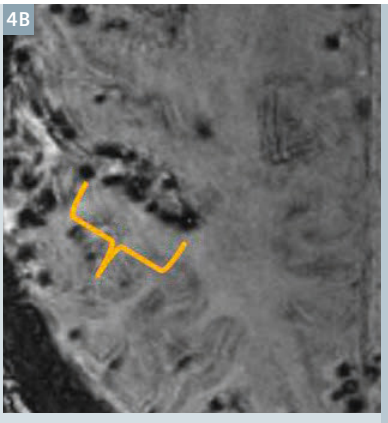

7T SWI 0.49 x 0.49 x 0.80 mm

4 Example of combination of increased spatial resolution and lesion conspicuity, enabling improved colocalization of small lesions on underlying anatomy. While this 64-year-old female already had a known diagnosis of cerebral amyloid angiopathy, manifest with innurable microhemorrhages (CMH) throughout the brain, the high spatial resolution of 7T revealed a strong colocalization of the CMH with the cortical ribbon. At lower field, this association could not be appriciated on the SWI sequence. Similar studies have shown the utility of 7T in the localization of microhemorrhages to the cortex in patients with cebebral amyloid angiopathy [10-12].



3T T2-TSE 0.55 x 0.55 x 4 mm thick



7T T2*-GRE 0.375 x 0.375 x 1.5 mm thick

5 Example of clinical utility in a multiple sclerosis patient. This 23-year-old female has a four-year history of progressive MS, whose diagnosis is not in question. This image examplifies a characteristic of MS well visualized with the high resolution of 7T, namely the central vein coursing through the middle of the MS plaque [14, 15]. The arrows point to the same plaque on a 3T T2-weighted sequence **(5A)**, and a 7T T2* GRE sequence **(5B)**. This imaging feature can be very useful in patients with lesser disease, where the diagnosis of MS is uncertain.



3T T2w 0.43 x 0.43 x 4 mm thick

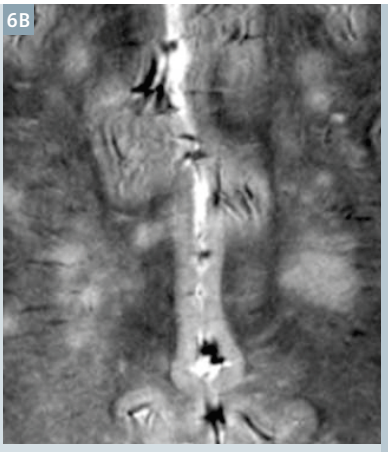

7T T2* GRE 0.375 x 0.375 x 1.5 mm thick

6 Counter-example to the previous patient of Figure 5 who had established MS. This 63-year-old female with cognitive issues has a heavy burden of white matter disease, and was referred to our mutiple sclerosis clinic for possible MS due to a 3T MRI. Images show a heavy burden of white matter disease, from a 3T T2-weighted sequence on the left **(6A)**, and a 7T T2* GRE sequence on the right **(6B)**. In distinction to the MS patient of Figure 5, no definitive central vein is seen at either field strength, and the diagnosis of MS was lowered, while the diagnosis of non-specific vasculopathy was raised [16]. A subseqent paratid biopsy revealed underlying Sjogren's disease, whose chronic small vessel disease likely caused the findings.

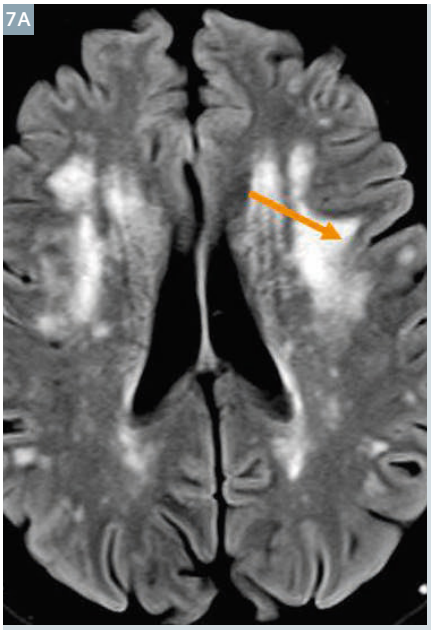

3T FLAIR 0.69 x 0.69 x 4 mm thick

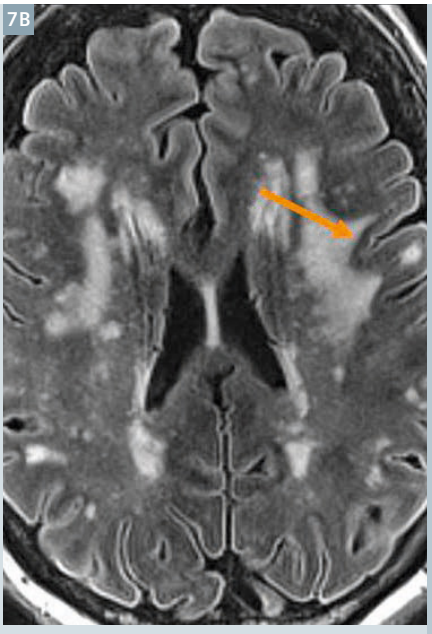

7T FLAIR 0.75 x 0.75 x 2 mm thick

7 Example of another discriminator of MS vs vasculopathy, using the same patient as in Figure 6. The subcortical U-fibers have a dual arterial blood supply (from both the adjacent capillary plexus occupying the gray matter ribbon, and from deep arterial penetrators coursing through the gray matter). This redundant supply of blood make this tissue more resiliant to ischemic injury, unlike deeper white matter. However, this tissue still remains as vulnerable to demyelinating disease as deeper white matter. Thus, careful delination of a preserved subcortical U-fibers can help discrimiate vasculopathy from demyelinating disease. In this case, the arrows point to a segment of subcortical U-fibers, which is better defined throughout (compare the segment just inferior to the arrows) with the high spatial resolution of 7T.

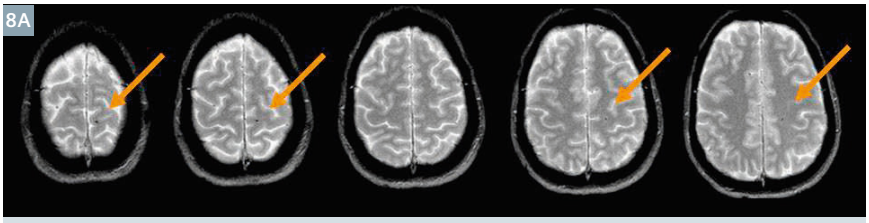

1.5T GRE 0.875 x 0.875 mm x 4 mm thick

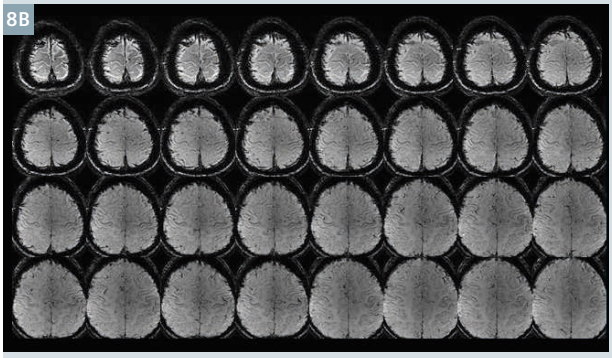

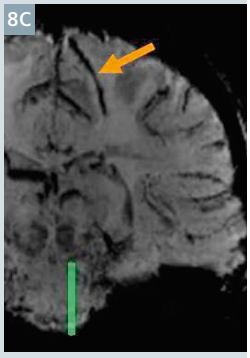

7T SWI 0.49 x 0.49 x 0.8 mm thick

8 Example of clinical value of small voxels and thin slices. A 43-year-old female presents six months after falling from a horse with headaches and presumed post-concussive syndrome. Several continuous slices from a 1.5T GRE sequence are shown in the top panel **(8A)**, with arrows pointing to small foci of susceptibility effect felt to be microhemorrhages. A 7T MRI was then obtained, bottom two panels **(8B, C)**. The lower panel shows an axial SWI sequence, whose 24 slices span the same axial distance as the 5 axial GRE slices at 1.5T. An advantage of the smaller voxels is that a high resolution MPR image was obtained in a coronal oblique direction **(8C)**, clearly revealing the dots of presumed microhemorrhage to be a linear morphology, and most likely a benign developmental venous anomaly, which is not related to traumatic brain injury (TBI). The patient has since been treated for chronic migraine headache, rather than post concussive syndrome. One similar study showed increased detection of developmental venous anomalies at 7T compared to 3T in patients with cavernous malformations [13].

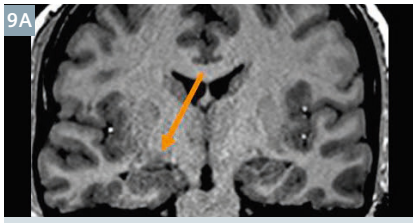

3T 0.41 x 0.41 x 1 mm

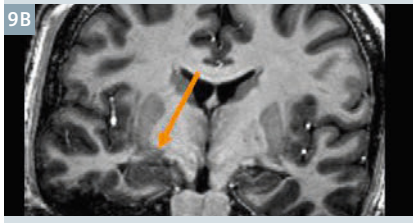

7T 0.75 x 0.75 x 0.75 mm

9 Example of a subtle heterotopia, never before appreciated at lower field MRI. The patient is a 30-year-old female, suffering from seizures since birth. A 7T T1 MP2RAGE **(9B)** revealed a previously unnoticed periventricular gray matter focus (arrow), lying adjacent to the right amygdala and hippocampus, which also appeared mildly enlarged. In addition, 7T revealed extensive periventricular heterotopias filling bilateral occipital horns (not shown). The patient recently underwent a right temporal lobectomy, and currently remains seizure free.

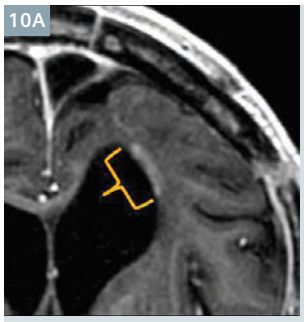

3T MPRAGE post gadolinium
0.45 x 0.45 x 2 mm thick



7T MP2RAGE post gadolinium
0.75 x 0.75 x 0.75 mm thick

10 Example of imaging recurrent tumor. This 65-year-old male has a known anaplastic oligodendroglioma, status post prior resection and radiation treatment. These post-gadolinium images (**10A**: 3T T1 MPRAGE; **10B**: 7T T1 MP2RAGE) show a thin segment of enhancement along the periventricular margin (shown by the bracket), indicative of tumor recurrence. While this 7T did not alter any clinical management, the high resolution and increased tissue contrast characteristics show better detail of the recurrence and adjacent tissue. This capability could potentially help patients because recurrence can be detected at a smaller level, earlier in the disease. Similarly, other studies have also shown increased tumor detection using different sequences at 7T compared to 3T [17-19].



3T SWI
0.43 x 0.43 mm x 2 mm thick



7T SWI
0.49 x 0.49 x 0.80 mm thick

11 Example of microhemorrhages not reported at lower field. This 54-year-old male experienced a motor vehicle accident 18 months earlier, and presents with persistant chronic headache. It is unclear if the headache is post-concussive syndrome, or a seperate headache syndrome. His 3T clinical MRI **(11A)** was reported as normal, however the 7T MRI **(11B)** showed several microhemorrhages with increased conspicuity. In retrospect, those microhemorrhages were visible with lower conspicuity at 3T. This example shows the practical importance of improved conspicuity of lesions, which is just as important as 7T revealing new lesions: if lesions with low conspicuity are present but not detected by the radiologist, they are effectively not present. On review of literature, one study has also shown 7T SWI improves identification of small hemorrhagic diffuse axonal injury compared to 3T [20].

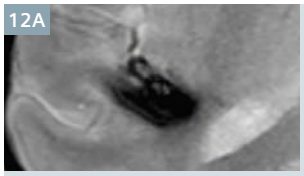

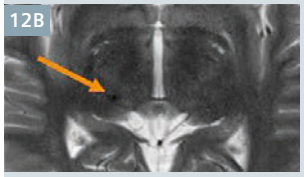

3T GRE 0.66 x 0.66 mm x 3 mm
and 3T T2-TSE
0.55 x 0.55 x 3 mm thick

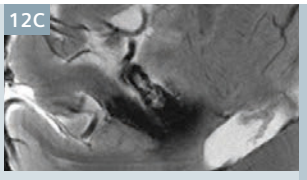

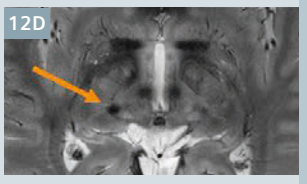

7T T2*-GRE
0.375 x 0375 x 2.00 mm thick

12 Another example of increased lesion conspicuity showing additional lesions. This 47-year-old male with a known cavernous malformation (shown on **12A, B** at 3T) had a 7T scan shown on **12C, D**. While the known large cavernous malformation in the posterior right insula shows increased detail at 7T, a second cavernous malformation not previously appreciated was seen in the right thalamus. In retrospect, this focus was present before but its marginal conspicuity was insufficient for a radiologist's detection. This lesion is now known and being followed. Prior earlier 7T studies using SWI have shown increased detection of a significant number of cavernous malformations and better definition of cavernous angioma angioarchitecture compared to lower fields [13, 21].

3T 0.28 x 0.28 x 3 mm

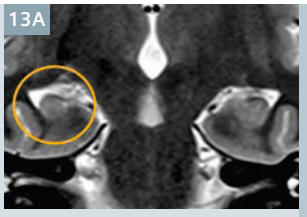

7T 0.375 x 0.375 x 1.50 mm

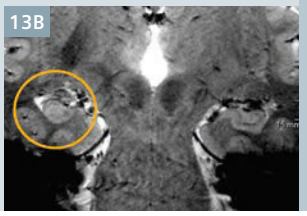

13 Example of high resolution confirming a diagnosis of mesial temporal sclerosis (MTS) in epilepsy. The patient is a 26-year-old male, who had a 3T MRI **(13A)** showing a rounded right hippocampal head (circled), slightly hyperintense, with indistinct internal architecture (compare those features with the patient's normal left hippocampus). 7T image **(13B)** provides superior definition of the rounded morphology and hyperintensity. This hippocampus was subsequently resected and the patient has now been seizure-free for over 2 years. While 7T did not change the diagnosis in this case, this example illustrates its potential to improve the diagnosis of MTS due to its superior resolution. Similarly, one study of 6 patients using 7T T2*-weighted sequence to evaluate hippocampal sclerosis showed greater anatomic detail than 1.5T [25].

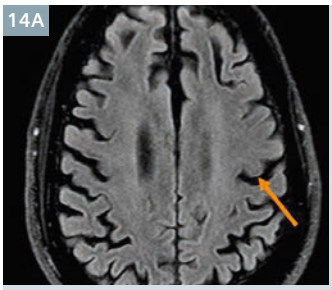

3T FLAIR
0.66 x 0.66 x 3 mm thick

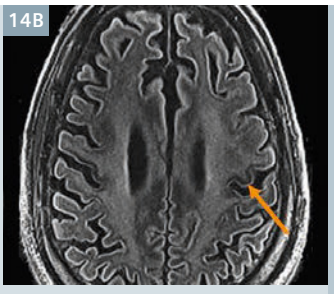

7T FLAIR
0.75 x 0.75 x 2 mm thick

14 Example of 7T applied to amytrophic lateral sclerosis (ALS), also known as Lou Gehrig's disease. The patient is a 68-year-old with ALS diagnosed 3 months earlier. **14A** is a 3T axial FLAIR, and **14B** a 7T axial FLAIR. The arrow points to the 'hand knob' of the motor strip in the left precentral gyrus. Note the gyriform decreased signal seen in the 7T, which is not well apparent at 3T. While this finding did not alter diagnosis or medical management, it has the potential to affect patients earlier in their disease when diagnosis may be ambiguous, as shown in other 7T studies [22-24].

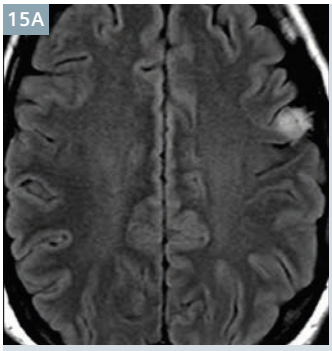

3T FLAIR
0.35 x 0.35 x 3 mm thick

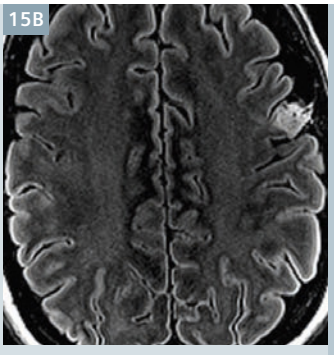

7T FLAIR
0.75 x 0.75 x 2.0 mm thick

15 Example left frontal lesion suspicious for a mass. This 31-year-old female presents with her first seizure in 25 years, after a history of childhood seizures. Images at 3T **(15A)** showed a left frontal lesion thought to be a low grade tumor, and was referred for possible resection. A 7T image **(15B)** provided sufficient detail to suggest the lesion is actually a post-traumatic lepto-meningeal cyst with subjacent scarring. The patient subsequently reported a prior history of head trauma at age 3 years. Surgery has been postponed and her seizures will be managed medically. This example shows increased lesion detail was able to alter the diagnosis of a tumor to a post-traumatic scar.

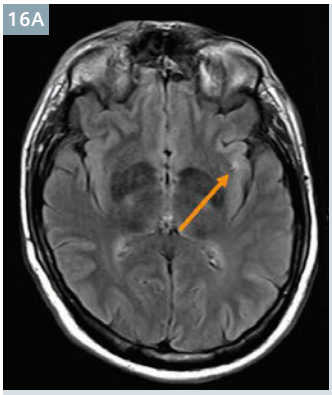

3T FLAIR
0.36 x 0.36 x 4 mm thick

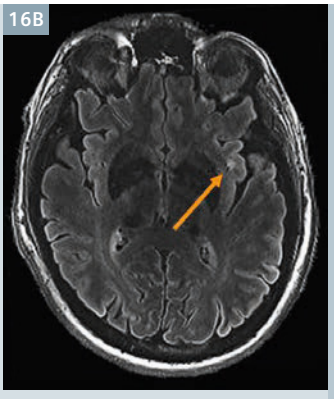

7T FLAIR
0.75 x 0.75 x 2.0 mm thick

16 Example of a lesion thought to be epilepstogenic, but determined to be benign with high resolution images. The patient is a 56-year-old male with epilepsy for 32 years, now medically refractory and being evaluated for surgery. A 3T FLAIR **(16A)** showed left subcortical gray-white indistinction of the insular cortex, suspicious for a focal cortical dysplasia. While this location was inconsistant with EEG findings, the patient was scheduled for an invasive neurosurgical evaluation to explore the lesion and other possible areas for seizure generation. A 7T FLAIR **(16B)** was obtained whose high resolution revealed the lesion to be a vascular abnormality causing adjacent scar that mimiced the appearance of a dysplasia. The patient's surgical plan was altered to not include the left insula.

3T FLAIR
0.35 x 0.35 x 3 mm thick

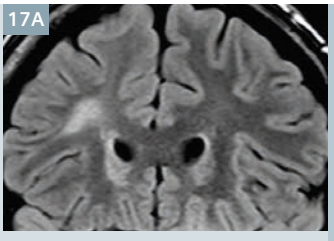

7T FLAIR
0.375 x 0.375 x 2 mm thick

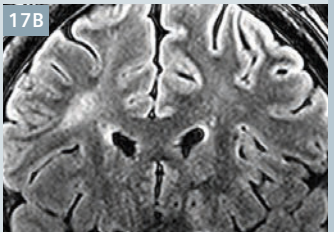

17 Example of ambiguous white matter lesion. The patient is a 24-year-old male with18 years of epilepsy. His 3T MRI image **(17A)** shows an unusual lesion in the right frontal lobe suggestive of a form of malformation of cortical development called a transmantle dysplasia. It was unclear if the lesion was related to his epilepsy because all his other tests pointed to posteriorly to this region. Higher detail due to smaller voxels from a 7T image **(17B)** verified that the lesion has no frank connection to the cortex, the adjacent cortex is normal with no gray-white indistinction, and the abnormality is most likely a vascular lesion. These features could be best appreciated by scrolling through the thin 7T sections. This suggestion was confirmed at 3T, and altered the patient's surgical plan to focus on other areas of the brain.

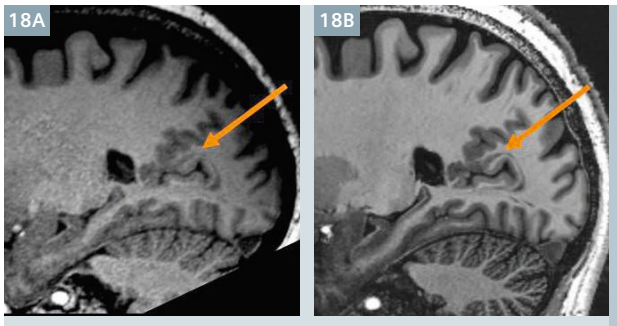

3T MPRAGE
0.41 x 0.41 x 1 mm

7T MP2RAGE
0.75 x 0.75 x 0.75 mm

18 Example of malformation of cortical development (MCD), not appreciated on imaging. The patient is a 37-year-old male with a 5-year history of epilepsy. His previous MRIs (typically 3T) only revealed a right thalamus cyst, which was known to be not epileptic. A 7T T1 MP2RAGE image **(18B)** showed an abnormal projection of gray matter signal extending into the white matter, compatible with a subcortical heterotopia (a form of MCD). In retrospect, guided by the 7T finding, subtle correlates could be found on 3T MRI **(18A)**. This identification of a subtle lesion started at 7T, and confirmed at 3T, altered the patient's management by making him a surgical candidate. This patient is currently undergoing intracranial EEG to confirm the epileptogenicity of the lesion.

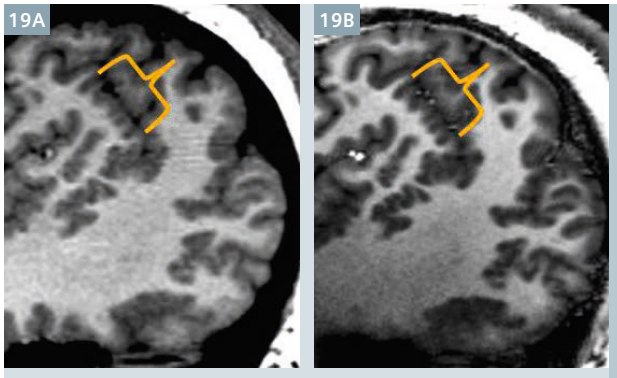

3T 0.46 x 0.46 x 0.94 mm

7T 0.75 x 0.75 x 0.75 mm

19 Example of improved conspicuity of Polymicrogyria (PMG). The patient is a 20-year-old male with a known congenital malformation of cortical development called PMG, manifest as abnormally small and tightly packed gyri (as an example, see cortex within interval of bracket). While the 3T sagittal MPGR image **(19A)** reveals the presence of PMG, the 7T MP2RAGE **(19B)** shows superior definition, due to combination of smaller voxels and increased CNR of gray to white matter. Occasionally regions of PMG are surgically removed, and accurate visualization of the extension is very important to clear surgical margins and potential cure. A study conducted by De Ciantis and colleagues also showed 7T provided additional details and greater involvement of cortical polymicrogyria compared to 3T, this was attributed to increased signal-to-noise and increased magnetic susceptibility [27].

3T T1-weighted
0.65 x 0.65 x 4 mm thick

7T MP2RAGE
0.75 x 0.75 x 0.75 mm

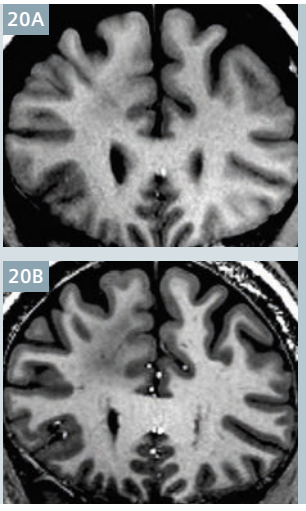

20 Example of low-grade brain tumor. The patient is a 50-year-old female, with a 15-year history of biopsy proven low grade astrocytoma, which had been grossly stable during that time. In addition, she had a 40-year history of epilepsy, well controlled until recently, and was now under consideration for surgery. A 3T coronal T1-weighted image **(20A)** shows subtle signal abnormality in the right frontal lobe white matter. The corresponding 7T image **(20B)** redemonstrates this finding with greater conspicuity. This detail improved visualization of the tumor's margins, which were more extensive than originally thought, and guided the decision to continue medical management rather than undergo a larger brain surgery. Another 7T study used a different approach and different set of sequences to evaluate 15 patients with astrocytomas (WHO grades II-IV) – greater susceptibility was used to detect tumor margins by observation of tumor vascularity which was only present at lower grade as diffusely infiltrating astrocytoma [18].

Discussion

One weakness of this method of using a gallery of side-by-side image comparisons of 7T to lower field to assess any clinical utility is that it only assesses the two-dimensional image. Our experience is that when actively viewing images on a DICOM viewer, with the ability to scroll up and down through lesions, and actively window, markedly increased lesion conspicuity, as opposed to simply viewing one static image. Thus, any conspicuity of images shown in this paper should be qualitatively considered a lower limit.

Another weakness is that the 7T protocols used in this study are not clincally optimized in terms of scanning time, as are the refined protocols on clinical MRIs at lower field. Imaging slots on the 7T do not face the same adminstrative pressures for patient throughput as clinical magnets, and are currently more liberal with scan times. Note this increased time is not unexpected at this early stage in the evolution of clinical sequence and protocol development at 7T. Thus, in the future, a more valid clinical comparison might involve using common sequences and protocols at 7T and lower field that require the same scan time.

Another limitation of the clinical utility of 7T is the increased B_1 inhomogeneities compared with lower field strength scanning. This presents a problem for interpretation of

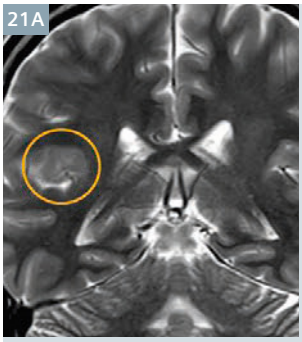

3T 0.28 x 0.28 x 3 mm



7T 0.375 x 0.375 x 2 mm

21 Example of subtle right peri-insular malformation of cortical development. This patient is a 26-year-old male who had intractable epilepsy for 19 years. EEG showed that seizures were originating from the left frontotemporal area. Coronal 3T T2-weighted image **(21A)** showed a suspicious lesion in the right posterior insular/parietal operculum region. 7T coronal GRE image **(21B)** delineated the lesion with much better conspicuity. The patient underwent surgery with complete resection of the subtle right peri-insular lesion and is now seizure free. Pathology confirmed a severe focal cortical dysplasia. A similar 7T study of patients with intractable focal epilepsy and unrevealing lesions, showed 26% improved detection of epileptogenic lesions not seen on 1.5T or 3T [26].

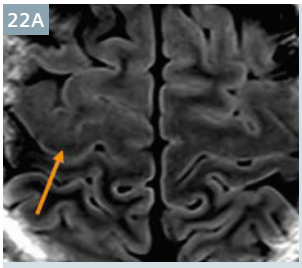

3T 0.82 x 0.82 x 4 mm

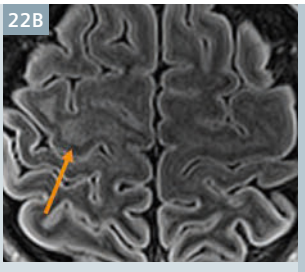

7T 0.75 x 0.75 x 2 mm

22 Example of subtle cortical dysplasia in epilepsy. The patient is an 18-year-old female with refractory focal epilepsy, with multiple prior 3T MRIs all read as normal. A 7T axial FLAIR image **(22B)** showed abnormally increased and asymmetric subcortical hyperintensity (arrow), which was also hypointense with indistinct gray-white margins on T1 MPRAGE sequence (not shown). In retrospect, a subtle abnormality could be seen at 3T **(22A)**, but with much less conspicuity and only on the exact same slice. The lesion was resected, with pathology confirming a focal cortical dysplasia. The patient remains seizure free.

whole-brain images, particularly in the lower parts of the temporal lobe, an important region for consideration of surgical intervention in epilepsy. Head coils incorporating multiple parallel transmission coil elements show considerable promise to improve the whole-brain B_1 homogeneity [28].

This paper presents a gallery of images of various neurological diseases, portrayed as a side-by-side comparison of 7T to lower field, each obtained in the same patient. This wide ranging comparison is made possible by an IRB permitting imaging of clinical patients at 7T for the expressed comparison of those imaging findings to those already obtained at lower field. Often this prompted a reappraisal of the earlier lower field findings and occassionally affected patient management.

The visualization of a lesion at 7T that was frankly not visible at lower field was infrequent, and typically the lesion was visible on the lower field image but less conspicuous. Sometimes this decerased conspicuity meant the lesion was not noticed at lower field by the radiolgoist. Therefore, in a busy clinical practice, there could be value for 7T imaging that increases lesion conspicuity that enables a radiolgist's detection, and this improvement is just as important as any de novo appearance of new lesions at 7T.

This series of cases includes clinical vignettes decribing how 7T findings influenced clinical management. While a few cases showed new, or de facto new lesions (such as Figure 8 microhemorrhages in TBI), the majority simply showed lesions visible at lower field, but with greater conspicuity. This increase is mainly due to smaller voxels providing higher spatial resolution, perhaps accentuated by intrinsically increased contrast-to-noise ratio of different tissue types. While the linear decrease in voxel size at 7T may seem modest (around 25%), this small increase nonetheless greatly aids lesion discrimiation to the radiologist's eye.

It is difficult to exactly predict the future clinical niche of 7T in neurological imaging. Some guidance of the extension from 3T to 7T may come from our prior experience from the extension from 1.5T to 3T [29-33]. Today 3T clincial image quality is superb but the initial MRIs suffered from inhomogenities. There were early concerns about differences of tissue contrast, gadolinium contrast, and poor coils [34, 35]. Today with over a decade of continued development and experience, 3T MRI addressed these issues and is now a mainstay of clinical imaging when high resolution and quality are required, for example in epilepsy. While the costs for 7T will be considerably more than 3T, there may likely evolve many clinical applications where 7T imaging will be specifically sought, especially after an analogous decade of continued developement and improvement [36].

Lastly, the role of 7T could borrow from an analogy in the technology of television, and its recent adoption of high-definition television (HDTV): 7T could viewed as 'high definition MRI'. In this analogy, whereas a television viewer can generally enjoy a program in both low-definition and high-definition TV, occassionally the extra detail makes a difference, for example when viewing the scores displayed during a sports broadcast. Similarly with MRI, both low-field and 7T can show important radiological features, but occassionally the extra resolution makes an important clinical difference.

Conclusion

The greatest clinical utility of 7T may be its improved spatial resolution, which can aid in the clinical diagnosis of pathologies that contain fine detail. A second utility may be its increased sensitivity to susceptibility effects. Finally, while 7T infrequently showed new lesions not frankly visible at lower field, it shows lesions better, and this can provide clinical significance.

References

1 Hua J, Qin Q, van Zijl PCM, et al. Whole-brain three-dimensional T2-weighted BOLD functional magnetic resonance imaging at 7 Tesla. Magn Reson Med 2014;72:1530–40.
2 Harmer J, Sanchez-Panchuelo RM, Bowtell R, et al. Spatial location and strength of BOLD activation in high-spatial-resolution fMRI of the motor cortex: a comparison of spin echo and gradient echo fMRI at 7 T. NMR Biomed 2012;25:717–25.
3 van der Zwaag W, Francis S, Head K, et al. fMRI at 1.5, 3 and 7 T: characterising BOLD signal changes. Neuroimage 2009;47:1425–34.
4 Olman CA, Yacoub E. High-field FMRI for human applications: an overview of spatial resolution and signal specificity. Open Neuroimag J 2011;5:74–89.
5 Vaughan JT, Garwood M, Collins CM, et al. 7T vs. 4T: RF power, homogeneity, and signal-to-noise comparison in head images. Magn Reson Med 2001;46:24–30.
6 Pohmann R, Speck O, Scheffler K. Signal-to-noise ratio and MR tissue parameters in human brain imaging at 3, 7, and 9.4 tesla using current receive coil arrays. Magn Reson Med 2016;75:801–9.
7 Shin W, Shin T, Oh S-H, et al. CNR improvement of MP2RAGE from slice encoding directional acceleration. Magn Reson Imaging 2016;34:779–84.
8 Seiger R, Hahn A, Hummer A, et al. Voxel-based morphometry at ultra-high fields. a comparison of 7T and 3T MRI data. Neuroimage 2015;113:207–16.
9 Fujimoto K, Polimeni JR, van der Kouwe AJW, et al. Quantitative comparison of cortical surface reconstructions from MP2RAGE and multi-echo MPRAGE data at 3 and 7 T. Neuroimage 2014;90:60–73.
10 Ni J, Auriel E, Martinez-Ramirez S, et al. Cortical localization of microbleeds in cerebral amyloid angiopathy: an ultra high-field 7T MRI study. J Alzheimers Dis 2015;43:1325–30.
11 van Veluw SJ, Biessels GJ, Klijn CJM, et al. Heterogeneous histopathology of cortical microbleeds in cerebral amyloid angiopathy. Neurology 2016;86:867–71.
12 De Reuck J, Deramecourt V, Cordonnier C, et al. Superficial siderosis of the central nervous system: a post-mortem 7.0-tesla magnetic resonance imaging study with neuropathological correlates. Cerebrovasc Dis 2013;36:412–7.
13 Frischer JM, Göd S, Gruber A, et al. Susceptibility-weighted imaging at 7 T: Improved diagnosis of cerebral cavernous malformations and associated developmental venous anomalies. NeuroImage Clin 2012;1:116–20.
14 Tallantyre EC, Morgan PS, Dixon JE, et al. 3 Tesla and 7 Tesla MRI of multiple sclerosis cortical lesions. J Magn Reson Imaging 2010;32:971–7.
15 Ge Y, Zohrabian VM, Grossman RI. Seven-Tesla magnetic resonance imaging: new vision of microvascular abnormalities in multiple sclerosis. Arch Neurol 2008;65:812–6.
16 Kilsdonk ID, Wattjes MP, Lopez-Soriano A, et al. Improved differentiation between MS and vascular brain lesions using FLAIR* at 7 Tesla. Eur Radiol 2014;24:841–9.
17 Noebauer-Huhmann I-M, Szomolanyi P, Kronnerwetter C, et al. Brain tumours at 7T MRI compared to 3T--contrast effect after half and full standard contrast agent dose: initial results. Eur Radiol 2015;25:106–12.
18 Moenninghoff C, Maderwald S, Theysohn JM, et al. Imaging of adult astrocytic brain tumours with 7 T MRI: preliminary results. Eur Radiol 2010;20:704–13.
19 Paek SL, Chung YS, Paek SH, et al. Early experience of pre- and post-contrast 7.0T MRI in brain tumors. J Korean Med Sci 2013;28:1362–72.
20 Moenninghoff C, Kraff O, Maderwald S, et al. Diffuse axonal injury at ultra-high field MRI. PLoS One 2015;10:e0122329.
21 Dammann P, Wrede K, Zhu Y, et al. Correlation of the venous angioarchitecture of multiple cerebral cavernous malformations with familial or sporadic disease: a susceptibility-weighted imaging study with 7-Tesla MRI. J Neurosurg http://doi.org/10.3171/2016.2.JNS152322.
22 Cosottini M, Donatelli G, Costagli M, et al. High-Resolution 7T MR Imaging of the Motor Cortex in Amyotrophic Lateral Sclerosis. AJNR Am J Neuroradiol 2016;37:455–61.
23 Versluis MJ, van der Grond J, van Buchem MA, et al. High-field imaging of neurodegenerative diseases. Neuroimaging Clin N Am 2012;22:159–71, ix.
24 Kwan JY, Jeong SY, Van Gelderen P, et al. Iron accumulation in deep cortical layers accounts for MRI signal abnormalities in ALS: correlating 7 tesla MRI and pathology. PLoS One 2012;7:e35241.
25 Breyer T, Wanke I, Maderwald S, et al. Imaging of patients with hippocampal sclerosis at 7 Tesla: initial results. Acad Radiol 2010;17:421–6.
26 De Ciantis A, Barba C, Tassi L, et al. 7T MRI in focal epilepsy with unrevealing conventional field strength imaging. Epilepsia 2016;57:445–54.
27 De Ciantis A, Barkovich AJ, Cosottini M, et al. Ultra-high-field MR imaging in polymicrogyria and epilepsy. AJNR Am J Neuroradiol 2015;36:309–16.
28 Zhu, Y: Parallel excitation with an array of transmit coils. Magnetic resonance in medicine, 51, 775-84, (2004).
29 Lin W, An H, Chen Y, et al. Practical consideration for 3T imaging. Magn Reson Imaging Clin N Am 2003;11:615–39, vi.
30 Frayne R, Goodyear BG, Dickhoff P, et al. Magnetic resonance imaging at 3.0 Tesla: challenges and advantages in clinical neurological imaging. Invest Radiol 2003;38:385–402.
31 Shapiro MD, Magee T, Williams D, et al. The time for 3T clinical imaging is now. AJNR Am J Neuroradiol 2004;25:1628–9; author reply 1629.
32 Pattany PM. 3T MR imaging: the pros and cons. AJNR Am J Neuroradiol 2004;25:1455–6.
33 Schmitz BL, Aschoff AJ, Hoffmann MHK, et al. Advantages and pitfalls in 3T MR brain imaging: a pictorial review. AJNR Am J Neuroradiol 2005;26:2229–37.
34 Runge VM, Case RS, Sonnier HL. Advances in clinical 3-tesla neuroimaging. Invest Radiol 2006;41:63–7.
35 Alvarez-Linera J. 3T MRI: advances in brain imaging. Eur J Radiol 2008;67:415–26.
36 Schmitt F, Grosu D, Mohr C, et al. [3 Tesla MRI: successful results with higher field strengths]. Radiologe 2004;44:31–47.

Contact

Stephen Jones, M.D., Ph.D.
Diagnostic Radiology
Cleveland Clinic Main Campus
Mail Code U15
9500 Euclid Avenue
Cleveland, OH 44195
USA
Phone: +1 216.444.4454
joness19@ccf.org



Compressed Sensing – the Flowchart

Mathias Blasche; Christoph Forman

Siemens Healthineers, Erlangen, Germany

The three key components of Compressed Sensing (CS)[1] are

1. Incoherent ('random') sub-sampling
2. Transform sparsity
3. Non-linear iterative reconstruction

The Compressed Sensing Flowchart provides a step-by-step visualization of the Compressed Sensing measurement and reconstruction process, explaining where and why these three key components are involved.

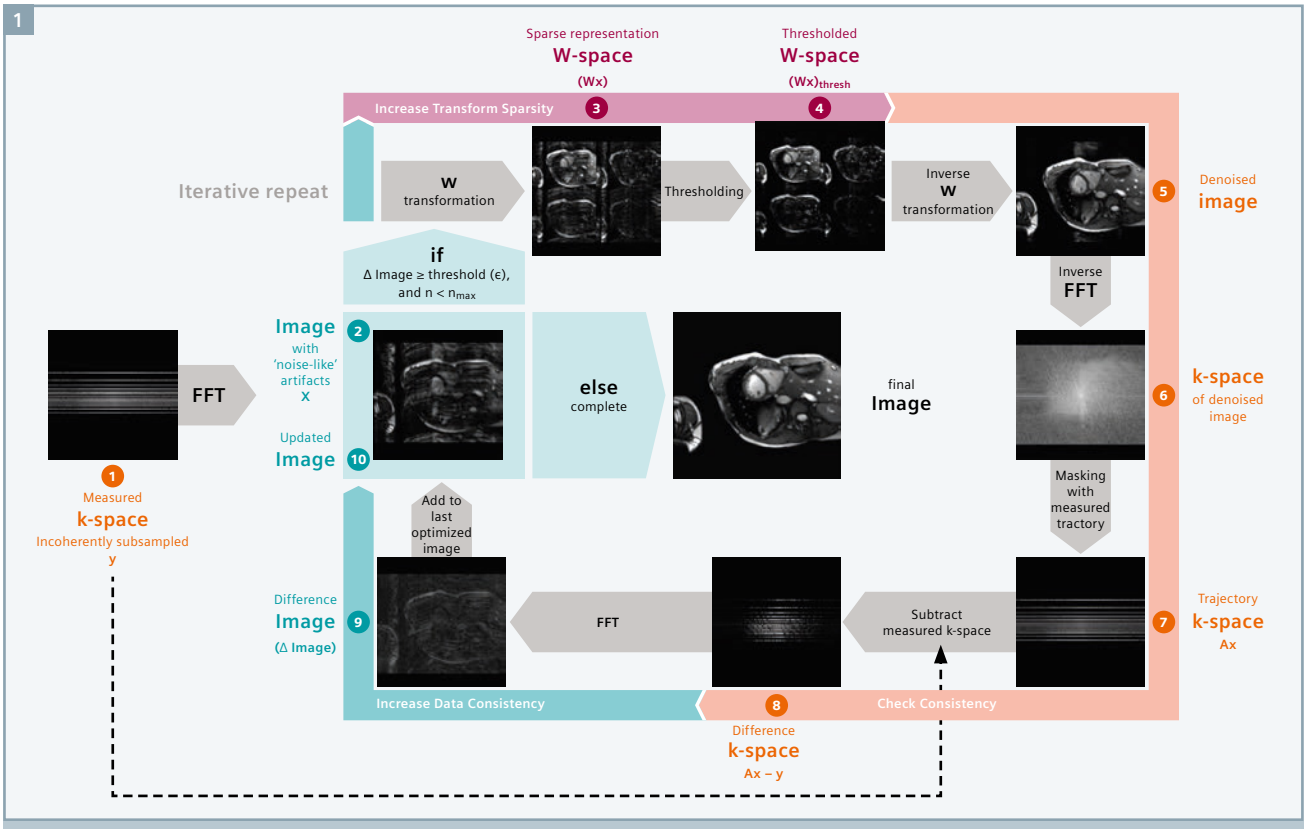

1 Compressed Sensing Flowchart. Some 'typical' images of the iterative reconstruction are depicted for visualization purposes.

Abbreviations and terminology

k-space '**y**'	Measured data (echoes), sorted in an m x n matrix; in the formulas denoted as '**y**'
Image '**x**'	Clinical image; in the formulas denoted as '**x**'
W-space	Different mathematical depiction of the image Examples: Wavelet, Total Variation
FFT	(Fast) Fourier transformation; transforms k-space into image space
FFT^{-1}	Inverse FFT, transforms image space into k-space
W	W transformation, transforms image space into W-space
W^{-1}	Inverse W Transformation, transforms W-space into image space
A	The transformation A consists of two steps, an inverse **FFT** and a 'trajectory masking', i.e. only depicting those pixels in k-space that were measured
λ	Weighting factor for the tradeoff between data consistency and transform sparcity
$\|\|...\|\|_1$	L1 norm: Sum of all absolute values (here: pixel intensities in W-space)
$\|\|...\|\|_2$	L2 norm, 'Euclidean norm': Square root of sum of squares

[1] 510(k) pending. Compressed Sensing Cardiac Cine is not commercially available. Future availability cannot be guaranteed.

The Compressed Sensing optimization formula

The following formula describes the optimization process of CS:

$$\min \| A x - y \|_2^2 + \lambda \| W x \|_1$$

This means that we are searching for an image **x** such that the term above is minimized.

The first term describes the 'data consistency'. It minimizes the least-squares difference (L2 norm, $\|\cdot\|_2^2$) between the estimated image x, and the acquired k-space data y. The smaller this (difference) term becomes, the better the consistency.

The second term describes the 'transform sparsity'. It is the L1 norm of the image transformed into a sparse representation (**W**-space). In this term, the sum of the absolute values of the pixels in the transform domain, denoted by the L1 norm ($\|\cdot\|_1$), is minimized. The smaller this L1 norm, the higher the sparsity. λ is an empirical (application-dependent) weighting factor for balancing data consistency vs. sparsity.

Hence, the optimization procedure minimizing this equation seeks to find a solution that fulfills both criteria, data consistency and transform sparsity. This is done in an iterative process.

1. Measured k-space

The first picture is the measured k-space. There are two differences compared to a 'conventional' scan:

1. Strong sub-sampling, i.e. significantly fewer echoes than in a conventional scan. This results in significantly higher scan speed. But since the Nyquist-Shannon sampling theorem [1] is violated, this will result in strong aliasing artifacts.
2. Incoherent ('random') sampling. This is necessary to create a noise-like appearance of the aliasing artifacts (resulting from the sub-sampling). The reason is that these noise-like artifacts (as opposed to structured artifacts) can then in a later step of the algorithm be removed with a thresholding procedure in W-space (see step 4). The random character of the sampling is essential for the success of the CS reconstruction – "*Randomness is too important to be left to chance*" [2].

   The incoherent sampling in CS is different from the (typically) coherent sub-sampling that is used in Parallel Acquisition Techniques, where the (structured) aliasing is removed by means of the knowledge of the coil sensitivity profiles.

The k-space in the formula is denoted as **y**.

2. Image

As a first step, the (incoherently) subsampled k-space is Fourier transformed into an image.

This image suffers from strong sub-sampling artifacts; but these aliasing artifacts are 'smeared' over the image, due to the incoherence of the sampling in step 1. The aliasing artifacts appear 'noise like'. The better the incoherence of the scan, the more 'homogeneous' the noise-like aliasing artifacts will appear, and the better the CS reconstruction will work.

This image serves as a starting point for the iterative optimization. Since we only covered a small part of k-space in step 1, we do not have the complete information about the image. This image **x** generated by a straightforward FFT is only one possible solution that is consistent with the measured data – but this solution suffers from strong artifacts. The following iterative process serves to find a better (artifact-free) solution that is also consistent with the measured data **y**.

The image in the formula is denoted as **x**.

3. W-space

The image is now transformed into a sparse representation (**W**-space). This is a different 'basis', i.e. a different mathematical depiction of the image. The goal of this transformation is to locally separate the 'wanted signal' from the noise (artifacts). **W**-space is a better-suited depiction of the image as the sparsity in **W**-space is higher. This means that the image 'informational content' is concentrated in few pixels in **W**-space, while most pixels have only a very low signal.

There are various different transformations that can be beneficial for this purpose. This depends on the application. A Wavelet transformation is a very common choice for MR imaging.

By the way, a Wavelet transformation is utilized in image compression with the JPEG 2000 format [3].

4. Thresholded W-space

After the **W** transformation (e.g. Wavelet transformation), the 'wanted signal' is now to a high degree separated from the noise (artifacts). This allows removing the noise by a thresholding procedure:

- Set all pixels with a value < threshold to zero;
- Subtract the threshold from all other pixel values.

This procedure is called 'soft thresholding'. It has been shown that 'soft thresholding' is beneficial for the solution [4]. The threshold is predefined, optimized for the application.

Since many pixels in **W**-space now have a value of 0, we have fewer non-zero pixels (coefficients). The 'transform sparsity', i.e. the sparsity of the image in **W**-space, is increased.

5. Denoised image

We now transform the **W**-space representation back into image space with the inverse **W** transformation ($\mathbf{W}^{-1}$).

By the thresholding procedure in **W**-space in the last step, we have now an image with less noise. This corresponds to a suppression of the noise-like aliasing artifacts, due to the incoherent sampling we applied in step 1.

However, with this denoising we have also 'fiddled' with the image content. The image has less noise (less artifact power) now, but does not exactly reflect the measurement anymore.

In the next steps 6-8, we will therefore check the image consistency (i.e. how well the denoised image still represents the measurement data).

6. k-space of denoised image

In order to compare the denoised image from step 5 with the measured k-space from step 1, we first apply an inverse Fourier Transformation (**FFT**$^{-1}$) to transform the image back to k-space.

Since the image in step 6 was modified, its k-space now consists of all spatial frequencies. This means that we have a 'complete k-space' (all pixels in k-space have non-zero values), as opposed to the measured (subsampled) k-space in step 1 which had only few non-zero values.

7. Trajectory k-space

Now follows a masking process. Remember that we measured only a small part of k-space in step 1. The k-space from step 6, on the other hand, is 'complete'. To compare the two, we filter the k-space (step 6) by only depicting the points (the 'measurement trajectory') of k-space (step 6) that were also measured in k-space (step 1). The rest of k-space (step 6) is set to zero.

The two steps inverse FFT (step 6) and masking (step 7) together are called the '**A** matrix' in the formula. The resulting k-space **Ax** can then be directly compared to the measured k-space **y**.

8. Difference k-space

We now create the 'Difference k-space' by subtracting the k-space **Ax** from step 7 from the measured k-space **y** from step 1.

The difference (**Ax – y**) corresponds to the error (non-consistency) that the thresholding from step 4 has created compared to the measured k-space **y**. The difference is a 'correction' k-space, so to speak.

9. Difference image

A simple Fourier transformation converts the 'Difference k-space' into a 'Difference image'.

This is used as a correction for the update of the image that we want to optimize.

10. Updated image

The image **x** from step 2 is now updated by adding the correction (difference) image from step 9.

This updated image now has less noise-like artifacts (corresponding to a higher sparsity in W-space) than the image had before the update, due to steps 3 and 4.

At the same time, it was made consistent with the measured k-space from step 1 by means of the correction from steps 8 to 9.

3-10. Iterative reconstruction

Steps 3 to 10 are now repeated. Each iteration will increase the sparsity (in W-space), corresponding to diminishing the aliasing artifacts in image space. At the same time, the consistency of the reconstruction with the measured k-space is taken care of.

This is an alternating optimization of data consistency and transform sparsity, i.e. the two terms in the formula. The factor λ in the formula is a weighting that defines the trade-off between data consistency and sparsity, it is pre-defined and optimized for the application.

As a metaphor:
One can think of scales rocking to and fro (between the optimization of the first term and the optimization of the second term in the formula). At the same time, the 'center of gravity' (the sum of both terms) is moving down (minimizing both terms in the formula simultaneously). The factor λ in the formula can be thought of as a 'lever', i.e. a shorter (small λ) or longer (large λ) bar of the scales for the sparsity term as compared to the data consistency term.

The iteration of steps 3 to 10 is repeated until:

- either the least-squares difference of the data consistency term, i.e., the Difference Image (step 9), is smaller than a predefined threshold ϵ,

$$\| Ax - y \|_2^2 < \epsilon$$

- or a predefined number of iterations N_{max} is reached.

In the end, we will have an image that is consistent with the measured data, but is denoised (i.e. the noise-like aliasing artifacts have been removed) due to the maximization of the transform sparsity. The final image will (very closely) look as if we had measured k-space completely – but at a much shorter scan time.

Optimization of Compressed Sensing

We have seen that there are many degrees of freedom for the optimization of the Compressed Sensing results. All these need to be taken care of in the application development.

The possible CS acceleration factor depends on the transform sparsity of the dataset. If the acceleration factor is chosen too high ("not justified by the sparsity"), the reconstruction will not yield acceptable results. The possible acceleration factor depends on the application.

The weighting factor λ for the balance between transform sparsity vs. data consistency (as described before) and the threshold for the sparsification in W-space (the soft thresholding in the W-space as discussed earlier) are related to each other in order to achieve optimal results. Also these depend on the application.

All the explanations above are a simplification. There are more 'intricacies' that were not discussed for the sake of simplicity, e.g. how the signals from multiple RF channels are handled, the combination of CS with PAT, higher dimensionality, etc.

The CS Flowchart only shows a depiction of a 2D scan (for the sake of simplicity), but Compressed Sensing can also (and better) be applied for multi-dimensional scans with other k-space trajectories. There are two important aspects for the improvement of the CS performance that define which applications benefit most from CS. These are the "Increase of Sparsity" and the "Increase of Randomness".

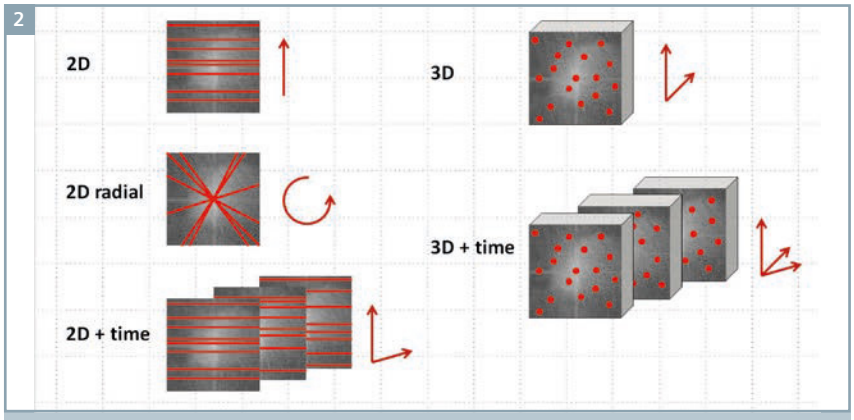

2 Dimensionality, k-space trajectory and degrees of freedom to improve incoherency ('randomness') of the scan.

Increase of Sparsity

An "Increase of Sparsity" will enable higher acceleration factors. If the (transform) sparsity of an MR dataset is low, no significant acceleration will be possible, i.e. it will not be possible to remove the noise-like artifacts while preserving an accurate anatomical depiction. For increasing the possible acceleration factor of the scan, a high 'dimensionality' of the MR scan helps.

A static 2D scan (like a conventional T2-weighted TSE scan) will typically not have a high sparsity (also not in its Wavelet representation). The achievable acceleration with CS for standard static 2D imaging will therefore not be very high.

But it is very different with e.g. Compressed Sensing Cardiac Cine (2D + time). Along the time dimension, the sparsity is quite high. In CS Cardiac Cine, only little changes are expected between sub-sequent time-frames due to the high temporal resolution and the static anatomy surrounding the heart. This increases the transform sparsity along the time dimension, and therefore high accelerations factors (such as 10) can be achieved in CS Cardiac Cine.

Other examples where the dataset has a high dimensionality and therefore higher sparsity with the potential for higher acceleration factors include, for example, 3D scans, dynamic '4D' scans (3D + time) and also diffusion imaging with multiple b-values and or multiple diffusion directions.

Increase of Randomness

Also improving the 'randomness' of the scan will help the performance and the possible acceleration factors of CS.

Figure 2 shows the number of degrees of freedom for different dimensionalities and different k-space trajectories, in order to improve the 'randomness' of the scan.

With static 2D imaging, there is only one degree of freedom, the spacing of the k-space line in phase-encoding direction. The potential for CS acceleration is therefore limited.

With 2D radial imaging, the angle between the different k-space lines can be freely chosen. Each line crosses the center of k-space. There are a couple of advantages for radial imaging vs. cartesian imaging; however, there are also a couple of disadvantages, such as potential aliasing in both directions and longer reconstruction times. The pros and cons of cartesian vs. radial sampling need to be weighed against each other to find the optimal solution, depending on the application.

2D + time (as in Compressed Sensing Cardiac Cine) also has high dimensionality. There are two degrees of freedom, along the phase-encoding direction and along time. The spatial phase-encoding steps can be chosen differently for each cardiac phase.

Static 3D has two degrees of freedom, since there are two phase-encoding directions. This allows a better 'randomness' than static 2D.

Dynamic 3D has an additional degree of freedom, along time. This high dimensionality of course holds great promise for future developments, already available as WIP packages from Siemens.

Overall, there is a wide potential for future Compressed Sensing applications with high acceleration factors and high clinical relevance.

References

1 https://en.wikipedia.org/wiki/Nyquist%E2%80%93Shannon_sampling_theorem
2 Marseille GJ, de Beer R, Fuderer M, Mehlkopf AF, van Ormondt D. Nonuniform phase-encode distributions for MRI scan time reduction. J Magn Reson 1996;111:70–75
3 https://en.wikipedia.org/wiki/JPEG_2000
4 David L. Donoho, De-noising by Soft-Thresholding, http://statweb.stanford.edu/~donoho/Reports/1992/denoiserelease3.pdf



Contact

Mathias Blasche
Siemens Healthcare GmbH
Karl-Schall-Str. 6
91050 Erlangen
Germany
Mathias.Blasche@siemens.com

Compressed Sensing: a Paradigm Shift in MRI

Christoph Forman[1]; Jens Wetzl[2]; Carmel Hayes[1]; Michaela Schmidt[1]

[1] Siemens Healthineers, Magnetic Resonance, Erlangen, Germany
[2] Pattern Recognition Lab, Friedrich-Alexander-University Erlangen-Nuremberg, Erlangen, Germany

Introduction

Reducing the complexity and length of examinations has been a major direction of research in magnetic resonance imaging (MRI) in recent years. With the introduction of the Dot engines, the complexity of MR examinations could be reduced through automatization and guidance, providing standardized and time-efficient workflows. Considerable effort has also been spent on developing methods to speed up data acquisition without degrading image quality. Accelerated imaging is a key factor to enable the visualization of rapid physiological or contrast changes in dynamic imaging. Moreover, short scans reduce the risk of artifacts due to any kind of motion during the scan. A significant speed-up of data acquisition allows both respiratory and cardiac motion to be frozen while maintaining an adequate temporal and spatial resolution. This in turn results in a high-quality and robust examination even for uncooperative patients, since data acquisition may be performed in free-breathing. Furthermore, reduced scan time and a decreased number of

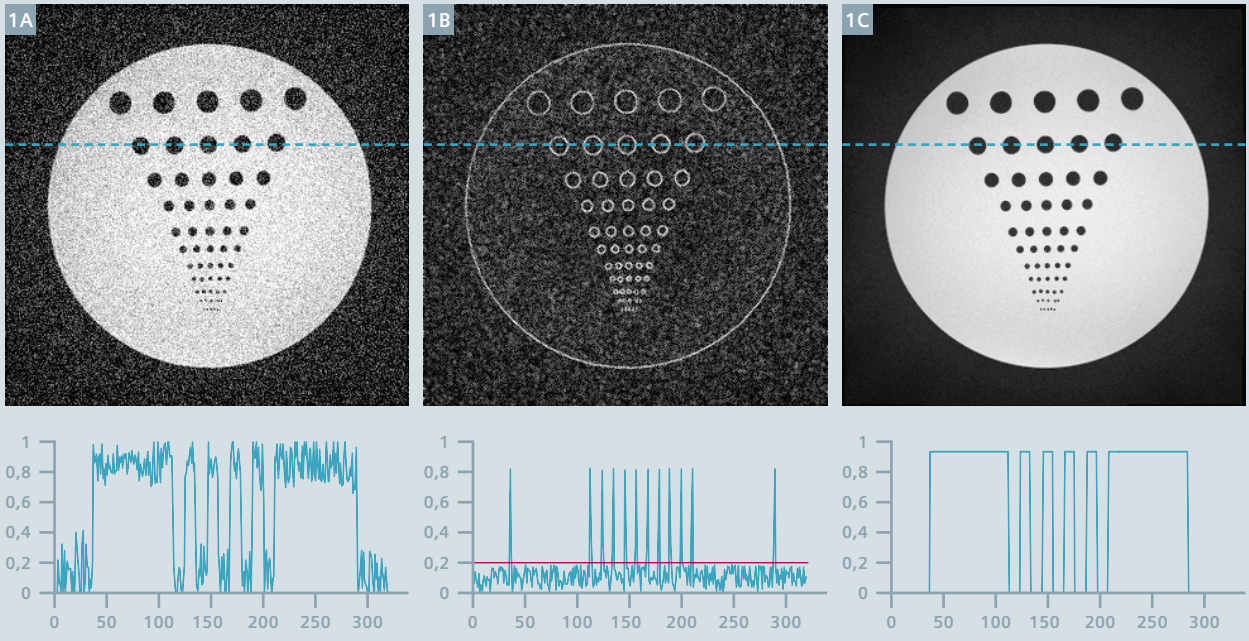

1 Additional noise reduces the homogeneity in the image of the resolution phantom **(1A)**, which can also be observed in the line plot along the dashed line. After transformation into a sparse representation using finite differences **(1B)**, the homogeneity can be restored by denoising, i.e., setting all pixels below a threshold level (red line) to 0. After the image is transformed back to its original domain, the phantom is piecewise constant **(1C)**.

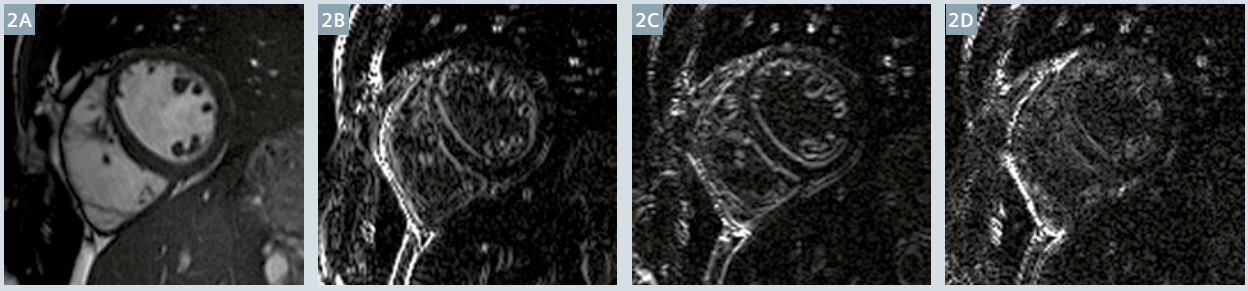

2 The short-axis view of the heart **(2A)** is transformed by the wavelet transform to achieve a sparse representation. In addition to the low-resolution representation of the original image, the wavelet transform results in three edge images **(2B-2D)**: While **(2B)** and **(2C)** contain the edges in horizontal and vertical direction, respectively, Figure 2D shows the diagonal edge components of the image. In the wavelet domain, the content of the image is sufficiently described by only few coefficients, i.e. the bright pixels.

breath-holds improve patient comfort. Last but not least, accelerated imaging means shorter examinations that can be invested in additional scans, higher resolution, or to improve the overall patient throughput. In this context, parallel imaging and compressed sensing techniques have been proposed to significantly speed up the acquisition time while maintaining diagnostic image quality.

Parallel imaging

Parallel imaging [1, 2] is well established in current clinical practice to speed up data acquisition in a large number of applications. With this technique, scan acceleration is usually achieved by uniformly sub-sampling *k*-space, for example, by skipping every other line. The resulting aliasing can be unfolded by incorporating the spatial encoding capabilities of multi-coil receiver arrays. However, the scan time reduction is often restricted to moderate acceleration factors between 2 and 4. This limitation is due to the restricted encoding capabilities in terms of number and position of the receiver coils. Additionally, acquiring less data also leads to a reduced signal-to-noise ratio (SNR).

Compressed sensing

In recent years, compressed sensing has gained large scientific attention. Originally, it was proposed as a general concept to accurately reconstruct a signal from a small number of random measurements [3, 4]. A few years later, compressed sensing[1] was introduced to MRI [5] and successfully combined with parallel imaging [6]. Exploiting the *compressibility* of medical images, this method promises to markedly exceed the acceleration rates that are feasible with parallel imaging. Although compressed sensing has denoising properties, it also has to deal with SNR loss from scan acceleration. Hence, possible acceleration factors scale with the native SNR of the scan. Up to now, the potential of compressed sensing has been shown in a large number of applications from 2D to 5D imaging [7-15].

The successful utilization of compressed sensing is a team play of data acquisition and image reconstruction. In the paper introducing compressed sensing to MRI, three criteria were identified as being essential to ensure successful image recovery from sub-sampled data [5]:

- First, the object that is acquired should have a *sparse representation* after conversion with a mathematical transformation.
- Second, *k*-space should be sub-sampled such that the aliasing results in *incoherent*, i.e. noise-like, artifacts in the image.
- Finally, image reconstruction requires a *nonlinear, iterative optimization* that simultaneously enforces a sparse representation of the resulting image. Thereby, it removes the noise-like artifacts, while it preserves its consistency to the acquired data.

These three essential requirements are discussed in detail below.

Transform sparsity

An image is considered as sparse when its informational content is represented by only a few pixels, while the contribution of the remaining majority of pixels is close to zero. In medical imaging, an angiogram provides a good example for such a sparse representation. However, in MRI, not all images are inherently sparse. But these images can also have a sparse representation utilizing a sparsifying transform. This transform provides an invertible mapping from an image to a sparse representation. Finite differences, i.e. images that contain only edge information, provide a simple technique to achieve a sparse representation, if the image is piecewise constant as shown in Figure 1. Discrete cosine transform and discrete wavelet transform are frequently used in the context of image compression, for example, in JPEG image compression. Utilizing such methods, images may be transformed into a sparse representation (see Fig. 2). In this domain, the content of the image is sufficiently described by only few coefficients,

[1] 510(k) pending. Compressed Sensing Cardiac Cine is not commercially available. Future availability cannot be guaranteed.

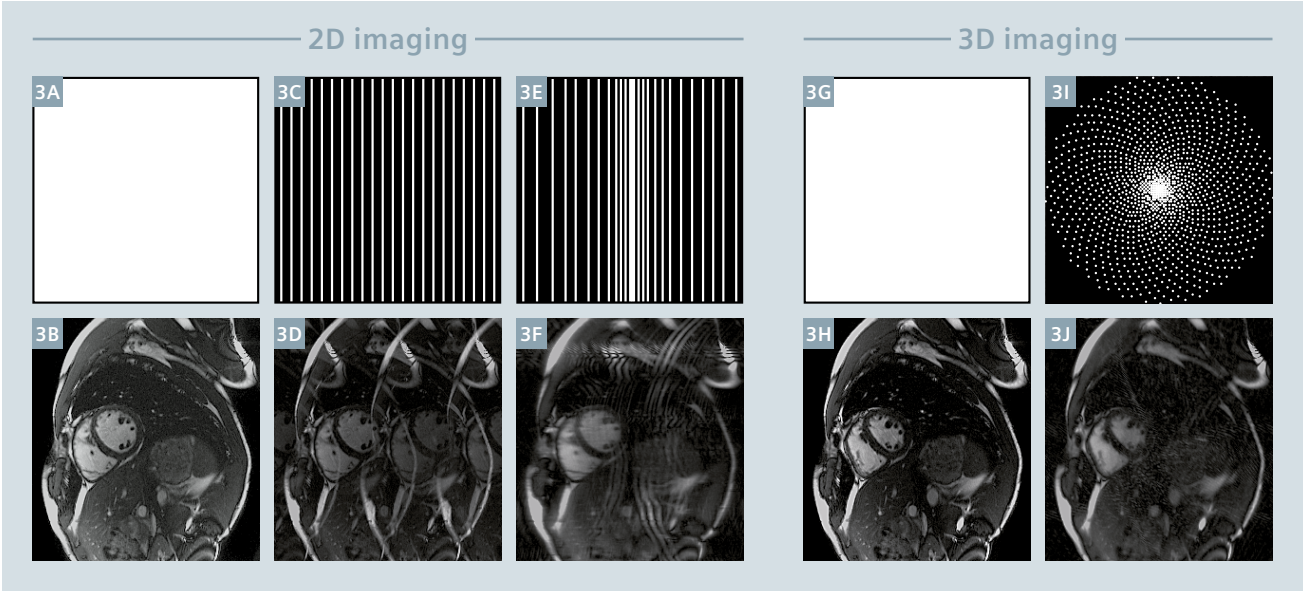

3 Examples of different sampling schemes, where *k*-space locations that are acquired are highlighted in white and the ones that are skipped are black (upper row) with corresponding image results and aliasing artifacts after Fourier transform (lower row). In 2D imaging, sub-sampling is limited to one phase-encoding direction whereas for 3D sub-sampling can be applied in two phase-encode directions. In case of CINE imaging, additional incoherence can be achieved in the temporal domain. **(3A, 3B)** Fully sampled *k*-space with artifact free result image; **(3C, 3D)** Regular subsampled *k*-space like PAT resulting in superposition of multiple ghosts; **(3E, 3F)** Irregular subsampled *k*-space as used in CS leading to incoherent aliasing artifacts similar to noise; **(3G, 3H)** Fully sampled *k*-space with artifact free result image; **(3I, 3J)** Irregular subsampled *k*-space as used in CS with noise-like artifacts.

i.e. the bright pixels. The percentage of these pixels relative to the total number of pixels defines the sparsity of the image. For image compression, pixels in this sparse representation that are below a certain threshold can be set to zero, which facilitates a compression of the signal. Once the compressed signal is converted back to its initial domain, the visual difference between the resulting image and its original version is negligible. In particular, the discrete wavelet transform has been shown to be a suitable sparsifying transform for many natural images, including MRI images, and is commonly used in compressed sensing applications. In the case of dynamic imaging, including CINE imaging, this transform can also be applied in the temporal dimension. The redundancy of information along this temporal dimension can be exploited, and often the sparsity is even higher compared to the spatial dimensions.

Incoherent sampling

Unlike the regular sub-sampling patterns used for parallel imaging, the data acquisition process for compressed sensing requires that *k*-space sub-sampling is irregular (see Fig. 3C for regular and 3E, 3I for irregular sampling). In conventional Cartesian parallel imaging, regular sub-sampling of *k*-space is advantageous in that the phase-encoding gradient is increasing linearly during the measurement, which is beneficial for physical and MRI hardware limitation reasons. However, violating the Nyquist sampling theorem in this manner results in a superposition of shifted replicas of the original signal as illustrated in Figure 3D. The number of replicas equals the chosen sub-sampling rate. This aliasing can then be unfolded utilizing the spatial encoding capabilities of the multi-coil receiver array and parallel imaging. In contrast, irregular, incoherent sub-sampling of *k*-space, as required for compressed sensing, would result in a noise-like appearance of sub-sampling artifacts (see Figs. 3F, 3J). Theoretically, completely random sub-sampling is optimal to ensure this noise-like behavior. However, purely random sampling is impractical in the case of MRI.

On the one hand, large and random steps in *k*-space may require large-amplitude gradient steps and should be avoided due to hardware limitations and physical reasons. On the other hand, the sampling trajectory must be repeatable to allow the same acquisition to be reproduced with consistent image quality. Therefore, sub-sampling patterns featuring deterministic properties that mimic random sampling within the given constraints are frequently used for compressed sensing data acquisition. In 2D Cartesian imaging with pure spatial coverage, the sub-sampling is limited to one dimension, as only the phase-encoding direction is sub-sampled in MRI. But in case of 2D dynamic imaging, the sampling pattern can be varied from one time frame to the next in order to maintain sufficient incoherence for compressed sensing. In 3D Cartesian imaging, sub-sampling can be applied in two phase-encoding directions. Alternatively, non-Cartesian sampling trajectories can be used, e.g., radial or spiral imaging, that already facilitate an incoherent sampling of *k*-space for 2D imaging.

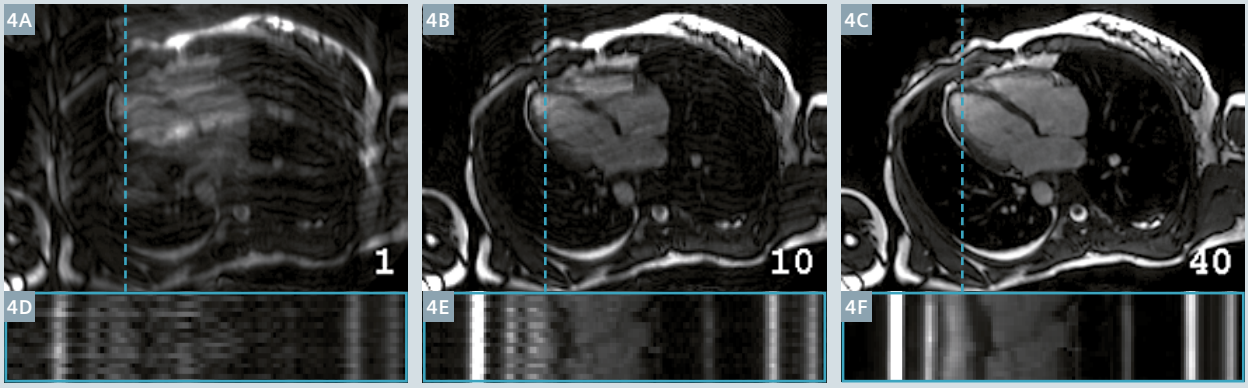

4 This Figure shows the progress of the optimization procedure to preserve data fidelity and reduce noise-like artifacts exemplarily in a Cardiac 2D CINE dataset **(4A-4C)**. While the top image shows one image of the time series, a temporal profile along the dashed line is plotted below. The incoherent sub-sampling in the spatio-temporal domain results in incoherent artifacts that dominate the image after the first iteration **(4A)**. Enforcing a sparse representation of the image and exploiting temporal redundancy, these artifacts are reduced with an increasing number of iterations **(4B)**. The compressed sensing reconstruction is terminated after 40 iterations and results in an aliasing-free image **(4C)**.

Nonlinear image reconstruction

If the two above-mentioned requirements are sufficiently met, the image can be recovered from the sub-sampled data by nonlinear, iterative reconstruction. In this reconstruction, a *data fidelity* term ensures consistency of the estimated image to the acquired data and a *transform sparsity* term enforces a sparse representation of the image in the transform domain by solving the following equation:

$$\min_{x} \underbrace{\|Ax-y\|_2^2}_{\text{data fidelity}} + \lambda \underbrace{\|\Phi(x)\|_1}_{\text{transform sparsity}}$$

The data fidelity term minimizes the least-squares difference ($\|\cdot\|_2^2$) between the estimated image, x, and the acquired *k*-space data, y. The system matrix, A, describes the data acquisition process, i.e., the transform from spatio-temporal to frequency domain, which is required for the comparison of the image and acquired data. Incorporating parallel imaging, it consists of the coil sensitivity maps of the individual receiver coil elements, the Fourier transform, and the applied sub-sampling pattern during data acquisition. In the transform sparsity term, the image is transformed into a sparse representation by $\Phi(\cdot)$, for example, using the discrete wavelet transform. In this term, the sum of the absolute values of the pixels in the transform domain, denoted by the ℓ_1 norm ($\|\cdot\|_1$), is minimized. Hence, the optimization procedure minimizing this equation seeks to find a solution that fulfills both criteria, data consistency and transform sparsity. This optimization procedure is more computationally intensive than conventional reconstruction, e.g., parallel imaging. The balance between data fidelity and sparsity is adjusted with the regularization parameter λ, which is usually found empirically. While small values of λ lead to an image that is closer to the acquired data, increasing this value tends to produce an image that is in favor of the sparse solution. When λ is too low, the image will be noisy, and when λ is too high a strongly filtered image appearance may be the consequence. The equation described above is iteratively minimized until a convergence criterion is met or a fixed number of iterations is reached. Figure 4 illustrates this optimization in the example of real-time CINE imaging of the heart.

Transition into clinical routine

Compressed sensing acquisition and reconstruction have been completely integrated into our clinical MRI scanners. Works-in-progress packages have been developed and tested by our clinical cooperation partners world-wide for various applications in the fields of cardiovascular [16-19], neurological [20], musculoskeletal [21-23] and oncological [24] imaging. The additional parameters needed to compose the compressed sensing protocols, for both acquisition and reconstruction, have been seamlessly integrated into our user interface (UI). A selection of possible continuous acceleration factors takes the place of discrete numbers that were familiar from parallel imaging. This facilitates a UI experience with a low level of complexity. The award-winning algorithm for compressed sensing reconstruction [8], ranking first at the ISMRM 2014 "sub-Nyquist" reconstruction challenge, has been fully integrated into the Siemens image reconstruction environment. Without the need for additional hardware, the images are directly calculated inline utilizing the full computational power of the reconstruction computer. Compressed

sensing reconstruction is performed on a graphics processing unit, which provides a significant speed-up in processing time. For example, the image series of one cardiac real-time CINE slice is processed in 10 to 15 seconds.

Thanks to its high acceleration rate due to compressed sensing, real-time sequences allow for a temporal and spatial resolution comparable to that of conventional segmented acquisitions. For example, compressed sensing in cardiac imaging permits fast quantification of left-ventricular (LV) function in a single breath-hold [25]. As demonstrated in Figure 5, this sequence still provides diagnostic images for LV function quantification even in challenging scenarios, such as in the presence of arrhythmia, where conventional sequences usually fail. This sequence may also be applied in free-breathing, which is beneficial for patients who are not able to hold their breath sufficiently and, in general, allows for a simplified and more patient-friendly examination workflow.

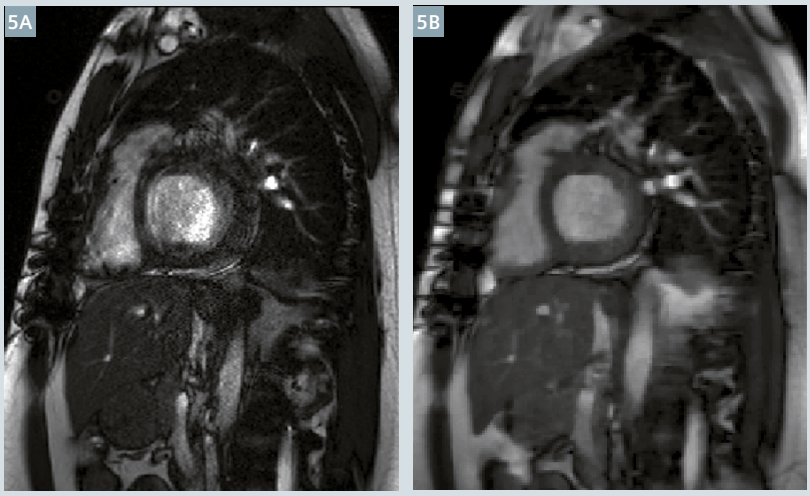

5 In cardiac imaging, the high acceleration rate due to compressed sensing enables real-time CINE imaging with a temporal and spatial resolution in a comparable range as conventional segmented acquisitions. While conventional imaging might fail in challenging scenarios, like in case of arrhythmia **(5A)**, the compressed sensing real-time sequence preserves a diagnostic image quality that still enables the quantification of LV function **(5B)**. *Images courtesy of Dr. François Pontana, Lille University Hospital, Lille, France.*

Conclusion

Compressed sensing facilitates rapid MR imaging by exploiting the fact that medical images have a sparse representation in a certain transfer domain. Representing a team play of data acquisition and image reconstruction, this allows for the reconstruction of artifact-free images following incoherent data acquisition. The acceleration enables a reduction in the acquisition time or an improvement in the spatial and/or temporal resolution. Real-time imaging featuring compressed sensing helps to reduce the need for breath-holding or ECG triggering. The integration of protocols based on compressed sensing in clinical workflows allows a significant reduction in the examination time for each patient. Our generalized integration of compressed sensing in the scanner environment will allow for the straightforward introduction of further applications that are likely to come in the near future.

References

1 M. A. Griswold, P. M. Jakob, R. M. Heidemann, M. Nittka, V. Jellus, J. Wang, B. Kiefer, and A. Haase. "Generalized Autocalibrating Partially Parallel Acquisitions (GRAPPA)". Magnetic Resonance in Medicine, Vol. 47, No. 6, pp. 1202–1210, June 2002.

2 K. Pruessmann, M. Weiger, M. B. Scheidegger, and P. Boesiger. "SENSE: Sensitivity Encoding for Fast MRI". Magnetic Resonance in Medicine, Vol. 42, No. 5, pp. 952–962, Nov. 1999.

3 D. Donoho. "Compressed Sensing". IEEE Transactions on Information Theory, Vol. 52, No. 4, pp. 1289–1306, Apr. 2006.

4 E. Candes and J. Romberg. "Sparsity and incoherence in compressive sampling". Inverse problems, Vol. 23, No. 3, pp. 969–985, Apr. 2007.

5 M. Lustig, D. Donoho, and J. M. Pauly. "Sparse MRI: The Application of Compressed Sensing for Rapid MR Imaging". Magnetic Resonance in Medicine, Vol. 58, No. 6, pp. 1182–1195, Dec. 2007.

6 D. Liang, B. Liu, J. Wang, and L. Ying. "Accelerating SENSE Using Compressed Sensing". Magnetic Resonance in Medicine, Vol. 62, No. 6, pp. 1574–1584, Dec. 2009.

7 G. Adluru, L. Chen, S. Kim, N. Burgon, E. G. Kholmovski, N. F. Marrouche, and E. V. R. DiBella. "Three-dimensional late gadolinium enhancement imaging of the left atrium with a hybrid radial acquisition and compressed sensing". Journal of Magnetic Resonance Imaging, Vol. 34, No. 6, pp. 1465-1471, Dec. 2011.

8 J. Liu, J. Rapin, T.-C. Chang, A. Lefebvre, M. O. Zenge, E. Mueller, and M. S. Nadar. "Dynamic cardiac MRI reconstruction with weighted redundant Haar wavelets". In: Proceedings of the 20th Annual Meeting of ISMRM, p. 4249, Melbourne, Australia, May 2012.

9 F. Han, S. Rapacchi, S. Kahn, I. Ayad, I. Salusky, S. Gabriel, A. Plotnik, J. P. Finn, and P. Hu, "Four-dimensional, multiphase, steady-state imaging with contrast enhancement (MUSIC) in the heart: A feasibility study in children". Magnetic Resonance in Medicine, Vol. 74, No. 4, pp. 1042-1049, Oct. 2015.

10 S. T. Ting, R. Ahmad, N. Jin, J. Craft, J. Serafim da Silveira, H. Xue, and O. P. Simonetti. "Fast Implementation for Compressive Recovery of Highly Accelerated Cardiac Cine MRI Using the Balanced Sparse Model". Magnetic Resonance in Medicine, doi: 10.1002/mrm.26224.

11 D. Stäb, T. Wech, F. A. Breuer, A. M. Weng, C. O. Ritter, D. Hahn, and H. Köstler, "High resolution myocardial first-pass perfusion imaging with extended anatomic coverage". Journal of Magnetic Resonance Imaging, Vol. 39, No. 6, pp. 1575–1587, Jun. 2014.

12 X. Chen, M. Salerno, Y. Yang, and F. H. Epstein, "Motion-compensated compressed sensing for dynamic contrast-enhanced MRI using regional spatiotemporal sparsity and region tracking: Block low-rank sparsity with motion-guidance (BLOSM)", Magnetic Resonance in Medicine, Vol. 72, No. 4, pp. 1028-1038, Oct 2014.

13 H. Xue, S. Inati, S. Sørensen, P. Kellman, and M. S. Hansen, "Distributed MRI Reconstruction Using Gadgetron-Based Cloud Computing", Magnetic Resonance in Medicine, Vol. 73, No. 3, pp. 1015-1025, March 2015.

14 J. Wetzl, F. Lugauer, M. Schmidt, A. Maier, J. Hornegger, and C. Forman. "Free-Breathing, Self-Navigated Isotropic 3-D CINE Imaging of the Whole Heart Using Cartesian Sampling", In: Proceedings of the 24th Annual Meeting of ISMRM, p. 411, Singapore, May 2016.

15 L. Feng, L. Axel, H. Chandarana, K. T. Block, D. K. Sodickson, and R. Otazo. "XD-GRASP: Golden-angle radial MRI with reconstruction of extra motion-state dimensions using compressed sensing". Magnetic Resonance in Medicine, Vol. 75, No. 2, pp. 775–788, Feb. 2016.

16 C. Forman, D. Piccini, R. Grimm, J. Hutter, J. Hornegger, and M.O. Zenge. "Reduction of respiratory motion artifacts for free-breathing whole-heart coronary MRA by weighted iterative reconstruction", Magnetic Resonance in Medicine, Vol. 73, No. 5, pp. 1885-1895, May 2015.

17 A. F. Stalder, M. Schmidt, H. H. Quick, M. Schlamann, S. Maderwald, P. Schmitt, Q. Wang, M. S. Nadar, and M. O. Zenge. "Highly undersampled contrast-enhanced MRA with iterative reconstruction: Integration in a clinical setting", Magnetic Resonance in Medicine, Vol. 74, No. 6, pp. 1652-1660, Dec. 2015

18 T. Yamamoto, K. Fujimoto, T. Okada, Y. Fushimi, A. Stalder, Y. Natsuaki, M. Schmidt, and K Togashi, "Time-of-Flight Magnetic Resonance Angiography With Sparse Undersampling and Iterative Reconstruction: Comparison With Conventional Parallel Imaging for Accelerated Imaging", Investigative Radiology, Vol. 51, No. 6, pp. 372-378, Jun 2016.

19 J. Wetzl, C. Forman, B. J. Wintersperger, L. D'Errico, M. Schmidt, B. Mailhe, A. Maier, and A. F. Stalder. "High-resolution dynamic CE-MRA of the thorax enabled by iterative TWIST reconstruction", Magnetic Resonance in Medicine, doi: 10.1002/mrm.26146.

20 E. Mussard, T. Hilbert, R. Meuli, J.-P. Thiran, and T. Kober. "Accelerated MP2RAGE Imaging Using Sparse Iterative Reconstruction", In: Proceedings of the 24th Annual Meeting of ISMRM, p. 4216, Singapore, May 2016.

21 R. Otazo, M. Nittka, M. Bruno, E. Raithel, C. Geppert, S. Gyftopoulos, M. Recht, and L. Rybak. "Sparse-SEMAC: Rapid and Improved SEMAC Metal Implant Imaging Using SPARSE-SENSE Acceleration", Magnetic Resonance Imaging, July 2016, Early View, DOI: 10.1002/mrm.26342.

22 J. Fritz, S. Ahlawat, S. Demehri, G.K. Thawait, E. Raithel, W.D. Gilson, M. Nittka. "Compressed Sensing SEMAC: 8-fold Accelerated High Resolution Metal Artifact Reduction MRI of Cobalt-Chromium Knee Arthroplasty Implants", Investigative Radiology, October 2016, Vol. 51, Issue 10, pp 666–676.

23 J. Fritz, E. Raithel, G. K. Thawait, W. Gilson, and D. F. Papp. "Six-Fold Acceleration of High-Spatial Resolution 3D SPACE MRI of the Knee Through Incoherent k-Space Undersampling and Iterative Reconstruction – First Experience". Investigative Radiology, Vol. 51, No. 6, pp. 400-409, Jun 2016.

24 D. Nickel, X. Chen, B. Mailhe, Q. Wang, Y. Son, J. M. Lee, and B. Kiefer. "Motion-resolved 3D dynamic contrast enhanced liver MRI", In: Proceedings of the 24th Annual Meeting of ISMRM, p. 4253, Singapore, May 2016.

25 G. Vincenti, P. Monney, J. Chaptinel, T. Rutz, S. Coppo, M.O. Zenge, M. Schmidt, M.S. Nadar, D. Piccini, P. Chèvre, M. Stuber, and J. Schwitter, "Compressed Sensing Single–Breath-Hold CMR for Fast Quantification of LV Function, Volumes, and Mass" JACC: Cardiovascular Imaging, Vol. 7, No. 9, pp. 882–892, Sep. 2014.



Contact

Christoph Forman
Siemens Healthcare GmbH
HC DI MR PI TIO CARD
Postbox 32 60
91050 Erlangen
Germany
christoph.forman@siemens.com

For further information, articles, case studies and keynotes on the topic of Compressed Sensing please visit

www.siemens.com/Compressed-Sensing

Compressed Sensing – a Metaphor

Mathias Blasche

Siemens Healthineers, Erlangen, Germany

Compressed Sensing (CS)[1] is an exciting new method with the potential to accelerate MR scans beyond what is possible with any other method. However, the CS reconstruction method is more complicated than the straightforward Fourier transform used in conventional MR imaging.

[1] 510(k) pending. Compressed Sensing Cardiac Cine is not commercially available. Future availability cannot be guaranteed.

The three key components of CS – incoherent sub-sampling, transform sparsity, and iterative reconstruction – may sound 'unwieldy' to many readers.

The 'Washing Metaphor' described below compares the CS mechanism with the washing of a T-shirt. This might look a little funny (and in fact this is intended), but it is actually quite an accurate analogy. It might help understanding CS in a 'non-technical' sort of way. Enjoy!

The goal of Compressed Sensing is to remove the (noise-like) aliasing artifacts from the image (that are due to the incoherent sub-sampling of the measured *k*-space) while ensuring that the reconstructed image is still consistent with the measured data.

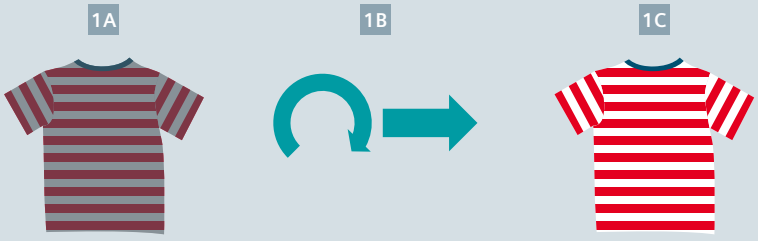

1 Goal of Compressed Sensing

(1A) MRI: We measure only a part of *k*-space (sub-sampling) in an incoherent ('random') way. This results in an image with noise-like aliasing artifacts.	**Metaphor:** We have a dirty T-shirt[1]. The dirt is homogeneously grey.
(1B) MRI: By maximizing transform sparsity[2], we remove the noise (= the aliasing artifacts) from the image. We take care that we keep the reconstructed image consistent with the measured data. The simultaneous improvement of sparsity and data consistency is done in an alternating fashion, iteratively until the optimum is achieved.	**Metaphor:** We wash the T-shirt in the rotating tub of the washing machine to remove the grey dirt. We take care not to wash out the colors.
(1C) MRI: The result is an anatomically correct image without aliasing artifacts (noise). The image looks virtually identical to an image with a completely measured *k*-space – but at much shorter scan time.	**Metaphor:** The T-shirt is clean, and the colors have been preserved. The T-shirt looks like new.

[1] Note: The red-white striped T-shirt was chosen as an arbitrary example. The stripes have nothing to do with any 'regular' sampling of *k*-space.
[2] 'Sparsity' stands for 'transform sparsity' in the remainder of the text, i.e. the sparsity in W-space, e.g. the Wavelet domain. Increasing sparsity in W-space corresponds to decreasing noise in image space.

In order to achieve the optimal result, the sum of sparsity and data consistency is maximized. This corresponds to a minimization of noise (= aliasing artifacts) while keeping anatomical accuracy. The sparsity needs to be optimally balanced with respect to the data consistency.

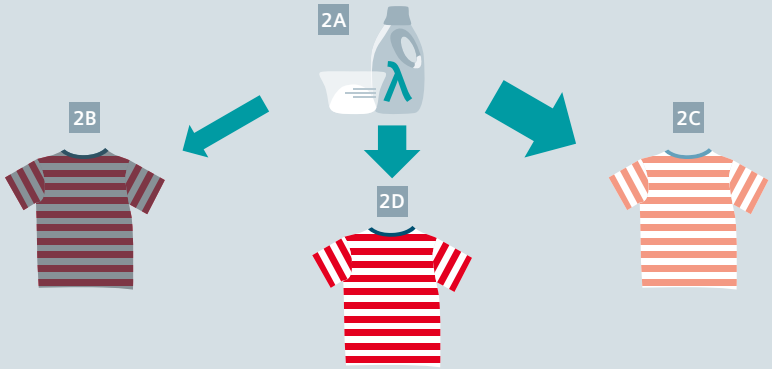

2 Sparsity vs. Data Consistency

(2A) MRI: For optimal balancing between sparsity and data consistency, the correct weighting factor λ needs to be applied. λ is application dependent and is optimized during the application development.[3]

Metaphor: The right amount of detergent has to be used.

(2B) MRI: If the sparsity weighting is too low (λ too small), there is still noise (aliasing artifacts) in the image.

Metaphor: With too little detergent, we will not remove the dirt on the T-shirt.

(2C) MRI: If the sparsity weighting is too high (λ too large), we will lose data consistency. The image is noise free but it does not show the true anatomy.

Metaphor: Using too much detergent, the dirt will be gone – but also the colors.

(2D) MRI: The right balance between sparsity and data consistency (optimal λ) results in the anatomy being depicted correctly, without noise (aliasing artifacts). The image looks as if we had measured *k*-space completely – but at much shorter scan time.

Metaphor: With the right amount of detergent, the dirt can be removed without affecting the colors. The T-shirt looks like new.

[3] To avoid misunderstandings: λ is preset, it is optimized for the application. It is not changed in the iterative reconstruction. Rather, the iterative reconstruction improves data consistency and sparsity in an alternating fashion, based on the preset λ.

Finally, we want to emphasize again the importance of incoherent ('random') scanning for a successful CS reconstruction.



3 The Importance of Incoherent Scanning

(3A) MRI: In case we do not sample *k*-space 'randomly enough', the aliasing artifacts will appear in a discrete way and not noise-like. Without this critical prerequisite for CS, the reconstruction will fail[4].

Metaphor: If we have concentrated stains instead of 'homogeneous dirt', it will not be possible to wash the stains off without destroying the colors.

(3B) MRI: If we concentrate on data consistency, we will not get rid of the artifacts (which are not noise-like but discrete).

Metaphor: If we concentrate on not washing off the colors (by using a low amount of detergent), we will not succeed in removing the concentrated stains completely.

(3C) MRI: If we emphasize sparsity (complete removal of the discrete high-intensity aliasing artifacts which are not noise-like), this will go at the expense of data consistency. The anatomy is not depicted correctly.

Metaphor: If we use enough detergent to wash off the stains, the colors will also fade out.

[4] For the sake of simplicity, we are discussing a pure CS reconstruction without the combination with parallel imaging. The combination with parallel imaging would also address discrete aliasing artifacts to a certain degree.

BioMatrix Tuners: CoilShim

Miriam R. Keil, Ph.D.; Jörg Rothard; Carmel Hayes, Ph.D.

Siemens Healthineers, Erlangen, Germany

A cervical spine or neck MRI can provide valuable diagnostic information for a wide range of different conditions. In particular, MRI's soft tissue contrast helps to detect and monitor a variety of pathologies, misalignments or injuries. It can be useful in evaluating symptoms such as pain, foreign body sensations, numbness, tingling or weakness in the arms, shoulder or neck area and can assist in detecting certain chronic diseases of the nervous system. It is also used in tumor diagnosis and in the assessment of bleeding, swelling, infections, or inflammatory conditions in the vertebrae or surrounding tissues.

In many patients, MR image quality in the neck or cervical spine region might be degraded by B_0 field distortions. These typically arise from tissue interfaces with different susceptibilities in this region, for example in the vicinity of the lung, between vertebrae, fluid-filled cavities, as well as from the body contour itself in the shoulders and neck area (Fig. 1). The low field homogeneity poses a challenge to MR imaging in this region and is often the source of image quality issues. Examples include insufficient fat saturation, spatial variations in the signal strength along the vertebrae, as well as regions showing complete signal loss.

With MAGNETOM Vida[1] a new technology platform, BioMatrix, is introduced, which combines the ability to adapt to the individual patient's biovariability and the established Tim integrated matrix coil technology. This, in particular, allows to substantially improve image quality in the neck area by utilizing CoilShim. CoilShim is one of the new BioMatrix technologies which allows for correction of patient-induced B_0 field inhomogeneities using dedicated shimming channels integrated into the Head/Neck coil.

Two new Head/Neck coils[1] support CoilShim: the BioMatrix Head/Neck 20 TCS (Tiltable, CoilShim) and the BioMatrix 64 CS (CoilShim)[1]. A first step in the compensation of patient-induced B_0 field inhomogeneities is the identification of the origin of these variations. Experiments indicate that there are two major sources of B_0 field inhomogeneities in head and neck MRI. These are the patients' shoulders on the one hand and the B_0 field distortion due to the neck on the other hand. The inhomogeneity pattern originates from the geometric shape of the human body in the head and neck area and the resulting difference in susceptibilities. Figure 1 shows a typical B_0 field inhomogeneity 'map' of the head and neck region. The map was generated from a principal component analysis performed on datasets from 19 volunteer scans. The analysis showed that only the first main component contains significant information. This suggests that the inhomogeneity pattern is likely to be the same for different body shapes and sizes and that only the magnitude of the inhomogeneity varies. To correct for B_0 field inhomogeneities in the shoulder and neck region, each of the two head and neck coils is equipped with two CoilShim channels (Fig. 2). The CoilShim channels are located in the posterior part of the Head/Neck coils,

[1] 510(k) pending. The product is still under development and not commercially available yet. Its future availability cannot be ensured.

1

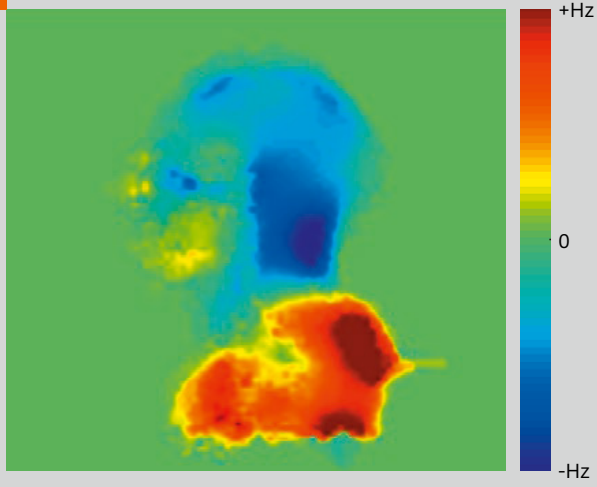

Figure 1: Typical B_0 field distortion pattern as seen in the sagittal orientation.

2

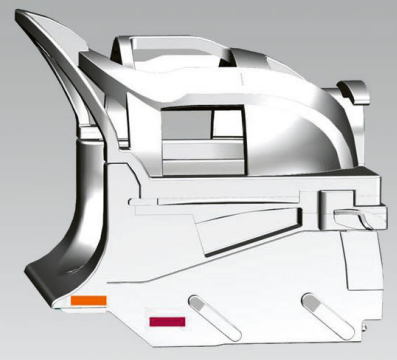

Figure 2: BioMatrix Head/Neck 20 TCS coil design and the location of the CoilShim elements in the BioMatrix Head/Neck 20 TCS coil.

allowing the CoilShim technology to be used even when the anterior part of the Head/Neck coils are detached. The magnitude of the B_0 field generated by each CoilShim channel can be adjusted independently with very fine resolution. This allows for best possible B_0 homogenization for each individual patient.

In order to ensure both adequate image quality and patient safety with the new Head/Neck coils with integrated CoilShim, special measures have been taken. These measures ensure decoupling of the CoilShim elements during the transmit phase and decoupling from the gradient system during the transmit and receive phase of the MR acquisition.

Applications

The usage of CoilShim requires no dedicated patient preparation: the patient can be positioned within the Biomatrix Head/Neck coil[1] as with any other head coil. When using the 20-channel TCS coil, the tilt angle may be adapted to the patients' needs, thereby providing increased patient comfort. Tilting the coil does not interfere with the CoilShim functionality but CoilShim may improve image quality degradations resulting from tilting.

CoilShim can be used with all clinical head and neck sequences and protocols, provided that the BioMatrix Head/Neck coil is plugged and active. "CoilShim" is turned on in the user interface by switching the respective parameter, which can be found on the tabcard "System", sub tab "Adjustments" from "Off" to "Auto". The actual enabling of CoilShim technology itself is therefore controlled automatically, depending on the slice geometry and the protocol parameters.

Results

The physical effect of the CoilShim feature on the B_0 field is illustrated in Figure 3, acquired in a healthy volunteer. The images compare B_0 field maps obtained using clinical state-of-the-art standard shimming with those which result from the usage of CoilShim technology.

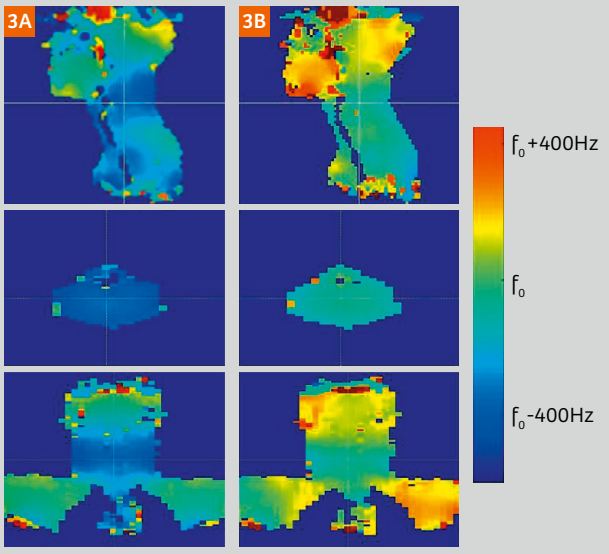

Figure 3: B_0 field map in the all three main orientations without **(3A)** and with CoilShim **(3B)**. The frequency shift relative to f_0 is shown in Hz.

The images show relative resonance frequency shifts in three orthogonal slice orientations. Once again, the two dominant sources of field inhomogeneity in the shoulder and in the neck area can be observed. In this example the frequency shift in the shoulder region is about 400 Hz and the frequency shift in the neck area is about -200 Hz. Given that the frequency shift between fat and water is 430 Hz at 3T, non-uniform fat saturation can be expected in such cases.

To further illustrate the impact of CoilShim on the quality of the shimmed region of interest, Figure 4 shows the frequency distribution of all voxels within the adjustment volume both with and without CoilShim. The spectrum of the frequencies within the adjustment volume is significantly narrowed on applying CoilShim.

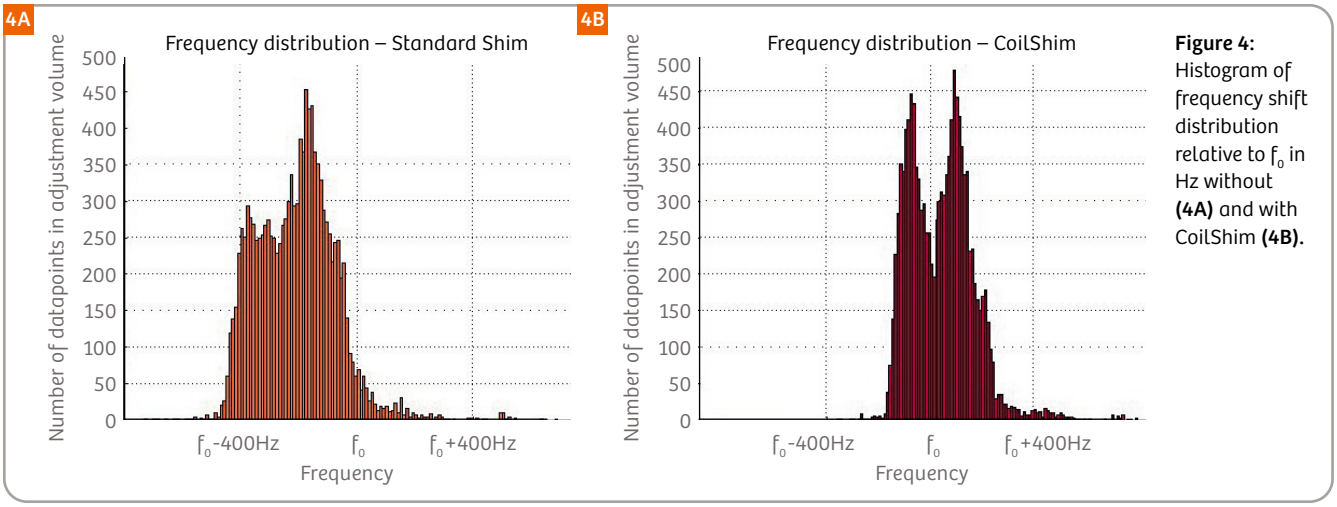

Figure 4: Histogram of frequency shift distribution relative to f_0 in Hz without **(4A)** and with CoilShim **(4B)**.

The improved field homogeneity is beneficial for all MR imaging studies in the head and neck. Applications which require a highly homogenous field, for example fat saturated or SPAIR images, or EPI-based imaging, benefit in particular from local shimming. Figures 5 and 6 show typical image examples obtained in several volunteers of different physical constitution. Figure 5 shows T1-weighted, fat saturated TSE images of the c-spine, Figure 6 illustrates the benefits of CoilShim in T2-weighted TSE images obtained with SPAIR preparation pulses. An axial T2-weighted BLADE image with SPAIR preparation pulses is shown in Figure 7. All examples show that more homogeneous fat saturation

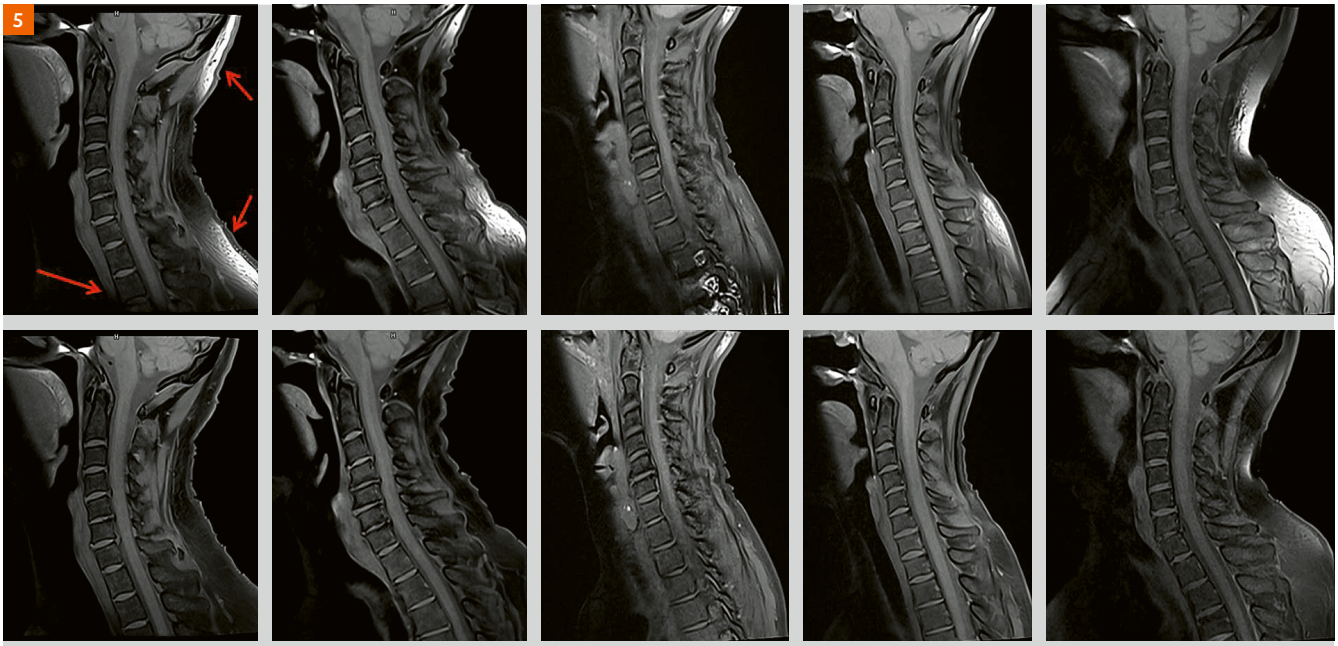

Figure 5: T1-weighted TSE images with fat saturation in five different volunteers. Using CoilShim (lower row) improved the fat saturation not only within the vertebrae but also in the posterior areas. The contrast between vertebrae and disk is also improved.

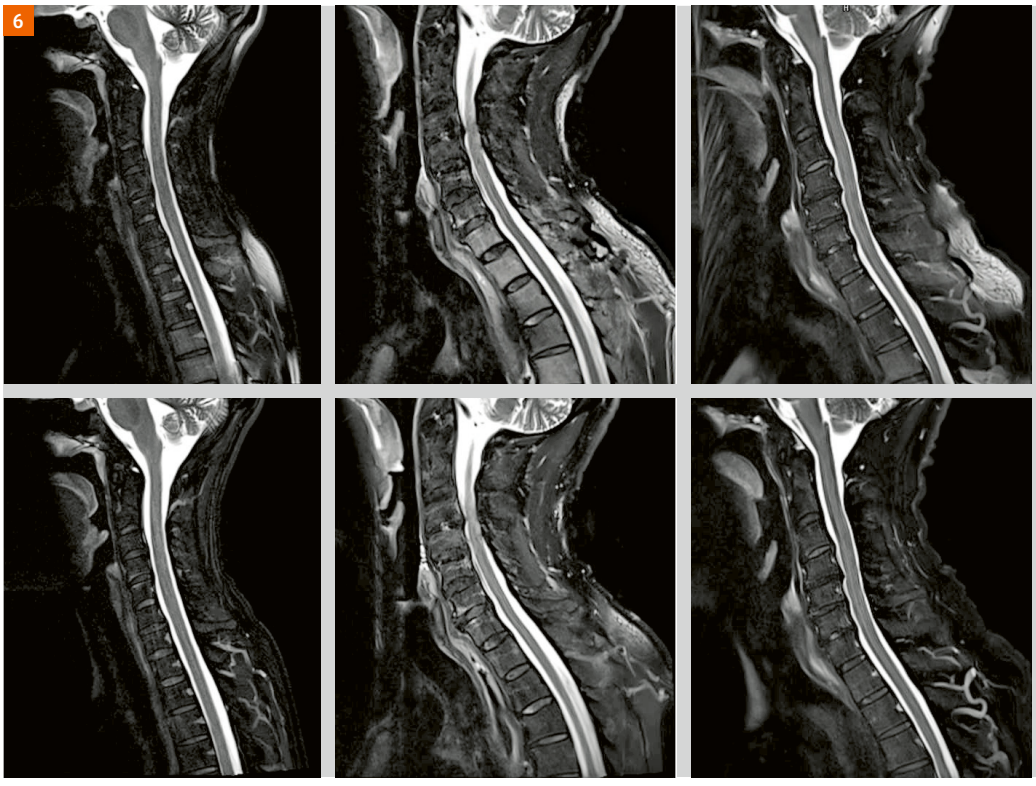

Figure 6: T2-weighted TSE images with SPAIR fat saturation in three different volunteers. Note the intensity gradient within the vertebrae without CoilShim (upper row). The image with active CoilShim on the right shows better homogeneity within the vertebrae and less contribution of unsaturated fatty tissue.

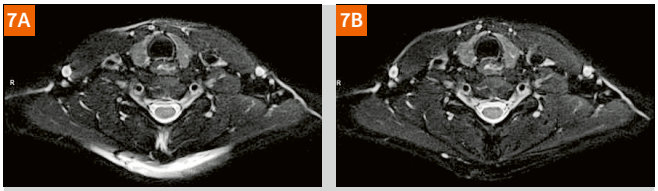

Figure 7: T2-weighted BLADE images with SPAIR fat saturation. The same imaging protocol was used with **(7A)** and without **(7B)** CoilShim. The fat saturation is more homogeneous when CoilShim is active.

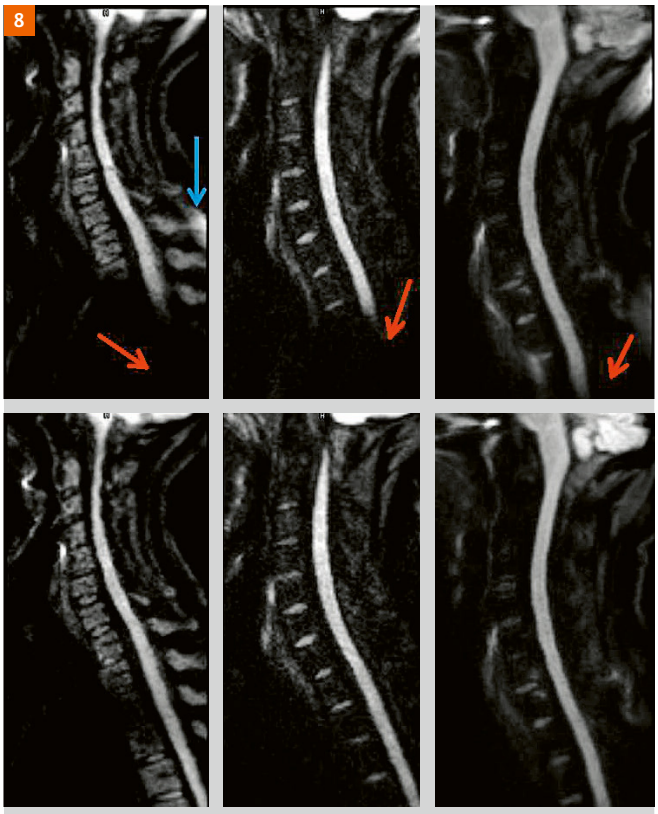

Figure 8: RESOLVE images of the c-spine with b=600 mm/s² in three volunteers. Note the lack of signal (red arrow) in the spinal canal when measured without CoilShim (upper row). Fat saturation is also more consistent (blue arrow).

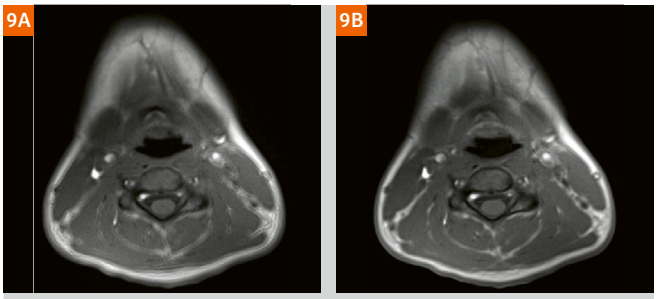

Figure 9: Radial sequences like the StarVIBE also benefit from higher field homogeneity. **(9A)** was measured without CoilShim, **(9B)** with active CoilShim. Note the increased image sharpness with CoilShim.

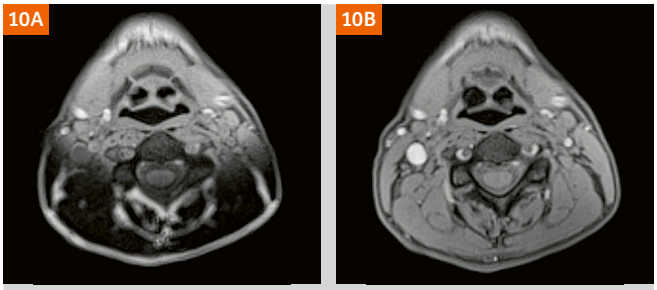

Figure 10: T1-weighted StarVibe images acquired in the neck. CoilShim **(10B),** can correct the field distortions which caused a shift in the frequency spectrum, inducing water saturation and corrupting image quality.

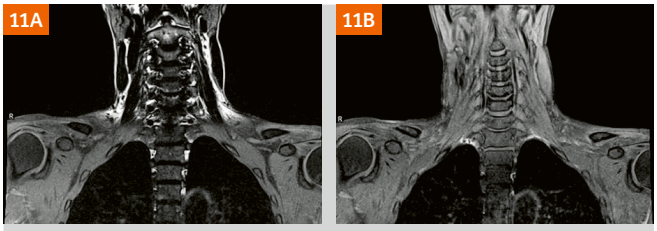

Figure 11: In rare cases, the field inhomogeneities at the border between neck and thorax are so severe, that the frequency is shifted. In these extreme examples, CoilShim **(11B)** also helps to mitigate the effects.

can be achieved with CoilShim. This in turn facilitates better lesion differentiation, in particular in the lower vertebrae.

Figure 8 shows RESOLVE diffusion-weighted images with a b-value of 600 mm/s² with and without CoilShim. Until now the display of the entire spinal canal was challenging, with CoilShim it becomes feasible to follow the spinal canal over the whole field-of-view.

Imaging methods which employ radial trajectories, for example the StarVIBE sequence, or methods such as TrueFISP, which demand a high field uniformity, also benefit from CoilShim technology and produce sharper or more homogeneous images. Figure 9 compares StarVIBE images obtained with and without CoilShim. Less homogeneous B_0 fields broaden the frequency spectra, leading to a shift in the readout direction. Since radial sequences sample *k*-space not in one, but in various directions, any off-resonance dephasing shift effect is propagated into a different direction, leading to blurred images. Larger variations in B_0 homogeneity can cause frequency shifts, which in turn lead to a degradation in image contrast, as shown in Figure 10 for a StarVIBE, and in Figure 11 for a TSE acquisition. Such issues can be avoided when using CoilShim.

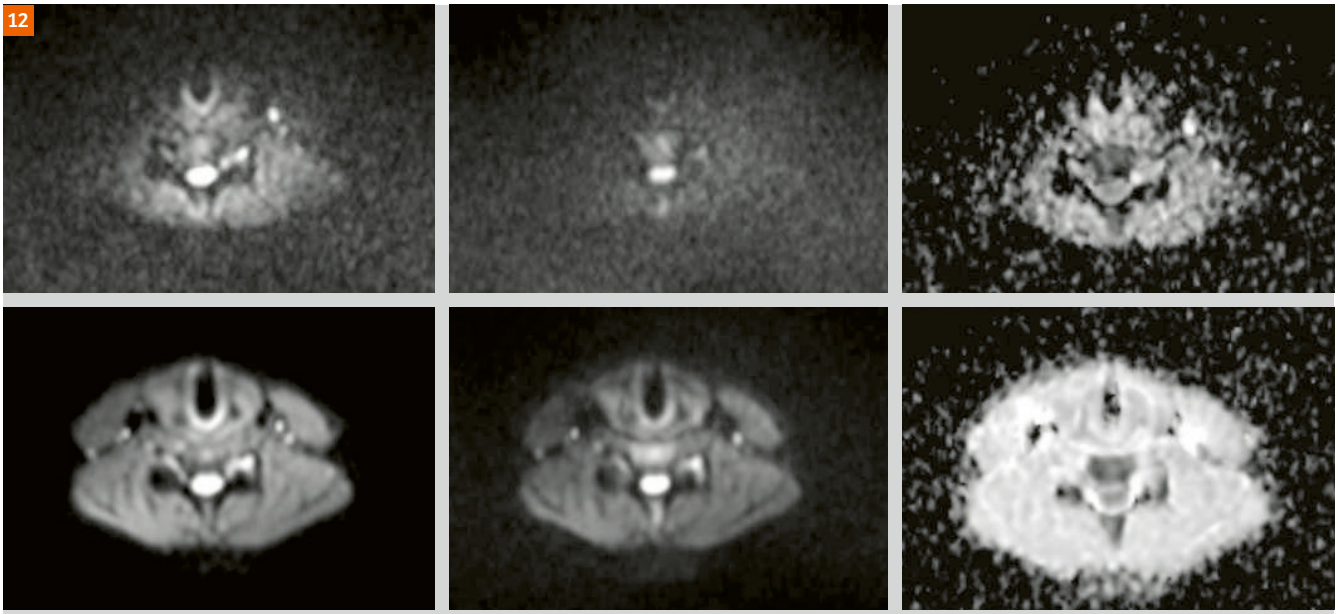

Figure 12: Combining CoilShim with SliceAdjust leads to significant image quality improvements in diffusion-weighted imaging. Less distortions and better spatial fidelity, significantly higher SNR for all b-values provides a new level of diagnostic reliability. The same slice is compared without CoilShim and SliceAdjust (upper row) and with active CoilShim and SliceAdjust (lower row). From left to right: b=50 s/mm², b=800 s/mm², ADC.

In combination with SliceAdjust, CoilShim technology allows for robust diffusion-weighted imaging (DWI) in the neck area. In the past, DWI imaging of the c-spine or neck soft tissue was challenged by distortions, low signal intensity and artefacts. On enabling the BioMatrix Tuners, the image quality can be improved significantly. Figure 12 illustrates the advantages of CoilShim and SliceAdjust when activated in a DWI image of the neck.

Practical tips

CoilShim is designed to optimize, in particular, the field homogeneity in the cervical spine. Therefore, it works best when imaging the cervical spine, especially in sagittal slice orientations. However, the whole neck area benefits when using CoilShim, although there are some physical limitations. First of all, as the CoilShim elements are located for safety reasons in the lower part of the Head/Neck coil, the scope of the feature is regionally restricted. For this reason, a drop in B_0 field homogeneity in the vicinity of the anterior part of the neck or the chin area may be observed. This effect may be manifested, as shown in Figure 13 for example, by inhomogeneous fat saturation in the chin area due to the regional limitations of the CoilShim field. The same applies to the shoulders, since the CoilShim elements cannot cover the entire shoulder region. This is shown in Figure 14. Another occasionally-observed effect is a frequency change in the t-spine next to the lung, seen usually in coronal images. As CoilShim optimizes the c-spine and cannot reach the vertebrae of the t-spine, the B_0 field

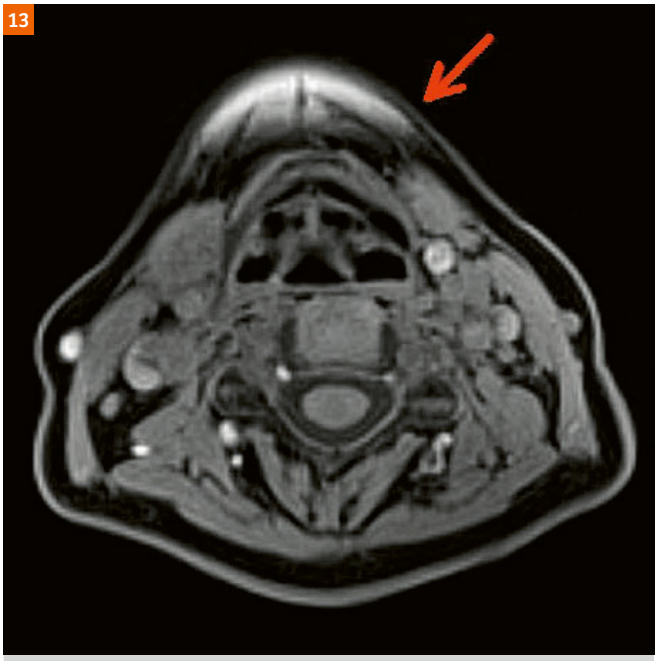

Figure 13: Anterior regions like the chin cannot be reached by CoilShim, which is located in the posterior neck coil region. Typically, in such cases, small regions with insufficient fat saturation are observed.

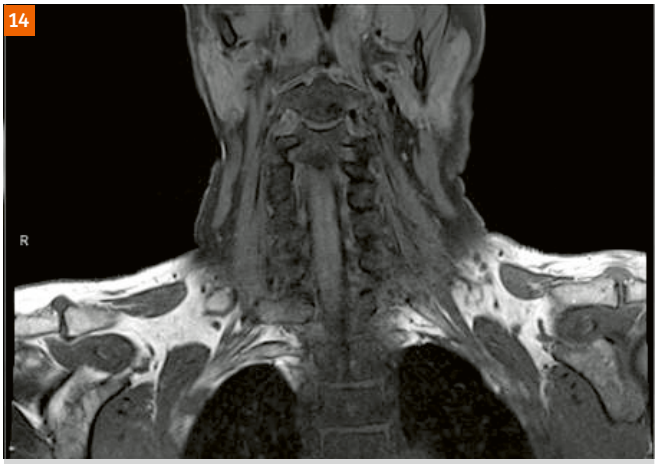

Figure 14: The local effectiveness of the CoilShim elements can lead to less efficient fat saturation in the lateral shoulder area.

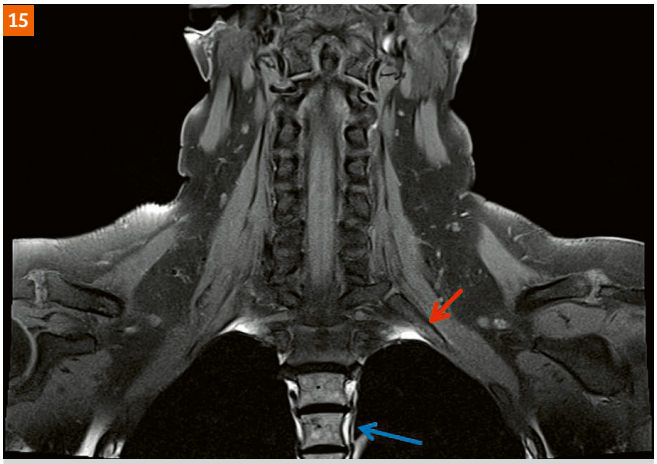

Figure 15: Typical lung-tip artefact (red arrow) and water saturation (blue arrow) in the t-spine. Note the homogeneous fat saturation in the neck/shoulder area.

is dominated by the lung, which might lead to lower field homogeneity with degradations in image quality in the t-spine as shown in Figure 15. The same image also shows the so called lung-tip artefact, which originates from local field distortions, leading to a less efficient fat saturation in a small area around the lung apex.

Summary

CoilShim addresses field disturbances within the head and neck region by local, patient-adapted shim currents. This helps to homogenize the static magnetic field in this region. Thereby the image quality can be improved. Typical benefits include more homogeneous fat saturation, less blurring in radial sequences and more signal with diffusion weighted imaging. Since CoilShim is based on new hardware and transmit pathways, it is currently only available with the BioMatrix Head/Neck coils. Nonetheless, this new technology might also be useful to improve B_0 homogeneity in other body regions in the future.

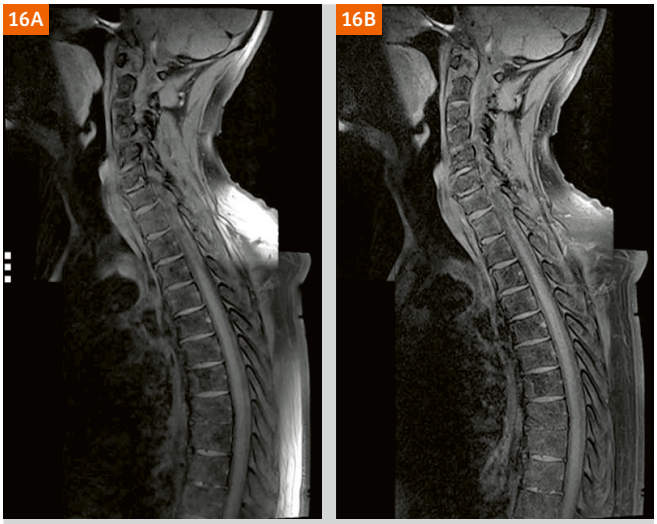

Figure 16: Composing for whole-spine representations also benefits from CoilShim **(16B).**

Contact

Miriam Keil

Siemens Healthcare GmbH

HC DI MR R&D SYS APPL
Post Box 91050
91050 Erlangen
Germany
Phone: +49 (9131) 84-4671
miriam.keil@siemens-healthineers.com

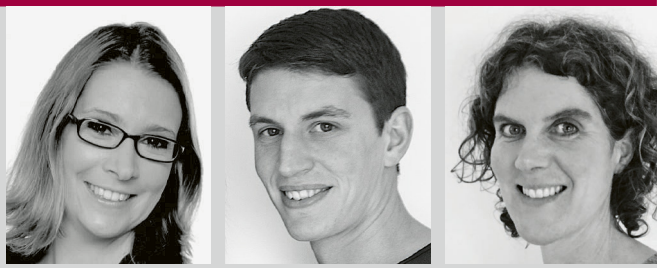

Miriam R. Keil | Jörg Rothard | Carmel Hayes

Rapid MR Susceptibility Imaging of the Brain Using Segmented 3D Echo-Planar Imaging (3D EPI) and its Clinical Applications

Pascal Sati[1]; Sunil Patil[2]; Souheil Inati[3,4]; Wen-Tung Wang[5]; J. Andrew Derbyshire[6]; Gunnar Krueger[7]; Daniel S. Reich[1,8]; John A. Butman[5,8]

[1] Translational Neuroradiology Section, National Institute of Neurological Disorders and Stroke, National Institutes of Health, Bethesda, MD, USA
[2] Siemens Healthineers, HC NAM USA DI MR COLLAB, Bethesda, MD, USA
[3] Functional MRI Core, National Institute of Mental Health, National Institutes of Health, Bethesda, MD, USA
[4] InatiAnalytics, Potomac, MD, USA
[5] Center for Neuroscience and Regenerative Medicine, Henry Jackson Foundation, Bethesda, MD, USA
[6] Section of Functional Imaging Methods, Laboratory of Brain and Cognition, National Institute of Mental Health, National Institutes of Health, Bethesda, MD, USA
[7] Siemens Healthineers, HC NAM USA DI MR COLLAB NE, Boston, MA, USA
[8] Radiology and Imaging Sciences, Clinical Center, National Institutes of Health, Bethesda, MD, USA

Abstract

MR susceptibility imaging (e.g., T2*, SWI, QSM) is a powerful tool for imaging blood vessels, hemorrhage, calcifications, and iron deposition in the normal and diseased brain with exquisite detail. To obtain such images at high resolution, very long image acquisition times are typically needed when using the conventional 3D gradient-echo sequence. Using a novel acquisition strategy called segmented (or multi-shot) 3D echo planar imaging (3D EPI)[1], we have found that MR susceptibility images can be produced with high resolution and no loss in diagnostic clarity. Our experience at the NIH across the range of field strengths indicates that the 3D EPI acquisition may be used to obtain very short scan times (1–3 min) at standard image resolutions or to increase the resolution to obtain submillimeter isotropic images in scan times on the order of 5–6 minutes. The ability to perform

[1] WIP, the product is currently under development and is not for sale in the US and in other countries. Its future availability cannot be ensured.

1

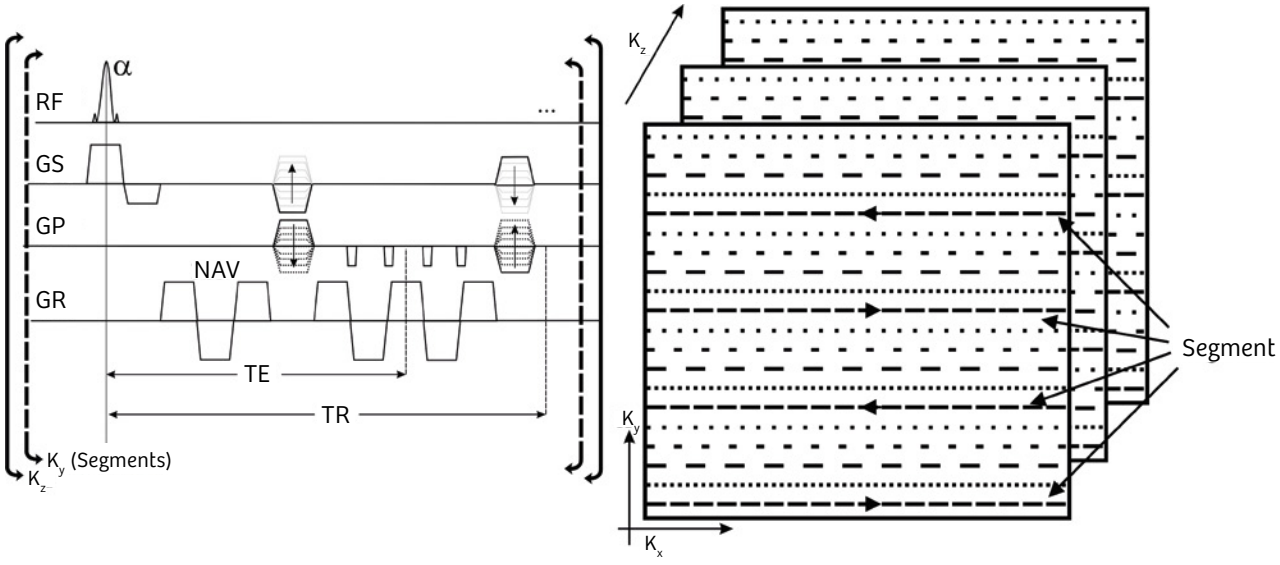

Figure 1: 3D EPI sequence diagram and its corresponding *k*-space trajectory.

rapid susceptibility imaging allows for its integration into routine clinical imaging, reduces the likelihood of motion artifact, and may be of particular benefit in the acute clinical setting such as stroke or traumatic brain injury where minimizing time in the scanner is paramount. Furthermore, the new capability to perform submillimeter isotropic imaging in clinically acceptable scan times opens up new avenues of clinical research in demyelinating diseases through the investigation of the relationship between central veins and white matter lesions.

Introduction

MR susceptibility imaging has become an essential clinical tool to visualize blood vessels, hemorrhage, calcifications, and iron deposits in the brains of people with neurological disorders. Susceptibility-based MR images can take various forms, including T2* contrast, susceptibility-weighted imaging (SWI), phase imaging, and quantitative susceptibility mapping (QSM). Because the image acquisition typically relies on a spoiled gradient echo (GRE) sequence with a relatively long TE to allow for susceptibility effects to influence contrast, scan time can be quite long, particularly when whole brain coverage and/or high resolution are required (e.g. > 15 min for 1 mm isotropic whole brain). Long acquisition times are problematic in a clinical setting, where subjects are likely to move during the scan resulting in blurred or unusable images. Therefore, slice thickness is usually limited to 2–4 mm while the field-of-view (FOV) covers only the supratentorial brain in order to maintain clinically compatible scan time.

To speed up the acquisition of MR susceptibility imaging, we recently developed a prototype volumetric (3D) segmented echo-planar imaging (EPI) sequence[1] that allows rapid imaging of the entire brain at submillimeter resolution. In a manner analogous to the use of an echo train in turbo spin echo to accelerate the acquisition of 3D spin echo, we use an echo train in segmented EPI to accelerate the acquisition of a 3D gradient echo. In this article, we describe this novel approach and present acquisition protocols developed across the range of magnetic field strengths to illustrate the application of this technique in different clinical and research applications.

MRI technique

The 3D EPI approach was originally introduced for whole-brain functional MRI with high-resolution at 7T [1]. It was then demonstrated to be a viable solution for fast high-resolution anatomical imaging of the brain at 7T when using a segmented approach with relatively short EPI train lengths in order to limit distortions and image blurring [2]. Through a collaboration between different institutes at the National Institutes of Health (NIH, Bethesda, MD) and Siemens MR, we implemented a segmented 3D EPI technique as a WIP on *syngo* MR E11A and as a prototype sequence on *syngo* MR B17A, B20P, D13A/D (available as C2P from NIH) and tested on a variety of Siemens scanners (1.5T MAGNETOM Aera, 3T Biograph mMR, 3T MAGNETOM Skyra, 3T MAGNETOM Prisma, and 7T Research System, Siemens Healthcare, Erlangen, Germany), all sited at the NIH Clinical Center. The pulse sequence diagram of the 3D seg EPI and its corresponding *k*-space trajectory are depicted in Figure 1. The segmentation used a conventional interleaved *k*-space trajectory along the primary phase encoding direction (K_Y), while the secondary phase encoding (K_Z) was used to select partitions. In order to reduce the artifacts due to B_0 variation and odd-even line discrepancy; which is typical in EPI, state-of-the-art navigator approach (shown as "NAV" in Figure 1) was integrated. The EPI factor was typically set to 15 which acquires 15 phase-encoded lines of *k*-space data for each excitation as a compromise between improving imaging efficiency while limiting the level of image distortion and blurring. Different acquisition protocols were setup according to the scanner field strength (Table 1) to produce high isotropic resolution T2*-weighted (T2*w) images of the brain under 6 min (Fig. 2). Despite a short TR, T2*-weighting is the dominant contrast on the magnitude images due to the use of prolonged TE and a low flip angle which minimize the T1-weighting. Although no obvious

	Plane	TR (ms)	TE (ms)	FOV (mm)	Phase FOV (%)	Slices	Voxel size (mm)	Matrix	Phase direction	EPI factor	TA (mins)
1.5T MAGNETOM Aera, Head/Neck 20 ch	Sag	64	37	228	94.1	256	0.75 iso	304	A >> P	15	5:23
3T MAGNETOM Biograph mMR, Head/Neck 16 ch	Ax	64	25	220	78.1	72	0.5 x 0.5 x 2.0	448	R >> L	15	1:30
	Sag	57	25	228	96.6	288	0.65 iso	352	A >> P	15	4:45
3T MAGNETOM Skyra, Head 32 ch & 3T MAGNETOM Prisma, Head 32 ch	Sag	64	35	250	81.3	256	0.65 iso	384	A >> P	15	5:46
7T research system, Head 32 ch	Ax	52	23	220	81.8	176	0.5 iso	440	R >> L	15	3:40

Table 1: 3D EPI acquisition protocols running on different Siemens scanners at NIH.

distortions could be detected on T2*w images, some noticeable areas of signal loss could be observed in the areas of poor B_0 field homogeneity (e.g. inferior frontal and temporal lobes). The 3D EPI protocol allows for reconstruction of magnitude, phase, SWI, and minimum intensity projection images which well depict the cerebral venous vasculature (Fig. 3). The phase images can be used to generate QSM images to map out the local magnetic susceptibility of brain tissues [3] (Fig. 3).

Application in multiple sclerosis

High-resolution T2*-weighted images are particularly useful to research clinicians for the purpose of detecting small veins inside cerebral white matter (WM) lesions, as this detection may aid with the diagnosis of multiple sclerosis (MS) [4]. When searching for central veins in WM lesions, whole-brain coverage is particularly important, since MS lesions can be found anywhere in the brain. Moreover, isotropic resolution is particularly useful to reformat images in any desired plane, a feature that is available on many radiology viewing platforms that enables veins to be well visualized irrespective of their orientation (Fig. 4).

Based on our experience with scanning 100+ MS patients using the high-resolution 3D EPI protocols at different field strengths, central veins are most conspicuous at 7T due to the increased resolution and contrast (Fig. 5). While central veins are visible at 1.5T and 3T, their detection can be facilitated by injecting a gadolinium-based contrast agent during the first minutes of the 3D EPI acquisition (Fig. 5). This is straightforward to implement when the MRI protocol already involves the use of contrast agent to detect newly enhancing MS lesions on T1-weighted images. Because there is usually a recommended 5-minute wait before running post-contrast imaging [5], the 3D EPI acquisition can be performed at that time, thus not prolonging the total scan time of the MRI exam.

Unlike T2-weighted fluid-attenuated inversion recovery (FLAIR) images, T2*-weighted and SWI images lack cerebrospinal fluid suppression and are, therefore, less able to demonstrate contrast between lesions and surrounding tissues, making the detection of lesions more difficult for the clinicians. To overcome these issues, our laboratory has developed and routinely generates an MR combined contrast, which we have called FLAIR* [6]. The FLAIR* approach uses the Siemens product sequence (SPACE IR) to acquire a 1 mm isotropic 3D FLAIR (for lesion detection) and our 3D EPI prototype sequence for 0.65 mm isotropic T2*-weighting (for vein detection); total acquisition time is <12 min. FLAIR* images are generated using simple processing steps: rigid co-registration, interpolation, and image multiplication (Fig. 6). Because of its close resemblance to the conventional FLAIR images, 3T FLAIR* can be readily interpreted by radiologists and neurologists.

Over the past couple of years, our fast, high-resolution 3D EPI protocols have been disseminated to a dozen

2

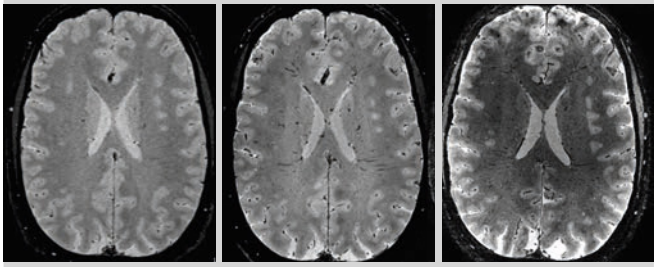

Figure 2: Representative 3D EPI images acquired on the same healthy volunteer at three different field strengths (1.5T, 3T and 7T). Submillimeter voxel dimensions were used for all scans (1.5T: 0.75 mm isotropic, 3T: 0.65 mm isotropic and 7T: 0.5 mm isotropic).

3

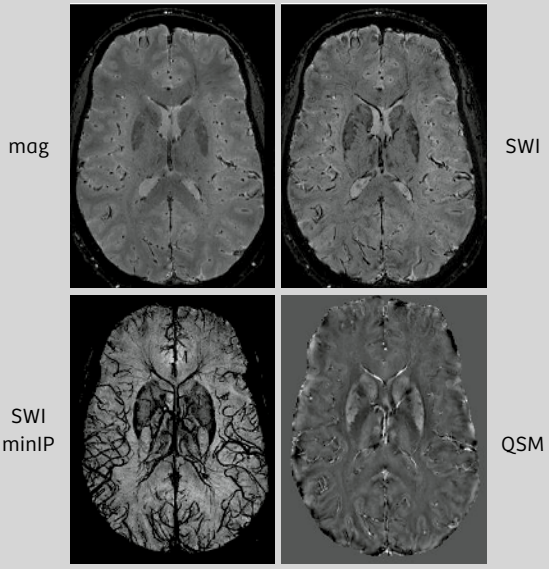

Figure 3: Different susceptibility-based contrasts obtained with 3D EPI protocol at 3T. T2*w contrast corresponds to the native magnitude images produced by the scanner. SWI and SWI mIP contrasts can also be generated by the scanner when using the WIP. QSM images are generated offline using the QSM reconstruction algorithm from Langkammer et al. (http://www.neuroimaging.at/pages/research/quantitative-susceptibility-mapping.php).

MRI centers specialized in MS across the US and Europe, resulting in several publications that illustrate its potential clinical value in MS [7–10]. Recent guidelines on the use of MRI in MS from the MAGNIMS group [5, 11] and the NAIMS cooperative [4] also mentioned 3D EPI and its combined FLAIR* contrast as promising MRI techniques for the clinical evaluation of the central vein sign in MS diagnosis.

4

3D EPI (3T), 0.65 mm iso

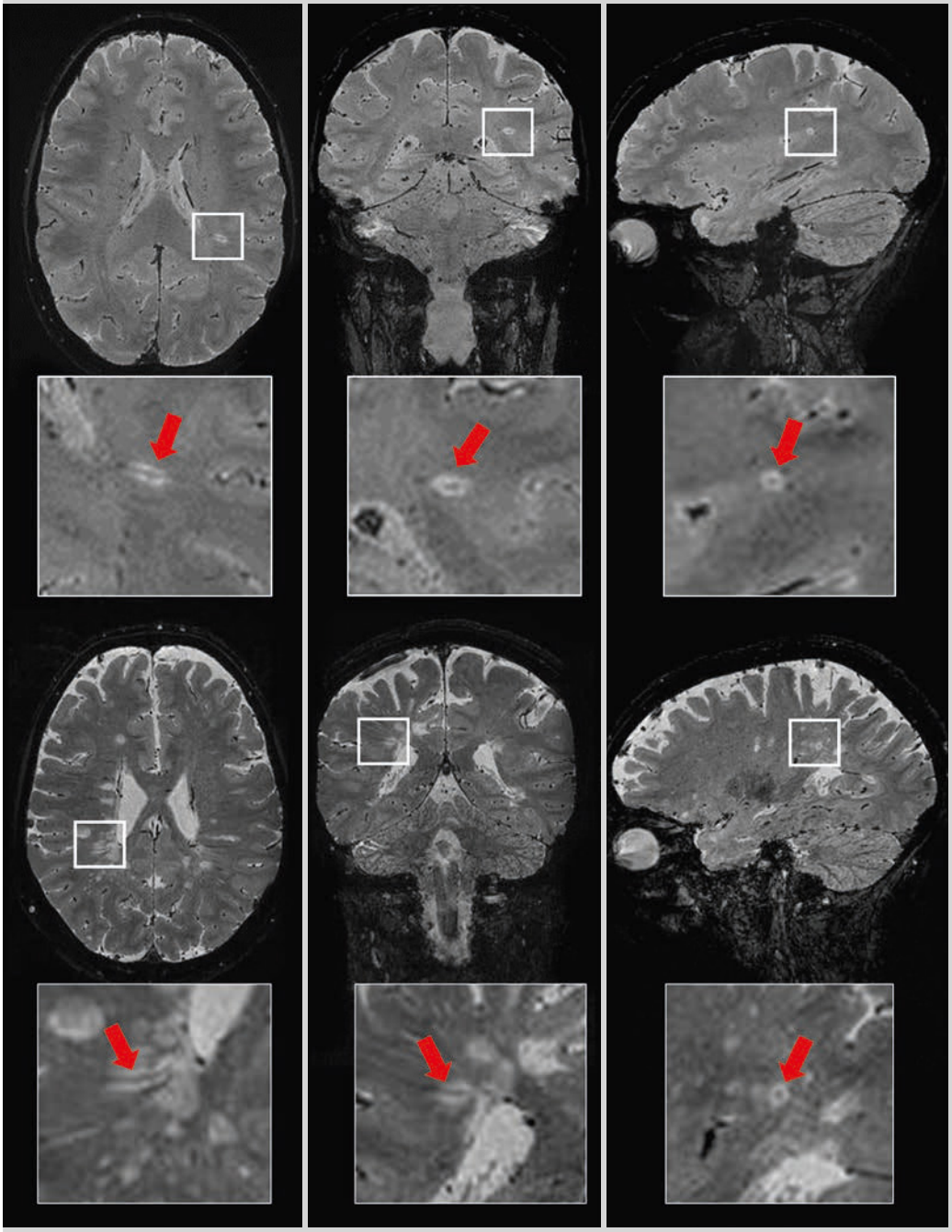

Figure 4: 0.65 mm isotropic 3D EPI (magnitude) T2*w images acquired at 3T in two different MS patients. Images can be reformatted for multiplanar viewing, thus allowing the identification of small parenchymal veins running centrally through MS lesions (red arrows in the magnified boxes).

Application in the acute clinical setting (e.g. traumatic brain injury (TBI) and stroke)

One major limitation of MRI in the acute clinical evaluation of traumatic brain injury and stroke is the simple fact that the extended MRI exam can be quite long. Thus, despite the additional information that may be gained by MRI relative to CT for these indications [12], clinicians continue to rely on CT to rule out intracranial hemorrhage and to rely on clinical evaluations to guide therapy. Any rapid and comprehensive MRI examination must be able to evaluate for intracranial hemorrhage using gradient echo based techniques [13]. In the setting of TBI, SWI is preferred over GRE T2* [14] due to its greater sensitivity for microhemorrhage and is typically performed as an axial acquisition with 2.0 mm slice thickness and in plane resolution of 0.5 to 1.0 mm.

5

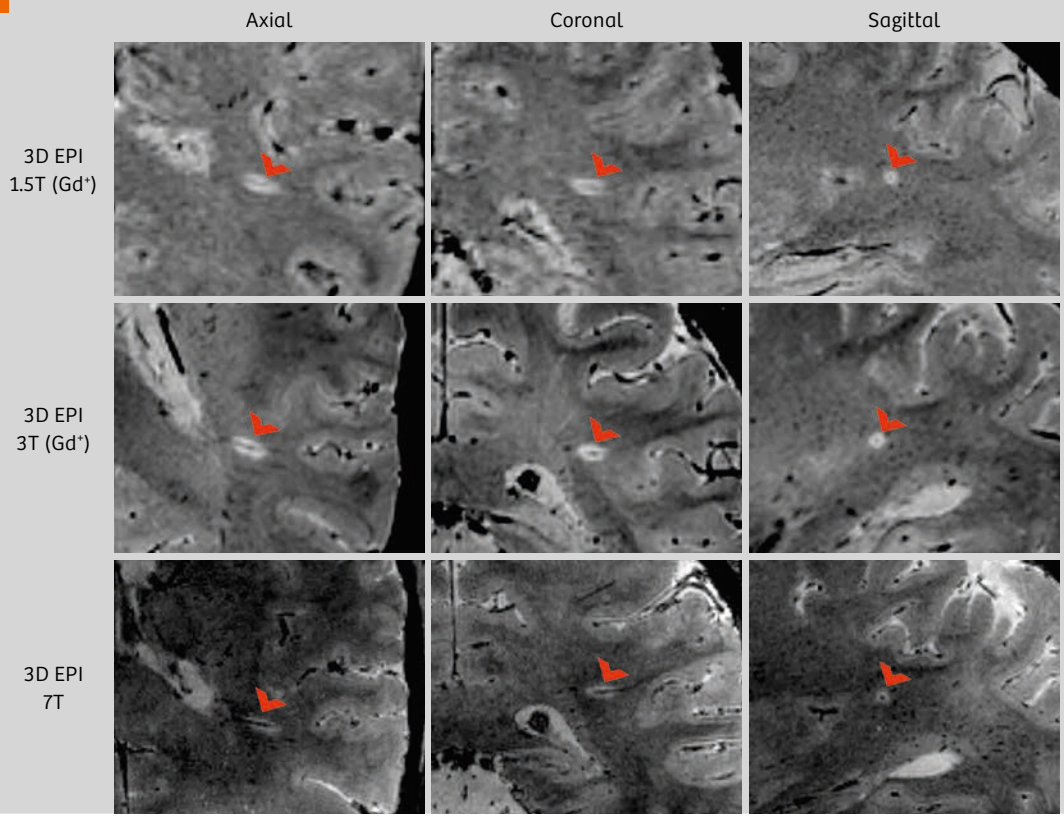

Figure 5: 3D EPI (magnitude) T2*w images in the same MS patient brain at three different field strengths (0.75 mm isotropic at 1.5T, 0.65 mm isotropic at 3T, and 0.5 mm isotropic at 7T). The same central vein inside an MS lesion can be detected at all field strengths and on all imaging planes (red arrows). Note that at 1.5T and 3T, images were acquired during the injection of gadolinium-based contrast agent (Gd+) to enhance the conspicuity of the parenchymal veins.

6

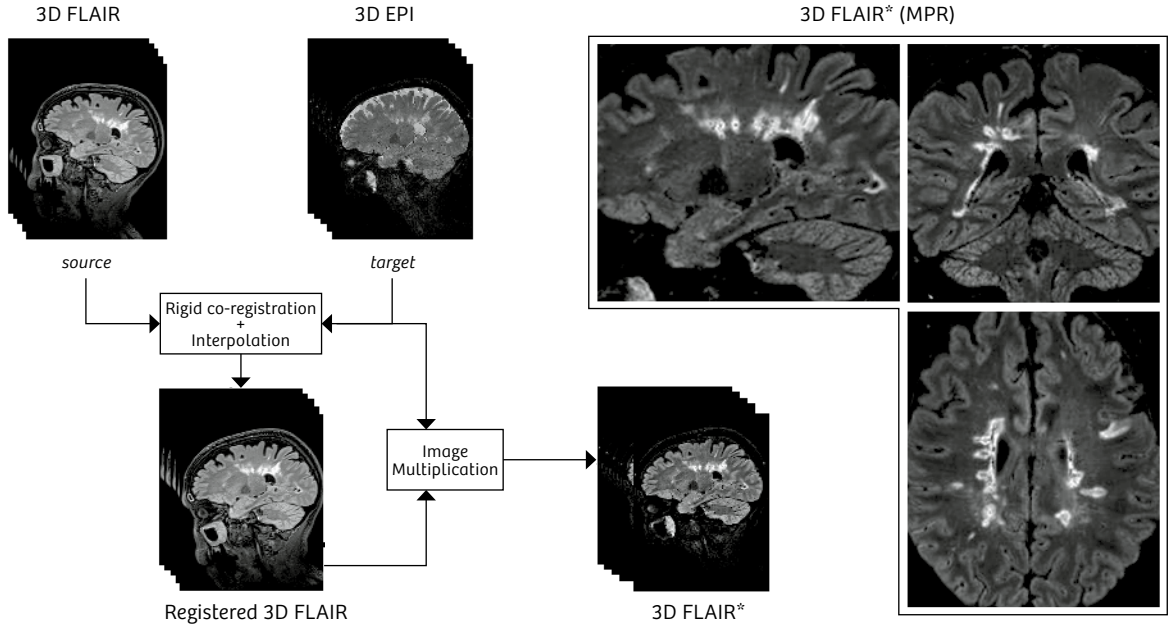

Figure 6: Workflow of the 3T FLAIR* processing pipeline. Native 3D FLAIR (1 mm isotropic) images are co-registered (rigid, 6 degrees of freedom) to native T2*w 3D EPI (0.65 mm isotropic) and interpolated (windowed sinc) to match the 3D EPI resolution. FLAIR* images are then generated by multiplying the registered 3D FLAIR images to the native 3D EPI images. Because FLAIR* images retain the high-isotropic-resolution from the native 3D EPI images, multiplanar reformatting (MPR) enables the reader to view FLAIR* images in any desired orientation. Our FLAIR* pipeline is currently performed offline after downloading the DICOM images from the NIH Radiology PACS system. Once the processing is completed, FLAIR* images are imported back into the PACS system to be read by NIH clinicians. Note that FLAIR* processing could also be done using the MR Arithmetics prototype[1] available under *syngo*.via Frontier.

7

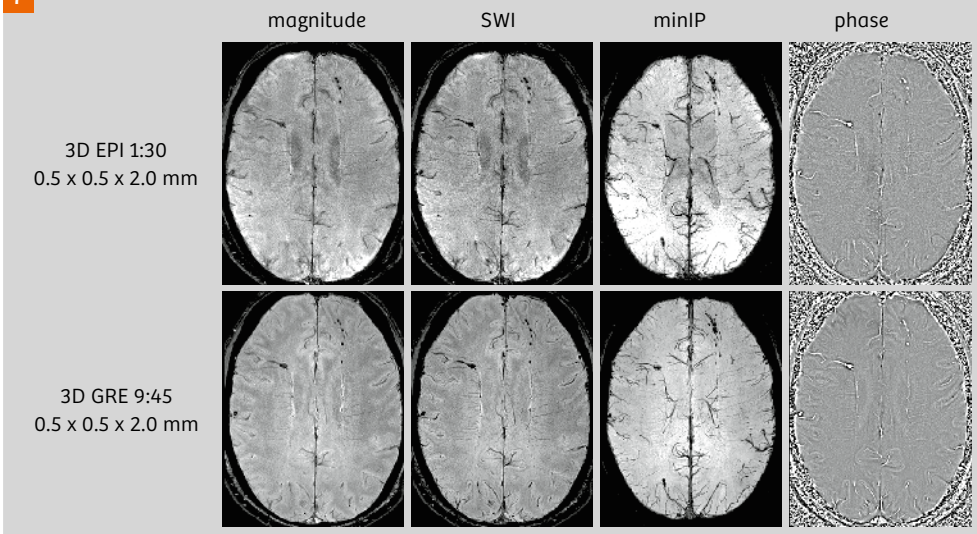

Figure 7: An ~ 1½-minute 3D EPI sequence compares favorably with an ~ 10-minute 3D GRE sequence for the depiction and characterization of traumatic axonal injury characterized by clustered curvilinear and punctate microhemorrhages scattered throughout the frontal lobes bilaterally. Identical image resolution and echo time (TE = 25 ms). 3D GRE was performed using iPAT2 and a TR of 40 ms and 6/8 partial phase encode. 3D EPI was performed with an EPI of 15 and a TR of 64 ms for a net ~ 6 fold acceleration. Minimum intensity projection (minIP) used a 10 mm slab thickness.

For the characterization of TBI associated microhemorrhage, consensus imaging protocols prefer GRE based SWI over the conventional 2D GRE T2*-weighted methods, but acknowledge, even using iPAT, that this demands imaging times on the order of 5–10 minutes for whole brain coverage [15]. With 3D EPI, equivalent or higher resolution is easily obtained in 1.5–3 minutes. Figure 7 compares 3D GRE based SWI to that of the 3D EPI SWI performed with identical in-plane resolution (0.5 × 0.5 mm) and slice thickness (2.0 mm) with imaging times of 9:45 and 1:30 respectively on a 3T Biograph mMR platform. Qualitatively, the images are quite similar, and, despite the somewhat lower SNR of the rapid SWI scan, the SNR is more than sufficient to detect and characterize small microhemorrhages and also to generate phase data and subsequent SWI processing.

Alternatively, one can spend more time imaging and obtain higher (e.g. 0.65 mm isotropic) resolution to allow for characterization of microhemorrhage in any plane of interest (Fig. 8) allowing for demonstration of the curvilinear microhemorrhages characteristic of traumatic axonal injury. In addition, such high resolution imaging can demonstrate other hemorrhagic pathologies such as subarachnoid hemorrhage, cortical contusion, and superficial siderosis.

Conclusions

In summary, we present a novel approach to acquire susceptibility-based MR images using a segmented 3D EPI prototype sequence. Our experience at the NIH has shown that this method can be used either to reduce the imaging time of standard resolution 3D GRE/SWI images, or to increase the resolution to acquire submillimeter isotropic images of the whole brain at a variety of field strengths, as low as 1.5T. One current limitation of our prototype sequence is the lack of parallel imaging capability acquisition (e.g., GRAPPA, CAIPIRINHA), which was recently demonstrated to be feasible at 7T [16]. Clinically, we believe

8

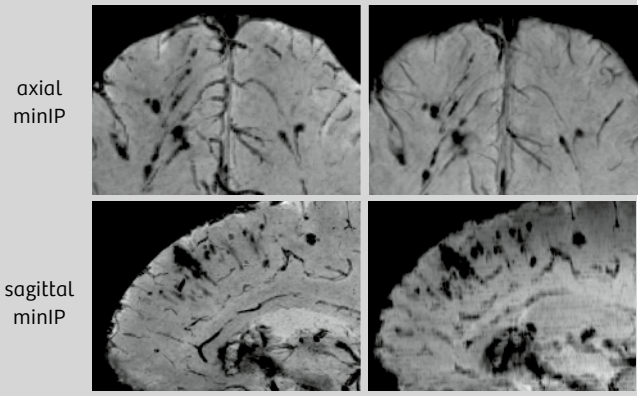

Figure 8: Comparison of microhemorrhage characterization using isotropic 0.65 mm 3D EPI vs. traditional 0.5 x 0.5 x 2.0 mm 3D GRE. Axial minimum intensity projections are comparable but the projections in the sagittal plane demonstrate the superiority of isotropic acquisition. Acquisition time for 3D EPI was 4:45 min and for GRE was 9:45 min.

the 3D EPI approach is a promising tool for MS diagnosis, but it could have many other applications in variety of neurological disorders, such as detecting microhemorrhage in neurovascular disease or traumatic brain injury, or assessing iron deposition in the substantia nigra in Parkinson's disease [17].

Acknowledgements

Research described in this article was supported in part by the Intramural Research Program of the National Institute of Neurological Disorders and Stroke, NIH. We also acknowledge the Center for Neuroscience and Regenerative Medicine for support.

Appendix

Currently, the 3D EPI prototype sequence[1] is available for *syngo* MR D13A/D through C2P exchange with NIH (Please contact Dr. Pascal Sati, satip@ninds.nih.gov). It is also available for *syngo* MR E11A as a WIP through Siemens (Please contact Dr. Sunil Patil, patil-sunil@siemens-healthineers.com). The collaborative work between the National Institute of Neurological Disorders and Stroke, the National Institute of Mental Health, and Siemens Healthcare USA was conducted under a Cooperative Research and Development Agreement.

References

1 B.A. Poser, P.J. Koopmans, T. Witzel, L.L. Wald, M. Barth, Three dimensional echo-planar imaging at 7 Tesla, Neuroimage, 51 (2010) 261-266.
2 J.J. Zwanenburg, M.J. Versluis, P.R. Luijten, N. Petridou, Fast high resolution whole brain T2* weighted imaging using echo planar imaging at 7T, Neuroimage, 56 (2011) 1902-1907.
3 C. Langkammer, K. Bredies, B.A. Poser, M. Barth, G. Reishofer, A.P. Fan, B. Bilgic, F. Fazekas, C. Mainero, S. Ropele, Fast quantitative susceptibility mapping using 3D EPI and total generalized variation, Neuroimage, 111 (2015) 622-630.
4 P. Sati, J. Oh, R.T. Constable, N. Evangelou, C.R. Guttmann, R.G. Henry, E.C. Klawiter, C. Mainero, L. Massacesi, H. McFarland, F. Nelson, D. Ontaneda, A. Rauscher, W.D. Rooney, A.P. Samaraweera, R.T. Shinohara, R.A. Sobel, A.J. Solomon, C.A. Treaba, J. Wuerfel, R. Zivadinov, N.L. Sicotte, D. Pelletier, D.S. Reich, N. Cooperative, The central vein sign and its clinical evaluation for the diagnosis of multiple sclerosis: a consensus statement from the North American Imaging in Multiple Sclerosis Cooperative, Nat Rev Neurol, 12 (2016) 714-722.

Contact

Pascal Sati, Ph.D.
Translational Neuroradiology Section
National Institute of Neurological Disorders and Stroke
National Institutes of Health

10 Center Drive MSC 1400
Building 10 Room 5C103
Bethesda, MD 20892-1400
USA
satip@ninds.nih.gov



Pascal Sati



John A. Butman

5 A. Rovira, M.P. Wattjes, M. Tintore, C. Tur, T.A. Yousry, M.P. Sormani, N. De Stefano, M. Filippi, C. Auger, M.A. Rocca, F. Barkhof, F. Fazekas, L. Kappos, C. Polman, D. Miller, X. Montalban, M.s. group, Evidence-based guidelines: MAGNIMS consensus guidelines on the use of MRI in multiple sclerosis-clinical implementation in the diagnostic process, Nat Rev Neurol, 11 (2015) 471-482.
6 P. Sati, I.C. George, C.D. Shea, M.I. Gaitan, D.S. Reich, FLAIR*: a combined MR contrast technique for visualizing white matter lesions and parenchymal veins, Radiology, 265 (2012) 926-932.
7 I.D. Kilsdonk, A. Lopez-Soriano, J.P. Kuijer, W.L. de Graaf, J.A. Castelijns, C.H. Polman, P.R. Luijten, J.J. Geurts, F. Barkhof, M.P. Wattjes, Morphological features of MS lesions on FLAIR* at 7 T and their relation to patient characteristics, J Neurol, 261 (2014) 1356-1364.
8 I.D. Kilsdonk, M.P. Wattjes, A. Lopez-Soriano, J.P. Kuijer, M.C. de Jong, W.L. de Graaf, M.M. Conijn, C.H. Polman, P.R. Luijten, J.J. Geurts, M.I. Geerlings, F. Barkhof, Improved differentiation between MS and vascular brain lesions using FLAIR* at 7 Tesla, Eur Radiol, 24 (2014) 841-849.
9 A.P. Samaraweera, M.A. Clarke, A. Whitehead, Y. Falah, I.D. Driver, R.A. Dineen, P.S. Morgan, N. Evangelou, The Central Vein Sign in Multiple Sclerosis Lesions Is Present Irrespective of the T2* Sequence at 3 T, J Neuroimaging, 27 (2017) 114-121.
10 A.J. Solomon, M.K. Schindler, D.B. Howard, R. Watts, P. Sati, J.P. Nickerson, D.S. Reich, "Central vessel sign" on 3T FLAIR* MRI for the differentiation of multiple sclerosis from migraine, Ann Clin Transl Neurol, 3 (2016) 82-87.
11 M. Filippi, M.A. Rocca, O. Ciccarelli, N. De Stefano, N. Evangelou, L. Kappos, A. Rovira, J. Sastre-Garriga, M. Tintore, J.L. Frederiksen, C. Gasperini, J. Palace, D.S. Reich, B. Banwell, X. Montalban, F. Barkhof, M.S. Group, MRI criteria for the diagnosis of multiple sclerosis: MAGNIMS consensus guidelines, Lancet Neurol, 15 (2016) 292-303.
12 M. Chiara Ricciardi, R.P. Bokkers, J.A. Butman, D.A. Hammoud, D.L. Pham, S. Warach, L.L. Latour, Trauma-Specific Brain Abnormalities in Suspected Mild Traumatic Brain Injury Patients Identified in the First 48 Hours after Injury: A Blinded Magnetic Resonance Imaging Comparative Study Including Suspected Acute Minor Stroke Patients, J Neurotrauma, 34 (2017) 23-30.
13 C.S. Kidwell, J.A. Chalela, J.L. Saver, S. Starkman, M.D. Hill, A.M. Demchuk, J.A. Butman, N. Patronas, J.R. Alger, L.L. Latour, M.L. Luby, A.E. Baird, M.C. Leary, M. Tremwel, B. Ovbiagele, A. Fredieu, S. Suzuki, J.P. Villablanca, S. Davis, B. Dunn, J.W. Todd, M.A. Ezzeddine, J. Haymore, J.K. Lynch, L. Davis, S. Warach, Comparison of MRI and CT for detection of acute intracerebral hemorrhage, JAMA, 292 (2004) 1823-1830.
14 K.A. Tong, S. Ashwal, B.A. Holshouser, L.A. Shutter, G. Herigault, E.M. Haacke, D.K. Kido, Hemorrhagic shearing lesions in children and adolescents with posttraumatic diffuse axonal injury: improved detection and initial results, Radiology, 227 (2003) 332-339.
15 C.A. Mutch, J.F. Talbott, A. Gean, Imaging Evaluation of Acute Traumatic Brain Injury, Neurosurg Clin N Am, 27 (2016) 409-439.
16 R. Stirnberg, J. Acosta-Cabronero, B.A. Poser, T. Stocker, 2D-segmented, multi-TE 3D-EPI for high-resolution R2* and quantitative susceptibility mapping at 7 Tesla, Proceedings of the International Society of Magnetic Resonance Imaging in Medicine, 2015.
17 C. Langkammer, L. Pirpamer, S. Seiler, A. Deistung, F. Schweser, S. Franthal, N. Homayoon, P. Katschnig-Winter, M. Koegl-Wallner, T. Pendl, E.M. Stoegerer, K. Wenzel, F. Fazekas, S. Ropele, J.R. Reichenbach, R. Schmidt, P. Schwingenschuh, Quantitative Susceptibility Mapping in Parkinson's Disease, PLoS One, 11 (2016) e0162460.

Assessing Brain Volumes Using MorphoBox Prototype

Alexis Roche[1,2,3]; Bénédicte Maréchal[1,2,3]; Tobias Kober[1,2,3]; Gunnar Krueger[4]; Patric Hagmann[1]; Philippe Maeder[1]; Reto Meuli[1]

[1] Department of Radiology, University Hospital (CHUV), Lausanne, Switzerland
[2] Advanced Clinical Imaging Technology, Siemens Healthineers, Lausanne, Switzerland
[3] Signal Processing Laboratory (LTS 5), École Polytechnique Fédérale de Lausanne, Lausanne, Switzerland
[4] Siemens Medical Solutions USA, Boston, MA

Introduction

Brain morphometry from routine structural MR images is useful to detect abnormal regional brain volumes that may be indicative of a disease [1]. For instance, hippocampus atrophy is known to be associated with memory impairment commonly experienced by individuals with dementia [2]. When combined with other volumetric measurements such as frontal lobe atrophy and white matter lesions, it may help diagnose a particular form of dementia (Alzheimer's disease, fronto-temporal or vascular dementia among others).

The MorphoBox algorithm[1] was developed by the Advanced Clinical Imaging Technology group in Lausanne in close collaboration with the University Hospital's Radiology Department. As an integral part of a Siemens prototype sequence, it automatically estimates a number of brain volumes from a single T1-weighted MR image acquired with the MPRAGE sequence, and compares these volumes with normative ranges adjusted for head size, age, and sex. The results are presented to the user in the form of a DICOM report, where brain structures that are found to be abnormally small (or abnormally large, e.g. for ventricular structures) are indicated with an asterisk.

Owing to its full incorporation into the MRI system, MorphoBox runs during image reconstruction. Results can be read with the *syngo* standard viewers or sent to the PACS system in order to seamlessly integrate into the radiological workflow. As of early 2016, more than 10,000 patients had benefited from this prototype worldwide.

[1] WIP, the product is currently under development and is not for sale in the US and in other countries. Its future availability cannot be ensured.

Methodology

Image processing

MorphoBox implements a processing pipeline consisting of several steps, as outlined in Figure 1. After the incoming MR scan has been checked for protocol compliance with a widely accepted standard for MPRAGE sequences [3], it is

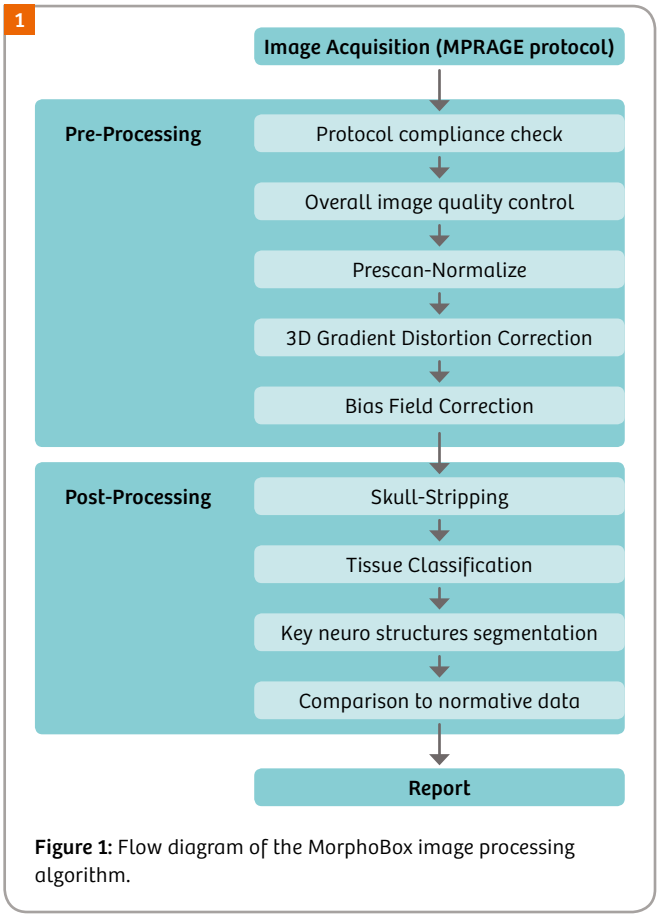

Figure 1: Flow diagram of the MorphoBox image processing algorithm.



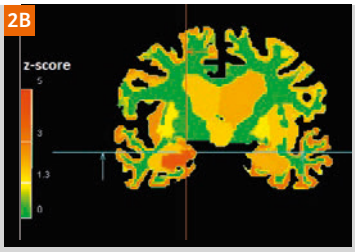

2C

Brain Morphometry Report - 4/7

Lobar GM/structure	Absolute [ml]	Normalized^ [%]	Normative Range^^ [%]
Frontal lobe			
GM left	67.4	* 4.93	[5.27 - 6.47]
GM right	64.2	* 4.69	[5.20 - 6.35]
Parietal lobe			
GM left	49.2	3.59	[3.48 - 4.46]
GM right	47.7	3.49	[3.41 - 4.31]
Occipital lobe			
GM left	15.4	* 1.12	[1.21 - 1.80]
GM right	15.9	* 1.16	[1.37 - 1.98]
Temporal lobe			
GM left	39.4	* 2.88	[3.32 - 4.00]
GM right	42.4	* 3.09	[3.52 - 4.30]
Cingulate gyrus			
GM left	6.3	0.46	[0.44 - 0.59]
GM right	6.5	0.47	[0.43 - 0.56]
Insula			
Left	3.8	* 0.28	[0.30 - 0.40]
Right	4.1	* 0.30	[0.34 - 0.44]

not approved for diagnostic purpose

Figure 2: Screenshots of MorphoBox results on the *syngo* viewer for an Alzeimer's Disease patient. **(2A)** an MRI coronal slice, **(2B)** the corresponding deviation map, and **(2C)** three pages from the report.

Brain Morphometry Report - 3/7

Patient Demographics 80 yrs Male

Image quality	high	0.72	[0 - 0.82]
Segmentation Quality	high	0.82	[0.7 - 1]

Tissue	Absolute [ml]	Normalized^ [%]	Normative Range^^ [%]
TIV	1368.4		
GM	474.8	* 34.7	[37.6 - 43.9]
cortical GM	349.5	* 25.5	[28.3 - 33.6]
WM	426.3	31.2	[26.0 - 31.4]
WMab	0.3	0.0	
CSF	467.3	34.2	[26.7 - 35.3]

^ Percentage of TIV (Total Intracranial Volume)
^^ 10th and 90th percentiles of healthy age-matched population
* Out-of-range volumes

not approved for diagnostic purpose

Brain Morphometry Report - 3/7

Structure	Absolute [ml]	Normalized^ [%]	Normative Range^^ [%]
Hippocampus	4.3	* 0.31	[0.38 - 0.48]
Hippocampus left	2.3	* 0.17	[0.19 - 0.24]
Hippocampus right	2.0	* 0.14	[0.19 - 0.24]
Ventricles	107.4	* 7.85	[1.94 - 5.38]
lateral ventricle left	55.3	* 4.04	[0.81 - 2.56]
lateral ventricle right	44.1	* 3.22	[0.79 - 2.41]
3rd ventricle	4.6	* 0.34	[0.14 - 0.29]
4th ventricle	3.5	0.25	[0.13 - 0.26]

not approved for diagnostic purpose

submitted to different image quality checks based on both signal-to-noise ratio and contrast-to-noise ratio assessments as well as motion-/aliasing-related artifact detection [4]. Subsequently, the images are corrected for gradient distortion [5] and radio-frequency field inhomogeneity [6, 7]. A tissue classification algorithm [8] is applied to the corrected image, the results of which are combined with a deformed anatomical template to segment various brain structures in the image [9], including: lobe-wise gray and white matter, insula, cingulate, hippocampi, central nuclei, subcortical white matter, corpus callosum, ventricular system, cerebellum, and different brainstem structures. Volumes are computed for each segmented structure.

Normative range analysis

A cohort of 437 subjects with balanced sex and age ranging from 19 to 91 years was used to construct normative ranges for each brain volume measure output by MorphoBox. Specifically, the volumes produced by MorphoBox on the normative cohort were divided by the corresponding total intra-cranial volume, also estimated by MorphoBox, and regressed against age and sex using a log-linear model [9]. The normative ranges were then defined depending on age and sex by the regression prediction intervals corresponding, respectively, to the 10th and 90th percentiles of the TIV-normalized volume distribution, as seen in Figures 2–7 for various brain structures.

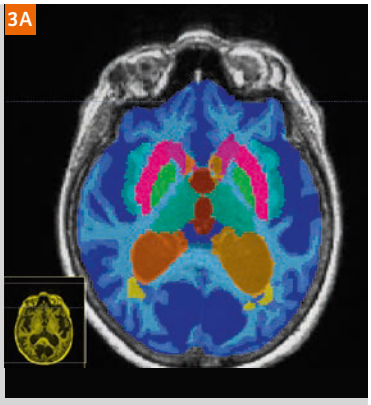

Figure 3: (3A) Axial slice of a 77-year-old woman with chronic vascular atrophy. Structures of interest segmented by MorphoBox and overlaid in color are the insula, putamen, pallidum, caudate nucleus, thalamus, lateral and third ventricles. In yellow are detected white matter lesions. **(3B–C)** Display of normative ranges for women as a function of age, respectively for the total normalized gray matter volume **(3B)** and the total normalized cerebrospinal fluid volume **(3C)**. The red dots indicate the volumes assessed by MorphoBox.

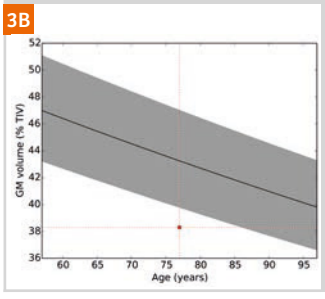

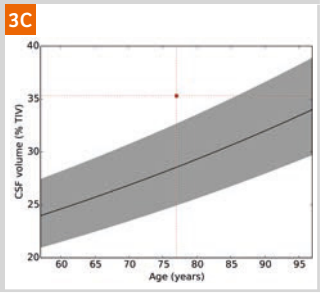

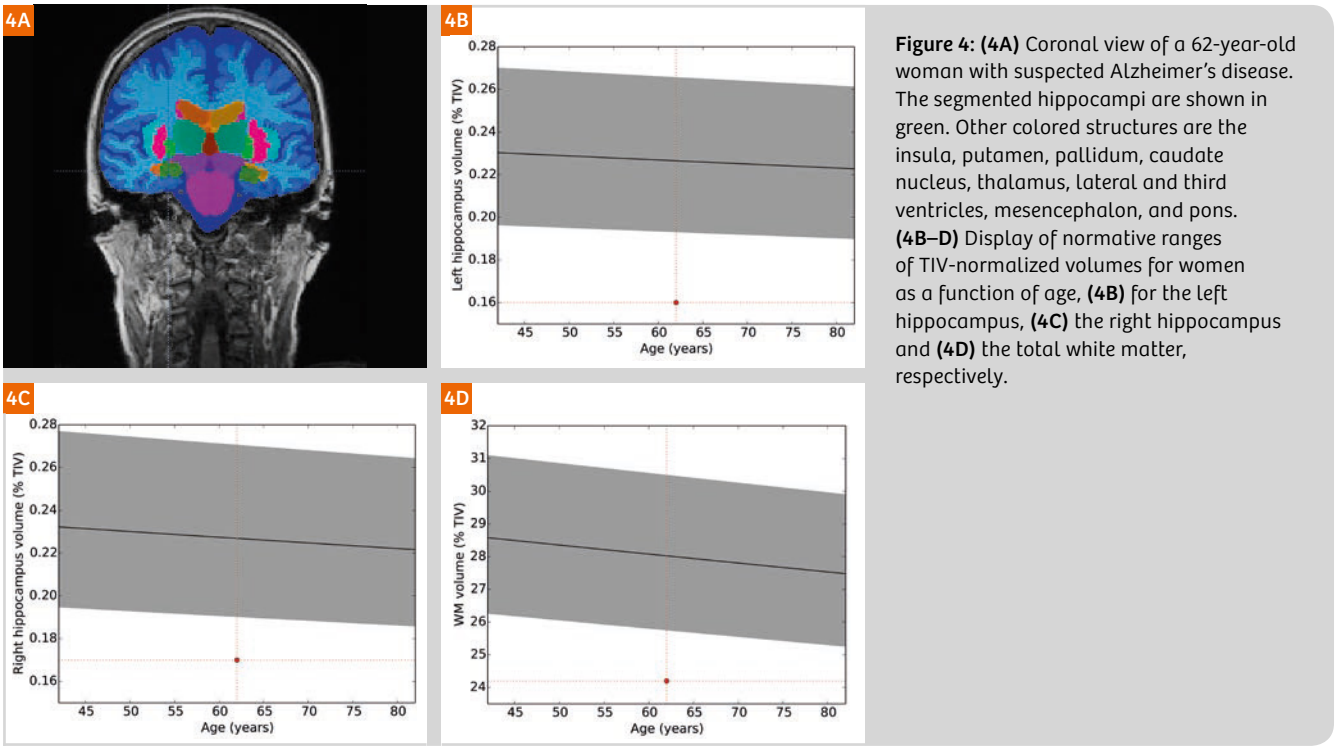

Figure 4: (4A) Coronal view of a 62-year-old woman with suspected Alzheimer's disease. The segmented hippocampi are shown in green. Other colored structures are the insula, putamen, pallidum, caudate nucleus, thalamus, lateral and third ventricles, mesencephalon, and pons. **(4B–D)** Display of normative ranges of TIV-normalized volumes for women as a function of age, **(4B)** for the left hippocampus, **(4C)** the right hippocampus and **(4D)** the total white matter, respectively.

Creation of report and deviation map

Finally, a report in form of a DICOM image is created containing patient identification, the result of the performed image quality assessment as well as a list of evaluated volumes, divided by hemispheres. Beside the absolute volumes, the TIV-normalized measures are reported and displayed in relation to the normative ranges. Detected deviations from the normative ranges are indicated with an asterisk (see Fig. 2). In addition, MorphoBox produces an image called "deviation map" displaying abnormal regions in hot colors (orange to red depending on the severity of deviation from normality). Since this information is stored as a DICOM image, it can be exported to the PACS like any other image and is available in other viewing software along with the imaging data.

Clinical examples

In the following examples, all brain MR slices are displayed in radiological convention (with the left hemisphere shown on the right of the image).

Results of applying MorphoBox on a 77-year-old female patient with chronic vascular atrophy are depicted in Figure 3A. Both global gray matter atrophy and global cerebrospinal fluid expansion, which are clearly visible in the MR scan, are appropriately detected by MorphoBox, as reflected in the normative range plots in Figure 3B. Other smaller structures are indicated as out-of-range in the MorphoBox report, including the ventricles, the frontal, temporal, parietal lobes, and the insula, in both hemispheres. Figure 4 shows the case of a 62-year-old woman with suspected Alzheimer's disease. Abnormal hippocampi are detected in both hemispheres, suggesting hippocampal atrophy. The total white matter volume is also flagged as abnormally low, which is common in early-age-of-onset Alzheimer's disease [10]. This case is in contrast with that of a 78-year-old woman with suspected early mild cognitive impairment, where the hippocampi like most brain structures are found normal, although insula atrophy is detected mainly on the left, see Figure 5.

As another example, the case of an 88-year-old man with probable cognitive disorder is shown in Figure 6A, for which cortical atrophy can be suspected from visual inspection of the MR scan. Quantitative analysis using MorphoBox (Fig. 6B) reveals that both frontal lobes are small, yet within the bounds of normality, and that both temporal lobes are clearly out-of-range, although the right hippocampus is normal and the left hippocampus is only slightly below the 10th percentile.

MorphoBox can also provide clinically relevant quantitative information on young patients, such as the 20-year-old woman with brain stem disorder shown in Figure 7A. The pons and medulla oblongata are found abnormal by MorphoBox, while the mesencephalon is borderline within normal range, as illustrated in Figure 7B.



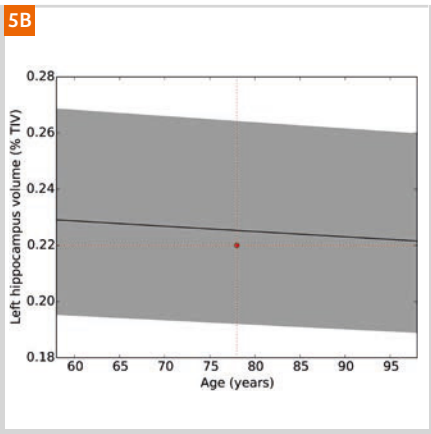

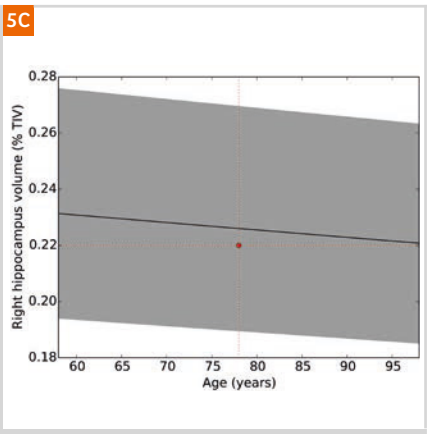

Figure 5: (5A) Coronal view of a 78-year-old woman with suspected MCI. The hippocampi (highlighted in green) are normal contrary to the left and right insulae (in light blue). Other structures shown in color (the central nuclei, ventricles, and brain stem) are normal. **(5B–E)** Display of normative ranges of TIV-normalized volumes for women as a function of age, **(5B)** for the left hippocampus, **(5C)** the right hippocampus, **(5D)** the left insula, and **(5E)** the right insula, respectively.

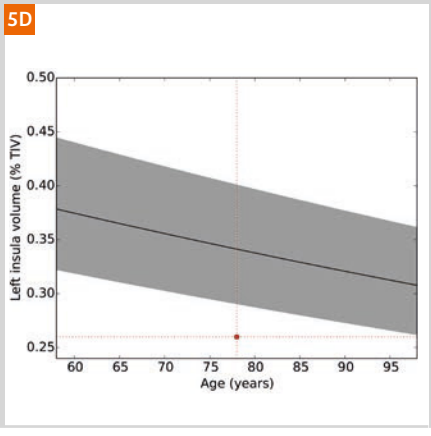

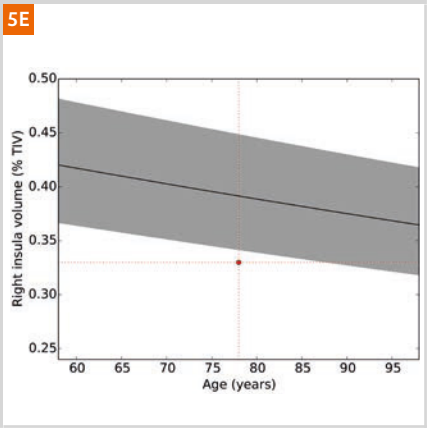

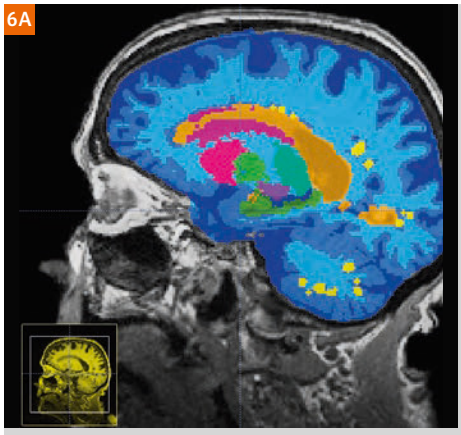

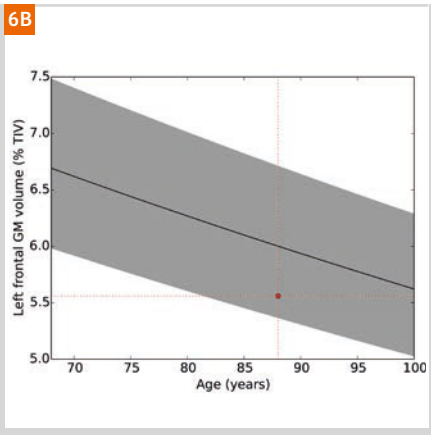

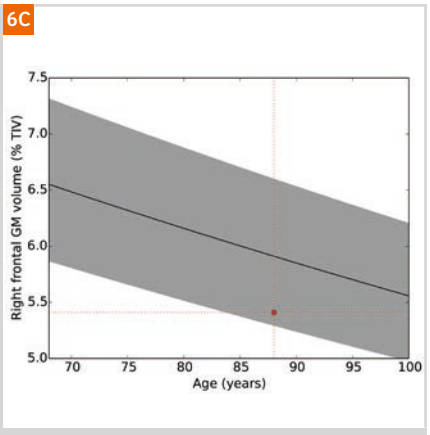

Figure 6: (6A) Sagittal view of an 88-year-old man with suspected cognitive disorder (left hemisphere). **(6B–E)** Display of normative ranges of TIV-normalized volumes for men as a function of age, **(6B)** for the left frontal lobe gray matter, **(6C)** the right frontal lobe gray matter, **(6D)** the left temporal lobe gray matter, and **(6E)** the right temporal lobe gray matter, respectively.

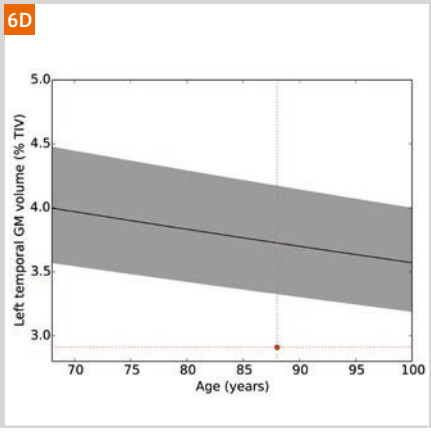

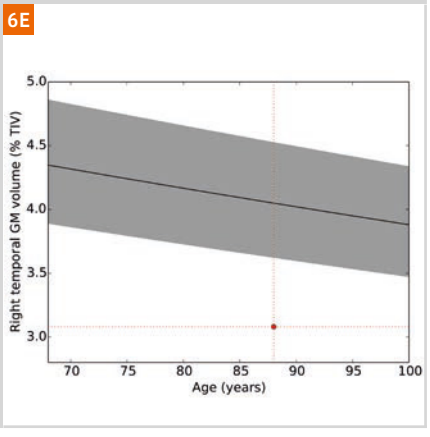

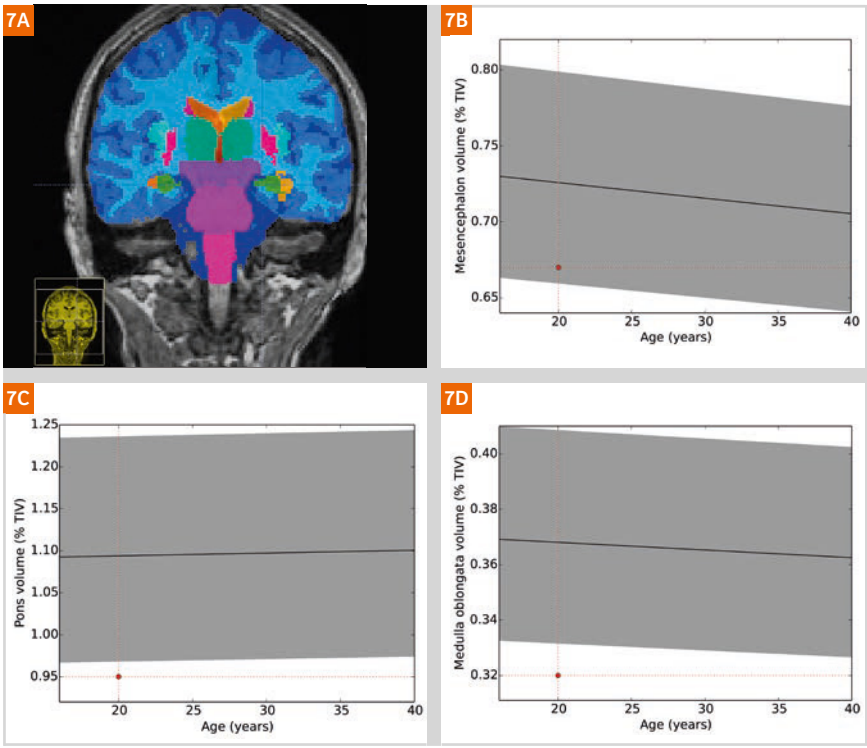

Figure 7: (7A) Coronal slice of a 20-year-old woman with brain stem disorder. The three brain stem substructures (mesencephalon, pons, medulla oblongata) are shown with distinct colors. **(7B–D)** Display of normative ranges of TIV-normalized volumes for women as a function of age, **(7B)** for the mesencephalon, **(7C)** the pons, and the medulla oblongata, **(7D)** respectively.

Conclusion

MorphoBox is a user-friendly brain volumetry prototype software compatible with clinical workflow constraints and intended for routine use. It provides quantitative information that can help radiological reading for patients with suspected neurodegeneration, as briefly exemplified in this article, and it is fully integrated in a clinical workflow. Our current objective is to further develop MorphoBox as a decision support tool for differential diagnosis of brain diseases.

References

1 D. Mietchen, and C. Gaser. Computational morphometry for detecting changes in brain structure due to development, aging, learning, disease and evolution. Frontiers in neuroinformatics 3: 25, 2009.

2 M.P. Laakso, et al. Hippocampal volumes in Alzheimer's disease, Parkinson's disease with and without dementia, and in vascular dementia: An MRI study. Neurology 46(3):678-681, 1996.

3 C.R. Jack, et al. The Alzheimer's disease neuroimaging initiative (ADNI): MRI methods. Journal of Magnetic Resonance Imaging 27(4):685-691, 2008.

4 B. Mortamet, M. Bernstein, J. C. Jack, J. Gunter, C. Ward, P. Britson, R. Meuli, J.-P. Thiran, and G. Krueger. Automatic Quality Assessment in Structural Brain Magnetic Resonance Imaging. Magnetic Resonance in Medicine 62:365–372, 2009.

5 P. Narayana, W. Brey, M. Kulkarni, and C. Sievenpiper. Compensation for surface coil sensitivity variation in magnetic resonance imaging. Magnetic Resonance Imaging 6:271–274, 1988.

6 K. Van Leemput, F. Maes, D. Vandermeulen, and P. Suetens. Automated model-based bias field correction of MR images of the brain. IEEE Transactions on Medical Imaging 18(10):885–896, 1999.

7 F. Schmitt. Correction of geometric distortion in MR Images. In Proceedings of the computer assisted radiology (CAR), pages 15–25. Springer, 1985.

8 A. Roche, D. Ribes, M. Bach-Cuadra, and G. Krueger. On the Convergence of EM-Like Algorithms for Image Segmentation using Markov Random Fields. Medical Image Analysis 15(6): 830–839, 2011.

9 D. Schmitter, A. Roche, B. Maréchal, D. Ribes, A. Abdulkadir, M. Bach-Cuadra, A. Daducci, C. Granziera, S. Klöppel, P. Maeder, R. Meuli, and G. Krueger. An evaluation of volume-based morphometry for prediction of mild cognitive impairment and Alzheimer's disease. NeuroImage: Clinical 7:7–17, 2014.

10 R. Migliaccio, et al. White matter atrophy in Alzheimer's disease variants. Alzheimer's & Dementia 8(5): S78-S87, 2012.

Contact



Alexis Roche, Ph.D.
Lead Clinical Research
Advanced Clinical Imaging Technology
Siemens Healthcare / CHUV / EPFL
HC CEMEA SUI DI BM PI

1015 Lausanne
Switzerland
Phone: +41 21 545 9972
alexis.roche@gmail.com

CS-VIBE – a Breakthrough in Ultrafast Dynamic Breast MRI

Ritse M. Mann; Suzan Vreemann

Radboud University Medical Centre, Department of Radiology, Nijmegen, the Netherlands

Abstract

In this article we present a compressed sensing (CS) – volume-interpolated breath-hold examination (VIBE) sequence[1] as a new approach for ultrafast dynamic breast MRI. Opposed to more common viewsharing techniques such as time resolved angiography with stochastic trajectories (TWIST), timepoints in CS-VIBE are independently obtained and therefore resolve the temporal blurring that is inherent to viewsharing techniques. The smart *k*-space filling of the CS-VIBE sequence allows for creation of high spatial resolution images from heavily undersampled data at an excellent temporal resolution of less than 5 seconds per volume obtained. As published previously [1] CS-VIBE allows acquisition of images at a similar quality as those obtained with TWIST at identical temporal resolution, but with a spatial resolution of 0.8 x 0.8 x 1.6 mm, thus more than halving the voxel size when compared to TWIST. This implies that CS-VIBE allows multiplanar reconstruction and assessment of morphologic lesion characteristics in multiple planes, which was so far not possible with viewsharing techniques.

Key points

- CS-VIBE allows ultrafast dynamic breast MRI at unprecedented spatial resolution
- CS-VIBE overcomes temporal blurring in ultrafast breast MRI
- Morphological lesion evaluation on CS-VIBE images is virtually identical to morphological lesion evaluation using conventional T1-weighted VIBE Dixon images

Background

Lately, interest in ultrafast dynamic breast MRI has surged. This is mainly due to the large improvements of MRI hardware and software that enabled the creation of high quality images at very high temporal resolution [2–5]. Already from studies in the early nineties it was evident that dynamic analysis of the inflow phase was more informative than late phase wash-out features [6]. However, initial approaches were single slice techniques and could therefore only be used to classify already known lesions at known locations. Around the shift of the century whole-breast acquisitions had become possible, albeit at spatial resolutions that still prevented most radiologists from actually looking at these images [7, 8]. Instead, the generated data was used for pharmacokinetic modeling using simple or more advanced iterations of the Tofts model [9, 10]. The thus obtained quantitative parameters were once again shown to yield more diagnostic information than wash-out features, and were complementary to morphologic assessment of lesion characteristics using the Breast Imaging Reporting and Data System (BIRADS) lexicon, or similar classification systems [7, 8, 11]. Especially K^{trans}, the transfer constant from the intravascular to the extravascular extracellular space proved to be a robust predictor of malignancy, being much higher in malignant than in benign lesions, which can be explained by the increased vascularization and the immaturity of these new-formed vessels in which the endothelial lining is often incomplete and sometimes even the basement membrane is lacking [12].

Nonetheless, the so-called 'quantitative' parameters still suffered from huge variation within patients and from site to site, mainly due to difficulties with the determination of a realistic arterial input function [13]. This is difficult due to the simple fact that in breast MRI no representative vessels that are large enough for measurements are present within the field-of-view. The common solution is to use a population based arterial input function, thus reducing the variation, but also the true quantitative aspect of the measurements. Alternative approaches make use of reference tissues, such as the pectoral muscle, but are likewise hampered by huge variations in the reference tissue due to the physical properties of the patients imaged [13, 14].

A further difficulty is that due to the limited spatial resolution maps of these pharmacokinetic parameters were not really sufficient for lesion detection, and use is therefore

[1] WIP. Cartesian CS-VIBE is currently under development and is not for sale in the US and in other countries. Its future availability cannot be ensured. CS GRASP-VIBE is 510(k) pending and may be used for the same purpose.

still limited to classification of otherwise detected lesions (and possible evaluation of the effects of primary systemic therapies), although the prerequisite of knowledge of lesion location is lifted by the whole-breast approach [7, 8, 11].

This largely shifted when modern viewsharing sequences became available that improved spatial and temporal resolution well beyond the borders of what was obtainable with keyhole based techniques [2–5]. In fact, it became possible to generate images within 5 seconds that met the international standards for diagnostic breast MRI, with a spatial resolution in plane of 1 x 1 mm, and a slice thickness of only 2.5 mm [5]. Suddenly it thus became possible to actually detect lesions on ultrafast dynamic breast MRI and perform classification based upon dynamic and morphologic features using the same images. By generating temporal maximum intensity projections (MIP), it has become possible to create an actual movie of contrast inflow; in general first highlighting the most suspicious finding in the breast ('the light bulb effect'), as these tend to enhance fastest.

In addition, a strong simplification of the interpretation of the dynamic data obtained, abandoning the pharmacokinetic model, but just looking at the slope of the enhancement curve, allows for much broader use of the ultrafast dynamic data, hardly without loss of its classifying properties [5, 15]. The rule of thumb is simple; the steeper the curve, the more likely that a lesion is malignant. Hence the maximum slope (MS) is an excellent tool for lesion classification. Furthermore, in analogy to the previously mentioned light bulb effect, the earlier a lesion enhances relative to the enhancement of the descending aorta, the more likely that it is malignant. This is captured in the 'time to enhancement' (TTE) [16]. In general most malignant lesions enhance within 15 seconds after aortic enhancement, whereas benign lesions enhance commonly later.

The excellent classifying properties of these simple inflow dynamics have since been confirmed by several studies using both radiologists and machine learning techniques. In one of the largest series to date, comparing 217 cancers to 172 benign lesions, Dalmis et al. reported that the overall classifying property of the inflow enhancement curve was 0.84, which compares favorably to most morphologic characteristics [17]. Moreover, this was robust over all types of malignant breast lesions, with only a slightly lower performance in ductal carcinoma in situ (DCIS) (Table 1).

Cancer type	n	Classifying property of dynamic features
DCIS	38	0.7690 (0.6728–0.8469)
IDC	141	0.8459 (0.7969–0.8893)
ILC	38	0.8673 (0.8018–0.9161)

Table 1: Classifying capacity of inflow dynamics for different types of malignant lesions. *Adapted from Dalmis et al. [17].*

Screening and abbreviated MRI

In the era of preventive and personalized medicine, screening for disease that is better treatable in its asymptomatic form is becoming more and more important. This is particularly true for breast cancer, which has an excellent prognosis when detected early [18].

Due to the excellent sensitivity of breast MRI for cancer screening trials already commenced in the late nineties, mainly in women at increased risk. Recent studies repeatedly report a sensitivity of MRI of approximately 90%, more or less doubling the sensitivity of mammography in the same populations [19, 20]. Also a stage shift of detected breast cancers is observed, making them smaller and thus easier to treat when detected by MRI [21].

Nonetheless, MRI screening, although internationally supported for all women with a lifetime risk of more than 20–25% [22], is in many countries reserved for women with hereditary breast cancer susceptibility genes or a history of chest radiation during puberty. This is mainly due to the inherent high costs of breast MRI, that have even increased over recent years by our aim to improve the specificity of the technique by adding sequences such as T2, diffusion and even spectroscopy on top of the conventional T1-weighted dynamic contrast-enhanced series.

This has led to the recent introduction of abbreviated scan protocols, that are aimed at lesion detection only, and are not specifically tailored to obtaining the best possible classification of eventual lesions. In screening this seems more than acceptable, as by far most of the scans are normal.

The simplest form of an abbreviated protocol was presented by Kuhl et al. in 2011 and suggested acquisition of only two T1-weighted acquisitions; one before, and one after contrast administration [23]. This acquisition protocol takes about 3 minutes and hence largely reduces the scan time needed for breast MRI that is in most practices at least a quarter of an hour. Subsequent generation of subtraction images and MIPs allowed for fast and accurate evaluation of the MRI acquisitions and did not reduce either sensitivity or specificity when compared to a full diagnostic protocol.

However, especially in screening women at somewhat increased risk morphological features of cancers can sometimes be deceptively benign. Hence abandoning all dynamic information on top of the lack of T2 and diffusion-weighted imaging (DWI) is unwanted if it is not really necessary.

Ultrafast breast MRI performed during and shortly after contrast examination might be used to overcome this issue. In women without lesions it is obviously unnecessary, but since it can be obtained without lengthening the protocol, it provides additional classification tools in women with breast lesions at no penalty in terms of acquisition time. In fact, when only ultrafast breast MRI is performed the acquisition time might be even further reduced to

approximately 2 minutes [5]. In a study presented by van Zelst et al. seven readers read 200 cases containing 31 MRI screen detected breast lesions and 54 biopsied benign lesions using only ultrafast breast MRI (TWIST) and using a full diagnostic protocol (FDP) consisting of high-resolution T1-weighted acquisitions before and after contrast administration, T2, and DWI [24]. Overall, sensitivity between the two techniques was equal (84%, vs 86%, ns.), whereas specificity was in fact higher using only TWIST than the FDP (81% vs 76%, p<0.001). This unambiguously shows that ultrafast breast MRI has high potential as screening technique.

Still, rather than choosing either the simple abbreviated approach or the ultrafast approach it is possible to combine the techniques in a short hybrid protocol, interleaving a number of ultrafast acquisitions in between the two high-resolution T1-weighted series during contrast administration, without lengthening the acquisition time of the simple approach. Such a hybrid protocol allows for very fast and simple evaluation in women without breast lesions, but enables both morphologic assessment and dynamic analysis of the contrast inflow in women with abnormalities.

Compressed sensing VIBE

The rationale for a hybrid protocol implies that there are still shortcomings of the current ultrafast techniques available. These are present both in the spatial and the temporal domain. In terms of spatial resolution TWIST might achieve a diagnostic level according to international standards; but the slice thickness of 2.5 mm still limits the possibility of multiplanar reconstruction, and thus assessment of morphological features and lesion extent in other planes than the axial slices usually obtained. In terms of temporal resolution viewsharing inherently causes some temporal blurring and thus less reliable dynamic information, despite the successes that have been achieved so far.

	CS-VIBE
TR (ms)	4.47
TE (ms)	2.06
FA (°)	15
Field-of-view (mm²)	358.4 x 358.4
Matrix size	448 x 381
TWIST central region A (%) / Sampling density B (%)	-
Slice thickness (mm)	1.6
Voxel volume (mm³)	1.024
Phase resolution (%)	85
Slice resolution (%)	70
Acceleration factor	20
Acceleration mode	CS
Time resolution per volume (s)	4.55
Total acquisition time (min)	1:40

Table 2: Parameters of the prototype CS-VIBE sequence.[1]

By shifting the acquisition from a viewsharing approach to compressed sensing several of these limitations are overcome. CS VIBE incoherently subsamples the phase-encoding plane with variable density, obeying a Gaussian distribution in which the density is higher in the center of *k*-space than at its borders. Despite the sparsity of the sampling technique adequate images can be reconstructed by optimization of a cost-function. Since volumes are independently obtained per time point no temporal blurring is present. Furthermore, a spatial resolution is achieved of 0.8 x 0.8 x 1.6 mm. Parameters of the prototype CS-VIBE sequence are presented in Table 2.

In a reader study by Vreemann et al. presented at this years ISMRM [25], it was shown that image quality of the CS-VIBE is equal to that of TWIST, despite the fact that the voxel volumes are more than halved. Artifacts between sequences are somewhat different. TWIST is particularly known for infolding and ghosting artifacts, likely directly caused by the viewsharing; CS-VIBE seems somewhat more prone to pulsation artifacts from the heart, which are particularly seen in the axillary region. The image quality of CS-VIBE almost approaches that of the conventional VIBE Dixon acquisitions with a spatial resolution of 0.9 x 0.9 x 1 mm, acquired in 91 seconds (Fig. 1).

Morphological lesion evaluation based on the CS-VIBE was compared to evaluation of lesion morphology on VIBE Dixon and results were virtually identical, showing the excellent capability of morphological assessment on CS-VIBE acquisitions alone, which is enabled by the possibility to create multiplanar reconstructions of the acquired volume. In addition it becomes possible to create rotating MIPs; although these might not be very essential for diagnostic practice, they certainly improve the clarity of the scan when explaining the findings to treating physicians, in particular surgeons (Fig. 2).

Currently, the implementation of CS-VIBE in clinical practice is still somewhat limited by the required reconstruction time of approximately 45 minutes on the scanner. This implies that images cannot be generated during the daily program, but instead image generation has to be performed over night. While for screening this might not be a real problem, in the sense that there is in general no reason why scans could not be read one day after acquisition. However, it still prevents the technologists from controlling the quality of their work. Future advances in the calculating capacity of work-stations used for image generation will however likely resolve this issue.

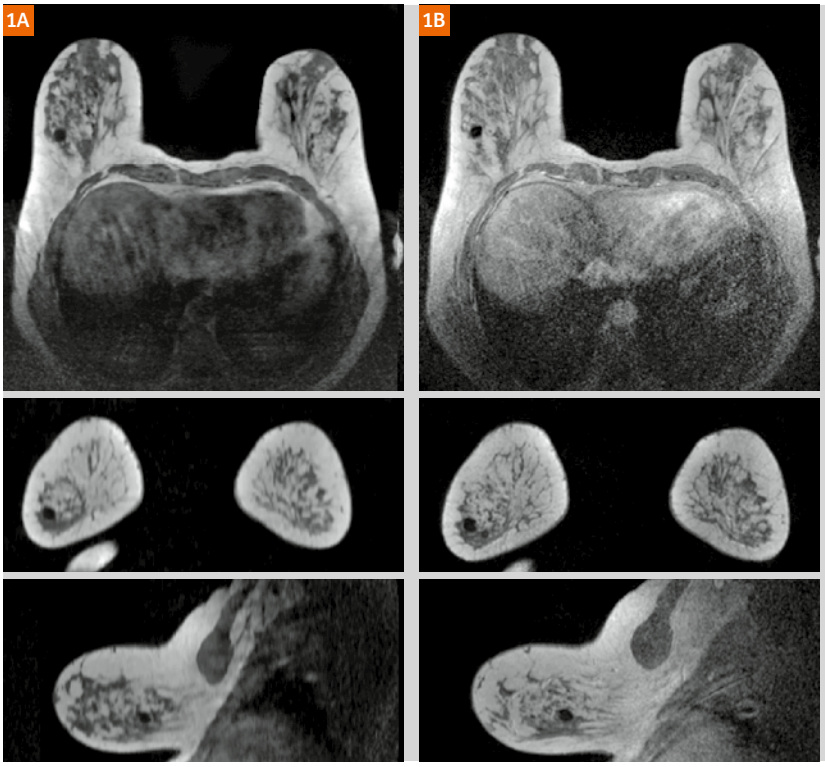

Figure 1: A comparison of image quality between the CS-VIBE **(1A)** and VIBE Dixon **(1B)** in multiple planes. Even though the VIBE Dixon acquisition is still somewhat sharper, morphological evaluation of structures within the breast is almost identical in all directions.

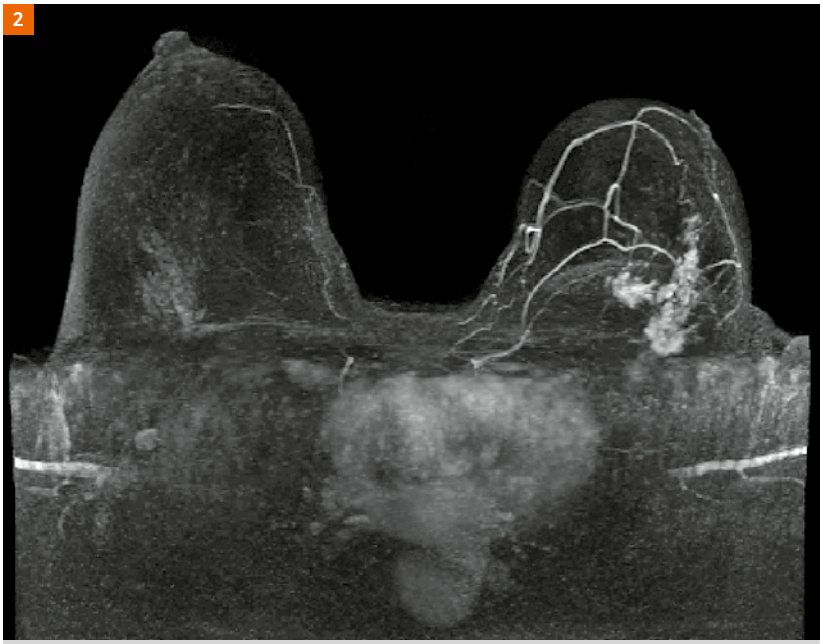

Figure 2: A maximum intensity projection image obtained from the first and last CS-VIBE acquisition, showing with high morphological detail a multifocal cancer in the left breast with marked vascular asymmetry.

In conclusion, CS-VIBE is a major step forward in ultrafast breast MRI; for the first time allowing high quality image generation at a spatial resolution that enables multiplanar reformatting, without temporal blurring and within 5 seconds. CS-VIBE therefore brings screening with ultrafast breast MRI alone one step closer.

References

1 Vreemann S, Rodriguez-Ruiz A, Nickel D, Maas M, Karssemeijer N, Weiland E, Kiefer B, Mann R. Advanced Ultrafast Dynamic Contrast Enhanced Breast MRI with Compressed Sensing VIBE. Proceedings of the 25th Annual Meeting of ISMRM, p. 2670, Honolulu, HI, USA, April 2017.

2 Herrmann KH, Baltzer PA, Dietzel M, Krumbein I, Geppert C, Kaiser WA, Reichenbach JR. Resolving arterial phase and temporal enhancement characteristics in DCE MRM at high spatial resolution with TWIST acquisition. J Magn Reson Imaging. 2011 Oct;34(4):973-82.

3 Tudorica LA, Oh KY, Roy N, Kettler MD, Chen Y, Hemmingson SL, Afzal A, Grinstead JW, Laub G, Li X, Huang W. A feasible high spatiotemporal resolution breast DCE-MRI protocol for clinical settings. Magn Reson Imaging. 2012 Nov;30(9):1257-67.

4 Le Y, Kipfer H, Majidi S, Holz S, Dale B, Geppert C, Kroeker R, Lin C. Application of time-resolved angiography with stochastic trajectories (TWIST)-Dixon in dynamic contrast-enhanced (DCE) breast MRI. J Magn Reson Imaging. 2013 Nov;38(5):1033-42.

5 Mann RM, Mus RD, van Zelst J, Geppert C, Karssemeijer N, Platel B. A novel approach to contrast-enhanced breast magnetic resonance imaging for screening: high-resolution ultrafast dynamic imaging. Invest Radiol. 2014 Sep;49(9):579-85.

6 Boetes C, Barentsz JO, Mus RD, van der Sluis RF, van Erning LJ, Hendriks JH, Holland R, Ruys SH. MR characterization of suspicious breast lesions with a gadolinium-enhanced TurboFLASH subtraction technique. Radiology. 1994 Dec;193(3):777-81.
7 Veltman J, Stoutjesdijk M, Mann R, Huisman HJ, Barentsz JO, Blickman JG, Boetes C. Contrast-enhanced magnetic resonance imaging of the breast: the value of pharmacokinetic parameters derived from fast dynamic imaging during initial enhancement in classifying lesions. Eur Radiol. 2008 Jun;18(6):1123-33.
8 Pinker K, Grabner G, Bogner W, Gruber S, Szomolanyi P, Trattnig S, Heinz-Peer G, Weber M, Fitzal F, Pluschnig U, Rudas M, Helbich T. A combined high temporal and high spatial resolution 3 Tesla MR imaging protocol for the assessment of breast lesions: initial results. Invest Radiol. 2009 Sep;44(9):553-8.
9 Tofts PS, Berkowitz B, Schnall MD. Quantitative analysis of dynamic Gd-DTPA enhancement in breast tumors using a permeability model. Magn Reson Med. 1995 Apr;33(4):564-8.
10 Brix G, Kiessling F, Lucht R, Darai S, Wasser K, Delorme S, Griebel J.Microcirculation and microvasculature in breast tumors: pharmacokinetic analysis of dynamic MR image series. Magn Reson Med. 2004 Aug;52(2):420-9.
11 Huang W, Tudorica LA, Li X, Thakur SB, Chen Y, Morris EA, Tagge IJ, Korenblit ME, Rooney WD, Koutcher JA, Springer CS Jr. Discrimination of benign and malignant breast lesions by using shutter-speed dynamic contrast-enhanced MR imaging. Radiology. 2011 Nov;261(2):394-403.
12 Saaristo A, Karpanen T, Alitalo K. Mechanisms of angiogenesis and their use in the inhibition of tumor growth and metastasis. Oncogene. 2000 Dec 11;19(53):6122-9.
13 Heisen M, Fan X, Buurman J, van Riel NA, Karczmar GS, ter Haar Romeny BM. The use of a reference tissue arterial input function with low-temporal-resolution DCE-MRI data. Phys Med Biol. 2010 Aug 21;55(16):4871-83.
14 Stoutjesdijk MJ, Zijp M, Boetes C, Karssemeijer N, Barentsz JO, Huisman H. Computer aided analysis of breast MRI enhancement kinetics using mean shift clustering and multifeature iterative region of interest selection. J Magn Reson Imaging. 2012 Nov;36(5):1104-12.
15 Platel B, Mus R, Welte T, Karssemeijer N, Mann R. Automated characterization of breast lesions imaged with an ultrafast DCE-MR protocol. IEEE Trans Med Imaging. 2014 Feb;33(2):225-32.
16 Mus RD, Borelli C, Bult P, Weiland E, Karssemeijer N, Barentsz JO, Gubern-Mérida A, Platel R, Mann RM. Time to enhancement derived from ultrafast breast MRI as a novel parameter to discriminate benign from malignant breast lesions. European Journal of Radiology, Vol. 89, p90–96
17 Dalmış MU, Gubern-Mérida A, Vreemann S, Karssemeijer N, Mann R, Platel B. A computer-aided diagnosis system for breast DCE-MRI at high spatiotemporal resolution. Med Phys. 2016 Jan;43(1):84.
18 Saadatmand S, Bretveld R, Siesling S, Tilanus-Linthorst MM. Influence of tumour stage at breast cancer detection on survival in modern times: population based study in 173,797 patients. BMJ. 2015 Oct 6;351:h4901.
19 Kuhl C, Weigel S, Schrading S, Arand B, Bieling H, König R, Tombach B, Leutner C, Rieber-Brambs A, Nordhoff D, Heindel W, Reiser M, Schild HH. Prospective multicenter cohort study to refine management recommendations for women at elevated familial risk of breast cancer: the EVA trial. J Clin Oncol. 2010 Mar 20;28(9):1450-7.
20 Sardanelli F, Podo F, Santoro F, Manoukian S, Bergonzi S, Trecate G, Vergnaghi D, Federico M, Cortesi L, Corcione S, Morassut S, Di Maggio C, Cilotti A, Martincich L, Calabrese M, Zuiani C, Preda L, Bonanni B, Carbonaro LA, Contegiacomo A, Panizza P, Di Cesare E, Savarese A, Crecco M, Turchetti D, Tonutti M, Belli P, Maschio AD; High Breast Cancer Risk Italian 1 (HIBCRIT-1) Study.. Multicenter surveillance of women at high genetic breast cancer risk using mammography, ultrasonography, and contrast-enhanced magnetic resonance imaging (the high breast cancer risk italian 1 study): final results. Invest Radiol. 2011 Feb;46(2):94-105.
21 Rijnsburger AJ, Obdeijn IM, Kaas R, Tilanus-Linthorst MM, Boetes C, Loo CE, Wasser MN, Bergers E, Kok T, Muller SH, Peterse H, Tollenaar RA, Hoogerbrugge N, Meijer S, Bartels CC, Seynaeve C, Hooning MJ, Kriege M, Schmitz PI, Oosterwijk JC, de Koning HJ, Rutgers EJ, Klijn JG. BRCA1-associated breast cancers present differently from BRCA2-associated and familial cases: long-term follow-up of the Dutch MRISC Screening Study. J Clin Oncol. 2010 Dec 20;28(36):5265-73.
22 Mann RM, Kuhl CK, Kinkel K, Boetes C. Breast MRI: guidelines from the European Society of Breast Imaging. Eur Radiol. 2008 Jul;18(7):1307-18.
23 Kuhl CK, Schrading S, Strobel K, Schild HH, Hilgers RD, Bieling HB. Abbreviated breast magnetic resonance imaging (MRI): first postcontrast subtracted images and maximum-intensity projection-a novel approach to breast cancer screening with MRI. J Clin Oncol. 2014 Aug 1;32(22):2304-10.
24 Van Zelst J, Gubern-Merida A, Vreemann S, Veltman J, Dorrius M, Loo C, Duvivier-van Hoof K, Karssemeijer N, Mann RM, High Risk Breast Cancer Screening with an Ultrafast High Spatiotemporal Resolution MRI Sequence; Less Costly and as Reliable as a Full Diagnostic MRI Protocol. Radiological Society of North America 2016 Scientific Assembly and Annual Meeting, November 27 - December 2, 2016, Chicago IL. archive.rsna.org/2016/16014917.html
25 Vreemann S, Rodriguez-Ruiz A, Nickel D, Maas MC, Karssemeijer N, Weiland E, Kiefer B, Mann RM. Advanced Ultrafast Dynamic Contrast Enhanced Breast MRI with Compressed Sensing VIBE. ISMRM 2017, abstract number 445

Contact

Ritse Mann
Radboud University Medical Centre
Department of Radiology

huispost 766
P.O. Box 9101
6500 HB
Nijmegen
the Netherlands
ritse.mann@radboudumc.nl

Suzan Vreemann
Radboud University Medical Centre
Department of Radiology

huispost 766
P.O. Box 9101
6500 HB
Nijmegen
the Netherlands
suzan.vreemann@radboudumc.nl



Pioneers of Connectome Gradients

Ralph Kimmlingen

Siemens Healthineers, HC DI MR TR R&D-PL, Erlangen, Germany

Abstract

A typical human brain contains 100 billion neurons which have about 10,000 individual connections with their neighbors. Being able to map structural and functional connectivity of an individual brain could be a first step on a new way of understanding and diagnosing mental illnesses. Continuous improvements on noninvasive magnetic resonance imaging (MRI) methods like functional MRI, resting-state MRI, and diffusion MRI enable this information (connectomics) to be obtained for the first time on a large human databasis. A key parameter is the available gradient field strength for diffusion-sensitive MRI sequences [1–3]. Siemens MR has developed two powerful prototype gradient systems for this purpose, which have been employed at five different locations in the US and Europe since 2011 (Fig. 1).

Up to today, the nervous system circuit diagram ('Connectome') of few creatures is known. Back in the early 1980s the little roundworm called *C. elegans* was discovered to have a nervous system of roughly 300 neurons showing a total of about 7,000 connections [4, 5]. Using invasive anatomical and neural-tracing techniques, mammalian brains like that of mice or primates are still under investigation. These methods are capable of an in-plane resolution of 40 µm [6, 7].

New non-invasive imaging methods which enable the study of brain connectivity of living humans have been developed since the beginning of this century. They are known as MR Imaging of anisotropic diffusion of water in the brain, and resting state fMRI [8–10]. The related advances in imaging technologies and data evaluation are empowering us today to study the human brain as an entire organ.

A group known as 'Blueprint for Neuroscience Research', a collaboration among 15 National Institutes of Health (NIH) in Bethesda, Maryland, USA, decided in 2009 to fund a five-year initiative for mapping the brain's long-distance communications network. The goal of the so called Human Connectome Project (HCP) was set to construct a map of the structural and functional neural connections *in vivo* within and across individuals. The HCP was funded with $40 million and comprised two research efforts: the first, a five-year project at the Center for Magnetic Resonance Research (CMRR) in Minneapolis, Minnesota, in collaboration with Washington University, St. Louis,

1

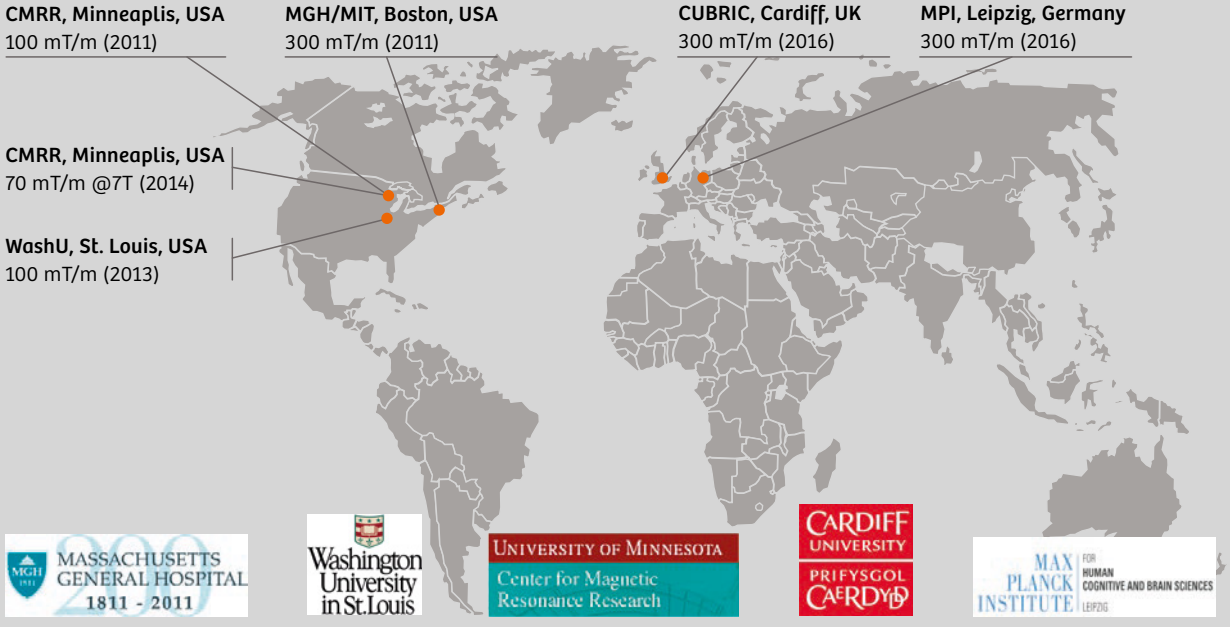

Figure 1: MAGNETOM Connectom scanners by Siemens Healthcare have been employed at five different locations since 2011.

2

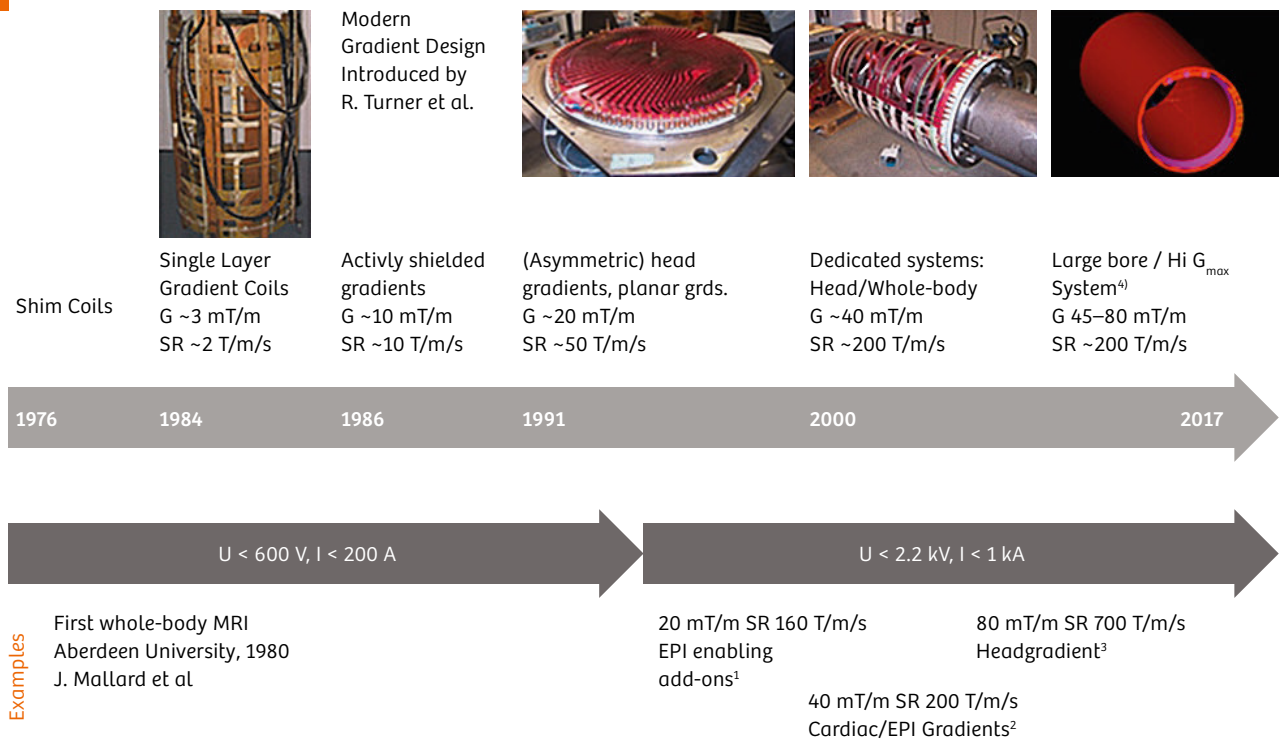

Figure 2: Gradient history of MRI systems.

[1] Cohen MS, Weisskoff RM. MRM. 1991; [2] Schmitt F, Eberlein E. et al. ISMRM, 1999; [3] Vom Endt A et al. ISMRM, 2006;
[4] Equals an increase of gradient power (slewrate x amplitude) of three magnitudes over 20 years.

Missouri, and the second a 3-year project at the Massachusetts General Hospital's (MGH) Martinos Center in cooperation with the University of California, Los Angeles. A comprehensive description for the HCP can be found in a 2012 *Nature* article [11].

In order to map the human connectomics, the Washington University & the University of Minnesota (WashU-Minn) consortium, utilized resting state fMRI and high angular resolution diffusion imaging (HARDI) – a special diffusion imaging technique. However, Diffusion Spectrum Imaging (DSI) – a general form of Diffusion Tensor Imaging that was pioneered in 2005 at the Massachusetts General Hospital (MGH) – was the method of choice for the MGH/University of California at Los Angeles (UCLA) consortium. To pursue this challenging task, both of these consortiums approached Siemens Healthineers to propose working together in hardware technology, more specifically in special gradient systems, which will enable the demanding diffusion imaging.

More recently, two European research centers have joined the exclusive club of Connectome gradient users. In 2016, the Cardiff University Brain Research Imaging Centre (CUBRIC), equipped with a 300 mT/m MAGNETOM Connectom, two 3T MAGNETOM Prisma and a MAGNETOM 7T system[1], was inaugurated by Queen Elizabeth II. At the end of 2016, the Max Planck Institute for Human Cognitive and Brain Sciences, Leipzig, Germany, also installed a MAGNETOM Connectom 3T MRI system[1].

Gradient technology

Siemens Healthcare introduced the first MAGNETOM 0.35T whole-body scanner in 1983 and has continuously extended the product portfolio with higher magnet and gradient field strengths. Starting with a peak amplitude (G_{max}) of 3 milli-Tesla per meter (mT/m) and a slew rate (SR) of 2 T/m/s in the early 1980s, today's (2017) clinical high-end 3T scanner MAGNETOM Prisma achieves a G_{max} of 80 mT/m and a SR of 200 T/m/s (see Fig. 2). Gradient system performance depends on many opposing factors including G_{max}, SR, linearity volume (LV) and available patient bore diameter. Highest performance demands are created by diffusion-weighted sequences which expect fast gradient switching for the readout pulses, highest peak amplitude / duty cycle for the diffusion pulses, and excellent shielding of eddy fields. As a consequence, gradient coils optimized for whole-body applications with a large linearity volume and inductance require high-voltage/-current power supplies. Starting with the first applications of the EPI imaging method in the early 1990s [12], especially gradient

[1] MAGNETOM Connectom and MAGNETOM 7T is ongoing research. All data shown are acquired using a non-commercial system under institutional review board permission. Siemens does not intend to commercialize the system.

3

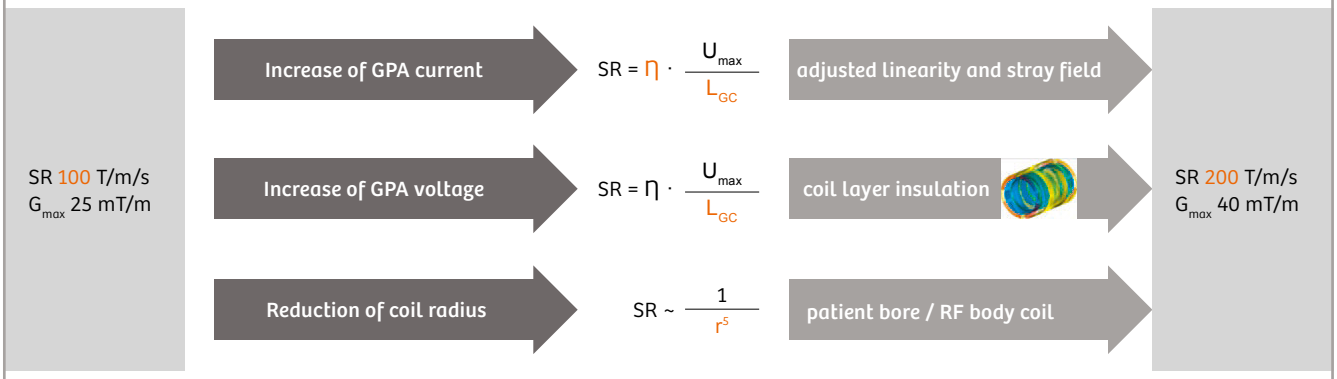

Figure 3: Improved gradient performance parameters (maximum gradient amplitude (G_{max}) or slew rate (SR)) can be achieved by either increasing gradient amplifier (GPA) power (via maximum voltage U_{max}) and adjusting the coil design (via field efficiency (Π) or inductance (L_{GC})) or by a reduction of the coil radius (r) and adjustments to the RF body coil and/or the patient bore diameter.

4

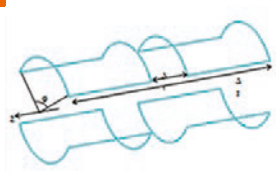

Biot Savart Methods
Maxwell / Golay design
analytical expressions
building blocks (still used)

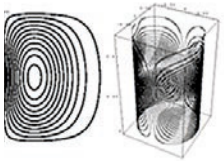

Current Density methods[2]
Target field / spherical harmonics
active screening / min. inductance
stream function discretization
(analytical & matrix based)

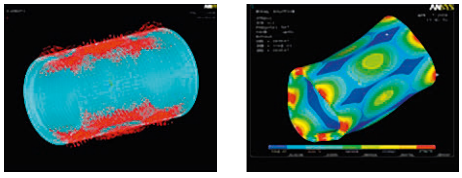

Additional methods
Lorentz force / moment compensation
stray field forming / eddy current reduction
heat & power minimization
geometry-specific (e.g. split/oval)

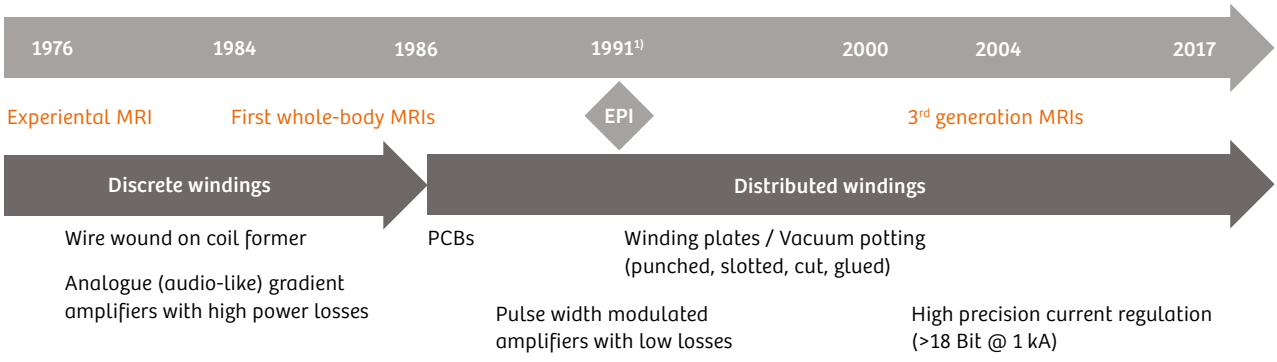

Figure 4: History of gradient coil design methods.

[1] In 1991, PNS (peripheral nerve stimulation) proves to limit gradient performance (predicted by T. Budinger 1979);
[2] R. Turner, Gradient Coil Design, A Review of Methods, MRM 11:903 (1993)

slew rate became a challenge for gradient system design. First attempts to reduce the rise time of EPI readout gradients involved additional resonant circuits, so-called 'EPI boosters' [13, 14].

With conventional gradient design methods [15, 16], SR increase (at otherwise constant parameters) can be achieved by either increasing the voltage of the power amplifier (GPA) or by reducing the inductance of the coil. Besides using more than a single amplifier and coil-set [17], the third alternative for higher SR is to reduce the inner radius of the coil system (Fig. 3). The strong (5th order) dependence of the SR from the coil radius leads to about a factor of two increase when changing from 70 cm to 60 cm patient bore. Thus, this parameter is a crucial part of the MR system concept definition. It emphasizes the importance of efficient use

of radial space inside the magnet bore. The best gradient performance is achieved by using only the necessary number of windings driven by the highest available current. In practice, the maximum current is mainly limited by power amplifier technology, forces on gradient connectors, wire cross section, and cooling efficiency. Additional design targets like shielding efficiency, force/torque compensation, and acceptable nonlinearities of the linear gradient field tend to increase the required number of windings, making up the challenge to the coil designer (Fig. 4).

5

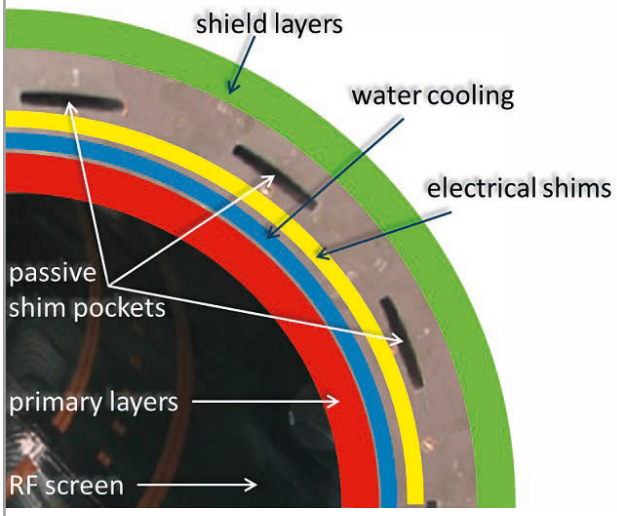

Figure 5: Layer breakdown of a cylindrical gradient coil system including passive iron shim.

Cylindrical symmetry dominates today's gradient coils. Coil geometry mostly follows the boundary conditions set by the main magnet design. Insert gradients could be designed without following the basic symmetry of the main magnet, but hardly do so. Due to the non-ideal nature of magnet and gradient fields (e.g. concomitant fields, forces, and torques), it is always advantageous to keep as many symmetries as possible. Dedicated insert gradients for different body parts are known (for example spine or knee [18]), but have not been successful in replacing their big brothers. Electrical and mechanical design aspects of non-cylindrical geometries are not very different from the standard configurations. For example, the target field method could be applied to calculate the primary and the shields' current density on a circular plane. The wire pattern and axial connections are generated by extracting the contour lines of their stream function. The same method can be applied to generate the wire pattern for the electrical shim coils. The gradient system thus consists of a variety of complex subcomponents, each forming a subsystem of its own (Fig. 6). The coil system (Fig. 5) comprises the linear field coils (X, Y, Z) including their shielding coils, higher-order shim coils, cooling layers, temperature sensors, RF screen, current and water connectors, the coil support structure, and its suspension.

Magnetic field generation with high amplitudes and large volumes is a difficult task. Considering that the natural

6

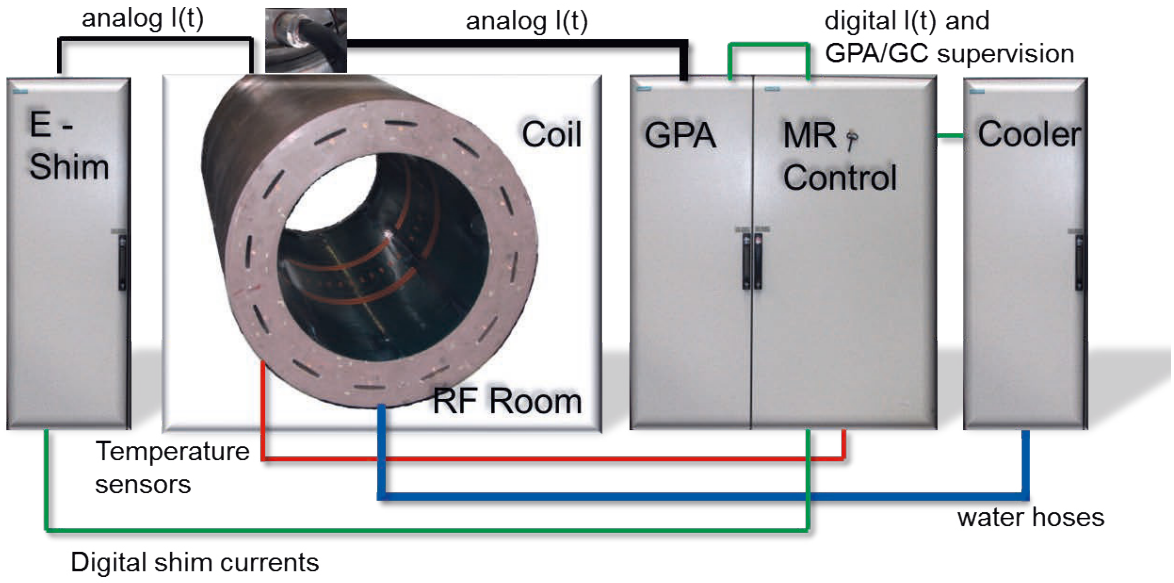

Figure 6: The gradient system consists of a coil system, a cooling system, a gradient power amplifier (GPA), a shim amplifier, and a gradient control system as part of the MR control system.

7

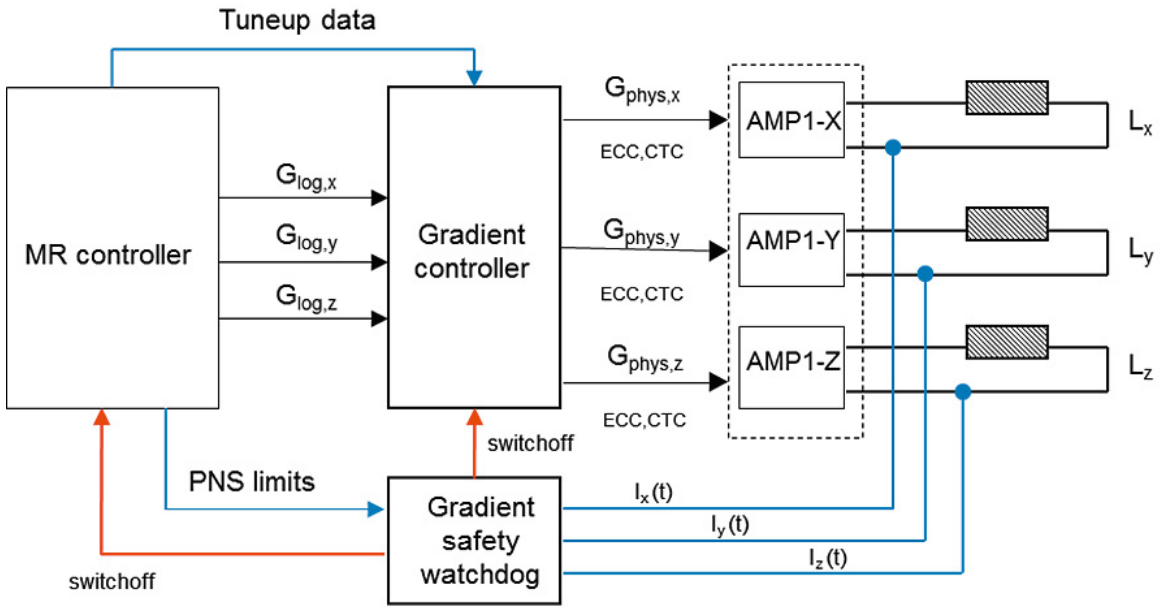

Figure 7: Control system of a typical MR scanner and its interface to the gradient controller. The gradient controller and the PNS safety watchdog are fed with logical gradient shapes (G_{log}) and gradient-coil-specific limits for peripheral nerve stimulation. The logical shapes are converted to physical shapes (G_{phys}) and modified by filter functions for eddy current and cross-term compensation (ECC and CTC) before being fed to the gradient amplifier's final stages (Amp X, Y, Z). The current in the gradient circuit with the coil impedance L is measured by high precision current probes and fed to the gradient safety watchdog unit. In case the PNS limit is exceeded, a safety switch-off signal is sent to the gradient and MR controller.

8

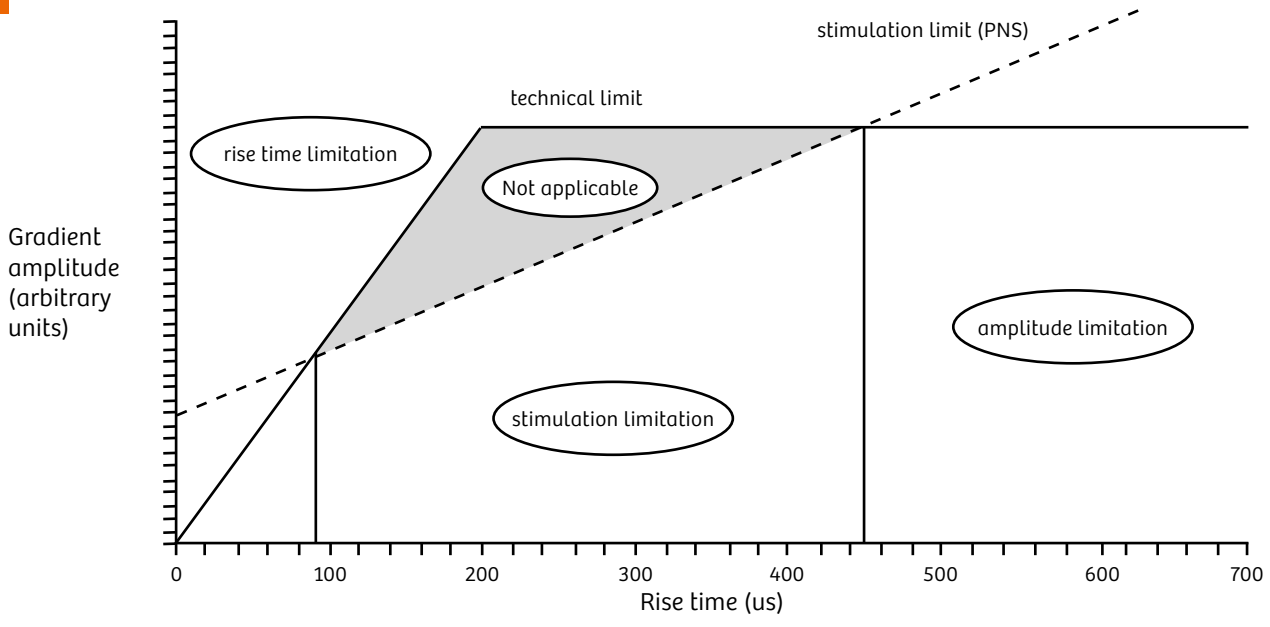

Figure 8: Limitations of gradient system performance for human use. The main limitation is given by the peripheral nerve stimulation threshold (PNS limit). If the technical performance of the gradient system is not adapted to this limit, a significant part of the parameter space is not applicable to human subjects.

(earth) magnetic field is about 50 uT in amplitude, the first whole-body gradient coils had to exceed this by two orders of magnitude. In one embodiment, wooden structures were used to support the race-track-like windings (Fig. 2). Furthermore, rapid gradient switching leads to strong vibrations due to the Lorentz forces of the conductors within the main magnetic field. This can be counteracted by increased stiffness of the support structures (e.g. with glass-fiber-reinforced plastic) and linking of all layers to a single body (e.g. with epoxy resin). In addition, dielectric strength of all gradient layers is required at minimal (<2 mm) radial distance of the conductors. Hence, today's gradient coils mainly consist of epoxy resin with excellent dielectric strength at low cost and high geometric flexibility. The challenge in the fabrication process is to ensure that all layers and subcomponents of the coil system are impregnated 100%. This can only be achieved with a complex vacuum potting procedure. Every step of this procedure needs to be defined and controlled thoroughly [19]. Process and material parameters like temperature profile, filling material, and filling percentage as well as curing time need to be adjusted to the geometry and inner structure of the gradient coil main body. A successful potting procedure is usually validated with a high voltage or electrical discharge test. This step ensures that the dielectric strength is good enough to withstand amplifier voltages of up to several kilovolts for an MR system's lifetime.

The control system of an MR scanner synchronizes and drives the activities of all hardware components (Fig. 7). The interface of the MR controller to a logical hardware component usually requires a sub control system of its own. The gradient controller and the Peripheral Nerve Stimulation (PNS [20]) safety watchdog are fed with logical gradient shapes (read, phase, slice) and gradient-coil-specific limits for PNS, respectively. Static correction data acquired during the first startup phase of the MR scanner ('Tune-up data') is transferred to the gradient controller and GPA before the start of the measurement sequence.

After the start of a gradient pulse sequence, the logical gradient shapes are converted into physical gradient shapes. In order to minimize eddy current effects, additional filters based on tune-up data may be applied to the gradient circuit current I(t) before transfer to the gradient amplifier component (e.g. eddy current pre-emphasis). The output of the gradient amplifier circuit is monitored by high-precision current sensors. Their signal is used for control and supervision of the gradient amplifier cabinet including PNS. The limits for human exposure to time-varying magnetic fields are defined by the IEC norm and need to be ensured based on calculations and measurements (Fig. 8).

Ultra-high gradient strength

The first decade of the new millennium brought the benefits of parallel imaging methods from research machines to clinical MRI scanners. Today (2017), most sequences make use of acquisition methods with measurement time reduction (or, in case of EPI, readout time reduction). Although the demand for high gradient amplitudes for diffusion imaging techniques is still unbowed, the advantage of ultra-high gradient slew rates now has a serious competitor.



Figure 9: Gradient insert 'AC88'. **(9A)** Test of the handling device at a 3T scanner. **(9B)** Reduced size of patient bore after installation of the coil.

Implementation of ultra-high gradient amplitudes with head-sized gradients inside a whole-body magnet bore is one approach to tackle the problem [21]. The advantage of simultaneous ultra-high slew rate and gradient amplitude is counteracted by the limited space inside the coil (Fig. 9). It is difficult to design a combined transmit/receive RF coil with >8 receive channels, good intra-channel decoupling, and high SNR due to the close proximity to the copper windings of the gradient coil. Separating the transmit coil is even more challenging, as this requires additional radial space for the RF return flux. In addition, patient handling is difficult. It is not easy to find volunteers who are willing to expose themselves to the near-claustrophobic conditions of such an experimental device. Even with asymmetric gradient design, the limited size of the shoulder cutouts will exclude part of the normal population from being scanned.

In diffusion imaging of the brain, long-lasting diffusion weighting gradient lobes are applied. The highest possible gradient amplitude is applied in the shortest possible time, combined with an echo-planar imaging (EPI) pulse sequence to encode diffusion and minimize head motion at the shortest possible echo time (TE). Typical TEs for b = 1,000 s/mm^2 on a 3T whole-body scanner are around 70–80 ms when Stejskal-Tanner encoding is applied without additional parallel imaging techniques. Higher b-values can only be achieved with a penalty in SNR, as TE increases with the duration of the diffusion lobe. Studies on mammals have indicated that much higher gradient strength than 40 mT/m would be required to produce sharp diffusion images of an adult human brain's wiring patterns [22]. Typical small-bore (about 100 mm) NMR scanners can apply 150–300 mT/m. Owing to the nonlinear increase of gradient strength with reduction of the inner diameter, even 1,000 mT/m (at 60 mm bore) are not uncommon. This reopened the question whether ultra-high gradient strength (>100 mT/m) may be achievable with a whole-body gradient design.

10

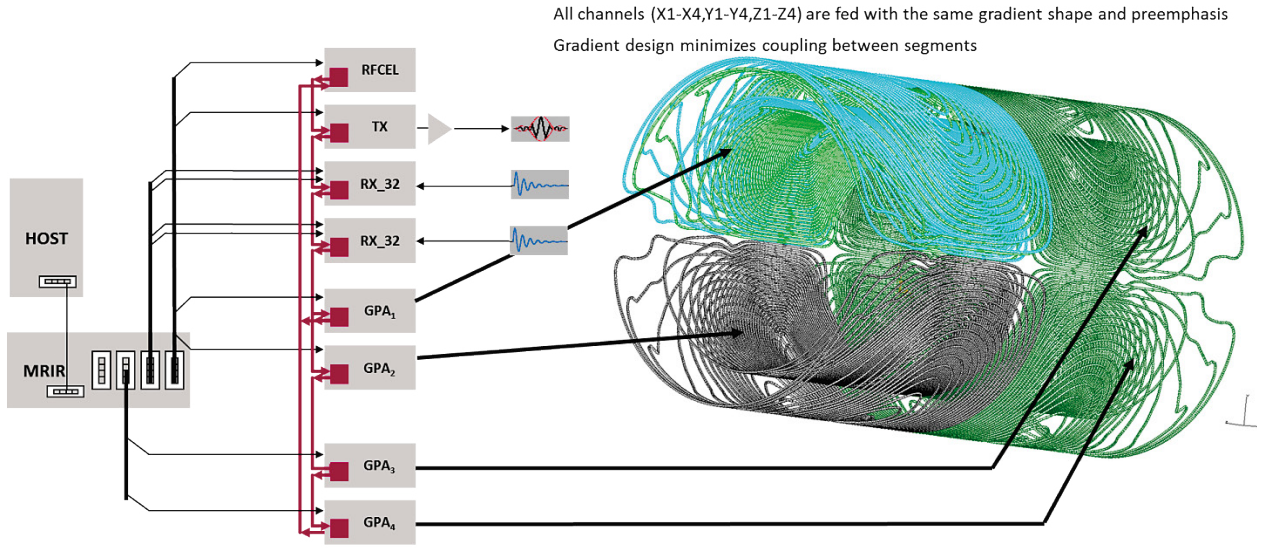

Figure 10: Control system concept for the 300 mT/m gradient. The MR control system (host computer HOST, image reconstruction computer MRIR) was extended to drive four sets of gradient amplifiers independently. The new architecture allows storing the calibration data for each of the 12 final stages driving the gradient coil segments.

The design target for a whole-body gradient was set to high gradient amplitudes with the linearity volume (LV) being limited to the brain volume (thus achieving less restrictive PNS thresholds). Two versions of this gradient design were designed and built. Version 1 (SC72) supports a G_{max} of 100 mT/m at SR 200 T/m/s with a single GPA cabinet (2 kV, 1 kA). It was designed to match forces and stray field of a 3T magnet and provide space for passive iron shims. It has a length of 158 cm, and an inner diameter of 64 cm. This yielded a robust, easy-to-use diffusion engine [23].

Version 2 (AS302) represents a quantum leap in whole-body gradient performance, i.e. G_{max} of 300 mT/m at SR 200 T/m/s. Design studies with reduced linearity constraints showed that up to 150 mT/m could be reached with a single gradient power amplifier. A further increase of gradient strength within conventional design constraints would have imposed duty cycle limitations, which are not favorable for diffusion applications. Due to the large volume of the coil body, the number of current density layers and thus the gradient strength could be doubled to 300 mT/m. As a consequence of the mutual coupling of the four primary and secondary layers per axis, coil inductance increased by more than a factor of two. To drive this high inductance at the SR 200 T/m/s needed for EPI readout, a new gradient system concept involving multiple gradient amplifiers was developed. In order to achieve the target slew rate, each of the three axes X, Y, Z was split into four independently driven segments (Fig. 10). Stray field and forces were matched to the 3T magnet used. The MR control system was extended to drive four sets of gradient amplifiers independently. The new architecture allows storing the calibration data for each of the 12 final stages driving the gradient coil segments. The gradient waveform is logically split and fed to four individual gradient controllers. This architecture also allows generating arbitrary field characteristics for each gradient coil axis, used to optimize eddy current compensation.

The GPA regulator architecture was extended to account for the dynamic differential control (D) of the driving signal. This allows counteracting the induced voltages in each segment coil due to mutual coupling. A new RF body coil was developed (capable of TrueForm excitation) which allows the use of the existing clinical patient table with minor

11

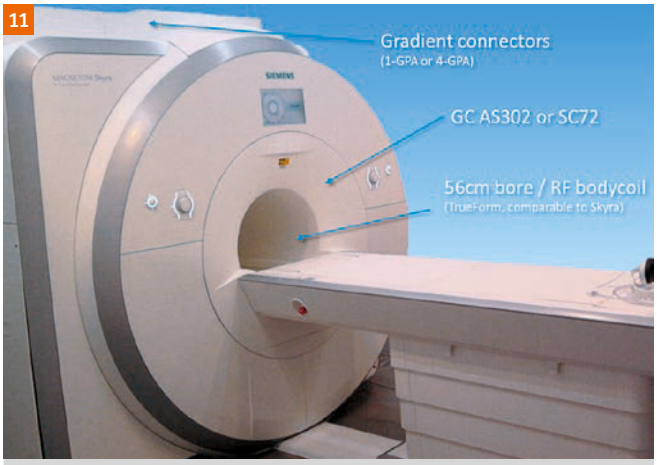

Figure 11: Modified MAGNETOM Skyra system. Dimensions of the RF body coil, patient table and cover were adjusted to the size requirements of both Connectom gradient coils.

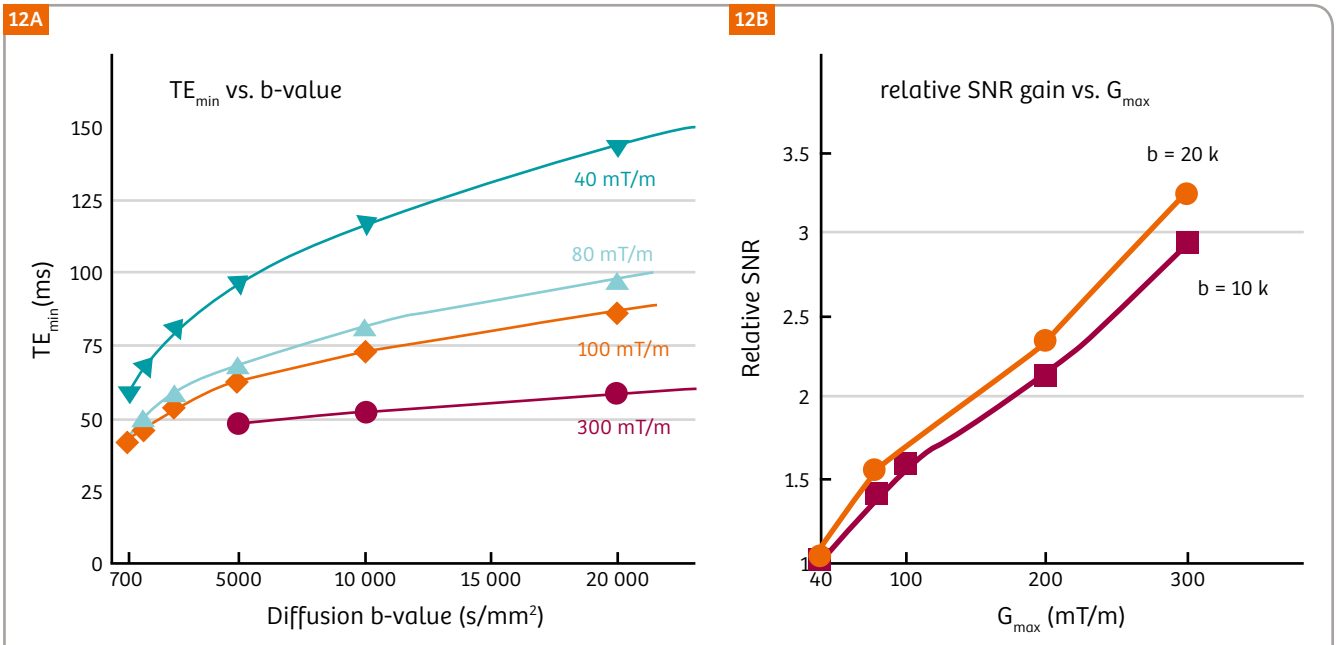

Figure 12: (12A) Minimum TE for a Skeskjal Tanner diffusion sequence (2 mm isotropic, FOV 200 mm). **(12B)** Measured SNR of the brightest sections of *in vivo* human white matter with 64-channel brain array coil (b = 10,000 s/mm² and 20,000 s/mm²).

mechanical modifications. The covers were modified accordingly (Fig. 11). Three cooling cabinets, four GPAs and a second filter panel were installed in the equipment room, before the first phantom images could be acquired in May 2011. Measurements of acoustic noise and vibrations showed lower amplitudes than typical 3T scanners, which is in line with the larger mass of the gradient coil body and the related higher net precision of torque and force balancing methods. The PNS studies performed on the AS302 and SC72 coils confirmed that it is possible to use high EPI readout amplitudes without PNS effects. Long rise times at high-amplitude pulses are limited by the regulatory-required cardiac monitor which was implemented in hardware.

Research in the US

Achieving the current state of connectomics has required a huge increase in MRI sensitivity, as well as much higher processing speeds to cope with the large amount of spatial data from water molecules. Unlike the BOLD effect which experiences enhanced contrast as field strength is increased, the diffusion contrast is set only by the displacement of the water and the applied field gradient and is thus independent of B_0. On the other hand, a more than two-fold sensitivity increase at 7T field strength would offer the opportunity to increase resolution for whole-brain studies towards one-millimeter isotropic voxel size. As the available methodologies in 2011 were not up to routinely coping with shorter T2 and T2* relaxation times, increased B_1(+) inhomogeneity and increased power deposition (SAR) at >7T field strength, both WU-Minn and MGH-UCLA teams set their main focus on 3T.

The MGH-UCLA consortium decided to re-engineer their scanner from the ground up to optimize diffusion imaging. Their efforts went into ultra-high gradient strength, sequence design and reconstruction, and high-channel receive coils. The gradient system with 300 mT/m was a major focus since gradient amplitude is central for the parameters diffusion contrast, T2 signal loss, and probability density function (PDF) of water. A field-of-view (FOV) shifting approach to Simultaneous Multi-Slice (SMS) EPI [25–27] was chosen to enable whole-brain coverage with low TR and TE. The group developed a 64-channel brain array coil showing a relative SNR gain of at least 40% compared to a sized-matched 32-channel brain array within the peripheral brain ROI [28]. The achieved efficiency gain is more than a factor of eight for high-b-value diffusion (3.5 x from shorter TE, 1.7 x from the slice acceleration factor of 3 from SMS, and 1.4 x from the RF coil) [29]. Average scan time for whole-brain diffusion was shown to be reduced from about one hour to 15 minutes (combined with compressed sensing, scan time was <5 minutes).

Increasing the gradient strength to the highest value ever attempted for human imaging also has significant impact on the concomitant field terms. In comparison to a conventional 45 mT/m scanner at 3T, the maximum field pertubation increases by a factor of ~$(300/45)^2$ = 44. The MGH-UCLA group successfully tackled this problem with the implementation of a fully refocusing Stejskal-Tanner scheme [1] and accompanying pre-processing eddy current correction. An unanticipated finding was that the increased gradient strength could induce magneto-phosphenes in the subjects' eye retina. Lowering the head coil vertically and

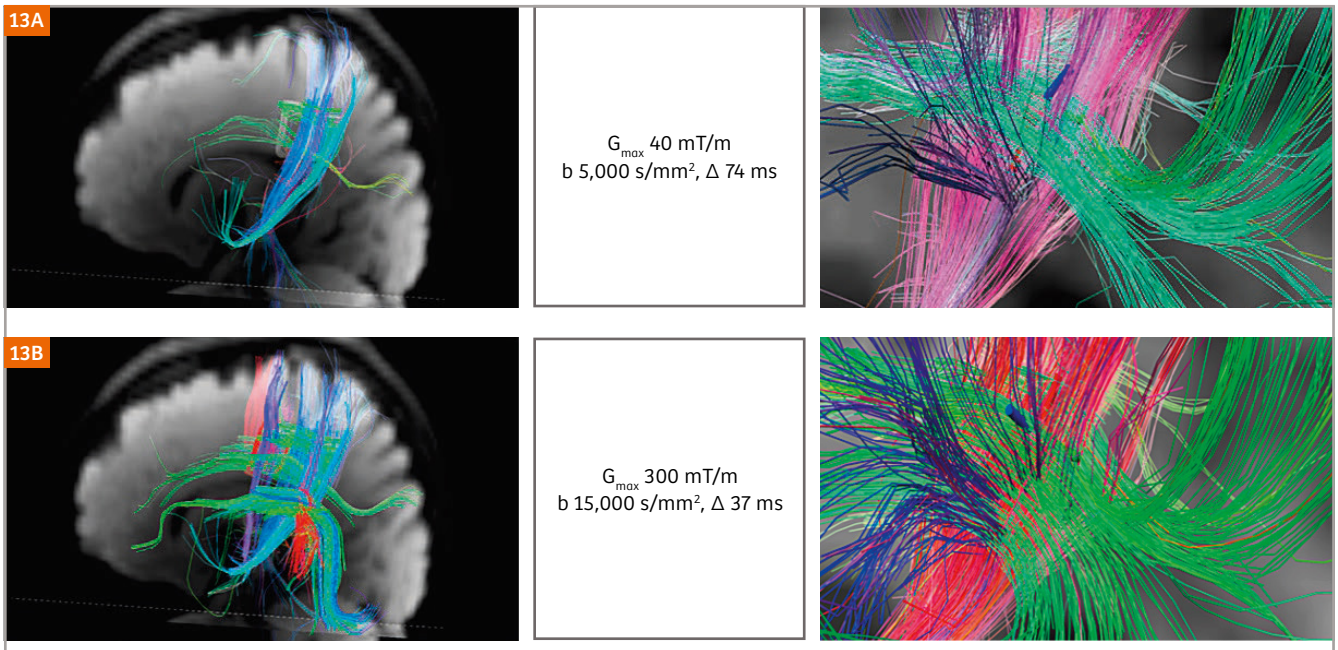

Figure 13: Micro-structural resolution with 40 mT/m **(13A)** and 300 mT/m **(13B)** gradients. dMRI data was aquired with a b-value of 5,000 s/mm² and 15,000 s/mm² respectively. Fiber pathways were computed with deterministic streamline integration and show a higher level of detail with a b-value of 15,000 s/mm². *Images courtesy of MGH, Boston, USA.*

positioning the eyes at isocenter in z was found to eliminate the induction of magneto-phosphenes within volunteer studies.

The ultra-high gradients yielded substantial and immediate gains in the sensitivity through reduction of TE while improved signal detection (Fig. 12) and increased efficiency of the DSI or HARDI acquisition, accuracy and resolution of diffusion tractography were illustrated (Fig. 13). Comparisons were performed across b-values based on q-ball orientation distribution function (ODF) metrics to investigate whether high-b-value dMRI (up to 10 k s/mm²) can improve resolving complex white-matter structures. The q-ball ODF features became sharper as the b-value increased. Crossing structures were detected in an increasingly larger fraction of white-matter voxels, and the spatial distribution of two-way and three-way crossing structures was found largely consistent with known anatomy (Fig. 14). Results indicate that dMRI with high diffusion encoding is a promising tool to characterize and understand the underlying structural organization and topological paths (motifs) in the human brain [30].

Relationships of adjacency and crossing between cerebral fiber pathways in humans and in nonhuman primate species are a major focus of the Connectomics department at the MGH. Whole-brain diffusion spectrum MRI was acquired with the 300 mT/m scanner *in vivo* in subjects (515 directions; pathways were computed with deterministic streamline integration, see Figs. 15–17) and *ex vivo*.

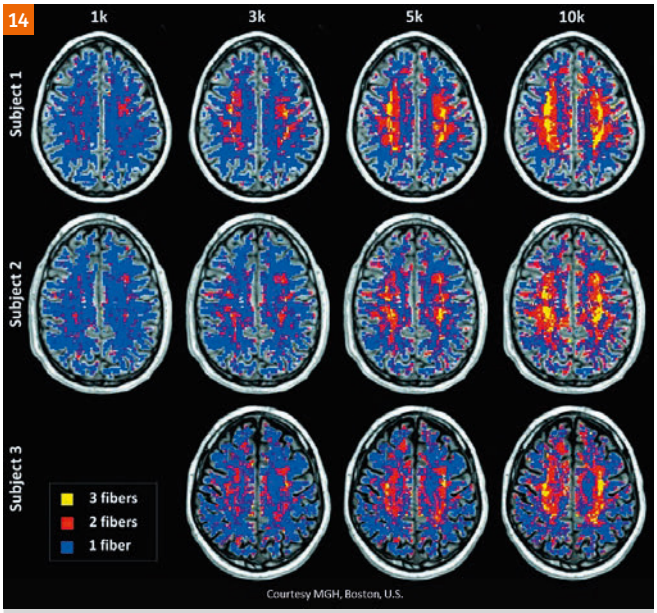

Figure 14: Spatial distribution of the number of fibers per voxel within the brain of three subjects (blue = 1, red = 2, yellow = 3 or more fibers). The orientation distribution function (ODF) peak threshold was selected to be two times the standard deviation above the mean of the noise peaks. A higher percentage of white matter voxels was identified as containing crossing fibers as b-value increased from 1,000 to 10,000 s/mm².

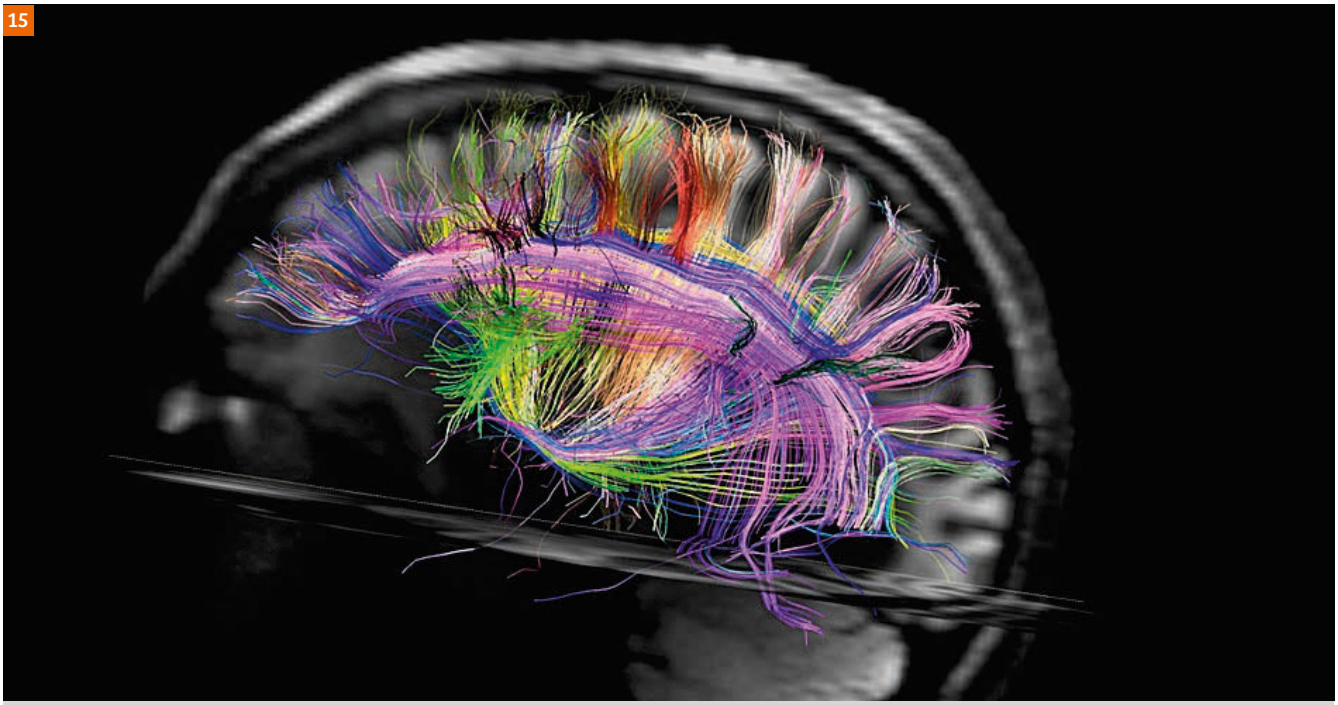

Figure 15: *In vivo* diffusion spectrum imaging (DSI) of the human brain. Reconstructed nerve fibers show the grid of corona radiata and SLF. Resolution 1.5 mm³, max b-value 15,000 s/mm², TA 20 min. *Image courtesy of V. Wedeen, MGH, Boston, USA.*

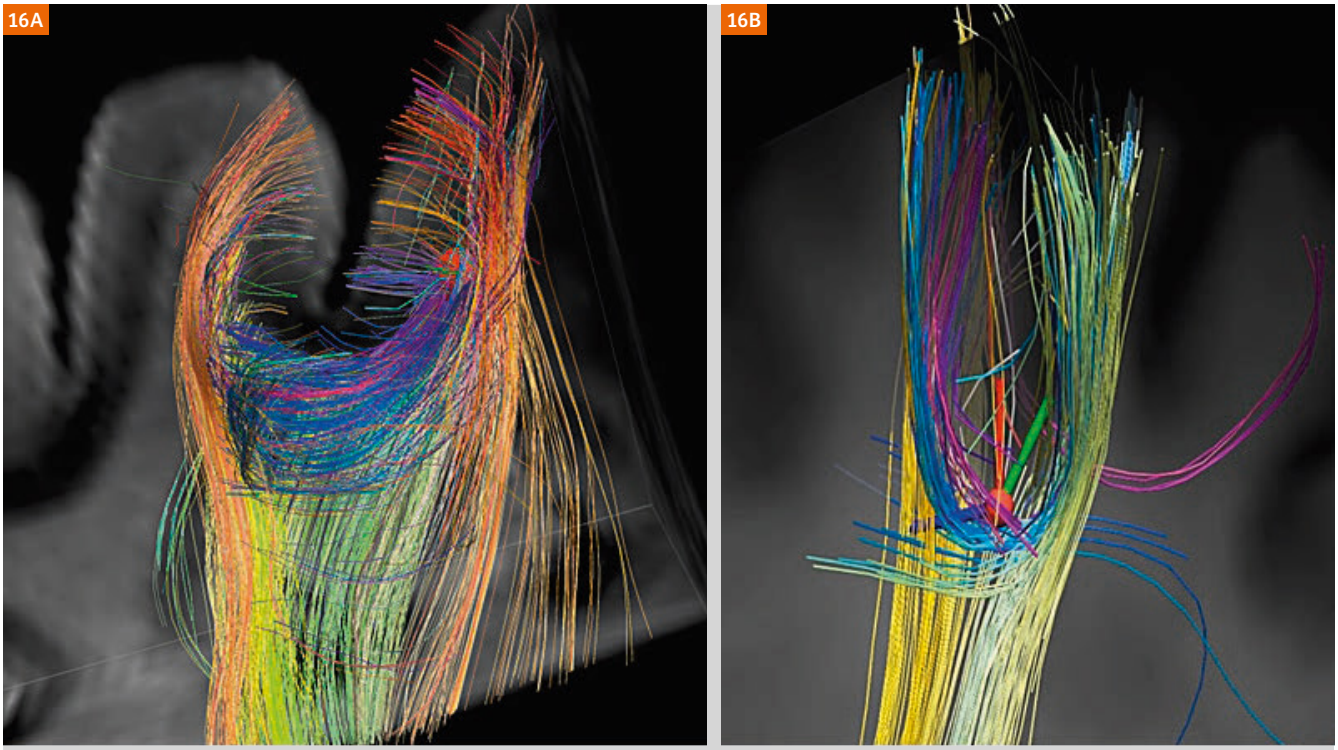

Figure 16: Diffusion spectrum imaging (DSI) of the human central sulcus U-fibers. **(16A)** *Ex vivo* data (b-value 40,000 s/mm², voxel size 0.5 mm³ isotropic, TA 12 h). **(16B)** *In vivo* data (b-value 15,000 s/mm², voxel size 2 mm³ isotropic, TA 20 min). *Images courtesy of V. Wedeen, MGH, Boston, USA.*

The cerebral fiber pathways were seen to form a rectilinear three-dimensional grid continuous with the three principal axes of early development. Cortico-cortical pathways were observed to form parallel sheets of interwoven paths in the longitudinal and medio-lateral axes, in which major pathways were local condensations. Details are covered by a *Science* publication from 2012 [31].

Beyond the immediate scope of the HCP, further applications like brain recovery after traumatic coma, axon diameter distributions [32, 33], and post-mortem diffusion tractography were explored. It could be shown that ultra-strong gradients enable human applications of techniques that were previously possible only in small-bore scanners. Detailed research results were published by Neuroimage

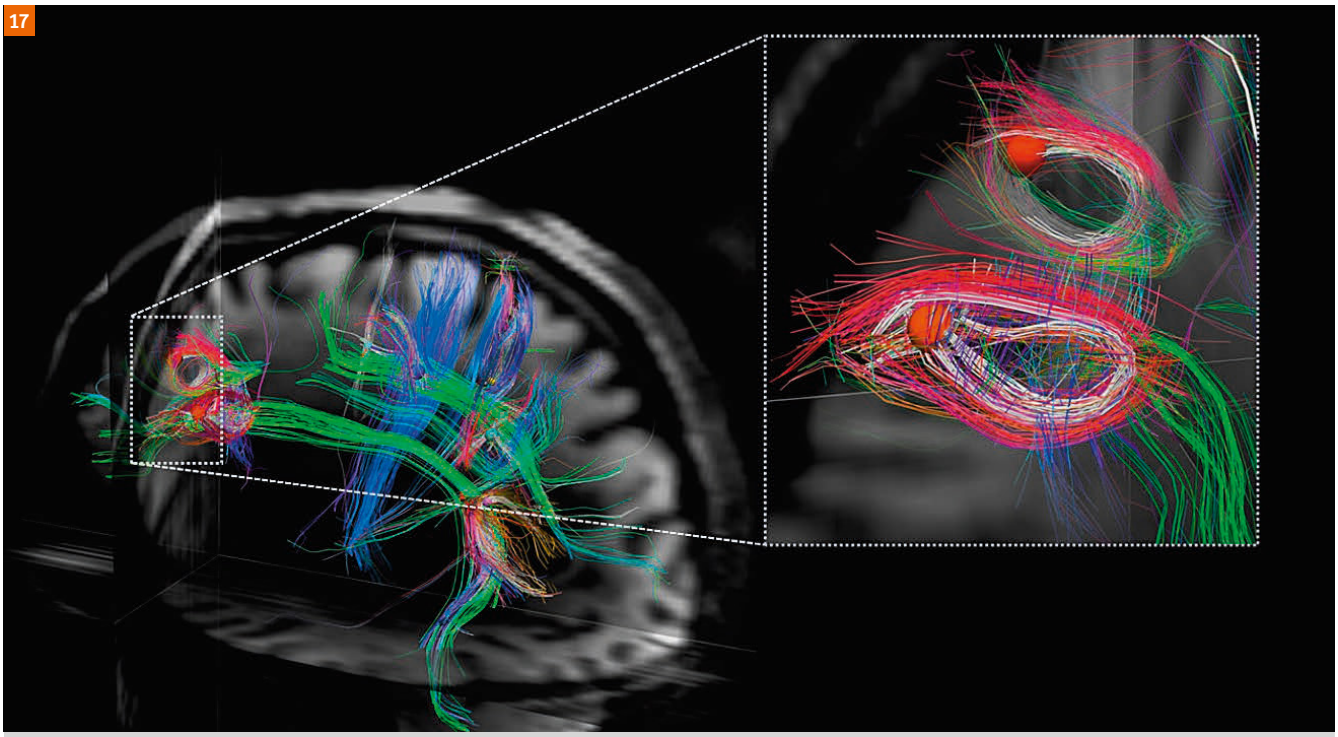

Figure 17: *In vivo* diffusion spectrum imaging (DSI) of the human gyri, and its continuity with deep white matter. (b-value 15,000 s/mm^2, voxel size 1.5 mm^3 isotropic, TA 20 min). *Image courtesy of V. Wedeen, MGH, Boston, USA.*

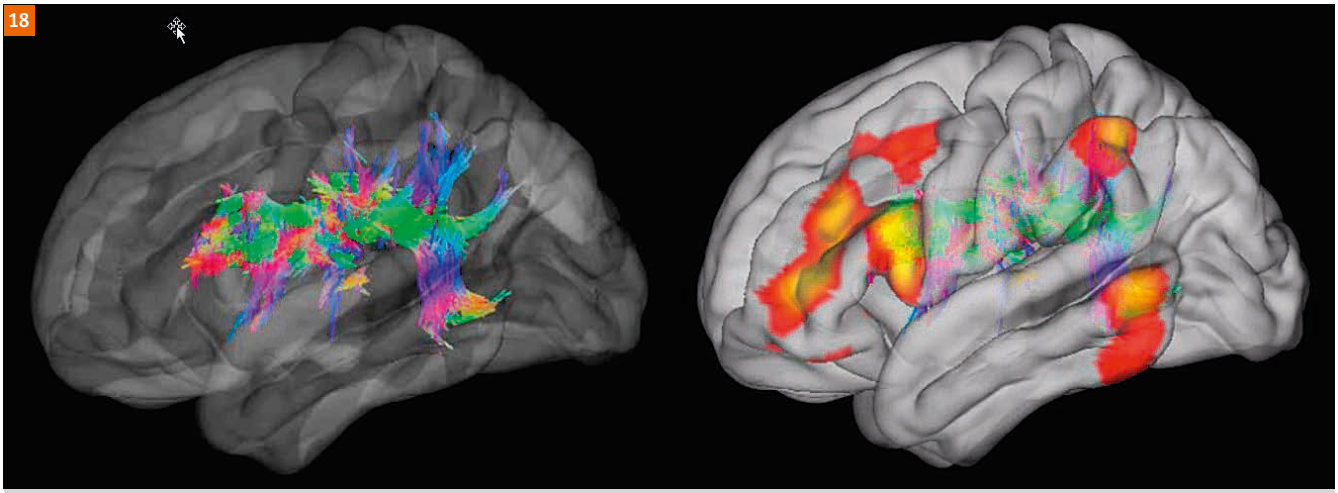

Figure 18: Interactive composite dataset of the human brain (180 areas per hemisphere). Red and yellow sections are based on data from resting state functional MRI, whereas the multicolored fibers were generated using probabilistic streamline tractography based on diffusion MRI. *Images courtesy of Washington University – University of Minnesota – Oxford University Human Connectome Project.*

[34] in 2013. More than 60 subjects were scanned with the 300 mT/m system by the MGH-UCLA consortium. The resulting reference data base was made publically available on the HCP internet homepage in 2016 [35].

The WU-Minn consortium focused on mapping long-distance brain connections [36] and their variability within healthy adults (twins and their non-twin siblings [37]). Three complementary methods were used, namely resting state functional MRI (rfMRI) which uses correlations in the temporal fluctuations in an fMRI time series to derive 'functional connectivity'; diffusion imaging (dMRI), which provides the input for axonal fiber tractography; and task-based fMRI (tfMRI), which is used together with T1- and T2-weighted imaging to identify functional parcellation in the human brain [38]. Improvements and optimization of these methods (Multiband/Simultaneous Multi-Slice Imaging) resulted in a whole-brain coverage with 2 mm isotropic resolution in 0.7 seconds for fMRI, yielding a data acquisition speed-up factor of up to nine. Applied to 1.25 mm isotropic dMRI data, a three-fold reduction in total data acquisition time was achieved. Using the HARDI [10] approach, diffusion encoding was performed with 270 q-points distributed over three shells of b = 1,000, 2,000, and 3,000 s/mm^2 (Fig. 20). Due to the targeted high number of subjects, the robust and easy-to-handle 100 mT/m gradient system was chosen.

The first half of the 5-year project focused on refining methods for data acquisition and processing [39] and resulted in robust fast pulse sequences and pre-processing pipelines providing substantial improvements for each of the MRI modalities [40]. The first pipeline provides correction algorithms for MRI raw data (e.g. eddy current and spatial distortion correction, reduction of temporal artifacts. The second pipeline involves mapping the data to cortical surfaces and subcortical gray-matter domains (Fig. 18), as understanding the human cerebral cortex requires a map (or parcellation) of its major subdivisions. Based on a pilot study of 10 healthy adults, an interactive composite dataset of the left and right cerebral hemispheres was created (Fig. 19). Red and yellow sections are strongly related to the seed location (black dot). The correlation factor is based on data from resting state functional MRI. This methodology could take research to a different level, considering that mental illnesses like autism might be related to abnormal brain circuits showing up a reduced functional connectivity in rsMRI scans.

Using multi-modal MRI images, 180 areas per hemisphere were delineated, bound by changes in cortical architecture, function, connectivity, and/or topography in a group average of 210 healthy adults. It has been possible to characterize 97 new areas and 83 previously reported areas. Automated delineation and identification of these areas was supported by a machine-learning classifier. This classifier detected the presence of >95% of the cortical areas in new subjects, replicated the group parcellation, and could correctly locate areas in individuals with atypical parcellations. These tools and datasets are part of the *'Connectome Workbench'* and *'ConnectomeDB'* database and were made available to the public [41].

After finalizing the HCP protocols in 2012, data was acquired using multiple imaging modalities, including customized 3T MRI (1,200 subjects) and 7T MRI (200 subjects) plus combined magneto- and electro-encephalography (MEG-248-channel/EEG-64-channel, 100 subjects). Technical optimizations in 7T image acquisitions for the HCP allowed to obtain high-quality, high-resolution whole-brain *in-vivo* dMRI data (Fig. 20). This data shows spatial details typically seen in *ex-vivo* studies and complement already very high-quality 3T HCP data in the same subjects [42]. More recently [43], it could

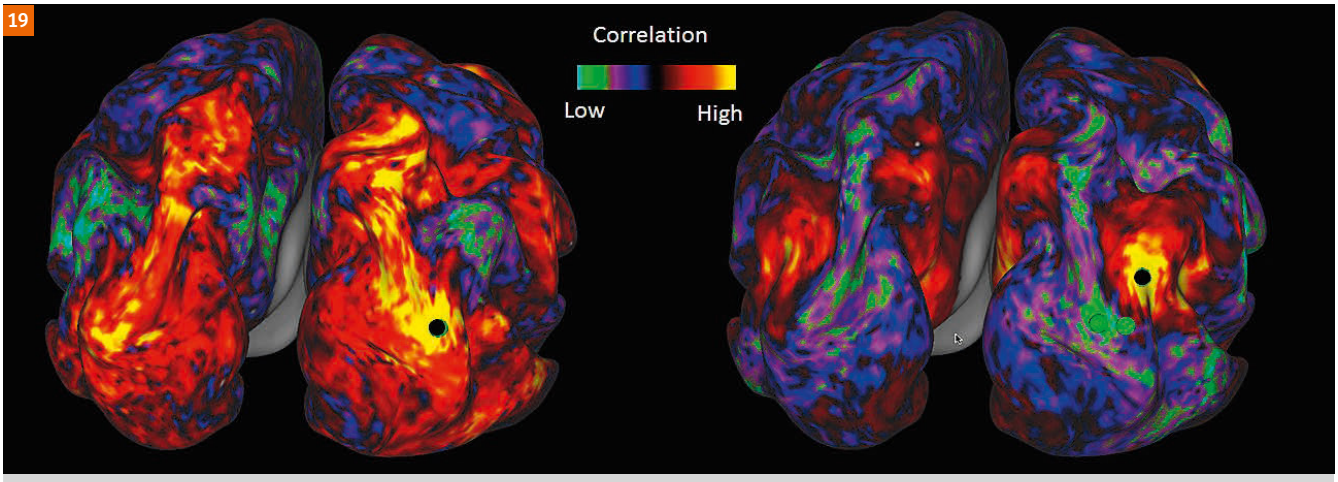

Group average, HCP Pilot-1 dataset (10 subjects, 14 scans), MB = 4, TR = 1.4 s, 2 mm voxels

Figure 19: Interactive composite dataset of the left and right cerebral hemispheres of the human brain (group average of 10 subjects). Red and yellow sections are strongly related to the seed location (black dot). The correlation factor is based on data from resting state functional MRI. *Images courtesy of Washington University – University of Minnesota – Oxford University Human Connectome Project.*

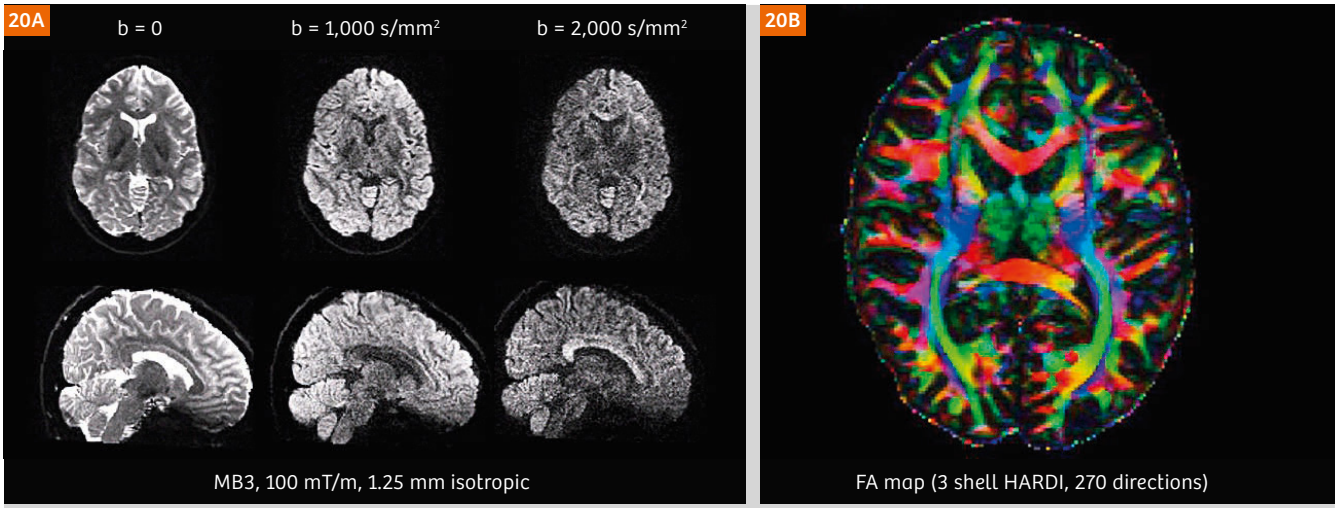

Figure 20: Representative examples of diffusion MRI with the finalized 3T HCP protocol (100 mT/m, MB3, 1.25 mm³ isotropic). Anatomical detail in comparison to a conventional 3T protocol (2 mm³ isotropic, not shown here) is significantly improved. **(20A)** Image intensities are presented in arbitrary units after distortion correction and averaging across paired phase encoding directions. **(20B)** Color fractional anisotropy (FA) maps. Colors depict the principal fiber orientation and gray scale intensities are defined by FA.
Images courtesy of Washington University – University of Minnesota – Oxford University Human Connectome Project.

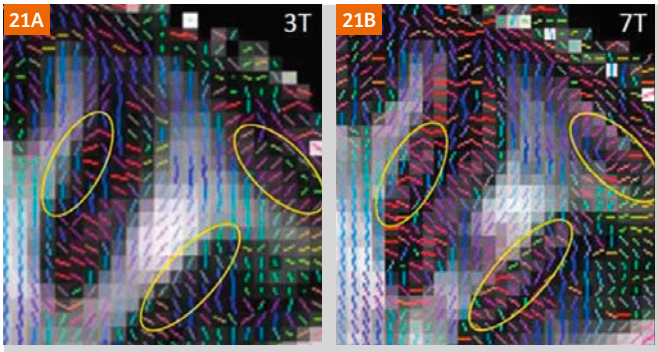

Figure 21: Zoomed-in coronal view of DTI principal direction of diffusion (PDD) maps overlaid on corresponding fractional anisotropy (FA) maps. HCP 3T **(21A)**. 7T **(21B)**. Due to the higher resolution and reduced partial volume effects, the 7T data recovers gray matter regions of low FA (yellow circles).
Images courtesy of Washington University – University of Minnesota – Oxford University Human Connectome Project.

be demonstrated that high-resolution images acquired at 7T provide increased functional contrast-to-noise ratios with significantly less partial-volume effects and more distinct spatial features (Figs. 21, 22). Studies of structural and functional brain connectivity were paired with behavioral and heritability measures. A detailed summary of the 5-year project result was published in *Nature Neuroscience* [44].

Research in Europe

The scientific success of the Connectome gradients has recently persuaded two major European research centers to extend their instruments parks with a 300 mT/m machine. **The Max Planck Institute for Human Cognitive and Brain Sciences, Leipzig, Germany**, plans to develop MRI methods to reliably characterize the detailed functional and anatomical micro- structure of the human brain. Their strategy is to combine the best data from 7T and the 3T Connectom scanner. They plan for imaging the intracortical microstructure, such as myeloarchitecture and intracortical connectomics, and fine structure in the white matter. The ultimate goal is to understand the structure-function relationship in the human brain, pathological changes in neurodegeneration (e.g. amyloid plaques in Alzheimer's disease) and provide early biomarkers. A first step in methodology development will comprise high-fidelity field mapping, optical prospective motion correction and new pulse sequences, in order to achieve a spatial resolution of 600 um or higher combined with high diffusion-weighting factors.

The **Cardiff University Brain Research Imaging Centre (CUBRIC), Cardiff, UK** plans to develop MRI methods for quantifying tissue structure at the microscopic scale. The principal approach looks at how fine tissue structure impedes the movement of water. Current MRI hardware (i.e. gradient strength) restricts measurement to relatively large molecular displacements and from tissue components

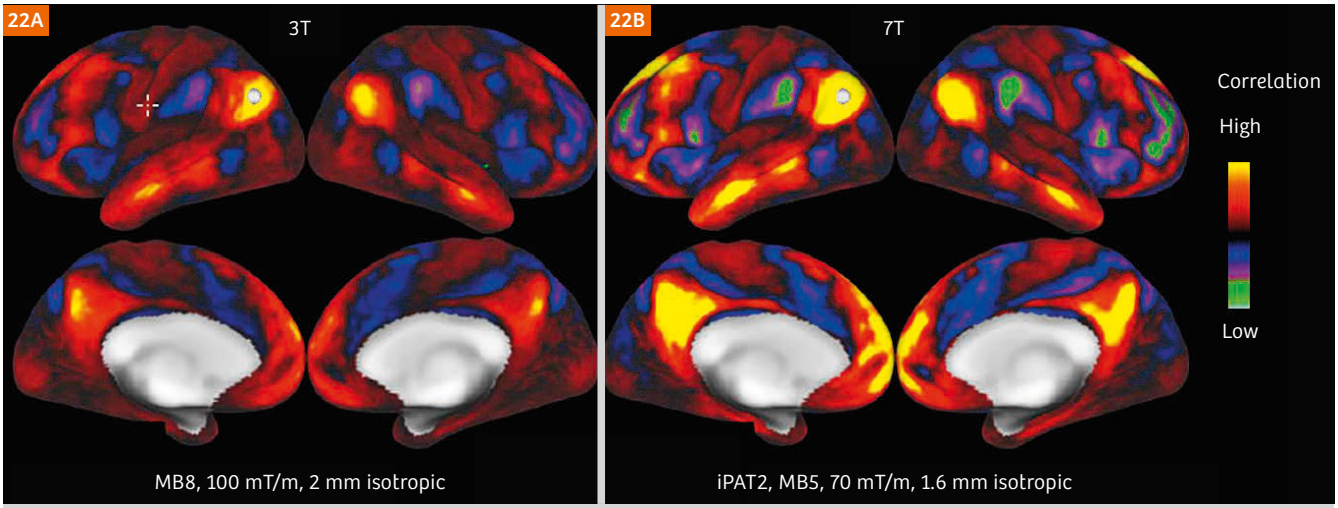

Figure 22: Exemplary composite dataset of the left and right cerebral hemispheres of the human brain (3T vs. 7T). Red and yellow sections are strongly related to the seed location in occipital parietal cortex (white dot). The correlation factor is based on data from resting state functional MRI. While the 3T data shows detailed connectivity / correlation throughout the brain, the correlation factor of 7T data is even more pronounced. *Images courtesy of Washington University – University of Minnesota – Oxford University Human Connectome Project.*

with a relatively strong and long-lived signal, prohibiting quantification of individual cell dimensions, or packing of nerve fibers. Once achieved with the new 300 mT/m machine, faster acquisition and access to newly-visible signal components will enable new mathematical models of microstructure on finer length-scales. This will help to increase understanding of tissue structure in health and disease, and to make testable predictions on important biophysical parameters such as nerve conduction velocities in the brain or cell structure in the liver. The ultimate goal is to develop the imaging software that brings this hardware to mass availability, in turn enabling a new generation of mainstream microstructure imaging and macrostructural connectivity mapping techniques to translate to frontline practice.

Conclusion

As of today, more than 140 studies have acknowledged the use of data generated by the Human Connectome Project. This reflects the goal of the NIH funding organization, which intended that the findings should be broadly applicable to clinical and scientific questions. Both MGH-UCLA and WU-Minn consortia, have successfully developed and applied new methods to map structural and functional connectivity of the brain. Gains in spatial sharpness and clarity are qualitatively analogous to those made in astronomy after the introduction of adaptive optics to overcome the atmospheric blurring. The initial thought that the human brain could be mapped in analogy to the Human Genome Project is now supported by a first, but important step. A promising next step is the extension of the Connectome user base with the new European sites, Cardiff University Brain Research Imaging Centre (CUBRIC) and Max Planck Institute for Human Cognitive and Brain Sciences, Leipzig. It remains to be seen in the future, which further methodical and instrumental steps need to be taken until the level of understanding of the human brain approaches that of *C. elegans*.

References

1 Stejskal EO, Tanner JE. Spin diffusion measurements: spin echoes in the presence of a time-dependent field gradient. Journal of Chemical Physics. 1965;42:288–292.
2 Le Bihan D, Breton E (1985). Imagerie de diffusion in-vivo par résonance magnétique nucléaire. C R Acad Sci (Paris). 301 (15): 1109–1112.
3 Basser PJ, Mattiello J, LeBihan D. Estimation of the effective self-diffusion tensor from the NMR spin echo. Journal of Magnetic Resonance. Series B. San Diego Cal 103.1994, 247–254.
4 Sulston JE, et al. The Embryonic Cell Lineage of the Nematode Caenorhabditis elegans. Developmental Biology 100, 64-119 (1983).
5 Towlson EK et al. The rich club of the C. elegans neuronal connectome. J Neurosci. 2013 Apr 10;33(15):6380-7.
6 Majka P et al. Towards a comprehensive atlas of cortical connections in a primate brain: Mapping tracer injection studies of the common marmoset into a reference digital template. J Comp Neurol. 2016 Aug 1;524(11):2161-81.
7 Zingg B, Hintiryan H, Gou L, Song MY, Bay M, Bienkowski MS, Foster NN, Yamashita S, Bowman I, Toga AW, Dong HW. Neural networks of the mouse neocortex. Cell 2014 156:1096–1111.
8 Biswal B, Yetkin FZ, Haughton VM, Hyde JS. Functional connectivity in the motor cortex of resting human brain using echo-planar MRI. Magn Reson Med. 1995 Oct; 34(4):537-41.
9 Wedeen VJ, Hagmann P, Tseng WY, Reese TG, Weisskoff RM. Mapping complex tissue architecture with diffusion spectrum magnetic resonance imaging. Magn. Reson. Med. 54, 1377–1386 (2005). (DSI).
10 Tuch D, Wedeen VJ, et al. High angular resolution diffusion imaging reveals intravoxel white matter fiber heterogeneity. MRM, 2002, 48(4):577-82.

11 Making connections. 396, Nature, vol 483, 22 March 2012.
12 Mansfield P. Multi-planar image formation using NMR spin echos. J. Phys. C, Solid State Physics 10:155 (1977).
13 Cohen MS, Weisskoff RM. Ultra-fast imaging. Magnetic Resonance Imaging 9:1 (1991).
14 Schmitt F et al. Echo-planar imaging of human brain perfusion at 1T. MRM: 116 (1991).
15 Turner R. A target field approach to optimal coil design. J Phys D 19:L147 (1986).
16 Siebold H. Gradient field coils for MR imaging with high spectral purity. IEEE Trans Magn 26:897 (1990).
17 Kimmlingen R, et al. Gradient System with Continously Variable Field Characteristics. Proc. Intl. Soc. Mag. Reson. Med. (1999).
18 Patz S et al. Novel encoding technology for ultrafast MRI in a limited spatial region. International Journal of Imaging Systems and Technology: 10.3:216 (1999).
19 Kaindl A, et al. Influence of chemo-rheological properties of silica-filled liquid epoxy resins on partial discharge behavior of coils. Proc. Coil Winding Conference (2001).
20 Irnich W. Electrostimulation by time-varying magnetic fields. MAGMA 2:43 (1994)
21 Kimmlingen R, et al. An easy to exchange high performance head gradient insert for a 3T whole body MRI system: First results. Proc. Intl. Soc. Mag. Reson. Med. (2004).
22 Takahashi E, Dai G, Wang R, Ohki K, Rosen GD, Galaburda AM, Grant PE, Wedeen VJ. Development of cerebral fiber pathways in cats revealed by diffusion spectrum imaging. Neuroimage 49(2): 1231-1240 (2010).
23 Kimmlingen R, et al. Concept and realization of high strength gradients for the Human Connectome Project. ISMRM conference (2012).
24 Budinger TF. Thresholds for physiological effects due to RF and magnetic fields used in NMR imaging. IEEE TransNucl.Sc., Vol. NS-26, No.2 April.1979.
25 Larkman DJ, Hajnal JV, Herlihy AH, Coutts GA, Young IR, Ehnholm G. Use of multicoil arrays for separation of signal from multiple slices simultaneously excited. J Magn Reson Imaging. 2001;13(2):313–317.
26 Feinberg DA, et al. Multiplexed Echo Planar Imaging for Sub-Second Whole Brain FMRI and Fast Diffusion Imaging. PLoS ONE, 2010. 5(12): p. e15710.
27 Setsompop K, Gagoski BA, Polimeni JR, Witzel T, Wedeen VJ, Wald LL. Blipped-controlled aliasing in parallel imaging for simultaneous multislice echo planar imaging with reduced g-factor penalty. Magn Reson Med. 2012 May; 67(5):1210-24.
28 Keil B, Blau JN, Biber S, Hoecht P, Tountcheva V, Setsompop K, Triantafyllou C, Wald LL. A 64-channel 3T array coil for accelerated brain MRI. Magn Reson Med. 2013 Jul; 70(1):248-58.
29 Setsompop K, Kimmlingen R, Eberlein E, Witzel T, Cohen-Adad J, McNab JA, Keil B, Tisdall MD, Hoecht P, Dietz P, Cauley SF, Tountcheva V, Matschl V, Lenz VH, Heberlein K, Potthast A, Thein H, Van Horn J, Toga A, Schmitt F, Lehne D, Rosen BR, Wedeen V, Wald LL. Pushing the limits of *in vivo* diffusion MRI for the Human Connectome Project. Neuroimage. 2013 Oct 15;80:220-33.

Contact

Ralph Kimmlingen, Ph.D.
Siemens Healthcare GmbH

Am Röthelheimpark 2
91052 Erlangen
Germany
ralph.kimmlingen@siemens.com



30 Fan Q, Nummenmaa A, Witzel T, Zanzonico R, Keil B, Cauley S, Polimeni JR, Tisdall D, Van Dijk K, Buckner RL, Wedeen V, Rosen BR, Wald LL. Investigating the capability to resolve complex white matter structures with high b-value diffusion MRI on the MGH-USC Connectome Scanner. Brain Connectivity, 2014 Nov; 4(9) p.718-26 PMID 25287963.
31 Van Wedeen J, Rosene DL, Wang R, Dai G, Mortazavi F, Hagmann P, Kaas JH, Tseng W-Y I. The Geometric Structure of the Brain Fiber Pathways: A Continuous Orthogonal Grid. Science. 2012 Mar 30; 335(6076): 1628–1634.
32 Huang SY, Nummenmaa A, Witzel T, Duval T, Cohen-Adad J, Wald LL, McNab JA. The impact of gradient strength on *in vivo* diffusion MRI estimates of axon diameter. Neuroimage 2014 Dec.9 Epub ahead of print. PMID: 25498429.
33 Huang, SY, Tobyne SM, Nummenmaa A, Witzel T, Wald LL, McNab JA, Klawiter EC Characterization of Axonal Disease in Patients with Multiple Sclerosis Using High-Gradient-Diffusion MR Imaging.
34 McNab JA, Edlow BL, Witzel T, Huang SY, Bhat H, Heberlein K, Feiweier T, Liu K, Keil B, Cohen-Adad J, Tisdall MD, Folkerth RD, Kinney HC, Wald LL. The Human Connectome Project and beyond: initial applications of 300 mT/m gradients. Neuroimage 2013;80:234-245.
35 Fan Q, Witzel T, Nummenmaa A, Van Dijk KR, Van Horn JD, Drews MK, Somerville LH, Sheridan MA, Santillana RM, Snyder J, Hedden T, Shaw EE, Hollinshead MO, Renvall V, Zanzonico R, Keil B, Cauley S, Polimeni JR, Tisdall D, Buckner RL, Wedeen VJ, Wald LL, Toga AW, Rosen BR. MGH-USC Human Connectome Project datasets with ultra-high b-value diffusion MRI. Neuroimage 2016;124(Pt B):1108-1114.
36 Smith SM, Miller KL, Moeller S, Xu J, Auerbach EJ, Woolrich MW, Beckmanna CF, Jenkinson M, Andersson J, Glasser MF, Van Essen DC, Feinberg DA, Yacoub ES, Ugurbil K. Temporally-independent functional modes of spontaneous brain activity. www.pnas.org/cgi/doi/10.1073/pnas.1121329109, 2011.
37 Van Essen DC, et al. The Human Connectome Project: A data acquisition perspective. NeuroImage (2012), j.neuroimage.2012.02.018.
38 Ugurbil K, et al. Pushing spatial and temporal resolution for functional and diffusion MRI in the Human Connectome Project. Neuroimage 80, 80–104 (2013).
39 Van Essen DC, et al. The WU-Minn Human Connectome Project: an overview. Neuroimage 80, 62–79 (2013).
40 Sotiropoulos SN, Jbabdi S, Xu J, Andersson JL, Moeller S, Auerbach EJ, Glasser MF, Hernandez M, Sapiro G, Jenkinson M, Feinberg DA, Yacoub E, Lenglet C, Van Essen DC, Ugurbil K, Behrens TE. Advances in diffusion MRI acquisition and processing in the Human Connectome Project. Neuroimage. 2013 Oct 15; 80:125-43.
41 Glasser MF, Coalson TS, Robinson EC, Hacker CD, Harwell J, Yacoub E, Ugurbil K, Andersson J, Beckmann CF, Jenkinson M, Smith SM, Van Essen DC. A multi-modal parcellation of human cerebral cortex. Nature 536, 171–178 (11 August 2016).
42 Vu AT, Auerbach E, Lenglet C, Moeller S, Sotiropoulos SN, Jbabdi S, Andersson J, Yacoub E, Ugurbil K. High resolution whole brain diffusion imaging at 7 T for the Human Connectome Project. Neuroimage. 2015 Nov 15; 122: 318–331.
43 Vu AT. High resolution whole brain diffusion imaging at 7T for the Human Connectome Project. NeuroImage (2016), http://dx.doi.org/10.1016/j.neuroimage.2016.11.049.
44 Glasser MF, Smith SM, Marcus DS, Andersson JLR, Auerbach EJ, Behrens TEJ, Coalson TS, Harms MP, Jenkinson M, Moeller S, Robinson EC, Sotiropoulos SN, Xu J, Yacoub E, Ugurbil K, Van Essen DC. The Human Connectome Project's neuroimaging approach. Nature Neuroscience 19, 1175–1187 (2016).

Gadgetron: Open Source Image Reconstruction

Michael S. Hansen; Hui Xue; Peter Kellman

Laboratory of Imaging Technology, National Heart, Lung, and Blood Institute, National Institutes of Health, Bethesda, MD, USA

Introduction

Image reconstruction plays a critical role in modern MRI methodology. Recent gains in imaging speed and quality have been driven by techniques such as parallel imaging [1–3] and compressed sensing [4]. Although there have been numerous innovations in image reconstruction, there are many new reconstruction techniques published in scientific journals that are not evaluated on a large scale and therefore never make it into clinical use. This is caused by challenges presented by the current development environments and paradigms. This paper reviews the development and deployment paradigm introduced by the Gadgetron [5] reconstruction framework as it has been used on the Siemens Healthcare platform. The concepts and information presented in this paper are based on research and are not commercially available.

While the field of image reconstruction continues to be very active, access to vendor reconstruction code has been limited. The Siemens Healthcare platform has traditionally provided a wide image reconstruction programming window through the Image Calculation Environment (ICE). This environment has enabled developers to use existing Siemens Healthcare reconstruction modules (Functors) as black box modules, but access to the source code of the full reconstruction pipeline has been limited. Modern reconstruction algorithms consist of several critical steps that form an image reconstruction pipeline [6], and when new reconstruction algorithms are developed, they must be compared to existing methodology to identify and analyze advantages and disadvantages. In many cases it is challenging to reproduce results from published papers on image reconstruction techniques. There are several reasons for this, but one important obstacle is the lack of access to the underlying source code used to produce the images. It is critical for researchers to be able to examine and reproduce each algorithmic step of previously developed methodology and consequently they have to attempt to replicate existing reconstruction methods from the descriptions in the publications. Given the cursory treatment that the actual implementation is frequently given in such publications, it can be a formidable challenge to produce a high quality, high performance implementation of existing algorithms. This makes any subsequent comparisons much less meaningful. Open access to source code of reference implementations will play an important role in advancing the field of MRI in general and MRI reconstruction in particular.

In addition to reproducibility problems, current MRI reconstruction development has also been hampered by the logistical and regulatory problems associated with deploying prototype reconstruction algorithms in a clinical environment. New techniques are often implemented in scripting environments such as MATLAB (MathWorks, Natick, MA, USA) or Python (Python Software Foundation, Wilmington, DE, USA) and they are not easily connected to clinical scanners. When researchers evaluate novel reconstruction algorithms, the workflow often involves

1

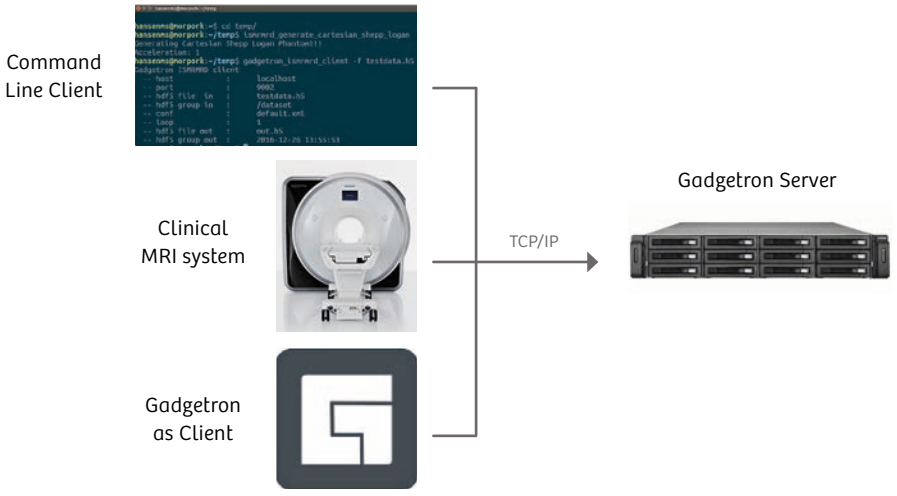

Figure 1: The Gadgetron uses a client-server architecture, where the server is the Gadgetron reconstruction engine. Clients make connections to the Gadgetron to send data and receive reconstructed images. Clients can be command line, stand-alone clients, imaging systems, or other Gadgetron instances.

transferring raw data for offline reconstruction and subsequent evaluation and comparison against existing techniques. This decouples the evaluation of reconstruction techniques from existing clinical workflows. The lack of tight scanner integration also creates a barrier for adoption and large scale testing of new techniques; the offline reconstruction workflow is manageable in small research settings where expert help is available, but it is not easily transferred to other sites. Ideally, images reconstructed with novel techniques should be available online on the scanner such that they can be used in the clinical analysis tools and immediate comparisons and evaluations become possible.

It is important to consider why developers use offline environment. One reason is that they need access to development tools and infrastructure that vendor environments such as ICE do not provide. The access to rapid prototyping scripting languages such as Python, MATLAB, or Julia (NumFocus, Austin, TX, USA) are examples of such tools, but more generally vendor reconstruction environments are relatively restrictive in terms of the hardware and software that they provide. As an example, the use of Graphical Processing Units (GPUs) was proposed [7–9] several years before such hardware became available on commercial MRI systems. Even today with the availability of the GPU hardware on commercial MRI systems, it is often older generation hardware and drivers that are not compatible with the latest development tools; the slow development cycles of commercial systems and the need to maintain backwards compatibility makes it challenging for commercial vendors to keep up with the rapidly changing field of computational hardware and software. There is a need for image reconstruction environments that can be deployed on platforms where developers can control the available hardware and the associated software components.

The Gadgetron was developed to provide solutions to the challenges outlined above. It is an open source, freely available image reconstruction server engine, which can be deployed as a stand-alone tool on a developers desktop computer or it can be connected directly and transparently to commercial Siemens Healthcare MRI systems. When connecting to a clinical MRI system, it can be deployed in several configurations:

a) directly on the available vendor hardware,

b) on a separate workstation connected to the scanner, or

c) on remote computer systems, which may provide cloud computing resources.

The framework enables developers to use the hardware and software platform of their choice. It is also modular and enables the users to use scripting languages for all or part of their image reconstruction pipeline. The following sections outline the architecture of Gadgetron and describe how it is connected to Siemens Healthcare MRI systems. A number of use cases and example applications are also provided.

Key points

- Reproducible research relies on Open Source software.
- Vendor reconstruction environments do not provide access to source code.
- It is challenging to deploy and test prototype reconstruction in a clinical environment.
- The Gadgetron is an Open Source image reconstruction framework which provides access to algorithm code, rapid prototyping, and transparent deployment on Siemens Healthcare MRI systems.
- Source code and documentation: https://gadgetron.github.io

Gadgetron architecture

The Gadgetron uses a client-server architecture as outlined in Figure 1. The reconstruction engine is the server and different types of clients can connect to the reconstruction server. Figure 1 illustrates three common scenarios. When the Gadgetron is used as a stand-alone reconstruction tool, the client would be a command line tool that reads a file with raw data and sends it to the Gadgetron. The Gadgetron instance can be local to the machine where the client is executing or it can be located on a remote server. Reconstructed images are returned to the client and written to an output file. When processing MRI datasets, the Gadgetron uses the ISMRM Raw Data (ISMRMRD) [10] format. The ISMRMRD format is a vendor neutral format for MR raw datasets and converters from most commonly used commercial vendors are available. Consequently, the ISMRMRD command line client, which is supplied with the Gadgetron source code, can be used to send data from any vendor to the Gadgetron engine for reconstruction after appropriate data conversion. The command line client is useful during reconstruction development and when processing datasets offline, but in a clinical setting, data must be sent directly by the scanner to the Gadgetron and images should be returned to the scanner host database for viewing and planning purposes. To facilitate this, an ICE based Gadgetron client (IceGadgetron) is available. The integration with Siemens Healthcare MRI systems is described in the *Siemens Healthcare Scanner Integration* section below. The Gadgetron engine itself can also act as a client. This use case is encountered when the Gadgetron is deployed in cloud computing platforms where multiple Gadgetron instances can collaborate on a reconstruction task. Some of these instances will be clients and some will be servers. This is discussed further in the *Deployment Strategies* below.

The reconstruction server engine is a pipeline architecture as shown in Figure 2. Each reconstruction program in the Gadgetron is a pipeline assembled from multiple modules

2

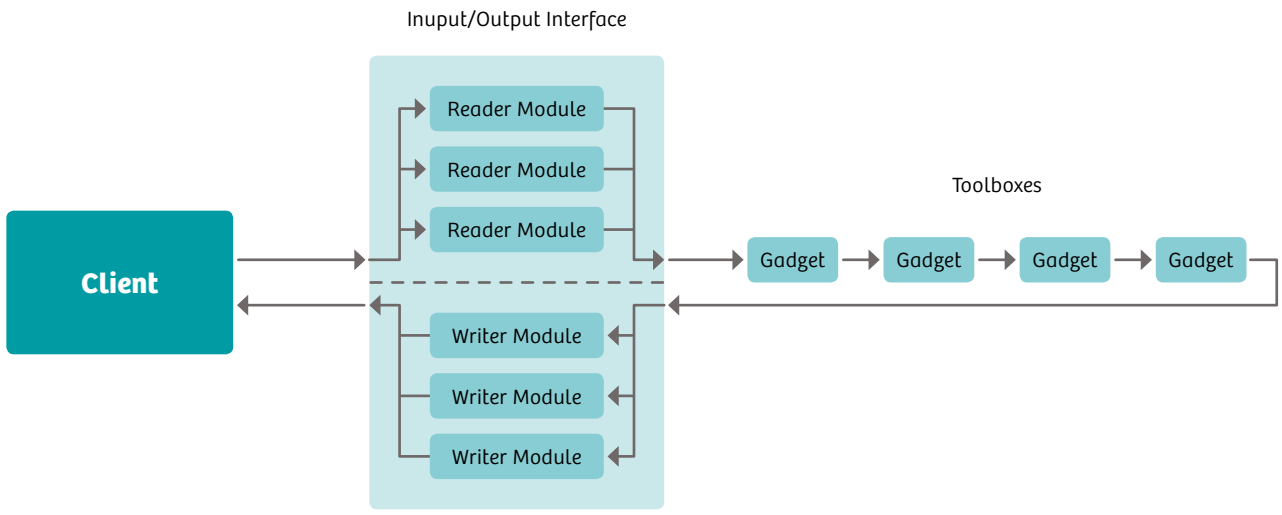

Figure 2: The Gadgetron pipeline architecture. The client connects to the Gadgetron reconstruction engine with a TCP/IP socket connection. The configurable input/output interface is responsible to deserializing incoming data and serializing outgoing data. Once data has been received, it is passed through a set of modules or Gadgets, which perform reconstruction steps. These Gadgets use a number of toolbox functions to perform the data processing.

that are assembled and configured at runtime. The data processing is modeled as a set of modules or Gadgets. As the data passes from Gadget to Gadget, it is modified and transformed until the final images are ready to be returned to the client. A configurable input/output interface is responsible for receiving data from the TCP/IP connection and transmitting reconstruction products back to the client. The configuration of this interface is done at runtime by assembling a set of modules that can handle the reading (deserialization) and writing (serialization) of particular datatypes. The Gadgetron framework does not put any restrictions on the type of data that can be sent and received, and as such it can be used to reconstruct any kind of imaging data. It can also receive and send data that it not related to the imaging experiment. Examples of such data could be physiological waveforms or other telemetry (such as subject motion data) that can be used in the reconstruction. To support a new data type, developers must implement the required reader/writer modules to deserialize/serialize the data.

The pipeline specification is provided to the Gadetron engine in the form of an XML document. This XML description lists the readers, writers, and Gadgets to include in the processing pipeline. The Gadgetron comes with a set of predefined reconstruction pipelines and the client can simply request which one to load. Alternatively, the client can transmit the XML description of the pipeline and assuming the requested Gadgets are available on the server, the pipeline will be loaded and raw data will be passed down the pipeline.

The Gadget modules are typically implemented in C/C++, but the framework also allows for modules to be implemented in scripting languages such as Python or MATLAB. The MATLAB integration requires that a MATLAB installation is available on the server that is running the Gadgetron engine. This MATLAB installation must be equipped with an appropriate license or access to a license server. The license requirements along with some performance issues associated with starting a MATLAB instance when MATLAB Gadgets load makes the MATLAB integration less attractive than the Python integration, but it is available as a prototyping tool. The scripting Gadgets provide a fast way to deploy existing prototype code on a clinical scanner. Subsequent development cycles can then be used to improve performance by moving critical pieces of the reconstruction to C/C++ Gadgets.

A set of C/C++ toolboxes are available as part of the Gadgetron framework. These toolboxes contain common components that are reused in several Gadgets. This includes data structures for storing and managing the acquisition data, filters, transforms (Fourier, wavelet, etc.), numerical solvers (conjugate gradient, nonlinear conjugate gradient, etc.), and other utilities. Much effort has been spent on tunings the computational efficiency and the use of parallel computing in these core components. The toolboxes can be used in stand-alone applications that do not use the Gadget pipeline architecture. The source code repository includes several such stand-alone applications that serve as examples of how to use key toolbox components. Of special note are several toolboxes that implement performance critical code on Graphical Processing Units (GPUs). One example is the non-Cartesian Fourier transform [7]. The GPU code uses NVIDIAs CUDA

framework [11]. The GPU based non-Cartesian FFT along with other key toolbox components (such as GPU solvers) form the basis for several high performance (real-time) implementations of non-Cartesian parallel imaging.

Siemens Healthcare scanner integration

The Gadgetron can be integrated with any commercial scanner platform, which allows sockets to be opened from the reconstruction pipeline in order to transmit data to the Gadgetron. The connection to the Gadgetron is achieved through a specialized ICE program called IceGadgetron. This ICE program is shared on the IDEA discussion board (https://www.mr-idea.com), where updated versions of binaries and source code are uploaded at regular intervals. The IceGadgetron package is known to work on *syngo* MR B, *syngo* MR D, and *syngo* MR E software versions.

The IceGadgetron package provides two key ICE Functors:
1) GadgetronEmitterFunctor (Emitter), and
2) GadgetronInjectorFunctor (Injector).
The role of these two Functors is illustrated in Figure 3. The Emitter is inserted into an existing ICE pipeline at the point where the developer would like the raw data (or images) to be transmitted to the Gadgetron and the Injector is inserted where the returned reconstruction products (usually images) are to be inserted back into the ICE pipeline. The location of the Emitter and the Injector can be controlled with a configuration file. In practice, each ICE reconstruction program that calls the IceGadgetron configurator is accompanied by a configuration document (in XML format) that specifies

3

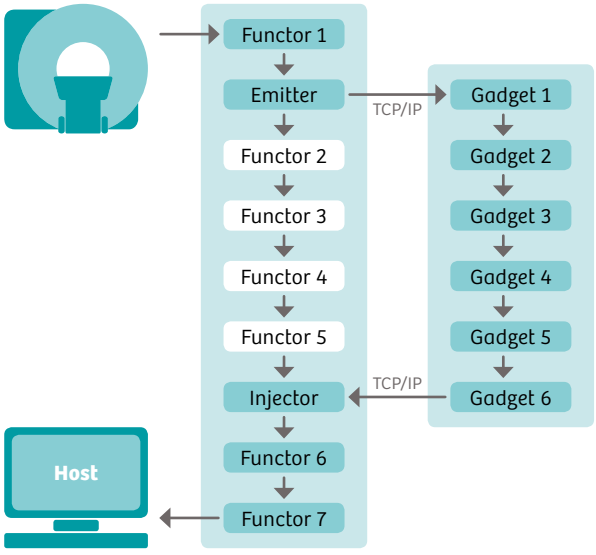

Figure 3: Schematic outline of the IceGadgetron package and connection to the Gadgetron. The IceGadgetron package provides two functors: The GadgetronEmitter, which translates the raw data to ISMRMRD format and sends it to the Gadgetron and the GadgetronInjector, which receives reconstructed images from the Gadgetron and injects them back into the ICE pipeline.

where the IceGadgetron Functors are to be inserted and other key configuration parameters such as which Gadgetron reconstruction program should be loaded. This allows the IceGadgetron program to be applied as an add-on to any existing reconstruction chain.

The Emitter plays multiple roles. Before sending any data from the current acquisition to the Gadgetron, it checks to see if there are any dependent measurements (such as noise measurements) for the current measurement and if so they are converted to ISMRMRD format and transmitted to the Gadgetron. It then converts the Siemens Healthcare specific raw data protocol (the sequences parameters) to an ISMRMRD header, which is transmitted to the Gadgetron. Finally, it does an on-the-fly conversion of each acquired raw data readout to ISMRMRD and transmits to the Gadgetron. Data is converted as it is acquired and transmitted to the Gadgetron immediately and consequently data processing on the Gadgetron starts immediately when data is available. This immediate transmission of data provides the Gadgetron framework with some performance advantages in a clinical setting compared to other prototyping environments that start data transmission when the acquisition is complete.

The Injector serves to receive images as they are returned to the Gadgetron. Once the images are back in the ICE environment, an appropriate header is attached to the images such that image numbering, timing information, etc., are attached to the image when they are inserted into the image database. After attaching a header to the images, they are passed down any remaining Functors in the ICE pipeline. This allows for post processing steps such as gradient distortion correction to be applied in the ICE environment where appropriate calibration information is available.

The Functors between the Emitter and the Injector are bypassed by default as indicated by the dotted outline in Figure 3, but it is also possible to operate IceGadgetron in such a way that the data is sent through both the Gadgetron and ICE pipelines. This may be useful for debugging and comparisons. However, since the Gadgetron is often used to deploy prototype reconstructions for which there may be no meaningful alternative in ICE, passing data through both pipelines is not always possible.

It is important to note that since conversion to DICOM images is done after the images return to the ICE environment, there is no need for patient identifying information (PII) to be sent to the Gadgetron. The ISMRMRD format defines header sections for PII (e.g., patient name), but when using the Gadgetron in conjunction with IceGadgetron, these header sections are not needed and are simply omitted. Consequently, the communication between the scanner and the Gadgetron is an anonymized stream of data. This is critical when considering deployment strategies where the Gadgetron engine is located outside the hospital firewalls. Such configuration options are discussed in more detail below.

Deployment strategies

The only requirement to connect a clinical MRI system to a Gadgetron instance is that the MRI system can open a TCP/IP network socket to either a local or remote Gadgetron instance. Some of the possible deployment topologies are outlined in Figure 4. The Siemens Healthcare reconstruction computer (the MRIR or MARS computer depending on software and hardware version) is equipped with a network interface, which is used to connect the ICE environment with the host. This network connection is configured with a local network IP address that only allows it to connect to the host, but there are two ways to utilize this network interface to provide access to a Gadgetron instance. A network switch can be inserted in the network between the MARS and the host computer. It should be noted that while such a switch used to be available *syngo* MR B line scanners, the newer *syngo* MR D and E systems do not ship with the switch since it is no longer needed. Inserting the switch is a modification of the system, which is not officially supported by Siemens Healthcare and may lead to loose the CE mark. Once the host and the reconstruction computer is connected via a switch, a Gadgetron reconstruction computer can be connected directly to this switch and given an IP address on the local network. This will allow the ICE environment to communicate directly with the Gadgetron computer. Alternatively, a Secure Shell (SSH) tunnel can be opened from the host computer and the ICE environment can connect to a remote Gadgetron through this tunnel; the connection will be made to the host, which will forward the connection. The ability to open a tunnel is built into the IceGadgetron package. Using a configuration file, the tunneling details can be specified such that the tunnel is automatically available in a way that is transparent to the user. When using a tunnel to connect to the Gadgetron, it is possible to use a Gadgetron server that is not directly connected to the MARS. This Gadgetron instance could be located somewhere else on network or it could be located at a remote location, e.g., in the cloud. Once a connection is made to cloud computing data center, it is possible to use Gadgetron topologies where multiple instances collaborate on the reconstruction thus reducing the reconstruction time of sophisticated algorithms to clinically acceptable reconstruction times [12].

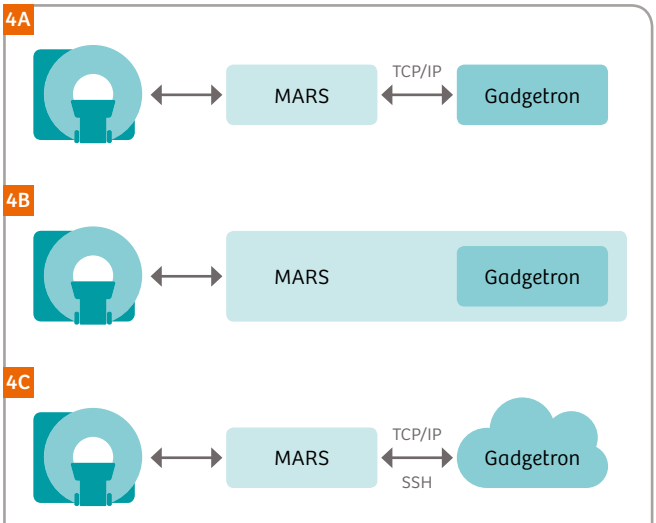

Figure 4: Gadgetron deployment topologies. The most straightforward way to connect the Gadgetron is with direct TCP/IP connection from the MARS to the Gadgetron **(4A)**. This requires a switch to be available on the local scanner network. Alternatively the Gadgetron may be deployed as a container directly on the MARS hardware **(4B)**. This enables Gadgetron operation without the installation of additional hardware. Finally the Gadgetron may be located on a remote system **(4C)**. When connecting to a remote system a Secure Shell (SSH) tunnel is opened from the host and the connection to the remote system is forwarded through this tunnel.

It is also possible to deploy the Gadgetron on Siemens Healthcare systems without installing any additional hardware. The Gadgetron development and deployment strategy (see Figure 4) makes heavy use of containers using either Docker [13] or chroot (https://en.wikipedia.org/wiki/Chroot) to manage application dependencies. It is possible to deploy such a container directly on the MARS computer and the IceGadgetron program can start and stop a Gadgetron instance automatically if configured to do so. This deployment strategy is a convenient way to deploy novel reconstruction algorithms directly on existing hardware. The Gadgetron containers can make full use of CPU and GPU hardware available on the MARS but the performance will ultimately be constrained by the hardware performance of the MARS. It should also be mentioned that ICE employs a proprietary memory management strategy that in general means that memory will not be released from the ICE environment once it has been allocated. On *syngo* MR E systems, IceGadgetron makes use of a mechanism to force the ICE environment to release reserved memory in order to make the memory available to the Gadgetron, but such a mechanism is not available on *syngo* MR D software releases. The deployment of the Gadgetron on the MARS system is only recommended for *syngo* MR E systems.

Development model

Open source software principles are key to the Gadgetron development model. The source code for the Gadgetron and ISMRMRD projects is freely available on Github (https://github.com). Changes to the source code are managed and reviewed through the online collaborative tools made available at that site. Changes are proposed as source code pull requests and after discussion and revision, they are merged into the source code. The development workflow is outlined in Figure 5. Modifications to the Gadgetron (or a dependency) triggers an automated build system to start compiling the source code on Windows, Linux, and Mac computers. If the code compiles, it is automatically tested. The test suite consists of a collection of unit tests for toolbox level components and a number of integration tests. The integration tests convert real raw data

5

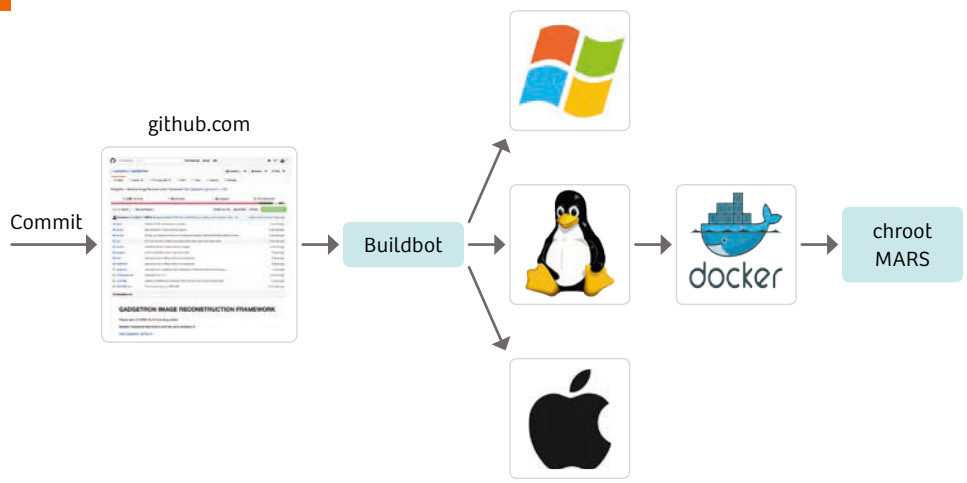

Figure 5: The Gadgetron development pipeline. Collaboration and code management is done using Github (https://github.com/gadgetron). Once code modifications are merged, the software is automatically built and tested on Windows, Linux, and Mac computers. Docker containers with all dependencies are generated and tested and the container images can be deployed directly on the Siemens Healthcare MARS computer.

sets to ISMRMRD format and reconstructs images with different image reconstruction pipelines. The reconstruction results are compared to a database with reconstruction results to detect any changes in reconstruction results. If all tests pass, the tested version of the Gadgetron with all dependencies is immediately released as a Docker image on Docker Hub (https://hub.docker.com/r/gadgetron). The build system tests multiple configuration options. In particular, multiple versions of NVIDIA CUDA are tested and Docker images based on different versions are released.

The Docker containers can be deployed immediately on any computer with the Docker engine installed. The containers will run natively on Linux and using a hypervisor on Windows and Mac computers. Consequently, it is relatively easy to install and run the Gadgetron, even for users with little or no experience in building software. The Gadgetron also comes with a script that allows the user to turn the Docker images into a chroot image that can be deployed directly on the Siemens Healthcare MARS computer as explained above. The conversion to chroot image is necessary at the moment because the MARS system does not have the required Docker engine installed.

Example applications

The Gadgetron supports a wide range of applications. Several of these applications are in the real-time imaging and cardiac imaging area due to the early developers of the Gadgetron, but as the community around the framework has grown, the applications have grown to be more generic and broadly applicable. The following sections describe four different use cases for the Gadgetron. Firstly, a generic, high performance parallel imaging reconstruction pipeline is discussed. It forms the backbone of several image reconstruction chains and provides image reconstruction performance metrics (such as g-factor maps from accelerated parallel imaging) in addition to high quality reconstructions. Secondly, interactive real-time imaging used in interventional image guidance is demonstrated. Thirdly, motion corrected, phase sensitive, inversion recovery reconstruction is highlighted as an application where the Gadgetron can be used to improve clinical workflow. Finally, retrospective respiratory motion correction for free breathing cardiac cine imaging is shown as an example of using the Gadgetron in the cloud.

Generic parallel imaging reconstruction pipeline

A multi-purpose, Cartesian parallel imaging pipeline forms the backbone of many clinical and research applications supported by the Gadgetron. The reconstruction algorithm is based on the GRAPPA algorithm [3], but the *k*-space kernels are Fourier transformed to image space and applied as coil combining coefficients in image space [14]. Based on the coil combining coefficients, parallel imaging related noise amplification is directly estimated in the form of *g*-maps. The reconstruction uses information about the receiver noise covariance matrix to maintain unit noise scaling throughout the image reconstruction pipeline and consequently, it can produce images that are reconstructed in signal-to-noise ratio (SNR) units [15, 16].

Figure 6 shows the Gadgets involved in this SNR scaled parallel imaging pipeline. Many of these Gadgets are reused in other reconstruction pipelines, which illustrates the modularity of the framework. Most Gadgetron reconstruction pipelines include the NoiseAdjust Gadget, which is responsible for noise prewhitening either based on noise samples acquired in a previous scan or inline noise measurements included with the data. After removing oversampling in the readout direction and partial Fourier (assymetric echo) adjustment, the data hits two commonly used Gadgets, the accumulation-and-triggering Gadget and the bucket-to-buffer Gadget. These two work in tandem to organize the incoming data before reconstruction. The accumulate-and-trigger Gadget simply stores the data while it waits for some trigger to occur. An example of such a trigger could be that the repetition number increases. Once the trigger occurs, the accumulated data (stored in

unorganized buckets) is passed on to the bucket to buffer mechanism, which will assemble the data in buffer structures that in the case of Cartesian imaging simply are *k*-spaces buffers. The buffers then pass into the reconstruction part of the pipeline where reference data is used to generate coil combining coefficients. After the image reconstruction there are multiple post-production steps that ready the images for return to the scanner. In this specialized reconstruction pipeline, there are also some additional Gadgets that output image and coil statistics, which are useful for evaluating reconstruction results.

Figure 7 shows example images from the generic parallel imaging reconstruction chain. The example is a rate 4 parallel imaging, real-time cine acquisition of a four-chamber view of the heart. The top image shows one frame of the real-time imaging series. The middle image is the *g*-map, which is produced by the reconstruction chain and the bottom image is the SNR scaled reconstruction. The SNR scaling feature of the Gadgetron reconstruction chain enables on-the-fly evaluation of reconstruction results and comparisons between patients and coils.

6

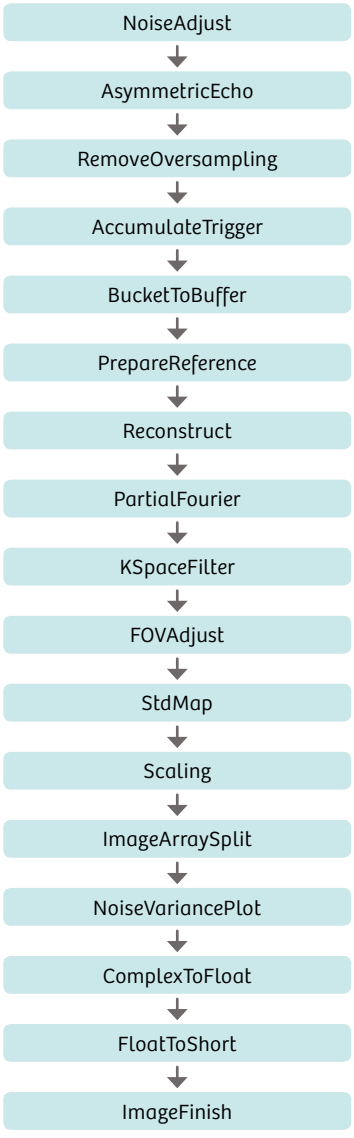

Figure 6: Generic parallel imaging reconstruction pipeline. Unit noise variance is established by the NoiseAdjust Gadget and maintained throughout the pipeline. The pipeline can produce images reconstructed in units of signal-to-noise ratio (SNR) [15].

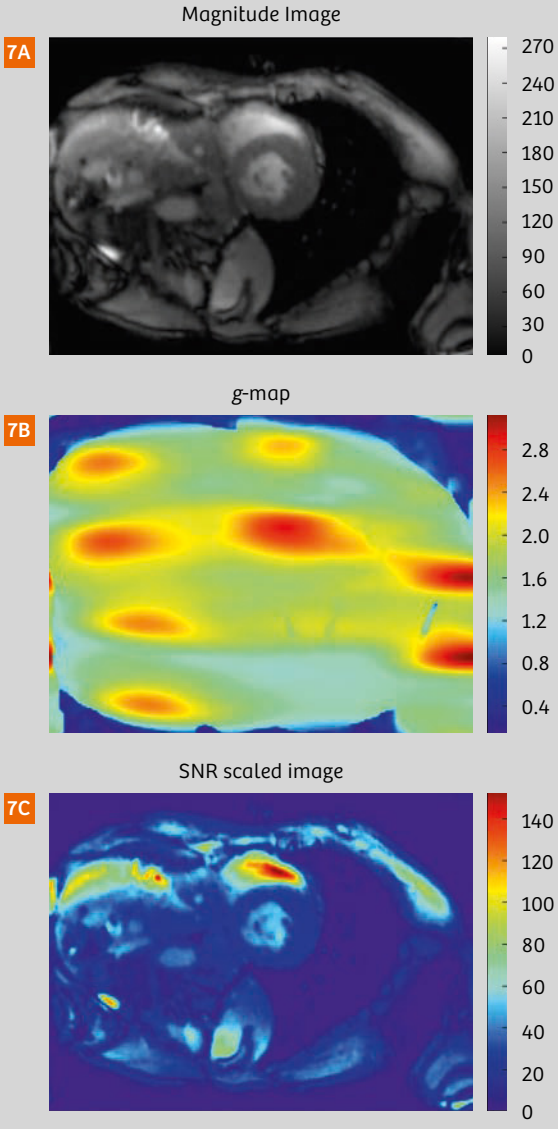

Figure 7: Example images from generic parallel imaging reconstruction pipeline. Data is from a real-time (acceleration rate 4) cardiac cine acquisition showing the heart in a four-chamber view. Top image **(7A)** is the magnitude image, middle image **(7B)** is the *g*-map, and bottom image **(7C)** is the image displayed in units of SNR. Notice how the SNR is higher closer to the coils on the chest.

8

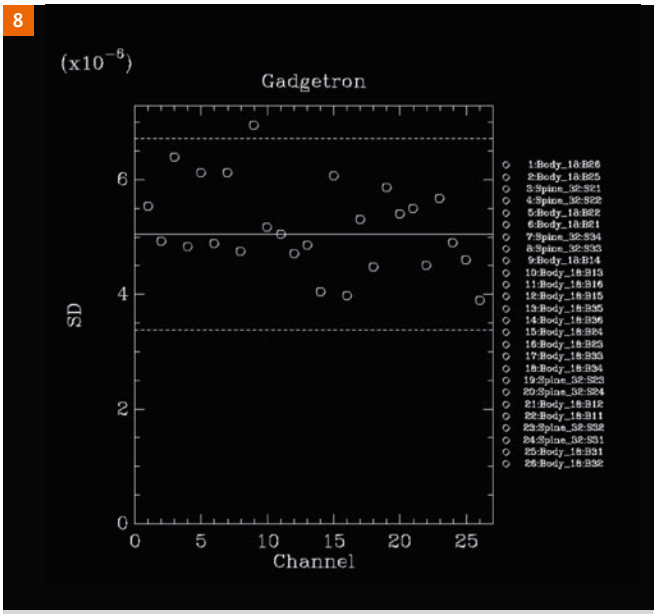

Figure 8: Noise standard deviation plot produced by the generic parallel imaging reconstruction chain. The plot shows the noise level in each employed channel and can be used to pinpoint faulty coil elements.

9

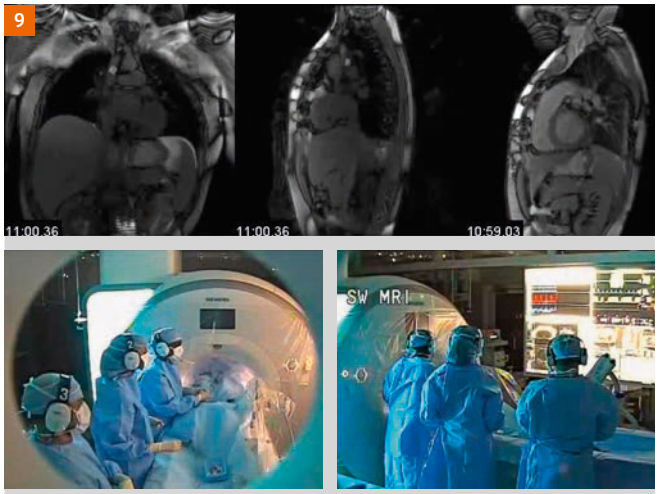

Figure 9: Real-time interventional MRI using the Gadgetron. The top row of images shows example real-time frames used to guide a passive catheter in the patient. The tip of the catheter is equipped with a balloon filled with a Gadolinium based contrast agent. An interactively controlled saturation pulse is used to provide contrast between balloon and surrounding tissue. Bottom row of images shows the interventional cardiologists using the real-time images for navigation.

Figure 8 shows another output from the generic reconstruction chain, which is a plot of the standard deviation of the noise in each channel used in the current reconstruction. This plot is useful in evaluating the performance of the currently used receive chain components. In the example plot, the coil elements have noise standard deviations in the same range, but faulty coil elements are quickly identified as having very high noise level or no noise at all. Users of the Gadgetron have found it useful to run at least one scan in each study, which outputs such an image. It can then be reviewed later as part of standard quality assurance procedures where it can help pinpoint faulty equipment.

Real-time interventional image guidance

One of the original motivations for creating the Gadgetron was to provide a high-performance environment in which to perform real-time reconstruction on the GPU. One of the driving applications for this was interventional MRI [17, 18]. For this application, real-time images must be reconstructed and displayed with low latency to allow the operator to manipulate instrumentation in the patient under MRI guidance. Figure 9 shows images from a diagnostic catheterization performed under MRI guidance. The top row shows example real-time guidance images and the bottom images show how the operator in the scanner room can use these images for navigating the catheters inside the patient. Typically one to three real-time slices are imaged simultaneously and the operator can manipulate the location of these slices interactively. Clinicians have also found it useful to be able to change imaging parameters such as parallel imaging acceleration factor on-the-fly. This enables interactive trade-off between SNR and imaging speed. The Gadgetron comes with a real-time reconstruction chain that can adapt when parallel imaging factor changes.

Siemens Healthcare has released a WIP for interventional MRI based on the BEAT_IRTTT sequence[1]. This sequence can be used with the Siemens Healthcare Interactive Front End (IFE) for interventional MRI. The distributed WIP does not ship with the Gadgetron, but the sequence has the required functionality to communicate with a Gadgetron installation running on either the MARS or an external workstation or server as described above.

Motion corrected, Phase Sensitive Inversion Recovery

Imaging of Late Gadolinium Enhancement (LGE) is the gold standard for assessing myocardial viability [19, 20]. The assessment has traditionally been done with a segmented, Inversion Recovery (IR) sequence acquired during a breath-hold [21]. It is possible to use a magnitude based reconstruction or Phase Sensitive Inversion Recovery (PSIR) [22]. The breath-holding technique can suffer from motion artifacts and thus motion corrected, free-breathing techniques [23] are gaining popularity. More recently, LGE imaging has also been combined with dark blood pre-paration to improve the blood to scar contrast [24].

[1] WIP, the product is currently under development and is not for sale in the US and in other countries. Its future availability cannot be ensured.

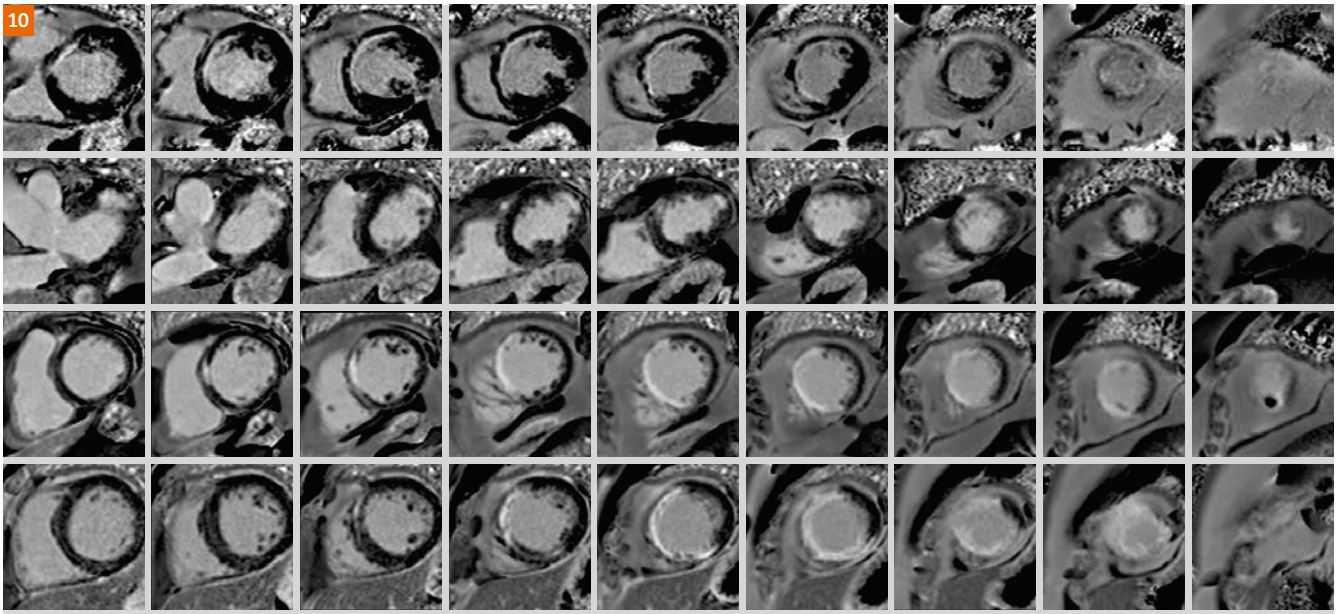

Figure 10: Example LGE stacks reconstructed with the motion corrected, PSIR reconstruction included in the Gadgetron. Stacks of 9 short-axis images can be acquired and reconstructed in approximately 2.5 minutes.

The Gadgetron incorporates reconstruction pipelines for all the popular LGE imaging options including non-rigid motion correction. The reconstruction has been implemented in such a way that multi-slice acquisitions can be reconstructed on-the-fly as they are acquired. While this is a small modification compared to current product pipelines, it has significant impact on workflow. Stacks of LGE images take a substantial amount of time to reconstruct when including motion correction. If this reconstruction does not start until the acquisition is done, it slows down the clinical workflow. Figure 10 shows example LGE short axis stacks, which have been acquired during free breathing and reconstructed using the Gadgetron. Acquisition time for a full stack of slices is on the order of 2.5 minutes. The reconstruction is complete approximately 5 seconds after the end of the scan.

Free-breathing, motion corrected cine imagine of the heart

Cardiac MRI is the gold standard for evaluating cardiac motion and function [25]. Traditionally, this evaluation has been done with a stack of short axis slices acquired during breath-holding. Typically 1–2 slices are acquired in a breath-hold and 9–13 slices are acquired to cover the ventricles. Multiple breath-holds are a significant challenge for cardiac patients in general and it represents a real impediment in pediatric[2] patients. Alternatively, a stack of real-time acquisitions can be prescribed, but the compromised spatial and/or temporal resolution makes it a less attractive option.

To overcome these problems, it was proposed that a series of real-time images acquired over multiple heart beats could be motion corrected, and the motion corrected data could be reassembled (also known as rebinning) with better temporal resolution [26, 27]. The techniques have been improved to use less data [28] and methods that handle non-Cartesian sampling have also been proposed [29]. Figure 11 shows example short axis images acquired with the free-breathing, motion corrected binning technique. The results are compared to breath-hold imaging and free-breathing with multiple averages. The motion correction algorithms increase the reconstruction time. It can be on the order of 1–2 minutes per slice, which is not tolerable clinically. The Gadgetron comes with an implementation of motion corrected binning, and it has been demonstrated that cloud computing can be used in conjunction with motion corrected binning [30]. With this approach, multiple instances of the Gadgetron collaborate on a given reconstruction, effectively assigning an independent computational node to each acquired slice. Since reconstruction of a given imaging slice can start as soon as the acquisition of that slice is complete, the reconstruction cost can be hidden by the acquisition such that the final images are reconstructed and back on the host computer within a minute of the acquisition finishing. Using the binning technique, the acquisition time of each slice is slightly longer than a breath-hold, typically 16–20 seconds, but it is acquired during free-breathing and no pause is needed between slices for the patient to catch their breath. The net result is an overall faster workflow and improved patient comfort.

[2] Siemens Healthcare Disclaimer: MR scanning has not been established as safe for imaging fetuses and infants less than two years of age. The responsible physician must evaluate the benefits of the MR examination compared to those of other imaging procedures.

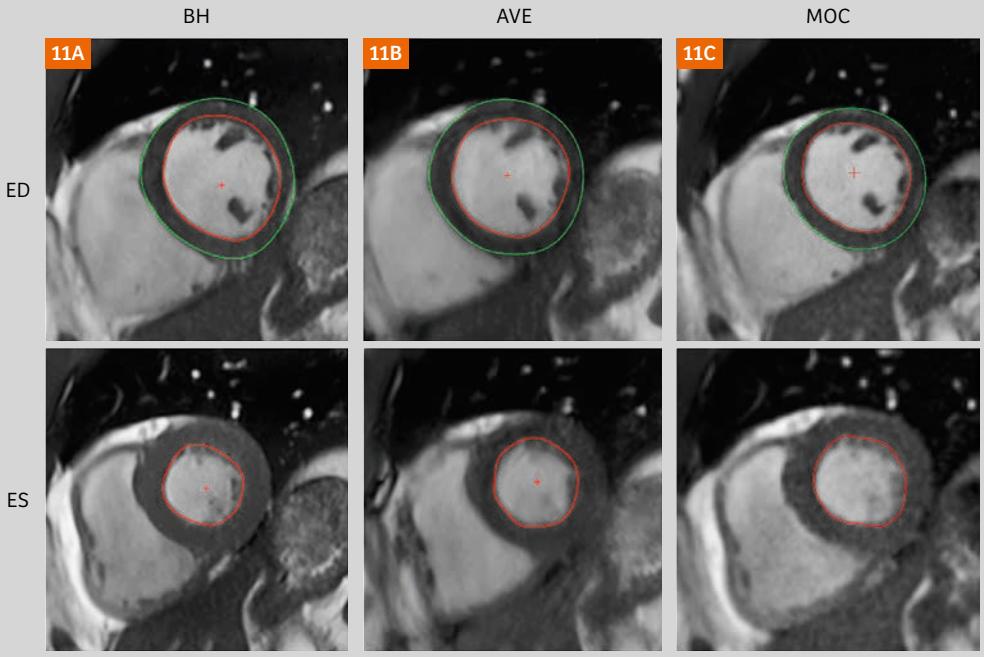

Figure 11: Example cardiac function images comparing three acquisition techniques: **(11A)** breath-hold (BH) segmented, **(11B)** free-breathing, multiple averages (AVE), **(11C)** free-breathing motion corrected (MOC) binning. Frames are shown for End Diastole (ED) and End Systole (ES).

Discussion and conclusions

The Gadgetron is an open source image reconstruction engine, which has been used extensively for MRI reconstruction. It is a client-server architecture that can be used as a stand-alone desktop image reconstruction system or it can be connected directly to clinical MRI systems by letting the vendor reconstruction act as a Gadgetron client. The internal MRI data format is the open ISMRM Raw Data standard and with converters being available for most major vendors, it can be used as a cross vendor image reconstruction platform. The framework is also cross-platform in the sense that it builds and runs on Windows, Linux, and Mac, which gives researchers flexibility to integrate it into existing work flows and infrastructure. Through the open development model, community contributions are encouraged and merged changes are continuously compiled, tested, and released for the community to use. The Gadgetron build systems produce containerized distributions that come with all necessary dependencies and can be deployed easily.

When used with Siemens Healthcare MRI scanners, a dedicated ICE program (IceGadgetron) can be used to add Gadgetron connectivity to any existing ICE program. The IceGadgetron program manages Gadgetron connection and measurement dependencies in a transparent way and the Gadgetron can be used in a clinical workflow without the need for expert research staff on site. This facilitates deployment of novel reconstruction algorithms in a clinical setting.

The Gadgetron is distributed with a wide range of ready-to-use reconstruction pipelines. These include generic parallel image reconstruction pipelines that support a wide range of parallel imaging strategies, including several commonly used strategies for acquiring calibration data. There are also several specialized reconstruction applications ranging from real-time non-Cartesian parallel imaging using GPU acceleration to cardiac imaging using free-breathing, motion correction strategies.

One of the main aims of the Gadgetron project is to provide the research community with access to completely open source implementations of robust, production quality reconstruction pipelines. The reconstruction components are a good place to start for new researches in the field and they provide a relevant reference point for reconstruction quality comparisons in scientific publications. Community participation is very much encouraged and software patches, bug fixes, and suggestions are welcomed by the growing group of people developing Gadgetron source code. The modularity of the Gadgetron also invites researchers to use it as a deployment vehicle for their own algorithms. The Gadgetron pipeline in combination with the IceGadgetron programs is a practical platform for deploying novel reconstruction algorithms in a clinical environment. External algorithms can be supplied as C/C++, Python, or Matlab code.

In conclusion, the Gadgetron aims to overcome some of the main limitations in current image reconstruction research; it provides open access to algorithm source code, is a rapid prototyping environment, and facilitates clinical deployment for rigorous testing.

References

1 Sodickson DK, Manning WJ. Simultaneous acquisition of spatial harmonics (SMASH): fast imaging with radiofrequency coil arrays. Magn Reson Med. 1997 Oct;38(4):591–603.
2 Pruessmann KP, Weiger M, Scheidegger MB, Boesiger P. SENSE: sensitivity encoding for fast MRI. Magn Reson Med. 1999 Nov;42(5):952–62.
3 Griswold MA, Jakob PM, Heidemann RM, Nittka M, Jellus V, Wang J, et al. Generalized autocalibrating partially parallel acquisitions (GRAPPA). Magn Reson Med. 2002 Jun;47(6):1202–10.
4 Lustig M, Donoho DL, Santos JM, Pauly JM. Compressed sensing MRI. Signal Process Mag IEEE. 2008;25(2):72–82.
5 Hansen MS, Sørensen TS. Gadgetron: An open source framework for medical image reconstruction. Magn Reson Med. 2012 Jul 12;
6 Hansen MS, Kellman P. Image reconstruction: An overview for clinicians. J Magn Reson Imaging. 2014 Jun 25;
7 Sorensen TS, Schaeffter T, Noe KO, Hansen MS. Accelerating the nonequispaced fast Fourier transform on commodity graphics hardware. Med Imaging, IEEE Trans. 2008;27(4):538–47.
8 Hansen MS, Atkinson D, Sorensen TS. Cartesian SENSE and k-t SENSE reconstruction using commodity graphics hardware. Magn Reson Med. 2008;59(3):463–8.
9 Sorensen TS, Atkinson D, Schaeffter T, Hansen MS. Real-time reconstruction of sensitivity encoded radial magnetic resonance imaging using a graphics processing unit. Med Imaging, IEEE Trans. 2009;28(12):1974–85.
10 Inati SJ, Naegele JD, Zwart NR, Roopchansingh V, Lizak MJ, Hansen DC, et al. ISMRM Raw data format: A proposed standard for MRI raw datasets. Magn Reson Med. 2017 Jan;77(1):411–21.
11 Nickolls J, Buck I, Garland M, Skadron K. Scalable parallel programming with CUDA. Queue. 2008 Mar 1;6(2):40.
12 Xue H, Inati S, Sørensen TS, Kellman P, Hansen MS. Distributed MRI reconstruction using gadgetron-based cloud computing. Magn Reson Med. 2015 Mar;73(3):1015–25.
13 Merkel, Dirk. Docker: lightweight Linux containers for consistent development and deployment. Linux J. 2014;2014(239):2.
14 Saybasili H, Kellman P, Griswold MA, Derbyshire JA, Guttman MA. HTGRAPPA: Real-time B 1 -weighted image domain TGRAPPA reconstruction. Magn Reson Med. 2009 Jun;61(6):1425–33.
15 Kellman P, McVeigh ER. Image reconstruction in SNR units: a general method for SNR measurement. Magn Reson Med. 2005 Dec;54(6):1439–47.
16 Kellman P. Erratum to Kellman P, McVeigh ER. Image reconstruction in SNR units: a general method for SNR measurement. Magn Reson Med. 2005;54:1439–1447. Magn Reson Med. 2007 Jul;58(1):211–2.
17 Razavi R, Hill DL, Keevil SF, Miquel ME, Muthurangu V, Hegde S, et al. Cardiac catheterisation guided by MRI in children and adults with congenital heart disease. Lancet. 2003 Dec 6;362(9399):1877–82.
18 Ratnayaka K, Faranesh AZ, Hansen MS, Stine AM, Halabi M, Barbash IM, et al. Real-time MRI-guided right heart catheterization in adults using passive catheters. Eur Heart J. 2013Feb;34(5):380–9.
19 Kim RJ, Fieno DS, Parrish TB, Harris K, Chen EL, Simonetti O, et al. Relationship of MRI delayed contrast enhancement to irreversible injury, infarct age, and contractile function. Circulation. 1999 Nov 9;100(19):1992–2002.
20 Fieno DS, Kim RJ, Chen EL, Lomasney JW, Klocke FJ, Judd RM. Contrast-enhanced magnetic resonance imaging of myocardium at risk: Distinction between reversible and irreversible injury throughout infarct healing. J Am Coll Cardiol. 2000;36(6):1985–91.
21 Kim RJ, Shah DJ, Judd RM. How we perform delayed enhancement imaging. J Cardiovasc Magn Reson. 2003 Jul;5(3):505–14.
22 Kellman P, Arai AE, McVeigh ER, Aletras AH. Phase-sensitive inversion recovery for detecting myocardial infarction using gadolinium-delayed hyperenhancement. Magn Reson Med. 2002 Feb;47(2):372–83.
23 Ledesma-Carbayo MJ, Kellman P, Arai AE, McVeigh ER, McVeigh ER. Motion corrected free-breathing delayed-enhancement imaging of myocardial infarction using nonrigid registration. J Magn Reson Imaging. 2007 Jul;26(1):184–90.
24 Kellman P, Xue H, Olivieri LJ, Cross RR, Grant EK, Fontana M, et al. Dark blood late enhancement imaging. J Cardiovasc Magn Reson. 2017 Jan 7;18(1):77.
25 Hundley WG, Bluemke DA, Finn JP, Flamm SD, Fogel MA, Friedrich MG, et al. ACCF/ACR/AHA/NASCI/SCMR 2010 Expert Consensus Document on Cardiovascular Magnetic Resonance. J Am Coll Cardiol. 2010 Jun 8;55(23):2614–62.
26 Kellman P, Chefd'hotel C, Lorenz CH, Mancini C, Arai AE, McVeigh ER. Fully automatic, retrospective enhancement of real-time acquired cardiac cine MR images using image-based navigators and respiratory motion-corrected averaging. Magn Reson Med. 2008 Apr;59(4):771–8.
27 Kellman P, Chefd'hotel C, Lorenz CH, Mancini C, Arai AE, McVeigh ER. High spatial and temporal resolution cardiac cine MRI from retrospective reconstruction of data acquired in real time using motion correction and resorting. Magn Reson Med. 2009 Dec;62(6):1557–64.
28 Xue H, Kellman P, LaRocca G, Arai AE, Hansen MS. High spatial and temporal resolution retrospective cine cardiovascular magnetic resonance from shortened free breathing real-time acquisitions. J Cardiovasc Magn Reson. 2013 Nov 14;15(1):102.
29 Hansen MS, Sørensen TS, Arai AE, Kellman P. Retrospective reconstruction of high temporal resolution cine images from real-time MRI using iterative motion correction. Magn Reson Med. 2012Sep;68(3):741–50.
30 Cross R, Olivieri L, O'Brien K, Kellman P, Xue H, Hansen M. Improved workflow for quantification of left ventricular volumes and mass using free-breathing motion corrected cine imaging. J Cardiovasc Magn Reson. 2016 Feb 25;18:10.

Contact



Michael S. Hansen, Ph.D.
Laboratory of Imaging Technology
National Heart, Lung, and
Blood Institute
National Institutes of Health

Building 10 Room B1D405
9000 Rockville Pike
Bethesda, MD 20814
USA
Phone: +1-301-496-1457
Cell: +1-301-412-9671
michael.hansen@nih.gov

MRI at UK Biobank

Niels Oesingmann[1]; Paul M. Matthews[2]; Karla Miller[3]; Stephen Smith[3]; Stefan Neubauer[4]; Steffen E. Petersen[5]; Jimmy Bell[6]

[1] UK Biobank, Stockport, Cheshire, UK
[2] Imperial College, Edmond and Lily Safra Chair, Division of Brain Sciences, Imperial College London, UK
[3] Oxford Centre for Functional Magnetic Resonance Imaging of the Brain (FMRIB), Oxford, UK
[4] John Radcliffe Hospital, Oxford, UK
[5] William Harvey Research Institute, London, UK
[6] University of Westminster, London, UK

Introduction

UK Biobank is a large prospective cohort study designed to understand the causes of common chronic disease with the aim of improving the prevention, diagnosis, and treatment of a wide range of serious and life-threatening illnesses – including cancer, heart diseases, stroke, diabetes, arthritis, osteoporosis, eye disorders, depression, and forms of dementia. UK Biobank recruited 500,000 people aged between 40–69 years in 2006–2010 from across Great Britain to take part in this project. They have undergone a range of physical measures, provided detailed information about themselves, and have given blood, urine, and saliva samples for future analysis. Also, participants agreed to have their health followed throughout their lives through linkage to their medical records. This will help scientists clarify why some people develop particular diseases and others do not.

In 2012, a proposal for an imaging enhancement in 100,000 participants was made to quantify detailed phenotypes that may be associated with disease and enhance the power to detect associations with incident health outcomes. The simultaneous imaging of brain, heart, arteries, abdomen, and bone in each individual participating in the imaging enhancement and the combination of these data would provide a dataset that is uniquely able to allow questions to be addressed regarding the relationships between phenotypes across organ systems and allowing assessment of pathophysiological mechanisms operating at a systemic level. For example, the relationships between obesity and aging-related macrostructural brain changes with later-life cognitive dysfunction [1] may suggest specific mechanisms and associations with incident disease and need further exploration in much larger datasets. Such correlations, which are based on prevalent disease, also need to be extended to studies of the associations of pre-symptomatic measures of body phenotype (e.g. body MRI and dual-energy X-ray absorptiometry (DXA)) with future brain health outcomes. The potential to relate longer term clinical and cognitive dysfunction outcomes to sensitive brain structural and functional markers, cardiac and body composition phenotypes (as well as to information on blood markers, lifestyle, and clinical history) would allow new depths of exploration of risk and pathogenic mechanisms, and the generation of new hypotheses regarding possible modifying factors. In the shorter term, value of the imaging enhancements in UK Biobank can be realised through cross-sectional case-control studies, e.g., relating brain imaging differences to prevalent brain disease or to independent phenotypic measures.

The pilot phase of imaging 5,500 participants was completed in September 2015. Further funding allowed for the main phase to start in 2016. In total, over 14,000 participants have already been scanned and imaging data from 10,000 subjects has been released for use by the international research community (http://www.ukbiobank.ac.uk/2017/02/new-data-from-brain-imaging-and-on-heart-attacks-and-strokes-available/). As many as 100 research groups are accessing the imaging data for their research.

The imaging methods employed are: magnetic resonance imaging (MRI), carotid ultrasound, and dual-energy X-ray absorptiometry. For MRI, three specific areas of interest were identified: brain, heart, and body imaging. The specifics of each MR application are described in the following sections.

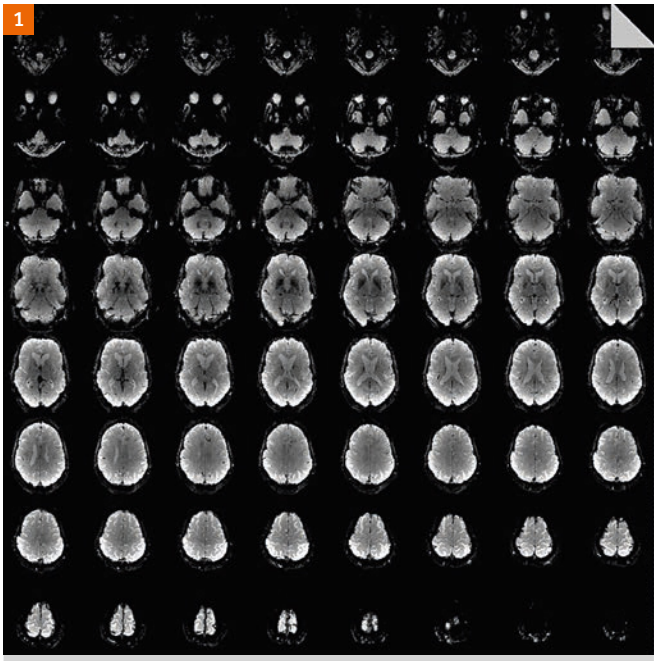

Figure 1: fMRI time point with simultaneous excitation of 8 slices.

MR imaging

To meet the temporal, financial, and geographic constraints of scanning 100,000 participants, the measurements are made in three different locations each fitted with two scanners (one 3T MAGNETOM Skyra and one 1.5T MAGNETOM Aera). Scanning sites were selected to allow maximize volunteer recruitment from UK Biobank participants across the UK. Currently, the primary site in Stockport, near Manchester, UK, is running with an average of 17 participants scanned per day (strictly within 12 h) on 7 days per week. The second site in Newcastle, UK, will be operational in April 2017 using the identical software and protocols. A third site in Reading, UK, will receive participants at the end of 2017. The brain program runs for about 30 minutes exclusively on the 3T systems, while an integrated body and cardiac program is measured on the 1.5T scanners for 10 and 20 minutes, respectively.

Major challenges, as one might expect, centre on the selection of the specific applications within each body region, the choice of measurement techniques, and the setting of protocol parameters. The need for data harmonization means that these decisions, which were made based on experience in the pilot phase, will be applied for all data acquisition in the next phase of development of the resource. Many developers and subject matter experts worldwide have contributed to the selection and optimization of the final imaging sequences and data management. An externally chaired imaging working group (constituted from leading UK academic researchers in relevant areas) has been responsible for the design of the imaging enhancements. Pre-piloting the feasibility of the proposed imaging protocols for each of the separate elements of the imaging assessment visit informed the final program further. There has also been careful consideration and consultation on the issue of providing feedback on incidental findings from imaging, including the implementation of a prospective study of unexpected findings of potential medical significance and both their clinical consequences and impact on lives of the volunteers affected.

Considerable effort within and outside Biobank is devoted to data transfer and security. This includes the encoding and separation of personal information to allow complete DICOM streams to be provided.

Along with the protocol for examinations, a quality assurance procedure was developed. There are three different quality aspects to consider over time: the status of the scanners, the actual scanning of participants, and the evaluation of data. The first aspect is realized by a regular high resolution phantom scan which detects B_0 and B_1 variations of the hardware as early as possible. Close cooperation with the service department is important in order to resolve potential issues as fast as possible and the proactive effort of the service employees is much appreciated. The second aspect requires the active participation of radiographers in an unconventional way. The scan protocol must change as little as possible while the circumstances and constancy of parameters must be checked as often as possible. While the orientation and position of an oblique protocol is slightly adjusted to the tilt of the head, none of the other scan parameters are modified. This also means, for example, that exactly 6 stages for the complete body are scanned irrespective of the height of the participant. This is a consequence of the decisions to keep both the measurement and acquisition time fixed. Hence, one must not underestimate the role of education and the challenges of an environment where the creative optimization and adjustment of protocols to the subject are neither desirable nor permitted. Tools are currently being developed to provide automatic checks against constancy of relevant parameters. The third aspect requires an evaluation of the resulting scans via the review of a number of defined image parameters. This depends on the evaluation chain of developers and it is important to establish a close feedback process.

Brain imaging

The brain MRI protocol will provide researchers with data concerning both brain structure and function from a single, short examination, including data to reconstruct the major white matter connection pathways. Each participant undergoes a 32-minute brain MRI protocol using a 3 Tesla MAGNETOM Skyra. This provides T1- and T2-weighted FLAIR structural 3D MRI, functional MRI during rest and task performance, whole-brain diffusion tensor imaging, susceptibility-weighted imaging (SWI), and arterial spin labeling (ASL).

The brain program comprises the following protocols:

- AutoAlign Scout images
- T1-weighted structural morphology MPRAGE with iPAT 2
- fMRI resting state protocol with simultaneous excitation of 8 slices
- fMRI task performance protocol with simultaneous excitation of 8 slices
- T2-weighted 3D FLAIR with iPAT 2
- Diffusion AP b = 0, b = 2 ms/μm^2 with 6 directions and simultaneous excitation of 3 slices
- Diffusion PA b = 0, 104 directions in total distributed over two shells with b = 1 and 2 ms/μm^2 with simultaneous excitation of 3 slices
- 3D SWI iPAT 2
- 3D pcASL

Highly efficient scanning protocols are needed to allow the full range of imaging and other phenotype measures to be obtained on each volunteer. To perform this imaging program within the limited time allocated, the use of acceleration techniques, in particular the simultaneous excitation of multiple slices, is required. It is also apparent

that the acquisition of data is tuned to the minimum required while the data quality and contrast aims to be the best per unit time of acquisition.

Cardiac imaging

Cardiovascular MRI is considered the most versatile and precise technique for simultaneous assessment of multiple cardiac parameters. Its reproducibility and non-invasiveness are key advantages for large-scale population studies over other imaging modalities such as echocardiography. An additional attractive feature for large scale population studies is that volunteers are not subjected to any potentially harmful radiation (as with cardiac CT). A major strength of CMR is the ability to obtain multi-parametric images in one imaging session related to both structure and function of the heart. A 20-minute protocol using a 1.5 Tesla scanner provides time-dependent heart chamber volumes, cardiac wall thickness and mass, tissue motion using tagging, and aortic size and compliance. In addition, the aortic flow quantitation is performed and the myocardial T1 is estimated.

The cardiovascular program consists of the following protocols:

- Cine scanning of the left ventricular long and short axis views
- Cine scan of the left ventricular outflow tract with ascending aorta
- Cine tagging of 3 short axis planes around the middle of the left ventricle
- Cine cross section of ascending aorta and proximal descending aorta
- Through-plane flow measurement of ascending aorta
- T1 mapping of mid-ventricular slice

Body imaging

There are a number of methods for estimating body fat content (such as the BMI, waist-hip circumference, and bio-impedance measures already included in UK Biobank). However, such estimates are imprecise (although still have predictive power) and cannot be used to assess adipose tissue distribution, which is both an individually distinctive phenotype and a determinant of relative disease risk. MRI can provide much more accurate information on fat content and distribution, muscle mass, and organ volume. A wide variation has been found between individuals in the amount of visceral, muscle, and liver fat for any given body mass index (BMI), waist-to-hip ratio (WHR), and total amount of body fat [5]. There is increasing evidence to suggest that fat distribution, rather than amount of fat, is important for determining an individual's risk of future disease [2, 3]. Body MRI provides an opportunity to examine the predictive importance of particular fat deposits (visceral, liver and pancreas) and the relative distribution of fat for the development of particular conditions (e.g. vascular disease, diabetes, and certain types of cancer). The 10-minute protocol on a 1.5 Tesla scanner provides quantitative information on subcutaneous-abdominal and visceral adipose tissue volumes and distribution and on intra-hepatocellular and intra-pancreatic lipid.

The body program comprises the following protocols:

- Dixon imaging of 6 contiguous stages beginning from neck downwards to the knees
- T1-weighted VIBE of pancreas

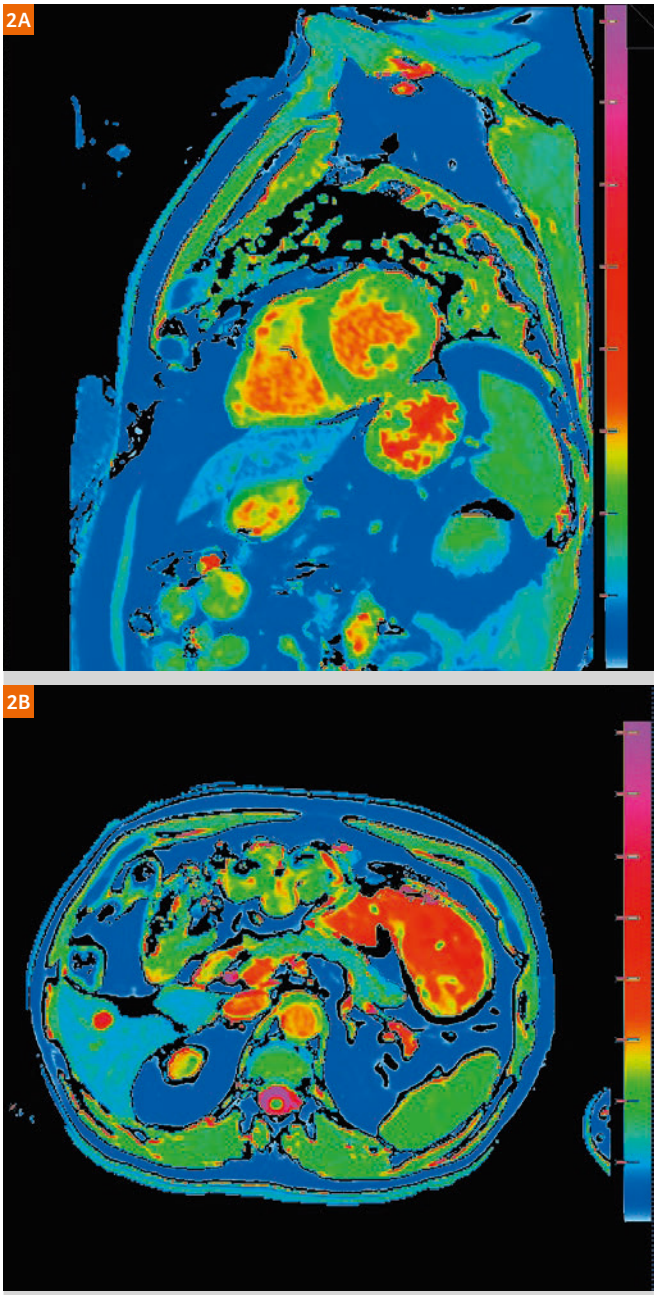

Figure 2: Computed T1 maps of heart and pancreas after acquisition of shMOLLI.

- T1 mapping of mid-liver axial cross-section
- T2*-weighted multi-echo imaging of liver cross-section
- T1-mapping of pancreas cross-section
- T2*-weighted multi-echo imaging of pancreas cross-section

Summary

The multi-modal imaging enhancement of 100,000 UK Biobank participants is well underway. This brief article presents an overview of the measurements within 1 hour of scan time with excellent quality. This, however, requires a strict regime of timing and scheduling to be performed successfully. UK Biobank solved a variety of challenges related to the infrastructure and logistics of the daily throughput. We would like to further stimulate the interest of researchers in using the unique dataset for research for many years to come. It is our hope that the community finds the data (depth, breadth, and quality) useful in answering a range of research questions.

The data and information UK Biobank presents is the result of the work of many people. The developers who programmed the sequences and those who provided the programming environment in the first place are as important as the final authors of the research publications that make use of the measurements. The insight and vision of funders provide a sound backbone of the activities of the many different departments of UK Biobank; MR images are now an exciting part of the growing data set within the UK Biobank data repository. We would like to thank and acknowledge the many contributors to this work inside and outside of UK Biobank. Specifically the use of the multiband implementation from CMRR (University of Minnesota) and the pcASL sequence from Fraunhofer MEVIS are acknowledged.

References

1 Stanek HM. Grieve SM, Brickman AM, et al. Obesity is associated with reduced white matter integrity in otherwise healthy adults. Obesity 2011; 19: 500-4.
2 Goldstone AP, Thomas EL, Brynes AE, et al. Elevated fasting plasma ghrelin in Prader–Willi syndrome adults is not solely explained by their reduced visceral adiposity and insulin resistance. J Clin Endocrinol Metab 2004; 89: 1718-26.
3 Thomas EL, Parkinson JR, Frost G, et al. The missing risk: MRI and MRS phenotyping of abdominal adiposity and ectopic fat. Obesity 2012; 20: 76-87.
4 Thomas EL, Hamilton G, Patel N, et al. Hepatic triglyceride content and its relation to body adiposity: a magnetic resonance imaging and proton magnetic resonance spectroscopy study. Gut 2005; 54: 122-7.
5 Thomas EL, Bell JD. Influence of undersampling on magnetic resonance imaging measurements of intra–abdominal adipose tissue. Int J Obes Relat Metab Disord 2003; 27: 211-8.

Further information

A primary portal for information on UK Biobank and how to access the data, which is available for all researchers, is:	www.ukbiobank.ac.uk/
In 2016, several milestones were achieved. Together, these describe the developing resource well:	www.ukbiobank.ac.uk/2016/11/scanning-study-launched/ www.ukbiobank.ac.uk/2016/09/brain-imaging-results-from-5000-subjects/ www.ukbiobank.ac.uk/2016/03/uk-biobank-looking-at-the-whole-person
Reports presented in annual UK Biobank meeting (2016) can be accessed through:	www.ukbiobank.ac.uk/listen-again-annual-meetings/
The actual publications can be found easily with a specific search term, for example, the cardiac, abdominal, and neuro publications, respectively, are listed here:	www.ukbiobank.ac.uk/published-papers/?tps=cardiac&tps_button=Search www.ukbiobank.ac.uk/published-papers/?tps=body&tps_button=Search www.ukbiobank.ac.uk/published-papers/?tps=neuro&tps_button=Search
Information on how to access the DICOM data and how to apply for downloading keys can be found at:	www.ukbiobank.ac.uk/register-apply/

Contact



Niels Oesingmann, Ph.D.
MR Physicist
UK Biobank

Units 1–4 Spectrum Way, Adswood
Stockport, Cheshire, SK3 0SA, UK
Phone: +44 (0)161.475 5360
Direct: +44 (0)161.475 1423
Mobile: +1 347.443 4328
Fax: +44 (0)161 475 5361
Niels.Oesingmann@ukbiobank.ac.uk



Professor Paul M. Matthews OBE, MD, DPhil, FRCP, FMedSci
Head of the Imaging Working Group
Imperial College London, Faculty of Medicine
Edmond and Lily Safra Chair
Head of Brain Sciences Division

E515
Burlington Danes
Hammersmith Campus

London SW7 2AZ, UK
Phone: +44 (0)20 7594 2855
P.Matthews@imperial.ac.uk

Benefits of Accelerated MR Imaging in Daily Routine

Val M. Runge, M.D.; Johannes K. Richter, M.D.; Hendrik von Tengg-Kobligk, M.D.; Johannes T. Heverhagen, M.D., Ph.D.

Department of Diagnostic, Interventional and Pediatric Radiology, Inselspital, University Hospital, University of Bern, Bern, Switzerland

Introduction

Clinical development in magnetic resonance imaging in recent years has focused on decreasing scan time, an important topic because of the greater length of time required for and cost therein of an MR exam when compared to computed tomography and ultrasound. The two relevant major technical innovations in the current decade, simultaneous multi-slice imaging and compressed sensing are discussed in depth by organ system in the following article, focusing in particular on four top areas in terms of number of exams performed, the brain, upper abdomen, musculoskeletal system and breast [1]. Additional relevant new imaging approaches – which in general are specific to a single area of the body – that can lend speed to the clinical exam are also included.

Brain

In clinical brain imaging, simultaneous multi-slice (SMS) today has major impact [2]. Diffusion-weighted echoplanar and T2-weighted turbo spin echo scans are acquired in nearly every patient exam. Due to the large number of elements employed in state-of-the-art head coils, SMS is easily adapted, most commonly with an acceleration factor of two. With current technology, in limited situations, a factor of three can also be employed. In the brain, for routine clinical imaging, both single shot and readout segmented (RESOLVE) EPI DWI are widely employed, with the choice often site-specific. Single shot EPI is substantially faster, but as a screening exam with thicker sections is limited at 3T due to bulk susceptibility artifacts. Readout segmented EPI scans take substantially longer, but at many sites are favored even for screening exams. When SMS is applied to screening single shot EPI diffusion exams of the brain, the improvement is minimal due to the fact that scan time is already short. This is not the case however for readout segmented EPI[1], where a substantial savings in scan time is possible (Fig. 1). In certain situations, where thinner sections would potentially improve diagnostic yield, the use of SMS is advocated, as also illustrated, not to decrease scan time with readout segmented EPI but to enable a decrease in slice thickness to be obtained within a reasonable scan time.

An alternative approach in routine clinical brain imaging for diffusion-weighted scans is that of acquiring the entire brain with thin section (1 mm) sections. Prior to the advent of SMS, this was not practical from a scan time point of view. With state-of-the-art coils at 3T, such a scan is today possible in an acquisition time under five minutes if SMS is employed (Fig. 2). The specific diffusion technique used is single shot EPI, with the small voxel size limiting bulk

[1] SMS and RESOLVE are products. The combination of the two technologies, SMS RESOLVE is works in progress, currently under development and is not for sale in the US and in other countries. Its future availability cannot be ensured.

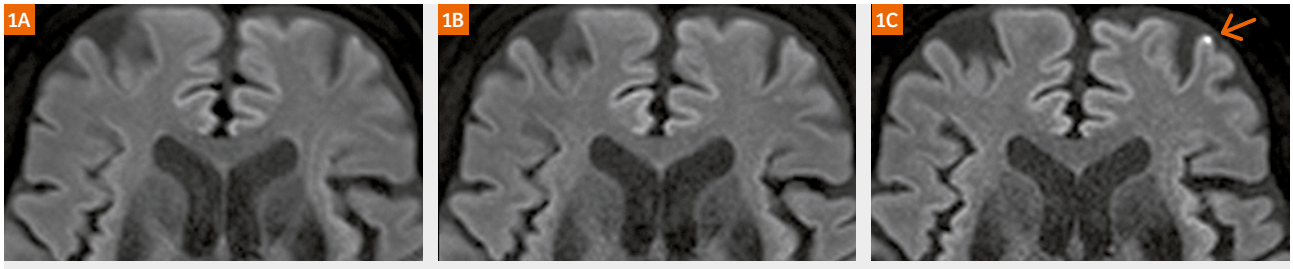

Figure 1:
The use of SMS with RESOLVE[1] for either reduced scan time or improved spatial resolution (specifically a reduction in slice thickness, while maintaining full brain coverage). A non-accelerated, 4 mm slice thickness, b 1000 RESOLVE image of the frontal lobes **(1A)** is compared to that with SMS2 (**1B**, 4 mm) and with SMS3 (**1C**, 2 mm). Scan times were 3:08 (min:sec) vs. 2:06 vs. 4:27. Image quality is equivalent between the conventional and SMS2 scans, however a small pinpoint cortical infarct (arrow) is visualized only with SMS3, due to the thinner slice thickness.

susceptibility artifact. Looking back at the history of the development of clinical MR, for brain screening exams, slice thickness decreased from 10 mm (initially) to 7 mm (with the advent of 1.5T) to 4 mm (with the advent of 3T). Given the possibilities offered by SMS, it is quite possible that high resolution thin section (1 mm) brain diffusion imaging will become routine in the future except for uncooperative patients.

TSE T2-weighted scans of the brain are typically fast, and thus at first glance not a likely candidate for the application of SMS. However, when thinner sections (< 4 mm) of the entire brain are desired, scan times often become substantial (over 4 minutes). This is due to the need to employ concatenations or other approaches such as extending TR in order to acquire the needed number of images to cover the entire brain. Although T2-weighted imaging is considered to be relatively robust to motion artifacts for brain imaging, this is generally a consequence of the relatively short scan time. With longer scan times, as well as with uncooperative patients, motion artifacts can be quite prominent and substantially degrade diagnostic image quality. Patients with acute ischemia are an important patient population in clinical brain MR imaging, with this population in particular benefiting by the use of SMS to achieve shorter scan times (Fig. 3).

Another approach to reducing overall exam time for a patient, specifically for brain imaging, involves the use of synthetic MRI [3]. If a specialized scan is acquired, then from this single acquisition, T1-, T2- and proton density-weighted images can be reconstructed (Fig. 4). Indeed, it is simply an issue of mathematics to calculate an image with any combination of TE and TR, or for example a FLAIR image that would for acquisition necessitate also the specification of an additional inversion pulse, and specifically TI. Likewise, parameter maps can be calculated, in the most simplistic approach

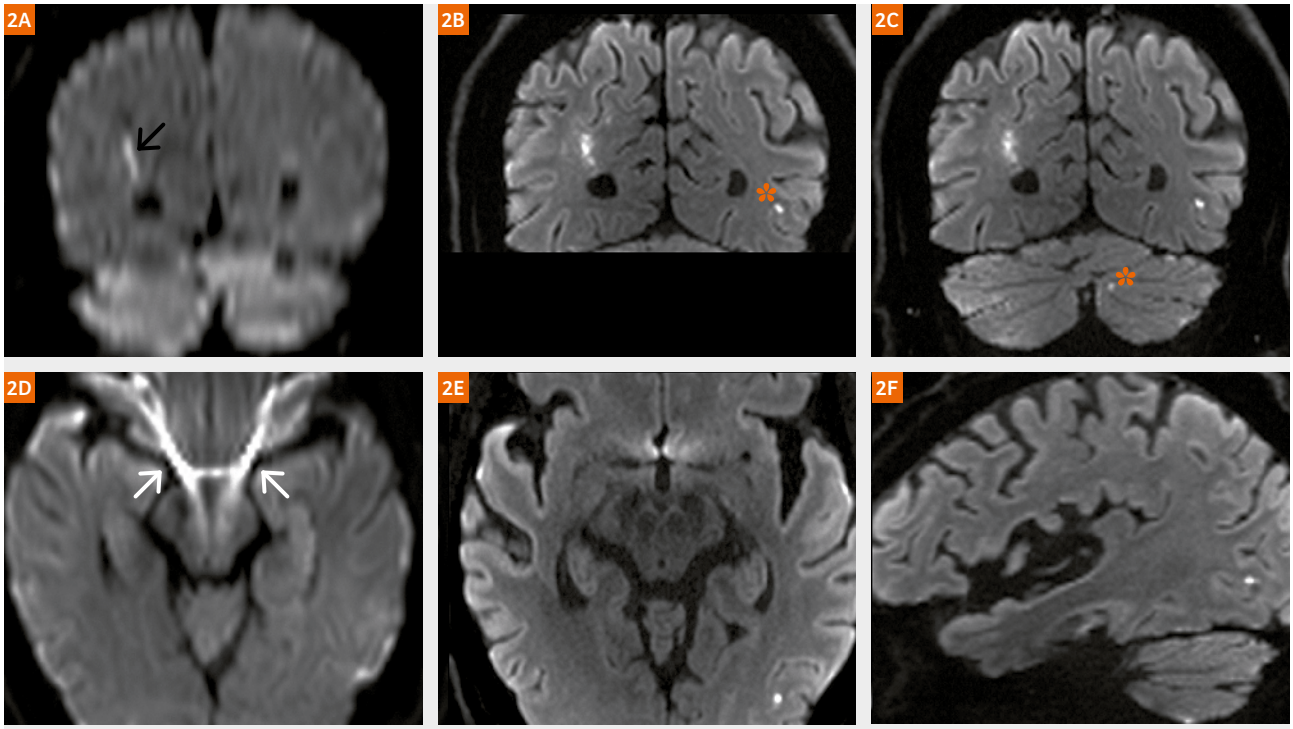

Figure 2:
Conventional 2D ss-EPI DWI (**2A, D** – 5 mm) vs. thin section (1 mm), high in plane resolution (0.6 x 0.6 mm^2) scans without SMS **(2B)** and with SMS2 **(2C, E, F)**. At 3T, bulk susceptibility artifacts (white arrows) degrade substantially conventional 5 mm section ss-EPI DWI, as seen in the axial scan (2D). A coronal reformat (2A) in this patient depicts, although poorly due to the low resolution, a small watershed infarct (black arrow). By reducing slice thickness and improving in-plane spatial resolution, bulk susceptibility artifacts are reduced and the infarct is well visualized on a reformatted coronal scan (2B, from a 62 image, 1 mm slice thickness, 4:24 min:sec scan). However, the entire brain cannot be scanned thus in a reasonable acquisition time. Employing SMS2, the entire brain can be imaged, with the acquisition time in this instance 4:39 min:sec, with high-resolution images and reformats possible in all planes (2C, E, F). These images reveal a pinpoint cerebellar infarct (*, 2C) in addition to the previously noted pinpoint occipital infarct (*, 2B, also visualized in 2E and F). Note also the marked reduction in bulk susceptibility artifacts in the axial plane (2E). Full brain imaging in this instance revealed multiple pinpoint acute infarcts, none visualized on the conventional 5 mm scan, and only that in the cerebral hemispheres seen on the high-resolution scan without SMS.

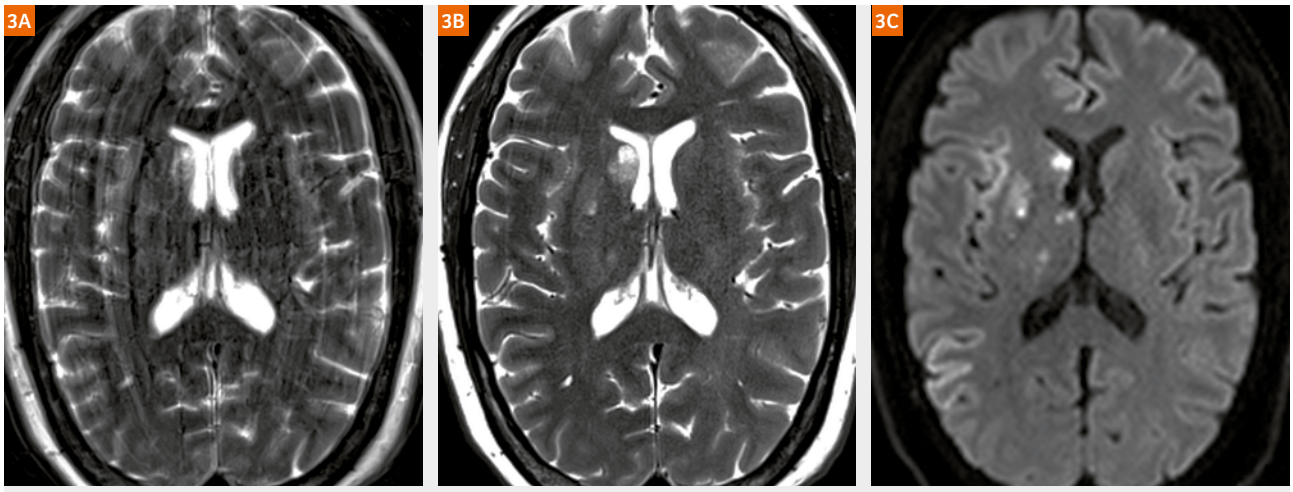

Figure 3:
Small infarcts of the caudate, putamen, and thalamus, **(3A, B)** T2-weighted TSE and **(3C)** diffusion-weighted ss-EPI scans. (3A) Conven-tional acquisition compared to (3B) SMS, using an acceleration factor of three. For the diffusion-weighted scan, (3C), SMS was also employed, with an acceleration factor of 2. Note the ghosting and image degradation on the conventional T2-weighted scan due tothe long acquisition time, with markedly improved image quality on the accelerated SMS T2-weighted scan. The SMS DWI scan was equivalent in terms of image quality to the scan acquired in a conventional fashion (not shown).

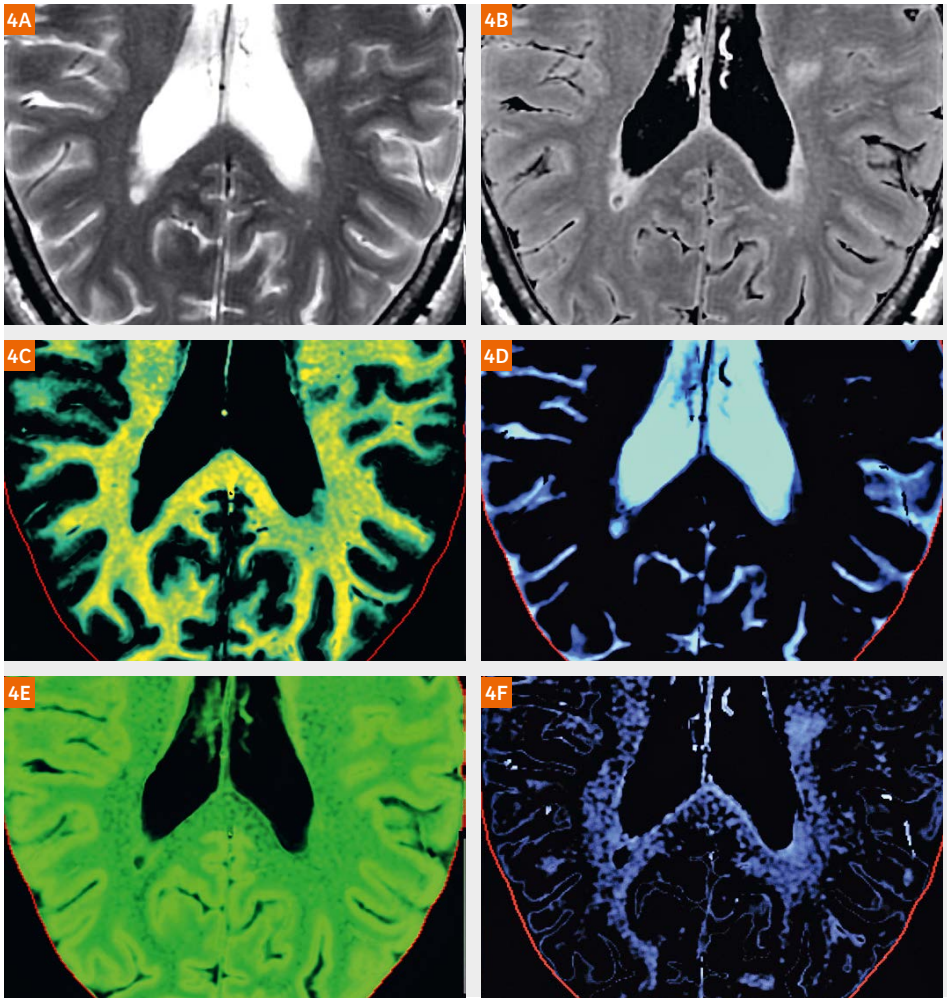

Figure 4:
Synthetic MRI, brain segmentation and myelin measurement in a patient with multiple sclerosis. From a scan requiring approximately six minutes for acquisition, R1, R2, and proton density maps are measured. This allows reconstruction of synthetic **(4A)** T2-weighted and **(4B)** FLAIR images. From the same data, myelin segmentation can be performed with calculation of **(4C)** myelin, **(4D)** free water, **(4E)** cellular, and **(4F)** excess parenchymal water partial volumes.
Reprinted with permission from Akifumi Hagiwara et al., Invest Radiol 2017;52 (10).

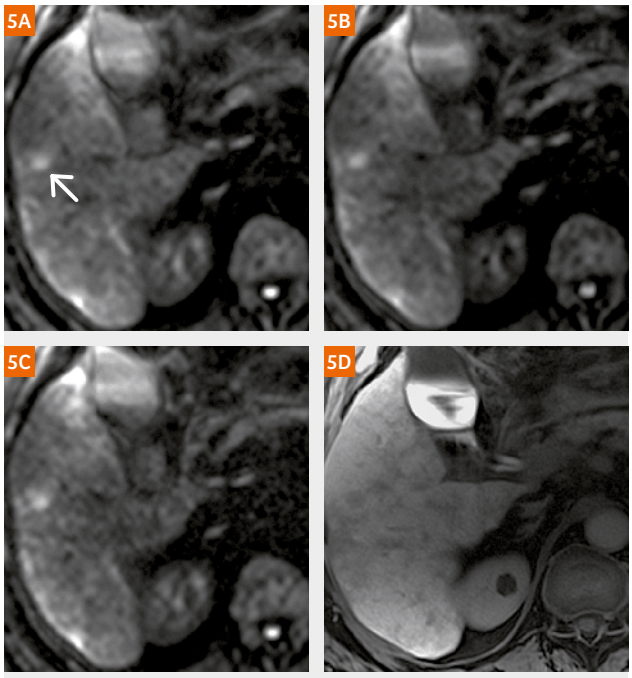

Figure 5:
SMS in liver imaging, in a patient with multifocal hepatocellular carcinoma (HCC), at 3T with 2D EPI DWI. SMS can be used, as illustrated, to either shorten scan time or acquire thinner sections without a substantial increase in scan time. Scan times were **(5A)** 2:41 (non-SMS), **(5B)** 1:38, and **(5C)** 2:54 min:sec (the latter both SMS with a 2-fold acceleration). The entire liver was covered in all scans, using a 5 mm slice thickness for **(5A, B)** and a 3 mm slice thickness for **(5C)**. A small HCC (arrow) with restricted diffusion is noted. For comparison, a delayed post-contrast scan after gadoxetic acid administration **(5D)** is also presented, using a non-breath-hold 2-minute acquisition radial VIBE scan. On the latter, the lesion is hypointense due to the lack of functioning hepatocytes.

T1, T2 and proton density maps. However, there is much more information available from such an acquisition, including volume estimations such as gray matter, white matter and ventricular volume. More sophisticated segmentation involves, as illustrated, evaluating myelin and the compartmentalization of water, which can be of value in the assessment of multiple sclerosis.

Image acquisition and reconstruction techniques that exploit data sparsity (compressed sensing) will also impact favorably brain imaging in the near future, and specifically contrast-enhanced MRA and time-of-flight (TOF) MRA – two common exams. Early clinical articles show the impact, with work in progress acquisition techniques readily available together with limited sequences for routine clinical use. Combining radial undersampling and sparse reconstruction, time resolved high-resolution contrast-enhanced MRA can be acquired, enabling improved characterization of arteriovenous malfor-mations, for example in determination of Spetzler-Martin grade as well as assessment of venous ectasia and deep venous drainage [4]. Data undersampling can also be combined with arterial spin labeling and 3D radial acquisition to improve the detection and characterization of intracranial arteriovenous shunts. 3D TOF MRA is employed clinically for brain aneurysm detection and evaluation, providing as well detection of intracranial stenoses and occlusions. This commonly used technique is also readily combined with data sparsity approaches in order to shorten scan time. Although development of specific techniques is still in its infancy, acceleration of the scan by a factor of five appears quite feasible [5].

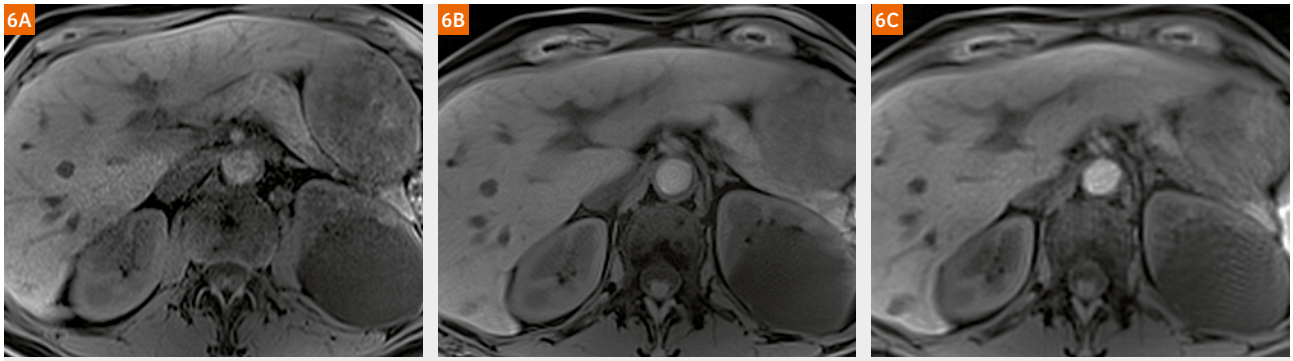

Figure 6:
Options for speed in liver T1-weighted imaging, comparison of ultrashort breath-hold and radial, free breathing, imaging. Images were acquired at 3T using a slice thickness of 3 mm without IV contrast administration. A large left renal cyst is noted. **(6A)** An ultrashort breath-hold Dixon VIBE sequence is compared to **(6B)** standard and **(6C)** scan time optimized (by restricting the number of radial views) radial VIBE scans. Scan times were 5 seconds, 2 minutes, and 21 seconds.

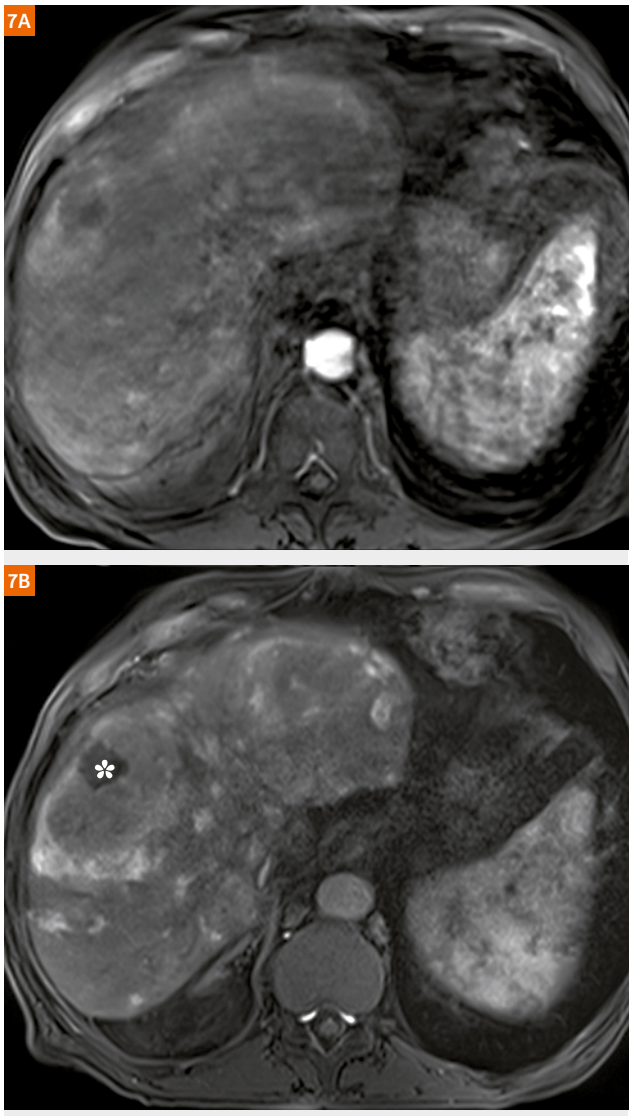

Figure 7:
Improved clinical liver imaging by utilization of ultrashort breath-hold T1-weighted imaging. Two early arterial phase T1-weighted exams in the same patient are compared. **(7A)** The first is a conventional CAIPIRINHA-VIBE sequence with fat saturation requiring an acquisition time of 16 seconds. **(7B)** The second is an accelerated Dixon VIBE sequence requiring a breath-hold time of only five seconds. A large partially necrotic hepatocellular carcinoma is noted in liver segment VIII (*) in this elderly male patient. The substantially reduced acquisition time for the latter scan (7B) enabled improved patient compliance, with the result being a marked increase in diagnostic image quality.

An important additional application of radial imaging with compressed sensing is for dynamic imaging of the pituitary (implemented with GRASP), providing both the high spatial and temporal resolution necessary for this evaluation. Very high image quality has been demonstrated in initial clinical implementation, providing improved recognition on the basis of differential contrast enhancement during the dynamic phase between the normal enhancing pituitary and microadenomas [1].

Upper abdomen

Diffusion-weighted imaging today is a vital sequence for routine abdominal MRI. Acquisition is normally during free breathing, using single shot EPI technique. SMS is easily applied, by using a shorter TR yet still enabling the desired anatomic coverage (Fig. 5) [6]. Although SMS could be used to achieve thinner sections or higher in-plane resolution, the focus for use of the technique in the upper abdomen has been to decrease scan time. Motion and the lower SNR in body imaging in general dictates the use in this manner.

Motion, primarily due to breathing, is likely the clinical factor with the greatest negative impact on the quality of MRI in the upper abdomen. Over the past 20 years, sequences have been optimized and new sequences have been developed allowing shorter and shorter breath-hold times. For example, on a state-of-the-art scanner today, the Dixon VIBE sequence can be acquired in as little as five seconds (Fig. 6). Many patients have difficulty holding their breath for even 20 seconds, with such a reduction in acquisition time improving greatly patient compliance and diagnostic image quality (Fig. 7). In patients unable to hold their breath at all, e.g. pediatric patients[2], radial imaging represents a further alternative direction for sequence development to combat breathing artifacts. As compared to a Cartesian acquisition, motion artifacts are reflected in the final image in a less prominent and more benign fashion (Fig. 6). This technique can be used to acquire high-resolution 3D post-contrast images in many regions where involuntary motion occurs, for example in the oral cavity. On the downside, however, the acquisition time for a high-resolution dataset is typically in the order of 2–3 minutes. If radial scans are optimized for scan time, the same SNR limitations as in all MR acquisitions apply. However, an additional consideration when shortening radial scans is the greater prominence of streak artifacts that reflect motion, if the approach used aims to decrease the number of phase-encoding steps.

Another consideration besides breath-hold capabilities is to gain more information in dynamic contrast-enhanced imaging with faster acquisition techniques. With CT, radiologists are largely limited by radiation dose considerations in terms of acquiring additional arterial phase images, while scan acquisition time has been the limitation in MRI.

[2] MR scanning has not been established as safe for imaging fetuses and infants less than two years of age. The responsible physician must evaluate the benefits of the MR examination compared to those of other imaging procedures.

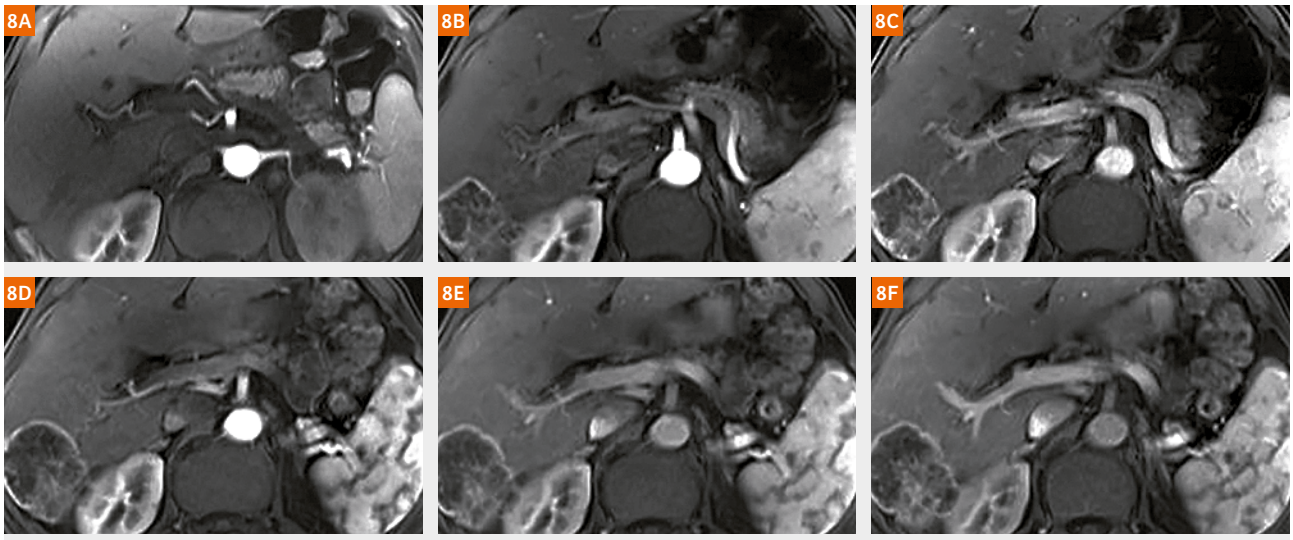

Figure 8:
Liver metastasis from rectal carcinoma, imaged with **(8A)** single phase, **(8B, C)** dual phase, and **(8D–F)** triple phase arterial acquisitions. The scans are separated in time by several months in each instance. CAIPIRINHA-VIBE with spectral fat saturation was employed for **(8A)**, CAIPIRINHA-VIBE, Dixon fat separation, and TWIST without view sharing for **(8B, C)**, and with view sharing for **(8D–F)**. Acquisition times for the three techniques per phase were 13 vs. 7.5 vs. 4.6 seconds. Use of the dual arterial phase acquisition led to well-timed arterial phase images with low respiratory motion artifact.
Adapted with permission from Yang Shin Park et al., Invest Radiol 2017;52 (10).

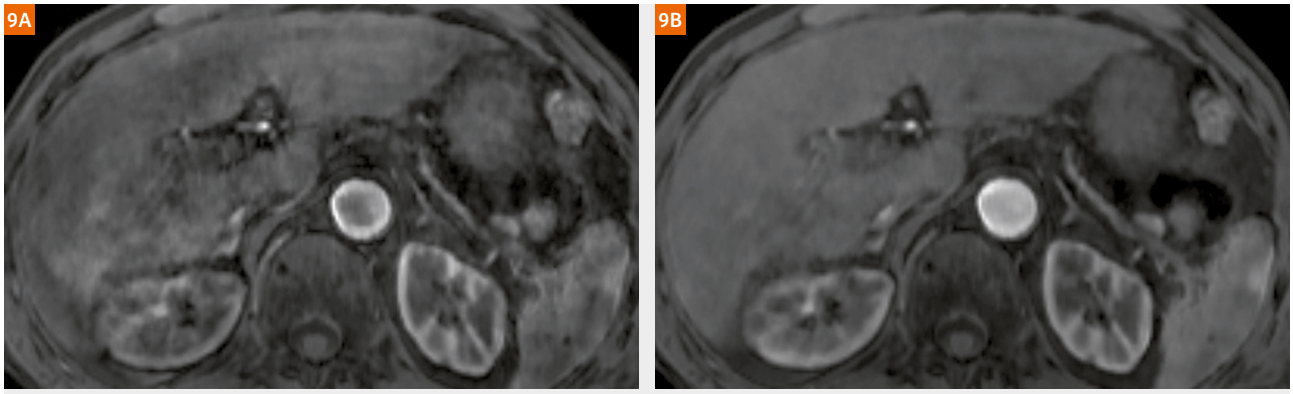

Figure 9:
Improved early arterial phase liver imaging using compressed sensing with respiratory-motion resolved reconstruction (XD-VIBE)[3].
The patient is an 81-year-old man with chronic hepatitis B and limited breath-holding capacity. The scans were acquired during free breathing. Pre-contrast, multi-arterial and portal venous phases were obtained with compressed sensing VIBE. Using a navigation signal acquired as part of the acquisition, two different image sets were reconstructed, **(9A)** the first using hard gating by either rejecting or accepting the echo train for reconstruction. For **(9B)** the second image set, with motion resolved reconstruction, the echo train was assigned to the motion state determined by the navigation signal. A substantial reduction in motion artifacts and improved image quality is achieved with (9B) XD-VIBE.
Reprinted with permission from Jeong Hee Yoon et al, Invest Radiol 2017;52 (10).

With the advent of new sequence types, however, multi-phase arterial acquisitions became possible, opening up a new diagnostic window for MRI of the upper abdomen (Fig. 8) [7]. By combining a view-sharing acquisition scheme with highly accelerated parallel imaging and fast T1-weighted 3D imaging (TWIST-VIBE), acquisition times of five seconds for imaging the entire upper abdomen are now possible. This allows for acquisition of early, mid and late arterial phase MR imagings in one 15-second breath-hold. In the past few years, many clinical studies have been published that advocate this approach and have shown the additional diagnostic information available in multi-arterial acquisitions.

[3] WIP, the product is currently under development and is not for sale in the US and in other countries. Its future availability cannot be ensured.

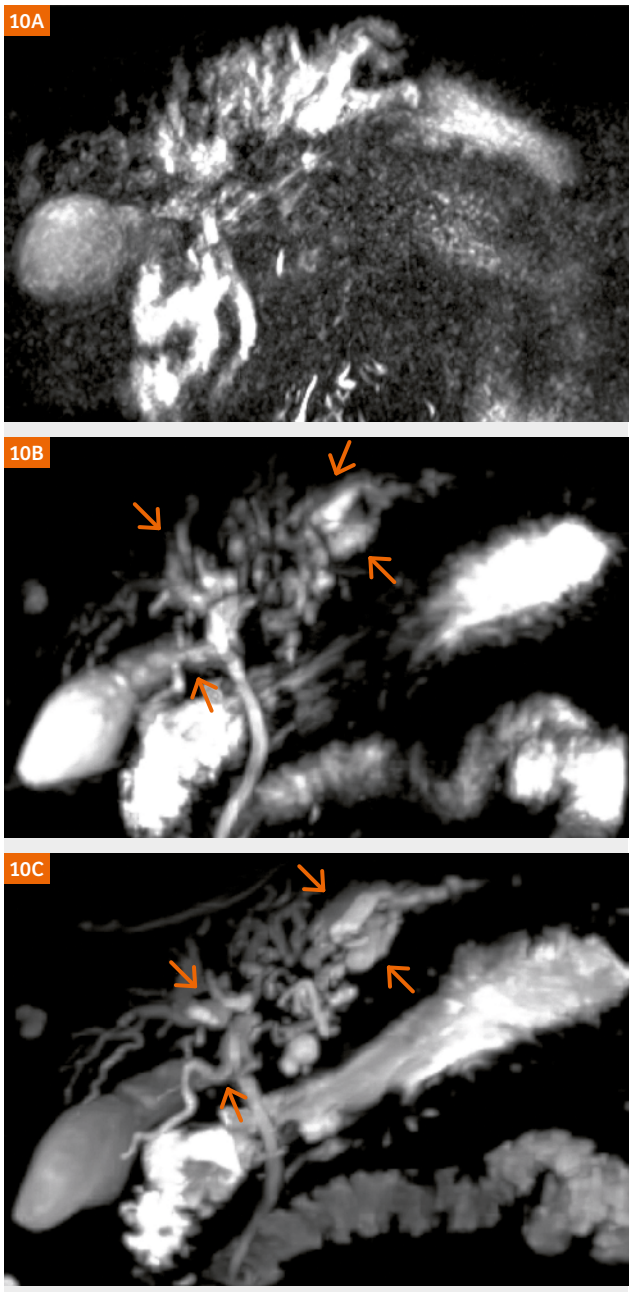

Figure 10:
3D MRCP exams of a patient with a hilar cholangiocarcinoma, comparing **(10A)** conventional and **(10B, C)** compressed sensing exams, with **(10C)** acquired during breath holding (16 sec). Conventional 3D MRCP exams require on the order of 5–10 minutes for acquisition, depending on the breathing pattern of the patient. On the conventional exam, dilatation of the intrahepatic ducts is evident, but the exam otherwise uninterpretable due to motion artifacts. Image quality with the non-breath hold compressed sensing exam is markedly improved. However, dilatation of the intrahepatic ducts and in particular second order branches (arrows) of the left hepatic duct are best visualized on the breath-hold compressed sensing exam.
Adapted with permission from Jeong Hee Yoon et al, Invest Radiol 2017;52 (10).

While beath-holds are still required with the TWIST-VIBE approach, the combination of radial image acquisition with compressed sensing reconstruction (GRASP-VIBE) was a seminal development in abdominal MRI in this decade. The previously mentioned streaking artifacts can be significantly reduced by introducing iterative reconstruction, thereby enabling reconstruction of 3D datasets that cover time frames of 5–10 seconds. This enables the acquisition of dynamic, contrast-enhanced scans of the liver during free-breathing in one continuous run. Studies have shown that this overcomes the timing challenges in dynamic imaging as well as limiting respiratory artifacts, expanding substantially the patient population eligible for abdominal MRI. A further improvement of image quality is achieved by applying self-gating, which recognizes the end-expiratory phase and rejects all other data.

The integration of compressed sensing into sequences optimized for imaging of the upper abdomen has already had a major impact upon clinical imaging, with further major developments anticipated in this rapidly developing field. XD-VIBE[3] is one such approach, using compressed sensing and simultaneous acquisition of a navigator signal for motion resolved reconstruction (Fig. 9) [8]. With this approach, excellent image quality and lesion detectability, together with a relative lack of motion artifacts, has been demonstrated in oncologic patients with images acquired during free breathing [9].

Turning to the biliary system, compressed sensing has a major impact as well in MR cholangiopancreatography. An important scan clinically is the heavily T2-weighted 3D acquisition which is used to visualize the biliary ducts. Due to the number of breath-holds required and the long TR, acquisition time is typically in the order of 4–6 minutes. This exam, when acquired with SPACE, may also be combined with compressed sensing. Depending upon the desired result, a substantial reduction in scan time can be achieved with the exam still acquired during quiet breathing, or the scan can be further optimized to allow acquisition in a single breath-hold [10]. Initial results favor clinical use of the latter (Fig. 10), reflecting as well the historical development of upper abdominal MR imaging.

Musculoskeletal system

As in other areas of the body, simultaneous multi-slice and compressed sensing go hand-in-hand in terms of improving the clinical exam in musculoskeletal imaging. For the knee in particular, due to the cylindrical, high number of elements design of the receiver coil, SMS is

[3] WIP, the product is currently under development and is not for sale in the US and in other countries. Its future availability cannot be ensured.





Figure 11:
High-resolution sagittal proton density-weighted images of a horizontal tear of the medial meniscus (posterior horn) demonstrating the value of SMS. Turbo spin echo exams acquired **(11A)** in a conventional fashion and **(11B)** using 2-fold SMS acceleration are compared. Voxel dimensions were 0.5 x 0.4 x 2.5 mm^3. Scan time was reduced from 6:36 to 3:27 min:sec by the use of SMS, with image quality and SNR maintained.

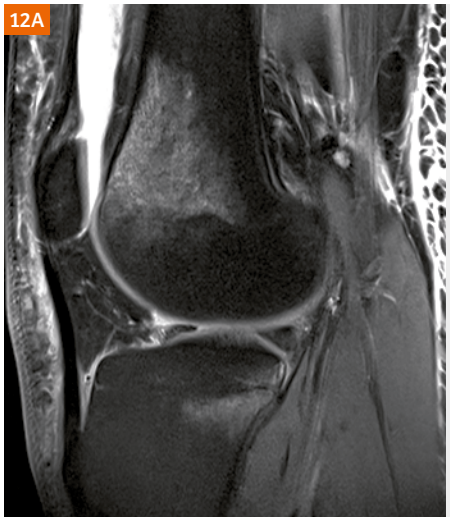



Figure 12:
SMS can be employed to markedly shorten scan time, which can be of high value either to increase patient throughput or as in the current example in the evaluation of a trauma patient. Extensive bone marrow edema (within the distal femur and proximal tibia) is seen, together with subcutaneous edema posteriorly and a large effusion within the suprapatellar bursa, on sagittal proton density-weighted images (with fat saturation) in this patient. As compared to **(12A)** the conventional scan, using **(12B)** an SMS factor of 2, the acquisition time was reduced by nearly a factor of two, to 1:34 min:sec.

highly applicable. The complex anatomy and numerous small critical components of the knee, all important for its proper function, have driven knee imaging clinically towards higher and higher resolution. The application of SMS enables a substantial reduction in scan time, making such desired high-resolution techniques viable (Fig. 11). Alternatively, if standard resolution scans will suffice for the clinical question and/or if possible patient movement limits the exam, for example in trauma patients, SMS can be critical to enable faster scans (Fig. 12). Both proton density and T2-weighted scans are commonly used in the musculoskeletal system, with SMS easily integrated in both instances. The use of two concatenations is often required, or a prolongation of TR, due to the number of slices needed to cover the structure anatomically using thin section imaging, with an SMS factor of 2 thus readily applicable.

The use of SEMAC for the reduction of metal[4] artifacts in orthopedic imaging is an ideal area for scan time reduction by the implementation of compressed sensing. Metal artifacts in many instances limit image interpretability, in particular at 3T. SEMAC corrects for metal artifacts by robust encoding of each excited slice. View angle tilting is incorporated to suppress most in-plane distortions, with *z*-phase encoding resolving the distorted excitation profiles which cause through-plane distortion. Unfortunately, the addition of *z*-phase encoding steps leads to longer scan times. To maintain feasible scan times, compressed sensing is incorporated into the SEMAC sequence. 8-fold acceleration through the implementation

[4] The MRI restrictions (if any) of the metal implant must be considered prior to patient undergoing MRI exam. MR imaging of patients with metallic implants brings specific risks. However, certain implants are approved by the governing regulatory bodies to be MR conditionally safe. For such implants, the previously mentioned warning may not be applicable. Please contact the implant manufacturer for the specific conditional information. The conditions for MR safety are the responsibility of the implant manufacturer, not of Siemens.

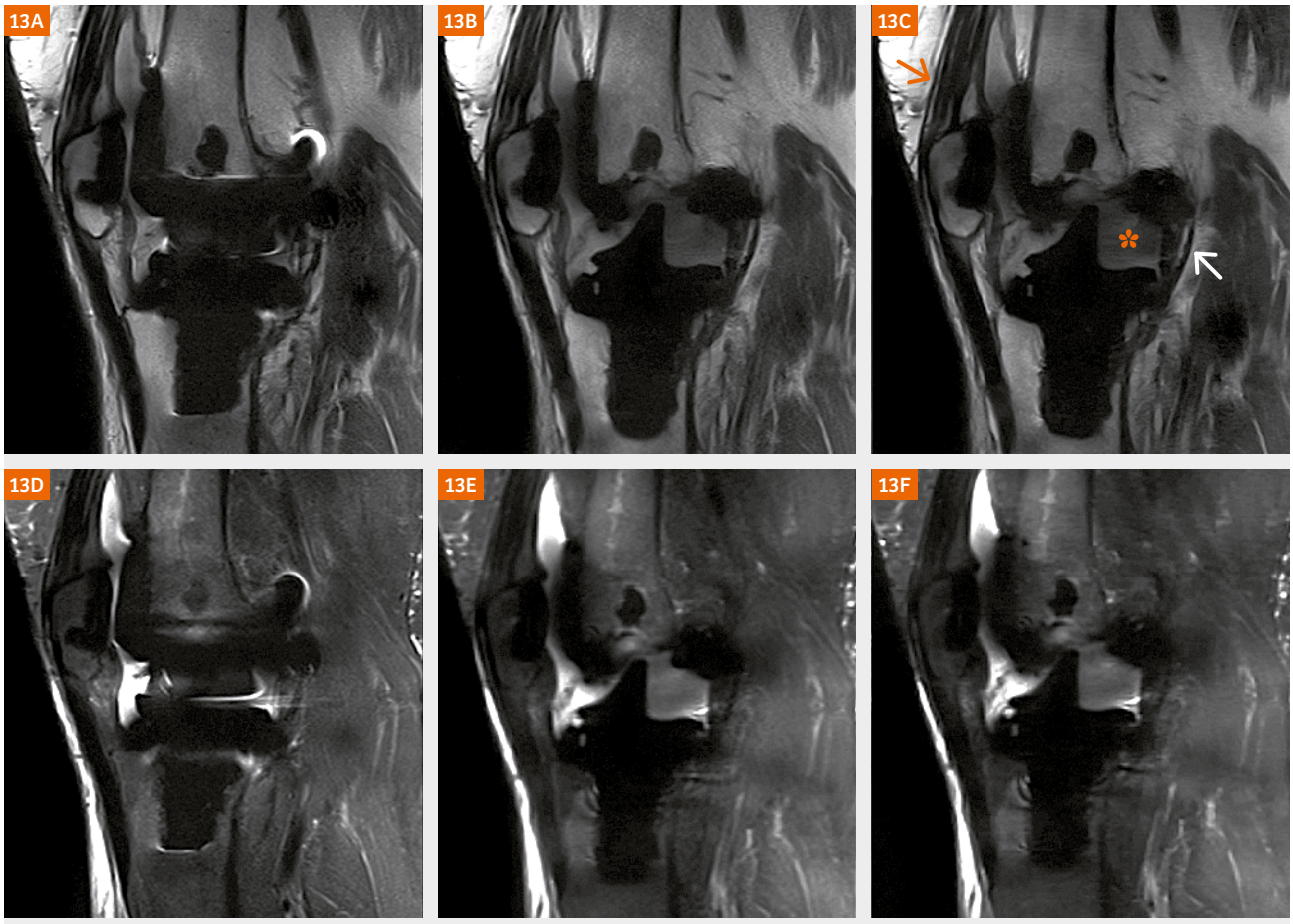

Figure 13:
Comparison of **(13A, D)** high-bandwidth TSE, **(13B, E)** SEMAC TSE, and **(13C, F)** compressed sensing SEMAC TSE[3] for metal artifact reduction. The (13A–C) upper row of images is with mild proton density-weighting and the (13D–F) lower row acquired with STIR. This older man had a cobalt-chromium knee arthroplasty implant. Scan times for the high-bandwidth sequences were five minutes, which with the application of SEMAC extended to 11 minutes in each instance. The application of compressed sensing allowed a reduction in scan time of the sequences with SEMAC to that of the high-bandwidth sequences. The extensor mechanism (orange arrow) is well seen on all scans, however the articular structures including specifically joint fluid (*) and the posterior capsule (white arrow) are best seen on the SEMAC images.
Adapted with permission from Jan Fritz et al., Invest Radiol 2016;51: 666–676.

of compressed sensing–based incoherent *k*-space undersampling has been demonstrated, yielding improved image quality relative to the use of high-bandwidth alone and equivalent image quality to the much longer conventional SEMAC acquisition (Fig. 13) [11]. This approach enables SEMAC to be extended in clinical application to the millions of patients with metallic implants.

Breast

Today breast MRI is an integral part of screening, diagnosis, and follow-up for breast cancer. For radiographic breast imaging, the direction of development has been towards increasingly complex and expensive methods [12]. Both SMS and compressed sensing offer an excellent way to move in the opposite direction, specifically in terms of shortening the exam. The application of SMS is simplistic, simply to decrease scan time for breast diffusion-weighted imaging, a crucial part of any breast evaluation (Fig. 14).

Dynamic contrast-enhanced (DCE) MR imaging is a vital tool in the diagnosis of breast cancer. To assess tumor morphology and contrast kinetics, ideally such an acquisition would have both high spatial and temporal resolution. The use of compressed sensing (CS), specifically in combination with VIBE, permits an increase in through-plane spatial resolution in dynamic exams with comparable visual assessment of lesions as with

[3] WIP, the product is currently under development and is not for sale in the US and in other countries. Its future availability cannot be ensured.

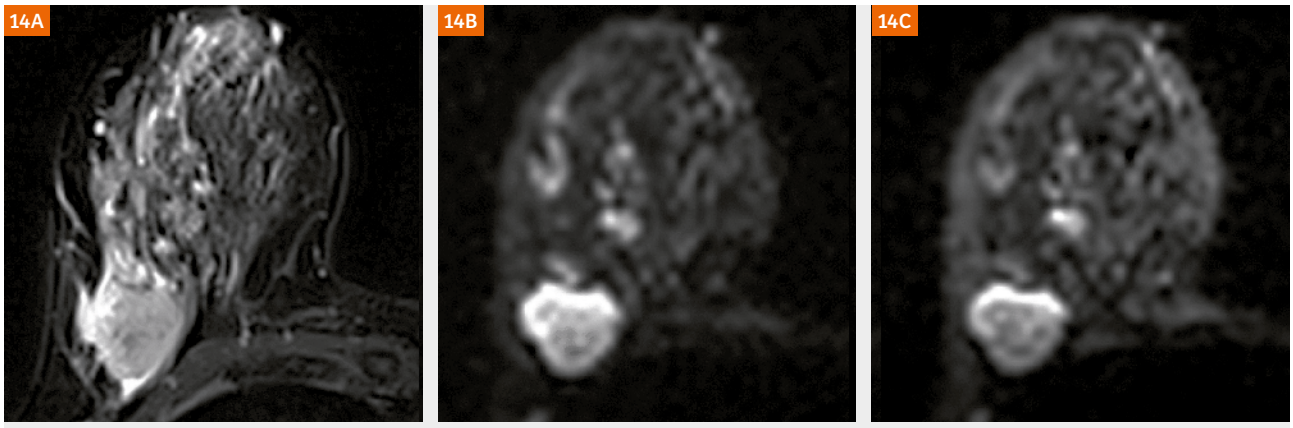

Figure 14:
The application of SMS to reduce scan time for readout segmented (rs, RESOLVE) EPI DWI in imaging of the breast. **(14A)** T2-weighted Dixon TSE and **(14B, C)** rs-EPI DWI scans of the right breast in a 45-year-old woman with invasive breast carcinoma are presented. The diffusion-weighted scans are 3 mm in slice thickness, with scan times of (14B) 7:28 and (14C) 3:17 min:sec. For (14C) an SMS factor of 2 was used.

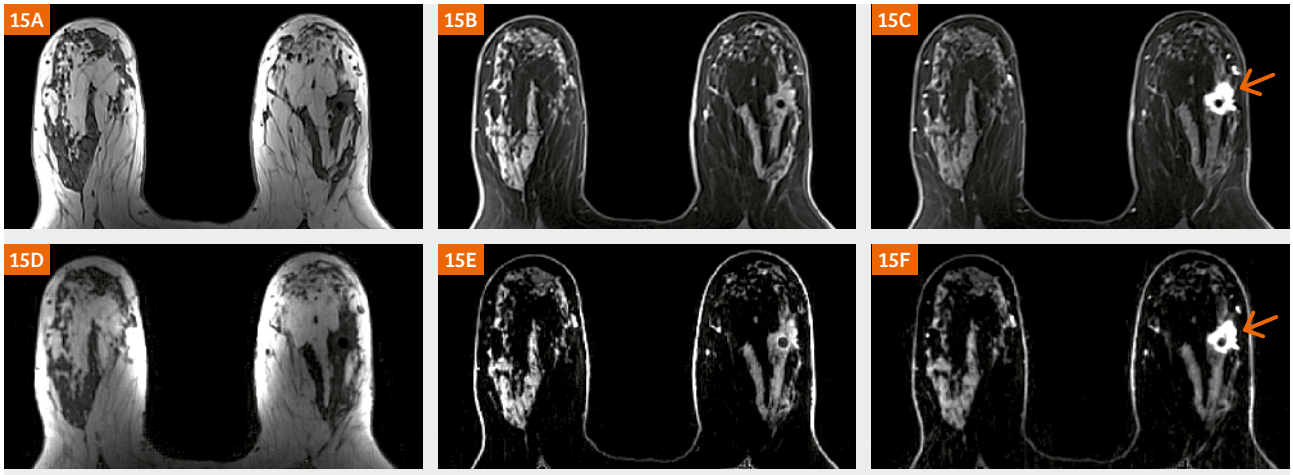

Figure 15:
Applicability of Dixon radial volumetric encoding (Dixon-RAVE[3]) for a comprehensive 3D dynamic contrast-enhanced MR exam of the breast. Conventional T1-weighted VIBE scans pre-contrast **(15A)** without and **(15B)** with fat suppression together with a **(15C)** post-contrast fat suppressed scan are illustrated on the top row. The images with equivalent tissue contrast on the bottom row **(15D–F)** are from a single continuous Dixon-RAVE scan performed during contrast injection, employing radial sampling and compressed sensing. This approach provides a diagnostic quality, comprehensive T1-weighted breast MR with high spatiotemporal resolution, reduced overall imaging time, and superior fat suppression. Illustrated are scans from a 61-year-old woman with invasive ductal carcinoma (arrow). *Reprinted with permission from Thomas Benkert et al, Invest Radiol 2017;52 (10).*

non-dynamic techniques such as VIBE-Dixon [13]. For example, in the clinical study just referenced, acquisition time was decreased by a factor of 18 in comparison to the T1-weighted Dixon sequence, yet with morphologic assessment not significantly different. CS-VIBE is a promising technique for ultrafast MR imaging, providing high spatial and temporal resolution, with image quality comparable to non-dynamic scans, providing in distinction to prior dynamic techniques reduced temporal blurring as well as the possibility of multiplanar lesion morphology assessment.

Another application of compressed sensing for dynamic contrast enhanced 3D breast imaging is with Dixon radial volumetric encoding (Dixon-RAVE)[3] [14]. Robust and uniform fat suppression improves the clinical applicability of DCE breast MRI. Dixon-RAVE combines compressed sensing, radial sampling and excellent fat suppression – providing scans with both high spatial and temporal resolution. In addition to contrast-enhanced images,

[3] WIP, the product is currently under development and is not for sale in the US and in other countries. Its future availability cannot be ensured.

from such an acquisition pre-contrast images with and without fat suppression can be extracted, enabling a comprehensive T1-weighted DCE exam with reduced overall scan time. Dixon-RAVE thus can serve as a one-stop-shop approach for comprehensive T1-weighted imaging of the breast (Fig. 15).

Conclusion

Improving the speed of MRI is important for its continued future widespread clinical use and success. Sparse imaging (compressed sensing, CS) and simultaneous multi-slice (SMS) are the two most important developments in the current decade to achieve this goal. These build upon the foundations laid by parallel imaging, VIBE, and radial imaging as well as many other innovations. CS and SMS have very general applications in routine clinical practice, together with improving several important subspecialty exams, covering the spectrum of what clinical MRI offers today, for example from pituitary imaging on the one hand to metal artifact reduction in musculoskeletal imaging on the other. Speed also improves the robustness of the technique, with these developments fundamentally impacting clinical utilization today and further developments extending at least into the next decade.

Contact

Val M. Runge, M.D.
Editor-in-Chief, Investigative Radiology
Department of Diagnostic, Interventional and Pediatric Radiology
University Hospital of Bern, Inselspital
Bern
Switzerland
ValMurray.Runge@insel.ch



References

1 Runge VM, Richter JK, Heverhagen JT. Speed in Clinical Magnetic Resonance. Invest Radiol. 2017;52(1):1-17.
2 Barth M, Breuer F, Koopmans PJ, Norris DG, Poser BA. Simultaneous multislice (SMS) imaging techniques. Magn Reson Med. 2016;75(1):63-81.
3 Hagiwara A, Warntjes M, Hori M, et al. SyMRI of the Brain: Rapid Quantification of Relaxation Rates and Proton Density, With Synthetic MRI, Automatic Brain Segmentation, and Myelin Measurement. Invest Radiol. 2017;52(10):647-657.
4 Schubert T, Wu Y, Johnson KM, et al. Time-of-Arrival Parametric Maps and Virtual Bolus Images Derived From Contrast-Enhanced Time-Resolved Radial Magnetic Resonance Angiography Improve the Display of Brain Arteriovenous Malformation Vascular Anatomy. Invest Radiol. 2016;51(11):706-13.
5 Fushimi Y, Fujimoto K, Okada T, et al. Compressed Sensing 3-Dimensional Time-of-Flight Magnetic Resonance Angiography for Cerebral Aneurysms: Optimization and Evaluation. Invest Radiol. 2016;51(4):228-35.
6 Taron J, Weiss J, Martirosian P, et al. Clinical Robustness of Accelerated and Optimized Abdominal Diffusion-Weighted Imaging. Invest Radiol. 2017;52(10):590-595.
7 Park YS, Lee CH, Kim JW, Lee YS, Paek M, Kim KA. Application of High-Speed T1 Sequences for High-Quality Hepatic Arterial Phase Magnetic Resonance Imaging: Intraindividual Comparison of Single and Multiple Arterial Phases. Invest Radiol. 2017;52(10):605-611.
8 Yoon JH, Yu MH, Chang W, et al. Clinical Feasibility of Free-Breathing Dynamic T1-Weighted Imaging With Gadoxetic Acid-Enhanced Liver Magnetic Resonance Imaging Using a Combination of Variable Density Sampling and Compressed Sensing. Invest Radiol. 2017;52(10):596-604.
9 Kaltenbach B, Bucher AM, Wichmann JL, et al. Dynamic Liver Magnetic Resonance Imaging in Free-Breathing: Feasibility of a Cartesian T1-Weighted Acquisition Technique With Compressed Sensing and Additional Self-Navigation Signal for Hard-Gated and Motion-Resolved Reconstruction. Invest Radiol. 2017;(11).
10 Yoon JH, Lee SM, Kang HJ, et al. Clinical Feasibility of 3-Dimensional Magnetic Resonance Cholangiopancreatography Using Compressed Sensing: Comparison of Image Quality and Diagnostic Performance. Invest Radiol. 2017;52(10):612-619.
11 Fritz J, Ahlawat S, Demehri S, et al. Compressed Sensing SEMAC: 8-fold Accelerated High Resolution Metal Artifact Reduction MRI of Cobalt-Chromium Knee Arthroplasty Implants. Invest Radiol. 2016;51(10):666-76.
12 Kuhl CK. The Changing World of Breast Cancer: A Radiologist's Perspective. Invest Radiol. 2015;50(9):615-28.
13 Vreemann S, Rodriguez-Ruiz A, Nickel D, et al. Compressed Sensing for Breast MRI: Resolving the Trade-Off Between Spatial and Temporal Resolution. Invest Radiol. 2017;52(10):574-582.
14 Benkert T, Block KT, Heller S, et al. Comprehensive Dynamic Contrast-Enhanced 3D Magnetic Resonance Imaging of the Breast With Fat/Water Separation and High Spatiotemporal Resolution Using Radial Sampling, Compressed Sensing, and Parallel Imaging. Invest Radiol. 2017;52(10):583-589.

Evolution of the Malignant Bone Marrow with Successful Therapy – Quantitative Analysis with Whole-body Diffusion-weighted MRI

Danoob Dalili[1]; Priya V. Joshi[2]; Robert Grimm[3]; Anwar R. Padhani[4]

[1] Imperial College Healthcare NHS Trust, St Mary's Hospital, London, United Kingdom
[2] Mount Vernon Cancer Centre and the East and North Herts NHS trust hospitals, Northwood, Middlesex, United Kingdom
[3] Siemens Healthineers, Erlangen, Germany
[4] Paul Strickland Scanner Centre, Mount Vernon Cancer Centre, Northwood, Middlesex, United Kingdom

Introduction

Bone disease is a common occurrence in metastatic breast cancer (MBC), but accurate evaluation of treatment benefit is notoriously difficult to do. There is a critical clinical need to develop non-invasive biomarkers to assess therapeutic effects of bone involvement in MBC. This is because the detection of primary non-responders and secondary therapy failure when disease burden is lowest, can help guide therapy decisions [1]. Currently, imaging assessments can only determine bone disease progression, because of which many patients with bone predominant disease receive ineffective medications for prolonged periods, and as a result do not change treatments until disease burdens become large, thus potentially hindering the effectiveness of follow-on treatments. It has been suggested, that aggressive disease detection methods and response monitoring could promote precision oncology in patients with bone involvement in MBC [2].

Guidelines from the American Society of Clinical Oncology and the European School of Oncology have recognized these limitations, advocating the use of serum tumor markers in addition to clinical assessments and imaging for monitoring MBC response [3, 4]. There is however, confusion regarding what constitutes suitable imaging for bone disease monitoring. All guidelines advocate the use of computed tomography (CT) and bone scans (BS), thus side stepping the limitations of CT/BS for assessing response in women with bone predominant metastatic disease.

Figure 1: Serial changes on morphological whole-spine sagittal T1-weighted images.

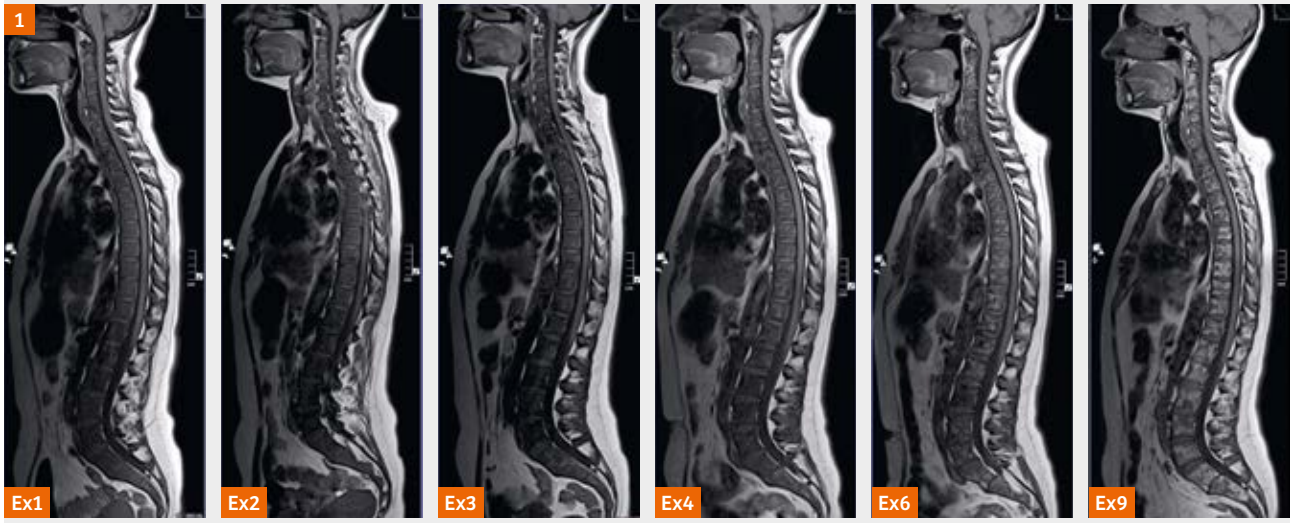

Diffuse metastatic infiltration throughout the spine, however note the small amount of fat on examination 6 (Ex6). The re-emergence of fat signal intensity is best appreciated on the last study (Ex9). The nature of the darker background signals on Ex9 is uncertain, but bone marrow (BM) scarring and/or residual active disease must be considered.

Figure 2: Serial changes on sagittal whole-spine STIR images.



Diffuse metastatic infiltration throughout the spine. Note no appreciable change in signal intensity between Ex1 and Ex2.
There is a marked increased in bone marrow signal between Ex3 and Ex6 consistent with increased BM water, which fades on the last examination (Ex9).

Figure 3: Serial changes on whole-body b = 900 s/mm^2 3D MIP images (inverted scale).

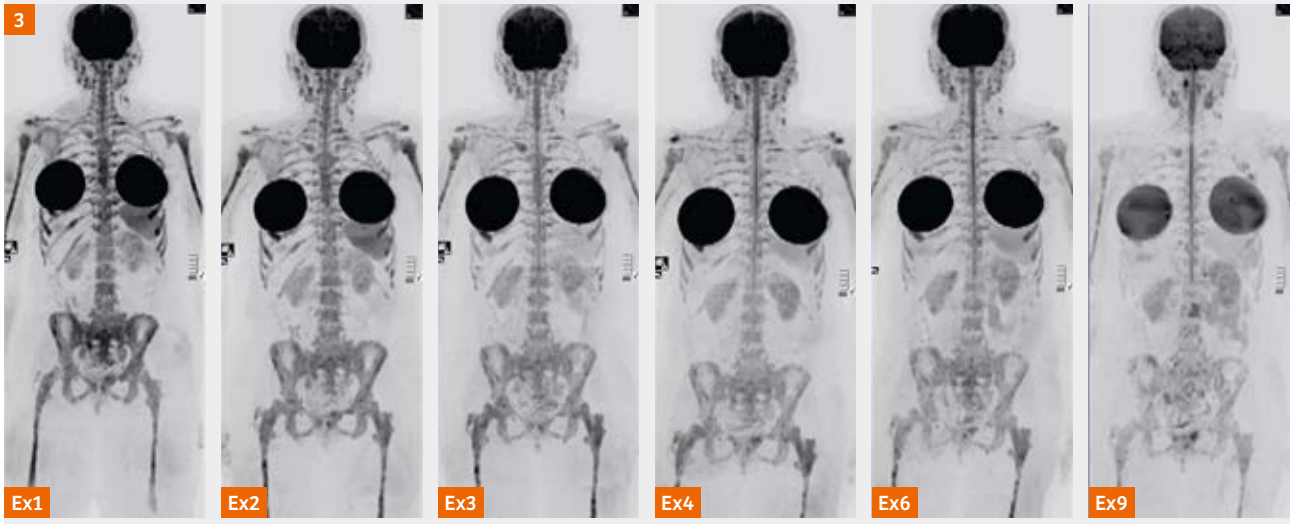

b900 3D MIP images (inverted scale) demonstrate a gradual reduction in signal intensity throughout the course of treatment, which is most evident between Ex1 and Ex2. The signal intensity is lowest on the last examination (Ex9). No extra-osseous disease is detected. Bilateral breast implants are seen in situ.

There is accumulating evidence showing the added value of PET/CT and whole-body MR imaging (WB-MRI) for decision making in metastatic breast cancer [5, 6]. WB-MRI with morphological and diffusion-weighted sequences has emerged as powerful tool for detecting and assessing the response of MBC with good efficacy in the assessment of bone metastases [7]. The key advantage of WB-MRI is that the success of therapies can be positively assessed (CT/BS scans use the 'no evidence of progression' category as meaning therapy success). As a result, WB-MRI has the potential to alter clinical diagnostic thinking when assessing bone disease response [6]. Uniquely, quantitative apparent diffusion coefficient values (ADC; unit μm^2/s) can bring objectivity to therapy response assessments.

Figure 4: Serial changes on MIP-ADC projection images.



Top row: ADC color projections focusing on response showing serial changes in voxels that are highly likely to be responding (green). Marked response is first observed on Ex3 in voxels co-localized to the axial skeleton. These high ADC voxels only decrease in extent on Ex9.

Bottom row: ADC color projections focusing on marrow showing serial changes in voxels that are likely to represent normal bone marrow (yellow). Their appearance is co-localized to the appendicular skeleton (proximal humeri and femora). The appearance of fat in the spine on Ex9 shown on T1w images in Figure 1 cannot be readily appreciated on these projection images.

Semi-automated threshold-based, quantitative ADC mapping and histogram analysis has been introduced as a viable and efficient tool for whole-body ADC mapping [8].

This case report applies the methodology of the companion article by Dalili et al. on the ability of the *syngo*.via Frontier MR Total Tumor Load software[1] to distinguish ADC changes ascribable to tumor response and bone marrow recovery [9]. We discuss how ADC changes can be explained by the mechanism of tumor cell death and introduce a biologic model that explains imaging observations during the repair phase after effective therapy [10].

[1] *syngo*.via Frontier is for research only, not a medical device. *syngo*.via Frontier MR Total Tumor Load is a released research prototype.

Case study

A 49-year-old peri-menopausal woman presented with bone only metastatic lobular carcinoma (ER-positive, HER2-neu negative) in 2013. Bilateral mastectomy (left breast for risk reduction), axillary node clearance and breast reconstructions were performed with completion radiotherapy to the right supraclavicular fossa and chest wall. She underwent initial systemic anticancer therapy with Tamoxifen and Zoledronic acid infusions. During treatment, she developed bone pain but CT scans were unhelpful regarding the status of her bone disease. Subsequently she was referred for a whole-body MRI scan to assess her disease status (volume and tumor viability). Nine WB-MRI studies were then performed every 3–4 months over the next 3.5 years for therapy response assessments.

Figure 5: ADC histogram changes with time.

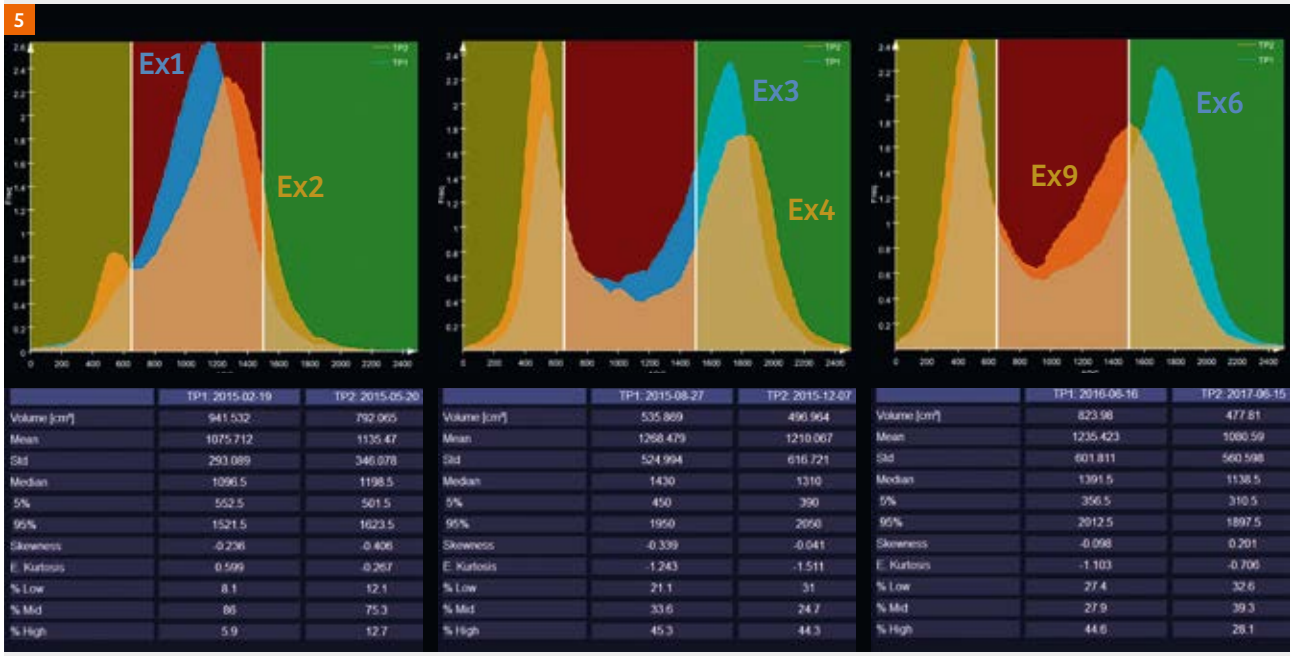

Histograms were created using the methodology of the accompanying article [9] at each time point. Fixed ADC thresholds were chosen (650 and 1500 µm²/s) because examination 1 was an 'on treatment' (Tamoxifen and Zoledronic acid) study (that is, no true pre-therapy baseline study was available). These default thresholds are based on literature values [12, 13]. Therefore, voxels in the red range are likely to represent untreated disease or those that have no-detected response. Green colored voxels have ADC values ≥ 1500 µm²/s (representing voxels that are 'likely' to be responding). Yellow voxels lie below 650 µm² and represent regions 'likely' to represent normal bone marrow.

Ex1 Ex2: At baseline (Ex1), the histogram is negatively skewed (tail to the left) consistent with the therapy effects of Tamoxifen, although 86% of segmented voxels are in the active range (between 650–1500 µm²/s). With the change of treatment to Anastrozole and Goserelin (Ex2), a positive therapy change effect can be detected with a small right sided shift of the histogram. The bulk of the voxels on Ex2 (75%), remain in the red-voxel range (650–1500 µm²/s). The emergence of a new peak below 650 µm²/s is noteworthy and, these yellow voxels seem confined to the limb bones (Fig. 4 – bottom row).

Ex3 Ex4: With the change of treatment to Everolimus and Exemestane (Ex3), a more dramatic histogram change becomes visible with 2 well separated peaks (below 650 µm²/s and above 1500 µm²/s). The peak above 1500 µm²/s indicates large cell kill and highly likely response and these green voxels can be located to the axial skeleton (Fig. 4 – top row). The enlarging peak below 650 µm²/s is consistent with further return of the mixed bone marrow depicted as yellow areas in the limb bones (Fig. 4 – lower row). This twin peak histogram pattern does not change much in the 6 month period between Ex4–Ex6.

Ex6 Ex9: A change of the histogram becomes visible 12 months later, on Ex9. At this point, the higher peak of the ADC histogram has begun to shift towards the red region, visible as increasing red regions on the MIP-ADC low projection images in Fig. 4. However, these emerging red voxels are unlikely to represent tumor regrowth because the b900 signal intensity has remained low (Fig. 3) and fat has remerged in the marrow spaces (Fig. 1). So, it's most likely that the emerging red regions on Ex9 are likely to represent bone marrow scarring/bone sclerosis according to the model in Fig. 6. This remains to be confirmed.

After the first WB-MRI examination (examination 1), therapy was changed to Anastrozole and Goserelin with Zoledronic acid infusions. She remained symptomatic and a follow-up WB-MRI (examination 2) did not demonstrate appreciable cell kill to the therapy change. Subsequently she was switched to Exemestane and Everolimus (mTOR inhibitor) with good symptomatic relief of bone pain. Symptomatic relief of bone pain was accompanied by a good therapy effect on whole-body MRI scans (examinations 3 and 4). However, her blood hemoglobin levels remained below the normal range at 90 g/L between examinations 1 and 4. Eventually she returned to work and currently, she suffers only from minor drug toxicity related side effects. Her hemoglobin recovered to the normal range by examination 6 (120 g/L) at 18 months, and improved further to 130 g/L by examination 9 at 30 months, thus confirming an overall good systemic response.

In this report, we illustrate six WB-MRI examinations, with the initial four studies performed consecutively at 3–4 month intervals (Ex1–Ex4) and the latter two (Ex6 and Ex9) at 18 months and 30 months respectively. All studies were undertaken using the same 1.5T MAGNETOM Avanto scanner, utilizing a published protocol [11]. The diffusion-

Figure 6: Biological model of the relationships between bone marrow state, high b-value signal intensity and ADC values in the setting of therapy response [10].

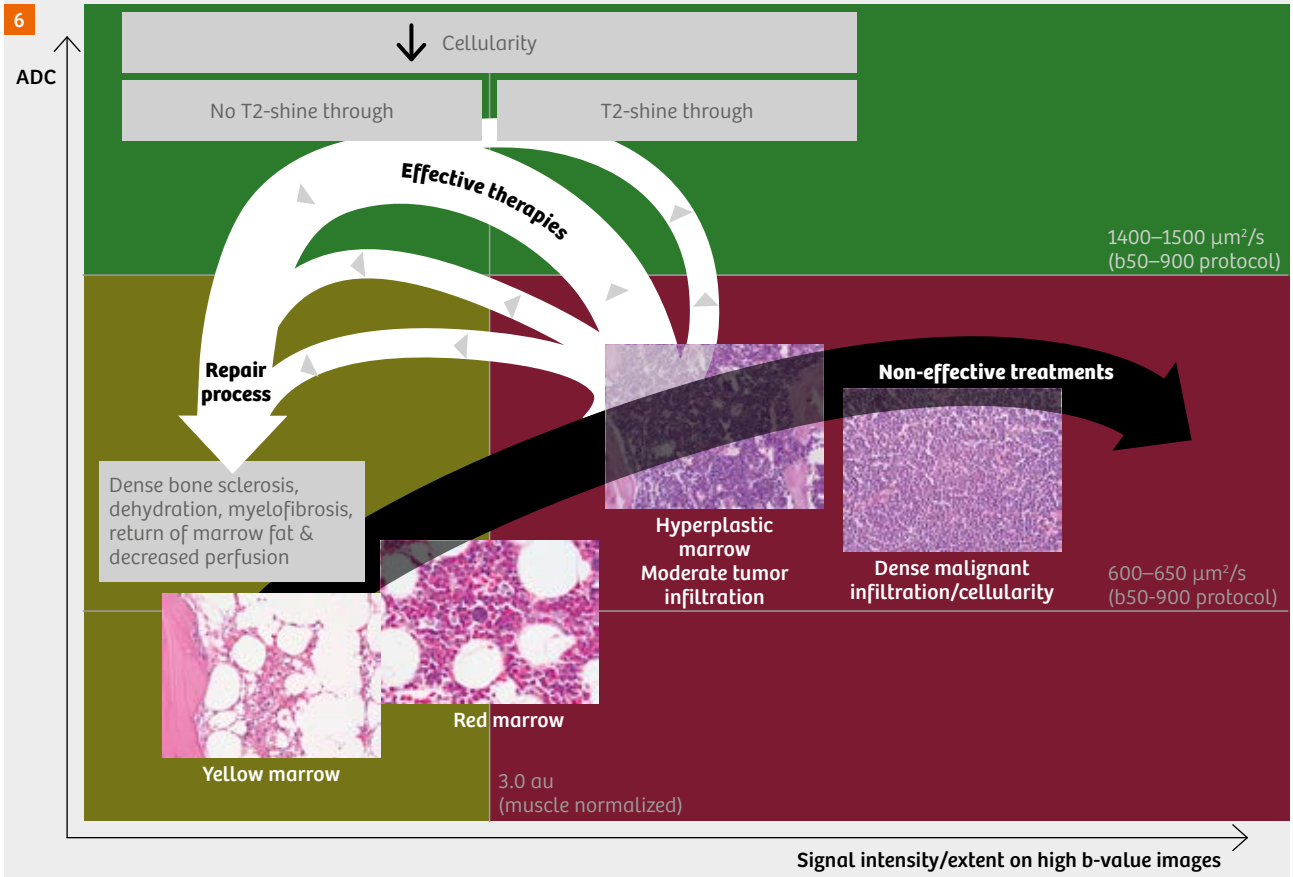

With therapy progression (black arrow), increases in the volume of abnormal signal intensity, new areas of abnormal signal intensity, or increased intensity of abnormalities on high b-value DW images can be seen. Modest increases, unchanged or slight decreases in ADC values compared to pre-therapy values can occur with disease progression. The initial modest increase in ADC values with disease progression occurs because tumor infiltration displaces bone marrow fat cells, increases bone marrow water (including water in the extracellular space) and increases tissue perfusion, thus returning higher ADC values compared to yellow or mixed bone marrow. The important point to note is that these increases in ADC values tend to be of small magnitude, provided that the metastatic lesions remain non-necrotic and in our experience rarely increases > 1400–1500 µm²/s. Stable ADC values occur when unchanged tumor cellularity occurs with increases in the geographic extent of disease. Reductions in ADC values are probably related to increasing cellularity within a fixed bone marrow space.

A variety of high b-value signal and ADC changes can be seen with effective therapy (white arrows). Decreases in signal intensity on high b-value images accompanied by increases in ADC values is the usual pattern (thick white arrow). The extent of ADC increases seems to depend on the type of treatment given with higher ADC values for treatments that cause greater tumor cell death especially when there is a strong inflammatory component. Occasionally, unchanged or minimally decreased high signal intensity on high b-value images associated with marked rises in ADC values is observed, as in this case (Ex2–Ex6). This is termed 'T2-shine through' which also indicates a successful response to therapy. T2-shine through appearances often can take a long time (often more than 1 year) for b-value signal intensity and ADC to decrease to the normal levels. The emergence of bone marrow sclerosis, fibrosis and/or return of bone marrow fat are part of repair processes. Note that these repair processes can decrease b-value signal intensity without affecting ADC values.

weighted images of examinations were analysed using threshold-based segmentation with *syngo*.via Frontier MR Total Tumor Load prototype software[1] [8]. Response to treatment was displayed using the methodology described in the accompanying article [9].

[1] *syngo*.via Frontier is for research only, not a medical device. *syngo*.via Frontier MR Total Tumor Load is a released research prototype.

Discussion

The premise for the use of ADC as a parameter of tissue characterization in the setting of treatment response, is that therapy-induced cell death precedes macroscopic lesion size changes. As a result of cellular necrosis, which results in loss of cell membrane integrity and increases in extracellular space water, ADC values typically increase.

During the following weeks to months, tumors may show shrinkage, with a resorption of the free extracellular fluid and fibrotic conversion leading to decreases in ADC values, although tumor recurrence can also result in reduced ADC values.

The degree of increase in ADC with successful therapy is highly dependent on the mode of cellular death with necrotic cell death resulting in higher ADC values due to associated inflammation and increased tissue water. Thus, chemotherapy typically results in greater degrees of tumor cell death and greater increases in ADC values [10]. With hormonal therapy, the mode of cell death is typically apoptotic and ADC value increases are smaller [12] as shown by the small ADC histogram shift between examinations 1 and 2 (Anastrozole and Goserelin therapy). When combination treatments are used, a synergistic, additive therapy effect can be observed clinically. This explains the greater ADC change in this case where Everolimus and Exemestane (mTOR inhibitor and hormonal therapy) were used together (examinations 3–6) resulting in two distinct peaks in the ADC histogram.

The phenomenon of 'T2-shine though' indicates a successful therapeutic effect with bone marrow edema. 'T2-shine through' can take a long time for high b-value signal intensity and ADC to decrease to normal levels [10]. The emergence of bone sclerosis, bone marrow fibrosis and/or return of bone marrow fat are part of repair processes, reducing high b-value signal intensity and lowering ADC values visible on the Ex9 images [10].

This latter phenomenon of decreasing ADC values with tissue repair highlights the need to evacuate all the acquired images (multiparametric assessments) for the correct interpretation of likely tissue disease status. So relying on ADC histograms alone may be misleading in the setting of tissue repair and recovery, making it necessary to take into account morphological appearances and quantitative parameters such as fat fraction and high b-value signal intensity to distinguish between healing processes from recurrent/residual cancer.

Contact

Dr. Danoob Dalili
Specialist Registrar Clinical Radiology
Imperial College Healthcare NHS Trust
St Mary's Hospital
Praed St
London W2 1NY
United Kingdom
Phone: +44 (0) 20 3312 6666
Dalili@doctors.org.uk



Prof. Anwar R. Padhani
Consultant Radiologist and
Professor of Cancer Imaging
Paul Strickland Scanner Centre
Mount Vernon Cancer Centre
Rickmansworth Road
Northwood, Middlesex HA6 2RN
United Kingdom
Phone (PA): +44-(0) 1923-844751
Fax: +44-(0) 1923-844600
anwar.padhani@stricklandscanner.org.uk



References

1 Lin NU, Thomssen C, Cardoso F et al. European School of Oncology-Metastatic Breast Cancer Task Force. International guidelines for management of metastatic breast cancer (MBC) from the European School of Oncology (ESO)-MBC Task Force: Surveillance, staging, and evaluation of patients with early-stage and metastatic breast cancer. Breast. 2013; 22(3):203-10.
2 Graham LJ, Shupe MP, Schneble EJ, et al. Current approaches and challenges in monitoring treatment responses in breast cancer. J Cancer. 2014 Jan 5;5(1):58-68.
3 Harris L, Fritsche H, Mennel R, et al. American Society of Clinical Oncology. American Society of Clinical Oncology 2007 update of recommendations for the use of tumor markers in breast cancer. J Clin Oncol. 2007; 20;25(33):5287-312.
4 Cardoso F, Costa A, Senkus E, et al. 3rd ESO-ESMO International Consensus Guidelines for Advanced Breast Cancer (ABC 3). Ann Oncol. 2017 Jan 1;28(1):16-33.
5 Riedl CC, Pinker K, Ulaner GA, et al. Comparison of FDG-PET/CT and contrast-enhanced CT for monitoring therapy response in patients with metastatic breast cancer. Eur J Nucl Med Mol Imaging. 2017 [epub].
6 Kosmin M, Makris A, Joshi PV, et al. The addition of whole-body magnetic resonance imaging to body computerised tomography alters treatment decisions in patients with metastatic breast cancer. Eur J Cancer. 2017; 77:109-116.
7 Woolf DK, Padhani AR, Makris A. Assessing response to treatment of bone metastases from breast cancer: what should be the standard of care? Ann Oncol. 2015; 26(6):1048-57.
8 Grimm R, Padhani AR. Whole-body Diffusion-weighted MR Image Analysis with syngo.via Frontier MR Total Tumor Load. MAGNETOM Flash 2017; 68(2), 73-75.
9 Danoob Dalili, Anwar R. Padhani, Robert Grimm. Quantitative WB-MRI with ADC histogram analysis for demonstrating complex response of bone marrow metastatic disease. MAGNETOM Flash 2017; 69(3): 38–42.
10 Padhani AR, Makris A, Gall P, et al. Therapy monitoring of skeletal metastases with whole-body diffusion MRI. J Magn Reson Imaging. 2014; 39(5):1049-78.
11 Padhani AR, Lecouvet FE, Tunariu N, et al. METastasis Reporting and Data System for Prostate Cancer (MET-RADS): Practical Guidelines for Acquisition, Interpretation, and Reporting of Whole-body MRI-based Evaluations of Multiorgan Involvement in Advanced Prostate Cancer. Eur Urol. 2017; 71(1):81-92.
12 Padhani, AR, Van Ree, K, Collins DJ, et al Assessing the Relation Between Bone Marrow Signal Intensity and Apparent Diffusion Coefficient in Diffusion-Weighted MRI. American Journal of Roentgenology 2013; 200(1), 163-170.
13 Messiou C, Collins DJ, Morgan VA, Desouza NM. Optimising diffusion weighted MRI for imaging metastatic and myeloma bone disease and assessing reproducibility. Eur Radiol. 2011; 21(8):1713-8.
14 Padhani AR. Observing endocrine therapy resistance in metastatic breast cancer with whole body MRI. Magnetom FLASH 2017; 68(2):80-83.

Imaging of the Pancreas: Technique and Clinical Applications

Giovanni Morana[1]; Alex Faccinetto[1]; Alberto Dorigo[1]; Pierluigi Ciet[2]; Silvia Venturini[1]; Michele Fusaro[1]

[1] Department of Radiology, General Hospital Ca' Foncello, Treviso, Italy
[2] Department of Radiology, Erasmus Medical Center, Rotterdam, the Netherlands

1. Introduction

MRI has assumed a leading role in imaging of the pancreas thanks to recent technical innovations with either breath-hold T1- and T2-weighted images or respiratory-triggered T2-weighted images. It also owes its success in this field to dynamic imaging with contrast media and secretin, as these techniques offer greater scope for noninvasive exploration of the pancreatic ducts and pancreatic parenchyma, and imaging of the pancreatic vessels.

2. MR technique

MR imaging of the pancreas requires high-field magnets, powerful and fast gradients, phased array surface coils, parallel imaging technology, and adapted sequences. Pancreas examinations are performed in both T2- and T1-weighted sequences, and in axial and coronal planes. MR imaging can provide multiple types of information on pancreatic diseases, such as morphology, vascularization, and water diffusion, as well as ductal imaging with functional information after secretin injection. With state-of-the-art MR equipment, a complete study of the pancreas takes about 30 to 40 minutes.

2.a T2-weighted sequences

2.a.1 Fast spin-echo sequence (HASTE, RARE)

These are axial and coronal single-shot, turbo spin-echo sequences with half k-space acquisition, a short echo time (40–80 ms) and a long echo time. Each slice is acquired in approximately one second. The main feature of this sequence is its low sensitivity to movement artifacts, which makes it suitable for uncooperative patients. Moreover, it is also highly sensitive to fluids, which appear as hyperintense in the pancreas (pancreatic duct, cystic lesions) and the peripancreatic area (stomach and duodenal content, peripancreatic fluid collections). Its main disadvantages are that the signal-to-noise ratio is lower than in fast multi-shot spin-echo sequences, and that it leads to slight blurring, which reduces its sensitivity in detecting small, low-contrast solid lesions. The signal of the normal pancreas is equal to or higher than that of the liver, whereas the ducts (biliary and pancreatic) appear strongly hyperintense.

2.a.2 Conventional T2-weighted fast spin-echo sequence

The latest sequences are acquired with fat suppression and respiratory compensation. They clearly show liquid infiltration in acute pancreatitis, but they are not particularly useful in studying focal solid or cystic pancreatic lesions.

2.b T1-weighted sequences

2.b.1 GRE T1-weighted 2D sequence with fat saturation

When using unenhanced imaging, this is the best sequence for differentiating between a normal and a diseased pancreas. A normal pancreas appears as homogeneously hyperintense. This is attributed to the presence of large quantities of aqueous protein in the acini of the pancreas, the abundance of endoplasmic reticulum in the acinar cells, and the paramagnetic ion-rich content, notably manganese [1, 2]. Fatty infiltration and fibrosis reduce the pancreas' high signal intensity. Focal or diffuse pancreatic diseases appear as hypointense areas. Thus, this sequence can be considered as very sensitive to pancreatic diseases, but with a low capacity for differentiating between lesions.

2.b.2 GRE T1-weighted 3D sequence with small flip angle, interpolation, and fat saturation

This sequence can be used for dynamic imaging after injection of gadolinium chelates. Its excellent contrast after bolus injection, combined with thin slices, makes it possible to reconstruct the vessels with maximum intensity projection (MIP) or volume rendering (VR) techniques. This

technique can be used as a way of combining parenchymal and vascular imaging.

Dynamic imaging of the pancreas is necessary for studying solid or cystic pancreatic lesions. After administering a test bolus to identify the correct acquisition timing, the operator consecutively acquires arterial, pancreatic (late arterial), venous, and delayed sequences. The arterial phase (15-20 seconds after injection of contrast medium) is useful in postprocessing to evaluate the arterial tree in the pancreatic region, and for evaluating solid hypervascular lesions. In this phase, pancreatic enhancement is stronger than liver enhancement. The pancreatic phase is usually obtained about 15 seconds after the peak bolus in the abdominal aorta [3] and is useful for identifying solid pancreatic lesions. The venous phase is acquired 45 seconds after contrast medium injection. When searching for delayed enhancement (such as in paraduodenal pancreatitis or autoimmune pancreatitis), a late sequence (180 seconds) can be added after injection [4].

2.b.3 Dynamic, multiphase contrast-enhanced MRI

FREEZEit TWIST-VIBE or CAIPIRINHA Dixon TWIST-VIBE is a novel, contrast-enhanced T1w-3D-fs-GRE sequence that makes it possible to acquire multiple arterial subphases during a single breath-hold. TWIST-VIBE facilitates the timing of the arterial phase and generates additional dynamic information on the vascular status of focal lesions [5]. Although research has primarily focused on hypervascular focal liver lesions [6], in pancreatic pathology TWIST-VIBE can be very useful for detecting small hypervascular lesions, such as neuroendocrine tumors (Fig. 1).

2.c Diffusion-weighted imaging (DWI)

DWI measures changes in the microscopic diffusion of water due to Brownian motion. DW images are acquired with the single-shot echoplanar technique (SE-EPI-SSh). When using this sequence, it is also possible to select a bipolar version that allows shorter TE – e.g., a spin-echo sequence to which two additional equal gradients with opposing directions are added immediately before and after the 180° impulse with diffusion sensitizing gradients. The breadth and duration of the diffusion gradients influences the diffusion weighting of the sequence, defined by the b-value and expressed in seconds per millimeters squared (s/mm^2) [7]. The sequence is generally repeated for various b-values, resulting in the acquisition of different diffusion weights for each section of the image. Finally, the different DW images are used to obtain the respective apparent diffusion coefficient maps (ADC maps) which allow a quantitative analysis of the signal by positioning a region of interest (ROI) on the structure being studied.

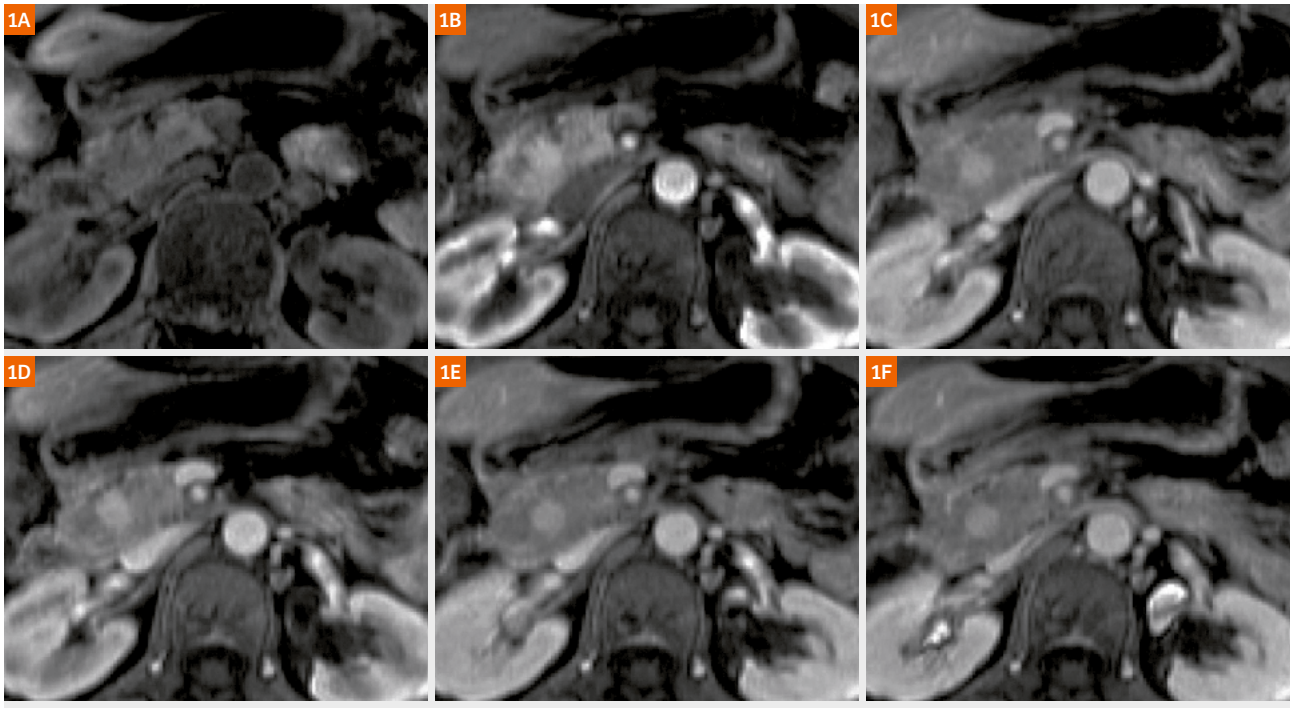

Figure 1A-F: PNET. Twist-VIBE can acquire up to six arterial phases and thus clearly visualize a hypervascular PNET.

DWI has been proposed as a diagnostic tool in neoplastic diseases because malignant lesions have a denser cellularity, a larger volume, and less extracellular space, which restricts the free movement of water molecules. This results in a lower ADC value and hyperintensity on diffusion-weighted (DW) images with high b-values. By contrast, benign lesions (such as benign tumors or inflammatory lesions) have more extracellular space, which preserves the diffusion of water molecules and results in high ADC values and hypointensity on DW images with high b-values.

Until recently, DWI of the pancreas and upper abdomen was of limited use due to major physiological motions. The long acquisition time meant that respiratory movements, bowel peristalsis, and blood flow all hindered the application of the sequence. The recent introduction of parallel imaging and respiratory triggering has allowed upper-abdomen DWI to become routine in state-of-the-art MR equipment [8].

However, some drawbacks remain: With low b-values (0–50), the long TR of the acquisition gives the sequence a T2-weighted appearance. This tends to decline with higher b-values (> 400) but can remain significant and therefore give a high water signal even in unrestricted diffusion conditions (T2 shine through).

Moreover, with low b-values, the signal is also sensitive to capillary perfusion, while the importance of water diffusion increases with high b-values [7]. Thus, ADC represents the microcirculation of blood (perfusion) and the molecular diffusion of water. Some authors suggest calculating ADC with lower b-values of ≥ 150 s/mm^2 and with an upper b-value of ≥ 700 s/mm^2 to avoid contamination by capillary perfusion [9]. With DWI, a normal pancreas has a signal intensity similar to that of the liver for the various b-values. The ADC value of a normal pancreas has been reported to be higher than in cases of pancreatic cancer and mass-forming pancreatitis [10]. A b-value of 1,500 s/mm^2 can improve the delineation of pancreatic adenocarcinomas at 3T [11].

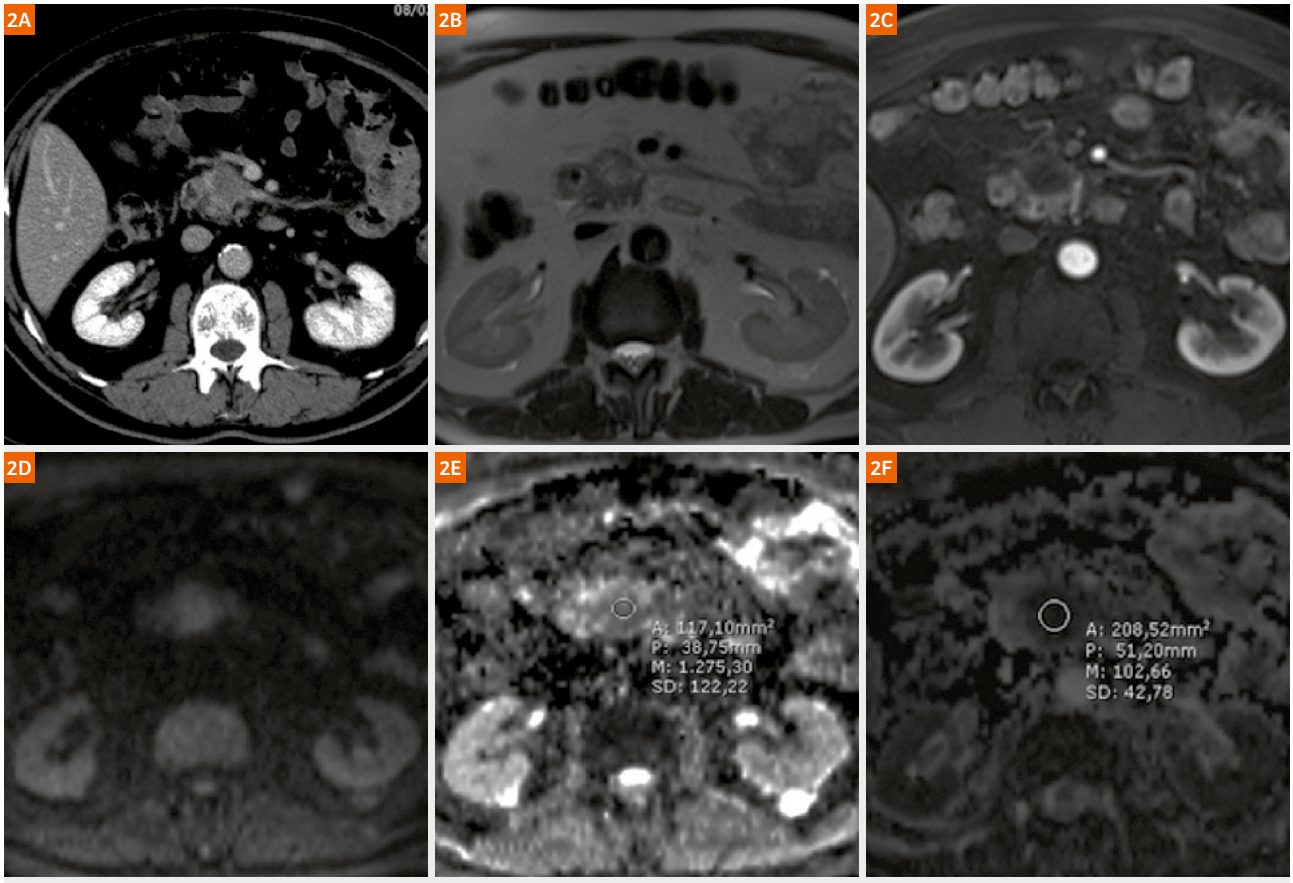

Figure 2: Pancreatic colloid adenocarcinoma. A small hypodense lesion is visible in the uncinate process on a CT image **(2A)**, and appears slightly hyperdense on T2w **(2B)** and remains hypovascular on contrast-enhanced MRI **(2C)**. With DWI (b = 800), the lesion is hyperintense **(2D)**, but the ADC map **(2E)** does not show restricted diffusion (1.2) due to colloid content. With IVIM, the lesion has a low perfusion fraction (10%), consistent with pancreatic carcinoma **(2F)**.

Intravoxel incoherent motion (IVIM) imaging is a method based on DWI with multiple b-values. It offers scope for separately analyzing pure molecular diffusion and microcirculation (or perfusion) with the IVIM-derived parameters of pure molecular diffusion coefficient (Dslow), perfusion fraction (f), and perfusion-related diffusion coefficient (Dfast) [12]. According to recent studies, the perfusion-related parameters f and Dfast are more helpful than ADC or Dslow in characterizing pancreatic diseases [13, 14] (Fig. 2).

IVIM models are based on the assumption that the probability displacement function of the water molecules follows a Gaussian distribution. However, studies show that this assumption is not valid when the acquisition is performed with b-values of > 1000 s/mm^2. This is due to the interaction of water molecules with membranes and other microstructural components, which in turn reduces the actual diffusion distance compared to free water.

Diffusion kurtosis imaging (DKI)[1] is an advanced DWI model that quantifies non-Gaussian behavior of diffusion and provides both a corrected ADC and the excess kurtosis of tissue (a measure of the extent to which tissue diffusion deviates from a Gaussian pattern). However, it is technically demanding, as it requires acquisition of b-values of > 1000 s/mm^2 [15]. Following some studies in different organs, only two papers have so far been published on the clinical application of DKI. One focused on pancreatic cancer [16], and showed that DKI had the highest area under the curve (AUC) when it came to differentiating tumorous from non-tumorous pancreatic parenchyma. The other focused on HbA1c levels in patients with suspected pancreatic disease. It showed that the mean Kurtosis measurement on DKI of the pancreas could be a potential biomarker for assessing HbA1c levels [17].

2.d T1 mapping

T1 mapping has been successfully used in a number of cardiac conditions, including myocardial fibrosis and myocardial deposition disease. Commercially available fast volumetric T1 mapping techniques then facilitated its application in other organs, such as in the liver to detect and quantify liver fibrosis [18]. Very recently, T1 mapping has also been used to detect early fibrotic changes in mild chronic pancreatitis (CP). It can differentiate patients with normal pancreas from those with mild CP and is thus a promising solution for the early diagnosis of CP [19].

[1] DKI postprocessing of standard DWI data is WIP, the product is currently under development and is not for sale in the US and in other countries. Its future availability cannot be ensured.

2.e MR cholangiopancreatography (MRCP)

Heavily T2-weighted sequences render static fluid or slow-flow structures very hyperintense with a very low signal from solid structures. Different and complementary approaches are used: 2D T2w single-shot fast spin echo, thick and/or thin multislice sequences, and 3D T2w (e.g., SPACE from Siemens Healthineers, and CUBE from GE).

A 2D T2w thick-slab sequence usually has a slice thickness of 40–70 mm so that it covers the whole pancreatic duct. It can be obtained in all planes, although it is generally acquired in the coronal plane, and requires breath-hold times of less than 3 seconds. The sequence provides excellent biliary and pancreatic mapping with no respiratory artifacts, few susceptibility artifacts, and good planar resolution.

3D T2w techniques have been implemented with respiratory triggering and free breathing. This provides a very high spatial resolution and isotropic voxels, allowing the acquired datasets to be reconstructed in different planes using maximum intensity projection postprocessing techniques. Images are of superior quality and achieve better delineation of pancreaticobiliary anatomy than conventional 2D images [20]. However, in the case of uncooperative patients, a 2D approach is more feasible and can obtain better results.

High image quality is obtained by orally administering contrast material that significantly decreases the signal of fluid contained in the stomach and duodenum – for instance, certain fruit juices (pineapple, blueberry, cranberry, etc.) or commercial oral superparamagnetic contrast agents based on iron oxide, such as Ferumoxil.

The IV administration of paramagnetic contrast agent prior to MRCP gives a superior image quality. This is thanks to the T2* effect of gadolinium, which suppresses the overlapping vessel signals and the signal from liquids in the interstitial compartment of the pancreatic gland, and does not affect the signal from the ducts [21].

2.f Secretin MRCP (S-MRCP)

Administering secretin stimulates the production of fluid and bicarbonate by the exocrine pancreas and increases the pancreas' flow rate almost immediately and for a few minutes after administration. At the same time, an increase in tension in the sphincter of Oddi (SO) is noted. In normal subjects, an increase in the main duct pressure is observed after one minute with an almost complete return to baseline values after five minutes and reversion of SO contraction [22]. The rise in the fluid volume of the main pancreatic duct (MPD) provides a clearer visualization of the duct in MRCP.

Serial acquisition of the pancreatic duct with a 2D thick-slab sequence and a time interval of 30–60 seconds for 10–15 minutes after IV administration of 1 mL/kg bodyweight of secretin provides a dynamic visualization of the pancreatic response to secretin [23–26].

The advantages of secretin-enhanced MRCP are therefore both morphological and functional:

- Morphological benefits: Better visualization of the MPD; easier detection of anatomical variants such as pancreas divisum; clear depiction of obstruction, stenosis, dilatation, and irregular contours of the duct. Overall, secretin-enhanced MRCP increases the negative predictive value of MR imaging of the pancreas [27].
- Functional benefits: Visualization of side branches at body/tail after secretin is a sign of early chronic pancreatitis; an abnormally prolonged dilatation of the MPD (> 3 mm 10 min after secretin injection) indicates a deficit of pancreatic juice outflow; the parenchymogram (parenchymal enhancement) is a sign of recurrent acute pancreatitis; reduced duodenal filling suggests a decrease in pancreatic exocrine reserve [26].

Secretin-stimulated MRCP images are in many ways better than those achieved with standard MRCP. They could help in diagnosing and making clinical decisions for patients with acute, acute recurrent, or chronic pancreatitis, and could improve the identification of patients in need of therapeutic endoscopic retrograde cholangiopancreato-graphy (ERCP) [28].

3. Clinical applications

3.a Acute pancreatitis

The robustness and availability of CT make it the most important technique in cases of acute pancreatitis (AP). CT is used to diagnose and stage AP, and has greatly improved and changed the clinical management of this condition. However, because it involves ionizing radiation and potentially nephrotoxic contrast agents, its use is subject to limitations in young patients and in patients with impaired renal function [29].

Given the critical conditions of these patients, MR protocols need to be adapted so that they become faster and require less cooperation from the patient.

Axial and coronal T2w HASTE sequences can usually provide sufficient information about the condition of the pancreatic gland and the presence and extent of peripancreatic fluid collections (Fig. 3) in the acute phase, and of pancreatic pseudocyst in the late phase. T2w HASTE sequences are also useful in detecting the small intrabiliary calculi that are most often the cause of AP (Fig. 4).

T1w GRE fat-saturated sequences can easily detect small hemorrhagic foci (Fig. 5), while contrast-enhanced MRI is essential in cases of suspected severe pancreatitis, where non-enhancing areas are defined as necrotic (Fig. 3).

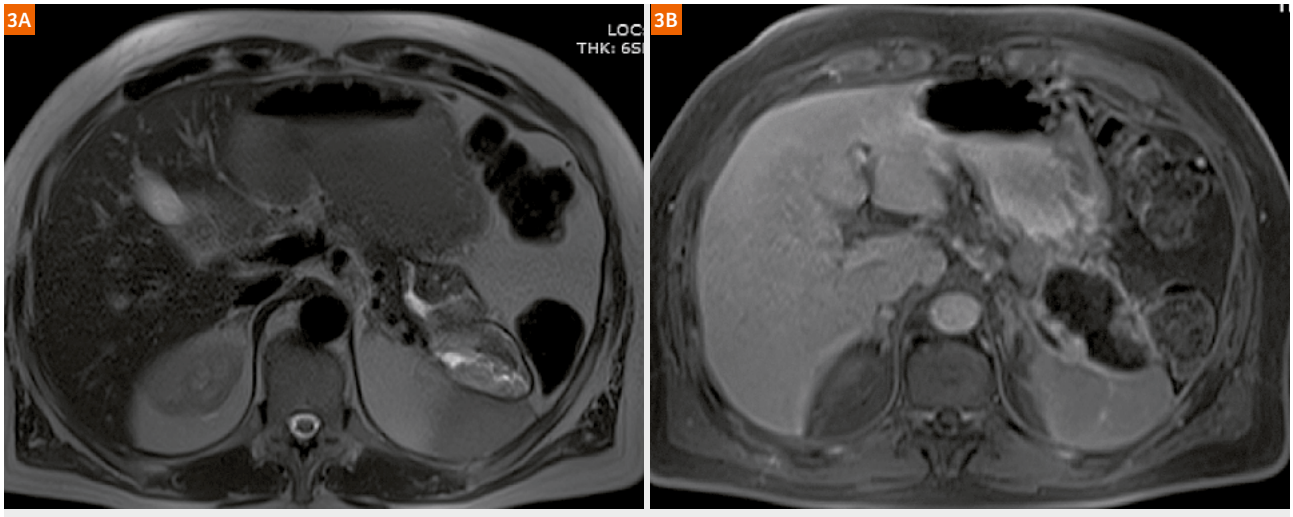

Figure 3: Peripancreatic fluid collection, recent severe pancreatitis. With HASTE T2w **(3A)**, a large collection with debris is visible in the tail of the pancreas. After Gd injection **(3B)**, a peripheral enhancement can be appreciated, while the internal debris does not show any significant enhancement.

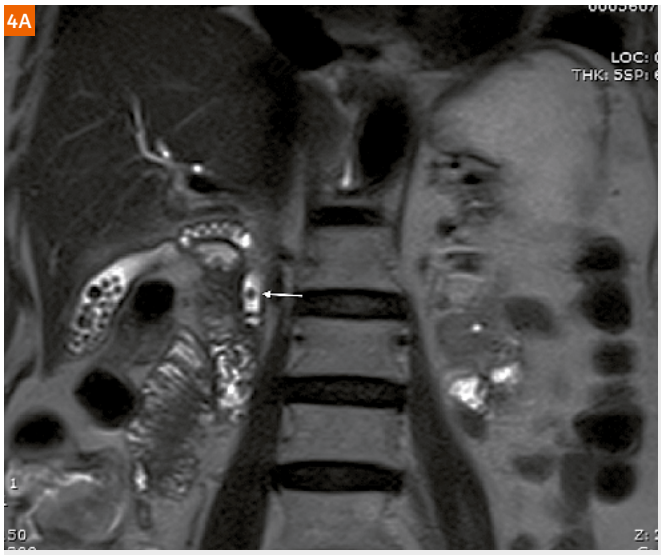

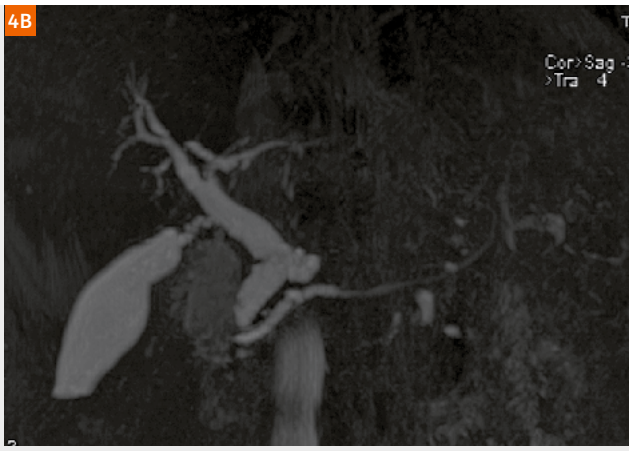

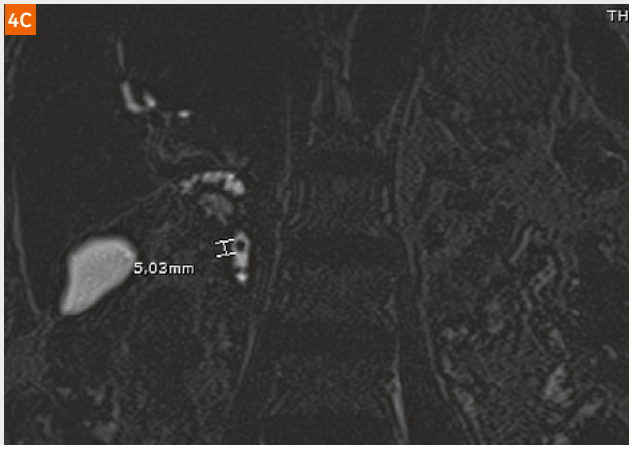

Figure 4: Biliary calculi. With coronal HASTE T2w **(4A)**, multiple calculi in the gallbladder can be appreciated. A small calculus is also visible in the intrapancreatic choledocus (arrow). The calculus cannot be seen in the MIP reformatted 3D MRCP images **(4B)**, as it is obscured by the bile signal. It can only be seen in a sub-MIP reformatted image **(4C)**.

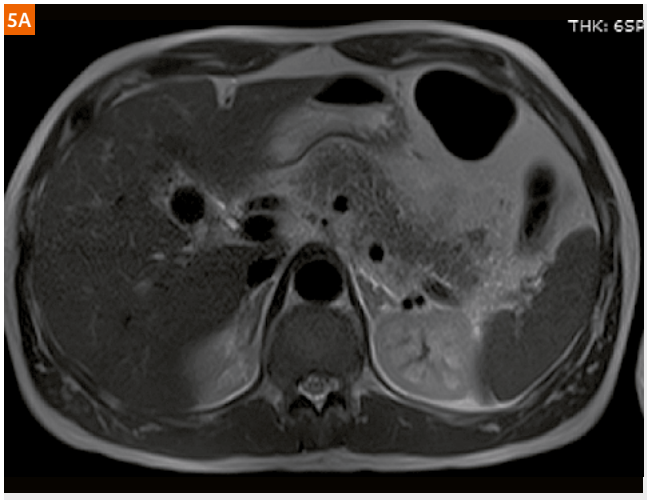

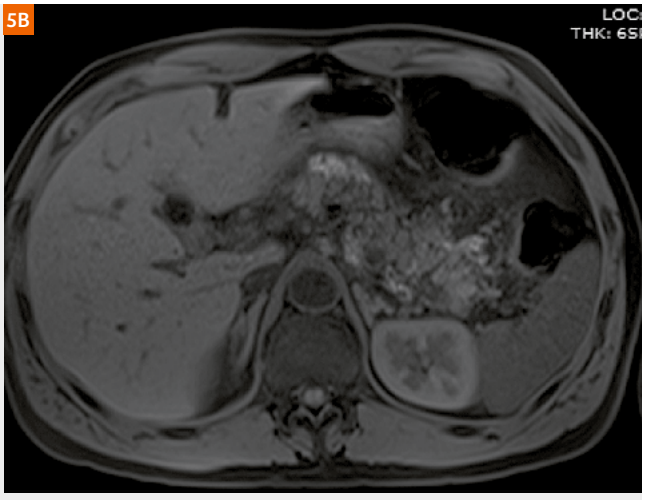

Figure 5: Acute pancreatitis. With T2w **(5A)**, an enlarged pancreatic gland is visible in the body-tail, with edema of the parenchyma. On T1w GRE fat-sat **(5B)**, the pancreatic gland is hypointense due to the edema. Small hyperintense foci are also visible, due to small hemorrhagic changes.

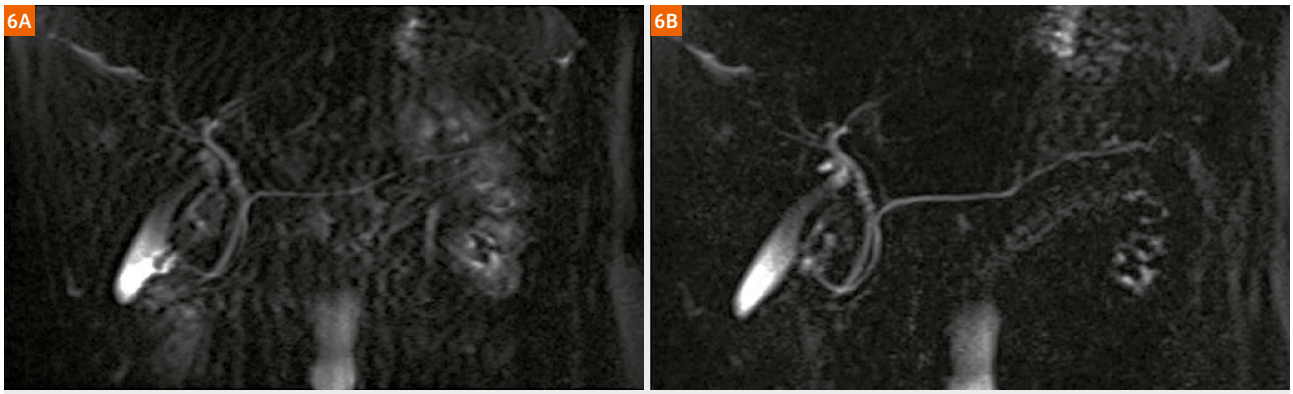

Figure 6: MRCP. On precontrast MRCP in a patient with recent edematous pancreatitis **(6A)**, the duct of Wirsung is obscured by the edema of the gland. Three minutes after injecting a Gd-based contrast agent **(6B)**, the edema has disappeared due to the T2* effect of the gadolinium in the interstitium, which results in better visualization of the duct.

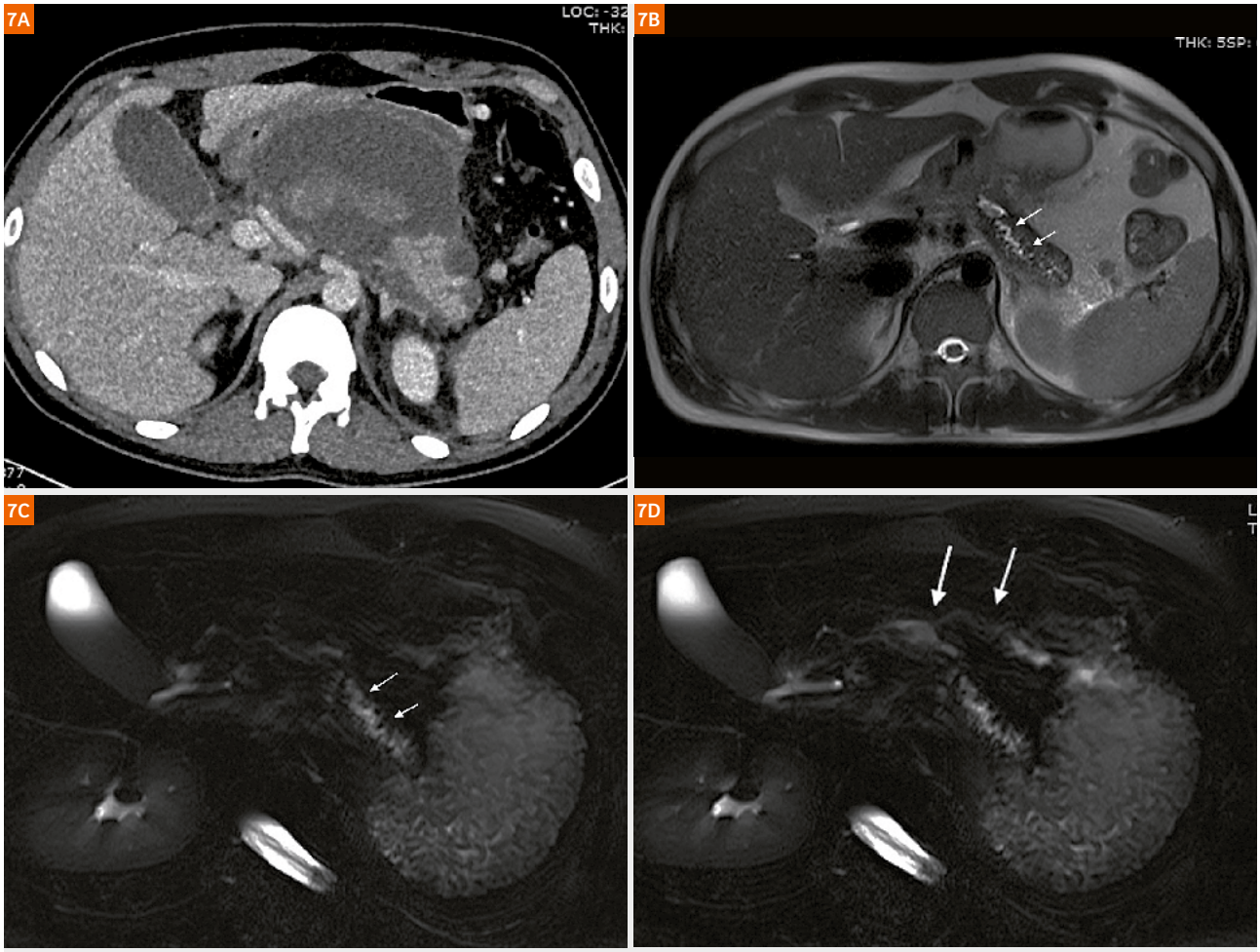

Figure 7: Pancreatic fistula. CT **(7A)** shows a large peripancreatic fluid collection in a patient with severe acute pancreatitis. After 3 months, the fluid has almost disappeared on HASTE T2w **(7B)** and slight dilatation of the duct of Wirsung is visible in the tail of the pancreas due to rupture of the duct (arrows). Axial MRCP (**7C)** confirms chronic obstructive pancreatitis in the tail (arrows). After secretin injection **(7D)**, pancreatic juice can be appreciated at the level of the duct rupture (arrows).

MRCP is often of low quality due to the significant interstitial edema of the pancreatic parenchyma. One way to improve image quality here is to perform MRCP five minutes after injecting paramagnetic gadolinium-based MR contrast agents. The T2* effect of gadolinium distributed in the interstitial space reduces the signal from interstitial fluids (i.e., edema), whereas the signal from the ducts remains unaffected (Fig. 6).

Secretin-enhanced MRCP is rarely used in these cases. When it is used, there must be a period of at least two weeks between the acute onset of symptoms and injection of secretin [26]. The technique is particularly useful for assessing pancreatic fistulas (Fig. 7).

MRI is particularly useful in cases of walled-off necrosis, an evolution of acute necrotic collection. In the presence of pancreatic necrosis, a collection that develops within four weeks of onset and lacks a discrete wall is defined as an acute necrotic collection. If the collection persists after four weeks and develops a discrete wall, it is then defined as walled-off necrosis (WON). With this type of necrosis, necrotic material often needs to be removed percutaneously or endoscopically, and this is often followed by surgical debridement. MRI can highlight the presence of abundant necrotic material, which can be difficult to drain percutaneously (Fig. 8).

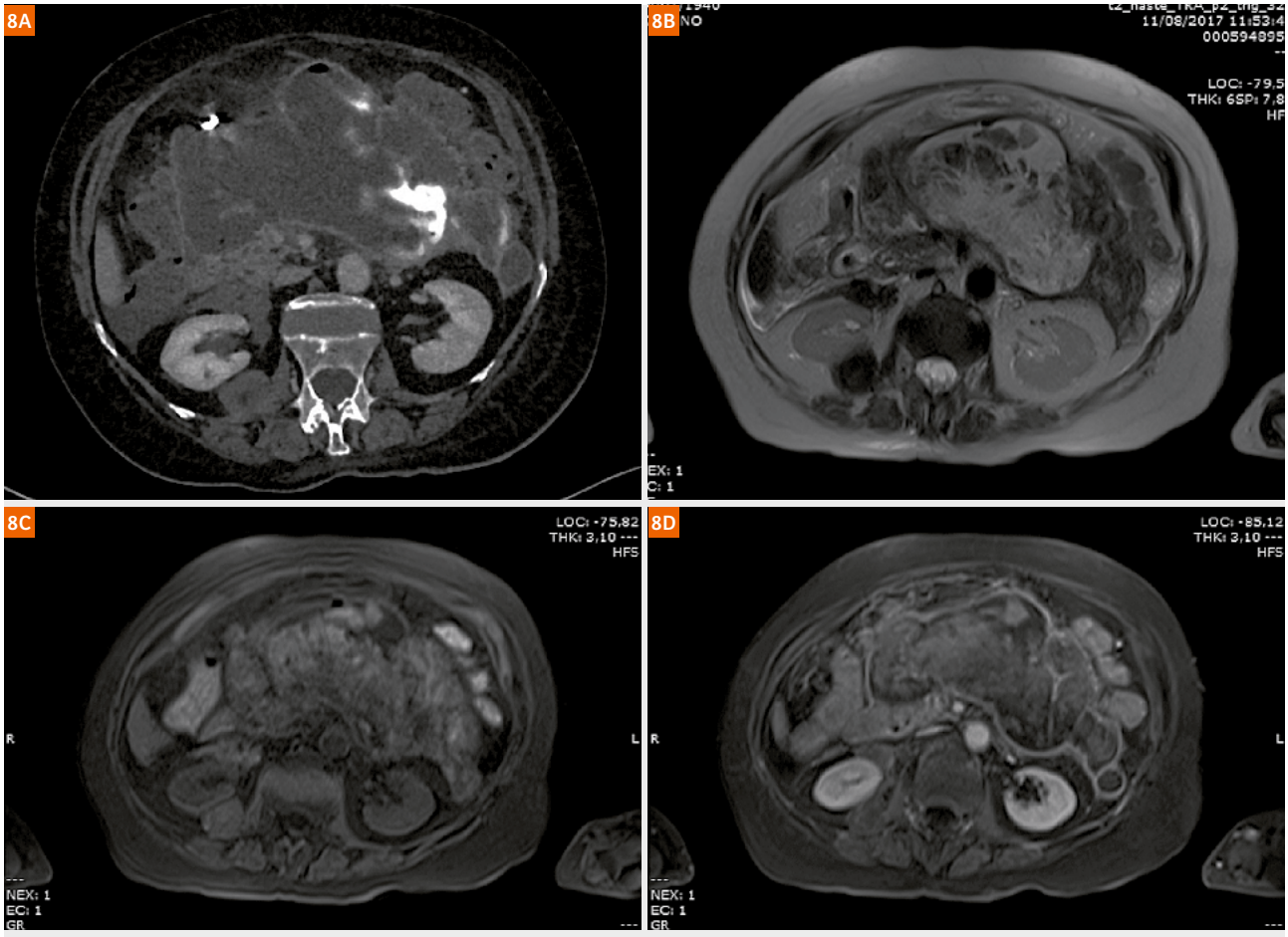

Figure 8: Walled-off necrosis (WON). CT **(8A)** shows a large collection with iodinated contrast material due to an unsuccessful attempt at endoscopic drainage. With HASTE T2w **(8B)**, the collection is well demarcated with necrotic material and hemorrhagic changes. T1w GRE fat-sat **(8C)** shows hyperintense foci caused by hemorrhagic changes. After Gd injection **(8D)** peripheral enhancement is visible, while the internal debris shows no significant enhancement.

3.b Recurrent acute pancreatitis (RAP)

Recurrent acute pancreatitis (RAP) is defined as the occurrence of two or more episodes of acute pancreatitis without concurrent clinical or imaging evidence of chronic pancreatitis. Irrespective of the etiology, RAP is independently associated with the development of chronic pancreatitis [32]. RAP can be caused by a variety of etiologies, including common bile duct stones or sludge, sphincter of Oddi dysfunction, pancreas divisum, anomalous pancreaticobiliary junction, genetic mutations, and alcohol-related issues. In approximately 30% of patients, the etiology of RAP is unclear and the term 'idiopathic' is used.

A standard MRI approach to RAP is used to detect the anatomical causes of the condition. However, secretin-enhanced MRCP also often plays a key role in diagnosing and managing RAP patients.

Secretin-enhanced MRCP is superior to conventional MRCP when it comes to detecting ductal abnormalities in RAP patients, particularly for findings related to early chronic pancreatitis. In addition, secretin-enhanced MRCP shows a reduction in exocrine function in up to one-third of RAP patients [33].

Moreover, these patients show a higher frequency of 'acinarization' (parenchymal blush), which is defined as a progressive increased signal intensity on T2-weighted images of the parenchyma on either side of the pancreatic duct in response to secretin-enhanced MRCP (Fig. 9) [33]. Acinarization probably occurs in patients with a propensity for increased pancreatic ductal pressure (i.e., patients with divisum, elevated basal pancreatic sphincter pressure, or an ampullary tumor) and adequate exocrine function (absence of severe chronic pancreatitis).

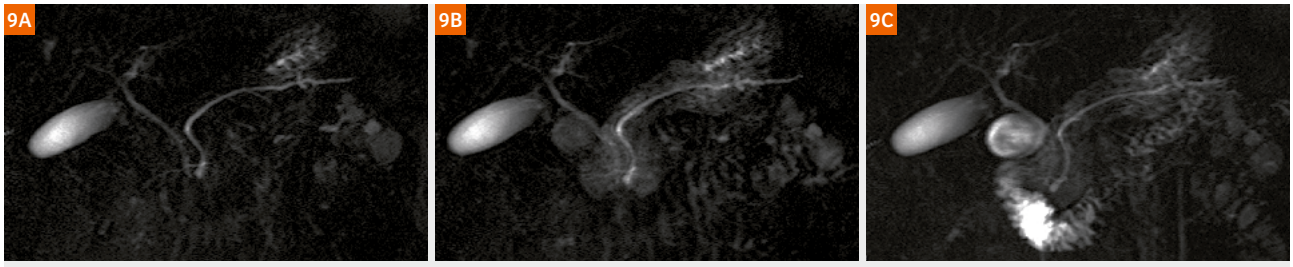

Figure 9: Recurrent acute pancreatitis, parenchymal blush. Patient with recurrent episodes of pain and increase of pancreatic enzymes. Presecretin MRCP **(9A)** shows no significant changes. Just 2 minutes after secretin injection **(9B)**, an increase in signal intensity of the parenchyma can be observed and persists for the full 17 minutes of the exam **(9C)**. This phase shows a good passage of pancreatic juice in the duodenum due to adequate exocrine function.

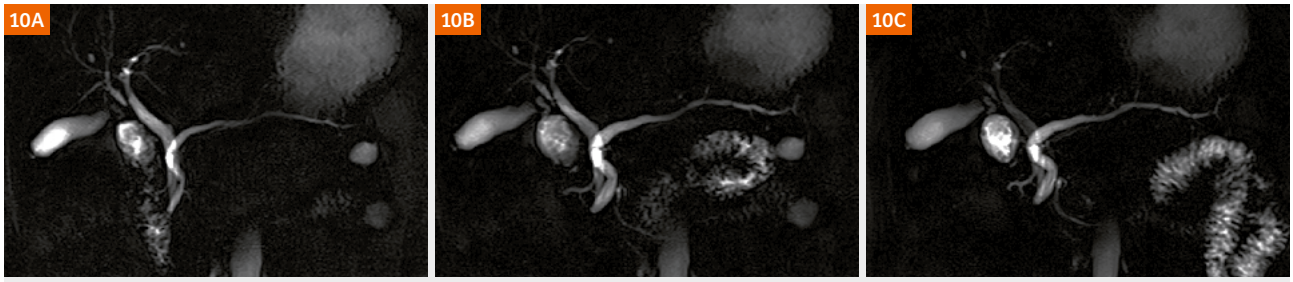

Figure 10: Recurrent acute pancreatitis, Sphincter of Oddi dysfunction (SOD). Patient with recurrent episodes of pain and increase of pancreatic enzymes. Presecretin MRCP **(10A)** shows a slight dilatation of the pancreatic duct. A further increase in the diameter of the pancreatic duct can be seen in the first few minutes after secretin injection (2 minutes: **10B**) and persists into the last phase of the study (8 minutes: **10C**).

Sphincter of Oddi dysfunction as a cause of idiopathic RAP remains controversial. In idiopathic RAP with nondilated ducts, an MRCP-S-guided approach achieved a diagnostic accuracy comparable to ERCP with regard to morphological lesions. The technique can be used as an alternative to ERCP and thus avoid ERCP-related complications in the diagnostic phase. The MRCP-S-guided approach provides details of the morphology of the pancreaticobiliary ductal system and permits indirect evaluation of sphincter of Oddi motility (Fig. 10). It is thus an alternative to more invasive tests such as manometry. However, the secretin test is less sensitive than manometry for intermittent sphincter motility disorders such as type II and III sphincter of Oddi dysfunction [34]. Therefore, a negative MRCP-S should be followed by manometry if clinically suspicions.

3.c Chronic pancreatitis

Chronic pancreatitis (CP) is a progressive inflammatory disease of the pancreas. It causes irreversible morphological changes and fibrotic replacement of the gland, and leads to gradual loss of exocrine and endocrine function [35].

Morphologically, CP is characterized by irregular sclerosis associated with the destruction and permanent loss of the exocrine parenchyma, which may be either focal, segmental, or diffuse. CP can involve various anatomical abnormalities of the pancreas, including atrophy or enlargement of the organ, ductal dilatation, and calcifications. The disease can be caused by alcohol abuse, smoking, gene mutations, autoimmune syndromes, metabolic disturbances, environmental conditions, and anatomical abnormalities. Most patients are found in industrialized countries, and approximately 80% suffer from alcoholism.

The pathology of CP was previously considered to be uniform, but now tends to be seen as varying according to the etiology of the disease. The rather vague term of 'chronic sclerosing pancreatitis' should be replaced by etiologically derived terms such as 'alcoholic chronic pancreatitis', 'hereditary chronic pancreatitis', 'obstructive chronic pancreatitis', 'autoimmune pancreatitis', and 'paraduodenal pancreatitis' (groove pancreatitis, cystic dystrophy of heterotopic pancreas) [36].

Imaging techniques are useful in both diagnosing CP (especially in the early stages) and classifying the disease. They can be used either to grade it, explain the etiology (even for rare forms), and differentiate the focal mass from ductal adenocarcinoma. CT, MRI, and ERCP each have a specific role to play in assessing CP, as each of the three techniques examines the pancreatic gland in different ways.

A recent meta-analysis showed that endoscopic ultrasound (EUS), ERCP, MRI, and CT all have comparably high diagnostic accuracy in the initial diagnosis of CP, although EUS and ERCP performed better than the rest [37]. However, the robustness and noninvasive nature of MRI means that it can compete with ERCP, which actually plays a more interventional role in cases of obstructive CP.

MRI with MRCP-S can detect early signs of CP. This is because MRCP-S can replicate the ERCP findings as set out in the Cambridge classification [38], with small ductal changes suggesting early CP (Fig. 11).

Very recently, T1 mapping has also been applied to detect early fibrotic changes in mild CP. In 98 patients who were grouped as having normal (n = 53) or mild CP (n = 45) – according to their history, presenting symptoms, and respective findings from MRCP-S and ERCP – inline T1 maps were acquired using a dual flip-angle 3D gradient echo technique and Siemens MapIt software to evaluate data for all patients. The mean T1 relaxation times of the pancreas differed significantly between the control (mean = 797 ms) and mild CP groups (mean = 1,099 ms). Using the area under the ROC curve analysis, a T1 relaxation time threshold value of 900 ms revealed 80% sensitivity and 69% specificity for the diagnosis of mild CP (area under the curve = 0.81). There was substantial interobserver agreement (kappa = 0.74, 95% CI: 0.65–0.82) between the two radiologists regarding the measurement of T1 relaxation times [19].

As CP progresses, parenchymal fibrosis reduces pancreatic function. The exocrine component can be viewed after secretin injection (Fig. 12). A decrease in pancreatic exocrine function can be visualized as a reduction in duodenal filling [39] and quantified by measuring changes in small-bowel water volume [40]. Parenchymal fibrosis also decreases the signal on T1 fat sat images. A strong correlation exists between MRI/MRCP-S findings and the histopathology of noncalcific CP [41].

In advanced stages, a diffuse dilatation of the duct of Wirsung can be observed, while ductal calcifications can be appreciated as a defect inside the duct (Fig. 13).

CP increases the risk of pancreatic cancer [42]. This is especially true for patients with hereditary pancreatitis, whose standardized incidence ratio is 67–87 [43]. These patients should therefore be subject to a long-term follow-up in order to detect the cancer in its earliest phase [43].

Moreover, some imaging manifestations of CP can simulate a pancreatic carcinoma. Differential diagnosis is therefore important in order to avoid unnecessary resections.

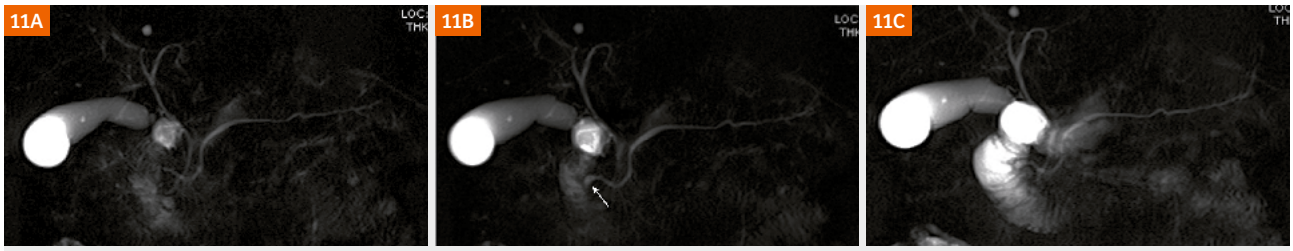

Figure 11: Early chronic pancreatitis. Pre-secretin MRCP **(11A)** shows a pancreas divisum with no signs of chronic pancreatitis. After secretin injection **(11B)**, a santorinicele is appreciable (arrow) with slight dilation of branch ducts in the body-tail. The excretory function of the pancreas is normal, with presence of pancreatic juice in the third portion of the duodenum **(11C)**.

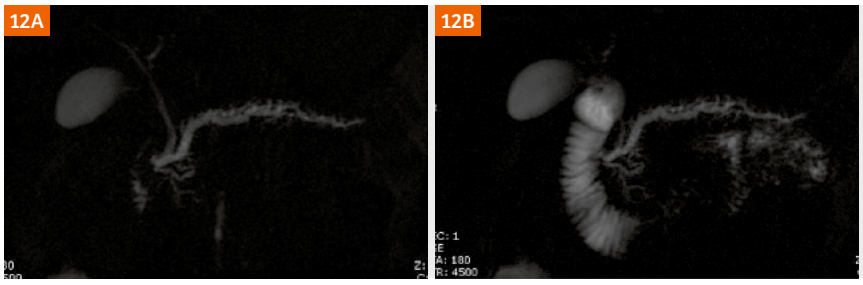

Figure 12A-B: Advanced chronic pancreatitis. MRCP **(12A)** shows diffuse dilatation of the pancreatic duct with ectasia of branch ducts. After secretin injection **(12B)**, the excretory function of the pancreas is normal, with presence of pancreatic juice in the third portion of the duodenum.

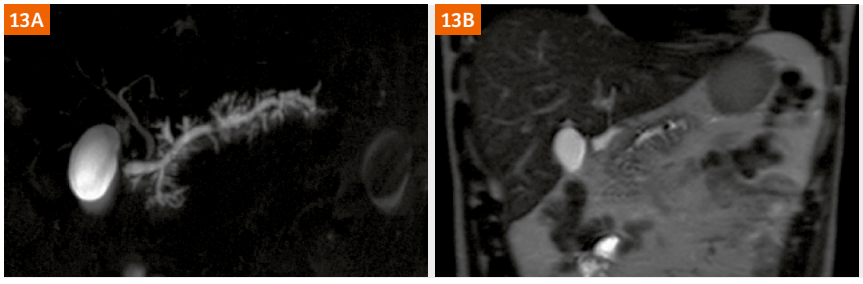

Figure 13A-B: Advanced chronic pancreatitis. MRCP **(13A)** shows diffuse dilatation of the pancreatic duct with ectasia of branch ducts and a small calculus in the tail of the pancreas. This is also well appreciable with coronal HASTE (**13B)**.

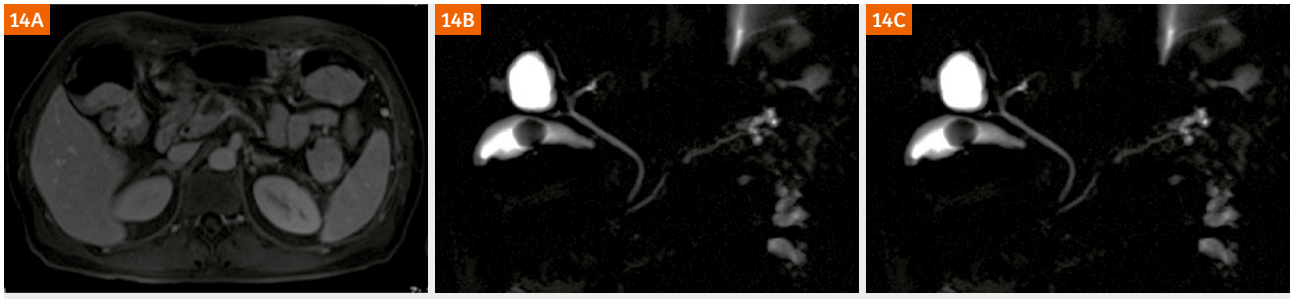

Figure 14: Pancreatic cancer. On T1w axial VIBE **(14A)**, a small hypovascular lesion is appreciable in the pancreatic head. MRCP **(14B)** shows a marked stenosis of the main pancreatic duct, with no visualization of the duct at the level of the lesion and dilatation of pancreatic duct upstream. After secretin injection **(14C)**, the duct is still not visible at the level of the mass.

3.c.1 Focal chronic pancreatitis

Approximately 20% of patients with chronic pancreatitis develop a focal inflammatory mass [44] which may closely mimic pancreatic cancer. The two may be virtually indistinguishable on the basis of morphological features or the enhancement pattern in MRI. Both will show hypointensity on unenhanced T1-weighted fat-suppressed images, hypovascularity in pancreatic arterial phase, and delayed enhancement with isointensity in venous and equilibrium phases. This is because an abundant fibrous stroma is present in both adenocarcinoma and focal pancreatitis [45].

MRCP is an important tool for differentiating most of these pancreatic lesions. Morphological changes in the main pancreatic duct may be one of the most useful ways of distinguishing focal chronic pancreatitis from adenocarcinoma. The most characteristic findings for cancer are complete obstruction of the main pancreatic duct and upstream dilatation of the duct (Fig. 14). A nonobstructed main pancreatic duct penetrates the mass more frequently in focal chronic pancreatitis ('duct-penetrating sign', Fig. 15) [46]. With a secretin injection, the best way of differentiating mass-forming pancreatitis from pancreatic carcinoma is via stenosis resolution, which was observed in 88.6% of mass-forming pancreatitis cases and in 0% of pancreatic carcinoma cases [47] (Fig. 15). This finding is not observed in malignant duct stenosis (Fig. 14).

DWI sequences do not seem to provide additional value in the differential diagnosis of pancreatic carcinoma and mass-forming chronic pancreatitis, with no significant differences in the signal intensity of DW images or ADC [48, 49]. However, the perfusion-related parameters f and Dfast are helpful in characterizing pancreatic diseases [13, 14].

3.c.2 Paraduodenal pancreatitis (PP)

Paraduodenal pancreatitis (PP) is a form of chronic pancreatitis involving the duodenal wall in the region of the minor papilla. It is considered a distinct entity with specific pathological findings.

Histologically, there is a thickening and scarring of the duodenal wall (particularly in the area corresponding to the minor papilla) that extends to the adjacent pancreatic tissue, and/or cystic changes in the duodenal wall. The cysts contain clear fluid, although granular white material and even stones can be present. Occasionally, some of the cysts may reach up to several centimeters in diameter. The fibrotic tissue that develops in the duodenal wall and also involves the groove between the duodenum and the pancreatic head might compress and indent the common bile duct [50].

The clinical profile of PP is middle-aged men who are heavy drinkers and smokers. They suffer from painful pancreatitis that is associated with vomiting and weight loss due to duodenal stenosis and impaired motility [51].

Although alcohol abuse appears to be an important risk factor, the location of the inflammatory process – the duodenal submucosa, the duodenal wall, and the adjacent pancreatic tissue – suggests that some anatomical variation in the region of the minor papilla makes this area particularly susceptible to alcohol injury. It is conceivable that the fluid outflow may be obstructed at the level of the minor papilla, as is the case in some instances of pancreas divisum. The frequent presence of heterotopic pancreatic tissue in the duodenal wall may reflect the incomplete involution of the dorsal pancreas in this region, and might contribute to an obstruction of the outflow in this area [36].

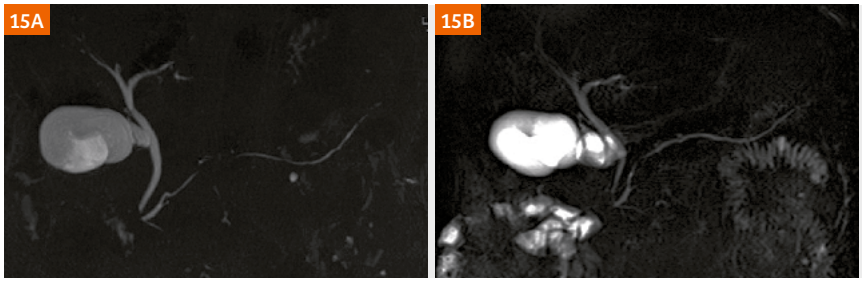

Figure 15: Benign duct stenosis. MRCP **(15A)** shows stenosis of the duct of Wirsung. After secretin injection **(15B)**, the stenosis is no longer recognizable.

The most characteristic finding on MR images is a sheet-like mass between the head of pancreas and the C-loop of the duodenum (the 'groove') (Fig. 16). The mass is hypointense to pancreatic parenchyma on T1-weighted images and can be hypointense, isointense, or slightly hyperintense on T2-weighted images. This variation in T2 signal can be attributed to the time of onset of the disease: Subacute disease shows brighter T2w images due to edema, while chronic disease has a lower signal due to fibrosis [52]. Fat-suppressed T1-weighted images reveal the

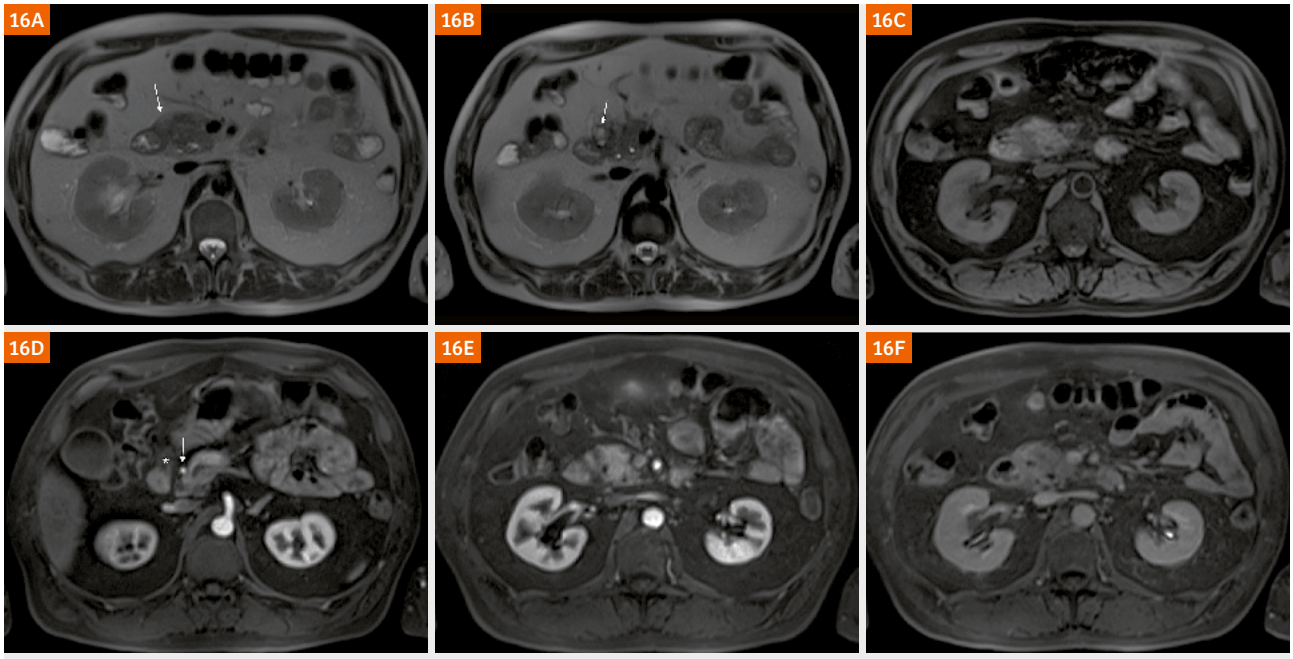

Figure 16: Paraduodenal pancreatitis. On T2w HASTE **(16A)**, an isointense sheet is visible between the duodenum and the pancreatic head (arrow). A more cranial slice **(16B)** shows some cystic lesions (arrow). On T1w GRE fat-sat **(16C)**, the lesion is hypointense. Arterial VIBE **(16D)** shows the gastroduodenal artery (arrow) between the pancreas and the lesion (*). The mass is hypointense in the arterial phase **(16E)**, but becomes isointense in the venous phase **(16F)**.

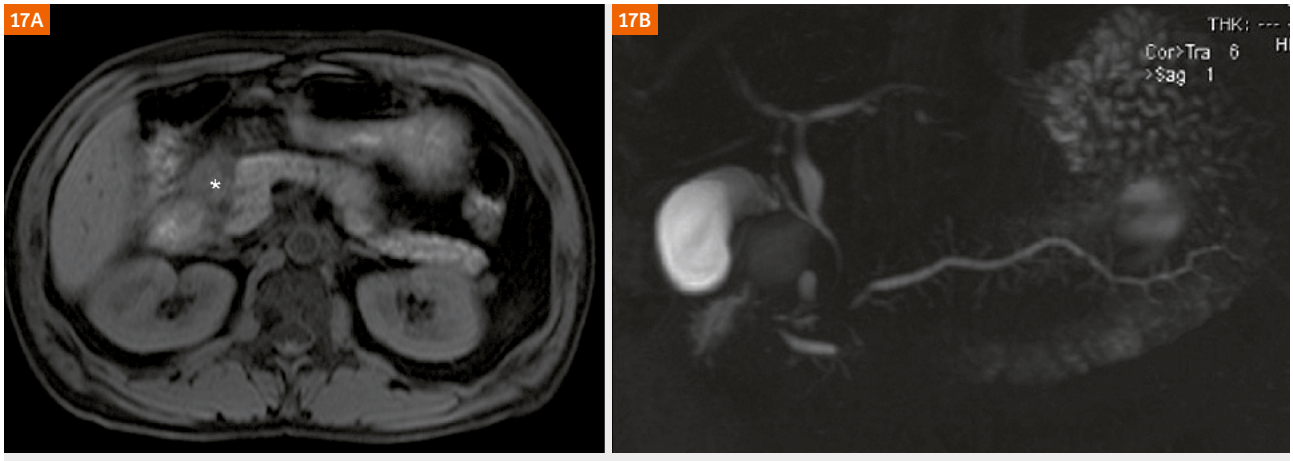

Figure 17: Paraduodenal pancreatitis. On T1w GRE fat-sat **(17A)**, the mass (*) appears hypointense with sharp delimitation from the pancreatic head. CWMR **(17B)** shows stenosis of the choledocus, but the tapering is regular in contrast to the abrupt aspect of stenosis in pancreatic cancer.

best delineation of the pancreatic head (normal hyperintensity if the pancreatic head is spared as in the pure form) from the hypointense mass in the pancreatico-duodenal groove [53]. Contrast-enhanced dynamic images show a delayed and progressive enhancement in the late phase that reflects the fibrous nature of the tissue (Fig. 16F). In the early stages, the main pancreatic duct is normal. An important differentiator is the absence of vascular encasement in groove pancreatitis, with leftward vascular (gastroduodenal artery) displacement without obstruction (Fig. 16D). The pancreatic carcinoma extending to the groove or duodenal wall invades along peripancreatic vessels [53].

Cystic lesions are well depicted in the groove or in the duodenal wall, especially in T2-weighted images (Fig. 16B). MRCP helps to show the relationship between the ductal system and the cystic changes.

In advanced cases, the pancreatic head or entire gland are involved and show hypointensity on T1-weighted images. A ductal dilatation with secondary duct ectasia is observed in some patients.

The duodenal wall is usually thickened and so the images should be evaluated carefully as it is not commonly associated with tumors in the pancreatic head.

Sometimes the common bile duct appears stenotic, but the tapering is regular, unlike the abruptness of stenosis in pancreatic cancer (Fig. 17) [52].

3.c.3 Autoimmune pancreatitis (AIP)

Autoimmune pancreatitis (AIP) is a relatively new condition and is increasingly being recognized. It accounts for 1–6% of cases of chronic pancreatitis [54]. Most of the affected patients are between 40 and 60 years old, with a strong male prevalence. AIP is associated with other autoimmune disorders such as Crohn's disease, Sjögren's syndrome, rheumatoid arthritis, primary sclerosing cholangitis, primary biliary cirrhosis, ulcerative colitis, systemic lupus erythematous, and retroperitoneal fibrosis [55].

By international consensus, AIP has been subdivided into two forms: Type 1 (> 60 years of age with male prevalence: 77%) and type 2 (40 years of age, no gender prevalence) [56]. However, more recent studies suggest that the natural history, diagnostic criteria, and treatment approach of the two conditions differ significantly. This has led to proposals for the term 'autoimmune pancreatitis' to be restricted to describing the clinical phenotype represented by lymphoplasmacytic sclerosing pancreatitis (LPSP), currently called type 1 AIP, and for type 2 AIP to be described as idiopathic duct-centric chronic pancreatitis (IDCP) [57].

LPSP is characterized by a systemic IgG4-associated disorder with elevated IgG4-positive cells in serology, the pancreas, and other organs (salivary glands, kidneys, and bile ducts). It is the most common form worldwide, accounting for almost all cases in Japan and Korea, and more than 80% of cases in Europe and the United States.

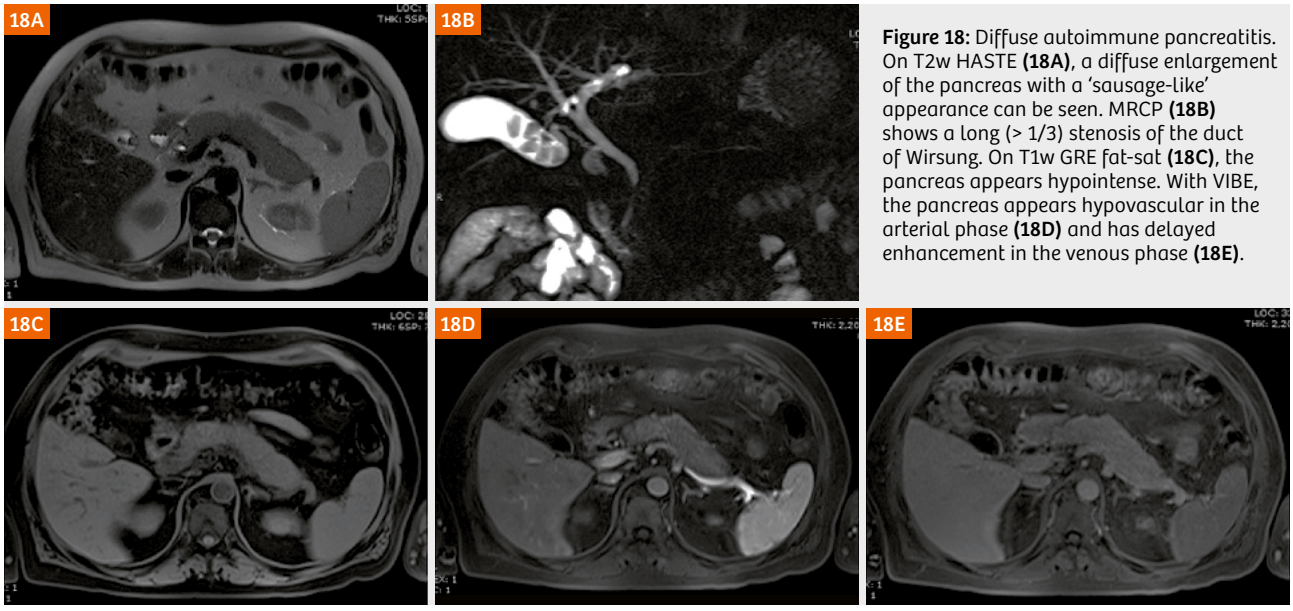

Figure 18: Diffuse autoimmune pancreatitis. On T2w HASTE **(18A)**, a diffuse enlargement of the pancreas with a 'sausage-like' appearance can be seen. MRCP **(18B)** shows a long (> 1/3) stenosis of the duct of Wirsung. On T1w GRE fat-sat **(18C)**, the pancreas appears hypointense. With VIBE, the pancreas appears hypovascular in the arterial phase **(18D)** and has delayed enhancement in the venous phase **(18E)**.

IDCP is primarily found in the pancreas and involves a lack of IgG4-positive cells.

The pathological gross appearance of AIP mimics pancreatic ductal adenocarcinoma because the inflammatory process commonly focuses on the head of the pancreas and results in a gray or yellowish-white induration of the affected tissue with loss of its normal lobular structure. The affected portion may be enlarged. These changes obstruct the main pancreatic duct and, usually, the distal bile duct including the papilla. In a minority of cases, the body or tail of the pancreas are involved. Diffuse involvement of the pancreas may also be observed.

The hallmark of the histological changes is an intense inflammatory cell infiltration of lymphocytes, plasma cells, some macrophages, and eosinophilic granulocytes. Vasculitis frequently affects the small veins [36]. Steroids are the cornerstone of treatment.

MR imaging shows an enlargement of the pancreas, which is usually diffuse ('sausage' shape) (Fig. 18) with a hypointense, capsule-like rim that is smooth and well-defined due to peripancreatic inflammation and fibrosis, but can be focal (Fig. 19). Some cases show minimal peripancreatic fat stranding [58]. On T2-weighted images, the pancreas shows an increased signal intensity

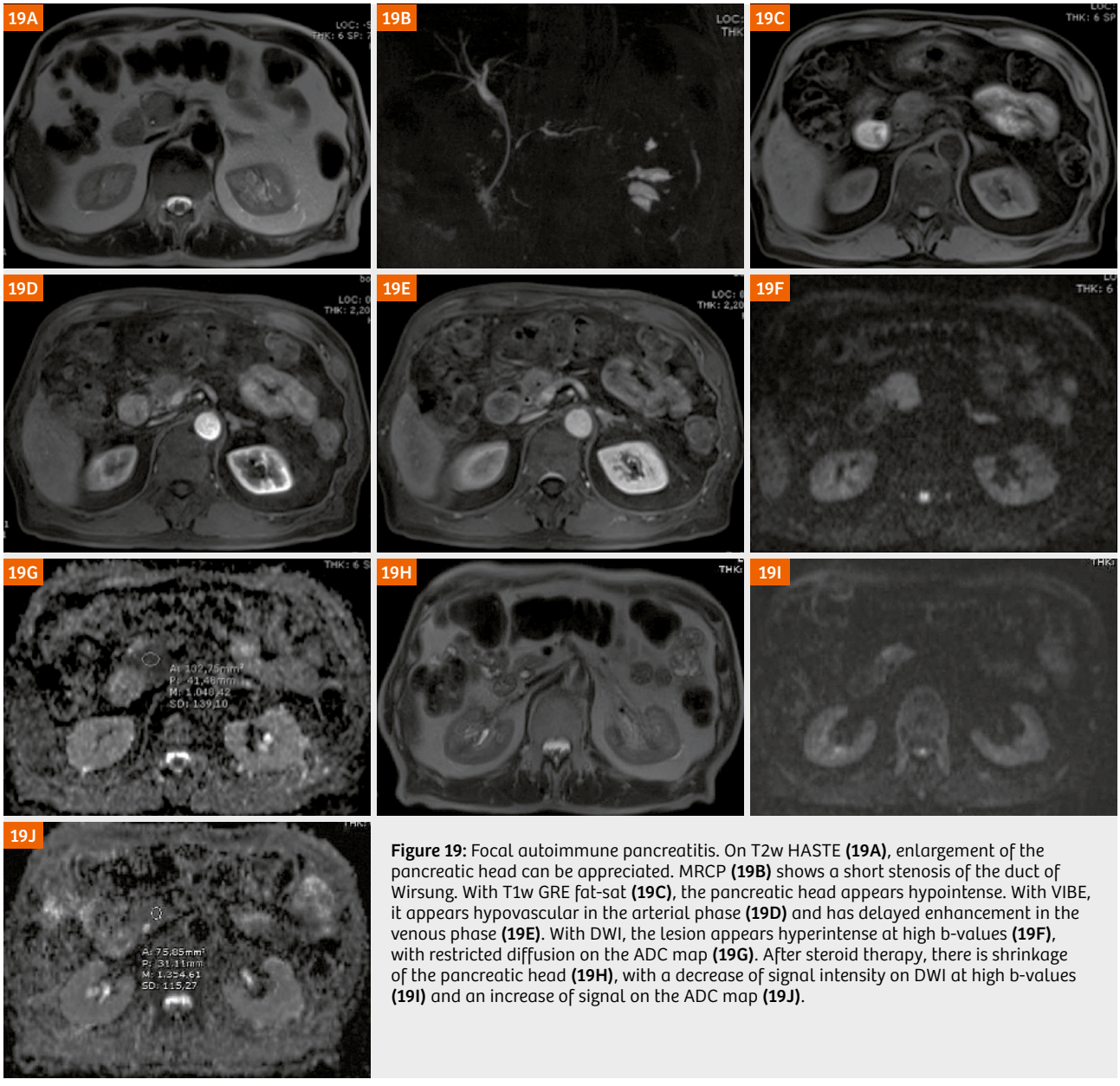

Figure 19: Focal autoimmune pancreatitis. On T2w HASTE **(19A)**, enlargement of the pancreatic head can be appreciated. MRCP **(19B)** shows a short stenosis of the duct of Wirsung. With T1w GRE fat-sat **(19C)**, the pancreatic head appears hypointense. With VIBE, it appears hypovascular in the arterial phase **(19D)** and has delayed enhancement in the venous phase **(19E)**. With DWI, the lesion appears hyperintense at high b-values **(19F)**, with restricted diffusion on the ADC map **(19G)**. After steroid therapy, there is shrinkage of the pancreatic head **(19H)**, with a decrease of signal intensity on DWI at high b-values **(19I)** and an increase of signal on the ADC map **(19J)**.

(Figs. 18A, 19A) compared with the signal intensity of the liver, with the hypointense capsule-like rim usually depicted best. The main pancreatic duct shows diffuse (Fig. 18B) or focal stenosis (Fig. 19B), where narrowing is usually longer than the stenosis of the main pancreatic duct in pancreatic cancer. Mild dilatation of the duct upstream of the affected area may occur (Fig. 19B).

On T1-weighted images, the affected pancreas shows decreased signal intensity compared with the signal intensity of the liver due to pancreatic fibrosis, with a distinctive reduction in signal on fat-saturated sequences (Figs. 18C, 19C). Contrast enhancement of the affected pancreatic parenchyma is usually reduced, with a delayed contrast enhancement (Figs. 18D-E, 19D-E) or a capsule-like rim [59]. Vessel invasion, vascular encasement, mass effect, and fluid collections are absent [58].

After steroid therapy, abnormal signal intensity of the pancreas improves to isointensity with that of the liver in both T1- and T2-weighted images. The pancreas returns to normal size or becomes atrophic (Fig. 19H), the capsule-like rim disappears, and stenosis of the lower common bile duct improves with subsequent decompression of the biliary tree and pancreatic duct [59].

Some studies suggest that DWI is helpful for differential diagnosis and control after steroid treatment. AIP shows DWI signal intensity and ADC values that are well correlated with the active symptoms of AIP patients, suggesting that DWI may be an objective biomarker for determining the indication for steroid therapy (Figs. 19F, G) [60]. Signal intensity decreases after therapy, thus reflecting disease activity (Figs. 19I, J) [61].

ADC values are significantly lower in AIP than in pancreatic cancer, and an ADC cut-off value may be useful for distinguishing AIP from pancreatic cancer [62, 63]. However, the DWI signal and ADC maps are similar to pancreatic carcinoma, making the differential diagnosis difficult. Although differentiating mass-forming AIP from pancreatic cancer is challenging, combining MRI findings (including contrast-enhanced dynamic images, MRCP, and DWI) can be helpful [64].

Finally, the IVIM parameter f is helpful in differentiating between AIP and pancreatic cancer, and could serve as an imaging biomarker during steroid treatment [65].

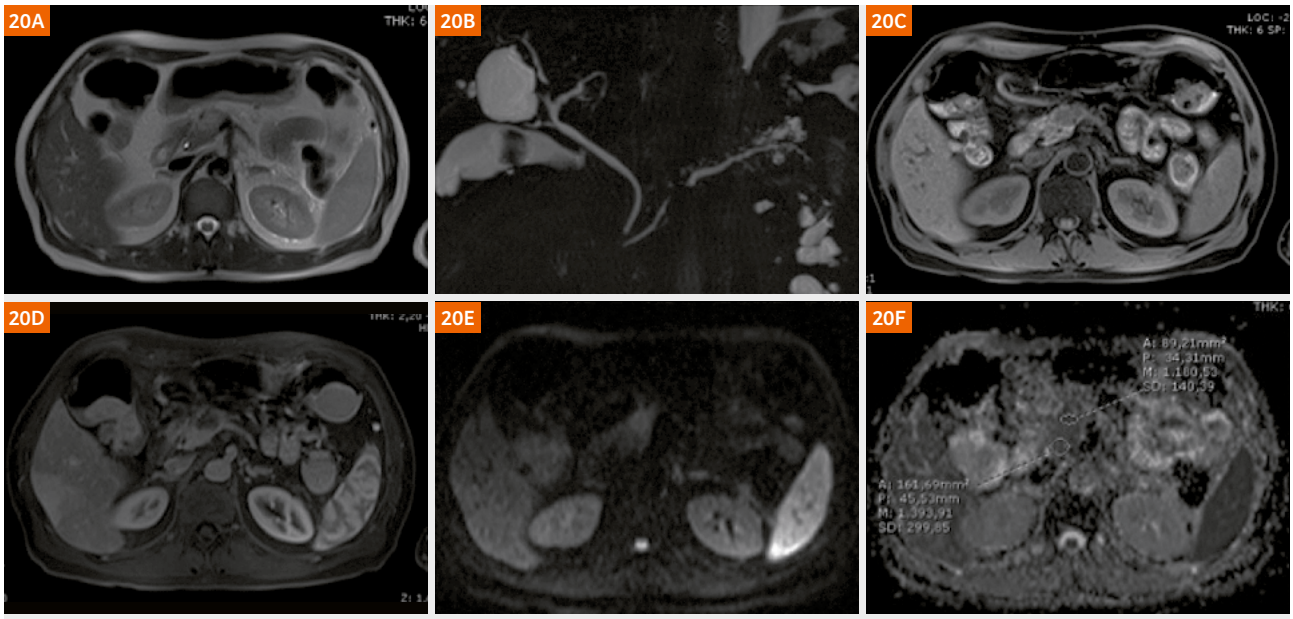

Figure 20: Pancreatic carcinoma. On T2w HASTE **(20A)**, a small hyperintense lesion is visible in the pancreatic head. MRCP **(20B)** shows a severe tight stenosis of the pancreatic duct with dilatation upstream. The lesion is hypointense on T1w GRE fat-sat **(20C)** and hypovascular with contrast-enhanced MRI VIBE **(20D)**. With DWI, the lesion shows high signal intensity at high b-values **(20E)** with restricted diffusion on the ADC map **(20F)**.

3.d Pancreatic carcinoma

Pancreatic carcinoma is the fourth most common cause of cancer death in the USA. The five-year survival rate is less than 5% [66]. About 60% of tumors occur in the head of the pancreas, 15% occur in the body, 5% occur in the tail, and 20% involve the pancreas diffusely [67]. At the time of diagnosis, tumors located in the head are usually smaller (2.5 to 3 cm) than those in the body-tail (5 to 7 cm) because of their earlier clinical manifestation due to the close contiguity with the choledochus.

The gross pathological features of pancreatic carcinoma are a mass with irregular, ill-defined contours and a significant fibrous component, and (less frequently) necrotic changes. The lack of a capsule is responsible for the early spread of the lesion to the surrounding structures, and particularly for vascular and neural invasion.

On unenhanced MR imaging (Fig. 20), pancreatic carcinoma shows a slightly different signal on T2w images from the surrounding pancreas, ranging from minimally hypointense to isointense to slightly hyperintense (Fig. 20A). This makes it difficult to identify the mass when it is small. Necrotic or cystic degeneration of the lesion can be easily identified by the hyperintensity on T2w images [68]. T2w images with fat saturation are considered useful in staging the lesion, and for evaluating the lymph node and peritoneal or hepatic metastases [69], where MRI is considered more sensitive than multidetector computed tomography [44]. The obstruction of the MPD is responsible for the dilatation of the duct upstream (Fig. 20B).

On T1w images, pancreatic carcinoma usually appears as a mass of lower signal than the normal pancreas (Fig. 20C). However, small tumors can show a late enhancement. Moreover, the obstruction of the main pancreatic duct is responsible for the dilatation of the duct with chronic obstructive pancreatitis of the pancreatic gland upstream. Since this has the same low signal on T1w images, it disguises the true extent of the tumor and makes it indiscernible from the pancreatic tumor on T2w and especially on T1w images [2]. Later, the obstruction of the main pancreatic duct causes the pancreatic gland upstream to atrophy (Fig. 21).

On dynamic imaging after injection of paramagnetic contrast agent, the presence of an abundant fibrous stroma within the tumor makes the tumor hypovascular and causes it to appear hypointense to the surrounding parenchyma (Fig. 20D). It can, however, be responsible for a delayed enhancement with secondary isointensity of the lesion (Fig. 21D) [45]. Isointensity of the tumor to the surrounding parenchyma, and coexisting or secondary chronic pancreatitis upstream can make it hard to identify the tumor and differentiate it from chronic pancreatitis [70].

In terms of DWI, most papers find that pancreatic carcinoma shows a restricted diffusion of free water with high b-values (> 500), which makes it appear hyperintense on diffusion-weighted images at high b-values (Fig. 20E). ADC maps show lower values for the tumor than for normal pancreatic parenchyma (Fig. 20F) [71]. However, similar findings have also been described with benign inflammatory lesions. The low ADC value of pancreatic cancer and mass-forming pancreatitis may stem from high cellularity and abundant fibrosis, which are common histopathological features of both pancreatic cancer and mass-forming pancreatitis. In chronic pancreatitis, fibrosis and chronic inflammation lead to the destruction and permanent loss of exocrine pancreatic tissue, and to the replacement of normal pancreatic parenchyma with fibrous tissue which may reduce the diffusion of tissue water and result in lower ADCs [72]. In autoimmune pancreatitis, the lymphocytic infiltration of the pancreatic gland restricts the movement of free water, with a DWI signal and ADC map similar to those of pancreatic carcinoma [61].

Although the DWI signal and ADC map are similar to those in pancreatic carcinoma and thus make the differential diagnosis difficult, combining MRI findings (including contrast-enhanced dynamic images, MRCP, and DWI) can be helpful [64]. ADC values are significantly lower in autoimmune pancreatitis (AIP) than in pancreatic cancer, and an ADC cut-off value may be useful for distinguishing AIP from pancreatic cancer [62, 63]. The IVIM parameters f and Dfast are also helpful in characterizing pancreatic diseases [13, 14].

With MRCP, stenosis of the main pancreatic duct can be easily identified with dilation upstream (Figs. 20B, 21B) [73]. In the case of a tumor in the head of the pancreas, stenosis of the intrapancreatic biliary duct can be seen, with dilation upstream and stenosis of both the biliary and pancreatic ducts (double duct sign) (Fig. 22), although it is not a specific sign of pancreatic carcinoma [74]. Stenosis of the biliary duct and main pancreatic duct are also visible in cases of chronic pancreatitis or inflammatory duodenal lesions [23]. An abrupt stenosis with sharp margins indicates malignant stenosis, while an irregular shape with beaded appearance is more indicative of chronic inflammation of the pancreas.

Some patients are at a high risk of developing pancreatic cancer [75]. According to preliminary studies, an MRI-based protocol for examining individuals at risk of pancreatic cancer seems to detect cancer or premalignant lesions with good accuracy. Compared with protocols based on more aggressive methods, using MRI exclusively can reduce costs, increase availability, and guarantee the safety of the individuals being examined [76].

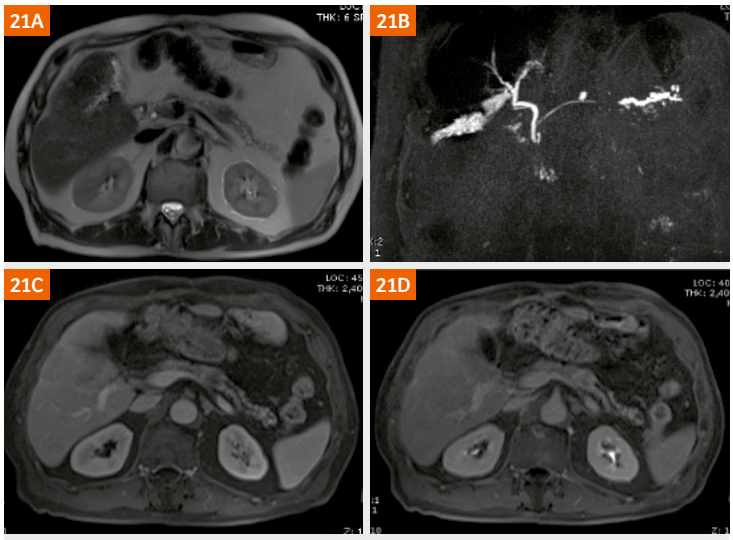

Figure 21: Pancreatic carcinoma. With T2w HASTE **(21A)**, a small hyperintense lesion is visible in the tail of the pancreas, with upstream dilatation of the duct of Wirsung and atrophy of the parenchyma. MRCP **(21B)** shows a severe tight stenosis of the pancreatic duct with dilatation upstream. The lesion is hypovascular on contrast-enhanced MRI VIBE during the arterial phase **(21C)** and shows contrast uptake in the late phase **(21D)**.

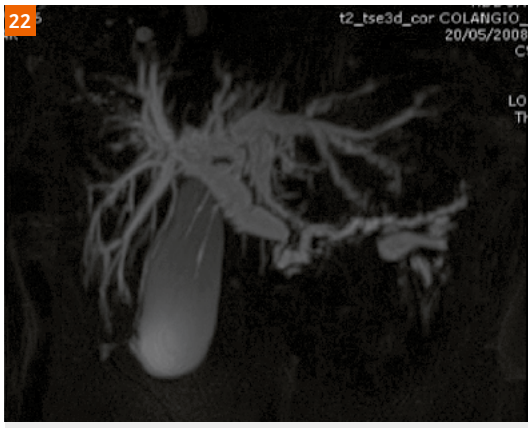

Figure 22: Pancreatic carcinoma. MRCP shows dilatation of the choledocus and the duct of Wirsung (double duct sign), which is caused by a carcinoma in the pancreatic head.

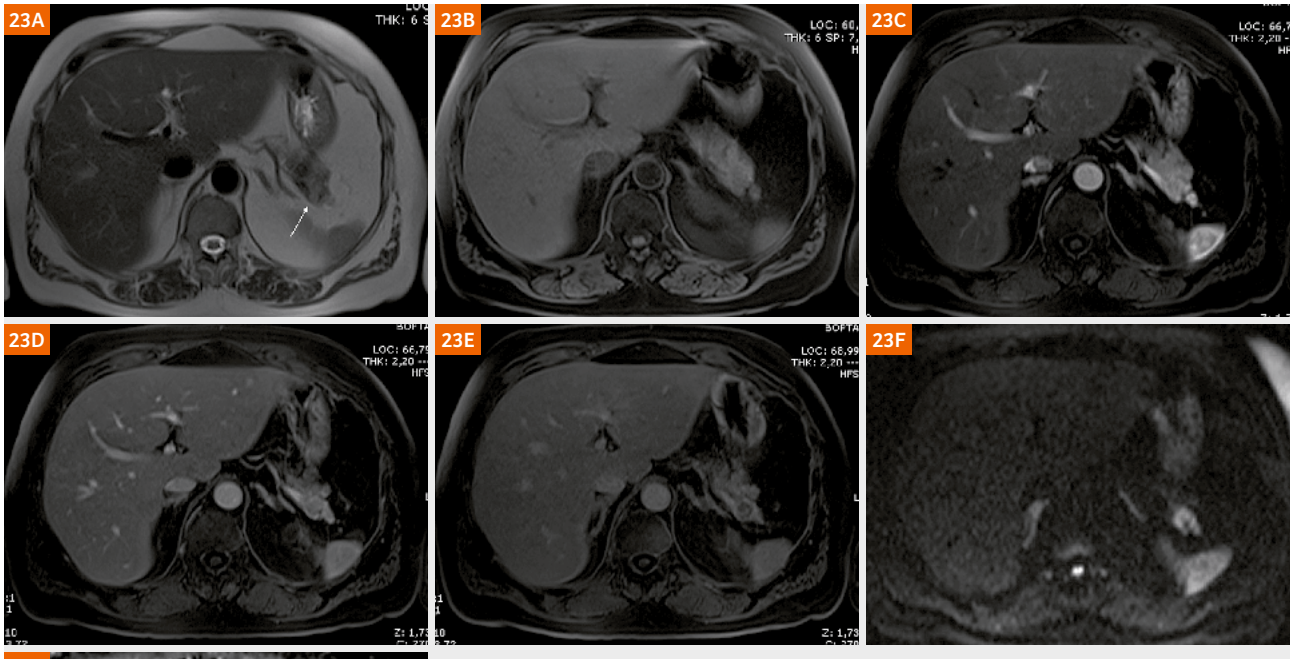

Figure 23: Neuroendocrine tumor G1. On T2w HASTE **(23A)**, a small, slightly hyperintense lesion is visible in the tail of the pancreas (arrow). The lesion is hypointense on T1 GRE fat-sat **(23B)** and appears hypervascular in the arterial phase **(23C)**, with washout in the venous phase **(23D)** and delayed phase **(23E)**. On DWI, the lesion shows high signal intensity at high b-values **(23F)** and appears hypointense on the ADC map **(23G)**.

3.e Neuroendocrine tumors

Pancreatic neuroendocrine tumors (PNETs) are relatively uncommon neoplasms. They account for 2% or fewer of all pancreatic neoplasms, with an estimated incidence of less than 1 per 100,000 people per year worldwide [77, 78]. PNETs can occur in people of all ages, with a peak incidence at between 30 and 60 years. Most PNETs are sporadic, but nearly 25% can occur in the context of genetic syndromes such as multiple endocrine neoplasia type 1 (MEN-1), Von Hippel-Lindau disease (VHL), neurofibromatosis type 1 (NF-1), and tuberous sclerosis [79, 80]. These tumors have a wide range of clinical, biological, morphological, and molecular features.

Compared with the other solid pancreatic neoplasms, PNETs take an overall more indolent course. Nonetheless, the biological behavior is extremely variable, ranging from more benign to highly malignant [81]. The revised World Health Organization (WHO) classification based on mitotic index and Ki-67 proliferation divides PNETs into three classes: Well-differentiated endocrine tumor or carcinoids (grade I, benign or uncertain behavior); well-differentiated endocrine carcinoma (grade II, low-grade malignant behavior); poorly differentiated endocrine carcinoma (grade III, high-grade malignant behavior) [77]. A Ki-67 index of less than 2%, between 3% and 20%, and above 20%, is characteristic of low-, intermediate-, and high-grade PNET respectively. WHO tumor grade is an independent prognostic factor of survival in patients with PNETs [77, 82, 83].

Nearly all well-differentiated PNETs secrete hormones, but most patients do not show a clinically apparent endocrinopathy as the hormones are produced in small quantities or are functionally inactive. Clinically, PNETs can be divided into hyperfunctioning (HF-PNET) and non-hyperfunctioning (NF-PNET) according to the presence or absence of a paraneoplastic endocrinopathy caused by uncontrolled hormone secretion.

HF-PNET is almost always diagnosed biochemically, and imaging is used to establish the location and extent of the primary tumor, assess potential metastatic spread, and plan surgery. Non-invasive techniques such as CT and MRI combined with nuclear medicine approaches are helpful here. Insulinomas and gastrinomas are the most common functional PNETs. Insulinomas are usually benign (in about 90% of cases) and small, whereas gastrinomas are larger and malignant in nearly 60% of cases. Nowadays, nearly 85% of PNETs are NF-PNETs and it is thought that their incidence has been increasing over recent years due to more frequent incidental detection [84–86]. Non-functional tumors tend to be symptomatic due to their large mass or to metastatic disease, and are malignant in most cases [87].

Morphologically, most PNETs have a predominantly intraparenchymal pattern of growth, presenting as a single lesion when sporadic, and ranging from 0.5 to 5 cm in size at diagnosis [83]. CT and MRI are typically the first choice of imaging modalities for evaluating most patients with suspected PNET. The appearance of PNETs can vary considerably and differs depending on whether the tumor is functional or non-functional. Like normal endocrine tissue, endocrine tumors often have a dense capillary network, and tumor growth is highly dependent on the development of a vascular supply. This high vascular density results in the characteristic enhancement feature of classic HF-PNETs: A uniformly hypervascular and well-defined lesion that is most prominent on arterial phases of contrast enhancement (Fig. 23).

However, while traditionally described as hypervascular solid masses, NF-PNETs vary considerably in terms of enhancement pattern and imaging appearance. Digital subtraction of late arterial phase with the unenhanced phase improves the detection and characterization of PNETs [88]. Recent data show how the majority of NF-PNETs are well defined or encapsulated, and predominantly solid and hypovascular in more than 50% of cases compared to the normal pancreas on late arterial and venous portal phases in CT and MRI [89]. However, no correlation was found between WHO grade and enhancement pattern [81, 90]. A strong correlation has been established between lesion size and tumor grade [91].

Generally, imaging characteristics are related to lesion size [92]. Smaller lesions tend to be more homogeneous, and larger lesions are more likely to demonstrate heterogeneous enhancement (Fig. 24), areas of cystic degeneration (Fig. 25), necrosis, fibrosis, and calcification (calcifications are seen in about 20% of NF-PNETs). NF-PNETs with an essentially completely cystic, unilocular appearance can also be observed. In these cases, a ring-like enhancing pseudocapsule is present and a similar-looking lesion in the pancreas raises the possibility of a diagnosis of NF-PNET [93]. On MRI, PNETs generally appear as relatively hypointense on T1-weighted images, and most have a signal intensity that is much higher than that of a normal pancreas on T2-weighted images. An abundance of intratumoral fibrosis accounts for the iso/hypointense T2-weighted images seen in some NF-PNETs. Main pancreatic duct dilatation is not a common finding, but it is possible. This, combined with a heterogeneous or non-classic enhancement pattern make PNET diagnosis more complex. Moreover, main pancreatic duct dilatation shows high specificity and positive predictive value for predicting PNETs of uncertain or malignant behavior [94].

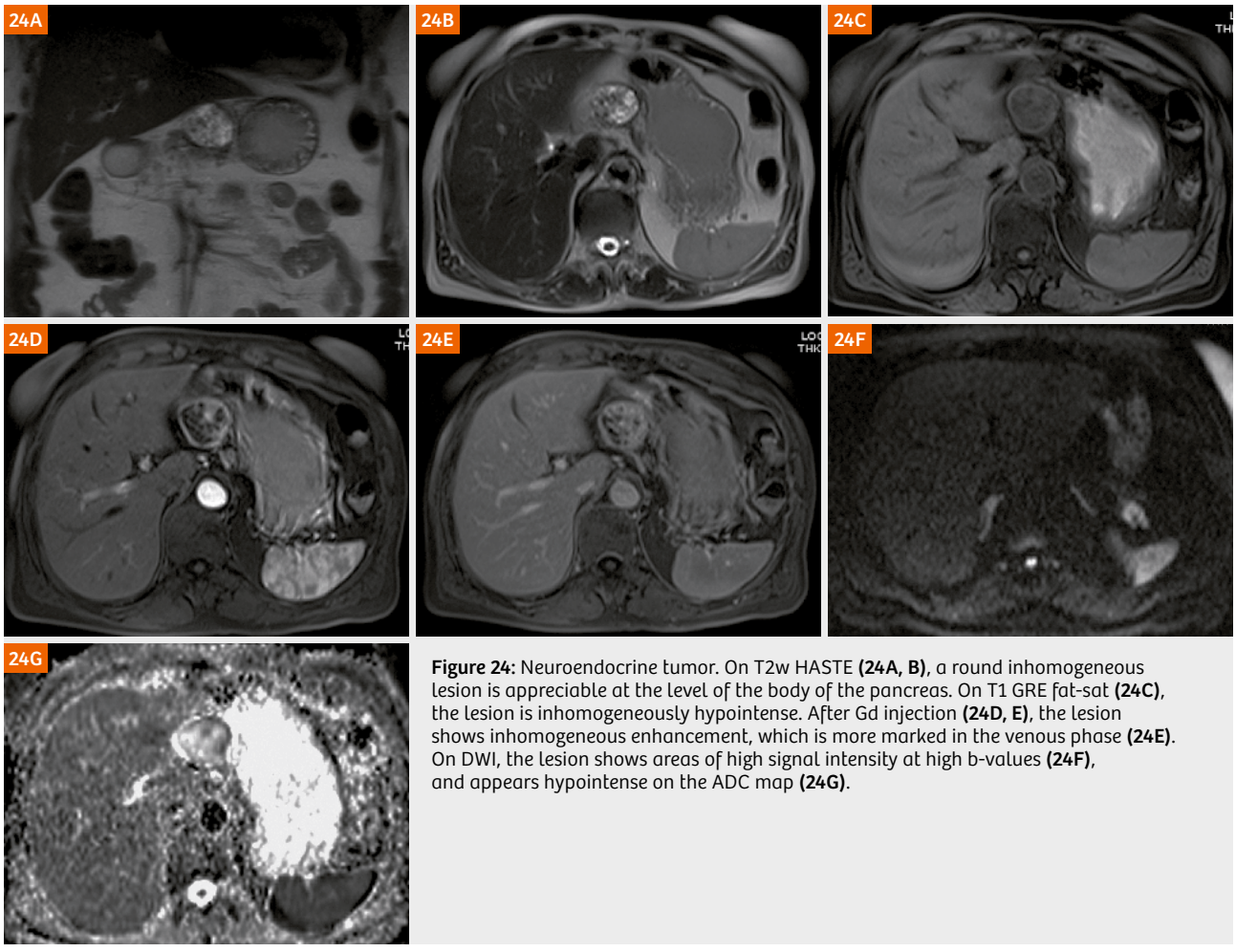

Figure 24: Neuroendocrine tumor. On T2w HASTE **(24A, B)**, a round inhomogeneous lesion is appreciable at the level of the body of the pancreas. On T1 GRE fat-sat **(24C)**, the lesion is inhomogeneously hypointense. After Gd injection **(24D, E)**, the lesion shows inhomogeneous enhancement, which is more marked in the venous phase **(24E)**. On DWI, the lesion shows areas of high signal intensity at high b-values **(24F)**, and appears hypointense on the ADC map **(24G)**.

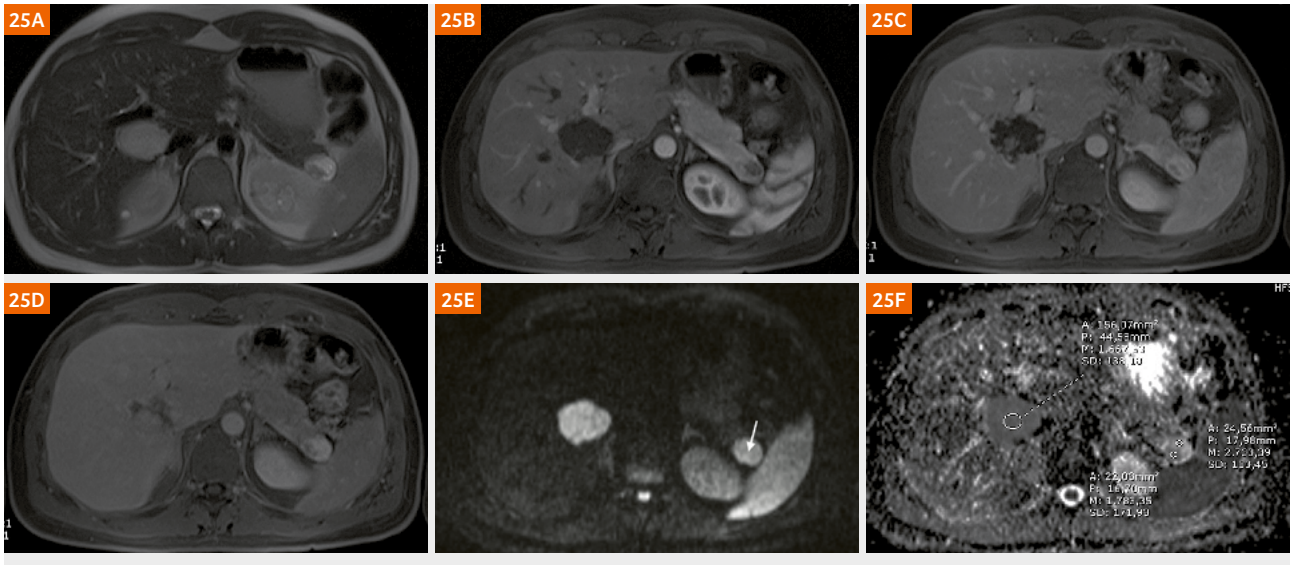

Figure 25: Neuroendocrine tumor. T2w HASTE **(25A, B)** shows a cystic lesion with a nodule in the tail of the pancreas. After contrast injection **(25B-D)**, the lesion shows inhomogeneous enhancement, starting from the nodule and with progressive enhancement of the cystic component. With DWI, the lesion shows areas of high signal intensity at high b-values **(25E)** and appears hypointense on the ADC map **(25F)**.

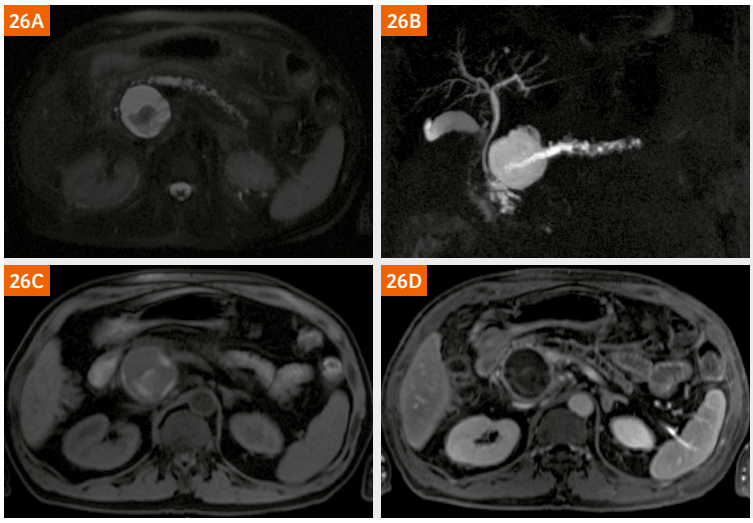

Figure 26: Pancreatic pseudocyst. On T2w HASTE **(26A),** a large inhomogeneous cyst is appreciable in the pancreatic head. The duct of Wirsung is dilated, with signs of chronic pancreatitis. MRCP **(26B)** clearly shows the morphological changes involved in chronic pancreatitis. On T1w GRE fat-sat **(26C)**, the content of the cyst is inhomogeneous due to the presence of internal debris, which appears hyperintense and does not enhance after contrast administration **(26D)**.

With DWI, PNETs usually show high signal intensity at high b-values and low ADC maps (Fig. 23F) [95]. Some studies show an inverse correlation between tumor grade and ADC map [91, 96, 97].

It has been suggested that the fusion of high b-value DWI and T2-weighted MR images can bring added value to the detection of pancreatic neuroendocrine tumors [98].

Histological diagnosis is mandatory in all cases and is usually obtained via surgical or endoscopic biopsies, or via ultrasound-guided liver biopsies. Endoscopic ultrasound-guided fine-needle aspiration (EUS-FNA) is effective for preoperatively determining Ki-67 expression, which is an important prognostic factor for PNET. EUS-FNA is highly accurate for neuroendocrine tumors, with a sensitivity above 90%, which means it is helpful for making a diagnosis [99].

3.f Cystic lesions (PCL)

With advances in diagnostic imaging, pancreatic cystic lesions (PCLs) are being detected with increasing frequency. At some referral centers, up to 30% of pancreatic resections are performed for cystic tumors [100]. It is important to accurately identify cystic tumors because they require different treatments according to their histological type and differentiation. However, the frequent lack of specific clinical and laboratory signs, and the overlap of imaging findings between different cystic tumors and between non-neoplastic and neoplastic cystic lesions of the pancreas mean that managing these patients is complex.

PCLs can be simply classified into two main groups: Non-neoplastic cysts and neoplastic cysts, which are commonly known as pancreatic cystic neoplasms (PCNs) (Tab. 1). Neoplastic cysts can be divided in non-mucinous and mucinous, with the latter considered premalignant lesions. In reality, non-mucinous neoplastic cysts also have lesions which need to be resected (Tab. 1). In general, non-neoplastic cysts account for up to 80% of all PCLs [101].

Although all pancreatic tumors, including ductal adenocarcinoma, may appear as cystic lesions, degenerative changes [102] mean that the classic cystic neoplasms of the pancreas are lined with a different epithelium whose morphology is the main diagnostic criterion and provides the prognostic value. Their macroscopic appearance (shape, volume, etc.), however, has no importance [103].

When dealing with a PCL, it is important to confirm or exclude communication between the cystic lesion and the main pancreatic duct. Radiologically, PCLs can be subdivided into non-communicating and communicating (Tab. 2). This section will only discuss the most frequent lesions.

In the differential diagnosis of benign and malignant pancreatic cystic neoplasms, MRI with MRCP has a sensitivity and specificity of 94% and 75% respectively [104], an accuracy of 73–81% [105, 106], and AUROC values of 0.73–0.91 [104–108]. MRI can exclude the malignancy of pancreatic cystic neoplasms with a negative predictive value (NPV) of 74–96% [105, 106].

3.f.1 Pancreatic pseudocyst (PPSC)

Pancreatic pseudocysts (PPSCs) are defined as a cystic cavity bound to the pancreas by inflammatory tissue and containing pancreatic juice or amylase-rich fluid. Typically, the wall of the pancreatic pseudocyst is fibrous and lacks an epithelial lining, making it different from a true pancreatic cyst. PPSCs are usually related to an acute

or chronic inflammatory process of the pancreas. Most PPSCs originate from large or small leaks in the ductal system and persist because of constant filling by pancreatic secretions [109], although communication is not always visible at imaging.

With increasing experience, it is becoming clear that the prevalence of PPSCs in pancreatic cystic lesions is lower than usually presumed [110, 111]. A presumptive diagnosis of PPSC based on imaging appearance alone can cause a diagnostic error in up to 50% of cases [110, 112, 113] Pancreatic cystic neoplasms are particularly susceptible to this misdiagnosis [114], which can result in inappropriate treatment.

In a comparison of incidental pancreatic cystic lesions [110], the incidence of pseudocyst was significantly higher in the group of symptomatic patients with a previous history of pancreatitis (26/29: 89.6%) than it was in the asymptomatic group (3/29: 10.4%). Therefore, to make a confident diagnosis of pseudocyst, it is necessary to have a correlation with the patient's clinical history. A previous clinical history of chronic or severe acute pancreatitis is a useful predictor for a pseudocyst. However, the same study showed that 25/42 (52%) of the patients with a history of pancreatitis had a cystic tumor of the pancreas, which means that previous pancreatitis cannot exclude the presence of a cystic tumor.

Endoscopic ultrasound-guided fine-needle aspiration (EUS-FNA) with cyst fluid analysis will differentiate between pseudocysts and neoplastic cysts in more than 90% of patients [115].

CT is the best imaging technique for detecting and diagnosing PPSC. Its sensitivity ranges from 90% to 100% [101]. However, a history of acute pancreatitis is essential for making a correct diagnosis of PPSC but is not always present [110]. PPSCs usually appear as a cystic lesion with a thick wall adjacent to the pancreas, which may show evidence of acute or chronic pancreatitis. The presence of debris or previous hemorrhage can cause an atypical appearance of the PPSC, which may be difficult to distinguish for mucinous cystic lesions.

With MRI, PPSCs appear as cystic lesions and are markedly hyperintense on T2w images and hypointense on T1w images. As a result of the underlying inflammatory process, heterogeneous intracystic content is commonly observed. Internal hemorrhage and hemoglobin sediments show high signal intensity on unenhanced T1-weighted MR images [116], thus simulating mucin content. One clue that favors the diagnosis of PPSC is the presence of layering, nonenhancing debris, especially on T2-weighted sequences [117]. The presence of internal debris is a highly specific imaging finding for the diagnosis of PPSC and is

Non-neoplastic cysts
Pseudocyst
Simple or congenital cyst
Retention cyst
Neoplastic cysts (pancreatic cystic neoplasms: PCNs)
Mucinous cystic lesions
Intraductal papillary mucinous neoplasm (IPMN)
Mucinous cystic neoplasm (MCN)
Non-mucinous cystic lesions
Serous cystic neoplasm (SCN)
Solid-pseudopapillary neoplasm (SPN)
Cystic neuroendocrine neoplasm
Acinar-cell cystic neoplasm
Other neoplastic lesions
Ductal adenocarcinoma with cystic degeneration

Table 1: Histological classification of pancreatic cystic lesions (PCLs)

Non-communicating pancreatic cyst
Non-neoplastic cysts
Pseudocyst
Simple or congenital cyst
Retention cyst
Neoplastic cysts (PCNs)
Mucinous cystic lesions
• *Mucinous cystic neoplasm (MCN)*
Non-mucinous cystic lesions
• *Serous cystic neoplasm (SCN)*
• *Solid pseudopapillary neoplasm (SPN)*
• *Acinar-cell cystic neoplasm (acinar cystadenoma)*
Other neoplastic lesions
• *Ductal adenocarcinoma with cystic degeneration*
• *Cystic neuroendocrine neoplasm*
Communicating pancreatic cyst
Non-neoplastic cysts
Pseudocyst
Neoplastic cysts (PCNs)
Mucinous cystic lesions
• *Intraductal papillary mucinous neoplasm (IPMN)*

Table 2: Radiological classification of pancreatic cystic lesions (PCLs)

related to necrotic portions of peripancreatic and pancreatic tissue that remain in the cyst cavity after cyst formation. Internal debris does not show enhancement after gadolinium injection and, when present, is a highly specific MR finding for the diagnosis of PPSC [117] (Fig. 26).

MRCP with secretin injection may be helpful before planning the therapeutic approach, as it can exclude communication between the PPSC and pancreatic duct, which is associated with an increased risk of treatment failure [118] (Fig. 27).

3.f.2 Serous cystadenoma (SCA)

Serous cystadenomas (SCA) represent around 1–2% of pancreatic neoplasms and 10–15% of cystic pancreatic lesions [119].

SCAs occur primarily in female patients in their fifties. They mainly affect the head of the pancreas, although they can be found in every part of the gland [120]. Histologically, SCAs are composed of multiple cysts formed by glycogen-rich, PAS-positive epithelial cells. They are benign lesions, and very few cases of serous cystadenocarcinoma have been published [121].

It is important to obtain a definite diagnosis of SCA noninvasively because if the lesion is asymptomatic, it can be left unresected and then followed up [120]. In a multinational review of 2,622 patients with SCA, the related mortality was almost nil, whereas operative mortality is not, which suggests conservative treatment for SCA [122]. A large lesion can cause obstructive chronic pancreatitis, and will thus need surgical resection [123]. In 15–30% of the cases, SCA is associated with Von Hippel-Lindau (VHL) disease [124].

Imaging findings of SCAs depend heavily on the macroscopic appearance. Typically, SCAs have three morphological patterns: Microcystic (or polycystic), honeycomb, and macrocystic (or oligocystic) [125].

A microcystic pattern is composed of multiple cysts measuring 2 cm or smaller and separated by fibrous septa that can coalesce into a central stellate scar that may calcify [126] (Fig. 28). In rare cases, some larger cysts (> 2 cm) can be observed in peripheral locations (mixed type).

The honeycomb pattern is characterized by numerous subcentimeter cysts that cannot be individually distinguished and thus appear as well-marginated lesions with soft-tissue or mixed attenuation, especially in CT. With MRI, the cystic content of the lesion is easily distinguishable with T2w sequences (Fig. 29).

The macrocystic pattern is characterized by a small number of cysts of > 2 cm which lack a central scar and are often indistinguishable from other cystic masses of the pancreas, especially mucinous cystic tumors (Fig. 30) [125–127].

In the multinational review of 2,622 patients with SCA, the microcystic pattern was seen in 45% of cases, the mixed type in 18%, the honeycomb in 5%, and the macrocystic in 32% [122].

Solid variant of serous cystadenoma has rarely been described. These lesions do not contain any cystic spaces on histopathology, and the cells are arranged in nests, sheets, and trabeculae separated by thick fibrous bands. The stroma demonstrates avid contrast enhancement showing a solid hypervascular appearance on CT, and can thus lead to an incorrect diagnosis of neuroendocrine tumor, especially with CT [128]. Only MRI can correctly characterize these lesions, thanks to its high sensitivity to static fluids (Fig. 31) [128, 129].

When associated with Von Hippel-Lindau disease, cystic lesions are multifocal and can diffusely involve the pancreatic gland (Fig. 32).

3.f.3 Mucinous cystic neoplasms (MCNs)

Mucinous cystic neoplasms (MCNs) account for 10% of all cystic pancreatic lesions. They are cyst-forming epithelial neoplasms composed of epithelial cells that produce mucin, and are supported by an ovarian-type stroma [130]. According to the grade of epithelial dysplasia, MCNs can be classified as follows: (I) MCN with low or intermediate-grade dysplasia; (II) MCN with high-grade dysplasia; and (III) MCN with an associated invasive carcinoma [101].

Peak occurrence is in the fifth decade, but MCNs can affect a wide range of ages. The malignancy of the lesions worsens with advanced age. This suggests that the lesions evolve from benign to malignant [130], as confirmed by the presence of differing degrees of differentiation, from benign to overtly malignant, in the same lesion [131].

In a review of 344 cases of MCNs with ovarian stroma, MCNs occurred almost exclusively in females (99.7%), were almost always located in the body or tail of the pancreas (94.6%), and rarely communicated with the pancreatic duct (6.8%). A total of 73.4% were benign and 26.6% were malignant [132].

As is the case with SCAs, symptoms of MCNs are nonspecific, with some degree of abdominal pain or discomfort that is seldom referred to the pancreatic region [133]. In the case of advanced malignant lesions, more evident clinical signs, such as dyspepsia, pain, weight loss, and jaundice, can be present [120].

Like SCAs, MCN imaging characteristics depend on the macroscopic appearance. MCNs appear as round masses

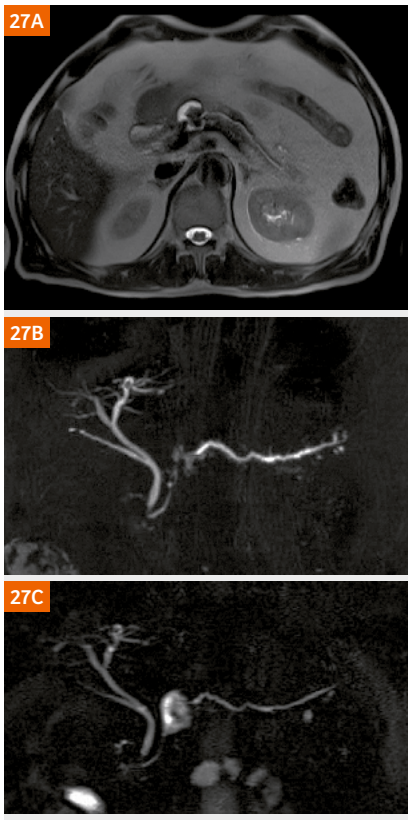

Figure 27: Pancreatic pseudocyst. T2w HASTE **(27A)** shows a fluid collection in the neck of the pancreas in a patient who previously had severe pancreatitis. MRCP **(27B)** shows the duct of Wirsung dilated upstream of the fluid collection. Soon after secretin injection **(27C)**, the fluid collection increases due to the passage of pancreatic juice in the pseudocyst.

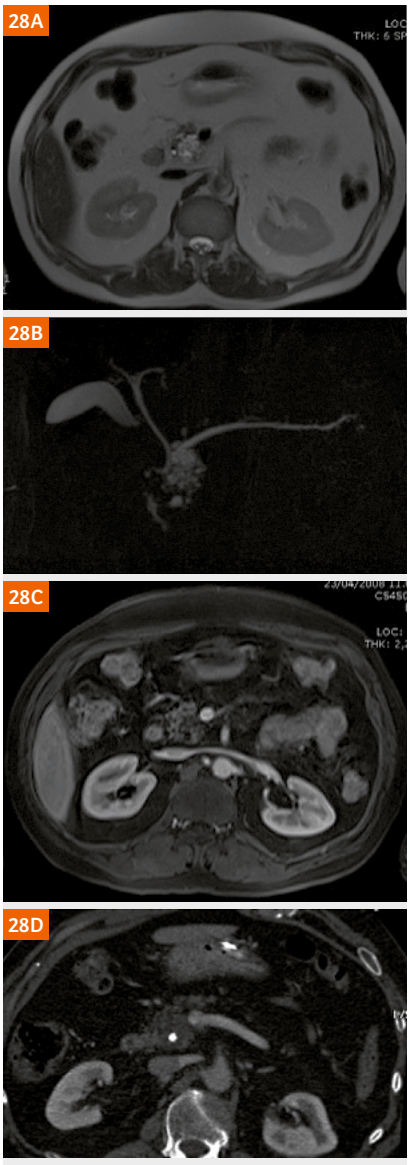

Figure 28: Serous cystadenoma, microcystic pattern. On T2w HASTE **(28A)**, several small (< 1 cm) cysts are visible in the uncinate process. On MRCP **(28B)**, the duct of Wirsung appears slight dilated upstream, with initial signs of chronic obstructive pancreatitis. After Gd injection, VIBE **(28C)** shows a slight enhancement in the fibrous septa. Unenhanced CT **(28D)** shows calcification in the central scar.

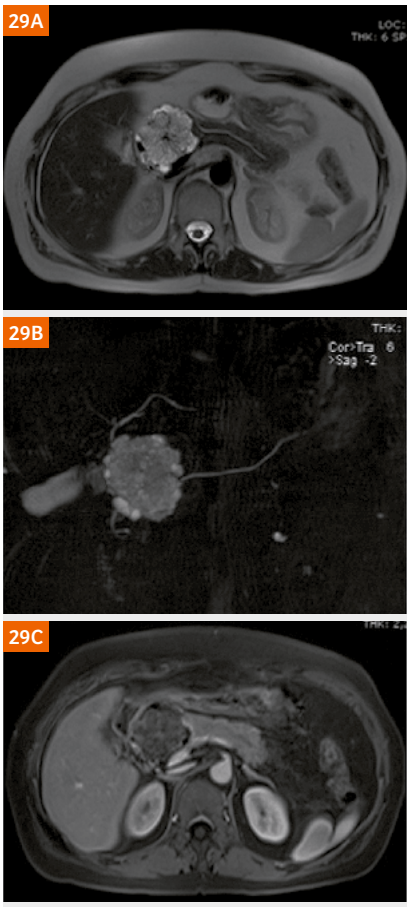

Figure 29: Serous cystadenoma, honeycomb pattern. On T2w HASTE **(29A)**, a large cyst with indistinguishable small cysts and some larger cysts at the periphery is visible in the pancreatic head. On MRCP (29B), the duct of Wirsung upstream appears normal. After Gd injection, VIBE **(29C)** shows a slight enhancement in the fibrous septa.

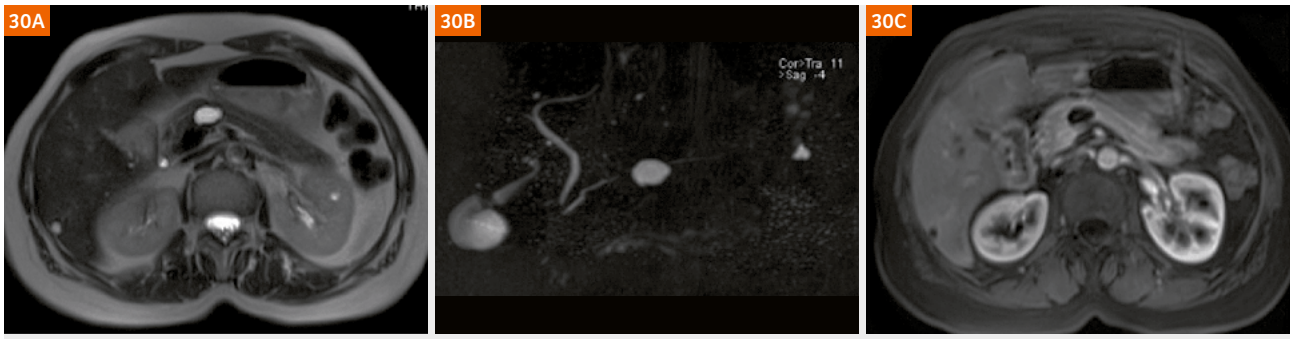

Figure 30: Serous cystadenoma, macrocystic pattern. On T2w HASTE **(30A)**, a 2.5-cm cyst with lobulated margins is visible in the neck of the pancreas. It is clearer on MRCP **(30B)**. The duct of Wirsung upstream appears normal. After Gd injection, VIBE **(30C)** shows no significant enhancement.

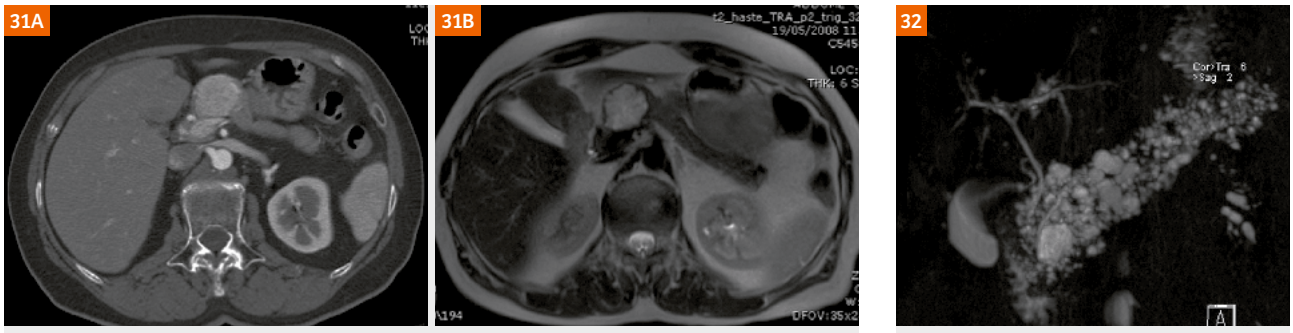

Figure 31: Serous cystadenoma, solid variant. CT in the arterial phase **(31A)** shows a large hypervascular lesion in the pancreatic head, simulating a neuroendocrine tumor. At T2w HASTE **(31B)**, the lesions clearly show microcystic content.

Figure 32: Von Hippel-Lindau disease. MRCP shows that the pancreatic parenchyma has been completely replaced by several cysts with diameters ranging from a few millimeters to 2 cm.

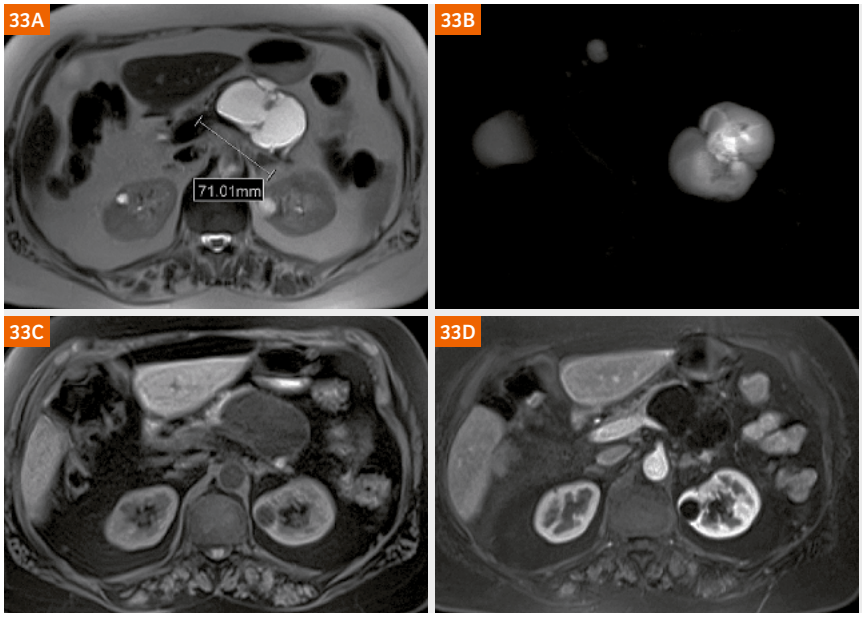

Figure 33: Mucinous cystic neoplasm, macrocystic multilocular pattern. On T2w HASTE **(33A)**, a large cyst with smooth margins and multilocular aspect is appreciable in the tail of the pancreas. MRCP **(33B)** clearly shows the multilocular pattern. With unenhanced VIBE **(33C)**, the content of the cyst is homogeneous. After Gd administration **(33D)**, the enhancement of the septa is clearly seen.

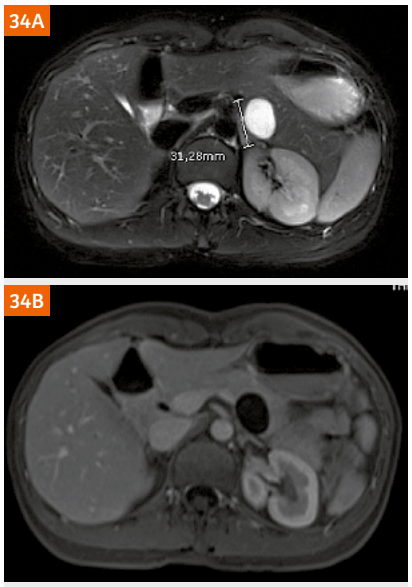

Figure 34: Mucinous cystic neoplasm, unilocular pattern. On T2w **(34A)**, a large unilocular cyst can be appreciated in the tail of the pancreas. It does not show any significant enhancement after Gd injection **(34B)**.

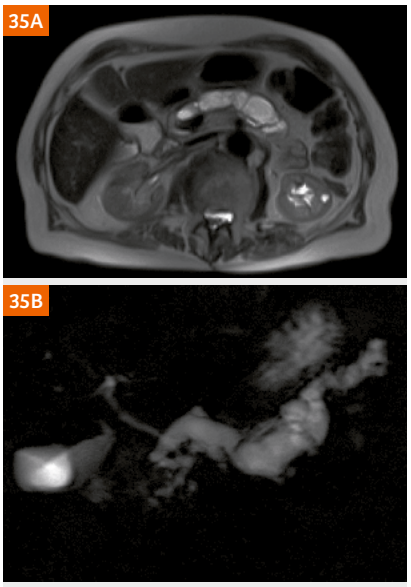

Figure 35: Diffuse MD-IPMN. T2w HASTE **(35A)** shows a diffuse dilatation of the main pancreatic duct with severe atrophy of the pancreatic parenchyma. MRCP **(35B)** shows the entire length of the dilated duct.

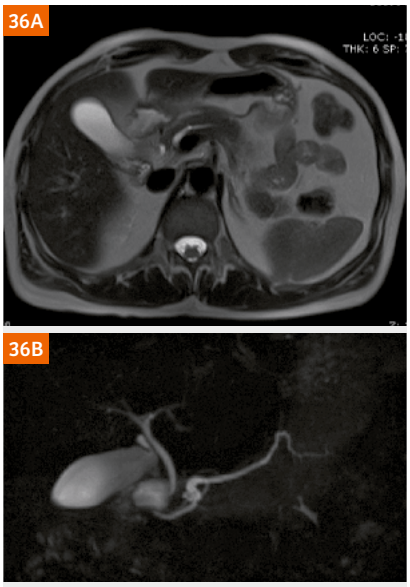

Figure 36: Segmental MD-IPMN. On T2w HASTE **(36A)**, a segmental dilatation of the main pancreatic duct is visible; pancreatic parenchyma is normal. MRCP **(36B)** provides a clearer image of the segmental dilated duct.

with sharp margins and two main patterns: Unilocular or multilocular macrocysts [134]. A macrocystic multilocular pattern is the most typical and common of the two (Fig. 33) [135], while a unilocular appearance (Fig. 34) is similar to many other cystic lesions.

Multicystic MCNs appear as a cystic mass with sharp margins. The wall varies in thickness, with mural vegetation or parietal calcifications [136]. Thick septa and/or papillary proliferations are suggestive of the malignant degeneration of the MCN [136]. MRI with heavily T2-weighted sequences allows for better identification of the thin septa than CT does (Fig. 33). However, it is less sensitive when it comes to identifying the calcifications. MRCP can easily demonstrate a lack of communication between the MCN and the main pancreatic duct and thus exclude an intraductal origin of the neoplasia [137]. The signal intensity of MCN on T1w images can be high due to hemorrhage or mucin content [136].

In a retrospective study of 65 patients with mucinous cystic adenoma (n = 43) and mucinous cystic adenocarcinoma (n = 22), a statistically significant difference was observed in some features: Size > 7 cm; septa and wall thickness > 3 mm; number of loculations > 4; nodules; hyperintensity of the cystic content on T1-weighted images; compression and/or infiltration of adjacent vessels or organs; and metastases. The best cut-off value to differentiate MCAs from mucinous cystadenocarcinoma was the presence of three features, with an accuracy of 91% [138].

3.f.4 Intraductal papillary mucinous neoplasm

Intraductal papillary mucinous neoplasms (IPMNs) are a group of exocrine mucin-producing tumors, diagnosed at a mean age of 60 years, with a male prevalence [139].

Improvements in imaging techniques have increased the incidental detection of IPMNs. In several studies, the prevalence of incidental cystic pancreatic lesions can be observed in up to 19.6% of imaging studies, with MR being the most sensitive [111]. The involvement or the communication of the cystic pancreatic lesion with the main pancreatic duct is crucial for the appropriate diagnosis of IPMN [140].

Three types of IPMNs have been described [141]: The main duct type (MD-IPMN), the branch duct type (BD-IPMN), and the mixed type, which meet the criteria for both MD-IPMN and BD-IPMN.

IPMNs arise from the epithelium of the pancreatic ductal system and can display the full spectrum of histologic dysplasia, including hyperplasia, adenoma, borderline tumor, and in situ or invasive carcinoma [142]. There are significant differences in frequencies of malignancy in

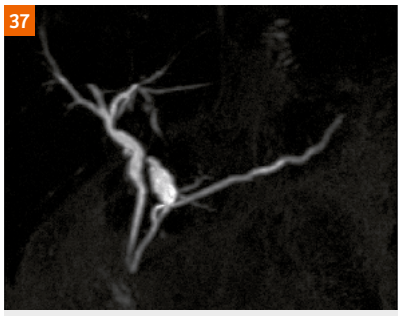

Figure 37: BD-IPMN. MRCP clearly shows a finger-type unilocular branch duct ectasia.

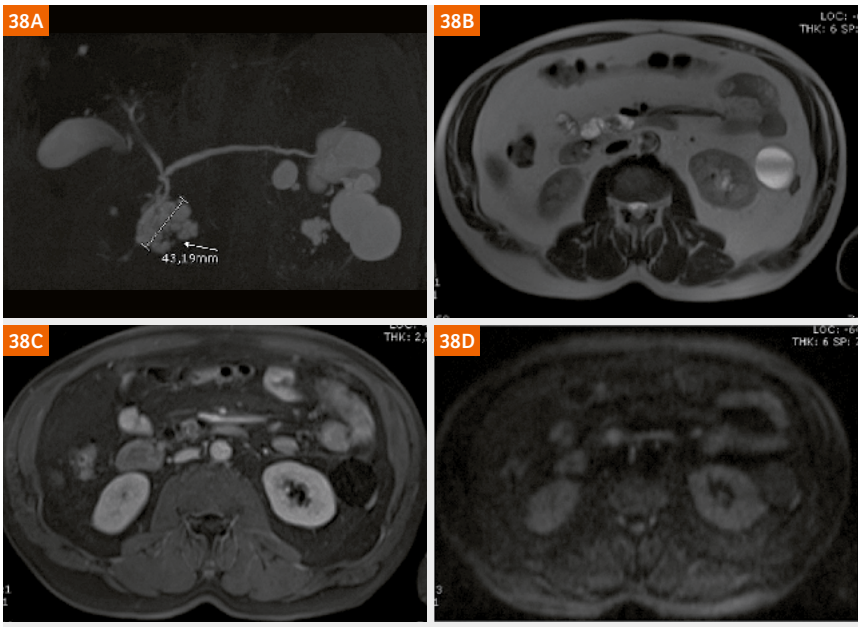

Figure 38: BD-IPMN with nodule. MRCP (**38A)** shows a multilocular BD-IPMN in the uncinate process with a small defect (arrow). This corresponds to a solid nodule visible with T2w HASTE **(38B)**, which enhances after Gd administration **(38C)** and shows high signal intensity at DWI at high b-values **(38D)**, due to restricted diffusion.

IPMNs depending on the morphological type. They are higher for MD-IPMNs (mean 61.6%) and lower for BD-IPMNs (25.5%) [141].

Due to the widespread use of non-invasive imaging of the abdomen (US, CT, MRI), IPMNs are now mostly detected incidentally when imaging is performed for unrelated indications [143]. Therefore, many patients with IPMNs are asymptomatic and incidentally identified. In other cases, the impaired outflow of pancreatic juice induced by the hypersecretion of mucin [144] may cause pain and produces the laboratory test abnormalities of pancreatitis, such as hyperamylasemia [145]. Thus, IPMNs can be discovered after an episode of pancreatitis. More severe symptoms such as jaundice, severe abdominal pain, weight loss, anorexia, and diabetes are more likely associated with malignant behavior.

The location and type of an IPMN determine its imaging appearance. IPMNs appear with a cystic dilation of the involved segment – either the main duct or branch duct. The production of mucin is the main cause of the dilation of the ducts.

MD-IPMN of the main pancreatic duct can present as segmental or diffuse. When diffused to the entire duct, this tumor can be confused with chronic pancreatitis [146]. Segmental IPMNs are very difficult to diagnose, as they present as an aspecific segmental dilation of the main pancreatic duct without any clear cause of obstruction or previous pancreatitis which can lead to a post-inflammatory stenosis. The affected segment tends to enlarge with dilation of the collateral ducts. When the lesion is localized in the head of the pancreas, there is a dilation of the main pancreatic duct upstream, secondary to the obstruction of the outflow of pancreatic juice, which simulates a diffuse IPMN [147]. In MD-IPMNs, ductal dilation is common and may be along the entire length of the duct (Fig. 33) or segmental (Fig. 36), and be with or without intraductal hypointense masses [139]. In advanced MD-IPMNs, adjacent parenchymal atrophy is frequently seen (Fig. 35) [144]. Mucin usually has the same pattern of pancreatic juice with the different imaging techniques, so it is not possible to differentiate mucin from pancreatic juice.

BD-IPMNs can present as unilocular (Fig. 37) or multilocular (Fig. 38) communicating cystic lesions with grapelike clusters that have a variable diameter ranging from a few millimeters to a few centimeters, and are unifocal (Fig. 37) or multifocal (Fig. 39). The cysts are separated by thin septa, which usually enhance after contrast media administration. For a correct diagnosis of BD-IPMN, communication with the main pancreatic duct must be demonstrated (Fig. 37) [148].

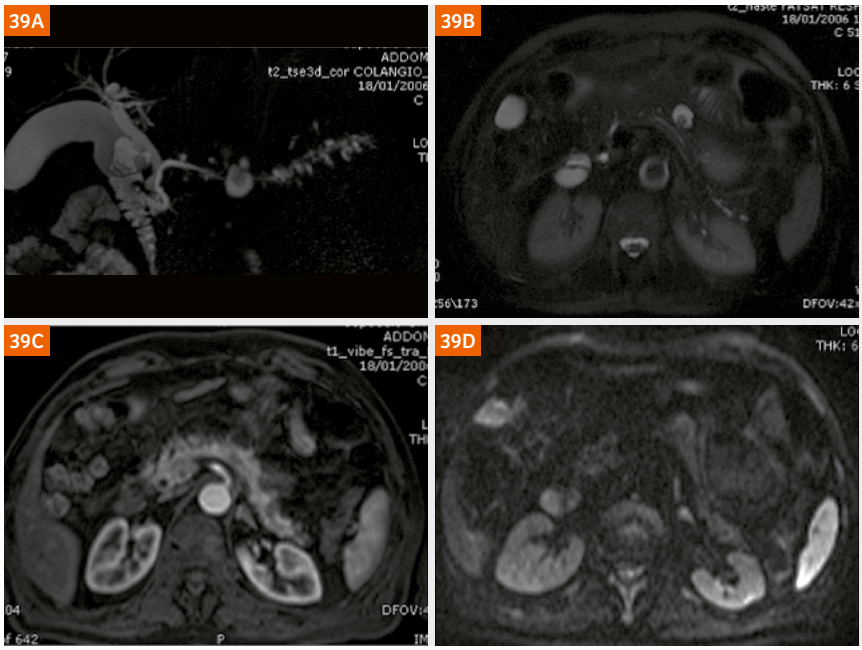

Figure 39: BD-IPMN with pseudonodule. MRCP **(39A)** shows a multifocal BD-IPMN in the body-tail of the pancreas. The largest cyst has a small defect, which corresponds to a solid nodule visible on T2w HASTE **(39B)**. It does not enhance after Gd administration **(39C)** and does not show high signal intensity at DWI at high b-values **(39D)**, due to unrestricted diffusion.

In mixed IPMNs, there is evidence of dilatation of the main pancreatic duct and branch ducts along its course (Fig. 42) [146]. However, in cases of BD-IPMNs where dilation of the main pancreatic duct is due to the overproduction of mucin by the tumor and not to the involvement of the main pancreatic duct, the differential diagnosis of mixed IPMNs can be difficult (Fig. 4) [146].

Clearly differentiating between IPMN lesions with different pathological expressions can be challenging unless clear evidence of malignancy is present [149]. However, some imaging findings can be suggestive of aggressive behavior of the IPMN.

According to international consensus guidelines, 'high-risk stigmata' and 'worrisome features' are useful imaging findings for lesion classification [141].

High-risk stigmata indicate a high possibility that the lesion is malignant, which means surgical resection is necessary if the patient is fit. The criteria for high-risk stigmata are as follows: Main duct diameter > 10 mm for MD-IPMN (Fig. 35); the presence of solid enhancing nodules within the cyst in BD-IPMN; obstructive jaundice in the presence of a cystic lesion of the pancreatic head. Proliferating nodules are characterized by the capacity to enhance after contrast media administration (Fig. 38C). With DWI sequences, the restricted diffusion of water molecules means that enhancing nodules appear as a focus of high signal intensity within the cystic lesions at high b-values (Fig. 38D). Non-enhancing nodules can be caused by dense mucin plugs, and do not show signal intensity with DWI (Fig. 39).

Worrisome features suggest the possibility that the lesion could become malignant, which would require further workup by EUS for better risk-stratification of the lesion, and a strict follow-up. The criteria for worrisome features are as follows: cyst > 3 cm; thickened and enhanced cyst walls; main pancreatic duct measuring 5–9 mm (Fig. 36); non-enhancing mural nodules (Fig. 39); abrupt change in the main pancreatic duct caliber with distal pancreatic atrophy; lymphadenopathy.

The management of IPMNs is mainly based on the location (MD and mixed IPMN versus BD-IPMN), the size of the largest cyst in BD-IPMN, and the presence of high-risk stigmata or worrisome features. Moreover, risk stratification for age and fitness for surgery must be considered [141].

Patients with BD-IPMN, cysts of > 3 cm, and no worrisome features can also be considered for EUS to verify the absence of thickened walls or mural nodules, particularly if the patient is elderly. If a patient is young and fit for surgery, then surgery should be strongly considered.

Patients with BD-IPMN, cysts of < 3 cm, and no worrisome features should be considered for observation according to size stratification.

MD-IPMNs with main pancreatic duct dilation of 5–9 mm can also be considered as a worrisome feature. The recommendation here is evaluation, but no immediate resection.

MR with MRCP has a sensitivity, specificity, and accuracy of 70%, 92% and 80% respectively in the diagnosis of benign vs. malignant IPMNs based on certain worrisome

features (nodules, main pancreatic duct > 10 mm, thick septa, calcifications) [150].

In patients with IPMN, pancreatic ductal carcinoma may develop independently in the pancreatic duct [151].

There have been rare reports of atypical appearances of complicated IPMNs with intraductal hemorrhage, perforation, and fistula formation [152]. Intraductal hemorrhage shows up as high signal intensity on T1 with fat saturation.

In some patients with BD-IPMN, follow-up can show a reduction in lesion size. This is due to the opening of the communication channel between the lesion and the main pancreatic duct, which was previously blocked by thick mucin. In such cases, the passage of mucin from the lesion to the main pancreatic duct reduces the pressure inside the lesion, causing it to shrink.

MD-IPMNs must be differentiated by the main duct dilation seen in chronic pancreatitis [146]. IPMNs affect patients in their 60s and 70s, with an equal distribution between men and women, while chronic pancreatitis is more frequent during one's 40s [153]. In a comparative study of IPMNs and chronic pancreatitis, specific findings for IPMNs were duct dilatation without stricture, bulging ampulla, nodule in a duct, grape-like secondary duct dilatation, and nodule in a cyst. Specific findings for chronic pancreatitis were duct dilatation with strictures, the presence of a stone, and side-branch ectasia with noncystic appearance.

3.f.5 Solid pseudopapillary tumors

Solid pseudopapillary tumors (SPTs) are the least frequent cystic tumors of the pancreas, and their origin is still uncertain. They have a low malignant potential and a favorable prognosis. They can occur in people of any age, but most often they affect women in their 30s [154]. In clinical terms, they are quite unspecific, with abdominal pain as the main symptom, sometimes together with a palpable mass. The low malignant potential of the lesion can account for its large size at the time of diagnosis [155]. The tumor appears as a round, well-encapsulated mass. The content of the lesion is solid with a variable amount of necrosis or hemorrhage, which is responsible for its frequently cystic appearance. In a group of 56 patients with SPT, calcifications were found in 29% of the cases [156]. After contrast agent administration, the solid component of the tumor appears well vascularized with all imaging techniques. When fresh hemorrhage is present, it is clearly visible on MR images, with high signal intensity on T1-weighted sequences and fluid-debris level [156]. When large cystic changes are present, SPTs appear as macrocystic unilocular or multilocular lesions, similar to mucinous cystic neoplasms; in this situation, the young age of the patient helps in the differential diagnosis.

6. Conclusion

Imaging of the pancreas represents a diagnostic challenge for both radiologists and clinicians because of overlapping clinical, radiological, and pathological features.

The wide pathological range of both solid and cystic lesions requires an in-depth knowledge of the pathology, and the application of the best imaging techniques in order to arrive at the correct diagnosis. The multiparametricity of MRI makes it possible to obtain morphological and functional images, which are useful in addressing most pathological conditions of the pancreas.

Contact

Giovanni Morana, M.D.
Radiology Department
General Hospital Ca' Foncello

31100 Treviso
Italy
Phone: +39-0422-322253
Fax: +39-0422-322202
giovanni.morana@aulss2.veneto.it



References

1 Pamuklar E, Semelka RC. MR imaging of the pancreas. Magn Reson Imaging Clin N Am. 2005 May;13(2):313-30. doi:10.1016/j.mric.2005.03.012.
2 Hakimé A, Giraud M, Vullierme MP, Vilgrain V. [MR imaging of the pancreas]. J Radiol. 2007 Jan;88(1 Pt 1):11-25. doi:10.1016/S0221-0363(07)89785-X.
3 Kanematsu M, Shiratori Y, Hoshi H, Kondo H, Matsuo M, Moriwaki H. Pancreas and peripancreatic vessels: effect of imaging delay on gadolinium enhancement at dynamic gradient-recalled-echo MR imaging. Radiology. 2000 Apr;215(1):95-102. doi:10.1148/radiology.215.1.r00ap1395.
4 Kalb B, Martin DR, Sarmiento JM, Erickson SH, Gober D, Tapper EB, et al. Paraduodenal pancreatitis: clinical performance of MR imaging in distinguishing from carcinoma. Radiology. 2013 Nov;269(2):475-81. doi:10.1148/radiol.13112056. Epub 2013 Jul 11.
5 Michaely HJ, Morelli JN, Budjan J, Riffel P, Nickel D, Kroeker R, et al. CAIPIRINHA-Dixon-TWIST (CDT)-volume-interpolated breath-hold examination (VIBE): a new technique for fast time-resolved dynamic 3-dimensional imaging of the abdomen with high spatial resolution. Invest Radiol. 2013 Aug;48(8):590-7. doi:10.1097/RLI.0b013e318289a70b.
6 Qu J, Han S, Zhang H, Liu H, Wang Z, Kamel IR, et al. Improved Detection of Recurrent Hepatocellular Carcinomas in Arterial Phase With CAIPIRINHA-Dixon-TWIST-Volumetric Interpolated Breath-Hold Examination. Invest Radiol. 2016 Oct;51(10):602-8. doi:10.1097/RLI.0000000000000281.
7 Colagrande S, Belli G, Politi LS, Mannelli L, Pasquinelli F, Villari N. The influence of diffusion- and relaxation-related factors on signal intensity: an introductive guide to magnetic resonance diffusion-weighted imaging studies. J Comput Assist Tomogr. 2008 May-Jun;32(3):463-74. doi:10.1097/RCT.0b013e31811ec6d4.
8 Kartalis N, Lindholm TL, Aspelin P, Permert J, Albiin N. Diffusion-weighted magnetic resonance imaging of pancreas tumours. Eur Radiol. 2009 Aug;19(8):1981-90. doi:10.1007/s00330-009-1384-8. Epub 2009 Mar 24.
9 Kallehauge JF, Tanderup K, Haack S, Nielsen T, Muren LP, Fokdal L, et al. Apparent Diffusion Coefficient (ADC) as a quantitative parameter in diffusion weighted MR imaging in gynecologic cancer: Dependence on b-values used. Acta Oncol. 2010 Oct;49(7):1017-22. doi:10.3109/0284186X.2010.500305.
10 Matsuki M, Inada Y, Nakai G, Tatsugami F, Tanikake M, Narabayashi I, et al. Diffusion-weighed MR imaging of pancreatic carcinoma. Abdom Imaging. 2007 Jul-Aug;32(4):481-3. doi:10.1007/s00261-007-9192-6.
11 Fukukura Y, Shindo T, Hakamada H, Takumi K, Umanodan T, Nakajo M, et al. Diffusion-weighted MR imaging of the pancreas: optimizing b-value for visualization of pancreatic adenocarcinoma. Eur Radiol. 2016 Oct;26(10):3419-27. doi:10.1007/s00330-015-4174-5. Epub 2016 Jan 6.
12 Koh D.M., Collins D.J. Diffusion-weighted MRI in the body: applications and challenges in oncology. AJR Am. J. Roentgenol. 2007 Jun;188(6):1622–35. doi:10.2214/AJR.06.1403.
13 Kang KM, Lee JM, Yoon JH, Kiefer B, Han JK, Choi BI. Intravoxel incoherent motion diffusion-weighted MR imaging for characterization of focal pancreatic lesions. Radiology. 2014 Feb;270(2):444-53. doi:10.1148/radiol.13122712. Epub 2013 Oct 28.
14 Kim B, Lee SS, Sung YS, Cheong H, Byun JH, Kim HJ, et al. Intravoxel incoherent motion diffusion-weighted imaging of the pancreas: Characterization of benign and malignant pancreatic pathologies. J Magn Reson Imaging. 2017 Jan;45(1):260-269. doi:10.1002/jmri.25334. Epub 2016 Jun 7.
15 Jensen JH, Helpern JA, Ramani A, Lu H, Kaczynski K. Diffusional kurtosis imaging: the quantification of non-gaussian water diffusion by means of magnetic resonance imaging. Magn Reson Med. 2005 Jun;53(6):1432-40. doi:10.1002/mrm.20508.
16 Kartalis N, Manikis GC, Loizou L, Albiin N, Zöllner FG, Del Chiaro M, et al. Diffusion-weighted MR imaging of pancreatic cancer: A comparison of mono-exponential, bi-exponential and non-Gaussian kurtosis models. Eur J Radiol Open. 2016 Apr 27;3:79-85. eCollection 2016. doi:10.1016/j.ejro.2016.04.002.
17 Noda Y, Kanematsu M, Goshima S, Horikawa Y, Takeda J, Kondo H, et al. Diffusion kurtosis imaging of the pancreas for the assessment of HbA1c levels. J Magn Reson Imaging. 2016 Jan;43(1):159-65. doi:10.1002/jmri.24982. Epub 2015 Jun 12.
18 Kim KA, Park MS, Kim IS, Kiefer B, Chung WS, Kim MJ, et al. Quantitative evaluation of liver cirrhosis using T1 relaxation time with 3 tesla MRI before and after oxygen inhalation. J Magn Reson Imaging 2012 Aug;36(2):405–10. doi:10.1002/jmri.23620. Epub 2012 Mar 5.
19 Tirkes T, Lin C, Fogel EL, Sherman SS, Wang Q, Sandrasegaran K. T1 mapping for diagnosis of mild chronic pancreatitis. J Magn Reson Imaging. 2017 Apr;45(4):1171-1176. doi:10.1002/jmri.25428. Epub 2016 Aug 13.
20 Zhang J, Israel GM, Hecht EM, Krinsky GA, Babb JS, Lee VS. Isotropic 3D T2-weighted MR cholangiopancreatography with parallel imaging: feasibility study. AJR Am J Roentgenol. 2006 Dec;187(6):1564-70. doi:10.2214/AJR.05.1032.
21 Takahashi S, Kim T, Murakami T, Okada A, Hori M, Narumi Y, et al. Influence of paramagnetic contrast on single-shot MRCP image quality. Abdom Imaging. 2000 Sep-Oct;25(5):511-3.
22 Matos C, Cappeliez O, Winant C, Coppens E, Devière J, Metens T. MR imaging of the pancreas: a pictorial tour. Radiographics. 2002 Jan-Feb;22(1):e2. doi:10.1148/radiographics.22.1.g02jae2e2.
23 Manfredi R, Costamagna G, Brizi MG, Maresca G, Vecchioli A, Colagrande C, et al. Severe chronic pancreatitis versus suspected pancreatic disease: dynamic MR cholangiopancreatography after secretin stimulation. Radiology. 2000 Mar;214(3): 849-55. doi:10.1148/radiology.214.3.r00mr24849.
24 Akisik MF, Sandrasegaran K, Aisen AA, Maglinte DD, Sherman S, Lehman GA. Dynamic secretin-enhanced MR cholangio-pancreatography. Radiographics. 2006 May-Jun;26(3):665-77. doi:10.1148/rg.263055077.
25 Manfredi R, Pozzi Mucelli R. Secretin-enhanced MR Imaging of the Pancreas. Radiology. 2016 Apr;279(1):29-43. doi:10.1148/radiol.2015140622.
26 Madzak A, Olesen SS, Wathle GK, Haldorsen IS, Drewes AM, Frøkjær JB. Secretin-Stimulated Magnetic Resonance Imaging Assessment of the Benign Pancreatic Disorders: Systematic Review and Proposal for a Standardized Protocol. Pancreas. 2016 Sep;45(8):1092-103. doi:10.1097/MPA.0000000000000606.
27 Hellerhoff KJ, Helmberger H 3rd, Rösch T, Settles MR, Link TM, Rummeny EJ. Dynamic MR pancreatography after secretin administration: image quality and diagnostic accuracy. AJR Am J Roentgenol. 2002 Jul;179(1):121-9. doi:10.2214/ajr.179.1.1790121.
28 Sherman S, Freeman ML, Tarnasky PR, Wilcox CM, Kulkarni A, Aisen AM, et al. Administration of secretin (RG1068) increases the sensitivity of detection of duct abnormalities by magnetic resonance cholangiopancreatography in patients with pancreatitis. Gastroenterology. 2014 Sep;147(3):646-654.e2. doi:10.1053/j.gastro.2014.05.035. Epub 2014 Jun 4.
29 Manikkavasakar S, AlObaidy M, Busireddy KK, Ramalho M, Nilmini V, Alagiyawanna M, et al. Magnetic resonance imaging of pancreatitis: an update. World J Gastroenterol. 2014 Oct 28;20(40):14760-77. doi:10.3748/wjg.v20.i40.14760.
30 Thoeni RF. Imaging of Acute Pancreatitis. Radiol Clin North Am. 2015 Nov;53(6):1189-208. doi:10.1016/j.rcl.2015.06.006. Epub 2015 Aug 5.
31 Shyu JY, Sainani NI, Sahni VA, Chick JF, Chauhan NR, Conwell DL, et al. Necrotizing pancreatitis: diagnosis, imaging, and intervention. Radiographics. 2014 Sep-Oct;34(5):1218-39. doi:10.1148/rg.345130012.
32 Md PS, Md UN. Role of ERCP in Patients With Idiopathic Recurrent Acute Pancreatitis. Curr Treat Options Gastroenterol. 2016 Sep;14(3):327-39. doi:10.1007/s11938-016-0096-9.
33 Sandrasegaran K, Tahir B, Barad U, Fogel E, Akisik F, Tirkes T, et al. The Value of Secretin-Enhanced MRCP in Patients With Recurrent Acute Pancreatitis. AJR Am J Roentgenol. 2017 Feb;208(2):315-321. doi:10.2214/AJR.16.16566. Epub 2016 Nov 8.
34 Testoni PA. Acute recurrent pancreatitis: Etiopathogenesis, diagnosis and treatment. World J Gastroenterol. 2014 Dec

7;20(45):16891-901. doi:10.3748/wjg.v20.i45.16891.
35 Brock C, Nielsen LM, Lelic D, Drewes AM. Pathophysiology of chronic pancreatitis. World J Gastroenterol. 2013 Nov 14;19(42):7231-40. doi:10.3748/wjg.v19.i42.7231.
36 Klöppel G. Chronic pancreatitis, pseudotumors and other tumor-like lesions. Mod Pathol. 2007 Feb;20 Suppl 1:S113-31. doi:10.1038/modpathol.3800690.
37 Issa Y, Kempeneers MA, van Santvoort HC, Bollen TL, Bipat S, Boermeester MA. Diagnostic performance of imaging modalities in chronic pancreatitis: a systematic review and meta-analysis. Eur Radiol. 2017 Sep;27(9):3820-3844. doi:10.1007/s00330-016-4720-9. Epub 2017 Jan 27.
38 Anaizi A, Hart PA, Conwell DL. Diagnosing Chronic Pancreatitis. Dig Dis Sci. 2017 Jul;62(7):1713-1720. doi:10.1007/s10620-017-4493-2. Epub 2017 Mar 17.
39 Cappeliez O, Delhaye M, Devière J, Le Moine O, Metens T, Nicaise N, et al. Chronic pancreatitis: evaluation of pancreatic exocrine function with MR pancreatography after secretin stimulation. Radiology. 2000 May;215(2):358-64. doi:10.1148/radiology.215.2.r00ma10358.
40 Gillams AR, Lees WR. Quantitative secretin MRCP (MRCPQ): results in 215 patients with known or suspected pancreatic pathology. Eur Radiol. 2007 Nov;17(11):2984-90. doi:10.1007/s00330-007-0708-9. Epub 2007 Jul 10.
41 Trikudanathan G, Walker SP, Munigala S, Spilseth B, Malli A, Han Y, et al. Diagnostic Performance of Contrast-Enhanced MRI With Secretin-Stimulated MRCP for Non-Calcific Chronic Pancreatitis: A Comparison With Histopathology. Am J Gastroenterol. 2015 Nov;110(11):1598-606. doi:10.1038/ajg.2015.297. Epub 2015 Sep 15.
42 Kirkegård J, Mortensen FV, Cronin-Fenton D. Chronic Pancreatitis and Pancreatic Cancer Risk: A Systematic Review and Meta-analysis. Am J Gastroenterol. 2017 Aug 1. doi:10.1038/ajg.2017.218. Epub ahead of print.
43 Raphael KL, Willingham FF. Hereditary pancreatitis: current perspectives. Clin Exp Gastroenterol. 2016 Jul 26;9:197-207. doi:10.2147/CEG.S84358. eCollection 2016.
44 Schima W, Ba-Ssalamah A, Kölblinger C, Kulinna-Cosentini C, Puespoek A, Götzinger P. Pancreatic adenocarcinoma. Eur Radiol. 2007 Mar;17(3):638-49. doi:10.1007/s00330-006-0435-7. Epub 2006 Oct 5.
45 Miller FH, Rini NJ, Keppke AL. MRI of adenocarcinoma of the pancreas. AJR Am J Roentgenol. 2006 Oct;187(4):W365-74. doi:10.2214/AJR.05.0875.
46 Ichikawa T, Sou H, Araki T, Arbab AS, Yoshikawa T, Ishigame K, et al. Duct-penetrating sign at MRCP: usefulness for differentiating inflammatory pancreatic mass from pancreatic carcinomas. Radiology. 2001 Oct;221(1):107-16. doi:10.1148/radiol.2211001157.
47 Boninsegna E, Manfredi R, Negrelli R, Avesani G, Mehrabi S, Pozzi Mucelli R. Pancreatic duct stenosis: Differential diagnosis between malignant and benign conditions at secretin-enhanced MRCP. Clin Imaging. 2017 Jan-Feb;41:137-143. doi:10.1016/j.clinimag.2016.10.020. Epub 2016 Oct 29.
48 Sandrasegaran K, Nutakki K, Tahir B, Dhanabal A, Tann M, Cote GA. Use of diffusion-weighted MRI to differentiate chronic pancreatitis from pancreatic cancer. AJR Am J Roentgenol. 2013 Nov;201(5):1002-8. doi:10.2214/AJR.12.10170.
49 Wiggermann P, Grützmann R, Weissenböck A, Kamusella P, Dittert DD, Stroszczynski C. Apparent diffusion coefficient measurements of the pancreas, pancreas carcinoma, and mass-forming focal pancreatitis. Acta Radiol. 2012 Mar 1;53(2):135-9. doi:10.1258/ar.2011.100252. Epub 2012 Jan 19.
50 Adsay NV, Zamboni G. Paraduodenal pancreatitis: a clinico-pathologically distinct entity unifying "cystic dystrophy of heterotopic pancreas", "para-duodenal wall cyst", and "groove pancreatitis". Semin Diagn Pathol. 2004 Nov;21(4):247-254.
51 de Pretis N, Capuano F, Amodio A, Pellicciari M, Casetti L, Manfredi R et al. Clinical and Morphological Features of Paraduodenal Pancreatitis: An Italian Experience With 120 Patients. Pancreas. 2017 Apr;46(4):489-495. doi:10.1097/MPA.0000000000000781.
52 Blasbalg R, Baroni RH, Costa DN, Machado MC. MRI features of groove pancreatitis. AJR Am J Roentgenol. 2007 Jul;189(1):73-80. doi:10.2214/AJR.06.1244.
53 Castell-Monsalve FJ, Sousa-Martin JM, Carranza-Carranza A. Groove pancreatitis: MRI and pathologic findings. Abdom Imaging. 2008 May-Jun;33(3):342-8. doi:10.1007/s00261-007-9245-x.
54 Pearson RK, Longnecker DS, Chari ST, Smyrk TC, Okazaki K, Frulloni L, et al. Controversies in clinical pancreatology: autoimmune pancreatitis: does it exist? Pancreas. 2003 Jul;27(1):1-13.
55 Okazaki K, Chiba T. (2002) Autoimmune related pancreatitis. Gut. 2002 Jul;51(1):1-4.
56 Zhang L, Chari S, Smyrk TC, Deshpande V, Klöppel G, Kojima M, et al. Autoimmune pancreatitis (AIP) type 1 and type 2: an international consensus study on histopathologic diagnostic criteria. Pancreas. 2011 Nov;40(8):1172-9. doi: 10.1097/MPA.0b013e318233bec5.
57 Majumder S, Takahashi N, Chari ST. Autoimmune Pancreatitis. Dig Dis Sci. 2017 Jul;62(7):1762-1769. doi:10.1007/s10620-017-4541-y. Epub 2017 Apr 1.
58 Sahani DV, Kalva SP, Farrell J, Maher MM, Saini S, Mueller PR, et al. Autoimmune pancreatitis: imaging features. Radiology. 2004 Nov;233(2):345-52. doi:10.1148/radiol.2332031436.
59 Manfredi R, Frulloni L, Mantovani W, Bonatti M, Graziani R, Pozzi Mucelli R. Autoimmune pancreatitis: pancreatic and extrapancreatic MR imaging-MR cholangiopancreatography findings at diagnosis, after steroid therapy, and at recurrence. Radiology. 2011 Aug;260(2):428-36. doi:10.1148/radiol.11101729. Epub 2011 May 25.
60 Oki H, Hayashida Y, Oki H, Kakeda S, Aoki T, Taguchi M, et al. DWI findings of autoimmune pancreatitis: comparison between symptomatic and asymptomatic patients. J Magn Reson Imaging. 2015 Jan;41(1):125-31. doi:10.1002/jmri.24508. Epub 2013 Nov 22.
61 Taniguchi T, Kobayashi H, Nishikawa K, Iida E, Michigami Y, Morimoto E, et al. Diffusion-weighted magnetic resonance imaging in autoimmune pancreatitis. Jpn J Radiol. 2009 Apr;27(3):138-42. doi:10.1007/s11604-008-0311-2. Epub 2009 May 3.
62 Kamisawa T, Takuma K, Anjiki H, Egawa N, Hata T, Kurata M, et al. Differentiation of autoimmune pancreatitis from pancreatic cancer by diffusion-weighted MRI. Am J Gastroenterol. 2010 Aug;105(8):1870-5. doi:10.1038/ajg.2010.87. Epub 2010 Mar 9.
63 Choi SY, Kim SH, Kang TW, Song KD, Park HJ, Choi YH. Differentiating Mass-Forming Autoimmune Pancreatitis From Pancreatic Ductal Adenocarcinoma on the Basis of Contrast-Enhanced MRI and DWI Findings. AJR Am J Roentgenol. 2016 Feb;206(2):291-300. doi:10.2214/AJR.15.14974.
64 Hur BY, Lee JM, Lee JE, Park JY, Kim SJ, Joo I et al. Magnetic resonance imaging findings of the mass-forming type of autoimmune pancreatitis: comparison with pancreatic adenocarcinoma. J Magn Reson Imaging. 2012 Jul;36(1):188-97. doi:10.1002/jmri.23609. Epub 2012 Feb 27.
65 Klauß M, Maier-Hein K, Tjaden C, Hackert T, Grenacher L, Stieltjes B. IVIM DW-MRI of autoimmune pancreatitis: therapy monitoring and differentiation from pancreatic cancer. Eur Radiol. 2016 Jul;26(7):2099-106. doi:10.1007/s00330-015-4041-4. Epub 2015 Oct 8.
66 Jemal A, Siegel R, Ward E, Murray T, Xu J, Smigal C et al. Cancer statistics 2006. CA Cancer J Clin. 2006 Mar-Apr;56(2):106–130.
67 Zamboni G, Capelli P, Pesci A, Beghelli S, Lüttges J, Klöppel G. Pancreatic head mass: what can be done? Classification: the pathological point of view. JOP. 2000 Sep;1(3 Suppl):77-84.
68 Balci NC, Semelka RC. Radiologic diagnosis and staging of pancreatic ductal adenocarcinoma. Eur J Radiol. 2001 May;38(2):105-12.
69 Zhong L. Magnetic resonance imaging in the detection of pancreatic neoplasms. J Dig Dis. 2007 Aug;8(3):128-32. doi:10.1111/j.1443-9573.2007.00297.x.
70 Zins M, Petit E, Boulay-Coletta I, Balaton A, Marty O, Berrod JL.

[Imaging of pancreatic adenocarcinoma] [Article in French]. J Radiol. 2005 Jun;86(6 Pt 2):759-79; quiz 779-80.
71 Fattahi R, Balci NC, Perman WH, Hsueh EC, Alkaade S, Havlioglu N, et al. Pancreatic diffusion-weighted imaging (DWI): comparison between mass-forming focal pancreatitis (FP), pancreatic cancer (PC), and normal pancreas. J Magn Reson Imaging. 2009 Feb;29(2):350-6. doi:10.1002/jmri.21651.
72 Akisik MF, Aisen AM, Sandrasegaran K, Jennings SG, Lin C, Sherman S, et al. Assessment of chronic pancreatitis: utility of diffusion-weighted MR imaging with secretin enhancement. Radiology. 2009 Jan;250(1):103-9. doi: 10.1148/radiol.2493080160. Epub 2008 Nov 10.
73 Sahani DV, Shah ZK, Catalano OA, Boland GW, Brugge WR. Radiology of pancreatic adenocarcinoma: current status of imaging. J Gastroenterol Hepatol. 2008 Jan;23(1):23-33. doi: 10.1111/j.1440-1746.2007.05117.x.
74 Oterdoom LH, van Weyenberg SJ, de Boer NK. Double-duct sign: do not forget the gallstones. J Gastrointestin Liver Dis. 2013 Dec;22(4):447-50.
75 Del Chiaro M, Zerbi A, Falconi M, Bertacca L, Polese M, Sartori N, et al. Cancer risk among the relatives of patients with pancreatic ductal adenocarcinoma. Pancreatology. 2007;7(5-6):459-69. doi:10.1159/000108963. Epub 2007 Oct 1.
76 Del Chiaro M, Verbeke CS, Kartalis N, Pozzi Mucelli R, Gustafsson P, Hansson J, et al. Short-term Results of a Magnetic Resonance Imaging-Based Swedish Screening Program for Individuals at Risk for Pancreatic Cancer. JAMA Surg. 2015 Jun;150(6):512-8. doi:10.1001/jamasurg.2014.3852.
77 Niederle MB, Hackl M, Kaserer K, Niederle B. Gastroenteropancreatic neuroendocrine tumours: the current incidence and staging based on the WHO and European Neuroendocrine Tumour Society classification: an analysis based on prospectively collected parameters. Endocr Relat Cancer. 2010 Oct 5;17(4):909–918. doi:10.1677/ERC-10-0152. Print 2010 Dec.
78 Klimstra DS, Arnold R, Capella C, et al. Neuroendocrine neoplasms of the pancreas. In: Bosman F, Carneiro F, Hruban RH, Theise N, editors. WHO Classification of Tumours of the Digestive System. Lyon: IARC Press; 2010. p. 322-6.
79 Oberg K. Pancreatic endocrine tumors. Semin Oncol. 2010 Dec;37(6):594-618. doi:10.1053/j.seminoncol.2010.10.014.
80 Horton KM, Hruban RH, Yeo C, Fishman EK. Multi-detector row CT of pancreatic islet cell tumors. Radiographics 2006 Mar-April;26(2):453-464. doi:10.1148/rg.262055056
81 Manfredi R, Bonatti M, Mantovani W, Graziani R, Segala D, Capelli P, et al. Non-hyperfunctioning neuroendocrine tumours of the pancreas: MR imaging appearance and correlation with their biological behavior. Eur Radiol. 2013 Nov;23(11):3029-39. doi:10.1007/s00330-013-2929-4. Epub 2013 Jun 21.
82 Pape UF, Jann H, Müller-Nordhorn J, Bockelbrink A, Berndt U, Willich SN, et al. Prognostic relevance of a novel TNM classification system for upper gastroenteropancreatic neuroendocrine tumors. Cancer 2008 Jul 15;113(2):256-65. doi:10.1002/cncr.23549.
83 Jann H, Roll S, Couvelard A, Hentic O, Pavel M, Müller-Nordhorn J, et al. Neuroendocrine tumors of midgut and hindgut origin: tumor-node-metastasis classification determines clinical outcome. Cancer. 2011 Aug 1;117(15):3332–41. doi:10.1002/cncr.25855. Epub 2011 Jan 18.
84 Rha SE, Jung SE, Lee KH, Ku YM, Byun JY, Lee JM. CT and MR imaging findings of endocrine tumor of the pancreas according to WHO classification. Eur J Radiol. 2007 Jun;62(3):371-7. doi:10.1016/j.ejrad.2007.02.036. Epub 2007 Apr 11.
85 Falconi M, Bartsch DK, Eriksson B, Klöppel G, Lopes JM, O'Connor JM, et al. ENETS Consensus Guidelines for the management of patients with digestive neuroendocrine neoplasms of the digestive system: well-differentiated pancreatic non-functioning tumors. Neuroendocrinology. 2012;95(2):120-34. doi:10.1159/000335587. Epub 2012 Feb 15.
86 Hruban RH, Pitman MB, Klimstra DS. Endocrine Neoplasms. In: Hruban RH, Pitman MB, Klimstra DS, editors. Tumors of the Pancreas: Afip Atlas of Tumor Pathology, Fourth Series. Washington DC: American Registry of Pathology; 2007. p. 251-304.
87 Tamm EP, Bhosale P, Lee JH, Rohren E. State-of-the-art Imaging of Pancreatic Neuroendocrine Tumors. Surg Oncol Clin N Am. 2016 Apr;25(2):375-400. doi:10.1016/j.soc.2015.11.007.
88 De Robertis R , Tinazzi Martini P, Cingarlini S, Ortolani S, Butturini G, Regi P, et al. Digital Subtraction of Magnetic Resonance Images Improves Detection and Characterization of Pancreatic Neuroendocrine Neoplasms. J Comput Assist Tomogr. 2017 Jul/Aug;41(4):614-618. doi: 10.1097/RCT.0000000000000552.
89 Humphrey PE, Alessandrino F, Bellizzi AM, Mortele KJ. Non-hyperfunctioning pancreatic endocrine tumors: multimodality imaging features with histopathological correlation. Abdom Imaging. 2015 Oct;40(7):2398-410. doi:10.1007/s00261-015-0458-0.
90 Manfredi R, Bonatti M, Mantovani W, Graziani R, Segala, D, Capelli P, et al. Non-hyperfunctioning neuroendocrine tumours of the pancreas: MR imaging appearance and correlation with their biological behaviour. Eur Radiol. 2013 Nov;23(11):3029-39. doi:10.1007/s00330-013-2929-4.
91 Lotfalizadeh E, Ronot M, Wagner M, Cros J, Couvelard A, Vullierme MP, et al. Prediction of pancreatic neuroendocrine tumour grade with MR imaging features: added value of diffusion-weighted imaging. Eur Radiol. 2017 Apr;27(4):1748-1759. doi: 10.1007/s00330-016-4539-4. Epub 2016 Aug 19.
92 Lewis RB, Lattin GE Jr, Paal E. Pancreatic endocrine tumors: radiologic-clinicopathologic correlation. Radiographics. 2010 Oct;30(6):1445-64. doi:10.1148/rg.306105523.
93 Bordeianou L, Vagefi PA, Sahani D, Deshpande V, Rakhlin E, Warshaw AL, et al. Cystic pancreatic endocrine neoplasms: a distinct tumor type? J Am Coll Surg. 2008 Jun;206(6):1154-8. doi:10.1016/j.jamcollsurg.2007.12.040. Epub 2008 Apr 14.
94 Gallotti A, Johnston RP, Bonaffini PA, Ingkakul T, Deshpande V, Fernández-del Castillo C, et al. Incidental neuroendocrine tumors of the pancreas: MDCT findings and features of malignancy. AJR Am J Roentgenol. 2013 Feb;200(2):355-62. doi:10.2214/AJR.11.8037.
95 Barral M, Taouli B, Guiu B, Koh DM, Luciani A, Manfredi R, et al. Diffusion-weighted MR imaging of the pancreas: current status and recommendations. Radiology. 2015 Jan;274(1):45-63. doi:10.1148/radiol.14130778.
96 Pereira JA, Rosado E, Bali M, Metens T, Chao SL. Pancreatic neuroendocrine tumors: correlation between histogram analysis of apparent diffusion coefficient maps and tumor grade. Abdom Imaging. 2015 Oct;40(8):3122-8. doi:10.1007/s00261-015-0524-7.
97 Woo S, Cho JY, Kim SY, Kim SH. Histogram analysis of apparent diffusion coefficient map of diffusion-weighted MRI in endometrial cancer: a preliminary correlation study with histological grade. Acta Radiol. 2014 Dec;55(10):1270-7.doi: 10.1177/0284185113514967. Epub 2013 Dec 6.
98 Brenner R, Metens T, Bali M, Demetter P, Matos C. Pancreatic neuroendocrine tumor: added value of fusion of T2-weighted imaging and high b-value diffusion-weighted imaging for tumor detection. Eur J Radiol. 2012 May;81(5):e746-9. doi: 10.1016/j.ejrad.2012.01.032. Epub 2012 Mar 3.
99 Nelsen EM, Buehler D, Soni AV, Gopal DV. Endoscopic ultrasound in the evaluation of pancreatic neoplasms-solid and cystic: A review. World J Gastrointest Endosc. 2015 Apr 16;7(4):318-27. doi:10.4253/wjge.v7.i4.318.
100 Salvia R, Festa L, Butturini G, Tonsi A, Sartori N, Biasutti T, et al. Pancreatic cystic tumors. Minerva Chir. 2004 Apr;59(2):185-207.
101 Brugge WR. Diagnosis and management of cystic lesions of the pancreas. J Gastrointest Oncol. 2015 Aug;6(4):375-88. doi: 10.3978/j.issn.2078-6891.2015.057.
102 Adsay NV, Klimstra DS. Cystic forms of typically solid pancreatic tumors. Semin Diagn Pathol. 2000; 17(1):81-8.
103 Klöppel G, Longnecker D, Capella C, Sobin L. Histological typing of tumours of the exocrine pancreas. Berlin: Springer-Verlag; 1996.
104 Kim JH, Eun HW, Park HJ, Hong SS, Kim YJ. Diagnostic

performance of MRI and EUS in the differentiation of benign from malignant pancreatic cyst and cyst communication with the main duct. Eur J Radiol. 2012 Nov;81(11):2927-35. doi:10.1016/j.ejrad.2011.12.019. Epub 2012 Jan 5.
105 Sainani NI, Saokar A, Deshpande V, Fernández-del Castillo C, Hahn P, Sahani DV. Comparative performance of MDCT and MRI with MR cholangiopancreatography in characterizing small pancreatic cysts. AJR Am J Roentgenol. 2009 Sep;193(3):722-31. doi:10.2214/AJR.08.1253.
106 Lee HJ, Kim MJ, Choi JY, Hong HS, Kim KA. Relative accuracy of CT and MRI in the differentiation of benign from malignant pancreatic cystic lesions. Clin Radiol. 2011 Apr;66(4):315-21. doi:10.1016/j.crad.2010.06.019. Epub 2011 Jan 8.
107 Visser BC, Yeh BM, Qayyum A, Way LW, McCulloch CE, Coakley FV. Characterization of cystic pancreatic masses: relative accuracy of CT and MRI. AJR Am J Roentgenol. 2007 Sep;189(3):648-56. doi:10.2214/AJR.07.2365.
108 Kim YC, Choi JY, Chung YE, Bang S, Kim MJ, Park MS, et al. Comparison of MRI and endoscopic ultrasound in the characterization of pancreatic cystic lesions. AJR Am J Roentgenol. 2010 Oct;195(4):947-52. doi:10.2214/AJR.09.3985.
109 Brun A, Agarwal N, Pitchumoni CS. Fluid collections in and around the pancreas in acute pancreatitis. J Clin Gastroenterol. 2011 Aug;45(7):614-25. doi:10.1097/MCG.0b013e318213ef3e.
110 Fernandez-del Castillo C, Targarona J, Thayer SP, Rattner DW, Brugge WR, Warshaw AL. Incidental pancreatic cysts: clinicopathologic characteristics and comparison with symptomatic patients. Arch Surg. 2003 Apr;138(4):427-3; discussion 433-424. doi:10.1001/archsurg.138.4.427.
111 Zhang XM, Mitchell DG, Dohke M, Holland GA, Parker L. Pancreatic cysts: depiction on single-shot fast spin-echo MR images. Radiology. 2002 May;223(2):547-53. doi:10.1148/radiol.2232010815
112 Lumsden A, Bradley EL, 3rd. Pseudocyst or cystic neoplasm? Differential diagnosis and initial management of cystic pancreatic lesions. Hepatogastroenterology. 1989 Dec;36(6):462-6.
113 Warshaw AL, Compton CC, Lewandrowski K, Cardenosa G, Mueller PR. Cystic tumors of the pancreas. New clinical, radiologic, and pathologic observations in 67 patients. Ann Surg. 1990 Oct; 212(4):432-43; discussion 444-5.
114 Le Borgne J, de Calan L, Partensky C. Cystadenomas and cystadenocarcinomas of the pancreas: a multiinstitutional retrospective study of 398 cases. French Surgical Association. Ann Surg. 1999 Aug; 230(2):152-61.
115 Brugge WR. Approaches to the drainage of pancreatic pseudocysts. Curr Opin Gastroenterol. 2004 Sep;20(5):488-92.
116 Barral M, Soyer P, Dohan A, Laurent V, Hoeffel C, Fishman EK, et al. Magnetic resonance imaging of cystic pancreatic lesions in adults: an update in current diagnostic features and management. Abdom Imaging. 2014 Feb;39(1):48-65. doi:10.1007/s00261-013-0048-y.
117 Macari M, Finn ME, Bennett GL, Cho KC, Newman E, Hajdu CH, et al. Differentiating pancreatic cystic neoplasms from pancreatic pseudocysts at MR imaging: value of perceived internal debris. Radiology. 2009 Apr;251(1):77-84. doi:10.1148/radiol.2511081286.
118 Arvanitakis M, Delhaye M, De Maertelaere V, Bali M, Winant C, Coppens E, et al. Computed tomography and magnetic resonance imaging in the assessment of acute pancreatitis. Gastroenterology. 2004 Mar;126(3):715-23.
119 Horvath KD, Chabot JA. An aggressive resectional approach to cystic neoplasms of the pancreas. Am J Surg. 1999 Oct;178(4):269-74.
120 Bassi C, Salvia R, Molinari E, Biasutti C, Falconi M, Pederzoli P. Management of 100 consecutive cases of pancreatic serous cystadenoma: wait for symptoms and see at imaging or vice versa? World J Surg 2003 Mar;27(3):319-23. Epub 2003 Feb 27.
121 Eriguchi N, Aoyagi S, Nakayama T, Hara M, Miyazaki T, Kutami R, et al. Serous cystadenocarcinoma of the pancreas with liver metastases. J Hepatobiliary Pancreat Surg 1998;5:467-70.
122 Jais B, Rebours V, Malleo G, Salvia R, Fontana M, Maggino L, et al. Serous cystic neoplasm of the pancreas: a multinational study of 2622 patients under the auspices of the International Association of Pancreatology and European Pancreatic Club (European Study Group on Cystic Tumors of the Pancreas). Gut. 2016 Feb;65(2)305-12. doi:10.1136/gutjnl-2015-309638. Epub 2015 Jun 4.
123 Tseng JF, Warshaw AL, Sahani DV, Lauwers GY, Rattner DW, Fernandez-del Castillo C. Serous cystadenoma of the pancreas: tumor growth rates and recommendations for treatment. Ann Surg. 2005 Sep;242(3):413-9; discussion 419-21.
124 Neumann HP, Dinkel E, Brambs H, Wimmer B, Friedburg H, Volk B, et al. Pancreatic lesions in the von Hippel-Lindau syndrome. Gastroenterology 1991 Aug;101(2):465-71.
125 Choi JY, Kim MJ, Lee JY, Lim JS, Chung JJ, Kim KW, et al. Typical and atypical manifestations of serous cystadenoma of the pancreas: imaging findings with pathologic correlation. AJR Am J Roentgenol. 2009 Jul;193(1):136-42. doi:10.2214/AJR.08.1309.
126 Procacci C, Graziani R, Bicego E, et al. Serous cystadenoma of the pancreas: report of 30 cases with emphasis on the imaging findings. J Comput Assist Tomogr. 1997; 21:373-382.
127 Procacci C, Biasiutti C, Carbognin G, Accordini S, Bicego E, Guarise A, et al. Characterization of cystic tumors of the pancreas: CT accuracy. J Comput Assist Tomogr. 1999 Nov-Dec;23(6):906-12.
128 Park HS, Kim SY, Hong SM, Park SH, Lee SS, Byun JH, et al. Hypervascular solid-appearing serous cystic neoplasms of the pancreas: Differential diagnosis with neuroendocrine tumours. Eur Radiol. 2016 May;26(5):1348-58. doi:10.1007/s00330-015-3961-3. Epub 2015 Sep 2.
129 Chu LC, Singhi AD, Haroun RR, Hruban RH, Fishman EK. The many faces of pancreatic serous cystadenoma: Radiologic and pathologic correlation. Diagn Interv Imaging. 2017 Mar;98(3):191-202. doi:10.1016/j.diii.2016.08.005. Epub 2016 Sep 7.
130 Zamboni G, Scarpa A, Bogina G, Iacono C, Bassi C, Talamini G, et al. Mucinous cystic tumors of the pancreas: clinicopathological features, prognosis, and relationship to other mucinous cystic tumors. Am J Surg Pathol. 1999 Apr;23(4):410-22.
131 Furukawa T, Takahashi T, Kobari M, Matsuno S. The mucus-hypersecreting tumor of the pancreas. Development and extension visualized by three-dimensional computerized mapping. Cancer. 1992 Sep 15;70(6):1505-13.

132 Goh BK, Tan YM, Chung YF, Chow PK, Cheow PC, Wong WK, et al. A review of mucinous cystic neoplasms of the pancreas defined by ovarian-type stroma: clinicopathological features of 344 patients. World J Surg. 2006 Dec;30(12):2236-45.

133 Bassi C, Molinari E, Falconi M, Pederzoli P. Clinical Manifestations and Therapeutic Management. In: Procacci C, Megibow AJ, editors. Imaging of the Pancreas. Cystic and Rare Tumors. Berlin: Springer; 2003. pp. 3-8.

134 Sperti C, Cappellazzo F, Pasquali C, Militello C, Catalini S, Bonadimani B, et al. Cystic neoplasms of the pancreas: problems in differential diagnosis. Am Surg. 1993 Nov;59(11):740-5.

135 Biasiutti C, Fornasa F, Venturini S, Pagnotta N, Schenal G, Procacci C. Mucinous Cystic Tumors. In: Procacci C, Megibow A, editors. Imaging of the Pancreas. Cystic and Rare Tumors. Berlin: Springer; 2003. pp. 57-74.

136 Buetow PC, Rao P, Thompson LD. From the Archives of the AFIP. Mucinous cystic neoplasms of the pancreas: radiologic-pathologic correlation. Radiographics. 1998 Mar-April;18(2):433-49. doi:10.1148/radiographics.18.2.9536488.

137 Koito K, Namieno T, Ichimura T, Yama N, Hareyama M, Morita K, et al. Mucin-producing pancreatic tumors: comparison of MR cholangiopancreatography with endoscopic retrograde cholangiopancreatography. Radiology. 1998 Jul;208(1):231-7. doi:10.1148/radiology.208.1.9646818.

138 Di Paola V, Manfredi R, Mehrabi S, Cardobi N, Demozzi E, Belluardo S, et al. Pancreatic mucinous cystoadenomas and cystoadenocarcinomas: differential diagnosis by means of MRI. Br J Radiol. 2016;89(1057):20150536. doi: 10.1259/bjr.20150536. Epub 2015 Nov 3.

139 Kim YH, Saini S, Sahani D, Hahn PF, Mueller PR, Auh YH. Imaging diagnosis of cystic pancreatic lesions: pseudocyst versus nonpseudocyst. Radiographics. 2005 May-Jun;25(3):671-85. doi:10.1148/rg.253045104.

140 Lewin M, Hoeffel C, Azizi L, Lacombe C, Monnier-Cholley L, Raynal M, et al. [Imaging of incidental cystic lesions of the pancreas]. [Article in French]. J Radiol. 2008 Feb;89(2):197-207.

141 Tanaka M, Fernandez-del Castillo C, Adsay V, Chari S, Falconi M, Jang JY, et al. International consensus guidelines 2012 for the management of IPMN and MCN of the pancreas. Pancreatology 2012 May-Jun;12(3):183-97. doi:10.1016/j.pan.2012.04.004. Epub 2012 Apr 16.

142 Ishida M, Egawa S, Aoki T, Sakata N, Mikami Y, Motoi F, et al. Characteristic clinicopathological features of the types of intraductal papillary-mucinous neoplasms of the pancreas. Pancreas. 2007 Nov;35(4):348-52. doi:10.1097/mpa.0b013e31806da090.

143 Berland LL, Silverman SG, Gore RM, Mayo-Smith WW, Megibow AJ, Yee J, et al. Managing incidental findings on abdominal CT: white paper of the ACR incidental findings committee. J Am Coll Radiol. 2010 Oct;7(10):754-73. doi:10.1016/j.jacr.2010.06.013.

144 Lim JH, Lee G, Oh YL. Radiologic spectrum of intraductal papillary mucinous tumor of the pancreas. Radiographics. 2001 Mar-Apr;21(2):323-37; discussion 337-40. doi:10.1148/radiographics.21.2.g01mr01323.

145 Procacci C, Graziani R, Bicego E, Bergamo-Andreis IA, Mainardi P, Zamboni G, et al. Intraductal mucin-producing tumors of the pancreas: imaging findings. Radiology. 1996 Jan;198(1):249-57. doi:10.1148/radiology.198.1.8539388

146 Procacci C, Megibow AJ, Carbognin G, Guarise A, Spoto E, Biasiutti C, et al. Intraductal papillary mucinous tumor of the pancreas: a pictorial essay. Radiographics. 1999 Nov-Dec;19(6):1447-63. doi:10.1148/radiographics.19.6.g99no011447.

147 Procacci C, Carbognin G, Biasiutti C, Guarise A, Ghirardi C, Schenal G. Intraductal papillary mucinous tumors of the pancreas: spectrum of CT and MR findings with pathologic correlation. Eur Radiol. 2001;11:1939-51. doi:10.1007/s003300100823.

148 Pilleul F, Rochette A, Partensky C, Scoazec JY, Bernard P, Valette PJ. Preoperative evaluation of intraductal papillary mucinous tumors performed by pancreatic magnetic resonance imaging and correlated with surgical and histopathologic findings. J Magn Reson Imaging. 2005 Mar;21(3):237-244. doi:10.1002/jmri.20254.

149 Campbell F, Azadeh B. Cystic neoplasms of the exocrine pancreas. Histopathology. 2008 Apr;52(5):539-51. doi:10.1111/j.1365-2559.2007.02856.x. Epub 2007 Sep 28.

150 Sahani DV, Kadavigere R, Blake M, Fernandez-Del Castillo C, Lauwers GY, Hahn PF. Intraductal papillary mucinous neoplasm of pancreas: multi-detector row CT with 2D curved reformations--correlation with MRCP. Radiology. 2006 Feb;238(2):560-9. doi:10.1148/radiol.2382041463.

151 Yamaguchi K, Kanemitsu S, Hatori T, Maguchi H, Shimizu Y, Tada M, et al. Pancreatic ductal adenocarcinoma derived from IPMN and pancreatic ductal adenocarcinoma concomitant with IPMN. Pancreas. 2011 May;40(4):571-80. doi: 10.1097/MPA.0b013e318215010c.

152 Yamada Y, Mori H, Hijiya N, Matsumoto S, Takaji R, Ohta M, et al. Intraductal papillary mucinous neoplasms of the pancreas complicated with intraductal hemorrhage, perforation, and fistula formation: CT and MR imaging findings with pathologic correlation. Abdom Imaging. 2012 Feb;37(1):100-9. doi: 10.1007/s00261-011-9723-z.

153 Cavallini G, Frulloni L, Pederzoli P, Talamini G, Bovo P, Bassi C, et al. Long-term follow-up of patients with chronic pancreatitis in Italy. Scand J Gastroenterol. 1998 Aug;33(8):880-9.

154 Klöppel G, Morohoshi T, John HD, Oehmichen W, Opitz K, Angelkort A, et al. Solid and cystic acinar cell tumour of the pancreas. A tumour in young women with favourable prognosis. Virchows Arch A Pathol Anat Histol. 1981;392(2):171-183.

155 Megibow AJ, Francis IR. Unusual Pancreatic Neoplasms: Imaging. In: Procacci C, Megibow AJ, editors. Imaging of the Pancreas. Cystic and Rare Tumors. Berlin: Springer; 2003. pp. 249-65.

156 Buetow PC, Buck JL, Pantongrag-Brown L, Beck KG, Ros PR, Adair CF. Solid and papillary epithelial neoplasm of the pancreas: imaging-pathologic correlation on 56 cases. Radiology. 1996; Jun;199(3):707-11. doi:10.1148/radiology.199.3.8637992.

GOKnee3D – Fully-automated One-button-push High-resolution MRI of the Knee

Jan Fritz, M.D., P.D., D.A.B.R.; Filippo Del Grande, M.D., MBA, MHEM; Neil Kumar, M.D.; Derek F Papp, M.D.; Rushyuan J Lee, M.D.

Johns Hopkins University School of Medicine, Baltimore, MD, USA

Magnetic resonance imaging (MRI) plays a key role in the workup of acute and chronic injuries, pain syndromes, and dysfunction of the knee. While radiographic and computed tomography evaluations provide excellent osseous detail, MRI is most accurate for the detection of bone marrow edema in the setting of radiographically occult bone contusion injuries and osseous stress reactions, non-displaced fractures, acute chondral shear injuries, and degenerative cartilage defects, tears of the collateral and cruciate ligaments, muscle-tendon injuries, and meniscal tears. Also, MRI can diagnose synovitis not only by the presence of a joint effusion, but also by visualizing synovial thickening, edema pattern, and frond-like hypertrophy.

Most MRI protocols of the knee for the assessment of internal derangement include pulse sequences that are tailored for the morphological assessment of anatomic structures, as well as pulse sequences that are tailored to maximize the conspicuity of findings with long T2 constants, such as fluid and edema.

For morphological assessment of the integrity of anatomical structures, intermediate-weighted MR images with echo times around 30 ms and no fat suppression are ideally suited due to their high signal yield, intermediate-to-high fluid signal, and high contrast-to-noise ratios of low signal intensity structures such as menisci, ligaments, and cartilage. The addition of a T1-weighted pulse sequence to the protocol can be beneficial for bone marrow assessment due to their exquisite specificity for fat signal, including osteomyelitis, marrow replacing diseases, and possibly fractures. However, T1-weighted pulse sequences have a lower sensitivity for detecting cartilage defects, ligamentous injuries, and meniscal tears due to absent fluid signal. Structural pulse sequences are often designed with a higher spatial resolution to maximize structural detail and the detection of small abnormalities, such cartilage fissures, and coapted tears.

For the assessment of signal abnormalities, pulse sequences with longer echo times and fat suppression

1

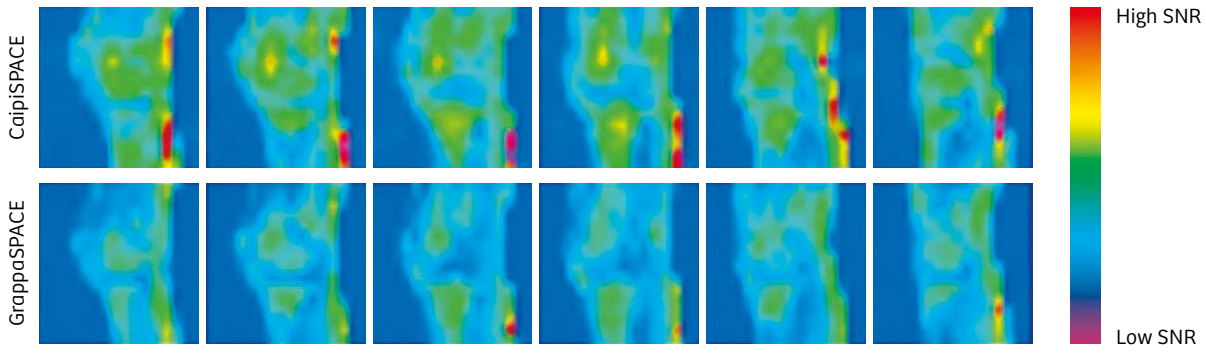

Figure 1:
3-Dimensional Signal-to-Noise Ratio maps illustrate the higher signal yield of CAIPIRINHA-accelerated 3D SPACE over GRAPPA-accelerated 3D SPACE.

510(k) pending. The product is not commercially available. Future availability cannot be guaranteed.

are typically used to increase the conspicuity of findings with long T2 constants, such as joint fluid, collections, and edema. The presence of an edema pattern in bone, ligaments, muscles, and fatty tissues often allows the differentiation of an acute injury or inflammation from chronic remodeling. Abnormally T2 hyperintense areas also have a higher suspicion to be a pain generator. Fast and turbo spin echo (TSE) pulse sequences with effective echo times of 60–70 ms and spectral fat suppression result in exquisite fluid sensitivity. The use of Spectral Attenuated Inversion Recovery (SPAIR) technique, instead of conventional spectral fat suppression can improve the homogeneity of fat suppression across the field-of-view [1]. Alternatively, STIR (Short Tau Inversion Recovery) technique may be used. Fluid sensitive sequences can be designed with less spatial resolution, as it does not interfere with their fluid-sensitivity but can improve efficiency and compensate for the lack of signal from suppressed fat-bound protons.

Two-dimensional (2D) TSE pulse sequences can be acquired with a high in-plane spatial resolution, e.g., with a pixel size of 0.5 x 0.5 mm^2 and less. However, to gain enough MR signal, a slice thickness of 2–4 mm is required, which lowers the effective spatial resolution and results in partial volume effects. The anisotropic voxel size prevents multiplanar reformations and requires the separate acquisition of images in axial, sagittal, and coronal orientation, which can be a time-consuming process and often requires total protocol acquisition times of 20 minutes.

Three dimensional (3D) TSE techniques such as Sampling Perfection with Application optimized Contrast using different flip angle Evolutions (SPACE) yield markedly more MR signal, due to volume-based excitation and use of multiple additional phase-encoding steps in a second direction. Together with the much higher signal yield, 3D data sets allow for the generation of much thinner slices partitions and facilitate 3D MRI with isotropic voxels size.



Figure 2:
Normal left knee of a 37-year-old healthy man. Sagittal isotropic 0.5 mm intermediate-weighted and 0.6 mm T2-SPAIR-weighted 3D CAIPIRINHA SPACE source MR images **(2A, B)** with standard axial **(2C, D)** and coronal **(2E, F)** reformats.

3

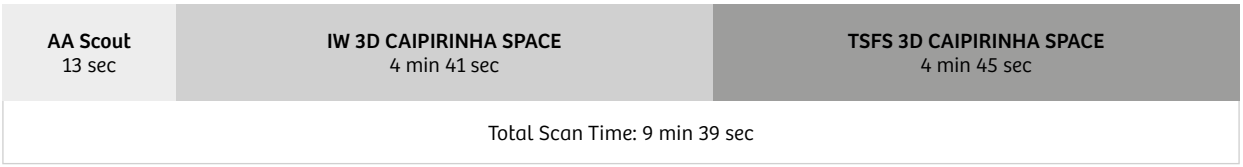

Figure 3:
GOKnee3D protocol for 3T MRI of the knee in under 10 minutes.

Such isotropic data sets with sufficiently small voxel size virtually eliminate partial volume effects and provide an opportunity for the improved display of small anatomic detail. Also, virtually any imaging plane can be reformatted from a single parent dataset (Fig. 1), including standard axial, sagittal, and coronal MR images, as well as oblique and curved planar reformations and 3D volume-rendered MR images.

The two phase-encoding directions of 3D SPACE provide an opportunity for bi-directional acceleration. A 2 x 2 parallel imaging using a Generalized Autocalibrating Partial Parallel Acquisition (GRAPPA) sampling pattern facilitates a 4-fold acceleration without the occurrence of acceleration and aliasing artifacts. As a further development, the use of a shifted Controlled Aliasing In Parallel Imaging Results IN Higher Acceleration (CAIPIRINHA) sampling pattern results in the optimized use of differential coil spatial sensitivities and improved geometry (g) factor performance [2, 3]. When compared to GRAPPA SPACE, CAIRPINIHA SPACE is characterized by increased image quality and 10–20% higher signal-to-noise ratios (Fig. 1). CAIPIRINHA-based 4-fold acceleration substantially reduces the time required for data acquisition and eliminates the need for compromises, including long echo trains, partial Fourier undersampling, and anisotropic data acquisition (Fig. 2) [4–6]. CAIPIRINHA SPACE with integrated anatomical landmark-based AutoAlign Knee technology, which provides automatic field-of-view and slice positioning, builds the foundation for GOKnee3D – a fully automated, one-button-push, high-resolution, 3D isotropic diagnostic knee exam with intermediate- and T2-SPAIR-weighted image contrasts and a total acquisition time of fewer than 10 minutes (Fig. 3).

The development of GOKnee3D adopted a similar strategic approach as earlier GO (Generalized Optimized) strategies [7–9]. The clinical validation study of GOKnee3D included head-to-head comparisons with conventional exams of 100 patients that were scanned at the MAGNETOM Skyra (3T) and 50 patients that were scanned at the MAGNETOM Aera (1.5T) [10]. All patients underwent the 10-minute GOKnee3D exam as well as a high-quality conventional 20-minute 2D exam that included six separately acquired pulse sequences of standard non-fat-suppressed and fat-suppressed clinical contrasts in three orientations. All images were independently evaluated by two board-certified, fellowship-trained musculoskeletal radiologists. The images were assessed for the presence or absence of joint effusion, joint bodies, popliteal cysts, lateral and medial meniscal tears, medial and lateral collateral ligament tears, anterior and posterior cruciate ligament tears, quadriceps and patella tendon tears, cartilage defects, bone marrow edema, and fractures. Additionally, the overall image quality and severity of motion artifact were also evaluated.

The study results indicate that the images generated by the 10-minute GOKnee3D protocol are at least diagnostically equivalent to the images of a 20-minute 2D TSE standard of reference protocol. There were no significant differences in the diagnosis of abnormal findings between GOKnee3D and the 2D TSE exams at both 1.5T and 3T. For both, 1.5T and 3T GOKnee3D protocols, the inter-reader agreement was consistently higher for the 3D images when compared to the 2D images.

An ongoing study evaluating the diagnostic accuracy of GOKnee3D for the detection of internal derangement in children[1] and adolescents, with arthroscopy as the standard of reference, indicates sensitivities of 83–100% and specificities of 93–100% for the diagnoses of discoid menisci, meniscus tears, ligament injuries, and osteochondritis dissecans lesions [11]. This study is currently being extended to adult patients.

The following clinical cases with surgical correlation illustrate the application of GOKnee3D for the evaluation of internal derangement in adults and children. All images were acquired on a 3T MAGNETOM Skyra MR imaging system (Siemens Healthcare, Erlangen, Germany) and Tx/Rx Knee 15 (QED, Mayfield Village, OH, USA) surface coil.

[1] MR scanning has not been established as safe for imaging fetuses and infants less than two years of age. The responsible physician must evaluate the benefits of the MR examination compared to those of other imaging procedures.

Case 1

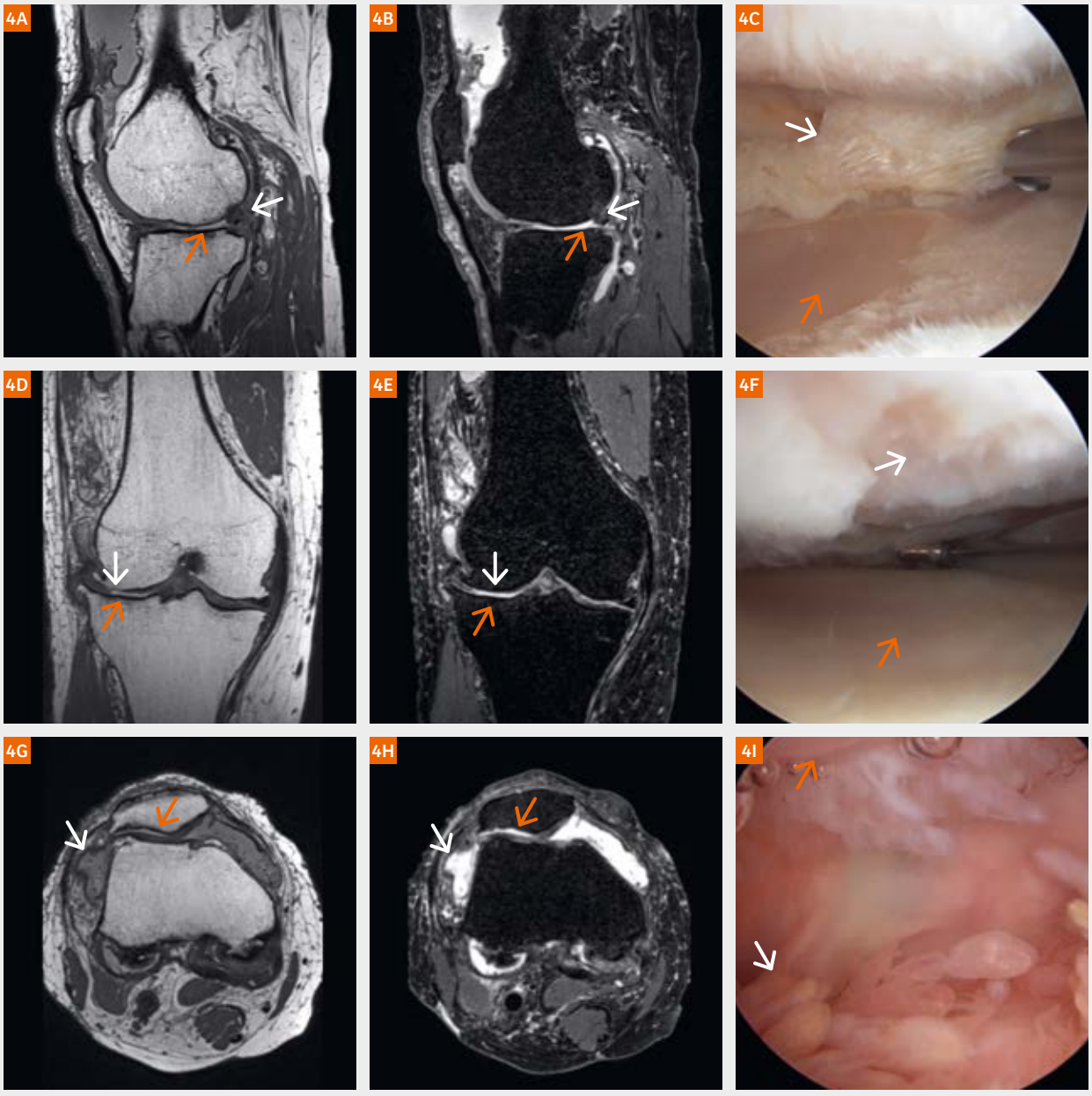

Indication: 60-year-old woman with intermittent pain and swelling of the right knee.

MRI findings: Sagittal, coronal, and axial intermediate-weighted and T2-SPAIR GOKnee3D images demonstrate a degenerative, complex tear of the posterior lateral meniscus (white arrows, **4A and 4B**). There is full-thickness cartilage loss over the lateral femoral condyle and lateral tibia plateau with focal bone-on-bone apposition (orange arrows, **4A and 4B**; white and orange arrows, **4D and 4E**). There is full-thickness cartilage loss of the lateral facet of the patella (orange arrow, **4G and 4H**) and synovitis with frond-like proliferations (white arrow, **4G and 4H**).

Arthroscopy findings: Degenerative, complex, tear of the posterior lateral meniscus (white arrow, **4C**). Full-thickness cartilage defects of the central femur (orange arrow, **4C and 4F**), tibia plateau (white arrow, **4F**), and lateral patella (orange arrow, **8I**) with synovitis (white arrow, **4I**).

Case 2

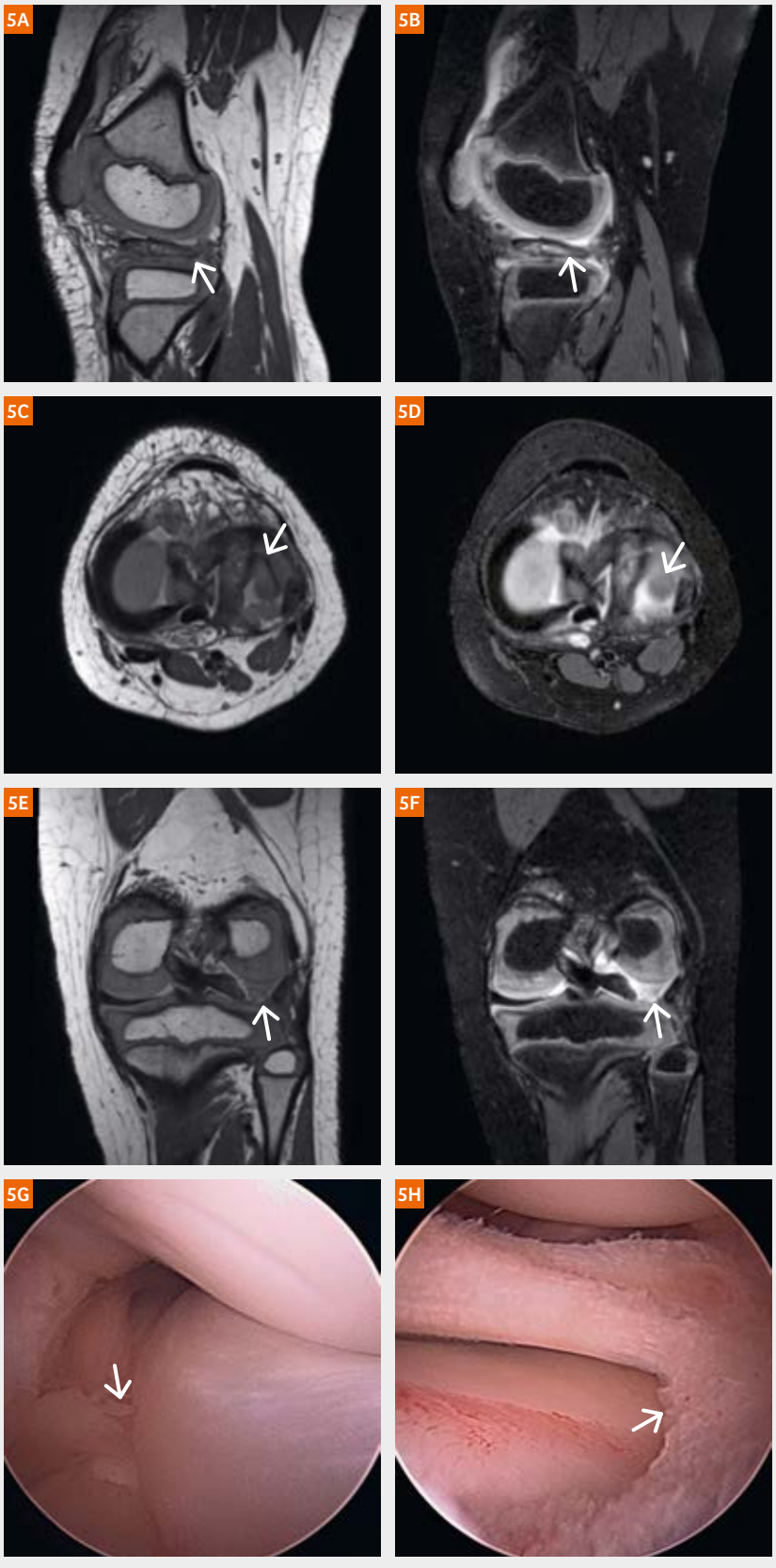

Indication: 4-year-old girl with mild knee pain and locking with motion.

MRI findings: Sagittal, coronal, and axial GOKnee3D images demonstrate a near complete discoid lateral meniscus with a complex tear (arrows). The medial meniscus, anterior and posterior cruciate ligaments, medial and lateral collateral ligaments, and articular cartilage are intact. There is a mild synovitis with small joint effusion.

Arthroscopy findings: Discoid lateral meniscus with a complex tear (arrow, **5G**), which was treated with resection of the tear and saucerization to create the crescent shape of a normal lateral meniscus **(5H).**

Case 3

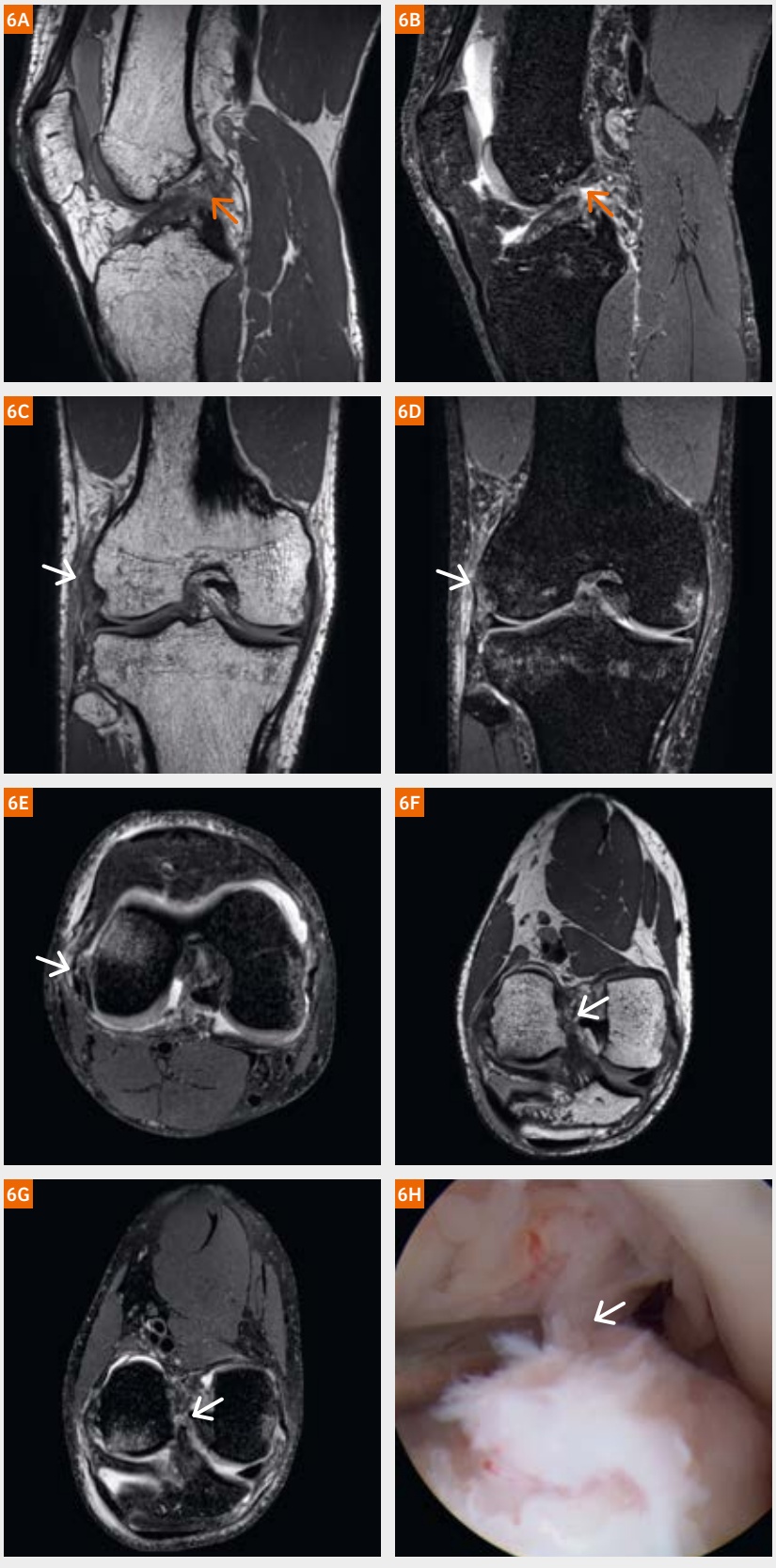

Indication: 30-year-old man with pain, swelling, and instability of the right knee following an American football injury.

MRI findings: Sagittal, coronal, axial and axial oblique GOKnee3D images demonstrate a full-thickness tear of the anterior cruciate ligament near the femoral attachment (arrow, **6A, B, F, G**). Additionally, there is a hemorrhagic joint effusion, a partial thickness tear of the lateral collateral origin (arrow, **6C–E**), and bone contusions of the femur and tibia.

Arthroscopy findings: Full-thickness tear of the anterior cruciate ligament near the femoral attachment (arrow, **6H**).

Case 4

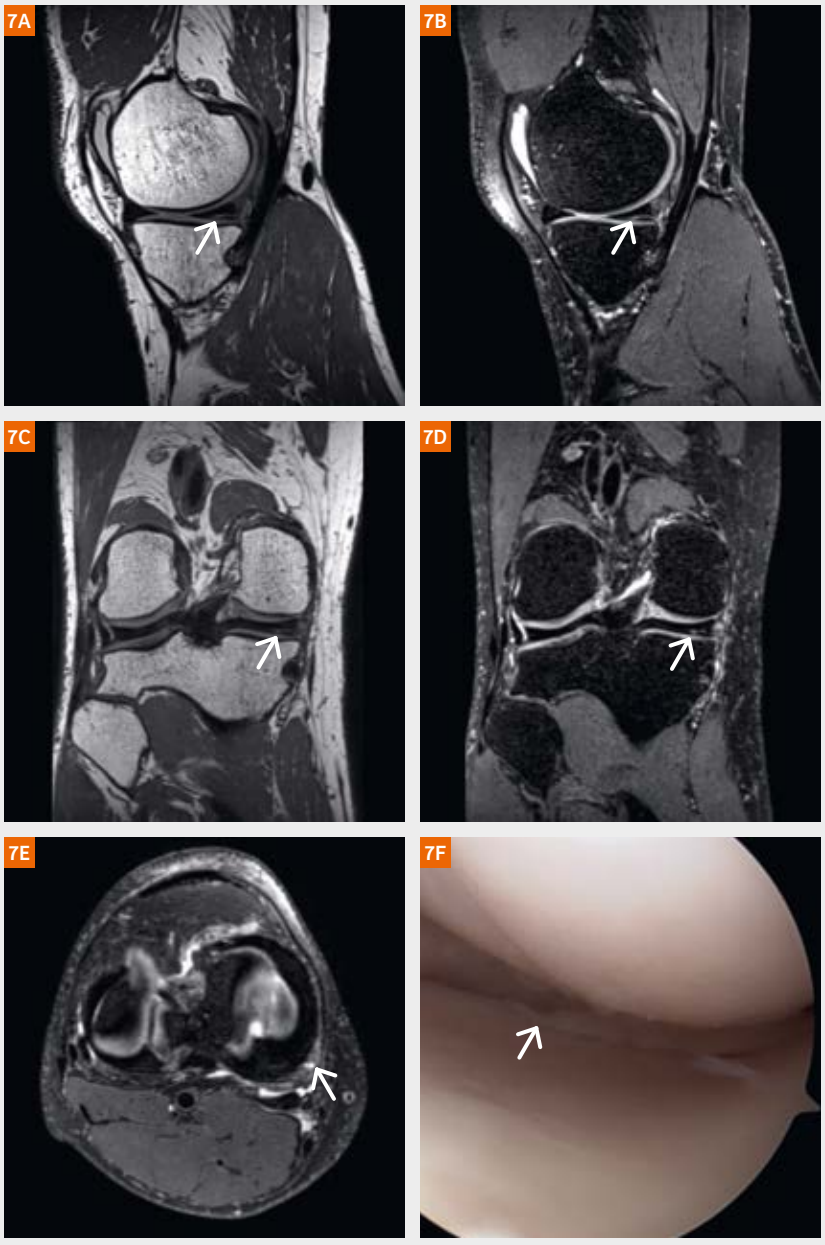

Indication: 52-year-old man with intermittent pain along the medial joint line of the knee.

MRI findings: Sagittal, coronal, and axial intermediate-weighted and T2-SPAIR GOKnee3D images demonstrate a complex, partial depth tear of the peripheral zone 1 of the posterior medial meniscus (arrows, **7A–D**). The meniscal tissue quality appears preserved. Additionally, there are small paramensical cysts at the location of the tear (arrow, **7E**).

Arthroscopy findings: Complex, partial depth tear of the peripheral zone 1 of the posterior medial meniscus (arrow, **7F**).

References

1 Horger W, Kiefer B. Fat suppression techniques – a short overview. MAGNETOM Flash 2011; 46: 56-59.
2 Breuer FA, Blaimer M, Mueller MF, Seiberlich N, Heidemann RM, Griswold M, Jakob PM. Controlled aliasing in volumetric parallel imaging (2D CAIPIRINHA). Mag Reson Med 2006; 55: 549-556.
3 Breuer F, Blaimer M, Griswold M, Jakob P. Controlled aliasing in Parallel Imaging Results IN Higher Acceleration (CAIPIRINHA). MAGNETOM Flash 2012; 49: 135-142.
4 Thawait GK, Lee RJ, Papp DF, Fritz J. High resolution isotropic 3D CAIPIRINHA SPACE MRI of the musculoskeletal system. MAGNETOM Flash 2016; 66: 30-38.
5 Fritz J, Fritz B, Thawait GG, Meyer H, Gilson WD, Raithel E. Three-Dimensional CAIPIRINHA SPACE TSE for 5-Minute High-Resolution MRI of the Knee. Invest Radiol. 2016 Oct;51(10):609-17.
6 Kalia V, Fritz B, Johnson R, Gilson WD, Raithel E, Fritz J. CAIPIRINHA accelerated SPACE enables 10-min isotropic 3D TSE MRI of the ankle for optimized visualization of curved and oblique ligaments and tendons. Eur Radiol. 2017 Sep;27(9):3652-3661.

Case 5



Indication: 14-year-old boy with anterior knee pain.

MRI findings: Sagittal, coronal, and axial oblique GOKnee3D images demonstrate patella alta alignment, hypoplasia of the trochlea, lateral patellar shift, and a full-thickness cartilage defect (arrows, **8A–D**) of the central patella with subcortical cyst formation and a small area of bone marrow edema pattern. There is a small joint effusion. The lateral and medial meniscus (arrows, **8E**) are intact.

Arthroscopy findings: Patellar chondromalacia with full-thickness cartilage defect (arrow, **8F**).

7 Rapalino O, Heberlein K. New strategies for protocol optimization for clinical MRI: Rapid examinations and improved patient care. MAGNETOM Flash 2016; 65: 22-25.

8 Prakkamakul S, Witzel T, Huang S, Boulter D, Borja MJ, Schaefer P, Rosen B, Heberlein K, Ratai E, Gonzalez G, Rapalino O. Ultrafast brain MRI: Clinical deployment and comparison to conventional brain MRI at 3T. J Neuroimaging 2016; 26(5): 503-510.

9 Fagundes J, Longo MG, Huang SY, Rosen BR, Witzel T, Heberlein K, Gonzalez RG, Schaefer P, Rapalino O. Diagnostic performance of a 10-minute gadolinium-enhanced brain MRI protocol compared with the standard clinical protocol for detection of intracranial enhancing lesions. Am J Neuradiol 2017; 38(9): 1689-1694.

10 Del Grande F and Fritz J. GOKnee3D Study. Unpublished data.

11 Fritz J, Ahlawat S, Thawait GK, Raithel E, Gilson W, Lee RJ. 3D MRI of Knee in Pediatric Patients with CAIPIRINHA SPACE: Diagnostic Performance Assessment with Arthroscopic Correlation. 25th ISMRM Annual Scientific Meeting & Exhibition; 2017; Hawaii, USA.

Case 6

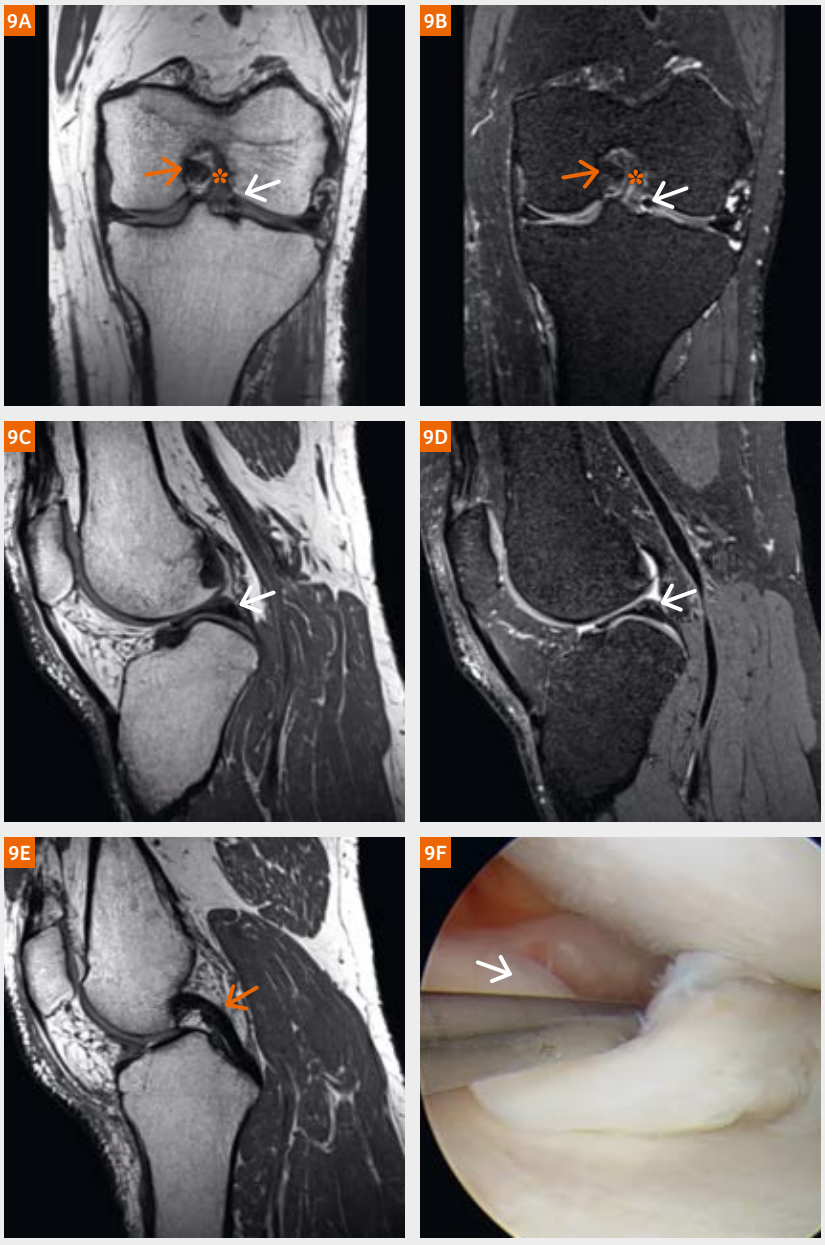

Indication: 51-year-old man with intermittent pain and locking of the left knee.

MRI findings: Sagittal and coronal intermediate-weighted and T2-SPAIR GOKnee3D images demonstrate a bucket handle tear of the lateral meniscus (white arrow, **9A–D**). The anterior cruciate ligament (asterisk, **9A–D**) and the posterior cruciate ligament (orange arrow, **9A** and **9B**) are intact.

Arthroscopy findings: Bucket handle tear of the lateral meniscus (arrow, **9F**).



Contact

Jan Fritz, M.D., P.D., D.A.B.R.
Director of Interventional MR Imaging
Associate Director MSK Fellowship
Assistant Professor of Radiology and Radiological Sciences
Johns Hopkins University School of Medicine
Russell H. Morgan Department of Radiology
and Radiological Science
Musculoskeletal Radiology

601 N. Caroline Street, JHOC 3140A
Baltimore, MD 21287
USA
jfritz9@jhmi.edu

A Within-subject Comparison of Common Neuroimaging Protocols on MAGNETOM Prisma^{fit} and MAGNETOM Trio Scanners

Ross W. Mair[1, 2]; Stephanie McMains[1]

[1] Center for Brain Science, Harvard University, Cambridge, MA, USA
[2] Athinoula A. Martinos Center for Biomedical Imaging, Massachusetts General Hospital, Charlestown, MA, USA

Introduction

The Center for Brain Science – Neuroimaging Facility (CBS) at Harvard University is a key imaging resource for a wide array of university psychology department and medical school faculty in the Boston area. Started with the installation of a MAGNETOM Trio (Siemens Healthcare, Erlangen, Germany) in 2008, the center achieves a funded average usage by researchers of ~2000 hours per year with an approximately 1000 additional hours per year of use for maintenance, development, and educational purposes. As such, the scanner is used consistently and at near-capacity by an active and diverse group of scientists from Harvard and from other institutions, including Harvard teaching hospitals, in the Boston community.

The vast majority of this MRI data is task-based or resting-state functional MRI employing T2*-weighted echo-planar imaging, or blood-oxygen level dependent (BOLD) techniques. Sessions also include a T1-weighted high-resolution structural or anatomical scan for co-registration to the BOLD images, and sometimes for brain morphometry. Many researchers also supplement their sessions with a short diffusion-weighted MRI scan. While most user-groups are eager to embrace new imaging technology and techniques when there is an appropriate benefit to the quality of their neuroimaging data, a key factor to ensuring quality data over studies that may run over periods stretching from 2 months to 2 years

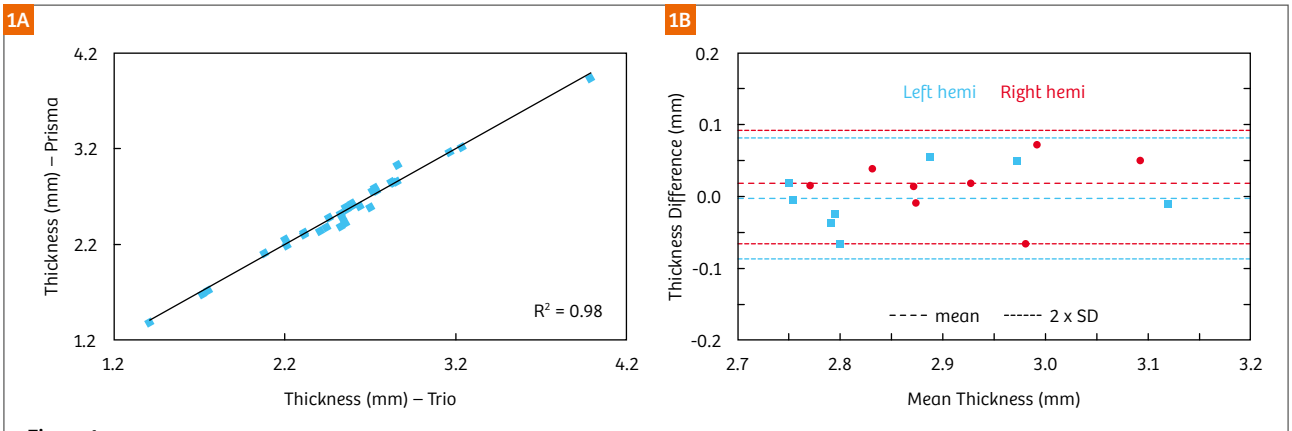

Figure 1:
(1A) Example correlation of cortical thickness of all 33 cortical regions of the Desikan-Killiany atlas from a single subject from T1-weighted images acquired on the MAGNETOM Trio and the MAGNETOM Prisma^{fit}. **(1B)** Example Bland-Altman difference plot of cortical thickness in the temporal lobes for 8 subjects from T1-weighted images acquired on the MAGNETOM Trio and the MAGNETOM Prisma^{fit}.

is stability and consistency of scanner performance, and continuity in image acquisition protocols and the resultant MRI data itself. At CBS, we have placed a very high priority on maintaining a stable and consistent scanning environment. As a result, when major imaging advances and hardware or software upgrades arrive, there are equal parts anticipation and trepidation for many of our user groups.

We upgraded the MAGNETOM Trio to the MAGNETOM Prisma^{fit} in the summer of 2015. The Prisma^{fit} represented a significant upgrade in performance capability over the Trio. The MAGNETOM Prisma platform included a major advance in gradient strength (80 mT/m, up from 45 mT/m), new highly-parallel array receive coils for the head, a digital RF transmit/receive architecture, and a much faster reconstruction computer. While the new gradient coil was expected to offer significant improvements in diffusion experiments, any change to the gradient system has the potential to bias brain morphometry data if there were changes in gradient linearity and performance. We believed the digital RF chain had the potential to significantly improve BOLD imaging with improved RF fidelity and a reduction in spurious noise pick-up, however it was unclear whether such benefits would hold up in the human head with its attendant physiological noise effects. In addition, as Simultaneous Multi-Slice imaging techniques were beginning to be adopted, the improved reconstruction system was seen as a key component that would allow routine use of this technique for high-temporal resolution BOLD imaging with real-time image reconstruction, rather than suffering often intolerable reconstruction lags, as was the case on the Trio.

To quantify the impacts and improvements offered by such a significant system upgrade, we scanned 8 subjects using a variety of anatomical, functional and diffusion protocols commonly employed at the time on the Trio platform, and then repeated the same scans with the same protocols on the Prisma^{fit} after the upgrade process. In addition, we devoted effort to assessing where the new hardware would permit improvements to temporal and spatial resolution in conventional BOLD imaging, both immediately after the hardware upgrade, and again following the software upgrade from *syngo* MR D13D to E11C in late 2016.

Methods

8 subjects were scanned on the 3T MAGNETOM Trio in July 2015. The same 8 subjects were scanned a second time on the MAGNETOM Prisma^{fit} in October 2015, after the scanner conversion. The relevant 32-channel head coil was used on each system. The scans included a 1.0 mm resolution multi-echo MPRAGE [1] anatomical scan acquired with FreeSurfer-recommended parameters (6:03 min, TR/TI = 2530/1100 ms, matrix 256 x 256 x 176, resolution = 1 x 1 x 1 mm (no partial fourier), parallel imaging acceleration (GRAPPA) = 2, pre-scan normalize enabled). Two resting state BOLD scans of 8-min duration were acquired, one with 3 mm resolution and TR = 3 s, the other with 2 mm nominal resolution, slice-acceleration [2, 3] (SMS) of 8 and TR = 750 ms. Additionally, a third BOLD scan employing a protocol commonly used for task studies at the time was acquired: 2 mm nominal resolution, SMS 3 and TR = 2 s. Two diffusion MRI protocols were employed, both with nominal 2 mm resolution: no SMS, 30 *b* directions, b = 1000 mm^2/s; and SMS 2, 64 *b* directions, b = 1000 mm^2/s. On the Prisma^{fit}, the diffusion protocols were reproduced exactly as implemented on the Trio, and then repeated utilizing the monopolar diffusion encoding scheme available in *syngo* MR D13 and E11, the performance gradient mode allowed by the Prisma^{fit} gradient set, and then optimizing the echo spacing and minimizing TE and TR. No changes were made to spatial resolution, number of *b* directions or *b* values, although it is widely expected such advances will become commonly employed on Prisma^{fit} system and similar scanners.

Anatomical images were analyzed using a FreeSurfer [4] processing stream. They were first corrected for gradient non-linearities according to the different scanner gradient coil parameters, after which the pairs of scans from each subject were aligned using the FreeSurfer robust registration tool [5]. FreeSurfer v.5.3 was used to perform an automated parcellation of the cortex, subcortical and white matter structures. The 33 cortical regions of the Desikan-Killiany atlas [6] were combined into five principal cortical lobes for simpler analysis [7]. Correlation and Bland-Altman difference plots were made for the thickness and volume of each principal cortical lobe determined from each scan, and for the volume of key sub-cortical structures. Surface-based plots were made to show regions of thickness difference and significance of difference. Diffusion scans were analyzed from raw DWI images and ADC and FA maps generated by the scanner software at the scanner console. In addition, diffusion scans were post-processed with a detailed stream that included gradient non-linearity correction, motion correction/realignment, eddy-current distortion correction, and registration to the anatomical space of the T1-weighted image. This alignment enabled the ADC and FA to be probed in the parcellated corpus callosum only, while the whole brain and white-matter-only masked images were analyzed for stability. BOLD scans were analyzed by assessing tSNR for each voxel, and averaged over the whole brain, after motion correction and detrending. Functional-connectivity

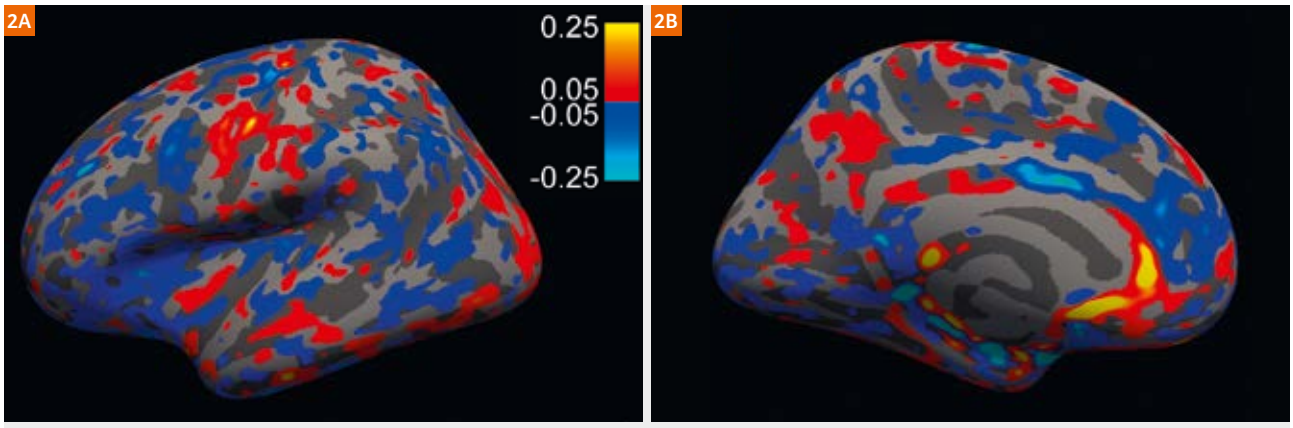

Figure 2:
Surface plots of average cortical thickness difference for pairs of T1-weighted images acquired on the MAGNETOM Trio and the MAGNETOM Prisma^{fit}. Thickness differences are threshold at ± 50–250 µm, color bars are in mm. The left hemisphere is shown – results are similar for the right hemisphere.

analysis was performed on the two resting-state BOLD scans with a seed-based correlation procedure using correlations between major network seeds [8].

Results/discussion – anatomical scans

The anatomical scans from each subject, acquired on the MAGNETOM Trio and on the MAGNETOM Prisma^{fit} appeared visually very similar. The offline gradient non-linearity correction modified the appearance of the neck/spine region on scans acquired on the Trio, but the brain and skull appeared unaffected. On the Prisma^{fit}, in addition to modification of neck/spine region, a slight extension to the crown of the skull and the parietal cortex just below it could be observed for some subjects following gradient non-linearity correction. Therefore, for comparison of brain morphometric data, gradient non-linearity correction was performed on the anatomical scans from each scanner, prior to robust registration of the pairs of scans to an unbiased base-space, after which the standard FreeSurfer processing stream was performed.

Figure 1A shows an example correlation plot for the thickness of all 33 cortical regions of the Desikan-Killiany atlas, from a single subject, as determined from images acquired on the Trio and on the Prisma^{fit}. Similar correlation plots were obtained for gray matter volume for the 33 cortical regions, and for the volumes of sub-cortical/white matter structures. Correlation Coefficients (R^2) were routinely ~0.95–1.00 for all subjects, and were especially high for the sub-cortical/white matter structure volumes. However, while intuitively simple, correlation plots can hide systematic biases, and so a Bland-Altman difference analysis was also performed. Figure 1B shows an example Bland-Altman difference plot, plotting the difference of the measured average cortical thickness of the temporal lobes for all eight subjects, when scanned on the Trio and on the Prisma^{fit}. The average thickness value was obtained from aggregating the relevant cortical regions from the Desikan-Killiany atlas for each subject [7]. The mean difference for both the left and right hemispheres was close to zero, with a standard-deviation inside ± 0.1 mm. Similar plots were obtained for the other principal cortical lobes, with differences always considerably less than ± 50 µm. Such differences are on the order of those seen for test-re-test scans on the same scanner on the same day [9]. For the sub-cortical/white matter structures, a wider range of differences were observed – up to ± 5%, but again were respectable compared to prior studies of variation between head coils or repeated measures on different days [10].

Figure 2 shows inflated-surface plots of cortical thickness difference for groups of scans on the Trio and on the Prisma^{fit}. Cortical thickness difference was determined using all 33 cortical regions of the Desikan-Killiany atlas for each scan, with each subject registered to FreeSurfer average-space, so differences can be analyzed on a single surface. Thickness differences are thresholded at ± 50 µm – the vast majority of difference observed is either below 50 µm (masked out), or between 50 and 100 µm. Only the inner surface of the temporal lobe and a spot in the central gyrus shows values higher. However, a t-test determined that none of the thickness differences are statistically relevant ($p > 0.01$).

In combination, the results from Figures 1 and 2 indicate that, with careful control for gradient non-linearity and

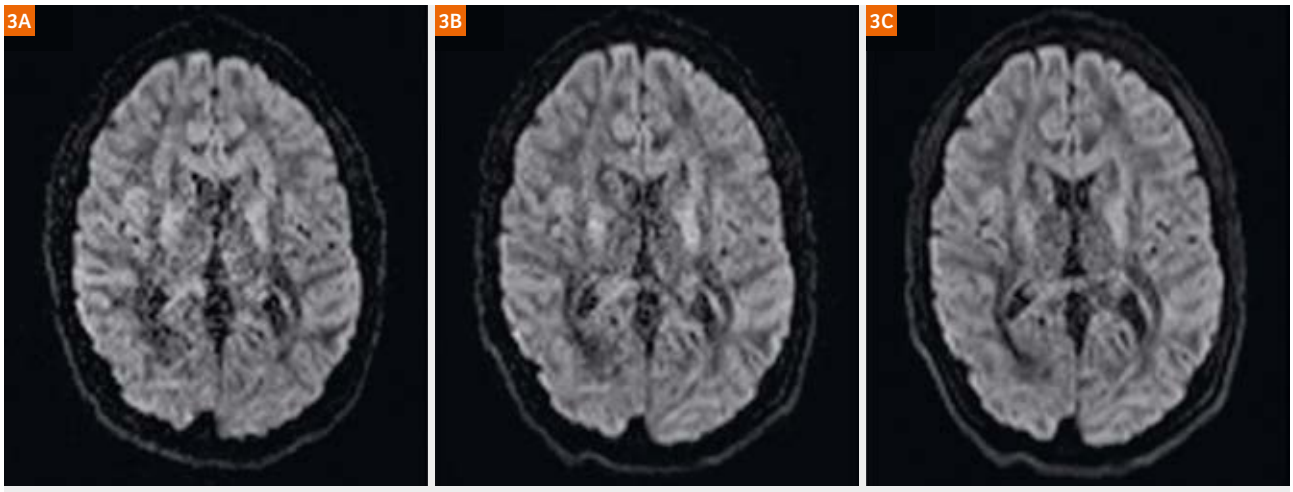

MAGNETOM Trio

MAGNETOM Trio protocol on MAGNETOM Prisma^{fit}

MAGNETOM Prisma^{fit} optimized

Figure 3:
Representative DWI images, as displayed at the scanner console, from the same subject acquired on the MAGNETOM Trio and the MAGNETOM Prisma^{fit}. A 2 mm isotropic, SMS = 2, 64-direction, *b* = 1000 s/mm^2 DTI protocol was used. **(3A)** Image from the Trio. **(3B)** Image from the Prisma^{fit} when the Trio protocol was implemented. **(3C)** Image from the Prisma^{fit} after optimizing echo-spacing, bandwidth, and TE as permitted by the Prisma^{fit} hardware.

robust registration, brain morphometric data should not be biased by scanner whether a Trio or Prisma^{fit} is used, or when the former is upgraded to the latter.

Results/discussion – diffusion scans

For the diffusion scans, the protocols used on the Trio were implemented exactly on the Prisma^{fit} without modification, to check for between-scanner variation, being cognizant of reducing bias for ongoing studies that straddled the upgrade period. Using "fast" gradient mode on the Sequence/Part 2 tab restricts the Prisma^{fit} gradient to the maximum strength and slew-rates employed on the Trio. These scans are referred to as "Trio protocol on Prisma", which we hoped would show insignificant variation from the scan on the Trio. The scans were then repeated employing the hardware and software advances of the Prisma^{fit}, principally the use of the monopolar diffusion encoding scheme which significantly reduces TE; the performance gradient mode allowed by the Prisma^{fit} gradient set allowing stronger gradient strengths with shorter gradient durations; and then optimizing the echo spacing and minimizing TE and TR as a result of the above changes. These scans are referred to as "Prisma optimized", although no changes were made to the spatial resolution, number of *b* directions or *b* values, as is likely for diffusion protocols truly optimized for the Prisma^{fit}.

Figure 3 shows a single slice from a diffusion-weighted image on the Trio, and the two corresponding scans on the Prisma^{fit}, all acquired with the 64-direction / SMS = 2 protocol. The reduction in TE, from 90 to 57 ms in the "Prisma optimized" protocol, results in a noticeable improvement in SNR in the DWI. The same impact is seen in the color-coded FA maps as generated by the scanner software without offline processing, which are shown in Figure 4. Again, the "Prisma optimized" protocol results in a noticeable improvement in SNR in the FA map. For the three marked ROI's shown in the images, which were chosen to comprise regions of highly uniform fiber orientation and density, an average reduction in the standard-deviation of FA in the three ROIs in the "Prisma optimized" image was found to be ~25%. For the same three ROI's, the average ADC standard-deviation fell by ~40% with the "Prisma optimized" protocol, but were otherwise similar for the Trio and the "Trio protocol on Prisma" scan.

To more carefully quantify the effect of the SNR increase and improved signal stability with the "Prisma optimized" protocol, the diffusion scans were also processed offline using a conventional processing stream including alignment to the T1-weighted image native space before recalculation of the ADC and FA images. The resultant ADC and FA images were then masked by the corpus callosum as derived from the FreeSurfer-processed T1-weighted image for each subject. Figure 5 shows the average of the standard-deviation of ADC and FA within the corpus callosum for the 8 subjects, using the two

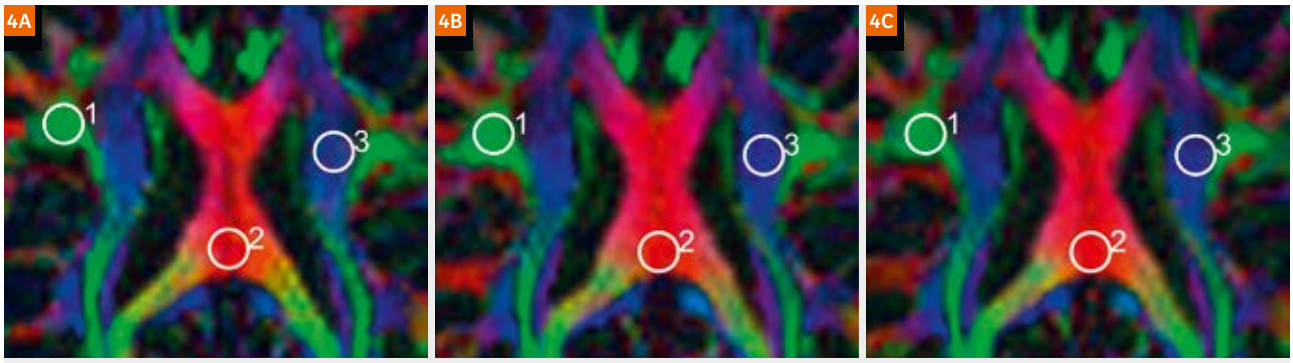

MAGNETOM Trio

MAGNETOM Trio protocol on MAGNETOM Prisma^{fit}

MAGNETOM Prisma^{fit} optimized

Figure 4:
A portion of the scanner-generated Color-FA maps from the same subject acquired on the MAGNETOM Trio and the MAGNETOM Prisma^{fit}. The same protocol from Figure 3 was used. **(4A)** FA image from the Trio. **(4B)** FA image from the Prisma^{fit} using the Trio protocol without modification. **(4C)** FA image from the Prisma^{fit} after optimizing as permitted by the Prisma^{fit} hardware. In the three ROIs shown, the ADC std-dev is ~40% lower and the FA std-dev is ~25% lower when the Prisma^{fit}-optimized protocol was used with this subject.

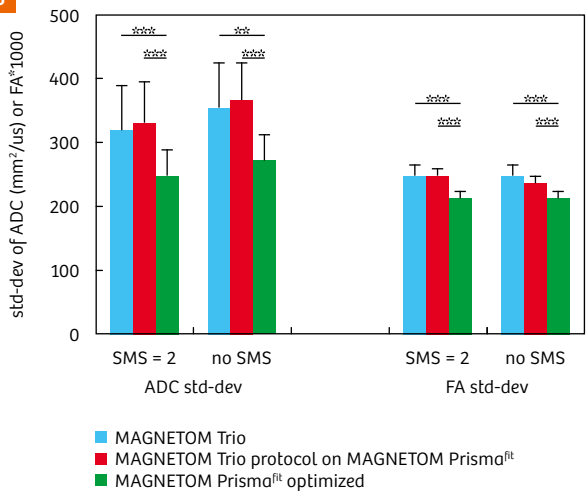

Figure 5:
Standard-deviation of the values of ADC and FA in the segmented corpus callosum, after detailed offline processing, for the three different scan procedures described in Figures 3 and 4 on the MAGNETOM Trio and MAGNETOM Prisma^{fit}, averaged over 8 subjects. Here, data from the SMS = 2 / 64-direction and the no SMS / 30-direction DTI protocols are shown.

acquisition protocols (SMS 2 / 64 directions, and no SMS / 30 directions) on the Trio, and for the "Trio protocol on Prisma" and "Prisma optimized" scans on the Prisma^{fit}. Noticeable reductions are seen in both the ADC and FA standard-deviations for the "Prisma optimized" scans for both protocols (all $p < 0.001$, except, "Trio protocol on Prisma" versus "Prisma optimized", $p < 0.01$); while the "Trio protocol on Prisma" and the original scan on the Trio essentially give indistinguishable results ($p > 0.05$).

Signal stability was also assessed from the repeated $b = 0$ images in each diffusion scan, in the same way it would be done for BOLD scans – dividing the mean image (after realignment) by the standard-deviation, to give a "time-series SNR" or tSNR image. This was done with 5 $b = 0$ images from each scan for the no SMS / 30 direction protocol, and 10 $b = 0$ images for the SMS 2 / 64 direction protocol. In each case, the metric was calculated on the whole brain after brain extraction, and on an image masked to show only the segmented white matter from the FreeSurfer-processed T1-weighted image for each subject. As shown in Figure 6, the "Prisma optimized" scans for both protocols exhibited improvements in tSNR of ~30–40% compared to the "Trio protocol on Prisma" and the original scan on the Trio (all $p < 0.001$), while the "Trio protocol on Prisma" and the original scan on the Trio were similar ($p > 0.05$).

These results show that the new, high-performance gradient coil that is the heart of the Prisma indeed delivers the expected boost of SNR to MRI diffusion scans, when the acquisition protocols are optimized to take full use of the new gradient strength and slew rate. The reduction in TE of ~30–40% for a commonly employed acquisition protocol can yield similar increases in diffusion-scan signal stability, and reduce the uncertainties in derived diffusion metrics by similar amounts. Of course, these new gradient capabilities are also being used to bring more advanced diffusion acquisition protocols into the mainstream, employing higher, and multiple, b values, and more diffusion directions; to improve fiber-tracking definition in areas where fibers cross. The multi-site Human Connectome Projects on Aging and Development, and the Adolescent Brain Cognitive Development (ABCD)

6

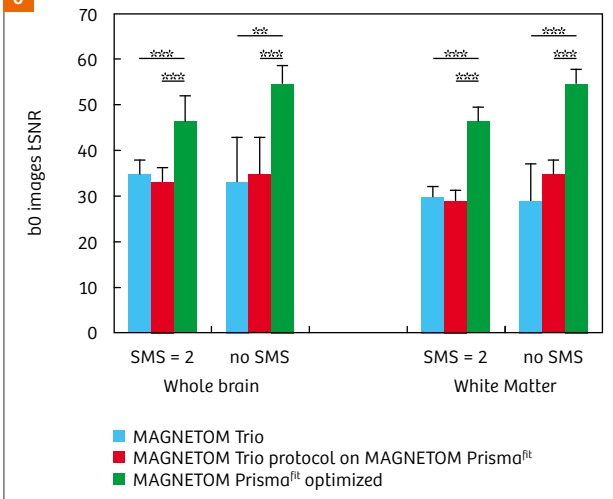

Figure 6:
DTI signal stability from repeated *b* = 0 images (labeled "tSNR"), averaged over 8 subjects, in the whole brain and in masked white matter, for the three different scan procedures described in Figures 3 and 4 on the MAGNETOM Trio and MAGNETOM Prisma^fit. The SMS = 2 / 64-direction protocol acquired 10 *b* = 0 images, and the no SMS / 30-direction protocol acquired 5 *b* = 0 images.

7

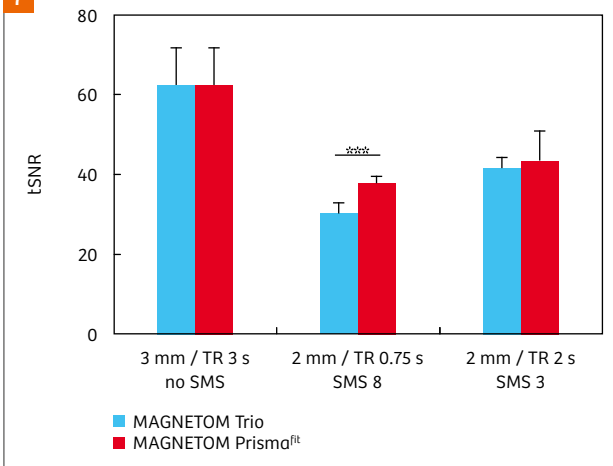

Figure 7:
Average whole-brain tSNR values measured in BOLD scans acquired on the MAGNETOM Trio and the MAGNETOM Prisma^fit.

study, both in the US, are both employing *b* values up to 3000 s/mm² with 100–200 *b*-vectors for routine use in studies that will scan thousands of subjects. Alternatively, for those wishing to replicate the diffusion protocol and data quality for studies ongoing from Trio scanners, the identical implementation of a protocol, with the gradient mode restricted to "Fast" mode, should give equivalent data on the Prisma.

Results/discussion – functional scans

Although Siemens Healthcare had not promised improvement to the quality and stability of EPI-BOLD scanning, we had initial hopes that some of the other hardware improvements, such as the all-optical transmit/receive chain between the magnet and the equipment room, the new sold-state RF amplifier system on the side of the magnet, and the fact that BOLD imaging would use a lower % of the maximum gradient strength (same gradient strength as used on the Trio, to avoid severe peripheral nerve and possibly cardiac stimulation) might serve to reduce instrumental noise and so increase the time-series SNR (tSNR) that determines the ability to detect BOLD activations.

Initial tests with the standard water phantom bore this expectation out. Using the 32-channel head coil, and the 3 mm / 500-timepoint EPI-stability protocol we run daily for scanner quality assurance, we observed a ~25% increase in tSNR when the protocol was first implemented on the Prisma^fit. However, the BOLD scans conducted on the 8 human subjects suggest that physiological noise in humans, at this frequency and field strength, is a great equalizer [11]. Figure 7 summarizes the tSNR results. The 3 mm / TR = 3 sec / no SMS resting state BOLD scans showed no change in average tSNR across the whole brain for the 8 subjects ($p > 0.05$). At higher spatial resolution, there were small gains in tSNR observed with the Prisma^fit. The TR = 2 s / SMS 3 protocol showed a ~5% gain in tSNR – although not statistically significant given the number of subjects ($p > 0.05$). The high temporal resolution resting-state BOLD scans (TR = 750 ms / SMS = 8) showed a modest gain of ~20% when averaged across all subjects ($p < 0.001$). However, benefits for resting-state network analysis were minimal, with improved definition of the networks seen in some subjects, but no quantifiable improvement observed in other subjects, or when averaged over all eight subjects. It is possible that certain tasks that yield weak activations may provide better results on the Prisma^fit under conditions of high spatial and/or temporal resolution. But for routine BOLD scans as commonly carried out in neuroimaging studies, with a spatial resolution of ~2.5–3 mm and TR of 2–3 sec, the Prisma will provide similar quality BOLD data to the Trio.

However, the new hardware of the Prisma^fit led us to re-evaluate what should be baseline acquisition protocols for BOLD scanning for routine use, with respect to either spatial or temporal resolution. The full details of this BOLD optimization is beyond the scope of this article. However, one example warrants brief mention, for it relies on a combination of improvements in the gradient coil and the improved speed of the new reconstruction

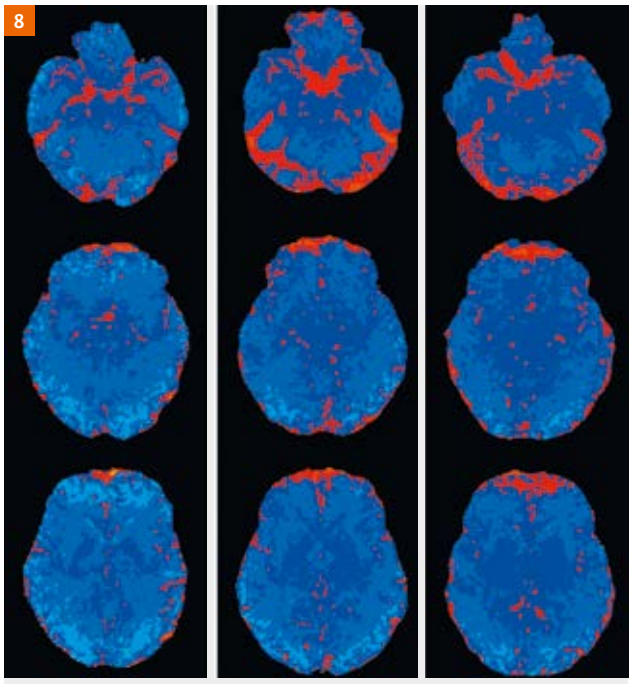

Figure 8:
Maps of tSNR difference in resting-state BOLD scans from three axial slices in three subjects, acquired on the MAGNETOM Prisma^{fit}. Red / orange indicates regions where tSNR is higher using a 1.7 mm resolution / GRAPPA = 2 / SMS = 3 protocol. Blue indicates regions where tSNR is higher with a 2.2 mm / no GRAPPA / SMS = 3 protocol.

computer, combined with simultaneous multi-slice techniques, which allowed us to push the envelope of spatial resolution for whole-brain BOLD scanning beyond what was routinely possible on the Trio, and achieve 1.5 mm and 1.7 mm isotropic resolution that our psychology faculty are now using successfully in standard neuroimaging studies. While not technically impossible on the Trio, the improved slew rate of the Prisma gradient coil and the higher "forbidden echo spacing" range due to acoustic resonances (0.78–0.93 ms vs ~0.58–0.69 ms on the Trio), enable the very large matrix size required for this spatial resolution with only two-fold GRAPPA acceleration to keep the TE to around 30 ms. Along with the improved echo-spacing that makes each echo train slightly shorter, the use of SMS allows the ~80–90 slices required for full brain coverage to be acquired in a 2-second TR, while the improved reconstruction system enables the data to be reconstructed without lagging behind the acquisition, despite the large matrix size and number of slices. Acquiring such data would certainly tax the older reconstruction hardware of the Trio.

The main benefits of using such a high spatial-resolution is to reduce partial volume effects over the cortical surface and to further ameliorate susceptibility-induced dropout and distortion in high-susceptibility areas of the human brain such as the orbital frontal cortex and the temporal poles. In these areas, EPI signal, and BOLD activations, may be seen from brain regions that are often not detected at 3T. (The benefits of higher spatial resolution, while maintaining high MR signal despite using smaller voxels, is one of the benefits of using an ultra-high field MRI system such as the 7T MAGNETOM Terra.) While the tSNR is lower in much of the brain than for acquisition protocols with ~2.0–2.5 mm spatial resolution, on the MAGNETOM Prisma^{fit}, we found the tSNR remained high enough to detect robust BOLD activations such as those of the principal resting-state networks with similar BOLD sensitivity to what was achieved at coarser spatial resolutions. In addition, not only was tSNR improved in the frontal and temporal regions, but we have detected – in numerous subjects – increased tSNR around much of the cortical surface, specifically in visual and parietal regions, where we did not initially expect significant benefit. This improved tSNR at high resolution presumably results from decreased partial-volume effects around the cortical surface, where larger voxels are contaminated by significant amounts of CSF with inherent physiological fluctuations. Figure 8 shows, for 3 axial slices in 3 different subjects, areas in red where tSNR is higher when using a 1.7 mm / TR 2 sec protocol than when using a 2.2 mm / TR 2 sec protocol (2.2 mm being the highest spatial resolution we could achieve without using in-plane acceleration, while keeping TE below 35 ms). The blue regions indicate where the 2.2 mm protocol had higher tSNR, as a result of higher mean signal in the larger voxels. Figure 9 shows group-average functional connectivity maps for 2 different protocols trialed on the Prisma^{fit}, namely the 2.2 mm spatial resolution protocol used in Figure 8 and the 1.5 mm protocol described above. The network maps, from two different seed regions, were remarkably similar despite the reduction in voxel size. Work from some of CBS's psychology faculty users employing the 1.5 mm spatial resolution protocol at 3T is already appearing in the literature [12], while others have employed increased temporal resolution in new studies [13].

Conclusions

The MAGNETOM Prisma^{fit} has been an incredible resource and superb tool for high-quality neuroimaging studies at Harvard's Center for Brain Science Neuroimaging facility. The hardware advances in the MAGNETOM Prisma^{fit}, as compared to the MAGNETOM Trio, provide the potential for significant improvements in diffusion imaging acquisition protocols, while functional (BOLD) imaging can benefit in a narrower range of optimized high-resolution protocols making higher spatial or temporal

9

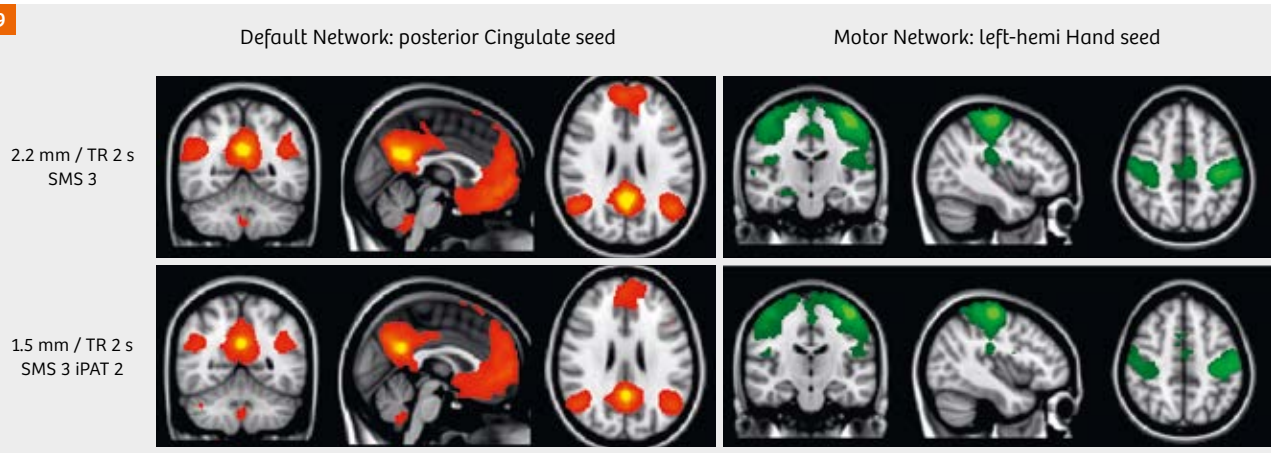

Figure 9:
Group average maps over 8 subjects of two different functional connectivity networks (Default Network from the posterior Cingulate cortex seed, and the Motor network from the left hemisphere Hand region seed) acquired with 2 different acquisition protocols on the MAGNETOM Prisma^{fit}: 2.2 mm / TR 2 sec / SMS = 3, and 1.5 mm / TR 2 sec / iPAT (GRAPPA) = 2 / SMS = 3.

resolution routinely attainable. However, of importance to those running long-term studies that require system stability, we have shown that coarser-resolution BOLD protocols and older, simpler diffusion protocols can be translated from the Trio to the Prisma^{fit} and provide data of a similar quality in terms of signal stability (tSNR), resting state BOLD activation, and standard-deviation of ADC and FA for fixed ROIs of ordered white matter. Additionally, minimal variation is observed in brain morphometric data derived from T1-weighted images from the same subjects, acquired over a 4-month interval, on the Trio and the Prisma^{fit}, indicating that scanner upgrade, in this case, should not bias long-running morphometric studies, provided gradient non-linearity is accounted for.

Acknowledgements

Harvard Center for Brain Science; NIH Shared Instrumentation Grant S10OD020039; NIH Grants P41-RR14075, U24-RR021382.

References

1 van der Kouwe AJ, Benner T, Salat DH, Fischl B. Brain morphometry with multiecho MPRAGE. NeuroImage, 40(2):559–569 (2008).
2 Moeller S, Yacoub E, Olman CA, Auerbach E, Strupp J, Harel N, Uğurbil K. Multiband multislice GE-EPI at 7 Tesla with 16-fold acceleration using Partial Parallel Imaging with application to high spatial and temporal whole-brain fMRI. Magnetic Resonance in Medicine, 63(5);1144–1153 (2010).
3 Setsompop K, Gagoski BA, Polimeni JR, Witzel T, Wedeen VJ, Wald LL. Blipped-controlled aliasing in parallel imaging for simultaneous multislice echo planar imaging with reduced g-factor penalty. Magnetic Resonance in Medicine, 67(5);1210-1224 (2012).
4 Fischl B, Dale AM. Measuring the thickness of the human cerebral cortex from magnetic resonance images. Proceedings of the National Academy of Sciences USA, 97(20):11050-11055 (2000).
5 Reuter M, Rosas HD, Fischl B. Highly Accurate Inverse Consistent Registration: A Robust Approach. NeuroImage, 53(4):1181–1196 (2010).
6 Desikan RS, Segonne F, Fischl B, Quinn BT, Dickerson BC, Blacker D, Buckner RL, Dale AM, Maguire RP, Hyman BT, Albert MS, Killiany RJ. An automated labeling system for subdividing the human cerebral cortex on MRI scans into gyral based regions of interest. NeuroImage, 31(3):968-980 (2006).
7 surfer.nmr.mgh.harvard.edu/fswiki/CorticalParcellation
8 Yeo BT, Krienen FM, Sepulcre J, Sabuncu MR, Lashkari D, Hollinshead M, Roffman JL, Smoller JW, Zöllei L, Polimeni JR, Fischl B, Liu H, Buckner RL. The organization of the human cerebral cortex estimated by intrinsic functional connectivity. Journal of Neuropyhsiology, 106(3);1125-1165 (2011).
9 Mair RW, Reuter M, van der Kouwe AJ. Validation of Cortical Thickness/Volume Data from Multi-Echo MPRAGE Scans with Variable Acceleration in Young and Elderly Populations. Proceedings of ISMRM, 22:1795 (2014).
10 Mair RW, Reuter M, van der Kouwe AJ, Fischl B, Buckner RL. Quantitative Comparison of Morphometric Data from Multi-Echo MPRAGE Variable Acceleration and Different Head Coils. Proceedings of ISMRM, 21:947 (2013).
11 Triantafyllou C, Polimeni JR, Wald LL. Physiological noise and signal-to-noise ratio in fMRI with multi-channel array coils. NeuroImage, 55(2):597-606 (2011).
12 Thakral PP, Benoit RG, Schacter DL. Imagining the future: The core episodic simulation network dissociates as a function of timecourse and the amount of simulated information. Cortex, 90(1):12-30 (2017).
13 Braga RM, Buckner RL. Parallel Interdigitated Distributed Networks within the Individual Estimated by Intrinsic Functional Connectivity. Neuron, 95(1):457–471 (2017).



Contact

Ross W Mair, Ph.D.
Harvard University
Center for Brain Science

NW 231.10
52 Oxford St
Cambridge, MA, 02138
USA
rmair@fas.harvard.edu

Whole-body MR diffusion imaging in oncology: origins, practice, and outlook

Giuseppe Petralia, M.D.[1,2,3]; Fabio Zugni, M.D.[4]; Marco Martinetti B.Sc.[3]; Paola Pricolo, M.D.[1]; Massimo Bellomi, M.D.[1,2,3]

[1] Department of Radiology, European Institute of Oncology (IEO), Milan, Italy
[2] Department of Oncology and Hematology, University of Milan, Milan, Italy
[3] Scientific Committee, Advanced Screening Centers – ASC Italia, Castelli Calepio (Bergamo), Italy
[4] Postgraduate School in Radiodiagnostics, University of Milan, Milan, Italy

Background

1905 was one of Albert Einstein's most productive years, his acclaimed *annus mirabilis* (from Latin meaning "extraordinary year"), in which he made a substantial contribution to the foundation of modern physics. In addition to other findings and innovations, Einstein extended Brown's theory about the random motion of particles [1]. Robert Brown, a Scottish botanist, was the first to notice the motion of particles in water; but he was not able to determine the underlying mechanisms of this motion. This was not the case for the German-born Nobel Prize winner. The first part of Einstein's theory was to determine how far a particle travels in a given time interval, and the second related the diffusion constant to physically measurable quantities, such as the mean squared displacement of a particle in a given time interval. Einstein observed, understood, and ultimately quantified water diffusion.

In 1974, R.V. Damadian patented the first magnetic resonance (MR) scanner as a "method for detecting cancer in tissue [2]." In this context, diffusion-weighted imaging played no significant role. This technical innovation was widely reported in the international media and had a significant impact on public opinion. In fact, with this new electronic device, Damadian claimed to be able to locate cancer across the whole body, raising expectations of the potential benefits of this innovation for oncology.

More than a decade later, a French physician named Denis Le Bihan came up with the intuitive idea of merging these two findings. Le Bihan showed that water diffusion could be displayed in the human brain through magnetic resonance imaging and, in 1985, produced the first diffusion-weighted image with MRI [3]. Since 1990, diffusion-weighted imaging (DWI) has become a standard neuroradiology tool for diagnosing ischemia. In 2004, Takahara et al. made a pioneering contribution to the development of DWI, by introducing a technology called diffusion-weighted whole-body imaging with background suppression (DWIBS), in which radiological images are acquired during free respiration, suppressing background signals and allowing volumetric acquisitions and multiple section excitations of the whole body [4]. Thanks to these developments regarding the role of diffusion in magnetic resonance imaging, the scientific community finally had a method for quantifying the microscopic motion of water molecules in biological tissues over the entire body. Over the past decade, medical technology suppliers have launched incredible technological developments enabling whole-body MRI (WB-MRI), including morphological and diffusion-weighted images, to be performed in just 30–45 minutes. Moreover, clinicians have found many exciting uses for this radiation free technique for the management of malignancies and cancer screening.

Guidelines and key uses of WB-MRI by cancer histotype

Following growing evidence of its effectiveness in the management of cancer patients, the use of WB-MRI has increased exponentially over the last decade [5]. Encouraging results in the management of a variety of different cancer histotypes, in some cases substantiated

1

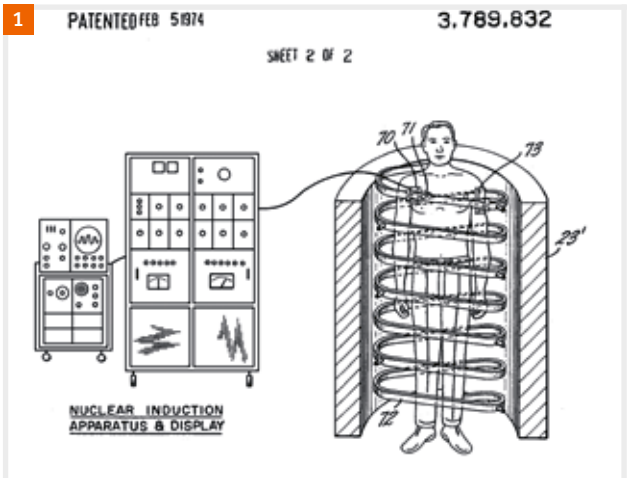

Figure 1:
Damadian's whole body MRI device, excerpt from the original U.S. Patent No. 3789832, Feb. 5, 1974.

by the highest level of scientific evidence [6], consolidated the role of WB-MRI in the management of several malignancies. In recent years, certain clinical guidelines have recommended the use of WB-MRI and important uses for this technique have been found in modern oncology.

Multiple myeloma

Multiple myeloma (MM) is a haematological cancer characterized by the accumulation of neoplastic plasma cells in the bone marrow. Bone disease, distinguished by the presence of bone fractures, osteolytic lesions, or osteoporosis, is a significant cause of morbidity and mortality in multiple myeloma [7]. Thus, according to the guidelines of the International Myeloma Working Group (IMWG), the presence of even asymptomatic bone disease on conventional radiography should be considered a criterion of symptomatic MM requiring treatment [8]. In a series of 611 MM patients, MRI detected more focal lesions than lytic lesions in whole-body X-rays of the spine (78% versus 16%; P 0.001), pelvis (64% versus 28%; P 0.001), and sternum (24% versus 3%; P 0.001) [9], which are the most common areas of MM systemic spread. Moreover, in a study of 41 patients with newly-diagnosed multiple myeloma, WB-MRI proved superior to conventional whole-body CT screening in detecting lesions of the skeleton. WB-MRI should thus be used to detect regions with bone marrow infiltration for both diagnosis and monitoring of treatment response. According to the guidelines on the role of imaging in patients with MM, produced by the British Society for Haematology [10], WB-MRI is recommended for staging all forms of multiple myeloma (Grade of Recommendation A, GR A, reflecting the highest level of evidence-based medicine). It is also recommended for the monitoring of oligosecretory and non-secretory myelomas (Level of Evidence, LoE 1B [11]) as well as for extramedullary disease (LoE 1B [12]). The GR A recommendation also indicates that WB-MRI should be used for the staging of solitary bone plasmacytoma (SBP), an early stage malignancy with a clinical course between MGUS and multiple myeloma.

Prostate cancer

Prostate cancer is the most common histotype among men. While some types of prostate cancer grow slowly and may need only minimal or even no treatment, others may develop aggressive behavior, requiring accurate systemic staging and follow up.

In high-risk patients, guidelines developed by the European Association of Urology recommend cross-sectional abdominopelvic imaging and a bone-scan, as a minimum (GR A, LoE 2A [14]). However, the guidelines suggest that MRI is more sensitive (97%) than choline PET/CT (91%) and bone scans (78%) for detecting bone metastasis. This was confirmed in a recent meta-analysis conducted by Shen et al. on 18 studies comparing the diagnostic accuracy of these three imaging techniques [15]. Moreover, the radiological assessment of metastasis also has prognostic value and changes treatment management protocols [16].

In advanced prostate cancer (APC) the management of metastasis is crucial: skeletal metastases are present in more than 90% of patients who die of the disease. In metastatic castrate-resistant prostate cancer (mCRPC) patients being treated with enzalutamide and abiraterone and radium-223, up to one disease progression in three is detected radiologically with no clinical symptom or PSA (prostate serum antigen) progression [17, 18]. Moreover, PSMA PET/CT may fail to provide information on tumor viability during androgen receptor inhibition. Two recent reviews identified the potential of WB-MRI to address the unmet need for robust imaging that allows us to monitor the response of bone metastases to treatment [19, 20]. The St Gallen Advanced Prostate Cancer Consensus Conference (APCCC) presented clear recommendations about castrate-resistant patients. The recommendations confirm that PSA alone is not reliable enough for monitoring disease activity in mCRPC (since metastases may develop without a rising PSA) and that imaging should be conducted before starting a new line of treatment [21]. Moreover, the APCCC recommendations affirm that "disease monitoring in the bone is especially difficult with well-described bone lesion are phenomena both on CT and bone scans, [...] and it is recognised that planar bone scintigraphy has short-comings and is less sensitive than other newer imaging technologies such as MRI of the whole body." Finally, although it acknowledged the "limited availability of these newer imaging technologies," the APC Consensus Conference confirmed that "advanced spinal/whole-body MRI techniques are also better able to identify and gauge the extent of bone disease than planar bone scans."

Melanoma

Although we have seen significant developments in the clinical management of advanced melanoma in recent years, most patients with stage IV melanoma will still die of the disease. For this reason, guidelines for the treatment of malignant melanoma have been published since 2001, providing feasible practical recommendations for clinicians and surgeons. Several meta-analysis and systematic reviews have established WB-MRI as a valid alternative method to PET/CT in oncology [22, 23]. Further studies have confirmed that WB-MRI is highly sensitive in detecting extracranial metastases in melanoma patients [24]. Although MRI with hepatobiliary contrast agents is

considered the best imaging strategy for identifying hepatic secondary lesions, small liver metastases can also be confidently detected with diffusion-weighted imaging as the sole method, as briefly reported in the case study (Fig. 2).

Moreover, studies are investigating recent developments in non-standard ultra-short TE (UTE)[1] MRI sequences [25] as a viable radiation-free alternative to reference CT scans in detecting small metastatic lesions in the lungs from melanoma (Fig. 3). In a study conducted on behalf of the German Dermatological Society and the Dermatologic Cooperative Oncology Group [26], Pflugfelder et al., strongly recommend WB-MRI for cross-sectional imaging of advanced melanoma (stage III or worse), asserting that the efficacy of this method is equivalent to whole-body CT and PET/CT. Moreover, WB-MRI is also recommended for the follow-up in patients with melanoma staged from IIC to IV [27].

[1] WIP, the product is currently under development and is not for sale in the US and in other countries. Its future availability cannot be ensured.

Figure 2: Hepatic metastases: do we really need contrast?

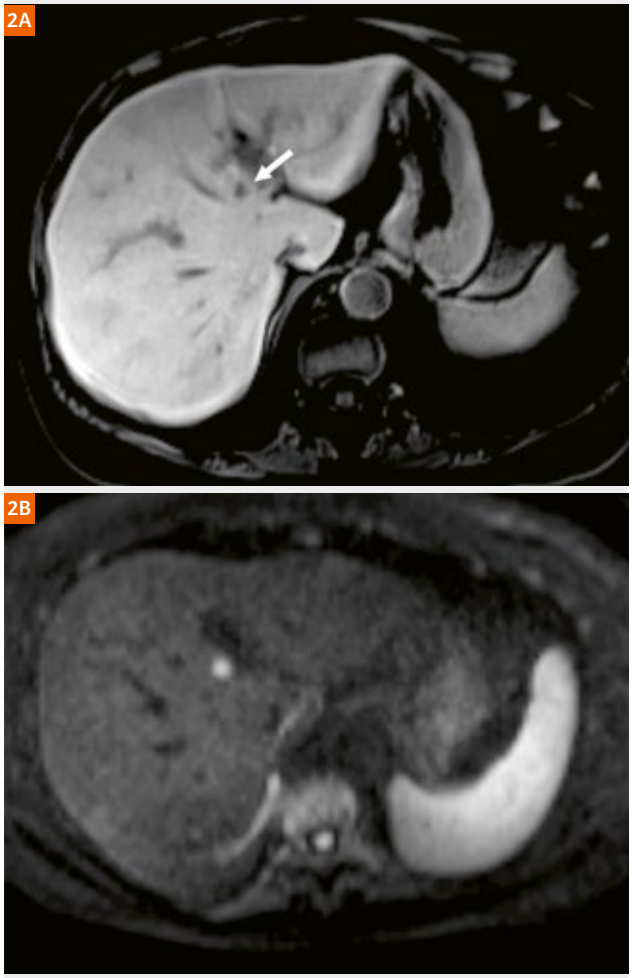

A patient with a stage III melanoma undergoes WB-MRI with hepatobiliary-specific contrast agent (gadolinium-ethoxybenzyl-diethylenetriamine penta-acetic acid, Gd-EOB-DTPA). The late hepatobiliary phase, 20 minutes after injection **(2A)**, reveals the presence of a 9 mm metastasis in the fourth segment (white arrow). The same lesion is clearly detectable in the high b-value (900 s/mm^2) diffusion-weighted image performed in the same session **(2B)**.

Breast

Breast cancer is the second leading cause of death among women. An epidemiological study based on 25,336 women diagnosed with primary invasive breast cancer, confirmed bone as the most common site of metastasis [28]. The widely accepted RECIST criteria (Response Evaluation Criteria in Solid Tumors) should not be used for monitoring bone lesions, as they are considered non-measurable. Moreover, the revised RECIST 1.1 failed to fully address this point. According to the new criteria bone metastases are only measurable once they have spread to the surrounding soft tissue with a mass larger than at least 10 mm in diameter [29]. This does not occur in the majority of the cases.

Since being introduced in clinical practice, conventional MRI has proven capable of supplying extremely precise imaging of the bone marrow which, in some cases, would be unachievable using other imaging techniques [30]. In

Figure 3: Lung metastasis in CT and MRI



A patient with stage IV melanoma undergoes a follow-up examination with low-dose CT of the lung and WB-MRI. A subcentimetric metastasis in the left inferior lobe is identified on the axial CT image (arrow in **3A**) as well as on the axial T1-weighted image (arrow in **3B**).

a meta-analysis conducted by Yang et al. on 145 studies comprising 15,221 patients with bone metastasis, WB-MRI showed better sensitivity for lesion detection (97%) than FGD-PET (91%)and bone scan (79%) [31]. In some instances conventional MRI could have shortcomings, however. For instance, a phenomenon known as T1 pseudo-progression can occur. This is when a strong response to therapy results in a bone marrow edema, which is visible as a T1 hypo-intensity and can be misclassified as progression. In such cases, the addition of DWI to T1-weighted images allows both the presence of the bone marrow edema and an absence of restrictions for water molecules to be identified, thus avoiding misdiagnosis [32]. The sclerotic response occurs when, after treatment, bone metastases appear unchanged on morphologic T1 images, but a response is clearly visible on the ADC map. The response is identified by an increase in the ADC value to over 1,500 µm²/s, which is a well-documented threshold for response to therapy (Fig. 4).

Studies are underway to evaluate the impact of the superior diagnostic performance of WB-MRI compared to conventional imaging techniques on the management of cancer patients and, ultimately, on their survival. In a recent study, Kosmin et al. [33] compared the findings of 210 paired WB-MRI scans and computed tomography of chest, abdomen, and pelvis (CT-CAP) performed at the same time (within 14 days) for follow-up in patients with metastatic breast cancer. They observed that therapy changes were made due to progressive disease (PD) detected in the imaging in 46 pairs of scans; in 16 of these pairs (34.7%), PD was only visible in the WB-MRI scans and was not diagnosed by CT examination. This observation emphasizes the additional value of performing WB-MRI scans as opposed to CT-CAP in actual clinical practice. There are several recognized breast cancer histotypes that have different gene expression profiles and thus need to be managed differently. In some cases, these types of breast cancer benefit from targeted therapies [34]. Clinical practice in treating invasive lobular breast cancer (ILC) has recently revealed an important use for WB-MRI scans in breast cancer patients. In ILC, the second most common histological subtype, the spread of metastases differs from invasive ductal breast cancer (IDC), the most common histological subtype. ILC is

Figure 4: Pseudo-progression of bone metastases

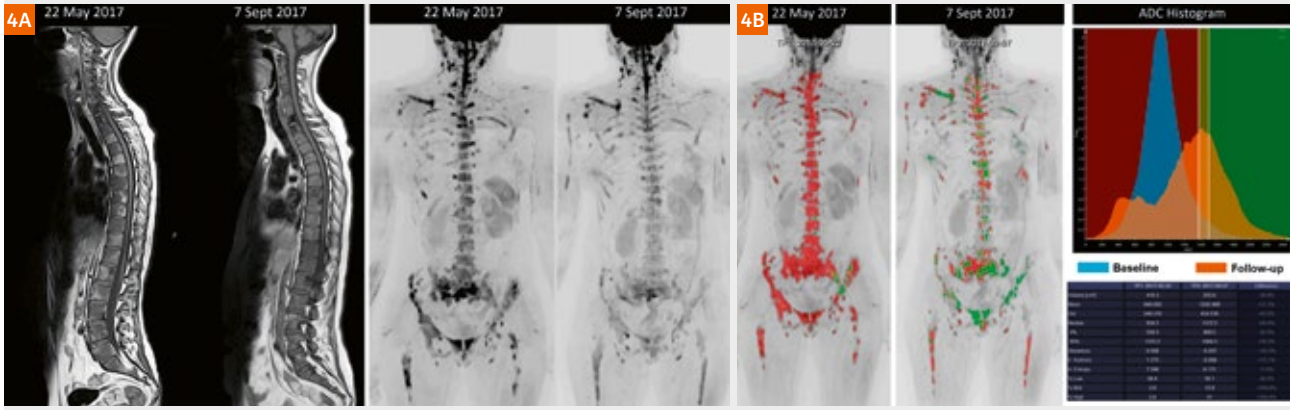

45-year-old woman with metastatic breast cancer. WB-MRI examinations before and after third-line systemic treatment with capecitabine and vinorelbine.

(4A) On T1-weighted sagittal images a diffuse reduction in signal intensity is identified in the whole spine following chemotherapy. However, it is impossible to assess whether this is consistent with progressive disease, stable disease, or response to therapy. This finding can sometimes be observed when bone metastases respond to cytotoxic chemotherapy. It is due to the increase in extracellular water in the bone marrow, which reduces signal intensity on T1-weighted images thus mimicking disease progression. Maximum intensity projection (MIP) in the high b-value (900 s/mm²) diffusion-weighted images reveal a decrease in signal intensity after therapy, related to decreased cellularity that is in fact consistent with response to therapy.

(4B) WB-tumor load segmentation undertaken on *syngo*.via Frontier[2] MR Total Tumor Load software (Siemens Healthcare; released research prototype). The MIP images in the high b-value (900 s/mm²) are overlaid with ADC value color classes using the thresholds indicated. The green voxels are values ≥1500 µm²/s (representing voxels that are 'highly likely' to be responding). The yellow voxels are set to lie between the 95th centile ADC value of the pre-treatment histogram (1390 µm²/s) and 1500 µm²/s thus representing voxels 'likely' to be responding. Red voxels represent mostly untreated and still active disease. A reduction in the volume of the active disease is measured (418 mL before therapy and 255 mL after therapy), with an overall increase in ADC values (946 µm²/s and 1742 µm²/s) on the corresponding relative frequency histograms. Note: the decreased extent and volume of red voxels are consistent with disease response (94% before therapy and 56% after therapy). The residual red regions on the post-therapy scan are likely to represent residual active disease with low ADC value, in the spine, pelvis, and limbs.

[2] *syngo*.via Frontier is for research only, not a medical device.

statistically more likely than IDC to spread to gastrointestinal (GI) organs, the peritoneum and retroperitoneum, the gynecological system, and the pleura, which are anatomical sites that are notoriously challenging to explore using PET and CT techniques [35]. Moreover, metastases from ILC are less FDG avid than other breast cancer histotypes [36] and therefore less visible on FDG-PET scans. This is associated with the reduced (to absent) E-cadherin membrane expression, which provides cell-to-cell adhesion and facilitates permeation through tissue planes. In ILC cancer cells this feature is responsible for the characteristic spread of the disease. This is known as "Indian file" neoplastic growth and involves neoplastic cells infiltrating the parenchyma around non-neoplastic ducts of GI organs or spreading to the peritoneum or retroperitoneum [37]. In our experience, thanks to the superior contrast resolution in WB-MRI compared to CT scans and the 'aspecific' nature of diffusion-weighted imaging (hyper-cellular lesions are always visible irrespective of the glucose metabolism), they are often able to depict the presence of neoplastic spread of disease into GI organs or the peritoneum/retroperitoneum earlier and more effectively than CT and FDG/PET-CT scans (see Fig. 5). Lastly, WB-MRI has demonstrated extraordinary results in detecting and staging breast cancer during pregnancy. In 40% of these cases, breast cancer presents at an advanced stage, which is 2.5 times the rate of the general breast cancer population. This means that accurate staging of bone, liver, and chest malignancies is crucial. However, imaging techniques involving ionizing radiation and the administration of intravenous contrast agents should be limited during pregnancy making WB-MRI the imaging technique of choice for systemic staging in pregnant women with breast cancer [38].

Lymphoma

FDG-PET/CT is the recommended imaging technique for the most common lymphomas, including DLBCL, follicular lymphoma, and Hodgkin lymphoma [39]. However, its diagnostic performance depends on glucose metabolism and patients with severely altered glucose metabolism may not be ideal candidates for this imaging technique. The aim of WB-MRI, on the other hand, is to investigate hypercellularity across the whole body. This technique is thus likely to be less histology-dependent than FDG-PET and therefore more suitable for patients with lymphomas with poor or no FDG avidity. In a prospective study of 140 patients, WB-MRI demonstrated better diagnostic performance than both FDG-PET/CT and CE-CT in patients with lymphoma subtypes with variable FDG avidity (the majority were MALT lymphomas) [40].

Another important use that is on the rise for WB-MRI is in young (< 35-year-old) lymphoma patients. Over the last decade, there have been promising increases in the survival rates for lymphomas, particularly among young patients. Nevertheless, NCCN guidelines still recommend repeated CT or PET/CT examinations every year, including in the clinical management of low stage lymphomas [41]. WB-MRI has shown diagnostic performance comparable

Figure 5: Gastric and peritoneal metastases from lobular breast cancer

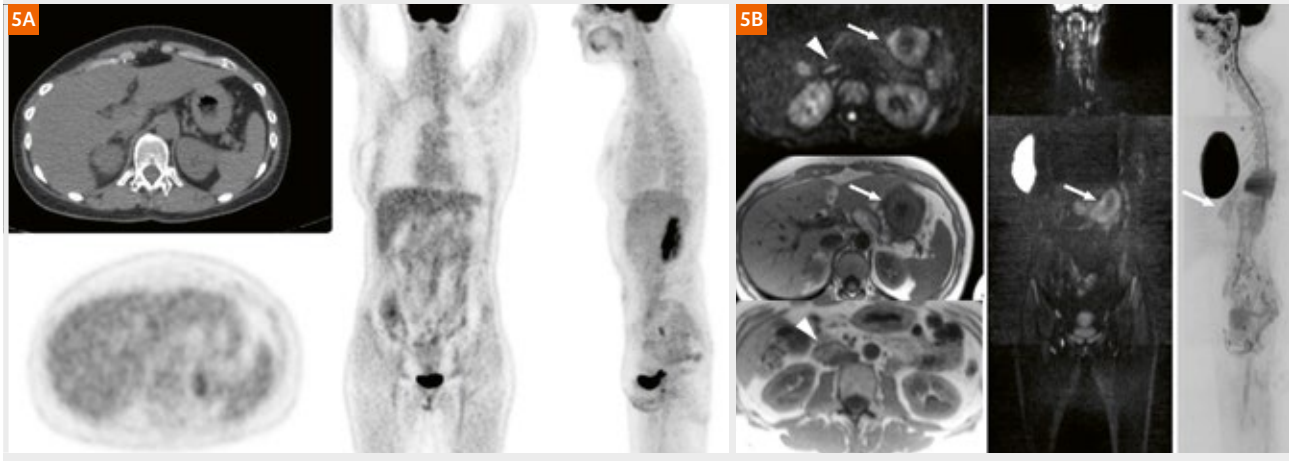

A 44-year-old woman with lobular breast cancer post-surgery undergoes several FDG PET/CT scans due to suspected disease recurrence based on a persistent and continuous rise in CA 15.3. No suspicious findings are visible on FDG PET/CT **(5A)**. A WB-MRI performed 15 days later **(5B)** reveals a thickening of the gastric wall, with corresponding abnormally high signal intensity in the high b-value images b-900 DWI (white arrows), and suspicious solid tissue on the right anterior renal fascia (white arrowhead). A second WB-MRI examination performed two months later showed the same findings. Gastroscopy with multiple punch biopsies of the gastric wall has been performed, confirming the presence of malignant infiltration of lobular breast cancer cells.

to that of PET/CT both in staging and follow-up. Thus, following the introduction of a dose-saving criterion for the younger patients, WB-MRI could be considered as an alternative to PET/CT and CT in the young lymphoma patient subgroup.

Cancer screening and WB-MRI

The aim of cancer screening is to detect cancer before symptoms appear. Several screening tests have proven to help detect cancer early and reduce the chance of dying from that disease [42]. Having saved thousands of lives, Pap tests, breast mammography for women, and FOBT for both women and men therefore became standard in many countries [43]. However, standard screening tests are not considered adequate for subjects genetically predisposed to cancer, such as those with Li-Fraumeni syndrome (LFS) and neurofibromatosis (NF). For patients with these conditions, advanced screening using WB-MRI is recommended. Moreover, there are high expectations of the benefits of advanced screening for the general population of asymptomatic subjects.

Li-Fraumeni syndrome

First described in 1969, Li-Fraumeni syndrome (LFS) is a highly penetrant cancer prone syndrome [44] caused by germline mutations of the TP53 tumor suppressor gene. Essentially, this rare, autosomal dominant, hereditary disorder, pre-disposes carriers to the development of a wide variety of cancer types. For this reason, it is also known as the sarcoma, breast, leukaemia, and adrenal gland (SBLA) syndrome. A recent meta-analysis validates the first statistically robust estimate of the clinical utility of WB-MRI in screening TP53 mutation carriers [45]. In addition, results from the UK SIGNIFY study on the cancer detection rate in this group of subjects argue for the adoption of at least a baseline whole body MRI scan [46]. Furthermore, the MD Anderson Cancer Center jointly with LFSA, the world largest LFS patients association, produced the first screening guidelines for the early detection of the syndrome. Guidelines developed by LEAD (Li-Fraumeni Syndrome Education and Early Detection) recommend WB-MRI for pediatric patients[1] between the age of 1 and

[1] Siemens Healthineers Disclaimer does not represent the opinion of the authors: MR scanning has not been established as safe for imaging fetuses and infants less than two years of age. The responsible physician must evaluate the benefits of the MR examination compared to those of other imaging procedures.

Figure 6: Assessment of post-treatment response

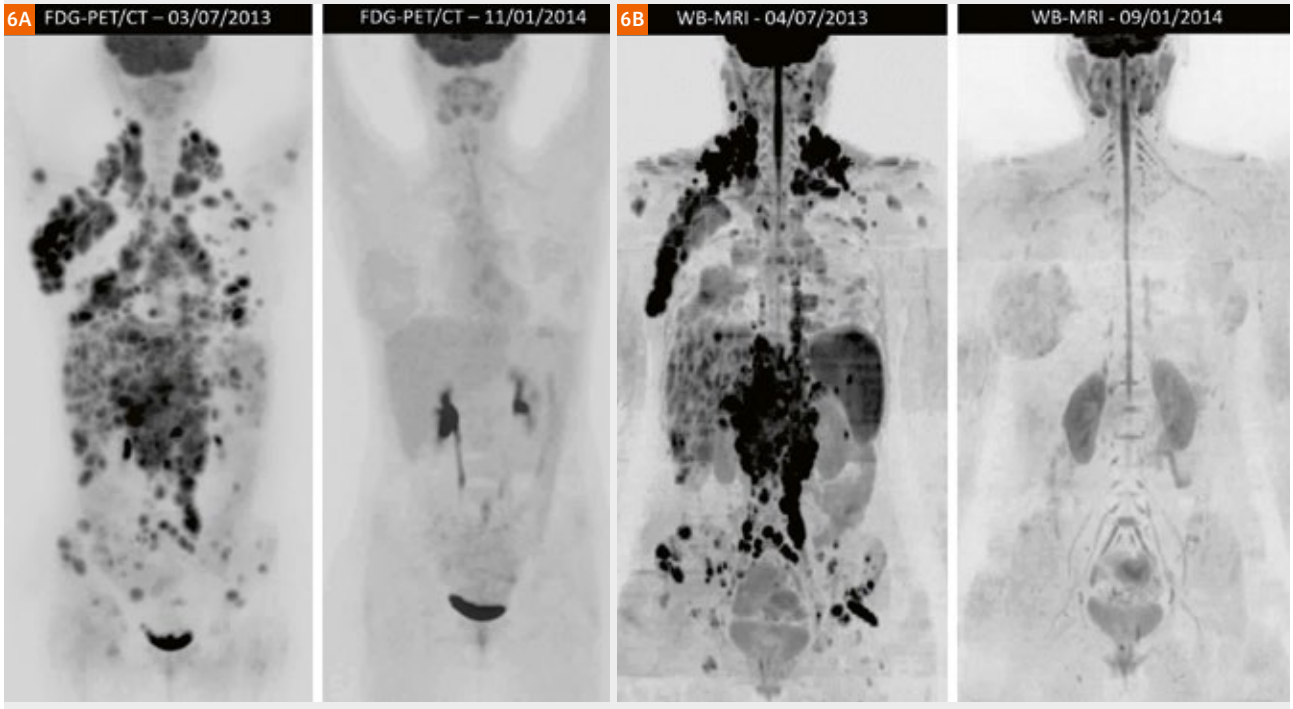

After multiple lines of systemic treatments, a 22-year-old woman with a relapse of non-Hodgkin lymphoma (Ann Arbor stage IVb) undergoes new chemotherapy combined with the ESHAP scheme and peripheral blood stem cell transplant. The patient undergoes FDG PET/CT and WB-MRI scans before treatment and six months post-treatment. Response assessment with PET/CT **(6A)** reveals a complete resolution of the abnormal FDG uptake across all body regions consistent with complete response (CR). Response assessment using WB-MRI at the same points in time **(6B)** is equally effective at showing CR.

10 years affected by sarcomas related to LFS, as well as for patients aged 10 or above, suffering from sarcomas, brain or adrenocortical tumors [47].

Lastly, according to a recent National Comprehensive Cancer Network (NCCN) recommendation, annual screening of LFS patients including WB-MRI should be a reference standard [48].

Neurofibromatosis

Neurofibromatosis is a genetic disorder causing tumors to form on nerve tissue. These tumors can develop anywhere across nervous system, including the brain, spinal cord, and nerves. Neurofibromatosis is usually diagnosed in childhood or early adulthood. Identifying pre-malignant and malignant tumors is essential for the clinical management of patients with NF, yet achieving this goal has remained challenging because of the heterogeneity of neurofibromas. Diffusion-weighted imaging is a particularly attractive technique for children[1] as most pediatric malignancies are small round cell tumors with impeded water diffusion. Moreover, WB-MRI has proven its efficacy in detecting and staging the three main clinical manifestations of NF: neurofibromatosis type 1 (NF1), neurofibromatosis type 2 (NF2), and schwannomatosis (SWN).

The National Cancer Institute has already recommended the development of practical guidelines to introduce WB-MRI for the detection of malignant peripheral nerve sheath tumors (MPNST) [49]. About half of all MPNST are diagnosed in people with neurofibromatosis and the lifetime risk of patients with NF1 developing this rare malignancy is between 8 and 13%. Moreover, a study conducted by Cashen et al. [50] showed an overall survival rate of 84% among treated patients emphasizing the key role of advanced imaging in early diagnosis and treatment management. The Response Evaluation in Neurofibromatosis and Schwannomatosis International Collaboration (REiNS) is in the process of developing official recommendations for the use of WB-MRI in NF [51]. The Neuro Foundation, the largest NF patient foundation in the UK, already recommends MRI for investigating preliminary signs of neurofibromatosis across the whole body [52].

Asymptomatic subjects and screening

Although current paradigms and treatments for cancer have resulted in substantial progress, oncologic diseases frequently evade long-term monitoring and cure. Thus, early detection and diagnosis in asymptomatic patients, before the systemic spread of the primary neoplasm, are critical. Early detection of subclinical disease may enable more efficient and effective initiation of preventive measures and treatment interventions at the early rather than later stages of disease. Imaging findings may thus result in the identification of early, and potentially curable, disease. Moreover, the role of the radiologist is crucial in deciding whether an image feature is normal or whether it potentially needs further examination.

The implementation of advanced imaging techniques in large cohort studies is an approach that has increasingly been used in epidemiologic research. The Framingham Heart study [53], the Multi-Ethnic Study of Atherosclerosis [54], and the Rotterdam study [55] have already demonstrated the invaluable scientific contribution of such techniques. In addition, advanced imaging has also improved our understanding of complex disease processes, as well as our ability to identify novel imaging biomarkers as precursors for subsequent disease states. The largest study using WB-MRI in asymptomatic subjects is the currently ongoing German National Cohort, a multicentric population-based study on 30,000 asymptomatic subjects. The study aims to identify risk and protective factors for population-relevant diseases and to provide new information that can be translated into primary prevention measures [56].

Several other studies regarding the use of WB-MRI for cancer screening have appeared in recent years. The first, published in 2008 by Gladys Lo et al. [57], described the incidental findings in a population of 132 doctors at Hong Kong Sanatorium and Hospital, who volunteered to undergo a WB-MRI for cancer screening. Various other studies have also been published over the last decade. The largest of these included 666 asymptomatic subjects in which a 1.05-percent rate of malignant cancers was determined [58].

Similar preliminary observations were made by the Advanced Screening Centers (ASC Italy), a recently founded social enterprise, originating from a collaborative partnership between a group of entrepreneurs and long-term supporters of cancer research, the European Institute of Oncology of Milan, and a panel of international experts in oncological WB-MRI, devoted exclusively to performing WB-MRI for cancer screening in asymptomatic subjects. From January 2017, when it was opened, to October 2017, ASC performed WB-MRI for cancer screening on 394 asymptomatic subjects.

The scans showed no abnormalities in just 12 of these subjects, which is actually consistent with the abnormality rates reported in the scientific literature. At least one abnormality was reported per 382 subjects (97% of the total).

However, for almost 80 percent of these subjects, no further investigation was requested, while 75 subjects were referred for follow-up. Further examinations were only requested for 9 subjects, and in 4 of these (1%) the presence of malignant cancer was confirmed histologically and the subject was informed.

However, the introduction of WB-MRI for screening the general population of asymptomatic subjects is still a long way off. First, it has to be proven that advanced cancer screening using WB-MRI, as opposed to screening that targets the most common malignancies (as per current standard practice) is scientifically relevant. Second, the diagnostic performance of WB-MRI in many cancer histotypes is well known, but it still needs validation for use in different populations (such as asymptomatic subjects). Third, there are practical issues associated with the relatively high cost of the equipment as well as the examination itself that present obstacles for the widespread use of WB-MRI. Lastly, but equally important, as with every practice in medicine, interpreting WB-MRI scans is heavily dependent on the experience of the reader. There is still inadequate standardization of image interpretation and reporting, as well as a lack of proper understanding of the learning curve required to be able to read an image effectively. Research to examine these issues is ongoing.

References

1 Einstein A. On the motion of small particles suspended in liquids at rest required by the molecular-kinetic theory of heat. Annalen der Physik. 1905;17:549-60.
2 Damadian RV. Apparatus and method for detecting cancer in tissue. US patent 3789832, filed 1972 March 17, issued 1974, February 5.
3 Le Bihan D, Breton E. Imagerie de diffusion in-vivo par résonance magnétique nucléaire. Comptes-Rendus de l'Académie des Sciences. 1985;93(5):27-34.
4 Takahara T, Imai Y, Yamashita T, Yasuda S, Nasu S, Van Cauteren M. Diffusion weighted whole body imaging with background-body signal suppression (DWIBS): technical improvement using free breathing, STIR and high-resolution 3D display. Matrix. 2004;160(160):160.
5 Koh DM, Blackledge M, Padhani AR, Takahara T, Kwee TC, Leach, et al. Whole-body diffusion-weighted MRI: tips, tricks, and pitfalls. American Journal of Roentgenology. 2012;199(2):252-62.
6 Wu LM, Gu HY, Zheng J, Xu X, Lin LH, Deng X, et al. Diagnostic value of whole-body magnetic resonance imaging for bone metastasis: a systematic review and meta-analysis. Journal of Magnetic Resonance Imaging. 2011;34(1):128-35.
7 Kristinsson SY, Minter AR, Korde N, Tan E, Landgren O. Bone disease in multiple myeloma and precursor disease: novel diagnostic approaches and implications on clinical management. Expert review of molecular diagnostics. 2011;11(6):593-603.
8 Kumar S, Paiva B, Anderson KC, Durie B, Landgren O, Moreau P, et al. International Myeloma Working Group consensus criteria for response and minimal residual disease assessment in multiple myeloma. The Lancet Oncology. 2016;17(8): e328-e346.
9 Walker R, Barlogie B, Haessler J, Tricot G, Anaissie E, Shaughnessy Jr JD, et al. Magnetic resonance imaging in multiple myeloma: diagnostic and clinical implications. Journal of Clinical Oncology. 2007;25(9):1121-28.
10 Dimopoulos MA, Hillengass J, Usmani S, Zamagni E, Lentzsch S, Davies FE, et al. Role of magnetic resonance imaging in the management of patients with multiple myeloma: a consensus statement. Journal of Clinical Oncology. 2015;33(6):657-664.
11 Oxford Centre for Evidence-based Medicine - Levels of Evidence (March 2009). 2016 February 19. [Internet]. [Cited 2018 March 03]. Available from: https://www.cebm.net/2009/06/oxford-centre-evidence-based-medicine-levels-evidence-march-2009/
12 Chantry A, Kazmi M, Barrington S, Goh V, Mulholland N, Streetly M, et al. Guidelines for the use of imaging in the management of patients with myeloma. British Journal of Haematology. 2017.
13 Myeloma: diagnosis and management. [Internet]. [Cited 2018 March 03]. Available from: https://www.nice.org.uk/guidance/ng35
14 Mottet N, Bellmunt J, Bolla M, Briers E, Cumberbatch MG, De Santis M, et al. EAU-ESTRO-SIOG guidelines on prostate cancer. Part 1: screening, diagnosis, and local treatment with curative intent. European Urology. 2017;71(4):618-29.
15 Shen G, Deng H, Hu S, Jia Z. Comparison of choline-PET/CT, MRI, SPECT, and bone scintigraphy in the diagnosis of bone metastases in patients with prostate cancer: a meta-analysis. Skeletal Radiology. 2014;43(11):1503-13.
16 Wang X, Pirasteh A, Brugarolas J, Rofsky NM, Lenkinski RE, Pedrosa I, et al. Whole-body MRI for metastatic cancer detection using T2-weighted imaging with fat and fluid suppression. Magnetic Resonance in Medicine. 2018.
17 Morris MJ, Molina, A., Small, E. J., De Bono, J. S., Logothetis, C. J., Fizazi, K., et al. Radiographic progression-free survival as a response biomarker in metastatic castration-resistant prostate cancer: COU-AA-302 results. Journal of Clinical Oncology. 2015;33(12):1356-63.
18 Bryce AH, Alumkal JJ, Armstrong A, Higano CS, Iversen P, Sternberg CN, et al. Radiographic progression with nonrising PSA in metastatic castration-resistant prostate cancer: post hoc analysis of PREVAIL. Prostate Cancer and Prostatic Diseases. 2017;20(2):221.
19 Padhani AR, Lecouvet FE, Tunariu N, Koh DM, De Keyzer F, Collins DJ, et al. Rationale for modernising imaging in advanced prostate cancer. European Urology Focus. 2017;3(2-3) :223-239.
20 Lecouvet FE, Talbot JN, Messiou C, Bourguet P, Liu Y, de Souza NM. Monitoring the response of bone metastases to treatment with Magnetic Resonance Imaging and nuclear medicine techniques: a review and position statement by the European Organisation for Research and Treatment of Cancer Imaging Group. European Journal of Cancer. 2014;50(15):2519-31.
21 Gillessen S, Attard G, Beer TM, Beltran H, Bossi A, Bristow R, et al. Management of patients with advanced prostate cancer: the report of the Advanced Prostate Cancer Consensus Conference APCCC 2017. European Urology. 2018;73(2):178-211.
22 Li B, Li Q, Nie W, Liu S. Diagnostic value of whole-body diffusion-weighted magnetic resonance imaging for detection of primary and metastatic malignancies: a meta-analysis. European Journal of Radiology. 2014;83(2):338-44.
23 Ciliberto M, Maggi F, Treglia G, Padovano F, Calandriello L, Giordano A, et al. Comparison between whole-body MRI and Fluorine-18-Fluorodeoxyglucose PET or PET/CT in oncology: a systematic review. Radiology and Oncology. 2013;47(3):206-18.
24 Petralia G, Padhani A, Summers P, Alessi S, Raimondi S, Testori A, et al. Whole-body diffusion-weighted imaging: is it all we need for detecting metastases in melanoma patients? European Radiology. 2013;23(12):3466-76.
25 Grodzki DM, Jakob PM, Heismann B. Ultrashort echo time imaging using pointwise encoding time reduction with radial acquisition (PETRA). Magnetic Resonance in Medicine. 2012;67(2):510-18.
26 Pflugfelder A, Kochs C, Blum A, Capellaro M, Czeschik C, Dettenborn T, et al. Malignant Melanoma S3-Guideline "Diagnosis, Therapy and Follow-up of Melanoma". JDDG: Journal der Deutschen Dermatologischen Gesellschaft. 2013;11(s6):1-116.

27 Dummer R, Siano M, Hunger R, Lindenblatt N, Braun R, Michielin O, et al. The updated Swiss guidelines 2016 for the treatment and follow-up of cutaneous melanoma. Swiss Medical Weekly. 2016;146:w14279.
28 Kwast AB, Groothuis-Oudshoorn KC, Grandjean I, Ho VK, Voogd AC, Menke-Pluymers MB, et al. Histological type is not an independent prognostic factor for the risk pattern of breast cancer recurrences. Breast Cancer Research and Treatment. 2012;135(1):271-80.
29 Eisenhauer EA, Therasse P, Bogaerts J, Schwartz LH, Sargent D, Ford R, et al. New response evaluation criteria in solid tumours: revised RECIST guideline (version 1.1). European Journal of Cancer. 2009;45(2):228-47.
30 Mehnati P, Tirtash MJ. Comparative efficacy of four imaging instruments for breast cancer screening. Asian Pac J Cancer Prev. 2015;16(15):6177-86.
31 Yang HL, Liu T, Wang XM, Xu Y, Deng SM. Diagnosis of bone metastases: a meta-analysis comparing 18FDG PET, CT, MRI and bone scintigraphy. European Radiology. 2011;21(12):2604-17.
32 Padhani AR, Makris A, Gall P, Collins DJ, Tunariu N, Bono JS. Therapy monitoring of skeletal metastases with whole-body diffusion MRI. Journal of Magnetic Resonance Imaging. 2014;39(5):1049-78.
33 Kosmin M, Makris A, Joshi PV, Ah-See ML, Woolf D, Padhani AR. The addition of whole-body magnetic resonance imaging to body computerised tomography alters treatment decisions in patients with metastatic breast cancer. European Journal of Cancer. 2017;77:109-16.
34 Romond EH, Perez EA, Bryant J, Suman VJ, Geyer Jr CE, Davidson NE, et al. Trastuzumab plus adjuvant chemotherapy for operable HER2-positive breast cancer. New England Journal of Medicine. 2005;353(16):1673-84.
35 Kwast AB, Groothuis-Oudshoorn KC, Grandjean I, Ho VK, Voogd AC, Menke-Pluymers MB, Siesling S. Histological type is not an independent prognostic factor for the risk pattern of breast cancer recurrences. Breast Cancer Research and Treatment. 2012;135(1):271-80.
36 Hogan MP, Goldman DA, Dashevsky B, Riedl CC, Gönen M, Osborne JR, et al. Comparison of 18F-FDG PET/CT for systemic staging of newly diagnosed invasive lobular carcinoma versus invasive ductal carcinoma. Journal of Nuclear Medicine. 2015;56(11):1674-80.
37 Goldstein NS. Does the level of E-cadherin expression correlate with the primary breast carcinoma infiltration pattern and type of systemic metastases? American Journal of Clinical Pathology. 2002;118(3):425-34.
38 Peccatori FA, Codacci-Pisanelli G, Del Grande M, Scarfone G, Zugni F, Petralia G. Whole body MRI for systemic staging of breast cancer in pregnant women. The Breast. 2017;35:177-81.
39 National Comprehensive Cancer Network Lymphoma. [Internet]. [Cited 2018 March 03]. Available from: https://www.tri-kobe.org/nccn/guideline/hematologic/english/hodgkins.pdf
40 Mayerhoefer ME, Karanikas G, Kletter K, Prosch H, Kiesewetter B, Skrabs C, Hoffmann M. Evaluation of diffusion-weighted MRI for pretherapeutic assessment and staging of lymphoma: results of a prospective study in 140 patients. Clinical Cancer Research. 2014;20(11):2984-93.
41 Hoppe RT, Advani RH, Ai WZ, Ambinder RF, Aoun P, Bello CM, et al. Hodgkin lymphoma, version 2.2012 featured updates to the NCCN guidelines. Journal of the National Comprehensive Cancer Network. 2012;10(5):589-97.
42 Cancer Screening. (n.d.) [Internet]. [Cited 2018 March 03, 2018]. Available from: https://www.cancer.gov/about-cancer/screening
43 Kamangar F, Dores GM, Anderson WF. Patterns of cancer incidence, mortality, and prevalence across five continents: defining priorities to reduce cancer disparities in different geographic regions of the world. Journal of Clinical Oncology. 2006;24(14):2137-50.
44 Li FP, Fraumeni JF. Soft-tissue sarcomas, breast cancer, and other neoplasms: a familial syndrome? Annals of internal medicine. 1969;71(4):747-52.
45 Ballinger ML, Best A, Mai PL, Khincha PP, Loud JT, Peters JA, et al. Baseline surveillance in Li-Fraumeni syndrome using whole-body magnetic resonance imaging: a meta-analysis. JAMA Oncology. 2017;3(12):1634-9.
46 Saya S, Killick E, Thomas S, Taylor N, Bancroft EK, Rothwell J, et al. Baseline results from the UK SIGNIFY study: a whole-body MRI screening study in TP53 mutation carriers and matched controls. Familial Cancer. 2017;16(3):433-40.
47 MD Anderson Cancer Centre and LFSA [Internet]. [Cited 2018 March 03]. Available from: http://www.livinglfs.org/wp-content/uploads/2016/03/LEAD-Pediatric-screening-program-2016.pdf
48 National Comprehensive Cancer Network (n.d.) [Internet]. [Cited 2018 March 03]. Available from: https://www.nccn.org/about/news/ebulletin/ebulletindetail.aspx?ebulletinid=535
49 Reilly KM, Kim A, Blakely J, Ferner RE, Gutmann DH, Legius E, et al. Neurofibromatosis Type 1–Associated MPNST State of the Science: Outlining a Research Agenda for the Future. JNCI: Journal of the National Cancer Institute. 2017;109(8).
50 Cashen DV., Parisien RC, Raskin K, Hornicek FJ, Gebhardt MC, Mankin HJ. Survival data for patients with malignant schwannoma. Clinical Orthopaedics and Related Research®. 2004;426:69-73.
51 Widemann BC, Blakeley JO, Dombi E, Fisher MJ, Hanemann CO, Walsh KS, et al. Conclusions and future directions for the REiNS International Collaboration. Neurology. 2013;81(21 supplement 1):S41-4.
52 NF1 Facts. [Internet]. [Cited 2018 March 03]. Available from: https://www.nfauk.org/what-is-neurofibromatosis/nf-type-1/nf1-facts/
53 Splansky GL, Corey D, Yang Q, Atwood LD, Cupples LA, Benjamin EJ, et al. The third generation cohort of the National Heart, Lung, and Blood Institute's Framingham Heart Study: design, recruitment, and initial examination. American Journal of Epidemiology. 2007;165(11):1328-35.
54 Bild DE, Bluemke DA, Burke GL, Detrano R, Diez Roux AV, Folsom AR, et al. Multi-ethnic study of atherosclerosis: objectives and design. American journal of epidemiology. 2002;156(9):871-81.
55 Hofman A, Brusselle GG, Murad SD, van Duijn CM, Franco OH, Goedegebure A, et al. The Rotterdam Study: 2016 objectives and design update. European Journal of Epidemiology. 2015;30(8):661-708.
56 Bamberg F, Kauczor HU, Weckbach S, Schlett CL, Forsting M, Ladd SC, et al. Whole-body MR imaging in the German National Cohort: rationale, design, and technical background. Radiology.2015;277(1):206-20.
57 Lo GG, Ai V, Au-Yeung KM, Chan JK, Li KW, Chien D. Magnetic resonance whole body imaging at 3 Tesla: feasibility and findings in a cohort of asymptomatic medical doctors. Hong Kong Medical Journal. 2008;14(2):90.
58 Cieszanowski A, Maj E, Kulisiewicz P, Grudzinski IP, Jakoniuk-Glodala K, Chlipala-Nitek I, et al. Non-contrast-enhanced whole-body magnetic resonance imaging in the general population: the incidence of abnormal findings in patients 50 years old and younger compared to older subjects. PLOS One. 2014;9(9):e107840.

Contact

Dr. Giuseppe Petralia, M.D.
Deputy Director Division of Radiology
IEO Istituto Europeo di Oncologia
Via Ripamonti, 435
20141 Milano
Italy
Phone +39 (0)257489915
giuseppe.petralia@ieo.it



MR Elastography – Pearls and Pitfalls

Bradley Bolster Jr, Ph.D.[1]; Ning Jin, Ph.D.[1]; Stephan Kannengiesser, Ph.D.[2]

[1] Siemens Healthineers, Malvern, PA, USA
[2] Siemens Healthineers, Erlangen, Germany

Introduction

Obesity is one of the most common lifestyle diseases in many countries and has led to a dramatic increase in patients diagnosed with non-alcoholic fatty liver disease (NAFLD). Within just half a decade, prevalence of NAFLD among a general population in the United States increased from 15% in 2005 to 25% in 2010 [1]. The picture is even more dramatic in the obese population with the reported prevalence ranging from 30–37% [2].

The clinical appearance of NAFLD encompasses a broad spectrum ranging from mild fatty liver disease, steatosis, inflammation, fibrosis, cirrhosis, and, finally, to hepatocellular carcinoma. Early detection and grading of fibrosis, therefore, has important implications for the management of patients with NAFLD to retard the progression to more severe stages of liver disease.

Percutaneous liver biopsy and histopathological analysis used to be the standard method to confirm and classify nonalcoholic steatohepatitis (NASH). This has now been widely replaced by noninvasive tests such as Ultrasound Elastography and MR Elastography (MRE) of the liver. In several comparison studies of MRE with different Ultrasound Elastography techniques, and MRE with functional MR imaging, MRE has been shown to exceed all other techniques in terms of diagnostic accuracy, sensitivity, specificity, and organ coverage [3–5].

Commercially available solutions for MRE allow the assessment of liver stiffness to be seamlessly integrated into a normal MR examination, including automated processing of the data[1].

How does MRE work? MRE depicts motion of mechanical shear waves in tissue using motion-sensitized sequences, followed by 'inverting' the wave pattern to deduce tissue stiffness. External motion is induced by an acoustic driver system (Resoundant Inc., Rochester, MN, USA). MRE requires additional hardware, and mechanical wave propagation varies inter-individually, so in practical application MRE does have some pitfalls, which if ignored, may lead to e.g., improper tissue actuation, offset slice positioning, and, ultimately, suboptimal results. Another challenge is posed by patients with marked iron deposits in the liver: In these cases, T2*-mediated signal loss can make it impossible to sufficiently capture the shear wave propagation through tissue using MRI. According to the literature, the technical failure rate is about 10% for conventional GRE-based MRE [6].

Alternative ways to overcome this problem include the use of fractional encoding [7] to allow a shorter echo time (TE) and the use of spin-echo-based MRE sequences [8].

Therefore, it is essential to set up the MRE equipment carefully, prepare patients properly, and choose the right MRE sequence for the given case. And ensure that the evaluation of stiffness values follows established procedures. This article provides some practical guidance and tips on how to perform MRE successfully in daily clinical practice.

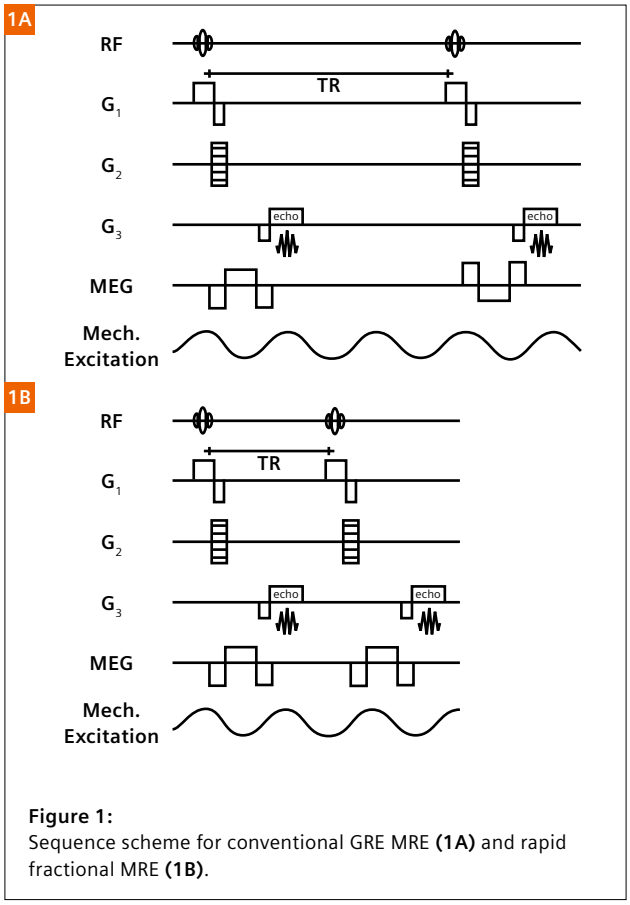

Figure 1:
Sequence scheme for conventional GRE MRE **(1A)** and rapid fractional MRE **(1B)**.

[1] *WIP, the product is currently under development and is not for sale in the US and in other countries. Its future availability cannot be ensured.*

MRE sequence improvements tailored to different use cases

Rapid MRE[2]

In the original version, MRE is performed with a phase-contrast gradient recalled echo (GRE) sequence, which applies motion-encoding gradients (MEGs) in synchronization with a 60 Hz external shear wave induced to the abdomen (Fig. 1A). This scheme is repeated every 50 ms with alternating polarity of the MEGs, resulting in a total acquisition time of about 20 seconds per slice, depending on the spatial resolution [9].

With rapid GRE (RF-GRE, [9]) this scheme is optimized as follows: Instead of applying MEGs with different polarity every 50 ms in the same phase of the mechanical excitation, the MEGs are played out with the same polarity every 25 ms, matching with opposite phases of the mechanical excitation (Fig. 1B).

The 50% shorter TRs dramatically reduce the required breath-hold duration. This means that patients have to hold their breath for just ~10 seconds rather than ~20 seconds, positively impacting the robustness of the method.

Fractional MRE encoding[3]

Motion encoding is normally done with a gradient waveform matching the mechanical wave period, i.e. a "1-2-1" MEG of 16.6 ms duration at 60 Hz driver frequency. This puts a lower limit on the achievable minimum TE, which may be too long for livers with iron overload, or at 3T. Alternatively, shortened, 'fractional' MEGs can be used. These have a lower motion-encoding strength, but the resulting shorter TE makes the GRE sequence less prone to T2*-induced signal loss, giving a net benefit for the final MRE result [10].

Spin Echo EPI MRE[4]

As an alternative to a GRE-type sequence for MRE, a Spin Echo (SE) sequence with a fast Echo-planar imaging (EPI) readout can also be used for MRE [8]. Due to the rapid readout, all required *k*-space data for several slices can typically be acquired within a 10–12 second breath-hold. Other advantages of the SE-EPI based approach are a higher robustness in patients with iron overload and a higher signal-to-noise ratio of the wave images compared with GRE-based MRE. SE-EPI MRE can also be combined with fractional encoding.

	Conventional GRE	RF-GRE	SE-EPI
Breath-hold duration	~20 sec	~10 sec	~10 sec
Measureable area of liver stiffness		+	+
Robustness against iron overload		+	++

[2]Rapid MRE is available with the syngo MR E11C software version.
[3]Rapid and fractional gre-MRE are available with syngo MR E11C. (There are no new protocols in the Siemens tree, but recommended protocols are available from application support.)
[4]Spin Echo MRE is available with the syngo MR E11E software version. The product is still under development and not commercially available yet. Its future availability cannot be ensured.

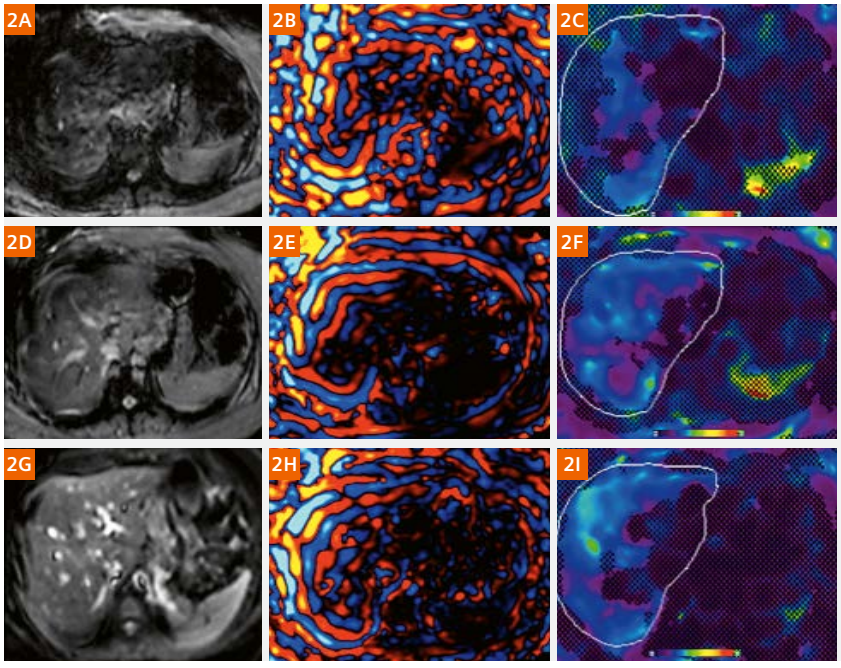

Figure 2:
41-year-old woman with NAFLD. Magnitude, wave, and liver stiffness maps with 95% confidence masks (left to right) for GRE **(2A-C)**, RF-GRE **(2D-F)**, and SE-EPI **(2G-I)** demonstrating largest area of measurable liver stiffness for the RF-GRE sequence with ROI areas of 15 mm², 27 mm², and 24 mm², respectively. *Figure reprinted from [11], with friendly permission of ER Felker and American Journal of Roentgenology (AJR).*

Comparison of methods

A recently published study [11] has compared conventional GRE, RF-GRE, and SE-EPI for MRE. While the study found no equivalent measures of liver stiffness for all techniques, significant differences in terms of failure rates and measureable areas of liver stiffness were found: Both RF-GRE and SE-EPI yielded larger measureable areas than conventional GRE, with RF-GRE having the largest measureable areas. Among patients with iron overload, there was a trend toward a larger measurable area of liver stiffness with SE-EPI. A corresponding example is shown in Figure 2.

Given that liver fibrosis is often spatially heterogeneous, the volume of liver sampled is considered one of the key advantages of MR Elastography compared with liver biopsy and ultrasound elastography. Therefore, RF-GRE appears to be the best choice in patients with normal iron concentrations in the liver, while SE-EPI appears to be superior for patients with iron overload.

3



4



MR Elastography workflow

Elastography can be performed at the beginning or end of a routine liver examination, this is a site preference.

1. Prior to positioning the patient turn on the Active Driver (Figure 3 – found in the equipment room).
   Note: The Active Driver goes into sleep mode after approximately one hour of inactivity.

2. Position the patient for an abdominal examination. Position the black Velcro Band directly underneath the liver.

3. Place the paddle (Passive Driver) on patient's right upper abdomen so that 1/4 of the paddle is over midline and 1/3 of the paddle is below the bottom of the rib cage (Fig. 4).
   Note: The tubing from the paddle can be placed coming from head or feet depending on scan room configuration.

4. Secure the paddle on the patient using the black Velcro Band. Please ensure that the entire paddle has good contact with the upper abdomen and is flat against the body surface. If the paddle has improper contact or is rocking back and forth try to adjust the position slightly for better contact.
   Note: Please make sure that the black Velcro Band is secured very tight on patient and paddle.

5. Prepare the patient mentally for the examination.
   a. Inform the patient that Elastography is performed at end expiration.
   b. Notify the patient, that she/he will feel pressure coming from the paddle during the examination.

6. Place the Body Array coil on the patient for a liver examination.

7. Register the patient and select the appropriate abdominal imaging protocol.

8. As indicated before, MRE can either be performed at the beginning or in the end of the abdominal examination.
   Note: Please make sure, that the localizer images / images used for planning the MRE exam are acquired in end expiration.

9. Planning of MRE scans: Position the MRE acquisition slice in the mid of the liver as indicated in the images (Fig. 5).

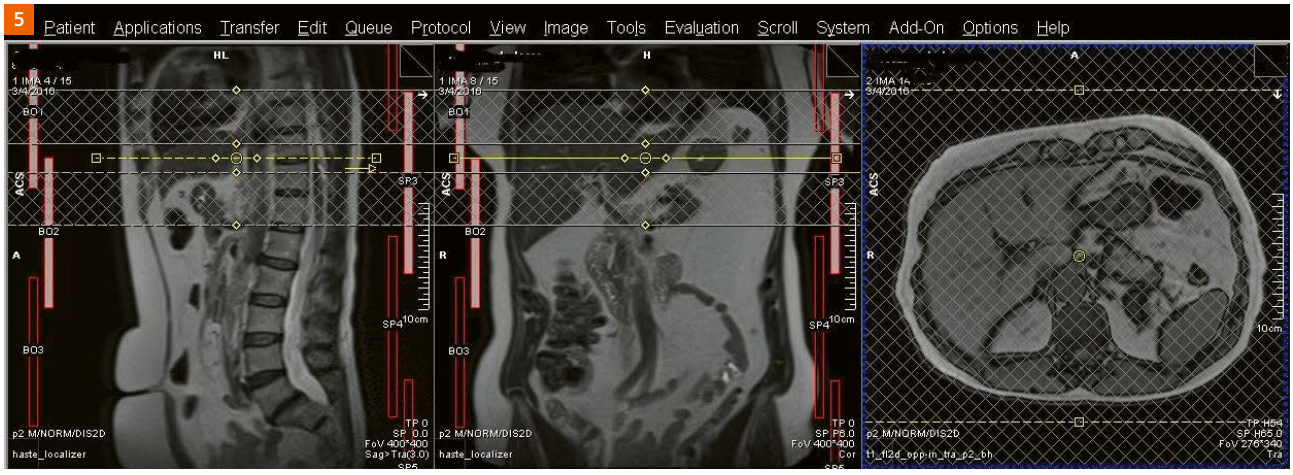

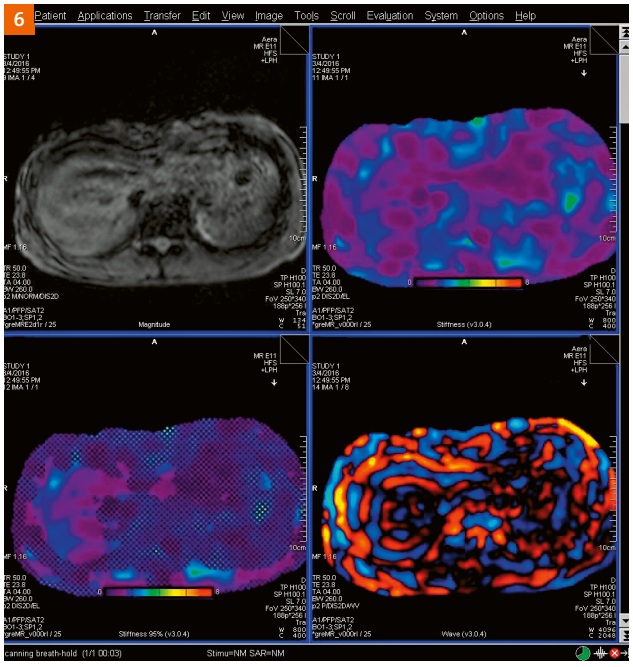

10. Instruct the patient again, that during the exam vibrations will be felt from the paddle.

11. Apply MR Elastography sequence. Perform the breath-holds in the exam at the end expiratory state.

12. Load and review images in Viewing Task Card to assess image quality. The following four series will be displayed (clockwise order):
Magnitude image: standard MRI image to evaluate general image quality such as breath-hold quality or SNR.
Stiffness Map / Elastogram: The elastogram is calculated from the shear wave images and represents the relative shear stiffness of tissue. The color scale indicates shear stiffness values in kPa ranging from 0–8 kPa.
Stiffness Map with 95% confidence mask overlay (hatched areas): With the confidence mask, areas where the calculated relative shear wave stiffness values are unreliable, are hashed out. This allows exclusion of areas of insufficient data quality.
Wave images: Wave images illustrate the propagation of shear waves through tissue with different speed and wave length. Based on this information, the Stiffness Maps are automatically calculated by the software (Fig. 6).

13. Image quality assurance: Check Magnitude images for image quality.
a. Check if the patient held the breath properly.
b. Check if the signal quality is sufficient, i.e. signal drops, inhomogeneities.
- Is the liver very dark?
- Is there a lot of lung tissue, but not much liver tissue in the FOV?

Note: If the quality is sub-optimal repeat the acquisition after checking proper slice positioning and reminding the patient to follow the instructions carefully.

14. Depending on the local preferences, repeat the MRE acquisition in different locations of the liver in H-F direction.
Note: Typically, 3–4 contiguous slices near the center of the liver are used.

15. Image analysis / post-processing: Select the Stiffness 95% Map and draw an ROI inside the grid area, avoiding meshed areas. Ensure that the ROI is drawn in liver tissue only. To draw an ROI select the "Tools" subtask card in the Viewing Task Card. Select the Circle ROI or Freehand ROI tool (Fig. 7).

16. Draw an ROI as described above. The displayed "Mean Value" divided by 100 shows the Relative Shear Stiffness in kPA in the ROI (Fig. 8).

17. Repeat this process for all acquired slices and average the resulting stiffness values.

Image quality troubleshooting tips

Anatomical Masking Failure – occurs when signal levels in the liver are lower than other structures in the slice. Review the GRE Magnitude image.

- Is there tissue that has brighter tissue then the liver (see Figure 9)?
- Does the tissue in the posterior peripheral tissue have brighter signal intensity then the liver does?
- Is the patient's stomach full?
- Tip: Repeat series with Sat band over bright signal (Fig. 9).
- If the entire liver is rejected by the confidence mask, shear waves may be missing in the tissue.
- Is the Active Driver turned off or in sleep mode?
- Did one of the hoses come undone?

7

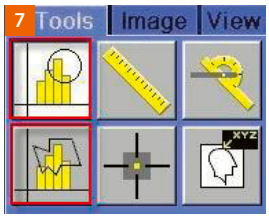

8

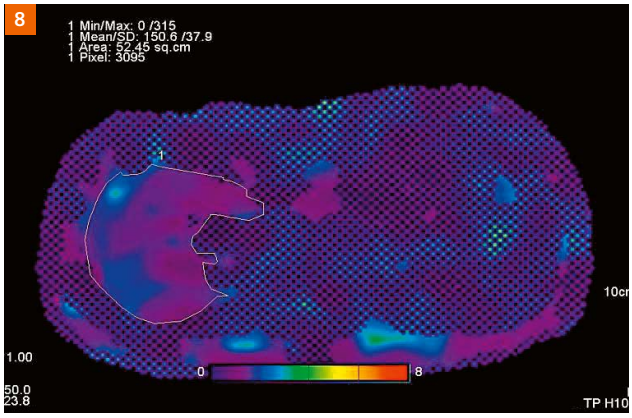

9

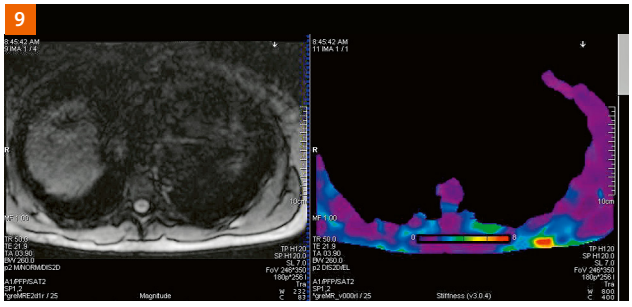

References:

1 Perumpail B, Khan MA, Yoo ER, Cholankeril G, Kin D, Ahmed, A. Clinical epidemiology and disease burden of nonalcoholic fatty liver disease. World J Gastroenterol. 2017 Dec 21; 23(47): 8263–8276.
2 Vernon G, Baranova A, Younossi ZM. Systematic review: the epidemiology and natural history of non-alcoholic fatty liver disease and non-alcoholic steatohepatitis in adults. Aliment Pharmacol Ther. 2011;34:274–285.
3 Tang A, Cloutier G, Szeverenyi NM, Sirlin CB. Ultrasound Elastography and MR Elastography for Assessing Liver Fibrosis: Part 1, Principles and Techniques. American journal of roentgenology. 2015;205:22–32.
4 Rizzo L, Calvaruso V, Cacopardo B, et al. Comparison of transient elastography and acoustic radiation force impulse for non-invasive staging of liver fibrosis in patients with chronic hepatitis C. Am J Gastroenterol. 2011;106:2112–2120.
5 Yoon JH, Lee JM, Joo I, et al. Hepatic fibrosis: prospective comparison of MR elastography and US shear-wave elastography for evaluation. Radiology. 2014;273:772–782.
6 Kim YS, Song JS, Kannengiesser S, Seo SY. Comparison of spin-echo echoplanar imaging and gradient recalled echo-based MR elastography at 3 Tesla with and without gadoxetic acid administration. Eur Radiol 2017;27(10):4120-4128.
7 Garteiser P, Sahebjavaher RS, Ter Beek LC, et al. Rapid acquisition of multifrequency, multislice and multidirectional MR elastography data with a fractionally encoded gradient echo sequence. NMR Biomed 2013; 26:1326-1335
8 Mariappan YK, Dzyubak B, Glaser KJ, et al. Application of Modified Spin-Echo-based Sequences for Hepatic MR Elastography: Evaluation, Comparison with the Conventional Gradient-Echo Sequence, and Preliminary Clinical Experience. Radiology 2017; 282:390-398.
9 Chamarthi SK, Raterman B, Mazumder R, Michaels A, Oza VM, Hanje J, Bolster B, Jin N, White RD, Kolipaka A. Rapid acquisition technique for MR elastography of the liver. Magn Reson Imaging. 2014 Jul;32(6):679-83.
10 Rump J, Klatt D, Braun J, Warmuth C, Sack I. Fractional Encoding of Harmonic Motions in MR Elastography. Magnetic Resonance in Medicine 2007(57):388-395.
11 Felker ER, Choi KS, Sung K, Wu HH, Raman SS, Bolster BD Jr, Kannengiesser S, Sorge K, Lu DSK. Liver MR Elastography at 3 T: Agreement Across Pulse Sequences and Effect of Liver R2* on Image Quality. AJR Am J Roentgenol. 2018 Sep;211(3):588-594.



Contact

Bradley Bolster Jr, Ph.D.
Siemens Healthineers
40 Liberty Boulevard
19355 Malvern, PA
USA
Phone: +1 (507) 993-0509
bradley.bolster@siemens-healthineers.com

Fetal MR Imaging: An Overview

Xianyun Cai[1]; Xin Chen[1]; Cong Sun[1]; Tuantuan Wang[1]; Hong Tang[1]; Jinxia Zhu[2]; Guangbin Wang[1]

[1]Department of MR, Shandong Medical Imaging Research Institute, Shandong University, China
[2]Siemens Healthineers, MR Collaboration, Beijing, China

The primary objective of prenatal diagnosis is to obtain genetic, anatomical, biochemical, and physiological information about the fetus that will allow the detection of any abnormalities that may have implications for the fetal and postnatal periods. This will make it possible to offer the family information, genetic counseling, and therapeutic alternatives. The main imaging method used for routine fetal examinations is ultrasonography (US). It is noninvasive, inexpensive, widely available, and can provide real-time studies without ionizing radiation. However, in cases of advanced gestational age, patient obesity, oligohydramnios, improper fetal position, and interposition of intestinal gas or pelvic acoustic shadows, US might have technical limitations and be unable to confirm findings. In our department, we consider using MRI when the US findings are equivocal or when the US images are difficult to interpret due to factors such as late pregnancy or an inaccessible fetal position. Fetal MR imaging[1] is regarded as a valuable adjuvant imaging tool for dedicated cases at field strengths of 3T or less. In general, with appropriate sequence adaptations, examinations of the fetus at 3T are comparable with images obtained at 1.5T. Also, because of the higher image resolution and signal-to-noise ratio (SNR), finer structures and lesions can be delineated at 3T. However, a major drawback is that examinations at 3T are more prone to artifacts, which complicates imaging the fetus for traditional referrals (maternal obesity, polyhydramnios). It is therefore important to decide which system might be better suited to address certain indications [1]. Investigation of normal organ development with fetal MRI has been described by Prayer et al. [2]. Maturational processes in utero are characterized by changes in the shape, size, and content/composition of organs, and by their relationship to each other.

In our institution, all the MRI examinations were performed on a 1.5T MAGNETOM Amira (Siemens Shenzhen Magnetic Resonance, Shenzhen, China) with spine and body array coils positioned over the lower pelvic area. Since our department introduced fetal MRI in June 2006, a total of 15,000 pregnant women with various anomalies (screened by ultrasonography) have been referred for fetal MRI examinations at our institution. The cases include brain, spine, chest, and abdominal anomalies. A placental MRI scan was performed for the first time in 2009, and 1,102 such scans have been performed to date. A total of 235 fetal spine scans have been performed since 2015, when susceptibility-weighted imaging (SWI) – a technique developed by Siemens [3], which conventionally uses the BOLD mechanism to generate venograms of the brain and to quantify venous oxygenation levels [4] – was first modified for fetal spine imaging with fast data acquisition by Robinson et al. [5]. In recent years, the development of MR sequences has led to major changes in fetal MRI imaging in our unit.

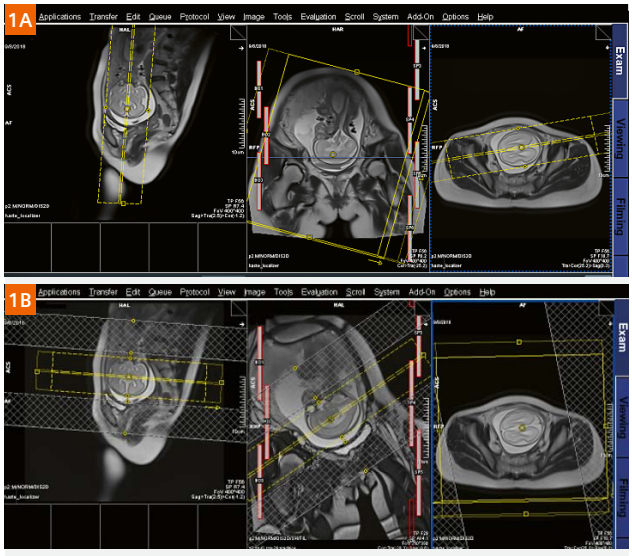

Figure 1:
Sagittal and coronal localizer images of the fetal brain.

[1]*Siemens Healthineers disclaimer does not represent the opinion of the authors: MR scanning has not been established as safe for imaging fetuses and infants less than two years of age. The responsible physician must evaluate the benefits of the MR examination compared to those of other imaging procedures.*

The rise and development of fetal magnetic resonance imaging

Origins

Since fetal MR imaging was first used in 1983 [6], no consistent or convincing evidence has emerged to suggest that briefly exposing a fetus to the changing electromagnetic fields of MR imaging has any harmful effects. In the early days, however, the acquisition time was too long and the motion artifacts were severe, which resulted in poor image quality and hindered the development of fetal MRI. With the development of ultrafast sequences in the 1990s, such as single-shot steady-state free precession (SSFP), half-fourier acquisition single-shot turbo spin echo (HASTE), fast T1-weighted gradient echo, and echo planar imaging, MR imaging became a noninvasive modality that could complement US in detecting fetal abnormalities, establishing prognoses, and assisting in perinatal management.

Safety

With fetal MRI, safety considerations such as exposure times, gradient field switching, noise, and radiofrequency power deposition should be kept in mind while following established guidelines [5–9]. No documented indications exist for using contrast agents in fetal MR imaging. Generally speaking, fetal MR imaging should be avoided in the first trimester, since the fetal cells are rapidly dividing and differentiating, and the influence of MRI on organogenesis is still unclear. Also, it is difficult to obtain good-quality images in very young fetuses.

Another important issue to consider in fetal MRI concerns gadolinium-based intravenous contrast media. These agents have been shown to cross the placenta and may appear in the fetal bladder, which means they are reabsorbed from the amniotic fluid by swallowing. The use of gadolinium-based contrast agents for MR imaging in pregnant women remains controversial. Recently, an animal experiment was conducted to determine whether gadolinium remains in juvenile nonhuman primate tissue after maternal exposure to intravenous gadoteridol during pregnancy. The study concluded that gadoteridol could cross the placenta. Given the similarities between human and nonhuman primate placental physiology, the study suggests there could be relatively little deposition in human fetal tissues after maternal gadoteridol injection. However, the long-term risk of such low levels of gadolinium deposition is still unknown. At our institution, no intravenous injection (of gadolinium agents or sedation agents) was used for any of the examinations, and specific absorption rate limits were in keeping with departmental protocols.

Moreover, maternal indications for prenatal MRI also need to be taken into account.

Fetal MR imaging

All the patients were imaged in supine or left-lateral position, depending on what was most comfortable. Fetal images are obtained in three orthogonal planes in the mother to plan the sagittal, coronal, and axial views of the fetus. The last sequence is used as a reference for planning the next sequence to compensate for fetal movement. All sequences are performed in all three planes through the fetus. Additional imaging planes, such as oblique sagittal or coronal positions, were obtained as needed. An axial T2-weighted sequence may be performed through the fetal brain for purposes of gestational dating. In recent years, ultrafast MR imaging sequences have provided short image acquisition times and usually prevent fetal motion from degrading image quality.

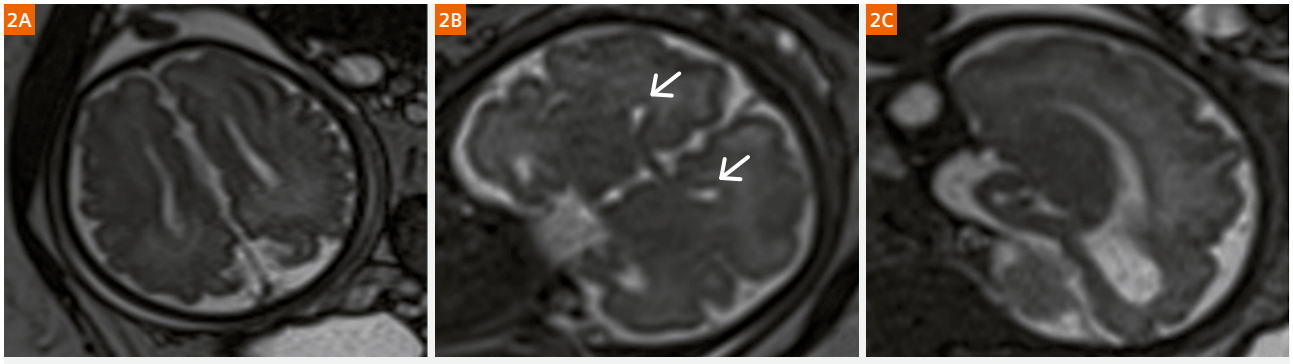

Figure 2: Corpus callosum agenesis
Sagittal HASTE **(2C)** shows complete absence of the corpus callosum. Axial TrueFISP **(2A)** shows parallel orientation of lateral ventricles. Coronal TrueFISP **(2B)** shows steer-horn-shaped frontal horns (arrows) resulting from the impression of Probst bundles.

1. **T2-weighted sequences**
   T2-weighted imaging (T2WI) includes single-shot, and half-Fourier single shot turbo spin echo (SSTSE, HASTE) T2-weighted sequences, and balanced sequences such as true fast imaging with steady-state precession (TrueFISP), which produces high tissue contrast and highlights the hyperintense amniotic fluid. At our institution, T2 HASTE and T2 TrueFISP were the most frequently used sequences for evaluating fetal anatomy. The TrueFISP sequence also allows vascular studies that require no intravenous contrast agent and can reveal hyperintense fetal vessels (vessels appear hypointense on SSTSE T1-weighted and T2-weighted images).

2. **T1-weighted sequences**
   T1-weighted imaging (T1WI), including 3D dual gradient echo (GRE), 2D fast spoiled GRE (FISP), and 3D liver acquisition and volume acquisition (3D VIBE), show less tissue contrast than T2WI sequences. T1WI sequences are primarily used to identify subacute bleeding, calcification, and lipoma, which appear as hyperintense loop structures in studies of congenital diaphragmatic hernia (CDH). T1WI sequences are also used to assess the presence and distribution of meconium, which enables accurate diagnosis of gastrointestinal abnormalities, reveals the size and location of the fetal liver, and can identify fetal, placental, or maternal hemorrhage.

3. **Susceptibility-weighted imaging**
   Susceptibility-weighted imaging (SWI) uses the intrinsic nature of local magnetic fields to enhance image contrast and thereby improve the visibility of various susceptibility sources and facilitate diagnostic interpretation [7]. It is worth mentioning that calcification is strongly diamagnetic and therefore decreases the magnetization in bone compared to the applied magnetic field. The technique results in a high contrast between bone and soft tissue, but a low contrast between different types of soft tissue. The low-signal bone is therefore easily distinguishable from the surrounding soft tissue.

4. **Diffusion-weighted imaging**
   As well as being used to diagnose cerebral infarction, diffusion-weighted imaging (DWI) sequences are currently being developed for fetal applications. The technique is already being used to study the maturity of lung parenchyma.

Fluid-sensitive short T1 inversion recovery (STIR), intravoxel incoherent motion imaging (IVIM), MR hydrography, and other sequences are not part of the routine fetal protocol but may be performed in specific cases where necessary.

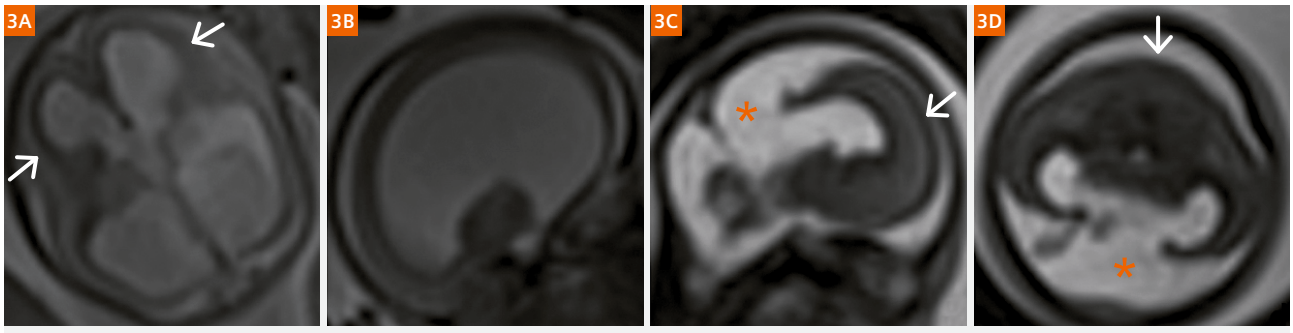

Figure 3: Severe hydrocephalus (3A, B) and alobar holoprosencephaly (3C, D)
Axial and coronal **(3A)** T2 HASTE imaging shows the marked dilation of the cerebral bilateral ventricle stenosis with only a thin mantle of overlying cerebral cortex (arrows). Sagittal **(3C)** and coronal **(3D)** T2 TrueFISP imaging shows only minimal frontal cerebral mantle (white arrows in 3A and B) and replacement of the majority of the brain with CSF (star). Coronal **(3C)** and axial **(3D)** T2 TrueFISP show a complete absence of falx, an interhemispheric fissure, and corpus callosum. Also visible is a horseshoe-shaped monoventricle communicating with a dorsal cyst (star).

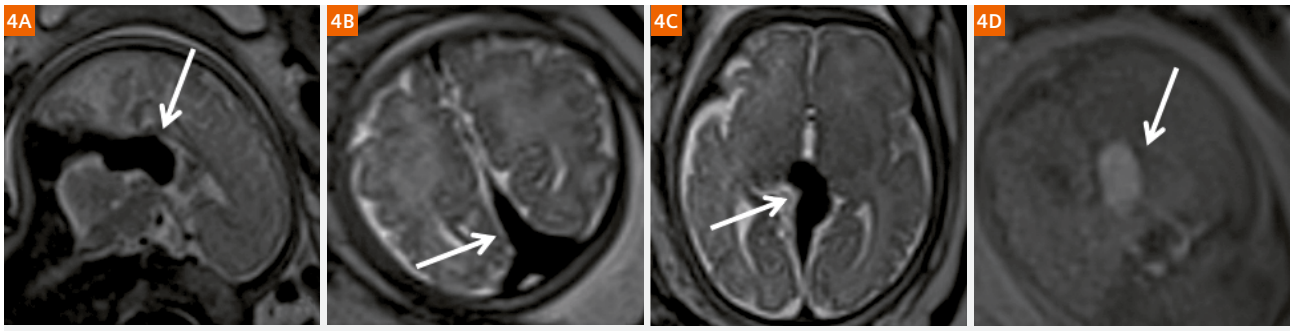

Figure 4: Galen vein malformation
Sagittal **(4A)** and coronal and axial **(4B)** T2 HASTE show a large varix (arrow) replacing the Galen vein, which exhibits hyperintensity on T1WI (**4D**, arrow).

The anatomy and anomalies in fetal MRI

Brain and spine

Imaging the central nervous system (CNS) anatomy and relevant pathology is clinically important for the early identification of cranial and spinal malformations and anomalous development. Fetal MRI has been shown to have higher contrast resolution and SNR than ultrasonography when it comes to illustrating the morphological changes in cranial and spinal brain abnormalities [8]. Most of the literature describing the results of MRI in large series of fetuses with CNS abnormalities deals with cerebral pathology. Spinal anomalies are usually described using examinations of smaller groups of patients or in case reports.

MR images of the developing fetal brain reflect changes in histogenesis and myelination. Subsequent changes are seen in the brain volume, surface configuration (sulcation), and internal configuration. Detailed information provided by MRI is necessary to evaluate the differentiation of white and gray matter, migration and myelination disorders, brain morphology and pathologies, and cranial posterior fossa and midline structures. Here, localizer brain scans (Fig. 1) provide the basis for images demonstrating different developmental deformities (Figs. 2–4).

The spinal canal and cord anomalies are among the CNS abnormalities which occur as a result of disruptions in formation and maturation. During the first three to five weeks of gestation (neurulation period), the neural tube, notochord, spine, and cranium develop. Disorders that occur at this stage of gestation (i.e., most spinal canal defects) are called "dorsal induction abnormalities". The dysraphic spinal canal and spinal cord disorders are divided into three groups: open dysraphic abnormalities, occult dysraphic abnormalities, and latent dysraphic abnormalities (e.g., diastematomyelia, hydromyelia, syringomyelia, dorsal dermoid sinus, teratoma, hamartoma, lipoma, dermoid/epidermoid cyst, and caudal regression syndrome).

Congenital anomalies of the spine occur at four to six weeks of gestation due to abnormal vertebral development that causes asymmetric growth of the spine. Anomalies in the ossification center of the fetal vertebral body result in bony defects such as hemivertebrae, butterfly vertebrae, and block vertebrae, which cause congenital scoliosis. MRI of fetuses diagnosed with osseous anomalies of the spine remains largely unexplored. Recently, we adapted and improved a clinically available SWI sequence for fetal spine imaging to evaluate vertebral malformations and anomalous vertebral development (in bony structures). We also typically used T2 TrueFISP and HASTE sequences to evaluate the recognition of the fetal spinal canal and spinal cord pathologies, as described in previous studies [9].

For MR imaging of the fetal spine, the protocol first involved a scout imaging sequence to gather information about the orientation of the fetus. Subsequent routine clinical sequences included T1WI, DWI, HASTE, T2-weighted TrueFISP, and SWI sequences. The HASTE, TrueFISP, and SWI sequences were obtained in the axial, coronal, and sagittal planes. The axial plane is best for assessing the neural arches, the coronal plane allows an additional assessment of the ribs and of pedicular widening in cases of spina bifida, and the sagittal plane is best for assessing the whole spine lengthways. The SWI sequence is best run immediately after routine HASTE or TrueFISP sequences, depicting the required anatomy by simply copying the slice parameters and thereby minimizing the time between sequences and reducing the chance of fetal motion. Here, localizer spine scans (Fig. 5) provide the basis for demonstrating various developmental deformities as follows (Figs. 5–9).

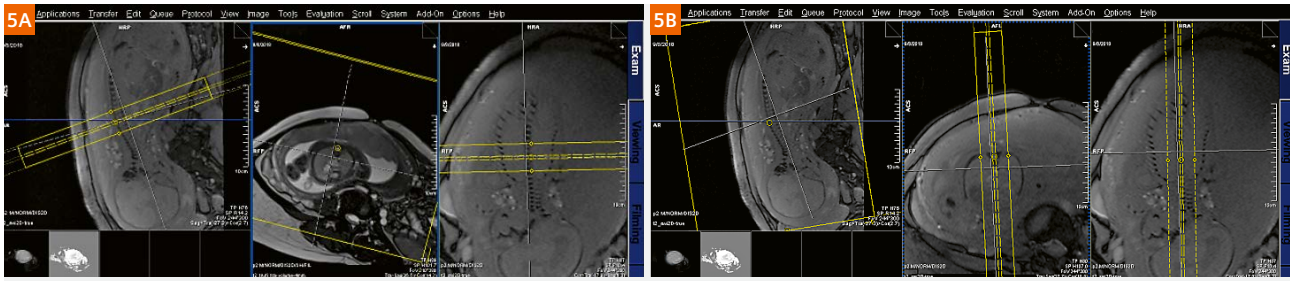

Figure 5:
Axial, sagittal, and coronal localizer images of the fetal spine.

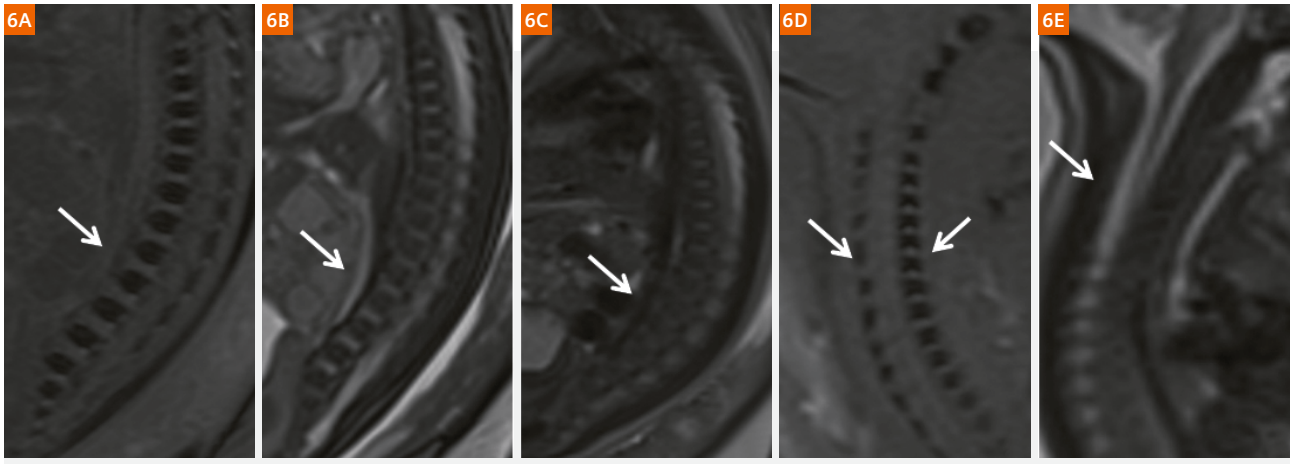

Figure 6:
Images at 32 weeks' gestation (6A–C) and 26 weeks' gestation (6D–E) with normal fetal spine structures. Sagittal view of the thoraco-lumbar spine, MR images including SWI (6A), TrueFISP (6B), and HASTE (6C). The SWI **(6A, D)** clearly shows the vertebral bodies and the posterior elements (arrows). On a similar plane in the same position using TrueFISP **(6B, E)** and HASTE **(6C)**, the vertebral column (arrows) is shown poorly but could reveal the structures of the intraspinal canal.

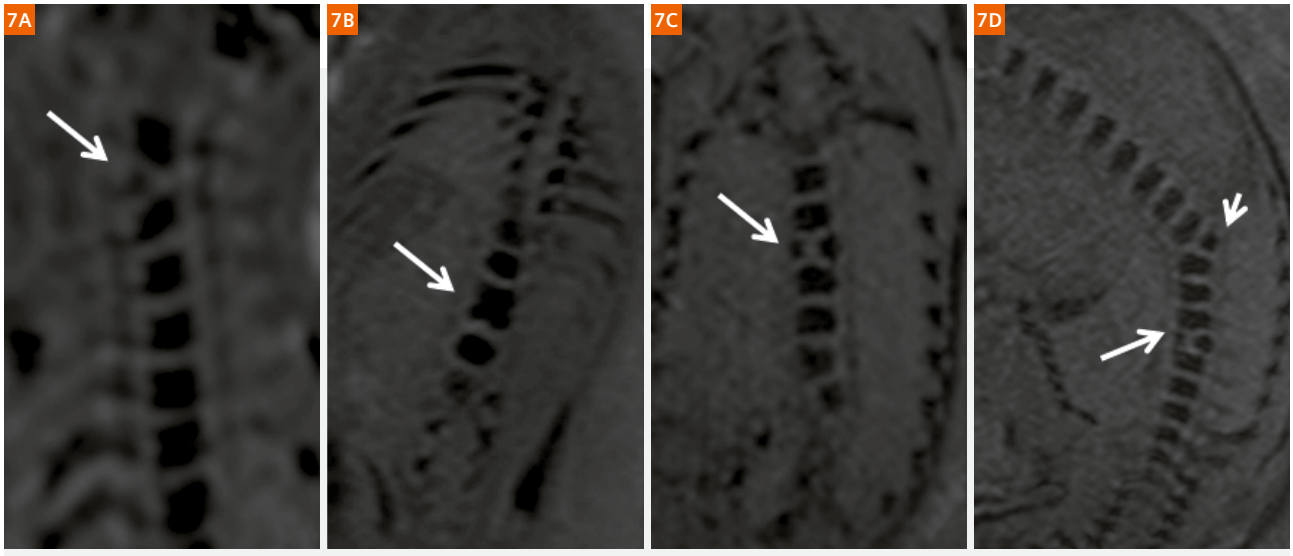

Figure 7:
SWI images at 26 weeks' gestation (7A), 25 weeks (7B), 33 weeks (7C), and 34 weeks with fetal vertebral anomalies. Coronal views of the cervical **(7A)**, lumbar **(7B)**, and thoracic **(7C)** spine show hemivertebrae, block vertebrae, and butterfly vertebrae. Multiple vertebral anomalies with hemivertebrae (short arrows) and butterfly vertebrae (long arrows) are clearly visible in coronal 2D SWI **(7D)**.

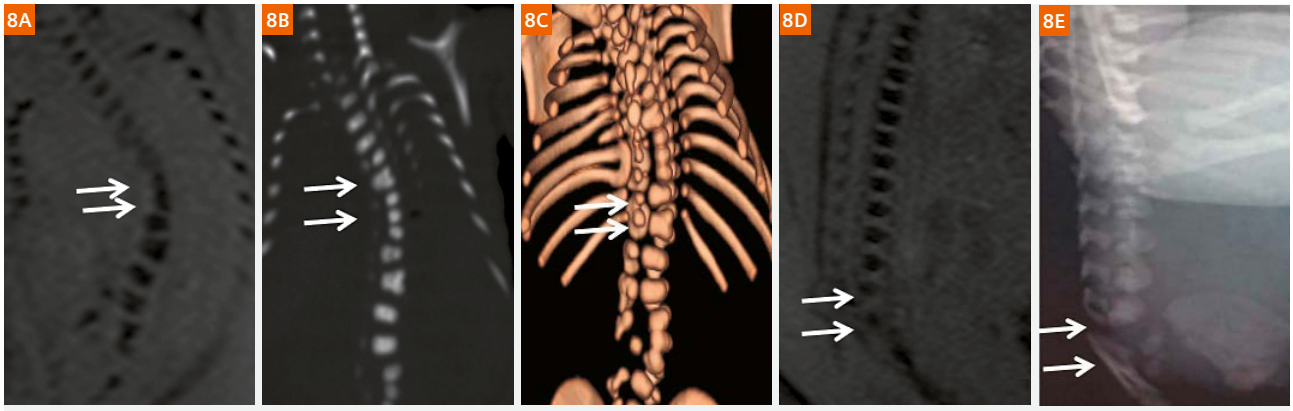

Figure 8:
Images at 24 weeks' gestation (8A–E) with multiple vertebral anomalies (8A–C) and at 32 weeks' gestation (8D–E) with caudal regression syndrome. SWI **(8A)** shows multiple vertebral anomalies (arrows) that were consistent with the postmortem CT (**8B**, **C**, arrows). SWI shows dysplasia of the sacrococcygeal vertebrae (arrows) that was consistent with the postmortem X-ray (**8E**, arrows).

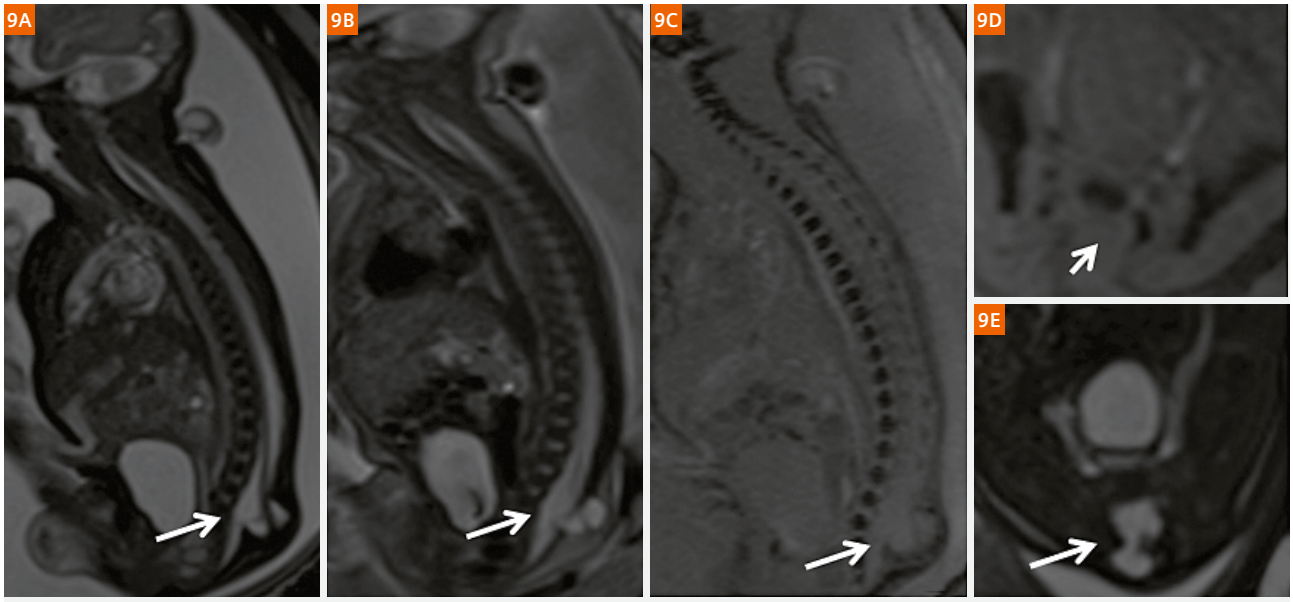

Figure 9:
Images at 32 weeks' gestation with spinal dysraphism (9A–E). Sagittal view of the MR images include HASTE **(9A)**, TrueFISP **(9B, E)**, and SWI **(9C, D)**. The pocket-like processes protruding from the sacrococcygeal spinal canal were all visible, and the spinal cord was found to extend from the spinal canal to the dilated dural capsule (9A, B, E, long arrow), which could not be seen with SWI (9C, D). However, SWI showed excellent osseous spinal structures and demonstrates the pedicular widening (9C, long arrow; 9D, short arrow).

Chest

At present, ultrasound and MRI are the only diagnostic tools that can examine fetal lungs noninvasively. MRI provides additional biochemical and functional information that cannot be obtained by ultrasound as well as detailed structural information. This therefore makes it a valuable diagnostic adjunct for assessing fetal lung development [10]. Congenital chest malformations can range from small and asymptomatic entities to large, space-occupying masses that require immediate surgical treatment. An understanding of fetal chest masses is essential for appropriate monitoring during pregnancy, and for treatment recommendations and delivery management. The most common congenital chest anomalies include congenital cystic adenomatoid malformation (CCAM), congenital diaphragmatic hernia (CDH), bronchopulmonary sequestration (BPS), congenital hydrothorax, and congenital lobar emphysema. Less common entities include congenital high airway obstruction syndrome (CHAOS), congenital bronchogenic cyst, bronchial atresia, pulmonary arteriovenous malformation (PAVM), congenital pulmonary lymphangiectasia, pulmonary hypoplasia-aplasia, mediastinal teratoma, and mediastinal lymphangioma. These pulmonary abnormalities are not mutually exclusive; they frequently occur together as hybrid conditions.

The MRI sequences used to evaluate the fetal chest include HASTE, fast single-shot echo, and TrueFISP. In our unit, HASTE and TrueFISP images are the most useful for evaluating the lung anatomy. The lungs typically contain a significant amount of alveolar fluid, which is homogeneously hyperintense relative to the chest wall muscle on T2-weighted images.

Congenital diaphragmatic hernia and extralobar pulmonary sequestration were demonstrated as follows (Figs. 10, 11).

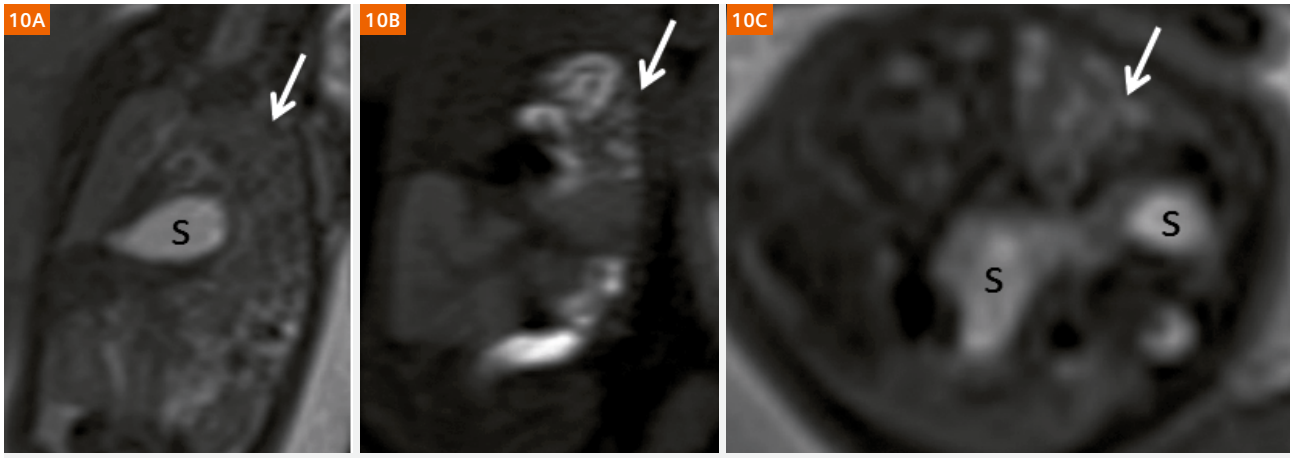

Figure 10: Congenital diaphragmatic hernia at 28 weeks' gestation
Coronal **(10A)** and axial **(10C)** T2 HASTE, and T1w imaging **(10B)** show herniated content (arrow) displacing the heart and compressing the unilateral lung and portions of the bowel (10B, arrow) and stomach (S) occupying the unilateral hemithorax.

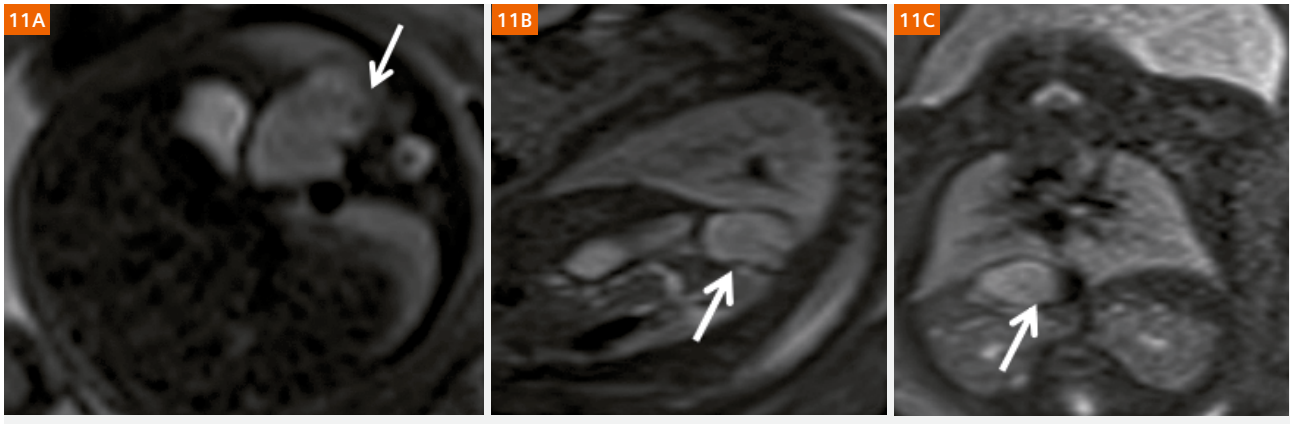

Figure 11: Extralobar pulmonary sequestration at 32 weeks' gestation
Axial **(11A)**, sagittal **(11B)**, and coronal **(11C)** T2 HASTE show a homogeneous, high T2WI signal between the left subphrenic space and left kidney with a clear boundary (arrow). Postnatal CT (not shown) enhancement shows a vascular shadow connected to the aorta.

Abdominal abnormalities and tumors

Fetal abdominal deformities and tumors vary in their location, and can be derived from the gastrointestinal tract, liver, kidney, and retroperitoneum. Congenital tumors are defined as those that are present during the fetal stage or at birth. In some cases, MRI can provide important information and even add important findings to prenatal US for perinatal management by visualizing fetal tumors with common tumor-related complications and other exceptional congenital abnormalities [11]. Common indications for fetal gastrointestinal (GI) MRI include suspected esophageal, small bowel, and large bowel obstruction, bowel malrotation, and bowel perforation resulting in meconium peritonitis or meconium pseudocyst. MRI is also particularly useful for evaluating rare GI abnormalities, such as megacystis microcolon intestinal hypoperistalsis syndrome (MMIHS), cloacal exstrophy, and cloacal malformation. Although US remains the modality of choice for investigating fetal anomalies, the findings are often nonspecific and may relate to transient normal variants [12]. In addition, urine and fluid in the colon beyond 24 weeks may have a similar sonolucent appearance on US and opposite appearances on MR images, allowing better identification and discrimination. In our department, a T1-weighted breath-hold sequence is completed in the coronal plane and, if necessary, in the sagittal and axial planes.

Different developmental deformities in the abdomen were demonstrated as follows (Figs. 12–16).

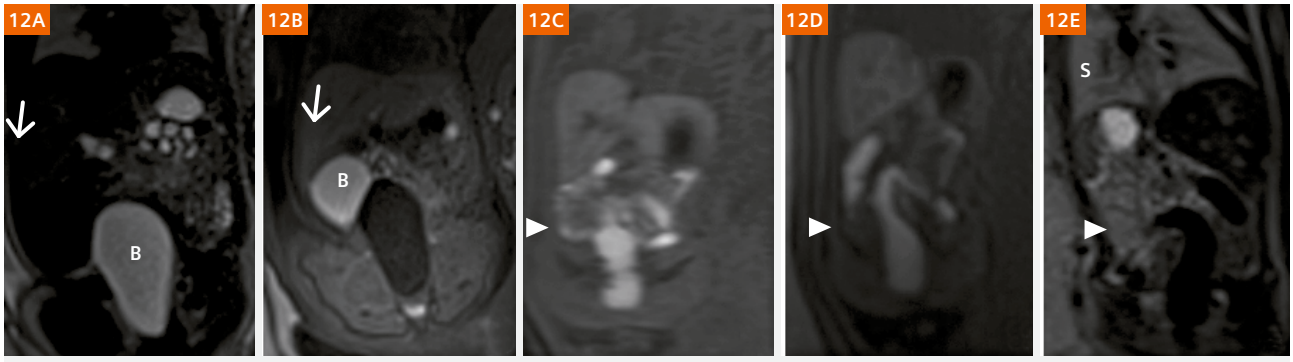

Figure 12: Localized intestinal dilatation at 30+4 weeks' gestation, and imperforate anus at 28 weeks' gestation
Coronal T2 HASTE **(12A)** and T1w **(12B)** images show the dilated loops of one part of the gastrointestinal tract. It is markedly hyperintense on T1WI (arrow) and hypointense on T2WI (arrow). Coronal T1WI **(12C, D)** and T2 TrueFISP **(12E)** images show a prominent rectum (arrowhead) with high T1 signal intensity and low T2 signal intensity. The abnormality of the large bowel was identified and diagnosed as rectal atresia during a postnatal physical examination. B = urinary bladder, S = stomach

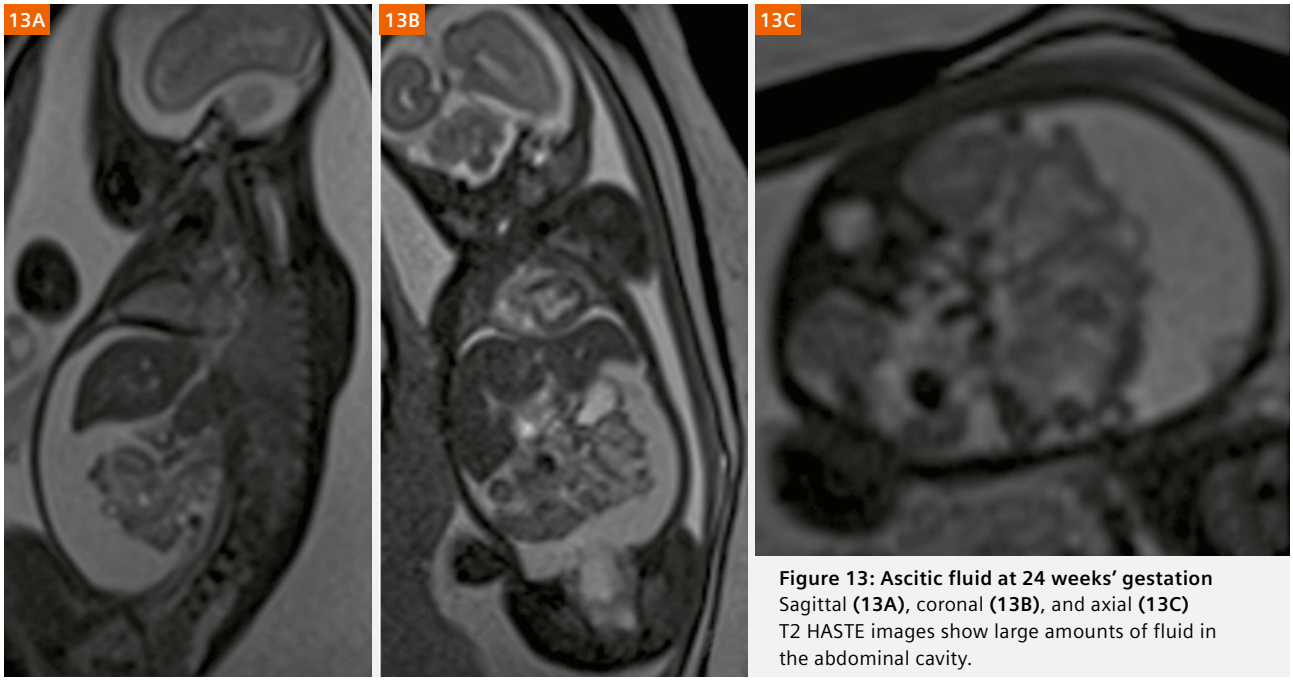

Figure 13: Ascitic fluid at 24 weeks' gestation
Sagittal **(13A)**, coronal **(13B)**, and axial **(13C)** T2 HASTE images show large amounts of fluid in the abdominal cavity.



Figure 14: Neuroblastoma at 28 weeks' gestation
Axial **(14A)**, sagittal **(14B)**, and coronal **(14C)** T2 HASTE images show a solid mass with a clear boundary above a lateral kidney that is hyperintense on a T2-weighted sequence (arrow) and was found to be neuroblastoma after birth.

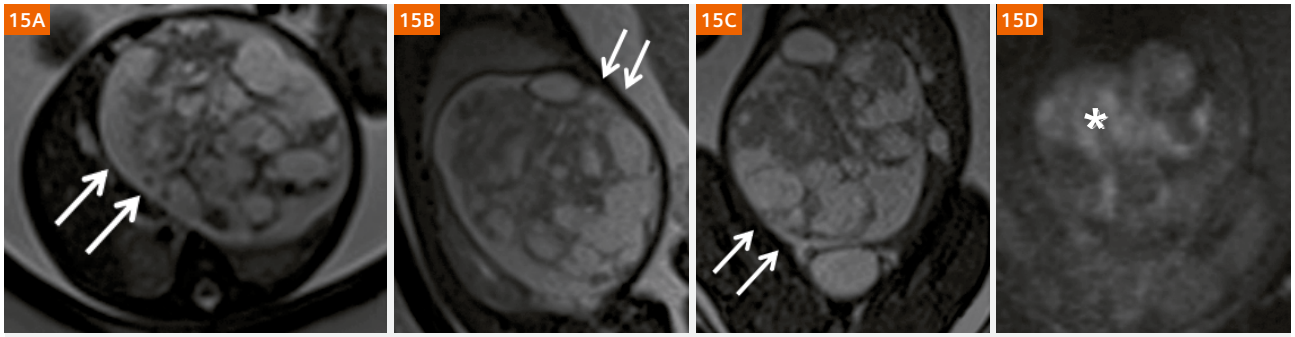

Figure 15: Teratoid tumors at 30 weeks' gestation
Axial T2 HASTE **(15A)**, sagittal **(15B)**, and coronal **(15C)** T2 TrueFISP images show a heterogeneous solid cystic mass with a high-intensity heterogeneous signal (arrows), and surrounding tissue that was markedly squeezed. The giant lesions showed restricted diffusion with DWI (**15D**, star). A histopathological diagnosis of teratoid tumors was made after birth.

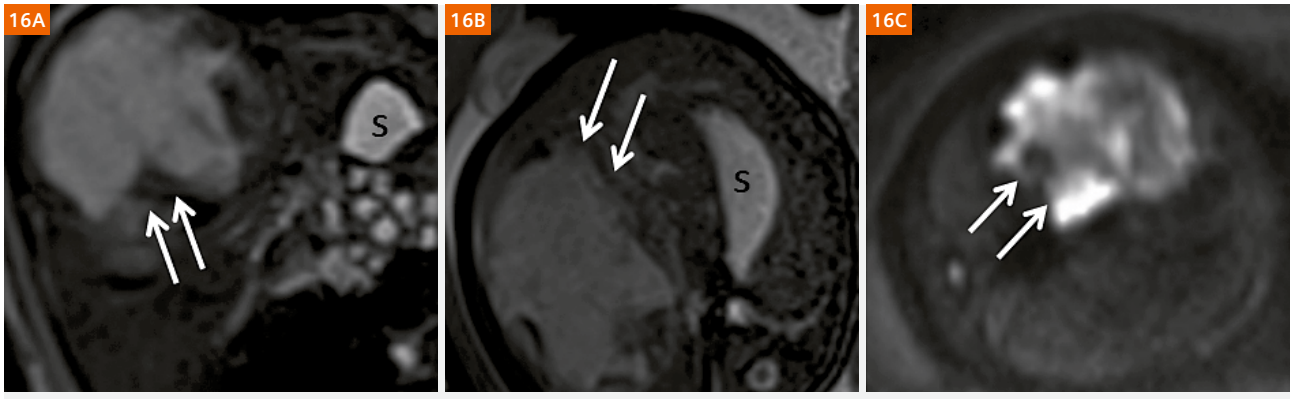

Figure 16: Hepatic hemangioendothelioma at 32 weeks' gestation
Coronal T2 HASTE **(16A)** and axial T2 TrueFISP **(16B)** images show a large heterogeneous and high-signal mass in the liver parenchyma, and highly restricted diffusion with DWI **(16C)**. A histopathological diagnosis of hepatic hemangioendothelioma was made after birth.

Maternal indications for prenatal MRI

In addition to fetal indications, there are several maternal indications for prenatal MR imaging. They include the possibility of uterine rupture, the need to differentiate between placenta accreta and percreta, a large myoma interfering with the pregnancy, and MR pelvimetric measurements. In our unit, the technique of placental MRI and the diagnostic level are increasingly convincing and compelling.

Abnormal invasive placenta (AIP) is a disease with a spectrum of severity characterized by abnormal, firmly adherent placental implantation into the uterus at varying depths. It is typically referred to as placenta accreta, increta, and percreta [13]. When AIP occurs, the placenta may not be completely separated from the uterus at the time of delivery, resulting in potentially life-threatening intrapartum or postpartum massive hemorrhage and associated morbidity such as multisystem organ failure, disseminated intravascular coagulation, and even death. Placenta percreta (PP) is the most dangerous type of AIP. It is characterized by trophoblasts fully penetrating the myometrium and in some cases extending to or breaching the serosa and even invading surrounding structures [14]. An accurate prenatal diagnosis of PP is therefore imperative.

In 2017, our team published an article on placenta accreta [15] that aimed to identify specific MRI features for differentiating PP from placenta accreta (PA), and to characterize the features of invasive placenta previa. Our studies showed a series of MRI features, including myometrial thinning, interrupted myometrium, loss of the placental-myometrial interface, marked placental heterogeneity, dark intraplacental bands, abnormal intraplacental vascularity, abnormal uterine bulge, placental bulge (type I and type II, Fig. 2), uterine serosal hypervascularity, bladder wall nodularity, and extrauterine placental extension. Our results suggest that type II placental bulge and uterine serosal hypervascularity are useful MRI features for differentiating PP from PA. Profoundly abnormal vessels are associated with greater blood loss during caesarean section. Our results could contribute to accurate prenatal diagnosis of PP and help minimize the risk of massive hemorrhage [15].

In our center, all the patients with suspected invasive placenta previa (IPP) were imaged in the supine or left-lateral position with bladders moderately full. T2-weighted HASTE and T2-weighted TrueFISP images were obtained without breath-hold in the axial, coronal, sagittal, and oblique sagittal planes. Additional imaging planes perpendicular to the placenta-uterus interface or uterus-bladder interface were obtained in the region of the suspected AIP.

Several placenta increta and placenta percreta were demonstrated as follows (Figs. 17–20).

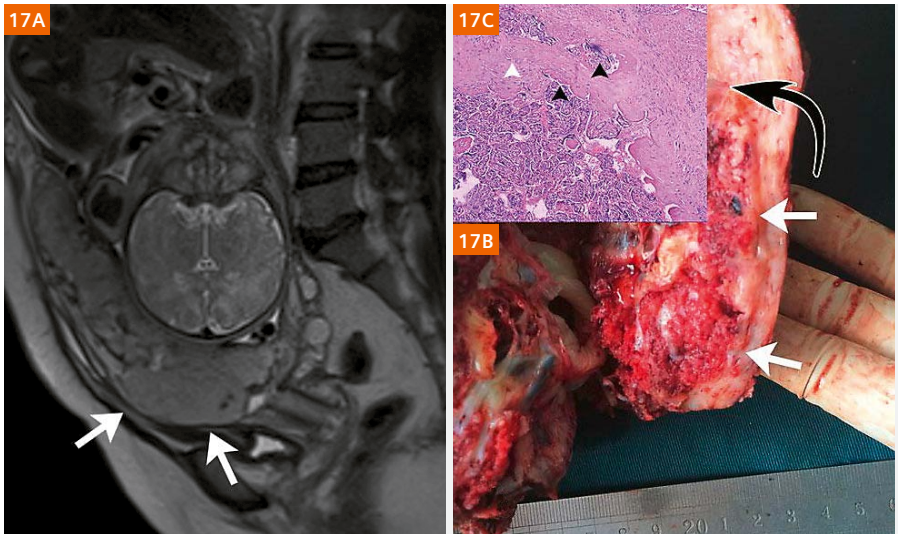

Figure 17: Placenta increta (PI) in a 40-year-old woman at 35 weeks' gestation
A sagittal T2 HASTE MR image **(17A)** demonstrates type I placental bulge (white arrows) with an intact uterine outline. A photograph **(17B)** of gross specimens after hysterectomy shows that the placenta has invaded the myometrium (white arrows) with intact uterine serosa, consistent with PI. A photomicrograph (**17C**, magnification x 400, hematoxylin and eosin stain) shows chorionic villi (black arrowheads) implanted in the myometrium (white arrowhead), consistent with PI.

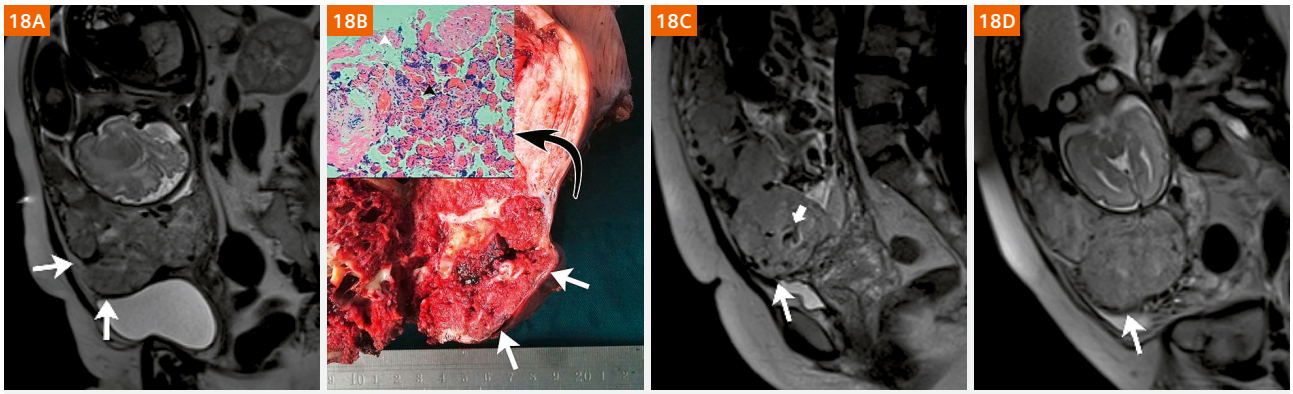

Figure 18: Placenta percreta (PP, 18A, B) in a 39-year-old woman at 30 weeks' gestation
A sagittal T2 HASTE MR image **(18A)** shows type II placental bulge (white arrows) protruding from the uterine outline. A photograph **(18B)** of gross specimens after hysterectomy shows placental invasion (white arrows) through the uterine wall, consistent with PP. A photomicrograph (magnification: x 400, hematoxylin and eosin stain) shows chorionic villi (black arrowhead) penetrating the myometrium (white arrowhead), consistent with PP. Sagittal T2 HASTE MR images show a type IIa placental bulge (long arrow, a focal outward bulge protruding from the uterine outline) with bridging vessels (short arrow) in a 31-year-old woman at 35 weeks' gestation with PP **(18C)** and type IIb placental bulge (long arrow) without bridging vessels in a 29-year-old woman at 32 weeks' gestation with PP **(18D)**.

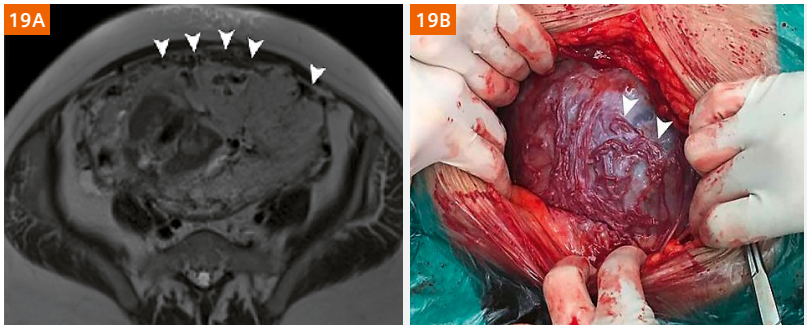

Figure 19: Placenta percreta (PP) in a 35-year-old woman at 29 weeks' gestation
An axial T2 HASTE image **(19A)** shows uterine serosal hypervascularity (arrowheads, tortuous and closely packed vessels along the uterine serosa) in the lower uterine segment.
A photograph **(19B)** taken during cesarean delivery shows the tortuous abnormal vessels in the uterine serosa (arrowheads), consistent with their appearance on MR images.

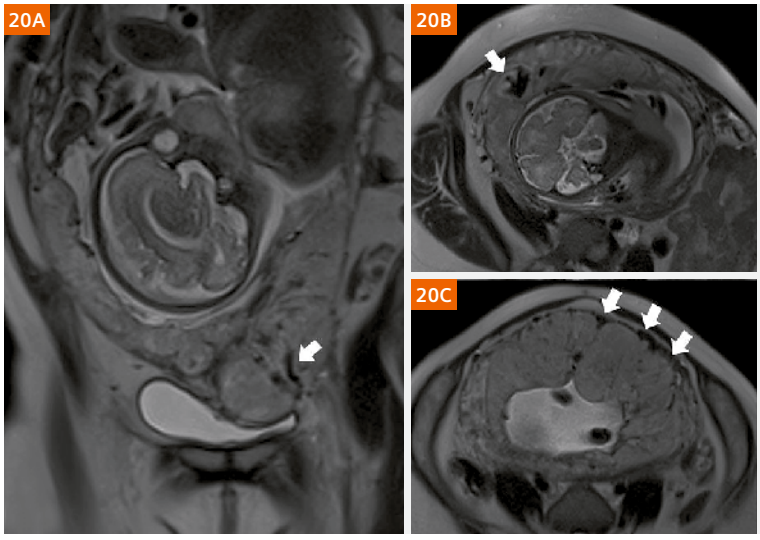

Figure 20:
A coronal T2 HASTE MR image **(20A)** shows bridging vessels (arrow) through the bulging placenta in a 25-year-old woman at 32 weeks' gestation with placenta percreta (PP). An axial T2 HASTE MR image **(20B)** shows abnormal intraplacental vascularity (arrow) in a 28-year-old woman at 30 weeks' gestation with placenta increta (PI). An axial T2 HASTE MR image **(20C)** demonstrates uterine serosal hypervascularity (arrows) in a 34-year-old woman at 35 weeks' gestation with PP.

As outlined in this article, fetal MR imaging is playing an increasingly important role in prenatal diagnostics. Nevertheless, US will and should remain the first choice for prenatal screening due to its low cost, ease of availability, and superb safety profile. Advances in fetal MRI have given clinicians powerful tools to identify fetal pathologies. These can range from small and symptomatic abnormalities to large, space-occupying masses that require immediate surgical treatment. The information obtained with fetal MR imaging can be helpful and allow early planning of prenatal management.

References

1 Weisstanner C, Gruber GM, Brugger PC, et al. Fetal MRI at 3T – ready for routine use? Br J Radiol. 2017; 90(1069):20160362.
2 Prayer D, Brugger PC. Investigation of normal organ development with fetal MRI. Eur Radiol. 2007; 17(10):2458-2471.
3 Haacke EM, Xu Y, Cheng YC, et al. Susceptibility weighted imaging (SWI). Magn Reson Med. 2004; 52(3):612-618.
4 Reichenbach JR, Jonetz-Mentzel L, Fitzek C, et al. High-resolution blood oxygen-level dependent MR venography (HRBV): a new technique. Neuroradiology 2001; 43(5):364-369.
5 Robinson AJ, Blaser S, Vladimirov A, et al. Foetal "black bone" MRI: utility in assessment of the foetal spine. Br J Radiol. 2015; 88(1046):20140496.
6 Smith FW, Adam AH, Phillips WD. NMR imaging in pregnancy. Lancet. 1983; 1(8314-5):61-62.
7 Reichenbach JR, Venkatesan R, Schillinger DJ, et al. Small vessels in the human brain: MR venography with deoxyhemoglobin as an intrinsic contrast agent. Radiology. 1997; 204(1):272-277.
8 Coakley FV, Glenn OA, Qayyum A, et al. Fetal MRI: a developing technique for the developing patient. AJR Am J Roentgenol. 2004; 182(1):243-252.
9 Duczkowska A, Bekiesinska-Figatowska M, Herman-Sucharska I, et al. Magnetic resonance imaging in the evaluation of the fetal spinal canal contents. Brain Dev. 2011; 33(1):10-20.
10 Kasprian G, Balassy C, Brugger PC, et al. MRI of normal and pathological fetal lung development. Eur J Radiol. 2006; 57(2):261-270.
11 Nemec SF, Horcher E, Kasprian G, et al. Tumor disease and associated congenital abnormalities on prenatal MRI. Eur J Radiol. 2012; 81(2):e115-e122.
12 Veyrac C, Couture A, Saguintaah M, et al. MRI of fetal GI tract abnormalities. Abdom Imaging. 2004; 29(4):411-420.
13 Belfort MA. Placenta accreta. Am J Obstet Gynecol. 2010; 203(5):430-439.
14 Silver RM, Barbour KD. Placenta accreta spectrum: accreta, increta, and percreta. Obstet Gynecol Clin North Am. 2015; 42(2):381-402.
15 Chen X, Shan R, Zhao L, et al. Invasive placenta previa: Placental bulge with distorted uterine outline and uterine serosal hypervascularity at 1.5T MRI – useful features for differentiating placenta percreta from placenta accreta. Eur Radiol. 2018; 28(2):708-717.

Contact

Guangbin Wang
Department of MR
Shandong Medical Imaging Research Institute
Shandong University
324, Jingwu Road, Jinan
Shandong 250021
China
wgb7932596@hotmail.com


Guangbin Wang


Xianyun Cai

Small Structures Big Challenges: Fetal Cardiac Magnetic Resonance Imaging

Veronica Bianchi[1]; Jérôme Yerly[1,2]; Jerome Chaptinel[1]; Yvan Mivelaz[3]; Milan Prsa[3]; Leonor Alamo[1]; Chantal Rohner[1]; Jean-Baptiste Ledoux[1,2]; Davide Piccini[1,5]; Chris Roy[1]; Matthias Stuber[1,2]

[1] Department of Radiology, University Hospital (CHUV) and University of Lausanne (UNIL), Lausanne, Switzerland
[2] Center for Biomedical Imaging (CIBM), Lausanne, Switzerland
[3] Department of Pediatrics, University Hospital (CHUV) and University of Lausanne (UNIL), Lausanne, Switzerland
[4] Department of Gynecology-Obstetrics, University Hospital (CHUV) and University of Lausanne (UNIL), Lausanne, Switzerland
[5] Advanced Clinical Imaging Technology, Siemens Healthineers, Lausanne, Switzerland

Introduction

Congenital heart disease (CHD) is the most common birth defect affecting nearly 1% of pregnancies in Europe [1, 2]. Gestational screening has greatly improved antenatal diagnosis of heart malformations and several prenatal interventions now exist to treat CHD in utero, or soon after birth. The timing and type of treatment relies heavily on the ability to accurately visualize a given cardiac malformation. Echocardiography is the gold standard for fetal cardiac imaging [3]. This imaging technique is safe and non-invasive but, despite the progress made in the field of fetal ultrasonography, its quality varies in the presence of maternal obesity, oligohydramnios, multiple gestations, or imaging during late gestation, among other conditions [4]. Since its early applications [5], cardiac magnetic resonance imaging (MRI) has been increasingly investigated for fetal[1] heart imaging in the last decade and has now become an active area of research. A growing number of studies are exploring its applicability in the evaluation of cardiac morphology and function for both normal and abnormal hearts [6–13]. Despite encouraging advances, there remain significant challenges for fetal cardiac MRI, including the small size and the high rate of the fetal heart, the absence of a conventional fetal cardiac gating signal, and the numerous sources of motion artifacts, such as gross fetal movement, and maternal respiration [4]. However, if these challenges can be addressed, it has been shown that MRI has the potential to provide complementary information to echocardiography, improve our ability to monitor CHD diagnosed *in* utero, and better help guide treatments and decision making.

The aim of this project was to develop an MR image acquisition and reconstruction framework that can overcome the aforementioned challenges and visualize the fetal heart with high spatial and temporal resolution [8]. In this article, we describe such an approach, which combines maternal breath-hold, compressed sensing, and self-gating to produce high quality CINE images of the fetal heart. In addition, here we show preliminary results using our reconstruction framework to produce high quality CINE images of the fetal heart. For comparison, we include ultrasound images in the same orientation of those acquired with MR.

Image reconstruction framework

Our reconstruction framework for golden angle radial acquisitions is composed of three main steps. First, intermediate low-resolution images are reconstructed using compressed sensing. Second, an ECG-like self-gating signal is extracted from the intermediate images. Third, the acquired data are reordered into the identified cardiac phases (Fig. 1) [8].

Initially, low spatial and temporal resolution images are reconstructed with a sliding window approach using 15 radial readouts per window and 70% view-sharing, leading to a temporal resolution of 18.5 ms (Fig. 1B). Subsequently, the obtained images are analyzed off-line with a custom-built semi-automatic tool in MATLAB[2] (MathWorks, Natick, MA, USA). The gating signal that reproduces the contraction cycles of the fetal heart is computed by cross-correlating each intermediate frame to a diastolic and a systolic reference image, focusing on a region of interest circumscribed around the fetal heart (Fig. 1C). Finally, and owing to the characteristics that the golden angle acquisition scheme is providing us with,

[1] *Siemens Healthineers disclaimer does not represent the opinion of the authors: MR scanning has not been established as safe for imaging fetuses and infants less than two years of age. The responsible physician must evaluate the benefits of the MR examination compared to those of other imaging procedures.*

[2] *The information shown herein refers to products of 3rd party manufacturers and thus are in their regulatory responsibility. Please contact the 3rd party manufacturer for further information.*

the radial readouts are retrospectively binned into different cardiac phases (Fig. 1D) with a bin width of 25 ms and a view-sharing equal to 50%, improving the temporal resolution to 12.5 ms. Both intermediate and retro-gated images are reconstructed using an in-house script implementing a *k-t* sparse SENSE algorithm model [14].

Image acquisition and analysis

To validate the proposed framework, six pregnant patients (gestational age 29.7 ± 2.1 weeks at the time of the MRI exam) with a suspicion of fetal non-cardiac pathology were recruited to undergo both MRI and fetal echocardiography. Written informed consent, according to the recommendations of the local ethics committee, was obtained from all subjects prior to examination.

MR acquisition was performed on a 1.5T clinical MR scanner (MAGNETOM Aera, Siemens Healthcare, Erlangen, Germany) with a 32-channel spine coil and an 18-channel body array coil for signal measurement. Data were collected under maternal breath-hold with a prototype radial golden angle bSSFP sequence (Fig. 1A) and acquisition parameters are summarized in Table 1 [8]. For each patient, three standard views (four-chamber, three-vessel and short-axis view), that are routinely targeted in the clinical fetal echocardiographic examination, were acquired (Fig. 2) in 20.1 s each. Echocardiographic images were acquired on a Voluson E8 Expert or Voluson E10 (GE Healthcare, Waukesha, WI, USA)

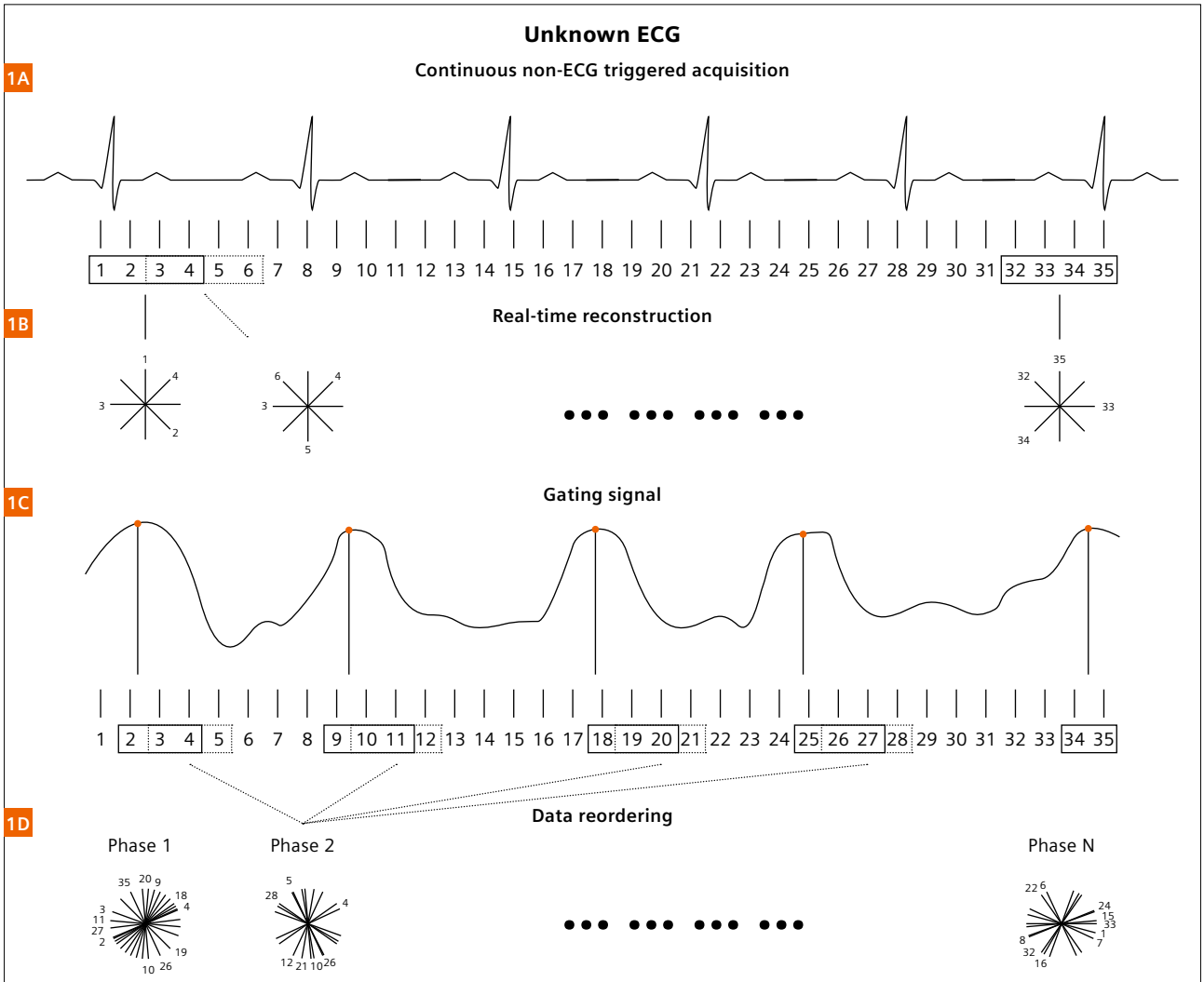

Figure 1:
Schematic overview of the MRI acquisition and reconstruction framework. The data, acquired with a golden angle continuous acquisition technique **(1A)**, were reconstructed applying a sliding window binning **(1B)** and intermediate images were obtained. The low-resolution images were subsequently analyzed to extract an ECG-like gating signal that represents the contraction cycles of the fetal heart **(1C)**. The self-gating signal was then used to retrospectively bin the radial data in different cardiac phases during which they were acquired **(1D)**.
(Figure adapted from Chaptinel et al. [8], with permission according to https://creativecommons.org/licenses/by/4.0/).

Parameter	Value
Field-of-view	260 x 260 mm²
Base resolution	256 x 256 pixels
Pixel size	1.0 x 1.0 mm²
Slice thickness	4.0 mm
TE/TR	1.99/4.1 ms
RF excitation angle	70°
Slices	3
Shot per slice	1
Radial readouts per slice	1600
Acquisition time per slice	6.7 s
Bandwidth	1028 Hz/pixel
Reconstructed temporal resolution	12.5 ms (shared phases)

Table 1: Values of the MR acquisition parameters.

with the RM6C 3D/4D curved array transducer with a frequency comprised in the range 1.0–7.0 MHz. Finally, MR and echocardiographic images were qualitatively and quantitatively compared to demonstrate the capability of both imaging techniques to visualize and measure heart structures. Two experienced pediatric cardiologists visually evaluated the quality of the images obtained with both modalities. Subsequently, they measured the diameter of aorta, main pulmonary artery, mitral valve annulus and tricuspid valve annulus using ClearCanvas (Synaptive Medical, Toronto, Canada) on both MR and echocardiographic images for each patient.

Results and discussion

MR images were successfully acquired on all patients. Figure 3 shows an example of fetal heart images in a 4-chamber (Fig. 3A), a short-axis (Fig. 3B) and a three vessel view (Fig. 3C) acquired in a 31-week-old fetus. MR images (columns on the left) are visually compared to the images obtained with the gold standard, echocar-

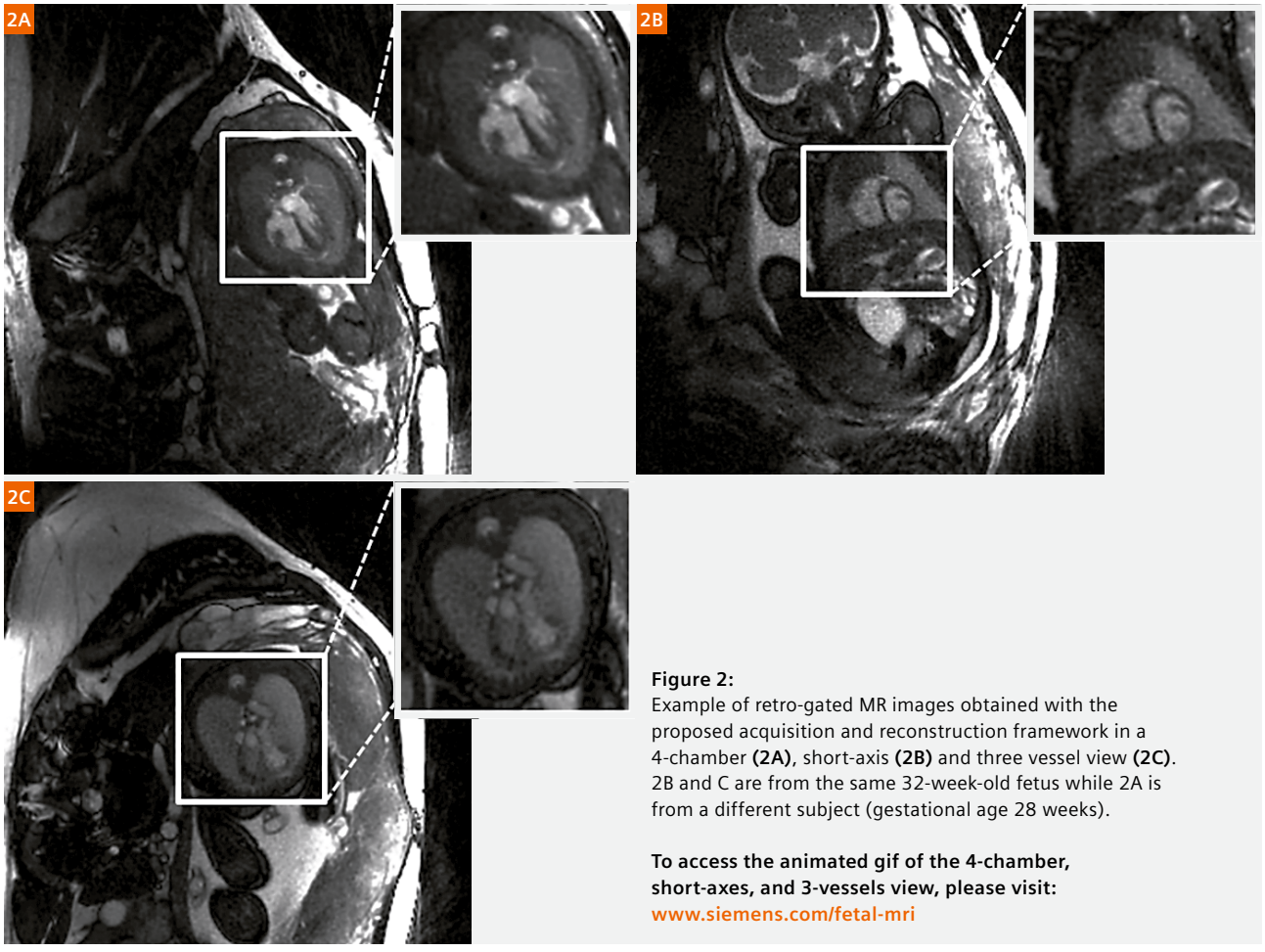

Figure 2:
Example of retro-gated MR images obtained with the proposed acquisition and reconstruction framework in a 4-chamber **(2A)**, short-axis **(2B)** and three vessel view **(2C)**. 2B and C are from the same 32-week-old fetus while 2A is from a different subject (gestational age 28 weeks).

To access the animated gif of the 4-chamber, short-axes, and 3-vessels view, please visit:
www.siemens.com/fetal-mri

diography (column on the right). The two imaging techniques proved to be comparable in terms of qualitative visualization of cardiac structures. The overall MR image quality was considered satisfying to perform quantitative measurements for all patients except for one in which the mitral valve and the tricuspid valve were not clearly recognizable. Moreover, one patient was excluded from the quantitative comparison because the echocardiographic images were not compatible with the software used for the analysis. Therefore, the diameter of aorta and main pulmonary artery were measured in five patients, while instead mitral valve annulus and tricuspid valve annulus were measured on the images of four patients. As shown in Figure 4, the quantitative measurements performed on the MR images are in good agreement with the measurements by

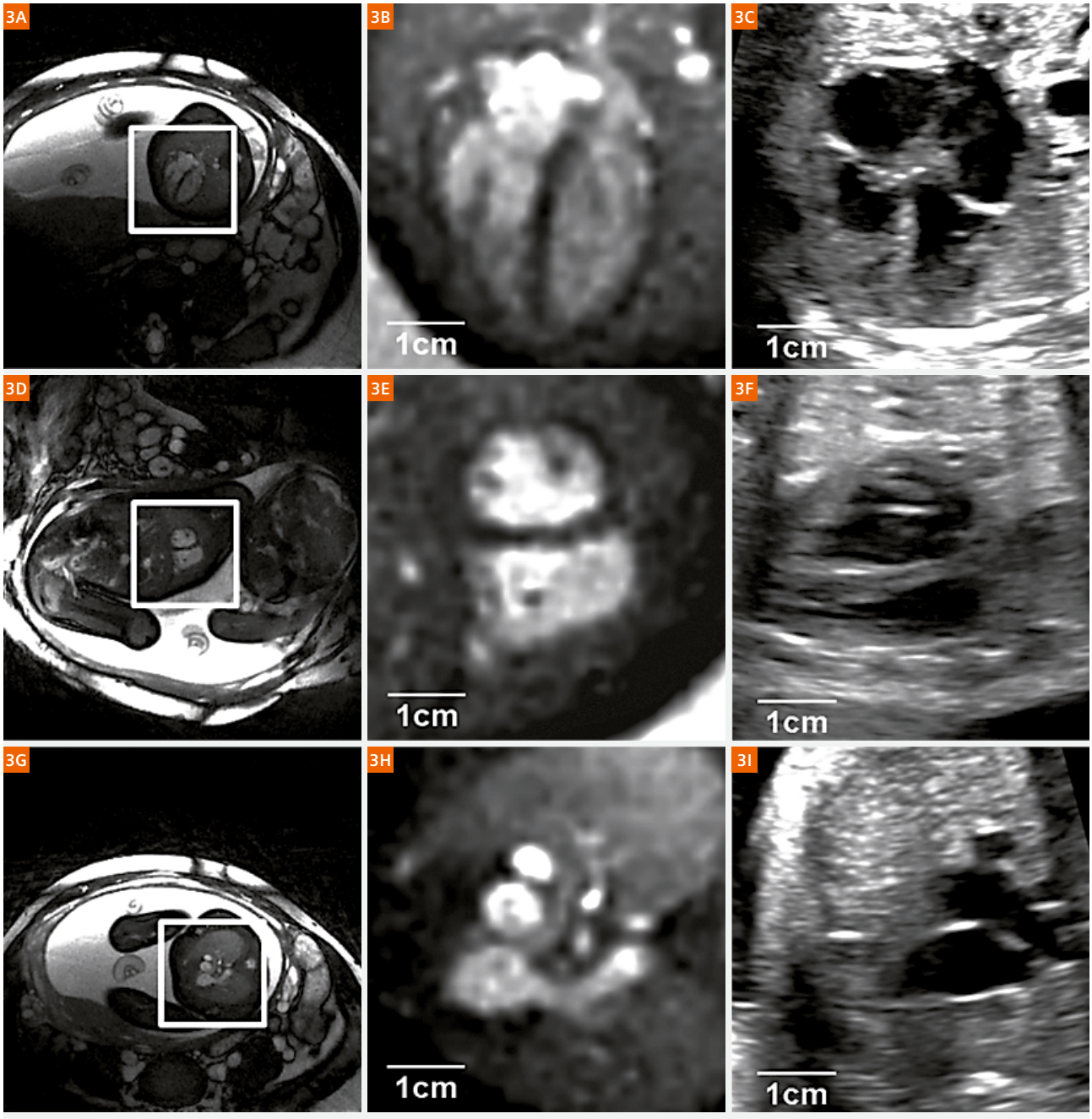

Figure 3:
Comparison between MR and echo images in 4-chamber **(3A–C)**, short-axis **(3D–F)** and three vessel view **(3G–I)** from one of the patient. *(Figure adapted from Chaptinel et al. [8] with permission according to https://creativecommons.org/licenses/by/4.0/).*

echocardiography. This study demonstrated that MRI is a promising technique for acquiring high spatial and high temporal resolution images of the fetal heart, and that it is critically enabled by advanced acquisition and reconstruction schemes that have recently been developed. These include golden angle acquisition, self-gating that obviates the need for an ECG, and compressed sensing reconstruction. Preliminary results show the potential of our acquisition and reconstruction framework for the visualization and measurement of normal fetal cardiac structures. MRI could offer a reliable easily repeatable and safe complementary imaging modality for patients in whom echocardiography is inconclusive. Further study is now required to assess the diagnostic capability of fetal cardiac MRI in the presence of cardiac abnormalities.

4

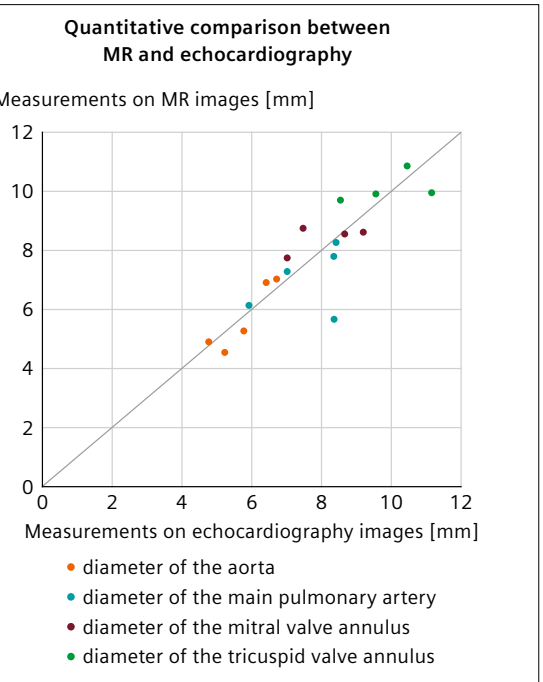

Figure 4:
Comparison between quantitative measurements performed on MR and echocardiographic images of normal fetal hearts. The graph shows the average values of the measurements performed by two pediatric cardiologists on the best-quality image for each methodology. The diameter of aorta and main pulmonary artery were measured on five fetal patients, while the mitral valve annulus and the tricuspid valve annulus were quantified for four fetal patients.

Contact

Prof. Matthias Stuber
Center for BioMedical Imaging (CIBM)
Centre Hospitalier Universitaire Vaudois (CHUV)
Rue de Bugnon 46, BH 8.80
1011 Lausanne
Switzerland
Matthias.stuber@chuv.ch



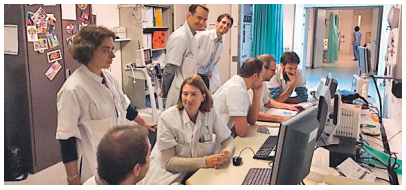

References:

1 Dolk H, Loane M, Garne E, for the European Surveillance of Congenital Anomalies (EUROCAT) Working Group. Congenital heart defects in Europe: prevalence and perinatal mortality, 2000 to 2005. Circulation 2011; 123:841–9.
2 EUROCAT Access Prevalence Tables. Available at: http://www.eurocatnetwork.eu/ACCESSPREVALENCEDATA/PrevalenceTables. Accessed September 11, 2018.
3 Donofrio MT, Moon-Grady AJ, Hornberger LK, et al. Diagnosis and treatment of fetal cardiac disease: A scientific statement from the american heart association. Circulation 2014; 129:2183–2242. doi: 10.1161/01.cir.0000437597.44550.5d.
4 Wielandner A, Mlczoch E, Prayer D, Berger-Kulemann V. Potential of magnetic resonance for imaging the fetal heart. Seminars in fetal & neonatal medicine 2013; 18(5):286-297.
5 Meyer-Wittkopf M, Cook A, McLennan A, Summers P, Sharland GK, Maxwell DJ. Evaluation of three-dimensional ultrasonography and magnetic resonance imaging in assessment of congenital heart anomalies in fetal cardiac specimens. Ultrasound Obstet Gynecol 1996; 8(5):303–8. doi: 10.1046/j.1469-0705.1996.08050303.x.
6 Votino C, Jani J, Damry N, Dessy H, Kang X, Cos T, Divano L, Foulon W, De Mey J, Cannie M. Magnetic resonance imaging in the normal fetal heart and in congenital heart disease. Ultrasound Obstet Gynecol 2012; 39(3):322-329. doi: 10.1002/uog.10061.
7 Manganaro L, Savelli S, Di Maurizio M, et al. Assessment of congenital heart disease (CHD): Is there a role for fetal magnetic resonance imaging (MRI)? Eur J Radiol 2009; 72:172-180. doi: 10.1016/j.ejrad.2008.06.016.
8 Chaptinel J, Yerly J, Mivelaz Y, Prsa M, Alamo L, Vial Y, Berchier G, Rohner C, Gudinchet F Stuber M. Fetal cardiac cine magnetic resonance imaging in utero. Sci Rep 2017; 7(1):15540. doi: 10.1038/s41598-017-15701-1.
9 Gorincour G, Bourliere-Najean B, Bonello B, Fraisse A, Philip N, Potier A, Kreitmann B, Petit P. Feasibility of fetal cardiac magnetic resonance imaging: preliminary experience. Ultrasound Obstet Gynecol 2007; 29:105-108. doi: 10.1002/uog.3924.
10 Tsuritani M, Morita Y, Miyoshi T, Kurosaki K, Yoshimatsu J. Fetal Cardiac Functional Assessment by Fetal Heart Magnetic Resonance Imaging. J Comput Assist Tomogr 2018; 00:00–00. doi: 10.1097/RCT.0000000000000781.
11 Roy CW, Seed M, Kingdom JC, Macgowan CK. Motion compensated cine CMR of the fetal heart using radial undersampling and compressed sensing. J Cardiovasc Magn Reson 2017;19:1–14. doi: 10.1186/s12968-017-0346-6.
12 Amerom JFP, Lloyd DFA, Murgasova K, et al. King's Research Portal Fetal Cardiac Cine Imaging Using Highly Accelerated Dynamic MRI with Retrospective Motion Correction and Outlier Rejection. doi: 10.1002/mrm.26686.
13 Haris K, Hedström E, Bidhult S, et al. Self-gated fetal cardiac MRI with tiny golden angle iGRASP: A feasibility study. J Magn Reson Imaging 2017 doi: 10.1002/jmri.25599.
14 Yerly J, Ginami G, Nordio G, Coristine AJ, Coppo S, Monney P, Stuber M. Coronary endothelial function assessment using self-gated cardiac cine MRI and k-t sparse SENSE. Magn Reson Med 2016; 76:1443–1454. doi: 10.1002/mrm.26050.

Three Years of PI-RADS v2: Achievements, Open Questions and Future Perspectives

Bernd Hamm, M.D.

Department of Radiology, Charité University Hospital, Humboldt-Universität zu Berlin and Freie Universität Berlin, Germany

The Prostate Imaging-Reporting and Data System version 2 (PI-RADS v2) was designed to set requirements for multiparametric MR (mpMRI) imaging of the prostate, to optimize image quality and standardize prostate MRI reporting and to reduce variability in image interpretation by proposing assessment categories for detection or exclusion of clinically significant cancer of the prostate. Three years after the introduction of PI-RADS v2, Anwar Padhani and other members of the PI-RADS committee summarize the current state of research and clinical experience with PI-RADS v2, name the strengths and weaknesses and propose directions for future research and improvements of the standard to contribute to value-based health care [1].

Summary

The range of genomic diversity and prognosis of prostate cancer (PCa), the variable prevalence in different populations as well as known limitations of established diagnostic tools, e.g., non-cancer-specific reasons for increased prostate-specific antigen (PSA) levels, and the semi-randomness of transrectal ultrasound (TRUS) biopsies lead to major challenges in the diagnostic management of these patients:

1. Men without clinically significant prostate cancer but elevated PSA levels undergo unnecessary biopsies with attendant morbidity [2].
2. Men with indolent (non-significant) cancers are diagnosed with the disease and undergo therapies which are not positively affecting their overall survival but instead may have severe side effects that significantly impact their quality of life [3].
3. Men having clinically significant cancer are underdiagnosed or the disease may even remain undiagnosed, resulting in suboptimal treatment decisions due to poor tissue sampling.

While there are several diagnostic options besides imaging, including molecular diagnostics, that allow more accurate PCa diagnosis, prostate mpMRI plays an increasingly important role in ruling out or detecting clinically significant cancer in men with elevated PSA levels.

The promotion of PI-RADS v2 as a global standard reduces variation in the acquisition, interpretation and reporting of prostate mpMRI exams and has thus made an important contribution to overcoming the limitations associated with highly variable imaging protocols (and quality of studies), high intra-reader variability and in particular the difficulties in communicating findings to referring urologists. Today, PI-RADS v2 has developed into the universal standard for prostate mpMRI interpretation and reporting, significantly improving communication among radiologists and urologists.

Multiple patient- and lesion-level analyses have shown that PI-RADS v2 assessment categories are effective and improve sensitivity for detection of clinically significant prostate cancer compared to PI-RADS v1. On the lesion level, however, studies indicate that non-index lesions tend to be overlooked (e.g., low-grade and very small prostate cancers). Furthermore, there

is a large body of evidence that both PI-RADS v2 and non-PI-RADS standardized scoring systems (Likert) have a very high "rule out" performance for clinically significant PCa. This has important implications for men with negative MRI findings and may help to significantly reduce the number of patients undergoing random biopsy of the prostate. Two recent prospective studies with excellent study designs – the PROMIS (2017, published in Lancet) and the PRECISION study (2018, published in NEJM) – have shown that mpMRI detects more significant prostate cancers and fewer non-significant cancers compared with random TRUS biopsy [4, 5]. These results will lead to the wider use of mpMRI prior to the first transrectal prostate biopsy in the mid-term.

Beyond summarizing recent studies and developments, the authors also point out limitations of PI-RADS v2, such as the still high intra-reader variability, vaguely defined assessment categories for the transition zone, and the unclear role of dynamic contrast-enhanced (DCE) MRI. While the authors announce some improvements in this regard with the pending update of PI-RADS (version 2.1), general questions and challenges remain and require further investigation.

Accordingly, there is a call to action to address the lack of quantitative metrics in the assessment of diffusion-weighted imaging (DWI) and DCE MRI, to improve the performance of MRI in the transition zone and to work on an expansion of PI-RADS, i.e., for Active Surveillance and recurrent cancer.

Conclusion

PI-RADS v2 was designed to assist in the selection of patients who should undergo prostate biopsy and to establish standards for imaging. It has been shown that the test performance of PI-RADS v2 in research and clinical practice is improved, retaining higher accuracy over systematic TRUS biopsies for PCa diagnosis. Another advantage of PI-RADS is that it markedly improves communication and understanding among radiologists and urologists. Diagnostic strategies that include imaging detect more clinically significant prostate cancers and less low-risk disease. PI-RADS has facilitated the standardization of mpMRI acquisition, interpretation and reporting but open questions and tasks remain.

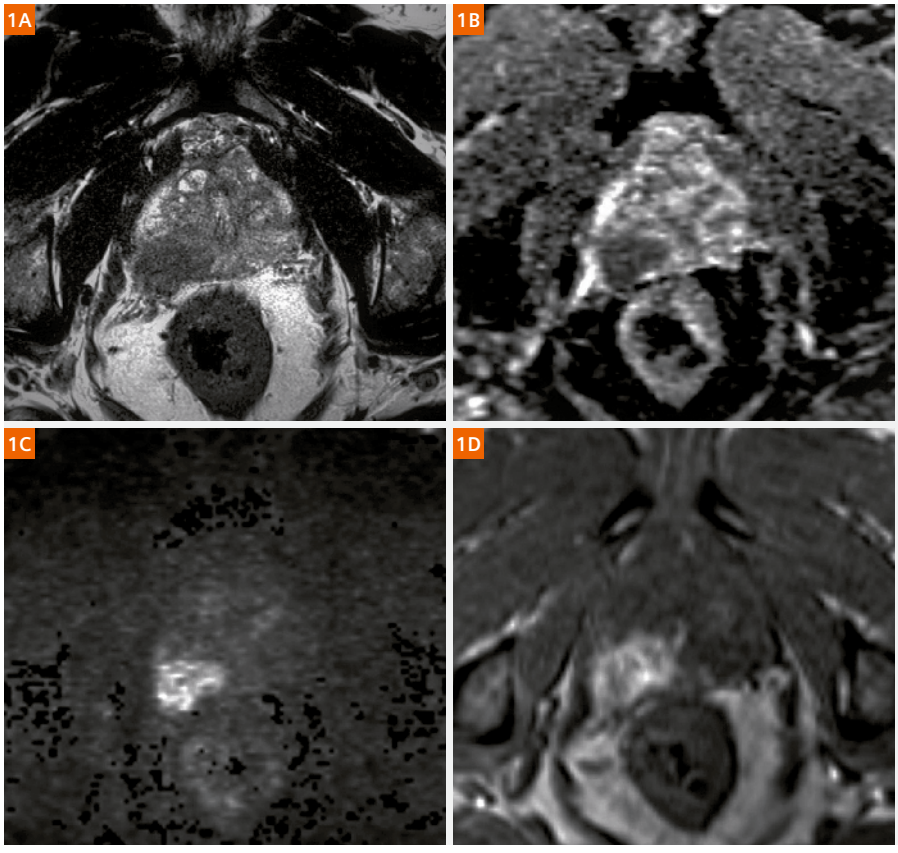

Figure 1:
63-year-old patient with a PSA increase from 5.6 ng/ml to 11.8 ng/ml over a 6-month period. Multiparametric MRI at 3 Tesla (MAGNETOM Skyra). Transverse T2-weighted TSE sequence **(1A)**, diffusion-weighted EPI sequence (ADC map) **(1B)** and calculated b-value of 1400 mm/s^2 **(1C)**, and dynamic contrast-enhanced sequence (TWIST) **(1D)**.

Focal lesion in the posterolateral peripheral zone on the right-hand side with extraprostatic extension and invasion of the neurovascular bundle (1A); there is corresponding marked diffusion restriction (1B, C) and focal early enhancement following contrast agent administration (1D); PI-RADS 5 (histology: Gleason 4+4=8).

Personal comment

Multiparametric prostate MRI is one of the biggest success stories of radiology in the last decade. While we started using MRI as a problem-solving tool in patients with multiple negative biopsies and to assess whether or not patients had extracapsular extension (with sub-optimal results), prostate MRI is clinically used in a much broader scope now. It is no longer questioned whether mpMRI can detect and localize clinically significant PCa and it has been shown that negative MRI findings (in case of high-quality examinations!) allow to safely avoid biopsies and further follow-ups in a significant number of patients. Urologists appreciate the clarity of a PI-RADS report with a standardized prostate pictogram, clearly indicating where to target a biopsy.

On the other hand, however, PI-RADS v2 is reducing our flexibility in imaging interpretation as expert readers, and the recommendations remain vague, for example, with regard to apparent diffusion coefficient (ADC) cutoff values or the assessment of the transition zone. Practical aspects in clinical management of patients such as: "What do we do about mpMRI-negative patients?", "Who should follow up PI-RADS 1-2 patients not undergoing biopsy – what should be the regimen for follow-up?", and "How should we deal with PI-RADS 3 patients?" remain unanswered so far and have to be addressed individually. Hopefully, these issues will be solved in one of the future PI-RADS versions. Therefore, the scientific community is called to action and to address these issues in future studies. Researchers around the globe can contribute and influence the development of future versions of PI-RADS into an even more refined tool in diagnosing and managing prostate cancer.

References

1 Padhani AR, Weinreb J, Barentsz J, et al. Prostate Imaging-Reporting and Data System Steering Committee: PI-RADS v2 Status Update and Future Directions. EUR Urology 2018, https://doi.org/10.1016/j.eururo.2018.05.035.
2 Loeb S, Vellekoop A, Ahmed HU, Catto J, Emberton M, Nam R, et al. Systematic review of complications of prostate biopsy. Eur Urol 2013;64:876–92. doi:10.1016/j.eururo.2013.05.049.
3 Ilic D, Neuberger MM, Djulbegovic M, Dahm P. Screening for prostate cancer. In: Ilic D, editor. Cochrane Database Syst. Rev., Chichester, UK: John Wiley & Sons, Ltd; 2013, p. 78. doi:10.1002/14651858.CD004720.pub3.
4 Ahmed HU, El-Shater Boaily A, Brown LC et al., the PROMIS study group. Diagnostic accuracy of multi-parametric MRI and TRUS biopsy in prostate cancer (PROMIS): a paired validating confirmatory study. Lancet. 2017. doi.org/10.1016/S0140-6736(16)32401-1.
5 Kasivisvanathan V, Rannikko AS, Borghi M, et al. MRI-targeted or standard biopsy for prostate-cancer diagnosis. N Engl J Med 2018;378:1767–77. doi: 10.1056/NEJMoa1801993.



Contact

Bernd Hamm, M.D.
Professor and Chairman
Department of Radiology
Charité University Hospital
Humboldt-Universität zu Berlin
and Freie Universität Berlin
Charitéplatz 1, 10117 Berlin
Germany
Tel.: +49 30 450 527 082
bernd.hamm@charite.de

Get your free copy of the PI-RADS 2 poster

Visit us at
www.siemens.com/magnetom-world

Go to > Publications
> Subscriptions
> MRI Poster

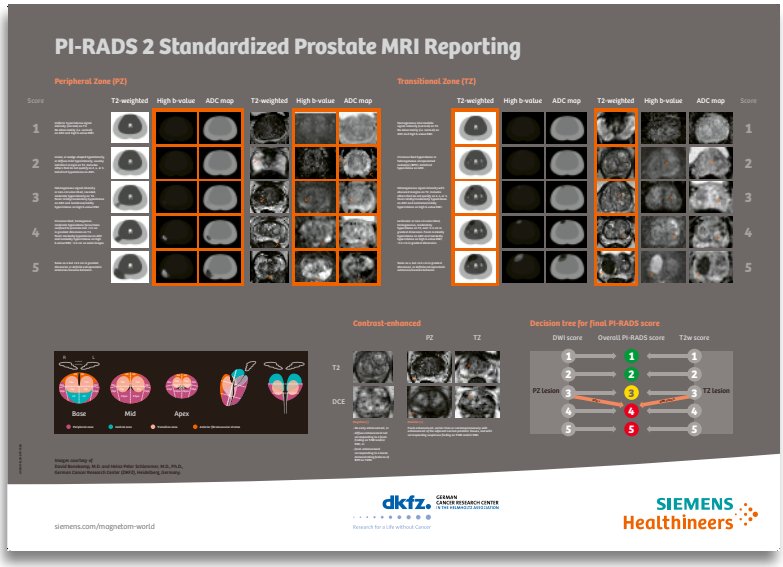

Cardiotoxicity in Cancer Therapy – the Role of Cardiovascular Magnetic Resonance

Christian P. Houbois[1,2]; Paaladinesh Thavendiranathan, MD SM[1,3,4]; Bernd J. Wintersperger, MD EBCR FAHA[1,2]

[1] Department of Medical Imaging, Peter Munk Cardiac Centre, University Health Network, Toronto, Canada
[2] Department of Medical Imaging, University of Toronto, Toronto, Canada
[3] Division of Cardiology, Peter Munk Cardiac Centre, University Health Network, Toronto, Canada
[4] Department of Medicine, University of Toronto, Toronto, Canada

Introduction

Cardiovascular magnetic resonance (CMR) imaging has become a mainstay in the assessment of various cardiac pathologies including ischemic and non-ischemic cardiomyopathies. Beyond the sole aspect of functional deterioration, CMR has convincingly demonstrated to provide further information on the underlying cause contributing sufficient information to narrow the differential diagnosis. Furthermore, insight into the myocardial composition may shed light into the risk prediction of certain diseases and may also allow monitoring of therapeutic interventions and their effects on the heart.

In recent years, the link between tumor therapies and cardiac disease has gained substantial attention and is currently focus of multiple ongoing large-scale studies. With the continuous improvement of survival rates of patients with various malignancies, potential detrimental effects on cardiac function and outcome including increased morbidity and mortality has become the center of such investigations. Outside study settings, major centers with large oncology and cardiac programs have started to establish Cardio-Oncology clinics, in order to help guide oncologists in their treatment planning in patients with pre-existing cardiac disease as well as taking care of patients with potential tumor therapy regimen related cardiovascular effects and potential development of heart failure (HF).

Tumor therapy and heart failure

Todays' therapy regimens in patients with malignant neoplasms may be based on surgical approaches, local or extended radiation therapy (RT) as well as systemic tumor therapies or a combination thereof. While surgical approaches and RT generally affect structures within the application field, systemic therapies may not only result in anti-tumor effects but may also affect otherwise normal body tissue, including the heart. Such negative effects of tumor-related therapy on the heart are generically referred to as cardiotoxicity. The known impact of anthracycline (AC) related tumor therapy possibly resulting in HF may often also be referred to as anthracycline induced heart failure (AIHF).

While modern personalized medicine approaches result in the continuous development of new anti-tumor drugs amongst different drug classes, AC still remain a mainstay of modern tumor therapy regimens. They are commonly used in treatment of breast malignancies, sarcomas and also hematologic malignancies. It is estimated that up to 60% of childhood cancer survivors have been exposed to AC therapy regimens and/or chest radiation [1; 2].

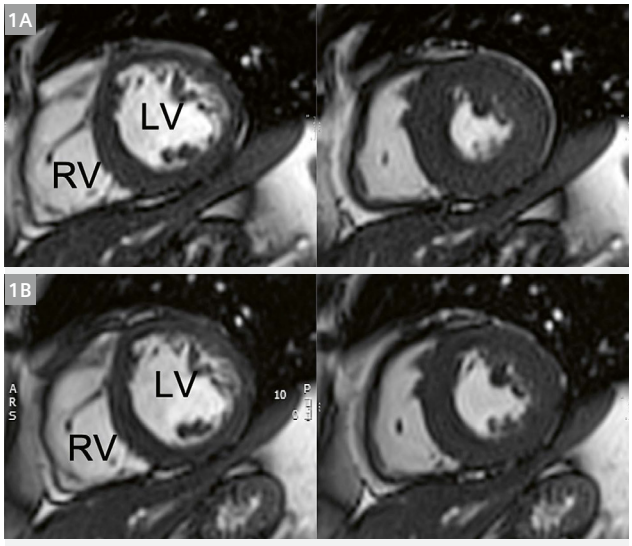

Figure 1:
Standard cine imaging in a patient with breast cancer **(1A)** prior to chemotherapy and **(1B)** one year after the end of anthracycline/trastuzumab combination therapy. Images demonstrate almost identical slice positioning (Cardiac Dot Engine) in diastole (left), but already visually a clear reduction in global ejection fraction is seen in systolie (right). The ejection fraction had dropped by ≥ 10% to < 50%.

LV = left ventricle; RV = right ventricle

Up to ~20% of patients undergoing AC based tumor therapy (with or without combination therapy) may experience AC related cardiotoxicity with the development of HF. The incidence generally increases with increasing cumulative AC dosing. Specifically designed studies employing short interval imaging (echocardiography) based monitoring of the ventricular function, the vast majority (up to 98%) of cardiotoxicity related HF developed either during the systemic cancer therapy or within one year after the end of therapy [3] (Fig. 1). Among patients experiencing such detrimental effects, the vast majority of patients will not entirely recover their cardiac function despite initiation of HF therapy [3]. The risk of cardiac events in this population is significantly increased and in case of confirmed AIHF, mortality may exceed 50% within two years.

Anthracyclines (e.g. doxorubicin, epirubicin) have been known from early use to potentially cause HF and still remain the drug class most commonly related to HF. However, also other drug classes may result in negative cardiovascular effects or may increase the risk of HF in combination with AC based therapy schemes. These classes include monoclonal anti-bodies (MAB) such as trastuzumab, tyrosine kinase inhibitors (TKI) as well as immune checkpoint inhibitors (ICI).

Meanwhile, guidelines have been developed helping to identify patient populations who are specifically at risk for cardiotoxicity related HF [4]. In general, the risk is specifically depending on the dosage of AC therapy, but also the amount of potentially applied additional radiation, potential cardiovascular risk factors as well as the combination of certain drug classes (e.g. anthracycline-trastuzumab combination therapy) [4].

Of specific interest is also the class of aforementioned ICI's, a group of agents that has generally demonstrated lower rates of cardiotoxicity, but that may specifically cause autoimmune myocarditis in rare instances resulting in high complication rates [5].

Cardiovascular magnetic resonance and cardiotoxicity

The breadth of techniques available in CMR for assessment of cardiac function, myocardial deformation and myocardial tissue characterization makes it a potentially ideal tool for assessment and monitoring of patients with increased risk of developing cancer therapy related cardiotoxicity.

Functional cardiac imaging

Today's definitions of cardiotoxicity are almost exclusively based on the assessment of the left ventricular (LV) ejection fraction (EF). As such, the known high accuracy and precision of CMR in the assessment of cardiac volume and function is perfectly suited to guide clinicians according to current definitions of cardiotoxicity [6]. With little variation, published criteria of cardiotoxicity follow a change in LVEF with main cut-offs at a drop of ≥ 10% to under 50% or 55%/53% respectively (Fig. 1) [7–9]. More subtle changes in LVEF (≥ 5%) should be considered as possibly related to cardiotoxicity in patients with symptoms of heart failure (HF) [8]. However, it is important to keep in mind that such thresholds are generally based on echocardiography or multigated acquisition (MUGA) radionuclide ventriculography, modalities that generally suffer from a higher inter-scan and inter-observer variability. Although there is no separate cut-off criterion based on CMR, recent study data suggests that MUGA results may potentially result in misclassification of patients [10].

In any of the above LVEF based definitions of cardiotoxicity, proper baseline assessment and follow scans are required; single time assessment of the cardiac function would not allow adequate judgement. In addition to standard imaging approaches, CMR may play an increasingly important role in the monitoring of such patients. Various clinical experiences report cases where echocardiography based functional assessment would have missed a significant drop in LVEF.

However, from decades of imaging experience it is known that LVEF changes may only occur as a delayed relation to local changes. Therefore, assessment of myocardial deformation may provide a more sensitive and earlier insight into myocardial changes. In the field of echocardiography, the application of speckle tracking echocardiography (STE) has pushed the use of strain imaging towards clinical use including assessment of cardiotoxicity. CMR offers various techniques for myocardial deformation imaging including myocardial tagging, sensitivity encoding (SENC) and displacement encoding with stimulated echoes (DENSE). However, such techniques have never been established on a larger scale in clinical routine CMR.

Most recently, developments of techniques that allow assessment of myocardial strain in routinely acquired cine balanced steady state free precession (bSSFP) data sets have opened a whole new avenue of myocardial deformation assessment. The different available techniques rely either on feature tracking algorithms or employ motion correction techniques for calculation of deformation in cine bSSFP [11–15]. Especially, prototype deformation map-based techniques such as TrufiStrain[1] (Siemens Medical Imaging Technologies, Princeton, US) demonstrated promising and highly

[1] *WIP, the product is currently under development and is not for sale in the US and in other countries. Its future availability cannot be ensured.*

reproducible results compared to accepted standard of reference such as myocardial tagging (Figures 2–4) [12; 14]. In the application of cardiotoxicity evaluation, CMR based strain has also demonstrated great promise aiming at early detection of changes.

Tissue characterization

Qualitative tissue characterization techniques such as T2-weighted imaging or Late Gadolinium Enhancement (LGE) imaging have long played a role in the assessment of various cardiomyopathies and inflammatory changes such as myocarditis [16, 17]. However, the use of LGE imaging in assessment of cardiotoxicity appears limited. As an exception, LGE may play a role in assessment of possible autoimmune myocarditis/pericarditis which may occur during ICI therapy and is considered a bad prognostic marker (Fig. 5).

As a potential new marker of cardiotoxicity related tissue level changes, cardiac relaxometry techniques such as T1 mapping, T2 mapping as well as derived markers such as extracellular volume fraction (ECV) have been proposed and evaluated in various experimental and clinical studies predominately focused on the effects of anthracycline therapy.

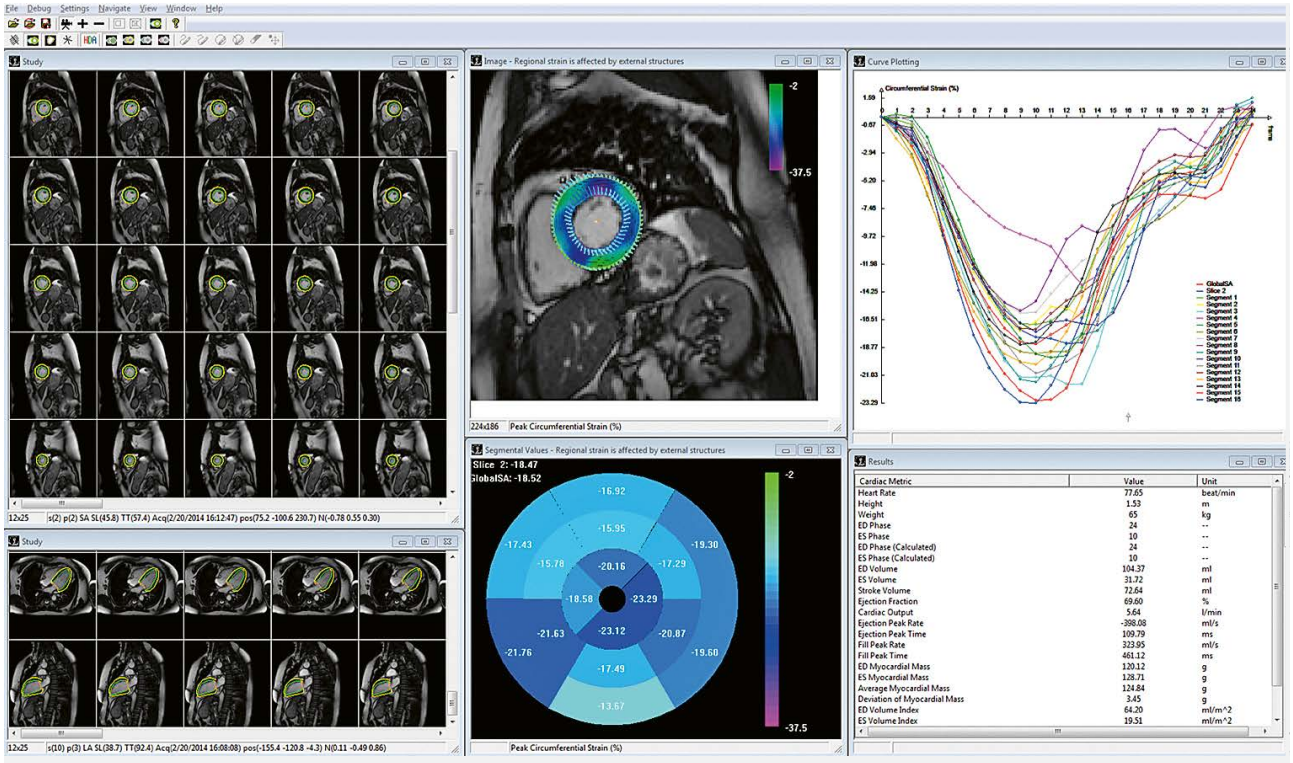

Figure 2:
Standard screen overview of TrufiStrain[1], a prototype software for cine derived strain analysis. The left part of the layout demonstrates the fully automated (short axis) and semiautomated (long axis) segmentation of the endo- and epicardial contours. The center part highlights a visual overlay of strain data onto cine data as well as a bullseye plot of AHA segment strain results. On the right, a visual display of the strain curves (circumferential in this case) for all 16 AHA segments as well as the entire slice with additional results of automated functional analysis at the bottom.

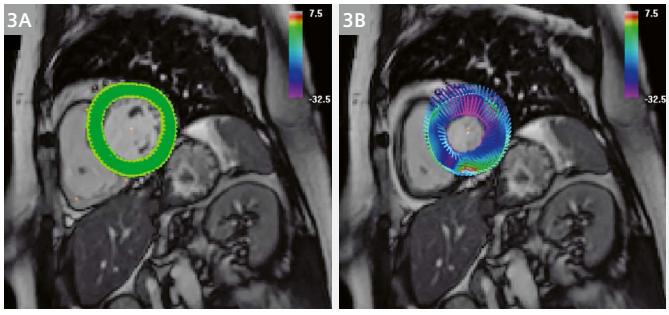

Figure 3:
Single short axis slice in a healthy volunteer in **(3A)** diastole and **(3B)** systole with time point related strain result overlay; the colored lines on the systolic display visualize the direction and magnitude of endo- as well as epicardial motion from diastole to systole.

In animal studies, the repeated application of anthracycline doses lead to a continuous increase in native T1 values over the course of 12–14 weeks while other studies have demonstrated that T2 values are increased in the early phase (~4–6 weeks) suggesting myocardial edema [18, 19]. However, the later study also demonstrated that despite elevated T2 values in early stages, ECV was not elevated until later stages. A possible explanation of elevated T2 and normal ECV might be the occurrence of intracellular edema.

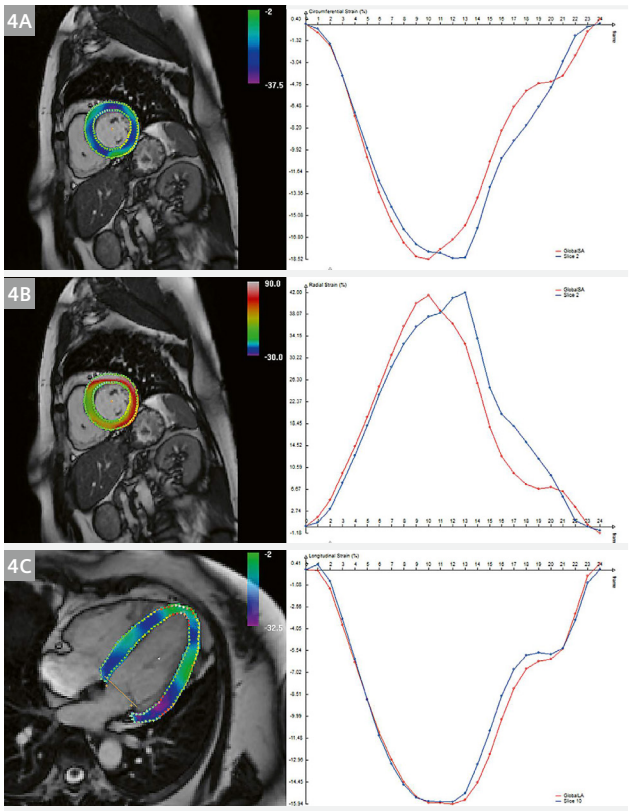

Figure 4:
Demonstration of three major directions/orientations of myocardial strains typically evaluated; **(4A)** circumferential strain, **(4B)** radial strain and **(4C)** longitudinal strain. As strain is a measure of length changes in relation to an applied force, the typical shortening in evaluation on circumferential and longitudinal strain result in negative strain values while the thickening during systole results in positive values for radial strain.

Changes in myocardial T1 as well as ECV values have also been demonstrated in patient studies. As in many other cardiomyopathies, pre-contrast T1 values as well as ECV increase after chemotherapy, likely related to development of interstitial fibrosis [20]. However, hyperacute reactions within the myocardium may result in an initial T1 value decrease possible indicating worse outcome [21]. Currently, there is still limited data from prospective longitudinal studies available to clearly describe potential differences in quantitative cardiac relaxometry in patients with and without development of functional deterioration after chemotherapy. Similar to functional analysis, likely sequential longitudinal imaging, including pre-therapy assessment of T1 and T2 data, is required to identify and differentiate true tissue changes from imaging related variability. A possibly even more promising use of cardiac relaxometry techniques may again relate to patients under ICI therapy with possible autoimmune myocarditis changes (Fig. 5). Similar to recent recommendations regarding the diagnosis of myocarditis in general, changes in quantitative tissue markers may help earlier and more accurate diagnosis [22].

Conclusion

While the playing field of potentially cardiotoxic tumor therapy generally hasn't substantially changed, decades of study results have helped to better understand risk factors and relationships between tumor therapy and cardiac failure. Furthermore, there is a much-increased awareness of the potential interaction between tumor

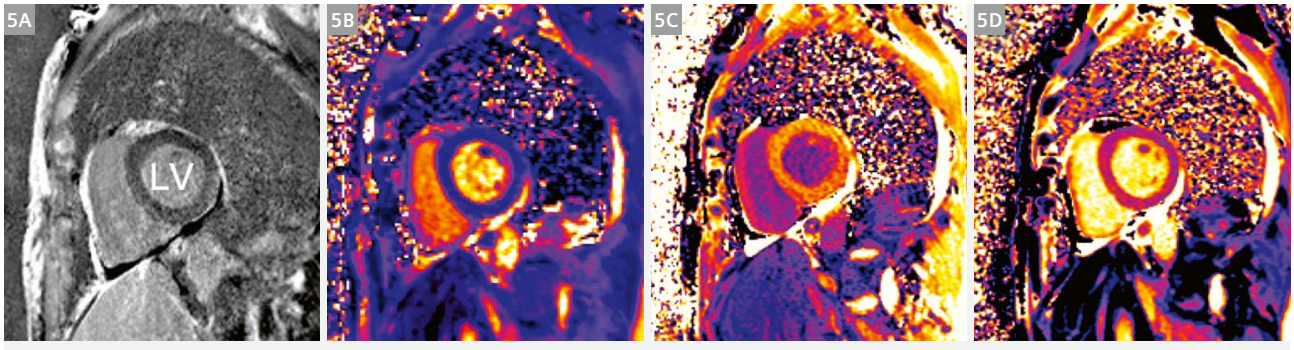

Figure 5:
Patient undergoing immune checkpoint inhibitor (ICI) cancer therapy with troponin elevation and suspicion of immune myocarditis. While **(5A)** LGE imaging possible demonstrates very faint diffuse enhancement, cardiac relaxometry with T1 and T2-mapping (1.5T) provides further information. **(5B)** T2 mapping reveals a T2 time of 55 ms while **(5C)** pre-contrast T1 values were 1184 ms and **(5D)** post-contrast T1 values 519 ms (0.15 mmol/kg Gadobutrol). Based on the patient's hematocrit the ECV is calculated to 38%.

therapy and heart failure resulting in the new subspecialty of 'Cardio-Oncology'. While imaging has long played a role in cancer patients undergoing chemotherapy, CMR is rapidly entering the field and is more frequently being employed. The accuracy and precision of CMR functional assessment proves beneficial in early identification of functional deterioration. Added information might be gathered from cine CMR based strain analysis and quantitative myocardial tissue markers (T1/T2/ECV mapping). However, the timing and specific application of CMR during the course of cancer therapy, especially in patients at risk, has yet to be determined. For a better understanding of that role, additional data on the general test-retest variability of such quantitative markers is still required. Furthermore, society guidelines and definitions of cardiotoxicity would need to further extend beyond the sole criteria of cardiac function.

References:

1 Smith LA, Cornelius VR, Plummer CJ et al. (2010) Cardiotoxicity of anthracycline agents for the treatment of cancer: systematic review and meta-analysis of randomised controlled trials. BMC Cancer 10:337.
2 Armenian SH, Hudson MM, Mulder RL et al. (2015) Recommendations for cardiomyopathy surveillance for survivors of childhood cancer: a report from the International Late Effects of Childhood Cancer Guideline Harmonization Group. Lancet Oncol 16:e123-136.
3 Cardinale D, Colombo A, Bacchiani G et al. (2015) Early detection of anthracycline cardiotoxicity and improvement with heart failure therapy. Circulation 131:1981-1988
4 Armenian SH, Lacchetti C, Barac A et al (2017) Prevention and Monitoring of Cardiac Dysfunction in Survivors of Adult Cancers: American Society of Clinical Oncology Clinical Practice Guideline. J Clin Oncol 35:893-911.
5 Escudier M, Cautela J, Malissen N et al. (2017) Clinical Features, Management, and Outcomes of Immune Checkpoint Inhibitor-Related Cardiotoxicity. Circulation 136:2085-2087.
6 Grothues F, Smith GC, Moon JC et al. (2002) Comparison of interstudy reproducibility of cardiovascular magnetic resonance with two-dimensional echocardiography in normal subjects and in patients with heart failure or left ventricular hypertrophy. Am J Cardiol 90:29-34.
7 Schwartz RG, McKenzie WB, Alexander J et al. (1987) Congestive heart failure and left ventricular dysfunction complicating doxorubicin therapy. Seven-year experience using serial radionuclide angiocardiography. Am J Med 82:1109-1118.
8 Seidman A, Hudis C, Pierri MK et al. (2002) Cardiac dysfunction in the trastuzumab clinical trials experience. J Clin Oncol 20:1215-1221.
9 Plana JC, Galderisi M, Barac A et al. (2014) Expert consensus for multimodality imaging evaluation of adult patients during and after cancer therapy: a report from the American Society of Echocardiography and the European Association of Cardiovascular Imaging. J Am Soc Echocardiogr 27:911-939.
10 Huang H, Nijjar PS, Misialek JR et al. (2017) Accuracy of left ventricular ejection fraction by contemporary multiple gated acquisition scanning in patients with cancer: comparison with cardiovascular magnetic resonance. J Cardiovasc Magn Reson 19:34.
11 Lamacie MM, Thavendiranathan P, Hanneman K et al. (2017) Quantification of global myocardial function by cine MRI deformable registration-based analysis: Comparison with MR feature tracking and speckle-tracking echocardiography. Eur Radiol 27:1404-1415.
12 Lamacie MM, Houbois CP, Greiser A, Jolly MP, Thavendiranathan P, Wintersperger BJ (2019) Quantification of myocardial deformation by deformable registration-based analysis of cine MRI: Validation with tagged CMR. Eur Radiol. DOI: 10.1007/s00330-019-06019-9.
13 Keller EJ, Fang S, Lin K et al (2017) The consistency of myocardial strain derived from heart deformation analysis. Int J Cardiovasc Imaging 33:1169-1177
14 Jolly MP, Jordan JH, Melendez GC, McNeal GR, D'Agostino RB, Jr., Hundley WG (2017) Automated assessments of circumferential strain from cine CMR correlate with LVEF declines in cancer patients early after receipt of cardio-toxic chemotherapy. J Cardiovasc Magn Reson 19:59.
15 Barreiro-Perez M, Curione D, Symons R, Claus P, Voigt JU, Bogaert J (2018) Left ventricular global myocardial strain assessment comparing the reproducibility of four commercially available CMR-feature tracking algorithms. Eur Radiol. 10.1007/s00330-018-5538-4.
16 Cummings KW, Bhalla S, Javidan-Nejad C, Bierhals AJ, Gutierrez FR, Woodard PK (2009) A pattern-based approach to assessment of delayed enhancement in nonischemic cardiomyopathy at MR imaging. Radiographics 29:89-103.
17 Friedrich MG, Sechtem U, Schulz-Menger J et al. (2009) Cardiovascular magnetic resonance in myocarditis: A JACC White Paper. J Am Coll Cardiol 53:1475-1487.
18 Hong YJ, Park HS, Park JK et al. (2017) Early Detection and Serial Monitoring of Anthracycline-Induced Cardiotoxicity Using T1-mapping Cardiac Magnetic Resonance Imaging: An Animal Study. Sci Rep 7:2663.
19 Farhad H, Staziaki PV, Addison D et al. (2016) Characterization of the Changes in Cardiac Structure and Function in Mice Treated With Anthracyclines Using Serial Cardiac Magnetic Resonance Imaging. Circulation Cardiovascular imaging 9:e003584.
20 Jordan JH, Vasu S, Morgan TM et al. (2016) Anthracycline-Associated T1 Mapping Characteristics Are Elevated Independent of the Presence of Cardiovascular Comorbidities in Cancer Survivors. Circulation Cardiovascular imaging 9
21 Muehlberg F, Funk S, Zange L et al. (2018) Native myocardial T1 time can predict development of subsequent anthracycline-induced cardiomyopathy. ESC Heart Fail. 10.1002/ehf2.12277.
22 Ferreira VM, Schulz-Menger J, Holmvang G et al. (2018) Cardiovascular Magnetic Resonance in Nonischemic Myocardial Inflammation: Expert Recommendations. J Am Coll Cardiol 72:3158-3176.

Contact

Bernd J. Wintersperger, MD EBCR FAHA
Department of Medical Imaging
Toronto General Hospital, 1 PMB-273
585 University Avenue
Toronto, Ontario, M5G 2N2
Canada
Tel.: 416-340-4800 ex. 8593
Bernd.Wintersperger@uhn.ca


Bernd Wintersperger


Christian Houbois


P. Thavendiranathan

Musculoskeletal and Body MRI in Children

Sarah D. Bixby, M.D.; Reid C. Nichols, RT (R) MR; Ali Gholipour, Ph.D.

Department of Radiology, Boston Children's Hospital, Boston, MA, USA

MRI imaging in pediatric patients is as much about the process as it is about the result. While high-quality images are the ultimate goal, for children an imaging study is a success if diagnostic images are obtained while minimizing the risk to the patient, which includes reducing the risk of anesthesia [1–2]. There are many ways to improve spatial resolution and gain signal-to-noise ratio (SNR) in MRI, though most strategies cost time. In clinical practice there are limitations on patient cooperation and magnet utilization that require a practical approach to imaging. While working with children is enormously satisfying, there are also challenges that come with pediatric imaging which require minimizing exam times, eliminating labor-intensive breath-holding instructions, and imaging through motion (respiratory and gross motion). Motion is a major obstacle when it comes to imaging young children. In many instances, the difference between a non-diagnostic exam and a successful exam may simply require reducing sequence time by half. While this used to require unacceptable compromise in image quality, this is no longer true. With increased field strength magnets (i.e. 3T), appropriate selection of multichannel phased array coils, and parallel imaging techniques, scan times have decreased considerably from where they started. With a few additional strategies it is not only possible, but more than likely that a complete exam can be performed in a young child[1] without sedation.

Advanced protocol planning, sequence prioritization, real-time exam monitoring, and skilled patient handling are also critical elements of a successful MRI examination in a young child.

A fundamental principle in imaging pediatric patients is to limit sequences to only those that are necessary, acquiring the most high yield sequences first. Patient cooperation is limited and young patients often have tolerance for two or three sequences. Radiologists should assume the most critical diagnostic information must be obtained in the first ten minutes of an exam. If those first sequences are diagnostic, the patient will be spared a follow-up exam under anesthesia. MRI is increasingly being used to screen patients with certain symptoms for presence or absence of disease, such as fracture detection in limping toddlers, evaluation for infection in children with fever of unknown origin, or appendicitis screening in patients with right lower quadrant pain. MRI may be the best means of detecting fractures in certain locations when the bones have not yet ossified (Fig. 1), and for localizing disease when patients are unable to verbalize symptoms.

[1] *MR scanning has not been established as safe for imaging fetuses and infants less than two years of age. The responsible physician must evaluate the benefits of the MR examination compared to those of other imaging procedures. Note: This disclaimer does not represent the opinion of the authors.*

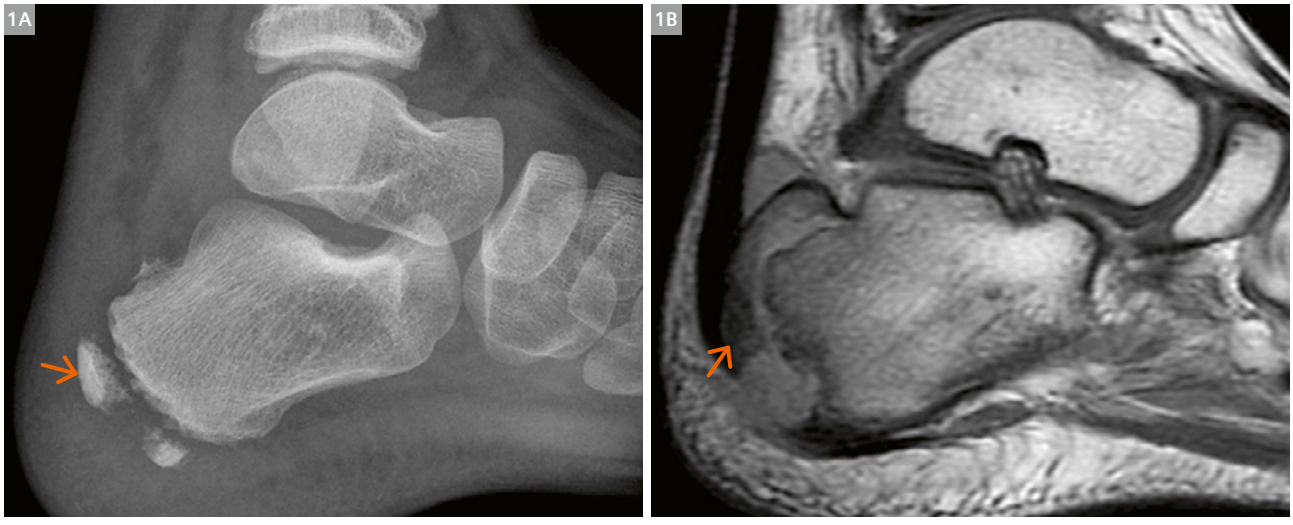

1 6-year-old female with calcaneal apophyseal fracture **(1A)** Lateral radiograph of the ankle reveals a normal-appearing apophysis (orange arrow). **(1B)** Sagittal PD-weighted TSE sequence reveals avulsion of the calcaneal apophysis, not appreciated on radiographs secondary to the lack of ossification.

It is more important to acquire images quickly to allow actionable diagnosis, rather than spending additional time enhancing imaging quality at the expense of patient cooperation.

Monitoring MRI examinations in real-time allows for adjustment of imaging parameters as the study unfolds [3]. As toddlers are often unable to articulate the location and nature of their symptoms, imaging requires looking far and wide initially and focusing down on an abnormality once identified. Setting up an MRI in a toddler with an unexplained limp, for example, often requires using one or more body matrix coils (depending on the child) to perform initial sequences with a large field of view (FOV) from the pelvis to the feet (Fig. 2). These sequences can be performed quickly, with need for additional sequences determined by the presence or absence of abnormal findings. Without real-time radiologist supervision, these protocol modifications would not be possible and the examination may need to be repeated.

While vigilant exam monitoring, careful protocoling, and adept patient handling are critical to successful imaging of children, these efforts may still fall short of the goal without additional sequence advancements. Accelerated acquisitions and motion robust sequences are, therefore, particularly valuable in pediatric imaging. Acceleration techniques allow for substantial reductions in imaging times so that they may be tolerated by young patients; in our experience this generally means shorter than two minutes per sequence. In pediatric musculoskeletal imaging, MRI protocols rely heavily on turbo spin-echo (TSE) sequences which include proton density (PD), intermediate weighted (IW), and T2-weighted images. Accelerated TSE acquisitions can be obtained through *k*-space undersampling in parallel imaging [4]; however a reduction or acceleration factor of R comes with a reduction of $1/\sqrt{R}$ in (SNR). In addition, SNR is also reduced by the noise amplification factor, or the *g*-factor (geometry factor) penalty that varies by the location in an image depending on the number of aliased replicates per voxel based on coil sensitivities [5]. The *g*-factor penalty depends on the receive coil design and coverage, and the geometry of imaging and can vary between 1 and 2 across the image. Simultaneous multi-slice (SMS) is another technique to accelerate imaging that excites multiple spatially distributed slices simultaneously by using a multi-band radiofrequency pulse and techniques to control aliasing and reduce the *g*-factor penalty [5–11]. Data obtained from receive coils from simultaneously excited slices are separated to reconstruct images. When parallel imaging and SMS are both applied, imaging times can be reduced 4- to 8-fold over traditional methods. In our routine knee MRI protocol we compared an accelerated T2-weighted TSE sequence using a parallel imaging iPAT factor of 2 with an SMS factor of 2 to achieve 4-fold acceleration against our traditional sequence without the SMS acceleration (Figs. 3, 4). We found both the SMS TSE and the TSE were equivalent in identifying pertinent imaging findings [12]. Compared to the traditional sequence, the SMS accelerated sequence is nearly twice as fast (Table 1). Further reduction in imaging time can be gained by increasing the SMS factor, with incremental cost to SNR. In our patient population we found that 4-fold acceleration is sufficient for most patients, and additional acceleration can be reserved for patients who are extremely nervous or fidgety, given the modest reduction in SNR.

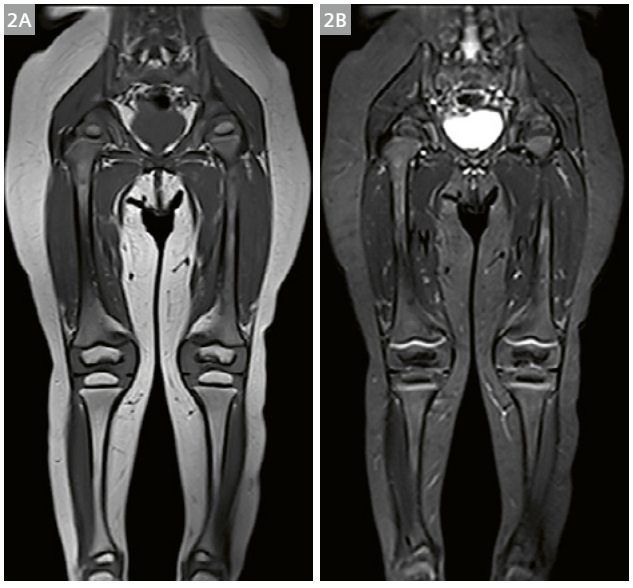

2 2-year-old female with limp. Coronal T1 **(2A)** and STIR **(2B)** sequences through the entire pelvis and lower extremities were performed using a body matrix coil as an initial screen to identify areas of pathology. No abnormality was identified.

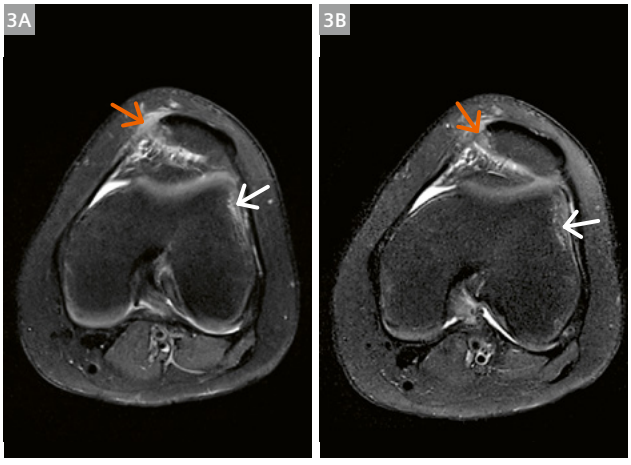

3 11-year-old female with patellar dislocation. **(3A)** Axial T2-weighted TSE image with fat suppression and **(3B)** corresponding axial T2-weighted SMS TSE image demonstrates a tear of the medial retinaculum (orange arrow) and a bone contusion at the lateral femoral condyle (white arrow).

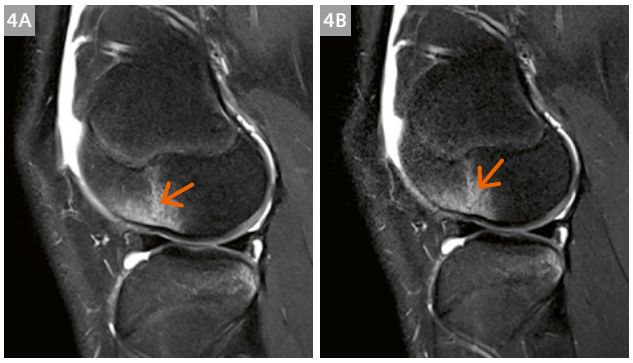

4 14-year-old boy with lateral femoral contusion (orange arrow) undergoing MRI. **(4A)** Sagittal T2-weighted TSE sequence and **(4B)** corresponding sagittal T2-weighted SMS TSE sequence for comparison.

The 3D TSE volumetric SPACE (Sampling Perfection with Application optimized Contrasts using different flip angle Evolution) acquisition is integral for imaging of large joints (knee and ankle) in children [13–18]. The three-dimensional, high-spatial resolution, isotropic images can be reconstructed into any imaging plane from a single volumetric data set, making it helpful for identifying subtle cartilage defects or ligamentous injuries. The imaging time, however, is relatively long which makes it particularly vulnerable to motion. The standard PD-weighted SPACE sequence in the knee protocol at our institution is 7 minutes and 40 seconds. Parallel imaging techniques can be applied to the acquisition but may cause aliasing artifacts and increase noise. CAIPIRINHA "Controlled Aliasing in Parallel Imaging Results in Higher Acceleration" [19] is a parallel imaging strategy that uses *k*-space sampling patterns designed to reduce aliasing and overlap on reconstructed images. While aliasing artifacts are still present, they are shifted to the corners of the image space.

Parameters	T2-weighted TSE	T2-weighted SMS TSE
Plane	Sagittal	Sagittal
Acquistion time (min:sec)	2:45	1:50
TR (ms)	4500	3000
TE (ms)	53	53
Echo train length	34	33
Matrix	384	384
Parallel imaging acceleration factor and reconstruction	2 (GRAPPA)	2 (GRAPPA)
FOV (mm)	140	140
Voxel dimension (mm)	0.4 x 0.4 x 3.0	0.4 x 0.4 x 3.0

Table 1: MRI parameters for T2-weighted TSE sequence versus T2-weighted SMS TSE sequence in the knee.

Parameters	PD-weighted 3D SPACE	PD-weighted 3D CAIPIRINHA SPACE
Plane	Sagittal	Sagittal
Acquistion time (min:sec)	7:40	4.00
TR (ms)	1000	1000
TE (ms)	49	49
Echo train length	41	41
Flip angle (°)	120	120 (variable)
Matrix	320 x 320 x 240	320 x 320 x 240t
Parallel imaging acceleration factor and reconstruction	2 (GRAPPA)	2 (GRAPPA)
FOV (mm)	162 x 249	162 x 249
Voxel dimension (mm)	0.54 x 0.54 x 1	0.54 x 0.54 x 1

Table 2: MRI parameters for Proton Density (PD)-weighted 3D SPACE sequence versus PD-weighted 3D CAIPIRINHA SPACE sequence in the knee.

Combined CAIPIRINHA and SPACE allows for 4-fold acceleration through undersampling in both the phase and partition encoding directions [14]. We compared the standard PD-weighted SPACE sequence in the knee with the CAIPIRINHA PD-weighed SPACE sequence (Table 2). Applying CAIPIRINHA to SPACE reduced our scan time from 7:40 minutes to 4:00 minutes without compromise in image quality (Figs. 5, 6). We reserve this sequence for slightly older patients (above the age of 8) who are able to cooperate for the 4 minute long acquisitions. In the younger patients, 2D sequences are still generally preferred. Anticipated pathologies in our youngest patients do not typically require such fine spatial resolution, and these patients reap greatest benefit from short acquisitions that require periodic opportunities for breaks.

Motion robust imaging alternatives are highly valuable in pediatric patients, particularly for abdominal and pelvic imaging [20]. Examinations that require breath-held sequences often require the child to be anesthetized and intubated to allow for periods of suspended respiration. With the aim of reducing need for anesthesia and/or the depth of anesthesia, free-breathing imaging capabilities are imperative. In the abdomen, 3D volumetric interpolated breath-hold examination (VIBE) imaging offers the most robust approach to acquiring T1-weighted imaging. VIBE allows for high spatial resolution with relatively fast imaging acquisitions of the entire abdomen [21, 22]. Depending on parameter selection, it is possible to acquire images through the entire field of view in approximately 20 seconds in a cooperative patient. Even adult patients may have difficulty breath-holding for a 20 second sequence [23], and children are even less likely to manage this. Cartesian VIBE obtained during free-breathing produces motion artifact within the image (Fig. 7) which limits the diagnostic quality of the sequence [24, 25]. T1-weighted images can be acquired with respiratory navigation, though this is less developed than navigated T2-weighted sequences, and image quality is inferior to the conventional breath-hold sequences [26–28]. Additionally, navigated T1-weighted imaging is not possible with fat suppression, which limits its utility for post-contrast imaging. A modified version of the VIBE sequence is a radial VIBE sequence that uses rectilinear sampling in the *z*-direction and radial sampling in the *xy* plane [24]. This sequence can be performed during free-breathing, and the radial sampling of *k*-space mitigates the effect of respiratory motion such that image quality is superior to the traditional breath-hold Cartesian VIBE [24]. The product version of this sequence is called StarVIBE, which is our standard for T1-weighted imaging in pediatric patients. Although the acquisition time is longer than a traditional VIBE sequence, the respiratory motion is distributed throughout the image such that there is little perception of the motion within the image. This technique is especially helpful for post-gadolinium enhanced imaging in the liver, kidneys, and bowel (Fig. 8). The ability to obtain high spatial-resolution, motionless imaging in patients who are freely breathing has dramatically altered our approach to sedating patients. We utilize the StarVIBE sequence in any child undergoing abdominopelvic imaging, for both pre and post-contrast fat-suppressed imaging.

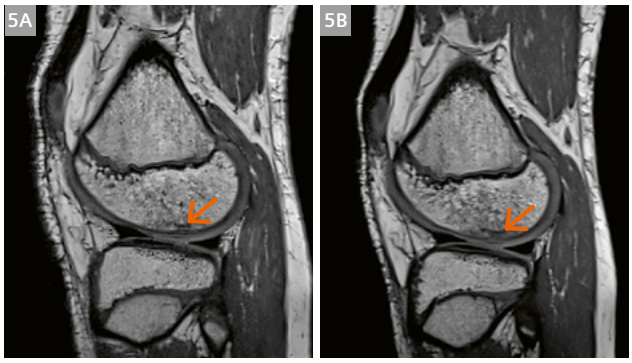

5 11-year-old female with lateral femoral condylar impaction fracture (orange arrow) seen on both **(5A)** sagittal PD-weighted SPACE sequence, and **(5B)** corresponding sagittal PD-weighted CAIPIRINHA SPACE sequence for comparison.



6 15-year-old female with ACL tear (white arrow). **(6A)** Sagittal PD-weighted SPACE sequence and **(6B)** corresponding sagittal PD-weighted CAIPIRINHA SPACE sequence through the ruptured ACL for comparison.

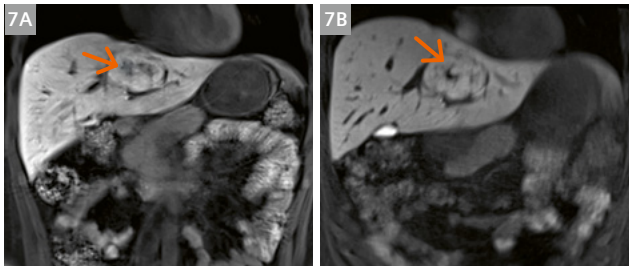

7 20-year-old female with FNH-like liver lesion. **(7A)** Coronal T1 VIBE with breath-holding after administration of Eovist contrast media reveals delayed uptake in a liver lesion (orange arrows), though images are degraded by motion. **(7B)** Sequence repeated with StarVIBE sequence with free-breathing demonstrates reduced motion artifact with better depiction of the lesion.

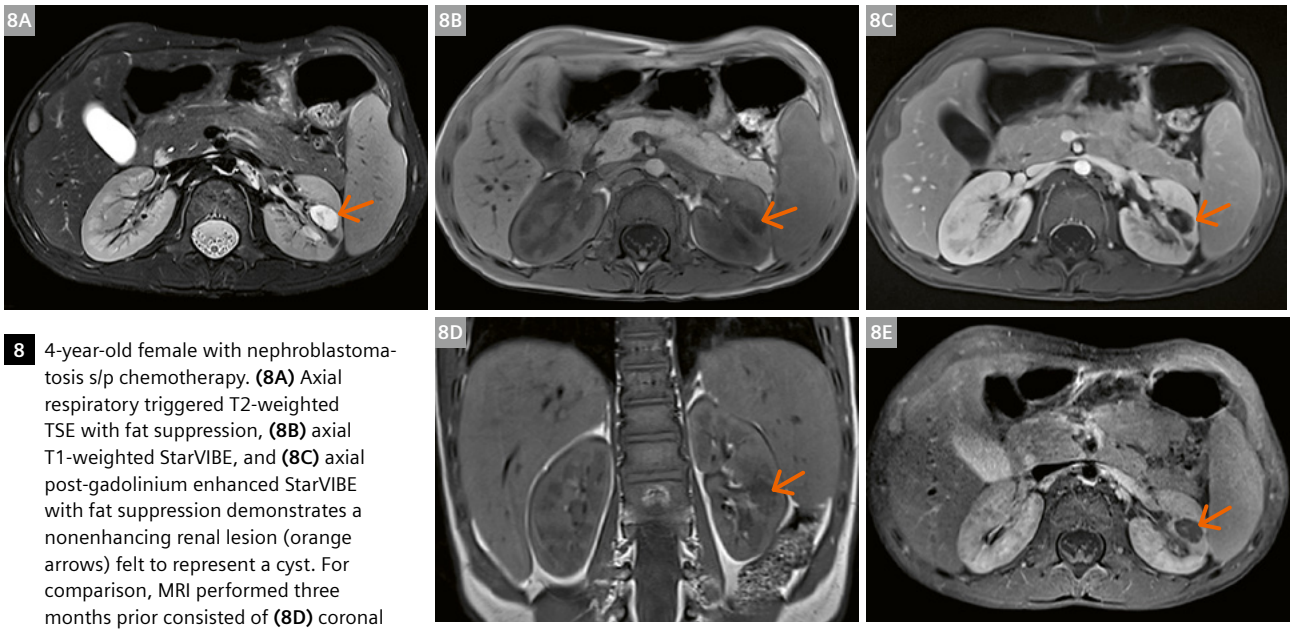

8 4-year-old female with nephroblastomatosis s/p chemotherapy. **(8A)** Axial respiratory triggered T2-weighted TSE with fat suppression, **(8B)** axial T1-weighted StarVIBE, and **(8C)** axial post-gadolinium enhanced StarVIBE with fat suppression demonstrates a nonenhancing renal lesion (orange arrows) felt to represent a cyst. For comparison, MRI performed three months prior consisted of **(8D)** coronal respiratory triggered T1-weighted TSE, **(8E)** axial post-gadolinium enhanced T1 TSE with fat suppression. Motion artifact is noted in the image from respiration.

The lack of breath-holding as a requirement for imaging obviates the requirement for endotracheal intubation, unless there are other reasons for which it would be required. A dynamic StarVIBE sequence is also available which allows for both high temporal resolution in addition to high spatial resolution images during dynamic contrast injection [29, 30], using compressed sensing techniques as a means to vastly undersample the data and reduce imaging times [20]. We are currently investigating this technique in the pediatric population, particularly with regard to renal, hepatic and bowel wall imaging.

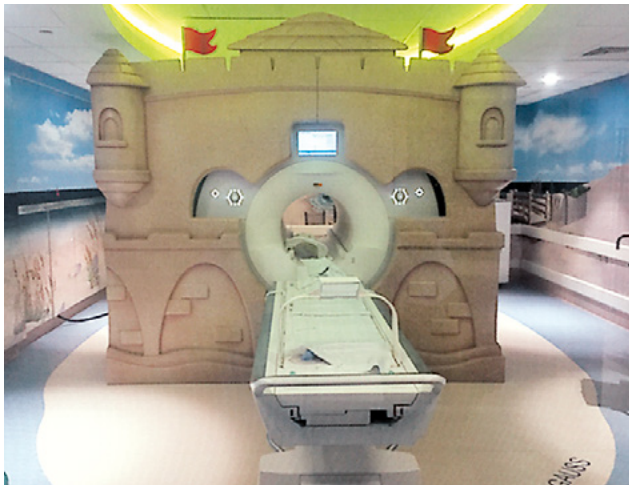

9 3T MAGNETOM Prisma MR scanner embedded in a sandcastle design. The room is decorated with decals in the theme of an ocean scene.

MR imaging in pediatric patients requires a team approach and collective efforts toward reducing our dependency upon sedation as a mechanism to acquire diagnostic, motion-free images. These include tailored protocoling, real-time monitoring, and utilization of accelerated or motion robust sequences. With the use of SMS TSE and CAIPIRINHA SPACE, MSK imaging examinations in children can be dramatically shortened without compromising image quality. StarVIBE imaging in the abdomen allows for high-resolution, free-breathing, T1-weighted imaging thereby eliminating requirement for endotracheal intubation for abdominal MRI in sedated patients. Reducing the anxiety and apprehension around the scanner and the scan room is also important in achieving patient cooperation. This can be achieved through embedding the scanner in a structure, such as a sandcastle, train, or boat (Fig. 9), decorating the room with colorful designs, distracting the patient with a movie during the scan, or preparing prior to the scan at a mock scanner or simulating the experience with virtual reality headsets. All of these strategies are currently employed at our hospital, oftentimes in combination. Further developments in prospective motion correction using motion cameras embedded in the magnet and sensors on the patient are currently being developed through collaborations with KinetiCor (Honolulu, HI, USA), with broad applications in the pediatric population. Our hope is that through these collective efforts we will drastically reduce the number of children requiring sedation for MRI, and improve the patient experience by reducing exam lengths and delays.

References

1 Callahan MJ, MacDougall RD, Bixby SD, Voss SD , Robertson RL, Cravero JP. Ionizing radiation from computed tomography versus anesthesia for magnetic resonance imaging in infants and children: patient safety considerations. Pediatr Radiol 2018; 48(1):21-30.
2 Paterson N, Waterhouse P. Risk in pediatric anesthesia. Paediatr Anaesth 2011; 21:848-857.
3 Robertson RL, Silk S, Ecklund K, Bixby SD, Voss SD, Robson CD. Imaging optimization in children. J Am Coll Radiol 2018; 15(3 Pt A):440-443.
4 Griswold MA, Jakob PM, Heidemann RM, Nittka M, Jellus V, Wang J, Kiefer B, Haase A. Generalized autocalibrating partially parallel acquisitions (GRAPPA). Magn Reson Medicine 2002 Jun; 47(6):1202-1210.
5 Breuer FA, Kannengiesser SA, Blaimer M, Seiberlich N, Jakob PM, Griswold MA. General formulation for quantitative G-factor calculation in GRAPPA reconstructions. Magn Reson Med 2009 Sep; 62(3):739-746.
6 Setsompop K, Gagoski BA, Polimeni JR, Witzel T, Wedeen VJ, Wald LL. Blipped-controlled aliasing in parallel imaging for simultaneous multislice echo planar imaging with reduced g-factor penalty. Magn Reson Med 2012 May 1; 67(5):1210-1224.
7 Barth M, Breuer F, Koopmans PJ, Norris DG, Poser BA. Simultaneous multislice (SMS) imaging techniques. Magn Reson Med 2016 Jan; 75(1):63-81.
8 Feinberg DA, Setsompop K. Ultra-fast MRI of the human brain with simultaneous multi-slice imaging. J Magn Reson 2013; 229:90-100.
9 Fritz J, Fritz B, Zhang J, Thawait GK, Joshi DH, Pan L, Wang D. Simultaneous multislice accelerated Turbo Spin Echo magnetic resonance imaging comparison and combination with in-plane parallel imaging acceleration for high-resolution magnetic resonance imaging of the knee. Invest Radiol 2017; 52:529-537.
10 Poser BA, Anderson RJ, Guerin B, Setsompop K, Deng W, Mareyam A, Serano P, Wald LL, Stenger VA. Simultaneous multislice excitation by parallel transmission. Magn Reson Med 2014; 71:1416-1427.
11 Gagoski BA, Bilgic B, Eichner C, Bhat H, Grant PE, Wald LL, Setsompop K. RARE/Turbo Spin Echo imaging with simultaneous multislice wave-CAIPI. Magn Reson Med 2015; 73:929–938.
12 Benali S, Johnston PR, Gholipour A, Dugan ME, Heberlein K, Bhat H, Bixby SD. Simultaneous multi-slice accelerated turbo spin echo of the knee in pediatric patients. Skeletal Radiol 2018 Jun; 47 (6):821-831.
13 Fritz J, Fritz B, Thawait GG, Meyer H, Gilson WD, Raithel E. Three-Dimensional CAIPIRINHA SPACE TSE for 5-Minute High-Resolution MRI of the Knee. Invest Radiol 2016; 51:609-617.
14 Fritz J, Ahlawat S, Fritz B, Thawait GK, Stern SE, Raithel E, Klyce W, Lee RJ. 10-min 3D Turbo Spin Echo MRI of the knee in children: arthroscopy-validated accuracy for the diagnosis of internal derangement. J Magn Reson Imaging 2018; doi: 10.1002/jmri.26241. epub ahead of print.

Contact

Sarah D. Bixby, M.D.
Associate Professor of Radiology
Department of Radiology
Boston Children's Hospital
300 Longwood Avenue,
Main Building, 2nd Floor
Boston, MA 02115
USA
Tel.: +1 857 218 4006
sarah.bixby@childrens.harvard.edu



15 Fritz J, Raithel E, Thawait GK, Gilson W, Papp DF. Six-fold acceleration of high-spatial resolution 3D SPACE MRI of the knee through incoherent k-space undersampling and iterative reconstruction – first experience. Invest Radiol 2016; 51:400–409.
16 Fritz J, Ahlawat S, Thawait GK, Raithel E, Gilson W, Lee RJ. 3D MRI of knee in pediatric patients with CAIPIRINHA SPACE: diagnostic performance assessment with arthroscopic correlation. Proc Intl Soc Mag Reson Med 2017; 25:1151.
17 Kalia V, Fritz B, Johnson R, Gilson WD, Raithel E, Fritz J. CAIPIRINHA accelerated SPACE enables 10-min isotropic 3D TSE MRI of the ankle for optimized visualization of curved and oblique ligaments and tendons. Eur Radiol 2017; 27:3652–3661.
18 Del Grande F, Delcogliano M, Guglielmi R, Raithel E, Stern SE, Papp DF, Candrian C, Fritz J. Fully automated 10-minute 3D CAIPIRINHA SPACE TSE MRI of the knee in adults. A multicenter, multireader, multifield-strength validation study. Invest Radiol 2018; 53:689-697.
19 Breuer FA, Blaimer M, Heidemann RM, Mueller MF, Griswold MA, Jakob PM. Controlled aliasing in parallel imaging results in higher acceleration (CAIPIRINHA) for multi-slice imaging. Magn Reson Med 2005 Mar 1; 53(3):684-691.
20 Jaimes C, Kirsch KE, Gee MS. Fast, free-breathing and motion-minimized techniques for pediatric body magnetic resonance imaging. Pediatr Radiol 2018; 48:1197-1208.
21 Rofsky NM, Lee VS, Laub G, Pollack MA, Krinsky GA, Thomasson D, Ambrosino MM, Weinreb JC. Abdominal MR imaging with a volumetric interpolated breath-hold examination. Radiology 1999; 212:876-884.
22 Lee VS, Lavelle MT, Krinsky GA, Rofsky NM. Volumetric MR imaging of the liver and applications. Magn Reson Imaging Clin N Am 2001; 9(4):697-716.
23 Krinsky GA, Lee VS, Theise ND, Weinreb JC, Rofsky NM, Diflo T, Teperman LW. Hepatocellular carcinoma and dysplastic nodules in patinets with cirrhosis: prospective diagnosis with MR imaging and explanation correlation. Radiology 2001; 219(2):445-54.
24 Chandarana H, Block TK, Rosenkrantz AB, Lim RP, Kim D, Mossa DJ, Babb JS, Kiefer B, Lee VS. Free-breathing radial 3D fat-suppressed T1-weighted gradient echo sequence. A viable alternative for contrast-enhanced liver imaging in patients unable to suspend respiration. Invest Radiol 2011; 46:648-653.
25 Chandarana H, Block KT, Winfeld MJ, Lala SV, Mazori D, Giuffrida E, Babb JS, Milla SS. Free-breathing contrast-enhanced T1-weighted gradient-echo imaging with radial k-space sampling for paediatric abdominopelvic MRI. Eur Radiol 2014; 24:320-326.
26 Vasanawala SS, Iwadate Y, Church DG, Herfkens RJ, Brau AC. Navigated abdominal T1-W MRI permits free-breathing image acquisition with less motion artifact. Pediatr Radiol 2010; 40:340-344.
27 Young PM, Brau AC, Iwadate Y, Vasanawala S, Daniel BL, Tamrazi A, Herfkens RJ. Respiratory navigated free breathing 3D spoiled gradient-recalled echo sequence for contrast-enhanced examination of the liver: diagnostic utility and comparison with free breathing and breath-hold conventional examinations. Am J Roentgenol AJR 2010; 195:687-691.
28 Azevedo RM, Campos ROP, Ramalho M, Heredia V, Dale BM, Semelka RC. Free-breathing 3D T1-weighted gradient echo sequence with radial data sampling in abdominal MRI: preliminary observations AJR Am J Roentgenol 2011; 197:650-657.
29 Kim KW, Lee JM, Jeon YS, Kang SE, Baek JH, Han JK, Choi BI, Bang Y-J, Kiefer B, Block KT, Ji H, Bauer S, Chin K. Free-breathing dynamic contrast-enhanced MRI of the abdomen and chest using a radial gradient echo sequence with K-space weighted image contrast (KWIC). Eur Radiol 2013; 23:1352–1360.
30 Kaltenbach B, Roman A, Polkowski C, Gruber-Rouh T, Bauer RW, Hammerstingl R, Vogl TJ, Zangos S. Free-breathing dynamic liver examination using a radial 3D T1-weighted gradient echo sequence with moderate undersampling for patients with limited breath-holding capacity. Eur J Radiol 2017; 86:26-32.

Unprecedented Echo Times for Diffusion MRI Using Connectom Gradients, Spiral Readouts and Field Monitoring

Lars Mueller; Chantal MW Tax; Derek K Jones

Cardiff University Brain Research Imaging Centre (CUBRIC), Cardiff, UK

Summary

- Using a unique combination of the ultra-strong (300 mT/m) magnetic field gradients provided on the MAGNETOM Connectom[1] scanner, a diffusion-weighted MRI sequence with spiral EPI read-out, and a field camera to monitor and correct for deviations from prescribed *k*-space trajectories, we present high quality images with unprecedented short echo times for diffusion MRI in the living human brain
- For b = 1000 s/mm^2, the echo time is 21.7 ms
- These short echo times confer two advantages:
  - Enhanced signal to noise ratio (SNR) due to reduced T2-weighted signal loss (which makes measurement of tissue with short T2, e.g., muscle, more robust)
  - Sensitivity to species previously 'invisible' in diffusion MRI, e.g., the myelin water, opening up the possibility of measuring their diffusion properties for the first time.
- In summary, this unique combination of hardware, sequence, field monitoring and reconstruction opens up a new window into tissue microstructural properties in the living human brain.

[1] *MAGNETOM Connectom is ongoing research. All data shown are acquired using a non-commercial system under institutional review board permission. Siemens does not intend to commercialize the system.*

The challenge of diffusion MRI

The introduction of diffusion-weighted imaging [3] into the armoury of quantitative MRI techniques, has revolutionised our understanding of tissue properties *in vivo* across a wide range of organs. Characterizing the *anisotropic* diffusion of water in tissue, allows properties such as density, shape, size, and orientation of different tissue compartments to be inferred [e.g., 1, 2, 6, 9].

A successful diffusion MRI sequence has two key components:

1. The application of sufficient diffusion-weighting (through the application of magnetic field gradients for a finite duration) that makes the sequence sensitive to **microscopic** displacements.
2. A very rapid read-out of the image, to effectively 'freeze' the physiological motion (**macroscopic** displacements) that would otherwise corrupt the diffusion-weighted image.

Regarding the first point, the field of diffusion MRI has been a key driver in the development of gradient technologies, providing higher and higher gradient amplitudes [10, 19]. The amount of diffusion weighting depends on the **product** of the amplitude and duration of the gradient pulses, and thus the stronger the gradient, the less time it needs to be applied to achieve the same diffusion-weighting. Regarding the second point, by far the most prevalent read-out is echo planar imaging (EPI), introduced into diffusion MRI by Turner et al. [21] (Fig. 1).

Thus, both stronger gradients and echo-planar readouts have improved the robustness and utility of diffusion

MRI since its initial inception. However, both of these pulse components take time to play out. In the most commonly-used pulse sequence, the diffusion-weighted **spin echo**, during these times the signal is constantly being lost due to an additional mechanism, i.e., transverse (T2) relaxation. Not only does this reduce the signal to noise ratio (SNR), but it also means that the signal from species with shorter T2 will contribute much less than species with longer T2.

The motivation for myelin

In the brain, the white matter fibres form the 'motorways' that transport packets of information between different brain regions. The white matter derives its name from the color of the myelin, a fatty layer that wraps around the axons, serving multiple functions (including speeding conduction velocity and reducing the energy requirements for signal transmission). The myelin is a key component of the white matter, and deficits in myelin have been implicated in a wide range of neurological, psychiatric, and developmental disorders, and it has thus been the focus of investigation and key-driver of a number of methodological advances in MRI, including multi-component relaxometry (looking at the water trapped between the layers of myelin, i.e. the 'myelin water' [13, 14, 22]), magnetization transfer imaging (looking at the macromolecules in the myelin *per se* [24], and quantitative susceptibility imaging [7]. However, myelin is rarely considered in diffusion MRI experiments [8]. The ultra-short T2 of the macromolecules themselves is too short (80 ms) to contribute to the spin echo signal, but also the myelin water (T2 ≤ 20 ms) for the echo times **typically** used in a diffusion-weighted spin echo sequence (TE ~80 ms), contributes around 2% of the signal (Fig. 2). Therefore, the contribution of myelin to the diffusion MRI signal in most human MRI experiments is effectively negligible.

If, however, we were able to **shorten** the echo times of the diffusion-weighted experiment to the point that the contribution from the myelin-water becomes non-negligible, the ability to quantify microstructural properties of the myelin space could offer new windows into the pathophysiology of a number of neurological and psychiatric diseases, provide earlier, differential diagnoses, and provide earlier access to treatment.

This article explores how we can achieve those shorter echo times in diffusion MRI, through manipulation of the two key components:

1. the gradient amplitude; and
2. the imaging read-out strategy.

We consider the challenges in implementation of this new approach, and the solutions we have developed to ameliorate them.

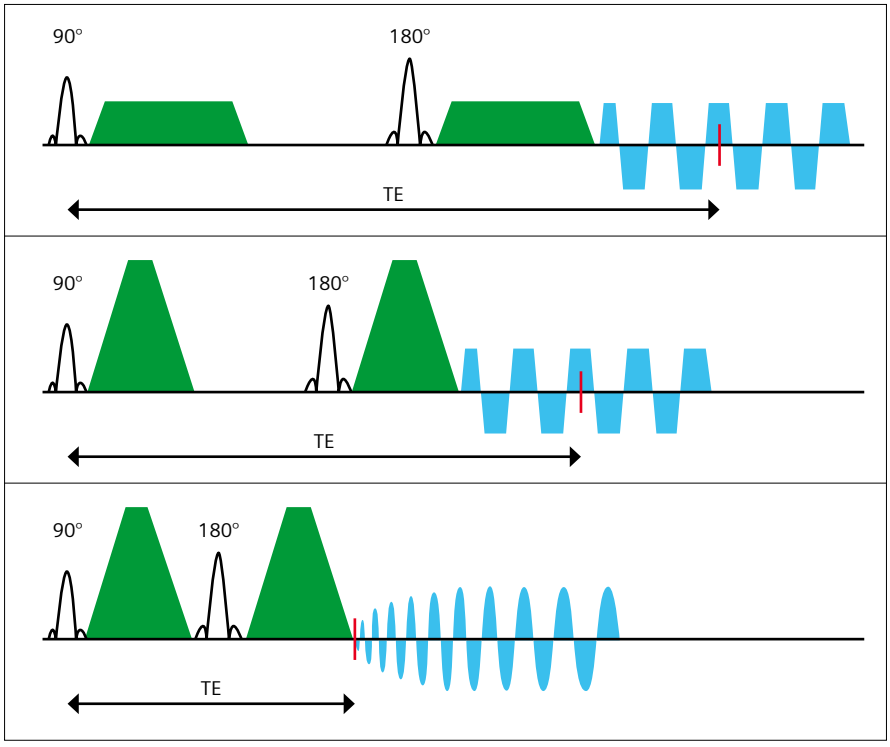

1 Sequence diagrams for different diffusion sequences. The diffusion encoding gradients are shown in green, the readout gradients are blue and the time of the spin echo is marked in red. Ultra-strong gradients and spiral readout are both needed to achieve the shortest possible echo times (TE). Top: Diffusion weighted spin echo (DWSE) sequence with echoplanar imaging (EPI) readout with normal gradient amplitude. Middle: DWSE-EPI with ultra-strong gradients. Bottom: DWSE sequence with ultra-strong gradients and spiral readout.

1. Stronger gradients to reduce the time for diffusion-encoding

The key component that reduces the diffusion-encoding time is an ultra-strong gradient system that enables stronger diffusion weightings per unit time compared to conventional gradient systems. In a typical Stejskal-Tanner experiment (Fig. 1), the amount of diffusion-weighting is determined by two factors: First, the gradient strength and duration of the diffusion-pulse (which can be expressed by q, where $q = \gamma G\delta$); and second, the duration between the diffusion-pulses during which molecular displacements take place (or the diffusion time, which can be expressed by τ, where $\tau = (\Delta - \delta/3)$). The amount of diffusion-weighting in an experiment can then be summarised by the b-value $b = q^2\tau = \gamma^2 G^2 \delta^2 (\Delta - \delta/3)$ [15]. From this equation, it becomes apparent that increasing the gradient-strength allows a much wider range of experiments, in that:

1. for a given b-value, a higher gradient strength allows to reduce the pulse-duration δ and the time between pulses Δ, overall shortening the time needed for diffusion-encoding. The reduction of the shortest possible TE is a direct consequence of this, and thus a wider range of TEs can be achieved;
2. for a given pulse-duration δ, a higher gradient strength provides higher q-values, and thus a wider range of q-values can be sampled;
3. for a given diffusion time, a wider range of b-values can be maintained.

While this clearly outlines the advantages of ultra-strong gradients for the usage for diffusion MRI, there are also challenges; image artifacts can become amplified or

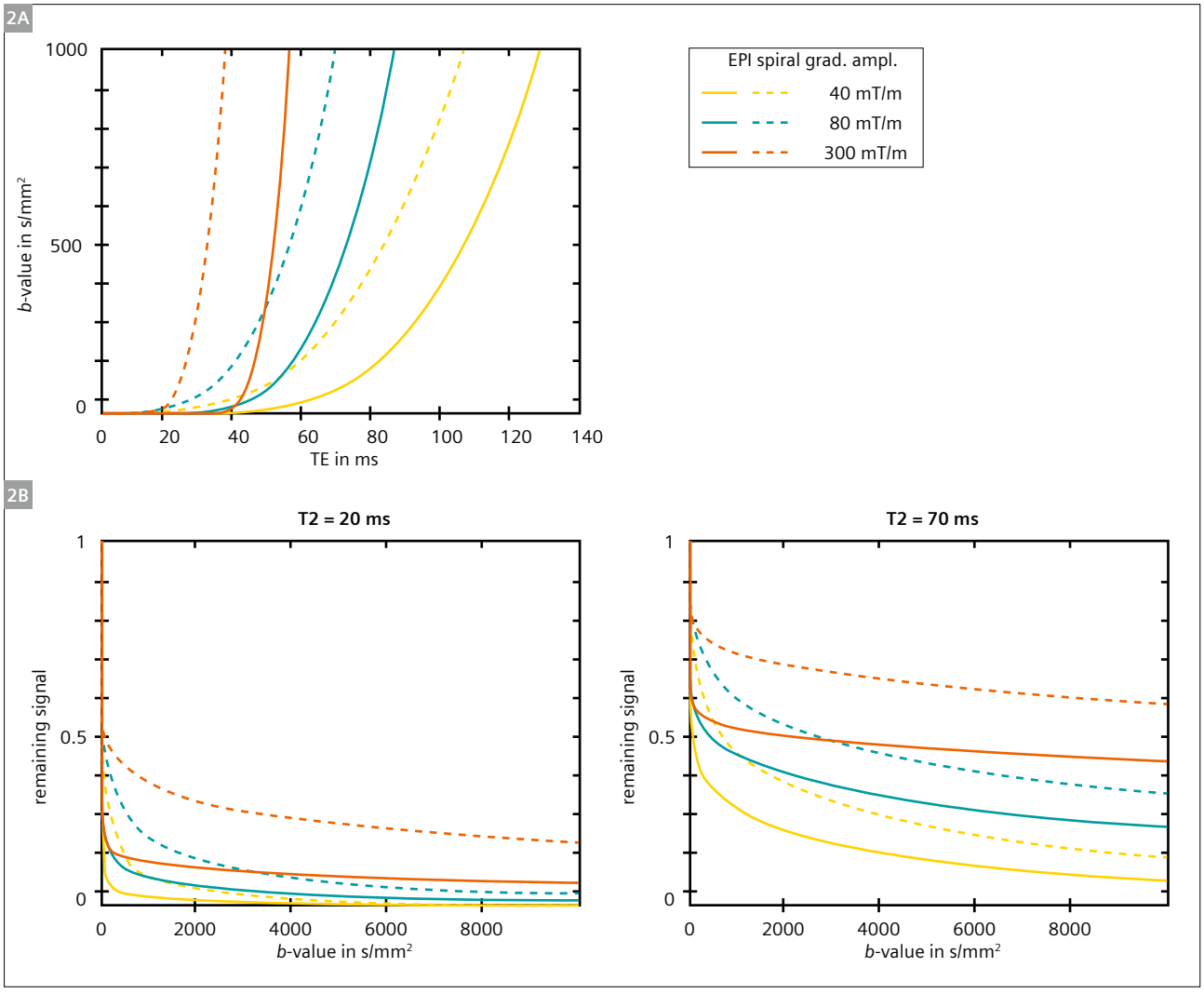

2 Relationships between b-value, echo time (TE), and T2-decay for spiral and EPI with different gradient amplitudes. For the EPI Grappa factor 2, partial fourier 6/8 and bandwidth per pixel of 2004 Hz (1536 Hz for 40 mT/m) were assumed at a resolution of 1.5 mm and FOV of 230 mm. **(2A)** Achievable b-value in given TE. **(2B)** Remaining normalized signal due to T2-decay at the shortest TE for the b-value.

additional artifacts can be observed compared to moderate gradient strengths [10, 19]. The stronger the gradient, the higher the amplitude of the long-time constant eddy currents. This will interfere with the readout gradients, which will lead to a deviation of the prescribed gradients for image readout and thus to image distortions. Achieving ultra-high gradient amplitudes furthermore comes at the cost of reducing the region over which the gradient system behaves linearly [10, 19]. In regions where the gradients exhibit nonlinearity, additional image distortions are to be expected [4, 11]. Geometrical distortions resulting from eddy currents and gradient nonlinearities are commonly corrected during post-processing; while eddy current-distortions can be ameliorated by registering the diffusion images non-rigidly, distortions from gradient nonlinearities require knowledge on the nonuniformities so that the images can be unwarped. It should be noted that eddy currents and gradient-nonlinearities distort the images in concert with B_0 inhomogeneity, and disentangling these effects is challenging.

Gradient nonlinearities additionally mean that the *b*-matrix as imposed by the diffusion gradients is spatially varying depending on the degree of nonlinearity. This means that, even when designed as such, *b*-vectors can become non-uniformly distributed over the hemisphere and *b*-values can deviate from the 'shell'. This can significantly impact diffusion measures when such deviations are not appropriately taken into account [4]. By estimating diffusion models or representations where the *b*-matrix associated with each DWI is adjusted voxel-wise, the adverse effects can be minimized at the cost of longer computation times. The situation is further exacerbated if the participant moves during the scan, as the *b*-value at a given position (after motion correction), is effectively changing over time, requiring *spatiotemporal tracking* of the *b*-matrix [17].

2. Reducing the time between diffusion encoding and *k*-space centre readout

In standard diffusion MRI, the image is read out with EPI, which traverses the *k*-space from one end to the other in parallel lines. Since the centre of *k*-space mostly determines the signal level in the final image, it is acquired at the time of the spin echo. Therefore, part of the *k*-space needs to be acquired beforehand, prolonging TE. Changing

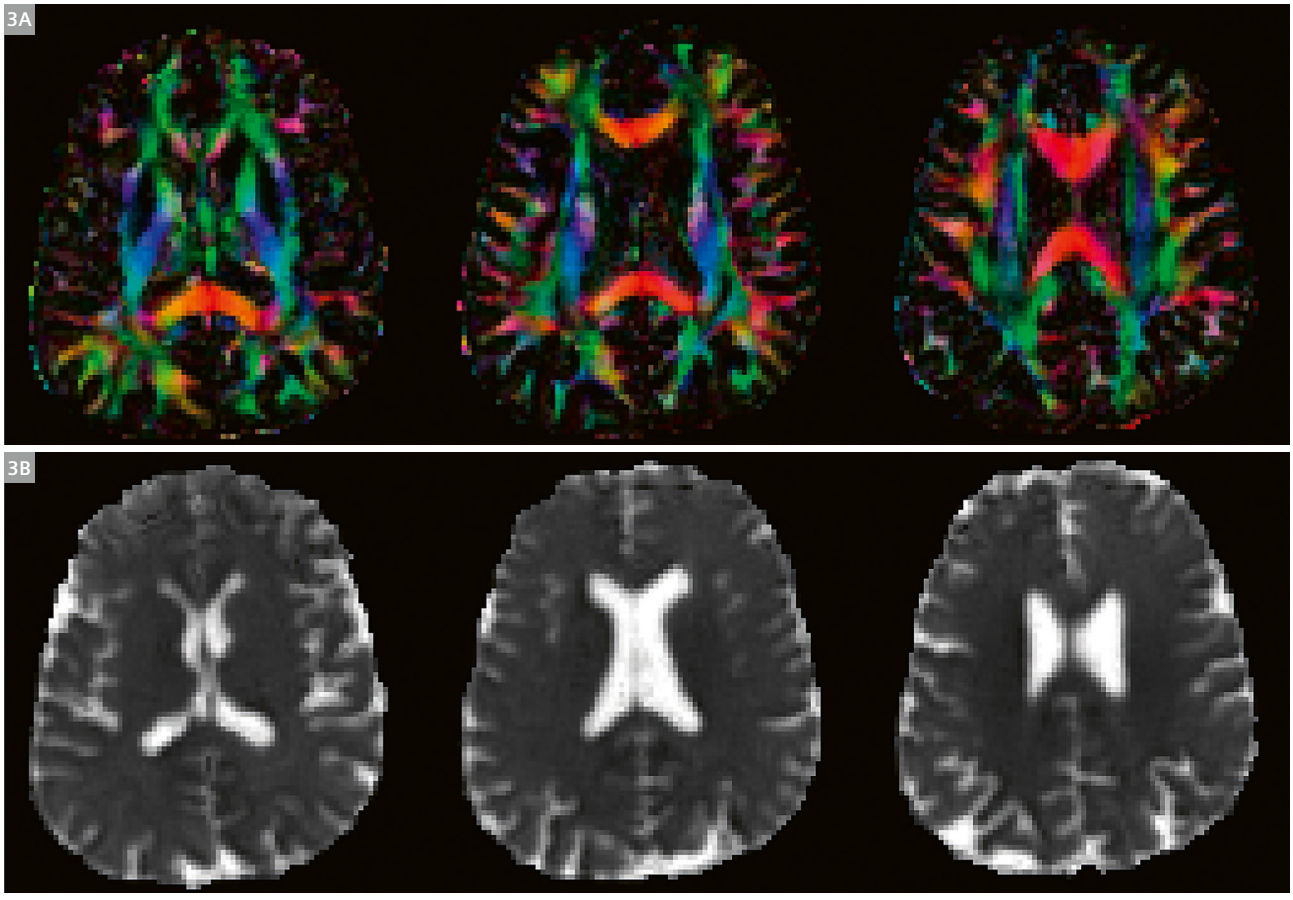

3 Direction-encoded fractional anisotropy **(3A)** and mean diffusivity **(3B)** calculated from diffusion data acquired with TE = 21 ms and b = 1000 s/mm².

the readout trajectory to a spiral starting at the centre negates this necessity of data acquisition before the spin echo. The use of a spiral readout allows shorter TE, compared to EPI, but introduces new difficulties in the imaging process. While the typical artefacts for an EPI readout (e.g., distortions due to eddy currents or B_0 inhomogeneities, ghosting due to gradient imperfections) can be handled in image processing, the artefacts with spiral readouts are often corrected during the image reconstruction. The main sources for artefacts in spiral imaging are:

1. B_0-inhomogeneities
2. T2* decay during the readout
3. Eddy currents and other gradient imperfections leading to a mismatch between prescribed and actual gradients.
4. Gradient nonlinearities (similar to EPI)

To measure the B_0 inhomogeneities, a B_0-map can be estimated by using a multi echo gradient echo sequence. This requires a few minutes additional acquisition time but is essential to reduce blurring. If an additional image with the same timing is acquired with the body coil, they can be combined to estimate the coil sensitivities necessary for a SENSE-type reconstruction. SENSE enables the undersampling of the spiral data and thus shorter readout times leading to less T2* blurring.

The gradients during the readout were measured with a spatio-temporal field monitoring approach [5] with a commercially available field camera. Knowledge of the B_0-map and the real *k*-space trajectory were combined with the knowledge of gradient nonlinearities in a single reconstruction pipeline [16], expanding on a previously introduced approach [23].

Unprecedented echo times and opportunites they present

Bringing together the ultra strong-gradients of the Connectom and a spiral readout with a proper reconstruction pipeline enables diffusion-weighted imaging at unprecedented TE *in vivo*. For b = 1000 s/mm^2, TE = 21.7 ms (see Fig. 3). This opens up new and exciting possibilities in diffusion imaging. Obviously, by reducing the (unwanted) T2-related signal decay during the diffusion encoding, the SNR is enhanced. This can be particularly important for species where diffusion MRI is challenging, e.g., in muscle, because the T2 is short.

Beyond the enhanced SNR, such a reduction in TE opens up new opportunities for exploration of brain microstructure and physiology. For example, with this short TE it might become feasible to measure the diffusion of myelin water [20]. Another promising new avenue is to explore the new contrast mechanism of diffusion-weighted fMRI, by looking into the TE dependence [18] or acquiring gradient echo and diffusion-weighted spin echo at the same TR with only tens of milliseconds between [18]. At present, we have only explored single shot spiral-EPI readouts. Future work will explore the combined use of multi-shot, navigated interleaved acquisitions [12], and external field monitoring to provide enhanced spatial resolution, while maintaining short echo times for diffusion MRI.

Overall objective	Shorten the echo time	
	Encoding	**Readout**
Objective	Shorten diffusion-encoding time	Shorten the time between diffusion encoding and the image readout of the center of *k*-space
Method	Increase the gradient strength	Spiral readout
Challenges	• Gradient nonlinearities and eddy currents cause geometrical distortions • Gradient nonlinearities cause spatiotemporally varying *b*-matrices	Interactions of readout gradients with • gradient nonlinearities and eddy-current induced fields cause geometrical distortions • mechanical vibrations cause signal loss and geometrical distortions
Solution	Image registration to correct for geometrical distortions. Compute spatiotemporally varying *b*-matrices from gradient nonlinearity information	Use field camera measurements to derive the actual readout trajectories

Table 1: Summary of key objectives, the methods, challenges, and solutions.

References

1 Assaf Y, Basser PJ. Composite hindered and restricted model of diffusion (CHARMED) MR imaging of the human brain. Neuroimage. 2005 Aug 1;27(1):48-58.
2 Assaf Y, Blumenfeld-Katzir T, Yovel Y, Basser PJ. AxCaliber: a method for measuring axon diameter distribution from diffusion MRI. Magn Reson Med. 2008 Jun;59(6):1347-54.
3 Le Bihan D, Breton E. Imagerie de diffusion in vivo par résonance magnétique nucléaire CR Acad. Sci. Paris T. 1985, 301 (Série II) (1985), pp. 1109-1112.
4 Bammer R, Markl M, Barnett A, Acar B, Alley MT, Pelc NJ, Glover GH, Moseley ME. Analysis and generalized correction of the effect of spatial gradient field distortions in diffusion-weighted imaging. Magn Reson Med. 2003 Sep;50(3):560-9.
5 Barmet C, De Zanche N, Pruessmann KP. Spatiotemporal magnetic field monitoring for MR. Magn Reson Med. 2008 Jul;60(1):187-97.
6 Basser PJ, Mattiello J, Le Bihan D. MR diffusion tensor spectroscopy and imaging. Biophys J. 1994 Jan;66(1):259-67.
7 Duyn JH, Schenck J. Contributions to magnetic susceptibility of brain tissue. NMR Biomed. 2017 Apr;30(4).
8 Harkins KD, Does MD. Simulations on the influence of myelin water in diffusion-weighted imaging. Phys Med Biol. 2016 Jul 7;61(13):4729-45.
9 Jespersen SN, Lundell H, Sønderby CK, Dyrby TB. Orientationally invariant metrics of apparent compartment eccentricity from double pulsed field gradient diffusion experiments. NMR Biomed. 2013 Dec;26(12):1647-62.
10 Jones DK, Alexander DC, Bowtell R, Cercignani M, Dell'Acqua F, McHugh DJ, Miller KL, Palombo M, Parker GJM, Rudrapatna US, Tax CMW. Microstructural imaging of the human brain with a 'super-scanner': 10 key advantages of ultra-strong gradients for diffusion MRI. Neuroimage. 2018 Nov 15;182:8-38.
11 Jovicich J, Czanner S, Greve D, Haley E, van der Kouwe A, Gollub R, Kennedy D, Schmitt F, Brown G, Macfall J, Fischl B, Dale A. Reliability in multi-site structural MRI studies: effects of gradient non-linearity correction on phantom and human data. Neuroimage. 2006 Apr 1;30(2):436-43.
12 Liu C, Bammer R, Kim DH, Moseley ME. Self-navigated interleaved spiral (SNAILS): application to high-resolution diffusion tensor imaging. Magn Reson Med. 2004 Dec;52(6):1388-96.
13 MacKay A, Whittall K, Adler J, Li D, Paty D, Graeb D. In vivo visualization of myelin water in brain by magnetic resonance. Magn Reson Med. 1994 Jun;31(6):673-7.
14 MacKay A, Laule C, Vavasour I, Bjarnason T, Kolind S, Mädler B. Insights into brain microstructure from the T2 distribution. Magn Reson Imaging. 2006 May;24(4):515-25.
15 Mattiello J, Basser PJ, Le Bihan D. The b matrix in diffusion tensor echo-planar imaging. Magn Reson Med. 1997 Feb;37(2):292-300.
16 Mueller L, Rudrapatna SU, Tax CMW, Wise RG, Jones DK. Diffusion MRI with b = 1000 s/mm² at TE < 22 ms using single-shot spiral readout and ultra-strong gradients: Implications for microstructure imaging. International Society for Magnetic Resonance in Medicine, Montreal, 2019.
17 Rudrapatna SU, Parker G, Roberts J, Jones DK. Strategies for correcting gradient-nonlinearity effects in ultra-high gradient Diffusion MRI experiments. International Society for Magnetic Resonance in Medicine, Paris, 2018.
18 Rudrapatna SU, Mueller L, Wright ME, Jones DK, Wise RG. A GRANDIOSE sequence to time-lock BOLD and diffusion-weighted fMRI contrasts in humans using ultra-strong gradients and spirals. International Society for Magnetic Resonance in Medicine, Montreal, 2019.
19 Setsompop K, Kimmlingen R, Eberlein E, Witzel T, Cohen-Adad J, McNab JA, Keil B, Tisdall MD, Hoecht P, Dietz P, Cauley SF, Tountcheva V, Matschl V, Lenz VH, Heberlein K, Potthast A, Thein H, Van Horn J, Toga A, Schmitt F, Lehne D, Rosen BR, Wedeen V, Wald LL. Pushing the limits of in vivo diffusion MRI for the Human Connectome Project. Neuroimage. 2013 Oct 15;80:220-33.
20 Tax CMW, Rudrapatna SU, Mueller L, Jones DK. Characterizing diffusion of myelin water in the living human brain using ultra-strong gradients and spiral readout. International Society for Magnetic Resonance in Medicine, Montreal, 2019.
21 Turner R, Le Bihan D, Maier J, Vavrek R, Hedges LK, Pekar J. Echo-planar imaging of intravoxel incoherent motion. Radiology. 1990 Nov;177(2):407-14.
22 Whittall KP, MacKay AL, Graeb DA, Nugent RA, Li DK, Paty DW. In vivo measurement of T2 distributions and water contents in normal human brain. Magn Reson Med. 1997 Jan;37(1):34-43.
23 Wilm BJ, Barmet C, Gross S, Kasper L, Vannesjo SJ, Haeberlin M, Dietrich BE, Brunner DO, Schmid T, Pruessmann KP. Single-shot spiral imaging enabled by an expanded encoding model: Demonstration in diffusion MRI. Magn Reson Med. 2017 Jan;77(1):83-91.
24 Wolff SD, Balaban RS. Magnetization transfer contrast (MTC) and tissue water proton relaxation in vivo. Magn Reson Med. 1989 Apr;10(1):135-44.


Lars Mueller

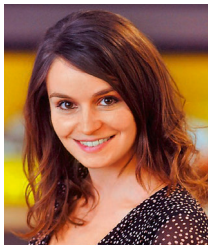
Chantal Tax


Derek Jones

Contact

Professor Derek Jones, BSc, MSc, PhD
Director of CUBRIC
Cardiff University Brain Research Imaging Centre
Outram Road, Block 2, Level 1
Maindy Road
Cardiff, CF24 4HQ
UK
Tel.: +44(0)29 2087 9412
jonesd27@cardiff.ac.uk

Deep Learning for Parallel MRI Reconstruction: Overview, Challenges, and Opportunities

Kerstin Hammernik[1,2]; Florian Knoll[3]; Daniel Rueckert[1]

[1]Department of Computing, Imperial College London, United Kingdom
[2]Institute of Computer Graphics and Vision, Graz University of Technology, Graz, Austria
[3]Department of Radiology, New York University, New York, NY, USA

With the success of parallel imaging [1–4] and compressed sensing [5–7], we have achieved a breakthrough in the field of routine clinical MR imaging to tremendously accelerate the inherently slow acquisition process. However, with the currently available technologies, we have reached a plateau in terms of acquisition speed. The next paradigm shift is already looming: During the past years, we have seen a tremendous development and impressive results of deep learning [8] algorithms in the field of medical imaging. There are many opportunities how deep learning tools can change the world of clinical examinations, ranging from precision medicine, computer aided diagnosis, image classification and segmentation to data acquisition and image reconstruction. Deep learning leverages the potential to change the complete workflow of clinical imaging, however, many algorithms have been developed regardless of practical relevance. In this article, we focus on the application of deep learning tools for parallel MR image reconstruction. We show how the limits of acquisition speed in MR imaging can be pushed even further, with improved image quality and reduced image reconstruction times compared to current state-of-the-art methods and we provide insights into this highly demanding, clinical standard application from different perspectives.

Deep learning for image reconstruction

Image reconstruction aims at recovering a clean, high-quality MR image from a set of acquired *k*-space measurements from multiple receiver coils. This process involves inverse Fourier transforms to map the measured *k*-space data to the image space. However, this is an ill-posed problem due to measurement errors, low signal-to-noise ratios, sparsely sampled data and limitations of

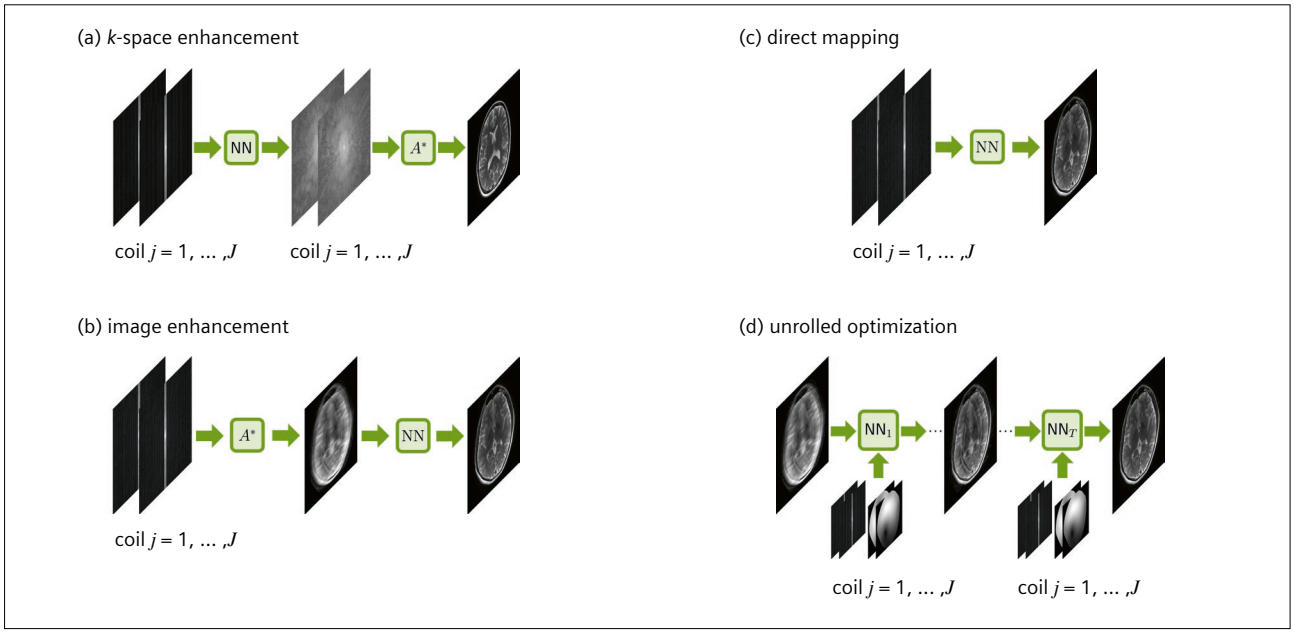

1 Overview of deep learning for parallel MR image reconstruction.

the hardware itself. Two great categories exist for MR image reconstruction, which are in fact closely related: Sensitivity encoding (SENSE) [1, 2] operates in image domain, while generalized autocalibrating partial parallel acquisitions (GRAPPA) [3] fills the missing information of undersampled acquisitions in *k*-space. Similar to the question if one would prefer SENSE or GRAPPA for image reconstruction, deep learning can improve image reconstruction both in *k*-space and image space. In this article, we introduce the basic idea of how deep learning can be used for parallel MR image reconstruction, which is illustrated in Figure 1. We refer the interested reader to [9, 10] for a more detailed insight into this topic.

Learning *k*-space enhancement

To learn improved *k*-space enhancement, both supervised learning methods that depend on training data and self-supervised methods, that learn an interpolation function from the fully sampled autocalibration lines, are reported. DeepSPIRiT [11] is based on *k*-space convolutional neural networks (CNN) that are trained on a reference database and does not depend on explicit coil sensitivity maps, *k*-space interpolation kernels or collection of autocalibration lines. In contrast, GRAPPA-based methods learn a relationship between the coils from an autocalibration signal. While GRAPPA, which is the most clinically used reconstruction method, is based on linear kernel methods and known to suffer from severe noise amplification at higher acceleration rates, it was improved by non-linear kernel methods (RAKI) [12]. RAKI is based on training a CNN from the autocalibration signal to interpolate missing *k*-space lines, resulting in less severe noise amplification compared to GRAPPA as illustrated in Figure 2.

Learning image enhancement

The first group of image-based algorithms learns to enhance a, possibly coil-sensitivity-weighted, zero-filling solution [13–18]. The zero-filling solution is mapped to a fully-sampled reference and does not require any further prior knowledge, hence, consistency to the measured *k*-space data is not ensured. To train these architectures successfully, large amounts of training samples and huge network architectures are required.

Learning the direct transform

The second group of image-based algorithms directly learn a transformation from the undersampled *k*-space data to the fully sampled image. This approach was presented as AUTOMAP by Zhu et al. [19] and is especially useful to overcome errors in the physical model, i.e., imperfect forward operator. The AUTOMAP architecture is characterized by a combination of fully-connected layers with convolutional layers on top and can be applied to any sampling trajectory in MR. The training requires a huge amount of memory due to the fully connected layers, hence, AUTOMAP is limited to small image size. This scaleability issue can be improved by decomposing AUTOMAP as shown in [20]. Although preliminary results are promising, it is practically not applicable yet as the trained networks are limited to specific input sizes which do not meet the requirements for heterogeneous training data in clinical practise.

Learning unrolled optimization

The third and largest group of image-based algorithms learns a fixed unrolled scheme in a supervised end-to-end manner. These fixed, unrolled schemes alternately update the image and impose data consistency. Data consistency can be realized in various ways: By performing gradient steps as in Variational Networks [21] or by solving the proximal mapping [22, 23]. We also find various other optimization schemes, not only for parallel MRI reconstruction, but for medical imaging in general. These schemes range from ADMM-net [24] to variable-splitting schemes [25] and primal-dual optimization [26].

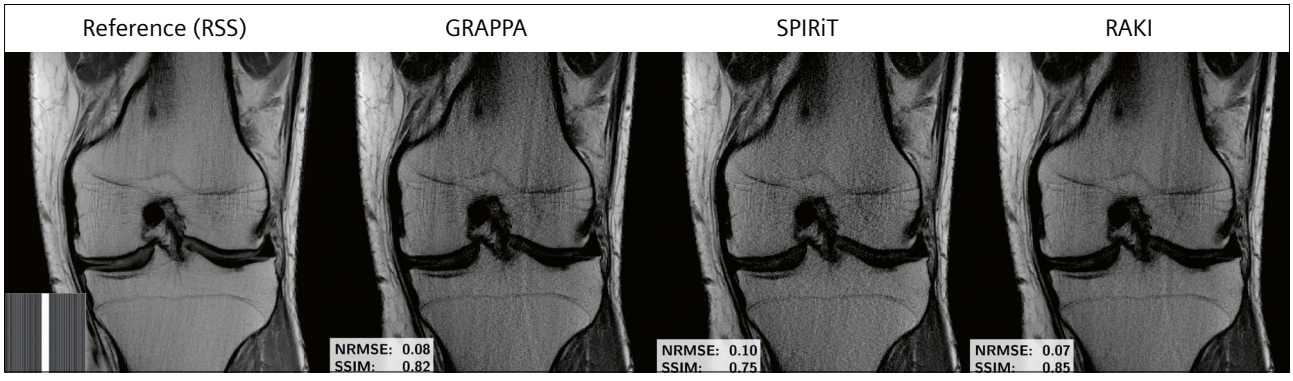

2 GRAPPA-type reconstructions for 4-fold Cartesian undersampling: Comparison of classic GRAPPA, SPIRiT [32] and learning-based RAKI [12] to the root-sum-of-squares (RSS) reference. While GRAPPA suffers from residual artifacts and SPIRiT from noise amplification, RAKI reconstructions achieve both better noise suppression and less residual artifacts. This observation is supported by the quantitative values.

An example for the impact of learning unrolled optimization for accelerated Cartesian imaging is depicted in Figure 3. Here, a variational network reconstruction [21] is compared to a linear CG-SENSE reconstruction [1] and a combined parallel-imaging-compressed sensing (PI-CS) approach [27]. We can clearly see the benefits of the learning-based reconstruction algorithm.

Another question which arises at this stage is if it is really necessary to incorporate the original *k*-space data into the learning-based reconstruction process or if learning image enhancement is enough. A first answer to this question is depicted in Figure 4. Here, a Unet [28] architecture is trained to enhance an initial sensitivity-combined zero-filling solution [16]. This architecture has about 14 million parameters. In comparison, a simple variational network with 140,000 parameters was trained as an unrolled gradient descent scheme with 10 iterations according to [21]. Indeed, we observe that the learned unrolled scheme outperforms the image enhancing network, hence, it is beneficial to include any available prior knowledge in the reconstruction process, which makes the learning task easier and might require less training data to achieve descent results.

High demands for learning-based MRI reconstruction approaches

Many research papers show promising results for learning-based MR image reconstruction, however, these results are often presented for a specific sequence and a simulated environment, e.g., single-coil MR data. We also feel that the image content for a specific sequence is very similar over a wide range of data. In fact, the data is highly inhomogenous and the radiologists' expectations differ from the researchers' perspective in terms of evaluation.

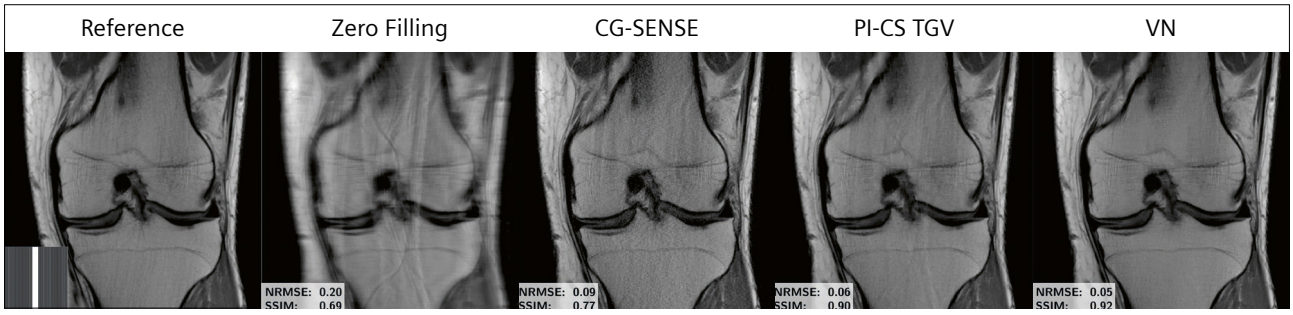

3 SENSE-type reconstructions for 4-fold Cartesian undersampling. Comparison of linear CG-SENSE reconstruction, a parallel imaging-compressed sensing combined Total Generalized Variation (PI-CS TGV) reconstruction [27], and a learning-based Variational Network (VN) reconstruction [21]. The learning-based VN approach reaches superior image quality and reduced artifacts.

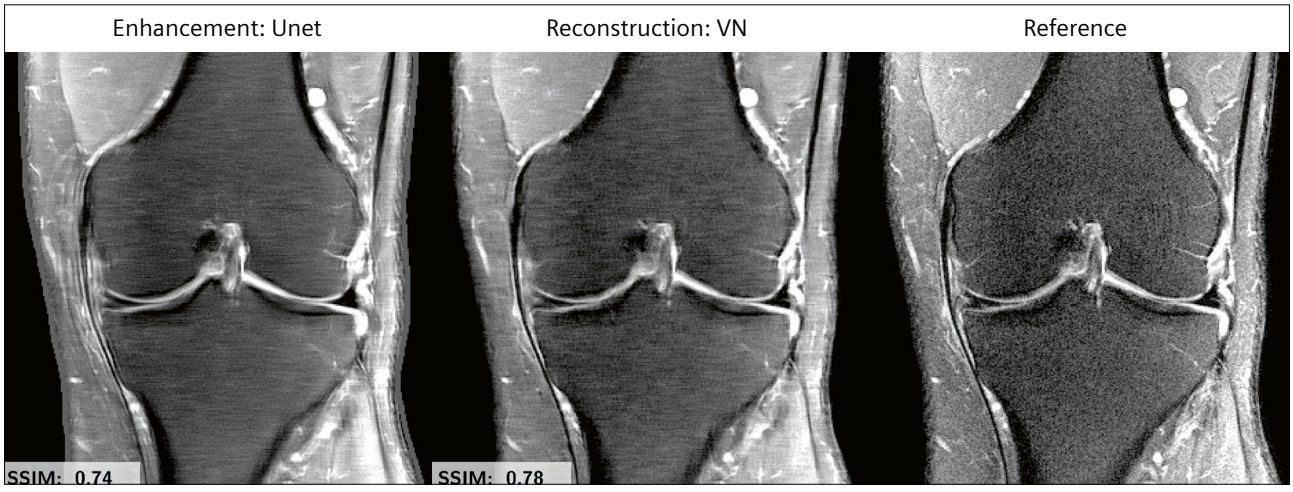

4 Comparison of learning-based image enhancement with a Unet to learning-based image reconstruction with a variational network (VN). The VN that uses the acquired *k*-space data achieves better SSIM scores and has only a fraction (1%) of the parameters compared to the Unet.

More than inverse Fourier transforms

When addressing MR data we often have a simplified picture in mind, telling us that we just have to perform an inverse Fourier transform to obtain the reconstructed image. Indeed, inverse Fourier transforms are the main ingredient for image reconstruction, however, many more aspects have to be considered when building learing-based solutions. The data are acquired in Fourier domain, hence, are complex-valued, which has to be addressed. A common approach here is to handle the complex-valued images as a two-channel real image. Further research points towards addressing the complex-valued issue by complex convolutions and complex activations [29].

In the case of SENSE-based approaches, the explicit estimation of coil sensitivity maps is still a pre-processing step and the final reconstruction quality highly depends on the quality of the coil sensitivity maps. The joint estimation of reconstructed image and coil sensitivity maps is still an open question in deep learning.

Heterogenous MRI data acquisition

Case study

A 42-year-old female patient had to undergo a clinical knee examination. The patient was referred to institution A, where a full clinical protocol (consisting of coronal PDw, coronal PDw with fat saturation, sagittal PDw, sagittal T2w with fat-saturation, axial T2w with fat saturation) was acquired using a 3T MAGNETOM Skyra (Siemens Healthcare, Erlangen, Germany) and a 15-channel knee coil. The patient moved to another country and had to undergo further treatment due to reappearing medical issues at institution B, where the same clinical protocol was acquired using a 1.5T MAGNETOM Aera (Siemens Healthcare, Erlangen, Germany) and a 15-channel knee coil. The patient, who is a computer scientist, was astonished when comparing the two protocols: Why do the images have different size? Why are some parts of the knee cropped and folded back on the other side in certain images of institution A? Why is so much noise in the images of institution B? You can hardly see anything! Why are there some artifacts in the images of institution A?

Using this case study, we can already identify common challenges in every day clinical MRI examinations: There is no universal acquisition scheme and even standard acquisition protocols vary not only from institution to institution, but also within the institution. These variations include changes in sequence parameters, matrix size, and base resolution. Furthermore, the radiographers acquiring the images have to adapt characteristic parameters individually for each patient. This includes for example the setting for phase encoding oversampling to ensure that the entire field-of-view is considered during acquisition and no backfolding occurs. Not only the sequence setting but also the hardware setting itself has a huge impact on the final image quality. The image quality depends on the coil load and the field strength of the MRI scanner. Other sources that influence the image quality are any kind of artifacts, including patient motion. The fastMRI dataset [16] is a great example for a heterogeneous dataset. The protocols for this dataset were adapted to fit the individual scanner hardware and imaged patient as optimal as possible. Figure 5 shows examples from this dataset for varying field strengths, noise levels and artifacts. The images have a different dimension in phase encoding (x) direction. The number of phase encoding steps are individually adjusted during acquisition, hence, introduce another degree of inhomogeneity for learning-based reconstruction approaches.

We see that learning-based approaches have to deal with highly heterogeneous data. Most of the currently available approaches are tested on high SNR data of the same scanner and sequence. Furthermore, for supervised learning approaches, we have to define a "ground truth" reconstruction. This becomes even more challenging, when an additional dynamic component is added or quantitative imaging is performed using learning-based approaches.

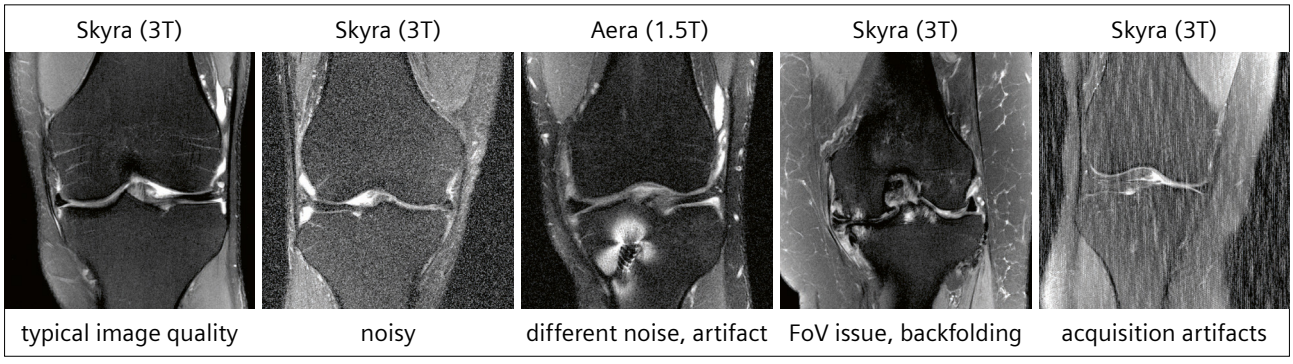

5 Examples of coronal PD-weighted knee scans with fat saturation from the fastMRI dataset [16]. The dataset contains heterogeneous data in terms of varying field strength, number of phase encoding steps and artifacts.

Researchers' evaluation

From a researchers' perspective, quantitative evaluation metrics are required to benchmark different approaches objectively. Common evaluation metrics here are the Peak-Signal-to-Noise ratio (PSNR) or the Structural Similarity Index (SSIM) [30]. Furthermore, supervised machine learning approaches require a qualitative image metric for network training which is reflected in the final image quality. The major drawback of most commonly used quantitative image metrics is their over-smoothing behaviour and the incapability to reflect small, subtle details in the metric. The images might have high quantitative scores, but appear unpleasant from a radiologists' perspective, hence, the insights into the true nature of MR images are still limited. Another obvious issue is to compare GRAPPA-based and SENSE-based algorithms, especially when no additional noise measurement is available to obtain the optimal weighting between the individual coils. Although Figures 2 and 3 show the same image slice, they cannot be compared directly as in this case the SENSE-based algorithms require explicit coil sensitivity maps and GRAPPA-based methods use implicit coil sensitivities for reconstruction. Hence, it is still an open question how to compare these algorithms from a researchers' perspective and it might require a more thorough evaluation of radiologists.

Radiologists' evaluation

In a diagnostic setting, the evaluation of diagnostic content, hence, the presence or absence of small subtle structures is inevitable. This requires large-scale studies to prove if all information are still available for the correct diagnosis if the acquisitions are accelerated. This includes a subjective evaluation of the image quality itself: Many learning-based approaches suffer from blurred images and residual artifacts, however, are these degraded images sufficient for correct diagnosis? Up to now, only small-scale studies in terms of image quality [21] and diagnostic content [31] were performed. Future opportunities include an evaluation on more diverse MR data, sample size and imaging exams.

Opportunities

A major concern in deep learning for medical imaging in general is the need for big data itself. While for computer vision applications, large databases and benchmarks exist, big data are only slowly arriving in medical imaging, mostly associated with dedicated image challenges. In the field of image reconstruction, the fastMRI dataset [16] provides a huge step towards a more generalized raw data archive, currently containing about 1000 fully sampled knee training datasets acquired with different Siemens Healthineers scanners. This rises the questions if we can train a universal network that is able to deal with the heterogeneous data, various anatomies and intra-/inter-vendor hardware settings. Are we able to train a universal network? Or might semi-supervised and unsupervised approaches provide a way to adapt to patient- and acquisition-specific clinical scenarios?

We experience that deep learning, and artificial intelligence in general, have the capability to change the complete imaging workflow in radiology. However, many of the existing approaches so far are based on simulated scenarios and have limited clinical value. Considering parallel imaging in image reconstruction provides a first step towards clinical applicability. While we focus here only on imaging data, there is also a vast amount of medical records, patients' history and even other sensor data available, which might be included and improve the image acquisition and reconstruction workflow.

Conclusion

The current developments in deep learning for medical image reconstruction reminds one of the hype we have experienced with compressed sensing. While compressed sensing started to change image reconstruction almost 20 years ago, it is only now a commercial product and established in clinical routine. Similarly, deep learning approaches for image reconstruction are not yet established in clinical examinations and will require a thorough evaluation, but they already provide a huge potential for the future of MR image reconstruction.

Acknowledgements

We want to thank Jo Schlemper for providing the Unet reconstruction and Mehmet Akçakaya for providing the GRAPPA, SPIRiT, and RAKI reconstructions. We also acknowledge research support by the EPSRC Programme Grant EP/P001009/1 and the National Institutes of Health under grants R01EB024532 and P41EB017183.

References

1 Klaas P Pruessmann, Markus Weiger, Markus B Scheidegger, and Peter Boesiger. SENSE: Sensitivity encoding for fast MRI. Magn Reson Med, 42(5):952–962, 1999.
2 K P Pruessmann, M Weiger, P Boernert, and P Boesiger. Advances in sensitivity encoding with arbitrary k-space trajectories. Magn Reson Med, 46(4):638–651, 2001.
3 Mark A Griswold, Peter M Jakob, Robin M Heidemann, Mathias Nittka, Vladimir Jellus, Jianmin Wang, Berthold Kiefer, and Axel Haase. Generalized autocalibrating partially parallel acquisitions (GRAPPA). Magn ResonMed, 47(6):1202–1210, 2002.
4 D K Sodickson and W J Manning. Simultaneous Acquisition of Spatial Harmonics (SMASH): Fast Imaging with Radiofrequency Coil Arrays. Magn ResonMed, 38(4):591–603, 1997.
5 Michael Lustig, David Donoho, and John M Pauly. Sparse MRI: The application of compressed sensing for rapid MR imaging. Magn Reson Med, 58(6):1182–1195, 2007.

6 Kai Tobias Block, Martin Uecker, and Jens Frahm. Undersampled radial MRI with multiple coils. Iterative image reconstruction using a total variation constraint. Magn Reson Med, 57(6):1086–1098, 2007.
7 Michael Lustig, David L. Donoho, Juan M. Santos, and John M. Pauly. Compressed Sensing MRI. IEEE Signal Processing Magazine, 25(2):72–82, 2008.
8 Yann LeCun, Yoshua Bengio, and Geoffrey Hinton. Deep Learning. Nature,521(7553):436–444, 2015.
9 Kerstin Hammernik and Florian Knoll. Machine learning for image reconstruction. In S. Kevin Zhou, Daniel Rueckert, and Gabor Fichtinger, editors, Handbook of Medical Image Computing and Computer Assisted Intervention. Academic Press, 2019.
10 Florian Knoll, Kerstin Hammernik, Chi Zhang, Steen Moeller, Thomas Pock, Daniel K. Sodickson, and Mehmet Akcakaya. Deep Learning Methods for Parallel Magnetic Resonance Image Reconstruction. Accepted for publication in IEEE Signal Processing Magazine, 2019.
11 Joseph Y. Cheng, Morteza Mardani, Marcus T. Alley, John M. Pauly, and Shreyas S. Vasanawala. Deep-SPIRiT: Generalized parallel imaging using deep convolutional neural networks. In Proc. 26th Annual Meeting of the ISMRM, Paris, France, 2018.
12 Mehmet Akçakaya, Steen Moeller, Sebastian Weingärtner, and Kâmil Uğurbil. Scan-specific robust artificial-neural-networks for k-space interpolation (RAKI) reconstruction: Database-free deep learning for fast imaging. Magn Reson Med, 81(1):439–453, 2019.
13 Yoseob Han, Jaejun Yoo, Hak Hee Kim, Hee Jung Shin, Kyunghyun Sung, Jong Chul Ye. Deep learning with domain adaptation for accelerated projection-reconstruction MR. Magn Reson Med, 80:1189–1205, 2018.
14 Chang Min Hyun, Hwa Pyung Kim, Sung Min Lee, Sungchul Lee, and Jin KeunSeo. Deep learning for undersampled MRI reconstruction. Physics in Medicine and Biology, 63(13), 2018.
15 Guang Yang, Simiao Yu, Hao Dong, Greg Slabaugh, Pier Luigi Dragotti, Xu-jiong Ye, Fangde Liu, Simon Arridge, Jennifer Keegan, Yike Guo, and David Firmin. DAGAN: Deep De-Aliasing Generative Adversarial Networks for Fast Compressed Sensing MRI Reconstruction. IEEE Transactions on Medical Imaging, 2018.
16 Florian Knoll, Jure Zbontar, Anuroop Sriram, Matthew J. Muckley, Mary Bruno, Aaron Defazio, Marc Parente, Krzysztof J. Geras, Joe Katsnelson, Hersh Chandarana, Zizhao Zhang, Michal Drozdzal, Adriana Romero, Michael Rabbat, Pascal Vincent, James Pinkerton, Duo Wang, Nafissa Yakubova, ErichOwens, C. Lawrence Zitnick, Michael P. Recht, Daniel K. Sodickson, and Yvonne W. Lui. fast MRI: a publicly available raw *k*-space and DICOM dataset for accelerated MR image reconstruction using machine learning. Radiology AI, page in press, 2019.
17 Jong Chul Ye, Yoseob Han, and Eunju Cha. Deep Convolutional Framelets: A General Deep Learning Framework for Inverse Problems. SIAM Journal in Imaging Sciences, 11(2):991–1048, 2018.
18 Kyong Hwan Jin, Michael T. McCann, Emmanuel Froustey, and Michael Unser. Deep convolutional neural network for inverse problems in imaging. IEEE Trans Image Proc, 26(9):4509–4522, 2017.
19 Bo Zhu, Jeremiah Z. Liu, Stephen F. Cauley, Bruce R. Rosen, and Matthew S. Rosen. Image reconstruction by domain-transform manifold learning. Nature 555 (7697), pp. 487-492, 2018.
20 Jo Schlemper, Ilkay Oksuz, James Clough, Jinming Duan, Andrew King, Julia Schnabel, Joseph Hajnal, and Daniel Rueckert. dautomap: Decomposing automap to achieve scalability and enhance performance. In ISMRM 27th Annual Meeting, page 0658, 2019.
21 Kerstin Hammernik, Teresa Klatzer, Erich Kobler, Michael P Recht, Daniel K Sodickson, Thomas Pock, and Florian Knoll. Learning a variational network for reconstruction of accelerated MRI data. Mag Reson Med, 79:3055–71, 2018.
22 Jo Schlemper, Jose Caballero, Joseph Hajnal, Anthony Price, and Daniel Rueckert. A deep cascade of convolutional neural networks for MR image reconstruction. In Proceedings of the International Society of Magn Reson Med (ISMRM), page 643, 2017.
23 Hemant K. Aggarwal, Merry P. Mani, and Mathews Jacob. MoDL: Model-Based Deep Learning Architecture for Inverse Problems. IEEE Transactions on Medical Imaging, 2019.
24 Yan Yang, Jian Sun, Huibin Li, and Zongben Xu. Deep ADMM-Net for Compressive Sensing MRI. In Advances in Neural Information Processing Systems (NIPS), pages 10–18, 2016.
25 Jinming Duan, Jo Schlemper, Chen Qin, Cheng Ouyang, Wenjia Bai, Carlo Biffi, Ghalib Bello, Ben Statton, Declan P O'Regan, and Daniel Rueckert. Vs-net: Variable splitting network for accelerated parallel mri reconstruction. Medical Image Computing and Computer Assisted Intervention (MICCAI), pp. 713-722, 2019.
26 Jonas Adler and Ozan Öktem. Learned Primal-Dual Reconstruction. IEEE Transactions on Medical Imaging, 37(6):1322–1332, 2018.
27 Florian Knoll, Kristian Bredies, Thomas Pock, and Rudolf Stollberger. Second order total generalized variation (TGV) for MRI. Magnetic Resonance in Medicine, 65(2):480–491, 2011.
28 Olaf Ronneberger, Philipp Fischer, and Thomas Brox. U-Net: Convolutional Networks for Biomedical Image Segmentation. Medical Image Computing and Computer-Assisted Intervention (MICCAI), pp 234-241, 2015.
29 Chiheb Trabelsi, Olexa Bilaniuk, Dmitriy Serdyuk, Sandeep Subramanian, João Felipe Santos, Soroush Mehri, Negar Rostamzadeh, Yoshua Bengio, and Christopher J. Pal. Deep complex networks. arXiv preprint arXiv:1705.09792,2017.
30 Zhou Wang, Alan Conrad Bovik, Hamid Rahim Sheikh, and Eero P. Simoncelli. Image quality assessment: From error visibility to structural similarity. IEEE Trans Image Proc, 13(4):600–612, 2004.
31 Florian Knoll, Kerstin Hammernik, Elisabeth Garwood, Anna Hirschmann, Leon Rybak, Mary Bruno, Tobias Block, James Babb, Thomas Pock, Daniel Sodickson, and Michael Recht. Accelerated Knee Imaging Using a Deep Learning Based Reconstruction. In Proceedings of the International Society of Magn Reson Med (ISMRM), page 645, 2017.
32 Michael Lustig and John M Pauly. SPIRiT: Iterative self-consistent parallel imaging reconstruction from arbitrary *k*-space. Magn Reson Med, 64(2):457–471, 2010.



Contact

Kerstin Hammernik
Imperial College London
Department of Computing
South Kensington Campus
London SW7 2AZ
United Kingdom
k.hammernik@imperial.ac.uk

Experience after One Year with MRgFUS

Marta Vidorreta, Ph.D.[1]; Miguel Fernández, MSc.[2]; Pablo D. Domínguez, M.D.[2]; Arantza Gorospe, M.D.[3]; Iciar Avilés-Olmos, M.D., Ph.D.[3]; María Cruz Rodríguez-Oroz, M.D., Ph.D.[3]; Jorge Guridi, M.D., Ph.D.[4]

[1]Siemens Healthineers, Madrid, Spain
[2]Department of Radiology, Clínica Universidad de Navarra, Pamplona, Spain
[3]Department of Neurology, Clínica Universidad de Navarra, Pamplona, Spain
[4]Department of Neurosurgery, Clínica Universidad de Navarra, Pamplona, Spain

Introduction

Essential tremor [1] is the most common neurological movement disorder. It causes involuntary and uncontrollable rhythmic shaking, most frequently in the hands, but other body parts can also be affected.

Severe tremor can seriously impair quality of life. It usually appears while doing everyday activities such as writing, eating or tying a shoelace – interfering with a patient's ability to live an independent and active lifestyle.

Essential tremor is a progressive disorder, and until very recently surgical treatment was the last resort when medication becomes ineffective. The preferred surgical method is Deep Brain Stimulation (DBS), in which electrodes are implanted into the target brain region and are controlled by a subcutaneous Implantable Pulse Generator (IPG) implanted at the subclavicular region. Albeit effective, this procedure requires extensive post-operative care, and incurs the risks of any open surgical procedure.

MR-guided Focused Ultrasound (MRgFUS) [2] is a novel, groundbreaking technology that allows incisionless surgery. Insightec's Exablate Neuro™ (Insightec, Tirat Carmel, Israel)[1] (Fig. 1) uses up to 1024 High-Intensity

[1] *The information shown herein refers to products of 3rd party manufacturers and thus are in their regulatory responsibility. Please contact the 3rd party manufacturer for further information.*



1 **MRgFUS setup**
In the MR room, MRgFUS treatment requires: **(1)** The MRI system, **(2)** the HIFU transducer helmet with its positioning system, **(3)** the patient's leg positioner, **(4)** the Exablate Neuro frontend cabinet, containing the power amplifiers that drive the transducer, **(5)** the water system cabinet that provides degassed, cold water at 15 °C, to serve as interface between the patient's head and the transducer, and **(6)** the silicon membrane that seals the transducer and permits water filling. Additional elements outside the MR room are the Exablate Neuro console, from which the neurosurgeon operates the procedure, and the equipment cabinet, containing the control PC and other electronics.

Focused Ultrasound waves (HIFU waves) to heat and precisely ablate the target spot with no surgical incisions or burr holes. Integration with the MRI system allows precise, patient-specific treatment planning and real-time monitoring. Moreover, MR temperature mapping is essential for careful temperature control of the target spot. At first the target area is heated gently, remaining below the 55–60 °C threshold that would produce irreversible effects, allowing a neurologist to evaluate patient response including tremor relief and potential side effects. This information is used by the treating physician to perform adjustments if necessary. Once the target is confirmed, the heating is gradually increased to create a highly accurate and controllable lesion. As a result, most patients experience immediate reduction of tremor with minimal complications.

Pre-treatment protocol

Patients diagnosed with severe essential tremor, which is incapacitating and resistant to medication, may be candidates for DBS or MRgFUS treatment. Depending on age and the physical state of the patient, MRgFUS may be recommended over DBS. As in any MRI scan, contraindications to MRgFUS include:

- Claustrophobia
- Inability to lie still for a long time
- Presence of non-MRI-compatible metallic/electronic objects in body

Subjects must also undergo a high-resolution head CT-scan prior to the procedure, to estimate their skull density ratio (SDR), defined as the averaged ratio between the skull's cancellous and cortical bones mean Hounsfield units. Patients with very low SDR scores, as determined by the Exablate Neuro's algorithm, are not suitable for MRgFUS, as the energy required to complete a successful treatment would be too high for existing safety standards.

Cardiovascular diseases must also be considered before recommending MRgFUS, as it can cause deep vein thrombosis due to the long immobilization time, and carries other CV risks.

A pre-treatment MRI scan is always performed to discard other neurological diseases and plan the MRgFUS ablation target. The MRI scan is done in our 3T intra-operative MAGNETOM Skyra (Siemens Healthcare, Erlangen, Germany), software version *syngo* MR E11C-AP03, with 32-channel head coil. The imaging protocol includes a high-resolution T1 MPRAGE, T2 FLAIR, T2 SPACE, and a DTI scan.

In essential tremor, the target spot is the Ventralis Intermidius Thalamic (Vim) nucleus, located in the hemisphere contralateral to the affected body part.

Vim planning can be performed on the T1 or T2 anatomical MR images, following these steps [3]:

- Find the intercommisural plane, i.e. the axial plane including both the anterior commissure (AC) and posterior commissure (PC)
- Draw the midline, and calculate the AC-PC distance, i.e. the length of the third ventricle
- Locate the Vim starting from the PC, measuring 25% of this distance in the anterior direction, 14–17 mm lateral from the midline, and 0–2 mm above the intercommissural plane

In our center, the Vim location calculation also uses information from the DTI scan [4]. The neuroradiologist processes this data at the *syngo*.via station and extracts the dentato-rubro-thalamic and cortico-thalamic tracts, which connect the motor centers from cerebellum and cortex, through the Vim nucleus in the thalamus. The tract information is fused with the anatomical image, to visualize the tract crossing at the AC-PC plane (Fig. 2). The final target is selected by the neurosurgeon based on all this information.

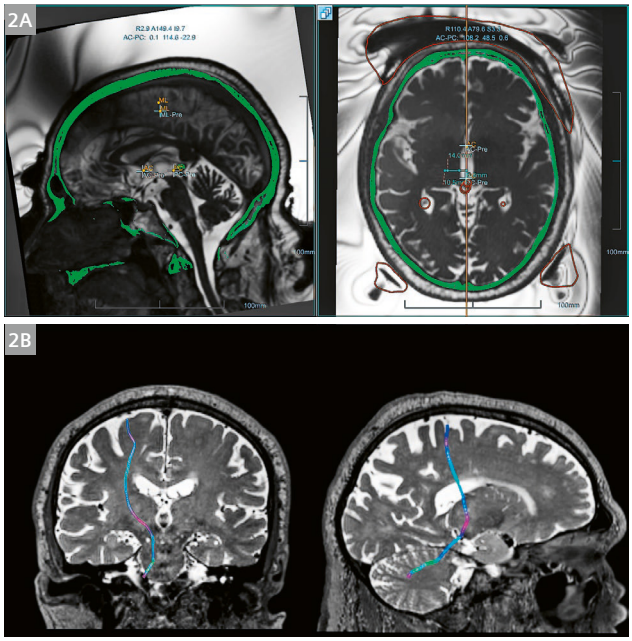

2 Target planning
Target planning is performed at the Exablate Neuro console, after the CISS sequence is acquired **(2A)**. The anterior and posterior commissures (AC and PC) are located on the sagittal and axial views, and the image is reformatted to the AC-PC plane. The Vim area is then identified 25% anterior to the PC and typically 14 mm lateral from the midline [3], although the third-ventricle wall can also be used as reference. If information about the crossing of the dentato-rubro-thalamic tract on the AC-PC plane is available, it can help refine the target location. The coronal and sagittal projections of the tract **(2B)** are extracted from pre-scan DTI data and postprocessed using *syngo*.via's Neuro 3D workflow. The tract can be exported as a DICOM series to be used at the time of planning.

Treatment day

Patients must be fully awake and responsive during treatment. Before starting, the only medications that may be administered are corticosteroids (dexamethasone), as a preventive measure, and analgesics in case of reported back pain or headache.

MRgFUS is a multi-departmental activity. On the day of treatment, the first thing to be done is the Daily Quality Assurance (DQA) scan at our 3T MAGNETOM Skyra. Communication between the MR and Exablate Neuro's console (Model Exablate 4000 Type 1.1, software version 7.2) is performed through the Access-i remote control feature, which allows the MR system to be operated from another client.

The DQA scan is performed on a special DQA phantom gel provided by Insightec. This checks that all functionalities are running smoothly (B_1 calibration, geometric alignment, temperature control, steering verification and cavitation control). The DQA protocol lasts about 15 minutes and is always performed by one of our team MR techs, trained and certified by Insightec's neuro application specialists.

Once the DQA is completed successfully, patient preparation begins. The scalp is shaved to prevent trapping of air that could absorb heat during treatment, causing skin burns. Then the neurosurgeon places the stereotactic frame on the patient's head. Compression stockings are recommended to reduce the chances of deep vein thrombosis. Finally, a silicon membrane is placed on the head. This seals the transducer, which is then filled with cold water at 15 °C, preventing skin damage during high-energy sonications. In between imaging and sonications this water is constantly circulating to keep the temperature low.

Once the patient is lying on the MR table, the frame is attached to the transducer to ensure no head motion during treatment.

Before starting the procedure, the anesthesiology team ensures that vital signs will be monitored at all times. Their main goal is to control potential symptoms. To this end, an intravenous line is placed in the non-treated arm in case medication needs to be administered during treatment. The most commonly used medications are:

- Antiemetics, if nausea is reported by the patient
- Steroids, to prevent and control edema
- Opioids, occasionally, for pain management
- Dexmedetomidine, an optional sedative administered always in low doses to perform Monitored Anesthesia Care (MAC) to manage anxiety

Prior to treatment, the patient's CT scan is loaded onto the Exablate Neuro's console. The neuroradiologist tags all air sinuses and calcifications as "no-pass" regions, as they can dissipate and deflect energy. The tagged CT scan will later be fused with the intra-operative MR images, using Exablate's semi-automatic registration method (Fig. 3). As a safety measure, transducer elements with orientations that cross the no-pass regions are automatically detected and switched off.

The complete MR procedure is carried out using the Tx-Rx body coil, as the Exablate Neuro transducer does not currently allow for a dedicated receive coil. After careful shimming and B_1 calibration, the planning scan is acquired using a 3D CISS sequence with the following parameters:

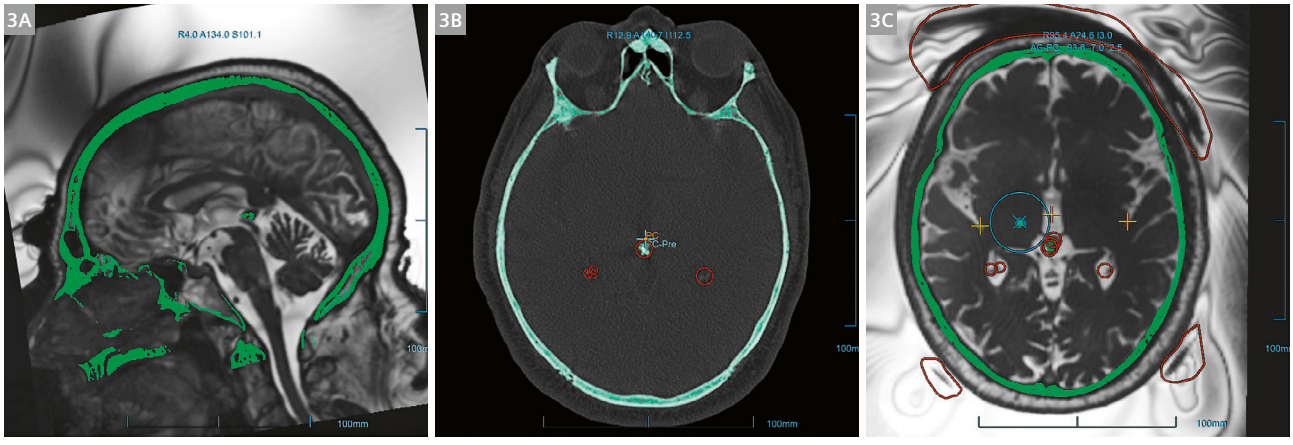

3 **Additional pre-planning steps**
Before proceeding to target planning, the CT and MRI scans must be fused **(3A).** This is performed using Insightec's semi-automatic method, and the result is always verified and corrected if necessary by the neurosurgeon. Calcium spots must be marked on the CT scan as "no-pass" regions **(3B)**, as they can dissipate and deflect energy. Membrane folds must be marked as they can contain trapped air bubbles **(3C)**. Motion trackers (orange crosses in 3C) are also placed throughout the brain at high-contrast interface areas to detect patient movement during treatment.

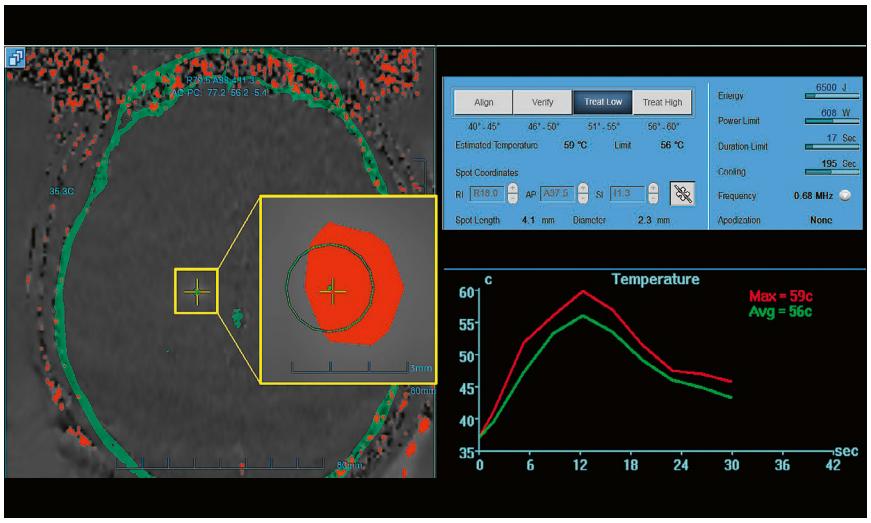

4 Sonication control
There are four sonication modes to choose from during a MRgFUS treatment: **Align** (40–45 °C), **Verify** (46–50 °C), **Treat-low** (51–55 °C) and **Treat-high** (56–60 °C). The total energy, maximum power and maximum duration of a sonication can be chosen by the neurosurgeon. Sonication stops automatically if the maximum temperature (determined by the chosen mode) is reached before the total energy is delivered. Real-time mean and maximum temperature graphs at the target spot are displayed for evaluation. After each sonication, there is a cooling pause of variable length, depending on the total energy applied.

TE/TR 2.4/5.6 ms, BW 300 Hz/px, FA 35–40°, FOV 240 x 240 mm², matrix 218 x 256, 144 sagittal slices, 1.35 mm slice thickness, 22%/50% slice/phase oversampling, slab-selective excitation, TA 8.5 min. MR frequency adjustment, critical to minimize imaging and thermal shifts, is also controlled in the Exablate's console.

The next steps are CISS image reformatting, MR-CT fusion, MR image screening of membrane folds (which also need to be avoided by the HIFU waves), motion tracker placement and target spot location. Once these are done, the transducer position is manually updated to bring the target center coordinates to the magnet's isocenter in order to minimize distortions.

At least four sonications are needed to complete a MRgFUS treatment (Fig. 4):

- **Align:** 40–45 °C sonication for target location
- **Verify:** 46–50 °C sonication for target localization and shape verification
- **Treat-low:** 51–55 °C sonication for clinical evaluation of the patient response to the stimulated target
- **Treat-high:** 56–60 °C sonication for permanent target ablation

In between each sonication there is a cooling pause of variable length. A specialized neurologist assesses the patient during these breaks, right at the bore of the MR, to ensure the effectiveness of the treatment. For instance, the patient may be asked to lift the affected limb and keep it still, write their name on a piece of paper, or mimic a drinking movement. Potential adverse effects, such as other limbs' numbness, are closely monitored. In case of side effects or insufficient clinical response, the target may be relocated and the sonication chain repeated.

Real-time temperature monitoring is carried out during each sonication by MR thermometry (Fig. 4). MR temperature maps are acquired with a time resolution of 3.5 s by means of a 2D FLASH phase image, with the following parameters: TE/TR 12.7/27.1 ms, BW 44 Hz/px, FA 30°, FOV 280 x 280 mm², matrix 128 x 256, 1 mm slice thickness. Real-time mean and maximum temperature graphs at the target spot are displayed at the Exablate's console for evaluation.

The desired power, duration and total energy delivered during a sonication can be freely chosen by the neurosurgeon. Each of the four sonication modes has a maximum threshold temperature, and real-time MR thermal mapping ensures that the sonication is automatically stopped if this temperature is reached before the total energy is delivered.

The whole treatment can last between 2 and 3 hours, depending on many factors including the patient's skull density score, the duration of the cooling pauses, and the number of sonications needed for successful treatment.

Post-treatment evaluation

A post-treatment MRI scan is always performed immediately after completing the HIFU procedure. This is done to evaluate lesion location and volume, before post-procedural symptoms appear as a result of the disrupted blood-brain barrier. Increased edema and petechial hemorrhage around the lesion area are common transitory symptoms that appear a few hours after treatment and gradually disappear in the following weeks [5].

The water is emptied from the system, the plastic membrane and stereotactic frame are removed from the patient, and the Exablate's transducer is replaced by the

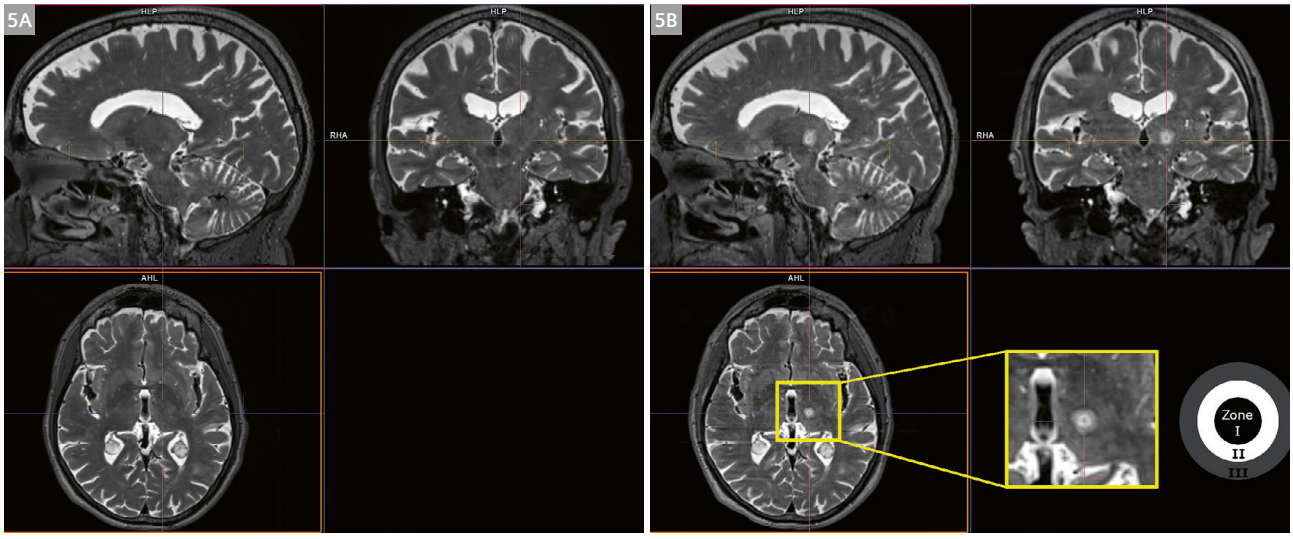

5 **Lesion evaluation**
T2-weighted SPACE images obtained from a representative patient pre- **(5A)** and 30 minutes post- MRgFUS treatment **(5B)**. Note the three concentric regions that appear in the treated hemisphere at the target spot, each with a distinct T2 contrast. The inner, hypointense region represents zone I, indicating necrosis; the mid, hyperintense region represents zone II, indicating cytotoxic edema; and the outer, mid-intense concentric region is zone III, and indicates the area of vasogenic edema [4].

32-channel coil on the MR table. Then the patient gets back in the scanner for approximately 30 minutes. As in the pre-treatment scan, the post-treatment examination consists of an anatomical 3D T1 MPRAGE, a 3D T2 SPACE, 2D T2 TSE, SWI, and a DTI scan.

The T2-weighted images are key to evaluate the extent of the lesion (Fig. 5). Typically, the lesion will show a circular shape of 3–6 mm diameter. We can distinguish up to three concentric zones in the T2 images [5]:

- **Zone I, necrotic:** the inner, T2 hypointense region shows the necrotic core
- **Zone II, cytotoxic:** the mid, T2 hyperintense region is cytotoxic edema
- **Zone III, vasogenic:** the outer, moderately T2 hyperintense ring shows the vasogenic portion of the edema

The lesion will extend through zones I and II, as cytotoxic edema is a premorbid cellular process, and thus irreversible. This process is confirmed in the diffusion scan, as cytotoxic edema causes increased restricted diffusion on MRI due to the cellular swelling and extracellular volume reduction.

Most patients stay overnight for further observation and are discharged the next day after receiving positive clinical evaluation from both the neurology and neurosurgery teams.

Personal experience

Looking back, we are proud to be the first institution worldwide to start treating patients with a Siemens Healthineers MRI scanner compatible with Exablate Neuro. This highly precise, minimally invasive treatment presents a great opportunity to improve many people's quality of life. As proof we have performed over 100 MRgFUS treatments within a year, with highly satisfactory results in most cases, and only a small percentage of patients with procedure-related complications, mostly transient.

Evolving from traditional surgery methods to MR-guided therapy was a challenge that we are happy to have successfully overcome as a team. During the first few procedures, Insightec's application specialists were with us on site, as well as our local Siemens Healthineers MR clinical scientist, to provide support.

Our close relationship with both Insightec and Siemens Healthineers allows us to solve any arising issues quickly, and we have now formed an effective multidisciplinary team that can perform much shorter, faster and safer procedures.

Future directions

Although essential tremor patients are the largest target group for this kind of therapies, MRgFUS is not limited to this condition. We will soon start treating Parkinson's disease tremor by targeting the subthalamic nucleus (STN).

The STN is proven as a beneficial therapeutic target [6], although its use for MRgFUS poses a challenge as it is difficult to reliably image even with 3T MRI. Other targets, including the internal globus pallidus, will also be explored.

Acknowledgments

MRgFUS is a multidisciplinary effort, and our treatments required a tight collaboration between the neurosurgeon and neurologist. But it could not be completed without the cooperation of the MR tech team, who were specifically trained for this procedure, the engineer on site, and the valuable contribution of the anesthesiologists Dr. Cristina Honorato and Dr. Antonio Martínez-Simón, who ensured the patient's well-being throughout the whole time.

We also thank the Insightec neuro apps team, led by Paul Wragg in Europe, for their valuable help during the training process.

References

1 Zesiewicz TA, Chari A, Jahan I, et al. Overview of essential tremor. Neuropsychiatr Dis Treat. 2010;6:401-408.
2 Lipsman N, Schawartz M, Huang Y, et al. A MR-guided focused ultrasound thalamotomy for essential tremor; A proof of concept study. Lancet Neurol. 2013;12:462-468.
3 Moser D, Zadicario E, Schiff G et al. MR-guided focused ultrasound technique in functional neurosurgery: targetic accuracy. J Ther Ultrasound. 2013;1:17.
4 Ezponda et al. Mapping the cortical connections of the ventral intermediate nucleus (VIM) with tractography in patients undergoing MRI-guided intensity focused ultrasound (HIFU) thalamotomy. RSNA. 2019;19008221.
5 Wintermark M, Druzgal DS, Huss MA et al. Imaging findings in MR imaging-guided focused ultrasound treatment for patients with essential tremor. Am J Neuroradiol. 2014;35:891-896.
6 Magara A, Bühler R, Moser D, et al. First experience with MR-guided focused ultrasound in the treatment of Parkinson's Disease. J Ther Ultrasound. 2014;2:11.



Contact

Jorge Guridi, M.D., Ph.D.
Head of the Neurosurgery Department
Clínica Universidad de Navarra
Avda. Pío XII, 36
31008 Pamplona (Navarra), Spain
+34 948 255 400
jguridi@unav.es

Advertisement

Your smarter connection to knowledge

PEPconnect

The Personalized Education Plan (PEP) platform is designed to provide self managed training in order to increase staff competency, efficiency and productivity. PEPconnect offers product training, clinical training, and instant access to performance support material. You can use your computer or mobile device to flexibly access the educational information. You can decide how to personalize your learning and share your experience with others: anytime, anywhere and from any device.



For MRI PEPconnect offers many e-clips, online trainings and job aids. They can be easily accessed from any device with Internet connection:
1) Go to www.siemens.com/pepconnect
2) Click **Explore PEPconnect**
3) Click **Medical Imaging and Therapy**
4) Select the **Magnetic Resonance Imaging** section you're interested in and enjoy

PEPconnect includes content of both standard and optional features on the different products.
Depending on your licenses and configuration, not all of the functions shown in the videos may be available on your system.

How a Bell Pepper Convinced the Siemens Med Board

Arnulf Oppelt, Ph.D.; Wilfried Loeffler, Ph.D.

Siemens Healthineers, Erlangen, Germany

"The best way to predict the future is to invent it."

Theodore Edward Hook, 1825

In 1983, the first Siemens MRI system bearing the MAGNETOM name was installed at the Mallinckrodt Institute of Radiology, in St. Louis, Missouri, USA. Ever since those early days, the name MAGNETOM has been associated with technological innovation and advances, such as the first wide bore 70-cm MRI system, new coil concepts like Tim and Tim4G ("from local to total") and, most recently, with the innovations of the BioMatrix platform. This allows the operator to adapt scanning to patient individuality via special sensors and interfaces and, thanks to the most modern acceleration techniques, also makes MRI faster and more patient friendly, for example with free breathing examinations.

This is the first part in a series of articles that take a retrospective view to see how we got to MRI of today.

Without doubt, Magnetic Resonance Imaging, or MRI for short, is the most flexible of all imaging methods and the diagnostic modality of choice for many clinical indications. Siemens Healthineers is the global leader in this technology. However, in the beginning MRI at Siemens was not mainly driven by market analysis or scientific progress.

In 1973, the British recording company EMI presented a completely new X-ray device at the RSNA Annual Meeting: the first computer tomograph. For established X-ray manufacturers like Siemens Medical and most of its competitors, there did not seem to be much future in such a development. Spatial resolution was of outmost importance, while few realized the benefit of significantly improved soft tissue contrast. Therefore, a tiny focal spot and a high-resolution image amplifier seemed to be what the market craved for.

When in 1976 the London Evening Standard published the headline "EMI on brink of a super scanner" in its June 11 edition, readers learned that the company was working on another revolutionary scanner, this time based on high-frequency radio waves, alarm bells started ringing: This time Siemens was not going to miss this trend.

Siemens, in fact, had its very own dedicated researcher, Dr. Alexander Ganssen, who had been investigating the possibilities of electromagnetic waves below the X-ray frequency spectrum for some time. Yet, there was little interest in Dr. Ganssens's proposals (Fig. 1) for the medical application of NMR (nuclear magnetic resonance) to determine blood flow, cystic fibrosis, and blood viscosity.

However, the article in the Evening Standard provided reason enough to visit Paul Lauterbur, a later recipient of the Nobel Prize, in the U.S. and Dr. Mansfield in England, on a fact-finding mission about advances in this field.

As a result, it was proposed that Siemens start its own work. In the fall of 1977, high-level preliminary discussions took place between Dr. Schittenhelm, Dr. Ganssen,

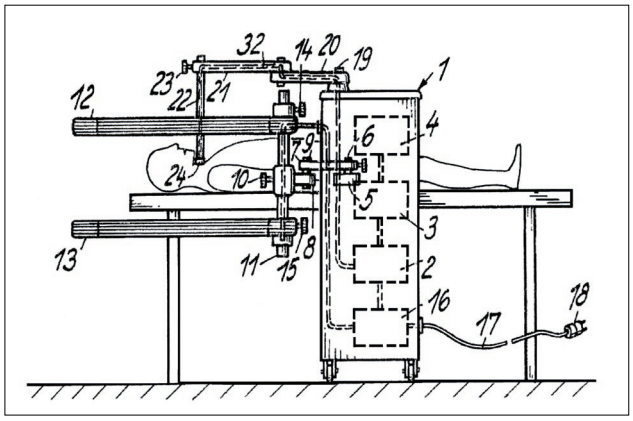

1 Dr. Ganssen's diagnostic equipment for determining the distribution of substances using nuclear magnetic resonance.

Mr. Kuckuck, Mr. Schmidt (Siemens), Dr. Mansfield (University of Nottingham, UK), Dr. Maudsley (Zürich University, Switzerland), and Dr. Oppelt (Technical University Darmstadt, Germany). This marked the beginning of the Siemens project.

The managing board now also approved the proposal. Dr. Mansfield was hired as a consultant, and Andrew Maudsley, who as part of his dissertation under Mansfield had been the first person to scan a human finger in vivo using NMR, and Arnulf Oppelt, one of the authors of this article, joined Siemens on February 1, 1978.

Development costs of some two million German Mark (DM) were approved, the head of the X-ray development department, Professor Gudden, was able assert himself amid strong protests from the X-ray CT sales department who would have liked to see that money used to further CT development. However, an image of a head presented by EMI at the RSNA in 1978 (Fig. 2) was too powerful an argument.

Specifications were drawn up for a trial scanner and an air-core whole-body magnet was ordered from Oxford Instruments (OI) in England. The gradient coils and power supply were developed at the Siemens research laboratories, RF and control electronics as well as the software were tasked to Siemens Med. A number of components were already available from Dr. Ganssen's preliminary work, such as a Magnion iron core experimental magnet, a frequency synthesizer, a 10 W RF power amplifier. A state-of-the-art PDP 11 minicomputer was available from the CT group. These components were combined to form a small imaging test set-up to develop and test the software for the planned large scanner. In particular, an experimental device for "spectroscopic imaging" was developed in order to allow fast measurements of the magnetic field homogeneity. This was published in 1979 in the Siemens Research and Development Reports [1]. At the end of 1978, the resistive whole-body magnet with a field strength of 0.1 Tesla was delivered (Fig. 3) and installed in the research system on the grounds of the Siemens research center housed in a purpose-built wooden hut, which contained no ferromagnetic parts, not even iron nails (Figs. 4 and 5).

By this time, Andrew Maudsley had again left Siemens to head an even more ambitious MRI project in the U.S. using superconducting magnets. He was succeeded by Dr. Wilfried Loeffler from CT development, the other author of this article. 1979 was spent eliminating faults in the software and hardware. It took rather a long time before we realized that the radio-frequency interference that caused us such a headache was entering via the magnet

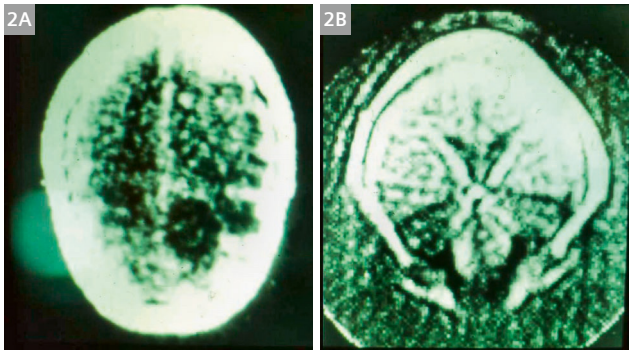

2 Comparison of an early CT image and an image of the head made with a new "radio wave scanner" at the EMI booth at RSNA 1978.

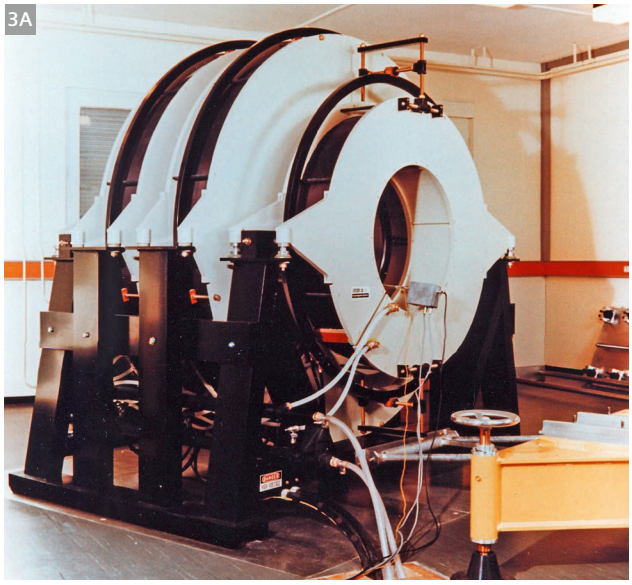

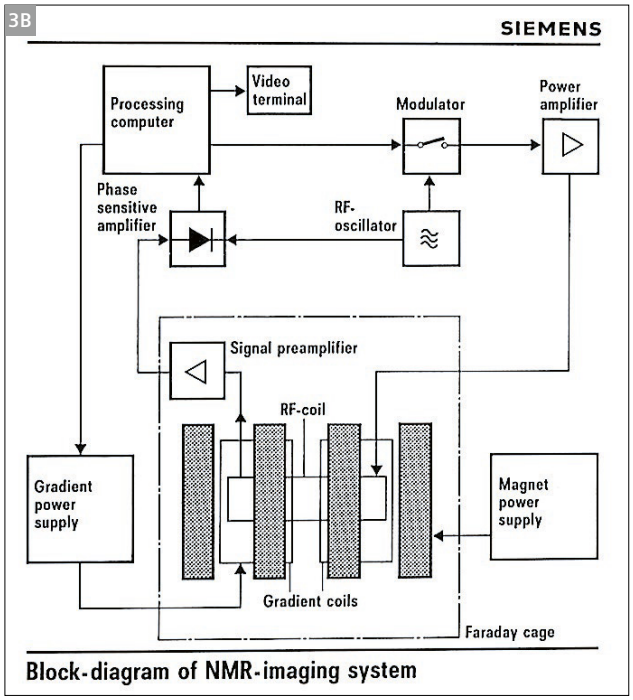

3 (3A) 0.1T whole-body magnet manufactured by Oxford Instruments for Siemens in 1978. (3B) Block diagram of an NMR imaging system.



4 First MRI measuring system at Siemens 1978.



5 RF Faraday cage built around the 0.1T magnet.

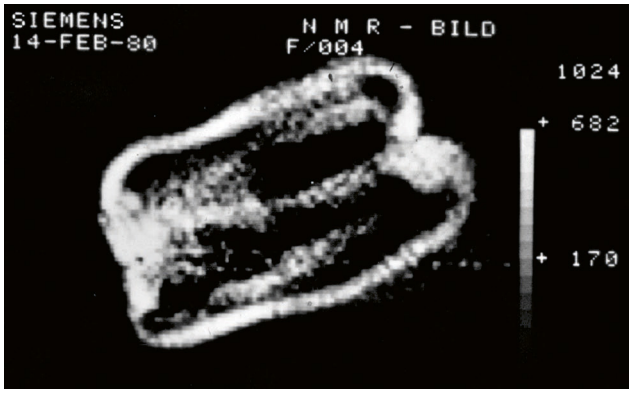

6 First Siemens MRI image of a bell pepper, 1979.

power supply cables. Although an RF filter for a current of 80 A was a product available from Siemens, the delivery time was three months. Time was running out. The business and budget negotiations for the coming year were about to begin and we were told in no uncertain terms that immediate proof of the functioning of the system in the form an image was the precondition for continuing the project. Luckily, this hard ultimatum did not shock us into forgetting all our basic physics and we remembered that random signal disturbances can be averaged out by repeated measurement. We would need an hour of measurement time to resolve this problem but the result proved worth waiting for.

We chose a green bell pepper as our measurement object, suitable because it would certainly keep still, contained water, was large enough to represent a human organ, and could be cut open to demonstrate the similarity between image and true anatomy of the object.

Since scanning took such a long time, we were not able to present the results to the managing board until the next day (Fig. 6).

Everyone involved was extremely happy with the image produced by the measurement. Little image noise, only one artifact. It took a few weeks before the cause of the artifact in image reconstruction was found. That is why the date of reconstruction that appears on the image is February 14, 1980, even though the object was scanned in November 1979.

A bell pepper had been instrumental in convincing the Siemens Med board of the potential of MRI. The decision to approve continuation of the project was a wise one, as history has shown.

Development moved fast, the first head images were presented at the annual meeting of the German Society of Neuroradiology in 1980 in Munich and at the German Röntgen congress in 1981 in Munich. Device developments were reported on in 1981 [2]. A year later, the business unit MR Tomography was established and product development started.

References

1 A.A. Maudsley, A. Oppelt, A. Ganssen Rapid Measurement of Magnetic Field Distributions Using Nuclear Magnetic Resonance Siemens Forsch. u. Entwickl. Ber. Vol. 8 (1979), No. 6, pp. 325–331.
2 A. Ganssen, W. Loeffler, A. Oppelt, F. Schmidt Kernspin-Tomographie Computertomographie 1, pp. 10–18 (1981).

Contact

Dr. Arnulf Oppelt
oppelt_arnulf@t-online.de

Dr. Wilfried Loeffler
G.W.Loeffler@t-online.de



Dr. Oppelt



Dr. Loeffler

Automated and Standardized CMR Exams Using Cardiac Dot Engine and Short CMR Protocols

Dr. Valentina Puntmann, M.D., Ph.D., FRCP

Institute for Experimental and Translational Cardiovascular Imaging
DZHK Centre for Cardiovascular Imaging,
Department of Cardiology, Division of Internal Medicine
University Hospital Frankfurt, Germany

Which cardiac MRI protocol do I use for which purpose? This question remains an unresolved riddle for many users, whether they are new to CMR or are experienced imagers. For many the ease of image acquisition and the quality of the heart views – rarely experienced by any other cardiac imaging modalities – creates a strong temptation to dive deeper and image more. This position is often strengthened by the comparative harmlessness of MRI exams compared with imaging modalities which require ionizing radiation. However, there is seldom benefit and little clinical evidence that would justify doing more individual scans or introducing additional techniques. In fact, for many patients currently, the most lasting impression of a cardiac MRI scan is how very long it took. What comes to mind for many clinicians is the high cost, relative complexity, and lack of immediate therapeutic benefit.



1 Cardiac Dot Engine
Courtesy of Siemens Healthineers.

It is also important to realize that the complexity of cardiac MRI, with additional scouts as well as planning views and procedures, is unlike that for any other imaging modality. This calls for an efficient core strategy that is first targeted to the clinical question, and, second, supported by validation-qualification evidence. Any additional views need to be used sparingly, if at all, and best regarded as elective views, they need to be decided upon by the attending physician and performed under their direct supervision. In practice, this is often best performed by doctors themselves, which mandates a doctor's own personal scanning capability to competently decide between responsible and (excessive) defensive scanning.

Third, in imaging environments with shared arrangements over equipment and staff where cardiac MRI is squeezed between the 'knees and spines' with an expectation of 'scanning as usual', the opportunity to consider many cardiac-specific issues in patient preparation is often lost. Attending physicians must be integrated into patient preparation, principally to conduct efficient and competent patient communication, as they must make a judgment on the scan plan that fits best to address the clinical question based on a real person and not on paper-based information. Sufficient investment of time to explain the details of the scan procedures and the importance of breath-holding sets the expectations and motivates patients to cooperate positively. A healthy dose of simple humanity, such as in-room presence when administering adenosine or regadenosone is often what defines the outcome in terms of diagnostic image quality and overall patient experience.

At the Institute for Experimental and Translational Cardiovascular Imaging at the University Hospital Frankfurt we have developed Goethe CVI® Cardiovascular Imaging approaches[1] that addressed these considerations in creating standard operating procedures and imaging protocols for everyday use. Notably, our approach greatly benefits from Cardiac Dot Engine technology (Siemens Healthcare, Erlangen, Germany). This highly automated planning tool is, in our view, an essential 'must-have' for cardiac MRI. The Cardiac Dot Engine is based on a traditional feature, the placement of the '3 points' that define a 2-dimensional plane, and as such the imaging slice. There are several advantages to using the Cardiac Dot Engine. First, its built-in automation simplifies cardiac planning steps, thus importantly reducing the overall onboarding training period for new users. Second, although still far from a self-driving experience, planning with the Cardiac Dot Engine can reduce the concentration-burnout from a full day of cardiac scanning, which can require multiple exchanges of personnel. Third, it allows for greater standardization of all procedures, reducing the variation between patient studies as well as between centers. The Cardiac Dot Engine recognizably reduces the complexity of cardiac scanning, and helps to mitigate the current scarcity of doctors with advanced cardiac MRI training. In centers with more doctors at hand, shorter examination times and overall greater engagement of the doctors allows for their fully autonomous scanning and reporting – as in echo – reducing the reliance on even scarcer radiographer availability.

In the Goethe CVI® exam cards[1], we incorporated a 3-dimensional SSFP localizer allowing for isocenter definition and shim box positioning. This is followed by the Heart Scout, a rough oblique localizer of the heart's position in the chest, which is essentially a combination of the vertical and horizontal long-axis views. Then comes the crucial Cardiac Dot Engine step: Definition of the long-axis views, which involves the positioning of the dots on the relevant anatomical landmarks. This uses a combination of 3 dots per slice to achieve the three true long-axis views for 2, 3, and 4 chambers. These geometries are then acquired as cines. Next comes the short-axis geometry definition, whereby the whole heart stack is planned alongside the subset of 3 short-axis slices (basal, mid, and the apical). Crucially, both are planned perpendicular to the centerline of the long-axis views, with concordance of the middle slice between them. With just these 3 steps, the planning of basic cardiac geometries is complete.

The Goethe CVI® Examcards include acquisition of native maps, (stress-only) myocardial perfusion and late gadolinium enhancement in basic cardiac geometries. The three basic protocols then differ by reductionist approach

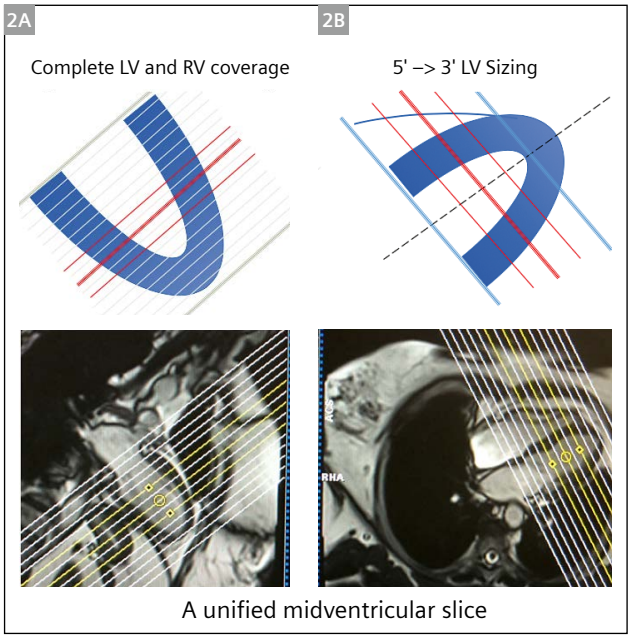

2 A unified midventricular slice with **(2A)** complete LV and RV coverage and **(2B)** 3' LV sizing.

[1]*The information shown herein refers to products of a 3rd party and thus are in their regulatory responsibility. Please contact the 3rd party for further information.*

to target the clinical question, for instance myocardial perfusion is performed when ischemia is suspected, or microvascular disease is deemed likely based on the pretest likelihood. In practice, most patients will undergo examination with myocardial perfusion imaging, as illustrated by examples of typical patients with either known coronary artery disease (previous stents, ongoing symptoms), those with multiple risk factors (e.g., metabolic syndrome), or systemic conditions where coronary vascular involvement is likely (e.g., systemic lupus erythematosus). Patients with atypical symptoms, commonly profound dyspnoea, will benefit from myocardial perfusion to clarify whether their symptoms correspond with 'angina equivalent'.

Patients with known pathological cardiac anatomy or cardiomyopathies and those who have had previous scans excluding significant myocardial ischemia, however, will undergo shorter protocols without myocardial perfusion. Patients who need repeat scans to follow up on myocardial inflammation/fibrosis and/or volumes/function will undergo native examinations only. Some patients will require a targeted expansion of the core protocols with MR angiography (aorta and renal arteries in hypertension scans), flows (Qp:Qs) or transaxial slices for congenital indications. The table time of a native scan is approximately 15 minutes, whereas other protocols (with myocardial perfusion and late gadolinium enhancement) are generally completed in under 30 minutes. This is an important contributor to an improved patient experience.

Goethe CVI® Approaches relate to a specific set of standard operating procedures and imaging protocols for cardiovascular magnetic resonance imaging and cardiac contrast tomography in everyday clinical use. Goethe CVI® exam cards are available for use, subject to a sharing agreement and a license fee. This arrangement with us involves two important considerations: First, the quality assurance when importing an exam card, as well as its maintenance to ensure that all functional parameters are preserved as originally envisaged. The second aspect encompasses the hands-on training of users for confident application. We offer several approaches to prospective users, either by Goethe CVI® fellowships or by way of a personalized, week-long observership training in collaboration with Siemens Healthineers. The details are provided on our website.



Contact

Assoc. Prof. Dr. Valentina Puntmann, MD, PhD, FRCP
Deputy Head
Goethe CVI® Fellowship Programme Lead
Consultant Physician, Cardiologist and Clinical Pharmacologist
Institute for Experimental and Translational Cardiovascular Imaging
DZHK Centre for Cardiovascular Imaging – Goethe CVI®
Department of Cardiology, Division of Internal Medicine
University Hospital Frankfurt
Theodor-Stern Kai 7
60590 Frankfurt-am-Main
Germany
valentina.puntmann@kgu.de
https://www.cardiac-imaging.org/goethe-cvi-approaches.html

Ultrafast Multi-contrast High-resolution 3D Brain MRI: a Technical Description of Wave-CAIPI

Daniel Polak[1,2]; Stephen Cauley[1,3]; Berkin Bilgic[1,3,4]; Lawrence Wald[1,3,4]; Kawin Setsompop[1,3,4]

[1]Martinos Center for Biomedical Imaging, Department of Radiology, Massachusetts General Hospital, Charlestown, MA, USA
[2]Siemens Healthineers, Erlangen, Germany
[3]Department of Radiology, Harvard Medical School, Boston, MA, USA
[4]Harvard-MIT Health Sciences and Technology, Massachusetts Institute of Technology, Cambridge, MA, USA

Introduction

Parallel imaging techniques (e.g., SENSE [1], GRAPPA [2], etc.) have enabled substantial scan time reduction in Magnetic Resonance Imaging (MRI) while retaining high spatial resolution and appropriate imaging contrast. These methods leverage the spatial information afforded by multi-channel receiver arrays to minimize the time-consuming gradient encoding. However, the performance of these acceleration techniques is limited by the spatial encoding capability of the coil sensitivities which are related to the coil design and coil geometry (adjacent coil elements typically have similar coil sensitivity). In the case of conventional 2D slice-by-slice imaging, the close spatial proximity of aliased voxels usually constrains clinical applications to moderate acceleration factors, even when a modern high-channel-count receive array is used.

Several new imaging technologies have been developed to address the increasing encoding burden at high resolution and enable faster scanning. This represents a move towards volumetric imaging, where Simultaneous MultiSlice (SMS) and efficient 3D-encoding have enabled dramatic increases in acquisition speed. These imaging techniques can also make better use of the coil sensitivity information in multi-channel receiver arrays, i.e. through employing controlled aliasing along multiple spatial dimensions. The 2D-CAIPIRINHA technique [3] was developed to enable higher acceleration for 3D acquisitions by employing a staggered k_y-k_z undersampling pattern. This increases the distance between aliased voxels in the phase-partition encoding plane allowing for better utilization of the available variation in the coil sensitivity profiles.

The recently proposed Wave-CAIPI[1] technique [4] expands controlled aliasing to the full 3D extent. This has enabled even greater parallel imaging encoding capability for structural scans while retaining good image quality and SNR.

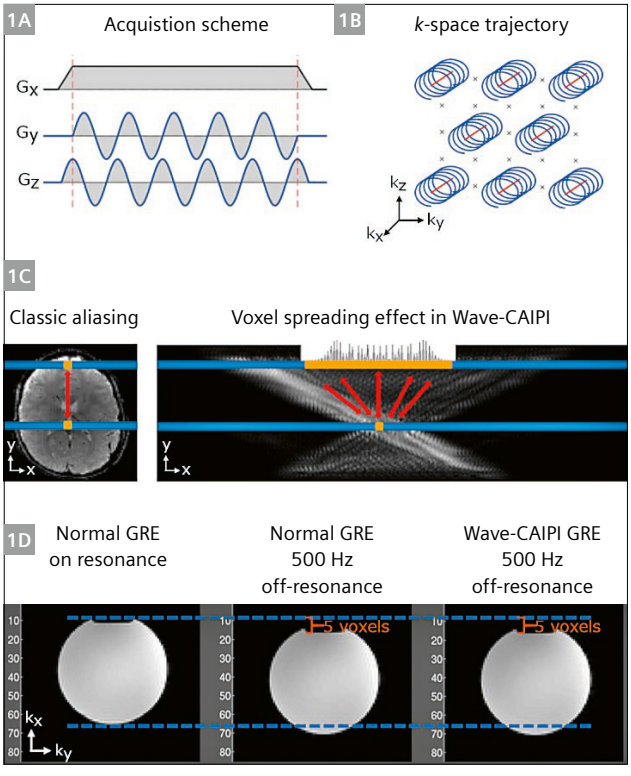

1 Wave-CAIPI:
(1A) Wave-CAIPI utilizes sinusoidal gradients during the frequency encoding. **(1B)** The sinusoidal waveforms incur corkscrew trajectories in *k*-space which are staggered due to the 2D-CAPIRINHA sampling **(1C)** In the image domain Wave-encoding results in voxel spreading along the readout direction. This increases the distance between collapsing voxels when compared to classic aliasing. **(1D)** Wave-CAIPI exhibits the same off-resonance shifts along the readout direction as standard Cartesian acquisitions (here shown for GRE at 500 Hz off-resonance and bandwidth 100 Hz/px).

[1]*Work in progress: the application is currently under development and is not for sale in the U.S. and in other countries. Its future availability cannot be ensured.*

Wave-CAIPI

Wave-CAIPI [4] generalizes 2D-CAIPIRINHA and Bunch Phase Encoding/Zig-Zag sampling [5, 6] to create a controlled aliasing concept that encompasses all three spatial dimensions (including the readout direction). Figure 1A demonstrates the acquisition scheme for Wave-CAIPI. Two sinusoidal gradients G_y and G_z are played during the readout with a quarter cycle phase shift. Combined with 2D-CAIPIRINHA sampling, this results in staggered corkscrew trajectories through *k*-space (Fig. 1B). In the image domain the additional phase deposition results in voxel-spreading along the readout direction which varies linearly as a function of the spatial y and z position (Fig. 1C). When combined with the interslice shifts from 2D-CAIPIRINHA, a well distributed aliasing pattern is created across all three spatial dimensions. This allows Wave-CAIPI to take full advantage of the 3D coil sensitivity information and enables up to an order of magnitude increase in acquisition speed with negligible parallel imaging noise amplification and artifact penalty [4, 7–9].

Wave-CAIPI also has several desirable properties that enable high quality reconstruction. In contrast to other rapid acquisition techniques such as EPI or spiral imaging, Wave-CAIPI is not susceptible to image blurring and distortion artifacts caused by inhomogeneity of the main magnetic field (B0) [9]. This can be attributed to the constant rate of *k*-space traversal along the readout direction (k_x) for Wave-CAIPI. As a result, phase evolution from B0 inhomogeneity only evolves as a function of k_x, resulting in the same chemical shift effect as observed in conventional Cartesian imaging sequences. This effect is demonstrated in Figure 1D. At 500 Hz off-resonance a Wave-CAIPI gradient echo (GRE) acquisition shows the same voxel shift along the readout direction as a standard acquisition. Moreover, intravoxel dephasing is negligible in Wave-CAIPI acquisitions as sinusoidal waveforms prevent large accrual of the gradient moment [4].

Figure 2 compares the encoding efficiency of Wave-CAIPI, 2D-CAIPIRINHA and standard acquisitions at R = 3 x 3 acceleration and 1 mm³ isotropic resolution using a Siemens Healthineers 32-channel head coil. Wave-CAIPI offers high quality reconstructions and negligible noise amplification penalty as evidenced by the reciprocal *g*-factor maps (measure of noise amplification due to lack of spatial encoding). In contrast, 2D-CAIPIRINHA and standard sampling provide insufficient encoding capability at R = 9-fold acceleration causing residual aliasing artifacts and large noise amplification especially in the center of the brain.

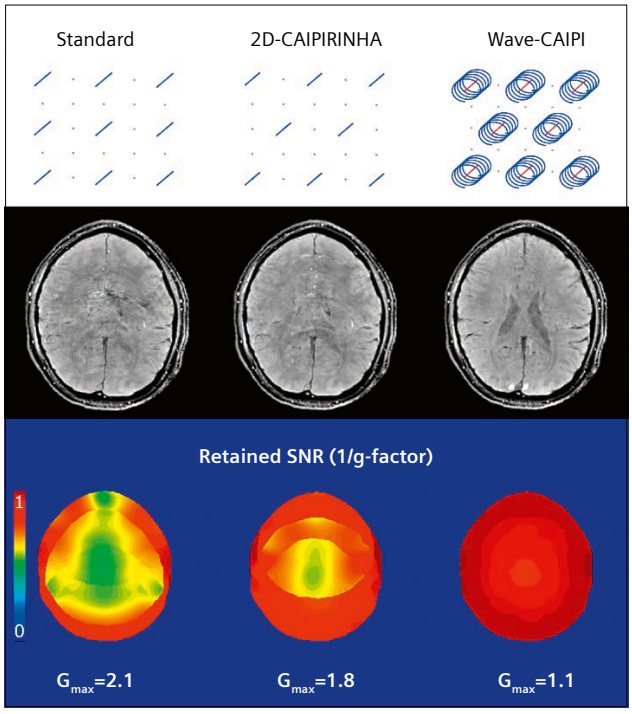

2 ***G*-factor comparison at R = 3 x 3:**
At R = 3 x 3 acceleration, standard and 2D-CAIPIRINHA sampling result in residual aliasing artifacts and large noise amplification especially in the center of the brain. In contrast, Wave-CAIPI yields high quality reconstructions without artifacts and close to perfect *g*-factor.

Auto-calibrated image reconstruction

Wave-CAIPI acquisitions can be reconstructed efficiently using a generalized SENSE framework thus avoiding the need for *k*-space gridding [4]. This is made possible as the non-Cartesian corkscrew trajectory can be represented as additional phase deposition in Cartesian *k*-space. Using a simple point spread function framework, the voxel spreading effect from Wave-CAIPI is either modeled as a spatially varying convolution in the image domain or more efficiently as a phase modulation in hybrid space (k_x, y, z). Due to this spatially invariant encoding property, the SENSE-based reconstruction also remains highly separable. This allows for efficient parallelization as separate linear systems can be solved for each set of collapsing readout lines. Moreover, Wave-CAIPI does not require internal calibration data, as volumetric ESPIRiT [10] coil sensitivity maps are typically computed from a rapid low-resolution 3D gradient echo (GRE) scan (acquisition time roughly two seconds).

The separable Wave-CAIPI reconstruction also facilitates the automatic estimation and correction of any minor gradient deviations from the nominal trajectory without the need for additional calibration scans. This auto-calibrated technique [11] relies on a compact representation of the Wave-encoding's sinusoidal phase modulation (including minor deviations) which can be accurately described using a limited number of frequency coefficients. To accurately determine the exact *k*-space

trajectory, the auto-calibrated reconstruction optimizes the frequency coefficients and aliased voxels jointly to reduce the data consistency error of the generalized SENSE encoding model. By limiting this non-linear search to a small representative set of collapsing readout lines, the computational demand of this optimization problem is substantially reduced while mitigating artifacts globally. This has enabled rapid convergence (roughly after 10 seconds) for arbitrary acquisition protocols using standard scanner computation hardware.

Applications

The Wave-CAIPI acquisition and reconstruction framework can be broadly applied and has been shown to enable up to an order of magnitude higher acceleration for both SMS and 3D imaging sequences [4, 7–9] with negligible *g*-factor noise amplification. This scan efficiency has allowed for the development of a six-minute high-resolution volumetric brain exam comprising of the clinical contrasts T1w MPRAGE, T2w SPACE, T2w SPACE-FLAIR and T2*w SWI. Detailed optimization of the Wave corkscrew was performed for each structural scan to achieve optimal performance with respect to SNR and image quality [8]. Figure 3 illustrates example slices acquired at 3T (MAGNETOM Skyra, Siemens Healthcare, Erlangen, Germany) using a product Siemens Healthineers 32-channel head coil. Good SNR and contrast are provided in each of the rapid volumetric acquisitions (scan time 1–2 minutes each). Due to the isotropic resolution ($1 \times 1 \times 1$ mm^3) of MPRAGE and SPACE (T2w and FLAIR) these datasets can also be reformatted and viewed in arbitrary orientations without loss of spatial resolution.

The encoding capability of Wave-CAIPI can also be deployed in clinical standard protocols with high in-plane resolution and thick slices [12]. In Figure 4, Wave-CAIPI SPACE-FLAIR (R = 3 x 2, 0.8 x 0.8 x 3 mm^3) was acquired in axial orientation and compared to standard clinical T2w TSE (R = 2). Despite substantial speed-up from Wave-encoding, comparable contrast and image quality is maintained.

At present, clinical validation of the rapid Wave-CAIPI sequences for brain imaging is being led by the Neuroradiology Department of the Massachusetts General Hospital (Boston, MA, USA). The objective of these ongoing assessments is to establish non-inferior diagnostic quality between the Wave-CAIPI and standard clinical protocols routinely used at this institution. Progress towards this goal has been reported in several clinical evaluations [13–16] and is also summarized in "Ultrafast Multi-contrast

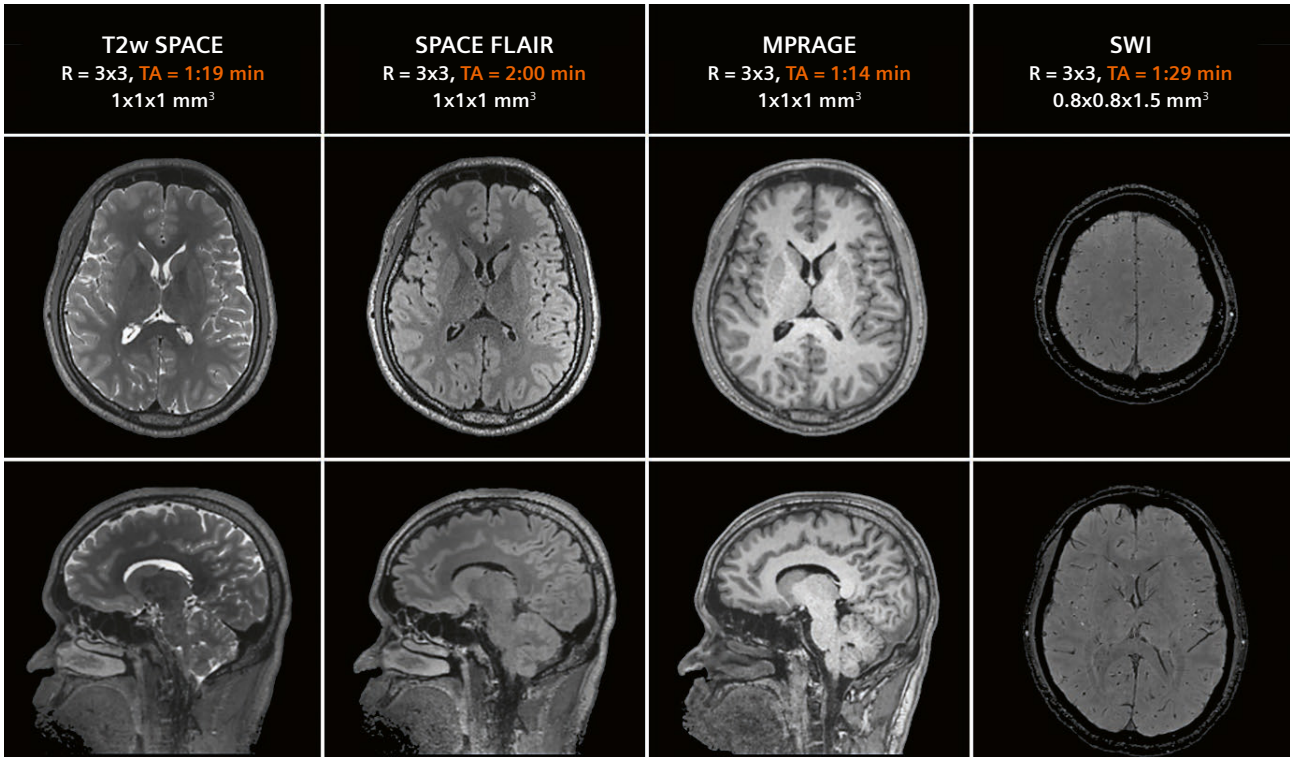

3 **Six-minute volumetric whole brain exam using Wave-CAIPI:**
Six-minute high-resolution whole-brain exam comprised of T2w SPACE, T2w SPACE-FLAIR, T1w MPRAGE and T2*w SWI at R = 9-fold acceleration.

High-resolution 3D Brain MRI: Clinical Evaluation of Wave CAIPI Acceleration in SWI, MPRAGE, FLAIR, SPACE" by Susie Huang et al. on page 21 of this issue.

Acknowledgments

The authors would like to thank Wei Liu, Daniel Nicolas Splitthoff, Borjan Gagoski, Wei-Ching Lo, Sinyeob Ahn, Thomas Beck, Thorsten Feiweier, Himanshu Bhat, Yulin Chang, Shivraman Giri and Keith Heberlein for their valuable support.

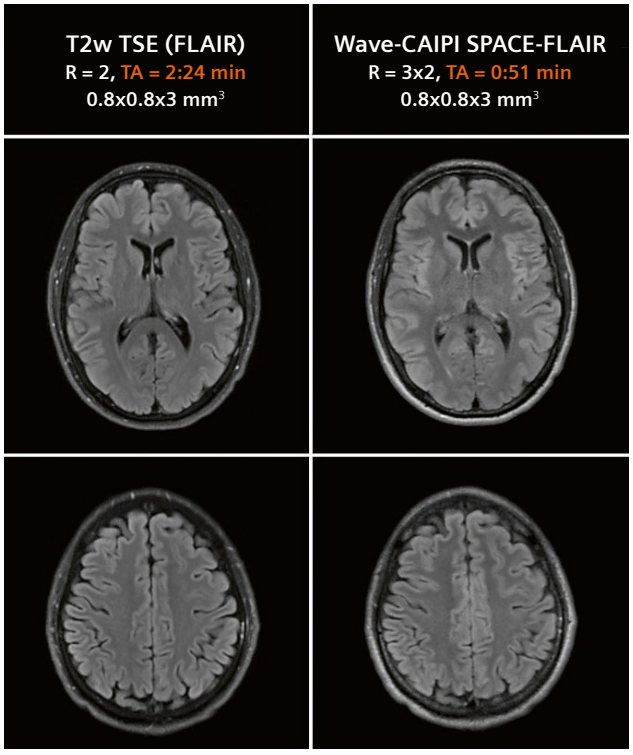

4 **Comparing standard T2w TSE versus Wave-CAIPI SPACE-FLAIR:** Standard clinical T2w TSE scan is compared to highly accelerated 3D Wave-CAIPI SPACE-FLAIR acquisition with high in-plane resolution and thick slices.

Contact

Kawin Setsompop
Massachusetts General Hospital
Martinos Center for Biomedical Imaging
Building 75, Room 2.102, 13th Street
Charlestown, MA, 02129, USA
Phone: +1 617-669-6640
kawin@nmr.mgh.harvard.edu



Daniel Polak
Siemens Healthineers
DI MR DL ORTH
daniel.polak@siemens.healthineers.com



References

1 K. P. Pruessmann, M. Weiger, M. B. Scheidegger, and P. Boesiger, "SENSE: Sensitivity encoding for fast MRI," Magn. Reson. Med., vol. 42, no. 5, pp. 952–962, 1999.
2 M. A. Griswold et al., "Generalized Autocalibrating Partially Parallel Acquisitions (GRAPPA)," Magn. Reson. Med., vol. 47, no. 6, pp. 1202–1210, 2002.
3 F. A. Breuer et al., "Controlled aliasing in volumetric parallel imaging (2D CAIPIRINHA)," Magn. Reson. Med., vol. 55, no. 3, pp. 549–556, 2006.
4 B. Bilgic et al., "Wave-CAIPI for highly accelerated 3D imaging," Magn. Reson. Med., vol. 73, no. 6, pp. 2152–2162, 2015.
5 H. Moriguchi and J. L. Duerk, "Bunched Phase Encoding (BPE): A new fast data acquisition method in MRI," Magn. Reson. Med., vol. 55, no. 3, pp. 633–648, 2006.
6 F. A. Breuer et al., "Zigzag sampling for improved parallel imaging," Magn. Reson. Med., 2008.
7 D. Polak et al., "Wave-CAIPI for highly accelerated MP-RAGE imaging," Magn. Reson. Med., vol. 79, no. 1, pp. 401–406, 2018.
8 D. Polak et al., "Highly-accelerated volumetric brain examination using optimized wave-CAIPI encoding," J. Magn. Reson. Imaging, vol. 50, no. 3, pp. 961–974, 2019.
9 B. A. Gagoski et al., "RARE/Turbo Spin Echo imaging with Simultaneous MultiSlice Wave-CAIPI," Magn. Reson. Med., vol. 73, no. 3, pp. 929–938, 2015.
10 M. Uecker et al., "ESPIRiT--an eigenvalue approach to autocalibrating parallel MRI: where SENSE meets GRAPPA.," Magn. Reson. Med., vol. 71, no. 3, pp. 990–1001, Mar. 2014.
11 S. F. Cauley, K. Setsompop, B. Bilgic, H. Bhat, B. Gagoski, and L. L. Wald, "Autocalibrated wave-CAIPI reconstruction; Joint optimization of k-space trajectory and parallel imaging reconstruction," Magn. Reson. Med., vol. 78, no. 3, pp. 1093–1099, 2017.
12 Wei-Ching Lo, et. al., "A comprehensive distortion-free 2-minute brain MR examination using BUDA and Wave-CAIPI", Accepted for oral presentation at ISMRM Annual Meeting 2020, Paris, France.
13 Conklin J, Longo MGF, Cauley SF, et al. Validation of Highly Accelerated Wave–CAIPI SWI Compared with Conventional SWI and T2*-Weighted Gradient Recalled-Echo for Routine Clinical Brain MRI at 3T. AJNR Am J Neuroradiol. 2019, 40:2073–80.
14 Longo MGF, Conklin J, Tian Q, et al. Validation of ultrafast Wave-CAIPI magnetization prepared rapid gradient-echo (MPRAGE) for quantitative evaluation of brain tissue volume in the workup of suspected neurodegenerative disease. American Society of Neuroradiology, 2019. Boston, MA.
15 Ngamsombat C, Longo MGF, Goncalves Filho ALM, et al. Evaluation of Ultrafast Wave-CAIPI Three-Dimensional Fluid-attenuated Inversion Recovery (3D FLAIR) Compared to Standard 3D FLAIR for Quantitative Analysis of Cerebral White Matter Lesions. Accepted for oral presentation at the Annual Meeting of the American Society of Neuroradiology, Las Vegas, Nevada. May 30–June 04, 2020.
16 Goncalves Filho ALM, Longo MGF, Conklin J, et al. Evaluation of Highly Accelerated Wave-CAIPI Post-Contrast 3D-T1 Sampling Perfection With Application Optimized Contrast Using Different Flip-Angle Evolutions (Wave-3D-T1 SPACE) Compared to Standard Post-Contrast 3D-T1 SPACE for Detection of Intracranial Enhancing Lesions. Accepted for oral presentation at the Annual Meeting of the American Society of Neuroradiology, Las Vegas, Nevada. May 30–June 04, 2020.

A Path to Establishing MRSI as a Clinical Standard Imaging

Mohammed Goryawala[1]; Hui Han[2]; Zahra Hosseini[3]; Sinyeob Ahn[3]; Gerald R. Moran[4]; Hyunsuk Shim[5]

[1]Department of Radiology, University of Miami, Miami, FL, USA
[2]Biomedical Imaging Research Institute, Cedars-Sinai Medical Center, Los Angeles, CA, USA
[3]Siemens Healthineers, Malvern, PA, USA
[4]Siemens Healthineers, Oakville, ON, Canada
[5]Department of Radiation Oncology and Radiology and Imaging Sciences, Winship Cancer Institute, Emory University School of Medicine, Atlanta, GA, USA

Abstract

This article introduces the evolution of technology for magnetic resonance spectroscopic imaging (MRSI) of the brain, and in particular describes 3D proton spectroscopic MRI with whole-brain coverage and its application to patients with brain tumors. Unfortunately, vendor-provided MRS technology for clinical use typically lags behind the capabilities developed in research labs and to date is limited to either single voxel or multi-voxel localization with very limited spatial coverage and resolution. Here, a multisite effort to transform this technology toward clinical standard imaging is described.

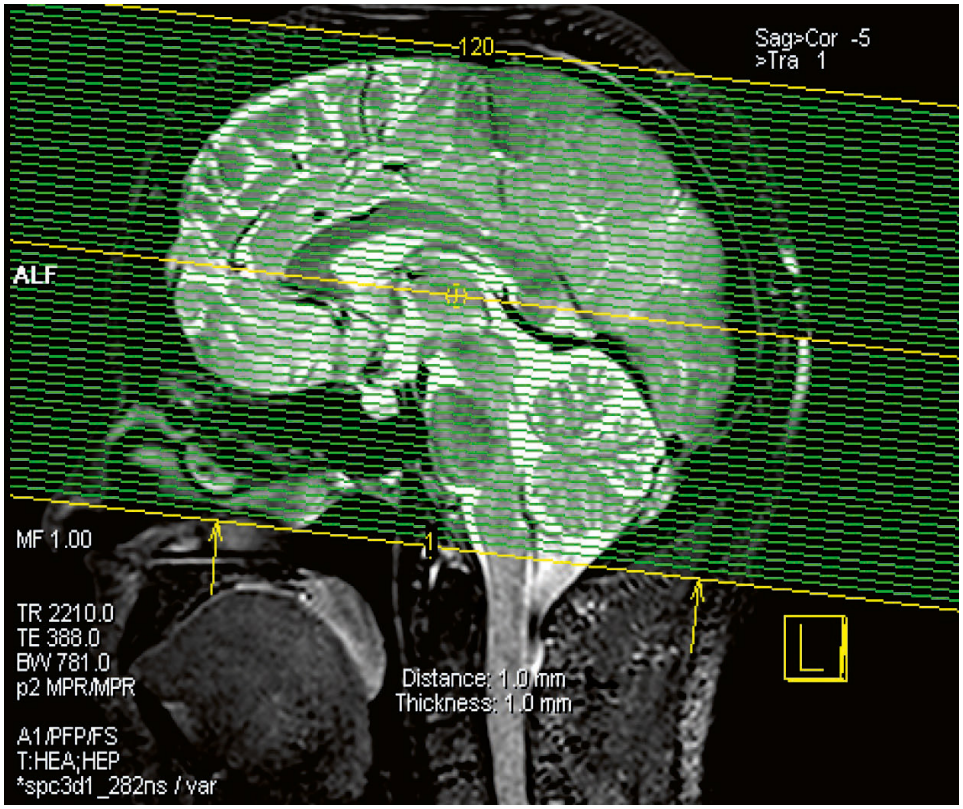

1 Example setup (graphical prescription) for a GRAPPA-encoded EPSI acquisition as described in the text.

The concepts and information presented in this paper are based on research and not commercially available.

Proton MRS-detectable metabolites of brain

Because of the relatively low sensitivity of *in vivo* ^{1}H magnetic resonance spectroscopy (MRS), in order for a compound to be detectable following successful water and lipid suppression, its concentration must be in the millimolar range, and it must be a small, mobile molecule. The information from a brain spectrum depends on several factors, such as the field strength used, echo time, and type of pulse sequence. On a 1.5T scanner with long echo times (e.g., 140 or 280 ms), only choline (Cho), creatine (Cr), and N-acetyl aspartate (NAA) are observable in the healthy brain, while compounds such as lactate (Lac), alanine, or others may be detectable if their concentrations are elevated above normal levels due to abnormal metabolic processes [1–3]. At short echo times (≤ 35 ms), more compounds become detectable. These include glutamine and glutamate, but these are not resolved from each other at 1.5T. In addition, myo-inositol, lipids, and macromolecules are detectable.

The largest signal in the healthy brain spectrum is the acetyl group of NAA that resonates at 2.0 ppm [4, 5]. NAA is often referred to as a healthy neuronal biomarker. The Cho signal (3.2 ppm) is involved in membrane synthesis and degradation and is commonly elevated in many types of tumors, including the brain, prostate, breast, liver, and other tumors [6]. The Cr at 3.0 ppm is involved in energy metabolism via the Cr kinase reaction, generating ATP. Cr shows quite large regional variations, with lower levels in white matter than gray matter in normal brain, as well as higher levels in the cerebellum compared to supratentorial regions [7]. The individual/regional variations in Cr levels are higher than NAA or Cho in normal brains. In a healthy brain, the methyl resonance of Lac (1.33 ppm) is barely detectable under normal conditions. Increased levels of brain lactate have been observed in a variety of conditions, including ischemia and tumor [1, 8]. Lac may be difficult to distinguish from overlapping lipids which have similar chemical shifts, either originating from the brain itself, or spatial contamination from the scalp. Myo-inositol (mI) is one of the larger signals in short echo time spectra (≤ 35 ms), occurring around 3.5–3.6 ppm. mI is a pentose sugar, which is part of the inositol triphosphate intracellular second messenger system. mI levels have been found to be increased in Alzheimer's dementia [9] and demyelinating diseases [10]. The exact pathophysiological significance of alterations in mI is uncertain, but a leading hypothesis is that elevated mI reflects increased populations of glial cells [11, 12], which may be linked to both degenerative and inflammatory diseases. mI has also been reported to be elevated in low-grade gliomas [13] and also correlates with depression status of GBM patients [14–16]. There are more than 25 additional compounds that have been assigned in ^{1}H MRS of the human brain. Some of these compounds are present in the normal brain but are difficult to detect routinely because they are too small and/or have overlapping peaks. Some examples of these compounds include aspartate, glycine, glutathione, ethanolamine, purine nucleotides, GABA, histidine, taurine, scyllo-inositol, and glucose [17]. Others may only be present under abnormal or pathological conditions, for instance, alanine, 2-hydroxyglutarate, phenylalanine, and ketone bodies. Occasionally exogenous compounds such as mannitol, ethanol or methyl-sulfonyl methane, all of which freely cross the blood-brain barrier, may also be observed in the spectrum.

Current state-of-the-art 3D MRSI

Multi-voxel (2D, or 3D) MRSI sequences are commonly available on commercial MR scanners [18], but their application has a number of problems, such as chemical shift displacement effects and restricted coverage due to the rectangular excitation of the voxel. Lipid signal bleeding from these effects can confound data quality and difficulty of appropriate data analysis. To avoid these problems, an alternative approach is to use a spin-echo sequence with outer volume suppression (OVS) pulses to suppress the lipid signals from the scalp, which can be readily extended to a multi-slice approach to obtain improved brain coverage [19]. These conventional Cartesian 2D or 3D phase-encoding approaches can give excellent quality data but are too time-consuming for clinical routine use because of the large number of phase-encoding steps to be collected. Therefore, a number of different approaches for fast MRSI have been developed (reviewed in [20–22]); however, so far these techniques have had a limited clinical impact, mainly because they are not commercially available nor mature enough for clinical applications. To reduce scan time, several *k*-space under-sampling strategies such as parallel imaging or compressed sensing have been applied to conventional MRSI, which involve tradeoffs for data quality, scan time, and spatial resolution [23–25].

Echo-planar spectroscopic imaging (EPSI) is a promising method for acceleration of whole-brain MRSI [26–29]. 3D EPSI has been used to study numerous different brain pathologies over the last two decades [30, 31]. The data displayed in the remainder of this chapter were obtained using 3D EPSI with whole-brain coverage, combined with GRAPPA and elliptical *k*-space encoding on a 3T MRI scanner with either 20- or 32-channel head coil arrays (Fig. 1). After the routine field map-based automated shim procedure on the scanner [32], it is strongly recommended to check the water linewidth to be less than ~25–28 Hz. If it is higher than 30 Hz, a brief 1st order manual shimming (x-, y-, and z-directions only) is recommended to reduce water linewidth, which can significantly improve the signal-to-noise ratio (SNR) and water/lipid suppression,

thus critical to obtain high-quality 3D data. A 3 pulse 'WET' [33] water suppression scheme is used along with lipid suppression by using a slab selective short TI (198 ms) inversion recovery (STIR) scheme [34, 35]. The EPSI pulse sequence also includes an interleaved small flip angle (20˚) water reference excitation [36] and GRAPPA spatial encoding [37] to shorten scan time (~15 minutes). The scan parameters used for images presented in this article are as follows: TR/TE/TI = 1710/17.6/198 ms, matrix size 50 x 50 x 18; 280 x 280 x 180 mm^3 FOV; 155 mm excitation slab thickness; interpolated matrix of 64 x 64 x 32 (Fig. 1) [38]. The quality of an acquired spectrum is critically dependent on the success of adjusting the field homogeneity (shimming), setting the scanner center frequency (on-resonance with water), and adjusting the flip angle(s) of the water suppression pulses. The failure of any one of these processes can lead to an uninterpretable spectrum. In the early days of MRS, many of these steps were performed manually by an operator, but for the current sequence, these steps are usually performed in an automated procedure offering greater ease and versatility for the application of the developed imaging methods in clinical environments.

Raw data are processed using the Metabolite Imaging and Data Analysis System (MIDAS[1], University of Miami, USA) [39]. This included B_0 and phase correction using the water reference data prior to any further processing in the frequency domain. The relative gray- and white-matter tissue and cerebrospinal fluid (CSF) contents in each SI voxel were estimated by downsampling the tissue segmentation maps, which were obtained using FSL/FAST algorithm [40], using the spatial response function of the EPSI acquisition. Additional processing included generating masks for brain and lipid regions, *k*-space extrapolation to reduce the contribution of extracranial lipid into the brain [41], linear registration between the T1-weighted MR and MRSI (TE = 50 ms), and signal intensity normalization following the creation of individual metabolite maps. Automated spectral analysis was carried out for 3 metabolites (NAA, Cr, Cho) or 6 metabolites (NAA, Cr, Cho, mI, lactate, and Glu/Gln (Glx)) [42]. Additional maps are generated for the fitted spectral linewidth and the Cramer-Rao lower bounds (CRLB) of fitting for each metabolite. Generated metabolite maps are overlaid on clinical images with a nominal voxel size of 4.4 x 4.4 x 5.6 mm are shown in Figure 2. The red contour represents two times elevated Cho/NAA ratio compared to the contralateral side. As apparent in Figure 2, not all metabolically active tumors are visible in standard MRIs (contrast-enhanced T1w-MRI and T2-SPACE). The MIDAS program package[1], developed by Dr. Maudsley and his team at the University of Miami is distributed together with the EPSI sequence at no cost under the GNU General Public License. For further information, the readers can reach out to their local Siemens Healthineers Collaborations Scientist.

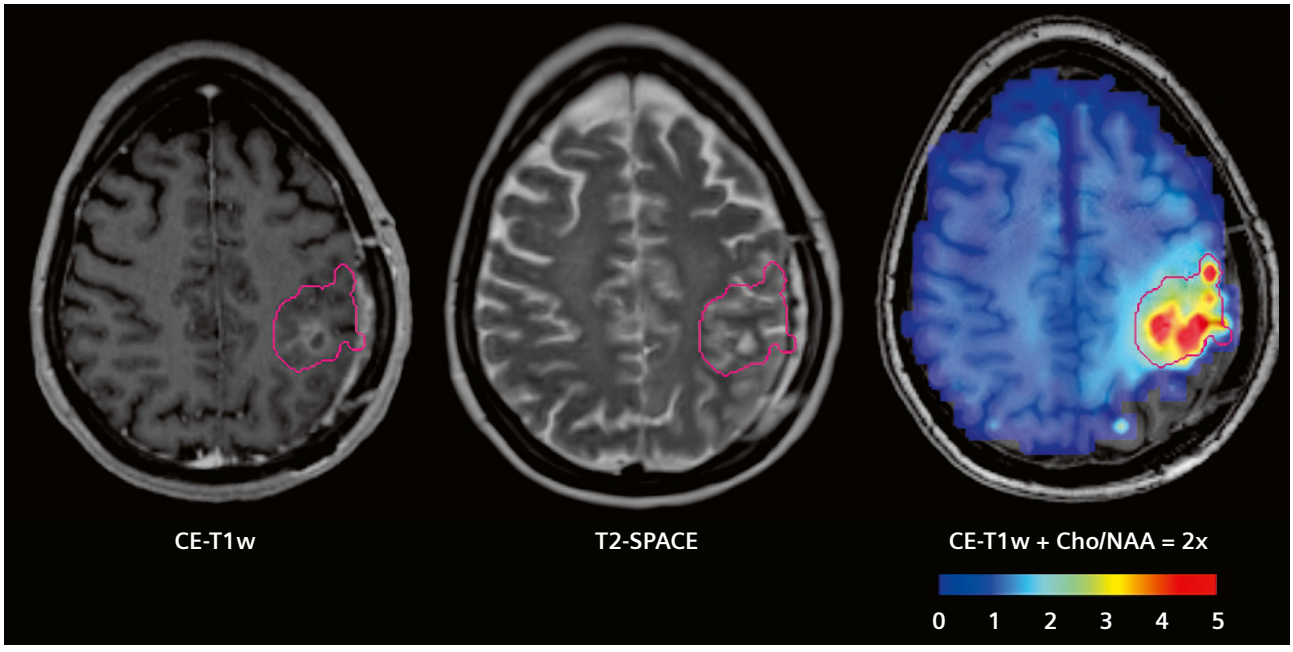

2 Views of anatomical and metabolite data with Cho/NAA ratio contour in red (2-fold over normal contralateral white matter). **(2A)** Contrast-enhanced T1w MRI; **(2B)** T2-SPACE MRI; **(2C)** Cho/NAA ratio map overlaid on T1w MRI. Cho/NAA ratio heat map shows metabolic abnormalities beyond CE-T1w or T2-SPACE MRIs and gives insight into the metabolic heterogeneity of the tumor and surrounding tissue. TE = 50 ms was used.

[1]The information shown herein refers to products of a 3rd party and thus are in their regulatory responsibility. Please contact the 3rd party for further information.

Developing the next generation of clinical spectroscopic MRI for patients with brain tumors

During the past decade, technological developments have transformed a single slice or multislice collection of 2D multivoxel chemical shift imaging (CSI) into a robust 3D imaging modality with the increased availability of 3T scanners, multichannel detector systems, new encoding methods, accelerated processing methods, automated artifact removal, and new approaches for obtaining whole-brain metabolite maps co-registered/overlaid with other clinical MR images. These developments allow MRSI to be addressed as "spectroscopic MRI", which is a significant improvement over standard vendor-provided 2D CSI techniques.

While MRSI has been shown to be capable of providing clinically useful information associated with disease processes or treatment, it has not had much impact on clinical care and its use remains largely confined to the research community. Technological advancements are required towards the acquisition, processing, interpretation, and dissemination of the MRSI data for true integration of spectroscopic MRI in the clinic. The current methods in whole-brain EPSI for water and lipid suppression are limited in their performance and are difficult to use for high-resolution whole-brain metabolite mapping due to SNR constraints. Improvements in methods for lipid and water suppression can offer a significant improvement in spatial resolution. Further, the adoption of methods that do not rely on inversion recovery for lipid suppression can improve imaging time and spatial coverage. The addition of these changes to the acquisition methods has the potential to elevate MRSI to true whole-brain technique with > 85% brain coverage with enhanced performance in critical cortical areas that are vital to a number of neurological applications.

Together with improved imaging, optimized reconstruction techniques play a vital role in more effective integration of spectroscopic imaging in the clinical environment. The current pipelines for EPSI data processing require time-consuming data transfer of multi-gigabyte datasets and processing on offline computers/servers which can be challenging for wider adaptation. In addition, to be able to fit the clinical workflow, the entire processing pipeline, including co-registration of metabolite and ratio maps with conventional anatomical MR images, should take less than an hour in order for the timely generation of the radiology report in the clinic. In currently available processing packages (such as MIDAS), one of the major bottlenecks is the time taken by the quantitative fitting routines which extract information on metabolite peak areas (proportional to concentrations) from the spectral data. As most fitting methods are based on iterative parametric modeling and the incorporation of a priori metabolite spectral information, one voxel at a time, and since high-resolution EPSI with whole-brain coverage generates several thousand spectra that need to be fit, it is virtually impossible to complete the entire processing pipeline in one hour on commonly available scanner computers. Furthermore, the complexity of MRSI technology requires on-site MRS experts to supervise the scanning of patients, process and analyze the data, and interpret the results with the clinicians involved. A particularly important role of on-site MRS experts is to recognize artifactual spectra and eliminate them before clinical decision making. Finally, the programs developed to process and display MRSI results are primarily for MRS experts, and not appropriate for general use by clinicians or other staff who do not have specialist training in MRS. Current multisite efforts at improving MRSI focus on a multi-faceted approach that aim to significantly improve processes from acquisition to the clinical deployment of spectroscopic MR imaging for its wider acceptance in clinical workflows based on NIH/NIBIB U01 funding (Han/Maudsley/Li/Cooper/Shim).

I. High-resolution mapping of brain metabolites

Brain metabolite concentrations are on the order of 10 mM or less, whereas water protons in the brain at approximately 80 M and lipid protons in peri-cranial fat, also at very high concentrations, are also present. The current methods in whole-brain EPSI for water and lipid suppression are limited in their performance and are difficult to use for high-resolution whole-brain metabolite mapping due to SNR constraints. To overcome these issues a novel acquisition scheme that increases SNR to enable the generation of higher-resolution MRSI metabolite maps using dual-band water and lipid suppression has been developed. Volumetric whole-brain MRSI can be acquired with TR = 950 ms and TE of 17.6 or 50 ms. Water and lipid suppression were carried out using the hypergeometric dual-band pulses [43] to create a passband between 1.8 and 4.2 ppm with Mz/Meq > 0.99 with Bloch equation simulations to derive the parameters for the individual hypergeometric pulses. Real-time frequency measurement and adjustment were carried out by sampling the water frequency every TR. The removal of inversion-based lipid nulling resulted in a significant improvement in SNR that enabled higher spatial sampling in the phase encoding direction to yield nominal voxel volume of 75.16 mm^3 and a zero-filled interpolated resolution of 1.3 x 2.0 x 2.5 mm with a FOV of 170 x 260 x 120 mm left-right, anterior-posterior, and head-foot directions, respectively with an acquisition time of 15 minutes using a GRAPPA factor of 1.3 in the phase-encoding direction. In conjunction with new sequence development, novel post-processing methods for tissue segmentation to improve masks for brain and lipid, lipid suppression using a frequency-

selective filtering technique using Hankel Lanczos singular value decomposition (HLSVD), and methods for estimation of regional metabolite ratios significantly improve the quality of generated high-resolution metabolite maps. The new acquisition methods have delivered excellent spectral quality as seen in Figure 3 with Figure 3A showing a short TE spectrum from normal white matter areas in a control subject whereas Figure 3B shows a TE 50 ms spectrum from a patient with high-grade glioma. The Ernst angle of the excitation pulse was set according to the TR for both acquisitions. SNR estimated as the ratio of the area under the NAA (or Cho in the absence of NAA) peak to the standard deviation of the noise, estimated between 0 to 1.2 ppm [44] is reported besides the spectra. SNR is expressed in decibels (dB) as 10*log10 (SNR).

Good coverage was observed across the brain with improved performance compared to previous lower resolution implementations of the EPSI sequence as evident from metabolite maps for a patient with high-grade glioma (Fig. 4). Brain coverage (defined as the percentage of brain voxels with linewidths of < 13 Hz) of as high as 80% was obtained in control subjects. Previous MRSI methods that employ multiple OVS bands to reduce lipid signals, or those using sparse reconstruction-based techniques, are often limited in their ability to map cortical regions. Moreover, lower resolution whole-brain approaches also perform poorly in cortical regions due to lipid signal bleeding and partial volume effects [45]. The high-resolution MRSI in the glioma case of Figure 4 shows the potential for better delineation of tumor boundaries, for instance for improved guidance of biopsies or radiation treatment planning.

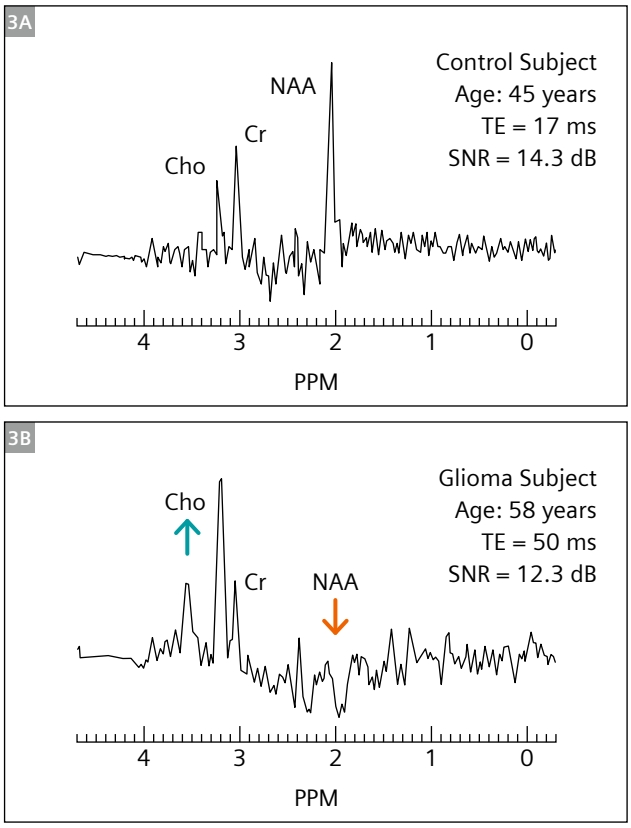

3 Representative spectra obtained using the proposed whole-brain MRSI. **(3A)** White matter spectra in a control subject acquired at TE = 17.6 ms. **(3B)** Tumor spectra in a high-grade glioma patient acquired at TE = 50 ms. Tumor spectra show lowered NAA (red arrow) and increased Cho (blue arrow).

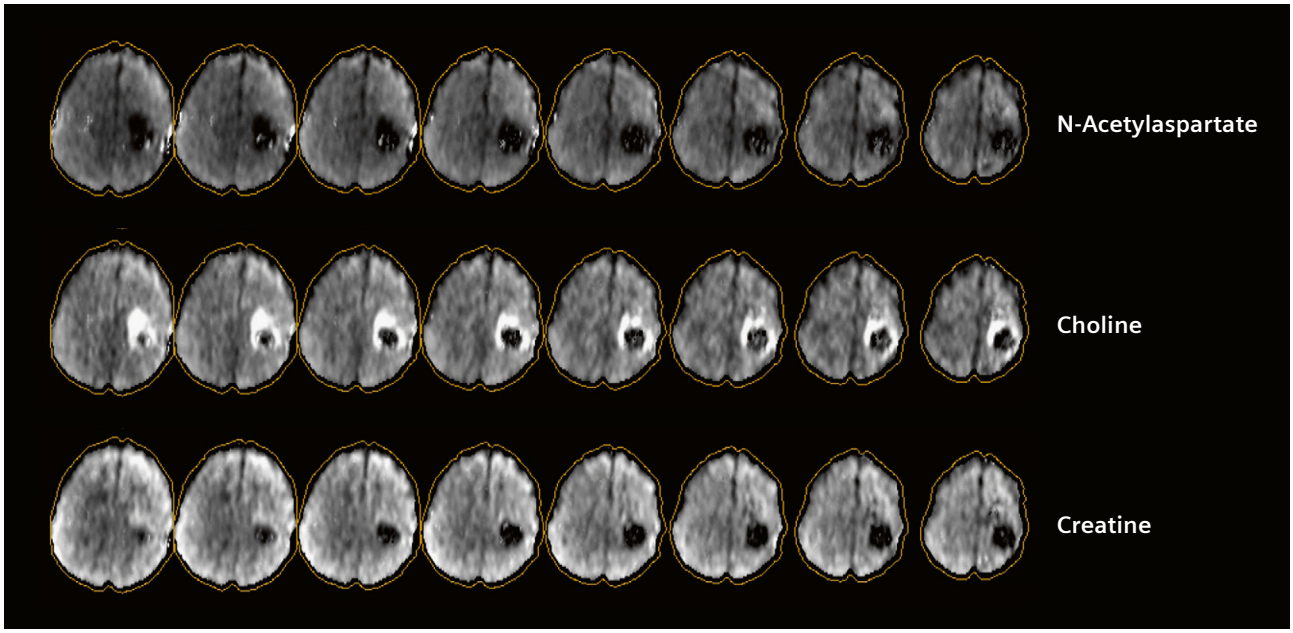

4 N-Acetylaspartate, Choline, and Creatine maps obtained using the high-resolution whole-brain MRSI sequence in a high-grade glioma patient acquired at TE = 50 ms.

II. Accelerated processing for rapid reconstruction
With the aim of fitting the entire MRSI pipeline, from the acquisition of the data to presentation of metabolite maps to the neuroradiologist within a clinically acceptable timeline (1 hour), the EPSI sequence was enhanced to perform the bulk of the time-consuming post-processing components on Siemens Healthineers platform. On-scanner processing pipelines were developed to perform data curation, echo correction, GRAPPA reconstruction and coil combination. The advantages of performing the operations on the scanner is a significant reduction (4-fold) of reconstruction time as compared to using remote systems in addition to significant reduction of data size needed to be transferred to secondary systems that fit the spectra for metabolite quantification. In this scenario, the on-scanner reconstructed data are of the order of 1 gigabyte in size as compared to ~30 gigabytes of raw data which results in significant reductions in transfer times. Moreover, intelligent pipelines have been developed that perform data reconstruction during the acquisition of other clinical sequences allowing complete on-scanner reconstruction possible before a patient leaves the facility. Furthermore, automated data transfer can be achieved by utilizing the Siemens Healthineers provided BOLD addin to transfer on-scanner processed data to remote computers/servers for further processing. Further processing carried out on the remote computer (or clouds) using MIDAS the Brain Imaging Collaboration Suite (BrICS) can be fully automated and generates metabolic images that can be sent to the institutional Picture Archiving and Communication System (PACS) for review by a radiologist in time to generate radiology report.

III. Accelerated spectral fitting using machine learning
A variety of methods have been developed for frequency domain analysis for single or multivoxel MRS [42, 46, 47]. Common analysis methods include parametric curve-fitting routines, using various model functions such as Lorentzian and Gaussian [48, 49] and fitting algorithms (simplex, non-linear least squares, etc.). The most sophisticated method, and one which is widely used, is the linear combination model ('LCModel') that fits the spectrum as a linear combination of the spectra of pure compounds known to exist in the spectrum [50]. Although LCModel works well for single-voxel and conventional MRSI data, it cannot process other types of fast MRSI data (such as EPSI). The MIDAS package for processing EPSI data [26] includes a spectral fitting routine that utilizes iterative expectation-maximization algorithms to estimate peak area parameters; however, it currently takes 40–60 minutes to execute on a high-end multicore workstation, which hampers the adaptation of MRSI into the routine clinical workflow. To overcome this, a novel fitting algorithm based on convolutional networks (FastFit) was developed, which provides rapid fitting of thousands of spectra from each EPSI data set in under 1 min using typical-performance computers that are found on MR scanners [51]. FastFit incorporates a priori knowledge of spectral physics into a deep learning algorithm that computes coefficients for a wavelet-based baseline and Lorentzian-Gaussian peak functions, published by Soher et al. [42]. Results suggest that this method is also more tolerable to baseline and other artifacts than traditional curve-fitting methods, and can effectively produce maps of metabolites and metabolite ratio 3D volumes for clinical interpretation in a timely manner [51].

IV. Development of automated artifact removing filter
As stated above, the clinical application of MRSI has been hampered due to challenges arising from: (a) artifacts in the data, which can produce erroneous classifications of tissue; and (b) a lack of consistent and validated models for spectral quality assessment.

The MIDAS program package includes first-pass multiple filters to eliminate poor quality spectra; (1) data are not included for spectral analysis if the water linewidth is > 18 Hz; and (2) following spectral fitting measures of linewidth (typically < 13 Hz), Cramer-Rao lower bounds (CRLB) (e.g., < 20% for Cr), and spectral outlier detection are used. Despite these first-pass filtering, many exceptions still occur and can lead to false-positive or false-negative detection of 'abnormal' spectra (e.g., based on ratios of Cho/NAA). Therefore, confirmation of true metabolic abnormality requires a manual review of individual spectrum by MRS experts, rather than a mere observation of maps of metabolite distributions alone. However, with several thousands of spectra in a single whole-brain EPSI scan, manual review by qualified MRS expert(s) is impractical and not scalable. To adopt whole-brain EPSI data into the clinical workflow, it is, therefore, necessary to develop additional automated spectral quality algorithms. Since there are no consistently accepted metrics for spectral quality [52], a novel algorithm for identifying and filtering spectral artifacts that arise from field inhomogeneities has recently been developed and validated [53]. This approach uses a convolutional neural network (CNN) trained using a curated dataset of 10,000 voxels derived from GBM patients and labeled by multiple MRS experts. The resulting filter can accurately recognize the broad range of spectral artifacts (e.g., due to poor water suppression, lipid suppression, low SNR, or baseline shifts) and provides highly specific and sensitive (AUC = 0.95) artifact classification to remove voxels with poor quality. This CNN-based filter complements the existing quality evaluation methods currently provided by MIDAS. In addition, an anatomical filter can exclude spectra from certain regions of the brain that have different normal metabolite levels and ratios than the cerebrum, using atlas-based registration [54].

V. Development of image viewing platform specialized for EPSI acquisition for non-MRS experts

Most programs to process/display EPSI data are not user-friendly and require significant training. They are challenging for clinicians or other non-MRS experts to use. To better facilitate the use of 3D whole-brain spectroscopic information in a clinically useful manner and promote real-time collaboration/support from MRS experts who are not necessarily available on-site, a web-based software platform has been developed for EPSI data display and real-time collaborative use in multisite clinical trials [55]. The Brain Imaging Collaboration Suite enables clinicians to manage, analyze, and visualize volumetric spectroscopic MRI (sMRI) with data from other clinical imaging sequences [55]. BrICS currently overlays metabolic information on anatomical images (i.e. CT or MRI) and enables browsing in whole-brain volumes, automated lesion segmentation, and spectral quality and fitting of individual spectrum all within a web browser. Metabolite information first gets co-registered into the space of a high-resolution T1w MRI and FLAIR. The end-user can select from various individual metabolite maps (in the case of GBM: NAA, Cho, Cr, and the Cho/NAA ratio maps) with interchangeable panels for enlarged views with editing capability of the segmented lesions (Fig. 5).

In order to make BrICS available to a larger collaboration community, we intend to exploit digital platforms that can support multiple users as well as a scanner-to-PACS interface without compromising patient information. MRI vendors have started to offer such digital solutions. For example, Siemens Healthineers teamplay platform enables the interfacing of MRI scanners with PACS and offers various FDA approved digital tools, called "Companions", that are specifically designed to facilitate such manual operations by radiologists as segmentation. BrICS can be built into the teamplay platform, as a radiation therapy planning Companion, to enable a large network of collaborators to work together in improving upon and translating this tool into the clinic.

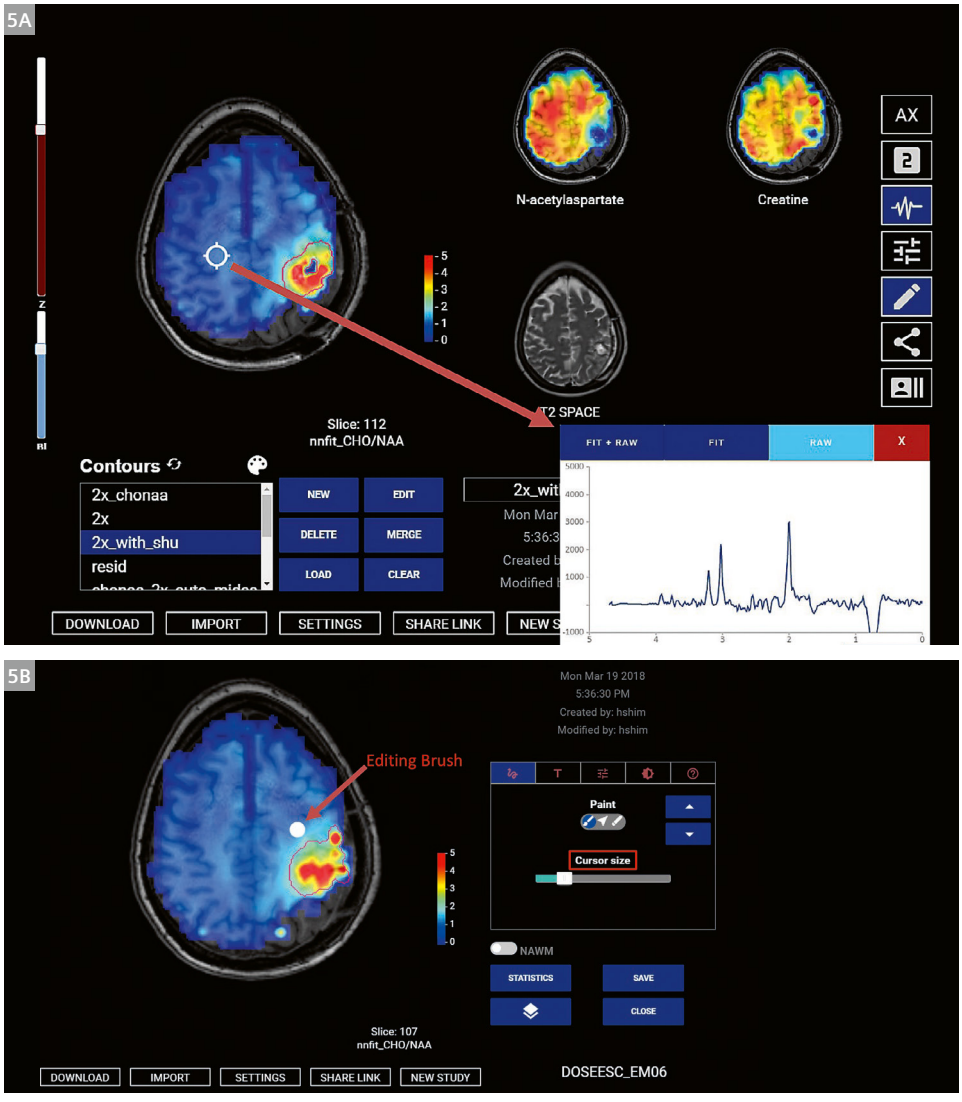

5 An example screenshot of BrICS (the same patient as Figure 2). BrICS allows metabolic information overlaid on anatomical images (i.e. CT or MRI), browsing the whole-brain volume, automated lesion segmentation, and spectral quality and fitting/viewing of individual spectrum for selected location (red arrow), all within a web browser. Metabolite information first gets co-registered into the space of a high-resolution T1w MRI and FLAIR (or any clinical MRIs). The end-user can select from various individual metabolite maps (in the case of GBM: NAA, Cho, Cr, and the Cho/NAA ratio maps) with interchangeable panels **(5A)** and edit the segmented lesions using various cursor size of paint brush (red arrow) in a separate screen in enlarged views **(5B)**.

VI. Advancing magnetic field B_0 homogeneity to improve MRSI quality and reproducibility

Owing to the theoretical doubling of overall signal-to-noise ratio (SNR), 3T MRI now plays the same role for clinical imaging that was occupied by 1.5T systems in the past. The static main (B_0) field inhomogeneity is mostly caused by magnetic susceptibility differences between soft tissues, air, and bone and is proportional to the B_0 field strength, which can lead to image distortion and signal loss. Static field (frequency) variations found at 3T are twice as large as those at 1.5T. To address this problem, advanced MR scanners use built-in shim coils in the magnet bore to provide shimming capability up to the 2nd order spherical harmonics (SH) for brain scans. Although this can address part of the issue, organs with an air-tissue interface or larger field-of-view, such as the heart, abdomen and the whole brain, are often subject to higher-order magnetic field disturbance and make the current vendor-provided solution insufficient. This remains a major challenge in spectroscopic MRI. The primary limitation to more widespread clinical implementation of spectroscopic MRI technology has been the inability to achieve good magnetic field homogeneity over the entire brain volume, as well as the variability in shimming between patients. Recently a new concept has been proposed and developed, so-called integrated parallel reception, excitation, and shimming (iPRES) [56, 57], using the same single coil array for simultaneous B_0 shimming and RF reception by adding DC currents to RF reception coil loops (Fig. 6). The close proximity of the shared shim-RF loops to the subject allows to increase the RF reception sensitivity and also provide additional local B_0 shimming. It relies on a novel circuit design (Fig. 6A) that allows an RF current (for reception) and a DC current (for B_0 shimming) to coexist independently in the same coil element. Compared to conventional RF array coils [58], the integrated RF-Shim array provides a powerful add-on ability for multi-coil local B_0 shimming [59]. The integrated shim-RF technology is currently pursued by several groups [60–63]. The innovative circuit design first implemented in a proof-of-concept two-channel RF/shim array [56], was applied to arrays with more channels [61, 62], where either 16 or 32 elements of commercial 32-channel RF head coils were modified for successful experiments on humans. The RF sensitivity was found not largely compromised compared to conventional RF array coil [58]. The iPRES concept has received considerable attention in the community and its potential impact in several MR applications recognized, including fMRI, MRS, and ultra-high-field MRI [64–72]. It also draws considerable attention from vendors since it can simplify scanner design and considerably improve its shimming function. The decreased distance from shim coils to the targeted organ increases shimming effectiveness compared to distantly located magnet bore shim coils. The integrated shim-RF coil does not compromise patient comfort compared to a clinical coil (Fig. 6). Additionally, the novel coil based shimming does not require more scan times, sequence modification or additional image reconstruction. The local shimming protocol essentially has no significant difference from vendor-supplied shimming protocols. The only difference is the shim coils being changed from the shim coils built in the magnet bore to a local shim-RF coil. As such, there will be no increase in exam times compared to existing protocols after the software is integrated into the MR scanner console.

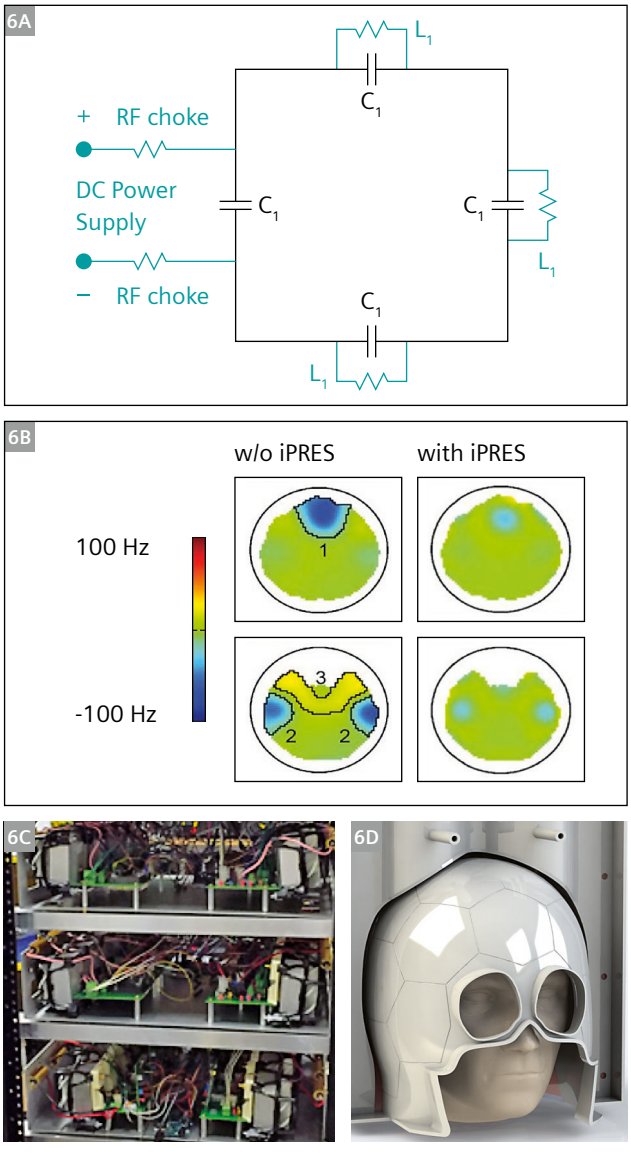

6 Integrated shim-RF head coil as a potential clinical technology. **(6A)** Shared RF/shim loop as used in iPRES. **(6B)** Field homogenization in frontal and temporal lobes. **(6C)** Homemade low cost multi-channel shim current amplifiers. **(6D)** The helmet CAD model for 3D printing has similar geometry as for product coils. Integrated coils have no compromise in patient comfort by integrating shim/RF into a standard-size head coil assembly.

Further advanced technology such as Unified Coil (UNIC) can provide even higher-order local shimming using a standard-size coil assembly, which may potentially achieve the true full brain coverage and allow metabolic evaluation of the entire brain. Such coils can be widely used and thus benefit the entire MR community by advancing B_0 shimming technology, and negligible eddy current effects make it very suitable for dynamic shimming. It will help catalyze the clinical acceptance of spectroscopic MRI. As a background, Siemens Healthineers has introduced the new generation MRI scanner MAGNETOM Vida with BioMatrix technology in 2017. Such integrated shim-RF coils fit the scope of the endeavor in better addressing one of the greatest challenges of imaging – variability of anatomies and physiologies among different patients – and further advance initiatives in precision medicine in MRI.

Conclusions and future prospects

To be able to utilize spectroscopic MRI in routine clinical workflow, there are still a number of improvements to be made, including; (1) accelerated processing pipeline to meet neuroradiology reading time; (2) whole-brain coverage; (3) fully automated and reliable artifact removal; and (4) improvement in resolution. Excitingly, an ultrahigh-resolution EPSI sequence is under development by Maudsley et al., which provides improved interpolated resolution of 1.3 x 2.0 x 2.5 mm^3 with 128 x 128 x 48 *k*-space points (currently under validation). This will enable imaging smaller tumors/regions of the brain and provides better brain coverage due to decreased sensitivity to field inhomogeneity and better fat suppression using smaller voxel size. Acquisition time is reduced by optimizing the sequence to acquire 50% fewer spectral points without affecting spectral quality and the field-of-view is decreased by 1/3 in the z-direction. With a shorter TR (950 ms) (previously 1700 ms), there was no increase in imaging time compared to the earlier sequence. On-scanner preprocessing modules are also under development to perform echo combination, GRAPPA reconstruction, coil combination, and spatial Fourier transform. Running these preprocessing modules on the scanner can significantly reduce post-processing times and the size of data required to be transferred, stored and processed. Since the ultrahigh-resolution sequence has more demanding computational requirements and may prolong reconstruction times, the reconstruction pipelines are modified to use parallel/distributed computing, which promises a significant reduction in processing times along with implementing the recently developed neural-network-based accelerated spectral fitting [51]. The value of spectroscopic MRI becomes evident when considering the shortcomings of conventional MRI exams in delineating disease progression versus treatment effect. Figure 7 shows the Cho/NAA = 2x volume in BrICS from a 16-year-old patient with high-grade glioma, using the ultrahigh-resolution sequence (the same patient in Figure 4) with an interpolated resolution of 6.5 µl. While there was hardly any enhancement visible in the CE T1w-MRI following surgery, the Cho map shows a significant elevation of choline in the anterior aspect of the resection cavity and the Cho/NAA ratio map revealed a 19.2 ml region consistent with a residual tumor. It is expected that by combining the software and improved hardware technologies described above, many of the obstacles of the implementation of MRSI in the clinic will be overcome, and it will gradually become accepted as an important modality for the evaluation of patients with brain tumors and other neurological diseases.

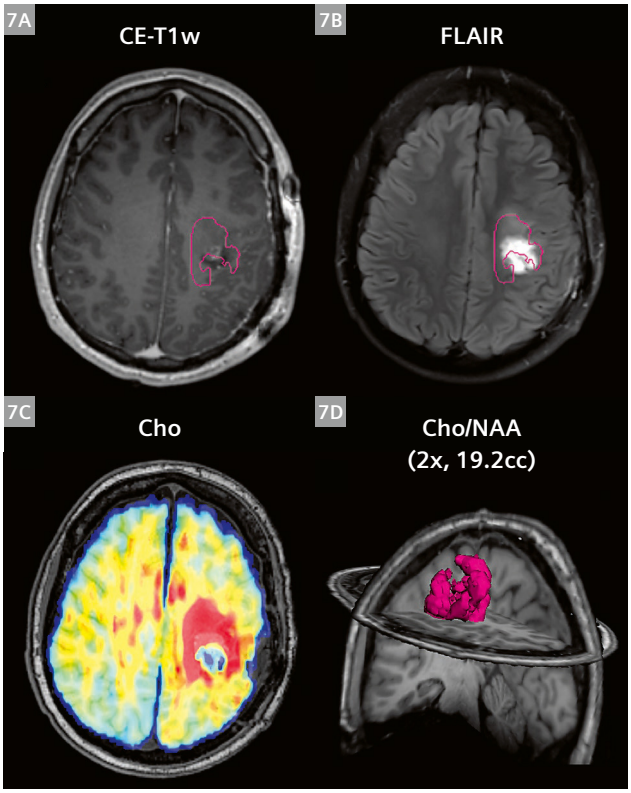

7 Conventional MRI including T1w **(7A)** and FLAIR **(7B)** showing an infiltrative mass in the left insula and posterior limb of the internal capsule. The complete extent of the mass is difficult to appreciate. Cho sMRI **(7C)** shows much larger spectroscopic abnormality encompassing a significant region of elevated Cho involving the temporal stem, insula, and cerebral peduncle **(7D)**.

Acknowledgment

This work has been supported by the National Institutes of Health grant: U01 EB028145.

References

1 Barker PB, Gillard JH, van Zijl PC, Soher BJ, Hanley DF, Agildere AM, Oppenheimer SM, Bryan RN. Acute stroke: evaluation with serial proton MR spectroscopic imaging. Radiology. 1994;192(3):723-32.
2 Lin DD, Crawford TO, Barker PB. Proton MR spectroscopy in the diagnostic evaluation of suspected mitochondrial disease. AJNR Am J Neuroradiol. 2003;24(1):33-41.
3 Remy C, Grand S, Lai ES, Belle V, Hoffmann D, Berger F, Esteve F, Ziegler A, Le Bas JF, Benabid AL, Decorps M, Segebarth CM. 1H MRS of human brain abscesses in vivo and in vitro. Magn Reson Med. 1995;34(4):508-14.
4 Frahm J, Michaelis T, Merboldt KD, Hanicke W, Gyngell ML, Bruhn H. On the N-acetyl methyl resonance in localized 1H NMR spectra of human brain in vivo. NMR Biomed. 1991;4(4):201-4.
5 Pouwels PJ, Frahm J. Differential distribution of NAA and NAAG in human brain as determined by quantitative localized proton MRS. NMR Biomed. 1997;10(2):73-8.
6 Barker P, Breiter S, Soher B, Chatham J, Forder J, Samphilipo M, Magee C, Anderson J. Quantitative Proton Spectroscopy of Canine Brain: In vivo and in vitro correlations. Magn Reson Med. 1994;32:157-63.
7 Jacobs MA, Horska A, van Zijl PC, Barker PB. Quantitative proton MR spectroscopic imaging of normal human cerebellum and brain stem. Magn Reson Med. 2001;46(4):699-705.
8 Petroff OA, Graham GD, Blamire AM, al-Rayess M, Rothman DL, Fayad PB, Brass LM, Shulman RG, Prichard JW. Spectroscopic imaging of stroke in humans: histopathology correlates of spectral changes. Neurology. 1992;42(7):1349-54.
9 Shonk TK, Moats RA, Gifford P, Michaelis T, Mandigo JC, Izumi J, Ross BD. Probable Alzheimer disease: diagnosis with proton MR spectroscopy. Radiology. 1995;195(1):65-72.
10 Kruse B, Hanefeld F, Christen HJ, Bruhn H, Michaelis T, Hanicke W, Frahm J. Alterations of brain metabolites in metachromatic leukodystrophy as detected by localized proton magnetic resonance spectroscopy in vivo. J Neurol. 1993;241(2):68-74.
11 Brand A, Richter-Landsberg C, Leibfritz D. Multinuclear NMR studies on the energy metabolism of glial and neuronal cells. Dev Neurosci. 1993;15(3-5):289-98.
12 Flogel U, Willker W, Leibfritz D. Regulation of intracellular pH in neuronal and glial tumour cells, studied by multinuclear NMR spectroscopy. NMR Biomed. 1994;7(4):157-66.
13 Castillo M, Smith JK, Kwock L. Correlation of myo-inositol levels and grading of cerebral astrocytomas. AJNR Am J Neuroradiol. 2000;21(9):1645-9.
14 Gurbani SS, Yoon Y, Weinberg BD, Salgado E, Press RH, Cordova JS, Ramesh KK, Liang Z, Velazquez Vega J, Voloschin A, Olson JJ, Schreibmann E, Shim H, Shu HG. Assessing Treatment Response of Glioblastoma to an HDAC Inhibitor Using Whole-Brain Spectroscopic MRI. Tomography. 2019;5(1):53-60.
15 Shim H, Wei L, Holder CA, Guo Y, Hu XP, Miller AH, Olson JJ. Use of high-resolution volumetric MR spectroscopic imaging in assessing treatment response of glioblastoma to an HDAC inhibitor. AJR Am J Roentgenol. 2014;203(2):W158-65.
16 Wei L, Hong S, Yoon Y, Hwang SN, Park JC, Zhang Z, Olson JJ, Hu XP, Shim H. Early prediction of response to vorinostat in an orthotopic glioma rat model. NMR Biomed. 2012; In Press.
17 van Zijl PCM, Barker PB. Magnetic Resonance Spectroscopy and Spectroscopic Imaging for the Study of Brain Metabolism. Imaging Brain Structure and Function. Annals of the New York Academy of Sciences. 820. New York, N.Y.1997. p. 75-96.
18 Nelson SJ. Analysis of volume MRI and MR spectroscopic imaging data for the evaluation of patients with brain tumors. Magn Reson Med. 2001;46(2):228-39.
19 Duyn JH, Gillen J, Sobering G, van Zijl PC, Moonen CT. Multisection proton MR spectroscopic imaging of the brain. Radiology. 1993;188(1):277-82.
20 Pohmann R, von Kienlin M, Haase A. Theoretical evaluation and comparison of fast chemical shift imaging methods. J Magn Reson. 1997;129(2):145-60.
21 Kurhanewicz J, Vigneron DB, Nelson SJ. Three-dimensional magnetic resonance spectroscopic imaging of brain and prostate cancer. Neoplasia. 2000;2(1-2):166-89.
22 Zhu H, Barker PB. MR spectroscopy and spectroscopic imaging of the brain. Methods Mol Biol. 2011;711:203-26.
23 Nassirpour S, Chang P, Avdievitch N, Henning A. Compressed sensing for high-resolution nonlipid suppressed (1) H FID MRSI of the human brain at 9.4T. Magn Reson Med. 2018;80(6):2311-25.
24 Strasser B, Povazan M, Hangel G, Hingerl L, Chmelik M, Gruber S, Trattnig S, Bogner W. (2 + 1)D-CAIPIRINHA accelerated MR spectroscopic imaging of the brain at 7T. Magn Reson Med. 2017;78(2):429-40.
25 Thomas MA, Nagarajan R, Huda A, Margolis D, Sarma MK, Sheng K, Reiter RE, Raman SS. Multidimensional MR spectroscopic imaging of prostate cancer in vivo. NMR Biomed. 2014;27(1):53-66.
26 Ebel A, Soher BJ, Maudsley AA. Assessment of 3D proton MR echo-planar spectroscopic imaging using automated spectral analysis. Magn Reson Med. 2001;46(6):1072-8.
27 Ebel A, Maudsley AA. Improved spectral quality for 3D MR spectroscopic imaging using a high spatial resolution acquisition strategy. Magn Reson Imaging. 2003;21(2):113-20.
28 Mansfield P. Spatial mapping of chemical shift in NMR. Magn Reson Med. 1984;1:370-86.
29 Posse S, Cuenod CA, Risinger R, Le Bihan D, Balaban RS. Anomalous transverse relaxation in 1H spectroscopy in human brain at 4 Tesla. Magn Reson Med. 1995;33(2):246-52.
30 Govindaraju V, Gauger GE, Manley GT, Ebel A, Meeker M, Maudsley AA. Volumetric proton spectroscopic imaging of mild traumatic brain injury. AJNR Am J Neuroradiol. 2004;25(5):730-7.
31 Pelletier D, Nelson SJ, Grenier D, Lu Y, Genain C, Goodkin DE. 3-D echo planar (1)HMRS imaging in MS: metabolite comparison from supratentorial vs. central brain. Magn Reson Imaging. 2002;20(8):599-606.
32 Nassirpour S, Chang P, Fillmer A, Henning A. A comparison of optimization algorithms for localized in vivo B_0 shimming. Magn Reson Med. 2018;79(2):1145-56.
33 Ogg RJ. WET, a T1- and B1-Insensitive Water-Suppression Method for in Vivo Localized 1H NMR Spectroscopy. J Magn Reson B. 1994;104:1-10.
34 Ebel A, Maudsley AA. Comparison of methods for reduction of lipid contamination for in vivo proton MR spectroscopic imaging of the brain. Magn Reson Med. 2001;46(4):706-12.
35 Hetherington HP, Mason GF, Pan JW, Ponder SL, Vaughan JT, Twieg DB, Pohost GM. Evaluation of cerebral gray and white matter metabolite differences by spectroscopic imaging at 4.1T. Magn Reson Med. 1994;32(5):565-71.
36 Maudsley AA, Domenig C, Govind V, Darkazanli A, Studholme C, Arheart K, Bloomer C. Mapping of brain metabolite distributions by volumetric proton MR spectroscopic imaging (MRSI). Magn Reson Med. 2009;61(3):548-59.
37 Zhu X, Ebel A, Ji JX, Schuff N. Spectral phase-corrected GRAPPA reconstruction of three-dimensional echo-planar spectroscopic imaging (3D-EPSI). Magn Reson Med. 2007;57(5):815-20.
38 Cordova JS, Shu HK, Liang Z, Gurbani SS, Cooper LA, Holder CA, Olson JJ, Kairdolf B, Schreibmann E, Neill SG, Hadjipanayis CG, Shim H. Whole-brain spectroscopic MRI biomarkers identify infiltrating margins in glioblastoma patients. Neuro Oncol. 2016;18(8):1180-9.

39 Maudsley AA, Darkazanli A, Alger JR, Hall LO, Schuff N, Studholme C, Yu Y, Ebel A, Frew A, Goldgof D, Gu Y, Pagare R, Rousseau F, Sivasankaran K, Soher BJ, Weber P, Young K, Zhu X. Comprehensive processing, display and analysis for in vivo MR spectroscopic imaging. NMR Biomed. 2006;19(4):492-503.
40 Zhang Y, Brady M, Smith S. Segmentation of brain MR images through a hidden Markov random field model and the expectation-maximization algorithm. IEEE Trans Med Imaging. 2001;20(1):45-57.
41 Haupt CI, Schuff N, Weiner MW, Maudsley AA. Removal of lipid artifacts in 1H spectroscopic imaging by data extrapolation. Magn Reson Med. 1996;35(5):678-87.
42 Soher BJ, Young K, Govindaraju V, Maudsley AA. Automated spectral analysis III: application to in vivo proton MR spectroscopy and spectroscopic imaging. Magn Reson Med. 1998;40(6):822-31.
43 Zhu H, Ouwerkerk R, Barker PB. Dual-band water and lipid suppression for MR spectroscopic imaging at 3 Tesla. Magn Reson Med. 2010;63(6):1486-92.
44 Goryawala MZ, Sheriff S, Maudsley AA. Regional distributions of brain glutamate and glutamine in normal subjects. NMR Biomed. 2016;29(8):1108-16.
45 Goryawala MZ, Sheriff S, Stoyanova R, Maudsley AA. Spectral decomposition for resolving partial volume effects in MRSI. Magn Reson Med. 2018;79(6):2886-95.
46 Soher BJ, van Zijl PC, Duyn JH, Barker PB. Quantitative proton MR spectroscopic imaging of the human brain. Magn Reson Med. 1996;35(3):356-63.
47 Mierisova S, Ala-Korpela M. MR spectroscopy quantitation: a review of frequency domain methods. NMR Biomed. 2001;14(4):247-59.
48 Marshall I, Bruce SD, Higinbotham J, MacLullich A, Wardlaw JM, Ferguson KJ, Seckl J. Choice of spectroscopic lineshape model affects metabolite peak areas and area ratios. Magn Reson Med. 2000;44(4):646-9.
49 Soher BJ, Maudsley AA. Evaluation of variable line-shape models and prior information in automated 1H spectroscopic imaging analysis. Magn Reson Med. 2004;52(6):1246-54.
50 Provencher SW. Estimation of metabolite concentrations from localized in vivo proton NMR spectra. Magn Reson Med. 1993;30(6):672-9.
51 Gurbani SS, Sheriff S, Maudsley AA, Shim H, Cooper LAD. Incorporation of a spectral model in a convolutional neural network for accelerated spectral fitting. Magn Reson Med. 2019;81(5):3346-57.
52 Kreis R. Issues of spectral quality in clinical 1H-magnetic resonance spectroscopy and a gallery of artifacts. NMR Biomed. 2004;17:361-81.
53 Gurbani SS, Schreibmann E, Maudsley AA, Cordova JS, Soher BJ, Poptani H, Verma G, Barker PB, Shim H, Cooper LAD. A convolutional neural network to filter artifacts in spectroscopic MRI. Magn Reson Med. 2018.

Contact

Hyunsuk Shim, Ph.D.
Winship Cancer Institute
of Emory University
Department of Radiation Oncology
1701 Uppergate Drive
Atlanta, GA 30322
USA
hshim@emory.edu



54 Schreibmann E, Gurbani S, Shim H, editors. Building an anatomical filter to facilitate 3D whole brain spectroscopic MRI into GBM treatment planning. American Association for Physicists in Medicine Annual Meeting; 2017; Denver, CO.
55 Gurbani S, Weinberg B, Mellon E, Schreibmann E, Sheriff S, Maudsley A, Cooper L, Shu HK, Shim H. The brain imaging collaboration suite (BrICS): a cloud platform for integrating whole-brain spectroscopic MRI into the radiation therapy planning workflow. Tomography. 2019;5(1):184-91.
56 Han H, Song AW, Truong TK. Integrated parallel reception, excitation, and shimming (iPRES). Magn Reson Med. 2013;70(1):241-7.
57 Han H, Truong TK, Song AW. Magnetic resonance imaging systems for integrated parallel reception, excitation and shimming and related methods and devices. US Patent 9,874,6162018.
58 Roemer PB, Edelstein WA, Hayes CE, Souza SP, Mueller OM. The NMR phased array. Magn Reson Med. 1990;16(2):192-225.
59 Juchem C, Nixon TW, McIntyre S, Boer VO, Rothman DL, de Graaf RA. Dynamic multi-coil shimming of the human brain at 7 T. J Magn Reson. 2011;212(2):280-8.
60 Darnell D, Truong TK, Song AW. Integrated parallel reception, excitation, and shimming (iPRES) with multiple shim loops per radio-frequency coil element for improved B_0 shimming. Magn Reson Med. 2017;77(5):2077-86.
61 Stockmann JP, Witzel T, Keil B, Polimeni JR, Mareyam A, LaPierre C, Setsompop K, Wald LL. A 32-channel combined RF and B_0 shim array for 3T brain imaging. Magn Reson Med. 2016;75(1):441-51.
62 Truong TK, Darnell D, Song AW. Integrated RF/shim coil array for parallel reception and localized B_0 shimming in the human brain. Neuroimage. 2014;103:235-40.
63 Winkler SA, Schmitt F, Landes H, de Bever J, Wade T, Alejski A, Rutt BK. Gradient and shim technologies for ultra high field MRI. Neuroimage. 2018;168:59-70.
64 Budinger TF, Bird MD, Frydman L, Long JR, Mareci TH, Rooney WD, Rosen B, Schenck JF, Schepkin VD, Sherry AD, Sodickson DK, Springer CS, Thulborn KR, Ugurbil K, Wald LL. Toward 20 T magnetic resonance for human brain studies: opportunities for discovery and neuroscience rationale. MAGMA. 2016;29(3):617-39.
65 Cloos MA, Knoll F, Zhao T, Block KT, Bruno M, Wiggins GC, Sodickson DK. Multiparametric imaging with heterogeneous radiofrequency fields. Nat Commun. 2016;7:12445.
66 Deistung A, Schweser F, Reichenbach JR. Overview of quantitative susceptibility mapping. NMR Biomed. 2017;30(4).
67 Esmaeili M, Bathen TF, Rosen BR, Andronesi OC. Three-dimensional MR spectroscopic imaging using adiabatic spin echo and hypergeometric dual-band suppression for metabolic mapping over the entire brain. Magn Reson Med. 2017;77(2):490-7.
68 Feinberg DA, Vu AT, Beckett A. Pushing the limits of ultra-high resolution human brain imaging with SMS-EPI demonstrated for columnar level fMRI. Neuroimage. 2018;164:155-63.
69 Hangel G, Strasser B, Povazan M, Heckova E, Hingerl L, Boubela R, Gruber S, Trattnig S, Bogner W. Ultra-high resolution brain metabolite mapping at 7 T by short-TR Hadamard-encoded FID-MRSI. Neuroimage. 2018;168:199-210.
70 Ma C, Lam F, Ning Q, Johnson CL, Liang ZP. High-resolution (1) H-MRSI of the brain using short-TE SPICE. Magn Reson Med. 2017;77(2):467-79.
71 Sclocco R, Beissner F, Bianciardi M, Polimeni JR, Napadow V. Challenges and opportunities for brainstem neuroimaging with ultrahigh field MRI. Neuroimage. 2018;168:412-26.
72 Webb AG, Van de Moortele PF. The technological future of 7 T MRI hardware. NMR Biomed. 2016;29(9):1305-15.

The Prostate Dot Engine – a System-Guided and Assisted Workflow to Improve Consistency in Prostate MR Exams

Wilhelm Horger, Gregor Thoermer, Elisabeth Weiland, Bernd Kuehn, Berthold Kiefer

Siemens Healthineers, Magnetic Resonance Imaging, Erlangen, Germany

The "PROMISe" of mpMRI

PROMIS, PRECISION, 4M and MRI-FIRST [1–4] are four landmark studies that are changing the way we screen for prostate cancer.

Evidence presented in these studies has already impacted guidelines on imaging prostate cancer issued by the European Association of Urology and national guidelines in the UK (NICE) and the Netherlands toward a scheme where prostate MRI serves a first-line triage test in biopsy-naïve men with elevated PSA levels.

These studies consistently provide Level 1A evidence that using multiparametric MRI (mpMRI) of the prostate can reduce the number of biopsies required in men with elevated PSA levels.

Due to the excellent negative predictive value of prostate mpMRI, men without suspicious MRI findings do not require further examinations. At the same time, the mpMRI pathway does not result in an under-detection of clinically significant cancer, but will reduce the number of clinically insignificant cancers picked up by chance in a "systematic TRUS-biopsy-only" care scheme (see Table 1). It has been shown for – quite differently organized – healthcare systems that the MRI pathway will reduce the overall healthcare expenditure per clinically significant cancer diagnosed. This advantage is largely driven by the reduced number of biopsies [5–7], resulting in fewer infections and sepsis, the latter presenting a huge financial burden [8]. The potential long-term effects on patient management of reduced detection of clinically insignificant disease have not even been modelled in studies of this kind.

Performance of mpMRI pathway in comparison with TRUS-bx pathway	PRECISION[1] (500 men)	MRI-FIRST[2]	4M Study[3]	PROMIS[4]
Avoid biopsy after negative mpMRI in (%) of patients	28 %	18 – 21 %	49 %	27 %
Increase in detection of significant cancers (%)	+12 %	No difference in significant cancer (+2 %)	No difference in significant cancer (+2 %)	No difference in significant cancer (+2 %)
Diagnosis of insignificant cancer	-13 %	-14 %	-11 %	-5 %
Reduction of biopsy cores per patient (relevant for infections and side effects	11 → 4 (= -64 %)	12 → 3 (= -75 %)	12 → 3 (= -75 %)	n.a.

Table 1: Summary of recently published landmark mpMRI prostate cancer detection studies and their impact on patient management.

The challenge in scaling up mpMRI

Expert panels are, however, aware that the MRI pathway puts an additional burden on radiologists and imaging providers and the potential risks and challenges associated with the increasing demand. Most radiologists have limited expertise in interpreting and reporting prostate MRI, and the consistent acquisition of high-quality mpMRI prostate examinations is a challenge for technologists not used to performing the exam routinely according to the PI-RADS recommendations.

In 2019, Engels et al. [9] and Barrett et al. [10] published excellent papers on how to perform high-quality mpMRI and which pitfalls to consider. They concluded that training of skilled professionals is key; but also that imaging vendors should provide tools and workflows that help tailor and optimize the exam for the individual patient, to maximize scan quality and consistency.

Respective software automatically detecting characteristic landmarks with machine learning trained algorithms to adjust size and angulation of FOVs to the individual anatomical conditions with high consistency and reproducibility has been successfully established for various applications, literarily ranging from head to toe with the Brain, Spine, Hip, Knee, Breast, Cardiac, Abdomen, and Whole-Body Dot Engines. Studies specifically investigating the value of such software for assisted and guided brain, liver and whole-body examinations have clearly shown relevant reduction of examination time compared to standard workflows [11–13]. In addition, for liver examinations, assisting features including automated bolus detection (ABLE) with an automatically positioned bolus tracker in the descending aorta allow technologists to achieve optimal arterial phase quality in dynamic contrast-enhanced scans in 94% of cases, where a fixed-time approach only achieves 73% of optimally timed arterial phase images [12].

Prostate Dot Engine[1] – from prototype to product

Such novel automated scanner software has recently been prototyped and evaluated for MRI examinations of the prostate. The aim is to standardize scan volume positioning, tilting and coverage, in order to ensure high consistency between operators, and to better support Active Surveillance with repeated MR scans [14]. Although the evaluation did not show a statistically significant time advantage of the assisted workflow over the manual workflow (26 versus 28 minutes median examination time), the overall imaging quality was superior with the assisted MRI scans, achieving an average rating of 4.6 out of 5 versus 3.8 out of 5 points for the manual workflow.

In the light of developing evidence and changing guidelines, the planned introduction of the Prostate Dot Engine as part of the software version *syngo* MR XA30A is timely.

The Prostate Dot Engine is designed for fast, reproducible and standardized prostate MR examinations and supports multi-parametric, multi-plane MR imaging according to the latest PI-RADS v2.1 recommendations [15]. The operator is guided through one comprehensive workflow with decision points to adapt the strategy to individual patient conditions (see Figure 1), while artificial intelligence aids in planning and performing the procedure steps.

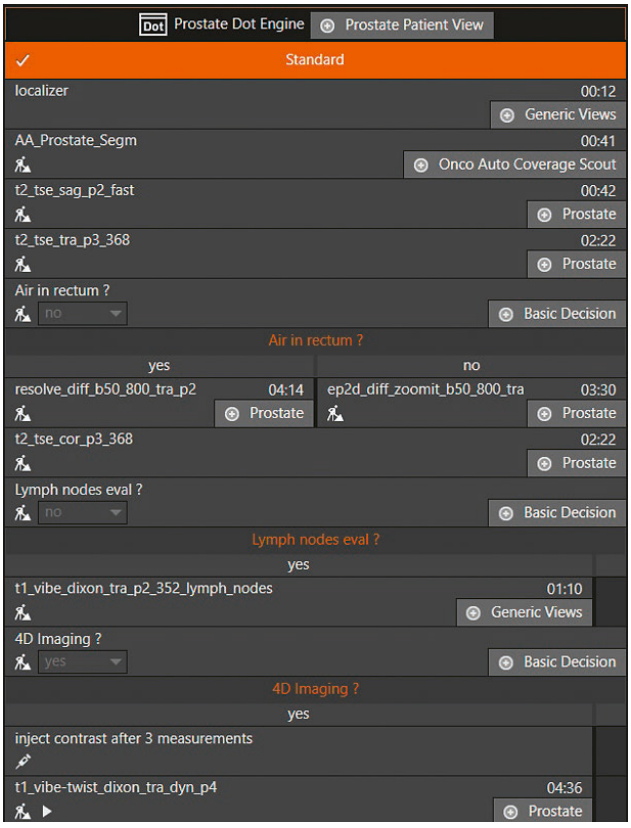

1 Workflow of the Prostate Dot Engine with different decision points.
For example, based on initial morphological scans the operator may be asked to decide whether a patient has a lot of gas in the rectum. If there is considerable gas, a highly robust RESOLVE DWI scan is acquired. If not, zoomed diffusion-weighed images are acquired. These are more prone to distortions, but offer higher spatial resolution and better contrast in shorter time.

Work in progress: the product is currently under development and is not for sale in the U.S. and in other countries. Its future availability cannot be ensured.

AI-assisted planning, angulation, and coverage

Before image acquisition, the operator has the choice between two general approaches for acquiring the data. In "Patient View" (Fig. 2) slice orientation can be chosen to be either "Anatomical" or "Axial". Anatomical means that the acquisition volumes are tilted to match the actual, individual angulation of the prostate in the body, which can be affected by factors such as bladder and rectal filling, or how the patient lies on the bed. Most recommendations and committees suggest acquiring either axial scans "perpendicular to the long axis of the prostate" or "true axial" images, the latter aimed at improving reproducibility in Active Surveillance [9, 15, 16].

A recent study has investigated the robustness of AI-derived axial slice angulation with the Prostate Dot Engine. Subjects underwent MRI scans of the prostate with full and empty bladder, with excellent reproducibility of the angulation [17], indicating that the assisted planning approach might increase consistency in Active Surveillance without compromising fidelity in anatomical coverage. The preferred angulation strategy can be predefined and set as a default, so it does not have to be selected in every patient.

The short AutoAlign prostate segmentation scan at the beginning of the exam facilitates the detection of certain landmarks in the small pelvis to derive the angulation and coverage required for the subsequent mpMRI of the prostate. For the angulation, the entry point of the bladder neck into the prostate and the exit of the urethra from the apex of the prostate are used as highly reproducible landmarks. In addition, the prostate gland is automatically segmented, and if the PSA value has been specified an estimate of PSA density (ng/ml) is provided in the generated report. Another feature of the Prostate Dot Engine is to support asymmetric anatomical coverage or a shift in the field-of-view direction as illustrated in Figure 3.

By default, images in the sagittal plane are acquired before the axial T2-weighted and diffusion-weighted images. This approach has repeatedly been reported to be beneficial as it gives the patient some time to relax and calm down, so they are less likely to move during the most relevant axial scans.

Diffusion-weighted imaging

After acquiring T2-weighted images in sagittal and transverse orientation, diffusion-weighted images are automatically pre-planned and acquired, using either RESOLVE or a

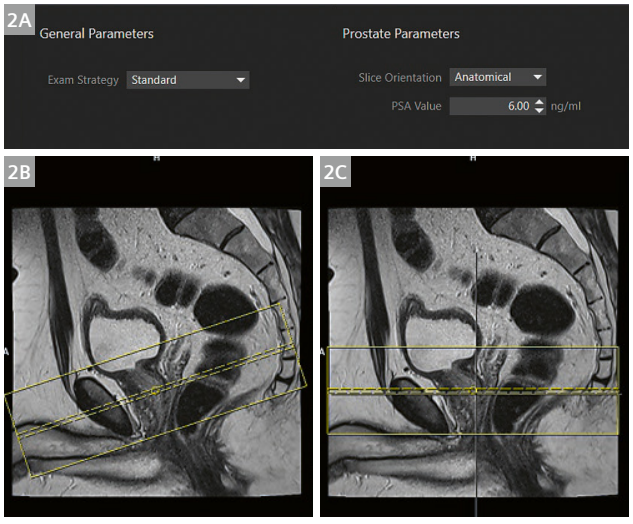

2 The Patient View of the Prostate Dot Engine **(2A)** is displayed before the examination. The operator can specify the desired slice orientation ("Anatomical" or "Axial"), which will result in the acquisition orientations shown in **2B** and **2C**, respectively. Coronal and sagittal acquisitions are acquired perpendicular to the chosen axial orientation. The PSA value can be entered in order to get an automated estimation of the PSA density.

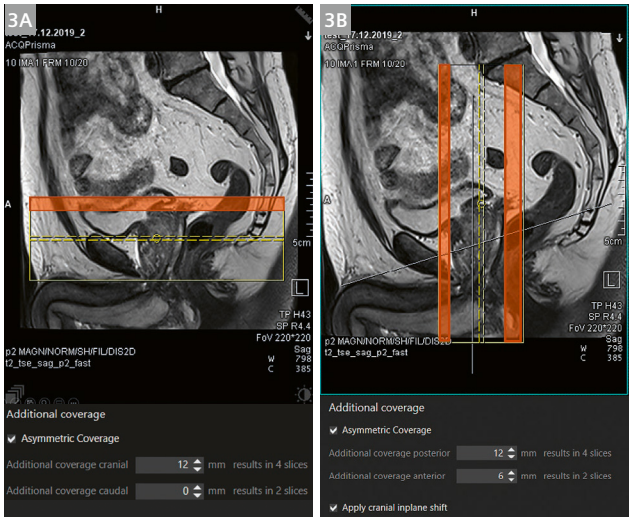

3 Based on the segmentation of the prostate gland, the required number of slices to cover the entire organ is automatically derived and adjusted. In particular with straight axial acquisitions, the seminal vesicles may expand more in the cranial direction than the prostate base **(3A)**. To ensure complete coverage of the seminal vesicles, the user interface allows to specify additional "asymmetric coverage", for example with 4 more slices in the cranial direction (corresponding to the orange area). The same can also be applied to other orientations, e.g., to coronal planes **(3B)**. In addition, a FOV shift to better cover lymph nodes in the small pelvis can be achieved by ticking the option "Apply cranial inplane shift" thus ending the FOV 5 cm below the apex of the prostate.

single-shot EPI method with reduced FOV (ZOOMit^{PRO}). The strengths of both techniques are specified in Table 2 and an illustrative case can be found in Figure 4.

Following the PI-RADS v2.1 recommendation, two *b*-values (b = 50 s/mm^2 and b = 800 s/mm^2) are scanned and ultra-high *b*-value images at b = 1400 s/mm^2 are automatically calculated. The often-suggested additional acquisition of a supporting *b*-value in the range of 400–500 s/mm^2 for improved ADC calculation is not recommended here, since a linear fitted ADC value is hardly influenced by this choice and the scan time may more effectively be invested in additional averages at the higher *b*-value.

With regards to the ultra-high *b*-value (> 1400 s/mm^2) there is some disagreement in the international community whether to acquire or extrapolate images, and on the optimal choice of the ultra-high *b*-value [18]. UK consensus guidelines are most specific in proposing b ≥ 1400 s/mm^2 at 1.5T and b ≥ 2000 s/mm^2 at 3T, both "preferentially acquired". Rosenkrantz et al. [20] provide some guidance on the choice of an optimal *b*-value, suggesting that "computed *b*-values in the range of 1500–2500 s/mm^2 (but not higher) are optimal for prostate cancer detection" providing high sensitivity for lesions and sufficient anatomical clarity.

The Prostate Dot Engine provides a flexible framework where protocol steps can be modified and added to best serve individual institutional expectations.

Dynamic contrast-enhanced imaging

After acquiring diffusion-weighted and coronal T2-weighted images, T1-weighted scans of the small pelvis and dynamic contrast-enhanced (DCE) images may be acquired. Some studies [20, 21] suggest that the detection rate of clinically significant cancer may not be negatively affected with a bi-parametric screening protocol, but the detection rate of insignificant cancer and the number of biopsies may go up due to a tendency to upgrade indecisive cases without DCE information. On the other hand, bi-parametric protocols have the clear advantage of being completely non-invasive and substantially shorter, there-

	ZOOMit^{Pro}	RESOLVE
TE (ms)	72	51
FOV (mm x mm)	100 x 100	200 x 200
Resolution (mm^3)	0.82 x 0.82 x 3.0	0.85 x 0.85 x 3.0
Acquisition time (min:sec)	3:30	4:14

Table 2: Comparison of protocol parameters of ZOOMit^{Pro} and RESOLVE with b = 50, 800 s/mm^2 at 3T (MAGNETOM Prisma). While ZOOMit provides higher SNR and resolution in shorter acquisition time, the readout segmented RESOLVE is more robust in patients with susceptibility issues (especially caused by gas in rectum) due to a substantially shorter echo train.

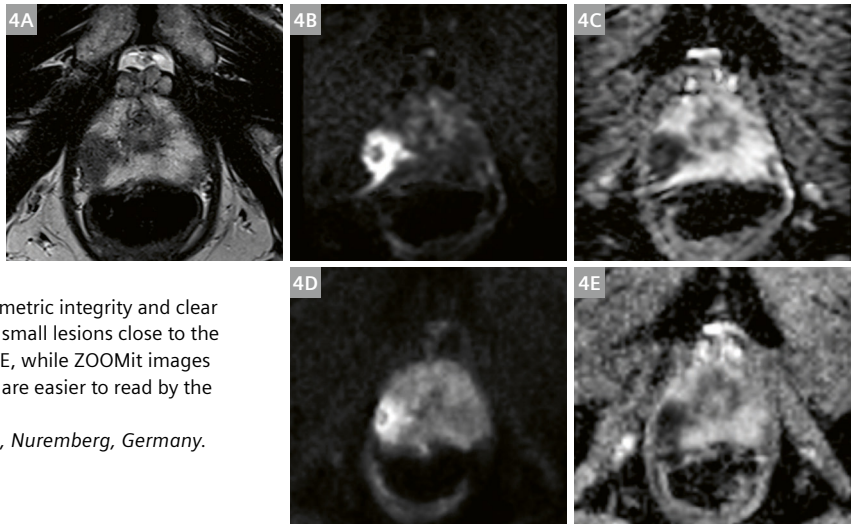

4 72-year-old patient with suspected prostate cancer. A clearly visible lesion in the right peripheral zone in the apical aspect of the prostate **(4A)** represented with a corresponding diffusion restriction in calculated high *b*-value images and ADC maps. Due to a substantial amount of gas in the rectum, ZOOMit images **(4B, D)** suffer from a distortion in phase-encoding-direction (here: L-R), sometimes also referred to as "comet tail sign" while the RESOLVE images **(4C, E)** expose high geometric integrity and clear lesion delineation. It can be argued that very small lesions close to the capsule may only be seen properly in RESOLVE, while ZOOMit images appear to have higher lesion conspicuity and are easier to read by the radiologists.
Images courtesy of Prof. Karlheinz Engelhard, Nuremberg, Germany.

fore more cost efficient. While the role of DCE in prostate cancer detection is debated and may be subject to change in a later version of PI-RADS, DCE remains integral part of PI-RADS v2.1 conform mpMRI for now. This is also reflected in the workflow of the Prostate Dot Engine: by default, DCE imaging is included but may be deselected (i.e. in follow-ups) or removed if this is the institutional preference. As for the other scans, positioning of the imaging volume is automatically adjusted and imaging parameters, such as temporal and spatial resolution, are kept constant to fulfill the requirements of the PI-RADS standard.

Summary

The Prostate Dot Engine aims to standardize mpMRI of the prostate, to assist less experienced users in performing the scans with consistent high quality, and to facilitate high reproducibility in repeated scans, for example in Active Surveillance. The Prostate Dot Engine is one of several intelligent solutions designed to scale up prostate MRI in the light of a globally rising demand for this procedure.

References

1 Kasivisvanathan V, Rannikko AS, Borghi M, et al. PRECISION Study Group Collaborators. MRI-Targeted or Standard Biopsy for Prostate-Cancer Diagnosis. N Engl J Med. 2018;378(19):1767-1777.
2 Rouvière O, Puech P, Renard-Penna R, et al. Use of prostate systematic and targeted biopsy on the basis of multiparametric MRI in biopsy-naive patients (MRI-FIRST): a prospective, multicentre, paired diagnostic study. Lancet Oncol 2018; http://dx.doi.org/10.1016/S1470-2045(18)30569-2.
3 van der Leesta M, Cornelb E, Israëla B, et al. Head-to-head comparison of transrectal ultrasound guided prostate biopsy versus multi-parametric prostate resonance imaging with subsequent MR-guided biopsy in biopsy-naïve men with elevated PSA; a large prospective multicenter clinical study. Eur Urol. 2018; in press.
4 Ahmed HU, El-Shater Bosaily A, Brown LC, et al. Diagnostic accuracy of multi-parametric MRI and TRUS biopsy in prostate cancer (PROMIS): a paired validating confirmatory study. Lancet. 2017;389: 815–22.
5 de Rooij M, Crienen S, Witjes JA, et al. Cost-effectiveness of magnetic resonance (MR) imaging and MR-guided targeted biopsy versus systematic transrectal ultrasound-guided biopsy in diagnosing prostate cancer: a modelling study from a health care perspective. Eur Urol. 2014;66(3):430-436.
6 Pahwa S, Schlitz NK, Ponsky LE, et al. Cost-effectiveness of MR Imaging-guided Strategies for Detection of Prostate Cancer in Biopsy-Naive Men. Radiology. 2017;285(1):157-166.
7 Faria R, Soares MO, Spackman E, et al. Optimising the Diagnosis of Prostate Cancer in the Era of Multiparametric Magnetic Resonance Imaging: A Cost-effectiveness Analysis Based on the Prostate MR Imaging Study (PROMIS). Eur Urol. 2018;73(1):23-30. doi: 10.1016/j.eururo.2017.08.018. Epub 2017 Sep 19.
8 Gross MD, Alshak MN, Shoag JE, et al. Healthcare Costs of Post-Prostate Biopsy Sepsis. Urology. 2019;133:11-15.
9 Engels RRM, Israël B, Padhani AR, et al. Multiparametric Magnetic Resonance Imaging for the Detection of Clinically Significant Prostate Cancer: What Urologists Need to Know. Part 1: Acquisition. Eur Urol. 2019 in press; DOI: https://doi.org/10.1016/j.eururo.2019.09.021.
10 Caglic I, Barrett T. Optimising prostate mpMRI: prepare for success. Clin Radiol. 2019 ;74(11):831-840.
11 Moenninghoff C, Umutlu L, Kloeters C, et al. Workflow efficiency of two 1.5T MR scanners with and without an automated user interface for head examinations. Acad Radiol. 2013;20(6):721-30.
12 Sharma P, Kalb B, Kitajima HD, et al. Optimization of single injection liver arterial phase gadolinium enhanced MRI using bolus track real-time imaging. J Magn Reson Imaging. 2011;33(1):110-8.
13 Stocker D, Finkenstaedt T, Kuehn B, et al. Performance of an Automated Versus a Manual Whole-Body Magnetic Resonance Imaging Workflow. Invest Radiol. 2018;53(8):463-471.
14 Esser M, Zinsser D, Kündel M, et al. Performance of an Automated Workflow for Magnetic Resonance Imaging of the Prostate: Comparison With a Manual Workflow. Invest Radiol. 2019. doi: 10.1097/RLI.0000000000000635
15 American College of Radiology. PI-RADS® Prostate Imaging – Reporting and Data System 2019, Version 2.1. https://www.acr.org/-/media/ACR/Files/RADS/Pi-RADS/PIRADS-V2-1.pdf
16 Appayya MB, Adshead J, Ahmed HU. National implementation of multi-parametric magnetic resonance imaging for prostate cancer detection – recommendations from a UK consensus meeting. https://doi.org/10.1111/bju.14361.
17 Cui Y, Han S, Li C, et al. Performance and Reproducibility of a Day Optimizing Throughput (Dot) Workflow Engine in Automated Prostate MRI Positioning. Proceedings of the 28th Annual Meeting of the ISMRM, Abstract No. #4546.
18 Kordbacheh H, Seethamraju RT, Harisinghani MG, et al. Image quality and diagnostic accuracy of complex-averaged high b value images in diffusion-weighted MRI of prostate cancer. Abdominal Radiology. 2019 June;44(6):2244-2253.
19 Brizmohun AM, Adshead J, Ahmed HU, et al. National implementation of multi-parametric magnetic resonance imaging for prostate cancer detection – recommendations from a UK consensus meeting. BJU Int. 2018;122:13-25. https://doi.org/10.1111/bju.14361.
20 Rosenkrantz AB, Parikh N, Kierans AS, et al. Prostate Cancer Detection Using Computed Very High b-value Diffusion-weighted Imaging: How High Should We Go? Acad Radiol. 2016;23(6):704-11.
21 Kuhl CK, Bruhn R, Krämer N, et al. Abbreviated Biparametric Prostate MR Imaging in Men with Elevated Prostate-specific Antigen. Radiology. 2017;285(2):493-505.
22 Van der Leest M, Israël B, Cornel EB, et al. High Diagnostic Performance of Short Magnetic Resonance Imaging Protocols for Prostate Cancer Detection in Biopsy-naïve Men: The Next Step in Magnetic Resonance Imaging Accessibility. Eur Urol. 2019;76(5):574-581.



Contact

Wilhelm Horger
MR Application Development
Siemens Healthineers
wilhelm.horger@siemens-healthineers.com

A Fully Automated, End-to-End Prostate MRI Workflow Solution Incorporating Dot, Ultrashort Biparametric Imaging and Deep-Learning-based Detection, Classification, and Reporting

David J. Winkel, M.D.[1]; Robert Grimm, Ph.D.[2]; Thomas Benkert, Ph.D.[2]; Berthold Kiefer, Ph.D.[2]; Daniel T. Boll, M.D.[1]

[1]Department of Radiology, University Hospital Basel, Switzerland
[2]MR Applications Predevelopment, Siemens Healthineers, Erlangen, Germany

Introduction

For more than a decade, magnetic resonance imaging (MRI) has been established as a powerful tool for prostate cancer diagnosis. The PROMIS study has demonstrated that prostate MRI is a suitable triage tool for biopsy-naïve men, reducing the number of unnecessary biopsies by a quarter while improving the detection of clinically significant cancer [1]. The PRECISION study randomized patients to either systematic biopsies or MRI; with no biopsy if MRI was negative, and targeted biopsy if MRI was positive. Targeted biopsies guided by MRI detected significantly more clinically significant cancers while reducing the number of clinically insignificant cancers [2]. Because of these findings, MRI for prostate cancer diagnosis has been integrated into established guidelines [3].

Increasing demand for prostate MRI examinations can be expected, as the incidence of prostate cancer increases with age and life-expectancy in developed countries is rising. Furthermore, prostate MRI has been discussed in the literature as a screening tool, similar to breast cancer screening [4]. However, several limitations need to be addressed in order to prepare for this increasing prostate MRI workload. Variation in MRI data acquisitions could be reduced [5]. Another limitation is the relatively long acquisition time of multiparametric MRI examinations (mpMRI) employing T2-weighted (T2w), diffusion-weighted imaging (DWI) and dynamic-contrast enhanced (DCE) MRI. Several studies have shown that an approach without DCE MRI, called biparametric MRI (bpMRI), yields comparable results to mpMRI of the prostate [6]. Potentially even more important topic is the varying interpretation performance based on the expertise level. However, even among expert radiologists, agreement on prostate cancer classification based on established guidelines is imperfect [7, 8].

This all points to a clear need for

1. Efficient, reproducible, and robust data acquisition workflow
2. Optimized and fast sequence design
3. Automated detection, classification, and reporting workflows in prostate MRI examinations

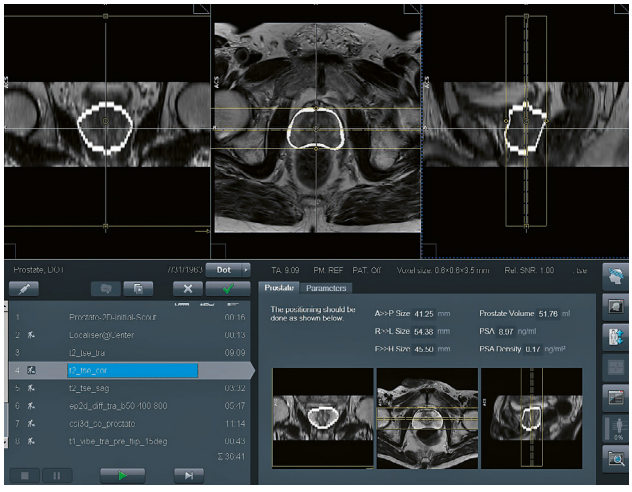

1 Image acquisition using the Prostate Dot Engine[1] including automated prostate contour detection, prostate centering, field of view adaption and three-dimensional correction of spatial axes.

This is a chain of independent, yet highly interlinked stages. Well-registered and reformatted images with reproducible high image quality are a key prerequisite for optimal and reproducible artificial intelligence-based analyses.

In this article, we outline an end-to-end solution that addresses all the limitations above, incorporating day optimizing throughput (Dot), ultrashort bpMRI and deep-learning-based lesion detection, classification and reporting. We present two example cases using the proposed workflow in order to illustrate its feasibility.

Material and methods

Prostate Dot Engine

The Prostate Dot Engine[1] is a prototype software tool designed to provide a fast, robust, and standardized image acquisition workflow. After acquiring the Turbo-Spin Echo (TSE) scout, the Prostate Dot automatically centers the prostate in the field of view, adapts the size of the field of view and performs a three-dimensional correction of spatial axes. Slices can be aligned either strictly orthogonal or automatically defined by the orientation of the urethra, i.e., perpendicular to the urethra for the axial planes. Furthermore, the prostate is segmented for standardized volume assessment. After coil placement, the Dot workflow does not require further adaptations by technicians, and it allows interruptions and corrections of the scan process at any time. A screenshot of the Prostate Dot Engine can be found in Figure 1.

[1]*Work in progress: the application is currently under development and is not for sale in the U.S. and in other countries. Its future availability cannot be ensured.*

Sequence specifications

The biparametric protocol consists of a T2-weighted turbo spin-echo (TSE) pulse sequence in axial, sagittal and coronal orientations and an improved single shot DWI EPI sequence (ZOOMit^{PRO}, Siemens Healthcare, Erlangen, Germany) with consecutive computation of the apparent diffusion coefficient. Unlike other DWI techniques, ZOOMit^{PRO} magnifies the prostate (in the phase-encoding direction) and is free of infolding artifacts. Either a smaller quadratic FOV or only a reduced FOV in the phase-encoding direction ('stripe') is excited (see Figure 2A). As there is no signal from the non-excited regions, only the small stripe needs to be encoded (see Figures 2B, C). That means the encoding time can be decreased while maintaining spatial resolution, or the spatial resolution can be increased, or a combination of the two. Furthermore, decreased encoding time reduces spatial distortion.

Prostate AI

The output of the Prostate Dot Engine goes into the AI prototype (Prostate AI[1], Siemens Healthcare, Erlangen, Germany) for fully automatic prostate lesion detection, classification and reporting.

As illustrated in Figure 3, Prostate AI contains two parts:

1. A preprocessing pipeline
2. A component for lesion detection and classification, based on deep learning

The preprocessing pipeline takes the acquired bpMRI sequences and generates the required well-formatted and transformed data volumes. From the DWI series, a logarithmic extrapolation method is adopted to compute a new DWI volume with *b*-value of 2000 s/mm^2. This step

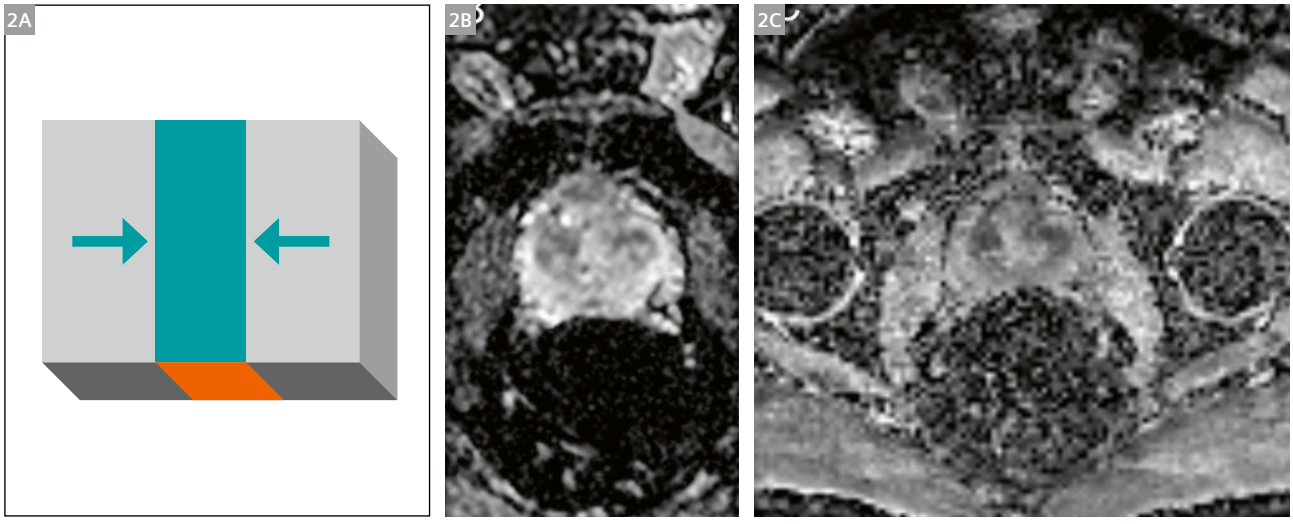

2 Single-shot DWI EPI sequence (ZOOMit^{PRO}) with image examples from one study object: **(2A)** reduced FOV in phase-encoding direction (blue stripe); **(2B)** resulting image in comparison to **(2C)** the conventional RESOLVE technique.

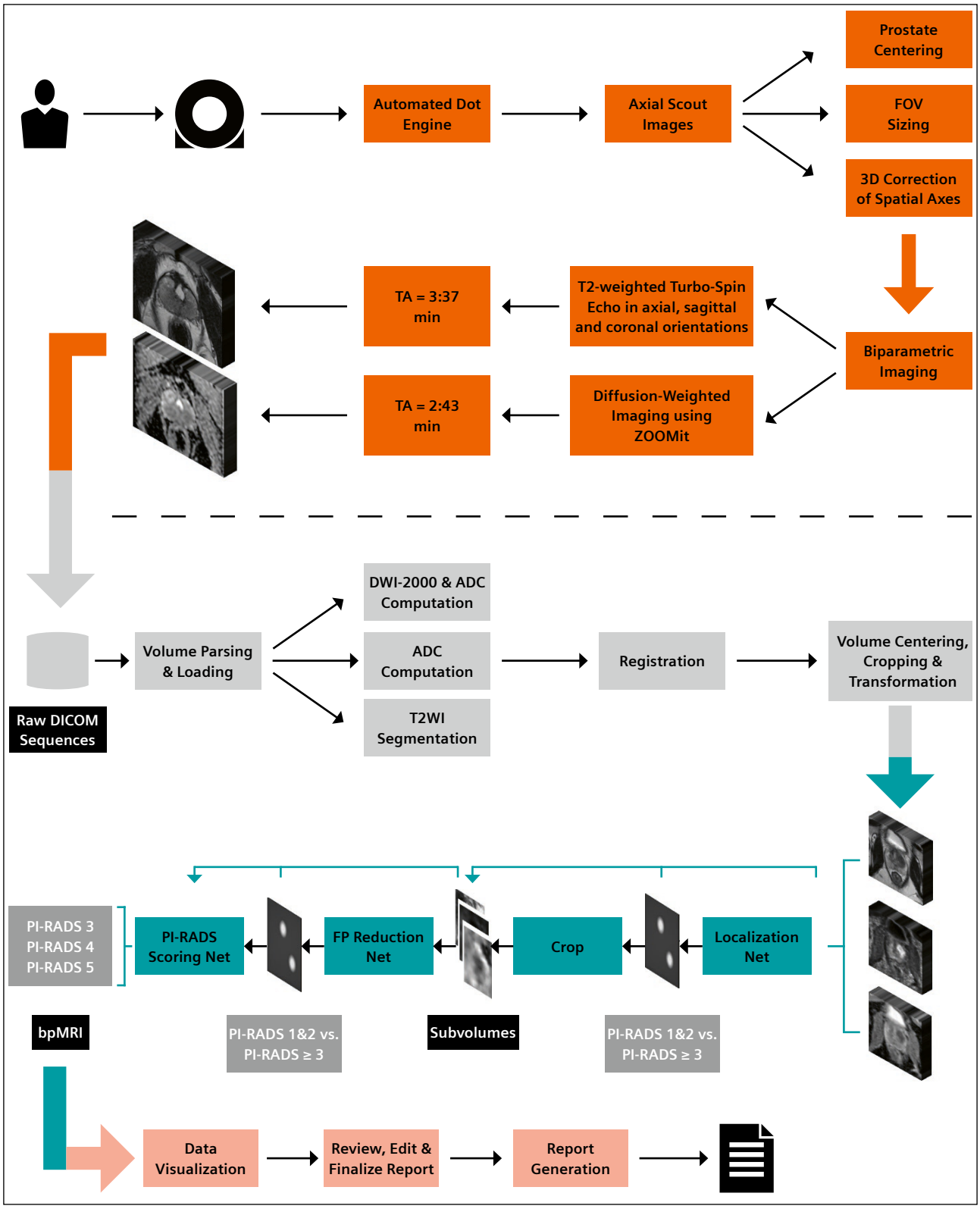

3 Image acquisition workflow using the automated Prostate Dot Engine and biparametric imaging (orange); deep learning architecture with preprocessing pipeline (gray); deep learning-based lesion detection and classification component (blue).

Dot = day optimizing throughput, FOV = field of view, 3D = three-dimensional, TA = time of acquisition, DICOM = Digital Imaging and Communications in Medicine, ADC = apparent diffusion coefficient, FP = false positive, PI-RADS = Prostate Imaging Reporting- and Data System

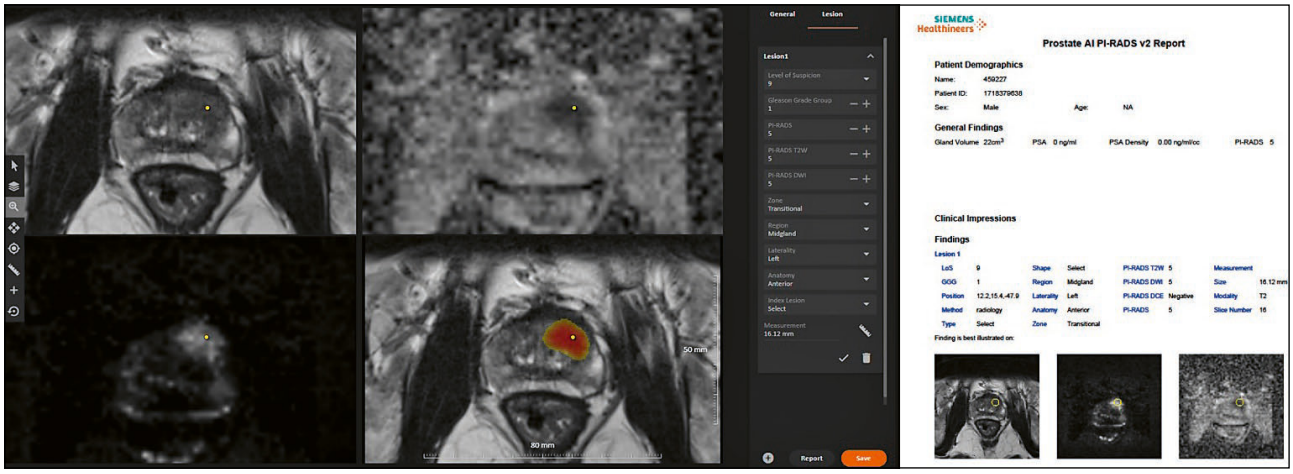

4 Data visualization platform with the T2w images, ADC map, and high *b*-value image as well as the T2w image overlaid with the AI-generated heatmap (in red and yellow). Prostate AI automatically detected the suspect lesion in the transition zone (TZ, yellow dot) and pre-populated all relevant information according to current PI-RADS guidelines. Next, a machine-readable report based on this information is generated.

can eliminate the *b*-value variances among the datasets and also improve lesion detection performance [10]. Also, apparent diffusion coefficient (ADC) maps are computed. Next, whole-organ gland segmentation is performed on the T2w volume using a learning-based method as presented in Yang et al. [11]. After segmentation, a rigid registration is conducted to align T2w and DWI images. The preprocessing pipeline can eliminate both geometric and intensity variances across sequences and patient studies.

Prostate AI then automatically detects clinically relevant lesions and classifies each detected lesion according to PI-RADS categories. This is achieved by a sequence of coupled deep neural networks that are trained separately. First, a fully convolutional localization net is able to generate a semantic lesion candidate heatmap (see Figures 5 and 6); then a sub-volume-based false positive reduction net further improves detection accuracy by removing the false positives; finally another sub-volume-based PI-RADS scoring net stages the level of malignancy for each detection according to PI-RADS categories.

In a last step, Prostate AI displays the detection and classification results on a dedicated platform. As the ability of the interpreting radiologist to accept or reject AI-based findings has been identified as a prerequisite for adoption of these techniques [12], these capabilities have been implemented. The user is then able to create a machine-readable report with all relevant information for the referring physician (see Figure 4). This report can be sent to the local RIS/PACS system.

Cases

Case 1

Figures 5A-D demonstrate a lesion in the right midgland PZpl/PZa of a 62-year-old man, with a maximum diameter of 30.2 mm and a mean ADC-value of 758 µm²/s. Prostate AI detected the lesion and assigned a PI-RADS 5 category. Biopsy results revealed a Gleason 4+3 = 7 pattern.

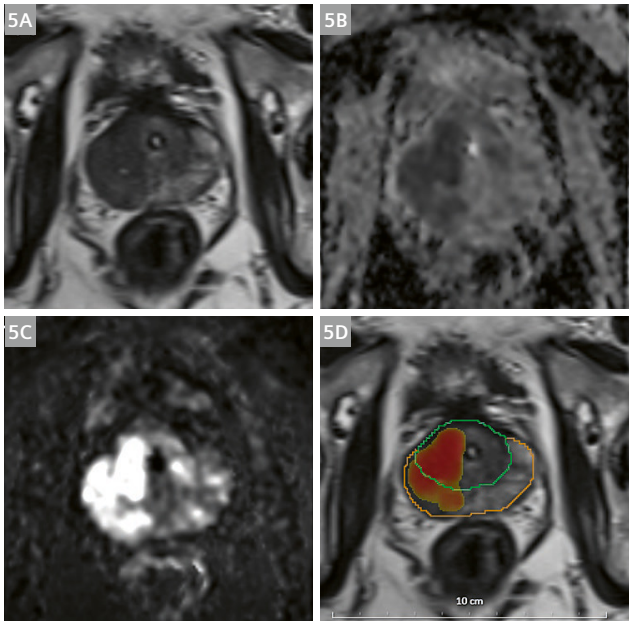

Case 2

Figures 6A-D demonstrate a lesion in the left apical PZpl of a 51-year-old man, with a maximum diameter of 10.2 mm and a mean ADC-value of 961 µm²/s. Prostate AI detected the lesion and assigned a PI-RADS 4 category. Biopsy results revealed a Gleason 3+3 = 6 pattern.

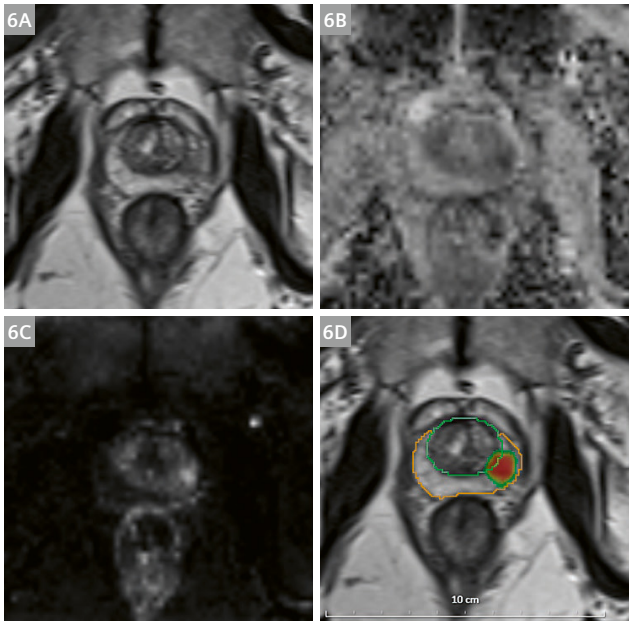

Conclusion

In this article, we outlined an end-to-end concept to allow a standardized workflow with a reproducible and fast data acquisition with optimized imaging sequences and an AI-empowered data analysis including automated detection, classification and reporting of suspicious lesions in biparametric prostate MRI examinations.

Reproducible and fast data acquisition concepts are not only contributing to a standardized reporting performed by human readers but would also help artificial intelligence-based solutions to reliably process input data. Preliminary results from a study conducted at the University of Innsbruck in Austria including 50 patients referred for a prostate MRI examination, compared the tilting angle of the auto-alignment of the Prostate Dot Engine against axes determined manually by an experienced radiologist, serving as the reference-standard. The investigators were able to show a mean ± SD deviation of the tilting angle of 5.5 ± 4.4 degrees (Ch. Kremser, W. Judmaier, Med. Uni Innsbruck, unpublished results). However, to date, there is no study investigating workflow differences, such as time-saving metrics, between Dot-guided and conventional, technician-guided workflows. Those studies are currently planned, and their results will contribute to reveal the value of Dot engines in clinical routine.

Concerning the use of abbreviated protocols consisting of T2-weighted and DWI only – so-called biparametric prostate MRI – several studies [6, 13, 14] have shown comparable results as obtained with conventional, mpMRI protocols including DCE-MRI. We added another component to our suggested workflow, that is performing DWI with the ZOOMit^{PRO}. As shown in Figure 2, ZOOMit^{PRO} uses a reduced FOV in the phase-encoding direction compared with either standard single shot DWI EPI or RESOLVE (REadout Segmentation Of Long Variable Echo trains). The resulting decreased acquisition time can be invested in a superior spatial resolution. Future studies are needed to systematically investigate differences between different types of DWI acquisition schemes compared to the ZOOMit^{PRO} technique.

The last component in our workflow is the use of AI-based lesion detection and classification. Schelb et al. [15] used the input from T2w sequences and DWI to train a deep learning algorithm (Unet) on the histopathological outcome, serving as ground truth. They were able to show that this algorithm achieved a similar performance to human readers using the PI-RADS assessment score. Cao et al. [16] used the input of mpMRI images to build a convolutional neural network trained on histopathological data and used this algorithm to detect suspicious lesions and to predict the Gleason score. The results were promising, with a high sensitivity for lesion detection – comparable to expert human readers – and a high classification performance with regards to clinically significant cancer. However, the usefulness of these algorithms needs to be proven in larger multi-reader, multi-case (MRMC) studies, systematically examining their influence on interpretation performance and speed, with and without those solutions.

We have identified a need to re-structure existing prostate MRI workflows, as patient or – in case of screening approaches – participant throughput is expected to increase. In our vision, current workflows need more reliable, reproducible and fast data acquisition steps. Furthermore, recent research has shown that deep learning algorithms can compete with human intelligence in prostate MRI reporting. We outlined a possible end-to-end solution and demonstrated its feasibility with two case examples. Future research will investigate what impact the individual components or the combination of those components will have on the future of prostate MRI.

References

1 Ahmed HU, El-Shater Bosaily A, Brown LC, et al. Diagnostic accuracy of multi-parametric MRI and TRUS biopsy in prostate cancer (PROMIS): a paired validating confirmatory study. Lancet. 2017;389:815–822. https://doi.org/10.1016/S0140-6736(16)32401-1

2 Kasivisvanathan V, Rannikko AS, Borghi M, et al. MRI-Targeted or Standard Biopsy for Prostate-Cancer Diagnosis. N Engl J Med. 2018;378:1767–1777. https://doi.org/10.1056/NEJMoa1801993

3 EAU Guidelines. Presented at the EAU Annual Congress Barcelona 2019. ISBN 978-94-92671-04-2.

4 Kim SJ, Vickers AJ, Hu JC. Challenges in Adopting Level 1 Evidence for Multiparametric Magnetic Resonance Imaging as a Biomarker for Prostate Cancer Screening. JAMA Oncol. 2018;4:1663–1664. https://doi.org/10.1001/jamaoncol.2018.4160

5 Padhani AR, Barentsz J, Villeirs G, et al. PI-RADS Steering Committee: The PI-RADS Multiparametric MRI and MRI-directed Biopsy Pathway. Radiology. 2019;292:464–474. https://doi.org/10.1148/radiol.2019182946

6 Weiss J, Martirosian P, Notohamiprodjo M, et al. Implementation of a 5-Minute Magnetic Resonance Imaging Screening Protocol for Prostate Cancer in Men with Elevated Prostate-Specific Antigen before Biopsy. Invest Radiol. 2018;53:186–190. https://doi.org/10.1097/RLI.0000000000000427

7 Weinreb JC, Barentsz JO, Choyke PL, et al. PI-RADS Prostate Imaging - Reporting and Data System: 2015, Version 2. Eur Urol. 2016;69:16–40. https://doi.org/10.1016/j.eururo.2015.08.052

8 Rosenkrantz AB, Ginocchio LA, Cornfeld D, et al. Interobserver Reproducibility of the PI-RADS Version 2 Lexicon: A Multicenter Study of Six Experienced Prostate Radiologists. Radiology. 2016;280:793–804. https://doi.org/10.1148/radiol.2016152542

9 Maas MC, Fütterer JJ, Scheenen TW. Quantitative evaluation of computed high b value diffusion-weighted magnetic resonance imaging of the prostate. Invest Radiol. 2013;48:779.

10 Rosenkrantz AB, Parikh N, Kierans AS, et al. Prostate Cancer Detection Using Computed Very High b-value Diffusion-weighted Imaging: How High Should We Go? Acad Radiol. 2016;23:704–711. https://doi.org/10.1016/J.ACRA.2016.02.003

11 Yang D, Xu D, Zhou SK, et al. Automatic Liver Segmentation Using an Adversarial Image-to-Image Network. In: Descoteaux M, Maier-Hein L, Franz A, et al (eds) Medical Image Computing and Computer Assisted Intervention – MICCAI 2017. Springer International Publishing, Cham. 2017; pp 507–515.

12 Padhani AR, Turkbey B. Detecting Prostate Cancer with Deep Learning for MRI: A Small Step Forward. Radiology. 2019;192012. https://doi.org/10.1148/radiol.2019192012

13 Kuhl CK, Bruhn R, Krämer N, et al. Abbreviated Biparametric Prostate MR Imaging in Men with Elevated Prostate-specific Antigen. Radiology. 2017;282:493–505. https://doi.org/10.1148/radiol.2017170129

14 Woo S, Suh CH, Kim SY, et al. Head-to-head comparison between biparametric and multiparametric MRI for the diagnosis of prostate cancer: A systematic review and meta-analysis. Am J Roentgenol. 2018;211:W226–W241. https://doi.org/10.2214/AJR.18.19880

15 Schelb P, Kohl S, Radtke JP, et al. Classification of Cancer at Prostate MRI: Deep Learning versus Clinical PI-RADS Assessment. Radiology. 2019;190938. https://doi.org/10.1148/radiol.2019190938

16 Cao R, Bajgiran AM, Mirak SA, et al. Joint Prostate Cancer Detection and Gleason Score Prediction in mp-MRI via FocalNet. IEEE Trans Med Imaging. 2019;38:2496–2506. https://doi.org/10.1109/TMI.2019.2901928



Contact

David J. Winkel, M.D.
Department of Radiology
University Hospital Basel
Spitalstrasse 21
4031 Basel
Switzerland
Tel.: +41 61 328 65 22
davidjean.winkel@usb.ch

An Attempt to Reconstruct the History of Gradient-System Technology at Siemens Healthineers

Franz Schmitt; Stefan Nowak; Eva Eberlein

Siemens Healthineers, Erlangen, Germany

Reprinted from MAGNETOM Flash (77) 2/2020

Introduction

The development of clinical MRI was a journey into engineering terra incognita. Although the basic components were known through building MRI prototypes in the early 1980s [1], driving this technology to perfection demanded innovations aplenty. Entirely new technological paths had to be navigated to perfect magnets, gradients, and RF excitation and reception.

This article explores how Siemens Healthineers learned to make good gradients. It charts the amazing technological advances from 1983, when Siemens Medizintechnik, as it was called then, began to develop their first MRI product, the MAGNETOM; until today, when Siemens Healthineers provide MAGNETOM Prisma, MAGNETOM Terra, and MAGNETOM Connectom[1] to the clinical and research community.

To get the story straight, we have revisited old memos and lab books, and consulted colleagues from the early days of MR at Siemens and also other companies. Technological progress comes through the ingenuity of many people, so we also tell the personal stories that reveal why one and not another path was taken.

[1] *MAGNETOM Connectom is ongoing research. All data shown are acquired using a non-commercial system under institutional review board permission. Siemens Healthcare GmbH does not intend to commercialize the system.*

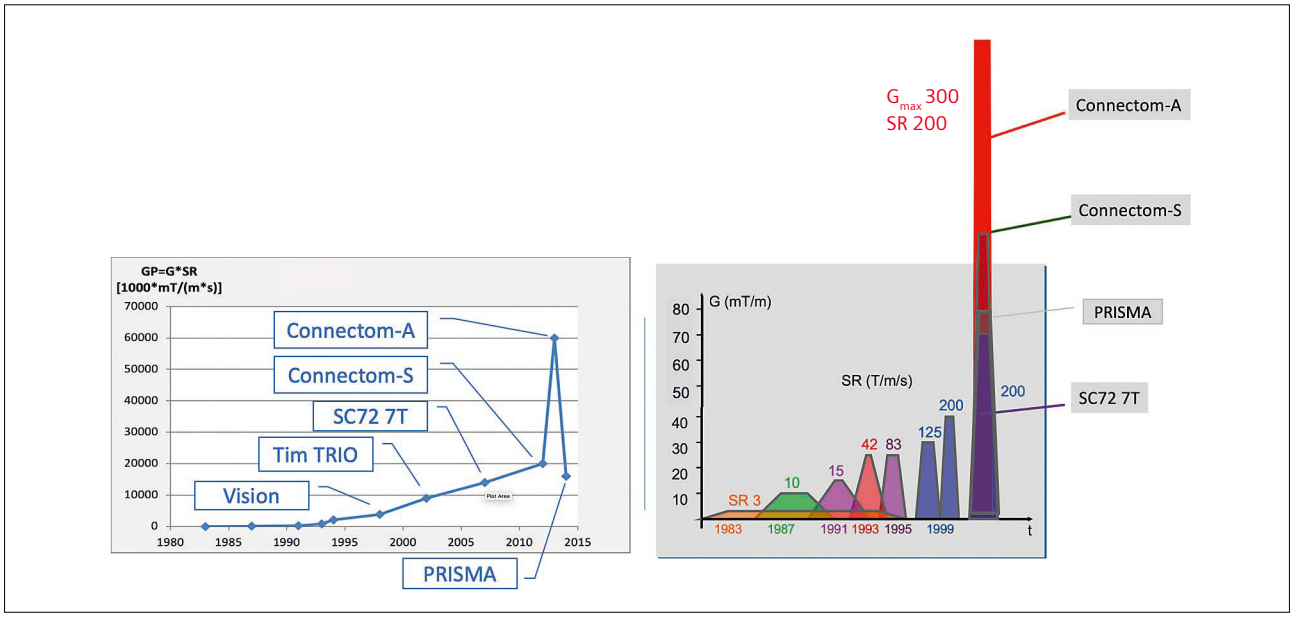

1 Evolution of gradient performance.

Gradient performance over the years

Since the introduction of MRI as a commercially available diagnostic tool in 1983, dramatic improvements have been achieved in all features defining image quality, such as resolution, signal-to-noise ratio (SNR), and speed. Initially, spin echo (SE) images with 128 x 128 pixels per slice were acquired in several minutes. Nowadays, the standard matrix size for musculoskeletal and neuro studies using TSE-based techniques is 512 x 512 with similar imaging times, but covering the entire volume of interest. Echo-planar imaging (EPI) [2] techniques has made it possible to acquire 128 x 128 images in less than 100 ms. Most recently, Simultaneous Multi-Slice (e.g., SMS-EPI for BOLD fMRI) allows the acquisition of an entire volume of 100 slices with resolution of $(1.2\ mm)^3$ at a repetition time (TR) of 1.3 seconds. That is CT-like speed [3, 4]. Here, high-speed gradients and novel RF excitation and reception techniques are combined, allowing resolution and throughput only dreamed of a few years ago.

At the beginning of clinical MRI, maximum achievable gradients G_{max} were typically in the range of 1 to 2 mT/m amplitude, with rise times of 1 to 2 ms. In terms of slew rate (SR), in units of T/m/s, that is on the order of SR 1. Over almost four decades, amplitudes and slew rates have increased by orders of magnitude. Present-day technology provides gradient pulses up to 80 mT/m for whole-body applications, with SR 200 T/m/s. This slew rate is the physiological limit for peripheral nerve stimulation (PNS) in whole-body applications, but not a technical limit. The slew rate is regulated by PNS thresholds [13]: When shortening a pulse sequence, the regulatory limits of PNS need to be observed. Higher SR is possible through higher voltages in principle, although it would present other technical challenges such as high voltage resilience of the entire gradient system. More on this later.

By reducing the linearity volume of a gradient coil, faster switching at higher amplitudes is possible. This has been introduced with the MAGNETOM Sonata [5] and with the SC72 gradient coil (70 mT/m at SR 200 T/m/s) in our 7T whole-body system [6]. This development has been pushed furthest for the Human Connectome project [7–9], with two gradient systems: the Connectom-S, a redesign of the SC72 for the 3T MAGNETOM Skyra magnet performing with 100 mT/m at SR 200 T/m/s; and the Connectom-A, also for the MAGNETOM Skyra magnet, which has a peak performance of 300 mT/m at SR 200 T/m/s [10]. Both systems sacrificed the patient bore, reducing it to 580 mm diameter.

So the performance of gradient systems has improved enormously. The product of maximum gradient strength times the slew rate, $GP = G_{max} * SR$, reflects the gradient performance GP [11]. The entire evolution of gradient performance is demonstrated in Figure 1.

Gradient and its leading role in fast MRI

Before we dive deeper into the technological intricacies of gradient systems, let's have a look what the major drivers of gradient performance were over the years.

First, the attainable spatial resolution in MRI (δx, the pixel size) is inversely proportional to the gradient-time integral

Equation 1

$$\delta x = \frac{2\pi}{\gamma \int G(t)dt}$$

integrated over the readout period T_{RO} (Fig. 2A), with γ representing the gyromagnetic ratio. Please note that integration is over the entire RO gradient pulse including the up and down ramp, and simultaneous acquisition of the MR signal: an extreme case, usually used for EPI, to show the need for higher and faster gradients. To shorten T_{RO} for a particular MR pulse sequence type without sacrificing resolution, the gradient amplitude G_{RO} must increase, and rise time T_{Rise} decrease.

Note the gyromagnetic ratio γ in the denominator of Equation 1. The vast majority of MRI is performed with protons, but with emerging ultra-high fields, such as 7T, other nuclei such as Sodium (^{23}Na) are becoming interesting [12]. As these nuclei have lower gyromagnetic ratio, gradient amplitude must be increased to maintain resolution.

When shortening gradient pulses, the limit to gradient amplitude is not set by technical feasibility, but mainly by the SNR, as extremely high bandwidth while acquiring the MR signal results in poor SNR:

Equation 2

$$SNR \sim \sqrt{\frac{1}{BW}}$$

A fast GRE example is shown in the lowest part of Figure 2B, illustrating the benefits of faster and stronger gradients to achieve shorter echo times (TE).

The development of echo-planar imaging (EPI) required extreme gradient performance (Fig. 2C). While normal SE and GRE imaging techniques could easily live with 10 T/m at SR 50 T/m/s or even below, EPI for neuro applications requires 30 mT/m and SR of 200 T/m/s in order to gather the T2*-weighted MR signal with a decent SNR, and minimize susceptibility artifacts.

Second, gradient power far beyond even EPI requirements became desirable when diffusion-weighted MR Imaging (DWI) was developed. For DWI, usually in combination with an EPI readout, strong and short gradient pulses, as described with the Stejskal-Tanner pulse scheme [14], yield high b-values in the shortest possible time to optimize SNR (Fig. 3). Until 2012,

the MR community used 45 mT/m at SR 200 T/m/s. Then the introduction of the Connectom gradients, which provided up to 300 mT/m at SR 200 T/m/s for experimental purposes, spurred the major vendors to improve their clinical scanners to 80 mT/m peak gradient strength, reflecting the needs of high-resolution MR diffusion imaging techniques such as diffusion spectral imaging (DSI) [15]. SNR in diffusion-weighted imaging can thereby improve considerably (Figure 3 left). The MGH group headed by Lawrence Wald and Van Wedeen showed a 3-fold SNR boost compared with G_{max} = 40 mT/m, which is excellent for an SNR-weak technique such as diffusion-weighted MRI (see Figure 3 right).

Third, moving from unshielded to shielded gradients, the number of wires almost doubles and the inductance slightly increases, resulting in a lower sensitivity (G/I_G) with G the gradient strength reached with a certain current I_G. Thus higher voltage and currents are needed to drive a gradient coil for given G_{max} and SR_{max}. That explains in part the historic performance increase in the first decade of clinical MRI, from 120 V_{peak} / 150 A_{peak} for the MAGNETOM (i.e. the first-generation Siemens MR system) and 250 V / 160 A_{peak} for the MAGNETOM SP (both with unshielded gradient coils) to the MAGNETOM Impact (shielded) which needed 300 V / 250 A_{peak} power supplies.

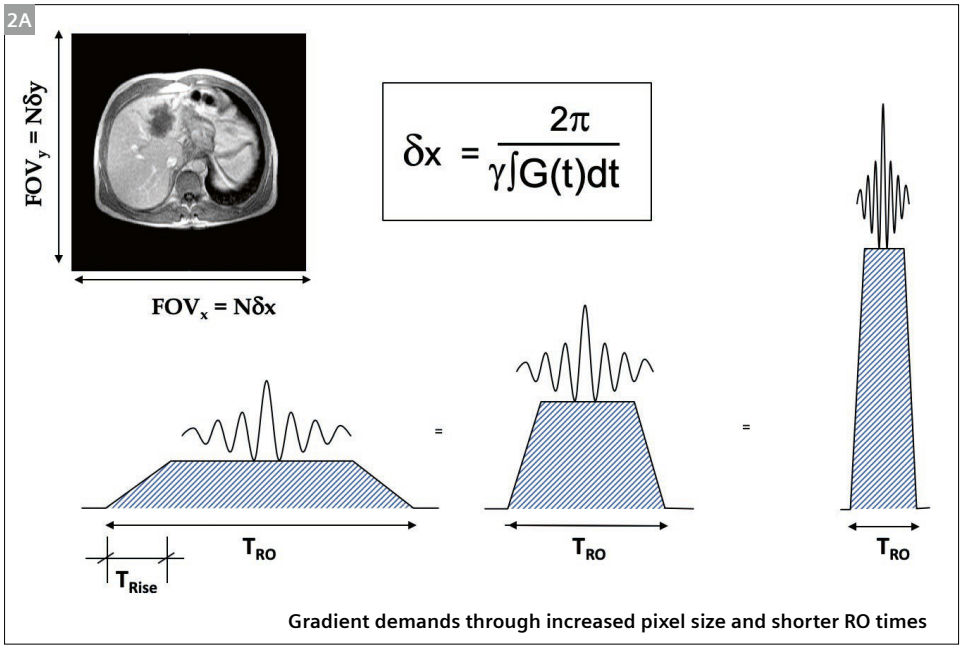

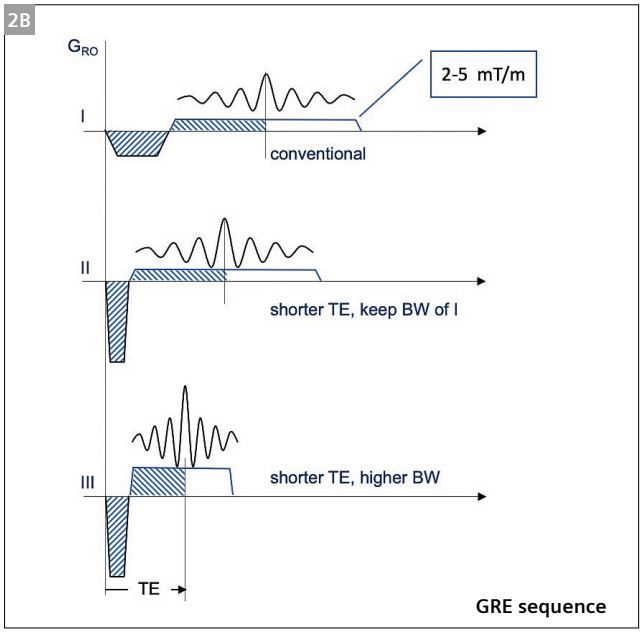

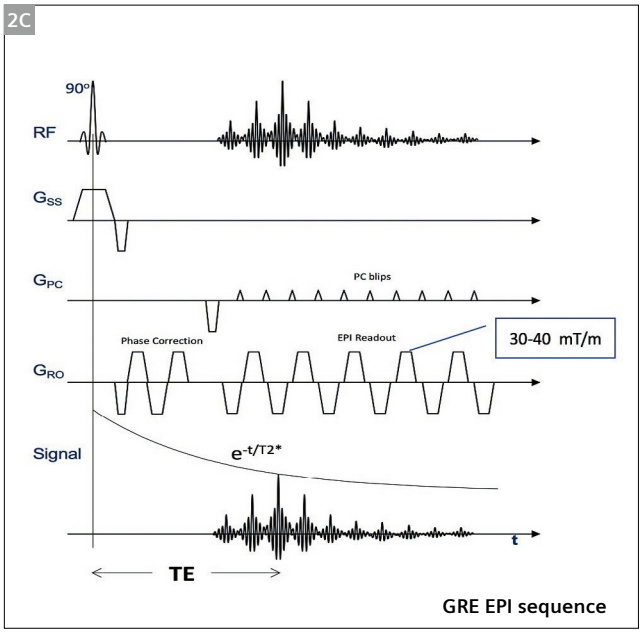

2 **(2A)** Image resolution and its correlation to the gradient-time integral. Gradient amplitude G_{RO} and slew rate must increase to maintain resolution while shortening T_{RO}. Lower row: increasing amplitude and slew rate is the key to shorter TE. **(2B)** Shortening a readout pulse with pre-dephaser to increase speed, with and without changing signal BW. **(2C)** Typical EPI pulse sequence timing.

Forth, the trend to shorter and wider MR systems also has to be noted here. The power required for a given gradient performance is approximately proportional to r^5 [16] where r represents the radius of the gradient coil. This is reflected in the higher currents provided by gradient power amplifiers in the last 15 years, since the MAGNETOM Espree (70 cm bore diameter with a length of 1.2 m) was introduced. The first Siemens 70 cm wide-bore 3T system, the MAGNETOM Verio, provided 2250 V / 900 A_{peak}, while the very successful MAGNETOM Trio with its 60 cm bore needed only 2000 V / 650 A_{peak}. Now, with the XT gradients of the MAGNETOM Vida (70 cm bore size), 2250 V / 1200 A are available to match modern MR imaging requirements. One thing is for sure: the electricity bill is increasing.

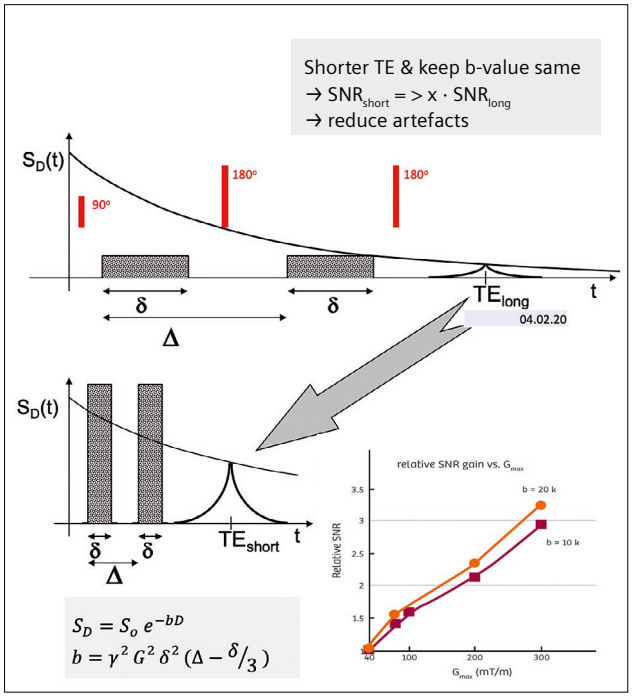

3 Diffusion imaging and its dependence on gradient performance.

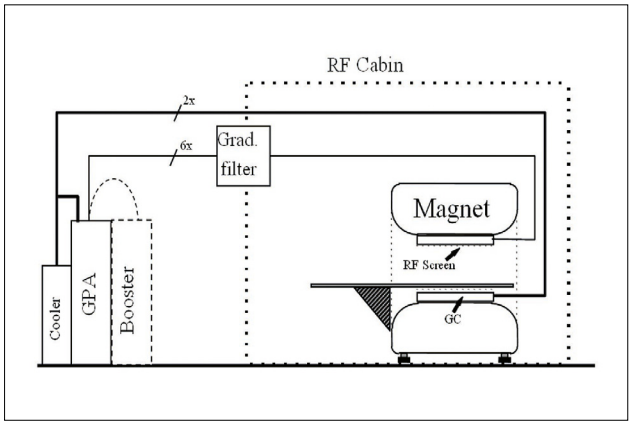

4 The MR gradient system.

The gradient system

The gradient system (Fig. 4) is composed of components generating the gradient field, including gradient coil and its driving power devices (gradient amplifier; and booster if available, as used in the early days of EPI); as well as connecting elements such as cables, gradient wall filters and cooling. The whole-body RF coil must also be considered, as eddy currents induced within its conductive elements may affect the quality of the gradient field, resulting in image quality degradation. Typically, gradient coils also house the shim system, which includes the space to place shim iron and a set of shim coils.

Let's now have a closer look at the two major components, the gradient power amplifier (GPA), sometimes also called gradient power supply (GPS), and the gradient coil (GC).

Gradient power amplifiers

From the very beginning of MR product development, Siemens kept the engineering and manufacturing of gradient amplifiers inside the company. The authors think that this was essential for the high performance of our gradient systems, as the integration of amplifier and coils requires close collaboration beyond just bit specs.

The purpose of a GPA is to supply the required voltage, V, and current, I, at a reasonable duty cycle, DC, (on/off ratio) to the gradient coil of inductance L and resistance R, according to

Equation 3

$$V(t) = R \cdot I(t) - L \frac{dI(t)}{dt}$$

For the very first MRI scanner generation, Siemens used linear high-precision music amplifiers. Their duty cycles are limited because the transistors are basically always on, and therefore experience excessive resistive losses.

Very early on, the Siemens Gradient Amplifier lab had focused on pulse-width modulated (PWM) amplifiers, and the first switch-mode GPA. The main advantage of a PWM amplifier is its high duty cycle (compared with linear amplifiers) as the transistors are being switched on and off only when needed, thereby minimizing resistive losses. It is quite impressive how PWM amplifiers perform compared to linear amplifiers. The latest Siemens Vida GPA performing at peak 2250 V and 1200 A built as a linear amplifier would have to face a total power dissipation of 3 x 2.7 MW = 8.1 MW, while realized as a PWM amplifier a transformer of 100 kVA (representing the total power dissipation for clinical and research scanning) is only required!

That is the reason why PWM amplifiers quickly became the standard for MRI gradient drivers, although they came with challenges due to switching noise and ripple, which

can reach up to the MR frequency and degrade MR image quality. More on this topic later.

The basic idea behind PWM amplifiers is that short voltage packages are switched to the gradient coil with frequencies up to 200 kHz (the switching frequency evolution of our GPAs is shown in Table 1). The voltage required to drive a certain slew rate, according to Equation 3, is supplied as described by the integral in Figure 5, as the average over many switching cycles with various on/off times. The semiconductors (switches) and the gradient inductance are configured in an H-bridge (Fig. 6). Each transistor T has an associated freewheel diode D [17]. Transistor T1 and T4 have D2 and D3 functioning as freewheel diodes, respectively; while T2 and T3 have D1 and D4.

With every new MR system platform, the latest reliable semiconductor technology was always used to build the best performing GPAs (Fig. 7).

The first generation, the Siemens MAGNETOM (internally called GBS I) with its linear amplifier, used 240 transistors in parallel in TO3 housing. The deionized water for cooling was at transistor potential. The performance was very meager, with peak values of 120 V and 150 A at a DC current of 30 A, meaning a duty cycle of 20%. A three-axis GPA required three full-sized cabinets (60 x 60 x 200 cm), one per gradient direction plus one for cooling (see Fig. 22B).

In 1987, this GPA was replaced with a PWM amplifier for the new MAGNETOM SP (GBS II) using stacked disk transistors which provided improved performance of 250 V and 160 A_{peak}, at a DC current of 80 A. The deionized water for cooling was still at transistor potential. All three gradient axes were now packaged into only one cabinet, a significant step forward in performance, space requirement, and costs. The drawback there was that the driver

Siemens MR system	Transistor switching frequency	Output ripple frequency
MAGNETOM (GBS II)	12.5 kHz	25 kHz
MAGNETOM Impact	25 kHz	50 kHz
MAGNETOM Vision	25 kHz	50 kHz
MAGNETOM Harmony & Symphony	50 kHz	100 kHz
MAGNETOMs with Cascade GPAs	20 kHz	200 kHz

Table 1: Switching frequency and residual output ripple frequency of Siemens gradient amplifiers.

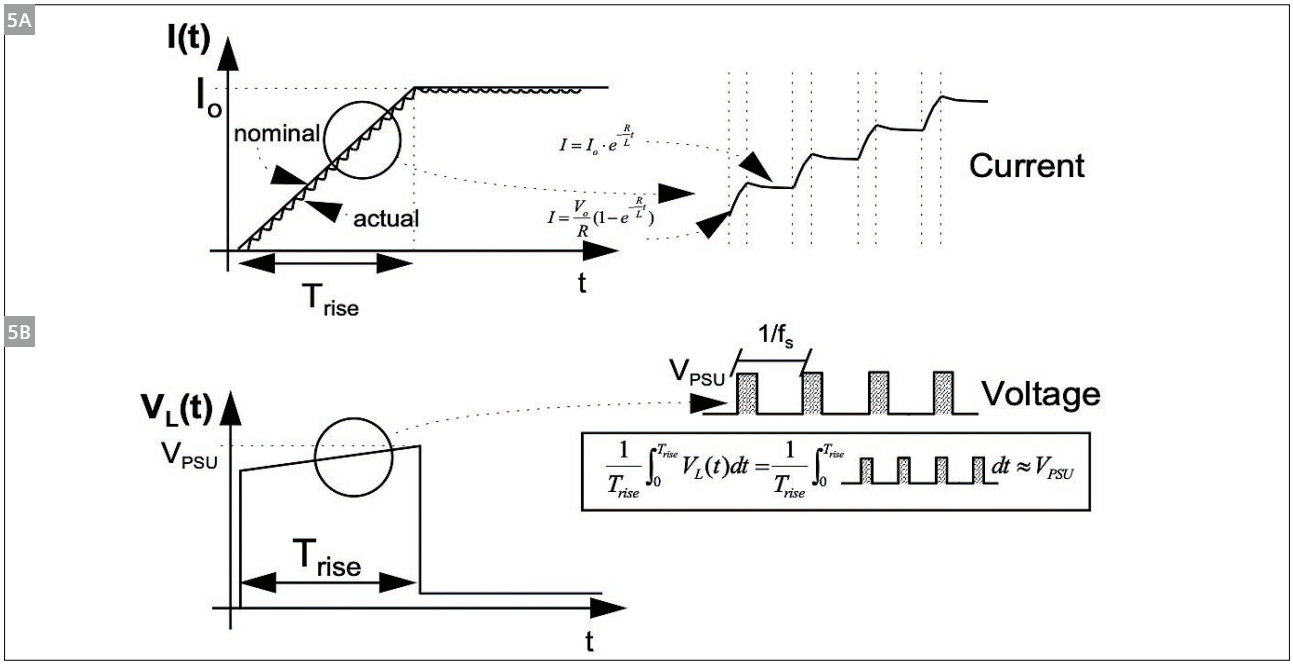

5 Principle of pulse-width modulated (PWM) amplifiers. **(5A)** Gradient current corresponding to a linear ramp (magnified version upper right). In reality these rise and falls are much smoother, and ripples cannot be seen in the current. **(5B)** Voltage required to perform the linear ramp, and integral conditions for the PWM voltage packages.

circuitry alone needed 200 W, due to the current-driven bipolar transistors. Today's MOSFETs and IGBTs are voltage driven, and need much less power.

A real leap in performance was made in 1991 with the introduction of MOSFETs (specifically BUZ325 transistors) for the MAGNETOM Impact [18]. With the circular design of the power stage, synchronous control was possible: Each semiconductor had the same driver signal transmission time and thermal conditions. Even this MOSFET was not perfect, as its intrinsic diodes had to be deactivated through tricky electric circuitry and external freewheel diodes. The digital gradient pulse form was transmitted via optical fibers, a first for Siemens and standard since then[2]. The power stages were air cooled but provided 300 V and 300 A_{peak}, resulting in a gradient strength of 10 mT/m for the first actively shielded gradient coil used in Siemens MRI systems (further information in the section on Gradient Coils). The Impact GPA was designed very conservatively with its circular arrangement. There was no prior knowledge on how to switch MOSFETs in parallel, as we used them as soon as they were available. Later, the peak amplitude was increased to 20 mT/m simply by changing some resistors in the control electronics, an easy upgrade for the installed machines. This caused some stir through the ranks at Siemens MR, as it seemed to be classical German over-engineering. Since then, every new system GPA had margins just big enough to handle local variations in electric power and slight increases in MR application demands, but not a 50% performance increase as happened with the MAGNETOM Impact.

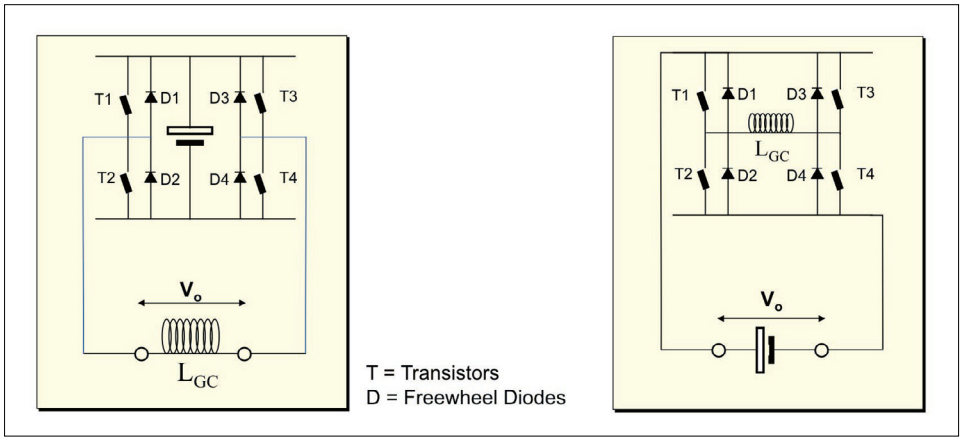

6 H-bridge configuration for PWM amplifiers. Both circuitry schemes are equivalent, but are shown because both are used in this paper.

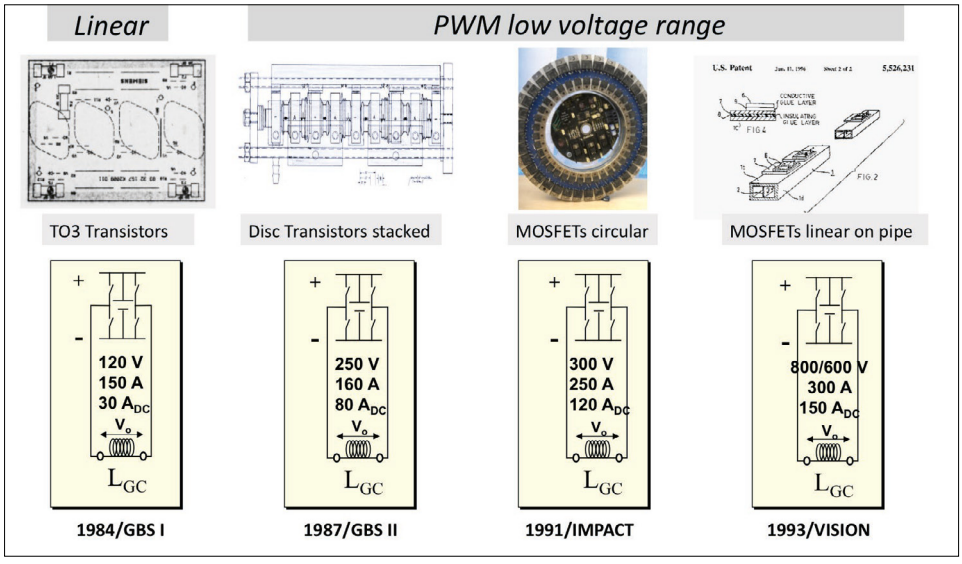

7 Single H-bridge PWM evolution at Siemens.

[2]*At about the same time Siemens started using direct current current transducers (DCCT) for measuring and controlling the output currents of the GPA. Günther Theil and Gunther Petzold convinced the Danish company Danfysik to integrate all necessary electronic components into one board with the current conductor to be probed running through the middle. Overall the precision for measuring the applied current in a gradient coil improved from 1% (as it is the case for classical music amplifiers) to ppm precision, which is essential for precise gradient pulses required for MRI.*

The next generation MRI was the MAGNETOM Vision in 1993. This also used MOSFETs, but as the ground plate was isolated from the cooling plate, it was water cooled again. Learning from the circular Impact design, we now used a rectangular pipe about 70 cm long. The cooling water was forced through that pipe. Each pipe had 36 transistors and 36 free-wheel diodes glued on and were all switched in parallel to achieve the peak current of 300 A. One such pipe resembled a half H-bridge. With its 600 V (originally 800 V, but more on this later) to drive the actively shielded gradient coil AS25, it reached 25 mT/m at SR 42 T/m/s. That design also had its challenges, and stabilizing it was quite a technological roller coaster. Nonetheless, the MAGNETOM Vision provided unique performance in the MR market. The peak amplitudes of 25 mT/m prepared the road towards EPI, but didn't reach the SR that would be required, yet.

Reaching the SR needed for EPI was an adventure that started in the late eighties at the Siemens Corporate research laboratory in Erlangen. When calculating the required gradient strength and switching speed, we concluded that at 2 Tesla, due to the short T2* of brain tissue, the total readout time for 128 x 128 EPI image should be no longer than 64 ms [19]. That required about 37 mT/m with a pure sinusoidal gradient pulse train to achieve a pixel size of about 2 mm. Sine gradient pulses were used as they could easily be achieved in a serial resonance circuit (Fig. 8). The capacitance C was tuned to match the inductance L of the gradient coil to reach a frequency of 1 kHz, according to

Equation 4

$$f = \frac{1}{2\pi} \cdot \frac{1}{\sqrt{LC}}$$

The capacitor was charged and discharged by cycling up and down, respectively (Fig. 8A). This is what we called "poor man's EPI", as it fixed the fast EPI RO to the X-axis. That up and down cycling caused parasitic times, which were avoided with the design shown in Figure 8B. Bipolar thyristor switches were switched in series and parallel to the capacitor, allowing to move the charge and discharge cycles outside the MR-relevant pulse sequence. By-passing the capacitor, any arbitrary gradient pulse-shape could be applied. Thyristors were precise enough to drive the rather slow 1 kHz RO pulses.

The next step was to move on to IGBT transistors [20] which in the meantime had become very powerful and far superior to thyristors. An H-bridge design was employed with the capacitor as dynamic voltage supply inside the bridge as shown in Fig. 8C. Figure 8E provides a look into the EPI booster box with its roll type capacitors. Karl-Heinz Ideler designed and build the first 3-axis EPI booster prototype [21] which was eventually installed at Beth Israel Hospital in Boston, MA, USA in 1992. Robert Edelman [22], Steve Warach, Paul Finn, Piotr Wielopolski [23] and others achieved landmark results beyond just using it for EPI-based imaging such as EPI-STAR [24] and diffusion imaging for stroke [25].

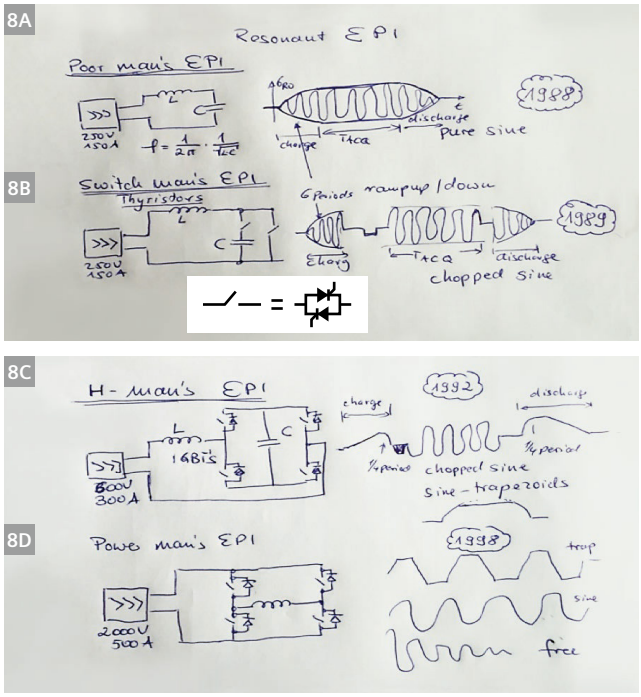

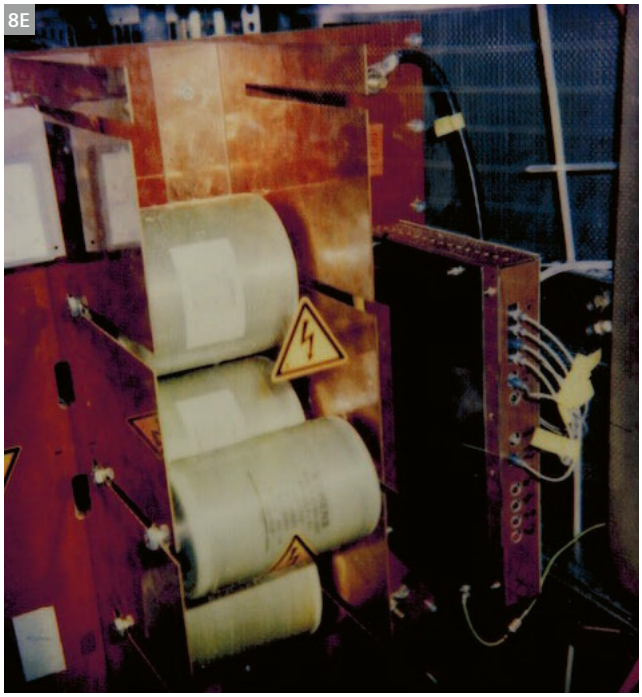

8 Left: The technological path of EPI at Siemens, from poor man's EPI to state-of-the-art. Right: A view into the booster box showing the capacitors for the resonance circuit.

Another group, the startup company Advanced NMR Systems was working independently on the challenge of EPI, under the direction of Richard Rzedzian and Ian Pykett, both trainees of Sir Peter Mansfield. While at first, ANMR intended to build their own imaging system, they instead contracted with General Electric to provide EPI capabilities as a retrofit to the Signa platform. In fact, their electronic solution to the problem of fast gradient switching was similar to (ours at) Siemens, using a series resonant circuit under tight control by IGBT transistors. ANMR chose to operate at a higher frequency of 1.4 kHz, thereby requiring proportionately higher peak gradient amplitudes. On the ANMR system, only the X and Y gradients could be used in echo planar mode. While this still allowed echo-planar imaging in all planes, it did not have the flexibility to switch phase and readout axes arbitrarily.

In its early phases ANMR partnered closely with the Massachusetts General Hospital NMR Center, collaborating with the applications team at ANMR, with the focus on diffusion and perfusion imaging [27]. The first ANMR "Instascan" product system was placed at the MGH-NMR center, where the first EPI based functional MRI, fMRI, experiments were performed. Jack Belleveau [28] and Ken Kwong [29] performed their seminal human BOLD experiments in 1991 with that EPI scanner.

When ANMR folded, its technology became the property of GE Medical Systems, who instead developed their own EPI booster technology [31] using inductive, as opposed to capacitive energy storage.

A similar resonant EPI booster was explored in Nottingham [30] at Sir Peter Mansfield's Lab, employing multiple serial resonance circuits to mimic a Fourier coefficient series.

Our resonant booster technology was eventually used for the MAGNETOM Vision, tuned to 833 Hz EPI (Echo Spacing = 600 µs), which brought EPI into the realm of clinical MR imaging. The 3-axis booster was housed in an extra cabinet, so all the gradient amplifier electronics were held in two cabinets (Fig. 4) and had no restrictions in use for conventional clinical MRI. Only the EPI application was restricted to sinusoidal ramps.

The MAGNETOM Vision system allowed to explore clinical stroke diagnostics using EPI diffusion imaging, and was also used in the now starting wave of fMRI research. Things moved on, however, with the MAGNETOM Harmony and MAGNETOM Symphony systems. More or less from scratch, we were able to develop a platform of components that could be integrated into different scanner types and field strengths.

For advancing GPA technology, we understood that performance needed to improve with output voltage and current, but the cost figure also needed to be improved.

A modular system was developed that allowed voltage stacking. The basic building block provided 400 V at 300 A_{peak}, so putting them in series provided 800 V, which doubled the SR. All 3-axis, including the 800 V upgrade, were packaged into one cabinet (Fig. 9, left). The base power module was still the pipe design we had used for the MAGNETOM Vision system.

As long as the MAGNETOM Vision existed as our EPI scanner, there was no need to increase the output voltage of this modular system to suffice for EPI. Yet sooner or later that challenge had to be tackled as by the end of the 90s MAGNETOM Vision was getting old and a new EPI capable MRI scanner needed to be developed. We had to face the challenge of how to continue: either boost the many-

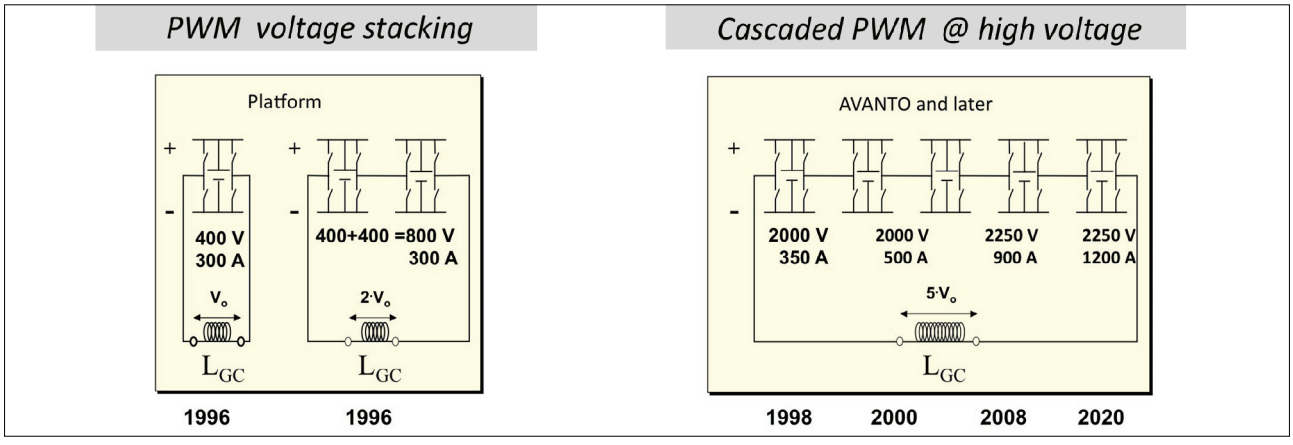

9 Voltage-stacked and cascaded PWM evolution at Siemens.

MOSFET technology that started with the Vision system (but without a booster), or find new more compact semiconductors such as IGBTs [32].

Stefan Nowak (one of the authors) spent 3 years at Siemens Semiconductors and saw the new IGBT module evolving. When returning to the MR R&D division in 1996, he focused on that technology. Two of us, Stefan Nowak and Franz Schmitt, still recall vividly the decisive experiment: the old but still very powerful many-MOSFET vs. the new IGBT modules. The later was humming away at significantly higher DC currents while the old overheated and went bust. A new era in GPA power electronics had come. The top right of Figure 9 shows the power electronics of half of an H-bridge of that new GPA.

With these platform GPAs, we could double the output voltage by adding another power stage (putting them in series; Fig. 9, left), while the switching frequency overall did not change. However, putting 5 power stages in series, as planned for the new GPA to reach 2000 V, would not be enough for high-performance imaging, and would have created challenges with RF spikes. Cascading [33], as we called it, helped to increase the switching frequency. The trick is that each H-bridge is time shifted by $1/5*1/f_s$, where f_s is the switching frequency of a single H-bridge. This gave five times the switching frequency of a single power stage at the output terminals. That allowed us to build very effective filters, as the inductances for such filter circuits decrease with increasing switching frequency, which reduced the size and resistive losses significantly. The new IGBT could handle much higher currents than MOSFETs. The series of cascade GPAs we have built over the years started at 350 A (throttled from 500 A) and has reached 1200 A, while the voltage has also increased to 5 x 450 V = 2250 V.

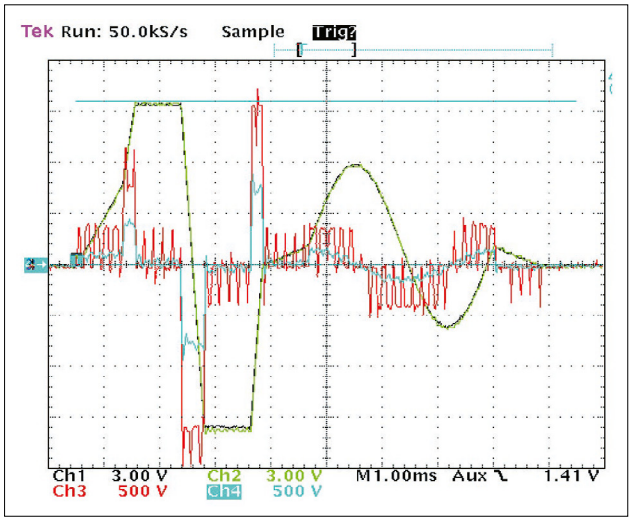

10 Oscilloscope trace: mixed trapezoidal and sinusoidal gradient pulse (green), unfiltered GPA output voltage (red), filtered output voltage (blue).

Figure 10 shows an oscilloscope trace, displaying the current and the unfiltered output voltage. The modulation of these H-bridges is cascaded until they reach the maximum voltage of 2000 V, i.e. when all stages (each supplying 400 V) are involved. Due to cascading switching frequency of 200 kHz at the output terminals is resulting.

It is remarkable to note that between 1983 and today the total power increase of several magnitudes was realized in one single cabinet.

Gradient coils

Gradient coil design also has changed significantly over the last decades. At the beginning, in MRI only Golay coils [34] were used, consisting of a continuous assembly of circular arc and straight-line conductors. However, they lacked good field linearity and efficiency. Further design steps were governed by a balance of computability and manufacturability, spiced with some imagination.

The next coil design employed polygons wrapped on a cylinder, connecting straight and curved conductors piece by piece (Fig. 11, bottom left). That offered more mechanical degrees of freedom to eliminate confounding higher orders in the field series.

At Siemens, these designs were first executed by Georg Frese, based on methods developed at the Erlangen Corporate Research lab (known in German as the "Forschungslabor") under Horst Siebold, Peter Henninger and Laxmikant Urankar in the "Feldkonfigurationen" team.

They had developed a mathematical library based on the Biot-Savart law, internally called the Urankar Routines. These routines provide the magnetic flux at any location in space generated by a piece of straight or arc segment wire carrying a unit current. The other tool developed here was MFB3D, used to evaluate a complete gradient coil design, calculating the magnetic flux B(r) inside the FOV. On top of these, the program called GOPT optimized the coil geometry automatically until specific goals such as field quality and field energy were achieved, under technical restrictions such as maximum coil length and diameter [35]. The z-component is of particular interest for MRI and is optimized to achieve the desired linearity. The transverse x and y components of the gradient magnetic flux, called Maxwell terms, unavoidable in nature are useless for MRI purposes, and are generally considered troublemakers as they contribute to eddy currents, PNS, can create imaging artifacts [37] and therefore also need to be considered when designing a gradient coil. In the early 80s, remote mainframe computers used for design calculation and optimization had a performance similar to today's smart watches, so you waited until the next morning for the result of a run – or for a short output saying "compiler error" because you had mistyped an O for a 0. For details on the mathematics see [36].

Unshielded designs were common in the early product lines. Siemens used them for the first two generations of the MAGNETOM systems. Internally these were called GBS I and GBS II, where GBS stands for Grund-Bau-Stein, loosely translating to basic building block, a modular concept that was seriously taken up later with the platform systems MAGNETOM Harmony and MAGNETOM Symphony. Commonality of components was essential to decrease the cost figure of an MRI scanner, so the same components could be used for different MAGNETOM systems and field strengths.

With the development of MAGNETOM Impact, actively shielded (AS) gradient coils were introduced at Siemens. This was driven by the 100% eddy-current overshoot needed for unshielded gradient coils, and by the growing pains of dealing with "incurable" higher-order eddy currents, generated by the outer fringe field of a gradient coil in the conductive environment, most prominently the cooling shields of the magnet and the cryostat wall. On the other hand, eddy currents in the RF screen could be cured by means of slotting it, as was explored during the development of EPI.

The idea of actively shielded gradient coils was invented around 1985 at the University Nottingham [38], the Massachusetts Institute of Technology [39] and General Electric [40] more or less simultaneously. Each axis of an actively shielded gradient coil is modelled as a primary (inner) and a secondary (outer) mesh layer (Fig. 12, right). Individual loop currents are optimized so that the required field quality, a linear gradient field, is achieved inside the FOV, while the magnetic flux outside the gradient coil at the location of the cryostat (for cylindrical superconducting magnets) is minimized (see Fig. 12) at the lowest possible inductance L. That prevents or at least minimizes the generation of eddy currents inside the cooling shields and cryostat,which is essential for good image quality in fast MRI.

The MAGNETOM Impact gradient coil, although shielded, was still based on the polygon train design. Primary and secondary coils were separated by blocks of wood and plastic formers and bandaged together (Fig. 13, left) into one unit. The space between primary and secondary coil was air filled. The coil could only be forced-air cooled. Water cooling was not yet necessary due to the low G_{max} and moderate duty cycle of the pulse sequences in these early days.

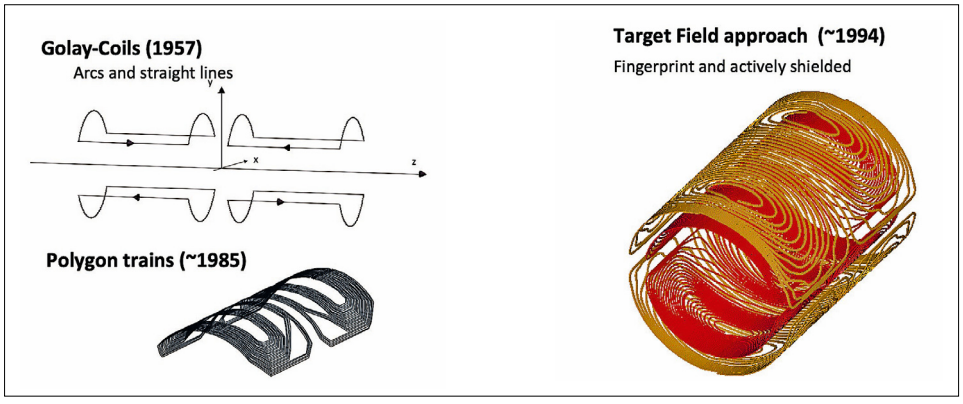

11 Winding design of a transverse gradient coil (Y). Upper left: Golay coil. Lower left: polygon design. Right: fingerprint design of an actively shielded y gradient.

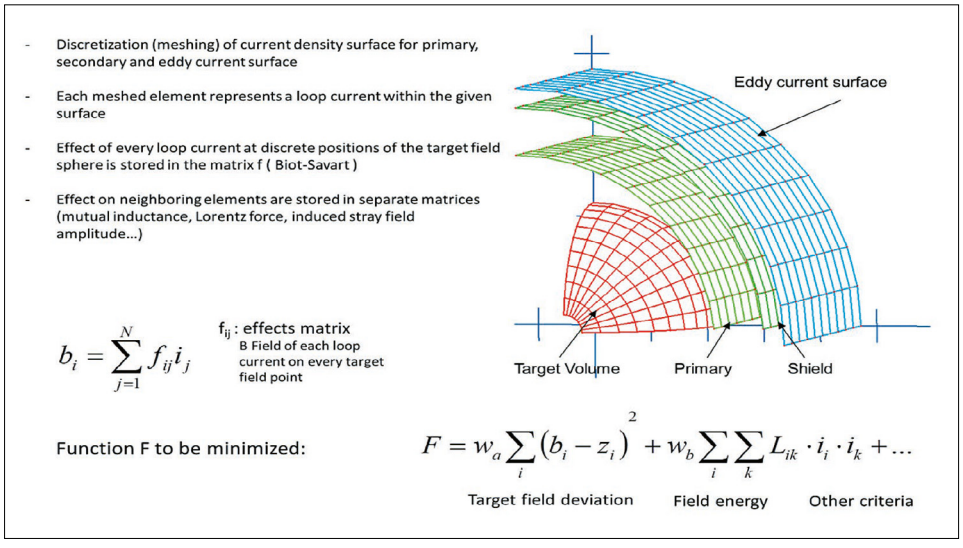

12 The current distribution in the primary and screen surface is calculated such that the required field quality is reached in the linearity volume, and the flux is minimized at the eddy current surface. Some numerical design principles and equations are shown.

From the EPI experiments performed at FL, we had learned that when driving a gradient coil with high voltages, extra measures must be taken to prevent the gradient coil from arcing and sparking (spiking as we called it; or white pixel noise according to GE). Voltage on our experimental EPI gradient systems was then already in the kV range. Due to the not perfectly filtered switching ripples of the gradient amplifier, RF spikes were making EPI almost impossible. EPI was geared towards cardiac imaging at that time, as it potentially allowed MR scaning of a beating heart. The first results were devastating, as the raw data were covered with bright pixels. These spikes rendered the image useless, unless you eradicated them from the raw data, which was a very tedious job that could take hours to produce a single decent image. This problem was solved with the next gradient coil, which we called Herz-EPI-II. It was still unshielded, but vacuum potting and using Litz wires cleared up the RF spikes, and allowed great EPI imaging [41]. This coil was high-voltage proof beyond 1 kV and was therefore an engineering target for the clinical product gradient coils to come.

Günther Pausch, a math and physics teacher, started working at Siemens in the gradient design group in 1984. He designed the MAGNETOM Impact gradient coil under the guidance of Georg Freese, exploring the field of numerical design methods. This eventually led to fingerprint designs, which are now state of the art. The numerical methods he developed, called target-field design, are still the basis of gradient coil design at Siemens – of course with significant improvements, for example to match general, complex geometric shapes, not only cylinders. The target-field design method can be seen as independent to the stream-function method developed at Peter Mansfield's lab in Nottingham by Robert Turner [42], which is an analytic method, while Günther Pausch's method is fully numerical.

The first realization of an efficient fingerprint design was the MAGNETOM Vision gradient coil, internally called AS25 (Fig. 13, right). New ways in building a gradient coil have been explored. As the Z gradient was directly wound on the cylindrical surface, transverse saddle shaped X and Y gradients, were laid out flat, fixed and then brought into a cylindrical shape by proper bending. The key person behind this technology development was Johan Schuster, who joined the MR business unit in the early 90s. This was also the first fully vacuum-potted product gradient coil, an adventure in itself. Setting up a manufacturing line for such a coil took special efforts. The first prototypes took 6 weeks from start to finish. When quality problems occurred – and they were plentiful in the beginning – it took quite some time to get them under control[3]. Eventually we managed to do so when Dietmar Lehne took control of the newly formed gradient factory, MRG. I (F.S.) joined MRG in 1994 to head the gradient and RF body coil design team.

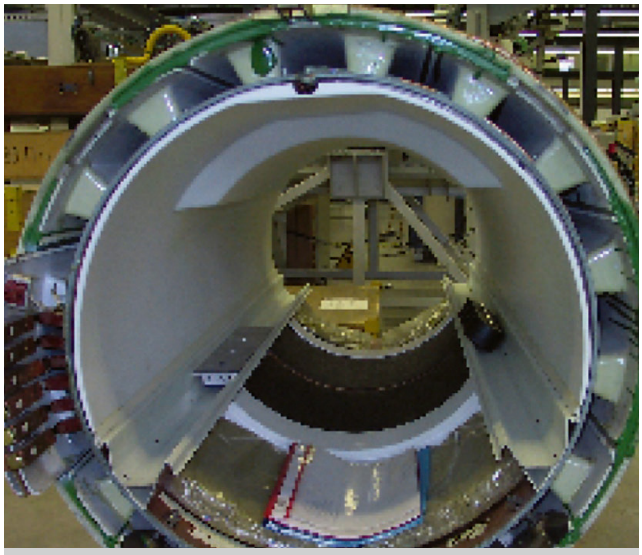

IMPACT

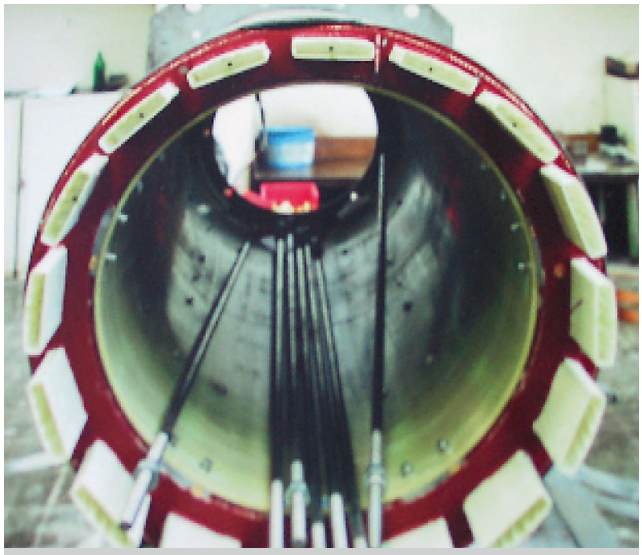

VISION

13 MAGNETOM Impact gradient coil on the left, and fully potted MAGNETOM Vision gradient coil AS25 on the right. Note the use of the space between primary and secondary coils for placing the shim irons, the 16 rectangular pieces sticking out of the body of the coil, visible because this coil was still unfinished.

[3] *An aspect we have experienced during the SARSCOV-2 outbreak: any measure being done to stop the outbreak took at least two weeks to see how the number of infected people changed and even four weeks and more to see how the number of deaths has changed. The logic is the same, i.e. you wait for 6 weeks to see if the changes on the make of the gradient coil has an effect on its quality build. Stay put and stick to the concept of clear thinking while you go through such challenging times.*

The gradient factory consisted of the design teams for gradient coil magnetic field, the gradient power supply, and the RF body coil. The RF body coil was considered an integral part of the gradient coil, as its shield was directly attached to the gradient coil body. Also within MRG were the mechanical design team and the entire manufacturing line for gradient coils, gradient amplifiers, and RF body coils. The manufacturing line was about 4 km away from the offices of the design groups, which seems close when compared to the other MR vendors. When Siemens MR moved into the new facility at the Roethelheim Park in 2000, however, it brought us all very close together. The design teams on one side of the corridor, the manufacturing line on the other. A new era had begun. We think it is no exaggeration to say that this is the secret to the dominance of Siemens gradient performance.

MAGNETOM Vision used the first fully EPI-capable clinical whole-body gradient coil, which performed at 25 mT/m and up to SR 125 T/m/s in the EPI configuration using a resonant booster running at 833 Hz. This gradient coil weighed about 600 kg and was more than two meters long.

Already in the mid 90s, there was a desire to shorten the overall length of MR systems. This was then combined in the mid 2000s with a demand for bores wider than the usual 60 cm diameter, mainly to improve patient comfort and lower anxiety [43].

Large-scale GC manufacturing accelerated with the platform systems, when Manufacturing and R&D moved into the same building at the Roethelheim Park. Major investment in a modern vacuum potting system paid off quickly. We also had to learn how to test the quality of gradient coils. Partial-discharge measurement, previously used for large electrical transformers, was the key to this. It was applied to the MAGNETOM Vision gradient coil and is now an established part of quality assurance.

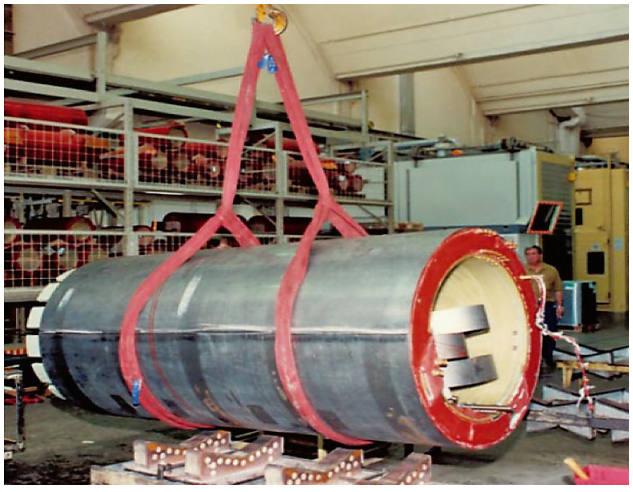

14 AS25 gradient coil right out of the potting chamber.

Head gradients

So far, we have described whole-body gradients. Now we turn to head gradient sets to highlight the Siemens activities in that field also. With dedicated head gradient insert coils, gradient performance can be increased substantially, as there is no practical physiological bound for amplitudes and SR.

Designing and building such coils goes back to the mid 90s, almost always driven by customer requests. We built our first head gradient coil, the HC40, in 1996, and delivered it to Mark Haacke's group at the Mallinckrodt Institute of Radiology in Saint Louis [44, 45]. The special feature of that coil was being directly cooled with deionized water through its hollow conductors which became again popular over the last 5 years [46]. That unshielded head gradient set reached 45 mT/m peak at SR 300 T/m/s. Due to its very low inductance, it needed an extra inductor in series with the gradient coil to match the overall inductance to the capabilities of the GPA regulator.

Another of our sets, the HC40seg, used segment coils [47] instead of saddle-shaped coils. We built and stacked segments with inner (primary) and outer (secondary) path to create the transverse gradients. That design was driven by the idea of minimizing acoustic noise. In the end, we did not follow it up, as a well shielded coil would have needed far too large a diameter, not a viable solution for the precious and restricted real estate inside the magnet.

For the 3T MAGNETOM Allegra, a head-only MR scanner, we designed the AC44 gradient coil which performed at 40 mT/m and SR 400 T/m/s. This coil was asymmetric in design to allow a shoulder cut-out for better positioning of the head in the sweet spot of the gradient coil and of the magnet [48]. The MAGNETOM Allegra was very popular in the neuroscience community since it provided the best EPI scanning available at that time, but it was not really suitable as a clinical machine for plain neuro scanning, as its FOV reached only two or three vertebrae bodies of the C-spine.

The asymmetric design continued with our unshielded AC88 head gradient line [49], which we used for our MAGNETOM Trio A Tim System. The coil was by intention unshielded, as the fringe fields in the cryostat and cooling shield of the 3T magnet were minimal due to large separation of gradient windings and cryostat. Eddy currents could be compensated by the classical method. This gradient system was conceived through discussion with the MGH Martinos Center, Van Wedeen, and Lawrence Wald, in particular. Its major focus was to increase G_{max} and decrease the echo time for DSI (see Figure 3). It used a special cradle system to wheel it in and out of the magnet (Fig. 15) and fitted inside the standard 600 mm patient bore without removing anything. It also used a huge mechanical switch (the Frankenstein switch as we called it) to switch between the clinical Trio gradient system and the experimental

AC88 system. The performance of G_{max} = 80 mT/m and SR 400 T/m/s was unique, and along with the Connectom gradient systems set the path for whole-body gradient system requirements to come.

For our 7T and 9.4T[4] research systems we used a redesigned MAGNETOM Avanto whole-body gradient coil (the Avanto-7T GC) which had beefed-up shim coil channels to match the required shimming needs at 7T. It gave 45 mT/m at SR 200 T/m/s. Some researchers considered it not fit for neuro imaging and fMRI at 7T. Therefore, we designed and built another fixed-mount asymmetric shielded head gradient set, the AC84, which fitted snugly into the bore of the Avanto-7T GC when the patient bore liner was removed. Its inner diameter was 400 mm and its outer diameter was 670 mm. With its 80 mT/m and SR 400 T/m/s, it matched the performance of the AC88. Kamil Ugurbil's group, at the University of Minnesota's Center for Magnetic Resonance Research, used that coil heavily, and exchanged it on a monthly basis with the Avanto-7T GC. That head gradient set was eventually abandoned when we built a better performing whole-body gradient coil, the SC72, for our UHF system. The bore size was chosen not to fit the AC84, as we were convinced that 70 mT/m at SR 200 T/m/s should be fine particularly for neuro imaging. That performance was possible by reducing the inner diameter (to 640 mm) and the linearity volume to avoid PNS. The reduction of the inner diameter of the gradient coil was possible as we saw no need for a whole-body RF coil for our UHF system – an assessment that still holds true today.



15 Handling of the insertable head gradient set AC88.

GE also demonstrated several head gradient systems for 1.5T [50] and for 3T systems as an introduction to the Connectom world [46].

Overall, head gradient systems allow unmatched performance for neuro imaging research purposes, but there is the limited use to brain imaging only, patient comfort, and the extra effort required to provide modern head RF coils that will fit in a head gradient coil.

Fight the heat

Gradient coils consist of current patterns in 3D space, usually in cylindrical layers. For a saddle coil, the current pattern can be water-jet cut into copper or aluminum sheets. Alternatively, wires (these may be block, filament or litz wires) can be laid out on a flat surface and fixed in place. Either of the conductors chosen is then bent over a cylindrical surface. Then, the layers and segments are connected to provide the desired gradient field.

The type of conductor material used is often a company secret. The questions are, what material offers the best performance with respect to power dissipation, including the skin effect due to driving frequencies beyond 1 kHz; and what material is best for manufacturing? Every conductor type experiences some ohmic losses and therefore produces heat. Minimizing these losses is key to high-performance gradients. Existing gradient system designs need electric line power of 50 kVA and more. This is quite a high number, since this heat must also be removed by the cooling system.

Conductor choice defines the heat generated in a coil. Figure 16 shows schematic impedance curves of four different wire types. As gradients are driven in a whole variety of pulsing schemes, the spectral bandwidth of gradient sequences is important. EPI is a perfect technology to demonstrate this, with an oscillating RO gradient in the region of 1 kHz. At this frequency, wire type 3 is clearly superior to type 2, which produces nearly twice as much heat.

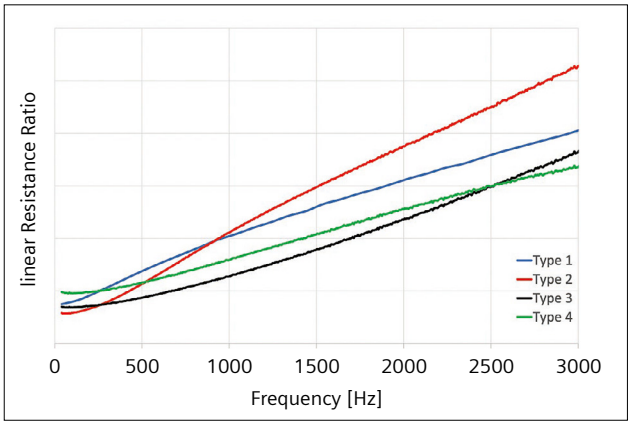

16 Impedance curves for 4 different wire types used in a gradient coil.

[4] *Work in progress: the application is currently under development and is not for sale in the U.S. and in other countries. Its future availability cannot be ensured.*

Hooking up a coil to scan human subjects

So far, we have described the development and manufacturing of the major gradient components at Siemens. When we hooked them up inside a magnet and entered the performance space of EPI, another adventure began.

Lorentz forces

A gradient coil experiences stresses caused by Lorentz forces

Equation 5

$$\underline{F} = q^* (\underline{v} \times \underline{B}_o)$$

with q being a charge (i.e, an electron) moving with speed $\underline{v}$ through the coil, and $\underline{B}_o$ the magnetic flux of the MR magnet. For saddle-shaped coils, there is typically a dominant banana-shaped bending mode (Fig. 17, top left, indicated by the force arrows). Here an unshielded gradient coil is shown. Actively shielded coils have the same bending modes, but internally the forces of the primary and the secondary layer oppose each other, and therefore create local compression and expansion also (Fig. 17, bottom left), which potentially can rip the coils apart if they are not properly potted. A variety of geometric modes are possible (Fig. 17, right). As Lorentz forces scale linearly with the magnetic field, it is obvious that gradient coil failures are more likely at high field. Entering the ultra-high-field world at 7T, we faced a learning curve that helped to improve the quality of coil manufacturing for the lower, clinical field strengths.

Vibration causes acoustic noise, so the higher the field, the higher the acoustic noise. Yet we have always managed to stay inside regulatory limits [51], even with our UHF systems.

Spikes

Early in the development of MAGNETOM Vision, Lorentz forces presented us with a nerve-wracking challenge. With the introduction of EPI, significantly higher currents and shorter pulses were applied, which led to friction of metallic and nonmetallic layers and caused charging and discharging. The poorly filtered switching ripples of the PWM power stages made this problem even more severe. While developing EPI at the Corporate Research lab we considered this period as very disturbing and somehow hopeless. I recall a time when due to the unfiltered switching ripple every metallic structure in and around the magnet was electrically charged up. Knocking on the RF cabin from the outside created an amazing blue sparking corona. That was eventually fixed by proper grounding and filtering the gradient power amplifiers better but did not solve all the troubles.

During testing of our first EPI prototype at the Beth Israel Hospital in Boston in early October 1992, I (F.S.) recall a time when the spikes were so devastating that EPI imaging was useless. After bringing in RF experts from the lab in Erlangen to help fix it, we gave up after a long week of tedious, yet unsuccessful work and decided to head to Cape Cod on Sunday instead. It was raining cats and dogs that weekend and humidity was significantly higher when we gave it a last try on Monday morning. Suddenly all the spikes were gone. The humid air suppressed electric

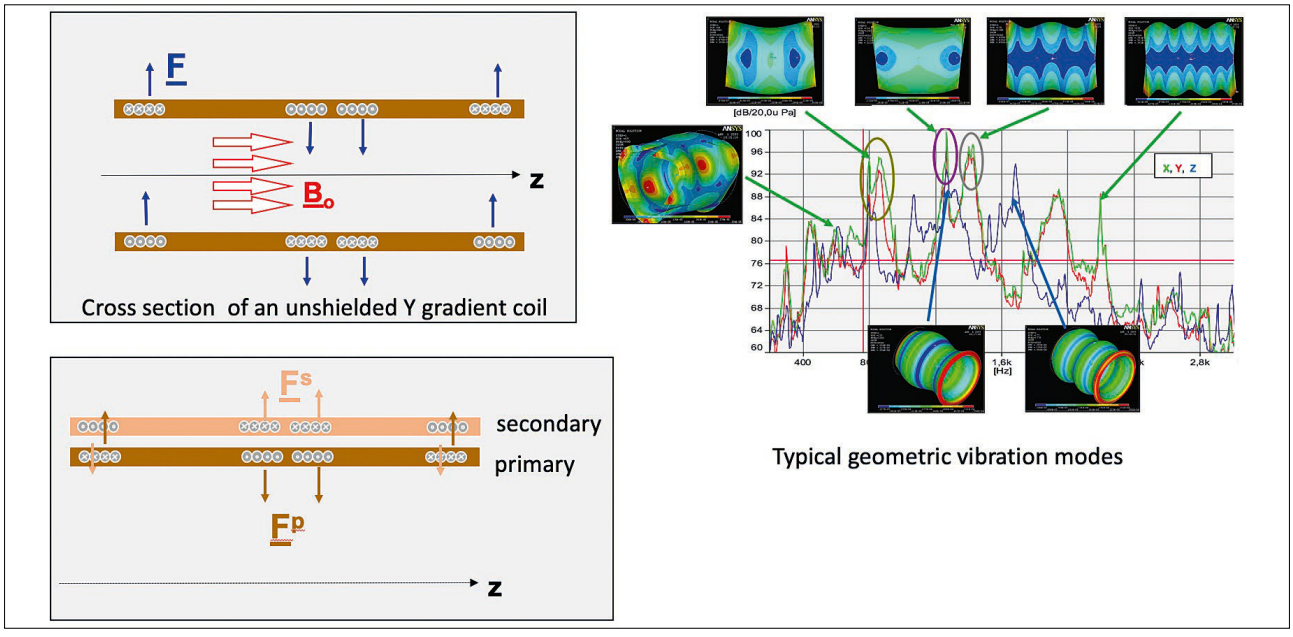

17 Lorentz forces and their effect on stresses and geometric modes of gradient coils.

discharges and therefore avoided spikes. This was one of those "aha" moments that lucky people sometimes have. A humidifier was brought into the RF cabin, and spikes were no longer a threatening issue – although they still pop up occasionally during the testing phases of early product prototypes.

When developing the Vision gradient system, we originally intended to start with 800 V PWM switching voltage. In the end it was not wise to continue with 800 V due to severe spiking. So we reduced the output voltage of the PWM stages to 600 V, which allowed us to fix the arcing and sparking. We eventually fixed the problem by cleaning up the materials inside the potted gradient coil, firmly grounding what needed to be grounded, properly galvanically seperating what needed to be insulated, and improving the mounting of the gradient coil inside the magnet. We also had to tackle air pockets inside the potted gradient coil. They are a major source of high electric field, as the permittivity ratio ϵ of epoxy to air is on the order of 4, and so increase the likelihood of arcs and sparks. A pot-pourri of spike trouble makers is shown in Figure 18.

Overall, this was the most challenging technological hurdle we have faced in our professional careers in MRI.

Coupling

Since the introduction of MAGNETOM Vision, Siemens gradient coils have electric shim coils as well as slots for placing ferromagnetic shim iron (Fig. 13, right). Shims are

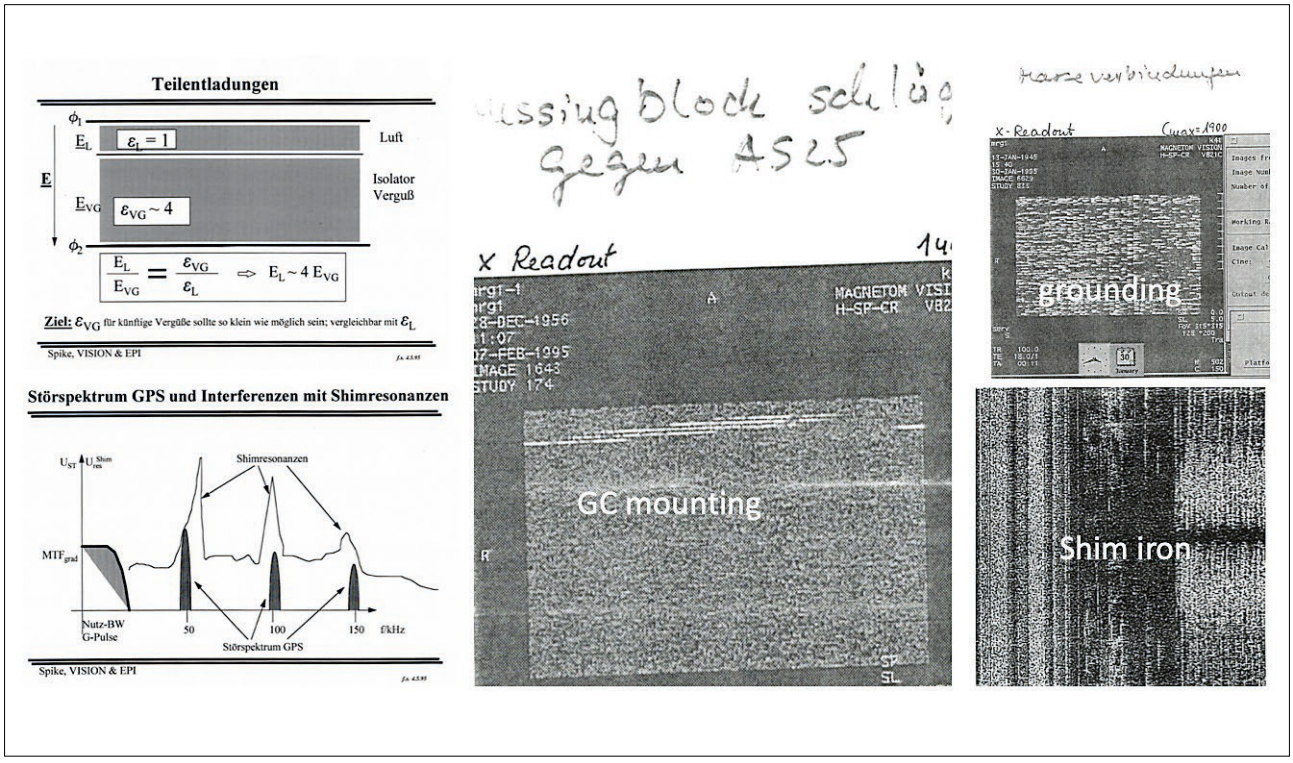

18 Spike phenomenas.

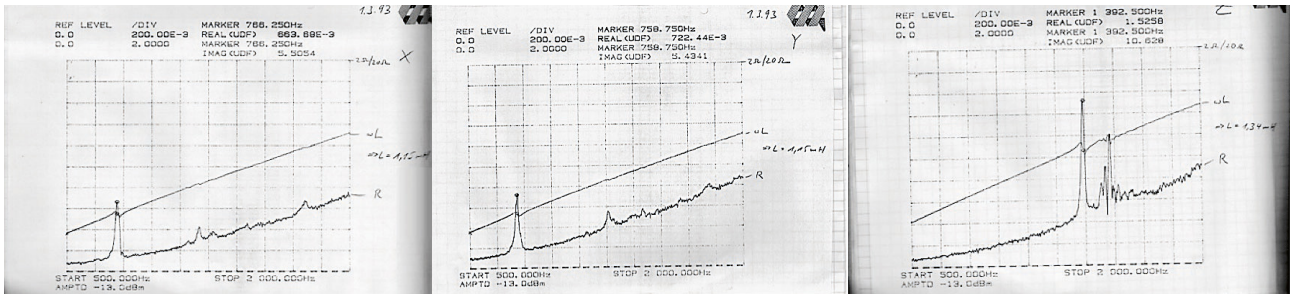

19 Effects of Lorentz forces on the impedance of a gradient coil. G_x, G_y, G_z from left to right. Transverse gradients (G_x & G_y) typically show resonance peaks at 700–800 Hz, depending on the diameter, wall thickness and length of the potted gradient coil, while for axial gradients (z-gradient shown on the right) the first dominant resonance is around 1400 Hz.

typically placed between the primary and the secondary layers, and so experience strong magnetic flux changes dB/dt. When the harmonics of GPA switching frequency coincide with resonances of a shim coil (A20 was the biggest trouble maker), arcing and sparking could occur at the shim coil terminals. Large filter networks helped on the Vision system. Later product generations solved this by decoupling the shim fields and reducing the switching ripples through output filtering at the GPA.

Electro magnetics-mechanics coupling into the shim iron itself was also possible. On our EPI prototype in Boston, the shim iron was attached to the magnet bore. Eddy currents could be induced even in the iron shim plates (some were about 10 x 25 cm) which vibrated and generated incredibly high acoustic noise levels (140 dB!), but only when one particular frequency was excited. That problem was solved by shrinking the shim plates and insulating each one from the others, and is no longer an issue.

Plotting impedance of the gradient coil against frequency reflects these mechanical resonances, where impedance can increase about 5-fold (Fig. 19). Each peak represents one of the bending modes shown in Figure 17. If I (F.S.) recall correctly, the shim iron peak was much broader (no screenshot exists from that unfortunately).

The electromagnetic-mechanical coupling described above is dependent on the magnetic field strength (Equation 5). Figure 20 shows impedance coupling results of a whole-body gradient coil and a head GC, spanning field ranges from 0 to 3T and 0 to 7T, respectively.

Driving an EPI RO gradient in such a peak frequency range could increase acoustic noise beyond legal limits, and also imaging would be degraded, as the GPA regulator (the feedback control system to assure that currents are correct) would be outside its normal range. In principle, this problem persists on modern systems, as vibration is unavoidable, but the total effect on image quality is very small, as todays GPA regulator compensates for it. However, the best remedy is to stay out of those vibration frequency bands to avoid excessive noise.

PNS

Our initial EPI experiments at the Siemens lab were performed on a head gradient system. Running EPI at 1 kHz and higher worked well, and no side effects were seen. As EPI was the only MR technique that appeared to allow single-shot imaging of a beating heart we run into another unexpected road block. The EPI RO at 1 kHz for a FOV of 400 mm required G_{max} on the order of 30 mT/m. I (F.S.) recall being the first subject of an EPI cardiac scan, and I experienced strong muscle contractions. I crawled out of the scanner while the EPI was still running and reported that unpleasant experience to my colleagues, who still thought I was in the scanner. We stopped any EPI activity while we tried to work out what was the root cause of these contractions. Soon we understood that due to a changing magnet flux, dB/dt, an electric field E is induced in the human body, and we had crossed a motor sensory threshold. To further understand this twitching phenome-

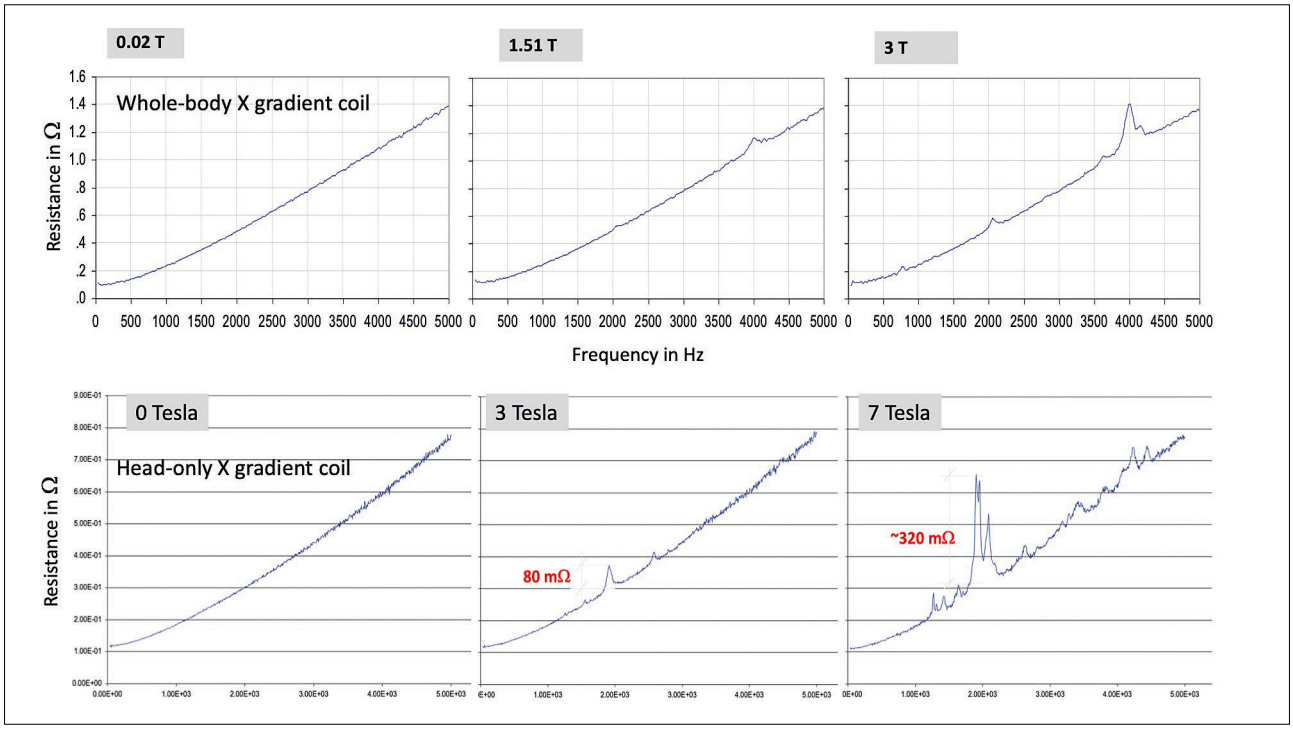

20 Resistance over frequency for head GC and whole-body GC for various magnetic field strengths.

non, we asked Tom Budinger, an MR pioneer from UC Berkeley, to help us explore the field of peripheral nerve stimulation (PNS).

Figure 21 shows some early experimental results from the Vision gradient coil, with a graph on the lower right showing all relevant physiological phenomena caused by dB/dt pulses. More details on this can be found in [10].

The results were published simultaneously with our main competitor, ANMR, at the RSNA 1989 [53, 54] and in 1991 in the Journal of Computed Tomography [55]. Nottingham University, where EPI was invented, later reported their view on PNS in 1993 [58], as did other groups in the U.S. who worked close with GE on that subject [56, 60].

In 1990, we performed animal experiments at UC Berkeley with Tom Budinger's group, equipped with a Siemens gradient system. The conclusion was that with MR gradients we could not induce any hazardous cardiac stimulation, such as extra heart beats or arrhythmia. We were at least a factor of 10 away from any cardiac risk.

Further explorations of PNS, together with Werner Irnich of the University of Giessen [57], eventually gave a clear picture of how EPI scanning and any fast switching gradient pulse sequences could be employed [59]. Based on that result, all product MRI scanners after the MAGNETOM Vision incorporated a PNS monitor (the SAFE monitor [62]), which would switch off the gradients when a certain threshold was exceeded, and also allowed look-ahead functionality.

The essence of all PNS experiments is that for EPI pulse trains (the worst case), be they trapezoidal or sinusoidal, there is a linear relationship between gradient rise time and gradient threshold amplitude (the amplitude at which the subject will feel muscle twitching). From a practical point of view, PNS is the limiting factor for fast switching gradients. In a whole-body environment, EPI can be comfortably deployed up to 40 mT/m at SR 200 T/m/s for x and z axis gradients. Faster switching is not permitted, and the PNS monitor will switch off the gradient. Higher gradient amplitudes are possible only with lower slew rates.

Summary

Since its clinical appearance, MRI underwent tremendous changes and improvements in applications from head to toe. This was mainly due to the numerous innovations and improvements in the MR system hardware. The RF system is considered the basis for the increased speed in MRI through parallel imaging (pRX) techniques such as SENSE and GRAPPA which allow in-plane speed up. Over the last 10 years Multiband (MB), and Simultaneous Multi-Slice (SMS) imaging has spread pRX techniques also across slices

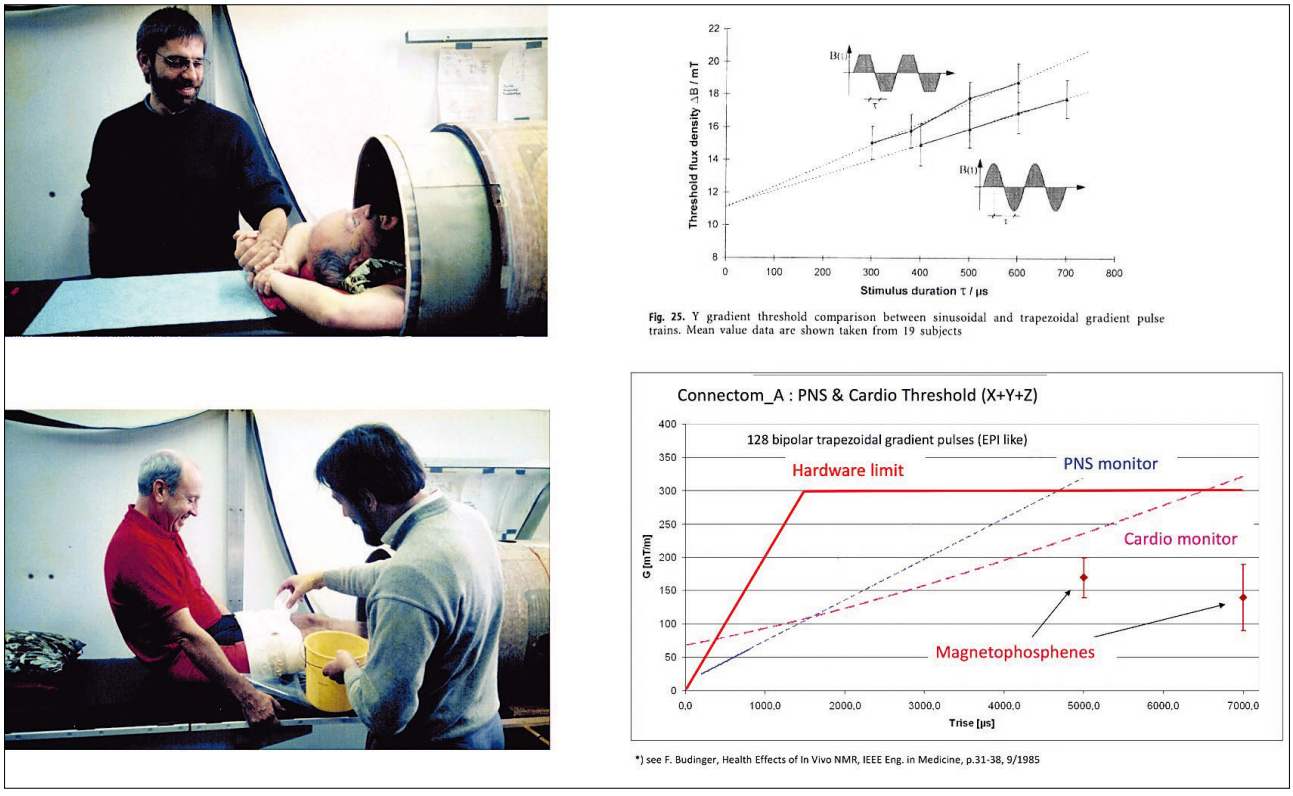

21 PNS experiments with an experimental gradient coil (MAGNETOM Vision) outside the magnet (left). The subject here is Tom Budinger. Top right shows PNS results on 19 subjects for sine and trapezoidal gradient pulses; vertical axis is B_{max} in units of mT. Lower right shows thresholds; gradient strength is shown in mT/m.

and allows 10fold and more speed up. Gradients on the other side also were essential to faster imaging. In particular EPI needs to be mentioned here. As a pure gradient echo technique the goal is to measure the entire heavily T2*-weighted FID in a time well below 100 ms. As EPI is SNR and PNS limited the gradient performance is limited to round about 40 mT/m at SR 200 T/m/s in whole-body settings. EPI is considered the work horse for fMRI research and is employed on hundreds if not thousands of human subjects per day around the globe. Combine EPI with diffusion weighting then we are rooted deeply in the clinical world for stroke and tumor diagnosis. For diffusion



22 **(22A)** Siemens Corporate Research "Feldkonfiguration" Team (~1984): Laxmikant Urankar, Peter Henniger, Horst Siebold.
(22B) GPA R&D team (~1984): from left to right: Harald Hofmann, Karl-Heinz Ideler, Gunther Petzold, Robert Bleisteiner, Stefan Nowak, Helmut Lenz, Günther Theil. In the background is the very first 3-axis gradient amplifier consisting of a total of 4 cabinets, one per gradient axis and one common cabinet for cooling.
(22C) GPA R&D team (~1983): from left to right: Helmut Lenz, Robert Bleisteiner, Stefan Nowak with a home build electrical model of a gradient coil to estimate the inductance of such coils. This was needed as at that time no whole-body gradient coil was existing for setting the PI regulator parameters of the gradient amplifier.
(22D) MR Physics including gradient coil design team (~1984): Jochen Abarth, Eckhardt Stetter, Franz Schmitt, Georg Frese, Angelika Mitzinek, Peter Heubes, Paul Margosian, Georg Ladwein, Paul Angstenberger, Günther Pausch, David Faul.
(22E) Gradient coil mechanical design team: Walter Derndinger, Tihomir Hudak, Christine Albert, Gerhard Nagengast, Günther Zebelein, Steffi Hammerl, Heinz Hahn, Elfriede Schönecker, Dietmar Lehne, Johann Baier.
(22F) GPA Electronics mechanical design team: Günther Pförtsch, Gernot Kwapil, Robert Zachmann, Karin Georgiatis, Bernd Räbiger, Klaus Albrecht, Norbert Hübler, Birgit Gmeinwieser, Karin Galster, Anne Kraus, Walter Rothmann, Peter Zöbelein.
(22G) Gradient coil design team (~2018): Peter Dietz, Stefan Stocker, Chris Ströhlein, Jörg Riegler, Andreas Krug, Sabrina Kreher-Harder, Martin. Sattler, Sascha Fath. Andrew Dewdney, Eva Eberlein, Anne Kraus, Simon Bauer, Axel vom Endt.
(22H) Connectom team (~2014): Herbert Thein, Johann Schuster, Franz Schmitt, Johannes Stadter, Eva Eberlein, Ralph Kimmlingen, Kevin Riedel. Helmut Lenz, who was very essential in getting the four GPAs synchronized should also be named here.

in clinical whole-body MRI systems we have now reached 80 mT/m gradient strength at SR 200. However, in the MR research world there seems to be no limit in requesting nearly unlimited gradient strength. We now have reached 300 mT/m in whole-body and head only set ups for targeted high-resolution neuro diffusion imaging. The Siemens Healthineers gradient development reflects that EPI route very nicely.

Acknowledgments

The authors would like to thank Horst Siebold, Georg Frese, Günther Pausch, Eckart Stetter, Robert Bleisteiner, Helmut Lenz, Mathias Blasche, Sascha Fath and Mark Cohen, UCLA, for their valuable support.

References

1 Oppelt A, Loeffler W. MAGNETOM Flash 2019;75(4):106-108.
2 Mansfield P. Multi-planar image formation using NMR spin echoes. J. Phys. C. 1977;10:L55-L58.
3 Moeller S, Yacoub E et al. MULTIBAND. Mag Res Med 2010;63(5):1144.
4 Setsompop K. Gagoski BA et al. Blipped-CAIPIRINHA for simultaneous multi-slice EPI with reduced g-factor penalty. Proceedings of the 18th Annual Meeting of ISMRM. 201018
5 Schmitt F, Arz W, Eberlein E et al. An ultra-high performance gradient system for cardiac and neuro MR Imaging. Proceedings of the ISMRM. 1999.
6 vom Endt A, Riegler J, Eberlein E et al. A High-Performance Head Gradient Coil for 7T Systems. Proceedings of the Joint Annual Meeting ISMRM-ESMRMB. 2007;15:451.
7 Kimmlingen R et al. Concept and realization of high strength gradients for the Human Connectome Project. Proceedings of the ISMRM. 2012;20:696.
8 http://www.humanconnectomeproject.org/
9 http://www.humanconnectome.org/
10 Kimmlingen R. Pioneers of Connectome Gradients. MAGNETOM Flash 2017 (68)2:122-136.
11 Blasche M. Whitepaper on Gradient Performance and Gradient Amplifier Power. Available at www.siemens.com/magnetom-world go to Publications > Whitepapers
12 Nagel AM, Laun FB, Weber M-A, Matthies C, Semmler W, Schad LR. Sodium MRI using a density-adapted 3D radial acquisition technique. MRM. 2009;(62)6:1565-1573
13 McRobbie DW. Occupational exposure in MR. Br J Radiology. 2012;85(1012):293-312.
14 Stejskal EO, Tanner JE. Spin diffusion measurements: Spin echoes in the presence of a time-dependent field gradient. J Chem Phys. 1965;42:288-92.
15 Tuch DS, Reese TG, Wiegell MR, Makris N, Belliveau JW, Wedeen VJ. High angular resolution diffusion imaging reveals intravoxel white matter fiber heterogeneity. Magn Reson Med. 2002;48:577-582.
16 Jin J. Electromagnetic Analysis and Design in Magnetic Resonance Imaging. 1998. ISBN 9780849396939.
17 https://www.elprocus.com/freewheeling-or-flyback-diode-circuit-working-functions/
18 https://en.wikipedia.org/wiki/MOSFET
19 Cohen MS, Schmitt F. Echo planar imaging before and after fMRI: A personal history. NeuroImage 2012;62(2):652-659.
20 https://en.wikipedia.org/wiki/Insulated-gate_bipolar_transistor
21 Ideler KH, Nowak S, Borth G, Hagen U, Hausmann R, Schmitt F. A resonant multi purpose gradient power switch for high performance imaging. Proceedings of the 11th Annual Scientific Meeting of the SMRM. 1992;11:4044.
22 Edelman RR et al. Qualitative mapping of cerebral blood flow and functional localization with echo-planar MR imaging and signal targeting with alternating frequency. Radiology. 1994;192:513-20.
23 Warach S, Gaa J, Siewert B, Wielopolski P, Edelman RR. Acute human stroke studied by whole brain echo planar diffusion-weighted magnetic resonance imaging. Annals of Neurology. 1995;37(2):234-241. https://doi.org/10.1002/ana.410370214
24 Edelman RR, Chen Q. EPI STAR MRI: Multislice mapping of cerebral blood flow. Magn Reson Med. 1998;(40)6:800-885.
25 Kolata G. New Brain Scanning Technique Can Show Strokes in Progress. New York Times. April 6, 1992.
26 Cohen MS, Weisskoff RM. Ultrafast MR Imaging. Magn Reson Imaging. 1991;9(1):1-37.
27 Rosen B, Belliveau J, Vevea J, Brady T. Perfusion imaging with NMR contrast agents. Magn Res Med. 1990;14(2):249-265.
28 Belliveau JW, Kennedy DN Jr, McKinstry RC, Buchbinder BR, Weisskoff RM, Cohen MS, Vevea JM, Brady TJ, Rosen BR. Functional mapping of the human visual cortex by magnetic resonance imaging. Science. 1991;254(5032):716-719.
29 Kwong, KK et al. Dynamic magnetic resonance imaging of human brain activity during primary sensory stimulation. Proc Natl Acad Sci USA. 1992;89(12):5675-5679.
30 Mansfield P, Harvey PR, Coxon RJ. Multi-mode resonant gradient coil circuit for ultra-high speed NMR imaging. Measurement Science and Technology. 1991;2(11).
31 Mueller OM, Roemer P, Park JN, Souza SP. A general purpose non-resonant gradient power system. Proceedings of the 10th Annual Scientific Meeting of the SMRM. 1991;10:130.
32 https://www.infineon.com/dgdl/Infineon-IGBT_or_MOSFET_Choose_Wisely-ART-v01_00-EN.pdf?fileId=5546d462533600a40153574048b73edc
33 Nowak et al. CASCADE IP ISMRM Syllabus
34 Golay MJE. Magnetic field control apparatus. US Patent 3515979A. Priority date 1957-11-04.
35 Frese G, Siebold H. Gradient coil system for a nuclear magnetic-resonance technique device. European Patent EP0073402B1. Priority date 1981-08-27.
36 Siebold H. A Computer Program for Optimizing Homogenous Field Magnets with Iron Yoke. IEEE Trans on Magn. 1988;24(1):408-410.
37 Bernstein MA, et al. Concomitant gradient terms in phase contrast MR: Analysis and correction. MRM. 1998;39(2):300-308.
38 Mansfield P, Chapman B, Turner R, Bowley R. Magnetic field screens. UK Patent GB2180943B. Priority date 1985-09-20.
39 Punchard W, Pillsbury RB. Magnetic resonance imaging systems. US Patent 4733189A. Priority date 1986-06-03.
40 Roemer P, Edelstein WA, Hickey J. Self-shielded gradient coils. Proceedings of the 5th Annual Meeting of the SMRM. 1986;(5):1067.
41 Schmitt F, Stehling MK, Ladebeck R, Fang M, Quaiyumi A, Bärschneider E, Huk W. Echo-planar imaging of the central nervous system at 1.0 T. JMRI. 1992;2:473-478.
42 Turner R. A target field approach to optimal coil design. J Phys D. 1986;19:L147
43 Heid O, Magnetic Resonance Imaging Magnet Assembly System with Improved Homogeneity. US Patent Application US20040178796A1.
44 Thompson MR, Kuppusamy K, Venkatesan R, Lin W, Haacke EM, Celik A. High resolution EPI imaging with a head gradient coil insert: applications to diffusion and functional MRI. Proceedings of the Fast MRI Workshop of the ISMRM. 1997:p181.

45 Tompson MR et al. Increased-Contrast, High-Spatial-Resolution, Diffusion-weighted, Spin-Echo, Echo-planar Imaging. Radiology. 1999;210:253-259.
46 Foo T, Lee SK, Tan ET, Mathieu J-B. Development of a Head-only Gradient Coil Prototype. GESIGNAPULSE.COM, Academic Issue 2015.
47 Zwanger MS, Porter D, Feiweier T, Reese T, Benner T, Kirsch JE. Compensation for Maxwell Cross-Terms in Diffusion-Weighted Imaging. Proceedings of the ISMRM. 2004;p101.
48 Meier C, Zwanger M, Feiweier T, Porter D. Concomitant Field Terms for Asymmetric Gradient Coils: Consequences for Diffusion, Flow, and Echo-Planar Imaging. Magnetic Resonance in Medicine. 2008;60:128-134.
49 Kimmlingen R, et al. An easy to exchange high performance head gradient insert for a 3T whole-body MRI system: first results. Proceedings of the ISMRM. 2004;p1630.
50 Alejski A, Chen Y, Rutt BK. Ultra-high-resolution Imaging with a clinical MRI. IEE Instrumentation & Measurement Magazine. 2002;5(2):18-22.
51 Foo T, Lee S-K, Tan ET, Mathieu J-B. Development of a Head-only Gradient Coil Prototype. GESIGNAPULSE.COM Academic Issue Spring 2015;11-15.
52 NEMA MS 4-2010: Acoustic Noise Measurement Procedure for Diagnostic Magnetic Resonance Imaging (MRI) Devices.
53 Goldfarb JW, Schmitt F. A robust method to remove spike artifacts through HPF post-processing. Book of abstracts ISMRM. 1996;3:1646
54 Cohen MS, Weisskopf RM, Kantor ML. Evidence of peripheral stimulation by time-varying magnetic fields. Proceedings of RSNA. 1989;75:1188.
55 Fischer et al. Physiological effects by fast oscillating field gradients. Proceedings of RSNA. 1989;75:1189.
56 Budinger TF, Fischer H, Hentschel D, Reinfelder H-E, Schmitt F. Physiological effects of fast oscillating magnetic flux gradients. J Comp Ass Tomog. 1991;15:909-914.
57 Reilly JP. Electrical Stimulation and Electro-pathology. Cambridge University Press, Cambridge-New-York-Oakleigh. 1992.
58 Irnich W. Magnetostimulation in MRI. Magn.Reson.Med. 1995;33(5):619-23.
59 Mansfield P, Harvey P. Limits of neural stimulation in echo-planar imaging. MRM. 1993;29:746-758
60 Schmitt F, Wielopolski P, Fischer H, Edelman RR. Peripheral Stimulations and their Relation to Gradient Pulse Shapes. Proceedings of the SMRM. 1994;p102.
61 Schaefer DJ, Bourland DJ, Nyenhuis JA, Foster KS, Licato PE, Geddes LA. Effects of simultaneous gradient combinations on human peripheral nerve stimulation thresholds. Proceedings of the Society of Magnetic Resonance. 1995 (Vol. 1220).
62 Hebrank F, Gebhardt M. SAFE model – a new method for predicting peripheral nerve stimulation in MRI. In Proceedings of the 8th Annual Meeting of ISMRM, Denver, CO, 2000. p. 2007.

About the Authors

All three authors have been hired in the beginning of the MR product development.

Eva Eberlein, a physicist, started in 1986 in the gradient design team. Eva first focused on shim coil optimization (part of the gradient coil assembly) as well as the shim measurement tool. She later focused on designing gradient coils. Today she is heading the gradient coil design team.

Stefan Nowak, an electrical engineer, started in 1982 as an intern and later for his Diploma thesis in Electrical Engineering (actually RF engineering!) on building a GPA prototype to become the first product gradient amplifier. When finished with his thesis he joined Siemens in 1984. With some years off the MR gradient amplifier electronics development to work at Siemens Semiconductors on high power semiconductors (1990–1993). He then worked as a consultant for MR to develop the product EPI booster. In 1995 he joined MR again as an engineer in the GPA electronics lab and was transferred to the healthcare central component factory, CO. Stefan headed the GPA design group until 2015 and at the end of his career worked at Siemens Corporate Research.

Franz Schmitt, a physicist, started in 1983 to work in the physics group of Wilfried Loeffler and Eckhardt Stetter playing with the first experimental MR scanner (0.1T open resistive magnet) in the so-called "Spanienhalle", learning from Peter Heubes in particular what MR-technology means, do trouble shooting and how to get it running. His first closer contact with gradients started when he worked on developing methods to measure the gradient modulation transfer function. Later he focussed on hardware and physics of faster MR imaging, culminating in the development of Echo-Planar Imaging, EPI, at the Siemens Corporate Research Lab, together with Hubertus Fischer, Helmut Barfuss, Dietmar Hentschel, Ralf Ladebeck and Erich Reinfelder under the leadership of Arnulf Oppelt. This is when Stefan and Franz joint forces from 1989 on to fulfill the EPI gradient power demands. From 1994 until 1999 Franz was in charge of the gradient development. After spending 4 years at the MGH Martinos Center in Charlestown, MA to learn about neuro imaging he returned to be the head of the gradient manufacturing until 2006 and then also headed the gradient design team again until 2008 before diving into MR collaboration and Ultra High Field until he retired in 2014. In every of these steps, gradients always have been a core of his activities.

Contact

Franz Schmitt
schmittfranz53@gmail.com

Eva Eberlein
Eva.Eberlein@Siemens-Healthineers.com

Stefan Nowak
stfrno@gmx.de

Revisiting the Physics behind MRI and the Opportunities that Lower Field Strengths Offer

André Fischer, Ph.D.

Global Segment Manager Neurology, Siemens Healthineers, Erlangen, Germany

This article outlines why moving to higher magnetic fields may not always be advantageous in MRI. We focus on phenomena that have a substantial impact on daily routine, and aim to provide a solid insight into underlying physical mechanisms. Some discussions have been simplified in the interest of addressing a broad range of readers.

Introduction

When MRI first transitioned from research into clinical practice in the early 1980s, typical magnetic fields were between 0.2 and 0.5T, mainly due to technical limitations. The clinical MRI community quickly moved towards higher fields, converging on 1.5T, which became the new standard. Later, around the turn of the millennium, 3T magnets started to penetrate the market, fueled by the quest for higher signal to noise ratio (SNR) with higher field strength. Today, 1.5T and 3T are the clinical workhorses, present in almost every large hospital radiology department. Lately, Siemens Healthineers have pushed for even higher field, introducing the MAGNETOM Terra – the first clinical 7T scanner with FDA clearance.

There was an immediate clinical advantage in moving to higher field. It increases the magnetization available for imaging, which improves SNR. The increased signal can be invested into either higher spatial resolution or reduced imaging time. For human MR imaging in general, SNR increases linearly with the field [1]. However, in order to maintain image quality, the chemical shift between different nuclei can be kept constant by adjusting the receiver bandwidth, in which case SNR is proportional to the square root of the field [1, 2]. Recent research in ultra-high-field human brain MRI suggests faster than linear increase of SNR with field [3].

Then again, there is no such thing as a free lunch. Increasing the field increases radiofrequency absorption in tissue, increases artifacts, and degrades imaging in various other ways, through the physical phenomena described below.

Radiofrequency absorption

MRI scanners use high-power radiofrequency pulses to manipulate nuclear spins. This RF energy would become a health hazard if it were intense enough to overheat tissue, so scans have to stick to safety limits.

Specific absorption rate (SAR) is the relevant measure of RF absorption, in watts per kilogram of body tissue. The International Electrotechnical Commission [4] sets maximum SAR of 2 W/kg in normal mode, and of 4 W/kg in first-level mode (both for whole-body SAR averaged over 6 minutes).

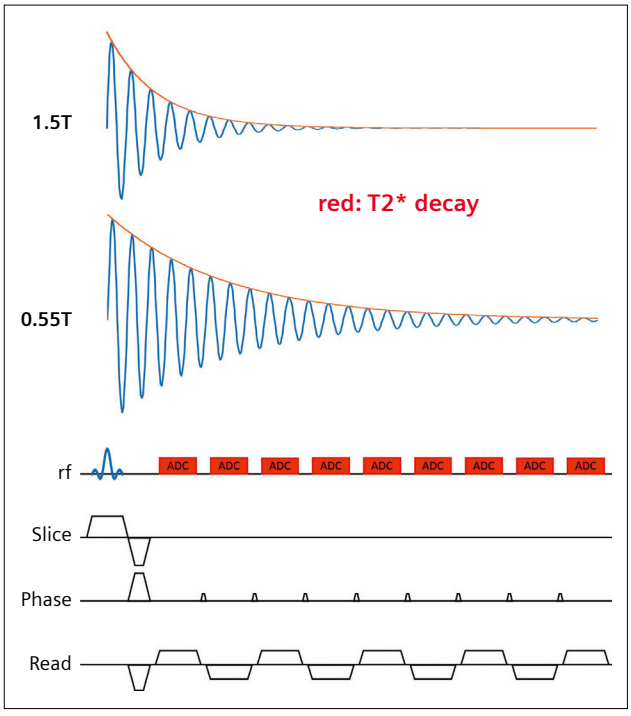

1 During a typical EPI gradient echo readout, the later echoes suffer from low signal intensity at 1.5T compared with 0.55T, and the resulting images are blurred (see Figure 2). The red envelope in the upper two sinusoids corresponds to the observed T2* decay (neglecting gradient-induced dephasing).

The absorbed energy depends on the square of the field, so it increases by a factor of 4 when doubling the field. Most clinicians and researchers have faced SAR limitations, e.g., in SAR "heavy" examinations such as Cardio or MSK, especially with the advent of 3T scanners in clinical routine. Operating in first-level mode is often mandatory at 3T, but even then the SAR threshold limits the use of clinically relevant sequences.

Using 0.55T instead of 1.5T or 3T reduces SAR by a factor of 7.5 or 30, respectively. Consequently, many SAR-intense sequences, e.g., TrueFISP or TSE, do not hit the SAR limit at 0.55T. This can help increase SNR by applying higher flip angles (e.g., 180° instead of lower flip angles such as 150° at 3T for TSE imaging; 90° flip angle for TrueFISP possible), or shortening radiofrequency (RF) pulses to minimize echo time (TE) and TR.

Relaxation times

The relaxation of spins is the main mechanism for the observed image contrast in MRI. In this section, we will review the types of relaxation and their impact on clinical routine.

T1 relaxation

The spin of a proton gives it a magnetic moment. Just as a compass needle aligns with the magnetic field of the Earth, the proton spin tends to align parallel to an external magnetic field B_0; this is the lower energy state of the proton spin, while the anti-parallel state is higher energy. In an MRI, a radiofrequency pulse can be used to convert parallel proton spins to their anti-parallel state; then spin-lattice relaxation (also known as T1 relaxation) gradually brings them back to their energetically preferred parallel state.

This is triggered by the random magnetic field fluctuations – sometimes referred to as "magnetic noise" – of the surrounding magnetic moments caused by, e.g., protons, electrons, and various molecules. The energy difference between the parallel and anti-parallel state corresponds to a resonance frequency, proportional to the field, and relaxation is triggered by "magnetic noise" close to that frequency. Generally speaking, this "noise" at lower frequencies is stronger than at higher frequencies – so at lower field, relaxation is more efficient.

The time constant of this relaxation, T1, is defined by [5]

Equation 1

$$T1 \propto \frac{B_0^b}{a}$$

with constants a and b that must be determined by experiment. Recent investigations [6] across a range of clinical fields (0.55T, 1.5T, 3T, 7T) revealed the following linear dependency between T1 and B_0:

Equation 2

$$T1 \propto \frac{B_0}{12.2}$$

with a = 12.2 and b = 1. This means that T1 gets shorter if the field decreases.

How does this help us from a clinical point of view? If T1 is shorter, the repetition time (TR) can be reduced, resulting in decreased scan time. For example, T1 for gray matter decreases from 1000–1300 ms at 1.5T down to 700–800 ms at 0.55T [7]. Due to this, TR can be reduced by the same proportion, at least 25%.

We can address the loss of SNR by averaging. SNR scales with the square root of the field [1, 2], so to have SNR at 0.55T comparable to that at 1.5T, three averages are necessary. Instead of tripling your imaging time, it will only increase your scan time by a factor of 2.25 because TR could be selected 25% shorter than at 1.5T. Physics comes in favorably from the T1 perspective at lower field strength.

T2 relaxation

Spin-spin relaxation, commonly referred to as transverse or T2 relaxation, does not show high dependency on field.

To observe T2 relaxation, a radiofrequency pulse first flips proton spins so that their net magnetization is perpendicular to the external field. Magnetization then precesses around the B_0 direction at the Larmor frequency

Equation 3

$$\omega = \gamma \cdot B_0$$

where γ is the gyromagnetic ratio of the proton.

The RF pulse also puts proton spins in phase. Gradually, magnetic noise knocks some spins out of phase, which decreases the net magnetization (the vector sum of all spins). After time T2 magnetization decreases by a factor of *e*, so after approximately 5T2 it has effectively vanished. By this argument the strength of the field does not affect T2 relaxation.

Nonetheless, empirical research shows that T2 increases slightly as the field falls. For gray matter, T2 values at 1.5T are 90–110 ms, while at 0.55T they are 110–120 ms

[5]. This would allow turbo spin echo (TSE) imaging to employ longer echo trains at 0.55T, reducing the number of required readouts, potentially reducing the required scan time compared with 1.5T – if the SNR penalty is neglected.

T2* relaxation

Imaging the diffusion of water molecules is one phenomenon that often relies on T2* contrast, and other applications such as BOLD imaging and DSC neuro perfusion suffer from T2* loss or blurring as well. All gradient-echo readouts, such as echo planar imaging (EPI), are modulated by T2* decay.

Several phenomena are affected by both regular T2 decay and another decay process known as T2'. T2' is caused by static inhomogeneities in the magnetic field, such as susceptibility-induced magnetic field gradients, which combine to form T2* relaxation.

The overall timescale is

Equation 4

$$T2^* = \left(\frac{1}{T2} + \frac{1}{T2'} \right)^{-1}$$

By employing TSE sequences, T2' can be recovered and true T2 decay can be observed.

Susceptibility-induced magnetic field gradients scale with B_0, so at high field T2* is shorter than at low field. In gray matter, T2* at 1.5T is typically 70–80 ms, while at 0.55T it is 80–90 ms [5]. This allows more SNR-efficient EPI sampling at 0.55T, since the available echo signal amplitude is relatively large for later echoes in the EPI train (see Figure 1). A side effect is reduced blurring (see Figure 2).

Susceptibility

Magnetic susceptibility measures how a material responds to an external magnetic field. The induced magnetization inside a material under external magnetic field strength *H* is:

Equation 5

$$\vec{M} = \chi \vec{H}$$

where χ is magnetic susceptibility[1].

The induced magnetization *M* and the external magnetic field *H* result in the magnetic flux density *B*:

Equation 6

$$\vec{B} = \mu_0 \vec{H} + \vec{M} = (\mu_0 + \chi)\vec{H}$$

where $\mu_0 = 4\pi \cdot 10^{-7}$ is the magnetic permeability of vacuum.

Eq. 6 tells us that as *H* increases, the change in *B* depends on the value of χ. If $\chi > 0$, *B* increases; if $\chi < 0$, *B* decreases; and if $\chi = 0$, *B* doesn't change.

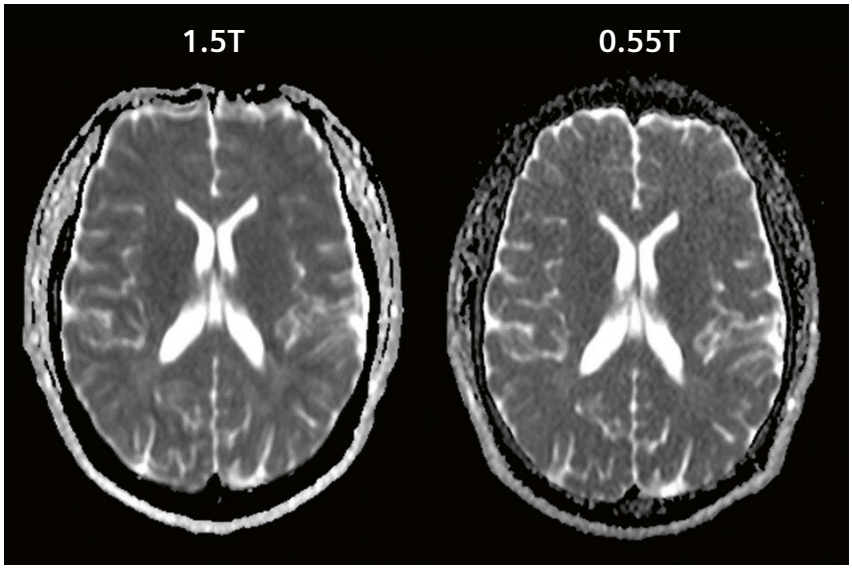

2 Due to faster T2* decay at higher field (see Figure 1), the apparent diffusion coefficient map at 1.5T is slightly blurred along the anterior-posterior direction. This is particularly apparent in the hyperintense gyri. Both images were acquired on the same volunteer. Also, a slight geometric distortion in the anterior brain region is visible at 1.5T (see Susceptibility).

[1] *There are different physical phenomena behind susceptibility. Diamagnetism is a universal property of any material which decreases the magnetic field inside it. It is often "hidden" underneath the stronger phenomenon of paramagnetism, which increases the magnetic field. Both dia- and paramagnetism can only be observed when an external magnetic field is present. As a side note, ferromagnetism is a property that is maintained even when the external magnetic field has been turned off.*

Susceptibility changes can be a valuable contrast source. Susceptibility-weighted imaging (SWI) exploits slight differences in χ to visualize veins in the brain, enabling the diagnosis of cerebral hemorrhage, for example. Quantitative susceptibility mapping (QSM) produces a map of susceptibility that might constitute a new biomarker [8–10].

At the same time, susceptibility is a source of artifacts. Near the sinuses and auditory canal, for example, the changes in susceptibility moving from air to tissue cause geometric distortions in conventional EPI-based imaging, including diffusion-weighted imaging (DWI) and functional MRI (fMRI). Eq. 6 shows that reducing the external field also reduces the absolute differences in local magnetic fields, which makes susceptibility-induced artifacts much less prominent. This can be seen in Figure 3, showing the results of DWI scans on the same volunteer performed on a 3T, a 1.5T, and a 0.55T system. While SNR clearly decreases as field decreases, the geometric distortions are significantly reduced as well.

Diffusion imaging of the optic nerves is also substantially improved at lower field (see Figure 4). A similar behavior is to be expected for imaging of metallic implants such as hip implants. This has been shown in the literature [11–13] and might have a significant impact on clinical practice in the aging societies of industrialized nations.

B_0 and B_1 Homogeneity

B_0 homogeneity is of utmost importance for image quality, and less effort is required to guarantee this homogeneity at lower B_0 values.

B_1 homogeneity is also crucial, to ensure homogenous excitation of the desired slice or volume. B_1 – or more precisely B_1^+ – is the transmitted radiofrequency field that excites the protons at their Larmor frequency. The flip angle is directly related to B_1 through:

Equation 7

$$\alpha = \gamma \cdot B_1 \cdot t_p$$

where α is the targeted flip angle of the applied RF pulse, γ is the gyromagnetic ratio of the proton, B_1 is the magnetic field of the applied RF pulse, and t_p is the pulse duration.

From this equation, it is clear that if B_1 is not homogenous, the excited slice or volume will show varying flip angle, leading to variations in contrast and SNR.

When the Larmor frequency ω increases, the associated wavelength λ decreases. At 3T, the wavelength within the human body is approximately 25–30 cm [14], close to the dimensions of a human torso. This results in construc-

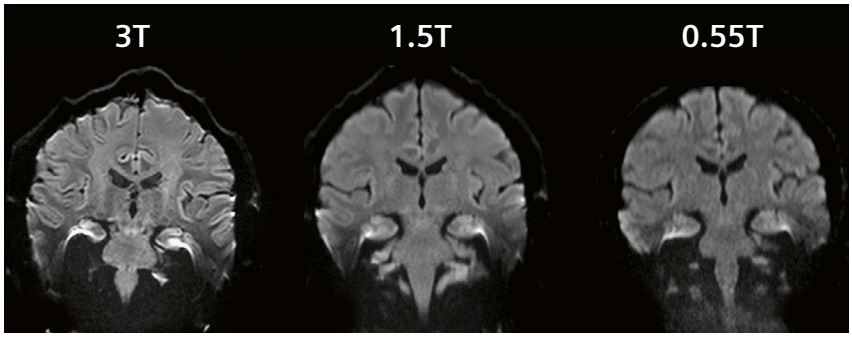

3 Coronal EPI diffusion scans (b = 1000 s/mm²) acquired on the same volunteer with three different fields. Moving to lower field typically comes with a reduction in SNR; but at the same time susceptibility artifacts near the temporal lobe due to vicinity of the air-filled internal auditory canal are substantially reduced.

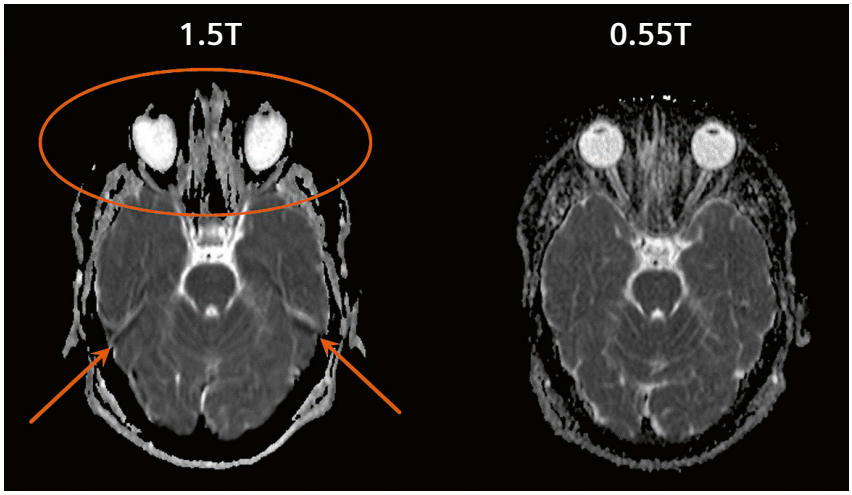

4 Geometric distortions caused by the air-filled sinuses and internal auditory canal are substantially reduced at lower field. In this example on the same volunteer at 1.5 and 0.55T, the eyeballs maintain their almost spherical shape, and the optic nerves are clearly visible (ellipse); the susceptibility artifacts near the temporal lobes (arrows) are almost invisible at 0.55T.

tive and destructive interference within the body, leading to inhomogeneous B_1 excitation. This phenomenon has triggered lots of research efforts to mitigate this problem and can now be considered understood; countermeasures such as B_1 shimming are available, but come with increased costs and hardware requirements.

Conversely, at lower field, the Larmor frequency is lower, so the associated RF wavelength is longer. This reduces or even eliminates the effect of interference. For example, at 0.55T, the wavelength is approximately 130–140cm, much larger than typical body diameter. So B_1 will be more homogeneous at lower field, giving more homogeneous contrast and SNR behavior.

Summary

For more than 20 years, the clinical standard for MR imaging has been either 1.5T or 3T. While many of the physical advantages of low field have been well known in the scientific community, the push for higher SNR favored higher fields. However, in the light of technical improvements made over the last 20 years, other metrics may be favored. Improvements in image reconstruction – from parallel imaging [16,17] and compressed sensing [18] to deep learning [19] – mean that clinicians can make optimal use of the available signal while exploiting the physical advantages of low-field MRI, such as reduced artifacts.

If SNR is sufficient at two different fields, then the focus may fall instead on diagnostic or financial value. Scientific literature even back in the mid 1990s showed no significant difference in diagnostic sensitivity or specificity between 1.5T and lower-field systems [20, 21]. Low-field machines are also less expensive, which is particularly relevant given the cost pressure in many healthcare systems.

All these factors could help bring MRI to places it has not been before – spreading into new geographical and clinical areas. The future of low-field MRI looks bright.

Contact

André Fischer, Ph.D.
Global Segment Manager Neurology
Siemens Healthineers
SHS DI MR M&S CSM
Allee am Roethelheimpark 2
91052 Erlangen, Germany
andre.fischer@siemens-healthineers.com



References

1 Hoult DI et al. The field dependence of NMR imaging. Magn Reson Med. 1986;3:722-746.
2 Boska MD et al. Comparison of P-31 MRS and H-1 MRI at 1.5 and 2.0 T. Magn Reson Med. 1990;13:228-238.
3 Pohmann R et al. Signal-to-noise ratio and MR tissue parameters in human brain imaging at 3, 7, and 9.4 tesla using current receive coil arrays. Magn Reson Med. 2016;75:801-809.
4 IEC 60601-2-33
5 Korb JP, Bryant RG. The physical basis for the magnetic field dependence of proton spin-lattice relaxation rates in proteins. J Chem Phys. 2001;115:10964–10974.
6 Wang Y et al. B0-field dependence of MRI T1 relaxation in human brain. Neuroimage. 2020;213:116700.
7 Campbell-Washburn A et al. Opportunities in Interventional and Diagnostic Imaging by Using High-performance Low-Field-Strength MRI. Radiology 2010;293:384-393.
8 Wang Y, Liu T. Quantitative Susceptibility Mapping (QSM): Decoding MRI Data for a Tissue Magnetic Biomarker. Magn Reson Med. 2015;73:82-101.
9 Tan H et al. Quantitative Susceptibility Mapping in Cerebral Cavernous Malformations: Clinical Correlations. Am J Neuroradiol. 2016;37:1209-1215.
10 Zeineddine HA et al. Quantitative susceptibility mapping as a monitoring biomarker in cerebral cavernous malformations with recent hemorrhage. J Magn Reson Imaging. 2018;47:1133-1138.
11 Gray CF et al. Low-field magnetic resonance imaging for implant dentistry. Dentomaxillofacial Radiology. 1998;27:225-229.
12 Klein H-M. Clinical Low Field Strength Magnetic Resonance Imaging - A Practical Guide to Accessible MRI. New York: Springer; 2016.
13 Klein H-M. Low-Field Magnetic Resonance Imaging; Fortschr Röntgenstr. 2020;192:537-548.
14 Choi J-Y et al. Abdominal Applications of 3.0-T MR Imaging: Comparative Review versus a 1.5T system. Radiographics. 2008;28:e30.
15 Moelker A et al. Relationship between magnetic field strength and magnetic-resonance-related acoustic noise levels. MAGMA. 2003;16:52-55.
16 Pruessmann KP et al. SENSE: sensitivity encoding for fast MRI; Magn Reson Med. 1999;42:952-962.
17 Griswold MA et al. Generalized autocalibrating partially parallel acquisitions (GRAPPA). Magn Reson Med. 2002;47:1202-1210.
18 Lustig M et al. Sparse MRI: The application of compressed sensing for rapid MR imaging. Magn Reson Med. 2007;58:1182-1195.
19 Hammernik K et al. Learning a variational network for reconstruction of accelerated MRI data. Magn Reson Med. 2018;79:3055-3071.
20 Lee DH et al. MR Imaging Field Strength: Prospective Evaluation of the Diagnostic Accuracy of MR for Diagnosis of Multiple Sclerosis at 0.5 and 1.5T. Radiology. 1995;194:257-262.
21 Vellet AH et al. Anterior cruciate ligament tear: prospective evaluation of diagnostic accuracy of middle- and high-field-strength MR imaging at 1.5 and 0.5 T. Radiology. 1995;197:826-830.

MAGNETOM Free.Max: from Concept to Product, a Brief History of the DryCool Magnet Development

Simon Calvert, CEng FIMechE

Head of Product Innovation & Chief Technology Officer, Siemens Healthineers, Oxford, UK

Introduction

Our new DryCool magnet is a key enabling element of our ground-breaking MAGNETOM Free.Max MRI system. The development and production program for the new generation magnet has lasted four years but was preceded by a research program lasting seven years, focussed on completely transforming our superconducting MRI magnet technologies. The program included developing new magnet coil technology and structural concepts as well as realising a dramatic reduction in our dependency on increasingly expensive, and sometimes scarce, liquid helium coolant. The highly innovative technologies used in the DryCool magnet are complimentary, and deliver a robust, reliable, and lightweight "plug and play" magnet solution to you.

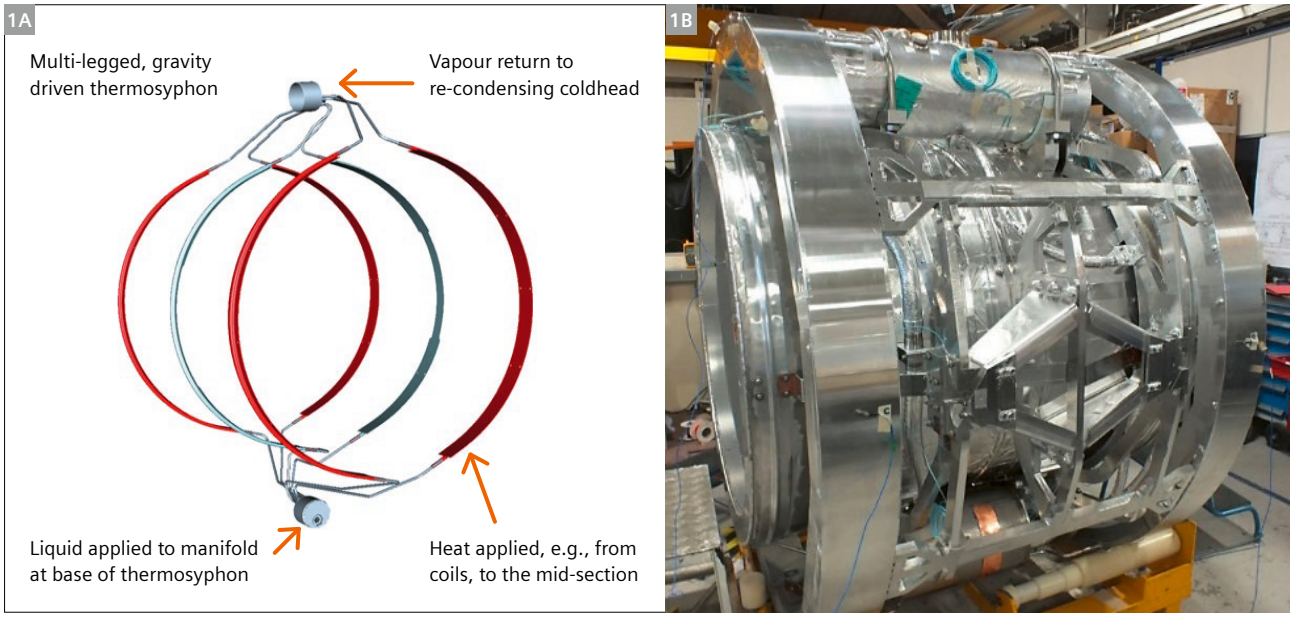

1 1.5 Tesla demonstrator showing the cryogenic concept and the superconducting magnet structure. **(1B)** 4K mass during build.

MAGNETOM Free.Max is currently under development and is not for sale in the U.S. and in other countries. Its future availability cannot be ensured.

1.5T Minimum Helium Inventory (MHI) research program (2008–2015)

In 2008 we started a program to transform our magnet technology and to reduce our dependency on helium. A key requirement for conduction-cooled superconducting magnets is to minimize the mass of the cold parts of the structure. Our focus was to use only the magnet's own refrigerator to cool down to operating temperature, thus avoiding the requirement for complex installation procedures.

The focus of the research program was to realize a 1.5T "Minimum Helium Inventory" magnet, which could later be integrated into an MRI system for imaging trials. Half scale, pipe-cooled magnets were developed and tested to prove the various technical concepts which were to be used in the 1.5T demonstrator. All tests were successful, and these technologies were then incorporated into the full-size magnet. The demonstrator was not intended to lead directly to a product but was a testbed to evaluate our new ground-breaking technologies. The magnet worked reliably and was also extensively tested in a MAGNETOM Aera MRI system in 2014 where it performed as well as the conventional "wet" magnet. New magnet electronics and software concepts were also developed and evaluated as part of the 1.5T MHI demonstrator program.

Simplification and focus on manufacturability

A great deal was learnt from the 1.5T research program, including how to develop a "dry" magnet which was optimized for cost and manufacturability. Much was also learnt about how conduction-cooled magnets interact with the MRI system and, in particular, the gradient system.

DryCool magnet development program (2016–2020)

It was decided to focus the magnet development program on a 0.55T magnet. This lower field also enabled the first 80 cm patient bore in the market without a substantial impact on the product cost. The lower field also keeps the mass low and so enables a short cool-down time. The very low mass of the magnet also reduces the installation cost and enables siting in non-traditional locations. The lower field also results in better compatibility with implants and interventional devices such as catheters.

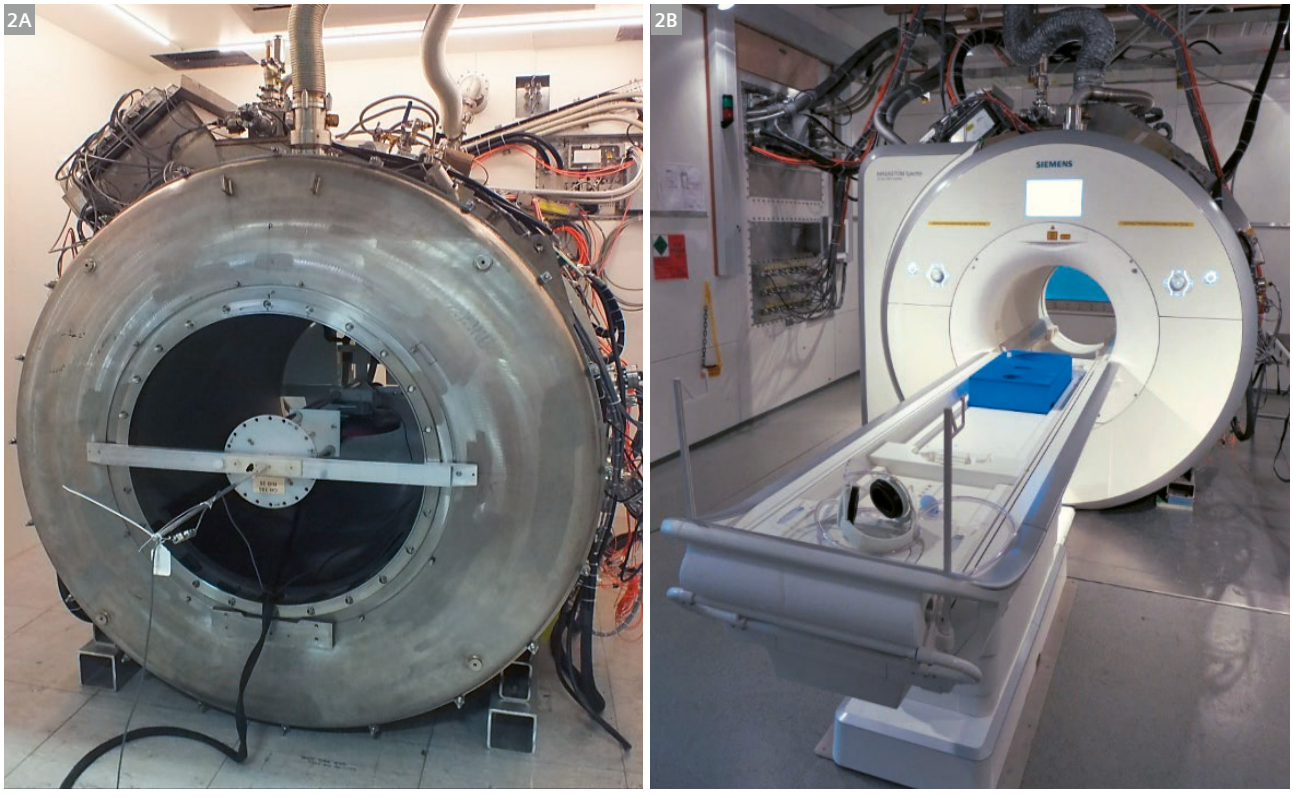

2 1.5 Tesla demonstrator during magnet testing and MRI system testing in 2014. **(2A)** Magnet tests in Oxford. **(2B)** System tests in Erlangen.

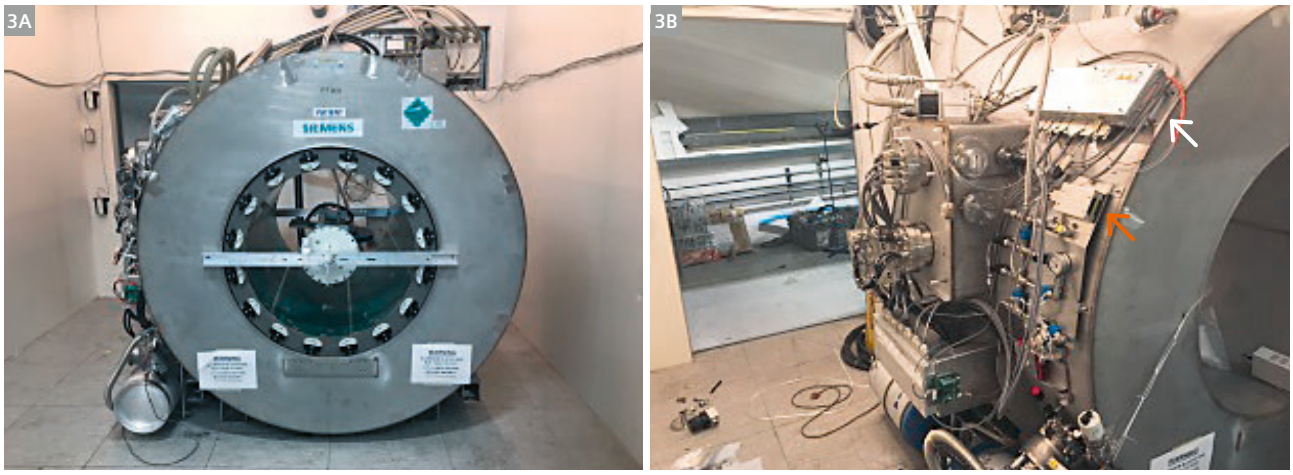

3 Prototype DryCool 0.55 Tesla magnet with close-up of electronics and cryogenic package. RDL (Run-down Load, orange arrow). MSCU (white arrow).

DryCool magnet specification

• Field strength:	0.55 Tesla
• Field temporal stability:	< 0.1 ppm/hour
• 5 gauss contours (from isocentre):	Axial 4.0 m, Radial 2.5 m
• Homogeneity:	See table 1
• Magnet length:	1.48 m
• Magnet warm bore:	1.060 m
• Magnet mass (installed):	1635 kg
• Liquid helium inventory:	0.7 litres (under normal operation)
• Helium boil-off rate:	Zero (under all imaging conditions)
• Cryogenic system:	Sealed helium system, no quench line
• Cooldown time from warm:	< 14 days (using the magnet's refrigerator)
• Designed acceleration limits:	5g vertical, 2g lateral
• Magnet current leads:	Fixed leads with HTS elements
• Automatic ramp-down:	Yes, if refrigeration is off for a period.
• Auto ramp-up:	Yes. Controlled by the magnet supervisory.
• Remote monitoring of the magnet:	Yes. Diagnostics on magnet and refrigerator.

Homogeneity Vrms (based on highly accurate 24 plane, 20 point plot)	Guaranteed
10 cm DSV	0.02 ppm
20 cm DSV	0.075 ppm
30 cm DSV	0.3 ppm
40 cm DSV	1.4 ppm
50 x 50 x 45 cm DEV	5.0 ppm

Table 1

DryCool magnet features

Advanced superconducting magnet structure with very low mass

The new superconducting magnet structure has a mass of approximately 300 kg. To achieve this exceptionally low mass in a large bore, the actively shielded magnet required the use of several new and innovative technologies. A completely new structural concept was used for the coils and supporting structure which, while very robust, allowed the use of very thin, yet stiff, structures. Since the volume of superconductor in the coil is low, a new ultra-fast quench propagation system was also developed to ensure that the magnet was not damaged if the Emergency Run Down Unit (ERDU) button was pressed. New superconducting joints, superconducting switches and other components were also developed. These components are no longer immersed in liquid helium and so need to be cooled by conduction only. Another key aspect of the magnet structure was to ensure that the coils had very low heating due to interaction with the gradient coil. New and innovative technologies were adopted to ensure that gradient coil-induced heating of the coils was minimized, and subsequent testing showed that the approach adopted was highly effective.

Simplified, manufacturable, and robust DryCool cryogenic system

The 1.5 Tesla demonstrator magnet had a cryogenic system which used pipes encircling the superconducting structure. While quite effective, such a system is complex to manufacture with many joints in the helium system. For the DryCool magnet, we adopted a simpler and more robust approach which was suitable for manufacture in high volumes. The cryogenic package is a separate sub-system which is integrated into the superconducting magnet structure by use of an innovative and highly optimized thermal connection system. This system efficiently removes heat from the coils and supporting structure giving a fast cool-down time, a low base temperature, and excellent tolerance of gradient coil interaction. Even with the most challenging imaging sequences, there is minimal heating of the magnet coils. The cryogenic package contains 0.7 litres liquid helium and is sealed, and so requires no quench pipe. Charging of the helium system is by high pressure gas only and no liquid helium is required. Once charged, and provided with power, the magnet will automatically cool down to operating temperature in less than 14 days. If the magnet arrives at the installation site partially cold, as will often be the case, the cool down time will be shortened.

DryCool magnet cryostat

The magnet cryostat is the sub-system that keeps the magnet coils cold and well protected. It has been highly optimized to minimize weight, minimize heat input to the superconducting magnet, and to ensure a high level of robustness during shipment, installation, or in seismic events when on site. Since we intend the DryCool magnet to be shipped to a wide range of locations across the globe, we have designed the cryostat to meet the same specifications as our wet magnets. The magnet can withstand sustained loads of 5g in the vertical direction and 2g in both lateral directions. This very robust specification ensures that the magnet is well protected during shipment to site.

Magnet electronics package and software

Since the DryCool magnet has a small inventory of helium and the heat capacity of most materials at 4 Kelvin is negligible, the tolerance of loss of refrigeration is less than a conventional “wet” magnet. Conventional superconducting magnets typically contain hundreds of litres of liquid helium and this gives a tolerance of refrigeration failure measured in days before magnet ramp-down is required. For the DryCool magnet, we have developed a sophisticated electronics and software system which monitors the magnet and refrigeration system and makes decisions about when to ramp the magnet down to avoid a quench. If the refrigeration system is off for a significant time period, the Magnet Supervisory and Control Unit (MSCU) will execute a magnet ramp down to avoid dissipating the magnet stored energy in the cold mass. The magnet energy is instead dissipated in a passive Run Down Load (RDL). Once the

magnet has been run down, and the power and cooling water is available again, the RDL is actively cooled to reduce the temperature so that the magnet can be ramped back to field. The MSCU also monitors many other magnet parameters to determine when the magnet can be automatically ramped back to field. The magnet has an integrated Magnet Power Supply (MPS) which is used to automatically ramp the magnet to its precise current for field, before putting the magnet into persistent mode. The MSCU also monitors many magnet and refrigeration parameters which can be monitored remotely by our service organisation. This allows preventative maintenance to be planned to ensure maximum "uptime" for the magnet and MRI system.

Product Life Cycle (PLC) and Total Cost of Ownership (TCO) savings

One key focus of the development of the DryCool magnet was to minimize Product Lifecycle Cost and Total Cost of Ownership for the customer. The very low magnet mass reduces the shipping costs, and reduces the logistics carbon footprint as, in many cases, sea or road shipments can be used rather than air freight. The low mass also reduces installation costs and allows the magnet to be sited on upper floors. The low mass and small size of the magnet also allows the MAGNETOM Free.Max MRI system to be sited in non-traditional locations such as ER departments and clinics. The lack of a quench pipe further reduces the installation costs and enables the magnet to be sited in locations where quench pipe runs would be too long, or very difficult and expensive to install. The lack of a large helium inventory reduces the magnet purchase price and reduces the servicing costs for the customer. Since the magnet has its own magnet power supply, the customer can, in most cases, ramp the magnet up and down when required without a service visit being required.

Conclusions

The DryCool magnet is a highly innovative development which incorporates many new technologies and concepts. The magnet delivers the first 80 cm patient bore in the industry and is a key enabler for the ground-breaking MAGNETOM Free.Max 0.55 Tesla MRI scanner. The magnet minimizes PLC and TCO and virtually eliminates the complex superconducting magnet servicing procedures which have been in place for several decades. The magnet is enabled for siting outside of traditional imaging suites and will undoubtably be used for many new applications in the future.

Contact

Simon Calvert
Siemens HC Ltd. MR Magnet Technology
SHS DI MR R&D MD
Wharf Road
OX29 4BP Oxford
United Kingdom
simon.calvert@siemens-healthineers.com



Improving Productivity in MRI – Clinical Experience in a Multisite Outpatient Practice Setting

Mike Notohamiprodjo, M.D., MHBA; Gerwin Schmidt, M.D.

DIE RADIOLOGIE, Munich, Germany

Introduction

Magnetic resonance imaging (MRI) is one of the most commonly performed procedures and the financial backbone of diagnostic imaging. Since the populations of industrial countries are continuously aging and average morbidity is therefore increasing, demand for diagnostic procedures is growing. Labor and operating costs, however, are rising while reimbursement for medical procedures is declining. This makes efficient exploitation of the available resources of pivotal importance in an increasingly competitive healthcare market.

Expanding the number of examined patients per MR scanner will help to meet the growing clinical demand and reliably improve profitability [1].

For this reason, an efficient and productive workflow with short patient changeover and acquisition times is essential. MR protocols should be sufficiently short, without losing time for planning and setting up the examinations. At the same time, high image quality has to be maintained to ensure diagnostic relevance. Investing in new acceleration techniques and workflow solutions will help to achieve these goals and bring forward the break-even point.

The recently introduced BioMatrix Technology and *syngo* MR XA software provide several methods to streamline the daily workflow of MR technologists. In order to shorten patient changeover times, automated selection and positioning of coils have been integrated, as has automation of image acquisition using Dot engines. In addition to established parallel imaging techniques such as GRAPPA and CAIPIRINHA, advanced acceleration methods have been integrated into the clinical protocols: Simultaneous Multi-slice (SMS) imaging employs complex RF pulses to simultaneously acquire several sections along the z-axis, allowing a significant reduction in the image acquisition time by shortening the required TR time with little SNR penalty [2], while Compressed Sensing (CS) rapidly accelerates MR imaging by reconstructing sparse data from a highly undersampled *k*-space [3].

DIE RADIOLOGIE, a large radiology network in the Munich area, recently installed a 1.5T MAGNETOM Sola scanner equipped with BioMatrix Technology and the newest acceleration techniques, as provided by the *syngo* MR XA20 software. Recent studies have shown that these methods can shorten individual sequences and entire examinations. However, we were interested to know whether the integrated technology is also effective in daily clinical routine and whether it could potentially increase the profitability of an MR scanner.

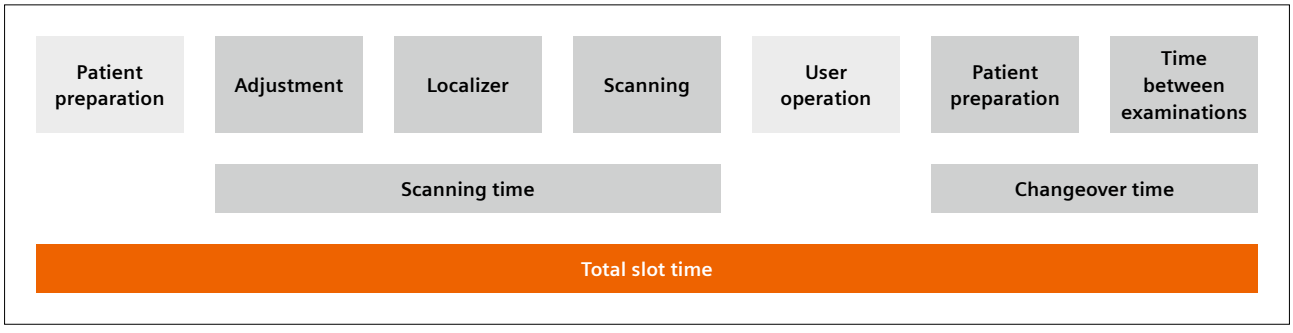

1 Definition of the components of an examination slot.

To study the effects of these novel techniques on patient throughput and subsequently on profitability, we performed a retrospective study that compared a 1.5T MAGNETOM Sola scanner with its predecessor, the 1.5T MAGNETOM Aera, in daily clinical routine.

Material and methods

MR scanners

DIE RADIOLOGIE is one of Germany's largest diagnostic imaging service providers with currently 13 outpatient practice sites in and around the Munich area. It operates 15 MR scanners, performing over 150,000 examinations per year. Over 250 healthcare professionals working as physicians, technologists, front-desk and administrative staff ensure that diagnostic and interventional procedures are performed to a high level.

The MAGNETOM Sola and MAGNETOM Aera (both Siemens Healthcare, Erlangen, Germany) are operated at different but similar sites in Munich. At each of these sites, another 1.5T scanner is operated in an adjacent suite.

The MAGNETOM Sola (software version *syngo* MR XA20; XJ gradients with 33 mT/m at 125 T/m/s, 32 channels) was installed mid-2019 and is equipped with a full coil set (20-channel tiltable head-neck-coil, 24-channel spine coil, 12-channel body coil, 16-channel Shoulder Shape coil, 18-channel Tx/Rx knee coil, 18-channel UltraFlex coil, 16-channel hand/wrist-coil, and 16 channel foot/ankle-coil), as well as the Turbo Suites Essential (iPAT, tPAT, PAT^2, CAIPIRINHA VIBE, CAIPIRINHA SPACE) and Excelerate (SMS EPI for DWI / DTI / BOLD, SMS TSE, CS TOF, CS SPACE), so that, in particular, Simultaneous Multislice imaging for DWI and TSE sequences and Compressed Sensing for MRCP and 3D time-of-flight sequences can now be integrated into clinical protocols. Furthermore, automated coil selection and patient positioning was applied.

The MAGNETOM Aera (software version *syngo* MR D13D, XQ gradients with 45 mT/m at 200 T/m/s, 48 channels) has been in operation since 2013, and features a similar coil set to the MAGNETOM Sola (20-channel head-neck coil, 32-channel spine coil, 18-channel body coil, 16-channel shoulder large/small, 15-channel Tx/Rx knee coil, 4-channel flex coil, 16-channel hand/wrist-coil and 16-channel foot/ankle coil). The most recent acceleration techniques, SMS and CS, are not available on this scanner.

Core examination times were between 8 a.m. and 6 p.m. on both systems. During core times, both scanners are usually operated by two technologists. The standard examination slot is 20 minutes long, so that three patients are examined per hour on average.

Usually, several examination slots are grouped by body region to minimize coil setup and examination times. There is no scheduled break during the day. The standard examination schedule for both scanners mainly consists of musculoskeletal and body imaging slots.

Prior to the study, internal and external application specialists matched the image quality of the MAGNETOM Sola to the MAGNETOM Aera, applying available acceleration techniques to shorten examination times. Image quality was approved by the authors of the study.

Data collection

Capacity utilization of the scanners was monitored using the cloud-based service teamplay (Siemens Healthcare, Erlangen, Germany) from August to October 2019. The extracted data comprised the body region examined, the coils used, the timepoints of patient registration, and all acquired sequences, including localizers and completion of the examination.

Using this data, parameters such as average patient preparation time before examination, average scanning time, average user operating time, average patient preparation time after examination, average time between examinations, and changeover time (sum of the last two items) could be derived (Fig. 1).

Only data collected during the core time between 8 a.m. and 6 p.m. was included. Days on which scanners were out of operation for more than one hour due to maintenance, for example, were excluded from the analysis.

Statistical analysis

Scanner operating times were found to exhibit normal distribution based on visual evaluation and were therefore summarized as mean values. To investigate differences between scanner operating times, one-tailed *t*-tests were performed on two independent samples with null hypotheses of time differences that equal zero and alternative hypotheses of greater time values for the MAGNETOM Aera than for the MAGNETOM Sola. Due to multiple testing, a p-value of < 0.001 (Bonferroni-corrected) was considered statistically significant. Time savings as a percentage were calculated as a time difference in relation to the operating times of the MAGNETOM Aera. Statistical analyses were conducted using Stata 16.1 (Stata Corporation, College Station, TX, USA).

Results

Examination mix

The most commonly performed examination on both scanners was MRI of the knee (Sola vs. Aera; 23% vs. 18%), of the lumbar spine (15% vs. 18%), of the cervical spine (12% vs. 16%), and of the shoulder (11% vs. 10%). Significantly more brain MRIs were performed on the MAGNETOM Aera than on the MAGNETOM Sola (6% vs. < 1%) (Fig. 2).

Clinical throughput

The average number of patients examined during the core time was significantly higher ($p < 0.001$) for the MAGNETOM Sola, n = 30 as opposed to n = 26 for the MAGNETOM Aera. This is a difference of 16%. On the busiest day, the number of examined patients was n = 33 for the MAGNETOM Sola and n = 29 for the MAGNETOM Aera.

The highest reduction in total slot time was achieved for MRI of the thoracic spine (21:55 vs. 28:09 minutes), lumbar spine (18:49 vs. 22:46 minutes), and the abdomen (22:23 vs. 26:57 minutes). The highest reduction in the average scan time was achieved for MRI of the knee (10:56 vs. 13:31 minutes), abdomen (14:20 vs. 17:34 minutes), and thoracic spine (14:41 vs. 17:18 minutes). The average slot time length was significantly shorter ($p < 0.001$), with 19:58 minutes for the MAGNETOM Sola and 22:35 minutes for the MAGNETOM Aera. The total slot time for the most commonly performed regions knee, lumbar and cervical spine, shoulder and ankle was reduced by between 10% and 17% on the MAGNETOM Sola (Fig. 3).

The overall average scanning time (adjustment, localizers, and measurement) on the MAGNETOM Sola was significantly, that is 12%, shorter ($p < 0.001$) than on the MAGNETOM Aera (12 minutes vs. 15 minutes). The average operating time (time for planning, patient communication during measurement) was also significantly, that is 22%, shorter ($p < 0.001$) for the MAGNETOM Sola (1:45 minutes vs. 2:15 minutes). The average changeover time (patient preparation after examination and time between examinations) was 3:42 minutes for the MAGNETOM Sola and 3:54 for the MAGNETOM Aera (Fig. 4), and therefore not significantly different.

Discussion

Our clinical productivity study shows that clinical throughput was significantly higher on the MAGNETOM Sola when compared with a similarly equipped MAGNETOM Aera. The average examination slot time was shortened by 2.5 minutes, which can be largely attributed to a shorter scanning time. The most frequently performed MR procedures were shortened by 11–17%, while maintaining similar image quality. These findings are of interest because the MAGNETOM Aera features stronger gradients and a higher number of channels while the MAGNETOM Sola is equipped with more recent accelerated acquisition techniques and coils.

The results of this study are significant because diagnostic imaging providers are also financial units, which are expected to achieve a certain profitability to meet the economic agenda of their respective shareholders. DIE RADIOLOGIE is still privately owned by its associate physicians, so that medical aspects such as high-quality examinations and precise diagnostic tests, an appropriate working environment, and comfortable patient experience still take precedence over purely financial aspects. In principle, a further shortening of the protocols is still potentially possible if necessitated by financial circumstances. However, for the time being we have decided against further accelerating MR protocols.

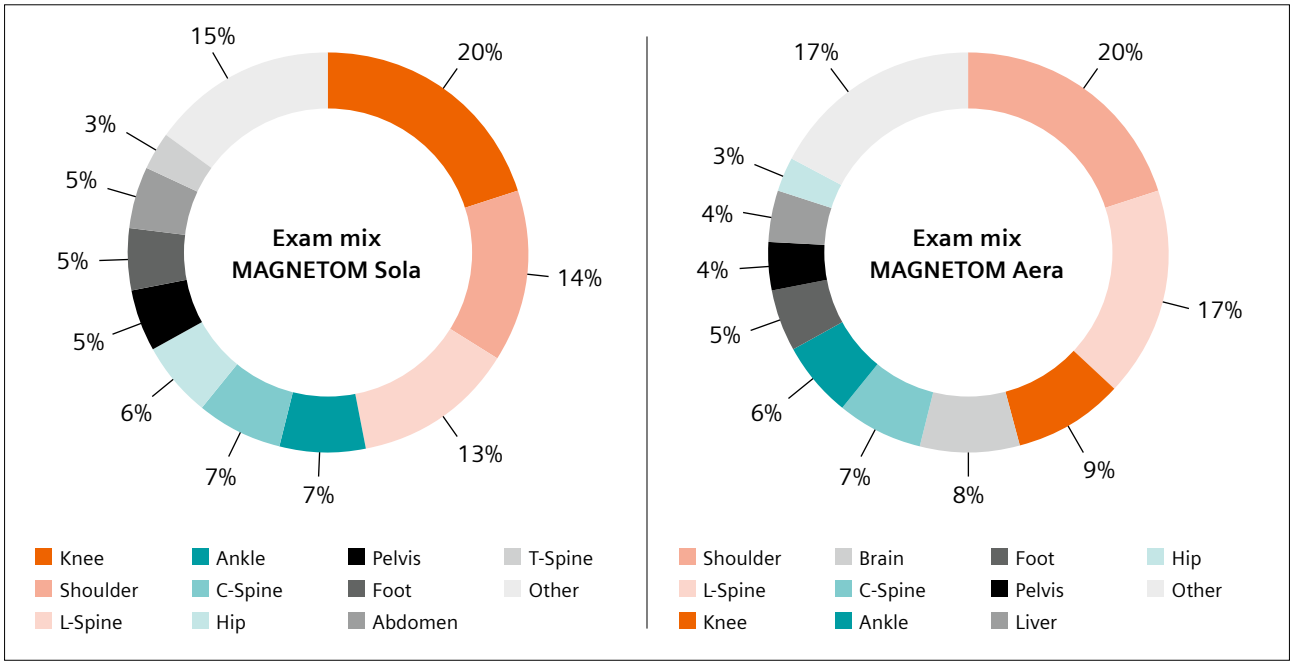

2 Exam mix of the MAGNETOM Sola and Aera.

With increasing patient throughput, a reduction in patient scanning time is one of the key components for shortening the examination slot time. While parallel imaging, usually with a GRAPPA acceleration factor of R = 2, is applied to most acquisition sequences, we have also integrated SMS acceleration into our clinical routine protocols on the MAGNETOM Sola to allow for a four-fold acceleration (achieved by combining GRAPPA R = 2 and SMS = 2). We have found that SMS acquisition is particularly helpful in examinations in which several slices are acquired, such as transversal sections of extremities or pelvic MR examinations. These findings corroborate previous studies, showing a significant reduction in the examination time when using this respective technique for rapid musculoskeletal imaging [4, 5] or diffusion-weighted imaging, particularly of abdominal organs [2, 6] and the prostate [7].

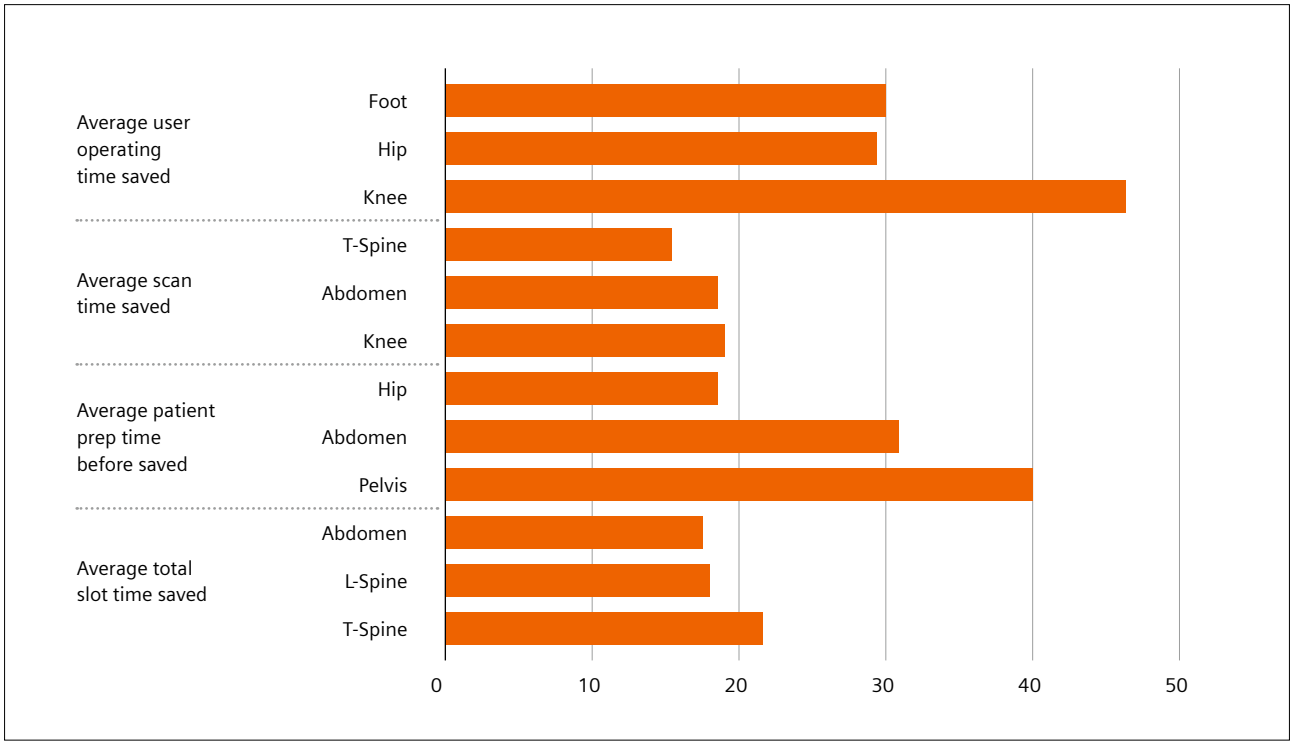

3 Top three savings in % by time category.

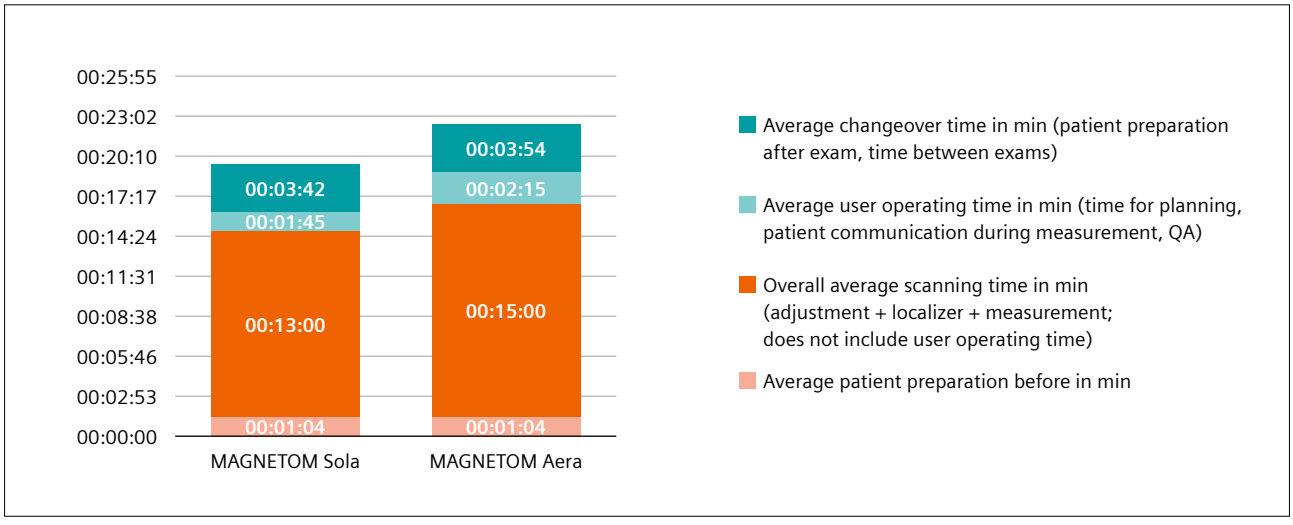

4 Time allocation comparison.

Alternatively, sequences accelerated with Compressed Sensing may lead to a significant reduction in acquisition time, such as for musculoskeletal imaging [1, 8, 9] or body imaging [3, 10, 11]. In our study, Compressed Sensing was applied for the acquisition of MRCP sequences in one breath-hold [3], providing excellent image quality in a considerably shortened acquisition time compared with the lengthy standard navigator-triggered acquisition technique, which is also susceptible to respiratory motion. The significantly shorter acquisition time of MRCP sequences most likely contributed considerably to the reduction in scan time for abdominal MRI on the MAGNETOM Sola.

Another important factor when attempting to accelerate patient throughput is shortening the non-scanning time, which consists of the changeover time and the operating time. The average changeover time was slightly shorter for the MAGNETOM Sola, which features automated coil detection and positioning. The operating time was shortened by 22%, presumably by exploiting the automated positioning of sequences in spine and knee examinations.

On average, the MAGNETOM Sola permitted the examination of four additional patients during the core scanning time. If we extrapolate the results of this study, we can expect to scan approximately one thousand additional patients each year, or save more than 300 hours of labor time. Both scenarios mean a significant increase in profitability of the scanner with a quick return on investment, while diagnostic image quality is maintained. It should be noted, however, that the additional examinations cause additional workload for the radiologists, so that any further acceleration of complex examinations would require the assistance of artificial intelligence to support quick and reliable diagnosis [12].

This study has its limitations. First, the study was performed three months after installation of the

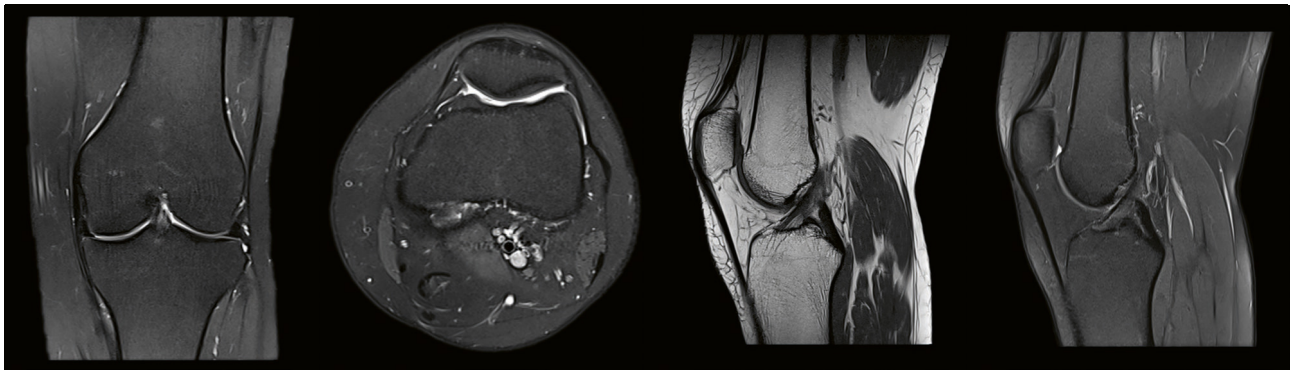

5 Example MRI of the knee acquired with the MAGNETOM Sola: Fat-saturated PD-weighted images in three planes (matrix 384 / slice thickness 3 mm / scan time 2 minutes approx. each / GRAPPA 2 / SMS2) and sagittal T1-weighted sequence (matrix 448 / slice thickness 3 mm / scan time 1:30 minutes / GRAPPA 2). Total scan time was approximately nine minutes including localizers / shimming / user operation.

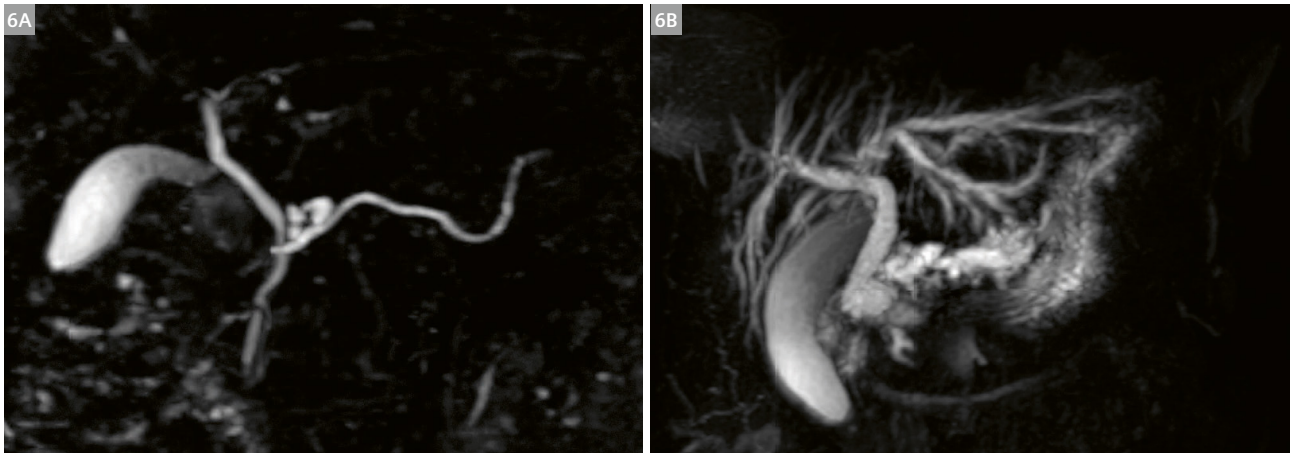

6 Example MRCP accelerated with CS acquired with the MAGNETOM Sola: **(6A)** Examination of a 56-year-old male patient with a branch duct type intraductal papillary mucinous neoplasia. **(6B)** Examination of a 62-year-old female patient with a papillary mass obstructing the common bile duct and pancreatic duct. Scan time was 18 seconds each.

MAGNETOM Sola, which was compared with a system that had been in operation for seven years, so further refinement of protocols and therefore acceleration is to be expected. Second, each scanner was operated by a different team of technologists, so that changeover and operating times, for example, could also be dependent on the individual speed of the technologist. However, the reduction in slot duration was largely achieved by adjusting the scanning time. Thirdly, we did not factor in repetition of sequences, for example, due to motion artifacts, or canceled examinations, which resulted in an increased time between examinations.

In summary, the advanced acceleration techniques of the MAGNETOM Sola allowed for a significant reduction in examination time, leading to a higher throughput during clinical routine and therefore dramatically increasing profitability of the scanner.

Acknowledgments

We would like to thank Dr. Roberto Lorbeer from Ludwig-Maximilians-University (LMU) Munich for advice on the statistical analysis.

References

1 Bratke G, Rau R, Weiss K, Kabbasch C, Sircar K, Morelli JN, et al. Accelerated MRI of the Lumbar Spine Using Compressed Sensing: Quality and Efficiency. J Magn Reson Imaging. 2019;49(7):e164-e75.
2 Taron J, Martirosian P, Schwenzer NF, Erb M, Kuestner T, Weiss J, et al. Scan time minimization in hepatic diffusion-weighted imaging: evaluation of the simultaneous multislice acceleration technique with different acceleration factors and gradient preparation schemes. MAGMA. 2016;29(5):739-49.
3 Taron J, Weiss J, Notohamiprodjo M, Kuestner T, Bamberg F, Weiland E, et al. Acceleration of Magnetic Resonance Cholangiopancreatography Using Compressed Sensing at 1.5 and 3 T: A Clinical Feasibility Study. Invest Radiol. 2018;53(11):681-8.
4 Fritz J, Fritz B, Zhang J, Thawait GK, Joshi DH, Pan L, et al. Simultaneous Multislice Accelerated Turbo Spin Echo Magnetic Resonance Imaging: Comparison and Combination With In-Plane Parallel Imaging Acceleration for High-Resolution Magnetic Resonance Imaging of the Knee. Invest Radiol. 2017;52(9):529-37.
5 Kaller S, Rullmann M, Patt M, Becker GA, Luthardt J, Girbardt J, et al. Test-retest measurements of dopamine D1-type receptors using simultaneous PET/MRI imaging. Eur J Nucl Med Mol Imaging. 2017;44(6):1025-32.
6 Taron J, Weiss J, Martirosian P, Seith F, Stemmer A, Bamberg F, et al. Clinical Robustness of Accelerated and Optimized Abdominal Diffusion-Weighted Imaging. Invest Radiol. 2017;52(10):590-5.
7 Weiss J, Martirosian P, Taron J, Othman AE, Kuestner T, Erb M, et al. Feasibility of accelerated simultaneous multislice diffusion-weighted MRI of the prostate. J Magn Reson Imaging. 2017;46(5):1507-15.
8 Fritz J, Fritz B, Thawait GK, Raithel E, Gilson WD, Nittka M, et al. Advanced metal artifact reduction MRI of metal-on-metal hip resurfacing arthroplasty implants: compressed sensing acceleration enables the time-neutral use of SEMAC. Skeletal Radiol. 2016;45(10):1345-56.
9 Fritz J, Raithel E, Thawait GK, Gilson W, Papp DF. Six-Fold Acceleration of High-Spatial Resolution 3D SPACE MRI of the Knee Through Incoherent k-Space Undersampling and Iterative Reconstruction-First Experience. Invest Radiol. 2016;51(6):400-9.
10 Weiss J, Notohamiprodjo M, Taron J, Martirosian P, Nickel D, Bamberg F, et al. Continuous Hepatic Arterial Multiphase Magnetic Resonance Imaging During Free-Breathing. Invest Radiol. 2018;53(10):596-601.
11 Weiss J, Notohamiprodjo M, Martirosian P, Taron J, Nickel MD, Kolb M, et al. Self-gated 4D-MRI of the liver: Initial clinical results of continuous multiphase imaging of hepatic enhancement. J Magn Reson Imaging. 2018;47(2):459-67.
12 Rueckel J, Kunz WG, Hoppe BF, Patzig M, Notohamiprodjo M, Meinel FG, et al. Artificial Intelligence Algorithm Detecting Lung Infection in Supine Chest Radiographs of Critically Ill Patients With a Diagnostic Accuracy Similar to Board-Certified Radiologists. Crit Care Med. 2020.



Gerwin Schmidt



Mike Notohamiprodjo

Contact

Prof. Mike Notohamiprodjo
Deputy Managing Partner
DIE RADIOLOGIE
Sonnenstr. 17
80331 München
Germany
Phone: +49 (89) 550596-0
Mike.Notohamiprodjo@die-radiologie.de

MAGNETOM Free.Max: Access to MRI – How to Make it Big Inside and Small Outside

Stephan Biber, Ph.D.

Senior System Architect & Principal Key Expert at Siemens Healthineers, R&D AEP, Erlangen, Germany

MR systems have always been known to be large, heavy machines that require a complex infrastructure such as the supply of liquid helium and a highly reliable supply of electricity and cooling. While the new DryCool magnet technology has been presented in detail by Simon Calvert [1], this article will focus on how the MAGNETOM Free.Max[1] system is able to be big on the inside with the first-ever 80 cm patient bore on the market, making it at the same time one of the smallest whole-body MRI systems on the market. With a footprint of just 23 m², a transportation height of less than 2 meters, and a weight of only 3.2 tonnes we believe the system defines a new class of MRI systems. This paper will present a number of technical innovations, which in isolation could be seen as simple engineering tasks, but together they help to overcome long-established issues with the installation process and therefore can realize unmet customer needs. Furthermore, we would like to demonstrate how only a holistic system-perspective, which aligns all the engineering disciplines behind a common goal, is able to accomplish this.

How to make it big: Combining field strength and gradient power with new imaging techniques

MR systems with solenoid magnets have been available with 60 cm patient bores since the early 1990s. In 2004, Siemens Healthineers introduced MAGNETOM Espree, the first 1.5T system with a 70 cm bore and MAGNETOM Verio in 2007, the first 3T system with a 70 cm bore. This broadened access to MRI for growing patient groups by improving comfort, counteracting claustrophobia, and accommodating obese patients in the bore. Despite the larger bore on the 70 cm systems, the need remained for even more space in the bore for the same reasons that first triggered the development of 70 cm systems. But whereas 20 years ago, the market was able to deal with the associated increased costs of 70 cm systems versus 60 cm systems, the situation is different today. Radiology is under severe cost pressure, which calls for new ways of providing high-value imaging with improved patient access at an affordable cost.

The belief in MRI has long been that higher field strengths and gradient powers together with a high receive system channel count delivers better image quality and higher speeds. This belief still holds true but there are other ways to serve markets that require the diagnostic quality of a 1.5T system but not necessarily at exactly the same speed and contrast. A larger bore diameter is essentially what drives up the costs of MRI systems. This, in turn, reduces the accessibility of MRI to a large part of the worldwide population. The costs of the magnet (mainly the superconductive wire) increase rapidly as the size rises. Gradient coil power increases with ~R^5, which would quadruple the power needed when going from a 60 to 80 cm patient bore. The only way out is to go against the grain and question existing assumptions on field strength and gradient power.

During an early prototyping phase back in 2016, a 1.5T MAGNETOM Aera system was ramped down to 0.55T and equipped with modified RF-electronics. With *in vivo* imaging, it was then possible to assess image quality and analyze the impact of different types of gradient engines.

Designed as our most compact whole-body MRI MAGNETOM Free.Max



Open	Small	Light	Low
80 cm	23 m²	< 3.2 t	< 2 m

[1] *MAGNETOM Free.Max is pending 510(k) clearance, and is not yet commercially available in the United States.*

The in-house prototype and a replica of this system installed at the National Institutes of Health (NIH) helped to demonstrate that routine clinical questions in general radiology can be answered at a field strength of 0.55T [2]. Our internal analysis indicated that acceptable image quality and measurement times could be achieved with a gradient engine of 45 T/m/s and a gradient field of approximately 26 mT/m for this application field. In contrast to the 1990s, we were able to combine this MRI system with new imaging techniques that help overcome some of the drawbacks of mid-field imaging. These negative aspects had originally stimulated the design of 1.5T scanners, e.g., DeepResolve Gain and Sharp are image reconstruction methods enabling intelligent, iterative denoising using individual noise maps and an increase in image resolution using a deep neural network. These technologies can be used to reduce acquisition times and improve image quality simultaneously. At the same time, Deep Resolve can be combined with image acceleration techniques such as parallel imaging – which was not available in the 90s – and Simultaneous Multi-slice (SMS) on MAGNETOM Free.Max. In addition, Compressed Sensing has also proven to be a valuable tool for acquisition acceleration. For clinical examples, please refer to the Image Gallery [3].

The unique combination of a 0.55T scanner with various powerful new acquisition and reconstruction techniques laid the foundation for the innovation, MAGNETOM Free.Max. The reduced field strength on both the magnet and the gradient engine allowed the bore diameter to be scaled up from 60 to 80 cm, while still keeping the superconductive wire length and gradient power within a range that would make the system more affordable.

Figure 1A shows the optimization in the multiparameter space: superconductive wire length and costs increase with field strength and magnet bore diameter. When starting with an 80 cm patient bore (1), the thickness needed for the gradient coil and the body coil dictate the magnet bore diameter. For the sake of simplicity here, we assume a range of different thicknesses shown by the blue and green areas, with a slight tendency of gradient coils with higher G_{max} and SR to also require more radial space (2). With the magnet bore diameter derived from the outer diameter of the gradient coil, the impact on wire length for 0.5T and 1.5T are shown by the yellow and red curves (3), assuming similar boundary conditions on the stray field. These two curves show the huge scale of the nonlinear increase in the superconductive wire for the magnet when field strength and bore diameter are increased.

Starting from the 80 cm bore diameter, looking into the lower right quadrant (4), it becomes evident that the gradient power not only increases with higher SR and G_{max}, but it increases disproportionally with patient bore diameter.

Increased gradient power usually goes hand in hand with the additional power needed for the cooling system, which has to extract the heat from the gradient coil and the gradient power amplifier (GPA) and dissipate it in the

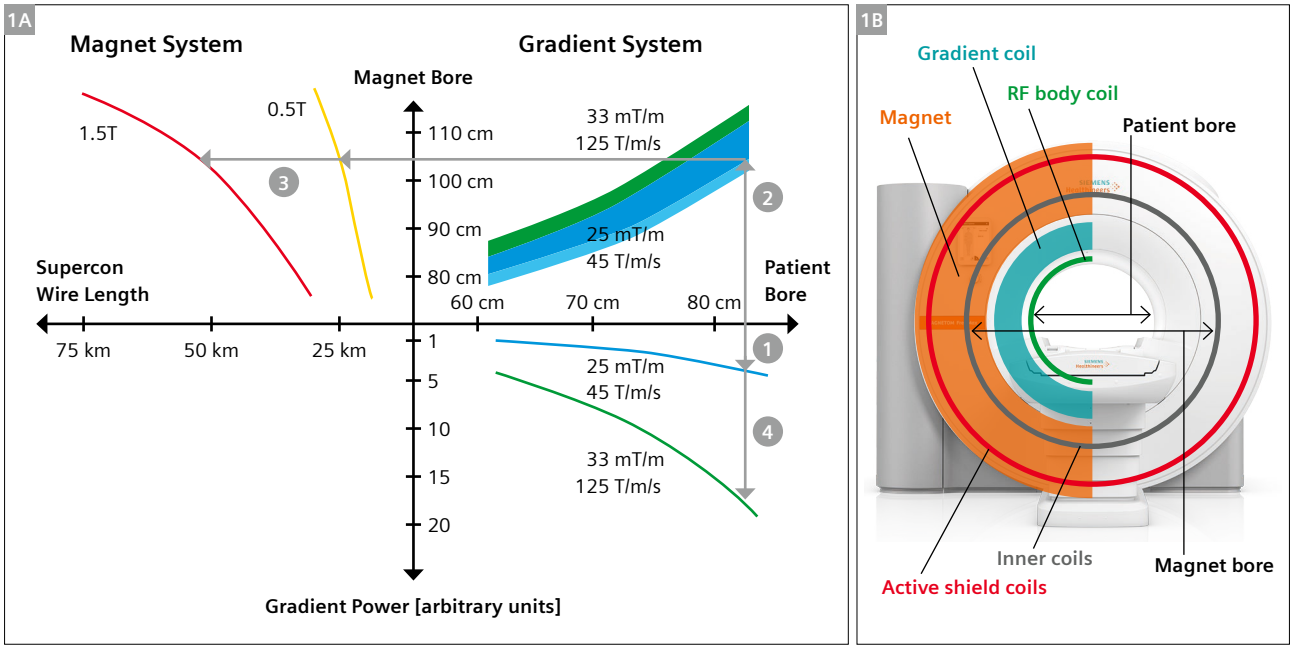

1 **(1A)** Scaling of superconductive wire length and gradient power with patient bore and field strength. Figures are merely illustrative to show the main correlations. Please note that the numbers in this article are also indicative to explain the physics and not related to a special design. **(1B)** When starting with an 80 cm patient bore, the thickness needed for the gradient coil and the body coil dictate the magnet bore diameter.

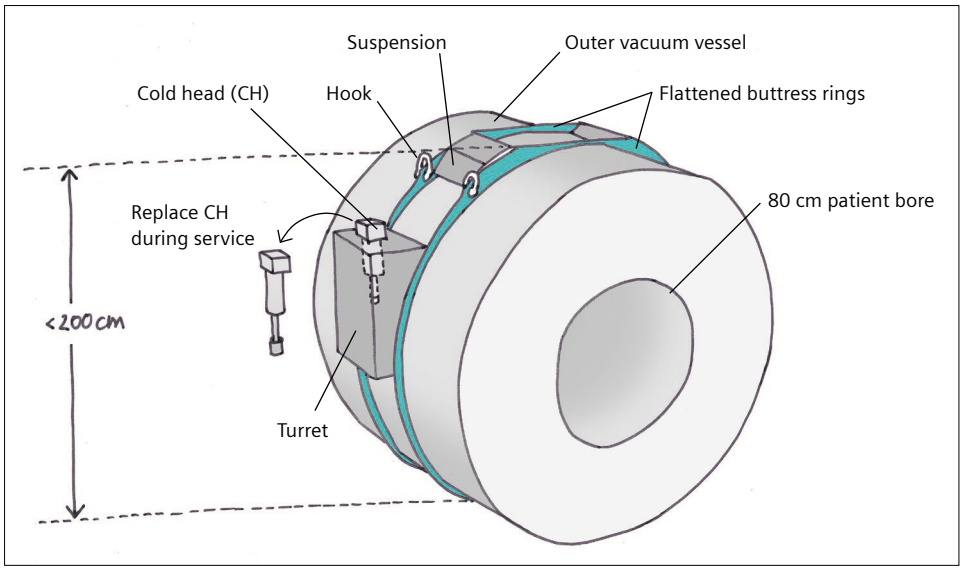

2 Figure 2 shows the flattened buttress rings, the outer vacuum vessel (OVC) with the shield coils, and the turret with the cold head that is moved further down on the side of the system.

air. Therefore, stronger gradients have a quadruple effect on the system design: They require more power to generate the fields, they require more cooling to extract the resulting heat and together this drives needs on local infrastructure up (connection power, space for chiller, etc.). They tend to also drive the gradient coil thickness and therefore the inner diameter (4) of magnet.

Scaling the Tx subsystem to provide sufficient B_1 amplitude on a 23 MHz system with an 80 cm patient bore is – compared with the magnet and gradient design – the easiest piece in this puzzle. Luckily, a lower Lamor frequency also requires less power to achieve the same B_1 field. Therefore, an existing 63 MHz amplifier can be tuned to 23 MHz and the additional power can be invested in overcoming the lower efficiency $\eta = B_1/P_{BC}$ of a body coil with a larger diameter. The lower conductivity of tissue at a lower frequency also makes SAR an almost negligible issue.

How to keep it small

While the inside of an MRI system should be as large as possible to provide space for the patient, it is more difficult to identify what the system should look like from the outside. When observing an installation process, it immediately becomes clear that the height of the system is a critical parameter: The system should be easily movable through doors. In the past, even removing doors often did not help and MRI installations frequently meant breaking up concrete structures, affecting the structural integrity of the building. Naturally, this was often associated with high costs and organizational efforts as well as other unwanted consequences. In many countries, two-meter high door openings are standard. Here is the simple but effective recipe with five major ingredients how to make sure the MRI system stays below 2 m height:

1. Outer vacuum vessel: Limit shield coil diameter
Underneath the plastic cover of an MRI system is the outer vacuum chamber (OVC), which contains the cryoshield and the superconductive magnet coils (dry magnets do not need a helium vessel). When the inner coils of the magnet are moved outward to accommodate the large patient bore, the shield coils also tend to move further out. Setting a boundary of ~1.95 m for the diameter of the OVC sets a clear design goal for the position of the shield coils. If the OVC is to be within the two-meter limit, it is essential that no other parts of the system design exceed this limit.

2. Buttress rings and magnet suspension
For the OVC to withstand the 1 bar atmospheric pressure from the outside, it is reinforced using circumferential buttress rings. These rings are flattened at the top of the magnet without any negative impact on their structural stiffness, which in turn allows the shield coils to be moved out as far as possible inside the OVC. Another structure that potentially affects the overall height of the system are the suspensions that hold the magnet coils in place. A tensile suspension connects the 4 K cold inside of the magnet with the warm outer vacuum chamber (OVC). The mechanical structure required to mount the tensile suspension to the outside of the OVC needs to be very slim so that this is not the highest point.

3. Quench pipe
The dry magnet does not need a quench pipe. It follows that there is no pipework on top of the magnet that could require extra height on top of the OVC and would require the connection of the magnet to the ceiling. This makes the new SkyView option possible (Fig. 3), which gives the system a unique visual impression by removing any connection between the MR scanner and the ceiling.

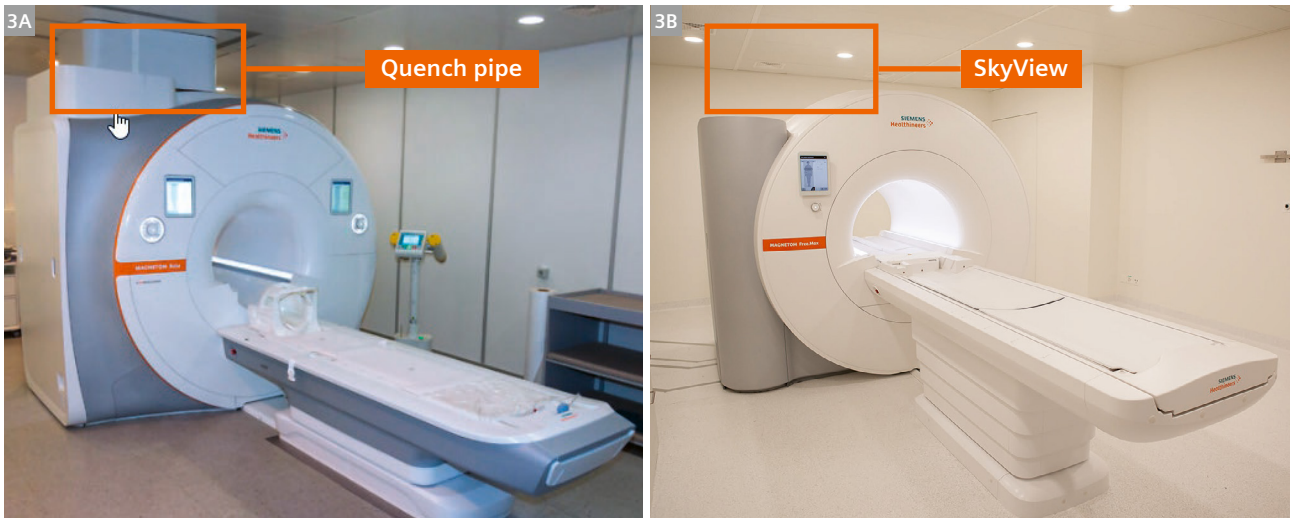

3 **(3A)** Conventional system with quench pipe. **(3B)** MAGNETOM Free.Max with DryCool magnet technology and easy siting.

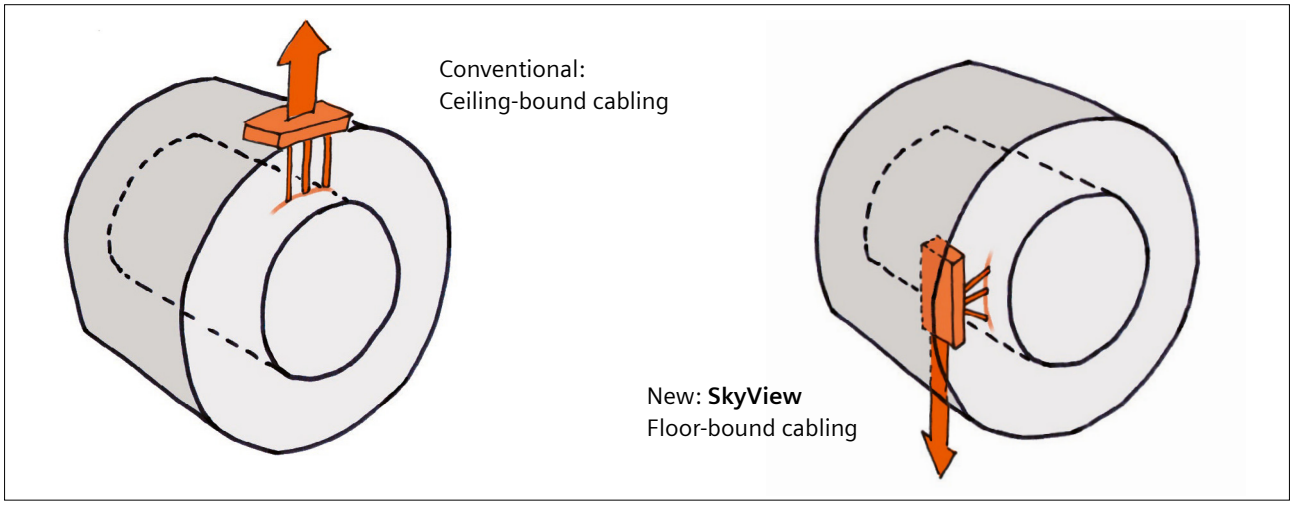

4 Gradient connection and SkyView

4. Gradient connections

The gradient coil needs to be connected to the gradient cables that deliver the current from the gradient power amplifier (GPA). As in every electrical connection, the point where two cables are joined together is critical to maintaining good electrical contact. The gradient cables carry currents over 300 A and voltage up to 1200 V, so any loose connections could generate sparks that must be avoided. The connection of gradient cables is particularly critical due to the high Lorenz forces:

$$|\vec{F}_L| = |I|\,|\vec{\ell}|\,|\vec{B}|\,\sin\alpha$$

Locally, the actual field at the end of the magnet can be higher by up to a factor of 2–3 than the nominal field at the isocenter. For a 1.5T system with a strong gradient engine (I = 900 A), a 40 cm long gradient cable at the end of the magnet will experience a force of approx. 500–1500 N (equaling 50–150 kg) oscillating with the gradient pulses. This is why, historically, the connection of the gradient cables from the GC to the cables from the GPA on scanners from Siemens Healthineers was on top of the magnet. Here, the fields perpendicular to the wires and the resulting Lorenz forces are lower. This location for the gradient connection was never an issue on wet MRI magnets, because other parts (e.g., the cold head or pipework for the quench line) were located even higher.

I = current, ℓ = length of wire/cable, B = magnetic flux density aka magnetic field, α = angle between wire/cable and B



5 MAGNETOM Free.Max installation at University Hospital Basel in Switzerland. Even during one of the very first installations, the small size of the system and the eliminated quench pipe paid off to make the installation process much easier.

With the lower field strength and the lower gradient current, it was possible to reduce the forces by almost one order of magnitude. This facilitates a gradient connection on the rear side of the magnet rather than on the top. This is also required for the SkyView siting option. Here, gradient cables are routed together with all other cables through the floor rather than the ceiling (Fig. 3B).

5. Cold head

The cold head in conventional MRI magnets, where the superconductive coils are submerged in a liquid helium bath, needs to be located above the liquid helium level to allow recondensation of the gaseous helium. In dry magnets that have just a small helium reservoir as a liquid heat buffer rather than a large helium vessel, the cold head can sit in any vertical position. On MAGNETOM Free.Max, the cold head is located inside a turret, mounted on the side ~30 cm below the upper boundary of the OVC. This not only allows unhindered transportation through 2 m high doors, but also means that all later service activities (e.g., cold head replacement) can be performed within a ceiling height of just 2.2 m – even after the system has been installed in its final location. Since MAGNETOM Free.Max can be both installed and serviced in low-height premises, MR diagnostics can now be brought to new places such as small imaging centers. These are often located in residential buildings with limited available space.

This overview shows how a complete design overhaul of the magnet and gradient system together with the use of new imaging and reconstruction techniques results in an MRI system that achieves somewhat contradictory goals: A large 80 cm bore for the patient with a scanner that delivers diagnostic image quality AND easy installation with a small physical footprint and low connection power.

More background information on MAGNETOM Free.Max and DryCool magnet technology will be available soon on: www.siemens-healthineers.com/magnetom-world.

Contact

Stephan Biber, Ph.D.
Siemens Healthineers
SHS DI MR R&D AEP
Postbox 32 60
91050 Erlangen
Germany
stephan.biber@siemens-healthineers.com



References

1 Calvert S. A Brief History of the DryCool Magnet Development. MAGNETOM Flash. 2020; MAGNETOM Free.Max special issue. Available at https://www.magnetomworld.siemens-healthineers.com/hot-topics/lower-field-mri
2 Campbell-Washburn AE, Ramasawmy R, Restivo MC, et al. Opportunities in Interventional and Diagnostic Imaging by Using High-Performance Low-Field-Strength MRI. Radiology. 2019;293(2):384-393.
3 MAGNETOM Free.Max Image Gallery. MAGNETOM Flash (78) 1/2021. Available at https://www.magnetomworld.siemens-healthineers.com/publications/magnetom-flash

Deep Resolve – Mobilizing the Power of Networks

Nicolas Behl, Ph.D.

Global Marketing Manager MRI Systems, Siemens Healthineers, Erlangen, Germany

The limitations of conventional image reconstruction

MRI is established as one of the key modalities in diagnostic imaging. The absence of ionizing radiation and the unmatched soft tissue contrast distinguish MRI from other imaging modalities. While these features have helped to establish MRI as the method of choice for the diagnosis of many pathologies, the main limitation of MRI is the acquisition time.

With conventional reconstruction methods, the acceleration of an acquisition can only be achieved by accepting compromises with respect to image resolution or signal-to-noise ratio (SNR). In general, acquisition speed, image resolution, and SNR are tightly linked and increasing one of the three automatically has a negative effect on at least one of the two others (Fig. 1).

The use of receive arrays and parallel imaging has been an important breakthrough in MR image reconstruction and is an essential part of clinical routine in MRI [1, 2].

Parallel imaging, however, usually comes at the price of higher image noise, especially in regions further away from the receive coils. This results in inhomogeneous noise distribution, especially if high acceleration factors are used. Compressed Sensing was another major development when it comes to image acceleration [3]. It benefits especially dynamic and non-cartesian 3D imaging but comes at the cost of a higher computational burden. Also, 2D cartesian imaging, which still is building the backbone of routine MR imaging, benefits less from Compressed Sensing.

Over the last years, artificial intelligence (AI) technologies have made their appearance in a various research publications [4, 5]. Especially the use of deep neural networks has proven to be helpful when trying to address the limitations of conventional MR image reconstruction, especially also for routine 2D imaging. Deep learning image reconstruction has the potential to tackle all three limiting factors of MR imaging simultaneously: image resolution, SNR, and acquisition speed.

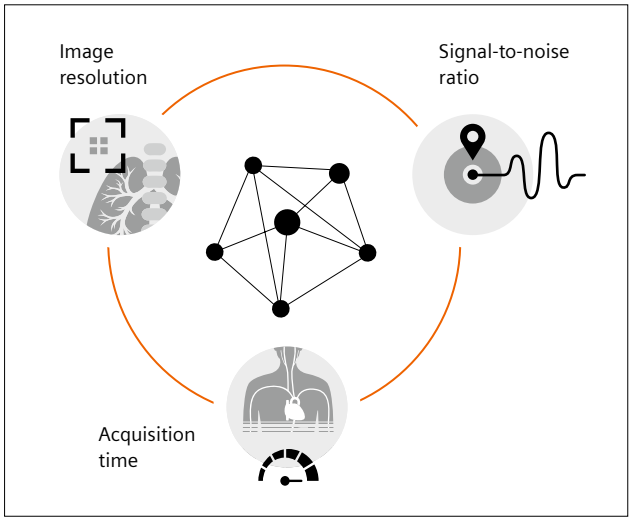

1 Image resolution, SNR, and acquisition time are the three limiting factors of MRI. Using conventional methods, changing one of them directly affects at least one of the two others. Deep learning reconstruction has the potential to disrupt this convention.

Deep Resolve Gain & Deep Resolve Sharp

Deep Resolve brings deep learning and AI to the MR image reconstruction process. Deep Resolve is an advanced reconstruction technology, which in its first step brings intelligent denoising and deep-learning-based image reconstruction directly to the core of the imaging chain.

Deep Resolve Gain is a solution for intelligent denoising. As mentioned above, in MRI, image noise is not uniformly distributed across the image. This can be due to coil array geometries since the SNR is usually higher close to the receive coils. Also the use of parallel imaging reconstruction techniques can lead to varying noise levels in the reconstructed image. These local variations in image noise can not be addressed by conventional noise filters, as these operate globally on the entire reconstructed image. Deep Resolve Gain incorporates specific noise maps, which are acquired together with the original raw data, directly into the image reconstruction [6].

These noise maps are generated without needing to spend additional scan time and can be extracted from the raw data. The reconstruction algorithm takes local noise variations into account and enables stronger denoising where noise would be most dominant when reconstructing with conventional methods.

Deep Resolve Gain helps to mitigate noise that is introduced when accelerating the acquisition e.g. by reducing

the number of averages or by increasing the acceleration factor in parallel imaging.

As the noise maps can be generated from the originally acquired raw data, no additional acquisition time is needed, and the results are available in real-time. Figure 2 shows how Deep Resolve Gain can be employed to accelerate an entire knee exam. Images acquired with increased acceleration and reconstructed with Deep

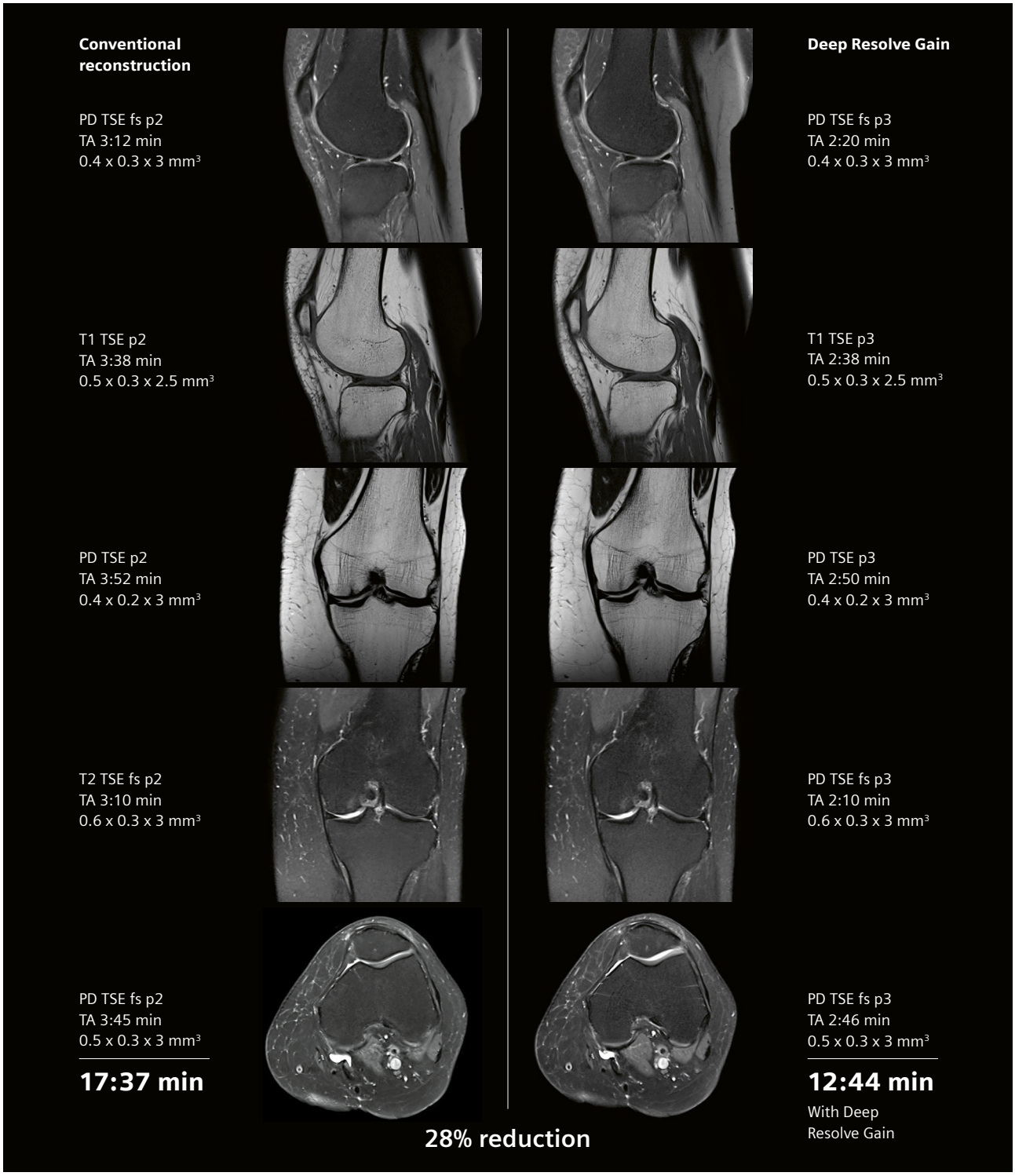

2 The increase in SNR achievable with Deep Resolve enables you to accelerate entire knee exams. The targeted reduction of image noise allows for the use of higher acceleration factors, without having to pay with increased image noise. Images are acquired on a MAGNETOM Vida 3T scanner.

Resolve Gain are similar in quality to the standard protocols which are conventionally reconstructed. In this example it results in an acceleration by 28% over the entire exam.

Deep Resolve Sharp is a novel image reconstruction technology to generate images with increased sharpness. The deep neural network at the core of Deep Resolve Sharp generates a high-resolution image from low resolution input data. The network was trained on a large number of pairs of low-resolution and high-resolution data.

As the training data for Deep Resolve Sharp covered a wide range of anatomies, the reconstruction network can be applied to all body regions. Deep Resolve Sharp can increase the matrix size by a factor of up to two along both in-plane axis, resulting in substantially increased image sharpness.

To ensure robust results, the acquired raw data is directly incorporated into the reconstruction and ensures consistency with the data from the scanner. The inclusion of the cross-check with the acquired raw data is essential for the robustness of the reconstruction and to ensure that contrasts are correctly represented in the final output. Figure 3 shows how Deep Resolve Sharp can be used to increase the sharpness of reconstructed images, without having to extend the acquisition time. Deep Resolve Sharp

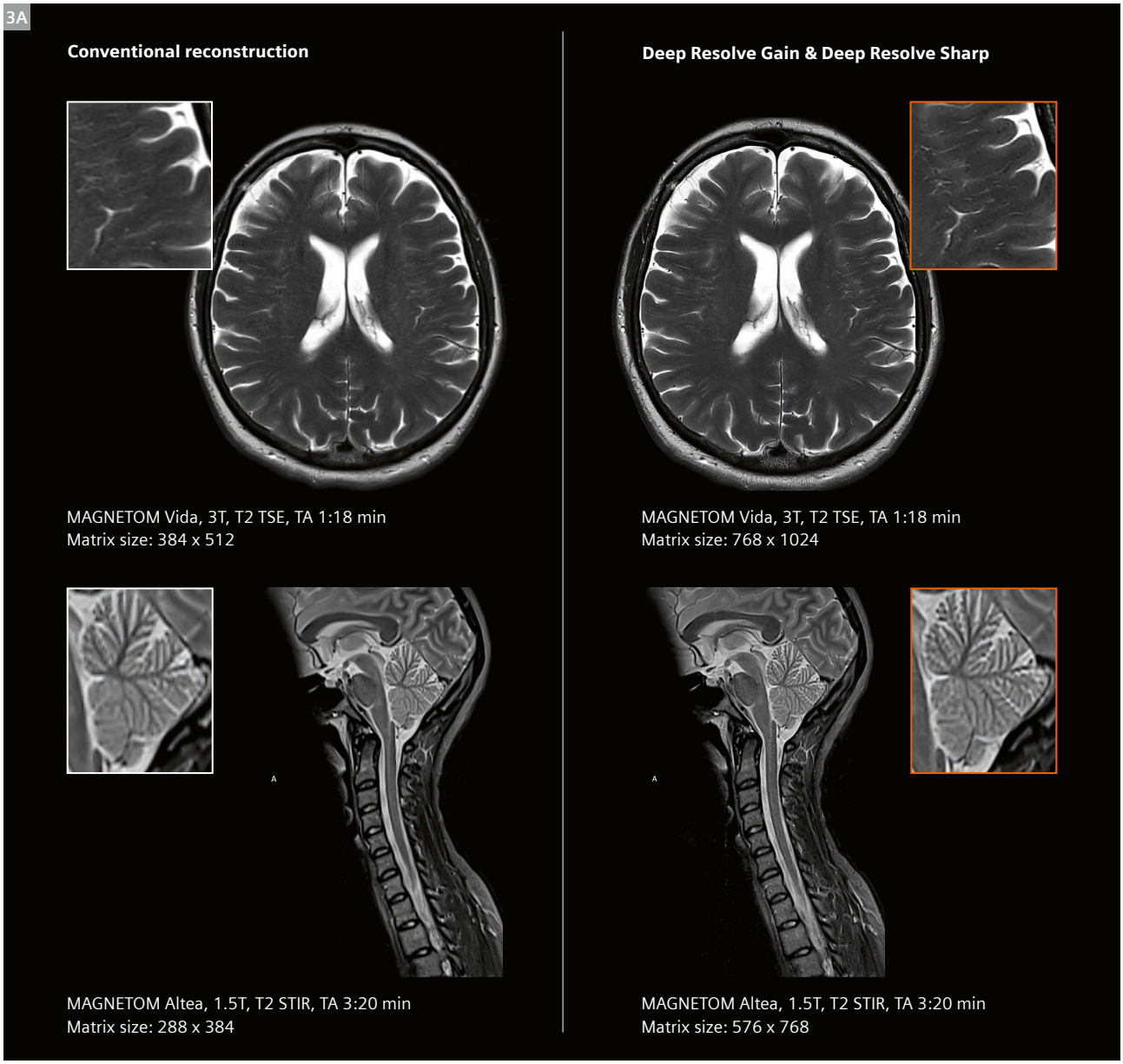

3 Deep Resolve Sharp uses a deep neural network to generate sharper images than ever before, enabling a clear depiction of fine structures and sharp edges. The use of raw data within the reconstruction process ensures robust results.

3B

Conventional reconstruction

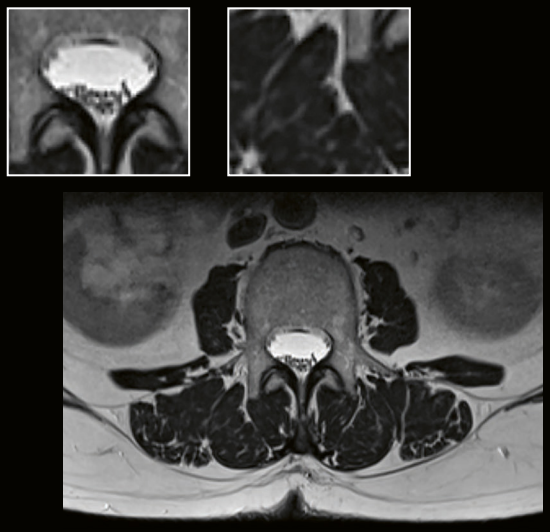

MAGNETOM Sola, 1.5T, T2 TSE, TA 3:45 min
Matrix size: 256 x 320



MAGNETOM Sola, 1.5T, T2 TSE, TA 2:24 min
Matrix size 307 x 384

Deep Resolve Gain & Deep Resolve Sharp

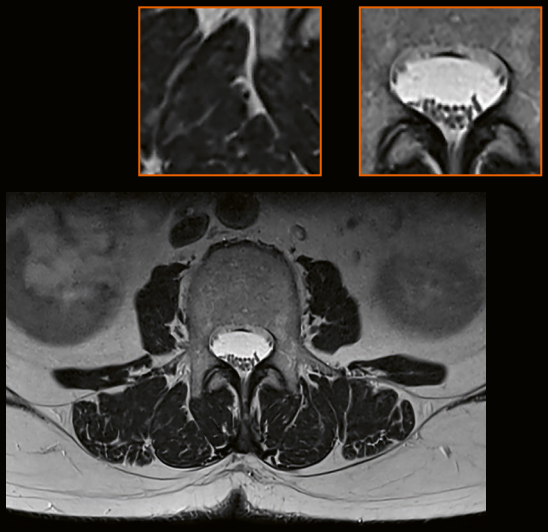

MAGNETOM Sola, 1.5T, T2 TSE, TA 3:45 min
Matrix size: 512 x 640

1aaaa3595



MAGNETOM Sola, 1.5T, T2 TSE, TA 2:24 min
Matrix size 614 x 768

1aaaa3588

can also be used to enable quicker scans. The phase resolution can be reduced in the acquisition and Deep Resolve Sharp can be employed to recover the resolution in the reconstruction process. An example is given in Figure 4B.

In Figure 4 you can see how Deep Resolve enables accelerated acquisition while simultaneously increasing image quality and sharpness.

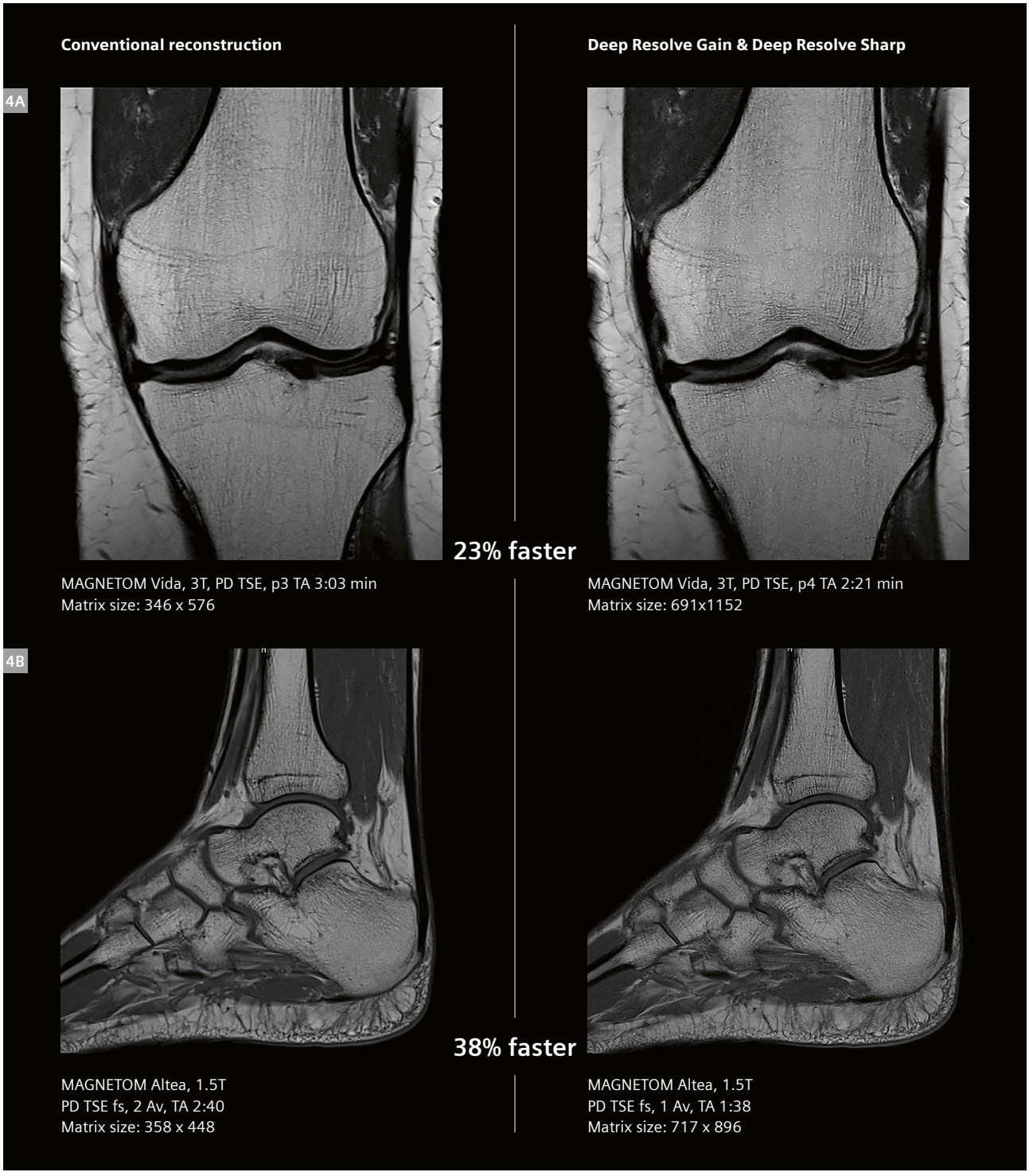

4 Together, the Deep Resolve technologies enable faster acquisitions, while increasing the image sharpness simultaneously. The targeted denoising achieved with Deep Resolve Gain allows for the use of higher acceleration, while Deep Resolve Sharp increases the sharpness of the image by increasing the matrix size.

Technology corner

Deep Resolve Gain uses individual noise maps as input for an iterative reconstruction process. This iterative process, together with the noise maps as prior knowledge reflecting where more noise is to be expected in the image, enables an effective denoising in the reconstruction process. This is similar to the reconstruction process used in Compressed Sensing, extending it to cartesian 2D imaging. For Deep Resolve Gain, the denoising in every iteration step takes place in the wavelet-domain. Denoising in the wavelet domain is more efficient than denoising in image or frequency domain. It enables a better separation between noise and small structures that are part of the image to be reconstructed. The denoising strength of Deep Resolve Gain can be adjusted, depending on the amount of noise and personal preference.

Deep Resolve Sharp uses a deep neural network to increase the sharpness in reconstructed images. The convolutional neural network operates on complex data and enables a reduction of the voxel size by up to a factor of two along each axis in-plane compared to conventional reconstruction. During the reconstruction using Deep Resolve Sharp, the information content corresponding to the originally acquired raw data remains unaffected. Incorporating the acquired raw data along the reconstruction process ensures robust results and correct representation of image contrast. The deep neural network used in Deep Resolve Sharp is rather used to predict the contents of remote areas within *k*-space. Conventional reconstruction using interpolation expands *k*-space with zeros, therefore not adding any information or contributing to image sharpness. The neural network at the core of Deep Resolve Sharp, on the other hand, was trained with a large number of pairs of low- and high-resolution data. It can therefore enhance the image with meaningful information corresponding to the outer parts of *k*-space, beyond the originally acquired data.

Open innovation platform[1]

Deep learning reconstruction is a very active field for researchers, demonstrating great potential for the future of MR image reconstruction, including denoising, artifact reduction, and possibly even the reconstruction of multiple contrasts from one single acquisition [7]. Deep Resolve gives you access to the plentitude of deep learning applications being developed in the field. Via an open innovation interface, Deep Resolve is planned to enable our partners to position their solutions in the Digital Marketplace, powered by the teamplay Digital Health Platform.

Currently, prototyping for image reconstruction algorithms is usually done offline, which means that the raw data has to be transferred from the scanner to a workstation, where they are finally reconstructed using a prototype developed e.g. in MATLAB or Python. These reconstructions then have to be converted to DICOM again if a clinician wants to evaluate them for a clinical study. Deep Resolve is planned to facilitate clinical transition for image reconstruction prototypes by enabling online reconstruction, directly at the scanner. The open innovation protocol is designed to support open community standards, such as the ISMRM raw data format and Gadgetron (Fig. 5).

[1] *The product is still under development and not commercially available yet. Its future availability cannot be ensured.*

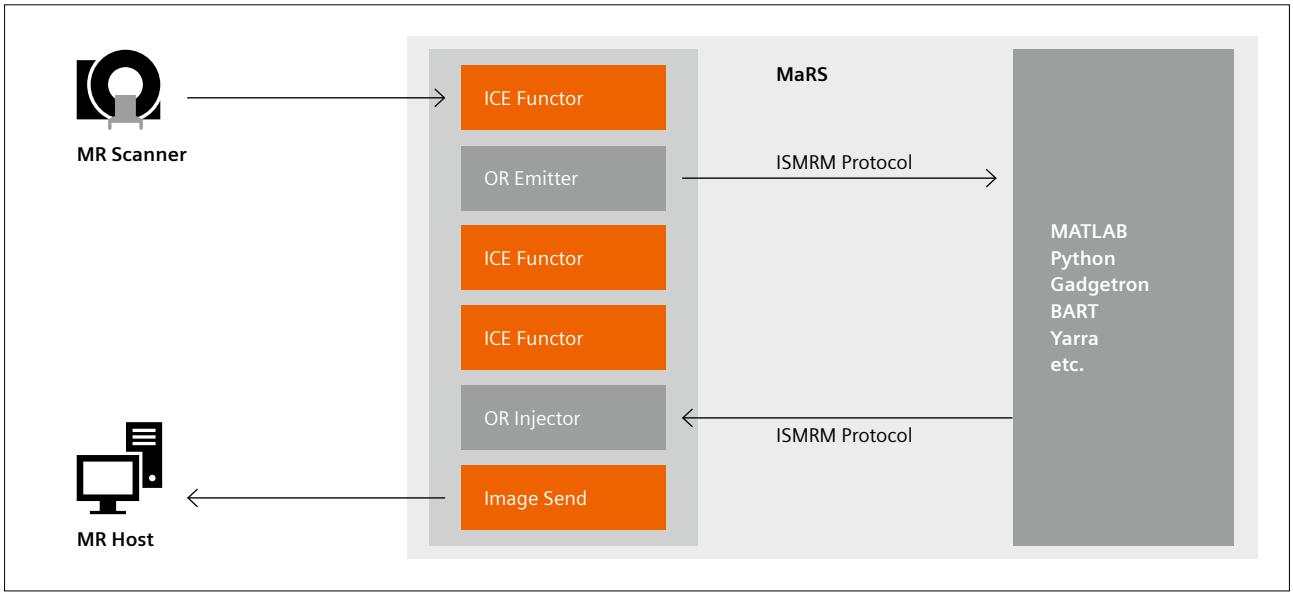

5 With an open innovation protocol, Deep Resolve is planned to facilitate translational research by enabling researchers to run their image reconstruction prototypes directly on the scanner.

Conclusion

Deep Resolve Gain and Deep Resolve Sharp introduce targeted, iterative denoising and deep learning reconstruction into clinical imaging. These technologies enable us to reduce acquisition times and improve image quality simultaneously. The unique inclusion of individual noise maps in an iterative reconstruction process enables intelligent, targeted denoising and Deep Resolve Sharp leverages the potential of deep learning reconstruction to achieve image resolutions beyond what is possible with conventional reconstruction methods. All this is done while including the acquired raw data along the entire reconstruction process, therefore ensuring robust and consistent results.

The potential of deep learning image reconstruction is immense, and current research is indicating a multitude of fascinating applications to come. Collaboration is key in MRI, so let us join our efforts in driving this exciting technology forward!

References

1 Pruessmann KP, Weiger M, Scheidegger MB, et al. SENSE: sensitivity encoding for fast MRI. Magn Reson Med. 1999;42(5):952-962.
2 Griswold MA, Jakob PM, Heidemann RM, et al. Generalized autocalibrating partially parallel acquisitions (GRAPPA). Magn Reson Med. 2002;47(6):1202-1210.
3 Lustig M, Donoho D, Pauly JM. Sparse MRI: The application of compressed sensing for rapid MR imaging. Magn Reson Med. 2007;58(6):1182-1195.
4 Hammernik K, Klatzer T, Kobler E, et al. Learning a variational network for reconstruction of accelerated MRI data. Magn Reson Med. 2018;79(6):3055-3071.
5 Hammernik, Kerstin, et al. Deep Learning for Parallel MRI Reconstruction. MAGNETOM Flash (75) 4/2019:10–15.
6 Kannengiesser SAR, Mailhe B, Nadar M, et al. Universal iterative denoising of complex-valued volumetric MR image data using supplementary information. Proceedings of the ISMRM, Abstract 1776, 2016.
7 Knoll F, Hammernik K, Zhang C, et al. Deep-learning methods for parallel magnetic resonance imaging reconstruction: A survey of the current approaches, trends, and issues. IEEE Signal Processing Magazine 37.1 (2020): 128–140.



Contact

Nicolas Behl, Ph.D.
Siemens Healthineers
DI MR M&S SYS
Erlangen
Germany
nicolas.behl@siemens-healthineers.com

The DICOM files of the figures in this article are available for download

www.magnetomworld.siemens-healthineers.com > Clinical Corner > Protocols > DICOM Images



Phoenix is a unique *syngo*-tool that allows you to click on an image, drag it into the measurement queue, and instantly duplicate the extracted protocol – TR, TE, bandwidth, number of slices, echo spacing, etc.

- Phoenix ensures reproducibility, e.g., for patient follow-up.
- Phoenix shares optimized protocols on the different MAGNETOM systems you work with.
- Phoenix supports multi-center protocol standardization.

You'll find DICOM images from various systems and all aspects of MRI at magnetomworld.siemens-healthineers.com **> Clinical Corner > Protocols > DICOM Images**

Pushing the Limits of Accuracy in MRI – A Perspective

John E Kirsch, Ph.D.

Athinoula A Martinos Center for Biomedical Imaging, Massachusetts General Hospital, Department of Radiology, Charlestown, MA, USA

Introduction

I am pretty sure that magnetic fields were never intended to be perfectly homogeneous or to vary precisely linearly in space at exactly a certain moment in time. At the very least, it is probably plausible to say that it was not what James Clerk Maxwell was thinking when he formulated his famous equations. Yet in 2021, magnetic resonance imaging (MRI) is used to do just about everything in healthcare, including guiding the placement of an electrode deep into the interior of the human brain at better than 1 mm accuracy to help patients with epilepsy, or producing exquisite anatomical information at 100 micron isotropic resolution (Fig 1).

MRI is based on magnetic fields throughout the entire measurement and imaging process, starting with a static external magnetic field that magnetizes the hydrogen nuclei in the body and ending with producing an image from that magnetization. The accuracy of those fields therefore ultimately determines the precision of the image outcome. The position of a voxel in a digital image representation of the anatomy is based on the singular assumption that the magnetic fields are precisely known everywhere in space and time. Deviation from this and there will be a proportional inaccuracy associated with the position of that voxel.

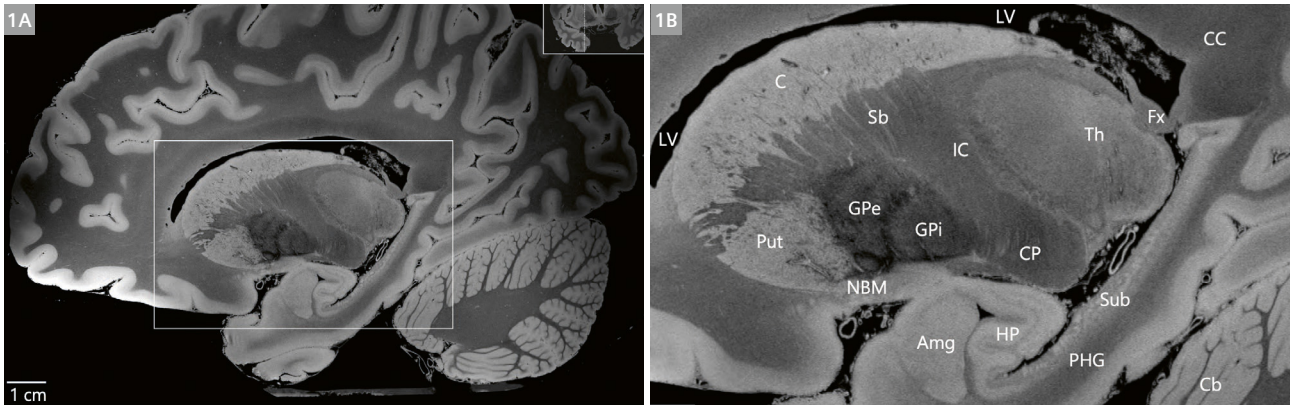

1 100 micron thick sagittal slice through an ex-vivo human brain acquired with the MAGNETOM 7T Classic showing delineation of basal ganglia, diencephalon, and medial temporal neuroanatomy at 100 micron resolution **(1A)**. A zoomed view of the striatum, amygdala (Amg), and hippocampus (HP) (within the white rectangle in 1A) is shown in **(1B)**.
Neuroanatomic abbreviations: C = caudate; Cb =cerebellum; CC = corpus callosum; CP = cerebral peduncle; Fx = fornix; GPe = globus pallidus externa; GPi = globus pallidus interna; IC = internal capsule; LV = lateral ventricle; NBM = nucleus basalis of Neynert; PHG = parahippocampal gyrus; Put = putamen; Sb = striatal bridges; Sub = subicular cortices; Th = thalamus.
With permission: Brian L Edlow, MD, Massachusetts General Hospital. BL Edlow, A Mareyam, A Horn, et al., 7 Tesla MRI of the ex vivo human brain at 100 micron resolution. Sci Data 6, 244 (2019). https://doi.org/10.1038/s41597-019-0254-8.

There are many applications now that rely on the informational accuracy of MRI, whether it be with its signal amplitude, phase, or position in space. Nowhere is this more evident than when using MRI for stereotactic planning, where spatial accuracy is paramount. High resolution isotropic 3D MR imaging has become the modality of choice for radiation treatment planning or surgical implantation procedures. Inaccuracies in the spatial position of the anatomy with respect to external fiducial markers can lead to potentially catastrophic outcomes. Spatial precision is also a requirement for personalized prosthetic modeling, where localized errors in position can cause painful misalignment for the recipient. Tissue morphometry and segmentation are being used more and more for medical and therapeutic evaluation that relies heavily on the volumetric precision not only in a given dataset but also longitudinally over time.

But spatial accuracy is not the only thing that relies on magnetic fields. In recent years, MRI is becoming more quantitative where accuracy in its signal amplitude and phase are necessary as well. Flow quantification in vascular and cardiac applications relies heavily on the precision of the signal phase, as does high-intensity focused ultrasound (HIFU) and other therapeutic procedures that use the phase information for MR thermometry to monitor tissue response. MR elastography requires the phase information to measure tissue stiffness in liver disease. Applications that demand accuracy and reproducibility in the signal amplitude also exist. Quantitative biomarkers such as the Apparent Diffusion Coefficient (ADC) in diffusion-weighted MRI rely on the signal amplitude decay associated with diffusion sensitization of water motion to probe tissues on a microscopic scale. And, fMRI requires extreme temporal stability of the signal magnitude to detect the statistical significance of the blood oxygen level dependence (BOLD) response in brain activity.

In the early days of MRI, we pretty much focused on just trying to maximize the signal-to-noise ratio (SNR) and simply hoped that after a 15-minute acquisition the scan would yield a reasonable facsimile of the human anatomy, whether it be of the brain, a knee, or the liver. But in this age of precision medicine, MRI is becoming much more quantitative, requiring equally greater accuracy. Just getting an image is no longer a reasonable expectation. MRI is now expected to be perfect in every way. Let us take a brief look into just how perfect, or not-so-perfect, it is.

Signal encoding

MRI of course begins with an external static B_0 magnetic field to create the initial magnetization. The MR signal that eventually is generated will possess characteristics of amplitude, phase, and frequency. Essentially, all three of these features are based on magnetic fields as described by the Larmor equation. For them to be accurate, this means that the magnetic fields that they are based on must also be accurate. Note that there are three magnetic fields that we deal with in MRI: B_0, B_1^+, and B_1^-. B_1^+ and B_1^- are the transmission and reception fields, respectively, and are perpendicular to the B_0 field in order to rotate the magnetization and detect it. Although the B_1 fields are clearly important and deserving of discussions about their accuracy, it is the B_0 field that is the focus here since it is ultimately what encodes the MR signal that gets detected and generates the image. Therefore, for the remainder of this paper only the B_0 magnetic fields will be discussed.

The MR experiment can be viewed as having four basic time-sequential elements – preparation, excitation, encoding, and readout. During preparation, the initial state of the magnetization for the experiment becomes defined. This may be an inversion preparation that might be applied for a specific type of tissue contrast, or it might be a type of saturation to suppress the magnetization from a specific tissue such as fat. In this stage, the accuracy of the B_0 field could be argued as playing a lesser role, primarily associated with the spatial uniformity of the outcome.

After the initial preparation, excitation is then carried out to rotate the magnetization out of the B_0 direction to create a transverse component which eventually becomes detected. This process relies on the resonance condition between RF transmission and magnetization, whereby their frequencies must be matched to produce the action of excitation and the rotation of the magnetization. By applying a spatially varying gradient field (G) during excitation one can then selectively excite a specific region in space. Here, the total magnetic field, $B_{0,tot}$ (comprised of the summation of the main magnetic field, B_0, and the gradient field, G) plays a significant role, since a one-to-one relationship will exist between the excitation of a physical location in space that matches the resonance condition according to the Larmor equation. Transmission at a specified frequency and bandwidth will produce excitation anywhere in physical space with a given slice thickness where it matches the Larmor frequency of the magnetization. For this to be accurate requires precision of $B_{0,tot}$ and therefore the main magnetic field, B_0, and the gradient field, G.

The encoding process is facilitated by applying G magnetic fields that spatially vary the B_0 magnetic field in a well-behaving manner so that signal can be mapped uniquely to different points in physical space. Gradient pulses of a given direction, amplitude, and duration encode the signal in *k*-space, the Fourier counterpart of image space, with the coordinates of k_x, k_y, and k_z. The action of the encoding process is to define the starting point coordinates in *k*-space for the readout process to follow, and the value of *k* will be based on the time

integration of the gradient pulsing. That said, the accuracy of the *k*-space encoding will therefore be defined by the accuracy of the gradient pulsing. In addition, however, since the transverse magnetization experiences the *total* magnetic field $B_{0,tot}$, the uniformity of the main magnetic field B_0 also plays an important role in the accuracy.

The final step of the MR experiment is the signal readout when the magnetization is detected and digitally sampled. *k*-space gets sampled according to the gradient pulsing that is applied simultaneously during the detection process. The *k*-space trajectory in readout will be based on the direction, amplitude, and duration of the gradient pulsing. Therefore, the trajectory will be determined by the precision of the gradient pulsing. And, as with the encoding process, the transverse magnetization experiences $B_{0,tot}$, so the readout accuracy will also depend on the uniformity of B_0 as well.

Historical progression

The spatial accuracy and temporal stability of the main static B_0 magnetic field and the pulsed G gradient magnetic fields has gone through different progression through the years. Early magnets were very large and heavy, and their spatial uniformity, or homogeneity, was in general quite poor. As the engineering design and manufacturing improved, magnet homogeneity also improved. However, other factors did not necessarily always allow continual improvement in the homogeneity. For example, a demand existed for wider and shorter bore designs to increase patient comfort, and siting requirements became more challenging for installing magnets in much smaller footprints. As a result, even though magnets progressively have become higher in field strength and more reliable and efficient, attaining the greatest homogeneity across a large imaging volume is not the only factor that is considered in present magnet technology.

Some amount of compensation for this can come from the implementation of active shimming with coils that generate 2nd-order spatial – or more recently even 3rd-order – harmonic correction of the static B_0 field. But it takes space to accommodate these extra shim coils in the bore, and this may be counterproductive with the ever-increasing demand for wider bore systems. For accuracy and precision, magnet homogeneity is what matters. But the final design will ultimately consider these other factors as well.

Probably what has progressed the most in the past decades is the gradient performance (on this point, readers can refer to the recent comprehensive historical summary *"An Attempt to Reconstruct the History of Gradient-System Technology at Siemens"* by Franz Schmitt et al. in the 2020 ISMRM issue of MAGNETOM Flash (77) 2/2020). In the early- to mid-1980s, gradient coils were unshielded, which meant that without compensation the field errors were on the order of 20% of the nominal amplitude of the gradient pulsing. Performance-wise, pulse rise times were typically 1500 µsecs or even longer in duration, and the maximum gradient amplitudes were no greater than about 3 mT/m. Since that time, continual improvements in power amplifiers, gradient coil design, and manufacturing have led to actively shielded configurations that have force compensation to minimize mechanical torque and vibrations, as well as counter windings to minimize higher-spatial-order eddy currents. Errors are reduced by several orders of magnitude or more, and gradient performance on contemporary whole-body clinical systems now have 200 T/m/s slew rates that allow pulse rise times of less than 100 µsecs and amplitudes up to 80 mT/m amplitudes. Digital precision to control arbitrary and complex gradient waveforms and their pre-emphasis to minimize eddy currents has steadily improved over the years, from 12 bits, to 16 bits, and up to 20 bits or higher.

Specialized gradient coil designs have most recently dramatically increased performance to as high as an astonishing 600 T/m/s and 500 mT/m. However, such fantastic improvements have not come without some compromises as well. In order to achieve these levels and stay within safe limits of peripheral nerve stimulation in the human body, the accuracy and extent of the spatial linearity of such gradient fields can be constrained.

The steady improvements in magnet, shim, and gradient coil design over the decades have allowed for rapid expansion of the types of acquisitions and applications that are now achievable with MRI. However, spatial and quantitative accuracy has not necessarily been the only metric by which contemporary systems are judged. Yet it can be considered just as critical and just as important.

Confounding factors (and where things can go wrong)

To have an appreciation for what it actually means to achieve better than 1 mm spatial accuracy or to produce an image with 100 micron resolution is to also have a realistic appreciation for what can go wrong. This became readily apparent to me very early in my career as an MRI scientist. My first role was to develop new applications, and what I found more times than not was that theory rarely behaved the same way in actual practice. And when it comes to the magnetic fields there are many things that can occur to cause these fields to distort in the real world, as shown in Table 1.

The primary objective of the magnet static B_0 magnetic field is to possess perfect uniformity everywhere in space. Since the B_0 field defines the initial state of the magnetization and its encoding, spatial non-uniformities and imperfections are a fundamental source of error. The

magnet itself is of course finite in size. As such, it will possess a nominal field strength in the middle of the bore and zero field strength at some distance far away. Therefore, at some point as you move away from the isocenter yet still are within the imaging field of view of spatial encoding, the B_0 field will taper off and the required homogeneity is lost. There exists a so-called "sweet spot" where the uniformity of the field is the highest.

One of the most common things that can lead to errors in the static magnetic field are the spatial distributions of the different magnetic susceptibility (χ) that exist in tissues and objects (Fig. 2). This physical property determines the B_0 magnetic field that that medium experiences. Most soft tissues are quite similar, so the distortions of the field are negligible. However, the χ of bone and air are quite different from soft tissue and their presence can cause significant local distortions in B_0. And of course, foreign objects such as surgical or therapeutic implants that might be made of a type of metal possessing very different properties of χ can produce very large spatial distortions of B_0 near the object.

Static and dynamic B_0 magnetic field	Dynamic G magnetic field
Finite shim volume	Eddy currents
Magnetic susceptibility	Concomitant fields
Chemical shift	Finite spatial linearity
External influences	Calibration and regulation
	Mechanical vibration
	Heating and drift

Table 1: Some of the sources of static B_0 and dynamic G errors.

The molecular environment that surrounds hydrogen nuclei causes small but observable changes in the microscopic magnetic field environment known as chemical shift. Because fat and water in tissues have a frequency shift that equates to roughly 3.5 ppm of magnetic field difference, this means that the signal from each will originate from different locations in space. The most common example of this is pixel misregistration where fat will be located at slightly different positions in the field-of-view from water. Excitation of fat will also occur at different positions from water.

These are static B_0 factors. But what about dynamic errors that are caused by external influences or the pulsing of the gradient G fields necessary to encode the MR signal? In urban areas like New York City, the environment can be a "firestorm" of magnetic fields that are constantly fluctuating all around you. A common source are subways, not so much because of the moving metallic trains but because of power lines that can produce strong magnetic fields from surges needed to move the trains. Although Siemens Healthineers has a unique solution for protecting the magnet from such external B_0 perturbations, if an MRI scanner is simply too close it can lead to measurable errors if it occurs when a scan is being done at that time.

Faraday's law tells us that a magnetic field that changes in time will generate an electric field. When a gradient is pulsed, it changes the total magnetic field $B_{0,tot}$ dynamically over time at a given point in space. This will therefore produce a countering eddy-current induced magnetic field on conductive surfaces that can then distort G and in turn $B_{0,tot}$ dynamically. Such eddy-current fields can come from implants or objects that have conductive components

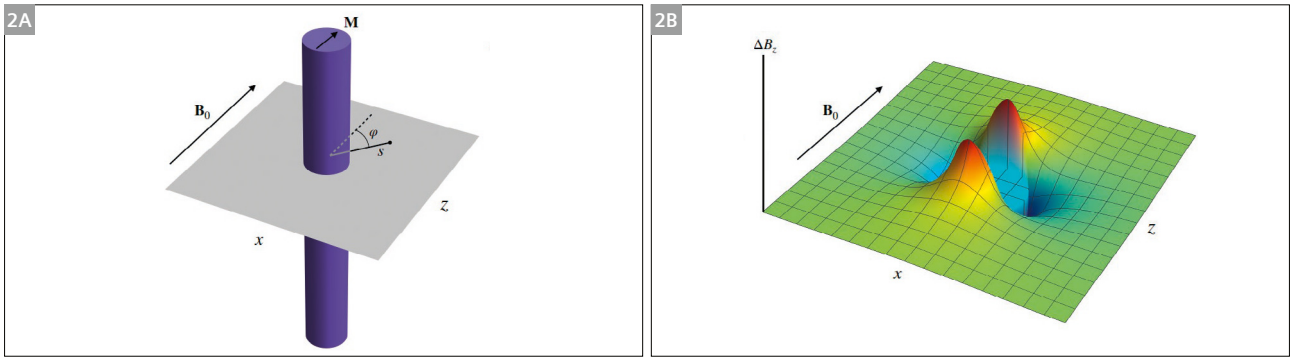

2 Localized magnetic susceptibility induced B_0 distortion in the presence of a cylinder containing uniform susceptibility that is greater than the surrounding external environment. **(2A)**: mathematical model showing the orientation of the cylinder relative to the main static B_0 magnetic field. **(2B)**: theoretical simulation of the distortion of the B_0 field. This model demonstrates the origins of the Blood Oxygen Level Dependent (BOLD) effect in the microvasculature in regions of brain activation.
With permission: Bradley R Buchbinder, MD, Massachusetts General Hospital. BR Buchbinder. Chapter 4: Functional magnetic resonance imaging. Handbook of Clinical Neurology. Vol 135. Neuroimaging, Part I. pp 61-92, JC Masdeu and RG Gonzalez, Editors, Elsevier BV (2016). https://doi.org/10.1016/B978-0-444-53485-9.00004-0

and surfaces, but the dominant source is from the conductive cryoshields within the magnet itself. As previously mentioned, actively shielded gradient coils are designed to minimize this, but the high performance of modern systems will still generate measurable errors within the imaging volume caused by these eddy currents.

Another source of error caused by pulsing the gradients is the additional terms commonly referred to as Maxwell concomitant gradients. According to Maxwell's equations, it can be shown that when producing a spatially varying gradient field, the actual total effect contains higher-spatial-order mathematical terms that are secondary or "concomitant" fields over and above the spatial linear term we wish to produce for encoding purposes. The extent of their contribution to errors are primarily proportional to the square of the magnitude of the gradient strength, the square of the position away from isocenter, and are inversely proportional to the main magnetic field strength. Therefore, large-gradient amplitudes of pulsing such as what are used in diffusion applications can produce appreciable errors from this source.

Aside from these physics-based phenomena, there are also several engineering factors that also can contribute to the overall errors associated with the gradient fields. First, like the magnet, the gradient coil is finite. As such, this will mean that the fields that it generates will eventually fall off away from the isocenter. Additionally, with the increased performance of modern gradients it is necessary to consider peripheral nerve stimulation and other safety constraints that will limit the extent of spatial linearity of the gradient fields. Figure 3 demonstrates how significant the spatial distortion can be if corrections of these errors are not applied.

Calibration and regulation of the amplifier output that drives the production of the gradient field are important aspects of accurate field generation. When a pulse sequence instruction specifies the amplitude and duration of a gradient pulse, this information is sent to the amplifier to convert the digital instruction to an analog electrical current which then drives the gradient coil generating the requested G field. Too much current will produce a G that is higher than what the instruction calls for. Calibrating this is therefore necessary to ensure accurate field generation (Fig. 4). And proper regulation is required to make sure that the baseline current always remains zero when no gradient field is being pulsed.

Rapidly changing magnetic fields associated with gradient pulsing also induce Lorentz forces that in turn produce mechanical vibrations. This of course also leads to the quite familiar knocking sounds associated with all MRI scanners. But it also can produce physical displacement. Although minor in most cases now that modern gradient coils are designed with force compensation to mitigate these vibrations, it cannot be completely ruled out as a potential factor.

The amount of current required to generate the gradient fields can be quite large, which over time produces a lot of heat that must be mitigated with cooling. However, state-of-the-art applications that exploit the maximum gradient performance over longer periods of time can lead

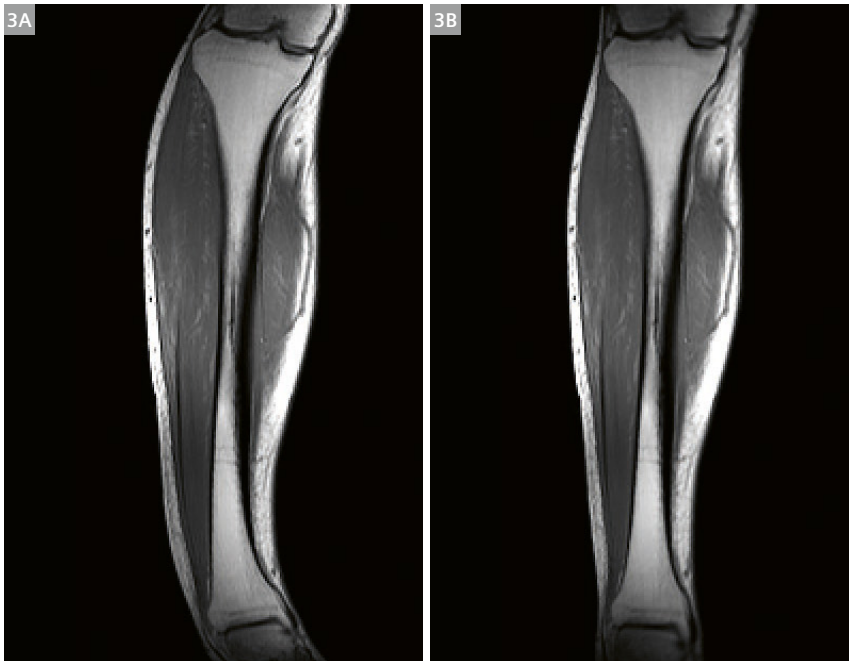

3 Large FOV coronal T1-weighted spin echo slice through the lower leg and calf muscle. Without correcting for the spatial nonlinearity of the gradient field, the image is geometrically distorted **(3A)**. Gradient related nonlinearity distortion is completely predictable if the gradient field is known and can therefore be corrected by pixel reformatting/ remapping **(3B)**.

to gradual drifting of the total B_0 field over the duration of the MR experiment.

And finally, with all these things that can go awry, when it is all said and done, Siemens Healthineers continues to strive to improve and perfect things, and we are therefore able to achieve some of the most astounding diagnostic images and remarkable outcomes with MRI, that continues to significantly make a positive impact on healthcare.

MRI applications

Once magnetization is transverse after the excitation process, it becomes vulnerable to all the inaccuracies of the B_0-related magnetic fields, whether from the main static magnetic field or from the pulsing of the gradients. This will be true regardless of the application. However, it is the application and what information it is trying to extract from the human body that ultimately determines whether the errors in $B_{0,tot}$ make a difference or not. For a given B_0 error somewhere in space, the spatial distortion or signal phase deviation may be large or small at that location based on the technique of measurement and its application.

Specific details of the myriad of MRI applications that now exist on modern scanners are beyond the scope of this paper. But there are several basic aspects that can make an application more or less sensitive to the $B_{0,tot}$ field and its errors. One of these is the MR signal readout. How fast one samples the signal and encodes it in *k*-space defines the field sensitivity of the MR experiment. The longer this duration, the more time passes for the transverse magnetization to evolve in the $B_{0,tot}$ field that it experiences. Errors in the field increase the magnitude of the error in the signal, as the magnetization continues to evolve during the sampling process.

Single-shot echo-planar-imaging (EPI) applications such as functional MRI (fMRI), diffusion tensor imaging (DTI), and dynamic susceptibility contrast (DSC) are at one extreme of the sensitivity spectrum where the entire readout of the MRI signal and complete sampling of *k*-space is done with a single magnetization preparation. Ironically, although this provides the ability to produce rapid "freeze-frame" results in a matter of 20 or 40 ms per image, on the scale of evolution of the transverse magnetization this is quite slow. These techniques are therefore extremely sensitive to B_0 errors leading to substantial spatial distortions, and signal magnitude and phase deviations.

In the more traditional steady-state Cartesian sampling used in gradient echo (GRE), spin echo (SE) or turbo spin echo (TSE) techniques, the duration of the readout of a line in *k*-space, and thus the sensitivity of the scan, is determined by different factors. On the one hand, high-bandwidth sampling associated with short readout durations offers the ability to shorten timing such as echo time (TE) or echo spacing with less sensitivity to B_0 errors, but is accomplished at the expense of increased noise and thus lower SNR. On the other hand, longer durations of lower bandwidth sampling improve the SNR but at the

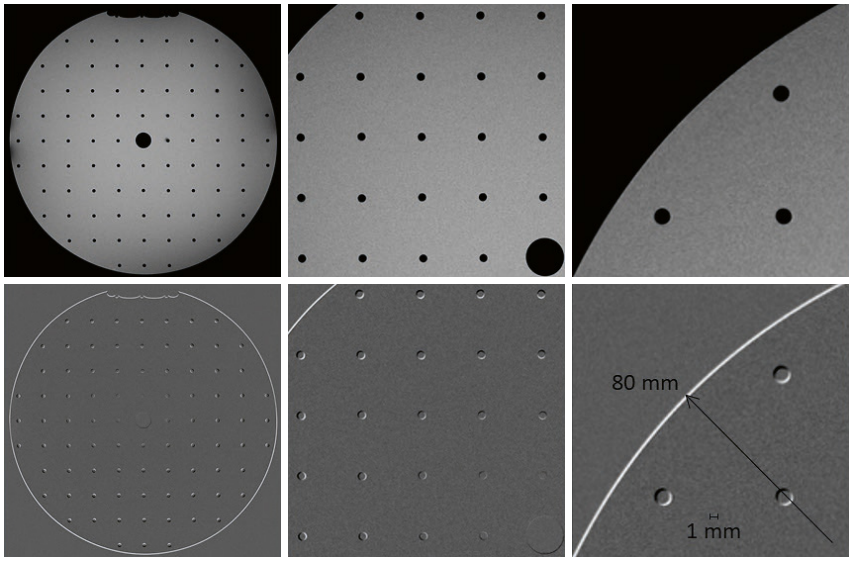

4 Effect of gradient calibration. A high resolution image of a phantom specially designed to assess spatial accuracy is shown in the upper row at various magnifications. The bottom row is a difference map between two slightly different calibrations. Note that since calibration is relative, the absolute spatial error will depend on the distance away from isocenter.

expense of increased sensitivity to B_0 errors. And, what fights against this is that higher spatial resolution necessitates higher *k*-space sampling of the information requiring larger gradient pulsing which can introduce greater error. So, although one may spatially encode an image with high resolution, the inaccuracy in the spatial position may also be higher.

Cartesian sampling is not the only method used to sample and fill *k*-space. Depending on the application, spiral or radial sampling trajectories can be of benefit. For example, ultrashort echo times are necessary to catch the MR signal before it rapidly decays away in solids such as cortical bone, or regions of interest that contain large localized susceptibility-based B_0 inhomogeneities, such as lung parenchyma. Each sampled data point in *k*-space will only be as accurate as the gradient pulsing that is required to encode that sample with the correct *k*-space coordinates. The more complex the *k*-space trajectory and the longer the readout of the sampling, the greater the potential for error in the mapping.

And finally, as perfect as we might strive to make the magnetic fields and signal encoding, the cooperation of the subject may end up being the single most important confounding factor. The longer the scan is, the greater the probability that the patient will move during the scan which can compromise the accuracy of the outcome. Navigator signals and tracking devices are prospective strategies used to attempt to mitigate some of these inevitable errors due to motion, but these as well ultimately rely on the accuracy of the B_0 fields to correct things.

On the not-so-distant horizon

As the MRI applications become more sophisticated, so do the ways to produce more accurate and reliable results. Clearly, engineering and manufacturing continues to improve the performance of MRI scanners, and Siemens Healthineers leads the way on this front. The scanner is no longer just a diagnostic device that produces images, but is a quantitative measurement system of biomarkers in the age of precision medicine.

In a different approach that accepts the premise that complicated four-dimensional B_0 errors will always exist, dynamic field cameras are devices that measure these complicated fields and either retrospectively or prospectively correct for such errors so that the result is completely corrected of the deviations that occur during the measurement process.

And of course, artificial intelligence (AI) has made great strides in recent years to become integrated in healthcare, radiology applications, and workflow. MRI is not excluded from this. AI is being assessed across a broad range of applications from improving lesion conspicuity, to increasing SNR without the typical compromise in spatial resolution, and using deep-learning algorithms to correct for B_0-related errors and producing super-resolution results.

Concluding remarks

At the beginning of my career, it was extremely important to me that I never stop learning in whatever field I chose. If I stopped learning, I vowed that I would change my direction. I never anticipated that when I chose to be a scientist in the field of magnetic resonance imaging that I would still be here today 35 years later where never a day passes that I am still fascinated by what can be accomplished with this incredible technology.

James Clerk Maxwell may not have ever expected that magnetic fields would be exploited in this way, but I am pretty sure he would be quite pleased to see what we have done with them.



Contact

John E Kirsch, Ph.D.
Director, Human Imaging Core
Athinoula A Martinos Center for Biomedical Imaging
Massachusetts General Hospital
Department of Radiology
149 Thirteenth Street, Room 2301
Charlestown, MA 02129
USA
jkirsch@mgh.harvard.edu

Initial Experience with Automatic Knee Cartilage Segmentation using MR Chondral Health

Vladimir Juras, Ph.D.; Pavol Szomolanyi, Ph.D.; Veronika Janáčová, MSc; Siegfried Trattnig, M.D.

High Field MR Centre, Department of Biomedical Imaging and Image-guided Therapy, Medical University of Vienna, Vienna, Austria

Abstract

Osteoarthritis (OA) is a degenerative disease affecting the articular cartilage characterized by slow cartilage loss over time. Magnetic resonance imaging (MRI) provides a noninvasive and sensitive tool for examining structures involved in OA disease. Both morphological and quantitative MRI techniques are helpful in the diagnosis and treatment monitoring of OA patients. In MR imaging, cartilage segmentation is an important evaluation step to define cartilage loss in disease progression or cartilage volume increase as a response to treatment. This step, however, presents a significant and substantial burden in large cohort trials. Here, we present our initial experience using automated segmentation software, MR Chondral Health[1], which is capable of automatically segmenting the whole knee cartilage on isotropic MRI scans.

Key points

1. Automated cartilage segmentation is an essential tool for improving the detection of early osteoarthritis in patients at risk of OA and, in particular, in treatment monitoring of newly developed cartilage regenerative drugs.
2. MR Chondral Health[1] provides robust and reproducible automated knee cartilage segmentation that can be performed on the most common 3D isotropic MR sequences.
3. Automated quantitative MRI data extraction can be added to the automated cartilage segmentation as it provides valuable information about collagen fibers and glycosaminoglycans.

Background

Osteoarthritis (OA), the most common form of arthritis, is a complex, multifactorial condition that causes disability in the older population [1]. In terms of pathophysiology, OA refers to disease of the entire joint including breakdown of cartilage and the associated alterations in the underlying bone. This leads to joint deformity, disability, and debilitating joint symptoms of all joint structures such as cartilage, bone, menisci, ligaments, and tendons. Studies have shown that the morphometric assessment of the cartilage structure, such as volume and thickness, from MR images provides an accurate measurement of OA progression [2–4]. Although a number of quantitative MRI techniques [5–8] have recently been developed for the detection of early cartilage degeneration, one of the major hurdles for clinical translation of these advanced quantitative techniques is the time-consuming and tedious task of manual or semiautomatic cartilage segmentation. In addition, manual segmentation is typically subject to relatively high inter- and intra-reader variability. Over the years, a number of different techniques for automated cartilage segmentation have been developed, including deformable models [9], clustering [10], intensity and edge detection-based [11, 12] approaches, and atlas-/graph-based methods [13]. The use of convolutional neural networks (CNNs) in knee articular cartilage segmentation has become very popular in recent years [14]. The model-based cartilage segmentation approach developed by Fripp et al. [15] has been implemented in the MR Chondral Health application (Siemens Healthcare, Erlangen, Germany) and provides

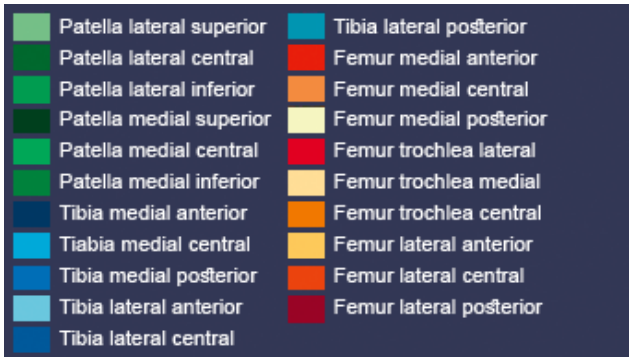

1 The color codes of 21 cartilage regions automatically segmented using MR Chondral Health.

[1] *Work in progress. The product is still under development and not commercially available yet. Its future availability cannot be ensured.*

automated knee cartilage segmentation, which is further divided into twenty-one subregions. Here we present an overview of the basic features of MR Chondral Health and our experience of its application in clinical trials.

Segmentation workflow

Knee cartilage was segmented using the prototype MR Chondral Health software (version 2.1.0, Siemens Healthcare, Erlangen, Germany), which uses a model-based segmentation algorithm [15]. The basic scheme consists of four stages: preprocessing (bone-cartilage interface (BCI) determination), atlas alignment, bone segmentation, and cartilage segmentation [15]. According to anatomical landmarks introduced by Surowiec et al., knee cartilage is divided into six patellar, six tibial, and nine femoral subregions [16]. These anatomical landmarks are visible on MR images as well as during arthroscopy. The color codes used are shown in Figure 1. Each segment can be further divided into three layers defined as three-thirds along the surface bone-cartilage interface (BCI) axis, if needed. The software is also capable of calculating a global and mean volume and thickness for each region – it is calculated as an average of the thickness values of the pixels lying on the BCI through all slices of a certain cartilage region. If a quantitative MRI measurement is available, it can be loaded into the software along with the morphological image, and after image registration, quantitative MRI values can be automatically extracted. Any of the 3D morphological sequences can be used for automated segmentation, preferably 3D-DESS (Double-Echo Steady State), but we successfully segmented cartilage on 3D-GRE (Gradient Echo), 3D-TrueFISP (Balanced Steady-State GRE), 3D-MERGE (Multiple Echo Recombined Gradient Echo), and 3D-WAT images (T1-weighted gradient echo with water-selective excitation). On average, a single knee segmentation step takes approximately 5–15 minutes, depending on the pixel resolution and number of slices (tested on a standard workstation equipped with an Intel Xeon W-2225 CPU @ 4.10 GHz with 4 cores, 16 GB of physical memory and an AMD Radeon R7 450 graphical unit). The example of automated cartilage segmentation from 3D-DESS and 3D-GRE morphological images are shown in Figure 2 and 3 respectively.

After coarse initial segmentation, the software allows the user to edit the individual cartilage regions manually. Two editing modes are available: paint mode, which uses brushes of selectable size and shape and adds or removes parts of the selected region, and nudge mode, which is applied to the contours of the selected region, which can

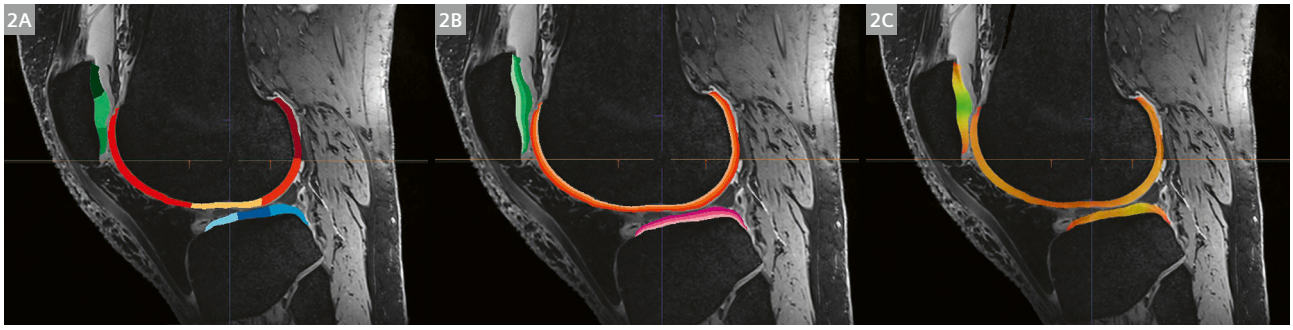

2 **(2A)** Automated segmentation of the knee cartilage on 3D-DESS images (7-tesla MRI, echo time 2.55 ms, repetition time 8.68 ms, acquisition matrix 320 x 320, pixel spacing 0.25 x 0.25 mm, slice thickness 0.5 mm). **(2B)** Three-layer representation of the segmentation (deep, middle, and superficial cartilage zones), **(2C)** cartilage thickness map.

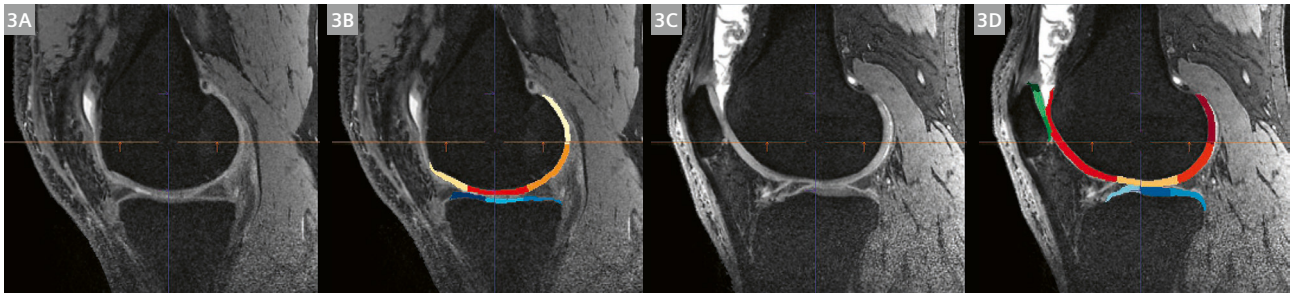

3 **(3A, B)** Automated segmentation of the medial condyle on 3D-GRE images (3-tesla MRI, echo time 4.92 ms, repetition time 16.3 ms, acquisition matrix 320 x 320, pixel spacing 0.5 x 0.5 mm, slice thickness 0.7 mm). **(3C, D)** Automated segmentation of the lateral condyle on 3D-GRE images of the same subject scanned with the same protocol.

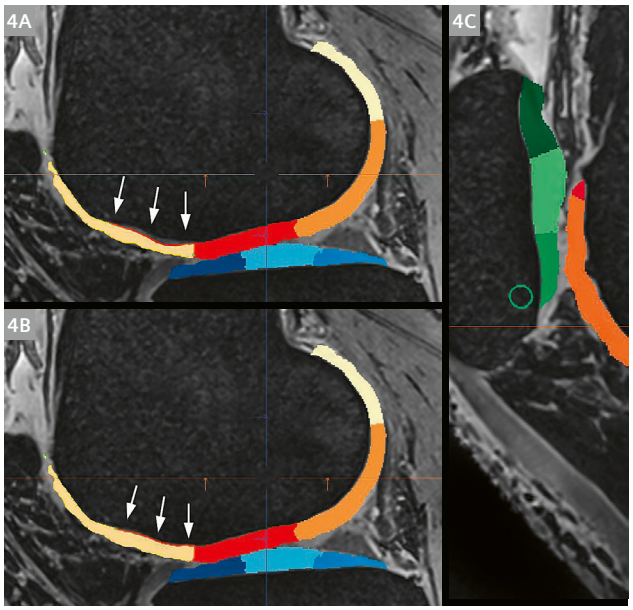

4 Segmentation post-editing in nudge mode – an inaccurately segmented region can be selected **(4A)** and dragged as required **(4B)**, the white arrows point to the selected region. Alternatively, post-editing in paint mode can be used; in this example, a circular six-pixel diameter brush was selected **(4C)**.

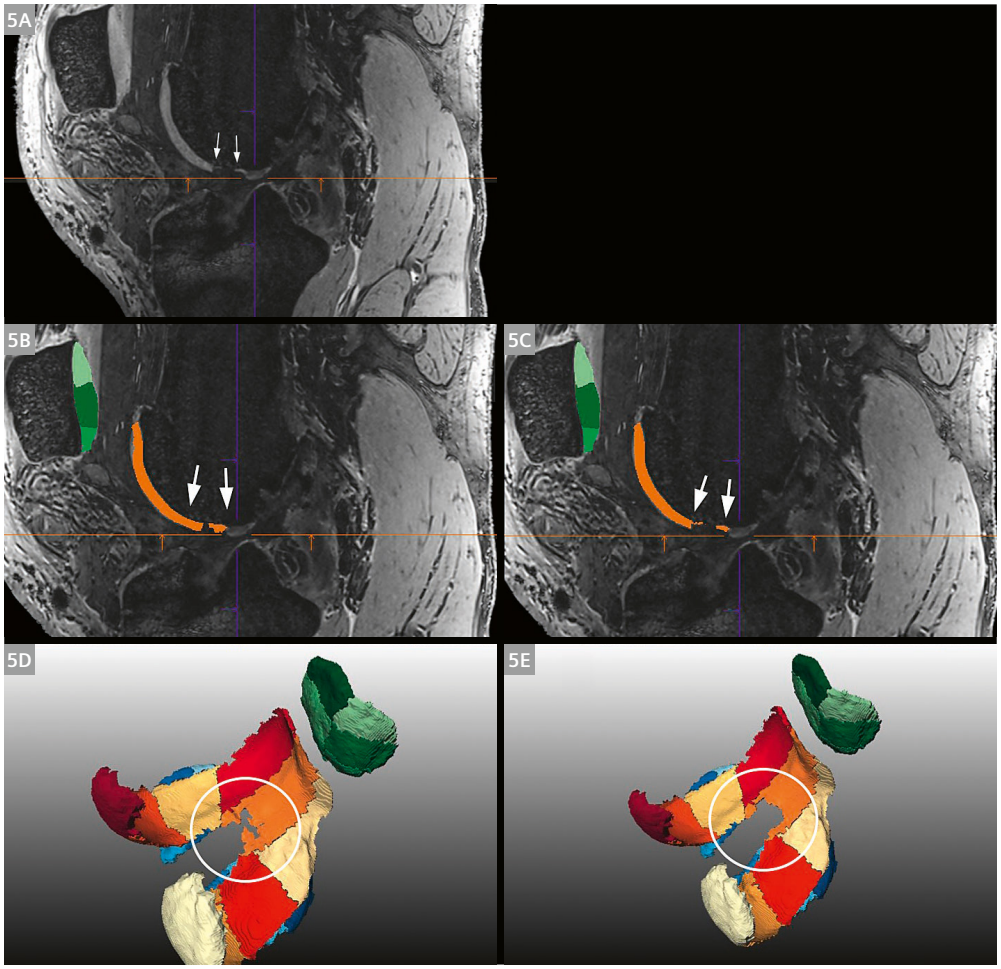

5 A 39-year-old female patient after ACI procedure; **(5A)** 3D-DESS image (7-tesla MRI, echo time 2.55 ms, repetition time 8.23 ms, acquisition matrix 384 x 384, pixel spacing 0.22 x 0.22 mm, slice thickness 0.45 mm), arrows indicate the donor site from which the cartilage was harvested. **(5B)** Unedited automated segmentation of the corresponding slice; **(5C)** Edited automated segmentation of the corresponding slice using paint mode; 3D rendering of an unedited **(5D)** and edited **(5E)** automated segmentation (donor site in the white circle).

be altered using a Bézier curve. An example of the editing mode is shown in Figure 4. Typically, post-editing is not necessary if high-quality DESS images are used. If low-resolution or low SNR images are used, editing takes approximately 5 to 20 minutes.

Automated cartilage segmentation in patients with autologous chondrocyte implantation

Autologous chondrocyte implantation (ACI) is a surgical procedure used to treat full-thickness articular cartilage defects of the knee [17]. It is a two-stage procedure: In the first stage, the surgeon harvests a small piece of articular cartilage from the patient's knee from which the chondrocytes are enzymatically isolated. In the second stage, open surgery is performed in which a scaffold of a different type, seeded with cells that have been harvested and cultivated, is inserted into in the articular cartilage defect. The chondrocytes should induce matrix synthesis and, at best, produce hyaline cartilage repair tissue. The transplanted part of cartilage typically fills the whole lesion and hence does not cause any problems for automated segmentation. The harvested part of the cartilage in a non-weight bearing region leaves a full-thickness hole in the cartilage which gradually fills up with fibrous tissue. Segmentation of the cartilage subregion encompassing the donor site can be used to indirectly assess refilling of the cartilage defect over time. The software clearly identifies cartilage interruption. However, the boundaries are not accurately segmented. In the example shown in Figure 5, the donor site was covered by approximately 15 slices, hence post-editing took less than five minutes per case.

Automated segmentation in patients treated with disease-modifying osteoarthritis drugs

The key potential of automated cartilage segmentation lies in the evaluation of patients treated with newly developed chondrotherapies, which can have a direct or indirect

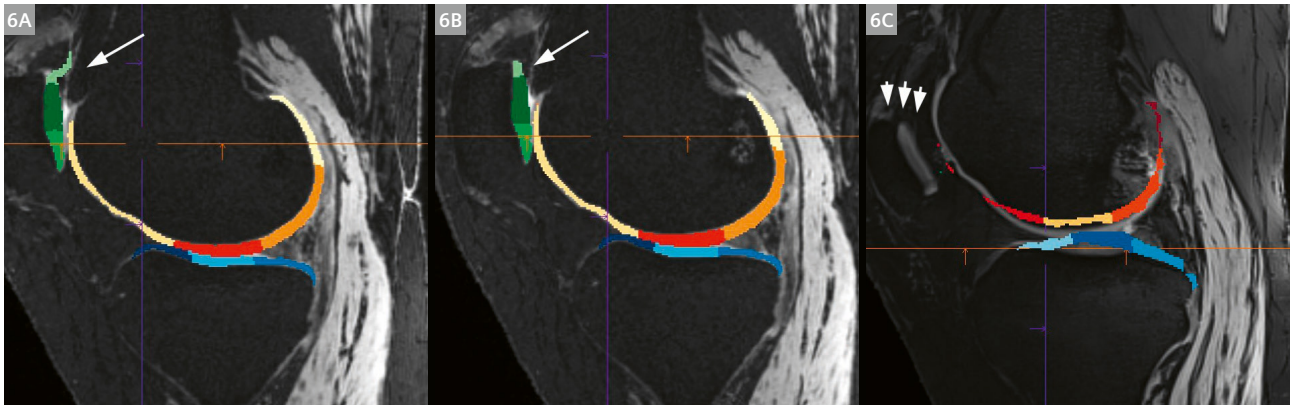

6 Automated knee cartilage segmentation of cadaver knees. If the patella (long arrow) has not substantially shifted **(6A)**, the resulting automated segmentation can be relatively easily edited **(6B)**. However, if the patella has shifted several centimeters caudally (three short arrows), further editing is needed **(6C)**.

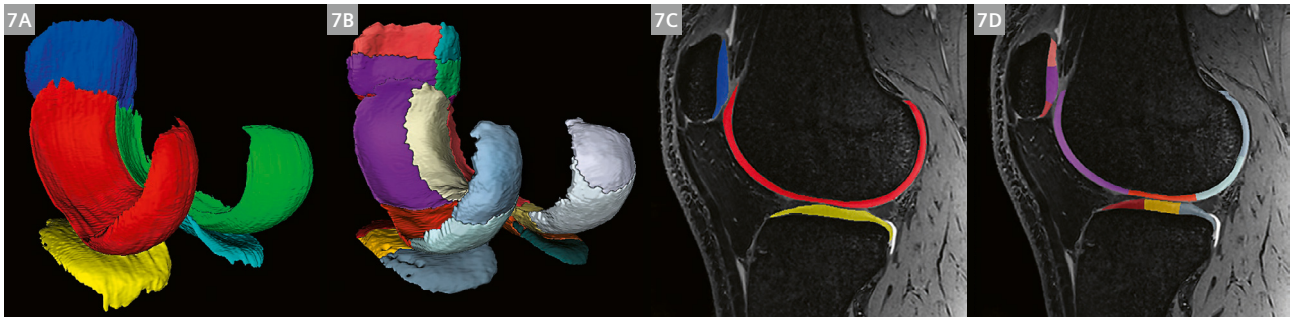

7 3D rendering of a manual **(7A)** and automated **(7B)** knee cartilage segmentation and example slices of manual **(7C)** and automated **(7D)** segmentation overlaid on 3D-DESS images (7-tesla MRI, echo time 2.55 ms, repetition time 8.86 ms, acquisition matrix 320 x 320, pixel spacing 0.25 x 0.25 mm, slice thickness 0.5 mm).

	Fully-automated cartilage segmentation		Fully-automated cartilage segmentation with post-editing	
Cartilage region	Jaccard	Dice	Jaccard	Dice
Patella	0.706	0.855	0.823	0.879
Lateral tibia	0.700	0.850	0.788	0.861
Medial tibia	0.702	0.825	0.832	0.828
Femur	0.722	0.882	0.845	0.895
All regions combined	0.710	0.834	0.822	0.866

Table 1: A comparison of automated and manual cartilage segmentation using the Jaccard coefficient and the Dice coefficient. Both options, fully automated and fully automated with post-editing, are listed. *Reproduced from [19]*.

Smallest detectable change

PATELLA

	LatSup	LatCent	LatInf	MedSup	MedCent	MedInf	all combined
T2 (in ms)	2.62	2.42	2.35	4.11	2.26	2.60	2.73
Volume (in mm^3)	75.9	70.9	51.6	101.6	102.6	38.6	73.5
Thickness (in mm)	0.14	0.22	0.26	0.17	0.25	0.12	0.19

TIBIA

	MedAnt	MedCent	MedPost	LatAnt	LatCent	LatPost	all combined
T2 (in ms)	2.55	3.23	3.07	1.85	3.05	2.73	2.74
Volume (in mm^3)	47.66	68.14	39.43	64.18	63.00	96.07	63.08
Thickness (in mm)	0.11	0.21	0.05	0.12	0.24	0.12	0.14

FEMUR

	MedAnt	MedCent	MedPost	TrochLat	TrochMed	TrochCent	LatAnt	LatCent	LatPost	all combined
T2 (in ms)	3.28	1.92	1.89	0.81	1.67	1.56	1.53	1.96	2.47	1.90
Volume (in mm^3)	45.81	201.04	187.04	73.93	64.20	178.29	88.72	165.68	151.05	128.42
Thickness (in mm)	0.18	0.20	0.21	0.09	0.12	0.09	0.21	0.22	0.18	0.16

Table 2: Test-retest of automated cartilage segmentation and automated 3D-TESS T2 extractions from baseline scan and scan repeated after eight days. *Reproduced from [19]*.

effect on the cartilage volume. Therefore, the MR Chondral Health (MRCH) software was employed for MRI knee examinations (3-tesla) performed at baseline and at a few follow-up timepoints over the course of one year after treatment. The effect of the treatment was assessed in an exploratory analysis of the additive volume within the weight-bearing area of the medial femur [18]. The data generated from the MRCH software in this study was found to be potentially more sensitive than that obtained by the manual segmentation approach.

Automated cartilage segmentation of cadaver knees

MR Chondral Health was also tested on cadaver knees from six donors. Automated segmentation of such knees can be challenging for several reasons. First, the MRI image contrast differs from in-vivo knees even when the same MRI protocol is used because of post-mortem changes of the soft tissue. Second, as the patellar tendon is typically cut in cadaver knees, the patella slips caudally, which results in unusual knee anatomy. The example of automated cartilage segmentation of cadaver knees with dislocated patella is shown in Figure 6.

Validating segmentation

In order to evaluate the accuracy of automated knee cartilage segmentation, the images of thirteen patients with a grade I and grade II femoral cartilage defect in the lateral or medial condyle (six females, 50.8 ± 4.4 years and seven males, 50.2 ± 6.1 years) were manually segmented by an experienced radiologist and automatically segmented using the MR Chondral Health application. To calculate test-retest variability, the MRI examinations were performed twice: at baseline and after eight days. The MRI protocol consisted of 3D-DESS, 3D-TESS T2 mapping (triple-echo steady state) [19], and CPMG T2 mapping (Carr-Purcell-Meiboom-Gill, i.e. multiecho spin-echo sequence). Manual segmentation was performed for bulk femoral, patellar, and tibial lateral and medial cartilage rather than for all twenty-one cartilage subregions separately, since reproducing the exact perimeters of the subregions defined automatically is a difficult task and might introduce a significant bias (Fig. 7). While testing for the similarity between the manual and automatic datasets, a mean Jaccard coefficient of 0.709 ± 0.010 and a mean Dice coefficient of 0.848 ± 0.025 were found when using the unedited data from the automated segmentation. When using data from the edited automated segmentation, the mean Jaccard and Dice coefficients increased to 0.822 ± 0.024 and 0.863 ± 0.027 respectively [20]. Details of the Jaccard and Dice coefficients for individual cartilage regions are listed in Table 1. The test-retest variability was also expressed as the smallest detectable change individually for cartilage volume, thickness, and T2 values (listed in Table 2).

Validating the accuracy of biochemical image registration

When biochemical images (such as those acquired with T2 mapping) are loaded into MR Chondral Health, the software registers the images, extracts the values, and displays them in the final output table (Fig. 8). In order to validate the accuracy of the registration, it was compared with an algorithm developed in MATLAB (version 2019b, The MathWorks, Inc, Natick, MA, USA). This algorithm uses a multimodal co-registration method, which was applied using spatial mapping of fixed images (DESS) and moving images (T2-TESS and T2-CPMG). Affine transformation with 12 degrees of freedom was used. Optimizer function parameters were determined by a previous iterative process, while a similarity index map was used as a quantitative co-registration quality marker (initial radius = 0.001; epsilon = 1.5e-4; growth factor = 1.01; and maximum iterations = 300). Two registering methods were compared across the twenty-one subregions in seven subjects using descriptive statistics and the Pearson correlation coefficient (Fig. 9). In the case of 3D-TESS T2 mapping, there was a high correlation between MR Chondral Health and MATLAB registration. However, in the case of 3D-CPMG T2 mapping, the correlation was substantially lower. In 3D-CPMG T2

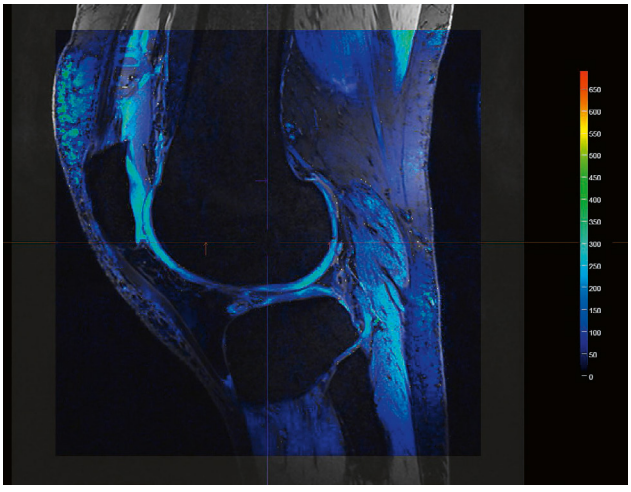

8 A screenshot from MR Chondral Health depicting a 3D-DESS image overlaid with a registered CMPG-T2 map.

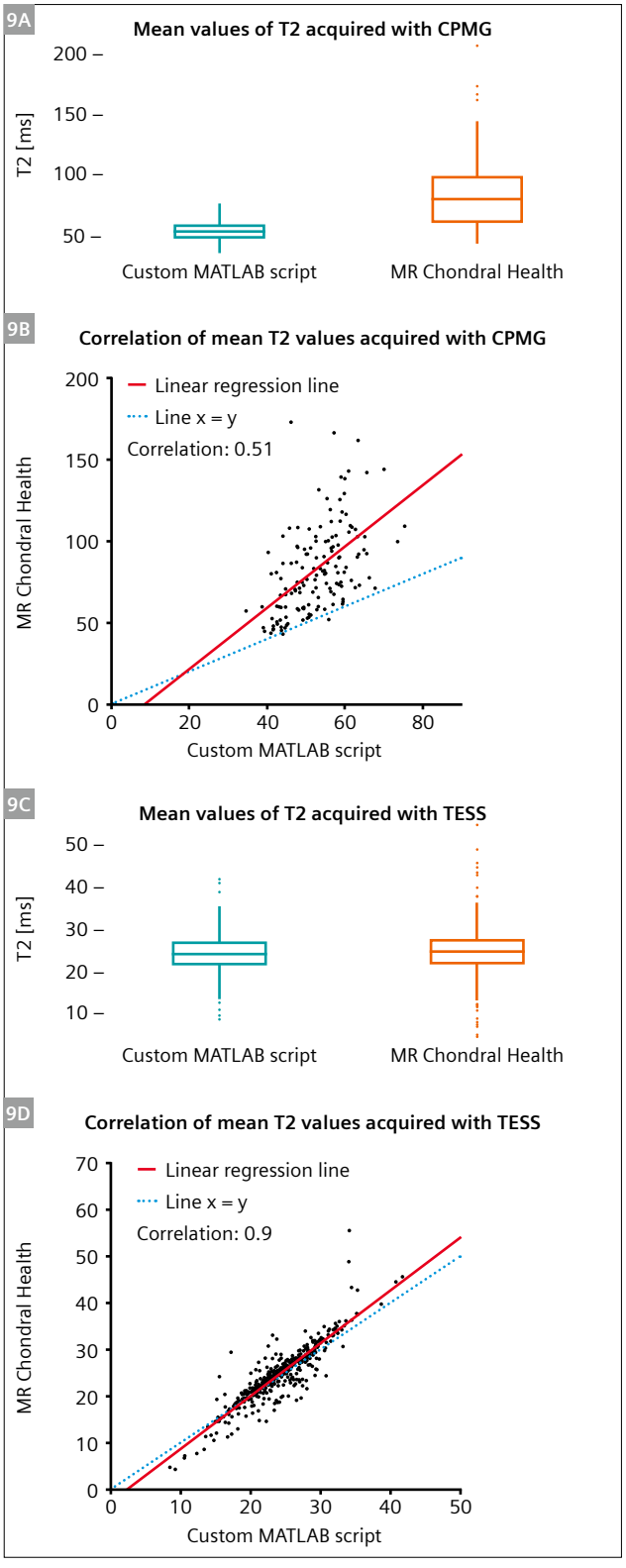

9 The comparison of two biochemical image (T2 mapping) registration methods: MR Chondral Health and custom-written MATLAB script; mean values of T2 acquired with TESS **(9A)** and CPMG **(9C)**, and a correlation between these two methods of CPMG-T2 **(9B)** and TESS-T2 **(9D)**.

mapping, MR Chondral Health slightly misregistered the maps onto bone; this introduced some outliers resulting in T2 overestimation. MR Chondral Health allows the user to adjust registration manually; however, this tool is rather cumbersome.

Conclusion and outlook

Fully automatic tissue segmentation is an essential step toward applying quantitative MRI techniques in a clinical setting. These advances in MR imaging may contribute to the development and evaluation of effective therapeutic strategies that target early structural changes. MR Chondral Health provides robust and reproducible automated segmentation of articular knee cartilage images from wide range of 3D MRI sequences. Automated extraction of quantitative MRI values is a promising feature of the software, but the registration algorithm used in this version still requires some improvement. (According to our information, this issue has been resolved with MR Chondral Health Version 2.2, which is to be released soon).
A remaining question still to be evaluated is the accuracy of automated cartilage segmentation in late-stage OA, which is manifested by cartilage thinning and forming of osteophytes.

References:

1 Sarzi-Puttini, P., M.A. Cimmino, R. Scarpa, R. Caporali, F. Parazzini, A. Zaninelli, F. Atzeni, and B. Canesi, Osteoarthritis: an overview of the disease and its treatment strategies. Semin Arthritis Rheum, 2005. 35(1 Suppl 1): pp. 1–10.

2 Ambellan, F., A. Tack, M. Ehlke, and S. Zachow, Automated segmentation of knee bone and cartilage combining statistical shape knowledge and convolutional neural networks: Data from the Osteoarthritis Initiative. Med Image Anal, 2019. 52: pp. 109–118.

3 Hou, W., J. Zhao, R. He, J. Li, Y. Ou, M. Du, X. Xiong, B. Xie, L. Li, X. Zhou, P. Zuo, E. Raithel, Z. Zhang, and W. Chen, Quantitative measurement of cartilage volume with automatic cartilage segmentation in knee osteoarthritis. Clin Rheumatol, 2021. 40(5): pp. 1997–2006.

4 Iranpour-Boroujeni, T., A. Watanabe, R. Bashtar, H. Yoshioka, and J. Duryea, Quantification of cartilage loss in local regions of knee joints using semi-automated segmentation software: analysis of longitudinal data from the Osteoarthritis Initiative (OAI). Osteoarthr Cartil, 2011. 19(3): pp. 309–14.

5 Liess, C., S. Lusse, N. Karger, M. Heller, and C.C. Gluer, Detection of changes in cartilage water content using MRI T-2-mapping in vivo. Osteoarthr Cartil, 2002. 10(12): pp. 907–913.

6 Watkins, L.E., E.B. Rubin, V. Mazzoli, S.D. Uhlrich, A.D. Desai, M. Black, G.K. Ho, S.L. Delp, M.E. Levenston, G.S. Beaupre, G.E. Gold, and F. Kogan, Rapid volumetric gagCEST imaging of knee articular cartilage at 3 T: evaluation of improved dynamic range and an osteoarthritic population. Nmr in Biomedicine, 2020. 33(8).

7 Welsch, G.H., S. Trattnig, K. Scheffler, P. Szomonanyi, S. Quirbach, S. Marlovits, S. Domayer, O. Bieri, and T.C. Mamisch, Magnetization transfer contrast and T2 mapping in the evaluation of cartilage repair tissue with 3T MRI. J Magn Reson Imaging, 2008. 28(4): pp. 979–986.

8 Zbyn, S., V. Mlynarik, V. Juras, P. Szomolanyi, and S. Trattnig, Evaluation of cartilage repair and osteoarthritis with sodium MRI. Nmr in Biomedicine, 2016. 29(2): pp. 206–215.
9 Tang, J., S. Millington, S.T. Acton, J. Crandall, and S. Hurwitz, Surface extraction and thickness measurement of the articular cartilage from MR images using directional gradient vector flow snakes. IEEE Trans Biomed Eng, 2006. 53(5): pp. 896–907.
10 Folkesson, J., E.B. Dam, O.F. Olsen, P.C. Pettersen, and C. Christiansen, Segmenting articular cartilage automatically using a voxel classification approach. IEEE Trans Med Imaging, 2007. 26(1): pp. 106–15.
11 Cashman, P.M., R.I. Kitney, M.A. Gariba, and M.E. Carter, Automated techniques for visualization and mapping of articular cartilage in MR images of the osteoarthritic knee: a base technique for the assessment of microdamage and submicro damage. IEEE Trans Nanobioscience, 2002. 1(1): pp. 42–51.
12 Kshirsagar, A.A., P.J. Watson, J.A. Tyler, and L.D. Hall, Measurement of localized cartilage volume and thickness of human knee joints by computer analysis of three-dimensional magnetic resonance images. Invest Radiol, 1998. 33(5): pp. 289–99.
13 Shim, H., S. Chang, C. Tao, J.H. Wang, C.K. Kwoh, and K.T. Bae, Knee cartilage: efficient and reproducible segmentation on high-spatial-resolution MR images with the semiautomated graph-cut algorithm method. Radiology, 2009. 251(2): pp. 548-56.
14 Ebrahimkhani, S., M.H. Jaward, F.M. Cicuttini, A. Dharmaratne, Y. Wang, and A.G.S. de Herrera, A review on segmentation of knee articular cartilage: from conventional methods towards deep learning. Artif Intell Med, 2020. 106: pp. 101851.
15 Fripp, J., S. Crozier, S.K. Warfield, and S. Ourselin, Automatic segmentation and quantitative analysis of the articular cartilages from magnetic resonance images of the knee. IEEE Trans Med Imaging, 2010. 29(1): pp. 55–64.
16 Surowiec, R.K., E.P. Lucas, E.K. Fitzcharles, B.M. Petre, G.J. Dornan, J.E. Giphart, R.F. LaPrade, and C.P. Ho, T2 values of articular cartilage in clinically relevant subregions of the asymptomatic knee. Knee Surg Sports Traumatol Arthrosc, 2014. 22(6): pp. 1404–14.
17 Harris, J.D., R.A. Siston, X. Pan, and D.C. Flanigan, Autologous chondrocyte implantation: a systematic review. J Bone Joint Surg Am, 2010. 92(12): pp. 2220–33.
18 Trattnig, S., C. Scotti, D. Laurent, D. Juras, S. Hacker, B. Cole, L. Pasa, R. Lehovec, P. Szomolanyi, E. Raithel, F. Saxer, J. Praestgaard, F. La Gamba, J. L. Jiménez, D. Sanchez Ramos, R. Roubenoff, and M. Schieker, POS0277 Anabolic effect of LNA043, a novel disease-modifying osteoarthritis drug candidate: results from an imaging-based proof-of-concept trial in patients with focal articular cartilage lesions, in Annals of the Rheumatic Diseases. 2021, BMJ Publishing Group Ltd., http://dx.doi.org/10.1136/annrheumdis-2021-eular.447: Online. p. 277.
19 Heule, R., C. Ganter, and O. Bieri, Triple echo steady-state (TESS) relaxometry. Magn Reson Med, 2014. 71(1): pp. 230–7.
20 Juras, V., P. Szomolanyi, M.M. Schreiner, K. Unterberger, A. Kurekova, B. Hager, D. Laurent, E. Raithel, H. Meyer, and S. Trattnig, Reproducibility of an Automated Quantitative MRI Assessment of Low-Grade Knee Articular Cartilage Lesions. Cartilage, 2020: pp. 1947603520961165.

Contact

Vladimir Juras, Ph.D.
Medical University of Vienna
Department of Biomedical Imaging and Image-guided Therapy
High Field MR Centre
Währinger Gürtel 18–20
1090 Vienna
Austria
Phone: +43 1 40 400 64660
vladimir.juras@meduniwien.ac.at


Vladimir Juras


Pavol Szomolanyi


Veronika Janacova


Siegfried Trattnig

Clinical Implementation of Deep Learning-Accelerated HASTE and TSE

Judith Herrmann[1]; Andreas Lingg[1]; Matthias Kündel[1]; Sebastian Gassenmaier[1]; Saif Afat[1]; Haidara Al-Mansour[1]; Dominik Nickel[2]; Gregor Koerzdoerfer[2]; Ahmed Othman[1,3]

[1]Department of Diagnostic and Interventional Radiology, Tuebingen, Germany
[2]MR Applications Predevelopment, Siemens Healthineers, Erlangen, Germany
[3]Department of Neuroradiology, University Medical Center, Mainz, Germany

Introduction

Magnetic resonance imaging (MRI) has become a modality of choice for the diagnosis of several diseases and is currently indispensable in healthcare. One big disadvantage of MRI is the long duration of the examination, usually ranging between 20 and 60 minutes for body trunk imaging. Long acquisition times come with downsides, such as decreased image quality due to motion artifacts, increased costs, and reduced patient throughput [1]. In view of the limited availability of MRI scanners in general, MRI remains a scarce and more expensive resource than other imaging techniques with limited access to patients in need.

In order to improve this situation, over the past few decades, different acceleration strategies such as compressed sensing (CS) and parallel imaging (PI) have been proposed and established. Recently a revolutionary development based on artificial intelligence has been implemented to further accelerate the acquisition and improve the image quality at the same time: Deep Learning (DL) reconstruction has come to the fore and is gradually being implemented in clinical routine [2–4].

The aim of this report is to describe the first clinical implementation of DL-accelerated, T2-weighted (T2w) half-Fourier single-shot turbo spin echo (HASTE)[1] sequences of the upper abdomen as well as T2w and proton density (PD)-weighted turbo spin echo (TSE) sequences for musculoskeletal imaging in routine daily workflow. The novel DL-accelerated sequences are evaluated in terms of feasibility and image quality compared to standard sequences.

[1]*Work in progress. The application is currently under development and is not for sale in the U.S. and in other countries. Its future availability cannot be ensured.*

MRI technique

Acceleration strategies for Deep Learning-reconstructed TSE and HASTE[1]

To accelerate the image acquisition, a conventional undersampling pattern known from parallel imaging is used for both sequences [5, 6]. Besides the data acquisition for the actual image data, calibration data for the coil-sensitivity estimation need to be acquired. For the TSE sequence, these data are acquired as part of the imaging scan. For the HASTE sequence, these are separately acquired using a second echo train covering only the region around the *k*-space center. In both sequences, a fraction of the *k*-space's periphery is not acquired to further reduce the acquisition time.

For TSE acquisitions, DL-reconstructed MRI can be used to improve on a combination of image resolution, acquisition time, and SNR, while maintaining the original contrast. In contrast to this, for the HASTE sequence, the improved DL reconstruction enables an improved image

Demographics	
Total (male/female), n	20 (8/12)
Age, mean ± SD (range), y	59 ± 13 (27–79)
Sequence and body region, n	HASTE, upper abdomen, 10 PD TSE, knee, 5 PD TSE, shoulder, 5

Table 1: Demographics of participating individuals
SD indicates standard deviation; y, years; n, number; HASTE, half-Fourier single-shot turbo spin echo; PD, proton density; TSE, turbo spin echo.

contrast. Specifically, with a higher acceleration factor the duration of the echo train can be shortened and therefore the effect of T2 decay can be reduced. As an additional benefit, the specific absorption rate (SAR) is reduced along with the number of refocusing pulses required. This allows for further sequence optimizations in the form of larger gaps between consecutively acquired slices and reduced repetition time.

Deep Learning image reconstruction

For both sequences, the image reconstruction comprises a fixed iterative reconstruction scheme or variational network [6, 7], alternating between data consistency and a Convolutional Neural Network (CNN)-based regularization. The regularization model's architecture is based on a novel hierarchical design of an iterative network that repeatedly decreases and increases the resolution of the feature maps, allowing for a more memory-efficient model than conventional CNNs. Coil sensitivity maps are estimated from the calibration data in advance as a pre-processing step. For the image reconstruction, undersampled *k*-space data, bias field correction, and coil sensitivity maps are inserted into the variational network.

The reconstruction was trained using volunteer acquisitions consisting of about 10,000 slices for each sequence type using conventional HASTE and TSE protocols acquired on various clinical 1.5T and 3T scanners (MAGNETOM scanners, Siemens Healthcare, Erlangen, Germany).

Implementation of DL image reconstruction in clinical workflow

To apply the DL reconstruction on clinically used MRI scanners, the network was converted to a C++ implemented inference framework. For the CPU-only reconstruction, inference needed about 2 seconds per slice for the protocol settings used. As the reconstruction was triggered after the end of the acquisition, the resulting perceived reconstruction time was 2–3 minutes including additional pre and post-processing. A GPU-based reconstruction is expected to reduce this duration to approximately 10 seconds, but was not available on the clinical scanners used.

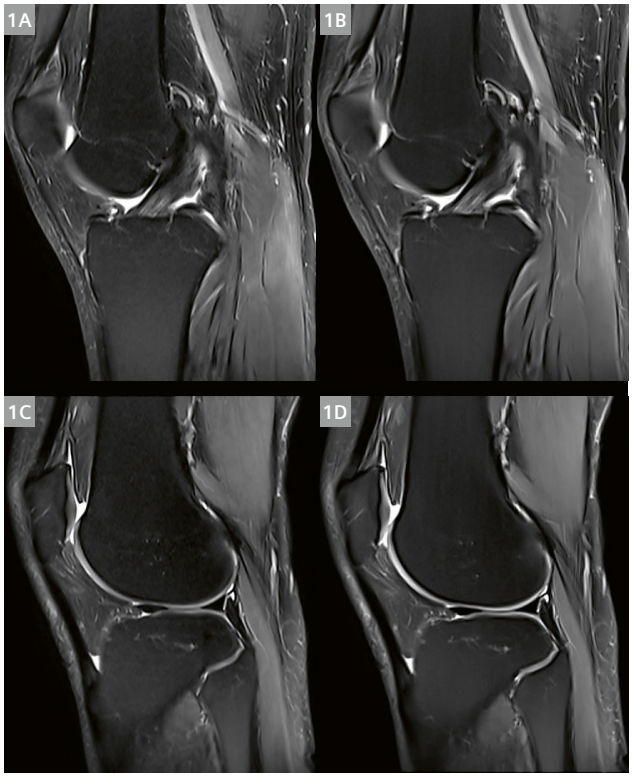

1 31-year-old female participant with MRI of the knee in coronal (upper row) and sagittal (lower row) plane at 3T. Standard reconstructed PD-weighted TSE **(1A** and **1C)** show more noise compared to Deep Learning-reconstructed PD-weighted TSE **(1B** and **1D)**. The delineation and assessment of anatomic structures, such as the anterior cruciate ligament, is comparable in both reconstructions.

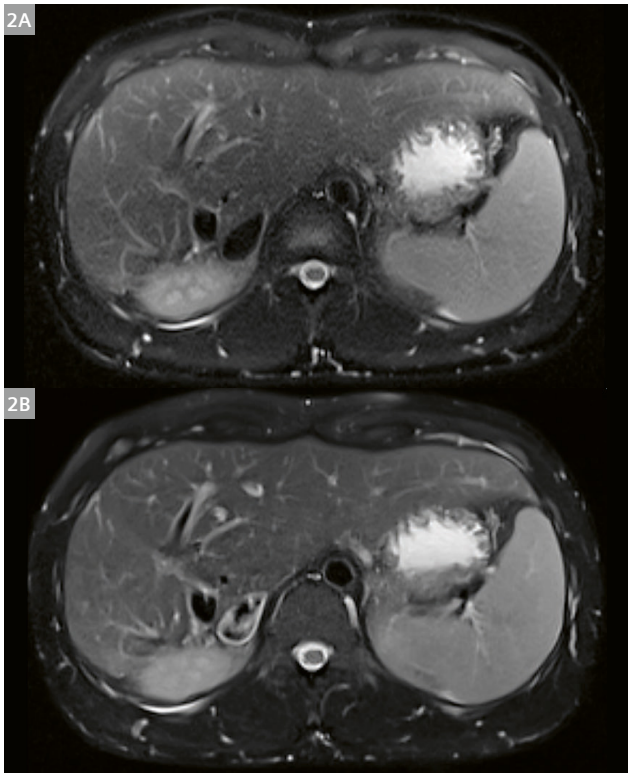

2 20-year-old male participant with MRI of the liver in axial plane at 1.5T. Image noise and edge sharpness of anatomical structures are improved in Deep Learning-reconstructed HASTE **(2B)** compared to standard reconstructed HASTE **(2A)**. Furthermore, the acquisition of the Deep Learning-reconstructed HASTE is possible within just one breath-hold.

Image quality analysis

Institutional review board approval was obtained for this prospective monocentric study. All study procedures were conducted in accordance with the ethical standards as laid down in the 1964 Declaration of Helsinki and its later amendments.

Accelerated MR images with DL reconstruction were prospectively acquired along with standard MR images on 1.5T and 3T MRI scanners (MAGNETOM Prisma^{fit}, MAGNETOM Vida, MAGNETOM Skyra, MAGNETOM Avanto, and MAGNETOM Aera, Siemens Healthcare, Erlangen, Germany) and an exemplary sample of 20 participants were included in this analysis (see Table 1). Two radiologists with three to ten years of experience in MRI who were blinded to participant information, acquisition parameters, and image reconstruction rated in consensus both standard MR images and accelerated MR images with DL reconstruction by using a random order. Overall image quality, artifacts, edge sharpness, and diagnostic confidence ratings were performed on an ordinal 5-point Likert scale ranging from one to five, with five being best. Reading scores were considered sufficient when reaching ≥ 3.

Image analysis was performed on a PACS workstation (GE Healthcare Centricity™ PACS RA1000, Milwaukee, WI, USA).

Statistical analysis was performed using SPSS version 26 (IBM Corp, Armonk, NY, USA). Besides descriptive statistics, comprising median and interquartile range (IQR), nonparametric paired Wilcoxon signed-rank tests were used to analyze Likert scores for image quality, artifacts, edge sharpness, and diagnostic confidence assessments. P-values less than 0.05 were considered statistically significant.

Results

The aim of this report was to describe the implementation of a DL image reconstruction in clinical workflow and evaluate its obtainable image quality in daily clinical routine. All sequences with DL image reconstruction were successfully implemented in clinical workflow and DL sequences were successfully acquired in all participants in all body parts. Fat suppression could be applied successfully for the TSE and HASTE sequences implemented with DL image reconstruction.

For TSE sequences, DL enabled a time saving of ≥ 50%. As expected, SAR did not exceed normal levels. For HASTE sequences, DL allowed for an acquisition time reduction of > 50%. As a single-shot sequence with a long train of refocusing pulses, HASTE is impaired by high power deposition, which limits its use at high resolutions and high field strengths, particularly if combined with acceleration techniques such as PI [8]. The DL algorithm used effectively reduced TA while staying within the SAR limitations. An overview of exemplary acquisition parameters is displayed in Table 2.

Radiologists rated the overall image quality of HASTE and PD TSE with DL reconstruction as excellent (median 5, IQR 4.25–5) and even superior to standard HASTE and

Sequence	HASTE		PD TSE FS	
	standard	DL	standard	DL
Body part	upper abdomen	upper abdomen	knee	knee
Tesla	1.5T	1.5T	3T	3T
Orientation	axial	axial	coronal	coronal
TA, min	1:28–1:44	0:16	3:11	1:33
FOV, mm	293 × 360	293 × 360	150	150
Voxel size, mm	1.13 × 1.13 × 6.0	1.13 × 1.13 × 6.0	0.2 × 0.2 × 3.0	0.2 × 0.2 × 3.0
TR, ms	1400	500	3790	3580
TE, ms	94	94	44	41
FA, degree	160	160	150	150

Table 2: Exemplary acquisition parameters of standard and vv sequences

HASTE indicates half-Fourier single-shot turbo spin echo; PD, Proton Density; TSE, turbo spin echo; FS, fat saturation; DL, deep learning; T, Tesla; TA, time of acquisition; FOV, field of view; TR, repetition time; TE, echo time; FA, flip angle.

PD TSE sequences (median 4, IQR 4–5, p<0.05). No severe artifacts occurred when using DL reconstruction as no difference was found in the extent of artifacts between standard (median 5, IQR 4–5) and DL-reconstructed sequences (median 5, IQR 4.25–5, p=0.157). Edge sharpness was improved with the DL reconstruction (median 5, IQR 5–5) compared to standard sequences (median 5, IQR 4–5, p<0.05). Diagnostic confidence was rated as comparable between the sequences (median 5, IQR 4.25–5. p=0.317). Image examples are given in Figures 1–3.

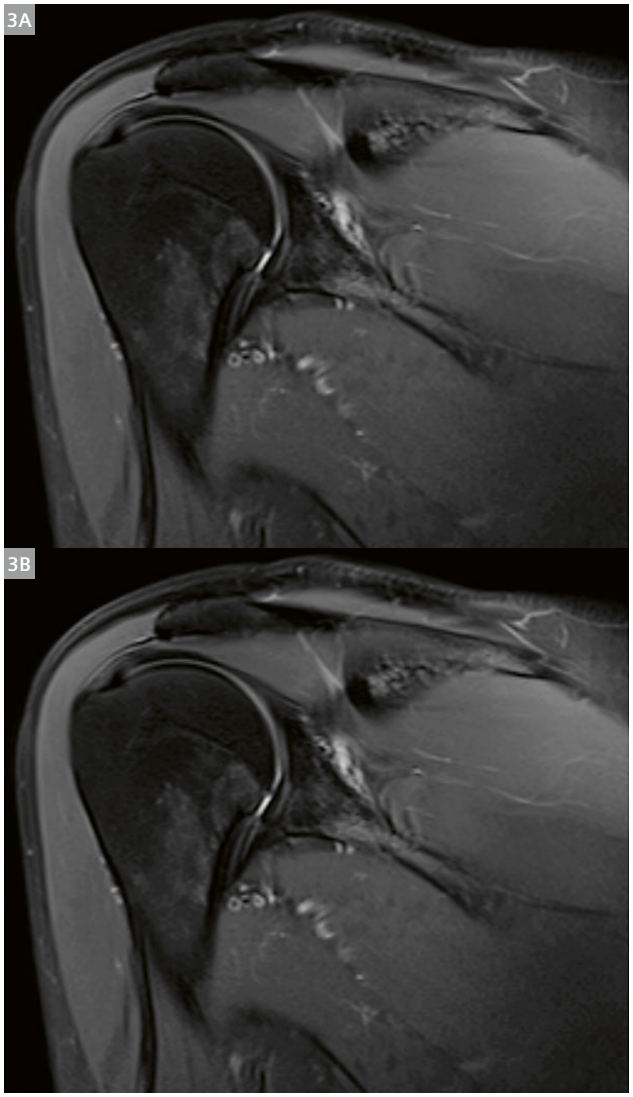

3 35-year-old female participant with MRI of the shoulder in coronal plane at 3T. Image noise and edge sharpness are improved in Deep Learning-reconstructed PD-weighted TSE **(3B)** compared to standard reconstructed PD-weighted TSE **(3A)**.

Discussion

Although MRI has evolved to become a modality of choice for the diagnosis of several diseases, its availability is still limited for reasons closely related to long examination times [1]. One promising approach to solve this shortcoming is to use novel techniques, including artificial intelligence (AI) and machine learning, to accelerate the acquisition of MR images. AI is in the public focus more than ever due to enormous innovations in the last decade, especially in the field of radiology. Novel AI techniques and new algorithms have not only been developed and trained to detect pathologies, but also to improve and accelerate image acquisition and reconstruction [9, 10]. Despite the rapid progress of all technological advances, especially in radiology, there is still a lack of widespread implementation in daily clinical routine. Therefore, the aim of this report was to describe the implementation of DL image reconstruction in daily routine and evaluate the obtainable image quality.

Our investigation demonstrates the successful implementation of DL reconstruction techniques in daily clinical workflow with a substantial reduction of TA and at the same time even higher image quality and improved edge sharpness compared to standard sequences. Effects of the implementation of these new techniques are primarily based on the reduction of TA without compromising regarding the extent of artifacts and diagnostic confidence. The reduction in TA of more than 50%, in particular, yields enormous potential for workflow optimization, increased availability of MRI, and improvement of healthcare.

One central issue in MRI has always been the shortage of scanners. Drastic acceleration and reduction of examination times might provide one piece of the big puzzle of how to enhance healthcare and balance the weight of supply and demand. This is of particular interest in low-income countries where there is only limited access to high-quality diagnostic MRI. DL reconstructions are mostly not very demanding regarding the technical specifications and can therefore also be applied in countries with less-developed technical infrastructures. Another issue that merits consideration is the increasing importance of MRI in standard of care diagnostic procedures. MRI has become increasingly important in many pathologies for diagnosis, biopsy planning, therapy surveillance, and follow-up [11-14].

One of the most challenging tasks in medicine has always been finding a compromise between best medical care and best economic outcome. As most healthcare systems worldwide are insurance based, they all face the same problem: shortage of money versus increase in

demand due to development of new expensive therapies, increased life expectancy, and new diagnostic possibilities. Reduction in acquisition time might allow a higher number of examinations per day.

As we successfully implemented DL sequences in imaging of different body regions, this report is intended to motivate radiologists to establish new AI techniques in everyday clinical practice to further accelerate MRI and improve access to MRI for more patients. For this report we selected some illustrative examples of the DL examinations conducted to provide a brief introduction into how DL sequences are implemented in daily routine. Systematic analyses of the different body regions are in progress and will be outlined in separate studies.

To conclude, DL image reconstruction can be implemented in clinical workflow and enables accelerated image acquisition while maintaining excellent image quality.

References

1 Vanderby S, Badea A, Pena Sanchez JN, Kalra N, Babyn P. Variations in Magnetic Resonance Imaging Provision and Processes Among Canadian Academic Centres.
Can Assoc Radiol J. 2017 Feb;68(1):56–65.

2 Knoll F, Hammernik K, Zhang C, Moeller S, Pock T, Sodickson DK, et al. Deep-Learning Methods for Parallel Magnetic Resonance Imaging Reconstruction: A Survey of the Current Approaches, Trends, and Issues. Ieee Signal Proc Mag. 2020 Jan;37(1):128–140.

3 Lin DJ, Johnson PM, Knoll F, Lui YW. Artificial Intelligence for MR Image Reconstruction: An Overview for Clinicians.
Journal of Magnetic Resonance Imaging. 2020 Feb 12.

4 Hyun CM, Kim HP, Lee SM, Lee S, Seo JK. Deep learning for undersampled MRI reconstruction. Phys Med Biol. 2018 Jul;63(13).

5 Knoll F, Hammernik K, Kobler E, Pock T, Recht MP, Sodickson DK. Assessment of the generalization of learned image reconstruction and the potential for transfer learning.
Magn Reson Med. 2019 Jan;81(1):116–128.

6 Hammernik K, Klatzer T, Kobler E, Recht MP, Sodickson DK, Pock T, et al. Learning a variational network for reconstruction of accelerated MRI data.
Magn Reson Med. 2018 Jun;79(6):3055–3071.

7 Schlemper J, Caballero J, Hajnal JV, Price AN, Rueckert D. A Deep Cascade of Convolutional Neural Networks for Dynamic MR Image Reconstruction. IEEE Trans Med Imaging. 2018 Feb;37(2):491–503.

8 Schulz J, Marques JP, Ter Telgte A, van Dorst A, de Leeuw FE, Meijer FJA, et al. Clinical application of Half Fourier Acquisition Single Shot Turbo Spin Echo (HASTE) imaging accelerated by simultaneous multi-slice acquisition.
Eur J Radiol. 2018 Jan;98:200–206.

9 Wichmann JL, Willemink MJ, De Cecco CN. Artificial Intelligence and Machine Learning in Radiology: Current State and Considerations for Routine Clinical Implementation.
Invest Radiol. 2020 Sep;55(9):619–627.

10 Weikert T, Cyriac J, Yang S, Nesic I, Parmar V, Stieltjes B. A Practical Guide to Artificial Intelligence-Based Image Analysis in Radiology.
Invest Radiol. 2020 Jan;55(1):1–7.

11 Petralia G, Padhani AR, Pricolo P, Zugni F, Martinetti M, Summers PE, et al., Italian Working Group on Magnetic R. Whole-body magnetic resonance imaging (WB-MRI) in oncology: recommendations and key uses.
Radiol Med. 2019 Mar;124(3):218–233.

12 Gillessen S, Omlin A, Attard G, de Bono JS, Efstathiou E, Fizazi K, et al. Management of patients with advanced prostate cancer: recommendations of the St Gallen Advanced Prostate Cancer Consensus Conference (APCCC) 2015.
Ann Oncol. 2019 Dec;30(12):e3.

13 Beets-Tan RG, Beets GL, Vliegen RF, Kessels AG, Van Boven H, De Bruine A, et al. Accuracy of magnetic resonance imaging in prediction of tumour-free resection margin in rectal cancer surgery.
Lancet. 2001 Feb 17;357(9255):497–504.

14 Balleyguier C, Sala E, Da Cunha T, Bergman A, Brkljacic B, Danza F, et al. Staging of uterine cervical cancer with MRI: guidelines of the European Society of Urogenital Radiology.
Eur Radiol. 2011 May;21(5):1102–10.



Contact

Judith Herrmann, M.D.
Eberhard Karls University Tuebingen
Department of Diagnostic and Interventional Radiology
Hoppe-Seyler-Strasse 3
72076 Tuebingen
Germany
judith.herrmann@med.uni-tuebingen.de

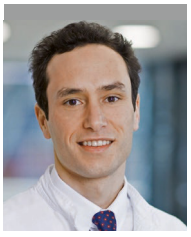

Ahmed Othman, M.D.
University Medical Center
Department of Neuroradiology
55131 Mainz
Germany
ahmed.e.othman@googlemail.com

Ultrafast Brain Imaging with Deep Learning Multi-Shot EPI: Preliminary Clinical Evaluation

Azadeh Tabari[1], Bryan Clifford[2], Augusto Lio M. Goncalves Filho[1], Zahra Hosseini[3], Thorsten Feiweier[4], Wei-Ching Lo[2], Min Lang[1], Maria Gabriela Figueiro Longo[1], Kawin Setsompop[5], Berkin Bilgic[6], Otto Rapalino[1], Pamela Schaefer[1], Stephen Cauley[6], Susie Huang[1], John Conklin[1]

[1]Department of Radiology, Massachusetts General Hospital, Boston, MA, USA
[2]Siemens Medical Solutions USA, Boston, MA, USA
[3]Siemens Medical Solutions USA, Atlanta, GA, USA
[4]Siemens Healthineers, Erlangen, Germany
[5]Department of Radiology / Department of Electrical Engineering, Stanford University, Stanford, CA, USA
[6]Department of Radiology, A. A. Martinos Center for Biomedical Imaging, Massachusetts General Hospital, Harvard Medical School, Boston, MA, USA

MR imaging (MRI) is an integral part of the diagnosis and treatment planning of various neurological diseases. However, the long scan time of brain MRI is a major factor that limits its effectiveness, especially in patients who are prone to motion and frequently require sedation. Thus, fast brain MRI protocols with acceptable diagnostic image quality are desired to enable wider clinical application of MRI [1, 2]. There is an ongoing clinical need to reduce the scan time of brain MRI, especially for uncooperative or motion-prone patients, and patients with diseases requiring rapid diagnosis such as stroke.

Various efforts have been made to achieve ultrafast MRI for brain imaging by using pulse sequences that rapily acquire images. One well-known approach is to use

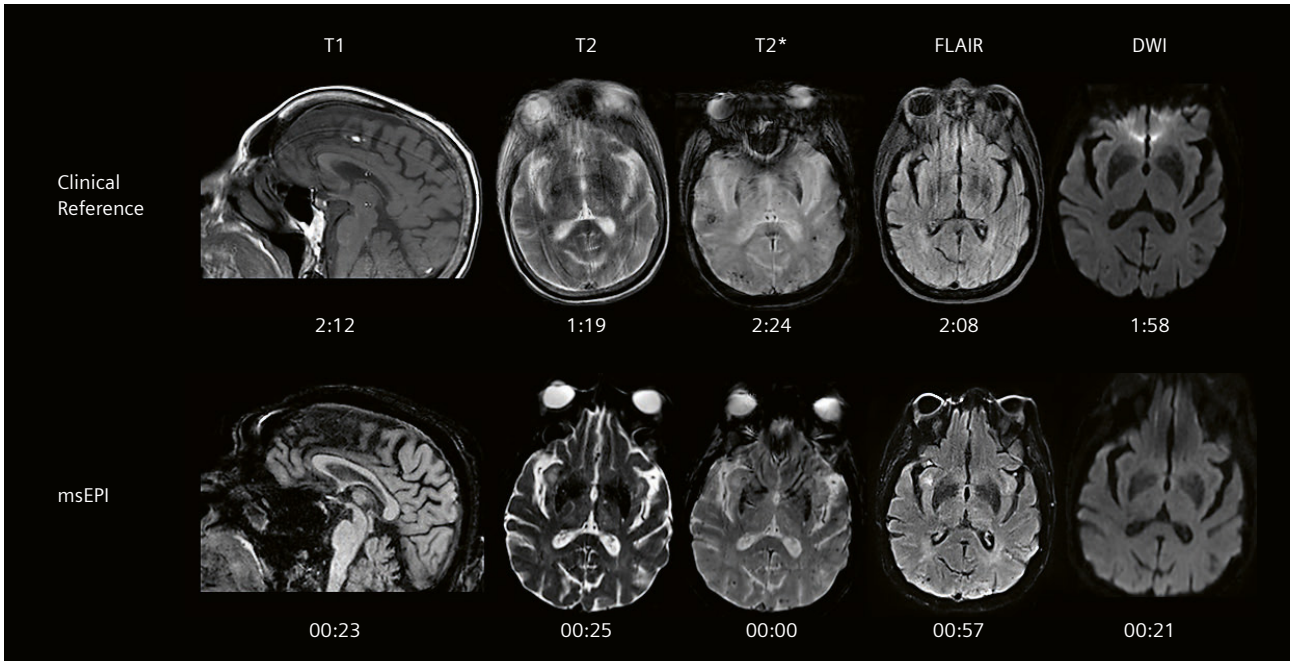

1 Illustrative example on the comparison of the motion-degraded exam of a 10-minute clinical reference protocol to the proposed 2-minute msEPI protocol in a 73-year-old female with no pathologic findings.

single-shot echo-planar imaging (ssEPI), which acquires *k*-space data for an entire 2D image in a single, long readout (shot), following a single RF-excitation pulse [3, 4]. The number of *k*-space lines (echoes) collected in a single shot is called the "EPI factor". The technical advances in the design of echo-planar imaging have made ultrafast brain MRI protocols, including a combination of anatomic and functional sequences, possible [5, 6]. ssEPI methods have recently been used to create rapid screening exams with total durations of 1–2 minutes. However, these rapid ssEPI approaches come at the cost of significant geometric distortion, low signal-to-noise ratio (SNR), and reduced tissue contrast [6–8]. In addition, these approaches offer limited flexibility to acquire in different image orientations or to repeat individual contrasts.

Multi-shot EPI (msEPI) acquisitions have been exploited to address these shortcomings. In a msEPI acquisition, data from multiple highly-undersampled shots are combined together. This approach results in reduced geometric distortion, but at the cost of slightly longer scan times. Higher acceleration factors can be used to compensate for this, but can lead to increased *g*-factor noise and residual aliasing [9–11]. Recent advancement in artificial intelligence (AI)-powered reconstruction algorithms have proved successful in denoising accelerated MRI data. Deep learning (DL) models, can be applied to reduce noise and residual aliasing during reconstruction [12].

In this article we show preliminary results from a clinical translational study being performed at Massachusetts General Hospital (MGH) for validating the feasibility of prototype DL-accelerated msEPI-based rapid brain protocols[1] in a high-volume emergency and inpatient care setting. The rapid imaging technique combines a novel deep learning algorithm to limit *g*-factor noise amplification, magnetization transfer preparation to improve brain tissue contrast, and high per-shot EPI undersampling factors to minimize geometric distortion [12, 13]. A multidisciplinary team of neuroradiologists, MR physicists, and Siemens Healthineers engineers at MGH have developed and optimized acquisition parameters for each of these prototype msEPI-based MRI protocols. Following the optimization of sequence parameters and DL-based reconstruction, an Institutional Review Board approved study was executed. The validation approach comprised prospective comparative studies of emergency and inpatient examinations with a variety of indications. The imaging protocol included T1-, T2-, T2*-weighted, T2-FLAIR, and DW imaging sequences from the prototype msEPI protocol and the clinical reference standard. Imaging was performed on 3T MRI scanners (MAGNETOM Skyra and MAGNETOM Prisma, Siemens Healthcare, Erlangen, Germany) using a 20-channel head coil. Fully sampled msEPI training data were acquired with two averages and eight shots across 16 healthy subjects (8 men, 8 women, aged 19–67). A single FLASH auto calibration scan, acquired at the start of each acquisition, allowed for the calculation of coil sensitivity maps, GRAPPA and/or SMS kernels. The data were split into training and validation datasets with 12 and 4 subjects, respectively. The use of fully sampled data allowed networks to be trained for different acceleration factors through retrospective undersampling.

Two board-certified neuroradiologists, blinded to the clinical history and the imaging protocols, evaluated the head-to-head image quality, scan time, and diagnostic performance of DL-accelerated msEPI-based MRI protocols against the respective clinical standard protocols. For diagnostic performance, they assessed six clinically relevant imaging findings in each protocol (intracranial mass-like lesion, intracranial hemorrhage, white matter hyperintensities, subarachnoid FLAIR hyperintensities, diffusion restriction, and hydrocephalus). For image quality, the raters used a 3-point score to evaluate image degradation by noise and artifacts. Qualitative assessment was compared using Wilcoxon signed-rank tests, and the intraclass correlation coefficients (ICCs) were used to test interobserver reproducibility on the diagnostic concordance between two readers.

Initial clinical experience

The prototype msEPI protocols (T1-, T2-, T2*-weighted, T2-FLAIR, and DWI) required only 2 minutes of scan time (not including adjustments), while the rapid reference protocols (turbo spin-echo (TSE)-based acquisitions) took 10 minutes for the same number of image contrasts. A total of 26 patients (Male:Female 12:14, mean age 58 ± 19 years old) were included in this preliminary study.

Two board-certified neuroradiologists performed an initial clinical subjective evaluation of the DL-accelerated msEPI-based images. Aside from noticeable mild distortion of soft facial tissues, the msEPI images contained only very minimal distortion of the pons and temporal lobes – areas which are critical for diagnosis. The limited artifacts we observed were most prevalent in the longer echo-time T2* data and corresponded to cases where patient motion could be identified. Figure 1 illustrates how shorter scan time allows for lower motion artifacts.

Interobserver agreement was 'almost perfect' for the evaluation of intracranial masses (ICC = 1), WM hyperintensities (ICC = 0.83), diffusion restrictions (ICC = 0.83), and hydrocephalus (ICC = 1); and 'substantial' for intracranial hemorrhage (ICC = 0.76) and subarachnoid FLAIR

[1] *Work in progress. The application is currently under development and is not for sale in the U.S. and in other countries. Its future availability cannot be ensured.*

hyperintensities (ICC = 0.65). Head-to-head comparisons of image quality showed increased noise on the msEPI exams for T1, FLAIR, and DWI ($p < 0.05$) and increased artifacts on T2, T2*, and FLAIR ($p < 0.05$), without compromising the detection of the imaging findings.

Figures 2–6 demonstrate examples of the msEPI images and the corresponding clinical reference images for each image contrast, highlighting the clinical findings in each. As these cases illustrate, the 2-minute DL-accelerated msEPI prototype sequences can offer high clinical efficacy at a significantly shorter acquisition time.

Conclusion

We have successfully used a DL-accelerated 2-minute msEPI protocol to enable rapid, comprehensive brain MRI evaluation of emergency department and hospitalized patients. In this preliminary study we found high interobserver agreement for major brain MRI findings, similar to that of a 10-minute conventional protocol. The DL-accelerated 2-minute msEPI protocol provided clear depiction of pathologic intracranial findings and comparable tissue contrast to that observed with the five-fold slower clinical reference exam. The msEPI technique is currently being evaluated in a larger clinical study of inpatient and emergency department patients at our institution, which

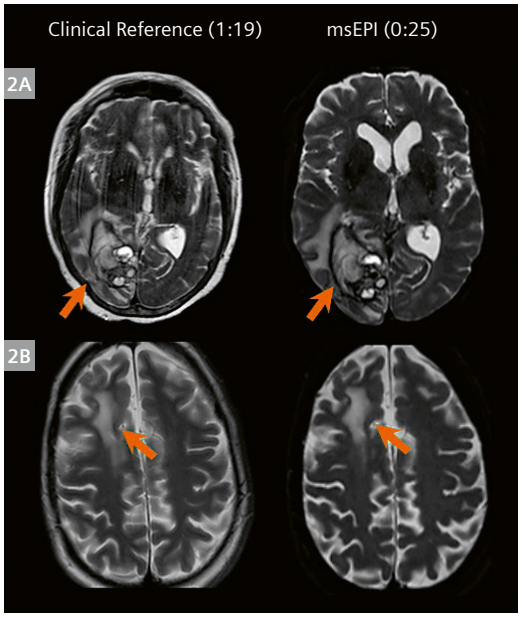

T2 Sequence	Acquisition Time (m:s)	Resolution (mm³)	TR (ms)	TE (ms)	PAT Factor	No. shots	Echo spacing (ms)
TSE	1:19	0.9×0.9×5.0	7060	85	2	–	9.42
msEPI	0:25	1.0×1.0×4.0	4500	86	2	4	1.2

2 **(2A)** Large complex hemorrhagic mass-like lesion within the right occipital lobe that is better seen on msEPI exam. The clinical reference exam that was performed with > 3-fold increase in scan time demonstrates intense motion artifacts.
(2B) Post-surgical changes from right frontal craniotomy with right frontal lobe encephalomalacia.

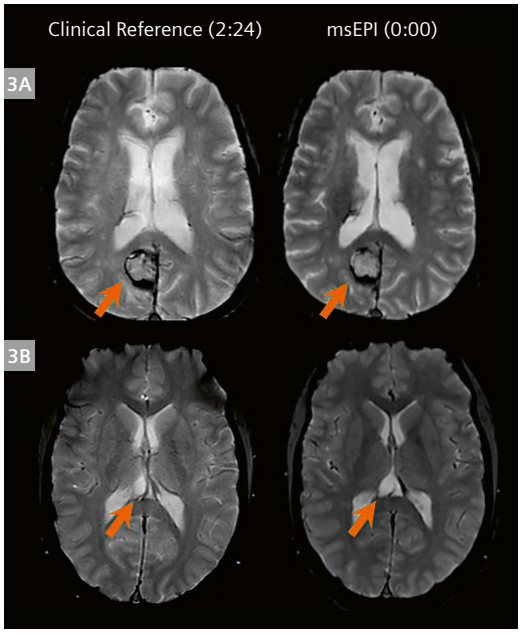

T2* Sequence	Acquisition Time (m:s)	Resolution (mm³)	TR (ms)	TE (ms)	PAT Factor	No. shots	Echo spacing (ms)
GRE	2:24	0.9×0.9×5.0	694	20	1	–	–
msEPI	0:00[2]	1.0×1.0×4.0	4500	21.2	2	4	1.2

3 **(3A)** Right parietal lobe intraparenchymal hematoma with dependent T2* hypointense blood products.
(3B) Non-enhancing cystic lesion in the right aspect of the pineal gland.

[2] *Acquired in combination with the T2 sequence.*

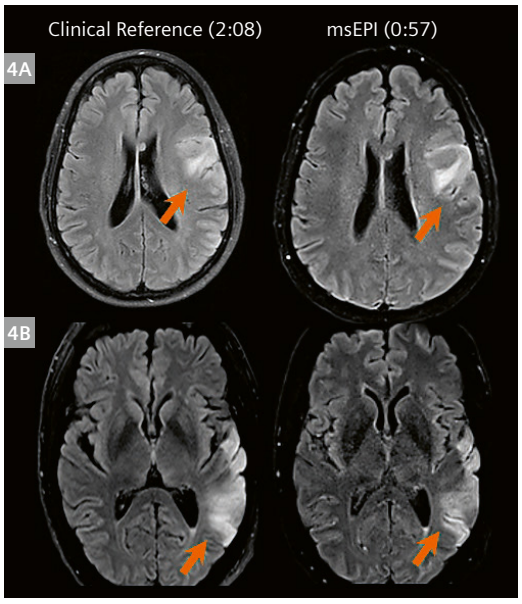

FLAIR Sequence	Acquisition Time (m:s)	Resolution (mm³)	TR (ms)	TE (ms)	PAT Factor	No. shots	Echo spacing (ms)
TSE	2:08	0.9×0.9×5.0	9000	85	2	–	7.49
msEPI	0:57	1.0×1.0×4.0	9000	86	2	2	1.19

4 **(4A)** Left frontal high-grade glioma.
(4B) Subacute left temporal lobe infarct (left middle cerebral artery territory).

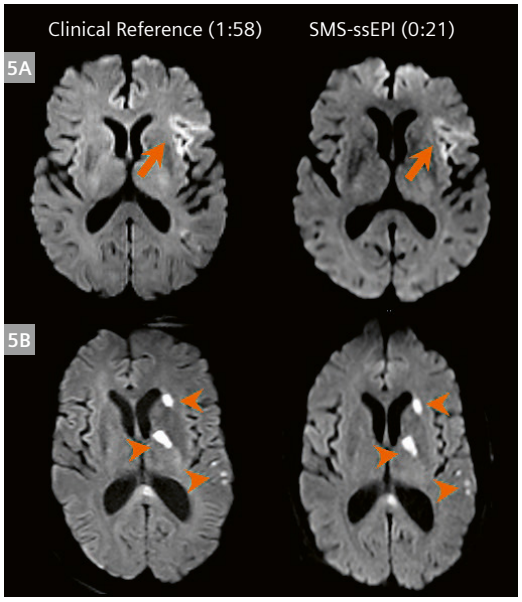

DWI Sequence	Acquisition Time (m:s)	Resolution (mm³)	TR (ms)	TE (ms)	PAT Factor	No. shots	Echo spacing (ms)
ssEPI	1:58	1.4×1.4×5.0	3800	72	2	1	0.72
SMS-ssEPI	0:21	1.4×1.4×4.0	2000	63	2	2	0.93

b-value 1000 s/mm²

5 **(5A)** Subacute infarct involving left frontal lobe and insula.
(5B) Multiple infarcts involving left cerebral hemisphere.

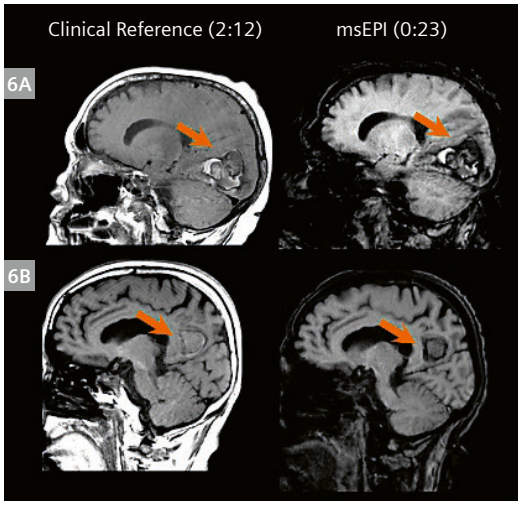

T1 Sequence	Acquisition Time (m:s)	Resolution (mm³)	TR (ms)	TE (ms)	PAT Factor	No. shots	Echo spacing (ms)
SE	2:12	0.9×0.9×4.0	400	8.4	1	–	–
msEPI	0:23	1.0×1.0×4.0	1670	12	2	4	1.18

6 **(6A)** Hemorrhagic neoplastic lesion in the right occipital lobe.
(6B) Right parietal lobe intraparenchymal hematoma.

will provide further insight into the advantages and trade-offs of ultrafast, high-quality brain imaging in this patient population. We envision this protocol could be an effective rapid screening tool for acute intracranial pathology in these often difficult to image and neurologically unstable patients.

References

1 Blystad I, Warntjes JB, Smedby O, et al. Synthetic MRI of the brain in a clinical setting. Acta Radiol 2012; 53:1158–1163
2 Raja, A. S. et al. Radiology Utilization in the Emergency Department: Trends of the Past 2 Decades. Am J Roentgenol. 203, 355–360 (2014).
3 Sun K, Zhong Z, Xu Z, et al. In-plane simultaneous multisegment imaging using a 2D RF pulse. Magn Reson Med. 2021 Aug 4. doi: 10.1002/mrm.28956. Epub ahead of print. PMID: 34350601.
4 Feinberg DA, Moeller S, Smith SM, et al. Multiplexed echo planar imaging for sub-second whole brain FMRI and fast diffusion imaging. PLoS One. 2010 Dec 20;5(12):e15710. doi: 10.1371/journal.pone.0015710. Erratum in: PLoS One. 2011;6(9).
5 Ha JY, Baek HJ, Ryu KH, et al. One-Minute Ultrafast Brain MRI With Full Basic Sequences: Can It Be a Promising Way Forward for Pediatric Neuroimaging? AJR Am J Roentgenol. 2020 Jul;215(1):198-205. doi: 10.2214/AJR.19.22378. Epub 2020 Apr 7. PMID: 32255685.
6 Setsompop K, Feinberg DA, Polimeni JR. Rapid brain MRI acquisition techniques at ultra-high fields. NMR Biomed. 2016 Sep;29(9):1198-221. doi: 10.1002/nbm.3478. Epub 2016 Feb 2. PMID: 26835884; PMCID: PMC5245168.
7 Skare S, Sprenger T, Norbeck O, et al. A 1-minute full brain MR exam using a multicontrast EPI sequence. Magn Reson Med. 2018;79(6):3045-3054. doi:10.1002/mrm.26974
8 Ryu KH, Choi DS, Baek HJ, et al. Clinical feasibility of 1-min ultrafast brain MRI compared with routine brain MRI using synthetic MRI: a single center pilot study. J Neurol. 2019;266(2):431-439. doi:10.1007/s00415-018-9149-4
9 Liao C, Bilgic B, Tian Q, et al. Distortion-free, high-isotropic-resolution diffusion MRI with gSlider BUDA-EPI and multicoil dynamic B 0 shimming. Magn Reson Med. March 2021:mrm.28748. doi:10.1002/mrm.28748
10 Chen N, Guidon A, Chang H-C, Song AW. A robust multi-shot scan strategy for high-resolution diffusion weighted MRI enabled by multiplexed sensitivity-encoding (MUSE). NeuroImage. 2013;72:41-47. doi:10.1016/j.neuroimage.2013.01.038
11 Conklin, J. et al. A comprehensive multi-shot EPI protocol for high-quality clinical brain imaging in 3 minutes. Proc. Intl. Soc. Magn. Reson. Med. 6691 (2020).
12 Clifford B, Conklin J, Huang S, et al. Clinical evaluation of an AI-accelerated two-minute multi-shot EPI protocol for comprehensive high-quality brain imaging. In: Proceedings of the 28th Annual Meeting of ISMRM, virtual, USA, 2020.
13 Demir S, Clifford B, Feiweier T, et al. Optimization of magnetization transfer contrast for EPI FLAIR brain imaging. International Society for Magnetic Resonance in Medicine, 2021. Online virtual meeting.

Contact

John Conklin, M.D., MS
Diagnostic Radiologist
Director of Emergency MRI
Division of Emergency Imaging
Department of Radiology
Massachusetts General Hospital
326 Cambridge St #410
Boston, MA 02114
USA
Phone: +1617-726-8323
John.Conklin@MGH.HARVARD.EDU



Advertisement

Prepare your patients mentally for their MRI exam

Tap the full potential of your facility by preparing your patients for the scan with our Patient Education Toolkit. A video, poster, meditation, and a book for children explain the process of an MRI exam in simple words and answer common questions.





Download the Patient Education Toolkit in your preferred language here:

magnetomworld.siemens-healthineers.com/toolkit/mri-patient-education

Magnetic Resonance Fingerprinting – The Future of Quantitative MR Neuroimaging

Gregor Kasprian, M.D.; Victor Schmidbauer, M.D.

Division of Neuroradiology, Department of Biomedical Imaging and Image-guided Therapy, Medical University of Vienna, Austria

By providing the possibility to acquire a variety of unique tissue contrasts, magnetic resonance imaging (MRI) is the gold standard for diagnostic brain imaging. However, current MRI strategies are compromised by time-consuming image data acquisitions, limitations in the comparability of quantitative imaging data, artifacts, and inter-scanner variability.

Improvements in quantitative imaging techniques will guide us toward a new era in diagnostic neuroradiology. The possibility to complement the subjective assessment of non-invasive brain imaging by quantitative data will lead to better, more reliable, and objectifiable diagnoses of diseases of the central nervous system. Moreover, robust quantitative data will serve as ideal input for artificial intelligence-based algorithms, which – in combination with radiological expertise – will improve diagnostic and prognostic precision and thereby optimize personalized treatment for many patients. To date, quantitative MR techniques have been time consuming and complex in data post-processing, and thus limited to research. To achieve clinical practicability and feasibility, these traditional approaches had to be reinvented.

MR signals translated into tissue-specific fingerprints

Magnetic Resonance Fingerprinting (MRF)[1] is a pioneering approach in the field of MR technology. MRF relies on the principle that each tissue examined evolves its own unique signal – *fingerprint* – after the application of a technically appropriate stimulus [1]. In contrast to conventional MRI, MRF is characterized by variation of the technical parameters, e.g., repetition time, and radiofrequency excitation angle, throughout the sequence acquisition to generate the evolution of the tissue's *fingerprint* [2]. Initially, this tissue fingerprint appears as complex and abstract data, which needs to be translated into an image. As for any translation, a pre-existing standard of reference or dictionary is required. A dictionary-based recognition process connects the acquired signal-derived information to quantitative MR metrics – such as, but not limited to, relaxation parameters and diffusion properties – in a voxel-wise manner [1, 2]. The MRF dictionary contains a collection of simulated fingerprints to represent all tissue-specific properties within the physiological range [3]. Since MRF pattern recognition takes a variety of different parameters into account, the tissue characterization process is considered highly accurate and robust [2]. In summary, three hallmarks characterize the entire MRF process. The first step – signal evolution and acquisition – is MR scanner and sequence dependent. The second and third steps are characterized by automatized data processing: dictionary-based pattern recognition and tissue-specific, property-based visualization [2, 3].

Quantitative MRI and multiple image contrasts in less than eight minutes

Based on a single sequence acquisition of less than eight minutes, MRF provides a variety of multiparametric imaging information for qualitative and quantitative non-invasive neuro MR diagnostics. By choosing physical MR properties as the bedrock of the technical concept, MRF demonstrates excellent inter-scanner reproducibility [4]. This approach allows a robust and objective method to detect, characterize, and quantify physiological and pathological changes of the central nervous system [5, 6]. Furthermore, MRF is regarded as a highly promising technique for eliminating artifacts in MR imaging [2, 7], as each voxel is subjected to the pattern recognition process individually. Overall, MRF is leading the way into the future of MRI, providing structural diagnostic, quantitative, robust, less artifact prone imaging data in a short imaging time.

[1] *MR Fingerprinting is not commercially available in some countries. Due to regulatory reasons its future availability cannot be ensured.*

Clinical experiences in MRF

Clinical experiences using this novel approach are still scarce. At the same time, as MRF technology is continuously improving, specific areas of interest in the neuroradiological application of this technology are currently being identified. MRF will be particularly valuable in diagnosing diseases that were previously difficult to assess and evaluate based on the subjective impression of individual radiologists. As MRF is sensitive to multiple MR parameters at once, it offers a variety of in-depth MR imaging markers of pathologically altered brain parenchyma. Pathological brain tissue, which so far might have been categorized as "normal-appearing" brain parenchyma by traditional subjective visual radiological assessment, could be detected more sensitively using MRF. This will allow better quantification and evaluation of the burden of disease in individual patients and will help better understand the current status and progress in a variety of neurological disorders. As a consequence, MRF can help monitor the effect of treatment more reliably than ever before.

Furthermore, time-saving, in-depth multiparametric characterization of pathologically altered brain tissue – after acquisition of a single MRF sequence – may further improve the diagnostic specificity of MRI, allowing to optimize the differentiation of similar-appearing signal changes into specific pathological entities. Ultimately, the resulting reduction in overall MR scan time may also grant easier and faster access to high-end MR diagnostics to the benefit of many patients.

Here, we would like to demonstrate some initial clinicoradiological experiences with MRF in different areas of diagnostic neuroimaging.

Basic MRF findings in normal subjects

MRF allows characterization of the fingerprint of specific brain compartments. Figure 1 shows the MR images of a 45-year-old normal subject. The upper row depicts sequentially acquired conventional T1-weighted (1A) and fluid-attenuated T2-weighted 3D sequences at 3 Tesla (MAGNETOM Vida, Siemens Healthcare, Erlangen, Germany) totaling an imaging time of up to 8 minutes. The results of a single acquisition using MRF (7 minutes acquisition time) are shown in Figure 1. A T1 map (1C) and a T2 map can be visualized with color coding according to the local T1 and T2 values. Advanced quantitative analysis using the MR Robust Quantitative Tool (MR RoQT) allows characterization of specific gray (dark colors) and white matter (bright colors) compartments, which can be distinguished from each other on the scatterplot graph (bottom row). The scatterplot indicates the T2 (x-axis) and T1 (y-axis) values of the analyzed regions of interest and

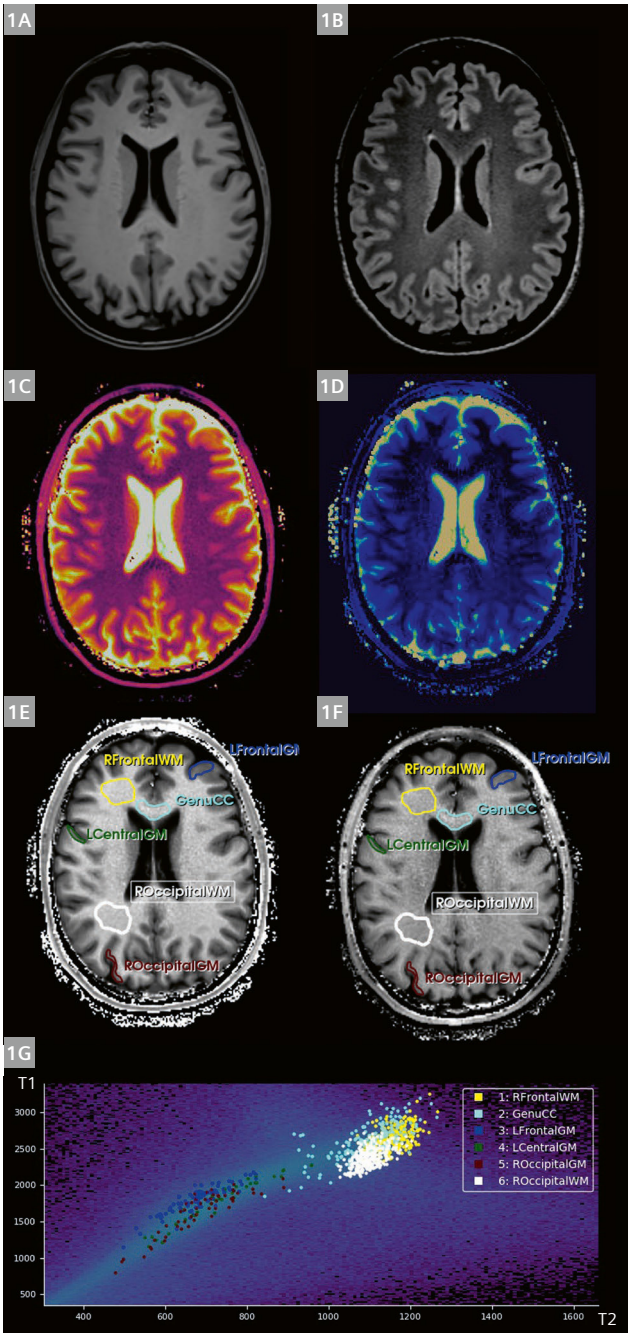

1 45-year-old healthy subject. **(1A, B)** T1-weighted (1A) and fluid-attenuated T2-weighted 3D sequences (1B) at 3T. **(1C, D)** MR Fingerprinting acquisition. **(1E, F)** T1 map (1E) and T2 map (1F) with color coding according to the local T1 and T2 values. **(1G)** MR RoQT scatterplot characterizing specific gray (dark colors) and white matter (bright colors) compartments. The scatterplot indicates the T2 (x-axis) and T1 (y-axis) values of the analyzed regions of interest and shows the normal variation of values within one tissue compartment.

shows the normal variation of values within one tissue compartment. Except for distinct differences between white and gray matter, there are also regional differences in the quantified T1 and T2 values. In addition to structural MR data, MRF also provides quantitative data, which cannot be extracted from conventional T2-weighted and T1-weighted MRI sequences, without investing further acquisition time. MRF is quite a robust quantitative MR technology, which is feasible in a clinical setting.

MRF findings in brain pathologies

In addition to the quantitative characterization of regional variations of brain tissue fingerprints, a detailed analysis of the MR characteristics of abnormal brain regions is also possible. Figure 2 depicts a 67-year-old patient with severe vascular leukoencephalopathy. Conventional FLAIR (2A) sequences depict the T2-weighted hyperintense white matter alterations, which are less conspicuous on T1-weighted sequences (2B). By using MRF and generating T2 maps (2C, D), lesional (yellow) and non-lesional (turquoise) brain regions can be automatically segmented based on their T1 and T2 quantitative characteristics, shown in the scatterplots (2E, F). By either selecting the lesional (yellow) or non-lesional (turquoise) range of T1/T2 values, these tissue types can be distinguished and separated as well as quantified. This will allow a more accurate semi-automated follow-up analysis of brain imaging data, and allows better monitoring of the course of a disease or the effectiveness of therapeutic measures.

MRF in amyotrophic lateral sclerosis

MRF can be particularly valuable if qualitative findings need to be objectified. This may be especially important in cases of neurodegenerative disorders such as amyotrophic lateral sclerosis (ALS). The hyperintense T2-weighted signal change of the corticospinal tract has been a useful sign of Wallerian degeneration in ALS. However, the sign is often subtle and sometimes non-specific. A reliable quantitative analysis of these changes might help to identify this sign with greater confidence and diagnostic certainty. Figure 3 shows the results of an MRI examination of a 71-year-old patient with clinically suspected ALS: The T1-weighted (3A), T2-weighted (3B), and FLAIR (3C) 3D sequences were sequentially acquired at 3 Tesla. The second row shows the results of the MRF analysis in the same patient, depicting the T1 map (3D) and the T2 map (3E). The arrows point to the left internal capsule. Please note the slight T2-weighted hyperintense signal alteration of the

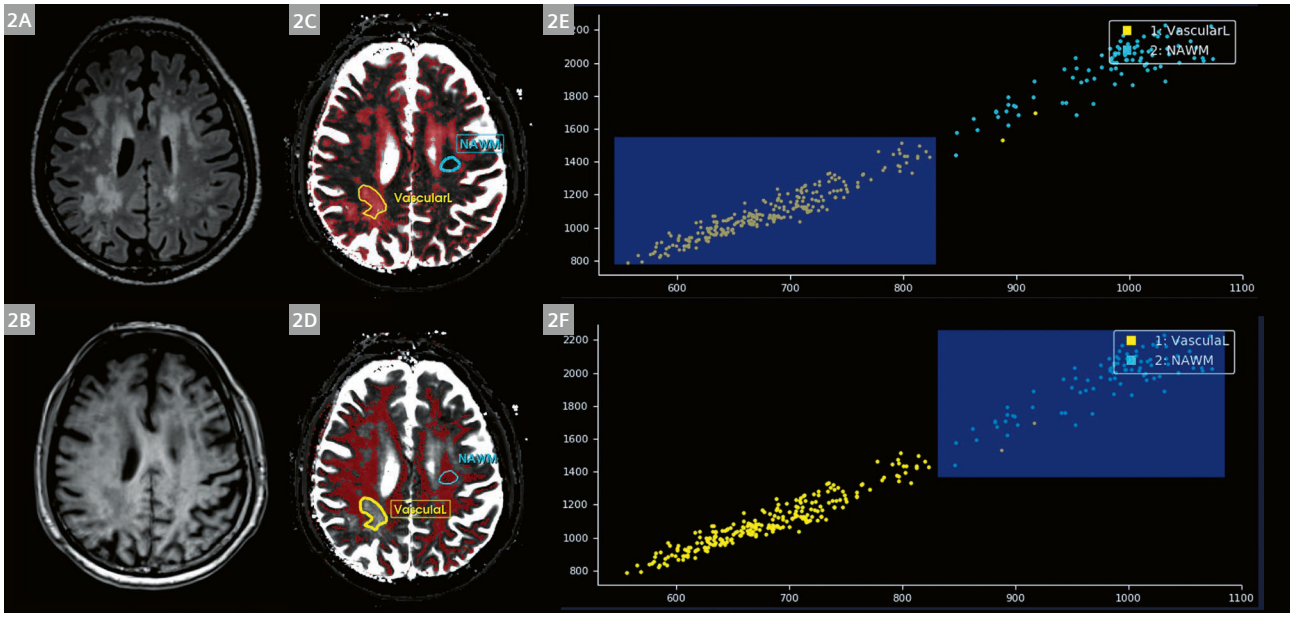

2 A 67-year-old patient with severe vascular leukoencephalopathy. **(2A)** Conventional FLAIR depict the T2-weighted hyperintense white matter alterations, which are less conspicuous on **(2B)** T1-weighted sequences. **(2C, D)** By using MRF lesional (yellow) and non-lesional (turquoise) brain regions can be automatically segmented based on their quantitative R1 (x-axis) and R2 (y-axis) characteristics, shown in the scatterplots **(2E, F)**.

corticospinal tract, which is confirmed on the T2 map of the MRF analysis.

If the local T1 (x-axis) and T2 (y-axis) values are analyzed using the postprocessing software MR RoQT, an unequivocal difference between the corticospinal tract fingerprints (red and yellow) and those of the optic radiation (pink) or the frontal white matter (blue) can be identified (Fig. 4). This improves the diagnostic confidence of the radiologist and leads to a smaller interrater variability in the imaging assessment of this disorder. Further, these findings can be combined with diffusion tensor imaging (DTI) based parameters (FA, diffusivity) or diffusion-weighted imaging (DWI) based ADC measurements to increase the diagnostic sensitivity of this sign.

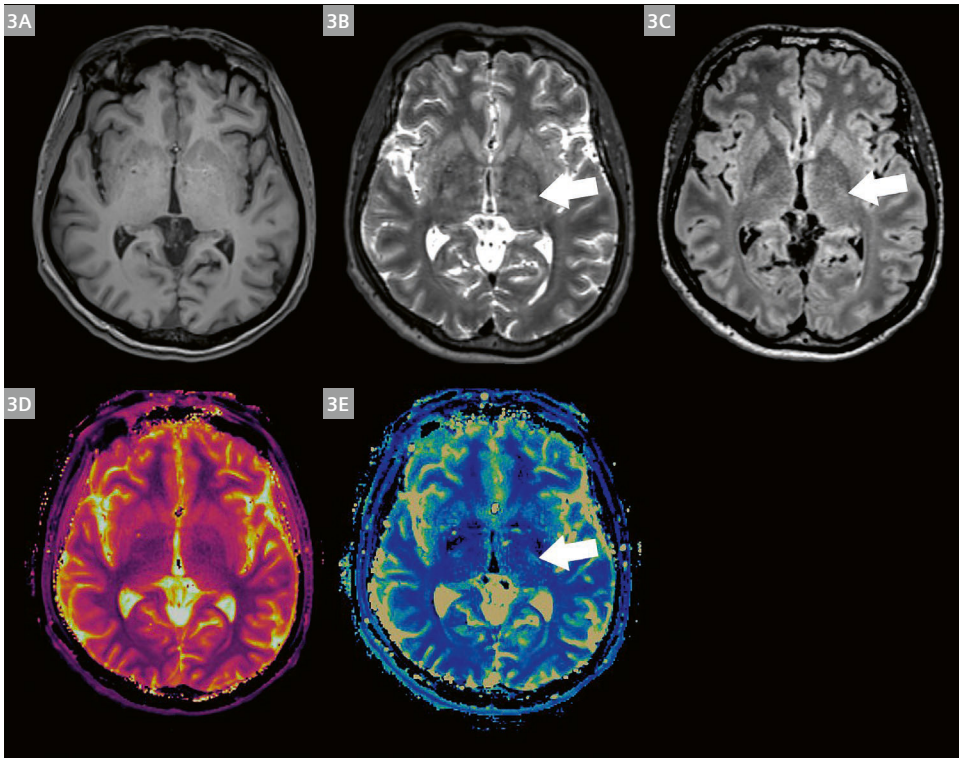

3 A 71-year-old patient with clinically suspected ALS. T1-weighted **(3A)**, T2-weighted **(3B)**, and FLAIR **(3C)** 3D sequences sequentially acquired at 3T. (3D, E) show the results of the MRF analysis in the same patient, depicting the T1 map **(3D)** and the T2 map **(3E)**. The arrows point to the left internal capsule. The slight T2-weighted hyperintense signal alteration of the corticospinal tract is confirmed on the T2 map of the MRF analysis.

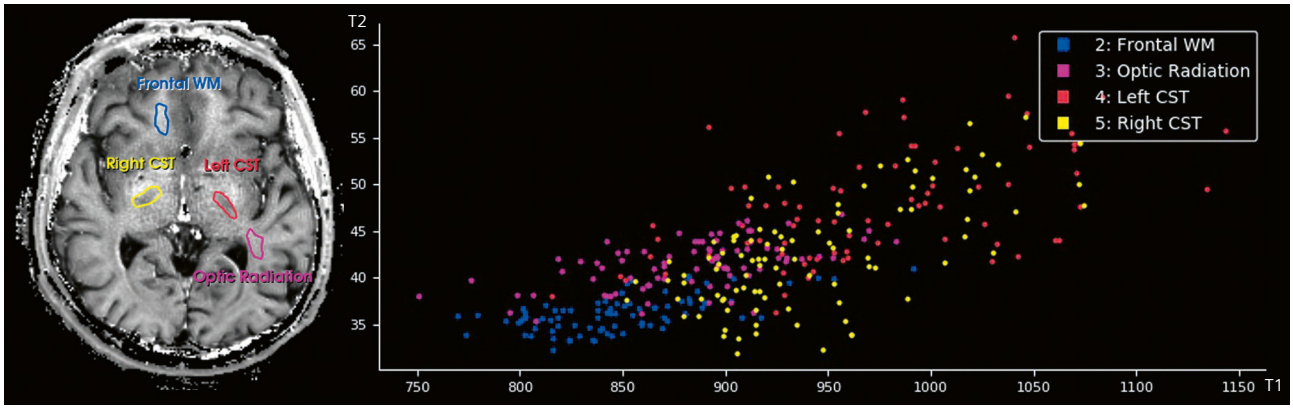

4 Postprocessing of the patient data shown in Figure 3 using the MR Robust Quantitative Tool (MR RoQT). T1 values are indicated on the x-axis, T2 values are plotted on the y-axis. The left and right corticospinal tracts show a distinctive difference in their T1 and T2 fingerprints compared to other white matter regions.

MRF in metabolic disorders or leukodystrophies

MRF may also be beneficial in neurological disorders, characterized by widespread signal alterations of the gray and white matter, such as leukodystrophies or mitochondriopathies. Figure 5 shows the MR images of a 6-year-old girl with glutaric aciduria type I – a metabolic disorder/mitochondriopathy. Please note the extensive white matter signal alterations on T1 (5A) FLAIR (5B) and DWI (5C, D). There is extensive white matter diffusion restriction. MRF (5E, F) quantifies the regional signal changes on T1 (5E) and T2 (5F) maps, indicating the relative sparing of the corticospinal tract and basal ganglia.

Using MRF-based quantification on T1 and T2 maps (Figure 6), regional variations in the pathology associated fingerprints can be identified. There is massive T1 and T2 shortening (turquoise) of the right frontal white matter. The optic radiation (pink) is less severely affected and the left corticospinal tract shows T2 (x-axis) and T1 (y-axis) values, which are in the normal range (compare Fig. 1). Combined with semiautomated segmentation tools (MR RoQT), this approach helps monitor disease progression and further refine specific disease-related patterns and fingerprints.

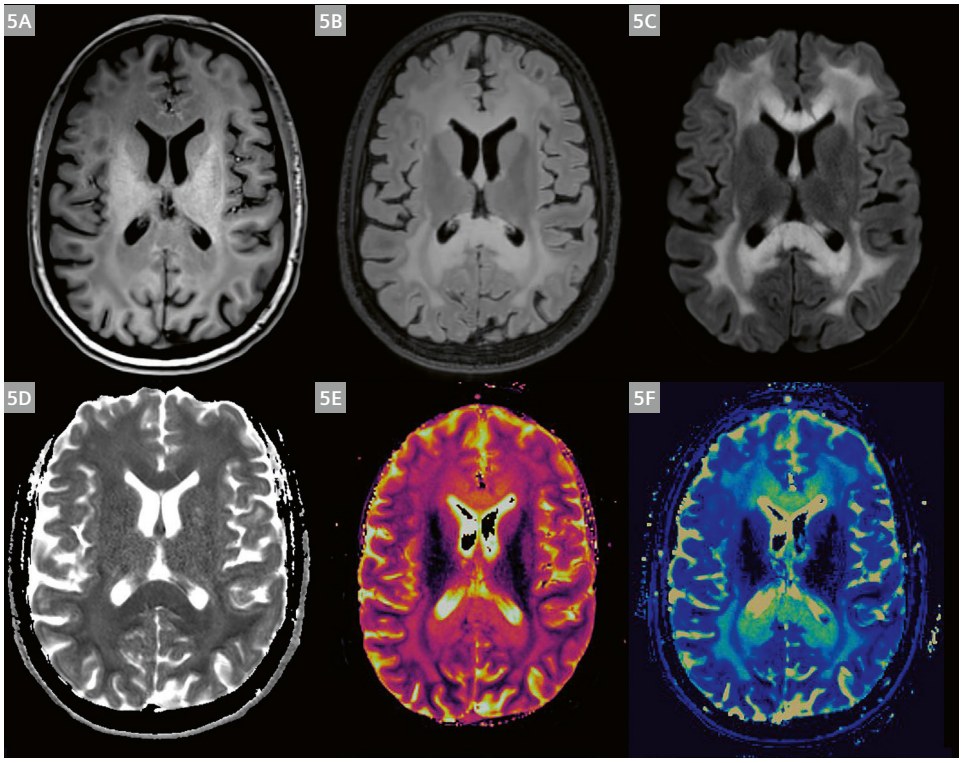

5 A 6-year-old girl with glutaric aciduria. Extensive white matter signal alterations on T1 **(5A)** FLAIR **(5B)** and DWI **(5C, D)**. MRF **(5E, F)** quantifies the regional signal changes on T1 (5E) and T2 (5F) maps indicating the relative sparing of the corticospinal tract and basal ganglia.

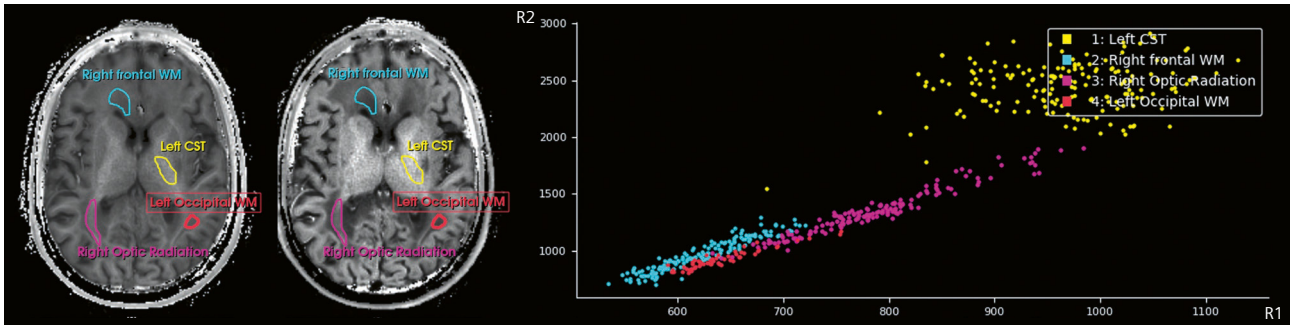

6 MRF-based quantitative R1 (x-axis) and R2 (y-axis) values show a severe shortening of the right frontal WM (turquoise). The right optic radiation (pink) as well as the left occipital WM (red) are less affected. Normal-appearing R1 and R2 values can be found in the left corticospinal tract (yellow).

Summary

MRF leads the way into a new era of neuro MRI. The possibility to provide multiple quantitative MR parameters based on a single data acquisition in less than 8 minutes results in quantitative data suitable for characterizing normal and pathologically altered tissue compartments of the central nervous system. As the regional neuroanatomical tissue diversity can be mapped non-invasively, MRF opens new possibilities in the non-invasive characterization of normal brain structure and its developmental changes across human lifespan. Further, pathological processes can be objectified and quantified, leading to greater confidence in the diagnosis of metabolic and neurodegenerative disorders. The extent of tissue pathology can be mapped and monitored over time, which is helpful in neurovascular disorders and inflammatory and/or demyelinating conditions. Lastly, disease-specific fingerprints of metabolic disorders and abnormal myelination processes are quantifiable and will be easier to identify. In the future, MRF will serve as an important backbone for artificial intelligence-based algorithms, aiming to automatically identify lesion-specific fingerprints. This will ultimately change the daily practice of neuroradiology.

References

1 Ma D, Gulani V, Seiberlich N, Liu K, Sunshine JL, Duerk JL, et al. Magnetic resonance fingerprinting. Nature. 2013 Mar;495(7440):187–92.
2 Panda A, Mehta BB, Coppo S, Jiang Y, Ma D, Seiberlich N, et al. Magnetic resonance fingerprinting – An overview. Curr. Opin. Biomed. 2017 Sep;3:56–66.
3 Tippareddy C, Zhao W, Sunshine JL, Griswold M, Ma D, Badve C. Magnetic resonance fingerprinting: an overview. Eur J Nucl Med Mol Imaging [Internet]. 2021 May 26 [cited 2021 Aug 19]; Available from: https://link.springer.com/10.1007/s00259-021-05384-2
4 Körzdörfer G, Kirsch R, Liu K, Pfeuffer J, Hensel B, Jiang Y, et al. Reproducibility and Repeatability of MR Fingerprinting Relaxometry in the Human Brain. Radiology. 2019 Aug;292(2):429-437.
5 Dubois J, Alison M, Counsell SJ, Hertz-Pannier L, Hüppi PS, Benders MJNL. MRI of the Neonatal Brain: A Review of Methodological Challenges and Neuroscientific Advances. J Magn Reson Imaging. 2021 May;53(5):1318–43.
6 Badve C, Yu A, Dastmalchian S, Rogers M, Ma D, Jiang Y, et al. MR Fingerprinting of Adult Brain Tumors: Initial Experience. AJNR Am J Neuroradiol. 2017 Mar;38(3):492–9.
7 Cloos MA, Knoll F, Zhao T, Block KT, Bruno M, Wiggins GC, et al. Multiparametric imaging with heterogeneous radiofrequency fields. Nat Commun. 2016 Nov;7(1):12445.

Contact

Associate Professor Gregor Kasprian, M.D., MBA
Department of Biomedical Imaging and Image-guided Therapy
Medical University of Vienna
Währinger Gürtel 18-20
1090 Vienna
Austria
Tel.: (+43) 1 40400 48950
gregor.kasprian@meduniwien.ac.



Gregor Kasprian



Victor Schmidbauer

Advertisement

Learn more about
Magnetic Resonance Fingerprinting

For technical explanations, articles, lectures, imaging examples and much more on MR Fingerprinting, visit us at

magnetomworld.siemens-healthineers.com/hot-topics/mr-fingerprinting



MR Fingerprinting is not commercially available in some countries. Due to regulatory reasons its future availability cannot be ensured.

MAGNETOM Free.Max: Keeping a Hot System Cool

Stephan Biber, Ph.D.

Senior System Architect & Principal Key Expert at Siemens Healthineers, R&D AEP, Erlangen, Germany

Helium is a rare element on Earth. Once released into the atmosphere, it is so lightweight that it leaves Earth's gravitational field and diffuses into space. DryCool technology, one of the key innovations on MAGNETOM Free.Max, reduces the helium demand in MR systems and removes the need to handle liquid helium during system installation. It also saves helium and prevents it from being released into the atmosphere during both normal system operation and failures such as quench events. However, the dramatic reduction of liquid helium to 0.7 liters contained in each MR magnet reduces the heat capacity of the magnet. If a conventional magnet loses cooling – e.g., due

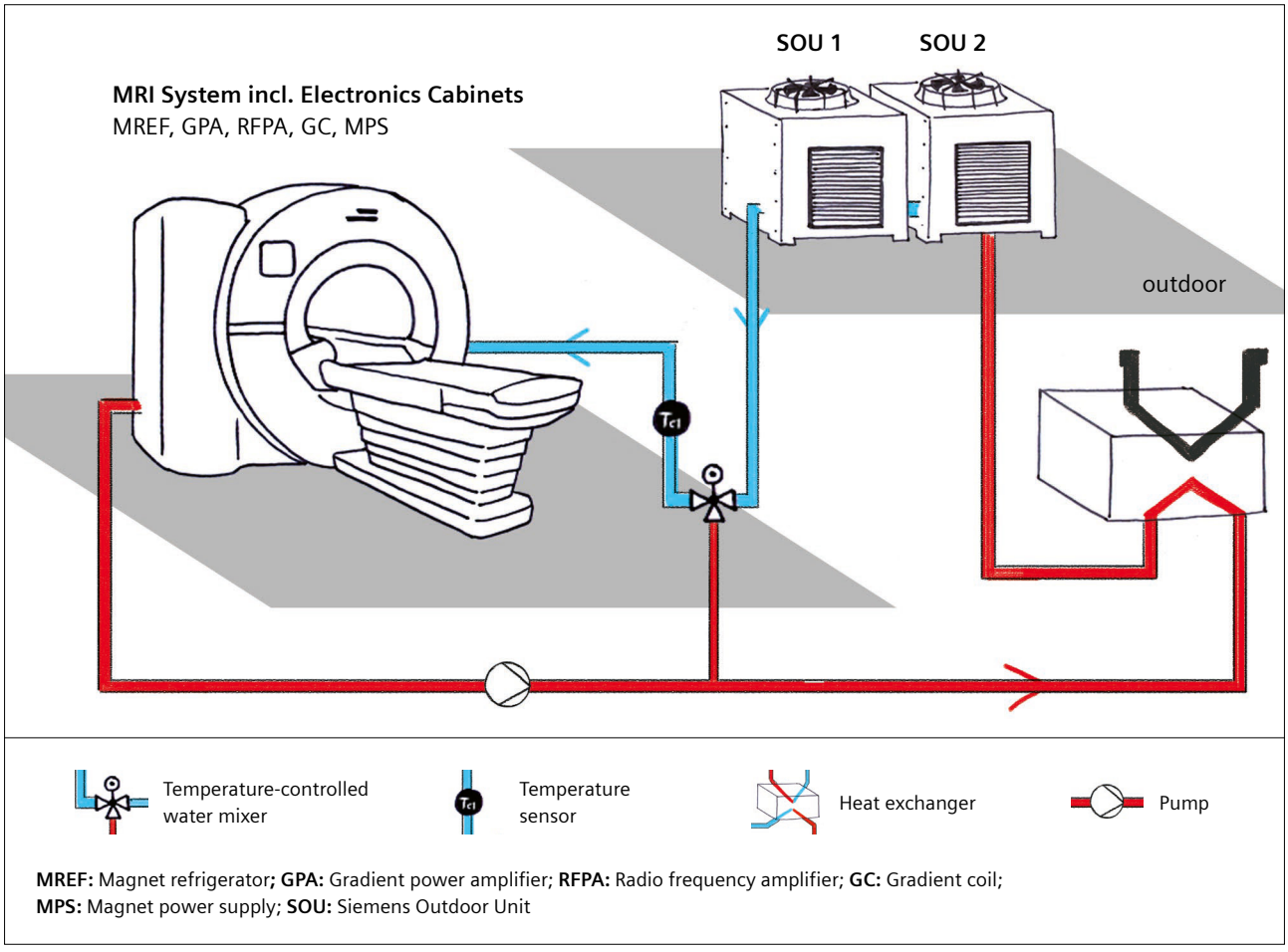

1 Active cooling system with external chillers.

to a power outage or a failure of the cooling system – the liquid helium slowly starts evaporating. Once a certain pressure threshold is exceeded (usually after less than 1 hour), the magnet loses helium into the ambient atmosphere. Depending on the filling level, a conventional magnet can stay cold by continuously evaporating its helium reservoir for many days without losing superconductivity. This is because the helium reservoir contains several hundred liters of helium. Reducing the helium down to less than 1 liter for DryCool magnets therefore also reduces the tolerance of such systems against infrastructure failures. The main types of failure are power outages and failures of the cooling system. This paper describes how MAGNETOM Free.Max can provide high availability of the MRI scanner despite a liquid helium inventory of only 0.7 liters.

Power outages

Power outages are external events, out of control of the MRI system. The system can only react accordingly; it cannot avoid the situation itself. With DryCool technology, a small integrated uninterruptible power supply (UPS) keeps the magnet electronics running even during a power outage. If the power outage persists, the magnet electronics will ramp down the magnet after a certain waiting time in order to avoid a quench event, which would turn all the energy in the magnetic field into heat and warm up the system significantly. With MAGNETOM Free.Max, ramping the magnet down and then back up to field is now an automatic procedure which no longer requires an onsite visit from a service technician, due to the integrated magnet power supply. After a controlled ramp down, the magnet heats up very slowly. Once power returns, it can be recooled and ramped up again [1]. In regions where power reliability is poor, the system can also be buffered with a large UPS which not only keeps the system cold, but also enables continuous scanning even during brownouts or blackouts of the power grid.

Cooling system failures

Unlike power outages, the reliability of the cooling system is very much under the control of the MRI system design. For an imaging modality like MRI, which relies so much on cooling, the reliability of the cooling system is essential for guaranteeing high availability of the MRI system. The MAGNETOM Free.Max cooling system was developed with the need for high reliability in mind from the very beginning. The following section explains the redundancy-focused architectural measures which were applied to MAGNETOM Free.Max.

A liquid helium temperature of 4 K is achieved using a cryocooler (“cold head”) which is driven by a compressor. The compressor (magnet refrigerator = MREF) requires approximately 6–8 kW of power to generate ~1 W cooling power on the 4 K level. In order to ensure permanent operation of the compressor, which keeps the magnet cold, the MREF must be supplied with electricity and cooling water. Cold water for MAGNETOM Free.Max can be provided by two different options:

Active cooling system

One option is to buy an external chiller which is tailored to operate with the MRI system. The flow diagram in Figure 1 shows that, in this case, the same water running through the MR components (MREF, gradient coil, amplifiers) is also running through the outdoor units SOU 1 and SOU 2. In such a configuration, the MRI system is self-contained and does not rely on any external water supply. This makes the setup very reliable because it avoids clogging of water flow or corrosion due to dirt and debris from external cooling water.

Chillers are located outside the building, often on rooftops or parking lots, where they use the ambient air to dissipate the heat from the MRI system. As they are located outdoors, chillers are exposed to all kinds of weather conditions: Temperatures can range from -20°C to +45°C, and dirt, dust, or leaves can block the heat exchangers. In highly reliable cooling systems, the outdoor units are a weak point in the chain. If an outdoor unit fails, the helium compressor will stop working and this will soon cause the magnet to ramp down. For the new DryCool technology, the chillers were designed with built-in redundancy to overcome this problem. During heavy-load scanning (mainly diffusion imaging) MAGNETOM Free.Max can



2 Active cooling system with two ~17 kW Siemens Outdoor Units (SOU).

require up to 33 kW of cooling power, with demand primarily coming from the gradient system (coil and amplifier), the magnet cooling, and the RF amplifier. The cooling power is provided by two separate ~17 kW outdoor units (Siemens Outdoor Unit: SOU 1 and SOU 2; Fig. 2), which can work mostly independently from one another. During times when the system is in standby or scanning with less power-demanding sequences (TSE, GRE), only one of the two chillers is needed and the other one is turned off to save energy. If there is a failure with one of the 17 kW chillers, the second one automatically takes over to guarantee a permanent cold water supply and avoid a magnet ramp-down and the associated system downtime. The system can even continue scanning in this mode. Furthermore, during normal operation when one chiller is enough, the chillers are switched on and off in alternating mode to make sure both chillers are always operational and the energy consumption is optimized.

The splitting of the cooling modules requires little additional effort, as the 33 kW cooling power is needed anyway for system operation. This means that there is no extra cooling power added to provide redundancy for the magnet cooling, because the 6–8 kW required for magnet cooling is less than half of the total cooling power of a single unit. Redundancy can therefore be achieved just by providing the overall cooling power from two separate units with half the total system power – without the need to install any unused cooling power, which would add extra effort and costs.

Passive cooling system

In many large institutions, cooling water is centrally supplied and the MRI system can profit from the fact that no extra chillers are needed. The so-called "passive cooling option" cools the MRI system using a heat exchanger which separates the water provided by the central cooling supply from the water circulating through the MRI system components (Fig. 3A).

In cases where the central water supply from the hospital is not considered to be reliable enough, there is also a possibility to connect a locally sourced "backup chiller" to the system. This can provide the cooling power needed to keep only the magnet refrigeration running in case the central water supply fails. The cold water for the MREF coming from the backup chiller is provided to the system through an additional heat exchanger. The system automatically detects cases where the cooling power from the central water supply is insufficient and sends a signal to trigger the backup chiller (Fig. 3B).

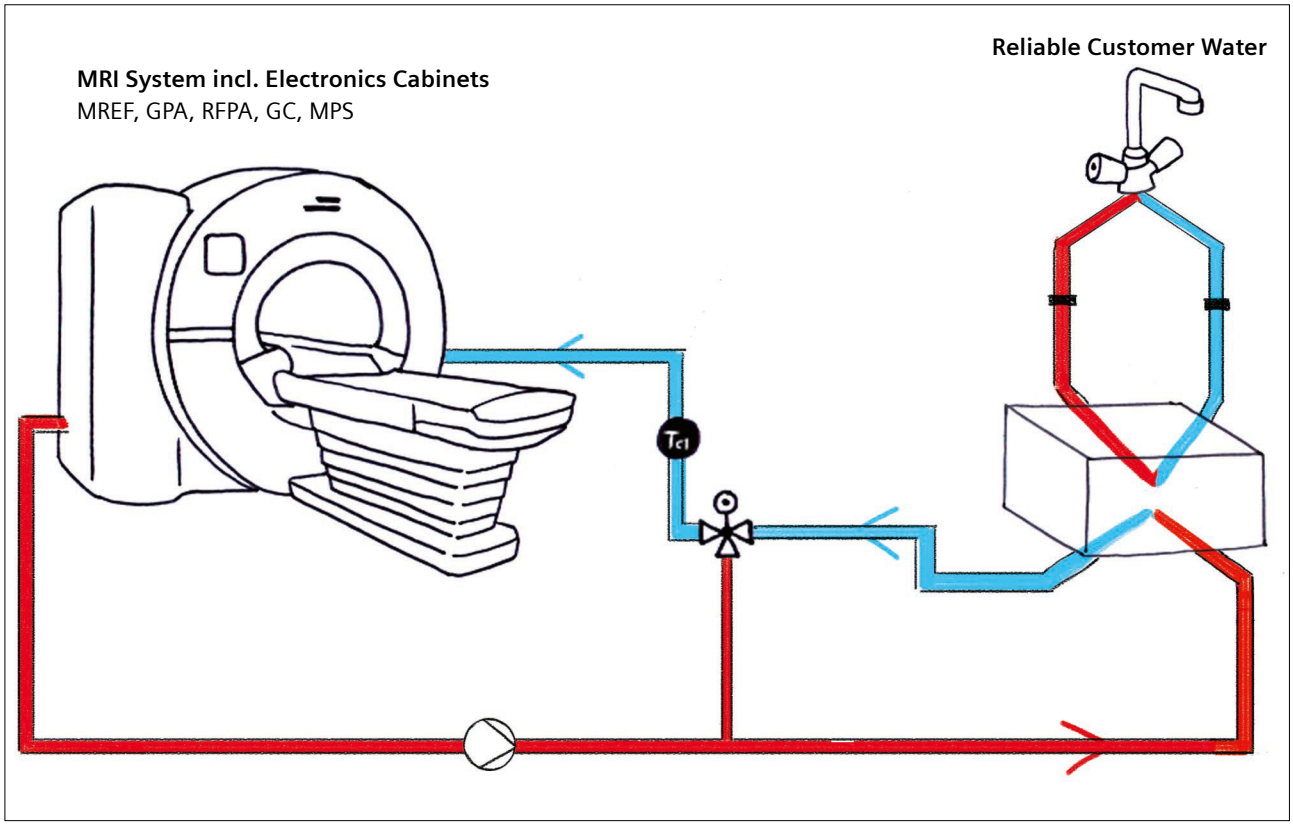

3A Passive cooling system with reliable water from a central customer supply.

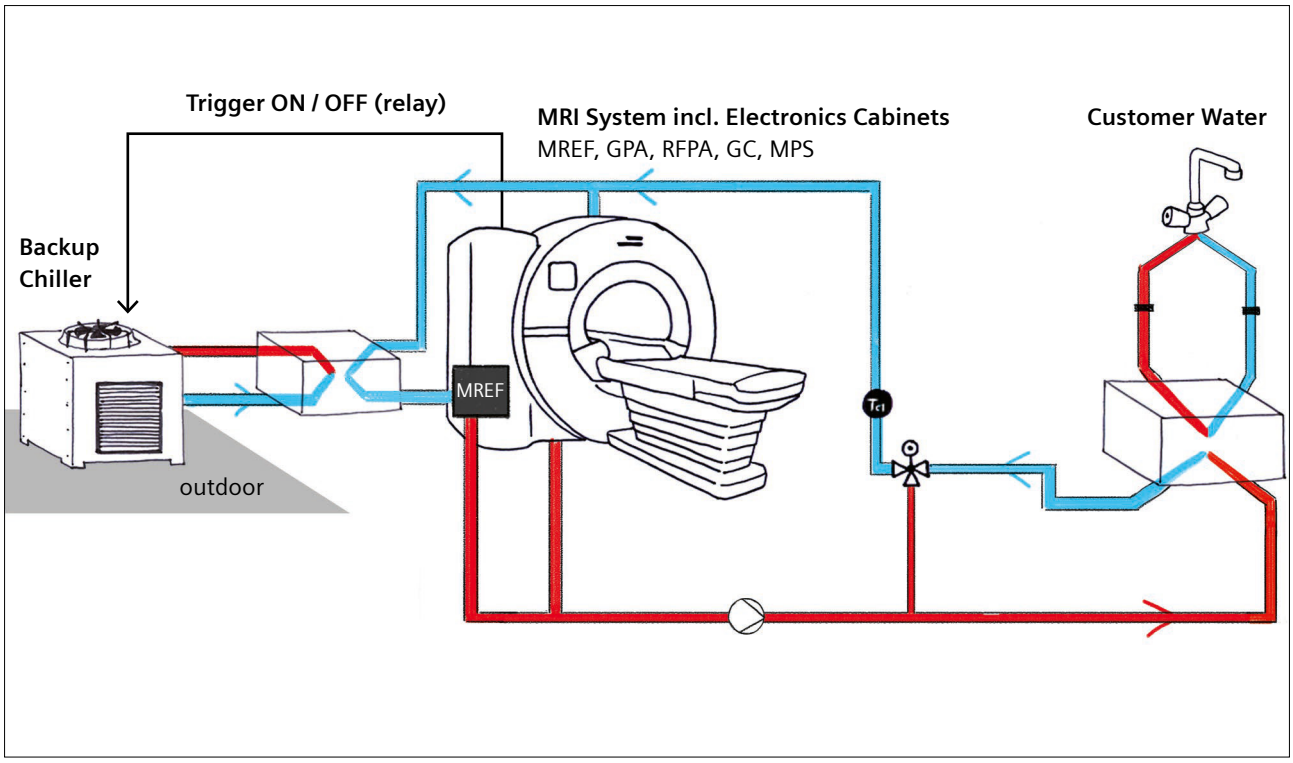

3B Passive cooling system with automatically triggered backup chiller.

Remote monitoring and service

Despite the best efforts to ensure high reliability, cooling systems with high water flow rates and pressure – such as those used in MRI systems – require regular service. With the MR cooling system running 24/7, most failures (leakage, clogging, corrosion, dirt on outdoor units) can be detected and solved by qualified service personnel before they cause the system to stop working. Furthermore, the built-in cooling system is connected to our online service and all parameters available via sensors are also transmitted and evaluated online to allow remote diagnostics and preventive maintenance. In particular, the magnet refrigerator (MREF) is equipped with sophisticated temperature and pressure sensors. Preventive maintenance makes it possible to detect problems by watching the trends of these parameters over time. As a result, many problems can be detected before they lead to a complete failure of a component.

Contact

Stephan Biber, Ph.D.
Siemens Healthcare GmbH
SHS DI MR R&D AEP
Postbox 32 60
91050 Erlangen
Germany
stephan.biber@siemens-healthineers.com



Summary

The above overview shows how the system architecture, both for the cooling system and the system control, is tailored to deal with the new challenges of DryCool magnets and deliver maximum availability. Three different configurations are provided to achieve a high-reliability cooling system adapted to the individual needs and conditions of different sites. The basic principle is to provide redundancy for those parts that have an unacceptably high chance of failure. Combining this with remote monitoring, regular servicing, and automatic ramping guarantees extremely high availability for DryCool systems and independency of the scarce natural resource helium.

Reference

1 Calvert S. MAGNETOM Free.Max: from Concept to Product, a Brief History of the DryCool Magnet Development. MAGNETOM Flash. 2021; MAGNETOM Free.Max special issue: 44–48. Available from: https://www.magnetomworld.siemens-healthineers.com/hot-topics/lower-field-mri

Complete Free-breathing, High-resolution Cardiac MR Studies and their Clinical Impact in Non-ischemic Cardiomyopathies

Guillem Pons-Lladó, M.D., Ph.D.

Cardiac Imaging Unit, Department of Diagnostic Imaging, Clínica Corachán, Barcelona, Spain

Abstract

Cardiovascular magnetic resonance imaging (CMR) has become an irreplaceable tool since it was introduced in clinical practice in the 1990s. Useful in every aspect of cardiac diseases, its role is particularly valuable in the study of non-ischemic cardiomyopathies (NICMs), due to the unique body of information it provides on these diseases. Referential data on morphology and function of the ventricles and, notably, on myocardial tissue characterization mean that the technique is now ordered in every patient with NICM.

The performance of studies, however, has traditionally required a large number of breath-hold maneuvers from the patient. These, combined with an uncomfortable position in the magnet, have resulted in the test being perceived as rather unpleasant, particularly among cardiac patients.

Recent advances in the field of sequence acceleration and the development of motion-correction algorithms, however, have turned into reality the option of a whole cardiac exam without the need for patients to hold their breath during acquisitions.

As illustrated in the present article, a complete study of patients with NICM can be performed during free breathing, including cine sequences accelerated with Compressed Sensing reconstruction and adaptive triggering, and tissue characterization studies using late gadolinium enhancement and T1/T2 mapping sequences with motion correction. When available in an MR system, in this case a 3T MAGNETOM Vida scanner, this exam can be done within 30 minutes, and may provide the same valuable information as that obtained with conventionally equipped systems.

Introduction

Since the integration of cardiovascular magnetic resonance imaging (CMR) into the field of diagnostic imaging in the late 1990s [1], the technique has become a true subspecialty in itself [2]. Continuous technical developments have widened its scope and have led to its present consideration as a first-line diagnostic tool.

Some inconvenient aspects of the acquisition of exams, however, have been recognized: isolation of the patient within the magnet in an uncomfortable position, need for repeated breath-holding, and a relatively long



1 Window of the physiology signal during the planning of a study with short-axis cine images and a free-breathing RT sequence. For a mean heart rate of 69 bpm in this case, slab of 10 prospectively gated, contiguous slices will be executed in 18 seconds. As 25 phases of the heart cycle are extracted by INTP, the resulting temporal resolution is 35 seconds.

exam duration. Considering the relevant information provided by the technique, these drawbacks are considered a tolerable burden by operating personnel and well-informed patients alike. Despite this, when patients are asked about their acceptance of the examination, some say they would prefer to undergo a different kind of non-invasive diagnostic imaging exam. Moreover, in the case of patients with cardiac conditions, maintaining the supine position and holding their breath repeatedly can be particularly strenuous.

Manufacturers and investigators have therefore both made efforts to counteract these inconveniences by devising strategies for acquiring and processing sequences aimed at shortening the exam time and minimizing the number and duration of breath-hold periods required. As a general rule, however, speeding up the acquisition results in ill-defined images [3]. Therefore, advances in faster acquisition schemes can only be realized if the resolution of the reconstructed images is preserved [4].

The present state of the art in CMR has notably achieved this goal, and the purpose of this brief article is to illustrate how these improvements have been integrated into clinical routine for the benefit of patients undergoing CMR, in this case on a 3T MAGNETOM Vida system. We have chosen to focus on the diagnostic workup of patients with suspected non-ischemic cardiomyopathy (NICM), as they represent a subset of patients for whom a CMR study is most frequently prescribed.

Planning of a conventional CMR study in patients with known or suspected NICM

CMR is considered as a Class I indication in patients who present with signs, symptoms, and/or findings from other diagnostic techniques consistent with NICM [5]. This is because CMR may provide, in every case, a body of information potentially useful for diagnosis, prognosis, and therapeutic decisions.

NICMs are a group of fairly distinct diseases that include hypertrophic, dilated, and restrictive cardiomyopathies – either primary or secondary. The CMR study protocols to be applied in each of these cases are detailed in official guidelines [6] and essentially aim to cover two aspects: data on the structure and function of the heart chambers and, importantly, information on myocardial tissue characteristics.

Most conventional MR systems equipped for cardiovascular applications are able to perform these studies nowadays. In addition to the pilot scans, the required sequences are as follows:

1. A complete series of cine sequences in both long and short axis views, usually obtained by a segmented, retrospectively ECG-gated, balanced steady-state free precession (bSSFP) technique.
2. Late gadolinium enhancement (LGE) sequences in the same orientations as those of the cine slices, obtained 10 minutes after the injection of a gadolinium-based contrast agent.

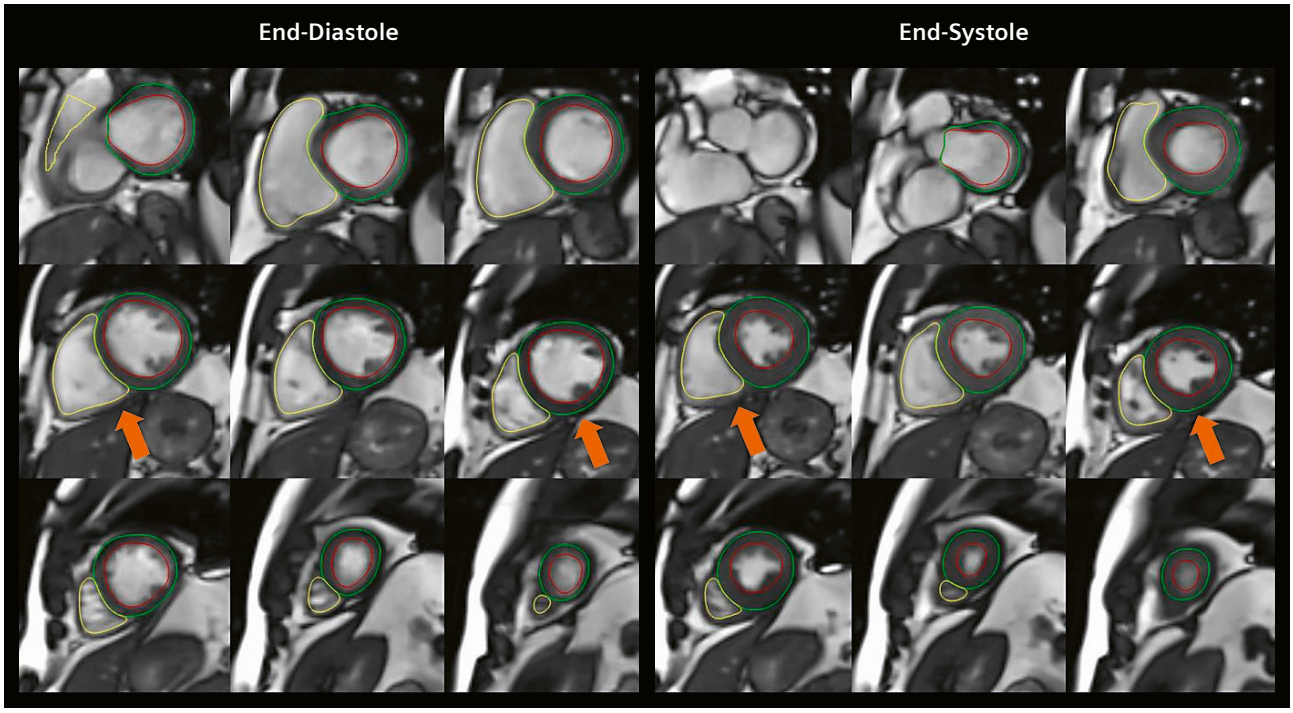

2 Free-breathing Compressed Sensing Cardiac Cine RT sequence obtained with adaptive ECG triggering and interpolative reconstruction to 25 phases of the cardiac cycle. Note the variable position of the diaphragm in the different slices (arrows) due to spontaneous breathing, and how the efficient tracking of the acquisition enables reliable border detection.

3. T1 and T2 mapping sequences. Each slice from these sequences must be acquired during breath-hold to achieve appropriate image quality, free of movement interference.

A standard study comprising all these sequences might require the performance of at least 30 breath-hold maneuvers, with a total exam time of nearly 45 minutes.

Advantages of a CMR exam performed with advanced technology to study NICM

The study of morphology and function

The acceleration of bSSFP cine sequences using parallel imaging techniques that allow for simultaneous (rather than sequential) gathering of data has contributed to a significant improvement in the acquisition of functional studies

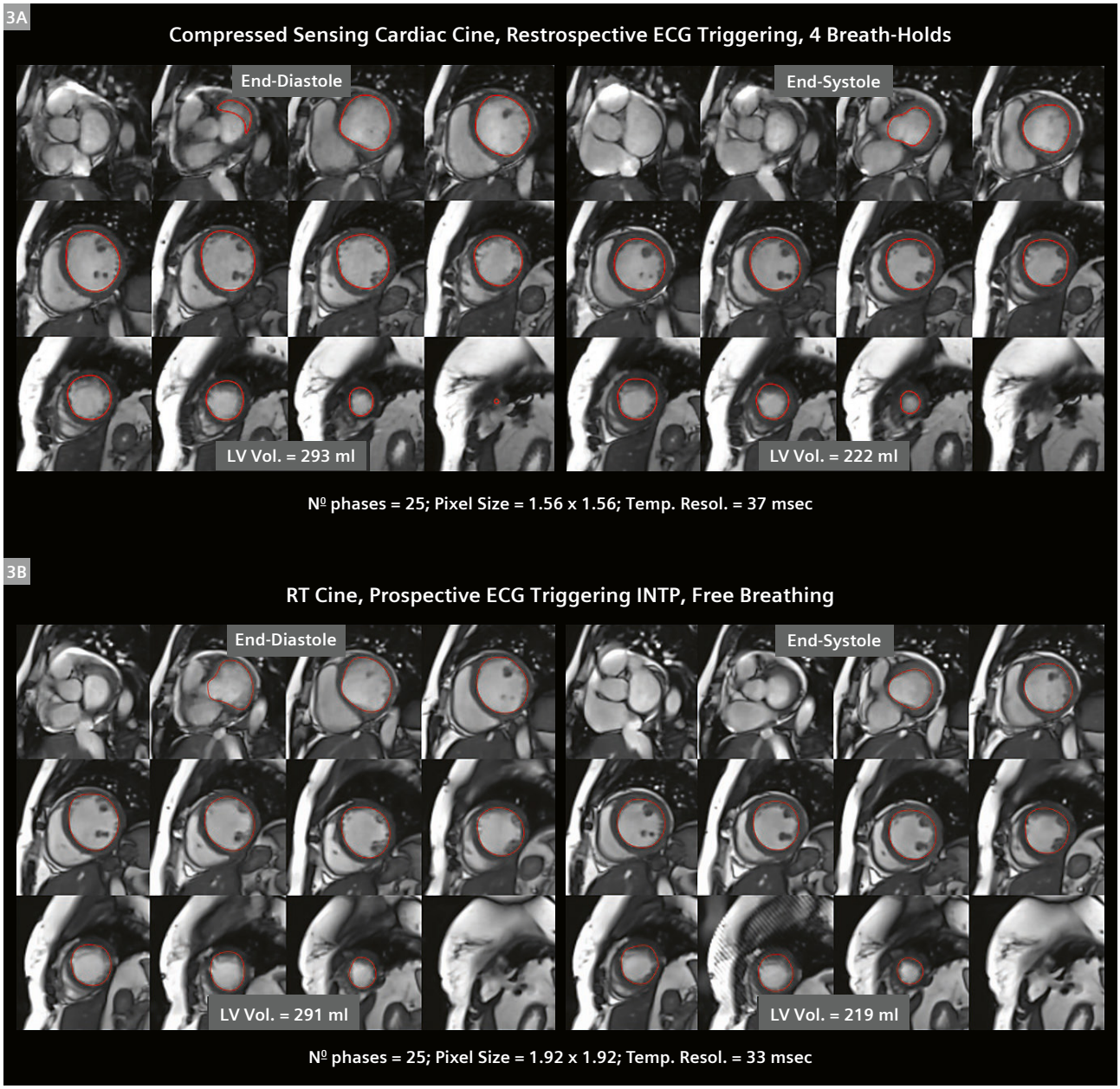

3 **(3A)** End-diastolic and end-systolic frames, and calculated LV volumes using a Compressed Sensing Cardiac Cine sequence obtained with four breath-hold periods in a patient with dilated NICM. **(3B)** The corresponding study with a free-breathing RT INTP cine sequence. Both sequences render a cardiac cycle with 25 phases with a temporal resolution of 35 ms, the spatial resolution being slightly higher in the case of the CS sequence. Pixel sizes are 1.56 vs 1.92 mm^2 for the RT sequence. Note the excellent agreement between volume calculations and, therefore, between values of ejection fraction: 24.2 and 24.7%, respectively.

of the heart [7]. Really fast and efficient cine sequences, however, have become an option in CMR with the implementation of acceleration schemes based on Compressed Sensing (CS), which reconstructs good-quality sparse images from highly undersampled *k*-space data [8]. By applying CS, the slab of short-axis cine images with complete ventricular coverage can be obtained with 1–2 breath-holds [9], instead of the 10–12 required by conventional techniques.

Real-time (RT) free-breathing cine sequences using CS on our 3T MAGNETOM Vida system are prospectively gated and render 15–20 phases per slice (depending on the heart rate), with an in-plane pixel size of around 1.5 mm^2 and a temporal resolution between phases of nearly 60 milliseconds. In addition, the option of adaptive triggering (AT) enables real-time adaptation of the acquisition to changes in heart rate. This strategy detects and reacts to changes in the cardiac cycle, effectively acquiring data between triggers. Combined with retrospective temporal interpolation (INTP) during postprocessing [10], it enables calculation of a predefined number of cardiac phases in cine acquisitions (usually 25), which further increases temporal resolution to nearly 30 milliseconds. The acquisition of every slice takes just 1–2 seconds, meaning that the total scan of the short-axis slab (10–12 slices) requires only 20–25 continuous heart beats during free breathing (Figs. 1, 2).

Comparisons of free-breathing RT sequences with conventional breath-hold cine studies have shown adequate agreement regarding volume calculations and ejection fraction values [10, 11], which validates the technique as a true alternative in practice (Fig. 3).

Although useful as a routine in most patients with NICM, the RT cine sequences still have some inherent limitations. As a prospective acquisition, there can still be slight differences in the number of reconstructed phases per slice and, particularly, in the time points of end-diastolic and end-systolic frames [11]. AT and INTP techniques are efficient for reconstructing robust, homogeneous sets of cine slices, but may also lead to some spatial blurring of images [10], which can be prominent in the case of the right ventricle [12] due to its complex anatomy. Finally, the presence of arrhythmias – particularly atrial fibrillation, which is frequent in NICM patients – poses a further challenge to RT cine imaging. While prospective acquisition has advantages in this case, highly increased heart rates drastically reduce the number of reconstructed cardiac phases and, therefore, the reliability of volume calculations at end-diastole and end-systole.

These drawbacks account for the need to have operator supervision for every study in order to guarantee the acquisition of adequately reconstructed images. In particular cases, this may lead to a move to breath-hold and/or retrospective types of acquisition, either with CS or RT cine sequences [13].

The study of tissue characterization

This part of the exam for patients with NICM is essential, as it provides information with proven prognostic value [14, 15]. Fortunately, it poses fewer challenges than cine studies for a free-breathing acquisition. LGE imaging, the cornerstone of myocardial tissue characterization, can be easily performed by sequences that retrospectively combine and average images at different respiratory phases using motion correction (MOCO) algorithms [16] (Fig. 4). A complete free-breathing LGE study on the short axis may be taken in 2–3 minutes, depending on the heart rate.

Myocardial T1 and T2 maps constitute an essential part of the study of tissue composition nowadays. These sequences are easy to perform as they require a single acquisition, which is recommended to be obtained during breath-hold, as MOCO algorithms in this case are less efficient at correcting through-plane motion [17]. In patients with difficult apnea maintenance, however, these sequences may be obtained in free breathing, asking the patient to keep a regular, calm respiratory pattern (Figs. 5, 6). Inspection of the resulting set of source images, however, is recommended in order to detect potential co-registration failure.

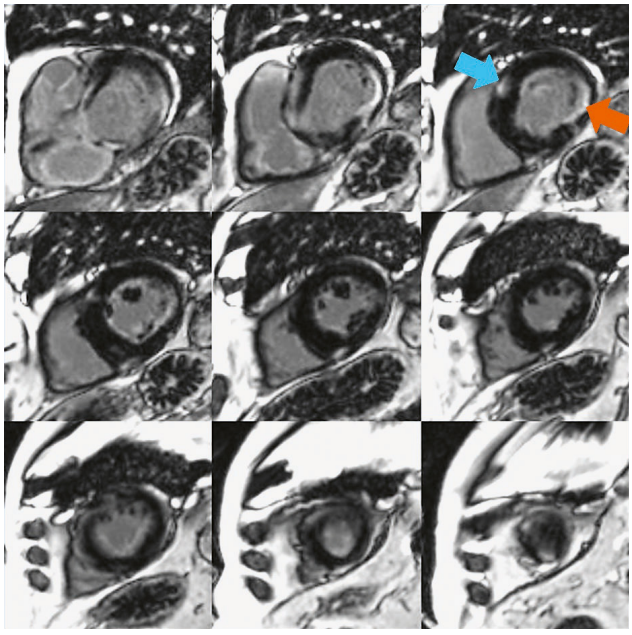

4 Single shot PSIR-SSFP free-breathing MOCO LGE in short-axis orientation in a patient with hypertrophic cardiomyopathy. Note the presence of focal, intramyocardial fibrosis (blue arrow) and, also, of subendocardial enhancement (orange arrow) indicating the coexistence of ischemic necrosis.

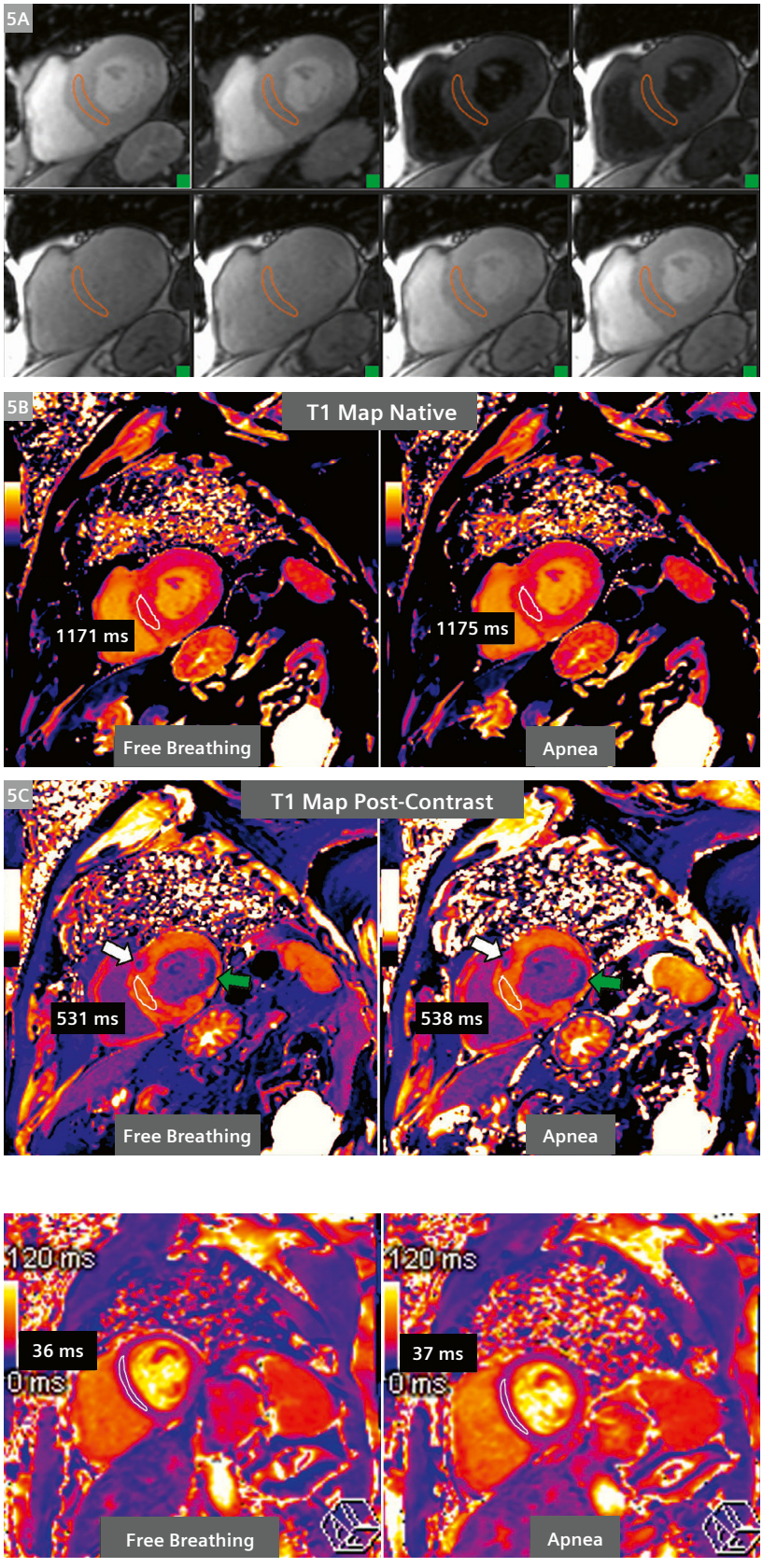

5 **(5A)** Set of raw source images from a T1 mapping sequence obtained during free breathing in the same patient as in Figure 4. Note the adequate co-registration of images. **(5B)** Resulting parametric image compared with a repeat measurement using breath-hold. Note the close agreement of native T1 values. **(5C)** The same studies after contrast: observe also the comparable resolution in the detection of areas of striking T1 reduction due to myocardial fibrosis (white arrow) and ischemic necrosis (green arrow).

6 Parametric images of T2 mapping sequences obtained during free-breathing and with breath-holding on the same patient showing comparable results.

Final comments

A complete CMR study of patients with NICM can currently be performed with sequences obtained during free breathing when using the most updated technology – in this case, a 3T MAGNETOM Vida system, as illustrated here. This makes the examination particularly comfortable for the patient and reduces the total exam time to 30 minutes (including the time lapse of waiting for the LGE study), which should impact positively on overloaded workflows. It is worth noting that the set of sequences discussed here, although robust, are more sensitive than conventional breath-hold sequences to interference caused by either an irregular pattern of respiration or arrhythmias, which might lead to suboptimal image reconstruction. This underlines the role of the operator, who should supervise the output of images after each acquisition to check for proper quality.

Acknowledgements

The author wishes to recognize the kind assistance provided by Marta Vidorreta, MR Clinical Scientist at Siemens Healthineers Spain, on technical aspects of the article.

References

1 Budinger TF, Berson A, McVeigh ER, Pettigrew RI, Pohost GM, Watson JT, Wickline SA. Cardiac MR imaging: report of a working group sponsored by the National Heart, Lung, and Blood Institute. Radiology. 1998;208(3):573–6.
2 Pohost GM. Certification of competence in cardiovascular magnetic resonance. J Cardiovasc Magn Reson. 1999;1(2):ix–x.
3 Xu J, Kim D, Otazo R, Srichai MB, Lim RP, Axel L, Mcgorty KA, Niendorf T, Sodickson DK. Towards a five-minute comprehensive cardiac MR examination using highly accelerated parallel imaging with a 32-element coil array: feasibility and initial comparative evaluation. J Magn Reson Imaging. 2013;38(1):180–8.
4 Hansen MS, Kellman P. Image reconstruction: an overview for clinicians. J Magn Reson Imaging. 2015;41(3):573–85.
5 Leiner T, Bogaert J, Friedrich MG, Mohiaddin R, Muthurangu V, Myerson S, Powell AJ, Raman SV, Pennell DJ. SCMR Position Paper (2020) on clinical indications for cardiovascular magnetic resonance. J Cardiovasc Magn Reson. 2020;22(1):76.
6 Kramer CM, Barkhausen J, Bucciarelli-Ducci C, Flamm SD, Kim RJ, Nagel E. Standardized cardiovascular magnetic resonance imaging (CMR) protocols: 2020 update. J Cardiovasc Magn Reson. 2020;22(1):17.
7 Mascarenhas NB, Muthupillai R, Cheong B, Pereyra M, Flamm SD. Fast 3D cine steady-state free precession imaging with sensitivity encoding for assessment of left ventricular function in a single breath-hold. AJR Am J Roentgenol. 2006;187(5):1235–9.
8 Lustig M, Donoho D, Pauly JM. Sparse MRI: The application of compressed sensing for rapid MR imaging. Magn Reson Med. 2007 Dec;58(6):1182–95.
9 Vincenti G, Monney P, Chaptinel J, Rutz T, Coppo S, Zenge MO, Schmidt M, Nadar MS, Piccini D, Chèvre P, Stuber M, Schwitter J. Compressed sensing single-breath-hold CMR for fast quantification of LV function, volumes, and mass. JACC Cardiovasc Imaging. 2014;7(9):882–92.
10 Saybasili H, McNeal GR, Zuehlsdorff S, Schmidt M, Kellman P, Zenge MO. Temporal interpolation of real-time cine images for ventricular function assessment. J Cardiovasc Magn Reson. 2014;16(Suppl 1):O42.
11 Haji-Valizadeh H, Rahsepar AA, Collins JD, Bassett E, Isakova T, Block T, Adluru G, DiBella EVR, Lee DC, Carr JC, Kim D; CKD Optimal Management with Binders and NicotinamidE (COMBINE) Study Group. Validation of highly accelerated real-time cardiac cine MRI with radial *k*-space sampling and compressed sensing in patients at 1.5T and 3T. Magn Reson Med. 2018;79(5):2745–2751.
12 Rahsepar AA, Saybasili H, Ghasemiesfe A, Dolan RS, Shehata ML, Botelho MP, Markl M, Spottiswoode B, Collins JD, Carr JC. Motion-Corrected Real-Time Cine Magnetic Resonance Imaging of the Heart: Initial Clinical Experience. Invest Radiol. 2018;53(1):35–44.
13 Xue H, Kellman P, Larocca G, Arai AE, Hansen MS. High spatial and temporal resolution retrospective cine cardiovascular magnetic resonance from shortened free breathing real-time acquisitions. J Cardiovasc Magn Reson. 2013;15(1):102.
14 Halliday BP, Baksi AJ, Gulati A, Ali A, Newsome S, Izgi C, Arzanauskaite M, Lota A, Tayal U, Vassiliou VS, Gregson J, Alpendurada F, Frenneaux MP, Cook SA, Cleland JGF, Pennell DJ, Prasad SK. Outcome in Dilated Cardiomyopathy Related to the Extent, Location, and Pattern of Late Gadolinium Enhancement. JACC Cardiovasc Imaging. 2019;12(8 Pt 2):1645–1655.
15 Puntmann VO, Carr-White G, Jabbour A, Yu CY, Gebker R, Kelle S, Hinojar R, Doltra A, Varma N, Child N, Rogers T, Suna G, Arroyo Ucar E, Goodman B, Khan S, Dabir D, Herrmann E, Zeiher AM, Nagel E; International T1 Multicentre CMR Outcome Study. T1-Mapping and Outcome in Nonischemic Cardiomyopathy: All-Cause Mortality and Heart Failure. JACC Cardiovasc Imaging. 2016;9(1):40–50.
16 Kellman P, Arai AE. Cardiac imaging techniques for physicians: late enhancement. J Magn Reson Imaging. 2012;36(3):529–42.
17 Messroghli DR, Moon JC, Ferreira VM, Grosse-Wortmann L, He T, Kellman P, Mascherbauer J, Nezafat R, Salerno M, Schelbert EB, Taylor AJ, Thompson R, Ugander M, van Heeswijk RB, Friedrich MG. Clinical recommendations for cardiovascular magnetic resonance mapping of T1, T2, T2* and extracellular volume: A consensus statement by the Society for Cardiovascular Magnetic Resonance (SCMR) endorsed by the European Association for Cardiovascular Imaging (EACVI). J Cardiovasc Magn Reson. 2017;19(1):75.



Contact

Guillem Pons-Lladó, MD, PhD
Cardiac Imaging Unit
Department of Diagnostic Imaging
Clínica Corachán
Buigas 19
08017 Barcelona
Spain
Phone: +34 607 26 38 48
gponsllado@gmail.com

Ultrafast Brain Imaging with Deep-Learning Multi-Shot EPI: Technical Implementation

Bryan Clifford[1], John Conklin[2], Susie Y. Huang[2], Thorsten Feiweier[3], Zahra Hosseini[4], Azadeh Tabari[2], Augusto Lio M. Goncalves Filho[2], Serdest Demir[2], Wei-Ching Lo[1], Stephan Kannengiesser[3], Dominik Nickel[3], Min Lang[2], Maria Gabriela Figueiro Longo[2], Michael Lev[2], Pam Schaefer[2], Otto Rapalino[2], Kawin Setsompop[5], Berkin Bilgic[6], Stephen Cauley[6]

[1]Siemens Medical Solutions USA, Boston, MA, USA
[2]Department of Radiology, Massachusetts General Hospital, Boston, MA, USA
[3]Siemens Healthineers, Erlangen, Germany
[4]Siemens Medical Solutions USA, Atlanta, GA, USA
[5]Department of Radiology and Department of Electrical Engineering, Stanford University, Stanford, CA, USA
[6]Department of Radiology, A. A. Martinos Center for Biomedical Imaging, Massachusetts General Hospital, Harvard Medical School, Boston, MA, USA

This work was performed using a prototype that led to the development of the Deep Resolve Swift Brain product.

Introduction

MRI is a crucial tool for the diagnosis and treatment planning of neurological diseases. Compared to CT and ultrasound, however, the underlying physics of the MR imaging process necessitates relatively long acquisition times. This has limited the use of brain MRI in time- or motion-sensitive settings, such as the emergency department, where long or repeated scans can delay urgently needed treatment [1–4].

The integration of parallel imaging (PI) and simultaneous multi-slice (SMS) imaging techniques [5–8] into standard turbo-spin-echo (TSE)-based clinical protocols has allowed for exam times of approximately 10 minutes. Advances in 3D volumetric encoding schemes [9], compressed sensing [10], and deep-learning (DL) reconstruction techniques [11–13] have helped alleviate the geometry-factor (*g*-factor) noise amplification of standard PI and SMS techniques to provide additional acceleration and further reduce exam times. Current application of these techniques to standard TSE-based protocols has lead to exam times of approximately 5 minutes [14–16].

Recently, single-shot echo-planar imaging (ssEPI) has been used to enable ultrafast multi-contrast exams on the order of 1–2 minutes [17, 18]. ssEPI acquisitions acquire all *k*-space lines after a single excitation or "shot" and allow for very rapid scan times, but require longer readout durations and echo times. As such, ssEPI images often suffer from susceptibility-induced geometric distortion as well as signal dropout and pileup artifacts.

To take advantage of the efficiency of EPI while mitigating signal-to-noise (SNR) and susceptibility-induced losses to image quality, we have developed a multi-shot EPI (msEPI)-based prototype[1] that leverages a DL-based image reconstruction to provide high-SNR T1w, T2w, T2*, and T2-FLAIR, complemented by ssEPI diffusion imaging within a 2-minute exam. The prototype's msEPI acquisition acquires readout lines in an interleaved fashion across several shots to achieve shorter echo times and reduce geometric distortion. At the same time, the DL-based image reconstruction produces high-SNR images and limits *g*-factor noise amplification. To provide greater flexibility and robustness to variations in the clinical workflow, the prototype allows each contrast to be acquired individually, in any orientation, and the DL-reconstruction includes a tunable parameter which can be automatically selected to optimize image quality and data fidelity.

In the following sections, we describe the prototype's data acquisition and image reconstruction methods, and provide performance evaluation metrics and preliminary results on clinical data not included during training.

Data acquisition

Prototype sequences were developed for acquiring T1w, T2w, T2*, FLAIR, and diffusion-weighted imaging data. Multi-shot acquisitions with high per-shot undersampling factors were used for all but the DWI sequence, which was

[1]*Work in progress. The application is currently under development and is not for sale in the U.S. and in other countries. Its future availability cannot be ensured.*

acquired using an SMS ssEPI acquisition. T2w and T2* contrasts are obtained before and after the refocusing pulse of the same msEPI scan, which further increases the sampling efficiency. To provide robustness against intra-scan motion and allow for the individual acquisition of any contrast, each scan was preceded by a fast FLASH reference scan [19], which was used to compute coil sensitivity maps, GRAPPA [5], and/or SMS kernels [20]. Additional information on the data acquisition is provided in [21].

Clinical evaluation data were acquired on patients and healthy volunteers using a 20-channel head/neck coil and a 64-channel head coil on 3T systems (MAGNETOM Prisma and Vida, Siemens Healthcare, Erlangen, Germany) with informed written consent and in accordance with local IRB guidelines. Clinical reference data were acquired for comparison immediately before the prototype exam using a standard 10-minute clinical exam. Protocol parameters from both exams are shown in Figure 1.

A deep-learning network was trained using a dataset consisting of more than 26,000 images across T1w, T2w, T2*, and T2-FLAIR contrasts in axial, coronal, and sagittal orientations (Fig. 2). The 2-average data for network training and validation were acquired on a 3T system (MAGNETOM Skyra, Siemens Healthcare, Erlangen, Germany) using a 20-channel head/neck coil.

Deep-learning hybrid image reconstruction

The prototype sequences use a novel image reconstruction algorithm that integrates DL priors into an iterative SENSE [22] reconstruction (Fig. 3). Undersampled data acquired from the scanner are first passed through a standard

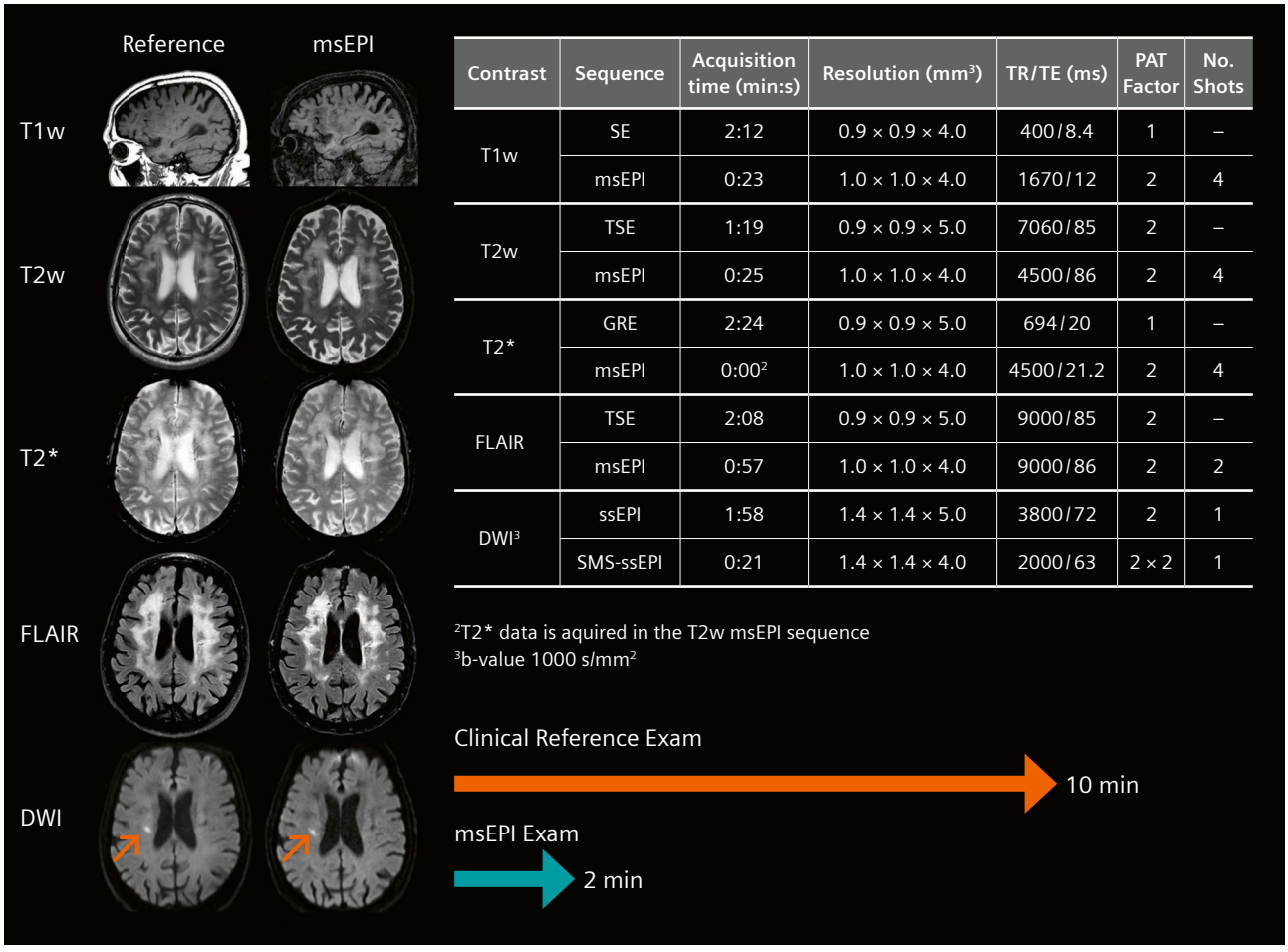

Contrast	Sequence	Acquisition time (min:s)	Resolution (mm³)	TR/TE (ms)	PAT Factor	No. Shots
T1w	SE	2:12	0.9 × 0.9 × 4.0	400/8.4	1	–
	msEPI	0:23	1.0 × 1.0 × 4.0	1670/12	2	4
T2w	TSE	1:19	0.9 × 0.9 × 5.0	7060/85	2	–
	msEPI	0:25	1.0 × 1.0 × 4.0	4500/86	2	4
T2*	GRE	2:24	0.9 × 0.9 × 5.0	694/20	1	–
	msEPI	0:00[2]	1.0 × 1.0 × 4.0	4500/21.2	2	4
FLAIR	TSE	2:08	0.9 × 0.9 × 5.0	9000/85	2	–
	msEPI	0:57	1.0 × 1.0 × 4.0	9000/86	2	2
DWI[3]	ssEPI	1:58	1.4 × 1.4 × 5.0	3800/72	2	1
	SMS-ssEPI	0:21	1.4 × 1.4 × 4.0	2000/63	2 × 2	1

[2]T2* data is aquired in the T2w msEPI sequence
[3]b-value 1000 s/mm²

1 Preliminary clinical results and protocol parameters of the msEPI and clinical reference exam. Images were obtained from a patient not included in the training or validation datasets, with a recent right corona radiata lacunar infarct (DWI images, arrows) and extensive white matter T2-FLAIR hyperintense signal abnormality likely related to cerebral small vessel disease. A graphical representation of the total acquisition times in the clinical reference and msEPI exams is included below the parameter table.

parallel imaging reconstruction, e.g., SENSE, which is used as input to an unrolled gradient-descent network (UGDN) [11]. The UGDN removes residual aliasing artifacts and noise from the initial reconstruction by iteratively passing the image through a deep neural network followed by a data-fidelity increasing operation which incorporates the physics of the acquisition and original measured data. The output of the UGDN, which will have good SNR but may be overly smooth, is then refined in a second iterative SENSE reconstruction, referred to as the DL-SENSE hybrid reconstruction [21].

The DL-SENSE hybrid reconstruction uses the image from the UGDN to regularize an iterative SENSE reconstruction and so generate a high-SNR image with good data fidelity and preservation of fine details. Specifically, the DL-SENSE hybrid reconstruction is a generalization of the methods in [23, 24] and computes the final image by solving the following optimization problem:

$$\min_{\boldsymbol{\rho}} || \boldsymbol{d} - \Omega \mathrm{FC}\boldsymbol{\rho} ||_2^2 + \lambda || \mathrm{WFC}(\boldsymbol{\rho}_{\mathrm{UGDN}} - \boldsymbol{\rho}) ||_2^2$$

where $\boldsymbol{d}$ and $\boldsymbol{\rho}$ are vectors of the measured data and image values, respectively; $\boldsymbol{\rho}_{\mathrm{UGDN}}$ is the output of the UGDN; F and C are the Fourier encoding and coil sensitivity operators; Ω is the *k*-space sampling operator; λ is a tunable denoising parameter; W is a diagonal weighting matrix.

A key feature of the DL-SENSE hybrid reconstruction is its ability to provide explicit control over the way the UGDN influences the final reconstructed image, which allows the same network to be applied to data acquired under novel noise conditions without the need for costly retraining. The user can control the balance between the fidelity of the final image with the measured data (left term in the above optimization problem) and with the output of the UGDN (right term in the above optimization problem) by tuning the denoising parameter λ. Similarly, the weighting matrix W controls the spectral mixing of information from the UGDN image and the measured data. In the current prototype, W was chosen as a sampling operator with the same undersampling factor as Ω but with complementary sample locations. For a given value of λ, this choice of W provided a desirable tradeoff between data fidelity and image quality and helped to focus the UGDN's representational power on unsampled *k*-space regions during training.

Network training and validation

The UGDNs used by the prototype were trained using images from a dataset consisting of more than 26,000 images across all contrasts and orientations (Fig. 2). During training, simulated training examples were generated by retrospectively undersampling high-SNR images, and noise was added to the simulated data to match clinical SNR levels. Separate UGDNs were trained for undersampling (PAT) factors of 2, 3, and 4. Networks were trained to minimize a loss function consisting of a weighted combination of the structural similarity index measure (SSIM) – known to correlate with radiologist quality rating [25, 26] – and the mean absolute error between the reconstructed images and their corresponding ground-truths.

Approximately 6,500 images in the dataset were excluded from training and reserved for validation of the trained networks. Following the same procedure used during training, noisy, undersampled data were generated from these images and reconstructed using the DL-SENSE hybrid scheme. The mean ± SD of the SSIM values between the reconstructed images and their corresponding ground-truth images are shown in Figure 2, sorted by contrast and PAT factor. These results indicate that the proposed method can reliably generate high-quality images, even at higher (≥ 3) acceleration factors.

Automatic selection of the denoising parameter

It can be challenging to select an appropriate denoising parameter given the variability seen in clinical settings. For a given protocol, the denoising parameter can be manually tuned according to radiologist preference; however, the ideal choice can vary with changes to protocol parameters, coil loading, coil selection, etc., which are common in the clinic. The parameter that yields the best results in one scenario may lead to overly smooth or noisy images in another scenario.

This problem was addressed by training a model to automatically select the denoising parameter based on estimated data SNR. The prototype computes the noise level using acquisition-specific noise calibration data and combines this with an estimate of the signal intensity to compute the SNR. A trained model then uses the estimated SNR to predict the denoising parameter preferred by radiologists [27]. This automatic, data-driven adaptation of the denoising parameter makes the prototype robust to changes in protocol parameters and automatically reduces the impact of the DL prior on the reconstruction in higher SNR (or lower PAT factor) scenarios, to maximize data fidelity while preserving image quality.

Figure 4A shows both the GRAPPA and DL-SENSE hybrid reconstructions of T2-FLAIR data (the contrast with lowest SNR) acquired from a healthy volunteer at PAT 2, 3, and 4. The GRAPPA reconstructions show the expected noise amplification with increasing PAT factor, but in the DL-SENSE hybrid reconstruction, the noise levels remain

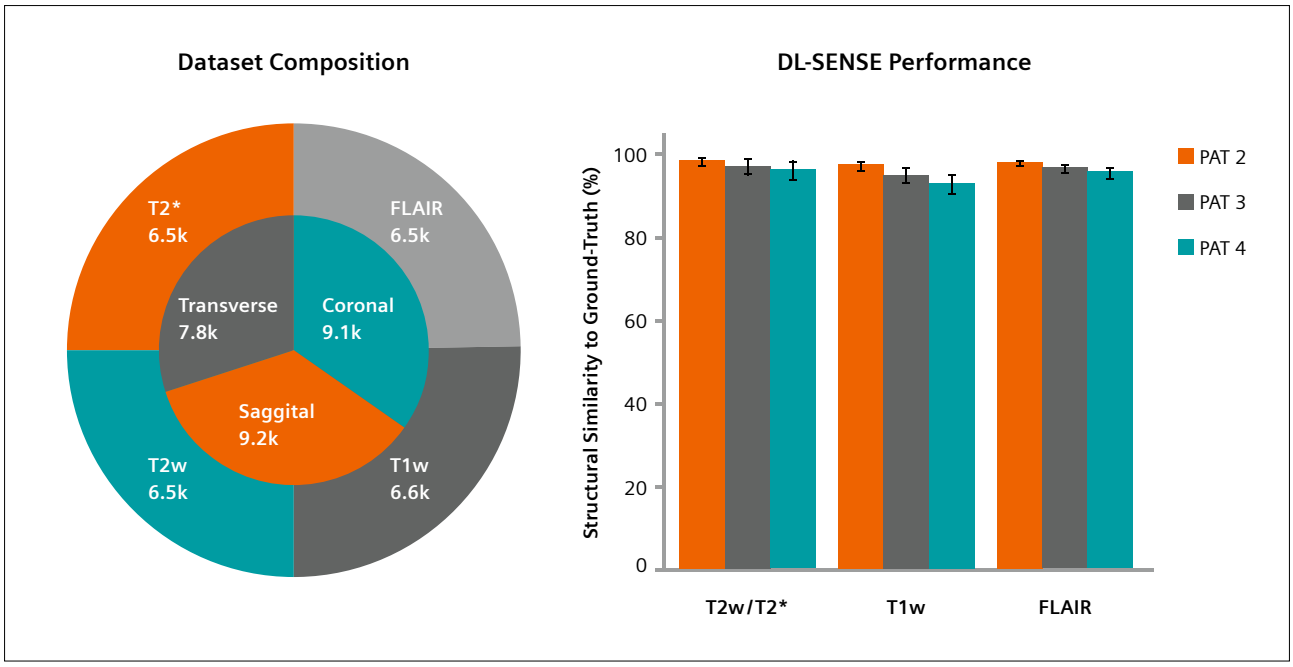

2 Dataset composition and validation results. The dataset consisted of more than 26,000 images and included T1w, T2w, T2*, and T2-FLAIR contrasts as well as coronal, sagittal, and transverse orientations, as shown in the pie chart. The bar chart shows the mean ± SD structural similarity index measure (SSIM) between DL reconstructions and the corresponding ground-truth validation images.

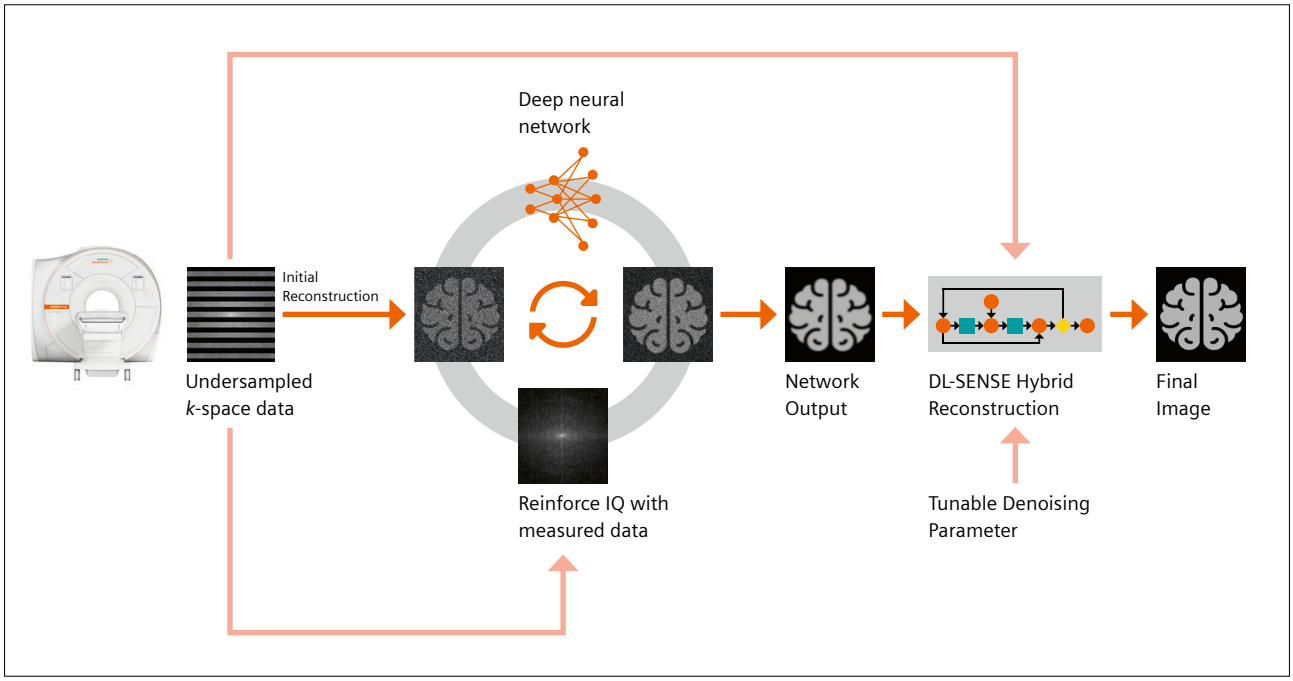

3 Illustration of the proposed reconstruction scheme. An initial SENSE reconstruction is generated from the undersampled *k*-space data and used as input to an unrolled gradient descent network (UGDN). The UGDN repeatedly alternates between deep neural-network denoising and data-fidelity updates to remove noise and residual aliasing while preserving the information in the acquired data. The UGDN output image and the measured data are then used in a regularized DL-SENSE hybrid reconstruction to produce the final image. By incorporating a tunable denoising parameter, the DL-SENSE hybrid reconstruction can be tailored to radiologist preference and also allows the same network to be applied to data acquired under noise conditions not previously seen without retraining.

relatively constant. Examination of representative denoising parameter values (orange markers in Figure 4B) shows that the trained model (orange line in Fig. 4B) automatically adjusts the denoising parameter as the PAT factor increases, using higher values for higher PAT factors. Figure 4B also shows example denoising parameter values from different contrasts and demonstrates how the model uses lower values for higher SNR contrasts (e.g., T2*) as well.

Reconstructions of T2-FLAIR data acquired on the same healthy volunteer using 20- and 64-channel coils are shown in Figure 5. Overall, the SNR of the two images is similar, but in the cortical region, the SNR of the 64-channel image is noticeably higher. These results suggest that the prototype can also adapt to changes in coil selection, allowing users to make the most out of higher density array coils.

Preliminary clinical results

We compared the proposed 2-minute prototype protocol to a standard TSE-based, 10-minute clinical reference protocol on a patient suffering from a recent right corona radiata lacunar infarct (DWI with restricted diffusion, Fig. 1 arrowheads) and extensive patchy and confluent

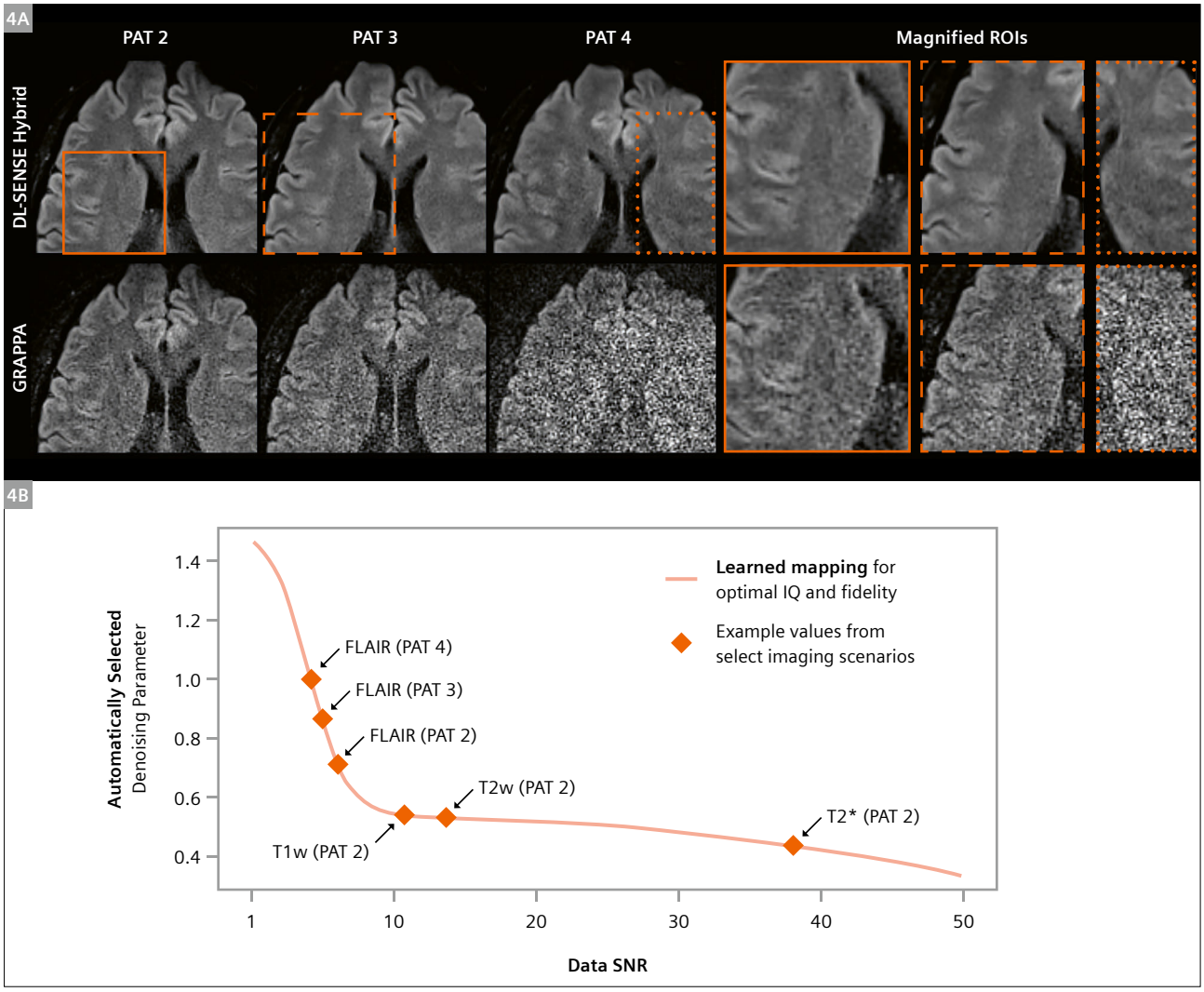

4 Generalization of the DL-SENSE hybrid reconstruction to higher undersampling (PAT) factors and varying SNR levels. **(4A)** Reconstructions of T2-FLAIR data acquired from a healthy volunteer at different PAT factors using the DL-SENSE hybrid reconstruction and GRAPPA. Magnified ROIs displayed on the right show how the proposed DL-SENSE reconstruction automatically adapts the denoising parameter to maintain image quality despite variations in the undersampling factor. **(4B)** The learned mapping between data SNR and optimal denoising parameter (orange line). The mapping was trained to predict parameters chosen by board-certified radiologists. The parameter values for the T2-FLAIR reconstructions in (4A) as well as for representative T1w, T2w, and T2* acquisitions are depicted by orange markers. The trained model tries to provide an optimal balance between image quality and data fidelity; in high-SNR scenarios, the model chooses lower values to maintain image quality while increasing data fidelity.

T2-FLAIR hyperintense white matter signal abnormality likely related to cerebral small vessel disease (T2-FLAIR, Fig. 1). Evaluation of the Figure 1 images by board-certified neuroradiologists indicated that, despite the nearly 5-fold reduction in exam time, the diagnostic quality of the images produced by the prototype was similar to that of the standard 10-minute exam. The white matter signal abnormality as well as the DWI/FLAIR mismatch (indicating a recent infarct) in the infarcted region can be clearly observed in the T2w, T2*, FLAIR, and DWI images from each protocol. Moreover, the gray/white differentiation of the msEPI T1w acquisition is similar to that of the reference SE T1w scan, despite the differences in the respective contrast mechanisms.

Although msEPI T1w images do not optimally depict facial soft tissues, which can be useful in certain diagnostic situations, it is interesting to note that the msEPI T1w images appear to depict the white matter lesions with greater conspicuity than the reference SE acquisition (possibly due to the increased T2* weighting). Regardless, future development will include the evaluation of a GRE-based T1w prototype sequence for the purposes of providing a nearly distortion-free reference, suitable for observing facial soft tissues.

In addition to the results presented here, clinical evaluations of earlier versions of this prototype have also been performed, with similar results [21, 28]. In particular, the report by Tabari et al. [28] provides initial results from a clinical evaluation on a large cohort of inpatients and emergency department patients, which indicate a high degree of interobserver agreement for major diagnostic findings, similar to that of the 5-fold slower clinical reference exam.

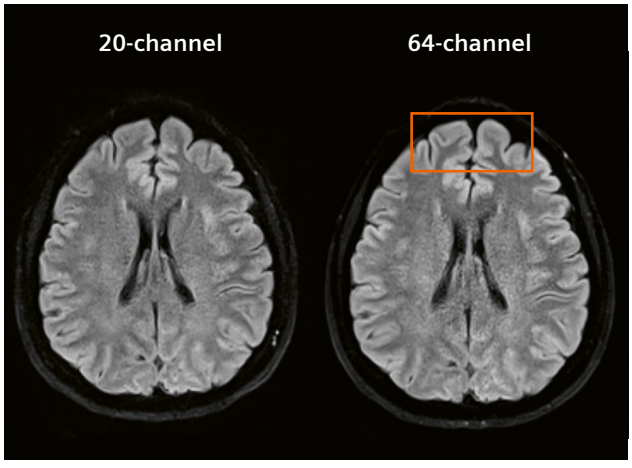

5 T2-FLAIR images acquired at 3T with the msEPI prototype sequence using the 20-channel head/neck coil and the 64-channel head coil from Siemens Healthineers. The msEPI prototype automatically adjusts the denoising level according to the SNR in each acquisition scenario, which makes it robust to variations in coil selection. To take advantage of the increased cortical sensitivity of the 64-channel coil, the prototype automatically reduces the denoising parameter in the DL-SENSE hybrid reconstruction to maximize IQ and data fidelity (see highlighted ROI).

Conclusions

We have developed an ultrafast MRI prototype that integrates a highly efficient msEPI acquisition with DL-based image reconstruction techniques to provide comprehensive brain MR imaging in a 2-minute exam. Although clinical evaluation on large patient cohorts is still ongoing, preliminary results indicate that the prototype can automatically adapt its DL reconstruction to variations in protocol parameters and coil selection to produce T1w, T2w, T2*, T2-FLAIR, and diffusion-weighted imaging with diagnostic quality similar to that of a standard 10-minute TSE-based acquisition.

References

1 Agarwal R, Bergey M, Sonnad S, Butowsky H, Bhargavan M, Bleshman MH. Inpatient CT and MRI utilization: trends in the academic hospital setting. J Am Coll Radiol. 2010;7(12):949–955.
2 Selvarajan SK, Levin DC, Parker L. The Increasing Use of Emergency Department Imaging in the United States: Is It Appropriate? AJR Am J Roentgenol. 2019;213(4):W180–W184.
3 Goyal M, Menon BK, van Zwam WH, Dippel DW, Mitchell PJ, Demchuk AM, et al. Endovascular thrombectomy after large-vessel ischaemic stroke: a meta-analysis of individual patient data from five randomised trials. Lancet. 2016;387(10029):1723–1731.
4 Berkhemer OA, Fransen PS, Beumer D, van den Berg LA, Lingsma HF, Yoo AJ, et al. A randomized trial of intraarterial treatment for acute ischemic stroke. N Engl J Med. 2015;372(1):11–20.
5 Griswold MA, Jakob PM, Heidemann RM, Nittka M, Jellus V, Wang J, et al. Generalized autocalibrating partially parallel acquisitions (GRAPPA). Magn Reson Med. 2002;47(6):1202–1210.
6 Pruessmann KP, Weiger M, Scheidegger MB, Boesiger P. SENSE: Sensitivity encoding for fast MRI. Magn Reson Med. 1999;42(5):952–962.
7 Glover GH. Phase-offset multiplanar (POMP) volume imaging: A new technique. J Magn Reson Imaging. 1991;1(4):457–61.
8 Barth M, Breuer F, Koopmans PJ, Norris DG, Poser BA. Simultaneous multislice (SMS) imaging techniques. Magn Reson Med. 2016;75(1):63–81.
9 Bilgic B, Gagoski BA, Cauley SF, Fan AP, Polimeni JR, Grant PE, et al. Wave-CAIPI for highly accelerated 3D imaging. Magn Reson Med. 2015;73(6):2152–2162.
10 Liang D, Liu B, Wang J, Ying L. Accelerating SENSE using compressed sensing. Magn Reson Med. 2009;62(6):1574–84.
11 Hammernik K, Schlemper J, Qin C, Duan J, Summers RM, Rueckert D. Systematic evaluation of iterative deep neural networks for fast parallel MRI reconstruction with sensitivity-weighted coil combination. Magn Reson Med. 2021;86(4):1859–1872.
12 Schlemper J, Caballero J, Hajnal JV, Price AN, Rueckert D. A Deep Cascade of Convolutional Neural Networks for Dynamic MR Image Reconstruction. IEEE Trans Med Imaging. 2018;37(2):491–503.

13 Aggarwal HK, Mani MP, Jacob M. MoDL: Model Based Deep Learning Architecture for Inverse Problems. IEEE Trans Med Imag. 2019;38(2):394–405.
14 Prakkamakul S, Witzel T, Huang S, Boulter D, Borja MJ, Schaefer P, et al. Ultrafast Brain MRI: Clinical Deployment and Comparison to Conventional Brain MRI at 3T. J Neuroimaging. 2016;26(5):503–510.
15 Recht MP, Zbontar J, Sodickson DK, Knoll F, Yakubova N, Sriram A, et al. Using Deep Learning to Accelerate Knee MRI at 3T: Results of an Interchangeability Study. AJR Am J Roentgenol. 2020;215(6):1421–1429.
16 Gassenmaier S, Afat S, Nickel D, Mostapha M, Herrmann J, Othman AE. Deep learning-accelerated T2-weighted imaging of the prostate: Reduction of acquisition time and improvement of image quality. Eur J Radiol. 2021;137:109600.
17 Skare S, Sprenger T, Norbeck O, Rydén H, Blomberg L, Avventi E, et al. A 1-minute full brain MR exam using a multicontrast EPI sequence. Magn Reson Med. 2018;79(6):3045–3054. doi:10.1002/mrm.26974
18 Delgado AF, Kits A, Bystam J, Kaijser M, Skorpil M, Sprenger T, et al. Diagnostic performance of a new multicontrast one-minute full brain exam (EPIMix) in neuroradiology: A prospective study. J Magn Reson Imaging. 2019;50(6):1824–1833.
19 Wang D, Deshpande V, Li X, Urgurbil K. Siemens Healthcare GmbH, Regents of the University of Minnesota, assignee. Multiband Slice Accelerated Imaging With Balanced Slice-Selective Gradients. United States patent 9,989,610. June 5, 2018.
20 Cauley SF, Polimeni JR, Bhat H, Wald LL, Setsompop K. Interslice leakage artifact reduction technique for simultaneous multislice acquisitions. Magn Reson Med. 2014;72(1):93–102.
21 Clifford B, Conklin J, Huang SY, Feiweier T, Hosseini Z, Goncalves Filho ALM, et al. An artificial intelligence-accelerated 2-minute multi-shot echo planar imaging protocol for comprehensive high-quality clinical brain imaging. Magn Reson Med. 2022;87(5):2453–2463. Epub 2021 December 31.
22 Pruessmann KP, Weiger M, Börnert P, Boesiger P. Advances in sensitivity encoding with arbitrary k-space trajectories. Magn Reson Med. 2001;46(4):638–651.
23 Hyun CM, Kim HP, Lee SM, Lee S, Seo JK. Deep learning for undersampled MRI reconstruction. Phys Med Biol. 2018;63(13):135007.
24 Wang S, Su Z, Ying L, Peng X, Zhu S, Liang F, et al. ACCELERATING MAGNETIC RESONANCE IMAGING VIA DEEP LEARNING. In: Proc IEEE Int Symp Biomed Imaging. 2016;2016:514–517.
25 Mason A, Rioux J, Clarke SE, Costa A, Schmidt M, Keough V, et al. Comparison of Objective Image Quality Metrics to Expert Radiologists' Scoring of Diagnostic Quality of MR Images. IEEE Trans Med Imaging. 2020;39(4):1064–1072.
26 Muckley MJ, Riemenschneider B, Radmanesh A, Kim S, Jeong G, Ko J, et al. Results of the 2020 fastMRI Challenge for Machine Learning MR Image Reconstruction. IEEE Trans Med Imaging. 2021;40(9):2306–2317.
27 Hosseini Z, Feiweier T, Conklin J, et al. A data-driven method for automatic regularization selection in a hybrid DL-SENSE reconstruction. In: Proc. Intl. Soc. Magn. Reson. Med. 2022:0206.
28 Tabari A, Clifford B, Goncalves Filho ALM, Hosseini Z, Feiweier T, Lo WC, et al. Ultrafast Brain Imaging with Deep Learning Multi-Shot EPI: Preliminary Clinical Evaluation. MAGNETOM Flash. 2021;79(2):66–70.

Contact

Bryan Clifford, Ph.D.
Siemens Medical Solutions USA
149 13th St, Suite 2301
Boston, MA 02129
USA
Bryan.Clifford@siemens-healthineers.com



→ Don't miss the clinical aspects of Deep Resolve Swift Brain

John Conklin, Azadeh Tabari, et al. (Massachusetts General Hospital, Boston, MA, USA)

"Ultrafast Brain Imaging with Deep Learning Multi-Shot EPI: Preliminary Clinical Evaluation"

The article is available at www.magnetomworld.siemens-healthineers.com/clinical-corner/case-studies/deep-resolve-swift-brain

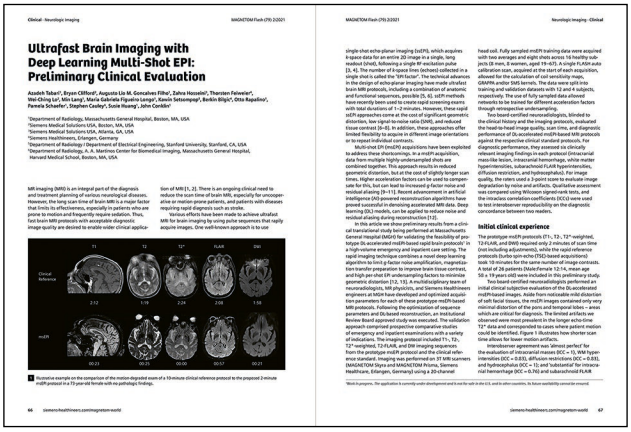

Ultrafast Brain Imaging with Deep Learning Multi-Shot EPI: Preliminary Clinical Evaluation

Distortion-free Diffusion-weighted Imaging Based on a TGSE BLADE Sequence: Technique and Clinical Application

Kun Zhou, Ph.D.; Wei Liu, Ph.D.

Siemens Shenzhen Magnetic Resonance Ltd., Shenzhen, China

Introduction

Diffusion-weighted imaging (DWI) is a powerful tool for probing tissue microstructures by measuring the Brownian motion of water molecules. It has been widely used for diagnosing a broad spectrum of pathologies. Single shot echo planar imaging (ssEPI) is the most commonly used sequence for DWI, due to its high data acquisition rate and low sensitivity to bulk motion and physiological movement. However, this technique often suffers from geometric distortion caused by susceptibility change at tissue interfaces, and image blurring caused by signal decay in the long acquisition window.

In the ssEPI sequence, the time between sampling points in phase encoding (PE) direction is relatively long, so the phase caused by static B_0 inhomogeneity accumulates, leading to geometric distortion [1]. Two variants of multishot techniques – interleaved EPI (iEPI) and readout segmented EPI (rsEPI) – can be applied to mitigate image distortion by reducing effective echo spacing. iEPI accelerates the *k*-space traversal by interleaving EPI trajectories along the PE direction [2], while rsEPI divides the full *k*-space into multiple segments along the readout direction [3]. However, significant residual problems still exist where strong B_0 inhomogeneities are present, such as in the inner ear, skull base, orbit, and sinuses. This is particularly true at higher field strengths since susceptibility artifacts increase along with the field strength.

To further reduce geometric distortion, DWI can also be carried out by turbo spin echo (TSE) sequences, which are free of phase error accumulation. These techniques fall into two categories: single-shot and multishot. Half-Fourier acquisition single shot turbo spin echo (HASTE) DWI belongs to the first category and has been used for cholesteatoma detection at 1.5T for many years [4]. It was recently rolled out to 3T because of the excellent lesion conspicuity [5]. HASTE DWI has some limitations: e.g., because a different diffusion encoding scheme is applied, the contrast is different from other DWI techniques. It is also more prone to blurring due to the relatively long echo train.

To overcome those limitations, multi-shot DWI sequences are introduced. However, shot-to-shot variations introduced by motion during the diffusion encoding gradients can impact image quality. Thus special acquisition strategies like BLADE are usually the method of choice, as the *k*-space center region in each shot can be used to correct these variations [6].

However, the application of TSE-BLADE-based DWI is limited due to its relatively long scan time, high specific

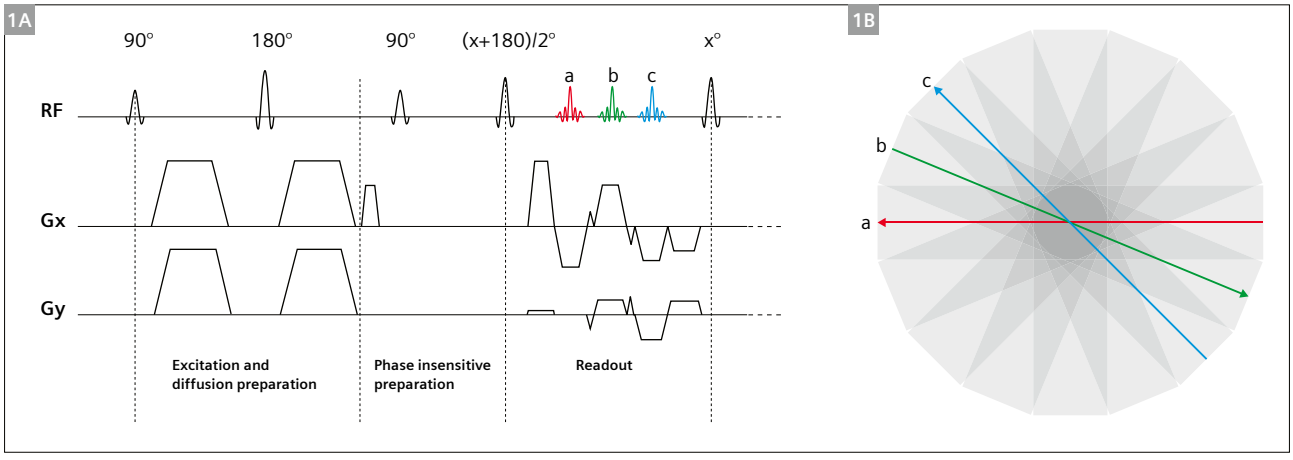

1 Sequence diagram and *k*-space filling order with EPI factor = 3. Note that only one echo spacing is shown.

absorption rate (SAR), and issues caused by violation of Carr-Purcell-Meiboom-Gill (CPMG) conditions. Several techniques have been developed to address these challenges. For example, a phase cycling method can be used to stabilize the echo train by reducing the interference coming from the non-CPMG components [7]. However, this scheme requires that the flip angles of refocusing pulses are as close to 180° as possible. Therefore, SAR is still high, especially at high fields, and B_1 field variation may result in unstable image quality. The turbo gradient spin echo (TGSE, or GRASE) technique, which generates and acquires gradient echoes and spin echoes via EPI-like bipolar gradients, can speed up the acquisition and reduce SAR accordingly. The gradient echoes and spin echoes sampled in one shot can be placed in one blade [8, 9] or distributed in different blades [10, 11]. In any case, the EPI factor should be kept in a moderate range to avoid off-resonance effects.

To provide a distortion-free DWI sequence that has high image quality and reasonable measurement time, the TGSE BLADE-based DWI sequence (TGSE BLADE DWI) was developed and rolled out to the 3T systems MAGNETOM Vida and MAGNETOM Lumina with software version *syngo* MR XA50A. This sequence is based on the TGSE sequence and acquires *k*-space with a BLADE trajectory [12]. A phase-insensitive preparation method [13] is used to handle the non-CPMG problem. Besides the TGSE readout technique, Simultaneous Multi-Slice (SMS) and the integrated parallel acquisition technique (iPAT) are applied to further reduce the measurement time [14].

Method

Diffusion encoding and phase-insensitive preparation

In diffusion imaging, physiological fluctuation and even tiny amounts of motion during the application of diffusion-sensitizing gradients introduce spatially varying and unknown phases to the spins in the transversal plane. If TSE-based sequences are used to sample the signals, the CPMG condition is not fulfilled and hence the echo amplitudes in the echo train attenuate rapidly. This results in image artifacts, e.g., severe inhomogeneity and signal loss in regions affected by the motion.

To address this problem, a phase-insensitive preparation module is applied between the diffusion preparation and the following refocusing pulses as shown in the sequence diagram in Figure 1.

EPI readout

To accelerate the conventional BLADE sequence, EPI-like readout gradients and blips are played out on both readout and phase encoding directions, producing radial-like *k*-space lines which are placed into separate blades, as shown in Figure 1. The readout is repeated throughout the whole echo train, producing all *k*-space lines for each blade. These blades cover *k*-space completely.

SMS and iPAT

SMS and iPAT is implemented to speed up the acquisition. To reduce the *g*-factor penalty, blipped-controlled aliasing [15] is used.

The time to acquire the necessary SMS calibration data is kept to a minimum by applying a quick separate TSE-based reference scan for the first blade. For other blades, the calibration data are interpolated from the acquired data.

This reference scan is also compatible with in-plane GRAPPA. In-plane GRAPPA makes it possible to acquire a wider blade, which can speed up the acquisition and can increase the robustness against motion.

Results of internal volunteer test

Figure 2 shows images of b = 0 s/mm², 1000 s/mm², and an ADC acquired with the TGSE BLADE DWI sequence on a MAGNETOM Vida with a 20-channel head-neck coil. With the application of SMS, in-plane GRAPPA, and TGSE readout, distortion-free diffusion-weighted images covering the whole brain can be acquired in a reasonable time.

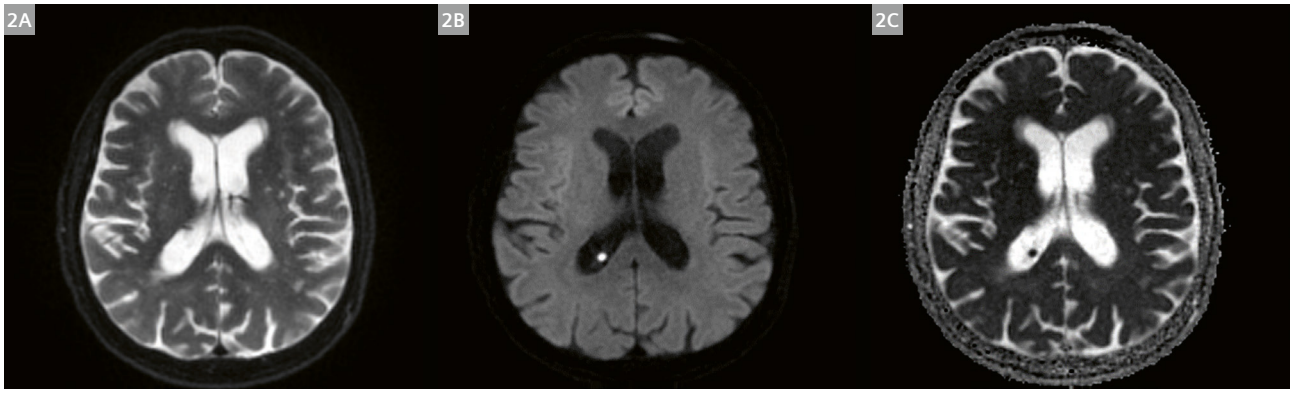

2 b = 0 s/mm², 1000 s/mm², and ADC from the TGSE BLADE diffusion sequence with a PE acceleration of 2 and a slice acceleration factor of 2. Other parameters are TE = 55 ms, TR = 4000 ms, FOV = 220 × 220 mm², matrix size = 176 × 176, and TA= 3:12 min.

Figure 3 shows a comparison between RESOLVE DWI and TGSE BLADE DWI of b = 1000 s/mm². Residual geometric distortions and signal pile-ups (arrows) are seen in the RESOLVE diffusion images and are less noticeable in the BLADE diffusion images.

Clinical applications

The application of EPI-based DWI is well established for many body regions. However, its ability to diagnose lesions could be compromised in regions with strong local susceptibility variations caused by magnetic field inhomogeneities. Several studies on the performance of TGSE BLADE DWI in these challenging regions were performed during the evaluation phase of this sequence, indicating that this sequence could be a promising solution for those challenging regions [16–20].

Cholesteatoma

Cholesteatoma is a benign, gradually expanding, and destructive epithelial lesion of the temporal bone that results in the erosion of adjacent bony structures and can lead to various complications [5].

Although CT imaging has traditionally been the method of choice, MRI with DWI is becoming more and more important in the evaluation of cholesteatoma, due to its superior soft tissue contrast. To evaluate the performance of RESOLVE and TGSE BLADE in this application, Sheng et al. performed a study to compare image quality qualitatively and quantitatively between TSGE BLADE and RESOLVE on a MAGNETOM Prisma with a 64-channel head-neck coil [16]. 42 patients with surgically confirmed cholesteatoma in the middle ear were enrolled in this study.

The results indicate that TGSE BLADE DWI significantly improved the image quality of cholesteatoma imaging by reducing B_0 inhomogeneity related artifacts and blurring. The authors found that TGSE BLADE DWI is more valuable than RESOLVE DWI for diagnosing small (2 mm) cholesteatoma lesions. As shown in Figure 4, axial TGSE BLADE DWI could completely and clearly show a small lesion (1.9 mm in width) located in the left tympanic cavity with less geometric distortion than was observed using RESOLVE DWI.

Although the study also found that the signal-to-noise ratio (SNR) of TGSE BLADE DWI is lower than RESOLVE, this is anticipated because the same acquisition time is used while the SNR efficiency of TGSE BLADE DWI is lower, since it has to compensate for the non-CMPG condition.

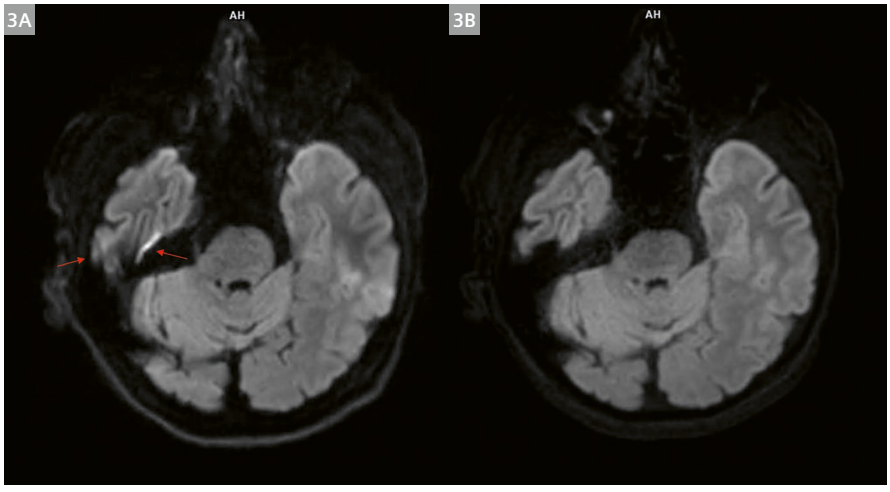

3 Example of the b = 1000 s/mm² trace-weighted images acquired with a product RESOLVE sequence **(3A)** and TGSE BLADE diffusion sequence **(3B)** at 3T.
Common parameters:
Matrix = 160 × 160,
FOV 220 × 220 mm²,
slice thickness = 4 mm,
in-plane Grappa factor = 2.
RESOLVE: TR = 5240 ms,
TE = 58 ms, TA = 1:57 min;
TGSE BLADE: TR = 5500 ms,
TE = 44 ms, TA = 3:50 min.

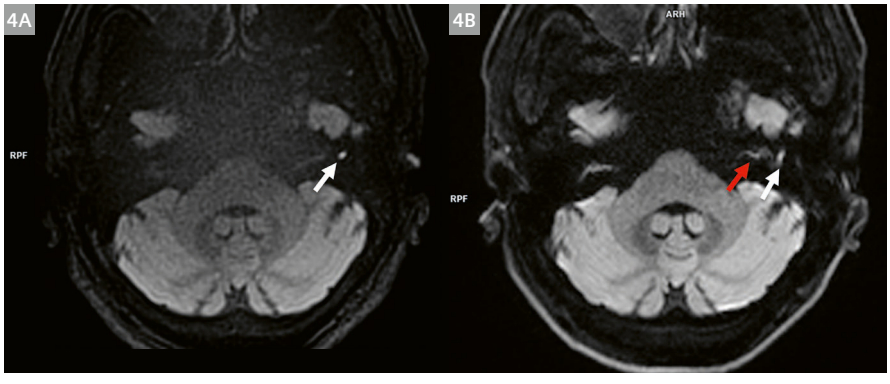

4 A 44-year-old male with a small cholesteatoma (1.9 mm width) in the left tympanic cavity (white arrow). **(4A)** Axial TGSE BLADE DWI (b = 1000 s/mm²) clearly shows a markedly high signal intensity for the small cholesteatoma (white arrows) without artifacts. **(4B)** Axial RESOLVE DWI (b = 1000 s/mm²) shows the high signal intensity of a small lesion (white arrow) with light geometric distortion, and the bilateral middle ear mastoid process with a few artifacts (red arrow).

Orbital tumor

DWI is also an essential MR sequence for diagnosing orbital diseases. Geometric fidelity is important for depicting small lesions in orbital DWI. Moreover, accurately characterizing the extent of invasion of orbital tumors is essential for clinical treatment planning or even prognosis of the orbital tumors.

Fu et al. performed a study that qualitatively and quantitatively compared the image quality and diagnostic performance of TGSE BLADE DWI and RESOLVE on a MAGNETOM Skyra with a 20-channel head-neck coil [17]. 43 patients with suspected orbital tumors were enrolled in this study.

TGSE BLADE DWI significantly outperformed RESOLVE on scores for geometric distortions, susceptibility artifacts, lesion conspicuity, and overall image quality. Three cases are shown in Figure 5.

Pediatric

In a preliminary study of 53 patients (10.4 ± 7.9 years), Hu et al. compared the diagnostic image quality of TGSE BLADE DWI versus ssEPI DWI in pediatric patients* on a

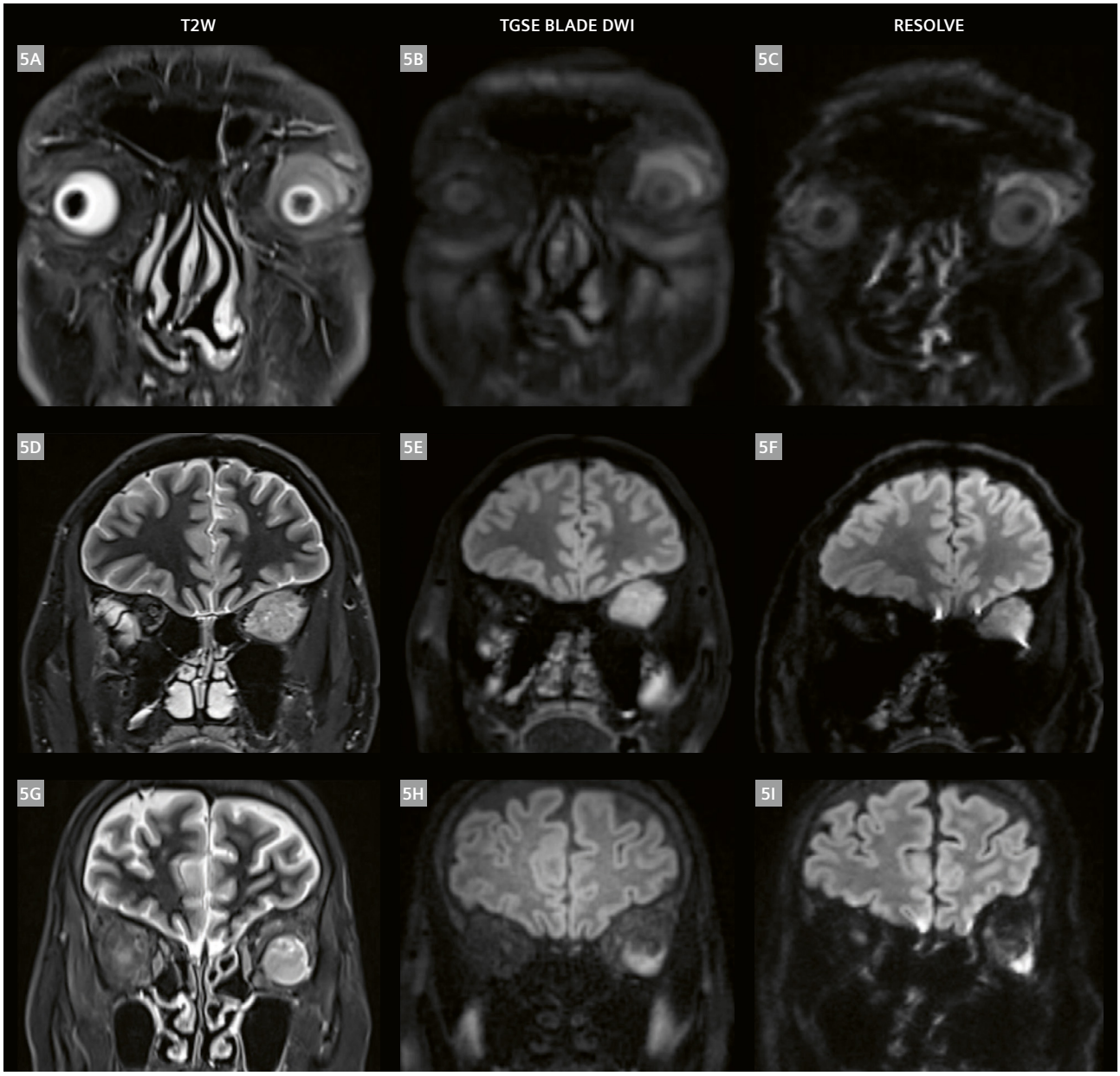

5 Coronal T2-weighted images **(5A, D, G)**, TGSE BLADE DWI b = 1000 s/mm² images **(5B, E, H)**, and RESOLVE b = 1000 s/mm² images **(5C, F, I)**. Patient 1 (5A–C), 62-year-old male, left orbital lymphoma; Patient 2 (5D–F), 50-year-old male, left orbital fibroma; Patient 3 (5G–I), 61-year-old female, left orbital hemangioma.

MAGNETOM Prisma with a 20-channel head-neck coil or a 64-channel head-neck coil [18]. The results show the feasibility of TGSE BLADE DWI in pediatric patients and children at 3T. Since there are fewer geometric distortions and signal pile-ups, it could be a viable first-choice alternative for ssEPI DWI in areas around air–tissue interfaces or in the presence of shunts/orthodontia.

Figure 6 shows a representative example from a 5-year-old boy with a right frontal lobe craniotomy for epileptic focus resection. Distortion and pile-ups can be seen in the ssEPI data in the anterior part of the resected area (solid arrows), but are not visible in the TGSE BLADE image. ADC maps highlight postsurgical contusion tissue along the resection margins and within the extra-axial spaces (hollow arrow). The TGSE BLADE ADC map (6D) appears less grainy centrally than the ssEPI ADC map (6C, square highlighted region).

Figure 7 shows an example from a 10-year-old girl with braces. TGSE BLADE images demonstrate reduced susceptibility-related artifacts compared to ssEPI.

Sinonasal lesions

Application of EPI-based DWI has been limited in the sinonasal regions, which contain many bone and air-tissue interfaces.

Geng et al. investigated the feasibility of TGSE BLADE DWI for assessing sinonasal lesions and compared the quality of TGSE BLADE with RESOLVE both qualitatively and quantitatively [19]. The study included 36 patients and was performed on a MAGNETOM Prisma with a 64-channel head-neck coil. The results show that TGSE BLADE can produce better image quality than RESOLVE in sinonasal lesions by reducing susceptibility artifacts and geometric distortion.

**MR scanning has not been established as safe for imaging fetuses and infants less than two years of age. The responsible physician must evaluate the benefits of the MR examination compared to those of other imaging procedures.*

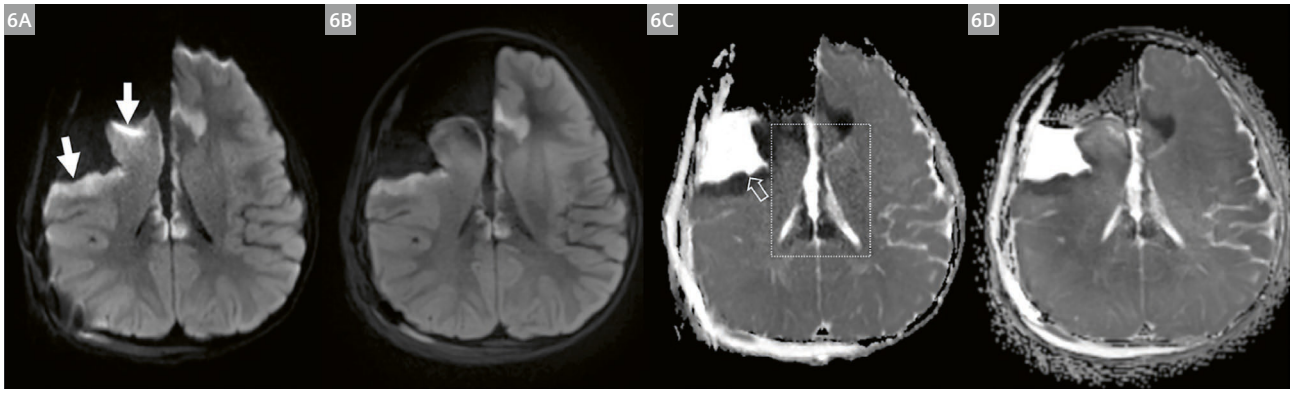

6 Images from a 5-year-old boy with right frontal lobe craniotomy for epileptic focus resection. DWI trace-weighted images and ADC maps are shown for ssEPI **(6A, C)** and TGSE BLADE **(6B, D)**.

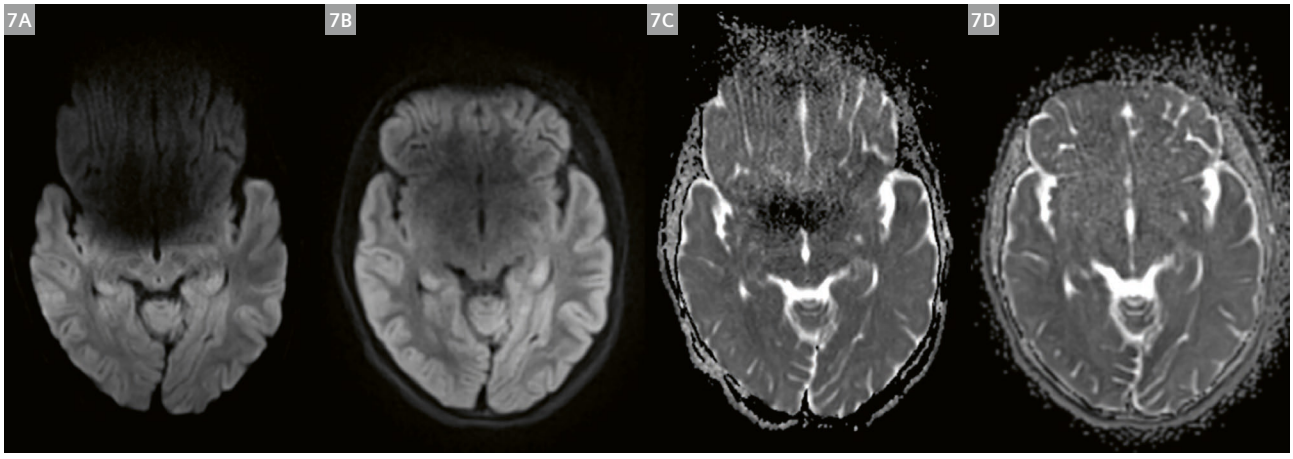

7 Images from a 10-year-old girl with braces. DWI trace-weighted images and ADC maps shown for ssEPI **(7A, C)** and TGSE BLADE **(7B, D)**.

Figure 8 shows an example of a 73-year-old woman with a schwannoma. The RESOLVE images have increased artifacts and distortion at the edge of the lesion (arrow), while TGSE BLADE has fewer artifacts.

Cerebellopontine angle tumors

The cerebellopontine angle (CPA) is the area bound by the pons and anterior aspect of the cerebellum medially, the petrous temporal bone laterally, and the tentorium superiorly. The complex anatomical structures of CPA pose a unique challenge to EPI-based DWI.

Fu et al. compared the clinical utility of TGSE BLADE DWI with RESOLVE DWI and ssEPI DWI for visualizing anatomical structures of CPA and depicting CPA tumors [20]. Eight volunteers and 36 patients with CPA tumors were enrolled. The results show that, compared with RESOLVE and ssEPI, TGSE BLADE minimized geometric distortions and ghosting artifacts and demonstrated an improved ability for depicting CPA tumors with better lesion conspicuity.

Figure 9 shows the images from a 50-year-old female patient with an acoustic neuroma located in the left internal auditory canal (IAC). Compared with the lesion depicted by the T2W image and contrast-enhanced T1W image (long white arrows, 9A, B), the lesion was visualized clearly in the trace-weighted image from TGSE BLADE DWI and ADC map without geometric distortion (long white arrows, 9C, D). Moderate and severe distortion can be observed on RESOLVE and ssEPI images (9E–H), respectively (long red arrows), which impacted demonstration of this small lesion. Moreover, signal pile-ups (short arrows) in the bone-air interfaces in TGSE BLADE were absent (9C), but were present both in RESOLVE (9E) and ssEPI (9G). The visualization of anatomical structures (triangular arrows) in TGSE BLADE (9C) was superior to RESOLVE (9E) and ssEPI (9G).

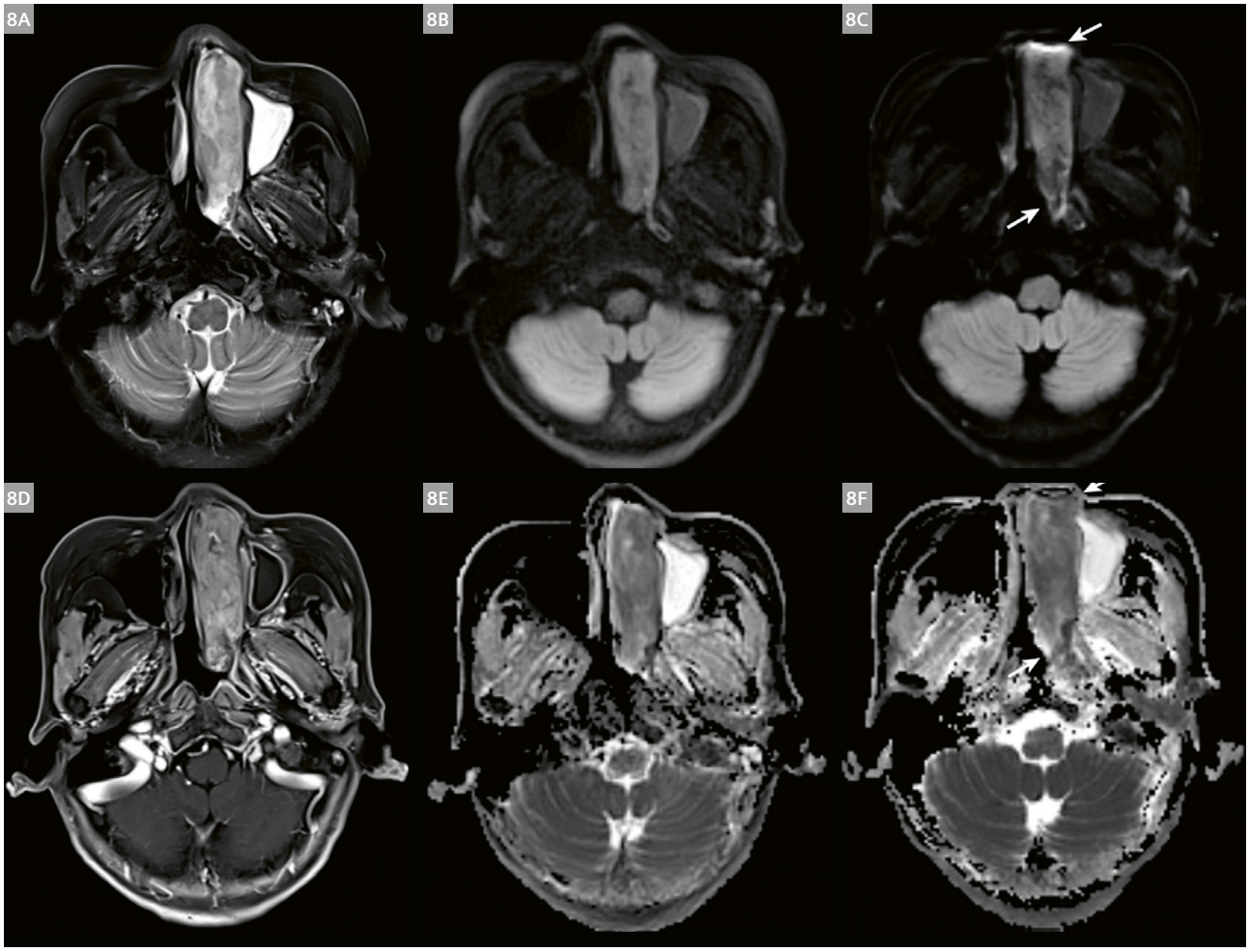

8 A schwannoma in a 73-year-old woman. **(8A)**: Axial T2W imaging, **(8D)**: contrast-enhanced T1W imaging, **(8B, E)**: TGSE BLADE, and **(8C, F)**: RESOLVE showed a mass that mainly involved the left nasal cavity. The image quality of (8B) TGSE BLADE b = 1000 s/mm² and (8E) ADC maps was significantly higher than that of (8C) RESOLVE b = 1000s/mm² and (8F) ADC maps.

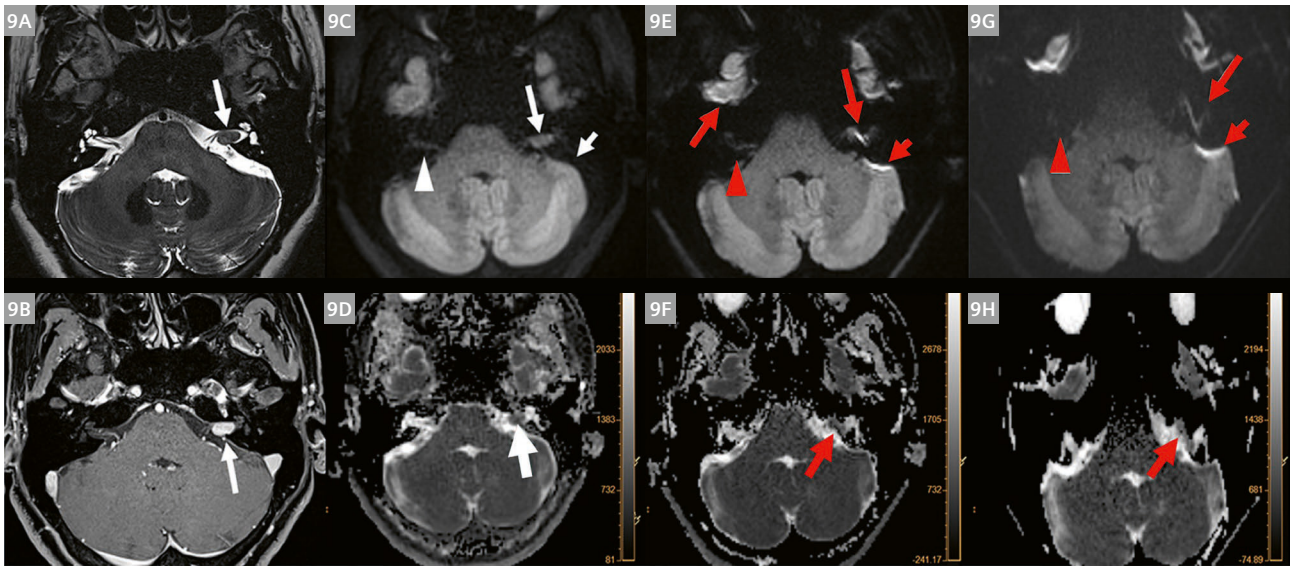

9 A 50-year-old female with an acoustic neuroma located in the left internal auditory canal (IAC). **(9A)** T2W image; **(9B)** contrast-enhanced T1W image; **(9C, E, G)** trace-weighted images of b = 1000 s/mm^2 of TGSE BLADE, RESOLVE and ssEPI; **(9D, F, H)** the corresponding ADC images.

Discussion

EPI-based sequences remain the clinical workhorse and default method for DWI in many applications. However, their image quality could be compromised and the feasibility of diagnosis could be challenged in regions or situations where strong B_0 inhomogeneities are present.

The TGSE BLADE DWI sequence samples a train of spin echoes and gradient echoes, and can generate distortion-free DWI images. Several studies have compared the image quality and diagnostic performance of TGSE BLADE DWI and EPI-based DWI, e.g. for cholesteatoma, orbital tumors, sinonasal lesions, and cerebellopontine angle tumors. The results show that TGSE BLADE DWI yields superior diagnostic quality to EPI-based methods in these challenging applications.

However, TGSE BLADE DWI sequences also have some limitations.

While the SNR efficiency of TGSE BLADE Diffusion is lower than that of EPI-based DWI sequences, because it has to compensate for the non-CPMG-condition, acceleration techniques like SMS and iPAT can reduce the additional scan time needed to achieve similar SNR.

The scan time can also be influenced by changing the EPI factor, but can also impact T2* and off-resonance effects. A factor of 3 to 5 is recommended as a good compromise between speed and undesired effects.

Conclusion

TGSE BLADE DWI is not sensitive to B_0 inhomogeneities while keeping a reasonable scan time. It is therefore a promising alternative to EPI DWI for detecting pathologies in regions with strong B_0 inhomogeneities.

Acknowledgments

We would like to thank all the institutions and individuals who evaluated this sequence and provided valuable feedback.

We are also grateful to all the collaborating scientists for their support and key observations: Benjamin Schmitt, Fu Cai Xia, Zhang Zhong Shuai, Jin Ning, Guo Yi Hao, Tobias Kober, Frederik Testud, Peter Kollasch, Vicky Sherwood, Pedro Itriago Leon, Gerald R. Moran, Yuta Urushibata, and Shani Ben-Amitay.

Thank you to Alto Stemmer, Thorsten Feiweier, Dominik Paul, and George W. Ferguson for the important discussions regarding the early development and productization of this sequence.

And thank you to Heiko Meyer and Weng De He for supporting this project.

References

1 Jezzard P, Balaban RS. Correction for geometric distortion in echo planar images from B_0 field variations. Magn Reson Med. 1995;34(1):65–73.
2 Chen NK, Guidon A, Chang HC, Song AW. A robust multi-shot scan strategy for high-resolution diffusion weighted MRI enabled by multiplexed sensitivity-encoding (MUSE). Neuroimage. 2013 15;72:41–7.
3 Porter DA, Heidemann RM. High resolution diffusion-weighted imaging using readout-segmented echo-planar imaging, parallel imaging and a two-dimensional navigator-based reacquisition. Magn Reson Med. 2009;62(2):468–75.
4 De Foer B, Vercruysse JP, Pilet B, Michiels J, Vertriest R, Pouillon M, et al. Single-shot, turbo spin-echo, diffusion-weighted imaging versus spin-echo-planar, diffusion-weighted imaging in the detection of acquired middle ear cholesteatoma. AJNR Am J Neuroradiol. 2006;27(7):1480–2.
5 Troalen T, Pellerin A, Bertrand D, Michelot Y, Svensson J, Testud F. HASTE diffusion-weighted imaging at 3 Tesla: evaluation of non-EPI diffusion for the detection of cholesteatomas. MAGNETOM Flash. 2021;79(2):83–88.
6 Pipe JG, Farthing VG, Forbes KP. Multishot diffusion-weighted FSE using PROPELLER MRI. Magn Reson Med. 2002;47(1):42–52. Erratum in: Magn Reson Med 2002;47(3):621.
7 Le Roux P. Non-CPMG Fast Spin Echo with full signal. J Magn Reson. 2002;155(2):278–92.
8 Lee CY, Li Z, Pipe JG, Debbins JP. Turboprop+: enhanced Turboprop diffusion-weighted imaging with a new phase correction. Magn Reson Med. 2013;70(2):497–503.
9 Pipe JG, Zwart N. Turboprop: improved PROPELLER imaging. Magn Reson Med. 2006;55(2):380–5.
10 Srinivasan G, Rangwala N, Zhou XJ. Steer-PROP: a GRASE-PROPELLER sequence with interecho steering gradient pulses. Magn Reson Med. 2018;79(5):2533–2541.
11 Li Z, Pipe JG, Lee CY, Debbins JP, Karis JP, Huo D. X-PROP: a fast and robust diffusion-weighted propeller technique. Magn Reson Med. 2011;66(2):341–7.
12 Zhou K, Liu W, Cheng S. Non-CPMG PROPELLER diffusion imaging: comparison of phase insensitive preparation with split acquisition. Proc Int Soc Magn Reson Med. 2018;26:5320.
13 Alsop DC. Phase insensitive preparation of single-shot RARE: application to diffusion imaging in humans. Magn Reson Med. 1997;38(4):527–33.
14 Zhou K, Liu W, Dong F, Cheng S. Slice-GRAPPA calibration using pre-scan data and application to simultaneous multi-slice PROPELLER. Proc Int Soc Magn Reson Med. 2017;25:3842.
15 Setsompop K, Gagoski BA, Polimeni JR, Witzel T, Wedeen VJ, Wald LL. Blipped-controlled aliasing in parallel imaging for simultaneous multislice echo planar imaging with reduced *g*-factor penalty. Magn Reson Med. 2012;67(5):1210–24.
16 Sheng Y, Hong R, Sha Y, Zhang Z, Zhou K, Fu C. Performance of TGSE BLADE DWI compared with RESOLVE DWI in the diagnosis of cholesteatoma. BMC Med Imaging. 2020;20(1):40.
17 Fu Q, Kong XC, Liu DX, Zhou K, Guo YH, Lei ZQ, et al. Turbo Gradient and Spin Echo PROPELLER-Diffusion Weighted Imaging for Orbital Tumors: A Comparative Study With Readout-Segmented Echo-Planar Imaging. Front Neurosci. 2021;15:755327.
18 Hu HH, McAllister AS, Jin N, Lubeley LJ, Selvaraj B, Smith M, et al. Comparison of 2D BLADE Turbo Gradient- and Spin-Echo and 2D Spin-Echo Echo-Planar Diffusion-Weighted Brain MRI at 3 T: Preliminary Experience in Children. Acad Radiol. 2019;26(12):1597–1604.
19 Geng Y, Shi Y, Chen W, Tang Z, Zhang Z, Zhou K, et al. BLADE turbo gradient- and spin-echo in the assessment of sinonasal lesions: a comprehensive comparison of image quality in readout-segmented echo-planar imaging. Acta Radiol. 2021:2841851211041820. Epub ahead of print.
20 Fu Q, Kong XC, Liu DX, Zhou K, Guo YH, Wang MF, et al. Clinical comparison of single-shot EPI, readout-segmented EPI and TGSE-BLADE for diffusion-weighted imaging of cerebellopontine angle tumors on 3 tesla. Magn Reson Imaging. 2021;84:76–83.3.



Contact

Kun Zhou, Ph.D.
Siemens Shenzhen Magnetic Resonance Ltd.
Hi-Tech Industrial Park
518057 Shenzhen
China
kun.zhou@siemens-healthineers.com



Wei Liu, Ph.D.
Siemens Shenzhen Magnetic Resonance Ltd.
Hi-Tech Industrial Park
518057 Shenzhen
China
weiwlliu@siemens-healthineers.com

Update on FLAIR Fusion in Multiple Sclerosis Follow-up and Beyond: An Indispensable Tool in Clinical Routine

Andreas Bartsch, M.D.[1]; Thomas Illigen[2]

[1]Radiologie Bamberg, Germany
[2]Siemens Healthineers, Erlangen, Germany

This is an update on the article "FLAIR Fusion in Multiple Sclerosis Follow-Up: An Indispensable Tool in Clinical Routine" by Stéphane Cantin and Emeline Lamain (Groupe Clinique du Mail, Grenoble, France), and Thomas Troalen and Melisa Bakir (Siemens Healthineers, Saint-Denis, France) that was published in MAGNETOM Flash (69) 3/2017.

Background

Modern radiologists face the challenge of managing a rising number of examinations (which, with more focus on 3D imaging and multiplanar reconstructions, themselves include an increasing number of images) without compromising the quality of their reports. *syngo*.via offers solutions to meet this challenge.

Radiologie Bamberg is a German radiological practice with a focus on neuroradiology and inflammatory CNS diseases like multiple sclerosis (MS), in particular. Its MR scanner primarily used to address the related clinical-radiological challenges is a 64-channel 3T MAGNETOM Skyra, now running on Numaris X with software version *syngo* MR XA30. Established core brain MR recordings for monitoring MS are a sagittal 3D FLAIR at 1 mm isotropic resolution or sagittal and axial 2D FLAIR at 3 mm slice thickness and submillimeter in-plane resolution.

For follow-up studies and comparisons, we generally recommend and use the AutoAlign functionality, since it is very beneficial for recording subsequent studies in good initial alignment, especially if anisotropic 2D recordings are used.

Follow-up of MS patients primarily consists of comparing current and prior examinations. The European Collaborative Research Network Magnetic Resonance Imaging in Multiple Sclerosis (MAGNIMS), has – together with the Consortium of Multiple Sclerosis Centers (CMSC) and the North American Imaging in Multiple Sclerosis Cooperative (NAIMS) – just recently published consensus recommendations on the use of MRI in MS [1], both for establishing the diagnosis and specifically for longitudinal follow-ups and monitoring the effectiveness and safety of treatment. To support detection of new MS- or treatment-related progressive multifocal leukoencephalopathy (PML) lesions, *syngo*.via can be used.

Inspired by the article "FLAIR Fusion in Multiple Sclerosis Follow-Up" by Stéphane Cantin, Thomas Troalen, Emeline Lamain, and Melisa Bakir published in MAGNETOM Flash 69 [2], we introduce further modifications, improvements and simplifications to the workflow and extend it to other applications, such as the detection of T2-progress in gliomas.

Goals

Using the previously described MPR/MPR overlay and the parathyroid-blue Color look-up table (LUT) recommended by Cantin et al. we were able to replicate their identification of new lesions. Yet, our goal and purpose for further development and improved *syngo*.via application was

1. to fully meet and comply with the new 2021 MAGNIMS-CMSC-NAIMS recommendations, which emphasize the clinical utility of co-registration, fusion, and subtraction techniques, especially if T2 lesion load is high and to increase the sensitivity for detecting new T2 lesions [1] (Panel 4, p. 10 and Appendix p. 7);
2. to provide a visualization of the registration quality between successive scans (prior and current) for QA/QC purposes; and
3. to enable the (neuro)radiologist to clearly differentiate between
   a) new or progressive lesions;
   b) unchanged lesions ("no evidence of disease activity" = NEDA according to radiological criteria);
   c) potentially decreasing lesions,

not only in MS, based on the information we can extract from the MR images.

Method

Evaluation of intramodal registration quality, see above, is essential for QA/QC in serial assessments because even at the same scanner and coil, using the same software and sequences, image co-registration/fusion is never perfect. In theory, intra-individual image registration upon follow-up is an affine problem requiring six (three translations and three rotations, "rigid-body co-registration") or seven (+ global scaling) degrees of freedom (DoF). However, gradient nonlinearities and image distortions pose challenges for this model and may lead to suboptimal results after image registration. Naturally, registration accuracy tends to be more limited for anisotropic 2D than isotropic 3D recordings, but 3D pulse sequences are more vulnerable to image intensity variations across the acquired volume. Notably, the quality of image registration between current and prior scans will influence both the sensitivity and specificity for detecting changes in lesion load or volume. Sufficient image registration accuracy is currently one of the main obstacles limiting the technological availability and widespread use of serial subtraction scans for MS follow-up, treatment, and pharmacovigilance safety monitoring as recommended by the 2021 MAGNIMS-CMSC-NAIMS consensus. Another main challenge is, due to the non-quantitative nature of standard scans, to achieve a common image intensity scaling to a best denominator between previous and follow-up scans.

We relinquished the use of color overlays as proposed by Cantin et al. and instead use an inverted grayscale. Numaris X software now provides *syngo*.via functionalities also on the scanner. One benefit is the automated grayscale adaption with no need for individual windowing using the MPR/MPR overlay, especially with the images from the prior examination being displayed at inverted grayscale on top of the current scans. The idea behind this approach was to

a) highlight new lesions,
b) obscure those that did not change in comparison and
c) obtain opposed contrast to a) for areas that decreased in size.

The latter and QA/QC evaluation of the image registration quality is not sufficiently feasible using color volume overlays.

Workflow

To establish our new workflow on *syngo*.via or directly on the scanner in View&GO, you need to simultaneously load the current and prior examinations. This can be achieved automatically with *syngo*.via using the prefetch functionality.

We would recommend a 2 x 3 layout to display the images in axial and sagittal orientations. Depending on your examination strategy and/or monitor settings, other layouts might be more expedient.

As a next step, an MPR/MPR overlay is created as described by Cantin et al.

For the reasons detailed above, we do not use the parathyroid-blue Color LUT. Instead, we recommend using the inverted grayscale overlay, which effectively yields an intensity-normalized subtraction between the current and

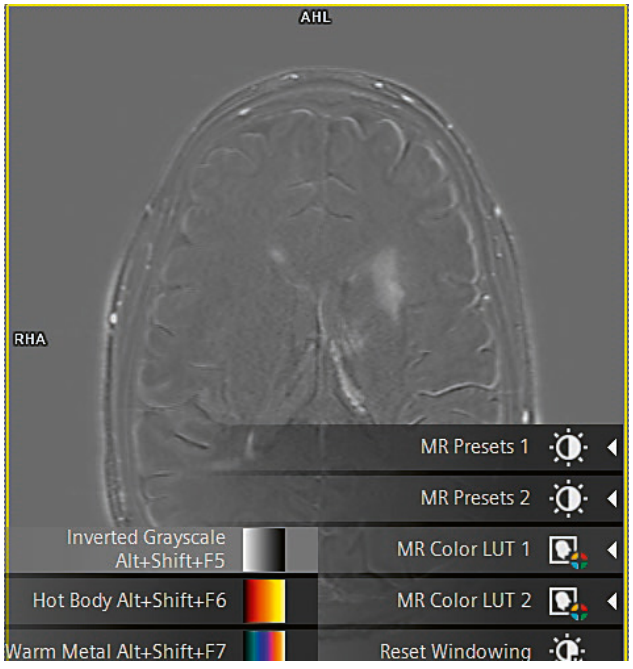

1 Assigning the MR Color LUT 1 Inverted Grayscale.

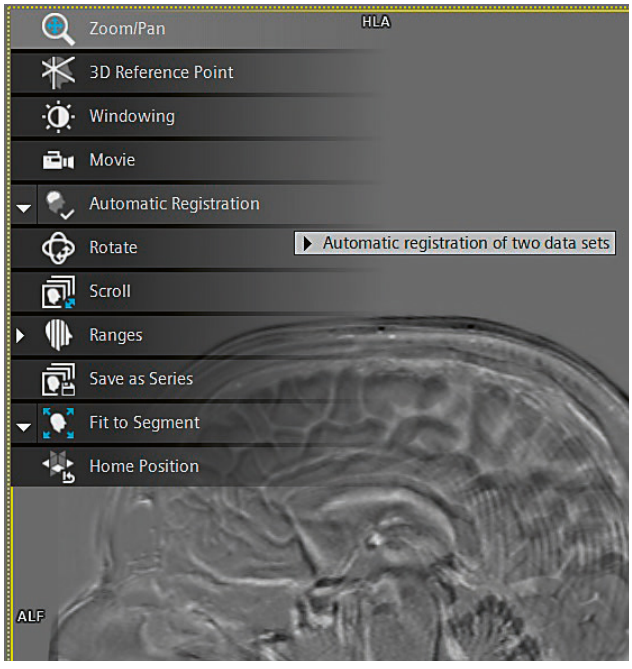

2 Top-left menu with Automatic Registration tool.

prior examination. Please note that Color LUT 1 will be used for the second loaded dataset; usually this will be the prior examination (Fig. 1).

It is essential to co-register the datasets. The Automatic Registration tool can be used for this next step.

The automatic registration is applied for all datasets simultaneously, so axial and sagittal images will be coregistered together just with one click.

Automatic registration will only work if both the current as well as prior exam have either been distortion corrected or not. We recommend 2D distortion correction per default. However, if this was disabled for one of the exams it can be reset in syngo.via for the other to generate a new series to match the two for registration.

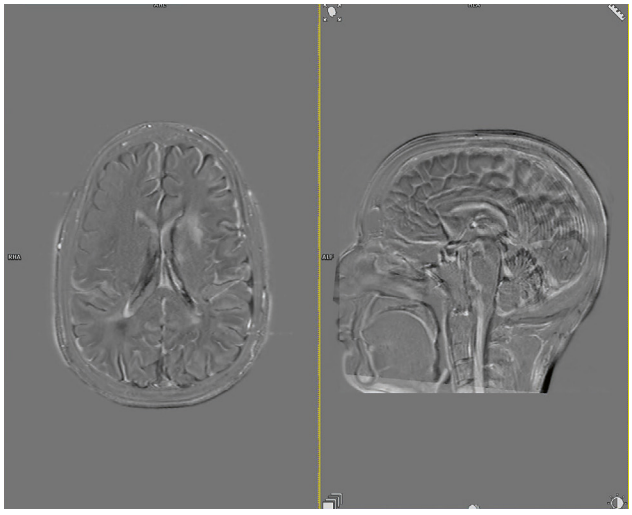

3 Axial and sagittal MPR/MPR inverted grayscale overlays before co-registration.*
** Although the initial overlay is reasonable, due to AutoAligned acquisitions, it should be further improved.*

If the automatic registration should not meet the expectations, there is still the opportunity to perform a visual alignment or manual registration of the two datasets (Fig. 5).

The proposed layout now offers, at rapid and convenient glance, a fast and easy comparison and reliable appraisal of lesions according to our primary goals a) to c) (see above).

The arrows and arrowheads in Figure 6 mark new FLAIR-hyperintense lesions in the current dataset as compared to the previous examination. The MPR/MPR overlay of our workflow properly highlights those lesions as white hyperintense areas at high contrast.

The red arrow in Figure 7 depicts an unchanged lesion in the current as compared with the previous examination. It is "zeroed out" in the MPR/MPR overlay, confirming that there is no radiological evidence of disease activity with regards to this particular lesion.

The following slice from another case in Figure 8 shows the conceivable lesion behavior of new or enlarging, unchanged, and decreasing lesions all in one image.

On the slice from the current data, the red arrow indicates an unchanged lesion which is "zeroed out" in the overlay subtraction (right), while the pink arrow reveals a new, expanding lesion juxtacortical to the insular cortex. The green arrow on the slice of the prior examination shows a lesion that was decreasing in the current compared with prior examination and which is visualized hypointense (black) on the MPR/MPR overlay.

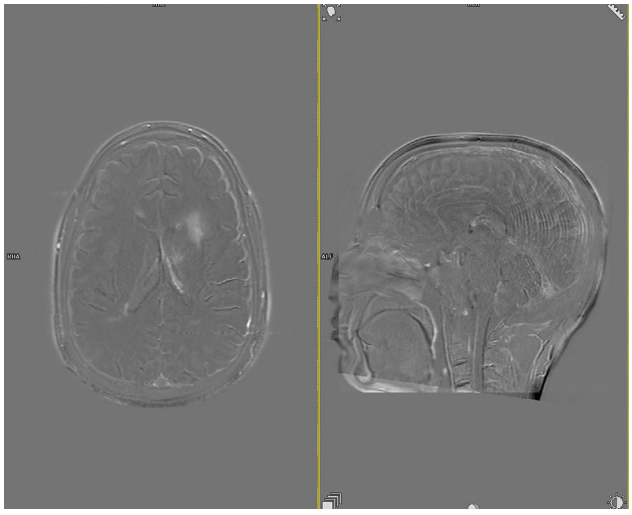

4 Axial and sagittal MPR/MPR inverted grayscale overlays after automatic registration.*
** Better (though not perfect) alignment between the current and prior scans becomes obvious at the outer and inner (ventricular) brain edges.*

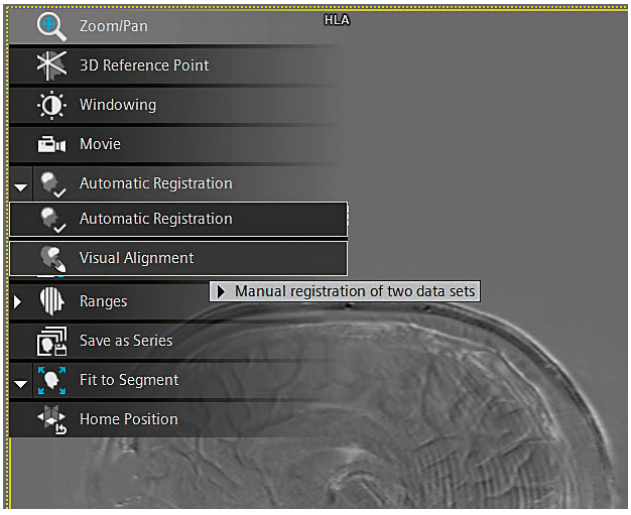

5 Top-left menu with Visual Alignment tool.*
** In our experience, a visual alignment was never necessary; automatic registration is recommended.*

Registration accuracy is best judged on the outer and inner (ventricular) brain edges. Here, misalignments will show up as hyper- and/or hypointense bands, respectively, in subtraction images. Such misalignments also affect the appearance of lesions in the overlay images and can, if not judiciously accounted for, lead to false-positive and false-negative detections. Compared to color overlays, our use of an inverted grayscale in a 2 x 3 layout substantially facilitates the recognition of such registration errors and thereby enhances both sensitivity and specificity.

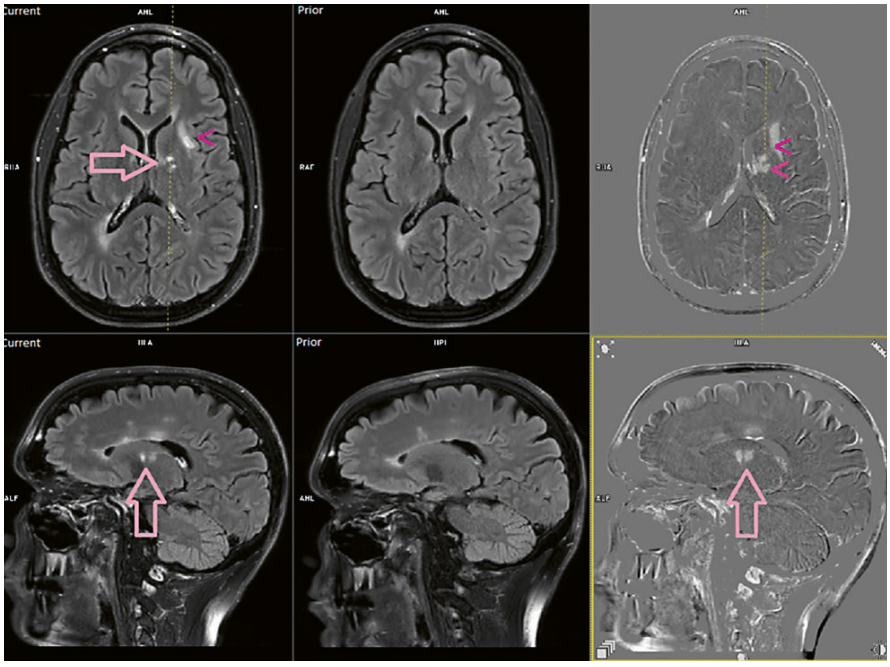

6 Detection of new lesions upon MS follow-up according to our workflow.*
** Note that for the current but not prior examination, gadolinium agent has been applied IV before the FLAIR acquisitions to prolong the delay to improve contrast enhancement as per the latest MAGNIMS 2021 recommendations. Therefore, there is positive contrast in the overlay subtraction images on the right in the choroid plexus.*

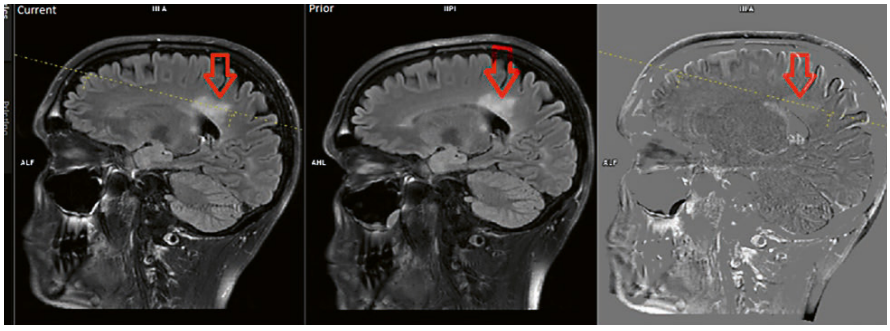

7 Concealing unchanged lesions upon MS follow-up in our workflow.*
** Also note the regression of mucosal swelling in the maxillary sinus in the current as compared to the prior exam, which therefore shows up hypointense in the overlay subtraction image on the right.*

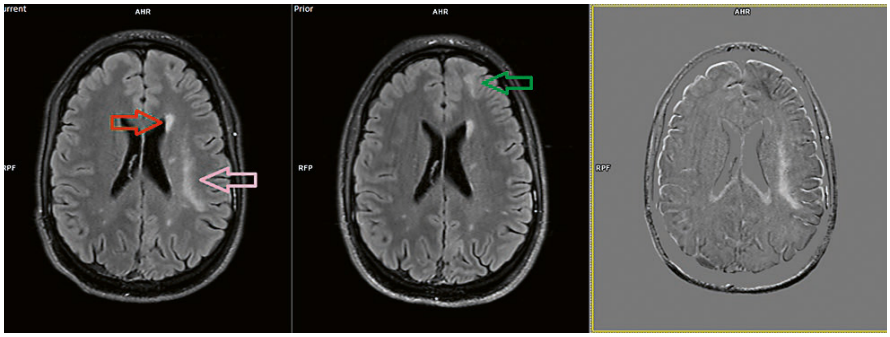

8 New (pink arrow), unchanged (red arrow), and decreasing (green arrow) lesions in a patient positive for the John Cunningham polyomavirus (JCV) with MS who developed an inflammatory PML after his 81st natalizumab infusion. Unchanged lesions are "zeroed out" in the MPR/MPR overlay, while new or enlarging lesions appear hyperintense, and regressive lesions hypointense. This is the desired behavior.*
** Slight misalignments between the current and prior scans appear as hyper/hypointense bands at brain edges and allow to assess the quality of image registration.*

In theory, optimal alignment of prior and follow-up scans would involve an unbiased, robust, inverse consistent co-registration into a mid-space between both images (in order to apply the same amount of interpolation to both) that iteratively deweights areas of high variance (i.e., differences/changes) between the two time points [3–5]. However, in our experience automatic registration of current and prior exams using MPR/MPR with inverted grayscale overlay works quite well if the same scanner and sequence were used for follow-up.

For 3D sequences recorded at 3T, particular care is required to avoid variable image intensity biases in the serial scans. If image alignment is sufficiently accurate according to visual QA/QC judgement, new lesions well below the 3 mm scale (reference size according to QBK-RL 2020 [6]) can be detected, in our experience even at the 1 mm scale.

Conclusion

In summary, our new proposed workflow enables the user to rapidly perform image co-registration, fusion, and intensity-normalized inverted grayscale overlay of serial scans that allows for good quality control and visualizes differences in lesion load/volume (i.e., numerical and in lesion extent) at opposite contrast while "zeroing out" unchanged

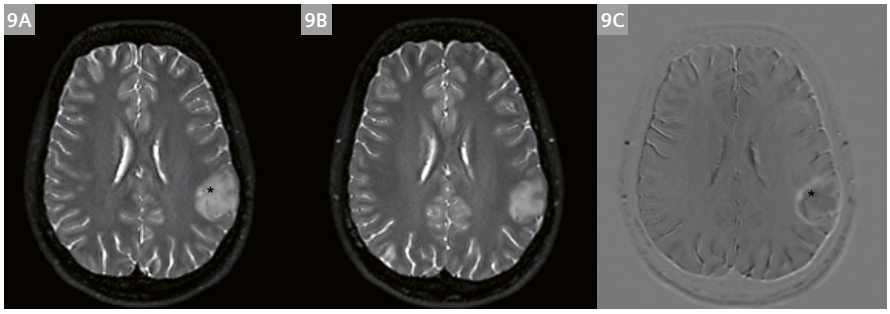

9 Detection of long-term T2 progression in a left supramarginal oligodendroglioma using co-registered 1 mm isotropic fat-saturated 3D T2 SPACE scan subtraction.
(9A) Current exam (March 2021).
(9B) Prior exam, not yet registered to (9A) but displaying approximately the same location at the tumor level, dating back 44 months (June 2017; and prior to stereotactic biopsy).
(9C) T2 scan subtraction using co-registered and inverted grayscale overlay of (9B) on (9A).

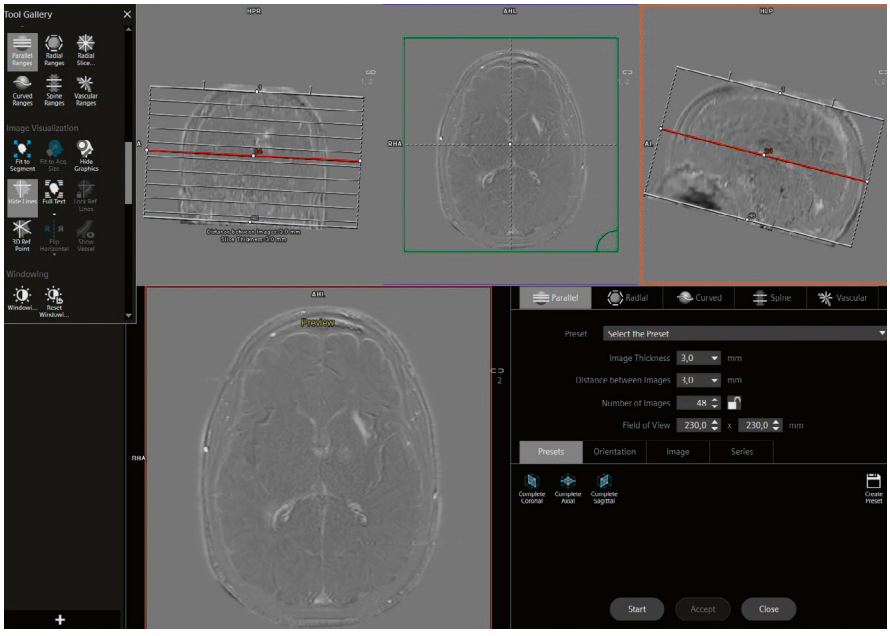

10 Axial reconstruction using the Parallel Ranges tool.

lesions as in subtraction images. This meets the recently published MAGNIMS-CMSC-NAIMS 2021 consensus recommendations on the clinical utility of co-registration, fusion, and subtraction techniques for monitoring disease activity, treatment response, and treatment safety in MS, especially if T2 lesion load is high, and to increase the sensitivity for detecting new T2 lesions [1].

According to in-house experience during the past year, our workflow may lead to several MS lesion detections which would have otherwise, due to high lesion load of the patient or, similarly, high work load of the reporting radiologist, been missed.

Furthermore, the technique can equally be applied to monitor T2 progress and treatment responses in intra-axial brain tumors, such as gliomas. In Figure 9 long-term, crescent-shaped T2 progression of the primary brain tumor became apparent comparing (Fig. 9A) and (Fig. 9B) and is accurately visualized in (Fig. 9C). Previously, it was missed on the short-term comparison of successive scans. The tiny dot (*) of a hypointense signal loss in the medial aspect of the tumor is due to a microbleed from the biopsy and also detectable on (Fig. 9C). The main tumor bed comes out slightly hypointense (i.e., with negative overlay values) due to discrete changes of the signal characteristics of the oligodendroglioma.

Additionally, any on a suitable given sequence/contrast hyper- (or even hypo-) intense lesion can be longitudinally monitored by our method (e.g., epidermoid cysts on diffusion or arachnoid cysts on T2/FLAIR) and, at least in theory, even the development of brain atrophy (which will present as “misregistration bands”; see OA/QC of registration accuracy in the Workflow section above). Global (and local) atrophy development is generally considered to reflect a neurodegenerative component of MS [7] but its assessment is not part of the current MAGNIMS 2021 recommendations [1].

For documentation and storage, the created MPR/MPR overlays can easily be reconstructed and saved in a separate series using the Parallel Ranges functionality (Fig. 10). To avoid interpolation artifacts, we recommend to reconstruct the subtraction overlays at no less than 2 mm slice thickness (we routinely use 3 mm). These subtraction series (“delta maps” or “change maps”) are then exported to the institution’s PACS.

The overlay subtractions generated by our workflow are – aside from pure radiological disease, treatment, and safety monitoring itself – well suited to present the detected changes to the patient in an intuitive manner that is easy to understand in order to argue for treatment options, to obtain informed consent, and to potentially improve compliance with the suggested management during further personalized care.

Acknowledgment

We are very grateful for the long-standing collaboration, support, and regular suggestions and requests for improvements provided by Dr. Boris-Alexander Kallmann, M.D., from the Multiple Sclerosis Center Bamberg (MSZB).

References

1 Wattjes MP, Ciccarelli O, Reich DS, Banwell B, de Stefano N, Enzinger C, et al. 2021 MAGNIMS-CMSC-NAIMS consensus recommendations on the use of MRI in patients with multiple sclerosis. Lancet Neurol. 2021;20(8):653–670.
2 Cantin S, Troalen T, Lamain E, Bakir M. FLAIR Fusion In Multiple Sclerosis Follow-Up. MAGNETOM Flash. 2017;69(3):100–103. Available from https://www.magnetomworld.siemens-healthineers.com/clinical-corner/application-tips/flair-fusion-in-multiple-sclerosis-follow-up.html
3 Reuter M, Rosas HD, Fischl B. Highly accurate inverse consistent registration: a robust approach. Neuroimage. 2010;53(4):1181–1196.
4 Reuter M, Schmansky NJ, Rosas HD, Fischl B. Within-subject template estimation for unbiased longitudinal image analysis. Neuroimage. 2012;61(4):1402–1418.
5 Reuter M, Gerstner ER, Rapalino O, Batchelor TT, Rosen B, Fischl B. Impact of MRI head placement on glioma response assessment. J Neurooncol. 2014;118(1):123–129.
6 Richtlinie des Gemeinsamen Bundesausschusses über Kriterien zur Qualitätsbeurteilung in der Kernspintomographie nach § 135b Absatz 2 SGB V [Internet]. Berlin, Germany: Gemeinsamer Bundesausschuss [cited February 10, 2022]. Available from: https://www.g-ba.de/downloads/62-492-2036/QBK-RL_2019-10-17_iK_2020-01-01.pdf
7 De Stefano N, Stromillo ML, Giorgio A, Bartolozzi ML, Battaglini M, Baldini M, et al. Establishing pathological cut-offs of brain atrophy rates in multiple sclerosis. J Neurol Neurosurg Psychiatry.2015;0:1–7.



Contact

PD Dr. med Andreas Bartsch, M.D.
Radiologie Bamberg
Heinrichsdamm 6
96047 Bamberg
Germany
bartsch@radvisory.net



Thomas Illigen
SHS EMEA CWE DI MR
Karlheinz-Kaske-Str. 2
91052 Erlangen
Germany
thomas.illigen@siemens-healthineers.com

Translation of Computer-Assisted MRI Assessments of Multiple Sclerosis to Clinical Care

Hagen H Kitzler[1]; Paul Kuntke[1]; Caroline Köhler[1]; Jennifer Linn[1]; Maria-Laura Blefari[2]; Sara Makaretz[2]; Adrian Tsang[2]; Till Hülnhagen[3]; Jonathan A Disselhorst[3]; Rodrigo Perea[2]; Ricardo A. Corredor-Jerez[3]; Punith B Venkategowda[4]; Sowmya Devdas[4]; Tjalf Ziemssen[5]; Elizabeth Fisher[2]; Tobias Kober[3]; on behalf of the MS PATHS* Investigators

*Multiple Sclerosis Partners Advancing Technology and Health Solutions

[1]Institute of Diagnostic and Interventional Neuroradiology, University Hospital Carl Gustav Carus, Technische Universität Dresden, Germany
[2]Biogen Digital Health, Biogen, Cambridge, MA, USA
[3]Advanced Clinical Imaging Technology, Siemens Healthineers, Lausanne, Switzerland
[4]Siemens Healthcare Pvt. Ltd., Bangalore, India
[5]Multiple Sclerosis Center, Center of Clinical Neuroscience, Department of Neurology, University Hospital Carl Gustav Carus, Technische Universität Dresden, Germany

MSPie served as a prototype platform to optimize and validate the performance of parts of the AI-Rad Companion Brain MR product solution.

Key points

- Standardized volumetric MRI follow-up protocols
- Fully automatic MRI data routing
- Immediate volumetric MRI analysis
- Computer-assisted monitoring
- Approval/rejection of results and report generation

Background

The Multiple Sclerosis Partners Advancing Technology and Health Solutions (MS PATHS; https://www.mspaths.com) is a Biogen-sponsored network that aims to standardize and quantify clinical, radiological, and biomarker assessments of MS in routine clinical practice, with the ultimate goals of enabling personalized medicine and large-scale real-world research. For the imaging assessments, the intention is to provide highly precise, automated quantification of disease-specific volumetric changes of both MS lesions and normalized brain volume. Mainly sub-clinical in nature, these MRI changes over time can provide important information on disease severity and response to disease modifying therapies [1].

In 2009, the concept of an MS treatment target termed, "no evidence of disease activity" (NEDA) arose from a retrospective analysis of clinical trial data [2], with the original definition consisting of no relapses, no disability progression, and no MRI-based disease activity markers, i.e., no gadolinium enhancing lesions or new or enlarging T2 lesions. Subsequently, further

Parameter	3D FLAIR MS-P	3D T1 MS-P
Brain coverage	Full	Full
Acquired pre-contrast	Pre-contrast	Pre-contrast
Orientation	Sagittal	Sagittal
MR acquisition type	3D	3D
Repetition time (ms)	5000	2300
Echo time (ms)	392–394	2.96–2.98
Inversion time (ms)	1800	900
Flip angle (deg)	120	9
Read FOV (mm)	256	256
Phase FOV (mm)	240	240
Percent FOV (%)	93.8	93.8
No. phase encoding steps	221	239
Phase encoding direction	A >> P	A >> P
Slice thickness (mm)	1	1
Pixel spacing (mm)	1 × 1	1 × 1
Pixel bandwidth (Hz/Px)	780	240

Table 1: The standardized MS PATHS acquisition protocol. This MRI protocol was implemented on available 3T scanners from Siemens Healthineers within all participating MS PATHS centers allowing optimal regional monitoring and inter-institutional comparison.

development of the NEDA definition led to the incorporation of the annualized rate of brain volume loss [3]. Based on recent imaging protocol and monitoring recommendations [4, 5], standardized imaging data acquisition forms the basis towards individual precision medicine monitoring in MS when supplemented by computer-aided evaluation technology.

The concept of new or enlarging T2 lesions (NET2L) as a marker of MS inflammatory activity is based on the understanding that the vast majority of gadolinium-enhancing lesions evolve into permanent T2 lesions. In addition, the growth of chronic inflammatory active lesions is yet another recognized marker of disease activity. The occurrence of NET2L in MS under treatment is considered evidence of therapy insufficiency or even failure [3].

The gradual loss of brain volume over lifetime represents a physiological process termed atrophy. Brain atrophy however intensifies and accelerates in MS, constituting the accumulative result of tissue destruction [6]. Therefore, (1) the cross-sectional comparison of individual brain volume measures with age-matched control groups and (2) the determination of the brain atrophy rate over defined intervals are measurable determinants of non-physiological brain atrophy. To normalize overall brain volume measures, brain tissue volume is typically normalized using the individually stable intracranial volume. The resulting ratio is called brain parenchymal fraction (BPF) and thus allows inter-individual comparison [7]. Although disease-modifying therapies attenuate brain volume loss in MS [8], the use of brain atrophy as a clinical marker of disease progression in individual patients is still subject of debate [9].

To realize the goals of reliable, quantitative MRI metrics in the MS PATHS network, Biogen initiated a collaboration with Siemens Healthineers to jointly develop the MS PATHS image evaluation (MSPie) software.[1] This *syngo*.via Frontier-based prototype enabled optimization and validation of the employed algorithms within the clinical workflow in a close collaboration between the University Hospital Dresden, other MS PATHS partners, Biogen and Siemens Healthineers. To this end, the prototype has an interactive user interface and means to correct the results. The final product which will be available within the AI-Rad Companion Brain MR suite incorporates the learnings which were gained from MSPie and is a fully automatic, non-interactive solution. Here, we present the results of our initial experience with translating this development to the point of care.

[1] *Work in progress. The application is currently under development and is not for sale in the U.S. and in other countries. Its future availability cannot be ensured.*



1 The graphical user interface provides a full screen presentation of segmentation and comparison results combined with a collection of numerical and graphical evaluations and a separate articulated control area for interactive lesion editing. Reformats can be adapted to coronal or sagittal viewing habits.

Methods

Standardized follow-up brain MRI acquisition

The use of MRI to measure MS disease activity and progression required minimal adjustments in primary data acquisition to ensure high sensitivity to changes over time [10]. The MS PATHS network therefore agreed to harmonize their institutional scanner protocols across all 3T MRI scanners from Siemens Healthineers at participating centers.

Core sequences are a 3D fluid-suppressed T2 contrast (FLAIR SPACE; "3D FLAIR MS-P") and a 3D T1 contrast (MPRAGE; "3D T1 MS-P") for detection of changes in T2 lesion burden and brain volume (for protocol details, see Table 1).

These two contrasts are taken as input for generating the imaging biomarkers (most importantly NET2L and BPF change) needed for the assessment. The lesion segmentation is a novel, fully automated prototype software, which showed good robustness and detection performance both cross-sectionally and longitudinally since it also takes partial volume effect into account [11–13].

During the development of MSPie, the BPF calculation was highly optimized in order to be able to robustly measure smallest volume changes, as the average rate of brain atrophy in MS is only about 0.5%/year.

The *syngo*.via Frontier setup is configured to allow an automated routing of the sequences described in Table 1 to *syngo*.via which then retrieves the prior MRI (if available) from the PACS and sends it to MSPie. The images are immediately analyzed and results are available approximately 10 minutes after the acquisition without any user interaction. They can then be viewed and evaluated in a graphical user interface (GUI) which was specifically designed for the application in the MS PATHS centers. The experiences gathered during its design and optimization in the clinical testing workflow were incorporated into the reports which are output by the product solution.

The MSPie GUI consists of two panels and a separate control area (Fig. 1). The main page provides the processed prior and current standardized "3D FLAIR MS-P" and "3D T1 MS-P" images overlaid with T2 lesions (blue) and whole brain parenchyma segmentations (green), respectively. A grey scale difference map presents highlighted changes over time accompanied by a color-coded map, where new or enlarging T2 lesions are marked differently (red) from stable lesions (blue). NET2L volume, total T2 lesion volume, T2 lesion volume fraction per total brain volume as well as the sub-volumes of juxtacortical, periventricular, infratentorial, and remaining other lesion types are provided together with their percentage change since the prior MRI.



2 The automatically generated report contains all the quantitative metrics displayed in the user interface. Subdivided into T2 lesion metrics and morphometry, i.e., volume measurements, the aim was to create an overview to inform referring neurologists of processing and evaluation results. Supplementary information documents technical constraints and quality impairments.

Brain volume is provided as BPF, alongside with the segmented grey matter (GM) and white matter (WM) fractions and their percent change. Additionally, volume fractions of cortical and deep GM and of the thalamus are generated.

The separated control area allows the evaluating neuroradiologist to edit the detected NET2L separately, i.e., NET2L can be removed from the results or added in case they were missed. In the latter case, a single click on the missed lesion is sufficient to activate a local segmentation, thus no manual segmentation needs to be conducted. In addition, both qualitative dials describing total lesion volume and BPF severity are provided based on a comparison with MS patients collected within the MS PATHS network.

All results are included in the report (see Fig. 2) to inform on the quantitative analysis. The report is created only after completion of the interactive review and, if the results are accepted by the neuroradiologist, it is sent to the PACS to accompany MSPie annotated lesion and brain masks.

Results

MSPie deployment into the MS radiology workflow

At our institution, we established an exploratory workflow to evaluate the integration of such a solution in our routine work while it was made sure that the standard radiological reading was not affected. The integration required minor adaptation of the institutional radiology workflow for follow-up MRI evaluation. For comparison with the MSPie results, the 3D FLAIR and T1 sequences were simultaneously reviewed in at least two perpendicular reformats in conventional setup. Furthermore, registered T2 and proton density acquisitions of the institutional protocol allowed infratentorial constraints of the 3D FLAIR-based lesion segmentation to be overcome. Reading using the MSPie prototype was arranged to follow conventional visual evaluation to avoid over-reliance on technical processing.

Since the MSPie evaluation was an additional procedure step of the application it initially prolonged the workflow. Whereas getting used to the MSPie handling compensated and subsequently even increased evaluation speed, some delay persisted in conjunction with institutional information technology performance restrictions. With growing confidence in the algorithm performance, we anticipate that evaluations can considerably accelerate today's routine reading.

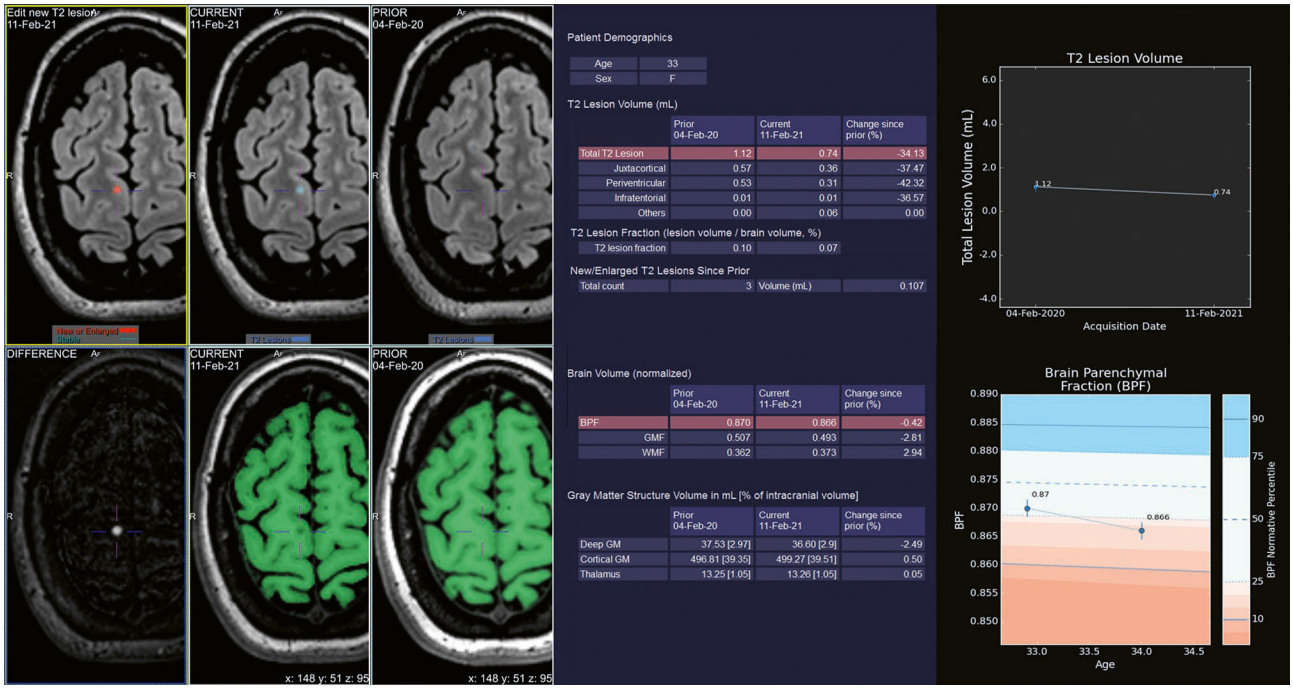

3 Within the standardized annual follow-up examination of this example MS patient a new juxtacortical T2 lesion appeared in the right frontal location (crosshairs), visible in the difference map and classified as NET2L (red) in the upper left segment used for lesion editing. In this segment, lesions can be deleted or added if necessary (see Fig. 4).

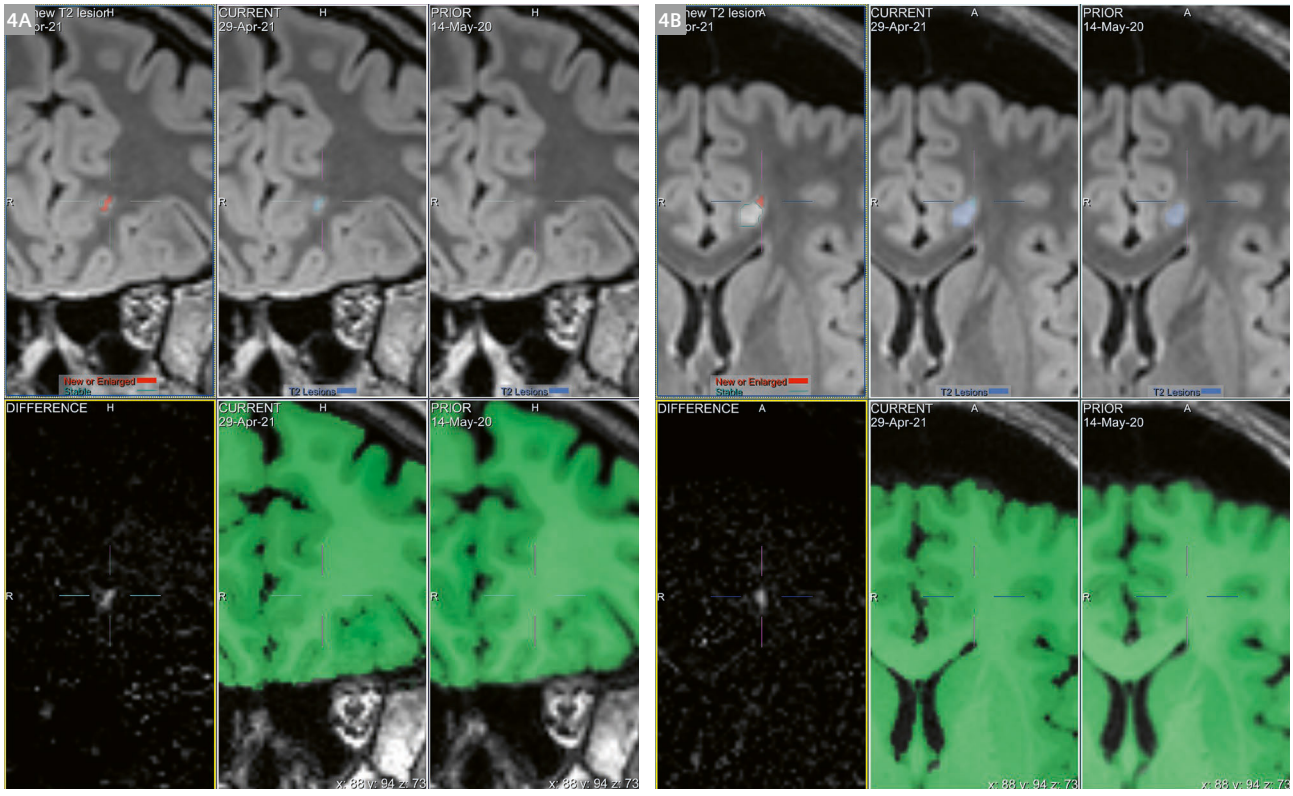

4 Two example patients with lesion growth of different geometry in standardized follow-up examination. The volume increase can be quaquaversal, i.e., resulting in a volume inflation in all directions **(4A)**, but more often regional outgrowth can be detected **(4B)**, resulting in an annex exceeding the prior lesion boundary.

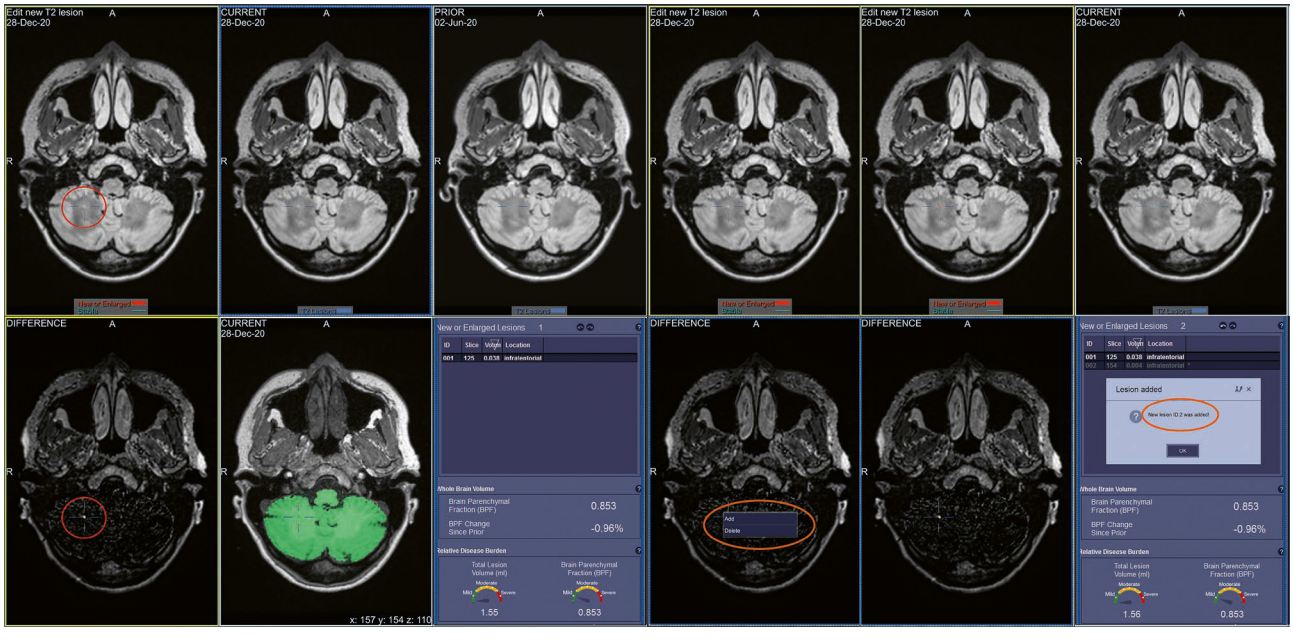

5 The MSPie prototype allows corrections to the automatically detected new or enlarging lesions. The difference map visualizes highlighted changes that occurred between the two time points (red circle; left half of the panel). Missed NET2L can be selected by an interactive window (orange ellipse) to add it to the NET2L segmentation.

Automated detection of new or enlarging T2 lesions

The detection of NET2L represents the essential task of the MRI evaluation in MS neuroradiology. Optimal MRI acquisition quality is thereby crucial to enable high precision of visual inspection. However, in MS patients with high lesion load, or with very small lesion size, juxtacortical lesions, or new lesions located adjacent to pre-existing lesions, visual detection can be challenging. Computer-assisted detection ensures high precision of the evaluating neuroradiologist even in difficult cases.

The software immediately provides all detected lesion differences with a clear visualization of stable lesions and NET2L volumes using well-distinguishable color-coding. Upon completion of conventional visual evaluation, it allowed checking for completeness, i.e., the review of perceived NET2L and other changes. This double-pass approach likely increases diagnostic certainty.

Besides newly forming lesions, lesion growth is also common in MS. Detection of enlarging lesions represents the more difficult task for the evaluating neuroradiologist since growth can be subtle, of complex geometry or ill-defined margins, and the surrounding diffusely abnormal WM might obscure the lesion formation and size change. However, lesion growth provides an important marker of subclinical inflammatory activity. The detection rate of enlarging lesions using conventional visual evaluation is therefore relatively low in comparison to new T2 lesions.

As with any image analysis software, automated lesion segmentation and change detection are subject to error. The interactive review of MSPie results was therefore deemed a significant feature when the prototype was in its planning stages. Thus, within MSPie, lesions missed (false negatives) and falsely detected NET2L (false positives) can be added or deleted using single mouse clicks in the GUI prior to being stored in the PACS or patient medical record (see Fig. 5). The generated corrections were consecutively used to optimise the final, non-interactive product solution.

Upon finalization of the editing process and completed PACS archiving, all results are summarized in an embedded report (see Fig. 2).

Brain volume assessment

In later adulthood, continuous decrease of brain volume is observed in normal aging. In MS, brain volume loss, or brain atrophy, begins at disease onset and progresses at an accelerated rate compared to healthy controls throughout the disease course. Within MS PATHS, normative values for the BPF were established, which allow volumetric changes exceeding normal brain aging to be detected.

In the prototype software, the BPF is automatically calculated and plotted against an age-matched healthy control subgroup which indicates age-specific percentiles. This already allowed visual perception and immediate age-appropriate and age-inappropriate classification for a single time point (see Fig. 6).

Further details of brain parenchyma volumes are provided, i.e., the normalized GM and WM volume fraction, as well as the compartmental volumes of cortical, deep and thalamic GM, including their shares in overall brain tissue volume.

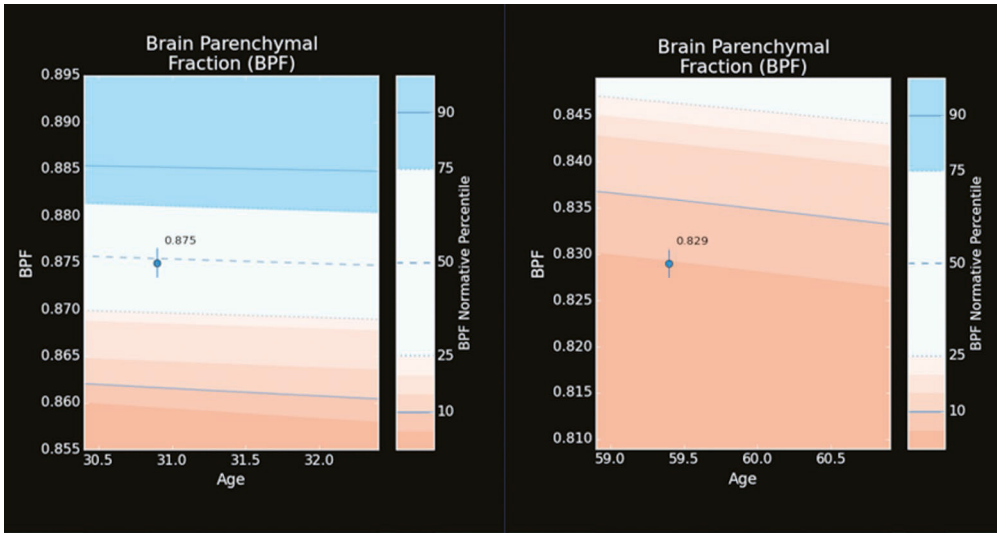

6 Cross-sectional evaluation to classify age-appropriateness of brain tissue volume for a given examination age using BPF percentiles. For quick reference the color-coded percentile score is displayed beside each plot for contextualization. Whereas the left case showed an age-appropriate BPF of 0.875 at the age of approx. 31 years, the right case clearly demonstrated an age-inappropriate BPF of 0.829 at the age of 59 years.

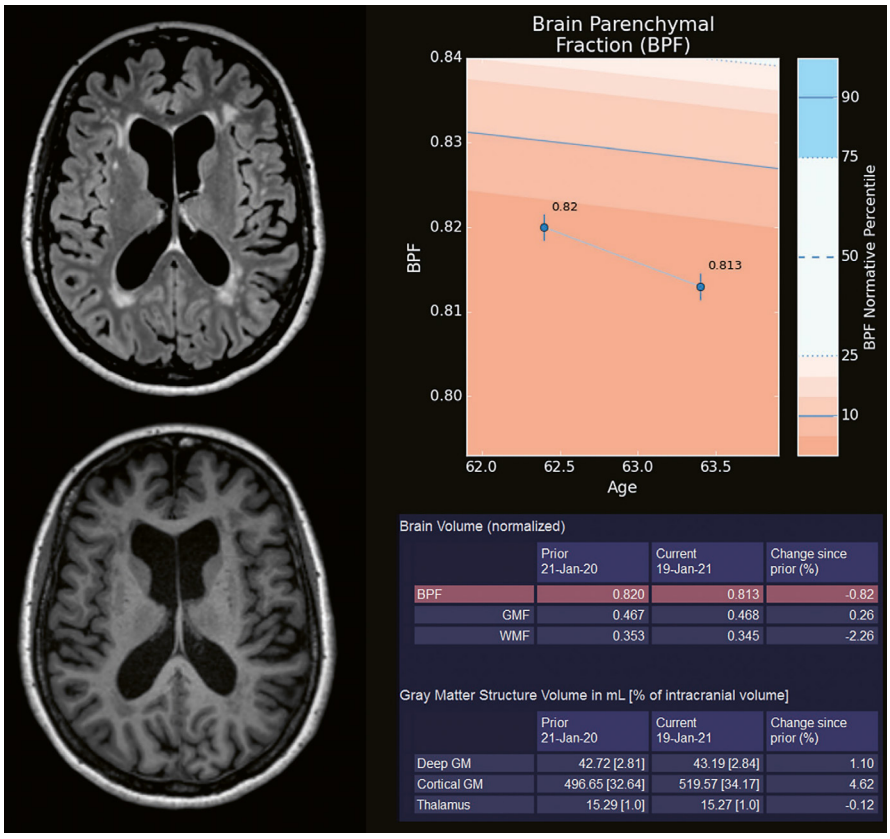

7 The natural course of MS is characterized by an accelerated loss of brain parenchyma resulting in age-inappropriate brain volume denominated as atrophy. The transition from age-appropriate to age-inappropriate normalized brain parenchyma volumes (BPF) is depicted in Figure 2. In the example on the left, BPF was already age-inappropriate at the prior MRI and further decreased by 0.82% in the annual follow-up, illustrating an explicitly increased acceleration of brain volume loss over time. The example FLAIR and T1 reformats below corpus callosum level visually demonstrated a predominant WM loss numerically confirmed by a relative 2.26% decrease.

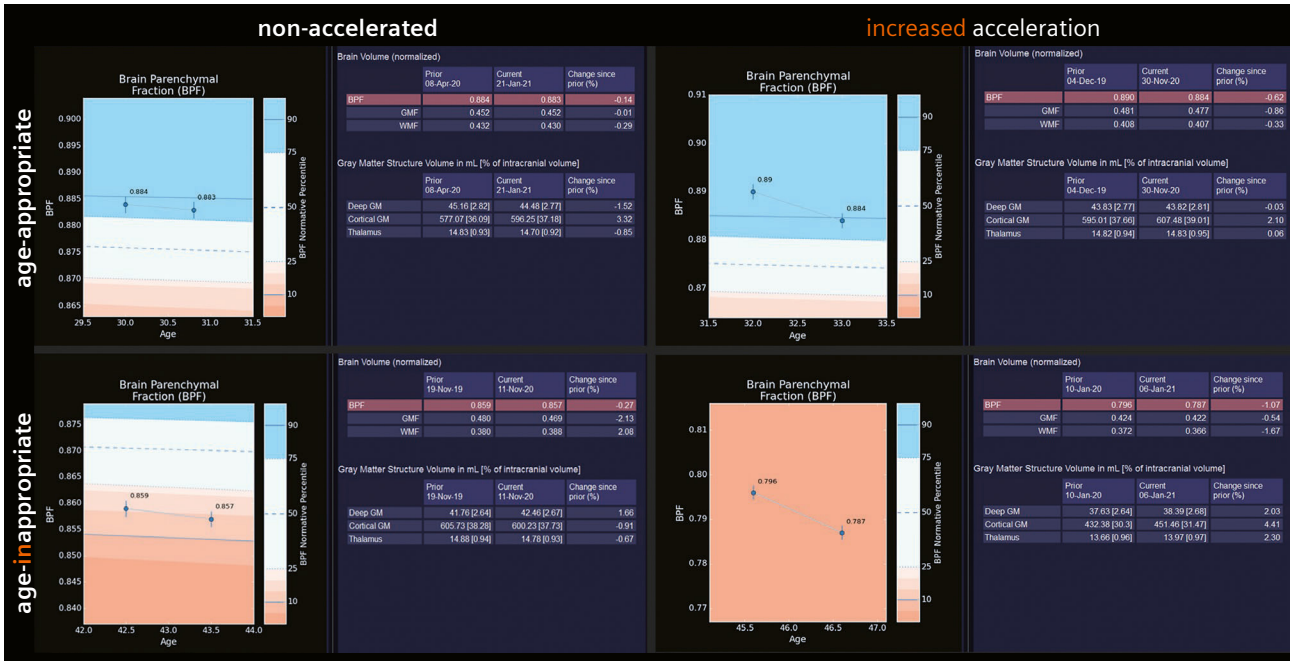

8 A classification in categories attempt of MS brain volume conditions and slopes of parenchymal volume loss.

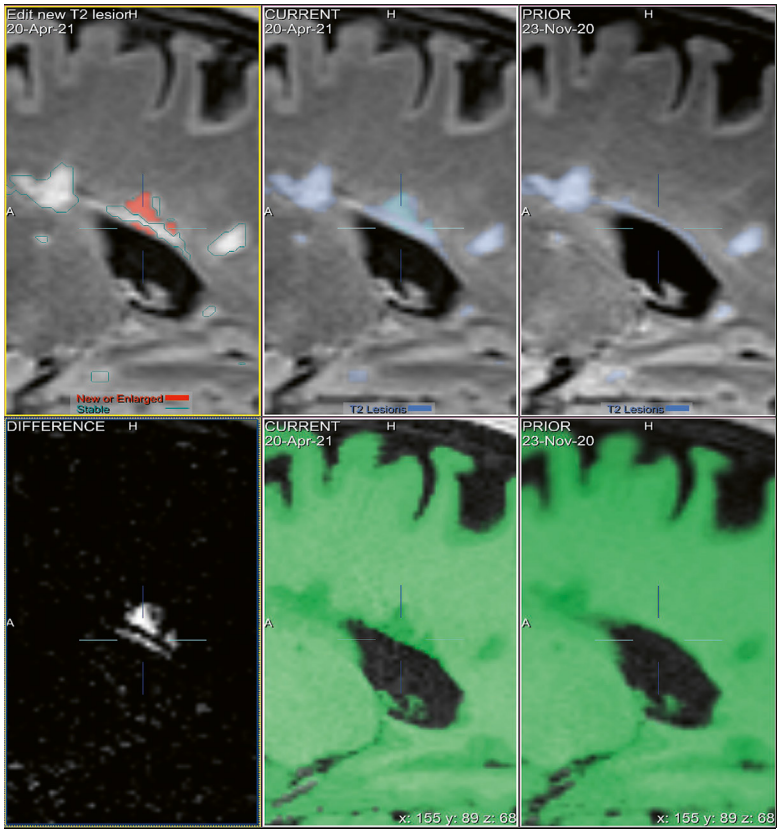

9 Multifocal growths of a stable periventricular lesion resembling three different NET2Ls selected by the prototype but effectively being separate growth zones of the same lesion.

Assessment of annual normalized brain volume change

To determine brain atrophy at the point of care in individual MS patients, the combined assessment of current state and rate of change is necessary. Based on the approach seen in Figure 8, four different descriptive classifications can be distinguished:

1. Age-appropriate and non-accelerated,
2. Age-inappropriate and non-accelerated,
3. Age-appropriate and increased acceleration, and
4. Age-inappropriate and increased acceleration, of BPF and BPF annual change, respectively.

It should be noted that the normative data for the BPF change over time are generated from single-time point assessments; it is thus assumed that the resulting rate of change describes healthy brain aging accurately on a group level.

Perils and pitfalls

The evaluation of the well-defined new T2 lesion segmentation results did not represent a problem. A couple of conditions, however, require careful interpretation of computer assisted tools for MS.

First, new MSPie users had to become acquainted with assessing lesion growth, especially in confluent lesions. If lesion/conglomerate growth was multifocal, as is shown in an illustrative case in Figure 9, NET2L segmentation resulted in multiple separated growth areas, i.e., erroneously classified growing lesions. Hence, the NET2L number was artificially increased. More sophisticated editing is currently being discussed to mitigate this issue in future software versions.

The change of a stable lesion location between two consecutive scans due to temporary displacement led to anomalous segmentation. Since only growth but not shrinkage was detected, this resulted into erroneously classified lesion growth (Fig. 10).

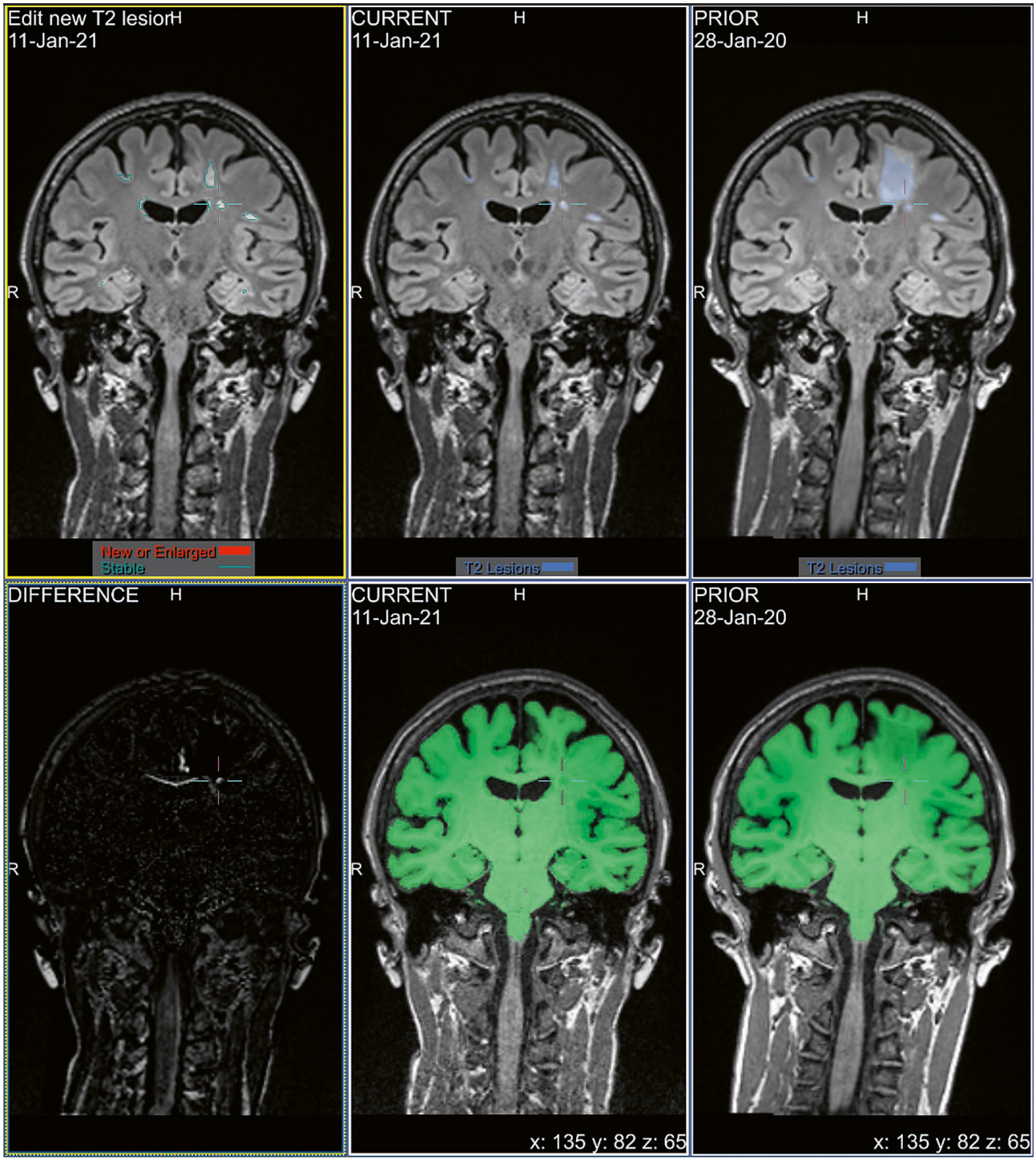

10 Due to a left frontal hyperacute lesion with perifocal edema and swelling, an adjacent lesion (crosshairs) was displaced in the prior scan. When edema and space occupation are resolved in the current scan this lesion held a slightly different position (note the shift within the cross hairs). As a result, a difference due to the lesion position change was detected during follow-up of this, in fact, unchanged lesion.



11 A case of long-standing Baló's sclerosis with clinical progression. No new or growing lesions were found, but there was an annualized 1.87% BPF change. Since the absolute T2 lesion volume decreases, such extreme atrophy may result in concomitant total apparent lesion volume reduction.

The quantification of the T2 lesion burden and brain tissue loss may also not be independent from each other, since in severe atrophy, an apparent overall T2 lesion volume reduction may emerge, as observed in Figure 11. However, this issue might be expected in severe and predominant WM atrophy only, but may be overcome by correction.

Finally, co-morbid diseases in MS patients may complicate both conventional and computer-assisted image evaluation. The cause of possible confusion is the limited specificity of the T2 signal and lesions. Stroke residues, brain tumors, and post-traumatic gliosis (see example in Fig. 12) may resemble lesions detected by the prototype. To prevent erroneous inclusion, the respective patients need to be evaluated with caution to exclude all non-MS pathology in computer-assisted segmentation.

Discussion

MSPie provides automatic data routing, longitudinal processing, and visualization of the results, as well as report generation, integrated into the neuroradiologist's workflow. The immediate, automated analysis represents the most important development for efficient translation, since results are ready for evaluation promptly after the acquisition. Retrieving results directly after scanning will allow the integration into standard radiological reporting that immediately follows. For the evaluating neuroradiologist it can increase reading speed for most MS cases.

The integration of quantitative cross-sectional and follow-up information on imaging MS pathology, including NET2L and brain atrophy rates, in so-called subclinical disease activity monitoring after definite clinical diagnosis and under treatment, fulfills an increasing demand for translation of highly specific volumetric assessments to routine reading by treating MS neurologists [3, 6].

To achieve precise volumetric measurements and especially reliable assessments of their change over time, the standardization of imaging data acquisition is mandatory [14]. This was recently reiterated in recommendations on the use of MRI in patients with MS, with a particular focus on follow-up MRI protocols in established disease and under immune-modulating treatment [5].

Based on our preliminary experience, this software can provide distinct benefits for MS image evaluation precision and reliability. In MS cases with extensive MRI pathology, visual evaluation can be laborious and prone to neurora-

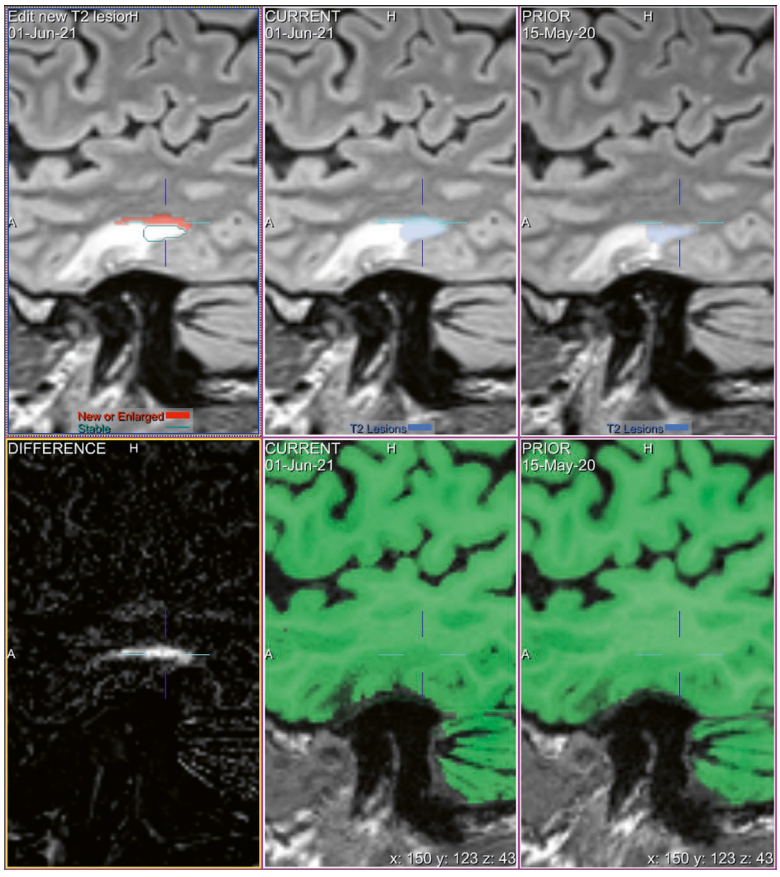

12 Post-traumatic temporal gliosis in an MS patient analyzed with the software prototype. The residue of a contusion resembles a T2 signal similar to an MS lesion and therefore was partly segmented. Progressing within the observation period, the prototype even detected lesion growth. However, this lesion needed to be excluded from the analysis.

diological misjudgment. Here, MSPie may ensure precision for follow-up MRI reading.

In particular, the MS imaging feature of subtle T2 lesion growth has likely been missed by conventional visual evaluation without computer aid. Hence, the importance of precision increase in clinical follow-up is obvious. However, this also identifies the need of common definitions of variants of MS lesion growth which are so far not incorporated into the neuroradiological repertoire of disease-related changes in MS [15].

The longitudinal quantification of brain tissue volume in MS allows the observation of increased rate of brain volume loss, exceeding the age-dependent acceleration. So far, conventional neuroradiology has been unable to quantify this characteristic feature of MS pathology in routine assessment. Thus, the precise determination of accelerated atrophy rates here appears to be the greatest translational advancement achieved.

However, the still incomplete clinical definition of MS imaging surrogates of subclinical disease activity and their clinical meaning [16, 17] presents neuroradiologists with a situation where precise characteristic alterations are provided at the diagnostic point of care that are still subject of debate in clinical MS neurology [18, 19].

Conclusions

Automated quantification of MS imaging metrics has long been a challenge, and the lack of standardization and highly precise techniques hindered its translation into clinical care. Insufficient MRI data quality, resolution, and limited reproducibility further impeded such application at the diagnostic point of care.

In combination with a perpetual standardized MR imaging protocol, the prototype may enable robust and fully integrated assessment of MS cases. While the neuroradiologist must remain vigilant with respect to machine-generated results, the software proves to support advanced clinical care and could serve the high information demand in MS neurology.

References

1 Mowry EM, Bermel RA, Williams JR, Benzinger TLS, de Moor C, Fisher E, Hersh CM, Hyland MH, Izbudak I, Jones SE, Kieseier BC, Kitzler HH, et al. Harnessing Real-World Data to Inform Decision-Making: Multiple Sclerosis Partners Advancing Technology and Health Solutions (MS PATHS). Front Neurol. 2020 Aug 7;11:632.
2 Havrdova E, Galetta S, Hutchinson M, Stefoski D, Bates D, Polman CH, O'Connor PW, Giovannoni G, Phillips JT, Lublin FD, Pace A, Kim R, Hyde R. Effect of natalizumab on clinical and radiological disease activity in multiple sclerosis: a retrospective analysis of the Natalizumab Safety and Efficacy in Relapsing-Remitting Multiple Sclerosis (AFFIRM) study. Lancet Neurol. 2009 Mar;8(3):254-60.
3 Kappos L, De Stefano N, Freedman MS, Cree BA, Radue EW, Sprenger T, Sormani MP, Smith T, Häring DA, Piani Meier D, Tomic D. Inclusion of brain volume loss in a revised measure of 'no evidence of disease activity' (NEDA-4) in relapsing-remitting multiple sclerosis. Mult Scler. 2016 Sep;22(10):1297-305.
4 Sastre-Garriga J, Pareto D, Battaglini M, Rocca MA, Ciccarelli O, Enzinger C, Wuerfel J, Sormani MP, Barkhof F, Yousry TA, De Stefano N, Tintoré M, et al.; MAGNIMS study group. MAGNIMS consensus recommendations on the use of brain and spinal cord atrophy measures in clinical practice. Nat Rev Neurol. 2020 Mar;16(3):171-182.
5 Wattjes MP, Ciccarelli O, Reich DS, Banwell B, de Stefano N, Enzinger C, Fazekas F, et al.; Magnetic Resonance Imaging in Multiple Sclerosis study group; Consortium of Multiple Sclerosis Centres; North American Imaging in Multiple Sclerosis Cooperative MRI guidelines working group. 2021 MAGNIMS-CMSC-NAIMS consensus recommendations on the use of MRI in patients with multiple sclerosis. Lancet Neurol. 2021 Aug;20(8):653-670.
6 Giovannoni G, Butzkueven H, Dhib-Jalbut S, Hobart J, Kobelt G, Pepper G, Sormani MP, Thalheim C, Traboulsee A, Vollmer T. Brain health: time matters in multiple sclerosis. Mult Scler Relat Disord. 2016 Sep;9 Suppl 1:S5-S48.
7 Rudick RA, Fisher E, Lee JC, Simon J, Jacobs L. Use of the brain parenchymal fraction to measure whole brain atrophy in relapsing-remitting MS. Multiple Sclerosis Collaborative Research Group. Neurology. 1999 Nov 10;53(8):1698-704.
8 Tsivgoulis G, Katsanos AH, Grigoriadis N, Hadjigeorgiou GM, Heliopoulos I, Papathanasopoulos P, Dardiotis E, Kilidireas C, Voumvourakis K. The efect of disease-modifying therapies on brain atrophy in patients with clinically isolated syndrome: a systematic review and meta-analysis. Ther Adv Neurol Disord. 2015;8(5):193–202.
9 Andravizou A, Dardiotis E, Artemiadis A, Sokratous M, Siokas V, Tsouris Z, Aloizou AM, Nikolaidis I, Bakirtzis C, Tsivgoulis G, Deretzi G, Grigoriadis N, Bogdanos DP, Hadjigeorgiou GM. Brain atrophy in multiple sclerosis: mechanisms, clinical relevance and treatment options. Auto Immun Highlights. 2019 Aug 10;10(1):7.
10 Simon JH, Li D, Traboulsee A, Coyle PK, Arnold DL, Barkhof F, Frank JA, Grossman R, Paty DW, Radue EW, Wolinsky JS. Standardized MR imaging protocol for multiple sclerosis: Consortium of MS Centers consensus guidelines. AJNR Am J Neuroradiol. 2006 Feb;27(2):455-61.
11 Fartaria MJ, Bonnier G, Roche A, Kober T, Meuli R, Rotzinger D, Frackowiak R, Schluep M, Du Pasquier R, Thiran JP, Krueger G, Bach Cuadra M, Granziera C. Automated detection of white matter and cortical lesions in early stages of multiple sclerosis. J Magn Reson Imaging. 2016 Jun;43(6):1445-54.
12 Fartaria MJ, Todea A, Kober T, O'brien K, Krueger G, Meuli R, Granziera C, Roche A, Bach Cuadra M. Partial volume-aware assessment of multiple sclerosis lesions. Neuroimage Clin. 2018 Feb 28;18:245-253.
13 Fartaria MJ, Kober T, Granziera C, Bach Cuadra M. Longitudinal analysis of white matter and cortical lesions in multiple sclerosis. Neuroimage Clin. 2019;23:101938.
14 Suthiphosuwan, Suradech & Kim, David & Bharatha, Aditya & Oh, Jiwon. (2017). Imaging Markers for Monitoring Disease Activity in Multiple Sclerosis. Curr Treat Options Neurol. 2017 May;19(5):18.
15 Köhler C, Wahl H, Ziemssen T, Linn J, Kitzler HH. Exploring individual multiple sclerosis lesion volume change over time: Development of an algorithm for the analyses of longitudinal quantitative MRI measures. Neuroimage Clin. 2019;21:101623.
16 Lublin FD. Disease activity free status in MS. Mult Scler Relat Disord. 2012 Jan;1(1):6-7.
17 Hegen H, Bsteh G, Berger T. 'No evidence of disease activity' – is it an appropriate surrogate in multiple sclerosis? Eur J Neurol. 2018 Sep;25(9):1107-e101.
18 Monschein T, Salhofer-Polanyi S, Altmann P, Zrzavy T, Dal-Bianco A, Bsteh G, Rommer P, Berger T, Leutmezer F. Should I stop or should I go on? Disease modifying therapy after the first clinical episode of multiple sclerosis. J Neurol. 2021 Apr;268(4):1247-1253.
19 Mayssam EN, Eid C, Khoury SJ, Hannoun S. No evidence of disease activity: Is it an aspirational therapeutic goal in multiple sclerosis? Multiple sclerosis and related disorders. 2020;40:101935.



Contact

Dr. Hagen H. Kitzler, M.D.
Institute of Diagnostic and Interventional Neuroradiology
Universitätsklinikum Carl Gustav Carus an der Technischen Universität Dresden
Fetscherstrasse 74
01307 Dresden
Germany
Tel.: +49 (0)351 458-18331
Hagen.Kitzler@ukdd.de

PASTEUR: Package of Anatomical Sequences Using Parallel Transmission Universal Pulses Now Available for MAGNETOM Terra

Aurélien Massire, Ph.D.[1]; Franck Mauconduit, Ph.D.[2]; Vincent Gras, Ph.D.[2]; Marc Lapert, Ph.D.[1]; Mathieu Naudin, Ph.D.[3,4,5]; Rémy Guillevin, M.D., Ph.D.[3,4,5]; Alexandre Vignaud, Ph.D.[2]; Nicolas Boulant, Ph.D.[2]

[1]Siemens Healthineers, Saint-Denis, France
[2]Université Paris-Saclay, CEA, CNRS, BAOBAB, NeuroSpin, Gif-sur-Yvette, France
[3]CHU Poitiers, France
[4]LRCOM I3M, University and University Hospital of Poitiers, France
[5]Laboratory of Applied Mathematics, UMR CNRS 7348, University of Poitiers, France

Introduction

In MRI, ultra-high-field (UHF) strengths (≥ 7T) provide a higher signal-to-noise ratio, enabling increased spatial resolution and/or reduced acquisition time as compared to lower-field MR systems [1–3]. As more and more patients have been scanned with UHF systems over the last decade, 7T MRI has markedly demonstrated its added value for diagnosing and characterizing two key diseases of the central nervous system: multiple sclerosis (MS) and focal epilepsy [4, 5]. With MS, 7T structural MRI successfully detects smaller and earlier lesions in both white matter (WM) and gray matter (GM), and provides improved characterization of lesion localization, formation, and resulting damage [4]. As for epilepsy, 7T structural MRI successfully increases the diagnosis success rate in patients with drug-resistant focal onset epilepsy for whom lesions could not be found using lower-field MR systems [5].

However, certain anatomies can be more challenging to acquire with UHF MRI, especially when examining larger volumes. This is due to destructive field interferences that can lead to spatial inhomogeneity in the radiofrequency (RF) excitation profile. In the head, the cerebellum and the temporal lobes can be affected by such inhomogeneities [6].

The use of parallel transmission (pTx) technology with an array of transmit coil elements has proven to be very efficient in addressing these challenges [7]. With pTx, the amplitudes and phases of the RF pulses transmitted by the channels of the coil array are independently modulated in time to homogenize the excitation profile over the volume of interest, provided the actual transmit RF field (B_1^+) and static field offset (ΔB_0) distributions are known. For non-selective excitations used in 3D anatomical MR sequences,

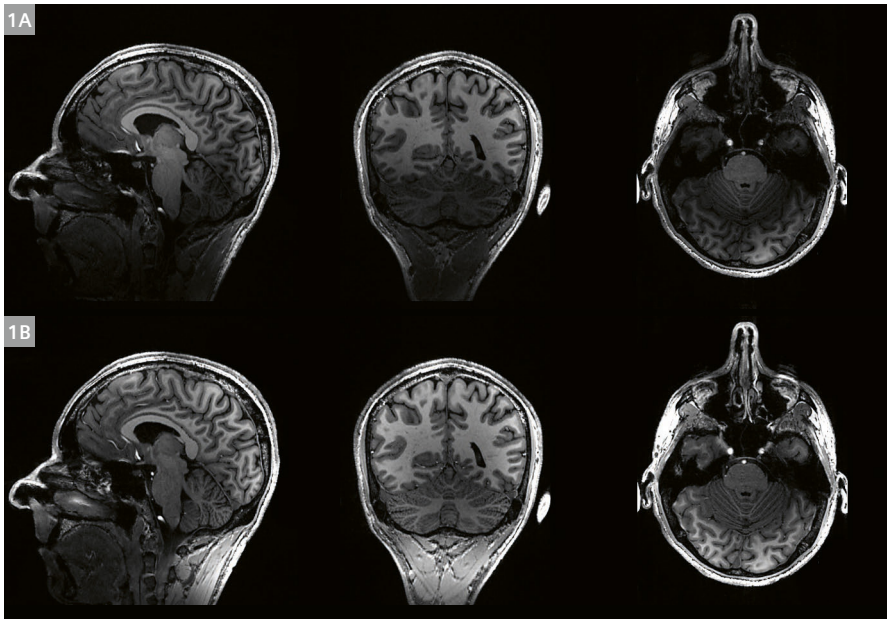

1 T1-weighted MPRAGE (Magnetization-Prepared Rapid Acquisition Gradient-Echo) sequence
(1A) Proposed MPRAGE protocol in standard non-pTx excitation. **(1B)** Same protocol with Universal Pulses (GRAPE RF pulses were used for magnetization inversion and excitation). Note how GM/WM contrast is specifically improved in the cerebellum and temporal lobes with UP imaging. The sequence SAR is lower using UPs than non-pTx excitation, since the inversion UP is less energetic than the conventional adiabatic RF pulse.

various parametrization approaches, such as k_T-points [8] or GRAPE [9, 10], have been proposed to design optimized RF and magnetic field gradient waveforms. The design of such subject-tailored RF pulses results in very homogeneous RF excitation profiles, but this is at the cost of the extra scan time required to map the patient field distributions and to design the RF pulses. It also demands specific expertise from the MR user [11, 12].

Alternate methods for a subject-tailored approach can avoid systematic measurement of the RF and static field distributions for each subject and subsequent RF pulse computation. Recently, an original approach that uses "Universal Pulses" (UP) for calibration-free pTx neuroimaging was developed by CEA NeuroSpin [13–15]. To ensure universality, the RF pulses of the PASTEUR package [16] were designed offline using a database of B_1^+ and ΔB_0 brain distributions experimentally acquired from a representative cohort and using state-of-the art optimization algorithms. Several key 3D MR sequences providing anatomical imaging were reprogrammed to host these UPs. The PASTEUR workflow is therefore completely transparent to the 7T radiographer, who can focus on the MR exam with no time penalty or need for advanced sequence parametrization.

In this work, the PASTEUR package, originally designed for the investigational MAGNETOM 7T, was brought to the latest generation of the 7T MR system from Siemens Healthineers: MAGNETOM Terra[1]. To demonstrate the power and versatility of UPs for neuroimaging, the PASTEUR package was deployed in the clinical environment of Poitiers University Hospital (CHU Poitiers) in France. The image quality achieved using conventional non-pTx excitation (i.e., circularly polarized (CP) mode) brain imaging was compared with that from PASTEUR UP brain imaging for MPRAGE, MP2RAGE, FLASH, and SPACE sequences performed on healthy volunteers.

Theory

To design the non-selective RF pulses of the PASTEUR package, two different *k*-space parametrizations were chosen according to the desired properties of the pulses: k_T-points [8] and GRAPE [9]. Briefly, k_T-points consist of multiple rectangular RF sub-pulses interleaved with gradient blips. The resulting degrees of freedom are therefore amplitude, phase, and the *k*-space position of each RF sub-pulse. The GRAPE pulses are made of simultaneously applied RF and gradient waveforms that vary at every time step. The additional degrees of freedom enable shorter GRAPE pulses compared to the k_T-points.

The MR sequences considered here require diverse RF pulses to influence spin magnetization, and each type has specific properties (e.g., small flip angle (FA), large FA, refocusing, inversion). Nevertheless, the general problem with FA homogenization is relatively similar and related to the pTx MR system, which is equipped with N_c transmitters. It usually involves optimizing the N_c RF complex temporal shapes and the G_X-G_Y-G_Z gradient temporal shapes (defining the locations in *k*-space during transmission) so as to minimize the deviation of the resulting FA map from the desired nominal value (as prescribed in the MR protocol).

For one subject, this problem is often (but not always) written as a magnitude least-squares (MLS) problem [17]. To generalize the concept of simultaneous FA homogenization over multiple subjects and thereby promote universality, the optimal RF / gradient shapes that minimize the root mean square error over N_s subjects are sought [13]. In the case of the PASTEUR package, the database consisted of 20 brain field distributions (male and female Caucasian healthy adult volunteers, age range: between 20 and 50 years old), acquired using MAGNETOM 7T MR systems equipped with 8Tx/32Rx Nova brain coils at CEA NeuroSpin (n = 10) and DZNE Bonn (n = 10). Due to evolutions in MAGNETOM Terra hardware and software, several modifications were made to UPs originally designed for MAGNETOM 7T, in order to update the original RF pulses (details and illustration of these "travelling pulses" are provided in [18]). Lastly, as designed RF pulses must respect hardware and safety limits for all patients [19], a set of explicit constraints on SAR and power per channel should be added [13–16]. For the PASTEUR package currently available for MAGNETOM Terra, the default RF power limits set by Siemens Healthineers were enforced. Design examples of UPs included in the PASTEUR package using GRAPE and k_T-point parametrizations are illustrated in Figure 2.

MR imaging

Data were acquired at CHU Poitiers on a 7T MR system[1] (MAGNETOM Terra, Siemens Healthcare, Erlangen, Germany) equipped with an 8Tx/32Rx transmit/receive coil (Nova Medical, Wilmington, MA, USA). The MR protocol, which consisted of 3D non-selective anatomical sequences, was approved by the local ethics committee. Informed consent was obtained for each subject prior to the MR examination. Exclusion criteria followed the GUFI recommendations [20].

[1] *For MAGNETOM Terra, pTx technology is included in Research mode (as part of the optional Dual mode) and is not intended for clinical use. Research operation may require observation of national regulations.*

MR sequences supported by the PASTEUR package are MPRAGE [21], MP2RAGE [22], FLAWS [23], FLASH, and SPACE [24], with several magnetization preparations (dark fluid, DIR). The main sequence parameters used at CHU Poitiers are summarized in the table below. Specific sequence information and additional observations are provided, along with images acquired from several healthy volunteers (Figs. 1, 3–9).

Results

High image quality over the whole brain was obtained for all MR sequences and imaging contrasts when UPs were activated (Figs. 1, 3–9). Where applicable (Figs. 1, 4, 7–9), image quality was significantly improved when compared to conventional non-pTx excitation (i.e., CP: circularly polarized mode). It should be noted that no additional image filters were used to reduce signal bias or to smooth images. Improvements were particularly visually striking in the cerebellum and the temporal lobes, notably on SPACE-based imaging. This is already a well-known phenomenon since the 3D SPACE sequence uses multiple refocusing RF pulses to maintain magnetization along a long echo train. Errors in FA profiles are additive, ultimately creating signal voids within the brain. Regarding sequence-specific absorption rate (SAR), SPACE protocols were usually close to the Level 1 limit. Nevertheless, all MR sequences could be run on millimetric or sub-millimetric spatial isotropic resolution. UP SAR is usually higher than standard rectangular RF pulses, but significantly lower than adiabatic RF pulses. As a result, sequence SAR was sometimes lower when using UPs than with conventional non-pTx excitation (for instance, in MPRAGE or DIR). The radiographers encountered no additional time penalties caused by pTx during the MR exams.

MR sequences	MPRAGE	MPRAGE HR	MP2RAGE	FLAWS	T2* FLASH	T2 SPACE	Dark Fluid $T2_p$ SPACE	DIR SPACE
TA (min)	4:59	9:54	12:20	9:40	5:12	6:00	7:12	7:06
TR (ms)	2600	3000	5000	5000	22	9000	9000	8000
TE (ms)	2.48	3.84	2.06	1.6	16	383	270	320
TI (ms)	1100	1200	740/2430	620/1430	–	–	2300	3500/650
FA (°)	5	6	5/4	4/8	15	T_2 var	T_2 var	T_2 var
FOV (mm^2)	224x224	224x224	230x230	230x230	224x224	230x230	230x230	240x240
Matrix size	320x320	448x448	384x384	288x288	448x376	288x288	288x288	240x240
Resolution (mm^3)	0.7 iso	0.5 iso	0.6 iso	0.8 iso	0.5 iso	0.8 iso	0.8 iso	1.0 iso
Number of partitions	256	320	288	208	320	240	240	192
Parallel imaging technique	GRAPPA	GRAPPA	GRAPPA	GRAPPA	GRAPPA	CAIPIRINHA	CAIPIRINHA	GRAPPA
Parallel imaging factor	3	3	3	3	2x2	3x3	3x3	3x3
Partial Fourier	7/8 (phase)	7/8 (slice)	7/8 (slice)	6/8 (slice)	6/8	allowed	allowed	allowed
Number of averages	1	1	1	1	1	1	1	2
Turbo Factor	256	280	252	156	–	218	180	180
Bandwidth (Hz/px)	210	220	350	500	200	827	599	401

Table 1: The main sequence parameters used at CHU Poitiers.

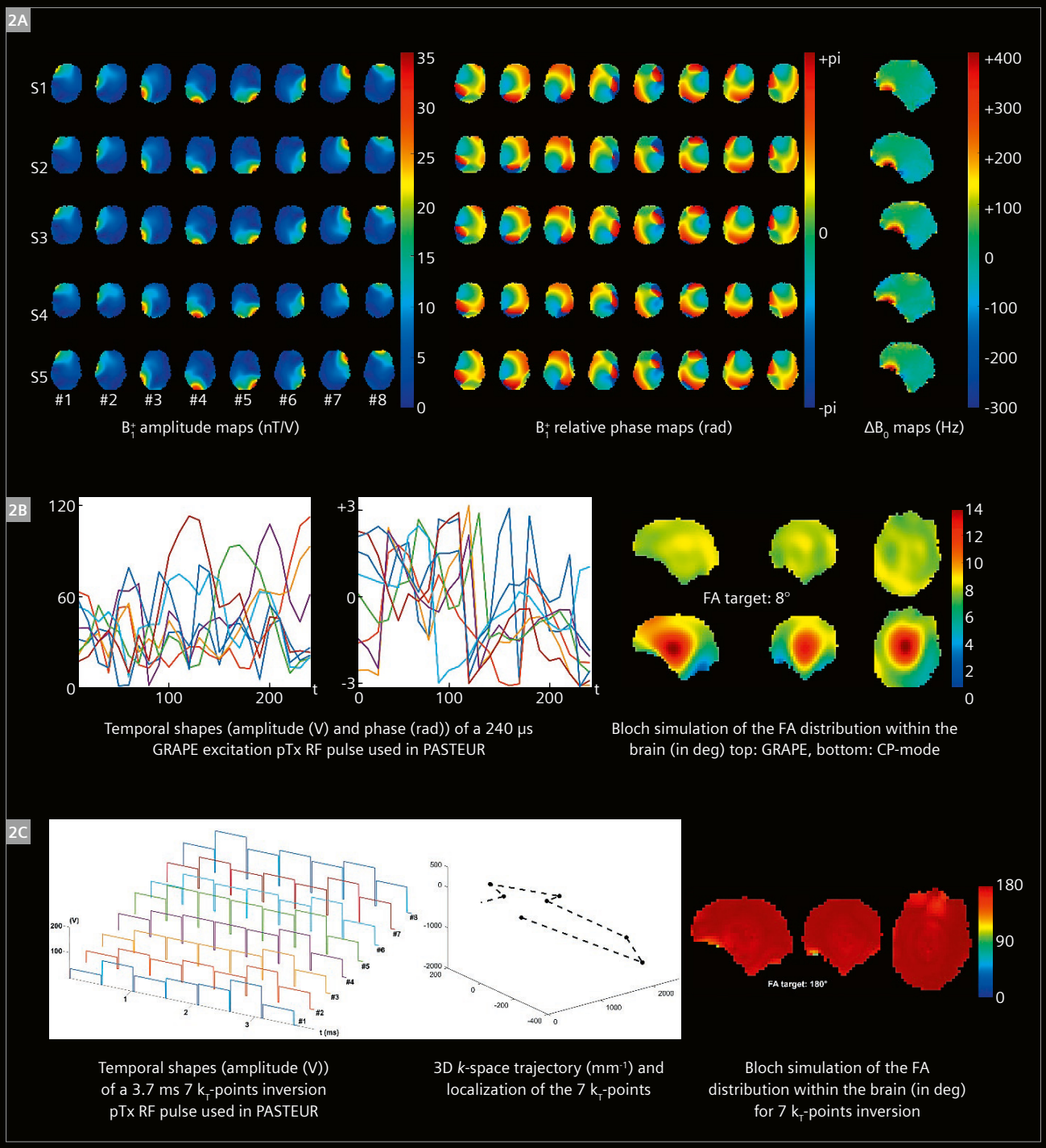

2 **Design examples of Universal Pulses of the PASTEUR package using GRAPE and K_T-points**

(2A) Extract of the database of brain B_1^+ and ΔB_0 distributions (n = 5 subjects) experimentally acquired on a representative cohort. Measured B_1^+ maps amplitude (nT/V) and relative phase (rad) are displayed in axial view at isocenter. Images are sorted by subjects from top to bottom and by channel indexes from left to right. Measured ΔB_0 offset maps (Hz) are displayed in sagittal view at isocenter. Qualitatively, the B_1^+ maps reveal a high degree of similarity across subjects, with typical spatial correlations of about 0.95 throughout channels. Additional technical details on the database construction can be found in [13].

(2B) Example of excitation UP RF temporal shapes designed with the GRAPE algorithm (different color indicates different transmit channel), along with the corresponding FA distribution in the brain simulated with Bloch equations (results from non-pTx excitation – circularly polarized mode – are also provided below to demonstrate the expected improvement).

(2C) Example of inversion Universal Pulses RF temporal shapes and *k*-space trajectory designed with k_T-points, along with the corresponding FA distribution in the brain simulated with Bloch equations.

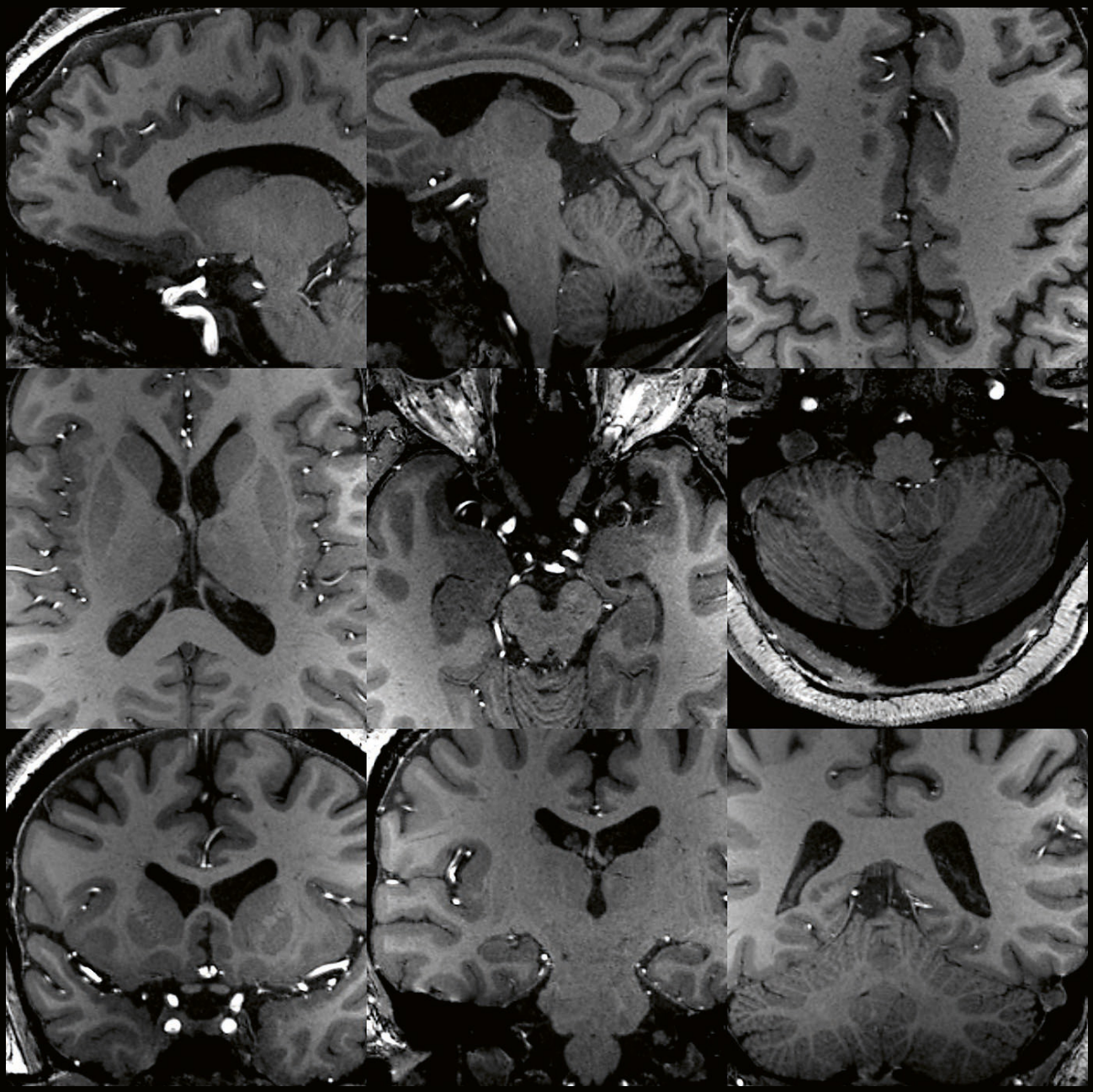

3 **High-resolution T1-weighted MPRAGE imaging using PASTEUR package**
Representative zoomed images in all orientations (sagittal, transverse, coronal) of a 500 µm isotropic spatial resolution MPRAGE sequence acquired in 10 minutes with Universal Pulses. Note the very high image quality over the whole brain, which could be further improved using image filters to mitigate the reception field bias.

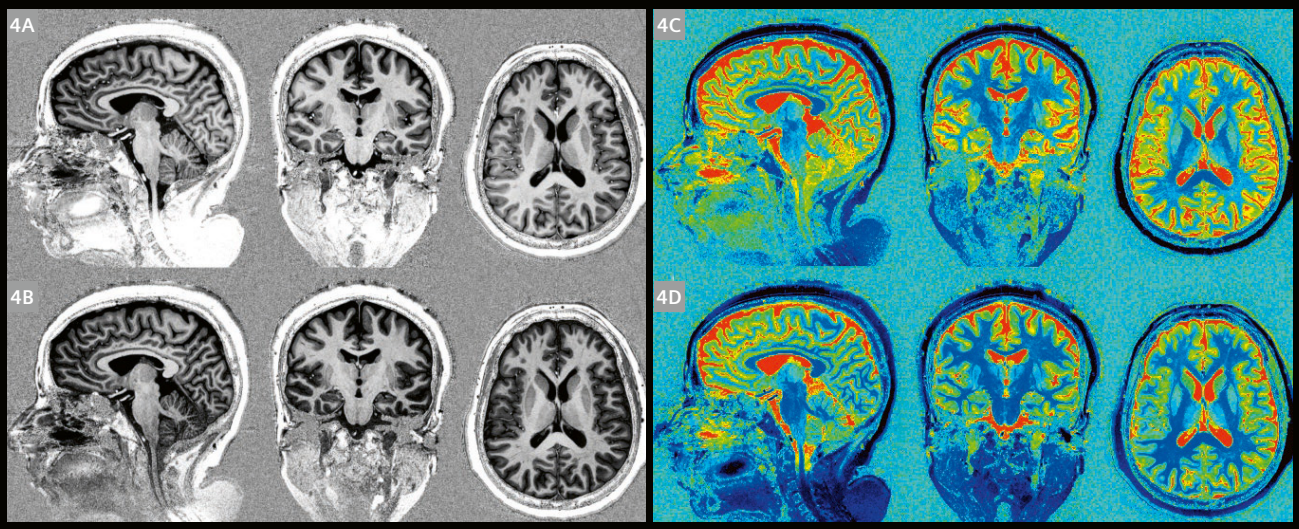

4 **T1-weighted MP2RAGE (Magnetization-Prepared 2 Rapid Acquisition Gradient-Echoes) sequence**
(4A) Uniform (UNI) images obtained with the proposed MP2RAGE protocol in standard non-pTx excitation. Note that MP2RAGE UNI images are inherently corrected for reception bias field, so the resulting signal inhomogeneity only comes from B_1^+ excitation bias. **(4B)** UNI images obtained with the same protocol using Universal Pulses. Signal homogeneity within the brain is improved (see, for instance, the signal homogeneity of the cortex). **(4C)** Associated quantitative T1 map (in ms) in colormap obtained with non-pTx excitation imaging. **(4D)** Associated T1 map obtained with UPs. The improvement in excitation homogenization significantly improves the accuracy of T1 measurement, as T1 values are computed with Bloch equation integration, notably in the WM and in the cortex.

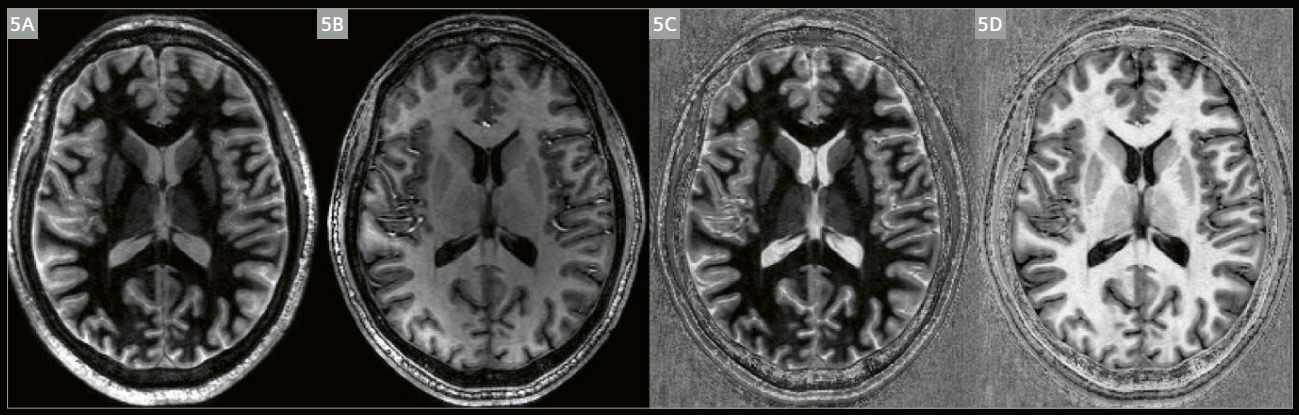

5 **T1-weighted FLAWS (FLuid And White matter Suppression) sequence**
Proposed protocol with Universal Pulses. **(5A)** Inversion 1 volume (equivalent to fast gray matter acquisition T1 inversion recovery, FGATIR), **(5B)** Inversion 2 volume (equivalent to MPRAGE), **(5C)** synthetic high contrast (HC), and **(5D)** synthetic high contrast opposite (HCO). Note that synthetic contrasts were computed offline. These synthetic contrasts are relevant for deep brain structure and/or cortex visualization, though they do amplify image noise [23].

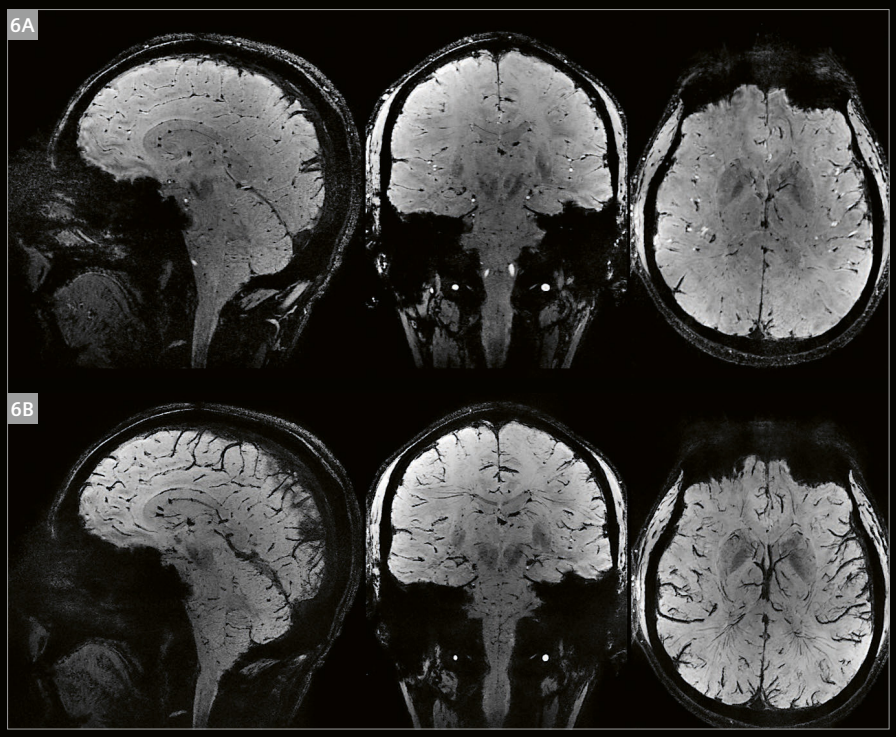

6 **T2*-weighted FLASH sequence (6A)** Proposed GRE protocol with Universal Pulses. **(6B)** Associated minimum-intensity projection (minIP), with 4 mm slice thickness. Note the high image quality, including in the lower part of the brain. This type of protocol could be used for quantitative susceptibility mapping (QSM).

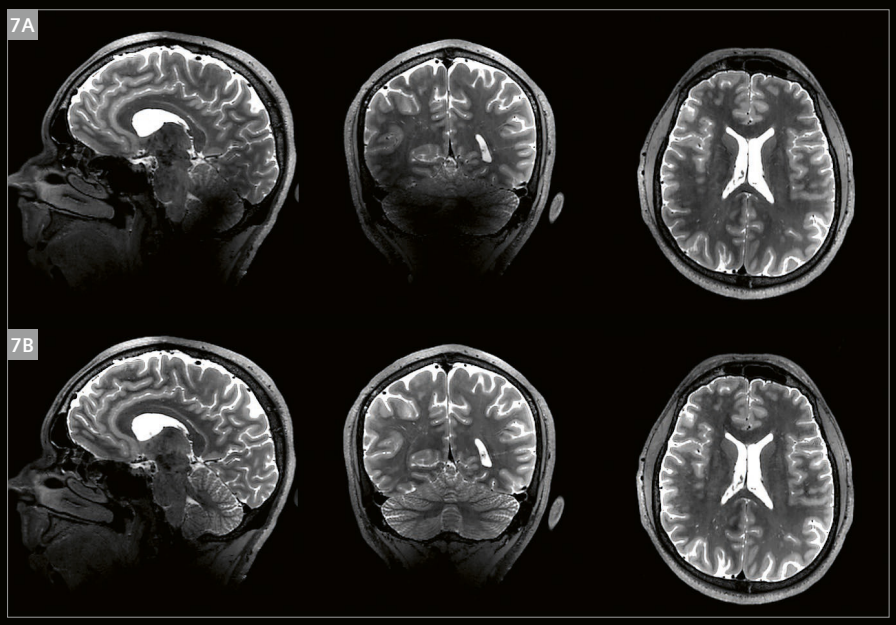

7 **T2-weighted SPACE (Sampling Perfection with Application optimized Contrasts using different flip angle Evolution) sequence (7A)** Proposed protocol in standard non-pTx excitation. **(7B)** Same protocol with Universal Pulses. The 3D SPACE sequence generates one T2-weighted volume. The chosen refocusing train option was T2 var (with target T1: 1400 ms, target T2: 50 ms). The improvement in excitation and refocusing homogenization significantly enhances signal homogeneity, notably in the cerebellum and temporal lobes.

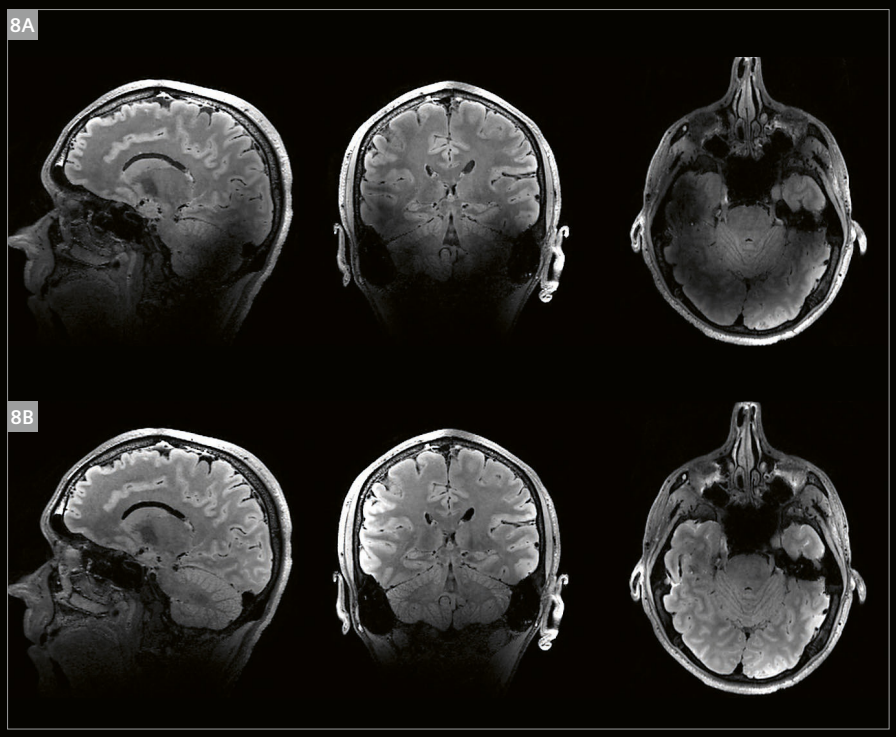

8 Dark fluid T2-weighted SPACE sequence with T2 magnetization preparation
(8A) Proposed protocol in standard non-pTx excitation. **(8B)** Same protocol with Universal Pulses. This sequence generates one T2-weighted volume with suppressed cerebrospinal fluid (CSF) signal. The preparation consisted of a 90°-τ-180°-τ-90° module (τ = 50 ms) to achieve an effective inversion of the CSF signal and a saturation in the brain tissues. This module is described in detail in [25]. The chosen refocusing train option was T2 var (with target T1: 1400 ms, target T2: 50 ms). The multiple improvements in preparation, excitation, and refocusing RF pulses results in an efficient signal restoration in the cerebellum and temporal lobes.

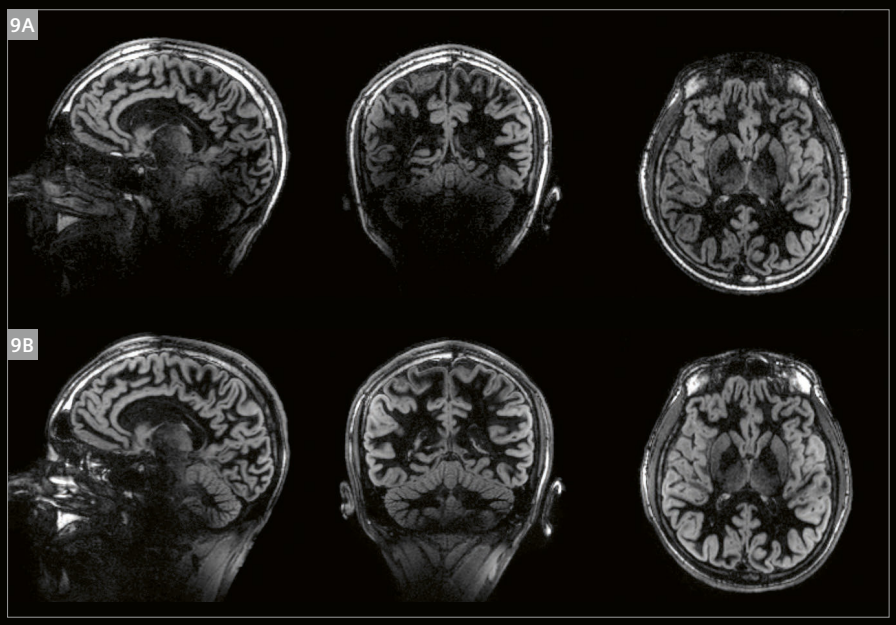

9 Double Inversion Recovery (DIR) SPACE sequence
(9A) Proposed protocol in non-pTx excitation. **(9B)** Same protocol with Universal Pulses. The 3D SPACE sequence generates one T2-weighted volume with both WM- and CSF-suppressed signals. The chosen refocusing train option was T2 var (with target T1: 1400 ms, target T2: 50 ms). The sequence SAR is lower with UP than with standard non-pTx excitation, since the inversion GRAPE pulses are less energetic than the standard adiabatic RF pulses. The multiple improvements in preparation, excitation, and refocusing RF pulses significantly enhances signal homogeneity and achieves efficient signal restoration in the cerebellum.

Discussion

In this work, the PASTEUR package was successfully deployed in a clinical site equipped with a MAGNETOM Terra and with no previous expertise in pTx or RF pulse design. The easy-to-use package allowed the team to acquire high-quality, high-resolution, whole-brain 3D structural images from several healthy volunteers, with various clinically relevant MR contrasts and at strictly zero workflow penalty. The results were very favorably received by the local radiologists, who concluded that typical UHF image artifacts were "gone for good".

The Universal Pulses presented here rely on a representative field database acquired in advance, and designed offline once by MR experts using thorough optimization approaches (since the offline computation time is irrelevant, increased pulse-design performance was achieved). UPs are thus valid for a given field strength (7T), body part (head), patient position (headfirst supine), and pTx RF coil. Assuming a certain degree of similarity in the B_1^+ and ΔB_0 maps among the population, UPs could be successfully applied to new patients without personalized field map measurements and RF pulse calculations. The PASTEUR package therefore makes the use of the underlying pTx hardware completely transparent to the operator.

While earlier work showed that increasing the size of the database improves UP robustness, the pulses' universality appears to converge rather quickly with the number of subjects [13]. Nevertheless, the idea of introducing database subgroups based, for instance, on gender, age, body mass index, or disease condition should be investigated in the future. Additional improvements could be made to further improve the universality, based on either of the following:

1. the latest machine-learning approaches to categorize the patients (Smart Pulse) [26];
2. fast subject- and exam-specific calibration using standardized UPs (SUPs) [27];
3. a combination of UPs with fast, tailored approaches (FOCUS) [28].

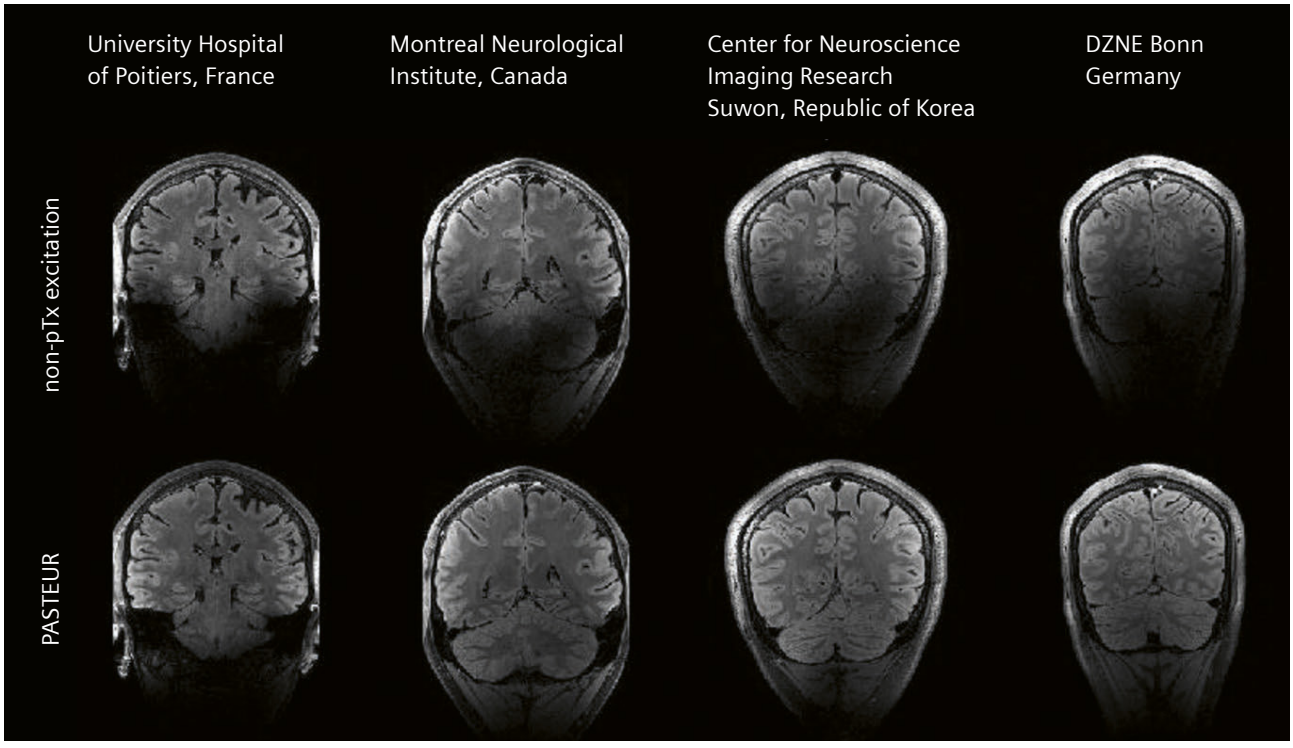

10 **Dark fluid T2-weighted SPACE imaging with PASTEUR in four testing sites**
Comparisons of standard non-pTx excitation and PASTEUR images from several research centers equipped with MAGENTOM Terra and MAGENTOM 7T^{Plus} systems (Figure adapted from [18]), illustrating the universality and reliability of UPs. From left to right: University Hospital of Poitiers in France; Montreal Neurological Institute in Canada; Center for Neuroscience Imaging Research in Suwon, Republic of Korea; and German Center for Neurodegenerative Diseases (DZNE) in Bonn, Germany.

Lastly, UP advantages were soundly demonstrated for brain imaging [9, 13–16, 25], yet other organs could likely also benefit from this approach, accounting for increased anatomical variability [29].

As already stated, image quality of the whole brain was always significantly improved with UPs compared to standard non-pTx excitation, in all considered imaging contrasts. Occasionally, small image artifacts remained in UP imaging. These hyper-signal artifacts arise from very localized and strong off-resonance effects, which have more variability among individuals (see also Figure 2). This is a known limitation of UPs, and radiologists should be aware of it. Note that the proposed imaging protocols could likely be improved, especially to reduce acquisition time. For instance, the latest acceleration techniques, such as compressed sensing, were not yet available for MPRAGE and MP2RAGE [30].

Additional MR sequences and supported features are planned for the PASTEUR package in the future: Several non-selective 3D MR sequences could be added, an important milestone would be the ability to excite arbitrary slabs with UPs [31], and 2D imaging should also be addressed while still maintaining the universality of the approach [32]. Importantly, all PASTEUR developments will be deployed to operate on the Iseult MAGNETOM 11.7T MRI system [33] recently installed at CEA NeuroSpin, a world-leading R&D collaboration between CEA and Siemens Healthineers.

The PASTEUR package is currently available for the 7T MAGNETOM Terra on the C2P platform[2] from Siemens Healthineers. At the time of writing, the PASTEUR package has already been distributed to 15 sites around the world (Fig. 10). Its adoption by the UHF community could help pave the way for pTx integration in clinical workflows.

Acknowledgments

This project received funding from the European Union's Horizon 2020 research and innovation program under Grant Agreement No 885876 (AROMA project). The authors would like to thank Iulius Dragonu, Carole Guillevin, Rene Gumbrecht, Robin Heidemann, Patrick Liebig, and Eberhard Pracht for their support. The authors are also grateful to Ilana Leppert, Christine Lucas Tardif, Sugil Kim, Kamil Uludag, and Tony Stöcker for providing PASTEUR images from their respective institutions.

[2]Access to the C2P platform from Siemens Healthineers is possible for collaboration partners who have signed the associated IDEA agreement. Please contact your local collaboration manager for more information.

References

1 Trattnig S, Bogner W, Gruber S, Szomolanyi P, Juras V, Robinson S, et al. Clinical applications at ultrahigh field (7 T). Where does it make the difference? NMR Biomed. 2016;29(9):1316–34.
2 Kraff O, Fischer A, Nagel AM, Mönninghoff C, Ladd ME. MRI at 7 tesla and above: Demonstrated and potential capabilities. J Magn Reson Imaging. 2015;41(1):13–33.
3 Van der Zwaag W, Schäfer A, Marques JP, Turner R, Trampel R. Recent applications of UHF-MRI in the study of human brain function and structure: a review. NMR Biomed. 2016;29(9):1274–88.
4 Bruschi N, Boffa G, Inglese M. Ultra-high-field 7-T MRI in multiple sclerosis and other demyelinating diseases: from pathology to clinical practice. Eur Radiol Exp. 2020;4(1):59.
5 Opheim G, van der Kolk A, Markenroth Bloch K, Colon AJ, Davis KA, Henry TR, et al. 7T Epilepsy Task Force Consensus Recommendations on the Use of 7T MRI in Clinical Practice. Neurology. 2021;96(7):327–341.
6 Van de Moortele PF, Akgun C, Adriany G, Moeller S, Ritter J, Collins CM, et al. B(1) destructive interferences and spatial phase patterns at 7 T with a head transceiver array coil. Magn Reson Med. 2005;54(6):1503–18.
7 Padormo F, Beqiri A, Hajnal JV, Malik SJ. Parallel transmission for ultrahigh-field imaging. NMR Biomed. 2016;29(9):1145–61.
8 Cloos MA, Boulant N, Luong M, Ferrand G, Giacomini E, Le Bihan D, et al. kT-points: short three-dimensional tailored RF pulses for flip-angle homogenization over an extended volume. Magn Reson Med. 2012;67(1):72–80.
9 Van Damme L, Mauconduit F, Chambrion T, Boulant N, Gras V. Universal nonselective excitation and refocusing pulses with improved robustness to off-resonance for Magnetic Resonance Imaging at 7 Tesla with parallel transmission. Magn Reson Med. 2021;85(2):678–693.
10 Khaneja N, Reiss T, Kehlet C, Schulte-Herbrüggen T, Glaser SJ. Optimal control of coupled spin dynamics: design of NMR pulse sequences by gradient ascent algorithms. J Magn Reson. 2005;172(2):296–305.
11 Massire A, Vignaud A, Robert B, Le Bihan D, Boulant N, Amadon A. Parallel-transmission-enabled three-dimensional T2 -weighted imaging of the human brain at 7 Tesla. Magn Reson Med. 2015;73(6):2195–203.
12 Cloos MA, Boulant N, Luong M, Ferrand G, Giacomini E, Hang MF, et al. Parallel-transmission-enabled magnetization-prepared rapid gradient-echo T1-weighted imaging of the human brain at 7 T. Neuroimage. 2012;62(3):2140–50.
13 Gras V, Vignaud A, Amadon A, Bihan D, Boulant N. Universal pulses: A new concept for calibration-free parallel transmission. Magn Reson Med. 2017;77(2):635–643.
14 Gras V, Mauconduit F, Vignaud A, Amadon A, Le Bihan D, Stöcker T, et al. Design of universal parallel-transmit refocusing kT -point pulses and application to 3D T2 -weighted imaging at 7T. Magn Reson Med. 2018;80(1):53–65.
15 Gras V, Boland M, Vignaud A, Ferrand G, Amadon A, Mauconduit F, et al. Homogeneous non-selective and slice-selective parallel-transmit excitations at 7 Tesla with universal pulses: A validation study on two commercial RF coils. PLoS One. 2017;12(8): e0183562.
16 Gras V, Mauconduit F, Vignaud A, Le Ster C, Leroi L, Amadon A, et al. PASTeUR: Package of Anatomical Sequences using parallel Transmission UniveRsal kT-point pulses. In: Proceedings of the 27th Annual Meeting of ISMRM. Montréal, QC, Canada. 2019; p. 4626.

17 Idrobo AH, Weiss P, Massire A, Amadon A, Boulant N. On variant strategies to solve the magnitude least squares optimization problem in parallel transmission pulse design and under strict SAR and power constraints. IEEE Trans Med Imaging. 2014;33(3):739–748.
18 Mauconduit F, Massire A, Gras V, et al. Traveling pulses visit 7T Terra sites: Getting ready for Parallel Transmission in routine use. Submitted to ISMRM 2022. London, United Kingdom. 2022; p. 2488.
19 International Electrotechnical Commission. Medical electrical equipment - Part 2–33: Particular requirements for the basic safety and essential performance of magnetic resonance equipment for medical diagnosis. 3rd ed. Geneva. 2010;603:2–33.
20 German Ultrahigh Field Imaging (GUFI). Approval of subjects for measurements at ultra-high-field MRI [Internet]. Germany [cited August 12, 2021]. Available from: https://mr-gufi.de/index.php/en/documents.
21 Mugler III JP, Brookeman JR. Three-dimensional magnetization-prepared rapid gradient-echo imaging (3D MP RAGE). Magn Reson Med. 1990;15(1):152–7.
22 Marques JP, Kober T, Krueger G, van der Zwaag W, Van de Moortele P-F, Gruetter R. MP2RAGE, a self bias-field corrected sequence for improved segmentation and T1-mapping at high field. Neuroimage. 2010;49(2):1271–81.
23 Beaumont J, Gambarota G, Saint-Jalmes H, Acosta O, Ferré JC, Raniga P, et al. High-resolution multi-T1 -weighted contrast and T1 mapping with low B1>+ sensitivity using the fluid and white matter suppression (FLAWS) sequence at 7T. Magn Reson Med. 2021;85(3):1364–1378.
24 Mugler III JP. Optimized three-dimensional fast-spin-echo MRI. J Magn Reson Imaging. 2014;39(4):745–67.
25 Gras V, Pracht ED, Mauconduit F, Le Bihan D, Stöcker T, Boulant N. Robust nonadiabatic T2 preparation using universal parallel-transmit kT-point pulses for 3D FLAIR imaging at 7 T. Magn Reson Med. 2019;81(5):3202–3208.
26 Tomi-Tricot R, Gras V, Thirion B, Mauconduit F, Boulant N, Cherkaoui H, et al. SmartPulse, a machine learning approach for calibration-free dynamic RF shimming: Preliminary study in a clinical environment. Magn Reson Med. 2019;82(6):2016–2031.
27 Le Ster C, Mauconduit F, Massire A, Boulant N, Gras V. Standardized Universal Pulse: a fast RF calibration approach to improve flip angle accuracy in parallel transmission. Magn Reson Med. 2022; 10.1002/mrm.29180
28 Herrler J, Liebig P, Gumbrecht R, Ritter D, Schmitter S, Maier A, et al. Fast online-customized (FOCUS) parallel transmission pulses: A combination of universal pulses and individual optimization. Magn Reson Med. 2021;85(6):3140–3153.
29 Aigner C Stefan, Dietrich S, Schaeffter T, Schmitter S. Calibration-free pTx of the human heart at 7T via 3D universal pulses. In: Proceedings of the 29th Annual Meeting of ISMRM. Online conference. 2021; p. 777.
30 Mussard E, Hilbert T, Forman C, Meuli R, Thiran J-P, Kober T. Accelerated MP2RAGE imaging using Cartesian phyllotaxis readout and compressed sensing reconstruction. Magn Reson Med. 2020;84(4):1881–1894.
31 Jamil R, Mauconduit F, Gras V, Boulant N. General gradient delay correction method in bipolar multispoke RF pulses using trim blips. Magn Reson Med. 2021;85(2):1004–1012.
32 Gras V, Poser BA, Wu X, Tomi-Tricot R, Boulant N. Optimizing BOLD sensitivity in the 7T Human Connectome Project resting-state fMRI protocol using plug-and-play parallel transmission. Neuroimage. 2019;195:1–10.
33 Le Bihan D, Schild T. Human brain MRI at 500 MHz, scientific perspectives and technological challenges. Supercond Sci Technol. 2017;30(3):033003.

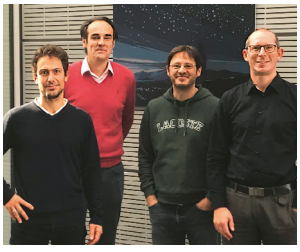

Contact

The METRIC team (from left to right: Vincent Gras, Alexandre Vignaud, Nicolas Boulant, Franck Mauconduit)
Université Paris-Saclay, CEA, CNRS, BAOBAB, NeuroSpin
91191, Gif-Sur-Yvette
France
nicolas.boulant@cea.fr
franck.mauconduit@cea.fr
https://joliot.cea.fr/drf/joliot/recherche/neurospin



Aurélien Massire, Ph.D.
MR Clinical Scientist
Siemens Healthcare SAS
40 Avenue des Fruitiers
93210, Saint Denis
France
aurelien.massire@siemens-healthineers.com

Magnetic Resonance Elastography of the Liver: Best Practices

Manjunathan Nanjappa, Ph.D.[1]; Bradley Bolster, Ph.D.[2]; Ning Jin, Ph.D.[2]; Stephan Kannengießer, Ph.D.[3]; Robert Sellers, RT(R)(MR)(CT)[2]; Arunark Kolipaka, Ph.D., FAHA, FSCMR[1]

[1]The Ohio State University, Columbus, OH, USA
[2]Siemens Healthineers, US MR R&D Collaborations, Malvern, PA, USA
[3]Siemens Healthineers, MR DL ONCO, Erlangen, Germany

Introduction

Liver is the largest solid internal organ of the human body. It performs a wide range of functions including aiding digestion, storing energy, removing metabolic waste and microorganisms from the circulatory system, and producing blood-clotting components. The liver can repair, regenerate and/or regrow itself to maintain its structure and functions, yet certain health conditions can overwhelm these capabilities leading to the progression of liver disease [1]. Alcohol abuse, obesity, and chronic illness can lead to excessive accumulation of extracellular matrix proteins including collagen. This results in diminished blood flow and the subsequent build-up of scar tissue in the liver known as liver fibrosis [2].

Liver fibrosis in its initial and moderate stages causes no clinical symptoms by itself and can often be missed by routine blood tests or by medical imaging examinations. Fibrosis can be treated and reversed on early detection; however, if this condition is left untreated for a long time, it may lead to a severe condition called cirrhosis. Once cirrhosis has developed, clinical symptoms and their associated problems may begin to appear, and eventually liver damage becomes permanent and irreversible [3]. Therefore, early detection of liver fibrosis plays an important role in treatment and disease management.

Traditionally, liver fibrosis is diagnosed and staged by percutaneous liver biopsy, an invasive technique. Lately, non-invasive methodologies such as blood serum tests and medical imaging techniques have emerged as an alternative to biopsy. However, serum tests such as APRI, FIB-4, and other commercial assays have proven less accurate than the imaging modalities [4] such as ultrasound (US) elastography and magnetic resonance elastography (MRE) for staging fibrosis. Several studies comparing MR- and US-based elastography techniques concluded that the MRE has been shown to exceed all other diagnostic methods in terms of accuracy, sensitivity, specificity, and organ coverage [5].

Magnetic Resonance Elastography

MRE is a non-invasive technique to estimate the stiffness of soft tissues. Given the non-invasive nature and accuracy of diagnostic results, in recent years MRE has become a standard clinical tool to stage liver fibrosis on both 1.5T and 3T scanners [6]. MRE can be acquired with or without contrast agent on board [8], meaning it can be performed at any point in a standard clinical examination, depending on site preference.

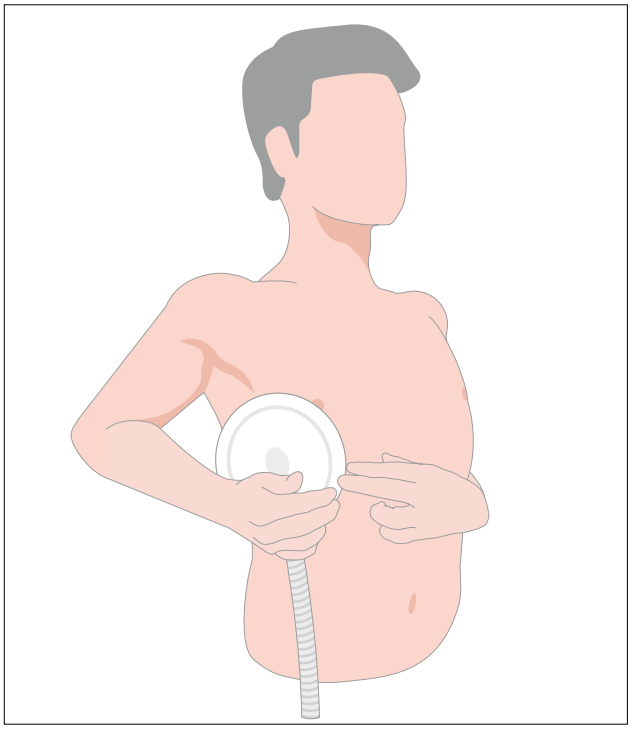

1 Illustration of the passive driver placement for liver MRE imaging. The entire flat surface of the drive should be in contact with the subject's upper abdomen at the fifth intercostal space and lateral to the mid-clavicular line.

The liver MRE technique can be separated into four elements as described below.

1. Inducing shear wave motion into the liver using an external mechanical driver
2. Acquiring wave images of the liver via motion encoding and phase-contrast imaging
3. Reconstructing stiffness maps from the wave images using an inversion algorithm
4. Reporting average stiffness values in ROIs identified in the liver stiffness maps as having good wave quality and no artifacts

Liver MRE has been described in a QIBA profile [10], which also gives practical guidance for performing MRE and interpreting the results. Conformance to this profile supports the claim that a change in measured hepatic stiffness of at least 19% is considered to be real with 95% confidence.

This article reviews the essentials of MRE and provides best practice for its routine clinical usage. To clinicians, the MRE technique offers the special benefit that all major MR manufacturers adopted the same standard solution, hardware and inversion algorithm, and high reproducibility has been demonstrated [6]. This uniformity makes the interpretation of diagnostic results much easier, especially in centers where multiple platforms are used. However, some image acquisition sequences and workflow options may differ, so in the following, the focus will be on the Siemens Healthineers platform.

The most commonly used and commercially available solution (Resoundant Inc, Rochester, MN, USA) induces continuous single frequency mechanical shear wave motion in the liver using a special hardware complement to the MR system that consists of an active driver (frequency generator) and a passive driver (plastic drum), and a standardized inversion algorithm implementation [17].

Insert 1: Best practice workflow

Pay attention to the following workflow elements to improve chances of performing a high quality MRE exam.

1. Inspect the hardware regularly for any damage to the passive driver diaphragm, or air leakage in the tubing system.

2. Turn the active driver (off and) on prior to each examination to wake it up from standby mode.

3. Place the elastic belt on the MR patient table at liver level and position the patient in a supine position with head-first. Position and secure the passive driver as explained in the section *Driver setup for liver MRE*. Lateral placement is preferred over anterior placement but good contact between the driver face and the subject's abdomen is critical.

4. Direct the end of the passive driver tubing towards where it will connect to the tubing from the active driver. In some cases this may be at the back of the bore.

5. Fasten the belt tightly. Ask the subject if they can breathe normally with the belt; if not, adjust the belt. Inform them about expected examination duration, order of sequences, that the Elastography is performed at end-expiration, and that they will feel vibrations coming from the driver during the activation. Repeat the latter to the patient just before the MRE sequence to avoid them being startled.

6. Verify passive driver positioning in scout images in relation to the liver at end-expiration and other landmarks. Adjust the driver as necessary.

7. Run the MR Elastography sequence and acquire the images at end-expiration.

8. Load the results into the Viewing Task Card and review image quality as described in the section *Postprocessing and evaluation* (magnitude for breathing artifacts, wave images for good propagation along with depth penetration, and confidence mask for successful inversion). In case of insufficient quality, check driver positioning and repeat, using a modified protocol where appropriate, e.g., in case of iron overload.

9. Measure stiffness via ROI evaluation as described in the section *Postprocessing and evaluation*.

Driver setup for liver MRE

Positioning of the passive driver on the subject (Figure 1) is one of the most critical steps in an MRE examination. Optimal driver positioning ensures that the externally generated mechanical waves are transferred to the subject efficiently and thereby penetrate deep into the liver. This helps achieve the desired anatomical coverage and obtain stiffness measurements with high quality.

To enable the performance of reliable human liver MRE, the passive driver is placed on the upper abdomen centered at the fifth intercostal space but lateral to the midclavicular line as shown in Figure 1. While positioning the passive driver it is necessary to make sure that the driver's flat surface area is fully in contact with the body close to the liver.

To maintain the passive driver in one fixed position throughout the imaging session, it is necessary to immobilize it with a dedicated elastic belt firmly while ensuring the subjects' comfort to breathe normally. To improve contact between the subject and the passive driver it is advisable to use extra cushioning material such as a sponge or clothing materials (as shown in Figure 2) in between the passive driver and the belt to tightly hold the driver against the body. This enables mechanical waves to be delivered to the region of interest uniformly throughout the imaging session. Finally, it is important to ensure that the passive driver is connected tightly to the active driver via plastic tubing so that there is no air leakage. It may be advantageous to connect the remaining tubing only after the subject has been moved into the scanner.

After placing the driver, it is important to verify that the driver is positioned correctly, i.e., centered in H-F direction with respect to the liver. If collected at end expiration localizer images of sagittal and axial views like those in Figure 3 will show the placement of the driver. The indentation on the sagittal view indicates that the driver is placed at the center with respect to the liver. Similarly, the axial view will show the indentation anterior to the liver. If the position of the driver is not correct, then the driver must be adjusted with respect to these landmarks.

Sequence optimization and image acquisition

The Siemens Healthineers MRE product consists of two sequence options, a GRE based sequence with an optional rapid acquisition mode (see Figure 4) and a sequence based on single-shot spin-echo echo planar imaging (SE-EPI). Both sequences acquire 2D axial slices in the center of the liver at end-expiration with through-slice motion encoding and include a fractional encoding option to shorten TE (Figure 4). The SE-EPI MRE acquisition is more efficient and should be the default acquisition where possible. The primary benefit of SE-EPI is that multiple slices are acquired in a single 11–13 seconds breath-hold and the SE-EPI component makes the sequence more robust to susceptibility that occurs with liver iron loading or with higher field strengths. Fat saturation is very important for SE-EPI; SPAIR-strong is the preferred fat suppression setting for this sequence. GRE MRE requires multiple breath-holds (one per slice), however, in some situations such as where implants exist and lower radio frequency flip angles are necessary, or if referencing previous GRE MRE studies, it can be the sequence of choice. Standard imaging parameters for the two sequences are shown in Table 1 and the standard Siemens Healthineers protocol tree for



2 Demonstration of MRE setup and driver placement for liver imaging, using the dedicated elastic belt, plus cushioning material (arrow).
Watch the videos on https://www.magnetomworld.siemens-healthineers.com/clinical-corner/protocols/body-pelvis/mr-elastography

MR Elastography is shown in Figure 5. As previously mentioned, an MRE protocol can be added either at the beginning (pre-contrast) or the end (post-contrast) of a measurement program.

The mechanical excitation frequency is fixed at 60 Hz, and the amplitude of the active driver is typically set to 40%, which will work well, irrespective of body habitus, in 85% of the patients. If the current driver amplitude should lead to either too much or too little motion encoding, some control over the motion encoding strength is possible using the Gradient mode UI parameter, since the amplitude of the motion encoding gradient (MEG) will scale with it: It is lower for Normal and higher for Fast Gradient mode.

The active driver is activated ("triggered") via the sequence, and automatic breath-hold commands can be used. Make sure that both MRE and the localizer are acquired in end-expiration.

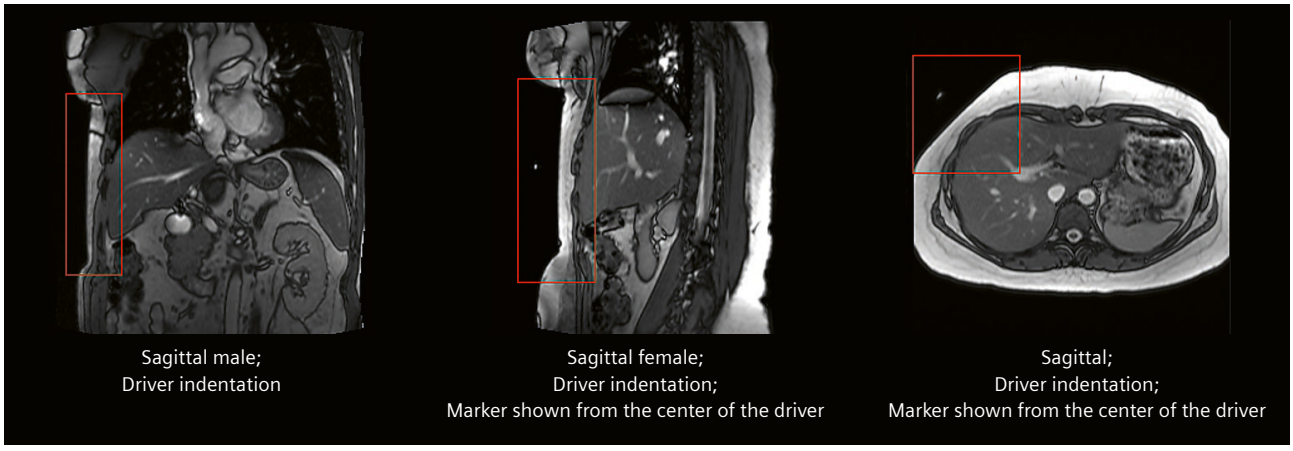

3 Localizers illustrating the driver placement for an optimized MRE liver examination. Positioning the driver center to the liver facilitates uniform propation of waves in the region of interest. (An MR visible fiducial has been added to the passive driver in this case showing the center of the passive driver in these images.)



4 Example parameter card for a GRE MRE protocol in Rapid mode (TR 25 instead of 50 ms, petrol highlight). Shortening the TE below the gap in the range bar (orange highlight) would activate fractional motion encoding (which may boost signal at the expense of sensitivity, but this is only recommended for cases with short T2*).

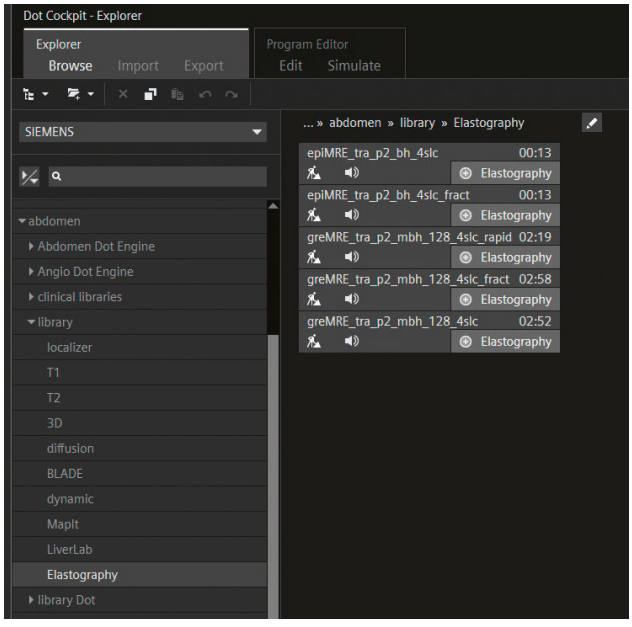

5 The Siemens Healthineers protocol tree for Elastography representing all MRE options: epiMRE with and without fractional encoding, and greMRE in its standard, rapid and fractional encoding configuration.

Parameter	SE-EPI MRE	GRE MRE
FOV	420 mm (x 100%)	420 mm x 70–100%
TR	1000–1200 ms	25[a] or 50 ms
TE	47 ms or lower[b]	21 ms or lower[b]
Slice thickness	8 mm, 25% gap	10 mm, no gap
Acquisition matrix	100 x 100%	128 x 80%
Bandwidth	2170 Hz/pixel	399 Hz/pixel
Gradient Mode	Normal, Fast[c]	Normal, Fast[c]
GRAPPA factor	2	2
GRAPPA reference lines	24 GRE/separate	12 integrated
Fat saturation	SPAIR – strong	none
Other key settings	Prescan Normalize, Adaptive Coil Combination	

Table 1: Typical sequence parameters for MRE.
[a] Selecting a TE of 25 ms will put the GRE MRE sequence into "Rapid" mode [14] (see Figure 4).
[b] Selecting TE lower than the gap in the sequence UI (see Figure 4) will cause the motion encoding gradients to be shortened to 65% of full ("fractional" encoding [15]); this is beneficial for short T2 / T2*, but will also reduce motion encoding, so it is only recommended for problem-solving.
[c] The gradient mode will influence the motion encoding via the MEG amplitude; start with Normal, and if there is not enough motion encoding, go to Fast.
Protocols (.exar1 files) are available for download at https://www.magnetomworld.siemens-healthineers.com/clinical-corner/protocols/body-pelvis/mr-elastography

Insert 2: Trouble shooting

No waves or inadequate waves in the liver (Figure 6)

1. Check tubing for disconnection and pneumatic pressure leakage. Make sure that the passive driver diaphragm (flat surface) is not damaged.
2. Make sure the passive driver has a good contact with the subject's body and is positioned correctly as shown in Figure 2.
3. Make sure the active driver is turned on and not in standby mode.

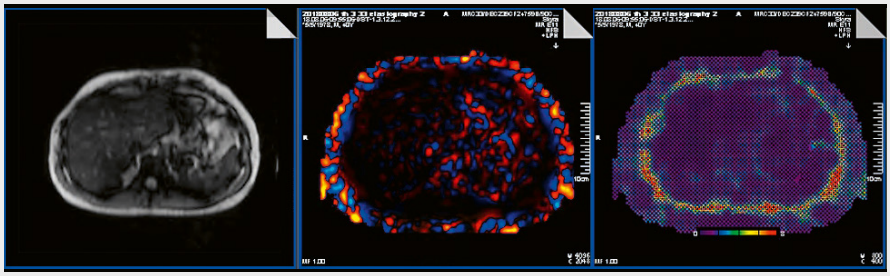

6 Example of a scan without mechanical vibration. The reason could be a disconnected pressure hose, or an active driver in standby mode.

No planar waves (Figure 7, Figure 8)

1. Adjust the driver position lateral to the center of Xiphoid as shown in Figure 1.
2. Check the localizer images as shown in Figure 3 to ensure the driver position is correct. If not adjust the driver position accordingly.
3. Additional care must be taken in imaging women and obese subjects in placing the driver laterally by moving the breast to have adequate planar waves in the liver.

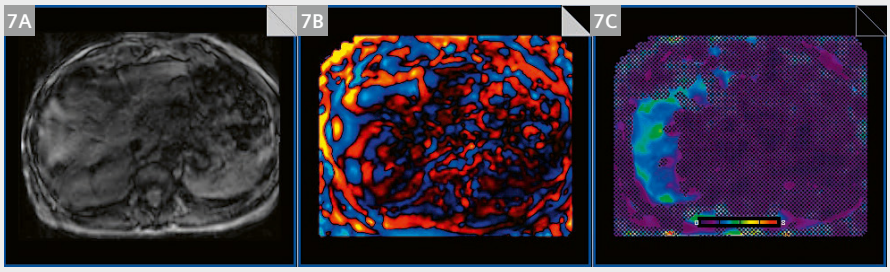

7 Volunteer example at 1.5T with bad placement of the passive driver. **(7A)** Magnitude, **(7B)** wave image with incoherent wave pattern, **(7C)** elastogram with 95% confidence markings.

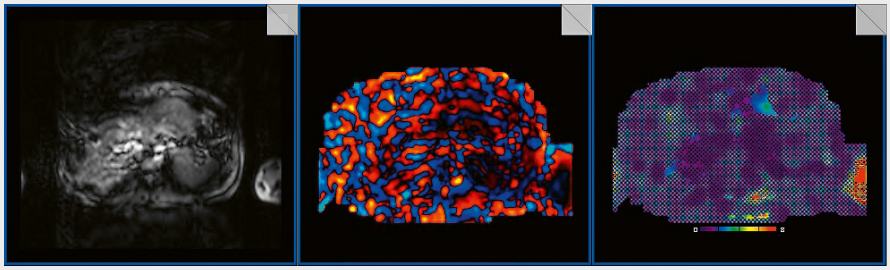

8 Example of a scan with erroneous driver triggering (Rapid GRE). The reason could be a wrongly set mechanical frequency on the active driver, or a wrongly configured trigger output (optical-to-electrical converter).

Signal loss through transverse relaxation (Figure 9)

The motion encoding gradient between excitation and acquisition in the sequence timing causes echo times to be comparatively long, e.g., ~20 ms for gradient-echo sequences and ~50 ms for SE-EPI sequences. Long echo times in turn make the sequences prone to signal loss if the transverse relaxation times (T2 or T2*) are short, which can be the case at 3T or with hepatic iron overload. Image acquisition parameters should be adjusted for these scenarios. The GRE based MR elastography technique does not perform well on iron overload liver; however, the SE-EPI based technique can be deployed with customized parameter settings [11] to obtain diagnostic quality images.

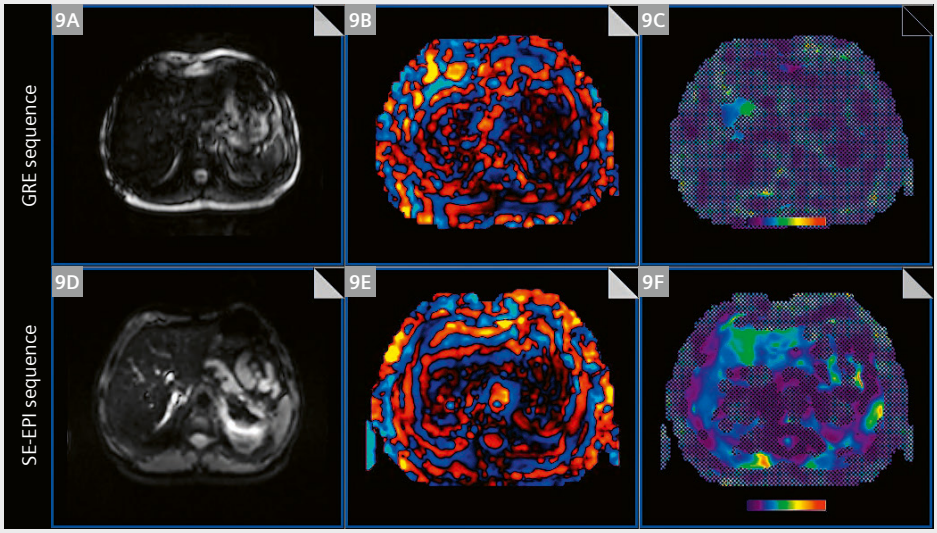

9 Volunteer example at 3T with R2* ~ 90 s-1, corresponding to a liver iron content of ~1.5 mg/g dry weight. **Top row**: GRE sequence, **bottom row**: SE-EPI sequence. **(9A, D)** magnitude, **(9B, E)** wave image, **(9C, F)** elastogram with 95% confidence markings.

Postprocessing and evaluation

The phase difference images are processed for the standard MRE option using an inline implementation of Resoundant's MMDI inversion algorithm to generate the stiffness maps called elastograms. Stiffness is calculated as the magnitude of the complex shear modulus [18]. The output further contains the original magnitude and phase difference images, and additional computed output: confidence map, stiffness map with confidence markings, and finally colored interpolated wave images. The confidence map is based on the wave quality, i.e., which includes wave signal-to-noise-ratio (SNR) wave amplitude and shape. Then, the stiffness map uses a 95% threshold of the confidence map (shown as unhatched area) to determine the regions to trust within the liver parenchyma and report the stiffness values. Figure 10 shows an example of output series obtained in one healthy volunteer.

The image quality of the data should be analyzed further to determine if any motion artifacts exist which are typically a result of improper breath-hold. The artifacts appear in the magnitude image as blurring or ghosting in the phase encoding direction. Additionally, the wave images (colored images of the output from the scanner) are also qualitatively analyzed to determine discernible waves propagating in the liver as connected wave fronts as shown in Figure 10.

The stiffness map is generated using a color scale from 0–8 kPa; a grayscale reading of 100 corresponds to 1 kPa. Note that all colorized maps are natively grayscale images displayed using a color lookup table; hence, they can be windowed, and ROI measurements can be made directly from them[1].

For repeatable measurements, a large region of interest is drawn in the liver parenchyma excluding the hatched region, avoiding the large vessels and at least 1 cm in from the edge of the liver. Note that the cross-hatched regions contain pixels of value zero, so they must not be included in ROI measurements. If in doubt, propagate ROIs to the stiffness map without cross-hatching. Make sure that the wave images show planar wave propagation in the selected region and avoid areas close to the liver edge and the left lobe. Divide ROI mean values by 100 to report the mean stiffness value in kPa. Hot spots in the stiffness maps that occur under the MRE driver or at the liver periphery are typically due to over driving or wave reflections respectively and should be avoided when drawing the ROIs. However, it is acceptable to include small artificial hot spots in the center region of the parenchyma as these may not change the mean stiffness value significantly. In Figure 10, it can be observed that planar waves penetrate throughout the liver and the stiffness map shows sufficient coverage of the liver to report the mean stiffness. Table 2 shows typical stiffness values used to stage liver fibrosis [19]; a meta-analysis [20] reported slightly different values. We advise the user to consult the scientific literature for latest studies which best match their clinical environment.

Stiffness values are generally independent of field strength. However, increased sensitivity to susceptibility effects such as iron overload cause signal loss in the liver parenchyma to be more prevalent at higher field strengths.

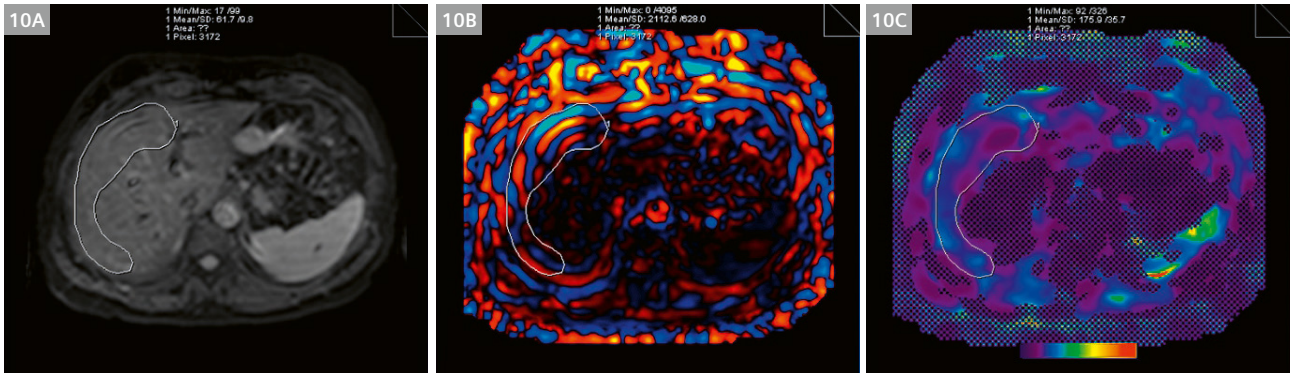

10 Scan results (SE-EPI) from a healthy volunteer. **(10A)** Magnitude, **(10B)** wave image, **(10C)** stiffness map with 95% confidence mask overlay; note the color bar indicating the color map distribution across the 0–8 kPa range. Planar wave propagation can be inferred from the uninterrupted wave pattern in the ROI. The manual free-hand ROI contours select regions of high wave quality while observing anatomical placement and the confidence mask.

[1]*Some PACS systems may not be able to retain these properties. Depending on syngo MR software version, there may be transfer/export settings to manage this.*

F0	F1	F2	F3	F4
3.00 ± 1.12 kPa	3.11 ± 0.82 kPa	3.87 ± 1.85 kPa	4.78 ± 1.89 kPa	6.52 ± 2.34 kPa

Table 2: Mean ± standard deviation values of MRE-derived liver stiffness for different fibrosis stages from 289 patients according to [19].

Insert 3: Setup and configuration

The hardware part of the MRE option is set up by a service engineer. Settings of the active driver can typically be configured once and remain unchanged thereafter. Details can be found in the operator manual [16]; some of them are given here for reference.

Figure 11 is a screenshot of the active driver's configuration page which can be accessed via a web browser and Ethernet connection, which may be a special research configuration[2]. The number of cycles per trigger is set to 3 for both GRE and SE-EPI MRE sequences as they are each designed to trigger the active driver every 50 ms. In pediatric patients[3] or in the 15% of adult patients with very large or very small body habitus, it can be beneficial to change the driver amplitude.

Note: If you have an older driver with earlier firmware (< version 2.0 as shown in the lower right-hand corner of the configuration screen), the driver frequency will need to be set to 60.1 Hz in order to sync correctly with the incoming triggers from the sequence. Additionally, the driver has a sleep timer configured in the lower part of the right-hand column on the configuration page. After the preset amount of time, the amplifier will go to sleep and no longer respond to triggers. To wake up the unit either depress the Trigger button on the configuration page or manually cycle the power on the unit. Without this sleep timer, damage to the driver can occur, greatly limiting its lifespan.

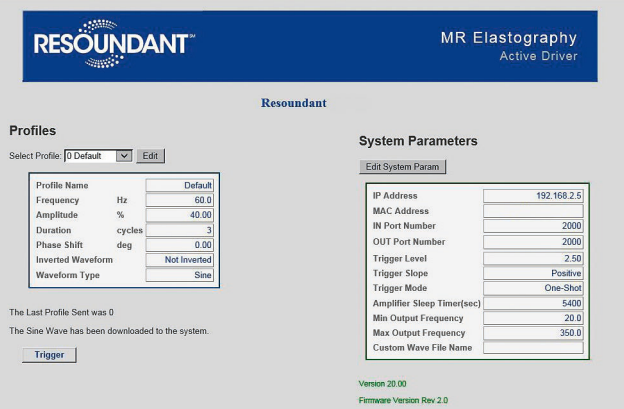

11 Screenshot showing the MRE active driver setting card (Resoundant Inc, Rochester, MN, USA) containing all necessary parameters for either MRE sequence at the proper frequency and amplitude.

[2]Please work with your MR Collaborations scientist and your service engineer if this special configuration is necessary at your site.
[3]MR scanning has not been established as safe for imaging fetuses and infants less than two years of age. The responsible physician must evaluate the benefits of the MR examination compared to those of other imaging procedures.

Summary and take away points

It was the intent of this article to give Siemens Healthineers MRE users, both new and experienced, guidance on how to consistently perform MRE with high-quality results. The content is weighted heavily on achieving a good patient setup with proper passive driver positioning. We have found that driver positioning can be highly variable in practice and is a major contributor to non-diagnostic MRE exams. Using the described workflow, however, it was shown that achieving measurable areas from 65% to 85% of liver coverage, our definition of a successful exam, is possible. Further, reproducibility of the results not only depends on patient setup and scanning workflow, but also on standardized image interpretation, quality checks, and ROI measurements. Therefore, the guidance provided includes these topics as well.

Once the MRE option is set up and configured correctly (see Insert 3), and the workflow for scanning, reading, and reporting is established, the procedure should be kept

unchanged to achieve low variability between examinations. In Insert 1 we summarize a best-practice workflow that includes some elements that may not be commonly considered. With its additional hardware and patient setup, the MRE acquisition has some inherent complexities not present in other MR imaging applications. Optimal wave propagation can depend on multiple factors ranging from hardware functionality to setup to exiting patient pathology. To address some of the more common scenarios we have provided a troubleshooting guide as Insert 2.

Finally, it should be noted that the current standard MRE solution is tailored to breath-hold liver applications by only acquiring a low number of slices and only encoding a single (through-slice) motion direction. This implicitly makes simplifying assumptions of in-plane, planar wave propagation without reflections. This also makes localized stiffness readings, e.g., by liver segment, less reliable. Thus, this "2D" standard solution cannot easily be transferred to other organs in the abdomen, or to other body regions. There exist prototypes with contiguous coverage of larger regions and "3D" motion encoding in all three spatial directions [12], as well as dedicated applications in other body regions [13].

References

1 Michalopoulos GK, DeFrances MC. Liver regeneration. Science. 1997;276(5309):60-6.
2 Bataller R, Brenner DA. Liver fibrosis. J Clin Invest. 2005;115(2):209-18. Erratum in: J Clin Invest. 2005;115(4):1100.
3 Sharma S, Khalili K, Nguyen GC. Non-invasive diagnosis of advanced fibrosis and cirrhosis. World J Gastroenterol. 2014;20(45):16820-30.
4 Wang XP, Wang Y, Ma H, Wang H, Yang DW, et al. Assessment of liver fibrosis with liver and spleen magnetic resonance elastography, serum markers in chronic liver disease. Quant Imaging Med Surg. 2020;10(6):1208-1222.
5 Tana MM, Muir AJ. Diagnosing Liver Fibrosis and Cirrhosis: Serum, Imaging, or Tissue? Clin Gastroenterol Hepatol. 2018;16(1):16-18.
6 Trout AT, Serai S, Mahley AD, Wang H, Zhang Y, Zhang B, Dillman JR. Liver Stiffness Measurements with MR Elastography: Agreement and Repeatability across Imaging Systems, Field Strengths, and Pulse Sequences. Radiology. 2016;281(3):793-804.
7 Venkatesh SK, Wang G, Lim SG, Wee A. Magnetic resonance elastography for the detection and staging of liver fibrosis in chronic hepatitis B. Eur Radiol.2014;24(1):70-8.
8 Hallinan JT, Alsaif HS, Wee A, Venkatesh SK. Magnetic resonance elastography of liver: influence of intravenous gadolinium administration on measured liver stiffness. Abdom Imaging. 2015;40(4):783-8.
9 Bolster Jr B, Jin N, Kannengiesser S, MR Elastography – Pearls and Pitfalls. MAGNETOM Flash (71) 2/2018:19-23.
10 QIBA Profile, Magnetic resonance elastography of the liver. Stage 2: consensus profile. Radiological Society of North America https://qibawiki.rsna.org/images/a/a5/MRE-QIBAProfile-2018-05-02 CONSENSUS.pdf (2018).
11 Barrera CA, Otero HJ, Hartung HD, Biko DM, Serai SD. Protocol optimization for cardiac and liver iron content assessment using MRI: What sequence should I use?, Clin Imaging, Volume 56, 2019, Pages 52-57. 2019;56:52-57.
12 Shi Y, Glaser KJ, Venkatesh SK, Ben-Abraham EI, Ehman RL. Feasibility of using 3D MR elastography to determine pancreatic stiffness in healthy volunteers. J Magn Reson Imaging. 2015;41(2):369-75.
13 Dong H, White RD, Kolipaka A. Advances and Future Direction of Magnetic Resonance Elastography. Top Magn Reson Imaging. 2018;27(5):363-384.
14 Chamarthi SK, Raterman B, Mazumder R, Michaels A, Oza VM, Hanje J, Bolster B, Jin N, White RD, Kolipaka A. Rapid acquisition technique for MR elastography of the liver. Magn Reson Imaging. 2014;32(6):679-83.
15 Rump J, Klatt D, Braun J, Warmuth C, Sack I. Fractional encoding of harmonic motions in MR elastography. Magn Reson Med. 2007;57(2):388-95.
16 Siemens Healthineers MR. Operator manual MR Elastography.
17 Resoundant Inc. Technical report. Available from https://www.resoundant.com/technical-report. [Accessed Feb 23, 2022].
18 Manduca A, Bayly PJ, Ehman RL, Kolipaka A, Royston TJ, Sack I, Sinkus R, Van Beers BE. MR elastography: Principles, guidelines, and terminology. Magn Reson Med. 2021;85(5):2377-2390.
19 Yin M, Glaser KJ, Talwalkar JA, Chen J, Manduca A, Ehman RL. Hepatic MR Elastography: Clinical Performance in a Series of 1377 Consecutive Examinations. Radiology. 2016;278(1):114-24.
20 Singh S, Venkatesh SK, Wang Z, Miller FH, Ehman RL, et al. Diagnostic performance of magnetic resonance elastography in staging liver fibrosis: a systematic review and meta-analysis of individual participant data. Clin Gastroenterol Hepatol. 2015;13(3):440-451.



Contact

Arunark Kolipaka, Ph.D., FAHA, FSCMR
Associate Professor & Technical Director,
Magnetic Resonance Imaging
The Ohio State University
Wexner Medical Center
Department of Radiology
395 West 12th Ave, 4th Floor
Columbus, OH 43210
USA
Phone: +1 614-366-0268
arunark.kolipaka@osumc.edu

MRI's Helium Footprint – And How to Make it Harder to Spot

Philipp Grätzel von Grätz, M.D.

Berlin, Germany

Helium is a finite resource. In fact, it is exceedingly rare on our planet, which is why efforts are underway to make helium-dependent industries more sustainable. Magnetic resonance imaging (MRI) is among these industries: One out of every seven litres of liquid helium consumed annually worldwide is used for cooling superconducting magnets in MRI machines. There are ways to get this figure down, both on the product and on the delivery side of the business. Achieving real helium sustainability for MRIs requires that several approaches be taken simultaneously.

Helium is what makes party balloons fly, and this is all that many people know about it. But while it is true that party balloons account for a relevant – albeit variable – share of the annual global helium consumption, there is much more to know about this inert, noble gas. Were you aware, for example, that helium is among the most abundant elements that exist? Bar hydrogen, it is actually the second most abundant one in the universe. The sun, for example, consists of 73 percent hydrogen and 23 percent helium, while other elements only account for the remaining 4 percent.

The global helium economy

So there is definitely no shortage of helium out there in space. But not every celestial body is a thermonuclear fusion reactor. The sun is. The Earth is not. Down on Earth, helium is extremely scarce. It is, in fact, one of the rarest naturally occurring elements. The majority of Earth's helium comes from natural radioactive processes, i.e., decaying heavy elements. This process is as slow as it sounds, which means that helium is a non-renewable, finite resource.

Where does helium come from? There is no such thing as helium-specific mining. Rather, helium is a by-product of natural gas mining. "The US has traditionally been the largest source of helium worldwide," says Andrew Wade, Helium Commodity Manager at Siemens Magnet Technology in Oxford, UK. In recent years, though, the helium supply from the US has dried up, and Wade has had to turn to other countries for procurement: "The biggest producers at the moment are Qatar and Algeria. There will also be some large gas fields opening in Siberia soon."

Helium is not only finite, it is also volatile: When a helium balloon pops, its helium escapes into the atmosphere, from where it cannot be retrieved. In other words:



1 Container compressor facility to retrieve helium from old MRI systems that undergo refurbishing.



2 Looking into the 20-foot-long container.

Unless recycled, any cuts into our planet's helium reserves will be final cuts. The end of Earth's helium supply is not imminent: At current rates of consumption, the global reserves might in fact last some three centuries. But end they will, and thus there is a strong case to improve sustainability in helium-dependent industries.

Magnetic resonance imaging and helium

What is helium currently used for? There are several industries that cannot do without helium at the moment. Helium is a shielding gas for welding and for laser processing in industrial manufacturing, especially in the aviation industry. The space industry, too, uses helium for pressurisation and purging. Helium is needed for producing semiconductors and optical fibres, which makes it indispensable for the IT and microelectronics industry. Appreciable quantities go into gas chromatography analytics and into producing the breathing mixture for deep-sea diving. Finally, helium serves as a cryogenic cooling liquid for superconductors. The latter may in fact be the single most important use of helium today, with the MRI industries accounting for the biggest share: "About 15 percent of the total global helium production is consumed by MRI," says Wade.

The MRI industry uses superconducting magnets to create strong and dynamic magnetic fields for modern-day MRI machines. Helium, which liquifies at about 4 K or −269° C, can create the low temperatures needed for supraconductivity. In essence, copper and niobium wires in MRI magnets are embedded in a bath of liquid helium. "The trick is stopping that helium from boiling," explains Wade. To do so, MRI machines use a cold head within a vacuum flask which recondenses any gas that arises. "The total amount of helium needed is different from MRI system to MRI system. As a rule of thumb, traditional MRI systems contain 1,500 litres of helium. About 2,000 litres are needed to get to a stable system. And after ten years, another 500 litres or so might have to be refilled. In the meantime, a well-managed magnet should not need any refilling."

Does it have to be that much?

If that sounds like a lot, that's because it is, especially given that the MRI industry is growing. "At the moment, the installed base increases at about 4,000 systems per year globally," estimates Wade. Under these conditions, the finite nature of helium means there is a need to act. There are three roads that can be taken toward better helium sustainability, and Siemens Healthineers is proceeding on all three of them.

"An important lever is trying to improve logistics and delivery," says Karlheinz Hörner, Director Magnetic Resonance Supply Chain Management at Siemens Healthineers in Erlangen, Germany. To get an MRI machine from the production site to the customer, whether by ship, by air cargo, or by lorry, is a challenging task. The problem is that as soon as the cooling is switched off for transport, the helium starts to evaporate. "Without cooling, we lose about 3% helium per day," says Hörner.

This is not a problem in the first couple of days, but it becomes a problem at a certain point: "We aim to ship any of our MRI machines to the customer within 20 days. The critical time frame is around 25 days, which is when 70 to 80% of the helium is lost." Once at the target destination, such a helium-drained magnet has to be re-cooled with liquid nitrogen and, depending on the amount of helium lost, potentially re-filled with liquid helium. Refilling can come with its own challenges, especially in remote

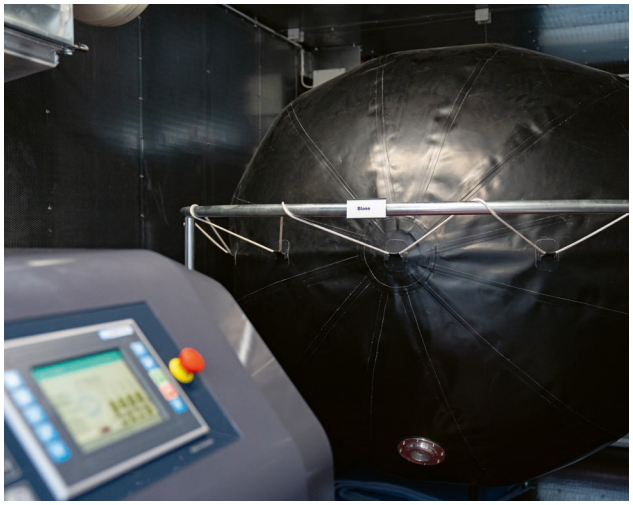

3 Helium bubble connected to a compressor that densifies helium up to a pressure of 200 bar.



4 Highly compressed recycling helium is filled into gas bottles and returned to gas vendors.

destinations. Helium is a diva. The COVID-19 crisis hasn't made life smoother for MRI shipping, either.

Helium cooling to go

In order to reduce helium losses during transport and to gain more overall flexibility, Siemens Healthineers started to introduce innovative cooling containers for long-distance MRI shipping from 2016 onwards. "There are 25 of these containers now – seven in Germany and the rest in China. This fleet will grow in the years to come," says Hörner. The cooling containers essentially mirror the MRI cooling on-site, in the hospital. There is a cooling unit at the front end of the container that keeps the MRI's cold head working all the way to customer. Avoiding breaks in the cooling chain means that no helium evaporates or needs to be refilled.

With MRI cooling containers, MRI machines can be shipped to remote countries without using air freight. This is why MRI cooling containers not only increase helium sustainability; avoiding air transport is also better for the climate. "This is especially relevant for India, where we had to use planes until recently. Australia and New Zealand have already told us that they won't accept MRI deliveries by air cargo at all anymore."

Cooling trucks are the siblings of cooling containers for shipping when it comes to overland transport by lorry. Cooling trucks are especially important in Brazil, where Siemens Healthineers operates a small factory for the local market. The cooling trucks are used to ship MRI machines to cities in the Amazon region, like Manaus, or to Recife and other cities on the north-eastern coast of South America. The benefits are the same as with cooling containers for cargo ships: No planes needed. Helium refilling avoided.

Helium recycling: from bench to balloon

A second important method of ensuring helium sustainability is recycling. This is done at the Siemens Healthineers facility in Forchheim, Germany, where old MRI systems undergo refurbishing. Originally, MRI refurbishing was done without helium retrieval. But this has changed in summer 2021, says Hörner: "We are now using a specifically designed, 20-foot-long container. It features a helium bubble which is connected to a compressor that densifies the collected helium up to a pressure of 200 bar." In the end, the highly compressed helium is filled into gas bottles, which gas vendors like Linde in turn sell to welders, divers, or indeed party balloon providers.

How much helium can be retrieved from a magnet that comes in for refurbishing depends on the type of MRI machine and on its overall condition. "Typically, MRI machines arrive at Forchheim with 25 to 30% of their original helium load," says Hörner. With 50 to 80 magnets finding their way back to Forchheim per year, this adds up to a substantial amount of recycled helium. Between July and September 2021 alone, nearly 20,000 litres of helium were retrieved with the help of the new container-compressor facility.

Rethinking MRI by draining the magnet

In addition to transport and logistics as well as recycling, there are the magnets themselves. This is where most can be gained in terms of helium sustainability, but it is also a technically demanding avenue to go. Over the years, the helium consumption of MRI machines has improved substantially, says Andrew Wade. During a ten-year lifecycle, an MRI system from the late 1980s required about 14,500 litres of helium in total. In a system produced in the early years of the 21st century, that value is down to around 3,100 litres on average. This translates into global statistics: "As an estimate, the MRI industry has managed to reduce overall helium consumption by around 25% during the last seven years – even though the installed base increased," Wade believes.

But 3,000 litres of helium per machine is by no means the upper limit of possible reductions. These days, Siemens Healthineers is pioneering an entirely new MRI platform that can be considered a moonshot from a helium sustainability perspective. Presented to the public at RSNA 2020, it is not the next evolutionary step towards less helium consumption. Rather, it marks the beginning of a totally new class of MRI systems that are radically different from their predecessors.

At the heart of the new platform is a newly designed magnet, the DryCool magnet. In the MAGNETOM Free.Max and MAGNETOM Free.Star systems, it comes with a field strength of 0.55T. The new magnet is much lighter and requires much less niobium-titanium wire, which means that cooling can be reduced to a minimum: The system contains no more than 0.7 litres of liquid helium under normal operation. Needless to say, this platform has the potential to change the world's helium sustainability equations completely. MRI's helium footprint, which was once as conspicuous as a dinosaur track, may soon become much harder to spot.

Further reading

Keeping a Hot System Cool by system architect Stephan Biber available from https://www.magnetomworld.siemens-healthineers.com/hot-topics/lower-field-mri

Scanning Faster: Application in Pediatric Neuroimaging

Michael Kean

Chief MR Technologist at The Royal Children's Hospital / Murdoch Children's Research Institute, Melbourne, Australia

How many of the MR community can remember neuroimaging pre-MRI or pre-CT, when highly skilled neuroradiologists performed air studies to outline the ventricles or CSF pathways to visualize the impact of intracranial or intraspinal pathology on normal anatomy? That was my introduction to pediatric neuroimaging in 1979.

How far we have come in such a short time is an extraordinary accomplishment, and the review by Runge [1] looking at the 50 years of innovation in imaging puts it all in perspective.

As a member of the MR community, I celebrated 30 years of pediatric MRI during the early phases of the COVID-19 pandemic, and every new advance in hardware, clinical applications, and pulse sequences still continues to amaze me – with a diverse and eclectic group of scientists and engineers working within academia and Siemens Healthineers taking us to places most of us never dreamed possible. If I reflect on my early days with my first Siemens system in the early 1990s I would never have imagined just how far this amazing imaging modality would develop. My first system was a MAGNETOM 63SP 4000 with no array coils, fast spin echo was only just being talked about, MPRAGE didn't exist, the gradient strength was 10 mT/m with an almost glacial slew rate of 10 T/m/s. When you compare that to our latest scanner, a MAGNETOM Prisma^{fit} with 80/200 gradients, it brings to reality how far we have come (Fig. 1).

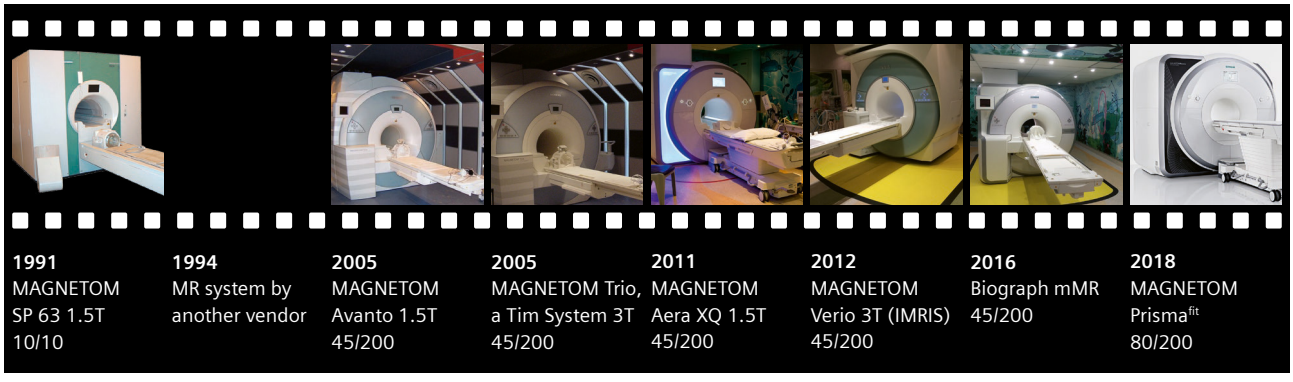

1 Evolution of MRI systems utilized by The Royal Children's Hospital for scanning pediatric patients from 1991 to present. Gradient strength represented by max gradient amplitude (mT/m) / slew rate (T/m/s).

[1] *MR scanning has not been established as safe for imaging fetuses and infants less than two years of age. The responsible physician must evaluate the benefits of the MR examination compared to those of other imaging procedures. Note: This disclaimer does not represent the opinion of the author.*

The use of MRI in the evaluation of pediatric neuroimaging has grown over the past 30 years, going from a clinical problem-solving tool after an equivocal CT to the imaging modality of choice in the majority of pediatric neuroimaging protocols.

This change in clinical focus has been due largely to the increasing availability of the modality and an explosion of technical advancements in areas such as field strength, system hardware, coil design, image reconstruction, pulse sequences, and more user-intuitive operating systems that have unleashed the potential to reduce scan times and, in some instances, correct for motion.

The requirement to make MR faster is driven by many factors within the clinical or research community. These range from patient compliance, pressure on the MR facility to scan more patients in a shorter time based on the rising costs of healthcare or unacceptable waiting lists, the requirement to add newer sequences into the protocol, and a reduction in sedation or anesthesia times.

The most common question for MR users is: Why can't we scan faster? And the processes that underlie that very simple but emotive question are complex and there is no one solution. To answer that question, we need to look at the basic equation that defines scan time in MRI, and at the complexity of interrelated components that define it. The scan time in MRI in its most basic form is

Equation 1

$$T_A = TR \cdot N_{Ave} \cdot N_y \cdot N_z$$

with TR being the repetition time, and N_{Ave}, N_y, and N_z being the the number of averages, phase encoding steps and partition encoding steps or slices, respectively. All these individual components contribute to image contrast, spatial resolution, and foremost the signal-to-noise ratio (SNR). While the latter may be affected by many factors, such as the coil, the object to be imaged, and relaxation, it is fundamentally defined by the voxel size V_{Voxel} and the time that is used to sample data T_S [2]:

Equation 2

$$SNR \propto V_{Voxel} \cdot \sqrt{T_S} \propto V_{Voxel} \cdot \sqrt{N_{Ave} N_y N_z}$$

The fact that SNR is not abundant in MRI leads, as can easily be seen from the above equation, to the well-known trade-off between spatial resolution, scan time, and SNR. Any small change of the above parameters will likely have an impact on image quality and it is ultimately the image quality that determines our success or failure on our quest to reduce scan times.

However, what is ultimately determined to be a diagnostic image of sufficient spatial resolution, signal-to-noise, and contrast-to-noise to adequately display the anatomical structure or pathology is not standardized. Our acceptance of image quality is mainly based on a radiologist's perception and their qualitative or semi-quantitative assessment of the data. Rofsky [3] wrote an editorial in JMRI in 2015 looking at this issue and its implications for how we construct our MR imaging protocols.

The goal for the MR team is to redefine the protocol to reduce the scan time whilst maintaining image quality consistent with the internal standards of the department, system hardware, and needs of the patient. In our attempts to make scan times shorter, the historical perception was that to successfully shorten scan times we needed to compromise on image quality. This is an unacceptable compromise, and we should be investigating methodologies that either produce images of an equivalent standard as our basic protocols or in some instances a higher quality, understanding the complexities involved in reducing our scan times (Fig. 2).

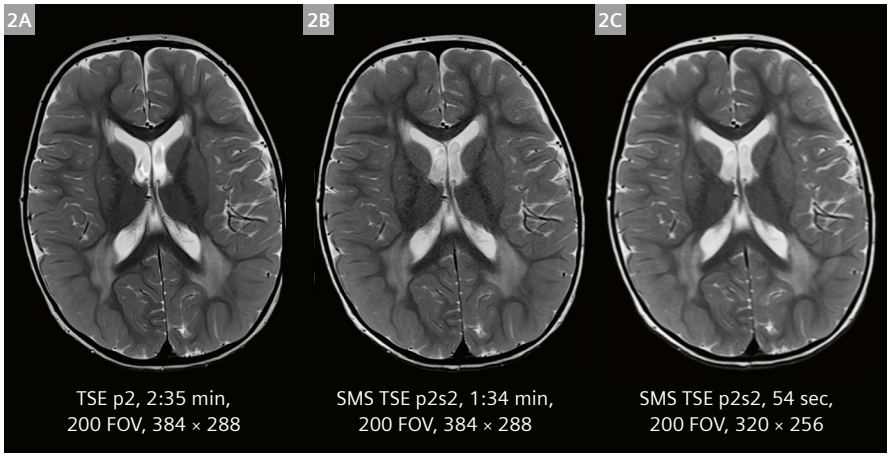

2 Three T2 images acquired with different scan times demonstrating that it is possible to balance a scan time reduction whilst maintaining diagnostic integrity.

Our longstanding collaboration with Siemens Healthineers has been instrumental in refining the internal parameters of new research applications or pre-product sequences and translating them into standard-of-care pediatric imaging. One of the most significant of these was the development of our Code Stroke protocol, in which MRI and not CT is considered as the first-line imaging modality in pediatric stroke (Fig. 3). But as we know, as soon as this article is published there will be newer and faster options available to the MR community and the acquisitions presented in this article will be considered slow.

Understanding the pulse sequence and the reconstruction method is crucial to a facility's ability to make informed adjustments within the protocol to reflect the speed and image quality they require. Many of these faster scanning sequences or iterative reconstruction techniques have the potential to introduce artifacts into the images, so it is imperative that all the information about the method is available locally, prior to implementing significant change.

So reducing scan time is just not as simple as changing one parameter. It is essential that we as end users understand the reliance on maintaining overall image quality and the potential consequences of producing unacceptable image quality based on these changes.

How many times has a member of the team come back from a meeting such as ISMRM with a new ultrafast scanning protocol, but when you try it the images look bad? Most of the time, not all the information is available during the presentation and often crucial information isn't shared. It's like baking a cake with only half the recipe and you must guess the rest. My advice would be: In your earliest foray into these new techniques, don't go jumping into the freezing lake. Instead, take it slowly and ease your way in. Initially work within the protocol tree from Siemens Healthineers. Or if it's a C2P agreement between two sites, adopt their protocol as they have done all the development work; once you have some local experience with the sequence, then and only then should you modify the parameters.

Every MRI scanning facility has its own definition of what is acceptable image quality, and that is ultimately how we all must define the success or failure of implementing any new sequence or reconstruction methodology designed to facilitate more efficient or faster scanning.

I would strongly advise all MR facilities to run their own side-by-side comparison of any new sequence or reconstruction technique before redefining your standard protocols. The qualitative evaluation of the data should include these questions:

1. Maintaining image sharpness – is there more image blurring?
2. Artifacts – comparable to previous protocol, or are there new artifacts based on the internals of the new sequence?
3. Maintenance of soft-tissue contrast that you would expect?
4. Is there more noise in the image than you are used to?
5. Is there image distortion of the anatomy within the FOV?
6. Are you getting the reduction in scan time you would expect?
7. How does it affect patient compliance?
8. Reconstruction times – are these slowing your booking allocations?

During the early 1990s, turbo spin echo was introduced based on the work by Hennig et al. [4]. It made significant reductions to scan times, but as a consequence drew a

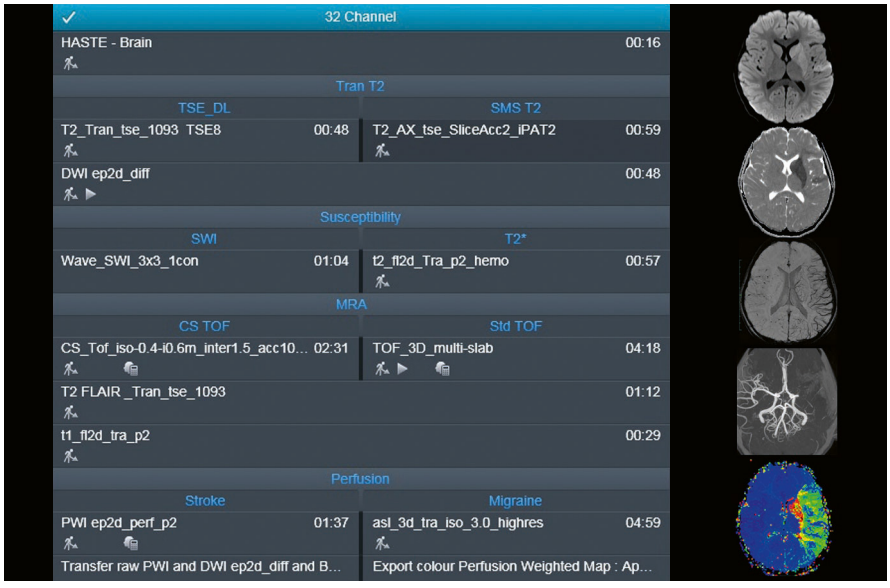

3 A screenshot of the Code Stroke protocol. MAGNETOM Prisma^{fit} with *syngo* MR E11C software using a 32-channel coil incorporating our latest modification to the protocol using advanced sequences.

considerable amount of criticism from the MR community because the image contrast, apparent image sharpness, and the appearance of fat wasn't the same as conventional spin echo imaging, leading to multiple comparative studies appearing in the literature [5, 6]. The experience gained from the very passionate debate brought about by this significant advance in MR sequences has served as a reminder to the members of the MR community who lived through it how slow we are to change. To quote John Maynard Keynes: "The difficulty lies not so much in developing new ideas as in escaping from old ones".

In the late 1990s and early 2000s, there were several major developments that had a significant impact on our ability to scan faster, and further refinements of these techniques have been the mainstay of our clinical and research imaging protocols. The development of multi-element phased array coils for brain and spine imaging enabled the development of parallel acquisition techniques. The introduction of techniques to undersample data using the characteristics of the individual coil elements in the coil array to reconstruct the data, i.e., SENSE by Pruessman et al. [7, 8] and GRAPPA by Griswold et al. [9], form the building blocks of our current parallel imaging techniques. The undersampling of data in the phase encoding direction within the imaging slice will directly impact the scan time as shown by Equation 1, but at the same time will reduce overall SNR (see Equation 2). In addition to that, we must account for noise amplification due to imperfections during the image reconstruction process. The equation for the SNR in parallel imaging is given by

Equation 3

$$SNR_{PAT} = \frac{SNR}{g\sqrt{R}}$$

where SNR refers to the SNR of non-accelerated data, R to the acceleration factor, and *g* to the geometry factor or *g*-factor. The latter essentially describes the capability of the coil array to reconstruct the given image in its specific orientation from undersampled data by exploiting the intrinsic spatial information encoded in their individual receiver sensitivities. The observed *g*-factor varies across the reconstructed image and is influenced by the coil geometry, i.e., by the number and location of the individual coil elements in the array with respect to the imaging volume, the phase encoding direction, the coil loading, and the applied acceleration factor R.

Apart from this *g*-factor noise amplification, parallel imaging has the potential to generate different and distinct types of image artifacts, which are often dependent on the parallel imaging technique used [10, 11]. Understanding the formation and characteristics of those artifacts can be complicated [12, 13], but is crucial.

The incorporation of parallel imaging into imaging protocols is standard nowadays, and acceleration factors of up to 3 can typically be achieved without impacting the resultant SNR and image quality.

In 3D imaging, the earliest implementations of parallel imaging only utilized data undersampling in the phase encoding direction. As demonstrated by Breuer et al. [14, 15], looking at parallel imaging from a more volumetric perspective opens up opportunities for modifying or distinctively controlling the aliasing that arises from the undersampling of *k*-space. The technique, which became known by the acronym CAIPIRINHA makes efficient use of the encoding capabilities of the coil array by exploiting the coil sensitivity variations not only along the phase encoding direction but also along the partition encoding direction, which results in reduced *g*-factors when compared to standard in-plane parallel imaging.

As we travel through the history of MRI, there are several very distinct periods of time in which vendors competed based on their ability to redefine the technology, and these translated to imaging protocols that produced scans of higher quality in less time.

The introduction of higher field strengths and higher density coil combinations redefined how we scanned our patients. It unleashed the potential of the significant increase in signal-to-noise and overcame some of the limitations of standard parallel imaging.

In 2005 we took delivery of our 3T MAGNETOM Trio, A Tim System, and 6 months later our 32-channel head coil [16]. These two components took our imaging to the next level. The combination of the high-SNR, high-coil-density array and 3 Tesla enabled us to confidently accelerate our acquisitions with higher acceleration factors whilst maintaining exquisite image quality.

As history has shown, nothing stands still in MRI. The evolution of new sequences or hardware from benchtop to clinic can be extremely short, and this has enabled the ongoing refinement of our clinical protocols.

The fundamental principle of CAIPIRINHA can also be applied in 2D imaging, where it has become a cornerstone of what today is known as simultaneous multi-slice (SMS) or multiband (MB) imaging [16, 17]. Notably, the simultaneous acquisition of multiple slices was explored well before the advent of parallel imaging. Mueller [18], Glover (with POMP) [19], and Larkman [20] investigated the concept in the context of acceleration and this early work underpinned the development of the SMS or MB sequences we use today.

By simultaneously exciting multiple slices rather than undersampling *k*-space, SMS doesn't shorten the time that is used to sample data. As such, it doesn't suffer the reduction in SNR generally associated with conventional

parallel imaging. In particular, SMS has proven useful for applications that intrinsically suffer from limited slice coverage or where long TRs or breath-holds render fast sequential scanning impossible [21–25].

The earliest adopters of these new SMS sequences were academic research centers that were probing the inner workings of the brain using DWI, and resting state and functional MRI. Depending on the encoding strategy, the excitation of multiple slices within the imaging volume comes with some inherent issues, such as interslice leakage degrading imaging, slice aliasing, Nyquist ghosts, and SAR. Given that TSE and DWI acquisitions are already relatively high-SAR sequences at 3T, sequence developers looked at methods to address the issue of peak RF load.

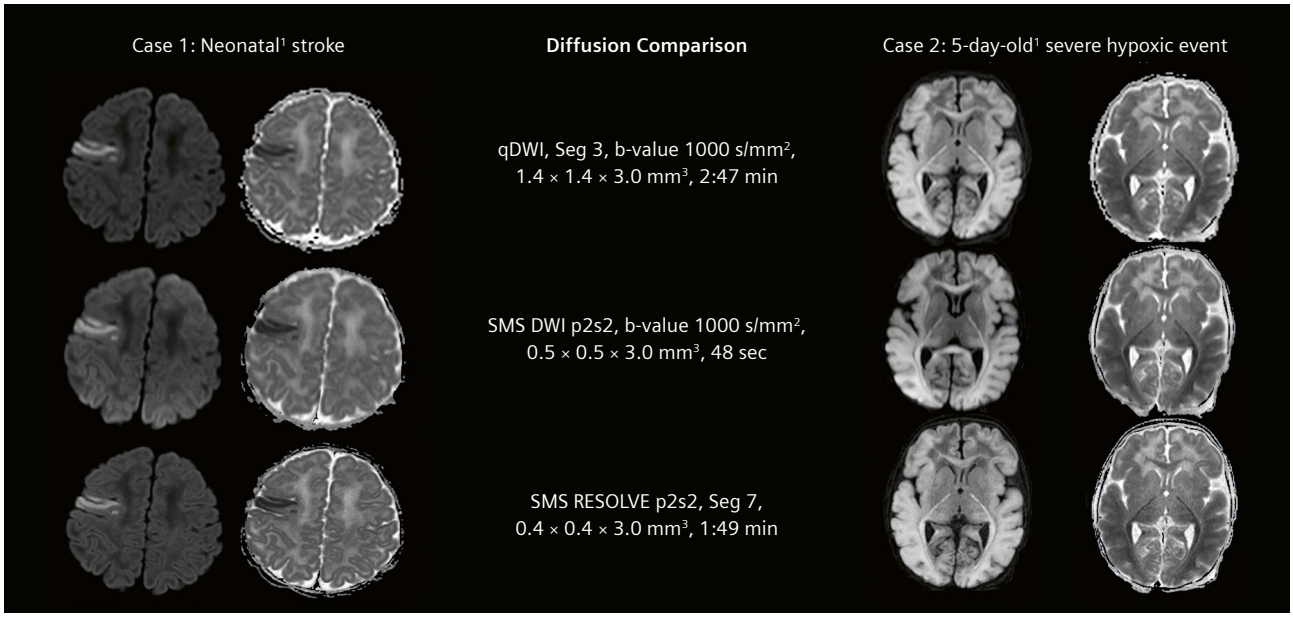

4 A comparison of different diffusion-weighted imaging (DWI) sequences demonstrating equivalent diagnostic sensitivity.

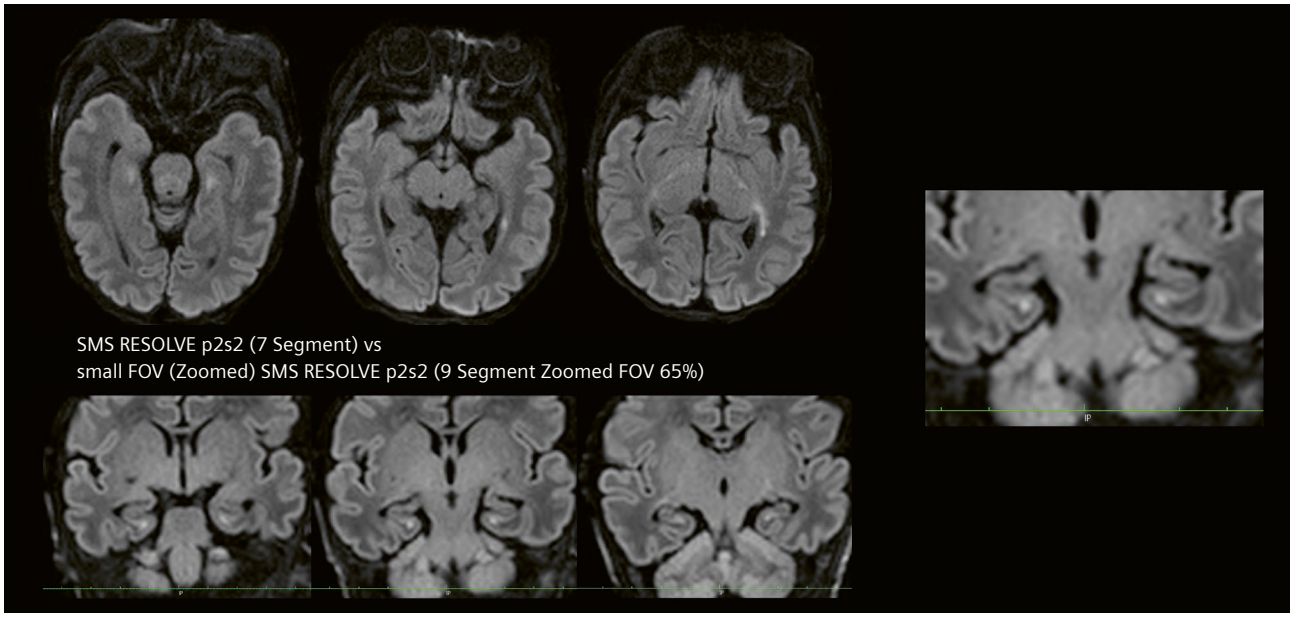

5 An example of SMS RESOLVE diffusion-weighted imaging (DWI) in a baby[1] with hypoxic ischemic encephalopathy (HIE). The images demonstrate the flexibility of the sequence to perform high diagnostic quality acquisitions in transverse and coronal.

One of the methods was to modify the original VERSE [26] pulse to meet the demands required of SMS imaging.

Our unit's first foray into SMS imaging was in 2012 and involved adapting the C2P sequence from CMRR to enhance our research studies (resting state and fMRI) and multi-direction multi-shell high b-value DTI examinations for epilepsy surgical planning. Although over the past 10 years there have been multiple modifications and enhancements to the SMS sequences, they still form an important component of our patient care.

In regards to clinical imaging, the introduction of SMS ssDWI acquisitions and later SMS RESOLVE has altered our clinical protocols. Currently we only perform accelerated ssDWI acquisitions in Code Stroke or for patients requiring a quick DWI. The use of SMS RESOLVE [24, 27, 28] is standard in all our other protocols, due to the reduction in scan time when compared to standard RESOLVE. The resultant scan time is equivalent to a ssDWI with the added benefits of significantly reduced image degradation at bone–air interfaces and areas of calcification or hemorrhage, and reduced T2* blurring based on the segmented acquisition. The beauty of the acquisition is that you can balance the number of segments and acquisition time to improve image quality in non-transverse acquisitions. We also opted to use the advanced shimming mode to further enhance our image quality (Figs. 4, 5).

With the diffusion imaging sorted, we turned our attention to implementing SMS TSE [29, 30] sequences into our standard neuroimaging protocols at 3T, primarily focusing on our epilepsy protocol. The T2 acquisitions in the protocol were required to cover the whole brain with a resolution of 0.2 × 0.2 × 2.5 mm^3 and a scan time less

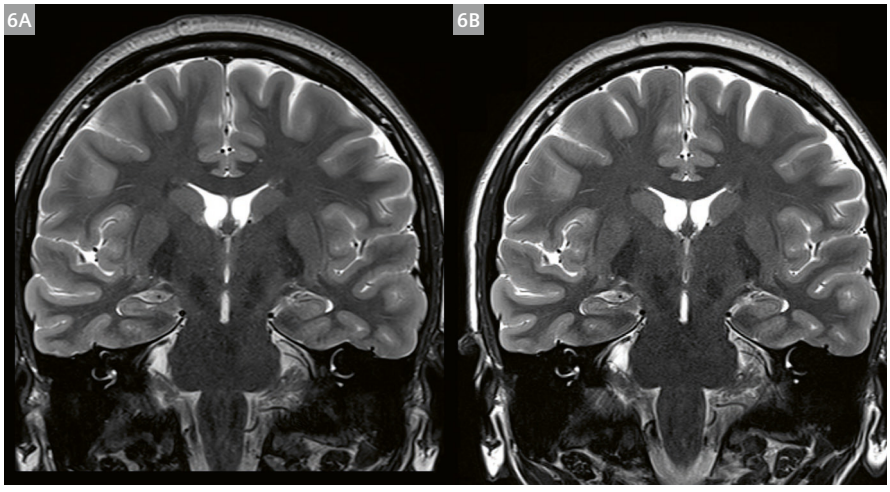

6 Two coronal T2 TSE acquisitions with matched slice thickness (2.5 mm) and resolution parameters (0.2 × 0.2 × 2.5 mm^3) demonstrating similar image quality. Image **(6B)** appears to have a higher spatial resolution but this is due to a slightly higher level of noise in the final image. **(6A)** Std T2 p2 TSE with **(6B)** SMS T2 TSE p2s2.

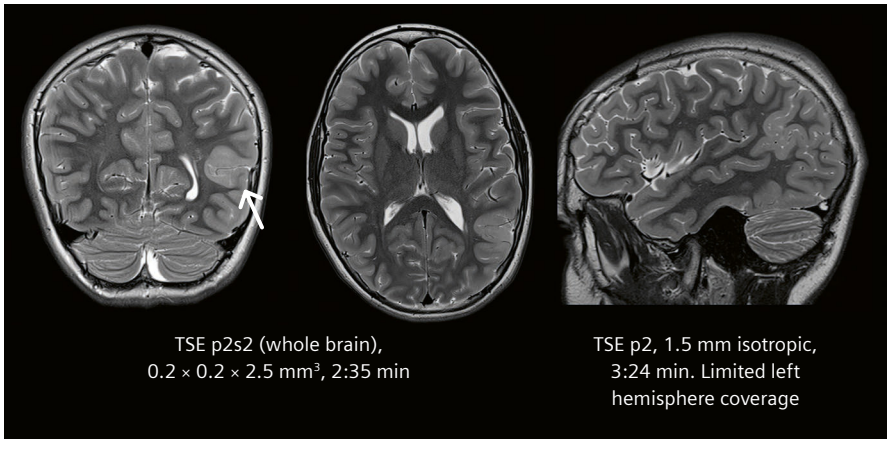

7 Clinical example from our epilepsy Dot protocol demonstrating the image quality using SMS p2s2 turbo spin echo (TSE) in a case of suspected bottom-of-sulcus dysplasia (BOSD), using MAGNETOM Prisma^{fit} with *syngo* MR E11C and the 32-channel Head Coil.

than the current standard TSE. The implementation of SMS into the diffusion components of our protocols was relatively straight forward, but SMS TSE was far more challenging in terms of addressing the SAR issues, interslice aliasing, matching similar image contrasts, and patient compliance. At our institution, we keep the scanner in normal mode and SAR management proved challenging; it required a reduction in flip angle and the utilization of normal or low SAR RF. The RF associated with the multi-slice excitation also has an impact on the image contrast and especially on the signal intensity of CSF through magnetization transfer effects. In the initial phase of trialing the sequence, the radiologists preferred the non-accelerated version, but increasing TR and TE values brought the image contrasts closer and made them acceptable to the radiologists whilst still reducing scan times by 45% (Figs. 6, 7). SMS is an extremely flexible addition to the pulse sequence and can be used with PAT or without. Most of the initial trials regarding the introduction of SMS or MB into clinical T2 imaging was using the standard TSE sequence. However, a variant was used for diffusion in cholesteatomas using the turbo gradient spin echo (TGSE) sequence, and the parameters could be modified to obtain T2 TGSE SMS BLADE acquisitions. This was extremely useful in reducing the scan time of T2 BLADE (Fig. 8). We currently use SMS TSE in non-longitudinal studies such as general screening,

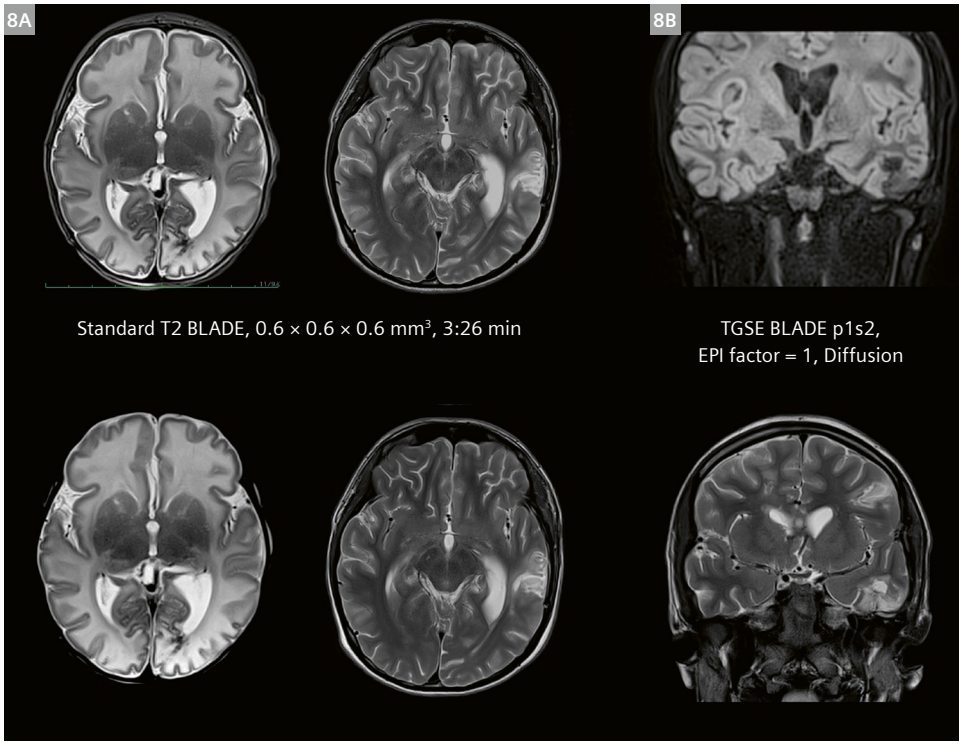

8 Two clinical examples of using TGSE SMS BLADE to reduce scan time.
(8A) Neonate with multiple congenital vascular malformations.
(8B) Follow-up postarterial stroke including coronal DWI.

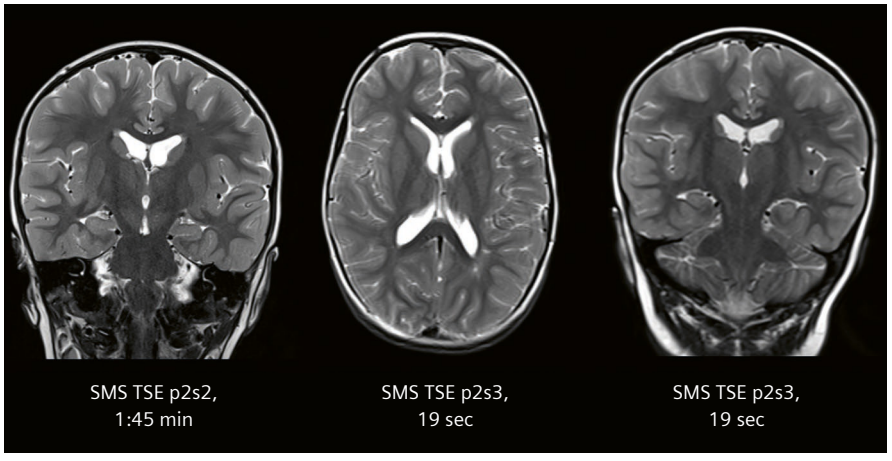

9 Due to referrer preferences, MRI is proving to be the examination of choice in pediatrics to look at hydrocephalus and shunt malfunction in patients with hydrocephalus – in reality: How fast can we go?

hydrocephalus follow-up, and Code Stroke. Not all our 3T scanners have the SMS option, so tumor monitoring still requires standard TSE. We have developed an extremely quick 3-plane T2 protocol using SMS TSE to evaluate shunt dysfunction in patients with hydrocephalus (Fig. 9).

The next phase of MRI technical developments heralded the arrival of higher density 4G coils, in particular the 64-channel coil [31] for head and neck imaging, and MAGNETOM Prisma^{fit} with its industry-leading gradients with a maximum gradient amplitude of 80 mT/m and a slew rate of 200 T/m/s. The ongoing development at Siemens Healthineers culminating in MAGNETOM Prisma^{fit} was covered by Schmitt [32] in a recent article in MAGNETOM Flash. In our efforts to reduce scan times the narrative is normally focussed on novel pulse sequences and complex image reconstruction algorithms but the complex interactions of the gradient sub-system that drives many of these advances is often ignored. Many of our standard clinical protocols utilize complex diffusion scans or fast scanning applications require the gradient sub-system to deliver acquisitions that produce smaller field of view (FOV), higher spatial resolution, shorter echo spacing (ESP), and minimum echo times (TE) to minimize image blurring and distortion artifacts.

3D imaging is the mainstay of numerous protocols within our institution, ranging from MR angiography, high-resolution T1 and FLAIR in our epilepsy protocols, and post-contrast black blood imaging in our neuro-oncology protocols, to volumetric T1 and T2 in research studies, or a basic T1 in screening brains.

Historically these acquisitions, even with standard PAT and the inclusion of 3D acceleration, have long resulted in many studies being degraded by patient motion.

In 2007 Michael Lustig et al. [33, 34] introduced their work on Compressed Sensing (CS). The technique, initially proposed as a concept to accurately reconstruct signals from small numbers of random measurements, exploits the inherent redundancy of MRI data and thus facilitates significant scan time reductions. CS requires that the acquired image is compressible. In other words, it needs to have a sparse representation in a well-known transform domain. If this condition is met, and *k*-space is undersampled such that the undersampling artifacts have a noise-like appearance in this transform domain, the image can be reconstructed using a nonlinear iterative optimization [35–37]. The level of scan acceleration is governed by the compressibility of the image rather than the factors that affect standard parallel imaging and may highly depend on the application and the basic SNR conditions at hand. While CS is typically suited to 3D applications and excellent results are obtained in 2D functional cardiac studies, the sparsity requirements are often not met with static 2D sequences.

Our first introduction to CS imaging was with 3D TOF MRA [38–40], which has a high degree of sparsity that gives us the possibility to use higher acceleration factors based on the inherent differences in MR contrast based on the TOF acquisition. We learned very quickly that CS was a very different entity from standard acceleration techniques and it presented us with many challenges on the road to

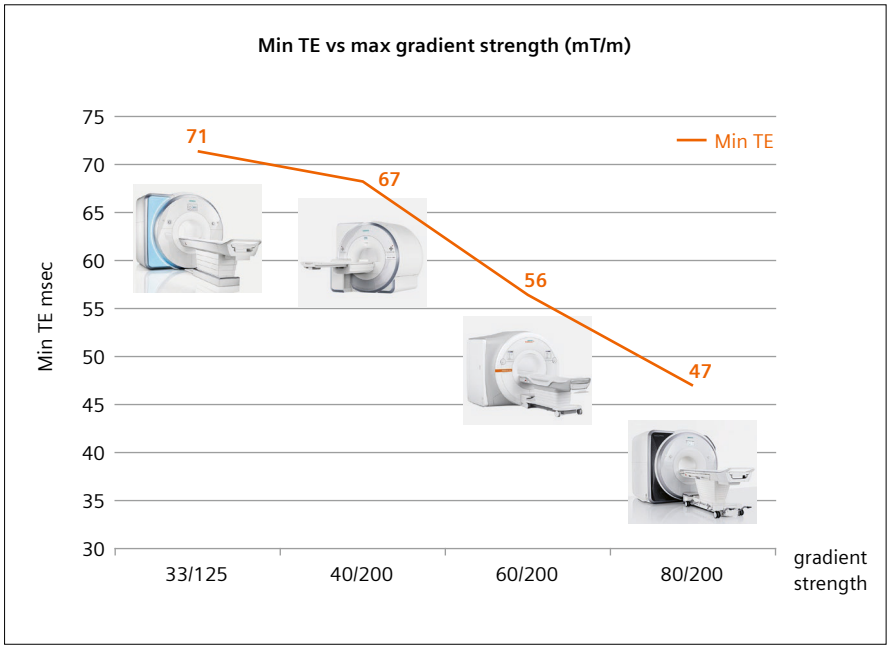

10 A comparison of the minimum TE obtained across several clinical systems with differing gradient performance (maximum gradient amplitude and slew rates) using a standardized acquisition protocol: TR 5 sec minTE, FOV 380 × 81%, Res 128 × 100%, p2, 1.5 × 1.5 × 5.0 mm^3, Monopolar Bw 2442 Hz, Normal RF, Max Performance Gradients, b-values 50/400/800 s/mm^2.

clinical acceptance – including very slow reconstruction times due to the complex image reconstruction pipeline. As with all our research sequences, we performed intensive cross-technique comparisons to optimize the data quality. We were introduced to new image reconstruction parameters that had dramatic effects on image quality. Many hours of retrospective data reconstruction were undertaken and involved varying the number of iterations and regularization factor to find the best trade-off between data consistency and mathematical data optimization. If the regularization factor was set too high, the images appeared over-filtered. If it was set too low, the images were noisy. We also found that if we changed the number of iterations, the regularization factor needed to be adjusted (Fig. 11). This process was undertaken for the acceleration factors, and our preferences for these were determined by clinical presentation. We opted for two acceleration factors: one of 7.2 for vascular follow-up cases and for moyamoya and vasculitis scans; and one of 10.2 in AVM and Code Stroke. This resulted in considerable reductions in scan times (Figs. 12–14). An added bonus from the reconstruction process was an increase in spatial resolution, which went from 0.3 × 0.3 × 0.5 mm³ (5:48 min) using standard 3D TOF to 0.4 × 0.4 × 0.4 mm³ (3:20 min) using 3D CS TOF (Fig. 15).

The translation of 3D CS TOF acquisition, although challenging at times, presented us with fewer challenges than developing protocols for our other 3D sequences. Each 3D acquisition posed different challenges in relation to overall image quality and our perceptions of how far we could take the acceleration factors. The beauty of optimizing CS protocols is that you can retrospectively reconstruct the data by modifying the regularization factor and number of iterations until you have reached that level of data consistency. The optimization of the CS T2 SPACE acquisition was the most straightforward and resulted in significant reductions in scan time. Similar to the 3D CS TOF, an added bonus was an increase in spatial resolution from 0.9 × 0.9 × 0.9 mm³ (5:20 min) for the standard 3D T2 SPACE to 0.8 × 0.8 × 0.8 mm³ (2:30 min) for the compressed sensing version (Fig. 16).

[2] *CS MPRAGE is work in progress. The application is currently under development and is not for sale in the U.S. and in other countries. Its future availability cannot be ensured.*

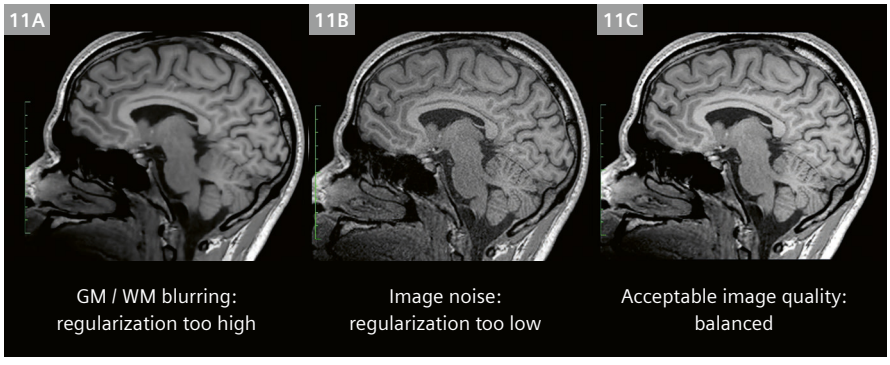

11 These images demonstrate the importance of optimizing the regularization factor in Compressed Sensing (CS) reconstruction and the impact it has on image quality. The images shown are CS MPRAGE[2] acquired on a MAGNETOM Prisma^{fit} with *syngo* MR E11C with a spatial resolution of 0.8 mm isotropic acquired in 2:30 min using a standard 32-channel Head Coil.

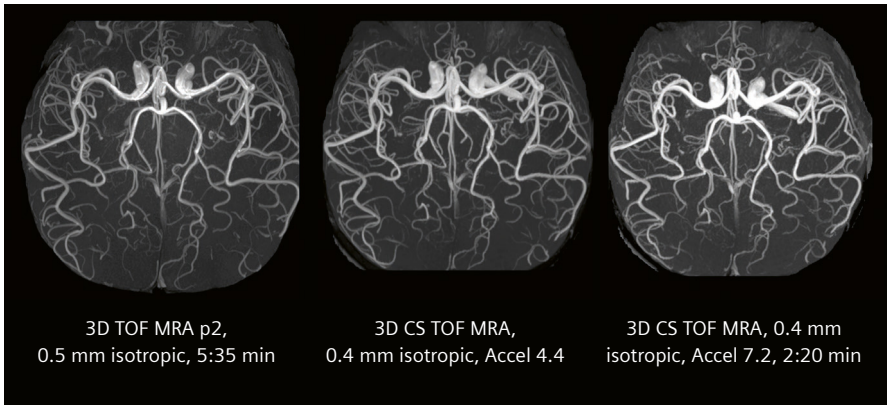

12 The image quality achieved in our internal quality assurance testing prior to our implementation of Compressed Sensing 3D Time of Flight (CS 3D TOF) into our standard protocols. The images shown are acquired on a MAGNETOM Prisma^{fit} with *syngo* MR E11C using a standard 32-channel Head Coil with previously determined regularization factor and number of iterations. These images represent the image quality achieved at differing levels of acceleration when compared to our standard 3D TOF MRA.

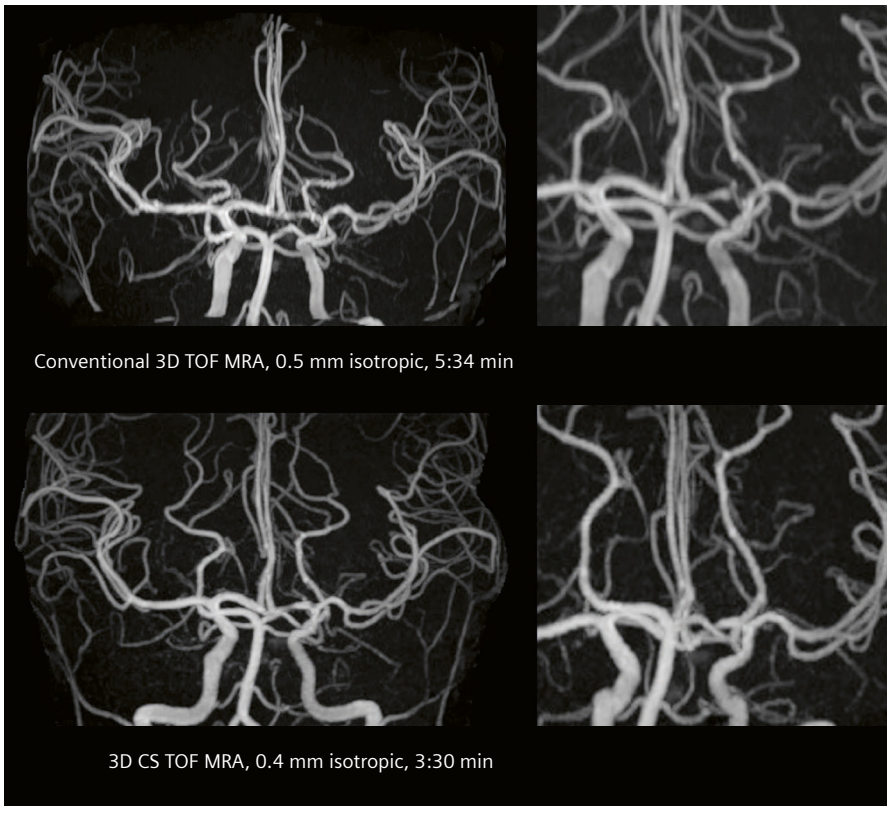

13 A comparison of two MRA techniques in a follow-up study of intracranial vasculitis.

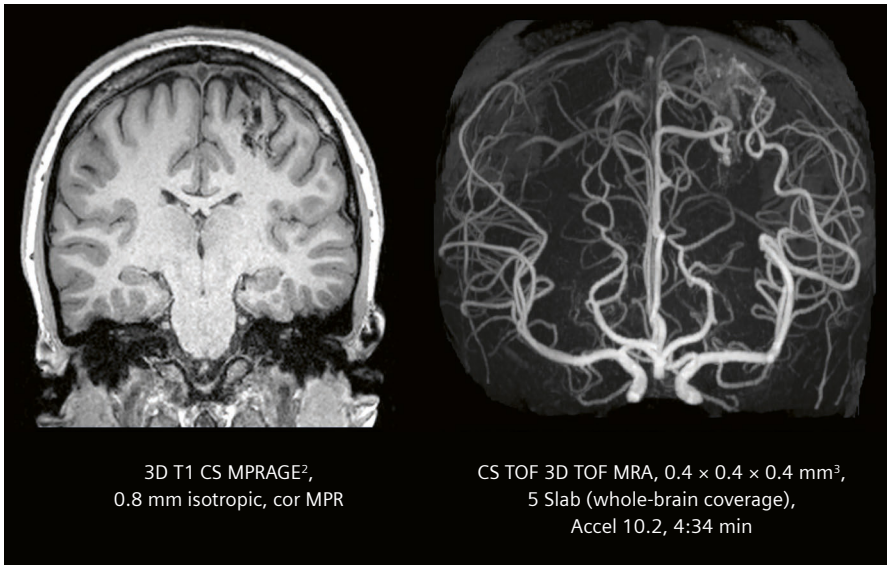

14 A clinical case of pre-operative planning in a patient with an arteriovenous malformation (AVM) acquired using CS MPRAGE² and CS 3D TOF MRA. The MRA was acquired with an acceleration of 10.2, which is our standard acceleration factor for AVMs balancing whole-head vessel coverage in an acceptable scan time whilst maintaining high quality data.

Our center has a very busy epilepsy surgery program and we have become reliant upon high-resolution fat-suppressed 3D SPACE FLAIR for our comprehensive imaging protocol in these patients [41, 42]. High resolution? Our previous standard of care protocol acquired 0.9 × 0.9 × 0.9 mm³ p2 FLAIR in 6:20 minutes, so the challenge was to see if we could obtain the same degree of scan time reduction as we did with T2 SPACE. Based on the information we obtained working with the T2 SPACE, it was clear that this wouldn't be possible. We settled on a protocol that provided a modest reduction in scan time, but as we experienced with the T2 SPACE, the SNR in acquisition enabled us to obtain a higher resolution of 0.8 × 0.8 × 0.8 mm³ (4:10 min) for the CS version compared to 0.9 × 0.9 × 0.9 mm³ (6:20 min) for the standard 3D T2 SPACE (Fig. 17).

3D T1 MPRAGE acquisitions are an integral component when constructing our pediatric brain protocols, and the flexibility to modify scan parameters based on the patient's age, clinical presentation, and compliance whilst preserving image quality is critical. If we apply our original question – can we reduce scan time whilst maintaining image quality that is equal to or better than the original? – I believe that with the majority of applications for MPRAGE we have met the brief, with the exception of epilepsy, where the image sharpness at the cortical grey matter–white matter junctions is slightly inferior to standard MPRAGE imaging, which reduces our diagnostic confidence

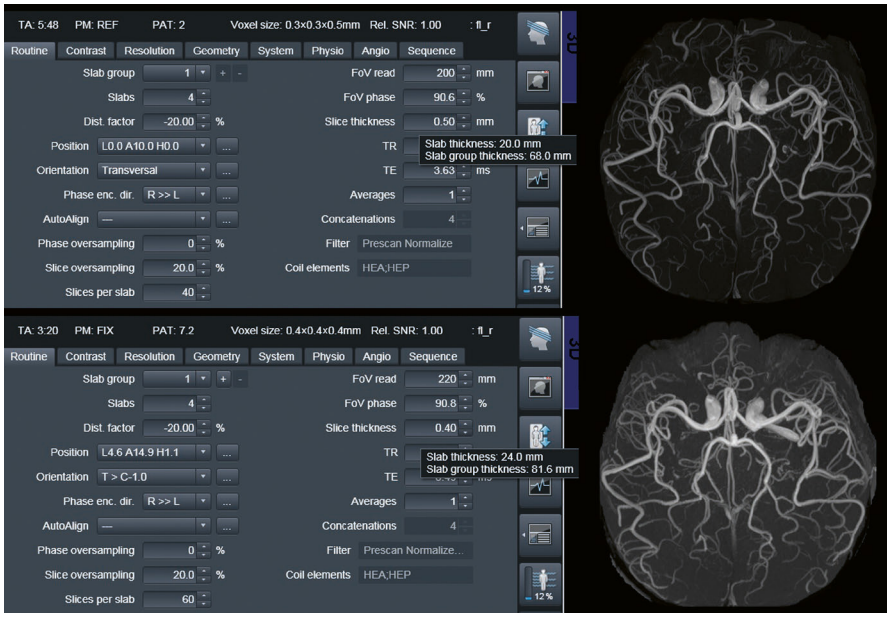

15 A screenshot of our Dot protocols for MRA demonstrating the protocol variations between our old standard 3D TOF MRA and the updated Compressed Sensing 3D Time of Flight (CS 3D TOF). The screenshots demonstrated the difference in spatial resolution, acceleration (shown as PAT) which equates to scan time reduction, volume coverage, and importantly image quality.

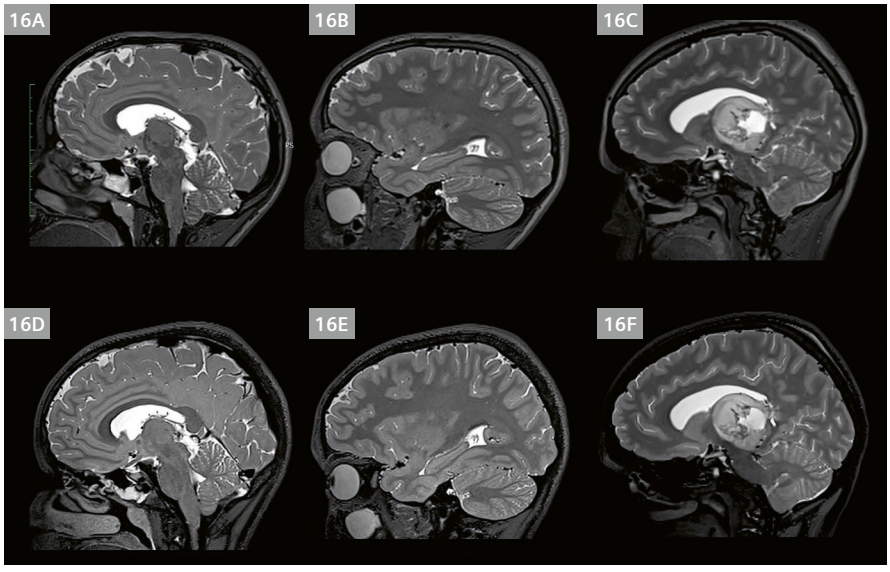

16 MAGNETOM Prisma^{fit} with *syngo* MR E11C and 32-channel Head Coil, 3D T2 SPACE, 0.9 mm isotropic, 5:20 min vs. 3D T2 CS SPACE, 0.8 mm isotropic, 2:30 min. **(16A, B, D, E)** 13-year-old normal control research participant. **(16C, F)** High-grade glioma.

in finding small cortical dysplasias (Figs. 18, 19). In contrast studies, the Compressed Sensing version of MPRAGE had the same degree of diagnostic accuracy when compared to standard MPRAGE [43, 44] (Fig. 20).

Our most challenging and definitely most frustrating task was the implementation of post-contrast, fat-suppressed black blood T1 SPACE in oncology. The sensitivity and specificity when evaluating metastatic disease in pediatric brain tumors dictates that this sequence is included in our protocols. Our initial attempts at developing this protocol failed due to inconsistent image quality resulting from a lack of inherent image contrast that introduced

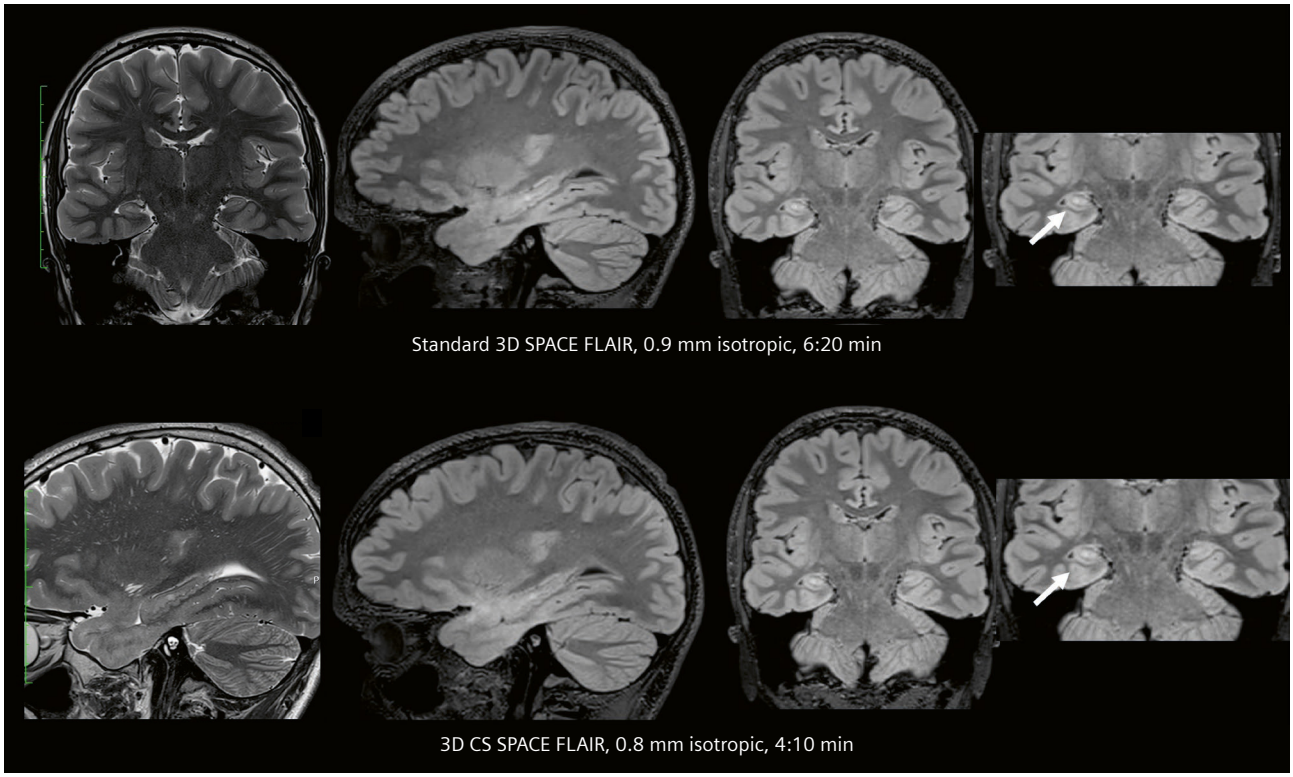

17 Comparison of 3D T2 FS SPACE and 3D T2 FS CS SPACE in a 16-year-old female with hippocampal lesion on outside imaging. Acquired on 3T MAGNETOM Prisma^{fit} with *syngo* MR E11C and the 32-channel Head Coil.

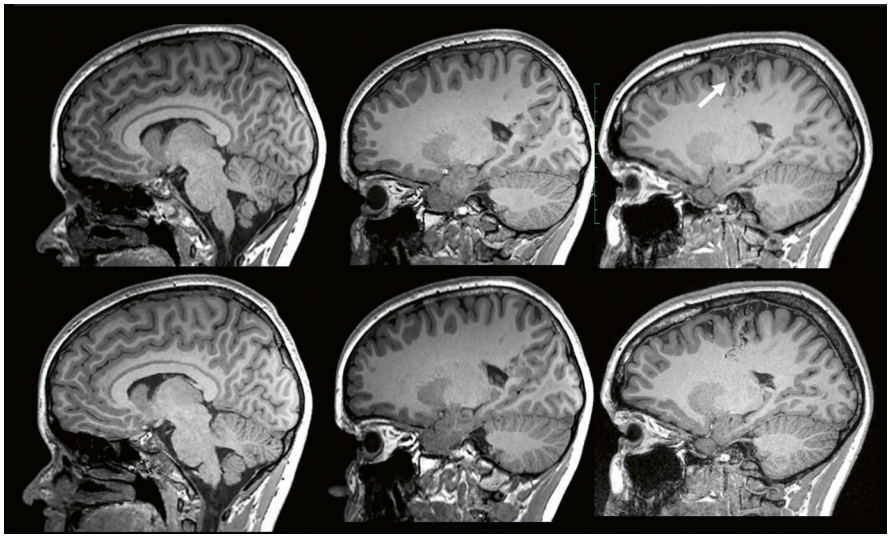

18 Comparison of standard 3D MPRAGE p2, 0.9 mm isotropic, 4:20 min (top row) and 3D CS MPRAGE, acceleration factor 3.5, 0.8 mm isotropic, 2:30 min (bottom row) in a patient with an AVM (arrow) demonstrating higher spatial resolution in a shorter scan time.

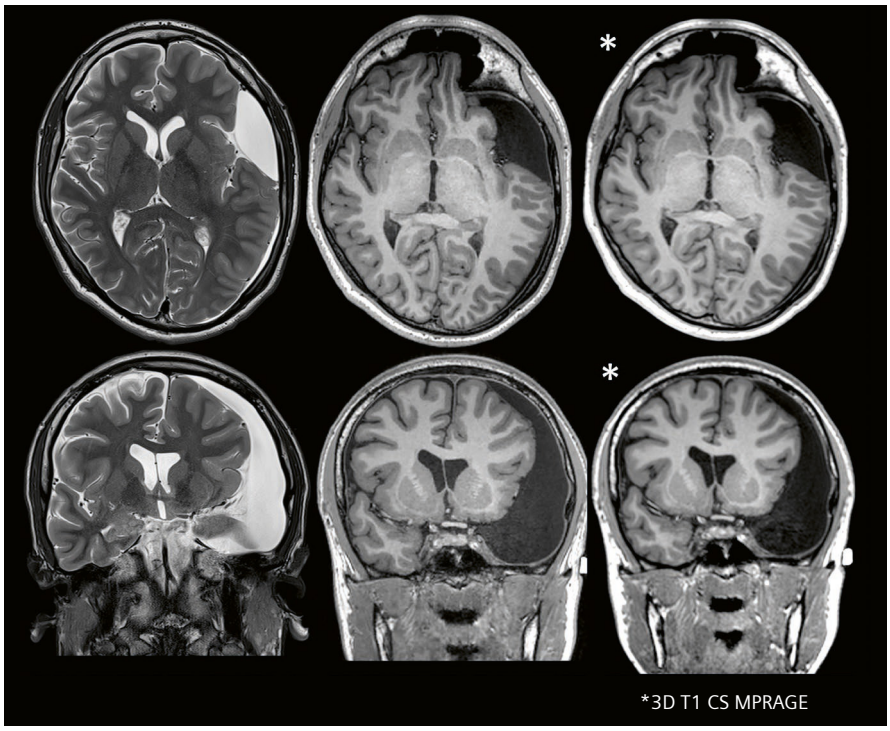

19 A clinical example of a patient with an arachnoid cyst comparing 3D MPRAGE p2, 0.9 mm isotropic, 4:20 min, and 3D CS MPRAGE[2], acceleration factor 3.5, 0.8 mm isotropic, 2:30 min, resolution in a shorter scan time. The T2 images were acquired with SMS TSE.

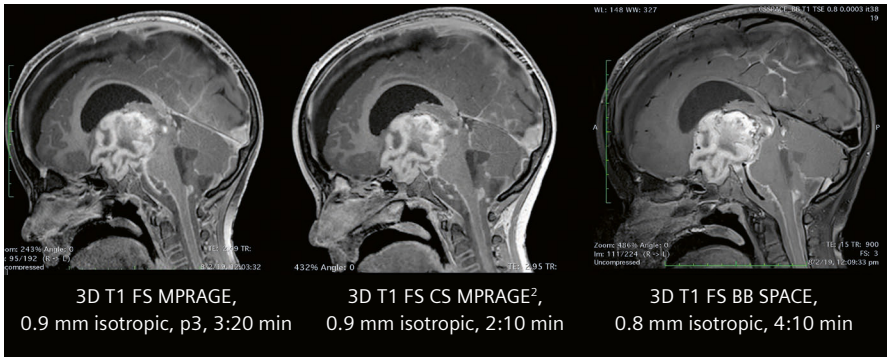

20 A side-by-side comparison of three fat-suppressed (FS) 3D T1 volumetric sequences in a patient with metastatic pilocytic astrocytoma following the administration of 0.05 ml/kg 1 mmol gadolinium contrast agent.

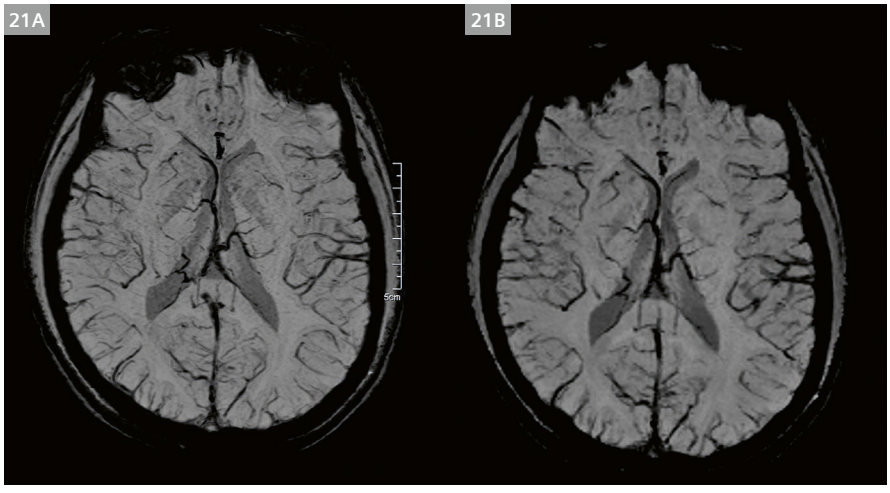

21 Our first clinical case comparing our standard susceptibility-weighted sequence (SWI) to 3D Wave CAIPI SWI. The standard SWI protocol **(21A)** uses a parallel imaging (PAT) factor of 3 and a minimally higher interpolated spatial resolution (0.6 × 0.6 × 1.8 mm³) acquired in 3:05 minutes compared to **(21B)** the Wave CAPI SWI (0.7 × 0.7 × 1.5 mm³) acquired with an acceleration of 3 × 2 and a resultant scan time of 1:32 min.

artifacts from a lack of data fidelity due to undersampling effects, motion and pulsatile artifacts, and ultimately lower acceleration rates.

On reflection, the introduction of Compressed Sensing into our standard protocol has achieved our goals by reducing scan times whilst maintaining imaging quality and diagnostic integrity [45–48]. But outside of a scan time perspective, CS also represents a paradigm shift in MRI. Unlike conventional imaging, the image reconstruction operation is non-linear, which renders this process less comprehensible. Artifacts and pitfalls may be much harder to detect and understand. The variation in our ability to reduce scan times was dictated by the weighting of the sequence (T1, T2) and the level of sparsity from the inherent tissue contrasts rather than the system hardware. The technique does require optimization of critical reconstruction parameters to maintain data fidelity when compared to standard acquisitions, and the introduction of different artifacts based on low-sparsity data and movement needs to be recognized and where necessary repeated. In some cases, a non-accelerated acquisition will produce data of higher consistency and the skill is to determine when to make that call. Remember that going faster isn't always the best option – understand the limitations and consequences of all the options you choose for scanning your patient.

The earliest attempts to accelerate 3D imaging by applying parallel imaging in both phase encoding directions produced images of varying degrees of quality and it was not until the development of CAIPIRINHA and more recently Wave CAIPI [49, 50] that it has been possible to produce high-quality data in reduced scan times without the use of computer-intensive iterative reconstruction techniques. CAIPIRINHA can be applied to SPACE and VIBE sequences within the standard 3D tree, Wave CAIPI is available also for GRE with SWI and for research applications in MPRAGE[2] and SPACE[2] [49]. This produces imaging protocols with significant reductions in time depending on the matrix coil, which ultimately defines the limitations on acceleration in both phase encoding directions. A review of the literature [51–56] supports our conclusions that the implementation of Wave CAIPI sequences into standard pediatric imaging protocols is possible and the reduction in scan times is consistent with other techniques without

[2]*Work in progress. The applications are currently under development and not for sale in the U.S. and in other countries. Their future availability cannot be ensured.*

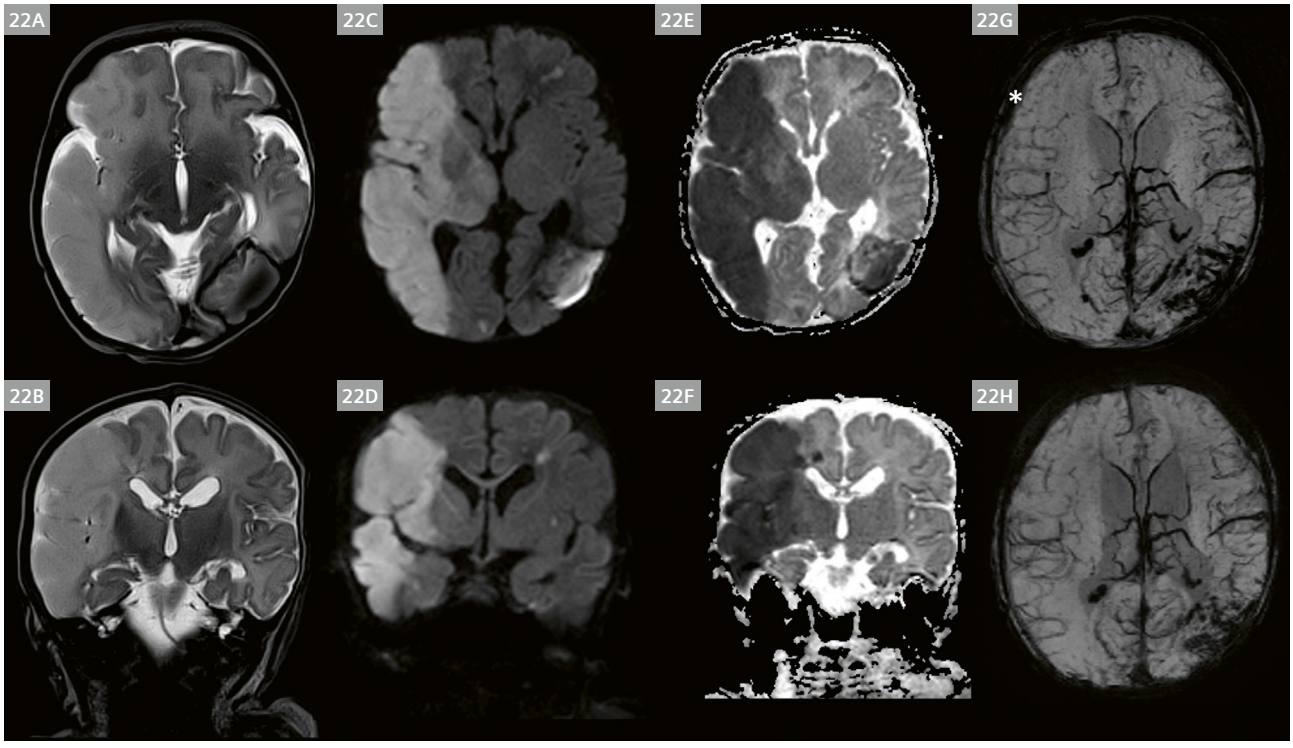

22 Clinical case of a 2-week-old baby[1], complex congenital heart disease (CHD) post 1st phase corrective surgery – clinical presentation floppy. Comparing our standard susceptibility-weighted sequence (SWI) to 3D Wave CAIPI SWI. The standard neonatal SWI protocol **(22A)** uses a parallel imaging (PAT) spatial resolution (0.6 × 0.6 × 1.6 mm³) acquired in 3:47 min compared to **(22B)** the Wave CAPI version (0.6 × 0.7 × 1.6 mm³) acquired with an acceleration of 2 × 2 and a resultant scan time of 2:30 min.
(22A,B) BLADE T2, 0.6 × 0.6 × 2.5 mm³; **(22C–F)** SMS RESOLVE DWI b 1000 s/mm², **(22G)** SWI p2, 0.6 × 0.6 × 1.6 mm³, 3:47 min; **(22H)** Wave CAIPI SWI 2 × 2, 0.6 × 0.6 × 1.6 mm³, 2:30 min

the long reconstruction times attributed to the iterative reconstruction methods. We currently use tgre_wave with SWI and MPRAGE[2]. Depending on the resolution required, the minimum reduction in scan time is 50% and higher in some other instances. In standard applications of Wave CAIPI SWI we use an acceleration factor of 3 × 2, but in neonatal[1] cases we use a more modest 2 × 2 as shown in the images. We haven't fully evaluated the application of Wave CAIPI SPACE[2] to pediatrics, as we have primarily focused our work on the compressed sensing applications (Figs. 21, 22).

Currently our preferred choices are 3D TOF, T2 SPACE, and FS SPACE FLAIR where we use Compressed Sensing and for MPRAGE and SWI we use the Wave CAIPI sequences

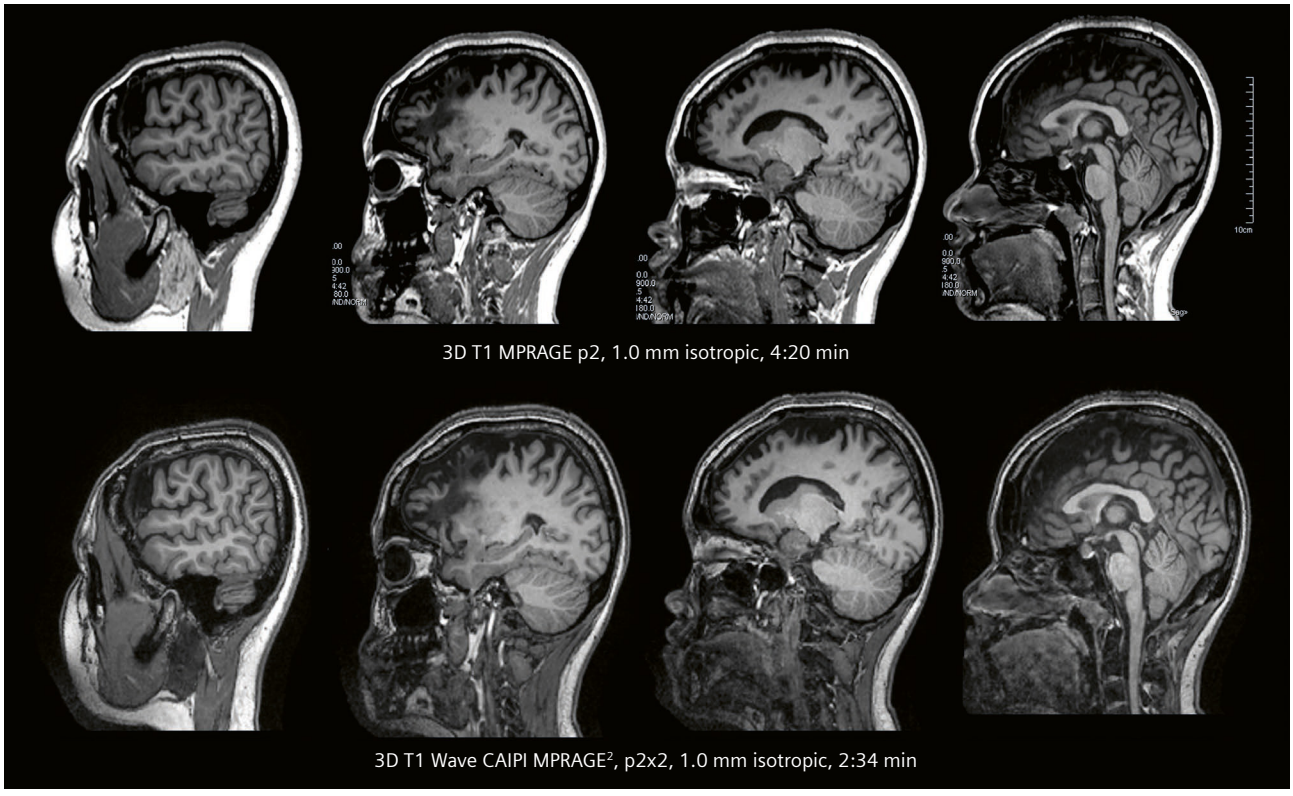

23 Clinical case of stroke follow-up in a 17-year-old girl with moyamoya disease comparing our standard 3D T1 MPRAGE (p2, 1 mm isotropic, 4:20 min) protocol to 3D Wave CAIPI MPRAGE[2] with a moderate PAT factor (p2x2, 1 mm isotropic, 2:34 min).

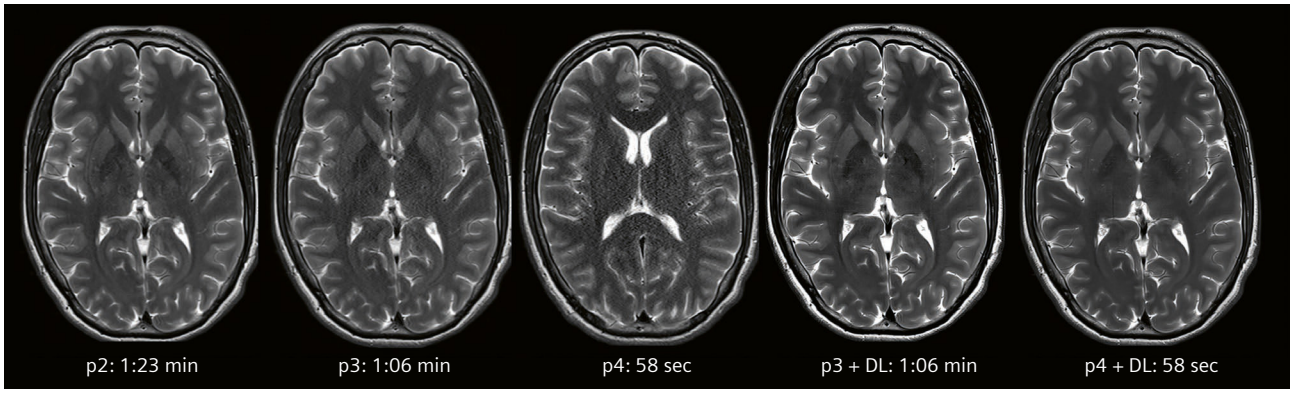

24 This is an illustration of the effect of varying the parallel imaging factor (PAT) on the scan time and subsequent reduction in signal-to-noise (SNR). All parameters remained locked except for the PAT factor. A deep learning algorithm (DL) was applied during image reconstruction to denoise the images and improve image quality.

(Fig. 23). We currently still prefer to use standard MPRAGE for neonatal imaging.

The most recent innovation and potentially the most exciting is the use of artificial intelligence (AI) image reconstruction techniques to denoise and sharpen our data in our quest to reduce scan times. Two recent articles published in MAGNETOM Flash by Behl [57] and Hammernik [58] describe the potential to dramatically reduce imaging time while maintaining image quality by using deep learning techniques. We know from the literature and every MR lecture we attend that the final MR image is a compromise between three tightly associated factors:

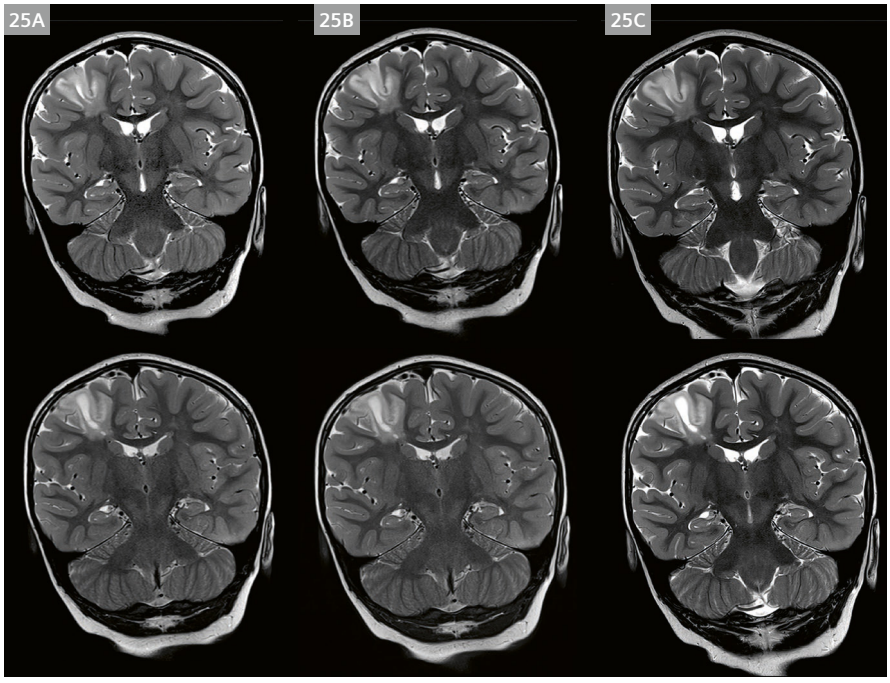

25 Clinical case of patient presenting with seizures requiring MRI for evaluation of suspected focal cortical dysplasia (FCD).
Three whole-brain coronal T2 scans were acquired where spatial resolution was matched (0.2 × 0.2 × 2.5 mm^3).

25A: TSE p2, 4:23 min
25B: SMS TSE p2s2, 2:36 min
25C: TSE p4 DL, 2:27 min

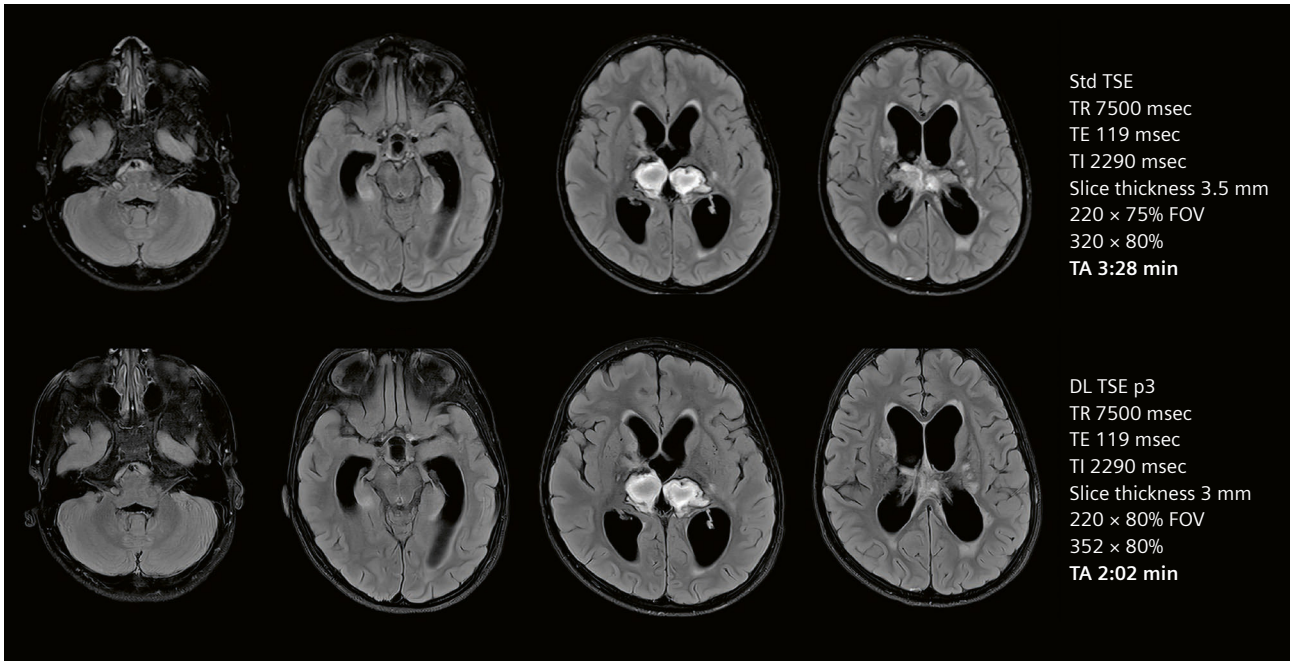

26 Clinical example comparing standard (std) 2D FS FLAIR and 2D FS FLAIR with deep learning (DL) in a patient with bilateral infarcts from venous sinus thrombosis.

SNR, resolution, and acquisition time. Minor modifications of one factor significantly affect the others – and AI or deep learning (DL) reconstruction methods have the potential to minimize these effects [59, 60].

We know that the use of PAT options introduces noise within the image, and the use of high-density coils introduces an inhomogeneous distribution of noise, which combined will degrade image quality. Deep learning solutions have the potential to denoise these images and dramatically improve image quality (Fig. 24).

By using deep learning we can increase the resolution, introduce higher PAT factors, or reduce the number of averages. We can intentionally create an image with more noise present in the data and use DL in the reconstruction phase to produce images of diagnostic quality. These techniques have enabled us to reduce the scan times of our 2D acquisitions that were previously not suitable for iterative reconstruction techniques (Fig. 25). 2D FLAIR acquisitions are used in many pediatric brain protocols and, based on conventional TSE acquisition strategies, they are considered slow when compared to other TSE sequences. The use of higher PAT factors and denoising of the image using DL has enabled a minimum 50% reduction in scan time (Figs. 26–28). This reduction in scan time is like all our 2D TSE sequences, but users should be aware that because we are potentially increasing the degree of data undersampling by using higher PAT factors, there is the potential for ringing artifacts, more prominent pulsatile effects, and more evident image degradation from movement.

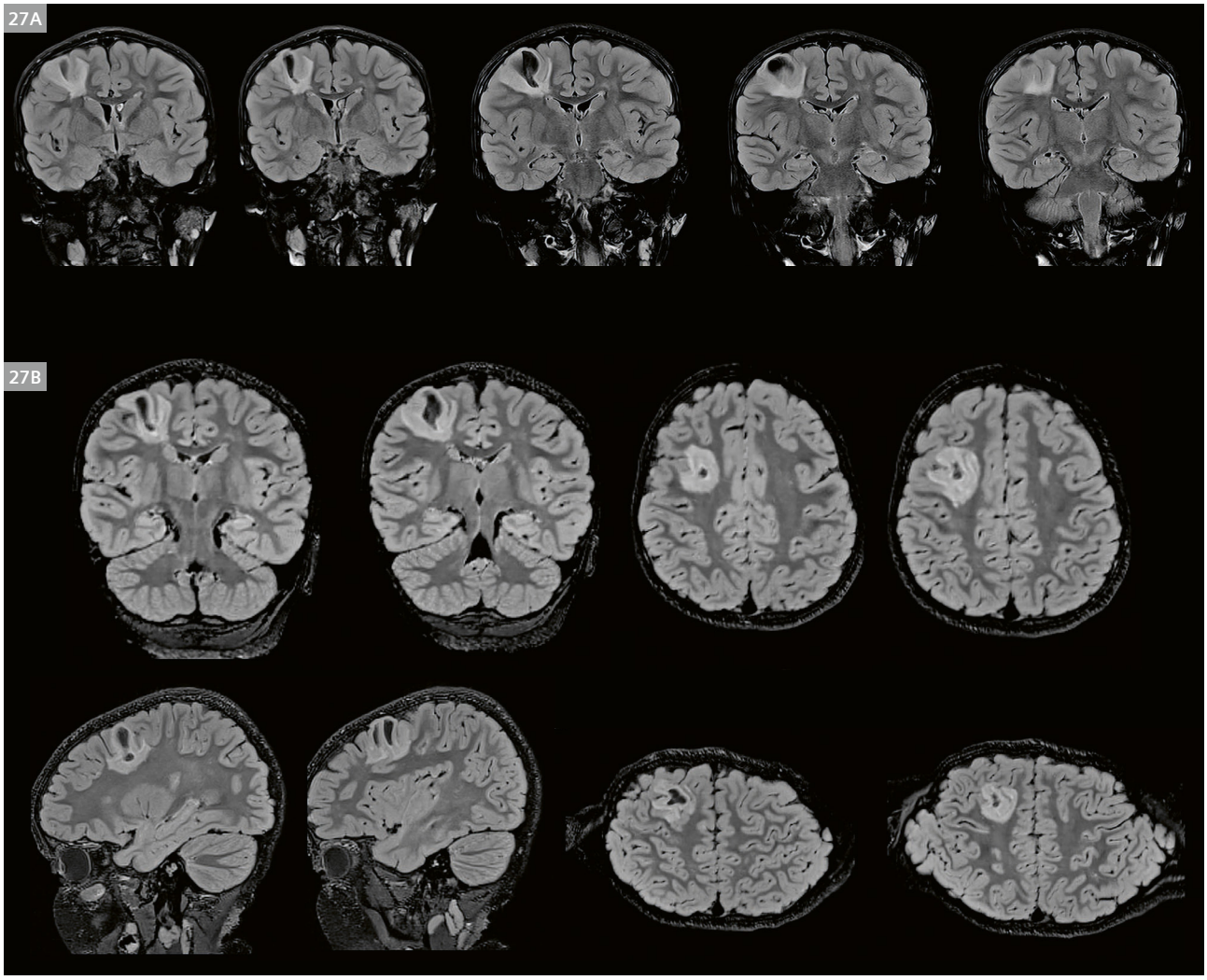

27 Same patient as in Figure 26, comparing DL 2D TSE FLAIR with 3D SPACE FS FLAIR CS. Patient presenting with seizure, clinical question: Focal Cortical Dysplasia (FCD)?
(27A) DL 2D T2 TSE FLAIR, 0.4 × 0.4 × 3.0 mm^3, 2:23 min
(27B) 3D SPACE FS FLAIR CS, 0.8 × 0.8 × 0.8 mm^3, 3:48 min

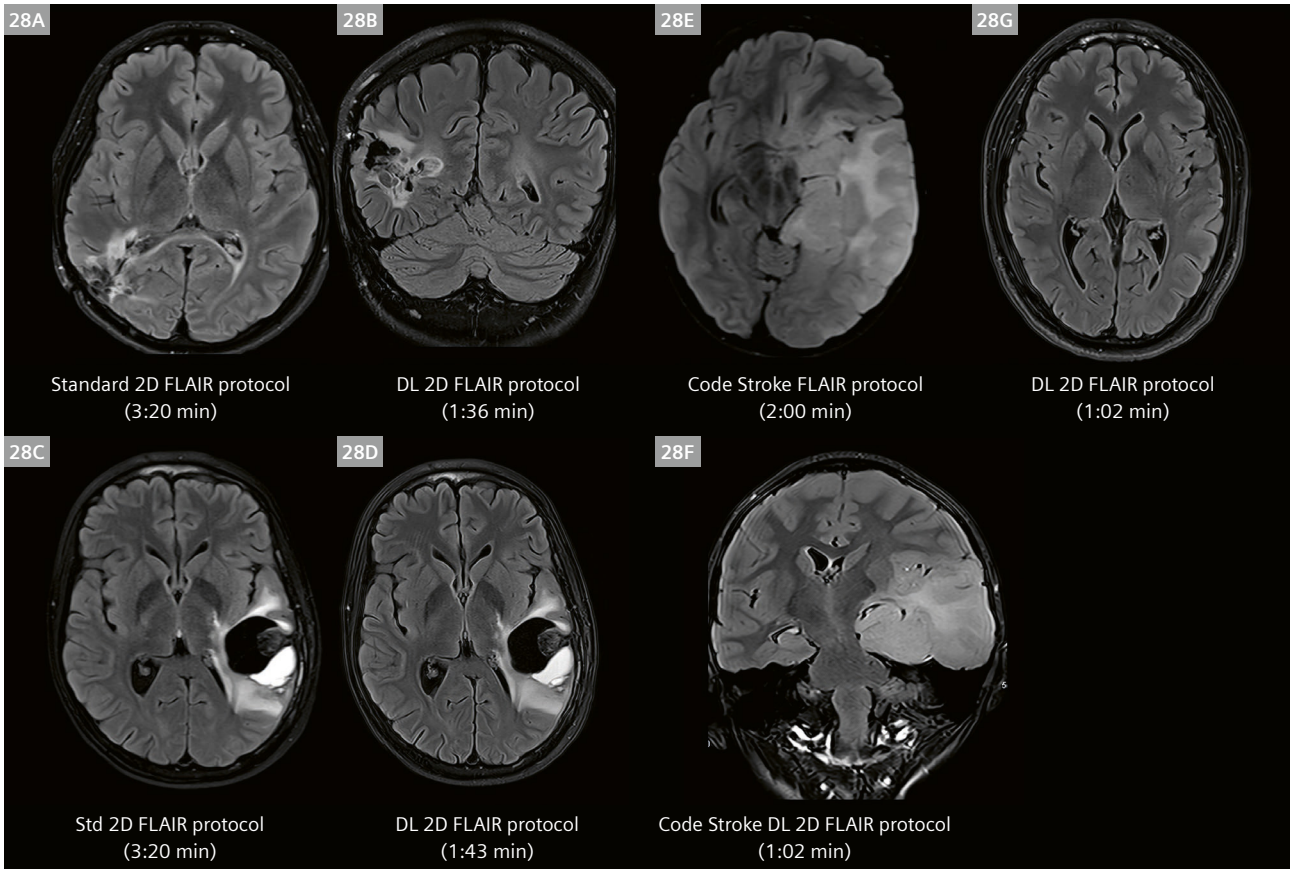

28 Standard 2D FS FLAIR has been one of the roadblocks to faster clinical brain protocols. These examples **(28A, B)** post operative DNET **(28C, D)** post operative Ewings sarcoma and **(28E, F)** Code Stroke that turned out to be high grade glioma demonstrate the utility of applying deep learning (DL) to 2D FLAIR to provide a strategy to reduce scan times and improve image quality. **(28G)** is an example of our 1 min Code Stroke FLAIR protocol.

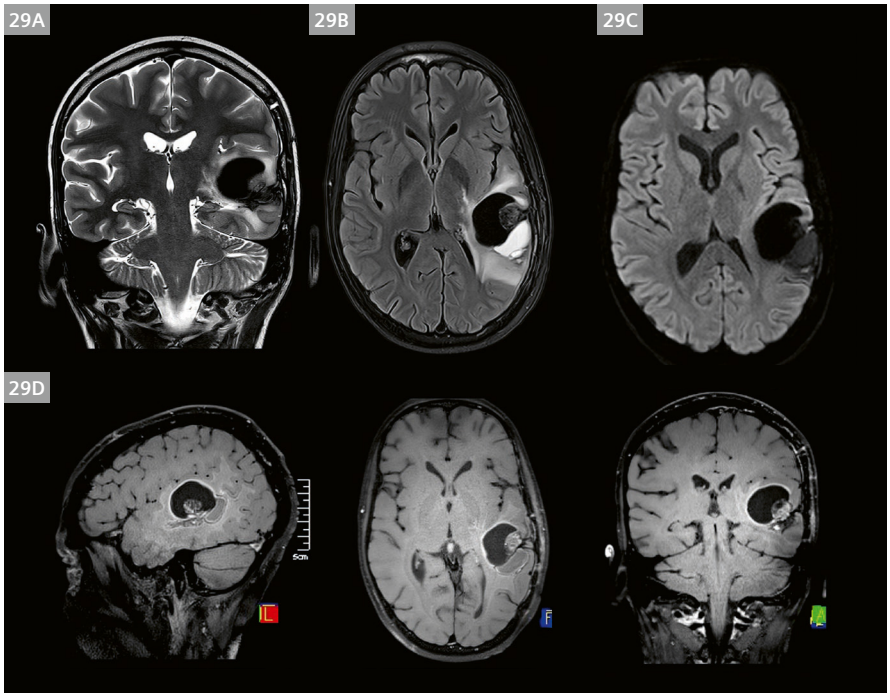

29 Putting it all together into a clinical neuro-oncology protocol. Recurrent supra tentorial Ewings Sarcoma.

29A: T2 TSE DL p3,
0.2 × 0.2 × 2.5 mm^3, 2:20 min
29B: T2 FS FLAIR DL, 1:43 min
29C: SMS RESOLVE p2s2 DWI,
b-value 1000 s/mm^2
29D: CS FS T1 SPACE BB,
0.8 mm isotropic, 4:12 min

Conclusion

The introduction of faster scanning techniques into routine pediatric protocols is possible and the scan time reductions can be significant. Whilst there may not be a single solution for each clinical protocol, the tools are available to customize your sequences to match the requirements of your department (Fig. 29). The MR team must have a basic understanding of the technique and, importantly, of any limitations associated with it before blindly implementing it into your daily protocols. There is the potential to introduce new artifacts with many of these methods, so you need to have a basic understanding of the underlying pulse sequence and reconstruction processes so you can perform quality assurance on your images. A caveat to introducing faster techniques is that some of the options available may use gradient-intensive pulse sequences that could produce a different acoustic noise profile or higher volume and induce more vibration that may disturb some patients.

Disclaimer

All images and author comments relate to the research versions of the Compressed Sensing, Wave CAIPI, and deep learning applications scanned on a MAGNETOM Prisma^{fit} with *syngo* MR E11C software.

Acknowledgments

The author acknowledges and recognizes the Wurundjeri people as the Traditional Custodians of the land in which we are located. We respect all Aboriginal and Torres Islander peoples and honor their cultural and spiritual relationships of the land and water, and their rich contribution to society.
Staff of the Children's MRI and PET Centre.
Staff and patients of RCH.
Siemens Healthineers Erlangen, Germany; Dr Heiko Meyer and the Neuroimaging team for having the confidence in our unit to enable multiple collaboration projects; Michaela Schmidt, Dr Christoph Forman and Dr Peter Speier for their help with CS 3D TOF MRA; Dr Daniel Staeb, Dr Kieran O'Brien, Jonathan Richer, and Peter Zammit from Siemens Healthineers Australia for their ongoing scientific support.

The author also acknowledges the support provided through our C2P agreement with the CMRR at the University of Minnesota, Minneapolis, MN, USA, for the SMS TSE and MB diffusion sequences.

References

1 Runge VM, Aoki S, Bradley WG Jr, Chang KH, Essig M, Ma L, et al. Magnetic Resonance Imaging and Computed Tomography of the Brain-50 Years of Innovation, With a Focus on the Future. Invest Radiol. 2015;50(9):551–556.
2 Macovski A. Noise in MRI. Magn Reson Med. 1996;36(3):494–497.
3 Rofsky NM. The importance of image quality: in the eyes of the beholder? J Magn Reson Imaging. 2015;41(4):861–865.
4 Hennig J, Nauerth A, Friedburg H. RARE imaging: a fast imaging method for clinical MR. Magn Reson Med. 1986;3(6):823–833.
5 Prenger EC, Beckett WW, Kollias SS, Ball WS Jr. Comparison of T2-weighted spin-echo and fast spin-echo techniques in the evaluation of myelination. J Magn Reson Imaging. 1994;4(2):179–184.
6 Patola WB, Coulter BA, Chipperfield PM, Lingawi SS. A comparison of conventional spin-echo and fast spin-echo in the detection of multiple sclerosis. J Magn Reson Imaging. 2001;13(5):657–667.
7 Pruessmann KP, Weiger M, Scheidegger MB, Boesiger P. SENSE: sensitivity encoding for fast MRI. Magn Reson Med. 1999;42(5):952–962.
8 Pruessmann KP, Weiger M, Börnert P, Boesiger P. Advances in sensitivity encoding with arbitrary k-space trajectories. Magn Reson Med. 2001;46(4):638–651.
9 Griswold MA, Jakob PM, Heidemann RM, et al. Generalized autocalibrating partially parallel acquisitions (GRAPPA). Magn Reson Med. 2002;47(6):1202–1210.
10 Yanasak NE, Kelly MJ. MR imaging artifacts and parallel imaging techniques with calibration scanning: a new twist on old problems. Radiographics. 2014;34(2):532–548.
11 Glockner JF, Hu HH, Stanley DW, Angelos L, King K. Parallel MR imaging: a user's guide. Radiographics. 2005;25(5):1279–1297.
12 Polimeni JR, Wiggins GC, Wald LL. Characterization of artifacts and noise enhancement introduced by GRAPPA reconstructions. Proc Intl Soc Mag Reson Med. 2008; p. 1286.
13 Larkman DJ, Nunes RG. Parallel magnetic resonance imaging. Phys Med Biol. 2007;52(7):R15–55.
14 Breuer FA, Blaimer M, Heidemann RM, Mueller MF, Griswold MA, Jakob PM. Controlled aliasing in parallel imaging results in higher acceleration (CAIPIRINHA) for multi-slice imaging. Magn Reson Med. 2005;53(3):684–691.
15 Breuer FA. CAIPIRINHA – Revisited. MAGNETOM FLASH 2015;63(3):7–15.
16 Wiggins GC, Triantafyllou C, Potthast A, Reykowski A, Nittka M, Wald LL. 32-channel 3 Tesla receive-only phased-array head coil with soccer-ball element geometry. Magn Reson Med. 2006 Jul;56(1):216–223.
17 Setsompop K, Gagoski BA, Polimeni JR, Witzel T, Wedeen VJ, Wald LL. Blipped-controlled aliasing in parallel imaging for simultaneous multislice echo planar imaging with reduced g-factor penalty. Magn Reson Med. 2012; 67(5):1210–1224.
18 Müller S. Simultaneous multislice imaging (SIMUSIM) for improved cardiac imaging. Magn Reson Med. 1989;10(1):145–155.
19 Glover GH. Phase-offset multiplanar (POMP) volume imaging: a new technique. J Magn Reson Imaging. 1991;1(4):457–461.
20 Larkman DJ, Hajnal JV, Herlihy AH, Coutts GA, Young IR, Ehnholm G. Use of multicoil arrays for separation of signal from multiple slices simultaneously excited. J Magn Reson Imaging. 2001;13(2):313–317.
21 Moeller S, Yacoub E, Olman CA, Auerbach E, Strupp J, Harel N, Uğurbil K. Multiband multislice GE-EPI at 7 tesla, with 16-fold acceleration using partial parallel imaging with application to high spatial and temporal whole-brain fMRI. Magn Reson Med. 2010;63(5):1144–1153.

22 Feinberg DA, Moeller S, Smith SM, Auerbach E, Ramanna S, Gunther M, Glasser MF, Miller KL, Ugurbil K, Yacoub E. Multiplexed echo planar imaging for sub-second whole brain FMRI and fast diffusion imaging. PLoS One. 2010;5(12):e15710.
23 Stäb D, Ritter CO, Breuer FA, Weng AM, Hahn D, Köstler H. CAIPIRINHA accelerated SSFP imaging. Magn Reson Med. 2011;65(1):157–164.
24 Setsompop K, Cohen-Adad J, Gagoski BA, Raij T, Yendiki A, Keil B, et al. Improving diffusion MRI using simultaneous multi-slice echo planar imaging. Neuroimage. 2012;63(1):569–580.
25 Barth M, Breuer F, Koopmans PJ, Norris DG, Poser BA. Simultaneous multislice (SMS) imaging techniques. Magn Reson Med. 2016;75(1):63-81.
26 Conolly SM, Nishimura DG, Macovski A, Glover GH. Variable-rate selective excitation. J Magn Reson.1969;78(3):440–458.
27 Porter DA, Heidemann RM. High resolution diffusion-weighted imaging using readout-segmented echo-planar imaging, parallel imaging and a two-dimensional navigator-based reacquisition. Magn Reson Med 2009;62(2):468–475.
28 Runge VM. Simultaneous Multi-Slice (Slice Accelerated) Diffusion EPI: Early Experience for Brain Ischemia and Cervical Lymphadenopathy. MAGNETOM Flash 2015;63(3):92–95.
29 Gagoski BA, Bilgic B, Eichner C, Bhat H, Grant PE, Wald LL, Setsompop K. RARE/turbo spin echo imaging with Simultaneous Multislice Wave-CAIPI. Magn Reson Med. 2015;73(3):929–938.
30 Wang D. Multiband Slice Accelerated TSE: Application in Brain Imaging. Proc Int Soc Mag Reson Med. 2014;22, 4317.
31 Keil B, Blau JN, Biber S, Hoecht P, Tountcheva V, Setsompop K, et al. A 64-channel 3T array coil for accelerated brain MRI. Magn Reson Med. 2013;70(1):248–258.
32 Schmitt F. An attempt to reconstruct the history of Gradient-System technology at Siemens. MAGNETOM Flash 2020;76(1). Available online from https://marketing.webassets.siemens-healthineers.com/f3ba149b97c25738/939f80bd2cc4/siemens-healthineers_magnetom-world_case-studiesSchmitt_Gradient_Development_ISMRM_2020.pdf
33 Lustig M, Donoho DL, Santos JM, Pauly JM. Compressed sensing MRI. IEEE Signal Processing Magazine. 2008;25(2):72–82.
34 Lustig M, Donoho D, Pauly JM. Sparse MRI: The application of compressed sensing for rapid MR imaging. Magn Reson Med. 2007;58(6):1182–1195.
35 Yang AC, Kretzler M, Sudarski S, Gulani V, Seiberlich N. Sparse Reconstruction Techniques in Magnetic Resonance Imaging: Methods, Applications, and Challenges to Clinical Adoption. Invest Radiol. 2016;51(6):349–364.
36 Hollingsworth KG. Reducing acquisition time in clinical MRI by data undersampling and compressed sensing reconstruction. Phys Med Biol. 2015;60(21):R297–322.
37 Forman C. Compressed Sensing: a Paradigm Shift in MRI. Compressed Sensing Supplement to MAGNETOM Flash 2016; 66(3) 8–13.
38 Natsuaki Y, Bi X, Zenge MO, Speier P, Schmitt P, Laub G. Time-Of-Flight with Sparse undersampling (TOFu): towards practical MR applications of the Compressed Sensing. Proc. ISMRM. 2014;#660.
39 Stalder AF, Natsuaki Y, Schmidt M, Bi X, Zenge MO, Nadar M, et al. Accelerating TOF MRA in Clinical Practice using Sparse MRI with Variable Poisson Density Sampling. Proc. ISMRM 2015;#3606.
40 Yanamoto T, Togashi K, Fujimoto K, Fushimi Y, Yamamoto A, Togashi K. Compressed Sensing: Application to Time-of-Flight MR Angiography. Compressed Sensing Supplement to MAGNETOM Flash. 2016;66(3):36–39.
41 Toledano-Massiah S, Sayadi A, de Boer R, Gelderblom J, Mahdjoub R, Gerber S, et al. Accuracy of the Compressed Sensing Accelerated 3D-FLAIR Sequence for the Detection of MS Plaques at 3T. AJNR Am J Neuroradiol. 2018;39(3):454–458.
42 Eliezer M, Vaussy A, Toupin S, Barbe R, Kannengiesser S, Stemmer A, et al. Iterative denoising accelerated 3D SPACE FLAIR sequence for brain MR imaging at 3T. Diagn Interv Imaging. 2022;103(1):13–20.
43 Benjamin AJV, Bano W, Mair G, Thompson G, Casado A, Di Perri C, et al. Diagnostic quality assessment of IR-prepared 3D magnetic resonance neuroimaging accelerated using compressed sensing and k-space sampling order optimization. Magn Reson Imaging. 2020;74:31–45.
44 Meister RL, Groth M, Jürgens JHW, Zhang S, Buhk JH, Herrmann J. Compressed SENSE in Pediatric Brain Tumor MR Imaging: Assessment of Image Quality, Examination Time and Energy Release. Clin Neuroradiol. 2022. doi: 10.1007/s00062-021-01112-3. Epub ahead of print.
45 Sartoretti T, Reischauer C, Sartoretti E, Binkert C, Najafi A, Sartoretti-Schefer S. Common artefacts encountered on images acquired with combined compressed sensing and SENSE. Insights Imaging. 2018;9(6):1107–1115.
46 Kayvanrad M, Lin A, Joshi R, Chiu J, Peters T. Diagnostic quality assessment of compressed sensing accelerated magnetic resonance neuroimaging. J Magn Reson Imaging. 2016;44(2):433–444.
47 Takatsu Y, Nakamura M, Yamashiro T, Ikemoto A, Sawa S, Nakamura M, et al. Evaluation of contrast and denoising effects related to imaging parameters of compressed sensitivity encoding in contrast-enhanced magnetic resonance imaging. Radiol Phys Technol. 2021;14(2):193–202.
48 Vranic JE, Cross NM, Wang Y, Hippe DS, de Weerdt E, Mossa-Basha M. Compressed Sensing-Sensitivity Encoding (CS-SENSE) Accelerated Brain Imaging: Reduced Scan Time without Reduced Image Quality. AJNR Am J Neuroradiol. 2019;40(1):92–98.
49 Polak D, Cauley S, Bilgic B, Wald L. Setsompop K. Ultrafast Multi-contrast High-resolution 3D Brain MRI: a Technical Description of Wave-CAIPI. MAGNETOM Flash 2020;76(1):21–27.
50 Polak D, Setsompop K, Cauley SF, Gagoski BA, Bhat H, Maier F, et al. Wave-CAIPI for highly accelerated MP-RAGE imaging. Magn Reson Med. 2018;79(1):401–406.
51 Chung MS, Lee EJ, Kim S, Kim SO, Byun JS. Wave-CAIPI susceptibility-weighted imaging achieves diagnostic performance comparable to conventional susceptibility-weighted imaging in half the scan time. Eur Radiol. 2020;30(4):2182–2190.
52 Filho ALG, Conklin J, Rapalino O, Schaefer P, Huang S. Ultrafast Multi-Contrast High-Resolution 3D Brain MRI: Clinical Evaluation of Wave-CAIPI Acceleration in SWI, MPRAGE, FLAIR, SPACE. MAGNETOM Flash 2020;76(1):21–27.
53 Conklin J, Longo MGF, Cauley SF, Setsompop K, González RG, Schaefer PW, Kirsch JE, Rapalino O, Huang SY. Validation of Highly Accelerated Wave-CAIPI SWI Compared with Conventional SWI and T2*-Weighted Gradient Recalled-Echo for Routine Clinical Brain MRI at 3T. AJNR Am J Neuroradiol. 2019;40(12):2073–2080.
54 Conklin J, Tabari A, Longo MGF, Cobos CJ, Setsompop K, Cauley SF, et al. Evaluation of highly accelerated wave controlled aliasing in parallel imaging (Wave-CAIPI) susceptibility-weighted imaging in the non-sedated pediatric setting: a pilot study. Pediatr Radiol. 2022;52(6):1115–1124.
55 Lin DJ, Johnson PM, Knoll F, Lui YW. Artificial Intelligence for MR Image Reconstruction: An Overview for Clinicians. J Magn Reson Imaging. 2021;53(4):1015–1028.
56 Baek HJ, Heo YJ, Kim D, Yun SY, Baek JW, Jeong HW et al. Usefulness of Wave-CAIPI for Postcontrast 3D T1-SPACE in the Evaluation of Brain Metastases. AJNR Am J Neuroradiol. 2022;43(6):857–863.
57 Behl N. Deep Resolve – Mobilizing the Power of Networks. MAGNETOM Flash 2021;78(1):29–35.

58 Hammernik K, Knoll F, Rueckert D. Deep Learning for Parallel MRI Reconstruction: Overview, Challenges, and Opportunities. MAGNETOM Flash 2019;75(4):10–15.
59 Hammernik K, Schlemper J, Qin C, Duan J, Summers RM, Rueckert D. Systematic evaluation of iterative deep neural networks for fast parallel MRI reconstruction with sensitivity-weighted coil combination. Magn Reson Med. 2021;86(4):1859–1872.
60 Knoll F, Hammernik K, Zhang C, Moeller S, Pock T, Sodickson DK, et al. Deep-Learning Methods for Parallel Magnetic Resonance Imaging Reconstruction: A Survey of the Current Approaches, Trends, and Issues. IEEE Signal Process Mag. 2020;37(1):128–140.
61 Koonjoo N, Zhu B, Bagnall GC, Bhutto D, Rosen MS. Boosting the signal-to-noise of low-field MRI with deep learning image reconstruction. Sci Rep. 2021;11(1):8248.
62 Chandra SS, Bran Lorenzana M, Liu X, Liu S, Bollmann S, Crozier S. Deep learning in magnetic resonance image reconstruction. J Med Imaging Radiat Oncol. 2021 Aug;65(5):564–577.
63 Eliezer M, Vaussy A, Toupin S, Barbe R, Kannengiesser S, Stemmer A, et al. Iterative denoising accelerated 3D SPACE FLAIR sequence for brain MR imaging at 3T. Diagn Interv Imaging. 2022 Jan;103(1):13–20.



Contact

Michael Kean, FISMRT, Chief MR Technologist
Children's MRI and PET Centre, Department of Medical Imaging
Honorary Fellow, Developmental Imaging, Murdoch Children's Research Institute
Honorary Senior Research Fellow, Department of Paediatrics, The University of Melbourne
Royal Children's Hospital
Flemington Road
Parkville, Australia
Tel.: +61 411681198
Michael.Kean@rch.org.au

Advertisement

Learn more about Deep Learning Image Reconstruction

Introduction to Deep Learning for MR Image Reconstruction
Florian Knoll, PhD
(New York University, New York, NY, USA)

Deep Learning Image Reconstruction – State of the Art
Kerstin Hammernik, PhD
(Imperial College London, UK)

Iterative Denoising and Increased Acquisition Speed
Johan Dehem, MD
(Yan Yperman Ziekenhuis, Ieper, Belgium)

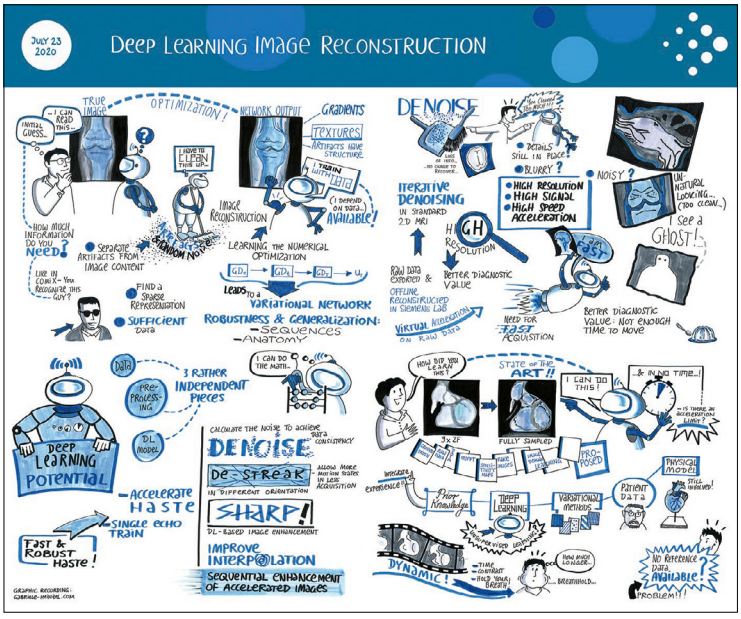

Graphic Recording: www.gabriele-heinzel.com

Don't miss this valuable source of information
www.siemens-healthineers.com/MWS2020-recordings

Pediatric Whole-Body MRI: How I Do It

Bac Nguyen, BSc; Lil-Sofie Muller, M.D., Ph.D.

Oslo University Hospital, Rikshospitalet, Oslo, Norway

Introduction

At Oslo University Hospital we have a high rate of pediatric patients, which can often pose a technical and diagnostic challenge. Indications for MRI in children at our institution include brain, spine, heart, abdomen, pelvis, MSK, and whole body. In non-cooperative children or children under 5 or 6 years of age[1], the examinations are most often performed under general anesthesia. For the older children, entertainment on a TV screen is offered and the examination is then generally well tolerated. In infants under 3 months of age, the feed and wrap technique is used, sometimes in combination with light sedation.

As the name indicates, whole-body MRI (WB-MRI) can image the entire body in one scan. It gives a full overview of multifocality, and favors detection of disease over characterization, sometimes even before symptoms develop. Although the entire body is not always imaged, the term whole-body MRI is normally used when three or more anatomical areas are included in one scan. There are numerous indications for WB-MRI [1]. In our institution, it is most often used for cancer staging, for early detection of cancer in children with genetic predisposition syndromes, or in cases of relapse in children with treated malignancy. It is also widely used in inflammatory disorders like chronic non-bacterial osteomyelitis and in children with juvenile idiopathic arthritis (JIA). Sometimes WB-MRI is used in children with non-specific symptoms and unknown underlying pathology.

[1] *MR scanning has not been established as safe for imaging fetuses and infants less than two years of age. The responsible physician must evaluate the benefits of the MR examination compared to those of other imaging procedures.*

Equipment

Modern high-end systems like the 3T MAGNETOM Vida and 1.5T MAGNETOM Sola (Siemens Healthcare, Erlangen, Germany) are equipped with BioMatrix technology, which facilitates WB-MRI with exquisit image quality within a short scan time. At our hospital, we mostly perform WB-MRI on our 1.5T systems. We currently only have one 3T scanner, which is prioritized for other uses. Our 1.5T scanners are a MAGNETOM Aera and a MAGNETOM Avanto^{fit} (Siemens Healthcare, Erlangen, Germany). The protocols are highly optimized regarding image quality and total scan time. The coils available for these scanners are designed for WB-MRI and consist of a Head/Neck 20, a Spine 32, two Body 18, and a peripheral angiography coil



1 The TV screen is behind the bore. A mirror (not shown here) allows the patient to see the screen while lying in the bore.

with 36 channels. These coils make our workflow faster, and we use the time saved to invest in the image quality.

TV entertainment is offered through our NordicNeuroLab solution (Fig. 1). The child can choose to watch a movie, YouTube, Netflix, etc. (Fig. 2). In our experience, being able to watch TV drastically reduces the need for sedation or anesthesia, and most patients manage to complete a WB-MRI examination with sufficient image quality.

Protocols

With a team of 26 MRI radiographers, it is important to have robust protocols that are easy to set up and have minimal need for adjustment. For optimal and consistent image quality, we decided to make the protocols according to weight rather than age (Fig. 3). It is easier to tailor each



2 Children can choose from various entertainment options.

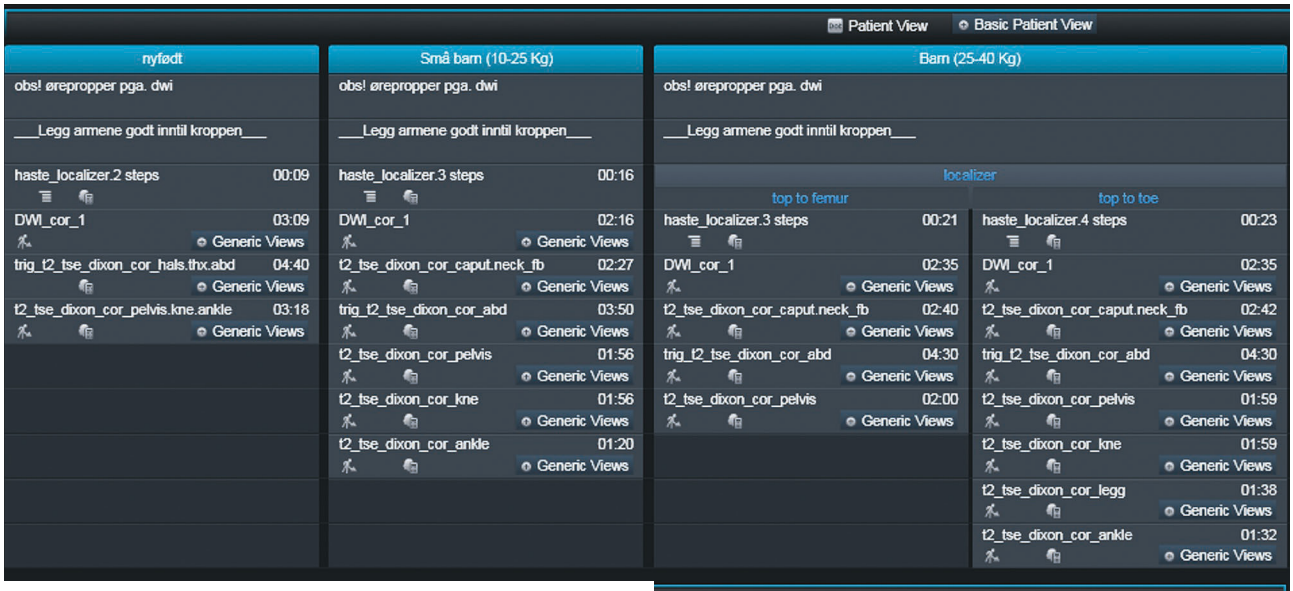

3 Screenshots showing how our WB-MRI are set up. We sometimes perform head-to-femur scans, and sometimes head-to-toe. The protocols are optimized according to weight rather than age.

protocol according to weight, because children with the same age can vary considerably in size.

There is no unifying protocol for WB-MRI in children. The sequences and planes are chosen according to the clinical question. However, WB-MRI is most often used as a screening tool for detecting pathology or identifying multifocality. This means that almost all protocols include a water-sensitive sequence with fat suppression, most often performed in the coronal plane. Historically, the STIR sequence was used most frequently due to its homogenous fat suppression [1]. In recent years, the Dixon fat-suppression technique has become readily available and

	0–10 kg		10–25 kg		25–40 kg		> 40 kg	
	T2w TSE Dixon	DWI	T2w TSE Dixon	DWI	T2w TSE Dixon	DWI	T2w TSE Dixon	DWI
Orientation	coronal	coronal	coronal	coronal	coronal	coronal	coronal	coronal
FOV read (mm)	350	300	350	400	450	450	450	450
FOV Phase (%)	90.6	98.5	112.5	74.6	131.3	69.3	140.6	69.3
FOV Phase Oversampling (%)	0	50	0	50	0	50	0	50
Phase direction	R-L	F-H	R-L	F-H	R-L	F-H	R-L	F-H
Base resolution	384	130	384	134	384	150	384	150
Phase resolution (%)	100	100	100	100	100	100	100	100
Slice thickness (mm)	3	3.5	3.5	3.5	4	4	4	4
Slices	30*	28*	38*	38*	46*	46*	46*	46*
Voxel size, interpolated (mm)	0.5 × 0.5	1.2 × 1.2	0.5 × 0.5	1.5 × 1.5	0.5 × 0.5	1.5 × 1.5	0.5 × 0.5	1.5 × 1.5
Scantime	2.5 min – 3 min	2.5 min – 3 min	2 min – 2.5 min	2 min – 2.5 min	2 min – 2.5 min	2.5 min – 3 min	2 min – 2.5 min	2.5 min – 3 min
TR (ms)	3540*	4560*	4470*	5320*	5400*	7290*	5200*	7290*
TE (ms)	109*	96*	109*	78*	109*	78*	109*	78*
Concatenations	2	1	2	1	2	1	2	1
Averages	3	10 (b50) / 30 (b1000)	1	2 (b50) / 15 (b1000)	1	4 (b50) / 15 (b1000)	1	4 (b50) / 15 (b1000)
Flip Angle (degree)	150		150		150		150	
Restore magnetization	yes	no	yes	no	yes	no	yes	no
PAT (GRAPPA)	2	2	2	2	2	2	2	2
Bandwidth (Hz/Px)	521	2024	512	2488	512	2380	512	2380
Turbo Factor	20		20		20		20	
b-values		b50 / b1000		b50 / b1000		b50 / b1000		b50 / b1000
TI		180		180		180		180
DWI mode		3D diagonal		3D diagonal		3D diagonal		3D diagonal
Diffusion scheme		monopolar		monopolar		monopolar		monopolar

Table 1: An overview of our parameter settings on a 1.5T MAGNETOM Aera. Keep in mind these settings can be different depending on scanner model. Also, this table only shows one step, while WB-MRI uses multiple steps.
*varies due to coverage

enables the combination of robust Dixon fat suppression with the image quality from the T2-weighted TSE sequence. In addition, this produces in-phase, out-of-phase, water-sensitive and fat-sensitive images in one acquisition. Our WB-MRI protocol now consists of T2w coronal TSE Dixon and coronal DWI (b-values 0 and 1000 s/mm^2, and ADC map) because we mainly use WB-MRI for detection rather than characterizing lesions. Previously, we included T1w coronal TSE in our WB-MRI protocol, mainly for bone-marrow pathology, but this is now no longer included in the standard protocol because we get all the information we need from T2w coronal TSE Dixon fat-only images [2].

Leaving out T1 sequences saves time that we can then invest in other dedicated sequences depending on the region of interest. For instance, we can add a T1-weighted sequence for T1 characterization. The setup for our protocol parameters can be seen in Table 1.

WB-DWI is often performed in transverse plane because it results in fewer distortion artifacts and better image quality. We later reconstruct and compose the images in the coronal plane, often in inverted scale to resemble PET images (Fig. 4). The big drawback of transverse acquisition is the long scan time, especially if two or more b-values with an ADC map are required. We have worked on optimizing the DWI in order to obtain the sequence directly in the coronal plane with two b-values and an ADC map. The main benefit is that this is time-efficient, but the coronal images are also better quality than the ones reconstructed from the transversal acquisition. We have protocols for both 3T and 1.5T systems, but we mainly use 1.5T scanners because it results in less distortion and inhomogeneity on the DWI sequence. Another important reason for using 1.5T is that it allows us to cover more of each step in the coronal plane than we can with 3T.

Shorter scan times in coronal acquisition are possible due to less coverage in the A-P direction, which means fewer slices and shorter TR. Due to inhomogeneity and distortion when acquiring images in the coronal plane, you need to use a FOV phase of around 60–70% (scanner dependent). If you choose a larger FOV phase, it will cause distortion in the periphery of the images. Phase direction is F-H to cope with distortion, and a phase oversampling of up to 50% helps to avoid aliasing artifacts (Fig. 5).

A good tip is to start the protocol with coronal DWI. However, this comes with advantages and disadvantages. One advantage is that you get a fast overview with the help of DWI to draw your attention to the area of pathology. Then, subsequent sequences can be focused on the area of interest. Another point is that coronal DWI requires more post-processing time compared to other sequences in the protocol. This includes composing, multiplanar reconstruction, and maximum intensity projection. The post-processing can be performed during the acquisition of the morphological sequences to save time.

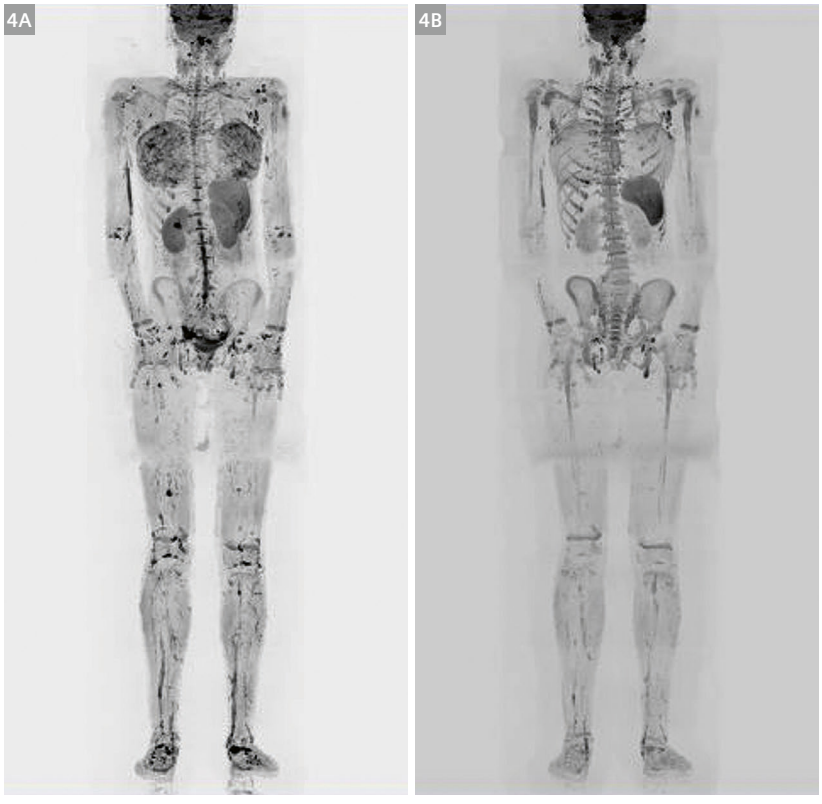

4 WB-DWI with inverted scale to resemble PET images. **(4A)** b-value 50 s/mm^2 and **(4B)** b-value 1000 s/mm^2. Performed directly in the coronal plane with multiple steps and then composed.

The disadvantage of starting with DWI is that the intense noise from the sequence at the very beginning of the protocol can scare children. Therefore, we always talk to the children to prepare them for the noise and also stay open to the option of starting with morphological sequences such as T2w coronal TSE Dixon if needed. We give the children headphones and earplugs. For younger children, earplugs can be fitted by cutting them in half, but this is not something we do at our institution. Instead, we use "Putty Soft", which can be sized to fit any ear (Fig. 6).

Conclusion

It is feasible to perform WB-MRI in children of all ages. The protocol must be robust and adjusted to patient weight. For specific indications, WB-MRI may give a good overview of disease burden in multifocal disease. It can also be useful in follow-ups for disease recurrence, and is occasionally used to look for disease focus in non-specific findings or symptoms.

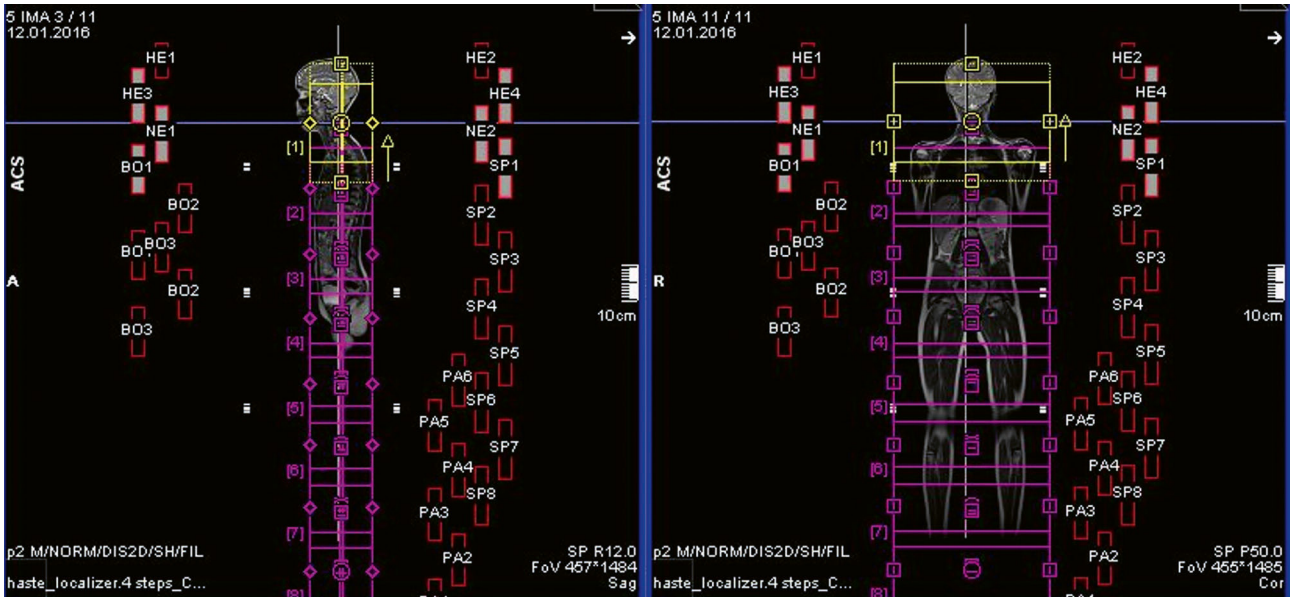

5 Our setup of WB-DWI for direct coronal imaging. In this case, we had eight multiple steps and then composed later.

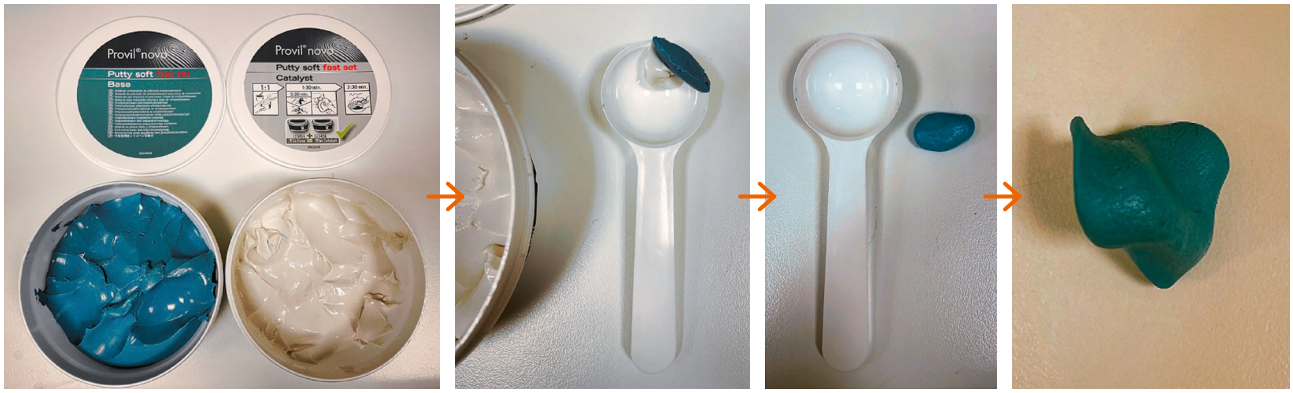

6 We mix the Putty Soft to shape earplugs that fit any patient perfectly. It is easy and fast to use, and reduces noise in combination with the headphones.

Case 1

A 5-month-old baby[1] with suspected multifocal Langerhans cells (LCH). WB-MRI was performed for disease staging with general anesthesia on a 1.5T MAGNETOM Avanto^{Fit}. The examination showed multiple lesions throughout the skeleton and lesions in the spleen, skin, and retroperitoneum.

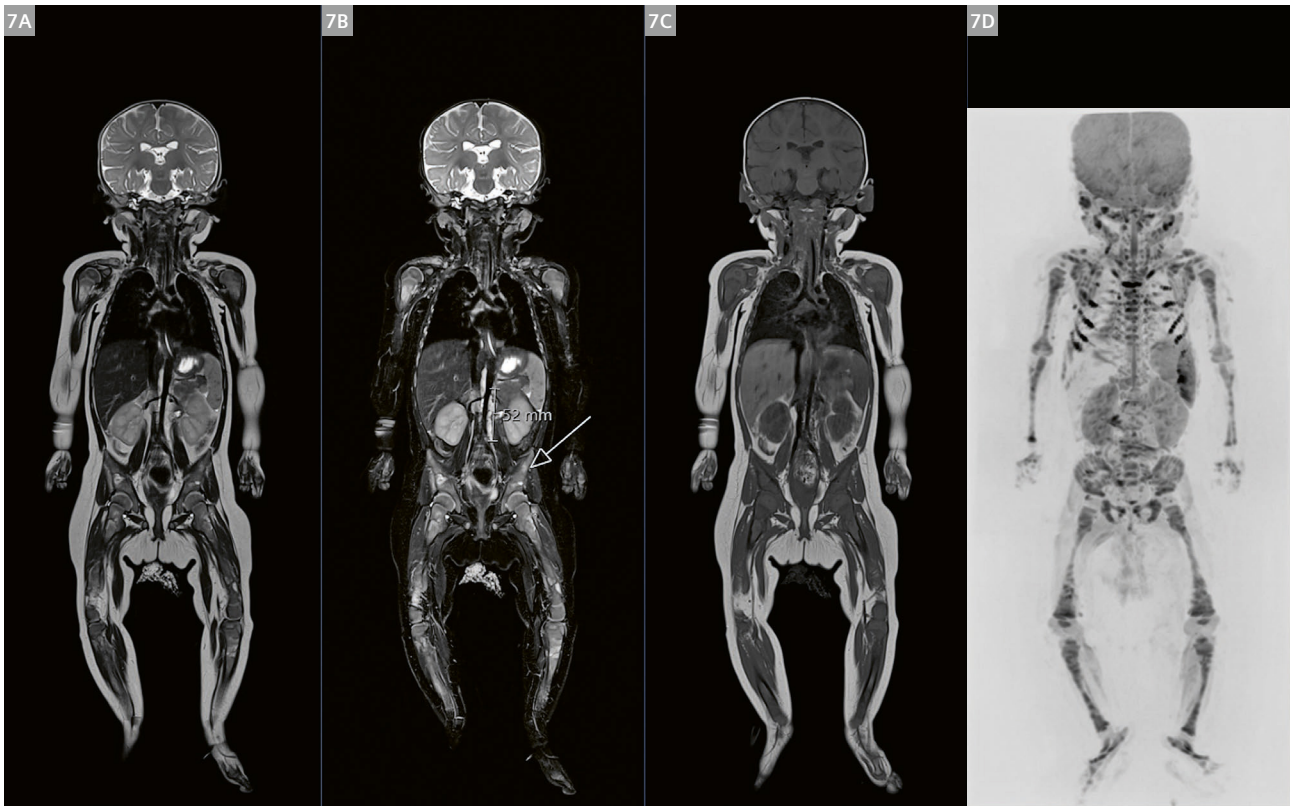

7 **(7A)** T2w TSE Dixon in-phase coronal, 0.45 × 0.45 × 3.5 mm, TA 2–2.5 min. Multiple steps, composed.
(7B) T2w TSE Dixon water-only coronal.
(7C) T1w TSE coronal, 0.45 × 0.45 × 3.5 mm, TA 2–2.5 min. Multiple steps, composed.
(7D) EPI DWI STIR coronal, 1 × 1 × 3 mm, b-value 1000 s/mm², TA 3–3.5 min. Multiple steps, composed.

[1] *MR scanning has not been established as safe for imaging fetuses and infants less than two years of age. The responsible physician must evaluate the benefits of the MR examination compared to those of other imaging procedures.*

Case 2

A 10-month-old baby[1] treated for neuroblastoma with an intra-abdominal tumor, and lymph-node and liver metastases. WB-MRI was performed three months post-treatment under general anesthesia on a 1.5T MAGNETOM Avanto^{Fit}.

The coronal WB-MRI images provide an overview of the total disease burden, with both the primary tumor and the metastasis. Dedicated sequences of the abdomen were performed as part of the pre-operative assessment.

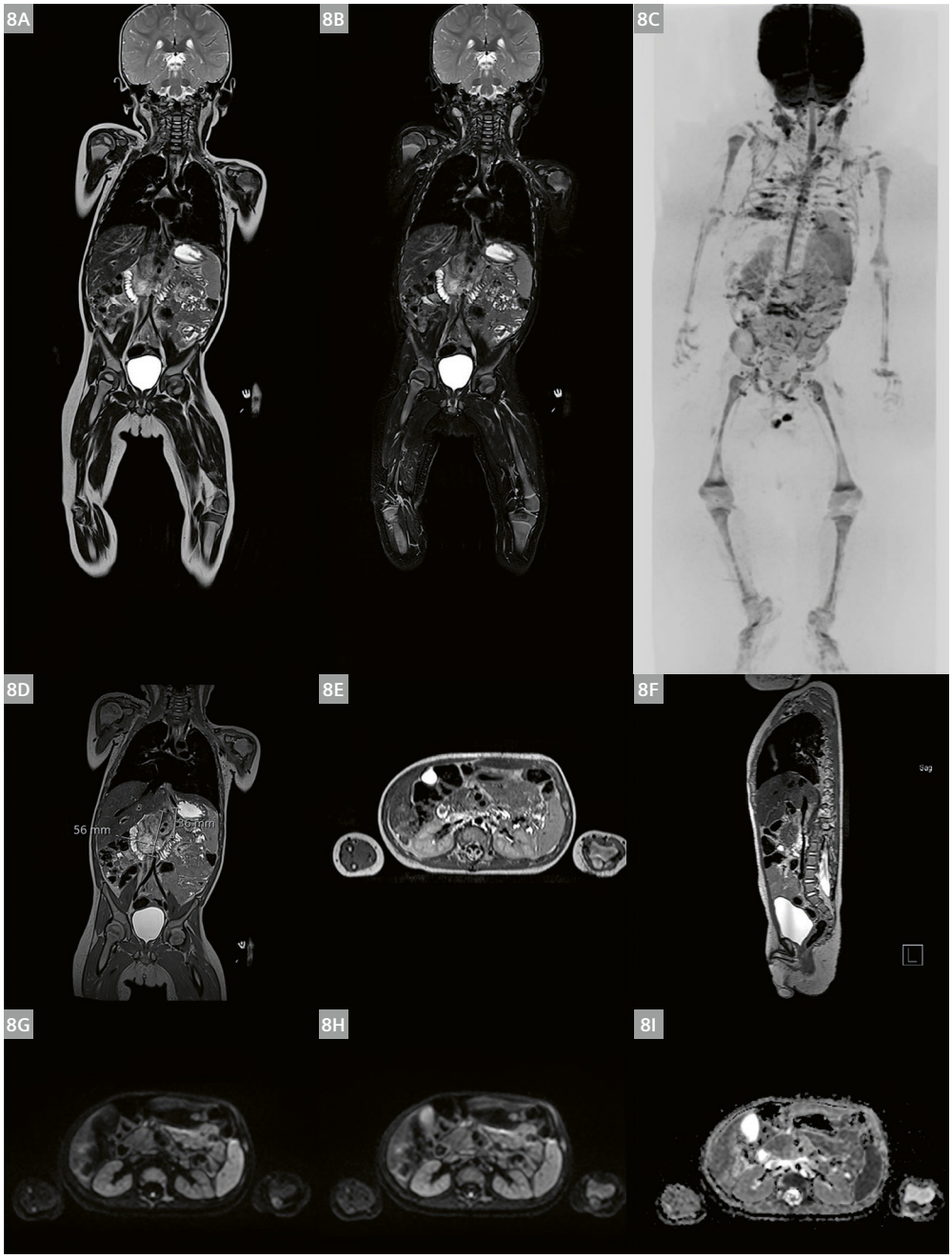

8 **(8A)** T2w TSE Dixon in-phase coronal, 0.45 × 0.45 × 3.5 mm, TA 2–2.5 min. Multiple steps, composed.
(8B) T2w TSE Dixon water-only coronal.
(8C) EPI DWI STIR coronal, 1 × 1 × 3 mm, b-value 1000 s/mm^2, TA 3–3.5 min. Multiple steps, composed.
(8D-F) T2w 3D SPACE coronal with MPR of transversal and sagittal, 1 × 1 × 1 mm isotropic, TA 5 min.
(8G-I) EPI DWI transversal, 1 × 1 × 4 mm, TA 3 min.

Case 3

A 2-year-old girl with neuroblastoma from the left adrenal gland with lymph-node and skeletal metastases. One initial and two follow-up WB-MRI scans were performed under general anesthesia on a 1.5T MAGNETOM Avanto^{Fit}. The scans were performed at approximately four-week intervals. The composed WB-DWI images give a good overview of the evolution of the primary tumor arising from the left adrenal gland, and of the lymph-node and skeletal metastases during the treatment course.



9 **(9A)** First WB-MRI. EPI DWI STIR coronal, 1 × 1 × 3 mm, b-value 1000 s/mm², TA 3–3.5 min. Multiple steps, composed.
(9B) First follow-up WB-MRI. EPI DWI STIR coronal, 1 × 1 × 3 mm, b-value 1000 s/mm², TA 3–3.5 min. Multiple steps, composed.
(9C) Second follow-up WB-MRI. EPI DWI STIR coronal, 1 × 1 × 3 mm, b-value 1000 s/mm², TA: 3–3.5 min. Multiple steps, composed.

Case 4

A 12-year-old boy with relapse of neuroblastoma and progressive disease in his legs, pelvis, and abdominal lymph nodes. The patient was awake during WB-MRI, with the TV screen as entertainment, on a 1.5T MAGNETOM Aera. The examination was aborted due to patient discomfort and pain, so some images are distorted by motion artifacts. Nonetheless, the examination indicates progressive changes in the tibia, lymph-node metastasis, and multiple lesions in the spine.



10 **(10A)** T2w TSE Dixon water-only coronal, 0.45 × 0.45 × 4.5 mm, TA 2–2.5 min. Multiple steps, composed.
(10B) T2w TSE Dixon fat-only coronal.
(10C) EPI DWI STIR coronal, 1.5 × 1.5 × 4.5 mm, b-value 1000 s/mm², TA 2–2.5 min. Multiple steps, composed.

Case 5

A 10-year-old boy with shoulder pain. Prior CT examination showed mediastinal lymph nodes and a lesion in the spina scapula. WB-MRI was performed for screening of multifocal disease, malignancy, or other pathology. The patient was awake during WB-MRI, with the TV screen as entertainment, on a 1.5T MAGNETOM Aera. The initial WB-MRI shows additional pathological locations in the skeleton, such as in the left humerus, left tibia, and distal femur. The second WB-MRI was performed approximately 5 months post-treatment and indicates no residual disease and no new pathology.



11 **(11A)** First WB-MRI. EPI DWI STIR coronal, 1.5 × 1.5 × 4.5 mm, b-value 1000 s/mm², TA 2–2.5 min. Multiple steps, composed.
(11B) Last WB-MRI. EPI DWI STIR coronal, 1.5 × 1.5 × 4.5 mm, b-value 1000 s/mm², TA 2–2.5 min. Multiple steps, composed.

References

1 Zadig P, von Brandis E, Lein RK, Rosendahl K, Avenarius D, Ording Müller LS. Whole-body magnetic resonance imaging in children – how and why? A systematic review. Pediatr Radiol. 2021;51(1):14–24.
2 Maeder Y, Dunet V, Richard R, Becce F, Omoumi P. Bone Marrow Metastases: T2-weighted Dixon Spin-Echo Fat Images Can Replace T1-weighted Spin-Echo Images. Radiology. 2018;286(3):948–959.



Contact

Bac Nguyen, BSc
Senior MRI Radiographer
Glenneveien 94
1476 Rasta
Norway
Tel.: +47 97702111
og_23@hotmail.com



Lil-Sofie Muller, M.D., Ph.D.
Consultant Paediatric Radiologist
Øvre Smestadvei 37 c
0378 Oslo
Norway
Tel.: +47 92828097
lilsofie.ording@gmail.com

Building a Global Power of Experience in Diagnostic Imaging – Lessons from Africa's COVID-19 Response

Udunna Anazodo, Ph.D.[1,2]; Iris Asllani, Ph.D.[3,4]; Abiodun Fatade, MBBS[2]

[1]Montreal Neurological Institute, McGill University, Montreal, Quebec, Canada
[2]Medical Artificial Intelligence (MAI) Lab, Crestview Radiology Ltd, Lagos, Nigeria
[3]Department of Biomedical Engineering, Rochester Institute of Technology, New York, NY, USA
[4]Department of Neuroscience and Imaging, Brighton and Sussex Medical School, University of Sussex, Brighton, UK

Nigeria's experience with Ebola shows us how having trained experts in place can make the difference when confronting unexpected health threats.

The U.S. Centers for Disease Control and Prevention (CDC), 2016

As we collectively resume our daily life in the post-pandemic 'new normal' and reflect on the varying trials and tribulations brought on by the COVID-19 pandemic, some have argued that what we lived through in the past two years was a 'syndemic' – the aggregation of the acute infectious SARS-CoV-2 and chronic noncommunicable diseases (NCDs), with their interaction increasing disease susceptibility and worsening health outcomes [1, 2]. In all likelihood, the poor management of the growing prevalence of NCDs, due primarily to a fragmented global public health policy, created the perfect storm for a COVID-19 syndemic [1]. Nonetheless, as the number of COVID-19 cases worldwide continue to trend downwards, the growing burden of NCDs, especially in low resourced areas, remains a threat to post-pandemic recovery and to the sustainability of health systems worldwide [3].

The pandemic highlighted the need for "medicine without borders", including development of accurate and easily implementable diagnostic tools. Here, we focus on high value diagnostic imaging, particularly CT and MRI services, as the global demand has risen over the past two decades as the technological innovations of these services become rapidly adopted as standard of care to manage the growing burden of NCDs. Thirteen of the twenty leading causes of deaths worldwide are NCDs, with cardiovascular diseases, cancers, respiratory diseases, and dementia leading the way (Fig. 1) [4, 5]. A staggering majority (70–80%) of these deaths occur in low-to-middle income countries (LMICs) [4]. Even in Sub-Saharan Africa, premature mortality from NCDs is on track to outpace the combined deaths from communicable, maternal, neonatal, and nutritional diseases by 2030 [4]. Not surprising, deaths from heart disease and cancer in 2019 (the latest global numbers available) were far greater than the total number of deaths attributed to COVID-19 from January 2020 to September 2022 (Fig. 1) [6].

What's even more surprising is that Africa seems to have fared relatively well with the COVID-19 pandemic, or syndemic, with a fewer number of COVID-19 cases and deaths compared to other regions of the world [6, 7], despite having the lowest vaccination rate in the world [7]. This is quite remarkable given early predictions of worse outcomes considering Africa's notoriously weak healthcare systems and its perennial lack of health infrastructure and skilled workforce [8–10]. Although the jury is still out as to why Africa seemingly weathered the COVID-19 storm, wave after wave, there is a general understanding that the region's level of preparedness from lessons of decades of battling epidemic infectious diseases may have conferred the *Power of Experience* to manage COVID-19 relatively well [7–12].

Are there lessons from Africa's COVID-19 experience that can be gleaned to inform pragmatic strategies that will strengthen diagnostic imaging services to address global threats from NCDs? Given that 80% of the world's population who largely resides in low-resourced areas is the most vulnerable but do not have access to adequate diagnostic imaging and must contend with poorly maintained equipment sporadically centralized in major cities in centers that are understaffed and lack skilled personnel, it is crucial that any wins in one health sector in LMICs is unweariedly and efficiently adapted to other sectors.

COVID-19 lessons from Africa: Think Omicron!

Precisely one year before COVID-19 took the world by storm, Nature ran a news feature on February 20, 2019, with the following headline, "This Nigerian doctor might just prevent the next deadly pandemic" [13]. The author, Amy Maxmen, was writing about Dr. Chikwe Ihekweazu, the first Director General of Nigeria Centre for Disease Control (NCDC), who completed his medical training at the University of Nigeria in Nsukka, Nigeria, prior to receiving his Master's in Public Health from Heinrich Heine University of Düsseldorf, Germany, and subsequent stints as a Medical Epidemiologists in Germany and the UK. The article described the 'step change' in Nigeria's pandemic preparedness with the arrival of Dr Ihekweazu as head of the fledging NCDC in 2016, during the 2014–16 Ebola crisis [13]. Armed with a measly $4 million budget in 2018 (0.036% of the US CDC's annual budget in the same year) and lessons from several epidemics (2016 Polio, 2016–17 Meningitis, 2018 Yellow fever, Lassa fever and Cholera), as well as a healthy political will from the Nigerian Government to support the NCDC and their leadership, Dr Ihekweazu did what Africans generally do – do much with little. The good doctor at the outset made "careful choices" [13] with his scarce resources and created a power of experience in COVID-19 management by:

I. Forming "real partnerships not a master-servant relationship" with US CDC [14] and other international public health institutions [15] to **train** epidemiologists and biologists in place at the NCDC and use his sheer dedication to attract Nigerians abroad to join the NCDC – "an experiment in brain gain" [13].

II. Building a regional **network** of molecular labs with the capacity to monitor pathogens and surveillance offices in each state in Nigeria linked to the national NCDC headquarter in the nation's capital, Abuja to prevent and respond to infectious disease outbreaks in a coordinated manner.

III. Strategically equipping regional labs with **infrastructure** for high quality diagnostics capacity including Polymerase Chain Reaction (PCR) machines, rapid antibody sensitivity diagnostic systems, and genomic sequencing and immunological testing systems.

When COVID-19 hit Nigeria in March of 2020, the NCDC had 6 molecular labs judiciously distributed across the country with capacity for PCR COVID-19 testing and other 6 in the process of being completed [16]. By May 2020, the test capacity had jumped to 23 labs across the country and, within 10 months, in January 2021, all 36 states in the country had molecular labs equipped with skilled

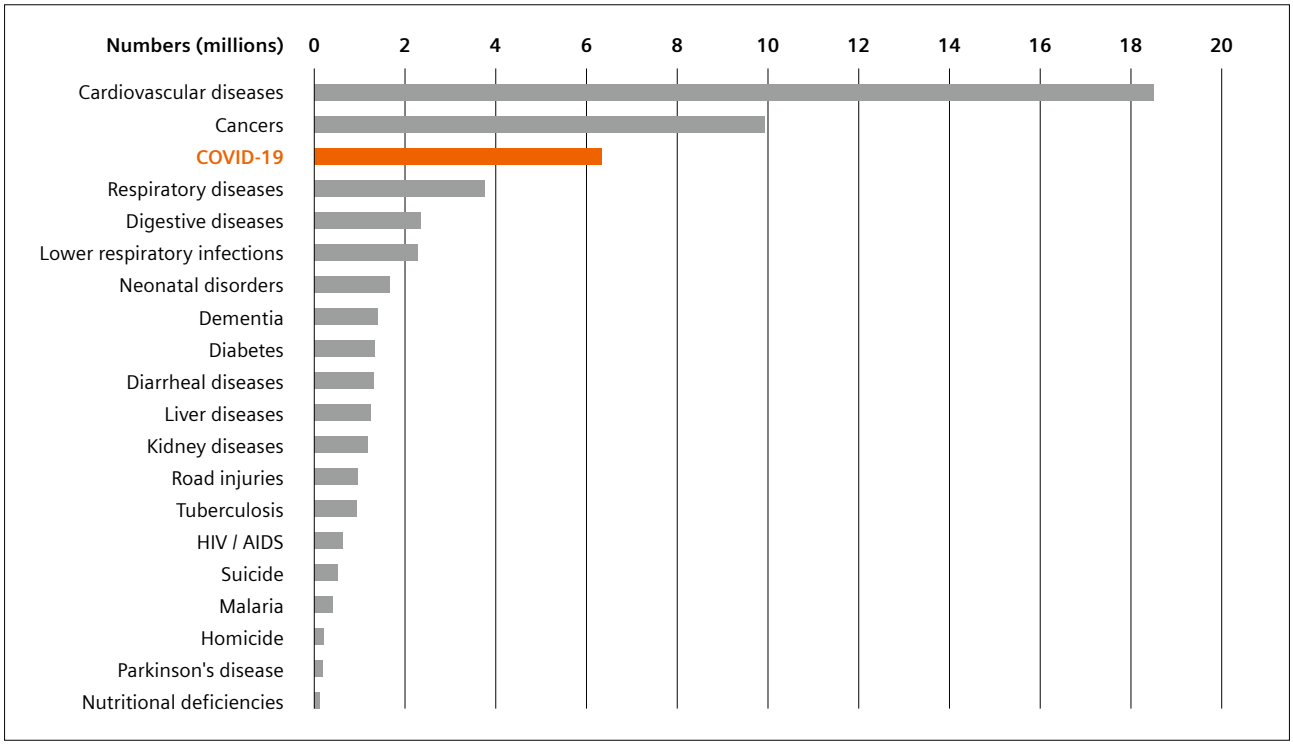

1 2019 worldwide number of deaths by cause [5].

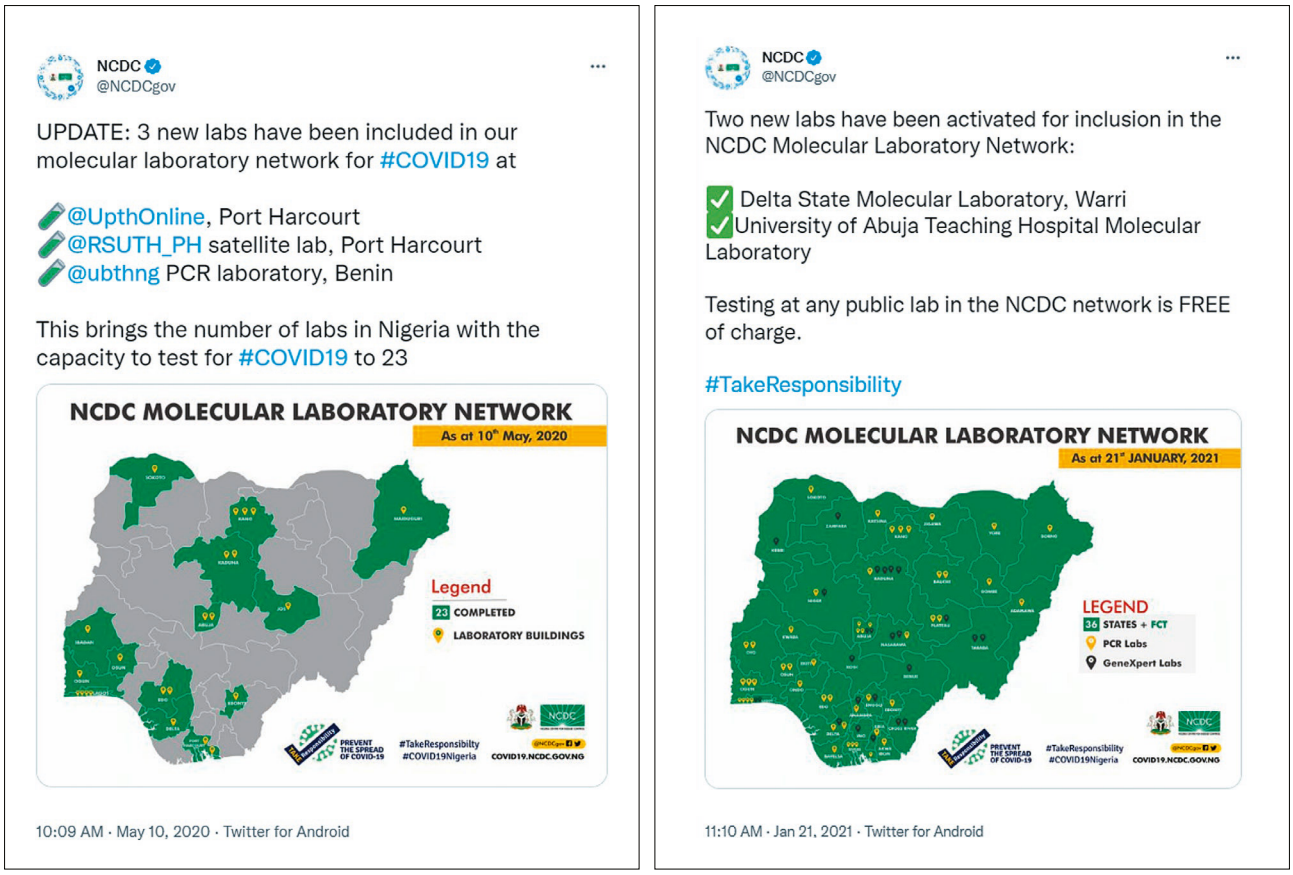

2 Strategically equipping regional labs with infrastructure for high quality diagnostics capacity.

personnel, infrastructure for COVID-19 testing, and linkage to rapid viral genome sequencing centers (Fig. 2). These resources were rapidly deployed to detect and track the emerging COVID-19 threat [16].

While Dr Ihekweazu and his team at NCDC were preparing Nigeria to address COVID-19, the Africa Center for Disease Control and Prevention (Africa CDC), formed in 2017, following the Ebola crisis, leaped into action in February 2020, days after the 1st case of COVID-19 was reported in Egypt [7], to form a Joint Continental Strategy with national public health institutions across the region. This continent-wide collaboration, still in place, provided the coordinated platform to share resources, work together in a pan-regional network, and communicate efforts, including implementation of lockdowns and restrictions [5]. More importantly, this continent-wide network, supported by scaled-up local capacity in surveillance and genomics, resulted in rapid discovery of several COVID-19 variants across Africa, including the now infamous Omicron variant, sampled in Botswana, and sequenced by the Network for Genomic Surveillance in South Africa [7, 17].

Now, imagine if Africa had the standard global support – the mismatched donated low-cost and low-resolution health technology, in this case, rapid kits or PCR with limited and isolated capacity for viral genome sequencing – if that were the case, the world would not have benefited from the African discovery of Omicron. Generally speaking, if low-resourced settings around the world were not empowered to develop and sustain their own local public health systems, the COVID-19 pandemic/syndemic may have had a more dire outlook. Therefore, we must lose no time to adopt this winning strategy to other healthcare sectors in LMICs.

Closing global gaps in diagnostic imaging

What Africa got right [7] with COVID-19 and a global lesson with clear relevance to diagnostic imaging is the need to work together as a global community to create the power of experience, the rich local expertise and capacity that will enable each country and each region to meet their pertinent and unique health care challenges.

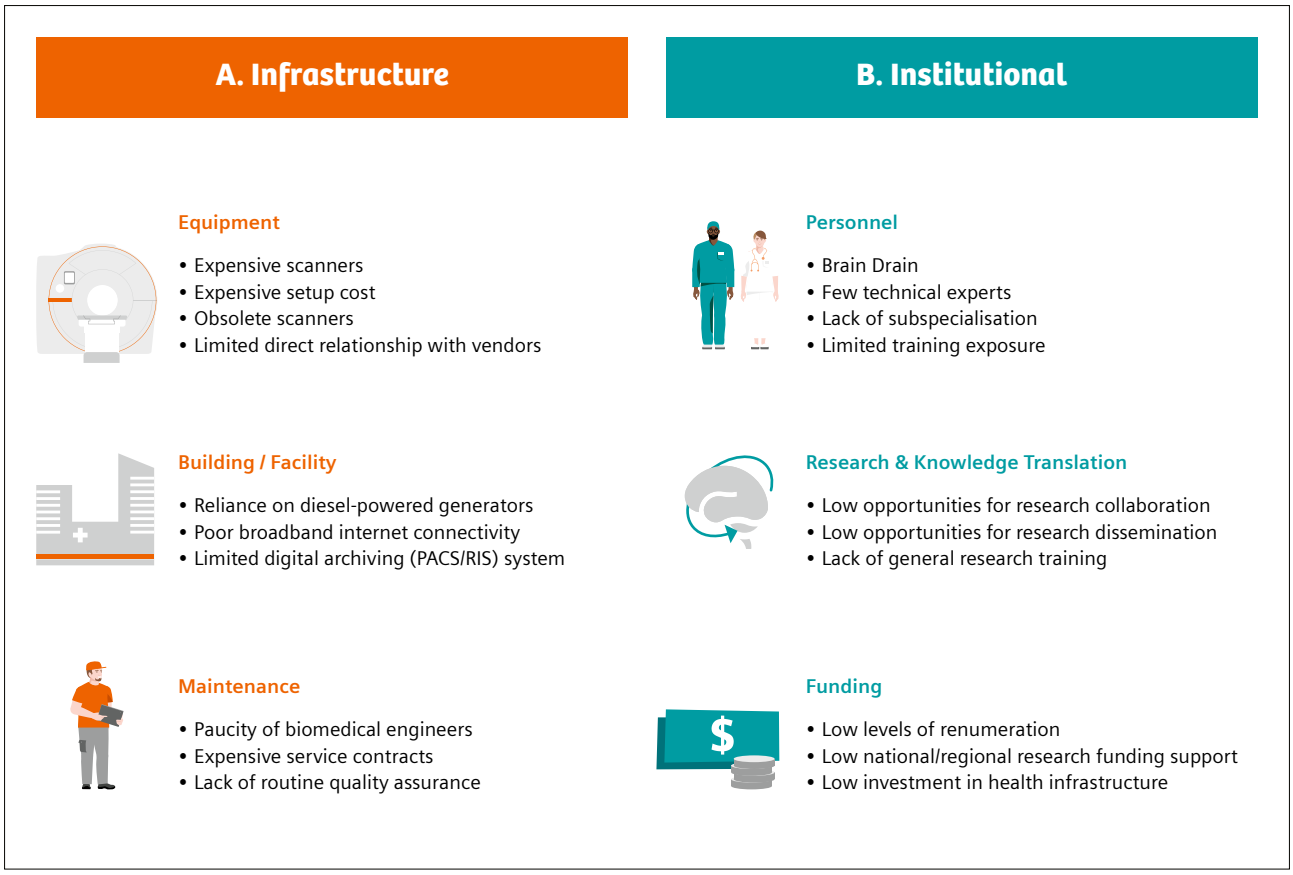

3 Drivers of limited access to MRI in Africa. *Figure adapted from [19].*

The question then is: How do we, as a global imaging community, work with those from the least-resourced areas to close longstanding inequities and enable our colleagues in Africa to address their overlapping complex imaging barriers (Fig. 3) so that the region's poor are provided with adequate access to clinically valuable diagnostic imaging?

In October 2019, we set out to do just that. We formed the Consortium for Advancement of MRI Education and Research in Africa (CAMERA), as a working group of the European Society of Magnetic Resonance in Medicine and Biology (ESMRMB), to address challenges to MRI access in Africa by strengthening local capacity for clinical use of MRI and expediting research translation of local MRI innovations. Since then, we have grown to become a global network of MRI experts from all disciplines (radiology, radiography, physics, biomedical engineering) and emerging fields (computational imaging and artificial intelligence) with a clear vision [18] and strategy, gleaning from Africa's COVID-19 lessons, to create the unbroken chain of resources and expertise in MRI across Africa [19]. In 2020 and 2021, we leveraged the general slowdown in radiology services during the COVID-19 lockdowns to conduct a Needs Assessment Study (NAS) to identify MRI capacity gaps and understand the general landscape of MRI in the region [19]. Our NAS captured needs as well as opportunities along four central priorities:

1) availability and access,
2) personnel training and education,
3) research translation, and
4) sustainable technology [19].

Based on the NAS findings, we formulated a framework (Fig. 4) to address these four priorities and the intricate barriers that accompany them (Fig. 3) [19].

We discovered that overall, the percentage of high field 1.5T MRI in Sub-Saharan Africa is growing and predominantly installed and operated at private clinics [19]. Furthermore, these scanners are severely (92%) underutilized, scanning less than 15 patients per day, per scanner, a far cry from the potential capacity of MRI, especially for clinics that service relatively large geographical areas [19]. Our study found that one of the major contributors to the under-utilization of MRI in the region is the perpetual and persistent lack of trained expertise to scan (radiographers), interpret (radiologists), develop,

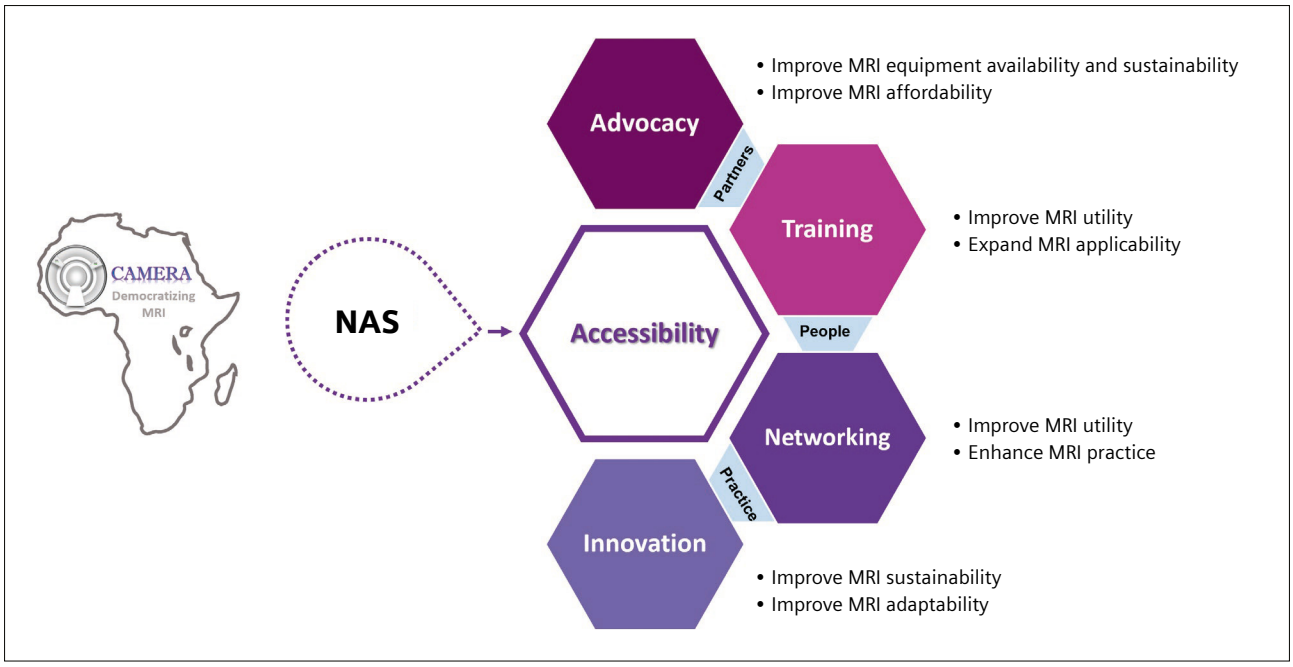

4 The CAMERA conceptual framework. *Figure adapted from [19].*

or optimize protocols, as well as process high quality images (physicists) and maintain (engineers) the scanners [19]. To address these issues, we are leveraging the existing MRI infrastructure in the region to develop local training and continuing education programs and create regional networking opportunities to provide our African colleagues with the power of experience in MRI diagnostics [19].

Training game changers and creating catalysts for MRI innovation in Africa

In October 2022 at the Association of Radiologists in Nigeria (ARIN) annual meeting, we launched the Africa Neuroimaging Archive (AfNiA), one of the key initiatives at CAMERA and funded by the Lacuna Fund [20], with the overarching aim of providing the power of experience in artificial intelligence (AI) applications in MRI diagnostics in low-resourced settings [21]. Specifically, AfNiA is a collaborative framework to enable ethical data share and aggregation of fragmented expertise, disciplines, resources, and pipelines required to effectively apply AI imaging solutions to transform diagnostic imaging care in the African setting (Fig. 5).

We have created the AfNiA ecosystem using glioma MRI diagnostics as an optimal use case and catalyst for the design, implementation, and validation of its 12 nodes (Fig. 5B). We chose glioma diagnostics to leverage the decade-long collaborative global efforts in glioma AI imaging applications by the computational imaging community through the RSNA/ACR/MICCAI Brain Tumor Segmentation (BraTS) challenge [22]. Although the BraTS challenge has provided several promising models, some segmenting tumors with precision comparable to manual expert reads [23], it is unclear if these models can be applied to African populations who need AI-assisted diagnosis the most [22]. Starting with data, we are aggregating retrospective brain MRI scans from clinics across Africa, including clinics that do not have access to PACS to curate, annotate, and archive the data for public use in the upcoming BraTS challenge.

Moreover, to address the lack of region-specific data governance provisions, policies for ethical use are being developed to govern access to curated data and ensure that AI solutions created using AfNiA will directly benefit the local communities who own and provide the data. This effort is crucial in Africa, where medical data is overwhelmingly provided from out-of-pocket patient expenses, and as such require direct benefit considerations [19]. Using the data governance mechanism, we will link local clinics to the wider imaging community and among themselves to enable co-creation of AI solutions in a global peer-to-peer collaborative network.

Lastly, to meaningfully create a rich local experience in AI imaging capacity, as part of AfNiA, we have developed the SPARK (Sprint AI Training for African Medical Imaging Knowledge Translation) program as a train-the-trainer workshop and hackathon (Fig. 6) to rapidly establish game changers that will drive AI imaging innovations locally.

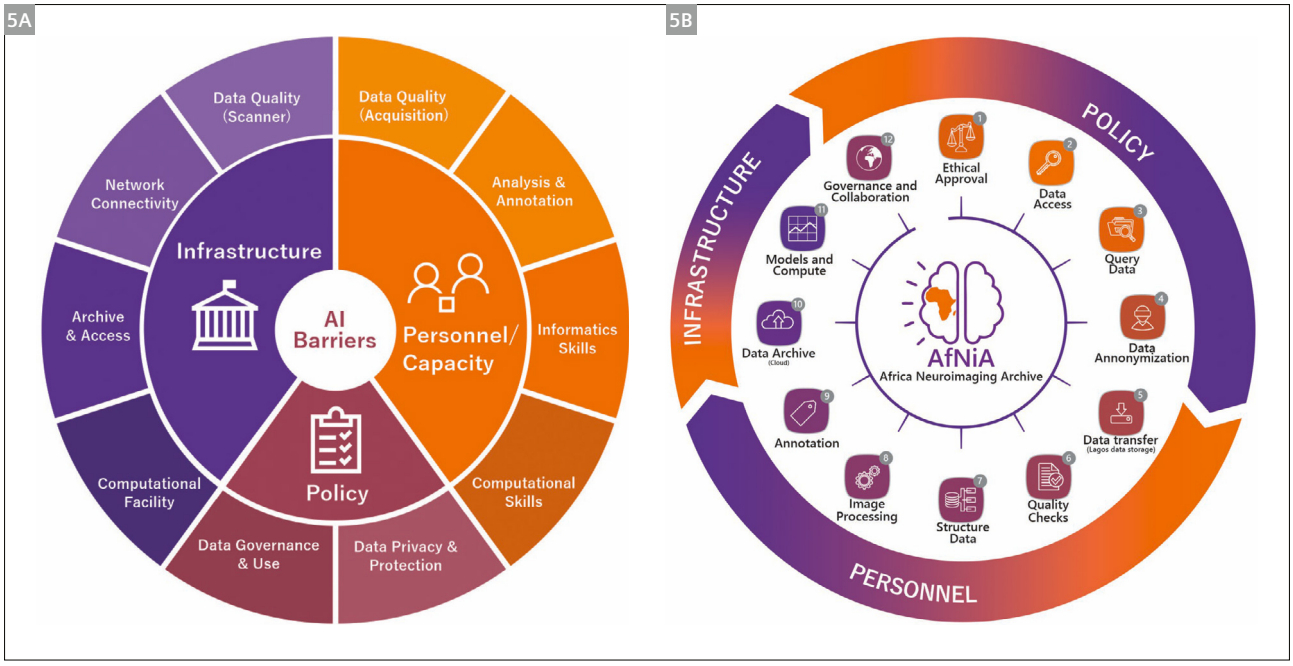

5 **(5A)** AI challenges in healthcare. **(5B)** The AfNiA ecosystem.

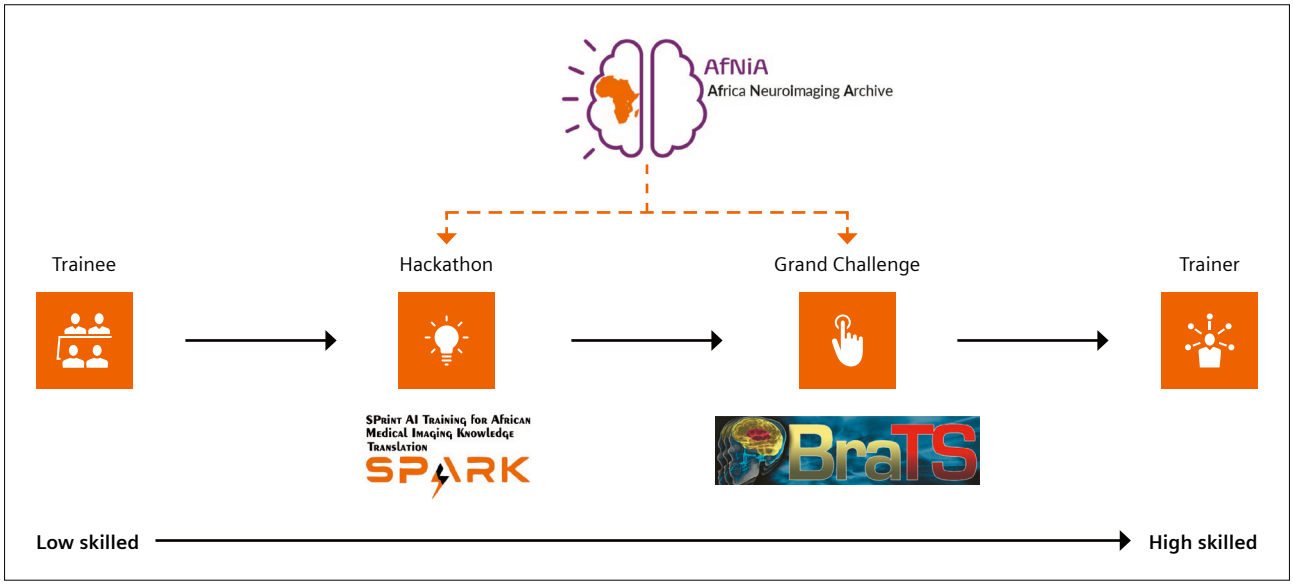

6 Train-the-trainer concepts to meaningfully create a rich local experience in AI imaging capacity.

The SPARK training program, which is planned to run for the first time in Summer 2023, will use RAD-AID's *Teach-Try-Use* [24] approach to train a multi-disciplinary team on data collection, AI model development, and clinical evaluation. The aim is to equip the trainees with competent skills to participate in the next 2023 BraTS challenge with models that have a clear chance of winning the challenge.

SPARK and AfNiA will operate out the Medical Artificial Intelligence (MAI) lab, strategically situated within Crestview Radiology Ltd, Lagos, Nigeria – a local clinic not affiliated with an academic institution, to ensure that AI models being developed can be swiftly and directly deployed to clinic (i.e., rapid model-to-clinic or bench-to-bedside).

Democratizing diagnostic imaging to advance global health

As novel innovations in mobile and low-cost imaging technology such as the 0.55T MRI system MAGNETOM Free.Max (Siemens Healthcare, Erlangen, Germany) continue to make their way into clinics, especially those in low-resourced settings, imaging communities such as the Radiological Society of North America, can partner with vendors who are starting to break barriers with these systems, to provide local communities around the world with the power of experience to address their global health challenges using high value diagnostic imaging. Considering how crucial low field MRI is to the democratization of diagnostic imaging and the surge of research and development in this field, collaborative multi-national and multi-institutional efforts should be strongly encouraged, especially those aimed at open sharing of resources, to readily include low-resourced settings. One such exemplary effort is the recent in situ assembly of a low field MRI system [25] at Dr Johnes Obungoloch's MRI lab at the Mbarara University of Science and Technology (MUST), Uganda (Fig. 7). The MRI system was developed at Leiden University Medical Center, the Netherlands, by Professor Andrew Webb and constructed at MUST by a team of international MRI scientists (Fig. 7) supported by Professor Steven Schiff's group at Yale University, New Haven, CT, USA. This first MRI system collaboratively built in Africa under a resource-limited setting and the accompanying MRI training provided to local scientists is the power of experience that will catalyze research projects pertinent to increasing MRI capacity to meet the region's healthcare needs and ambitions.

If COVID-19 has taught us anything, it is that we must now practice 'medicine without borders', to Think Globally while Acting Locally, to now go further together, so we can as Professor Daniel K Sodickson, former President of ISMRM eloquently stated at the ISMRM-ESMRMB 2018 Mansfield Lecture, marshal all our disruptive innovative forces to continue to create new ways of seeing [26].



7 Assembly of a low field MRI system at Mbarara University of Science and Technology (MUST), Uganda, Africa.

References

1 Horton R. Offline: COVID-19 is not a pandemic. Lancet. 2020;396(10255):874.
2 Di Guardo G. CoViD-19, a "syndemic" rather than a "pandemic" disease. BMJ. 2020;370:m3702.
3 Wilkinson E. UK Government urged to recognize post-COVID cancer backlog. Lancet Oncology. 2021;22(7):910.
4 Ezzati M, Pearson-Stuttard J, Bennett JE, Mathers CD. Acting on non-communicable diseases in low- and middle-income tropical countries. Nature. 2018;559(7715):507-516.
5 Our World in Data. Deaths by cause, World 2019. https://ourworldindata.org/causes-of-death [Accessed on September 27, 2022].
6 World Health Organization (WHO) Coronavirus (COVID-19) Dashboard. https://covid19.who.int/ [Accessed on September 27, 2022].
7 Happi CT, Nkengasong JN. Two years of COVID-19 in Africa: lessons for the world. Nature. 2022;601:22-25.
8 Nordling L. The Pandemic appears to have spared Africa so far. Scientists are struggling to explain why. Science. 2020 Aug 11.
9 Ofotokun I, Sheth AN. Africa's COVID-19 Experience – A Window of Opportunity to Act. JAMA Network Open. 2021;4(9):e2124556.
10 Chitungo I, Dzobo M, Hlongwa M, Dzinamarira T. COVID-19: Unpacking the low number of cases in Africa. Public Health Pract (Oxf). 2020:100038.
11 Tessema GA, Kinfu Y, Dachew BA, Tesema AG, Assefa Y, Alene KA, et al. The COVID-19 pandemic and healthcare systems in Africa: a scoping review of preparedness, impact and response. BMJ Global Health. 2021;6:e007179.
12 Soy A. Coronavirus in Africa: Five reasons why COVID-19 has been less deadly than Elsewhere. Global Development Commons. United Nations International Children's Emergency Fund (UNICEF). October 9, 2020. https://gdc.unicef.org/resource/coronavirus-africa-five-reasons-why-covid-19-has-been-less-deadly-elsewhere [Accessed on September 27, 2022].
13 Maxmen A. This Nigerian doctor might just prevent the next deadly pandemic. Nature 2019;566,310-313.
14 Centers for Disease Control and Prevention (CDC). CDC in Nigeria. https://www.cdc.gov/globalhealth/countries/nigeria / [Accessed on September 27, 2022].
15 German Federal Ministry of Health. Fighting COVID-19: Support to West Africa-Module https://ghpp.de/en/projects/afrolabnet/fighting-covid-support-to-west-africa/ [Accessed on September 27, 2022].
16 Nigeria Centre for Disease and Control (NCDC). COVID-19 Dashboard. https://covid19.ncdc.gov.ng/report/ [Accessed on September 27, 2022].
17 Tegally H, Wilkinson E, Giovanetti M, Iranzadeh A, Fonseca V, Giandhari J, et al. Detection of a SARS-CoV-2 variant of concern in South Africa. Nature. 2021;592(7854):438-443.
18 https://www.cameramriafrica.org/ [Accessed on September 27, 2022].
19 Anazodo UC, Ng JJ, Ehiogu B, Obungoloch J, Fatade A, Mutsaerts HJMM, et al. The Consortium for Advancement of MRI Education and Research in Africa (CAMERA). A Framework for Advancing Sustainable MRI Access in Africa. NMR Biomedicine. 2022. doi: 10.1002/nbm.4846
20 Lacuna Fund. Announcing Awards for Health Datasets. https://lacunafund. org/announcing-awards-for-health-datasets/. Published May 19, 2022. [Accessed May 22, 2022].
21 Anazodo U C, Adewole M, Dako F. AI for Population and Global Health in Radiology. Radiol Artif Intell. 2022;4(4):e220107.
22 Menze BH, Jakab A, Bauer S, Kalpathy-Cramer J, Farahani K, Kirby J, et al. The Multimodal Brain Tumor Image Segmentation Benchmark (BRATS). IEEE Trans Med Imaging. 2015;34(10):1993-2024.
23 Kouli O, Hassane A, Badran D, Kouli T, Hossain-Ibrahim K, Steele JD. Automated brain tumor identification using magnetic resonance imaging: A systematic review and meta-analysis. Neurooncol Adv. 2022;4(1):vdac081.
24 https://rad-aid.org/artificial-intelligence/ [Accessed September 27, 2022].
25 de Vos B, Parsa J, Abdulrazaq Z, Teeuwisse WM, Van Speybroeck CDE, de Gans DH, et al. Design, Characterisation and Performance of an Improved Portable and Sustainable Low-Field MRI System. Front Phys. 2021.9:701157.
26 Warnert EAH, Nayak K, Menon R, Rice C, Port J, Morris EA, et al. Resonate: Reflections and recommendations on implicit biases within the ISMRM. J Magn Reson Imaging. 2019;49(6):1509-1511.

Contact

Udunna C. Anazodo, Ph.D.
Assistant professor of neurology and neurosurgery
Montreal Neurological Institute at McGill University
3801 Rue University
Montréal, QC H3A 2B4
Canada
udunna.anazodo@mcgill.ca


Udunna Anazodo, Ph.D.


Iris Asllani, Ph.D.


Abiodun Fatade, MBBS

High-Resolution Accelerated Prostate TSE Axial Imaging with Deep Learning Reconstruction at 3 Tesla

Edouard Reizine, M.D.[1]; Wafa Boughanmi, M.D.[1]; Aurélien Massire, Ph.D.[2]; Elisa Roccia, Ph.D.[3]; Dominik Nickel, Ph.D.[3]; Thomas Benkert, Ph.D.[3]; Alain Luciani, Ph.D., M.D.[1,4,5]

[1]Service d'Imagerie Médicale, AP-HP, Hôpitaux Universitaires Henri Mondor, Créteil, France
[2]Siemens Healthcare SAS, Saint-Denis, France
[3]Siemens Healthineers, Erlangen, Germany
[4]Faculté de Santé, Université Paris-Est Créteil, Créteil, France
[5]INSERM IMRB, U 955, Equipe 18, Créteil, France

Introduction

Multiparametric MRI is a crucial tool for prostate cancer detection, staging, active surveillance, and now also prior to biopsies (MRI-targeted biopsies). The guidelines for prostate imaging (PI-RADS [1]) currently recommend a protocol that consists of several MR sequences: T2-weighted (T2w), diffusion-weighted imaging (DWI), and dynamic contrast-enhanced (DCE) imaging. Notably, the T2w turbo spin echo (TSE) sequence should be acquired in the axial plane, with a slice thickness of 3 mm without gaps, and high in-plane spatial resolution. The increased demand for prostate MRI examinations observed in the past years requires to adequately respond by reducing the examination times in order to increase throughput on the one hand and to minimize the table time for the patient on the other. Indeed, this is especially problematic as prostate cancer commonly affects elderly men, who may have difficulties remaining motionless during long MRI examinations.

Deep learning reconstruction has played a key role in tackling this challenge, as it has been proven to reduce acquisition times with comparable, and often improved, image quality and diagnostic accuracy compared to standard reconstruction techniques [2–4]. Initially Siemens Healthineers' deep learning reconstruction solution, Deep Resolve, consisted of Deep Resolve Gain and Deep Resolve Sharp.

- Deep Resolve Gain [5] mitigates thermal noise by incorporating prior knowledge of the noise characteristics into the image reconstruction, performing denoising of the data in image space. The enhanced SNR can be used to accelerate the acquisition by either increasing the acceleration factor in parallel imaging or by reducing the number of averages.
- Deep Resolve Sharp improves the image sharpness by reconstructing a high-resolution image from low-resolution data using a deep neural network. In particular it suppresses truncation artifacts in *k*-space and allows to avoid conventional *k*-space filtering. This enables to achieve image resolutions that would not be possible to achieve using conventional reconstruction.

When we first tested Deep Resolve Gain and Sharp at the Henri Mondor hospital, we were convinced by the results and decided to immediately implement it in our clinical practice. Deep Resolve is indeed now the standard of operation for prostate MR imaging at our institution.

This deep learning reconstruction technology has now gone one step further with the introduction of Deep Resolve Boost, which is even more powerful, bringing the results to a new level.

Deep Resolve Boost for TSE

Deep Resolve Boost replaces the conventional image reconstruction with a deep neural network [2]. The network architecture has similarities to an iterative image reconstruction and receives undersampled raw data as well as pre-estimated coil sensitivity maps as input. High quality images are then obtained by alternating between a parallel imaging model that relates images to acquired data and a deep learning-based regularization that enhances image quality. The main benefit of this technology is the ability to reduce the acquisition time without compromising SNR or image quality, as described in several publications [3, 6]. The outcome of the reconstruction can be further improved by combining Deep Resolve Boost with Deep Resolve Sharp.

Materials and methods

At our institution we had access to a research implementation of Deep Resolve Boost for TSE[1]. All patients underwent a prostate examination in our clinical 3T MR system (MAGNETOM Vida; Siemens Healthcare, Erlangen, Germany) with XT gradients, an 18-channel body array and a 72-channel spine array. We acquired three MR sequences:

- Transverse 2D T2w TSE reconstructed with Deep Resolve Gain and Sharp
- Transverse 2D T2w TSE reconstructed with the research implementation of Deep Resolve Boost[1]
- Transverse 2D diffusion single-shot EPI with 3 b-values (50, 1000, 1500 s/mm^2)

The acquisition parameters of the T2-weighted sequences are shown in Table 1.

We present a series of clinical cases which show that Deep Resolve Boost for TSE provides at least similar image quality and diagnostic information as the more time-intensive Deep Resolve Gain and Sharp TSE acquisition, which is now the clinical standard at our institution.

[1] *With software version syngo MR XA50 Deep Resolve Boost is available for MAGNETOM Vida.*

	Deep Resolve Gain and Sharp TSE	Deep Resolve Boost TSE
Scan time (min:s)	**3:16**	**1:50**
FOV (mm^2) / phase oversampling	160 × 160 / 145%	180 × 180 / 200%
TE (ms)	116	104
TR (ms)	3380	3850
Reconstructed voxel size (mm^3)	0.26 × 0.26 × 3	0.24 × 0.24 × 3
Nb excitations	**2**	**1**
Matrix size	304 × 304 × 26	368 × 368 × 26
Acceleration technique	GRAPPA 2 (Auto -32)	GRAPPA 3 (TSE/Sep -24)
Flip angle (°)	133	160
Turbo factor	23	25
Phase resolution (%)	85	85
Bandwidth (Hz/Px)	201	200
Nb concatenations	2	2

Table 1: Acquisition parameters of the T2-weighted sequences.

Cases

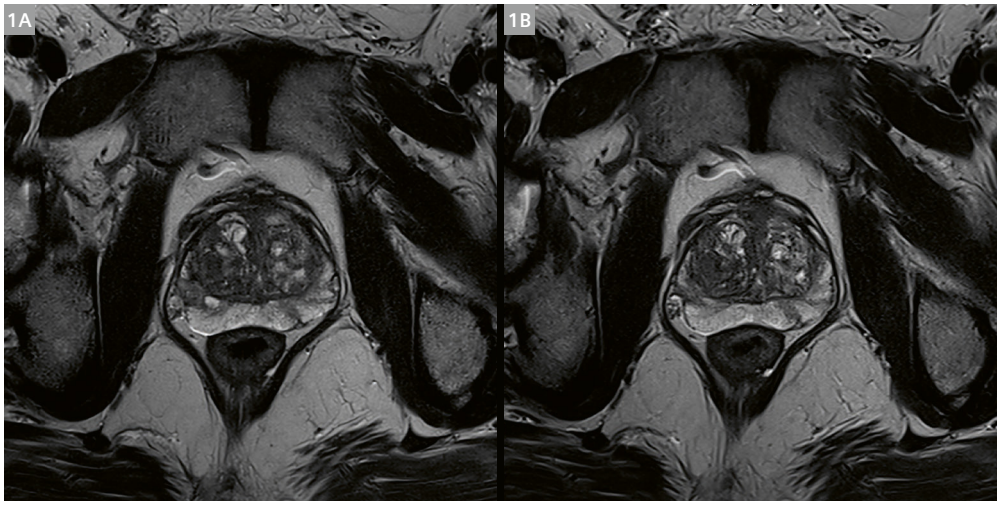

1 A 72-year-old patient (Density PSA = 0.09 ng/ml²) with bilateral PI-RADS 2 lesions in the middle peripheral zones of the prostate. T2-weighted TSE using **(1A)** Deep Resolve Gain and Sharp and **(1B)** Deep Resolve Boost. Deep Resolve Boost provides comparable image quality with a 41% scan time reduction.

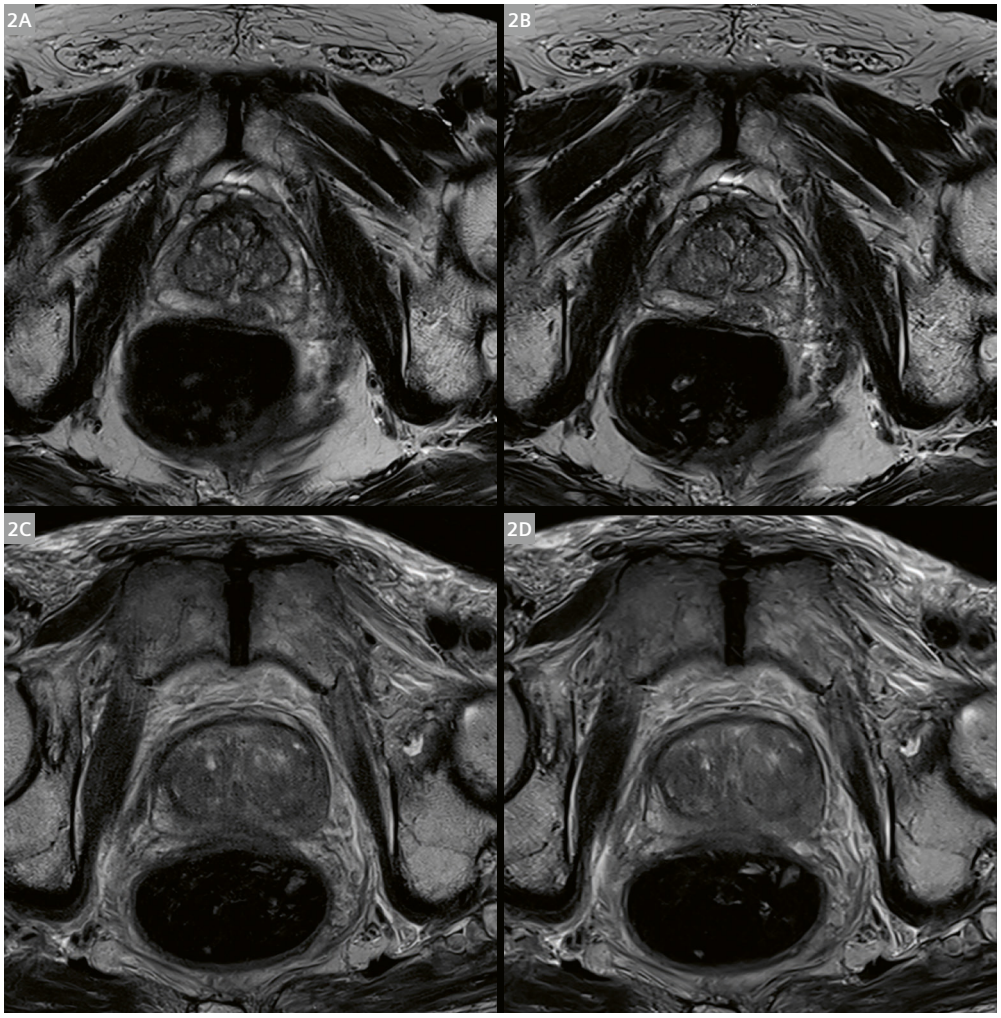

2 A 77-year-old patient (PSA = 1.7 ng/ml; density PSA = 0.05 ng/ml²) with bilateral PI-RADS 2 lesions in the middle peripheral zones of the prostate. T2-weighted TSE using **(2A)** Deep Resolve Gain and Sharp and **(2B)** Deep Resolve Boost.

An 83-year-old patient (PSA =14.8 ng/ml; density PSA = 0.29 ng/ml²) with a PI-RADS 4 lesion in the right postero-medial middle peripheral zone of the prostate. T2-weighted TSE using **(2C)** Deep Resolve Gain and Sharp and **(2D)** Deep Resolve Boost.

For both patients, motion artefacts in the Deep Resolve Boost images are reduced thanks to the shorter acquisition time (1 average), allowing sharper delineation of the anatomical structures.

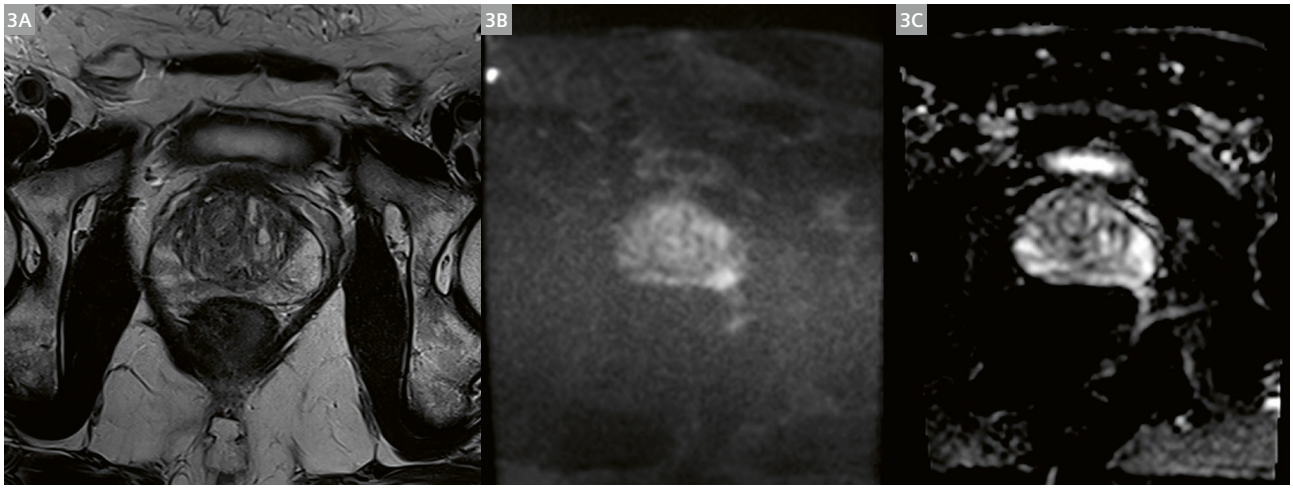

3 A 59-year-old patient (PSA: 4.2 ng/mL; density PSA = 0.10 ng/ml^2) with bilateral PI-RADS 2 lesions in the middle peripheral zones of the prostate. T2-weighted TSE using **(3A)** Deep Resolve Boost. **(3B)** Trace DWI image with b-value 1500 s/mm^2, **(3C)** ADC map.

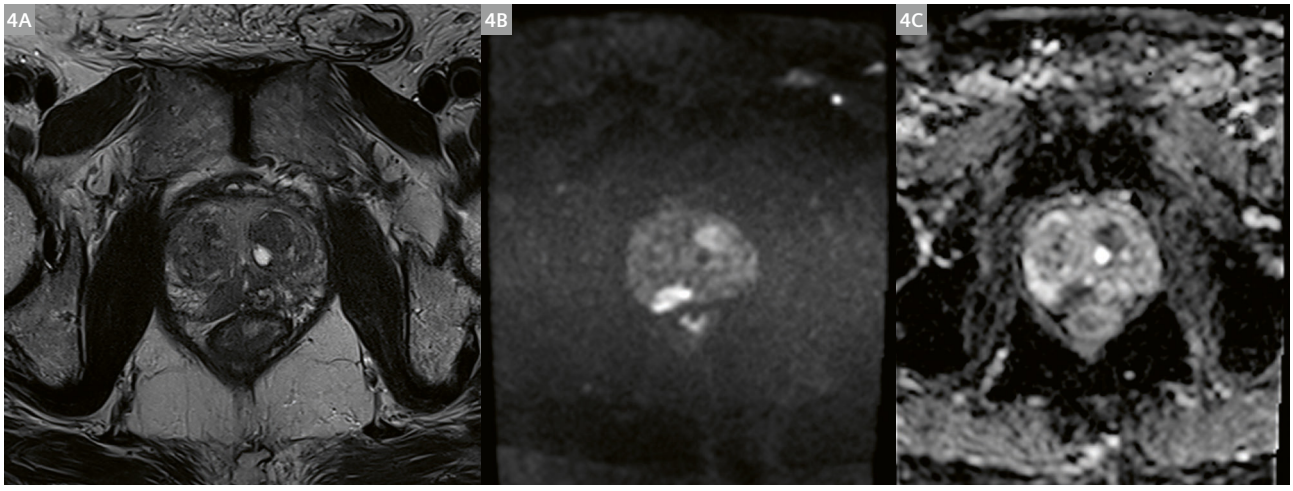

4 A 81-year-old patient (PSA: 12 ng/mL; density PSA = 0.33 ng/ml^2) with a PI-RADS 5 lesion in the right posteromedial apical peripheral zone of the prostate. T2-weighted TSE using **(4A)** Deep Resolve Boost. **(4B)** Trace DWI image with b-value 1500 s/mm^2, **(4C)** ADC map.

Conclusion

Compared to Deep Resolve Gain and Sharp, Deep Resolve Boost allowed us to decrease the acquisition time of the T2w TSE acquisition by 41% (Fig. 1), as only 1 average was acquired compared to the 2 averages of the Deep Resolve Gain and Sharp scan, with comparable image quality. One of the benefits of the shorter acquisition time was the reduction of artefacts due to either voluntary or involuntary patient motion (Fig. 2), which is one of the challenges of prostate imaging. No evident artefacts were observed. There is an increasing body of evidence from clinical studies and scientific publications that these physics-guided deep learning reconstruction approaches provide reliable and robust image information with anatomical fidelity.

These results are also in line with the published literature, which has reported significant time savings, as well as comparable image quality and diagnostic confidence for staging prostate lesions when compared to conventional acquisitions [2–4, 7].

The adoption of Deep Resolve in our clinical workflow has helped us to match the increased demand of prostate MRI examinations at our institution and we are confident that further improvements in acquisition time and spatial resolution can be achieved.

References

1 Weinreb JC, Barentsz JO, Choyke PL, Dornud F, Haider MA, Macura KJ, et al. PI-RADS Prostate Imaging – Reporting and Data System: 2015, Version 2. Eur. Urol. 2016, 69, 16–40.
2 Gassenmaier S, Afat S, Nickel D, Mostapha M, Herrmann J, Othman AE. Deep learning-accelerated T2-weighted imaging of the prostate: Reduction of acquisition time and improvement of image quality. Eur J Radiol. 2021;137:109600.
3 Gassenmaier S, Afat S, Nickel MD, Mostapha M, Herrmann J, Almansour H, Nikolaou K, Othman AE. Accelerated T2-Weighted TSE Imaging of the Prostate Using Deep Learning Image Reconstruction: A Prospective Comparison with Standard T2-Weighted TSE Imaging. Cancers (Basel). 2021;13(14):3593.
4 Kim EH, Choi MH, Lee YJ, Han D, Mostapha M, Nickel D. Deep learning-accelerated T2-weighted imaging of the prostate: Impact of further acceleration with lower spatial resolution on image quality. Eur J Radiol. 2021;145:110012.
5 Dehem J, Kannengießer S, Hoelscher UC. Initial Clinical Experience with an Iterative Denoising Algorithm Applied to Reduced-data 2D Turbo Spin Echo Acquisitions. ↗MAGNETOM Flash. 2021;(78)2:22-28.
6 Herrmann J, Gassenmaier S, Nickel D, Arberet S, Afat S, Lingg A, et al. Diagnostic Confidence and Feasibility of a Deep Learning Accelerated HASTE Sequence of the Abdomen in a Single Breath-Hold. Invest Radiol. 2021;56(5):313–319.
7 Johnson PM, Tong A, Donthireddy A, Melamud K, Petrocelli R, Smereka P, Qian K, Keerthivasan MB, Chandarana H, Knoll F. Deep Learning Reconstruction Enables Highly Accelerated Biparametric MR Imaging of the Prostate. J Magn Reson Imaging. 2022;56(1):184-195.

Contact

Professor Alain Luciani, Ph.D., M.D.
HU Henri Mondor
Medical Imaging Department
APHP, UPEC University
51 Avenue Mal De Lattre De Tassigny
94000 Créteil
France
alain.luciani@aphp.fr


Alain Luciani, Ph.D., M.D.


Edouard Reizine, M.D.

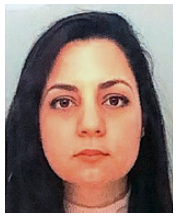
Wafa Boughanmi, M.D.

Advertisement

PI-RADS 2.1 Standardized Prostate MRI Reporting

David Jean Winkel, M.D. and Hanns-Christian Breit, M.D.

University Hospital Basel, Switzerland

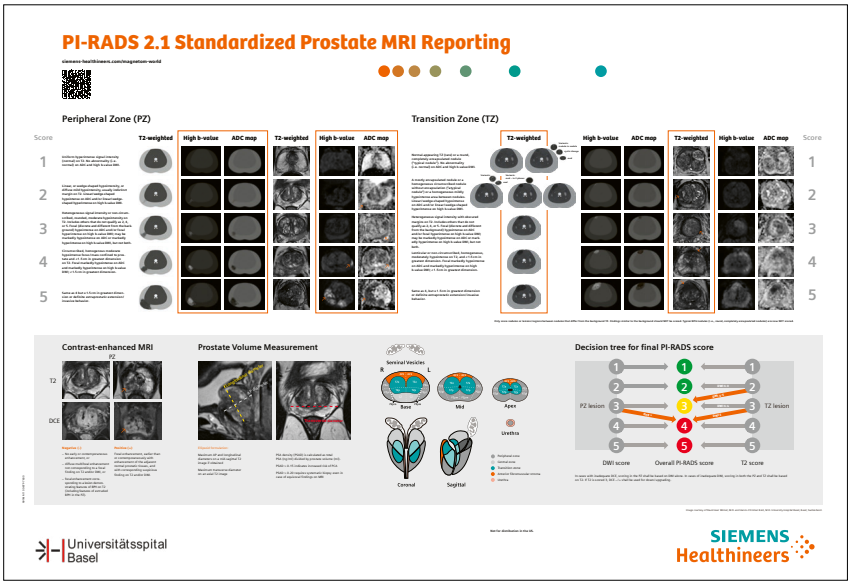

Get your free copy of the PI-RADS poster at
www.magnetomworld.siemens-healthineers.com/publications/subscriptions/mri-poster

Improving Patients' Experience of MRI: Why and How Reducing Stress and Anxiety in Patients May Enhance Clinical Operations

Janika Madl[1,2]; Susanne Bay[2]; Rolf Janka[3]

[1]Chair of Health Psychology, Friedrich-Alexander-Universität Erlangen-Nürnberg, Erlangen, Germany
[2]Siemens Healthineers, Erlangen, Germany
[3]Department of Radiology, Universitätsklinikum Erlangen, Germany

Introduction

Magnetic resonance imaging (MRI) is non-invasive and painless, with excellent spatial resolution and soft-tissue contrast. These numerous benefits have rendered MRI one of the most important diagnostic tools in modern medicine. In Germany, 150 MRI examinations are performed per 1,000 inhabitants every year [1]. Yet, MRI also has substantial drawbacks: Most MRI protocols are time-consuming and very dependent on the patient's cooperation and ability to lie motionless. One of the main roots for disruptions to MRI workflows is stress and anxiety in patients, who often experience MRI as uncomfortable and frightening [2, 3]. Beyond creating a negative patient experience, feelings of anxiety and stress may relate to unexpected patient-related events such as motion artifacts, the need for sedation, or failed scans; these events result in a substantial amount of revenue lost [4–6]: Andre et al. [4] calculated that US$ 115,000 are lost per scanner every year due to unexpected patient behavior.

The aim of this article is to provide a holistic picture of patients' experience of MRI, related unexpected behaviors and consequences, and approaches to improve the situation for all concerned: patients, healthcare staff, and the medical institutions. The focus is to provide insights into the "Patient Experience (PX) in MRI" collaboration project between Siemens Healthineers, the Chair of Health Psychology (FAU Erlangen-Nürnberg), and Universitätsklinikum Erlangen, Department of Radiology. During this collaboration project, two empirical studies and one systematic review with meta-analysis were conducted and will be presented in the following.

Take-home points

- Although most patients tolerate MRI well, a substantial number of patients experience clinically relevant levels of anxiety; related unexpected patient behaviors disturb clinical workflows and impede efficiency of healthcare providers.
- Patients' response to MRI depends on many different factors; previous negative experiences with MRI and female sex seem to be particularly predictive of a negative patient experience.
- In order to address individual patients' needs, different materials for patient preparation should be offered: Not only informational material, but also measures to support active modulation of anxiety, e.g., relaxation exercises.
- Patients who experience high levels of stress or anxiety tend to lie less still, which may provoke motion artifacts and the need for scan repetitions, thereby prolonging procedural times. Therefore, reducing stress and anxiety in patients might not only improve the patient experience, but also lead to clinical workflows running more smoothly.

Patients' experience of MRI: An introduction

How patients experience MRI has been a topic of interest since the very beginnings of MRI. In the course of MRI paving its way from the 1980s on, it soon became apparent that many patients fear this medical "coffin" [7]; Figures 1A and 1B show that, indeed, early MRIs resembled "mechanical monster[s]" [7]. Since then, many technological advancements have made MRI more patient-friendly: Recent MRI machines produce less noise, are equipped with shorter, wider bores that are open at both ends, and acquire images much quicker, thereby reducing scan duration [8, 9]. Some studies report that these advancements have resulted in reduced levels of stress and anxiety, as well as related operational issues [6, 10, 11]. Yet, others find that – although most patients tolerate MRI well – stress and anxiety are still widespread phenomena reaching levels that are considered clinically relevant in around 30% of patients [12, 13]. Two questions arise from these findings:

1) What factors differentiate patients who fear MRI from the rest?
2) To what extent have technical advancements brought about improvements regarding the patient experience of MRI examinations and related behaviors?

Adequate patient preparation seems to be most decisive in preventing a negative patient experience and fostering smooth clinical workflows

In our "baseline" study, our aim was to analyze patients' response to MRI in detail including influencing factors and consequences [12]. We thereby considered patients' psychological response (i.e., anxiety), the physiological response (i.e., salivary stress markers), and operational effects on clinical processes (i.e., scan repetitions due to motion artifacts, scan duration).

The study was conducted in the department of radiology of Universitätsklinikum Erlangen. We examined anxiety and physiological stress markers in 96 patients undergoing MRI (M = 49 years, 61.5% female). Anxiety was assessed via questionnaires before and after MRI; at the same timepoints, we took saliva samples to measure salivary stress markers (cortisol, alpha-amylase).

In general, most patients tolerated MRI well. Yet, every third patient experienced moderate to severe levels of anxiety in anticipation of the examination and experienced relief only after having endured the examination. As suggested by Ahlander et al. [14], this implies that efforts to improve the patient experience might be most effective



1 **(1A, B)** While the first MAGNETOM MRI scanner from 1983 [41] might have been a scary sight, only a few years later product development focused also on patient comfort. **(1C)** In 1993, Siemens introduced the 0.2T MAGNETOM Open. **(1D, E)** In 1996 the product line around MAGNETOM Symphony featured a flared bore. **(1F)** In 2004 MAGNETOM Espree was the world's first 1.5-tesla system with a 70-centimeter opening. **(1G)** Today a relaxing atmosphere, noise reduction and fast sequences make MRI easier to tolerate.

when applied in advance. Materials for patient preparation can only reduce anticipatory anxiety when given with sufficient lead time, ideally a few days/weeks before the examination.

We examined a broad range of potentially influencing factors (sex, age, positioning, accompanying persons, pain, previous experiences, examined body part) and found them to interact with patients' response in a complex way. Women receiving breast examinations had a particularly high risk of anxiety. This is in line with previous studies that reported a more negative response to MRI in women vs. men [6, 12, 15]. Further, we found that negative experiences made during previous MRI examinations significantly predicted a negative experience during the current examination. That means that patients who once have a negative MRI experience tend to keep on having bad experiences. When integrating our results on the impact of age and positioning with other studies, the state of research appears to be less clear [6, 12, 16–18]. Most certainly, it can be deduced that patients differ considerably regarding their response to MRI and their needs, which is why they also require different approaches to address these needs.

Furthermore, we found evidence of a link between patients' experience and clinical workflows: Patients' response to MRI predicted the probability of scan repetitions and scan duration [12], thereby supporting previous results that reported a connection between the patient experience and the prevalence of unexpected patient-related events [5, 19–22]. For example, an increase of 1 nmol/L in the stress marker salivary cortisol predicted a prolongation of the scan duration of more than 4 minutes [12].

Apart from individual factors that influence patients' experience of MRI, technological advancements have been proposed that aim to have a positive impact on stress and anxiety as well as related behavioral issues in patients. Yet, until now, no systematic review has summarized the patient experience of MRI, related unexpected patient behaviors, and their evolution along with technological advancements holistically. We sought to overcome this research gap in a systematic review with a meta-analysis that we conducted on patients' response to MRI, its effects (i.e., unexpected patient behaviors related to stress and anxiety), and their evolution over time [20].

Evolution of patients' experience of MRI and related unexpected patient behaviors over time: A systematic review and meta-analysis

We searched four databases and screened more than 12,000 studies. Meta-analysis of 44 studies revealed that, despite the common understanding of patient anxiety, there have been no significant improvements over time in the amount of anxiety experienced: Average values of reported anxiety were close to the cut-off considered as clinically relevant and around 4% of patients reported to be unwilling to undergo further MRI examinations. Similarly, the rates of unexpected patient-related events such as no-shows, failed scans, motion artifacts, and sedation, have not significantly reduced over time. While these findings could be traced back to statistical issues or the fact that we had to use the year of study publication as an indicator of MRI technology as more exact data on scanner technology was unavailable for most studies, it might as well reflect the fact that patients still experience substantial stress and anxiety in the context of MRI. An additional interesting finding was that claustrophobia significantly moderated the overall number of unexpected patient events. The rates of unexpected behaviors such as no-shows, motion artifacts, failed scans, and sedation were higher in patient groups with higher levels of claustrophobia. This supports the notion of a link between the patient experience and clinical workflows as has been postulated previously [5, 19, 21, 22].

Based on the results of the baseline study and meta-analysis, it can be concluded that stress and anxiety in patients have always been and still are a relevant topic in the context of MRI. In short, technological advancements of the MRI scanners alone might not be sufficient to improve the patient experience of MRI or related unexpected events – at least until now. There seems to be a need for interventions that target patients' needs more explicitly. The evidence generally suggests that MRI-related patient anxiety and related effects can be prevented when we enrich standard care and properly address patients' needs.

How patient's experience of MRI can be improved: An overview

A wide variety of interventions to improve patients' experience of MRI has been developed and tested in the past. Approaches range from easy-to-implement measures to very elaborate and complex ones: From the supply of music or having someone accompany the patient, to variations in patient positioning or the environment, mock MRI, aromatherapy, amended patient information, distraction via VR, hypnosis and other relaxation strategies, to communication training for the medical personnel.

Many of these approaches have been proven to be effective (see Munn et al. [17] for an overview), but this article will focus on interventions specifically targeted at patient preparation.

Two major types of interventions for patient preparation can be distinguished:

- The aim of informational interventions is to reduce ambiguity and feelings of uncertainty that may constitute a stressor for patients [2, 23, 24]. Although

many studies report beneficial effects of additional information, others find even negative effects when information is provided exclusively [17].

- A different approach aims at enhancing a patient's ability to cope with the stressful situation more successfully, e.g., via relaxation techniques [25, 26]. Although consistently positive, the effect sizes of these interventions vary considerably [17].

The majority of the literature points toward substantial benefits of interventions to improve the MRI patient experience; yet, some questions remain unresolved: Why do some studies report positive effects of informational interventions but others don't? Where do the considerable variations in the reported effect sizes of coping interventions trace back to? And is there a link between patient experience and clinical processes?

Patient preparation should cover different needs of patients

In order to address these questions and help to enhance the patient experience of MRI, we developed a patient education toolkit (see Fig. 2) in collaboration with Siemens Healthineers MR marketing and tested it in clinical trial. We based our approach on the assumptions of the "Model of Coping Modes" [27, 28], which may contribute to explaining the inconsistencies described above. The model describes different ways of coping with stress-inducing situations that people tend to employ habitually. The model proposes vigilance and cognitive avoidance as two basic dimensions of how attention shifts when facing stressful situations. While cognitive avoidance means the tendency to divert attention from threatening cues to reduce the bodily arousal induced by these, vigilance refers to the opposite: An increased focus on threatening cues to enhance knowledge about the situation and reduce feelings of uncertainty [25, 27]. Figure 3 depicts the four coping styles that can be differentiated on the basis of these two dimensions. According to this scheme, it can be expected that sensitizers benefit from receiving additional information: It should enable them to reduce feelings of uncertainty successfully. By contrast, repressers should benefit from distraction and relaxation, which supports distracting attention away from the threatening cues that induce arousal.

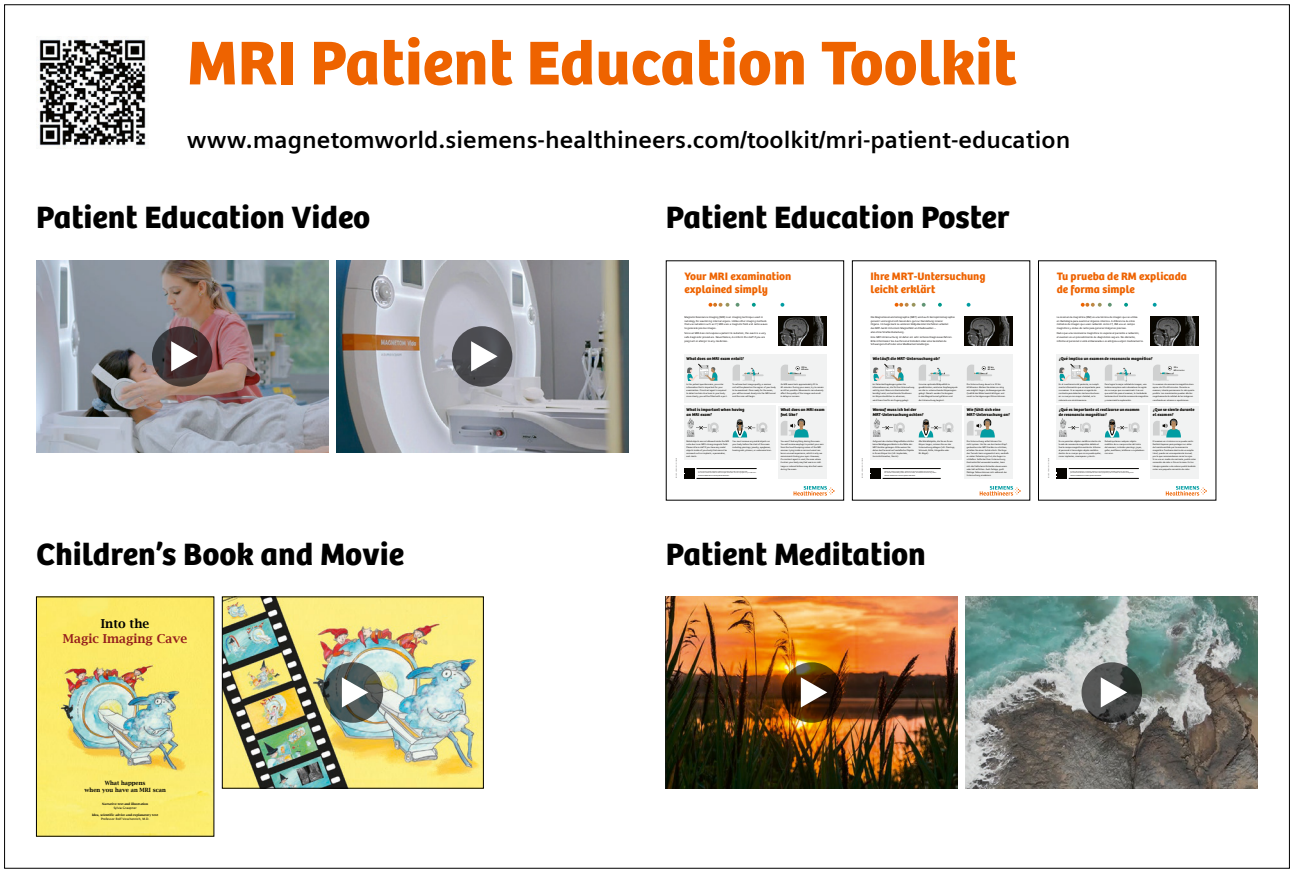

2 QR code for access to the Patient Education Toolkit including the two patient preparation videos and the MRI book for children.

Patient preparation that matches the coping style ("congruent preparation") has been shown to improve patient-related outcomes such as pain, anxiety, and adaptation in other medical fields like surgery [29, 30], cardiac catheterization [31], cancer survivorship care [32], or coloscopy [33]. We therefore hypothesized the same pattern to apply to MRI patients: We expected the psychological and physiological response of patients to improve when they received an intervention congruent with their coping style vs. when they received incongruent preparation or no additional preparation (i.e., standard care control group).

We tested this assumption in a study with a randomized controlled design with 142 patients. While sitting in the waiting room, the patients randomly watched one of two videos developed to address the needs of sensitizers (information video) or repressors (relaxation video) or received standard care (no video). Both videos can be accessed via the QR code presented in Figure 2. We assessed the patients' psychological and physiological responses to the examination, their evaluation of the videos, and recorded procedural outcomes (scan duration, repeated scans, interruptions). Anxiety was assessed via questionnaires on arrival at the hospital, after watching the video (or after a comparable amount of time in the control group), and after MRI. Cortisol as a physiological stress marker was assessed on arrival and after the MRI scan.

We found that cortisol levels were elevated compared with a "normal" day, which meant that undergoing MRI induced physiological stress in patients [34]. As cortisol still followed its normal circadian rhythm, we concluded that this elevation most likely reflected anticipatory effects, which is in line with our findings from the baseline study [12]. The videos were very well received by the patients [35]: Almost all reported that they found them helpful and that they increased their confidence regarding the examination; whereby the information video was evaluated even more positively. When the patients' preparation matched their coping style, anxiety decreased even before MRI, whereas this relief was only observed after the examination in patients whose preparation did not fit their needs. Beyond the positive effects at the patient level, we also found scan duration to be 10–20% shorter in the interventional groups and, descriptively, rates of scan repetitions or interruptions were 30–50% lower. Although our hypotheses were supported on a descriptive level, results failed to reach statistical significance. We believe that this is most likely due to power issues but there has, as yet, been no statistical confirmation of the effects on clinical processes and results must be interpreted with caution.

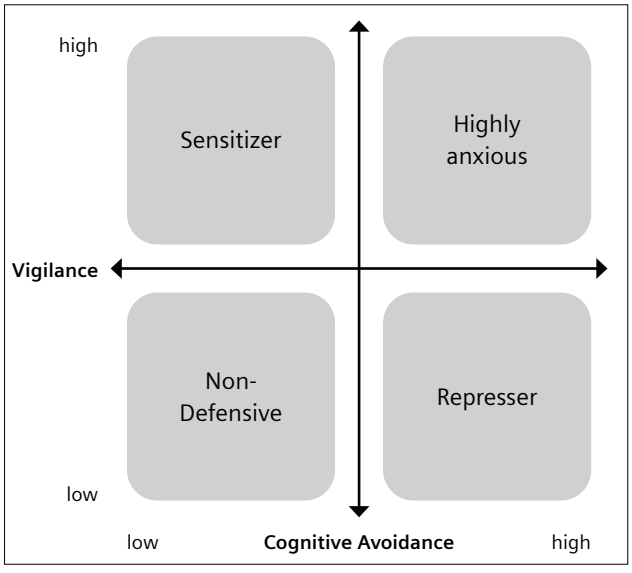

3 The Model of Coping Modes (based on Krohne [42]).

Improving patients' experience of MRI by addressing individual needs in advance can reduce stress and anxiety in patients and support smooth clinical workflows

Anxiety and stress in patients have always been and still are relevant phenomena in the context of MRI examinations. Based on the results of our studies [12, 34, 35] and the consideration of Ahlander et al. [14], we suggest that patients' response to MRI is most negative in anticipation of the examination. Therefore, changing the way patients are prepared for MRI seems to be a crucial step for improving MRI-related healthcare. Enriching standard care with additional patient preparation can have a positive impact on patients' experience of MRI. Our research suggests that patients vary greatly regarding their needs. Therefore, considering interindividual differences in patients' needs may be a promising approach to reduce stress and anxiety in patients most effectively. We therefore suggest that medical institutions should start providing tailored medicine, also in respect to the patient experience. This may be achieved by providing a variety of different materials for patients to choose from – or amendments of standard care, when thinking more generally. Thereby, it seems to be crucial to reach out to patients in advance: Providing patients with the opportunity to prepare themselves according to their own needs in a calm environment has the potential to maximize the beneficial effects.

Apart from being a relevant end in itself, we found in line with previous research that improving the patient experience could also have beneficial effects on clinical

workflows [5, 12, 17, 19, 21, 35–37]. Research suggests that patients who are calmer are less likely to be no-shows, have a lower need for sedation, premature terminations are less likely to happen, and patients move less, which could result in less need for scan repetitions and therefore shorter scan duration times [17, 19, 21, 36–40]. These effects might be even more pronounced when considering that time for patient education and preparation could also be reduced if patients were to arrive in an enhanced state of preparation. We therefore propose that improving the patient experience could result in positive effects for all stakeholders: Patients will be more relaxed, which also reduces stress for the medical personnel; furthermore, workflows will run more smoothly, thereby also increasing the revenue of an institution.

References

1 OECD. Magnetic resonance imaging (MRI) exams 2021.
2 Carlsson S, Carlsson E. 'The situation and the uncertainty about the coming result scared me but interaction with the radiographers helped me through': a qualitative study on patients' experiences of magnetic resonance imaging examinations. J Clin Nurs 2013;22:3225–3234.
3 Törnqvist E, Månsson A, Larsson E-M, Hallström I. It's like being in another world – patients' lived experience of magnetic resonance imaging. J Clin Nurs 2006;15:954–961.
4 Andre JB, Bresnahan BW, Mossa-Basha M, Hoff MN, Smith CP, Anzai Y, et al. Toward quantifying the prevalence, severity, and cost associated with patient motion during clinical MR examinations. J Am Coll Radiol 2015;12:689–695.
5 Dantendorfer K, Amering M, Bankier A, Helbich T, Prayer D, Youssefzadeh S, et al. A study of the effects of patient anxiety, perceptions and equipment on motion artifacts in magnetic resonance imaging. Magn Reson Imaging 1997;15:301–306.
6 Dewey M, Schink T, Dewey CF. Claustrophobia during magnetic resonance imaging: Cohort study in over 55,000 patients. J Magn Reson Imaging 2007;26:1322–1327.
7 Notini E. Panic. JAMA J Am Med Assoc 1988;259:897.
8 Brunnquell CL, Hoff MN, Balu N, Nguyen XV, Oztek MA, Haynor DR. Making magnets more attractive: Physics and engineering contributions to patient comfort in MRI. Top Magn Reson Imaging 2020;29:167–174.
9 Rinck PA. Magnetic resonance in medicine: A critical introduction. 12th ed. 2018.
10 Enders J, Zimmermann E, Rief M, Martus P, Klingebiel R, Asbach P, et al. Reduction of claustrophobia with short-bore versus open magnetic resonance imaging: A randomized controlled trial. PLoS ONE 2011;6:e23494.
11 Michel SC, Rake A, Götzmann L, Seifert B, Ferrazzini M, Chaoui R, et al. Pelvimetry and patient acceptability compared between open 0.5-T and closed 1.5-T MR systems. Eur Radiol 2002;12:2898–2905.
12 Madl J, Janka R, Bay S, Rohleder N. MRI as a stressor: The psychological and physiological response of patients to MRI, influencing factors, and consequences. J Am Coll Radiol 2022;19:423–432.
13 Sadigh G, Applegate KE, Saindane AM. Prevalence of unanticipated events associated with MRI examinations: A benchmark for MRI quality, safety, and patient experience. J Am Coll Radiol 2017;14:765–772.
14 Ahlander B-M, Engvall J, Maret E, Ericsson E. Positive effect on patient experience of video information given prior to cardiovascular magnetic resonance imaging: A clinical trial. J Clin Nurs 2018;27:1250–1261.
15 Harris LM, Menzies RG, Robinson J. Predictors of panic symptoms during magnetic resonance imaging scans. Int J Behav Med 2001;8:80–87.
16 Eshed I, Althoff CE, Hamm B, Hermann K-GA. Claustrophobia and premature termination of magnetic resonance imaging examinations. J Magn Reson Imaging 2007;26:401–404.
17 Munn Z, Jordan Z. Interventions to reduce anxiety, distress and the need for sedation in adult patients undergoing magnetic resonance imaging: a systematic review: Int J Evid Based Healthc 2013;11:265–274.
18 Tazegul G, Etcioglu E, Yildiz F, Yildiz R, Tuney D. Can MRI related patient anxiety be prevented? Magn Reson Imaging 2014;33:180–183.
19 Ladapo JA, Spritzer CE, Nguyen XV, Pool J, Lang E. Economics of MRI Operations After Implementation of Interpersonal Skills Training. J Am Coll Radiol 2018;15:1775–1783.
20 Madl JEM, Nieto Alvarez I, Amft O, Rohleder N, Becker L. The psychological, physiological, and behavioral responses of patients to magnetic resonance imaging (MRI): A systematic review and meta-analysis. Under Revision.
21 Powell R, Ahmad M, Gilbert FJ, Brian D, Johnston M. Improving magnetic resonance imaging (MRI) examinations: Development and evaluation of an intervention to reduce movement in scanners and facilitate scan completion. Br J Health Psychol 2015;20:449–465.
22 Thompson MB, Coppens NM. The effects of guided imagery on anxiety levels and movement of clients undergoing magnetic resonance imaging: Holist Nurs Pract 1994;8:59–69.
23 Krohne HW. Stress und Stressbewältigung bei Operationen. 1. Auflage. Berlin Heidelberg: Springer; 2017.
24 Mackenzie R, Sims C, Owens RG, Dixon AK. Patients' perceptions of magnetic resonance imaging. Clin Radiol 1995;50:137–143.
25 Krohne, de Bruin JT. Stress bei medizinischen Eingriffen: Kritischer Überblick über verschiedene Interventionsansätze. Z Für Med Psychol 1998;7:3–39.
26 Miller SM, Combs C, Stoddard E. Information, coping and control in patients undergoing surgery and stressful medical procedures. In: Steptoe A, Appels A, editors. Stress Pers. Control Health, Chichester, UK: Wiley; 1989, p. 107–130.
27 Krohne HW. Vigilance and cognitive avoidance as concepts in coping research. In: Krohne HW, editor. Atten. Avoid. Strateg. Coping Aversiveness, Seattle: Hogrefe & Huber; 1993, p. 19–50.
28 Krohne HW. Individual differences in emotional reactions and coping. In: Davidson RJ, Goldsmith HH, Scherer KR, editors. Handb. Affect. Sci., New York: Oxford University Press; 2003, p. 698–725.
29 Krohne HW, El-Giamal M. Psychologische Operationsvorbereitung, Stressbewältigung und perioperativer Status. Z Für Gesundheitspsychologie 2008;16:183–195.
30 Martelli MF, Auerbach SM, Alexander J, Mercuri LG. Stress management in the health care setting: Matching interventions with patient coping styles. J Consult Clin Psychol 1987;55:201–207.
31 Ludwick-Rosenthal R, Neufeld RWJ. Preparation for undergoing an invasive medical procedure: Interacting effects of information and coping style. J Consult Clin Psychol 1993;61:156–164.

32 de Rooij BH, Ezendam NPM, Vos MC, Pijnenborg JMA, Boll D, Kruitwagen RFPM, et al. Patients' information coping styles influence the benefit of a survivorship care plan in the ROGY Care Trial: New insights for tailored delivery. Cancer 2019;125:788–797.
33 Morgan J, Roufeil L, Kaushik S, Bassett M. Influence of coping style and precolonoscopy information on pain and anxiety of colonoscopy. Gastrointest Endosc 1998;48:119–127.
34 Madl JEM, Sturmbauer SC, Janka R, Bay S, Rohleder N. Preparing patients according to their individual coping style improves patient experience of magnetic resonance imaging. J Behav Med 2022. https://doi.org/10.1007/s10865-022-00361-y.
35 Madl JEM, Janka R, Bay S, Sturmbauer S, Rohleder N. Effects of video-based patient preparation for MRI on clinical processes and patient experience. Under Revision.
36 Ali SH, Modic ME, Mahmoud SY, Jones SE. Reducing clinical MRI motion degradation using a prescan patient information pamphlet. Am J Roentgenol 2013;200:630–634.
37 Norbash A, Yucel K, Yuh W, Doros G, Ajam A, Lang E, et al. Effect of team training on improving MRI study completion rates and no-show rates: Improving MRI Study Completion Rates. J Magn Reson Imaging 2016;44:1040–1047.
38 Andre JB, Johansson K. Relaxed patients, reduced motion, improved productivity. FieldStrength 2016;1:11–15.
39 Lang EV, Ward C, Laser E. Effect of team training on patients' ability to complete MRI examinations. Acad Radiol 2010;17:18–23.
40 Törnqvist E, Månsson A, Larsson E-M, Hallström I. Impact of extended written information on patient anxiety and image motion artifacts during magnetic resonance imaging. Acta Radiol 2006a;47:474–480.
41 Zenger I. Magnetic Resonance Imaging at Siemens. A success story. Erlangen, Germany: Siemens Healthcare AG; 2014. https://marketing.webassets.siemens-healthineers.com/1800000001929766/ef6a5e27aaf7/Siemens_MRI_MAGNETOM-World_Case-Study_success-story-Hellwich_1800000001929766.pdf
42 Krohne HW. Angst und Angstbewältigung. Stuttgart: Kohlhammer; 1996.



Contact

Janika Madl, M.Sc.
Chair, Health Psychology
Friedrich-Alexander-University
Erlangen-Nürnberg
Nägelsbachstrasse 49a
91052 Erlangen
Germany
janika.madl@fau.de

Advertisement

What happens when you have an MRI scan?

Help your little patients lose their fear – with Lottie

Lottie is an adventurous little lamb that loves to skateboard. But poor Lottie had an accident and may have broken her ankle. Now instead of leaping, she can only limp. Lottie is off to the hospital for an MRI scan. This engaging story by Professor Rolf Vosshenrich and Sylvia Graupner explains to children what it's like to have an MRI scan in a way they can understand.

We offer Lottie's story as a children's book in 15 languages (PDF) and as video in 5 languages. You can also order hard copies of the book in German, English, and Spanish.

The material is available at
www.siemens-healthineers.com/magnetom-world

Go to **> Publications > MR Basics**



Artificial Intelligence: Learning About the Future of Cardiovascular MR

Kerstin Hammernik, Ph.D.[1] and Thomas Küstner, Ph.D.[2]

[1]Technical University of Munich, Germany / Imperial College London, UK
[2]University Hospital Tübingen, Germany

Over the past 40 years, cardiovascular magnetic resonance (CMR) has evolved from an esoteric research tool to an indispensable clinical tool that routinely changes patient management across the breadth of modern cardiovascular practice. CMR is a versatile, non-invasive imaging modality that provides a comprehensive assessment of multiple parameters for cardiac function and morphology in a single protocol. It plays a major role in the diagnosis and management of cardiovascular disease (CVD). The prevalence of CVD is increasing annually and the conditions are among the leading causes of morbidity and mortality worldwide. This requires improvements in assessing, diagnosing, treating, and monitoring CVD patients. CMR will play a central role in achieving these goals. However, there remain major challenges for the widespread use of this technique:

(a) Complex technology with many pulse sequences and parameters to choose from
(b) Manual data analysis and interpretation
(c) Inherent cardiac and respiratory motion
(d) Duration of the examination

Methods using artificial intelligence (AI) have been proposed to address these challenges, but have also given rise to new questions about the methods' reliability, accuracy, generalizability, and robustness. In order to shape the future of CMR and establish where and how AI can play a role in it, we will showcase some CMR applications and scenarios that reflect the abovementioned challenges. We will highlight some AI methods for each step of the CMR processing chain and conclude with thoughts on remaining challenges and opportunities.

Learning about the heart in higher dimensions

CMR enables the acquisition of morphological, functional, and quantitative tissue parameters. Various sequences are devised that represent powerful tools for the non-invasive characterization of congenital or acquired CVDs, including ischemia, valvular diseases, and ischemic and non-ischemic cardiomyopathies. Cardiac function is commonly assessed with continuous acquisitions (cine, real-time) over multiple cardiac cycles. Perfusion imaging permits the assessment of physiologic and pathophysiologic functional parameters. First-pass perfusion is the clinical standard for measuring myocardial blood flow and detecting myocardial ischemia. Cardiac viability is traditionally studied with a gadolinium-based contrast agent in late gadolinium enhancement. Cardiovascular flow by phase-contrast imaging measures the velocity of blood in the cardiac chambers and great vessels. Coronary magnetic resonance angiography (CMRA) has the potential to diagnose coronary artery diseases. Quantitative CMR techniques like T1, T2, or T1rho mapping provide characterization of tissue properties that distinguish healthy from diseased tissue. More recently, MR fingerprinting[1] and MR multitasking have been proposed to provide multi-parametric data in a continuously measured acquisition under a free-movement scenario (with respiration and a beating heart). Multi-parametric CMR offers the promise of a more accurate diagnosis, early disease detection, and monitoring over time or of response to therapy [1].

These applications require either high spatial and/or temporal resolution, should ideally be acquired in 3D with whole-heart coverage to avoid slice misalignments or to allow reformatting into arbitrary image orientations, or are susceptible to cardiac and respiratory motion. The achievable image quality must be sufficient to detect and characterize CVDs, and is thus an inherent trade-off between imaging resolution, scan time, and signal-to-noise ratio (SNR), which are overall challenging requirements to meet. Moreover, to fully utilize the available information and/or to resolve the individual factors (motion, relaxivity, perfusion, etc.), joint data processing of all acquired data should be performed. This in turn yields high-dimensional data processing for CMR. To give an example, 5D cine imaging provides 3D spatial information of respiratory (1D) and cardiac (1D) motion-resolved data. If we jointly reconstruct motion-resolved data, we can share spatiotemporal information, i.e., sharing samples at a spatial location

[1]*MR Fingerprinting is not commercially available in some countries. Due to regulatory reasons its future availability cannot be ensured.*

between different respiratory/cardiac motion states by accounting for the underlying motion between motion states. The benefit is increased sampling efficiency and higher sampling density, which in turn can result in improved image quality. Furthermore, high-dimensional data processing naturally lends itself to the combination of several data processing steps, as shown in Figure 1. In our 5D cine example, the image reconstruction is combined with a motion correction/estimation procedure. The combination could also expand across several processing steps and we could develop a single AI network that performs this task for us. Let us say we are actually interested in assessing the left ventricular function using the 5D cine imaging. We could thus combine reconstruction, motion estimation, and image segmentation (to obtain left ventricular functional parameters) using as input the acquired MR raw data and outputting the left ventricular functional parameters (ejection fraction, end-systolic volume, and so on). While joint processing has its benefits, one could also be interested in obtaining the intermediate results of this joint processing chain – to perform quality assurance, for instance, or to further visually assess morphology and function. However, depending on the selected setup, architecture, and scenario, this may no longer be easily possible. On the other hand, we could have developed individual and finely tuned AI networks for each of the tasks. For the 5D cine example, an image reconstruction network is followed by an image registration network that merges individually reconstructed motion states on which a subsequent image segmentation network is performed. Intermediate results (reconstructed image, motion fields, segmentation masks) would be available, but we would lose the possibility to share information between and within processing steps.

While the concepts of joint processing sound intriguing and have already been studied in several research settings, applying them to a clinical scenario in a reliable fashion is challenging. Furthermore, high-dimensional AI-based data processing is not trivial and currently still limited in most cases by the available graphics processing unit (GPU) memory and the availability of network building blocks to process data beyond 3D [2].

AI forming the CMR workflow

For a conventional CMR examination, several individual sequences are acquired, for which different processing steps are conducted. These include image acquisition, image formation, and diagnosis, as illustrated in Figure 1. These processing steps could be performed individually with highly optimized and tuned AI networks, or several steps could be combined end-to-end for outputting multiple results in so-called multi-tasking networks. While AI has the potential to improve each step of the imaging pipeline, it should be seen as a support for clinicians, not a replacement.

Scanning and planning

The most tedious and time-consuming part of CMR is planning the cardiac scan. The image quality depends on the experienced technician responsible for acquiring the data, and uncertainties might be introduced by incorrect planning. AI has the potential to speed up the whole planning workflow, resulting in increased patient comfort and reduced healthcare costs. Also, AI-supported planning allows for more standardized cardiac scans and reduces the complexity of cardiac view planning. Siemens Healthineers provides a solution for AI-based view planning with its myExam Cardiac Assist tool [3, 4].

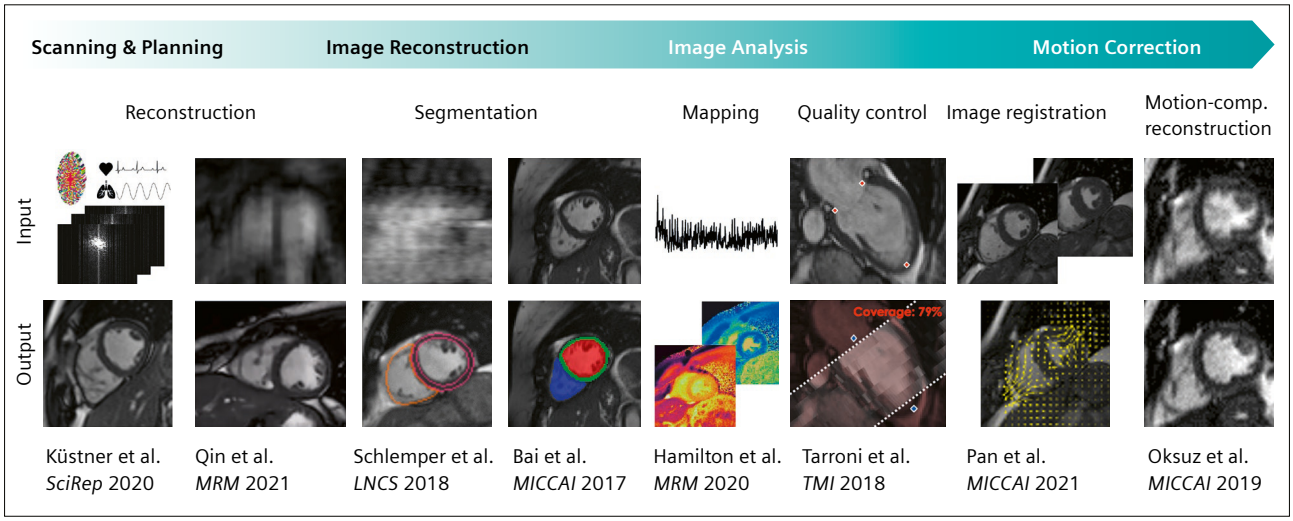

1 Overview of clinical workflow supported by several artificial intelligence (AI) methods. Different AI solutions along the imaging and processing chain are illustrated for cardiac cine imaging. The inputs and outputs of the proposed AI techniques are also shown.

Image reconstruction

Traditional image reconstruction techniques suffer from long reconstruction times and limitations in acceleration under Cartesian sampling patterns. Furthermore, prior knowledge of the reconstructed images needs to be incorporated into the reconstruction procedure. However, this prior information is often too simple to characterize the complex medical images. AI provides the opportunity to gain this prior knowledge directly from the data. Dictionary learning is an early example of data-driven learning in Compressed Sensing (CS)-based MRI reconstruction, and involves learning directly from undersampled data how the individual dictionary entries should be combined. AI-based solutions now achieve image quality similar or superior to classic CS-based approaches, while reducing the reconstruction time tremendously from minutes and hours to seconds. Furthermore, the learned priors can deal with the characteristic, coherent backfolding artifacts that appear in Cartesian sampling schemes, which are standard in the clinical workflow.

However, learning only a data-driven image prior is not enough, and special care needs to be taken with the acquired *k*-space data. While purely image-driven networks are able to produce realistic-looking images, the images themselves are not consistent with the acquired *k*-space data. We refer the interested reader to a previous article in MAGNETOM Flash and to book chapters [5, 6] for more information on how to include the acquired *k*-space into a reconstruction network. In the current article, we focus on the application of AI-based solutions to (high-dimensional) CMR, including static and dynamic imaging.

Fuin et al. proposed a multi-scale variational network for CMRA [7]. For this static application, the reconstruction time could be reduced from ~5 minutes for a CS-based approach to ~14 seconds for the proposed learning-based approaches. Comparable image quality was achieved between the fully sampled reference scan and the 9× accelerated scan. The results show that the acquisition time can be reduced from 18:55 minutes for the fully sampled reference scan to 2:34 minutes for the 9× accelerated acquisition, while the image quality stays comparable.

An alternative approach for shortening the scan time while simultaneously increasing spatial resolution is to use AI-based super resolution. Images are acquired at a low image resolution and retrospectively reconstructed to the high-resolution target. This approach has been successfully applied to cardiac cine [8, 9] and CMRA [10, 11].

In the context of cine image reconstruction, Schlemper et al. proposed a data-consistent convolutional neural network (CNN), performing alternating single-coil data-consistency steps and image denoising with a 5-layer CNN [12]. This approach was improved by a recurrent approach to propagate information through the time dimensions and between iterations [13]. Separated convolutions in the spatial domain and temporal domain further improve reconstruction quality, yielding more accurate functional

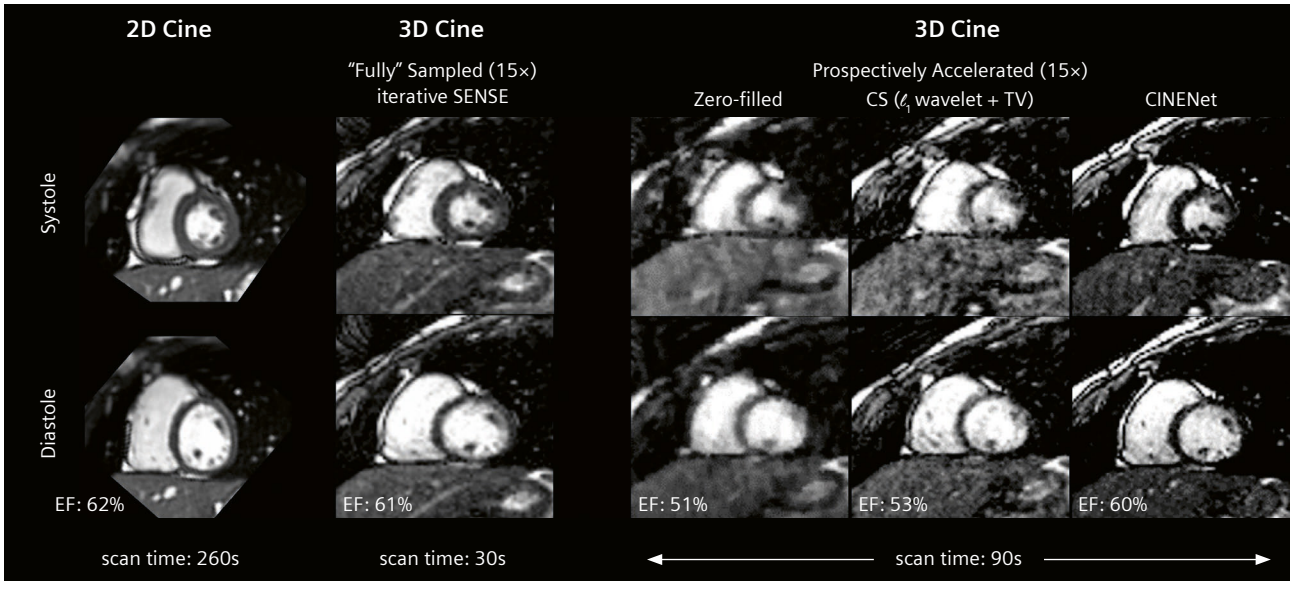

2 Physics-guided deep learning-based image reconstruction for cardiac cine imaging. High imaging acceleration (15×) enables the acquisition of a 3D cardiac cine with isotropic resolution and left ventricular coverage in a single breath-hold of < 10 seconds. A deep learning-based image reconstruction, CINENet, provides high image quality in contrast to the zero-filled reconstruction (input to network) or a Compressed Sensing (CS) reconstruction. CINENet reconstruction of accelerated scan (9 seconds) is in good accordance with a separate (slightly accelerated, 2.5×) 3D cine (30 seconds) and a conventional multi breath-hold 2D cine (260 seconds). The 3D cine with CINENet reconstruction shows high agreement with the conventional 2D cine in terms of left ventricular ejection fraction (EF).

parameters [14] and allowing for accelerated 3D cine reconstruction [15]. An example for accelerated single-breath-hold 3D cine reconstruction compared to conventional multi-slice multi-breath-hold 2D reconstruction is depicted in Figure 2. The aforementioned approaches operate directly on the full image, but low-rank and sparse priors are less frequently studied. Building on the success of unrolled networks, recent works focus on learning a structured low-rank prior [16] or low-rank plus sparse decomposition [17] in the context of dynamic MRI reconstruction.

While most approaches apply CNNs primarily in the image domain, hybrid networks exploit information in complementary domains. Due to the dynamic component in cine images, we can exploit the data in various domains. Exploiting all available data in various spaces pushes the reconstruction results further. El-Rewaidy et al. use both *k*-space and image domain information for radial imaging, implementing CNNs in both domains [18]. Complementary information in *k-t* and *x-f* space was studied in Qin et al. [19].

All aforementioned reconstruction approaches assume that fully sampled training data are available. The fully sampled data serve as a reference during training. However, training data is not always available, and is sometimes even impossible to acquire. Yaman et al. proposed a self-supervised learning approach that uses only the acquired training data points, with application to late gadolinium enhancement as depicted in Figure 3 [20]. The sampled data points are split into two disjoint sets, where the first set is used in the data consistency units of the unrolled reconstruction network, and the second set is used to evaluate the loss function during training directly in *k*-space.

Image analysis

CMR image segmentation and quantitative evaluation can be a challenging, time-consuming, and operator-intensive task. Segmentation of the chambers and myocardium is a mandatory postprocessing task. Automation of these tasks can therefore significantly reduce the time required for CMR image assessment.

AI-based solutions for image segmentation have been shown to be highly accurate and fast [21]. Considerable efforts have been directed toward cine imaging, as it is considered the gold standard for the assessment of cardiac chamber volumes and function [22]. The work of Morales et al. provided additional myocardial strain measures [23]. Segmentation methods have also been paired with predictions of important markers for cardiovascular disease, such as volume of pericardial adipose tissue [24] and scar-tissue areas [25]. Fahmy et al. automatically quantified left ventricular mass and scar volume in late gadolinium enhanced imaging [26], which showed strong agreement between the automated segmentations and the manual delineations. Farrag et al. [27] investigated the propagation of segmentation masks derived from cine imaging for the accurate segmentation of myocardial tissue in T1 mapping of a shMOLLI sequence. In contrast, the work of Hann et al. [28] segmented the myocardium directly in the shMOLLI data.

Segmentations have also been shown to provide valuable information for image reconstruction and motion correction tasks. Joint learning of motion estimation and segmentation for cine imaging was proposed by Qin et al. [29]. The results suggested that an efficient motion estimation network can bypass the need for high-quality reconstructions to achieve accurate image segmentation,

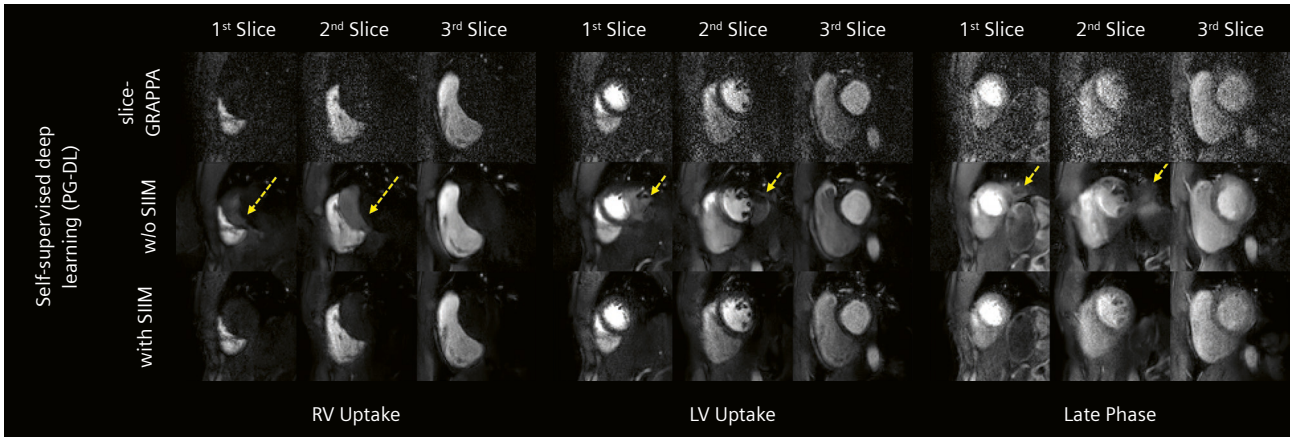

3 Physics-guided deep learning-based image reconstruction for dynamic contrast-enhanced MRI. A three-slice myocardial perfusion in the right ventricle (RV) uptake, left ventricle (LV) uptake and late phase is shown for different reconstruction techniques. A split slice-GRAPPA (top row) is compared to two self-supervised deep learning solutions (middle and bottom row) [63]. The difference between the deep learning methods is the use of signal intensity informed multi-coil (SIIM) encoding, which better models the underlying MR physics as indicated by the yellow arrows. *Image courtesy of Mehmet Akçakaya.*

indicating the superiority of high-dimensional data processing. Sun et al. [30] proposed a unified deep network architecture for joint image reconstruction and segmentation. The reconstruction and segmentation networks share network parts, acting as intrinsic regularizers for each other, while unshared network parts act specifically to the task (reconstruction or segmentation). Their results suggest that training a joint network is beneficial for high-quality segmentation of undersampled *k*-space data. While most multi-task networks aimed for an intermediate reconstructed image, Schlemper et al. [31] bypassed this step and directly predicted segmentation maps from highly undersampled dynamic CMR images of the UK Biobank data. Their results indicate that clinical parameters can be computed within an error of 10% if at least 10 lines are acquired for each cardiac phase using Cartesian sampling.

As sufficient image quality is a crucial factor in any further downstream task, Tarroni et al. devised an automated cardiac quality control [32]. The heart coverage, existence of inter-slice motion, and myocardial to blood pool contrast are automatically assessed. Their findings enable a reproducible and objective setting for large-scale and automated data processing.

Neural networks have also been proposed for quantitative CMR imaging to allow for accelerated myocardial tissue characterization. Jeelani et al. estimated quantitative T1 maps from a MOLLI sequence [33, 34]. The work of Fahmi et al. paired the quantification network with a segmentation to target the maps toward the myocardium [35].

For multi-parametric acquisitions in MR fingerprinting, AI solutions have been initially proposed for non-cardiac applications [36] in order to bypass dictionary simulation and pattern matching and thereby reduce computation time and memory requirements. In CMR fingerprinting, sequence timings depend on the subject's cardiac rhythm. Hamilton et al. proposed an estimation of T1 and T2 maps directly from undersampled spiral images showcasing rapid and robust predictions [37], as depicted in Figure 4.

Myocardial tissue characterization has also been studied in the context of radiomics. In radiomics, the image data is converted into mineable high-dimensional data using a large number of handcrafted features targeted toward the image intensity, and structural and textural information. These features are then used to perform segmentation of myocardial tissue [38], differentiate between acute and chronic infarction [39], differentiate between causes of myocardial hypertrophy [40], discriminate between hypertensive heart disease and hypertrophic cardiomyopathy patients [41], and quantify myocardial inflammation [42].

Beyond purely imaging-focused approaches, AI methods have also been used to predict outcomes in patients with various cardiovascular diseases [43] and identify relationships between cardiac morphology and non-imaging information as provided by genetic variations [44].

Motion correction

Physiological motion is still one of the major extrinsic sources of image artifacts and requires appropriate handling during acquisition or reconstruction. In the case of CMR, we are primarily dealing with respiratory and cardiac motion, which result in non-rigid deformations of the heart and its surrounding environment. Respiratory motion and cardiac motion are in most solutions regarded as periodic, but they do not necessarily have a fixed frequency throughout the scan. In other words, a subject might hold their breath, or a heartbeat might be skipped and should therefore be treated as cyclic rather than periodic. Simplifications in modeling and correcting motion may be necessary to handle the motion problem and to build an appropriate AI solution.

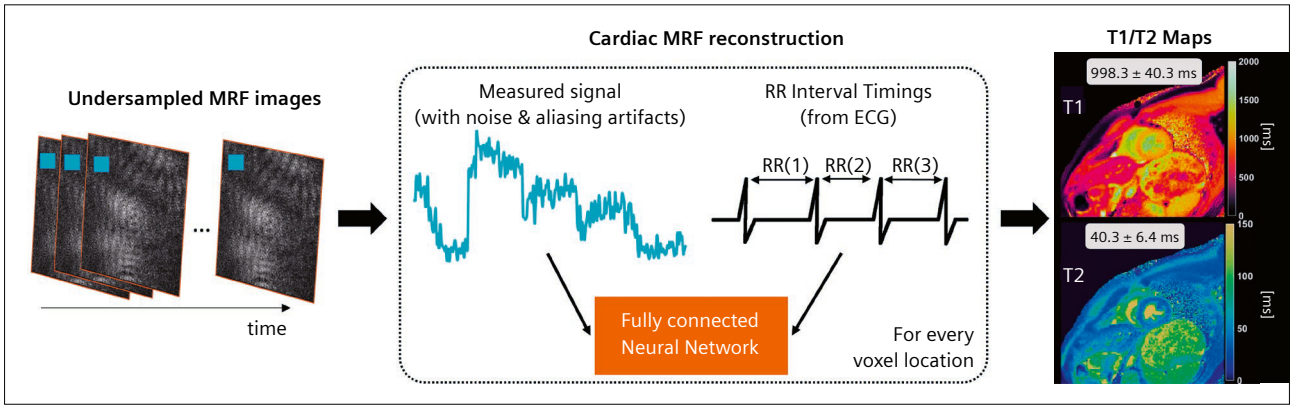

4 Deep learning-based magnetic resonance fingerprinting (MRF) for myocardial tissue mapping [37]. A cardiac MRF sequence collects data within an ECG-triggered window under breath-hold from which the temporal fingerprint (measured signal) can be extracted for every voxel location. Together with the heart-rate interval timings, a fully connected neural network estimates the T1 and T2 values at each voxel location. *Image courtesy of Jesse Hamilton.*

AI-based image registration methods have been proposed to map motion states in motion-resolved images, outputting a motion field of the moving anatomies. Mappings can be expressed between a pair of images (e.g., end-systolic frame to end-diastolic frame), known as pairwise registration, or between a group of images (several diastolic frames) to a target image (end-systolic frame), known as groupwise registrations. Large non-rigid motion across multiple temporal frames can occur, and in the case of 2D imaging the existence of through-plane motion complicates the motion estimation process. Moreover, estimated motion fields should be diffeomorphic, i.e., a forward motion (end-systolic to end-diastolic) can be easily inverted to a backward motion (end-diastolic to end-systolic).

A fast and reliable motion estimation is therefore required that correlates these short- and long-term correspondences. AI methods have been proposed to operate on the reconstructed motion-resolved images (i.e., in the image domain) for pairwise registrations [45–47] or groupwise registrations [48]. Alternatively, registration could be carried out directly on the acquired raw *k*-space data [49]. Since it is often of interest to estimate motion from as little data as possible (providing high temporal motion resolution), motion estimation procedures have been challenged with data from accelerated acquisitions [49–51].

Instead of outputting a motion field, joint motion-compensated image reconstruction networks have been studied. Motion estimations are embedded with the reconstruction process in order to exploit the high-dimensional data [52–54], as highlighted in Figure 5. Further combinations with segmentation have been studied in [55], which introduced a joint framework for motion artifact detection, correction in *k*-space, and image segmentation. In this setting, the motion correction problem is reformulated as a reconstruction task. The motion artifact network detects motion-affected lines in *k*-space, which are then signaled to the reconstruction part for removal, yielding a motion-corrected image from which segmentations are derived. The results showed that joint processing was superior to sequential processing.

Adversarial training strategies as proposed in [56, 57] aim to correct for the motion in the image domain. These networks consist of two parts: a generator network which predicts motion-corrected images from simulated motion-corrupted ones, and a discriminator which tries to distinguish between the generated motion-corrected images (from generator) and real motion-corrected images. The goal is to fool the discriminator network to generate images that look like real motion-corrected images. Alternatively, motion embeddings can be learned with variational autoencoders that allow to distinguish between motion-affected and motion-corrected scans [58].

Current challenges, opportunities, and limitations

CMR imaging offers a great opportunity for deep learning due to the redundancy and the high dimensionality of the data. However, we also face challenges regarding acquisition time, SNR, the trade-off between spatial and temporal resolutions, and different types of motion, e.g., cardiac and respiratory motion, which makes the application of deep learning techniques more demanding. While deep learning approaches often outperform CS-based approaches in terms of pixel-wise quantitative scores, these approaches might tend to over-blur the temporal component. However, a

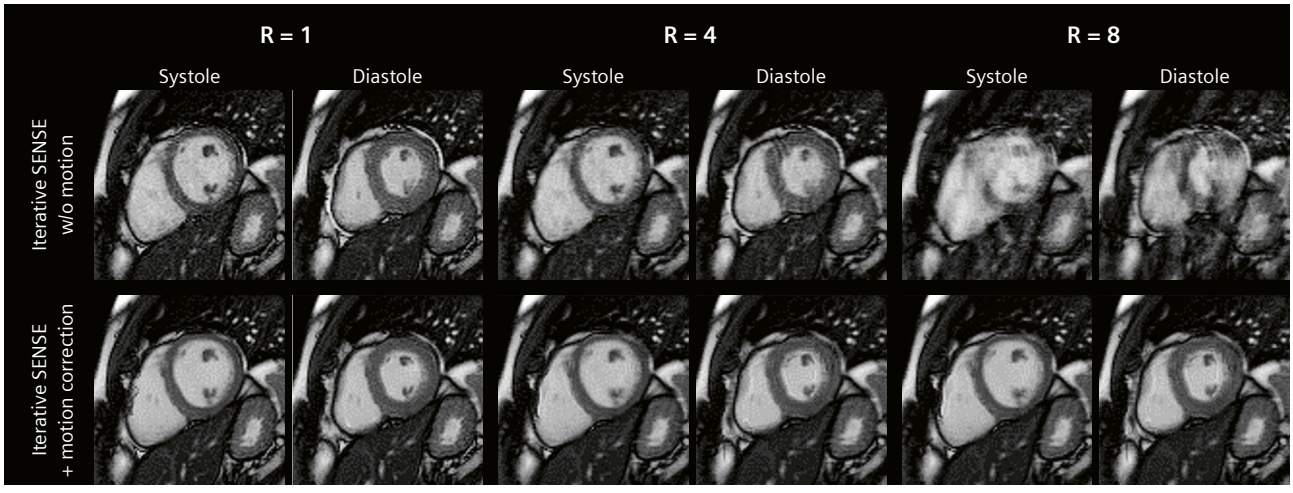

5 Motion-compensated image reconstruction for cardiac cine imaging. An image reconstruction is paired with a motion estimation network. The impact of sharing the available spatiotemporal information in a motion-corrected image reconstruction (bottom row) is shown in comparison to performing only a non-motion-informed image reconstruction (top row). For higher accelerations, sharing spatiotemporal data allows to increase sampling density and thereby improve image quality.

high resolution of the temporal dynamics is crucial for diagnosis and to detect subtle pathologies.

When using deep learning techniques, it is challenging to evaluate the quality and robustness of reconstruction approaches, especially in the case of subtle pathologies. However, we might get trapped in overly optimistic results if we use simulated data and neglect the unprocessed raw *k*-space data [59]. In a different line of work, the robustness of neural networks to small adversarial perturbations at the input was investigated [60]. Robustness of neural networks to changes in anatomy was studied in the context of static 2D imaging in [61], showing that domain shift has a marginal impact on image reconstruction when using unrolled networks and moderate acceleration. This observation regarding domain shift is different to image analysis tasks, where a subtle change might lead to mis-segmentation, for instance.

Deep learning approaches were intensively and individually studied in the context of scan planning, accelerated acquisition and reconstruction, and image analysis. While we often focus only on one part of this full imaging pipeline, deep learning provides many more opportunities to improve the whole workflow of CMR image acquisition for analysis and diagnosis. Future investigations of deep learning approaches will go deeper in supporting the choice of exam based on actual physiological scan parameters such as heart rate, or on the patient information obtained during the scan. Deep learning techniques will also support further acceleration in scan time to enable real-time interventional cardiac MRI [62]. We also observe a trend towards embedding different elements of the imaging pipeline into a deep learning approach and training this network end-to-end as shown in multi-task networks, or exploiting the available data, e.g., via motion fields, which will form the future of learning-based CMR imaging.

Acknowledgments

The authors would like to thank Jesse Hamilton and Mehmet Akçakaya for providing materials for the figures, and Teresa Correia, Tevfik Ismail, Wendy Strugnell, Chiara Coletti, Masa Bozic-Iven, Sebastian Weingärtner, and Gastao Cruz for the discussions.

References

1 Ismail TF, Strugnell W, Coletti C, Božić-Iven M, Weingärtner S, Hammernik K, et al. Cardiac MR: From Theory to Practice. Front Cardiovasc Med. 2022;9:826283.
2 Hammernik K, Kuestner T, Rueckert D. Machine Learning in MRI Reconstruction. In: Akcakaya M, Doneva M, Prieto C, editors. Magnetic Resonance Image Reconstruction Theory, Methods, and Applications. Elsevier; 2022. ISBN: 9780128227268. In press.
3 Thomas SJ, Bryant MG, Radvan J, Speier P, Mueller E, Schmidt M, et al. The need for speed – adenosine stress MRI in less than 30 minutes. J Cardiovasc Magn Reson. 2013;15(Suppl 1):E24.
4 Wang K, Zhang W, Li S, Bi X, Schmidt M, An J, et al. Free-Breathing 10-Min Cardiac MRI Protocol at 3.0t: Single-Center Experience. Biomedical Journal of Scientific & Technical Research. 2022;41(1):32365-32373.
5 Hammernik K, Knoll F, Rueckert D. Deep Learning for Parallel MRI Reconstruction: Overview, Challenges, and Opportunities. MAGNETOM Flash. 2019;75:10-15.
6 Hammernik K, Knoll F. Chapter 2 – Machine learning for image reconstruction. In: Zhou SK, Rueckert D, Fichtinger G, editors. Handbook of Medical Image Computing and Computer Assisted Intervention. Academic Press; 2020. p. 25–64.
7 Fuin N, Bustin A, Küstner T, Oksuz I, Clough J, King AP, et al. A multi-scale variational neural network for accelerating motion-compensated whole-heart 3D coronary MR angiography. Magn Reson Imaging. 2020;70:155–167.
8 Lin JY, Chang YC, Hsu WH. Efficient and Phase-aware Video Super-resolution for Cardiac MRI. arXiv. 10626 [eess.IV].
9 Steeden JA, Quail M, Gotschy A, et al. Rapid whole-heart CMR with single volume super-resolution. J Cardiovasc Magn Reson. 2020;22:56.
10 Küstner T, Munoz C, Psenicny A, Bustin A, Fuin N, Qi H, et al. Deep-learning based super-resolution for 3D isotropic coronary MR angiography in less than a minute. Magn Reson Med. 2021;86(5): 2837–2852.
11 Ishida M, Nakayama R, Uno M, et al. Learning-based super-resolution technique significantly improves detection of coronary artery stenoses on 1.5T whole-heart coronary MRA. J Cardiovasc Magn Reson. 2014;16 (Suppl 1), P218.
12 Schlemper J, Caballero J, Hajnal JV, Price AN, Rueckert D. A Deep Cascade of Convolutional Neural Networks for Dynamic MR Image Reconstruction. IEEE Trans Med Imaging. 2018;37(2):491–503.
13 Qin C, Schlemper J, Caballero J, Price AN, Hajnal JV, Rueckert D. Convolutional Recurrent Neural Networks for Dynamic MR Image Reconstruction. IEEE Trans Med Imaging. 2019;38(1):280–290.
14 Sandino CM, Lai P, Vasanawala SS, Cheng JY. Accelerating cardiac cine MRI using a deep learning-based ESPIRiT reconstruction. Magn Reson Med. 2021;85(1):152–167.
15 Küstner T, Fuin N, Hammernik K, Bustin A, Qi H, Hajhosseiny R, et al. CINENet: deep learning-based 3D cardiac CINE MRI reconstruction with multi-coil complex-valued 4D spatio-temporal convolutions. Sci Rep. 2020;10:13710.
16 Ke Z, Huang W, Cui ZX, Cheng J, Jia S, Wang H, et al. Learned Low-Rank Priors in Dynamic MR Imaging. IEEE Trans Med Imaging. 2021;40(12):3698–3710.
17 Huang W, Ke Z, Cui ZX, Cheng J, Qiu Z, Jia S, et al. Deep low-Rank plus sparse network for dynamic MR imaging. Medical Image Analysis. 2021;73:102190.
18 El-Rewaidy H, Fahmy AS, Pashakhanloo F, Cai X, Kucukseymen S, Csecs I, et al. Multi-domain convolutional neural network (MD-CNN) for radial reconstruction of dynamic cardiac MRI. Magn Reson Med. 2021;85(1):1195–1208.
19 Qin C, Duan J, Hammernik K, Schlemper J, Küstner T, Botnar R, et al. Complementary time-frequency domain networks for dynamic parallel MR image reconstruction. Magn Reson Med. 2021;86(6):3274–3291.
20 Yaman B, Shenoy C, Deng Z, Moeller S, El-Rewaidy H, Nezafat R, et al. Self-Supervised Physics-Guided Deep Learning Reconstruction for High-Resolution 3D LGE CMR. IEEE 18th International Symposium on Biomedical Imaging (ISBI), 2021, pp. 100–104.
21 Bernard O, Lalande A, Zotti C, Cervenansky F, Yang X, Heng PA, et al. Deep Learning Techniques for Automatic MRI Cardiac Multi-Structures Segmentation and Diagnosis: Is the Problem Solved? IEEE Trans Med Imaging. 2018;37(11):2514–2525.
22 Bai W, Sinclair M, Tarroni G, Oktay O, Rajchl M, Vaillant G, et al. Automated cardiovascular magnetic resonance image analysis

with fully convolutional networks.
J Cardiovasc Magn Reson. 2018;20(1):65.
23 Morales MA, van den Boomen M, Nguyen C, Kalpathy-Cramer J, Rosen BR, Stultz CM, et al. DeepStrain: A Deep Learning Workflow for the Automated Characterization of Cardiac Mechanics. Front Cardiovasc Med. 2021;8:730316.
24 Bard A, Raisi-Estabragh Z, Ardissino M, Lee AM, Pugliese F, Dey D, et al. Automated Quality-Controlled Cardiovascular Magnetic Resonance Pericardial Fat Quantification Using a Convolutional Neural Network in the UK Biobank. Front Cardiovasc Med. 2021;8:677574.
25 Chen J, Yang G, Gao Z, Ni H, Angelini E, Mohiaddin R, et al. Multiview two-task recursive attention model for left atrium and atrial scars segmentation. arXiv:1806.04597 [cs.CV].
26 Fahmy AS, Rausch J, Neisius U, Chan RH, Maron MS, Appelbaum E, et al. Automated Cardiac MR Scar Quantification in Hypertrophic Cardiomyopathy Using Deep Convolutional Neural Networks. JACC Cardiovasc Imaging. 2018;11(12):1917–1918.
27 Farrag NA, White JA, Ukwatta E. Semi-automated myocardial segmentation in native T1-mapping CMR using deformable non-rigid registration of CINE images. In: Medical Imaging 2019: Biomedical Applications in Molecular, Structural, and Functional Imaging. SPIE Conference Series. 2019;10953.
28 Hann E, Ferreira VM, Neubauer S, Piechnik SK. Deep Learning for Fully Automatic Contouring of the Left Ventricle in Cardiac T1 Mapping. CMR 2018 – A Joint EuroCMR/SCMR Meeting Abstract Supplement. ID# 376365.
29 Qin C, Bai W, Schlemper J, Petersen SE, Piechnik SK, Neubauer S, et al. Joint Learning of Motion Estimation and Segmentation for Cardiac MR Image Sequences. arXiv;2018.1806.04066 [cs.CV].
30 Sun L, Fan Z, Ding X, Huang Y, Paisley J. Joint CS-MRI Reconstruction and Segmentation with a Unified Deep Network. Lecture Notes in Computer Science (including subseries Lecture Notes in Artificial Intelligence and Lecture Notes in Bioinformatics). 2019;11492 LNCS:492-504.
31 Schlemper J, Oktay O, Bai W, Castro DC, Duan J, Qin C, et al. Cardiac MR Segmentation from Undersampled *k*-space Using Deep Latent Representation Learning. In: Frangi A, Schnabel J, Davatzikos C, Alberola-López C, Fichtinger G (eds). Medical Image Computing and Computer Assisted Intervention – MICCAI 2018. MICCAI 2018. Lecture Notes in Computer Science. 2018;11070.
32 Tarroni G, Bai W, Oktay O, Schuh A, Suzuki H, Glocker B, et al. Large-scale Quality Control of Cardiac Imaging in Population Studies: Application to UK Biobank. Sci Rep. 2020;10:2408.
33 Jeelani H, Yang Y, Zhou R, Kramer CM, Salerno M, Weller DS. A Myocardial T1-Mapping Framework with Recurrent and U-Net Convolutional Neural Networks. In: IEEE 17th International Symposium on Biomedical Imaging (ISBI). 2020:1941–1944.
34 Martini N, Della Latta D, Santini G, Valvano G, Barison A, Avogliero F, et al. Automatic AHA model segmentation of cardiac T1 maps with deep learning. Proc Intl Soc Mag Reson Med. 2018;26:1047.
35 Fahmy AS, El-Rewaidy H, Nezafat M, Nakamori S, Nezafat R. Automated analysis of cardiovascular magnetic resonance myocardial native T1 mapping images using fully convolutional neural networks. J Cardiovasc Magn Reson. 2019;21(1):7.
36 Cohen O, Zhu B, Rosen MS. MR fingerprinting Deep RecOnstruction NEtwork (DRONE). Magn Reson Med. 2018;80(3):885–894.
37 Hamilton JI, Currey D, Rajagopalan S, Seiberlich N. Deep learning reconstruction for cardiac magnetic resonance fingerprinting T1 and T2 mapping. Magn Reson Med. 2021;85(4):2127–2135.
38 Kotu LP, Engan K, Skretting K, Måløy F, Orn S, Woie L, et al. Probability mapping of scarred myocardium using texture and intensity features in CMR images. Biomed Eng Online. 2013;12:91.
39 Larroza A, López-Lereu MP, Monmeneu JV, Gavara J, Chorro FJ, Bodí V, et al. Texture analysis of cardiac cine magnetic resonance imaging to detect nonviable segments in patients with chronic myocardial infarction. Med Phys. 2018;45(4):1471–1480.
40 Schofield R, Ganeshan B, Kozor R, Nasis A, Endozo R, Groves A, et al. CMR myocardial texture analysis tracks different etiologies of left ventricular hypertrophy. J Cardiovasc Magn Reson. 2016;18(Suppl 1):O82.
41 Neisius U, El-Rewaidy H, Nakamori S, Rodriguez J, Manning WJ, Nezafat R. Radiomic Analysis of Myocardial Native T1 Imaging Discriminates Between Hypertensive Heart Disease and Hypertrophic Cardiomyopathy. JACC Cardiovasc Imaging. 2019;12(10):1946–1954.
42 Baeßler B, Schaarschmidt F, Treutlein M, Stehning C, Schnackenburg B, Michels G, et al. Re-evaluation of a novel approach for quantitative myocardial oedema detection by analysing tissue inhomogeneity in acute myocarditis using T2-mapping. Eur Radiol. 2017;27(12):5169–5178.
43 Kotu LP, Engan K, Borhani R, Katsaggelos AK, Ørn S, Woie L, et al. Cardiac magnetic resonance image-based classification of the risk of arrhythmias in post-myocardial infarction patients. Artif Intell Med. 2015;64(3):205–15.
44 Biffi C, de Marvao A, Attard MI, Dawes TJW, Whiffin N, Bai W, et al. Three-dimensional cardiovascular imaging-genetics: a mass univariate framework. Bioinformatics. 2018;34(1):97–103.
45 Pan J, Rueckert D, Kuestner T, Hammernik K. Efficient Image Registration Network for Non-Rigid Cardiac Motion Estimation. In: Haq N, Johnson P, Maier A, Würfl T, Yoo J (eds). Machine Learning for Medical Image Reconstruction. MLMIR 2021. Lecture Notes in Computer Science. 2021;12964. Springer, Cham.
46 Morales MA, Izquierdo-Garcia D, Aganj I, Kalpathy-Cramer J, Rosen BR, Catana C. Implementation and Validation of a Three-dimensional Cardiac Motion Estimation Network. Radiol Artif Intell. 2019;1(4):e180080.
47 Upendra RR, Wentz BJ, Shontz SM, Linte CA. A Convolutional Neural Network-based Deformable Image Registration Method for Cardiac Motion Estimation from Cine Cardiac MR Images. Comput Cardiol (2010). 2020;47:10.22489/CinC.2020.204.
48 Qi H, Hajhosseiny R, Cruz G, Küstner T, Kunze K, Neji R, et al. End-to-end deep learning nonrigid motion-corrected reconstruction for highly accelerated free-breathing coronary MRA. Magn Reson Med. 2021;86(4):1983–1996.
49 Küstner T, Pan J, Qu H, Cruz G, Gilliam C, Blu T, et al. LAPNet: Non-Rigid Registration Derived in *k*-Space for Magnetic Resonance Imaging. In: IEEE Transactions on Medical Imaging. 2021;40(12):3686–3697.
50 Hammernik K, Pan J, Rueckert D, Küstner T. Motion-Guided Physics-Based Learning for Cardiac MRI Reconstruction. In: 55th Asilomar Conference on Signals, Systems, and Computers. 2021:900–907.
51 Huttinga NRF, van den Berg CAT, Luijten PR, Sbrizzi A. MR-MOTUS: model-based non-rigid motion estimation for MR-guided radiotherapy using a reference image and minimal *k*-space data. Phys Med Biol. 2020;65(1):015004.
52 Seegoolam G, Schlemper J, Qin C, Price A, Hajnal J, Rueckert D. Exploiting Motion for Deep Learning Reconstruction of Extremely-Undersampled Dynamic MRI. In: Shen D, Liu T, Peters TM, Staib LH, Essert C, Zhou S, et al. (eds). Medical Image Computing and Computer Assisted Intervention – MICCAI 2019. MICCAI 2019. Lecture Notes in Computer Science. 2019;11767. Springer, Cham.
53 Küstner T, Pan J, Gilliam C, Qi H, Cruz G, Hammernik K, et al. Self-Supervised Motion-Corrected Image Reconstruction Network for 4D Magnetic Resonance Imaging of the Body Trunk. APSIPA Transactions on Signal and Information Processing. 2022;11(1):e12.

54 Qi H, Hajhosseiny R, Cruz G, Kuestner T, Kunze K, Neji R, et al. End-to-end deep learning nonrigid motion-corrected reconstruction for highly accelerated free-breathing coronary MRA. Magn Reson Med. 2021;86(4):1983–1996.
55 Oksuz I, Clough JR, Ruijsink B, Anton EP, Bustin A, Cruz G, et al. Deep Learning-Based Detection and Correction of Cardiac MR Motion Artefacts During Reconstruction for High-Quality Segmentation. IEEE Trans Med Imaging. 2020;39(12):4001–4010.

Contact



Kerstin Hammernik, Ph.D.
AI in Healthcare and Medicine
Technical University of Munich
Boltzmannstr. 3
85748 Garching
Germany
k.hammernik@tum.de



Thomas Küstner, Ph.D.
University Hospital Tübingen
Hoppe-Seyler-Straße 3
72076 Tübingen
Germany
thomas.kuestner@med.uni-tuebingen.de

56 Zhang Y, Zhang W, Zhang Q, Yang J, Chen X, Zhao S. CMR motion artifact correction using generative adversarial nets. arXiv:1902.11121 [cs.CV].
57 Küstner T, Armanious K, Yang J, Yang B, Schick F, Gatidis S. Retrospective correction of motion-affected MR images using deep learning frameworks. Mag Reson Med. 2019;82(4):1527-1540.
58 Ghodrati V, Bydder M, Ali F, Gao C, Prosper A, Nguyen KL, et al. Retrospective respiratory motion correction in cardiac cine MRI reconstruction using adversarial autoencoder and unsupervised learning. NMR Biomed. 2021;34(2):e4433.
59 Shimron E, Tamir JI, Wang K, Lustig M. Implicit data crimes: Machine learning bias arising from misuse of public data. Proc Natl Acad Sci U S A. 2022;119(13):e2117203119.
60 Antun V, Renna F, Poon C, Adcock B, Hansen AC. On instabilities of deep learning in image reconstruction and the potential costs of AI. Proc Natl Acad Sci U S A. 2020;117(48):30088–30095.
61 Hammernik K, Schlemper J, Qin C, Duan J, Summers RM, Rueckert D. Systematic evaluation of iterative deep neural networks for fast parallel MRI reconstruction with sensitivity-weighted coil combination. Magn Reson Med. 2021;86(4):1859–1872.
62 Jaubert O, Montalt-Tordera J, Knight D, Coghlan GJ, Arridge S, Steeden JA, et al. Real-time deep artifact suppression using recurrent U-Nets for low-latency cardiac MRI. Magn Reson Med. 2021;86(4):1904–1916.
63 Yaman B, Hosseini SAH, Moeller S, Ellermann J, Uğurbil K, Akçakaya M. Self-supervised learning of physics-guided reconstruction neural networks without fully sampled reference data. Magn Reson Med. 2020;84(6):3172–3191.

Advertisement

Learn more about Deep Learning Image Reconstruction

Introduction to Deep Learning for MR Image Reconstruction
Florian Knoll, Ph.D.
(New York University, New York, NY, USA)

Deep Learning Image Reconstruction – State of the Art
Kerstin Hammernik, Ph.D.
(Imperial College London, UK)

Iterative Denoising and Increased Acquisition Speed
Johan Dehem, M.D.
(Yan Yperman Ziekenhuis, Ieper, Belgium)

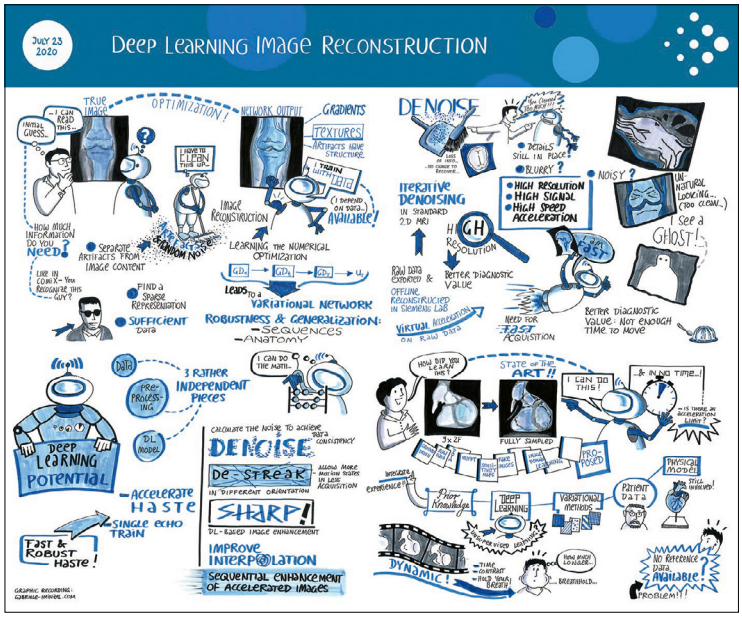

Graphic Recording: www.gabriele-heinzel.com

Don't miss this valuable source of information
siemens-healthineers.com/MWS2020-recordings

3D Whole Heart Applications: Angiography and Delayed Enhancement

Jason Craft[1], Joshua Y. Cheng[1], Nancy Diaz[1], Karl P. Kunze[2], Michaela Schmidt[3]

[1]St. Francis Heart Hospital, DeMatteis Research Center, Greenvale, NY, USA
[2]Siemens Healthcare Limited, Frimley, UK
[3]Siemens Healthineers, Erlangen, Germany

Introduction

It has become more important than ever before to diversify non-invasive imaging methods that involve contrast media administration. Compared to CT imaging, MRI does not involve nephrotoxic iodinated contrast or ionizing radiation. However, ungated first pass magnetic resonance angiography (MRA) cannot effectively freeze cardiac motion; and provides reduced quality of segmentation compared to CT pulmonary vein angiography [1]. Diaphragmatic navigator (dNAV) used for motion correction is associated with unpredictable scan times when respiration is irregular, and imperfect slab tracking ratio [2]. Furthermore, approximately 50–100 Hz off-resonance is frequently observed at the interface of the pulmonary veins and left atrium due to susceptibility effects and inflow from the lungs [3]. Therefore, the use of balanced steady-state free precession (bSSFP) and fat saturation pulses, particularly at higher field strengths, can be technically unsatisfactory for this application. Thus, the unmet clinical need is to provide robust clinical angiographic methods that can effectively image complex patients with arrhythmias, while minimizing image artifacts.

Instead of tracking the diaphragmatic interface, image navigators (iNAV) track the blood pool contrast of the left ventricle [4]. 2D translational motion in the head-to-foot direction can be extracted and estimated on a per cardiac cycle basis and is used to bin data with

Imaging parameters for whole heart MRA and LGE			
Sequence	Inversion recovery GRE	Saturation recovery GRE	Inversion recovery Dixon GRE
FOV	320 mm (axial)	320 mm (axial)	320 mm (axial)
Spatial resolution	1.3 × 1.3 mm	1.3 × 1.3 mm	1.3 × 1.3 mm
Slice thickness	1.4 mm	1.4 mm	1.4 mm
Slice resolution	90%	90%	90%
Fat Sat	No	Yes	No
Acceleration Factor	2.9	2.9	2.8
Bandwidth	579 Hz/px	579 Hz/px	453 Hz/px
Flip angle	18°	18°	15°
TI/Saturation time	220–260 ms (systolic) 290 ms (diastolic)	150 ms	According to scout
TE/TR	1.42 ms/3.89 ms	1.42 ms/3.89 ms	2.38, 4.76 ms/6.97 ms
Data window duration	62–130 ms	62–130 ms	62–130 ms

Table 1: 3D whole heart sequence parameters.

respect to respiration. 3D image volumes are obtained using a non-rigid motion-compensated reconstruction of all binned data [5, 6], leading to 100% scan efficiency and predictable scan time. The sampling pattern consists of spiral-like interleaves acquired alternately based on the golden angle of rotation (variable-density golden-step Cartesian trajectory with spiral profile order sampling, or VD-CASPR)[1] [7].

As a result of scanning more efficiently, the predictable scan time translates into less gadolinium-based contrast agent (GBCA) use. Specifically, compared to dNAV based applications, we can use 33% less contrast [8, 9], and we can do it without the need for higher field strengths. Furthermore, we can acquire angiography and delayed enhancement at higher near isotropic spatial resolution. We acquire all 3D datasets at a true spatial resolution of $1.3 \times 1.3 \times 1.5$ mm^3, with a reconstructed slice thickness of 1.4 mm (Table 1).

Pulmonary vein angiography and arterial delayed enhancement using iNAV

At our institution, we are asked to provide pulmonary vein anatomical imaging for segmentation and importation into the electro-anatomical mapping system. With MRI, not only is anatomical information obtained, but functional information such as atrial and ventricular volumetrics, left atrial delayed enhancement, and quantification of valvular heart disease. Obtaining one MRI examination is simply more logistically efficient than obtaining CT angiography plus echocardiography imaging. Our 3D MRA and late gadolinium enhancement (LGE) imaging is performed on a 1.5T MAGNETOM Sola, but our institution also has experience with the 3D inversion recovery Dixon multi-echo gradient recalled echo (GRE)[1] performed on the 3T MAGNETOM Skyra platform.

Concerning the MRA and LGE exam workflow, the image navigator and saturation band position can be automatically determined using free-breathing 3 plane localizers and the AI cardiac scan companion (AICSC)[1] prototype. The diastolic or systolic rest period of the left atrium can be determined using the included high temporal resolution free breathing 4-chamber (or HLA) cine [10]. The user can manually determine the data window duration, or this can be automatically determined based on the rest period of the right coronary artery by the AICSC. Given the diastolic rest period is longer at slower ventricular rates, we prefer diastolic imaging at regular heart rhythms < 80 BPM. When the ventricular rate is > 80 BPM or significant arrhythmia such as atrial fibrillation is present, systolic imaging is preferential.

In addition to the prototype sequence[1] for *syngo* XA20 featuring 3D inversion recovery Dixon multi-echo GRE, 3D T2 prep bSSFP, and 3D T2 Prep Dixon multi-echo GRE, the user can configure different preparatory pulses to manipulate image contrast. We acquire pulmonary vein angiography using either inversion recovery GRE or saturation recovery GRE. Both methods have respective strengths and weaknesses. Inversion recovery maintains vessel sharpness and is compatible with the 1500 Hz wideband pulse which mitigates device artifacts. Furthermore, inversion recovery can be used without fat saturation, which makes this option especially attractive at higher field strengths. The inversion time parameter at 1.5T represents a balance between SNR and background suppression-values range from 220 ms to 300 ms at 1.5T [11–14]. Similar to previous literature [15], we have observed that image contrast is quite consistent even with irregular rhythms; iNAV tracking similarly remains quite robust despite the dependence of the beat-to-beat image contrast on the RR interval. Figure 1 depicts excellent image quality despite underlying atrial fibrillation, using inversion recovery GRE. Saturation recovery images have overall higher signal-to-noise, and can be used without manipulation of the inversion time parameter.

Simplifying the contrast injection scheme is important to reduce human error and to optimize workflow. Our contrast injection scheme does not involve the use of look-up tables, saline dilution, or manipulation of extra tubing and/or stop cocks. To provide adequate signal for iNAV tracking, 0.05 mmol/kg of 1 molar contrast agent is injected at 2 ml/sec, followed by 20 ml of saline at the same rate. Immediately after, the remaining 0.10 mmol/kg contrast is administered as a slow infusion, followed by saline at the same rate (0.2 ml/sec). The contrast is injected after starting the first 3D scan, and after observing satisfactory cardiac gating and appropriate iNAV placement prescription. This scan is solely run for the iNAV functionality in order to visualize contrast passage and arrival. The first, second pass, and continuous infusion dose is observed passing through the heart (Fig. 2). The first 3D scan is stopped as soon as the contrast peaks in the pulmonary artery. The exact same protocol is restarted by using STOP/CONTINUE on the inline display (which was linked by the copy reference "copy everything"). We target a maximum scan duration of 4 minutes given the length of the contrast administration and need to perform other imaging prior to delayed enhancement. 15 minutes after the initial injection of GBCA, we perform delayed enhancement of the left atrium using the inversion recovery Dixon multi-echo GRE whole heart sequence at identical spatial resolution. If desired, residual fat can be subtracted from the 3D MRA using the inversion recovery Dixon multi-echo.

[1] *Work in progress. The application is currently under development and is not for sale in the U.S. and in other countries. Its future availability cannot be ensured.*

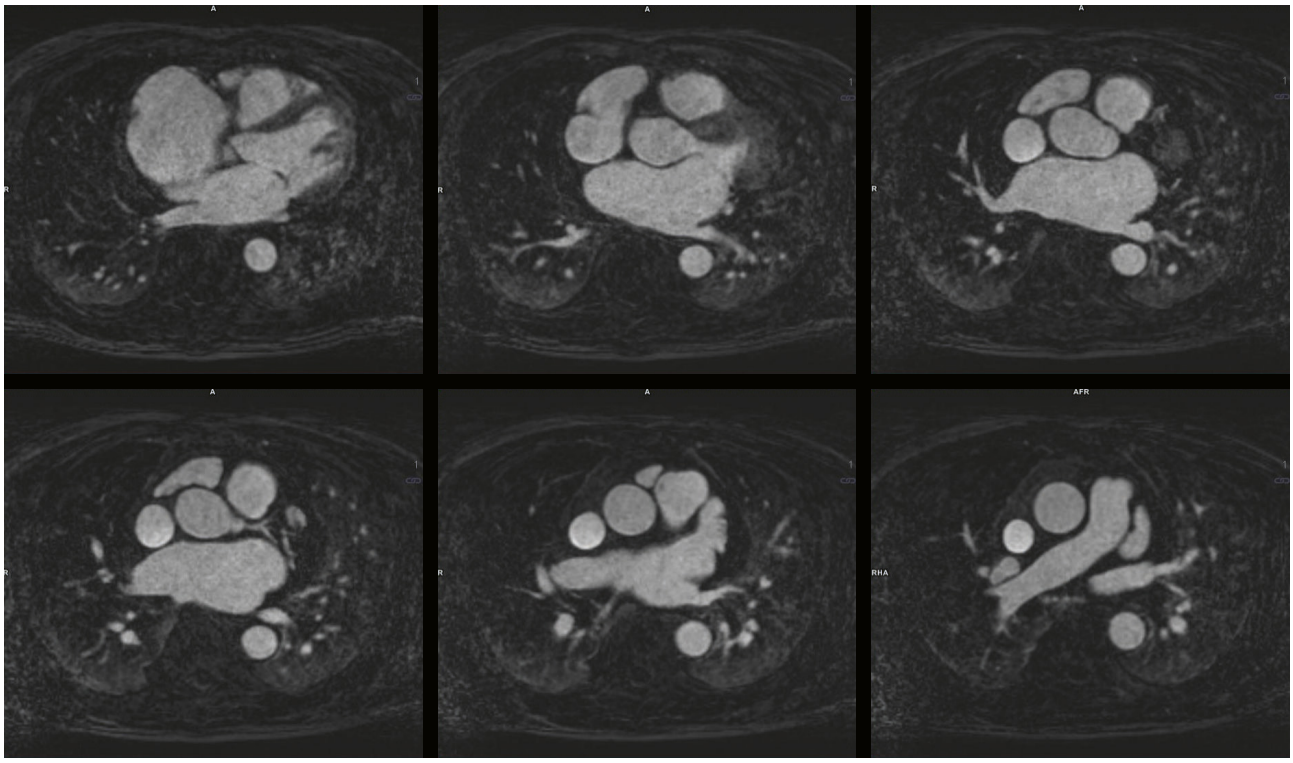

1 3D whole heart MRA inversion recovery subtracted images from a patient in atrial fibrillation.

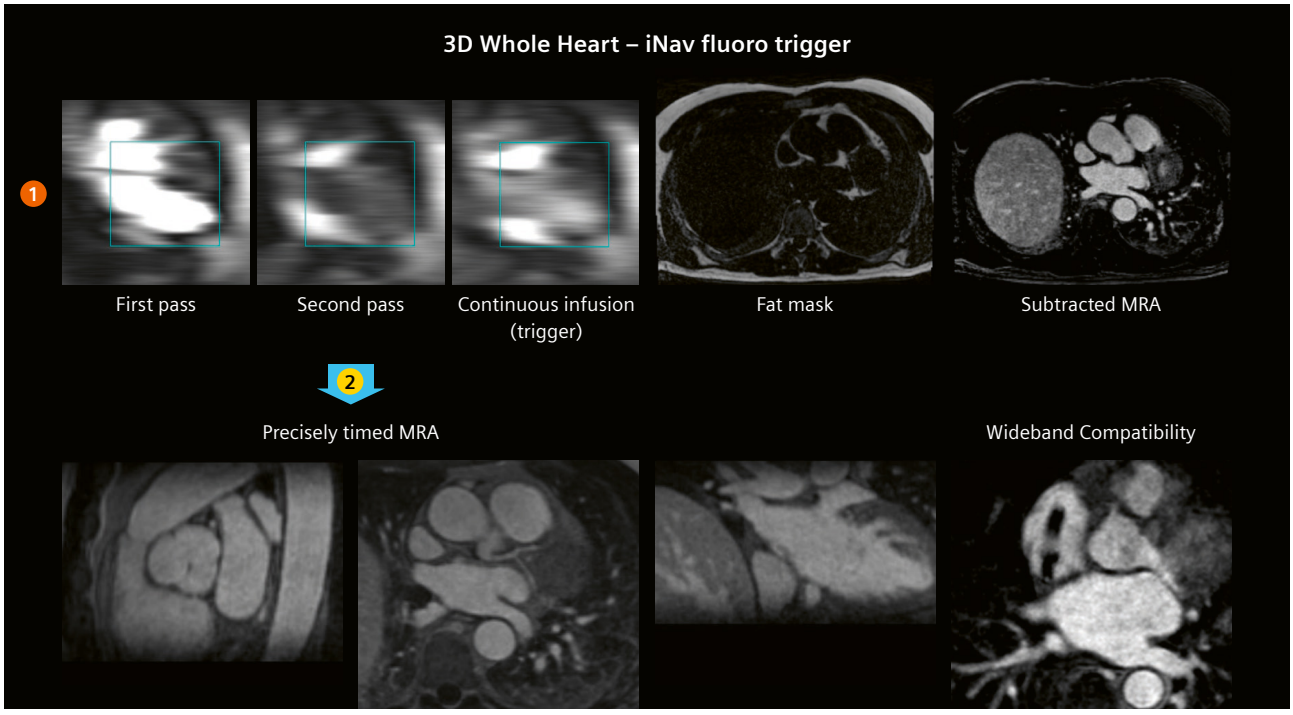

2 The iNAV fluoro trigger method for MR angiography. Two identical 3D whole heart program steps are created in the workflow. The first step (1) is used only for monitoring the passage of contrast with the iNAV. The second step (2), which will run to completion, is triggered at the peak of the continuous infusion in the pulmonary artery.

GRE fat image as a mask. As mentioned, because of the scan efficiency of the iNAV and precision timing of the contrast infusion, we are able to reduce contrast from 0.20 mmol/kg to 0.15 mmol/kg while still providing robust image quality whether patient is in sinus rhythm or has atrial fibrillation.

Case 1

A 59-year-old male was referred for evaluation of COVID-19 myocarditis and to evaluate the left atrial appendage. The patient contracted COVID-19 three weeks prior; one week prior to cardiac MRI imaging, the patient had new onset atrial fibrillation and dyspnea on exertion. Ventricular function with bSSFP cine demonstrated enlargement of the right ventricle with mildly reduced systolic function. Revised Lake Louise criteria was not met for acute myocarditis; however the patient had bilateral pulmonary emboli involving the right middle, right upper, right lower, and left lower segmental branches, with thrombus extending into the right main pulmonary artery. There was no evidence of left atrial appendage thrombus. Figure 3 illustrates the findings on 3D whole heart saturation recovery angiography and inversion recovery Dixon multi-echo GRE. Subsequent CT pulmonary angiogram agreed with MRI findings, and ultrasound Doppler was positive for

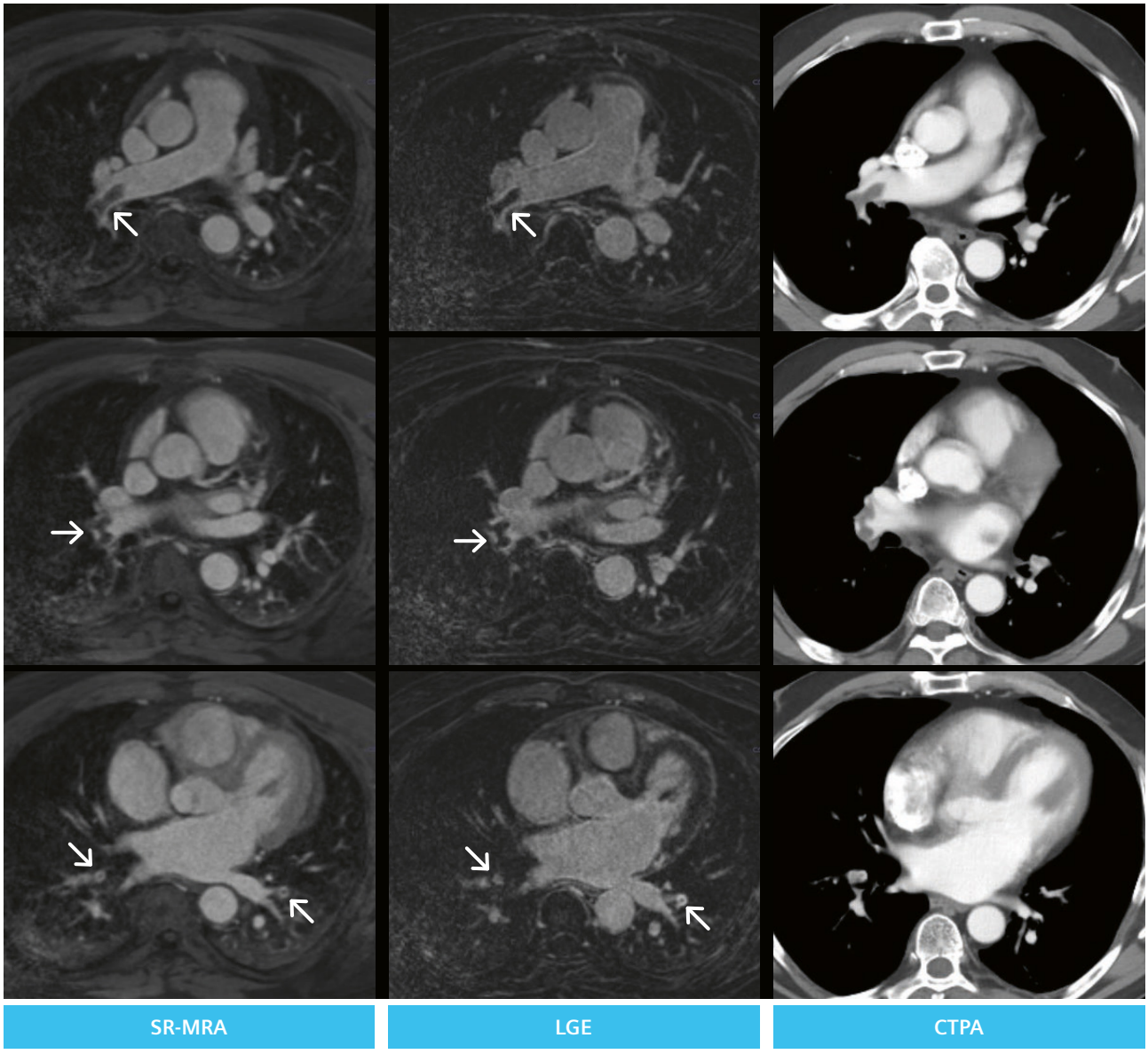

3 Incidentally discovered bilateral pulmonary emboli (arrowheads). From left to right column: saturation recovery MRA, inversion recovery Dixon multi-echo GRE, and CT pulmonary angiography.

acute right popliteal deep venous thrombosis. It is important to understand that CT pulmonary venography is timed to opacification of the left atrium; therefore abnormalities involving the pulmonary arteries may be incompletely characterized. Imaging with 3D whole heart, however, does not suffer from this limitation.

3D left ventricular delayed enhancement

In most cases, 2D PSIR LGE can provide sufficient detail and quantification of left ventricular scar burden. However there are clinical scenarios where providing a 3D dataset is beneficial, such as pre-planning for electrophysiology procedures, or for improved visualization of the right ventricle [16]. Specifically, 3D high resolution LGE can identify substrate features that may be subtle or absent on 2D imaging. By acquiring these 3D datasets in high resolution and reduced partition thickness we can minimize partial volume effects, allow for visualization of heterogeneity within regions of enhancement, scar channels, and the presence of epicardial components. Here, the user has flexible options: the 3D inversion recovery Dixon multi-echo GRE which provides more robust fat separation and is most beneficial at 3T; whereas fat saturated inversion recovery GRE can be used for scan efficiency at 1.5T. Both methods are compatible with the 1500 Hz wideband pulse which suppresses metallic artifacts caused by implanted devices such as ICDs or pacemakers.[2]

Case 2

A 67-year-old male referred for evaluation of non-sustained ventricular tachycardia (NSVT). The patient has frequent ventricular arrhythmia throughout the study, and ventricular function was only possible by using compressed sensing real time cine. Whole heart inversion recovery with fat sat LGE demonstrates heterogenous inferolateral scar with clear borders, scar channels, and epicardial component. A transmural segment of enhancement is also demonstrated in the mid anterolateral wall. 3D LGE with a restrictive temporal window is able to capture small and relevant details missing in the traditional 2D approach. This is only possible due to the 100% efficiency of the iNAV since we can trade acquisition efficiency for a smaller data acquisition window. In contrast, 2D PSIR LGE effectively freezes cardia

[2]The MRI restrictions (if any) of the metal implant must be considered prior to patient undergoing MRI exam. MR imaging of patients with metallic implants brings specific risks. However, certain implants are approved by the governing regulatory bodies to be MR conditionally safe. For such implants, the previously mentioned warning may not be applicable. Please contact the implant manufacturer for the specific conditional information. The conditions for MR safety are the responsibility of the implant manufacturer, not of Siemens Healthineers.

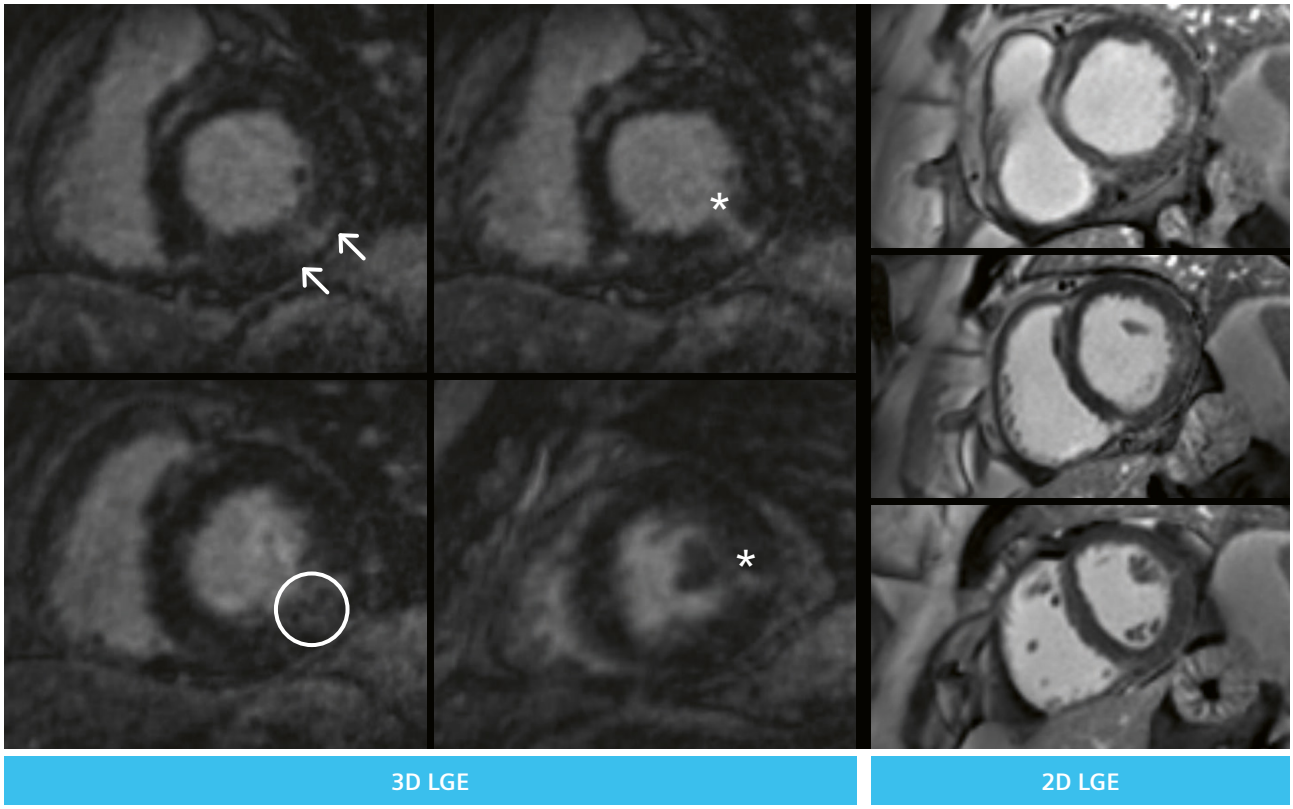

4 Comparison of 3D LGE vs 2D LGE. 3D LGE clearly demonstrates a heterogenous rim-like area of enhancement (circle), scar channels (asterisks), and epicardial component to scar (arrows). Features are ill-descript on 2D LGE.

motion, but incompletely characterizes respective areas of enhancement (Fig. 4).

Summary

In addition to what has already been described in this article, the potential for 3D whole heart to similarly accelerate coronary MRA has also been explored [17]. Submillimeter isotropic spatial resolution, with faithful representation of detail compared with the fully sampled reference can be obtained in a fraction of the time. Likewise, whole chest non-contrast MRA can be acquired more efficiently with 3D T2 prep fat saturated bSSFP at 1.5T [18] or using 3D T2 prep Dixon GRE at 3T. In conclusion, 3D whole heart is a versatile and robust package that overcomes the limitations of traditional dNAV methods for motion correction, combining VD-CASPR and iNAVs for acquisition and SNR efficiency as well as predictable scan time. Furthermore, AI based automatic positioning features and rest period scout facilitate ease of use for new and experienced users alike.

References

1 Dong J, Dickfeld T, Dalal D, Cheema A, Vasamreddy CR, Henrikson CA, Marine JE, Halperin HR, Berger RD, Lima JA, Bluemke DA, Calkins H. Initial experience in the use of integrated electroanatomic mapping with three-dimensional MR/CT images to guide catheter ablation of atrial fibrillation. J Cardiovasc Electrophysiol. 2006;17: 459-66.
2 Moghari MH, Hu P, Kissinger KV, Goddu B, Goepfert L, Ngo L, Manning WJ, Nezafat R. Subject-specific estimation of respiratory navigator tracking factor for free-breathing cardiovascular MR. Magn Reson Med. 2012;67(6):1665-72.
3 Hu P, Peters DC, Stoeck C, Kissinger KV, Goddu B, Goepfert L, Manning WJ, Nezafat R. Off-resonant pulmonary vein imaging. J Cardiovasc Magn Reson. 2009;11(Suppl 1):P185.
4 Henningsson M, Koken P, Stehning C, Razavi R, Prieto C, Botnar RM. Whole-heart coronary MR angiography with 2D self-navigated image reconstruction. Magn Reson Med. 2012;67(2):437-45.
5 Cruz G, Atkinson D, Henningsson M, Botnar RM, Prieto C. Highly efficient nonrigid motion-corrected 3D whole-heart coronary vessel wall imaging. Magn Reson Med. 2017;77(5):1894-1908.
6 Zeilinger MG, Kunze KP, Munoz C, Neji R, Schmidt M, Croisille P, Heiss R, Wuest W, Uder M, Botnar RM, Treutlein C, Prieto C. Non-rigid motion-corrected free-breathing 3D myocardial Dixon LGE imaging in a clinical setting. Eur Radiol. 2022;32(7):4340-4351.
7 Munoz C, Bustin A, Neji R, Kunze KP, Forman C, Schmidt M, Hajhosseiny R, Masci PG, Zeilinger M, Wuest W, Botnar RM, Prieto C. Motion-corrected 3D whole-heart water-fat high-resolution late gadolinium enhancement cardiovascular magnetic resonance imaging. J Cardiovasc Magn Reson. 2020;22(1):53.
8 Bustin A, Sridi S, Gravinay P, Legghe B, Gosse P, Ouattara A, Rozé H, Coste P, Gerbaud E, Desclaux A, Boyer A, Prevel R, Gruson D, Bonnet F, Issa N, Montaudon M, Laurent F, Stuber M, Camou F, Cochet H. High-resolution Free-breathing late gadolinium enhancement Cardiovascular magnetic resonance to diagnose myocardial injuries following COVID-19 infection. Eur J Radiol. 2021;144:109960.
9 Tandon A, James L, Henningsson M, Botnar RM, Potersnak A, Greil GF, Hussain T. A clinical combined gadobutrol bolus and slow infusion protocol enabling angiography, inversion recovery whole heart, and late gadolinium enhancement imaging in a single study. J Cardiovasc Magn Reson. 2016;18(1):66.
10 Yoon SS, Hoppe E, Schmidt M, Forman C, Chitiboi T, Sharma P, Tillmanns C, Maier A, Wetzl JA. Robust Deep-Learning-based Automated Cardiac Resting Phase Detection: Validation in a Prospective Study. Proc Intl Soc Mag Reson Med. 2020;28:2210.
11 Dabir D, Naehle CP, Clauberg R, Gieseke J, Schild HH, Thomas D. High-resolution motion compensated MRA in patients with congenital heart disease using extracellular contrast agent at 3 Tesla. J Cardiovasc Magn Reson. 2012;14:75.
12 Lam CZ, Pagano JJ, Gill N, Vidarsson L, de la Mora R, Seed M, Grosse-Wortmann L, Yoo SJ. Dual phase infusion with bolus tracking: technical innovation for cardiac and respiratory navigated magnetic resonance angiography using extracellular contrast. Pediatr Radiol. 2019;49(3):399-406.
13 Febbo JA, Galizia MS, Murphy IG, Popescu A, Bi X, Turin A, Collins J, Markl M, Edelman RR, Carr JC. Congenital heart disease in adults: Quantitative and qualitative evaluation of IR FLASH and IR SSFP MRA techniques using a blood pool contrast agent in the steady state and comparison to first pass MRA. Eur J Radiol. 2015;84(10):1921-1929.
14 Zheng J, Bae KT, Woodard PK, Haacke EM, Li D. Efficacy of slow infusion of gadolinium contrast agent in three-dimensional MR coronary artery imaging. J Magn Reson Imaging. 1999;10(5):800-805.
15 Groarke JD, Waller AH, Vita TS, Michaud GF, Di Carli MF, Blankstein R, Kwong RY, Steigner M. Feasibility study of electrocardiographic and respiratory gated, gadolinium enhanced magnetic resonance angiography of pulmonary veins and the impact of heart rate and rhythm on study quality. J Cardiovasc Magn Reson. 2014 ;16(1):43.
16 Ghonim S, Ernst S, Keegan J, Giannakidis A, Spadotto V, Voges I, Smith GC, Boutsikou M, Montanaro C, Wong T, Ho SY, McCarthy KP, Shore DF, Dimopoulos K, Uebing A, Swan L, Li W, Pennell DJ, Gatzoulis MA, Babu-Narayan SV. Three-Dimensional Late Gadolinium Enhancement Cardiovascular Magnetic Resonance Predicts Inducibility of Ventricular Tachycardia in Adults With Repaired Tetralogy of Fallot. Circ Arrhythm Electrophysiol. 2020;13(11):e008321.
17 Bustin A, Ginami G, Cruz G, Correia T, Ismail TF, Rashid I, Neji R, Botnar RM, Prieto C. Five-minute whole-heart coronary MRA with sub-millimeter isotropic resolution, 100% respiratory scan efficiency, and 3D-PROST reconstruction. Magn Reson Med. 2019;81(1):102-115.
18 Hajhosseiny R, Rashid I, Bustin A, Munoz C, Cruz G, Nazir MS, Grigoryan K, Ismail TF, Preston R, Neji R, Kunze K, Razavi R, Chiribiri A, Masci PG, Rajani R, Prieto C, Botnar RM. Clinical comparison of sub-mm high-resolution non-contrast coronary CMR angiography against coronary CT angiography in patients with low-intermediate risk of coronary artery disease: a single center trial. J Cardiovasc Magn Reson. 2021;23(1):57.



Contact

Jason Craft, M.D.
Department of Cardiovascular Imaging
St. Francis Heart Hospital
DeMatteis Research Center
101 Northern Blvd
Greenvale NY, 11548
USA
Jason.craft@chsli.org

Advertisement

Expert Talks

Don’t miss the talks of experienced and renowned experts on all aspects of MR imaging





Advancing (Clinical) Insights Through Imaging of Complex Brain Structures Using 7T

Roy Haast
Center for Magnetic Resonance
(Marseille, France)

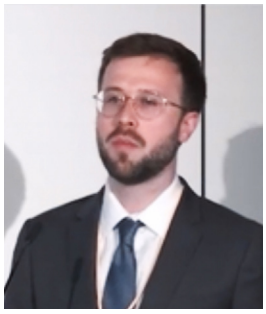

Real-life experience using a fully automated CMR planning sofware in a Swiss radiology department

Carl Glessgen
Geneva University Hospitals
(Geneva, Switzerland)



Unlocking Innovation: gammaSTAR’s Integration with the Open Sequence Interface

Daniel C. Hoinkiss
Fraunhofer Institute
(Bremen, Germany)



Opportunities for Functional and Vascular Imaging at 7T

Saskia Bollmann
The University of Queensland
(Brisbane, Australia)



Advancing Diffusion MRI for Comprehensive Characterisation of the Prostate Gland

Malwina Molendowska
CUBRIC, Cardiff, UK /
Lund University, Sweden

Visit us at
magnetomworld.siemens-healthineers.com

Go to
Clinical Corner > Clinical Talks

SIEMENS Healthineers

Skip the Electrodes, But Not A Beat: The Engineering Behind the Beat Sensor

Peter Speier, Ph.D. (manuscript) and Mario Bacher (box texts)

Siemens Healthineers, Erlangen, Germany

Introduction

Early in the development of cardiac MR, even long before bSSFP/TrueFISP made it clinically useful [1], the ECG was established as the standard trigger source [2] despite its well-known drawbacks of complex patient preparation and MR-related artifacts caused by the magnetohydrodynamic (MHD) effect and the radio frequency (RF) pulses of the MR measurement [3, 4]. Its main advantage is the early and well defined trigger time point based on the R-wave that precedes the ventricular contraction.

The only other clinically adopted cardiac trigger method is the finger-tip pulse sensor peripheral plethysmogram (PPG) [5], but its late and patient-state-dependent trigger position in the cardiac cycle reduces both its versatility and stability. Therefore, PPG is used only as a back-up.

Over the years, the reliability and ease of use of the ECG have been improved dramatically by the introduction of the vector ECG [6], wireless connections, and standardized handling procedures [3, 4]. Still, over the last 12 years, quite a few alternative methods of cardiac triggering have been proposed [7–12], indicating that there is still a need for more reliable and easier-to-use cardiac trigger methods. Some of these methods are based on optical or mechanical measurements. However, the MRI scanner is already a very sophisticated electromagnetic signal generation and sensing device. Therefore, trigger methods like the BioMatrix Beat Sensor (Glossary), which are based on electromagnetic effects are a good match as they can re-use already existing facilities of the MRI machine.

BioMatrix Beat Sensor – the Pilot Tone

The development of the BioMatrix Beat Sensor started with a power pitch presentation that I attended at the ISMRM 2014 in Milan, Italy. It was about respiratory noise navigation and was given by Anna Andreychenko [13]. It is well known that respiration modulates the electric load of the MR receiver coils. If the receivers are matched to maintain constant signal under load variations, this results in a modulation of the thermal noise power. Andreychenko demonstrated that respiratory navigation can be derived from measurements of the noise power. I was intrigued by this method and tried it out upon my return from the conference. I quickly realized that the number of noise data points required to characterize respiration is quite high and difficult to achieve during fast measurements like bSSFP. Luckily, I remembered a presentation that Lars Hanson had given at the IDEA developer conference in Freiburg, Germany, back in 2007 [14]. There, he described a system for "burning" electroencephalography (EEG) information into MR images by modulating the information onto a weak RF carrier close to Larmor frequency. The modulation is extracted by the MR receiver together with the MR data, and the EEG data appears as a stripe artifact in the image, or, if the carrier frequency is placed just outside of the frequency band of the image, i.e., in the oversampling region, the MR data remains uncontaminated by the additional signal. I postulated that any body-motion would modulate a constant coherent RF signal and that the achievable SNR per unit time would be higher than for noise navigation. I discussed the idea with a few experts in the factory in Erlangen who agreed that it should be feasible to use the signal for respiratory navigation. Markus Vester suggested the term "Pilot Tone" (PT) for the new motion-sensing method. In communication engineering, a Pilot Tone refers to a reference signal that is transmitted together with the payload signal to characterize the transmission path.

We presented our case and received approval from MR management for an initial cross-departmental investigation. We started the first volunteer tests with an off-the-shelf signal generator in the control room connected through the wave-guide hole to an untuned pickup loop taped to the funnel of a 1.5T MAGNETOM Espree. For the setup, see Figure 1A. The first experiment featured a series of breath-holds alternating between inspiration and expiration. We looked at the data in the command line tool *measdataviewer* directly on the scanner and could immediately see a strong and clean modulation with respiratory position. Over the year, we continued experiments and built an inline-processing module in our image reconstruction environment ICE that would generate live respiratory information and clean up the MR data. I presented the initial results at the ESMRMB 2015 in Edinburgh, UK [15].

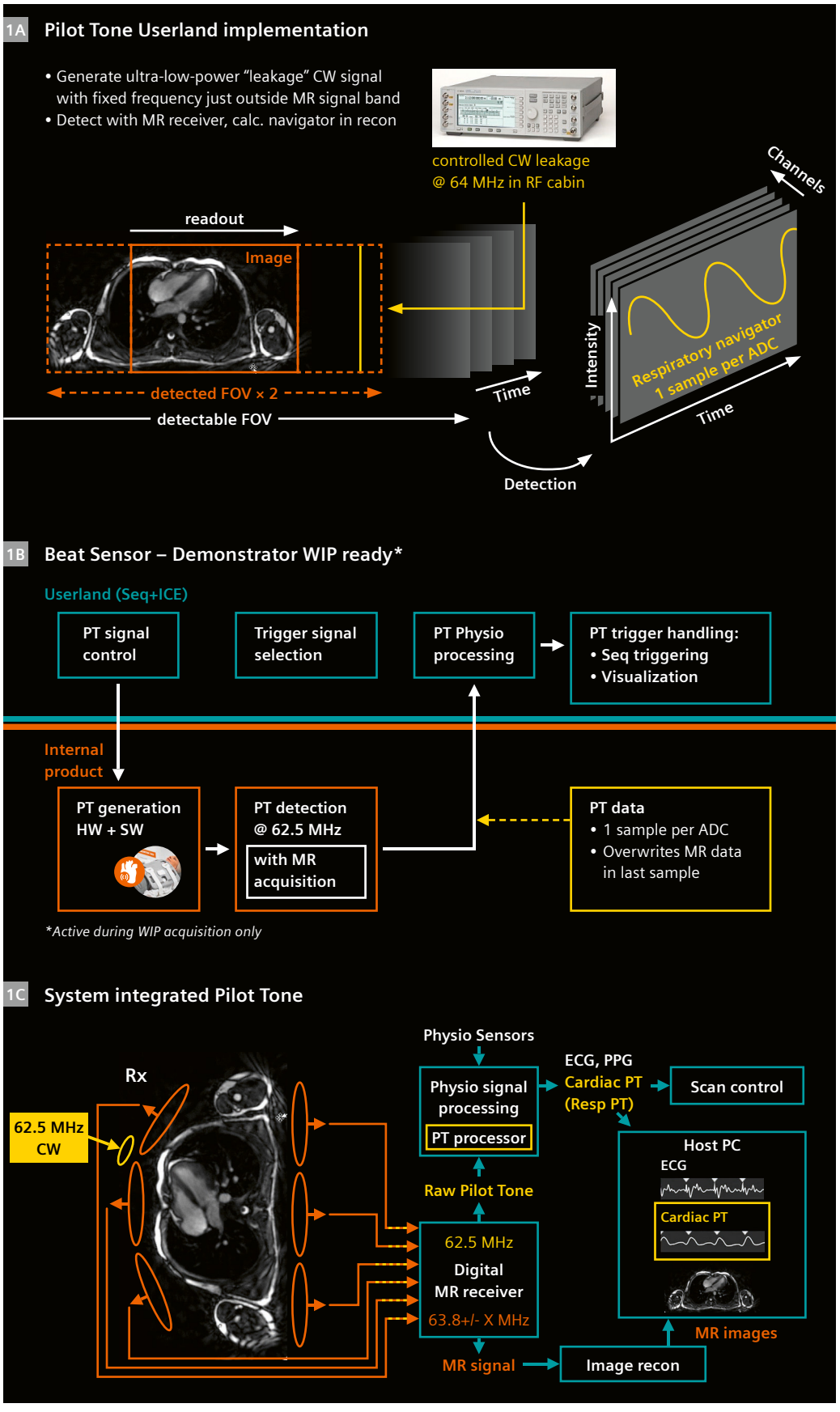

1 Three integration levels of the Pilot Tone subsystem: **(1A)** Vendor-independent "userland" implementation; **(1B)** Integrated PT generation and detection for increased signal stability for experimental use by collaboration partners; **(1C)** Fully integrated PT subsystem to continuously provide physiological information.

Since this abstract is difficult to obtain, it is reprinted with kind permission of ESMRMB in the Appendix.

In summer 2015, we started a collaboration with Fernando Boada's group at CAI2R at NYU. They set up their own version of the experiment on their Biograph mMR and published their first results at the ISMRM 2016 in Singapore [16]. They have continued to develop respiratory PT applications for MR-PET [41, 17] and they even offer their own version of a battery-powered PT generator[1]. Other sites also built their own PT setups for respiratory work and investigated its application to free-breathing MR Fingerprinting (MRF) [18] and prospective slice tracking in free-breathing cardiac MRI [19, 20].

This "userland"[2] approach to PT applications is vendor agnostic, but has three main drawbacks which introduce complications that can reduce their stability:

1. The PT data is acquired only when the sequence plays out an ADC. So, if the measurement is not continuous (e.g., a cine), but contains recovery periods or other pauses (e.g., TSE), no PT data is available in the pauses unless the sequence is modified to fill the gaps with ADCs. However, additional ADCs increase the raw data size significantly. Also, there is no PT data in pauses between measurements.
2. The frequency of the PT must be adapted to the frequency band used by the current protocol: It must fall into the oversampling region that is outside the reconstructed frequency band but inside the oversampled band. The width of the frequency band depends on the protocol (the receiver bandwidth). In addition, the band shifts with in-plane slice shifts in readout direction. The frequency selection becomes easier to fulfill if the oversampling factor (standard is factor 2) is increased, but this also increases the raw data size by the same factor and might not be possible for protocols that utilize high receiver bandwidth.

[1] *https://cai2r.net/resources/3t-pilot-tone*

[2] *The term "userland" is used here in analogy to the usage in the Linux community to denote functionality programmed only using the vendor-provided programming toolset, for MRI typically limited to sequence and image reconstruction.*

Box 1: A history of electromagnetic monitoring and MR

In 1958, YE Moskalenko, who worked on electroplethysmography in the context of the Russian space program, demonstrated that a radar transmission setup operating at 1 GHz (much higher than the operating frequency of a clinical MRI scanner) could be used to observe respiration and cardiac activity [33].

The first report on an electromagnetic navigation (EMN) signal at low frequency observed in humans was published ten years later by Tarjan and McFee [34]. Their goal was a contactless measurement of blood volume. They adapted a method known in geophysics as an "induction measurement": They projected a magnetic field with a frequency of only 100 kHz into the chest of a volunteer and observed the resulting field with a set of two coaxially aligned receive coils while suppressing direct coil-to-coil coupling. A change in body conductivity would result in a modulation of the received field. They observed a modulation of a few percent due to respiration and a smaller modulation due to cardiac motion of about one percent. They also noted that the signal seems to represent cardiac volume change.

While it has been known in NMR and MRI that an electrically conductive sample loads the coil, and that for optimal efficiency and SNR, the coil must be tuned and matched to the sample, the effect was not exploited for physiologic monitoring until 1988, when Buikman et al. proposed to measure the modulation of the reflection of an RF pulse in the body coil to record respiratory and cardiac information [35].

However, the idea was not picked up widely until quite recently, when new developments enabled robust separation of the different modulation sources: the availability of near-infinite computing power, the availability of massively parallel receive systems on virtually all clinical MRI scanners, and the availability of highly parallel transmit systems on high-field MRI scanners. Where highly parallel transmit systems are available, the reflection of all their elements can be monitored during RF pulses [36]. When measuring the coupling between all elements, high-quality rich data is obtained that allows separation of multiple motion contributions [37], but only while transmitting RF pulses.

The noise navigator [13] and the Pilot Tone [15] require multi-channel capability on the receive side only. Therefore, they can be implemented on all modern MRI systems and while the MR receiver operates, navigation data can be obtained.

The most recent development in EMN for MRI is the "Beat Pilot Tone" [38]: The method removes the requirement that the PT frequency be near the Larmor frequency by generating the signal close to the Larmor frequency only in the MR receive chain as an intermodulation product of two electromagnetic signals with higher frequencies, where these two frequencies are separated by approximately the Larmor frequency. This approach allows low-cost integration of EMN at radar frequencies into the MR scanner by using the MR receive system as a continuous wave (CW) radar detector.

3. The PT appears as a peak in the Fourier-transformed ADC. The peak position is a function of the PT frequency and the scanner's detection frequency; thus, it depends on the slice geometry, i.e., on the off-center shift in readout direction. This correction is deterministic and can be calculated exactly from protocol parameters and raw data headers. However, the eddy current compensation contains a B_0 correction, which is realized by varying the receive frequency. The correction thus generates additional, small transient shifts in the PT peak position when gradients are applied. These will become noticeable when the eddy current steady state changes markedly, e.g., when toggling between slice orientations. To avoid this problem, the PT peak position must be redetermined with every substantial change in the gradients, e.g., when switching slice orientations or when playing out large phase encoding jumps. In addition, the PT frequency from a generator that is not synchronized to the MR scanner will drift with time, and the detection frequency must be adapted if the drift is too large.

To eliminate these problems, we integrated the Pilot Tone generation into the MAGNETOM architecture as a prototype. The solution was to generate the PT at a fixed frequency and detect it directly after digitization before the "userland" signal with all corrections is derived. This made it necessary to implement the PT detection in firmware. To save field-programmable-gate-array (FPGA) resources we picked as frequency Nyquist/2 in the digitized frequency band, where the detection algorithm would not require multiplications but only additions. This led to the currently used PT frequency 62.5MHz @ 1.5T. To avoid drifts of the PT signal in frequency and phase, and thus enable complex valued processing, the PT signal is generated by the scanner itself using a "spare" frequency generator.

In parallel, we continued to explore the possibilities of the new method in a master's thesis in the cardiac predevelopment team, together with the local university [21]. Our department head, Lars Lauer, challenged us to extend the scope of the thesis beyond respiratory navigation and aim for cardiac triggering. At that time, we had no indication that this would be feasible, as we had never seen a cardiac signal with our remote generator set-up. If we had studied the scientific literature better (Box 1), we might have been more hopeful, but this only happened in the following master's thesis [22]. Halfway into Lea Schröder's thesis, Jan Bollenbeck built a battery-powered PT generator that could withstand the RF pulses of the MR experiment. The aim was to place the generator closer to the patient's chest to reduce sensitivity to non-respiratory motion, e.g., head or foot movement. We first attached the generator to the scanner's inner bore cover over the chest and didn't see anything new. However, when we placed it directly on the chest of the volunteer, we could see the cardiac signature directly in the raw data. These results were presented at ISMRM 2016 in Singapore [23] (Fig. 2). Internally, they also raised a lot of interest because of the potential for developing the new method into an alternative to ECG.

These initial results were seen promising enough to start the product integration. The first goal was to enable collaboration sites to start their own PT experiments with an integrated, stable, and easy-to-use system that featured local PT generation. I was able to convince Peter Gall, the product manager of the new system platform that was in the planning stage at that time, to include the necessary hardware (HW) and software (SW) in the system project.

Early in 2016, we started a second master's thesis on PT, this time with the Graz University of Technology in Austria, to further develop the cardiac application of the PT [22]. Using a second generation of the battery-powered PT generator, Mario Bacher ran a volunteer cohort study and developed signal processing SW for retrospective and

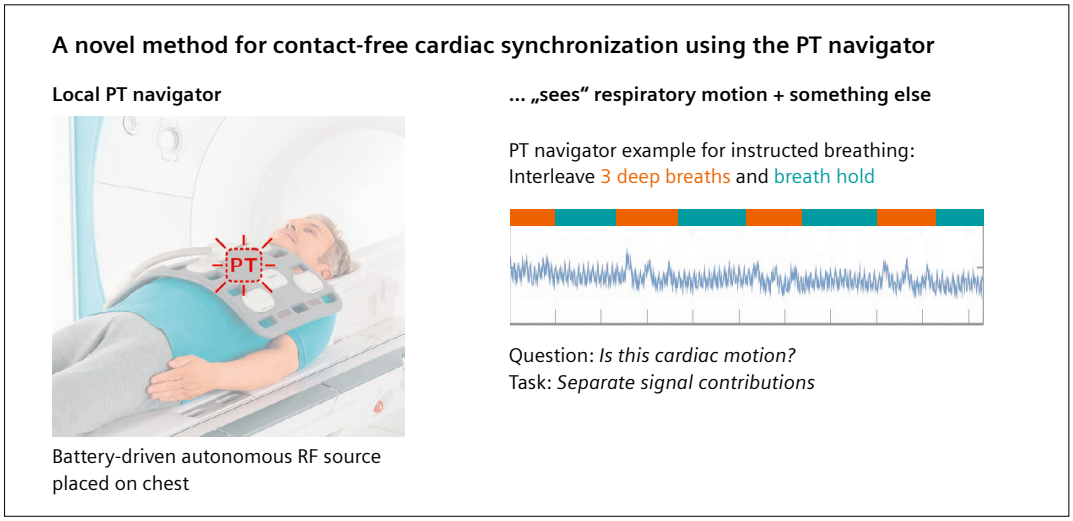

2 The key slide from [23] demonstrates that cardiac motion can be detected using a locally generated Pilot Tone.

Box 2: PT physics: The transformer model

The PT signal, like all electromagnetic applications, is a result of the Maxwell equations ;-) To understand real-world scenarios, especially complex ones like humans, numerical simulations are required. However, insight into the basic principles can be obtained with idealized, simple models: the main mechanism of the PT modulation by cardiac motion can be understood by comparing the setup to an electric transformer. The pre-condition is that the PT-generating loop is much smaller than the electromagnetic wavelength and thus mainly generates a magnetic field and only a negligibly small electric field. Thus, the PT is a purely magnetic signal which exists only as a near field; contrary to radar, which is a self-propagating electromagnetic wave, used in its far field.

A transformer consists of two coils: The primary driving coil (yellow, left side) produces an oscillating magnetic field. The resulting flux through the second coil (yellow, right side) induces a voltage. The flux between the coils is maximized by connecting the two coils with a magnetic, but non-conductive medium. Luckily for us MRI people, the human body is only weakly magnetic and it conducts electricity quite well. Therefore, the body can be seen as a magnetically transparent but lossy transformer core. The primary magnetic field (blue) will generate eddy currents in the tissues (orange), depending on the local conductivity. These eddy currents in turn generate secondary magnetic fields (orange). The secondary field opposes the primary field at the point of origin. In this example we observe the superposition of both fields in the receive coil on the right where both field lines point in different directions. Thus, depending on the geometry the secondary field can cause decreasing or increasing amplitude and/or phase shifts.

The body consists of tissues that have different electrical conductivity and change their position during motion. When conductive tissues move, the eddy current distribution changes and the net secondary field with it. The resulting modulation of the received fields is observed as the Pilot Tone signal. Even though the heart is relatively small, its motion is clearly observable because during cardiac contraction, highly conductive heart muscle and blood are replaced by weakly conductive fat and lung tissue.

As mentioned earlier, the Pilot Tone frequency needs to be chosen fairly close to the Larmor frequency: 62.5 MHz for 1.5T systems. Again, we were lucky: These frequencies hit a sweet spot where on the one hand wavelengths are long enough (2.4 m to 4.8 m in a vacuum, a few dezimeters in tissues) so that the signal penetrates the body quite freely and can therefore be described by this simple model, and where, on the other hand the frequency is high enough that the induced eddy currents and consequently the secondary magnetic fields are strong enough to be easily detected.

All these factors together enable reliable detection of cardiac, respiratory, and even head motion at standard clinical field strengths. However, as Anand et al. [38] have shown, exciting opportunities also await at very high frequencies! When venturing into the GHz range, the transformer model is no longer applicable, as we are entering the domain of radar. Here, higher order interactions start to dominate the signal and limit its penetration into the body, which is expected to optimize the detection of rigid motion.

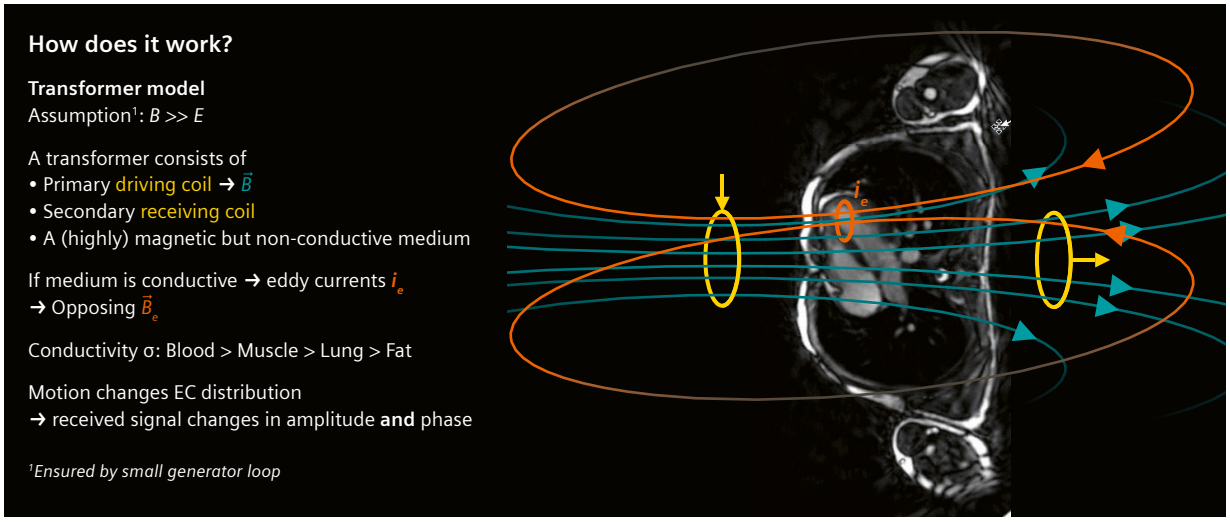

finally also for prospective cardiac triggering (Box 3). He obtained his first prospectively triggered cardiac cine still with a battery-powered generator and a pure "userland" implementation. He went on to work on a PhD thesis on the topic at Lausanne University Hospital (CHUV) in Switzerland. In his work, he also unearthed the early history of electromagnetic navigation and its use in MRI (Box 1), and the physics of signal generation (Box 2).

For the first version of the integrated PT-generation and detection system, (Fig. 1B) the PT was generated inside the new BioMatrix 12 coil. The PT was still detected only during ADCs and evaluated in ICE, but it was already much more stable. In this context, the term "Beat Sensor" was introduced to describe the cardiac application of the Pilot Tone (Glossary). This system was subsequently used at the Royal Brompton Hospital (RBH) in London, UK, to acquire the first cardiac PT patient data [24], and at CHUV and Ohio State University (OSU), Columbus, OH, USA, to develop and evaluate respiratory and retrospective cardiac applications (see e.g., Falcão [25] and Chen [26]).

Developing a robust and complete cardiac PT application takes time, and we went through several releases that gradually moved us closer to the current product. First, we implemented a general PT framework (see Fig. 1C) with the following main features:

- An acquisition-independent and continuously acquired PT data stream, with samples being flagged as invalid during RF pulses
- Pairing each PT sample with information about the preceding RF pulse to enable spike subtraction
- A PT-processing framework that can be exchanged and reconfigured for individual measurements to enable rapid prototyping and work-in-progress packages.

The first point amounts to quite a substantial paradigm shift: Before, the MR receiver had to be configured and active only during measurements. Now, the receiver had to be always configured and active to receive PT data during and between measurements. To achieve this, a dedicated team spent much of the development time

Box 3: Signal processing basics

A key advantage of the PT method is the use of all connected coil elements for receiving the PT signal. Each receive coil "sees" a different combination of cardiac, respiratory and other motion, depending on its location. Since we are interested in observing cardiac and respiratory motion by themselves, these components must be separated first.

This can be accomplished by a class of algorithms known as "Blind Source Separation". The problem statement is simple: Given a multitude N of sensors measuring signals x which are a combination A of M < N independent signals, separate the underlying signals s.

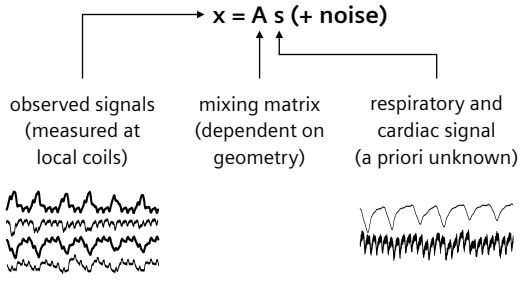

In other words: the equation needs to be solved for A, the so-called mixing matrix. Initially we used FastICA (Independent Component Analysis, [39]), in which the non-Gaussianity is optimized as a proxy for statistical independence [22]. While this algorithm worked well for Cine sequences, which are not affected by RF interference, a new PCA-based algorithm was developed in collaboration with the Shenzhen team, based on [27], in which the RF contamination of the PT signals is minimized by mixing vectors that are orthogonal to the main principal components of the eigenspace of interference signals.

To enable robust cardiac triggering, the cardiac motion signal needs to be de-noised in real-time. Classical digital filters, however, would introduce an unacceptably large time delay for the cardiac application (e.g., > 600 ms for an 80 dB stopband FIR lowpass at 6 Hz).

In [12, 22], we proposed to use a Kalman filter to denoise the signal. A Kalman filter, named after Rudolf E. Kalman, is an algorithm that uses a series of measurements, including noise and other inaccuracies, and attempts to fit these measurements in a least-squares sense to a predefined signal model. In our case, the signal is modeled using a constant velocity motion model similar to Spincemaille et al. [40], in which the signal evolution is modeled as the 1D motion of a particle with constant velocity. This approach has two additional advantages: First, it does not only provide a de-noised signal, but also an estimation of the signals first derivative, i.e., velocity, which is subsequently used for trigger detection (see Box 4). And second, it can interpolate over short gaps in the data that occur while sending RF pulses.

on writing and debugging the HW–SW interconnectivity. The flexible processing framework drastically sped up the subsequent development by enabling us to test new code on previous stable baselines and SW versions. To minimize porting efforts, we kept interfaces constant and minimized dependencies on other modules.

In 2021, we released the first clinical application: Beat Sensor triggering for Cines only. The limitation to Cine was necessary because we had not yet implemented a general RF-artifact compensation, and for Cine a simple signal average is sufficient. Most of the development time was spent on optimizing signal processing and workflow. For about one year we had regular volunteer shifts to test stability and usability of the latest developments. A lot of time was spent on the special coil handling required for Beat Sensor-triggered measurements: The PT signal is acquired using the coil elements currently selected for imaging, and signal-processing training is valid for one coil select only. Therefore, Beat Sensor-triggered protocols must automatically select the coils used in training.

While the team in Erlangen, Germany, had been working towards productization of the cardiac application of PT, the Siemens Healthineers development team in Shenzhen, China, had been developing the respiratory application of PT. After an initial ramp-up phase, the team in Shenzhen independently developed and released a first product for respiratory triggering on MAGNETOM Amira – A BioMatrix System. After this release, the two groups intensified their collaboration: Yan Tu Huang in Shenzhen integrated his respiratory processing into the PT framework, and several algorithms were exchanged between the sites and applications. The cardiac application benefited most by rebasing on the robust method for RF-artifact suppression [27] that Shenzhen had developed for the respiratory application. We jointly extended this algorithm for the cardiac application. Based on this algorithm we were able to stabilize

Box 4: PT signal characteristics and trigger time point

The cardiac component of the Pilot Tone closely follows the cardiac volume curve without a delay: At the time of the R-wave, in end-diastole, when the heart is fully expanded, it assumes its maximum value. During end-systole, when the heart is fully contracted, it assumes its minimum value, and during the static mid-diastolic period it plateaus at an intermediate value. The Beat Sensor signal, shown on the right, is the inverted time derivative of this cardiac component. It has the advantage that it features a rather narrow positive peak at the beginning of the cardiac cycle and provides additional suppression of respiratory contamination.

The Beat Sensor triggers when the systolic contraction starts (specifically, when the derivative reaches 40% of its maximum value). This trigger point was chosen for its stability and occurs approximately 100 ms after the R-wave. This wave delay is learned during the Beat Sensor training phase using only the waveform of the cardiac component as the distance between trigger point and the preceding maximum. Low-pass filters in the signal processing add roughly 100 ms to this, resulting in a total delay of about 200 ms. If a finger pulse sensor (PPG) is present as well, its delay with respect to the R-wave is also determined.

One crucial functionality for cardiac exams is "Capture Cycle": based on the current heart rate, an algorithm places the acquisition in the end-diastolic cardiac phase where motion is minimal. For the ECG, that triggers on the R-wave, this placing is achieved by maximizing the trigger delay. For Beat Sensor and PPG triggering, the algorithm has been modified to account for the trigger delays learned during Beat Sensor training. Thus, after the training "Capture RR" can be used for all three trigger sources.

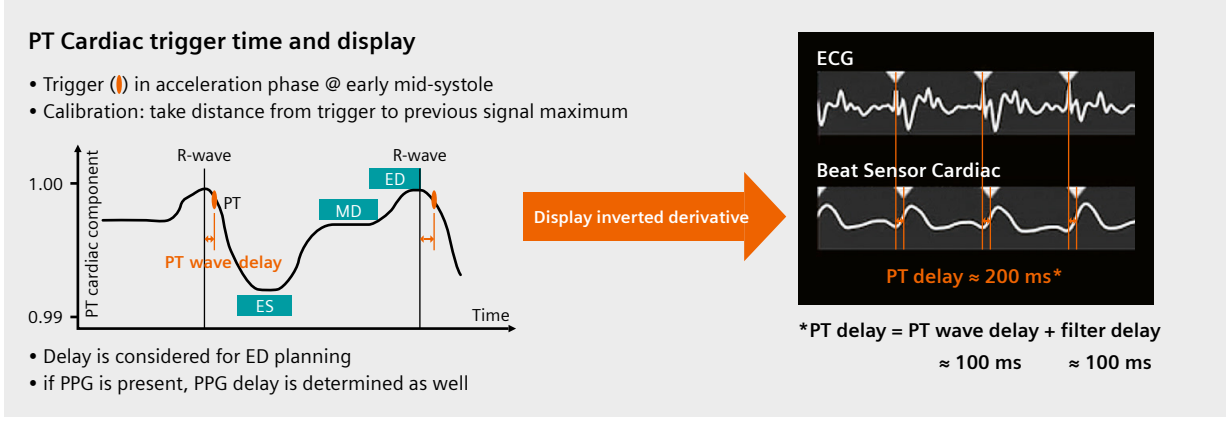

cardiac triggering for all cardiac protocols. The signal characteristics of the current implementation are described in Box 4.

To collect customer feedback early, we developed a work-in-progress package (WIP) of Beat Sensor triggering for the whole cardiac exam. The WIP was initially installed at four different sites (Jan Yperman Hospital, Ieper, Belgium; Royal Brompton Hospital, London, UK; Ohio State University, Columbus, OH, USA; and Northwestern University (NWU), Evanston, IL, USA). While the feedback on clinical performance was positive [28–30], the calibration workflow proved to be too complex and error-prone. Thus, we reworked and hardened the calibration workflow just before the development deadline and could release Beat Sensor triggering for the whole cardiac exam for the current SW version *syngo* MR XA51A for the 1.5T BioMatrix Systems MAGNETOM Sola, MAGNETOM Altea, and MAGNETOM Sola Fit. The next SW version for 3T systems will bring this functionality to MAGNETOM Vida and MAGNETOM Lumina.

The development of PT-based methods is ongoing. The clinical use of the first complete release of the Beat Sensor will certainly reveal limitations, but it will also show distinct advantages when compared with the ECG. We are committed to removing limitations and turning the advantages into clinically useful features. So please try out the Beat Sensor in your clinical routine and let us know about your experiences.

Looking beyond cardiac to general motion management, the use of Pilot Tone is still in its infancy and we have only scratched the surface of many aspects and applications. Two examples are two-dimensional characterization of respiration [31] and characterization of head motion [32]. The scanner-integrated PT with its continuous data stream and its flexible processing framework is a powerful tool to enable these upcoming investigations and developments.

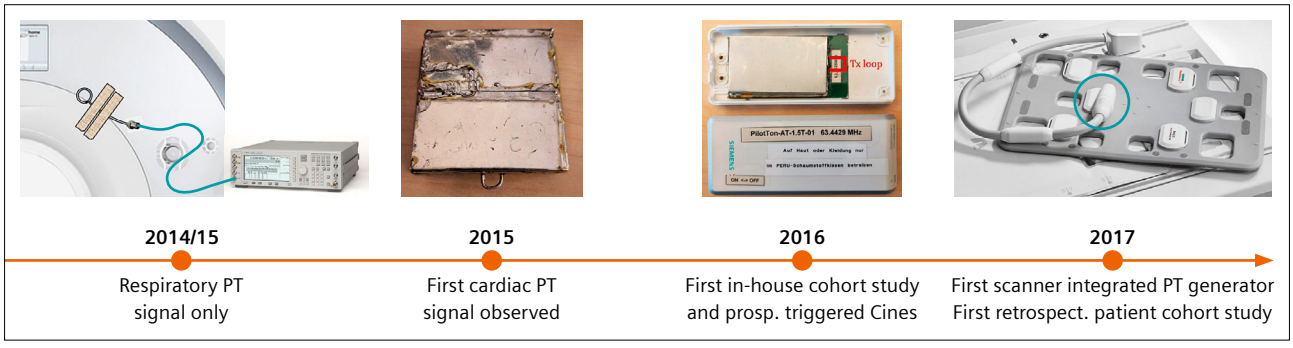

3 Four generations of Pilot Tone generators: From initial respiratory experiments to a scanner-integrated solution.

Acknowledgment

A big Thank you to all contributors. Especially:

- **Generator hardware:** Jan Bollenbeck
- **Physio-SW:** Michael Schwertfeger
- **PT processing:** Mario Bacher, Yan Tu Huang
- **Sequences, exam prototypes and data analysis:** Carmel Hayes, Randall Kroeker
- **Volunteer data:** Manuela Rick
- **Early patient data:** Peter Gatehouse (RBH)



Appendix: Reprint of Ref. 15

PT-Nav: a novel respiratory navigation method for continuous acquisitions based on modulation of a pilot tone in the MR-receiver

P. Speier[1], M. Fenchel[1], R. Rehner[2]

[1]MR PI, Siemens Healthcare, Erlangen, Germany
[2]MR R&D, Siemens Healthcare, Erlangen, Germany

Purpose/Introduction

High-resolution 3D abdominal or cardiac MR imaging requires synchronization to respiratory motion. The motion can be tracked by dedicated respiratory sensors, MR navigators, selfgating algorithms, or, as recently proposed, by analyzing the received noise [1] or measuring load changes of the transmit coil [2]. These methods increase setup complexity, require interruption of steady state, special k-space trajectories and high SNR per scan, long averaging times, or additional scanner-integrated hardware. We hypothesize that a coherent signal from an independent source, received in parallel with the MR signal, can be used as a high-quality navigator that does not suffer from the drawbacks of the previous methods.

Subjects and methods

Continuous series of sagittal bSSFP or GRE images (500...1000 images, 3...5 images/s, (1.5...2 mm)^2 × 10 mm) of the right liver dome were acquired with anterior and posterior multi-channel receive coils. Meanwhile, a continuous-wave (CW) RF signal, generated by a commercial signal generator, was transmitted as a pilot tone into the magnet bore by a non-resonant pickup coil, placed on the table or outer magnet cover, with a frequency outside of the frequency band of the MR signal and the FOV, but inside the received frequency band, and an amplitude adjusted to be detectable in the linear operating regime of the receiver.

Image reconstruction was modified in-house for pilot tone detection: During a learning phase, the pilot tone frequency f in the received data was determined. Then, for each k-space line and channel, the pilot tone was fit to the model $A \times \exp(i2\pi ft)$, the complex amplitude A logged as PT-navigator, and the model subtracted from the data (Fig. 1). Offline processing was performed in MATLAB (Math-Works). The positions of the liver dome (HF direction) or abdominal wall (AP direction) were tracked in the images, and their correlations to low-pass (1 Hz-Hann-window)-filtered PT-navigators were calculated for all channels.

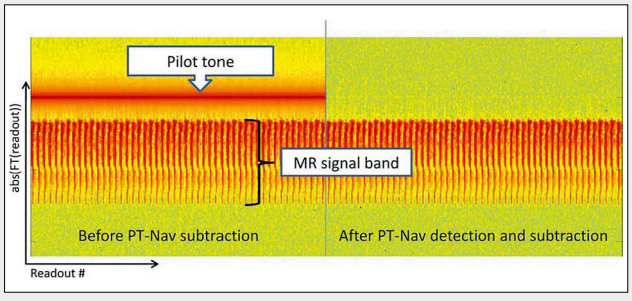

1 Exemplary Fourier-transformed raw data (one channel), demonstrating successful detection and elimination of a pilot tone placed next to the MR-signal band

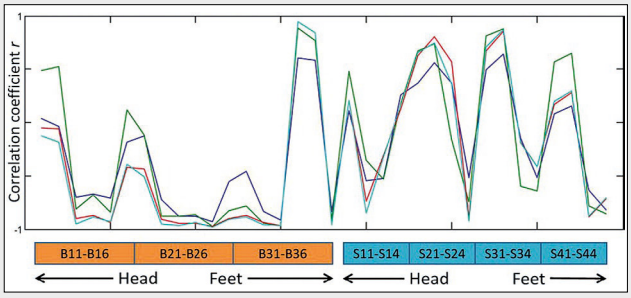

2 Exemplary correlation coefficients of anterior (orange) and posterior (blue) coil elements for 4 measurements of volunteer B

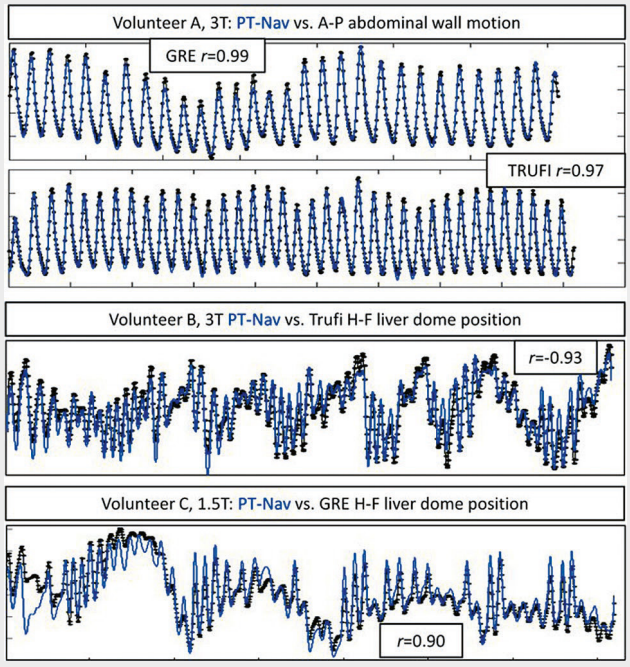

3 Exemplary correlations between best PT-Nav channel and image-based navigators (curves shown after mean subtraction and amplitude normalization)

Results

Measurements of 5 volunteers were performed on three systems (MAGNETOM Espree, Aera, and Skyra, Siemens Healthcare). Correlation factors varied in sign and amplitude between channels (Fig. 2). For all volunteers, receive channels with high correlation coefficients $r \geq 0.9$ were found while volunteers laid still, allowing precise characterization of even quite irregular respiratory patterns (Fig. 3). Correlations could be slightly improved by combining channels.

Discussion/Conclusion

Our early results suggest that the proposed PT-Nav method can provide, with minimal hardware requirements, respiratory information for continuous sequences that is comparable to that of "gold-standard" MR navigators.

References

1 A. Andreychenko, ISMRM 2014, #92.
2 I. Graesslin, ISMRM 2010, #3045.

Glossary

Electromagnetic navigation (EMN)
Characterizing motion by its influence on low-frequency electro-magnetic fields inside the body, used here with a focus on scanner-integrated methods

Pilot Tone (PT)
MR-integrated EMN, the only hardware part is the field generator

BioMatrix Beat Sensor
1. Cardiac application of Pilot Tone
2. Hardware integrated Pilot Tone generator (BioMatrix 12, BioMatrix 18 coils)

BioMatrix Respiratory Sensor
1. Respiratory Sensor hardware in BioMatrix Spine coils on 1.5T MAGNETOM Sola, and MAGNETOM Altea, as well as on 3T MAGNETOM Vida, and MAGNETOM Lumina (this is EMN, but not PT based)
2. Respiratory PT application on 1.5T MAGNETOM Amira - A BioMatrix System (uses a PT generator in the BioMatrix 13 coil)

Why is "Beat Sensor" an appropriate term for the Pilot Tone generator?
Like the finger pulse sensor, the Beat Sensor is an active sensing method: It emits a signal into the body and receives the motion-induced modulation of this signal. The Beat Sensor hardware, that is built into the BioMatrix 12 and BioMatrix 18 coils, fulfils the function of a signal generator but does not receive the signal. It can be likened to the light emitter in the finger pulse sensor. The role of the light receiver is implemented by modifying the SW of the already existing MR receive system.

HW	Pulse Sensor	Beat Sensor
Generator	Light emitter	PT generator: dedicated hardware in BioMatrix 12 and BioMatrix 18 coils
Receiver	Light detector	PT receiver (reuse MR receive system)

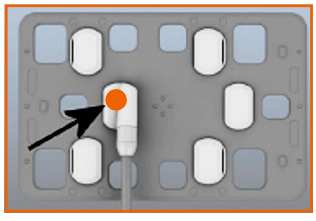



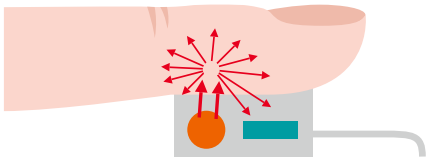

References

1 Carr JC, Simonetti O, Bundy J, Li D, Pereles S, Finn JP. Cine MR angiography of the heart with segmented true fast imaging with steady-state precession. Radiology. 2001;219(3):828-834.
2 Lanzer P, Botvinick EH, Schiller NB, Crooks LE, Arakawa M, Kaufman L, et al. Cardiac imaging using gated magnetic resonance. Radiology. 1984;150(1):121-7.
3 Niendorf T, Winter L, Frauenrath T. Electrocardiogram in an MRI Environment: Clinical Needs, Practical Considerations, Safety Implications, Technical Solutions and Future Directions. In: Millis RM (Editor). Advances in Electrocardiograms. IntechOpen.2012. doi:10.5772/24340.
4 MRI Questions: EKG Detection [Internet]. Elster LLC; 2021 [cited November 29, 2022]. Available from: https://mriquestions.com/ekg-problems.html
5 Denslow S, Buckles DS. Pulse oximetry-gated acquisition of cardiac MR images in patients with congenital cardiac abnormalities. AJR Am J Roentgenol. 1993;160(4):831-3.
6 Chia JM, Fischer SE, Wickline SA, Lorenz CH. Performance of QRS detection for cardiac magnetic resonance imaging with a novel vectorcardiographic triggering method. J Magn Reson Imaging. 2000;12(5):678-88.
7 Frauenrath T, Hezel F, Renz W, d'Orth Tde G, Dieringer M, von Knobelsdorff-Brenkenhoff F, Prothmann M, Schulz Menger J, Niendorf T. Acoustic cardiac triggering: a practical solution for synchronization and gating of cardiovascular magnetic resonance at 7 Tesla. J Cardiovasc Magn Reson. 2010 Nov 16;12(1):67. doi: 10.1186/1532-429X-12-67. PMID: 21080933; PMCID: PMC2998500.
8 Nedoma J, Fajkus M, Martinek R, Nazeran H. Vital Sign Monitoring and Cardiac Triggering at 1.5 Tesla: A Practical Solution by an MR-Ballistocardiography Fiber-Optic Sensor. Sensors (Basel). 2019;19(3):470.
9 Spicher N, Kukuk M, Maderwald S, Ladd ME. Initial evaluation of prospective cardiac triggering using photoplethysmography signals recorded with a video camera compared to pulse oximetry and electrocardiography at 7T MRI. Biomed Eng Online. 2016;15(1):126.
10 Kosch O, Thiel F, Seifert F, Sachs J, Hein MA. Motion detection In-Vivo by multi-channel ultrawideband radar. IEEE International Conference on Ultra-Wideband. 2012:392-396. doi: 10.1109/ICUWB.2012.6340451.
11 Kording F, Schoennagel B, Lund G, Ueberle F, Jung C, Adam G, et al. Doppler ultrasound compared with electrocardiogram and pulse oximetry cardiac triggering: A pilot study. Magn Reson Med. 2015;74(5):1257-65.
12 Bacher M, Speier P, Bollenbeck J, Fenchel M, Stuber M. ISMRM 2018 Paris, Abstract #2960, Pilot Tone Navigation Enables Contactless Prospective Cardiac Triggering: Initial Volunteer Results for Prospective Cine.
13 Andreychenko A, Crijns S, Raaijmakers A, Stemkens B, Luijten P, Lagendijk J, et al. ISMRM 2014 Milan, Abstract #0092, Noise variance of an RF receive array reflects respiratory motion: a novel respiratory motion predictor.
14 Hanson LG, Lund TE, Hanson CG. Encoding of electrophysiology and other signals in MR images. J Magn Reson Imaging 2007, 25(5), 1059-1066.
15 Speier P, Fenchel M, Rehner R. PT-Nav: a novel respiratory navigation method for continuous acquisitions based on modulation of a pilot tone in the MR-receiver. ESMRMB 2015, 32nd Annual Scientific Meeting, Edinburgh, UK, 1-3 October: Abstracts, Thursday, Magnetic Resonance Materials in Physics, Biology and Medicine. 2015; 28:1–135.
16 Koesters T, Brown R, Zhao T, Fenchel M, Speier P, Feng L, et al. ISMRM 2016 Singapore, Abstract #4250, Motion Correcting Complete MR-PET Exams Via Plot Tone Navigators.
17 Solomon E, Rigie DS, Vahle T, Paška J, Bollenbeck J, Sodickson DK, et al. Free-breathing radial imaging using a pilot-tone radiofrequency transmitter for detection of respiratory motion. Magn Reson Med. 2021;85(5):2672-2685.
18 Huang SS, Boyacioglu R, Bolding R, MacAskill C, Chen Y, Griswold MA. Free-Breathing Abdominal Magnetic Resonance Fingerprinting Using a Pilot Tone Navigator. J Magn Reson Imaging. 2021;54(4):1138-1151.
19 Ludwig J, Speier P, Seifert F, Schaeffter T, Kolbitsch C. Pilot tone-based motion correction for prospective respiratory compensated cardiac cine MRI. Magn Reson Med. 2021;85(5):2403-2416.
20 Ludwig J, Kerkering KM, Speier P, Schaeffter T, Kolbitsch C. Pilot tone-based prospective correction of respiratory motion for free-breathing myocardial T1 mapping. MAGMA. 2022 Aug 3. doi: 10.1007/s10334-022-01032-4. Online ahead of print. PMID: 35921020.
21 Schröder, L. Information content of a novel MR navigator relating to physiological activities. Advisors: Haderlein T, Maier A, Wetzl J, Speier P. Siemens Healthcare GmbH. Started June 2015. [Not accessible online].
22 Bacher M. Cardiac Triggering Based on Locally Generated Pilot-Tones in a Commercial MRI Scanner: A Feasibility Study [master's thesis. Graz: Graz University of Technology; 2017. 103 p.] https://diglib.tugraz.at, linked via https://graz.pure.elsevier.com/de/publications/cardiac-triggering-based-on-locally-generated-pilot-tones-in-a-co
23 Schroeder L, Wetzl J, Maier A, Lauer L, Bollenbeck J, Fenchel M, et al. ISMRM 2016 Singapore, Abstract #410: A Novel Method for Contact-Free Cardiac Synchronization Using the Pilot Tone Navigator.
24 Bacher, M. SCMR 2020 Orlando, FL, USA, co-workshop. [Not accessible online].
25 Falcão MBL, Di Sopra L, Ma L, Bacher M, Yerly J, Speier P, et al. Pilot tone navigation for respiratory and cardiac motion-resolved free-running 5D flow MRI. Magn Reson Med. 2022;87(2):718-732.
26 Chen C, Liu Y, Simonetti OP, Tong M, Jin N, Bacher M, et al. Cardiac and respiratory motion extraction for MRI using Pilot Tone-a patient study. arXiv:2202.00055 [eess.SP].
27 Inventors: Huang YT, Zhang QY, Li ZB. Using eigenvector algorithm to reduce RF interference in respiration or heartbeat detection. CN112415453-A. Publication: 2021-02-26.
28 Pan Y, Varghese J, Jin N, Hayes C, Speier P, Ahmad R, et al. ISMRM 2022 London, UK, Abstract #4770: Validation of Beat Sensor Cardiac Triggering against ECG Cardiac Triggering in both Volunteer and Patient Cohorts.
29 Hayes C, Huang YT, Rick M, Kroeker R, Bacher M, Pan Y, et al. ISMRM 2022 London, UK, Abstract #4786: Multi-center evaluation of the novel Beat Sensor Cardiac triggering technology,
30 Lin K, Sarnari R, Speier P, Hayes C, Davids R, Carr JC, et al. Pilot Tone-Triggered MRI for Quantitative Assessment of Cardiac Function, Motion, and Structure. Invest Radiol. 2022. doi: 10.1097/RLI.0000000000000922. Online ahead of print. PMID: 36070525.
31 Schroeder L, Wetzl J, Maier A, Rehner R, Fenchel M, Speier P. ISMRM 2016 Singapore, Abstract #3103: Two-Dimensional Respiratory-Motion Characterization for Continuous MR Measurements Using Pilot Tone Navigation.
32 Speier P, Bacher M, Bollenbeck J, Fenchel M, Kober T. ISMRM 2018 Paris, Abstract #4101: Separation And Quantification Of Head Motion Modes By Pilot Tone Measurements.

33 Moskalenko YE. Utilization of superhigh frequencies in biological investigations. Biophysics (USSR) (English translation).1958;3:619–26. [Only second hand knowledge! We have not been able to get a copy of the original article yet.]
34 Tarjan PP, McFee R. Electrodeless measurements of the effective resistivity of the human torso and head by magnetic induction. IEEE Trans Biomed Eng. 1968;15(4):266-78.
35 Buikman D, Helzel T, Röschmann P. The rf coil as a sensitive motion detector for magnetic resonance imaging. Magn Reson Imaging. 1988;6(3):281-9.
36 Graesslin I, Stahl H, Nehrke K, Harvey P, Smink J, Mens G, et al. An alternative concept for non-sequence interfering, contact-free respiration monitoring. In: Proceedings of the 17th Annual Meeting of ISMRM, Honolulu, HI, USA. 2009:753.
37 Jaeschke S, Robson MD, Hess AT. Cardiac gating using scattering of an 8-channel parallel transmit coil at 7T. Magn Reson Med. 2018;80(2):633–640.
38 Anand S, Lustig M. ISMRM 2021 online, Abstract #0568: Beat Pilot Tone: Exploiting Preamplifier Intermodulation of UHF/SHF RF for Improved Motion Sensitivity over Pilot Tone Navigators.
39 Hyvärinen A. Fast and Robust Fixed-Point Algorithms for Independent Component Analysis. IEEE Trans Neural Netw. 1999;10(3):626-634.
40 Spincemaille P, Nguyen TD, Prince MR, Wang Y. Kalman filtering for real-time navigator processing. Magn Reson Med. 2008;60(1):158-168.
41 Vahle T, Bacher M, Rigie D, Fenchel M, Speier P, Bollenbeck J, et al. Respiratory Motion Detection and Correction for MR Using the Pilot Tone: Applications for MR and Simultaneous PET/MR Examinations. Invest Radiol. 2020;55(3):153-159.



Contact

Peter Speier, Ph.D.
Cardiovascular Application Development
SHS DI MR RCT CLS CARD
Allee am Roethelheimpark 2
91052 Erlangen
Germany
peter.speier@siemens-healthineers.com

Advertisement

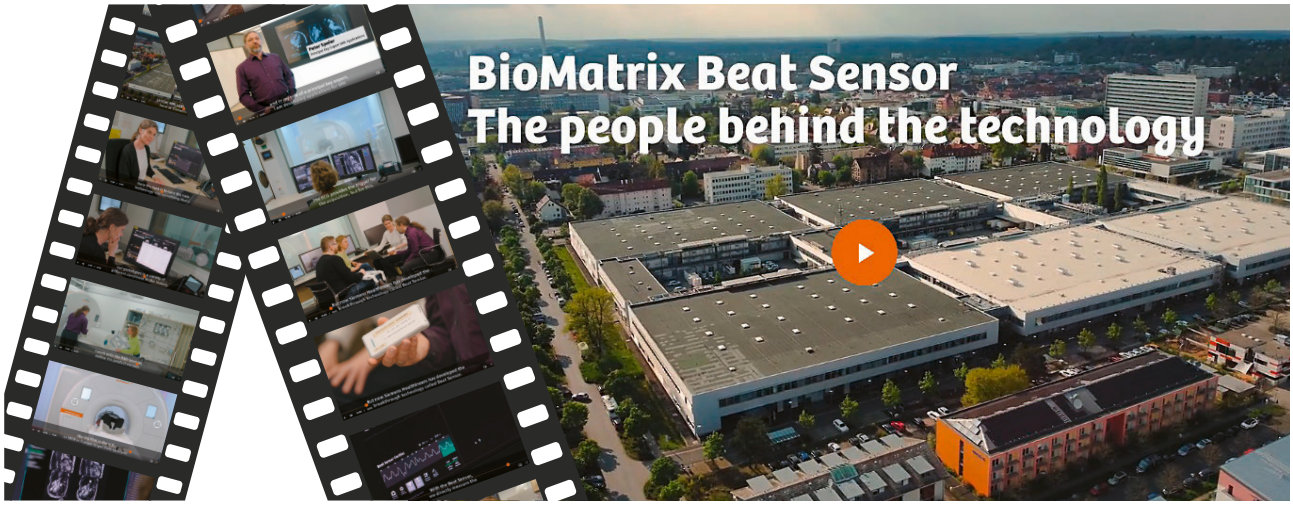

Watch as BioMatrix Beat Sensor developers Peter Speier, Mario Bacher, Carmel Hayes, and Manuela Rick explain the various stages of the development.

Visit us at:
www.siemens-healthineers.com/magnetic-resonance-imaging/clinical-specialities/cardiovascular-mri

Retrospective Motion Correction for Brain MRI: A Technical Description of SAMER

Daniel Polak[1], Daniel Nicolas Splitthoff[1], Bryan Clifford[2], Wei-Ching Lo[2], Yan Tu Huang[3], Nan Xiao[3], Heiko Meyer[1], Azadeh Tabari[4], Komal Awan[4], Min Lang[4], John Conklin[4], Susie Y. Huang[4,5], Lawrence L. Wald[4,5], Stephen Cauley[4,5]

[1]Siemens Healthcare GmbH, Erlangen, Germany
[2]Siemens Medical Solutions, Boston, MA, USA
[3]Siemens Shenzhen Magnetic Resonance Ltd., Shenzhen, China
[4]Department of Radiology, Massachusetts General Hospital, MA, USA
[5]Martinos Center for Biomedical Imaging, Massachusetts General Hospital, MA, USA

Introduction

Patient motion is a common source of artifacts in brain MRI and accounts for up to 20% of scans being repeated at U.S. hospitals [1]. Motion artifacts often appear as image blurring, ringing, and signal dropouts which may negatively affect image interpretation and diagnosis [2]. 3D volumetric scans with high isotropic spatial resolution are particularly prone to motion due to their long acquisition times. Faster scanning afforded by advanced encoding and reconstruction techniques can reduce the severity of motion [3]. However, even reducing scan times to 1–2 minutes does not solve the problem completely since patient motion typically occurs on the time scale of seconds.

Estimating and correcting for patient motion in clinical brain scans is an active area of research, but no method has found widespread clinical usage. Previously proposed techniques require accurate supplemental tracking data, which is often obtained from external hardware equipment [4, 5] or MRI motion navigators [6, 7]. The position information is used to either update the imaging field of view of the MRI scanner in "real time" (prospective correction) or to inform a motion-aware image reconstruction (retrospective correction). The use of additional tracking data to prospectively or retrospectively correct the image can mitigate motion artifacts, but adoption into clinical protocols is challenging due to the high demands for robustness, reliability, and minimal disruption to the workflow. Specifically, these techniques are expected to yield significant image quality improvement in the presence of moderate to strong patient motion, where the accuracy of the motion parameter measurements is high (measurement error is a small percentage of the motion amplitude). But high image quality must be retained when there is no or limited motion (the amplitude of the motion is below the uncertainty of the tracker's or navigator's measurement). Furthermore, the method must not disrupt the clinical workflow by, for instance, requiring extensive set-up, altering sequence parameters, or delaying image reconstruction. These demanding requirements must be met for all examinations to avoid adversely affecting the large percentage that can be completed with limited or no patient motion.

Data-driven retrospective motion correction provides an opportunity to meet many of these requirements, given that it can be formulated as a "do-no-harm" strategy. These methods extract the motion information and the motion-free image directly from the *k*-space data of the imaging scan without requiring additional tracking hardware or disruptive sequence modifications [8, 9]. This ensures that the baseline image quality and contrast will be maintained and that the motion-mitigation strategy only adds value to the exam. Radiologists also have the opportunity to directly compare the motion-modeled reconstruction against the original non-corrected images for improved diagnostic utility. Unfortunately, data-driven motion correction is computationally demanding because it often requires the inversion of a large and sophisticated nonlinear physics model that describes the effect of motion on the acquired *k*-space data. The challenging optimization required for this reconstruction is computationally prohibitive for standard clinical workflows where technologists need to make an intermediate informed decision.

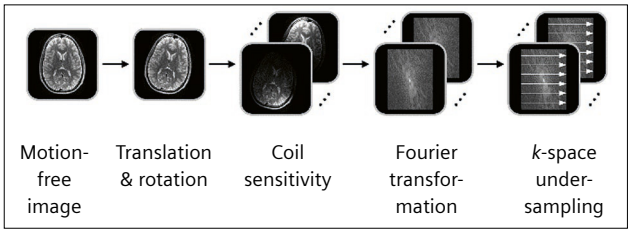

1 **Illustration of the SENSE+motion forward model.** The *k*-space data of a given shot is related to the image volume through image translation and rotation, coil sensitivity shading, Fourier transformation, and *k*-space undersampling.

[1]*Work in progress. The product is still under development and not commercially available. Its future availability cannot be ensured.*

The recently proposed scout accelerated motion estimation and reduction (SAMER)[1] algorithm [10, 11] will reduce the computational burden of motion estimation by leveraging an ultra-fast scout scan along with the repeated acquisition of a very limited number of additional *k*-space encoding lines. This approach will facilitate robust and highly efficient retrospective motion correction with clinically acceptable computation times.

SAMER

The SAMER[1] framework is based on SENSE [12] parallel imaging with rigid body motion operators added to describe motion within the forward model. Details of this SENSE+motion model are described in Figure 1. Estimating the motion trajectory and the motion-free image is achieved by minimizing the deviation between the physics model prediction and the acquired *k*-space data. Directly performing this estimation is a difficult and computationally costly joint optimization problem of both motion unknowns and the image voxels (Fig. 2A). The goal of SAMER is to decouple the motion trajectory and the motion-free image estimation. The iterative solution is aided by acquiring additional *k*-space encoding lines (motion guidance lines) and an ultra-fast scout scan. These serve as a prior and as a guide for the image/motion trajectory optimization problem (Fig. 2B).

The motion guidance lines and the scout are integrated into the standard data acquisition with minimal added acquisition length or timing disruption. In 3D multi-shot sequences such as MPRAGE, the data collection is divided into echo trains (shots), each containing about 100–200 phase/partition encoding lines. As illustrated in Figure 3, SAMER adds a small number of additional guidance lines to each echo train. This induces negligible effects on image quality, contrast, and sequence timing. The ultra-fast, low-resolution scout scan with matching contrast to the guidance lines is acquired only once before the imaging sequence (Fig. 3). It is obtained from a single echo train (single-shot) and can be considered motion-free.

The key computational benefit of SAMER is the ability to estimate the subject's motion for each motion state independently without requiring an intermediate re-estimation of the image volume. This enables very efficient motion estimation (~1 sec/shot) using standard scanner GPU hardware. Moreover, the per-shot motion optimizations can be initiated during the sequence acquisition. This makes efficient use of the scanning time and allows the final motion-aware image reconstruction to start shortly after scan completion.

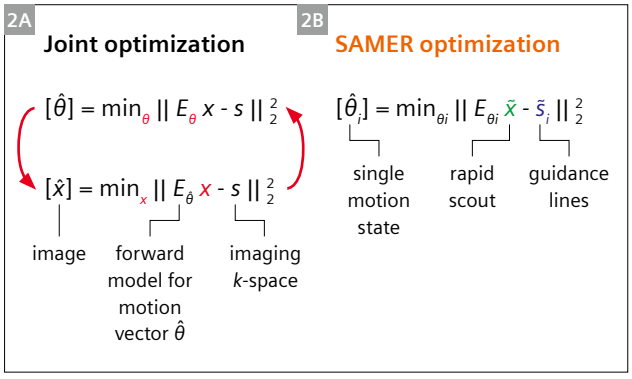

2 Comparison between joint and SAMER[1] motion optimization. Joint methods alternate between updating the motion parameters θ and the image estimate x. In SAMER, guidance lines $\tilde{s}_i$ and the rapid scout $\tilde{x}$ facilitate direct (non-joint) motion trajectory estimation. This avoids computationally costly updates of the image volume during the motion optimization and allows each motion state θ_i to be determined independently.

Applications

The SAMER framework was implemented into a T1-weighted 3D MPRAGE sequence. Scans were performed on two healthy volunteers using a 3T MRI scanner (MAGNETOM Vida; Siemens Healthcare, Erlangen, Germany) and a 20-channel head coil. Volunteers were trained to perform motion patterns that closely resemble clinical scenarios including (i) step motion between three natural positions, (ii) periodic nodding to mimic breathing, and (iii) unsupervised free motion. All reconstructions were performed online using the standard scanner GPU

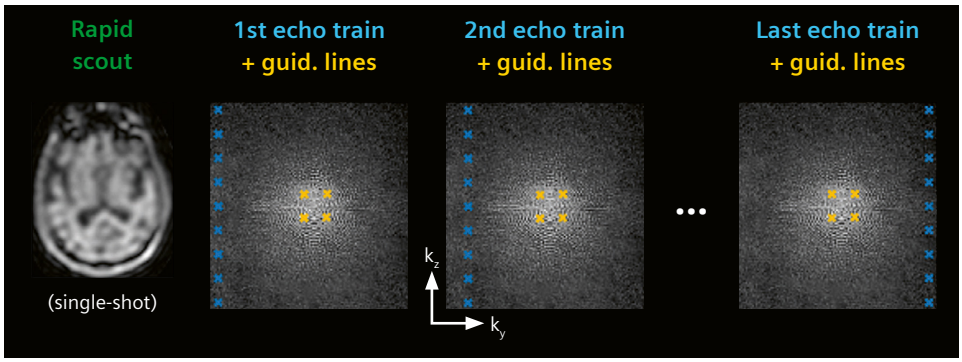

3 Illustration of the rapid scout and motion guidance lines in 3D MPRAGE. The low-resolution, single-shot scout is acquired once before the imaging scan. Guidance lines (yellow) are integrated into the standard data acquisition (blue) of each MPRAGE echo train.

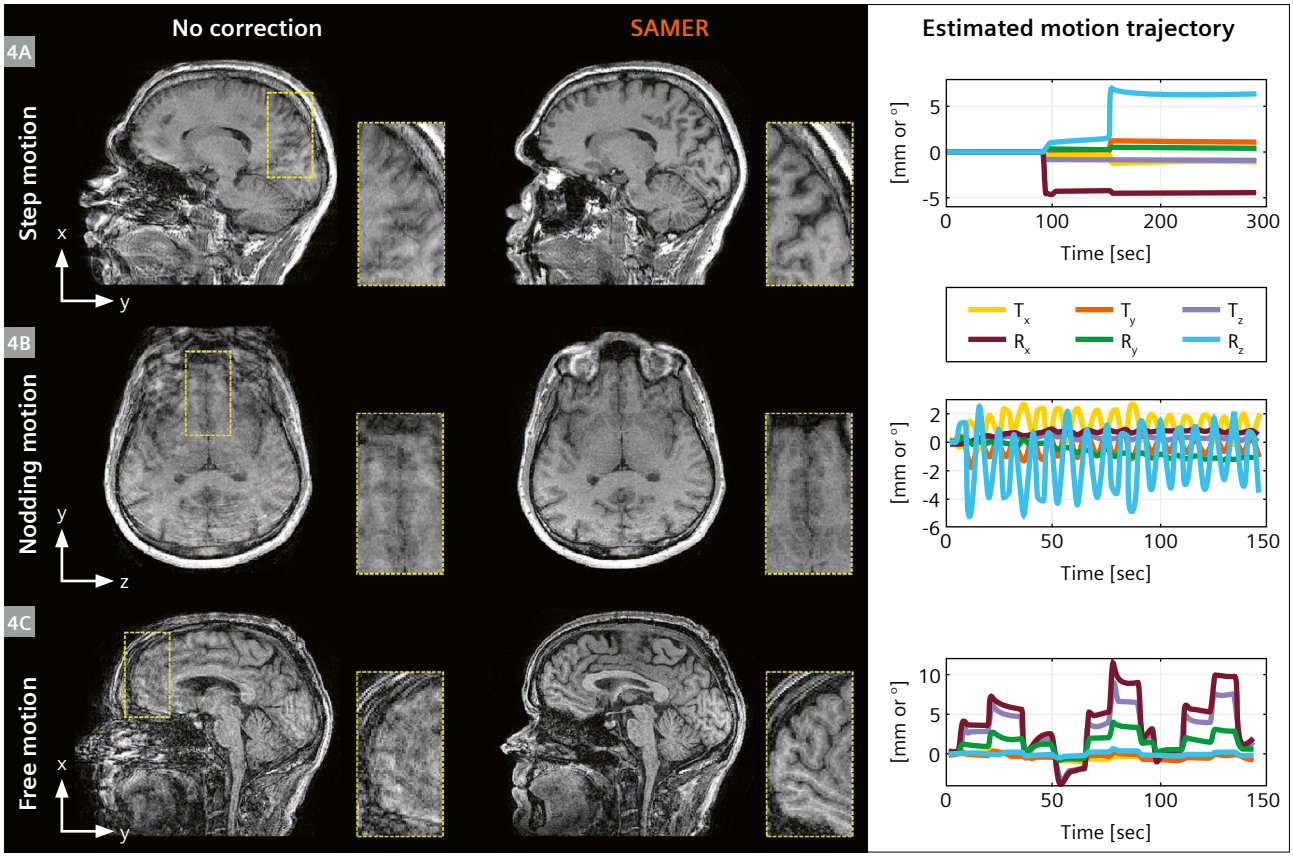

4 **In vivo motion correction of clinically representative motion patterns in 3D MPRAGE.** SAMER mitigated most ringing/blurring artifacts and reduced loss of spatial resolution.

hardware. Motion parameters were estimated once per TR with a temporal resolution of 2.5 seconds. The instructed step motion with up to 7° of rotation resulted in image blurring and loss of spatial resolution which was mitigated well by SAMER (Fig. 4A). A similar improvement in image quality was achieved in the scans with instructed nodding and unsupervised free motion, where better depiction of anatomical structures in the frontal cortex can be clearly observed (Fig. 4B, 4C). The efficient inline GPU implementation enabled rapid image-reconstruction times of about 1–2 minutes, which is within standard decision time windows for clinical workflows, i.e., less than a typical MRI scan duration.

Research on SAMER is currently being performed by the Neuroradiology department of the Massachusetts General Hospital (Boston, MA, USA). In a recent study [13], SAMER MPRAGE was explored in inpatient and emergency settings, comparing the level of motion severity with and without correction. It was noted that SAMER reduced the motion severity: 69% of nondiagnostic motion cases were considered diagnostic after correction; on the other hand, no significant adversary effect on the motion grade was reported in cases with minimal or no motion.

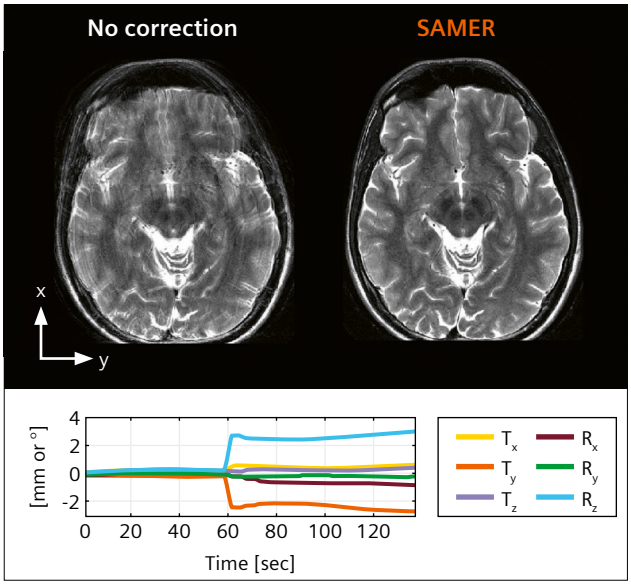

5 **In vivo motion correction of 2D TSE with instructed step motion.** SAMER removed most motion artifacts enabling improved delineation between gray and white matter.

The SAMER framework generalizes to many sequences and imaging scenarios. For example, a first attempt has been made to deploy SAMER into TSE to demonstrate retrospective motion correction with the most commonly used form of 2D imaging (high in-plane resolution, thick-slice protocols). For an initial assessment, T2-weighted TSE data was acquired with instructed step motion, and the SAMER reconstruction was performed offline. Figure 5 shows the improved spatial resolution and reduced ringing artifacts after the motion correction.

In conclusion, the SAMER approach will offer a computationally scalable solution for retrospective motion correction. The ultra-fast scout scan and motion guidance lines can be easily implemented into the standard sequence sampling, ensuring broad applicability across 2D and 3D sequences.

References

1 Andre JB, Bresnahan BW, Mossa-Basha M, Hoff MN, Smith CP, Anzai Y, et al. Toward Quantifying the Prevalence, Severity, and Cost Associated With Patient Motion During Clinical MR Examinations. J Am Coll Radiol. 2015;12(7):689-695.

2 van Heeswijk RB, Bonanno G, Coppo S, Coristine A, Kober T, Stuber M. Motion compensation strategies in magnetic resonance imaging. Crit Rev Biomed Eng. 2012;40(2):99-119.

3 Zaitsev M, Maclaren J, Herbst M. Motion artifacts in MRI: A complex problem with many partial solutions. J Magn Reson Imaging. 2015;42(4):887-901.

4 Zaitsev M, Dold C, Sakas G, Hennig J, Speck O. Magnetic resonance imaging of freely moving objects: prospective real-time motion correction using an external optical motion tracking system. Neuroimage. 2006;31(3):1038-1050.

5 Ooi MB, Aksoy M, Maclaren J, Watkins RD, Bammer R. Prospective motion correction using inductively coupled wireless RF coils. Magn Reson Med. 2013;70(3):639-647.

6 Tisdall MD, Hess AT, Reuter M, Meintjes EM, Fischl B, van der Kouwe AJ. Volumetric navigators for prospective motion correction and selective reacquisition in neuroanatomical MRI. Magn Reson Med. 2012;68(2):389-99.

7 Kober T, Marques JP, Gruetter R, Krueger G. Head motion detection using FID navigators. Magn Reson Med. 2011;66(1):135-43.

8 Cordero-Grande L, Teixeira RP, Hughes EJ, Hutter J, Price AN, Hajnal JV. Sensitivity Encoding for Aligned Multishot Magnetic Resonance Reconstruction. IEEE Trans Comput Imaging. 2016;2(3):266–280.

9 Haskell MW, Cauley SF, Wald LL. TArgeted Motion Estimation and Reduction (TAMER): Data consistency based motion mitigation for mri using a reduced model joint optimization. IEEE Trans Med Imaging. 2018;37(5):1253–1265.

10 Polak D, Splitthoff DN, Clifford B, Lo WC, Huang SY, Conklin J, et al. Scout accelerated motion estimation and reduction (SAMER). Magn Reson Med. 2022;87(1):163-178.

11 Polak D, Hossbach J, Splitthoff DN, Clifford B, Lo WC, Tabari A, et al. Motion guidance lines for robust data consistency-based retrospective motion correction in 2D and 3D MRI. Magn Reson Med. 2023;89(5):1777-1790.

12 Pruessmann KP, Weiger M, Börnert P, Boesiger P. Advances in sensitivity encoding with arbitrary k-space trajectories. Magn Reson Med. 2001;46(4):638-651.

13 Lang M, Tabari A, Polak D, Ford J, Clifford B, Lo WC, et al. Clinical Evaluation of Scout Accelerated Motion Estimation and Reduction Technique for 3D MR Imaging in the Inpatient and Emergency Department Settings. AJNR Am J Neuroradiol. 2023;44(2):125-133.



Contact

Daniel Polak, Ph.D.
Siemens Healthineers
DI MR RCT CLS NEUR
Allee am Roethelheimpark 2
91052 Erlangen
Germany
daniel.polak@siemens.healthineers.com

Fetal Low Field MRI – the First 150 Cases

Jana Hutter, Ph.D.[1,2]; Jordina Aviles Verdera[1,2]; Raphaël Tomi-Tricot, Ph.D.[3]; Kelly Payette, Ph.D.[1,2]; Alena Uus, Ph.D.[1,2]; Sara Neves Silva[1,2]; Sebastien Ourselin, FREng[2]; Shaihan Malik, Ph.D.[1,2]; Mary Rutherford, M.D.[1,2]; Joseph Hajnal, Ph.D.[1,2]

[1]Centre for the Developing Brain, School of Biomedical Engineering, King's College London, UK
[2]Biomedical Engineering Department, School of Biomedical Engineering, King's College London, UK
[3]MR Research Collaborations, Siemens Healthcare Limited, Camberley, UK

Introduction

Fetal[1] magnetic resonance imaging (fetal MRI) has continuously increased its prominence in both research and clinical applications. The wide range of available contrasts, the high resolution, the ability to image the entire fetus up until late gestation, and operator-independence make it an essential research tool and an ideal complementary modality to ultrasound for clinical care. Fetal MRI is mainly used to image suspected clinical abnormalities found through ultrasound that require further clarification, such as neurological, spine, thorax, and abdominopelvic malformations or masses. It can also be used for detailed evaluations in cases of abnormal placentation, for antenatal surgical planning of spinal lesion closure in fetuses with spina bifida, and for laser ablations in monochorionic twin pregnancies or fetuses with congenital heart disease.

While anatomical imaging using turbo spin-echo (HASTE) sequences originally dominated, functional contrasts are increasingly being employed for a variety of indications in both research and clinical settings. They are either adapted from other parts of radiology or developed specifically for fetal indications, and include diffusion-weighted MRI [1, 2], T2* relaxometry [3], T1 relaxometry [4], and perfusion MRI [5]. As these complex functional techniques are being developed, they further increase the range of indications and hence applicability of fetal MRI.

While the current trend in MRI is to image at higher field strengths, some of the significant challenges encountered in fetal MRI may be addressed by operating at a lower field strength.

Advanced imaging techniques may be hampered by geometric distortion artifacts arising at air–tissue interfaces. This is made worse by the need to run highly efficient EPI-based read-outs for diffusion MRI, functional MRI, and multi-echo gradient echo sequences for T2* relaxometry, which leads to an increasing need for specialist image-based shimming techniques [6]. This increases examination time and the need for specialized fetal MRI technologists. Further challenges include B_1 inhomogeneity-related artifacts

1A

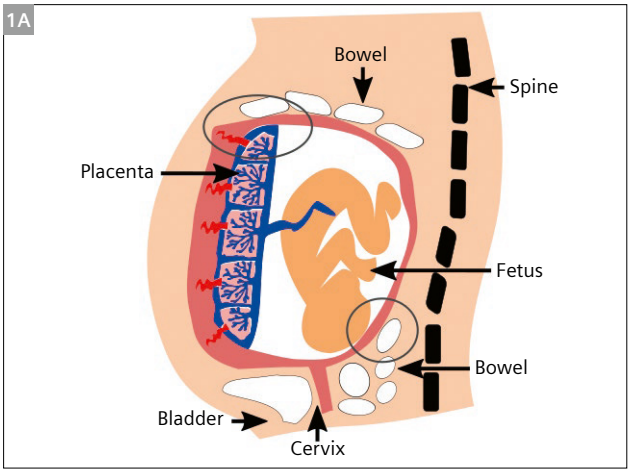

1B **Localizer**

Clinical protocol		
Anatomical MRI (T2-weighted HASTE)		11 min whole uterus
Diffusion MRI (Diffusion-weighted spin echo single shot EPI)		3 min whole uterus
Dynamic single-slice scan (cine)		1 min 1 slice
T2* Relaxometry (Multi-echo gradient echo single-shot (EPI)	*	4 min whole uterus
Research protocol		
T1 Relaxometry (Multi-echo gradient echo single-shot EPI)	*	3 min whole uterus
Combined T2*-Diffusion MRI (Multi-echo gradient echo single shot EPI)	*	8 min whole uterus
HARDI-Diffusion MRI (Diffusion-weighted spin echo single-shot EPI)	*	4 min placenta
No image-based shimming/calibration		

1 **(1A)** Schematic representation of the area of interest. The black circles signify areas of significant distortion due to air–tissue interfaces. **(1B)** Protocol overview for the clinical 20-minute exam and the research additions. The asterisks indicate custom-made sequences.

[1]*Siemens Healthineers disclaimer: MR scanning has not been established as safe for imaging fetuses and infants less than two years of age. The responsible physician must evaluate the benefits of the MR examination compared to those of other imaging procedures*

enhanced by the presence of amniotic fluid, and specific-absorption-rate (SAR) limitations [7] resulting in inefficiencies in the sequences. Both B_0 and B_1 inhomogeneities increase with higher field strengths. Therefore, lower field strengths reduce both the impact of the aforementioned artifacts and the need for specialist correction tools.

T2* is quickly becoming a widely used functional modality, especially to assess the placenta in major pregnancy complications such as pre-eclampsia and fetal growth restriction. The increase in T2* at lower field strengths provides a clinically beneficial T2* dynamic range that is ideal for these assessments. Similarly, shorter T1 times at low field can potentially increase acquisition speed for T1 relaxometry, facilitating its application in fetal MRI.

While comfort and space are paramount for any patient undergoing an MRI scan, pregnant women in the later weeks of pregnancy present a population where space and comfort is both particularly important and challenging to achieve in a standard-sized MRI bore. In addition, the number of obese pregnant women is rising – with 24% of all pregnant women in the UK and U.S. considered obese as of 2020 [8]. This presents a currently underserved population that could benefit from fetal MRI, as these women often do not receive adequate prenatal imaging due in part to the detrimental effect of increased abdominal fat on ultrasound imaging. Lower-field strength MRI typically allows a homogeneous field even with a wider bore. Increasing the bore size to 80 cm and reducing the required length of the magnet may enable MRI to complement ultrasound in the routine clinical screening of the obese pregnant patient.

Finally, a field strength-independent challenge concerns unpredictable and uncontrollable fetal motion, especially in early-to-mid gestation when fetuses have enough space for large displacements. This can be particularly problematic for fetal functional MRI modalities, which rely on the acquisition of the same slice location multiple times in a time-series format, to then be combined for spatiotemporal analysis. Both post-processing base techniques such as slice-to-volume registration (SVR) [9, 10] and prospective motion-correction techniques based on localization and tracking may be employed at low field strengths.

Main benefits:

- 20-minute efficient and robust clinical imaging workflow at low field
- Improved patient comfort due to wide bore
- Increased magnetic field homogeneity and reduced imaging artifacts
- First evidence proving the efficacy of low-field clinical fetal MRI

Materials and methods

Patient preparation and comfort

Pregnant patients are consented for research by either a research midwife or obstetrician and then prepared for the scan. The weight of the pregnant uterus on the vena cava in supine position can in rare cases lead to vasovagal episodes. To mitigate this and allow early detection, tight blood pressure controls are performed in multiple positions. A first blood pressure reading is taken while the patient is sitting on the scanner table, after which they lie on their left side for a second blood pressure reading, and then slowly the patient is eased onto their back in head first supine position to limit the compression of the vena cava. Padding for the lower back, the head, and the legs is provided as requested. Throughout the scan, blood pressure readings are performed automatically at 10-minute intervals, the maternal heart rate and saturation are continuously monitored, and frequent verbal interaction is maintained.

Clinical protocol

The protocol was crafted to allow assessment of the fetal brain and body, the placenta, and the cervix (see Figure 1A for an overview). It consists of a clinical session (Fig. 1B), which lasts about 20 minutes, and a research session of up to 40 minutes. Both are designed specifically with the advantages and challenges of 0.55T in mind and are therefore modified from our standard fetal imaging at 1.5T and 3T in the following way:

The resolution for the anatomical HASTE scans was reduced, using a slice thickness of 4.5 mm instead of 2.5 mm (in-plane resolution 1.4 × 1.4 mm^2) and 9 stacks (3 uterus stacks, 3 fetal brain stacks, and 3 fetal body stacks) instead of 6 to allow robust SVR.

A multi-echo gradient echo EPI sequence was modified to include multiple echoes, allowing for motion-robust T2* mapping of the entire uterus with 20 dynamics. T2* shortens with advanced gestational age and with most major pathologies. Compared to higher field strengths, the increased T2* at low field allows longer read-outs and the conservation of signal over longer echo times at later gestation and in cases with placental disease. A diffusion MRI scan, allowing both apparent diffusion coefficient (ADC) and intravoxel incoherent motion (IVIM) calculations as typically used for fetal imaging, was acquired covering the entire uterus. Finally, a dynamic (CINE) single-slice HASTE scan was acquired (TR = 4 seconds) to visualize cardiac activity and limb and head motion.

Research protocol

The gradient echo sequence was modified with a global adiabatic inversion pulse and slice-shuffling to reap the benefits of the reduced T1 at this field strength for an efficient quantitative fetal T1 acquisition. A previously

proposed multi-echo diffusion MRI scan [11] was used to sample a large parameter space, combined synergistically with the longer T2* and allowing sampling for a longer time.

Importantly, none of these elements included image-based shimming or any other advanced shimming of the kind required on higher-field scanners, thus saving scanning time.

Analysis and quantities obtained

An anatomical brain report is obtained from the HASTE stacks and includes bi-parietal diameter, transcerebellar diameter, ventricular sizes, presence of orbits, ears, and more. The cervical length and the lung are segmented individually to obtain respective quantitative values. The stacks are also reconstructed to 3D volumes using SVR resulting in automatic segmentations and volumes for 16 brain regions. Mono-exponential fitting is performed on the T2* and T1 data to obtain quantitative maps for the brain and placenta. Finally, the dynamic T2* scans are processed using SVR and AI-based localization and segmentation to obtain organ-specific T2* maps and values for 10 organs of interest.

Results

Comfort and success of the examination

In the first nine months, a total of 150 fetal scans from 16+0 to 40+2 weeks of gestational age were performed on the 0.55T scanner, including 25 patients referred for clinical indications. This cohort includes patients with either significant claustrophobia or a BMI that does not

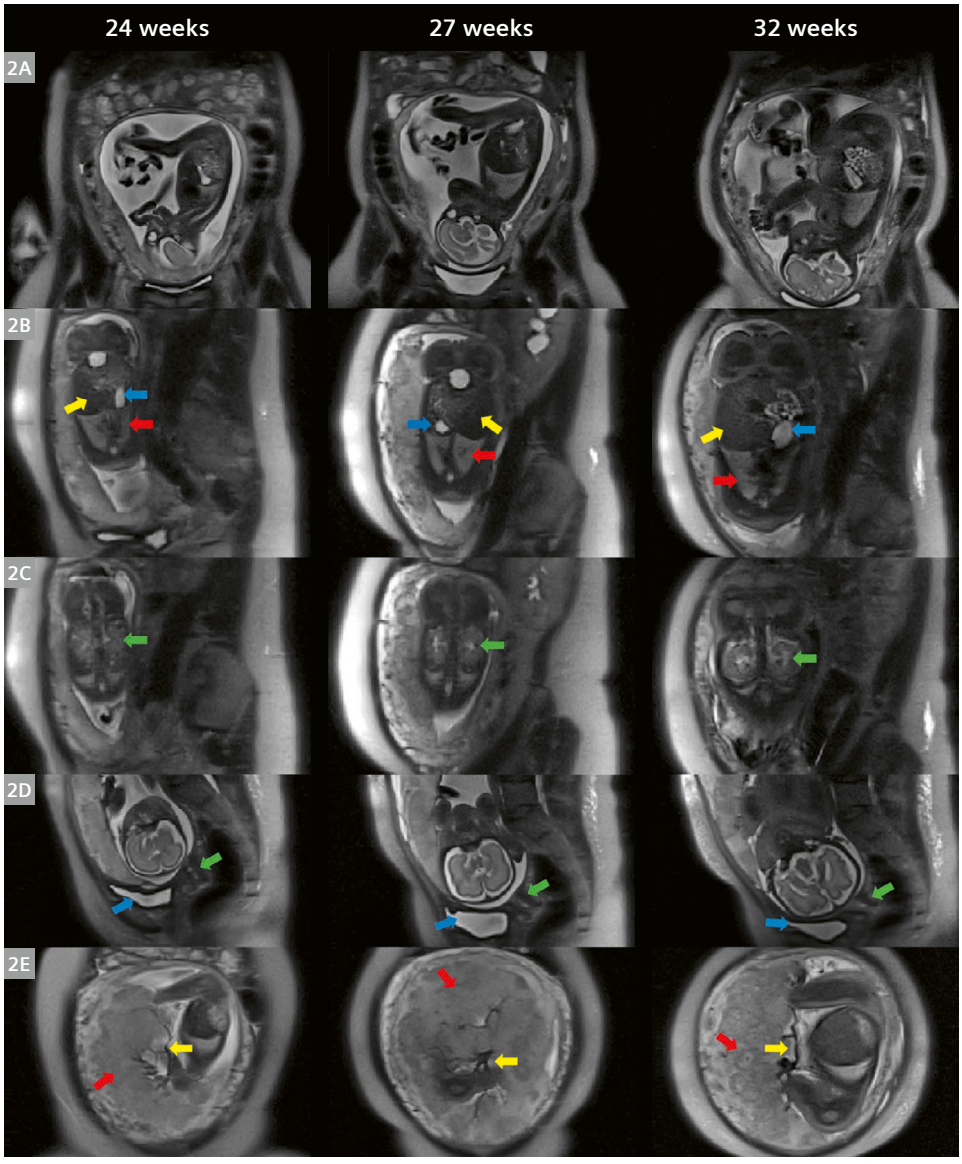

2 Fetal case scanned longitudinally at three time points during pregnancy (24, 27, and 32 weeks) illustrating **(2A)** a coronal whole uterus view; **(2B)** the fetal lung (red), stomach (blue), and liver (yellow); **(2C)** the kidney (green); **(2D)** the cervix (green arrow) and bladder (blue arrow); and **(2E)** a coronal whole uterus view through the placenta showing chorionic vessels connecting the placenta to the umbilical cord (yellow arrows) and the increasing heterogeneity with age within placental lobules (red arrow).

allow comfortable examination on any other available scanner (max BMI = 49.9 kg/m^2). The pathologies studied included neurological abnormalities (ventriculomegaly, midline cysts, mega cisterna magna, scalp tumor), fetal body abnormalities (cystic kidney), and big obstetrical syndromes associated with the placenta (pre-eclampsia, fetal growth restriction). They also included findings such as funnels in the cervix, endometrial cysts, and fibroids. Patient feedback from a small cohort of pregnant women who had both a low-field and a high-field MRI scan during the same pregnancy revealed an increase in comfort (from 2.9 to 4.3 on a scale of 1 "not comfortable" to 5 "very comfortable"). This was also reflected in the large number of research patients choosing to come back for up to four scans.

Anatomical data obtained as illustrated in a longitudinal case (the same fetus was scanned at 24, 27, and 32 weeks) shown in Figure 2 clearly depicts all fetal structures (lungs, liver, stomach, and kidney are marked with arrows), the placental vasculature (yellow arrow), heterogeneity (red arrow), and the cervix (green arrow). Figure 3 shows more detailed views of the brain in radiological planes and after SVR at three time points. The results from automatic regional segmentation on these SVR results are shown for 60 healthy control cases in the bottom row, illustrating the ability of the data to accurately assess growth. Finally, Figure 4 shows zoomed images of the described pathologies, illustrating the ability of the low-field data to robustly visualize and quantify these.

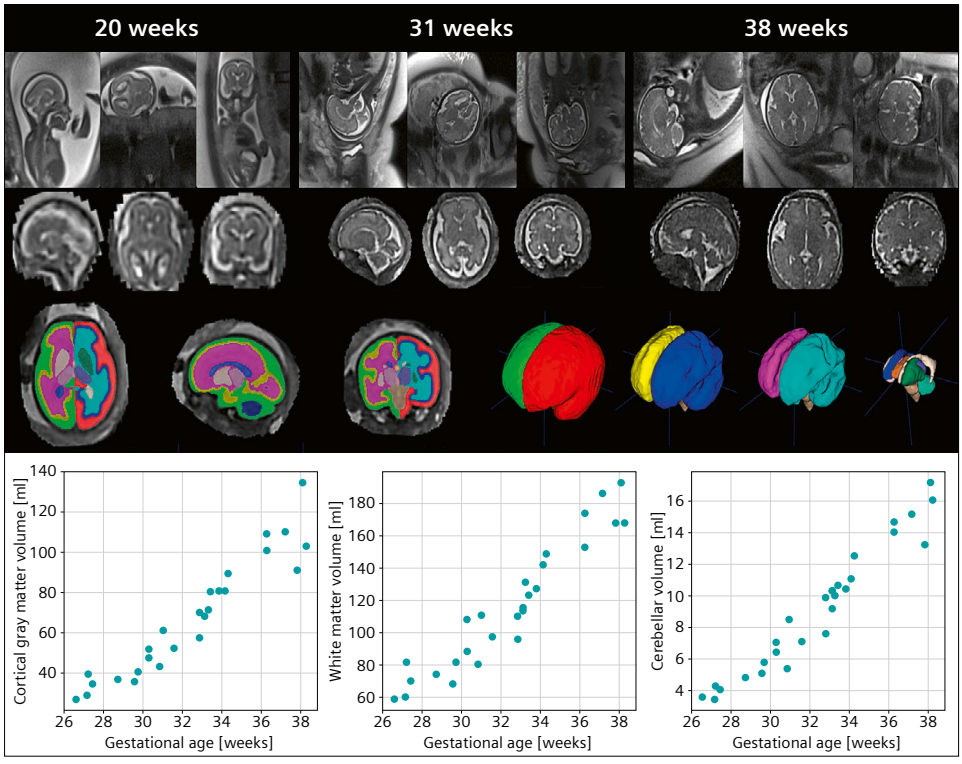

3 Detailed views of the HASTE data from the brain, acquired in radiological planes (top row) and after SVR (second row) at 20, 31, and 38 weeks. Results from the automatic subregion brain segmentation (third row) and volumetric brain assessment over gestational age (bottom row) from left to right: cortical grey matter volume, white matter volume, and cerebellar volume.

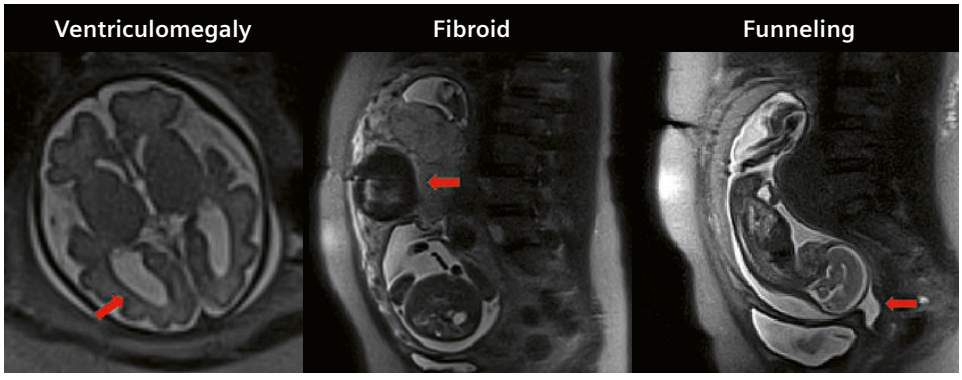

4 Fetal HASTE images of selected pathologies, including ventriculomegaly, an enlarged cisterna magna, a low signal-intensity fibroid, and funneling of the cervix.

Functional data and case study: BMI of 49.9 kg/m²

A total of 128 full sets of functional data were acquired, including T1 and T2* relaxometry and diffusion MRI. Imaging from a longitudinal case (same fetus scanned at 32 and 40 weeks) for T1 and for T2* (Fig. 5) depicts good delineation of major and fine brain structures. Finally, the T2* obtained for each fetal organ shows the ability of the proposed protocol at 0.55T to acquire quantitative information even for small fetal structures throughout gestation.

Results in a selected case with BMI = 49.9 kg/m² (Figure 6 for the anatomical and Figure 7 for the functional data) demonstrate the ability to obtain detailed results even in such challenging cases.

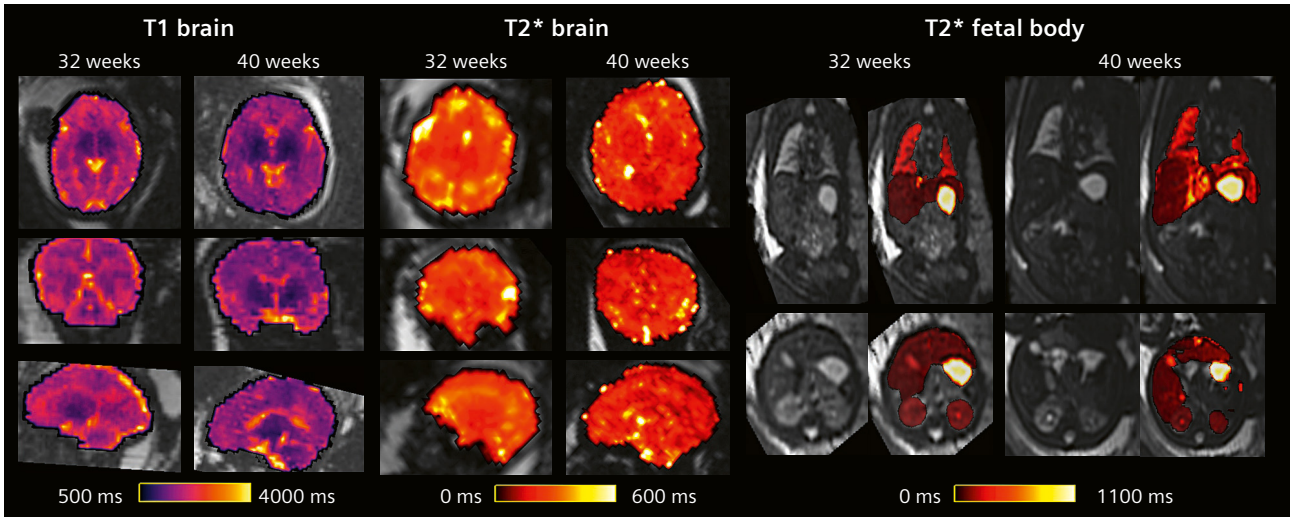

5 Longitudinal T1 (left) and T2* (middle) brain maps, and fetal organ T2* maps (right) for a subject scanned at 32 and 40 weeks' gestational age.

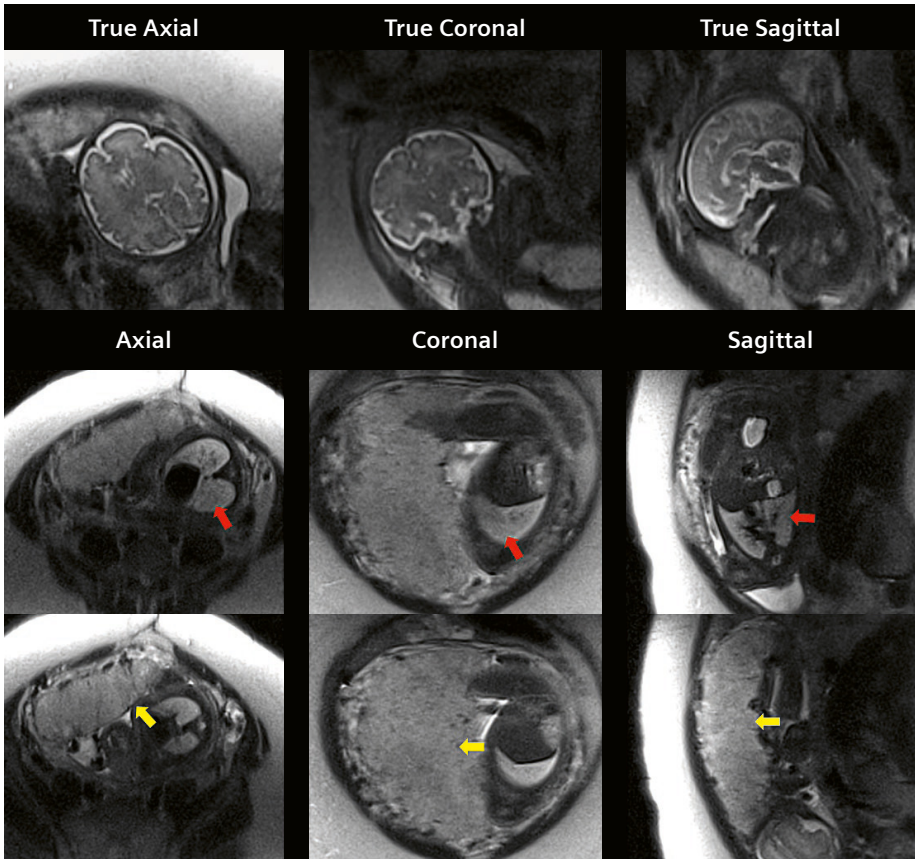

6 **Case study of fetal MRI at BMI 49.9 kg/m²: Part I:** Anatomical results for a participant with BMI = 49.9 kg/m² showing the ability to depict the brain structures (top row), the lungs (middle row, red arrows) and the placenta (bottom row, yellow arrows).

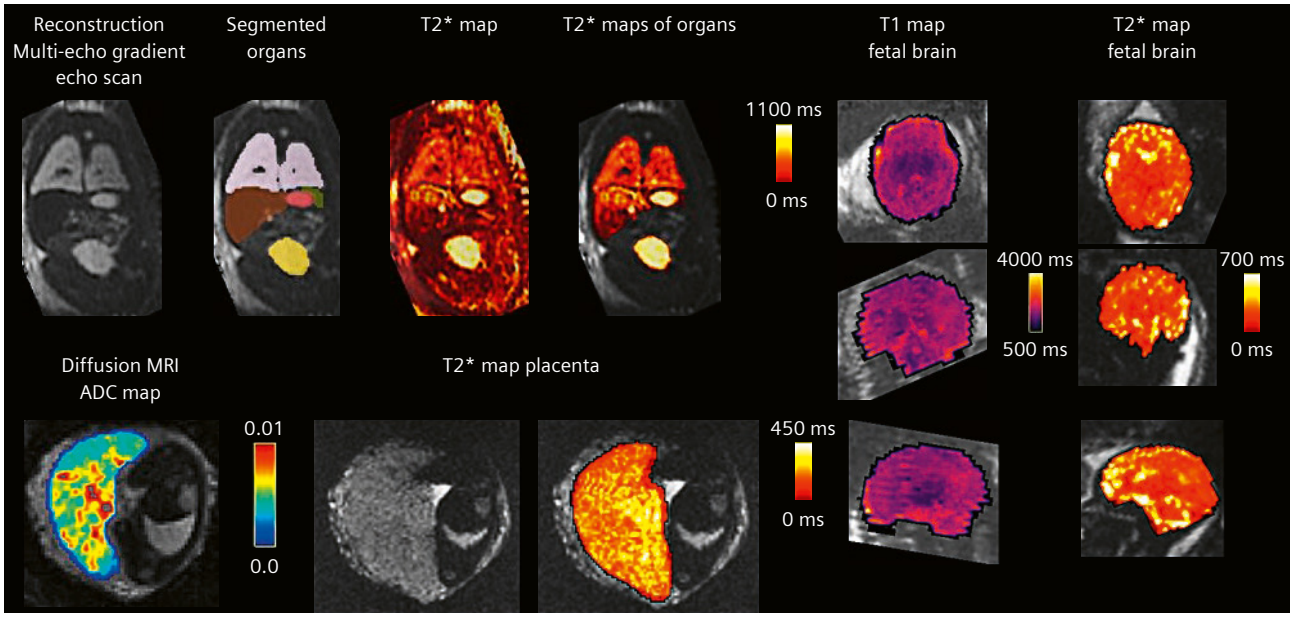

7 **Case study of fetal MRI at BMI 49.9 kg/m²: Part II:** Functional results from the same case for a participant with BMI = 49.9 kg/m² showing the individual organ T2* maps, the T1 and T2* maps of the brain, and the placental ADC and T2* map.

Discussion and conclusion

Fetal MRI at 0.55T is feasible, offers essential benefits, and is thus a promising direction for future antenatal imaging. The proposed short protocol allows anatomical and functional assessment of the fetus within 20 minutes. This is facilitated by foregoing any need for image-based shimming or other special correction tools, and carefully drafted to make use of the longer T2* and shorter T1 at low field. The research sequences allow further insights into desired regions of interest such as placental and lung microstructure and function. The wider bore size and shorter length increases comfort and thus increases access to fetal MRI until late gestation and in patients with higher BMIs. The fact that the scanner is a commercially available system makes it easy to integrate state-of-the-art techniques such as simultaneous multi-slice imaging, illustrated at 0.55T in Figure 8. Next steps will include adding fetal cardiac sequences; scanning further clinical cohorts such as patients with invasive placentation, preeclampsia, and congenital heart disease; and assessing the fetal placental unit prior to labor to assist in birth management. Other routinely used sequences for fetal MRI such as TrueFISP and T1-weighted contrasts will be added in the future.

An important future step is to further increase the availability of fetal MRI by allowing operation in hospitals and imaging centers without fetal MRI specialists. To come closer to this goal, a first step was the development of a prospective motion-correction technique that can detect fetal head translational displacements using deep learning and then feeds this information back to the scanner to continuously update the acquisition geometry in real time. This prospective motion correction shows great potential for applications that would highly benefit from precise correction of motion artifacts and immediate enhancement of the image quality during the scan. This can also be developed to be used to assess the tissue microstructure of the fetal brain through the quantification of the fetal brain's blood-oxygen-level-dependent (BOLD) response to maternal oxygenation and diffusion MRI.

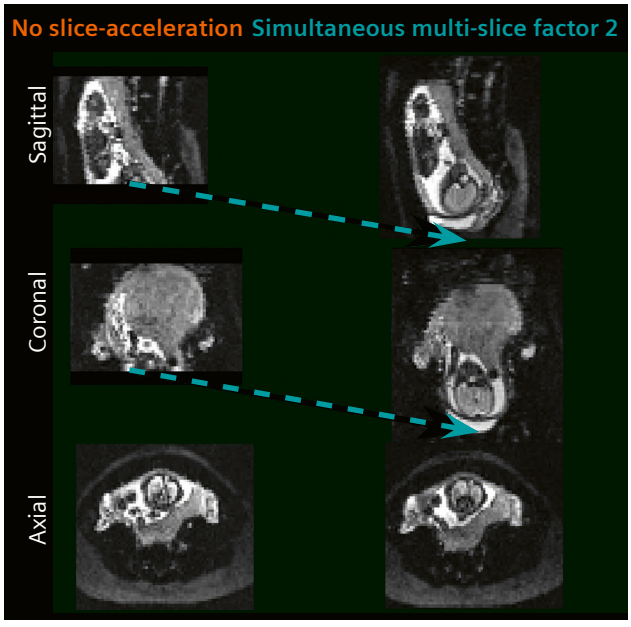

8 Simultaneous multi-slice imaging for T2* imaging at 0.55T illustrating the extension of the field of view by a factor of nearly two in the same scan time.

References

1 Bonel HM, Stolz B, Diedrichsen L, Frei K, Saar B, Tutschek B, et al. Diffusion-weighted MR imaging of the placenta in fetuses with placental insufficiency. Radiology. 2010;257(3):810–819.
2 Slator PJ, Hutter J, Palombo M, Jackson LH, Ho A, Panagiotaki E, et al. Combined diffusion-relaxometry MRI to identify dysfunction in the human placenta. Magn Reson Med. 2019;82(1):95–106.
3 Sørensen A, Hutter J, Seed M, Grant PE, Gowland P. T2*-weighted placental MRI: basic research tool or emerging clinical test for placental dysfunction?
Ultrasound Obstet Gynecol. 2020;55(3):293–302.
4 Gowland PA, Freeman A, Issa B, Boulby P, Duncan KR, Moore RJ, et al. In vivo relaxation time measurements in the human placenta using echo planar imaging at 0.5 T.
Magn Reson Imaging. 1998;16(3):241–247.
5 Zun Z, Limperopoulos C. Placental perfusion imaging using velocity-selective arterial spin labeling.
Magn Reson Med. 2018;80(3):1036–1047.
6 Gaspar AS, Nunes RG, Ferrazzi G, Hughes EJ, Hutter J, Malik SJ, et al. Optimizing maternal fat suppression with constrained image-based shimming in fetal MR.
Magn Reson Med. 2019;81(1):477–485.
7 Abaci Turk E, Yetisir F, Adalsteinsson E, Gagoski B, Guerin B, Grant PE, et al. Individual variation in simulated fetal SAR assessed in multiple body models.
Magn Reson Med. 2020;83(4):1418–1428.
8 Creanga AA, Catalano PM, Bateman BT. Obesity in Pregnancy.
N Engl J Med. 2022;387(3):248–259.
9 Uus A, Zhang T, Jackson LH, Roberts TA, Rutherford MA, Hajnal JV, et al. Deformable Slice-to-Volume Registration for Motion Correction of Fetal Body and Placenta MRI.
IEEE Trans Med Imaging. 2020;39(9):2750–2759.
10 Kuklisova-Murgasova M, Quaghebeur G, Rutherford MA, Hajnal JV, Schnabel JA. Reconstruction of fetal brain MRI with intensity matching and complete outlier removal.
Med Image Anal. 2012;16(8):1550–1564.
11 Hutter J, Slator PJ, Christiaens D, Teixeira RPAG, Roberts T, Jackson L, et al. Integrated and efficient diffusion-relaxometry using ZEBRA. Sci Rep. 2018;8(1):15138.

Contact

Jana Hutter, Ph.D.
Centre for the Developing Brain
School of Biomedical Engineering
King's College London
Westminster Bridge Road
London, SE1 7EH
United Kingdom
jana.hutter@kcl.ac.uk



Whole-Body MRI at 1.5T in the Era of Deep Resolve

Will McGuire; Marie Fennessy; Anwar R. Padhani

Paul Strickland Scanner Centre, Mount Vernon Hospital, Northwood, Middlesex, UK

Until recently it could take up to an hour to perform a whole-body MRI (WB-MRI). But what if you could cut that in half and make it better? Buckle up.

Around six years ago we shared a how-to guide hosted on the Siemens Healthineers *WB-MRI website*. Hopefully, many of you found this helpful in designing and refining your protocols to meet the increasing demand for WB-MRI for clinical indications including the diagnosis of multiple myeloma, the surveillance of patients with cancer predisposition syndromes, and for patients with bone predominant metastatic disease from prostate and breast cancer. Over the past few years several technological and software developments have improved access to this technique by significantly reducing scan times (TA) while maintaining (and in many cases improving) image quality.

In this article, we share our experience in developing WB-MRI protocols on the 1.5T MAGNETOM Sola emphasising how we have harnessed the power of Deep Resolve and the XA platform. For reference, previous guides and resources remain available online and as such we won't touch on the older software platforms and instead focus on how things have changed.

XA platform
The latest generation MAGNETOM scanners feature the new XA-platform scanner software. Previous-generation systems may also be offered upgrades (dependent on individual support agreements) enabling access to the library of the latest scanning techniques.

Sequence/ stations	TR (ms)	TE (ms)	FOV (mm)	Phase FOV (%)	Slice	Slice thick-ness (mm)	Gap (%)	Matrix (inter-polation)	Phase enc. direction (over-sampling)	iPAT / DRB / DRS / DRG	b-values (s/mm²)	Aver-ages	TA (min:sec)
FastView	n/a	n/a	n/a	n/a	Range 1350 mm	n/a	n/a	n/a	n/a	n/a	n/a	n/a	00:38
STIR spine sag (x2)	3500	89	380	100	15	4	20	272×218 (on)	H>F (80%)	2 / off / on / on	n/a	1	02:24 total
T1 spine sag (x2)	266	8.6	380	100	15	4	20	256×204 (on)	H>F (80%)	0 / off / on / on	n/a	1	02:08 total
T1 Dixon VIBE axial (x6)	6.8	2.39 / 4.77	430	93.8	44	5	0	256×204 (off)	A>P (PE – 0% SL – 45.5%)	CAIPI 4 (2×PE2×SL)	n/a	1	01:36 total
DWI axial (x6)	5370	63	430	90.6	40	5	0	128×128 (on)	A>P (0%)	2 / on / on / off	50, 900	3D diagonal 3, 8	07:42 total
T2 HASTIRM cor (x4)	1000	95	450	100	38	6	10	384×346 (off)	R>L (50%)	3	n/a	1	02:32
T2 HASTE axial (x6)	1000	96	430	93.8	40	5	0	320×240 (off)	A>P (0%)	3	n/a	1	02:48
												Total measurement time	**19:48**

Table 1: Key sequence parameters for MET-RADS [1] core sequences on 1.5T MAGNETOM Sola – excluding adjustment times.

Evolution, not revolution

This updated protocol relies heavily on the utilization of **Deep Resolve Boost** (DRB), **Gain** (DRG) and **Sharp** (DRS) which are available to current owners and new purchasers of the various Deep Resolve packages. DRB for DWI[1] will become available upon future upgrades to *syngo* MR XA60/61 – contact your local product specialist for details. Cases demonstrating the clinical use of DRB in whole-body DWI can be found in the article *"Initial experiences using DRB to accelerate whole-body diffusion MRI"* presented in this edition of MAGNETOM Flash.

Procedurally, many aspects of executing a whole-body examination remain the same as were set out in the previous guide – Table 1, detailing parameter selections, shows the familiar structure of the examination.

Software compatibility
A downloadable *.exar1 file from the *syngo* MR XA51 platform is available at *www.siemens.com/wb-mri*. Due to the inability to perform sequence conversion to an older software platform, *.pdf files are also available. Please note that, at the time of publishing, these files do not include the DRB DWI sequence – updates will be posted online as this becomes available.

[1] *Work in progress. The product is still under development and not commercially available. Its future availability cannot be ensured.*

Managing changes

As changes in quantitative measurements such as ADC values and bone marrow fat fraction are increasingly relied on by radiologists to assess the success of anticancer treatments [1], scan parameters must remain as consistent as possible between patient visits – we recommend this should include ensuring patients are scanned on the same hardware each time. Those managing a fleet of different scanner models will be familiar with the difficulties around standardization of acquisition in this context. Naturally, as scanners are replaced and upgrades are performed, it can be difficult to match exactly what was done before and this may mean the advantages of new techniques are overlooked in the pursuit of reproducibility.

Utilize the resources available to you, whether that be through the expertise of the Siemens Healthineers MR Applications team or via assistance from expert colleagues. You should ensure that whatever changes to image appearance manifest as a result of system upgrades, everyone in the team knows how to identify and interpret the effect of those changes.

You may find **teamplay Protocols** useful if managing more than one Siemens Healthineers MR system. This service allows you to distribute protocol changes remotely.

Minimum equipment requirements
- Spine 32
- BioMatrix Head/Neck 20
- Body 18 coils as required for coverage to knees (3× recommended)
- Optional: Peripheral Angio 36 if full-leg coverage is required without patient repositioning

Protocol set-up

As pointed out in the introduction, little has changed in the set-up for whole-body MRI examinations. However, as acquisition times become shorter, inefficient workflows can have a greater impact on the total examination time. Some sites will find the features of **MyExam Whole-Body Assist** useful particularly when designing user friendly protocols for less experienced operators.

The sequences presented here are ordered in such a way that ensures any post-processing (MIPs, MPRs) can be completed while the patient is being examined. Due to the decreased TAs, adjustments can occupy a greater proportion of the examination length (Fig. 1). Use the shim mode "Tune up" where appropriate for spine and HASTE sequences that do not require a comprehensive adjustment strategy to reduce the impact on examination duration.

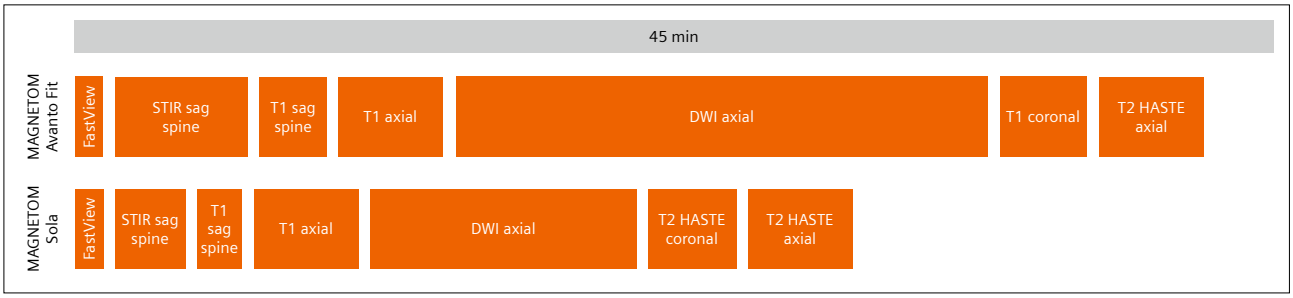

1 Comparison of example examination times on the MAGNETOM Avanto Fit (top) versus MAGNETOM Sola (bottom) scanners with approximate adjustment times included.

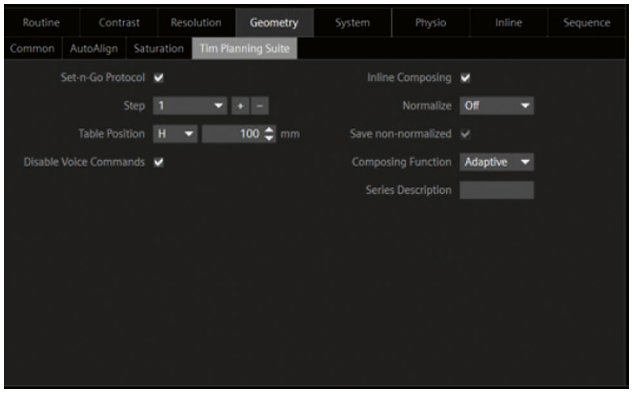

2 Location of disable voice commands tick box – this can be set on a per-step basis.



3 A colleague demonstrating vertex to knee coil coverage with three Body 18 coils.

During initial protocol setup, disable breath-hold instructions on slice groups positioned in the head, lower body and leg regions as there are minimal breathing artifacts in these anatomical regions (**Geometry: Tim Planning Suite:** Disable Voice Commands tick box, Fig. 2).

You may choose to have the T2 HASTE/HASTIRM sequences run without breath-holds as standard – the single-shot nature of the acquisition effectively eliminates motion artifact, however, there may be some slice-to-slice positional mismatch if this approach is selected. Including extras such a fast FLAIR brain sequence using Deep Resolve is optional but can serve as early asymptomatic lesion detection for some patient groups.

Patient and equipment set-up

It is important to ensure patients are as comfortable as possible so that they can tolerate the full examination without interruption. Use foam pads, pillows and knee supports where required for comfort and to protect patients from possible injury from a conductive loop or RF proximity burns. Changing patients into hospital gowns or other suitable clothing can help reduce the likelihood of discovering non-implanted metallic objects once the scan has begun.

Use of the anterior part of the Head/Neck 20 will improve image quality in the anterior head and neck region. All of the sequences in this protocol are fairly tolerant to the removal of these coil elements, so you can afford to be led by patient preference. Remember that BioMatrix Head/Neck 20 coil can be tilted to 9 or 18 degrees, enabling closer posterior coil positioning for kyphotic patients and thus greatly improving both patient comfort and image quality in the head and neck region. Place Body 18 and/or Peripheral Angio 36 coils as required to cover the desired length of scan (Fig. 3) – ensure the first Body 18 coil is positioned to cover the patient's shoulders superiorly.

If regularly used together you can prepare two of your Body 18 coils for whole-body placement using loosely connected Velcro straps – being careful not to damage the coils.

Depending on the height of the patient and the range of motion of your scanner table you may be able to achieve full head-to-toe coverage with the Peripheral Angio 36 coil. With this coil you may notice signal drop posteriorly which can be countered by positioning an upside-down Body 18 coil longways in the recess the removable table padding occupies. Ensure that excess pressure is not placed on this Body 18 coil by strategic placement of the foam pads supplied with your system.

AutoCoilSelect is now managed on a per-sequence basis (further details in Table 2) and you should set group graphics to ON before you start. If patients are unable to hold their breath remember to disable any automatic voice commands. Using the positioning laser, set the start position to a patient's chin and the FastView localizer will begin acquisition from above the skull vertex. You're now ready to scan – read on for sequence-specific tips and follow along with the video at *www.siemens.com/wb-mri*.

Sequence details	Positioning and ranges	Acquisition tips	Adjustable parameters	Notes
Step 1 **FastView localizer** **Range:** Vertex to knees **Plane:** Axial (MPRs are generated automatically)	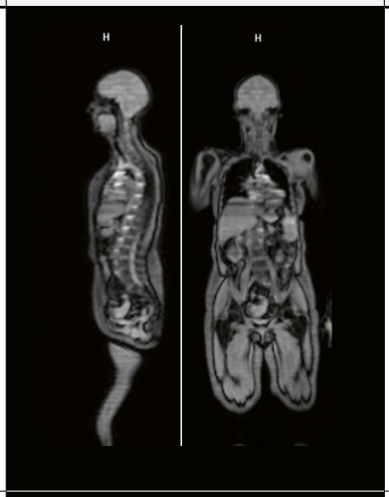	Set the acquisition range required for your study – the maximum range will vary depending on the table movement limits of your scanner		As before you should allow this localizer to fully complete before planning further. When complete your anterior elements will display on screen
Step 2 **STIR and T1 spine** **Range:** Whole spine **Plane:** Sagittal to patient's anatomy **Method:** Set-n-Go	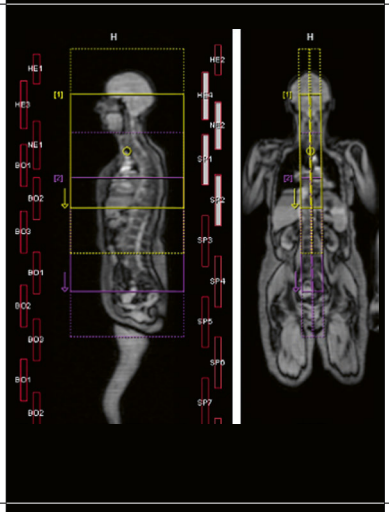	Enable spine or adaptive composing in the **Geometry: Tim Planning Suite** tab Ensure H>F coverage from skull base to at least S3 Angle to cover all vertebral bodies R>L for best fit Reduce artifact by setting AutoCoilSelect to "Restricted" and allowing only posterior elements to be used	Increase the number of slices to cover vertebral bodies R>L Increase phase FOV to a maximum of 120% to accommodate taller patients while maintaining resolution If this is still insufficient, add an additional slice group	Experiment with the amount of overlap required to maintain the quality of the composed images – be mindful that shorter bore scanners may have a more limited region of homogeneity
Step 3 **T1 Dixon CAIPI VIBE** **Range:** Vertex to knees **Plane:** Axial **Method:** Set-n-Go with automated breath-hold instructions	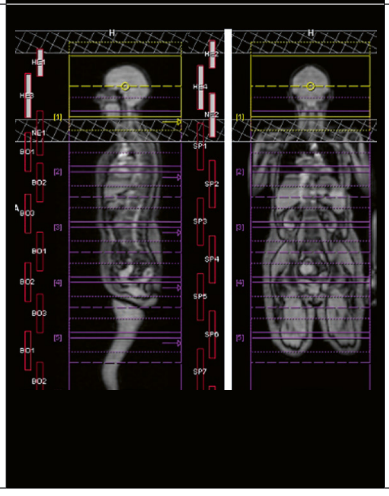	Position the Set-n-Go stack so that the first step has "spare" slices proud of the vertex – this ensures the DWI and HASTE axial series have the correct coverage Disabling breath-holds on those steps not affected by breathing motion can reduce TA and improve the patient experience	Add further steps if required for taller patients You may increase FOV for larger patients but be aware you will gain little additional anatomical coverage R>L due to edge-of-field artifact	Stacked 3D VIBE images benefit from a small amount of overlap – this is why the VIBE has 44 slices versus the 40 for DWI/HASTE which do not require overlap

Table 2: Step-by-step sequence positioning and acquisition tips (steps 4–6 on the next page).

Sequence details	Positioning and ranges	Acquisition tips	Adjustable parameters	Notes
Step 4 **DWI** **Range:** Vertex to knees **Plane:** Axial **Method:** Set-n-Go	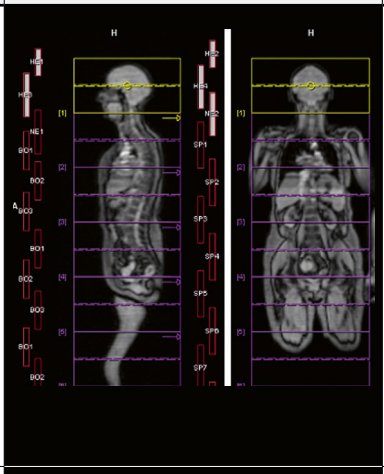	Applying copy reference functions to the DWI and HASTE axial sequences will ensure slice position match between series Experiment with setting the AutoCoilSelect range to "Generous" – you may find this improves SNR by activating additional receiver elements	Limit parameter changes to this sequence as the ADC values produced are increasingly relied on for quantitative response assessment – altering acquisition parameters may impact the ADC and make serial comparison more challenging	Removing b900 averages from the signal-rich head step and adding them to the abdomen steps can reduce stepping artifacts through the liver and spleen
Step 5 **T2 HASTIRM** **Range:** Vertex to knees **Plane:** Coronal **Method:** Set-n-Go	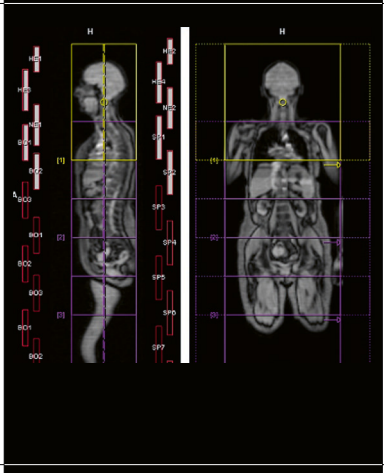	Leave some space above the level of the vertex – without this, the head will be affected by edge-of-field artifact If desired this sequence can be performed with breath-holds but typically motion artifact is not significant using this single-shot technique	Vary the inversion time (TI) to achieve the desired level of fat suppression For a HASTE, TR controls the spacing between shots rather than having a significant impact on image contrast – be wary of going too fast however as you can increase SAR issues and introduce artifact if the TR is too short	Where available, applying DRB will compensate for noise introduced by using an increased GRAPPA factor – this shortens the echo train and sharpens HASTE images
Step 6 **T2 HASTE** **Range:** Vertex to knees **Plane:** Axial **Method:** Set-n-Go	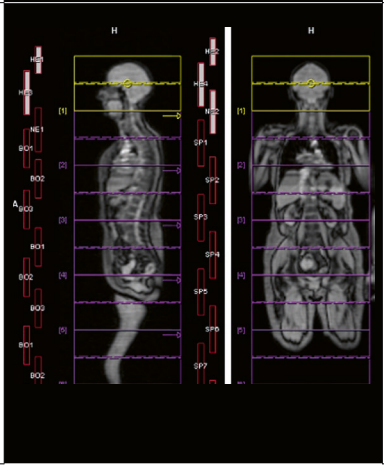	Use the copy reference function to ensure slice positions match with the DWI and T1 VIBE axial images As with step 5, this sequence can be performed with breath-holds if required	As above	In addition to the above, where available increase the interleaving step size to reduce any artifact from shorter TRs on image quality

Table 2: Step-by-step sequence positioning and acquisition tips.

Spine sequences (STIR and T1-weighted)

These sequences are used to evaluate bone lesions and reveal any lesions threatening the spinal canal. STIR remains the recommended approach for fat-suppressed whole-spine imaging due to its robustness against artifacts, and ability to tailor the degree of fat suppression by varying the inversion time (TI). The CoilShim feature, integrated into the BioMatrix Head/Neck 20 coil, improves local field homogeneity and has a role to play where spectral fat-suppression techniques are preferred, reducing or eliminating bright-fat artifact in the cervical and upper thoracic spine.

For T1-weighted imaging, setting a low TR can improve the contrast between normal and tumour-infiltrated bone marrow, spinal cord, and cerebrospinal fluid. When set to only activate posterior elements, the new per-sequence AutoCoilSelect setting "Restricted" allows operators the freedom to move scan volumes without inadvertent activation of anterior artifact-creating elements during spinal imaging.



4 STIR and T1 sagittal composed whole-spine images demonstrating improvements in image quality between conventional **(4A, 4C)** and DRG+DRS **(4B, 4D)** sequences.

Deep Resolve for TSE can facilitate marked reductions in TA while maintaining or improving image quality (Fig. 4). You may find DRB less useful for spine imaging due to infolding (SENSE) artifacts when an H>F phase encoding direction is selected. This protocol uses the image-based denoising technique DRG which (while less effective at denoising) avoids such infolding artifacts. DRG has several settings which require trialling using the retro-recon function to find the best balance for your readers. DRS permits a lower base resolution to be selected for equivalent or better reconstructed image resolution.

Utilizing simultaneous multi-slice (SMS) can allow you to quickly acquire large volume T1 and T2 TSE axial spine series in regions of concern (for example if impending cord compression is seen). If thinner slice resolution is required you might consider using Compressed Sensing (CS) on a SPACE axial sequence to reduce the comparatively lengthy TA.

Whole-body sequences (T1 Dixon, T2 HASTE, and HASTIRM)

T1 Dixon imaging allows the creation of quantitative fat-fraction images which are used to assess tumor response or progression. Previously, the creation of these images was a manual procedure involving the addition and division of image series but can now be generated inline (**Inline: Liver**: Fat Fraction (2pt) tick box, Fig. 5) and will be composed along with the chosen Dixon contrasts.

If enabled, DRB can improve the sharpness of HASTE images by compensating for noise introduced with the use of higher acceleration factors, reducing the echo train length and thus reducing blurring.

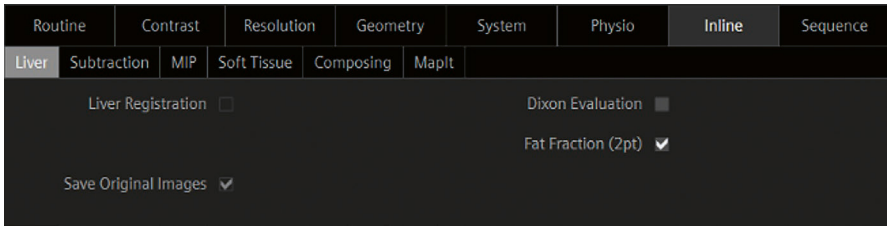

5 Tick box for automatic fat-fraction reconstruction.

Diffusion-weighted imaging

Previously, WB diffusion sequences were affected by broken spine artifacts, which were countered with awkward manual frequency-fixing techniques. This is now a thing of the past with the advent of SliceAdjust – a slice-by-slice shimming technique available on BioMatrix scanners. SliceAdjust should be used when acquiring and composing multiple large-volume DWI blocks.

Acquiring liver-lesion sensitive b-value images (between b500-b600 s/mm²) was previously recommended by the MET-RADS and MY-RADS guidelines. However, improvements in the signal-to-noise ratio enabled by the XA platform now allow good-quality b500-b600 s/mm² to be calculated rather than acquired, saving you time. Setting a calculated b value is straightforward – simply enable it in the **Diff**: tab on each DWI step.

DWI-SNR can be optimized by setting the bandwidth to allow minimum echo spacing, permitting the selection of an optimally minimized TE.

The diffusion parameters should be set to your team's preferred balance of SNR versus geometric distortion. Typically a 3D diagonal acquisition maximizes gradient performance resulting in greater SNR compared to the 3-scan-trace method. It's important to note that if the single-diffusion-direction 3D diagonal mode is selected, averages should be multiplied by 3 to reach an equivalent number of averages to a 3-directional 3-scan-trace. Additionally, the selection of a monopolar diffusion scheme will allow a shorter TE (and thus increased SNR) at the cost of increased geometric distortion.

When optimizing the sequence you may find a TR gap between a range of shorter, more SAR-intensive TRs and the next selectable TR (Fig. 6). Usually it is optimal to select the lowest TR however if SAR is an issue (e.g., if you are attempting to replicate this technique at 3T) an effective tactic is to select the minimum TR of the second "window" – reducing heating while minimizing TA.

Currently, SMS is an ineffective acceleration technique for WB-DWI. To maximize time-saving, one must either select a much shorter TR (which may have a significant negative impact on image contrast / DWI-SNR) or acquire more slices per step risking straying into the region of ADC drop-off as demonstrated by Winfield et al. [2]. SMS may however have a role to play in addressing the TA implications of a large TR "gap" as discussed above.

Deep Resolve Boost performs excellent denoising, enabling the selection of fewer averages per b-value resulting in a much shorter total TA versus conventional DWI (Fig. 7). Asymmetric averaging ensures the majority of time is spent acquiring high b-value data. Additionally, step-based averaging (e.g., more on the liver, fewer on the brain) helps to reduce the more conspicuous stepping artifact which can be seen in the liver and spleen with these shorter duration/fewer average sequences.

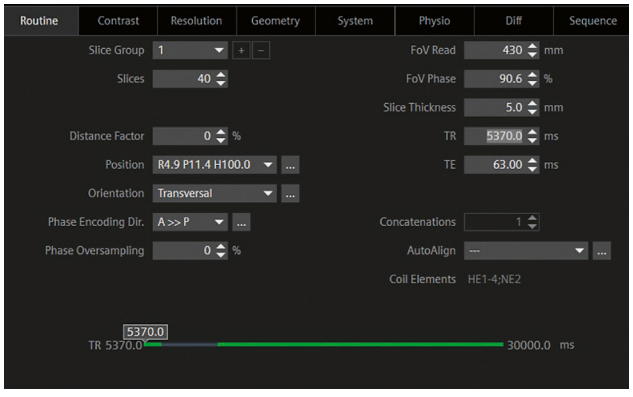

6 TR selection demonstrating interval between selectable TRs.

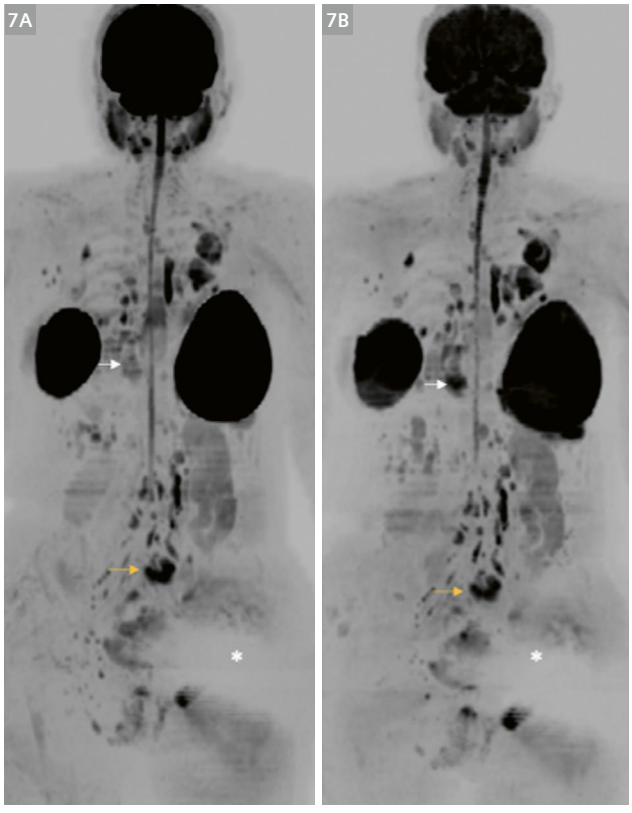

7 b900 inverted coronal MIP projections of conventional **(7A)** and DRB **(7B)** DWI.

Embrace the potential

Re-learning the relationships between SNR, scan time, and sequence parameters in the era of Deep Resolve has been a fascinating journey. Ultimately, you'll need to take that journey yourself to find what works best for you and your team.

By leveraging the power of these acceleration techniques, we've seen that patients' experience and image quality can be improved while allowing greater utilization of these often-limited resources.

While we'll always have fond memories of the MAGNETOM Avanto Fit, we've aimed to show that you too can make a huge impact for your patients by embracing the future of MRI. Good luck!

Visit www.siemens.com/wb-mri to watch the video tutorial.

References

1 Padhani AR, Lecouvet FE, Tunariu N, et al. METastasis Reporting and Data System for Prostate Cancer: Practical Guidelines for Acquisition, Interpretation, and Reporting of Whole-body Magnetic Resonance Imaging-based Evaluations of Multiorgan Involvement in Advanced Prostate Cancer. Eur Urol. European Association of Urology; 2017;71:81–92.

2 Winfield JM, Collins DJ, Priest AN, et al. A framework for optimization of diffusion-weighted MRI protocols for large field-of-view abdominal-pelvic imaging in multicenter studies. Med. Phys; 2016;43:95–110.



Contact

Will McGuire, MSc MRSO (MRSC™)
Deputy Superintendent Radiographer
Paul Strickland Scanner Centre
Northwood, UK
will.mcguire@stricklandscanner.org.uk

Advertisement

Prepare your patients mentally for their MRI exam

Most patients who undergo an MRI exam, experience some level of anxiety. As a result, some move so much that they cause motion artifacts, cannot complete the scan, or do not even show up for the exam. Up to 75%[1] of all unsatisfactory scan outcomes can be eliminated by educating patients on the MRI exam.

Tap the full potential of your facility by preparing your patients for the scan with our patient education toolkit. A **video, poster, meditation,** and a **book for children** explain the process of an MRI exam in simple words and answer common questions:

- What does an MRI exam entail?
- What is important when having an MRI exam?
- What does an MRI exam feel like?





Download the patient education toolkit in your preferred language here:
siemens-healthineers.com/mri-patient-education

[1] *Törnqvist, E., Månsson, A., Larsson, E.-M., & Hallström, I. (2006). Impact of extended written information on patient anxiety and image motion artifacts during magnetic resonance imaging. Acta Radiologica, 47(5), 474–480. https://doi.org/10.1080/02841850600690355.*

3D Whole-Heart Imaging: An Innovative Collaborative Solution

Karl P. Kunze[1,2], Jens Wetzl[3], Seung Su Yoon[3], Radhouene Neji[2], Gaia Banks[3], Rene Botnar[2,4,5], Claudia Prieto[2,4], Michaela Schmidt[3]

[1]MR Research Collaborations, Siemens Healthcare Limited, Camberley, United Kingdom
[2]School of Biomedical Engineering and Imaging Sciences, King's College London, United Kingdom
[3]Cardiovascular MR Predevelopment, Siemens Healthineers, Erlangen, Germany
[4]Escuela de Ingeniería, Pontificia Universidad Católica de Chile, Santiago, Chile
[5]Institute for Biological and Medical Engineering, Pontificia Universidad Católica de Chile, Santiago, Chile

Clinical need

A broad spectrum of clinical use cases for cardiovascular magnetic resonance imaging (CMR) profit from high isotropic resolution in three dimensions to show thoracic vasculature including the small and tortious coronary artery vessels and fibrosis/myocardial viability using the late gadolinium enhancement (LGE) measurement technique. Recent clinical studies have demonstrated the value of free-breathing, high-isotropic-resolution CMR to diagnose ischemic heart disease using coronary artery and vein [1, 2] or LGE imaging [3], cardiomyopathy [4], congenital [5] and structural [6] heart disease, and ablation lesion assessment [7].

Challenges

One challenge of using a high isotropic resolution in the range of 1 mm^3 to 1.3 mm^3 in the context of CMR exams is the prolonged scan time when compared to other imaging methods. Although CMR has several benefits including high tissue contrast and no need for radiation, it remains a comparatively slow imaging modality. For whole-heart coverage with high isotropic resolution, a novel imaging strategy is required to complete scans in 5 to 10 minutes.

Ideally, these measurements should be acquired in free breathing. Hence, cardiac and respiratory motion must be addressed. To minimize cardiac motion, scanning should be performed during a time in the cardiac cycle when the heart is in its quiescent phase, usually at end-diastole with a window of 80–160 ms, depending on the heart rate. To find the still phase of the heart, a 4-chamber cine is usually acquired. An experienced operator needs to manually define it and then enter it correctly in the 3D measurement protocol.

To account for respiratory motion, navigators are typically used to scan during free breathing. The frequently used 1D cross-paired diaphragm navigators are manually placed on the liver dome, and imaging data are accepted only in end-expiration. Depending on the breathing pattern, the acceptance rate can be between 20% and 60%. Therefore, scan time is unpredictable upfront, and a drift in breathing pattern during the scan may further decrease acquisition efficiency.

Moreover, accepting data only in end-diastole and in end-expiration makes data sampling very inefficient. Long scan times result in high institutional costs and are a discomfort for sick patients, meaning they can result in patient movement (reduced patient compliance) and non-diagnostic images.

One method to overcome this hurdle is the "free-running" acquisition approach, which samples and uses all data irrespective of the breathing and cardiac-motion states, with separation of these during image reconstruction [8, 9]. While this single-click method has numerous benefits that have been shown in multiple publications, it has not yet been widely distributed and tested clinically because it requires high-end computing, long reconstruction times, and often the use of contrast agent.

Another way to account for respiratory motion is to use image-based navigators [10] combined with non-rigid motion-compensated reconstruction. This enables predictable scan times and an acceptance rate of 100% of data irrespective of the breathing position. When combined with novel undersampling strategies [11, 12], a scan time of 5 to 8 minutes is possible, while the reconstruction only needs to address respiratory-motion compensation and *k*-space undersampling.

3D Whole Heart is work in progress. The application is still under development and not commercially available. Its future availability cannot be ensured.

A third challenge for 3D imaging is the workflow, including positioning of multiple objects like navigators, saturation bands, and imaging volume, and determining the appropriate resting phase in the cardiac cycle as mentioned above. For the LGE measurements, correctly estimating inversion time (TI) to null healthy myocardium is yet another task for operators.

Finally, robust fat saturation is key for high-contrast display of the coronary arteries, as they are embedded in epicardial fat. For certain LGE applications, the separation of fat and water is also essential, e.g., in patients with pericarditis or small endomyocardial fibrosis, where it can be difficult to distinguish between fat and lesion.

The solution

To overcome the limitations of 1D diaphragmatic navigators, 2D image navigators (iNAV) have been proposed to enable direct tracking of the impact of respiratory motion on the heart [9]. With iNAV imaging, it is possible to derive accurate quantitative motion information in two spatial dimensions. This enables retrospective motion correction rather than prospective gating, resulting in 100% respiratory scan efficiency and predictable scan times.

While iNAV imaging allows for direct correction of beat-to-beat translational respiratory motion in a predefined image region, accounting for non-rigid motion during the breathing cycle requires a more complex, non-rigid motion-compensated reconstruction framework. A first step in such approaches is often data binning, followed by reconstruction of different bin images representing the different respiratory motion states present in the data. As each bin image only contains a small fraction of the already undersampled 3D acquisition, reconstruction of the individual bin images requires a well-designed interplay of acquisition patterns and reconstruction algorithms.

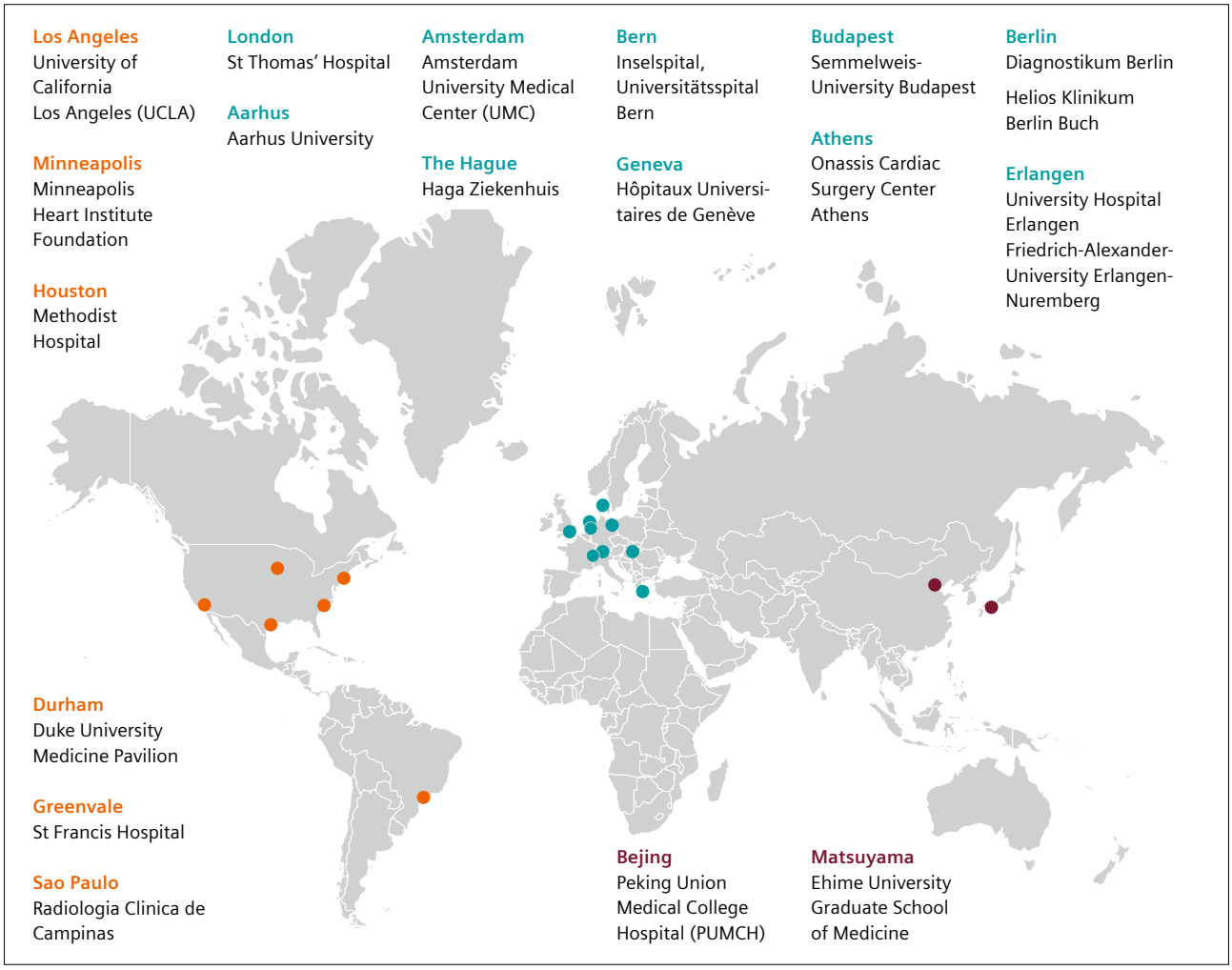

1 **Clinical partners for validating the 3D Whole-Heart application**
Our clinical partners helped us by sharing their experience so we could improve the research sequence and make it robust for a wide range of clinical questions and settings.

The variable-density Cartesian trajectory with spiral profile order sampling (VD-CASPR) [11, 12] provides high overall undersampling factors while maintaining favorable undersampling properties when data is split up into respiratory bins, enabling regularized reconstruction of artifact-free respiratory bin images [13]. These bin images can then be used to estimate 3D non-rigid motion between the motion states they represent, and motion information can be used in a final, non-rigid motion-compensated reconstruction of all data [14, 15]. Despite the large number of steps involved, the computational burden in the form of reconstruction time can be minimized to orders of 1 to 2 minutes using implementations with modern GPU technology [16].

In addition to standard chemical shift-based fat saturation methods, the described approach can be combined with Dixon-based fat-water separation. This provides a means to achieve robust elimination of fat from the final water-only image [17, 18], while also providing a fat-only image that can enable, e.g., discrimination between bright myocardial scar signal and fatty infiltration (Figure 2). Dixon fat-water separation enables improved visualisation of the coronary arteries [18], especially at 3T.

Workflow automation

As previously described, whole-heart imaging has typically increased the workload and requires more experienced operators given the need for precise positioning of saturation bands, image navigator, resting phase, and potentially TI. Together with the novel whole-heart sequence, we now offer workflow support for many of the planning steps that previously required manual user input.

In the following, we describe three modules for automating common planning tasks: AutoPositioning (for placement of graphical objects, e.g., the imaging volume, navigator, saturation bands) [19]; AutoRestingPhase (to determine a suitable acquisition window during the quiescent period in the cardiac cycle) [20]; and AutoTI (to set the proper inversion time for subsequent LGE imaging) [21].

AutoPositioning is based on localizer scans in coronal and transversal orientations. It uses deep learning to detect multiple anatomical structures, including the location and size of the heart and left ventricle, as well as the location of the liver dome and the arms. These are used to automatically perform the subsequent planning steps. Based on an initial localizer, the heart is placed into the isocenter, and further localizers centered on the heart can be acquired. Slices for thorax overview imaging and the AutoAlign scout can be positioned. For the whole-heart sequence, the imaging volume including slice coverage and position of the image navigator and saturation bands can be set automatically.

AutoRestingPhase is based on a 4-chamber-view cine to determine the quiescent phases of different cardiac structures within the cardiac cycle. First, the right coronary artery (RCA) and the four chambers of the heart are automatically detected. Subsequently, their motion throughout the cardiac cycle is tracked via image registration and then quantified and displayed as a motion curve. The valleys in this motion curve serve as suggestions for the whole-heart acquisition window. Different types of whole-heart acquisition can use the resting phase results of different anatomies of interest, e.g., the RCA for T2-prepared angiography or the left ventricle for 3D LGE.

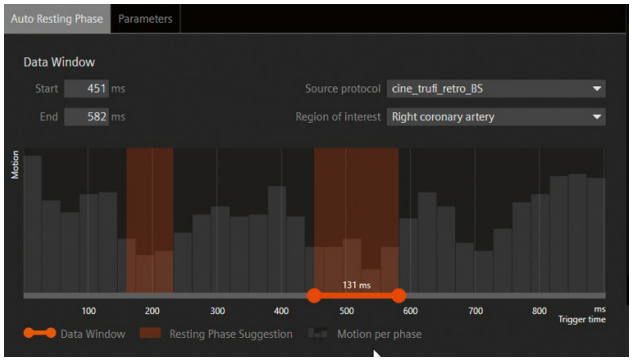

AutoTI is based on a TI scout in short-axis orientation, which is segmented to find the myocardial and blood-pool intensity values at each inversion time. The minimum of the myocardial intensity curve is first used to determine a TI with optimal myocardial nulling, then refined by finding an adjacent TI time with improved blood-myocardium contrast in case both have their zero crossings at similar times. An offset can then be applied automatically to subsequent LGE acquisitions to account for the time between TI scout and LGE acquisitions. This is applicable both to conventional 2D LGE and the novel 3D LGE acquisition.

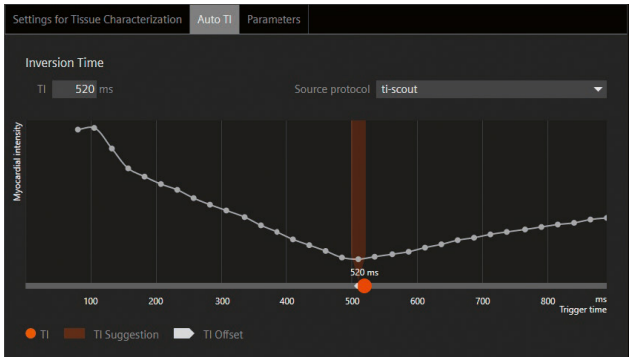

The combination of these modules significantly reduces the complexity and workload involved in performing high-quality whole-heart acquisitions, and simplifies or even improves the entire scan workflow.

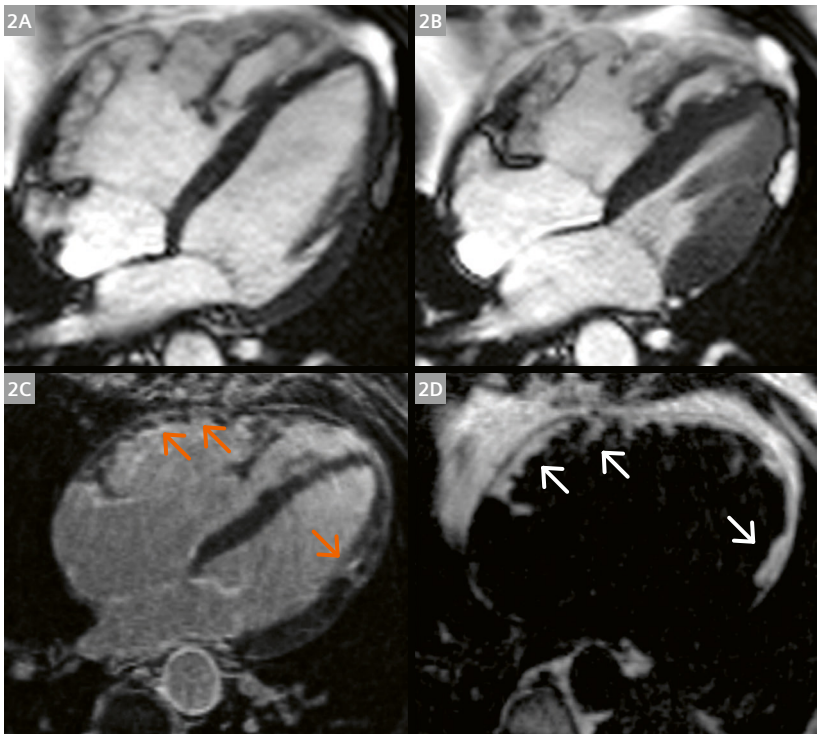

2 A 60-year-old male patient with fibrofatty replacement in LGE of the free wall of the RV and LV. Cine imaging 4-chamber view in a diastolic phase **(2A)** and systolic phase **(2B)**. The 3D whole-heart technique allows a differentiation between fibrosis **(2C)** in water-only LGE images and fat deposits **(2D)** in fat-only images. Fat deposition is depicted by the white arrows. Fibrosis is depicted by the orange arrows.
CMR imaging was performed on a 1.5 Tesla scanner (MAGNETOM Avanto fit, Siemens Healthcare, Erlangen, Germany) using cine imaging steady-state free precession (SSFP). After application of gadolinium-based contrast media (gadoteridol 0.2 mmol/kg), image-based navigated 3D whole-heart LGE sequence with fat–water separation was performed.
Images courtesy of Edyta Blaszczyk, MD[1,2,3], and Jeanette Schulz-Menger, MD[1,2,3,4]

[1]Charité – Universitätsmedizin Berlin, corporate member of Freie Universität Berlin and Humboldt-Universität zu Berlin, ECRC Experimental and Clinical Research Center, Berlin, Germany. [2]Working Group on Cardiovascular Magnetic Resonance, Experimental and Clinical Research Center, a joint cooperation between Charité Medical Faculty and the Max-Delbrück Center for Molecular Medicine. [3]DZHK (German Centre for Cardiovascular Research), partner site Berlin, Germany. [4]HELIOS Hospital Berlin-Buch, Department of Cardiology and Nephrology, Berlin, Germany.

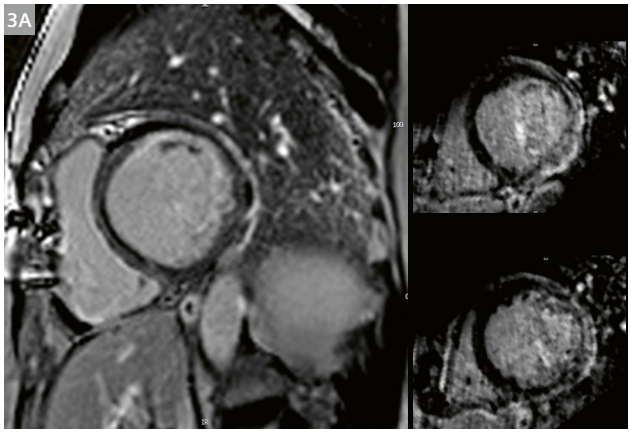

3 53-year-old male patient. **(3A)** Sustained VTs, MVR (MVP), DCM like phenotype of HF. **(3B)** Identify potential ablation targets from 3D corridors of border zone tissue and verify the detected corridors directly with the DICOM images. **(3C)** Import pre-procedural imaging into any electroanatomic mapping (EAM) system. Agreement of the structural arrhythmogenic substrate detected as corridors by CMR 3D LGE and the sites of electrical channels that may serve as the isthmus of VT. Late potentials and local abnormal ventricular activities at the areas of structural VT corridors.
CMR imaging was performed on a 1.5 Tesla MAGNETOM Sola (Siemens Healthcare, Erlangen, Germany).
Images courtesy of Evangelia Nyktari, M.D. (CMR); Athanasios Saplaouras, M.D. (EP lab); Konstantinos Letsas, M.D., Ph.D. (EP lab); Michalis Efremidis, M.D., Ph.D. (EP Lab); P Rozos and S Zarkadoulas (CMR) at Onassis Cardiac Surgery Center, Athens, Greece.

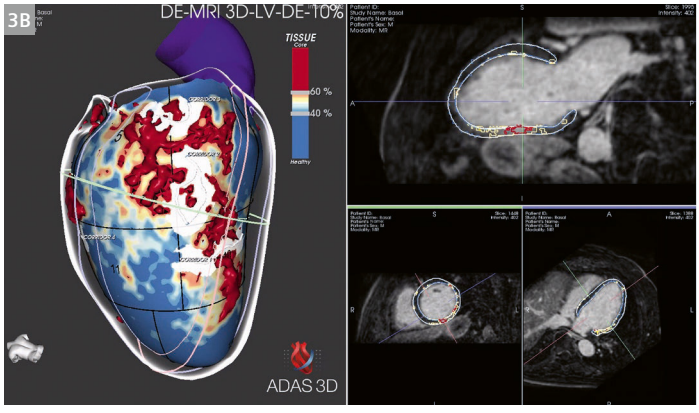

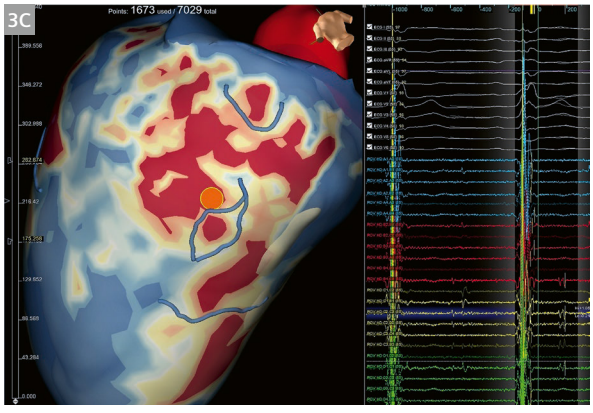

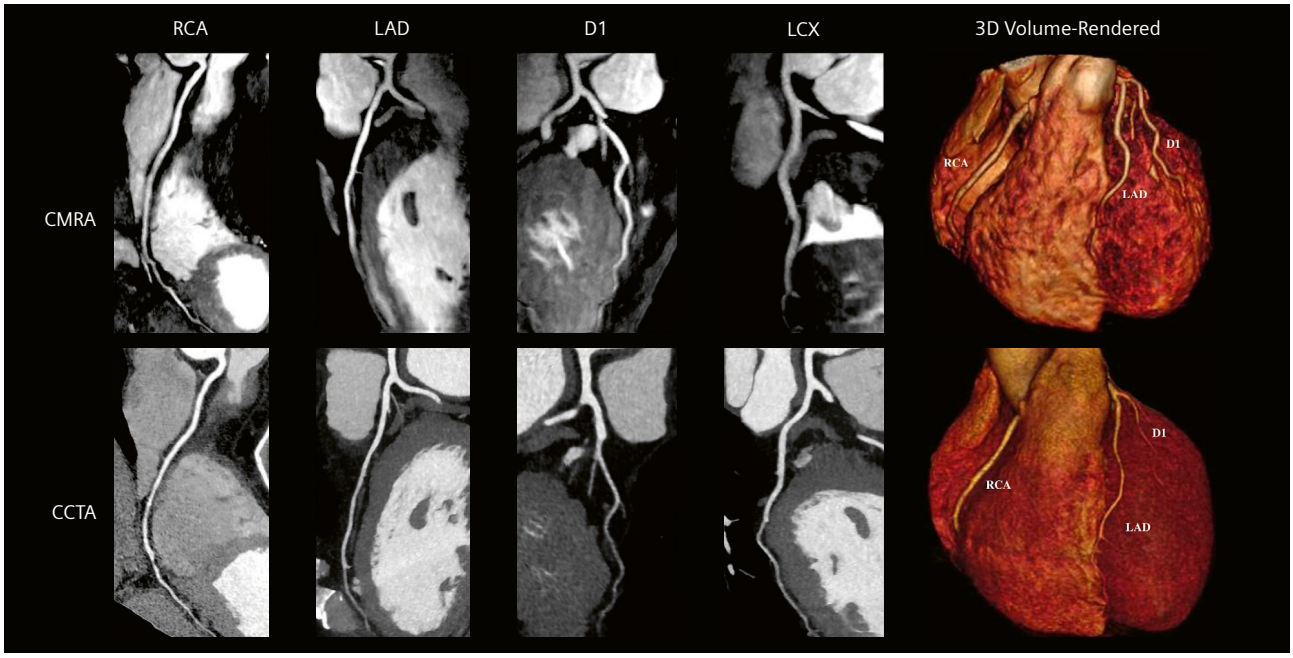

4 Curved multiplanar reformat and 3D volume-rendered non-contrast CMRA and contrast-enhanced CCTA in a 54-year-old male with no significant stenosis.
Abbreviations: CMRA = coronary magnetic resonance angiography; CCTA = coronary computed tomography angiography; RCA = right coronary artery; LAD = left anterior descending artery; D1 = first diagonal artery; LCX = left circumflex artery.
CMR imaging was performed on a 1.5 Tesla MAGNETOM Aera (Siemens Healthcare, Erlangen, Germany).
Images courtesy of Reza Hajhosseiny, M.D.[1]; Aurélien Bustin, Ph.D.[1]; Imran Rashid, M.D., Ph.D., FRACP[1]; Gastao Cruz, Ph.D.[1]; Ronak Rajani, M.D., Ph.D., FACC, FRCP[2]; Claudia Prieto, Ph.D.[1]; René M. Botnar, Ph.D.[1]; et al.
Adapted and reproduced from Hajhosseiny et al. [22].

[1]*School of Biomedical Engineering and Imaging Sciences, King's College London, United Kingdom*
[2]*School of Cardiovascular Medicine and Sciences, King's College London, United Kingdom*

Technical partner for developing the 3D Whole-Heart application

The whole-heart imaging sequence, image navigator, and image reconstruction framework described here were developed in close collaboration with the research groups of Professor René Botnar and Professor Claudia Prieto at King's College London, UK.

Conclusion and outlook

Clinical validation, resp. research studies, and feedback from numerous global sites indicate that implementing the novel 3D Whole-Heart sequence from Siemens Healthineers makes scans with whole-heart coverage and high isotropic resolution routinely possible in 5 to 10 minutes. Given the high level of automation available to support operators and achieve faster scan times, we expect rapid clinical adoption.

References

1 Hajhosseiny R, Rashid I, Bustin A, Munoz C, Cruz G, Nazir MS, et al. Clinical comparison of sub-mm high-resolution non-contrast coronary CMR angiography against coronary CT angiography in patients with low-intermediate risk of coronary artery disease: a single center trial. J Cardiovasc Magn Reson. 2021;23(1):57.
2 Nazir MS, Bustin A, Hajhosseiny R, Yazdani M, Ryan M, Vergani V, et al. High-resolution non-contrast free-breathing coronary cardiovascular magnetic resonance angiography for detection of coronary artery disease: validation against invasive coronary angiography. J Cardiovasc Magn Reson. 2022;24(1):26.
3 Peters AA, Wagner B, Spano G, Haupt F, Ebner L, Kunze KP, et al. Myocardial scar detection in free-breathing Dixon-based fat- and water-separated 3D inversion recovery late-gadolinium enhancement whole heart MRI. Int J Cardiovasc Imaging. 2023;39(1):135-144
4 Bustin A, Hua A, Milotta G, Jaubert O, Hajhosseiny R, Ismail TF, et al. High-Spatial-Resolution 3D Whole-Heart MRI T2 Mapping for Assessment of Myocarditis. Radiology. 2021;298(3):578-586.
5 Fotaki A, Pushparajah K, Hajhosseiny R, Schneider A, Alam H, Ferreira J, et al. Free-breathing, Contrast Agent-free Whole-Heart MTC-BOOST Imaging: Single-Center Validation Study in Adult Congenital Heart Disease. Radiol Cardiothorac Imaging. 2023;5(1):e220146.

6 Toupin S, Pezel T, Bustin A, Cochet H. Whole-Heart High-Resolution Late Gadolinium Enhancement: Techniques and Clinical Applications. J Magn Reson Imaging. 2022;55(4):967-987.
7 Sim I, Razeghi O, Karim R, Chubb H, Whitaker J, O'Neill L, et al. Reproducibility of Atrial Fibrosis Assessment Using CMR Imaging and an Open Source Platform. JACC Cardiovasc Imaging. 2019;12(10):2076-2077.
8 Di Sopra L, Piccini D, Coppo S, Stuber M, Yerly J. An automated approach to fully self-gated free-running cardiac and respiratory motion-resolved 5D whole-heart MRI. Magn Reson Med. 2019;82(6):2118-2132.
9 Roy CW, Di Sopra L, Whitehead KK, Piccini D, Yerly J, Heerfordt J, et al. Free-running cardiac and respiratory motion-resolved 5D whole-heart coronary cardiovascular magnetic resonance angiography in pediatric cardiac patients using ferumoxytol. J Cardiovasc Magn Reson. 2022;24(1):39.
10 Henningsson M, Koken P, Stehning C, Razavi R, Prieto C, Botnar RM. Whole-heart coronary MR angiography with 2D self-navigated image reconstruction. Magn Reson Med. 2012;67(2):437-445.
11 Prieto C, Doneva M, Usman M, Henningsson M, Greil G, Schaeffter T, et al. Highly efficient respiratory motion compensated free-breathing coronary MRA using golden-step Cartesian acquisition. J Magn Reson Imaging. 2015;41(3):738-746.

Contact

Michaela Schmidt
Siemens Healthineers
SHS DI MR RCT CLS CARD
Allee am Roethelheimpark 2
91050 Erlangen
Germany
michaela.schmidt@siemens-healthineers.com



Karl P. Kunze, Ph.D.
Siemens Healthineers
SHS EMEA GBI DI PI
Riverside Way
Camberley GU15 3YL
United Kingdom
karl-philipp.kunze@siemens-healthineers.com



12 Bustin A, Rashid I, Cruz G, Hajhosseiny R, Correia T, Neji R, et al. 3D whole-heart isotropic sub-millimeter resolution coronary magnetic resonance angiography with non-rigid motion-compensated PROST. J Cardiovasc Magn Reson. 2020;22(1):24.
13 Correia T, Ginami G, Cruz G, Neji R, Rashid I, Botnar RM, et al. Optimized respiratory-resolved motion-compensated 3D Cartesian coronary MR angiography. Magn Reson Med. 2018;80(6):2618-2629.
14 Batchelor PG, Atkinson D, Irarrazaval P, Hill DL, Hajnal J, Larkman D. Matrix description of general motion correction applied to multishot images. Magn Reson Med. 2005;54(5):1273-1280.
15 Cruz G, Atkinson D, Henningsson M, Botnar RM, Prieto C. Highly efficient nonrigid motion-corrected 3D whole-heart coronary vessel wall imaging. Magn Reson Med. 2017;77(5):1894-1908.
16 Zeilinger MG, Kunze KP, Munoz C, Neji R, Schmidt M, Croisille P, et al. Non-rigid motion-corrected free-breathing 3D myocardial Dixon LGE imaging in a clinical setting. Eur Radiol. 2022;32(7):4340-4351.
17 Munoz C, Cruz G, Neji R, Botnar RM, Prieto C. Motion corrected water/fat whole-heart coronary MR angiography with 100% respiratory efficiency. Magn Reson Med. 2019;82(2):732-742.
18 Munoz C, Bustin A, Neji R, Kunze KP, Forman C, Schmidt M, et al. Motion-corrected 3D whole-heart water-fat high-resolution late gadolinium enhancement cardiovascular magnetic resonance imaging. J Cardiovasc Magn Reson. 2020;22(1):53.
19 Wetzl J, Yoon S, Schmidt M, Haenel A-B, Weißgerber A, Barkhausen J, et al. AI-based Single-Click Cardiac MRI Exam: Initial Clinical Experience and Evaluation in 44 Patients. International Society for Magnetic Resonance in Medicine 2023.
20 Yoon S, Preuhs E, Schmidt M, Forman C, Chitiboi T, Sharma P, et al. Automated Cardiac Resting Phase Detection Targeted on the Right Coronary Artery. Machine Learning for Biomedical Imaging. 2023;2,arXiv:2109.02342:1-26.
21 Yoon S, Schmidt M, Rick M, Chitiboi T, Sharma P, Emrich T, et al. Validation of a deep learning based automated myocardial inversion time selection for late gadolinium enhancement imaging in a prospective study. International Society for Magnetic Resonance in Medicine 2021.
22 Hajhosseiny R, Rashid I, Bustin A, Munoz C, Cruz G, Nazir M.S, et al. Clinical comparison of sub-mm high-resolution non-contrast coronary MRA against coronary CTA in patients with low-intermediate risk of CAD: A single center trial. J Cardiovasc Magn Reson. 2021;23(1):57.

Optimizing Brachial Plexus Magnetic Resonance Neurography at 3 Tesla

Yenpo Lin, M.D.[1]; Ek T. Tan, Ph.D.[1]; Xiaoying Cai, Ph.D.[2]; Peter Kollasch, M.Sc.[2]; Alto Stemmer, Dipl.-Phys.[3]; Marcel Dominik Nickel, Ph.D.[3]; Guido Buonincontri, Ph.D.[3]; Andreas Schäfer, Ph.D.[3]; Tom Hilbert, Ph.D.[4,5]; Darryl B. Sneag, M.D.[1]

[1]Department of Radiology and Imaging, Hospital for Special Surgery, New York, NY, USA
[2]Siemens Healthineers, Malvern, PA, USA
[3]Siemens Healthineers, Erlangen, Germany
[4]Advanced Clinical Imaging Technology, Siemens Healthineers International AG, Lausanne, Switzerland
[5]LTS5, École Polytechnique Fédérale de Lausanne (EPFL), Lausanne, Switzerland

Introduction

At the Hospital for Special Surgery (HSS), ongoing efforts are made to improve image quality in magnetic resonance neurography (MRN). MRN comprises a specialized set of techniques focused on imaging peripheral nerves, which can be challenging given their small size and non-linear course throughout the body. When utilized in parallel with electrodiagnostic testing, MRN not only facilitates accurate localization of nerve injuries but also offers a comprehensive assessment of both the injured nerve and the end-organ muscle. MRN of the brachial plexus (BP) presents unique challenges due to inherent field inhomogeneities related to the neck/shoulder curvature and proximity to the lungs [1]. In 2021, the first Siemens Healthineers system was installed at our institution – a MAGNETOM Vida 3T. In this article, we share our experience in optimizing imaging quality for BP imaging on the MAGNETOM Vida.

Three-coil setup:
20-channel HNU +
18-channel UltraFlex +
posterior Spine Coil

Two-coil setup:
18-channel UltraFlex
(anterior: small,
posterior: large)



1 Comparison of coil types for unilateral, left brachial plexus MRN. **(1A)** Imaging with the neck at isocenter and the brachial plexus off isocenter using a combination of a 20-channel neurovascular array for the neck region, an 18-channel UltraFlex flexible coil array, and posterior spine elements. The BioMatrix Respiratory Sensor may be used for respiratory gating. **(1B)** An alternative setup with the left brachial plexus at isocenter, using two 18-channel UltraFlex arrays; the smaller coil is placed anteriorly while the larger coil is placed posteriorly (under the subject). An additional strap may be needed to deploy the respiratory pillow.

Sequence	2D IW-TSE	2D T2w-TSE	SPACE STIR	2D T2w-TSE
Deep Resolve Boost	Y	Y (Prototype)[1]	Y (Prototype)[1]	Y (Prototype)[1]
Orientation	Axial	Coronal	Double oblique-coronal	Oblique sagittal
Field of view, cm	28	32	30	16
TR/TE, ms	4000–6500/35	3000–9000/85	3000/161 (apparent TE = 60)	3000–6000/85
TI, ms	–	–	250	–
Matrix size (frequency × phase)	512 × 410	320 × 240	304 × 168	320 × 240
Pixel resolution (frequency × phase), mm^2	0.5 × 0.7	1.0 × 1.3	1.0 × 1.0	0.5 × 0.7
Slice thickness, mm (no spacing)	3.5	4.0	1.0	2.5
Slices	60	40–50	100–120	24–40
Bandwidth, Hz/Pixel	296	240	382	240
Turbo factor	14	14	130	14
Total acceleration factor (GRAPPA / CAIPIRINHA)	2	2	4	2
Gadolinium contrast	none	none	optional	none
Fat suppression	none	Dixon	STIR	Dixon/Fat saturation
Scan time, min:sec	2:00	3:45	4:40	4:00, variable with respiratory gating

Table 1: Unilateral brachial plexus protocol on MAGNETOM Vida 3T.
IW indicates intermediate-weighted; TSE: turbo spin echo; T2w: T2-weighted; TR: repetition time; TE: echo time; TI: inversion time; GRAPPA: generalized autocalibrating partial parallel acquisition; CAIPIRINHA: controlled aliasing in parallel imaging results in higher acceleration

[1]*Work in progress. The product is still under development and not commercially available. Its future availability cannot be ensured.*

Coil configuration

To maximize signal-to-noise ratio (SNR) for BP MRN, it is vital to use multichannel receiver arrays that cover the large anatomical regions of the neck, shoulder, and axilla, while also minimizing the distance between coil elements and the targeted anatomy [2]. At HSS, the BP is typically imaged unilaterally, rather than bilaterally, to optimize spatial resolution and coverage; if bilateral coverage is required, two unilateral scans are typically acquired. On the MAGNETOM Vida 3T, the preferred three-coil setup includes a combination of either a 20-channel neurovascular array for the neck region, an 18-channel UltraFlex flexible coil array (small or large, depending on coverage needed) over the chest wall/upper arm, and the posterior spine array (Fig. 1). Alternatively, two 18-channel UltraFlex arrays, the smaller version placed anteriorly and the larger placed posteriorly, can be placed (Fig. 1). The three-coil setup is easier to configure, in our experience, but the two-coil setup provides flexibility for positioning the targeted BP closer to magnet isocenter.

BP protocol – overview and rationale

Our current, unilateral BP protocol comprises acquisitions both longitudinal and orthogonal relative to the course of the nerve segments (Fig. 2). Following localizer scans, a two-dimensional (2D) axial intermediate-weighted (IW)-TSE is acquired to guide plotting of subsequent scans. Next, a large field of view 2D coronal T2-weighted Dixon TSE is acquired to assess the regional musculature. These two TSE sequences are used to plot the remaining nerve-sensitive scans: two, 2D oblique sagittal T2-weighted Dixon acquisitions for orthogonal, high in-plane

resolution and a single, coronal T2-weighted three-dimensional (3D) SPACE-STIR sequence for high through-plane resolution. For the SPACE-STIR, coverage is best optimized with a 'double oblique' prescription, which is first aligned parallel to the clavicle and includes cephalocaudal coverage from the C4 superior endplate to the axilla and anterior-posterior coverage from the chest wall to the posterior scapula. This is followed by a second alignment step, made off the 2D coronal T2-weighted Dixon TSE, from C4 to the axillary region.

Optimized 3D SPACE STIR

The SPACE sequence offers a significant advantage, compared to 2D imaging, by enabling higher through-plane spatial resolution (0.8–1.0 mm isotropic) and facilitating evaluation in any arbitrary plane without distortion, either using oblique or curved multiplanar reformations. We use a prototype SPACE-STIR sequence[1] with optimizations to improve B_0 and B_1+ robustness. These improvements include:

1. C-shaped frequency offset corrected inversion (C-FOCI) pulse for uniform fat suppression [3, 4],
2. variable flip angle train tailored with consideration of the B_1+ inhomogeneity and
3. deep-learning-based 3D reconstruction algorithm tailored for CAIPIRINHA sampling pattern for high-quality reconstruction.

In particular, 3D deep-learning reconstruction now facilitates acquisitions at 0.8 mm resolution, as compared to our default 1.0 mm-isotropic prescription (Fig. 3).

[1] *Work in progress. The product is still under development and not commercially available. Its future availability cannot be ensured.*

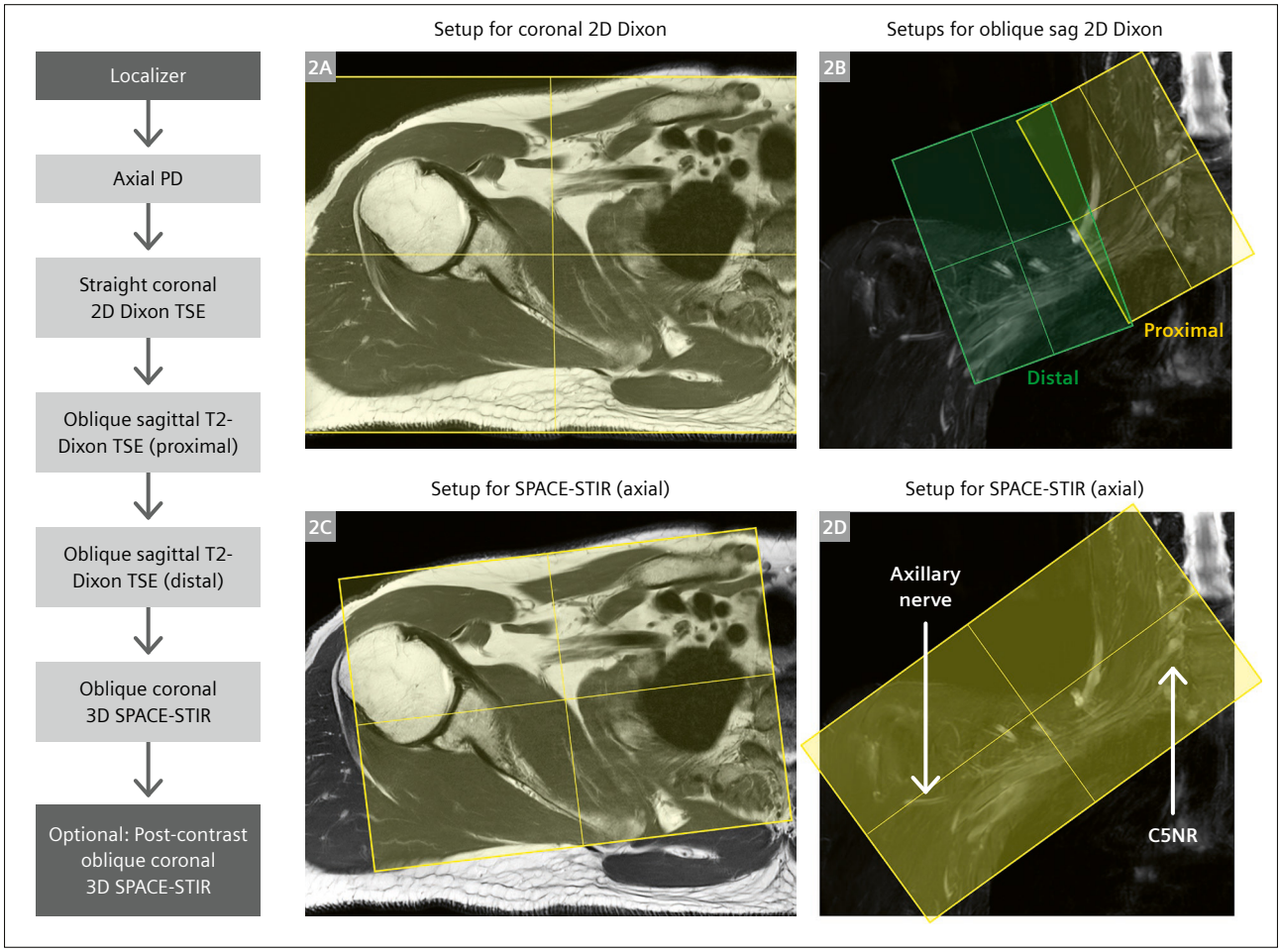

2 Suggested protocol for unilateral BP MRI, and illustration of prescription boxes. From the unilateral axial intermediate-weighted image **(2A)**, the straight coronal Dixon is plotted to cover 'skin-to-skin' (anterior to posterior) at the level of the subclavian vessels. Then two, 2D oblique sagittal T2-weighted Dixon scans are plotted off the coronal Dixon water image for proximal (yellow) and distal (green) coverages **(2B)**; two scans are needed to ensure the images are orthogonal to the BP. Finally, a double-oblique coronal 3D SPACE-STIR is plotted off the axial IW image, parallel to the clavicle **(2C)** and off the coronal Dixon, to include from the C5 nerve root to the axillary region (yellow box as shown in **2D**).

A SPACE-STIR sequence is sometimes acquired following intravenous gadolinium administration to improve vascular suppression, and to visualize small branch nerves of the plexus that may otherwise be obscured by venous contamination (Fig. 4) [5]. Gadolinium shortens the T1 of blood, thus bringing the blood T1 closer to that of fat, and reduces T2 transverse magnetization.

2D MRN

Orthogonal 2D MRN imaging typically provides higher in-plane spatial resolution, compared to 3D sequences, to better evaluate fascicular architecture [6]. However, achieving high in-plane spatial resolution (< 0.5 mm) within a clinically reasonable scan time (to mitigate respiratory motion artifact) while also maintaining adequate SNR poses a significant challenge. The Siemens Healthineers Deep Resolve Boost reconstruction algorithm helps mitigate these challenges by reducing noise amplification or blurring [7], when applying parallel imaging acceleration or partial Fourier acquisition.

Applying fat suppression techniques is also crucial in 2D MRN to enhance the contrast ratio between the peripheral nerves and surrounding fat. We typically employ the Dixon method in this context due to its ability to simultaneously provide homogenous fat suppression (despite field inhomogeneities) and high SNR efficiency. This is particularly important in the neck-shoulder region, which has high B_0-variation. For the 2D Dixon sequence on the MAGNETOM Vida system, one can choose between 'strong' and 'weak' fat suppression modes to modulate the degree to which the fat signal contributes to the MR images. Our preference is the 'strong' option to optimize nerve/muscle and nerve/fat contrast.

Respiratory triggering

Orthogonal imaging planes, particularly those through the infraclavicular segments of the BP, are prone to aliasing from respiratory motion due to the proximity of such segments to the lung apex. Respiratory motion artifacts are sometimes severe and may render the exam uninterpretable. Use of prospective respiratory

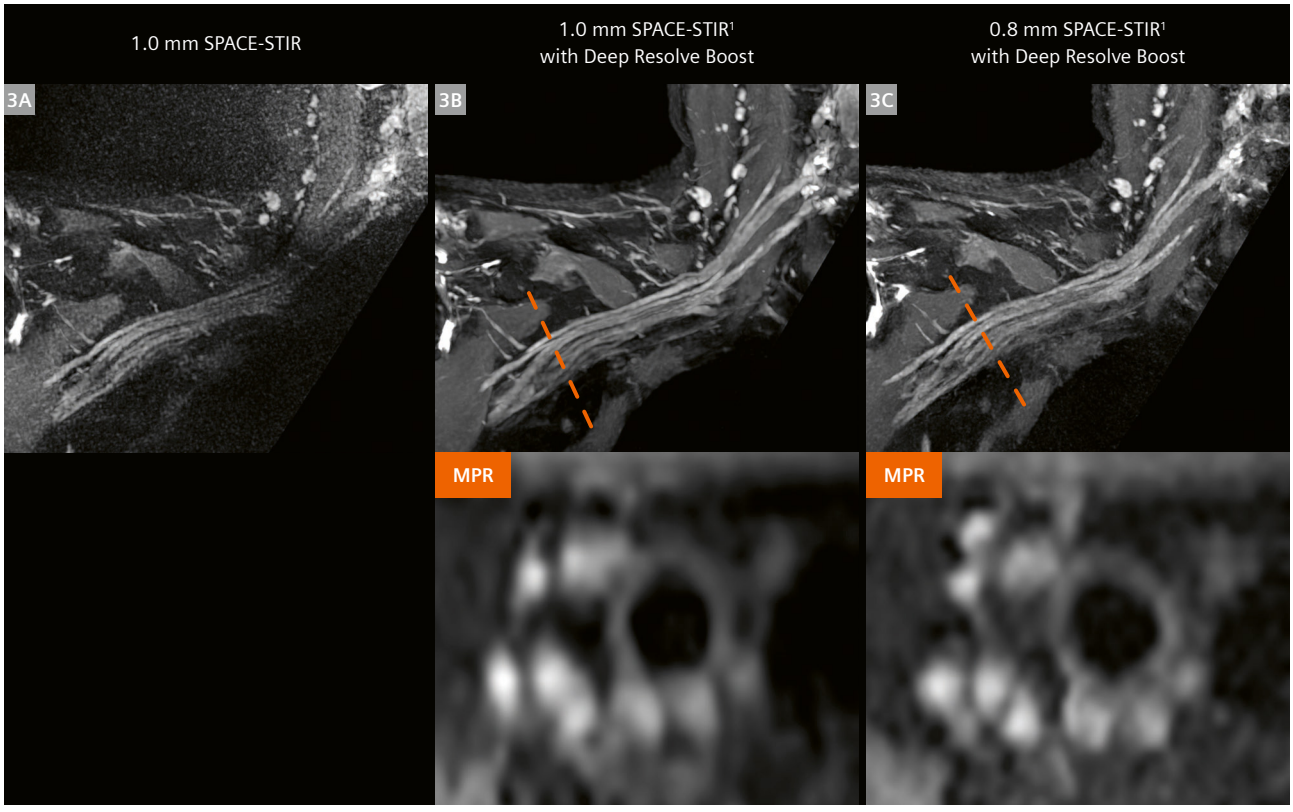

3 Comparison of SPACE-STIR acquired with standard reconstruction and with Deep Resolve (DR) Boost reconstruction. The top row images are all coronal SPACE-STIR images with 10 mm maximal intensity projection (MIP). **(3A)** Standard reconstruction of a 1.0 mm isotropic acquisition exhibits poor conspicuity of the brachial plexus. **(3B)** With DR Boost, improved conspicuity of the nerves is observed. **(3C)** DR Boost with 0.8 mm acquisition is feasible, providing sharper nerve definition, especially in the oblique-axial multiplanar reformation orthogonal to the brachial plexus at the level of the dashed lines (bottom row).

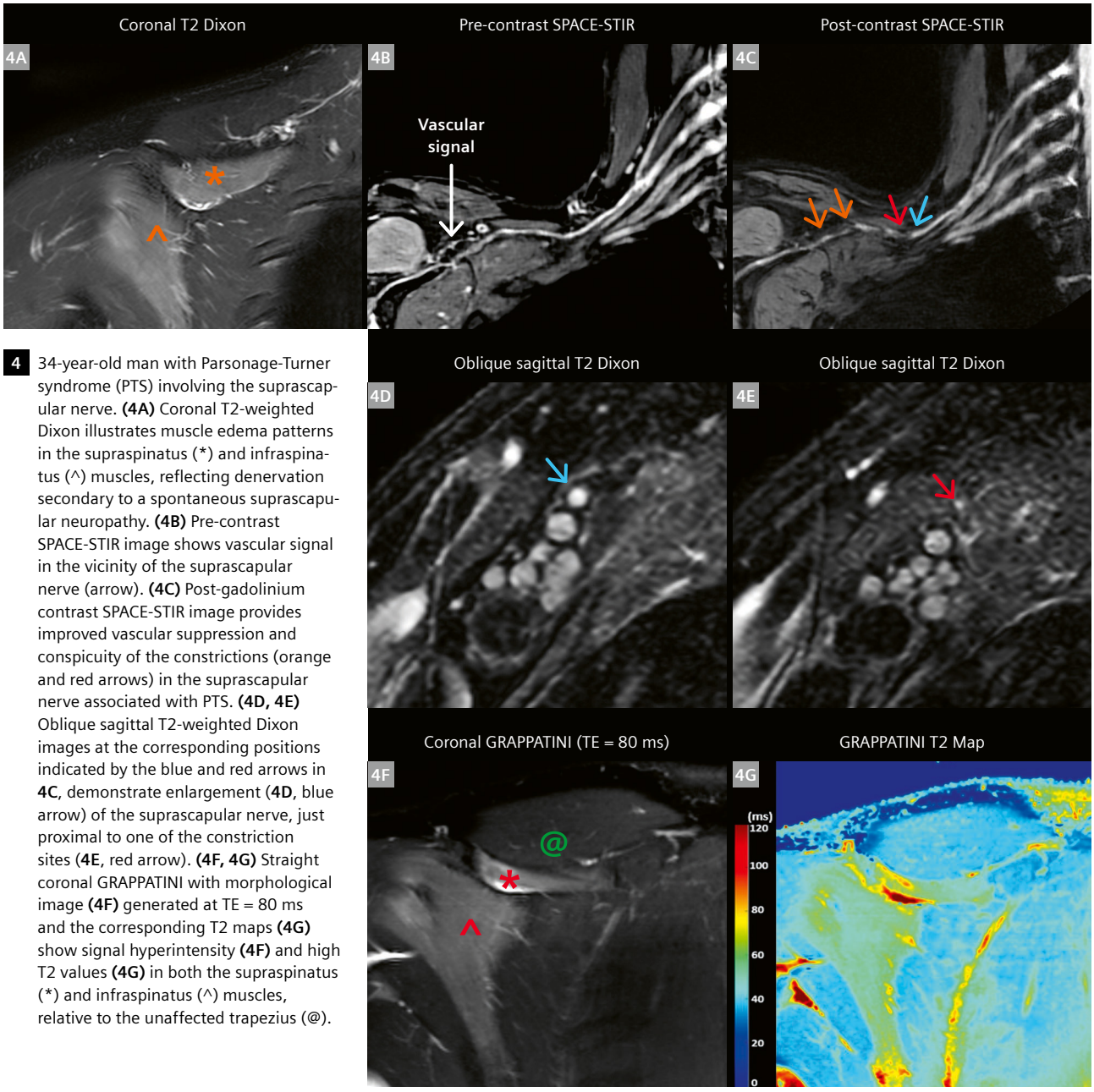

4 34-year-old man with Parsonage-Turner syndrome (PTS) involving the suprascapular nerve. **(4A)** Coronal T2-weighted Dixon illustrates muscle edema patterns in the supraspinatus (*) and infraspinatus (^) muscles, reflecting denervation secondary to a spontaneous suprascapular neuropathy. **(4B)** Pre-contrast SPACE-STIR image shows vascular signal in the vicinity of the suprascapular nerve (arrow). **(4C)** Post-gadolinium contrast SPACE-STIR image provides improved vascular suppression and conspicuity of the constrictions (orange and red arrows) in the suprascapular nerve associated with PTS. **(4D, 4E)** Oblique sagittal T2-weighted Dixon images at the corresponding positions indicated by the blue and red arrows in **4C**, demonstrate enlargement (**4D**, blue arrow) of the suprascapular nerve, just proximal to one of the constriction sites (**4E**, red arrow). **(4F, 4G)** Straight coronal GRAPPATINI with morphological image **(4F)** generated at TE = 80 ms and the corresponding T2 maps **(4G)** show signal hyperintensity **(4F)** and high T2 values **(4G)** in both the supraspinatus (*) and infraspinatus (^) muscles, relative to the unaffected trapezius (@).

triggering via bellows to enable acquisitions during maximal end-expiration has been shown to improve interobserver agreement and nerve conspicuity [8]. On the MAGNETOM Vida, prospective respiratory gating uses the BioMatrix Respiratory Sensor embedded into the posterior spine array. These sensors automatically detect and record respiratory and head movements once the patient is positioned on the table. This feature enhances workflow efficiency by enabling technologists to perform respiratory-triggered scans without incurring additional setup time (Fig. 5). Alternatively, the respiratory signal may also be obtained using the respiratory cushion complete with belt setup where an additional posterior phased-array coil is placed between the patient and the table in the two-coil setup.

Future directions

Quantitative MRI techniques, including T2 mapping, perfusion, and diffusion-weighted or diffusion tensor imaging (DWI/DTI), carry the potential to supplement qualitative BP assessment. A study of patients with chronic inflammatory demyelinating polyneuropathy found that not only were nerve root sizes enlarged but also demonstrated elevated

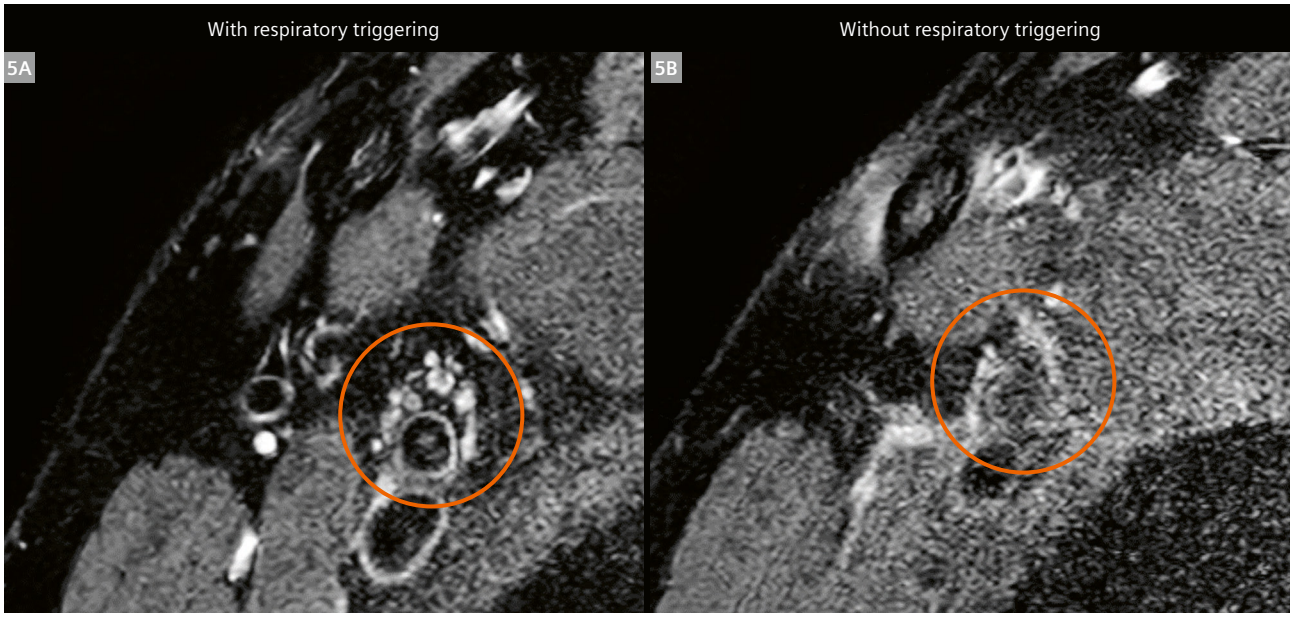

5 Oblique sagittal T2 Dixon imaging through the infraclavicular plexus (distal acquisition), demonstrates improved conspicuity of the cords with prospective respiratory gating (**5A**, using the imbedded BioMatrix Sensors) compared to the non-gated respiratory acquisition **(5B)**. Note that the gated scan requires approximately two minutes longer to acquire.

T2 relaxation times [9]. A quantitative Siemens Healthineers MRI prototype sequence, generalized autocalibrating partially parallel acquisition with the model-based accelerated relaxometry by iterative nonlinear inversion (GRAPPATINI)[1], can provide accurate T2 estimations and synthetic morphologic images [10, 11]. This technique may enable simultaneous qualitative and quantitative evaluation of both nerves and muscles in MR neurography, thereby shortening overall scan time and reducing registration errors between two separate acquisitions (Fig. 4F–G).

References

1 Davidson EJ, Tan ET, Pedrick EG, Sneag DB. Brachial Plexus Magnetic Resonance Neurography: Technical Challenges and Solutions. Invest Radiol. 2023;58(1):14-27.
2 Sneag DB, Queler S. Technological Advancements in Magnetic Resonance Neurography. Curr Neurol Neurosci Rep. 2019;19(10):75.
3 Ordidge RJ, Wylezinska M, Hugg JW, Butterworth E, Franconi F. Frequency offset corrected inversion (FOCI) pulses for use in localized spectroscopy. Magn Reson Med. 1996;36(4):562-566.
4 Wang X, Greer JS, Dimitrov IE, Pezeshk P, Chhabra A, Madhuranthakam AJ. Frequency Offset Corrected Inversion Pulse for B0 and B1 Insensitive Fat Suppression at 3T: Application to MR Neurography of Brachial Plexus. J Magn Reson Imaging. 2018;48(4):1104-1111.
5 Sneag DB, Daniels SP, Geannette C, Queler SC, Lin BQ, de Silva C, et al. Post-Contrast 3D Inversion Recovery Magnetic Resonance Neurography for Evaluation of Branch Nerves of the Brachial Plexus. Eur J Radiol. 2020;132:109304.
6 Sneag DB, Rancy SK, Wolfe SW, Lee SC, Kalia V, Lee SK, et al. Brachial plexitis or neuritis? MRI features of lesion distribution in Parsonage-Turner syndrome. Muscle Nerve. 2018;58(3):359-366.
7 Zochowski KC, Tan ET, Argentieri EC, Lin B, Burge AJ, Queler SC, et al. Improvement of peripheral nerve visualization using a deep learning-based MR reconstruction algorithm. Magn Reson Imaging. 2022;85:186-192.
8 Sneag DB, Mendapara P, Zhu JC, Lee SC, Lin B, Curlin J, et al. Prospective respiratory triggering improves high-resolution brachial plexus MRI quality. J Magn Reson Imaging. 2019;49(6):1723-1729.
9 Hiwatashi A, Togao O, Yamashita K, Kikuchi K, Momosaka D, Nakatake H, et al. Simultaneous MR neurography and apparent T2 mapping in brachial plexus: Evaluation of patients with chronic inflammatory demyelinating polyradiculoneuropathy. Magn Reson Imaging. 2019;55:112-117.
10 Roux M, Hilbert T, Hussami M, Becce F, Kober T, Omoumi P. MRI T2 Mapping of the Knee Providing Synthetic Morphologic Images: Comparison to Conventional Turbo Spin-Echo MRI. Radiology. 2019;293(3):620-630.
11 Wang F, Zhang H, Wu C, Wang Q, Hou B, Sun Y, et al. Quantitative T2 mapping accelerated by GRAPPATINI for evaluation of muscles in patients with myositis. Br J Radiol. 2019;92(1102):20190109.

Contact

Darryl B. Sneag, M.D.
Director of MRI Research & MR Neurography
Hospital for Special Surgery
535 East 70th Street
New York, NY 10021
USA
Tel.: +1 646 714 6043
sneagd@HSS.EDU



[1] *Work in progress. The product is still under development and not commercially available. Its future availability cannot be ensured.*

Clinical Experience with the BioMatrix Beat Sensor: Cardiac MRI Exams Without ECG Leads

Naokazu Mizuno[1]; Yuka Otaki[1]; Akihiro Manabe[2]; Nobuo Iguchi[3]

[1]Department of Radiology, Sakakibara Heart Institute, Tokyo, Japan
[2]Siemens Healthcare K.K, Tokyo, Japan
[3]Department of Cardiology, Sakakibara Heart Institute, Tokyo, Japan

Introduction

ECG gating is essential for performing cardiac MRI examinations. However, the accuracy of cardiac synchronization with ECG gating is significantly influenced by the patient's condition and characteristics, such as their body size, chest hair, cardiac location, motion, and arrhythmia. ECG gating aims to detect the variations in the electric potential of the heart, but it is often difficult to obtain the original ECG waveform due to radio frequency (RF) pulses or magnetic field interference. The BioMatrix Beat Sensor, which was recently launched by Siemens Healthineers, is an innovative technology that can acquire biological information including cardiac activity and diaphragmatic motion without placing ECG leads or respiratory belts. Therefore, this technique is expected to simplify patient preparation and reduce examination time in cardiac MRI examinations and improve the patient experience during the scan.

In this article, we introduce our experience with clinical patients and healthy volunteers who underwent cardiac MRI with the BioMatrix Beat Sensor on a 1.5T MAGNETOM Sola with BioMatrix Body 12-channel and Spine 32-channel coils.

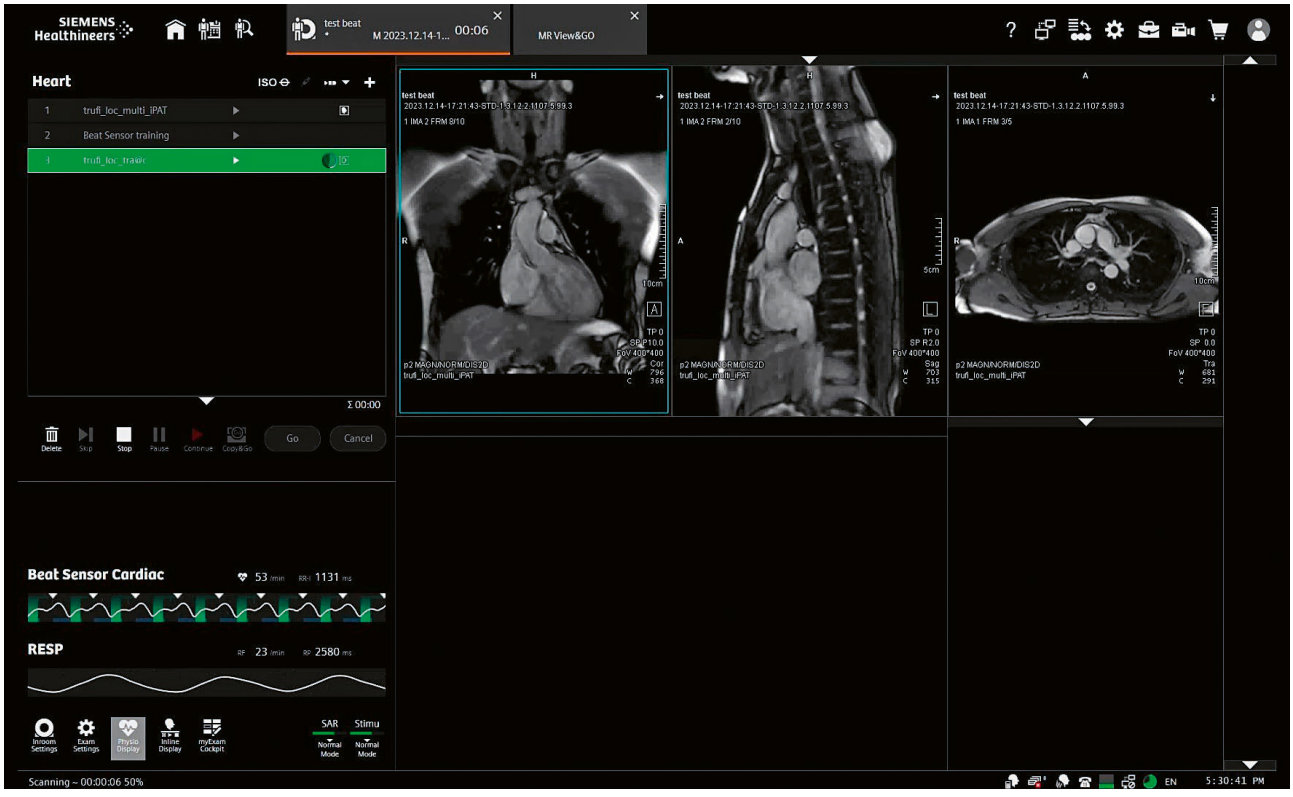

1 BioMatrix Beat Sensor interface for a cardiac MRI scan.

BioMatrix Beat Sensor

Pilot Tone (PT), which was developed based on the principle that a constant RF signal can be modulated by physiological, especially cardiac motion, enables the detection of cardiac motion when the BioMatrix Body coil (Fig. 1) is used. As mentioned earlier, since the Beat Sensor does not require ECG leads placed on chest walls, or respiratory belts, it is expected to improve the clinical workflow of MRI examinations by avoiding preparations involving direct skin contact. This is especially helpful for patients with chest hair. Before imaging with the BioMatrix Beat Sensor, a training scan ("learning") has to be performed to confirm the position of the heart, the appropriate type of coil, and to perform training of the signal processing for isolation of the cardiac signal component und suppression of RF artifacts. After the training scan, the trigger source Beat Sensor can be applied to all imaging protocols including cine, T2-weighted, myocardial mapping, and late gadolinium enhancement (Fig. 2). For comparison, in general, a vectorcardiography-based QRS detection algorithm is used for ECG gating, which aims to detect the R-wave at its peak by recognizing the R-wave's rising edge. However, the timing of cardiac triggers detected by the Beat Sensor is about 200 milliseconds delayed with respect to the R-wave, which is detected by ECG triggering. Triggering with the Beat Sensor in the acceleration phase of the cardiac contraction and subsequent low pass filter processing both contribute to this delay [1] (Fig. 3).

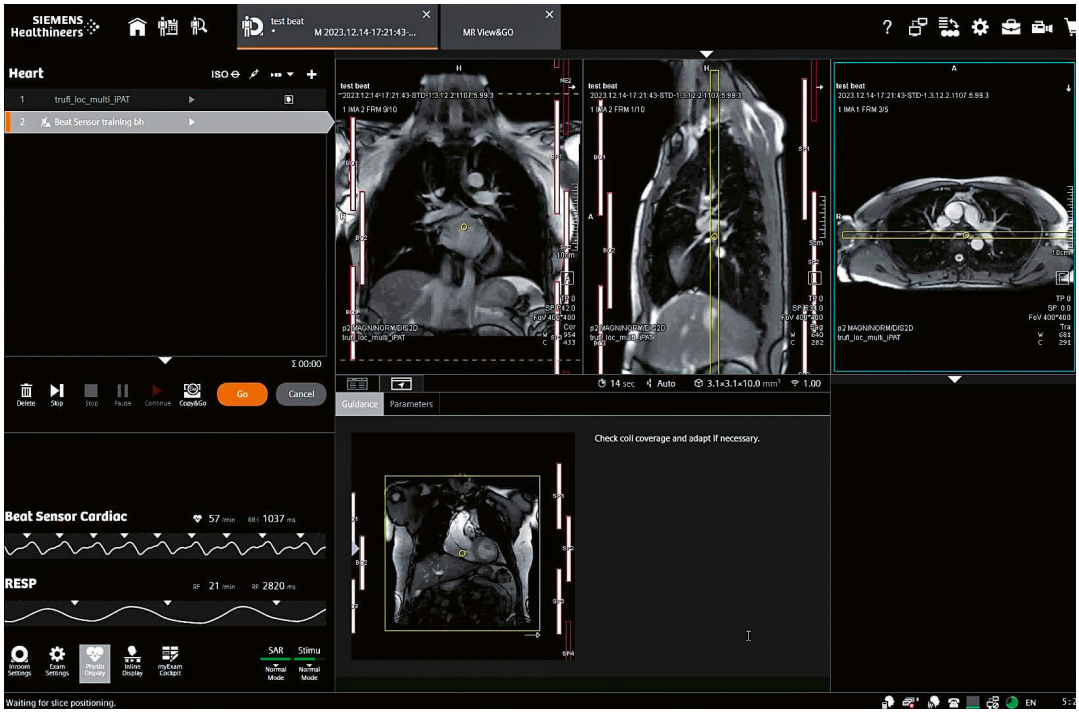

2 BioMatrix Beat Sensor interface for a training scan.

PT Cardiac trigger time and display

- Trigger ( ) in acceleration phase @ early mid-systole
- Calibration: take distance from trigger to previous signal maximum

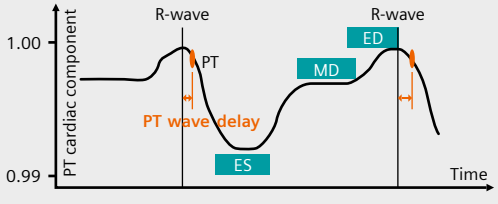

- Delay is considered for ED planning
- if PPG is present, PPG delay is determined as well

Display inverted derivative

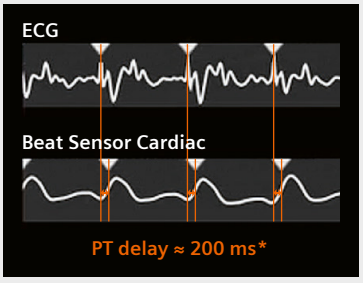

*PT delay = PT wave delay + filter delay
≈ 100 ms ≈ 100 ms

3 PT signal characteristics and trigger time point [1].

Left ventricular functional analysis in healthy volunteers

In 8 healthy volunteers, we compared left ventricular (LV) volumes derived by the Beat Sensor to those derived by ECG gating. We found that there were no significant differences in end-diastolic (EDV) and end-systolic volumes (ESV) between the two groups (not shown). The beginning of the LV volume filling curves recorded by the Beat Sensor was delayed by approx. 200 milliseconds as previously estimated [1] (Fig. 4). These characteristics of the Beat

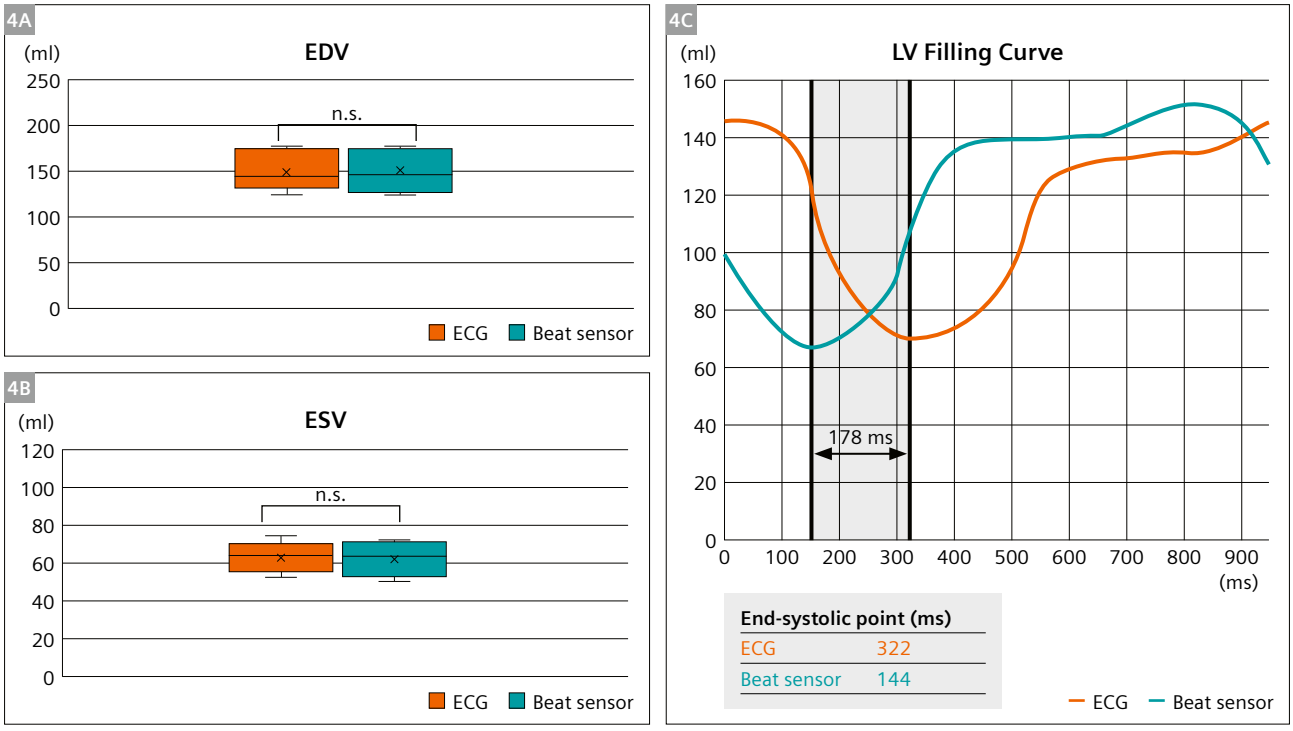

4 LV volume and filling curves in healthy volunteers undergoing cine cardiac MRI with Beat-Sensor and ECG gating. **(4A)** EDV, **(4B)** ESV, and **(4C)** example of LV filling curves. EDV = end-diastolic volume, ESV = end-systolic volume.

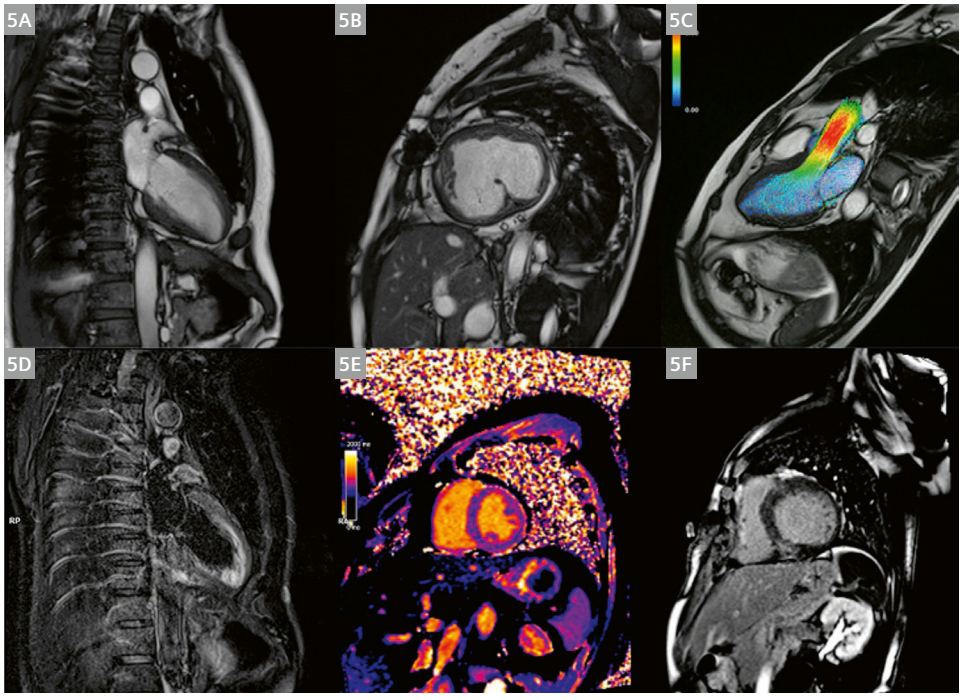

5 Example images of cardiac MRI with the BioMatrix Beat Sensor. Cine imaging, 4D-flow imaging, and T1 mapping using the Beat Sensor in a healthy volunteer are shown in Figures **5A**, **5C**, and **5D**, respectively. Figure **5B** shows cine imaging in a case with a single ventricle, and **5F** shows MOCO PSIR for the hypertrophic cardiomyopathy patient.

Sensor should be kept in mind, especially when scanning still-imaging protocols such as T2-weighted and myocardial mapping, and late-gadolinium enhancement with manual positioning of the scan window, which are often scanned in diastole.

Clinical patients

In our experience, reading physicians could adeptly evaluate cardiac motion through cine imaging and could conduct tissue characterization via myocardial mapping and late gadolinium enhancement, thereby effectively addressing the majority of clinical cases. Notably, the Beat Sensor has reliably achieved cardiac synchronization in a wide spectrum of cases, including patients with hypertrophic cardiomyopathy, complex congenital heart disease, and reduced ejection fraction (Fig. 5). Our observations extend published results of successful cardiac synchronization [2, 3] also to patients with arrhythmias, high heart rates, and pacing rhythms (Fig. 6). In an overweight patient [4] the Beat Sensor signal was more easily disturbed by other contributions, e.g., patient motion, but trigger time points corresponded very well to ECG (Fig. 7C).

In a newborn[1] the Beat Sensor training failed, resulting in unreliable triggering (Fig. 7A), likely due to the high heart rate and large size of coil elements of the BioMatrix Body 12. Figure 7 also shows results in patients with Wolff-Parkinson-White syndrome, bigeminy, and complete atrioventricular (AV) block.

[1] *Siemens Healthineers disclaimer: MR scanning has not been established as safe for imaging fetuses and infants less than two years of age. The responsible physician must evaluate the benefits of the MR examination compared to those of other imaging procedures. Note: This disclaimer does not represent the opinion of the author.*

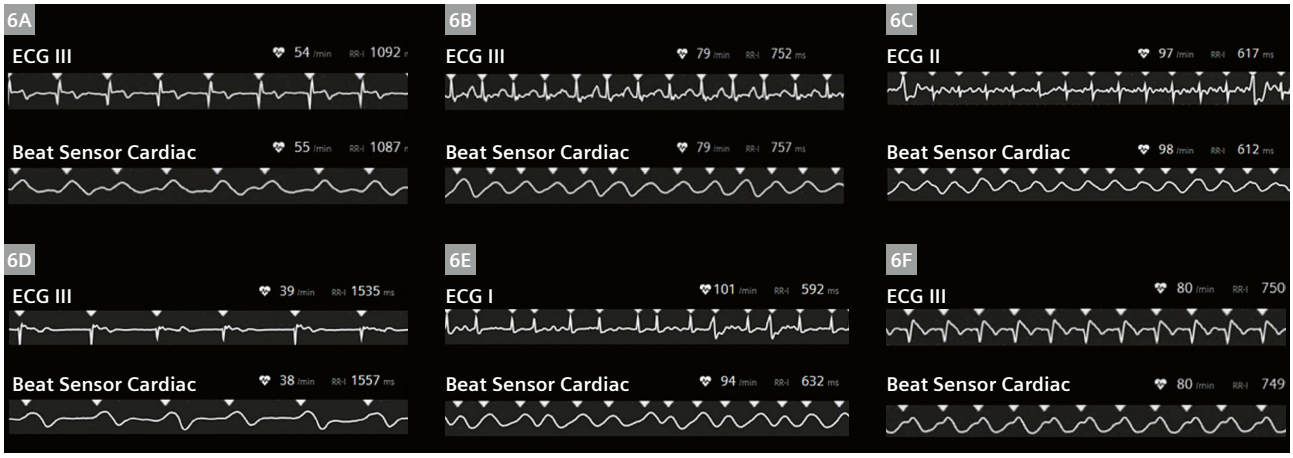

6 ECG waveform during cardiac MRI with ECG gating and the BioMatrix Beat Sensor. ECG waveform in patients with hypertrophic cardiomyopathy **(6A)**, a single ventricle **(6B)**, a reduced LV ejection fraction **(6C)**, atrial fibrillation with low heart rates **(6D)**, atrial fibrillation with high heart rates **(6E)**, and pacing rhythm (DDD implantation) **(6F)**.

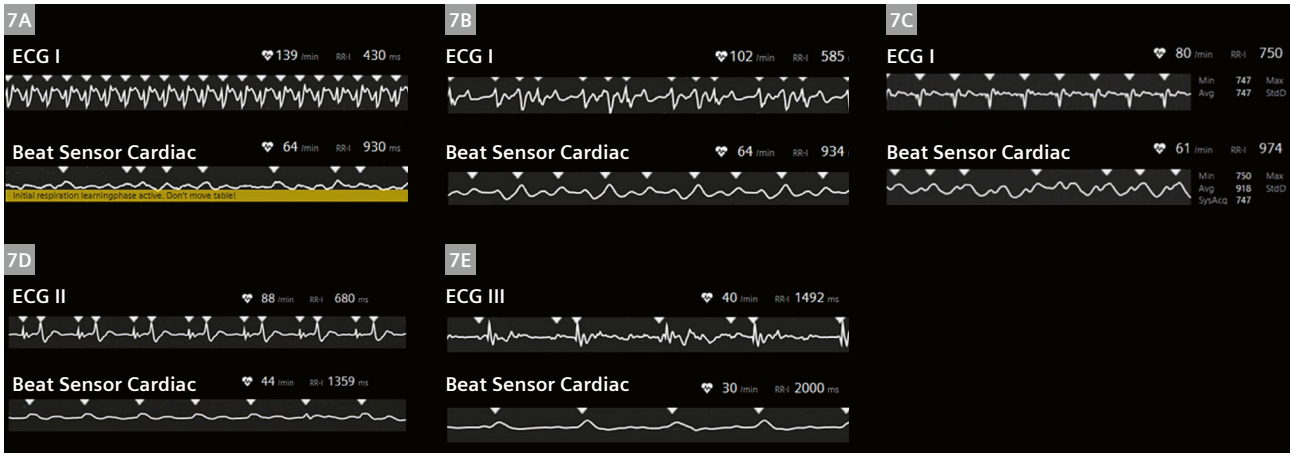

7 ECG waveform during cardiac MRI with ECG gating and the BioMatrix Beat Sensor. ECG waveform during cardiac MRI with ECG gating and the Beat Sensor in a newborn[1] with high heart rate **(7A)**, and in patients with Wolff-Parkinson-White syndrome **(7B)**, overweight **(7C)**, bigeminy **(7D)**, and complete AV block **(7E)** are shown.

The advantages of the BioMatrix Beat Sensor

Using the BioMatrix Beat Sensor provides a crucial advantage, in that it enables cardiac MRI scans even in challenging scenarios, such as with arrhythmias or difficulties in breath-holding, which are difficult conditions for ECG gating. Further, by conducting a preparatory training scan, the Beat Sensor facilitates imaging with both breath-holding and free breathing. Additionally, after the training, the operator can simply switch between ECG and Beat Sensor gating, eliminating the need for extra settings or preparation.

Cardiac MRI examinations do not aim to detect waveforms that detect the electrical potential difference of the heart. Rather, they aim to assess cardiac motion and perform tissue characterization. In our experience cardiac synchronization with the Beat Sensor is sufficient for these exams. ECG gating may not only acquire cardiac signals from heart motion, but also subtle electrical signals generated by muscles or arrhythmias, which can often cause reduced imaging quality. Since the Beat Sensor directly detects the heartbeat, it enables scanning at the cardiac phase without cardiac motion, especially for still cardiac imaging.

In the following section, we present clinical cases with bigeminy and complete atrioventricular block, for which the Beat Sensor provided efficient cardiac MRI scanning.

1. Bigeminy

Bigeminy is a cardiac arrhythmia that repeats ventricular premature contraction (VPC) every other beat. When patients with bigeminy are scanned with ECG triggering, all R-waves including VPCs are triggered, which results in motion artifacts. Motion artifacts can influence image quality and the values of the resulting quantitative parameters in cine imaging, T1, T2 mapping, and late gadolinium enhancement. Like the Beat Sensor, ECG gating includes retrospective and prospective gating. When scanning arrhythmic patients with ECG gating, a cardiac arrhythmia detection function with retrospective gating can be performed to remove the arrhythmia dataset during the preset R-R interval. However, the arrhythmia detection function involves determining the appropriate phase manually, especially in the case of bigeminy. Although prospective ECG gating is useful for severe cardiac arrhythmia, it is impossible to capture cardiac information during the entire cardiac cycle. When using the Beat Sensor, it is possible to accurately trigger the timing of the diastolic phase without detecting small contractions related to VPC (Fig. 8). Beat Sensor skipped every second trigger, thus the cine contained one bigeminy period (2 heart beats) and resolved both the short and long cardiac cycle. Interestingly, an LV filling curve could be generated for the case with bigeminy, which can be distorted with ECG gating. The resulting LV filling curve can be seen in Figure 9.

2. Complete atrioventricular block

Complete atrioventricular (AV) block is a type of arrhythmia characterized by an incomplete electrical AV dissociation, with independent atrial and ventricular rates, which are often seen in patients with coronary artery disease or cardiac sarcoidosis undergoing cardiac MRI. As atria and ventricles function independently of each other during imaging with a complete AV block, all R-waves, including irregular R-waves, generate ECG triggers, thus diastolic imaging is impossible. Since the Beat Sensor is sensitive to the contractile motion of the heart, and generates triggers only after irregular R-waves. Therefore the Beat Sensor allows to synchronize acquisition to the diastole for still imaging. In the example with complete AV block in Figure 10, Beat-Sensor triggering was successful in acquiring interpretable images from a motion-corrected phase-sensitive inversion recovery (MOCO PSIR) acquisition and acts as an automatic arrhythmia detection function.

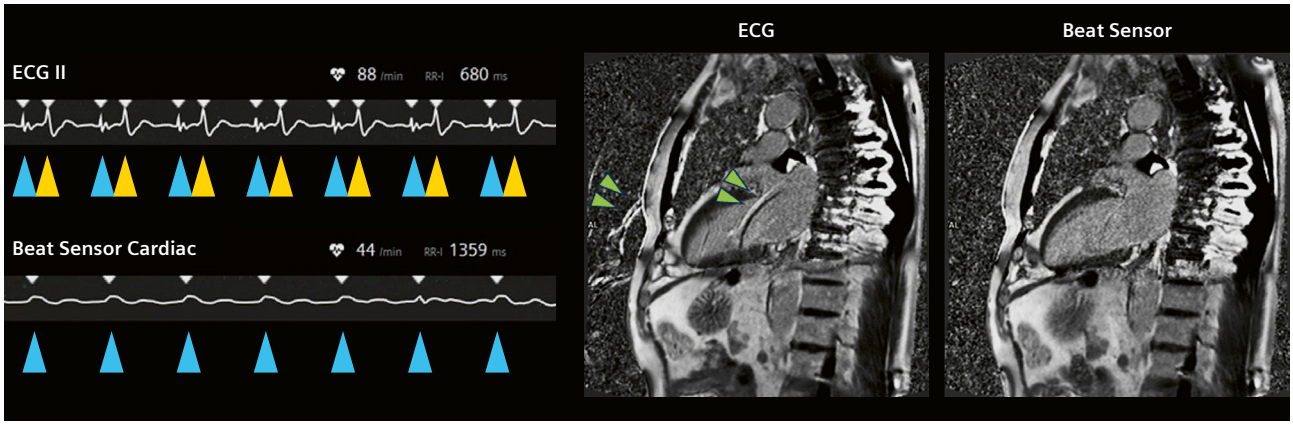

8 Comparison of late gadolinium enhancement images in a patient with bigeminy with ECG gating and the BioMatrix Beat Sensor. There is a motion artifact (green arrow) in late gadolinium imaging of the VPC patient using ECG gating, but no motion artifact with the Beat Sensor.

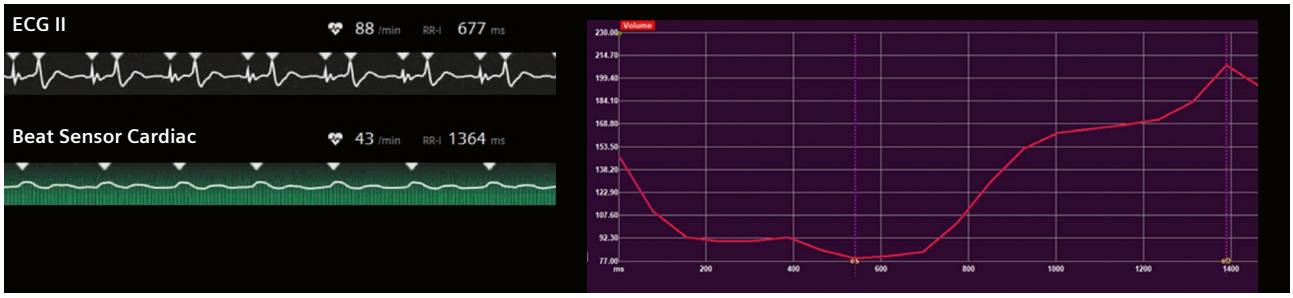

9 LV filling curve in a patient with bigeminy.

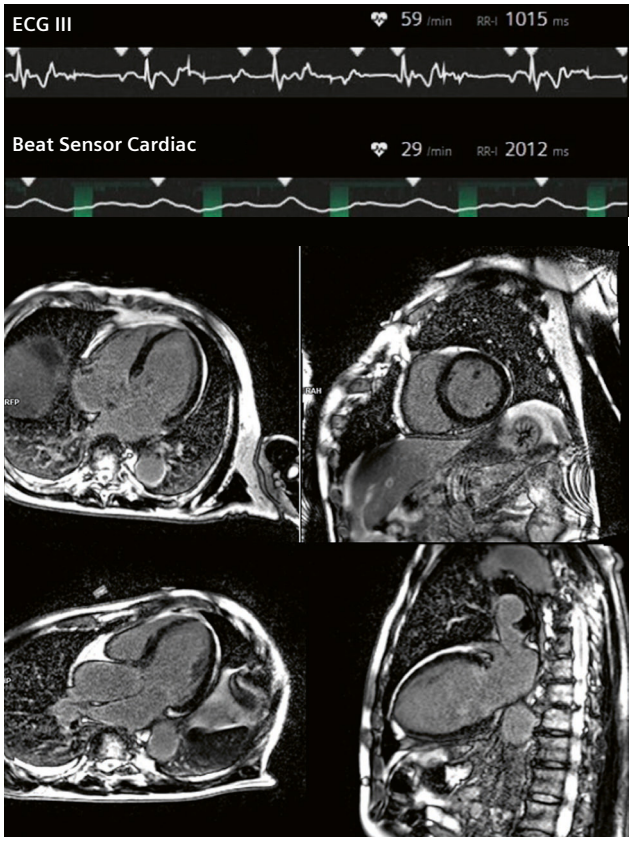

10 BioMatrix Beat Sensor with MOCO PSIR (free breathing). The Beat Sensor enabled capturing diastole with MOCO PSIR for the patient with complete atrioventricular block.

Conclusion

BioMatrix Beat Sensor is a new technology that enables cardiac MRI examinations without the need for ECG leads. Not only does it eliminate the need for electrodes and the discomfort of tape irritation and direct skin contact, but it also frees up technologists by streamlining the clinical workflow. By directly detecting cardiac motion, the Beat Sensor introduces novel cardiac synchronization with advantages in handling arrhythmic patient that were unattainable with ECG gating. Its efficacy warrants validation across multiple facilities to enhance clinical workflows by offering substantial support in advanced cardiac MR imaging.

References

1 Speier P, Bacher M. Skip the Electrodes, But Not A Beat: The Engineering Behind the Beat Sensor. MAGNETOM Flash. 2023;83(2):106–117. Available at https://www.magnetomworld.siemens-healthineers.com/clinical-corner/case-studies/biomatrix-beat-sensor
2 Lin K, Sarnari R, Speier P, Hayes C, Davids R, Carr JC, Markl M. Pilot Tone-Triggered MRI for Quantitative Assessment of Cardiac Function, Motion, and Structure. Invest Radiol. 2023;58(3):239-243.
3 Pan Y, Varghese J, Tong MS, Yildiz VO, Azzu A, Gatehouse P, et al. Two-center validation of Pilot Tone Based Cardiac Triggering of a Comprehensive Cardiovascular Magnetic Resonance Examination. Res Sq [Preprint]. 2023:rs.3.rs-3121723. doi: 10.21203/rs.3.rs-3121723/v1.
4 Karamarkou C, Thielmann C. Clinical Approach of BioMatrix Beat Sensor Cardiac Triggering. MAGNETOM Flash. 2023;83(1):7–10.
5 Axel L, Bhatla P, Halpern D, Magnani S, Stojanovska J, Barbhaiya C. Correlation of MRI premature ventricular contraction activation pattern in bigeminy with electrophysiology study-confirmed site of origin. Int J Cardiovasc Imaging.2023. 39:145–152. doi.org/10.1007/s10554-022-02707-8.
6 Chen C, Liu Y, Simonetti OP, Tong M, Jin N, Bacher M, et al. Cardiac and respiratory motion extraction for MRI using Pilot Tone – a patient study. Accepted at The International Journal of Cardiovascular Imaging. Eprint at arXiv:2202.00055.
7 Falcão MBL, Di Sopra L, Ma L, Bacher M, Yerly J, Speier P, et al. Pilot tone navigation for respiratory and cardiac motion-resolved free-running 5D flow MRI. Magn Reson Med. 2022;87(2):718-732.



Contact

Naokazu Mizuno, RT
Sakakibara Heart Institute
Department of Radiology
Asahi-cho 3-16-1, Fuchu-shi
Tokyo, 183-0003
Japan
Tel: +81 24-314-3111
Fax: +81 24-314-3199
nmizuno@shi.heart.or.jp

Can We See the Bottom? A Look into Deep Learning-Based Image Reconstruction

Dominik Nickel, Ph.D.

Principal Key Expert for Sequence and Reconstruction Techniques, Siemens Healthineers AG, Erlangen, Germany

In 2016, machine-learning pioneer Geoffrey Hinton suggested that "people should stop training radiologists now. It's just completely obvious within five years deep learning is going to do better than radiologists." Even though this has not happened so far and is unlikely to happen in the foreseeable future, the impact of deep learning on radiology and the way imaging is performed and interpreted is undeniable. For MR imaging (MRI), it has turned out that image reconstruction can benefit hugely from the inclusion of trained components and can generate better images from fewer data. Initial works on deep learning-based image reconstruction started around the time of Hinton's comment [1, 2]. With its capability to push MRI toward higher resolution, higher signal-to-noise, and/or shorter acquisition time, it only took a few years for the technique to transition from technical research into commercially available products that are widely used in clinical routine.

The fast clinical transition combined with the reputation of neural networks for being black boxes understandably raises questions and concerns about the loss or masking of relevant information and the hallucination of "beautiful" but false images. Users would like to have a better understanding of how the technique works, why it enables a significant performance improvement regarding image quality, and where its limitations are. Even though answering these questions about deep learning applications is generally difficult, it is important to be more explicit about the specific type of architecture being referred to. After various approaches were explored, the "physics-based" or "physics-informed" reconstructions have prevailed for generating an image from raw *k*-space data. This class of reconstructions is characterized by the fact that a conventional parallel imaging model is combined with trainable components that take care of image enhancement.

Physics-informed reconstructions

The idea of combining parallel imaging and image enhancement is not new. It is also a central aspect of Compressed Sensing (CS) as used in MRI. For Compressed

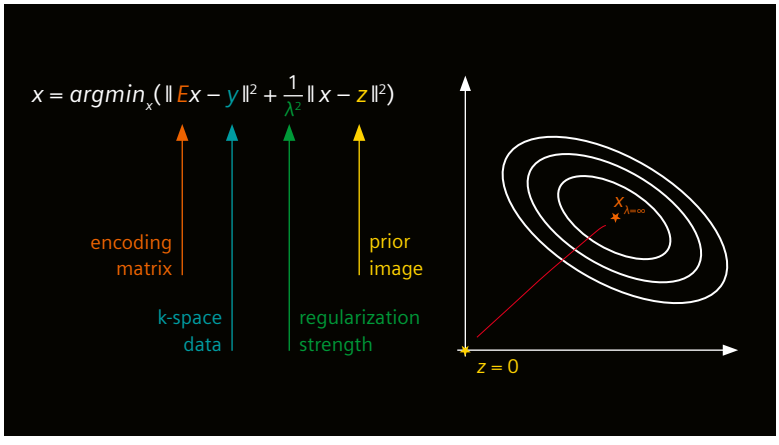

1 Illustration of regularized SENSE as a quadratic optimization problem, involving a data consistency term that relates the image x to k-space data y using an encoding matrix E involving sampling mask, Fourier transformation, and coil sensitivity maps. The data consistency term is balanced by a quadratic regularization involving a prior image z that is assumed to be zero. The definition of the regularization strength λ is such that the reconstruction provides images close to the prior for small values and close to the unregularized SENSE reconstruction for high values of λ. Therefore, the trajectory of solutions for varying regularization strength λ starts from the prior image and steps toward the minimum of the data consistency term.

Sensing, the reconstructed image is obtained by iteratively solving an optimization problem which includes a data consistency term based on a parallel imaging model and image regularization terms. Deep learning-based reconstructions (DLR) are often inspired by an explicit, iterative algorithm that is used for this kind of optimization. However, the connection to an optimization problem is removed in DLR, and some processing steps are replaced by trainable components. This is referred to as an unrolled architecture. Most notably, image regularizations are typically replaced by neural networks. As such, Compressed Sensing reconstructions may be considered a special case of a physics-informed deep learning reconstruction as they are in the space of allowed configurations that can be obtained through training. But there is a large space of possible configurations, such that the heuristically designed versions employed in Compressed Sensing are unlikely to be picked.

Once an architecture is specified, the optimal parameters need to be determined. This is where the data-driven aspect of deep learning comes in. The most established approach is supervised training based on fully sampled acquisitions serving as ground truth. For typically thousands of such datasets, a desired target image is generated. Furthermore, inputs that mimic an accelerated acquisition are synthesized. Additional inputs such as coil sensitivity maps needed for the parallel imaging component may be provided. The network parameters are then obtained by established training methods that stochastically optimize the model parameters by comparing the network output to the desired target using a similarity metric or loss function. Training typically lasts multiple days on dedicated GPU servers. Once finished, the obtained configuration or model parameters can be exported for prospective use on a scanner. Prospective execution has a numerical demand similar to an iterative reconstruction and is usually done on integrated GPUs.

A conceptionally intuitive network architecture

To gain insight into the performance of deep learning-based image reconstruction, an architecture that allows direct connection to parallel imaging and image-based denoising is presented in the following.

Starting off with conventional parallel imaging, a regularized SENSE [3] reconstruction is illustrated in Figure 1. Already in this reconstruction, an additional regularization term is introduced that allows to condition the inversion of the linear problem when the parallel imaging acceleration becomes too large for the available coil configuration.

At this point, it is worth mentioning the *g*-factor, which is often used to describe the additional local noise amplification in parallel imaging. It is sometimes suggested that the *g*-factor is purely determined by the acquisition and its acceleration. This is not correct because, for instance, a zero-padded Fourier transformation corresponds to ideal noise propagation and a *g*-factor of '1'. Of course, this is with unacceptable aliasing, but artifacts are not reflected in the *g*-factor. Any practical parallel imaging reconstruction therefore includes a regularization that helps to limit the noise amplification. The definition of the regularization strength λ in Figure 1 is such that it is also an upper bound on the noise amplification or *g*-factor. In that sense, it is interpretable, which will become relevant below. At the same time, λ is the step size on the trajectory from the prior image toward the unregularized SENSE reconstruction. Figure 2 shows a comparison of two reconstructions with and without regularization using aggressive retrospective acceleration. It is apparent that a regularization is required to reduce noise amplification, i.e., to restrict the *g*-factor.

Given a test dataset that is later also used for more involved networks, a first experiment is to evaluate metrics between regularized SENSE reconstructions and expected targets from the fully sampled acquisition as a function of



2 Unregularized SENSE reconstruction **(2A)** and regularized SENSE reconstruction with λ = 4 **(2B)** from retrospectively subsampling a fully sampled acquisition **(2C)**. The retrospective acceleration factor is 2 × 2 in AP and HF direction, deliberately chosen to be too aggressive for the given coil setup.

the regularization strength. This is presented in Figure 3. Interestingly, the best results are not achieved for the unregularized SENSE, but depending on acceleration and chosen metric for regularization strengths on the order of 5. Determining the optimal regularization this way may already be considered a machine learning reconstruction – possibly the simplest conceivable one, and with unimpressive performance.

For deep learning-based reconstruction, image-to-image networks are typically included for the enhancement of intermediate images. In the simplest case, this may be a denoising network after a parallel imaging reconstruction. A more general approach that alternates between parallel imaging reconstruction and deep learning-based enhancement is depicted in Figure 4.

The basic idea is to have regularized SENSE reconstructions where the regularization strength steps from a current prior image toward the unregularized SENSE reconstruction. The step sizes are then determined through training, and the network estimates the next prior image from the result of the previous SENSE reconstruction. So the task of the network appears constrained and the conventional parallel imaging reconstruction is a subset of the training architecture. Another advantage is that there is no requirement to have a larger number of iterations to ensure convergence. This is ensured by using the regularized SENSE reconstruction as an update mechanism.

To evaluate the potential of such an architecture, an unrolled network with 6 iterations and conventional U-nets [4] was set up and trained using about 5,000 training pairs from about 500 acquisitions. On the same test datasets used in Figure 3, the finally obtained reconstruction achieved PSNR values of 37.7 dB and 36.5 dB, as well as SSIM values of 0.93 and 0.92 for a retrospective acceleration of 4 and 6, respectively. This outperforms the conventional reconstruction drastically. In Figure 5, an example image is shown on the left, which visually comes close to the ground truth.

Most notably, the noise amplification in the center of the image and associated with an increased *g*-factor seems to be absent. This is a rather general behavior observed for unrolled, deep learning-based reconstructions. Some insight can be obtained when looking at the regularization strengths at each iteration. These are stated in Table 1.

It is apparent that the training leads to a parameterization where the first iterations perform a weakly regularized parallel imaging reconstruction whose output is taken to estimate the following prior using a neural network.

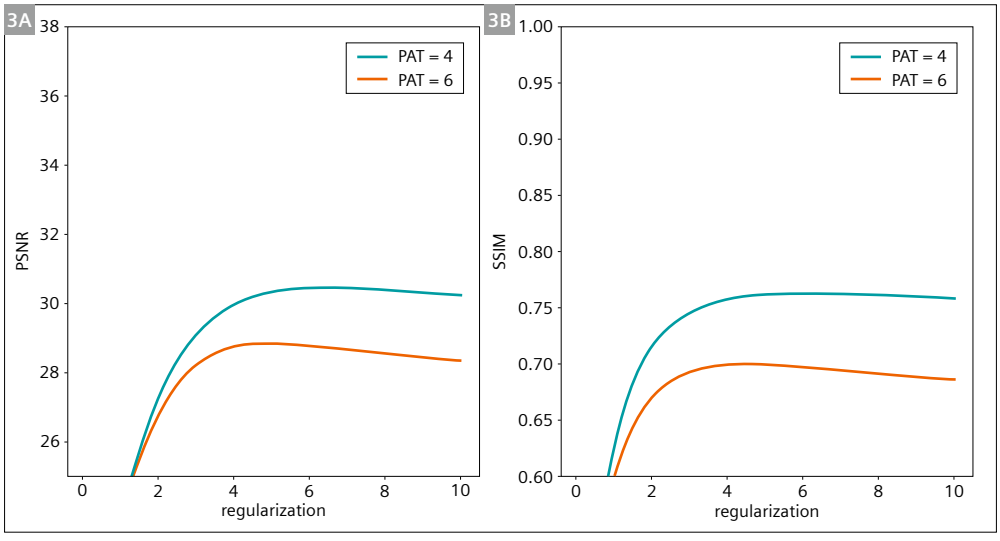

3 Average peak signal-to-noise ratio (**3A**, PSNR) and structural similarity index measure (**3B**, SSIM) of test datasets with retrospective subsampling with acceleration 4 (petrol) and 6 (orange) as a function of the regularization strength.

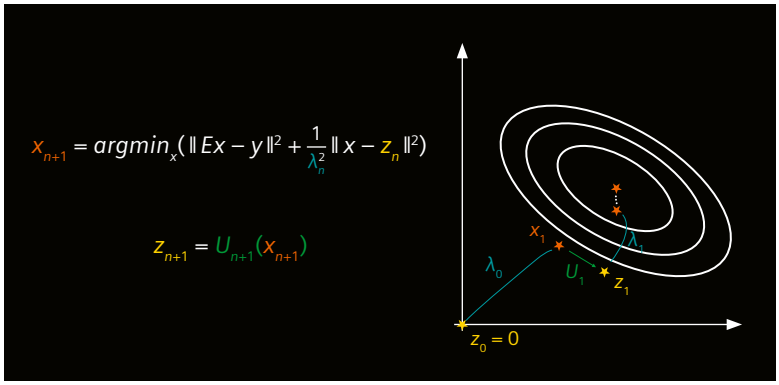

4 Illustration of an unrolled deep learning-based reconstruction that starts from a vanishing prior imaging ($z_0 = 0$) and then performs iterations comprising a regularized SENSE reconstruction followed by the estimation of a new image prior using a neural network U_n. The number of iterations is fixed. The regularization strengths for each iteration and the model parameters of the neural networks form the trainable parameters. The output of the final network is taken as the reconstructed image. The diagram on the right sketches a trajectory of the iterations through the image domain with indicated ellipsoidal hypersurfaces of the data consistency term.



5 Prediction of an unrolled network with 6 iterations **(5A)**, and regularized SENSE reconstruction with λ = 4 **(5B)** from retrospectively subsampling a fully sampled acquisition **(5C)**.

λ_1	λ_2	λ_3	λ_4	λ_5	λ_6
7.05	7.05	3.91	1.85	1.11	0.91

Table 1: Regularization strengths for each iteration of a trained network with 6 iterations.

Therefore, the reconstruction quickly comes close to solutions with acceptable data consistency. In the latter iterations, the steps toward the unregularized SENSE solution become smaller. Here, the conditioning of the data consistency starts to become more relevant. Areas with small noise propagation are also better conditioned, such that the step sizes affect the image more and make sure that the image is consistent with the data consistency. At the same time, this also restricts the solution in regimes with worse conditioning, and the image regularization has more influence there. Therefore, the last iterations mostly help to improve the image quality in the less well-conditioned regions, and the noise appearance in the final reconstruction is much more homogenous.

The presented behavior therefore gives a reasonable explanation for the significantly improved performance of unrolled deep learning-based reconstructions compared to pure post-processing approaches. Alternating between data consistency based on a parallel imaging model and deep learning-based image enhancement allows to iteratively optimize the output of the reconstruction. This is also a reasonable explanation for why the approach generalizes surprisingly well, or rather why it is less dependent on the image content seen during training, as the architecture is highly incentivized to be consistent with a physical model with freedom mostly for the ill-conditioned domains. This freedom seems to be in local image enhancement such as denoising and edge preservation, meaning that topics like hallucination have so far not surfaced for physics-informed deep learning-based image reconstructions. The magical aspect that remains unexplained is the performance of the individual neural networks for image enhancement. This is a general aspect of deep learning and is outside of the scope of this paper.

Validation of deep learning-based image reconstruction

Even though the performance of deep learning-based image reconstruction can be explained to some extent, it needs to be validated with care. Currently, the transition into clinical routine is focused on improving established sequence types and contrasts. Therefore, clinical evaluations that use qualitative and quantitative metrics for comparison to the established clinical sequences are typically used to establish evidence [5].

References

1 Hammernik K, Klatzer T, Kobler E, Recht MP, Sodickson DK, Pock T, et al. Learning a Variational Network for Reconstruction of Accelerated MRI Data.
Magn Reson Med. 2018;79(6):3055–3071. Epub 2017 Nov 8.
2 Schlemper J, Caballero J, Hajnal JV, Price AN, Rueckert D. A Deep Cascade of Convolutional Neural Networks for Dynamic MR Image Reconstruction.
IEEE Trans Med Imaging. 2018;37(2):491–503. Epub 2017 Oct 13.
3 Pruessmann KP, Weiger M, Scheidegger MB, Boesiger P. SENSE: sensitivity encoding for fast MRI.
Magn Reson Med. 1999;42(5):952–62.
4 Ronneberger O, Fischer P, Brox T. U-net: Convolutional networks for biomedical image segmentation. In: Navab, N, Hornegger, J, Wells, W, Frangi, A (eds) Medical Image Computing and Computer-Assisted Intervention – MICCAI 2015. 18th International Conference, Munich, Germany, October 5–9, 2015, Proceedings, Part III.
Springer International Publishing. pp. 234–241.
5 Afat S, Ursprung S, Herrmann J, Brendlin A, Werner S, Lingg A, et al. Deep Learning-based reconstruction in clinical MRI – How we do it in Tübingen. MAGNETOM Flash. 2024;87(2):14–25.



Contact

Dominik Nickel, Ph.D.
Siemens Healthineers AG
SHS DI MR RCT CLS BODY
Karl-Schall-Str. 6
91052 Erlangen
Germany
marcel.nickel@siemens-healthineers.com

Phase-Resolved Functional Lung (PREFUL) MRI of Ventilation and Perfusion in Premature Infants

Jonathan P. Dyke, Ph.D.[1,2]; Andreas Voskrebenzev, Ph.D.[3,4]; Filip Klimeš, Ph.D.[3,4]; Jens Vogel-Claussen, M.D.[3,4]; Robert Grimm, Ph.D.[6]; Arzu Kovanlikaya, M.D.[2]

[1]Citigroup Biomedical Imaging Center, Weill Cornell Medicine, New York, NY, USA
[2]Department of Radiology, Weill Cornell Medicine, New York, NY, USA
[3]Institute of Diagnostic and Interventional Radiology, Hannover Medical School, Hannover, Germany
[4]Biomedical Research in End-Stage and Obstructive Lung Disease (BREATH), Member of the German Center for Lung Research (DZL), Hannover, Germany
[5]Department of Pediatrics, Weill Cornell Medicine, New York, NY, USA
[6]Siemens Healthineers, Erlangen, Germany

Introduction

Challenges of lung MRI

Imaging the lung via MRI has proven challenging in the past due to several caveats. The bulk magnetization signal obtained in MRI is related to: $M_0 \sim PD\ \gamma^2\ B_0/T$ where PD represents the proton density of ^1H in the voxel, γ the gyromagnetic ratio, and B_0 the strength of the main magnetic field. Assuming that most soft tissues of interest (brain, muscle, etc.) have a density of 1.05 g/cm^3–1.1 g/cm^3, the average proton density of lung parenchyma is < 0.2 g/cm^3 during inspiration. This is a factor of 5 times lower, which directly reduces the signal-to-noise ratio of the lungs compared to other soft tissues, keeping all other factors the same [1]. The respiratory motion of the lungs requires rapid acquisition schemes, which were not always clinically available. During inspiration, the air we breathe contains only ~ 0.000055% ^1H, which eliminates any MRI signal in the alveoli and causes a reduction in signal intensity. Magnetic susceptibility also plays a role in image quality, as the bulk susceptibility difference between air in the lungs and parenchymal tissue is $\Delta X_0 \sim 8$ ppm. In this regard, imaging the lung at 1.5T reduces the artifact between the air–tissue interface that would occur at 3T. This, combined with the extremely short T2* of lung parenchyma (1.41 ms ± 0.41 ms at 1.5T), requires imaging with the lowest echo time (TE) possible (ideally < 1.0 ms) in order to achieve the maximum MRI signal before decay [2]. All of these factors must be taken into account when designing a lung imaging protocol for MRI.

Imaging of the neonatal lung

Clinical scanners now offer options which address some of the issues mentioned above, using advanced MRI pulse sequences and techniques to achieve excellent structural lung imaging in children[1] and adults in the clinic. However, additional challenges come with imaging neonates[1] either in the neonatal intensive care unit (NICU) or in a standard imaging suite. At our institution, we have imaged both premature and term infants in both the hospital imaging environment and on the 1.5T MAGNETOM Amira MRI scanner which is uniquely sited within our NICU [3, 4]. In this article, we will describe our clinical experience with neonatal lung imaging and the associated challenges, such as small patient size, patient motion, lack of breath hold, and reduction of auditory noise to protect the infant.

Patient size / neonatal-specific MRI receive coils

The size difference between adult and infant lungs (Fig. 1) requires a set of MRI coils that are optimized to receive signal from such a small volume. Several options are available, including the NORAS 16-channel VARIETY flex coil (NORAS MRI products, Höchberg, Germany), which provides a single 8-channel coil anterior and one 8 channel coil posterior on the infant. This coil provides optimal signal-to-noise in the infant lungs and includes a cylindrical foam insert to allow the infant to lie comfortably during the scan.

Patient motion

Since these infants are scanned without sedation using a feed-and-swaddle technique, patient motion in neonatal lung imaging periodically becomes an issue. However,

[1]*Siemens Healthineers disclaimer: MR scanning has not been established as safe for imaging fetuses and infants less than two years of age. The responsible physician must evaluate the benefits of the MR examination compared to those of other imaging procedures. This disclaimer does not represent the opinion of the authors.*

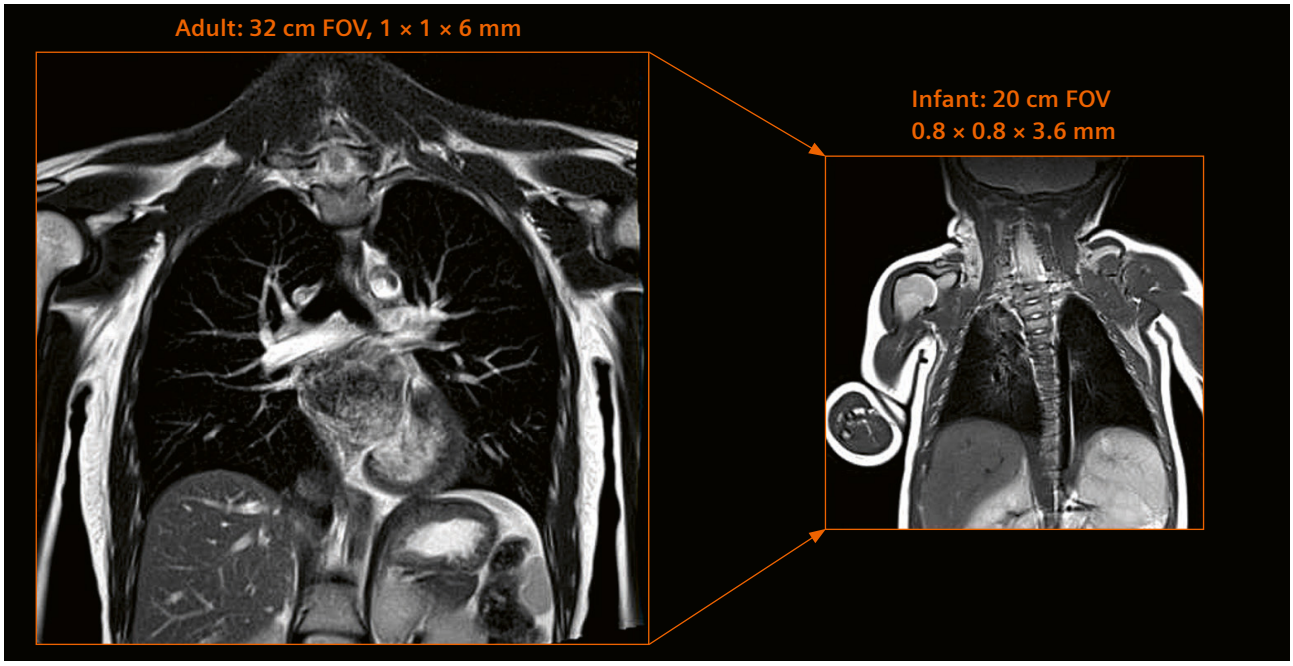

1 The raw size difference between the lungs of a healthy adult and those of a premature infant at term are shown with the same coronal T2 BLADE pulse sequence on the 1.5T MAGNETOM Amira MRI scanner.

during the phase-resolved functional lung (PREFUL) imaging sequence, which acquires 6.4 frames/s, one can immediately see whether the motion is severe enough to stop the scan. This is possible by enabling the in-line real-time display on the MRI scanner. Periodically, the infant will awaken and move significantly in-plane or even roll out of the single coronal plane of imaging. The scan can be immediately stopped, as they are only ~ 1 minute in length, and repeated later in the study once the infant has returned to a more relaxed state as shown by the patient monitoring unit. Moreover, in post-processing, images prone to through-plane motion may be retrospectively removed from the stack prior to analysis.

Noise reduction techniques for neonatal imaging

Limiting auditory noise to protect the infants' hearing is of prime importance. At our institution, we use multiple levels of hearing protection to reduce the scanner noise for neonates as much as possible. The first step is to insert half of a standard foam earplug into each ear. Another option is to use Mack's soft moldable silicone earplugs (McKeon Products, Inc., Warren, MI, USA), which can also be cut in half and fit to the infant ear. Earplugs in general can reduce the noise in the MRI by between 20 and 30 decibels (dB) and are always the first line of defense (Fig. 2A). The second layer of ear protection for the infants are the MiniMuff neonatal noise guards (Natus Medical, San Carlos, CA, USA) (Fig. 2B). These MRI-safe disposable



2 **(2A)** Mack's silicone putty earplugs, **(2B)** MRI MiniMuffs disposable neonatal noise guards, **(2C)** Ima·X noise-canceling MRI headphones.

noise guards have a gentle hydrogel adhesive to provide a secure fit and reduce sound levels by an additional 7 dB. The last layer of ear protection focuses on headphones that will not slip off the infant. We purchased the world's first noise canceling infant MRI headphones (Fig. 2C) (Ima·X, Luxembourg), which reduce the noise by an average of 22 dB and up to 30 dB @ 1kHz. Prior to purchasing these headphones, our in-house technique was to remove the center bar between an MRI-compatible set of adult headphones and to secure each side with Coban adhesive wrap (3M, Maplewood, MN, USA) to prevent sliding. Note that the earplugs, MiniMuffs, and headphones can be placed while the infant is feeding in the mother's room, before they are brought to the MRI scanner. This means that once the infant falls asleep after feeding, they do not have to be disturbed again to apply the ear protection.

Structural imaging of the neonatal lung

Imaging of the neonatal lung can be divided into two main categories: 1) anatomical or structural imaging, and 2) functional imaging. Typical standard-of-care structural imaging of the neonatal lung relies on chest X-rays (CXR), which are routinely ordered in neonates and were first reported in the literature in 1967 [5]. One main advantage of CXR in the NICU and hospital setting is accessibility. The radiographs can be performed using a portable X-ray unit which can be brought directly into the mother's room. Current diagnostic studies typically limit the dose to between 24 µG and 32 µG, and are associated with a very low risk of induced malignancy [6, 7]. However, CXRs provide only single-plane 2D images and have decreased sensitivity in detecting milder disorders of the lung. Many neonates in our NICU are also required to have multiple CXR exposures during their stay. Although this is generally considered safe, it does add to the cumulative radiation dose received in this vulnerable population early in life.

The modality without ionizing radiation that shows the most promise for structural imaging of the neonatal lung is MRI. The incorporation of 3D ultra-short echo-time (UTE) or even zero echo-time (ZTE) imaging has provided "CT-like" imaging of the lung using product MRI sequences available on Siemens Healthineers scanners [8]. These sequences compensate for the fast T2* decay time of lung parenchyma by acquiring echo times in the tens of µs. Specifically, Siemens Healthineers provide several pulse sequences for use in clinical lung imaging. These include a 3D stack-of-spirals VIBE UTE along with the pointwise encoding time reduction with radial acquisition (PETRA) [9]. Our group has incorporated the 3D PETRA sequence in the NICU for structural lung imaging (Fig. 3A). One advantage of the PETRA sequence in the neonate population is that it is completely silent and tends not to disturb the infant during scanning. We also acquire the free-breathing stack-of-stars radial VIBE (StarVIBE) product sequence in both axial and coronal planes to study the airway, lung parenchyma, and lung volume (Fig. 3B).

Functional imaging of the neonatal lung

While structural MRI of the lungs has gained ground in clinical use, assessment of lung function, especially in this vulnerable population, is lacking. The feasibility of acquiring quantitative ventilation and perfusion data in the newborn period without sedation or contrast administration is novel. This information is especially important in the NICU as the most common complication of preterm birth is bronchopulmonary dysplasia (BPD), also known as chronic lung disease of prematurity (CLDP). Premature infants represent approximately 10% of all births in

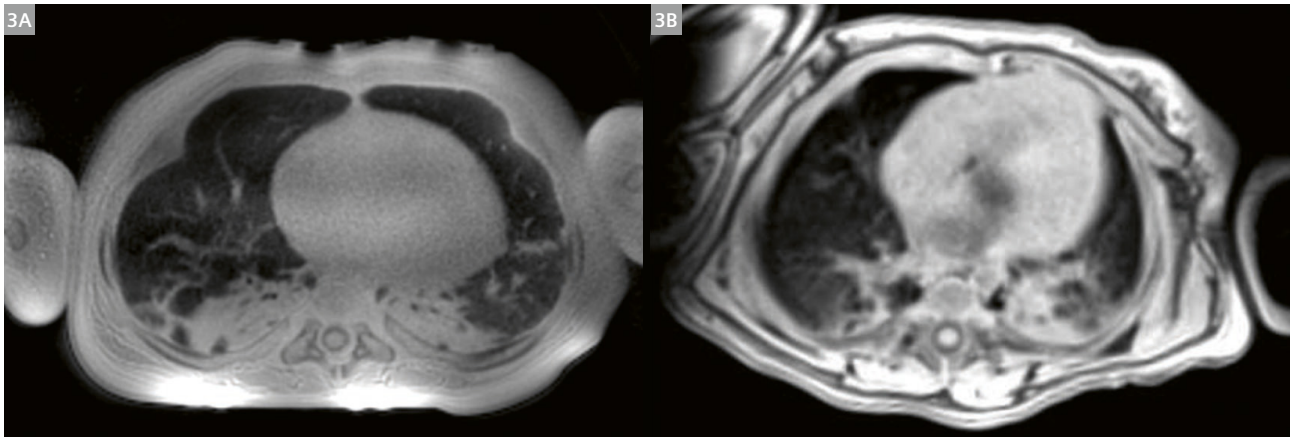

3 **(3A)** PETRA MR image from an infant born at 24 weeks 4/7 days with grade 3 BPD demonstrating bilateral bibasilar atelectasis. Acquired resolution was 0.78 mm isotropic showing an image reconstructed to 0.78 × 0.78 1.56 mm. **(3B)** A StarVIBE sequence from another infant with grade 2 BPD at 0.9 × 0.9 × 2.0 mm resolution.

developed countries and are associated with a mortality rate of up to 10% for very premature infants born at fewer than 29 weeks' gestation [13]. BPD is the major respiratory complication of premature birth, affecting 10,000 to 15,000 infants in the U.S. annually, and up to 50% of infants born < 1kg [10, 11]. This disease was first described more than 50 years ago, and was initially characterized by inflammation and fibrosis secondary to administration of oxygen and mechanical ventilation in moderately premature infants (~ 34 weeks' gestation) [5, 12].

Current means of non-invasively detecting BPD in premature infants in the NICU rely on the surrogate measure of whether respiratory ventilator support is required for more than three consecutive days (either invasive or non-invasive ventilation to maintain arterial oxygen saturation above 90%) [13]. Techniques such as lung spirometry and pulmonary function testing, which can be done in children and adults, cannot be performed in infants without the risk of sedation and intubation. Also, this technique is not available in most neonatal units, and lacks sensitivity to detect early lung disease [14, 15]. Currently, there is no other means of acquiring this information in this population; our group's work using phase-resolved functional lung (PREFUL) MRI technique[2] in premature infants meets this need.

In addition, there are no means in the clinic to identify the BPD phenotypes of airway, lung parenchyma, and perfusion in each infant. Clinical care only assesses the degree of respiratory support or oxygen that each infant needs and for what time period, without knowledge of the underlying cause of the disease. However, specific treatment would differ knowing that the large airways/tracheal area was decreased in comparison with an infant having pulmonary hypertension and perfusion abnormalities. Our group is the first to use the PREFUL MRI technique in premature infants to quantify perfusion defect % (QDP), ventilation defect % (VDP), V/Q defect, non-defect match %, and quantitative pulmonary perfusion values [mL/min/100mL]. Another group has also used PREFUL MRI in normal-term infants and toddlers with and without sedation in a pilot study [16].

PREFUL MR lung imaging technique

Phase-resolved functional lung (PREFUL) imaging is a method to evaluate dynamic MR data acquired in free breathing without any need for contrast agent administration [17]. Three coronal slices are placed at the level of the tracheal bifurcation, one slice anterior, and one posterior to this slice using a 2D spoiled gradient echo (TFL) sequence with a 1.57 ms TR, 0.99 ms TE, 5° FA, 10 mm slice thickness, 30 cm FOV and a 128 × 102 matrix reconstructed to 256 × 256 resulting in an in-plane resolution of 1.2 × 1.2 mm^2. A total of 512 images were acquired continuously (80 s) with a temporal resolution of 6.4 frames/s during free breathing. No respiratory or cardiac gating was done (Fig. 4).

A custom MATLAB based implementation of PREFUL (courtesy of Hannover Medical School) was utilized, first transforming the acquired image time series to a fixed lung volume with a group-oriented registration approach [18]. This enables the analysis of the signal time course in each voxel, which is mainly influenced by two variables: First, by proton density, which will change during inspiration and expiration. Second, by the time-of-flight effect, which describes the inflow of spins with a higher magnetization into the imaging plane. While the first effect is directly connected to ventilation, the second is related to perfusion. Since both signal changes occur at different frequencies (cardiac frequency vs. respiration frequency), they can be separated with an adequate filtering approach (Fig. 5). A low-pass filter is applied to evaluate the ventilation, and a high-pass filter is used for perfusion. Further, an image-guided, edge-preserving filter can be applied to increase the signal-to-noise ratio while preserving fine structural details [19]. Note that similar functionality is available in Siemens Healthineers' MR Lung research

[2] *The research application is currently under development and is not for sale in the U.S. and in other countries. Its future availability cannot be ensured.*

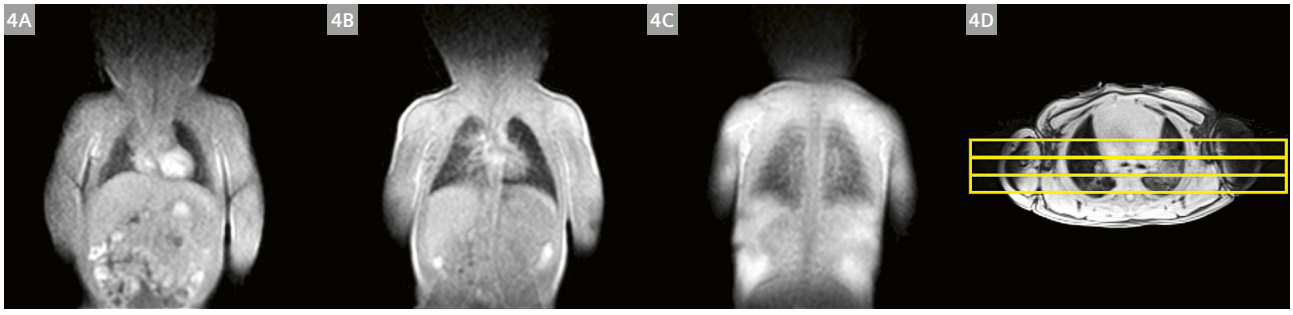

4 The three coronal slices are centered at the level of the tracheal bifurcation in the infant. Note that optimal signal intensity should be visibly centered on the lungs from the anterior and posterior flex coils on the infant. This should be confirmed in the localizer image at the beginning of the exam.

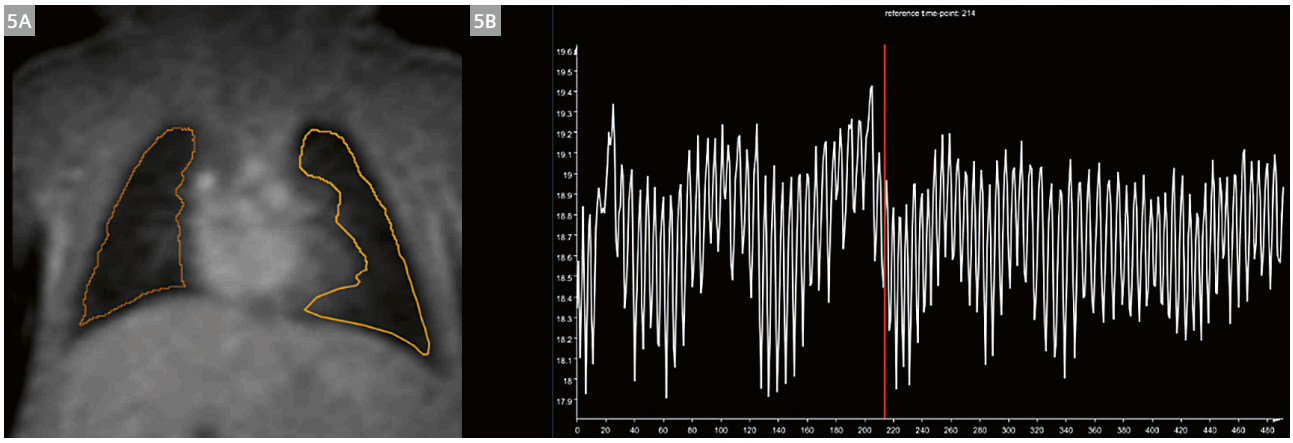

5 **(5A)** A single-slice PREFUL image of a neonate showing automated artificial intelligence (AI) segmentation of the lungs. Manual editing of the contours was performed to include minor regions at the periphery of the lung (MRLung 2.0, Siemens Healthineers, Erlangen, Germany). **(5B)** Inspiration and expiration cycles of the free-breathing acquisition are shown on the right with a temporal resolution of 200 ms/frame.

application.The Hannover group, which invented the processing algorithm, is also available for consultation at the company BioVisioneers GmbH in Germany (biovisioneers.com; info@biovisioneers.com).

In the next step, the respiratory and cardiac phase are estimated for each image with a sine-model. The sorting of the images allows one to interpolate a complete cardiac and respiratory cycle. This 3D ventilation (V) and perfusion (Q) information (2 spatial dimensions + 1 temporal dimension) can be further processed to calculate a series of V/Q parameters, including regional ventilation, quantified perfusion, and flow-volume correlation metric [20–22]. By applying thresholds, binary parameters can be derived and combined to V/Q maps, which can provide the percentage of lung volume affected by ventilation and perfusion defects, and the respective match and mismatch ratios. The thresholds for V/Q maps were determined by correlating with independent validation methods such as hyperpolarized ^{129}Xe MRI, dynamic contrast-enhanced (DCE) MRI, and SPECT.

Validation has been performed for the PREFUL MRI sequence by the Hannover group. The repeatability of the parameters was recently demonstrated in healthy subjects and in chronic obstructive pulmonary disease (COPD) patients [23]. Furthermore, comparisons with gold-standard and more established techniques were carried out. Specifically, PREFUL was validated with fluorinated and hyperpolarized xenon MRI (direct ventilation measurement), DCE MRI (perfusion measurement with contrast agent application), and standard single-photon emission computed tomography (SPECT) [24–28]. Recently, dynamic PREFUL parameters showed treatment response in COPD in the CLAIM trial: indacaterol/glycopyrronium (IND/GLY) improved the regional ventilation dynamics, perfusion, and V/Q match [29, 30]. Additionally, the dynamic parameter was able to predict survival using only a baseline scan [31].

PREFUL MRI results

The following parameters were calculated: perfusion defect % (QDP), ventilation defect % (VDP), V/Q defect and non-defect match %, and pulmonary perfusion [mL/min/100mL] [22, 28]. Defects < 30% are considered normal or mild (grade 1) for both ventilation and perfusion. Defects between 30% and 60% are categorized as moderate grade 2 BPD, and defects > 60% as severe grade 3 BPD. Figure 6 shows ventilation and perfusion maps from a normal infant. Figure 7 displays V/Q defects in an infant with grade 2 BPD, showing the mismatch between ventilation and perfusion.

The PREFUL MRI is used to evaluate lung ventilation and perfusion defects and to obtain quantitative estimates of pulmonary perfusion in units of mL/min/100mL. Of clinical interest is the ability to define a perfusion defect % and compare with the ventilation defect %. This allows independent assessment of these two components of BPD phenotypes in the same patient with the same scan.

Conclusion

PREFUL MRI is a non-invasive technique performed under free breathing without the need for sedation or exogenous contrast agents. It has the potential to identify localized defects in ventilation and perfusion in premature infants. There are currently no means to non-invasively quantify respiratory function in premature infants. PREFUL can be implemented with default MRI pulse sequences. Therefore, once a post-processing pipeline is implemented, the method can be applied in a multi-center or cooperative setting as an outsourced analysis pipeline without high technological prerequisites, and can be applied to studies in premature infants with BPD. Non-invasive functional lung imaging in infants can be done safely and routinely with the proper setup and staff.

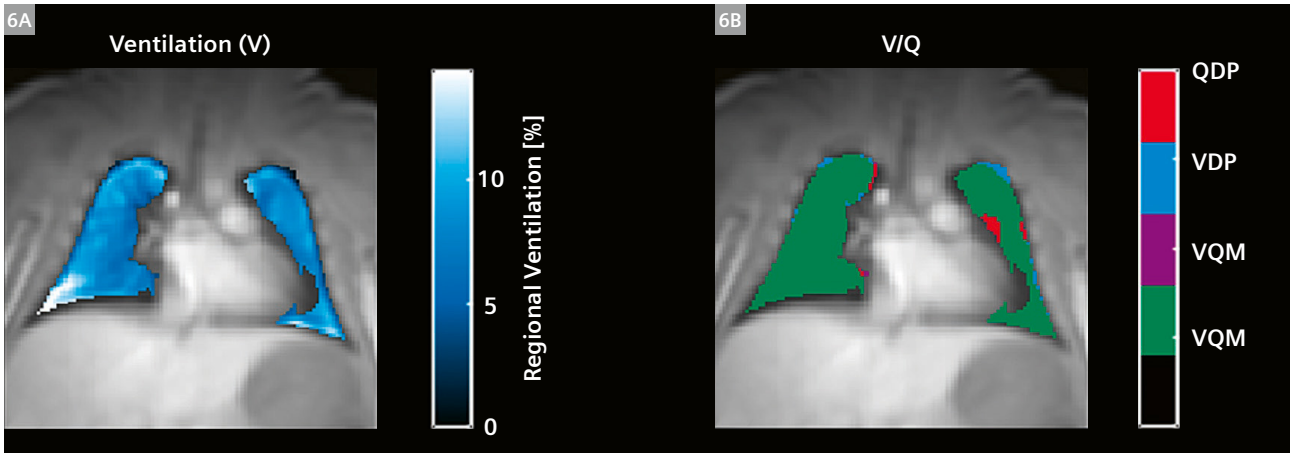

6 **(6A)** Ventilation and **(6B)** ventilation/perfusion(V/Q) defect maps are shown in a normal infant at term. Notice the homogeneity in the **(6A)** ventilation map shown in blue. **(6B)** V/Q defect map shows minimal ventilation defect percentage in blue and minimal perfusion defect percentage in red. Green = VQM non-defect; purple = VQM defect; VQM = ventilation/perfusion match

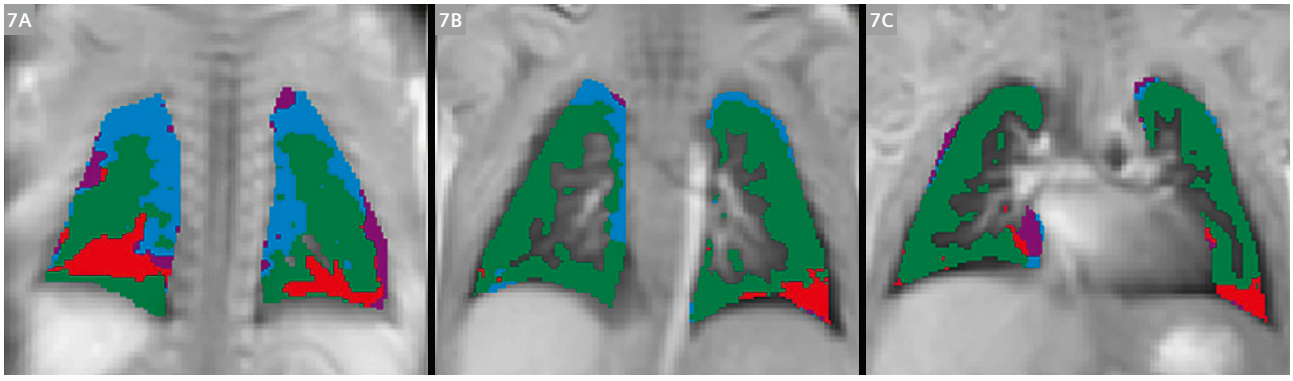

7 Functional lung. A perfusion map acquired using PREFUL MRI is displayed from an infant with grade 2 BPD. A 19% total ventilation defect percentage (VDP%) and a 13.3% total perfusion defect percentage (QDP%) is shown averaged across the three slices.
Red = QDP% exclusive; blue = VDP% exclusive; green = VQM non-defect, purple = VQM defect; VQM = ventilation/perfusion match

Acknowledgments

The authors would like to acknowledge the assistance of the pediatric and NICU nursing staff at NYP, who played an invaluable role in the success of this study. Funding for this work is provided under NHLBI R01HL167003-01A1. Research reported in this publication was supported by the National Heart, Lung and Blood Institute of the National Institutes of Health under award R01HL167003.

Statements and declarations

None of the authors have a competing financial interest in this study. Robert Grimm is employed by Siemens Healthineers, which manufactures the MRI scanner and provides the research analysis software. Filip Klimeš, Andreas Voskrebenzev, and Jens Vogel-Claussen are shareholders of BioVisioneers GmbH, a company which has interest in pulmonary MRI methods.

References

1 Van Dyk J, Keane TJ, Rider WD. Lung density as measured by computerized tomography: implications for radiotherapy. Int J Radiat Oncol Biol Phys. 1982;8(8):1363–1372.
2 Hatabu H, Alsop DC, Listerud J, Bonnet M, Gefter WB. T2* and proton density measurement of normal human lung parenchyma using submillisecond echo time gradient echo magnetic resonance imaging. Eur J Radiol. 1999;29(3):245–252.
3 Dyke JP, Voskrebenzev A, Blatt LK, Vogel-Claussen J, Grimm R, Worgall S, et al. Assessment of lung ventilation of premature infants with bronchopulmonary dysplasia at 1.5 Tesla using phase-resolved functional lung magnetic resonance imaging. Ped Radiol. 2023;53(6):1076–1084.
4 Dyke JP, Garfinkel AC, Groves AM, Kovanlikaya A. High-resolution rapid neonatal whole-body composition using 3.0 tesla chemical shift magnetic resonance imaging. Pediatr Res. 2018;83(3):638–644.
5 Northway WHJ, Rosan RC, Porter DY. Pulmonary disease following respirator therapy of hyaline-membrane disease. Bronchopulmonary dysplasia. N Engl J Med. 1967;276(7):357–68.
6 Liszewski MC, Lee EY. Neonatal Lung Disorders: Pattern Recognition Approach to Diagnosis. AJR Am J Roentgenol. 2018;210(5):964–975.

7 Higano NS, Ruoss JL, Woods JC. Modern pulmonary imaging of bronchopulmonary dysplasia. J Perinatol. 2021;41(4):707–717.
8 Renz DM, Herrman K-H, Kraemer M, Boettcher J, Waginger M, Krueger PC, et al. Ultrashort echo time MRI of the lung in children and adolescents: comparison with non-enhanced computed tomography and standard post-contrast T1w MRI sequences. Eur Radiol. 2022;32(3):1833–1842.
9 Grodzki DM, Jakob PM, Heismann B. Ultrashort echo time imaging using pointwise encoding time reduction with radial acquisition (PETRA). Magn Reson Med. 2012;67(2):510–518.
10 Jensen EA, Schmidt B. Epidemiology of bronchopulmonary dysplasia. Birth Defects Res A Clin Mol Teratol. 2014;100(3):145–157.
11 Jensen EA, Edwards EM, Greenberg LT, Soll RF, Ehret DE, Horbar JD. Severity of Bronchopulmonary Dysplasia Among Very Preterm Infants in the United States. Pediatrics 2021;148(1): e2020030007.
12 Stoll BJ, Hansen NI, Bell EF, Walsh MC, Carlo WA, Shankaran S, et al. Trends in Care Practices, Morbidity, and Mortality of Extremely Preterm Neonates, 1993–2012. JAMA. 2015;314(10):1039–1051.
13 Higgins RD, Jobe AH, Koso-Thomas M, Bancalari E, Viscardi RM, Hartert TV, et al. Bronchopulmonary Dysplasia: Executive Summary of a Workshop. J. Pediatr. 2018;197:300–308.
14 Davies G. Does newborn screening improve early lung function in cystic fibrosis? Paediatr Respir Rev. 2022;42:17-22. Epub 2020 Aug 20.
15 Shepherd EG, Clouse BJ, Hasenstab KA, Sitaram S, Malleske DT, Nelin LD, et al. Infant Pulmonary Function Testing and Phenotypes in Severe Bronchopulmonary Dysplasia. Pediatrics. 2018;141(5):e20173350.
16 Zanette B, Schrauben EM, Munidasa S, Goolaub DS, Singh A, Coblentz A, et al. Clinical Feasibility of Structural and Functional MRI in Free-Breathing Neonates and Infants. J Magn Reson Imaging. 2022;55(6):1696–1707.
17 Voskrebenzev A, Gutberlet M, Klimeš F, Kairet TF, Schonfeld C, Rotarmel A, et al. Feasibility of quantitative regional ventilation and perfusion mapping with phase-resolved functional lung (PREFUL) MRI in healthy volunteers and COPD, CTEPH, and CF patients. Magn Reson Med. 2018;79(4):2306–2314.
18 Voskrebenzev A, Gutberlet M, Kaireit TF, Wacker F, Vogel-Claussen J. Low-pass imaging of dynamic acquisitions (LIDA) with a group-oriented registration (GOREG) for proton MR imaging of lung ventilation. Magn Reson Med. 2017;78(4):1496–1505.
19 He K, Sun J, Tang X. Guided image filtering. IEEE Trans Pattern Anal Mach Intell. 2013;35(6):1397–1409.
20 Klimeš F, Voskrebenzev A, Gutberlet M, Kern A, Behrendt L, Kaireit TF, et al. Free-breathing quantification of regional ventilation derived by phase-resolved functional lung (PREFUL) MRI. NMR Biomed. 2019;32(6):e4088.
21 Alsady TM, Voskrebenzev A, Greer M, Becker L, Kaireit TF, Welte T, Wacker F, Gottlieb J, Vogel-Claussen J. MRI-derived regional flow-volume loop parameters detect early-stage chronic lung allograft dysfunction. J Magn Reson Imaging. 2019;50:1873–1882.
22 Glandorf, J , Klimeš F, Behrendt L, Voskrebenzev A, Kaireit TF, Gutberlet M, Wacker F, Vogel-Claussen J. Perfusion quantification using voxel-wise proton density and median signal decay in PREFUL MRI. Magn Reson Med. 2021;86:1482–1493.
23 Pöhler GH, Klimeš F, Behrendt L, Voskrebenzev A, Gonzalez CC, Wacker F, Hohlfeld JM, Vogel-Claussen J. Repeatability of Phase-Resolved Functional Lung (PREFUL)-MRI Ventilation and Perfusion Parameters in Healthy Subjects and COPD Patients. J Magn Reson Imaging. 2021;53:915–927.
24 Kaireit TF, Gutberlet M, Voskrebenzev A, Freise J, Welte T, Hohlfeld JM, et al. Comparison of quantitative regional ventilation-weighted fourier decomposition MRI with dynamic fluorinated gas washout MRI and lung function testing in COPD patients. J Magn Reson Imaging. 2018;47(6):1534–1541.
25 Kaireit TF, Kern A, Voskrebenzev A, Pöhler GH, Klimes F, Behrendt L, et al. Flow Volume Loop and Regional Ventilation Assessment Using Phase-Resolved Functional Lung (PREFUL) MRI: Comparison With 129 Xenon Ventilation MRI and Lung Function Testing. J Magn Reson Imaging. 2021;53(4):1092–1105.
26 Kaireit TF, Voskrebenzev A, Gutberlet M, Freise J, Jobst B, Kauczor HU, et al. Comparison of quantitative regional perfusion-weighted phase resolved functional lung (PREFUL) MRI with dynamic gadolinium-enhanced regional pulmonary perfusion MRI in COPD patients. J Magn Reson Imaging. 2019;49(4):1122–1132.
27 Behrendt L, Voskrebenzev A, Klimeš F, Gutberlet M, Winther HB, Kaireit TF, et al. Validation of Automated Perfusion-Weighted Phase-Resolved Functional Lung (PREFUL)-MRI in Patients With Pulmonary Diseases. J Magn Reson Imaging. 2020;52(1):103–114.
28 Marshall H, Voskrebenzev A, Smith LJ, Biancardi AM, Kern AL, Collier GJ, et al. 129 Xe and Free-Breathing 1 H Ventilation MRI in Patients With Cystic Fibrosis: A Dual-Center Study. J Magn Reson Imaging. 2023;57(6):1908–1921.
29 Vogel-Claussen J, Schönfeld CO, Kaireit TF, Voskrebenzev A, Czerner CP, Renne J, et al. Effect of Indacaterol/Glycopyrronium on Pulmonary Perfusion and Ventilation in Hyperinflated Patients with Chronic Obstructive Pulmonary Disease (CLAIM). A Double-Blind, Randomized, Crossover Trial. Am J Respir Crit Care Med. 2019;199(9):1086–1096.
30 Voskrebenzev A, Kaireit TF, Klimeš F, Pohler GH, Behrendt L, Biller H, et al. PREFUL MRI Depicts Dual Bronchodilator Changes in COPD: A Retrospective Analysis of a Randomized Controlled Trial. Radiol Cardiothorac Imaging 2022;4(2):e210147.
31 Vogel-Claussen J, Kaireit TF, Voskrebenzev A, Klimeš F, Glandorf J, Behrendt L, et al. Phase-resolved Functional Lung (PREFUL) MRI-derived Ventilation and Perfusion Parameters Predict Future Lung Transplant Loss. Radiology 2023;307(4):e221958.

Contact

Jonathan P. Dyke, Ph.D.
Citigroup Biomedical Imaging Center
Weill Cornell Medicine
1300 York Avenue, Box 234
New York, NY, 10021
USA
Tel.: +1 212 746 5781
jpd2001@med.cornell.edu
Orcid ID: 0000-0001-7170-488X


Jonathan P. Dyke, Ph.D.


Arzu Kovanlikaya, M.D.

Going Beyond DTI in the Clinic: The Appeal of Microstructural MRI

Ileana Jelescu, Ph.D.

Microstructure Mapping Lab, Department of Radiology, Lausanne University Hospital (CHUV) and University of Lausanne (UNIL), Lausanne, Switzerland

Diffusion MRI has established itself as a very powerful tool to detect and quantify cellular changes in tissue. The diffusion-weighted signal is sensitized to the random displacement of water molecules in the tissue. The mean squared displacement is on the order of a few microns to tens of microns and is largely dependent on the restrictions and hindrances encountered by the water molecules in the tissue, in the form of cell membranes or other obstacles. Diffusion MRI can thus inform about tissue microstructure features that are far below the image spatial resolution – typically still 1.5 to 2.5 mm isotropic voxel size on clinical MRI systems.

Notably, since the late 1980s, diffusion MRI has been the method of choice for the diagnosis of acute stroke [1]. The dramatic drop in apparent diffusion coefficient (ADC) happening within minutes of the stroke onset is a better feature than, e.g., the increase in T2 that only occurs ~24 hours later [2]. Another clinical success story for diffusion MRI is the use of tractography in surgical or radiotherapy treatment planning [3, 4]. Tractography enables the reconstruction of white matter fibers based on the principal direction(s) of diffusion in each voxel. The underlying assumption is that diffusion along axons is much faster than perpendicular to axons, where water molecules are highly slowed down by axon membranes, myelin sheaths, and a highly tortuous extracellular space.

To account for diffusion anisotropy across the brain or other organs, the formalism of diffusion tensor imaging (DTI) was introduced early on [5]. The diffusion tensor enables reconstruction of the ADC in any arbitrary direction of space. Four scalar metrics are typically derived from the tensor: mean diffusivity (MD), fractional anisotropy (FA), axial diffusivity (AD), and radial diffusivity (RD). MD represents the average ADC across all directions of space. AD represents the diffusivity along the fastest direction of diffusion (e.g., along the white matter bundle), and RD represents the diffusivity in the radial/perpendicular plane to that. Metrics such as MD and FA have become extremely useful in the evaluation/diagnosis of many normal and pathological conditions in the brain. Outside the brain, trace-weighted images (effectively, MD) are part of clinical protocols in the liver [6–8], prostate [9], breast [10, 11], etc. The clinical value of DTI is so overwhelming that it has become a common shortcut to consider "diffusion MRI" and "DTI" as synonyms.

Here, we want to argue that the field of diffusion MRI (dMRI) is much richer than DTI, and to encourage the clinical translation and widespread adoption of more advanced dMRI protocols that enable data analysis beyond the diffusion tensor. The compatibility of protocols with the clinic is largely driven by scan time and by feasibility across scanners and imaging centers. Recent technological advances now enable the acquisition of more comprehensive dMRI data than DTI in a clinically feasible scan time (< 10 min) [12]. These advances concern MRI scanner hardware and notably stronger gradients, acquisition acceleration techniques such as GRAPPA [13] or multiband [14], and processing strategies that boost data quality, such as denoising [15, 16].

What is the advantage of acquiring richer data than is needed for the DTI estimation? And what is meant by "richer data"? DTI assumes that the diffusion signature in any voxel can be modeled as an ellipsoid. This is commonly referred to as the "Gaussian Phase Approximation", which holds up to a moderate diffusion weighting of b ~1000 s/mm^2 in vivo[1] (Fig. 1). However, biological tissue contained in a voxel is in fact complex and heterogeneous. There is significant value in retrieving specific information about features such as cellular density, morphology, characteristic sizes, myelination, etc. This is the challenge that the field of microstructural MRI has taken on, with remarkable progress and success stories over the past few years [12, 17–19].

[1] *Please note that the Gaussian Phase Approximation does not imply isotropy. A medium can be Gaussian anisotropic.*

Beyond DTI: Diffusion kurtosis imaging

Firstly, sensitivity to tissue complexity and heterogeneity can already be gleaned from the behavior of the diffusion-weighted signal beyond the Gaussian Phase Approximation, i.e., for b-values > 1000 s/mm². This heterogeneity is measured by the "kurtosis" (Fig. 1). Diffusion Kurtosis Imaging (DKI) is thus a clinically feasible extension of DTI that estimates the kurtosis tensor jointly with the diffusion tensor [21]. Summary metrics derived from the kurtosis tensor are mean, axial, and radial kurtosis (MK, AK, RK). Qualitatively, high kurtosis suggests high diffusion heterogeneity in the voxel, or microstructural complexity. For example, radial kurtosis is high in aligned white matter fiber bundles, due to the two very different water populations – highly restricted in the intra-axonal space and more mobile in the extra-axonal space. Demyelination, axonal loss, or membrane permeation will reduce kurtosis. Inflammation on the other hand can increase kurtosis due to increased cellularity [20]. While diffusivity and kurtosis typically change in opposite directions with physiological and pathological processes (i.e., kurtosis decreases when diffusivity increases), numerous studies have shown DKI to provide complementary information to DTI about tissue microstructure. For example, in voxel-based or ROI-based analyses, kurtosis metrics can identify differences between patients and controls in brain regions where DTI metrics do not (Fig. 2). DKI is thus used to improve the detection of brain changes during, for instance, development [22, 23], aging [24], early psychosis and schizophrenia [25–27], cognitive impairment and Alzheimer's disease [28], multiple sclerosis [29], glioma [30], stroke [31, 32], traumatic brain injury [33, 34], and prostate and other body applications [35]. While DTI estimation can be done using typically ~30 directions of a single non-zero b-value referred to as a "shell" (usually b = 1000 s/mm²), two non-zero shells are needed for DKI estimation. A typical DKI protocol would thus include an additional b = 2000–2500 s/mm² shell with ~30 directions. It is critical that the entire protocol (b = 0, 1000, 2000) is set up as a single scan, such that the echo time (TE) is consistent across all diffusion-weighted images. Data compatible with the DKI estimation can

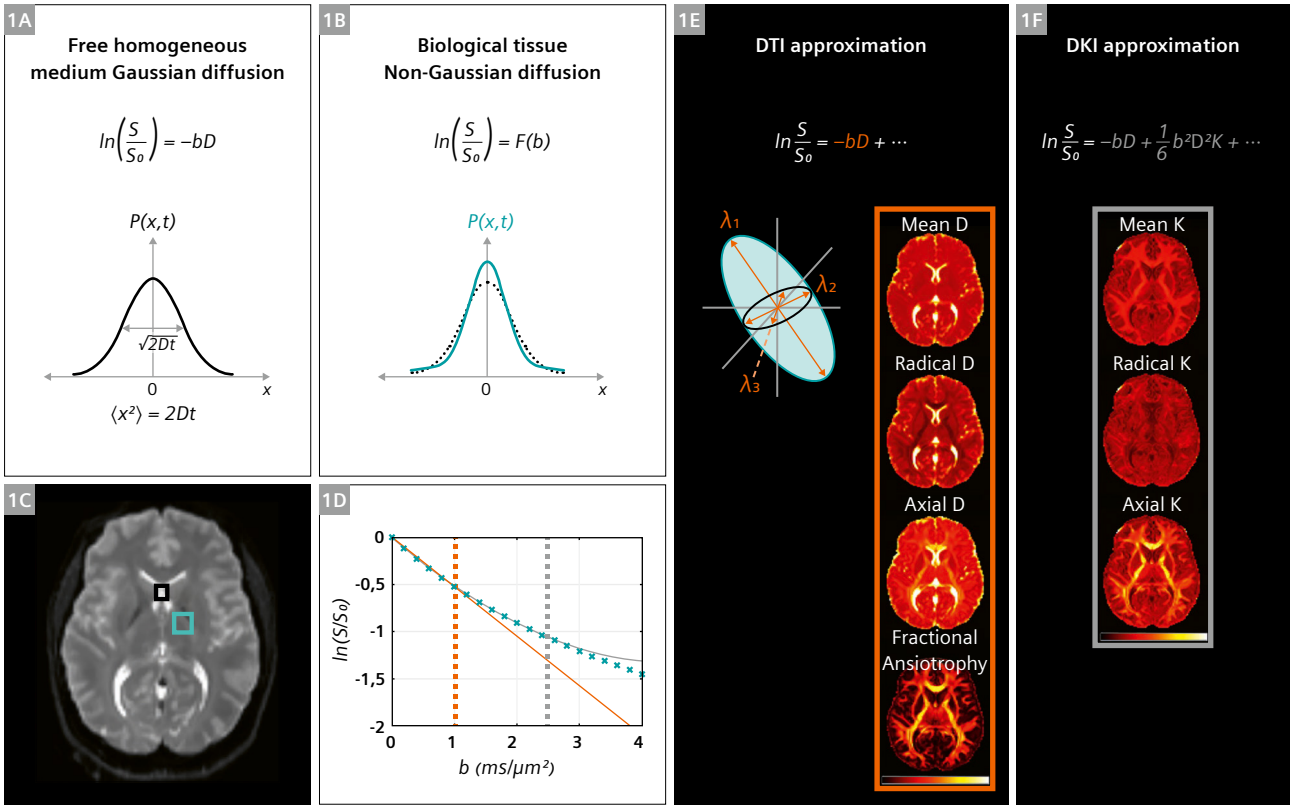

1 **(1A)** In a free homogeneous medium, such as cerebrospinal fluid (black box in (1C)), the displacement probability follows a Gaussian shape, whereby the diffusion process is referred to as Gaussian. **(1B)** In biological tissue, such as brain white matter (petrol box in (1C)), the displacement probability is no longer Gaussian; it is more peaked (positive kurtosis). **(1D)** The diffusion-weighted MRI signal (petrol) can be approximated as Gaussian (orange solid line, DTI) only up to a low b-value (~1 ms/μm² or 1000 s/mm², orange dashed vertical line), after which it deviates from a linear pattern and can be described by a quadratic function (gray solid line, DKI) up to moderate b-value (~2.5 ms/μm² or 2500 s/mm², gray dashed vertical line). Corresponding parametric maps are shown in **(1E)** for DTI and **(1F)** for DKI metrics of a 33-year-old female. Diffusivities scale bar: [0 3] μm²/ms, FA [0 1], and kurtosis [0 3]. *Figure adapted from [20], with permission.*

currently be acquired in a scan time of 6–7 minutes, at a resolution of 2 mm isotropic.

The availability of two-shell (or even better, multi-shell) dMRI data really boosts the number of analyses that the data are suitable for, as compared to single-shell. Aside from enabling DKI estimation, two or more shells also improve the estimation of the orientation distribution function (ODF) at every voxel, in order to refine tractography reconstructions [36, 37] and especially to make the data suitable for estimating biophysical models of diffusion, which are at the heart of microstructural MRI.

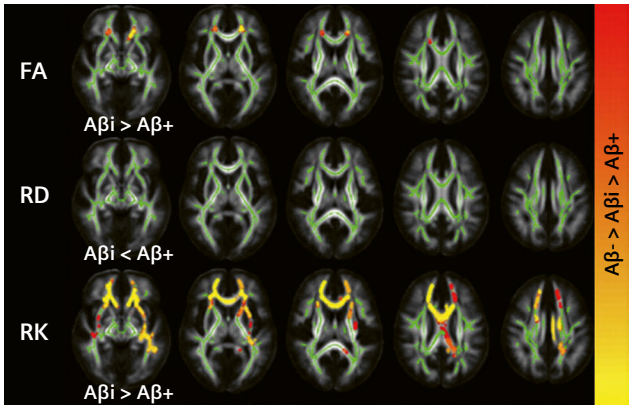

2 Axial views show significant differences between patients with intermediate beta-amyloid levels (Aβi) and amyloid-positive patients (Aβ+) for FA, RD, and RK. Significantly reduced RK in Aβ+ as compared to Aβi is more widespread in the brain than reduced FA or increased RD. *Figure adapted from [28], with permission.*

Indeed, the metrics provided by DTI and DKI analyses – MD, FA, and MK – are sensitive to physiological and pathological processes, but they lack specificity in the sense that various processes can yield the same signature in terms of these diffusion metrics. For example, a decrease in FA in white matter can be caused by mechanisms as varied as demyelination, axonal loss, microgliosis, etc. [38]. To retrieve specificity, biophysical models of diffusion in a given tissue type are introduced.

Brain white matter

The most popular and studied model is certainly the two- or three-compartment model of diffusion in white matter (Fig. 3). Here, one compartment represents the collection of axons, and the second compartment represents the extra-axonal space. The two-compartment model of diffusion in white matter thus captures five parameters [f, $D_{i,\parallel}$, $D_{e,\parallel}$, $D_{e,\perp}$, p_2], which can all be estimated independently using a two-shell acquisition similar to the DKI scheme. Each one has its own microstructural relevance and improves the specific characterization of white matter pathology, as summarized in Figure 3 and supported by several preclinical and human validation studies [20, 39–44].

A third compartment can sometimes be used to capture the cerebrospinal fluid (CSF) partial volume as a sixth parameter, with the additional f_{iso} for CSF fraction. However, recent evidence suggests that estimating the

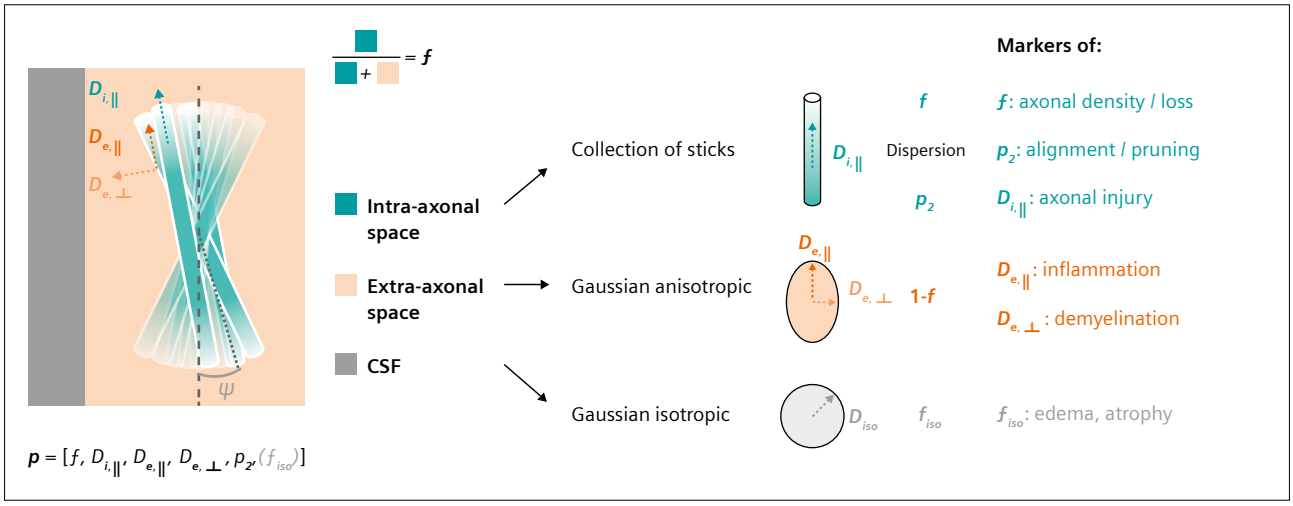

3 The Standard Model of diffusion in white matter. Axons are modeled as a collection of infinitely long sticks (cylinders with zero radius), where diffusion is unidirectional with diffusivity $D_{i,\parallel}$. They occupy a relative voxel water fraction f and their orientation distribution function (ODF) can be parametrized using an expansion in spherical harmonic coefficients; in practice, only the first coefficient p_2 is usually estimated, which gives a measurement of orientation dispersion (ranging between $p_2 = 0$ for isotropically distributed axons and $p_2 = 1$ for perfectly aligned axons). Extra-axonal water is modeled as a Gaussian anisotropic medium with diffusivities $D_{e,\parallel}$ and $D_{e,\perp}$ in the parallel and perpendicular directions, respectively. A third possible compartment is CSF, which is modeled as a Gaussian isotropic medium with fixed diffusivity $D_{iso} = 3\ \mu m^2/ms$ (the diffusivity of free water at body temperature), occupying a relative voxel water fraction f_{iso}. In this case, the fractions are normalized such that they add up to 1: $S_{tot} = (1 - f_{iso})(f \cdot S_{intra} + (1 - f) \cdot S_{extra}) + f_{iso} \cdot S_{CSF}$.

three-compartment model requires data beyond single-TE and linear diffusion encoding schemes to be robust [45].

We thus consider the two-compartment model of white matter to be compatible with clinical protocols. The estimation of the five parameters requires at least two shells with b-values (1000/2000) s/mm² sampled across at least 30 directions. Several implementations of this model have been proposed over the years using various acronyms, including NODDI [46], WMTI [47], WMTI-Watson [48, 49], and CHARMED [50]. However, they can all be unified under a Standard Model [51], which can be estimated using a choice of publicly available software tools: [45, 48] (Fig. 4). Importantly, these recommended implementations of the Standard Model estimation do not fix any parameters to arbitrary values to stabilize the fit. This maintains a high specificity of each parameter to its biological description. Indeed, pathology can, for example, alter compartment diffusivities (e.g., $D_{e,\parallel}$ decreases due to axonal injury [52]), an effect which can only be captured if $D_{e,\parallel}$ is a free model parameter. If it is fixed to an arbitrary value, the pathological change will be incorrectly absorbed by another parameter of the model [53].

The value of white matter microstructure characterization using the Standard Model vs. DTI has been demonstrated in several studies of clinical populations, and notably at early stages of change, such as in mild cognitive impairment, early psychosis, acute ischemia, multiple sclerosis, and early brain development [27, 28, 54]. For example, the Standard Model reveals mainly a decrease in axonal water fraction and an increase in extra-axonal diffusivities in early psychosis compared to controls, pointing to an extra-axonal-initiated pathology possibly with myelin damage [27]. The model reveals a decrease in axonal water fraction and in intra-axonal diffusivity in cognitive impairment, pointing to an intra-axonal-initiated pathology [28, 52]. Unfortunately, the model cannot be applied retrospectively to single-shell clinical data, despite what some implementations suggest [55]. Its broader use thus warrants a change in default diffusion clinical protocol from the single-shell DTI to two or three shells. We underline once more that the cost in scan time remains very moderate thanks to acceleration techniques, and is superseded by the benefits of a more refined white matter characterization.

Brain gray matter

Modeling diffusion in gray matter is more challenging than in white matter: The limited myelination does not guarantee that water will stay within the same compartment over typical clinical diffusion times ($\Delta > 20$ ms) and thus inter-compartment water exchange must be modeled. A recent model suitable for cortical gray matter has been proposed: Neurite EXchange Imaging (NEXI)[2]. It has been successfully demonstrated and validated, first on preclinical MRI systems [56, 57], then on Connectom scanners from Siemens Healthineers [58, 59] and recently also on a 3T MAGNETOM Prisma system from Siemens Healthineers

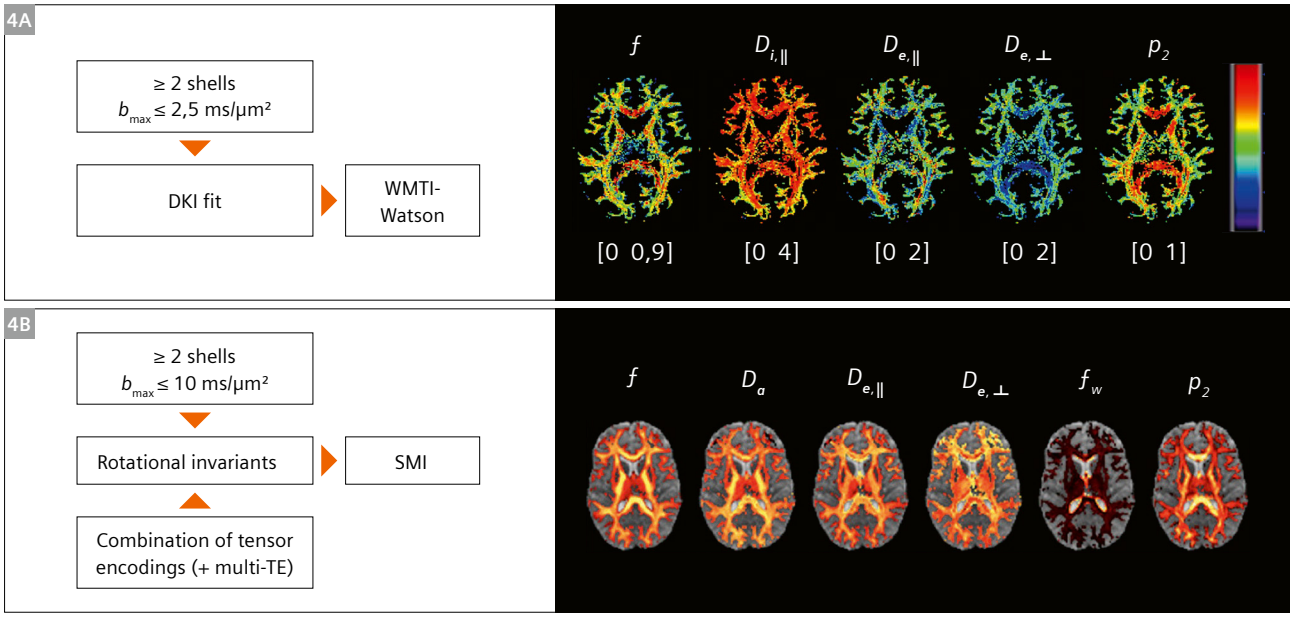

4 **(4A)** The WMTI-Watson implementation of the Standard Model can be estimated directly from a DKI fit using, for example, a deep-learning implementation in [48] available at https://github.com/Mic-map/WMTI-Watson_DL. **(4B)** The Standard Model Imaging (SMI) toolbox is suitable for both classical DKI data (2 shells, b_{max} up to 2500 s/mm²) as in **(4A)** or richer data such as multi-shell up to b_{max} = 10,000 s/mm² and/or combinations of measurements using linear and spherical diffusion encoding or multi-TE [45]. The toolbox is available at https://github.com/NYU-DiffusionMRI/SMI. *SMI maps adapted from [45], with permission.*

[60, 61] (Fig. 5). Briefly, NEXI is a two-compartment model that disentangles contributions from intra-neurite water and extra-neurite water and estimates the exchange time t_{ex} across the cellular membrane. Accounting for the exchange enables a more accurate estimation of neurite density (which would be otherwise underestimated), while the measurement of the exchange time itself is a relevant proxy for cell membrane integrity and gray matter myelination [56, 62]. The biomarker value of NEXI parameters remains to be thoroughly validated, though initial preclinical and clinical studies are encouraging [56, 60, 63].

However, the estimation of NEXI model parameters requires a diffusion protocol that can only be set up using research applications. Indeed, it requires sampling both dimensions of (q, t) space independently, as opposed to aggregated within the b-value.[3] In other words, the diffusion time t needs to be controlled directly in the sequence card, an option which is currently not available in the diffusion product sequences from Siemens Healthineers. NEXI is for now mainly suitable for research protocols, but it holds great promise for characterizing gray matter pathology in patient cohorts. This model could be extended to also account for cell bodies, which are more abundant in gray than white matter, but the feasibility of estimating all model parameters reliably is under investigation [57].

Beyond the brain: tumors, prostate, muscle

Moving away from the brain, biophysical models of diffusion MRI have been developed for other tissue types and organs. However, to unleash the potential of microstructural MRI for non-brain applications, advanced dMRI protocols also must be established prospectively.

Certainly, the reliable estimation of diffusion models outside the brain also requires data acquisition beyond what is typically feasible with the diffusion product sequence. Protocols need to span multiple diffusion times, and often also beyond the pulsed-gradient spin-echo (PGSE) scheme, using either OGSE (Oscillating-Gradient Spin-Echo)[4] [64] or STEAM (Stimulated Echo)[4] [65].

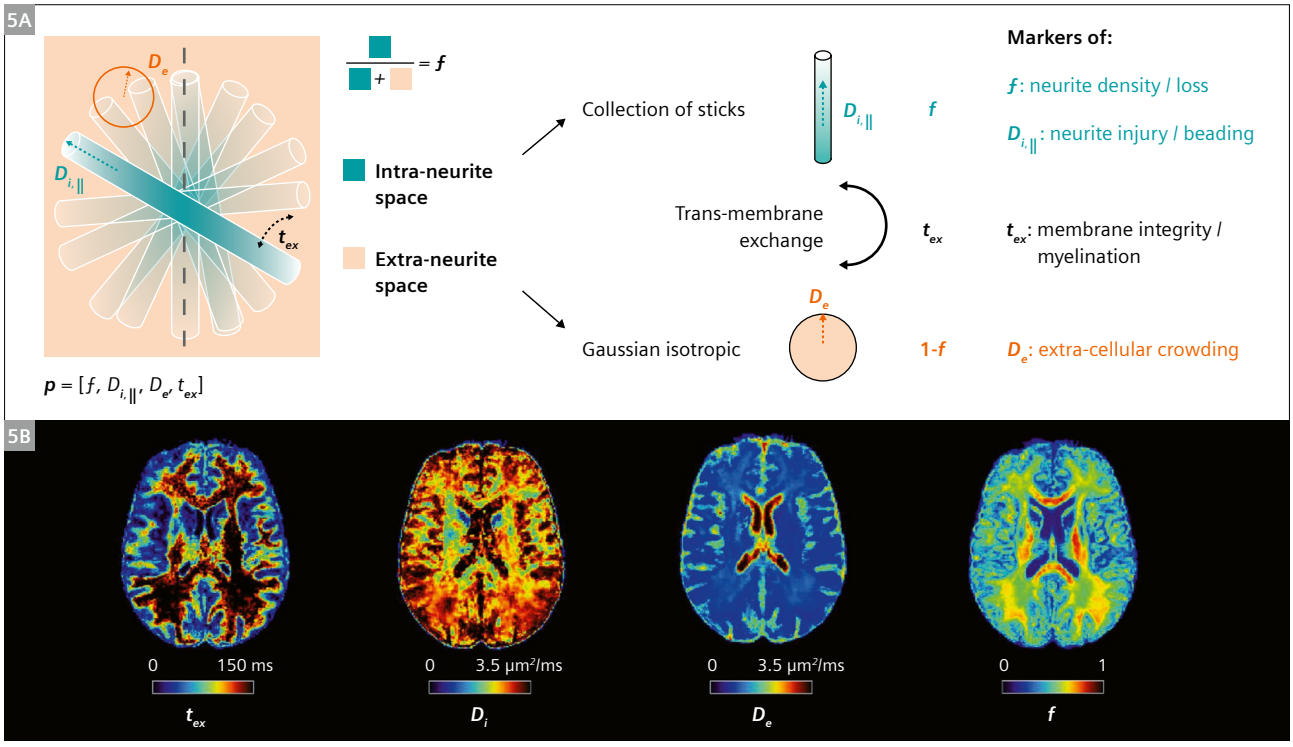

5 **(5A)**: NEXI is a two-compartment model capturing four parameters: the intra-neurite water fraction f, the intra-neurite diffusivity D_i (where neurites are modeled as infinitely long sticks, randomly oriented), the extra-cellular diffusivity D_e, assumed isotropic, and the water exchange time t_{ex} between the intracellular and extracellular compartments. **(5B)**: Example NEXI maps in the human brain. *Adapted from [59], with permission.* NEXI can be estimated using publicly available code: https://github.com/Mic-map/nexi.

[2]Siemens Healthineers Disclaimer: This article describes possible future ideas and concepts. It is not intended to describe specific performance and/or safety characteristics of currently planned or future products. Future realization and availability cannot be guaranteed.

[3]For the pulsed-gradient spin-echo (PGSE) diffusion weighting, and in the narrow pulse approximation: $b = (\gamma G\delta)^2 (\Delta - \delta/3) = q^2 t$, where q is the spatial phase warp and t is the diffusion time.

[4]The product is still under development and not commercially available. Its future availability cannot be ensured.

Compared to PGSE, OGSE and STEAM acquisitions give access to diffusion times that are much shorter or longer, respectively. These diffusion encoding schemes are available as part of research protocols. Beyond linear diffusion encoding (i.e., sensitizing the signal to diffusion along one specific direction at a time), diffusion gradient waveforms tailored to enable multi-dimensional diffusion encoding are sometimes also required [66]. They are available through C2P (https://github.com/filip-szczepankiewicz/fwf_seq_resources/tree/master/Siemens).

Tumors are a perfect application for microstructural MRI. Their heterogeneity is difficult to capture with DTI metrics alone. Usually, the tumor environment is modelled as impermeable spheres of a given radius within an extracellular space. Cell size can then be estimated through varying diffusion times, using PGSE or a combination of PGSE and OGSE measurements, depending on the time range that needs to be sampled. Two common models are IMPULSED (Imaging Microstructural Parameters Using Limited Spectrally Edited Diffusion) [67] and POMACE (Pulsed and Oscillating gradient MRI for Assessment of Cell size and Extracellular space) [68]. Several clinical studies have successfully exploited diffusion time-dependence to characterize glioma [69, 70] or prostate cancer [71]. Using multi-dimensional diffusion encoding, it is possible to also probe the shapes of the cells that constitute the tumor. Consider a voxel of spherical cell bodies vs. a voxel of isotropically oriented neurites. Both scenarios would yield similar diffusion signatures in single diffusion encoding (PGSE or OGSE) methods – e.g., a very low FA in both cases. Multi-dimensional diffusion encoding enables separating these two cases by extracting the "microscopic FA" (μFA), which would be very low for spherical cells and very high for neurites and astrocytic processes (Fig. 6). One approach to multiple diffusion encoding is *q*-space trajectory imaging, or diffusion tensor (b-tensor) encoding, which consists in using time-varying ("free") diffusion gradient waveforms to probe multiple directions at once [73, 74]. One of its most successful applications was in discriminating between various types of tumors characterized by different cell geometries [72, 75, 76] (Fig. 6). It has also been used to assess kidney microstructure [77] and to improve the estimation of the Standard Model of white matter [45].

The reader is referred to dedicated reviews on tumor microstructure characterization [76, 78, 79].

In the case of prostate microstructure, the model accounts for a densely packed cellular compartment (composed of stroma and epithelium), for which the fiber diameter and membrane permeability can be estimated using the random permeable barrier model (RPBM), and a luminal compartment with almost unrestricted water diffusion, for which the average lumen diameter can be estimated. The model therefore requires an acquisition where the diffusion time is varied using a STEAM scheme, and the echo time TE is also varied to separate water pools with different T2s [80]. This model has been successfully applied to the characterization of healthy and cancerous

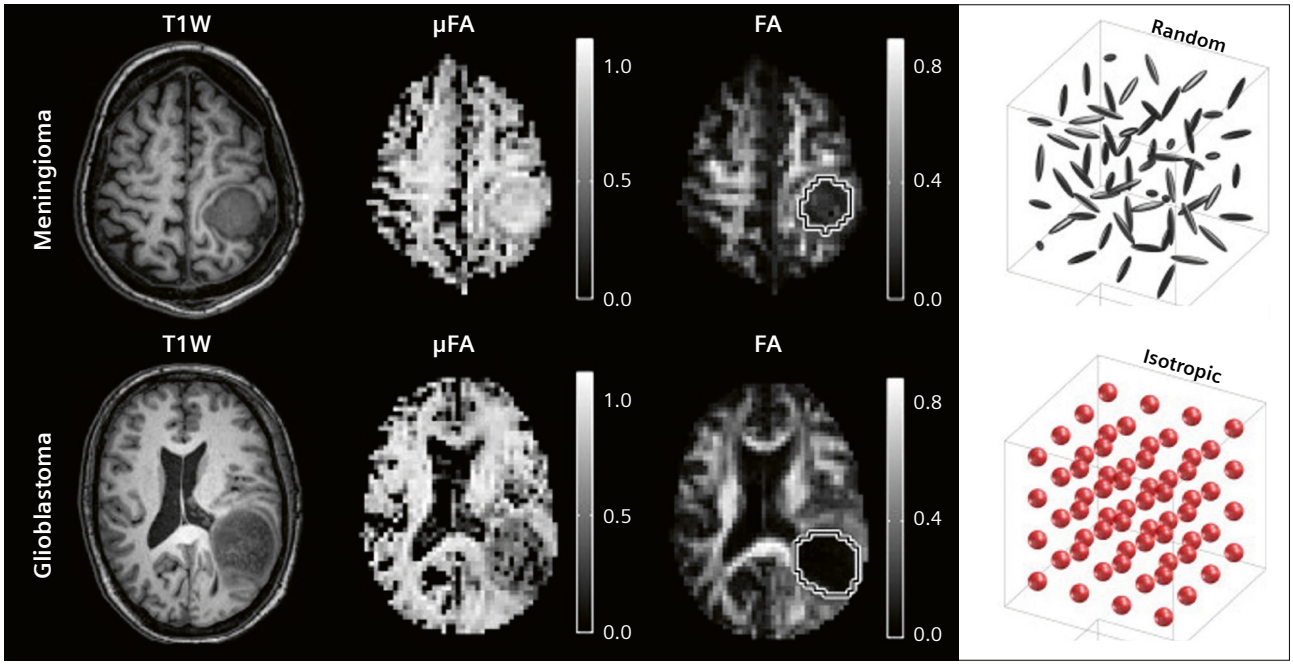

6 A meningioma (top row) and glioblastoma (bottom row) display similar contrast on T1w images and low FA. However, the μFA estimated from a combined acquisition of linear and spherical diffusion encoding is high in the meningioma and low in the glioblastoma. This is due to their underlying most abundant microstructure (sketched in the right-hand column). *Figure adapted from [86], with permission.*

prostate [81] with the potential of eventually foregoing the need for invasive biopsies.

Finally, time-dependent diffusion MRI also serves microstructural quantification of skeletal muscle. The RPBM model has been applied to estimate myofiber diameter changes due to injury-related atrophy and subsequent recovery [82]. Recently, clinical applications of time-dependent diffusion to Duchenne muscular dystrophy have also been performed [83].

Conclusion and future directions

The diffusion MRI signal contains very valuable information about tissue microstructure, and the regime that goes beyond the Gaussian Phase Approximation and DTI enables a more refined and specific characterization of cellular-level features. It is worthwhile acquiring multi-shell data routinely in clinical practice to improve sensitivity and specificity to pathology. We also encourage the widespread adoption of more advanced research protocols, which may include varying the diffusion time and/or the dimensionality of diffusion encoding, and which are particularly useful for brain gray matter and body imaging. A community-wide reflection on how to best integrate quantitative microstructure maps into the clinical workflow is much needed for radiologists and clinicians to make use of the available information. For example, normative databases for diffusion microstructure parameters like the ones developed for relaxometry [84] are currently in development [85]. They would enable evaluating the extent of alterations on a patient-by-patient basis.

References

1 Moseley ME, de Crespigny AJ, Roberts TP, Kozniewska E, Kucharczyk J. Early detection of regional cerebral ischemia using high-speed MRI. Stroke. 1993;24(12 Suppl):I60–5.
2 Lansberg MG, Thijs VN, O'Brien MW, Ali JO, de Crespigny AJ, Tong DC, et al. Evolution of apparent diffusion coefficient, diffusion-weighted, and T2-weighted signal intensity of acute stroke. AJNR Am J Neuroradiol. 2001;22(4):637–644.
3 Panesar SS, Abhinav K, Yeh FC, Jacquesson T, Collins M, Fernandez-Miranda J. Tractography for Surgical Neuro-Oncology Planning: Towards a Gold Standard. Neurotherapeutics. 2019;16(1):36–51.
4 Shahbandi A, Sattari SA, Haghshomar M, Shab-Bidar S, Lawton MT. Application of diffusion tensor-based tractography in treatment of brain arteriovenous malformations: a systematic review. Neurosurg Rev. 2023;46(1):115.
5 Basser PJ, Mattiello J, LeBihan D. Estimation of the effective self-diffusion tensor from the NMR spin echo. J Magn Reson B. 1994;103(3):247–254.
6 Chandarana H, Taouli B. Diffusion and perfusion imaging of the liver. Eur J Radiol. 2010;76(3):348–358.
7 Girardet R, Dubois M, Manasseh G, Jreige M, Du Pasquier C, Canniff E, et al. The combination of non-contrast abbreviated MRI and alpha foetoprotein has high performance for hepatocellular carcinoma screening. Eur Radiol. 2023;33(10):6929–6938.
8 Sobeh T, Inbar Y, Apter S, Soffer S, Anteby R, Kraus M, et al. Diffusion-weighted MRI for predicting and assessing treatment response of liver metastases from CRC – A systematic review and meta-analysis. Eur J Radiol. 2023;163:110810.
9 Padhani AR, Schoots IG. Prostate cancer screening-stepping forward with MRI. Eur Radiol. 2023;33(10):6670–6676.
10 Iima M, Honda M, Sigmund EE, Ohno Kishimoto A, Kataoka M, Togashi K. Diffusion MRI of the breast: Current status and future directions. J Magn Reson Imaging. 2020;52(1):70–90.
11 Partridge SC, Nissan N, Rahbar H, Kitsch AE, Sigmund EE. Diffusion-weighted breast MRI: Clinical applications and emerging techniques. J Magn Reson Imaging. 2017;45(2):337-355.
12 Jelescu IO, Palombo M, Bagnato F, Schilling KG. Challenges for biophysical modeling of microstructure. J Neurosci Methods. 2020;344:108861.
13 Griswold MA, Jakob PM, Heidemann RM, Nittka M, Jellus V, Wang J, et al. Generalized autocalibrating partially parallel acquisitions (GRAPPA). Magn Reson Med. 2002;47(6):1202–1210.
14 Feinberg DA, Setsompop K. Ultra-fast MRI of the human brain with simultaneous multi-slice imaging. J Magn Reson. 2013;229:90–100.
15 Moeller S, Pisharady PK, Ramanna S, Lenglet C, Wu X, Dowdle L, et al. NOise reduction with DIstribution Corrected (NORDIC) PCA in dMRI with complex-valued parameter-free locally low-rank processing. Neuroimage. 2021;226:117539.
16 Veraart J, Novikov DS, Christiaens D, Ades-Aron B, Sijbers J, Fieremans E. Denoising of diffusion MRI using random matrix theory. Neuroimage. 2016;142:394–406.
17 Alexander DC, Dyrby TB, Nilsson M, Zhang H. Imaging brain microstructure with diffusion MRI: practicality and applications. NMR Biomed. 2019;32(4):e3841.
18 Novikov DS, Fieremans E, Jespersen SN, Kiselev VG. Quantifying brain microstructure with diffusion MRI: Theory and parameter estimation. NMR Biomed. 2019;32(4):e3998.
19 Novikov DS, Kiselev VG, Jespersen SN. On modeling. Magn Reson Med. 2018;79(6):3172–3193.
20 Jelescu IO, Fieremans E. Chapter 2 - Sensitivity and specificity of diffusion MRI to neuroinflammatory processes. In: Laule C, Port JD (Eds.). Advances in Magnetic Resonance Technology and Applications. Imaging Neuroinflammation. Academic Press. 2023:31–50. https://doi.org/10.1016/B978-0-323-91771-1.00010-1
21 Jensen JH, Helpern JA, Ramani A, Lu H, Kaczynski K. Diffusional kurtosis imaging: the quantification of non-gaussian water diffusion by means of magnetic resonance imaging. Magn Reson Med. 2005;53(6):1432–1440.
22 Jelescu IO, Veraart J, Adisetiyo V, Milla SS, Novikov DS, Fieremans E. One diffusion acquisition and different white matter models: how does microstructure change in human early development based on WMTI and NODDI? Neuroimage. 2015;107:242–256.
23 Paydar A, Fieremans E, Nwankwo JI, Lazar M, Sheth HD, Adisetiyo V, et al. Diffusional kurtosis imaging of the developing brain. AJNR Am J Neuroradiol. 2014;35(4):808–814.
24 Benitez A, Jensen JH, Falangola MF, Nietert PJ, Helpern JA. Modeling white matter tract integrity in aging with diffusional kurtosis imaging. Neurobiol Aging. 2018;70:265–275.
25 Cho KIK, Kwak YB, Hwang WJ, Lee J, Kim M, Lee TY, et al. Microstructural Changes in Higher-Order Nuclei of the Thalamus in Patients With First-Episode Psychosis. Biol Psychiatry. 2019;85(1):70–78.
26 Kochunov P, Rowland LM, Fieremans E, Veraart J, Jahanshad N, Eskandar G, et al. Diffusion-weighted imaging uncovers likely sources of processing-speed deficits in schizophrenia. Proc Natl Acad Sci U S A. 2016;113(47):13504–13509.

27 Pavan T, Alemán-Gómez Y, Jenni R, Steullet P, Schilliger Z, Dwir D, et al. White Matter Microstructure Alterations and Their Link to Symptomatology in Early Psychosis and Schizophrenia. 2024. https://doi.org/10.1101/2024.02.01.24301979

28 Dong JW, Jelescu IO, Ades-Aron B, Novikov DS, Friedman K, Babb JS, et al. Diffusion MRI biomarkers of white matter microstructure vary nonmonotonically with increasing cerebral amyloid deposition. Neurobiol Aging. 2020;89:118–128.

29 de Kouchkovsky I, Fieremans E, Fleysher L, Herbert J, Grossman RI, Inglese M. Quantification of normal-appearing white matter tract integrity in multiple sclerosis: a diffusion kurtosis imaging study. J Neurol. 2016;263(6):1146–1155.

30 Bai Y, Lin Y, Tian J, Shi D, Cheng J, Haacke EM, et al. Grading of Gliomas by Using Monoexponential, Biexponential, and Stretched Exponential Diffusion-weighted MR Imaging and Diffusion Kurtosis MR Imaging. Radiology. 2016;278(2):496–504.

31 Hui ES, Fieremans E, Jensen JH, Tabesh A, Feng W, Bonilha L, et al. Stroke assessment with diffusional kurtosis imaging. Stroke. 2012;43(11):2968–2273.

32 Umesh Rudrapatna S, Wieloch T, Beirup K, Ruscher K, Mol W, Yanev P, et al. Can diffusion kurtosis imaging improve the sensitivity and specificity of detecting microstructural alterations in brain tissue chronically after experimental stroke? Comparisons with diffusion tensor imaging and histology. Neuroimage. 2014;97:363–373.

33 Chen J, Chung S, Li T, Fieremans E, Novikov DS, Wang Y, et al. Identifying relevant diffusion MRI microstructure biomarkers relating to exposure to repeated head impacts in contact sport athletes. Neuroradiol J. 2023;36(6):693–701.

34 Karlsen RH, Einarsen C, Moe HK, Håberg AK, Vik A, Skandsen T, et al. Diffusion kurtosis imaging in mild traumatic brain injury and postconcussional syndrome. J Neurosci Res. 2019;97(5):568–581.

35 Rosenkrantz AB, Padhani AR, Chenevert TL, Koh DM, De Keyzer F, Taouli B, et al. Body diffusion kurtosis imaging: Basic principles, applications, and considerations for clinical practice. J Magn Reson Imaging. 2015;42(5):1190–1202.

36 Guo F, Leemans A, Viergever MA, Dell'Acqua F, De Luca A. Generalized Richardson-Lucy (GRL) for analyzing multi-shell diffusion MRI data. Neuroimage. 2020;218:116948.

37 Jeurissen B, Tournier JD, Dhollander T, Connelly A, Sijbers J. Multi-tissue constrained spherical deconvolution for improved analysis of multi-shell diffusion MRI data. Neuroimage. 2014;103:411–426.

38 Jelescu IO, Budde MD. Design and validation of diffusion MRI models of white matter. Front Phys. 2017;28:61.

39 Guglielmetti C, Veraart J, Roelant E, Mai Z, Daans J, Van Audekerke J, et al. Diffusion kurtosis imaging probes cortical alterations and white matter pathology following cuprizone induced demyelination and spontaneous remyelination. Neuroimage. 2016;125:363–377.

40 Jelescu IO, Zurek M, Winters KV, Veraart J, Rajaratnam A, Kim NS, et al. In vivo quantification of demyelination and recovery using compartment-specific diffusion MRI metrics validated by electron microscopy. Neuroimage. 2016;132:104–114.

41 Mollink J, Kleinnijenhuis M, Cappellen van Walsum AV, Sotiropoulos SN, Cottaar M, Mirfin C, et al. Evaluating fibre orientation dispersion in white matter: Comparison of diffusion MRI, histology and polarized light imaging. Neuroimage. 2017;157:561–574.

42 Salo RA, Belevich I, Jokitalo E, Gröhn O, Sierra A. Assessment of the structural complexity of diffusion MRI voxels using 3D electron microscopy in the rat brain. Neuroimage. 2021;225:117529.

43 Sepehrband F, Clark KA, Ullmann JF, Kurniawan ND, Leanage G, Reutens DC, et al. Brain tissue compartment density estimated using diffusion-weighted MRI yields tissue parameters consistent with histology. Hum Brain Mapp. 2015;36(9):3687–3702.

44 Veraart J, Fieremans E, Novikov DS. On the scaling behavior of water diffusion in human brain white matter. Neuroimage. 2019;185:379–387.

45 Coelho S, Baete SH, Lemberskiy G, Ades-Aron B, Barrol G, Veraart J, et al. Reproducibility of the Standard Model of diffusion in white matter on clinical MRI systems. Neuroimage. 2022;257:119290.

46 Zhang H, Schneider T, Wheeler-Kingshott CA, Alexander DC. NODDI: practical in vivo neurite orientation dispersion and density imaging of the human brain. Neuroimage. 2012;61(4):1000–1016.

47 Fieremans E, Jensen JH, Helpern JA. White matter characterization with diffusional kurtosis imaging. Neuroimage. 2011;58(1):177–188.

48 Diao Y, Jelescu I. Parameter estimation for WMTI-Watson model of white matter using encoder-decoder recurrent neural network. Magn Reson Med. 2023;89(3):1193–1206.

49 Jespersen SN, Olesen JL, Hansen B, Shemesh N. Diffusion time dependence of microstructural parameters in fixed spinal cord. Neuroimage. 2018;182:329–342.

50 Assaf Y, Freidlin RZ, Rohde GK, Basser PJ. New modeling and experimental framework to characterize hindered and restricted water diffusion in brain white matter. Magn Reson Med. 2004;52(5):965–978.

51 Novikov DS, Veraart J, Jelescu IO, Fieremans E. Rotationally-invariant mapping of scalar and orientational metrics of neuronal microstructure with diffusion MRI. Neuroimage. 2018;174:518–538.

52 Tristão Pereira C, Diao Y, Yin T, da Silva AR, Lanz B, Pierzchala K, et al. Synchronous nonmonotonic changes in functional connectivity and white matter integrity in a rat model of sporadic Alzheimer's disease. Neuroimage. 2021;225:117498.

53 Jelescu IO, Veraart J, Fieremans E, Novikov DS. Degeneracy in model parameter estimation for multi-compartmental diffusion in neuronal tissue. NMR Biomed. 2016;29(1):33–47.

54 Liao Y, Coelho S, Chen J, Ades-Aron B, Pang M, Osorio R, et al. Mapping tissue microstructure of brain white matter in vivo in health and disease using diffusion MRI. ArXiv [Preprint]. 2023:arXiv:2307.16386v2.

55 Edwards LJ, Pine KJ, Ellerbrock I, Weiskopf N, Mohammadi S. NODDI-DTI: Estimating Neurite Orientation and Dispersion Parameters from a Diffusion Tensor in Healthy White Matter. Front Neurosci. 2017;11:720.

56 Jelescu IO, de Skowronski A, Geffroy F, Palombo M, Novikov DS. Neurite Exchange Imaging (NEXI): A minimal model of diffusion in gray matter with inter-compartment water exchange. Neuroimage. 2022;256:119277.

57 Olesen JL, Østergaard L, Shemesh N, Jespersen SN. Diffusion time dependence, power-law scaling, and exchange in gray matter. Neuroimage. 2022;251:118976.

58 Lee HH, Olesen JL, Tian Q, Ramos Llorden G, Jespersen SN, Huang SY. Revealing diffusion time-dependence and exchange effect in the in vivo human brain gray matter by using high gradient diffusion MRI. Proc. Intl. Soc. Mag. Reson. Med. 2022. London, UK, p. 254.

59 Uhl Q, Pavan T, Molendowska M, Jones DK, Palombo M, Jelescu I. Quantifying human gray matter microstructure using Neurite Exchange Imaging (NEXI) and 300 mT/m gradients. Imaging Neuroscience. 2024;2:1–19.

60 Uhl Q, Pavan T, Feiweier T, Piredda GF, Jespersen SN, Jelescu I. NEXI for the quantification of human gray matter microstructure on a clinical MRI scanner. Proc. Intl. Soc. Mag. Reson. Med. 2024. Singapore.

61 Uhl Q, Pavan T, Feiweier T, Canales-Rodríguez EJ, Jelescu I. Optimizing The NEXI Acquisition Protocol For Quantifying Human Gray Matter Microstructure On A Clinical MRI Scanner Using Explainable AI. Proc. Intl. Soc. Mag. Reson. Med. 2023. Presented at the Annual Meeting of the ISMRM, Toronto, Canada, p. 948.
62 Williamson NH, Ravin R, Cai TX, Falgairolle M, O'Donovan MJ, Basser PJ. Water exchange rates measure active transport and homeostasis in neural tissue. PNAS Nexus. 2023;2(3):pgad056.
63 Hertanu A, Uhl Q, Pavan T, Lamy CM, Jelescu IO. Quantifying features of human gray matter microstructure postmortem using NeuriteExchange Imaging (NEXI) at ultra-high field. Proc. Intl. Soc. Mag. Reson. Med. 2023. Toronto, Canada.
64 Xu J, Does MD, Gore JC. Quantitative characterization of tissue microstructure with temporal diffusion spectroscopy. J Magn Reson. 2009;200(2):189–197.
65 Merboldt KD, Hänicke W, Bruhn H, Gyngell ML, Frahm J. Diffusion imaging of the human brain in vivo using high-speed STEAM MRI. Magn Reson Med. 1992;23(1):179–192.
66 Szczepankiewicz F, Sjölund J, Ståhlberg F, Lätt J, Nilsson M. Tensor-valued diffusion encoding for diffusional variance decomposition (DIVIDE): Technical feasibility in clinical MRI systems. PLoS One. 2019;14(3):e0214238.
67 Jiang X, Li H, Xie J, McKinley ET, Zhao P, Gore JC, et al. In vivo imaging of cancer cell size and cellularity using temporal diffusion spectroscopy. Magn Reson Med. 2017;78(1):156–164.
68 Reynaud O, Winters KV, Hoang DM, Wadghiri YZ, Novikov DS, Kim SG. Pulsed and oscillating gradient MRI for assessment of cell size and extracellular space (POMACE) in mouse gliomas. NMR Biomed. 2016 Oct;29(10):1350–1363.
69 Zhang H, Liu K, Ba R, Zhang Z, Zhang Y, Chen Y, et al. Histological and molecular classifications of pediatric glioma with time-dependent diffusion MRI-based microstructural mapping. Neuro Oncol. 2023;25(6):1146–1156.
70 Zhu A, Shih R, Huang RY, DeMarco JK, Bhushan C, Morris HD, et al. Revealing tumor microstructure with oscillating diffusion encoding MRI in pre-surgical and post-treatment glioma patients. Magn Reson Med. 2023;90(5):1789–1801.
71 Wu D, Jiang K, Li H, Zhang Z, Ba R, Zhang Y, et al. Time-Dependent Diffusion MRI for Quantitative Microstructural Mapping of Prostate Cancer. Radiology. 2022;303(3):578–587.
72 Szczepankiewicz F, van Westen D, Englund E, Westin CF, Ståhlberg F, Lätt J, et al. The link between diffusion MRI and tumor heterogeneity: Mapping cell eccentricity and density by diffusional variance decomposition (DIVIDE). Neuroimage. 2016;142:522–532.
73 Topgaard D. Multidimensional diffusion MRI. J Magn Reson. 2017;275:98–113.
74 Westin CF, Knutsson H, Pasternak O, Szczepankiewicz F, Özarslan E, van Westen D, et al. Q-space trajectory imaging for multidimensional diffusion MRI of the human brain. Neuroimage. 2016;135:345–362.
75 Szczepankiewicz F, Lasič S, van Westen D, Sundgren PC, Englund E, Westin CF, et al. Quantification of microscopic diffusion anisotropy disentangles effects of orientation dispersion from microstructure: applications in healthy volunteers and in brain tumors. Neuroimage. 2015;104:241–252.
76 Nilsson M, Englund E, Szczepankiewicz F, van Westen D, Sundgren PC. Imaging brain tumour microstructure. Neuroimage. 2018;182:232–250.
77 Nery F, Szczepankiewicz F, Kerkelä L, Hall MG, Kaden E, Gordon I, et al. In vivo demonstration of microscopic anisotropy in the human kidney using multidimensional diffusion MRI. Magn Reson Med. 2019;82(6):2160–2168.
78 Fokkinga E, Hernandez-Tamames JA, Ianus A, Nilsson M, Tax CMW, Perez-Lopez R, et al. Advanced Diffusion-Weighted MRI for Cancer Microstructure Assessment in Body Imaging, and Its Relationship With Histology. J Magn Reson Imaging. 2023. doi: 10.1002/jmri.29144. Epub ahead of print.
79 Reynaud O. Time-Dependent Diffusion MRI in Cancer: Tissue Modeling and Applications. Front. Phys. 2017;5. https://doi.org/10.3389/fphy.2017.00058
80 Lemberskiy G, Fieremans E, Veraart J, Deng FM, Rosenkrantz AB, Novikov DS. Characterization of prostate microstructure using water diffusion and NMR relaxation. Front Phys. 2018;6:91.
81 Lemberskiy G, Rosenkrantz AB, Veraart J, Taneja SS, Novikov DS, Fieremans E. Time-Dependent Diffusion in Prostate Cancer. Invest Radiol. 2017;52(7):405–411.
82 Lemberskiy G, Feiweier T, Gyftopoulos S, Axel L, Novikov DS, Fieremans E. Assessment of myofiber microstructure changes due to atrophy and recovery with time-dependent diffusion MRI. NMR Biomed. 2021;34(7):e4534.
83 McDowell AR, Feiweier T, Muntoni F, Hall MG, Clark CA. Clinically feasible diffusion MRI in muscle: Time dependence and initial findings in Duchenne muscular dystrophy. Magn Reson Med. 2021;86(6):3192–3200.
84 Piredda GF, Hilbert T, Granziera C, Bonnier G, Meuli R, Molinari F, et al. Quantitative brain relaxation atlases for personalized detection and characterization of brain pathology. Magn Reson Med. 2020;83(1):337–351.
85 Pavan T, Alemán-Gómez Y, Jenni R, Cleusix M, Alameda L, Do KQ, et al. Normative Modelling of White Matter Microstructure in Early Psychosis and Schizophrenia. Proc. Intl. Soc. Mag. Reson. Med. 2023. Toronto, Canada, p. 651.
86 Szczepankiewicz F, Lasič S, van Westen D, Sundgren PC, Englund E, Westin CF, et al. Quantification of microscopic diffusion anisotropy disentangles effects of orientation dispersion from microstructure: applications in healthy volunteers and in brain tumors. Neuroimage. 2015;104:241-252.



Contact

Ileana Jelescu, Ph.D.
Assistant Professor, SNSF Eccellenza, and ERC Starting Fellow
Microstructure Mapping Lab
Dept of Radiology, Lausanne University Hospital (CHUV) and University of Lausanne (UNIL)
Centre de Recherche en Radiologie PET3, CHUV
Rue du Bugnon 46
1011 Lausanne
Switzerland
Tel.: +41 21 314 6020
Ileana.Jelescu@chuv.ch

Advances in Susceptibility-Weighted Imaging (SWI) and Quantitative Susceptibility Mapping (QSM)

Josef Pfeuffer[1], Korbinian Eckstein[2], Ashley Wilton Stewart[2], Marcel Dominik Nickel[1], Jin Jin[3], Heiko Meyer[1], Steffen Bollmann[2], Kieran O'Brien[3]

[1]Application Development, Siemens Healthineers AG, Erlangen, Germany
[2]The University of Queensland, Brisbane, Australia
[3]Siemens Healthcare Pty Ltd, Brisbane, Australia

Objectives

- Demonstrate enhanced performance of susceptibility-weighted imaging (SWI) in high-susceptibility brain regions (e.g., frontal lobe, ear canals) through improved phase processing.
- Achieve signal-to-noise improvements in SWI via the utilization of multi-echo SWI acquisition and processing techniques.
- Provide a comprehensive overview of processing methodologies and algorithms applied in the generation of quantitative susceptibility mapping (QSM) and susceptibility map-weighted imaging (SMWI).
- Demonstrate the advantages gained from using 3D deep learning *k*-space-to-image reconstruction (Deep Resolve Boost).
- Enable visualization of nigrosome 1 "swallow tail" patterns in the substantia nigra using a 0.65 mm isotropic protocol, accomplished within a three-minute acquisition.

The data shown in this article uses research sequences and scanner inline reconstructions at 3 Tesla[1] with software version *syngo* MR XA60. The 3T MR scanners include MAGNETOM Vida, MAGNETOM Skyra, and MAGNETOM Prisma. Three-dimensional gradient-echo imaging (3D-GRE) and 3D echo-planar imaging (3D-EPI) sequences are used in this article.

Introduction

There has been a growing interest in image contrasts derived from phase images obtained from T2*-weighted gradient-echo (GRE) acquisitions. The fundamental principles of Susceptibility-Weighted Imaging (SWI) were comprehensively expounded by J. R. Reichenbach and E. M. Haacke [1] in 2001. SWI is now a highly valuable contrast for a wide range of clinical applications. Valuable insights into the evolution and application of SWI principles can be found in the related references [2–5]. The recently proposed treatments for Alzheimer's disease will likely increase the utilization of SWI to regularly monitor potential side effects. These "Disease-Modifying Therapies" (DMT) rely on serial MR imaging with T2*-weighted and/or SWI imaging to check for the presence of microhemorrhages and superficial siderosis known as Amyloid-Related Imaging Abnormalities of Hemorrhage (ARIA-H) [6]. The recent Wave-CAIPI SWI product, illustrated in Figure 1, could be a useful addition to this clinical application.

Another phase imaging-based technique known as Quantitative Susceptibility Mapping (QSM) [4, 7–9] can also provide additional information about the apparent magnetic susceptibility of underlying tissues. QSM can provide information about the "biometal" content in tissues, including paramagnetic iron (Fe^{2+}), contrast agents (Gd, Fe^{2+}), and diamagnetic calcium (Ca^{2+}). QSM has the potential to provide new clinical insights into a variety of diseases, allowing for enhanced understanding and diagnosis. Examples include the following:

- Inflammation and Multiple Sclerosis (MS) [4, 10–13]
- Calcification [4] versus hemorrhaging in the brain [14] and in tumors [15]
- Support for presurgical planning for Parkinson's disease [16, 17]
- Iron accumulation in normal aging and in neurodegenerative diseases [18–24]
- Iron overload in the liver [25]
- Bone mineralization [26]

QSM reconstruction involves several sophisticated processing steps which are currently relegated to offline execution instead of using streamlined inline processing on the scanner. Furthermore, even though both SWI and QSM rely on the same underlying data, the lack of compatibility

[1]*Work in progress: The research application is currently under development and is not for sale in the U.S. and in other countries. Its future availability cannot be ensured.*

between the various processing techniques in existing software pipelines has hindered the seamless dual application of SWI and QSM post-processing steps.

In this work, we will showcase results from a research implementation which explored further enhancements to clinical GRE acquisitions attainable through the incorporation of parallel imaging in both directions with CAIPIRINHA acceleration, and adopting multi-echo acquisitions with suitable echo combinations. The SWI reconstruction pipeline on the scanner was extended to enable compatibility with advanced acceleration techniques, including CAIPIRINHA. The pipeline also utilizes an additional Laplacian unwrapping pre-processing step before high-pass filtering, and supports multi-echo datasets.

Magnitude and phase images were previously exported for processing in offline QSM packages. The reconstruction pipeline of the research implementation sequence includes two research QSM methods: TGV and MEDI, as detailed below. These methods run parallel to SWI, providing SWI, QSM maps, and QSM-derived images inline.

Lastly, the benefits of more efficient 3D-EPI sequences are also showcased for both SWI and QSM. This is made possible by integrating a novel deep learning *k*-space-to-image-space reconstruction. Through the utilization of the new 3D Deep Resolve Boost and super-resolution 3D Deep Resolve Sharp features, now available on MAGNETOM scanners, the imaging capabilities for both SWI and QSM applications are further amplified.

Improved Susceptibility-Weighted Imaging (SWI)

The recently available product Wave-CAIPI SWI is an innovative SWI technique exclusive to Siemens Healthineers [27, 28]. Figure 1 compares the speed and image quality of Wave-CAIPI SWI to current standard SWI, obtained using a MAGNETOM Vida with a voxel size of 0.6 × 0.6 × 2.0 mm³. This novel SWI approach allows for a substantial acceleration in diagnostic single-echo 3D-SWI, enabling imaging in half the acquisition time.

Multi-echo SWI data can be acquired with the research application, and it incorporates 3D Laplacian phase unwrapping for improved phase images. Imaging regions of high susceptibility result in phase shifts greater than ±π, characterized by black and white banding or aliasing in the phase image. This artifact is commonly seen above the paranasal sinuses and the ear canals. Adding a 3D Laplacian unwrapping pre-processing step before the conventional SWI reconstruction effectively removes the aliasing and reveals the smoother underlying phase change.

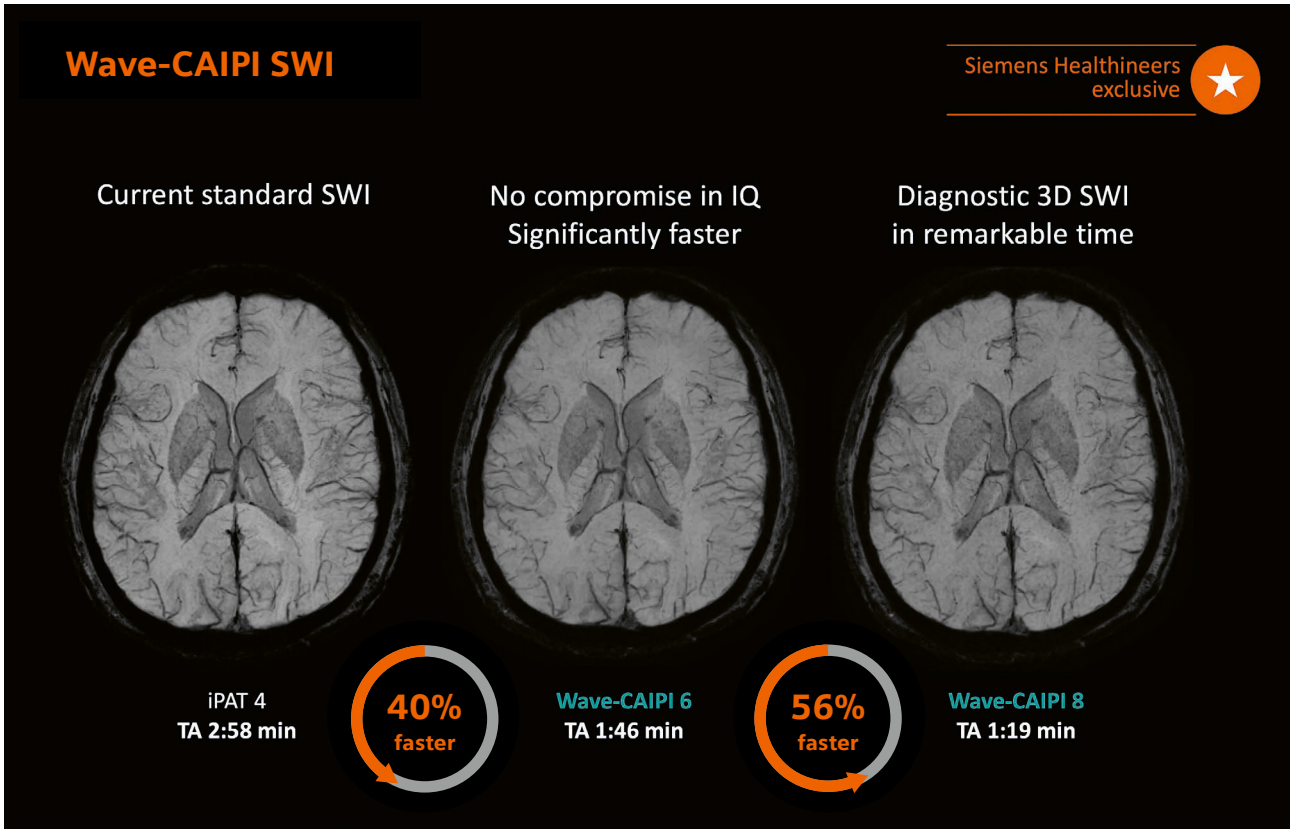

1 Comparison of product SWI and Wave-CAIPI SWI acquired on a 3T MAGNETOM Vida with a voxel size of 0.6 × 0.6 × 2.0 mm³. This novel SWI technique, unique to Siemens Healthineers, can significantly accelerate diagnostic 3D-SWI and enables imaging twice as fast as standard SWI.

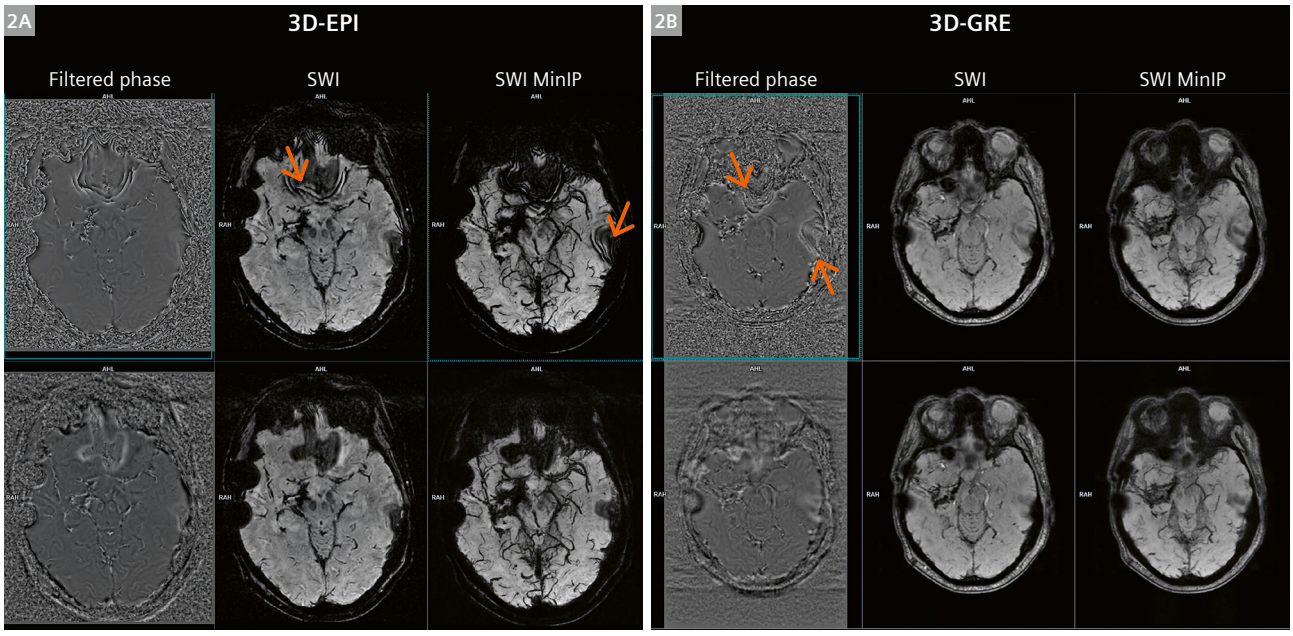

2 Effect of improved phase processing for susceptibility-weighted imaging (SWI): filtered phase (left), SWI image (middle) and minimum intensity projection MinIP (right). Artifacts are visible in regions with large off-resonances above the paranasal sinuses in the frontal lobe and ear canals (top row), causing sudden phase changes or aliasing (phase wraps). They are visibly improved using phase unwrapping (bottom row). The SWI images are from an MS patient scanned with 3D-EPI at an echo time of 40 ms **(2A)** and multi-echo 3D-GRE (ten TEs from 5 to 44 ms) **(2B)**.
Data courtesy of Dr. Sylvie Grand and Professor Alexandre Krainik (CHU Grenoble), and Marylene Delcey (Siemens Healthineers, France).

Imaging parameters:
3D-EPI: FOV 169 x 200 mm^2, 72 slices, resolution 0.39 × 0.39 × 1.5 mm^3 (interpolated), TE 40 ms, TR 80 ms, FA 20°, BW 369 Hz/px, no PAT, EF 11, TA 1:43 min.
3D-GRE: FOV 176 × 256 mm^2, 120 slices, resolution 0.41 × 0.39 × 1.0 mm^3 (interpolated), 10 TEs 5.3–44 ms, $TE_{average}$ 25 ms, TR 50 ms, FA 15°, BW 407 Hz/px, PAT 3, TA 5:25 min.

Consequently, the resultant SWI images show improved signal recovery with minimal artifacts in these areas of high susceptibility.

The impact of enhanced phase processing on SWI is illustrated in Figure 2. This MS patient was scanned using a product 3D-EPI at an echo time of 40 ms (Fig. 2A) and a product multi-echo 3D-GRE (ten echo times ranging from 5 to 44 ms) (Fig. 2B). In the first row, the filtered phase (left), SWI image (middle), and minimum intensity projection (MinIP) (right) depicts phase aliasing artifacts in regions with significant off-resonances (see arrows in the frontal lobe and ear canals). These artifacts result from the sudden phase wraps, which are difficult to resolve with conventional SWI processing. In the bottom row, the same images are presented after employing the Laplacian phase unwrapping pre-processing step. This process visibly improves the artifacts seen in the top row.

To further demonstrate the ability of the multi-echo 3D-GRE acquisition to enhance the signal-to-noise ratio compared to utilizing just a single echo, we present images from another MS patient. (Fig. 3A) SWI images (top panel) and SWI MinIP images (bottom) were captured using a multi-echo 3D-GRE acquisition with ten echoes ranging from 5 to 44 ms. Five out of the ten echo times are displayed, along with the combined images with an average echo time of 25 ms. A comparison is made with a single-echo acquisition on the left (Fig. 3B), highlighting the visibly improved signal- and contrast-to-noise observed in the combined images from the ten echoes. Various weightings for the echo combination can be chosen, such as equal weighting, echo-time-dependent weighting, or user-defined custom weighting.

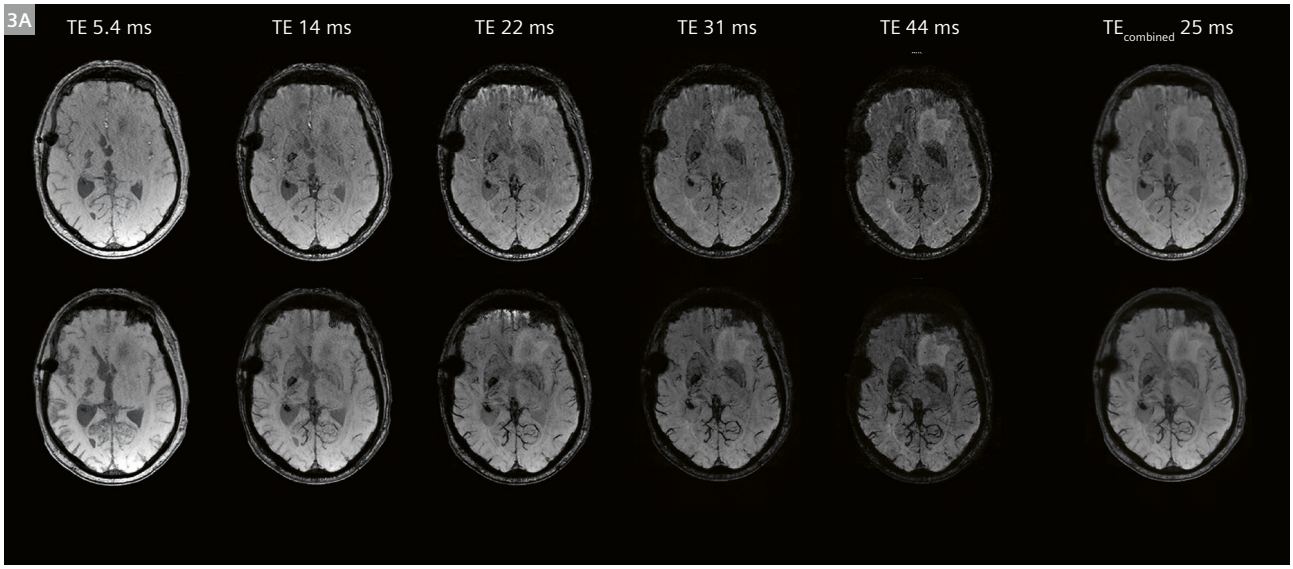

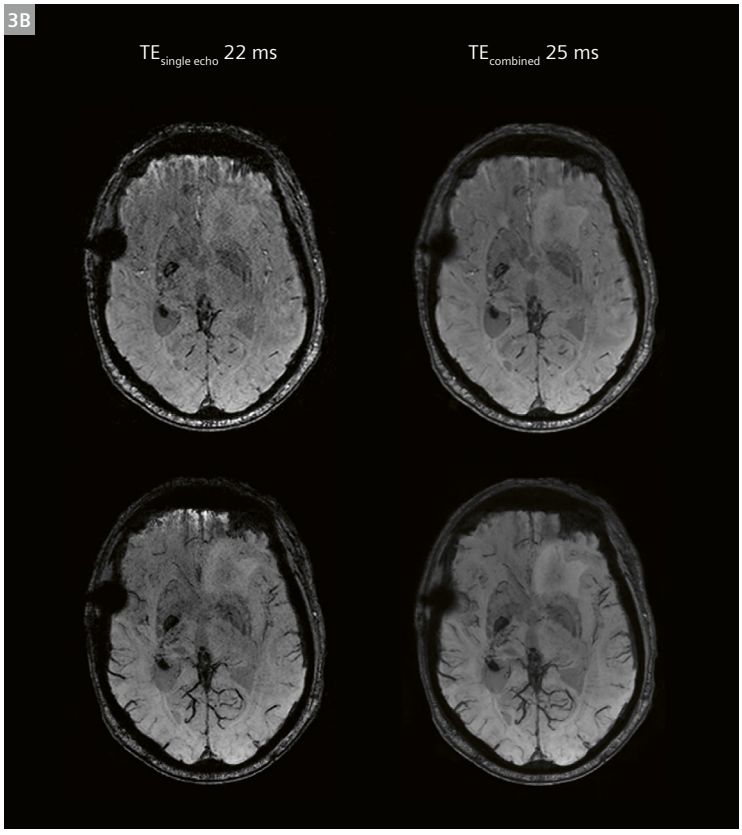

3 Signal-to-noise improvements for SWI using multi-echo 3D-GRE. **(3A)** SWI (top) and SWI MinIP (bottom) from an MS patient with a multi-echo 3D-GRE acquisition using ten echo times from 5 to 44 ms. Five images out of the ten echo times are shown, as well as the combined images with average TE 25 ms. **(3B**) Compared to a single-echo acquisition (left), the combined images from ten echoes show visibly improved signal- and contrast-to-noise.

Imaging parameters: Same 3D-GRE patient data as in Figure (2B) with a different slice shown.

Quantitative Susceptibility Mapping (QSM)

An overview of data acquisition and processing for SWI and QSM is shown in Figure 4. For QSM, the key steps include phase unwrapping, creating a mask from the magnitude image, and applying the background field correction and dipole inversion. In contrast, SWI involves filtering the signal phase, weighting it by the magnitude, and performing a MinIP across slices (Fig. 4A). In the SWI MinIP, the effects of susceptibility from the venous blood make it well-suited to visualizing veins in the brain. However, the processing steps required for SWI imaging make the data incompatible with the steps required to compute QSM. To overcome this, the research implementation reconstructs SWI and QSM in parallel pipelines.

This package now enables the inline post-processing of phase data to generate QSM data using two methods: **Total Generalized Variation (TGV)** [29–31] and **Morphology Enabled Dipole Inversion (MEDI)** [32]. For each method, either a morphological (for brain only) or phase-fidelity-based masking procedure like in ROMEO [31] is required to identify the region of interest for further processing. The package supports three different post processing methods:

- The **MEDI QSM algorithm** applies a choice of background field correction algorithms including the Projection onto Dipole Fields (PDF) and Laplacian Boundary Value (LBV) methods.
- The **TGV QSM algorithm** combines the Laplacian phase unwrapping, background phase removal, and dipole inversion into a single optimization problem. The TGV algorithm is implemented in the Compute Unified Device Architecture (CUDA, NVIDIA, Santa Clara, CA, USA) on the graphics processing unit (GPU) and can be configured by the number of iterations and the regularization parameters. GPU processing time for a 1 mm isotropic whole-brain data set is 5–10 seconds.
- In addition, the **two-step TGV QSM algorithm** [30] is a recent extension of the TGV method which performs two successive TGV reconstructions. The first reconstruction is processed with a mask that only contains reliable susceptibility sources. The second reconstruction applies an additional mask that includes both reliable and less-reliable sources. The different phase-based masks are determined using different thresholds applied to the phase-fidelity image – a normalized phase quality metric. The two-step TGV algorithm aims to be more robust to less-reliable or high-susceptibility sources, which often introduce streaking into the QSM image. The two successive reconstructions are subsequently combined to provide one resultant QSM image.

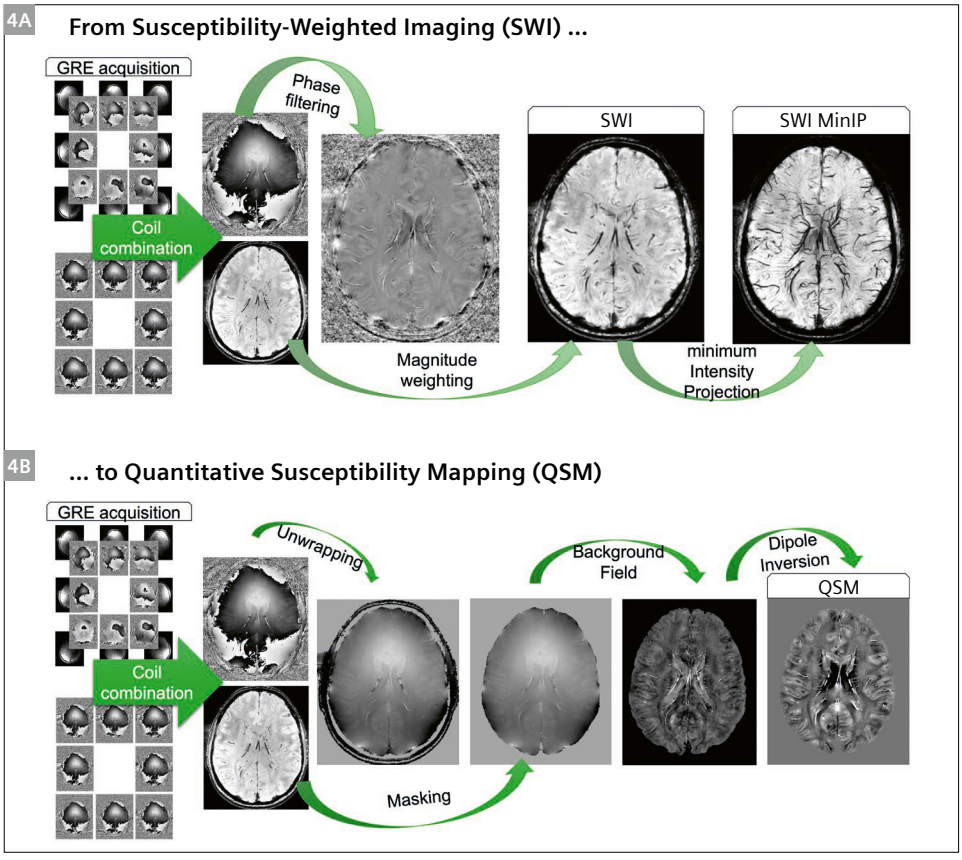

4 Overview of data acquisition and processing for SWI and QSM. **(4A)** SWI is computed from GRE data by filtering the signal phase, weighting it by the magnitude and then minimum intensity projection (MinIP) across slices. In the SWI MinIP, the susceptibility effects from the venous blood make it perfectly suited to visualizing veins in the brain. **(4B)** The steps that are typically required to compute QSM are phase unwrapping, calculating a brain mask, background field removal, and dipole inversion.

In Figure 5, three slices are presented, each processed with different QSM algorithms, along with a derived Susceptibility Map-Weighted Imaging (SMWI) contrast (see below). The QSM maps are scaled to the range of [-100, 300] ppb, which is equivalent to [-0.1, 0.3] ppm. In Figure 5A, the two-step TGV algorithm is featured. The processing mask is created from a phase fidelity map and is thereby independent from brain anatomy. In Figure 5B, the MEDI algorithm is employed, utilizing brain masking with slight erosion of image edges to mitigate artifacts in the dipole inversion process. The overall representation of deep brain structures is well-preserved in both QSM modalities, with MEDI showing a tendency for increased QSM values compared to TGV, while TGV images appear less regularized (smoothed) in comparison to MEDI.

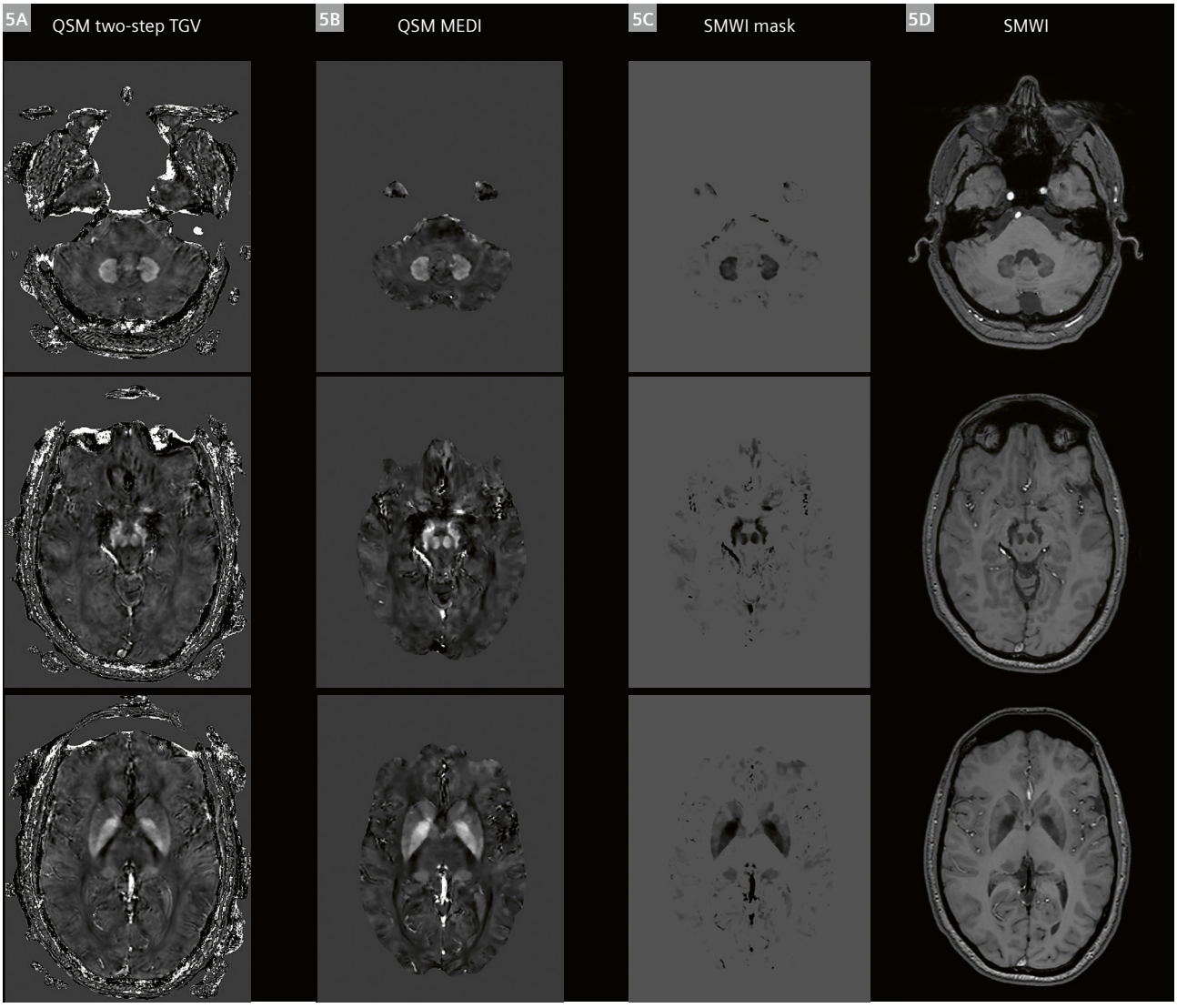

5 Three slices processed with different QSM algorithms and the derived SMWI contrast. The QSM maps are scaled to [-100, 300] ppb, equivalent to [-0.1, 0.3] ppm. **(5A)** The two-step TGV algorithm creates the processing mask from a phase fidelity map and is thus independent from brain anatomy. **(5B)** The MEDI algorithm uses brain masking, and the image edges are somewhat eroded to avoid artifacts in the dipole inversion process. Overall, deep brain structures are represented well in both QSM modalities. MEDI has a tendency for increased QSM values compared to TGV, while the TGV images appear less regularized (smoothed) compared to MEDI. **(5C)** SMWI mask with a weighting factor between [0, 1] calculated from Figure 5B, QSM MEDI images. **(5D)** SMWI images derived from the SMWI mask and the underlying magnitude image.

Imaging parameters:
3D-GRE: FOV 178 × 256 mm^2, 128 slices, resolution 0.5 × 0.5 × 1.0 mm^3 (interpolated), 6 s TE 5.4–27 ms, $TE_{average}$ 16 ms, TR 31 ms, FA 20°, BW 407 Hz/px, PAT 2, Deep Resolve Boost and Sharp, TA 4:25 min.

Susceptibility Map-Weighted Imaging (SMWI)

SMWI has recently been proposed to enhance the contrast-to-noise ratio for visualizing structures containing iron. Recent studies, such as the one conducted by Sung and colleagues in 2022, have demonstrated that SMWI surpasses SWI in assessing nigral hyperintensity at 3T [33].

SMWI images are generated from the QSM image, following the method outlined by Sung-Min Gho et al. in 2014 [34]. This involves combining the magnitude image with a QSM-based weighting factor, introducing an alternative yet analogous contrast to SWI.

The paramagnetic susceptibility mask (with positive susceptibility values, $th_{value} > 0$) is designed as follows [34]:

$$S_{mask}(x) = \begin{cases} 0 & th_{value} < S_{value}(x) \\ (th_{value} - S_{value}(x)) / th_{value} & 0 < S_{value}(x) \leq th_{value} \\ 1 & otherwise \end{cases}$$

By default, SMWI employs a paramagnetic susceptibility mask (pSMWI) with a preset threshold of 1 ppm (1000 ppb) and a multiplication factor denoted as m = 4. In the context of different pathologies, the utilization of a diamagnetic susceptibility mask (dSMWI) with negative susceptibility values is considered advantageous, although it is not explicitly illustrated in the present context.

The pSMWI mask is shown in Figure 5C and is characterized by a weighting factor within the range [0, 1], and is computed from the QSM MEDI images illustrated in Figure 5B. The SMWI images in Figure 5D are subsequently generated by combining the SMWI mask with the underlying magnitude image.

3D deep learning *k*-space-to-image reconstruction

The standard image reconstruction of the 3D-GRE and 3D-EPI sequences include GRAPPA and CAIPIRINHA. The research 3D-EPI application herein allows for flexible EPI train lengths, segmentation, and acceleration factors [35, 36]. Both sequences also include the 3D deep learning *k*-space-to-image reconstruction method Deep Resolve Boost, and the super-resolution method Deep Resolve Sharp.

The deep learning reconstruction comprises two independent, sequential processing steps. Firstly, Deep Resolve Boost images are generated on the acquired resolution using a variational network architecture with six iterations that alternate between parallel imaging reconstruction and 3D image regularizations using U-nets. The network parameters were determined through supervised training based on several hundreds of fully sampled 3D datasets of healthy volunteers from various body regions. Secondly, for Deep Resolve Sharp, the obtained images were interpolated using a deep learning-based super-resolution algorithm, with a factor-of-two interpolation. Both steps were implemented in PyTorch trained on a dedicated GPU cluster and with networks exported for prospective use in the scanner reconstruction pipeline.

Figure 6 displays QSM maps scaled within the [-100, 300] ppb range, obtained from the two sequences 3D-GRE and 3D-EPI, employing different image reconstructions. The QSM algorithm applied in this context was TGV.

The 3D-EPI protocol parameters were matched to those of the five-echo 3D-GRE, with an echo time set to 20 ms. The five-echo 3D-GRE had echo times ranging from 6.6 to 34 ms, with an average echo time of 20 ms. The acquisition time (TA) for the 3D-GRE sequence was 5:35 min. To align with the five echoes of the 3D-GRE, the EPI factor for 3D-EPI was set to five, rendering this sequence approximately four times faster (TA 1:41 min). The minimum repetition time (TR) was selected, specifically TR 39 ms for 3D-GRE, and TR 56 ms for 3D-EPI, respectively.

The signal- and contrast-to-noise ratio in the QSM maps exhibits a slight decrease when comparing 3D-GRE to the faster 3D-EPI acquisitions, as depicted in Figure 6A from left to right. This reduction aligns with our anticipated outcome from signal-to-noise calculations. However, when the data is reconstructed using the 3D deep learning *k*-space-to-image reconstruction method (Deep Resolve Boost), the QSM image quality and structural features are comparable to standard reconstruction. This holds true even with the approximate four-fold increase in speed, as illustrated in Figure 6B from left to right.

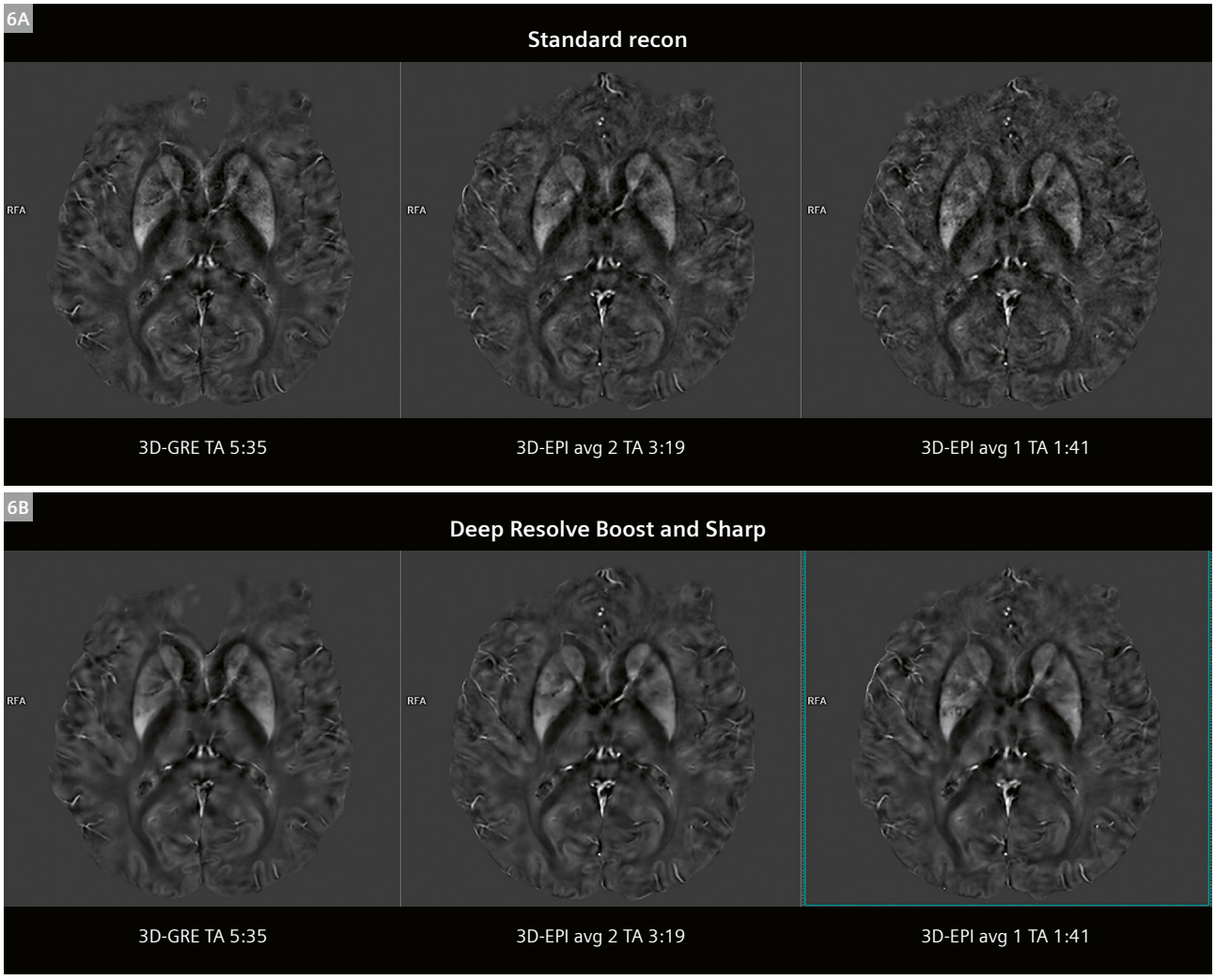

6 QSM maps scaled to [-100, 300] ppb from different sequences, 3D-GRE and 3D-EPI, and different image reconstructions. **(6A)** 3D-EPI used matched parameters with an echo time of 20 ms compared to 3D-GRE. The EPI factor of five in 3D-EPI compared to five echoes with 3D-GRE makes this sequence approx. four times faster. The QSM contrast-to-noise ratio decreases with the faster acquisition (left to right). **(6B)** Using the 3D deep learning *k*-space-to-image reconstruction (Deep Resolve Boost) could mostly preserve the QSM image quality even with an approx. 4-time increase in speed.

Imaging parameters: FOV 224 × 224 mm², 64 slices, resolution 0.35 × 0.35 × 2.0 mm³ (interpolated), PAT 3, standard reconstruction vs. Deep Resolve Boost and Sharp, TGV algorithm.
3D-GRE: 5 TEs 6.6 – 34 ms, $TE_{average}$ 20 ms, TR 39 ms, FA 15°, BW 200 Hz/px, TA 5:35 min.
3D-EPI: TE 20 ms, TR 56 ms, FA 21°, BW 284 Hz/px, EF 5, TA 3:19 / 1:41 min with avg 2 / 1.

Nigrosome 1 ("swallow tail") imaging in substantia nigra

Publications hint that SWI at 3T or 7T could potentially function as a novel imaging biomarker for idiopathic Parkinson's disease (IPD) [33] by improving the ability to observe the nigral hyperintensity or nigrosome 1. Recent studies [33] also propose that the novel SMWI methods may further enhance the ability to observe changes to nigrosome 1. These studies also provide evidence that the robust diagnostic performance of the novel SMWI methods remains consistent in a multicenter setting with various MRI scanners, indicating the potential applicability of SMWI in assessing nigrostriatal degeneration in individuals with parkinsonism.

Figure 7 displays QSM and SMWI images of a healthy subject, with slices planned along the AC–PC line. The nigrosome 1 "swallow tail" in the substantia nigra is clearly highlighted in both QSM and SMWI images (Fig. 7A). The SMWI image is presented in 3D orthogonal planes of nigrosome 1 (Fig. 7B).

Notably, using a 64-channel head-neck coil, the 0.65 mm isotropic dataset with whole-brain coverage was acquired in a total time of 3:12 min. This efficiency is achieved through (1) effective sampling with 3D-EPI and (2) employing 3D deep learning *k*-space-to-image reconstruction (Deep Resolve Boost).

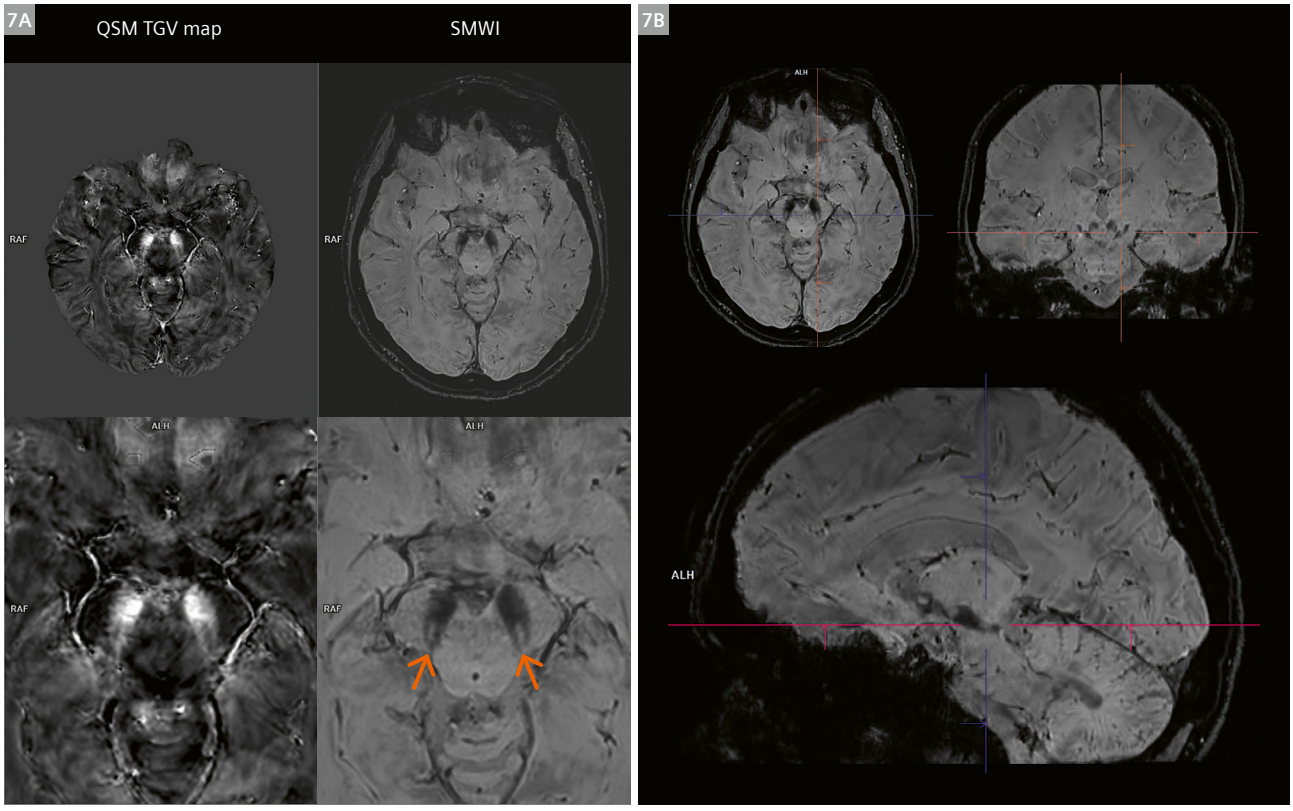

7 QSM and SMWI of a healthy subject with slices planned along the AC–PC line. **(7A)** The nigrosome 1 "swallow tail" in the substantia nigra is nicely contrasted in both QSM and SMWI images. **(7B)** SMWI image in 3D orthogonal planes of nigrosome 1. Remarkably, the 0.65 mm^3 isotropic dataset with whole-brain coverage could be acquired in 3:12 min using a 64-channel head-neck coil. This is made possible by using (1) efficient sampling with 3D-EPI and (2) 3D deep learning *k*-space-to-image reconstruction (Deep Resolve Boost).

Imaging parameters:

3D-EPI: FOV 250 × 250 mm^2, 196 slices, resolution 0.33 × 0.33 × 0.65 mm^3 (interpolated), TE 27 ms, TR 51 ms, FA 15°, BW_{RO} 651 Hz/px, BW_{PE} 30 Hz/px (46 Hz/mm), EF 19, slcOS 14%, slcPF 6/8, PAT 2, Deep Resolve Boost and Sharp, avg 2, TA 3:12 min.

Conclusions

In conclusion, this article showcases significant advancements in Susceptibility-Weighted Imaging (SWI) and Quantitative Susceptibility Mapping (QSM) techniques, offering notable improvements in image quality and diagnostic potential. Through utilization of 3D Laplacian phase unwrapping, SWI processing demonstrates enhanced signal recovery and reduced artifacts in areas of high susceptibility. The implementation of multi-echo 3D-GRE techniques further enhances signal-to-noise ratio in SWI images.

The introduction of QSM and SMWI emerges as a promising approach to achieve superior diagnostic performance compared to SWI alone. The synergy of efficient sampling techniques such as 3D-EPI and 3D deep learning *k*-space-to-image reconstruction (Deep Resolve Boost) can significantly accelerate the image acquisition while preserving image quality for these novel clinical imaging techniques.

These advancements contribute to the evolving landscape of neuroimaging, paving the way for enhanced diagnostic accuracy and efficiency in evaluating neurodegenerative disorders. The search for and validation of clinically valuable biomarkers, such as the improved visualization of nigrosome 1 and the "swallow tail" sign for idiopathic Parkinson's disease, are now more accessible through this research.

Acknowledgments

The collaborative development of the QSM and 3D-EPI research package involved Professor Markus Barth and his team at the Center for Advanced Imaging, The University of Queensland, Australia, which includes Monique Tourell and Saskia Bollmann.

Jinsuh Kim from Emory University School of Medicine, Atlanta, USA (present address), played a pivotal role in developing the TGV GPU code in collaboration with Christian Langkammer and Kristian Bredies from the University of Graz, Austria.

The ROMEO code was developed through a collaboration with Professor Simon Robinson from the High Field MR Center, Medical University of Vienna, Austria, and Barbara Dymerska from the Wellcome Centre for Human Neuroimaging, University College London, UK.

Professors Pascal Spincemaille and Yi Wang from the Cornell MRI Research Lab, NY, USA, provided the QSM MEDI code.

Dr. Sylvie Grand and Professor Alexandre Krainik from CHU Grenoble, France, and Marylene Delcey, Siemens Healthineers, France, contributed the patient SWI data presented in Figure 2. Protocol optimization and subject data for Figure 7 were provided by Melanie Adam, master's student at Siemens Healthineers, Erlangen, Germany.

The authors express their gratitude to Professor Jongho Lee from the Department of Electrical and Computer Engineering, and to Professor Eung Yeop Kim from Radiology at Samsung Medical Center, Seoul, Korea, for their insightful discussions about Susceptibility Map-Weighted Imaging.

References

1 Reichenbach JR, Haacke EM. High-resolution BOLD venographic imaging: a window into brain function. NMR Biomed. 2001;14(7–8):453–67.
2 Haacke EM, Mittal S, Wu Z, Neelavalli J, Cheng YC. Susceptibility-weighted imaging: technical aspects and clinical applications, part 1. AJNR Am J Neuroradiol. 2009;30(1):19–30.
3 Mittal S, Wu Z, Neelavalli J, Haacke EM. Susceptibility-weighted imaging: technical aspects and clinical applications, part 2. AJNR Am J Neuroradiol. 2009;30(2):232–52.
4 Wang Y, Spincemaille P, Liu Z, Dimov A, Deh K, Li J, et al. Clinical quantitative susceptibility mapping (QSM): Biometal imaging and its emerging roles in patient care. J Magn Reson Imaging. 2017;46(4):951–971.
5 Eckstein K, Bachrata B, Hangel G, Widhalm G, Enzinger C, Barth M, et al. Improved susceptibility weighted imaging at ultra-high field using bipolar multi-echo acquisition and optimized image processing: CLEAR-SWI. Neuroimage. 2021;237:118175.
6 Cummings J, Rabinovici GD, Atri A, Aisen P, Apostolova LG, Hendrix S, et al. Aducanumab: Appropriate Use Recommendations Update. J Prev Alzheimers Dis. 2022;9(2):221–230.
7 Duyn J. MR susceptibility imaging. J Magn Reson. 2013;229:198–207.
8 Haacke EM, Liu S, Buch S, Zheng W, Wu D, Ye Y. Quantitative susceptibility mapping: current status and future directions. Magn Reson Imaging. 2015;33(1):1–25.
9 Wang Y, Liu T. Quantitative susceptibility mapping (QSM): Decoding MRI data for a tissue magnetic biomarker. Magn Reson Med. 2015;73(1):82–101.
10 Chen W, Gauthier SA, Gupta A, Comunale J, Liu T, Wang S, et al. Quantitative susceptibility mapping of multiple sclerosis lesions at various ages. Radiology. 2014;271(1):183–92.
11 Langkammer C, Liu T, Khalil M, Enzinger C, Jehna M, Fuchs S, et al. Quantitative susceptibility mapping in multiple sclerosis. Radiology. 2013;267(2):551–9.
12 Li X, Harrison DM, Liu H, Jones CK, Oh J, Calabresi PA, et al. Magnetic susceptibility contrast variations in multiple sclerosis lesions. J Magn Reson Imaging. 2016 Feb;43(2):463–73.
13 Rahmanzadeh R, Galbusera R, Lu PJ, Bahn E, Weigel M, Barakovic M, et al. A New Advanced MRI Biomarker for Remyelinated Lesions in Multiple Sclerosis. Ann Neurol. 2022;92(3):486–502.
14 Schweser F, Deistung A, Lehr BW, Reichenbach JR. Differentiation between diamagnetic and paramagnetic cerebral lesions based on magnetic susceptibility mapping. Med Phys. 2010;37(10):5165–78.
15 Straub S, Laun FB, Emmerich J, Jobke B, Hauswald H, Katayama S, et al. Potential of quantitative susceptibility mapping for detection of prostatic calcifications. J Magn Reson Imaging. 2017;45(3):889–898.
16 Alkemade A, de Hollander G, Keuken MC, Schäfer A, Ott DVM, Schwarz J, et al. Comparison of T2*-weighted and QSM contrasts in Parkinson's disease to visualize the STN with MRI. PLoS One. 2017;12(4):e0176130.
17 Devos D, Moreau C, Devedjian JC, Kluza J, Petrault M, Laloux C, et al. Targeting chelatable iron as a therapeutic modality in Parkinson's disease. Antioxid Redox Signal. 2014;21(2):195–210.

18 Bilgic B, Pfefferbaum A, Rohlfing T, Sullivan EV, Adalsteinsson E. MRI estimates of brain iron concentration in normal aging using quantitative susceptibility mapping. Neuroimage. 2012;59(3):2625–35.
19 Acosta-Cabronero J, Williams GB, Cardenas-Blanco A, Arnold RJ, Lupson V, Nestor PJ. In vivo quantitative susceptibility mapping (QSM) in Alzheimer's disease. PLoS One. 2013;8(11):e81093.
20 Moon Y, Han SH, Moon WJ. Patterns of Brain Iron Accumulation in Vascular Dementia and Alzheimer's Dementia Using Quantitative Susceptibility Mapping Imaging. J Alzheimers Dis. 2016;51(3):737–45.
21 Hwang EJ, Kim HG, Kim D, Rhee HY, Ryu CW, Liu T, et al. Texture analyses of quantitative susceptibility maps to differentiate Alzheimer's disease from cognitive normal and mild cognitive impairment. Med Phys. 2016;43(8):4718.
22 van Bergen JM, Hua J, Unschuld PG, Lim IA, Jones CK, Margolis RL, et al. Quantitative Susceptibility Mapping Suggests Altered Brain Iron in Premanifest Huntington Disease. AJNR Am J Neuroradiol. 2016;37(5):789–96.
23 Deistung A, Stefanescu MR, Ernst TM, Schlamann M, Ladd ME, Reichenbach JR, et al. Structural and Functional Magnetic Resonance Imaging of the Cerebellum: Considerations for Assessing Cerebellar Ataxias. Cerebellum. 2016;15(1):21–25.
24 Schweitzer AD, Liu T, Gupta A, Zheng K, Seedial S, Shtilbans A, et al. Quantitative susceptibility mapping of the motor cortex in amyotrophic lateral sclerosis and primary lateral sclerosis. AJR Am J Roentgenol. 2015;204(5):1086–92.
25 Sharma SD, Fischer R, Schoennagel BP, Nielsen P, Kooijman H, Yamamura J, et al. MRI-based quantitative susceptibility mapping (QSM) and R2* mapping of liver iron overload: Comparison with SQUID-based biomagnetic liver susceptometry. Magn Reson Med. 2017;78(1):264–270.
26 He Q, Liu Z, Wang Y, Du J. Ultrashort Echo Time Quantitative Susceptibility Mapping (UTE-QSM) of Cortical Bone. Proceedings of the 23rd Annual Meeting ISMRM Toronto, ON, Canada. 2015. Vol. 1725.
27 Polak D, Cauley S, Bilgic B, Wald L, Setsompop K. Ultrafast Multi-contrast High-resolution 3D Brain MRI: a Technical Description of Wave-CAIPI. MAGNETOM Flash.2020;76(1):17–20.
28 Filho ALG, Conklin J, Rapalino O, Schaefer P, Huang S. Ultrafast Multi-Contrast High-Resolution 3D Brain MRI: Clinical Evaluation of Wave-CAIPI Acceleration in SWI, MPRAGE, FLAIR, SPACE. ↗ MAGNETOM Flash.2020;76(1):21–27.
29 Langkammer C, Bredies K, Poser BA, Barth M, Reishofer G, Fan AP, et al. Fast quantitative susceptibility mapping using 3D EPI and total generalized variation. Neuroimage. 2015;111:622–30.
30 Stewart AW, Robinson SD, O'Brien K, Jin J, Widhalm G, Hangel G, et al. QSMxT: Robust masking and artifact reduction for quantitative susceptibility mapping. Magn Reson Med. 2022;87(3):1289–1300.
31 Dymerska B, Eckstein K, Bachrata B, Siow B, Trattnig S, Shmueli K, et al. Phase unwrapping with a rapid opensource minimum spanning tree algorithm (ROMEO). Magn Reson Med. 2021;85(4):2294–2308.
32 Liu J, Liu T, de Rochefort L, Ledoux J, Khalidov I, Chen W, et al. Morphology enabled dipole inversion for quantitative susceptibility mapping using structural consistency between the magnitude image and the susceptibility map. Neuroimage. 2012;59(3):2560–8.
33 Sung YH, Kim JS, Yoo SW, Shin NY, Nam Y, Ahn TB, et al. A prospective multi-centre study of susceptibility map-weighted MRI for the diagnosis of neurodegenerative parkinsonism. Eur Radiol. 2022;32(5):3597–3608.
34 Gho SM, Liu C, Li W, Jang U, Kim EY, Hwang D, et al. Susceptibility map-weighted imaging (SMWI) for neuroimaging. Magn Reson Med. 2014;72(2):337–46.
35 Jin J, Tourell M, Sati P, Liu K, Derbyshire J, O'Brien K, et al. Segmented 3D EPI with CAIPIRINHA for Fast, High-Resolution T2*-weighted Imaging. Proceedings of the Annual Meeting ISMRM 2021.
36 Jin J, Nickel D, Pfeuffer J, Tourell M, Stewart A, Bollmann S. Fast, High-resolution Whole Brain SWI and QSM with CAIPIRINHA 3D-EPI and Deep Learning Reconstruction. Proceedings of the Annual Meeting ISMRM 2024.

Contact

Dr. Josef Pfeuffer
Siemens Healthineers AG
SHS DI MR RCT CLS NEUR
Erlangen
Germany
josef.pfeuffer@siemens-healthineers.com


Josef Pfeuffer


Steffen Bollmann


Korbinian Eckstein


Ashley Wilton Stewart

Canine and Feline MRI: How Does it Differ from Human MRI?

Zoe Lenard, BVSc (Hons) FANZCVS (Radiology)

Animalius Vet, Perth, Western Australia

The recognition of the importance of the human-animal bond has driven demand for veterinary services, with owners often prepared to seek out advanced diagnostics and treatments for their pets. Pandemic conditions saw a spike in pet ownership [1], with 69% of Australian households owning a pet. There has been a steady increase in the demand for advanced imaging (CT and MRI) in the last decade and the access to veterinary MRI has correspondingly increased. Companion animals (dogs and cats) are commonly affected by neurological and musculoskeletal conditions, which are suited to MR imaging.

Whilst principles for MRI remain the same regardless of species, there are several important differences between veterinary and human patients.

Anatomic considerations

Dogs and cats are typically smaller than the average adult human. Veterinary patient size may have similarities with pediatric imaging, with body weights ranging from 1 to 2 kg for small-breed dogs, puppies, and kittens, and 50 to 80 kg for large-breed dogs. Mammalian anatomy is similar, but there are several species-specific quirks. For instance, dogs and cats have 13 thoracic and 7 lumbar vertebrae, compared to 12 and 5 in humans.

The obvious size discrepancy between humans and veterinary patients is often amplified, particularly in the head. The relative size of the canine or feline brain is much smaller than the human brain, because much of the carnivorous head is occupied by masticatory muscles, significant frontal sinuses, and a relatively massive nasal cavity (Fig. 1). This makes sense in an evolutionary sense: Predators and carnivores have evolved to have 2 to 3 times the bite force of humans, necessitating a significant investment in masticatory muscles.

There is also considerable variation in skull length between individual dog breeds. And the length of the typical canine or feline nasal cavity puts a human's nose to shame. Intricate and delicate nasal turbinates fill a massive paired nasal cavity, opening to a cavernous paired frontal sinus. Many canine and feline nasal cavities are as long as (or longer) than the length of the brain. This can

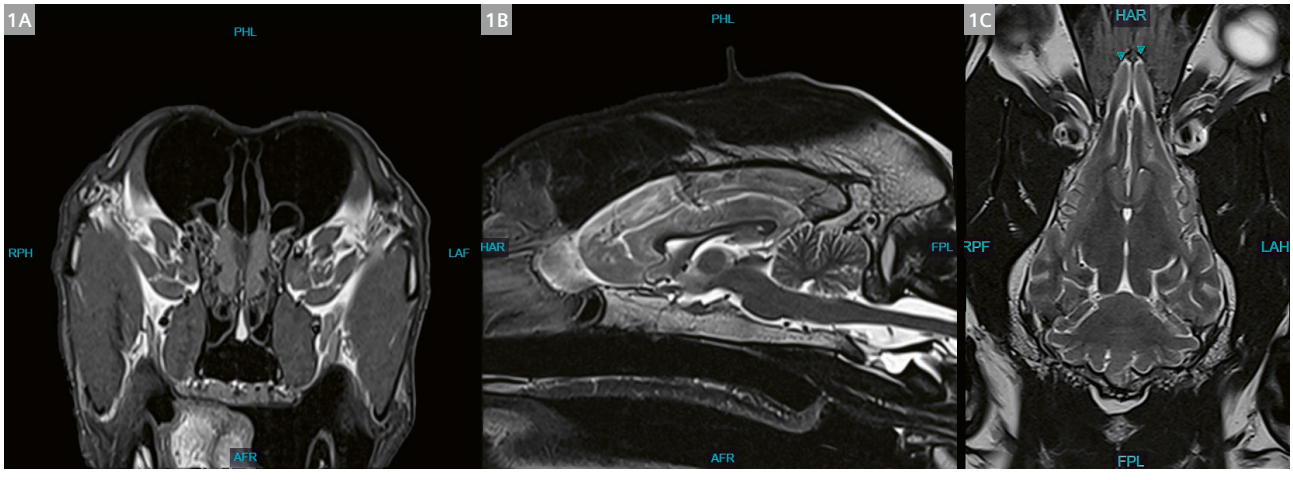

1 **Great Dane**
(1A) Transverse T1w image at the level of the interthalamic adhesion. Note the large masticatory muscles relative to the small size of the brain within the head. **(1B)** Sagittal T2w image at the level of the interthalamic adhesion. Note the long olfactory bulbs of the cerebrum (left, abutting the cribriform plate), the air-filled frontal sinuses dorsally, and the normal shape of the cerebellum caudally. **(1C)** Dorsal T2w image at the level of the interthalamic adhesion. Note the large olfactory bulbs of the cerebrum (arrow heads) and the large amount of muscle surrounding the skull.

lead to the development of massive nasal pathology, including nasal carcinomas or fungal rhinitis, which lend themselves to MRI evaluation (Figs. 2 and 3). Compare this to the human, where it would be unusual to have a nose longer than the diameter of the brain in any plane. The olfactory bulbs of the canine brain are significant structures on a large stalk (Fig. 1C), and the ability to detect smell (and emotion) far exceeds the analytical ability of modern instrumentation [2].

Recent decades have seen an increase in popularity of brachycephalic breeds as pets (including the French Bulldog or the British Shorthair cat). British sources suggest

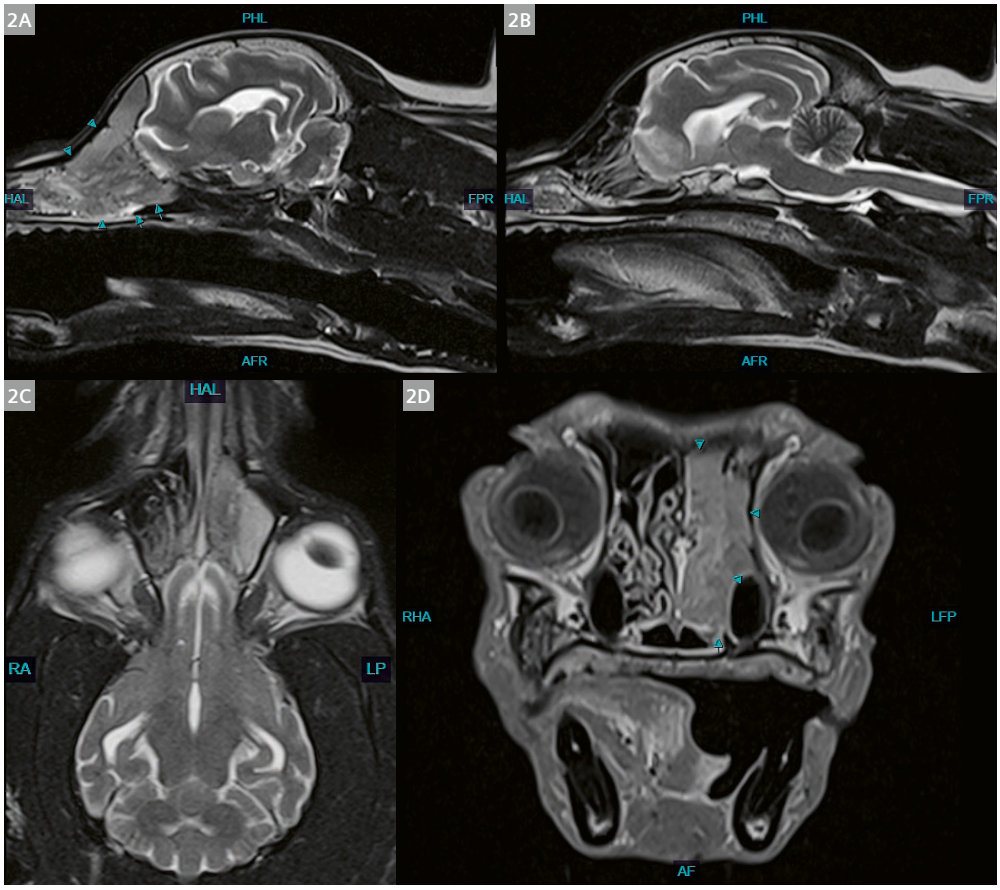

2 Maltese dog
(2A) Parasagittal T2w image through the left nasal cavity showing a large mass (arrows). **(2B)** Parasagittal T2w image through the right nasal cavity showing normal nasal turbinates. **(2C)** Dorsal T2w image showing normal right caudal nasal turbinate bones and the mass destroying the left nasal turbinate bones. Right is to the left. **(2D)** Transverse T1w with contrast showing left-sided nasal cavity mass (arrows).

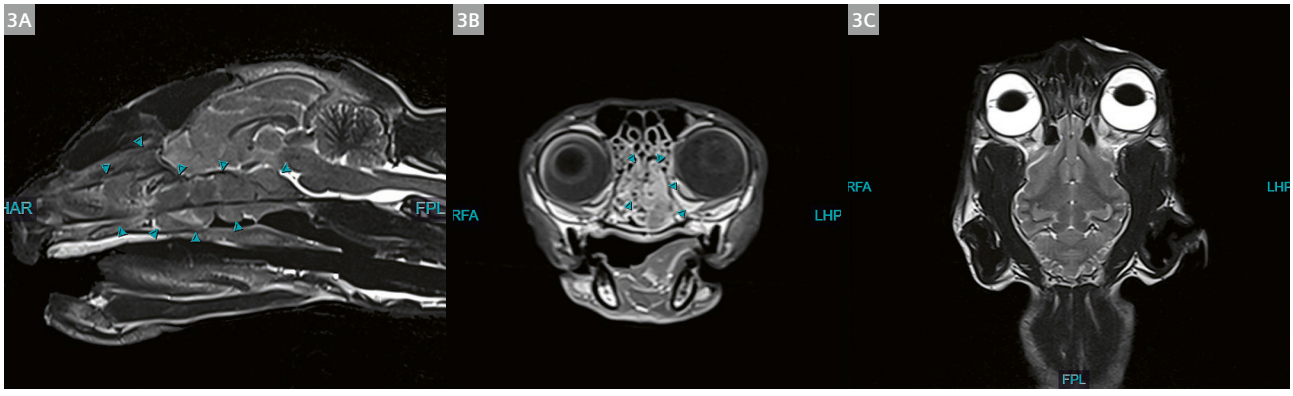

3 Cat
(3A) Sagittal T2w image showing large, isointense nasal cavity mass (arrows) throughout the ventral aspect of the nasal cavity and into the nasopharynx. **(3B)** Transverse T2w image showing isointense nasal cavity mass (arrows) throughout the ventral aspect of the nasal cavity and into the nasopharynx. **(3C)** Dorsal T2w image showing a normal dorsal feline nasal cavity with multiple fine turbinate bones.

a 400% increase in registrations of French Bulldogs over recent decades [3]. Their popularity is due to their appealing short, wide face and large eyes. The biomechanics of the canine and feline brachycephalic skull have been ethically disastrous, truncating the nasal cavity and obliterating frontal sinuses. Rather than emulating the human skull with its large brain, in these breeds, there is compression of the craniocaudal skull dimension, with the resulting deformation causing upper airway obstruction, caudal occipital malformation resulting in brain herniation, and ventriculomegaly and ocular abnormalities (Fig. 4). The results can be devastating and lead to conditions like hyperthermia, upper airway obstruction (asphyxiation), seizures, and neck pain.

The spinal cord of a small dog or cat is relatively small and may measure only 3–5 mm in diameter. In a larger-breed canine, it may measure up to 9–10 mm in diameter (Figs. 5, 6). The increased number of thoracic and lumbar

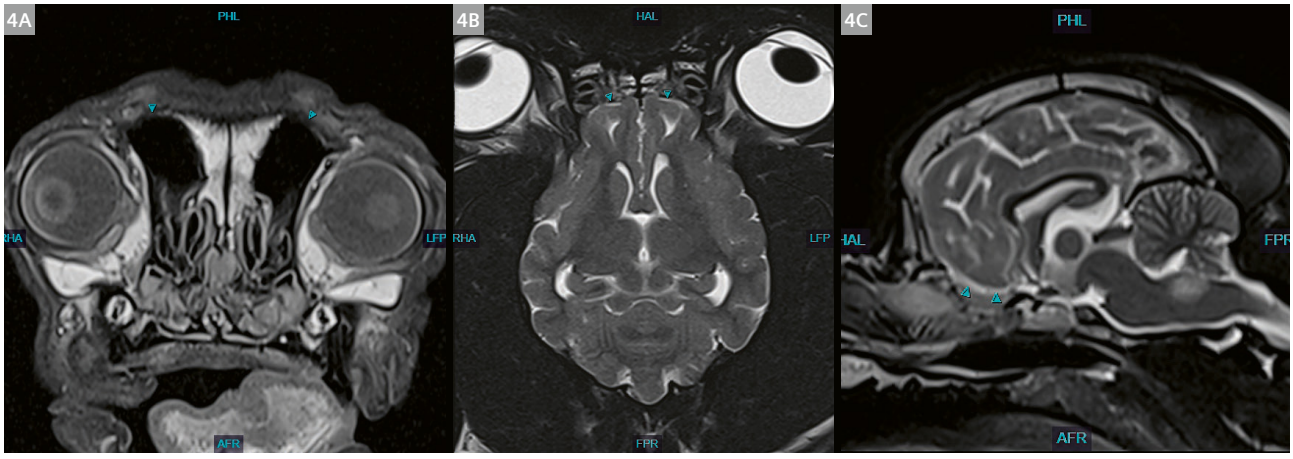

4 French Bulldog
(4A) Transverse T1w image through the caudal nasal cavity showing small frontal sinuses (arrowheads) and minimal nasal turbinates compared to the Great Dane (1A). **(4B)** Dorsal T2w image through the interthalamic adhesion showing truncated cerebral olfactory bulbs (arrows) and minimal nasal turbinates compared to the Great Dane (1B). **(4C)** Sagittal T2w image showing truncated cerebral olfactory bulbs (arrowheads) and minimal nasal cavity.

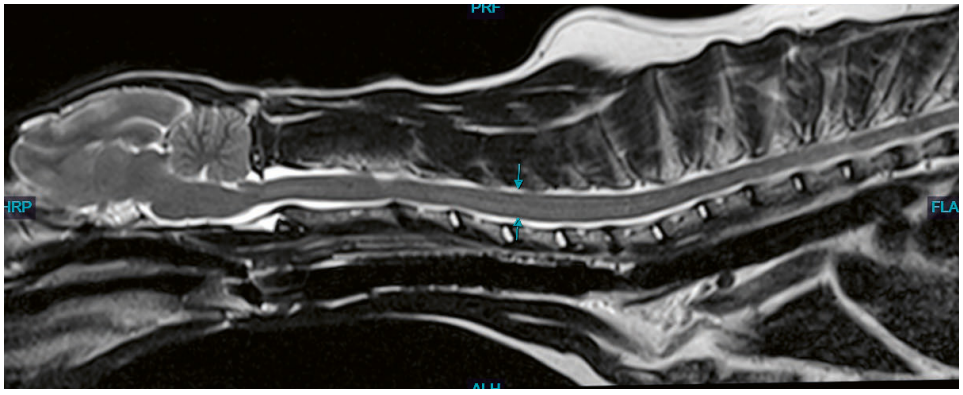

5 Cat
Sagittal T2w image:
The height of the spinal cord between the arrows is 4 mm.

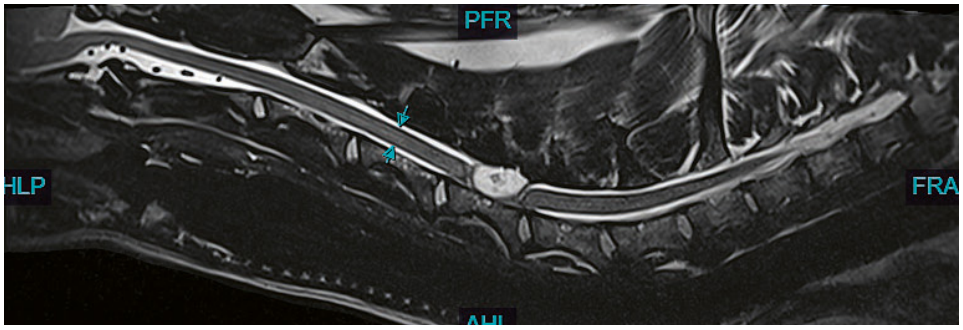

6 Labrador (35 kg)
Sagittal T2 image:
The height of the spinal cord between the arrows is 7 mm.

vertebrae in dogs and cats corresponds to an increased spinal cord length, with a relatively caudally located cauda equina (often caudal to L5–6, or indeed within the level of the sacrum). The longer spine and tiny cord can lead to challenges in maximizing signal from the small cord and may require longer scan times.

Anatomic planes

Anatomic planes in non-primate mammals are different from those in people because of a quadrupedal gait, compared to the bipedal gait of humans. In the head, there is a rotation of the anatomic plane reflected in a different nomenclature for veterinary patients. Whilst the sagittal plane is the same between species, the transverse plane in veterinary imaging correlates with the coronal plane in human imaging. Different terminology is used throughout the body (Fig. 7). For example, anterior and posterior planes are not routinely used in veterinary imaging (apart from some specific exceptions like the eye). The main planes are cranial (towards the head), caudal (towards the tail), dorsal (towards the spine), and ventral (towards the sternum). Differences like these can appear trivial but can lead to significant confusion when human terms are used in the veterinary context.

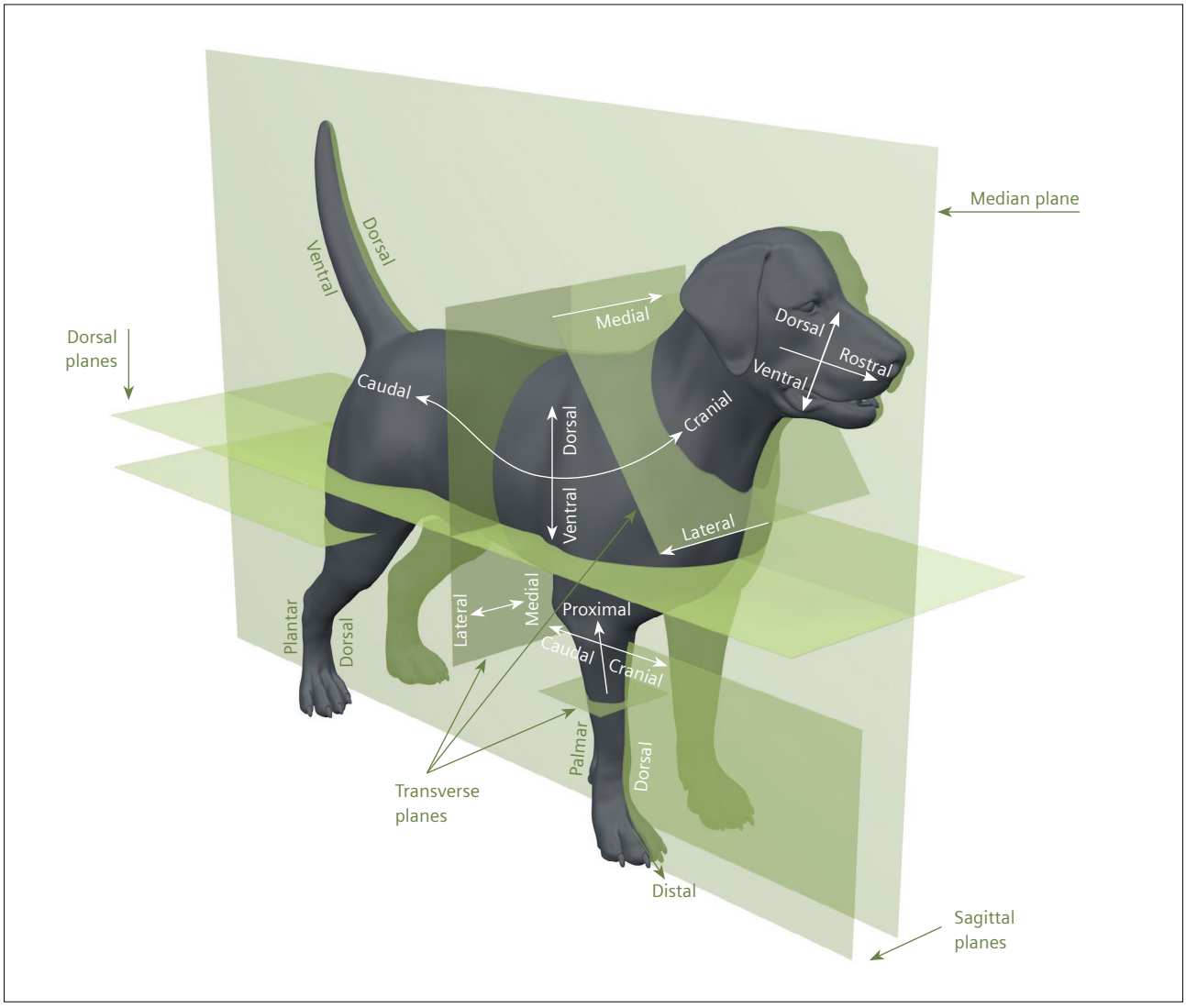

7 Orientations, planes of motion, and directional terms for the dog.

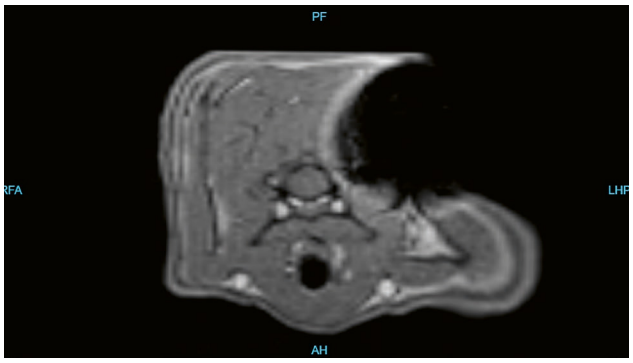

8 Transverse MPRAGE with contrast at the level of the caudal cervical spine of a cat. Note the left-sided magnetic susceptibility artifact created by the patient's microchip, typically placed in a deep subcutaneous location in the neck.

Artifacts

In many jurisdictions around the world, pet dogs and cats must be microchipped. Microchip placement is often in the subcutaneous tissue between the shoulder blades. This creates considerable signal void artifacts when imaging the caudal cervical spine (Fig. 8).

Anesthesia

Veterinary patients are usually completely anesthetized (with endotracheal intubation) for MRI studies. This results in still patients and excellent fidelity in positioning between different series. Anesthetized patients may still hear the noise in the magnet, so it is preferable to pack their ears with hearing protection.

Full anesthesia is useful for optimizing positioning without movement, but it comes at a cost. Body temperature tends to drop with anesthesia, which can prolong recovery time, and this effect is exacerbated in very small animals. Patients are commonly carefully wrapped in blankets for warmth, with particular attention on extremities (which, if exposed to the ambient temperature, can result in patient cooling).

Specific Absorption Rate (SAR) calculations are rarely helpful in veterinary patients. They are calculated based on assumptions about the cylindrical size of human body regions and may not correlate well with the different body size and shape of veterinary patients. Cats and dogs have smaller limbs (with much less muscle, particularly distally) than humans. Veterinary-specific calculations of SAR have not been developed. Early research suggests that body temperature tends to decrease in veterinary high-field MRI due to the effects of anesthesia [4], but careful monitoring (either way) is still required.

The best positioning for spinal imaging is dorsal recumbency, as it minimizes the effects of respiratory motion on the spine. Many veterinary centers may not have access to MRI-compatible anesthesia equipment, so the anesthetic machine (vaporizer and ventilator) is placed outside the RF cage, necessitating extra-long Bain or circle circuits with monitoring limited to heart rate, respiratory rate, expired CO_2, pulse oximetry, and blood pressure assessment. Intravenous fluid support similarly requires long extension sets to reach the patient if the fluid pumps are external to the RF cage.

Conclusion

Medical imaging technologists starting to work in the veterinary field face a steep learning curve as they adjust to different anatomy and body size, terminology, anesthesia requirements as well as different disease processes, and pathophysiology.

References

1 Animal Medicines Australia. Pets and the Pandemic: a social research snapshot of pets and people in the COVID-19 era. [Accessed Oct 24, 2023]. Available from: https://animalmedicinesaustralia.org.au/wp-content/uploads/2021/08/AMAU005-PATP-Report21_v1.4_WEB.pdf.
2 Kokocińska-Kusiak A, Woszczyło M, Zybala M, Maciocha J, Barłowska K, Dzięcioł M. Canine Olfaction: Physiology, Behavior, and Possibilities for Practical Applications. Animals (Basel). 2021;11(8):2463.
3 HSVMA Humane Society Veterinary Medical Association. The Cost of Cuteness. Health and Welfare Issues Associated with Brachycephalic Dog Breeds. [Accessed Oct 30, 2023]. Available from: https://www.hsvma.org/brachycephalic#:~:text=Increasing%20Global%20Popularity%20of%20Brachycephalic%20Dogs&text=The%20numbers%20of%20AKC%2Dregistered,respectively%2C%20from%202006%2D2016.
4 Paul F, Alef M. Variation of rectal temperature in dogs undergoing 3T-MRI in general anesthesia. Front Vet Sci. 2023;10: 1156773.

Contact

Dr Zoe Lenard,
BVSc (Hons) FANZCVS (Radiology)
Animalius Vet
6 Focal Way
Bayswater WA 6053
Australia
Tel.: +61 (0)8 6166 3770
zoe@animalius.vet



High-Resolution Imaging of the Hip Joint in the Age of Deep Learning

Ji Lin, M.D.[1]; Xiaoying Cai, Ph.D.[2]; Peter Kollasch, M.Sc.[2]; Nicolas Groß-Weege, Ph.D.[3]; Hollis G. Potter, M.D.[1]

[1]Department of Radiology and Imaging, Hospital for Special Surgery, New York, NY, USA
[2]Siemens Healthineers, Malvern, PA, USA
[3]Siemens Healthcare, Erlangen, Germany

Introduction

Magnetic resonance imaging (MRI) has proven to be an invaluable resource in the diagnosis and management of orthopedic conditions, given its superior soft tissue contrast, lack of ionizing radiation, and ability to obtain high-resolution imaging. In the face of declining reimbursement and rising pressure for increased patient throughput, efforts are ongoing to decrease scan times while maintaining image quality and resolution [1]. This is especially important when patients are unable to tolerate prolonged scan times due to claustrophobia or pain. In these instances, faster scan times may be paramount to patient care.

In recent years, studies have compared faster MRI sequences with a variety of standard protocols, yielding favorable results for the accelerated scans [2–7]. Improvements in imaging resolution and scan time were assisted by new artificial intelligence (AI) techniques. No difference was found in diagnostic confidence or capability and the scans utilizing deep learning (DL) reconstruction were indeed judged to be of better image quality [3–7].

One of the most frequently performed MR examinations at imaging centers specializing in orthopedic imaging, including at our institution, is MRI of the hip. The relatively thin cartilage of the hip requires superior in-plane and through-plane (slice) resolution to maintain diagnostic accuracy, which results in longer scan times [8]. Given the large number of these studies, the option for a more efficient hip MRI protocol would not only improve patient care at the individual level, but would also contribute to overall increased scanning capacity. We have partnered with Siemens Healthineers to use DL reconstruction, reduced echo spacing, and reduced specific absorption rate (SAR) with optimization of radiofrequency (RF) pulses to enable a hip MRI protocol that requires no more than

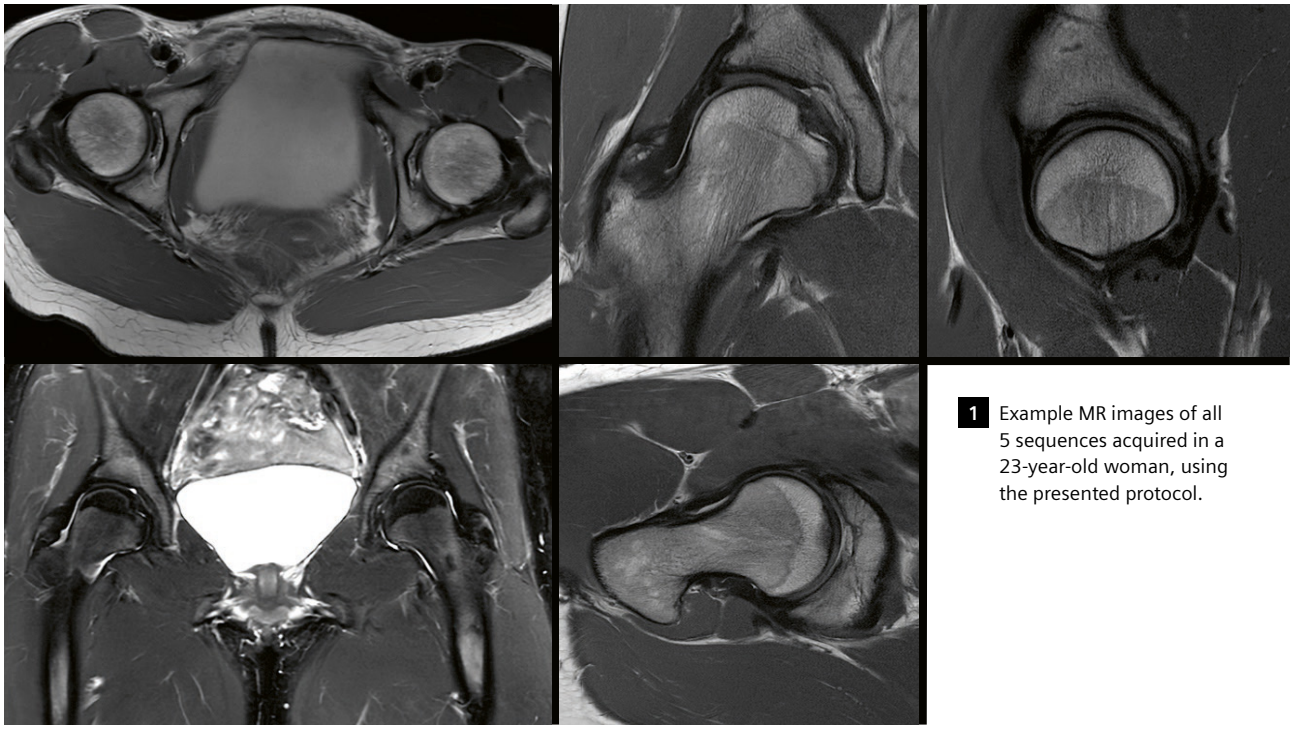

1 Example MR images of all 5 sequences acquired in a 23-year-old woman, using the presented protocol.

15 minutes of scan time but still maintains spatial resolution and signal-to noise ratio (SNR) on par with our standard-of-care studies. The suggested expedited protocol is outlined in this article, to make it available to any user of a 3T magnet from Siemens Healthineers.

Expedited hip MRI protocol with example images

The suggested protocol contains 5 essential acquisitions using a prototype turbo spin-echo (TSE) sequence. Table 1 lists the acquisition parameters in detail for implementation on a MAGNETOM Vida 3T scanner with an XT gradient system. Following a 3-plane fast localizer, a large field-of-view axial TSE sequence of the pelvis and bilateral hips is acquired with intermediate weighting. Next, a coronal unilateral TSE sequence is acquired focusing on the affected hip, followed by a bilateral hip coronal TSE short tau inversion recovery (STIR) sequence. Unilateral intermediate-weighted sagittal and oblique axial TSE acquisitions are obtained for assessing the hip joint. This protocol is acquired without contrast and with an 18-channel phased-array coil anteriorly and an in-table spine matrix coil posteriorly. All acquisitions utilize Deep Resolve Boost and Deep Resolve Sharp for algorithms for DL-enhanced image reconstruction. This protocol produces high-resolution diagnostic scans, as in Figure 1, which shows high-quality images from each sequence acquired in a 23-year-old woman.

The large field-of-view sequences provide an overview of pelvic and hip structures, allowing comparison to the contralateral side for symmetry of osseous structures and musculature about the hips, as well as identification of potential intrapelvic pathology that may present as groin pain. Inversion recovery weighting highlights areas of edema or fluid, including marrow or soft tissue edema, joint effusions, bursitis, or cysts. Smaller field-of-view intermediate-weighted sequences allow high-resolution anatomic evaluation of the symptomatic hip. The coronal plane optimizes evaluation of the superior joint cartilage, superior acetabular labrum, and hip abductors. The oblique axial plane grants superior visualization of the anterior and posterior cartilage and labrum, as well as the rectus femoris and iliopsoas tendons, and further provides an

Acquisition	Axial TSE	Coronal TSE	Coronal IR	Sagittal TSE	Oblique axial TSE
Coverage	Bilateral	Unilateral	Bilateral	Unilateral	Unilateral
Field of view, mm	380	190	380	190	190
TR/TE, ms	5600 / 30	3500–4800 / 35	3500–5500 / 24	4000 / 35	4000 / 34
TI, ms	–	–	240	–	–
Matrix size (frequency × phase)	512 × 384	512 × 384	352 × 282	512 × 410	512 × 358
Phase encoding direction	R > L	H > F	H > F	H > F	L > R
Acquired in-plane resolution (frequency × phase), mm²	0.74 × 0.99	0.37 × 0.49	1.08 × 1.35	0.37 × 0.46	0.37 × 0.53
Slice thickness/gap, mm	5.5 / 0	3 / 0	5.5 / 0	2.5 / 0	3 / 0
Slices	50	32	36	26	28
Bandwidth, Hz/pixel	257	222	219	222	233
Turbo factor	14	12	15	14	14
Echo spacing, ms	6.94	8.65	7.95	8.65	8.45
iPAT	3	2	3	2	2
DRB and DRS	Yes	Yes	Yes	Yes	Yes
Fat suppression	–	–	STIR	–	–
Scan time, min:sec	2:00	3:20	2:15	2:40	2:15

Table 1: Acquisition parameters of the recommended hip protocol on a MAGNETOM Vida 3T with an XT gradient system.
TSE: turbo spin echo; TR: repetition time; TE: echo time; TI: inversion time; iPAT: integrated Parallel Acquisition Technique; DRB: Deep Resolve Boost; DRS: Deep Resolve Sharp; STIR: short tau inversion recovery.

assessment of the neck-head offset. The sagittal plane provides another look at the anterior and posterior joint cartilage, and is the optimal plane for evaluating the anterior labrum.

The coronal STIR and intermediate-weighted TSE images of a 65-year-old woman in Figure 2 reveal hyperintense bursitis from low-signal calcium hydroxyapatite deposition as well as a small amount of joint fluid. Multiplanar intermediate-weighted TSE images show multifocal chondral and labral pathologies in the same subject in Figure 3. Figure 4 illustrates a labral tear with an associated paralabral cyst on an oblique axial intermediate-weighted TSE sequence in a 25-year-old woman.

The prototype TSE sequence includes several improvements to reduce echo spacing with improved sequence timing, and reduced SAR with variable-rate selective excitation [9]. The scan time of these acquisitions is between 1:30 and 3:00 minutes, depending on the desired spatial

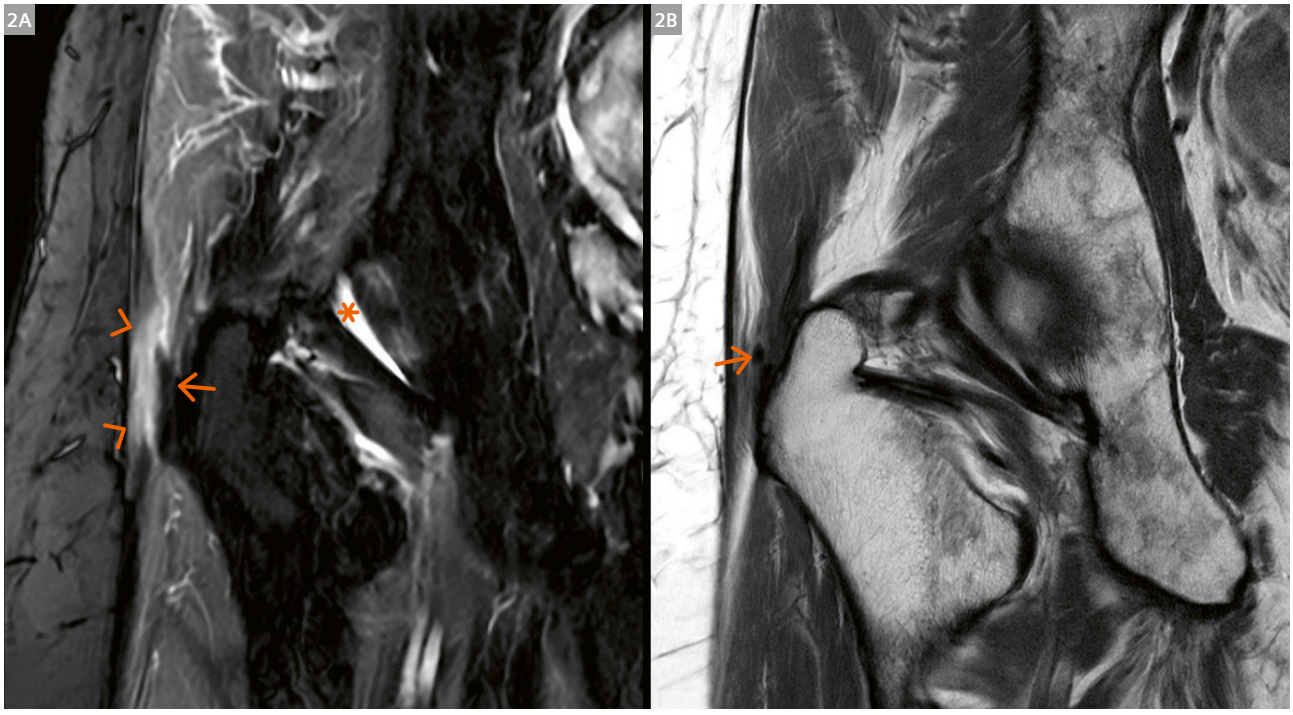

2 Coronal STIR **(2A)** and intermediate-weighted TSE **(2B)** images of the right hip in a 65-year-old woman, acquired in 1:30 minutes and 2:22 minutes respectively, show a low signal focus of calcium hydroxyapatite deposition along the gluteus medius insertion (arrows) with adjacent greater trochanteric bursa thickening (arrowheads), reflecting calcific tendinosis and bursitis. A small amount of fluid in the joint is indicated by an asterisk.



3 Coronal **(3A)**, sagittal **(3B)**, and oblique axial **(3C)** intermediate-weighted TSE sequences of the same woman, with acquisition times of 2:22 minutes, 2:28 minutes, and 2:22 minutes respectively, demonstrate areas of full thickness cartilage loss (arrowheads) over both the acetabulum and the femoral head. A subchondral cyst, high-grade chondral fissure, and anterior labral tear are indicated by arrows in 3A, 3B, and 3C, respectively.

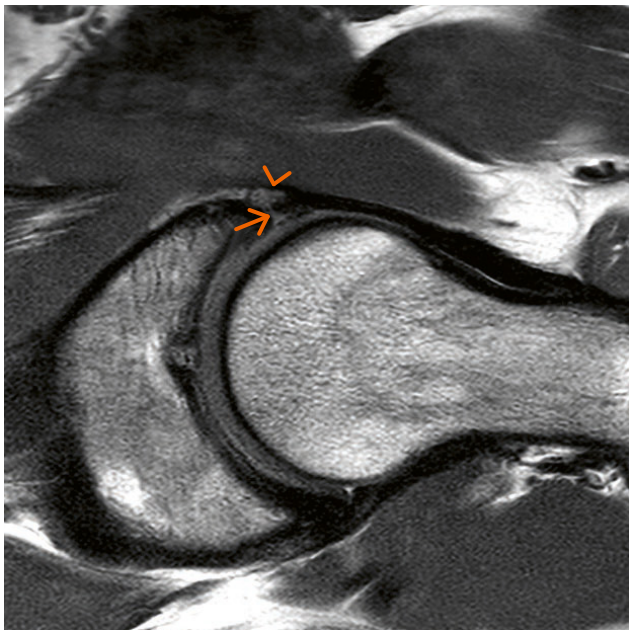

4 An oblique axial intermediate-weighted TSE sequence of the left hip in a 24-year-old woman, with an acquisition time of 2:05 minutes, shows an anterior labral tear (arrow) generating a small paralabral cyst (arrowhead).

resolution. The total exam time is estimated at 12 minutes, with slight variations from subject to subject due to coverage differences and prescribed SAR limits.

Conclusion and future directions

Advances in deep learning techniques have facilitated the development of new MRI protocols aimed at improving clinical outcomes and increasing throughput. As this technology evolves, it can continue to help us improve our protocols so we can keep up with increasing patient volumes while maintaining high diagnostic quality. To that end, we have presented a suggested protocol that allows users of 3T magnets from Siemens Healthineers to implement a faster and enhanced scan for hip MR evaluation.

References

1 Schartz E, Manganaro M, Schartz D. Declining Medicare Reimbursement for Diagnostic Radiology: A 10-Year Analysis Across 50 Imaging Studies. Curr Probl Diagn Radiol. 2022;51(5):693-698.
2 Del Grande F, Rashidi A, Luna R, Delcogliano M, Stern SE, Dalili D, et al. Five-Minute Five-Sequence Knee MRI Using Combined Simultaneous Multislice and Parallel Imaging Acceleration: Comparison with 10-Minute Parallel Imaging Knee MRI. Radiology. 2021;299(3):635-646.
3 Herrmann J, Afat S, Gassenmaier S, Koerzdoerfer G, Lingg A, Almansour H, et al. Image Quality and Diagnostic Performance of Accelerated 2D Hip MRI with Deep Learning Reconstruction Based on a Deep Iterative Hierarchical Network. Diagnostics (Basel). 2023 Oct 18;13(20).
4 Herrmann J, Feng YS, Gassenmaier S, Grunz JP, Koerzdoerfer G, Lingg A, et al. Fast 5-minute shoulder MRI protocol with accelerated TSE-sequences and deep learning image reconstruction for the assessment of shoulder pain at 1.5 and 3 Tesla. Eur J Radiol Open. 2024;12:100557.
5 Terzis R, Dratsch T, Hahnfeldt R, Basten L, Rauen P, Sonnabend K, et al. Five-minute knee MRI: An AI-based super resolution reconstruction approach for compressed sensing. A validation study on healthy volunteers. Eur J Radiol. 2024;175:111418.
6 Zerunian M, Pucciarelli F, Caruso D, De Santis D, Polici M, Masci B, et al. Fast high-quality MRI protocol of the lumbar spine with deep learning-based algorithm: an image quality and scanning time comparison with standard protocol. Skeletal Radiol. 2024;53(1):151–159.
7 Zhao Q, Xu J, Yang YX, Yu D, Zhao Y, Wang Q, et al. AI-assisted accelerated MRI of the ankle: clinical practice assessment. Eur Radiol Exp. 2023;7(1):62.
8 Gold SL, Burge AJ, Potter HG. MRI of hip cartilage: joint morphology, structure, and composition. Clin Orthop Relat Res. 2012;470(12):3321–31.
9 Conolly S ND, Macovski A. Variable-Rate Selective Excitation. Journal of Magnetic Resonance. 1988;78(3):440–458.



Contact

Ji Lin, M.D.
Department of Radiology and Imaging
Hospital for Special Surgery
535 East 70th Street
New York, NY 10583
USA
linji@hss.edu

Advertisement

MR Fingerprinting Development Kit

for Tailored Research Applications



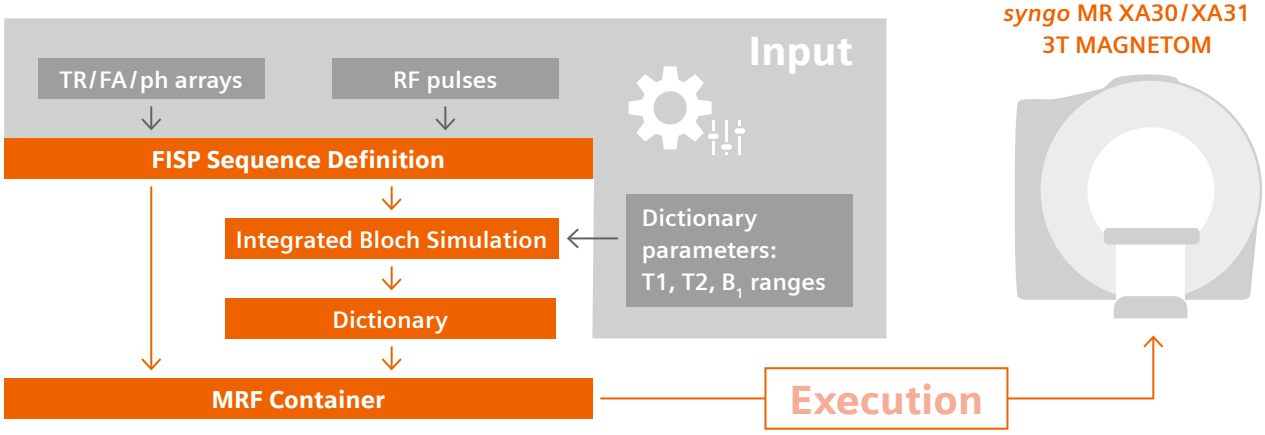

The MR Fingerprinting Development Kit[1] takes files describing the input parameters T1, T2, RF- flip angles and pulse phases. This input generates a customized MR Fingerprinting[1] sequence. The input also serves as the basis for a Bloch simulation, which creates a MR Fingerprinting dictionary unique to its input parameters.

In a final step, the new MR Fingerprinting sequence and its unique dictionary are bundled in the so-called MR Fingerprinting container. This container can be transferred and executed on a qualified MAGNETOM 3T scanner from Siemens Healthineers[2] with a valid MR Fingerprinting license.

The sequence generation, the Bloch simulation, and the creation of the MR Fingerprinting container are performed by running a Windows command line tool[3] provided with the MR Fingerprinting Development Kit.

The MR Fingerprinting Development Kit is available for download to all users of MR Fingerprinting at **www.magnetomworld.siemens-healthineers.com/hot-topics/mr-fingerprinting/mrf-developer-kit**

This unique MRF Development Kit empowers you to tailor the research application to your needs.

[1]The product / feature is not for sale in the U.S. Its future availability cannot be guaranteed.
[2]syngo MR XA30: MAGNETOM Prisma, MAGNETOM Prisma Fit, MAGNETOM Skyra; syngo MR XA31: MAGNETOM Vida
[3]The user needs to install the MR Fingerprinting Development Kit on a standalone Windows 10 PC. Installation on the host computer is not possible.

SIEMENS Healthineers

Expert Insights: Hidden Gems from Application Specialists at Siemens Healthineers

Tricia Thompson on optimizing TSE image quality

Tricia Thompson, MRT(R)(MR)

Tricia qualified as a radiographer MRT(R) in Canada in 2002. An opportunity to train in MRI in the UK took her first to Derby in 2004 for five years, where she worked on mobile MRI scanners across the whole of the UK and gained her second qualification in Canada of MRT(MR). She then worked in London for five years at various private hospitals and clinics before moving to Australia to become an MR Applications Specialist for Siemens Healthineers. Now in her 10th year, she is a Senior Applications and Demo Specialist with a focus on image quality/product development and special interest in Breast MRI and Breast Biopsy, MR in Radiotherapy, and PET-MR.

Contact

Tricia Thompson
Siemens Healthcare Pty Ltd. Australia
SHS AP AUS CS CS APP MR
Citylink Business Centre
153 Campbell Street
Bowen Hills QLD 4006
Australia
tricia.thompson@siemens-healthineers.com





As Applications Specialists, we actively work with MAGNETOM users to provide them with the best possible image quality in scan times appropriate for their needs. At times this requires some creativity by applying different approaches to achieve the best results. In Australia, most of our customers prefer an image that is less smooth and more resolute. Since the release of Deep Resolve Boost and Deep Resolve Sharp, we need to re-think our approach, since our conventional way of optimizing turbo spin-echo image quality has changed and there are new ways to utilize existing parameters. Here, we explore some key parameters, including iPAT factor, PAT reference scan mode, and denoising options.

Historically, when using iPAT, or more specifically GRAPPA, we have taken a more conservative approach when considering the use of higher acceleration factors, due to the resultant excess image noise. When applying our Deep Learning (DL) technology, this is less of an issue thanks to the denoising power of Deep Resolve Boost. Deep Resolve Boost is a DL reconstruction algorithm, which has been trained on a large number of data sets to reconstruct high signal-to-noise-ratio images from under-sampled raw data. As the deep neural network has been optimized to work on highly accelerated scans, a PAT factor of 4 is often now routinely used in clinical practice. An acceleration factor of 4 means only one quarter of the full *k*-space lines are acquired (depending on the reference scan mode). Reducing the acceleration factor to 3 has a minimal impact on scan time and results in improved visualization of finer anatomical detail as more lines of *k*-space are included (Fig. 1).

In DL applications using GRAPPA, the PAT reference scan mode can impact the perceived resolution of an image. As a quick reminder, the reference scan is necessary to provide the GRAPPA reconstruction weights to calculate the missing points/lines in *k*-space during image reconstruction. There are several reference scan types available, dependent on the sequence type and its application. In DL TSE, there are generally two options available: Integrated and TSE Separate (unless combined with Simultaneous Multi-Slice (SMS), then only TSE Separate). In our experience, TSE Separate tends to result in a smoother image appearance, while Integrated appears to result in a coarser image appearance (Fig. 2).

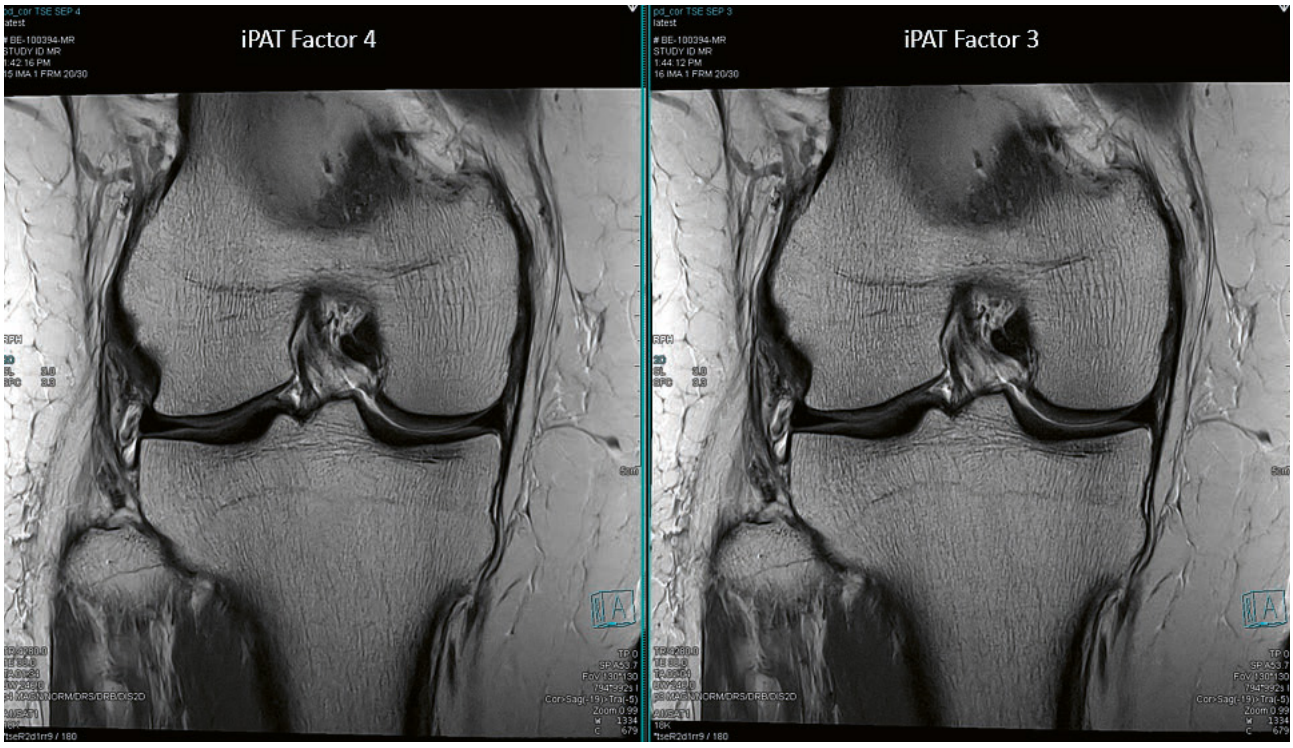

1 Denoising with Deep Resolve Boost, acquired on a 3T MAGNETOM Lumina.
Images courtesy of Beyond Radiology, Auckland, New Zealand.

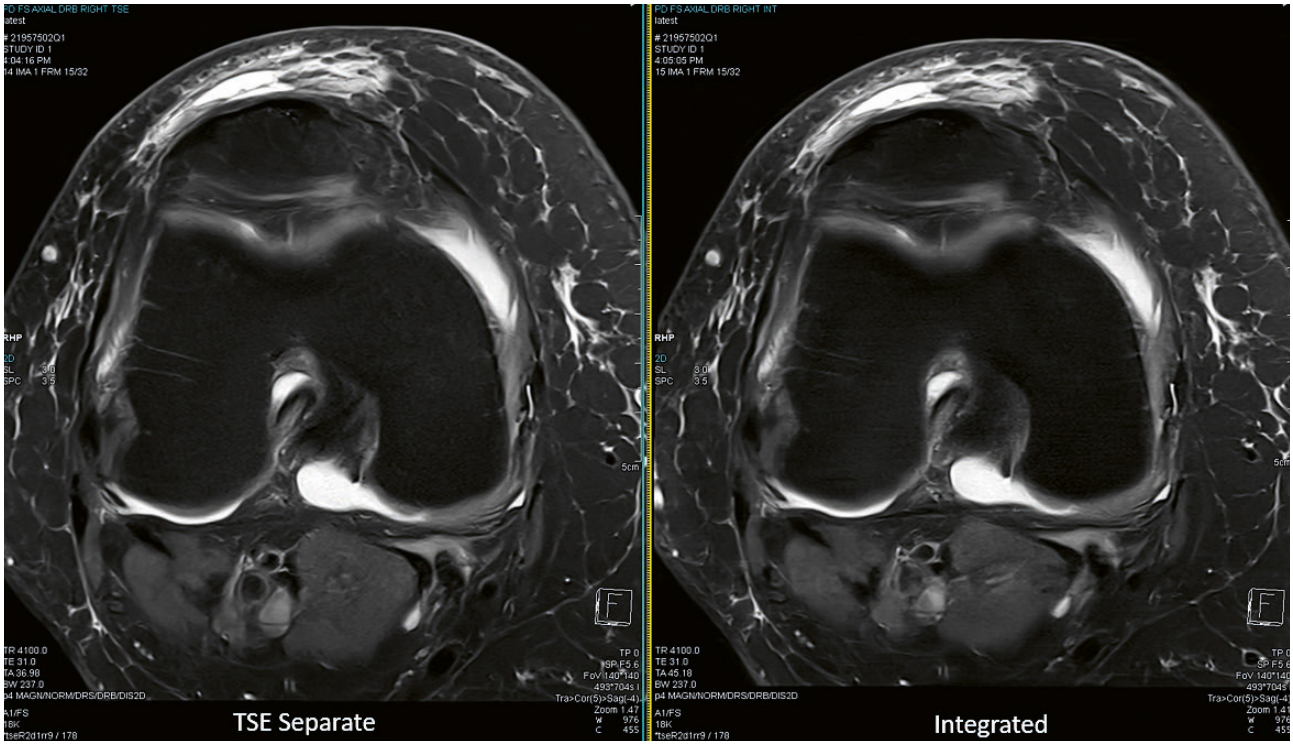

2 Reference scan types acquired on a 3T MAGNETOM Vida.
Images courtesy of Queensland X-Ray, Coorparoo and Brisbane, Australia.

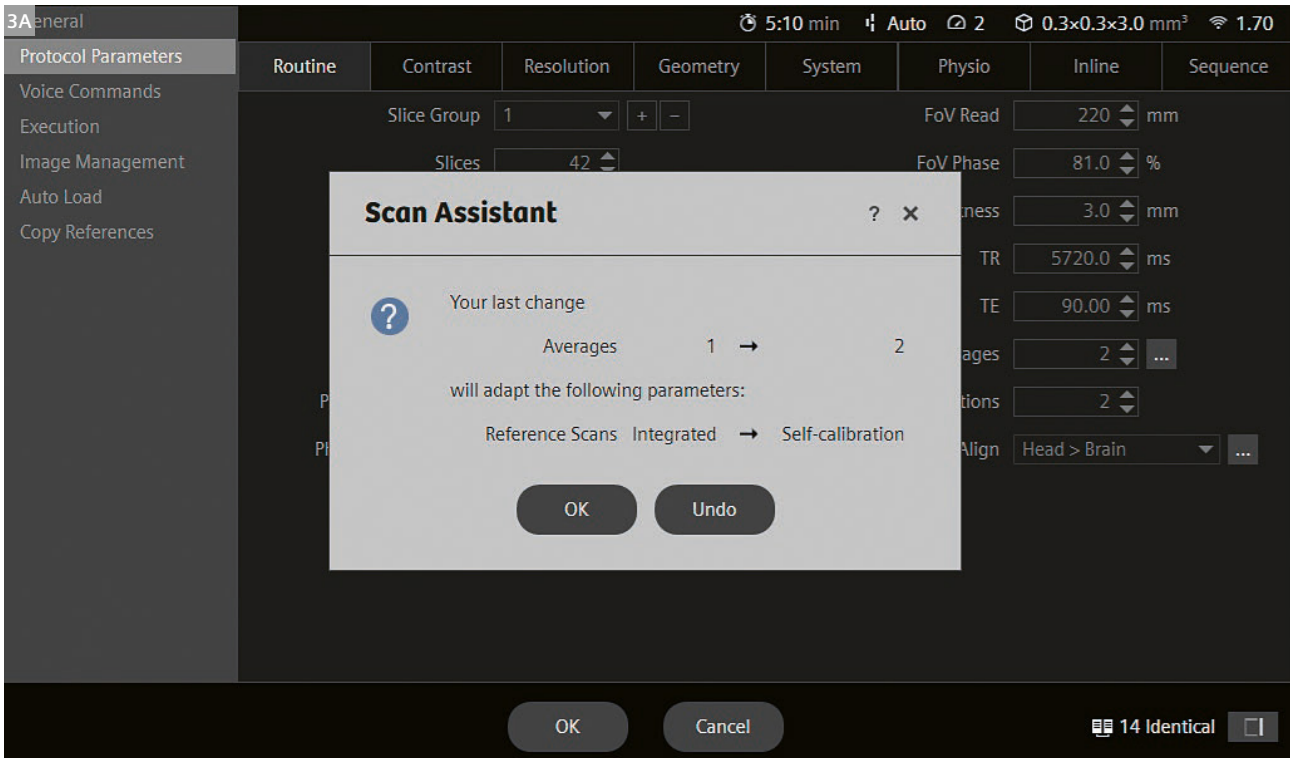

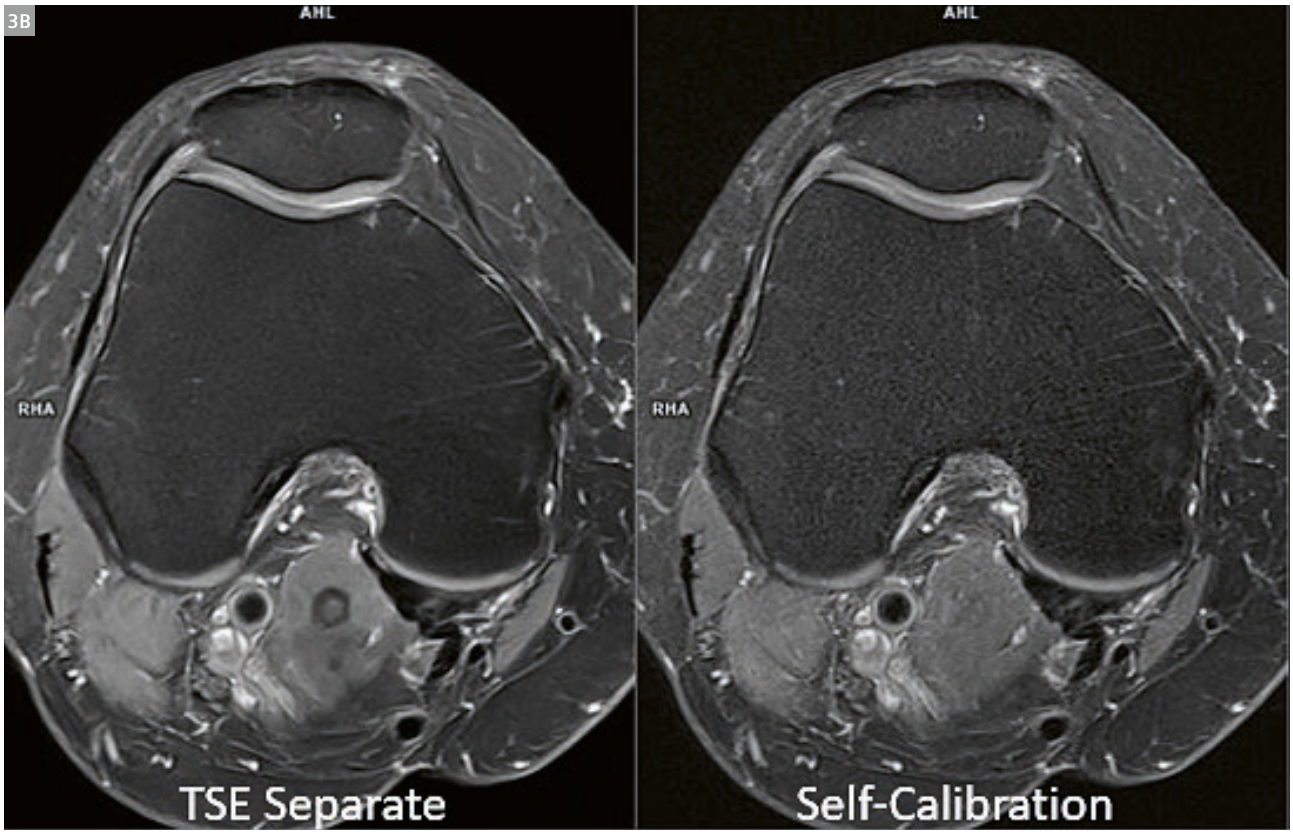

3 **(3A)** Self-calibration reference scan mode.
(3B) Choose the TSE Separate scan mode in combination with deep learning image reconstruction. Images acquired on a 3T MAGNETOM Vida.
Images courtesy of Queensland X-Ray, Coorparoo and Brisbane, Australia.

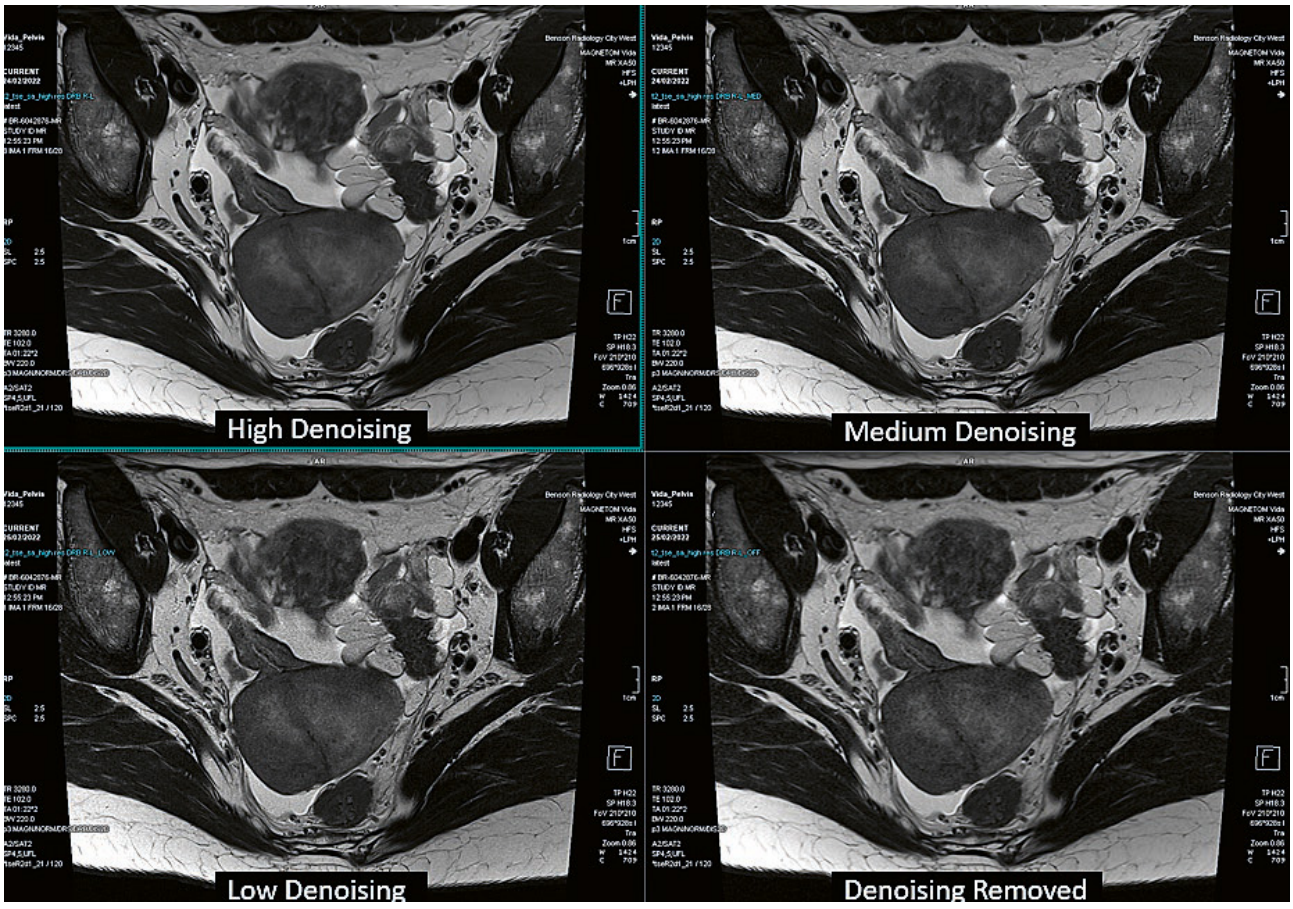

4 Denoising levels acquired on a 3T MAGNETOM Vida.
Images courtesy of Benson Radiology, City West, Adelaide, Australia.

It is worth remembering that Integrated reference scans are more tolerant to small amounts of motion, so it may be more appropriate than TSE Separate in some body regions, such as prostate, rectum, etc.

There is another reference scan mode to be aware of when using Deep Resolve Boost in some software versions prior to *syngo* MR XA60: Self-calibration. Historically, this parameter is automatically applied when the number of averages is equal to or greater than the acceleration factor (Fig. 3A). Self-calibration mode should be avoided as the deep neural network has not been trained with this type of data, and denoising does not behave as expected. Choose either the Integrated or TSE Separate reference scan mode in this scenario (Fig. 3B).

In addition to the parameters mentioned, there are also low, medium, and high denoising levels to choose from. The amount of denoising applied is often based on the radiologist's preference: High denoising results in a smoother image appearance than low denoising. Using our Retrospective Reconstruction tool, they are easily compared following only a single acquisition (Fig. 4). Please note that you can only do this on a Deep Resolve scan, it is not possible to retrospectively add Deep Resolve to the image reconstruction.

Acknowledgments

Special thanks to Jonathan Richer, Kylie Martin, and Georgia Peisker.

Building the Future of MRI: Workflow Optimization and Patient-Centered Design at Mass General Brigham's High-Efficiency Outpatient Facility

Alexander Herold[1,2]; Helen L. Piltner[1,3]; Arhaan Gupta-Rastogi[1]; Barbara D. Wichtmann[4]; Wei-Ching Lo[3]; Azadeh Tabari[1]; Andrew Sharp[1]; Sean P. Hartmann[1]; Lauren Melski[1]; Jeremy Herrington[1]; Shivraman Giri[3]; Waqas Majeed[3]; Jens Guehring[3]; Onofrio A. Catalano[1]; James A. Brink[1]; Oleg Pianykh[1]; Mukesh Harisinghani[1]; Jad S. Husseini[1]; Min Lang[1]; Susie Y. Huang[1]

[1]Department of Radiology, Massachusetts General Hospital, Boston, MA, USA
[2]Department of Biomedical Imaging and Image-guided Therapy, Medical University of Vienna, Austria
[3]Siemens Healthineers, Boston, MA, USA
[4]Department of Neuroradiology, University Hospital Bonn, Germany

Introduction

The growing global demand for magnetic resonance imaging (MRI) services [1] has created significant challenges for healthcare systems worldwide, leading to longer MRI wait times and increased burden on personnel and equipment. The expansion and maintenance of large fleets of MRI scanners may also be constrained by space and capital budgets. Given such constraints, healthcare systems benefit from greater focus on optimizing MRI workflows and facility designs to balance high-quality care with operational efficiency.

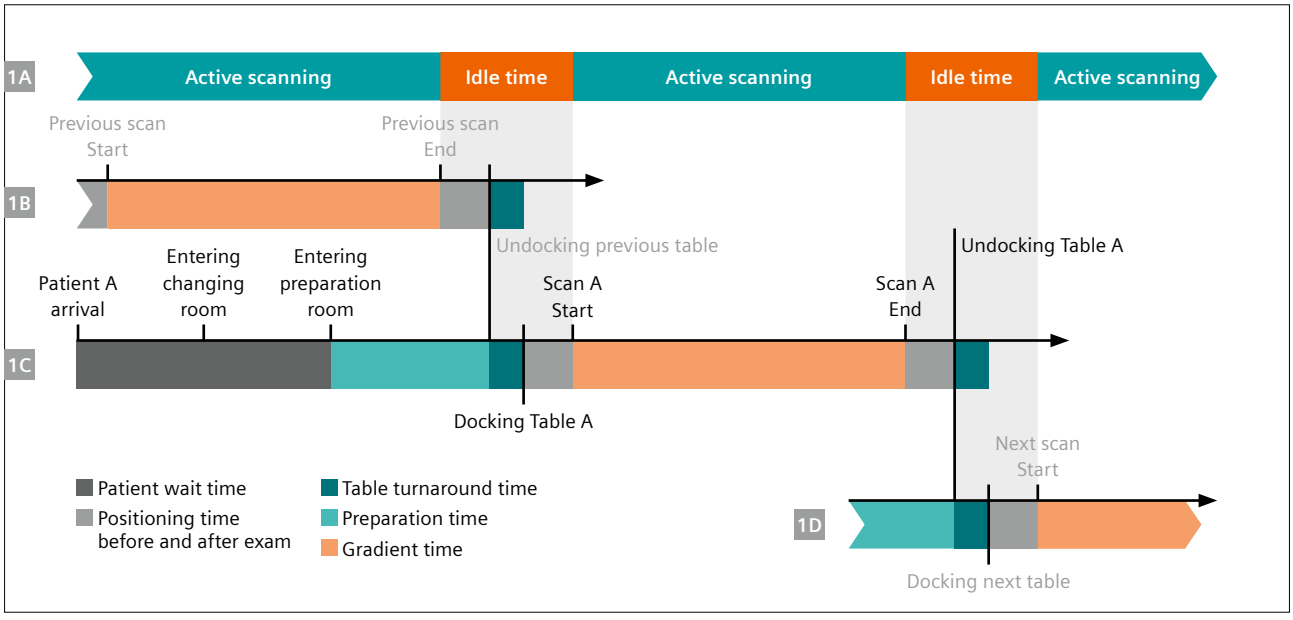

1 Schematic diagram outlining the stages of the MRI examination. **(1A)** displays the active scanning time (petrol) and idle time (orange). **(1C)** outlines the pathway taken by a representative patient (Patient A) through the imaging facility. The total MRI cycle encompasses: the wait time (dark gray), defined as the time from Patient A's arrival to their entry into the preparation room; the preparation time (light petrol), delineated by the entry and exit of Patient A from the preparation room; the table turnaround time (dark petrol), defined as the time from undocking of the table from the previous patient **(1B)** to docking of Patient A's table in the MRI scanner; additional positioning time (lighter gray) of Patient A once the table has been docked in the scanner; the gradient time (light orange), defined as the time when the patient is being actively scanned; and the corresponding positioning and table turnaround times after Patient A's examination has ended.

In 2019, the Department of Radiology at Mass General Brigham embarked on a three-year initiative to design and build a stand-alone outpatient MRI facility aimed at serving more patients, reducing MRI wait times, and enhancing patient satisfaction, all while maintaining and improving the quality of care. As part of the process, the team studied MRI workflows at various outpatient imaging facilities, both within their system and others [2, 3], to identify the most time-consuming processes and bottlenecks. Three key stages of the MRI examination were identified as the primary contributors to delays: patient preparation time, table turnaround time, and MRI gradient time (Fig. 1). The new MRI facility was specifically designed to address these critical rate-limiting steps by streamlining the workflow to improve efficiency and patient experience.

The new Mass General Brigham high-efficiency outpatient MRI facility opened in Assembly Row, Somerville, Massachusetts, USA, in March 2022. This article reviews the design and workflow optimization strategies implemented at this novel MRI facility and evaluates their impact on workflow efficiency as compared to reference MRI facilities. We examine how these design choices and operational procedures impact key performance metrics in MRI service delivery.

Facility design

The new outpatient MRI facility at Assembly Row features an innovative design and layout optimized for workflow efficiency and patient comfort. Spanning 8,000 square feet, the Assembly Row imaging center houses three identical 3 Tesla wide-bore scanners (MAGNETOM Vida, Siemens Healthineers, Erlangen, Germany). The scanner rooms situated across the hall from four standardized patient preparation bays, which are laid out in a direct path from the scanner rooms, separated by a spacious nine-foot-wide corridor (Figs. 2, 3).

This layout allows for concurrent patient scanning and preparation of the next patient in the bay across the hall. Each scanner is equipped with two interchangeable dockable tables, enabling seamless and rapid transitions between patients. The preparation bays serve as dedicated spaces for MRI staff to provide patients with instructions for the upcoming examination, position patients on the dockable table, place an intravenous catheter as needed, and position the radiofrequency receive coil(s) required for the upcoming examination. The design and layout of the preparation bays effectively shift the preparation steps of the examination, which can be time-consuming, out of the scanner room while allowing the MRI technologist and nursing staff to interact in a private setting with the patient, orienting the patient to the examination and answering any questions that they may have.

Identifying rate limiting steps in MRI workflow

Our radiology department embarked on a comprehensive three-year process in 2019 to design and build the stand-alone outpatient MRI facility at Assembly Row, as recently

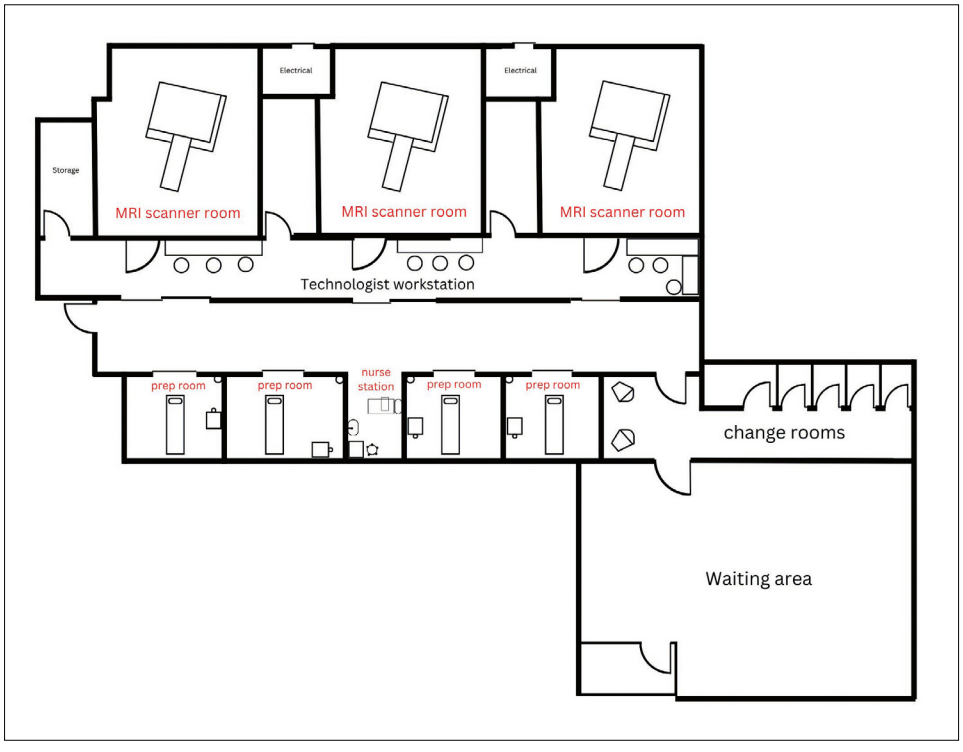

2 Floor plan of the new outpatient MRI facility at Assembly Row, featuring three MRI scanners, each equipped with two interchangeable dockable tables. Four patient preparation bays are positioned opposite the scanners, separated by a nine-foot corridor. This design enables concurrent patient preparation and scanning [4].



3 The new Assembly Row outpatient imaging center combines advanced technology with optimized workflows. **(3A)** Wide-bore MRI scanner with interchangeable patient table. The scanner is slightly angled towards the entrance to allow for faster table docking. **(3B)** Nine-foot corridor with patient preparation bays on the left and scanner room entrances on the right. This layout enables parallel patient preparation and scanning, allowing for seamless transitions between exams. *Images courtesy of Jeremy Herrington and Lauren Melski.*

described by Lang et al. [4]. The goal was to incorporate innovative architectural designs and operational processes to serve more patients, decrease MRI wait times, and increase patient satisfaction while maintaining and improving the quality of care. Prior to developing the new MRI facility, a team composed of radiologists, MRI technologists and technologist managers conducted extensive observations of MRI workflows at established outpatient imaging facilities within Mass General Brigham and at external sites. Through this analysis, they identified the most time-consuming processes and bottlenecks, which centered around three key metrics: patient preparation time, table turnaround time, and gradient time (see Fig. 1 for definitions). The new MRI site was specifically designed to address these critical rate-limiting steps.

Patient preparation and table turnaround time

In conventional MRI facilities, the processes of patient preparation and changeover are significant rate-limiting steps that often lead to inefficiencies and delays. Traditionally, these processes occur sequentially: after one scan concludes, the patient exits the scanner room, the table is cleaned, and only then is the next patient brought in for preparation. This preparation involves positioning the patient on the table, placing headphones or earplugs, and placing the appropriate coils – all while the scanner sits idle. This approach is time-consuming, especially for patients with limited mobility, and any delays cascade into subsequent appointments.

The new imaging facility at Assembly Row addresses these bottlenecks through innovative design features and workflow optimization. The imaging center incorporates dedicated preparation bays and utilizes dockable tables, enabling a parallel processing approach that significantly reduces the time spent in moving patients on and off the scanner. While one scan is in progress, technologists can efficiently prepare the next patient in a separate bay, including performing positioning and intravenous line and coil placement. When the current scan finishes, the dockable table system allows for a nearly seamless transition between patients. This system effectively decouples patient preparation from scanner occupancy, minimizing transition times and scanner idle time. The use of dockable tables eliminates the need for patients to walk into and out of the scanning room, which is particularly beneficial for those with mobility issues. Furthermore, it allows for more efficient cleaning between patients, as the table cleaning process occurs outside the scanner room while the next patient is being prepared on a separate table.

The impact of these innovations in design and workflow has been striking. Preliminary results of our ongoing workflow efficiency analyses demonstrate mean turnaround times of four minutes at the Assembly Row MRI facility, with almost 40% of exams having turnaround times of less than one minute, compared to a mean turnaround time of nine minutes at other outpatient MRI facilities within the hospital system, where typically only < 1% of exams have turnaround times of under one minute.

MR gradient time and impact of Deep Resolve

Most of the MRI examination is taken up by the MRI gradient time, the period when the scanner actively acquires

images. Traditionally, efforts to improve MRI efficiency focused on incorporating accelerated imaging techniques like parallel imaging, simultaneous multislice acquisition, and compressed sensing [5, 6], which reduce scan times but are constrained by fundamental trade-offs between signal, spatial resolution, and contrast. The introduction of deep learning into the image acquisition and reconstruction pipeline has revolutionized the landscape of fast MR imaging techniques [7]. At our new facility, we have incorporated Deep Resolve technology from Siemens Healthineers throughout MRI examinations in all anatomical regions. Our experience with Deep Resolve has shown its promise in enabling faster scans and improving image quality while extending the boundaries of the usual tradeoffs between signal-to-noise ratio, resolution, and scan time.

Comparative analysis with MRI scan times before and after the adoption of deep learning techniques has revealed significant improvements in gradient time and exam efficiency [4]. Neurological and musculoskeletal MRI examinations demonstrated mean gradient times ≤ 20 minutes with reductions ranging from 24%–46% compared to reference centers, while abdominal MRI examinations demonstrated mean gradient times of 22–25 minutes with reductions of 20%–35%. These findings align with previous efforts at our institution, where the concatenation of several highly accelerated sequences in the most performed brain MRI protocols yielded up to a 40% reduction in protocol length [8].

On-time performance and patient experience

The combination of facility design, workflow optimization, and adoption of fast MRI techniques including deep learning-enabled methods has led to significant improvements in on-time performance and overall patient experience. As a result, the Assembly Row MRI facility has demonstrated superior punctuality, with 80% of exams starting within five minutes of the scheduled appointment time, compared to 63–66% at reference outpatient MRI facilities. Patients at the Assembly Row imaging facility also experienced an average reduction in wait time of 6.6 minutes compared to reference facilities.

The improvements in workflow efficiency and quick patient turnaround have offered the serendipitous opportunity to make use of the time savings from early completion of many MRI examinations. Our technologist managers have taken advantage of the time savings by implementing a virtual scanner resource, which allows for dynamic, real-time adjustments to the examination schedule to accommodate add-on exams when scheduled exams finish ahead of schedule. This innovative approach effectively creates a fourth "virtual scanner" to aid in managing exam capacity and throughput, particularly during peak hours. The virtual scanner concept has specifically been used for scheduling additional patients with shorter examination times, such as routine brain, knee, shoulder, and non-contrast lumbar and cervical spine MRI scans, beyond the strict capacity limits of the three physical scanners. By strategically inserting these shorter (i.e., < 20 minute) examinations into potential gaps in the schedule created by early exam completion and/or underutilized time slots, the facility can accommodate variability in exam duration, thereby improving on-time performance and reducing patient wait times.

Survey data reveal higher patient satisfaction at the Assembly Row imaging facility compared to reference outpatient imaging facilities within our hospital system, underscoring the success of these patient-centered design elements and scheduling innovations. Anecdotal feedback from MRI technologists at the Assembly Row facility has also been positive, with many technologists recognizing the benefits of the additional time and space offered by the preparation bays for alleviating patient anxiety and developing good rapport and communication between the patient and provider.

Impact on slot times and patient throughput

The innovative design and operational strategies implemented at the Assembly Row imaging facility have yielded substantial improvements in efficiency and patient throughput. Most notably, the facility opened with 30-minute imaging appointment slots, which represents a 33% reduction in slot time compared to the 45-minute slots that were traditionally offered at our reference outpatient MRI facilities. This adjustment alone has the potential to increase daily patient capacity by up to 50%. The impact of the workflow improvements is clearly demonstrated in the facility's performance during direct comparison periods with reference facilities, as revealed in analyses reported in forthcoming publications.

Conclusion

The innovative design and operational strategies at our high-efficiency MRI facility have significantly enhanced patient throughput and satisfaction. By addressing key bottlenecks in the MRI workflow, focusing on shortening the time spent during key periods in the MRI examination, including the patient preparation, table turnaround, and gradient times, we have achieved substantial improvements in performance metrics. The optimized facility's ability to reduce appointment slots from 45 to 30 minutes, while improving on-time performance and patient experience, showcases the promise of this multi-faceted approach. As healthcare systems worldwide grapple with increasing demand for MRI services, the Assembly Row model offers a blueprint for optimizing imaging workflows without compromising image quality or patient care. This

integrated approach to facility design and process improvement could serve as a valuable template, with customizable workflows and fast imaging acquisitions that may be readily adopted by healthcare institutions seeking to enhance their imaging services and patient experience in the face of growing resource constraints.

Contact

Associate Professor Susie Y. Huang, M.D., Ph.D.
Radiologist in the Division of Neuroradiology
Department of Radiology
Massachusetts General Hospital
Harvard Medical School
55 Fruit St
Boston MA 02114
USA
susie.huang@mgh.harvard.edu



Alexander Johannes Herold, M.D.
Research Fellow in Radiology
Department of Radiology
Massachusetts General Hospital
Harvard Medical School
55 Fruit St
Boston MA 02114
USA
AHEROLD@mgh.harvard.edu



References

1 Smith-Bindman R, Kwan ML, Marlow EC, Theis MK, Bolch W, Cheng SY, et al. Trends in Use of Medical Imaging in US Health Care Systems and in Ontario, Canada, 2000-2016. JAMA.2019;322(9):843–856.
2 Lin DJ, Doshi AM, Fritz J, Recht MP. Designing Clinical MRI for Enhanced Workflow and Value. J Magn Reson Imaging. 2024;60(1):29–39.
3 Recht MP, Block KT, Chandarana H, Friedland J, Mullholland T, Teahan D, et al. Optimization of MRI Turnaround Times Through the Use of Dockable Tables and Innovative Architectural Design Strategies. AJR Am J Roentgenol. 2019;212(4):855–858.
4 Lang M, Lo WC, Sharp A, Hartmann SP, Pianykh OS, Melski LM, et al. Improving Workflow Efficiency at an Outpatient MRI Imaging Facility: A Case Study. J Am Coll Radiol. 2024:S1546–1440(24)00531–3.
5 Del Grande F, Rashidi A, Luna R, Delcogliano M, Stern SE, Dalili D, et al. Five-Minute Five-Sequence Knee MRI Using Combined Simultaneous Multislice and Parallel Imaging Acceleration: Comparison with 10-Minute Parallel Imaging Knee MRI. Radiology. 2021;299(3):635–646.
6 Fritz J, Fritz B, Zhang J, Thawait GK, Joshi DH, Pan L, et al. Simultaneous Multislice Accelerated Turbo Spin Echo Magnetic Resonance Imaging: Comparison and Combination With In-Plane Parallel Imaging Acceleration for High-Resolution Magnetic Resonance Imaging of the Knee. Invest Radiol. 2017;52(9):529–537.
7 Hammernik K, Klatzer T, Kobler E, Recht MP, Sodickson DK, Pock T, et al. Learning a variational network for reconstruction of accelerated MRI data. Magn Reson Med. 2018;79(6):3055–3071.
8 Lang M, Cartmell S, Tabari A, Briggs D, Pianykh O, Kirsch J, et al. Evaluation of the Aggregated Time Savings in Adopting Fast Brain MRI Techniques for Outpatient Brain MRI. Acad Radiol. 2023;30(2):341–348.

Download the optimized MSK protocols (upper and lower extremities) from the Assembly Row outpatient imaging center.
3T MAGNETOM Vida (software version XA50A), exar1 file and PDF

https://www.magnetomworld.siemens-healthineers.com/clinical-corner/protocols/musculoskeletal-mri/optimized-msk-protocols

Specific Absorption Rate (SAR) Supervision on MAGNETOM Systems

Lena Gast, Ph.D. and Hendrik Paysen, Ph.D.

Siemens Healthineers, Erlangen, Germany

What is SAR?

Magnetic resonance imaging (MRI) relies on the application of radiofrequency (RF) electromagnetic fields to excite the spins, and thus generate the measured MR signal. More precisely, the excitation is achieved by time-varying magnetic fields (B_1), which are always accompanied by changing electric (E) fields (Maxwell's laws). These E-fields interact with charged particles inside biological tissue, leading to energy dissipation and, consequently, tissue heating. Excessive heating can cause tissue damage, so the temperature increase due to RF fields must be limited. However, a direct monitoring of the global or local temperature increase in the patient during an MRI examination is generally not feasible. Therefore, the specific absorption rate (SAR) is introduced as a measure to limit tissue heating. The SAR describes the amount of energy that is absorbed by the tissue within a certain time – i.e., the absorbed power – per kg body weight (unit = W/kg). It is related to the electric field strength, the mass density, and the conductivity of the examined tissue. Generally, SAR is higher in tissues with a higher conductivity, such as muscle tissue, than in tissues with lower conductivity, such as fat. Therefore, tissue composition within the examined body region impacts SAR. Moreover, SAR increases with the square of the frequency of the excitation field (ω), or similarly the main magnetic field strength (B_0). For example, an approximately four-times higher SAR can be expected at 3T than at 1.5T. An overview of various factors influencing SAR is given in Table 1.

Finally, SAR can be linked to temperature increase – the relevant factor for patient safety – by Pennes' bioheat transfer equation [1]. This equation describes the tissue's physiological responses to energy deposition based on its thermoregulatory and heat-loss capabilities.

SAR limits

The SAR limits that must be adhered to during an MRI examination are defined in the International Electrotechnical Commission (IEC) standard for medical electrical equipment (IEC 60601-2-33) [2]. These limits apply to all MRI systems independent of vendor, field strength, or specific system type. The SAR limits are defined for an averaging

Category	Parameter	Impact on SAR
Hardware	• Field strength • RF transmit coil (volume vs. local RF transmit coil)	• Higher field strength → higher SAR ($SAR \propto B_0^2$) • Determines which SAR aspects are supervised by system
Protocol parameters	• Repetition time (TR) • Flip angle (α) • Number of slices	• Longer TR → lower SAR ($SAR \propto 1/TR$) • Higher flip angle → higher SAR ($SAR \propto \alpha^2$) • Higher number of slices → higher SAR
Patient registration input	• Patient weight • Patient height • Patient gender	• Used for cylinder model calculations • Used for cylinder model calculations • No direct impact on SAR, mostly used for consistency checks
Patient characteristics	• Tissue composition, tissue conductivity • Patient (head) positioning relative to transmit coil	• Influences measured absorbed power → scaling of SAR aspects • Used for cylinder model calculations → head SAR/partial-body SAR

Table 1: Summary of main factors influencing SAR.

time of 6 minutes with the aim of reducing the global temperature increase to 0.5 °C in normal operating mode, and 1.0 °C in first level controlled operating mode (see Table 2). When performing measurements in the first level controlled operating mode, permanent medical supervision of the patient is required due to the higher allowed SAR values and potentially higher temperature increase. Patients with reduced thermoregulatory capabilities (e.g., febrile patients, infants, or pregnant patients) should only be examined in normal operating mode.

The IEC standard differentiates between two types of RF transmit coils: volume RF coils with a homogeneous excitation field, such as the body or knee RF transmit coil; and local RF transmit coils with an inhomogeneous excitation field, such as surface RF coils used for spectroscopic applications. In the following, we will focus on volume RF transmit coils as they represent the most common use case in clinical MRI at field strengths ≤ 3T. For volume coils, the MR system must supervise three different SAR aspects[1]:

- **Whole-body SAR:** the complete RF power absorbed by the patient divided by the patient mass.
- **Head SAR:** the RF power absorbed by the head of the patient divided by the head mass.
- **Partial-body (or exposed-body) SAR:** the RF power absorbed by the patient mass within the effective volume of the transmit coil (i.e., the region in which 95% of the total RF field is deposited) divided by the exposed body mass.

Figure 1 depicts how head SAR and partial-body SAR depend on the patient positioning within the RF transmit coil. The specific limits for partial-body SAR vary depending on the ratio of the exposed body mass and the total body mass of the patient. If the entire patient mass is within the effective RF field (for example, if infants are examined using the body transmit coil), partial-body SAR equals whole-body SAR. Additionally, the IEC defines limitations for local SAR, i.e., SAR averaged over any 10 g of tissue, which are mainly relevant for non-volume transmit coils.

Depending on the positioning of the patient within the transmit coil, either whole-body SAR, head SAR or partial-body SAR is the limiting factor for SAR supervision. For example, if the patient's head is in the isocenter of the scanner during a brain examination, head SAR will have the highest value relative to the IEC limit, and will therefore be the limiting factor. In contrast, for a torso

[1] *Examinations of patients with MR-conditional implants may additionally require the supervision of the root mean squared B_1 field (B_{1rms}) averaged over 6 minutes and 10 seconds.*

Operating mode	Whole-body SAR (W/kg)	Partial-body SAR (W/kg)	Head SAR (W/kg)
Normal operating mode	2	2–10[a]	3.2
First level controlled operating mode	4	4–10[b]	3.2

Table 2: Limits for SAR averaged over 6 minutes according to the IEC standard. Twice the values may be applied within an averaging time of 10 seconds. For partial-body SAR, the limits vary depending on the exposed body mass relative to the total patient mass.
[a] Normal mode: SAR_{pb} = 10 W/kg – (8 W/kg × exposed patient mass / total patient mass);
[b] First level mode: SAR_{pb} = 10 W/kg – (6 W/kg × exposed patient mass / total patient mass).

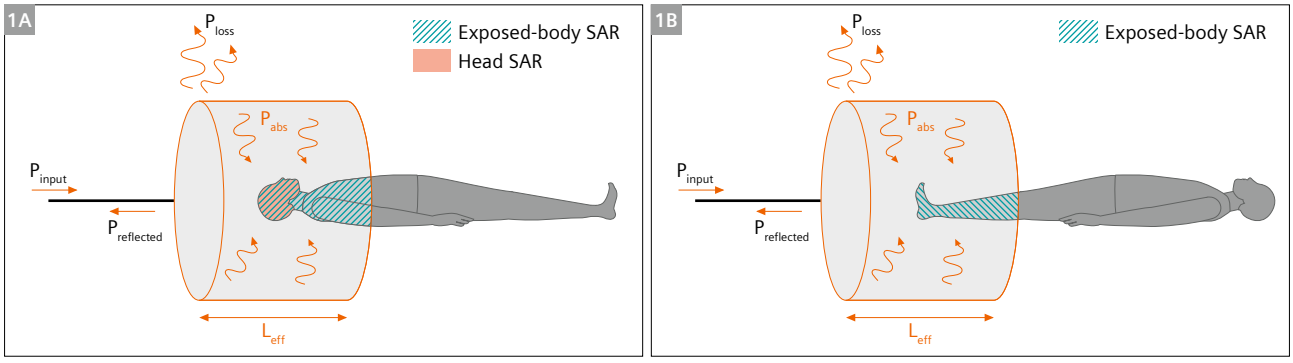

1 Schematic depiction of different SAR aspects depending on patient positioning within the RF transmit (body) coil. In general, SAR can be measured as the difference between the input power (P_{input}) and reflected power ($P_{reflected}$), as well as power losses (P_{loss}), divided by the (exposed) patient mass. The part of the body that is exposed to the RF field within the effective length of the transmit (body) coil (L_{eff}) is marked. **(1A)** In the case of a head examination with the head in the isocenter of the scanner (head first supine positioning), head SAR is the limiting SAR aspect. **(1B)** For a foot/ankle examination (feet first supine positioning), exposed-body SAR is the limiting SAR aspect. In the latter case, head SAR is zero, as the head of the patient is far outside of the effective coil length.

examination, whole-body SAR will be the limiting SAR aspect. Figure 2 shows the SAR information UI of a MAGNETOM system for an examination, in which head SAR was the limiting SAR aspect.

It should be noted that the thermoregulation of the patient may be reduced at high ambient temperatures. According to the IEC standard, the whole-body SAR limit in first level controlled operating mode must therefore be reduced by 0.25 W/kg per degree until 2 W/kg (= limit in normal operating mode) if the ambient temperature is > 25 °C. It is therefore important to control the temperature within the MR examination room by turning on the air ventilation system.

Local heating

Even if the global SAR limits are met, strong local heating may occur due to local enhancement of electric fields and locally induced eddy currents. Electrical field enhancements may, for example, arise near the RF transmit (body) coil or due to contact with an electrically conductive object. Moreover, current loops may form when there is direct skin-to-skin contact, e.g., between the thighs or calves, leading to strong heating at the contact point (see Fig. 3). Another reason for local heating is the "antenna effect." If the effective length of a conductive wire is approximately half the wavelength of the RF field, the wire functions as an antenna for the induced RF field, leading to strong heating. Overall, contact points (with an object, the bore wall, or skin-to-skin) are the most common reason for RF burns in MRI [3]. They must be prevented, for example, by using distance cushions.

SAR supervision for MAGNETOM systems

This section provides an overview of the fundamental concepts used in SAR supervision on a MAGNETOM system. A patient-specific SAR modeling approach is used, which relies on two key components:

1) A model to determine the SAR distribution inside the patient.
2) Refinement of these calculated model values based on patient specific adjustment measurements.

These two steps will be explained in the following sections. The main question that shall be answered is: "How does the scanner determine the three SAR values: whole-body SAR, partial-body SAR, and head SAR?"

To calculate SAR, we need to know the total power absorbed by the whole body, the exposed partial body, the head ($P_{abs,wb}$, $P_{abs,pb}$, $P_{abs,head}$), and the corresponding masses (m_{wb}, m_{pb}, m_{head}):

$$SAR_{wb} = \frac{P_{abs,wb}}{m_{wb}} \; ; \; SAR_{pb} = \frac{P_{abs,pb}}{m_{pb}} \; ; \; SAR_{head} = \frac{P_{abs,head}}{m_{head}}$$

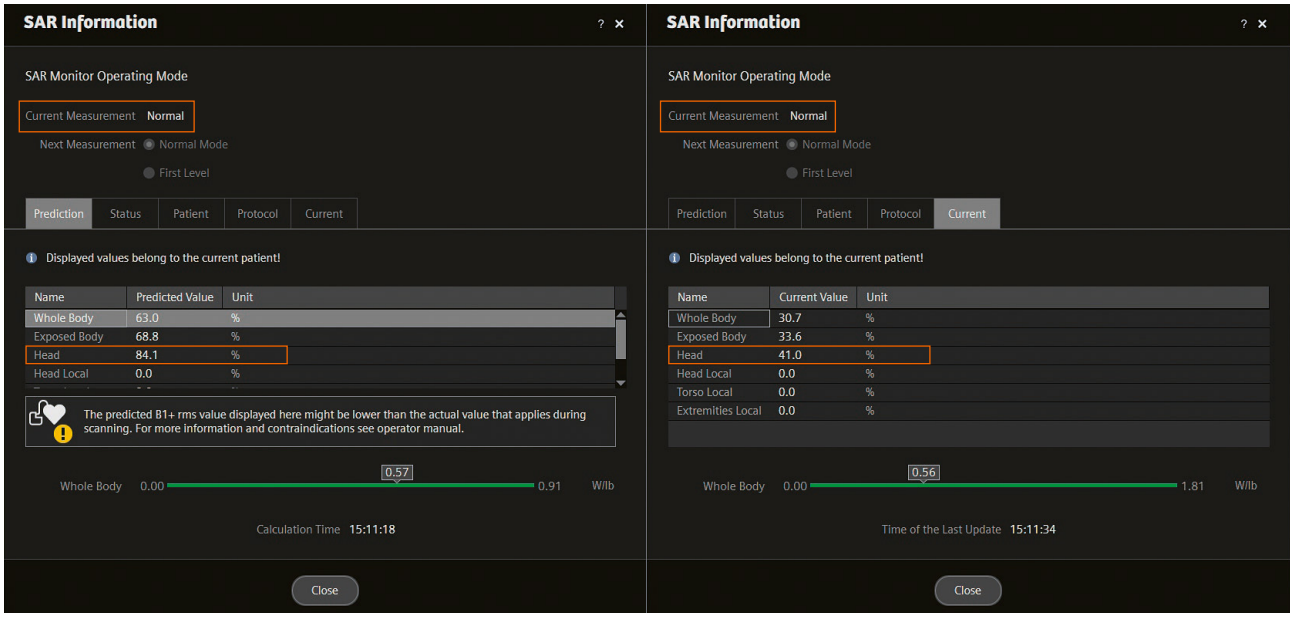

2 SAR information UI of MAGNETOM scanners. The whole-body, exposed-body, and head SAR values calculated based on the protocol parameters for the current protocol are shown in the "Prediction" tab. All values are given relative to the respective IEC limits and averaged over the entire run time of the protocol. The SAR values currently measured by the system are displayed in the "Current" tab. Measured values are averaged over time intervals of 6 min and 10 s. The higher of these two values is displayed. For the given measurement, head SAR yields the highest value. That means head SAR is the most critical aspect for SAR supervision.

Whole-body SAR is the only aspect that can directly be measured. The total mass of the patient m_{wb} is known from the patient registration. The total power absorbed by the patient $P_{abs,wb}$ is determined via direct power measurements:

$$P_{abs,wb} = P_{Input} - P_{Reflected} - P_{Losses}$$

The input power P_{Input} and all power losses, either by reflection $P_{Reflected}$ or by conversion into heat P_{Losses}, are constantly measured by the system (see Fig. 1). With that, whole-body SAR can be calculated for each scan using m_{wb} and $P_{abs,wb}$.

SAR-distribution model

Calculating partial-body and head SAR is more challenging, as it is not possible to directly measure the mass or absorbed power of specific body parts. To estimate these values, the patient's body is modeled using a "cylinder model" consisting of four homogeneous cylinders: one representing the head, one for the torso, and two for the legs (see Fig. 4). This approximation is simple but very reliable and explicitly encouraged by IEC 60601-2-33. The

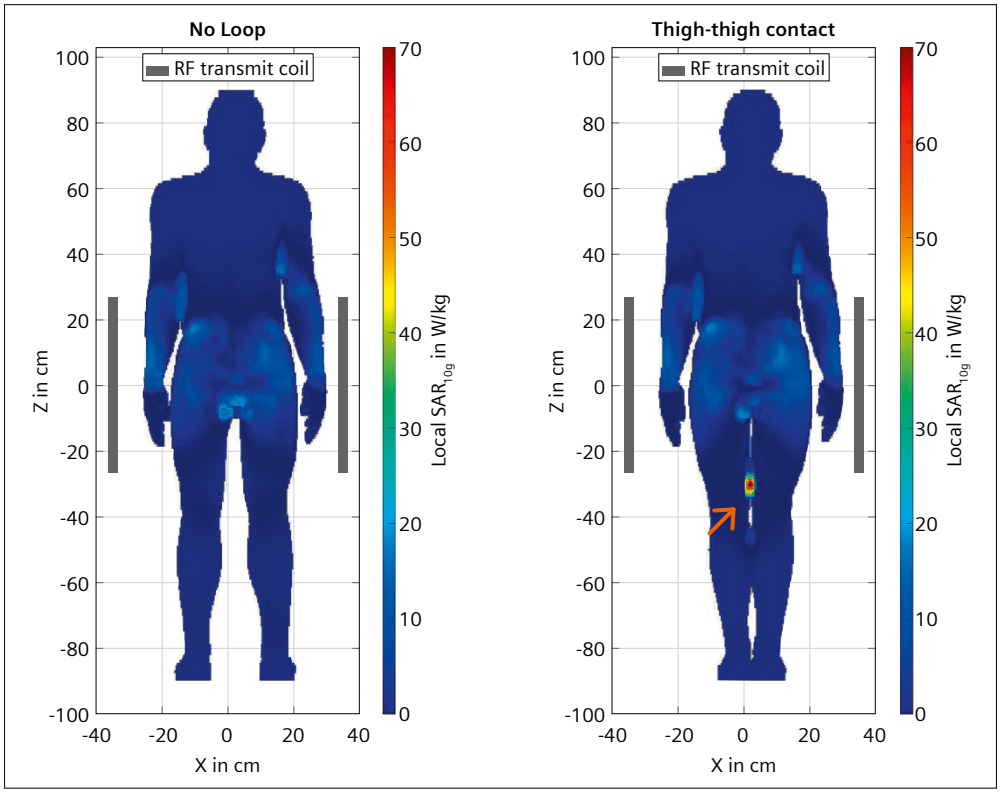

3 SAR simulation showing strongly increased local SAR values (10 g average) at the point of contact between the inner thighs. As a result, an RF burn might arise at the contact point.

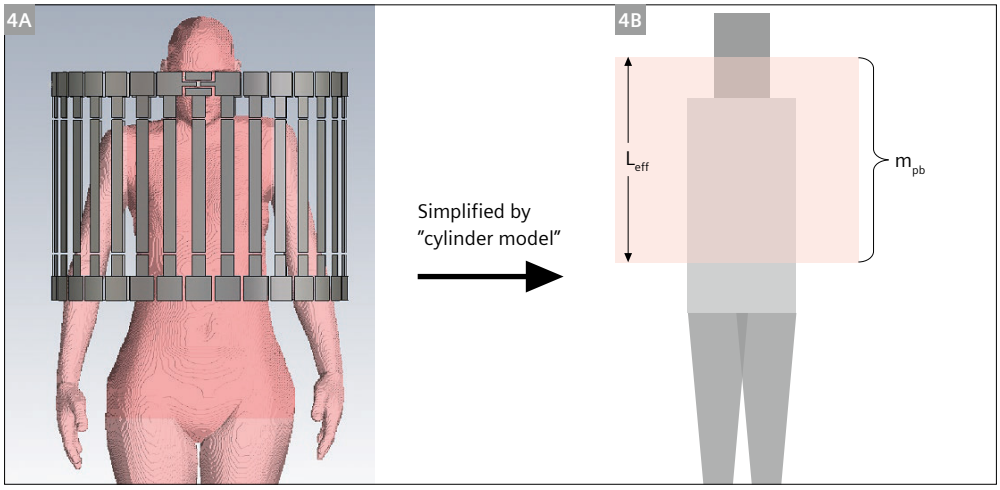

4 **(4A)** Actual situation of patient inside RF transmit coil. **(4B)** Cylinder model approximation of patient and RF transmit coil. The red rectangle shows the area in which 95% of the RF power is absorbed. The human anatomy is modeled with four cylinders.

dimensions of these cylinders (length and radius) are based on statistical data related to the patient's weight and height. Additionally, the patient's position relative to the transmit coil must be known to correctly align the cylinder model. The area in which 95% of the emitted power is absorbed is described by the effective length L_{eff} and is known for each transmit coil. With this information, the head mass and the exposed partial-body mass can be determined.

The big advantage of using the cylinder model is that there is an analytical formula to determine the power absorbed by a homogenous cylinder within a magnetic RF field [4]:

$$P_{cyl} \sim \omega^2 \times B_1^2 \times \sigma_{cyl} \times R_{cyl}^4 \times L_{cyl}$$

ω = Frequency of RF field;
B_1 = Magnetic RF field strength;
σ_{cyl} = Conductivity of homogenous cylinder;
R_{cyl} = Radius of cylinder;
L_{cyl} = Length of cylinder.

This basic formula was improved and refined over recent decades, and its validity is confirmed for each new transmit coil. Using this formula and the cylinder model, the absorbed power for each of the four cylinders can be calculated for a given reference magnetic field strength $|B_1^2|$. Because SAR ~ E^2 ~ B_1^2, this result can then be scaled for each measurement, as $|B_1^2|$ is known for each sequence. With the determined power and the estimated masses from the cylinder model, all SAR values can be calculated.

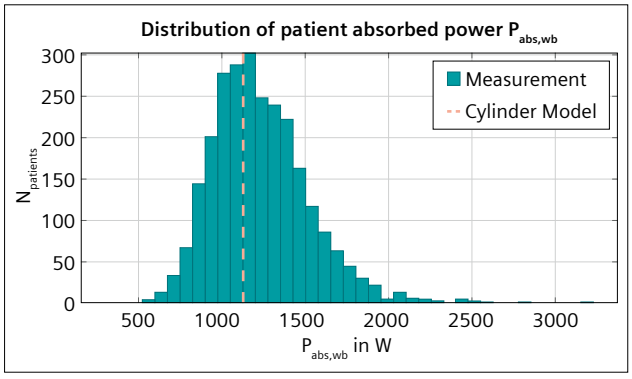

5 Distribution of N = ~2500 different patient examinations with patients of similar height, weight, and position relative to the RF transmit coil for a fixed reference $|B_1^2|$. The dashed red line represents the expected total absorbed power determined by the cylinder model.

Patient-specific adjustment

Although the cylinder model is a powerful approximation, it is insufficient to cover the large variety of human anatomies, postures, and tissue compositions. For a specific patient height, weight, and position, the cylinder model provides a single value for the total absorbed power corresponding to a given $|B_1^2|$ (e.g., a specific pulse sequence). However, if multiple patients with the same height and weight are scanned at the same position and using the same pulse sequence, the total absorbed power $P_{abs,wb}$, measured as described above, varies by factors ~ 3–5 (see Fig. 5).

To incorporate this huge variety into the SAR supervision, a short reference scan is performed at the beginning of an examination to measure the total absorbed power by the patient ($P_{abs,wb}$). If this measurement value is larger than the power determined from the cylinder model ($P_{abs,wb,cyl}$), the estimated power for each cylinder and all SAR values are scaled up by the factor s:

$$s = \frac{P_{abs,wb}}{P_{abs,wb,cyl}}$$

If, however, the measured value is smaller than the value determined from the cylinder model, the cylinder model values are used without scaling (no values $s < 1$ are applied), ensuring patient safety.

This feature of the SAR supervision allows patient-specific performance. For patients with very low absorbed power, high $|B_1^2|$ values are allowed, which improve the image quality or decrease the acquisition time. One drawback of this important safety mechanism is that no accurate SAR calculation can be done before the patient-specific adjustments are performed, which are usually triggered with the start of the first sequence and must be performed again for each new table position. This means that the same pulse sequence might run for one patient but will not be allowed for a different patient, even if the registered patient weight, height, and position are the same. In such a case, the "SAR Limit(s) Exceeded" window will appear after an attempted start of the measurement (see Fig. 6). There are features that enable a smoother workflow by avoiding disruptions from the "SAR Limit(s) Exceeded" pop-up windows. This is achieved by selecting ranges of allowed TR or flip-angle values and automatic modifications of the protocol parameters if necessary.

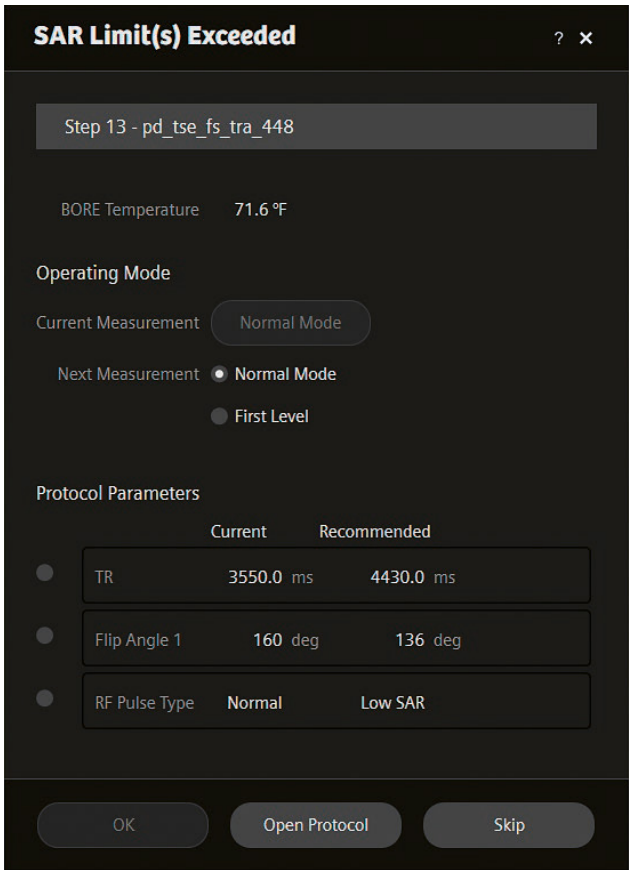

6 "SAR Limit(s) Exceeded" pop-up window on MAGNETOM scanners. This information will appear if the SAR supervision predicts a limit violation before the start of the measurement. Since patient-specific adjustments are needed for this information, the information will show up only after pressing "start" or "apply."

During the measurement, the applied SAR values are constantly supervised to check for deviations from the prediction by controlling the input power and by independent power measurement devices. If an SAR limit violation is detected, the measurement is stopped immediately.

An alternative SAR supervision approach is to establish a fixed $|B_1^2|$ limit that applies universally to all patients and positions. This method guarantees that the protocol will be applicable to every patient. However, the $|B_1^2|$ limit must be set very conservatively to ensure safety in all scenarios, which would significantly reduce performance for the majority of patients.

Conclusion/summary

Safe MRI examinations regarding RF heating are achieved by following the mandatory SAR limits outlined by IEC 60601-2-33. SAR supervision on MAGNETOM scanners relies on mathematical modeling of the SAR distribution ("cylinder model") in combination with direct power measurements to adapt the calculated aspects to the patient-specific conditions. This ensures safe scanning of the patient, while enabling maximum achievable B_1 depending on the individual tissue properties and patient positioning within the RF transmit coil.

The fundamental principles described in this article apply to all MAGNETOM scanners. However, for low-field scanners (0.55T), SAR is significantly less of a concern due to the threefold lower frequency compared to 1.5T, resulting in SAR values that are ~ 7.4-fold lower. Consequently, a more simplified SAR modeling approach is employed, as most cases are constrained by other factors such as component protection. For ultrahigh-field scanners (7T) the SAR supervision additionally includes modeling of local SAR, which will be described in more detail in a following article in a later issue of MAGNETOM Flash.

References

1 Pennes HH. Analysis of tissue and arterial blood temperatures in the resting human forearm. J Appl Physiol. 1948;1(2):93–122.
2 IEC 60601-2-33, edition 4.0 (2022-08).
3 Tang M, Yamamoto T. Progress in Understanding Radiofrequency Heating and Burn Injuries for Safer MR Imaging. Magn Reason Med Sci 2023; 22(1):7–25.
4 Bottomley PA, Redington RW, Edelstein WA, Schenck JF. Estimating radiofrequency power deposition in body NMR imaging. Magn Reson Med. 1985;2(4):336-49.

Contact

Lena Gast, Ph.D. and Hendrik Paysen, Ph.D.
SHS DI MR R&D TACE PHC
Siemens Healthineers
MR Research & Development
Allee am Röthelheimpark 2
91052 Erlangen
Germany
lena.gast@siemens-healthineers.com
hendrik.paysen@siemens-healthineers.com



Gradient-Free MRI for the Moon and Other Hard-To-Reach Places

Gordon E. Sarty, P.Eng., Ph.D.[1,2]; Logi Vidarsson, Ph.D.[3]

[1]Space MRI Lab, QuanTA Centre, University of Saskatchewan, Saskatoon, Canada
[2]Pelican MRI Inc., Saskatoon, Canada
[3]LT Imaging, Inc., Toronto, Canada

Introduction

We have proposed MRI for use in space to study the effects of the space environment on human health [1, 2]. Such an MRI scanner needs to be absolutely minimal in terms of size, weight, and power (SWaP). The requirement for a low SWaP leads to a scanner design with a permanent low-field magnet with a field of 50 mT to 60 mT. The spacecraft environment, with other sensitive electronic equipment onboard, also means that the stray field must be negligible. The requirement aboard the International Space Station (ISS) is less than 3.2 gauss at 7 cm from the MRI enclosure. Therefore, a Halbach magnet design is indicated because of its low radial stray field. A gradient-free design is also indicated, where radio frequency (RF) image encoding using B_1 is used instead of the traditional switched B_0 gradient image encoding. The elimination of the gradient sub-system considerably lowers the weight, complexity, and power requirements of the MRI scanner.

Many low-field, portable MRI scanner designs have been proposed and built recently [3–6]. These devices have been designed to improve the accessibility of MRI, especially in low- to middle-income countries (LMIC) [7]. However, they use switched B_0 field gradients to achieve imaging, making them less desirable for space MRI designs. Other designs use fixed non-uniform B_0 fields to achieve a B_0 Spatial Encoding Method (B_0 SEM) [8]. Our design for a wrist-sized MRI scanner for the Gateway lunar space station, to be launched later this decade, uses a combination of RF encoding, B_0 SEM, and a narrow B_1 receiver coil profile to achieve a one-slice imaging capability. The RF encoding method used is the Transmit Array Spatial Encoding (TRASE) [10, 11] method. One of our earlier TRASE MRI prototypes was built for 2D imaging encoding [12]. However, to simplify the design further, an approach that uses only one dimension of TRASE RF encoding has been proposed for the Gateway MRI scanner. Since a full 2D TRASE encoding is not used to achieve imaging, we call this a 1.5D TRASE MRI design. This Gateway MRI design, recently completed for a concept study for the Canadian Space Agency (CSA), can be added to the list of existing low-field, portable MRI designs for potential use in LMICs and in other remote locations like the Canadian north. In fact, an objective of the CSA is to see healthcare technology developed for space applied on Earth. On its website, the CSA summarizes its Health Beyond Initiative as follows:

"*The need for increased medical autonomy is not unique to space travellers. Remote and medically isolated populations – including northern and Indigenous communities – experience many of the same barriers found in space. These may include:*

- *limited medical equipment and resources*
- *communication delays or difficulties*
- *lack of access to medical expertise*
- *limited possibility of emergency evacuations*

These challenges make it more difficult for people living and working in remote communities to get the care they need. Doctors in these communities could use improved telemedicine technologies and other tools to provide a range of care, from routine exams to serious emergency treatment. Autonomous medical care could help the health professionals in these distant areas diagnose and treat patients right in their communities."

Here, we review the design of the proposed Gateway MRI scanner, looking at the hardware components as currently implemented in a couple of prototypes that we call Owl MRI scanners.

RF encoding approaches

Gradient-free MRI – that is, MRI designs that do not use switched B_0 gradient fields – can be accomplished through the use of Radio Frequency (RF) image encoding. The idea of using B_1 field variations for encoding spatial information into the Nuclear Magnetic Resonance (NMR) signal goes

Siemens Healthineers Disclaimer: This article describes possible future ideas and concepts. It is not intended to describe specific performance and/or safety characteristics of currently planned or future products. Future realization and availability cannot be guaranteed.

back to the concept of rotating frame zeugmatography by Hoult in 1979 [9]. For that original method, a linear variation of B_1 magnitude in one spatial direction was proposed to achieve a spatial tip angle encoding. Currently, there are three main approaches to RF encoding:

1. TRASE (TRansmit Array Spatial Encoding) [10, 11]: This method relies on the production of a B_1 field with a spatially varying phase gradient using specially designed RF transmit coils. Phase encoded data are generated using a train of 180° transmit pulses, with alternating pulses transmitted through coils with different spatial phase gradients.

2. FREE (Frequency-modulated Rabi-Encoding) [13, 14]: This method uses RF transmit pulses that have an FM modulation in addition to the usual AM pulse envelope. A transmit coil with a spatially varying B_1 magnitude is needed along with a train of 180° transmit pulses in which each pulse has a different FM profile.

3. BS-SET (Bloch-Siegert Spatial Encoding Technique) [15, 16]: This method uses a Bloch-Siegert off-resonance pulse in the presence of a spatially varying B_1 magnitude to impart a spatially varying phase into the NMR signal. A train of 180° transmit pulses, at the resonant frequency, is used with Bloch-Siegert off-resonance pulses transmitted after every other on-resonance pulse.

The design reviewed here only uses TRASE. When this and other RF encoding methods are more fully developed, we might see the abandonment of gradient systems in general for low-field MRI systems, for which RF encoding techniques are particularly suited. The frequent RF pulses needed for RF encoding, played out as trains of 180° pulses, mean that the specific absorption rate (SAR) may be too high at higher fields. But at lower fields, SAR is not a problem [17]. RF encoding methods nearly all need to deal with non-linearities in the production of spatially varying B_1 fields, so the simplicity of the hardware is somewhat traded off for the complexity of the software needed for image reconstruction. Complex software does not affect the SWaP characteristics of the MRI scanner, making this a good trade-off for systems destined for the Moon.

A 1.5D TRASE MRI scanner for the Gateway lunar space station

We have recently completed a concept study for the CSA, in which a design for a wrist-sized 1.5D TRASE MRI scanner was proposed for use on the planned Gateway lunar space station (Fig. 1). Spatial encoding of the NMR signal in the design is accomplished through the following:

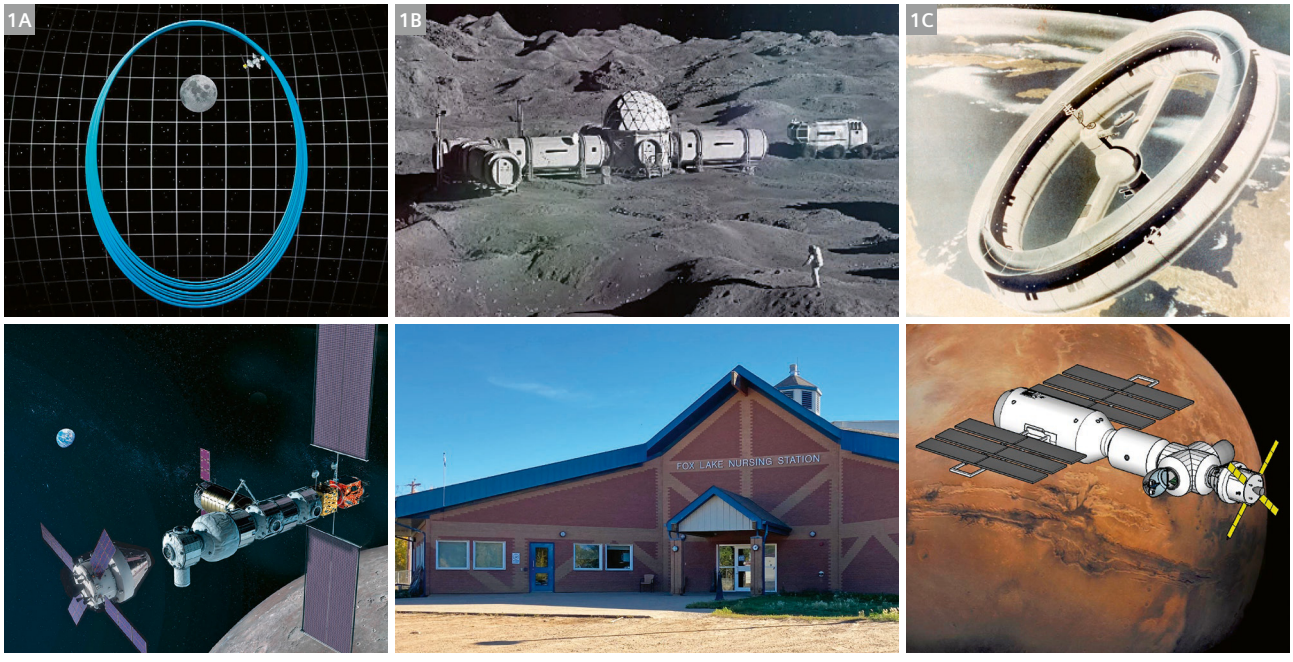

1 Hard-to-reach locations. **(1A)** The Gateway international lunar space station will orbit the Moon in a near-rectilinear halo orbit (NRHO), an orbit that interacts with an Earth-Moon Lagrange point where the Earth and Moon's gravitational pull are equal. **(1B)** Future gradient-free MRI systems could be developed in parallel for use in future lunar base hospitals (top) and for present-day northern community clinics (bottom). **(1C)** Other future destinations for gradient-free MRI scanners would be commercial space stations (top) and interplanetary transports to Mars (bottom).

1. RF TRASE encoding in the left-right (*x*) direction. We used an RF coil set consisting of a saddle coil and a twisted solenoid coil [18] as illustrated in Figure 2 for one of our Owl MRI prototypes.

2. Frequency encoding in the up-down (*y*) direction. The Halbach magnet used in our designs (Fig. 3) have built-in B_0 gradients to essentially achieve SEM encoding in the y direction.

3. Single slice selection on the axial (*z*) direction with a narrow B_1 profile receive coil. Through the use of a passive transmit/receive (T/R) switch, the saddle coil, with its narrow B_1 profile, is used to achieve slice selection.

Note that this MRI design can only produce one image slice. This is another trade-off made to achieve minimal SWaP. We have made several prototypes, two of which are illustrated in Figure 3. The hardware for the 1.5D TRASE MRI design is very simple and easily made. The coils (Fig. 2) and the magnet barrel (Fig. 3) were made using 3D printing; the parts were printed with polylactic acid (PLA). To further minimize weight and complexity, we used class D amplifiers for the transmitted RF instead of the more traditional, heavier, and less efficient class A/B amplifiers. Controlling the pulse sequences is a custom Software Defined Radio (SDR) board that is connected to a laptop computer via a Universal Serial Bus (USB) cable. The RF amplifiers and the SDR board are shown mounted into the USask Owl MRI prototype, along with the power supplies (5V for the SDR, 12V for the class D RF transmit amplifiers and the Low-Noise Amplifier (LNA) for reception), in Figure 4.

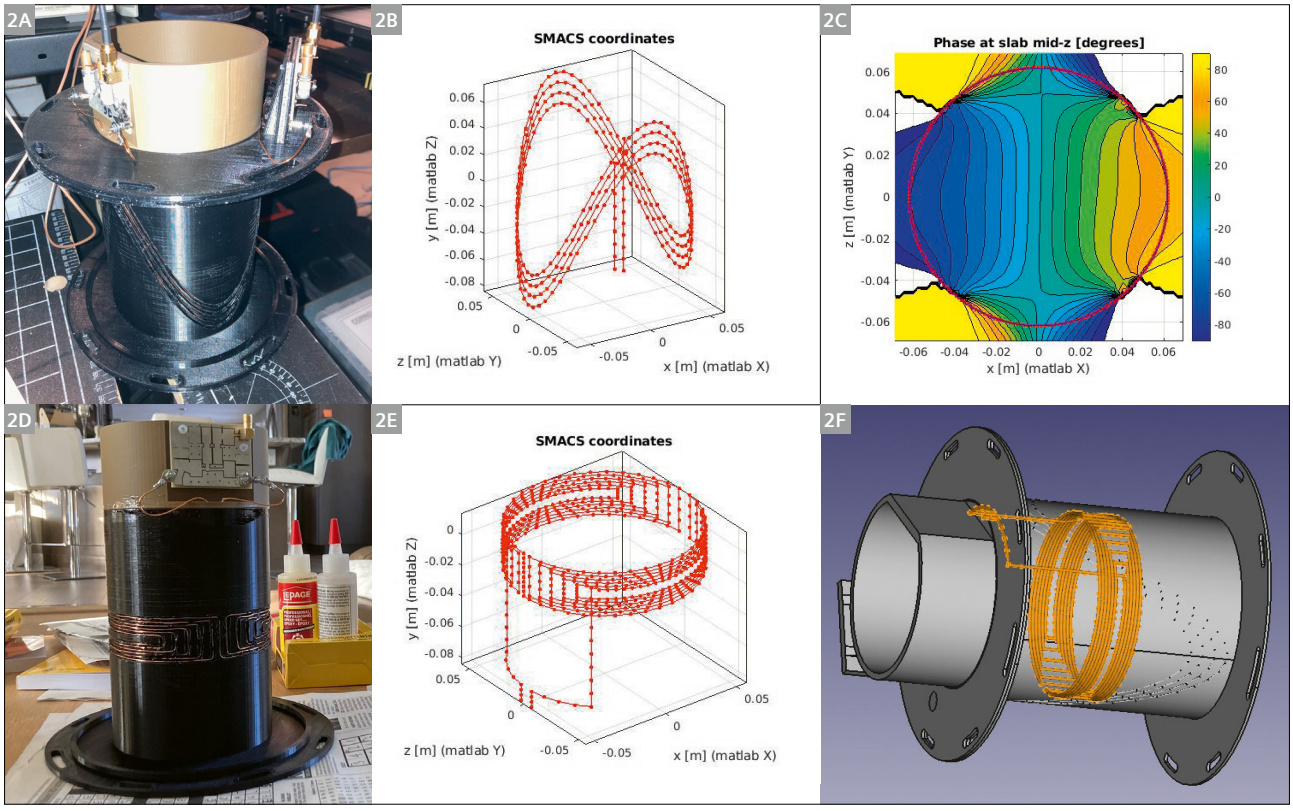

2 The RF coils used in the USask Owl MRI prototype. **Top row, the twisted solenoid coil. (2A)** 3D-printed coil; **(2B)** wire path; **(2C)** B_1 phase contours from a Biot-Savart calculation. **Bottom row, the saddle coil. (2D)** 3D-printed coil; **(2E)** wire path; **(2F)** the saddle coil is nested inside the twisted solenoid coil and provides a uniform B_1 field that has a narrow profile in the axial, z, direction to define a slice roughly 15 mm in thickness.

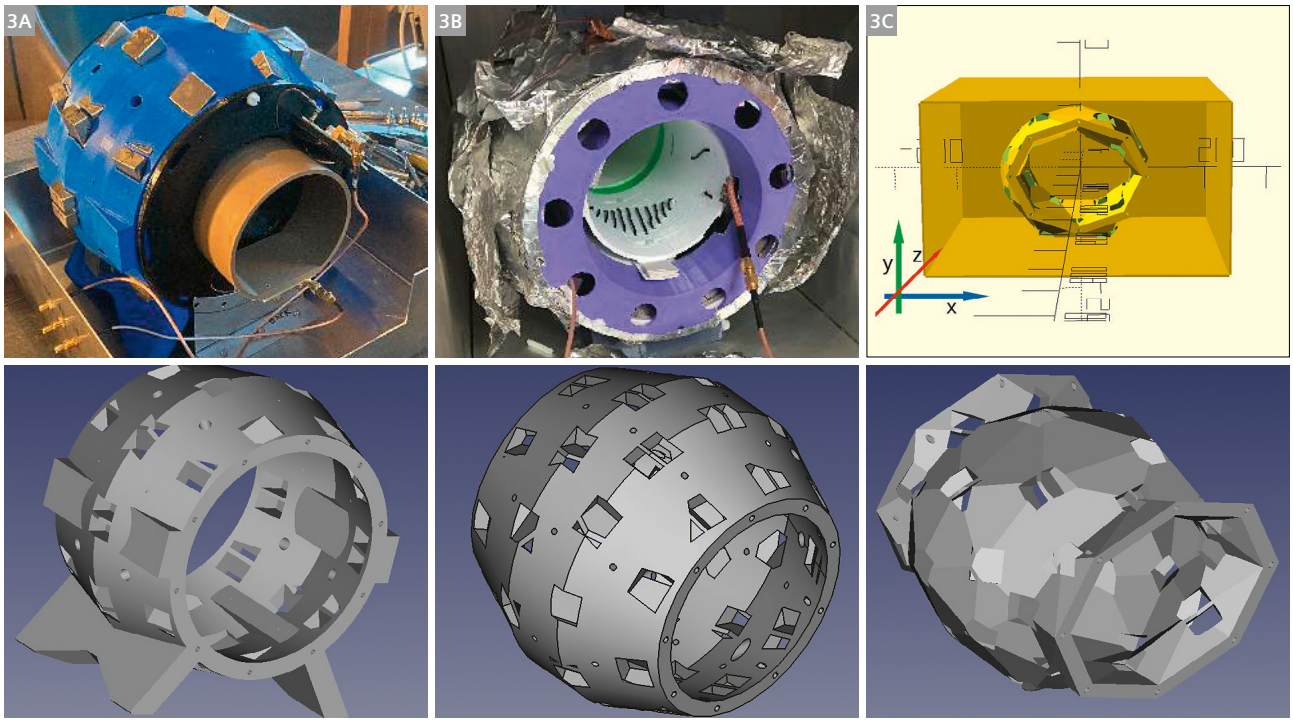

3 Three varieties of Owl MRI prototypes and designs. **(3A)** The USask Owl MRI prototype. The magnet is a Halbach magnet with three rings of magnet blocks. **(3B)** The LT Imaging Owl MRI prototype. Its Halbach magnet has four rings of magnet blocks. **(3C)** The Gateway Owl MRI concept. Its Halbach magnet will have four rings of magnets and has an elliptical shape in order to fit into the Gateway's provided experiment rack enclosure box. All magnets produce fields of approximately 50 mT with a built-in magnetic field gradient of about 10 mT/m in the vertical, *y*, direction.

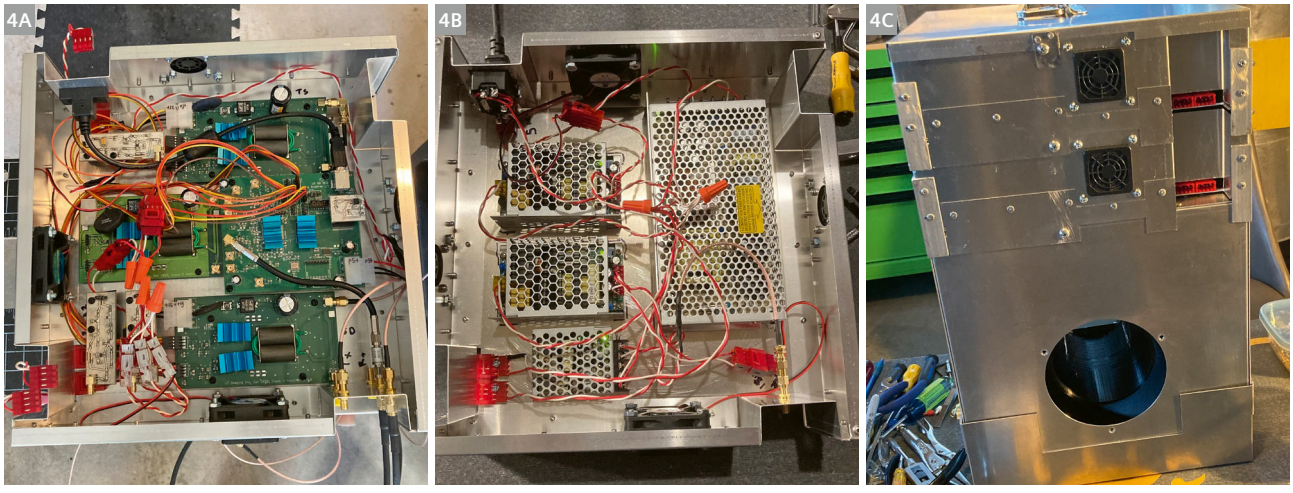

4 Hardware packaging for the USask Owl MRI. **(4A)** The electronics box for the class D RF amplifiers and the SDR board. The SDR board is in the middle row on the right. The other three boards are class D RF amplifiers of which only two are used for the 1.5D TRASE prototype. **(4B)** The power supply box. The large power supply on the right is 5V for the SDR board. The other three are 12V power supplies with the top two on the left being for the class D RF amplifiers and the one on the bottom left being for the receive LNA. **(4C)** The assembled unit. The magnet box is on the bottom, the power supplies are in the middle, and the electronics box is on top. Altogether, the unit has a mass of 11.9 kg and uses a measured 30 W average of power during imaging.

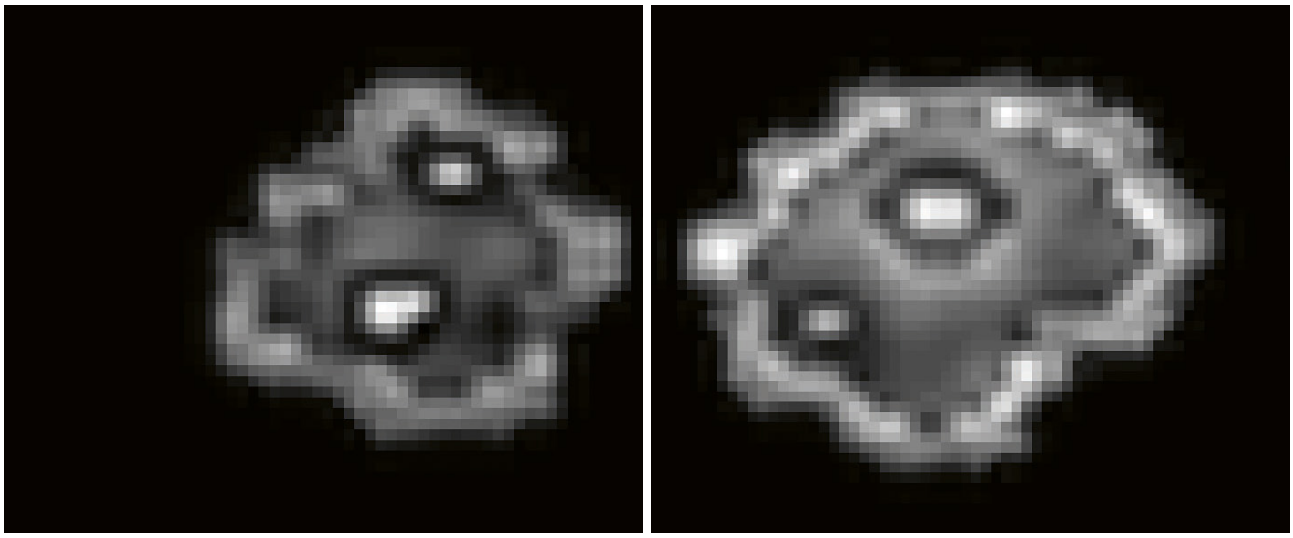

5 Preliminary wrist images produced by the LT Imaging Owl MRI prototype. They are clearly not ready for clinical application yet, and some basic image processing was used to clean up the raw images produced after Fourier transform. The image processing included dilution, erosion, thresholding, and clamping, but no AI was used. The radius and ulna, and their bone cortex, are clearly visible.

The images we get from our prototypes (Fig. 5) are not yet ready for clinical use. The non-linearities in the system referred to earlier necessitate creative software solutions that we are currently working to fully implement. The trade-off of software complexity for hardware simplicity means that these MRI scanners are perfect for student hardware building projects. Such projects have started at the Saskatchewan Indian Institute of Technologies (SIIT), and we are working toward expanding them into high schools in Saskatchewan's northern communities. Ultimately, we foresee that small, specialized MRI scanners will be built and maintained in the communities that use them, following the knowledge that you simply cannot just drop off complex medical equipment in a remote community and expect that it will function [7].

Conclusion

Gradient-free MRI technology that uses RF encoding has been advanced by a few research groups and is a promising approach for lightweight, portable MRI systems at low fields in the ~50 mT range. This approach to MRI design has the potential to complement and potentially supersede the low-field designs now being built in research labs for the purpose of making MRI more accessible and defining a new role for MRI as a point-of-care diagnostic tool. The field strength of 50 mT is at a frontier value below the 0.55T field strength of the MAGNETOM Free.Max and Free.Star MRI scanners. Our MRI scanners, designed originally for use in space, will fill a diagnostic niche opposite the very high field 14T MRI scanners now being planned [19].

Acknowledgment

Funding for the development of MRI technology suitable for use in space was provided by the Canadian Space Agency (CSA) and the Natural Science and Engineering Research Council (NSERC) of Canada.

References

1 Sarty GE, Obenaus A. Magnetic resonance imaging of astronauts on the International Space Station and into the solar system. Can Aeronaut Space J. 2012;58(1):60–68.
2 Sarty GE, Scott A, Turek K, Liszkowski P, Sharp J, Tomanek B. A Wrist MRI for the International Space Station. International Astronautical Federation, 65th International Astronautical Congress, Toronto, Canada, September 29–October 3, 2014.
3 O'Reilly T, Teeuwisse WM, de Gans D, Koolstra K, Webb AG. In vivo 3D brain and extremity MRI at 50 mT using a permanent magnet Halbach array. Magn Reson Med. 2021;85(1):495–505.
4 Cooley CZ, McDaniel PC, Stockmann JP, Srinivas SA, Cauley SF, Śliwiak M, et al. A portable scanner for magnetic resonance imaging of the brain. Nat Biomed Eng. 2021;5(3):229–239.
5 Liu Y, Leong ATL, Zhao Y, Xiao L, Mak HKF, Tsang ACO, et al. A low-cost and shielding-free ultra-low-field brain MRI scanner. Nat Commun. 2021;12(1):7238.
6 Guallart-Naval T, Algarín JM, Pellicer-Guridi R, Galve F, Vives-Gilabert Y, Bosch R, et al. Portable magnetic resonance imaging of patients indoors, outdoors and at home. Sci Rep. 2022;12(1):13147.
7 Webb A, Obungoloch J. Five steps to make MRI scanners more affordable to the world. Nature. 2023;615(7952):391–393.
8 Cooley CZ, Stockmann JP, Armstrong BD, Sarracanie M, Lev MH, Rosen MS, et al. Two-dimensional imaging in a lightweight portable MRI scanner without gradient coils. Magn Reson Med. 2015;73(2):872–883.
9 Hoult DI. Rotating Frame Zeumatography. J Magn Reson. 1979;33(1):183–197.

10 Sharp JC, King SB. MRI using radiofrequency magnetic field phase gradients. Magn Reson Med. 2010;63(1):151–161.
11 Sharp JC, King SB, Deng Q, Volotovskyy V, Tomanek B. High-resolution MRI encoding using radiofrequency phase gradients. NMR Biomed. 2013;26(11):1602–1607.
12 Sarty GE, Vidarsson L. Magnetic resonance imaging with RF encoding on curved natural slices. Magn Reson Imaging. 2018;46:47–55.

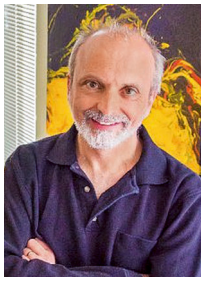

Contact

Gordon E. Sarty, P.Eng., Ph.D.
Professor, Department of Psychology and Health Studies
Director, Space MRI Lab, QuantTA Centre
University of Saskatchewan
105 Administration Pl
Saskatoon, SK S7N 5A2
Canada
ges125@usask.ca

I have the privilege of living on Treaty 6 Territory and the Homeland of the Métis.

13 Torres E, Froelich T, Wang P, DelaBarre L, Mullen M, Adriany G, et al. B1-gradient-based MRI using frequency-modulated Rabi-encoded echoes. Magn Reson Med. 2022;87(2):674–685.
14 Froelich T, DelaBarre L, Wang P, Radder J, Torres E, Garwood M. Fast spin-echo approach for accelerated B1 gradient-based MRI. Magn Reson Med. 2023;89(6):2204–2216.
15 Martin JB, Srinivas SA, Vaughn CE, Sun H, Griswold MA, Grissom WA. Selective excitation localized by the Bloch-Siegert shift and a B1+ gradient. Magn Reson Med. 2022;88(3):1081–1097.
16 Selvaganesan K, Ha Y, Sun H, Zhang Z, Sun C, Samardzija A, et al. Encoding scheme design for gradient-free, nonlinear projection imaging using Bloch-Siegert RF spatial encoding in a low-field, open MRI system. Sci Rep. 2024;14(1):3307.
17 Parsa J, Andrew Webb A. Specific absorption rate (SAR) simulations for low-field (< 0.1 T) MRI systems. MAGMA. 2023;36(3):429–438.
18 Sun H, Yong S, Sharp JC. The twisted solenoid RF phase gradient transmit coil for TRASE imaging. J Magn Reson. 2019;299:135–150.
19 Bates S, Dumoulin SO, Folkers PJM, Formisano E, Goebel R, Haghnejad A, et al. A vision of 14 T MR for fundamental and clinical science. MAGMA. 2023;36(2):211–225.

Accelerating Cardiac MRI with Inline Generative AI and Open Recon

Tess E. Wallace[1,2]; Manuel A. Morales[2]; Salah Assana[2]; Omer Burak Demirel[2]; Kelvin Chow[3]; Reza Nezafat[2]

[1]Siemens Medical Solutions USA, Inc., Boston, MA, USA
[2]Department of Medicine (Cardiovascular Division), Beth Israel Deaconess Medical Center and Harvard Medical School, Boston, MA, USA
[3]Siemens Healthcare Ltd, Calgary, Canada

Introduction

Cardiac MRI protocols often require challenging breath-holds, and the resulting motion artifacts can compromise imaging quality. Compressed Sensing (CS) can significantly shorten scan times compared to traditional parallel imaging but has limitations in both image quality and reconstruction time. AI-based techniques can further increase imaging efficiency [1]; however, seamlessly integrating these approaches into daily practice can pose challenges due to the substantial effort required for on-scanner implementation in vendor software environments. We recently proposed a generative AI-based model for resolution enhancement [2] that can be readily deployed using the Open Recon[1] platform (Siemens Healthineers, Erlangen, Germany) to provide fully automated inline integration without any modification to product sequences. The resolution enhancement generative adversarial inline neural network (REGAIN) is trained on cardiac cine images and has been successfully applied to both reduce breath-hold duration and enable free-breathing real-time imaging across multiple cardiac MRI applications (Fig. 1).

REGAIN acceleration

For the REGAIN acquisition, *k*-space is undersampled using existing uniform or non-uniform acceleration techniques, such as GRAPPA or CS. In addition, the operator prescribes a reduced spatial resolution along the phase-encoding direction to further reduce scan time. GRAPPA or CS is applied normally to estimate missing *k*-space lines and is zero-padded in the phase-encoding direction prior to inverse Fourier transform to reconstruct an anisotropic

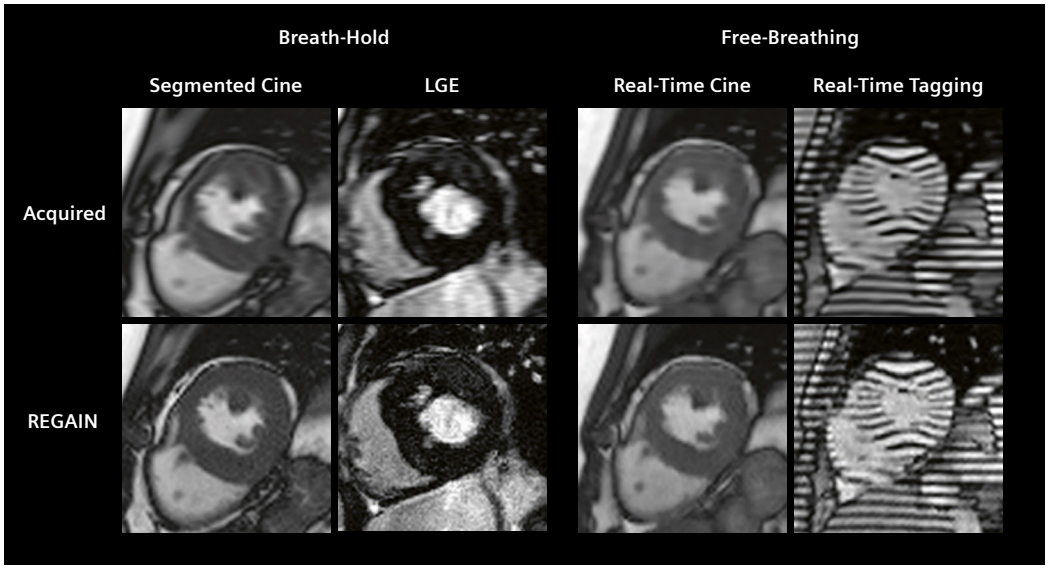

1 Acquired low-resolution data and AI-based resolution enhancement (REGAIN) using a pre-trained model based on seg mented cine images. REGAIN enables shorter breath-holds in segmented ECG-gated cine and LGE sequences, and free-breathing real-time cine and tagging images with high temporal resolution.

[1]*Open Recon is to add clinical reconstructions to the system, if signed and released for clinical use by SHS. Any other recon used e.g., by researchers is automatically labeled not for diagnostic use, which may require observation of national regulations.*

Siemens Healthineers Disclaimer: This article describes possible future ideas and concepts. It is not intended to describe specific performance and/or safety characteristics of currently planned or future products. Future realization and availability cannot be guaranteed.

low-resolution image with a matrix size corresponding to the desired high-resolution image. REGAIN subsequently restores the image sharpness of the reconstructed low-resolution images.

The REGAIN model was trained on retrospectively collected GRAPPA-accelerated, ECG-gated segmented bSSFP cine MRI from 1,616 patients with various cardiovascular indications [2]. Training data consisted of pairs of high resolution and low-resolution images, synthesized by discarding the outer phase-encoding lines. The generator is trained to sharpen the low-resolution image, while the discriminator estimates the probability that an image reconstructed from full *k*-space data appears "more realistic" than the resolution-enhanced image, to produce generated images that mimic true high-resolution images. REGAIN is implemented in Python using PyTorch (the Linux Foundation, San Francisco, CA, USA) and is open source: https://github.com/HMS-CardiacMR/REGAIN.

This proposed resolution enhancement model was validated on cine images prospectively collected from 126 patients and 55 healthy subjects. For ECG-gated segmented cine, REGAIN reduced the number of breath-holds required compared with GRAPPA parallel imaging (3.7 ± 1.0 vs 11.2 ± 1.4), while achieving similar diagnostic quality scores and excellent agreement for left ventricular function, volume, and strain measurements. Combining REGAIN with CS-facilitated 16-fold acceleration, enabling free-breathing real-time cine with $(1.8\ mm)^2$ in-plane spatial resolution, and 28 ms temporal resolution, with rapid inline image reconstruction [2]. The previously trained REGAIN model has also been successfully applied to enable highly accelerated real-time tagging to quantify myocardial deformation in response to physiological exercise in both healthy subjects and patients [3]. Most recently, REGAIN has also been applied without modification to reduce breath-hold duration in inversion-recovery 2D late gadolinium enhancement (LGE) acquisition (6 seconds vs. 16 seconds with GRAPPA acceleration) [4] and to improve image sharpness and quality of single-beat 2D LGE acquired with 4.7-fold acceleration [5].

Open Recon platform

The Open Recon platform is designed to provide a generalized interface for deploying advanced image reconstruction and analysis algorithms directly on the scanner with inline integration. Open Recon extends the existing reconstruction pipeline of Siemens Healthineers by either adding a third-party algorithm at the end of pipeline ("image to image") or replacing the Fourier transform ("raw-to-complex image") (Fig. 2). Data processed by the Open Recon application are converted to DICOM and displayed on the scanner, facilitating seamless integration. Open Recon processing can be selected for any sequence protocol through a customizable parameter card on the user interface, allowing developer-defined parameters to be adjusted for each acquisition for additional control of the processing pipeline.

Third-party algorithms may be implemented in any desired programming language and can communicate via the standardized open-source ISMRM raw data (MRD) format. Open Recon applications are packaged as Docker containers, which provide a consistent and isolated environment that can be deployed directly on the scanner's existing computer and enable unrestricted use of common software libraries. Open Recon apps are independent of the scanner software version, enabling the same application to be distributed to a fleet of scanners with Open Recon functionality.

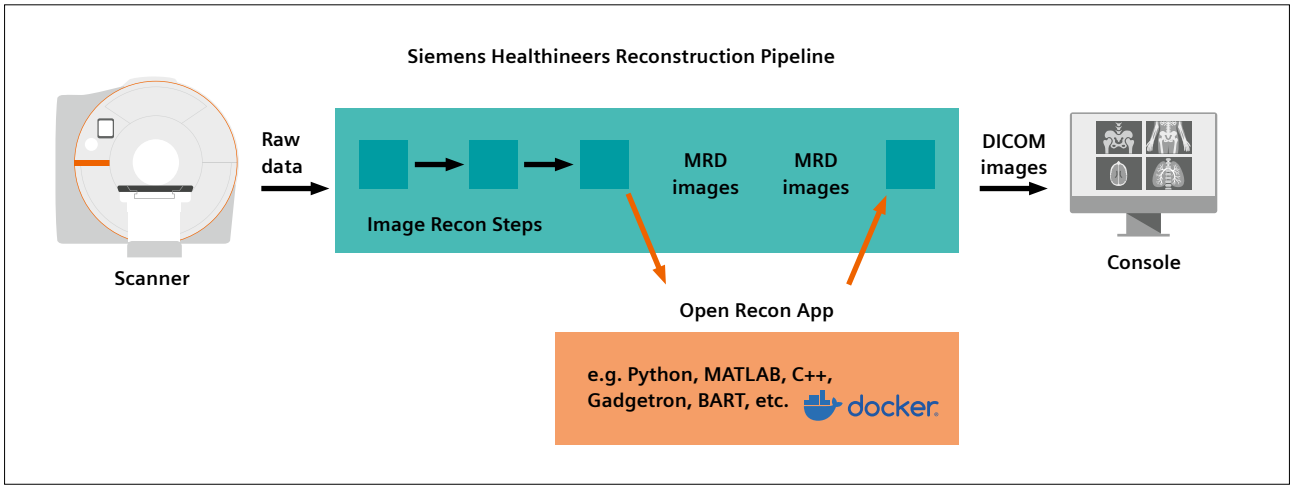

2 Conceptual overview of the Open Recon platform for image-to-image workflows.

Innovating with Open Recon

The inline integration of the REGAIN algorithm with Open Recon enables fully automated reconstruction with low latency. The immediate availability of reconstructed images on the scanner console streamlines the workflow, allowing the AI-based resolution enhancement to be run routinely. The packaging of Open Recon apps, such as REGAIN, as independent Docker containers simplifies deployment and sharing with other sites. In particular, the software independence of Open Recon apps may help facilitate multi-center clinical trials, potentially accelerating the validation of AI-based methods and enabling quicker translation of these research applications. Integration with Open Recon increases the accessibility of REGAIN as a promising AI-based resolution enhancement method for improving cardiac MRI by simplifying deployment, thereby enabling widespread distribution and further research studies.

References

1 Morales MA, Manning WJ, Nezafat R. Present and Future Innovations in AI and Cardiac MRI. Radiology. 2024;310(1):e231269.
2 Yoon S, Nakamori S, Amyar A, Assana S, Cirillo J, Morales MA, et al. Accelerated Cardiac MRI Cine with Use of Resolution Enhancement Generative Adversarial Inline Neural Network. Radiology. 2023;307(5):e222878.
3 Morales MA, Yoon S, Fahmy A, Ghanbari F, Nakamori S, Rodriguez J, et al. Highly accelerated free-breathing real-time myocardial tagging for exercise cardiovascular magnetic resonance. J Cardiovasc Magn Reson. 2023;25(1):56.
4 Demirel OB, Wallace T, Pierce P, et al. Rapid 2D myocardial late gadolinium enhancement imaging with resolution enhancement generative adversarial inline neural network. In: Proceedings of the ISMRM Annual Meeting. 2024 May 04–09. Singapore.
5 Demirel OB, Wallace T, Pierce P, et al. Free breathing single-beat myocardial late gadolinium enhancement imaging, In: Proceedings of the ISMRM Annual Meeting. 2024 May 04–09. Singapore.



Tess E. Wallace



Reza Nezafat

Contact

Reza Nezafat, Ph.D.
Cardiovascular MR Center
Beth Israel Deaconess Medical Center
330 Brookline Ave
Boston, MA 02215
USA
rnezafat@bidmc.harvard.edu

Next-Generation Cardiac MRI: Simplifying the Complex with AutoMate Cardiac

Seung Su Yoon; Michaela Schmidt; Manuela Rick; Dominik Rupp; Miriam Van de Stadt-Lagemaat; Jens Wetzl

Siemens Healthineers, Erlangen, Germany

Background

Two-dimensional cardiac magnetic resonance imaging (CMR) is a highly complex procedure, and the challenges are even greater in 3D CMR. The need to enable operators with varying levels of experience to produce precise, consistent results has driven the development of new solutions to simplify workflows. To make cardiac imaging accessible to a broader range of technologists, we introduced AutoMate Cardiac[1], an AI-powered platform that automates many of the manual steps required for robust CMR exams.

The foundation for AutoMate Cardiac was laid during the early development phase of 3D WholeHeart Pro. Initially focused on automating the detection of the beating heart's quiescent phase with AutoRestingPhase, the idea soon expanded to include other aspects of scan planning and execution.

Another crucial element of AutoMate Cardiac is AutoPositioning. This was developed during the global COVID 19 lockdown, when we had ample time to annotate data and train neural networks. The module automatically positions the patient's heart in the magnet isocenter and determines the correct anatomical locations for the imaging volume, navigators, and saturation volumes using AI.

Finally, a third module called AutoTI automates the selection of inversion times (TI) for late gadolinium enhancement (LGE) scans. This can be applied to standard 2D LGE imaging and to 3D LGE using 3D WholeHeart Pro.

The development journey of AutoMate Cardiac shaped the personal journey of one of our team members, Seung Su Yoon, who began implementing the first prototypes of these modules during his PhD studies. What started as an academic project evolved into a full-fledged product that he would help bring to market as a full-time employee of Siemens Healthineers.

Technical features

AutoMate Cardiac comprises three modules: AutoPositioning, AutoRestingPhase, and AutoTI. The modules automatically execute planning tasks that are typically performed manually by the technologist. Figure 1 illustrates a set of protocols commonly acquired during a CMR exam and shows how the modules interact to automate the scan workflow.

During the prototyping and productization phases, the modules were developed using diverse datasets obtained through close collaboration with various institutions, including Diagnostikum Berlin, Robert Bosch Krankenhaus Stuttgart, and Universitätsklinikum Hamburg-Eppendorf, all in Germany, Cardiovascular Institute Paris Sud (ICPS), Hôpital Privé Jacques Cartier, Massy in France, and Semmelweis University in Budapest, Hungary.

AutoPositioning uses the segmentation of coronal/transverse localizer images to detect bounding boxes of the arms, left ventricle, and whole heart. A UNet model was trained to segment these structures, as shown in Figure 2. A second model was trained to find the liver dome using a heat map regression. The isocenter position was determined by the transverse center of the detected

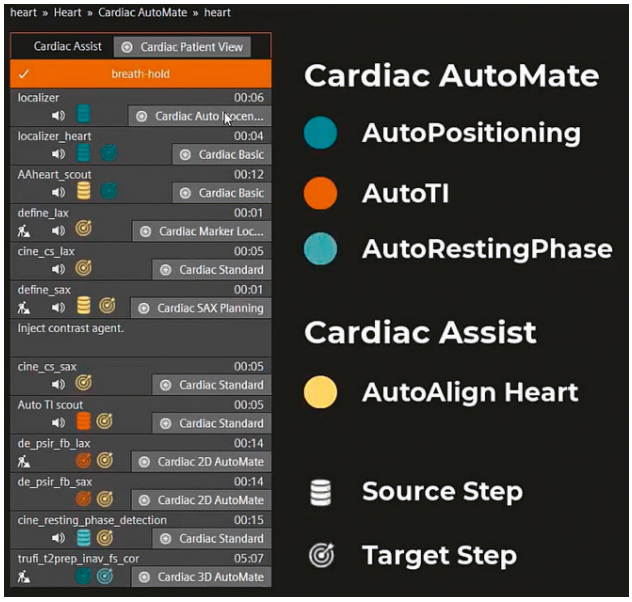

1 Overview of the clinical protocols with AutoMate Cardiac highlighted.

[1] *Work in progress. AutoMate Cardiac is currently under development and is not for sale in the U.S. and in other countries. Its future availability cannot be ensured.*

left ventricle, the size and location of the whole-heart bounding box was used to position the adjustment volume. The center of the whole-heart bounding box was used to position the slice groups for subsequent scans centered on the heart. For 3D WholeHeart Pro scans, saturation bands were placed over the arms, and the left ventricle bounding box was used for image navigator (iNav) placement. For respiratory-gated scans, the detected liver dome landmark served to position the diaphragmatic pencil-beam navigator.

AutoRestingPhase is based on the segmentation of regions of interest in a four-chamber view cine series and the application of motion quantification through image registration across the cine series, weighted on the localized regions, to detect quiescent periods in the cardiac cycle (Fig. 3). Two networks were trained for localizing the

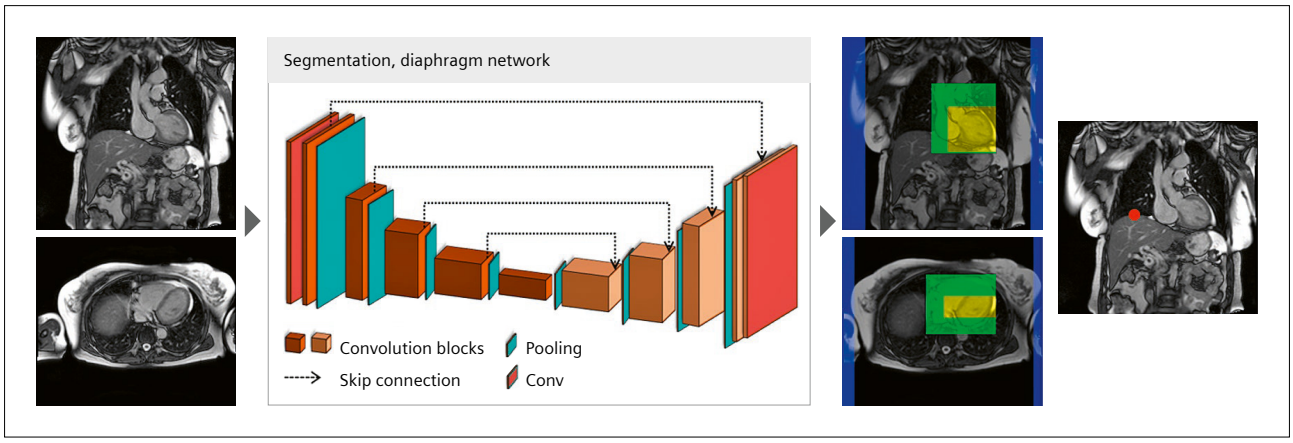

2 Overview of the AutoPositioning feature.

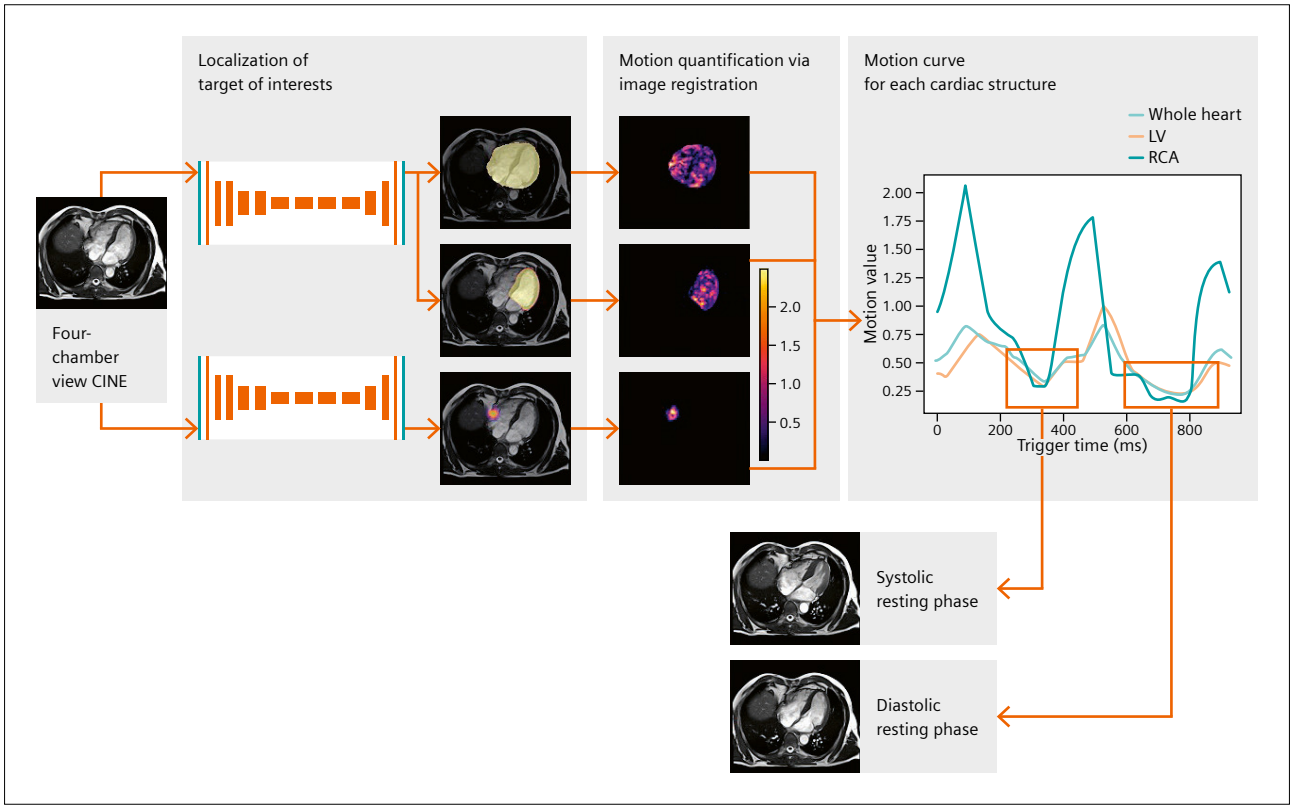

3 Overview of the AutoRestingPhase feature.

regions of interest (ROIs): a multi-region segmentation network for the left and right ventricles and atria; and the right coronary artery (RCA) detection network. UNet models were used for both the segmentation and RCA landmark detection tasks. Motion curves for each ROI could then be computed using the anatomical locations of these ROIs combined with image registration. Valleys in the motion curves represent quiescent phases of the corresponding anatomical structures and can be used to perform imaging without motion artifacts.

AutoTI is based on the segmentation of the myocardium and left-ventricular blood pool from a TI scout series of a mid-ventricular short-axis slice to detect the optimal TI for the subsequent LGE acquisitions (Fig. 4). After segmentation using a trained UNet model, the segmentation masks are used to compute the average tissue intensity of the myocardium and blood pool at each inversion time in the TI scout series. Based on the myocardial intensity curve, the TI is initially selected at the minimum intensity value. Starting from this initial TI time, the optimum TI is finally selected within a small time window after the initial TI, where the relative difference between blood pool and myocardium signal is highest to optimize blood-myocardium contrast.

Clinical evaluation and collaborations

The first deployment of AutoRestingPhase was at Diagnostikum Berlin, where it received positive feedback. According to Rolf Gebker, MD, the technologists were very happy with the automatic feature and almost never needed to adjust the trigger delay for the resting phase. Feedback from personnel at other sites, including Juliano Lara Fernandes, MD, at Radiologia Clinica de Campinas in Brazil, helped further refine the tool before it was distributed more broadly as part of the 3D WholeHeart research application.

A clinical paper from Ehime University [1] highlighted the tool's advantages: While manual detection of the resting phase took experts an average of 50 seconds, and less experienced operators up to 100 seconds, the neural network determined the resting phase almost instantly as cine images were acquired. Moreover, the study showed that the network detected the resting phase position and duration more accurately than less experienced operators, both as compared to the expert annotation using the root mean square error (RMSE).

The complete AutoMate Cardiac platform, which also includes AutoPositioning and AutoTI, was then rolled out as a research application on the Numaris X platform, together with the 3D WholeHeart research application. Early evaluations showed promising results, both in terms of

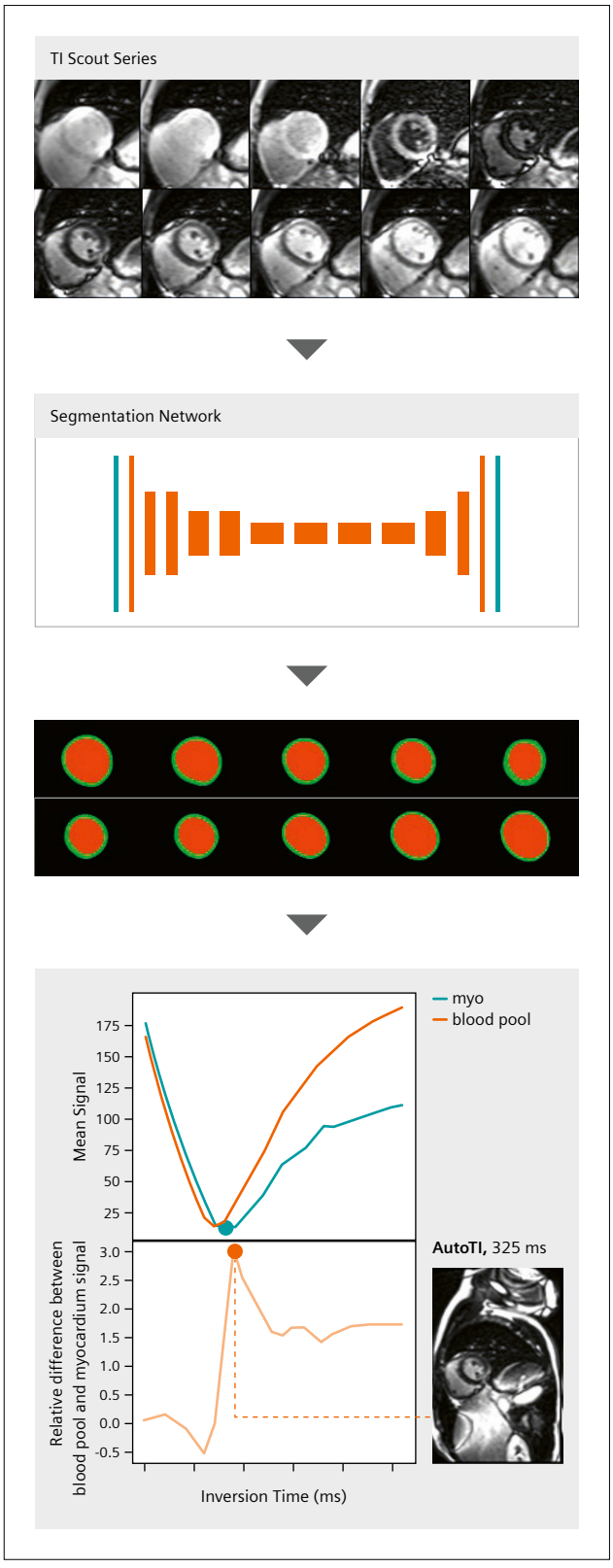

4 Overview of the AutoTI feature.

operator acceptance and validation studies. Jason Craft, MD, from St. Francis Heart Hospital, DeMatteis Research Center, Greenvale, NY, USA, commented that "the AI scout works well for rest-period detection and navigator placement." A study from Aarhus University [2] demonstrated the system's success with automatic resting phase detection, while AutoTI was validated in a study at Royal Bournemouth Hospital [3], which found that it accurately selected the correct inversion time in all 20 cases reviewed.

Single-click CMR workflow

Building on the individual modules of AutoMate Cardiac, our team explored the possibility of creating a fully automated, single-click CMR workflow inspired by the myExam Autopilot system for other body regions. By further automating missing components like short-axis subset planning, we developed a streamlined and modular single-click workflow for CMR.

Results from feasibility studies conducted at Campus Lübeck of University Hospital Schleswig-Holstein [4], Royal Bournemouth Hospital [3], and Geneva University Hospitals [5] have been encouraging. In Lübeck, only 4 out of 44 patient exams required manual intervention, while Bournemouth's comparison of the previous myExam Cardiac Assist and the single-click approach showed a five-minute time saving. Geneva's evaluations, currently under review, suggest that the single-click method results in fewer planning errors and provides time savings, particularly in free-breathing workflows.

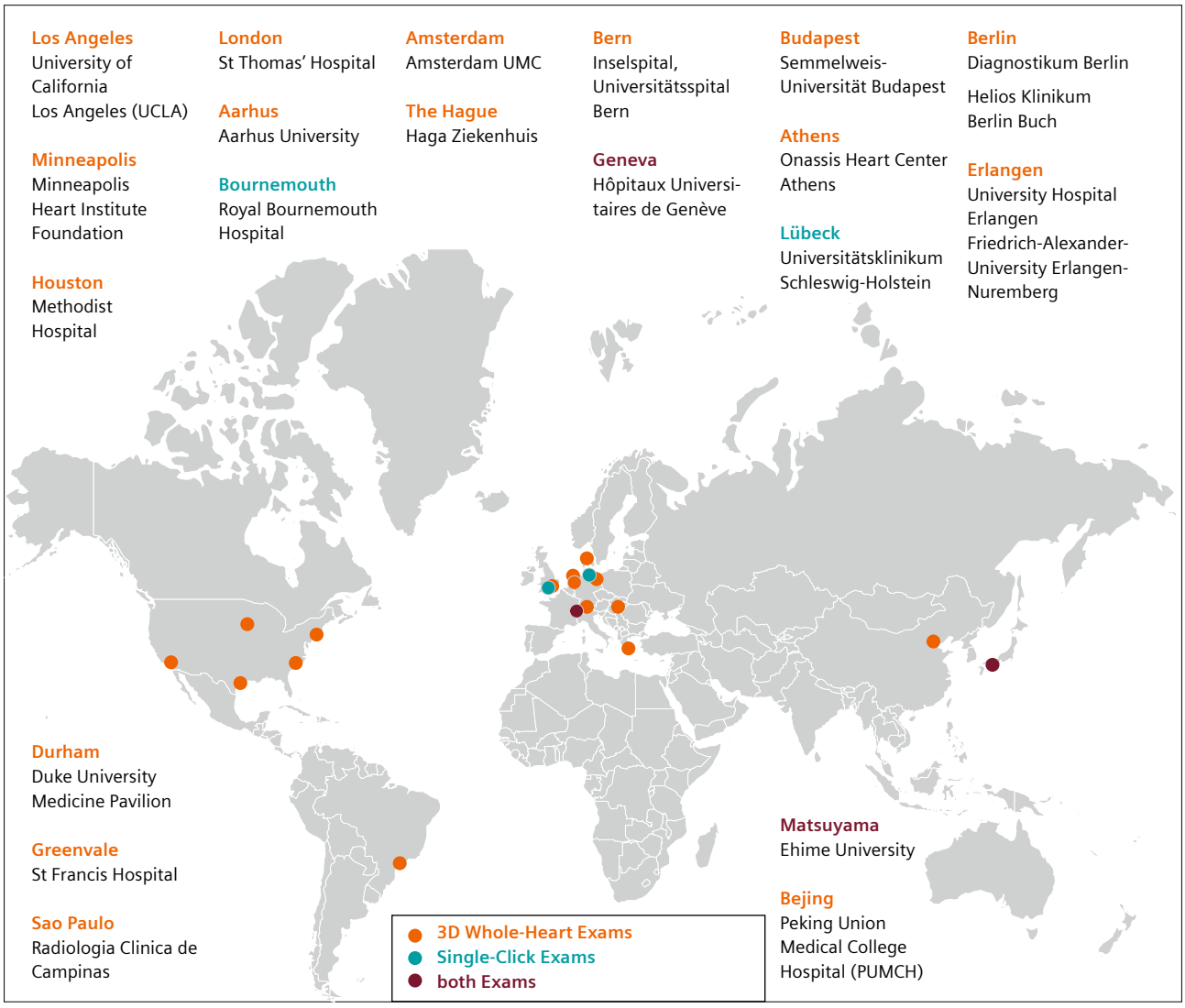

5 Clinical partners for validating the AI workflow features for 3D Whole-Heart and for Single-Click Exams.

From predevelopment to product

To integrate the research components into the product, their functionality had to be screened, understood, and brought into the context of existing software components of the Cardiac Assist. A concept was developed that involved consolidating the new AutoMate Cardiac features into fewer but configurable components. In practice, this meant merging the eight add-ins from the research application into three configurable product add-ins that enable the same variety of features as the research add-ins. For example, the resting-phase and AutoTI components can be switched on or off by configuration, instead of using different add-ins. The AutoPositioning component was added to the Cardiac Basic add-in.

The prototype code of the add-in components was partly refactored to adhere to product code quality requirements, and automated tests were added. The productization also involved adapting the user-interface (UI) styles to achieve a clean and consistent look-and-feel, as well as support for internationalization, which meant adding resources for translating interface texts into different languages, such as Chinese, French, German, Japanese, and Spanish.

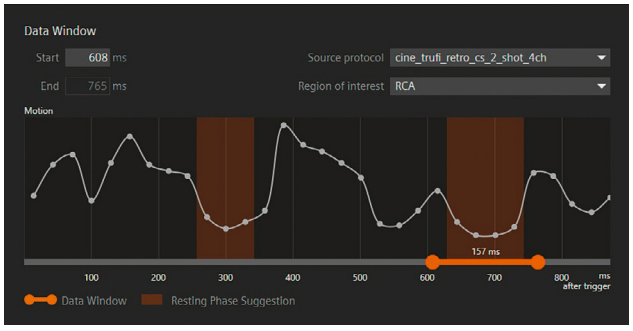

6 Screenshot of the early productization phase, where motion intensities were represented as continuous lines.

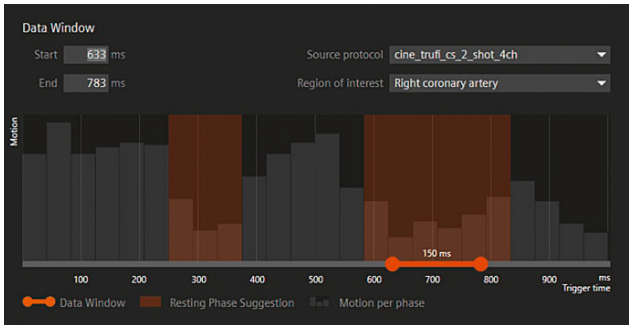

7 Screenshot of the final product. Axes were relabeled and arranged, and a bar chart shows concrete values of motion intensity between two cine images.

During the productization process, many details of the workflow and visualization were improved. This involved smaller changes, such as renaming the x- and y-axes, as well as more profound changes, such as altering the representation of the resting-phase data. Instead of using a line chart, the AutoRestingPhase user interface shows its data as a bar chart, which has the advantage of representing the intensity of motion between two cine images as discrete values rather than implying continuous values (Figs. 6 and 7).

User manual

The new AutoMate Cardiac scanning workflow with the newly implemented add-ins with their configuration options needed to be described in the user manuals so users can look up the necessary information. The development mandate included delivering the input for the user manual in English. Screenshots and texts were provided and set in the right context in the existing user manual. After final layout and a final native-speaker check, the adapted manuals were translated by professional translators into seven languages to meet the needs of users worldwide.

Training for application specialists and inhouse trainers

In the highly complex field of MR imaging, our inhouse trainers and application specialists need to be trained on each new functionality so they can explain the new options to our customers in detail.

With AutoMate Cardiac, we moved the complexity of the scan execution into the segmentation algorithms and the configuration of the add-ins. In the Siemens tree we provide a comprehensive set of protocols with the appropriate add-in configurations. Nevertheless, the installed-base community is highly diverse and varies enormously in terms of specific needs. The application specialists must therefore be able to customize the add-ins to suit these individual requirements. A deep understanding of the available options, the dependencies, and potential pitfalls is crucial. During product development, the task is to provide initial training for our multipliers at the training center, for our customer demo colleagues in the Customer Center, and for the application specialists who support the Customer Use Test sites. The input from these initial training courses is used to compile all further training materials.

Customer Use Test phase

The Customer Use Test (CUT) phase is mandatory for medical devices. Prior to final release, the new software is given to a small number of clinical sites so they can thoroughly test the new options in a clinical environment with real patients and scope to, for instance, apply contrast agent.

During the CUT phase, we gain first impressions about how customers are using the new options – once during in-person visits, and again from the official feedback given after the CUT phase. Unlike the users of research applications, who have a lot of expertise in the specific topic and are therefore chosen as collaboration partners from predevelopment, the CUT customers are not particularly specialized in a specific examination type, since they must test all regions and all new implementations in the new software version.

For software version *syngo* MR XA70A, four CUT sites were selected to test the new AutoMate Cardiac functionality. Two customers are located in Germany, one in Belgium, and one in Romania. Two of the customer sites were familiar with clinical cardiac examinations, one had only rarely performed them, and one had never done any before the CUT phase.

All four customers used the additional support from the AutoMate Cardiac functionality and will continue with the simplified workflow after the CUT phase. All three components – AutoPositioning, AutoTI, and AutoRestingPhase – were rated 1.68 on average (on a scale of 1 to 5, with 1 being the highest score).

After one day of onsite training, the customer that had no prior experience of CMR was able to use Cardiac Assist to perform comprehensive cardiac examinations. During the CUT phase, three out of four customers used the AutoMate Cardiac add-ins in combination with the Cardiac Assist workflows; and one customer used the AutoMate Cardiac support only. The test phase therefore proved that AutoMate Cardiac can be used either in combination or as standalone support to ease complex CMR examinations.

During the CUT phase, we experienced no serious issues with the newly implemented functionality. Minor problems were solved during the in-house test phase, before the final release.

Conclusion

AutoMate Cardiac is a significant advancement in CMR scan automation. Through AI-powered features like AutoPositioning, AutoTI, and AutoRestingPhase, we have created a comprehensive tool that simplifies the imaging process, enhances accuracy, and reduces operator variability. With ongoing validations and expanding clinical applications, AutoMate Cardiac is on track to transform the way CMR is performed globally, pushing the boundaries of what is possible with automated imaging solutions.

References

1 Ogawa R, Kido T, Shiraishi Y, Yagi Y, Yoon S, Wetzl J, et al. Neural network-based fully automated cardiac resting phase detection algorithm compared with manual detection in patients. Acta Radiologica Open. 2022;11(10):20584601221137772.

2 Wood G, Pedersen A, Kunze K, Neji R, Hajhosseiny R, Wetzl J, et al. Automated detection of cardiac rest period for trigger delay calculation for image-based navigator coronary magnetic resonance angiography. J Cardiovasc Magn Reson, 2023;25(1):52.

3 McDermott S, Wetzl J, Schmidt M, Benbow M, Yoon S, Geppert C, et al. AI-based Cardiac Scan Automation: A Prospective Comparison of Highly Automated Scan Workflows in 32 Patients. J Cardiovasc Magn Reson. 2024;26(1):100674.

4 Haenel A, Wetzl J, Yoon S, Schmidt M, Weißgerber AB, Barkhausen J. et al. Analysis of an AI-based prototype for user-independent automated cardiac MRI (CMR) scanning. Presented at: European Congress of Radiology; March 1–5, 2023; Vienna, Austria.

5 Glessgen C, Crowe L, Wetzl J, Schmidt M, Yoon S, Poletti PA, et al. Fully Automated vs. Manual Cardiac MRI: a Single-Center Prospective Evaluation of Quality and Scan Times. European Radiology [in revision].

6 Yoon S, Preuhs E, Schmidt M, Forman C, Chitiboi T, Sharma P, et al. Automated Cardiac Resting Phase Detection Targeted on the Right Coronary Artery. Machine Learning for Biomedical Imaging. arXiv. 2023;2:2109.02342.

7 Yoon S, Schmidt M, Rick M, Chitiboi T, Sharma P, Emrich T, et al. Validation of a deep learning based automated myocardial inversion time selection for late gadolinium enhancement imaging in a prospective study. Presentation at International Society for Magnetic Resonance in Medicine (ISMRM) 29th Annual Meeting & Exhibition, Virtual.



From left to right: Jens Wetzl, Manuela Rick, Seung Su Yoon, Michaela Schmidt, Miriam Van de Stadt-Lagemaat, Dominik Rupp

Contact

Jens Wetzl
Siemens Healthineers
DI MR RCT CLS CARD
Allee am Roethelheimpark 2
91052 Erlangen
Germany
jens.wetzl@siemens-healthineers.com

Seung Su Yoon
Siemens Healthineers
DI MR R&D SWI AFT APPL
Allee am Roethelheimpark 2
91052 Erlangen
Germany
seungsu.yoon@siemens-healthineers.com

Metals and More: The MRI Sustainability Lifecycle

Philipp Grätzel von Grätz, M.D.

Berlin, Germany

In a world of finite resources, the medical product industry needs to consider environmental aspects in all lifecycle phases – without compromising on product quality. As part of its MRI business, Siemens Healthineers has been exploring circular economy pathways for two decades now, including repair services, a leading refurbishment and upgrade portfolio that helps to reduce the need for raw materials and complex logistics – and, of course, recycling.

The main components of an MRI are the magnet, the gradient coils, the radio frequency coils, the local coils, the patient table, the electronics, and, of course, the cover that holds the various components together. When it comes to circular economy pathways in the MRI business, one important distinction is whether components can easily be replaced without disassembling the whole system. "Components that can be easily replaced are potentially repairable," says Martin Vitzthum, Head of Process Planning for coils at the Siemens Healthineers Magnetic Resonance Imaging Unit. "This is why we are offering repair services for a broad spectrum of MRI components, especially local coils, but also electronics, and patient tables."

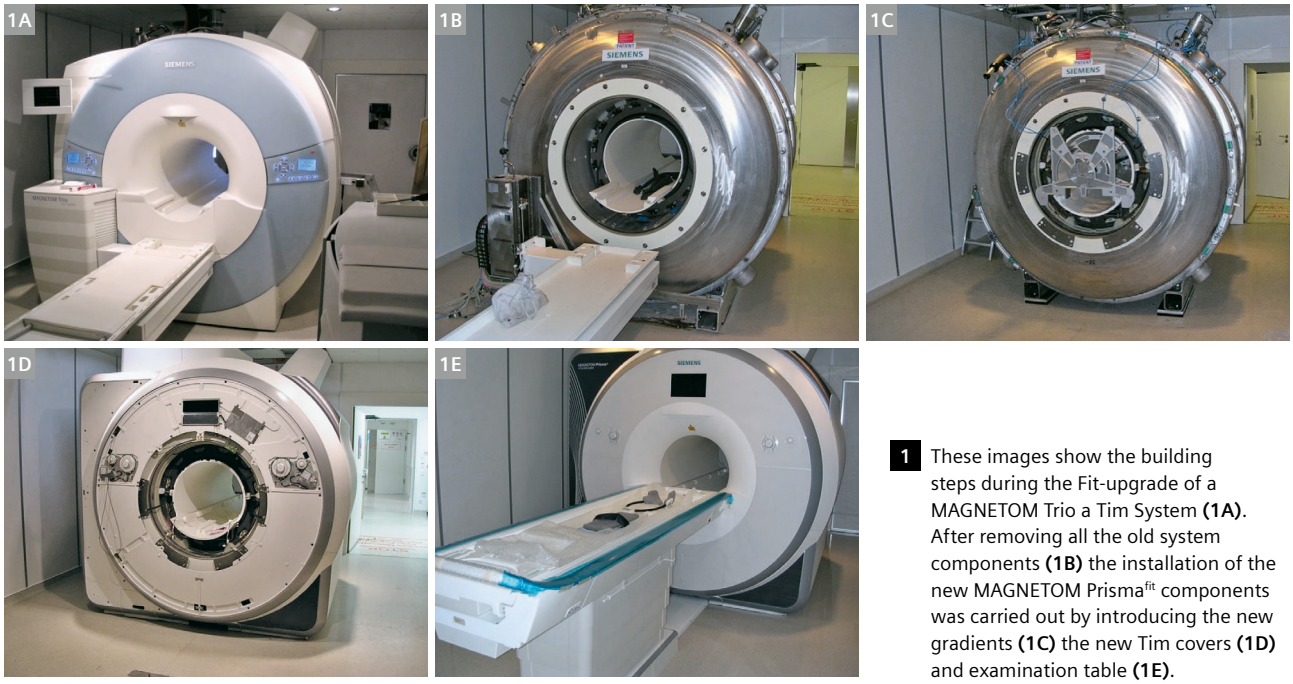

1 These images show the building steps during the Fit-upgrade of a MAGNETOM Trio a Tim System **(1A)**. After removing all the old system components **(1B)** the installation of the new MAGNETOM Prisma^{fit} components was carried out by introducing the new gradients **(1C)** the new Tim covers **(1D)** and examination table **(1E)**.

Local MRI coils: What can be repaired will be repaired

Repair services for components that are subject to regular wear and tear are not only about environment, but also about quality, according to Norbert Gebhardt, who heads the Local Coils Production Team at Siemens Healthineers in Erlangen. Damaged local coils sometimes return in a pretty dire state. But customers nevertheless expect to get them back as good as new: "Whether repaired or new, a coil that we deliver will be produced according to highest quality standards, and tested thoroughly. This is why the 60 employees who produce the new coils are the same who repair them."

Local coil production is a relevant subunit of the MRI business. Martin Vitzthum estimates that, on average, every MRI customer uses eight to ten different local coils for various types of examinations. Some might even need up to 15. There are head coils, body coils of all kinds, and contour coils, which are flexible like a blanket. All in all, about 21,000 local coils leave the Erlangen production site every year. About 11,000 of them are totally new, the other 10,000 have passed the repair cycle. "Approximately 40 percent of local coils with defects don't need to be thrown away but can be repaired," says Vitzthum. "This is a relevant contribution to better sustainability." In fact, the share of repaired coils could be even higher. But there are countries where regulators make it impossible for hospitals to accept repaired coils. In this case, there is no other option than to send new ones.

A circular economy approach for local coils makes a lot of sense, according to Gebhardt, because the coils contain finite resources. This includes standard metals like copper, but also several rare-earth elements. As important as reducing the use of finite resources is, Gebhardt emphasizes that the benefits they create go beyond sustainability: "Repairing helps us learn about how customers use our coils. If certain problems occur again and again, the product will be adjusted so that customers will receive a better product in the end." Quality, in other words, has a sustainability dimension in itself, since components that need fewer repairs will need less transport and less (re)packaging.

Packaging is another area that Siemens Healthineers employees are scrutinizing for potential waste reduction and improved sustainability: "We are thinking about moving away from foamed plastic towards more environmental-friendly materials," says Gebhardt. This would reduce the amount of chemicals needed, but has to be done carefully: "At the moment, there is practically no transport damage with the 21,000 local coils that we deliver." A 'greener' packaging that results in more damage during shipping and thus more reconsignments won't help Mother Nature.

The MRI sustainability lifecycle: From upgrading ...

We are leaving the world of mobile components and turn towards the MRI system itself. There are different avenues that Siemens Healthineers is exploring in order to limit the amount of raw materials required, to extend the lifetime of its scanners, and to re-use any components that can be re-used as often as reasonably possible. A very important service offered for many MRI machines is the on-site upgrade service. Take for instance a MAGNETOM Avanto 1.5T MRI system: first introduced in 2003, it can be 'rejuvenated' in the hospital where it is installed to become a MAGNETOM Avanto Fit or even a MAGNETOM Sola Fit – in other words, a scanner that is one or even two generations younger.

The sustainability dimension of this on-site upgrade service often goes underestimated, according to Lars Drüppel, Vice President Product Lifecycle Management at Siemens Healthineers. It means that a customer who requires a more modern MRI system does not necessarily have to order a completely new one. This will avoid energy-intensive shipping, and also all the construction work that comes with newly delivered MRI systems. "We are the only MRI company worldwide that is able to offer this kind of service on this scale," says Drüppel. "In fact, we are anticipating possible upgrades for every MRI that we bring to the market."

Upgrading an MRI scanner on-site takes approximately two to three weeks, says Jan Chudzik, Head of Installed Base Business MRI at Siemens Healthineers. This is considerably less than the construction work that would be needed when buying a new one. "Less down-time is an important argument for the upgrades," adds Patricia Gehrlein, Project Manager Market Access at Siemens Healthineers. "A MAGNETOM user can get back to business-as-usual quicker with an upgrade than with the purchase of a totally new system."

Going for an upgrade means that more or less every component of the old MRI is dismantled, bar the magnet. Leaving the magnet on-site is possible because it is extremely durable. "Such a magnet can last 20 years and more," explains Chudzik. "There are very few magnets that act up early on. These, we wouldn't upgrade. But once a magnet has been out in the field for ten years and worked reliably, it can easily be used for another ten."

... and refurbishing ...

Refurbishing is another option to make the MRI business more sustainable. In contrast to upgrading, refurbishing means that the MRI system returns to the production site. The result of the refurbishing process is an MRI scanner



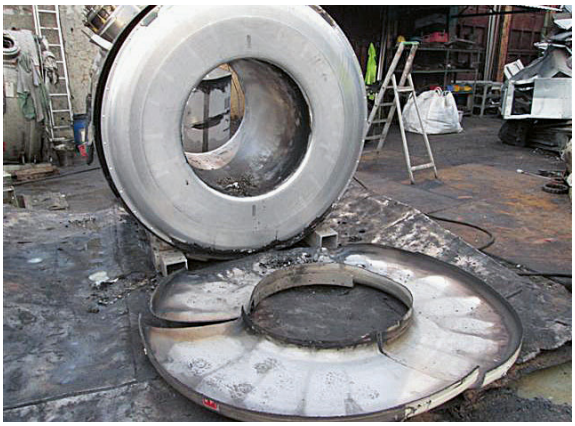


of the same type as the original one. It uses as many of the original systems components as possible, thereby balancing environmental as well as business perspectives. In the end, an "ecoline" label is added – which indicates that the MRI scanner is an environmentally-friendly, refurbished one.

"Refurbished MRIs are by no means just second-hand systems," says Lars Drüppel. "Our goal for ecoline MRIs is to provide MRI scanners that are as good as new." To get there, the original MRI is disassembled into its main components. And each component is refurbished at the production site of the original components. "This means, for example, that all returning magnets are sent back to our magnet factory in Oxford, UK, where our colleagues refurbish them and then return them to us." Similar to the repair service of the local coils, the ecoline MRIs run through the same production lines as the new MRIs, and they are assembled by the same teams of employees. "By doing so, we can guarantee highest quality standards. The expected lifetime of an ecoline system is similar to that of any other system. The same specifications need to be fulfilled, and customers get the same guarantees."

From a user perspective, refurbished systems are not only attractive because of the lower price. They can also be helpful in institutional consolidation efforts: If a hospital wants to standardize its MRI fleet, it might want to buy systems of a type that they own already instead of always going for the latest generation.

A problem remains, though, and this is again similar to the one faced by repair services: In some countries, China for example, regulators do not allow for refurbished or upgraded MRI systems at all. There are other countries, where only privately owned, but not public institutions can order refurbished medical products.

… towards professional recycling by experienced partners

Not every MRI can be refurbished, and not always is an on-site upgrade possible or sensible. At a certain point, late in the lifecycle of an MRI scanner, the most sustainable option is to buy a new one. Enter the recycling specialist, since, of course, an MRI system is not simply left at the landfill. "We process about 30,000 to 40,000 tons of electronic waste per year, and about 10 percent of these are medical products," says André Roth, managing director of the disposal company Westarp in Aschaffenburg, Germany, a recycling specialist focused, among others, on metals.

Roth is an old hand at this business. Westarp has been cooperating with Siemens Healthineers on recycling for more than two decades. In MRI recycling, step one is to send a lorry to the hospital that wants to dispose of its scanner: "We collect between one and three machines every three weeks or so," says Roth. "For each MRI, a specialized Westarp employee will have to work for about twelve hours to do the recycling." In the beginning, this requires heavy machinery like hydraulic shovels and plasma cutting systems. Towards the end, metals are crushed, sifted and melted, and chemicals are used to separate some types of materials.

Roth estimates that between 40 and 50 percent of a typical MRI is steel or other iron-containing metals. Aluminum metal sheets are another relevant component. They make up about 15 percent, according to Roth. Steel and aluminum are sold directly to steel and aluminum mills. But there is more to MRI metals than that. The coils and the superconducting magnet wires contain copper, niobium and titanium. The usual approach is to crush the wires into a granulate material that is then melted. The result is liquid copper in different purity levels.

From a sustainability perspective, niobium is especially interesting, since about 90 percent of this metal is mined in only one country, Brazil. Unfortunately, separating niobium from copper and titanium is rather difficult. Roth



says that some procedures were tried in the past to recycle niobium, but that they were too complex at the time. The tide could be turning now, though, with prices for raw materials on the rise: "Fact is, niobium is indispensable for medical products, so it is a good idea to try and recover it."

Composite metals are necessary for super-conducting wires. Roth is aware of this, but nevertheless he regrets the trend in some industries to use ever more composite materials: "The more composite materials are used, the more difficult the recycling gets." That said, he is glad to see that recycling research has been witnessing a renaissance in recent years. New technologies to separate raw materials are constantly being tested: "The goal is always to recover as many materials as possible, and to recover them as homogeneously as possible."

In conclusion, there can be no doubt that sustainability has to be addressed in all industries, including the MedTech industry. Repairing, recycling and refurbishing should be part of every sustainability agenda, and so should efforts to reduce energy consumption and the need for finite resources – topics that have been covered in the two articles preceding this one. At the moment, healthcare is a major contributor to climate change – being responsible, for example, for about five per cent of CO_2 emissions globally. The challenge is to improve this and other sustainability parameters without compromising on quality of medical care. This is not easy. But with proper expertise from companies that have a deep understanding of what medicine is about, it should be doable.

Visit **https://www.siemens-healthineers.com/company/sustainability** to learn how Siemens Healthineers help improve quality of life.

Further reading

Philipp Grätzel von Grätz, M.D.

"MRI in the Age of Sustainability – Reducing Energy Consumption Without Compromising"

"MRI's Helium Footprint – And How to Make it Harder to Spot"

These articles are available at
www.siemens-healthineers.com/magnetom-world

Go to > clinical-corner > case-studies
> sustainability-in-medical-technology



Open Sequence: An Introduction

Thomas Kluge and Christoph Forman

Siemens Healthineers, Erlangen, Germany

Background

In recent years, open innovation and reproducible research have become increasingly important in the research community. For image reconstruction, significant efforts have been made to establish a vendor-independent standard for the storage and transfer of MRI raw data (the ISMRMRD format) [1]. Reconstruction algorithms supporting this format can be distributed, enabling reproduction of results and application to new data. This can be performed offline for research purposes. On MAGNETOM scanners from Siemens Healthineers, these algorithms can be integrated into the clinical workflow at the scanner using containers and the Open Recon interface.

Several MR sequence development frameworks have been proposed for data acquisition [2–6]. While these

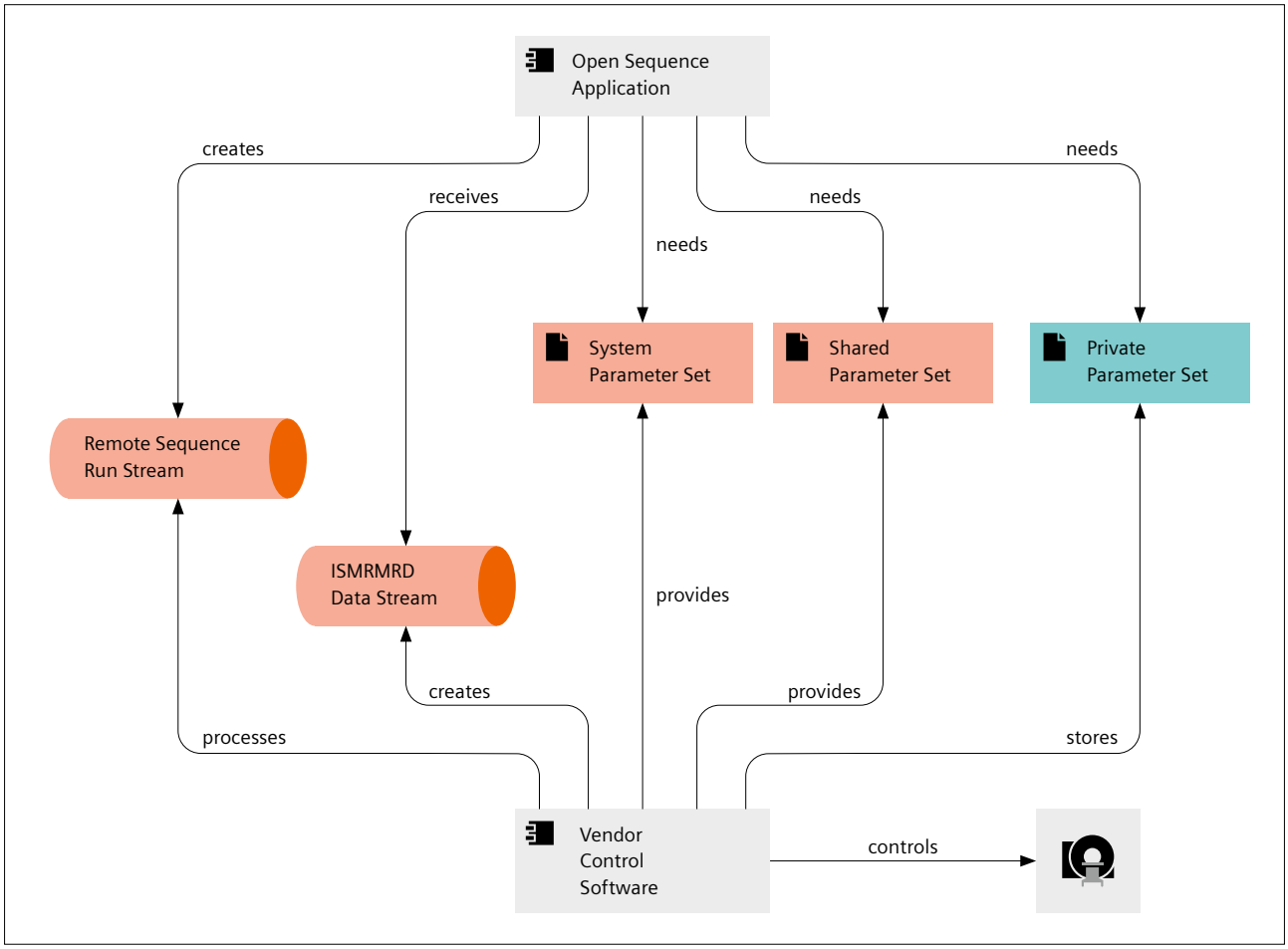

1 The Open Sequence application[1] overview connects an Open Sequence application with the vendor control software. Via the interface, the MR application is parameterized before it provides the MR sequence as a Remote Sequence Run Stream. The acquired data is sent back as an ISMRMRD data stream.

[1] *Open Recon is to add clinical reconstructions to the system, if signed and released for clinical use by Siemens Healthineers. Any other recon used (e.g., by researchers) is automatically labeled with "not for diagnostic use", which may require observation of national regulations.*
Open Sequence is work in progress. The application is currently under development and is not for sale in the U.S. and in other countries. Its future availability cannot be ensured.

environments claim vendor-independence, the integration on the scanner requires a vendor-specific adapter module provided with these environments. This module is deeply integrated into the vendor's scanner control software and must be adapted and re-released for each software update. This creates significant work for the developers and users of such an environment. To address these shortcomings and to fully support reproducible research, a software-version- and programming-language-independent interface for data acquisition on MAGNETOM scanners has been introduced [7].

The interface was announced at this year's ISMRM Annual Meeting. It will be released with the Open Sequence product on MAGNETOM scanners, providing all necessary interfaces to develop an application for MR data acquisition.

Open Sequence is primarily designed for those who maintain MR sequence programming environments, for researchers, and for developers of MR sequences. Eventually, it will provide physicians, researchers, and patients with access to a wide variety of MR sequence applications that will improve open innovation, reproducible research, and clinical diagnosis. While the interface physically decouples the MR application from the MR scanner and its control software via network communication, it enables the development of the MR sequence application in any programming language and with any sequence development environment or library. Furthermore, the Open Sequence interface allows to deploy the sequence application without the need to install any binaries on the MR scanner. The Open Sequence interface offers long-term stability and enables the deployment and execution of sequences on every supported MAGNETOM scanner without the need to modify the sequence application.

This article will provide an overview of the main components of the Open Sequence interface, and will then describe use cases for MR applications.

The Open Sequence interface

As illustrated in Figure 1, the Open Sequence interface has a central role by connecting the vendor control software to an Open Sequence application. The interface consists of three main components that are required to describe the MR application: Parameterization, Remote Sequence Run Stream, and the ISMRMRD Data Stream. These components will be discussed in more detail in the following.

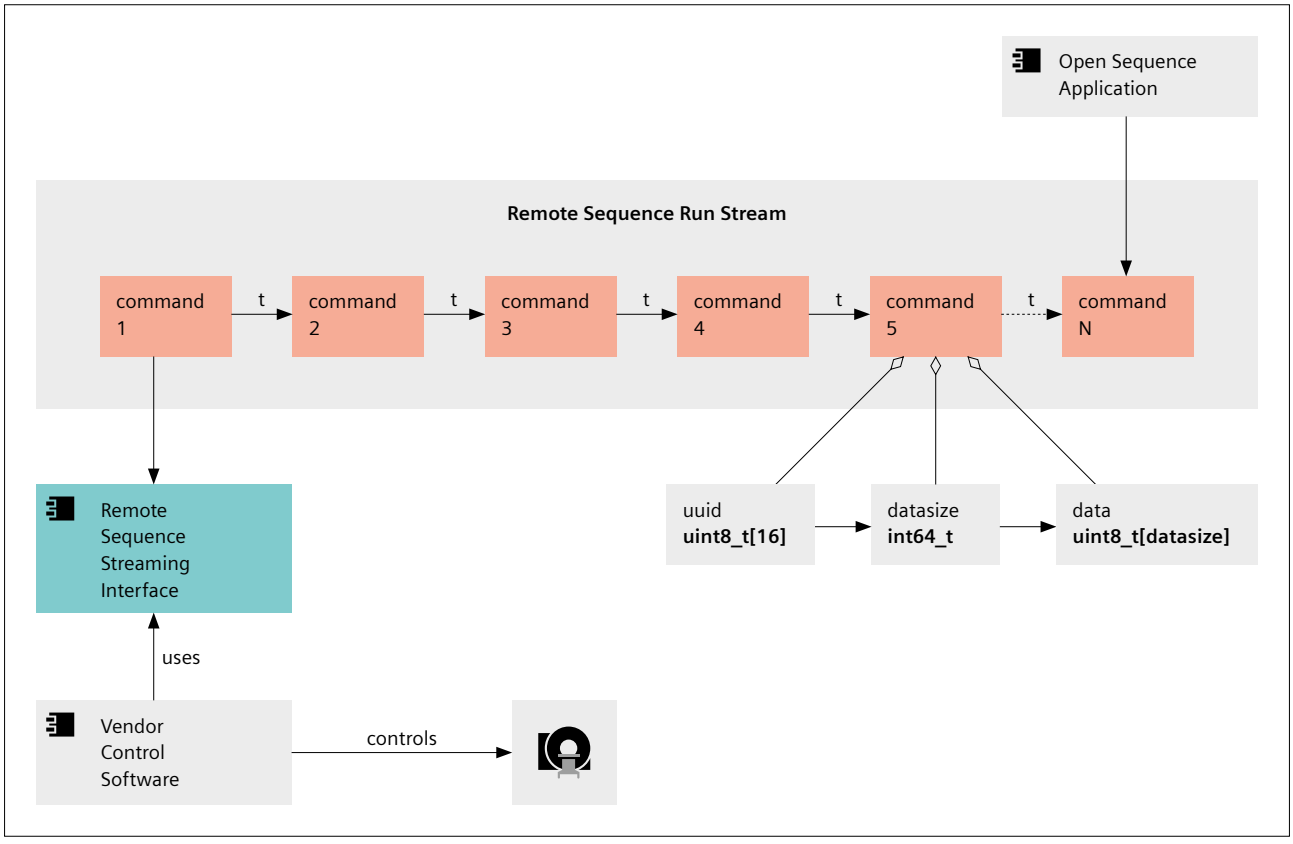

2 The MR sequence running on the vendor's scanner is defined by the Open Sequence application via a stream of commands. As shown for Command 5, each command has the same basic structure, i.e., a UUID identifying the command, the size of the data associated with the command, and the command content data.

Parameterization

The parameters required by the Remote Sequence are provided by three data structures: the System, Shared, and Private Parameter sets. The System Parameter Set contains parameters describing the MR system, e.g., gradient maximum amplitude and minimum rise time. The Shared Parameter Set provides parameters defined by the user interface of the MR scanner during the examination, e.g., position and orientation of the field of view. Finally, the parameters specific to the MR application are provided in the Private Parameter Set. These private parameters are stored by the MR scanner software and sent to the Remote Sequence without further interpretation by any software component of the MR scanner.

Streaming the MR sequence

As shown in Figure 2, the scanner control data is streamed as a series of commands that are each identified by a unique identifier (UUID) and remain stable across all software versions. With this design, new commands can be added later without the need to modify the interface and without rendering existing Remote Sequences invalid. Each command can be serialized and deserialized in a variety of supported programming languages. Once published, the structure of a single command should never change.

Figure 3 shows an example of such a command embedded in the sequence run stream in detail. The highlighted command represents the start of a time slice within the sequence diagram and provides its duration. The subsequent commands describe the content of the time slice, finalized by a command ending the time slice. A series of these blocks of commands organized in time slices is used for describing the complete MR sequence. Following this concept, the Remote Sequence Run Stream contains a complete serialized version of the MR sequence that is streamed to the MR scanner for execution.

ISMRMRD data stream

The data acquired by the MR scanner is streamed back to the Remote Sequence using the ISMRMRD format [1]. The Remote Sequence can implement image reconstruction or further process the acquired data.

Use cases for MR applications

The Open Sequence interface enables a variety of options for developing and deploying an MR application. In the following, two use cases are introduced.

Researcher plays MR sequence from file

This use case is interesting for the researcher or a student who want to run their – potentially very first – MR sequence on a real MR scanner.

The creation of the Remote Sequence Run Stream and the reconstruction of the data acquired is performed by software written by the researcher in the programming

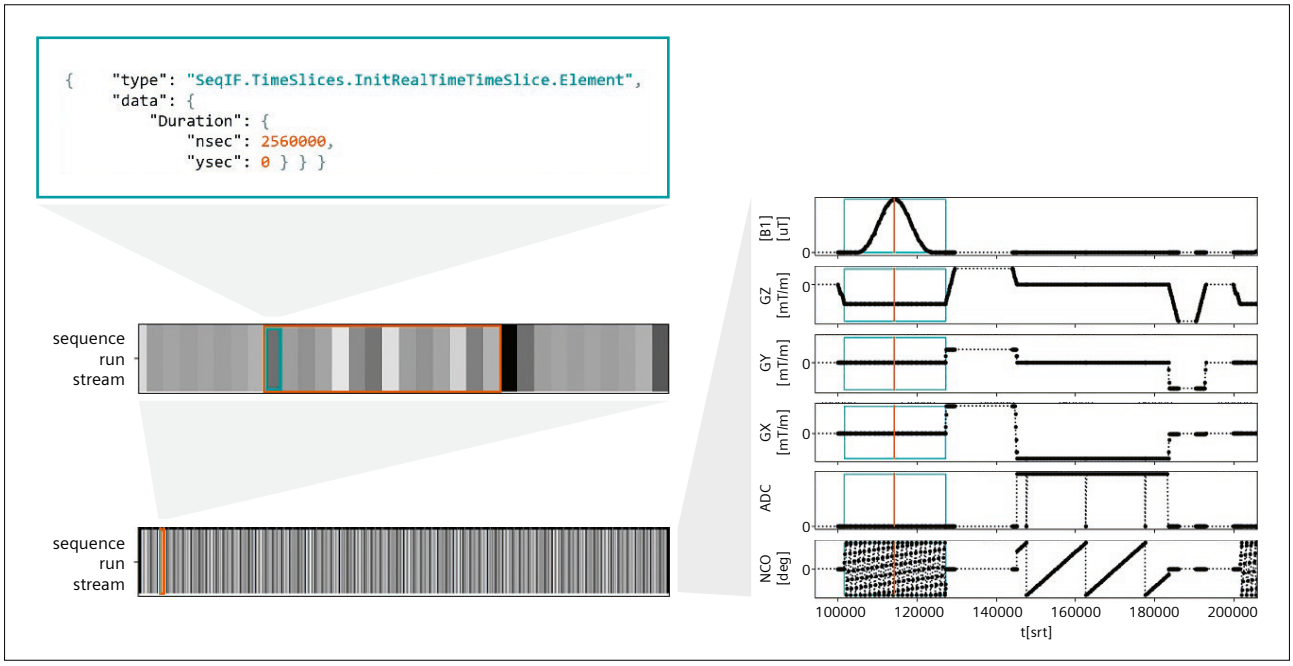

3 Example of a Remote Sequence command stream for a FLASH sequence. The highlighted command represents the start of a time slice within the sequence diagram and provides its duration. The subsequent commands describe the content of the time slice, followed by a command ending the time slice. A series of these commands is used to describe the complete sequence diagram.

language of their choice. On the MR scanner, a special File Player MR sequence can be used for accessing system and shared parameters, as well as for executing the MR sequence and retrieving the acquired data as a file. The individual steps of this approach are illustrated in Figure 4.

This approach easily provides sufficient scanner access for acquiring data for scientific publications, and supports reproducible research as the files can easily be shared between researchers.

The first activities for connecting the widely adopted Pulseq [5, 6] framework, in particular the Python version [12], to the MR scanner without using a binary adapter module are based on this use case and demonstrated in [11].

Use case: MR sequence streamed via network interface
In the long term, this use case is aimed at the maintainers of sequence development environments and developers of clinical MR applications.

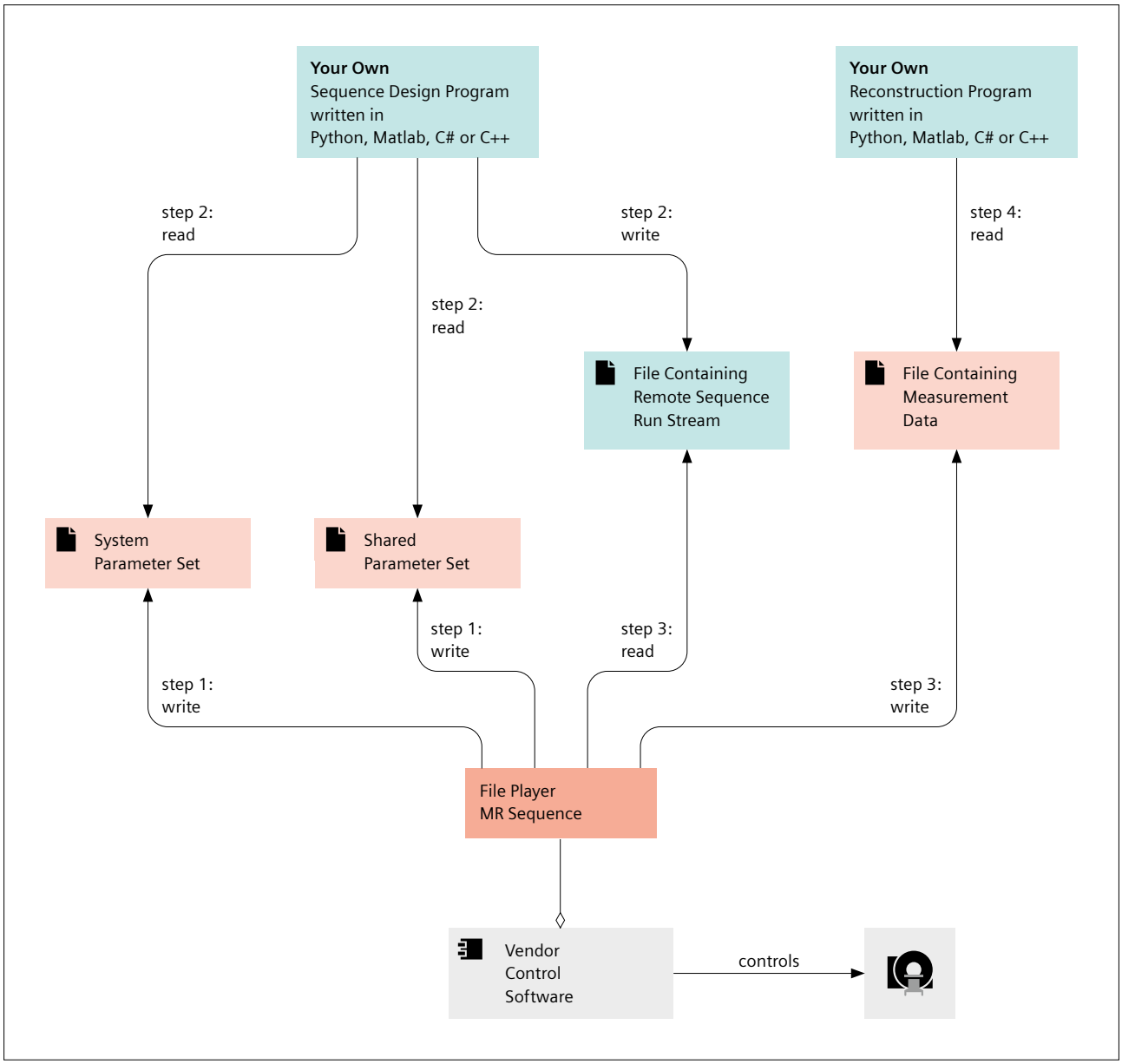

4 **File Player use case.**
Step 1: Export of the parametrization. Step 2: Creation of the MR sequence as a Remote Sequence Run Stream file. Step 3: Execution of the MR sequence and export of the acquired data. Step 4: Image reconstruction.

In this use case, the MR application is completely decoupled from the MR system via the Open Sequence network interface. It aims to develop and deploy MR applications independent of the software version of the MR scanner, while the MR application can be seamlessly integrated into the examination workflow on the MR scanner.

Based on the documentation of the Open Sequence network interface, the MR application can be developed in any programming language. In the first version of Open Sequence, the MR application is hosted on a computer connected to the MR system via a network cable.

This use case can already be demonstrated by the integration of the gammaSTAR framework [3, 4], developed by the Fraunhofer Institute for Digital Medicine MEVIS. Figure 6 shows an echo planar imaging (EPI) sequence streamed from the gammaSTAR framework to Open Sequence. This sequence has successfully been run on an MR scanner with gammaSTAR running on an external computer.

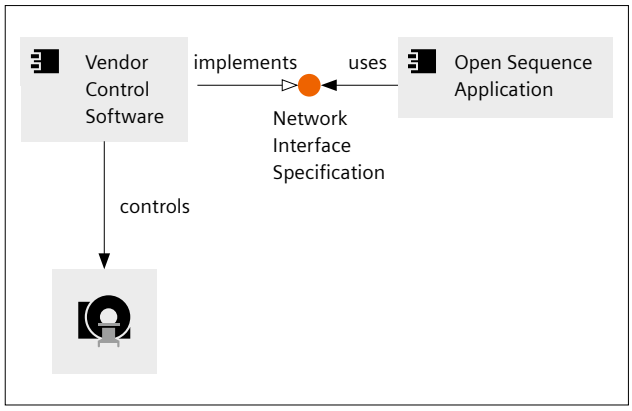

5 **Network streaming use case.**
The MR application is physically decoupled via the Open Sequence Network Interface. All communication between the vendor control software and the Open Sequence application is defined by this interface.

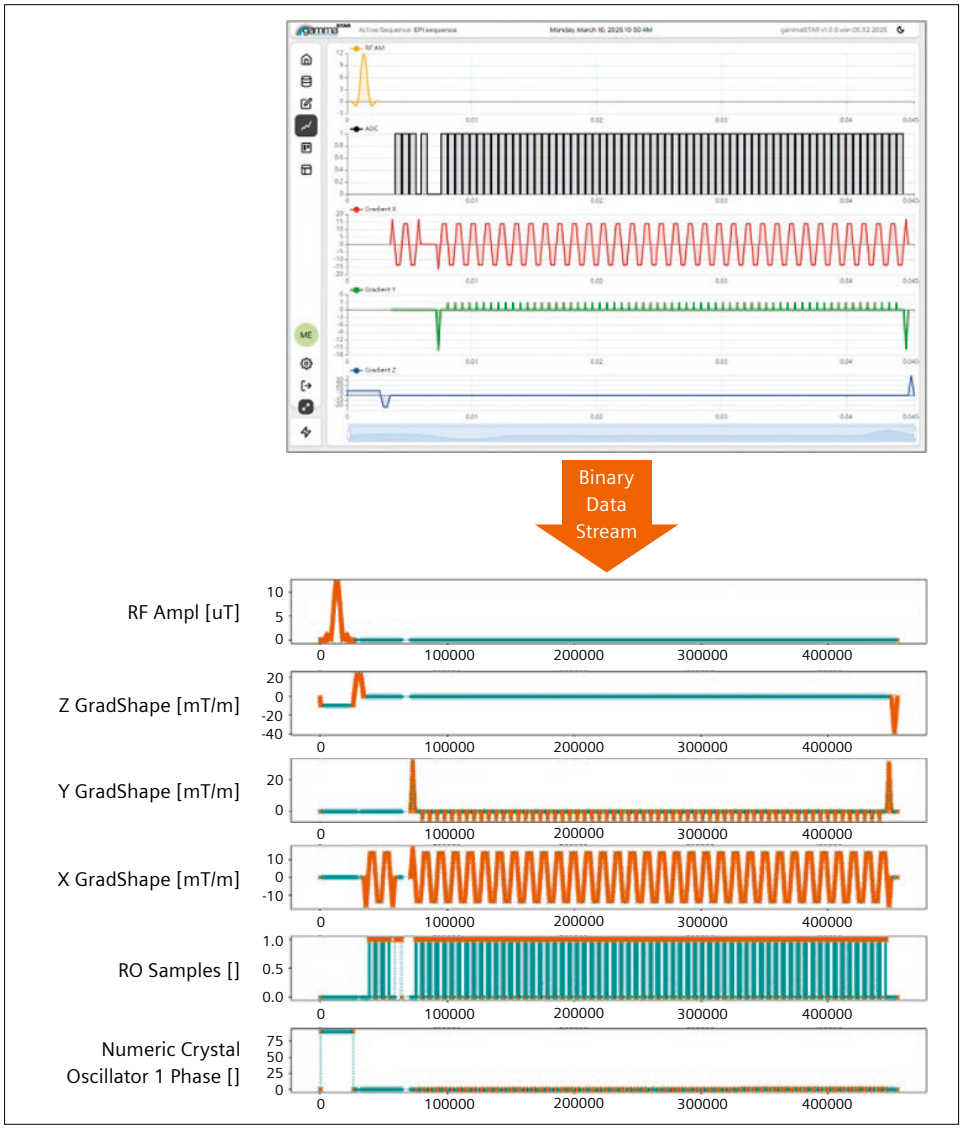

6 Example of an EPI sequence defined in gammaSTAR (top), which is streamed via the network interface to Open Sequence and plotted (bottom).

Next steps

The first version of Open Sequence is limited to the execution of predefined streams that have been completely transferred to the control software of the MR scanner before starting the execution. Consequently, the duration of the MR sequence could be limited by the amount of real-time compliant memory available to the control software, and the MR sequences cannot be dynamically defined by reacting to, e.g., physiological events or user interaction. This problem is in the process of being addressed and is described in [10].

The Remote Sequence Streaming Interface has a strong focus on software architecture. However, it is heavily related to work dealing with the question of how to efficiently and effectively develop MR sequences in general. The concept of time slices as small building blocks for MR sequences in particular plays an important role in the MR Fingerprinting Development Kit introduced in [8] and [9].

Contact

Thomas Kluge
Siemens Healthineers
SHS DI MR PPD DPS DIH
Allee am Roethelheimpark 2
91052 Erlangen
Germany
thomas.kluge@siemens-healthineers.com



Christoph Forman, Ph.D.
Siemens Healthineers
SHS DI MR PPD DPS DIH
Allee am Roethelheimpark 2
91052 Erlangen
Germany
christoph.forman@siemens-healthineers.com



Conclusion

The Open Sequence interface enables sequence development independent of the software version of the MR scanner. A wide range of development and deployment opportunities are enabled. Using established sequence development environments like gammaSTAR and Pulseq with the Open Sequence interface further supports open innovation and reproducible research.

Future versions will focus on enabling real-time MR applications and simplifying MR sequence development.

References

1 Inati SJ, Naegele JD, Zwart NR, Roopchansingh V, Lizak MJ, Hansen DC, et al. ISMRM Raw data format: A proposed standard for MRI raw datasets. Magn Reson Med. 2017;77(1):411–421.
2 Santos JM, Wright GA, Pauly JM. Flexible real-time magnetic resonance imaging framework. Conf Proc IEEE Eng Med Biol Soc. 2004;2004:1048–51.
3 Cordes C, Konstandin S, Porter D, Günther M. Portable and platform-independent MR pulse sequence programs. Magn Reson Med. 2020;83(4):1277–1290.
4 Fraunhofer Institute for Digital Medicine MEVIS. gammaSTAR [Internet]. Bremen, Germany: Fraunhofer MEVIS; 2025 [cited 2025 Mar 13]. Available from: https://www.mevis.fraunhofer.de/en/research-and-technologies/imaging-physics/gammastar.html
5 Layton KJ, Kroboth S, Jia F, Littin S, Yu H, Leupold J, et al. Pulseq: A rapid and hardware-independent pulse sequence prototyping framework. Magn Reson Med. 2017;77(4):1544–1552.
6 Pulseq. Open-source Pulse Sequences [Internet]. Pulseq. [cited 2025 Mar 13]. Available from: https://pulseq.github.io/
7 Kluge T, Forman C. A Remote Sequence Streaming Interface for Open Innovation. In: ISMRM Annual Meeting Proceedings. 2023:0401.
8 Körzdörfer G. Novelties in MR Fingerprinting. ↗ MAGNETOM Flash. 2020;76(1):28–33.
9 Kluge T, Nittka M, Kannengiesser S, Koerzdoerfer G, Grund C, Buonincontri G, et al. A Comprehensive MR Fingerprinting Development Kit (MRFDK) In: ISMRM Annual Meeting Proceedings. 2022:#4798.
10 Kluge T, Forman C. Sequence Description Language: Enabling Real-Time Applications in the Remote Sequence Interface for Open Innovation. In: ISMRM Annual Meeting Proceedings. 2025.
11 Shafiekhani M, et al. Python-based Pulseq Client to the Remote Sequence Streaming Interface. In: ISMRM Annual Meeting Proceedings. 2025.
12 Github. imr-framework/pypulseq [Internet]. Github, Inc. 2025 [cited 2025 Mar 13]. Available from: https://github.com/imr-framework/pypulseq

Optimizing Energy Efficiency in MRI Scanners

Florian Raab[1], Fabian Wagner[2], Julian Wohlers[2], Shreeja Varadarajan[2], Jens Gühring[2], Rainer Schneider[2], Judith Herrmann[3], Mike Notohamiprodjo[4], Konstantin Nikolaou[3], Saif Afat[3], Thomas Küstner[1]

[1]Medical Image and Data Analysis (MIDAS.lab), Department of Diagnostic and Interventional Radiology, University Hospital of Tübingen, Germany
[2]Siemens Healthineers, Erlangen, Germany
[3]Department of Diagnostic and Interventional Radiology, University Hospital of Tübingen, Germany
[4]Radiologische, Strahlentherapeutische und Nuklearmedizinische Partnerschaftsgesellschaft München, DIE RADIOLOGIE, Munich, Germany

Introduction

MRI scanners are essential in clinical diagnostics, but they are also among the most energy-intensive devices in healthcare [1, 2]. Their energy consumption has become a significant concern, particularly in light of rising energy costs in Europe, where the price more than doubled between December 2020 and December 2021 [3]. Radiology departments, which account for at least 4.2% of a hospital's total energy consumption, are major contributors to both energy costs and greenhouse gas emissions [1, 4–8]. Within these departments, MRI scanners consume more than 100 megawatt-hours (MWh) per year on average, making them the highest energy consumers compared to other equipment [4, 9]. As demand for MRI devices grows, finding ways to optimize their energy efficiency and operate them sustainably has become a pressing priority.

The primary drivers of MRI energy consumption are the magnet cooling system and the gradient system, with magnet cooling alone accounting for approximately 42% of total energy use [10]. Active scanner operation demands more energy than idling [6], with productive use accounting for up to 70% of the total energy consumed [9]. Hence, reducing energy consumption during active operation or shortening the duration of active scanner operations offers the most promising benefits. One way to achieve this is by shortening acquisition times, though maintaining diagnostic quality remains a critical consideration here. Optimizing protocols and incorporating artificial intelligence (AI)-accelerated sequences (undersampled acquisitions paired with AI-based image reconstructions) can contribute to energy savings. In this regard, AI-based reconstructions

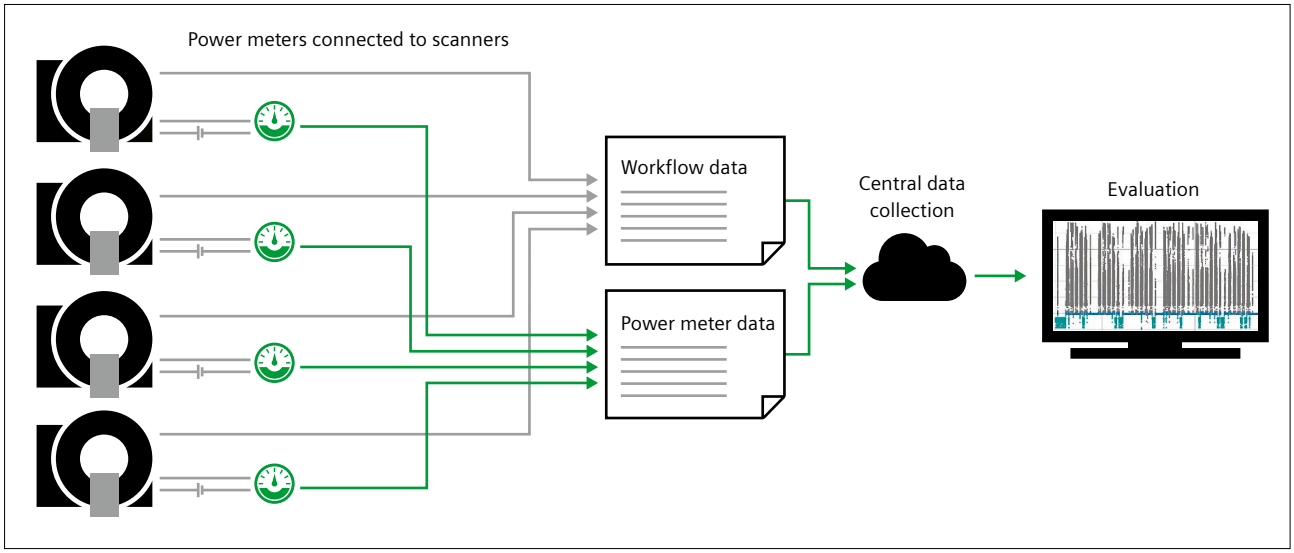

1 The MRI scanners are connected to power meters with a 1-hertz (Hz) sampling rate. Synchronized power-meter, sequence, parameter, and examination data are collected and centrally stored. Eventually, insights into workflow are gained and the impact of individual scan parameters on the scanner's power consumption is evaluated.

of undersampled or noisy data have demonstrated the ability to reconstruct high-fidelity images without compromising image quality [11–13]. These innovations thus provide promising opportunities to balance energy efficiency with reduced scan times. On the other hand, reducing acquisition times may result in the freed-up time being used for increased patient throughput, which would diminish the energy savings. Hence, it is critical to observe the complete workflow and propose energy optimizations along the whole imaging chain.

In a first study [10], we therefore investigated and analyzed energy consumption on two MRI scanners in a musculoskeletal setting when using optimized protocols and AI-accelerated sequences. Our findings showed that it was possible to achieve significant energy savings by optimizing protocol settings and implementing AI technologies. The outcomes motivated us to collect a more long-term and comprehensive database. We have therefore installed automatic energy measurement devices (power meters) in a fleet of MRI scanners (currently five scanners, with more being prepared) at our hospital to monitor the energy consumption behavior in a clinical setting during regular MRI workflows. We aim to identify the specific energy demands across different scanner models, operational modes, and imaging sequences. The findings will provide insights into which features drive energy consumption and where substantial efficiency improvements can be made. The focus will be on energy-saving optimizations, such as protocol refinement, AI-accelerated imaging, and cooling-system adjustments. Ultimately, the goal is to optimize the complete MRI workflow to enable more sustainable MRI operations while maintaining the high standards required for diagnostic quality.

Energy measurement

We are collecting and analyzing extensive data on energy consumption and scanner use from our primarily clinical MRI scanners, creating one of the most detailed datasets available to date. For this first-of-a-kind installation (Fig. 1), data collection began in June 2024 and is ongoing. Each scanner is equipped with a Siemens SENTRON 7KM power meter (Siemens AG, Chem, Germany) that allows continuous and precise energy tracking. General information, including the time of the measurements, scan duration, and the operated scanner, were collected. Further, detailed information such as the system and scan parameters for each sequence were documented. In total, 122 parameters are recorded, capturing detailed information that enables a granular analysis of power use relative to imaging requirements. Although not all parameters are relevant to every sequence, this exhaustive dataset allows to identify features driving energy consumption and facilitates in-depth correlation analysis between power consumption and specific protocol settings. This data on the operational use of MRI scanners is logged and automatically collected. Each piece of operational use data is time-synchronized and associated with its specific power consumption data.

We are interested in obtaining the following:

1. Observational insights into workflows and energy consumption, especially the influence of certain parameters
2. Insights into the potential benefits of AI-accelerated imaging to save energy
3. An estimate of potential power savings by identifying idle periods in which a scanner is "ready for measurement" but remains inactive (with high power demand)

We consider these extended idle periods to be potentially suitable for activating Eco Power Mode (switching off the helium pump during off-cycles and reactivating it based on temperature and pressure values), which could reduce energy consumption by optimizing the magnet cooling. Idle intervals longer than one hour, where Eco Power Mode was not activated, are flagged as opportunities for additional savings.

Findings

A first study focused on two scanners in a practice setting and investigated musculoskeletal imaging. The results indicate that reducing scan time significantly contributes to energy savings [10]. We found that, across all body regions, the average reduction in energy consumption was 72% with AI-accelerated sequences, and 31% with economic protocols (shortened imaging sequences using slightly increased acceleration factors or reduced resolution). This was accompanied by time reductions of 71% (AI) and 18% (economic protocols) compared to a conventional baseline. Optimizing the cooling system using Eco Power Mode during the non-scanning time showed a 30% lower energy consumption. In detail, we observed an average scan time reduction for optimized (economic) protocols of 34% (hip: 235 s, $p < 0.001$), 32% (knee: 148 s, $p < 0.001$), 11% (spine: 57 s, $p < 0.01$), and 25% (shoulder: 146 s, $p < 0.01$) compared to the baseline. AI protocols in turn resulted in an average scan time reduction of 81% (hip: 467 s, $p < 0.001$), 66% (knee: 268 s, $p < 0.001$), 49% (spine: 218 s, $p < 0.001$), and 77% (shoulder: 367 s, $p < 0.001$) over the baseline. This resulted in an average energy reduction of 21% (hip: 1.9 kilowatt-hours (kWh), $p = 0.31$), 48% (knee: 4.0 kWh, $p < 0.001$), 22% (spine: 2.3 kWh, $p < 0.01$), and 28% (shoulder: 2.9 kWh, $p < 0.01$)

for optimized protocols over baseline, and a reduction of 69% (hip: 5.2 kWh, $p < 0.001$), 89% (knee: 6.3 kWh, $p < 0.001$), 66% (spine: 5.8 kWh, $p < 0.001$), and 76% (shoulder: 6.5 kWh, $p < 0.001$) for AI protocols over baseline. The image quality of the optimized and AI-accelerated sequences was comparable to the baseline. Our results are depicted in Figure 2. Considering 250 working days with 10 hours of standby overnight, and 115 days without operation, this reflects an average energy saving per scanner and year of 14.1 MWh, which equates to 5,414 kg of CO2 (385 g CO2/kWh in Germany), if AI sequences are used. Whilst this is promising, several additional variables, such as sequence, application, and targeted body region, will impact the total energy consumption. To better understand these individual influences and to propose an evidence-driven parameter adjustment for energy reduction, we set up a second, larger-scale study.

In this ongoing study, we are currently analyzing data gathered during clinical examinations on five of our clinical MRI scanners, on which a variety of protocols are performed. An example of energy consumption over a three-month period is depicted in Figure 3. The most energy is consumed during the scanner's productive (non-idle) times (Fig. 3, top). Across the five scanners, we identified that activating Eco Power Mode during idle periods could yield savings of up to 48.7 MWh yearly, equating to 18,750 kg of CO2. As expected, scan duration significantly influences overall energy consumption (Fig. 4). However, the scan duration explains only 57% of the total variance in energy usage, indicating that other factors also influence energy consumption. Additionally, the field strength (1.5T vs 3T) has a considerable impact, with the 3T scanner consuming noticeably more energy (Fig. 4). The selected protocols (and the sequences they contain) have a substantial impact on energy consumption, with savings of up to 1 kWh per applied protocol. For nearly 1,919 unique protocols, we generalized and simplified them to identify some common behaviors. Adjustment sequences require little energy, but their frequent occurrence within the protocol can easily accumulate to a significant amount of energy use. Furthermore, the slice thickness influences energy consumption, with thinner slices resulting in higher energy use. Spin-echo sequences show a higher energy demand than gradient-echo sequences (Fig. 5). However, it should be noted that this is also linked to the imaged body region, for which sequences are optimized, and which subsequently have a different scan duration footprint (for example, comparing T1w TSE of several minutes in the brain versus single breath-hold Dixon imaging of a few seconds in the abdomen). For a comprehensive analysis, we thus need to include all features to find the best workflow optimizations to reduce energy consumption.

Conclusion

Our studies are the first to show in detail, in a fleet of MRI scanners over several months, the energy consumption correlated to MRI sequences and various features. We high-

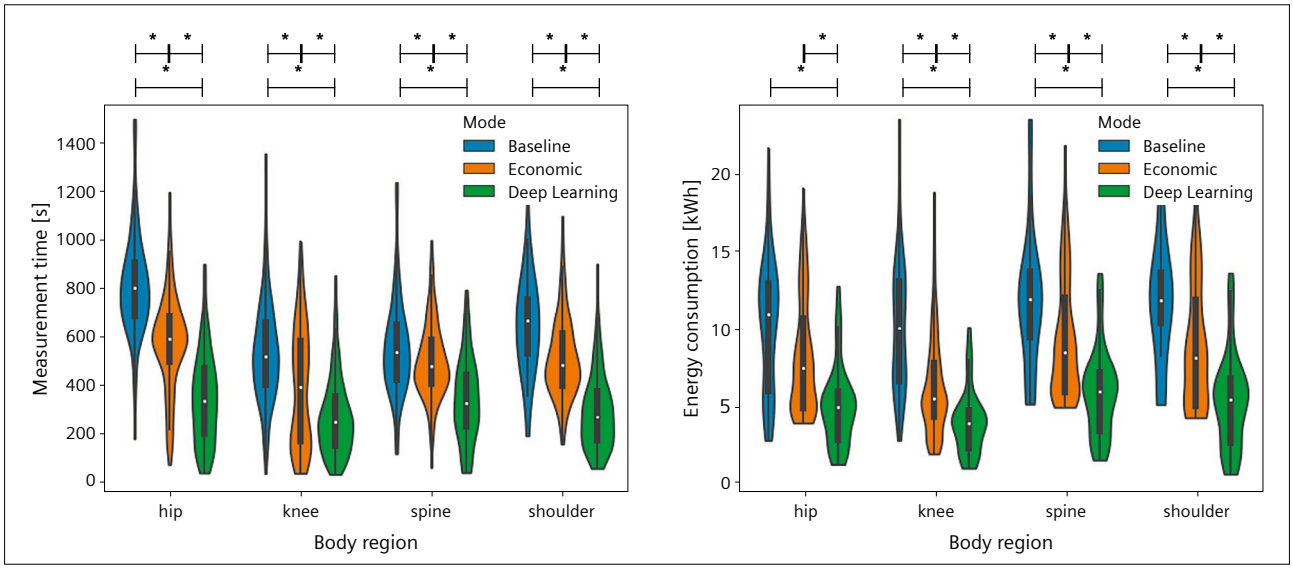

2 First study: Acquisition times (left) and energy consumption (right) for each body region (hip, knee, spine, and shoulder) of the musculoskeletal protocols in two MRI scanners. Energy consumption modes are depicted: baseline (no modifications), economic (shortened sequences), and deep learning (AI-accelerated sequences). Data distribution, mean (white dot), interquartile range (solid black vertical box), and standard deviation (thin black vertical bars) are shown. Statistical significance with a p-value of 0.05 is indicated by the asterisks.

light the potential of Eco Power Mode and of AI-accelerated sequences to significantly reduce energy consumption. The thorough analysis of features such as scanner type, scan duration, protocol, and scan parameters is the first step toward identifying factors contributing to energy consumption. In the future, these findings will enable us to improve energy efficiency and recommend workflow optimizations to reduce energy consumption. In addition, a closer examination of the interactions between the features is necessary to gain a deeper understanding and develop effective trade-offs. Overall, implementing these strategies will drive substantial energy and cost savings, and will support more sustainable MRI operation in clinical settings.

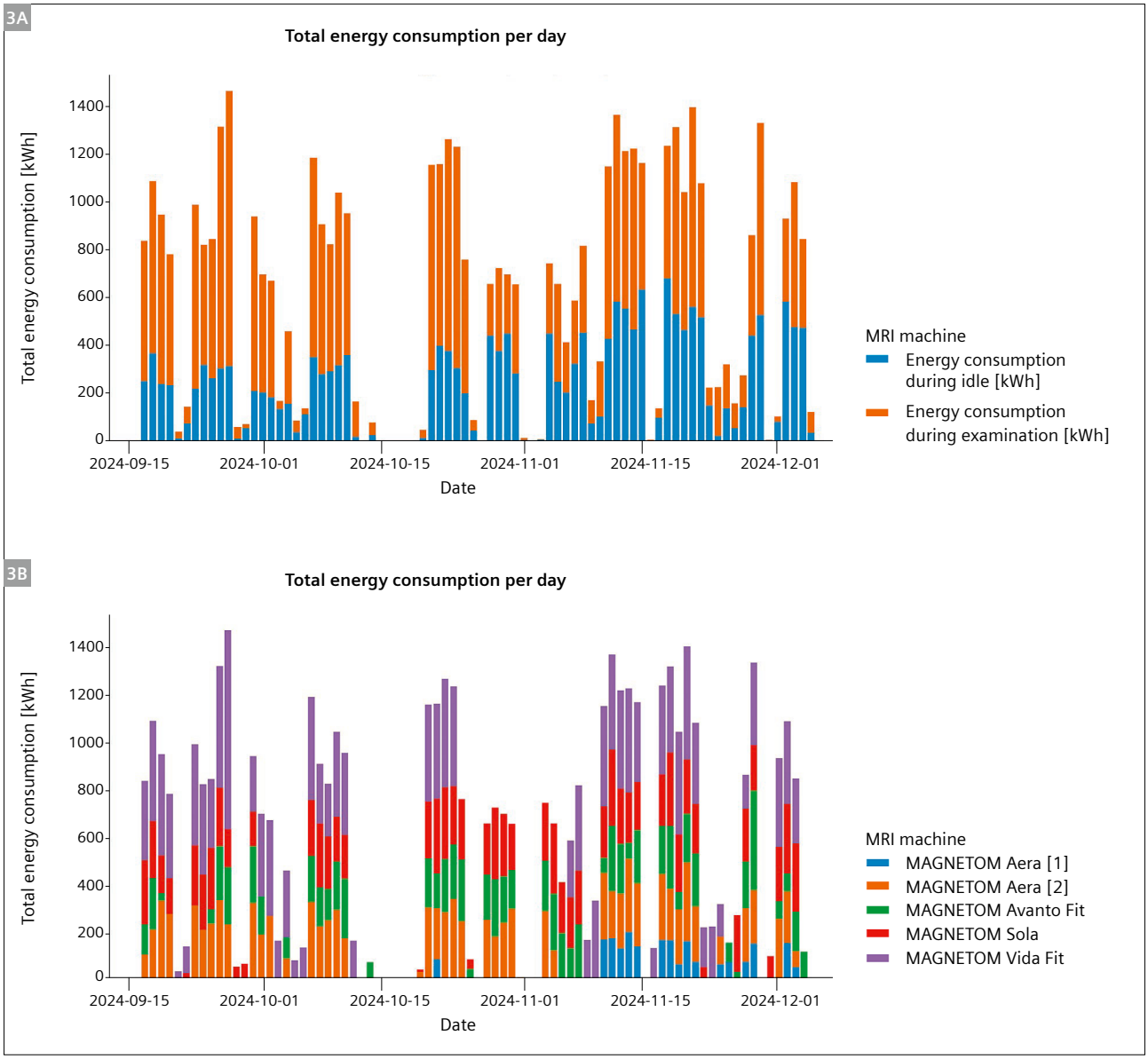

3 Second study: Example depiction of total daily energy consumption over three months. **(3A)** Total energy consumption divided into energy consumption during idle and productive (non-idle) states. The total energy consumption is the sum of the idle and productive states. **(3B)** Total energy consumption of the different MRI scanners.

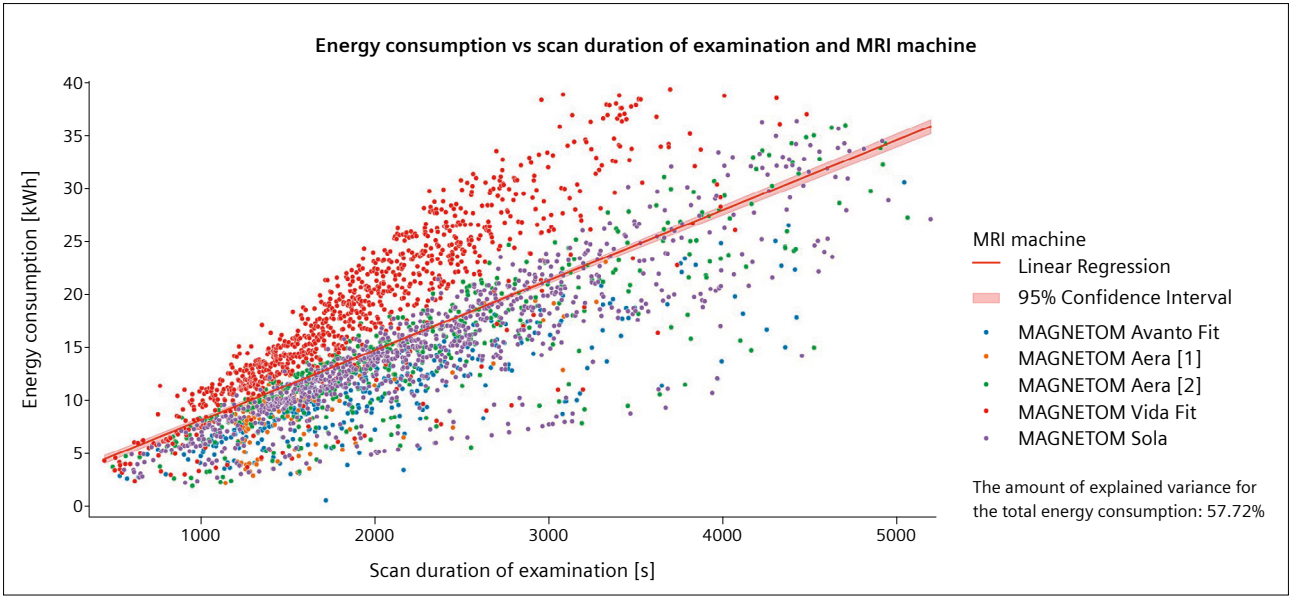

4 Second study: The scan duration of the entire examination/protocol shows a positive relationship with overall energy consumption. However, the scan duration explains only 57% of the total variance, indicating that other factors also influence energy consumption. The plot reveals two distinct groups: The MAGNETOM Vida Fit, a 3T scanner (Siemens Healthineers, Erlangen, Germany), exhibits a steeper slope in its relationship with scan duration, while the 1.5T scanners have a gentler slope.

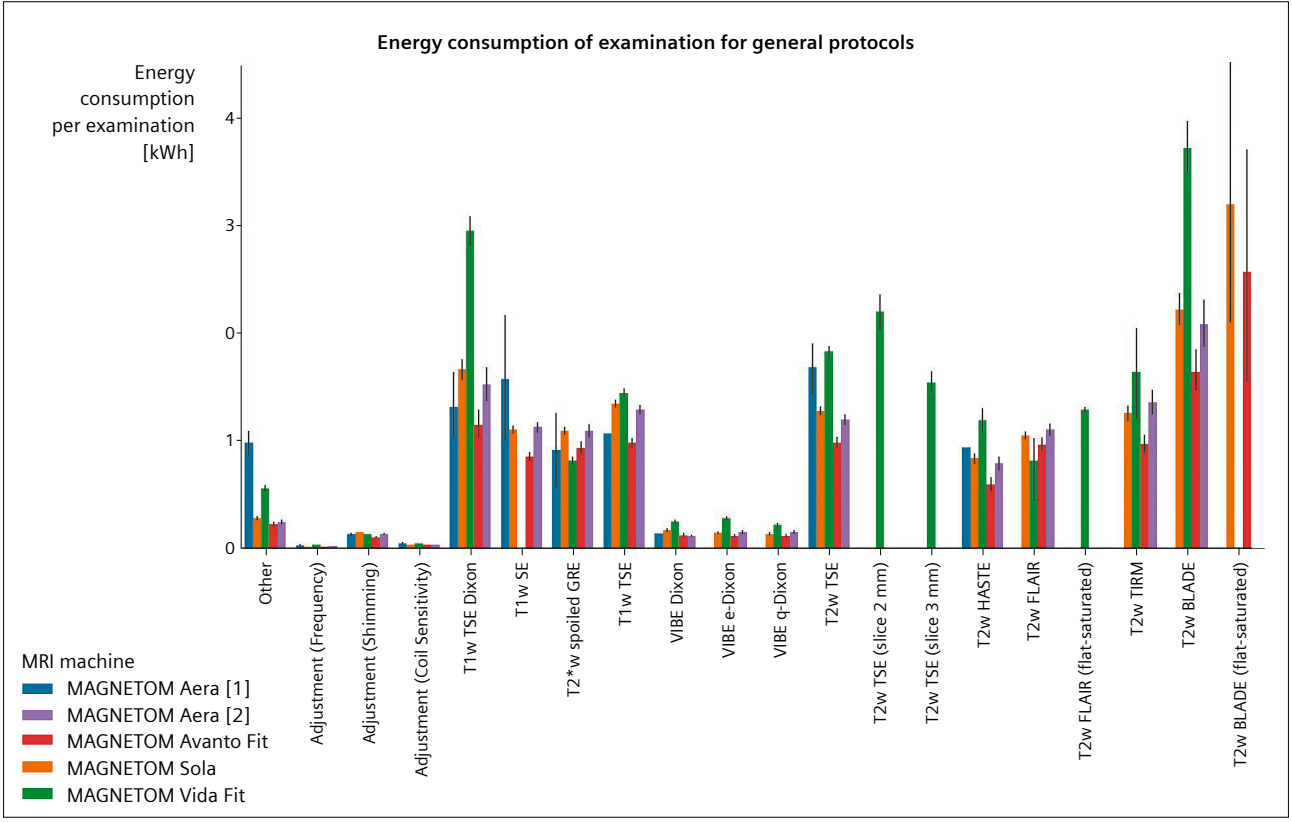

5 Second study: The harmonized sequences were plotted in relation to their energy consumption. Adjustment sequences generally consume less energy. Sequences with thinner slices require more energy – e.g., T2w TSE (2 mm) vs. T2w TSE (3 mm), where the number in brackets refers to the slice thickness. Spin-echo sequences demand in general more energy than gradient-echo sequences.

References

1 Aunión-Villa J, Gómez-Chaparro M, García-Sanz-Calcedo J. Study of the energy intensity by built areas in a medium-sized Spanish hospital. Energy Effic. 2021; 14(3):26.
2 Bawaneh K, Ghazi Nezami F, Rasheduzzaman M, Deken B. Energy Consumption Analysis and Characterization of Healthcare Facilities in the United States. Energies. 2019;12(19):3775.
3 Eurostat Home [Internet]. Europa.eu. [cited 2025 Mar 5]. Available from: https://ec.europa.eu/eurostat/web/main/home.
4 Heye T, Meyer MT, Merkle EM, Vosshenrich J. Turn It Off! A Simple Method to Save Energy and CO2 Emissions in a Hospital Setting with Focus on Radiology by Monitoring Nonproductive Energy-consuming Devices. Radiology. 2023;307(4):e230162.
5 Vosshenrich J, Heye T. Small Steps toward a More Sustainable and Energy-efficient Operation of MRI. Radiology. 2023;307(4):e230874.
6 Woolen SA, Becker AE, Martin AJ, Knoerl R, Lam V, Folsom J, et al. Ecodesign and Operational Strategies to Reduce the Carbon Footprint of MRI for Energy Cost Savings. Radiology. 2023;307(4): e230441. Erratum in: Radiology. 2023;308(1):e239020.
7 Brown M, Schoen JH, Gross J, Omary RA, Hanneman K. Climate Change and Radiology: Impetus for Change and a Toolkit for Action. Radiology. 2023;307(4):e230229.
8 Buckley BW, MacMahon PJ. Radiology and the Climate Crisis: Opportunities and Challenges- Radiology In Training. Radiology. 2021;300(3):E339–E341.
9 Sustainability In MRI: The power of less is more. 2023 [Internet]. Siemens Healthineers [cited 2025 Mar 5]. Available from: https://www.siemens-healthineers.com/magnetic-resonance-imaging/sustainability-in-mri.
10 Afat S, Wohlers J, Herrmann J, Brendlin AS, Gassenmaier S, Almansour H, et al. Reducing energy consumption in musculoskeletal MRI using shorter scan protocols, optimized magnet cooling patterns, and deep learning sequences. Eur Radiol. 2024. Epub ahead of print.
11 Hammernik K, Küstner T, Yaman B, Huang Z, Rueckert D, Knoll F, et al. Physics-Driven Deep Learning for Computational Magnetic Resonance Imaging: Combining physics and machine learning for improved medical imaging. IEEE Signal Process Mag. 2023;40(1):98–114.
12 Heckel R, Jacob M, Chaudhari A, Perlman O, Shimron E. Deep learning for accelerated and robust MRI reconstruction. MAGMA. 2024;37(3):335–368.
13 Wang S, Xiao T, Liu Q, Zheng H. Deep learning for fast MR imaging: A review for learning reconstruction from incomplete k-space data. Biomed Signal Process Control. 2021;68:102579.

Contact

Professor Thomas Küstner, Ph.D.
Medical Image and Data Analysis (MIDAS.lab)
University Hospital Tübingen
Hoppe-Seyler-Straße 3
72076 Tübingen
Germany
thomas.kuestner@med.uni-tuebingen.de



The statements and recommendations for energy and cost savings described herein are based on results that were achieved in settings possible due to certain standard and optional features available on Siemens MAGNETOM systems. Because there is no "typical" MRI suite or installation and many variables exist (e.g., MRI location, site specific installation requirements, case mix, level of IT and/or automation adoption) there can be no guarantee that customers will achieve the same results.

Phase-Resolved Functional Lung (PREFUL) MRI: The Next-Generation Ventilation-Perfusion Scan?

Andreas Voskrebenzev, Ph.D.[1,2,3]; Filip Klimeš, Ph.D.[1,2,3]; Jens Vogel-Claussen, M.D.[1,2,3]

[1]Institute for Diagnostic and Interventional Radiology, Hannover Medical School, Hannover, Germany
[2]Biomedical Research in End-Stage and Obstructive Lung Disease (BREATH), Member of the German Center for Lung Research (DZL), Hannover, Germany
[3]BioVisioneers GmbH, Laatzen, Germany

Introduction

Chronic pulmonary diseases – such as chronic obstructive pulmonary disease (COPD), cystic fibrosis (CF), and chronic thromboembolic pulmonary hypertension (CTEPH) – require accurate and sensitive diagnostic techniques to monitor progression and therapeutic response [1]. Traditional pulmonary function tests (PFTs), including the Tiffeneau-Pinelli index, provide global lung function parameters but lack the capacity to map region-specific changes [2]. Imaging approaches like computed tomography (CT) or single photon emission computed tomography (SPECT) can visualize lung morphology and function but inevitably involve ionizing radiation, making repeated examinations challenging [3, 4].

Magnetic resonance imaging (MRI) offers a promising, radiation-free alternative for lung function assessment. Although low proton density and rapid signal decay in the lung pose technical challenges [5], several methods have been developed to address these limitations. For instance, fluorinated ^{19}F or hyperpolarized gas MRI (e.g., ^{129}Xe) provides direct ventilation imaging [6] and, when paired with intravenous contrast [7], yields perfusion information. However, such techniques require specialized equipment, trained personnel, and contrast agents, and they may raise concerns over long-term safety.

Fourier decomposition (FD) is a contrast-free approach that uses conventional proton MRI and postprocessing to derive ventilation (V) and perfusion (Q) maps [8]. After image registration, the respiratory and cardiac frequency components of the time-series signal in each voxel are extracted, enabling simultaneous V/Q assessment. Soon, advanced versions of FD were developed [9–11], including self-gated non-contrast-enhanced functional lung imaging (SENCEFUL) [12]. Incorporating an additional DC acquisition in a quasi-random fast low-angle shot (FLASH) sequence allowed to sort each individual *k*-space line into one synthetic respiratory and cardiac cycle for higher temporal resolution and analysis of ventilation perfusion dynamics.

Following this idea, phase-resolved functional lung (PREFUL) MRI uses extended post-processing, allowing for retrospective image sorting according to respiratory and cardiac phases in combination with a conventional unmodified spoiled gradient-echo (GRE) or balanced steady state free precession (bSSFP) acquired in free breathing [13]. This allows dynamic V/Q assessment with commercially available sequences. Consequently, PREFUL MRI permits region-specific evaluations of dynamic lung function, including ventilation, perfusion, and even phase-based parameters such as flow-volume loop correlation metric (FVL-CM) [14] and pulse wave transit time or velocity measurements [15, 16]. Furthermore, many clinical studies have shown robust correlations with conventional methods [17–19, 15], reproducibility across different centers [20–22], and sensitivity in therapeutic and monitoring situations [23–29].

Despite these promising results, PREFUL remains restricted to a few specialized centers, partly due to limited awareness of the method's technical feasibility and clinical potential. This work aims to provide an overview of the current PREFUL methodology, thereby facilitating broader implementation.

Theory

Four main components – proton density, time-of-flight (TOF) effects, movement, and noise – primarily influence the pulmonary time-series MR signal in free-breathing spoiled gradient-echo acquisitions. Additional factors (e.g., T1, T2/T2* decay, diffusion, field inhomogeneities) are typically minimized through appropriate protocols (low flip angle, short TR, asymmetric echo, and dynamic parallel imaging [30]) and thus are omitted here. Pulmonary and cardiac motion during the MR acquisition is compensated by image registration. During expiration, shrinking lung volume increases proton density and thus raises the MR signal; during inspiration, the opposite occurs, forming the basis of ventilation measurements through the signal-volume relationship [31, 32]:

Equation 1

$$S \sim 1 / V$$

Pulsatile blood inflow induces further signal modulations known as TOF effect, which underpin perfusion measurements. Given the lung's inherently low signal, averaging and filtering improve signal-to-noise ratio so that the remaining variations predominantly reflect ventilation and perfusion. Because these variations occupy distinct frequency ranges, they can be separated by Fourier analysis [33]. Ventilation is then quantified via the inverse relationship between lung volume and proton signal, yielding the regional ventilation (RVent) [34] parameter:

Equation 2

$$RVent = \frac{V_{Insp} - V_{Exp}}{V_{Reg}} = \frac{S_{Reg}}{S_{Insp}} - \frac{S_{Reg}}{S_{Exp}}$$

During the initial transient phase of the acquisition, the MR signal has not yet reached steady state (SS) and thus briefly reflects near-maximal magnetization. By fitting these early

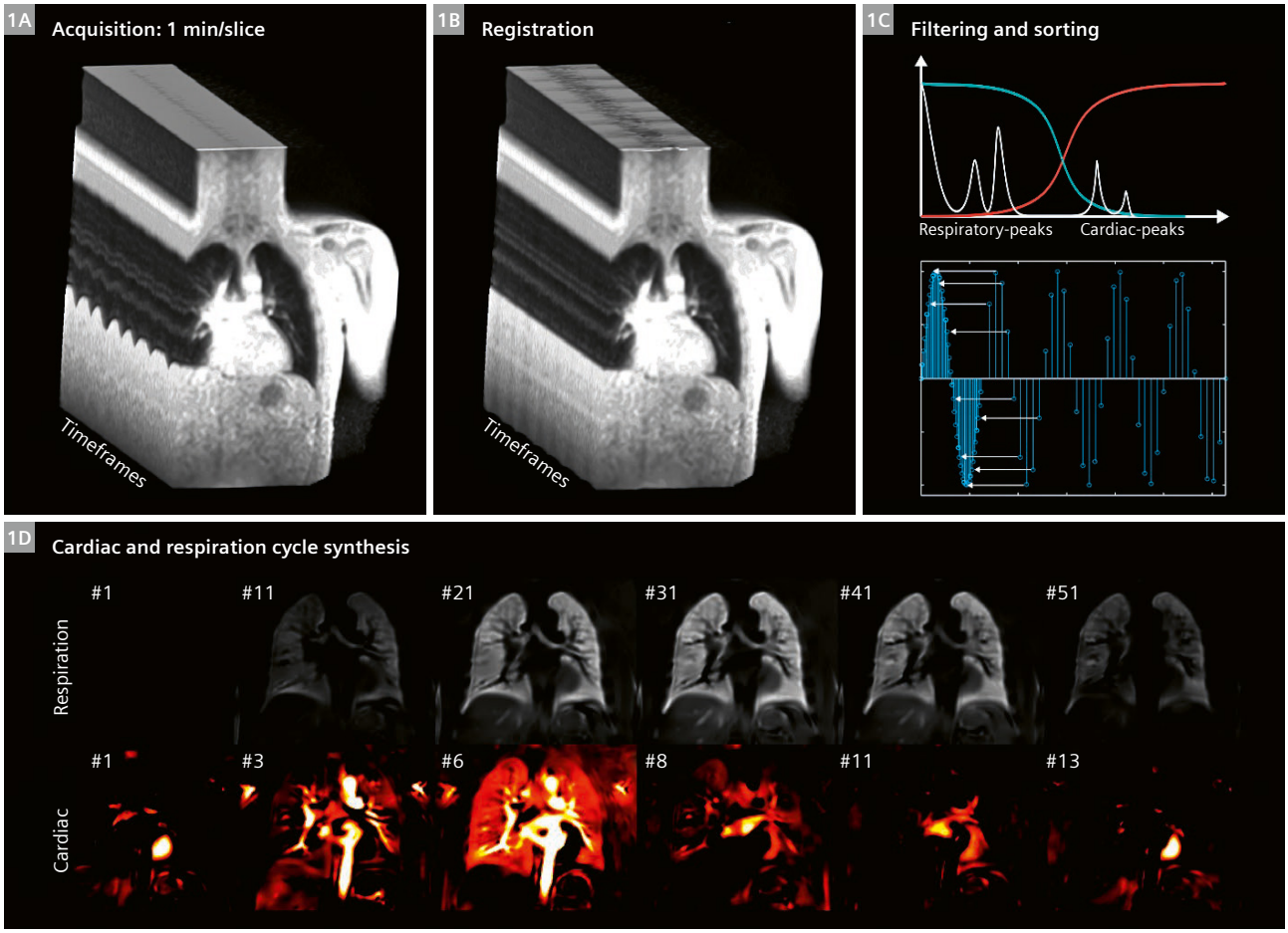

1 Simplified illustration of the phase-resolved functional lung (PREFUL)[1] MRI workflow: **(1A)** Free-breathing spoiled gradient-echo acquisition, **(1B)** motion correction via image registration, **(1C)** signal filtering (high-pass (red curve) and low-pass (blue curve)) and phase sorting, and **(1D)** synthesis of the cardiac and respiratory cycles (subset of phases provided). The resulting data are then quantified to yield various functional parameters and generate a final report.

data points to an exponential curve, it is possible to estimate the maximum signal (S_0). In addition, the signal drop between S_0 and steady state captures the potential effect if all voxels were moving. Together, these measurements serve as normalization factors for blood fraction (BF) content:

Equation 3
$$BF = S_{0,Map} / S_{0,Vessel}$$

and for flow-related signal difference Q in the steady state:

Equation 4
$$EF = Q / Median (S_0 - SS)$$

as fully detailed by Glandorf et al. [35], and allow full quantification of perfusion (QQ) in mL/min/100 mL:

Equation 5
$$QQ = EF \cdot BF \cdot VV \cdot f_{Heart} \cdot \frac{60\ s}{min} \cdot \frac{100}{VV \cdot 100}$$

with the heart frequency f_{Heart} determined from the fourier spectrum and the voxel volume (VV).

Methods

Figure 1 gives a simplified overview of the core protocol steps, consisting of acquisition, registration, filtering and sorting, and final cycle synthesis. Further details are described in the following sections. More in-depth information can be found in previous articles [13, 36].

For this article, retrospective evaluation of unpublished data from a healthy volunteer and a representative CF patient who participated in a previously published study on elexacaftor-tezacaftor-ivacaftor (ETI) therapy [28] was performed.

Acquisition

After standard MRI safety precautions and prescreening for contraindications, participants are placed head-first and supine on a 0.55T, 1.5T, or 3T scanner table. A multi-channel flex coil is positioned beneath the chin to optimize signal coverage of the lungs, and care is taken to secure it without restricting breathing. Localizer scans establish orientation, and a transversal morphological image is acquired to identify the tracheal bifurcation, which serves as a consistent landmark for coronal slices. Depending on the protocol length, either a limited number of slices (e.g., three slices spaced at 100%) or multiple slices with smaller spacing (20%–33%) are acquired to cover the lungs; each slice is acquired separately rather than interleaved. Typical temporal resolutions range from approximately 3 to 5 images/second. A representative protocol is provided in Table 1. Example slice positioning is shown in Figure 2.

Parameter	Setting
Sequence	SPGRE, bSSFP
Orientation	Coronal
Field of view (FOV)	500 × 500 mm²
Slice thickness (ST)	15 mm
Repetition time (TR)	3 ms or lower
Echo time (TE)	1 ms or lower
Bandwidth (BW)	1500 Hz/Pixel
Flip angle (FA)	~5° (Ernst angle)
Acceleration	T-GRAPPA 2×
Temporal resolution (dt)	> 3 frames/second
Frames/measurements	up to 500 depending on dt
Total duration / slice	1 minute

Table 1: Typical sequence settings for a PREFUL[1] acquisition. Please note that some settings such as TE, TR, and FA will depend on the field strength and gradient system.

Postprocessing

Following acquisition, images are corrected for respiratory and cardiac motion, filtered for noise reduction and V/Q separation, and sorted to generate phase-resolved data for both ventilation and perfusion.

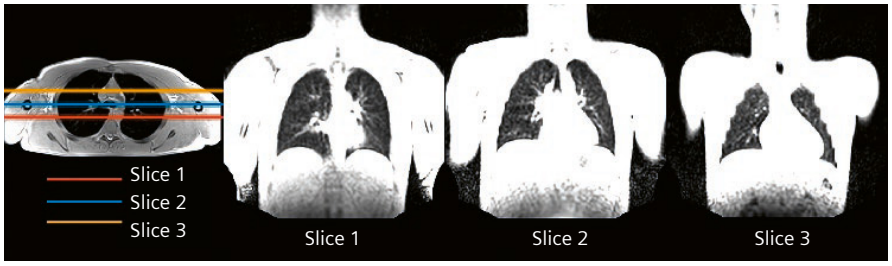

2 Example of slice positioning using a transverse volumetric interpolated breath-hold examination (VIBE) sequence for planning. Then, three coronal slices are acquired for PREFUL in free breathing with a 100% slice gap. The second slice is aligned with the tracheal bifurcation to serve as a repeatable anatomical landmark.

General segmentation

To enable a fully automated processing pipeline, all necessary segmentations are performed by either neural networks (nnU-Net/U-Net for lung boundaries [37] and vessel segmentation [38, 16]) or algorithmic methods for the large central vessel [18]. The final lung parenchyma region of interest (ROI) is then generated by subtracting the vessel segmentation from the lung boundary ROI. Figure 3 provides an illustration of the segmentation procedure.

Registration

Images are grouped into ten respiration-based categories (inspiration to expiration). Non-rigid registration is performed within each group toward an intermediate lung position, then progressively between groups until they converge to a mid-respiration reference (Group 5). This approach (GOREG) minimizes the deformation per registration step and enhances algorithmic stability [39]. As registration packages Advanced Normalization Tools (ANTs) [40] with BSplineSyN is known to deliver a good registration quality. However, the less-explored polynomial expansion-based algorithm ("Forsberg") [41, 42] can offer comparable results with shorter processing times [43, 44].

General filtering

Registered images are denoised using guided filtering [45] with the temporally averaged image as a guiding image. Low-pass and high-pass filters (cut-off around 0.7 Hz) are applied to separate perfusion- and ventilation-related components. The initial 20 images are discarded (except in quantified perfusion calculations) to ensure a steady-state signal.

Perfusion

Cardiac phase determination relies on algorithmically identifying strong perfusion-weighted signal regions in the lung and mediastinum (red ROI, Fig. 3) [18]. A piecewise sinusoidal fit of the corresponding time-series allows phase-sorting of the cardiac cycle, which is then interpolated (15 phases) to exceed the original sampling rate and generate high-temporal-resolution perfusion dynamics. This re-sorted dataset provides an entire cycle from diastole to systole, and back to diastole (Fig. 1).

Ventilation

Respiratory frequency and tidal volume can vary substantially, so a cosine model function is used to assign images to specific respiratory phases based on signal amplitude. The slope of the signal determines whether data belongs to inspiration or expiration. Nadaraya-Watson kernel regression then generates a uniformly sampled respiratory cycle. RVent is calculated by comparing the mid-respiration signal with inspiration and expiration signals (Equation 2) [34].

Parameter calculation and thresholding

The synthesized full cardiac and respiratory cycles enable derivation of additional functional parameters. RVent is computed at each phase, while FVL-CMs are calculated as an MRI analog to flow-volume loops of pulmonary function tests [14]. Quantified perfusion involves normalizing early transient-state images to account for proton density changes, fitting an exponential model to reach maximal magnetization, and then identifying cardiac phases with maximal lung parenchyma signal [46, 35]. Blood fraction and exchange fraction estimates are combined to calculate perfusion in mL/min/100 mL (Equation 5).

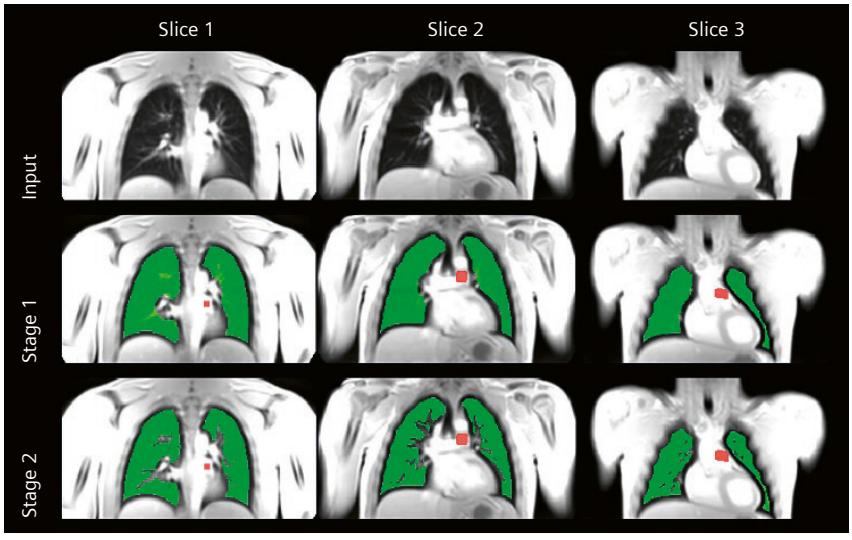

3 Illustration of the segmentation procedure for three slices. In the first stage, a neural network identifies the lung boundary (green). In the second stage, intraparenchymal vessels are excluded from the lung boundary. Separately, an algorithm segments a large vessel with a strong perfusion signal (red).

Parameter maps undergo static and dynamic thresholding to classify ventilation and perfusion defects (VD/QD). FVL-CM is thresholded with a fixed value of 90%. For the remaining parameters, the 90th percentile is used as an estimate for a normal value and multiplied with an empirical factor (0.4 for RVent and 0.15 for QQ).

Corresponding defect percentages are computed based on the proportion of voxels below the chosen thresholds relative to total lung parenchyma. Combining RVent and FVL-CM allows further subcategorization of V/Q defects according to a fourfold table (see Table 2).

Defect	VD	No VD
QD	VQM(D)	QDP(Ex)
No QD	VDP(Ex)	VQM(H)

Table 2: The resulting four combinations when comparing ventilation and perfusion defect (VD/QD): VQ match of defects (VQM(D)), VQ match of healthy regions (VQM(H)), and exclusive VDP and QDP.

All analyses in the results section use Forsberg registration and combine both RVent and FVL-CM metrics into a single VD measurement, classifying a voxel as VD if either RVent or FVL-CM (or both) met the defect criteria. Lung parenchyma parameters are summarized using mean values, and the complete set of ventilation/perfusion (V/Q) metrics is reported.

Results

Example data from a healthy volunteer (Fig. 4) demonstrate homogeneous ventilation and perfusion throughout the lung parenchyma, resulting in a 92% V/Q match. By contrast, a cystic fibrosis patient (Fig. 5) shows heterogeneous distribution before treatment, corresponding to a 40% V/Q match. Following therapy, all parameters improve markedly, culminating in a 93% V/Q match.

Discussion

In this article, we described the proton MRI technique known as PREFUL, providing example results to highlight its capabilities. A key distinction of PREFUL, compared to techniques like Fourier decomposition and its derivatives, is its combination with a conventional spoiled gradient echo (SPGRE) sequence. While balanced steady-state free precession (bSSFP) sequences deliver a signal-to-noise ratio advantage at 1.5T or lower, at 3T they suffer from reduced image quality and banding artifacts that hinder analysis [47]. Despite being developed for SPGRE, recent studies have demonstrated that PREFUL provides strong comparability with both sequences at 1.5T [48]. Besides the image sorting algorithm, as an additional major difference in post-processing, filtering is less restricted and amplitude calculation is carried out in time domain to account for frequency variations.

As outlined in the introduction, PREFUL has undergone validation against gold standards like SPECT, dynamic contrast-enhanced (DCE) MRI, and (hyperpolarized) gas MRI [49, 17, 18, 50, 19]. It has been tested in a variety of settings [51, 52, 20, 48, 44], including multi-center trials [21, 22, 53] and at 0.55T [25, 26, 54], demonstrating robust performance. PREFUL has proven capable of reflecting disease pathology and tracking disease progression and treatment responses [23, 55, 56, 24, 27, 57, 28, 16], making it a promising candidate for clinical translation. In particular, dynamic parameters like the spirometry-inspired FVL-CM have shown greater sensitivity as biomarkers compared to static measures that rely on only a limited portion of the synthesized cycles.

The main limitation of the PREFUL method lies in its coarse spatial resolution (4 × 4 × 15 mm^3) and moderate acquisition time (1 minute per 2D slice), which complicate detailed lung assessments. To address this, a 3D version of PREFUL has been developed, offering higher isotropic resolution (4 × 4 × 4 mm^3) and enabling more comprehensive ventilation dynamics measurements with a self-gated stack-of-stars VIBE or FLORET UTE sequence [58, 59] in about eight minutes. Despite being a relatively new technique, several studies have already validated the clinical applicability of 3D PREFUL [60, 43, 61]. However, a primary drawback of the 3D version is the lack of integrated perfusion information and the need for more specialized sequences. Consequently, 2D PREFUL remains a forward-looking technique, particularly as emerging biomarkers – such as pulse wave transit time or velocity measurements – gain traction. Ongoing advancements in image acceleration and protocol refinements may offer a near-term pathway to broader dissemination of the 2D PREFUL method.

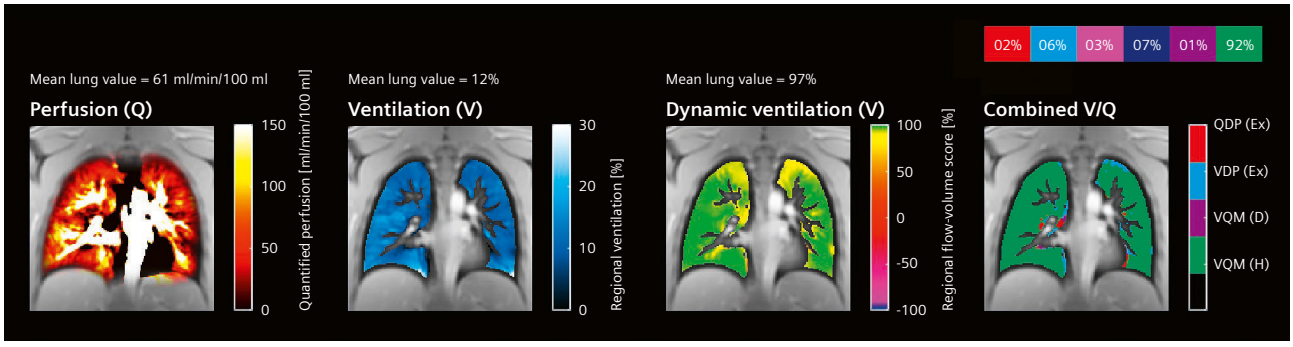

4 Example PREFUL maps of a healthy volunteer (male, age 36), showing perfusion in mL/min/100 mL, regional ventilation in %, flow-volume loop correlation metric (FVL-CM) in %, and a V/Q map obtained by thresholding and combining all maps. Please note the homogenous distribution of V/Q values in the lung parenchyma.

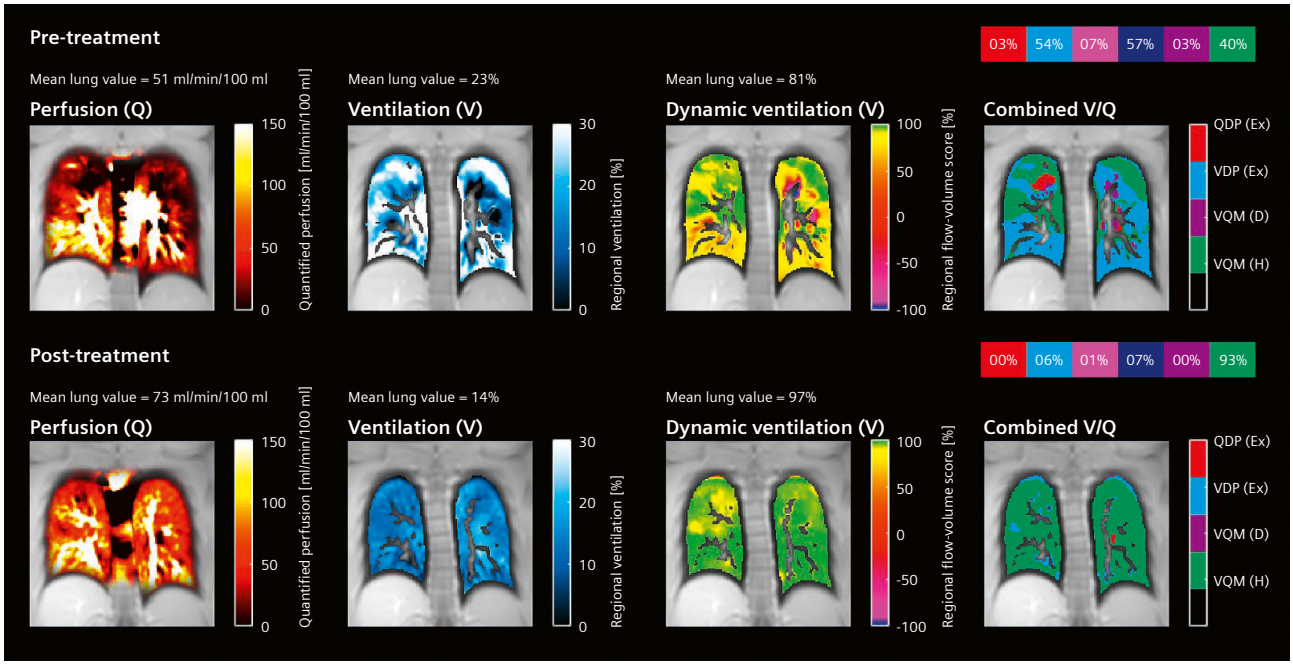

5 Pre- and post-treatment effect visualized for a CF patient (male, age 20) after ETI therapy. Please note the homogenization of V/Q after treatment, visible on all maps.

The LungMaps application from Siemens Healthineers

PREFUL technology will be available soon under the product name LungMaps[1] as a postprocessing application for MRI scanners from Siemens Healthineers. However, the nomenclature in the product is slightly different:

- RVent is called "Ventilation-weighted map" (Vw) without quantitative numbers.
- QQ is called "Perfusion-weighted map" (Qw) without quantitative numbers.
- FVL-CM is called "apparent flow volume loop correlation map" (aFVL).
- In the defect maps (see Table 2 and Figure 6), the product uses the following labels:
  - "Defect match" instead of VQM(D)
  - "Ventilation defect" instead of VDP(Ex)
  - "Perfusion defect" instead of QDP(Ex)
  - "No defect match" instead of VQM(H)

[1] *LungMaps is currently under development and not commercially available. Its future availability cannot be ensured.*

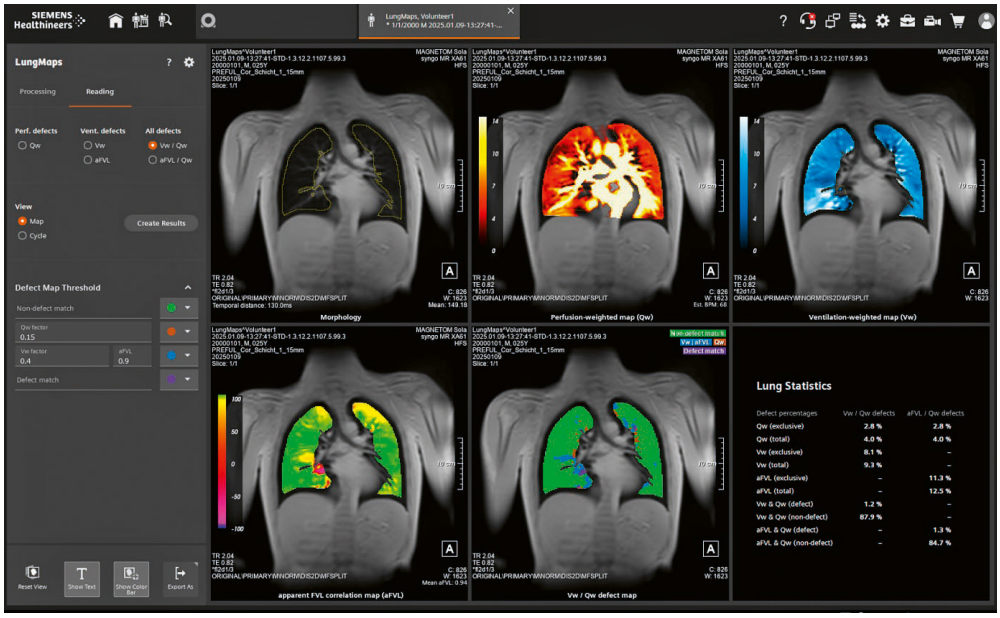

6 The LungMaps[1] application from Siemens Healthineers. This dataset from a healthy volunteer shows regular perfusion- and ventilation-weighted maps. The aFVL map and the Vw/Qw defect map show no signs of lung defects. The lower right corner displays a structured report of the defect percentages, which is also available as a PDF and as a secondary capture DICOM file.

To learn more about
LungMaps please visit us at

siemens-healthineers.com/magnetic-resonance-imaging/options-and-upgrades/clinical-applications/lungmaps

Figure 6 shows a screenshot of the application running on *syngo*.via, in this case on a healthy volunteer. All processing, including the neural network-based segmentation (see General segmentation) of the lungs and PREFUL analysis, is fully automated. However, the user can manually edit the lung segmentation if desired

Conclusion

PREFUL MRI provides a robust, radiation-free means of assessing ventilation and perfusion in a single free-breathing scan. Validation studies have consistently shown strong concordance with established methods like SPECT, DCE, and hyperpolarized gas MRI, underscoring its clinical potential. Although current 2D acquisitions use relatively coarse spatial resolution, the 3D version provides more detailed lung coverage, albeit without simultaneous perfusion and with less widespread sequences. Ongoing refinements in acquisition speed, resolution, and biomarker integration thus position 2D PREFUL as a promising candidate for next-generation V/Q scans using free-breathing proton-based pulmonary imaging.

References

1 Vogelmeier CF, Criner GJ, Martinez FJ, Anzueto A, Barnes PJ, Bourbeau J, et al. Global Strategy for the Diagnosis, Management, and Prevention of Chronic Obstructive Lung Disease 2017 Report: GOLD Executive Summary. Eur Respir J. 2017;49(3):1700214.
2 Ranu H, Wilde M, Madden B. Pulmonary Function Tests. Ulster Med J. 2011;80(2):84–90.
3 Galbán CJ, Han MK, Boes JL, Chughtai KA, Meyer CR, Johnson TD, et al. Computed tomography-based biomarker provides unique signature for diagnosis of COPD phenotypes and disease progression. Nat Med. 2012;18(11):1711–1715.
4 Roach PJ, Schembri GP, Bailey DL. V/Q Scanning Using SPECT and SPECT/CT. J Nucl Med. 2013;54(9):1588–1596.
5 Wild JM, Marshall H, Bock M, Schad LR, Jakob PM, Puderbach M, et al. MRI of the lung (1/3): methods. Insights Imaging. 2012;3(4):345–353.
6 Albert MS, Cates GD, Driehuys B, Happer W, Saam B, Jr CSS, Wishnia A. Biological magnetic resonance imaging using laser-polarized 129Xe. Nature. 1994;370(6486):199–201.
7 Berthezène Y, Vexler V, Clément O, Mühler A, Moseley ME, Brasch RC. Contrast-enhanced MR imaging of the lung: assessments of ventilation and perfusion. Radiology. 1992;183(3):667–672.
8 Bauman G, Puderbach M, Deimling M, Jellus V, Chefd'hotel C, Dinkel J, et al. Non-contrast-enhanced perfusion and ventilation assessment of the human lung by means of fourier decomposition in proton MRI. Magn Reson Med. 2009;62(3):656–664.

9 Bauman G, Bieri O. Matrix pencil decomposition of time-resolved proton MRI for robust and improved assessment of pulmonary ventilation and perfusion. Magn Reson Med. 2017;77(1):336–342.
10 Bondesson D, Schneider MJ, Gaass T, Kühn B, Bauman G, Dietrich O, et al. Nonuniform Fourier-decomposition MRI for ventilation- and perfusion-weighted imaging of the lung. Magn Reson Med. 2019;82(4):1312–1321.
11 Ilicak E, Ozdemir S, Schad LR, Weis M, Schoenberg SO, Zöllner FG, et al. Phase-cycled balanced SSFP imaging for non-contrast-enhanced functional lung imaging. Magn Reson Med. 2022;88(4):1764–1774. doi:10.1002/mrm.29302
12 Fischer A, Weick S, Ritter CO, Beer M, Wirth C, Hebestreit H, et al. SElf-gated Non-Contrast-Enhanced FUnctional Lung imaging (SENCEFUL) using a quasi-random fast low-angle shot (FLASH) sequence and proton MRI. NMR Biomed. 2014;27(8):907-917.
13 Voskrebenzev A, Gutberlet M, Klimeš F, Kaireit TF, Schönfeld C, Rotärmel A, et al. Feasibility of quantitative regional ventilation and perfusion mapping with phase-resolved functional lung (PREFUL) MRI in healthy volunteers and COPD, CTEPH, and CF patients. Magn Reson Med. 2018;79(4):2306–2314.
14 Voskrebenzev A, Klimeš F, Gutberlet M, Kaireit T, Schönfeld C, Renne J, et al. Imaging-Based Spirometry in Chronic Obstructive Pulmonary Disease (COPD) Patients using Phase Resolved Functional Lung Imaging (PREFUL). In: Proc Intl Soc Mag Reson Med. 26;2018:1079.
15 Pöhler GH, Löffler F, Klimeš F, Behrendt L, Voskrebenzev A, González CC, et al. Validation of Phase-Resolved Functional Lung (PREFUL) Magnetic Resonance Imaging Pulse Wave Transit Time Compared to Echocardiography in Chronic Obstructive Pulmonary Disease. J Magn Reson Imaging. 2022;56(2):605–615.
16 Wernz MM, Voskrebenzev A, Müller RA, Zubke M, Klimeš F, Glandorf J, et al. Feasibility, Repeatability, and Correlation to Lung Function of Phase-Resolved Functional Lung (PREFUL) MRI-derived Pulmonary Artery Pulse Wave Velocity Measurements. J Magn Reson Imaging. 2024;60(5):2216–2228. Epub March 9, 2024.
17 Kaireit TF, Voskrebenzev A, Gutberlet M, Freise J, Jobst B, Kauczor HU, et al. Comparison of quantitative regional perfusion-weighted phase resolved functional lung (PREFUL) MRI with dynamic gadolinium-enhanced regional pulmonary perfusion MRI in COPD patients. J Magn Reson Imaging. 2019;49(4):1122–1132.
18 Behrendt L, Voskrebenzev A, Klimeš F, Gutberlet M, Winther HB, Kaireit TF, et al. Validation of Automated Perfusion-Weighted Phase-Resolved Functional Lung (PREFUL)-MRI in Patients With Pulmonary Diseases. J Magn Reson Imaging. 2020;52(1):103–114.
19 Kaireit TF, Kern A, Voskrebenzev A, Pöhler GH, Klimes F, Behrendt L, et al. Flow Volume Loop and Regional Ventilation Assessment Using Phase-Resolved Functional Lung (PREFUL) MRI: Comparison With 129 Xenon Ventilation MRI and Lung Function Testing. J Magn Reson Imaging. 2021;53(4):1092–1105.
20 Pöhler GH, Klimeš F, Behrendt L, Voskrebenzev A, Gonzalez CC, Wacker F, et al. Repeatability of Phase-Resolved Functional Lung (PREFUL)-MRI Ventilation and Perfusion Parameters in Healthy Subjects and COPD Patients. J Magn Reson Imaging. 2021;53(3):915–927.
21 Behrendt L, Smith LJ, Voskrebenzev A, Klimeš F, Kaireit TF, Pöhler GH, et al. A dual center and dual vendor comparison study of automated perfusion-weighted phase-resolved functional lung magnetic resonance imaging with dynamic contrast-enhanced magnetic resonance imaging in patients with cystic fibrosis. Pulm Circ. 2022;12(2):e12054.
22 Marshall H, Voskrebenzev A, Smith LJ, Biancardi AM, Kern AL, Collier GJ, et al. 129Xe and Free-Breathing 1H Ventilation MRI in Patients With Cystic Fibrosis: A Dual-Center Study. J Magn Reson Imaging. 2023;57(6):1908–1921.
23 Alsady TM, Voskrebenzev A, Greer M, Becker L, Kaireit TF, Welte T, et al. MRI-derived regional flow-volume loop parameters detect early-stage chronic lung allograft dysfunction. J Magn Reson Imaging. 2019;50(6):1873–1882.
24 Voskrebenzev A, Kaireit TF, Klimeš F, Pöhler GH, Behrendt L, Biller H, et al. Pulmonary Dysfunction after Pediatric COVID-19. Radiology. 2023;306(3):e221250.
27 Vogel-Claussen J, Kaireit TF, Voskrebenzev A, Klimeš F, Glandorf J, Behrendt L, et al. Phase-resolved Functional Lung (PREFUL) MRI-derived Ventilation and Perfusion Parameters Predict Future Lung Transplant Loss. Radiology. 2023;307(4):e221958.
28 Dohna M, Voskrebenzev A, Klimeš F, Kaireit TF, Glandorf J, Pallenberg ST, et al. PREFUL MRI for Monitoring Perfusion and Ventilation Changes after Elexacaftor-Tezacaftor-Ivacaftor Therapy for Cystic Fibrosis: A Feasibility Study. Radiol Cardiothorac Imaging. 2024;6(2):e230104.
29 Ouyang T, Tang Y, Klimes F, Vogel-Claussen J, Voskrebenzev A, Yang Q. Phase-Resolved Functional Lung (PREFUL) MRI May Reveal Distinct Pulmonary Perfusion Defects in Postacute COVID-19 Syndrome: Sex, Hospitalization, and Dyspnea Heterogeneity. J Magn Reson Imaging. 2025;61(2):851–862. Epub June 17, 2024.
30 Breuer FA, Kellman P, Griswold MA, Jakob PM. Dynamic autocalibrated parallel imaging using temporal GRAPPA (TGRAPPA). Magn Reson Med. 2005;53(4):981–985.
31 Bankier AA, O'Donnell CR, Mai VM, Storey P, De Maertelaer V, Edelman RR, et al. Impact of lung volume on MR signal intensity changes of the lung parenchyma. J Magn Reson Imaging. 2004;20(6):961–966.
32 Zapke M, Topf HG, Zenker M, Kuth R, Deimling M, Kreisler P, et al. Magnetic resonance lung function – a breakthrough for lung imaging and functional assessment? A phantom study and clinical trial. Respir Res. 2006;7(1):106.
33 Deimling M, Jellus V, Geiger B, Chefd'hotel C. Time Resolved Lung Ventilation Imaging by Fourier Decomposition. Proc Intl Soc Mag Reson Med. 16; 2008:2639.
34 Klimeš F, Voskrebenzev A, Gutberlet M, Kern A, Behrendt L, Kaireit TF. Free-breathing quantification of regional ventilation derived by phase-resolved functional lung (PREFUL) MRI. NMR Biomed. 2019;32(6):e4088.
35 Glandorf J, Klimeš F, Behrendt L, Voskrebenzev A, Kaireit TF, Gutberlet M, et al. Perfusion quantification using voxel-wise proton density and median signal decay in PREFUL MRI. Magn Reson Med. 2021;86(3):1482–1493.
36 Voskrebenzev A, Klimeš F, Wacker F, Vogel-Claussen J. Phase-Resolved Functional Lung MRI for Pulmonary Ventilation and Perfusion (V/Q) Assessment. J Vis Exp. 2024;(210):e66380.
37 Isensee F, Jaeger PF, Kohl SAA, Petersen J, Maier-Hein KH. nnU-Net: a self-configuring method for deep learning-based biomedical image segmentation. Nat Methods. 2021;18(2):203–211.
38 Ronneberger O, Fischer P, Brox T. U-Net: Convolutional Networks for Biomedical Image Segmentation. In: Navab N, Hornegger J, Wells WM, Frangi AF, eds. Medical Image Computing and Computer-Assisted Intervention – MICCAI 2015. Lecture Notes in Computer Science. Springer Cham, Switzerland; 2015:234–241.
39 Voskrebenzev A, Gutberlet M, Kaireit TF, Wacker F, Vogel-Claussen J. Low-pass imaging of dynamic acquisitions (LIDA) with a group-oriented registration (GOREG) for proton MR imaging of lung ventilation. Magn Reson Med. 2017;78(4):1496–1505.

40 Avants BB, Tustison NJ, Song G, Cook PA, Klein A, Gee JC. A Reproducible Evaluation of ANTs Similarity Metric Performance in Brain Image Registration. Neuroimage. 2011;54(3):2033–2044.
41 Forsberg D, Andersson M, Knutsson H. Extending Image Registration Using Polynomial Expansion To Diffeomorphic Deformations. In: SSBA Symposium on Image Analysis. 2012:4.
42 Forsberg D. fordanic/image-registration. Published online 2022. Available at https://github.com/fordanic/image-registration. Accessed April 12, 2022.
43 Klimeš F, Voskrebenzev A, Gutberlet M, Grimm R, Wacker F, Vogel-Claussen J. Evaluation of image registration algorithms for 3D phase-resolved functional lung ventilation magnetic resonance imaging in healthy volunteers and chronic obstructive pulmonary disease patients. NMR Biomed. 2023;36(3):e4860.
44 Voskrebenzev A, Gutberlet M, Klimeš F, Kaireit TF, Shin HO, Kauczor HU, et al. A synthetic lung model (ASYLUM) for validation of functional lung imaging methods shows significant differences between signal-based and deformation-field-based ventilation measurements. Front Med (Lausanne). 2024;11:1418052.
45 He K, Sun J, Tang X. Guided Image Filtering. IEEE Trans Pattern Anal Mach Intell. 2013;35(6):1397-1409.
46 Behrendt L, Voskrebenzev A, Klimeš F, Gutberlet M, Winther HB, Kaireit TF, et al. Validation of Automated Perfusion-Weighted Phase-Resolved Functional Lung (PREFUL)-MRI in Patients With Pulmonary Diseases. J Magn Reson Imaging. 2020;52(1):103–114.
47 Bauman G, Pusterla O, Bieri O. Functional lung imaging with transient spoiled gradient echo. Magn Reson Med. 2019;81(3):1915–1923.
48 Hahn JJ, Voskrebenzev A, Behrendt L, Klimeš F, Pöhler GH, Wacker F, et al. Sequence comparison of spoiled gradient echo and balanced steady-state free precession for pulmonary free-breathing proton MRI in patients and healthy volunteers: Correspondence, repeatability, and validation with dynamic contrast-enhanced MRI. NMR Biomed. 2024;37(11):e5209. Epub July 12, 2024.
49 Marshall H, Voskrebenzev A, Biancardi A, Smith L, Tahir B, Wild J, et al. Comparison of 1H MRI and 3He MRI ventilation images in patients with cystic fibrosis and patients with lung cancer. Eur Respir J. 2018;52(suppl 62):PA387.
50 Couch MJ, Munidasa S, Rayment JH, Voskrebenzev A, Seethamraju RT, Vogel-Claussen J, et al. Comparison of Functional Free-Breathing Pulmonary 1H and Hyperpolarized 129Xe Magnetic Resonance Imaging in Pediatric Cystic Fibrosis. Acad Radiol. 2021;28(8):e209–e218.
51 Glandorf J, Klimeš F, Voskrebenzev A, Gutberlet M, Wacker F, Vogel-Claussen J. Effect of intravenously injected gadolinium-based contrast agents on functional lung parameters derived by PREFUL MRI. Magn Reson Med. 2020;83(3):1045–1054.
52 Glandorf J, Klimeš F, Voskrebenzev A, Gutberlet M, Behrendt L, Crisosto C, et al. Comparison of phase-resolved functional lung (PREFUL) MRI derived perfusion and ventilation parameters at 1.5T and 3T in healthy volunteers. PLOS ONE. 2020;15(12):e0244638.
53 Moher Alsady T, Voskrebenzev A, Behrendt L, Olsson K, Heußel CP, Gruenig E, et al. Multicenter Standardization of Phase-Resolved Functional Lung MRI in Patients With Suspected Chronic Thromboembolic Pulmonary Hypertension. J Magn Reson Imaging. 2024;59(6):1953–1964.
54 Kato RM, Chun S, Detterich J, Cui SX, Iyer NP, Lee NG, et al. Phase-Resolved Functional Lung 0.55T MRI Analysis Demonstrates Ventilation-perfusion Defects Driven by Abnormal Perfusion in Patients With Fontan Circulation. In: C59. PICKING UP THE KIDS AT BALBOA PARK: INSIGHTS IN PEDIATRIC PULMONARY HYPERTENSION. American Thoracic Society International Conference Abstracts. Am J Respir Crit Care Med. 2024;209:A6024.
55 Pöhler GH, Klimes F, Voskrebenzev A, Behrendt L, Czerner C, Gutberlet M, et al. Chronic Thromboembolic Pulmonary Hypertension Perioperative Monitoring Using Phase-Resolved Functional Lung (PREFUL)-MRI. J Magn Reson Imaging. 2020;52(2):610–619.
56 Munidasa S, Couch MJ, Rayment JH, Voskrebenzev A, Seethamraju R, Vogel-Claussen J, et al. Free-breathing MRI for monitoring ventilation changes following antibiotic treatment of pulmonary exacerbations in paediatric cystic fibrosis. Eur Respir J. 2021;57(4):2003104.
57 Friedlander Y, Munidasa S, Thakar A, Ragunayakam N, Venegas C, Kjarsgaard M, et al. Phase-Resolved Functional Lung (PREFUL) MRI to Quantify Ventilation: Feasibility and Physiological Relevance in Severe Asthma. Acad Radiol. 2024;31(8):3416–3426.
58 Klimeš F, Voskrebenzev A, Gutberlet M, Kern AL, Behrendt L, Grimm R, et al. 3D phase-resolved functional lung ventilation MR imaging in healthy volunteers and patients with chronic pulmonary disease. Magn Reson Med. 2021;85(2):912–925.
59 Klimeš F, Plummer JW, Willmering MM, Matheson AM, Bdaiwi AS, Gutberlet M, et al. Quantifying spatial and dynamic lung abnormalities with 3D PREFUL FLORET UTE imaging: A feasibility study. Magn Reson Med. 2025. Online ahead of print.
60 Klimeš F, Voskrebenzev A, Gutberlet M, Obert AJ, Pöhler GH, Grimm R, et al. Repeatability of dynamic 3D phase-resolved functional lung (PREFUL) ventilation MR Imaging in patients with chronic obstructive pulmonary disease and healthy volunteers. J Magn Reson Imaging. 2021;54(2):618–629.
61 Klimeš F, Voskrebenzev A, Gutberlet M, Speth M, Grimm R, Dohna M, et al. Effect of CFTR modulator therapy with elexacaftor/tezacaftor/ivacaftor on pulmonary ventilation derived by 3D phase-resolved functional lung MRI in cystic fibrosis patients. Eur Radiol. 2024;34(1):80–89.

Contact

Andreas Voskrebenzev, Ph.D.
Medizinische Hochschule Hannover
Carl-Neuberg-Str. 1
30625 Hannover
Germany
Voskrebenzev.Andreas@mh-hannover.de



Jens Vogel-Claussen, Andreas Voskrebenzev, Filip Klimeš

The CEA-Siemens Healthineers MAGNETOM Iseult 11.7-Tesla MRI System: A 20-year Odyssey to Image the Human Brain

The Iseult Consortium (in alphabetical order):
Jerome Allard[1], Alexis Amadon[2], Guy Aubert[1], Jean Belorgey[1], Christophe Berriaud[1], Cédric Bonnelye[2], Michel Bottlaender[2], Romain Boudoin[1], Nicolas Boulant[2], Thierry Boussuge[1], Philippe Brédy[1], Andrew Dewdney[3], Peter Dietz[3], Guillaume Dilasser[1], Yannick Drouen[1], Olivier Dubois[1], Sandrine Faict-Bastin[1], Ulrich Fontius[3], Graham Gilgrass[3], Ignazio Gonzales Insua[3], Vincent Gras[2], Quentin Guihard[1], Patrice Guiho[1], Jean-Christophe Guillard[1], Rene Gumbrecht[3], Robin Heidemann[3], Vincent Jannot[1], François-Paul Juster[1], Felix Köber[3], Brice Koestel[4], Denis Le Bihan[2], René Leboeuf[1], Matthieu Lepetit Coiffé[4], Frédéric Leprêtre[2], Caroline Le Ster[2], Ange Lotodé[1], Michel Luong[5], Aurélien Massire[4], Franck Mauconduit[2], François Nunio[1], Lionel Quettier[1], Hermann Landes[6], Hervé Lannou[1], Frédéric Molinié[1], Hubert Neyrial[1], Christophe Pallier[7], Cédric Péron[1], Cécile Rabrait[2], Luc Renou[4], Arnaud Roger[1], Philippe Rouffiat[4], Wolfram Ruth[3], Laure Sabatier[8], Thierry Schild[1], Martin Schroeder[3], Rebecca Schuster[3], Loris Scola[1], Patrick Sieber[3], Armand Sinanna[1], Vadim Stepanov[1], Mathieu Szmigiel[1], Xavier Tastet[4], Olivier Tellier[1], Robert Touzery[1], Pierre Védrine[1], Alexandre Vignaud[2], Christian Walter[1], Karsten Wicklow[3]

[1]Irfu, CEA, Paris-Saclay University, Gif-sur-Yvette, France
[2]NeuroSpin, CEA, CNRS, Paris-Saclay University, Gif-sur-Yvette, France
[3]Siemens Healthineers, Erlangen, Germany
[4]Siemens Healthineers, Courbevoie, France
[5]DACM, CEA, Paris-Saclay University, Gif-sur-Yvette, France
[6]Ensimtech, Buckenhof, Germany
[7]Cognitive Neuroimaging Unit, NeuroSpin, INSERM, CEA, CNRS, Paris-Saclay University, Gif-sur-Yvette, France
[8]DIREI, CEA, Paris-Saclay University, Gif-sur-Yvette, France

Ultra-high-field MRI: A tool to study the human brain

Understanding the human brain and its complex functions is instrumental for advancing medical science. Despite significant progress in neuroimaging [1, 2], many brain processes remain poorly understood due to their complexity and the limitations of current imaging technologies. Ultra-high-field (UHF) MRI offers supra-linear gains [3] in signal-to-noise ratio, which can be invested to achieve unprecedented spatial resolution [4, 5]. This allows for the visualization of smaller anatomical features, such as cortical layers and subcortical nuclei, which are often blurred in conventional MRI scans. By uncovering these features and processes, UHF MRI could contribute to a better global understanding of the physiopathology of several neurological disorders, and could help identify related biomarkers, leading to more accurate diagnoses and targeted treatments [6–8]. Reaching the "mesoscopic" scale in imaging [9] can help bridge the gap between molecular processes at the cellular level and whole-brain activity, fostering a more comprehensive understanding of the human brain.

Additionally, blood oxygenation level-dependent (BOLD) imaging [10] is based on variations in blood oxygenation, which are influenced by neuronal activity and are more detectable at UHF strengths. This boost in sensitivity, combined with increased spatio-temporal resolution, means BOLD significantly benefits from UHF MRI, enabling precise mapping of brain activity and providing insights into functional connectivity and neural pathways [11]. These advancements pave the way for studying more complex brain functions. Altogether, integrating UHF MRI into neuroscience research has the potential to revolutionize our knowledge of the brain and improve clinical outcomes for a variety of neurological conditions.

The Iseult project

Based on this idea, the Iseult project was launched in 2001 by the French Atomic Energy Commission (CEA) as an exceptional, visionary challenge. The project aimed to build an MRI magnet operating at 11.7T to investigate the human brain at a mesoscopic scale. After nearly 20 years of research and development mainly led by the Institute of Research into the Fundamental Laws of the Universe (IRFU) of the CEA, the 132-ton 11.7T magnet, with its imaging equipment, delivered its first images in 2021 [12].

The field homogeneity and temporal stability constraints for MRI were met thanks to a careful design of the magnet [13]. The core part of the Iseult MRI system is an actively shielded niobium-titanium (NbTi) magnet cooled with a superfluid helium (He) cryostable bath at 1.8 kelvin (K) [14], providing a homogeneous magnetic field within a 90 cm warm bore, operated in driven mode. A multi-strand wire magnet design was chosen to reduce the inductance of the main superconducting coil and thus reduce the maximum voltage induced in case of quench. The magnet consists of 170 double pancake wires, with about 250 superconductive joints, making it a unique design. A magnetic field intensity of 11.7T was the upper limit to use an NbTi alloy at 1.8 K. A dedicated cryogenic plant was installed in the basement of the NeuroSpin building to service superfluid helium and cool down the magnet at 1.8 K. Figure 1 displays the magnet and associated devices, while detailed specifications of the magnet are provided in Table 1.

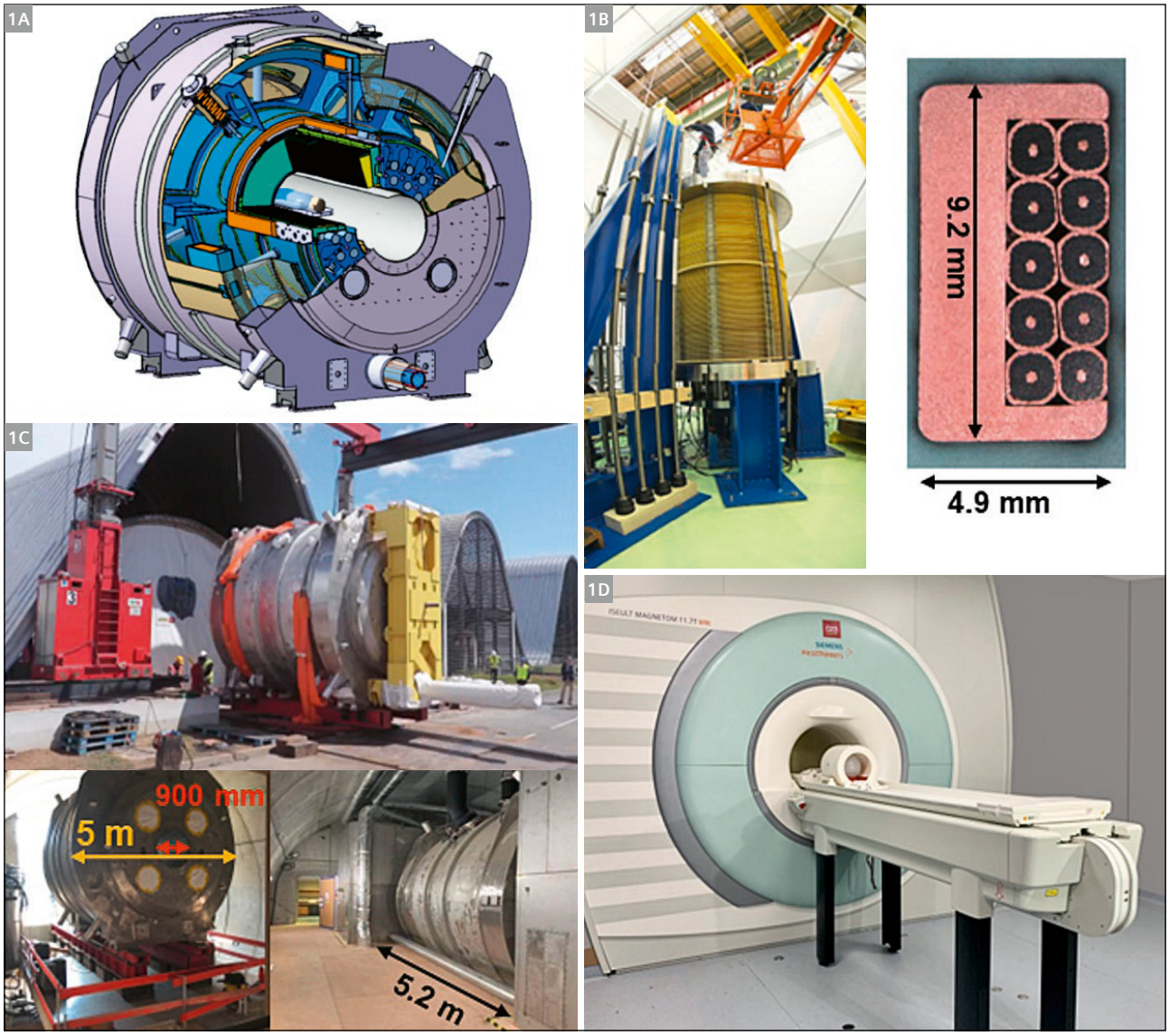

1 The Iseult magnet and installation set-up. **(1A)** Diagram of the magnet showing the main coil and the two actively shielding coils. The magnet weighs 132 tons, has an outer diameter and total length of just under 5 m, and the bore diameter is 90 cm. **(1B)** A view of the 170 double pancake wires at the manufacturing site in Belfort, France, and a cross-section of the magnet superconductor made of ten NbTi-Cu wires soldered into a copper channel. **(1C)** Installing the magnet in a dedicated NeuroSpin arch (10 m in diameter), and general views of the magnet inside the NeuroSpin arch. **(1D)** View of the front side of MAGNETOM Iseult[1], as seen by volunteers. A ramp is required to access the static patient table (not shown here).

[1] *MAGNETOM Iseult is an investigational device only and is not intended for sale or clinical use. Research operations may require observation of national regulations.*

Current	1470 A
Operating temperature	1.8 K
Central field	11.72 T
Inductance	308 H
Stored energy	338 MJ
Mass	132 tons

Table 1: Main parameters of the Iseult magnet.

The Iseult MRI system is currently equipped with a whole-body SC72 gradient coil (maximum gradient strength and slew rate: 80 mT/m and 200 T/m/s respectively; weight: 900 kg, length: 1.59 m, inner/outer diameter: 64/81 cm) designed and manufactured by Siemens Healthineers. A gradient coil-magnet interaction test campaign was carried out over a two-year period [12]. Gradient coils operate under oscillating currents, which generate eddy currents in the different metallic shells under a strong magnetic field, inducing significant forces and vibrations. If not well characterized and understood, their consequences can be disastrous and lead to magnet quench, hardware damage, or image artifacts. The objective of the test campaign was therefore:
1) to determine safe and optimal MR exploitation modes in terms of gradient frequency, strength, and duration;
2) to gather information to troubleshoot the system if artifacts are encountered during imaging. The tests covered acoustics, vibrations, power deposition in the helium bath, and field monitoring [15] measurements. For a comprehensive description and results of this study, see [12].

The last piece of equipment is a geometrically decoupled 16Tx/32Rx radiofrequency (RF) custom coil (combined to 8Tx/32Rx), which the CEA designed specifically for the Iseult 11.7T project [16]. The transmit-receive array is made of 15 linear resonators (dipoles) arranged in lower/

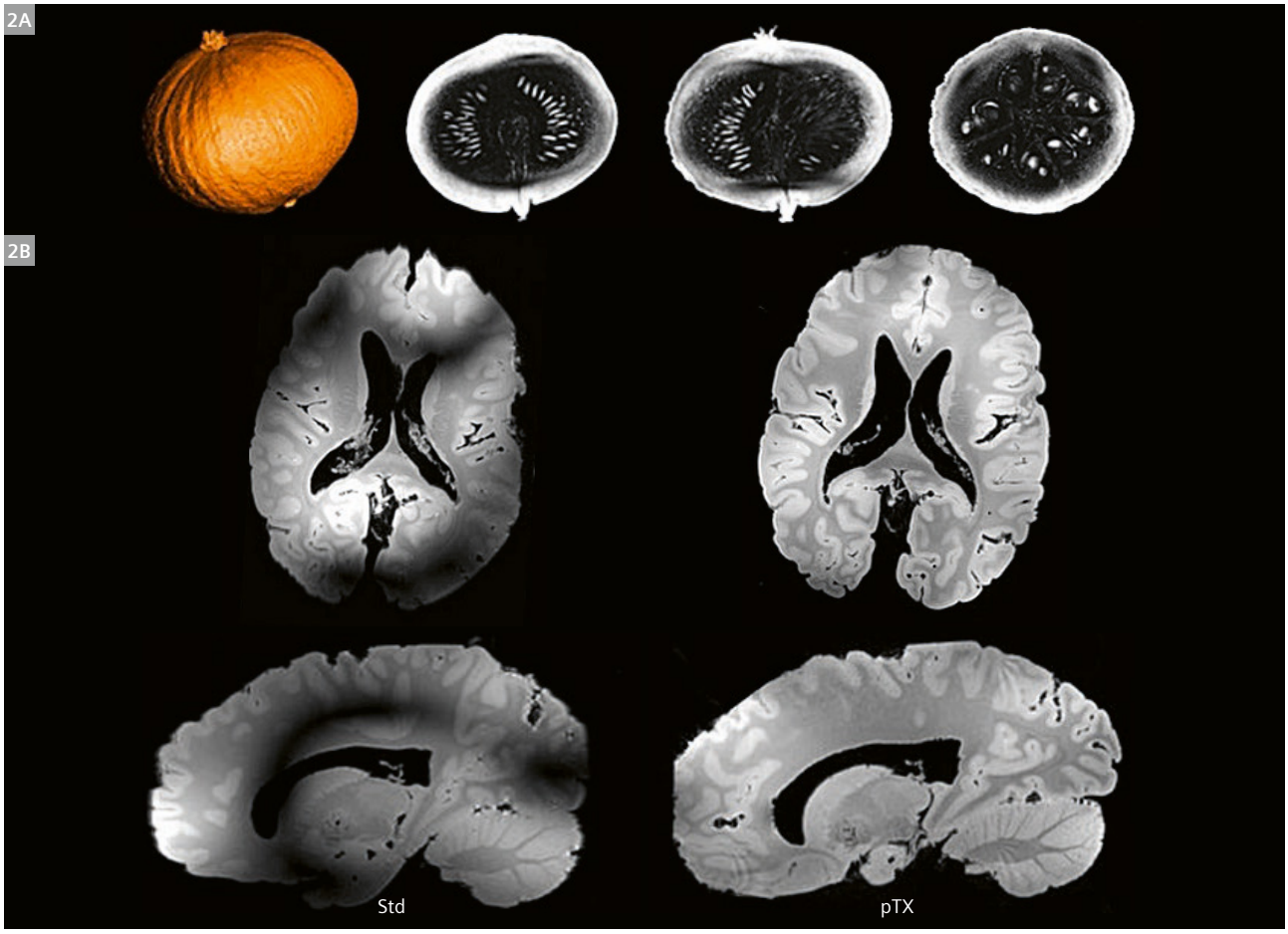

2 **(2A)** Gradient-echo (GRE) imaging of a pumpkin with a 400 µm isotropic resolution, acquired with the service coil from Siemens Healthineers (QED, birdcage architecture). The acquisition duration was about 4 hours (no acceleration). **(2B)** 3D GRE images acquired with the Iseult parallel transmission (pTx) RF coil on an ex vivo brain, with phase-shimming (left) and kT points (right). Axial (top) and sagittal (bottom) slices are shown, demonstrating the significant improvement in image quality with pTx.

upper rows in z-direction, and one patch resonator, while the receive array consists of 16 loops. Eight RF power amplifiers feed the RF transmit elements to mitigate the RF field inhomogeneity problem. This peculiar architecture satisfies two needs: compactness that enables compatibility with a local B0 shim insert [17], and easy tuning and performance prediction. Figure 2 shows the first images acquired with the system at the end of 2021.

Patient-Reported Experience Measures

Before the start-up of MAGNETOM Iseult[1], the highest magnetic field used for MRI on humans was 10.5T, at the University of Minnesota in the United States [18]. Approval from the French regulatory body, Agence Nationale de Sûreté et du Médicament, and a national ethics committee to perform initial tests in vivo on healthy adult participants was granted in early 2023 (IDRCB 2022-A02321-42). Whether humans could withstand 1.5-hour MRI exams at 11.7T was uncharted territory, the preliminary magnet study (PREMS) therefore proceeded cautiously to gather evidence for the absence of harmful effects in realistic conditions [19, 20]. Physiological, vestibular, and cognitive measurements were recorded to verify the innocuousness of the magnetic field on 20 participants scanned at 11.7T, and on another 20 participants with the magnetic field switched off (nocebo effect). The participants of the 0T control group were not informed of the absence of the magnetic field and received the same instructions as the volunteers scanned at 11.7T. The sound of MRI sequences was mimicked with recordings played by a loudspeaker hidden at the back of the magnet. Genotoxicity was assessed for the 11.7T group, with blood samples drawn before and after the 90-minute exposure. In all tests performed throughout the protocol, no significant differences between the 11.7T group and the 0T group could be identified (for a comprehensive description and results of this study, see [21]).

Radiofrequency pulse design and parallel transmission technology

In MRI, the B_1^+ field refers to the radiofrequency (RF) magnetic field that is used to excite the protons in the body. Achieving homogeneous B_1^+ distribution in the body becomes increasingly challenging at higher field strengths due to the shorter wavelength of the RF field [22]. Destructive interferences lead to significant spatial variations in the signal intensity, reducing image quality and causing artifacts in regions with complex geometries, like the human brain. One established method for mitigating these B_1^+ inhomogeneities is parallel transmission (pTx) technology, which uses multiple RF coil elements to independently control and modulate in time the amplitude and phase of the transmitted RF signals [23]. By employing pTx techniques, it is possible to tailor the RF fields to specific regions of interest, resulting in more uniform excitation and improved image homogeneity [24, 25]. With MAGNETOM Iseult, the use of pTx is mandatory to perform high-quality proton imaging of the human brain.

MR imaging at 11.7T

The first in vivo images of the human brain were acquired at 11.7T during the second half of 2023 on the PREMS cohort [21]. The magnetic resonance sessions were 90 minutes long and targeted anatomical T1-weighted, T2-weighted, and T2*-weighted contrasts, using gradient-echo (GRE) and spin-echo MR sequences (the main sequence parameters are provided in Table 2). The aforementioned homemade pTx RF coil with dedicated virtual observation points for specific-absorption-rate (SAR) monitoring was used for all imaging. All acquisitions were performed with up to second-order B_0 shimming using quadratic programming and brain masking. The RF and ΔB_0 field maps were acquired first for each participant for the pulse design and shimming using 2D interferometric saturated turboFLASH [26] at 5 mm isotropic resolution and 3D multi-GRE acquisitions at 2.5 mm isotropic resolution, respectively. RF pulses were designed with the k_T points [27], the "spokes" [28], and the gradient ascent pulse engineering (GRAPE) algorithm [29] approaches, respectively, using an active-set algorithm [30] with simultaneous *k*-space optimization [31] and under explicit hardware and SAR constraints. The GRAPE pulse was a universal RF pulse [32] and was designed offline on a database consisting of the first six participant field maps, while all other tailored RF pulses were designed using a dedicated workstation next to the MR system, during the exam. MR sequence source codes were modified to enable the use of the dynamic pTx RF pulses. No images were corrected for reception field bias (B_1^-). A gallery of images is shown in Figure 3 (to see more images, refer to [21], which is an open access article).

[1] *MAGNETOM Iseult is an investigational device only and is not intended for sale or clinical use. Research operations may require observation of national regulations.*

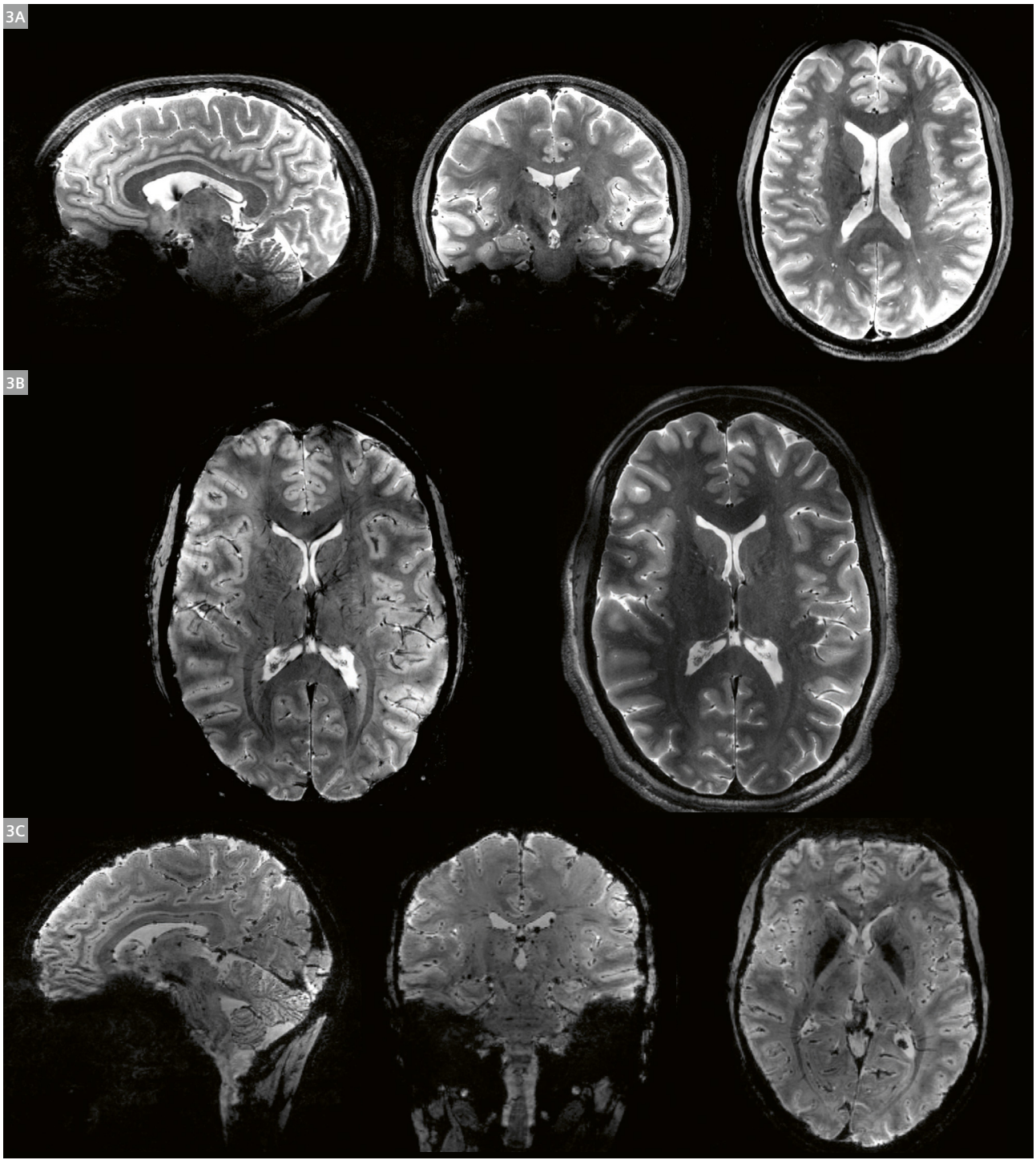

3 In vivo images of the human brain obtained at 11.7T. **(3A)** 3D T2-weighted variable flip angle turbo spin-echo (SPACE) acquisition, with parallel transmission GRAPE universal RF pulses reaching a high RF excitation homogeneity throughout the whole brain. **(3B)** In vivo T2*-weighted 2D GRE axial image, with multi-spoke RF pulses reaching a high B1+ field homogeneity on a slice-by-slice basis [33], juxtaposed with T2-weighted 2D TSE axial images, obtained by combining two complementary RF static shims [34]. **(3C)** In vivo T2*-weighted 3D GRE images, used to perform quantitative susceptibility mapping (QSM) [35].

	2D T2* GRE	3D T2* GRE	2D TSE	3D T2 SPACE
TA (min)	5:16	5:14	4:26	10:08
TR (ms)	600	25	7000	6000
TE (ms)	20	3.5 / 8.12 / 12.74 / 17.36	48	301
FA (°)	27	10	180	T_2 var
Matrix size	1032	276	640	400
Resolution $(mm)^3$	0.19 × 0.19 × 1	0.8 × 0.8 × 0.8	0.3 × 0.3 × 1	0.55 × 0.55 × 0.55
No. of slices/partitions	13	224	7	320
Acceleration	GRAPPA 2	GRAPPA 2×2	GRAPPA 4	GRAPPA 4×2
Turbo factor	–	–	9	165
Bandwidth (Hz/px)	40	430	130	250

Table 2: Main parameters of MR sequences used during the preliminary magnet study (PREMS).

A fruitful, ongoing collaboration between Siemens Healthineers and the CEA

The collaboration between the CEA and Siemens Healthineers in the field of MR essentially started with the first work packages for the Iseult project back in 2006, embodied by the signature of a master research agreement between the two entities. Siemens Healthineers has committed to providing MR instrumentation dedicated to this system, with the latest software and hardware technologies, bringing MAGNETOM Iseult to the highest standard of MR instrumentation from the outset. Several individual project agreements (IPAs) have also been signed to enable collaboration on specific topics. In particular, one IPA has been set up to develop and adapt a handful of state-of-the-art MR sequences provided by Siemens Healthineers to handle the specific pTx RF pulses designed using the tools of the CEA, so that they can be properly operated at 11.7T. Another IPA oversaw a collaboration to obtain key experimental data about the interaction between the gradient coil and the Iseult magnet to identify safe working conditions for using the MRI equipment.

Due to the magnitude of this project, people from different teams (project management, ultra-high-field development, MR collaboration) at Siemens Healthineers were involved. Customer service engineers were present at every stage of the installation, start-up, and operation of the MR system. The successful acquisition of the first in vivo images at 11.7T, with only 20 trials, is a perfect illustration of teamwork over many years and across the two organizations, with a great deal of preparation beforehand at 7T.

A promising future

The Iseult project is already 20 years old, yet somehow it feels as if this adventure is only just beginning. By producing the very first in vivo images of the human brain, this one-of-a-kind MR system has demonstrated great potential. While the PREMS study is now finished, more approvals from the regulatory body and national ethics committee are sought to perform new imaging sessions on healthy volunteers, particularly focusing on functional MRI (fMRI). Clinical research projects on patients are also envisioned. At this stage, many efforts are still ongoing to expand the current portfolio of pTx-compatible MR sequences, with more robust RF pulse design and additional sequence programming. For instance, designing robust inversion RF pulses was challenging due to the architecture of the present coil, and they left very localized artifacts despite achieving high overall performance [21]. More coils have also been designed and are ready to be tested [36]. One vision of CEA/NeuroSpin is to offer MAGNETOM Iseult as a unique international platform for the scientific community, making it accessible to any research project in the world, with dedicated on-site resources for support. Following the announcement of the first images, a number of sites have already approached the research center about launching new and ambitious clinical investigations.

Nevertheless, many of the challenges faced are further amplified at higher magnetic field strengths. The high spatial resolution aimed for makes imaging far more susceptible to blurring, and nearly two-thirds of the images acquired during the PREMS cohort had to be discarded because of motion artifacts. To tackle this wide range of challenges, the NeuroSpin team is working within the European Accurate, Reliable and Optimized Functional Magnetic Resonance Imaging (AROMA) consortium (https://aroma-h2020.com/) to assemble the necessary international expertise.

Increased static field inhomogeneities also are a burden for echo-planar imaging, the cornerstone of functional exploration of the human brain, causing unwanted image distortions and signal losses. A new multi-coil array prototype, named SCOTCH [17], has recently been designed by the CEA to shim the static field in the brain at 7T as if it were a partial seventh-order spherical harmonic conventional shimming system. Simulations showed promising artifact reduction at 11.7T with a 48-channel SCOTCH with a higher current amplitude. However, it would require a high-performance cooling system to dissipate the power. The implementation of such system and its positive impact on functional MR image quality is the subject of current research being carried out at CEA/NeuroSpin.

A central goal is to push the resolution of human fMRI to new levels, for instance by resolving individual cortical layers with spatial resolution on the order of 350–450 micrometers [4]. In view of the hardware needed to achieve such an ambitious target, MAGNETOM Iseult will be upgraded in the coming years with a powerful new gradient head coil designed by Siemens Healthineers (called Impulse, it is capable of achieving a maximum gradient strength of up to 200 mT/m for each axis and a slew rate of up to 700 T/m/s for each axis) and a state-of-the-art RF high density receiver array [4] that allows the system to quickly pick up fleeting MR signal before it decays.

Acknowledgments

This project received funding from the Banque Publique d'Investissement (BPIFrance), AROMA H2020 FET-Open (grant no. 885876) and Agence Nationale de la Recherche (ANR) (France 2030 Future Investment Program, grant no. ANR-21-ESRE-0006, ESR/EquipEx+, PRESENCE project). The authors would like to thank Siemens Magnet Technology (SMT) for their contribution to the magnet design, GE Alstom for magnet manufacturing, the Musée National d'Histoire Naturelle of Paris and Mathieu Santin from Paris Brain Institute for postmortem brain imaging, and the NeuroSpin platform team for organizing the MR exams.

References

1 Vogt N. Human brain mapping. Nat Methods. 2023;20(12):1869.
2 Finn ES, Poldrack RA, Shine JM. Functional neuroimaging as a catalyst for integrated neuroscience. Nature. 2023;623(7986):263–273.
3 Le Ster C, Grant A, Van de Moortele PF, Monreal-Madrigal A, Adriany G, Vignaud A, et al. Magnetic field strength dependent SNR gain at the center of a spherical phantom and up to 11.7T. Magn Reson Med. 2022;88(5):2131–2138.
4 Feinberg DA, Beckett AJS, Vu AT, Stockmann J, Huber L, Ma S, et al. Next-generation MRI scanner designed for ultra-high-resolution human brain imaging at 7 Tesla. Nat Methods. 2023;20(12):2048–2057.
5 Waks M, Lagore RL, Auerbach E, Grant A, Sadeghi-Tarakameh A, DelaBarre L, et al. RF coil design strategies for improving SNR at the ultrahigh magnetic field of 10.5T. Magn Reson Med. 2025;93(2):873–888.
6 Cosottini M, Frosini D, Pesaresi I, Costagli M, Biagi L, Ceravolo R, et al. MR imaging of the substantia nigra at 7 T enables diagnosis of Parkinson disease. Radiology. 2014;271(3):831–8.
7 Opheim G, van der Kolk A, Markenroth Bloch K, Colon AJ, Davis KA, Henry TR, et al. 7T Epilepsy Task Force Consensus Recommendations on the Use of 7T MRI in Clinical Practice. Neurology. 2021;96(7):327–341.
8 Sati P, Oh J, Constable RT, Evangelou N, Guttmann CR, Henry RG, et al. The central vein sign and its clinical evaluation for the diagnosis of multiple sclerosis: a consensus statement from the North American Imaging in Multiple Sclerosis Cooperative. Nat Rev Neurol. 2016;12(12):714–722.
9 Gulban OF, Bollmann S, Huber LR, Wagstyl K, Goebel R, Poser BA, et al. Mesoscopic in vivo human T2* dataset acquired using quantitative MRI at 7 Tesla. Neuroimage. 2022;264:119733.
10 Ogawa S, Lee TM, Kay AR, Tank DW. Brain magnetic resonance imaging with contrast dependent on blood oxygenation. Proc Natl Acad Sci U S A. 1990;87(24):9868–72.
11 Uğurbil K. ULTRAHIGH FIELD and ULTRAHIGH RESOLUTION fMRI. Curr Opin Biomed Eng. 2021;18:100288.
12 Boulant N, Quettier L. Commissioning of the Iseult CEA 11.7 T whole-body MRI: current status, gradient-magnet interaction tests and first imaging experience. MAGMA. 2023;36(2):175–189.
13 Le Bihan D, Schild T. Human brain MRI at 500 MHz, scientific perspectives and technological challenges. Supercond Sci Technol. 2017;30(3):033003.
14 Quettier L, Aubert G, Belorgey J, Berriaud C, Bredy P, Dilasser G. Commissioning Completion of the Iseult Whole Body 11.7 T MRI System. IEEE Transactions on Applied Superconductivity. 2020;30(4):1–5.
15 Vannesjo SJ, Haeberlin M, Kasper L, Pavan M, Wilm BJ, Barmet C, et al. Gradient system characterization by impulse response measurements with a dynamic field camera. Magn Reson Med. 2013;69(2):583–93.

16 Luong M, Ferrand G, Chazel E, Gapais PF, Gras V, Boulant N, et al. A Compact 16Tx-32Rx Geometrically Decoupled Phased Array for 11.7T MRI. In: Proceedings of the 2022 Annual Meeting of ISMRM. London, UK; p. 0707.
17 Meneses BP, Stockmann JP, Arango N, Gapais PF, Giacomini E, Mauconduit F, et al. Shim coils tailored for correcting B0 inhomogeneity in the human brain (SCOTCH): Design methodology and 48-channel prototype assessment in 7-Tesla MRI. NeuroImage. 2022;261:119498.
18 He X, Ertürk MA, Grant A, Wu X, Lagore RL, DelaBarre L, et al. First in-vivo human imaging at 10.5T: Imaging the body at 447 MHz. Magn Reson Med. 2020;84(1):289–303.
19 Grant A, Metzger GJ, Van de Moortele PF, Adriany G, Olman C, Zhang L, et al. 10.5 T MRI static field effects on human cognitive, vestibular, and physiological function. Magn Reson Imaging. 2020;73:163–176.
20 Le Ster C, Selingue E, Poirier R, Edeline J-M, Mériaux S, Boulant N. Behavioral and functional assessment of mice inner ear after chronic exposure to an ultrahigh B0 field of 11.7 T or 17.2 T. Magn Reson Med. 2023;90(2):699–707.

Contact

Nicolas Boulant, Ph.D.
Scientific director of the Iseult project
METRIC, BAOBAB, NeuroSpin, CEA, CNRS,
Paris-Saclay University
91191, Gif-Sur-Yvette
France
nicolas.boulant@cea.fr



Franck Mauconduit, Ph.D.
System manager of MAGNETOM Iseult
METRIC, BAOBAB, NeuroSpin, CEA, CNRS,
Paris-Saclay University
91191, Gif-Sur-Yvette
France
franck.mauconduit@cea.fr
https://joliot.cea.fr/drf/joliot/recherche/neurospin



Aurélien Massire, Ph.D.
MR Clinical Scientist
Siemens Healthcare SAS
6 rue du Général Audran
92400, Courbevoie
France
aurelien.massire@siemens-healthineers.com



21 Boulant N, Mauconduit F, Gras V, Amadon A, Le Ster C, Luong M, et al. In vivo imaging of the human brain with the Iseult 11.7-T MRI scanner. Nat Methods. 2024;21(11):2013–2016.
22 Webb AG, Collins CM. Parallel transmit and receive technology in high-field magnetic resonance neuroimaging. Int J Imaging Syst Technol. 2010;20(1):2–13.
23 Katscher U, Börnert P, Leussler C, van den Brink JS. Transmit SENSE. Magn Reson Med. 2003;49(1):144–50.
24 Padormo F, Beqiri A, Hajnal JV, Malik SJ. Parallel transmission for ultrahigh-field imaging: Parallel Transmission for Ultrahigh-Field Imaging. NMR Biomed. 2016;29(9):1145–61.
25 Massire A, Mauconduit F, Gras V, et al. PASTEUR: Package of Anatomical Sequences Using Parallel Transmission Universal Pulses Now Available for MAGNETOM Terra. MAGNETOM Flash. 2022;80(1):65–74.
26 Brunner DO, Pruessmann KP. B1(+) interferometry for the calibration of RF transmitter arrays. Magn Reson Med. 2009;61(6):1480–8.
27 Cloos MA, Boulant N, Luong M, Ferrand G, Giacomini E, Le Bihan D, et al. kT-points: Short three-dimensional tailored RF pulses for flip-angle homogenization over an extended volume. Magn Reson Med. 2012;67(1):72–80.
28 Setsompop K, Alagappan V, Gagoski B, Witzel T, Polimeni J, Potthast A, et al. Slice-selective RF pulses for in vivo B1+ inhomogeneity mitigation at 7 tesla using parallel RF excitation with a 16-element coil. Magn Reson Med. 2008;60(6):1422–32.
29 Van Damme L, Mauconduit F, Chambrion T, Boulant N, Gras V. Universal nonselective excitation and refocusing pulses with improved robustness to off-resonance for Magnetic Resonance Imaging at 7 Tesla with parallel transmission. Magn Reson Med. 2021;85(2):678–693.
30 Hoyos-Idrobo A, Weiss P, Massire A, Amadon A, Boulant N. On variant strategies to solve the magnitude least squares optimization problem in parallel transmission pulse design and under strict SAR and power constraints. IEEE Trans Med Imaging. 2014;33(3):739–48.
31 Gras V, Luong M, Amadon A, Boulant N. Joint design of kT-points trajectories and RF pulses under explicit SAR and power constraints in the large flip angle regime. J Magn Reson. 2015;261:181–9.
32 Gras V, Vignaud A, Amadon A, Bihan D, Boulant N. Universal pulses: A new concept for calibration-free parallel transmission. Magn Reson Med. 2017;77(2):635–643.
33 Mauconduit F, Gras V, Vignaud A, Boulant N. MetaPulse2D: methodology to enable universal slice specific spokes pulses in parallel transmission. In: Proceedings of the 2022 Annual Meeting of ISMRM. London, UK; Abstract #0454.
34 Orzada S, Maderwald S, Poser BA, Bitz AK, Quick HH, Ladd ME. RF excitation using time interleaved acquisition of modes (TIAMO) to address B1 inhomogeneity in high-field MRI. Magn Reson Med. 2010;64(2):327–33.
35 Santin M, Didier M, Mauconduit F, et al. In vivo R2* and QSM on the 11.7T whole-body Iseult MRI System using Universal Pulses Transmission and Virtual Coil Reconstruction. Submitted to the 2025 Annual Meeting of ISMRM. Honolulu, Hawaii, U.S.
36 Chu S, Gras V, Mauconduit F, Massire A, Boulant N, Gunamony S. Electromagnetic and RF pulse design simulation based optimization of an eight-channel loop array for 11.7T brain imaging. Magn Reson Med. 2023;90(2):770–783.

A Milestone in Medical Imaging: The Pioneering Development of the First Integrated PET/MR Scanner at Siemens Healthineers

Holger Schmidt[1]; Marc Lauterbach[1]; Manuel Schneider[1]; Hans Wehrl[1]; Matthias Schmand[2]; James Corbeil[3]; David Faul[4]; Silvia Dias Almeida[1]; Matthias Fenchel[1]

[1]Siemens Healthineers, Erlangen, Germany
[2]Siemens Healthineers, Knoxville, TN, USA
[3]Siemens Healthineers, Rockford, TN, USA
[4]Siemens Healthineers, New York, NY, USA

Introduction

Siemens was the first company to build and market a whole-body PET/MR for clinical imaging. The story of this landmark achievement is worth retelling. PET/MR is a powerful imaging technology that uses the strengths of both modalities synergistically, combining the submillimeter, anatomic resolution of MRI with the ultra-high sensitivity of molecular PET imaging. Due to the complementary nature of the information provided by each modality, PET/MR is ideal for complex disease characterization and radiomics. In contrast to PET/CT, PET/MR also allows for truly simultaneous and isocentric imaging. Therefore, fully synergistic applications like MR-guided PET motion correction and PET-guided MR motion correction are also possible. In addition, the technology allows multifunctional imaging, i.e., the combination of functional information derived from MR and PET, such as BOLD fMRI with ^{18}F-FDG PET [1].

Compared with PET/CT, which was already clinically available in 2000 [2], PET/MR had a slower start, with the first human images being published in 2008 [3]. This was mainly due to the high complexity and technical challenges of combining both modalities into a single system.

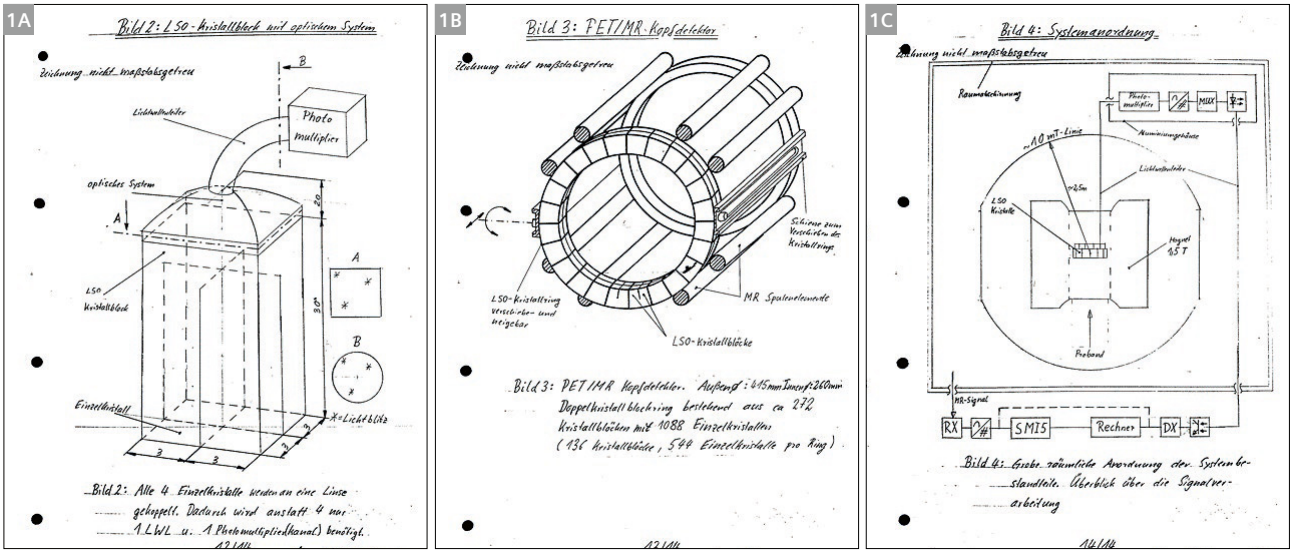

1 PET/MR idea from 1998. **(1A)** Shows the LSO crystals coupled via a light guide to a fiber-optic cable and PMTs outside the magnetic fringe field. **(1B)** The system was envisioned as a brain-PET detector with a movable detector ring for FOV selection. **(1C)** System layout with electronics installed inside and outside of the RF cabin. PET/MR image fusion was envisioned to be performed on an extra computer coupled with the Siemens Medical Imager Five (SMI5) image reconstruction computer of the MR system.

In addition, while PET/CT simplified the workflow of a PET exam by reducing the time to acquire an attenuation correction for the PET reconstruction, PET/MR first needed to establish applications, workflows, and protocols – some of which incorporate options unique to PET/MR.

This article aims to reconstruct part of the history of the technology from the point of view of Siemens Healthineers. It is not intended to give a full and exact account of the development of PET/MR itself, which has been the subject of considerable research and development work over the past 30 years.

Initial idea to combine PET and MR imaging

Engineers and physicists at Siemens Medical Solutions, as our company was then called, of course closely monitored the technological developments in both modalities as part of their daily routine. In the mid-to-late 1990s, the academic world was also studying the foundations of future PET/MR systems in the form of photomultiplier tube (PMT) detectors coupled with optical fibers [4], and semiconductor-based light detectors such as avalanche photodiodes (APDs) [5]. As early as 1998, the first idea for a combined PET/MR system was presented within Siemens. A system was described that operated in the form of a head coil with add-on PET detectors (Fig. 1), connected by optical fibers or APDs. Since 3T was by no means an established field strength in the clinical field, the improvement idea referred more specifically to systems like the 1.5T MAGNETOM Vision or one of its successors, such as the 1.5T MAGNETOM Symphony or the 1T MAGNETOM Harmony. The idea was ahead of its time, and the proposal was rejected. Nevertheless, the concept of PET/MR made a successful return within 10 years.

Testing the waters: The BrainPET system

By the mid-2000s, it was evident that PET/CT systems were often superior to standalone PET systems in clinical practice due to the combination of patient throughput, of physiological information and of anatomical detail. However, in certain applications, such as neurology and oncology, MRI [6] showed clear advantages over CT imaging due to its superior soft-tissue contrast and capabilities for functional imaging, such as blood-oxygen-level-dependent (BOLD) imaging. Small-animal PET/MR systems showed that it was possible to solve the basic technical challenges, such as crosstalk between the two modalities [7–9]. Therefore, the idea of a combined PET/MR system regained traction at Siemens. In 2005, Siemens Medical Solutions bought its longtime PET partner, CTI Molecular Imaging, with the goal of expanding its presence in the molecular imaging market [10]. Pioneering efforts to build solid-state detectors for PET/MR with APDs were already underway at CTI, so it was agreed to go forward with a combined PET/MR system to see if a suitably large PET/MR market existed. There was a clear vision to work toward a whole-body PET/MR system, but due to the many technical challenges and the disruptive nature of the system, it was decided to take an intermediate step via a research system to learn, and then to iterate from there.

The system later became known as BrainPET, which reflected its main application. Conventional PET systems at this time still used PMTs for photodetection. However, PMTs are very sensitive to external magnetic fields, rendering them unusable in the vicinity of an MRI system. Using long optical fibers to connect the scintillation crystals to the PMTs was deemed inefficient due to inherent light loss and signal shape changes. Fortunately, APDs were just becoming commercially available and were stable enough. They were used in the calorimeter at CERN (The Electromagnetic Calorimeter Project, Technical Design Report, CERN/LHCC97-31, 1997), so the Siemens developers knew that Hamamatsu APDs worked and were stable. In addition, preclinical systems existed [5]. The form factor and resolution of the APDs offered the possibility of resolving smaller crystals. It was therefore a natural step in detector development to move on to the APD technology. Ultimately, this was also a preliminary development for more advanced solid-state light detectors such as silicon photomultipliers (SiPMs), though these were not ready to use at that time.

Therefore, the system used CTI's newly developed PET detector, for which the pioneered APDs were coupled to a matrix of 2.5 × 2.5 × 20 mm^3 lutetium oxyorthosilicate (LSO) scintillation crystals. Six of these modules were combined into a detector cassette enabling a field of view (FOV) of 19.2 mm in the *z*-direction (axial). Thirty-two of these copper-shielded cassettes formed the cylindrical PET detector system. The inner diameter of the PET detector was 36 cm, with the outer diameter fitting inside the 60-cm bore of a 3T MAGNETOM Trio MRI scanner. To enable MR signal transmission and reception, a dedicated transmit receive coil was fit inside the PET ring – a birdcage transmission coil and an eight-channel receive coil.

This combination essentially transformed the whole-body MAGNETOM Trio MRI system into a head-only (and some body parts) PET/MR system [11]. The PET insert was completely retractable (although its cables were somewhat heavy) and, without the insert, the system could be used as a regular clinical MRI scanner. The PET detector cassettes were connected to the Siemens Medical Solutions QuickSilver data acquisition system [12] via 10-meter cables. A PET handling device mounted at the end of the patient bore allowed the setup of a PET/MR system or an MR-only system. The BrainPET prototype was designed mainly to gain experience of this new modality

and was therefore introduced at five sites. These were: Atlanta, GA, and Boston, MA, in the United States; and Jülich, Munich, and Tübingen in Germany. Two of these BrainPETs are still used for research in Boston and Jülich. Their image resolution makes them particularly attractive for neurological research. With the introduction of the BrainPET, Siemens Medical Solutions established a strong collaboration network to further develop PET/MR technology. Amongst the big successes of BrainPET were the first human PET/MR images obtained by a U.S.-German team in 2008 [3], and extensive and high-ranking research work published and presented by the respective sites [13–17]. Figure 2 depicts one of the first PET/MR images acquired on the BrainPET: the first patient scanned at the Athinoula A. Martinos Center for Biomedical Imaging on May 23, 2008. The patient was a 54-year-old man with glioblastoma with cutaneous extension and received 5.45 mCi of FDG for a clinical PET scan performed 2.5 hours before the PET/MR scan.

The BrainPET sparked many creative research projects and academic ambitions, and the nuclear-medicine and MRI communities were very positive about the marriage of these two modalities. However, the limitations of a dedicated system for neurology research were becoming obvious, as it was not intended as a PET/MR system for widescale use. Huge potential was predicted for the fields of oncology and cardiology, both of which would require a whole-body PET/MR system. Furthermore, the BrainPET was not yet a fully integrated system: The MR and PET images had to be acquired and reconstructed at two separate consoles and there was no integrated solution for attenuation correction.

Still, the BrainPET allowed the collection of important clinical and technical experience and feedback, enabling PET/MR development to take the next quantum leap toward a fully integrated, clinical whole-body system. This became known as the Biograph mMR.

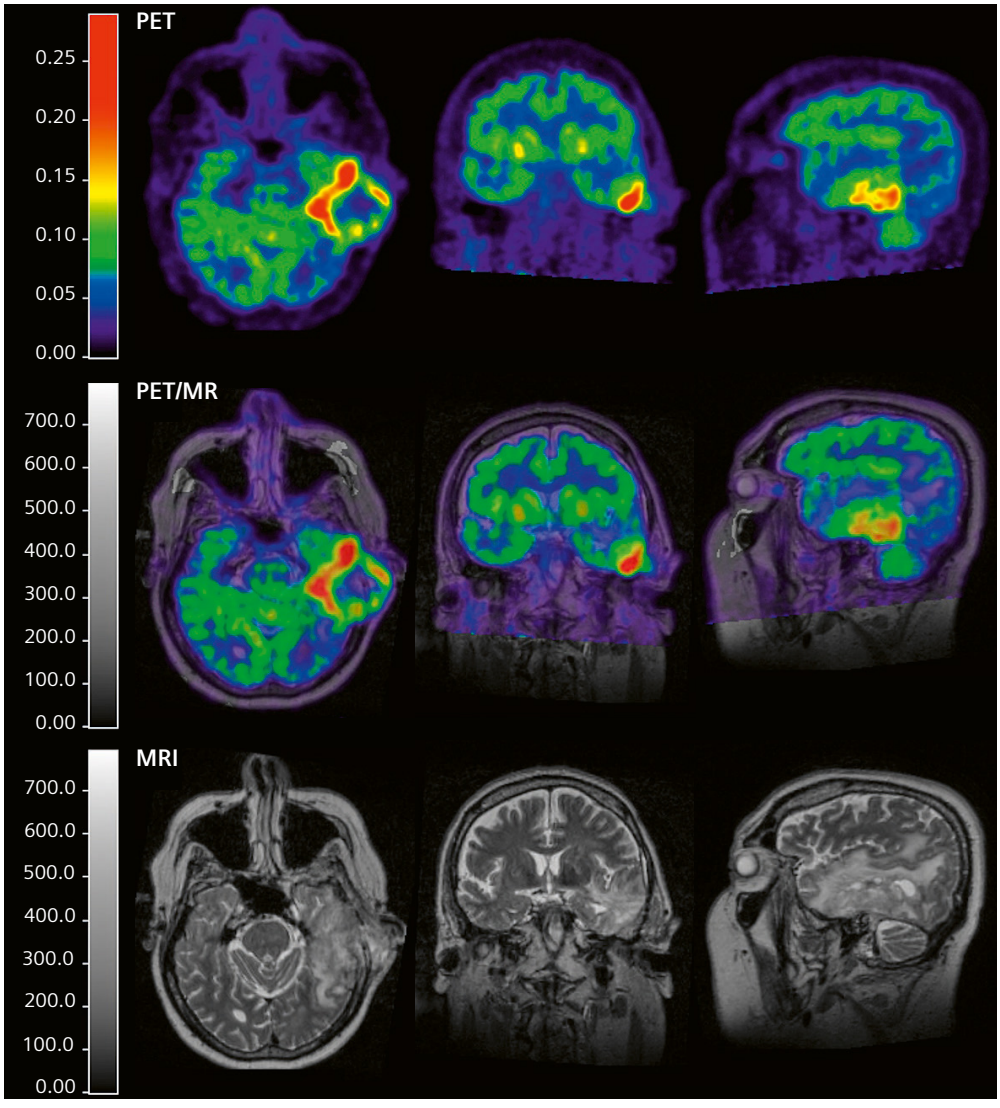

2 First simultaneous ^{18}F-FDG PET/MR scan at the Athinoula A. Martinos Center for Biomedical Imaging using the 3T MR-compatible BrainPET prototype. The subject was a 54-year-old man with glioblastoma with cutaneous extension. *Images courtesy of Ciprian Catana, MD, PhD; A.A. Martinos Center, Massachusetts General Hospital, Boston, MA, USA.*

From simultaneous to synergistic PET/MR: Biograph mMR

Siemens had developed concepts for a whole-body all-purpose scanner in parallel with the introduction of BrainPET and maintained this vision in ongoing dialog with the PET/MR clinical and research communities. Various challenges had to be overcome on the electronics and mechanical integration front.

In the transition from BrainPET to the Biograph mMR, APDs were still used, but the electronics were completely redesigned so they could sit inside the main magnetic field, inside the bore or near the end of the magnet rather than outside the main magnetic field. This forced further development in digitalization, including digital time measurement of PET annihilation photon events directly at the MRI scanner, which was a considerable innovation at the time.

The mechanical integration concept of the PET gantry into the MRI system was also a challenge. This included: the ability to service the PET subsystem in the magnetic field without disassembling the unit; an interleaved cooling concept; mutual shielding of each modality from the adverse effects of the other; a holistic concept for attenuation correction for both the patient, the patient table, and the MR coils; plus additional topics regarding hardware and software integration, including temporal and spatial registration of the acquired data and images.

It became clear early on that the whole-body PET/MR system had to be based on an MRI system with a 70-cm bore, and that the PET detector needed to fit within the MR scanner and have a field of view that did not extend out of the homogeneous field of the MR, to make an integrated solution possible.

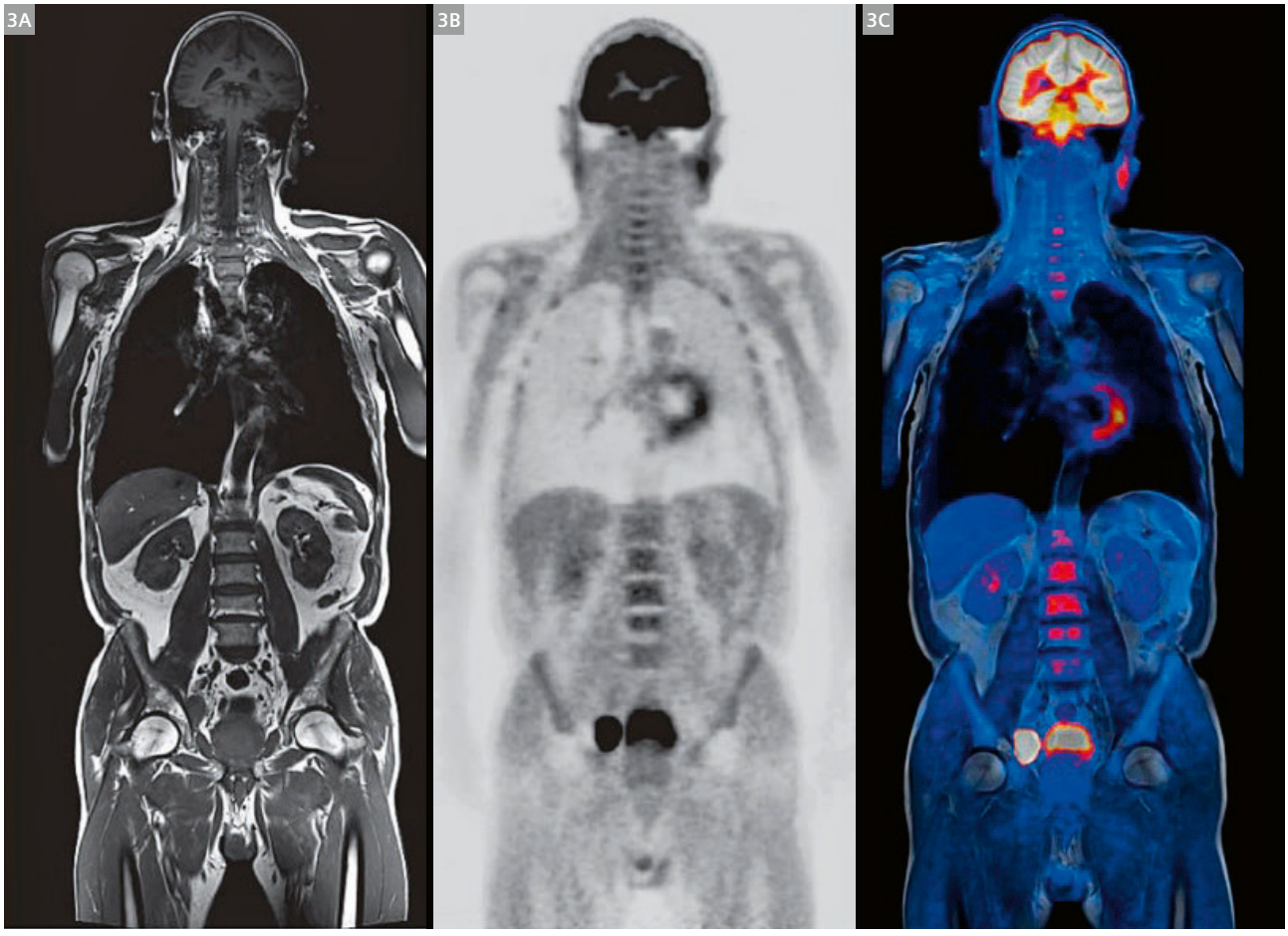

3 Patient with lymph node metastasis following a history of a penis carcinoma. Images show whole-body T1-weighted MR image **(3A)**, attenuation corrected PET **(3B)**, and MR/PET hybrid images **(3C)** in a coronal orientation, that were all simultaneously acquired in a multistation/multi-bed acquisition mode. MRI in this wholebody study (3A) displays anatomical structures with exquisite detail and excellent soft-tissue contrast. PET (3B) and the combined MR/PET hybrid image (3C) in this coronal overview show enhanced tracer activity in one lymph node on the right side of the patient.
Images from Quick HH, Ladebeck R, Georgi JC. Whole-Body MR/PET Hybrid Imaging: Technical Considerations, Clinical Workflow, and Initial Results. MAGNETOM Flash. 2011; 46(1):88–100.

Numerous discussions were also held regarding the MR field strength of such a system. The clinical standard was 1.5T, but 3T was the field strength preferred by researchers and clinicians with a focus on neurological imaging. Given the experiences and positive feedback from BrainPET users, the decision was made in favor of a 3T-based system. It is worth mentioning that Siemens conceived this system for both clinical and research use from the outset. The specification of the system was designed to compete with the high-end systems of each modality, and to allow for optimal clinical performance and excellent research. The PET detector of the Biograph mMR system was based on APD electronics and 4 × 4 × 20 mm LSO crystals; 8 × 8 crystals were coupled with 3 × 3 APDs on a detector block. Eight rings each with 56 detector blocks formed the PET detector with an axial FOV of 25.8 cm (head-feet direction). The integration of the detector reduced the bore size from 70 cm to 60 cm. The motivation was to enable the growing PET/MR community to pave the way for widespread PET/MR usage through pilot studies and by identifying the key advantages and most compelling clinical applications. The first whole-body scan was performed during a clinical investigation at the first external installation at the Technical University of Munich, Germany, in November 2010.

When the Biograph mMR was launched at the RSNA in 2010 and with the commercial system installation in 2011, it was a revolution. People were excited and could barely believe it was an integrated system with all the capabilities, but the small footprint of a regular MRI system. According to one anecdote, people walked past the conference booth wondering where to find the integrated PET/MR system, because the Biograph mMR looked just like a regular MRI scanner from the outside. Another anecdote shows the excitement that the Biograph mMR generated everywhere: For the first time in the history of Siemens Medical, the FDA's press statement saying the system was cleared for the U.S. market was issued *before* the Siemens marketing department was able to publish its own.

The progress of the Biograph mMR since 2011 can roughly be divided into three phases: During the first phase the installed base grew quickly. Most of the systems were installed at sites which used the system for research and where many innovative ideas were tried. Some proved successful, others were discarded. The community invested a lot of effort in proving and discussing equality with respect to PET/CT. Technical developments improved the performance of the system and led to the introduction of a new software version in 2014. A range of applications and protocols were proposed and tried. Additional features (truly synergistic applications, e.g., respiratory motion management and respiratory gating both with a matching attenuation correction) were introduced along with a first attempt at MR-driven PET head motion correction (BrainCOMPASS, with NEMA and ACRIN testing capabilities) and more.

In the second phase specific key applications emerged, e.g., indications for which a PET/CT and an MRI scan are generally ordered (epilepsy surgery planning, dementia evaluation, oncology staging, prostate cancer staging, neurodegenerative disease, cardiac sarcoidosis). Another important aspect was the reduction of radiation exposure from the CT component, making it particularly suitable for pediatric malignancy cases [18, 19]. Protocols were becoming more streamlined, and consensus papers on PET/MR protocols were published [20]. A new software version was introduced in 2017 with further improvements in attenuation correction (extended FOV, and bone attenuation correction) and truly synergistic motion correction (BodyCOMPASS), as well as improvements to the general PET/MR workflow (Fig. 4).

Roughly since 2017, patients with these key indications are being scanned in financially sustainable volumes, and new tracers are boosting PET/MR usage (tau- and amyloid-based tracers for Alzheimer's diagnostics, and PSMA for prostate imaging). Research is continuing extensively. The community is requesting further innovations in the areas of PET and MRI such as imaging pain or using MRI to anatomically guide the PET reconstruction of brain and prostate images.

For three or four years, the Biograph mMR was the only clinical whole-body PET/MR scanner on the market. Even 13 years after its introduction, it has retained its attractiveness as the most complete and mature commercial PET/MR system in the world. So far, an estimated 250,000 patients have been scanned on Biograph mMR systems, meaning a PET/MR system has helped write a quarter of a million personal healthcare stories. Many case studies and reports have been published [21–23] describing how complementary information acquired with PET and MRI has made a difference to the patient's diagnostic outcome and the chosen treatment path.

Shape the new era of personalized care: BIOGRAPH One

Since the introduction of Biograph mMR in 2011, the PET/MR market has experienced steady growth. Initially, the focus was primarily on research, but as the installed base expanded, clinical applications began to emerge, particularly in areas where the combined strengths of soft tissue contrast and resolution from MRI and metabolic insights from PET provided unique diagnostic value. Key application areas include neurology (e.g., neurodegenerative diseases), oncology (e.g., prostate cancer imaging), cardiology, and theranostics, with uses in oncology, inflammatory diseases, and novel Alzheimer's treatments.

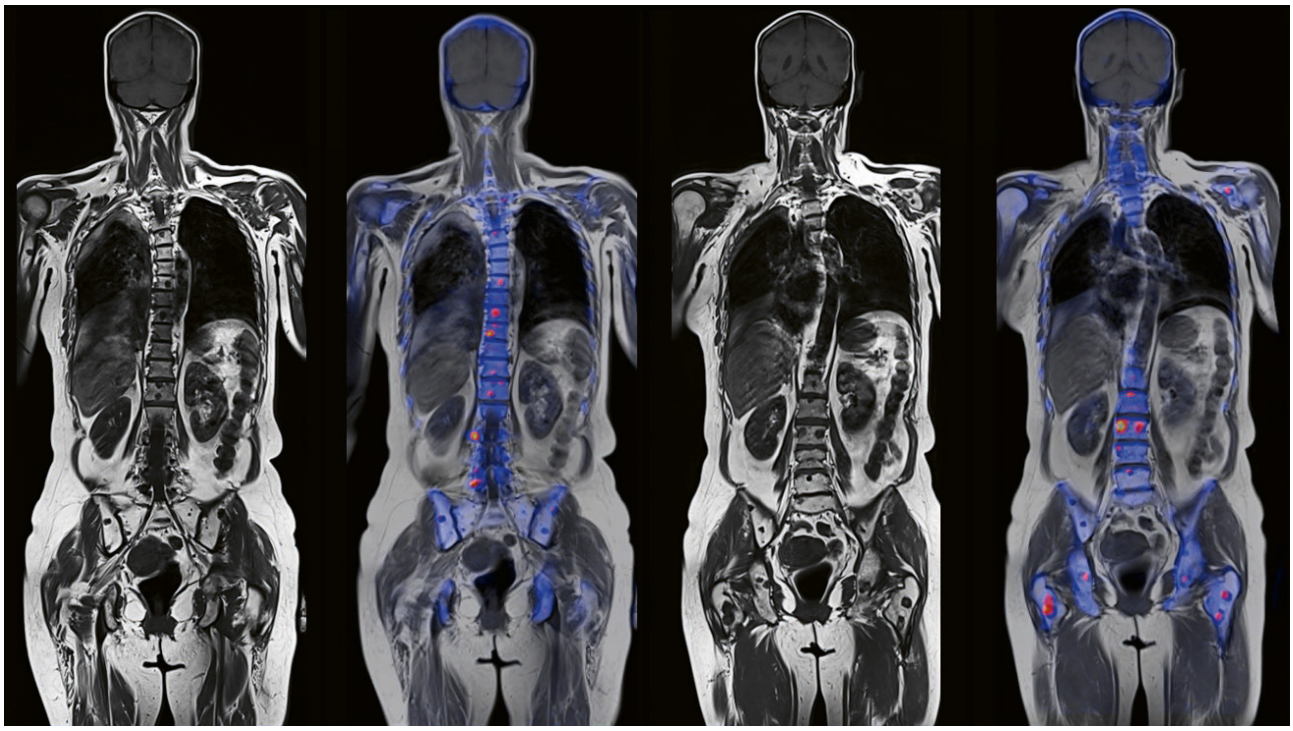

4 Metastatic breast cancer ^{18}F-NaF PET/MR (Biograph mMR). A patient with bone metastases demonstrates the potential of the Biograph mMR to help in the diagnosis of bone processes either osteoblastic, osteolytic or infiltrative. Fat suppressed MRI is advantageous to detect early marrow changes. PET overlapped with T1 TSE composed. *Images courtesy of NYU Langone Medical Center, New York, USA*.

Despite these successes, wider adoption of PET/MR was hindered by three main challenges identified a decade after its market introduction:

- Economic barriers: Longer scan times, higher costs compared to PET/CT, and limited reimbursement options.
- Complexity: Complex workflows, extensive patient preparation, high data volumes, and lengthy reading times.
- Technological gaps: Image resolution and contrast lagged behind the capabilities of the latest standalone PET and MRI systems.

To address these challenges, Siemens Healthineers leveraged flagship technologies from both PET and MRI modalities and added significant innovations. A great example is the PET detector where the novel approach to digitalize the signals already on the detector board level, all components except the LSO crystals and the SiPMs had to be newly designed. Thus developing the next-generation system, now introduced as BIOGRAPH One[1]. This new system is designed to integrate key technologies from the BIOGRAPH Vision PET/CT and the MAGNETOM Vida MRI scanner, while adding numerous innovations on top addressing the following:

Designed to promote high patient throughput:

- Boost PET performance by introducing SiPM technology and best-in-class time-of-flight (TOF) imaging
- Boost MRI performance by introducing deep learning image reconstruction
- Provide high-density channel MRI coils to allow for higher acceleration factors
- Extend the PET FOV to 35 cm to reduce the number of bed positions in whole-body acquisitions and to increase the PET sensitivity
- Improve the up time of the system by reducing the time for system calibration and detector replacement

Reduce system complexity:

- Introduce a new workflow to simplify planning and scan execution, bringing components from MR and PET/CT planning, in a unified user-interface
- Introduce protocol automation such as myExam Assist, AutoAlign, and the copy reference concept to reduce exam planning and user interaction and to improve workflow consistency
- Improve serviceability and operational aspects of the scanner, such as reducing siting requirements by utilizing only one filter plate

[1] *BIOGRAPH One is currently under development and not commercially available. It is not for sale in the U.S.A. and its future availability cannot be ensured.*

In the PET domain, the introduction of TOF technology and SiPM detectors has significantly enhanced imaging performance. By 2017, the BIOGRAPH Vision PET/CT was introduced, as one of the first in the industry to offer a TOF timing resolution below 250 ps, reducing time resolution by 50% compared to other PET/MR systems on the market. This leap improved effective sensitivity and localization accuracy – critical for clinical applications, especially in neurology. Additionally, the shift from analog to digital detectors reduced signal interference and increased overall robustness. These advancements along with additional key innovations, are now first introduced with BIOGRAPH One, designed to result in an order of magnitude improvement in PET sensitivity.

On the MR side, BIOGRAPH One is planned to incorporate the latest 3T technology with BioMatrix technology, advanced coil designs, and cutting-edge reconstruction methods like Compressed Sensing and deep learning-based image reconstruction (Deep Resolve). These upgrades enhance image quality, accelerate scans, and increase patient throughput, making the system well-suited for both clinical and research applications.

The development of BIOGRAPH One aimed to overcome economic and operational barriers, while also boosting clinical performance. Enhanced PET sensitivity is achieved through SiPM technology and TOF imaging. Deep learning-based image reconstruction improves MR image quality, and the extended PET field-of-view (FOV) reduces the number of bed positions required for whole-body scans. Improved calibration and streamlined maintenance processes further enhance system uptime and reliability.

The introduction of a unified user interface and automation tools such as myExam Assist and AutoAlign will simplify workflow, reducing the time needed for exam planning and improving consistency. By integrating these elements, BIOGRAPH One offers potential for a seamless, simultaneous PET/MR experience that addresses the demands of modern clinical environments.

The journey of BIOGRAPH One has reached an exciting new chapter with the first system installation in Rigshospitalet Copenhagen, Denmark (Fig. 5). The very first clinical scans were conducted as part of the system's initial evaluation. These included a scan of a patient undergoing assessment for suspected dementia (Fig. 6) and another of a patient with relapsed follicular lymphoma being evaluated for complications related to immunosuppression and chronic lung disease (Fig. 7). These are some of prime clinical applications of PET/MR. This is just the beginning – with more installations to follow, we look forward to continuing Siemens Healthineers' leadership in PET/MR imaging and shaping this new era in personalized care with BIOGRAPH One.

The evolution of PET/MR has not only advanced diagnostic capabilities but has also broadened the horizon for clinical and research applications. With every iteration, the technology has shifted closer to fulfilling its potential: delivering a comprehensive, efficient, and user-friendly diagnostic tool that combines the best of PET and MR into a single, seamless experience. Siemens Healthineers' dedication to overcoming technical and economic barriers continues to drive innovation, and the BIOGRAPH One stands as a testament to this ambition.

By blending cutting-edge developments in PET sensitivity, MR efficiency, and user workflow, Siemens Healthineers reaffirms its role as a pioneer in the imaging industry. The future holds new possibilities for PET/MR, promising expanded applications, improved patient outcomes, and a continued commitment to pushing the boundaries of what hybrid imaging can achieve. This new era of PET/MR will not only serve the needs of today's clinicians and patients but will lay the foundation for tomorrow's breakthroughs in precision medicine.



5 The first BIOGRAPH One. Assembled in the Siemens Healthineers headquarters in Erlangen, Germany and installed at University Hospital Erlangen, Germany, and at the Rigshospitalet, Copenhagen, Denmark.

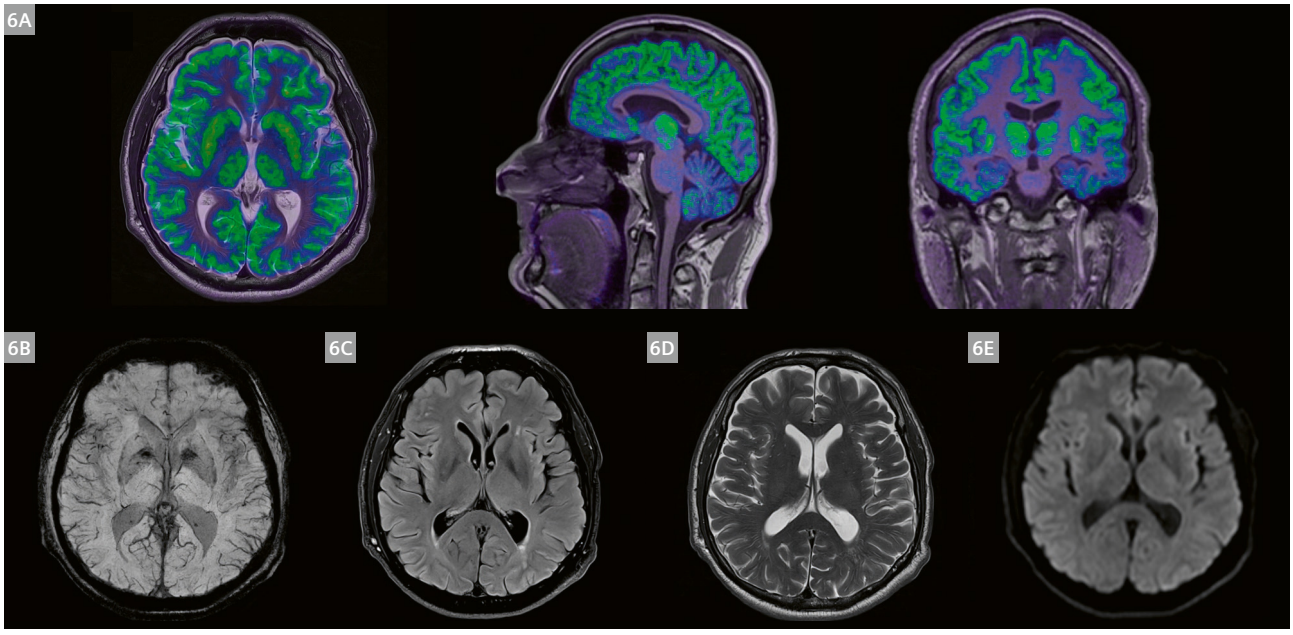

6 First-ever clinical images acquired using the new BIOGRAPH One system as part of the clinical investigation being conducted at the Rigs Hospital, Copenhagen, Denmark. A ^{18}F-FDG PET/MR scan was performed on a 63-year-old patient, who presented a history of progressive memory issues and was being assessed for suspected early neurodegenerative disease. The exam revealed slightly asymmetrical uptake in the frontal regions, with preserved cortical metabolism and symmetrical uptake in the basal ganglia, thalami, and cerebellar hemispheres. **(6A)** Fused PET and T2-weighted anatomical MR images displayed in axial, sagittal, and coronal views. **(6B)** Susceptibility Weighted Imaging provides high sensitivity for detecting vascular structures and micro-hemorrhages. **(6C)** T2-weighted Dark Fluid sequence enhances contrast for cerebrospinal fluid spaces, aiding in visualization of potential abnormalities. **(6D)** High-resolution T2-weighted anatomical scan, used for detailed structural assessment. **(6E)** Diffusion-weighted imaging at b = 1000 s/mm^2, offering insights into tissue microstructure without specific abnormalities detected.

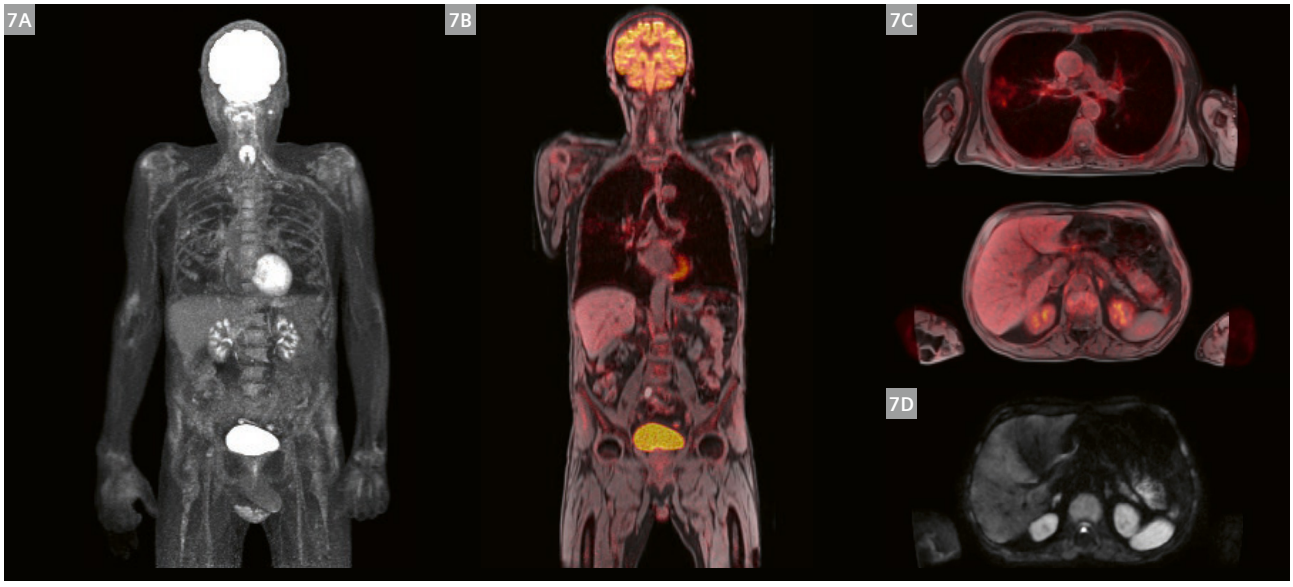

7 First clinical images from the BIOGRAPH One PET/MR system at Rigshospitalet, Copenhagen, Denmark.
A 75-year-old male patient with relapsed follicular lymphoma was scanned to assess immunosuppression-related complications, including recurrent pneumonia and Chronic Obstructive Pulmonary Disease (COPD). The imaging revealed unchanged metabolic remission of lymphoma but increased FDG uptake in the lungs, consistent with inflammatory or infectious changes. **(7A)** PET-only image showing metabolic activity in the lungs and parotid gland. **(7B)** Fused PET and MR attenuation-corrected image (PET+MRAC) for anatomical localization and **(7C)** axial views of increased FDG update. **(7D)** Diffusion-weighted imaging (DWI) sequence, providing additional information on tissue composition and potential microstructural changes.

References

1 Wehrl HF, Hossain M, Lankes K, Liu CC, Bezrukov I, Martirosian P, et al. Simultaneous PET-MRI reveals brain function in activated and resting state on metabolic, hemodynamic and multiple temporal scales. Nat Med. 2013;19(9):1184–9.
2 Beyer T, Townsend DW, Brun T, Kinahan PE, Charron M, Roddy R, et al. A combined PET/CT scanner for clinical oncology. J Nucl Med. 2000;41(8):1369–79.
3 Schlemmer HP, Pichler BJ, Schmand M, Burbar Z, Michel C, Ladebeck R, et al. Simultaneous MR/PET imaging of the human brain: feasibility study. Radiology. 2008;248(3):1028–35.
4 Shao Y, Cherry SR, Farahani K, Slates R, Silverman RW, Meadors K, et al. Development of a PET detector system compatible with MRI/NMRsystems. IEEE Trans Nucl Sci. 1997;44:1167–71.
5 Pichler BJ, Lorenz E, Mirzoyan R, Pimpl W, Roder, Schwaiger M, et al. Performance test of a LSO-APD PET module in a 9.4 Tesla magnet. IEEE Nuclear Science Symposium Conference Record. Vol 2. Piscataway, NJ: IEEE. 1997:1237–1239.
6 Seemann MD. Whole-body PET/MRI: the future in oncological imaging. Technol Cancer Res Treat. 2005;4(5):577–82.
7 Judenhofer MS, Wehrl HF, Newport DF, Catana C, Siegel SB, Becker M, et al. Simultaneous PET-MRI: a new approach for functional and morphological imaging. Nat Med. 2008;14(4):45965.
8 Catana C, Procissi D, Wu Y, Judenhofer MS, Qi J, Pichler BJ, et al. Simultaneous in vivo positron emission tomography and magnetic resonance imaging. Proc Natl Acad Sci U S A. 2008;105(10):3705–10.
9 Wehrl HF, Judenhofer MS, Thielscher A, Martirosian P, Schick F, Pichler BJ. Assessment of MR compatibility of a PET insert developed for simultaneous multiparametric PET/MR imaging on an animal system operating at 7 T. Magn Reson Med. 2011;65(1):269–79.
10 Ridley EL. Siemens to buy CTI for $1 billion. AuntMinnie.com. 2005. https://www.auntminnie.com/clinical-news/molecular-imaging/nuclear-medicine/article/15572274/siemens-to-buy-cti-for-1-billion (accessed Aug 12, 2024).
11 Herzog H. PET/MRI: challenges, solutions and perspectives. Z Med Phys. 2012;22(4):281–98.
12 Newport DF, Siegel SB, Swann BK, Atkins BE, McFarland AR, PressleyDR, et al. QuickSilver: a flexible, extensible, and high-speed architecture for multi-modality. IEEE NSS-MIC conf record. 2006:2333–4.
13 Catana C, Benner T, van der Kouwe A, Byars L, Hamm M, Chonde DB, et al. MRI-assisted PET motion correction for neurologic studies in an integrated MR-PET scanner. J Nucl Med. 2011;52(1):154–161.
14 Chonde DB, Abolmaali N, Arabasz G, Guimaraes AR, Catana C. Effect of MRI acoustic noise on cerebral fludeoxyglucose uptake in simultaneous MR-PET imaging. Invest Radiol. 2013;48(5):302–312.
15 Stegger L, Martirosian P, Schwenzer N, Bisdas S, Kolb A, Pfannenberg C, et al. Simultaneous PET/MR imaging of the brain: feasibility of cerebral blood flow measurements with FAIR-TrueFISP arterial spin labeling MRI. Acta Radiol. 2012;53(9):1066–72.
16 Kolb A, Wehrl HF, Hofmann M, Judenhofer MS, Eriksson L, Ladebeck R, et al. Technical performance evaluation of a human brain PET/MRI system. Eur Radiol. 2012;22(8):1776–88.
17 Boss A, Bisdas S, Kolb A, Hofmann M, Ernemann U, Claussen CD, et al. Hybrid PET/MRI of intracranial masses: initial experiences and comparison to PET/CT. J Nucl Med. 2010;51(8):1198–205.
18 Gatidis S, Bender B, Reimold M, Schäfer JF. PET/MRI in children. Eur J Radiol. 2017;94:A64–A70.
19 Kwatra NS, Lim R, Gee MS, States LJ, Vossough A, Lee EY. PET/MR Imaging: Current Updates on Pediatric Applications. Magn Reson Imaging Clin N Am. 2019;27(2):387–407.
20 Amorim BJ, Hong TS, Blaszkowsky LS, Ferrone CR, Berger DL, Bordeianou LG, et al. Clinical impact of PET/MR in treated colorectal cancer patients. Eur J Nucl Med Mol Imaging. 2019;46(11):2260–2269.
21 Musafargani S, Ghosh KK, Mishra S, Mahalakshmi P, Padmanabhan P, Gulyás B. PET/MRI: a frontier in era of complementary hybrid imaging. Eur J Hybrid Imaging. 2018;2(1):12.
22 Singnurkar A, Poon R, Metser U. Head-to-Head Comparison of the Diagnostic Performance of FDG PET/CT and FDG PET/MRI in Patients With Cancer: A Systematic Review and Meta-Analysis. AJR Am J Roentgenol. 2024;223(3):e2431519.
23 Umutlu L, Beyer T, Grueneisen JS, Rischpler C, Quick HH, Veit-Haibach P, et al. Whole-Body [18F]-FDG-PET/MRI for Oncology: A Consensus Recommendation. Rofo. 2019;191(4):289–297.



From left to right: Marc Lauterbach, Silvia Dias Almeida, Hans Wehrl, Holger Schmidt, Manuel Schneider. Not in the picture are Matthias Schmand, James Corbeil, David Faul, and Matthias Fenchel

Contact

Holger Schmidt, Ph.D.
Solution Owner PET/MR
SHS DI MR AS
Allee am Roethelheimpark 2
91052 Erlangen
Germany
holgerschmidt@siemens-healthineers.com

Evaluating Intraoperative Magnetic Resonance Imaging (ioMRI) Approaches in Neurosurgery: A Literature Review about Applications, Benefits, and Cost-Effectiveness

Victor Gabriel El-Hajj[1]; Victor E. Staartjes[1]; Magnus Kaijser[2]; Erik Edström[1]; Adrian Elmi-Terander[1]

[1]Department of Clinical Neuroscience, Karolinska Institutet, Stockholm, Sweden
[2]Department of Neuroradiology, Karolinska University Hospital, Stockholm, Sweden

Introduction

Since its introduction in the 1970s [1–3] magnetic resonance imaging (MRI) has become a cornerstone of medical imaging. In neurosurgery, the integration of MRI has revolutionized both preoperative planning and post-operative evaluation, enhancing treatment precision and decision-making guidance. This is particularly relevant in fields that strongly rely on high levels of precision and where operative accuracy directly translates into improved patient outcomes. These fields include neurosurgical oncology and functional neurosurgery [4].

Among the groundbreaking advancements in neuro-surgical technology of recent decades [5], intraoperative magnetic resonance imaging (ioMRI) has emerged as a transformative tool [6]. By integrating high-resolution imaging into the operating room (OR), ioMRI enables neurosurgeons to visualize critical anatomical structures and assess surgical progress in real time. While ioMRI has traditionally been achieved through a dedicated OR with ioMRI capability, emerging evidence suggests that using an external MRI machine outside the OR, in the radiology department for the same purpose, can serve as a viable alternative [7].

This review examines the applications, benefits, and cost-effectiveness of ioMRI in neurosurgery. It also explores the workflow associated with the use of ioMRI through either a dedicated ioMRI suite or an external, remote MRI suite.

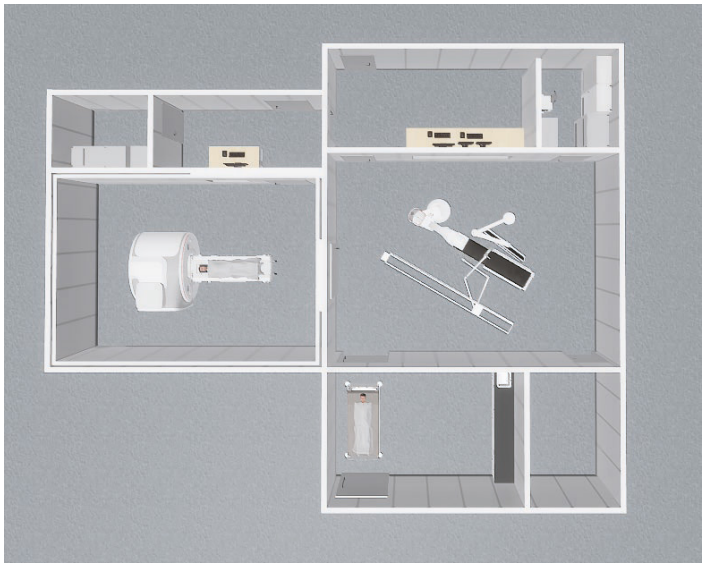

1 Setup for a twin-room OR concept. A conventional OR supplemented by a high-field MRI scanner in an adjacent room.

These images do not necessarily show realistic setups but are intended only to illustrate the concepts.

Results

Intraoperative MRI in neurosurgical applications and outcomes

Neurosurgical oncology

The most established application of ioMRI in neurosurgery is in the field of glioma surgery, where its role in enhancing the extent of safe resection is supported by solid evidence. During the past decade, three randomized controlled trials have studied the use of ioMRI for glioma surgery [8–10]. One meta-analysis pooling the results of these three studies found that ioMRI-guided surgery improved extent of resection (EOR), indirectly enhancing progression-free survival, in high-grade gliomas specifically [11]. Despite more extensive resection, there was no significant increase in postoperative neurological deficits. However, ioMRI did not significantly improve overall survival in glioblastoma. Although ioMRI extended surgery duration, it was not associated with an increase in postoperative complications.

These findings corroborate the results from several observational studies. In a study by Shah et al. [12] on 640 patients with glioblastoma, of whom 332 underwent surgery with ioMRI, the authors found that ioMRI significantly increased the EOR and gross total resection (GTR) rates, without affecting overall survival. Similarly, in a network meta-analysis of 11 studies comparing conventional neuronavigation to ioMRI, as well as to 5-aminolevulinic acid (5-ALA) guidance for high-grade glioma surgery, the authors concluded that ioMRI and 5-ALA were both superior to conventional neuronavigation for achieving GTR [13]. However, there were no significant differences in terms of EOR, when comparing ioMRI and 5-ALA.

Surgical treatment of other neurosurgical tumor subtypes has also benefited from the emergence of ioMRI within the field. They include pituitary tumors, meningiomas, and chordomas.

In transsphenoidal pituitary surgery, ioMRI provides real-time imaging that can assist in detecting residual tumor tissue and identifying suboptimal decompression of surrounding neurovascular structures. In addition, ioMRI can help identify hemorrhagic complications requiring immediate attention [14]. One study that included 27 patients undergoing transsphenoidal endoscopic resection of pituitary macroadenoma found the use of ioMRI to be associated with an increase in GTR rates from 60% to 80%.

In the context of meningiomas or skull base chordomas, where EOR is established as an independent predictor of outcomes [15–17], there has been evidence supporting the use of ioMRI. For meningiomas, the authors of a study of 70 meningioma resection surgeries guided by ioMRI found that up to 16% of patients had their surgery positively affected by intraoperative imaging either improving the resection or avoiding unnecessary additional dissection, which could potentially harm critical neurological structures [18]. Another study addressing the use of ioMRI for meningioma resection concluded that the use of real-time ioMRI aided in deciding on further tumor resection, as well as in evaluating the residual tumor volume at the end of the surgery and in assessing the need for further adjuvant radiotherapy [19].

Similarly, in one study on 11 patients with skull base chordomas and chondrosarcomas, the authors found ioMRI guidance to increase EOR from 93% to 98% on average [20]. In another study on 15 patients with skull base chordomas, ioMRI warranted further resection of margins in seven of the cases (47%), highlighting the role of real-time ioMRI in guiding surgical resection [21]. Both studies led to the conclusions that ioMRI is both safe and effective for intraoperative assessment of EOR and the presence of residual tumor when resecting skull base chordomas and chondrosarcomas. Furthermore, ioMRI proves valuable even when GTR is not feasible, as it facilitates surgical guidance toward achieving maximal safe resection.

Neurovascular surgery

Although ioMRI has been primarily established in the field of neurosurgical oncology, its benefits have also extended to other neurosurgical subspecialties [22]. In the field of neurovascular surgery, the resection of cavernous angiomas and arteriovenous malformations was one of the earliest procedures to be performed with ioMRI guidance, given the underlying similarities with tumor surgery. In these cases, ioMRI serves as both a navigation tool and a means to evaluate EOR in real-time during the procedure [23].

In addition, magnetic resonance angiography (MRA) during aneurysm clipping has enabled the visualization of aneurysm occlusion and parent vessel patency [24], while blood oxygenation level-dependent (BOLD) ioMRI allows for the assessment of brain hemodynamic changes following intracranial-extracranial bypass surgery [25]. Furthermore, ioMRI has been introduced in neurointerventional procedures, with Yan et al. describing the use of intraoperative MRA to assess residual aneurysm status after elective coiling. In that study, the authors deemed the quality of the ioMRI to be adequate to evaluate potential aneurysmal residues. In fact, no residual aneurysms on the angiogram were missed on the ioMRI. This has significant implications for efforts to reduce intraoperative radiation exposure [26].

Functional neurosurgery

The use of ioMRI has also made its way into the field of functional neurosurgery [27, 28]. Its role in improving the accuracy of electrode placement and in verifying final electrode position during deep brain stimulation (DBS) surgery has been extensively studied. In a cohort of 650 patients [29], the authors demonstrated a high level of accuracy,

precision, and safety associated with the use of ioMRI. Another study demonstrated that ioMRI could detect brain shifts, allowing for real-time adjustments during electrode implantation [30]. In addition, ioMRI has been reported to assist in detecting complications such as intraparenchymal hemorrhage and ventricular penetration during electrode placement [30]. A study comparing ioMRI-guided electrode placement with microelectrode-guided placement found that ioMRI was associated with superior clinical outcomes, while both techniques demonstrated a comparable safety profile [31]. This has also been highlighted in a study by Larson et al., which demonstrated submillimeter accuracy of ioMRI-guided electrode placement [27]. Intraoperative MRI has also been used to guide open epilepsy surgery. In fact, a systematic review on the topic found ioMRI guidance to be associated with significantly higher rates of GTR and seizure freedom, and with lower rates of postoperative neurological deficit and reoperations [32].

Spinal neurosurgery

Within the field of spinal surgery, ioMRI has yet to see the same kind of widespread adoption as it has in the other neurosurgical subspecialties. In spinal surgery, ioMRI has been primarily adopted to reduce intraoperative radiation exposure, typically associated with the use of fluoroscopy. For instance, Choi et al. described the use of ioMRI guidance during percutaneous transforaminal endoscopic lumbar discectomy [33], demonstrating feasibility and high precision regarding both the entry point and evaluation of the level of decompression. Similarly, Woodard et al. used ioMRI to confirm achievement of adequate decompression of the spinal cord [34].

Intraoperative MRI setup and workflow

There are three approaches to implementing ioMRI: in a dedicated OR equipped with MRI capabilities; using a portable MRI device in a conventional OR; or transporting the patient to an external MRI facility during surgery [7, 35].

Dedicated hybrid OR with MRI capability

An OR equipped with built-in MRI capabilities is typically designed and constructed specifically for this purpose from the outset [6]. This process involves the construction of an operating suite large enough to accommodate the MRI machine and capable of supporting its full use. This construction would therefore be reminiscent of an MRI suite (Fig. 2).

Another way of acquiring an OR with built-in MRI capability is by adapting an existing conventional OR [36]. While this process may be more suitable to most institutions, it remains costly and renders the operating room unusable for several months during the modification [36, 37]. Integrating an MRI machine into an OR requires consideration of several things, including adequate space management, safety requirements for patients and staff, and dedicated mechanical and electrical installations [36, 38]. In addition, the design and engineering of the room's ceiling, floor, walls, and doors must incorporate both magnetic and acoustic shielding. This is essential to prevent external electromagnetic interference and to minimize noise levels generated by the MRI machine [38].

Whether newly constructed or adapted from a conventional OR, the hybrid OR with MRI presents key challenges,

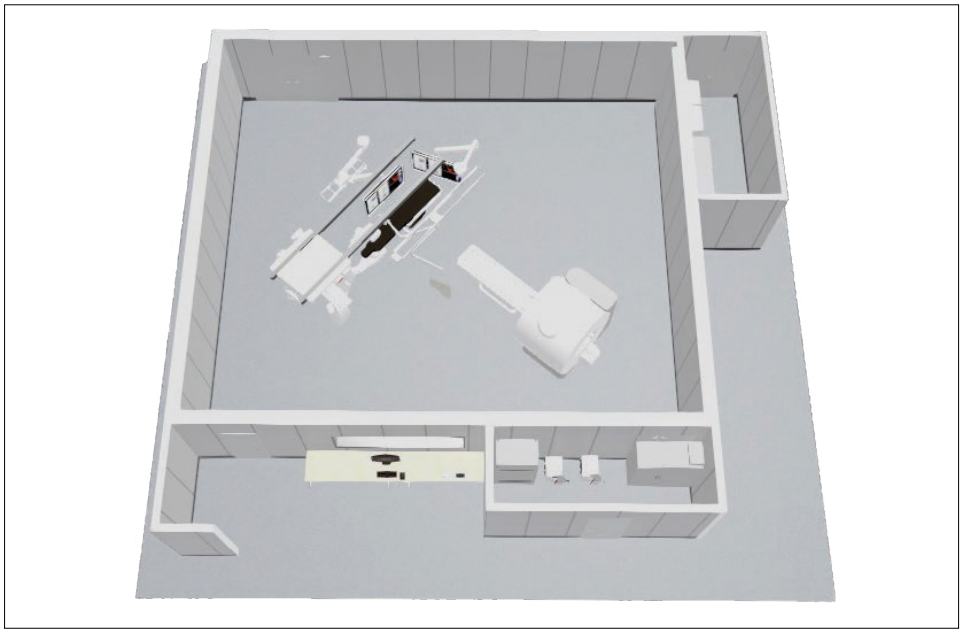

2 Single-room setup, a dedicated hybrid OR with MRI capability.

particularly for integrating MRI-compatible instrumentation within the OR. This applies not only to surgical instruments but also to instruments used by the anesthesia staff [39]. In fact, several studies have highlighted the unique anesthetic challenges related to anesthesia care and patient monitoring in the context of a hybrid OR with MRI [40]. Moreover, the constant high-level electromagnetic field emitted by the stationary MRI machine has the potential to interfere with other electronic equipment in the OR, which will need to be adapted or protected accordingly.

The development of MRI-compatible surgical equipment and tools, such as nonferromagnetic instruments, and MRI-compatible navigation devices and microscopes, is hence necessary.

Nonetheless, physical access constraints and the limited availability of MRI-compatible instruments restrict the range of surgical procedures that can be performed with the patient inside the scanner throughout the operation. A natural solution to this issue is therefore to conduct the surgery outside the scanner and either move the MRI scanner to the patient or use an operating table designed to move the patient into the scanner as needed [37, 41]. This approach has led to the development of innovative solutions, such as floor- or ceiling-mounted MRI systems that can be moved along rails to the operating table for imaging during surgical procedures [42–44].

Finally, it is worth noting that the use of high-field MRI systems intraoperatively necessitates the presence of highly trained personnel to ensure safe and adequate operation of the machine.

Conventional OR with the use of a portable MRI device

Conventional ORs equipped with portable MRI devices are a distinct approach to intraoperative imaging compared to hybrid ORs with stationary MRI machines. Portable MRI systems operate at significantly lower magnetic field strengths, typically ranging from 0.064T to below 0.5T [38, 45, 46]. While this results in inferior image quality compared to high-field stationary systems, it also reduces safety constraints and the need for extensive infrastructure, making them a practical choice in many clinical settings.

The reduced magnetic field strength of portable MRI devices minimizes the risks associated with non-MRI-compatible objects and the interference with other equipment. This inherent safety advantage allows them to be used in conventional ORs without the need for extensive modifications [46]. Portable systems are less obtrusive and can be brought into the OR when imaging is required and removed when no longer needed, preserving the versatility of the operating space.

Despite the limitations in image resolution due to the lower signal-to-noise ratio of low-field systems, portable MRI devices have proven effective, with their use being validated on a wide range of neurosurgical procedures [47–49].

Portable MRI devices also simplify the logistical and financial challenges associated with integrating advanced imaging into surgical workflows. Unlike stationary systems, they do not require the construction of dedicated MRI suites or the installation of advanced safety measures, significantly lowering the cost and complexity of implementation. This flexibility makes them particularly valuable

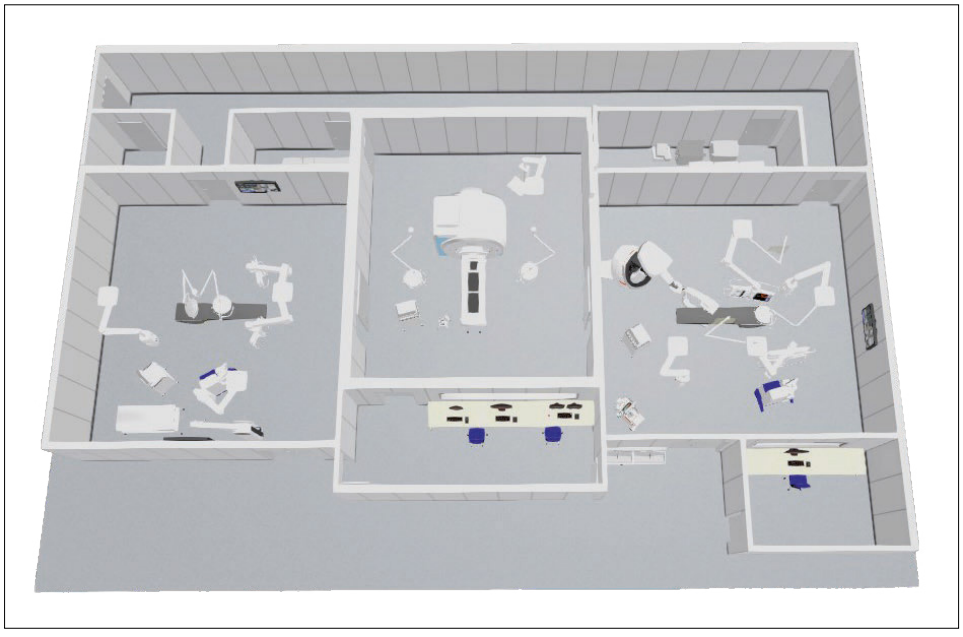

3 Three-room setup, where two ORs share the MRI.

These images do not necessarily show realistic setups but are intended only to illustrate the concepts.

in resource-constrained settings or hospitals seeking to expand their imaging capabilities without disrupting existing infrastructure. However, the operation of these devices typically requires trained personnel, an important factor that must be considered.

As technology advances, portable MRI systems are poised to become increasing clinically useful. Improvements in hardware and software continue to narrow the gap in image quality between portable and stationary systems, potentially broadening their scope of applications. For now, portable MRI devices remain a compelling option for conventional ORs, balancing the trade-off between image quality and practicality while enabling intraoperative imaging in a safe and flexible manner.

Conventional OR with intraoperative transport of the patient to an external MRI facility

The third option avoids disruptions to the existing OR infrastructure while still providing high-quality intraoperative imaging. It simply consists of transferring the patient to the external MRI facility at the radiology department or the hospital's MRI center during the surgery, when imaging is needed. While this approach requires the external MRI facility to be located reasonably close to the operating unit to ensure feasible patient transportation, in one study the total walking distance between the OR and MRI facility was reported to be approximately 140 meters and included an elevator ride of three floors [50]. Despite that, this option remains the most cost-efficient of all three, as it eliminates the need for any additional purchases or modifications to the OR infrastructure. This makes it a practical and accessible option for institutions in resource-limited settings that want to incorporate an ioMRI workflow. One study addressing the cost-effectiveness of this approach found that the costs of performing ioMRI in the OR compared to the external MRI facility may be up to 29 times higher and may demand more than three times as much time from radiology personnel per exam [51].

This approach typically involves temporarily pausing the surgery to transport the patient to the MRI facility, ensuring strict adherence to infection control protocols and that all essential monitoring and support equipment accompany the patient during the transit. A detailed workflow protocol for ioMRI using an external MRI facility has been described in a few studies [35, 50, 51] and includes the following:

1) **Initial surgical procedure**
   The surgery begins with the standard routine at the center. The patient's head is fixed in a Mayfield clamp, and neuronavigation is employed to guide the surgery. After craniotomy, the tumor resection is performed under a surgical microscope, with intraoperative neurophysiological monitoring such as transcranial and subcortical motor-evoked potentials (MEP) used in certain cases.
2) **Preparation for ioMRI**
   When the attending surgeon determines that the tumor removal is complete, the ioMRI procedure begins. Temporary wound closure is performed, with the dura sealed using sutures, and the craniectomy covered with hemostatic sponges. The skin is closed with a running suture, and the Mayfield clamp is removed. Sterile dressing is applied to the wound.

   The OR is then prepared for patient transfer. All equipment attached to the OR table is positioned on one side to facilitate movement. Instruments, including monopolar and bipolar cautery devices, drills, and cables, are covered to maintain their sterility for the second phase of surgery. The patient, under general anesthesia, is transferred to a hospital bed for transportation to the MRI facility.
3) **MR imaging**
   The patient is then transferred from the OR to an external MRI facility, where imaging is performed using the same scanners employed in the routine clinical workflow of the radiology department. This approach allows for comprehensive scans, encompassing all image contrasts typically used in the preoperative evaluation. The protocol includes various MR contrasts such as T1, T2, DWI, ADC, T2*, and T2 FLAIR sequences, with gadolinium contrast administered as needed. The radiology department coordinates the schedule to accommodate ioMRI patients efficiently without significantly disrupting regular imaging workflows. During imaging, consultant neuroradiologists and the attending neurosurgeon analyze the scans onsite. If resectable tumor remnants are identified, a new neuronavigation plan is promptly created in collaboration with the neuroradiologists.
4) **Return to the OR**
   After imaging, the patient is returned to the OR. For patients with no detectable tumor remnants, the wound is reopened, irrigated, and hemostasis is confirmed. Permanent closure of the dura, fixation of the bone flap, and closure of soft tissues and skin are then performed.

   For patients with resectable tumor remnants, the head is refixed in the Mayfield clamp using sterile pins, and neuronavigation is updated with the new imaging data. Additional tumor resection is performed, with all newly resected tissue sent for histopathological analysis. The wound is then permanently closed following the same protocol.

This protocol allows for the integration of ioMRI into neurosurgical workflows, balancing the need for high-quality imaging with operational efficiency and patient safety. However, it has notable limitations, including the inability to provide real-time or continuous imaging during surgery, as well as constraints on repeated imaging due to the logistical challenges and time required for patient transport to and from the MRI facility. Moreover, a significant limitation of this approach lies in the considerably prolonged operative and anesthesia durations. While this limitation is not unique to this technique, it may be more pronounced compared to other ioMRI approaches. Nonetheless, one study describing this ioMRI approach for glial tumor resection reported operative delays of approximately 68 minutes [50]. In comparison, studies using ioMRI in a dedicated OR have documented operative time extensions ranging from 72 to 120 minutes [9, 52–54]. These findings suggest that this approach may not necessarily result in longer delays compared to other ioMRI techniques. Other noteworthy challenges associated with this technique primarily involve those faced by the neuroanesthesia team, including ensuring stable hemodynamics during the transfer process, and maintaining adequate anesthetic depth and ventilation throughout the patient's transition to and from the MRI suite. Additional challenges pertain to ensuring the MRI compatibility of equipment. Staff training is a crucial consideration, particularly given the inherent learning curve associated with implementing this ioMRI workflow. Notably, a study involving 53 patients undergoing various neurosurgical procedures with external ioMRI demonstrated a significant reduction in transfer times when comparing the first and second halves of their cohort [35]. This finding underscores the importance of experience and structured training in optimizing workflow efficiency and reducing procedural delays.

Twin-room OR setup with intraoperative short-distance transfer

Similar to the remote MRI facility concept described above, so-called "twin-room" concepts have been described and successfully applied [55, 56]. As illustrated in Figure 1, a twin-room concept consists of an ordinary operating room with the addition of a separate room containing the MRI scanner, with a magnetically shielded door in between. While similar to the remote MRI concept, this particular setup has several advantages: First, the patient transport is drastically reduced to only a few meters, which minimizes some of the potential risks inherent to any transport of intubated patients [57]. Second, the transfer can occur directly from the operating table onto the MRI scanning bed, avoiding the need for a second bed-to-bed transfer. Third, the MRI scanner in a twin-room concept can – whenever intraoperative imaging is not currently being used – still be run continuously by the neuroradiology department, barring the logistical and coordinative challenges of scheduling outpatient versus intraoperative scanning slots efficiently. Fourth, the magnetically shielded door enables the use of the connected OR as a conventional OR at all other times, with no requirement to regularly use nonferromagnetic equipment, as would be the case in single-room concepts, for instance.

Conclusion

In conclusion, integrating ioMRI into neurosurgical workflows is a transformative advancement in achieving precise and safe surgical outcomes. Each approach to ioMRI – whether through hybrid ORs, portable MRI systems, or patient transport to external MRI facilities – offers unique benefits and challenges. Among these, the external MRI facility approach stands out as a particularly cost-efficient and accessible option. Despite its logistical complexities, including the need for meticulous planning and coordination, this method provides access to high-quality imaging without necessitating significant modifications to existing infrastructure. Moreover, with structured training and experience, workflow efficiency and safety can be substantially improved, making this approach increasingly viable. As technology and procedural protocols continue to evolve, ioMRI, in all its forms, will solidify its role as a cornerstone of modern neurosurgical practice, enhancing precision and ultimately leading to improved patient outcomes.

References

1 Geva T. Magnetic resonance imaging: historical perspective. J Cardiovasc Magn Reson. 2006;8(4):573–80.
2 Viard A, Eustache F, Segobin S. History of Magnetic Resonance Imaging: A Trip Down Memory Lane. Neuroscience. 2021;474:3–13.
3 Ai T, Morelli JN, Hu X, Hao D, Goerner FL, Ager B, et al. A historical overview of magnetic resonance imaging, focusing on technological innovations. Invest Radiol. 2012;47(12):725–41.
4 Filler A. The history, development and impact of computed imaging in neurological diagnosis and neurosurgery: CT, MRI, and DTI. Nature Precedings. 2009:1–11.
5 Gharios M, El-Hajj VG, Frisk H, Ohlsson M, Omar A, Edström E, et al. The use of hybrid operating rooms in neurosurgery, advantages, disadvantages, and future perspectives: a systematic review. Acta Neurochir (Wien). 2023;165(9):2343–2358.
6 Black PM, Moriarty T, Alexander E 3rd, Stieg P, Woodard EJ, Gleason PL, et al. Development and implementation of intraoperative magnetic resonance imaging and its neurosurgical applications. Neurosurgery. 1997;41(4):831–42; discussion 842–5.

7 Mislow JMK, Golby AJ, Black PM. Origins of intraoperative MRI. Neurosurg Clin N Am. 2009;20(2):137–46.
8 Senft C, Bink A, Franz K, Vatter H, Gasser T, Seifert V. Intraoperative MRI guidance and extent of resection in glioma surgery: a randomised, controlled trial. Lancet Oncol. 2011;12(11):997–1003.
9 Kubben PL, Scholtes F, Schijns OE, Ter Laak-Poort MP, Teernstra OP, Kessels AG, et al. Intraoperative magnetic resonance imaging versus standard neuronavigation for the neurosurgical treatment of glioblastoma: A randomized controlled trial. Surg Neurol Int. 2014;5:70.
10 Li Z, Song Y, Farrukh Hameed NU, Yuan S, Wu S, Gong X, et al. Effect of high-field iMRI guided resection in cerebral glioma surgery: A randomized clinical trial. Eur J Cancer. 2024;199:113528.
11 Wach J, Vychopen M, Basaran AE, Güresir A, Seidel C, Kühnapfel A, et al. Efficacy and safety of intraoperative MRI in glioma surgery: a systematic review and meta-analysis of prospective randomized controlled trials. J Neurosurg. 2024:1–12. Online ahead of print.
12 Shah AS, Sylvester PT, Yahanda AT, Vellimana AK, Dunn GP, Evans J, et al. Intraoperative MRI for newly diagnosed supratentorial glioblastoma: a multicenter-registry comparative study to conventional surgery. J Neurosurg. 2020;135(2): 505–514.
13 Golub D, Hyde J, Dogra S, Nicholson J, Kirkwood KA, Gohel P, et al. Intraoperative MRI versus 5-ALA in high-grade glioma resection: a network meta-analysis. J Neurosurg. 2020;134(2):484–498.
14 Stanton M, Antony J, Withers T. Intraoperative MRI in trans-sphenoidal surgery using frameless stereotaxis. Surg Neurol Int. 2021;12:179.
15 Ghaith AK, Nguyen R, El-Hajj VG, Montaser A, De Biase G, Ravindran K, et al. Proton versus photon adjuvant radiotherapy: a multicenter comparative evaluation of recurrence following spinal chordoma resection. Neurosurg Focus. 2024;56(5):E9.
16 Lemée JM, Corniola MV, Da Broi M, Joswig H, Scheie D, Schaller K, et al. Extent of resection in meningioma: Predictive factors and clinical implications. Sci Rep. 2019;9(1):5944.
17 Aizer AA, Bi WL, Kandola MS, ee EQ, Nayak L, Rinne ML, et al. Extent of resection and overall survival for patients with atypical and malignant meningioma. Cancer. 2015;121(24):4376-81.
18 Chakraborty S, Zavarella S, Salas S, Schulder M. Intraoperative MRI for resection of intracranial meningiomas. J Exp Ther Oncol. 2017;12(2):157–162.
19 Tuleasca C, Aboukais R, Vannod-Michel Q, Leclerc X, Reyns N, Lejeune JP. Intraoperative MRI for the microsurgical resection of meningiomas close to eloquent areas or dural sinuses: patient series. J Neurosurg Case Lessons. 2021;1(8):CASE20149.
20 Essayed WI, Juvekar P, Bernstock JD, Rassi MS, Almefty K, Zamani AA, et al. Multimodal intraoperative image-driven surgery for skull base chordomas and chondrosarcomas. Cancers (Basel). 2022;14(4):966.
21 Metwali H, Samii A, Gerganov V, Giordano M, Fahlbusch R, Samii M. The Significance of Intraoperative Magnetic Resonance Imaging in Resection of Skull Base Chordomas. World Neurosurg. 2019;128:e185–e194.
22 Tuleasca C, Aboukais R, Vannod-Michel Q, Lejeune JP. Microsurgical resection under intraoperative MRI guidance and diffusion tractography for a cavernous malformation of the primary motor cortex. Acta Neurol Belg. 2023;123(4):1591–1595.
23 Goren O, Monteith SJ, Hadani M, Bakon M, Harnof S. Modern intraoperative imaging modalities for the vascular neurosurgeon treating intracerebral hemorrhage. Neurosurg Focus. 2013;34(5):E2.
24 Sutherland GR, Kaibara T, Wallace C, Tomanek B, Richter M. Intraoperative assessment of aneurysm clipping using magnetic resonance angiography and diffusion-weighted imaging: technical case report. Neurosurgery. 2002;50(4):893–7; discussion 897–8.
25 Muscas G, Bas van Niftrik CH, Fierstra J, Piccirelli M, Sebök M, Burkhardt JK, et al. Feasibility and safety of intraoperative BOLD functional MRI cerebrovascular reactivity to evaluate extracranial-to-intracranial bypass efficacy. Neurosurg Focus. 2019;46(2):E7.
26 Yan Y, Kaderali Z, Chowdhury T, Shankar J. Feasibility of intraoperative MRI for endovascular coiling of intracranial aneurysms: A single centre experience. Interv Neuroradiol. 2023;29(5):520–524.
27 Larson PS, Starr PA, Bates G, Tansey L, Richardson RM, Martin AJ. An optimized system for interventional magnetic resonance imaging-guided stereotactic surgery: preliminary evaluation of targeting accuracy. Neurosurgery. 2012;70(1 Suppl Operative):95–103; discussion 103.
28 Roessler K, Hofmann A, Sommer B, Grummich P, Coras R, Kasper BS, et al. Resective surgery for medically refractory epilepsy using intraoperative MRI and functional neuronavigation: the Erlangen experience of 415 patients. Neurosurg Focus. 2016;40(3):E15.
29 Rajabian A, Vinke S, Candelario-Mckeown J, Milabo C, Salazar M, Nizam AK, et al. Accuracy, precision, and safety of stereotactic, frame-based, intraoperative MRI-guided and MRI-verified deep brain stimulation in 650 consecutive procedures. J Neurosurg. 2022;138(6):1702–1711. Print 2023 Jun 1.
30 Cui Z, Pan L, Song H, Xu X, Xu B, Yu X, et al. Intraoperative MRI for optimizing electrode placement for deep brain stimulation of the subthalamic nucleus in Parkinson disease. J Neurosurg. 2016;124(1):62–9.
31 Bezchlibnyk YB, Sharma VD, Naik KB, Isbaine F, Gale JT, Cheng J, et al. Clinical outcomes of globus pallidus deep brain stimulation for Parkinson disease: a comparison of intraoperative MRI- and MER-guided lead placement. J Neurosurg. 2020;134(3):1072–1082. Print 2021 Mar 1.
32 Englman C, Malpas CB, Harvey AS, Maixner WJ, Yang JYM. Intraoperative magnetic resonance imaging in epilepsy surgery: A systematic review and meta-analysis. J Clin Neurosci. 2021;91:1–8.
33 Choi G, Modi HN, Prada N, Ahn TJ, Myung SH, Gang MS, et al. Clinical results of XMR-assisted percutaneous transforaminal endoscopic lumbar discectomy. J Orthop Surg Res. 2013;8:14.
34 Woodard EJ, Leon SP, Moriarty TM, Quinones A, Zamani AA, Jolesz FA. Initial experience with intraoperative magnetic resonance imaging in spine surgery. Spine (Phila Pa 1976). 2001;26(4):410–7.
35 Manohar N, Mohapatra D, Balasubramaniam A, Rao K, Srinivas D, Chakrabarti D. Setting up workflow of an intraoperative MRI unit: A single-centre experience of first 53 cases. J Neuroanaesth Crit Care. 2018;5(03):177–183.
36 Mesko NW, Joyce DM, Ilaslan H, Joyce MJ. Creating an Intraoperative MRI Suite for the Musculoskeletal Tumor Center. Clin Orthop Relat Res. 2016;474(6):1516–22.
37 Lang MJ, Kelly JJ, Sutherland GR. A moveable 3-Tesla intraoperative magnetic resonance imaging system. Neurosurgery. 2011;68(1 Suppl Operative):168–79.
38 White MJ, Thornton JS, Hawkes DJ, ill DL, Kitchen N, Mancini L, et al. Design, operation, and safety of single-room interventional MRI suites: practical experience from two centers. J Magn Reson Imaging. 2015;41(1):34–43.
39 Gandhe RU, Bhave CP. Intraoperative magnetic resonance imaging for neurosurgery - An anaesthesiologist's challenge. Indian J Anaesth. 2018;62(6):411–417.
40 Schroeck H, Welch TL, Rovner MS, Johnson HA, Schroeck FR. Anesthetic challenges and outcomes for procedures in the intraoperative magnetic resonance imaging suite: A systematic review. J Clin Anesth. 2019;54:89–101.

41 Abernethy LJ, Avula S, Hughes GM, Wright EJ, Mallucci CL. Intra-operative 3-T MRI for paediatric brain tumours: challenges and perspectives. Pediatr Radiol. 2012;42(2):147–57.
42 Feigl GC, Heckl S, Kullmann M, Filip Z, Decker K, Klein J, et al. Review of first clinical experiences with a 1.5 Tesla ceiling-mounted moveable intraoperative MRI system in Europe. Bosn J Basic Med Sci. 2019;19(1):24–30.
43 Akutsu H, Yamamoto T, Masuda Y, Ishikawa E, Masumoto T, Matsuda M, et al. Movable intraoperative magnetic resonance imaging incorporating a seismic system. Clin Neurol Neurosurg. 2015;135:57–61.
44 Chicoine MR, Lim CCH, Evans JA, Singla A, Zipfel GJ, Rich KM, et al. Implementation and preliminary clinical experience with the use of ceiling mounted mobile high field intraoperative magnetic resonance imaging between two operating rooms. Acta Neurochir Suppl. 2011;109:97–102.
45 Patel KS, Yao Y, Wang R, Carter BS, Chen CC. Intraoperative magnetic resonance imaging assessment of non-functioning pituitary adenomas during transsphenoidal surgery. Pituitary. 2016;19(2):222–31.
46 Altaf A, Baqai MWS, Urooj F, Alam MS, Aziz HF, Mubarak F, et al. Intraoperative use of ultra-low-field, portable magnetic resonance imaging - first report. Surg Neurol Int. 2023;14:212.
47 Altaf A, Shakir M, Malik MJA, Arif A, Islam O, Mubarak F, et al. Intraoperative use of low-field magnetic resonance imaging for brain tumors: A systematic review. Surg Neurol Int. 2023;14:357.
48 Bossert S, Unadkat P, Sheth KN, Sze G, Schulder M. A Novel Portable, Mobile MRI: Comparison with an Established Low-Field Intraoperative MRI System. Asian J Neurosurg. 2023;18(3):492–498.
49 Altaf A, Shakir M, Irshad HA, Atif S, Kumari U, Islam O, et al. Applications, limitations and advancements of ultra-low-field magnetic resonance imaging: A scoping review. Surg Neurol Int. 2024;15:218.
50 Frisk H, Persson O, Fagerlund M, Jensdottir M, El-Hajj VG, Burström G, et al. Intraoperative MRI without an intraoperative MRI suite: a workflow for glial tumor surgery. Acta Neurochir (Wien). 2024;166(1):292.
51 Kaijser M, Frisk H, Persson O, Burström G, Suneson A, El-Hajj VG, et al. Two years of neurosurgical intraoperative MRI in Sweden - evaluation of use and costs. Acta Neurochir (Wien). 2024;166(1):80.
52 Eid H, Crevier-Sorbo G, Moreau JT, Saint-Martin C, Elzawawi MS, Mousa WA, et al. Eight-Year Experience With 3-T Intraoperative MRI Integration in Focal Pediatric Epilepsy Surgery: Impact on Extent of Resection, Residual Volumes, and Seizure Outcomes. AJR Am J Roentgenol. 2020;214(6):1343–1351.
53 Martin XP, Vaz G, Fomekong E, Cosnard G, Raftopoulos C. Intra-operative 3.0 T magnetic resonance imaging using a dual-independent room: long-term evaluation of time-cost, problems, and learning-curve effect. Acta Neurochir Suppl. 2011;109:139–44.
54 Sylvester PT, Evans JA, Zipfel GJ, Chole RA, Uppaluri R, Haughey BH, et al. Combined high-field intraoperative magnetic resonance imaging and endoscopy increase extent of resection and progression-free survival for pituitary adenomas. Pituitary. 2015;18(1):72–85.
55 Stienen MN, Fierstra J, Pangalu A, Regli L, Bozinov O. The Zurich checklist for safety in the intraoperative magnetic resonance imaging suite: Technical note. Oper Neurosurg (Hagerstown). 2019;16(6):756–765.
56 Staartjes VE, Serra C, Maldaner N, Muscas G, Tschopp O, Soyka MB, et al. The Zurich Pituitary Score predicts utility of intraoperative high-field magnetic resonance imaging in transsphenoidal pituitary adenoma surgery. Acta Neurochir (Wien). 2019;161(10):2107–2115.
57 Beckmann U, Gillies DM, Berenholtz SM, Wu AW, Pronovost P. Incidents relating to the intra-hospital transfer of critically ill patients. An analysis of the reports submitted to the Australian Incident Monitoring Study in Intensive Care. Intensive Care Med. 2004;30(8):1579–85.

Contact

Adrian Elmi-Terander
Department of Clinical Neuroscience
Karolinska Institutet
K8 Klinisk neurovetenskap
171 77 Stockholm
Sweden
adrian.elmi.terander@ki.se


Adrian Elmi-Terander


Victor Gabriel El-Hajj

Challenges with Operations using Intraoperative MRI: A Practical Perspective for Implementation in the Surgical Workflow

Monika Grimm, Vittorio Stumpo, Carlo Serra, Philipp Bardelli, Christian Möhrlen

Department of Neurosurgery, Clinical Neuroscience Centre, University Hospital Zurich and University of Zurich, Switzerland

Integrating intraoperative magnetic resonance imaging (ioMRI) into a neurosurgical operation requires adaptation of almost the entire workflow. Steps including arrival of the patient in the operating room (OR), anesthesia management, arrangement of staff and instruments in the OR, and preparation of the sterile field must all be rethought to address the logistical challenges introduced by ioMRI. These challenges can vary depending on the ioMRI setup (e.g., single room, dual-use single room, or twin room), and the OR management process must always have patient safety as its guiding principle.

The Department of Neurosurgery at University Hospital Zurich (NCH-USZ) has been using ioMRI for more than 20 years. In 2001, as the first center in Europe and among the first in the world, it introduced ioMRI using the PoleStar 0.25T system (Medtronic, Louisville, CO, USA). It replaced that system in 2013 with the MAGNETOM Combi Suite with 3T ioMRI (Siemens Healthineers, Erlangen, Germany), a choice dictated by several factors, including the desire to achieve better image quality while reducing the logistical impact of ioMRI on the surgical procedure (Fig. 1).

From a structural point of view, the transition required interinstitutional planning and coordination. This began in 2007 with the decision-making and planning phase, and ended in June 2013 with the first surgery. Then we upgraded to the Nexaris MR suite and now, twelve years and over one thousand operations later, we present an article that aims to illustrate the OR staff's experience of integrating intraoperative MRI at 3T into the Department of Neurosurgery at University Hospital Zurich. The article places a strong emphasis on the issues that the team had to resolve, and offers suggestions and solutions for quickly and smoothly integrating ioMRI into clinical surgical routine.

Intraoperative MRI at 3T

Both, the MAGNETOM Combi Suite and Nexaris MR are two-room solutions (Fig. 2) made up of a 3T MRI scanner



1 **Pioneering experiences with ioMRI at University Hospital Zurich**
The Department of Neurosurgery in Zurich introduced the PoleStar 0.25T MRI system as early as 2001. It was the first ioMRI system for conventional operating rooms, and featured an integrated image-guided navigation system.



2 **The MAGNETOM Combi Suite two-room solution**
When this solution was introduced in 2013, it allowed imaging with patient transfer, and 24-hour use with the possibility of additional outpatient examinations.

from Siemens Healthineers, and a surgical Maquet OR Table System (Getinge AB, Gothenburg, Sweden).

The twin-room system in the Department of Neurosurgery is made possible by the physical proximity between the department's operating block and the MR center in the Department of Neuroradiology. In the setup, an OR is separated from an MR room by a system of doors that allows both rooms to be used separately. When ioMRI is necessary, the logistics are coordinated with the Department of Neuroradiology, and the door separating the two rooms is opened. The patient is then transferred intraoperatively to the ioMRI room and then returned to the OR.

Measures before the first planned operation using 3T ioMRI

Over the years, this process has become known as "transfer." Back in 2013, it was a new innovation that had to be introduced into the perioperative surgical workflow. This required numerous interdisciplinary meetings, which had already begun in 2012.

Firstly, the issue of materials needed to be addressed: Everything that would accompany the patient into the ioMRI room had to be MR-compatible. This obviously concerned the patient-specific pre-operative assessment, the operating table used for the transfer, the head clamps, and the anesthesia hardware (Fig. 3).

Anesthesia considerations

Anesthesia-related compatibility issues must be carefully evaluated in terms of both the patient and the OR equipment. During the pre-anesthesia assessment, it is essential to determine whether the patient has any implanted prosthetic or foreign material that could be damaged or excessively heated by the magnetic field. For the same reason, all body jewellery must be removed. Additionally, any allergies or intolerances to contrast agents that may be used must be identified and considered preoperatively. When preparing the patient for anesthesia and surgery with ioMRI, an MR-compatible monitoring system must be used, ensuring it is approved for use in the magnetic-field environment. The specifics of the MRI magnet must be taken into account, and tesla-compatibility checked. The signals from these monitoring systems are typically transmitted via radio waves, and the small transmitters should be positioned as far from the magnet as possible, avoiding direct contact with the patient.

For medication administration, patient access lines should be equipped with sufficiently long extensions.

With respect to contrast agent administration, a line of 18-gauge or larger should be used and should be prepared with check valves to prevent backflow of contrast agent into the line. In the past, infusion pumps were sometimes kept outside the MRI room, with lines threaded through a small opening. However, modern pump holders are now designed as Faraday cages, allowing pumps to be safely stored and transported into the MRI suite without additional risks. Furthermore, an MR-compatible ventilator must be available and approved for use at the given magnetic field strength. It should be positioned as far from the magnet as possible, although the length of the breathing tubes remains a limiting factor. Care must always be taken to ensure that the patient has enough space for breathing tubes during transfer into the MRI scanner, to prevent accidental extubation. Nevertheless, a non-magnetic set of laryngoscopes in various sizes must always be readily available to facilitate emergency intubation in case of airway loss.

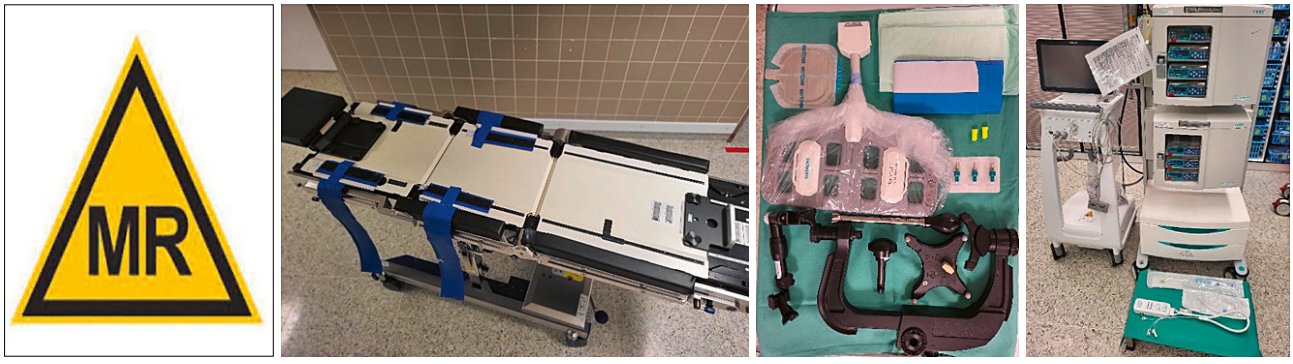

3 **Resolving ioMRI-OR compatibility issues**
To ensure a smooth intraoperative transfer, procedural steps had to be clearly defined, and MR-compatible materials had to be used. An OR table system with transfer plate was therefore employed. Concerning fixation and navigation systems, carbon head clamps, MRI safe skull pins, a carbon navigation system, and flex coils were used. From an anesthesia standpoint, the use of a Faraday cage for perfusors, and an MR-compatible monitoring system and respirator were adopted, avoiding Woodbridge tubes, temperature probes, and bispectral index and neuromuscular transmission monitoring.



4 **Before clinical implementation: Simulation phase with company support** A simulation phase with all necessary staff and with support from the relevant companies took place before the first ioMRI-guided surgery using the MR-compatible equipment discussed above. To simulate the patient's head for testing the MRI acquisition, a melon was placed in the MRI-compatible head clamp, and the images were acquired as normal.

Surgical considerations

Particular attention was paid to the patient-positioning design, as the combination of the characteristics of the surgical table and the MR-compatible head clamps does not allow for sitting or lateral positions. This conceptual design phase led to the preparation of a series of protocols that were then tested and subsequently refined by simulating a transfer to the MR room with all the professionals involved and with the help of the companies that produce the various materials (Fig. 4).

During the simulation phase, particular attention was also paid to simulating emergency situations and the corresponding responses in each peri- and intraoperative phase. The two phases of conceptual design and simulation thus allowed the team to develop collective expertise that is very effective for integrating ioMRI into clinical routine. The phases also identified some aspects that are essential for ensuring that this expertise is not lost and can remain a constant asset for the OR staff over the years, even with inevitable staff turnover. The need for regularly training the whole team was immediately apparent, as was the need to make the process reliably and easily controllable with checklists at the most relevant stages of the operation (from induction of anesthesia to positioning the patient and preparing them for transfer).

Challenges of ioMRI in daily routine

To ensure patient safety, a careful review and testing was carried out for the following: intraoperative transfer workflow, emergency during transfer, maintenance of sterility of the surgical site during transfer, and MR equipment for transfer. The smooth execution of the process involves a high level of specialist expertise and interdisciplinary collaboration between all groups involved, including the neurosurgeons, the neuro-anesthesia team, the OR nursing staff, the neurophysiologist, the specialized radiology technicians, and the neuroradiologists. Attention must also be paid to regular rotation of specialist staff, thus taking into account and ensuring the introduction of new employees and continued workflow training (Fig. 5).



5 Overcoming challenges in ioMRI patient transfer, ensuring patient safety and staff training.

The measures taken at an early stage, well before ioMRI was introduced into clinical routine, allowed all the professionals involved – medical and paramedical – to prepare themselves well for the actual test and to pass the exam of ioMRI in daily routine. It is worth emphasizing again the challenges that must be faced: On the one hand, the patient's safety is potentially endangered by the transfer, so maximum attention must be paid to the MR compatibility of all the material that accompanies the patient into the ioMRI room, and to the maintenance of the sterility of the operating field (with appropriate measures, as we will see shortly). Both phases lend themselves perfectly to being checked in a reliable and simple way by means of special checklists. On the other hand, the OR staff experience additional challenges caused by the introduction of ioMRI into the surgical workflow, which could be a source of errors and inefficiencies and which, in the experience of the Department of Neurosurgery, have been successfully addressed thanks to continuing professional training and a work culture favorable to team building, vertical and horizontal teaching, and constructive confrontation (a "speak-up" culture).

Surgery with ioMRI

We will now address – with abundant photographic documentation – the practical implications of introducing ioMRI into clinical routine. We will emphasize the most important aspects, and those that can lead to practical difficulties if not properly addressed.

Figure 6 shows the positioning of the patient and the immobilization of the head in the clamp. Doro or Noras head clamps are routinely used, depending on the clinical needs of the surgeon. Once the clamp has been secured, it is necessary to make sure that the patient's head, the head clamp, and their body can comfortably enter the MR tube. Since it is obviously not possible to bring the patient into the MRI scanner at this stage for this reason alone, the suppliers have devised a collision indicator in the form of a plastic structure shaped like a closed arch that simulates the dimensions of the MR bore. Once the collision indicator test has been successfully completed, the operating field is prepared by positioning the lower coil and protecting it with an adhesive sheet that is firmly attached to the patient's shoulders. Maximum attention must be paid to positioning, covering, and preparing the patient in such a way as to avoid, with all possible precautions, liquids of



6 Patient positioning and immobilization for ioMRI
Steps include (from top left to bottom right) head clamping, referencing for navigation, checking MRI fit with collision indicator, attaching adhesive cloth to patient's shoulders, positioning the flex coil, and preparing the incision site for disinfection.

any nature (whether surgical wash or bodily fluids) from getting under the sterile field and wetting the patient, as this could cause burns.

Particular attention must also be paid to removing any non-MR-compatible objects from under the sterile field, which must be strictly checked with the help of checklists (Fig. 7).

The surgery can now proceed as normal, taking care to inform the Department of Neuroradiology in advance of the time scheduled for the ioMRI. To allow colleagues sufficient time to adjust their schedules and to prepare the ioMRI system from a hospital-hygiene point of view, we regularly give one hour's notice. When the surgeon decides that it is time to perform the ioMRI to check the extent of resection, the most sensitive phase begins. At the Department of Neurosurgery, this process has been successfully implemented for 12 years, and the relevant steps are presented in Figure 8.

After adequate hemostasis, the surgical cavity is filled with Ringer's irrigation solution to avoid MR artifacts that can occur in the presence of pneumocephalus. The dura mater is then closed and covered first with Gelfoam (Pfizer, New York, NY, USA) and then with MR-compatible gauze so as to prevent dead space formation. This is followed by approximation of the wound margins and a temporary suture. At this point (Fig. 9), the surgical site is sealed with an additional MR-compatible gauze and a transparent airtight adhesive sheet. The same process is performed for the navigator reference. If present, the fluid containment bag, which is in the sterile fields at the Department of Neurosurgery, is cut and removed, as it contains a metal core.

The surgical wound, sealed with transparent adhesive tape, is further covered with two sterile adhesive drapes (Fig. 10), taking care to position more superficially the one that will later be taken out first. At this point, the surgical drapes are cut so that they do not fall below the lower line of the surgical table, and the patient is fully covered with an additional drape. The correctness of this step is verified with a dedicated checklist.

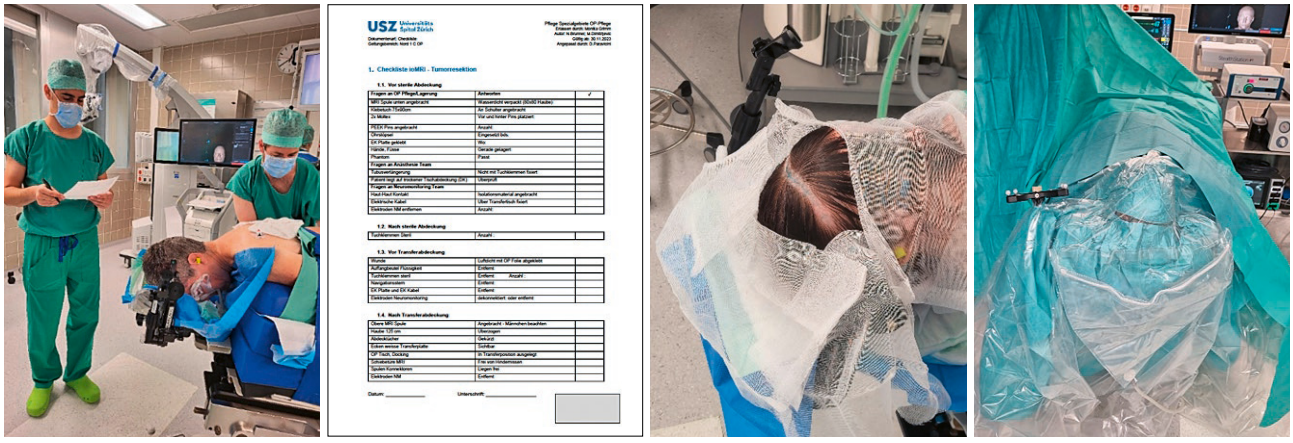

7 MR checklist before surgical draping
Before sterile surgical draping, staff must go through a checklist to ensure the patient's safety and the smooth running of the process. Specific attention must be paid to removing all metallic objects and avoiding moisture to exclude the risk of burns during ioMRI acquisitions. Gauzes without X-ray strips must also be avoided (as these cause artifacts), as must metallic strips.

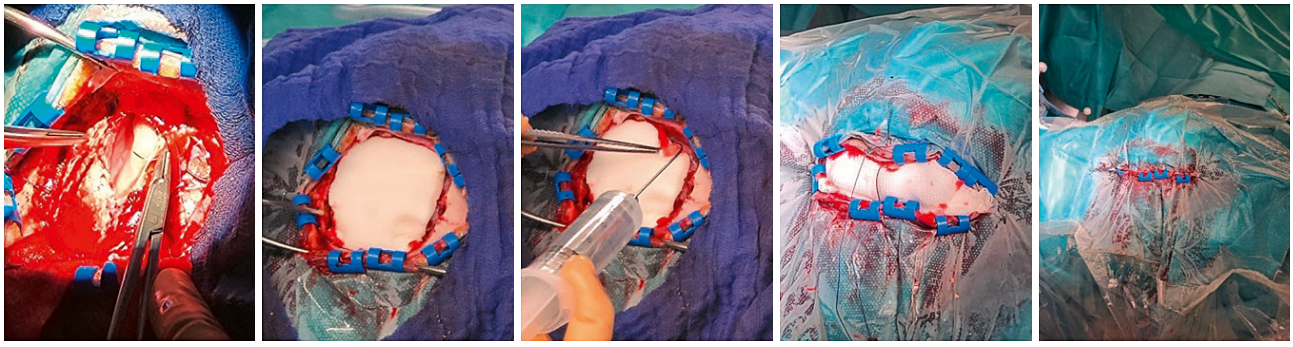

8 Temporary closure
Before initiating the sterile draping for transfer to the ioMRI room, temporary closure is performed. This includes the following steps, as displayed from left to right: temporary dura suture, dura seal with Spongostan (Ferrosan Medical Devices, Søborg, Denmark), filling of the surgical cavity with Ringer's irrigation solution, if necessary additional sealing with a gauze without X-ray strips, and provisional skin closure.

The surgical instruments in the OR are kept sterile, and the preparation for transfer is completed (Fig. 11) by covering the surgical site with an additional sterile plastic cap (in order to keep the sheets in this region compact) and then positioning the upper coil.



9 **Adapting the sterile field to ioMRI needs before sterile draping**
To ensure good image acquisition, before sterile draping, the wound is sealed airtight using gauze without X-ray strips, and OpSite drape (Smith & Nephew Medical Ltd., Hull, UK). The navigation reference star is removed, and the arm on which it is mounted is covered with sterile drape. The fluid bag must be cut and removed if it contains metal.

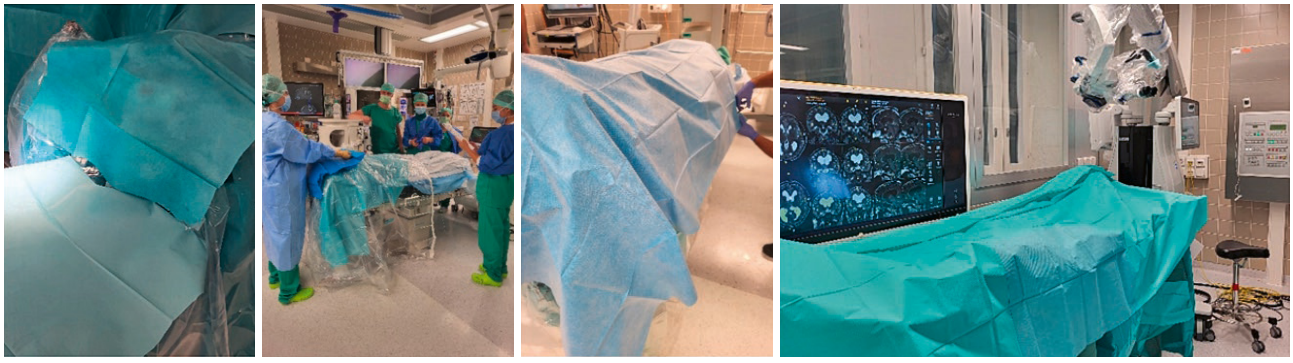

10 **Sterile draping**
After completing the previous steps, sterile draping is done in the following steps, from left to right: coverage of the wound with two additional adhesive drapes, execution of ioMRI checklist, coverage of the entire sterile patient surface with a sterile surgical cover, and coverage of sterile instruments with a sterile surgical cover.

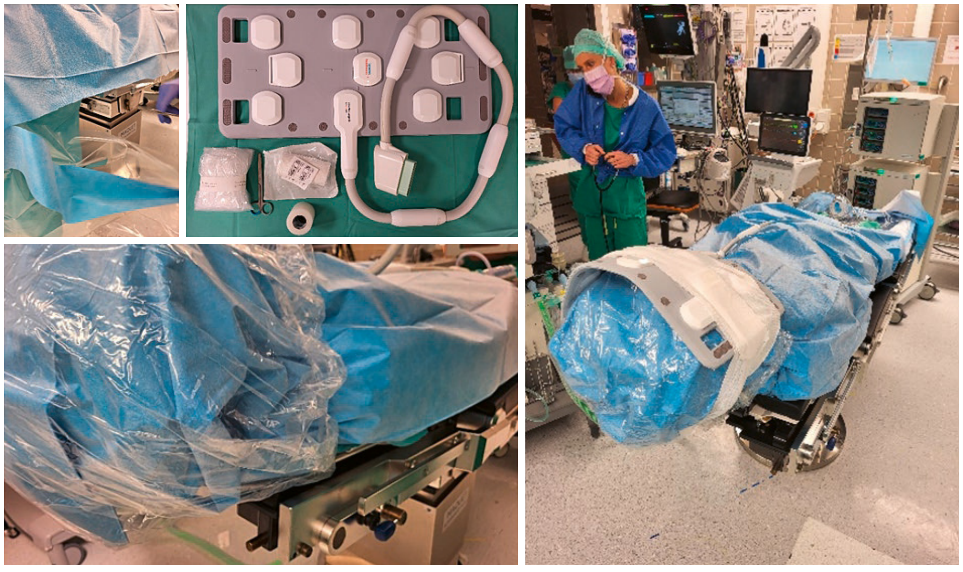

11 **Preparation for transfer after sterile covering**
Before proceeding to transfer, all sterile drapes are shortened to the height of the operating table, and an additional head section with an 80 × 125 hood is positioned on the head of the patient. Lastly, the flex coil with an elastic bandage and adhesive drape is positioned.



12 Transfer execution
After an additional checklist performed by the OR nurse and the neuroanesthesia team, the patient is ready to be transferred for acquisition of the ioMRI images. The steps are detailed in the figure and include door-opening, transfer of the MRI table to the OR, docking to the operating table, patient transfer, patient positioning and preparation of the MRI, and door-closing before image acquisition.



13 Return to the OR after ioMRI, and new preparation of the surgical field
Upon return in the OR, the surgical field is prepared to enable continuation of the surgery: The sterile patient drapes are removed, and to maximize sterility a new drape is applied. At this point, surgery can resume, with removal of the gauze from the surgical wound and reopening the temporary skin closure. Depending on the ioMRI results, additional tumor resection can be performed before assessing hemostasis again and closing the wound permanently.

The final checklist of the OR staff and the checklist of the anesthesia staff collectively serve as a prologue to the actual transfer (Fig. 12).

In the experience of the Department of Neurosurgery, the transfer is carried out by the neuroradiology staff in unison with the OR staff and the neuroanesthesia team. The latter remains inside the MR room for the entire MRI examination, and remains on standby to immediately manage an emergency if it arises. As previously stated, it must always be ensured that the patient's breathing tube is long enough when transferring them to the MRI. Patient movement represents the greatest risk in this regard.

The OR is kept sterile for the entire duration of the ioMRI examination. When the patient is returned to the OR, the operating table is reattached (Fig. 13) and the neuroanesthesia team check the correct position and function of the lines and monitoring. The surgical site is prepared again, removing in strict order and with the utmost attention to sterility the sheet that completely wrapped the patient (it is usually allowed to fall to one side), then the most superficial adhesive sterile sheet, and finally the second adhesive sterile sheet mentioned in Figure 10. At that point, the patient is covered with a new overall sterile drape, with a transparent sterile drape over the surgical site, and the rest of the OR is prepared as usual. The surgical wound can then be reopened under unaltered sterile conditions and the operation can be resumed.



Contact

Monika Grimm
Operating Theater Specialist
Department of Neurosurgery
Clinical Neuroscience Centre
University Hospital and University of Zürich
Rämistrasse 100
CH-8091 Zürich
Switzerland
monika.grimm@usz.ch

Flash Forward: Deep Learning-Enhanced Musculoskeletal MRI at the Speed of Thought

Jan Vosshenrich, M.D.[1,2]; Jan Fritz, M.D.[1]

[1]Department of Radiology, Grossman School of Medicine, New York University, New York, NY, USA
[2]Department of Radiology, University Hospital Basel, Switzerland

Musculoskeletal MRI represents the standard of care for the noninvasive diagnostic work-up and surveillance of a wide range of musculoskeletal conditions, offering unparalleled soft tissue contrast and anatomic detail. Over the past two decades, hardware and sequence design advancements have pushed the boundaries of image quality and diagnostic accuracy. But it is only recently that musculoskeletal MRI has entered a new era. Advanced acceleration techniques and deep learning-based image reconstruction methods have enabled us to trim minutes off lengthy image acquisition times and have redefined what is possible, much like Barry Allen gaining superhuman speed and becoming *The Flash*. Deep learning-enhanced rapid musculoskeletal MRI transforms clinical practice by providing shorter scan times, enhanced patient comfort, and better image quality than would ever be achievable with conventional MRI, while maintaining the diagnostic performance of established comprehensive imaging protocols. By exploring this evolving landscape and showcasing how these innovations can be gainfully applied in clinical practice, we aim to provide practical insights and spark excitement for this thrilling new chapter in musculoskeletal MRI.

Echo train compaction: The speed force of musculoskeletal MRI

In the race toward ultra-fast high-resolution musculoskeletal MRI, even the most advanced acceleration strategies rely on one critical foundation: a finely tuned pulse sequence. Just as *The Flash* channels the *Speed Force* to unlock his full potential, the performance of musculoskeletal MRI hinges on pulse sequence parameter optimization to maximize efficiency even before advanced acceleration techniques come into play. With meticulously designed pulse sequences, seemingly small time savings at the echo train level scale substantially through advanced acceleration techniques. Consider a modest 10-second gain from optimizing an echo train. Combined with a six-fold acceleration method, this can translate into a blazing 60-second reduction in acquisition time. Time savings further multiply with the number of acquired pulse sequences, for example, to five minutes for a five-sequence knee MRI protocol. Therefore, prepping and priming turbo spin-echo (TSE) pulse sequences like a speedster ready to sprint is key to realizing exponential speed gains.

Compact echo trains are crucial to optimizing TSE pulse sequences for peak performance. This involves configuring pulse-sequence parameters to fit the highest number of strong refocusing echoes into the shortest possible time window, minimizing image blur and maximizing signal. The shorter the echo spacing, the more echoes can be captured per unit of time. The three core elements enabling this compression are fast radiofrequency (RF) pulses, high-performance gradients, and high receiver bandwidth. Though not always mentioned in commonly cited pulse-sequence time equations, these factors are the hidden forces that drive image acceleration.

Modern clinical MRI systems allow the user to select fast RF pulses that occupy less time in the echo train, thereby shortening echo spacing and accelerating image acquisition. Though these rapid RF pulses do increase the specific absorption rate (SAR), they are key to unleashing the full potential of TSE pulse sequences. The "Performance" gradient mode lets users access the strongest and fastest gradients to further expedite the completion of an echo train by minimizing temporal gaps between RF pulses. Although strong gradients can occasionally induce peripheral nerve stimulation, this is generally well tolerated during musculoskeletal MRI. Finally, high receiver bandwidth also contributes to shorter echo spacing by minimizing individual echo length. While increased bandwidth may lower the signal-to-noise ratio (SNR), it brings crucial benefits for musculoskeletal imaging, including reduced chemical shift artifacts and sharper anatomical detail. Also, signal losses are limited through earlier sampling of stronger MR signals [1].

Combining fast RF pulses, high-performance gradients, and high receiver bandwidths shrinks echo spacing, shortens repetition times, and lengthens echo trains, thereby setting the stage for multiplicative time gains with advanced acceleration techniques.

Deep learning-enhanced parallel imaging: Shattering the speed limit

Parallel imaging represents the most effective and widely adopted method to accelerate TSE pulse sequences in musculoskeletal MRI. By leveraging the spatial sensitivity profiles of multi-element receiver coils, parallel imaging enables undersampling of phase-encoding data, historically the most time-intensive component of image acquisition. Time savings result from sampling only every second, third, or fourth line in *k*-space for twofold, threefold, or fourfold acceleration, respectively, while keeping the field of view, matrix size, and spatial resolution constant [2]. The relationship between the acceleration factor and acquisition time is direct: Omitting more phase-encoding steps reduces the scan duration proportionally. However, a predictable trade-off in SNR (proportional to the square root of the acceleration factor), as well as *g*-factor-related penalties (arising from coil geometry and spatial encoding limitations), have traditionally prevented the clinical use of acceleration factors higher than two to three for 2D TSE imaging, and four for 3D TSE imaging [2]. Faster acceleration typically introduces inhomogeneous noise amplification and aliasing artifacts, particularly when surpassing the effective number of available receive coil elements in the phase-encoding direction [3]. For example, a knee coil comprised of 18 individual coil elements may have the geometry of three longitudinal coil rings of six coil elements each, usually leading to uncorrectable aliasing artifacts when fourfold acceleration is applied across the three rings.

Recent developments in deep learning (DL)-based image reconstruction methods now allow us to overcome these longstanding limitations. Deep Resolve Boost enhances parallel imaging accelerated TSE pulse sequences and requires fewer sampled raw data to form diagnostic-quality images. Image reconstruction combines a physical MRI model with neural network-based regularization, incorporating *k*-space data and coil sensitivity maps to adaptively address heterogeneous noise patterns and aliasing artifacts while ensuring data consistency. [4]. The resulting ability of DL reconstruction methods to produce images from fourfold parallel imaging accelerated 2D TSE datasets, rivaling or even outperforming conventional image reconstruction from twofold accelerated data, is paradigm-shifting [5]. By mitigating SNR losses and correcting aliasing artifacts, these tools allow for greater acceleration flexibility without compromising diagnostic image quality, thereby redefining the speed and efficiency thresholds of modern musculoskeletal MRI [6]. Deep Resolve Boost for TSE imaging is clinically available at field strengths from 0.55T to 7T and offers unprecedented speed gains in musculoskeletal MRI while preserving image quality.

Deep learning-enhanced simultaneous multislice imaging: Breaking the slice barrier

Simultaneous multislice (SMS) is a key enabler of next-generation ultra-fast musculoskeletal MRI. Combined with parallel imaging and elliptical *k*-space scanning, it substantially amplifies acceleration, laying the foundation for DL-driven MRI at unprecedented speeds [7].

In contrast to traditional sequential slice acquisition patterns of TSE pulse sequences, SMS simultaneously excites and captures MR signals from more than one slice. Like parallel imaging acceleration, SMS relies on deconvolution algorithms such as CAIPIRINHA (Controlled Aliasing in Parallel Imaging Results in Higher Acceleration) to separate mixed MR signals for accurate reconstruction of slice-specific image data using coil sensitivity maps, field-of-view shifts, and gradient encoding [8, 9]. The SMS approach reduces the effective repetition time of a TSE pulse sequence, which can translate into both direct and indirect time savings. Direct benefits include reductions in repetition time, the obviation of concatenations, the ability to lengthen echo trains, and the simultaneous acquisition of in-phase and opposed-phase echoes for Dixon-based imaging. Indirect gains comprise time-neutral increases in slice coverage, reduced interslice gaps and slice thickness, and the incorporation of otherwise time-intensive fat suppression methods like SPAIR.

Perhaps most importantly, SMS synergizes particularly effectively with parallel imaging. While parallel imaging reduces scan time at the cost of both acceleration-factor-proportional and *g*-factor-related SNR losses, SMS introduces only minor *g*-factor-dependent reductions in SNR. However, simultaneously imparted RF pulses to excite more than one slice at a time increase energy deposition and SAR. In peripheral joint MRI, concerns regarding SAR can be mitigated using local transmit coils, optimized RF pulse designs, and moderate flip angles between 125° and 150° [3].

When applied in concert, SMS and parallel imaging yield multiplicative acceleration benefits. For example, combining twofold SMS acquisition with twofold parallel imaging of TSE pulse sequences enables fourfold TSE acceleration. Even without integrating DL reconstruction methods, this has enabled clinical five-minute, five-sequence knee MRI protocols at 1.5T and 3T with unchanged diagnostic performance compared with conventional twofold parallel imaging acceleration since 2020 [10].

In contrast, standalone fourfold parallel imaging in the knee exceeds the capabilities of conventional image reconstruction and leads to substantially degraded images with drastically reduced SNR and increased artifact burden [10].

The current development and future integration of end-to-end DL reconstruction methods for combined SMS-parallel imaging acceleration will further transform

the landscape. Extending DL-enhanced image reconstruction capabilities to simultaneously accelerated datasets, such as SMS2-PAT3, SMS3-PAT3, SMS2-PAT4, SMS3-PAT4, and SMS2-PAT6, may enable total acceleration factors exceeding 10, while preserving or enhancing image quality [11, 12]. The convergence of DL-enhanced SMS-parallel-imaging-accelerated musculoskeletal MRI is a powerful framework to build on. Much like a speedster breaking the dimensional barrier, these technologies allow musculoskeletal MRI to transcend former limits.

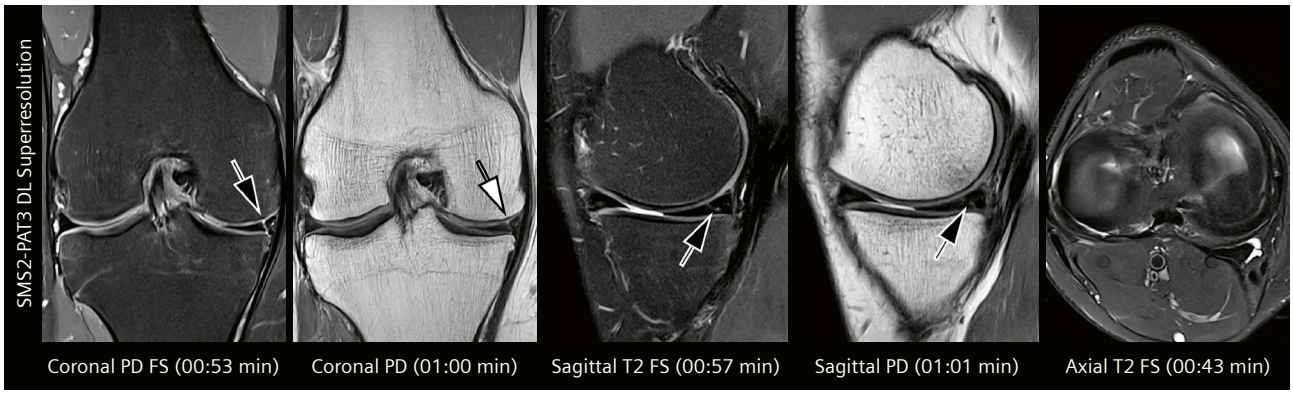

1 3-Tesla knee MRI with echo-train-compacted turbo spin-echo pulse sequences using combined twofold simultaneous multislice and threefold parallel imaging acceleration with deep learning-based image reconstruction and superresolution augmentation. The MR images show a vertical longitudinal medial meniscus tear (arrows).
MR images were obtained with a 3T MAGNETOM Vida MRI system and a 1-transmit-channel-18-receiver-channel knee coil. The MRI protocol is given in Table 1. PD = proton density weighting, PD FS = fat-suppressed proton density weighting, T2 FS = fat-suppressed T2 weighting.

Parameter	Ax T2 FS	Cor PD	Cor PD FS	Sag T2 FS	Sag PD
Gradient performance	high	high	high	high	high
Radiofrequency speed	fast	fast	fast	fast	fast
Repetition/echo time [ms]	3600 / 57	3700 / 24	3700 / 35	3700 / 56	3700 / 24
PI	3	3	3	3	3
SMS / FOV shift	2 / 2	2 / 2	2 / 2	2 / 2	2 / 2
Echo-train length	13	13	13	13	13
Bandwidth [Hz/pixel]	296	354	301	299	354
Echo spacing [ms]	7.1	8.0	7.1	8.0	8.0
FOV [mm]	140 × 140	140 × 140	140 × 140	140 × 140	140 × 140
Matrix	272 × 204	336 × 252	272 × 204	304 × 228	336 × 252
Slice thickness [mm]	3	3	3	3	3
Slices	38	36	36	38	38
Phase direction	right-to-left	head-to-foot	head-to-foot	head-to-foot	head-to-foot
Flip angle [°]	125	125	125	125	125
Acquisition time [mm:ss]	00:43	01:00	00:53	00:57	01:01

Table 1: NYU comprehensive rapid 3T sixfold SMS2-PAT3-accelerated knee MRI protocol.
Ax = axial, Cor = coronal, Sag = sagittal, PD = proton density weighted, FS = fat suppression, PI = parallel imaging acceleration factor, SMS = simultaneous multi-slice acquisition acceleration factor, FOV = field of view

Deep learning superresolution reconstruction: Precision at speed

Achieving higher spatial resolution in musculoskeletal MRI is essential for visualizing small anatomical details and detecting subtle pathology. However, the inherent trade-off between spatial resolution and SNR – defined by an inverse square-root relationship – posed a persistent challenge until recently. Higher-resolution acquisitions typically required longer scan times and came at the cost of reduced SNR, representing the well-known "no free lunch in MRI" theory.

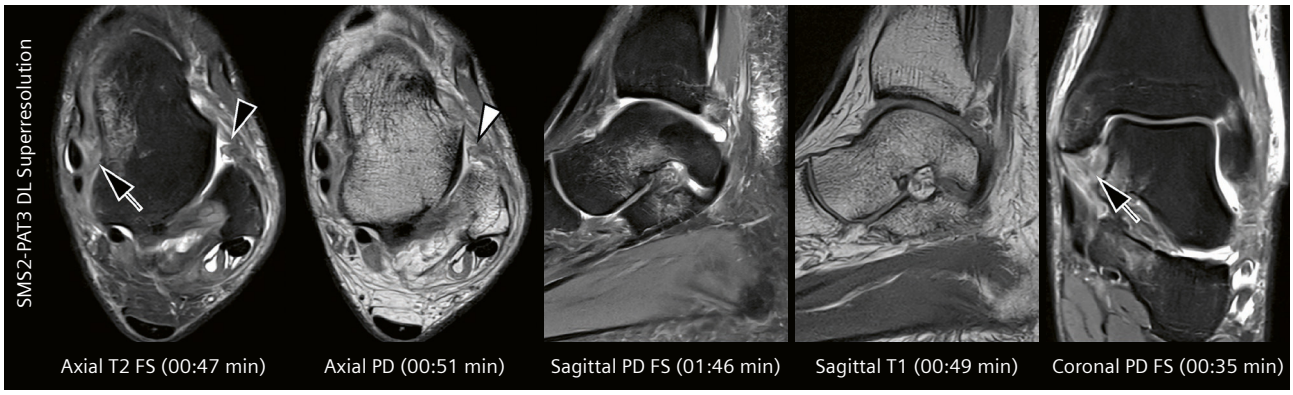

2 3-Tesla ankle MRI with echo-train-compacted turbo spin-echo pulse sequences using combined twofold simultaneous multislice and threefold parallel imaging acceleration with deep learning-based image reconstruction and superresolution augmentation. The MR images show sequela of a recent ankle sprain injury with tears of the deep fibers of the deltoid ligament complex (arrows) and the anterior talofibular ligament (arrowheads), as well as contusions of the medial talus and calcaneus without evidence of fracture.
MR images were obtained with a 3T MAGNETOM Vida MRI system and a 16-receiver-channel ankle/foot coil. The MRI protocol is given in Table 2. PD = proton density weighting, PD FS = fat-suppressed proton density weighting, T2 FS = fat-suppressed T2 weighting.

Parameter	Ax T2 FS	Ax PD	Sag PD FS	Cor PD FS	Sag T1
Gradient performance	high	high	high	high	high
Radiofrequency speed	low	low	normal	low	low
Repetition/echo time [ms]	4180 / 39	3800 / 19	5820 / 37	4000 / 39	400 / 8.9
PI	3	3	2	3	3
SMS / FOV shift	2 / 2	2 / 2	2 / 4	2 / 2	2 / 2
Echo-train length	14	14	16	14	4
Bandwidth [Hz/pixel]	305	354	304	305	347
Echo spacing [ms]	9.7	9.6	9.2	9.7	8.9
FOV [mm]	140 × 100	140 × 143	140 × 140	140 × 103	140 × 140
Matrix	304 × 228	336 × 252	336 × 252	304 × 228	272 × 204
Slice thickness [mm]	3	3	3	3	3
Slices	36	36	28	34	28
Phase direction	right-to-left	right-to-left	anterior-to-posterior	right-to-left	anterior-to-posterior
Flip angle [°]	138	121	160	126	127
Acquisition time [mm:ss]	00:47	00:51	01:46	00:49	00:35

Table 2: NYU comprehensive rapid 3T sixfold SMS2-PAT3-accelerated ankle MRI protocol.
Ax = axial, Cor = coronal, Sag = sagittal, PD = proton density weighted, FS = fat suppression, PI = parallel imaging acceleration factor, SMS = simultaneous multi-slice acquisition acceleration factor, FOV = field of view

The recent introduction of DL-based superresolution augmentation offers a transformative approach to breaking the interconnection of speed, image detail, and SNR. By computationally enhancing spatial resolution from lower-resolution acquisitions, these methods enable faster imaging without compromising diagnostic detail [11]. This allows MRI raw data to be acquired with lower matrix sizes in shorter acquisition windows while yielding high-resolution output image data. Alternatively, image detail can be improved beyond what is achievable with conventional techniques in the same scan time.

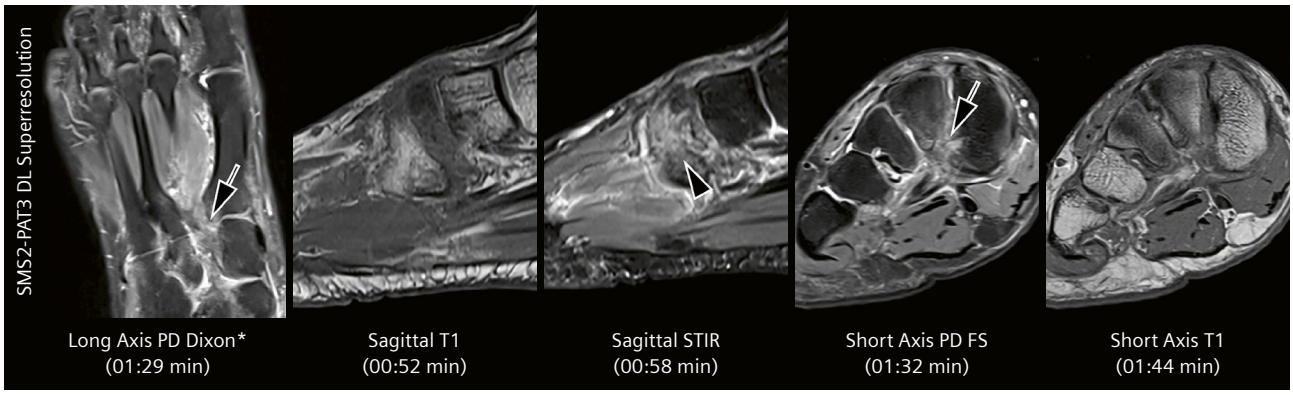

3 3-Tesla MRI of the midfoot with echo-train-compacted turbo spin-echo pulse sequences using combined twofold simultaneous multislice and twofold parallel imaging acceleration with deep learning-based image reconstruction and superresolution augmentation (*PD Dixon images were reconstructed with conventional methods because Deep Resolve Boost is not yet clinically available for Dixon-based fat-water separation). The MR images show high-grade tearing of the Lisfranc ligament (arrows) with surrounding soft tissue edema and adjacent osseous contusions (arrowhead).
MR images were obtained with a 3T MAGNETOM Vida MRI system and a 16-receiver-channel ankle/foot coil. The MRI protocol is given in Table 3. PD = proton density weighting, PD FS = fat-suppressed proton density weighting, STIR = short tau inversion recovery.

Parameter	Short axis PD FS	Short axis T1	Sag STIR	Sag T1	Long axis PD Dixon
Gradient performance	high	high	high	high	high
Radiofrequency speed	low	low	normal	low	normal
Repetition/echo time [ms]	6000 / 37	600 / 9.2	3030 / 33	600 / 8.6	3800 / 42
PI	2	2	2	2	2
SMS / FOV shift	2 / 4	2 / 4	2 / 4	2 / 4	2 / 2
Echo-train length	14	4	9	4	14
Bandwidth [Hz/pixel]	305	350	295	348	395
Echo spacing [ms]	9.2	9.2	8.3	8.6	10.4
FOV [mm]	120 × 109	120 × 108	200 × 138	200 × 141	200 × 144
Matrix	256 × 184	304 × 219	320 × 240	368 × 276	384 × 277
Slice thickness [mm]	3	3	3	3	3
Slices	54	54	34	32	30
Phase direction	right-to-left	right-to-left	head-to-foot	head-to-foot	right-to-left
Flip angle [°]	117	115	125	123	150
Acquisition time [mm:ss]	01:32	01:44	00:58	00:52	01:29

Table 3: NYU comprehensive rapid 3T fourfold SMS2-PAT2-accelerated forefoot/midfoot MRI protocol.
Sag = sagittal, PD = proton density weighted, FS = fat suppression, STIR = short tau inversion recovery, PI = parallel imaging acceleration factor, SMS = simultaneous multi-slice acquisition acceleration factor, FOV = field of view

Historically, interpolation methods such as zero-filling have been employed to estimate higher-resolution images, though these have shown limited effectiveness for musculoskeletal MRI [1, 13]. Deep Resolve Sharp, in contrast, has been trained on large datasets of paired low- and high-resolution images across various sequences and contrast settings, and seemingly enhances the level of image detail and visualization of small structural abnormalities [4]. Deep Resolve Sharp can effectively double the matrix size in both in-plane directions for 2D acquisitions and can augment slice resolution by a factor of two for 3D datasets to enhance image resolution.

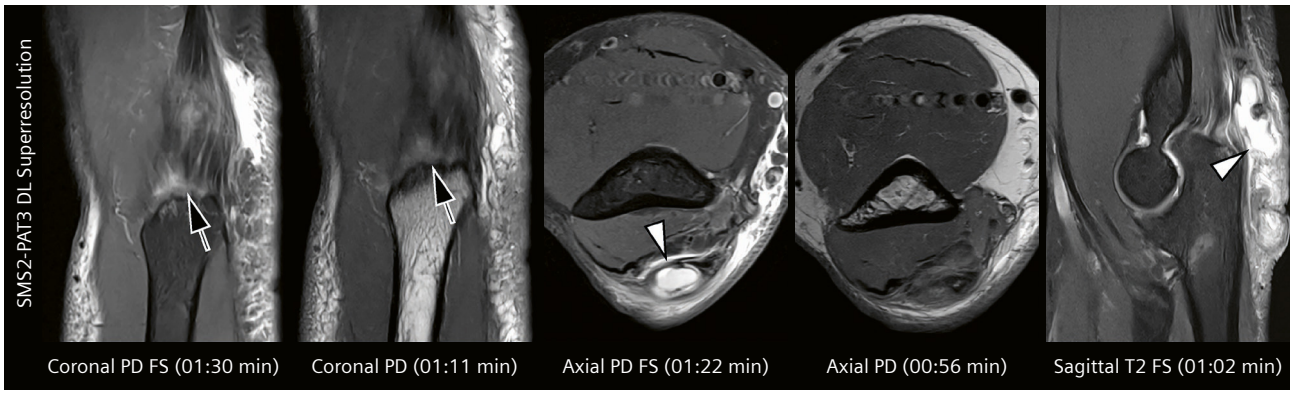

4 3-Tesla MRI of the elbow with echo-train-compacted turbo spin-echo pulse sequences using combined twofold simultaneous multislice and twofold parallel imaging acceleration with deep learning-based image reconstruction and superresolution augmentation. The MR images show a high-grade partial-thickness tear of the distal triceps tendon from the olecranon insertion (arrows) and associated moderate olecranon bursitis (arrowheads) with surrounding soft tissue edema.
MR images were obtained with a 3T MAGNETOM Vida MRI system and a 1-transmit-channel-18-receiver-channel knee coil. The MRI protocol is given in Table 4. PD = proton density weighting, PD FS = fat-suppressed proton density weighting, T2 FS = fat-suppressed T2 weighting.

Parameter	Ax PD	Ax PD FS	Cor PD FS	Cor PD	Sag T2 FS
Gradient performance	high	high	high	high	high
Radiofrequency speed	normal	normal	normal	normal	normal
Repetition/echo time [ms]	3800 / 28	3800 / 38	3800 / 38	3800 / 28	3800 / 46
PI	2	2	2	2	2
SMS / FOV shift	2 / 4	2 / 4	2 / 4	2 / 4	2 / 4
Echo-train length	15	11	11	15	15
Bandwidth [Hz/pixel]	281	294	299	286	299
Echo spacing [ms]	9.34	9.48	9.50	9.26	9.16
FOV [mm]	120 × 120	120 × 120	120 × 120	120 × 120	120 × 120
Matrix	336 × 252	288 × 216	288 × 216	336 × 252	288 × 216
Slice thickness [mm]	3	3	2.8	2.8	3
Slices	34	36	32	30	26
Phase direction	right-to-left	right-to-left	head-to-foot	head-to-foot	head-to-foot
Flip angle [°]	123	125	125	125	125
Acquisition time [mm:ss]	00:56	01:22	01:30	01:11	01:02

Table 4: NYU comprehensive rapid 3T fourfold SMS2-PAT2-accelerated elbow MRI protocol.
Ax = axial, Cor = coronal, Sag = sagittal, PD = proton density weighted, FS = fat suppression, PI = parallel imaging acceleration factor, SMS = simultaneous multi-slice acquisition acceleration factor, FOV = field of view

Most importantly, Deep Resolve Sharp can be integrated with advanced acceleration and image reconstruction methods, including parallel imaging, SMS acquisition, and Deep Resolve Boost, further enhancing the speed and quality of musculoskeletal MRI. This multi-layered approach enables the generation of superresolution images from rapidly acquired, undersampled datasets, delivering stunning visual improvements and meaningful real-life gains in diagnostic confidence [4].

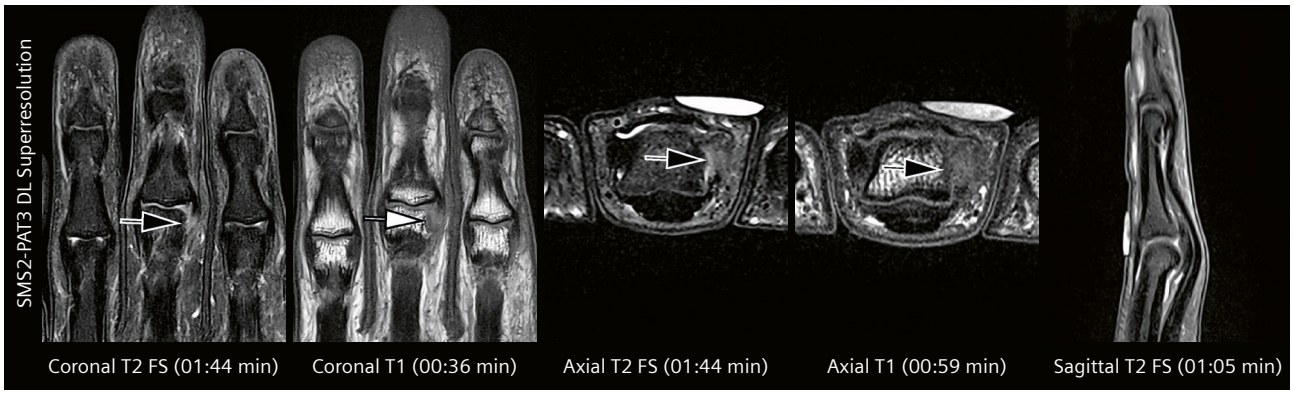

5 3-Tesla MRI of the fingers with echo-train-compacted turbo spin-echo pulse sequences using combined twofold simultaneous multislice and twofold parallel imaging acceleration with deep learning-based image reconstruction and superresolution augmentation. The MR images show a tear of the radial collateral ligament of the middle finger at the proximal insertion at the proximal phalanx (arrows).
MR images were obtained with a 3T MAGNETOM Vida MRI system and a 16-receiver-channel hand/wrist coil. The MRI protocol is given in Table 5. T2 FS = fat-suppressed T2 weighting.

Parameter	Ax T1	Sag T2 FS	Ax T2 FS	Cor T1	Cor T2 FS
Gradient performance	high	high	high	high	high
Radiofrequency speed	low	low	low	low	fast
Repetition/echo time [ms]	500 / 11	4000 / 43	4280 / 70	400 / 12	4500 / 65
PI	2	2	2	2	2
SMS / FOV shift	2 / 4	2 / 4	2 / 4	2 / 4	2 / 4
Echo-train length	3	16	11	3	11
Bandwidth [Hz/pixel]	363	301	289	289	284
Echo spacing [ms]	11.2	10.8	11.7	11.8	9.3
FOV [mm]	80 × 80	100 × 103	80 × 80	100 × 100	100 × 100
Matrix	320 × 288	272 × 204	304 × 228	320 × 256	320 × 256
Slice thickness [mm]	3	3	3	2.2	2.2
Slices	36	18	36	16	16
Phase direction	anterior-to-posterior	head-to-foot	right-to-left	right-to-left	right-to-left
Flip angle [°]	117	130	112	120	120
Acquisition time [mm:ss]	00:59	01:05	01:44	00:36	01:44

Table 5: NYU comprehensive rapid 3T fourfold SMS2-PAT2-accelerated finger MRI protocol.
Ax = axial, Cor = coronal, Sag = sagittal, FS = fat suppression, PI = parallel imaging acceleration factor, SMS = simultaneous multi-slice acquisition acceleration factor, FOV = field of view

Putting it all together: Where we stand and where we are headed

The combined use of finely tuned TSE pulse sequences with compact echo trains, advanced image acceleration techniques like parallel imaging and SMS acquisitions, and DL-based image reconstruction and superresolution augmentation methods facilitate clinical sixfold (SMS2-PAT3) accelerated DL superresolution MRI of the knee (Fig. 1, Table 1) with excellent diagnostic performance for the detection of intra-articular structural abnormalities [14]. Similarly, fourfold (SMS2-PAT2) to sixfold (SMS2-PAT3) accelerated DL superresolution MRI of the ankle (Fig. 2,

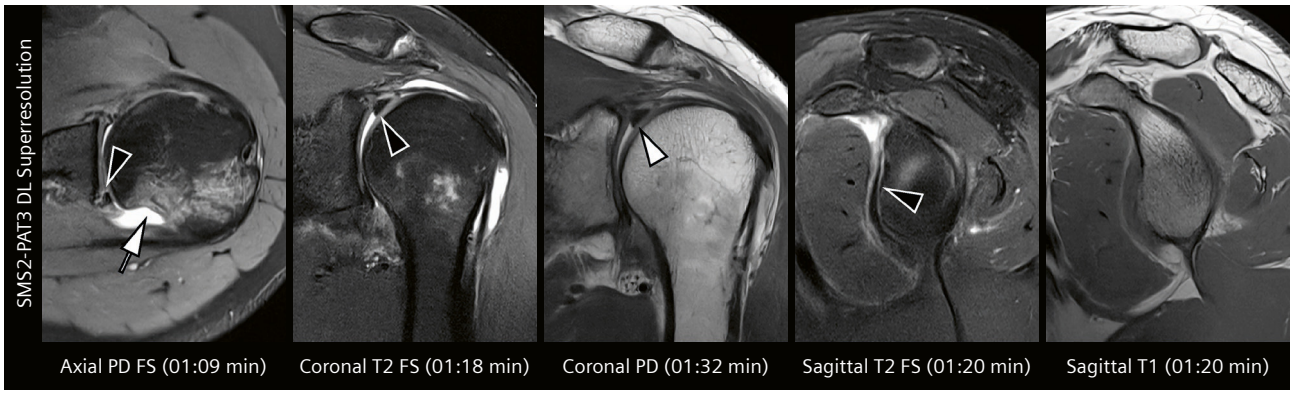

6 3-Tesla MRI of the shoulder with echo-train-compacted turbo spin-echo pulse sequences using threefold parallel imaging acceleration with deep learning-based image reconstruction and superresolution augmentation. The MR images show sequela of a recent anterior shoulder dislocation with a large Hill-Sachs fracture with adjacent bone marrow edema (arrow) and extensive, 360-degree labral tear, including displacement of the superior labrum (arrowheads).
MR images were obtained with a 3T MAGNETOM Vida MRI system and a 16-receiver-channel shoulder coil. The MRI protocol is given in Table 6. PD = proton density weighting, PD FS = fat-suppressed proton density weighting, T2 FS = fat-suppressed T2 weighting.

Parameter	Ax PD FS	Cor T2 FS	Cor PD	Sag T2 FS	Sag T1
Gradient performance	high	high	high	high	high
Radiofrequency speed	normal	low	low	low	low
Repetition/echo time [ms]	4200 / 31	4350 / 54	3970 / 35	5030 / 53	786 / 11
PI	3	3	3	3	3
SMS / FOV shift	0 / 0	0 / 0	0 / 0	0 / 0	0 / 0
Echo-train length	11	12	11	13	4
Bandwidth [Hz/pixel]	260	252	279	217	279
Echo spacing [ms]	10.3	10.8	11.5	10.6	10.6
FOV [mm]	140 × 140	140 × 140	140 × 140	140 × 140	140 × 140
Matrix	320 × 256	320 × 256	448 × 314	320 × 240	320 × 256
Slice thickness [mm]	3	3	3	3	3
Slices	30	28	28	28	28
Phase direction	anterior-to-posterior	head-to-foot	head-to-foot	head-to-foot	head-to-foot
Flip angle [°]	150	150	150	150	150
Acquisition time [mm:ss]	01:09	01:18	01:32	01:20	01:20

Table 6: NYU comprehensive rapid 3T threefold PAT3-accelerated shoulder MRI protocol.
Ax = axial, Cor = coronal, Sag = sagittal, PD = proton density weighted, FS = fat suppression, PI = parallel imaging acceleration factor, SMS = simultaneous multi-slice acquisition acceleration factor, FOV = field of view

Table 2), foot (Fig. 3, Table 3), elbow (Fig. 4, Table 4), and fingers (Fig. 5, Table 5) are routinely used in clinical practice with acquisition times of five to six minutes. Such comprehensive yet rapid MRI protocols can be accommodated in 10- to 15-minute MRI appointment times in architecturally optimized settings to maximize operational efficiency and sustainability [15, 16]. Imaging of peripheral joints benefits from closed coil designs and advantageous geometric arrangements of individual coil elements that prevent extensive aliasing artifacts and incomplete slice separation compared with central joints like the shoulder and hip, and in the spine. Combined parallel imaging and SMS acceleration for these joints may result in incomplete artifact removal during image reconstruction, even with current DL methods. However, three- to fourfold parallel imaging accelerated DL superresolution MRI, e.g., in the shoulder, can be achieved with excellent diagnostic performance in an acquisition time below seven minutes [17] (Fig. 6, Table 6). Future directions include the clinical implementation of currently developed end-to-end DL reconstruction methods for combined PI-SMS acceleration that promise to eliminate residual aliasing artifacts and make artifact-free eight- to twelvefold-accelerated DL superresolution musculoskeletal MRI with acquisition times below three minutes a clinical reality in the near future.

These developments have pushed through frontiers in musculoskeletal MRI by breaking physical interconnections with acceleration factors at a level of image detail that no one believed was possible a few years ago. However, the journey to new horizons has likely just started, and our excitement for enhancing the efficiency and value of musculoskeletal MRI is exponentially accelerating. We are on the verge of further bending the rules of time and physics and racing toward a future where ultra-fast superresolution MRI is not just possible, but also global routine clinical practice.

References

1 Del Grande F, Guggenberger R, Fritz J. Rapid Musculoskeletal MRI in 2021: Value and Optimized Use of Widely Accessible Techniques. AJR Am J Roentgenol. 2021;216(3):704–717.
2 Vosshenrich J, Koerzdoerfer G, Fritz J. Modern acceleration in musculoskeletal MRI: applications, implications, and challenges. Skeletal Radiol. 2024;53(9):1799–1813.
3 Fritz J, Guggenberger R, Del Grande F. Rapid Musculoskeletal MRI in 2021: Clinical Application of Advanced Accelerated Techniques. AJR Am J Roentgenol. 2021;216(3):718–733.
4 Walter SS, Vosshenrich J, Cantarelli Rodrigues T, Dalili D, Fritz B, Kijowski R, et al. Deep Learning Superresolution for Simultaneous Multislice Parallel Imaging-Accelerated Knee MRI Using Arthroscopy Validation. Radiology. 2025;314(1):e241249.
5 Recht MP, Zbontar J, Sodickson DK, Knoll F, Yakubova N, Sriram A, et al. Using Deep Learning to Accelerate Knee MRI at 3 T: Results of an Interchangeability Study. AJR Am J Roentgenol. 2020;215(6):1421–1429.
6 Fritz J, Kijowski R, Recht MP. Artificial intelligence in musculoskeletal imaging: a perspective on value propositions, clinical use, and obstacles. Skeletal Radiol 2022;51(2):239–243.
7 Fritz J, Fritz B, Zhang J, Thawait GK, Joshi DH, Pan L, et al. Simultaneous Multislice Accelerated Turbo Spin Echo Magnetic Resonance Imaging: Comparison and Combination With In-Plane Parallel Imaging Acceleration for High-Resolution Magnetic Resonance Imaging of the Knee. Invest Radiol. 2017;52(9):529–537.
8 Barth M, Breuer F, Koopmans PJ, Norris DG, Poser BA. Simultaneous multislice (SMS) imaging techniques. Magn Reson Med. 2016;75(1):63–81.
9 Breuer F, Blaimer M, Griswold MA, Jakob PM. CAIPIRINHA – Revisited. Simultaneous Multi-Slice Supplement. MAGNETOM Flash. 2025;63(3):8–15.
10 Del Grande F, Rashidi A, Luna R, Delcogliano M, Stern SE, Dalili D, et al. Five-Minute Five-Sequence Knee MRI Using Combined Simultaneous Multislice and Parallel Imaging Acceleration: Comparison with 10-Minute Parallel Imaging Knee MRI. Radiology. 2021;299(3):635–646.
11 Lin DJ, Walter SS, Fritz J. Artificial Intelligence-Driven Ultra-Fast Superresolution MRI: 10-Fold Accelerated Musculoskeletal Turbo Spin Echo MRI Within Reach. Invest Radiol. 2023;58(1):28–42.
12 Fritz J. Boldly Going Where No One Has Gone Before – The Roadmap to 10-fold Accelerated Routine Musculoskeletal MRI Exams. MAGNETOM Flash. 2021;79(2):4–14.
13 Bernstein MA, Fain SB, Riederer SJ. Effect of windowing and zero-filled reconstruction of MRI data on spatial resolution and acquisition strategy. J Magn Reson Imaging. 2001;14(3):270–80.
14 Vosshenrich J, Breit HC, Donners R, Obmann MM, Walter SS, Serfaty A, et al. Clinical Implementation of Sixfold-Accelerated Deep Learning Super-Resolution Knee MRI in Under 5 Minutes: Arthroscopy-Validated Diagnostic Performance. AJR Am J Roentgenol. 2025 Apr 23. doi: 10.2214/AJR.25.32878. Epub ahead of print.
15 Recht MP, Block KT, Chandarana H, Friedland J, Mullholland T, Teahan D, et al. Optimization of MRI Turnaround Times Through the Use of Dockable Tables and Innovative Architectural Design Strategies. AJR Am J Roentgenol. 2019;212(4):855–858.
16 Chaban YV, Vosshenrich J, McKee H, Gunasekaran S, Brown MJ, Atalay MK, et al. Environmental Sustainability and MRI: Challenges, Opportunities, and a Call for Action. J Magn Reson Imaging. 2024;59(4):1149–1167.
17 Vosshenrich J, Bruno M, Cantarelli Rodrigues T, Donners R, Jardon M, Leonhardt Y, et al. Arthroscopy-validated Diagnostic Performance of 7-Minute Five-Sequence Deep Learning Super-Resolution 3-T Shoulder MRI. Radiology. 2025;314(2):e241351.



Contact

Jan Vosshenrich, M.D.
University Hospital Basel
Department of Radiology
Spitalstrasse 21
4031 Basel
Switzerland
jan.vosshenrich@usb.ch

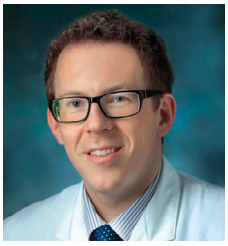

Jan Fritz, M.D.
New York University
Grossman School of Medicine
Department of Radiology
550 1st Avenue, 2nd Floor
New York, NY 10016
USA
jan.fritz@nyulangone.org

Exploring the T2-Mapping GRAPPATINI Technique for Qualitative and Quantitative Assessment of Orthopedic and Neuromuscular Conditions

Ek T. Tan, Ph.D.; Amy Z. Lu, BS; Darryl B. Sneag, M.D.

Department of Radiology and Imaging, Hospital for Special Surgery, New York, NY, USA
Weill Cornell Medical College, New York, NY, USA

Introduction

Quantitative T2 mapping has emerged as a promising tool for several diagnostic MRI applications, including the evaluation of orthopedic and neuromuscular pathology. Traditionally, T2 mapping has been constrained by long acquisition times and low spatial resolution, thereby requiring a separate acquisition added to routine scans. However, T2 mapping has seen renewed attention with the introduction of techniques for accelerating T2 mapping, such as GRAPPATINI[1] [1], which combines two acceleration techniques:

1) acceleration in *k*-space sampling using generalized autocalibrating partially parallel acquisition (GRAPPA) [2] and
2) acceleration in echo sampling using model-based accelerated relaxometry by iterative non-linear inversion (MARTINI) [3] (Fig. 1).

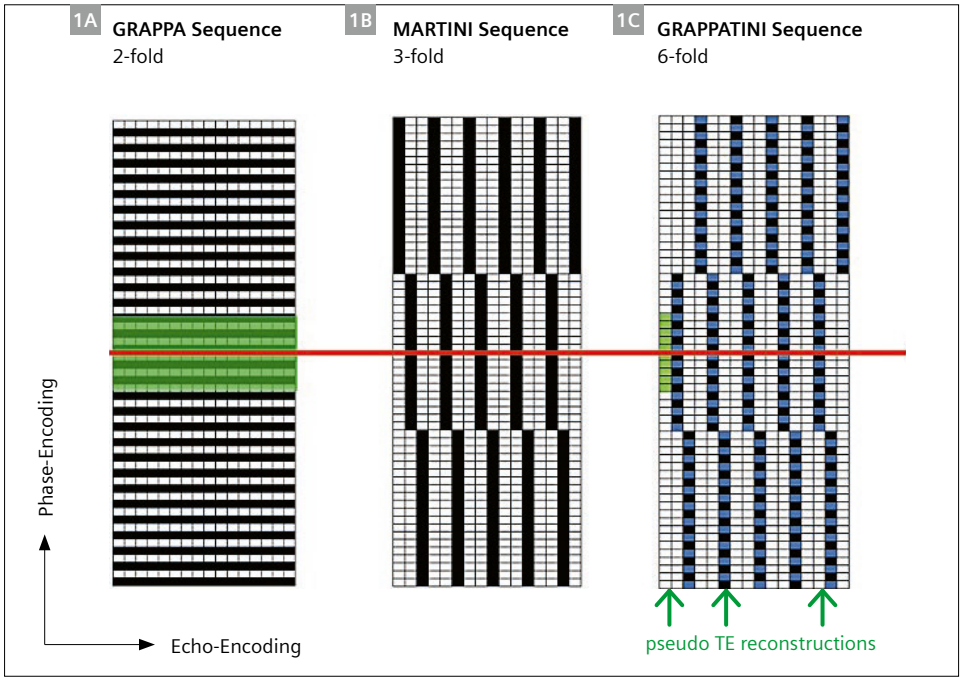

1 **(1A)** Standard, 2-fold GRAPPA compared to **(1B)** MARTINI and **(1C)** GRAPPATINI sampling patterns. The black squares indicate sampled *k*-space points in a 60 × 16 phase/echo-encoding matrix. The red line indicates the *k*-space center with zero phase encoding. The green samples in the GRAPPA and GRAPPATINI patterns indicate *k*-space points used for calibration. The blue squares indicate unsampled *k*-space points that are reconstructed using the GRAPPA method. Pseudo-TE reconstructions can be performed at arbitrary echo times (green arrows).

[1] *Work in progress. The application is currently under development and is not for sale in the U.S. and in other countries. Its future availability cannot be ensured.*

This hybrid acceleration method enables rapid T2 quantification while simultaneously producing synthetic T2-weighted images that can be used for diagnostic interpretation (Fig. 2).

Here, we share our initial clinical experiences of applying GRAPPATINI to neuromuscular and orthopedic imaging. This report includes key results from a recently published study applying GRAPPATINI to the lower extremity for assessment of foot drop [4], as well as additional examples for other conditions and anatomical regions. All subjects participating in studies involving the GRAPPATINI research sequence provided written informed consent under an institutional review board (IRB) approved protocol.

GRAPPATINI in neuromuscular imaging: peripheral nerve and muscle

Foot drop is a neurological condition frequently attributed to entrapment of the common peroneal nerve (CPN) as it courses through a fibro-osseous tunnel of the fibular neck at the knee [5]. In a recent study published in the *Journal of Magnetic Resonance Imaging* (JMRI) [4], we prospectively recruited 27 patients with suspected foot drop undergoing 3T magnetic resonance neurography (MRN) of the distal thigh and knee region and added a fat-suppressed GRAPPATINI sequence to routine, clinical sequences [5]. Specifically, the conventional T2-weighted (T2w) Dixon-fat-suppressed turbo spin echo (TSE) sequence was used to evaluate the distal sciatic nerve and its common peroneal and tibial nerve branches, and to detect active muscle denervation, primarily in the anterior tibialis that controls

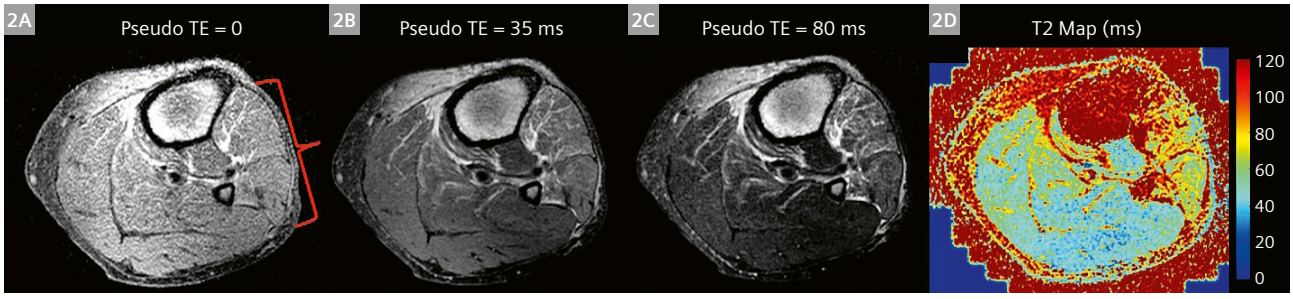

2 62-year-old male with prior total knee arthroplasty (TKA) and foot drop. Axial GRAPPATINI 3T imaging performed with chemical saturation fat suppression on the left calf region just distal to the TKA, demonstrates increased muscle signal in the anterior compartment with increased pseudo-echo times (TE) **(2A, 2B** and **2C)**, and elevated quantitative T2 values **(2D)**, corresponding to muscle edema related to active muscle denervation.

Parameter	T2w Dixon TSE	GRAPPATINI
Sequence type	T2w-TSE with Dixon fat suppression	Model-based T2 mapping (GRAPPATINI)
Scan orientation	Axial	Axial
TR (ms)	5000–11070	3000–9980
TE (ms)	80	10, 20, ..., 100
GRAPPA factor	2	2
MARTINI factor	–	3
Scan time (min)	3:00–7:00	3:09–6:49
FOV (cm)	14–15	14–15
Matrix	320 × 256	322 × 373
Slice thickness (mm)	3–3.5	3–3.5
Slices	48–92	22–50
Readout bandwidth (Hz/pixel)	240–425	243–354

Table 1: Pulse sequence parameters for T2w Dixon TSE and GRAPPATINI imaging techniques in neuromuscular imaging for foot drop assessment at 3T.

foot dorsiflexion. The GRAPPATINI sequence was added in the sections imaged with T2w-Dixon-TSE, and synthetic images were generated at TE = 80 ms for qualitative comparison (Table 1). The GRAPPATINI sequence provided high-resolution, synthetic T2-weighted images and quantitative T2 maps within a scan time of 3–6 minutes (variable depending on longitudinal coverage and slice thickness). Qualitative image assessments, including fascicular nerve architecture, muscle visualization, and diagnostic confidence, were found by three readers to be comparable to conventional T2w-Dixon imaging.

Importantly, GRAPPATINI also enabled quantitative T2 measurements of the common peroneal and tibial nerves (Fig. 2), as well as affected and unaffected lower extremity muscles (Fig. 3). Elevated T2 values in injured nerves and denervated muscle provide a quantitative depiction of pathology [6, 7]; for example, elevated T2 values in muscle denervation have been found to correlate better with electromyography results as compared to qualitative T2-weighted imaging [8]. In our study, a statistically significant T2 elevation was observed in denervated compared to non-denervated muscles (e.g., tibialis anterior:

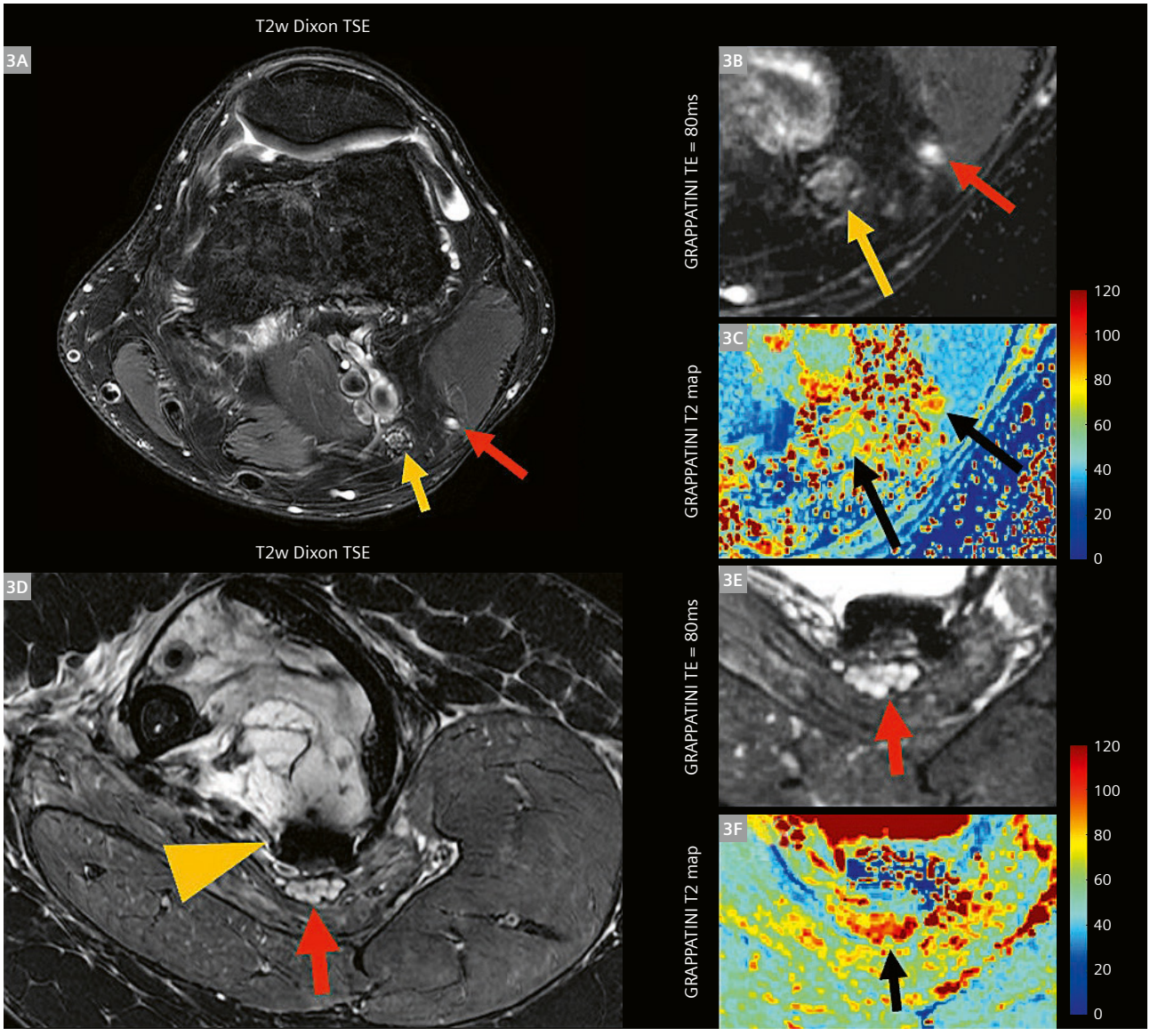

3 Two examples in the lower extremity at 3T. A 56-year-old male with left foot drop (3A–3C). **(3A)** Conventional T2-weighted Dixon TSE images demonstrate hyperintensity of the common peroneal nerve (red arrow) relative to the normal tibial nerve (yellow arrow). Fat-suppressed GRAPPATINI synthetic T2-weighted (T2w) magnified image **(3B)** at TE = 80 ms demonstrates signal hyperintensity corresponding to elevated T2 values **(3C)**. A 19-year-old male with synovial sarcoma post partial tibial resection, screw fixation, and radiotherapy (3D–3F). Conventional imaging **(3D)** and GRAPPATINI TE = 80 ms **(3E)** demonstrate a hyperintense, enlarged tibial nerve (red arrow) posterior to the fixation hardware (yellow arrowhead). T2 mapping shows corresponding high T2 of the tibial nerve (**3F**, arrow).

72.6 ms vs. 46.6 ms, p = 0.002), supporting the utility of GRAPPATINI T2 maps to identify neuromuscular pathology and possibly quantify denervation severity.

GRAPPATINI may also be readily applied to other anatomical regions, e.g., the brachial plexus, for evaluation of peripheral neuropathy such as Parsonage-Turner syndrome (PTS). This condition, also known as neuralgic amyotrophy, commonly involves hourglass-like constrictions of different nerves in the upper extremities and results in severe muscle denervation in the motor distribution of these nerves [6] (Figs. 4 and 5).

GRAPPATINI in orthopedics: intervertebral disc and cartilage

We further explored GRAPPATINI's potential in the spine. T2 mapping has been previously employed to quantify microstructural changes of the degenerated lumbar intervertebral disc, with decreased T2 corresponding with qualitative severity using the Pfirrmann grading scale [9]. A relatively quick 3-minute GRAPPATINI sequence can be similarly acquired to quantify T2 disc values, with pseudo-images generated at longer echo times considered

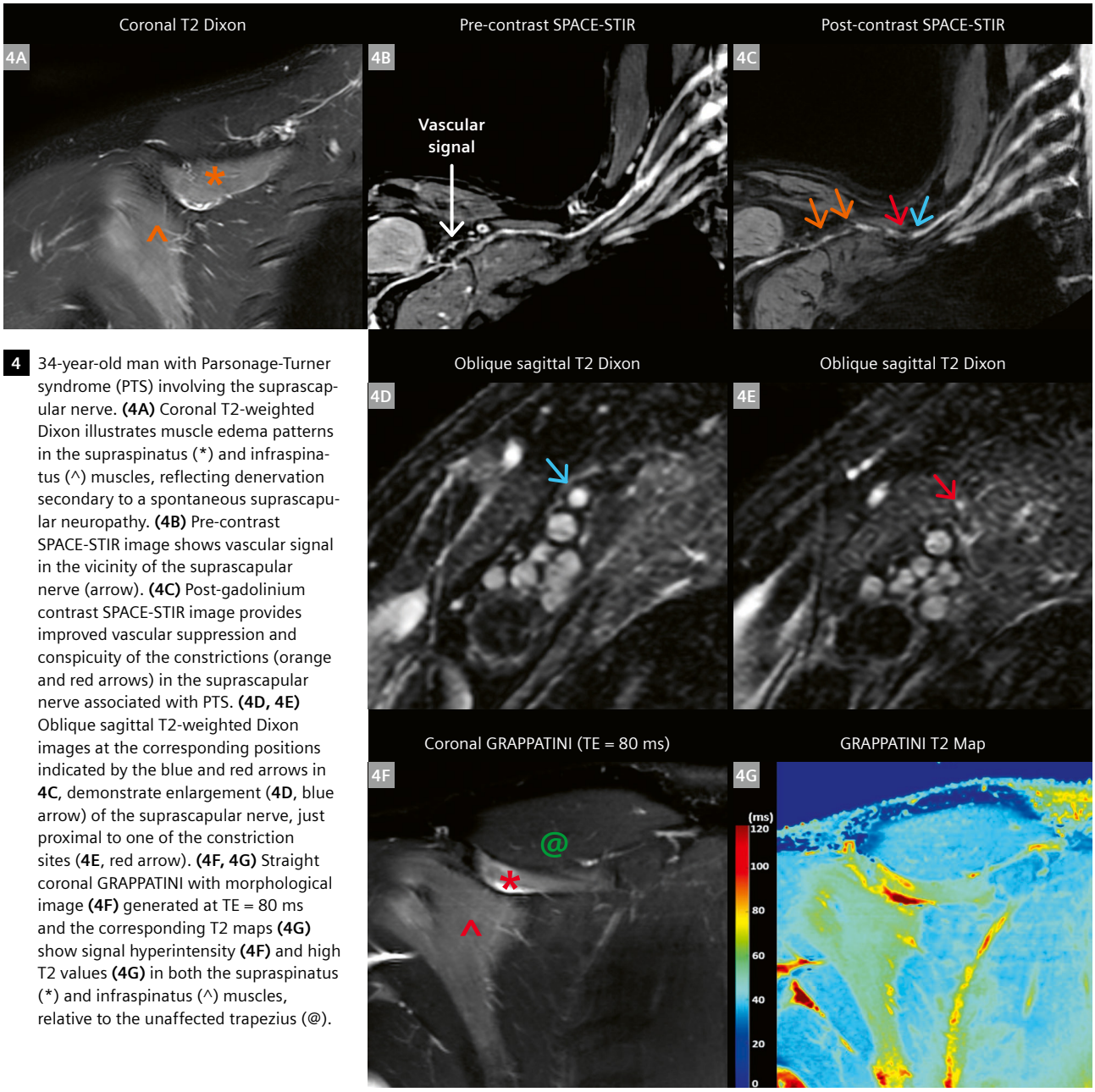

4 34-year-old man with Parsonage-Turner syndrome (PTS) involving the suprascapular nerve. **(4A)** Coronal T2-weighted Dixon illustrates muscle edema patterns in the supraspinatus (*) and infraspinatus (^) muscles, reflecting denervation secondary to a spontaneous suprascapular neuropathy. **(4B)** Pre-contrast SPACE-STIR image shows vascular signal in the vicinity of the suprascapular nerve (arrow). **(4C)** Post-gadolinium contrast SPACE-STIR image provides improved vascular suppression and conspicuity of the constrictions (orange and red arrows) in the suprascapular nerve associated with PTS. **(4D, 4E)** Oblique sagittal T2-weighted Dixon images at the corresponding positions indicated by the blue and red arrows in **4C**, demonstrate enlargement (**4D**, blue arrow) of the suprascapular nerve, just proximal to one of the constriction sites (**4E**, red arrow). **(4F, 4G)** Straight coronal GRAPPATINI with morphological image **(4F)** generated at TE = 80 ms and the corresponding T2 maps **(4G)** show signal hyperintensity **(4F)** and high T2 values **(4G)** in both the supraspinatus (*) and infraspinatus (^) muscles, relative to the unaffected trapezius (@).

in lieu of a separate, standard sagittal T2-TSE acquisition (Fig. 6). The addition of T2 mapping may potentially be beneficial for assessing early changes in disc microstructure to help guide non-surgical management of low back pain and training regimens in high-performance athletes.

Another potential application of GRAPPATINI is cartilage evaluation. Quantitative T2 mapping is a valuable tool for assessing cartilage and meniscus integrity and matrix composition, offering noninvasive insight into early degenerative changes before morphological defects manifest [10, 11]. In a series of 9 patients (4 females, 5 males, mean [range] age = 45 [27–72]) undergoing clinical knee MRI for cartilage and meniscal evaluation, a non-fat-suppressed GRAPPATINI sequence was added with a focus to obtain high-resolution, multiplanar T2 mapping at accelerated scan times and compare T2 values to those obtained using a conventional T2-mapping sequence (MapIt) (Table 2, Fig. 7). The GRAPPATINI technique not only provided high-resolution, synthetic proton-density-weighted and T2-weighted images, but also excellent agreement with standard T2 mapping (Table 3). While we did not explore the potential for qualitative evaluation in this study, the GRAPPATINI sequence can provide a synthetic image at a similar echo time as our conventional proton-density-weighted TSE sequence.

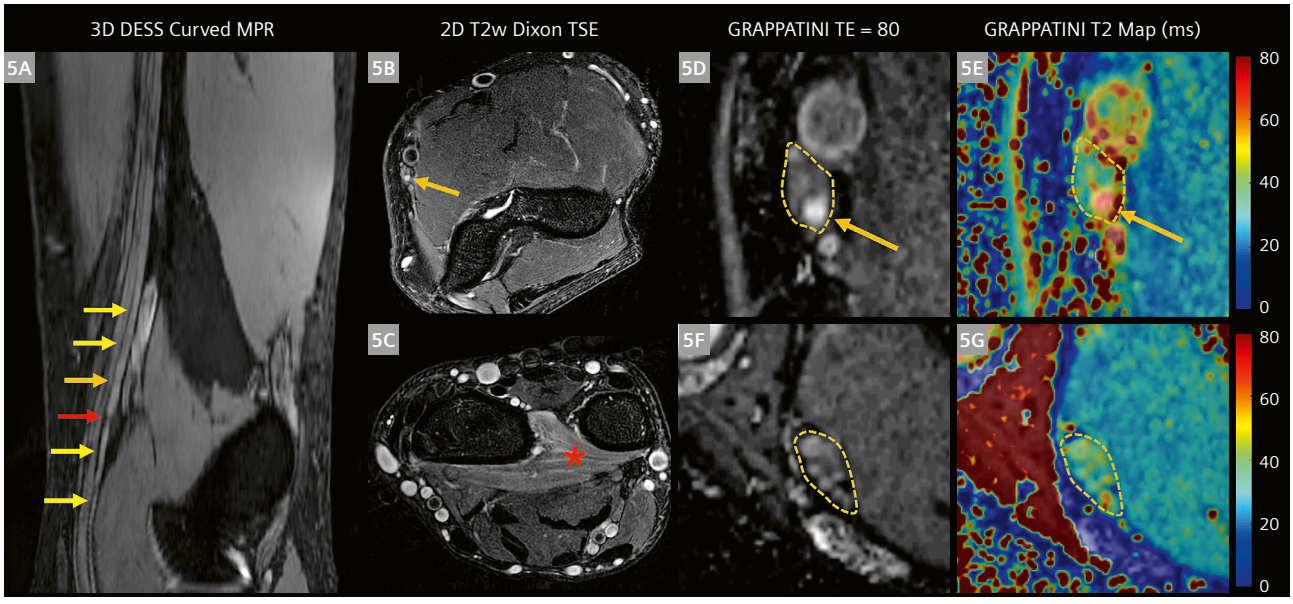

5 Arm and forearm 3T MRI exams (MAGNETOM Vida) in a 33-year-old male subject with left anterior interosseous nerve (AIN) syndrome. **(5A)** Curved maximum projection reconstruction (MPR) from a 3D double echo steady state (DESS) sequence demonstrates enlargement of the AIN bundle of the median nerve (yellow arrows), and a focal constriction (red arrow) characteristic of Parsonage-Turner syndrome and resulting in denervation of the pronator quadratus muscle (**5C**, red *). **(5B)** Axial T2-weighted, fat-suppressed imaging proximal to the constriction (corresponding to the orange arrow location on 5A) demonstrates hyperintensity of the AIN bundle, seen also with hyperintensity and high T2 in GRAPPATINI **(5D, 5E)**. By comparison, expected signal intensity and T2 values were detected in the asymptomatic, ulnar nerve **(5F, 5G)**.

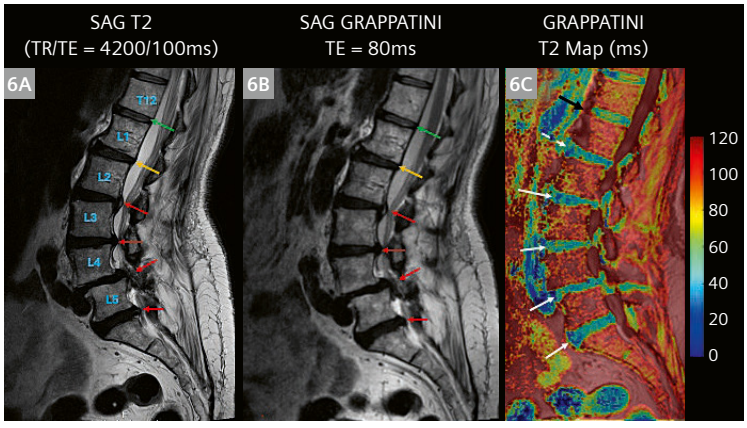

6 Lumbar spine 3T MRI (MAGNETOM Vida) in an 81-year-old female patient with chronic low back pain and claudication who is being considered for spinal fusion and decompression. Sagittal T2 TSE **(6A)** and GRAPPATINI pseudo-TE = 80 ms images **(6B)** demonstrate disc bulges and moderate-to-severe central narrowing from L2–3 to L5–S1 (red arrows), but no disc bulge at T12–L1 (green arrow) or at L1–2 (yellow arrow). Despite the absence of a disc bulge at L1–2, the intervertebral disc at this level demonstrates degeneration, manifest as a low T2 value (T2 = 49.9 ms, dashed arrow) similar to those measured from the L2–3 to L5–S1 discs (T2 = 46.7–50.7 ms, solid white arrows). Compare with the more normal T2 value at T12–L1 (61.9 ms, black arrow) **(6C)**.

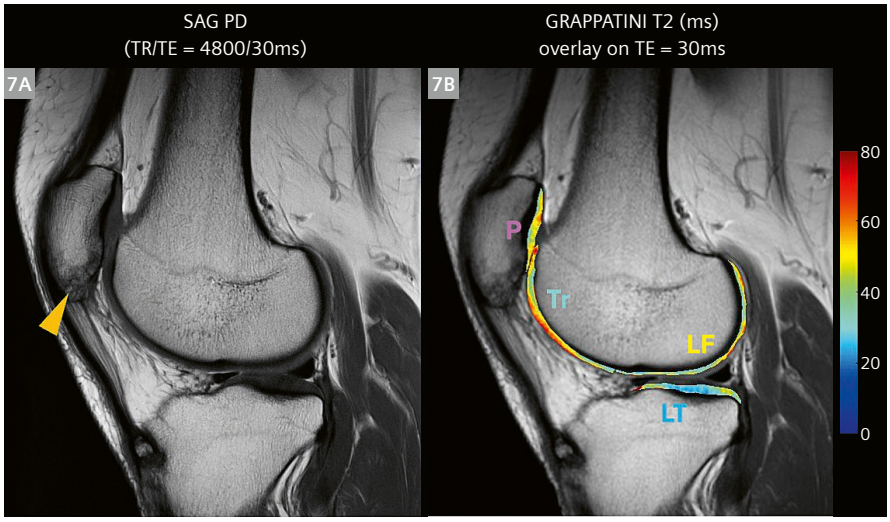

7 MRI at 3T (MAGNETOM Vida) in a 34-year-old female subject with chronic right knee pain demonstrates normal-appearing cartilage on the sagittal proton-density-weighted image **(7A)**. GRAPPATINI demonstrates inhomogeneity and higher mean T2 values of cartilage overlying the patella (P, T2 = 46.3 ms) and trochlea (Tr, T2 = 51.0 ms) **(7B)**, as compared to the lateral tibial and femoral cartilage (LT, LF, T2 = 35.9–42.6 ms), suggesting early chondral degeneration. Enthesopathic changes (yellow arrowhead, 7A), unrelated to chondral wear, are noted at the patellar tendon origin.

Parameter	PD	MapIt	GRAPPATINI
Sequence type	Proton-density-weighted TSE	Standard T2 mapping (multi-echo spin echo)	Model-based accelerated T2 mapping
Scan orientation	Sagittal	Sagittal	Sagittal
TR (ms)	3500–6000	2500	3500
TE (ms)	25–28	10, 20, ..., 80	10, 20, ..., 100
Echo train length	12	8	10
GRAPPA factor	2	2	2
MARTINI factor	–	–	3
Nominal scan time (min)	5:00	5:00	2:30
FOV (cm)	15–19	15–19	15–19
Matrix	512 × 400	336 × 236	336 × 236
Slice thickness (mm)	3.5	4.0	4.0
Readout bandwidth (Hz/pixel)	315	354	354

Table 2: MRI sequence parameters for proton-density-weighted (PD) TSE, MapIt, and GRAPPATINI for 3T knee imaging.

Metric	MapIt	GRAPPATINI	p-value
Mean patellar cartilage T2 (ms)	55.9	51.1	0.48
Mean trochlear cartilage T2 (ms)	71.1	61.8	0.028*
Mean medial femoral cartilage T2 (ms)	65.5	61.7	0.26
Mean medial tibial cartilage T2 (ms)	55.4	60.1	0.65
Mean lateral femoral cartilage T2 (ms)	52.7	51.2	0.65
Mean lateral tibial cartilage T2 (ms)	37.1	42.7	0.13
Scan time (min)	4:10	1:52	< 0.001*

Table 3: T2 values and scan times: MapIt vs. GRAPPATINI in nine knee MRI subjects.

Discussion

GRAPPATINI offers the potential to streamline neuromuscular and orthopedic clinical and research investigations via novel schemes for accelerating T2-mapping acquisition and reconstructions. The dual functionality of T2 mapping and output of synthetic magnitude images for qualitative evaluation is particularly valuable in clinical scenarios otherwise requiring relatively time-intensive, multiplanar, multi-contrast protocols for comprehensive evaluation of a particular condition, and where both qualitative assessment and objective biomarker quantiication may help guide care.

While we observed excellent performance in the examples provided here, further work will be needed to improve GRAPPATINI image reconstruction and to standardize acquisition parameters across anatomical regions and patient populations. This may include a more comprehensive study to determine the quantitative accuracy of GRAPPATINI in various phantom studies, as well as the scan-rescan reproducibility of GRAPPATINI-generated T2 maps. Future studies may explore integration with deep-learning-based reconstruction methods or expand GRAPPATINI to other pulse sequences.

Conclusion

The GRAPPATINI technique represents a valuable addition to the MRI toolbox, enabling fast, efficient, and multiparametric evaluation of musculoskeletal and neuromuscular pathology. We anticipate that ongoing refinement of GRAPPATINI protocols will continue to expand its role in clinical MRI, especially as the demand grows for efficient, quantitative imaging solutions that do not compromise image quality or diagnostic confidence.

Contact

Ek T. Tan, Ph.D.
Co-Director of the MRI Lab
Department of Radiology and Imaging
Hospital for Special Surgery
535 East 70th Street
New York, NY 10021
USA
tane@hss.edu



Darryl B. Sneag, M.D.
Director of MRI Research and
MR Neurography
Department of Radiology and Imaging
Hospital for Special Surgery
535 East 70th Street
New York, NY 10021
USA
sneagd@hss.edu



Acknowledgments

The authors thank Tom Hilbert, Ph.D. and Xiaoying Cai, Ph.D. from Siemens Healthineers for their invaluable technical support.

References

1 Hilbert T, Sumpf TJ, Weiland E, Frahm J, Thiran JP, Meuli R, et al. Accelerated T2 mapping combining parallel MRI and model-based reconstruction: GRAPPATINI. J Magn Reson Imaging. 2018;48(2):359–368.
2 Griswold MA, Jakob PM, Heidemann RM, Nittka M, Jellus V, Wang J, et al. Generalized autocalibrating partially parallel acquisitions (GRAPPA). Magn Reson Med. 2002;47(6):1202–10.
3 Sumpf TJ, Petrovic A, Uecker M, Knoll F, Frahm J. Fast T2 Mapping with Improved Accuracy Using Undersampled Spin-Echo MRI and Model-Based Reconstructions with a Generating Function. IEEE Trans Med Imaging. 2014;33(12):2213–22.
4 Lu AZ, Lin Y, Hilbert T, Igbinoba Z, Shakoor D, Cai X, et al. Feasibility of Qualitative Evaluation and Quantitative T2 Mapping of Peripheral Nerves and Muscles Using GRAPPATINI. J Magn Reson Imaging. 2025. doi: 10.1002/jmri.29803.
5 Bendszus M, Wessig C, Reiners K, Bartsch AJ, Solymosi L, Koltzenberg M. MR imaging in the differential diagnosis of neurogenic foot drop. AJNR Am J Neuroradiol. 2003;24(7):1283–9.
6 Sneag DB, Urban C, Li TY, Colucci PG, Pedrick EG, Nimura CA, et al. Hourglass-like constrictions on MRI are common in electromyography-confirmed cases of neuralgic amyotrophy (Parsonage-Turner syndrome): A tertiary referral center experience. Muscle Nerve. 2024;70(1):42–51.
7 Argentieri EC, Tan ET, Whang JS, Queler SC, Feinberg JH, Lin B, et al. Quantitative T2- mapping magnetic resonance imaging for assessment of muscle motor unit recruitment patterns. Muscle Nerve. 2021;63(5):703–709.
8 Tan ET, Serrano KC, Bhatti P, Pishgar F, Vanderbeek AM, Milani CJ, et al. Quantitative MRI Differentiates Electromyography Severity Grades of Denervated Muscle in Neuropathy of the Brachial Plexus. J Magn Reson Imaging. 2022;56(4):1104–1115.
9 Stefanou DE, Velonakis G, Karavasilis E, Argyropoulos G, Kelekis A, Kelekis N, et al. T2 mapping of lumbar intervertebral disc: quantitative evaluation of degeneration in relation to Pfirrmann grading system and a template for intervertebral disc segmentation. Hippokratia. 2023;27(3):75–81.
10 Eijgenraam SM, Bovendeert FAT, Verschueren J, van Tiel J, Bastiaansen-Jenniskens YM, Wesdorp MA, et al. T2 mapping of the meniscus is a biomarker for early osteoarthritis. Eur Radiol. 2019;29(10):5664–5672.
11 Baum T, Joseph GB, Karampinos DC, Jungmann PM, Link TM, Bauer JS. Cartilage and meniscal T2 relaxation time as non-invasive biomarker for knee osteoarthritis and cartilage repair procedures. Osteoarthritis Cartilage. 2013;21(10):1474–84.

StarVIBE for Bone Imaging

Eddie Song BS, RT(R)(MR)(MRSO)

Clinical Education Specialist at Siemens Healthineers, Durham, NC, USA

Abstract

Three-dimensional bony morphology assessment is an important part of diagnostic imaging. Computed tomography (CT) has been a leading modality in this field due to its high resolution and relatively fast scan times. However, CT imaging comes at the cost of ionizing radiation, which may not be an option for some patients. Magnetic resonance imaging (MRI) is another modality of choice and is free of ionizing radiation. However, bone morphology is not depicted in as much detail as in CT imaging, due to the extremely short T2 relaxation times [1]. Recently, ultra-short-TE and zero-TE sequences have begun to fill this gap. However, these sequences may not be readily available at all facilities. When choices are limited, another option for 3D bone imaging is the StarVIBE sequence.

Benefits of StarVIBE

StarVIBE is a sequence primarily designed for free-breathing body and pediatric imaging [2]. However, it also has several benefits in 3D bone imaging. Although StarVIBE does not have the very short echo times (TEs) of ultra-short-TE and zero-TE sequences, its repetition time (TR) and TE are still relatively short compared to other pulse sequences. This characteristic of volume interpolated breath-hold examination (VIBE) makes it a suitable candidate for 3D bone imaging. According to several studies, when compared to CT imaging, 3D MRI with VIBE in lumbar imaging showed fracture sensitivity, specificity, and accuracy of 97.7%, 92.3%, and 95.7%, respectively [1].

StarVIBE is robust against motion due to its stack-of-stars trajectory [1]. StarVIBE is a modified version of VIBE that uses radial sampling for in-plane imaging, and Cartesian sampling for through-plane imaging. The center of *k*-space is sampled multiple times due to the radial trajectory, making StarVIBE relatively motion-insensitive. Certain situations and body parts can benefit from motion-insensitive imaging, where StarVIBE becomes advantageous. Additionally, the radial trajectory of StarVIBE requires no phase oversampling, as a radial readout gradient is used inplane. This makes StarVIBE appealing for imaging any body part without aliasing artifacts. However, dedicated protocol modifications are necessary to optimize it for bone imaging.

Modifications for bone imaging

There are several protocols for StarVIBE within the software package from Siemens Healthineers, if availalbe. It is easier to begin with the version that has a smaller field of view and thinner slice thickness. Selecting StarVIBE under the head region is a good starting point (Fig. 1). It already has a 1.5 mm slice thickness and a 0.9 × 0.9 mm pixel dimension.

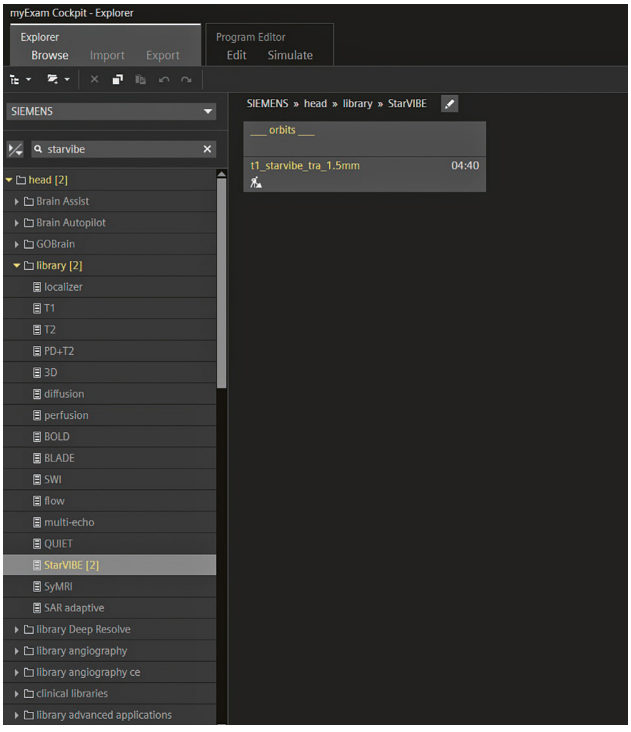

1 StarVibe sequence in the protocol tree from Siemens Healthineers.

The first modification is to turn off the fat saturation pulse and reduce the flip angle to 3° for 1.5T field strengths, and 2° for 3T field strengths (Fig. 2).

The sequence also needs to be optimized to achieve the shortest in-phase TE based on magnetic field strength. The shortest in-phase TE can be entered manually, or automatically selected by choosing the In Phase option under Part 1 of the Sequence tab (Fig. 3).

The shortest in-phase TEs are close to 4.7 ms on 1.5T scanners from Siemens Healthineers, and 2.4 ms on 3T scanners from Siemens Healthineers. Changes to the flip angle and TE help minimize T1 differences between soft tissue, chemical misregistration, and T2 signal loss, while maintaining optimal bone contrast [1]. The higher magnetic field strength of 3T allows for a smaller flip angle, reducing T1 soft tissue contrast due to its innately higher signal intensity.

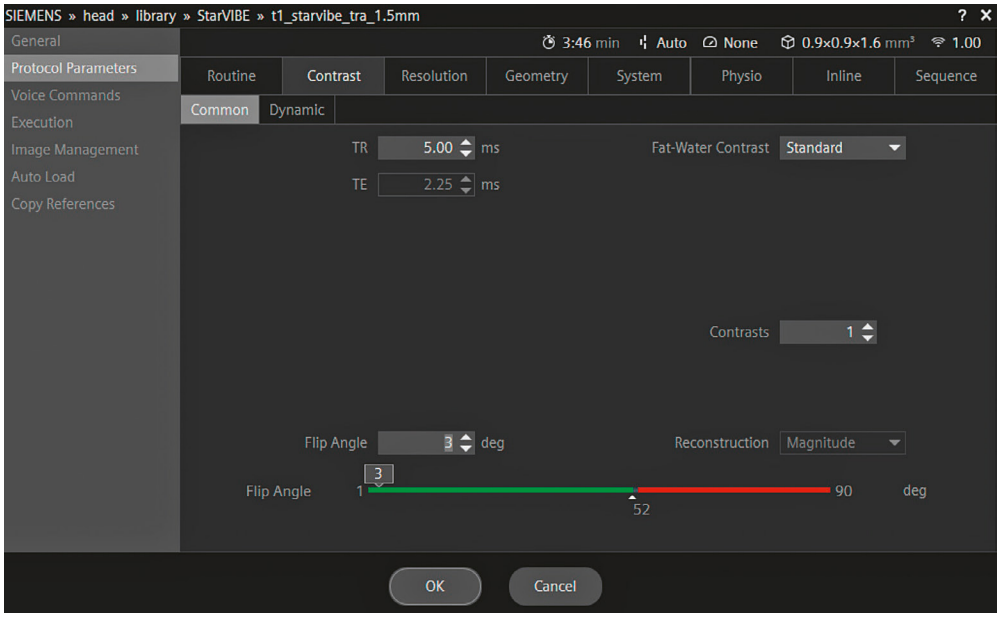

2 Turning off the fat saturation pulse and reducing the flip angle.

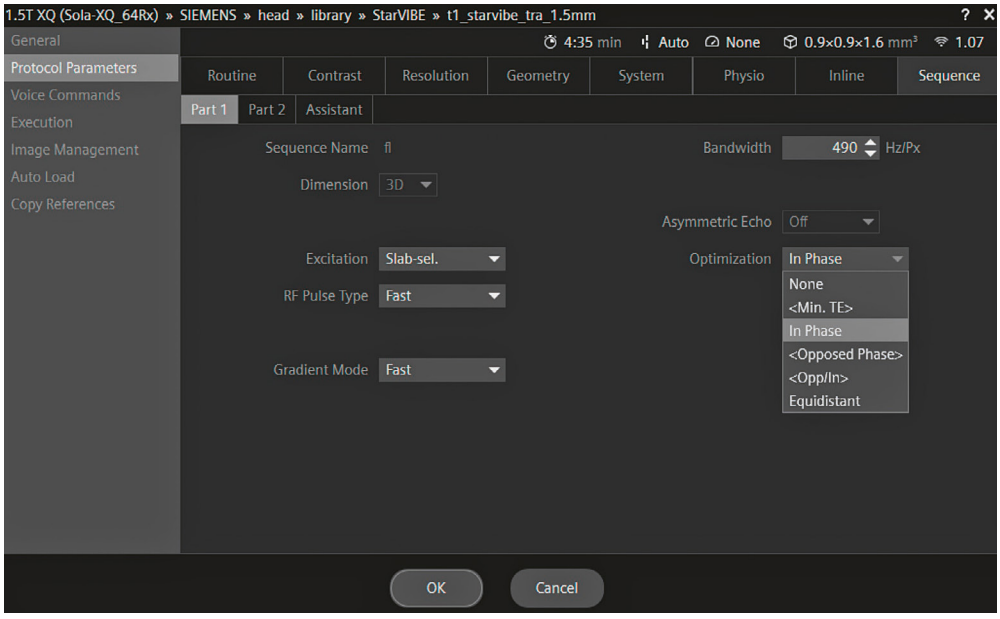

3 Selecting the In Phase option under Part 1 of the Sequence tab.

Ideally, the image should be isotropic to enable optimal reconstruction in any plane after the scan. Due to signal-to-noise-ratio limitations, a 1 × 1 × 1 mm voxel size is a good target for 1.5T. For 3T, it may be possible to reduce the voxel size to 0.8 × 0.8 × 0.8 mm. During this adjustment, the field of view may be limited. If the field of view needs to be reduced, the base matrix may need to be decreased first, due to gradient limitations. Slice resolution can be set to 75%–80% to interpolate and save scan time. Slice thickness should be adjusted to maintain an isotropic voxel size. If the user interface does not allow the desired thinner slice thickness, this can be solved by increasing the number of slices per slab to cover the body part of interest. An increase in slices should provide extra signal in 3D volume acquisition; however, the scan time may increase due to additional slice acquisition. Longer scan times can be balanced by decreasing the average to one. Once the desired voxel size is achieved, radial views should be optimized.

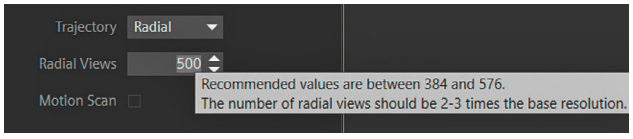

4 Recommended values for the number of radial spokes are displayed on the tooltip when you hover over the Radial Views parameter.

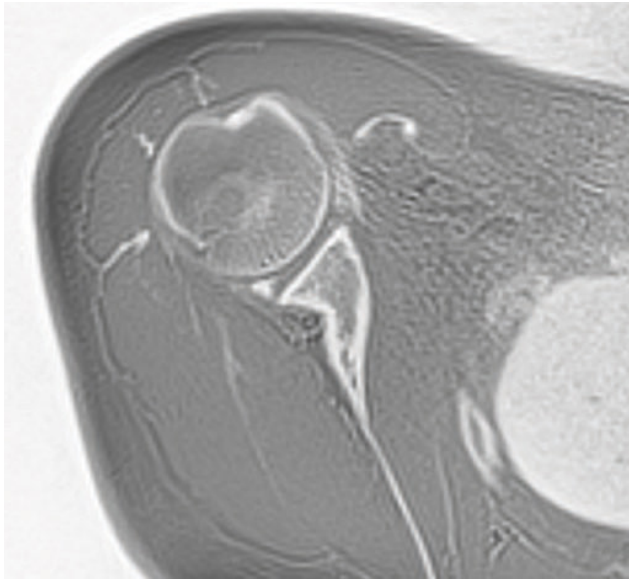

5 Modified StarVIBE for the bone imaging of a shoulder with inverted greyscale.

Radial views determine how many radial spokes are used in the radial sampling scheme of StarVIBE [2]. Recommended values for the number of radial spokes are displayed on the tooltip when you hover over the Radial Views parameter (Fig. 4). The range of recommended values can change depending on what base resolution is set. An optimal number of radial spokes allows for proper overlap in the center of *k*-space, thereby reducing motion artifacts. The correct radial views can also reduce streak artifacts. Therefore, bone imaging in motion-prone body regions may require a higher number of radial views than in relatively stationary body regions. Scan time is another factor to consider, as more radial views will require longer scan times.

Once the image is acquired, the grayscale can be inverted in View&GO by pressing F10 on the keyboard. Alternatively, radiologists can easily invert it from the PAC. This grayscale inversion provides a CT-like 3D bone imaging appearance (Figs. 5 and 6). The isotropic acquisition of StarVIBE bone imaging should allow the user to reconstruct it in any plane to evaluate the region of interest.



6 Modified StarVIBE for the bone imaging of an ankle with inverted greyscale.

Conclusion

MRI is a safe way to evaluate bone morphology. The isometric StarVIBE low TE sequence was designed to enhance osseous cortical and trabecular detail.

Like CT, it allows for a single sequence to be reformatted into multiple planes. This sequence offers numerous potential clinical applications, particularly in cases where a CT scan would traditionally be required alongside an MRI. Proper modification of StarVIBE enables flexible, optimal, and sensitive bone imaging.

References

1 Chong LR, Lee K, Sim FY. 3D MRI with CT-like bone contrast – An overview of current approaches and practical clinical implementation. Eur J Radiol. 2021;143:109915.
2 Chandarana H, Block TK, Rosenkrantz AB, Lim RP, Kim D, Mossa DJ, et al. Free-Breathing radial 3D Fat-Suppressed T1-Weighted gradient echo sequence: a viable alternative for contrast-enhanced liver imaging in patients unable to suspend respiration. Invest Radiol. [Internet]. 2011;46(10):648–53.



Contact

Eddie Song BS, RT(R)(MR)(MRSO)
Clinical Education Specialist
at Siemens Healthineers
109 Tuftin Drive
Durham, NC 27703
USA
eddie.song@siemens-healthineers.com

Pictorial Essay: Clinical Application of StarVIBE for Bone Imaging

Erin Moran, M.D.

Associate Professor of Radiology, Duke University, Durham, NC, USA

Over the last decade, the attempt to produce MR images that provide bony detail comparable to CT has resulted in multiple different techniques including various VIBE sequences, UTE/ZTE sequences, and synthetic CT. The StarVIBE sequence for bone imaging shares many of the benefits of those techniques. It is isometric and provides high-resolution images that are reformattable. The images also provide excellent cortical and trabecular detail in bony structures, as well as excellent visualization of soft tissue mineralization. The sequence also stands up well when dealing with metal[1] artifact and is comparable to metal reduction sequences in its ability to reduce metal artifact. Additionally, there is no loss of signal when relevant anatomy is distant from the isocenter, which is particularly useful when imaging joints such as the shoulder and the hip.

These images provide some examples of our initial experience using this sequence at Duke.

[1] *The MRI restrictions (if any) of the metal implant must be considered prior to patient undergoing MRI exam. MR imaging of patients with metallic implants brings specific risks. However, certain implants are approved by the governing regulatory bodies to be MR conditionally safe. For such implants, the previously mentioned warning may not be applicable. Please contact the implant manufacturer for the specific conditional information. The conditions for MR safety are the responsibility of the implant manufacturer, not of Siemens Healthineers.*

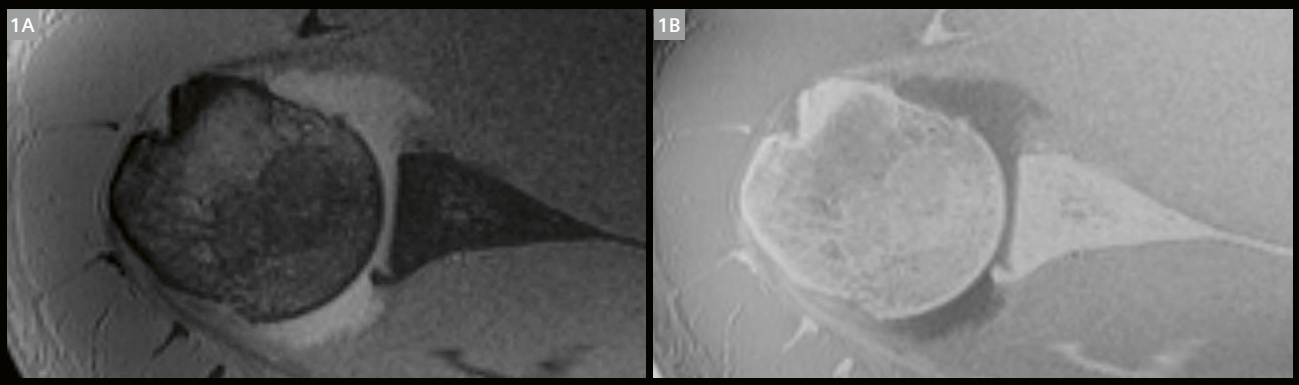

1 A modified StarVIBE axial sequence from an MR arthrogram in the original **(1A)** and in the inverted **(1B)** form shows bone loss in the anterior glenoid in a patient with recurrent dislocations.

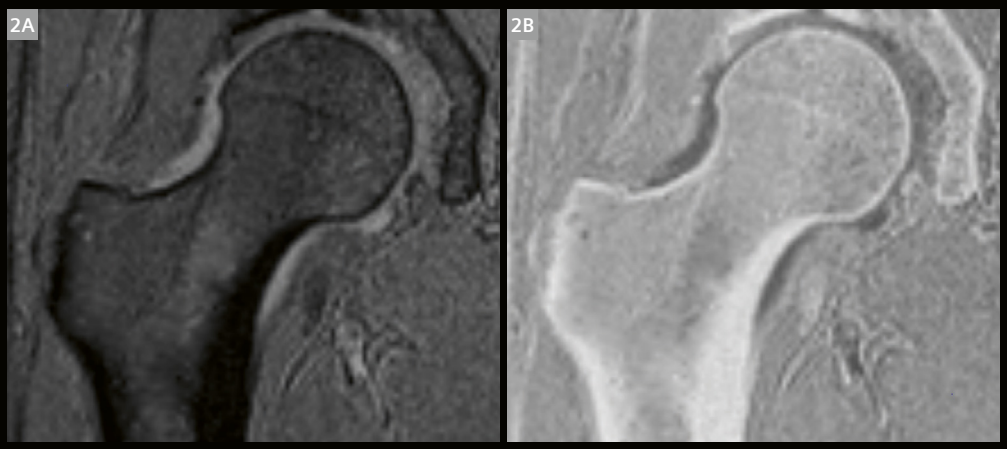

2 A modified StarVIBE coronal sequence from a hip arthrogram in a patient with prior surgery shows the post-surgical changes to the bone following a femoral osteochondroplasty.

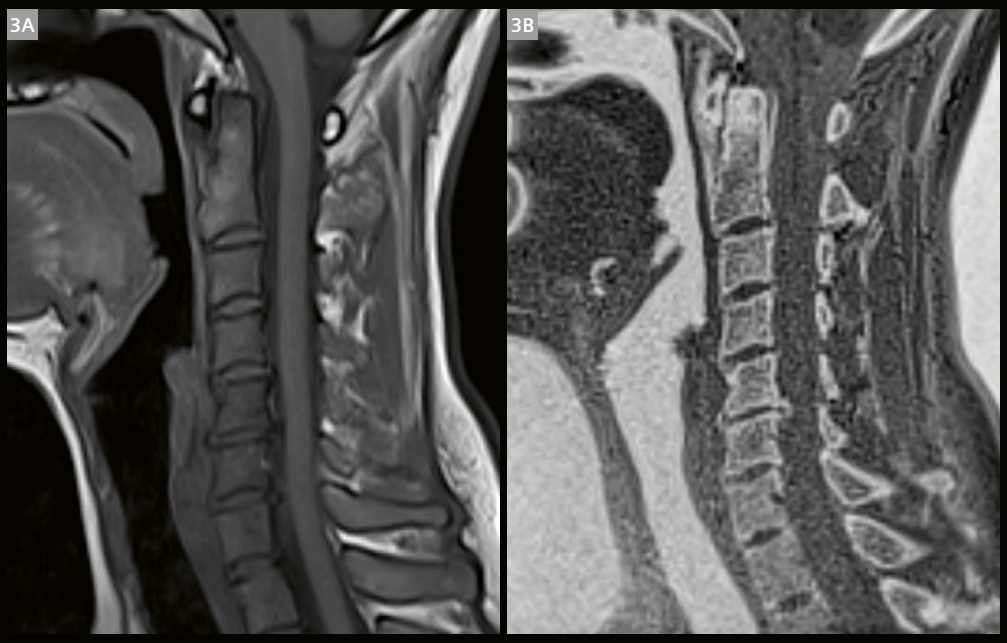

3 A modified StarVIBE sagittal sequence and sagittal T1 TSE. The posterior osteophytes at the level of C5–C6 are more clearly visualized on the StarVIBE sequence.

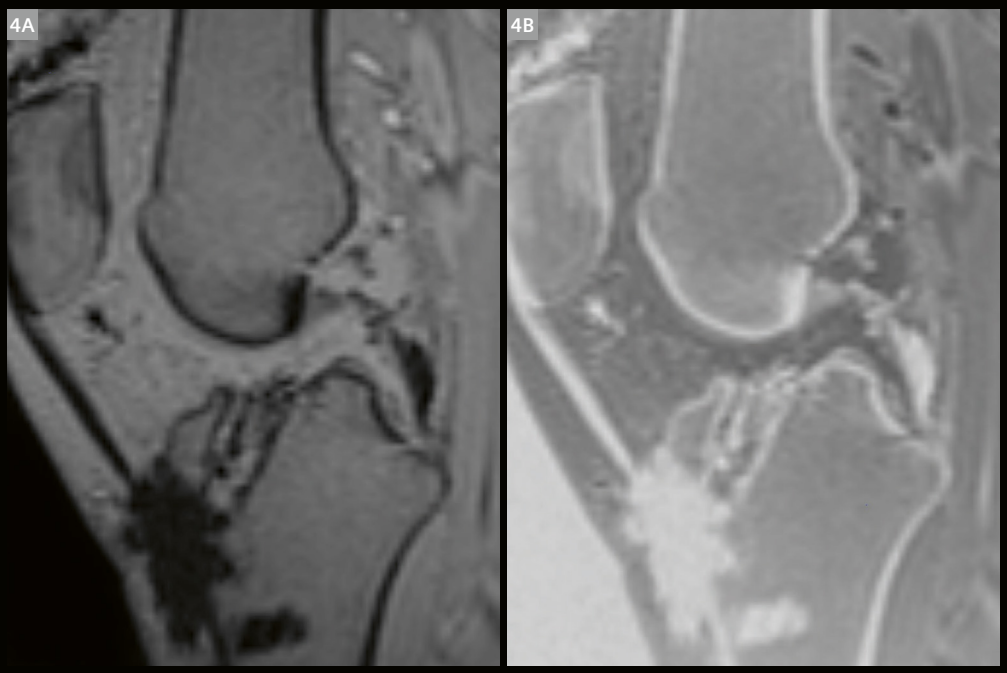

4 Modified StarVIBE sagittal images in a patient with a prior ACL reconstruction. The sequence delineates the bony detail of the tibial tunnel on par with CT in preoperative assessment for revision ACL reconstruction.

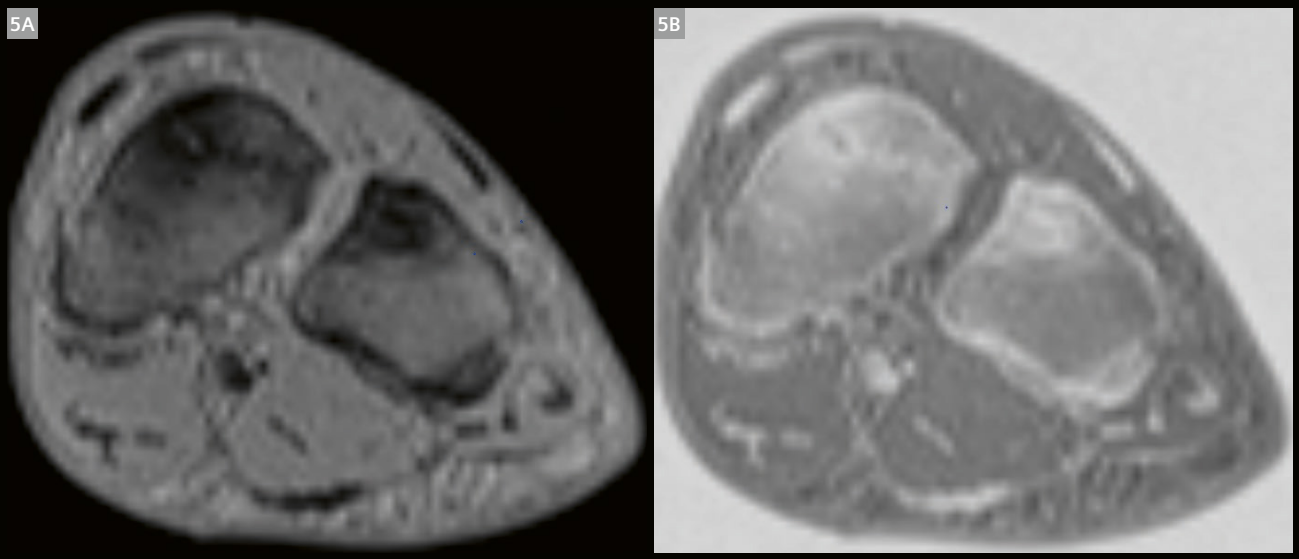

5 A modified StarVIBE coronal image from a midfoot MRI in a patient with suspected navicular stress reaction. On STIR sequences (not shown), bone marrow edema was present throughout the navicular, consistent with stress reaction. On the StarVIBE coronal sequence, linear signal is present within the navicular, consistent with a developing stress fracture.

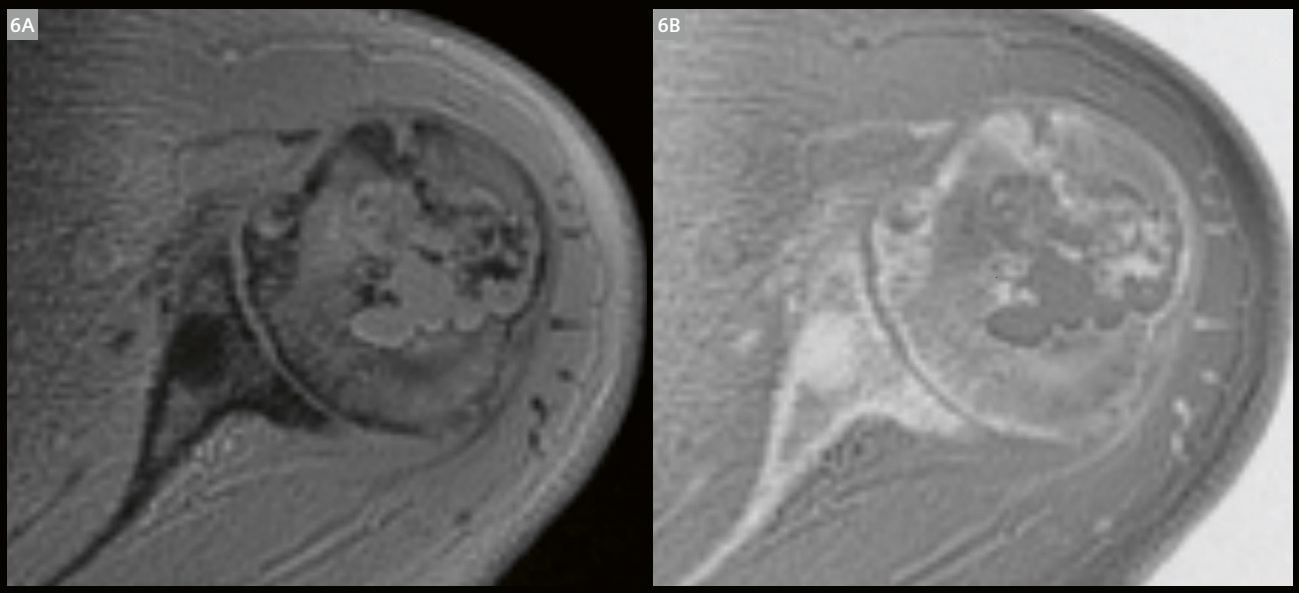

6 A modified StarVIBE axial image of the left shoulder in a patient with a chondroid lesion in the humeral head. The margins of the lesions, as well as the chondroid mineralization, are clearly delineated.

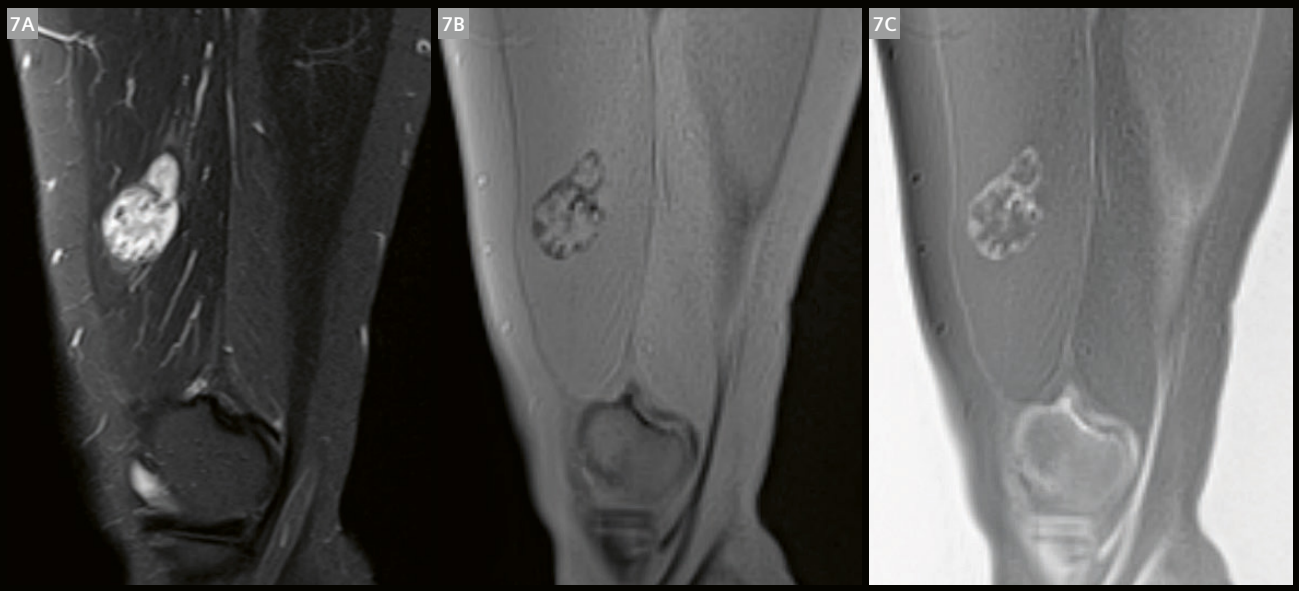

7 A sagittal STIR image and StarVIBE sagittal images of the right thigh in a patient with myositis ossificans. The peripheral rim of mineralization demonstrated on the modified StarVIBE sequences allows the diagnosis to be made on the MRI without the need for additional imaging.

Contact

Erin Moran, M.D.
Associate Professor of Radiology,
Duke University
Box 3808 DUMC
Durham, NC 27710
USA
Tel.: +1 (919) 684-2711
erin.moran@duke.edu



The Spectrum of Interventional MRI

David Woodrum, M.D., Ph.D.; Setayesh Sotoudehnia Korani, M.D.; Scott Thompson, M.D., Ph.D.

Mayo Clinic, Rochester, MN, USA

Abstract

Clinical use of magnetic resonance imaging (MRI) for image-guided procedures began in the late 1980s. However, early procedures were limited by tools, in-bore access to the patient, and MR imaging limitations. Interventional MRI (iMRI) offers some natural advantages including superior soft tissue resolution, ease of multiplanar imaging, lack of ionizing radiation, and the ability to re-image the same slice. MRI guidance is particularly advantageous when the pathology can be best or only visualized with MRI. There has been tremendous growth in clinical applications and positive patient outcomes of iMRI over the past three decades, and the community has benefited from close collaboration between interventional radiologists, MR physicists, and MR nurses. There has been tremendous growth in clinical applications of iMRI over the last 35+ years [1]. The purpose of this article is to give a high-level overview of the breadth of interventional MRI.

Introduction

Shortly after the introduction of clinical diagnostic magnetic resonance imaging (MRI) in the 1980s, diagnostic and interventional radiologists recognized the superior soft tissue contrast of MRI and began to explore the use of MRI guidance during interventional procedures, particularly for head and neck lesions [2–4]. However, early applications of interventional MRI (iMRI) were limited due to the lack of dedicated iMRI magnets, pulse sequences, procedural suites, and equipment. Over the next three decades, significant advancements in iMRI-conditional technology coupled with developments in dedicated iMRI procedural suites enabled significant growth and development of clinical body iMRI applications including aspiration, localization, biopsy, and ablation [5, 6]. MRI offers significant advantages including: superior soft tissue contrast and anatomic detail, leading to increased lesion conspicuity; ease of multiplanar imaging; multiparametric imaging capabilities; lack of ionizing radiation; the ability to monitor effects of treatment in near real time; and the ability to re-image the same slice [7, 8].

With the growth of dedicated clinical iMRI services, safety considerations in the iMRI environment have become paramount [9, 10]. Moreover, systematic physics and clinical safety testing have led to the safe use of previously MR-conditional and unsafe devices in the MR environment, further enabling expansion of clinical body iMRI applications [9, 11–13]. Likewise, with the growth of dedicated iMRI magnets, various MR pulse sequences have been optimized with tradeoffs between image acquisition speed, signal-to-noise ratio (SNR), and spatial and contrast resolution [14, 15].

Additionally in this time period, there has been tremendous development of commercially available MR-conditional needles, and biopsy and ablation devices, which has further enabled the growth of body iMRI applications [10, 16]. Currently, there are a variety of devices approved by the Food and Drug Administration (FDA) for performing MRI-guided and monitored cryoablation, laser ablation, microwave ablation (MWA), radiofrequency ablation (RFA), and focused ultrasound (MRgFUS). Current iMRI applications include localization, biopsy, and sclerotherapy of lesions with poor soft tissue contrast on other imaging modalities, and thermal ablation for benign and malignant neoplastic processes.

Clinical applications of body interventional MRI

There has been tremendous growth in applications of body iMRI, including localization, drainage, biopsy, and sclerotherapy of lesions poorly visualized with ultrasound (US) or computed tomography (CT) [7, 8, 16–18]. This review focuses on many, but not all, iMRI applications as these continue to grow.

Localization

Soft tissue pathology with poor soft tissue contrast on US or CT may be particularly amenable to MRI-guided wire localization when precise localization of a pathology with a patchy or heterogenous distribution is needed prior to targeted surgical biopsy. Examples include intramuscular lymphoma and juvenile dermatomyositis (Fig. 1) [19, 20].

Sclerotherapy

Traditionally, percutaneous sclerotherapy of venous malformations has been performed with a combination of US and fluoroscopic guidance. However, when venous malformations are poorly conspicuous on US, MRI guidance for needle placement prior to sclerotherapy may be utilized, particularly given the inherent high T2-weighted signal within most venous malformations (Fig. 2). Prior studies have shown that MRI-guided percutaneous sclerotherapy is safe, technically feasible, and effective in the treatment of peripheral soft tissue venous malformations at both 1.5T and 3T [21, 22].

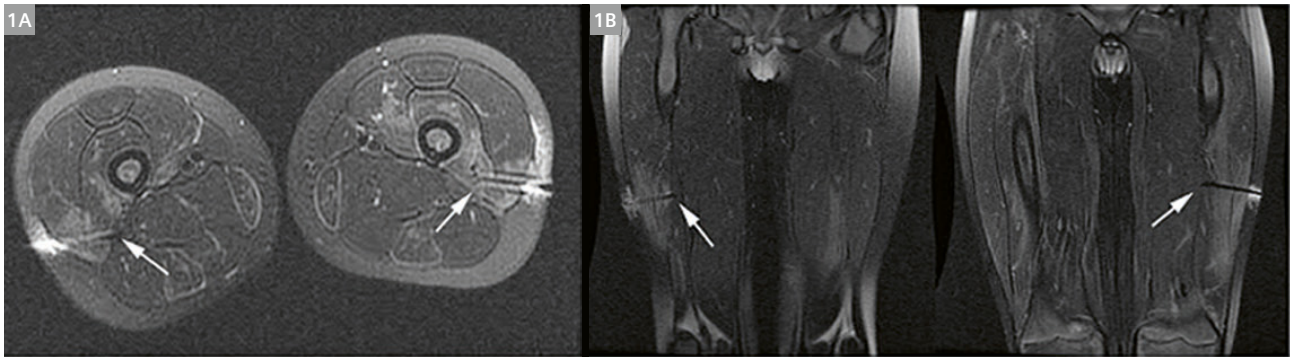

1 MRI of the needle position within the high T2 signal in the vastus lateralis. **(1A)** Axial and **(1B)** coronal with the localizing wire in place and subsequent surgical biopsy confirming juvenile dermatomyositis [40].

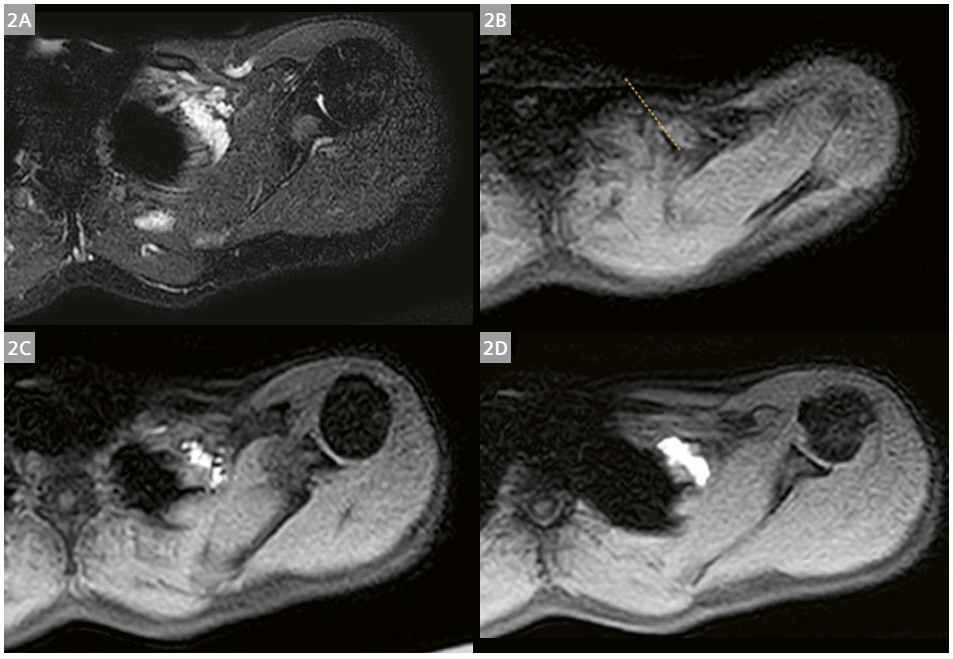

2 **(2A)** T2 with fat saturation demonstrates a bright slow-flow vascular malformation. **(2B)** shows a 22Ga ITP needle placed into the vascular malformation. **(2C)** demonstrates injection of dilute 1:10 gadolinium into the vascular malformation confirming the intra-luminal position. **(2D)** demonstrates injection of a gadolinium and bleomycin mixture into the lesion to perform sclerotherapy. (Unpublished images)

Biopsy

Similar to lesion localization, soft tissue masses with poor soft tissue contrast on US or CT may be suitable for MRI-guided biopsy. This may be performed using freehand, US-assisted or guidance-grid techniques depending on lesion location and organ movement [8, 16, 18, 23]. Prostate and seminal vesicle biopsy via a transperineal approach with a guidance grid is well suited for MRI-guided biopsy [23–25]. Small liver or soft tissue lesions (Fig. 3) seen on diagnostic MRI and positron emission tomography (PET) that cannot be localized by grayscale, color doppler, or contrast-enhanced US, US fusion, or CT are excellent candidates for MRI-guided freehand biopsy. For patients with prior non-diagnostic biopsies of small or technically difficult lesions, consideration can be given to having an on-site cytopathologist for immediate review of the diagnostic adequacy of the biopsy specimen.

Ablation

Image-guided percutaneous thermal ablation with MRI is enhanced with more precise lesion visualization and the ability to monitor ablation temperature: either heat or cold. While US, and to a lesser extent CT, can provide some real-time ablation monitoring, MRI has superior soft tissue contrast and, together with MR thermometry, offers a unique feature for monitoring the ablation procedure.

Kidney

Ablation of renal neoplasms is most commonly performed under US and/or CT guidance using cryoablation, RFA or MWA [26, 27]. However, MRI-guided cryoablation has been shown to be safe and effective for treatment of small renal neoplasms [28]. In our practice, MRI-guided cryoablation is reserved for ablation of renal neoplasms that are intra-parenchymal or endophytic and poorly visualized on US or non-contrast CT (Fig. 4).

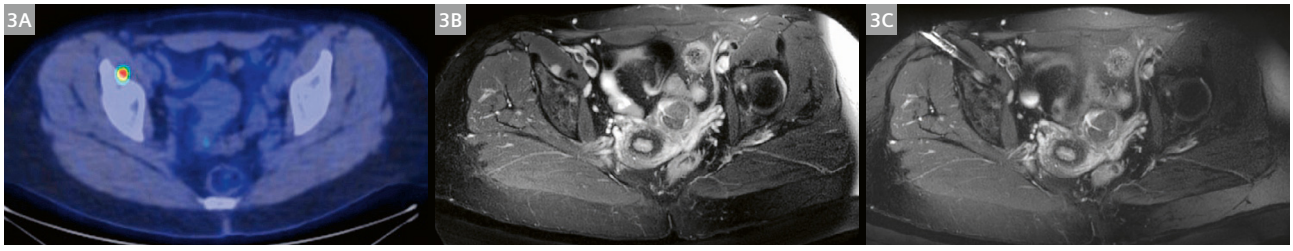

3 MRI-guided muscle lesion biopsy to determine benign versus malignant. **(3A)** shows an axial fluorodeoxyglucose (FDG) PET-CT image demonstrating a lesion with increased activity in the right iliopsoas muscle. CT-guided biopsy was unsuccessful. **(3B)** demonstrates a T2-weighted MR lesion in the same location as the abnormal PET activity. **(3C)** demonstrates an 18Ga ITP biopsy needle through the lesion. (Unpublished images)

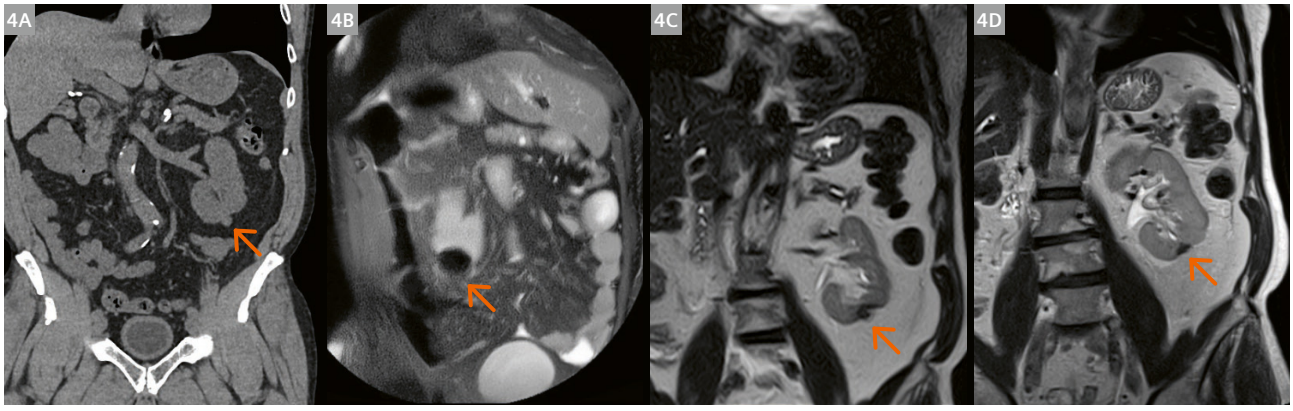

4 MRI-guided renal mass ablation for a 65-year-old man with a history of right kidney resection for renal cell carcinoma and development of a new left lower pole renal mass. **(4A)** shows a non-contrast CT image demonstrating a tiny mass on the lower pole of the left kidney. **(4B)** demonstrates T2-weighted MR images showing the iceball encompassing the tiny nodule. **(4C)** shows T2-weighted images three months post-ablation. **(4D)** shows T2-weighted images two years post-ablation. (Unpublished images)

Prostate and seminal vesicles

MRI-guided laser ablation of the prostate with MR thermometry in a 64-year-old man with rising prostate specific antigen (PSA) and biopsy-positive Gleason 7 (4+3) disease in the left mid prostate: MRI-guided thermometry allows continuous monitoring of the ablation heating during treatment (Fig. 5).

MRI-guided focal cryoablation of the prostate for Gleason 7 (3+4) disease in the left anterior prostate: Ice ball monitoring is achieved with a balanced HASTE updating every 10–20 seconds (Fig. 6).

MRI-guided focused transurethral ultrasound ablation (TULSA) of the prostate for Gleason 7 disease in the left posterior prostate: The TULSA treatment device (TULSA-PRO, Profound Medical Corp., Mississauga, Canada) was placed over the wire into the urethra and positioned with the transducers in the prostatic tissue. During treatment, the MR temperature mapping is used to guide and control the treatment frequency and the power, which is monitored continuously.

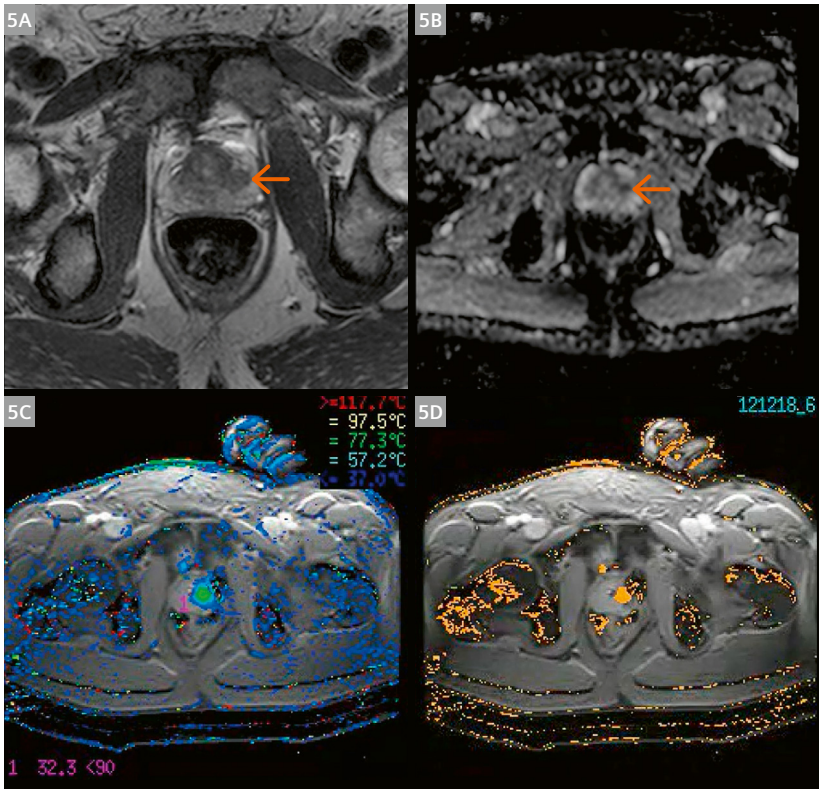

5 **(5A)** demonstrates T2-weighted imaging of the prostate showing a lesion in the left prostate. **(5B)** shows the ADC map demonstrating the restricted diffusion in the left prostate lesion. **(5C)** is the phase image during MR thermometry demonstrating heating in the left prostate. **(5D)** is the calculated damage map using time and temperature inputs into an Arrhenius equation. (Unpublished images)

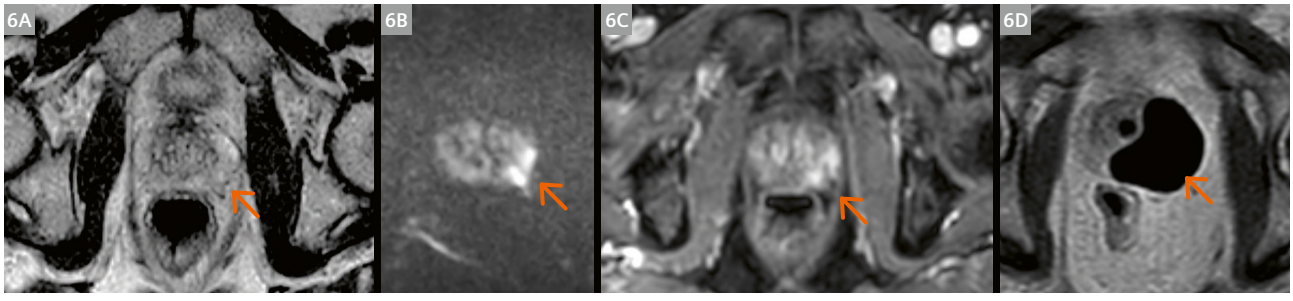

6 **(6A)** shows a T2-weighted image demonstrating decreased signal in the left posterior prostate (orange arrow). **(6B)** demonstrates restricted diffusion in this same area (orange arrow). **(6C)** demonstrates Gadolinium enhancement in this same area (orange arrow). **(6D)** demonstrates maximal ice ball formation encompassing the lesion (orange arrow). (Unpublished images)

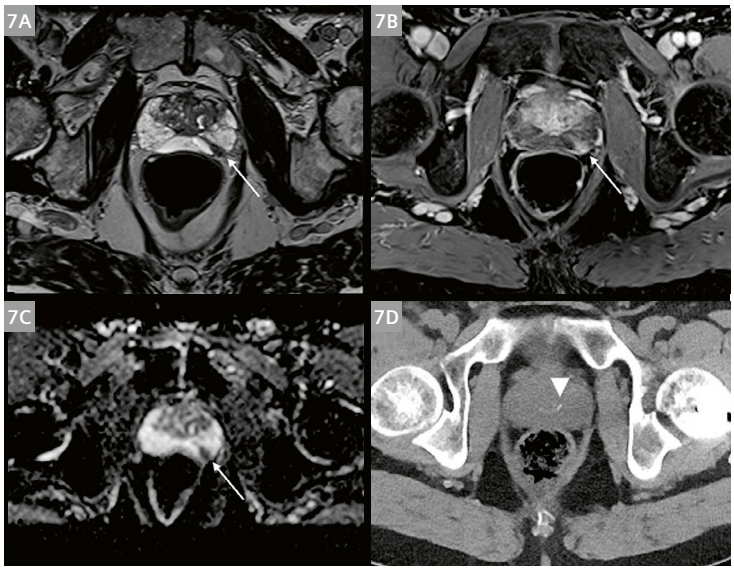

7 Pre-treatment workup for the MRI-guided TULSA for prostate cancer. **(7A)** demonstrates T2 abnormality in the left posterior peripheral zone of the prostate (white arrow). **(7B)** demonstrates hyperenhancement in a similar location after gadolinium (white arrow). **(7C)** demonstrates restricted diffusion in the ADC map for the lesion (white arrow). **(7D)** demonstrates some very tiny calcifications, which can be worked around with the TULSA device (white arrowhead). (Unpublished data)

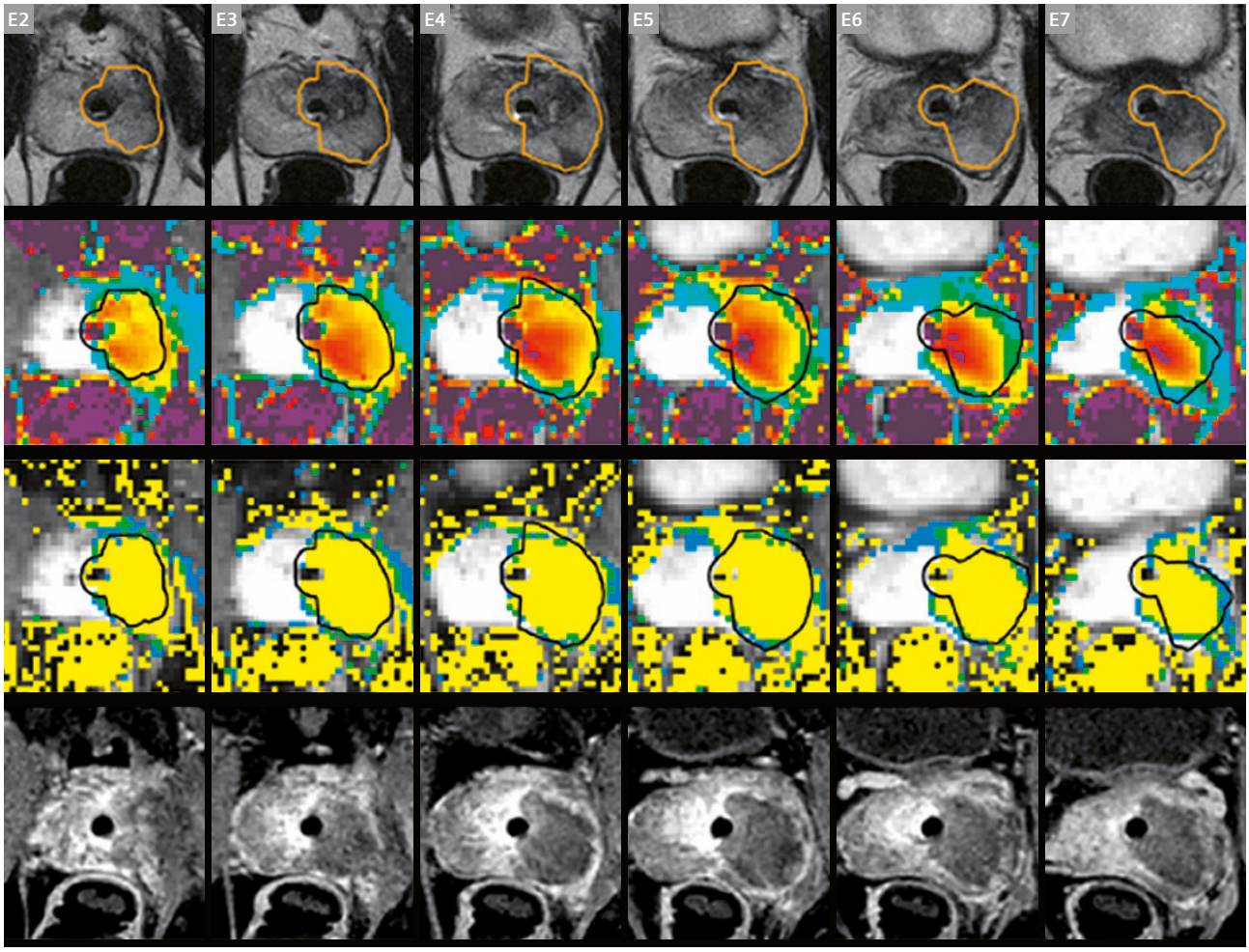

8 Summary images from the MRI-guided TULSA treatment. The first row shows the T2-weighted anatomic images corresponding to the location of the individual US transducers from E2–E7. The second row shows the maximal heat delivered by each US transducer at each level. The third row shows the calculated damage map based on the Arrhenius equation. The fourth row shows the postgadolinium images after the ablation, confirming the treatment zone at each level. (Unpublished data)

Hepatobiliary

Image-guided thermal ablation is considered a curative-intent treatment for very early or early stage hepatocellular carcinoma (HCC) [29]. Additionally, thermal ablation is used for treatment of a wide range of metastases to the liver, particularly colorectal liver metastases (CRLM) [30]. Historically, US and CT were the most common imaging modalities used for guidance and monitoring during hepatic radiofrequency or microwave ablation [31, 35]. However, in recent years, MRI-guided thermal ablation including RFA, MWA (Fig. 9), laser ablation, and cryo-ablation have emerged as safe and effective treatment options, particularly when the liver lesion is best visualized by MRI. We have found MRI guidance and monitoring for ablation particularly useful for small hepatic tumors that are poorly visualized by ultrasound, and for tumors deep in the liver such as in the caudate lobe, high up in the hepatic dome, or adjacent to critical structures such as central bile ducts, stomach, or colon, where monitoring of the ablation zone is critical.

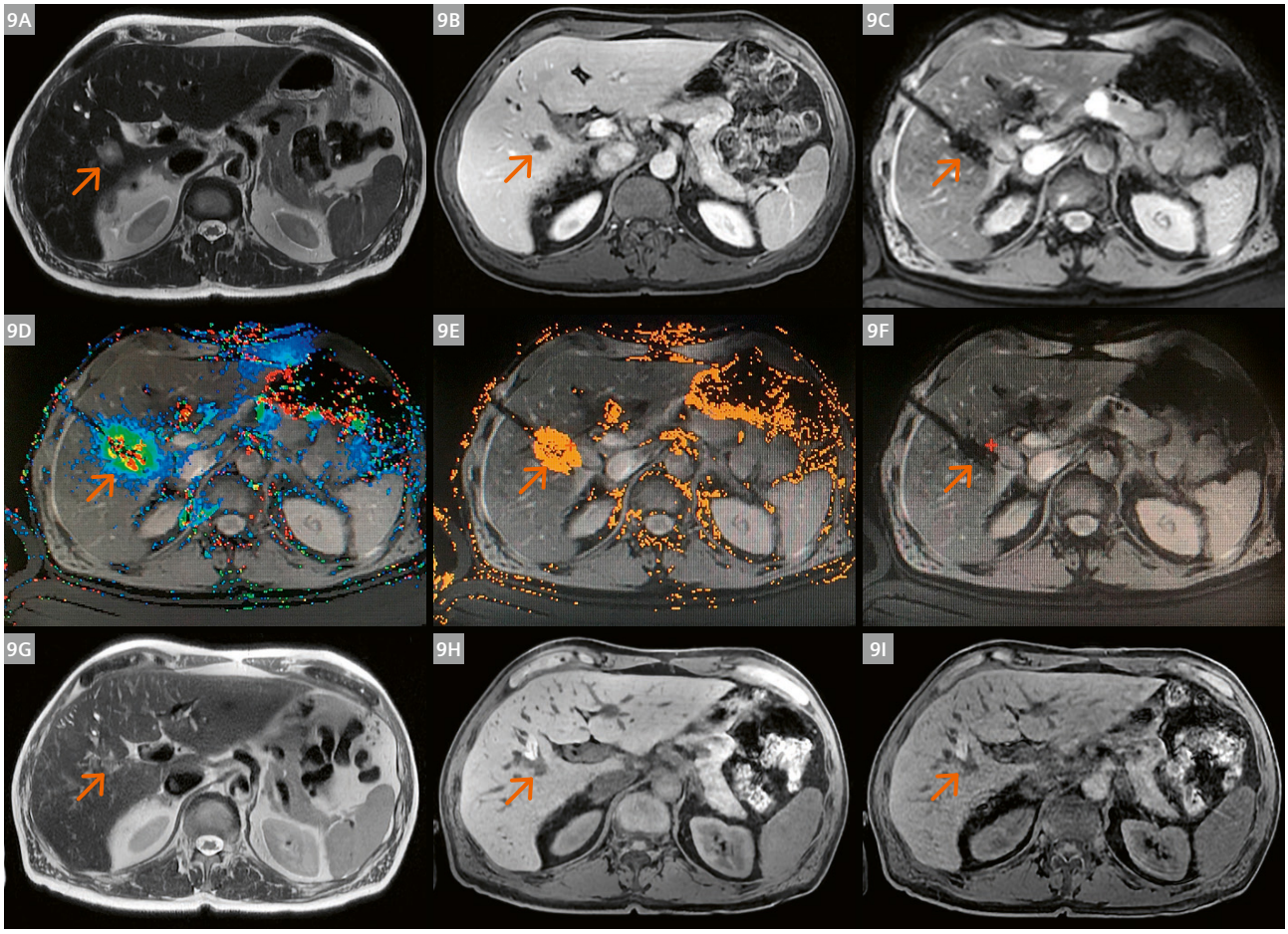

9 MRI-guided microwave ablation in a 72-year-old male for metastatic prostate cancer to the liver with central lesion. **(9A)** is the T2 weighted image demonstrating a small central lesion (orange arrow). **(9B)** shows the post-gadolinium image demonstrating delayed enhancement to the remaining liver typical of prostate cancer mets (orange arrow). **(9C)** demonstrates placement of the microwave antennae using a combination of US/MRI guidance (orange arrow). **(9D)** (phase imaging), **(9E)** (estimated damage map), and **(9F)** (T1 anatomic imaging) are from the temperature mapping proton resonance frequency imaging during the ablation. **(9D)** demonstrates the active temperature rise from the ablation (orange arrow). **(9E)** shows the damage map based on time and temperature change measurements using the Arrhenius equation (orange arrow). Followup MRI at three months post-ablation with **(9G)** (T2-weighted images), **(9H)** (pre-contrast T1 images), and **(9I)** (post-gadolinium images) demonstrating significant decrease in size since treatment consistent with evolving ablation changes. (Unpublished images)

Musculoskeletal and soft tissue

There has been an increasing role for image-guided thermal ablative therapies in the treatment of musculoskeletal and soft tissue tumors including the use of MRI guidance [36–38]. MRgFUS and cryoablation are feasible for treatment of focal metastatic disease to the bone. Additionally, several series have reported on the safety and effectiveness of percutaneous ablation for treatment of extra-abdominal desmoid tumors [39–41]. MRI-guided ablation is particularly beneficial when desmoid tumors are in close proximity to critical structures such as hollow viscus or nerves. Lastly, in patients with soft tissue oligometastatic disease, MRI-guided cryoablation offers a minimally invasive palliative treatment option [42, 43].

Peripheral soft tissue vascular anomalies

Peripheral soft tissue vascular anomalies (VA) include vascular tumors and vascular malformations. While percutaneous image-guided sclerotherapy and embolization are considered first-line treatments for symptomatic VA depending on size, location, and flow characteristics, emerging evidence suggests that MRI-guided laser ablation and cryoablation (Fig. 10) are safe and effective for treatment of symptomatic peripheral soft tissue VA [44–46]. In our practice, the most common vascular anomalies we treat with MRI-guided ablation include both pediatric and adult focal slow-flow venous or venolymphatic malformations, and focal vascular tumors, most commonly in the trunk or extremities. Less commonly, we have treated small focal high-flow arteriovenous malformations (AVMs) with MRI-guided ablation and a tourniquet proximal to the site of ablation to decrease the high flow, and focal cervicofacial slow-flow venous malformations.

Conclusions and future directions

Significant advancements in iMRI magnets, technology, and devices over the last three decades have enabled rapid growth of clinical body iMRI applications including lesion localization, biopsy, drainage, sclerotherapy, and ablation. Building a successful clinical iMRI practice requires

1. multidisciplinary collaboration and teamwork, including interventional and diagnostic radiologists, clinicians, MR physicists, technologists and nurses, anesthesiologists and nurse anesthetists, administrators and industry partners,
2. investment in personnel, space, equipment, and resources,
3. education of referring clinicians regarding the clinical safety and effectiveness of clinical body iMRI applications, particularly as a problem-solving tool when other image-guided procedures have failed or are deemed not technically feasible. Safety in the iMRI environment is paramount and requires close collaboration with MR physicists and MRI safety officers. Ongoing technological and technique advancements such as interventional PET/MRI, advanced navigation systems, and robotics will help interventional radiologists continue to push the frontiers of body iMRI applications in the coming decades [47, 48].

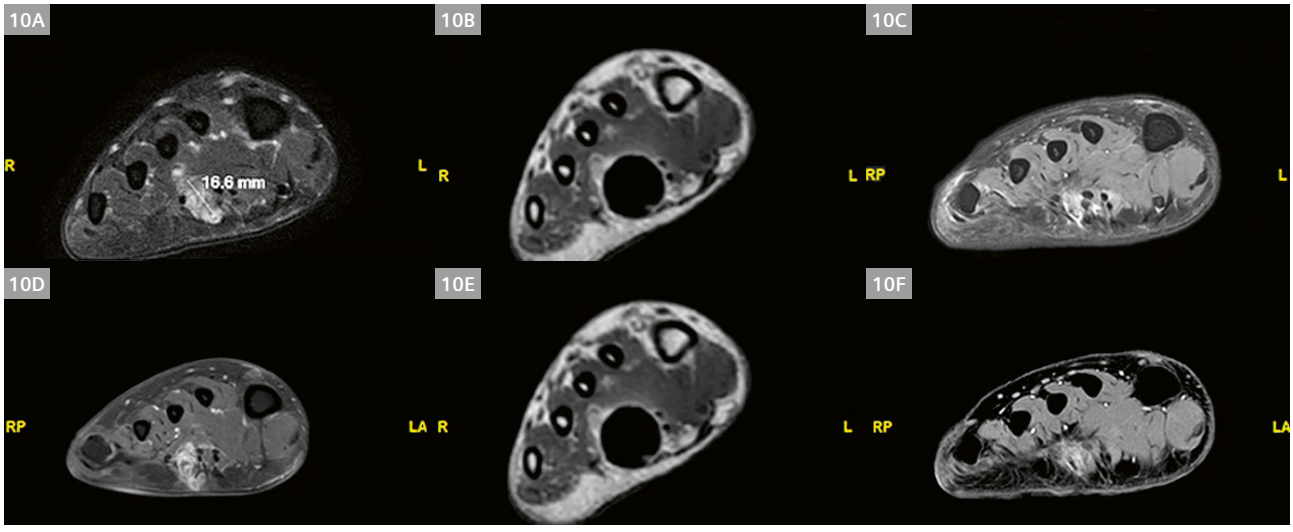

10 **(10A)** demonstrates high T2 signal in the plantar aspect of the foot, representing a slow-flow vascular malformation causing significant pain to the patient every day when walking. **(10D)** demonstrates the gadolinium enhancement within the vascular malformation. **(10B)** and **(10E)** demonstrate the ice ball formation during the MRI-guided cryoablation. **(10C)** represents the postablation T2 signal change, which usually decreases significantly. **(10F)** represents the postablation gadolinium lack of enhancement consistent with treatment and no flow. (Unpublished images)

References

1 Thompson SM, Gorny KR, Koepsel EMK, Welch BT, Mynderse L, Lu A, et al. Body Interventional MRI for Diagnostic and Interventional Radiologists: Current Practice and Future Prospects. Radiographics. 2021;41(6):1785–801.
2 Mueller PR, Stark DD, Simeone JF, Saini S, Butch RJ, Edelman RR, et al. MR-guided aspiration biopsy: needle design and clinical trials. Radiology. 1986;161(3):605–9.
3 Lufkin R, Teresi L, Chiu L, Hanafee W. A technique for MR-guided needle placement. AJR Am J Roentgenol. 1988;151(1):193–6.
4 Duckwiler G, Lufkin RB, Teresi L, Spickler E, Dion J, Vinuela F, et al. Head and neck lesions: MR-guided aspiration biopsy. Radiology. 1989;170(2):519–22.
5 Sedaghat F, Tuncali K. Enabling Technology for MRI-Guided Intervention. Top Magn Reson Imaging. 2018;27(1):5–8.
6 Busse H, Kahn T, Moche M. Techniques for Interventional MRI Guidance in Closed-Bore Systems. Top Magn Reson Imaging. 2018;27(1):9–18.
7 Sequeiros RB, Ojala R, Kariniemi J, Perala J, Niinimaki J, Reinikainen H, et al. MR-guided interventional procedures: a review. Acta Radiol. 2005;46(6):576–86.
8 Weiss CR, Nour SG, Lewin JS. MR-guided biopsy: a review of current techniques and applications. J Magn Reson Imaging. 2008;27(2):311–25.
9 White MJ, Thornton JS, Hawkes DJ, Hill DLG, Kitchen N, Mancini L, et al. Design, operation, and safety of single-room interventional MRI suites: practical experience from two centers. J Magn Reson Imaging. 2015;41(1):34–43.
10 Nour SG, Lewin JS. Creating a Clinical Interventional MRI Service. Top Magn Reson Imaging. 2018;27(1):25–31.
11 Lu A, Woodrum DA, Felmlee JP, Favazza CP, Gorny KR. Improved MR-thermometry during hepatic microwave ablation by correcting for intermittent electromagnetic interference artifacts. Phys Med. 2020;71:100–107.
12 Gorny KR, Favazza CP, Lu A, Felmlee JP, Hangiandreou NJ, Browne JE, et al. Practical implementation of robust MR-thermometry during clinical MR-guided microwave ablations in the liver at 1.5 T. Phys Med. 2019;67:91–99.
13 Ma C, Long ZY, Lanners DM, Tradup DJ, Brunnquell CL, Felmlee JP, et al. Protocol for testing suitability of compact US imaging systems for use inside MRI suites, and application to one commercial US system. Biomed Phys Eng Expr. 2016;2(4).
14 Yutzy SR, Duerk JL. Pulse sequences and system interfaces for interventional and real-time MRI. J Magn Reson Imaging. 2008;27(2):267–75.
15 Kahn T, Busse H. Interventional magnetic resonance imaging. Heidelberg: Springer; 2012. xvii, pp. 496.
16 Kaye EA, Granlund KL, Morris EA, Maybody M, Solomon SB. Closed-Bore Interventional MRI: Percutaneous Biopsies and Ablations. AJR Am J Roentgenol. 2015;205(4):W400–10.
17 Lewin JS, Nour SG, Duerk JL. Magnetic resonance image-guided biopsy and aspiration. Top Magn Reson Imaging. 2000;11(3):173–83.
18 Nour SG, Lewin JS. Percutaneous biopsy from blinded to MR guided: an update on current techniques and applications. Magn Reson Imaging Clin N Am. 2005;13(3):441–64.
19 Thompson SM, Gorny KR, Jondal DE, Rech KL, Mardini S, Woodrum DA. MRI-guided Wire Localization Surgical Biopsy in an Adolescent Patient with a Difficult to Diagnose Case of Lymphoma. Cardiovasc Intervent Radiol. 2017;40(1):135–138.
20 Tuen VC, Zingula SN, Moir C, Reed AM, Matsumoto JM, Woodrum DA. MRI guided wire localization muscle biopsy in a child with juvenile dermatomyositis. Pediatr Rheumatol Online J. 2013;11(1):15.
21 O'Mara DM, Berges AJ, Fritz J, Weiss CR. MRI-guided percutaneous sclerotherapy of venous malformations: initial clinical experience using a 3T MRI system. Clin Imaging. 2020;65:8–14.
22 Andreisek G, Nanz D, Weishaupt D, Pfammatter T. MR imaging-guided percutaneous sclerotherapy of peripheral venous malformations with a clinical 1.5-T unit: a pilot study. J Vasc Interv Radiol. 2009;20(7):879–87.
23 Woodrum DA, Gorny KR, Greenwood B, Mynderse LA. MRI-Guided Prostate Biopsy of Native and Recurrent Prostate Cancer. Semin Intervent Radiol. 2016;33(3):196–205.
24 Woodrum DA, Gorny KR, Mynderse LA. MR-Guided Prostate Interventions. Top Magn Reson Imaging. 2018;27(3):141–151.
25 Woodrum DA, Kawashima A, Gorny KR, Mynderse LA. Targeted prostate biopsy and MR-guided therapy for prostate cancer. Abdom Radiol (NY). 2016;41(5):877–88.
26 Atwell TD, Schmit GD, Boorjian SA, Mandrekar J, Kurup AN, Weisbrod AJ, et al. Percutaneous ablation of renal masses measuring 3.0 cm and smaller: comparative local control and complications after radiofrequency ablation and cryoablation. AJR Am J Roentgenol. 2013;200(2):461–6.
27 Thompson SM, Schmitz JJ, Thompson RH, Weisbrod AJ, Welch BT, Viers BR, et al. Introduction of Microwave Ablation Into a Renal Ablation Practice: Valuable Lessons Learned. AJR Am J Roentgenol. 2018;211(6):1381–1389.
28 Cazzato RL, De Marini P, Leonard-Lorant I, Leclerc L, Auloge P, Tricard T, et al. Safety and Oncologic Outcomes of Magnetic Resonance Imaging-Guided Cryoablation of Renal Cell Carcinoma: A 10-Year Single-Center Experience. Invest Radiol. 2021;56(3):153–162.
29 Weinstein JL, Ahmed M. Percutaneous Thermal Ablation for Hepatocellular Carcinoma. Semin Intervent Radiol. 2020;37(5):527–536.
30 Ruers T, Van Coevorden F, Punt CJ, Pierie JE, Borel-Rinkes I, Ledermann JA, et al. Local Treatment of Unresectable Colorectal Liver Metastases: Results of a Randomized Phase II Trial. J Natl Cancer Inst. 2017;109(9):djx015.
31 Yang N, Gong J, Yao L, Wang C, Chen J, Liu J, et al. Magnetic resonance imaging-guided microwave ablation of hepatic malignancies: Feasibility, efficacy, safety, and follow-up. J Cancer Res Ther. 2020;16(5):1151–1156.
32 Xiang J, Liu M, Lu R, Wang L, Xu Y, He X, et al. Magnetic resonance-guided ablation of liver tumors: A systematic review and pooled analysis. J Cancer Res Ther. 2020;16(5):1093–1099.
33 Winkelmann MT, Gohla G, Kubler J, Weiss J, Clasen S, Nikolaou K, et al. MR-Guided High-Power Microwave Ablation in Hepatic Malignancies: Initial Results in Clinical Routine. Cardiovasc Intervent Radiol. 2020;43(11):1631–1638.
34 Weiss J, Winkelmann MT, Gohla G, Kubler J, Clasen S, Nikolaou K, et al. MR-guided microwave ablation in hepatic malignancies: clinical experiences from 50 procedures. Int J Hyperthermia. 2020;37(1):349–355.
35 Chen J, Lin Z, Lin Q, Lin R, Yan Y, Chen J. Percutaneous radiofrequency ablation for small hepatocellular carcinoma in hepatic dome under MR-guidance: clinical safety and efficacy. Int J Hyperthermia. 2020;37(1):192–201.
36 Ahrar K, Sabir SH, Yevich SM, Sheth RA, Ahrar JU, Tam AL, et al. MRI-Guided Interventions in Musculoskeletal System. Top Magn Reson Imaging. 2018;27(3):129–139.
37 Nour SG, Monson DK. MRI-guided musculoskeletal soft tissue interventions. Top Magn Reson Imaging. 2011;22(4):197–205.
38 Kurup AN, Callstrom MR. Increasing Role of Image-Guided Ablation in the Treatment of Musculoskeletal Tumors. Cancer J. 2016;22(6):401–410.

39 Griffin MO, Kulkarni NM, O'Connor SD, Sudakoff GS, Lea WB, Tutton SM. Magnetic Resonance-Guided Focused Ultrasound: A Brief Review With Emphasis on the Treatment of Extra-abdominal Desmoid Tumors. Ultrasound Q. 2019;35(4):346–354.
40 Havez M, Lippa N, Al-Ammari S, Kind M, Stoeckle E, Italiano A, et al. Percutaneous image-guided cryoablation in inoperable extra-abdominal desmoid tumors: a study of tolerability and efficacy. Cardiovasc Intervent Radiol. 2014;37(6):1500–6.
41 Schmitz JJ, Schmit GD, Atwell TD, Callstrom MR, Kurup AN, Weisbrod AJ, et al. Percutaneous Cryoablation of Extraabdominal Desmoid Tumors: A 10-Year Experience. AJR Am J Roentgenol. 2016;207(1):190–5.
42 Vaswani D, Wallace AN, Eiswirth PS, Madaelil TP, Chang RO, Tomasian A, et al. Radiographic Local Tumor Control and Pain Palliation of Sarcoma Metastases within the Musculoskeletal System with Percutaneous Thermal Ablation. Cardiovasc Intervent Radiol. 2018;41(8):1223–1232.
43 McMenomy BP, Kurup AN, Johnson GB, Carter RE, McWilliams RR, Markovic SN, et al. Percutaneous cryoablation of musculoskeletal oligometastatic disease for complete remission. J Vasc Interv Radiol. 2013;24(2):207–13.
44 Thompson SM, Callstrom MR, McKusick MA, Woodrum DA. Initial Results of Image-Guided Percutaneous Ablation as Second-Line Treatment for Symptomatic Vascular Anomalies. Cardiovasc Intervent Radiol. 2015;38(5):1171–8.
45 Cornelis FH, Labreze C, Pinsolle V, Le Bras Y, Castermans C, Bader C, et al. Percutaneous Image-Guided Cryoablation as Second-Line Therapy of Soft-Tissue Venous Vascular Malformations of Extremities: A Prospective Study of Safety and 6-Month Efficacy. Cardiovasc Intervent Radiol. 2017;40(9):1358–1366.
46 Cornelis FH, Marin F, Labreze C, Pinsolle V, Le Bras Y, Midy D, et al. Percutaneous cryoablation of symptomatic venous malformations as a second-line therapeutic option: a five-year single institution experience. Eur Radiol. 2017;27(12):5015–5023.
47 Reich CM, Sattler B, Jochimsen TH, Unger M, Melzer L, Landgraf L, et al. Practical setting and potential applications of interventions guided by PET/MRI. Q J Nucl Med Mol Imaging. 2020;65(1):43–50.
48 Hata N, Moreira P, Fischer G. Robotics in MRI-Guided Interventions. Top Magn Reson Imaging. 2018;27(1):19–23.



Contact

David Woodrum, M.D., Ph.D.
Radiology and Vascular Centers
Mayo Clinic
200 First St. SW
Rochester, MN 55905
USA
woodrum.david@mayo.edu

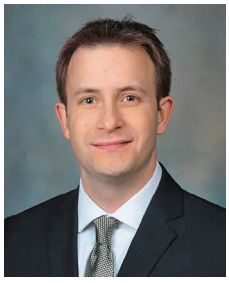

Scott M. Thompson, M.D., Ph.D.
Radiology
Mayo Clinic
200 First St. SW
Rochester, MN 55905
USA
thompson.scott@mayo.edu

Advanced Imaging-Based Medicolegal Death Investigation: Postmortem MRI and CT

Chris O'Donnell, MB BS[1,2]; Aoife Reid, BRadMedImag (Hons)[3]; Miranda Northey, Grad. Dip. MRT[1]; Catherine Vincent, BMedRadSci[1]; Felicity Barnes, MB BS (Hons)[1]; Joanna Glengarry, MB ChB (Dist.)[1,2]

[1]Victorian Institute of Forensic Medicine, Melbourne, Australia
[2]Department of Forensic Medicine, Monash University, Australia
[3]Siemens Healthcare Pty. Ltd., Australia

Abstract

Postmortem computed tomography (PMCT) is well established for medicolegal death investigation. There are deficiencies in PMCT that can be overcome with postmortem magnetic resonance imaging (PMMRI) especially in the brain, spinal cord, and heart, and in young children. MRI sequences need to be adapted to the deceased, mostly to compensate for body cooling. In this case of hypoxic ischemic brain injury, both PMCT and PMMRI provided information about the deceased. This included iodine leak into the basal ganglia following high-dose antemortem CT scanning confirmed on dual energy PMCT, and swelling and T2 hyperintensity in gray matter of the basal ganglia and cortex on PMMRI. These findings were confirmed as hypoxic ischemic encephalopathy at autopsy examination.

Introduction

Postmortem computed tomography (PMCT) has become the standard of practice at many forensic institutions for investigating cause and manner of death. All admissions to our institution are scanned from head to toe. PMCT is used to triage the body to decide if there is a probable cause of death or to exclude traumatic injury, and to aid in determining if autopsy is necessary to advance the diagnosis and further characterize pathology. PMCT-guided procedures can also be undertaken and include angiography, specimen sampling such as bladder aspiration or orogastric tube insertion, and organ biopsy. Pathologists use PMCT to guide the autopsy dissection, concentrating on the areas of suspected pathology and avoiding the need to open all body cavities such as the skull if CT findings are negative. Retrospective review of PMCT can aid in interpreting findings at autopsy. Magnetic resonance imaging (MRI) is rarely used in postmortem practice due to difficulties in access. However, it can provide more information as long as sequences are adapted to the deceased to compensate for reduced body temperature, decomposition, and absence of blood flow. Image interpretation in both PMCT and postmortem MRI (PMMRI) differs from clinical imaging due to changes that occur in the body after death, and requires specialized postmortem imaging experience.

Although PMCT is useful for the analysis of bones, chest, abdomen, and hemorrhage, it has limited application as intravenous radiographic contrast agent is not administered after death. Major areas of deficiency include the brain, spinal cord, heart, and young children, where there is minimal abdominal and peripheral fat to separate organs and other structures. MRI has excellent contrast resolution in these areas. It is therefore complementary to CT and can provide a complete analysis of the body contents for forensic purposes.

Case report

A middle-aged adult was found unconscious on the floor. Prolonged resuscitation ensued and they were transferred to a hospital emergency department. Imaging in hospital included a CT brain scan with angiography and a CT pulmonary angiogram (CTPA) with abdomen and pelvis examination using a total of 150 cc radiographic contrast (Omnipaque 350 iohexol: 113.25 g/150 mL, GE Healthcare Australia Pty Ltd, Melbourne, Australia). The CT brain scan showed diffuse brain swelling and no hemorrhage. The CTPA showed no pulmonary embolism, and examination of the abdomen/pelvis was otherwise normal. Clinical testing subsequently confirmed brain death, and the patient was extubated. Given the sudden and unexpected nature of the death, it was referred to the coroner for medicolegal death investigation, and the decedent was transferred to the Victorian Institute of Forensic Medicine (VIFM). A whole-body CT was performed on admission, followed by dedicated dual energy CT of the brain based on initial findings. A postmortem brain MRI was performed after the body had been stored in refrigeration at ~ 4 °C. A full autopsy examination was undertaken after the MRI.

Technique

The institute's mortuary-based CT scanner is a SOMATOM Drive with software version VB20A. The PMCT technique included whole-body imaging from head to toe, and dedicated imaging with a smaller field of view through the head and neck (see Table 1).

Dual energy PMCT of the head was performed (see Table 2) and analyzed on *syngo*.via (version VB80D) using the CT Dual Energy workflow and the Virtual Unenhanced application profile.

The institute's mortuary-based MRI system is a 3T MAGNETOM Vida with software version XA60. Images were analyzed on *syngo*.via (version VB80D) using the MR Basic workflow. For imaging parameters, see Table 3.

After review of the whole-body CT scan to exclude internal metallic hardware, the body bag is opened, and an external examination is undertaken to detect and remove any metallic devices or other accoutrements on the skin. The body bag is then closed, with any metallic zips moved to the foot end. The body is carefully transferred with a ceiling hoist onto the eDrive dockable table. The head is positioned in the 64-channel head/neck coil, and the table is maneuvered to the scanner and docked.

Scan parameter	Routine head	Routine whole body
Scan range	Vertex to T1	Vertex to toes
Slice thickness	1 mm	1.5 mm
Slice increment	0.8 mm	1.0 mm
FOV	300 mm	500 mm
Soft Tissue		
Kernel	H31s	B30f
Window	Base orbita	Abdomen
Bone		
Kernel	H70h	Vertex to toes
Window	Bone	
Lung		
Kernel		B70f
Window		Lung
Eff mAs	420	280
kV	120	120
Pitch	0.55	0.6
Care Dose4D	off	off
Care kV	off	off
Rotation time	1 sec	0.5 sec
Detector config.	128 x 0.6	128 x 0.6

Table 1: PMCT whole-body imaging.

Parameter	Dual energy head
Care kV	Tube A 100 / Tube B Sn 140
Quality ref mAs	119
Pitch	0.6
FOV	300
Detector config.	32 x 0.6
Slice thickness	1.5 mm
Slice increment	1.0 mm
Reconstruction kernel (s)	Qr 40
Reconstruction window	Cerebrum

Table 2: Dual energy PMCT of the head

Sequence	MPRAGE	T2 TSE axial	T2 TSE coronal	T2 TSE dark-fluid axial_fs	PD TSE axial	T2 SWI	Resolve (segmented DWI) axial
Echo time (ms)	2.32	87	87	80	11	20	TE1: 75 TE2: 125
Repetition time (ms)	2300	3600	3600	9000	2290	30	5650
Slice thickness (mm)	0.9	3.0	3.5	3.0	3.0	2.0	3.0
Acquisition matrix	256 x 256	312 x 512	312 x 512	174 x 304	243 x 400	270 x 352	200 x 200
Imaged field of view (mm)	240 x 240	187 x 230	187 x 230	187 x 230	187 x 230	196 x 230	230 x 230
Receiver bandwidth (Hz/pixel)	200	222	222	289	223	100	781
Acquisition time (min:sec)	5.21	2.18	2.47	1.50	2.00	1.45	3.48
Acceleration	GRAPPA 2	GRAPPA 4	GRAPPA 4	GRAPPA 2	GRAPPA 2	Wave CAIPI: 6	SMS:2,: GRAPPA 2
AI (Deep Resolve Boost, Deep Resolve Sharp)	n/a	DRB:med; DRS	DRB:med;	50, 800	0.5 × 0.5 × 3.0	1.5 × 1.5 × 4.0	1.0 × 1.0 × 3.0
Inversion time (ms)*	900	n/a	n/a	Variable*	n/a	n/a	n/a
Flip angle	8	150	150	150	150	15	180
b values (s/mm^2)	n/a	n/a	n/a	n/a	n/a	n/a	b0; b1500; Calc b2000

Table 3: Imaging parameters
* = depends on body temperature (see Fig. 4)
n/a = not applicable

Image review

The PMCT of the brain shows bilateral symmetrical hyperdensity in the basal ganglia, including caudate heads and lentiform nuclei. On dual energy CT (DECT), this hyperdensity is shown to represent iodine and disappears on the virtual non-contrast reconstruction (Fig. 1).

The PMMRI of the brain demonstrates swelling and increased T2 signal in the basal ganglia (Fig. 2). Further swelling and increased T2 signal indicative of edema is present within the cortical gray matter of both the frontal and parietal lobes, indicative of diffuse hypoxic ischemic brain injury. This was confirmed at autopsy.

Superimposition of colorized axial T2 TSE PMMRI and axial PMCT using *syngo*.via (Fig. 3).

Series of FLAIR sequences with differing inversion times (constant TR and TE) showing varying effects on T2 contrast and signal within the cerebrospinal fluid (CSF) to find the null point, i.e., net zero transverse magnetization of water (Fig. 4).

Discussion

Hypoxic ischemic injury to the brain occurs when there is generalized inadequate oxygenation leading to cell swelling and death (so-called hypoxic ischemic encephalopathy or HIE). This is often associated with cardiac arrest. Gray matter is more metabolically active than white, making it sensitive to hypoxemia and more likely to be affected. This includes the basal ganglia and cortical gray matter. On CT imaging, hypoxemia is manifested as edema within gray matter and the resultant swelling. Normally, intravenously injected radiographic contrast does not enter the brain tissue due to an intact blood-brain barrier that restricts it to the meninges and blood vessels. If the barrier is disrupted, as it is in hypoxic injury, the radiographic contrast can leak into the brain, especially the basal ganglia, leading to a phenomenon known as hyperdense basal ganglia (HBG).

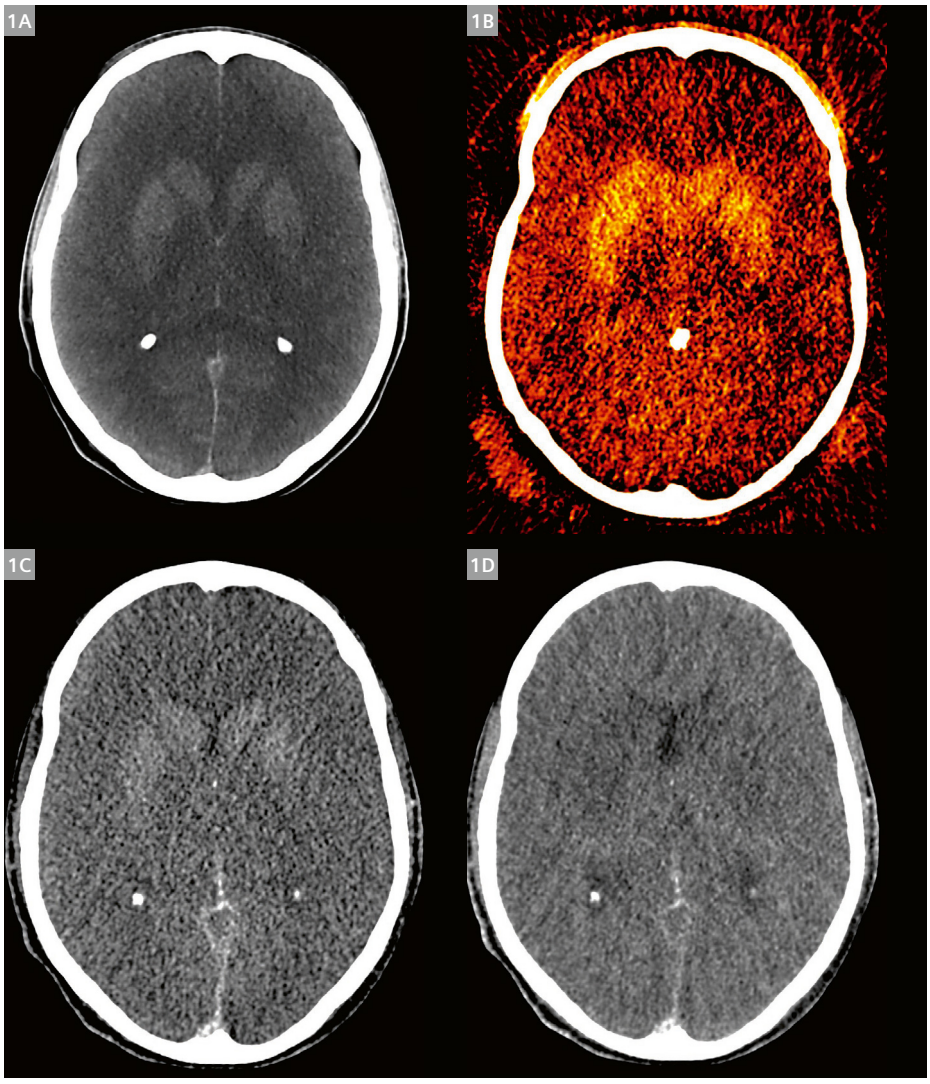

1 Axial PMCT brain **(1A)** showing bilateral symmetrical hyperdensity of basal ganglia. Axial PM DECT brain with iodine overlay **(1B)** shows that this hyperdensity is iodine deposition with a concentration of 1.5 mg/mL. Side-by-side comparison of DECT with iodine **(1C)** and virtual non-contrast **(1D)** showing loss of hyperdensity in the basal ganglia indicating the presence of iodine. Note how high-density blood in the superior sagittal sinus does not show loss of density on virtual non-contrast (VNC).



2 T2 TSE axial **(2A)** and coronal **(2B)** PMMRI showing bilateral symmetrical hyperintensity and swelling in basal ganglia indicative of hypoxic ischemic encephalopathy (HIE).

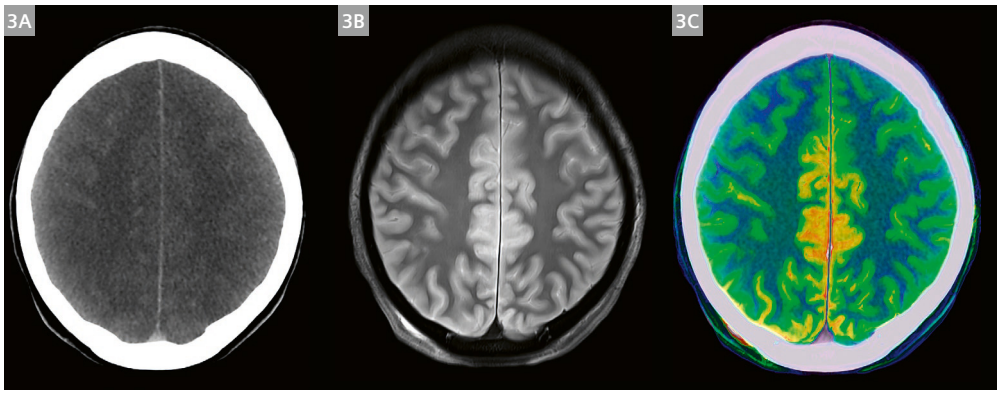

3 Axial PMCT **(3A)** shows minor swelling of the medial cortex. T2 TSE axial PMMRI **(3B)** shows significant swelling and abnormal T2 signal in the medial cortices. Fused colorized T2 TSE axial PMMRI and PMCT **(3C)**.

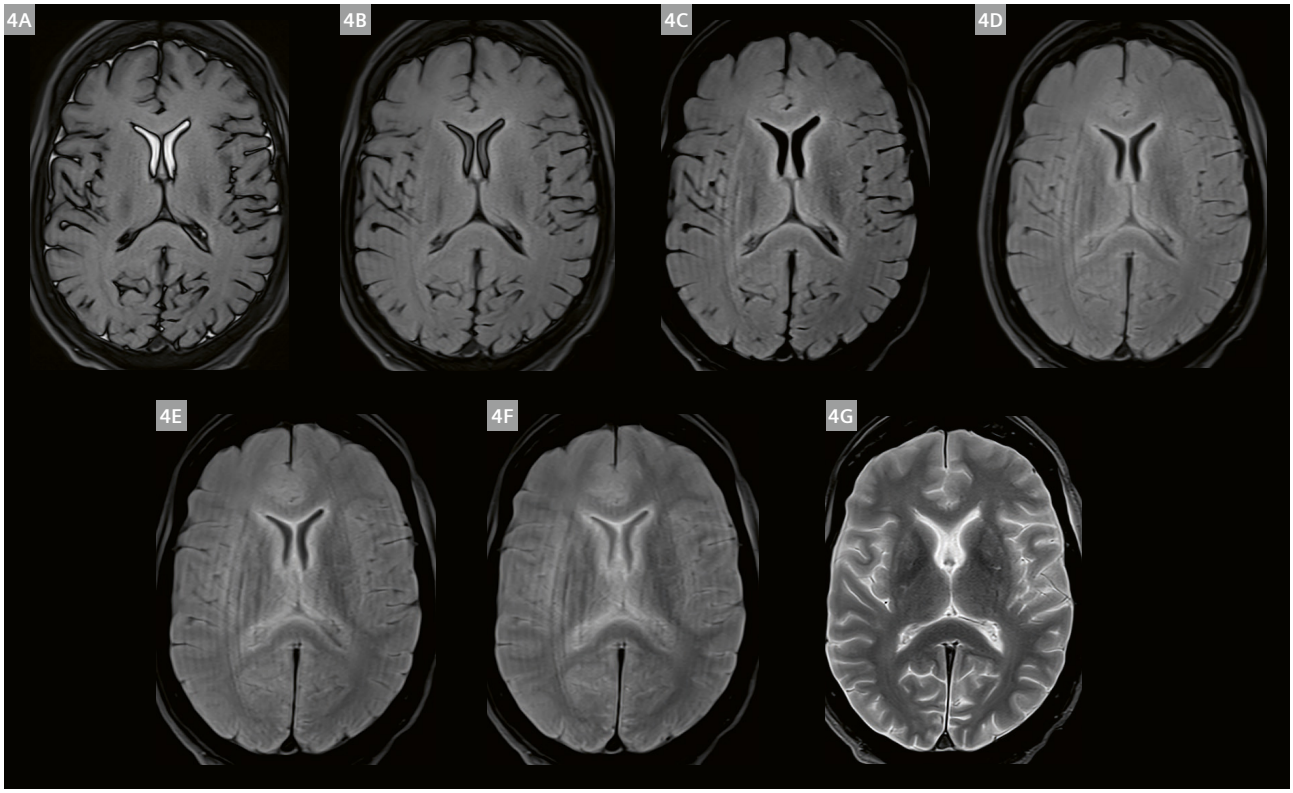

4 Axial T2 TSE dark-fluid FLAIR sequences with a TR of 9000, a TE of 80 ms, and a TI of **(4A)** 1000, **(4B)** 1200, **(4C)** 1400, **(4D)** 1600, **(4E)** 1800, **(4F)** 2000, and **(4G)** 2500 msec. The TI of 1400 ms produces the best signal suppression in CSF.

On PMCT, HBG is detected if an individual has an episode of severe hypoxic injury, is resuscitated to reestablish blood flow and oxygen to the brain, and then undergoes post collapse radiological imaging using large volumes of IV radiographic contrast (e.g., coronary angiography or a CT pan scan). Although not necessarily seen at the time of the antemortem CT, the contrast will progressively leak into the brain at sites where the blood-brain barrier is disrupted, such as the basal ganglia, and can be detected on PMCT as HBG.

Dual energy CT can detect iodine in tissues and can be used to confirm that this hyperdensity is iodine, distinguishing it from other causes such as nonketotic hyperglycemia, calcification, hemorrhage, and copper deposition (Wilson disease).

MR imaging is temperature sensitive, especially for T1-weighted sequences, leading to low signal intensity and tissue contrast [1]. T2 contrast and signal intensity are less affected. Deceased persons are routinely stored in fridges at ~ 4 °C. The temperature of the decedent at the time of scanning varies depending on body habitus and duration of refrigeration. If necessary, this can be quantified using rectal or forehead temperature measurements [2]. Limited T1-weighted sequences are performed in PMMRI and are not relied upon for diagnosis, apart from detection of methemoglobin and fat. T2-weighted sequences on PMMRI are most useful without flow artifacts. This means that time-of-flight MR angiography is not possible, but CSF is always universally white and brain edges are extremely sharp as there is no brain pulsation. FLAIR imaging is problematic due to temperature sensitivity, meaning inversion times differ from clinical practice [3]. We routinely perform a series of rapid preliminary FLAIR sequences with variable TI (1000–1600 ms) to determine the "sweet spot" or null point of CSF signal (Fig. 4). Once determined, this TI is then used for a full diagnostic sequence. A TI of 1400 ms is most commonly used on our magnet at 3T on bodies taken directly from refrigeration. This contrasts with the typical TI of 2500 ms used in clinical cases at body temperature.

Despite immediate changes to the body that occur following death, swelling and abnormal T2 signal in the brain on MRI are not a feature until decomposition progresses. It is somewhat counterintuitive that pathology such as HIE can be readily detected as swelling and increased T2 signal on PMMRI, although diffusion-weighted imaging is more problematic. This means that PMMRI of the brain is a particularly useful investigative tool for many fatal neurological conditions such as infarction, mass lesions, hemorrhage, and HIE.

Conclusion

Postmortem imaging is now highly sophisticated. It uses all the CT and MRI techniques available in clinical radiology, albeit with adjustments to allow for changes in the body after death and refrigeration. In medicolegal practice, interpretation must also be tempered by the requirements of investigators and the criminal justice system to answer questions, which may not always be obvious to clinically trained medical specialists, whose focus is diagnostic and therapeutic rather than forensic. Imaging specialists must therefore be experts in interpreting imaging of deceased persons, have an understanding of the law, and be able to engage with legal professionals and investigators, including providing expert evidence in court.

References

1 Berger C, Bauer M, Scheurer E, Lenz C. Temperature correction of post mortem quantitative magnetic resonance imaging using real-time forehead temperature acquisitions. Forensic Sci Int. 2023;348:111738.
2 Berger C, Bauer M, Wittig H, Gerlach K, Scheurer E, Lenz C. Investigation of post mortem brain, rectal and forehead temperature relations. J Therm Biol. 2023;115:103615.
3 Bruguier C, Magnin V, Knebel JF, Grabherr S, Dunet V, Genet P. Inversion time optimization in postmortem 1.5 tesla FLAIR brain imaging: a pilot study. Int J Legal Med. 2025. doi: 10.1007/s00414-025-03571-6. Epub ahead of print.



Contact

Dr. Chris O'Donnell, MB BS, FRANZCR, MMed, GradDipForMed, FFFPMI (RCPA)
Forensic Radiologist
Victorian Institute of Forensic Medicine
65 Kavanagh St
Southbank VIC 3006
Australia
chris.odonnell@vifm.org

Examining Musculoskeletal Implants with Lower-Field MRI

Bianca Samsula[1], Simon Balzer[2], Mathias Nittka, Ph.D.[2]; Markus Lentschig, M.D.[1]

[1]ZEMODI - MVZ Zentrum für moderne Diagnostik, Bremen, Germany
[2]Siemens Healthineers, Erlangen, Germany

Implant surgery for musculoskeletal diseases has been progressing steadily in recent years, and the number of operations is continually growing. In Germany alone, some 200,000 hip replacements are performed each year, along with roughly 150,000 knee replacements. Improvements and new developments in implant technology mean that other joint replacement surgeries (such as for the shoulder, elbow, ankle, or knuckles) are also being performed increasingly frequently [1].

This is leading to rising demand for diagnostic imaging connected to pathologies at or around these implants*. Since the established methods of X-ray and CT imaging are of limited diagnostic value, patients are increasingly being referred to MRI.

With conventional high-field MRI scanners, it is difficult to examine body regions that contain metallic implants: The large difference in magnetic susceptibility between metal and the surrounding tissue causes significant local distortion of the magnetic field, which produces the familiar image artifacts in the region of the implant. Even when using advanced applications like WARP and SEMAC, the image quality on conventional 1.5T and 3T MRI systems remains limited, making it difficult to diagnose the pathology.

With a low field strength of 0.55T, the systems of the MAGNETOM Free. Platform have the advantage of producing significantly fewer susceptibility artifacts than is commonly the case with high-field systems. With far fewer distortions and artifacts in the direct vicinity of implants, these lower-field scanners make it possible to identify pathologies better than with high-field systems, despite the lower resolution and signal-to-noise ratio. Like imaging at higher field strengths, these examinations use turbo spin echo (TSE) sequences with optimized acquisition parameters that are activated via the WARP option in the sequence. Increased excitation and readout bandwidths are crucial here, especially in combination with STIR technology as a more robust alternative to conventional spectral fat saturation for fat suppression.

In addition to established advanced acceleration techniques (parallel imaging and Simultaneous Multi-Slice acquisition), deep-learning-based image reconstruction methods offer enormous potential – now also at lower field strengths. This means that, even at these lower field strengths, it is possible to produce high-quality diagnostic MR images in very acceptable acquisition times.

The combination of lower field strength and deep learning therefore lends itself particularly well to imaging implants using 0.55T systems in clinical routine.

This article will present our experience using a selection of case studies. Full protocols for the hip and knee regions are available on MAGNETOM World: www.magnetomworld.siemens-healthineers.com/clinical-corner/protocols

The patients were examined on a 0.55T MAGNETOM Free.Max using only TSE sequences with the WARP option and Deep Resolve reconstruction. The main parameters are presented in the tables. We did not use more advanced WARP techniques such as VAT[1] and SEMAC[2]. Since there were already so few distortions compared to high-field imaging, these techniques offered us no diagnostically relevant advantage that would have justified the disadvantages.

For hip examinations, patients were positioned on their back and head first. The Spine coil and the Contour M/L coil were used for imaging.

For knee examinations, patients were positioned on their back and feet first. The Contour Knee coil was used for imaging.

[1]View-angle tilting (VAT): Slices are acquired at a tilt angle to partially compensate for the metal distortions. This can cause some blurring, but VAT is essential for the SEMAC technique.

[2]Slice encoding for metal artifact correction (SEMAC): This technique can at least partially correct even very severe distortions. However, it is very time-consuming and therefore generally associated with a loss of resolution and contrast.

**The MRI restrictions (if any) of the metal implant must be considered prior to patient undergoing MRI exam. MR imaging of patients with metallic implants brings specific risks. However, certain implants are approved by the governing regulatory bodies to be MR conditionally safe. For such implants, the previously mentioned warning may not be applicable. Please contact the implant manufacturer for the specific conditional information. The conditions for MR safety are the responsibility of the implant manufacturer, not of Siemens Healthineers.*

Example images showing the advantage of lower field over high field

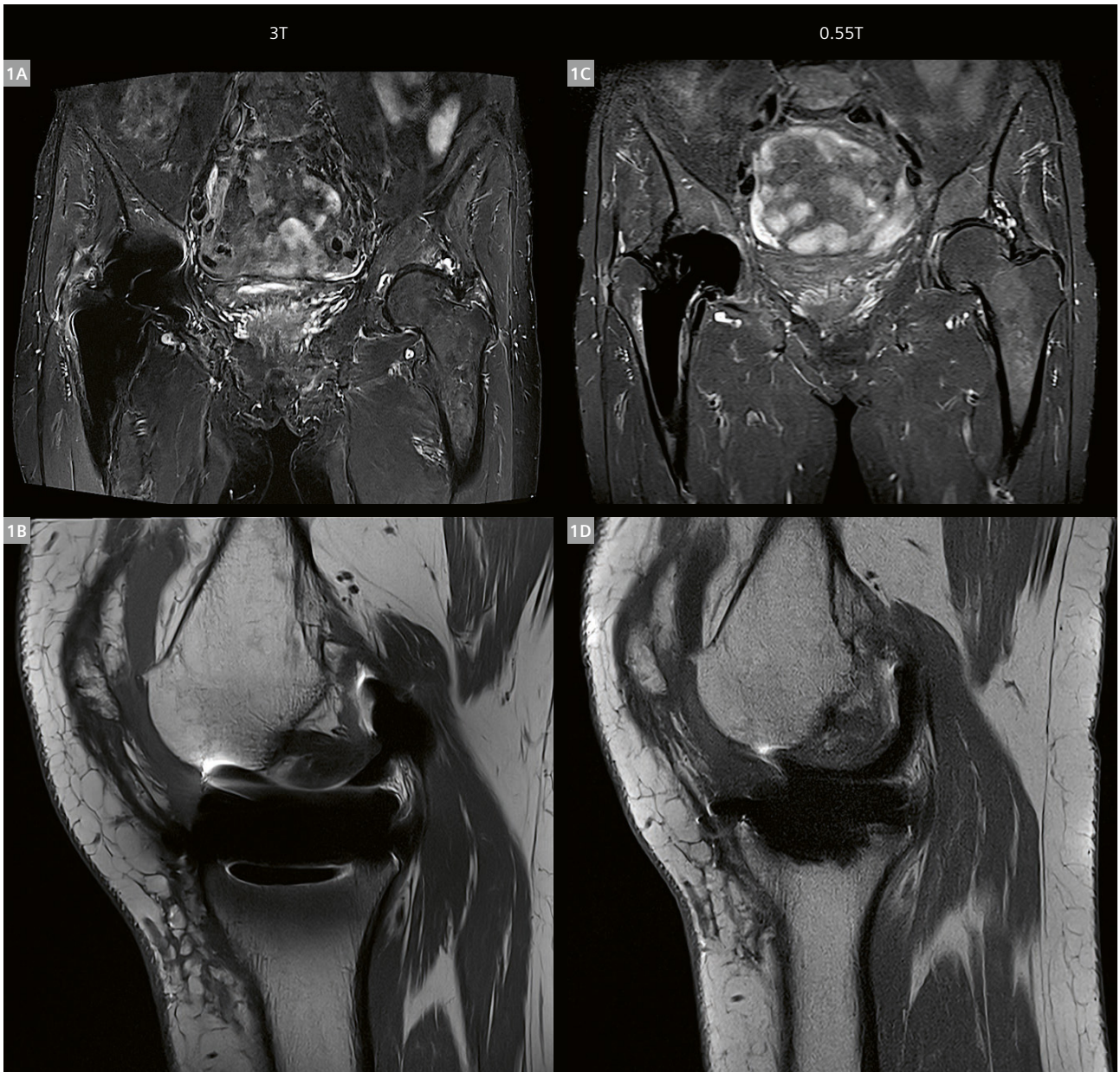

1 Left **(1A)** STIR cor and **(1B)** T1 TSE sag on a 3T system. Right **(1C)** STIR cor and **(1D)** T1 TSE sag on a 0.55T system.

Clinical case studies

Knee

Increasing pain after a partial knee replacement. Loosening? A Dual Energy CT scan showed no evidence of loosening. Bone marrow edema of the medial femoral condyle; stress reaction with joint effusion.

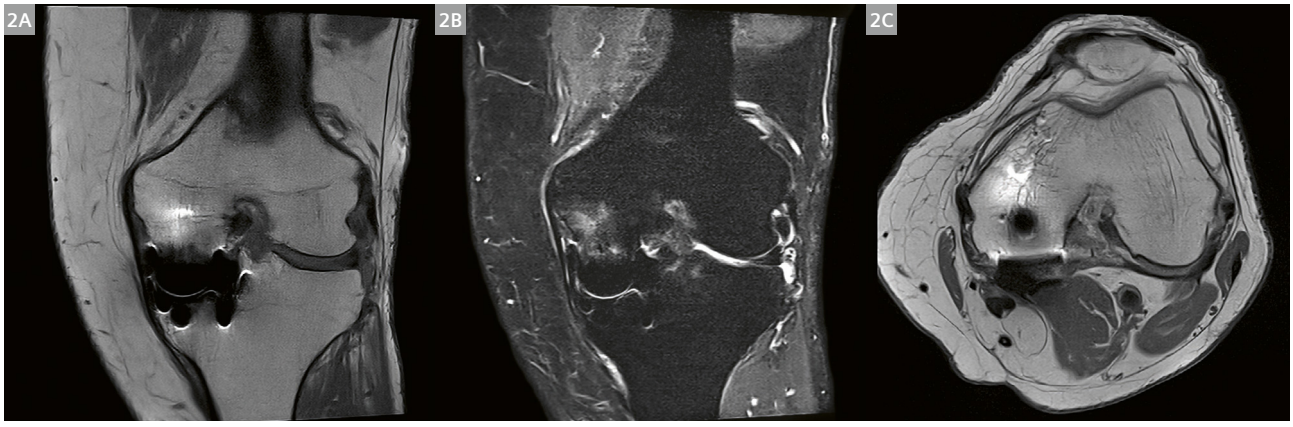

2 **(2A)** PD cor. **(2B)** STIR cor, bone marrow edema clearly visible. **(2C)** PD tra.

Knee

Increasing pain following partial knee replacement; establishing cause of pain. An examination on the 3T system was discontinued due to artifacts. Implant appears normal on MRI. Pronounced arthritic changes in the lateral joint cavity, Grade 3 lateral meniscus tear and Grade 4 chondromalacia at the lateral femoral condyle.



3 **(3A)** STIR cor, visible bone marrow edema with arthritic changes. **(3B)** STIR sag, visible bone marrow edema with arthritic changes. **(3C)** PD tra.

Hip

Pain after implantation of a gamma nail following femoral neck fracture approximately 12 months ago. Material intact. Fracture line still visible with significant soft tissue buildup.

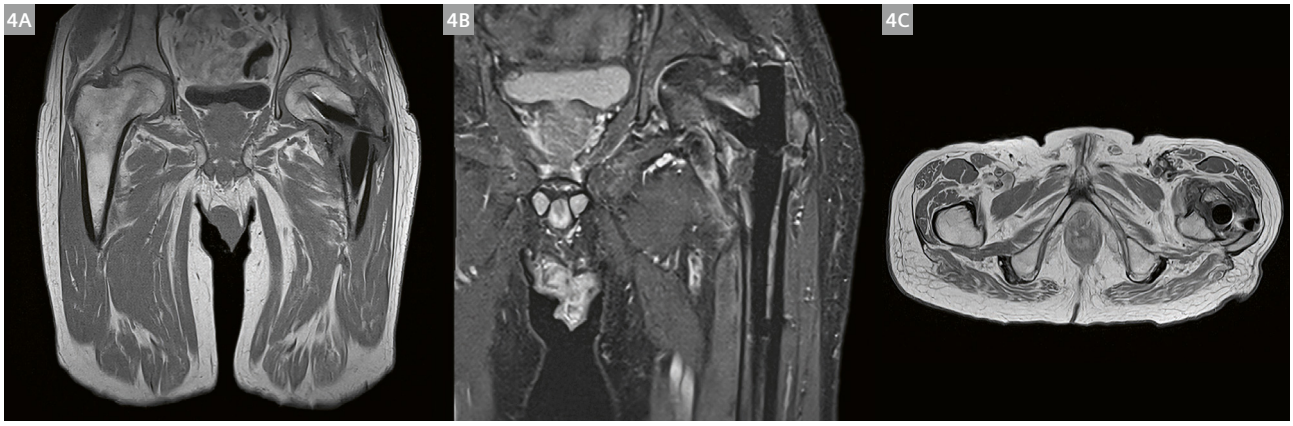

4 **(4A)** T1 cor. **(4B)** STIR cor, clearly visible soft tissue buildup. **(4C)** PD tra, clearly visible fracture line with soft tissue buildup.

Hip

Bilateral total hip replacement followed by recurring dislocation of the right hip prosthesis. Increasing pain in the right hip since falling eight months ago. No fracture, no loosening of the endoprosthesis, no bone lesion. Extensive joint effusion leaking into the trochanteric bursa.

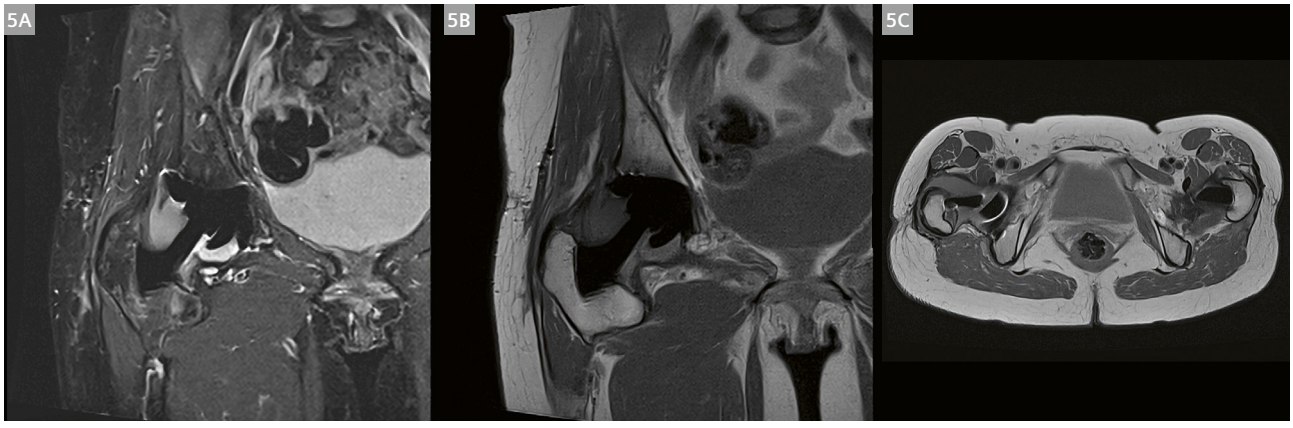

5 **(5A)** STIR cor, clearly visible effusion and hematoma. **(5B)** PD cor. **(5C)** PD tra, clearly visible effusion.

	T1 TSE sag	T1 TSE cor	STIR cor	STIR tra	STIR sag	PD TSE cor	PD TSE tra
Voxel size [mm³]	0.3 × 0.3 × 3.0	0.3 × 0.3 × 3.0	0.3 × 0.3 × 3.0	0.4 × 0.4 × 4.0	0.4 × 0.4 × 3.0	0.2 × 0.2 × 3.0	0.3 × 0.3 × 3.0
TR/TE [ms]	420 / 8.2	440 / 8.4	3800 / 39	3600 / 39	3500 / 38	2830 / 26	2710 / 25
PE-direction	H>>F	R>>L	R>>L	R>>L	H>>F	R>>L	R>>L
Phase oversampling [%]	150	150	130	200	200	140	150
Avg./Conc.	3 / 2	3 / 2	3 / 2	2 / 2	4 / 1	3 / 1	3 / 1
BW [Hz/px]	305	300	301	300	302	302	300
TA [min]	3:37	3:57	4:43	3:30	3:49	3:03	2:47

Table 1: Scan parameters, knee.

	PD TSE cor	T1 TSE cor	STIR cor
Voxel size [mm³]	0.5 × 0.5 × 3.0	0.5 × 0.5 × 3.0	0.6 × 0.6 × 3.0
TR/TE [ms]	2500 / 31	386 / 7.2	5000 / 45
PE-direction	R>>L	R>>L	R>>L
Phase oversampling [%]	100	200	200
Avg./Conc.	2 / 1	2 / 2	2 / 1
BW [Hz/px]	395	352	300
TA [min]	2:04	2:26	2:57

Table 2: Scan parameters, bilateral hip.

	PD TSE cor	T1 TSE cor	STIR cor	PD TSE sag	STIR sag
Voxel size [mm³]	0.5 × 0.5 × 3.0	0.5 × 0.5 × 3.0	0.7 × 0.7 × 3.0	0.5 × 0.5 × 3.0	0.7 × 0.7 × 3.0
TR/TE [ms]	2600 / 24	482 / 8	6100 / 35	3000 / 24	7100 / 35
PE-direction	R>>L	R>>L	R>>L	H>>F	H>>F
Phase oversampling [%]	170	170	200	200	200
Avg./Conc.	2 / 1	2 / 2	2 / 1	2 / 1	2 / 1
BW [Hz/px]	391	349	352	391	352
TA [min]	1:59	2:06	2:46	2:29	3:13

Table 3: Scan parameters, unilateral hip.

Hip

Total hip replacement in 2016. Increasing hip pain for roughly the past three years. Slight bone marrow edema along the stem of the prosthesis, markedly lateral, indicating loosening of the prosthesis.

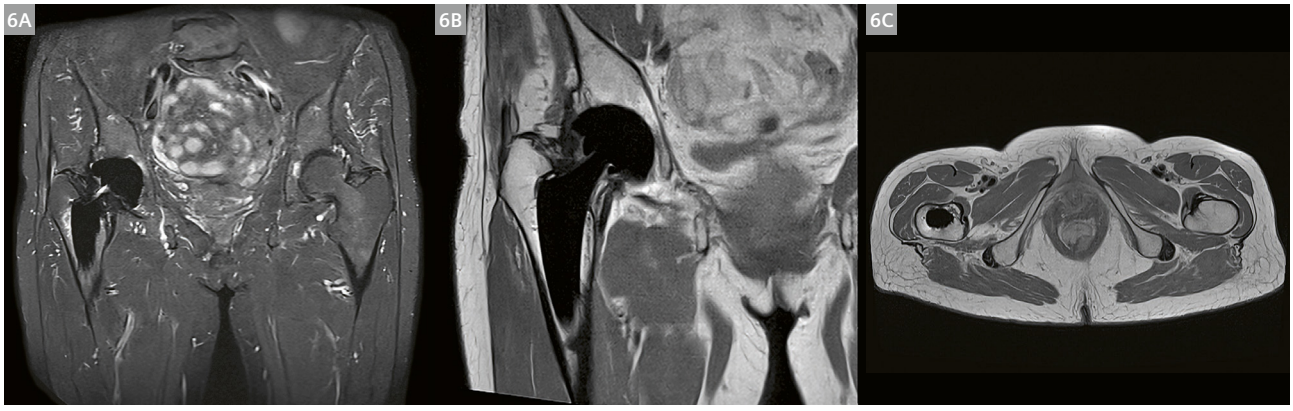

6 **(6A)** STIR cor, with visible bone marrow edema bordering the implant. **(6B)** PD cor. **(6C)** PD tra.

Conclusion

It has been three and a half years since our MAGNETOM Free.Max was installed, and we see the system as the perfect complement to our high-field scanners (a 3T MAGNETOM Skyra, a 3T MAGNETOM Lumina, a 1.5T MAGNETOM Altea, a 1.5T MAGNETOM Avanto Fit, and our PET/MR scanner, Biograph mMR). Thanks partly to its wide-bore design, our MAGNETOM Free.Max is ideal for examining claustrophobic or extremely overweight patients and is very popular among these populations. Particularly when it comes to examining patients with musculoskeletal implants, we find our lower-field system to be at a great advantage over the high-field systems. This means that diagnosing pathologies following implants is no longer limited to Dual Energy CT scanning: MR imaging can now supply crucial additional information for these cases.

References

1 Feuerriegel GC, Sutter R. Managing hardware-related metal artifacts in MRI: current and evolving techniques. Skeletal Radiol. 2024;53(9):1737–1750.



Contact

Bianca Samsula
ZEMODI - MVZ Zentrum für moderne Diagnostik
Schwachhauser Heerstraße 63a
28211 Bremen
Germany
bianca.samsula@zemodi.de



Markus Lentschig, M.D.
ZEMODI - MVZ Zentrum für moderne Diagnostik
Schwachhauser Heerstraße 63a
28211 Bremen
Germany
markus.lentschig@zemodi.de

Download the 0.55T MAGNETOM Free.Max protocols (**.exar1 and PDF**) at

www.magnetomworld.siemens-healthineers.com/clinical-corner/protocols

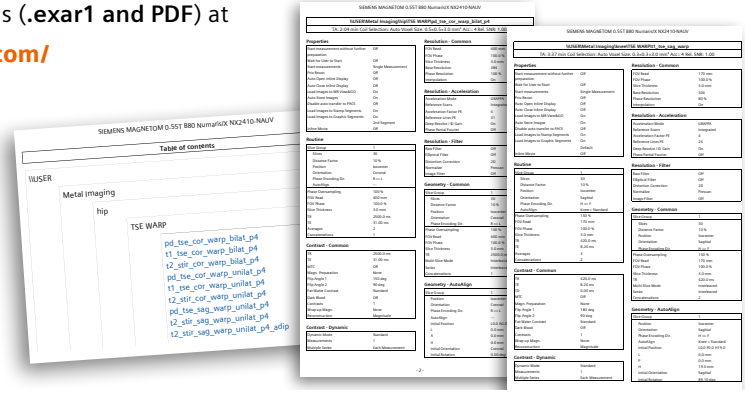

Mobile MRI: Revolutionizing Access to Advanced Imaging

Jakob Krebs Christensen

Agito Medical A/S, Nørresundby, Denmark

Historical development of mobile MRI units

The evolution of mobile MRI units represents a remarkable convergence of medical imaging technology and transportation engineering, driven by the fundamental challenge of bringing diagnostic capabilities to underserved populations and remote locations.

Early conceptualization (1980s)

The concept of mobile MRI emerged in the 1980s, shortly after magnetic resonance imaging became clinically established in major medical centers. As hospitals recognized the diagnostic value of MRI but faced significant capital investment barriers, the idea of shared mobile units began to take shape. Early pioneers faced considerable technical challenges: MRI systems needed precise magnetic field stability, extensive shielding from external electromagnetic interference, and substantial amounts of power, all of which seemed incompatible with mobile platforms.

The American FONAR Corporation tackled these obstacles with success and introduced the world's first mobile MRI unit in 1983. It received FDA approval in 1985 and began serving multiple separate hospital sites from 1986 [1].

The magnetic field strength on these first-generation mobile systems was typically limited to 0.5 Tesla or less, and image quality was compromised by vibrations and electromagnetic interference from the vehicle's systems.

Technological breakthroughs (1990s–2000s)

The mid-1990s marked a turning point, with several key technological advances. Improved superconducting magnet designs allowed for more compact systems while maintaining high field strength. Advanced shielding techniques, including both active and passive electromagnetic shielding, enabled mobile units to operate in various environments without significant image degradation. Vibration isolation systems were developed to minimize the impact of road transport and environmental factors on image quality.

During this period, manufacturers began producing purpose-built mobile MRI trailers with integrated power generation systems, patient areas, and operator consoles. The development of helium recapture systems (zero boil-off) reduced the operational costs associated with cryogenic coolant loss, making mobile units more economically viable and practical for routine clinical use.

Meeting current global healthcare challenges

Mobile radiology units provided by private companies are emerging as crucial solutions to one of the many pressing healthcare challenges facing the world today.

The World Health Organization (WHO) reports that over two-thirds of the global population lack access to radiology services [2]. This reflects a massive gap in diagnostic capabilities that mobile units are uniquely positioned to address. These flexible, transportable imaging solutions tackle inequities in healthcare access by bringing advanced diagnostic capabilities to underserved communities, rural hospitals, and regions with limited infrastructure.

The momentum gained during the last 10 years is attributed to the rising demand for decentralized healthcare, reflecting a broader shift toward more accessible, patient-centered care delivery models.

The growth of the mobile radiography industry is primarily driven by an increase in chronic diseases, necessitating more frequent diagnostic imaging. Another factor is its ability to address critical shortages in the healthcare workforce by providing imaging services without requiring investments in permanent facilities and long-term staffing commitments.

Mobile units offer rapid deployment capabilities for emergency situations, temporary coverage during equipment maintenance, and scalable solutions for varying patient volumes. In doing so, they provide a strategic response to the dual challenges of expanding healthcare access while maintaining cost-effectiveness in an increasingly resource-constrained global healthcare environment.

Operational models

Trailer units are true mobile MRI systems housed in large semi-trailers that operate as scanning rooms. They are magnetically shielded and can be transported with the magnet fully energized to minimize setup time at each location.

Trailer units are designed for maximum mobility and can be easily moved between facilities on a regular schedule. With an overall size of approximately 15 × 3 meters, the units are typically used in route-based operations. This means they follow predetermined routes between multiple healthcare facilities, spending days or weeks at each location before moving to the next site. They are ideal for serving rural areas, smaller hospitals, or facilities that need temporary MRI access during equipment maintenance, replacement, or surges in demand.

Relocatable units are oversized trailers that can be semi-permanently parked at a hospital or imaging facility and function as a bridge between mobile trailer units and fixed installations.

A relocatable unit provides ground-level access and a spacious environment for patients and staff. It is a good option if a facility is considering a long-term imaging solution, as the unit can be fully integrated into the hospital infrastructure, maintaining the patient pathway.

These units are typically deployed for months or years at a single location. Compared to the capital investment for a permanent installation, a relocatable MRI unit can provide the most cost-effective way of meeting increasing clinical demand.

Relocatable units are commonly used when facilities need expanded capacity but want to avoid the time and expense of permanent construction, or when testing market demand before committing to a permanent installation.

Each model has distinct advantages in terms of cost-effectiveness, scheduling flexibility, and resource utilization. The optimal choice will depend on factors such as patient volume, geographic distribution of facilities, and local healthcare infrastructure requirements.



1 A 1.5T MAGNETOM Viato.Mobile deployed in a trailer unit in Spain.



2 A 1.5T MAGNETOM Sola deployed in a relocatable unit in the UK.

Current state of mobile MRI technology

Mobile MRI technology has reached a significant level of maturity and adoption. The field has seen important technological breakthroughs, particularly in sustainability and operational efficiency.

In February 2024, we at Agito Medical received the world's first helium-free mobile MRI scanner for our fleet. It reduces environmental impact and operational costs and marks a significant step forward in sustainable healthcare technology. This development addresses one of the major operational and financial challenges of traditional MRI systems: helium dependency.

These sealed MRI systems also have practical advantages, allowing safe transport thanks to simple ramp-up/ramp-down procedures. They also enable optimized positioning, as they are not constrained by a quench pipe, which traditionally requires careful distancing from structures and personnel.

Another breakthrough concerns innovative measures for reducing power consumption, such as switching MRI units off and enabling power-save mode. The power-save mode works by cycling cooling components on and off when the MRI is not in use, rather than keeping all systems running continuously. This maintains the magnet's superconducting state while reducing energy consumption during idle periods. The technology is especially effective for facilities and mobile units that operate during specific hours, allowing significant energy savings overnight and during weekends.

These power-saving technologies are a win-win solution for healthcare providers: They substantially reduce costs while contributing to environmental sustainability goals without compromising imaging quality or patient care.

In addition, optimized system reliability and remote service capabilities enable real-time diagnostics, predictive maintenance, and instant technical support. This signifi-

cantly reduces downtime through proactive issue resolution and by eliminating the need for on-site technician visits for routine troubleshooting. In turn, this maximizes scanner availability and operational efficiency while lowering service costs.

All the above features are ideal for mobile MRI systems, which must operate reliably in challenging environments characterized by vibrations, frequent transportation between locations and regions, support from multiple technicians, and deployment across diverse clinical applications.

Outlook and emerging trends

The future of MRI technology is rapidly evolving, driven by several transformative trends that promise to continue revolutionizing mobile imaging over the next decade.

More helium-free systems

As mentioned above, the first "helium-free" unit was deployed in our fleet in 2024. We are excited to see other vendors either developing or offering such technology now too, as it is truly a match made in heaven for mobile MRI units.

The question now is whether and when the recent research into next-generation superconductivity with more-accessible nitrogen-cooled copper-free and nickel-based superconductors, or perhaps even the new LK-99 superconductor [3] that South Korean researchers claim can operate at room temperature, will become a reality in MRI technology.

Artificial intelligence

AI has significantly transformed clinical radiology by enhancing image quality, reducing scan times, and improving diagnostic accuracy and patient safety in MRI. These applications are streamlining workflows and increasing acquisition efficiency and speed, while maintaining superior image quality.

This is probably only the beginning of the AI evolution. In the near future, we are likely to encounter AI technology that can transform both the patient experience and diagnostic capabilities through, for instance, advanced Compressed Sensing and deep learning-based reconstruction that enable faster image acquisition without compromising quality. We are also likely to see AI technology offer fully automated image reconstruction, protocol optimization, and preliminary analysis to help radiologists focus on complex diagnostic decisions.

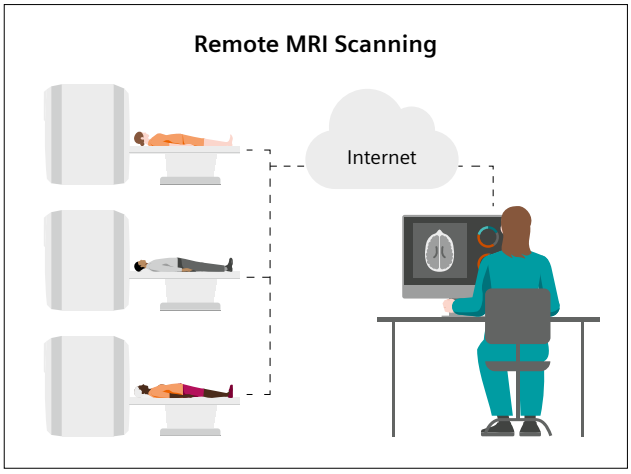

3 The concept of remote scanning.

Remote scanning

Remote MR and CT scanning has evolved significantly. Several key technological advances are now FDA approved and have been clinically implemented by both independent vendors and major MRI manufacturers. One such solution is *syngo* Virtual Cockpit from Siemens Healthineers, which reflects the broader trend toward remote scanning capabilities across the industry.

This infrastructure is very well suited for mobile scanners. It expands the reach of skilled technologists, especially in rural and underserved areas where these units are often in operation.

Assuming regulatory and compliance barriers are addressed, and the concept is optimized and fully adopted, we might very well see new mobile MRI or CT units developed specifically for remote use. They would have a different and optimized layout: Since less space would be needed for the technologist, patients would have a larger and better environment.

Patient-centric innovations

The industry is increasingly focusing on patient comfort and accessibility. Patient-centered technology, such as wide-bore systems, in-system entertainment, low-acoustic-noise scanning, lightweight coils, and free-breathing scanning, will continue to be an important goal for MRI in the 21st century and will greatly impact the mobile environment as well.

Conclusion

Today's mobile MRI units serve diverse populations worldwide, from rural communities in high-income nations to underserved regions in low- and middle-income countries. These systems have proven particularly valuable in disaster response scenarios, military medical support, and population health screening programs. The concept of mobile units continues to evolve with advances in artificial intelligence, power and helium optimization, and remote scanning.

Research estimates that the global mobile scan market will reach US$ 10.73 billion by 2034, up from US$ 6.52 billion in 2025, which represents a 7.4% annual growth rate [3]. Growth drivers include rising demand in underserved areas, and screening programs. North America and Europe currently dominate adoption, while Asia-Pacific markets are expanding rapidly.

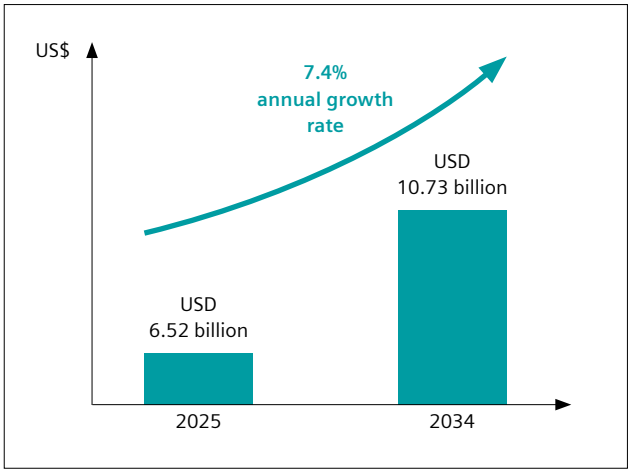

4 The global mobile scan market is estimated to reach US$ 10.73 billion by 2034, up from US$ 6.52 billion in 2025 – a 7.4% annual growth rate. *Figure reprinted with permission from [4].*

References

1 FONAR Corporation. FONAR History [Internet]. Melville, NY, USA: FONAR Corporation. [cited 2025 Sept 25]. Available from: https://www.fonar.com/history.html
2 Mariani G, Kasznia-Brown J, Paez D, Mikhail MN, H Salama D, Bhatla N, et al. Improving women's health in low-income and middle-income countries. Part II: the needs of diagnostic imaging. Nucl Med Commun. 2017;38(12):1024-1028.
3 Kim E, Luo W, Jho H. Perception and argumentation in the LK-99 superconductivity controversy: a sentiment and argument mining analysis. Sci Rep. 2025;15(1):13254.
4 Research and Markets. Mobile Scan Radiology Room Market Size, Share, Trends, Analysis, and Forecasts, 2024-2025 & 2026-2034 | Global Industry Growth, Competitive Landscape, Opportunities, and Challenges [Internet]. Dublin, Ireland: GlobeNewswire; 2025 [cited 2025 Sept 25]. Available from: https://www.globenewswire.com/news-release/2025/06/24/3103984/28124/en/Mobile-Scan-Radiology-Room-Market-Size-Share-Trends-Analysis-and-Forecasts-2024-2025-2026-2034-Global-Industry-Growth-Competitive-Landscape-Opportunities-and-Challenges.html



Contact

Jakob Krebs Christensen
Sales Manager, Nordics, Iberia, and CEE
AGITO Medical A/S
Bejlerholm 3B
9400 Nørresundby
Denmark
Tel.: +45 25 37 68 59
Jakob.Krebs@AgitoMedical.com

Unlocking the Heart's Microstructure: Cardiac Diffusion MRI with Ultra-Strong Gradients

Maryam Afzali, Ph.D.[1,2,3]; Lars Mueller, Ph.D.[1]; Sam Coveney, Ph.D.[1]; Fabrizio Fasano, Ph.D.[4,5]; Filip Szczepankiewicz, Ph.D.[6]; Derek K Jones, Ph.D.[2]; Jürgen E Schneider, Ph.D.[1]

[1]Biomedical Imaging Science Department, Leeds Institute of Cardiovascular and Metabolic Medicine, University of Leeds, Leeds, UK
[2]Cardiff University Brain Research Imaging Centre (CUBRIC), School of Psychology, Cardiff University, Cardiff, UK
[3]Division of Cardiovascular Sciences, College of Life Sciences, University of Leicester, the National Institute for Health Research Leicester Biomedical Research Centre and British Heart Foundation Leicester Centre of Research Excellence, Glenfield Hospital, Leicester, UK
[4]Siemens Healthcare Ltd, Camberley, UK
[5]Siemens Healthineers, Erlangen, Germany
[6]Department of Medical Radiation Physics, Lund University, Lund, Sweden

Abstract

Diffusion MRI of the human heart provides unique insight into myocardial microstructure but has been hampered by cardiac and respiratory motion, short T2 of the heart muscle, and limited gradient strength. Recent advances in ultra-strong gradient technology not only help to overcome these technical challenges but also allow higher diffusion weighting (i.e., b-values) with clinically compatible echo times. Our recent studies demonstrate how this enabled in vivo diffusion kurtosis imaging (DKI) and q-space trajectory imaging (QTI) in the beating human heart, therefore moving beyond the Gaussian assumptions of diffusion tensor imaging (DTI). These advances may pave the way for more sensitive biomarkers of pathological changes of the myocardium and bring microstructural imaging closer to clinical application.

Key points

- Ultra-strong gradients (300 mT/m) make cardiac diffusion MRI feasible at higher b-values.
- In vivo cardiac diffusion kurtosis imaging and q-space trajectory imaging (QTI) were demonstrated with clinically compatible echo times.
- Kurtosis and QTI metrics reveal non-Gaussian diffusion, offering access to new imaging biomarkers of myocardial microstructure.
- Translation to clinical systems is within reach with new 200 mT/m gradient scanners.

Clinical motivation: The unmet need for microstructural cardiac imaging

Cardiovascular disease remains one of the leading causes of death worldwide [1]. While conventional cardiac MRI has revolutionized non-invasive assessment of cardiac anatomy, function, perfusion, and viability, it offers only indirect surrogates of myocardial microstructure [2]. Yet microstructural remodeling – including cardiomyocyte disarray, hypertrophy, fibrosis, and altered cellularity – underpins the pathogenesis of cardiomyopathies, ischemic injury, heart failure, and arrhythmias [3].

Histology provides exquisite microstructural information but is invasive, destructive, and limited to the biopsied region. Clinicians have long sought a "virtual biopsy" tool that could provide microstructural insights non-invasively and reproducibly [4]. Diffusion MRI offers precisely this promise, with sensitivity to water motion at the cellular scale [5]. However, its potential has remained largely unrealized in the heart, where motion, limited gradient performance, and low signal-to-noise ratio (SNR) have posed formidable barriers [6].

Why standard diffusion MRI falls short in the heart

T2 in the brain tissue is about 69 ms in white matter and around 99 ms in gray matter [8] (using a 3T MRI system). T2 in the heart muscle (i.e., myocardium) is ~46 ms at 3T [7], which is about two-thirds to half of the values found

in the brain. It is therefore important to achieve shorter echo times in cardiac imaging compared to brain imaging. In addition, motion-compensated diffusion gradient waveforms are needed for cardiac diffusion-weighted MRI (due to the motion of heart), which adds to the required echo time. Finally, mean diffusivity in the myocardium (~1.5 μm²/ms) [9] is higher than in brain tissue (0.93 μm²/ms in white matter [10, 11]), which causes higher signal attenuation in the heart compared to the brain for the same b-value, and hence puts further constraints on the SNR. Therefore, short TE are essential for the successful application of cardiac diffusion MRI techniques, which in turn require higher gradient performance.

Ultra-strong gradients: A step-change for diffusion encoding

The advent of ultra-strong gradient systems, such as the 3T MAGNETOM Connectom[1] system equipped with a 300 mT/m gradient coil, has transformed what is experimentally possible. By enabling higher b-values at shorter echo times, these systems provide a new window into tissue microstructure. Originally developed for brain imaging, the MAGNETOM Connectom has subsequently become a unique platform for translational "below-the-neck" research, including the heart.

In our recent studies, we leveraged the capability of the MAGNETOM Connectom MR system to push the boundaries of cardiac diffusion MRI. We performed, for the first time, in vivo cardiac diffusion tensor imaging (DTI) on the MAGNETOM Connectom, which enabled higher b-value and higher-order motion compensation (up to third order; diffusion gradient waveforms were designed using the NOW toolbox [12, 13], see Fig. 1) [11] with an echo time comparable to what is commonly used on clinical scanners (such as the 3T MAGNETOM Prisma) for cardiac DTI. Diffusion-weighted imaging was performed with a prototype pulse sequence[2] that enabled diffusion encoding with user-defined gradient waveforms [14, 15]. This work already hinted at non-Gaussian behavior and potentially time-dependent diffusion effects [16], and showed that the myocardium can be probed more deeply and specifically than ever before. It also demonstrated that strong gradients do not merely "improve" existing methods, but also unlock qualitatively new experimental spaces.

Building on this foundation [16], our 2025 *Magnetic Resonance in Medicine* paper [17] reported the first successful implementation of diffusion kurtosis imaging (DKI) in the human heart. DKI extends beyond the Gaussian assumption of DTI, quantifying how water diffusion deviates from it due to microstructural heterogeneity.

We acquired multi-shell diffusion data in healthy volunteers using 300 mT/m gradients, fitted a DKI model, and obtained parametric maps of mean, axial, and radial kurtosis (see Fig. 2). These maps revealed measurable non-Gaussian behavior in the myocardium, consistent with the tissue's known complexity.

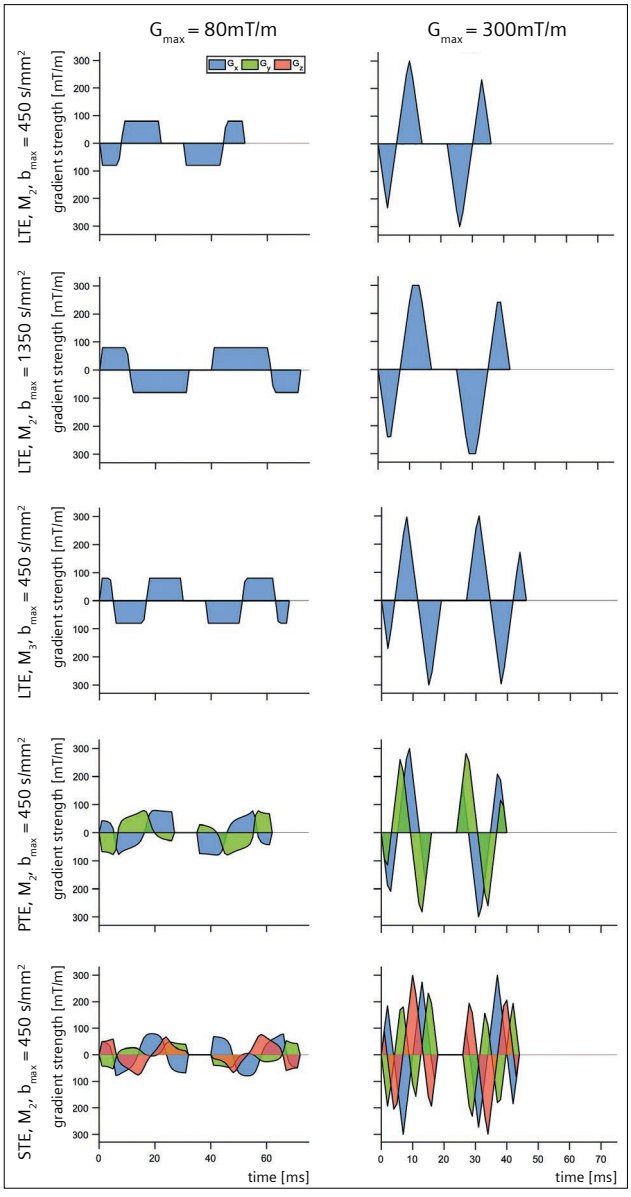

1 Gradient performance comparison. Schematic showing the difference between 80 mT/m and 300 mT/m gradient strength for different b-values, motion compensation order, and encoding schemes (LTE, PTE, STE).

[1] *MAGNETOM Connectom is ongoing research. All data shown are acquired using a non-commercial system under institutional review board permission. Siemens Healthineers does not intend to commercialize the system.*

[2] *Work in progress. The application is currently under development and is not for sale in the U.S. and in other countries. Its future availability cannot be ensured.*

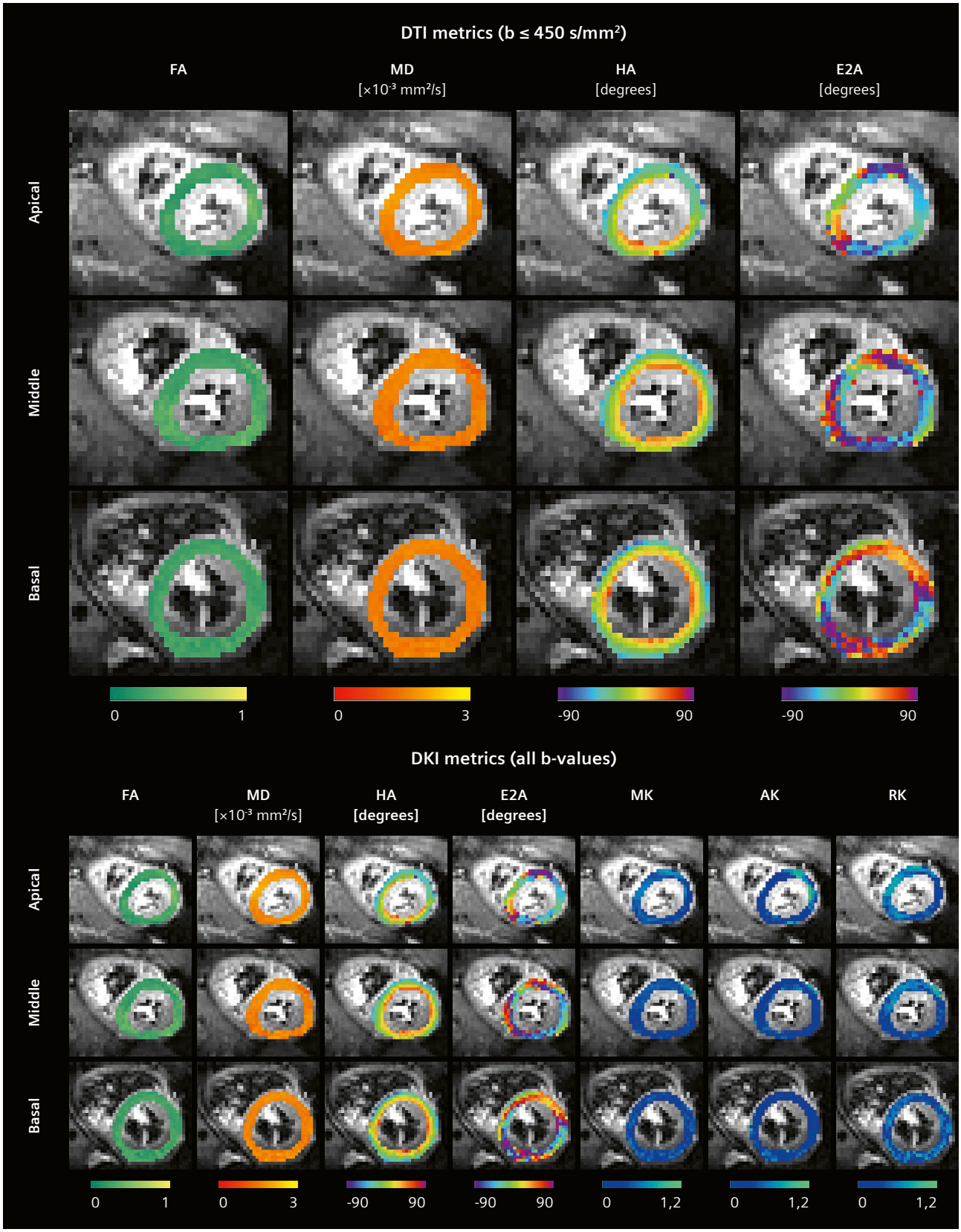

2 Example fractional anisotropy (FA), mean diffusivity (MD), helix angle (HA), and secondary eigenvector angle (E2A) maps using cardiac diffusion tensor imaging and mean, axial, and radial kurtosis maps (MK, AK, RK) using cardiac diffusion kurtosis imaging.

Together, these results provide a new set of imaging biomarkers for characterizing myocardial tissue – potentially sensitive to disease processes such as hypertrophy, fibrosis, and microstructural disarray.

Probing complex microstructure

Q-space trajectory imaging (QTI) represents a paradigm shift in (cardiac) diffusion MRI [16]. Unlike conventional DTI or DKI, which sample diffusion along a single encoding direction at a time (linear tensor encoding (LTE)), QTI explores diffusion along continuous or arbitrarily shaped trajectories in q-space, allowing direct estimation of higher-order diffusion moments and compartment-specific properties [18]. QTI can capture features such as microscopic anisotropy, isotropic and anisotropic kurtosis, heterogeneity, and orientation dispersion, providing a rich description of myocardial microstructure that is inaccessible with lower-order models.

Using an ultra-strong gradient system, we were able to acquire cardiac diffusion weighted images using advanced diffusion encoding schemes such as planar tensor encoding (PTE) and spherical tensor encoding (STE). These enable the quantification of microstructural features of the tissue such as microscopic anisotropy and isotropic and anisotropic kurtosis [19] (see Fig. 3).

Bridging to clinical translation

While the MAGNETOM Connectom system is unique (there are only four scanners of this kind worldwide), its insights are not destined to remain restricted to these highly specialized scanners. The emergence of new clinical systems with significantly improved gradient performance, such as the 3T MAGNETOM Cima.X system equipped with a 200 mT/m gradient coil, brings these advances closer to patients.

The implications could be profound:

- Microstructural biomarkers such as kurtosis could enrich clinical MRI protocols for cardiomyopathies and heart failure.
- Higher b-value DTI may improve sensitivity to remodeling processes, better guide therapies, and benefit prognosis.
- Motion-compensated encoding and novel readouts (e.g., spiral) should allow integration into clinically feasible scan times.

By demonstrating feasibility at the high gradient strengths, our work provides a roadmap for translating cardiac microstructural imaging to the new generation of clinical scanners.

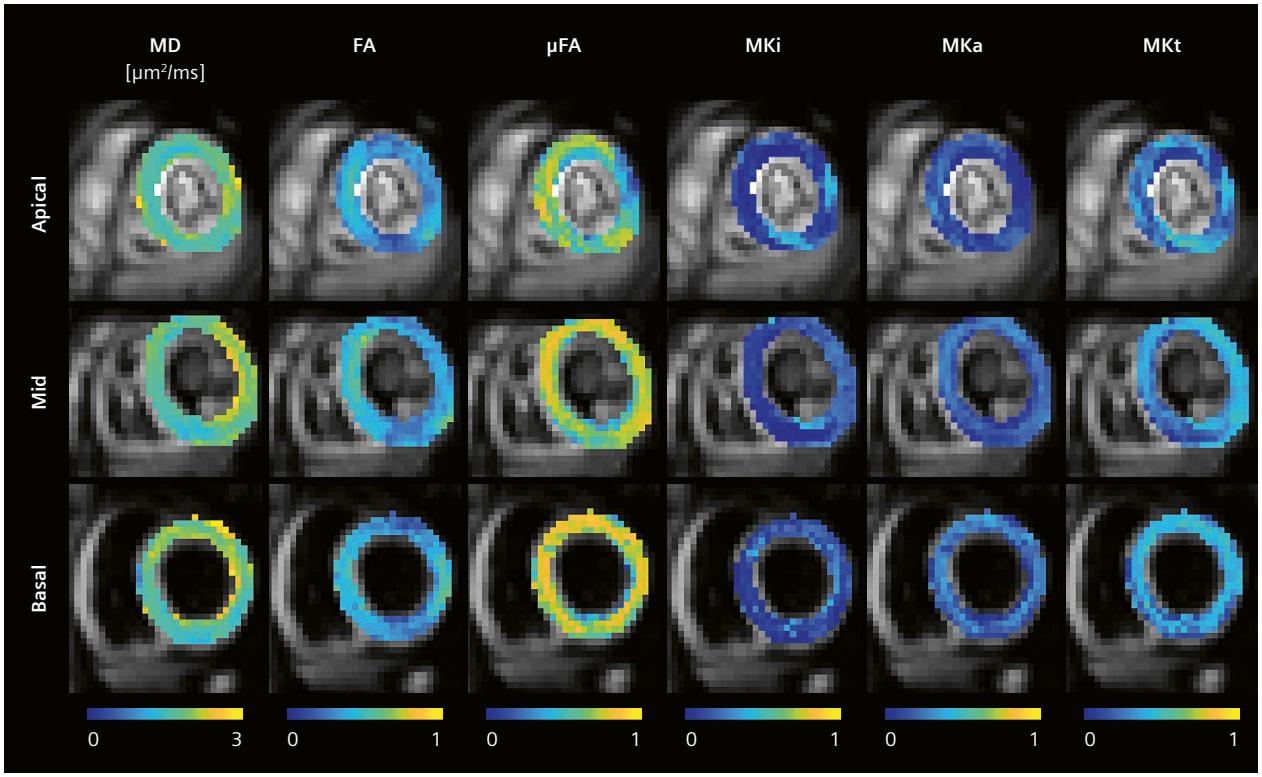

3 Example q-space trajectory imaging (QTI) metrics, microscopic fractional anisotropy (μFA), and isotropic (MKi), anisotropic (MKa), and total mean kurtosis (MKt).

Towards a virtual microscope for the heart

The ability to non-invasively probe myocardial microstructure represents a paradigm shift for cardiovascular imaging. With ultra-strong gradients, cardiac diffusion MRI is evolving from an experimental tool into a powerful research and diagnostic tool.

Future directions may include:

- Extending cardiac diffusion kurtosis imaging to patient populations with hypertrophic and dilated cardiomyopathy, ischemic heart disease, and arrhythmogenic disorders.
- Combining diffusion with relaxation dimensions, creating multidimensional "fingerprints" of cardiac tissue.
- Developing robust, motion-compensated sequences and advanced reconstruction strategies.
- Standardizing acquisition and analysis across centers, paving the way for multi-site clinical studies.

In essence, we are moving closer to a "virtual microscope" for the heart – a tool that could reveal the tissue-level signatures of disease, guide personalized treatment, and reduce reliance on invasive biopsies.

This research was funded by the Wellcome Trust Investigator Award (219536/Z/19/Z).

References

1 Lindstrom M, DeCleene N, Dorsey H, Fuster V, Johnson CO, LeGrand KE, et al. Global Burden of Cardiovascular Diseases and Risks Collaboration, 1990-2021. J Am Coll Cardiol. 2022;80(25):2372–2425.
2 Simkowski J, Eck B, Wilson Tang WH, Nguyen C, Kwon DH. Next-Generation Cardiac Magnetic Resonance Imaging Techniques for Characterization of Myocardial Disease. Curr Treat Options Cardiovasc Med. 2024;26(8):243–254.
3 Ashkir Z, Samat AHA, Ariga R, Finnigan LEM, Jermy S, Akhtar MA, et al. Myocardial disarray and fibrosis across hypertrophic cardiomyopathy stages associate with ECG markers of arrhythmic risk. Eur Heart J Cardiovasc Imaging. 2025;26(2):218–228.
4 Jelescu IO, Palombo M, Bagnato F, Schilling KG. Challenges for biophysical modeling of microstructure. J Neurosci Methods. 2020;344:108861.
5 Basser PJ, Pierpaoli C. Microstructural and physiological features of tissues elucidated by quantitative-diffusion-tensor MRI. 1996. J Magn Reson. 2011;213(2):560–70.
6 Gamper U, Boesiger P, Kozerke S. Diffusion imaging of the in vivo heart using spin echoes--considerations on bulk motion sensitivity. Magn Reson Med. 2007;57(2):331–7.
7 Hanson CA, Kamath A, Gottbrecht M, Ibrahim S, Salerno M. T2 Relaxation Times at Cardiac MRI in Healthy Adults: A Systematic Review and Meta-Analysis. Radiology. 2020;297(2):344–351.
8 Stanisz GJ, Odrobina EE, Pun J, Escaravage M, Graham SJ, Bronskill MJ, et al. T1, T2 relaxation and magnetization transfer in tissue at 3T. Magn Reson Med. 2005;54(3):507–12.
9 Nguyen C, Fan Z, Sharif B, He Y, Dharmakumar R, Berman DS, et al. In vivo three-dimensional high resolution cardiac diffusion-weighted MRI: A motion compensated diffusion-prepared balanced steady-state free precession approach. Magn Reson Med. 2014;72(5):1257–67.
10 Cercignani M, Inglese M, Pagani E, Comi G, Filippi M. Mean diffusivity and fractional anisotropy histograms of patients with multiple sclerosis. AJNR Am J Neuroradiol. 2001;22(5):952–8.
11 Afzali M, Mueller L, Coveney S, Fasano F, Evans CJ, Engel M, et al. In vivo diffusion MRI of the human heart using a 300 mT/m gradient system. Magn Reson Med. 2024;92(3):1022–1034.
12 Sjölund J, Szczepankiewicz F, Nilsson M, Topgaard D, Westin CF, Knutsson H. Constrained optimization of gradient waveforms for generalized diffusion encoding. J Magn Reson. 2015;261:157–68.
13 Szczepankiewicz F, Sjölund J, Dall'Armellina E, Plein S, Schneider JE, Teh I, et al. Motion-compensated gradient waveforms for tensor-valued diffusion encoding by constrained numerical optimization. Magn Reson Med. 2021;85(4):2117–2126.
14 Szczepankiewicz F, Sjölund J, Ståhlberg F, Lätt J, Nilsson M. Tensor-valued diffusion encoding for diffusional variance decomposition (DIVIDE): Technical feasibility in clinical MRI systems. PLoS One. 2019;14(3):e0214238.
15 Mueller L, Afzali M, Coveney S, Doring A, Fasano F, Evans J, et al. ZOOM and enhance: Zonally magnified Oblique Multi-slice for cardiac DTI with ultra-strong gradients. Proc Intl Soc Mag Reson Med. 2024:1269.
16 Teh I, Shelley D, Boyle JH, Zhou F, Poenar AM, Sharrack N, et al. Cardiac q-space trajectory imaging by motion-compensated tensor-valued diffusion encoding in human heart in vivo. Magn Reson Med. 2023;90(1):150–165.
17 Afzali M, Coveney S, Mueller L, Jones S, Fasano F, Evans CJ, et al. Cardiac diffusion kurtosis imaging in the human heart in vivo using 300 mT/m gradients. Magn Reson Med. 2025;94(5):2100–2112.
18 Westin CF, Knutsson H, Pasternak O, Szczepankiewicz F, Özarslan E, van Westen D, et al. Q-space trajectory imaging for multidimensional diffusion MRI of the human brain. Neuroimage. 2016;135:345–62.
19 Afzali M, Mueller L, Coveney S, Jones S, Evans J, Fasano F, et al. Quantifying microscopic anisotropy in the human heart in vivo using ultra-strong gradients. Proc Intl Soc Mag Reson Med. 2024:1267.



Contact

Maryam Afzali, Ph.D.
Lecturer
Division of Cardiovascular Sciences
University of Leicester
Glenfield Hospital, Groby Road,
Leicester, LE39QP
United Kingdom
mad37@leicester.ac.uk



Jürgen E Schneider, Professor
Leeds Institute of Cardiovascular and Metabolic Medicine
University of Leeds
Clarendon Way
Leeds, LS2 9JT
United Kingdom
J.E.Schneider@leeds.ac.uk

Enabling Cardiac MRI at 0.55T: Early Results from MAGNETOM Free.XL

Daniel Giese, Manuela Rick, Oskar Isay, Axel Joachim Krafft, Michaela Schmidt

Siemens Healthineers, Erlangen, Germany

Cardiac magnetic resonance imaging (CMR) is crucial in the diagnosis and management of many cardiovascular diseases. The newly released 2025 ESC Guidelines for the management of myocarditis and pericarditis now include Class 1 recommendations for the use of CMR as a first-line diagnostic tool [1]. However, the availability of CMR remains limited, mainly due to cost, siting requirements, and lack of experienced personnel [2].

With the advancement of technical innovations such as minimal helium inventory, strong gradients, improved receiver coils, and deep learning-based image reconstruction algorithms, a renewed interest in lower field strengths is emerging in the MRI community [3]. Following the launch of the first 0.55T system – MAGNETOM Free.Max – in 2020, the worldwide CMR community immediately put it to the CMR test. Although the system was not released for cardiac applications, several research sites have highlighted its great potential for nearly all CMR contrasts and acquisitions [4, 5]. The large 80 cm bore has additionally allowed imaging in challenging cases, such as obese or claustrophobic patients who would not have had access to CMR [6]. A study using an animal model has even demonstrated the feasibility of using this system in an interventional CMR setting [7] Yet two limitations of the MAGNETOM Free.Max configuration for CMR, namely the limited gradient performance and the lack of a physiological triggering unit for ECG synchronization, were still to be overcome.

With the arrival of the newest 0.55T system from Siemens Healthineers, MAGNETOM Free.XL[1] (Fig. 1), comprehensive CMR exams can now be performed at 0.55T. Thanks to the integrated physiological monitoring unit and stronger gradient performance, users will be able to take full advantage of the benefits of scanning at 0.55T. Shorter echo times can reduce B_0 artifacts around devices[2]. Furthermore, the stronger gradients allow shorter acquisition times of single-shot-based CMR images, such as myocardial mapping, real-time cine, and myocardial perfusion imaging. The system will be presented to the CMR community at SCMR 2026 in Rio de Janeiro, Brazil. With its 100 cm flared opening, MAGNETOM Free.XL is also designed to support the workflow of interventional procedures. Its widespread application in diagnostic CMR has been eagerly awaited, especially due to the stronger gradient performance compared to MAGNETOM Free.Max.



1 MAGNETOM Free.XL has a 100 cm flared opening and is fully equipped to allow unprecedented CMR imaging at 0.55T.

Field strength	0.55T
Bore size	> 100 cm flared opening with 80 cm bore
Max. amplitude per axis	34 mT/m
Max. slew rate per axis	160 T/m/s
Spine coil (table-integrated)	18 elements
Body surface coil M	12 elements
Body surface coil L	6 elements

Table 1: MAGNETOM Free.XL is equipped with hardware that allows users to take advantage of the physics at 0.55T.

[1]Work in progress. The application / the system is currently under development and is not for sale in the U.S. and in other countries. Its future availability cannot be ensured.
[2]The MRI restrictions (if any) of the metal implant must be considered prior to patient undergoing MRI exam. MR imaging of patients with metallic implants brings specific risks. However, certain implants are approved by the governing regulatory bodies to be MR conditionally safe. For such implants, the previously mentioned warning may not be applicable. Please contact the implant manufacturer for the specific conditional information. The conditions for MR safety are the responsibility of the implant manufacturer, not of Siemens Healthineers.

The hardware specifications of MAGNETOM Free.XL are listed in Table 1.

In this article, we present our initial experience of performing CMR scans in volunteers at 0.55T without contrast administration using a MAGNETOM Free.Max system and a MAGNETOM Free.XL system with its stronger gradients.

Due to the system's lower field strength and corresponding **reduced magnetohydrodynamic effect**, ECG synchronization is greatly simplified, as the ECG curve shows fewer artifacts. This can be seen in Figure 2, which shows an ECG signal outside the magnet, in a 3T system, in a 1.5T system, and in the 0.55T MAGNETOM Free.XL magnet.

The reduced main magnetic field and subsequent **reduction in B_0 distortions** can now be exploited with stronger gradient performance. In Figure 3, we show example images of three devices: a pacemaker[2], a transcatheter aortic valve replacement device[2], and a left atrial appendage closure implant[2], all acquired on a MAGNETOM Avanto Fit (1.5T), a MAGNETOM Free.Max (0.55T) and a MAGNETOM Free.XL (0.55T). Acquisitions were performed using a balanced steady-state free precession (bSSFP) contrast, as typically used for cine functional CMR assessment. Especially for the pacemaker, the banding artifacts (dark rim around the device) are reduced with the MAGNETOM Free.XL system.

The gradient performance and its influence on several CMR protocols can be seen in Table 2, which compares MAGNETOM Free.Max to MAGNETOM Free.XL.



2 The native ECG signal (top row), is barely distorted at 0.55T, whereas distortions become stronger with increasing magnetic field strengths (1.5T and 3T).

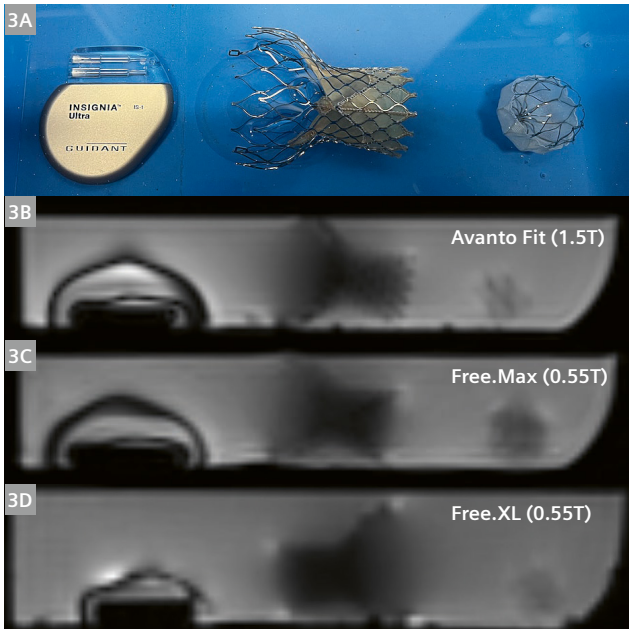

3 **(3A)** from left to right: pacemaker, transcatheter aortic valve replacement device, and a left atrial appendage closure implant. **(3B)** 1.5T MAGNETOM Avanto Fit; **(3C)** 0.55T MAGNETOM Free.Max; **(3D)** 0.55T MAGNETOM Free.XL.
The pacemaker exhibits fewer banding artifacts on MAGNETOM Free.XL, due to the combination of lower field strength and stronger gradient performance.

		MAGNETOM Free.Max	MAGNETOM Free.XL
Segmented cine	TE	1.7 ms	1.05 ms
	TR	4.2 ms	2.6 ms
	Breath-hold duration	9 s	5.2 s
Dynamic perfusion (3 slices)	TE	1.78 ms	1.1 ms
	Frame duration	252 ms	157 ms
	Maximum heart rate	79 bpm	125 bpm
3D bSSFP	Segments	28	39
	Acquisition duration	6.6 min	5.6 min
Interactive real-time cine	Frame duration	221 ms	132 ms
	Frame rate	4 fr/s	7 fr/s

Table 2: A comparison of several acquisition parameters achievable on the MAGNETOM Free.XL and MAGNETOM Free.Max systems. The 3D bSSFP is a T2-prepared 3D morphological acquisition with fat saturation, as typically used for coronary MR angiography (MRA). The interactive real-time cine is used for interventional imaging and allows real-time acquisition and inline reconstruction.

For all imaging protocols, the stronger gradients allow a **reduction in the echo times** (TE) and therefore in the echo spacing (TR). This time-reduction can be used for **shorter acquisition times** in the case of segmented cine or 3D bSSFP, or for **higher frame rates** for single-shot applications such as real-time cine or perfusion imaging. In the case of perfusion imaging, the stronger gradients allow the acquisition of three slices per heartbeat, even in situations of high (< 125 bpm) heart rates.

MAGNETOM Free.XL comes with the full portfolio of **planning and workflow features** from Siemens Healthineers. These include automatic cardiac view planning using myExam Cardiac Assist as shown in Figure 4.

Similarly, the resting phase is automatically detected based on a 4-chamber cine as part of the AutoMate Cardiac functionality. This is shown in Figure 5 for the automatic parametrization of a 3D iNAV-based acquisition on MAGNETOM Free.XL.

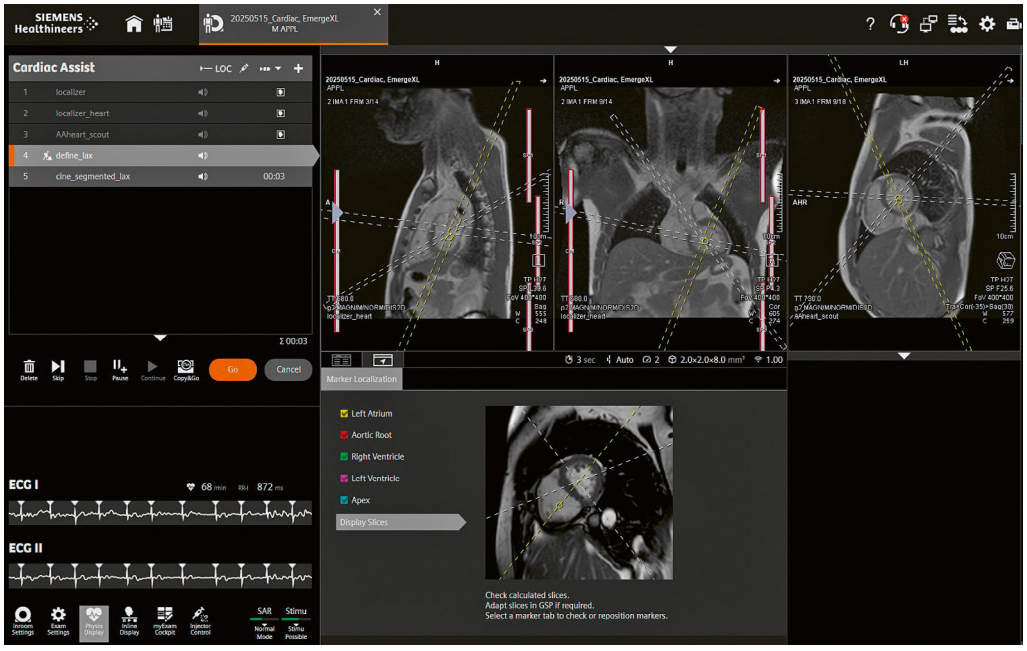

4 Scout images and planning results in a healthy volunteer. Landmarks and planes are automatically found using myExam Cardiac Assist.



5 Example of AutoRestingPhase detection in the AutoMate Cardiac feature of MAGNETOM Free.XL.

Figure 6 shows morphological short-axis dark-blood images using a TSE-based sequence with Deep Resolve (upper row: T2; lower row: turbo inversion recovery magnitude, TIRM) on MAGNETOM Free.XL.

Figure 7 shows functional cardiac assessment, including the automatic inline segmentation and ventricular function calculation on bSSFP cine imaging.

A direct comparison of cine images, acquired in the same volunteer on MAGNETOM Free.XL and MAGNETOM Free.Max, is shown in Figure 8. The images depict a single time frame of two segmented acquisitions with bSSFP contrast in the same volunteer. The images demonstrate that the stronger gradient performance allows the **reduction of flow-related dark-band artifacts** due to shortened echo spacing.

Figure 9 shows real-time cine images acquired on both systems. In real-time cine applications, where interactive slice modifications and inline reconstruction and visualization are needed, the improved gradient performance of MAGNETOM Free.XL helps to achieve substantially **higher frame rates**. For example, with the protocol settings for real-time cine with an in-plane resolution of 2.4 × 2.4 mm

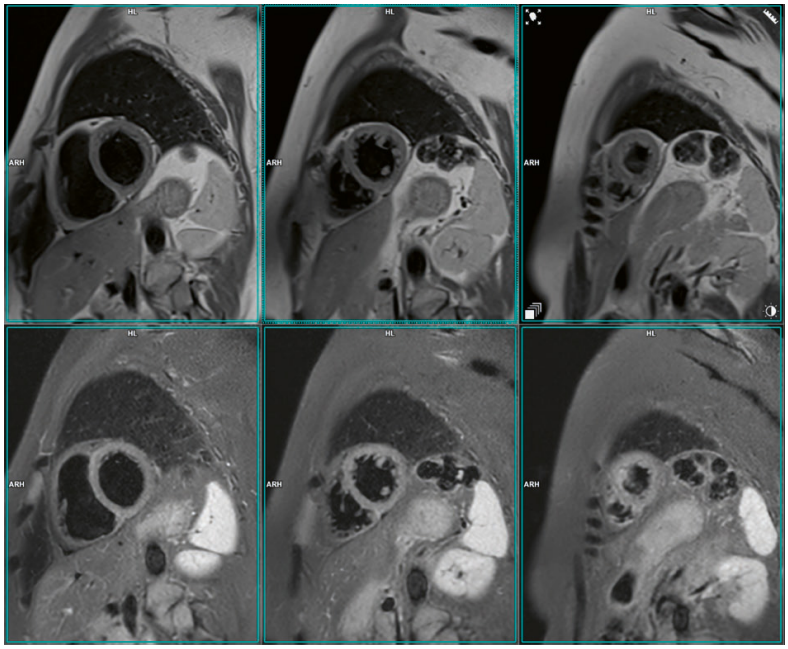

6 T2 TSE (top row) and TIRM (bottom row) acquisition with Deep Resolve on MAGNETOM Free.XL.

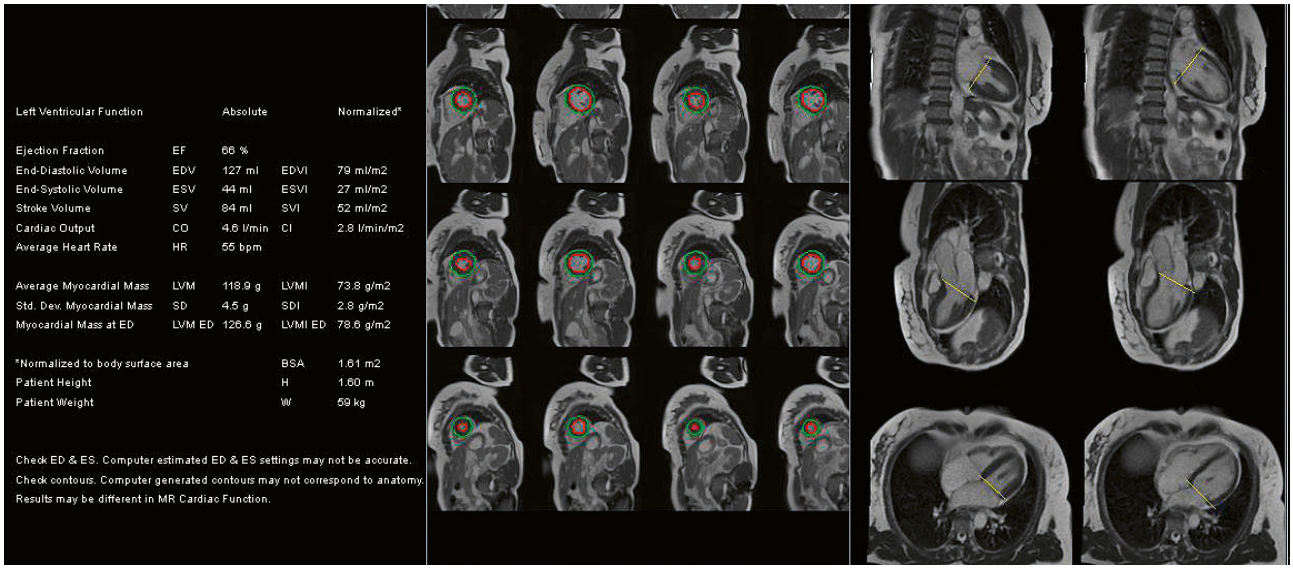

7 Results of the inline ventricular function assessment with automatic generation of a report (left) and visualization of the segmentation results (middle and right).

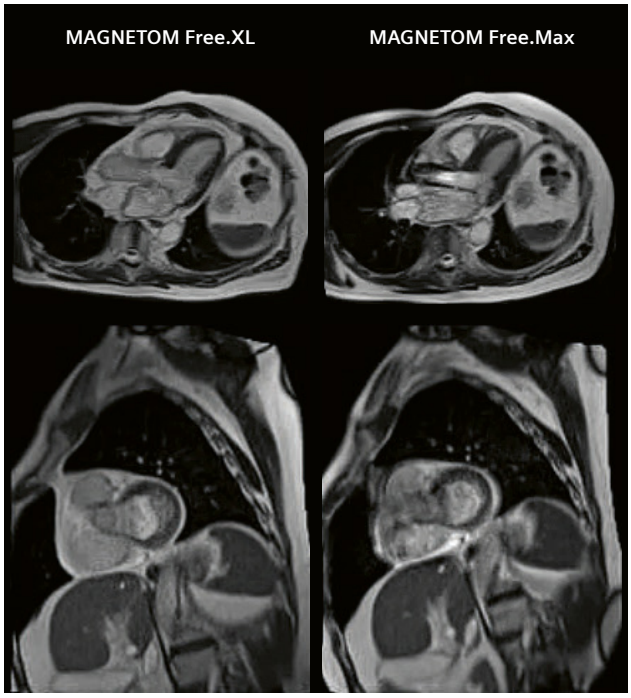

8 A single time frame of segmented bSSFP images in a 3-chamber view (top) and basal short-axis view (bottom) acquired in the same volunteer on MAGNETOM Free.XL and MAGNETOM Free.Max. The reduction in flow artifacts is visible on the MAGNETOM Free.XL images, due to decreased echo spacings.

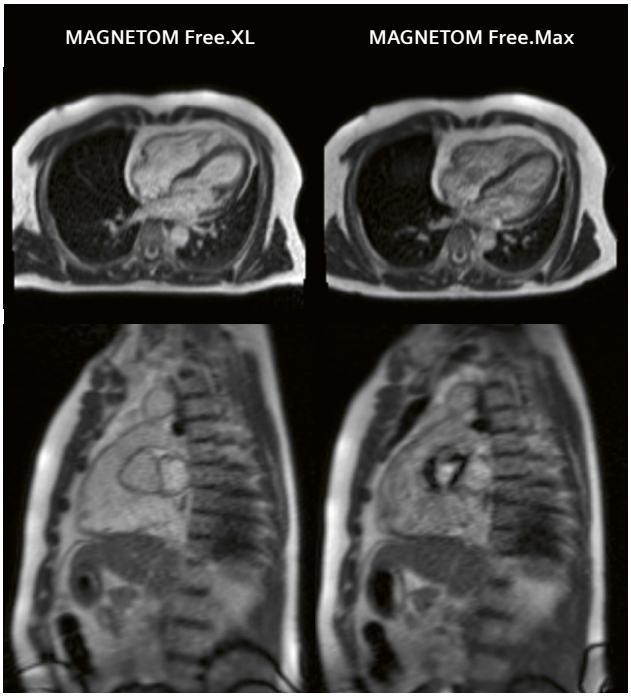

9 Single time-frame bSSFP images (in-plane: 2.4 × 2.4 mm, slice thickness: 7 mm) in 4-chamber view (top) and right ventricular outflow tract (bottom) in the same volunteer on MAGNETOM Free.XL (left) and MAGNETOM Free.Max (right). This demonstrates the improvement in image quality, e.g., reduced flow artifacts, obtained with the shorter acquisition times (132 ms with MAGNETOM Free.XL vs. 221 ms with MAGNETOM Free.Max).

and a slice thickness of 7 mm, the acquisition time of a single frame was reduced from 221 ms on MAGNETOM Free.Max to 132 ms with MAGNETOM Free.XL.

The ability to acquire **real-time cine at high frames rates** is an important step toward achieving applications that go beyond purely diagnostic examinations, e.g., interventional cardiac procedures such as right heart catheterizations. These applications require visualization of the device and the surrounding anatomy at high frame rates for safe navigation and procedural success. Together with the advantages of the lower field strength for device safety (e.g., reduced radiofrequency (RF)-induced heating), and improved patient access from the larger bore opening, this might pave the way for using MAGNETOM Free.XL as a versatile diagnostic and interventional[3] platform.

The combination of **Deep Resolve with Compressed Sensing** for cine bSSFP imaging on MAGNETOM Free.XL can be appreciated in Figure 10, which demonstrates a clear improvement in sharpness and reduced level of noise.

Multiparametric mapping using MyoMaps is also fully supported on MAGNETOM Free.XL. Due to the reduced T1 values at 0.55T, the acquisition scheme on

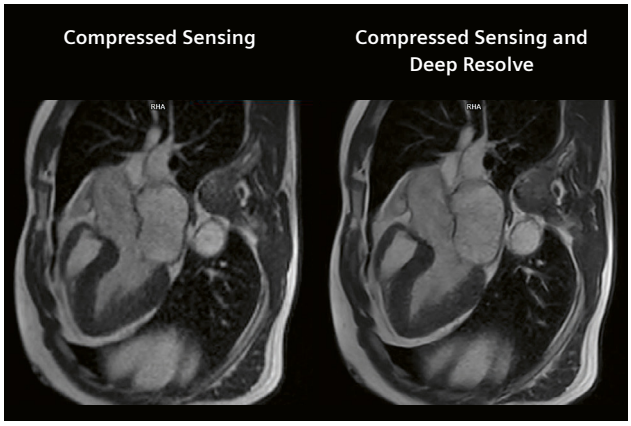

10 While Compressed Sensing allows the acceleration of cine acquisitions, the addition of Deep Resolve increases sharpness and reduces noise.

MAGNETOM Free.XL for native T1 mapping is currently set to 4-3-2-2 (as compared to 5-(3)-3 at 1.5T and 3T). Figure 11 shows example T1 and T2 images and maps acquired on MAGNETOM Free.XL.

[3]*Work in progress. The system is currently nor released for cardiac interventions.*

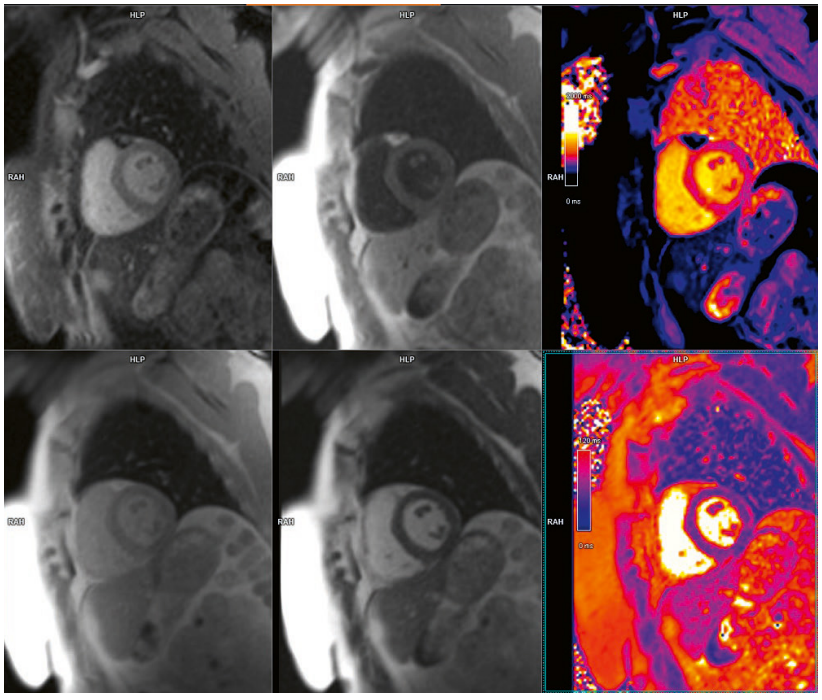

11 T1 and T2 mapping on MAGNETOM Free.XL is feasible. Nevertheless, reference values still need to be collected at 0.55T and this is a prerequisite for clinical use of MyoMaps.

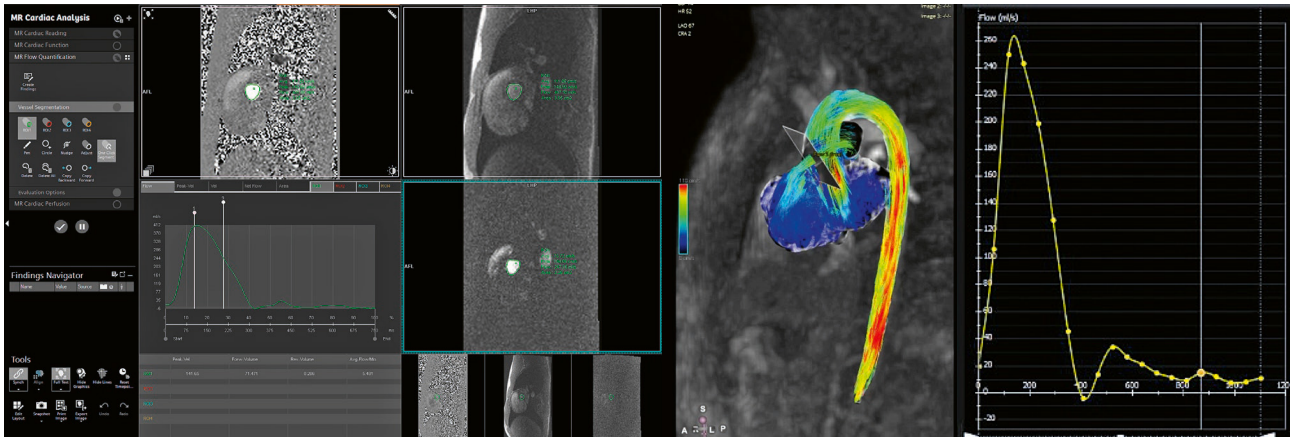

12 Phase-contrast imaging on MAGNETOM Free.XL. Although signal-to-noise ratio (SNR) is reduced at 0.55T compared to 1.5T and 3T, the values for 2D Flow and 4D Flow match, and advanced visualization on 4D Flow (here using cvi42) is feasible.

Although phase-contrast imaging is known to benefit from higher field strengths, Figure 12 demonstrates that classical **2D Flow** imaging is possible on MAGNETOM Free.XL, as is **4D Flow**, which was processed using cvi42 (Circle Cardiovascular Imaging, Calgary, Canada) in this case.

Finally, an image-based navigated 3D bSSFP with fat saturation using the **WholeHeart Pro** sequence is shown in Figure 13. This demonstrates high resolution, a large homogeneous signal, and good fat saturation.

In conclusion, MAGNETOM Free.XL showed consistent performance across all relevant CMR applications that we could test natively (imaging with contrast media is not permitted in volunteer scans at Siemens Healthineers). Not only was the image quality stable and met expectations throughout the image contrasts, but all AI-based workflow-support applications are also available and were shown to work successfully. These can be integrated into the examination, if needed. Workflow automation includes user support in planning the cardiac views, adapting protocols to the patient's physiology, and assuring a comparable, robust, and excellent image quality independent of the user. The AutoMate Cardiac AutoPositioning feature further supports users with automatic positioning of the heart in the isocenter and with planning of additional protocol parameters and geometries such as saturation bands, navigators, and coronal or transversal 2D or 3D slices or slabs. Additionally, AutoTI (which we are yet to test on the 0.55T system in patients after contrast agent

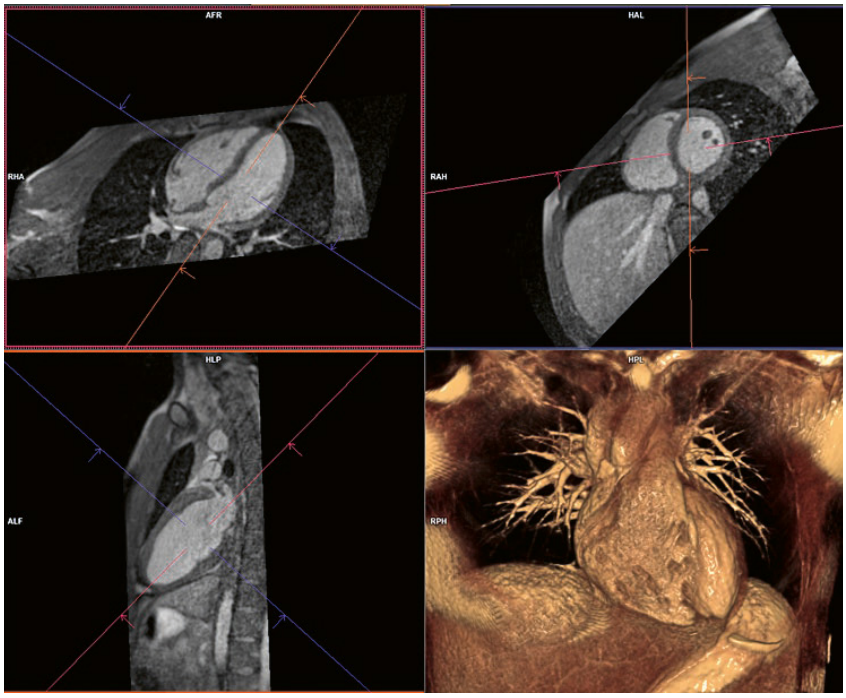

13 Acquisition of the 3D WholeHeart Pro sequence on MAGNETOM Free.XL exhibits excellent contrast and good fat saturation using 3D bSSFP.

administration) suggests an optimal inversion time (TI) for maximum signal intensity differentiation between healthy myocardium and scar. Finally, the AutoRestingPhase detection feature automatically detects the quiescent cardiac phase to enable optimized motion-free image acquisition. AI-based Deep Resolve Sharp is now also available in several CMR applications, including cine and black-blood imaging. This achieves improved sharpness and reduced noise, which is especially useful at 0.55T. Compared to 0.55T MAGNETOM Free.Max, the improved gradient performance of MAGNETOM Free.XL can improve speed, reduce artifacts, and enable all typical CMR acquisitions.

With its combination of the inherent advantages of low-field imaging, enhanced gradient performance, and advanced AI-driven automation and reconstruction, the MAGNETOM Free.XL system is well positioned for clinical adoption in cardiac MRI.

Contact

Daniel Giese, Ph.D.
Siemens Healthineers
SHS DI MR RCT CLS CARD
Research & Clinical Translation,
Magnetic Resonance
Allee am Roethelheimpark 2
91052 Erlangen
Germany
giese.daniel@siemens-healthineers.com



References

1 Schulz-Menger J, Collini V, Gröschel J, Adler Y, Brucato A, Christian V, et al. 2025 ESC Guidelines for the management of myocarditis and pericarditis. Eur Heart J. 2025;46(40):3952–4041.
2 Qin C, Murali S, Lee E, Supramaniam V, Hausenloy DJ, Obungoloch J, et al. Sustainable low-field cardiovascular magnetic resonance in changing healthcare systems. Eur Heart J Cardiovasc Imaging. 2022;23(6):e246–e260.
3 MAGNETOM Flash. MAGNETOM Free.Max special issue. RSNA Edition 2020. Available from: https://marketing.webassets.siemens-healthineers.com/90472072ae6f7648/3230ad37f3ce/MAGNETOM_Flash_Free-Max_Edition_RSNA_Edition.pdf?ste_sid=ebd817edf840e277fb20f2e1e0b1c4aa
4 Varghese J, Jin N, Giese D, Chen C, Liu Y, Pan Y, et al. Building a comprehensive cardiovascular magnetic resonance exam on a commercial 0.55 T system: A pictorial essay on potential applications. Front Cardiovasc Med. 2023;10:1120982.
5 Campbell-Washburn AE, Varghese J, Nayak KS, Ramasawmy R, Simonetti OP. Cardiac MRI at Low Field Strengths. J Magn Reson Imaging. 2024;59(2):412–430.
6 Kaushal A, Crawley R, Jeljeli S, Sequeiros T, Valapil R, Bolla R, et al. Use of a 0.55T 80cm-wide Bore Scanner for Cardiac Imaging in Bariatric and Claustrophobic Patients: A Preliminary Single Centre Experience. J Cardiovasc Magn Reson. 2024;26(1):101017.
7 Armstrong AK, Liu Y, Kelly JM, Krishnamurthy R, Swinning J, Liu Y, et al. Feasibility of magnetic resonance imaging-guided cardiac catheterization, angioplasty, and stenting in a commercial wide-bore 0.55T scanner. J Cardiovasc Magn Reson. 2025;27(1):101858.

Neurofeedback for Treating Depression: An Emerging Application of Real-Time Functional MRI

Rainer Goebel[1] and David Linden[2]

[1] Maastricht Brain Imaging Center, Department of Cognitive Neuroscience, Faculty of Psychology and Neuroscience, Maastricht University, the Netherlands
[2] Mental Health and Neuroscience Research Institute; Faculty of Health, Medicine and Life Sciences; Maastricht University, the Netherlands

Abstract

In functional MRI (fMRI) neurofeedback, a closed-loop brain-computer interface enables participants to learn self-regulating brain activity using real-time information from their brain (Fig. 1). This method is increasingly being used in scientific and clinical settings. Several 3 Tesla studies have shown the promise of this approach as an add-on treatment for depression, helping patients improve emotion regulation and self-efficacy. Traditional neurofeedback, which uses mean activity from emotion-related areas, cannot distinguish specific emotions. It is therefore unclear whether a patient is engaging in a positive or negative emotional mental state. To address this ambiguity, a new semantic neurofeedback approach maps individual emotions onto a two-dimensional space and visualizes the current emotional state as a moving point on that map. This technique allows participants to navigate their emotional space, thereby offering clearer and potentially more effective therapy for depression. A 7-Tesla proof-of-concept study shows promise for this new real-time fMRI neurofeedback method.

Introduction to functional MRI neurofeedback

Functional magnetic resonance imaging (fMRI) has revolutionized the study of the human brain. By enabling high-resolution, non-invasive recordings of the blood oxygenation level dependent (BOLD) response, it provides indirect measures of neuronal activity [1–4]. While in many cases, the fMRI analysis is being performed quite some time after the data has been acquired, real-time fMRI (rt-fMRI) systems were developed already shortly after the inception of fMRI [5]. They process the data during scanning — i.e., as soon as it is acquired. Although the potential of rt-fMRI for quality assurance, functional localizers, intra-operative studies, and teaching has long been recognized, the uptake has been rather slow. However, the interest in rt-fMRI increased with the invention of fMRI neurofeedback about 20 years ago. One of the first neurofeedback publications [6] describes how optimized brain-imaging software (developed by this paper's co-author, Rainer Goebel) performed incremental data analysis almost as comprehensively as standard offline data

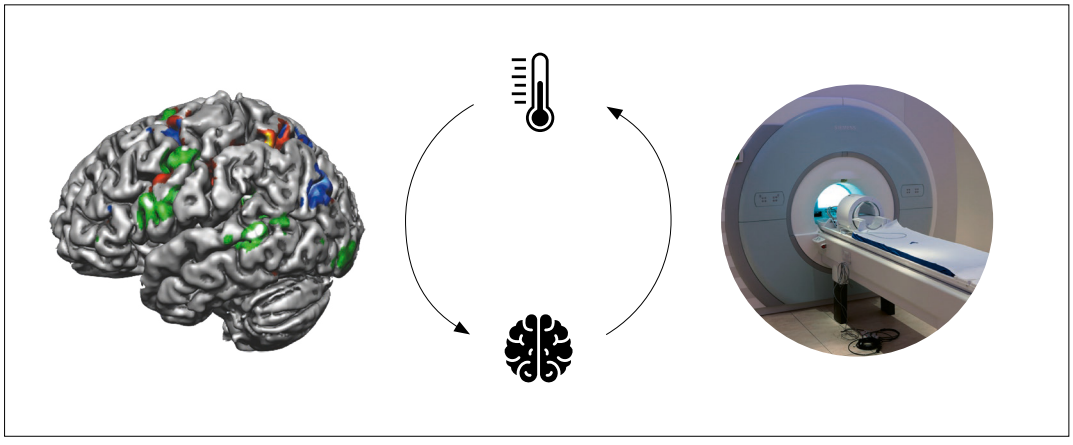

1 Real-time fMRI neurofeedback as a closed-loop system.

analysis. This included motion correction, spatial and temporal filtering, and statistical analysis of the fMRI signals from the entire brain using a recursive general linear model (for an overview of currently employed methods, see [7]). Most importantly, the software allowed to interactively select multiple brain regions, from which the neurofeedback signal was calculated and shown as visual feedback (time-course displays) to the participants in the scanner during ongoing functional scanning. The paper concluded that this novel approach meant fMRI-guided self-regulation would become feasible for healthy participants and patients.

Application in depression treatment

Despite this promising outlook, it took almost 10 years until the first psychiatric application of fMRI neurofeedback was published providing activity feedback from emotion-related brain areas in patients with depression [8]. In this 3-Tesla study, the mean activity from emotion-related areas was provided on a thermometer-like display that showed participants whether they had successfully engaged in emotional mental states during neurofeedback blocks. After only four neurofeedback practice sessions (separated by about a week), patients showed a significantly improved ability to regulate their emotions, which was accompanied in most patients by a substantial reduction of depression symptoms, as measured with the Hamilton Depression Rating Scale (HDRS). This proof-of-concept study laid the foundation for using fMRI neurofeedback to help patients self-regulate emotions in depression, and has had world-wide impact (seven active clinical trials are currently listed on clinicaltrials.gov). More generally, the increasing awareness about the high prevalence of neurological and psychological issues in society, and the limited therapeutic solutions available, has generated excitement for fMRI neurofeedback as a non-pharmacological, brain-driven, and precise treatment option. The rising interest in clinical neurofeedback has been accompanied by large-scale EU funding (e.g., the BRAINTRAIN project [9]) and an increasing number of promising clinical studies on neurofeedback applied to mental disorders such as PTSD [10] and anxiety [11], and to neurological conditions such as Parkinson's disease [12]. Because it provides direct access to (dysfunctional) brain circuits [13], neurofeedback has become a truly disease-modifying intervention, which are currently virtually absent in psychiatry and are rare in neurology.

While neurofeedback has been explored for many clinical disorders [14], depression treatment has proven to be one of its most successful applications in subsequent randomized clinical trials [15, 16]. Its clinical effect (reducing symptoms by approximately 40%) clearly surpasses that of commonly observed placebo or non-specific effects. Furthermore, it has been revealed that the reduction in depression symptoms correlates with an increase in reported self-efficacy, which is an important concept in the psychology of depression. Neurofeedback seems to positively influence two core symptoms of major depression: anhedonia and a perceived loss of control. It does this by teaching patients to engage in positive emotions and by boosting their self-efficacy, respectively. Importantly, after undergoing successful treatment sessions in the scanner, patients were able to apply the learned emotional regulation strategies also outside the scanner. This led to sustained outcome effects, as demonstrated by follow-up measurements recorded weeks or months after the intervention. Most depression neurofeedback studies have used 3-Tesla fMRI, including our studies on 3 Tesla MAGNETOM Prisma scanners in Cardiff (UK) and Maastricht (NL), but a large-scale study currently running at Stanford University is using a 7-Tesla MAGNETOM Terra.X system with impulse gradients to provide optimal feedback signals to patients [17].

Limitations of conventional neurofeedback

There are (at least) two ways of designing clinical protocols for fMRI neurofeedback. On the one hand, one could directly target pathological hyper- or hypoactivation with down- or upregulation. For this approach, stable patterns of abnormal fMRI activity that can be detected and modulated in single trials (without pooling data over longer timeframes) would need to be identified in patients, which is often not possible. On the other hand, one could use the real-time fMRI signal to reinforce particular (desirable) mental states, such as those from positive emotional imagery or memories [8, 15, 16]. This is the approach that most studies on depression have taken so far. However, these clinical studies on fMRI neurofeedback were based on mean activity in a target area or on functional connectivity between brain areas or networks (for example, partial correlation coefficients). In previous studies on neurofeedback for emotion regulation in depression treatment, this conventional approach was "blind" to the type of emotion, since it does not distinguish between specific emotions. Since both positive and negative emotions can lead to an increase in the mean activity in the emotion network, it is thus not automatically known whether a patient is engaging in a positive or negative emotional mental state, despite specific instructions. This lack of specificity presents a challenge for further optimizing therapeutic outcomes, because the feedback should ideally be specific to the targeted emotion. We can now move beyond such low-dimensional feedback signals and harness brain activity patterns that reflect semantic representations in the brain, especially on ultra-high-field (7-Tesla) MRI scanners [16, 18].

Semantic neurofeedback of emotions

To overcome the limitations of conventional neurofeedback for depression, a novel approach termed "semantic neurofeedback of emotions" has been recently proposed [20]. This method leverages multivariate brain activity patterns using representational similarity analysis (RSA) and multi-dimensional scaling (MDS) to capture the semantic structure of emotional representations in the brain (Fig. 2). The experimental protocol begins with an individualized mapping session, in which participants recall autobiographical memories associated with a range of emotions. Brain activation patterns in an emotion-related network are extracted and used to construct a personalized two-dimensional emotion map. In subsequent neurofeedback sessions, a participant's current emotional brain state is visualized as a moving point on the map. Patients are instructed to navigate their mental state toward a target emotion in a series of neurofeedback periods that are interspersed with rest periods. The distance between the current mental state and the other emotions on the map reflects pattern similarity; the size of the visual marker represents the intensity of the evoked emotion brain pattern (Fig. 3).

This semantic ("unblinded") continuous feedback allows participants to consciously explore and regulate their emotional states. It also trains engagement with negative emotions when therapeutically appropriate, particularly to help participants learn how to shift brain activity patterns from negative states toward desired positive emotions.

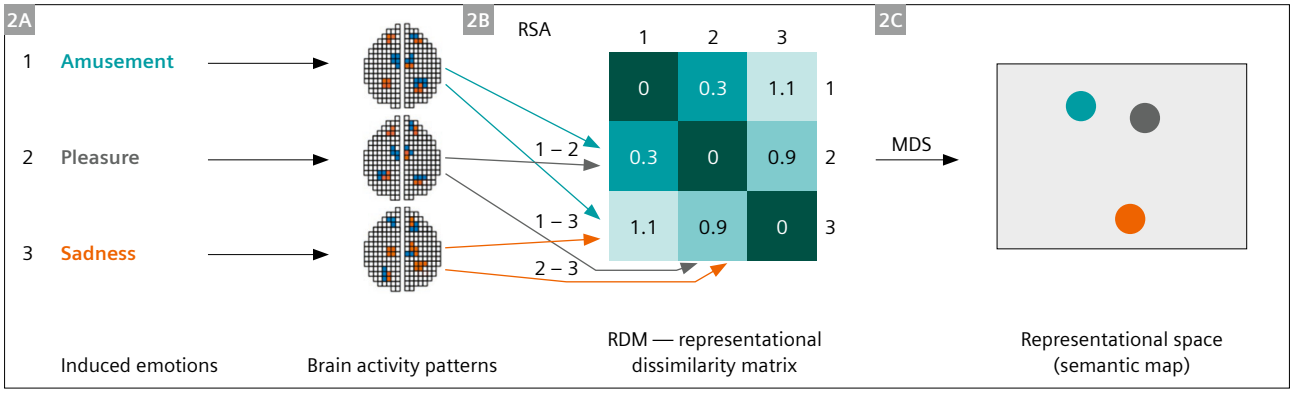

2 Illustration of representational (dis)similarity analysis (RSA) and semantic map creation with N = 3 conditions of induced emotions. **(2A)** Presented stimuli (e.g., pictures or recalled emotional autobiographical memories) evoke distributed activity patterns (N = 3). For voxels in a selected region of interest, the N patterns are compared pairwise (e.g., by calculating a linear correlation value). **(2B)** Similarity (e.g., correlation) values are converted into dissimilarity values d (e.g., d = 1 – correlation, ranging from perfect correlation (d = 0) over no correlation (d = 1) to perfect anticorrelation (d = 2)); pairwise dissimilarity values are placed in respective cells of the representational dissimilarity matrix (RDM) and are often color-coded (here: dark petrol for low dissimilarity, light petrol for high dissimilarity). **(2C)** Using multi-dimensional scaling (MDS), the high-dimensional similarity information in the RDM is projected onto a two-dimensional representational space or semantic map (adapted from [20]).

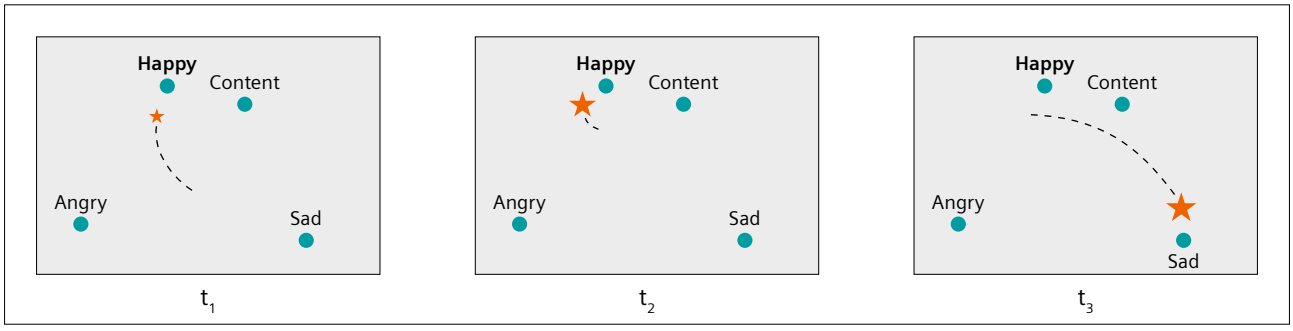

3 Schematic illustration showing semantic neurofeedback of emotions for depression treatment. After a localizer session, the (individual) semantic map contains the four mapped emotions 'happy', 'content', 'angry', and 'sad' as anchor points. After receiving the instruction "navigate to 'happy'", the participant engages in a happy emotional autobiographical memory. The red star, which represents the current mental state, moves from a relatively neutral emotional state (start of dashed line) toward the 'happy' emotion in the semantic map (t_1). By staying close to the target emotion, the participant increases the strength of the 'happy' emotion pattern, as indicated by the larger size of the red star (t_2). After subsequently receiving the instruction "navigate to 'sad'", the participant engages in a sad emotional state, and the current mental state star moves toward the 'sad' emotion in the semantic map (t_3) (adapted from [20]).

Feasibility and benefits of semantic neurofeedback

The feasibility of semantic neurofeedback of emotions has recently been demonstrated in a first proof-of-concept study with five participants [21]. The study consisted of two sessions per participant, conducted at 7 Tesla on a MAGNETOM 7T Plus scanner in Maastricht, the Netherlands. The first session was used to identify the patterns evoked by different emotions. In the second session, the participants practiced navigating to emotions using semantic neurofeedback. Out of nine emotions (contentment, gratitude, friendship love, enthusiasm, surprise, sadness, anger, disgust, and fear), four were selected for each participant to best reflect different valence and arousal categories. In the localizer runs, participants engaged in autobiographical memories matching the selected emotions. An individual mask was created by combining activation from each emotion within the emotional network [22]. Activation patterns were then extracted for the four emotions inside the mask and used to calculate the representational dissimilarity matrix, from which the individual two-dimensional map was created (Fig. 2). During the second session, this map was used to provide the participants with feedback on how their current emotional state was related to the emotion patterns from the first session. The calculated similarity was displayed by a moving red dot, the size of which represented the intensity of pattern activation (Fig. 4). The pilot results demonstrated that participants managed to regulate their brain activation and navigate closely to the emotional target (Fig. 5). These findings indicate the general feasibility of the approach, as high accuracy and

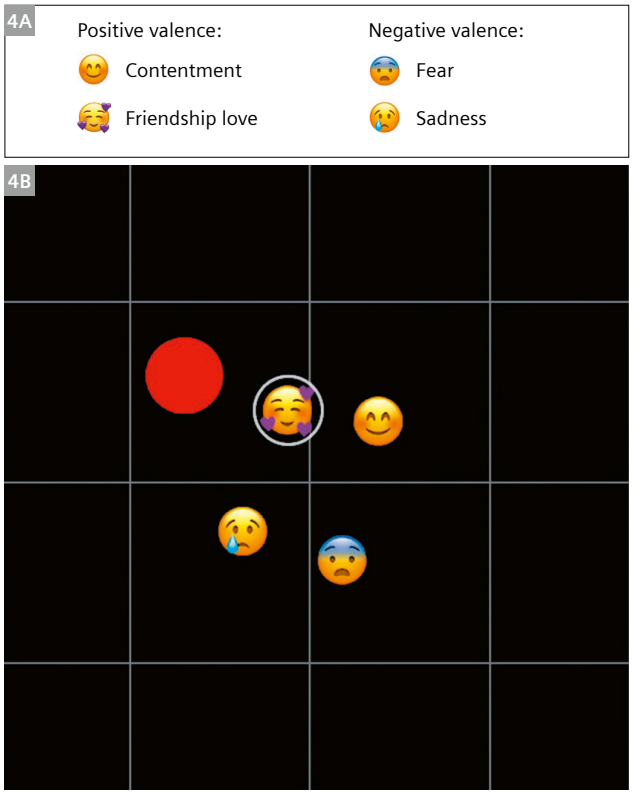

4 Snapshot of real-time fMRI semantic neurofeedback of emotion. **(4A)** Legend showing the four emotions that were selected for the participant and displayed as emojis in the semantic map. **(4B)** Snapshot of the display shown to a participant after they successfully navigated to the cued emotion (white circle) of 'friendship love'. The large size of the red dot indicates that the participant experienced a strong feeling of friendship love.

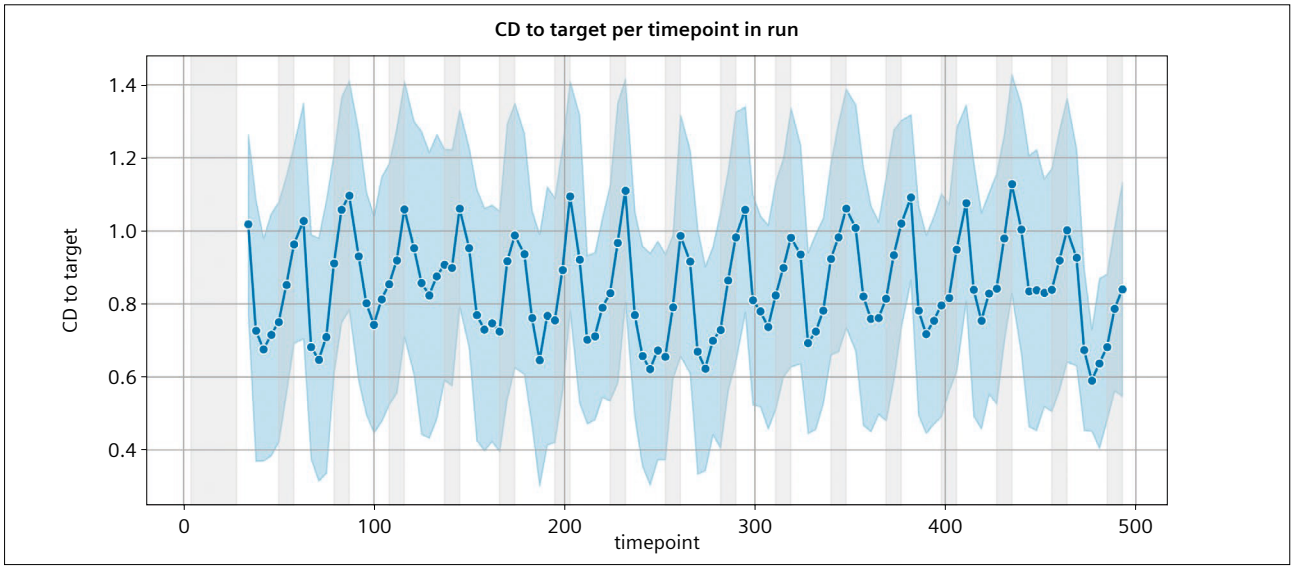

5 These results of semantic neurofeedback of emotion (average of five participants) show that the participants were able to navigate toward the target emotion in individual trials. The distance from the current mental state to the target emotion (y axis) is the correlation distance (CD), which corresponds well with the Euclidean distance (ED) shown on the semantic map. The CD decreases in the white sections (neurofeedback blocks) and rises in the gray sections (rest periods).

engagement were achieved even with non-optimized protocols and methods, suggesting substantial potential for future improvements.

We have not yet systematically compared semantic neurofeedback of emotions at 3-Tesla fMRI versus 7-Tesla fMRI. However, robustly discriminating between different emotion patterns to create a semantic map of emotions is challenging and will likely benefit from the enhanced signal-to-noise ratio or higher spatial resolution at 7 Tesla.

Overall, we believe that this new, transparent technique of navigating one's own emotional space has the potential to enable more specific training for future clinical studies on depression and, more generally, mood disorders.

While fMRI has revolutionized brain research in humans, clinical applications of fMRI are rare. Real-time fMRI neurofeedback for depression has the potential to become a routine application of fMRI in the future, benefitting patients who are not sufficiently responding to conventional interventions.

References

1 Ogawa S, Lee TM, Kay AR, Tank DW. Brain magnetic resonance imaging with contrast dependent on blood oxygenation. Proc Natl Acad Sci U S A. 1990;87(24):9868–72.
2 Ogawa S, Tank DW, Menon R, Ellermann JM, Kim SG, Merkle H, et al. Intrinsic signal changes accompanying sensory stimulation: functional brain mapping with magnetic resonance imaging. Proc Natl Acad Sci U S A. 1992;89(13):5951–5.
3 Bandettini PA, Wong EC, Hinks RS, Tikofsky RS, Hyde JS. Time course EPI of human brain function during task activation. Magn Reson Med. 1992;25(2):390–7.
4 Kwong KK, Belliveau JW, Chesler DA, Goldberg IE, Weisskoff RM, Poncelet BP, et al. Dynamic magnetic resonance imaging of human brain activity during primary sensory stimulation. Proc Natl Acad Sci U S A. 1992;89(12):5675–9.
5 Cox RW, Jesmanowicz A, Hyde JS. Realtime functional magnetic resonance imaging. Magn Reson Med. 1995;33(2):230–6.
6 Weiskopf N, Mathiak K, Bock SW, Scharnowski F, Veit R, Grodd W, et al. Principles of a brain-computer interface (BCI) based on real-time functional magnetic resonance imaging (fMRI). IEEE Trans Biomed Eng. 2004;51(6):966–70.
7 Goebel R. Analysis methods for real-time fMRI neurofeedback. In: Hampson M, editor. fMRI Neurofeedback. London, UK: Academic Press; 2021:23–55.
8 Linden DEJ, Habes I, Johnston SJ, Linden S, Tatineni R, Subramanian L, et al. Real-Time Self-Regulation of Emotion Networks in Patients with Depression. PLoS One. 2012;7(6):e38115.
9 CORDIS. Final Report Summary - BRAINTRAIN (Taking imaging into the therapeutic domain: Self-regulation of brain systems for mental disorders). CORDIS - EU research results. Content archived 2024, June 18. Cited 2026, March 19. Available from: https://cordis.europa.eu/project/id/602186/reporting
10 Fruchtman-Steinbok T, Keynan JN, Cohen A, Jaljuli I, Mermelstein S, Drori G, et al. Amygdala electrical-finger-print (AmygEFP) NeuroFeedback guided by individually-tailored Trauma script for post-traumatic stress disorder: Proof-of-concept. Neuroimage Clin. 2021;32:102859.
11 Zilverstand A, Sorger B, Sarkheil P, Goebel R. fMRI neurofeedback facilitates anxiety regulation in females with spider phobia. Front Behav Neurosci. 2015;9:148.
12 Subramanian L, Morris MB, Brosnan M, Turner DL, Morris HR, Linden DEJ. Functional Magnetic Resonance Imaging Neurofeedback-guided Motor Imagery Training and Motor Training for Parkinson's Disease: Randomized Trial. Front Behav Neurosci. 2016;10:111.
13 Krause F, Linden DEJ, Hermans EJ. Getting stress-related disorders under control: the untapped potential of neurofeedback. Trends Neurosci. 2024;47(10):766–776.
14 Tursic A, Eck J, Lührs M, Linden DEJ, Goebel R. A systematic review of fMRI neurofeedback reporting and effects in clinical populations. Neuroimage Clin. 2020;28:102496.
15 Mehler DMA, Sokunbi MO, Habes I, Barawi K, Subramanian L, Range M, et al. Targeting the affective brain-a randomized controlled trial of real-time fMRI neurofeedback in patients with depression. Neuropsychopharmacology. 2018;43(13):2578–2585.
16 Young KD, Siegle GJ, Zotev V, Phillips R, Misaki M, Yuan H, et al. Randomized clinical trial of real-time fMRI amygdala neurofeedback for major depressive disorder: Effects on symptoms and autobiographical memory recall. Am J Psychiatry. 2017;174(8):748–755.
17 ClinicalTrials.gov. fMRI Neurofeedback With Matter Neuroscience App. ClinicalTrials.gov ID: NCT06735885. National Library of Medicine. Last updated 2025, Dec 17. Cited 2026, March 19. Available from: https://clinicaltrials.gov/study/NCT06735885
18 Russo AG, Lührs M, Di Salle F, Esposito F, Goebel R. Towards semantic fMRI neurofeedback: navigating among mental states using real-time representational similarity analysis. J Neural Eng. 2021;18(4):046015.
19 Ciarlo A, Russo AG, Ponticorvo S, Di Salle F, Lührs M, Goebel R, et al. Semantic fMRI neurofeedback: a multi-subject study at 3 tesla. J Neural Eng. 2022;19(3):036020.
20 Goebel R, Lührs M, Ciarlo A, Esposito F, Linden DE. Semantic fMRI neurofeedback of emotions: From basic principles to clinical applications. Philos Trans R Soc Lond B Biol Sci. 2024;379(1915):20230084.
21 Goblirsch A. Applying Semantic Neurofeedback to Navigate Emotional Space. Master's research thesis. Maastricht University. 2025.
22 Lindquist KA, Wager TD, Kober H, Bliss-Moreau E, Barrett LF. The brain basis of emotion: A meta-analytic review. Behav Brain Sci. 2012;35(3):121–143.

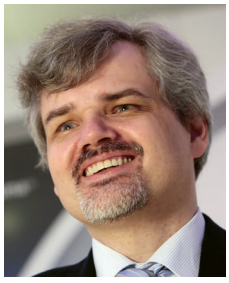

Contact

Professor Dr. rer. nat. Rainer Goebel
Maastricht Brain Imaging Center
Department of Cognitive Neuroscience
Faculty of Psychology and Neuroscience
Maastricht University
Oxfordlaan 55
6229 EV Maastricht
The Netherlands
r.goebel@maastrichtuniversity.nl



David Linden, M.D.
Director Mental Health and
Neuroscience Research Institute
Faculty of Health, Medicine and
Life Sciences
Maastricht University
Universiteitssingel 40
6229 ER Maastricht
The Netherlands
david.linden@maastrichtuniversity.nl

Optimized Susceptibility MRI Sequences for Novel Diagnostic Biomarkers of Multiple Sclerosis

Sreekanth Madhusoodhanan Nair[1], Jin Jin[2], Chang Gao[3], Nader Binesh[4], Thomas Benkert[5], Marcel Maya[4], Pascal Sati[1]

[1] Neuroimaging Program, Department of Neurology, Cedars-Sinai Medical Center, Los Angeles, CA, USA
[2] Siemens Healthineers Pty Ltd, Brisbane, Australia
[3] Siemens Healthineers, Los Angeles, CA, USA
[4] Department of Imaging, Cedars-Sinai Medical Center, Los Angeles, CA, USA
[5] Siemens Healthineers, Erlangen, Germany

Introduction

The 2024 revisions of the international diagnostic criteria for multiple sclerosis (MS) [1] provide an expanded role for magnetic resonance imaging (MRI) by incorporating two novel imaging biomarkers: the central vein sign (CVS) [2] and paramagnetic rim lesions (PRL) [3]. Recent MRI guidelines by the MAGNIMS-CMSC-NAIMS consortia provide practical guidance for the implementation of the different MRI sequences required for the accurate biomarker detection and precise identification of MS [4]. In this article, we focus specifically on the implementation of the susceptibility MRI sequences required for the detection of CVS and PRL.

Due to their paramagnetic properties, CVS and PRL can be detected non-invasively using susceptibility MRI sequences. More specifically, susceptibility-weighted imaging (SWI) has emerged as an important additional sequence to the diagnostic brain MRI protocol for MS since it is highly sensitive to venous features and iron-related signals in the white matter lesions that would be otherwise invisible on conventional T1- and T2-weighted sequences [5, 6]. Although standard SWI provides filtered phase images that are adequate for PRL detection, the SWI magnitude images are not optimized for standalone CVS detection. This complicates the diagnostic interpretation workflow for practitioners. Additionally, standard SWI relies on a gradient echo (GRE) acquisition, which cannot provide in a clinically feasible scan time the recommended submillimeter isotropic resolution for the highest confidence in CVS and PRL detection [4]. An alternative strategy for overcoming this issue for CVS detection is the use of T2*-weighted 3D-segmented echo-planar imaging (3D EPI) [7].

In this article, we will review these techniques and provide guidance for the clinical implementation of an optimized SWI-GRE protocol[1] for concomitant evaluation of CVS and PRL, and of a submillimeter T2* 3D EPI protocol for reaching highest detection confidence for CVS and PRL.

MRI acquisitions

All the cases presented here were imaged on 3T MRI scanners (MAGNETOM Skyra and MAGNETOM Vida) using 20-channel head/neck coils at Cedars-Sinai Medical Center (Los Angeles, CA, USA). Two different brain SWI protocols using the same spatial resolution and coverage were implemented: (a) standard SWI-GRE with a flip angle (FA) of 15°, and (b) optimized SWI-GRE with an FA of 5°. All other sequence parameters were the same in both the standard and optimized SWI-GRE protocols. Additionally, the 3D EPI sequence ('ep_seg_fid'), available in the default sequence tree from Siemens Healthineers (Fig. 1) for recent software versions (≥ VA31), was used to implement submillimeter isotropic T2*-weighted acquisition. Details of the sequence parameters used are shown in Table 1.

[1] 3D EPI SWI processing is provided via a research application[x] resulting in filtered phase images as well as SWI magnitude images.
[x] Work in progress. The application is currently under development and is not for sale in the U.S. and in other countries. Its future availability cannot be ensured.

Protocol	Standard SWI-GRE	Optimized SWI-GRE	T2* 3D EPI
TE (ms)	20	20	35
TR (ms)	27	27	65
FA (deg)	15	5	10
In-plane resolution (mm²)	0.7 × 0.7	0.7 × 0.7	0.7 × 0.7
Slice thickness (mm)	2	2	0.7
FOV Read (mm)	250	250	250
FOV Phase (%)	81.3	81.3	81.3
Base resolution	384	384	384
Acceleration factor	GRAPPA (2)	GRAPPA (2)	None
EPI factor	None	None	15
Bandwidth (Hz/px)	120	120	394
Reconstruction	Magn/Phase	Magn/Phase	Magn/Phase
Coil combination	Adaptive Combine	Adaptive Combine	Adaptive Combine
Scan time	3:50 minutes	3:50 minutes	5:08 minutes

Table 1: MRI acquisition parameters for standard SWI, optimized SWI, and T2* 3D EPI at 3-tesla.

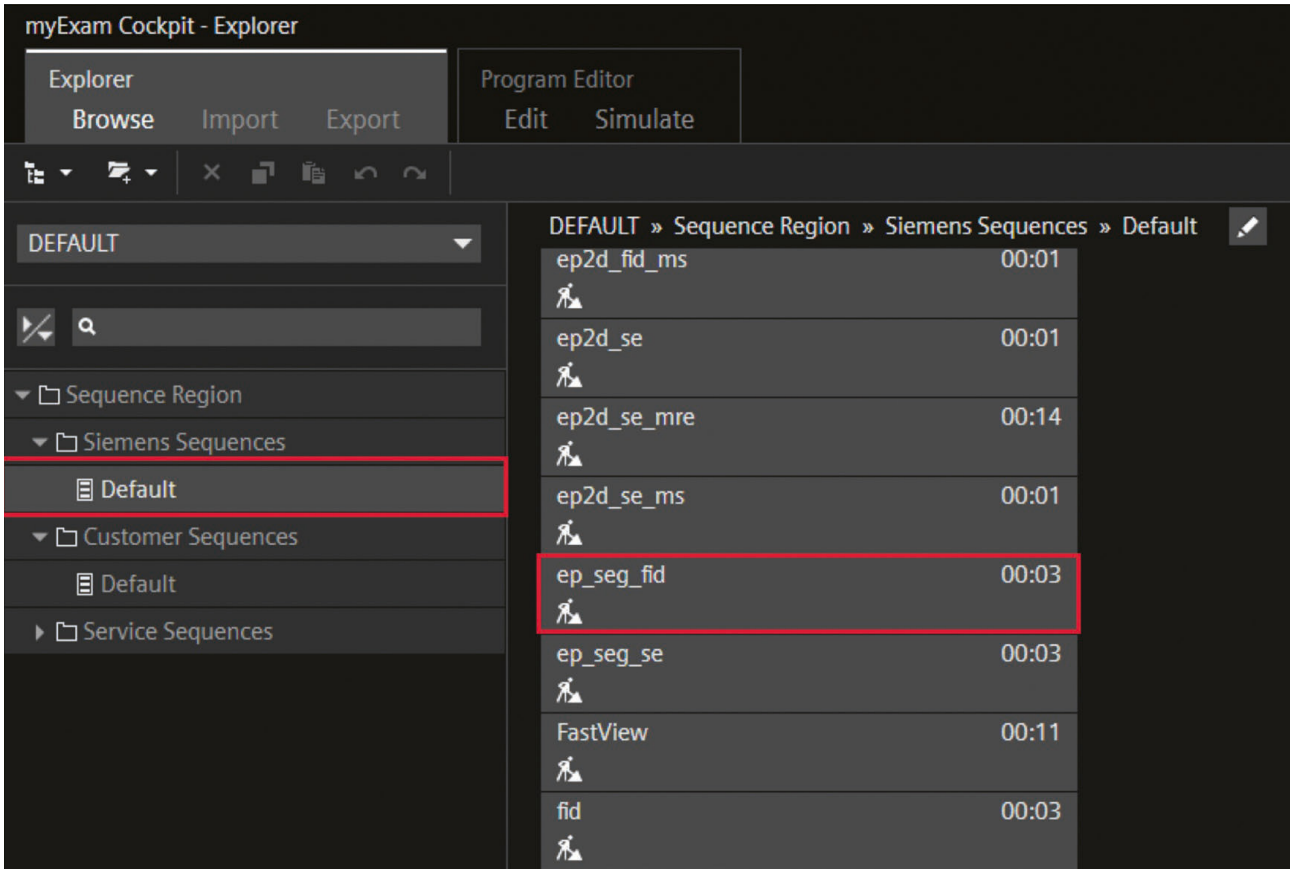

1 Product 3D EPI sequence ('ep_seg_fid') as it appears in the default sequence tree from Siemens Healthineers.

SWI-GRE

As a reminder, the standard SWI-GRE protocol was initially designed for assessing cerebral vasculature and hemorrhage [8, 9]. SWI is particularly useful for evaluating patients with stroke, vascular malformations, and venous diseases [6, 8], but it is not optimized for evaluating the CVS in patients with MS. Indeed, the standard SWI-GRE acquisition prioritizes maximal signal intensity with an FA near to the Ernst angle (between 15° and 20°), which introduces substantial T1-weighted contrast when repetition time (TR) is short. This T1 weighting significantly reduces the lesion-to-white-matter contrast and prevents the co-localization of MS lesions and central veins on SWI magnitude images. This issue is illustrated in Figure 2, where MS lesions appear largely isointense or hypointense on SWI magnitude images, thus requiring the use of T2 FLAIR images to co-localize the presence of T2 hyperintense lesions. In addition, the evaluation of CVS requires establishing the vein centrality using a precise co-registration between T2 FLAIR and SWI. This further complicates the interpretation workflow in clinical practice and reduces the reliability of the CVS rating if the T2 FLAIR and SWI images are inadequately aligned. On the other hand, SWI filtered phase images can be used for PRL evaluation and should be preferred over SWI magnitude images due to their higher sensitivity for PRL detection [10]. In Figure 2, a hypointense rim with isointense core depicting chronic active inflammation in the lesion is clearly visible in the filtered phase image. Note that the image intensity of the filtered phase images is displayed in the left-handed system by default on scanners from Siemens Healthineers. Therefore, the intensity of the filtered phase images needs to be inverted to match the right-handed convention recommended for the detection of PRL (e.g., paramagnetic rims and blood vessels appear dark) [3].

Optimized SWI-GRE

One way to improve diagnostic accuracy and workflow with SWI-GRE is to optimize the acquisition protocol for adequate detection of lesions and central veins on magnitude images. A simple protocol modification is to lower the FA (from 15° to 5° at 3T) to reduce T1 weighting and increase lesion visibility [11]. This single change in the sequence parameter does not affect the scan duration and enables the standalone detection of CVS. This is shown in

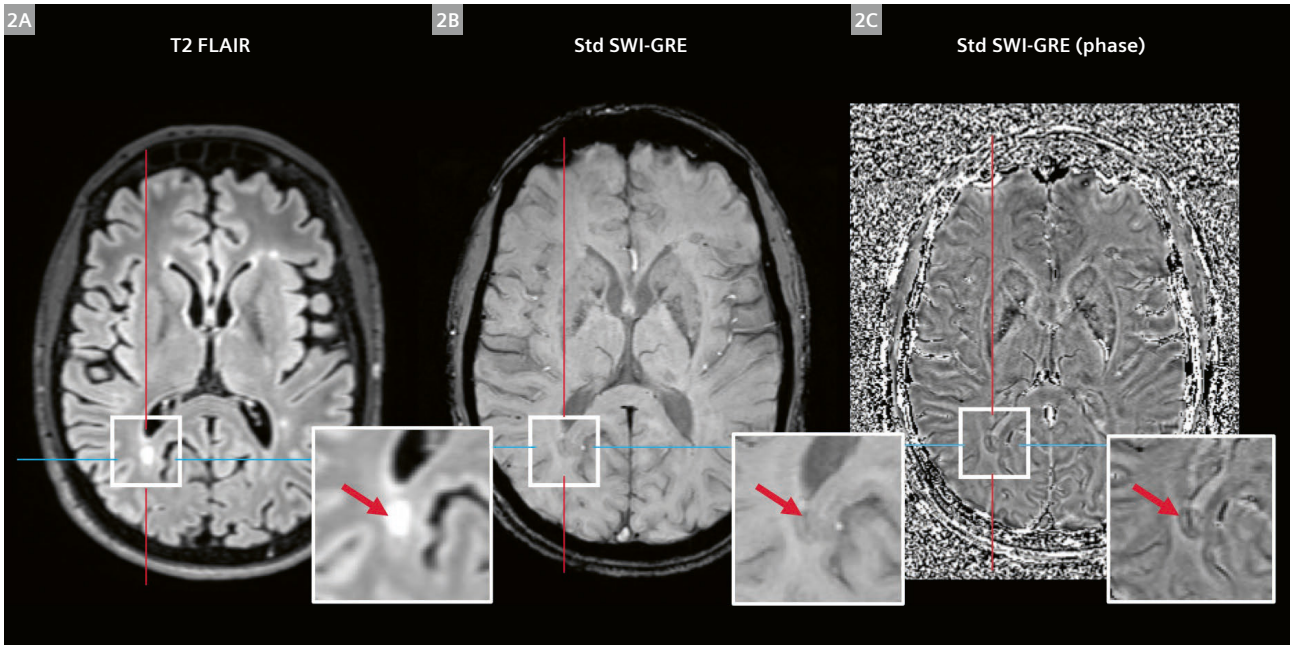

2 **(2A)** Focal hyperintense lesions on T2 FLAIR images, **(2B)** corresponding susceptibility-weighted (SWI) enhanced magnitude image and **(2C)** filtered phase image. Lesions appear isointense on the SWI enhanced magnitude image. For detection of the central vein sign (CVS), centrality of the vein needs to be confirmed using the crosshair. Paramagnetic rim lesion (PRL) is more clearly visible on the filtered phase image than the enhanced magnitude image.

Figure 3, which compares the two SWI protocols (standard and optimized[1]) acquired in the subjects with MS. Hyperintense focal white matter lesions identified on T2 FLAIR are invisible on standard SWI magnitude images but appear hyperintense on the optimized SWI magnitude images (red arrows). As a result, the presence of a central hypointense vein inside these focal white matter lesions can be demonstrated easily with the optimized SWI magnitude images. An important additional observation is that the change in FA does not impact the detection of incidental microbleed (yellow arrows). Moreover, the detection of PRL is not affected by the change in FA, as shown in Figure 3, where both SWI filtered phase images display similar detection sensitivity (white arrows). Additional examples illustrating the superior detection of CVS-positive lesions achieved with the optimized SWI are shown in Figure 4 (top two rows). Examples of the superior detection of PRL-positive lesions achieved with SWI filtered phase images over SWI magnitude images are also shown in Figure 4 (bottom two rows).

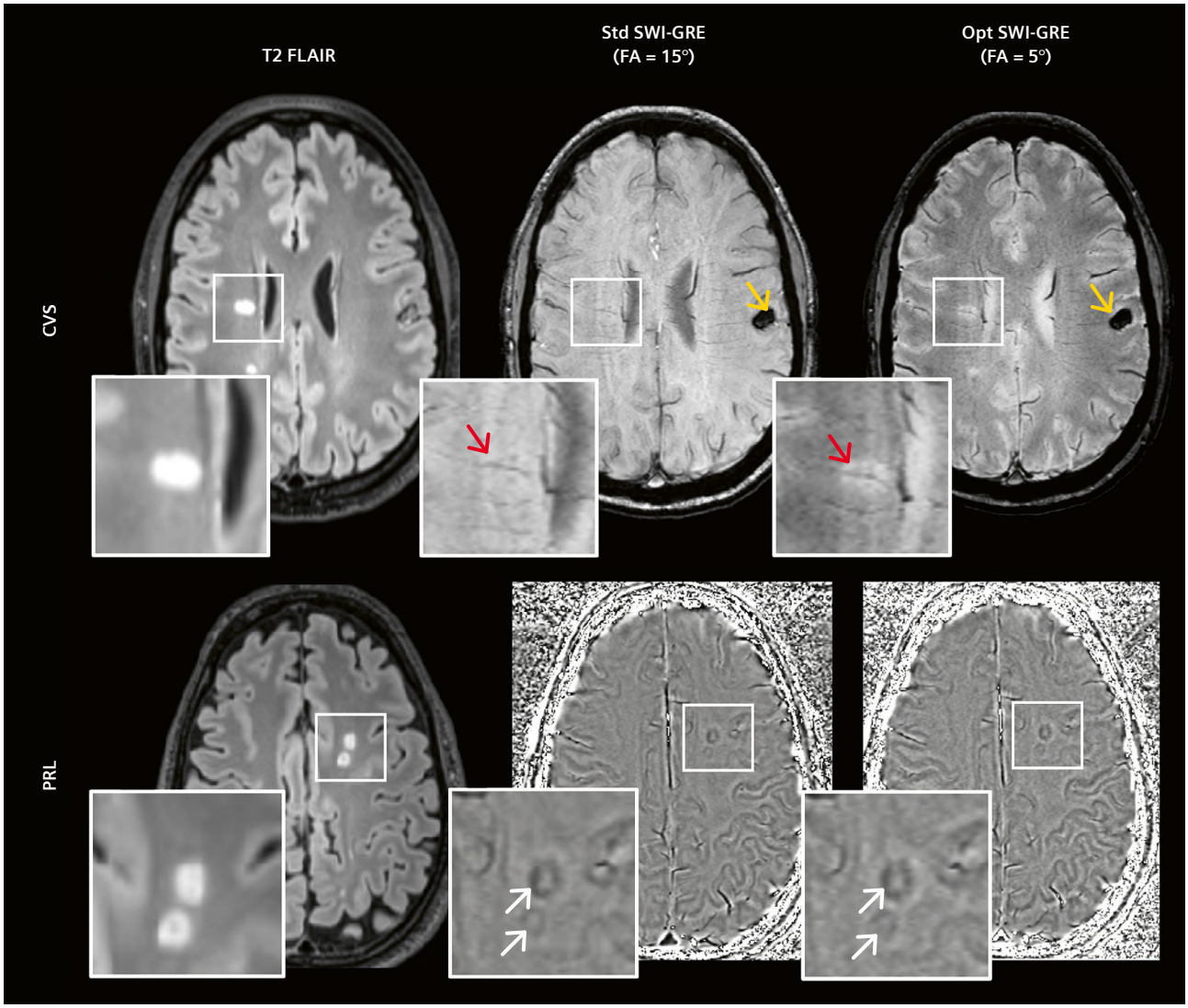

3 Head-to-head comparison of standard and optimized SWI-GRE images acquired in the same subjects with multiple sclerosis. T2 FLAIR images show focal hyperintense lesions in the periventricular and deep white matter areas. Standard SWI-GRE (FA = 15°) shows limited lesion conspicuity with isointense contrast, whereas optimized SWI-GRE (FA = 5°) clearly depicts CVS with high tissue contrast (hyperintense lesion with hypointense vein) (red arrow). A hemorrhagic bleed shows comparable sensitivity on both SWI acquisitions (yellow arrow). Bottom panels: On filtered phase images, PRL demonstrates equal sensitivity with both SWI protocols (white arrows).

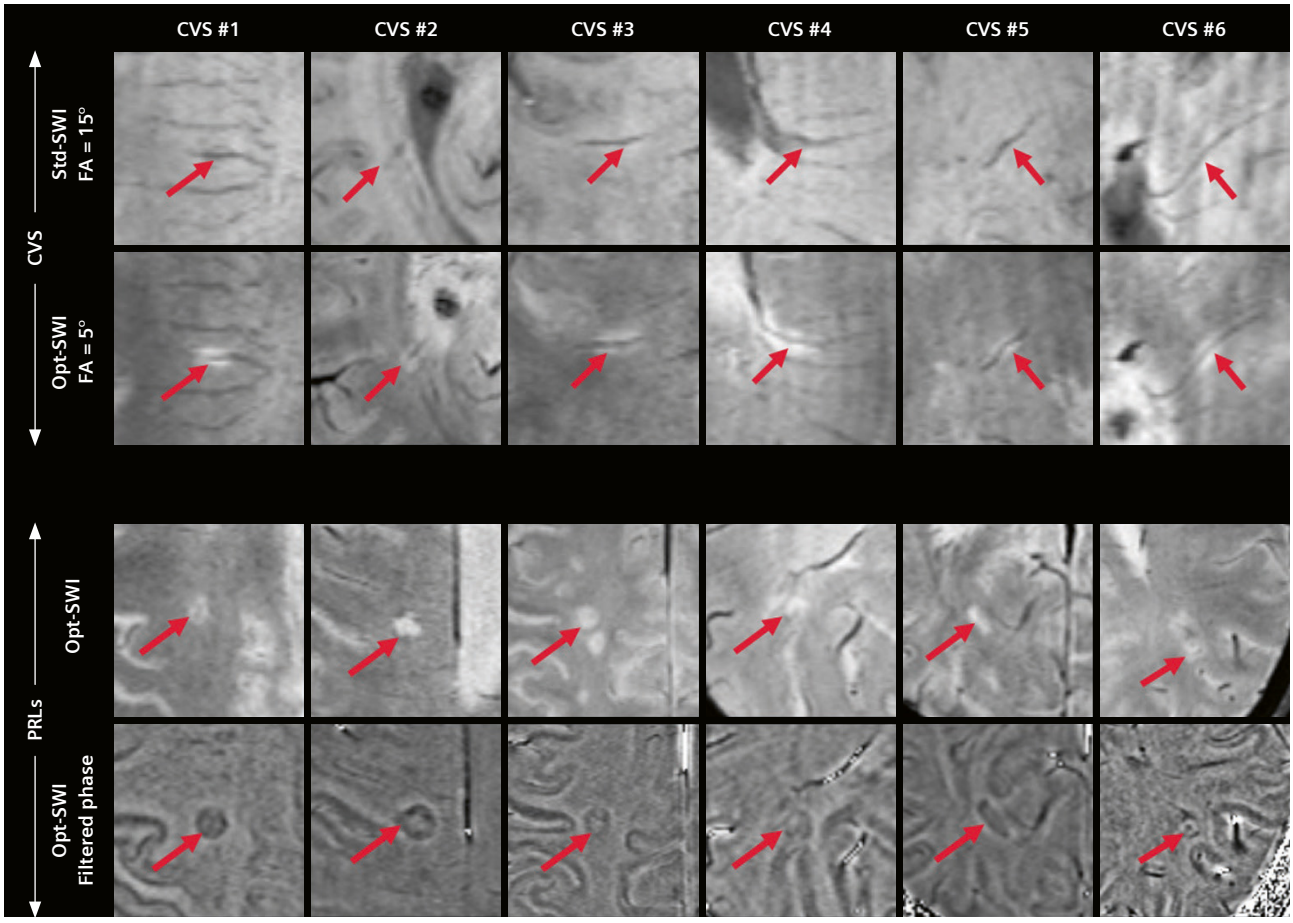

4 The top two rows demonstrate the standalone CVS detection sensitivity of SWI-GRE acquisition at two flip angles, illustrated in the same MS patient evaluated for Select6 criteria (6 or more CVS positive lesions as per the 2024 revised MS diagnostic criteria). The bottom two rows exhibit the superior PRL detection sensitivity, illustrated in six patients with MS. A hypointense rim with an isointense core indicating chronic active inflammation is clearly visible in the filtered phase images, unlike in the SWI magnitude images.

T2*-weighted 3D EPI

The international MRI guidelines recently published by the MAGNIMS-CMSC-NAIMS consortia recommend using submillimeter isotropic T2*-weighted and filtered phase images for more sensitive and reliable detection of the CVS and PRL [2–4]. The product version of the 3D EPI sequence [7, 12] (available for software versions ≥ *syngo* MR VA31) enables the acquisition of magnitude and phase images at 0.65–0.8 mm isotropic in a clinically feasible scan time of 4–6 minutes without the use of parallel imaging acceleration (Table 1). SWI processing is provided via a research application[×], resulting in filtered phase images as well as SWI magnitude images. Representative examples from an MS subject scanned with the 3D EPI protocol are shown in Figure 5. The CVS is clearly visible in all three planes of the T2*-weighted 3D EPI images (red arrows). Similarly, PRL is clearly visible in all three planes of the filtered phase images from 3D EPI (white arrows). This multi-planar evaluation increases reader confidence in rating the CVS and PRL, and reduces any potential false-positive detection. Note the difference in image quality when reformatting the SWI images in coronal and sagittal views. This is due to the anisotropic voxel dimensions which hinders the multi-planar assessment of CVS and PRL (Fig. 5, bottom two rows).

[×] *Work in progress. The application is currently under development and is not for sale in the U.S. and in other countries. Its future availability cannot be ensured.*

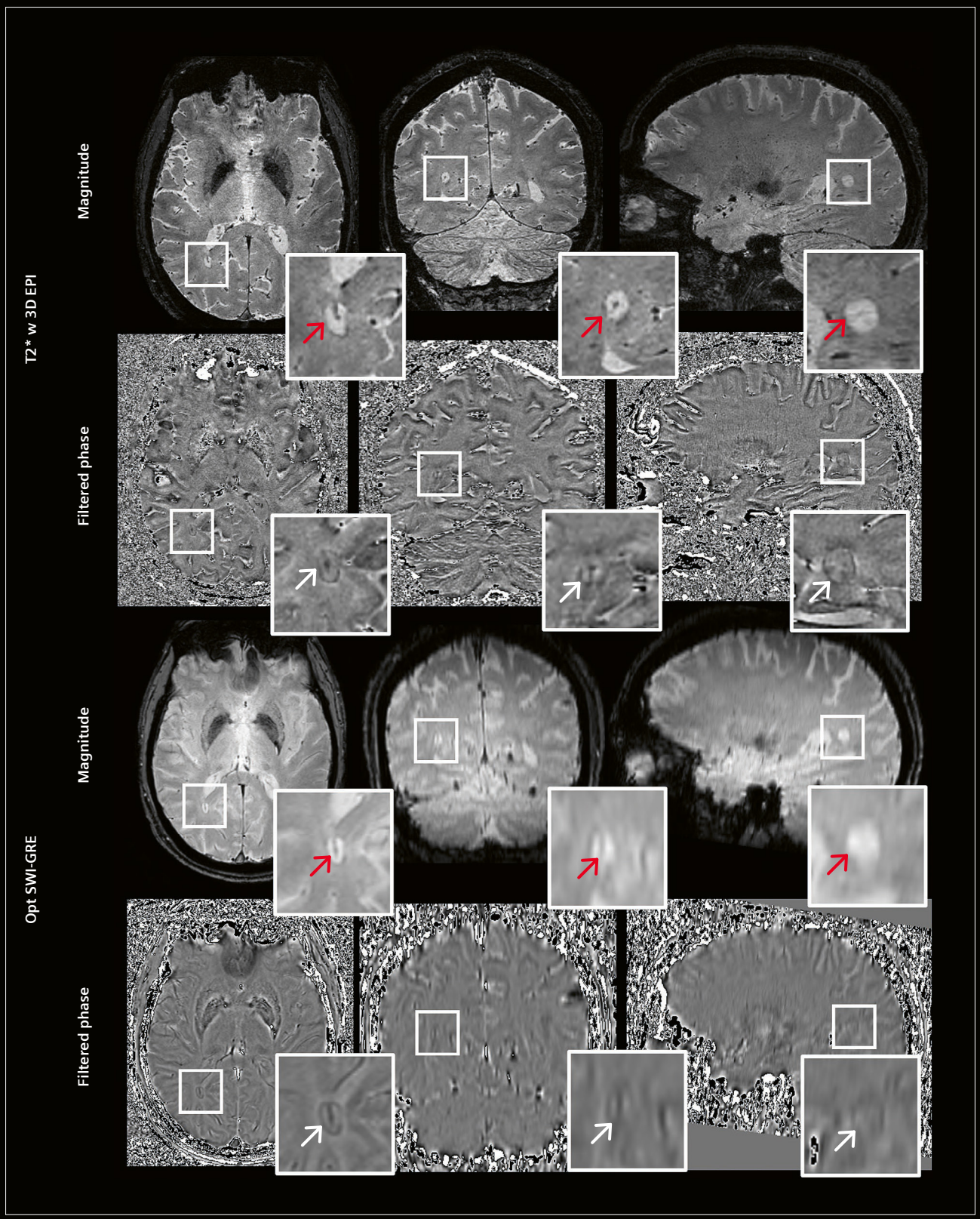

5 Multiplanar view of optimized T2*-weighted 3D EPI (top) and SWI-GRE (bottom) acquired on the same MS patient. High-resolution isotropic acquisition in T2*-weighted 3D EPI enables clear visualization of CVS and PRL in all imaging planes.

Discussion and conclusions

Given the need for rapid clinical adoption of the new imaging biomarkers recently included in the revised diagnostic criteria for MS, we provide here practical strategies to integrate adequate susceptibility MRI sequences into the diagnostic imaging workflow. We recommend using an optimized SWI protocol at 3-tesla to ensure sensitive detection of CVS, and filtered phase images for sensitive detection of PRL. When possible, the more advanced 3D EPI sequence is recommended to acquire submillimeter isotropic images. This enables multi-planar evaluation of T2*-weighted and filtered phase images and increases the radiologist's confidence in interpreting CVS and PRL. Our recommended MRI protocols for these sequences are available for download (see QR code) or can be requested directly via local Siemens Healthineers support. Finally, work is currently underway on technical developments that are using advanced acceleration strategies and deep-learning reconstruction methods to further reduce acquisition time and facilitate wider implementation of these sequences in the clinical setting.

Contact

Sreekanth Madhusoodhanan Nair, Ph.D.
Postdoctoral Scientist
Neuroimaging Program
Department of Neurology
Cedars-Sinai Medical Center
Atrium Building, 2nd Floor
8750 Beverly Blvd
Los Angeles, CA 90048
USA
Sreekanth.madhusoodhanan@cshs.org



Pascal Sati, Ph.D.
Associate Professor
Director of Neuroimaging Program
Department of Neurology
Cedars-Sinai Medical Center
Atrium Building, 2nd Floor
8750 Beverly Blvd
Los Angeles, CA 90048
USA
Pascal.sati@cshs.org



Marcel Maya, M.D.
Professor and Co-Chair
Department of Imaging
Cedars-Sinai Medical Center
8700 Beverly Blvd, Room M335
Los Angeles, CA 90048
USA
Marcel.maya@cshs.org



Acknowledgments

We acknowledge the support of the National Institute of Neurological Disorders and Stroke (NINDS), the National Multiple Sclerosis Society (NMSS), the Department of Defense (DoD), and the Erwin Rautenberg Foundation.

Appendix

Download the optimized SWI and T2* EPI protocol for different scanner models from:

magnetomworld.siemens-healthineers.com/clinical-corner/protocols/neurology-neurography/mri-sequences

References

1 Montalban X, Lebrun-Frénay C, Oh J, Arrambide G, Moccia M, Amato MP, et al. Diagnosis of multiple sclerosis: 2024 revisions of the McDonald criteria. Lancet Neur. 2025;24(10):850–865.
2 Sati P, Oh J, Constable RT, Evangelou N, Guttmann CR, Henry RG, et al. The central vein sign and its clinical evaluation for the diagnosis of multiple sclerosis: a consensus statement from the North American Imaging in Multiple Sclerosis Cooperative. Nat Rev Neurol. 2016;12(12):714–722.
3 Bagnato F, Sati P, Hemond CC, Elliott C, Gauthier SA, Harrison DM, et al. Imaging chronic active lesions in multiple sclerosis: a consensus statement. Brain. 2024;147(9):2913–2933.
4 Barkhof F, Reich DS, Oh J, Rocca MA, Li DK, Sati P, et al. 2024 MAGNIMS-CMSC-NAIMS consensus recommendations on the use of MRI for the diagnosis of multiple sclerosis. Lancet Neurol. 2025;24(10):866–879.
5 Clarke M, Pareto D, Pessini-Ferreira L, Arrambide G, Alberich M, Crescenzo F, et al. Value of 3T susceptibility-weighted imaging in the diagnosis of multiple sclerosis. AJNR Am J Neuroradiol. 2020; 41(6):1001–1008.
6 Mittal S, Wu Z, Neelavalli J, Haacke EM. Susceptibility-weighted imaging: technical aspects and clinical applications, part 2. AJNR Am J Neuroradiol. 2009;30(2):232–52.
7 Sati P, Patil S, Inati S, Wang W-T, Derbyshire JA, Krueger G, et al. Rapid MR susceptibility imaging of the brain using segmented 3D echo-planar imaging (3D EPI) and its clinical applications. ↗ MAGNETOM Flash. 2017;68(2):26–32.
8 Haacke EM, Xu Y, Cheng YCN, Reichenbach JR. Susceptibility weighted imaging (SWI). Magn Reson Med. 2004;52(3):612–8.
9 Haacke EM, Mittal S, Wu Z, Neelavalli J, Cheng Y-C. Susceptibility-weighted imaging: technical aspects and clinical applications, part 1. AJNR Am J Neuroradiol. 2009;30(1):19–30.
10 Lee JD, Renner B, Madhusoodhanan Nair S, Nakamura K, Luskin E, Shinohara RT, et al. Superior visibility of paramagnetic rim lesions on filtered phase versus SWI. AJNR Am J Neuroradiol. 2026:ajnr. A9295.
11 Madhusoodhanan Nair S, Hsu YC, Luskin E, Ayrapetyan D, Liu A, Binesh N, et al. Optimized Susceptibility Weighted Imaging for the Detection of Central Vein Sign in Multiple Sclerosis at 3-tesla. In: Proceedings of the Annual Meeting of ISMRM & ISMRT, Honolulu, Hawai'i, USA. 2025 May 10–15. ISMRM; 2025:3766.
12 Sati P, Thomasson DM, Li N, Pham DL, Biassou NM, Reich DS, et al. Rapid, high-resolution, whole-brain, susceptibility-based MRI of multiple sclerosis. Mult Scler. 2014;20(11):1464–70.

Radial UTE MRI in Musculoskeletal Diseases: Current Clinical Applications and Future Perspectives

Yun Sun Choi, M.D., Ph.D.[1]; Stefan Sommer, Ph.D.[2]; Jaekon Sung[3]

[1] Department of Radiology, Nowon Eulji Medical Center, Eulji University, Seoul, Korea
[2] Swiss Innovation Hub, Siemens Healthineers International, Zurich, Switzerland
[3] MR Research Collaboration, Siemens Healthineers Ltd, Seoul, Korea

Introduction

Magnetic resonance imaging (MRI) is the modality of choice for evaluating most soft-tissue structures in the musculoskeletal system because of its excellent soft-tissue contrast and lack of ionizing radiation. However, conventional MRI sequences typically use echo times longer than one millisecond and therefore fail to capture signal from tissues with ultrashort transverse relaxation times, such as cortical bone, calcified cartilage, fibrocartilage, the deep or enthesial portions of tendons and ligaments, and cartilaginous endplate at the discovertebral junction [1, 2]. Because these short-T2 tissues are frequently involved in musculoskeletal disease, conventional MRI leaves a diagnostic gap that has traditionally been addressed by radiography or computed tomography (CT).

Three-dimensional (3D) radial ultrashort echo time (UTE)* MRI helps bridge this gap by sampling the free induction decay within tens of microseconds after non-selective excitation, using a center-out radial *k*-space trajectory [3]. This technique enables visualization of tissues that are normally signal-void on conventional MRI, and can provide CT-like contrast for cortical bone and mineralized tissue while preserving the soft-tissue advantages of MRI. As a result, radial UTE MRI has emerged as a promising adjunct to standard musculoskeletal MRI protocols, particularly when simultaneous assessment of bone, mineralized tissue, marrow, and soft-tissue structures is clinically desirable.

Technical principles of radial UTE MRI

Three-dimensional ultrashort echo time (3D UTE) imaging was performed using a center-out radial research application sequence with TE 40 µs [3]. A short nonselective radiofrequency (RF) block pulse (40 µs) was followed by immediate data sampling after transmit/receive switching. To minimize TE, data acquisition was initiated during the ramp-up of the readout gradient. *k*-space was sampled from the center to the periphery using an isotropic 3D radial "kooshball" trajectory (Fig. 1). Image reconstruction was performed via a non-uniform fast Fourier transform using Cartesian gridding with a Kaiser-Bessel window function. To reduce trajectory deviations, the *k*-space locations of the samples were estimated using a gradient impulse response function [4]. The imaging parameters are summarized in Table 1.

Clinical applications

The clinical value of 3D radial UTE MRI lies in its ability to depict cortical bone and mineralized tissue with CT-like contrast while retaining the soft-tissue information available from conventional MRI. In current musculoskeletal imaging practice, UTE is best understood as an additional sequence within a standard MRI protocol, rather than a stand-alone examination. The following sections summarize representative clinical applications in which UTE MRI may provide incremental diagnostic value.

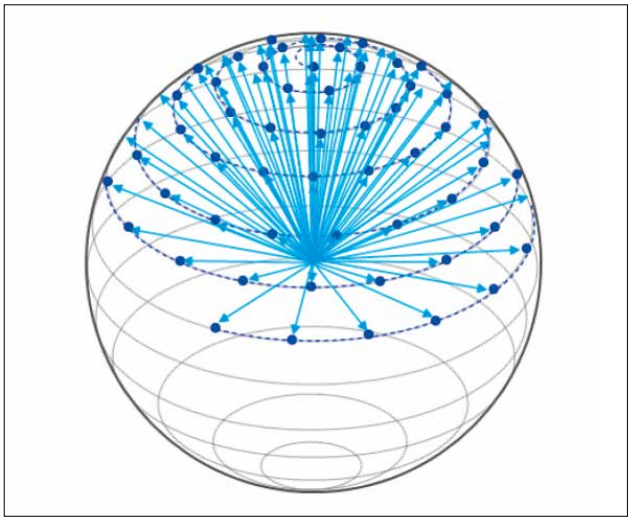

1 Schematic visualization of the radial sampling scheme.

*Work in progress. The application is currently under development and is not for sale in the U.S. and in other countries. Its future availability cannot be ensured.

Bone morphology and cortical contour assessment

Accurate depiction of cortical contour and osseous morphology is fundamental in many musculoskeletal diagnoses [5]. On conventional MRI, cortical bone is usually seen as signal-void structure, which can make subtle cortical irregularity, osseous remodeling, or complex bony anatomy difficult to assess. Radial UTE MRI can improve visualization of cortical margins and bone morphology by providing CT-like contrast within an MRI examination [6, 7].

This capability is particularly useful in joints and anatomic regions where both osseous morphology and soft-tissue status are clinically relevant. For example, in the spine and appendicular skeleton, UTE MRI can depict cortical contour abnormalities while conventional MRI sequences demonstrate marrow edema, disc disease, ligamentous injury, synovitis, or soft-tissue pathology (Fig. 2). Thus, UTE MRI may complement routine MRI by integrating osseous and soft-tissue information in a single radiation-free examination (Fig. 3) [7, 8].

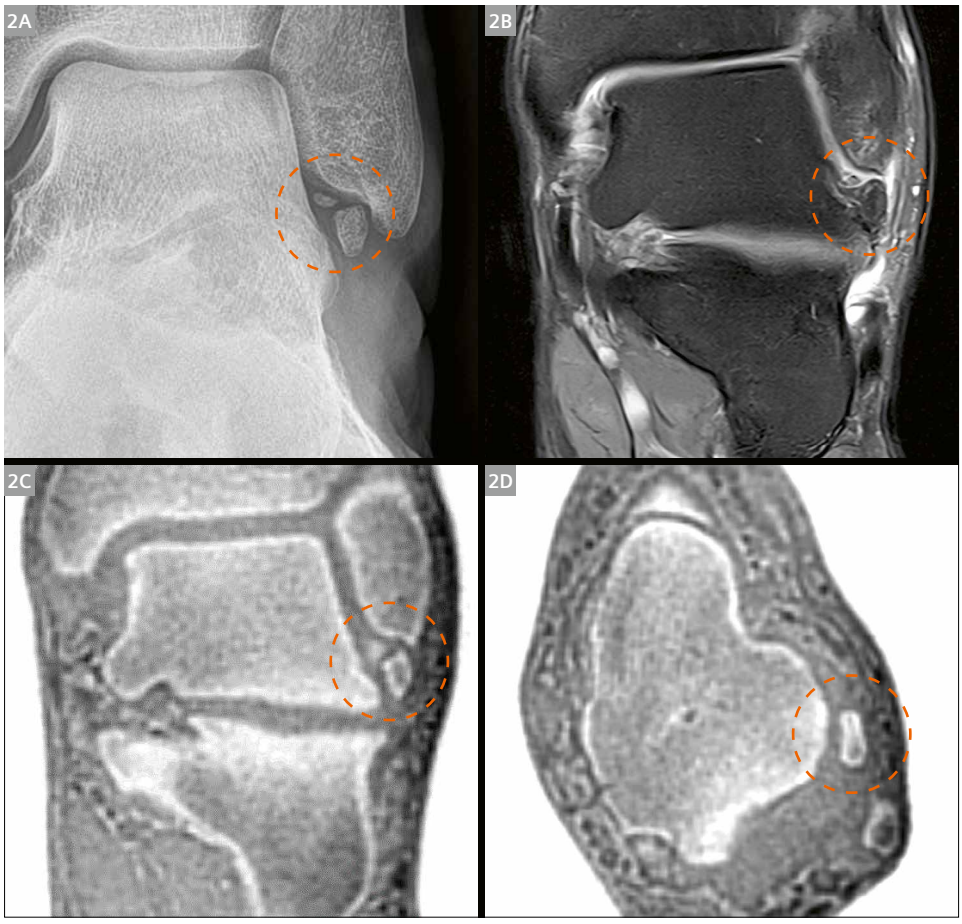

2 Symptomatic bipartite os subfibulare in a 22-year-old male with chronic ankle instability. Anteroposterior ankle radiograph **(2A)**, coronal fat-suppressed T2-weighted MR image **(2B)**, and coronal and axial UTE MR images **(2C, 2D)** demonstrate a bipartite os subfibulare. The ossicles (dotted circles) are more clearly delineated with CT-like cortical contrast on UTE than on the corresponding conventional MR image. The patient subsequently underwent surgical treatment.

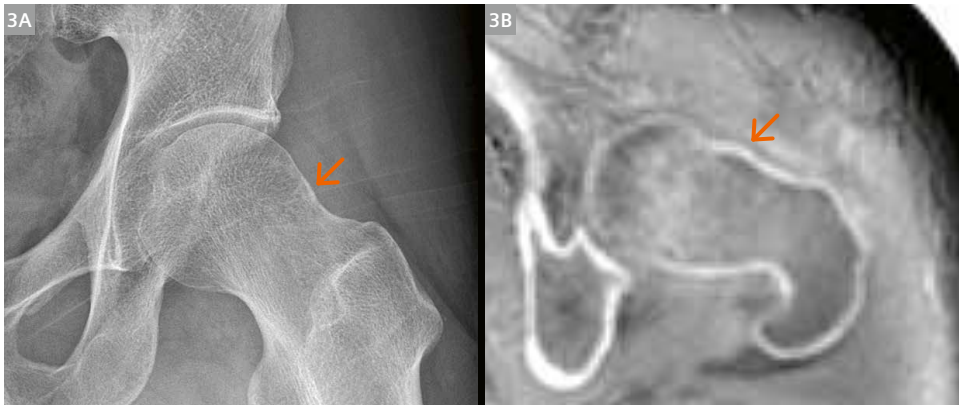

3 Femoroacetabular impingement (cam type) in a 51-year-old male. Dunn-view radiograph **(3A)** and axial UTE MR image **(3B)** of the left hip demonstrate an osseous prominence (arrows) at the femoral head–neck junction, which is clearly delineated with CT-like cortical contrast on UTE.

Fractures

Fracture evaluation is another important application of radial UTE MRI. Fracture lines, cortical disruption, and displaced osseous fragments are often defined by cortical bone, which is poorly visualized on conventional MRI but can be depicted more directly with UTE-based imaging [7, 8]. UTE MRI may therefore improve confidence in identifying cortical breaks or small osseous fragments when conventional MRI findings are equivocal.

This approach may be especially advantageous when radiation avoidance is desirable, such as in children, young adults, pregnant patients when appropriate, or patients requiring repeated follow-up examinations (Fig. 4) [6, 9]. In addition, UTE MRI may be useful when both fracture morphology and associated marrow or soft-tissue injury need to be assessed. However, because CT still provides superior spatial resolution, UTE MRI should currently be regarded as complementary to CT rather than a universal substitute.

Focal bone lesions

In focal bone lesions, radial UTE MRI can add information about cortical integrity and matrix mineralization to the marrow and soft-tissue information provided by conventional MRI [9, 10]. Conventional MRI is highly sensitive for marrow replacement, edema, soft-tissue extension, endosteal scalloping, and aggressive features. However, it is less specific for mineralized matrix, cortical detail, and small calcified or ossified components.

UTE MRI may help depict patterns of mineralization, including chondroid calcification, osteoid matrix, or nidus mineralization, while also demonstrating cortical involvement and associated pathologic fracture (Fig. 5). This information can be useful in lesion characterization, treatment planning, and follow-up. Nevertheless, CT remains superior when very fine mineralized matrix detail or subtle cortical destruction must be assessed with maximum spatial resolution.

Joint pathology

Radial UTE MRI may also contribute to the evaluation of degenerative, inflammatory, and infectious joint diseases by improving visualization of cortical and subchondral osseous abnormalities. These include osteophytes, subchondral sclerosis, erosions, osteolysis, and frank bony destruction [7, 8].

Parameters	3D radial UTE sequence
Radial view	40000
TR / TE (ms)	3.9 / 0.04
FOV (mm)	More than 200 mm
Flip angle (deg)	1.5°
Matrix	202 × 202
Slice thickness (mm)	0.7
Slices	288 slices per slab
Bandwidth (Hz/pixel)	1157
Acquisition time (min:sec)	5:13

Table 1: 3T MAGNETOM Vida imaging parameters



4 Tibial tuberosity avulsion fracture in a 13-year-old boy. Lateral knee radiograph **(4A)** and sagittal and coronal UTE MR images **(4B, 4C)** demonstrate a tibial tuberosity avulsion fracture extending through the proximal tibial physis and epiphysis with intra-articular extension. UTE MR images clearly delineate the fracture line and displaced fragment with CT-like cortical contrast.

In degenerative disease in the joints and spine, productive osseous changes such as osteophytes and subchondral remodeling are important markers of disease severity (Fig. 6). In this setting, UTE MRI may help provide a more comprehensive evaluation of both soft-tissue and osseous components of degenerative disease [7, 8].

In inflammatory arthritis, cortical erosions are clinically important because they reflect structural joint damage. UTE MRI may improve depiction of erosive change by better delineating cortical margins. Similarly, in infectious arthritis, early recognition and accurate mapping of cortical erosion or subchondral destruction are important

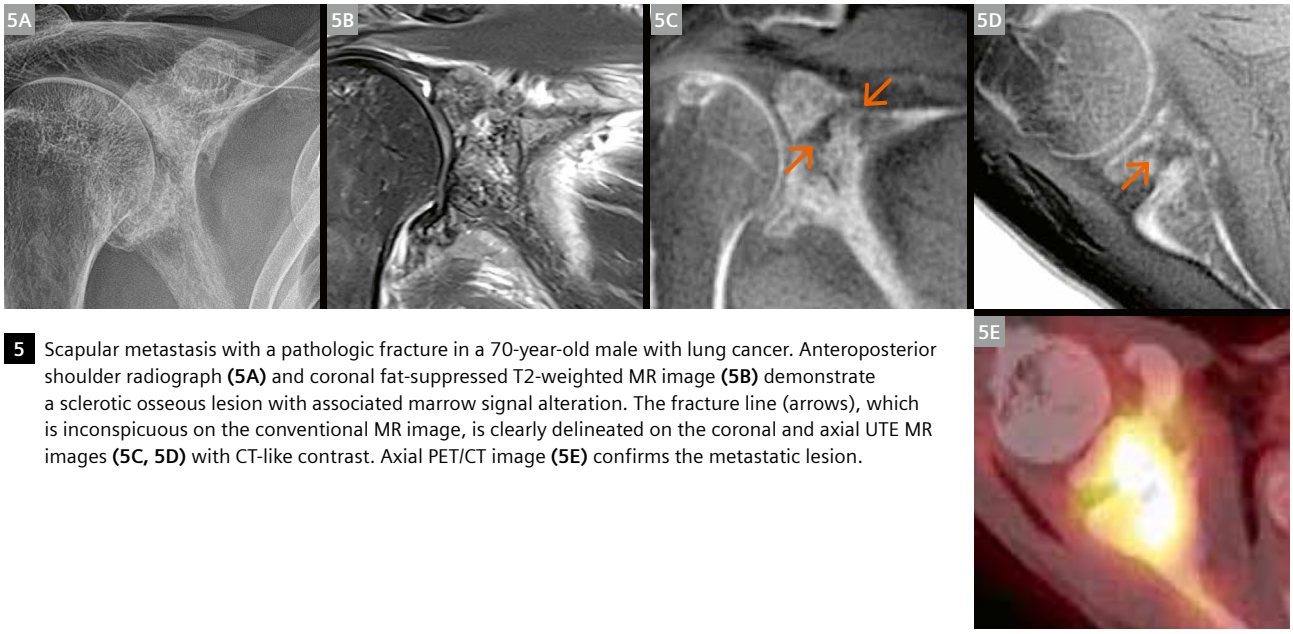

5 Scapular metastasis with a pathologic fracture in a 70-year-old male with lung cancer. Anteroposterior shoulder radiograph **(5A)** and coronal fat-suppressed T2-weighted MR image **(5B)** demonstrate a sclerotic osseous lesion with associated marrow signal alteration. The fracture line (arrows), which is inconspicuous on the conventional MR image, is clearly delineated on the coronal and axial UTE MR images **(5C, 5D)** with CT-like contrast. Axial PET/CT image **(5E)** confirms the metastatic lesion.

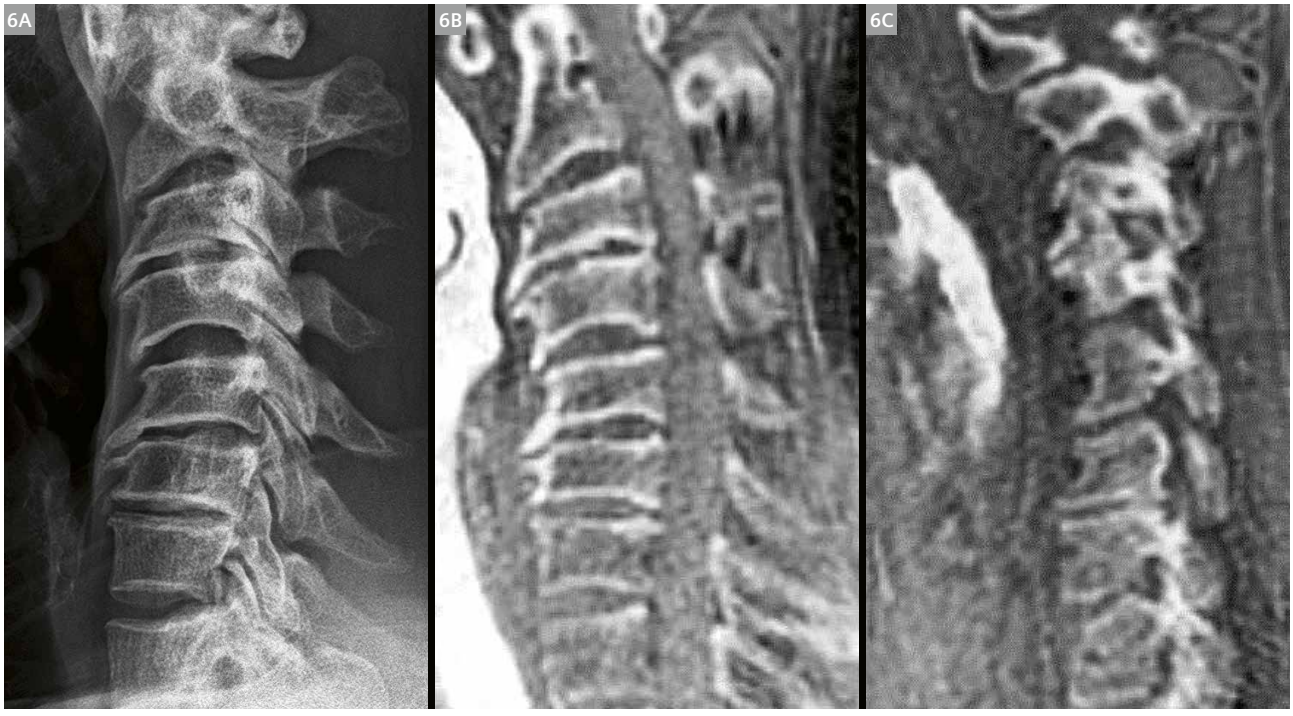

6 Cervical spondylosis in a 56-year-old male. Lateral cervical spine radiograph **(6A)** and sagittal UTE MR images **(6B, 6C)** demonstrate multilevel osteophytes, endplate sclerosis, and disc space narrowing. UTE clearly delineates these osseous degenerative changes with CT-like contrast.

for assessing disease severity and planning treatment. By combining UTE depiction of cortical destruction with conventional MRI findings such as joint effusion, synovitis, abscess, and marrow edema, MRI may provide a more complete radiation-free assessment of joint infection [6–8].

Soft-tissue calcification and ossification

Calcified and ossified soft-tissue deposits have short-T2 properties and may be difficult to characterize on conventional MRI, where they often appear as nonspecific low-signal foci. Radial UTE MRI can directly depict mineralized tissue and may therefore improve detection and characterization of soft-tissue calcification or ossification [8, 9].

This application is relevant in conditions involving calcific tendinopathy, heterotopic ossification, enthesopathic change, and other mineralized deposits within ligaments or periarticular soft tissues (Fig. 7). By clarifying whether a low-signal abnormality on conventional MRI represents mineralization, fibrosis, susceptibility artifact, or another process, UTE MRI may improve diagnostic specificity and help define disease extent [9].

Postoperative evaluation

Postoperative musculoskeletal imaging often requires assessment of both hardware and adjacent bone. Conventional MRI may be limited by susceptibility artifacts near metallic implants, while radiographs provide limited soft-tissue and marrow information. The very short echo time of UTE sequences can reduce susceptibility-related signal loss and distortion, and radial UTE-based approaches may improve visualization of bone and hardware-adjacent structures (Fig. 8) [11].

Advanced applications

Beyond morphologic imaging, UTE-based techniques enable quantitative assessment of short-T2 tissues. Quantitative UTE methods can estimate parameters such as T2*, T1, T1ρ, magnetization transfer ratio, macromolecular proton fraction, and porosity-related indices. These biomarkers are being investigated for evaluating cortical bone quality, tendon and ligament composition, cartilage degeneration, and other tissue-level changes that are difficult to assess with conventional MRI [2, 6, 8, 12–14].

Emerging UTE-based approaches, including quantitative susceptibility mapping, conductivity mapping, and accelerated 3D radial acquisitions with deep learning reconstruction, may further expand the role of UTE MRI in musculoskeletal imaging. These methods remain largely investigational, but they suggest that UTE MRI may eventually contribute not only to structural visualization but also to quantitative tissue characterization.

Limitations and future directions

Despite its advantages, radial UTE MRI has several important limitations. First, although UTE can provide CT-like contrast, it does not yet match the spatial resolution, speed, or robustness of CT for fine cortical detail and subtle mineralization [7, 8, 13]. Second, radial UTE MRI may require longer acquisition times than conventional sequences, increasing susceptibility to patient motion. Nevertheless, the radial nature of the sequence is less susceptible to motion due to repeated sampling of the *k*-space center. Third, radial acquisitions can produce specific artifacts, including streak artifacts, blurring, chemical shift, and artifacts related to gradient imperfections. These artifacts may mimic or obscure pathology



7 Calcific tendinitis of the supraspinatus in a 75-year-old female. The calcific deposit (arrows) is clearly depicted on the 30° caudal tilt radiograph **(7A)** and the inverted grayscale UTE MR image **(7B)**, which provides CT-like contrast; it appears ambiguous on the corresponding proton density (PD)-weighted MR image **(7C)**.

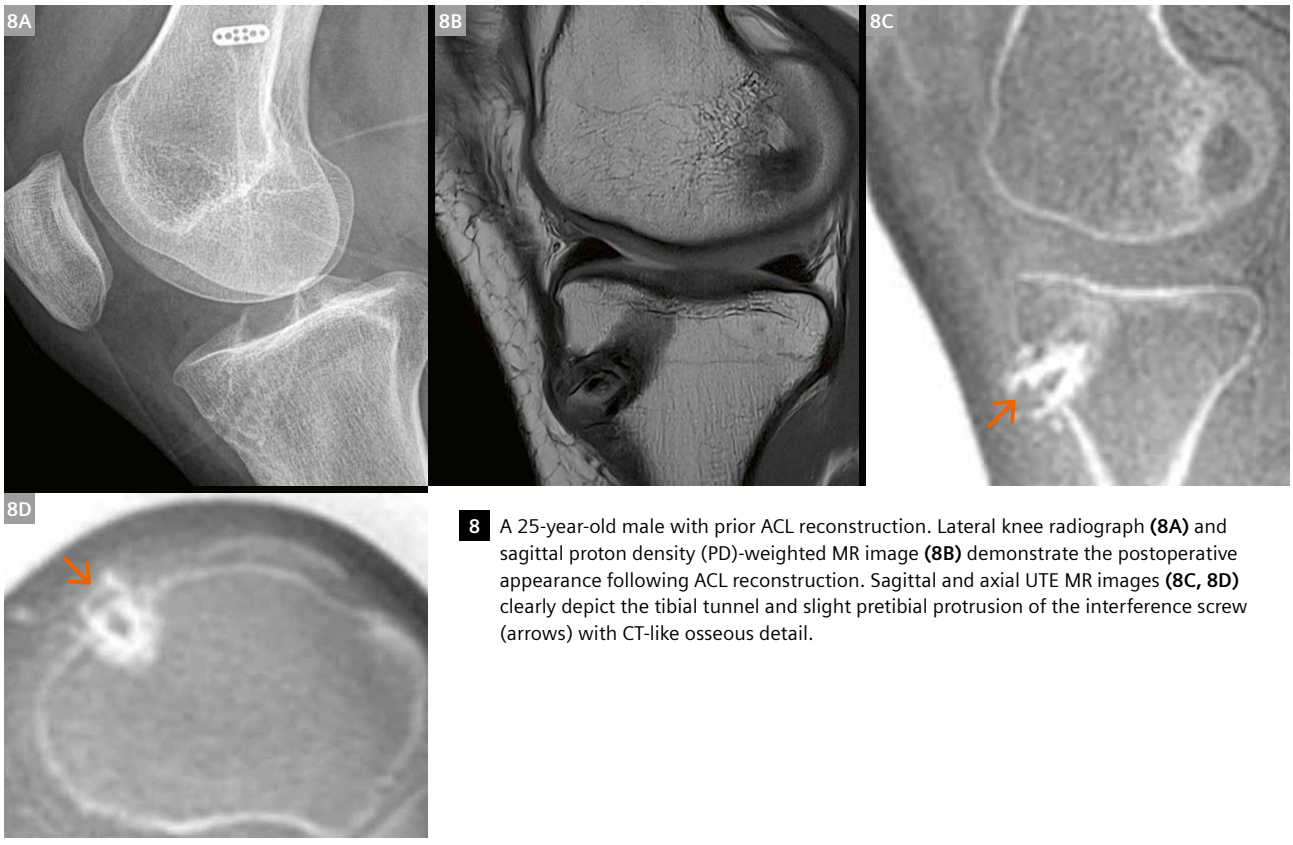

8 A 25-year-old male with prior ACL reconstruction. Lateral knee radiograph **(8A)** and sagittal proton density (PD)-weighted MR image **(8B)** demonstrate the postoperative appearance following ACL reconstruction. Sagittal and axial UTE MR images **(8C, 8D)** clearly depict the tibial tunnel and slight pretibial protrusion of the interference screw (arrows) with CT-like osseous detail.

if not recognized. Technical optimization and careful interpretation are therefore essential [12, 15, 16]. Finally, incomplete standardization remains a barrier to broader clinical adoption. However, ongoing advances in accelerated acquisition and image reconstruction, including deep learning-based reconstruction, are improving image quality while reducing scan times. Together with further clinical validation and protocol harmonization, these developments are expected to enhance the clinical feasibility of radial UTE MRI and facilitate its broader integration into routine musculoskeletal imaging across institutions [17].

Conclusion

Radial UTE MRI is a rapidly evolving technique that expands the diagnostic capability of musculoskeletal MRI by enabling visualization of tissues that are poorly seen on conventional sequences. By recovering signal from short-T2 structures and providing CT-like contrast for cortical bone and mineralized tissue, UTE MRI can complement standard MRI in the evaluation of bone morphology, fractures, focal bone lesions, joint disease, soft-tissue calcification or ossification, and postoperative changes.

At present, radial UTE MRI is best regarded as a powerful adjunct to, rather than a replacement for, CT or conventional MRI. Its clinical role is partially limited by longer acquisition times, sequence-specific artifacts, magic-angle effect, and lower spatial resolution compared with CT. Nevertheless, continuing advances in acquisition and reconstruction are likely to expand the role of radial UTE MRI in comprehensive, radiation-free musculoskeletal imaging.

Acknowledgments

We would like to thank Dr. Sugil Kim of MR Research Collaboration at Siemens Healthineers, Seoul, Korea, for his helpful discussion throughout this study.

References

1 Siriwanarangsun P, Statum S, Biswas R, Bae WC, Chung CB. Ultrashort time to echo magnetic resonance techniques for the musculoskeletal system. Quant Imaging Med Surg [Internet]. 2016;6(6):731–43. Available from: http://dx.doi.org/10.21037/qims.2016.12.06
2 More SS, Zhang X. Ultrashort echo time and zero echo time MRI and their applications at high magnetic fields: a literature survey. Investig Magn Reson Imaging [Internet]. 2024;28(4):153–73. Available from: http://dx.doi.org/10.13104/imri.2024.0009
3 Wu Z, Zaylor W, Sommer S, Xie D, Zhong X, Liu K, et al. Assessment of ultrashort echo time (UTE) T2* mapping at 3T for the whole knee: repeatability, the effects of fat suppression, and knee position. Quant Imaging Med Surg [Internet]. 2023;13(12):7893–909. Available from: http://dx.doi.org/10.21037/qims-23-459
4 Vannesjo SJ, Graedel NN, Kasper L, Gross S, Busch J, Haeberlin M, et al. Image reconstruction using a gradient impulse response model for trajectory prediction. Magn Reson Med [Internet]. 2016;76(1):45–58. Available from: http://dx.doi.org/10.1002/mrm.25841
5 Feuerriegel GC, Kronthaler S, Weiss K, Haller B, Leonhardt Y, Neumann J, et al. Assessment of glenoid bone loss and other osseous shoulder pathologies comparing MR-based CT-like images with conventional CT. Eur Radiol [Internet]. 2023;33(12):8617–26. Available from: http://dx.doi.org/10.1007/s00330-023-09939-9
6 Jerban S, Chang DG, Ma Y, Jang H, Chang EY, Du J. An update in qualitative imaging of bone using ultrashort echo time magnetic resonance. Front Endocrinol [Internet]. 2020;11:555756. Available from: http://dx.doi.org/10.3389/fendo.2020.555756
7 Florkow MC, Willemsen K, Mascarenhas VV, Oei EHG, van Stralen M, Seevinck PR. Magnetic resonance imaging versus computed tomography for three-dimensional bone imaging of musculoskeletal pathologies: a review. J Magn Reson Imaging [Internet]. 2022;56(1):11–34. Available from: http://dx.doi.org/10.1002/jmri.28067
8 Slawig A, Rothe M, Deistung A, Bohndorf K, Brill R, Graf S, et al. Ultra-short echo time (UTE) MR imaging: a brief review on technical considerations and clinical applications. Rofo [Internet]. 2024;196(7):671–81. Available from: http://dx.doi.org/10.1055/a-2193-1379
9 Teixeira PAG, Kessler H, Morbée L, Douis N, Boubaker F, Gillet R, et al. Mineralized tissue visualization with MRI: practical insights and recommendations for optimized clinical applications. Diagn Interv Imaging [Internet]. 2025;106(5):147–56. Available from: http://dx.doi.org/10.1016/j.diii.2024.11.001
10 Rahmer J, Börnert P, Groen J, Bos C. Three-dimensional radial ultrashort echo-time imaging with T2 adapted sampling. Magn Reson Med [Internet]. 2006;55(5):1075–82. Available from: http://dx.doi.org/10.1002/mrm.20868
11 Carl M, Koch K, Du J. MR imaging near metal with undersampled 3D radial UTE-MAVRIC sequences. Magn Reson Med [Internet]. 2013;69(1):27–36. Available from: http://dx.doi.org/10.1002/mrm.24219
12 Sedaghat S, Park JI, Fu E, von Drygalski A, Ma Y, Chang EY, et al. Ultrashort echo time quantitative susceptibility source separation in musculoskeletal system: a feasibility study. J Imaging [Internet]. 2026;12(1):28. Available from: http://dx.doi.org/10.3390/jimaging12010028
13 Rothe M, Riedel S, Slawig A, Deistung A, Bohndorf K, Brill R, et al. Fast 3D UTE in vivo T1 and T2* mapping of fast relaxing knee tissues at 3 T. Magn Reson Med [Internet]. 2026;95(2):693–705. Available from: http://dx.doi.org/10.1002/mrm.70099
14 Sedaghat S, Park JI, Fu E, Jung Y, Jang H. Ultrashort echo time double echo steady-state MRI for quantitative conductivity mapping in the knee: a feasibility study. Tomography [Internet]. 2026;12(2):18. Available from: http://dx.doi.org/10.3390/tomography12020018
15 Ferrari L, Bianchi T, Champendal M, Sá dos Reis C, Ghotra SS. Ultra-short and zero echo time MRI sequences for MSK investigation: a scoping review. Radiography (Lond) [Internet]. 2026;32(3):103334. Available from: http://dx.doi.org/10.1016/j.radi.2026.103334
16 Zhao X, Lee H, Song HK, Cheng CC, Wehrli FW. Impact of gradient imperfections on bone water quantification with UTE MRI. Magn Reson Med [Internet]. 2020;84(4):2034–47. Available from: http://dx.doi.org/10.1002/mrm.28272
17 Herrmann KH, Krämer M, Reichenbach JR. Time efficient 3D radial UTE sampling with fully automatic delay compensation on a clinical 3T MR scanner. PLoS One [Internet]. 2016;11(3):e0150371. Available from: http://dx.doi.org/10.1371/journal.pone.0150371

Contact

Yun Sun Choi, M.D., Ph.D.
Department of Radiology
Nowon Eulji Medical Center
Eulji University
68 Hangeulbiseok-ro, Nowon-gu
Seoul 01830
Republic of Korea
cys0128@eulji.ac.kr



The MAGNETOM World

Your portal to protocols, articles and case studies

Siemens Healthineers' global MRI community offers peer-to-peer support and information. Radiologists, physicists, cardiologists, and technologists, have all contributed with publications, protocols, training documents, case studies, and more – all freely available to you via this unique network.

The centerpiece of the MAGNETOM World Internet platform consists of our users' clinical results. Here you will find case reports and clinical methods.

Go to
Clinical Corner > Case studies



Here you can download clinical protocols, phoenix images and application tips including videos.

Go to
Clinical Corner > Protocols

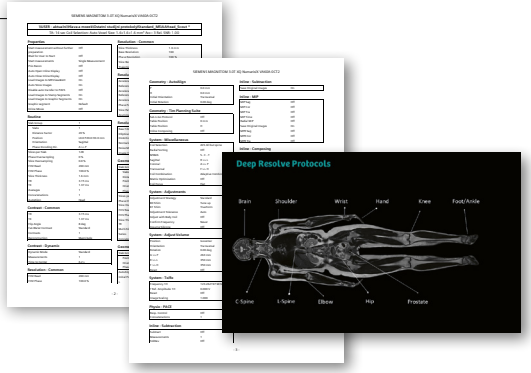

Just a mouse click away you will find application videos and useful tips allowing you to optimize your daily MR examinations.

Go to
Clinical Corner > Application Tips



Proactive Ergonomic Design for Interventional MRI: Insights from Digital Human Modeling

Justin Davidson, M.Sc., Ph.D.(c)[1]; Joshua Krieger, B.S.[2]; Sean Chambers, Ph.D.[2]; Jan-M. Brandt, Ph.D.[3]; Steven Fischer, Ph.D., RKin, CCPE[1]

[1] Faculty of Health, University of Waterloo, Waterloo, ON, Canada
[2] Cook Medical, Bloomington, Indiana, USA
[3] Siemens Healthineers, Erlangen, Germany

Abstract

Interventional MRI (iMRI) is increasingly recognized as a powerful platform for image-guided procedures, offering non-ionizing imaging and superior soft-tissue contrast compared with conventional CT-guided workflows [1, 2]. While the clinical benefits of iMRI are well established, less attention has been paid to the physical and ergonomic demands placed on interventional radiologists who must work within the geometric constraints of MRI systems. Longer bore lengths, narrower access, and constrained reach conditions can require clinicians to adopt sustained, non-neutral postures that may elevate musculoskeletal loading over time.

The solution is to apply digital human modeling (DHM) techniques to quantify ergonomic exposures during simulated needle-insertion tasks performed in CT and MRI environments. By integrating live human motion-capture data with predictive biomechanical simulation, this study demonstrates how scanner geometry, specifically bore length, bore diameter, bore flaring, and table height, interact with clinician anthropometry to influence physical (ergonomic) demands on the body.

The findings show that ergonomic risk in iMRI is not inherent to MRI as a modality but rather is highly design dependent. Certain MRI configurations, particularly those incorporating flared bore entries and elevated table heights, can substantially reduce low-back loading compared with both CT-guided workflows and more conventional MRI designs. Shoulder loading, often cited as a barrier to MRI-guided intervention, was found to be comparatively modest across systems and sensitive to access geometry rather than bore length alone.

This work underscores the value of embedding ergonomics early in scanner design and service planning. Digital human modeling provides a rigorous, evidence-based approach for proactively evaluating human–system interactions. It thereby supports the development of iMRI environments that optimize clinical performance while safeguarding the long-term occupational health of interventional radiologists.

Introduction

Interventional radiology has evolved around the principle of minimally invasive, image-guided therapy, with precision and safety as core objectives. MRI-guided interventions align strongly with these goals, offering real-time visualization without ionizing radiation exposure [3, 4]. Compared with CT guidance, MRI provides superior soft-tissue contrast, which can improve visualization of small



1 Motion-capture data were collected around the MAGNETOM Free.Max* as clinicians performed a simulated needle insertion using a torso phantom to parameterize and validate the digital human model.
** The MAGNETOM Free.Max would not normally be used for interventions. It was used here due to its greater in-bore access and availability.*

The products/features mentioned herein are not commercially available in all countries.Their future availability cannot be guaranteed.

lesions (< 1 cm) and targeting accuracy, particularly in complex anatomical regions [5].

As iMRI adoption increases, clinicians are spending more time performing procedures within MRI environments. Unlike CT scanners, which typically have short gantries and open access, MRI systems are characterized by longer bores and more restrictive entry geometries. To access targets that are positioned near the scanner isocenter, which is required for optimal image quality, interventional radiologists may need to reach deep into the bore while maintaining visual attention on external displays. These constraints shape the posture, reach strategy, and loading at the shoulder and low back, which can influence the risk of developing musculoskeletal disorders.

Why ergonomics matters in image-guided interventions

Musculoskeletal disorders are prevalent among interventional clinicians, with the shoulder and low back frequently identified as regions of vulnerability [2]. Tasks involving sustained arm elevation, asymmetric reaching, and trunk flexion are known to increase joint loading and fatigue potential [6]. In CT-guided procedures, these demands are compounded by the requirement to wear protective lead aprons, which typically add 4–5 kg of mass to the torso and increase spinal loading [7].

MRI-guided interventions eliminate ionizing radiation exposure and therefore the need for lead protection, offering an immediate ergonomic advantage. However, this benefit may be partially offset by the increased reach distances and constrained access imposed by MRI bore geometry and isocenter location. The net ergonomic outcome is therefore not obvious and cannot be inferred from imaging modality alone. Instead, it emerges from the interaction between human characteristics, task demands, and system design.

Digital human modeling provides a computational framework for representing human posture, movement, and biomechanical loading across a range of anthropometries. Modern digital human models can be integrated with computer-aided design (CAD) environments to simulate realistic human–system interactions and quantify joint torques, reach feasibility, and fatigue-related metrics [8, 9]. In this study, DHM was deployed to understand how scanner design elements shape the posture, reach strategy, and loading at the shoulder and low back.

Methodology

Phase 1: From motion capture to comparative simulation

The research followed a two-stage workflow. In the first stage, six clinicians with a range of experience levels and body sizes performed representative needle-insertion tasks in an MRI environment using a torso phantom. Tasks varied by reach depth (isocenter and 12 cm short of the isocenter) and needle orientation, reflecting common interventional scenarios. Whole-body kinematics were captured using an inertial measurement system (Fig. 1) and processed to define a representative "standard" posture.

The MAGNETOM Free.Max would not normally be used for interventions but was used due for greater in-bore access and availability. At the time of the study, the MAGNETOM Free.XL was not yet commercially available; therefore, clinician postures were collected using the MAGNETOM Free.Max during the first phase of the study. These experimentally captured postures were used to inform and calibrate the DHM workflow by providing representative reference postures for simulated needle insertion tasks. From these baseline postures, the DHM could then adapt the simulated clinician's anthropometry to the surrounding MRI geometry in order to predict likely working postures in other scanner configurations, including the MAGNETOM Free.XL. This approach allowed the model to be used to investigate the potential ergonomic implications of different MRI design features within the MAGNETOM Free.XL geometry.

Motion-capture data were used to parameterize and validate the DHM. DHM predicted joint angles for key degrees of freedom fell largely within one standard deviation of the in vivo measured means, indicating that the simulated postures were realistic representations of clinician behavior.

Phase 2: Comparative simulation to inform scanner design

In the second stage, the validated model was applied to comparative simulations of three imaging systems. One was a conventional CT scanner (including simulated lead apron loading) and two were MRI designs with distinct

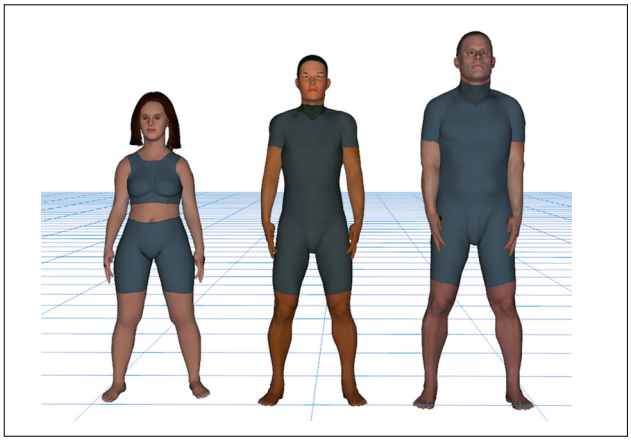

2 Avatars of a woman in the 5th percentile for height, a man in the 50th percentile, and a man in the 95th percentile were selected to understand how clinician anthropometry interacts with MR scanner design elements.

bore geometries: The 0.55T MAGNETOM Free.XL features a 100 cm flared bore design with a larger bore diameter (80 cm) and longer bore length (165 cm) than the 1.5T MAGNETOM Sola, which features no flaring, a smaller bore diameter (70 cm), and a shorter bore length (157 cm). The MAGNETOM Free.XL has a bore geometry specifically designed for interventions, whereas the MAGNETOM Sola represents a conventional MRI scanner.

Avatars representing a woman in the 5th percentile for height, a man in the 50th percentile for height, and man in the 95th percentile for height (Fig. 2) were used to explicitly examine the interaction between scanner design and anthropometry (Fig. 3).

Primary outcome metrics included joint torques at the shoulder and low back, as well as endurance times estimated using joint-specific fatigue models [10]. Joint torques serve as a metric to evaluate the intensity of effort on the shoulder and low back. Endurance time serves as a proxy measure for muscular fatigue, where muscular fatigue is difficult to model directly.

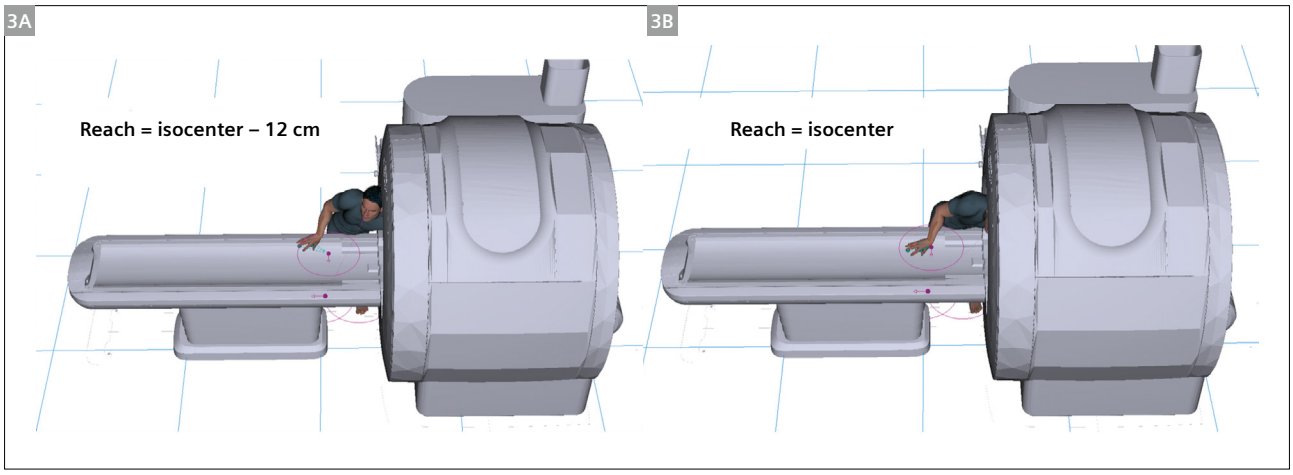

3 Simulation of a male clinician in the 50th percentile for height reaching into the bore to perform a needle ablation. The left panel **(3A)** illustrates a reach to a location that is 12 cm short of the isocenter (the maximum distance from isocenter that can provide strong contrast. The right panel **(3B)** illustrates a reach to isocenter.

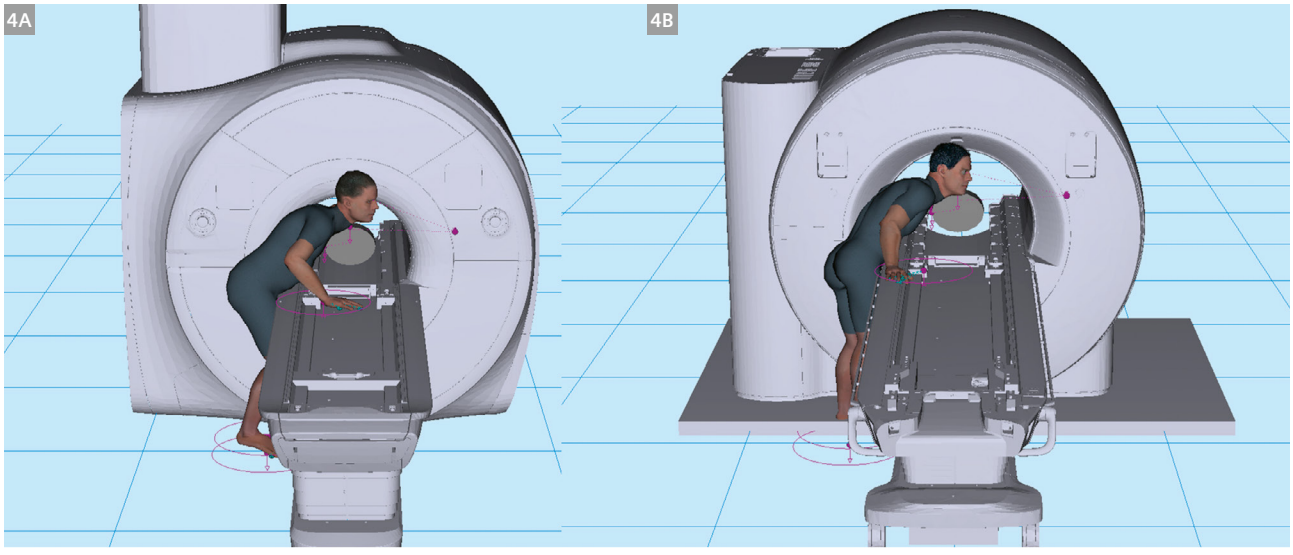

4 Bore height, diameter, and flare all influence the ways clinicians will move to perform needle targeting. The left panel **(4A)** illustrates a man in the 95th percentile for height reaching into a scanner with a lower height, narrower bore, and limited flare at bore entry. These design elements can limit the clinician's ability to lean into the bore. The right panel **(4B)** illustrates a man in the 95th percentile for height reaching into a scanner with a higher height, wider bore, and more pronounced flare at bore entry. This enables an easier lean into the bore and a more upright posture while monitoring the screen.

Results

Key findings I: Shoulder loading is modest and geometry dependent

Across all simulated systems, shoulder torques during needle-insertion tasks were relatively low, remaining below levels typically associated with elevated injury risk [6]. As expected, CT-based simulations exhibited the lowest shoulder torques overall, reflecting the shorter reach distances enabled by the compact gantry geometry.

Differences between the two MRI designs revealed important trade-offs. One configuration reduced shoulder abduction/adduction torque while increasing flexion/extension torque, whereas the other demonstrated the opposite pattern. These findings indicate that shoulder loading is influenced not only by bore length, but also by bore diameter, entry flaring, and table height. The 100 cm flared bore of the MAGNETOM Free.XL allows clinicians to position the shoulder closer to the target, reducing moment arms even in longer systems (Fig. 4).

Key findings II: Low-back loading and fatigue are strongly design dependent

The most pronounced differences between imaging systems were observed at the low back. In CT-guided simulations, low-back extensor torques were consistently higher when the additional mass of a typical protective lead apron was included (4.26 kg), despite the shorter reach distances. This finding aligns with established biomechanical evidence showing that external torso loads substantially increase spinal extensor demand [6]. At the low-back, about the lateral bend axis, endurance time was longest when performing a needle-insertion procedure in a CT scanner (Fig. 5). However, endurance time about the flexion/extension axis was lowest when simulating a needle-insertion task using the MAGNETOM Free.XL scanner, where endurance time was 46% lower (i.e. increased rate of fatigue) when simulating needle-insertion in CT relative to the MAGNETOM Free.XL.

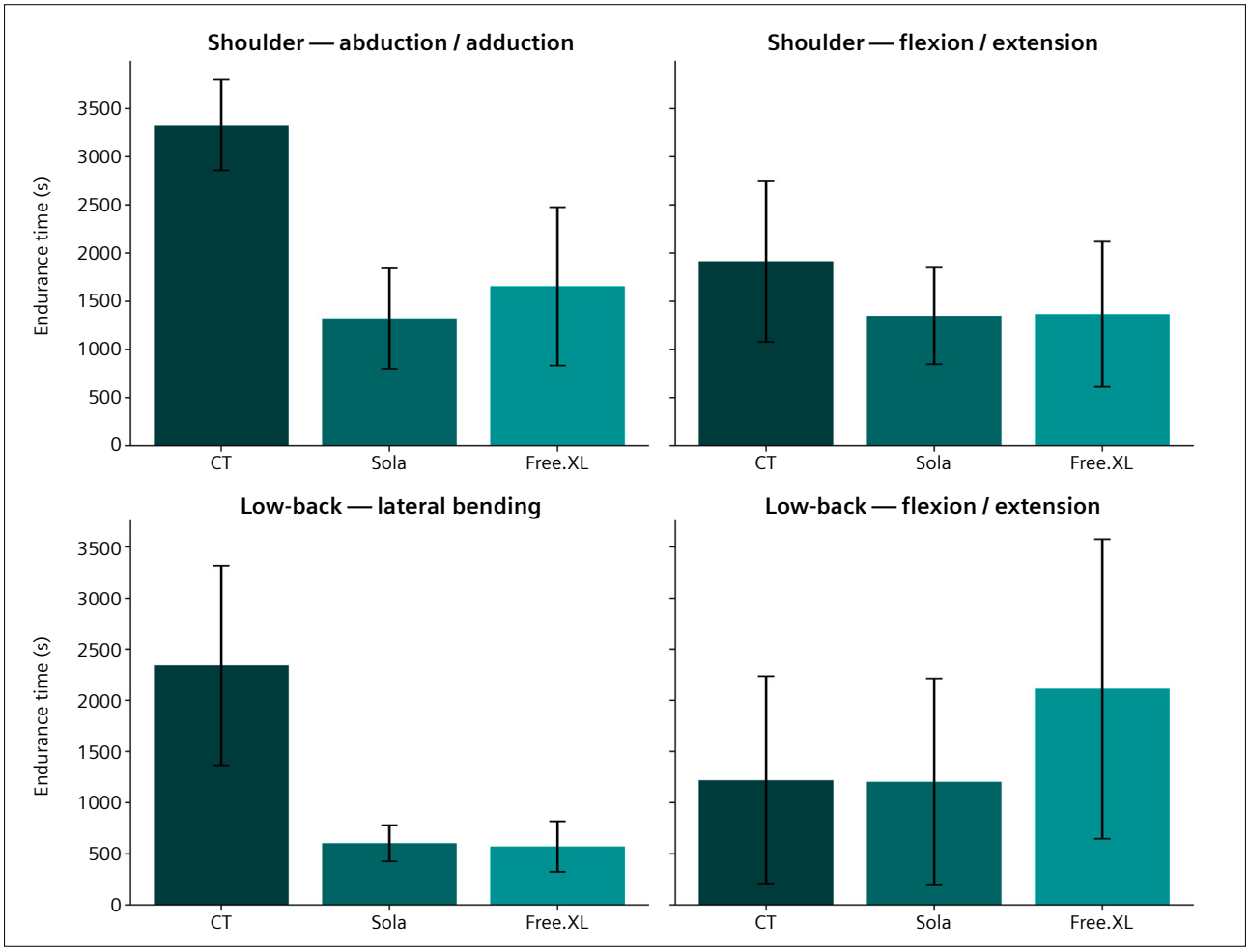

5 Shoulder abduction/adduction and flexion/extension endurance times and low-back lateral bending and flexion/extension endurance times across three scanner models aggregated across avatar anthropometry and needle-insertion location. Higher values are interpreted as less fatiguing (i.e., the task could be performed for a longer time without fatiguing).

The MRI design featuring a flared bore, larger diameter, and elevated table height (MAGNETOM Free.XL) demonstrated markedly lower low-back flexion/extension torques and substantially longer endurance times compared with both conventional CT and a more conventional MRI geometry. These reductions were attributed to the combined effects of eliminating the lead apron load, improving access geometry, and reducing forward trunk flexion.

Discussion

Inclusivity and anthropometry

A critical contribution of this work is its explicit consideration of anthropometric diversity. Simulations showed that certain reach tasks were not feasible for the smallest avatar under specific MRI configurations unless table height or clinician elevation was adjusted. This finding highlights the importance of adjustable system features in supporting an inclusive interventional workforce.

Rather than treating reach limitations as individual shortcomings, the results emphasize the role of design in enabling safe and effective performance across a wide range of statures (Fig. 6).

Implications for scanner design and clinical practice

The findings synthesized here reinforce that ergonomic outcomes in interventional imaging are design dependent rather than modality dependent. Bore length, bore diameter, bore flaring, and table height interact to shape musculoskeletal loading and fatigue potential.

For manufacturers, DHM provides a powerful framework for evaluating ergonomic trade-offs early in the design process, complementing traditional performance metrics such as image quality and throughput [8]. For healthcare organizations, these insights support more informed procurement and service planning decisions, particularly as iMRI programs scale.

Future directions

Future work can extend DHM-based evaluation to longer procedures, dynamic task sequences, and team-based workflows. Advances in fatigue modeling and predictive simulation may further enhance realism and applicability [9]. Beyond hardware design, DHM may support training, workflow optimization, and procedure-specific setup recommendations based on clinician anthropometry.

Conclusion

Interventional MRI offers clear clinical advantages, but its long-term success depends on designing systems that support the people who use them. The work summarized here demonstrates that ergonomic risk in iMRI is neither inevitable nor uniform. Through validated digital human modeling, it is possible to identify design features that meaningfully reduce musculoskeletal loading, particularly at the low back, while maintaining clinical functionality. The 100 cm flared bore geometry of the MAGNETOM Free.XL appears to have ergonomic advantages compared with conventional CT and conventional 70 cm bore MRI geometries.

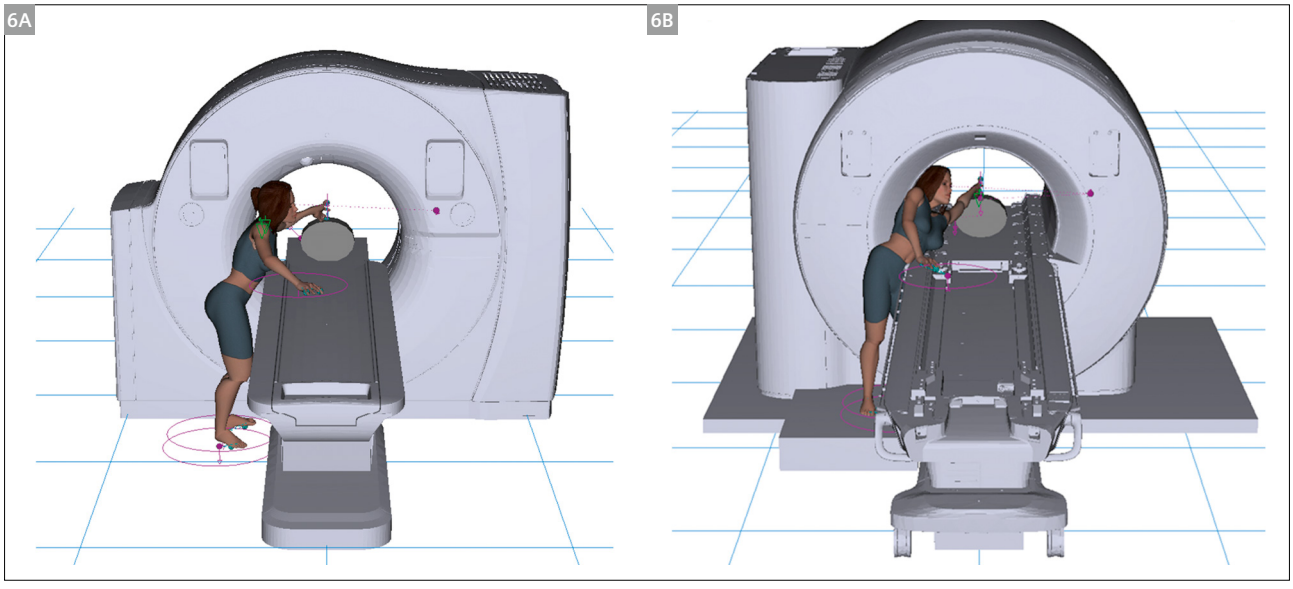

6 A lower scanner (left panel, **6A**) is more accessible for a woman in the 5th percentile for height. However, as illustrated in Figure 4, a lower scanner increases ergonomic risks for taller clinicians. However, the ability to match clinician hip height to the table height of the MAGNETOM Free.XL (right panel, **6B**), regardless of scanner height, offers an ideal solution.

By embedding ergonomics upstream in scanner design and service planning, the field can move beyond reactive mitigation and toward proactive prevention to support the sustainable, human-centered growth of interventional MRI.

References

1 Bock M, Wacker FK. MR-guided intravascular interventions: techniques and applications. J Magn Reson Imaging [Internet]. 2008;27(2):326–38. Available from: http://dx.doi.org/10.1002/jmri.21271

2 Cornelis FH, Razakamanantsoa L, Ben Ammar M, Lehrer R, Haffaf I, El-Mouhadi S, et al. Ergonomics in interventional radiology: Awareness is mandatory. Medicina (Kaunas) [Internet]. 2021;57(5):500. Available from: http://dx.doi.org/10.3390/medicina57050500

3 Kos S, Huegli R, Bongartz GM, Jacob AL, Bilecen D. MR-guided endovascular interventions: a comprehensive review on techniques and applications. Eur Radiol [Internet]. 2008;18(4):645–57. Available from: http://dx.doi.org/10.1007/s00330-007-0818-4

4 Saeed M, Wilson M. Value of MR contrast media in image-guided body interventions. World J Radiol [Internet]. 2012;4(1):1–12. Available from: http://dx.doi.org/10.4329/wjr.v4.i1.1

5 Fernández-Gutiérrez F, Martínez S, Rube MA, Cox BF, Fatahi M, Scott-Brown KC, et al. Comparative ergonomic workflow and user experience analysis of MRI versus fluoroscopy-guided vascular interventions: an iliac angioplasty exemplar case study. Int J Comput Assist Radiol Surg [Internet]. 2015;10(10):1639–50. Available from: http://dx.doi.org/10.1007/s11548-015-1152-y

6 Chaffin, DB, Andersson GBJ. Occupational Biomechanics. 2nd ed. Nashville, TN: John Wiley & Sons; 1991.

7 Barrier Technologies. How Much Does A Lead Apron Weigh & What Are The Effects On The Body? [Internet]. Barrier Technologies. 2022 [cited 2026 June 23]. Available from: https://barriertechnologies.com/how-much-does-a-lead-apron-weigh/

8 Chaffin DB. Improving digital human modelling for proactive ergonomics in design. Ergonomics [Internet]. 2005;48(5):478–91. Available from: http://dx.doi.org/10.1080/00140130400029191.

9 Abdel-Malek K, Arora JS. Human Motion Simulation: Predictive Dynamics. San Diego, CA: Academic Press; 2013.

10 Frey-Law LA, Avin KG. Endurance time is joint-specific: a modelling and meta-analysis investigation. Ergonomics [Internet]. 2010;53(1):109–29. Available from: http://dx.doi.org/10.1080/00140130903389068

Further reading

- Davidson JB, Cashaback JGA, Fischer SL. A response surface methodology to determine the optimal objective function weightings within a multi-objective optimization digital human model used to predict postures. Comput Methods Biomech Biomed Engin [Internet]. 2023;26(2):187–98. Available from: http://dx.doi.org/10.1080/10255842.2022.2052052
- Davidson JB, Fischer DSL. Predicting preferred motorcycle riding postures to support human factors/ergonomic trade-off analyses within a multi-objective optimisation-based digital human model. Ergonomics [Internet]. 2025;68(3):359–73. Available from: http://dx.doi.org/10.1080/00140139.2024.2329694
- Davidson JB. et al. Evaluating alternative MRI designs to support interventional radiology using an in-silico simulation approach. 2026. Manuscript under review.
- National Institute for Occupational Safety and Health. Hierarchy of Controls [Internet]. CDC. 2024 April 10 [cited 2026 June 23]. Available from: https://www.cdc.gov/niosh/hierarchy-of-controls/about/index.html?CDC_AA_refVal=https%3A%2F%2Fwww.cdc.gov%2Fniosh%2Ftopics%2Fhierarchy%2Fdefault.html



Contact

Steven Fischer, Ph.D., RKin, CCPE
Associate Professor, Associate Chair, Applied Research, Partnerships, & Outreach
Department of Kinesiology and Health Sciences, University of Waterloo
200 University Ave W
Waterloo, Ontario, Canada N2L 3G1
steven.fischer@uwaterloo.ca

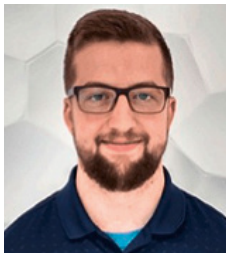

Justin Davidson, M.Sc., CSCS
Ph.D. Candidate
Department of Kinesiology and Health Sciences, University of Waterloo
200 University Ave W
Waterloo, Ontario, Canada N2L 3G1
justin.bryce.davidson@uwaterloo.ca








1993

3 **Why a Newsletter? The mission of the MAGNETOM Flash** Vol. 1 No. 1
Christine Harris, Children's Hospital of Philadelphia, USA

4 **Clinical Focus: Knee Imaging. MR Imaging the Anterior Cruciate Ligament of the Knee** Vol. 1 No. 1
Brian Murphy, Doctor's Hospital of Coral Gables, FL, USA

5 **Clinical Focus: Turbo Spin Echo. Principles and Clinical Applications** Vol. 1 No. 2
A.J. Martinez, Dir. of MRI, North Idaho Imaging, Coeur D'Alene, ID, USA

6 **Clinical Focus: Turbo Spin Echo. The Intricacies Explained** Vol. 1 No. 2
Dean Kaufman, Siemens Medical Systems, Inc.

7 **Cross word puzzle** Vol. 1 No. 2
Philip A. Femano, President, Medical Imaging Consultants, Inc., USA

1994

8 **Clinical Applications of Fat Suppression Techniques. Principles and Clinical Applications** Vol. 2 No. 1
Richard Patt, Goergetown University Medical Center, Washington, D.C., USA

9 **Fat Suppression In Magnetic Resonance Imaging** Vol. 2 No. 1
Helmuth Schultze-Haakh, Siemens Medical Systems, Inc.

10 **The Flash Word Bash!** Vol. 2 No. 1
Philip A. Femano, President, Medical Imaging Consultants, Inc., USA

1995

11 **Array coil design** Vol. 3 No. 1
Charles M. Anderson, and Ralph E. Lee, University of California, San Francisco, CA, USA

1996

13 **MR-guided procedures** Vol. 4 No. 3
Anne Deery Sheehan, Open Product Manager, Siemens Medical Systems, Iselin, NJ, USA

15 **MR Imaging of the prostate with the CP body array coil** Vol. 4 No. 3
Jeffrey C. Weinreb, New York University Medical Center, New York, NY, USA

16 **Principles of low field MR imaging** Vol. 4 No. 4
Helmuth Schultze-Haakh, Siemens Medical Systems, Tustin, CA, USA


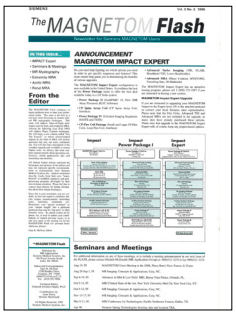





1997

18 **Clinical principles of diffusion imaging** Vol. 5 No. 3
Yuri Wedmid, Siemens Medical Systems, Tustin, CA, USA

19 **Technical principles of diffusion imaging** Vol. 5 No. 3
James Moore, Siemens Medical Systems, Tustin, CA, USA

1999

20 **Non-Echo-Planar Fast MR Imaging Techniques Part 1** Vol. 6 No. 1
D. Chien et al., Siemens AG, Medical Engineering Group, Erlangen, Germany

22 **Non-Echo-Planar Fast MR Imaging Techniques Part 2** Vol. 6 No. 2
D. Chien et al., Siemens AG, Medical Engineering Group, Erlangen, Germany

2001

29 **MRI in Pediatric Radiology[2] – Possibilities and limitations of low field magnetic resonance imaging** Vol. 8 No. 1
M. Wagner et al., Friedrich-Alexander University, Erlangen-Nuremberg, Germany

40 **Advancements in MRI scanner technology lead to improved functional imaging** Vol. 8 No. 1
A. G. Sorensen, MGH-NMR Center, Massachusetts General Hospital, Charlestown, USA

2002

44 **Product News: Maestro Class** Vol. 9 No. 1
M. Wagner et al., Friedrich-Alexander University, Erlangen-Nuremberg, Germany

52 **SENSE and SMASH: Physical principle, advantages** Vol. 9 No. 2
Matthias Blasche, Siemens AG, Medical Solutions, MR Marketing, Erlangen, Germany

2003

56 **20 Years of Development and a Constantly Improving Performance = MAGNETOM** Vol. 10 No. 1
Peter Kreisler, Collaborations and Applications, Erlangen, Germany

[1] Work in progress. The application is currently under development and is not for sale in the U.S. and in other countries. Its future availability cannot be ensured.

[2] MR scanning has not been established as safe for imaging fetuses and infants less than two years of age. The responsible physician must evaluate the benefits of the MR examination compared to those of other imaging procedures.

[3] The MRI restrictions (if any) of the metal implant must be considered prior to patient undergoing MRI exam. MR imaging of patients with metallic implants brings specific risks. However, certain implants are approved by the governing regulatory bodies to be MR conditionally safe. For such implants, the previously mentioned warning may not be applicable. Please contact the implant manufacturer for the specific conditional information. The conditions for MR safety are the responsibility of the implant manufacturer, not of Siemens Healthineers.








62 **iPAT Applications in Clinical Routine and Beyond: Imaging from Head to Toe** Vol. 10 No. 2
Olaf Dietrich, et al., Department of Clinical Radiology, Ludwig-Maximilians-University of Munich, Germany

78 **A Quantum Leap in MR Tomography: Tim [76x32]** Vol. 10 No. 2
Carol Milano and Christoph Zindel

82 **Introducing MAGNETOM Avanto: The Revolution Begins Now** Vol. 10 No. 2
Carol Milano and Christoph Zindel

2004

86 **Perfusion MRI and MRS for Brain Tumors** No. 28
Meng Law, et al, New York University school of Medicine, New York, NY, USA

96 **MAGNETOM C! is changing the face of mid-field MRI** No. 29
Stefan Domalski, Siemens AG Medical Solutions, Magnetic Resonance Division, Erlangen, Germany

102 **All You Want to Know about FatSat** No. 29
David Purdy, MR R&D, Research & Collaborations, USA

2005

108 **Diffusion-Weighted MR Imaging for Diagnosis of Liver Metastases** No. 30
Bachir Taouli, Department of Radiology, NYU Medical Center, New York, USA

112 **T2-Weighted 3D MR Imaging of the Torso –First Clinical Experiences with SPACE** No. 30
M. P. Lichy, et al., Department for Radiological Diagnostics, University Tübingen, Germany

115 **Advances in Cardiac MRI at 3T –Benefits of Multi-Channel MR Systems** No. 31
Bernd J. Wintersperger, Department of Clinical Radiology, University Hospitals-Grosshadern, Ludwig-Maximilians-University, Munich, Germany

2006

120 **Software Compensation for Patient Position Enabling Reproducible Slice Positioning – AutoAlign** No. 32
Katherine T. Scott, Siemens Medical Solutions, Inc., Malvern, PA, USA

126 **A Practical Approach to Lung MRI at 1.5T** No. 33
Jürgen Biederer, et al., University Hospital Schleswig-Holstein Campus Kiel (UKSH), Department of Diagnostic Radiology, Kiel, Germany and German Cancer Research Center (DKFZ), Department of Radiology, Heidelberg, Germany





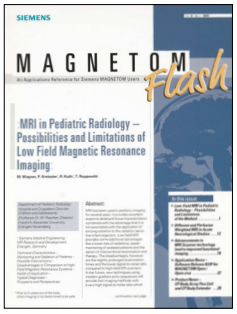







132 ***syngo* TimCT – Continuous Table Move, Powered by Tim** — No. 34 TimCT
Mathias Blasche, Siemens Medical Solutions, Erlangen, Germany

141 ***syngo* TimCT – a Novel Concept for Whole-Body MRI** — No. 34 TimCT
O. Schaefer, Department of Radiology, University Hospital Freiburg, Germany

2007

145 **Small Animal Imaging on 1.5T MR Systems** — No. 35 Spec. Ed.
J. Schulz, et al., DKFZ, Dept. of Medical Physics in Radiology, Heidelberg, Germany and Siemens Medical Solutions, Erlangen, Germany

153 **High-Resolution Small Animal Imaging on 3T Clinical MR Scanners** — No. 35 Spec. Ed.
Robin M. Heidemann, et al., Siemens Medical Solutions, Erlangen, Germany

158 **Pushing the Boundaries of MR with Siemens MAGNETOM 7T** — No. 35
John Grinstead, Siemens Medical Solutions USA, Inc.

163 **Parallel Transmission (pTX) Technology** — No. 35
Franz X. Hebrank, et al., Siemens Medical Solutions, Charlestown, MA, USA

168 **Diffusion-Weighted Imaging in Breast MRI – An Easy Way to Improve Specificity** — No. 37
Evelyn Wenkel and Rolf Janka, University Hospital Erlangen, Radiology, Erlangen, Germany

173 **Potential Role of Multi b Factor Diffusion-weighted Imaging of the Breast** — No. 37
Mitsuhiro Tozaki, Breast Center, Kameda Medical Center, Chiba, Japan and
Katsuya Maruyama, Siemens-Asahi Medical Technologies LTD., Tokyo, Japan

2008

177 **Arterial Spin Labeled Perfusion MRI** — No. 38
John A. Detre, Center for Functional Neuroimaging, Department of Neurology and Radiology, University of Pennsylvania, Philadelphia, PA, USA

181 **Highly Parallel Detection for MRI** — No. 38
Lawrence L. Wald, Massachusetts General Hospital and Harvard Medical School, Boston, MA, USA
Graham Wiggins, Harvard-MIT Division of Health Sciences and Technology, Cambridge, MA, USA

192 **Detection and Characterization of Focal Liver Lesions using Respiratory-Triggered Diffusion-Weighted MR Imaging (DWI)** — No. 39
Konstantin Holzapfel, et al., Department of Radiology, Technical University Munich, Germany

197 **Questions & Answers on Hardware Topics** — No. 39
Rolf Heinrichs and Matthias Nitka, Siemens Healthcare, Erlangen, Germany













2009

198 **Intravoxel Incoherent Motion (IVIM) *f*-maps of Pancreatic Lesions** No. 41
Thomas Joseph Re, et al., German Cancer Research Center (DKFZ), Heidelberg, Germany

206 **32-Channel Head Coil Imaging at 3T** No. 41
Thomas Benner, Athinoula A. Martinos Center for Biomedical Imaging, Department of Radiology, Massachusetts General Hospital and Harvard Medical School, Boston, MA, USA

216 **First Clinical Experiences with a Prototype of a Novel Cardiac Workflow Engine** No. 42
Russell Bull and Matthew Benbow, Royal Bournemouth Hospital, Bournemouth, UK

222 **IMRISneuro 70 cm Bore 3T in Intra-Operative Neurosurgery** No. 42
Jeanne Elliott, IMRIS, Winnipeg, Manitoba, Canada

2010

228 **Diagnostic Relevant Reduction of Motion Artifacts in the Posterior Fossa by *syngo* BLADE Imaging** No. 43
Thekla von Kalle, et al., Department of Pediatric Radiology, Olgahospital Klinikum Stuttgart, Germany

234 **4D Flow MR Imaging** No. 44
Alex Barker, et al., Department of Radiology, Medical Physics, University Hospital Freiburg, Germany

241 **3T MR Imaging of Peripheral Nerves Using 3D Diffusion-Weighted PSIF Technique** No. 45
Avneesh Chhabra, et al., Johns Hopkins University, Baltimore, MD, USA

244 **Advantages of MSK Imaging at 3 Tesla with special focus on Spine and Tumor Imaging** No. 45
Marc-André Weber, Diagnostic and Interventional Radiology, University Hospital Heidelberg, Germany

2011

255 **Fat Suppression Techniques – a Short Overview** No. 46
Wilhelm Horger, Berthold Kiefer, Siemens Healthcare, Erlangen, Germany

259 **Frequently Asked Questions: Diffusion-Weighted Imaging (DWI)** No. 46
Joachim Graessner, Siemens Healthcare, Hamburg, Germany

263 **Whole-Body MR/PET Hybrid Imaging: Technical Considerations, Clinical Workflow, and Initial Results** No. 46
Harald H. Quick, et al., Institute of Medical Physics (IMP), Friedrich-Alexander University Erlangen-Nürnberg, Erlangen, Germany













276 **Integrated Whole Body MR/PET Imaging. First Examples of Clinical Application** — No. 46
Rolf Heinrichs and Matthias Nitka, Siemens Healthcare, Erlangen, Germany

286 **Neuroimaging as a Clinical Tool in Surgical Planning and Guidance for Pediatric Epilepsy[2]** — No. 48
Binjian Sun, et al., Children's Healthcare of Atlanta, Department of Radiology, Atlanta, GA, USA

293 **3T MR Imaging of Cartilage using 3D Dual Echo Steady State (DESS)** — No. 48
Rashmi S. Thakkar, et al., Johns Hopkins University School of Medicine, Russell H. Morgan Department of Radiology and Radiological Science, Baltimore, MD, USA

2012

297 **Magnetic Resonance Elastography: Proven Indications, Challenges and Future Considerations** — No. 49
Sudharshan Parthasarathy, et al., Chicago Medical School, Rosalind Franklin University of Medicine, North Chicago, IL, USA

305 **Controlled Aliasing in Parallel Imaging Results in Higher Acceleration (CAIPIRINHA)** — No. 49
Felix Breuer, et al., Research Center, Magnetic Resonance Bavaria e.V (MRB), Würzburg, Germany

313 **The Signal-to-Noise Indicator or How to Navigate the 'Bermuda Triangle'** — No. 49
Joachim Graessner, Siemens Healthcare, Hamburg, Germany

318 ***syngo* WARP – Metal Artifact Reduction Techniques in Magnetic Resonance Imaging** — No. 50
Theresa Bachschmidt, et al., Siemens Healthcare, Erlangen, Germany

320 **Whole-Body Diffusion-Weighted MRI of the Bone Marrow in Health and Disease** — No. 50
Anwar Padhani, et al., Paul Strickland Scanner Centre, Mount Vernon Cancer Centre, Northwood, Middlesex, UK

326 **Biochemical MRI in Musculoskeletal Applications** — No. 50
Siegfried Trattnig, et al., MR Centre – High field MR, Department of Radiology, Medical University of Vienna/Vienna General Hospital, Vienna, Austria

338 **Magnetic Resonance Neurography – Techniques and Interpretation** — No. 50 Neuro Ed.
Avneesh Chhabra, et al., Department of Radiology & Radiological Science, Johns Hopkins University, Baltimore, MD, USA

343 **High-Resolution DWI in Brain and Spinal Cord with *syngo* RESOLVE** — No. 50 Neuro Ed.
Julien Cohen-Adad, Department of Electrical Engineering, Ecole Polytechnique de Montreal, QC, Canada and A. A. Martinos Center for Biomedical Imaging, Massachusetts General Hospital, Harvard Medical School, Charlestown, MA, USA













2013

352 **Myocardial First-Pass Perfusion Imaging with High Resolution and Extended Coverage Using Multi-Slice CAIPIRINHA** — No. 51
Daniel Stäb, et al., Institute of Radiology, University of Würzburg, Würzburg, Germany and Comprehensive Heart Failure Center (CHFC), Würzburg, Germany

359 **Introduction to Advanced Techniques in MR Neuroimaging** — No. 52
Bernhard Schuknecht, Krisztina Baràth, Diagnostic, Vascular and Interventional Neuroradiology, Medizinisch Radiologisches Institut MRI Zürich, Bethanien Hospital, Zürich, Switzerland

368 **MAGNETOM Aera – Combining Throughput and Highest Quality MRI in an Optimized Clinical Workflow** — No. 52
Johan Dehem, VZW Jan Yperman, Ieper, Belgium

379 **Parallel Transmission and its Clinical Implementation: Enabling new Clinical Imaging Paradigms** — No. 52
Fernando Boada, et al., Department of Radiology NYU Langone Medical Center, New York, NY, USA

386 **Bandwidth in MRI?** — No. 52
Joachim Graessner, Siemens Healthcare, Hamburg, Germany

392 **The New, High-Performance MR Gradient System XR 80/200. Design, Benefits and Safe Operation** — No. 52
Daniel Fischer, Eva Eberlein, Siemens Healthcare, Erlangen, Germany

396 **Optimizing MRI for Radiation Oncology: Initial Investigations** — No. 54
James Balter, et al., Department of Radiation Oncology, University of Michigan, Ann Arbor, MI, USA

401 **Improving the Robustness of Clinical T1-Weighted MRI Using Radial VIBE** — No. 55
Tobias Block, et al., Department of Radiology, NYU Langone Medical Center, New York, NY, USA

407 **Making MRI Scanning Quieter: Optimized TSE Sequences with Parallel Imaging** — No. 55
Eric Y. Pierre, et al., Biomedical Engineering, Case Western Reserve University, Cleveland, Ohio, USA

2014

412 **RESOLVE: A Powerful Tool for Imaging the Pediatric Spine²** — No. 57
Laura Hayes, Damian Grattan-Smith, et al., Department of Radiology, Children's Healthcare of Atlanta at Scottish Rite, Atlanta, GA, USA

420 **Amide Proton Transfer MRI in Patients with High-Grade and Low-Grade Gliomas** — No. 58
Meiyun Wang, et al., Department of Radiology, Henan Provincial People's Hospital, Zhengzhou, Henan, China













423 **Case Series: Minimally Invasive 3 Tesla Interventional MRI** — No. 59
Kemal Tuncali, Brigham and Women's Hospital, Dept. of Radiology, Boston, MA, USA

426 **GRASP: Tackling the Challenges of Abdominopelvic DCE-MRI** — No. 60
Kai Tobias Block, et al., Department of Radiology, NYU Langone Medical Center, New York, NY, USA

433 **Slice Order (Slice Timing) for fMRI Evaluation** — No. 60
Joachim Graessner, Siemens Healthcare, Hamburg, Germany

436 **Cardiac Dot Engine: Significant Time Reduction at Cardiac Magnetic Resonance Imaging** — No. 60
Jesús Ciro Pueyo, et al., Department of Radiology, Clínica Universidad de Navarra, Pamplona, Spain

440 **Magnetic Resonance Imaging at Siemens: A success story** — No. 60
Ingo Zenger and Antje Hellwich, Siemens Healthcare, Erlangen, Germany

2015

448 **Myocardial T1 Mapping – Comparison of Techniques** — No. 61
Kelvin Chow and Richard Thompson, Department of Biomedical Engineering, University of Alberta, Edmonton, Canada

455 **Practical Considerations for the Evaluation of the Neuroforamina in Routine Spine Imaging at 3T. A Case Series** — No. 62
Marc-André Weber, et al., Clinic of Diagnostic and Interventional Radiology, University Hospital Heidelberg, Germany

460 **MR-Guided Biopsies of the Prostate in Supine Patient Position** — No. 63
Florian Schneider, et al., Diagnostic Radiology, Martha-Maria Hospital Nürnberg, Germany

463 **Self-Navigated Free-Breathing High-Resolution 3D Cardiac Imaging: A New Sequence for Assessing Cardiovascular Congenital Malformations** — No. 63
Juerg Schwitter, et al., University Hospital of Lausanne (CHUV), Lausanne, Switzerland

470 **CAIPIRINHA – Revisited** — No. 63 SMS Ed.
Felix Breuer, et al., Research Center, Magnetic Resonance Bavaria, Würzburg, Germany

478 **Advancing Diffusion MRI Using SMS EPI** — No. 63 SMS Ed.
Kawin Setsompop, et al., Massachusetts General Hospital, Charlestown, MA, USA

485 **High-Resolution Diffusion-Weighted Neuroimaging at 3T and 7T with Simultaneous Multi-Slice RESOLVE** — No. 63 SMS Ed.
Robert Frost, et al., Oxford Centre for Functional MRI of the Brain (FMRIB), University of Oxford, UK

495 **Epilepsy Imaging with Simultaneous Multi-Slice Turbo Spin Echo** — No. 63 SMS Ed.
Michael Kean, et al., Royal Children's Hospital, Melbourne, Australia



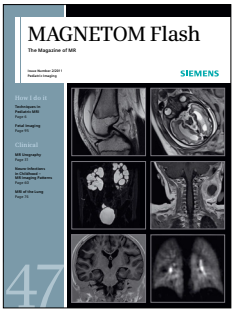









2016

499 **Cardiac Diffusion Tensor MRI Using Simultaneous Multi-Slice Acquisition with a Blipped-CAIPIRINHA Readout** — **No. 64**
Choukri Mekkaoui, et al., Massachusetts General Hospital, Harvard Medical School, Boston, MA, USA

502 **Overview of MR Fingerprinting** — **No. 65**
Vikas Gulani, et al., Case Western Reserve University, University Hospitals Case Medical Center, Cleveland, OH, USA

512 **Permeability Imaging of Parotid Tumors with Golden-Angle Radial Sparse Parallel MR Imaging (GRASP)** — **No. 65**
Sohil H. Patel, et al., New York University Langone Medical Center, New York, NY, USA

514 **Diffusion-Weighted MR Mammography (DWI-MRM) – Potential in the Clarification of Suspicious Lesions Detected by X-Ray Mammography** — **No. 65**
Sebastian Bickelhaupt, et al., German Cancer Research Center (DKFZ), Heidelberg, Germany

519 **Long-term Experience with MR Upgrades** — **No. 66**
Christos Loupatatzis, MRI AG Spital Maennedorf, Switzerland

525 **Iron Quantification with LiverLab** — **No. 66**
Stephan Kannengiesser, Siemens Healthineers, Erlangen, Germany

528 **Free-breathing Late Enhancement Imaging: Phase Sensitive Inversion Recovery (PSIR) with Respiratory Motion Corrected (MOCO) Averaging** — **No. 66**
Peter Kellman, et al., National Heart, Lung, and Blood Institute, National Institutes of Health, Bethesda, MD, USA

537 **Clinical Neuroimaging at 7T Compared to Lower Field: a Photo Essay** — **No. 66**
Stephen E. Jones, et al., Cleveland Clinic, Cleveland, OH, USA

546 **Compressed Sensing – the Flowchart** — **No. 66 CS Ed.**
Mathias Blasche, et al., Siemens Healthineers, Erlangen, Germany

550 **Compressed Sensing: a Paradigm Shift in MRI** — **No. 66 CS Ed.**
Christoph Forman, et al., Siemens Healthineers, Erlangen, Germany

556 **Compressed Sensing – a Metaphor** — **No. 66 CS Ed.**
Mathias Blasche, Siemens Healthineers, Erlangen, Germany







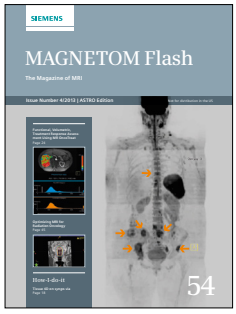





2017

558 **BioMatrix Tuners: CoilShim** — **MAGNETOM Vida Sp. Ed.**
Miriam R. Keil, et al., Siemens Healthineers, Erlangen, Germany

564 **Rapid MR Susceptibility Imaging of the Brain Using Segmented 3D Echo-Planar Imaging (3D EPI) and its Clinical Applications** — **No. 68**
Pascal Sati, et al., National Institutes of Health, Bethesda, MD, USA

571 **Assessing Brain Volumes Using MorphoBox Prototype** — **No. 68**
Alexis Roche, et al., Department of Radiology, University Hospital Lausanne, Switzerland

576 **CS-VIBE – a Breakthrough in Ultrafast Dynamic Breast MRI** — **No. 68**
Ritse M. Mann and Suzan Vreemann, Radboud University Medical Centre, Nijmegen, the Netherlands

581 **Pioneers of Connectome Gradients** — **No. 68**
Ralph Kimmlingen, Siemens Healthineers, Erlangen, Germany

596 **Gadgetron: Open Source Image Reconstruction** — **No. 68**
Michael S. Hansen, et al., National Institutes of Health, Bethesda, MD, USA

607 **MRI at UK Biobank** — **No. 68**
Niels Oesingmann, et al., UK Biobank, Stockport, Cheshire, UK

611 **Benefits of Accelerated MR Imaging in Daily Routine** — **No. 69**
Val M. Runge, et al., University Hospital Bern, Switzerland

622 **Evolution of the Malignant Bone Marrow with Successful Therapy – Quantitative Analysis with Whole-body Diffusion-weighted MRI** — **No. 69**
Danoob Dalili, et al., Imperial College Healthcare NHS Trust, St Mary's Hospital, London, UK

628 **Imaging of the Pancreas: Technique and Clinical Applications** — **No. 69**
Giovanni Morana, et al., General Hospital Ca' Foncello, Treviso, Italy

662 **GOKnee3D – Fully-automated One-button-push High-resolution MRI of the Knee** — **No. 69**
Jan Fritz, et al., Johns Hopkins University School of Medicine, Baltimore, MD, USA

671 **A Within-subject Comparison of Common Neuroimaging Protocols on MAGNETOM Prisma^{fit} and MAGNETOM Trio Scanners** — **No. 69**
Ross W. Mair and Stephanie McMains, Harvard University, Cambridge, MA, USA



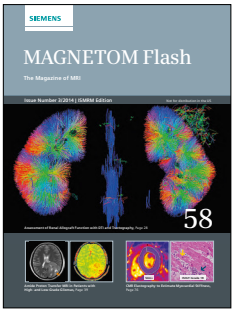









2018

679 **Whole-body MR diffusion imaging in oncology: origins, practice, and outlook** No. 70
Giuseppe Petralia, et al., European Institute of Oncology, Milan, Italy

688 **MR Elastography – Pearls and Pitfalls** No. 71
Bradley Bolster, Siemens Healthineers, Malvern, PA, USA

693 **Fetal² MR Imaging: An Overview** No. 71
Guangbin Wang, et al., Shandong University, Shandong, China

705 **Small Structures Big Challenges: Fetal Cardiac Magnetic Resonance Imaging** No. 71
Matthias Stuber, et al., University of Lausanne, CHUV, Lausanne, Switzerland

710 **Three Years of PI-RADS v2: Achievements, Open Questions and Future Perspectives** No. 71
Bernd Hamm, Charité University Hospital, Berlin, Germany

2019

713 **Cardiotoxicity in Cancer Therapy – the Role of Cardiovascular Magnetic Resonance** No. 72
Bernd J. Wintersperger, et al., University Health Network, Toronto, Canada

718 **Musculoskeletal and Body MRI in Children²** No. 73
Sarah Bixby, et al., Boston Children's Hospital, Boston, MA, USA

724 **Unprecedented Echo Times for Diffusion MRI Using Connectom Gradients, Spiral Readouts and Field Monitoring** No. 74
Derek Jones and Lars Mueller, et al., Cardiff University Brain Research Imaging Centre, Cardiff, UK

730 **Deep Learning for Parallel MRI Reconstruction: Overview, Challenges, and Opportunities** No. 75
Kerstin Hammernik, et al., Imperial College London, United Kingdom

736 **Experience after One Year with MRgFUS** No. 75
Jorge Guridi, et al., Clínica Universidad de Navarra, Pamplona, Spain

742 **How a Bell Pepper Convinced the Siemens Med Board** No. 75
Arnulf Oppelt and Wilfried Loeffler, Siemens Healthineers, Erlangen, Germany



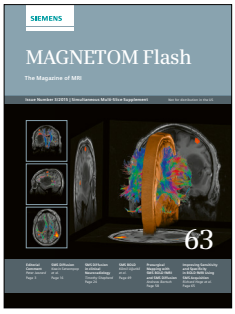





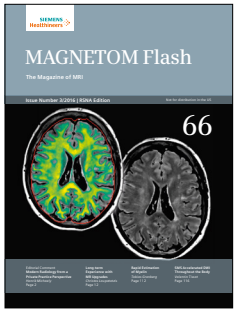



2020

745 **Automated and Standardized CMR Exams Using Cardiac Dot Engine and Short CMR Protocols** — SCMR 2020
Valentina Puntmann, University Hospital Frankfurt, Frankfurt/Main, Germany

748 **Ultrafast Multi-Contrast High-Resolution 3D Brain MRI: a Technical Description of Wave-CAIPI** — No. 76
Kawin Setsompop, et al., Massachusetts General Hospital, Charlestown, MA, USA

752 **A Path to Establishing MRSI as a Clinical Standard Imaging** — No. 76
Hyunsuk Shim, et al., Emory University School of Medicine, Atlanta, GA, USA

763 **The Prostate Dot Engine – a System-Guided and Assisted Workflow to Improve Consistency in Prostate MR Exams** — No. 76
Wilhelm Horger, et al., Siemens Healthineers, Erlangen, Germany

768 **A Fully Automated, End-to-End Prostate MRI Workflow Solution Incorporating Dot, Ultrashort Biparametric Imaging and Deep-Learning-based Detection, Classification, and Reporting** — No. 76
David J. Winkel, et al., University Hospital Basel, Switzerland

774 **An Attempt to Reconstruct the History of Gradient-System Technology at Siemens** — No. 76
Franz Schmitt, et al., Siemens Healthineers, Erlangen, Germany

794 **Revisiting the Physics behind MRI and the Opportunities that Lower Field Strengths Offer** — Free.Max 2020
André Fischer, Siemens Healthineers, Erlangen, Germany

799 **MAGNETOM Free.Max: from Concept to Product, a Brief History of the DryCool Magnet Development** — Free.Max 2020
Simon Calvert, Siemens Heatlhineers, Oxford, UK

804 **Improving Productivity in MRI – Clinical Experience in a Multisite Outpatient Practice Setting** — No. 77
Mike Notohamiprodjo and Gerwin Schmidt, DIE RADIOLOGIE, Munich, Germany

2021

810 **MAGNETOM Free.Max: Access to MRI – How to Make it Big Inside and Small Outside** — No. 78
Stephan Biber, Siemens Healthineers, Erlangen, Germany

815 **Deep Resolve – Mobilizing the Power of Networks** — No. 78
Pascal Sati, et al., National Institutes of Health, Bethesda, MD, USA

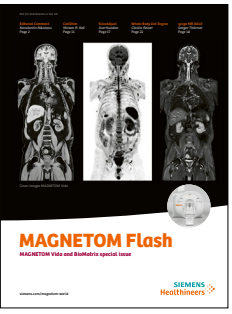



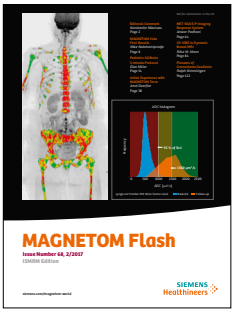



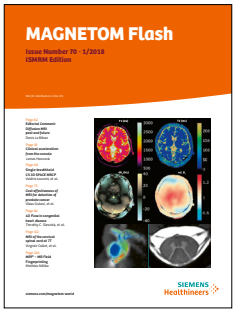

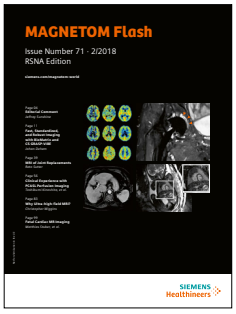

822 **Pushing the Limits of Accuracy in MRI – A Perspective** — No. 78
John E Kirsch, Athinoula A Martinos Center for Biomedical Imaging, Massachusetts General Hospital, Charlestown, MA, USA

829 **Initial Experience with Automatic Knee Cartilage Segmentation using MR Chondral Health** — No. 79
Vladimir Juras, Siegfried Trattnig, et al., High Field MR Centre, Medical University of Vienna, Austria

837 **Clinical Implementation of Deep Learning-Accelerated HASTE and TSE** — No. 79
Ahmed Othman, Judith Herrmann, et al., University Medical Center, Mainz / Eberhard Karls University Tuebingen, Germany

842 **Ultrafast Brain Imaging with Deep Learning Multi-Shot EPI: Preliminary Clinical Evaluation** — No. 79
John Conklin, et al., Massachusetts General Hospital, Boston, MA, USA

847 **Magnetic Resonance Fingerprinting –The Future of Quantitative MR Neuroimaging** — No. 79
Gregor Kasprian and Victor Schmidbauer, Department of Biomedical Imaging and Image-guided Therapy, Medical University of Vienna, Austria

853 **MAGNETOM Free.Max: Keeping a Hot System Cool** — No. 79
Stephan Biber, Siemens Healthineers, Erlangen, Germany

2022

857 **Complete Free-breathing, High-resolution Cardiac MR Studies and their Clinical Impact in Non-ischemic Cardiomyopathies** — SCMR 2022
Guillem Pons-Lladó, Cardiac Imaging Unit, Department of Diagnostic Imaging, Clínica Corachán, Barcelona, Spain

863 **Ultrafast Brain Imaging with Deep-Learning Multi-Shot EPI: Technical Implementation** — No. 80
Bryan Clifford, et al., Siemens Healthineers, Boston, MA, USA

870 **Distortion-free Diffusion-weighted Imaging Based on a TGSE BLADE Sequence** — No. 80
Kun Zhou and Wei Liu, Siemens Shenzhen Magnetic Resonance Ltd., Shenzhen, China

878 **Update on FLAIR Fusion in Multiple Sclerosis Follow-up and Beyond: An Indispensable Tool in Clinical Routine** — No. 80
Andreas Bartsch, et al., Radiologie Bamberg, Germany

884 **Translation of Computer-Assisted MRI Assessments of Multiple Sclerosis to Clinical Care** — No. 80
Hagen H. Kitzler, et al., University Hospital Carl Gustav Carus, Technische Universität Dresden, Germany

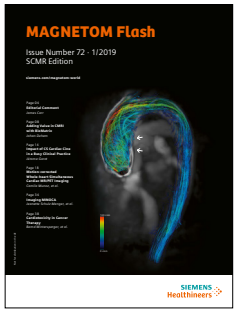



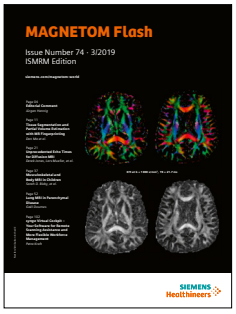

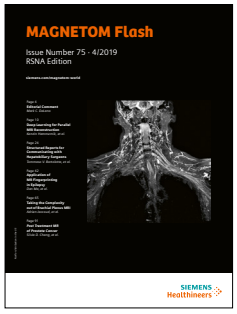



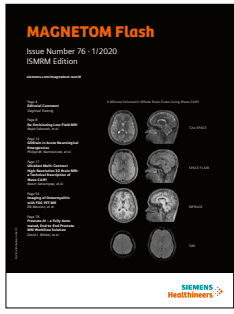

896 **PASTEUR: Package of Anatomical Sequences Using Parallel Transmission Universal Pulses Now Available for MAGNETOM Terra** No. 80
Nicolas Boulant, et al., Université Paris-Saclay, CEA, CNRS, BAOBAB, NeuroSpin, Gif-sur-Yvette, France

907 **Magnetic Resonance Elastography of the Liver: Best Practices** No. 80
Arunark Kolipaka, et al., The Ohio State University, Columbus, OH, USA

916 **MRI's Helium Footprint – and How to Make it Harder to Spot** No. 80
Philipp Grätzel von Grätz, Berlin, Germany

919 **Scanning Faster: Application in Pediatric Neuroimaging** No. 81
Michael Kean, Royal Children's Hospital, Melbourne, Australia

940 **Pediatric² Whole-Body MRI: How I Do It** No. 81
Bac Nguyen and Lil-Sofie Muller, Oslo University Hospital, Rikshospitalet, Oslo, Norway

950 **Building a Global Power of Experience in Diagnostic Imaging – Lessons from Africa's COVID-19 Response** No. 82
Udunna Anazodo, et al., McGill University, Montreal, Quebec, Canada

958 **High-Resolution Accelerated Prostate TSE Axial Imaging with Deep Learning Reconstruction at 3 Tesla** No. 82
Alain Luciani, et al., Hôpitaux Universitaires Henri Mondor, Créteil, France

963 **Improving Patients' Experience of MRI: Why and How Reducing Stress and Anxiety in Patients May Enhance Clinical Operations** No. 82
Janika Madl, et al., Universitätsklinikum Erlangen, Germany

970 **Artificial Intelligence – Learning About the Future of Cardiovascular MR** No. 82
Kerstin Hammernik, Technical University of Munich, Germany, and Thomas Küstner, University Hospital Tübingen, Germany

979 **3D Whole Heart Applications: Angiography and Delayed Enhancement** No. 82
Jason Craft, et al., St. Francis Heart Hospital, DeMatteis Research Center, Greenvale, NY, USA



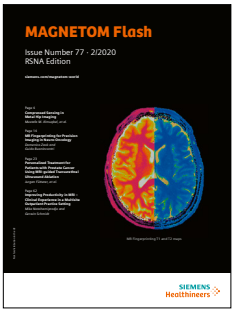



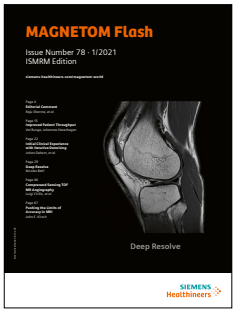

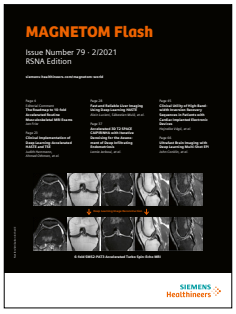



2023

986 **Skip the Electrodes, But Not A Beat: The Engineering Behind the Beat Sensor** — No. 83
Peter Speier and Mario Bacher, Siemens Healthineers, Erlangen, Germany

998 **Retrospective Motion Correction for Brain MRI: A Technical Description of SAMER** — No. 84
Daniel Polak, et al., Siemens Healthineers, Erlangen, Germany

1002 **Fetal² Low Field MRI – the First 150 Cases** — No. 84
Jana Hutter, et al., School of Biomedical Engineering, King's College London, UK

1009 **Whole-Body MRI at 1.5T in the Era of Deep Resolve** — No. 85
Will McGuire, et al., Paul Strickland Scanner Centre, Mount Vernon Cancer Centre, Northwood, Middlesex, UK

1017 **3D Whole-Heart Imaging: An Innovative Collaborative Solution** — No. 85
Michaela Schmidt, Karl P. Kunze, et al., Siemens Healthineers, Erlangen, Germany

1023 **Optimizing Brachial Plexus Magnetic Resonance Neurography at 3 Tesla** — No. 85
Darryl Sneag, et al., Hospital for Special Surgery, New York, NY, US

2024

1029 **Clinical Experience with the BioMatrix Beat Sensor: Cardiac MRI Exams Without ECG Leads** — No. 86
Naokazu Mizuno et al., Sakakibara Heart Institute, Tokyo, Japan

1035 **Can We See the Bottom? A Look into Deep Learning-Based Image Reconstruction** — No. 87
Dominik Nickel, Siemens Healthineers, Erlangen, Germany

1039 **Phase-Resolved Functional Lung (PREFUL) MRI of Ventilation and Perfusion in Premature Infants** — No. 87
Jonathan P. Dyke, et al., Weill Cornell Medicine, New York, NY, USA

1046 **Going Beyond DTI in the Clinic: The Appeal of Microstructural MRI** — No. 87
Ileana Jelescu, Microstructure Mapping Lab, Lausanne University Hospital (CHUV) and University of Lausanne (UNIL), Switzerland

1055 **Advances in Susceptibility-Weighted Imaging (SWI) and Quantitative Susceptibility Mapping (QSM)** — No. 87
Josef Pfeuffer, et al., Siemens Healthineers, Erlangen, Germany

1066 **Canine and Feline MRI: How Does it Differ from Human MRI?** — No. 87
Zoe Lenard, Animalius Vet, Perth, Australia



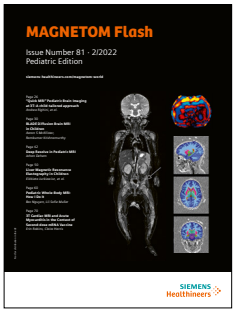



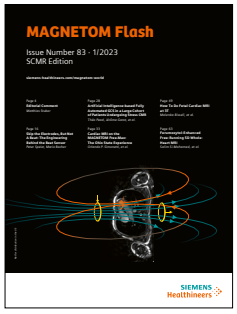

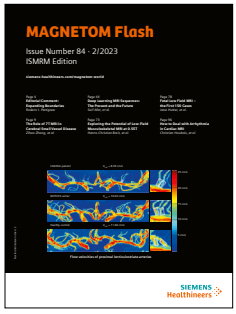

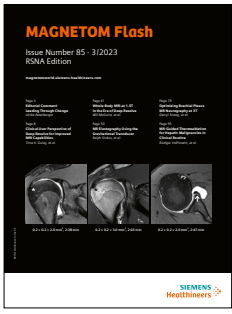

1071 **High-Resolution Imaging of the Hip Joint in the Age of Deep Learning** No. 89
Ji Lin, et al., Hospital for Special Surgery, New York, NY, USA

1076 **Expert insights: TSE image quality** No. 89
Tricia Thompson, Siemens Healthineers, Bowen Hills, QLD, Australia

1080 **Building the Future of MRI: Workflow Optimization and Patient-Centered Design at Mass General Brigham's High-Efficiency Outpatient Facility** No. 89
Susie Huang, Alexander Herold, et al., Massachusetts General Hospital, Boston, MA, USA

1085 **Specific Absorption Rate (SAR) Supervision on MAGNETOM Systems** No. 89
Lena Gast and Hendrik Paysen, Siemens Healthineers, Erlangen, Germany

1091 **Gradient-Free MRI for the Moon and Other Hard-To-Reach Places** No. 89
Gordon Eric Sarty, et al., Space MRI Lab, QuanTA Centre, University of Saskatchewan, Saskatoon, Canada

2025

1097 **Accelerating Cardiac MRI with Inline Generative AI and Open Recon** No. 90
Reza Nezafat, et al., Beth Israel Deaconess Medical Center, Boston, MA, USA

1100 **Next-Generation Cardiac MRI: Simplifying the Complex with AutoMate Cardiac** No. 90
Seung Su Yoon, Jens Wetzl, et al., Siemens Healthineers, Erlangen, Germany

1106 **Metals and More: The MRI Sustainability Lifecycle** No. 90
Philipp Grätzel von Grätz, Berlin, Germany

1110 **Open Sequence: An Introduction** No. 91
Thomas Kluge and Christoph Forman, Siemens Healthineers, Erlangen, Germany

1116 **Optimizing Energy Efficiency in MRI Scanners** No. 91
Thomas Küstner, et al., MIDAS.lab, University Hospital Tübingen, Germany

1122 **Phase-Resolved Functional Lung (PREFUL) MRI: The Next-Generation Ventilation-Perfusion Scan?** No. 91
Andreas Voskrebenzev, et al., Hannover Medical School, Germany

1131 **The CEA-Siemens Healthineers MAGNETOM Iseult 11.7-Tesla MRI System: A 20-year Odyssey to Image the Human Brain** No. 91
Nicholas Boulant, Franck Mauconduit, et al., Paris-Saclay University, Gif-Sur-Yvette, France



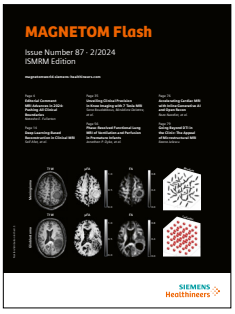

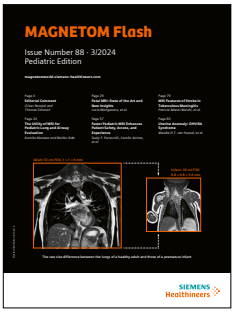



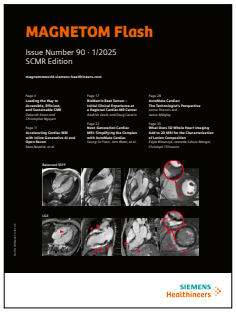

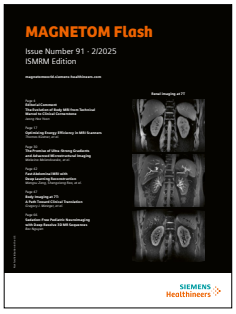

1139 **A Milestone in Medical Imaging. The Pioneering Development of the First Integrated PET/MR Scanner at Siemens Healthineers** — No. 91
Holger Schmidt, et al., Siemens Healthineers, Erlangen, Germany

1148 **Evaluating Intraoperative Magnetic Resonance Imaging (ioMRI) Approaches in Neurosurgery: A Literature Review about Applications, Benefits, and Cost-Effectiveness** — No. 92
Victor Gabriel El-Hajj, Adrian Elmi-Terander, et al., Department of Clinical Neuroscience, Karolinska Institutet, Stockholm, Sweden

1156 **Challenges with Operations using Intraoperative MRI: A Practical Perspective for Implementation in the Surgical Workflow** — No. 92
Monika Grimm, et al., Department of Neurosurgery, Clinical Neuroscience Center, University Hospital Zurich, University of Zurich, Switzerland

1163 **Flash Forward: Deep Learning-Enhanced Musculoskeletal MRI at the Speed of Thought** — No. 93
Jan Vosshenrich and Jan Fritz, Department of Radiology, Grossman School of Medicine, New York University, New York, NY, USA

1172 **Exploring the T2-Mapping GRAPPATINI Technique for Qualitative and Quantitative Assessment of Orthopedic and Neuromuscular Conditions** — No. 93
Ek T. Tan, Darryl B. Sneag, et al., Department of Radiology and Imaging, Hospital for Special Surgery, New York, NY, USA

1179 **StarVIBE for Bone Imaging** — No. 93
Eddie Song, Siemens Healthineers, Durham, NC, USA

1182 **Pictorial Essay: Clinical Application of StarVIBE for Bone Imaging** — No. 93
Erin Moran, Duke University, Durham, NC, USA

1186 **The Spectrum of Interventional MRI** — No. 94
David Woodrum and Scott Thompson, Mayo Clinic, Rochester, MN, USA

1195 **Advanced Imaging-Based Medicolegal Death Investigation: Postmortem MRI and CT** — No. 95
Chris O'Donnell, et al., Victorian Institute of Forensic Medicine, Melbourne, Australia

1201 **Examining Musculoskeletal Implants with Lower-Field MRI** — No. 95
Bianca Samsula, et al., ZEMODI - MVZ Zentrum für moderne Diagnostik, Bremen, Germany

1207 **Mobile MRI: Revolutionizing Access to Advanced Imaging** — No. 95
Jakob Krebs Christensen, Agito Medical A/S, Nørresundby, Denmark

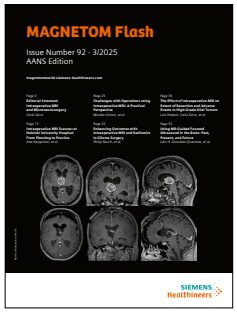

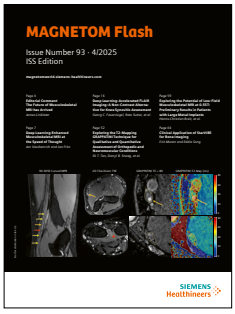

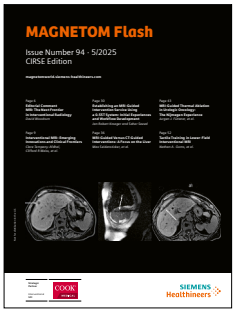

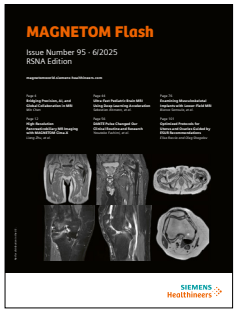

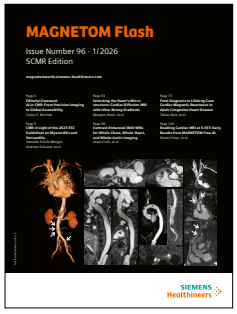

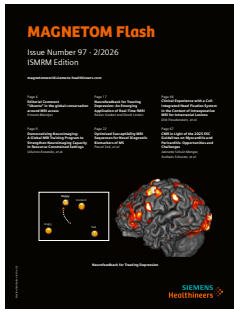

2026

1212 **Unlocking the Heart's Microstructure: Cardiac Diffusion MRI with Ultra-Strong Gradients** **No. 96**
Maryam Afzali, et al., Leeds Institute of Cardiovascular and Metabolic Medicine, University of Leeds, UK

1217 **Enabling Cardiac MRI at 0.55T: Early Results from MAGNETOM Free.XL** **No. 96**
Daniel Giese, et al., Siemens Healthineers, Erlangen, Germany

1224 **Neurofeedback for Treating Depression: An Emerging Application of Real-Time Functional MRI** **No. 97**
Rainer Goebel and David Linden, Maastricht University, the Netherlands

1229 **Optimized Susceptibility MRI Sequences for Novel Diagnostic Biomarkers of Multiple Sclerosis** **No. 97**
Pascal Sati, et al., Department of Neurology, Cedars-Sinai Medical Center, Los Angeles, CA, USA

1236 **Radial UTE[1] MRI in Musculoskeletal Diseases: Current Clinical Applications and Future Perspectives** **No. 98**
Yun Sun Choi, et al., Department of Radiology, Nowon Eulji Medical Center, Eulji University, Seoul, Korea

1244 **Proactive Ergonomic Design for Interventional MRI: Insights from Digital Human Modeling** **No. 99**
Steven Fischer, Justin Davidson, et al., Faculty of Health, University of Waterloo, Waterloo, ON, Canada

[1] Work in progress. The application is currently under development and is not for sale in the U.S. and in other countries. Its future availability cannot be ensured.
[2] MR scanning has not been established as safe for imaging fetuses and infants less than two years of age. The responsible physician must evaluate the benefits of the MR examination compared to those of other imaging procedures.
[3] The MRI restrictions (if any) of the metal implant must be considered prior to patient undergoing MRI exam. MR imaging of patients with metallic implants brings specific risks. However, certain implants are approved by the governing regulatory bodies to be MR conditionally safe. For such implants, the previously mentioned warning may not be applicable. Please contact the implant manufacturer for the specific conditional information. The conditions for MR safety are the responsibility of the implant manufacturer, not of Siemens Healthineers.

Not for distribution in the US

On account of certain regional limitations of sales rights and service availability, we cannot guarantee that all products included in this brochure are available through the Siemens Healthineers sales organization worldwide. Availability and packaging may vary by country and is subject to change without prior notice. Some/All of the features and products described herein may not be available in the USA.

The information in this document contains general technical descriptions of specifications and options as well as standard and optional features which do not always have to be present in individual cases, and which may not be commercially available in all countries. Due to regulatory reasons their future availability cannot be guaranteed. Please contact your local Siemens Healthineers organization for further details.

Siemens Healthineers reserves the right to modify the design, packaging, specifications, and options described herein without prior notice. Please contact your local Siemens Healthineers sales representative for the most current information.

Note: Any technical data contained in this document may vary within defined tolerances. Original images always lose a certain amount of detail when reproduced.

Siemens Healthineers Headquarters
Siemens Healthineers AG
Siemensstr. 3
91301 Forchheim, Germany
Phone: +49 9191 180
siemens-healthineers.com

Published by Siemens Healthineers AG · Order No. A91MR-1000-0007M-7600 · 17052 1126 · *©Siemens Healthineers AG, 2026*